



APCOM2013 & ISCM2013  
Conference Proceedings

**5<sup>th</sup> Asia Pacific Congress on Computational  
Mechanics (APCOM2013)  
&  
4th International Symposium on Computational  
Mechanics (ISCM2013)**

**11<sup>th</sup>-14<sup>th</sup> December 2013, Singapore**

**Edited by: G.R. Liu, Z.S. Liu**

Proceedings of 5<sup>th</sup> Asia Pacific Congress on Computational Mechanics (APCOM2013)  
& 4<sup>th</sup> International Symposium on Computational Mechanics (ISCM2013)

This volume contains full papers accepted by APCOM2013 and ISCM2013, 11<sup>th</sup>-14<sup>th</sup>  
December 2013, Singapore.

First Edition, December 2013.

Papers in this Proceedings may be identically cited in the following manner: Author  
names, *Paper title, Proceedings at the APCOM2013 & ISCM2013, 11<sup>th</sup>-14<sup>th</sup> December  
2013, Singapore*, Eds: G.R. Liu, Z.S. Liu, Scientech Publisher.

Note: The papers/data included in this volume are directly from the authors. The  
editors are not responsible of inaccuracy, error, etc. Please discuss with the author  
directly, if you have any question.

Published by

Scientech Publisher LLC, USA

<http://www.sci-en-tech.com/Books/>

## PREFACE

Dear Colleagues,

On behalf of the organising committees, we are delighted to welcome you to the 5th Asia Pacific Congress On Computational Mechanics (APCOM2013) & 4th International Symposium on Computational Mechanics (ISCM2013) at Singapore.

The APCOM/ISCM2013 is an international conference providing an international forum for exchange ideas on recent advances in areas related to mechanics, including computational methods, numerical modelling & simulation, as well as their applications in engineering and science. It will accommodate presentations on a wide range of topics to facilitate interdisciplinary exchange of ideas in science, engineering and related disciplines, and foster various types of academic collaborations in the Asia Pacific region and internationally. All papers accepted for publication in the proceedings has been peer reviewed. Papers may also be selected and invited to be developed into a full journal paper for publication in special issues of the journals.

The APCOM/ISCM2013 conference program covers over 600 presentations in about 100 technical sessions.

There will be 6 Plenary Lectures, 24 Thematic Plenary Lectures, 120 Keynote Lectures and 120 Invited Lectures at the conference. The conference sessions will cover a broad range of topics in relation to computational mechanics, including formulation theory, computational methods and techniques, modelling techniques and procedures, materials, deformation processing, materials removal processes, processing of new and advanced materials, welding and joining, surface engineering and other related processes.

We would like to express our gratitude to all the members of the Local Organising Committee, International Organization Committee, and the International Steering Committee who have provided advice and guidance in planning and executing this conference. Our sincere thanks and appreciation go to some 200 international reviewers for their prompt review reports on the submitted papers. Our appreciation goes also to all the Mini-Symposium Organizers for their effort and contribution in the organization. We must single out some members involved in the daily services to this conference, Dr. Fangsen Cui, Dr. Yuan Cheng, Miss Tracy Tang, and many others. A vote of thanks also goes to members at the Sciencetech Publisher USA for their management of the conference.

We hope that the proceedings of this conference will provide a great venue of presenting and exchanging information for your scientific work. We all of you have a great time in this beautiful garden city Singapore.

G.R. Liu (University of Cincinnati, USA)  
Z.S. Liu (National University of Singapore, Singapore)  
Conference Chairmen

## ORGANIZATION COMMITTEES

### Local Organization Committee

#### Chairmen:

Z.S. Liu (National University of Singapore; Xi'an Jiaotong University, China)

G.R. Liu (University of Cincinnati, USA)

#### Members:

F. S. Cui (IHPC, Singapore)

S. P. Joshi (National University of Singapore)

B. C. Khoo (National University of Singapore)

H. P. Lee (National University of Singapore)

S. C. Fan (Nanyang Technological University)

H. Li (Nanyang Technological University)

T. Y. Ng (Nanyang Technological University)

L. H. Poh (National University of Singapore)

R. K. Jaiman (National University of Singapore)

Z. D. Sha (IHPC, Singapore)

V. B. C. Tan (National University of Singapore)

### International Organization Committee

**Chairman:** G. R. Liu, **Co-Chairmen:** S. Valliappan and M. W. Yuan

#### Members:

W T Ang (Nanyang Technological University, Singapore)

A. K. Ariffin (Universiti Kebangsaan Malaysia, Malaysia)

S. W. Chae (Korea University, Korea)

C. S. Chen (University of Southern Mississippi, USA)

A. Cheng (University of Mississippi, USA)

D. Chen (National Taiwan University, Taiwan)

J. T. Chen (National Taiwan Ocean University, Taiwan)

X. Chen (Columbia University, USA)

Y. M. Cheng (Shanghai university, China)

C. K. Choi (KAIST, Korea)

R. De Borst (University of Glasgow, UK)

Raj Das (University of Auckland, New Zealand)

Z. C. Deng (Northwestern Polytechnical University, China)

Y. T. Gu (Queensland University of Technology, Australia)

X. Han (Hunan University, China)

K. Kashiyama (Chuo University, Japan)

M. Kawahara (Chuo University, Japan)

A. Korsunsky (University of Oxford, UK)

N. Khalili (University of New South Wales, Australia)

Y. Y. Kim (Seoul National University, Korea)

A. Leung (City University of Hong Kong, China)

M. Li (Taiyuan University of Technology, China)

Q. Li (University of Sydney, Australia)

Y. M. Li (Xi'an Jiaotong University, China)

C. S. Liu (National Taiwan University, Taiwan)

M. B. Liu (Chinese Academy of Sciences, China)

Y. J. Liu (University of Cincinnati, USA)

Z. S. Liu (XJTU, China and NUS, Singapore)

J. Lu (City University of Hong Kong, China)

T. J. Lu (Xi'an Jiaotong University, China)

V. P. Iu (University of Macau, China)

G. W. Ma (University of Western Australia, Australia)

N. Miyazaki (Kyoto University, Japan)

J. Orkisz (Cracow University of Technology, Poland)

E. N. Pan (University of Akron, USA)

D. Qian (University of Cincinnati, USA)

Q. H. Qin (Australian National University, Australia)

Q. Wang (University of Manitoba, Canada)

B. Sarler (University of Nova Gorica, Slovenia)

S. P. Shen (Xi'an Jiaotong University, China)

G. Q. Shi (Canada National Research Council, Canada)

S. Sloan (University of Newcastle, Australia)

K. Y. Sze (University of Hong Kong, China)

W. A. Wall (Technische Universität München, Germany)

Jane Wang (Northwestern University, USA)

T. J. Wang (Xi'an Jiaotong University, China)

D. L. Yang (National Taiwan University, Taiwan)

Y. B. Yang (Yunlin University, Taiwan)

Z. J. Yang (University of Manchester, UK)

W. B. Yao (University of Macau, China)

Z. H. Yao (Tsinghua University, China)

S. Yoshimura (University of Tokyo, Japan)

M. W. Yuan (Peking University, China)

C. Z. Zhang (University of Siegen, Germany)

H. W. Zhang (Dalian University of Technology, China)

Lihai Zhang (The University of Melbourne, Australia)

Y. Zheng (Zhejiang University, China)

**International Scientific Committee****Chairman:** G. Yagawa**Co-Chairmen:** Onate and G.R. Liu**Members:**

J. D. Achenbach (Northwestern University, USA)  
N. R. Aluru (UIUC, USA)  
J. S. Chen (University of California, Los Angeles, USA)  
W. Chen (Purdue University, Indiana, USA)  
R. M. Cotta (UFRJ, Brazil)  
S. De (Rensselaer Polytechnic Institute, USA)  
G. Dulikravich (Florida International University, USA)  
C. Farhat (Stanford University, USA)  
J. Fish (Columbia University, USA)  
Eliot Fang (Sandia National Laboratories, USA)  
H. J. Gao (Brown University, USA)  
A. Huerta (Universitat Politecnica de Catalunya, Spain)  
T. Hughes (Stanford University, USA)  
Sergio R. Idelsohn (CIMNE, Spain)  
W. Ju (University of California, Los Angeles, USA)  
T. Kant (Indian Institute of Technology Bombay, India)  
P. Krysl (University of California, San Diego, USA)  
P. Ladevèze (LMT-Cachan, France)  
G. Y. Li (Hunan University, China)

W. K. Liu (Northwestern University, USA)  
H. Mang (Vienna University of Technology, Austria)  
J. T. Oden (University of Texas at Austin, USA)  
H. R. B. ORLANDE (UFRJ, Brazil)  
D. R. J. Owen (University of Wales Swansea, UK)  
M. Papadrakakis (NTUA, Greece)  
P. M. Pimenta (Polytechnic School at University of São Paulo, Brazil)  
E. Ramm (Universität Stuttgart, Germany)  
J. N. Reddy (Texas A&M University, USA)  
O. Roger (CNAM, France)  
B. Schrefler (CISM, Italy)  
Z. G. Suo (Harvard University, USA)  
T. E. Tezduyar (Rice University, USA)  
Francis Thio (US Department of Energy, USA)  
P. Wriggers (Leibniz Universität Hannover, Deutschland)  
T. Yabe (Tokyo Institute of Technology, Japan)  
S. K. Youn (KAIST, Korea)

## TABLE OF CONTENTS

Preface	iii
Committees	iv
Table of Contents	vi
The effects of flexible fixation on early stage bone fracture healing <i>L. Zhang, S. Miramini, P. Mendis, M. Richardson, M. Pirpiris and A. Oloyede</i>	1
Dynamic Analysis of SSI Systems via a Coupled Finite-element/Scaled Boundary Finite-element Model <i>D. Chen, C. Birk, and S. Dai</i>	8
Crashworthiness Behaviour on Aluminum Foam Bumper Beam and Side Member System under Oblique Impact <i>F. Djamaluddin, S. Abdullah, A. K. Arrifin and Z. M. Nopiah</i>	18
An SBFEM element for thin-walled beams <i>J.D. Jung, W. Becker</i>	27
Application of DEM Simulation to drum type agitation mill for appropriate comminution <i>Yuki Tsunazawa, Kazuki Tahara, Chiharu Tokoro and Shuji Owada</i>	35
Dynamic analysis by a new family of time marching procedures based on numerically computed Green's functions <i>D. Soares Jr.</i>	43
High Pressure Zone Capture Wing Configuration for High Speed Air Vehicles <i>K. Cui, G.L. Li, S.C. Hu, Z.P. Qu</i>	51
A Method of Weighted Mean for Structural Random Loading Identification <i>Liao Jun, Jiang Bingyan, Xu Dafu, Liao He</i>	64
Application Optimization of Two-Dimensional Nozzle with Alloy Steel Structure in the Supersonic Wind Tunnel <i>Wang Ying, Bu Junhui, Wang Wei, and Chen Ding</i>	73
Numerical study of vortex-induced vibration by symmetric Lorentz forces <i>Hui Zhang, Bao-chun Fan, and Zhi-hua Chen</i>	80
Fluid-structure coupling analysis and simulation of viscosity effect on Coriolis mass flowmeter <i>Luo Rongmo, and Wu Jian</i>	88
Uncertainty Modeling and Simulation Highlighting on Tail Probability in Biomechanics Study on Pressure Ulcer <i>Samuel Susanto Slamet, Naoki Takano, and Tomohisa Nagasao</i>	96
Application Optimization of Regulating Valve in Wind Tunnel <i>Shen Feng Jing, Sun Tao, Bu Jun Hui, Sun Yong Tang, and Wang Tie Jing</i>	104

Molecular Dynamics Simulation of Shock Wave Propagation in Aluminum Single Crystal <i>Yuan-Yuan JU, Qing-Ming ZHANG</i>	110
Delamination Damage Propagation Behavior of Composite Laminate Plate Under Low-Velocity Impact Using a New Adhesive Layer Model <i>Y. ZHAO, K. DONG, Y. GAO</i>	116
Detonation diffraction in combustible high speed flows <i>M.Y. Gui, G. Dong, and B.C. Fan</i>	124
Comparison of PIM and RPIM solutions of Elasto-plastic Thick Beams <i>B. Kanber, N. F. Dogan</i>	129
Vibration of Thin Beams by PIM and RPIM methods <i>B. Kanber, and O. M. Tufik</i>	137
Parameter-free Shape Optimization Method for Natural Vibration Design of Stiffeners on Thin-walled Structures <i>Yang Liu, Masatoshi Shimoda</i>	144
Graph grammar based multi-frontal direct solver for isogeometric FEM simulations on GPU <i>M. Paszyński, K. Kuźnik, V.M. Calo and D. Pardo</i>	151
Dual boundary integral equations for three-dimensional rectangular crack problems <i>Guizhong Xie, Jianming Zhang</i>	159
Evaluation of radiative heat transfer effect on fire whirlwind <i>Seigo Sakai</i>	169
Vibration of Double-walled Carbon Nanotubes Predicted by Timoshenko Beam Models and Molecular Dynamics <i>Rumeng Liu, Lifeng Wang</i>	177
Numerical Simulation of Drag and Flow Noise Property on Structure for Carrier of Multi-loads AUV <i>Guang Pan, Yao shi, Baowei Song, Xiaoxu Du, Zhidong Yang, Jun Jiang</i>	185
A Framework for Auto-segmentation of Left Ventricle from Magnetic Resonance Images <i>Xulei Yang, Si Yong Yeo, Calvin Lim, Yi Su, Min Wan, Liang Zhong, and Ru San Tan</i>	193
Application of Digital Image Correlation for strain measurements of large masonry walls <i>A.H. Salmanpour and N. Mojsilović</i>	200
Discrete crack modeling of RC structure using hybrid-type penalty method <i>Y. Fujiwara, N. Takeuchi, T. Shiomi, and A. Kambayashi</i>	207
Numerical Simulations of Particle Deposition in Metal Foam Heat Exchangers <i>E. Sauret, S. C. Saha, and Y. T. Gu</i>	215
Seismic response of a concrete gravity dam considering hydrodynamic effects <i>A. Dey and M. B. Sawant</i>	222
Development of multi-phase-field crack model to express crack propagation in polycrystal <i>Kento Oshima, Tomohiro Takaki, and Mayu Muramatsu</i>	230

Low-dispersion sampling-based parameter importance measure analysis for anti-ice piccolo structure of anti-resonance design <i>ZHANG Feng, HE Xindang, NAN Hua, YAO Huiju</i>	236
A facade design idea generation support system through evolutionary computing <i>Hiroki Matsuda and Kazutoshi Tsutsumi</i>	243
Effect of Shear Deformation on Convergability of Simple Contact Analysis with Large Displacement <i>Z.M. Nizam, H. Obiya, K. Ijima, R. Tokubuchi, and K. Ishibashi</i>	249
The robustness of Timoshenko beam in geometrically non-linear frame analysis <i>Ryota Tokubuchi, Hiroyuki Obiya, Katsushi Ijima, Noriaki Kawasaki, Z.M.Nizam</i>	257
Interval identification of thermal parameters for convection-diffusion heat transfer problems <i>Xue Yanni, Yang Haitian</i>	263
Hybrid algorithm for inverse DC/AC resistivity logging measurement simulations <i>M. Paszyński, E. Gajda-Zagórska, M. Smółka, R. Schaefer, D. Pardo</i>	273
Characteristics of MFS analysis for finite plate problems with a hole <i>Wataru Fujisaki, T.Suetugu, and M. Takashima</i>	281
A Non-parametric Form-Finding Method for Designing Membrane Structure <i>Masatoshi Shimoda and Koichi Yamane</i>	286
Ultra-Accurate Isogeometric Structural Vibration Analysis with Novel Higher Order Mass Formulations <i>Dongdong Wang, Xiwei Li, Wei Liu, and Hanjie Zhang</i>	294
Numerical modeling on concrete debris ricocheting off sand ground <i>J. Xu, C.K. Lee, and S.C. Fan</i>	302
Molecular simulation of the influence of nickel coating on the interfacial bonding strength of carbon nanotube/magnesium composites <i>X. Zhou, S. Y. Song, L. Li, and J. Y. Wu</i>	310
A hybrid approach to structural topology optimization of vehicle for crashworthiness <i>Kun Yan, Gengdong Cheng</i>	314
Damage Identification of Beams based on Element Modal Strain Energy and Data Fusion with Reconstructed Modal Rotations <i>H Cao, T Liu</i>	322
Continued fraction formulation for infinite acoustic fluid with uniform cross section <i>S.M. Li</i>	331
Mechanisms of strain rate effect of metal foams with numerical simulations of D Voronoi foams during SHPB tests <i>B. Yang, Z.J. Liu, L.Q. Tang, Z.Y. Jiang and Y.P. Liu</i>	338
Experimental Study on High Damping Polymer Concrete <i>HUA Jianmin, HU Zhimao, CAO Hui, ZHENG Xing</i>	344



A new assumed strain beam element based on a sixth-order beam theory for static and dynamic analysis of composite beams <i>Xiaodan Wang, Guangyu Shi</i>	353
Computation of Hydrodynamic Coefficients of Portable Autonomous Underwater Vehicle <i>J. Jiang, Y. Shi, and G. Pan</i>	361
Experimental and numerical evaluation of fatigue behavior of foam core sandwich structure <i>Peiyan Wang, Xiaoyu Li, Zhufeng Yue</i>	367
Non-Parametric Shape Optimization of -D Frame Structures for Maximizing a Natural Frequency <i>Takashi Morimoto and Masatoshi Shimoda</i>	375
Analysis of Exterior Acoustics using the Edge-based Smoothed Finite Element Method (ES-FEM) <i>Wei Li, Ming Lei, Yingbin Chai and G.R. Liu</i>	383
Simulation of Nonlinear Magnetorheological Particle-filled Elastomers <i>Shulei Sun, Xiongqi Peng, Zaoyang Guo</i>	400
An Improved Genetic Algorithm with Two-level Approximation for Truss Topology and Size Optimization <i>Dongfang Li, Shenyang Chen, and Hai Huang</i>	406
Free vibration analysis of D FG plates by a meshfree boundarydomain integral equation method <i>Y. Yang, K.P. Kou, V.P. Lu, C.C. Lam, Ch. Zhang</i>	414
Direct determination of critical load combinations for elastoplastic structures subject to multiple load cases <i>S. Tangaramvong, and F. Tin-Loi</i>	424
Computational Method for Thermal Interactions between Compressible Fluids and Complicated-Shaped Structures with Multiphase Modeling <i>D.Toriu, S.Ushijima and K.Aoki</i>	432
Effects of Continuum Breakdown on Aerodynamics <i>Fei Huang, Liang Zhang, Wen-bo Miao and Xiao-li Cheng</i>	440
Optimization of stiffened shell structures with stability objective/constraint based on kriging surrogate model and the explicit FEM <i>Bin Wang, Jiandong Tian, Cheng Huang</i>	448
A STUDY OF THE OPTIMAL DESIGN AND MECHANICS SENSIBILITY IN THREE HINGE TRUSS "For two asymmetrical truss with different or equal component section sizes" <i>Toru Katori, Kazutoshi Tsutsumi</i>	455
Porohyperelastic Analysis of Single Chondrocyte Using AFM and inverse FEA <i>Trung Dung Nguyen, Yuantong Gu</i>	463
Fundamental study for seawall collapse simulation during Tsunami by using a particle method <i>Toshihiro Morimoto, Mitsuteru Asai, and Yoshimi Sonoda</i>	470
Subjective Evaluation of Crash Behavior of Muscle at Subsonic Level for Simulation of Bird Strike <i>Naoki Torii, Atsushi Sakuma, and Hirokazu Shoji</i>	476

Random vibration analysis of structures with uncertain-but-bounded parameters <i>Duy Minh Do, Wei Gao, and Chongmin Song</i>	483
Implementation of fundamental-solution based hybrid finite element model for elastic circular inclusions <i>H. Wang and Qing H. Qin</i>	490
Direct numerical simulation of unsteady natural convection boundary layers on an evenly heated plate with time-varying heating flux <i>Wenxian Lin, and S.W. Armfield</i>	498
Numerical Simulation of Nonlinear Acoustic Waves in Two-Phase Fluid <i>Yoshiaki Tamura, Nobuo Tsurumi, and Yoichiro Matsumoto</i>	506
Finite element modeling of a tunnel affected by dislocation of faults <i>Xingwen Luo, Zhenjun Yang</i>	511
Multi-objective optimization design of coronary stent based on kriging surrogate model <i>H.X. Li, B. Zhu and X.C. Wang</i>	519
A time-domain BEM for dynamic crack analysis of magnetoelastic composites <i>M. Wünsche, Ch.Zhang, J. Sladek, V. Sladek</i>	527
Application of Surface Mapping to Visualize Wall Shear Stress and Particles deposition in a Realistic Human Nasal Cavity <i>Yidan Shang, Kiao Inthavong, and Jiyuan Tu</i>	535
Time-Implicit Gas-Kinetic Scheme <i>S. Tan, Q.B. Li, and S. Fu</i>	542
Influence of boundary slip effect on thermal environment in thermochemical non-equilibrium flow <i>Wenbo Miao, Junming Lv, Fei Huang and Xiaoli Cheng</i>	550
Parameter Optimization of the Transition Zone of Large Thin-walled Tank Structure <i>Ling Zhang, Xi Zhang, Cheng Huang</i>	559
State Estimation Problem for the Action Potential Modeling in Purkinje Fibers <i>D. C. Estumano, H. R. B.Orlande and M. J.Colaço</i>	567
An iterative truly meshless coupling to solve embedded crack problems <i>E.F. Fontes Jr, J.A.F. Santiago, and J.C.F. Telles</i>	575
Computations of Compound Droplet Formation in a Flow Focusing Device <i>S. Homma</i>	584
Hybrid probabilistic interval dynamic analysis of vehicle-bridge interaction system with uncertainties <i>Nengguang Liu, Wei Gao, Chongmin Song and Nong Zhang</i>	589
Dynamic reliability based structural optimization <i>W. Gao, J. Ma, C.M. Song and F. Tin-L</i>	597

Research on structural optimization design for shield beam of hydraulic support based on response surface method <i>Dongchen Qin, Huiyu Li, Zhuli Liu, and Jiangyi Chen</i>	604
An Effective Level Set-based Method for the Design of Extrudable Structures <i>H. Li, L. Gao, P.G. Li and T. Wu</i>	611
Substructure dual reciprocity boundary element method for prediction of acoustic attenuation performance of silencers with potential flow <i>X. H. Miao, X. R Wang, D. Jia, D. J. Qian, and F. Z. Pang</i>	619
Simulations of Droplets falling on a solid surface Using Phase-Field Method <i>T. Sakakiabara, T.Takaki, and M.Kurata</i>	627
Uncertainty in long-term behavior and buckling of concrete-filled steel tubular columns <i>Xue Shi, Wei Gao, Yong-Lin Pi, Mark A. Bradford</i>	633
Direct Numeric Simulation of Sheared Convective Boundary Layer Entrainment with GPUs <i>Nicholas J. Stewart, David W. Holmes, Wenxian Lin, Steven W. Armfield and Michael P. Kirkpatrick</i>	641
Non-linear elastic in-plane buckling of crown-pinned arches with rotational end restraints <i>K. Luo, Y. L. Pi, W. Gao and M. A. Bradford</i>	648
Deformation Properties of Single Red Blood Cell in a Stenosed Microchannel <i>P.G.H. Nayanajith, S. C. Saha, and Y.T. Gu</i>	656
Natural convection in a reservoir induced by periodic thermal forcing at the water surface <i>Yadan Mao</i>	664
Development of a Steam Distribution Network Simulator for Enhanced Oil Recovery Systems <i>Tatsuro Yashiki, Yukinori Katagiri, Yoshikazu Ishii, Shunichi Kuba, Takayuki Mitadera, and Tomohiko Yoshida</i>	672
CIVA-Stabilized Finite Element Method for Tsunami Simulations <i>Yusuke Takahashi, Masaaki Sakuraba, and Kazuo Kashiwama</i>	680
Large-Scale Tsunami Simulation Based on Three-Dimensional Parallel SUPG-VOF Method <i>Taiki Fumuro, Seizo Tanaka, and Kazuo Kashiwama</i>	688
Effect of Temperature Gradient within Solid Particles for Dispersed Two-Phase Flow and Heat Transfer <i>Takaaki TSUTSUMI, Shintaro TAKEUCHI, and Takeo KAJISHIMA</i>	696
Mesh Modification System for Three Dimensional Unstructured Mesh Using VR Technology <i>Satoshi Tanaka, Kazuo Kashiwama, and Akira Kageyama</i>	704
Development of Simulation System for Tsunami Evacuation Using Virtual Reality Technology <i>Takeshi Kawabe, Kazuo Kashiwama, Hiroshi Okawa and Hideo Miyachi</i>	712
A Road Traffic Noise Evaluation System Considering A Stereoscopic Sound Field Using Virtual Reality Technology <i>Kou Ejima, Kazuo Kashiwama, Masaki Tanigawa and Masayuki Shimura</i>	720
Interval method for solving the dynamics problems of multibody system with uncertain parameters <i>Jinglai. Wu, Zhen. Luo, and Nong. Zhang</i>	728

Numerical evaluation of fluid force acted on bridge girders during tsunami by using particle method <i>Shoichi Tanabe, Mitsuteru Asai, and Yoshimi Sonoda</i>	736
Statistical Independence, Measures and Testing <i>Y. Unnisa, D. Tran and F. Huang</i>	744
A Linear Response Surface based on SVM for Structural Reliability Analysis <i>U. Alibrandi, C.Y. Ma, and C.G. Koh</i>	752
A novel MR device with variable stiffness and damping capability <i>Shiyu Zhao, Huaxia Deng, Jin Zhang, Shuaishuai Sun, Weihua Li, Lajun Zhou</i>	760
Error Analysis of Dynamical Measurement System Based on Binocular Vision <i>Yue Wang, Jin Zhang, and Huaxia D</i>	769
Large-deformation plasticity analysis using the edge-based smoothed finite element method <i>J. Liu, Z.Q. Zhang</i>	780
Numerical simulation of cross-flow around four cylinders by Local Domain Free Discretization-Immersed Boundary Method <i>Y.L. Wu, C. Shu, and H. Ding</i>	788
Solid-Fluid Interaction Analysis in Fixed Mesh and its Application to Functional Design of Component <i>Yuta Tamura, Atsushi Kawaguchi, Toru Hamasaki, Shigenobu Okazawa and Satoyuki Tanaka</i>	793
FTMP-based Simulation and Continuum Description of Discrete Dislocation System <i>Motoki Uematsu and Tadashi Hasebe</i>	799
DEM Simulation of a Screw Feeder Using the Adhesion Powder <i>M. Kimata, S. Kikai, T. Kagami and M. Hasegawa</i>	807
FTMP-based Simulation of Twin Nucleation and Substructure Evolution under Hypervelocity Impact <i>Tatsuya Okuda, Kazuhiro Imiya, and Tadashi Hasebe</i>	812
Inverse scattering analysis of an elastic half space by means of volume integral equation method <i>Terumi Touhei and Takuya Hinago</i>	820
Development of a triple-scale analysis method for plain-woven laminates based on a homogenization theory for time-dependent composites <i>Kohei Oide, Tetsuya Matsuda, and Fumiya Kawasaki</i>	826
FTMP-based Modeling and Simulation of Magnesium <i>Naoki Kajiwara, Kazuhiro Imiya and Tadashi Hasebe</i>	834
DEM simulation of agglomerated particle behavior in pan-type pelletizer using liquid bridge model <i>Daiki Fujihashi, Yuki Tsunazawa, Kazuki Tahara, Chiharu Tokoro and Shuji Owada</i>	842
Fast multi-scale simulations of a Step-and-Flash Imprint Lithography <i>M. Sieniek, P. Gurgul and M. Paszyński</i>	850
Thermal stress simulation of ultrafine plate-fin structures using a homogenization theory <i>Hiromu Kobori, Tetsuya Matsuda, and Masahiro Arai</i>	858

Combined Method for Rigid Bodies-Spring Model and Discrete Element Method <i>T.Yagi and N.Takeuchi , K.Yamamura, E.Hamasaki</i>	863
Effects of laminate misalignment on thermoelastoviscoplastic properties of ultrafine plate-fin structures <i>Yuki Yamanaka, Tetsuya Matsuda</i>	869
Computational Study of Reynolds Number Effect on Owl-like Wing Aerodynamics at Low Reynolds Numbers <i>K. Kondo, H. Aono, T. Nonomura, A. Oyama, K. Fujii, M. Yamamoto</i>	877
M-integral and configurational forces for Mode-I crack growth based on Gurson-Tvergaard model in elastoplasticity materials <i>B.H. Zhanga, , Q. Lia, Y.H. Chena, H.L. Wangb</i>	885
Simulation of D Free-surface Potential Flows Using a Robust Local Polynomial Collocation Method <i>Nan-Jing Wu, Ting-Kuei Tsay, Yang-Yih Chen, and I-Chen Tsu</i>	895
Multi-physics CFD simulation of three-phase flow with MPS method <i>Ryouhei Takahashi, Makoto Yamamoto and Hiroshi Kitada</i>	903
A Momentum Exchange-based Immersed Boundary-Lattice Boltzmann Method for Fluid Structure Interaction <i>Jianfei Yang, Zhengdao Wang, and Yuehong Qian</i>	910
A new scaled boundary finite element method using Fourier shape functions <i>Yiqian He, Haitian Yang, and Andrew J. Deeks</i>	916
Comparison of various numerical discretisation approaches for the scaled boundary method <i>Yiqian He, Haitian Yang, and Andrew J. Deeks</i>	922
Performance Analysis of a High Order Immersed Interface Method for CFD Applications <i>P. C. V. Paino, M. A. F. de Medeiros</i>	930
Parallel Implementation of Grammatical Evolution <i>E. Kita, Y. Lu, H. Sugiura and Y. Wakita</i>	939
Modeling of Wave Propagation in Unbounded Domains Using the Scaled Boundary Finite Element Method <i>Xiaojun Chen, Carolin Birk, Chongmin Song</i>	945
A quantitative method to determine the optimal stress field for D 8-node quadrilateral hybrid finite element <i>Canhui Zhang, Pei Liu, and Dongdong Wang</i>	955
Analytical solution for the transient response of functionally graded rectangular plates subjected to moving loads <i>Ta DuyHien, Hyuk-Chun Noh</i>	963
D Model Reconstruction of Patient-Specific Cardiac Mesh from Segmented Contour Lines <i>Chi Wan Lim, Yi Su, Si Yong Yeo, Gillian Maria Ng, Vinh Tan Nguyen, Liang Zhong, Ru San Tan, Kian Keong Poh, Ping Chai</i>	969

Earthquake Response Analysis of a Gravity Dam Considering the Radiation Damping of Infinite Foundation <i>Y.S. Liu and D.H. Chen</i>	977
Simple Method of Calculation of Statically Indeterminate Trusses <i>J. Rębielak</i>	985
A computational model of bone-cell interactions taking into account bone specific surface <i>Ch. Lerebours, P.R. Buenzli, C.D.L. Thomas, J.G. Clement, P. Pivonka</i>	991
Numerical Simulations of Shock Wave Reflection over Double Wedges <i>Z.L. Jiang and Y. Yang</i>	999
The distance sinh transformation for the numerical evaluation of nearly singular integrals over curved surface elements <i>Yu Miao, Jiahe Lv, Hongping Zhu</i>	1005
Numerical Simulation of Rigid Wheel Running Behavior on Sand Terrain <i>Mengyan Zang, Chunlai Zhao</i>	1016
Random Vibration Analysis for Impellers of Centrifugal Compressors Through the Pseudo-Excitation Method <i>Y.F. Wang, S. J. Wang, and L.H. Huang</i>	1030
Transient dynamical analysis of a dual-rotor system excited by a sudden loss of mass of blade <i>Jin Huang, Yuefang Wang</i>	1035
D Elastostatic Boundary Element Analysis of Ultra-Thin Structures with Planar Surfaces <i>Y.C. Shiah, Y.M. Lee , and R.B. Yang</i>	1042
A modified SPH method for modeling explosion and impact Problems <i>M. B. Liu, D. L. Feng and Z. M. Guo</i>	1057
Contact analysis for an anisotropic half-domain with micropatterns considering friction <i>Hideo Koguchi!, Shuma Suzuki, and Masahiro Taroura</i>	1064
Transition Phenomena in Turbulent Natural Convective Flow Using Subgrid Modeling <i>G.H. Yeoh, G.E. Lau , V. Timchenko and J.A. Reizes</i>	1072
A Finite Element Formulation of Minimization Problem for Steady Plastic Cycling <i>D.A. Tereshin</i>	1080
A multi-dimensional drift flux mixture model for gas-droplet two-phase flow <i>Zhi Shang, Hongying Li, Jing Lou</i>	1088
A semi-analytical model for predicting underwater noise radiated from offshore pile driving <i>Q. P. Deng, W. K. Jiang</i>	1096
Simulation to the Cyclic Deformation of Polycrystalline Aluminum Alloy Using Crystal Plasticity Finite Element Method <i>Juan Luo, Guozheng Kang, Mingxing Shi</i>	1104
The power loss and efficiency analysis of a DOFs planetary gear box <i>H.B. Yin, S. L. Li, H. Zhang, X.Y. Zhao and J. Zhang</i>	1110

Grid deformation based on macro-element and partitioning techniques for flapping mechanism <i>J. H. Ko, and T. Q. Le</i>	1115
Tensile properties of graphene nanotube hybrid structures: a molecular dynamics study <i>H.F. Zhan, K. Xia and Y.T. Gu</i>	1121
Recent Progress of NPLS Technique and Its Applications in Measuring Supersonic Flows <i>YI Shi-he, CHEN Zhi, HE Lin, ZHAO Yu-xin, TIAN Li-feng, WU Yu</i>	1129
A study on the cloud effect on debris trajectory <i>C.K. Lee, J. Xu, and S.C. Fan</i>	1139
General Ray Method and Rotating Projection Algorithm for Fast Recognition of Discrete Micro Scale Compound Structures <i>Grebennikov Alexandre</i>	1146
A Multi-Dimensional Limiter for Hybrid Grid <i>H. W. Zheng</i>	1153
Snoring as Markers for Obstructive Sleep Apnea – A Computational Multiphysics Investigation <i>M.R. Rasani, A.K. Ariffin, and J.Y. Tu</i>	1158
Investigation of a Shock-Detecting Sensor for Filtering of High-Order Compact Finite Difference Schemes <i>M. Khoshab, A. A. Dehghan, H. Mahmoodi Darian, and V. Esfahanian</i>	1163
An implicit multigrid solver for high-order compressible flow simulations on GPUs <i>V. Esfahanian, M. Hedayat, B. Baghapour, M. Torabzadeh and S.J. Hosseini</i>	1171
Strong-stability-preserving explicit Runge-Kutta methods for SPH elastodynamics <i>L. He, R.S. Crouch, M. Seaid and C.E. Augarde</i>	1179
Nonparametric Reliability-based Design Optimization Using Sign Test on Limited Discrete Information <i>W. Lim, J. Jang, S. Park, E. Amalnerkar and T.H. Lee</i>	1188
Simulation of Thermal behavior of a Two-speed Dual Clutch Transmission <i>Xingxing Zhou, Paul Walker, Nong Zhang, Bo Zhu, Jiageng Ruan</i>	1196
Design Optimization of Structures using A Nodal Density-Based SIMP Method <i>Y. Wang, Z. Luo, and N. Zhang</i>	1201
Stability Problem of Stadium Roof <i>P. Rosko, and A. Bekö</i>	1209
Meso-scale Fracture Modelling of Concrete Based on X-ray Computed Tomography Images <i>Wenyuan Ren, Zhenjun Yang, and Phil Withers</i>	1215
Computational Mechanics of a Coupled Flow-Structure Interaction Problem with Applications to Bio-inspired Micro Air Vehicles <i>Rohan Banerjee, Padmanabhan Seshaiyer</i>	1225
Modelling crack propagation using a non-matching SBFEM-FEM coupled method <i>X.F Wang, Z.J Yang, and D.S. Yin</i>	1233

Calibration of Constitutive Adhesion Models <i>E. B. Albuquerque, L.A. Borges and D.A. Castello</i>	1240
Some Considerations on the Appropriate Dimension in the Numerical Analysis of Geoengineering Structures <i>Ö. Aydan, M. Geniş, N. Tokashiki and H. Tano</i>	1246
Wind Tunnel Tests of the Counter-Rotating Propeller of Stratospheric Airship <i>Peiqing Liu, Jingwei Sun, and Zhihao Tang,</i>	1254
Relevancy of Peak Parameter Plots in Estimating Effects of Ground Shock <i>J.H. Chew, and E.C. Leong</i>	1263
Two- and Three-Dimensional Validation of Icing Model <i>Ryosuke Hayashi and Makoto Yamamoto</i>	1271
Numerical and Fundamental Study on Ice Growth of Ice Crystal Accretion <i>Koharu Furuta and Makoto Yamamoto</i>	1279
A rescaling method for generating inflow conditions in simulations of supersonic boundary layers <i>Ning Hu and Han-Dong Ma</i>	1286
Analysis of Acoustic-Fields generated by Supersonic Jet Impinging on an Inclined Flat Plate and a Curved Plate <i>Yuki Nagata, Taku Nonomura, Kozo Fujii, Makoto Yamamoto</i>	1292
Displacement Function Method of Space Problem for Transversely Isotropic Foundation Based on Damage Theory <i>Wang Baoshi, Liu Junqing, Chen Chengcheng</i>	1300
Analysis of Steel Moment Frames subjected to Vehicle Impact <i>Hyungoo Kang, Jeongil Shin, Jinkoo Kim</i>	1308
Formulation and development of the cell-based smoothed discrete shear gap plate element (CS-FEM-DSG) using three-node triangles <i>T. Nguyen-Thoi, P. Phung-Van, H. Nguyen-Xuan</i>	1316
A High-Order Unstructured Mixed Method for Aerodynamic Applications <i>Min Kyu Jung and Oh Joon Kwon</i>	1324
Investigation of Residual Stress Effect on Fatigue Life of Butt Weld Joints Subjected to Cyclic Bending <i>Ali Gharizadeh, Bijan Samali, Ali Saleh</i>	1332
Sequential Projection Maximin Distance Sampling Method <i>J. Jang, W. Lim, S. Cho, M. Lee, J. Na and T.H. Lee</i>	1340
Computational Fluid Dynamics (CFD) Simulations of Dispersed Flow of Viscous Oil in Water in a Horizontal Pipe <i>Robin Yap Miao Sin, Cary K Turangan</i>	1348
Grid Generation for Screw Compressors with Variable Geometry Rotors <i>A. Kovacevic, S. Rane and N. Stosic</i>	1356



Neural Network Prediction of Nonlinear Elastic Unloading for High Strength Steel <i>M. R. Jamli, A. K. Ariffin, and D. A. Wahab</i>	1366
Prediction of solid recirculation rate and solid volume fraction in an ICFB <i>Ravi Gujjula, Narasimha Mangadoddy</i>	1372
Coupled Reliability and S-version Finite-Element Model for Probabilistic Distribution of Surface Crack Growth under Constant Amplitude Loading <i>M.R.M. Akramin, A.K. Ariffin, Masanori Kikuchi, S. Abdullah, and N. Nikabdullah</i>	1382
Left Ventricle Segmentation by Circular Shape Constrained Clustering Algorithm <i>Xulei Yang, Si Yong Yeo, Yi Su, Calvin Lim, Min Wan, Liang Zhong, and Ru San Tan</i>	1390
Research on Energy-saving for two Different Cutter-head Drive System of Shield Tunneling Machine <i>H.Y. Liu, J.H. Bu, S.N. Wang, and Y.T. Sun</i>	1397
Simulation of Bubbly Flow in a Vertical Pipe Using Discrete Phase Model <i>H.Y. Li, J. Lou, Z. Shang and H. Tang</i>	1405
Numerical Studies of Gas-Liquid-Fueled Two-Phase Detonation by Using Improved CE/SE method <i>D. L. Zhang</i>	1414
A dual-reciprocity boundary element method for axisymmetric thermoelastodynamic deformations in functionally graded solids <i>W. T. Ang and B. I. Yun</i>	1425
OPTIMIZATION OF THE GAS FLOW IN A GEM CHAMBER AND DEVELOPMENT OF THE GEM FOIL STRETCHER <i>Francesco NOTO, Valerie DE SMET, Vincenzo BELLINI, Evaristo CISBANI, Francesco LIBRIZZI, Francesco MAMMOLITI, Maria Concetta SUTERA</i>	1434
Simulation of passive myocardium of rabbit ventricles, using selective smoothed finite element method(S-FEM) <i>C. Jiang, Zhi-Qian Zhang, X. Han, G.R. Liu</i>	1442
Theoretical and Numerical Analysis of Heat Transfer in Pipeline System <i>Xiaowei Zhu, Hui Tang, Hua Li, Jiahua Hong, Songyuan Yang</i>	1451
Simulation on separation flowing around cylinders with lattice Boltzmann method <i>Z.D. Wang, J.F. Yang, Y.H. Qian</i>	1460
Symbolic Calculation of Free Convection for Porous Material of Quadratic Heat Generation in a Circular Cavity <i>Kamyar Mansour</i>	1465
Combined explicit and implicit algorithms for dynamic problems using the numerical manifold method <i>X.L. Qu and G.W. Ma</i>	1471
Authors Index	1479

## The effects of flexible fixation on early stage bone fracture healing

**\*\*L. Zhang<sup>1</sup>, S. Miramini<sup>1</sup>, P. Mendis<sup>1</sup>, M. Richardson<sup>2</sup>, M. Pirpiris<sup>2</sup> and A. Oloyede<sup>3</sup>**

<sup>1</sup> Department of Infrastructure Engineering, The University of Melbourne, Australia.

<sup>2</sup> The Epworth Hospital, Richmond, Australia.

<sup>3</sup> Science and Engineering Faculty, Queensland University of Technology, Australia

\*Corresponding author: [lih Zhang@unimelb.edu.au](mailto:lih Zhang@unimelb.edu.au)

### Abstract

The mechanical microenvironment at a fracture site could potentially influence the outcomes of bone fracture healing. It is known that, should the fixation construct be too stiff, or the gap between the fracture ends be too large, bones are less likely to heal. Flexible fixation or so-called “biological fixation” has been shown to encourage the formation of fracture callus, and therefore result in better healing outcomes. However, till date the nature of the relationship between the degree of mechanical stability provided by a flexible fixation and optimal healing fracture healing outcomes has not been fully understood. This paper presents a computational model that can predict healing outcomes from early stage healing data under various fixation configurations. The results of the simulations demonstrate that the change of mechanical microenvironment of fracture site resulting from the different fixation configurations is of importance for the healing outcomes.

**Keywords:** bone fracture healing; locking compression plate (LCP); interfragmentary movements (IFM); mechanical microenvironment; computational modelling.

### Introduction

The flexibility of internal fixation systems affects the formation of fracture callus as a result of interfragmentary strain (IFS) at fracture site (Zhang et al. 2012). It has been demonstrated that the initial phase of healing is especially sensitive to IFS and influences the ultimate healing outcomes as the initial interfragmentary movements are higher at early stage of healing after surgery (Carter et al. 1988; Klein et al. 2003). For example, it has been established that there is a strong correlation between hydrostatic fluid pressure and tissue differentiation in the initial stages of fracture healing (Carter et al. 1988), and that bone healing is influenced by the stability of initial shear fixation (Chell et al. 1995). However, despite several research efforts around the world over the last decades, there still remains a significant gap in our understanding of the relationships between mechanical stability conditions and the biology of bone fracture healing processes (Perren 2002b).

Apparently, soft callus formation is especially important for the stabilization of the fracture site through the stages of healing, and if not properly formed could result in malfunctioning bone segment union. To improve the healing outcomes and avoid the risks of delayed union and non-union, various types of fixation have been developed in the last decades. Standard fixation plates which mainly focus on mechanical stability (so called “absolutely stability”) through the compression of standard plates against underlying bone using normal screws, could lead to delayed healing, damage to blood supply of fracture site and underlying periosteum (Szypryt and Forward 2009). With the development of locking plate, which acts as an internal splint and load sparing device, the compression between plate and bone becomes unnecessary. Particularly, the application of locking plate in osteoporotic patient reduces the risks of fixation failure resulting from the pull out of screws (Szypryt and Forward 2009). In addition, the core diameter of a locking head screw (LHS) is normally larger than that of a standard cortical screw, and so could provide much greater strength in bending (200%) and shear (100%). The purpose of locking plate is to promote formation of fracture callus via allowing a certain degree of IFM at the fracture gap without compromising the

overall mechanical stability of the fracture site (Perren 2002a). However, as the mechanical properties of widely used locking plate material (e.g. stainless steel and titanium) are normally much higher than that of bone, standard locking plate might still suppress interfragmentary movements required for indirect bone healing (Claes et al. 2011; Henderson et al. 2008; Lujan et al. 2010b). Further, although the locking plate allows some IFM to help simulate callus formation, the generated IFM is not uniformly distributed across the fracture site (i.e., much smaller IFM at near cortex in comparison to that at far cortex), and this spatially dependent IFM could lead to asymmetric tissue distribution within the callus, and ultimately delayed healing (Bottlang et al. 2010; Lujan et al. 2010b).

Several attempts have been made to further improve flexibility of locking plates with the aim of simulating the formation of callus. For example, recent studies have been increasingly focused on the development of innovative plate materials with material mechanical properties more similar to bone such as composite polymers (JH and SH 2007; Kim et al. 2010; Zdero and Bougherara 2010) and metal foams (Rabiei 2010; Rabiei 2012). However this new concept is still in its infancy and needs more biomechanical and clinical investigations in order to be widely accepted by the orthopaedic community. Clinically, the flexibility of the locking plates could be enhanced by adjusting the working length (WL), bone-plate distance (BPD) and number of screws (Ahmad et al. 2007; Claes 2011; Hak et al. 2010; Miller and Goswami 2007; Stoffel et al. 2003), however the limitations of these surgical techniques lie in their incapability of solving the problem of the significant difference between the IFM at the near and far cortex zones of the callus which leads to asymmetric callus formation and possibly delayed healing and non-union (Bottlang et al. 2010; Claes 2011; Lujan et al. 2010b). To tackle this issue, the dynamic locking screw (DLS) was recently developed with the aim of increasing the IFM in the near cortex zone, and ultimately uniform callus formation (Bottlang et al. 2009; Bottlang and Feist 2011; Bottlang et al. 2010; Döbele et al. 2010; Doornink et al. 2011; Gardner et al. 2009; Gardner et al. 2010; Plecko et al. 2012; Sellei et al. 2011). Different from LHS, DLS consists of an outer sleeve attached to the bone and an inner pin with reduced diameter at the near cortex resulting in the increase of the IFM on the near cortex side, and consequently enhancing callus formation in this area (Bottlang et al. 2010; Plecko et al. 2012; Sellei et al. 2011). However, none of these techniques has proved adequate till date due to the lack of fundamental understanding of the relationship between mechanical stability conditions and the biology of bone fracture healing process. Therefore, the objective of this paper is to develop a computational model that facilitates the understanding of the relationships between the change in the mechanical environment of a fracture site and varying fixation configurations of a locking plate system.

## Methods

After surgical installation of internal fixation, the fracture callus is developed within the fracture gap by filling with granulation tissue during the first several days of healing during which the biomechanical condition is of critical importance for the ultimate healing outcomes (Epari et al. 2006; Klein 2003; Thompson et al. 2002). At this stage, callus could be treated as a porous fluid saturated material (González-Torres et al. 2010) that could be modeled by the theory of porous media which is commonly used to study the mechanical behavior of biological soft tissues (e.g. cartilage and brain) (Oloyede and Broom 1991; Oloyede and Broom 1994; Zhang et al. 2007; Zhang et al. 2008; Zhang et al. 2009). Considering a particular constituent of a fluid-filled soft biological tissue (e.g. callus) occupies a domain  $\Omega_0^\alpha$ , i.e. solid phase ( $\alpha = s$ ) or fluid phase ( $\alpha = f$ ). The time-dependent position of the particle in the current Eulerian configuration  $\Omega$ , is given by

$$x(X^\alpha, t) = X^\alpha + u^\alpha(X^\alpha, t) \quad (1)$$

where  $u^\alpha$  is the  $\alpha$ -constituent displacement. The volume fraction of solid and fluid phase may be defined respectively as

$$\phi^s + \phi^f = 1 \quad (2)$$

Assuming intrinsically incompressible constituents, the Cauchy stress tensors of the solid and fluid phases are defined as

$$\boldsymbol{\sigma}^s = -\phi^s p \mathbf{I} + \boldsymbol{\sigma}_E^s \quad (3)$$

$$\boldsymbol{\sigma}^f = -\phi^f p \mathbf{I} \quad (4)$$

where  $\boldsymbol{\sigma}_E^s$  is the elastic stress resulting from solid deformation and  $\mathbf{I}$  is the identity tensor. If the solid constituent can be treated as hyperelastic, then

$$\boldsymbol{\sigma}_E^s = \frac{1}{J^s} \mathbf{F}^s \bullet 2 \frac{\partial U(\mathbf{u}^s)}{\partial \mathbf{C}^s} \bullet \mathbf{F}^{sT} \quad (5)$$

where  $U(\mathbf{u}^s)$  is the Helmholtz energy per unit reference volume stored in the solid,  $\mathbf{F}^s$  is the deformation gradient of the solid phase,  $\mathbf{C}^s = \mathbf{F}^{sT} \bullet \mathbf{F}^s$  is the right Cauchy-Green deformation tensor of the solid phase, and  $J^s = \det \mathbf{F}^s$  is the volume change of solid phase.

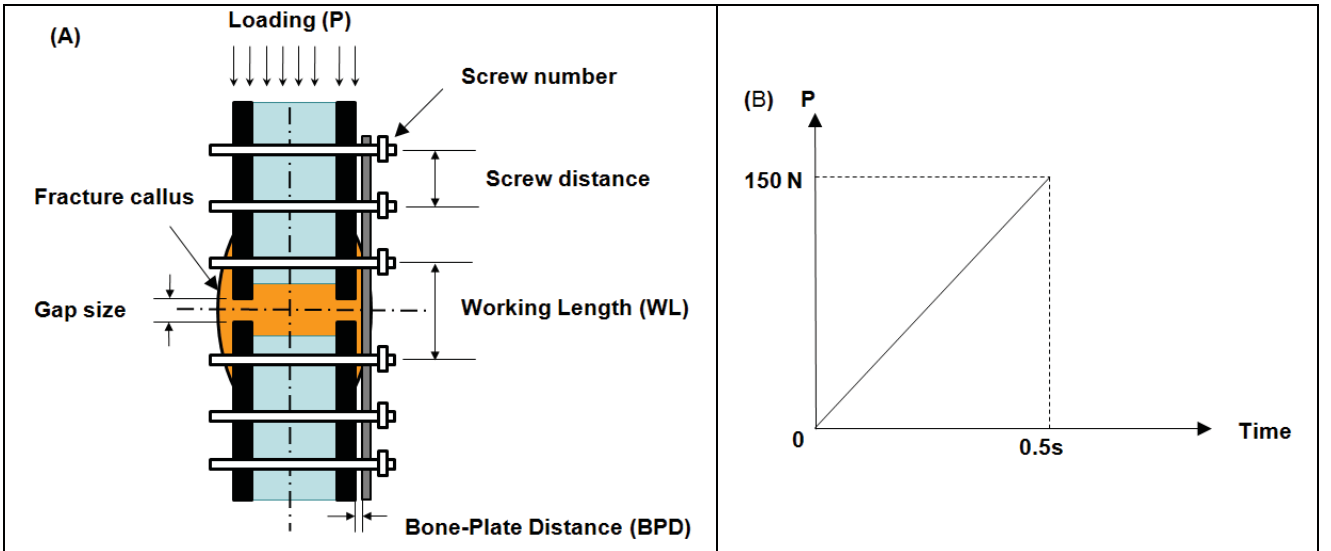
Ignoring the body and inertial forces, the momentum equation of the solid phase is given by

$$\nabla \bullet \boldsymbol{\sigma}^\alpha + \pi^\alpha = 0 \quad (6)$$

where  $\boldsymbol{\sigma}^\alpha$  is the Cauchy stress tensor for the  $\alpha$ -constituent,  $\pi^s$  and  $\pi^f$  are momentum exchange vectors describing the frictional interactions between the solid phase and fluid phase. That is,

$$\pi^s = -p \nabla \phi^f + (\phi^f)^2 \kappa^{-1} \bullet (\mathbf{v}^f - \mathbf{v}^s) \quad (7)$$

where  $\kappa$  is the symmetric Darcy permeability tensor.



**Figure 1** Fixation conditions of locking plate for computational modeling of bone fracture healing characteristics at early stage.

**Table 1 Parameters used in this study (Lacroix and Prendergast 2002; McCartney et al. 2005)**

	Young's modulus (MPa)	Poisson's Ratio	Porosity	Permeability (m <sup>4</sup> /Ns)	Fluid phase compression modulus (MPa)	Solid phase compression modulus (MPa)
Granulation Tissue	0.05	0.17	0.8	10 <sup>-14</sup>	2300	2300
Marrow	2	0.17	0.8	10 <sup>-14</sup>	2300	2300
Cortical Bone	20000	0.3	0.04	10 <sup>-17</sup>	2300	13920

This study will theoretically investigate the tissue development simulated by the change of mechanical microenvironment of the fracture site resulting from various locking plate conditions. **Error! Reference source not found.** is a schematic diagram of the fixation conditions of the locking plate used in our analysis, and the values of parameters used in this study are shown in Table 1. The fractured bone is subject to a time-dependent load ( $P$ ) applied over 0.5s simulating physiological walking load (approx. 20% of the normal body weight that a patient could withstand after surgery) (Goodship 1985).

#### *Mechanoregulation of bone healing*

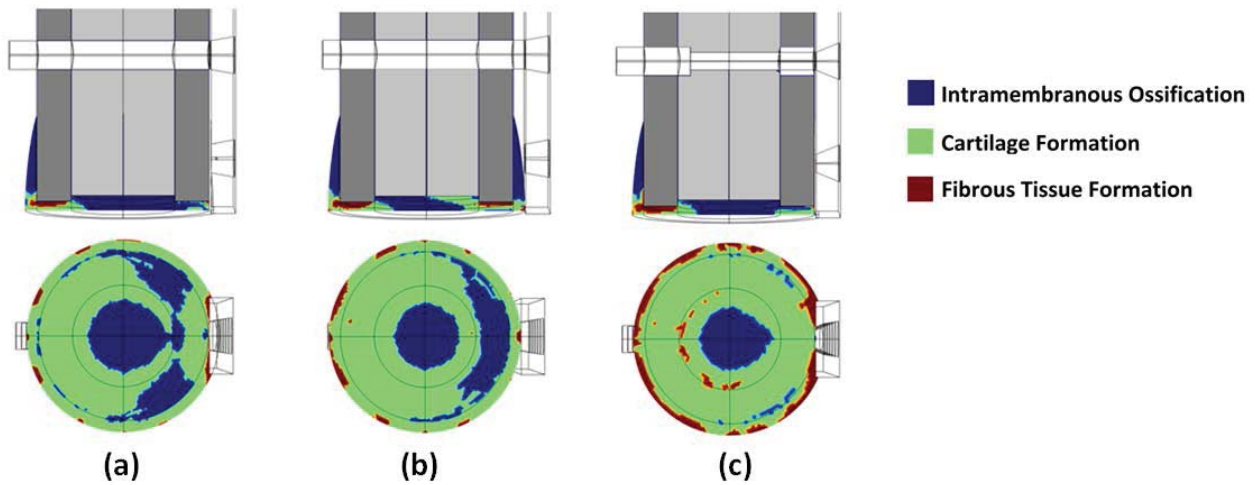
Assuming mesenchymal stem cell differentiation within fracture callus is simulated by the change of biomechanical microenvironment of cells, Prendergast et al suggested that the differentiation process of stem cells are governed by a so-called "Stimulus Index ( $S$ )", which is defined as (Prendergast et al. 2010)

$$S = \frac{\gamma}{a} + \frac{\nu}{b} \quad (8)$$

where  $a = 0.0375$ ,  $b = 3 \mu\text{m/s}$ ,  $\gamma$  is octahedral shear strain in callus and  $\nu$  is interstitial fluid flow within the callus. The values of  $\gamma$  and  $\nu$  can be obtained by solving the governing equations (3) – (7) using the commercial Finite Element software package COMSOL MULTIPHYSICS (2012). Therefore, the stem cells could exert spatially dependent differentiation behaviour within the callus depending on the magnitude of  $S$  in a particular region of callus. During the early stage of bone healing (*i.e.* first week after surgery), high magnitude of stimulus index ( $S > 3$ ) results in formation of fibrous tissue inside the callus, an intermediate  $S$  ( $1 < S < 3$ ) leads to cartilage tissue and bone formation via intramembranous ossification when the stimulus index  $S$  is small enough ( $S < 1$ ). During the next stages of bone healing, fibrous tissue is replaced by cartilage when  $1 < S < 3$  and the cartilage undergoes endochondral ossification and is replaced by woven bone when  $S < 1$ . The mechanoregulation theory proposed by Prendergast et al has been used in this study.

Synthes 4.5mm stainless steel Locking Compression Plate (224mm long, 17.5mm wide and 5.2mm thick with 12 locking holes) was used to compare the effects of various configurations of fixation using LHS, DLS and different BPDs on the healing outcomes. To promote indirect healing, intramembranous ossification is unfavourable at early stage of healing, in the meantime consistent and asymmetric callus formation is also of importance for ultimate healing outcomes (Lujan et al. 2010a).

## Results and Discussion



**Figure 2 Comparison of simulation results for callus formation in healing fracture sites under (a) LHS, BPD = 0mm (control); (b) LHS, BPD = 2mm; and (c) DLS, BPD = 2mm**

**Table 2 Tissue differentiation in the osteotomy gap**

Type	Intramembranous ossification	Cartilage formation	Fibrous tissue formation
(a)	37.10%	41.20%	21.70%
(b)	25.20%	44.70%	30.10%
(c)	15.10%	38.60%	46.30%

Figure 2 provides the prediction of tissue formation under (a) LHS, BPD = 0mm (control); (b) LHS, BPD = 2mm; and (c) DLS, BPD = 2mm, respectively. The amount of different tissues formation in the osteotomy gap (*i.e.* Intramembranous ossification, cartilage formation and fibrous tissue formation) is presented in Table 2. The simulation results demonstrate that under LHS, the increase of BPD by 2mm (Figure 2b) relative to the control (Figure 2a) has some beneficial effects in reducing intramembranous ossification by around 12%, however this increase of BPD is still unable to change the condition of asymmetrical tissue development within the callus due to the significant difference of interfragmentary strain between near and far cortex zones of the callus. In comparison to LHS, the use of DLS in combination with the increase of BPD produces the most encouraging results, *i.e.* reducing intramembranous ossification by more than 20%, and most importantly leading to more consistent and symmetric tissue development. The simulation results indicate that the application of DLS has substantial potential for improving bone healing outcomes.

## Conclusions

In this study, we have presented a computational model to predict bone fracture healing outcomes, demonstrating that the model could quantitatively describe tissue differentiation pattern in the early stages of fracture healing. Most importantly, the predicted results indicate that innovative fixation techniques such as DLS, could potentially lead to better healing outcomes via significantly reducing intramembranous ossification while promoting symmetric tissue development within the callus.

## Acknowledgments

The authors wish to acknowledge the support of Synthes Asia and Pacific and The Ian Potter Foundation, and The University of Melbourne.

## References

- (2012). "COMSOL Multiphysics." COMSOL Inc.
- Ahmad, M., Nanda, R., Bajwa, a. S., Candal-Couto, J., Green, S., and Hui, a. C. (2007). "Biomechanical testing of the locking compression plate: when does the distance between bone and implant significantly reduce construct stability?" *Injury*, 38, 358-64.
- Bottlang, M., Doornink, J., Fitzpatrick, D. C., and Madey, S. M. (2009). "Far cortical locking can reduce stiffness of locked plating constructs while retaining construct strength." *The Journal of bone and joint surgery. American volume*, 91, 1985-94.
- Bottlang, M., and Feist, F. (2011). "Biomechanics of far cortical locking." *Journal of orthopaedic trauma*, 25 Suppl 1, S21-8.
- Bottlang, M., Lesser, M., Koerber, J., Doornink, J., von Rechenberg, B., Augat, P., Fitzpatrick, D. C., Madey, S. M., and Marsh, J. L. (2010). "Far cortical locking can improve healing of fractures stabilized with locking plates." *The Journal of bone and joint surgery. American volume*, 92, 1652-60.
- Carter, D. R., Blenman, P. R., and Beaupré, G. S. (1988). "Correlations between mechanical stress history and tissue differentiation in initial fracture healing." *Journal of Orthopaedic Research*, 6(5), 736-748.
- Chell, H., Epari, D. R., Kassi, J. P., Bragulla, H., Bail, H. J., and Duda, G. N. (1995). "The course of bone healing is influenced by the initial shear fixation stability." *Journal of Orthopaedic Research*, 9, 324-332.
- Claes, L. (2011). "Biomechanical principles and mechanobiologic aspects of flexible and locked plating." *Journal of orthopaedic trauma*, 25 Suppl 1, S4-7.
- Claes, L., Reusch, M., Göckelmann, M., Ohnmacht, M., Wehner, T., Amling, M., Beil, F. T., and Ignatius, A. (2011). "Metaphyseal fracture healing follows similar biomechanical rules as diaphyseal healing." *Journal of Orthopaedic Research*, 29(3), 425-432.
- Döbele, S., Horn, C., Eichhorn, S., Buchholtz, A., Lenich, A., Burgkart, R., Nüssler, A. K., Lucke, M., Andermatt, D., Koch, R., and Stöckle, U. (2010). "The dynamic locking screw (DLS) can increase interfragmentary motion on the near cortex of locked plating constructs by reducing the axial stiffness." *Langenbeck's archives of surgery / Deutsche Gesellschaft für Chirurgie*, 395, 421-8.
- Doornink, J., Fitzpatrick, D. C., Madey, S. M., and Bottlang, M. (2011). "Far cortical locking enables flexible fixation with periarticular locking plates." *Journal of orthopaedic trauma*, 25 Suppl 1, S29-34.
- Epari, D. R., Taylor, W. R., Heller, M. O., and Duda, G. N. (2006). "Mechanical conditions in the initial phase of bone healing." *Clinical biomechanics (Bristol, Avon)*, 21, 646-55.
- Gardner, M. J., Nork, S. E., Huber, P., and Krieg, J. C. (2009). "Stiffness modulation of locking plate constructs using near cortical slotted holes: a preliminary study." *Journal of orthopaedic trauma*, 23, 281-7.
- Gardner, M. J., Nork, S. E., Huber, P., and Krieg, J. C. (2010). "Less rigid stable fracture fixation in osteoporotic bone using locked plates with near cortical slots." *Injury*, 41, 652-6.
- González-Torres, L. A., Gómez-Benito, M. J., Doblaré, M., and García-Aznar, J. M. (2010). "Influence of the frequency of the external mechanical stimulus on bone healing: A computational study." *Medical Engineering & Physics*, 32, 363-371.
- Goodship, A. E. (1985). "The influence of induced micromovement upon the healing of experimental tibial fractures." *Journal of Bone and Joint Surgery*, 67(4), 650.
- Hak, D. J., Toker, S., Yi, C., and Toreson, J. (2010). "The influence of fracture fixation biomechanics on fracture healing." *Orthopedics*, 33, 752-5.
- Henderson, C. E., Bottlang, M., Marsh, J. L., Fitzpatrick, D. C., and Madey, S. M. (2008). "Does locked plating of periprosthetic supracondylar femur fractures promote bone healing by callus formation? Two cases with opposite outcomes." *The Iowa orthopaedic journal*, 28, 73-6.
- JH, K., and SH, C. (2007). "Design of a flexible composite bone plate for bone fracture healing." 14th international conference on composite structures, Melbourne, Australia.
- Kim, S.-H., Chang, S.-H., and Jung, H.-J. (2010). "The finite element analysis of a fractured tibia applied by composite bone plates considering contact conditions and time-varying properties of curing tissues." *Composite Structures*, 92, 2109-2118.
- Klein, P. (2003). "The initial phase of fracture healing is specifically sensitive to mechanical conditions." *Journal of Orthopaedic Research*, 21(4), 662.
- Klein, P., Schell, H., Streitparth, F., Heller, M., Kassi, J.-P., Kandziora, F., Bragulla, H., Haas, N. P., and Duda, G. N. (2003). "The initial phase of fracture healing is specifically sensitive to mechanical conditions." *Journal of Orthopaedic Research*, 21, 662-669.
- Lacroix, D., and Prendergast, P. J. (2002). "A mechano-regulation model for tissue differentiation during fracture healing: analysis of gap size and loading." *Journal of Biomechanics*, 35, 1163-1171.
- Lujan, T. J., Henderson, C. E., Madey, S. M., Fitzpatrick, D. C., Marsh, J. L., and Bottlang, M. (2010a). "Locked plating of distal femur fractures leads to inconsistent and asymmetric callus formation." *Journal of Orthopaedic Trauma*, 24(3), 156-162.

- Lujan, T. J., Henderson, C. E., Madey, S. M., Fitzpatrick, D. C., Marsh, J. L., and Bottlang, M. (2010b). "Locked plating of distal femur fractures leads to inconsistent and asymmetric callus formation." *Journal of orthopaedic trauma*, 24, 156-62.
- Mccartney, W., Donald, B., and Hashmi, M. (2005). "Comparative performance of a flexible fixation implant to a rigid implant in static and repetitive incremental loading." *Journal of Materials Processing Technology*, 169, 476-484.
- Miller, D. L., and Goswami, T. (2007). "A review of locking compression plate biomechanics and their advantages as internal fixators in fracture healing." *Clinical biomechanics (Bristol, Avon)*, 22, 1049-62.
- Oloyede, A., and Broom, N. D. (1991). "Is classical consolidation theory applicable to articular cartilage deformation?" *Clinical Biomechanics*, 6(4), 206-212.
- Oloyede, A., and Broom, N. D. (1994). "The generalized consolidation of articular cartilage: an investigation of its near-physiological response to static load." *Connective Tissue Research*, 31(1), 75-86.
- Perren, S. M. (2002a). "Evolution of the internal fixation of long bone fractures. The scientific basis of biological internal fixation: choosing a new balance between stability and biology." *The Journal of Bone and Joint Surgery*, 1093-1110.
- Perren, S. M. (2002b). "Evolution of the internal fixation of long bone fractures: the scientific basis of biological internal fixation: choosing a new balance between stability and biology." *Journal of Bone and Joint Surgery*, British Volume, 1093-1110.
- Plecko, M., Lagerpusch, N., Andermatt, D., Frigg, R., Koch, R., Sidler, M., Kronen, P., Klein, K., Nuss, K., Bürki, A., Ferguson, S. J., Stoeckle, U., Auer, J. a., and von Rechenberg, B. (2012). "The dynamisation of locking plate osteosynthesis by means of dynamic locking screws (DLS)-An experimental study in sheep." *Injury*.
- Prendergast, P. J., Checa, S., and Lacroix, D. (2010). "Computational models of tissue differentiation " *Computational Modeling in Biomechanics*, 3, 353-372.
- Rabiei, A. (2010). "Recent developments and the future of bone mimicking: materials for use in biomedical implants." *Expert review of medical devices*, 7, 727-9.
- Rabiei, A. (2012). "Composite metal foam and methods of preparation thereof."
- Sellei, R. M., Garrison, R. L., Kobbe, P., Lichte, P., Knobe, M., and Pape, H.-C. (2011). "Effects of near cortical slotted holes in locking plate constructs." *Journal of orthopaedic trauma*, 25 Suppl 1, S35-40.
- Stoffel, K., Dieter, U., Stachowiak, G., Gächter, A., and Kuster, M. S. (2003). "Biomechanical testing of the LCP – how can stability in locked internal fixators be controlled?" *Injury*, 34, 11-19.
- Szypryt, P., and Forward, D. (2009). "The use and abuse of locking plates." *Orthopaedics and Trauma*, 23(4), 281-290.
- Thompson, Z., Miclau, T., Hu, D., and Helms, J. a. (2002). "A model for intramembranous ossification during fracture healing." *Journal of orthopaedic research : official publication of the Orthopaedic Research Society*, 20, 1091-8.
- Zdero, R., and Bougherara, H. (2010). "x Orthopaedic Biomechanics : A Practical Approach to Combining Mechanical Testing and Finite Element Analysis." 171-194.
- Zhang, L., Gardiner, B. S., Smith, D. W., Pivonka, P., and Grodzinsky, A. J. (2007). "The effect of cyclic deformation and solute binding on solute transport in cartilage." *Archives of Biochemistry and Biophysics*, 457(1), 47-56.
- Zhang, L., Gardiner, B. S., Smith, D. W., Pivonka, P., and Grodzinsky, A. J. (2008). "A fully coupled poroelastic reactive-transport model of cartilage." *Molecular & Cellular Biomechanics*, 5(2), 133-153.
- Zhang, L., Gardiner, B. S., Smith, D. W., Pivonka, P., and Grodzinsky, A. J. (2009). "Integrated model of IGF-I mediated biosynthesis in deforming articular cartilage." *Journal of Engineering Mechanics (ASCE)*, 135(3), 439-449.
- Zhang, L., Richardson, M., and Mendis, P. (2012). "Role of chemical and mechanical stimuli in mediating bone fracture healing." *Clinical and Experimental Pharmacology and Physiology*, 39, 706-710.



# Dynamic Analysis of SSI Systems via a Coupled Finite-element/Scaled Boundary

## Finite-element Model

\*D. Chen<sup>1</sup>, C. Birk<sup>2</sup>, and S. Dai<sup>3</sup>

<sup>1</sup>College of Civil Engineering and Architecture, China Three Gorges University, Yichang 443002, China

<sup>2</sup>School of Civil and Environmental Engineering, University of New South Wales, Sydney, NSW 2052, Australia

<sup>3</sup>College of Mechanics and Materials, Hohai University, Nanjing 210098, China

\*Corresponding author: chdenghong@gmail.com

### Abstract

A coupled model based on finite element method (FEM) and scaled boundary finite element method (SBFEM) for transient dynamic response of large-scale SSI systems is presented. The well-established FEM is used for modeling the near-field bounded domains. A local high-order transmitting boundary, which is based on SBFEM and the improved continued fraction solution for the dynamic stiffness matrix, is used for modeling the dynamic response of the far-field unbounded domains. The bounded and unbounded formulations are coupled via the interaction force vector at the interface. The standard equations of the coupled model in the time domain are obtained by combining the dynamic equations of bounded and unbounded domains, which can be solved by a direct time-domain integration method. The stability of the coupled system depends on the general eigenproblem of the coefficient matrices. Possible spurious modes can be eliminated using the spectral shifting technique. The validity of the coupled model is shown by means of two numerical examples.

Keywords: Dynamic soil-structure interaction, Coupled FEM-SBFEM model, High-order transmitting boundary, Spectral shifting technique.

### 1 Introduction

Dynamic soil-structure interaction plays an important role in the design and safety assessment of structures, especially for large-scale structures, such as concrete dams, nuclear power plants, bridges etc. A rational and commonly used approach for modeling the whole system is to divide it into two parts. The first part is the near-field bounded domain, which contains the structure and a part of the adjacent soil and can be efficiently modeled by the finite element method. The second part is the far-field unbounded domain, which includes the rest of the infinite foundation. The major challenge is the accurate description of radiation damping at infinity. Here, the well-established finite element method cannot be used straightforwardly, since outgoing waves are reflected at the artificial boundaries of the finite element mesh.

Over the past few decades, many numerical methods have been developed to model the wave propagation in unbounded domains. Generally, they can be classified into two groups, global and local procedures. The global procedures include the boundary element method (Beskos, 1987; Beskos, 1997), the thin layer method (Kausel, 1986; Kausel, 1994), exact non-reflecting boundaries (Keller and Givoli, 1989) and the scaled boundary finite element method (Wolf and Song, 1996). The local procedures include the viscous boundary (Lysmer and Kuhlemeyer, 1969), the viscous-spring boundary (Deeks and Randolph, 1994; Liu *et al.*, 2006), the artificial transmitting boundary (Liao *et al.*, 1984), infinite elements (Zhao, 2009) and high-order absorbing boundary conditions (Engquist and Majda, 1977; Higdon, 1986; Bayliss and Turkel, 1980). The advantages, disadvantages and some progresses of these methods have been summarized in the review literatures (Tsynkov, 1998; Givoli, 2004; Lou *et al.*, 2011) and are not repeated here.

The scaled boundary finite element method, developed by Wolf and Song in 1990s, is a semi-analytical technique which excels in modelling wave propagation in unbounded and bounded domains. This method has the following distinguished features. First of all, the radiation condition for unbounded domain is satisfied rigorously without requiring a fundamental solution. Secondly, only the boundary of the domain is discretized as in the boundary element method, and the spatial dimension is reduced by one. Moreover, this method can be coupled seamlessly with the standard finite element method. Utilizing the advantages of the scaled boundary finite element method, many scholars have adopted it to study dynamic soil-structure interaction problems.

Zhang *et al.* (1999) applied a piecewise linear approximation of the acceleration unit-impulse response matrix of the unbounded domain within one time step and simplified the solution of the time-consuming convolution integrals. Yan *et al.* (2004) coupled the finite element method and the scaled boundary finite element method for 3D dynamic analysis of soil-structure interaction in the time domain. Linear system theory was employed to improve the efficiency for solving the acceleration unit-impulse response matrix of the unbounded domain. Radmanovic and Katz (2012) made two improvements to the original method. Genes (2012) reported a coupled model for dynamic analysis of 2D large-scale SSI systems based on finite element method, boundary element method and scaled boundary finite element method, and presented a parallel computation algorithm for the coupled model. Schauer *et al.* (2011, 2012) introduced a parallel algorithm for a coupled finite element - scaled boundary finite element approach to study soil-structure-interaction problems. Due to high computational cost resulting from the application of SBFEM to large-scale problems, parallel computing based on PC clusters was employed to improve the computational efficiency.

The original solution procedure, which is based on the solution of the acceleration unit-impulse response matrix of the unbounded domain, was commonly used in the above references. It is global in time and space, and thus computationally expensive. Alternative procedures, which aim at avoiding the convolution integral altogether by developing the scaled boundary finite element method directly in the time domain, have been proposed recently. Song and Bazzyar (2008) proposed a Padé approximation for the dynamic stiffness matrix of an unbounded medium in the frequency domain, which has a large range and high rate of convergence. Bazzyar and Song (2008) then developed a high-order local transmitting boundary based on a continued-fraction solution of the dynamic stiffness matrix. But the method may fail for systems with a larger number of degrees of freedom and for approximations of higher order. Birk *et al.* (2012) presented an improved continued-fraction solution for the dynamic stiffness matrix of an unbounded domain, which is numerically more robust and suitable for large-scale systems and arbitrarily high orders of expansion.

This paper aims to develop a new coupled method that combines the bounded and unbounded domains in the time domain. Here, the bounded domain is modeled by the well-established finite element method. The unbounded domain is represented by the high-order transmitting boundary, which is based on the improved continued fraction solution for the dynamic stiffness matrix.

The rest of the paper is outlined as follows. Section 2 describes some basic equations about the scaled boundary finite element method. Section 3 presents a new coupled method of bounded and unbounded domains. Section 4 demonstrates the application of the proposed coupled method to two numerical examples. Section 5 summarizes some major conclusions from this contribution.

## **2 Summary of the scaled boundary finite element method**

The scaled boundary finite element method is introduced in detail by Wolf and Song (1996). For completeness, only some main equations are summarized in this part.

The scaled boundary finite element method is described in a local coordinate system,  $\eta$ ,  $\zeta$  on the boundary and the radial coordinate  $\xi$ . SBFEM defines the whole domain by scaling a boundary  $S$  relative to a scaling center  $O$ . The normalized radial coordinate  $\xi$  is a scaling factor, defined as 1 at the boundary  $S$  and 0 at the scaling center  $O$ . For a bounded domain,  $0 \leq \xi \leq 1$ ; whereas, for an unbounded domain,  $1 \leq \xi < +\infty$ .

The displacements at a point  $(\xi, \eta, \zeta)$  are interpolated as

$$\{u(\xi, \eta, \zeta)\} = [N(\eta, \zeta)] \{u(\xi)\} = [N_1(\eta, \zeta)[I], N_2(\eta, \zeta)[I], \dots] \{u(\xi)\} \quad (1)$$

where  $[N(\eta, \zeta)]$  are the shape functions in the circumferential directions.  $\{u(\xi)\}$  are the displacements along the radial lines and are analytical with respect to  $\xi$  only.

The strains are derived as

$$\{\varepsilon(\xi, \eta, \zeta)\} = [B^1(\eta, \zeta)] \{u(\xi)\}_{,\xi} + \frac{1}{\xi} [B^2(\eta, \zeta)] \{u(\xi)\} \quad (2)$$

where  $[B^1(\eta, \zeta)]$  and  $[B^2(\eta, \zeta)]$  represent the strain-nodal displacement relationship.

The stresses and strains are related by the elastic matrix  $[D]$

$$\{\sigma(\xi, \eta, \zeta)\} = [D] \{\varepsilon(\xi, \eta, \zeta)\} \quad (3)$$

After expressing the governing differential equations in the scaled boundary coordinates, Galerkin's weighted residual method or the virtual work formulation (Deeks and Wolf, 2002) is applied in the circumferential directions. In the frequency domain, the scaled boundary finite element equation in displacement is expressed as

$$[E^0] \xi^2 \{u(\xi)\}_{,\xi\xi} + ((s-1)[E^0] - [E^1] + [E^1]^T) \xi \{u(\xi)\}_{,\xi} + ((s-2)[E^1]^T - [E^2]) \{u(\xi)\} + \omega^2 [M^0] \xi^2 \{u(\xi)\} = 0 \quad (4)$$

where  $s$  ( $=2$  or  $3$ ) denotes the spatial dimension of the domain, and  $\omega$  is the excitation frequency. The coefficient matrices  $[E^0]$ ,  $[E^1]$ ,  $[E^2]$ , and  $[M^0]$  are obtained by assembling the element coefficient matrices calculated on the boundary. The coefficient matrices are written for three-dimensional elastodynamics as

$$[E^0] = \int_{-1}^{+1} \int_{-1}^{+1} [B^1(\eta, \zeta)]^T [D] [B^1(\eta, \zeta)] |J(\eta, \zeta)| d\eta d\zeta \quad (5a)$$

$$[E^1] = \int_{-1}^{+1} \int_{-1}^{+1} [B^2(\eta, \zeta)]^T [D] [B^1(\eta, \zeta)] |J(\eta, \zeta)| d\eta d\zeta \quad (5b)$$

$$[E^2] = \int_{-1}^{+1} \int_{-1}^{+1} [B^2(\eta, \zeta)]^T [D] [B^2(\eta, \zeta)] |J(\eta, \zeta)| d\eta d\zeta \quad (5c)$$

$$[M^0] = \int_{-1}^{+1} \int_{-1}^{+1} [N(\eta, \zeta)]^T \rho [N(\eta, \zeta)] |J(\eta, \zeta)| d\eta d\zeta \quad (5d)$$

### 3 Coupled method of bounded and unbounded domains

#### 3.1 Bounded domain

The equation of motion of the bounded domain in the time domain can be expressed as

$$\begin{bmatrix} [M_{ss}] & [M_{sb}] \\ [M_{bs}] & [M_{bb}] \end{bmatrix} \begin{Bmatrix} \{\ddot{u}_s\} \\ \{\ddot{u}_b\} \end{Bmatrix} + \begin{bmatrix} [K_{ss}] & [K_{sb}] \\ [K_{bs}] & [K_{bb}] \end{bmatrix} \begin{Bmatrix} \{u_s\} \\ \{u_b\} \end{Bmatrix} = \begin{Bmatrix} \{P_s\} \\ \{P_b\} \end{Bmatrix} - \begin{Bmatrix} \{0\} \\ \{R_b\} \end{Bmatrix} \quad (6)$$

where  $[M]$  and  $[K]$  are the mass and stiffness matrices of the bounded domain,  $\{\ddot{u}\}$ ,  $\{\dot{u}\}$ ,  $\{u\}$  are the acceleration, velocity and displacement vectors,  $\{P\}$  is an external force vector acting directly on the bounded domain, while  $\{R\}$  is an interaction force vector acting at the soil-structure interface. Subscript  $s$  describes the nodes belonging only to the bounded domain,  $b$  denotes the nodes at the boundary belonging to both, the bounded and unbounded domains. Here, the stiffness matrix  $[K]$  and mass matrix  $[M]$  are assembled by the finite element method (Zienkiewicz *et al.*, 2005).

### 3.2 Unbounded domain

For an unbounded domain, the scaled boundary finite element equation in dynamic stiffness is expressed as

$$([S^\infty(\omega)]+[E^1])[E^0]^{-1}([S^\infty(\omega)]+[E^1]^T)-(s-2)[S^\infty(\omega)]-\omega[S^\infty(\omega)]_{,\omega}-[E^2]+\omega^2[M^0]=0 \quad (6)$$

The continued fraction solution for  $[S^\infty(\omega)]$  at the high-frequency limit ( $\omega \rightarrow \infty$ ) is expressed as

$$[S^\infty(\omega)]=[K_\infty]+i\omega[C_\infty]-[X^{(1)}][Y^{(1)}(\omega)]^{-1}[X^{(1)}]^T \quad (7a)$$

$$[Y^{(i)}(\omega)]=[Y_0^{(i)}]+i\omega[Y_1^{(i)}]-[X^{(i+1)}][Y^{(i+1)}(\omega)]^{-1}[X^{(i+1)}]^T \quad (i=1,2,\dots,M_{cf}) \quad (7b)$$

where  $[K_\infty]$ ,  $[C_\infty]$ ,  $[Y_0^{(i)}]$  and  $[Y_1^{(i)}]$  are coefficient matrices to be determined recursively in the solution procedure.  $M_{cf}$  is the order of the continued fraction expansion. The solution of these coefficient matrices is described in detail in the work by Birk *et al.* (2012) and not repeated here. The additional factor matrices  $[X^{(1)}]$  and  $[X^{(i+1)}]$  are introduced to improve the numerical stability of the solution. In the original method (Bazyar and Song, 2008), the coefficient matrix  $[X^{(1)}]$  is taken as a unit matrix  $[I]$ . But it may cause numerical difficulty or even erroneous results, especially for the systems with many degrees of freedom and high orders of continued fraction expansion. So an improved continued fraction method (Birk *et al.*, 2012) is developed to overcome the numerical problem. Compared to the original approach, it leads to numerically more robust formulations and is therefore suitable for large-scale systems and arbitrarily high orders of expansion. The **LDL**<sup>T</sup> decomposition (Golub and Van Loan, 1996) is employed to obtain  $[X^{(i)}]$ .

Using the improved continued fraction solution of the dynamic stiffness and introducing auxiliary variables, the force-displacement relationship with  $\xi=1$  on the boundary is expressed in the time domain as

$$[K_u]\{z(t)\}+[C_u]\{\dot{z}(t)\}=\{f(t)\} \quad (8)$$

with

$$[K_u]=\begin{bmatrix} [K_\infty] & -[X^{(1)}] & 0 & \cdots & 0 & 0 \\ -[X^{(1)}]^T & [Y_0^{(1)}] & -[X^{(2)}] & \cdots & 0 & 0 \\ 0 & -[X^{(2)}]^T & [Y_0^{(2)}] & \cdots & 0 & 0 \\ \vdots & \vdots & \vdots & \ddots & -[X^{(M_{cf}-1)}] & 0 \\ 0 & 0 & 0 & -[X^{(M_{cf}-1)}]^T & [Y_0^{(M_{cf}-1)}] & -[X^{(M_{cf})}] \\ 0 & 0 & 0 & 0 & -[X^{(M_{cf})}]^T & [Y_0^{(M_{cf})}] \end{bmatrix} \quad (9a)$$

$$[C_u] = \begin{bmatrix} [C_\infty] & & & & & \\ & [Y_1^{(1)}] & & & & \\ & & [Y_1^{(2)}] & & & \\ & & & \ddots & & \\ & & & & [Y_1^{(M_{cf}-1)}] & \\ & & & & & [Y_1^{(M_{cf})}] \end{bmatrix} \quad (9b)$$

$$\{z(t)\} = \begin{Bmatrix} \{u_b\} \\ \{u^{(1)}\} \\ \{u^{(2)}\} \\ \vdots \\ \{u^{(M_{cf}-1)}\} \\ \{u^{(M_{cf})}\} \end{Bmatrix}, \quad \{f(t)\} = \begin{Bmatrix} \{R_b\} \\ \{0\} \\ \{0\} \\ \vdots \\ \{0\} \\ \{0\} \end{Bmatrix} \quad (9c)$$

where the vector  $\{z\}$  consists of the displacement vector  $\{u_b\}$  and the auxiliary variables  $\{u^{(i)}\}$  on the boundary. The vector  $\{f\}$  contains the coupling forces  $\{R_b\}$  on the boundary.

### 3.3 Coupled method of bounded and unbounded domains

The bounded and unbounded domain formulations are coupled via the interaction force vector  $\{R_b\}$ . For a linear system, the coupled equations of the bounded and unbounded domain in the time domain are obtained by combining Equation (6) and (8). It yields

$$[K_c]\{d_c\} + [C_c]\{\dot{d}_c\} + [M_c]\{\ddot{d}_c\} = \{f_c\} \quad (10)$$

with

$$[K_c] = \begin{bmatrix} [K_{ss}] & [K_{sb}] & & & & \\ [K_{bs}] & [K_{bb}] + [K_\infty] & -[X^{(1)}] & & & \\ & -[X^{(1)T}] & [Y_0^{(1)}] & -[X^{(2)}] & & \\ & & -[X^{(2)T}] & [Y_0^{(2)}] & & \\ & & & & \ddots & -[X^{(M_{cf}-1)}] \\ & & & & -[X^{(M_{cf}-1)T}] & [Y_0^{(M_{cf}-1)}] & -[X^{(M_{cf})}] \\ & & & & & -[X^{(M_{cf})T}] & [Y_0^{(M_{cf})}] \end{bmatrix} \quad (11a)$$

$$[C_c] = \begin{bmatrix} [0] & [0] & & & & \\ [0] & [C_\infty] & & & & \\ & & [Y_1^{(1)}] & & & \\ & & & [Y_1^{(2)}] & & \\ & & & & \ddots & \\ & & & & & [Y_1^{(M_{cf}-1)}] \\ & & & & & & [Y_1^{(M_{cf})}] \end{bmatrix} \quad (11b)$$

$$[M_c] = \begin{bmatrix} [M_{ss}] & [M_{sb}] & & & & & \\ [M_{bs}] & [M_{bb}] & & & & & \\ & & [0] & & & & \\ & & & [0] & & & \\ & & & & \ddots & & \\ & & & & & [0] & \\ & & & & & & [0] \end{bmatrix} \quad (11c)$$

$$\{d_c\} = \left( \{u_s\} \quad \{u_b\} \quad \{u^{(1)}\} \quad \{u^{(2)}\} \quad \dots \quad \{u^{(M_{cf}-1)}\} \quad \{u^{(M_{cf})}\} \right)^T \quad (11d)$$

$$\{f_c\} = \left( \{P_s(t)\} \quad \{P_b(t)\} \quad \{0\} \quad \{0\} \quad \dots \quad \{0\} \quad \{0\} \right)^T \quad (11e)$$

Equation (10) is a standard equation of motion with sparse symmetric matrices in the time domain. It can be converted to be a system of first-order ordinary differential equations with high-order stiffness and damping matrices.

$$[K_{global}] \{z_{global}\} + [C_{global}] \{\dot{z}_{global}\} = \{P_{global}\} \quad (12)$$

Equation (12) can be easily solved by a direct time-domain integration method (Adhikari and Wagner, 2004). It should be noted that the stability of Equation (12) depends on the general eigenproblem for the coefficient matrices  $[K_{global}]$  and  $[C_{global}]$ . If some positive real parts of the general eigenvalues are observed, the system will be unstable. Therefore, it is very important to eliminate these spurious modes using the spectral shifting technique (Trinks, 2004).

## 4 Numerical examples

### 4.1 Example 1: Dynamic response of an elastic block on a homogeneous half-space soil

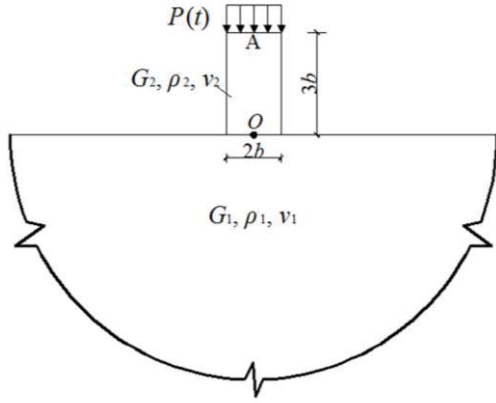
The dynamic response of an elastic block on a homogenous half-space soil as shown in Figure 1 is studied. The soil's properties are: shear modulus  $G_1=G$ , Poisson's ratio  $\nu_1=0.25$ , mass density  $\rho_1=\rho$ . The properties of the elastic block are: shear modulus  $G_2=G$ , Poisson's ratio  $\nu_2=0.25$ , mass density  $\rho_2=\rho$ . Plain strain state is considered. A uniformly distributed pressure  $P(t)$  with an amplitude  $P$  and a duration  $3b/c_s$ , as shown in Figure 2 is applied on the top surface of the elastic block. This series of two triangular force pulses of different duration represents a combination of high and low frequency loading. The fixed time step  $\Delta t=0.02b/c_s$  is selected.

In the coupled method, the block and soil are discretized with 288 four-node finite elements and 325 nodes as shown in Figure 3. The unbounded domain is modelled using the high-order transmitting boundary. It is discretized with 24 two-node line elements and 25 nodes. The scaling center of the unbounded domain is chosen at point O as shown in Figure 1. The dynamic analysis is performed using authors' Matlab code.

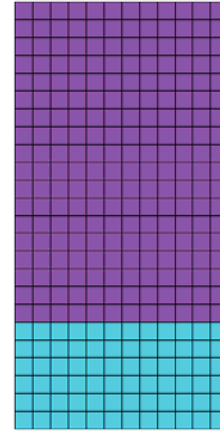
To evaluate the accuracy of the proposed coupled method, an extended mesh with a rectangle area  $21b \times 20b$  to the right of plain of symmetry is analysed using the finite element method. Only half of the symmetric system is discretized with 6768 eight-node elements of size  $0.25b \times 0.25b$ , yielding 20657 nodes. A fixed boundary condition is adopted in the reference finite element model. The implicit analysis is carried out using the commercial finite element software ABAQUS/Standard (ABAQUS, 2010).

The vertical displacement responses at points A, O (see Figure 1) are plotted in Figure 4. The

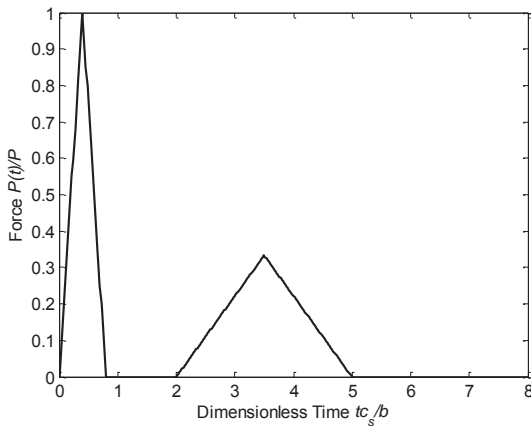
results are non-dimensionalised with  $P/G$ . In case of the order  $M_{cf}=9$ , the results agree very well with the reference solution for time up to  $\bar{t} = 10$ . After that, slight deviations can be observed. By increasing the order to  $M_{cf}=15$ , the agreement between the results of the coupled method and those of the extended mesh is excellent.



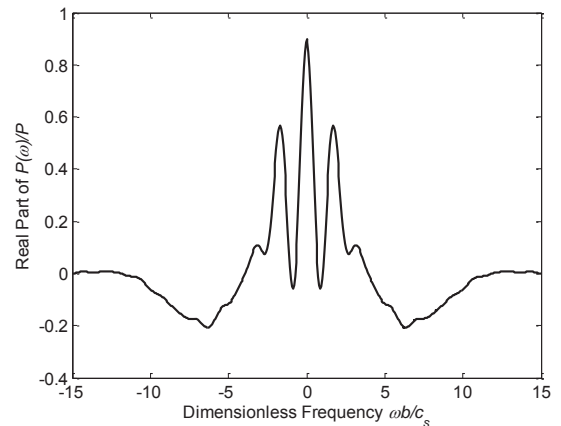
**Figure 1. Elastic block and half-space under strip loading**



**Figure 3. FE mesh of the coupled system**

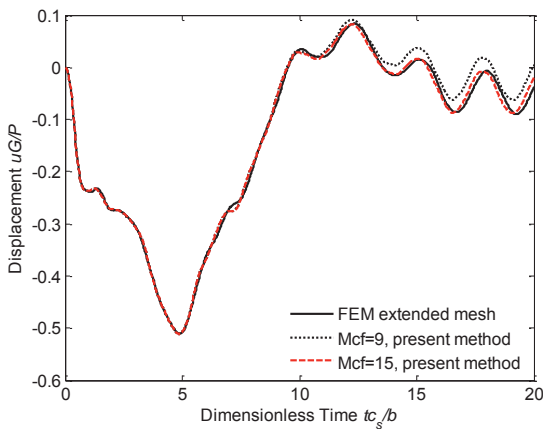


(a) Time domain

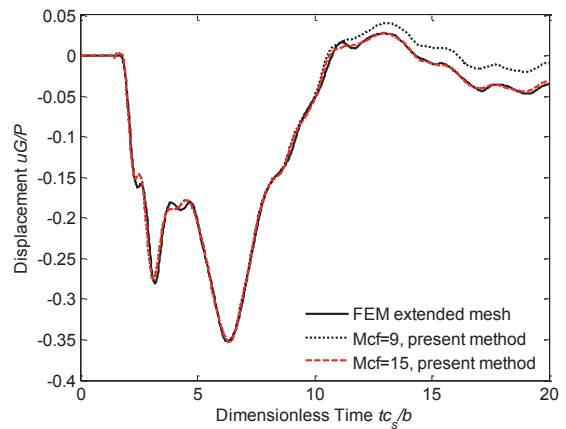


(b) Frequency domain

**Figure 2. Series of two triangular force pulses**



(a) Point A



(b) Point O

**Figure 4. Dimensionless vertical displacements**

#### 4.2 Example 2: Seismic response of a gravity dam-foundation system

As an application example, the seismic response of a concrete gravity dam as shown in Figure 5 is investigated. The concrete gravity dam of 89 m high is constructed on a homogenous semi-infinite rock foundation, which is extended to infinity. The dam's properties are: modulus of elasticity  $E_c=25.44$  GPa, Poisson's ratio  $\nu_c=0.20$  and unit weight  $\gamma_c=26.0$  kN/m<sup>3</sup>. The properties of the semi-infinite rock foundation are exactly the same as those of the concrete. Plain strain state is considered. The design peak ground accelerations are  $0.399g$  in the horizontal direction and  $0.266g$  in the vertical direction, where  $g$  is the gravitational acceleration. The horizontal and vertical (2/3 horizontal) components of the 1967 KOYNA earthquake records (see Figure 6) are applied to the nodes of the dam body. The performance of the dam for only empty reservoir condition is studied.

In the coupled method, the system is discretized with 288 four-node finite elements and 325 nodes as shown in Figure 7. The semi-infinite foundation is discretized with 24 two-node line elements and 25 nodes. The scaling center of the semi-infinite foundation is located at the center of the dam-foundation interface. The fixed time step  $\Delta t=0.02s$  is selected.

In order to obtain another reference solution that can be compared with the proposed solution, the range of the dam foundation is extended to  $2 \times 10^4$  m toward the upstream, downstream directions and  $2 \times 10^4$  m in the vertical direction. The dam and foundation are discretized with 186520 four-node elements and 187467 nodes.

Time histories of the horizontal and vertical displacements at dam crest are plotted in Figure 8. Clearly, the numerical results obtained from the coupled method ( $M_{cf}=12$ ) agree well with those obtained from the extended mesh. For the solutions of the extended mesh and the coupled method, the maximum horizontal displacements at dam crest are 3.44 cm and 3.33 cm, respectively. The maximum vertical displacements at dam crest are 1.09 cm and 1.05 cm, respectively. The relative errors of the horizontal and vertical displacements are 3.39% and 3.73%, respectively, which are both less than 5% and acceptable from an engineering point of view.

To evaluate the efficiency of the coupled method, the computer times spent on the above analyses are recorded on a computer with Intel(R) Pentium(R) CPU G840 @ 2.80GHz and 4GB RAM. The extended mesh and present approach in Example 1 take 37min41s and 7min57s, respectively. The computer times for the extended mesh and present approach of Example 2 are 2h13min46s and 7min2s, respectively. Obviously, the present approach is more efficient.

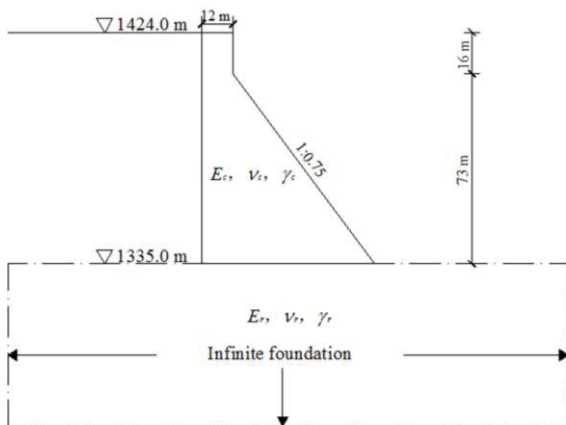


Figure 5. The gravity dam in section

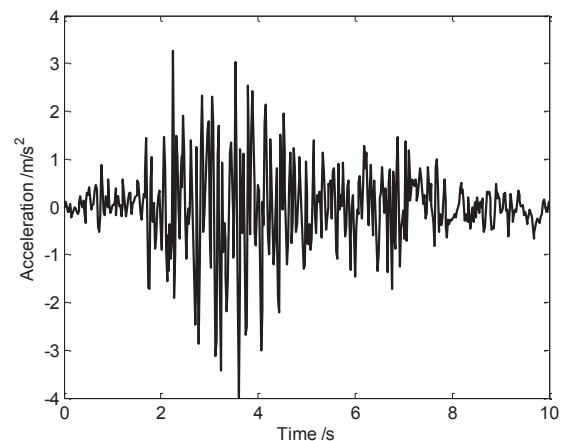
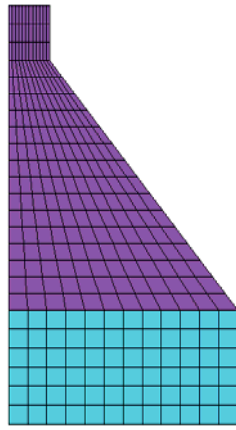
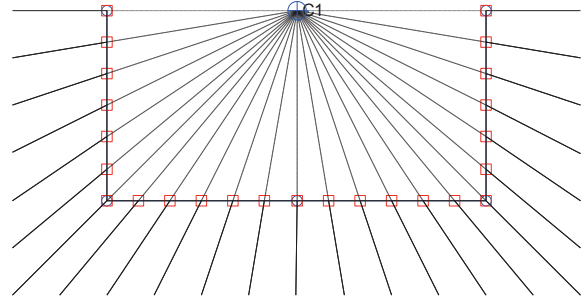


Figure 6. The input earthquake acceleration

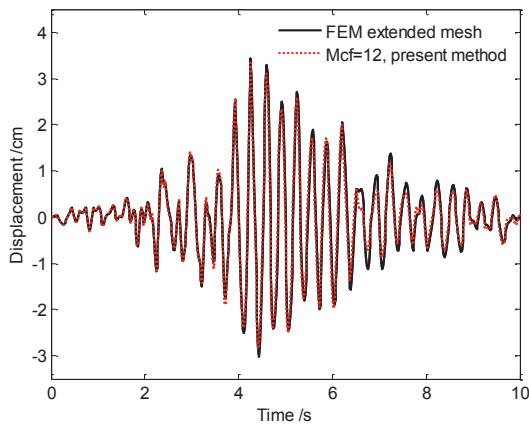




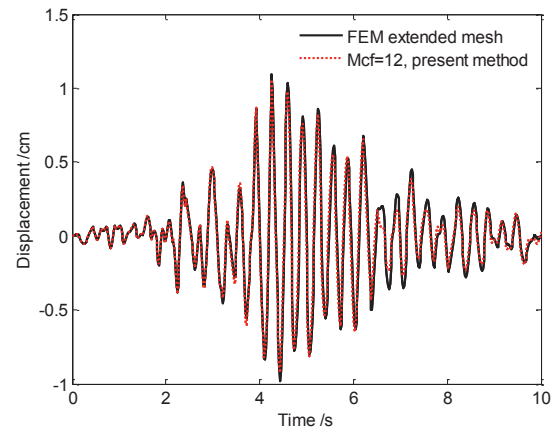
(a) FE mesh of the system



(b) SBFEM mesh of the unbounded domain

**Figure 7. Mesh of the gravity dam-foundation system**

(a) Horizontal



(b) Vertical

**Figure 8. Time histories of displacements at dam crest**

## 5 Conclusions

A novel coupled method of bounded and unbounded domains is presented. The near-field bounded domain is modeled by the well-established finite elements. The far-field unbounded domain is represented by the high-order transmitting boundary, which is based on the improved continued fraction solution for the dynamic stiffness matrix of the unbounded domain. The coupled standard equation of motion of a linear system in the time domain is obtained by combining the dynamic equations of bounded and unbounded domains, which can be solved by a direct time-domain integration method. The results of two numerical examples demonstrate that the coupled method is more accurate and efficient in the time domain. The approach presented in this paper can easily be extended to three-dimensional problems, further study is ongoing.

## Acknowledgements

This work was supported by the Science Foundation of China Three Gorges University (Grant No. KJ2013B003). This support is gratefully acknowledged.

## References

- Beskos, D. E. (1987), Boundary element methods in dynamic analysis. *Applied Mechanics Reviews*, 40, pp. 1–23.
- Beskos, D. E. (1997), Boundary element methods in dynamic analysis: Part II (1986-1996). *Applied Mechanics Reviews*, 50, pp. 149–197.

- Kausel, E. (1986), Wave propagation in anisotropic layered media. *International Journal for Numerical Methods in Engineering*, 23, pp. 1567–1578.
- Kausel, E. (1994), Thin-layer method: formulation in the time domain. *International Journal for Numerical Methods in Engineering*, 37, pp. 927–941.
- Keller, J. B and Givoli, D. (1989), Exact non-reflecting boundary conditions. *Journal of Computational Physics*, 82, pp. 172–192.
- Wolf, J. P. and Song, Ch. (1996), *Finite-element modeling of unbounded media*. Wiley: New York.
- Lysmer, J. and Kuhlemeyer, R. L. (1969), Finite dynamic model for infinite media. *Journal of Engineering Mechanics, ASCE*, 95, pp. 759–877.
- Deeks, A. J. and Randolph, M. F. (1994), Axisymmetric time-domain transmitting boundaries. *Journal of Engineering Mechanics, ASCE*, 120, pp. 25–42.
- Liu, J. B., Du, Y. X. and Du, X. L. (2006), 3D viscous-spring artificial boundary in time domain. *Earthquake Engineering and Engineering Vibration*, 5, pp. 93–102.
- Liao, Z. P., Wong, H. L. and Yang, B. (1984), A transmitting boundary for transient wave analyses. *Scientia Sinica Mathematica*, 27, pp. 1063–1076.
- Zhao, C. B. (2009), *Dynamic and transient infinite elements: theory and geophysical, geotechnical and geoenvironmental applications*. Springer: Berlin.
- Engquist, B. and Majda, A. (1977), Absorbing boundary conditions for the numerical simulation of waves. *Mathematics of Computation*, 31, pp. 629–651.
- Higdon, R. L. (1986), Absorbing boundary conditions for difference approximations to multi-dimensional wave equation. *Mathematics and Computation*, 47, pp. 437–459.
- Bayliss, A. and Turkel, E. (1980), Radiation boundary conditions for wave-like equations. *Communications on Pure and Applied Mathematics*, 33, pp. 707–725.
- Tsynkov, S. V. (1998), Numerical solution of problems on unbounded domains. A review. *Applied Numerical Mathematics*, 27, pp. 465–532.
- Givoli, D. (2004), High-order local non-reflecting boundary conditions: a review. *Wave Motion*, 39, pp. 319–326.
- Lou, M. L., Wang, H. F., Chen, X. and Zhai, Y. M. (2011), Structure-soil-structure interaction: Literature review. *Soil Dynamics and Earthquake Engineering*, 31, pp. 1724–1731.
- Zhang, X., Wegner, J. L. and Haddow, J. B. (1999), Three-dimensional dynamic soil-structure interaction analysis in the time domain. *Earthquake Engineering and Structural Dynamics*, 28, pp. 1501–1524.
- Yan, J. Y., Zhang, C. H. and Jin, F. (2004), A coupling procedure of FE and SBFEM for soil-structure interaction in the time domain. *International Journal for Numerical Methods in Engineering*, 59, pp. 1453–1471.
- Radmanovic, B. and Katz, C. (2012), Dynamic soil-structure interaction using an efficient scaled boundary finite element method in time domain with examples. *SECED Newsletter*, 23(3), pp. 3–14.
- Genes, M. C. (2012), Dynamic analysis of large-scale SSI systems for layered unbounded media via a parallelized coupled finite element/boundary element/scaled boundary finite element model. *Engineering Analysis with Boundary Elements*, 36, pp. 845–857.
- Schauer, M., Langer, S., Roman, J. E. and Quintana-Ortí, E. S. (2011), Large scale simulation of wave propagation in soils interacting with structures using FEM and SBFEM. *Journal of Computational Acoustics*, 19, pp. 75–93.
- Schauer, M., Roman, J. E., Quintana-Ortí, E. S. and Langer, S. (2012), Parallel computation of 3-D soil-structure interaction in time domain with a coupled FEM/SBFEM approach. *Journal of Scientific Computing*, 52, pp. 446–467.
- Song, Ch. and Bazyar, M. H. (2008), Development of a fundamental-solution-less boundary element method for exterior wave problems. *Communications in Numerical Methods in Engineering*, 24, pp. 257–279.
- Bazyar, M. H. and Song, Ch. (2008), A continued-fraction-based high-order transmitting boundary for wave propagation in unbounded domains of arbitrary geometry. *International Journal for Numerical Methods in Engineering*, 74, pp. 209–237.
- Birk, C., Prempramote, S. and Song Ch. (2012), An improved continued-fraction-based high-order transmitting boundary for time-domain analyses in unbounded domains. *International Journal for Numerical Methods in Engineering*, 89, pp. 269–298.
- Deeks, A. J. and Wolf, J. P. (2002), A virtual work derivation of the scaled boundary finite-element method for elastostatics. *Computational Mechanics*, 28, pp. 489–504.
- Zienkiewicz, O. C., Taylor, R. L. and Zhu, J. Z. (2005), *The finite element method: its basis and fundamentals (Sixth edition)*. Elsevier Butterworth-Heinemann: Oxford.
- Golub, G. H. and Van Loan, C. F. (1996), *Matrix Computations (Third edition)*. North Oxford Academic: Oxford.
- Adhikari, S. and Wagner, N. (2004), Direct time-domain integration method for exponentially damped linear systems. *Computers and Structures*, 82, pp. 2453–2461.
- Trinks, C. (2004), Consistent absorbing boundaries for time-domain interaction analyses using the fractional calculus. PhD Thesis, Dresden University of Technology: Dresden.
- ABAQUS Inc. (2010), *ABAQUS Theory Manual, Version 6.10*. Providence, RI, USA.

## Crashworthiness Behaviour on Aluminum Foam Bumper Beam and Side Member System under Oblique Impact

F. Djamaluddin, S. Abdullah, A. K. Arrifin and Z. M. Nopiah

Department of Mechanical and Materials Engineering, Faculty of Engineering and Built Environment,  
Universiti Kebangsaan Malaysia, 43600 UKM Bangi, Selangor, Malaysia.

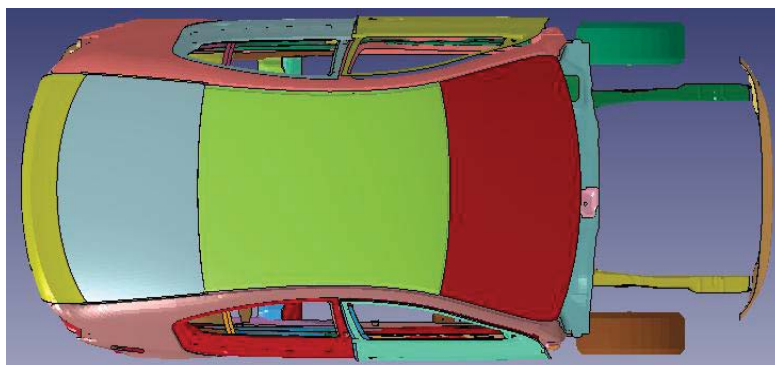
\*Corresponding author : fauzanman\_77@yahoo.com, shahrum.ukm @ gmail.com

### Abstract

This paper presents the simulation of crush behavior for side members and bumper beam under axial and angular impact loading. Recent issues of automotive industry are to reduce weight and to improve occupant safety. Aluminum foam as a lightweight material was selected due to its excellent energy absorption capacity. Various parameters have been considered, such as angles of load, geometry and the material selection, aluminum alloy (AA6063 and AA6060) . Bumper beam connected two side members were impacted load angles of  $0^\circ$  to  $30^\circ$  from longitudinal axis. The finite element analysis approach using the specific software package has determined the crashworthiness parameters, that were specific energy absorption (SEA) and crush force efficiency (CFE). The outcome of this study have formulated functions for calculating of crush parameters.

**Keywords:** Aluminum foam, bumper beam, crashworthiness, oblique impact, side member

Bumper beam side members system is main part of vehicle in absorbing of the kinetic energy under frontal impact. Figure 1. shows position of the bumper beam and side member system in the automobile.



**Figure 1.** Position of bumper beam and side member system at automobile

During the accident, this system not only endures a bending effect, but also a combination of bending and collapsing, especially under angle load. In this paper, we studied the combination of axial and angle loads of the system, which consists of two side members connected at the bumper beam. In accordance with standard safety regulations driving of the vehicle and federal safety standards (FMVSS), the loading angular is from  $0^\circ$  to  $30^\circ$  for rigid barrier tests at 48 km/h velocity.

Celullar material, such as foam, is used to fill thin-walled column. This column is expected to increase ability of the material energy absorption without adding excessive weight. Hansen et al (2000). have conducted experimental tests to find effective crushing distance in aluminum foam square and cylindrical column. Ahmad et al.(2010) studied whether the aluminum foam-filled conical tubes can improve energy absorption in their experiment test. Research on oblique impact on structure is limited. However, this load occurs in many vehicle accidents. Certain research, such as Reyes et al. (2002), Nagel et al. (2006), and Ahmad et al.(2010), have conducted oblique loading using experiment test.

This work determines crush behavior by considering a numerical solution. Finite element model set up used was ABAQUS software. Finally, we find correlation between crash behavior of bumper beam and side member system and their different parameters, such as length and thickness.

## **Theory Background**

Some parameters are applied to determine the ability to absorb energy of the material or structure. The specific energy absorption (SEA) and the crush force efficiency (CFE) are two parameters used to calculate the absorption level of material and structures. For this study, we focused on square columns filled with aluminum foam.

### ***Mean crush load***

we used mean crush load to calculate capability of material for energy absorption. In this study, displacement is used to determine the value of energy absorbed. In the numerical result, displacement is given by the node at the top end of the aluminum foam tube.

$$Pm = \frac{Ea}{\delta} \quad (1)$$

where  $\delta$  deformation of structure that the time after reach mean crush load . Peak crushing force should reduce energy and increase level of occupant safety in automotive accidents (Kurata et al. 2002).

### *Specific energy absorption (SEA)*

SEA shows energy ( $Ea$ ) per unit mass ( $m$ ) or,

$$SEA = \frac{Ea}{m} \quad (2)$$

### *Crush force efficiency (CFE)*

CFE is the ratio of the mean crush load to the peak crush load

$$CFE = \frac{Pm}{Pmax} \quad (3)$$

### **Model of Finite Element**

By considering the dynamic numerical solution, the model of simple bumper beam side members system under loading angle was formed, as seen in Figure 1. Both bottom parts of the side members was clamped, whereas the top left corner of the bumper beam under angle load had a velocity of 10 m/s.



**Figure 2. Simple model of aluminum foam bumper beam side member system under oblique impact**

Model and simulation used the ABAQUS explicit finite element code. The mechanical properties of the materials were obtained from experiments with the engineering curve of

stress-strain, as shown in Figures 2 and 3. Model of the system formed a square aluminum column using the Belytschko-Tsay. Deshpande and Fleck (2000) developed the crushable foam model for the foam core. The aluminum foam has mechanical properties such as Young's modulus  $E=64.8$  GPa, rate sensitivity damping coefficient is 0.05, Poisson's ratio of 0.01, and rate sensitivity damping coefficient of 0.05 (Song et al. 2005). The mechanical properties of AA6063 and AA6060 can be referred to in the table below.

Table 1. Mechanical Properties of aluminum alloy

PARTS	MATERIAL	$\nu$	$\rho$ (kg/m <sup>3</sup> )	$\sigma_u$ (N/mm <sup>2</sup> )	$\sigma_y$ (N/mm <sup>2</sup> )
Bumper beam	AA 6060	0.33	2700	160	120
Side member	AA 6063	0.30	2700	215	160

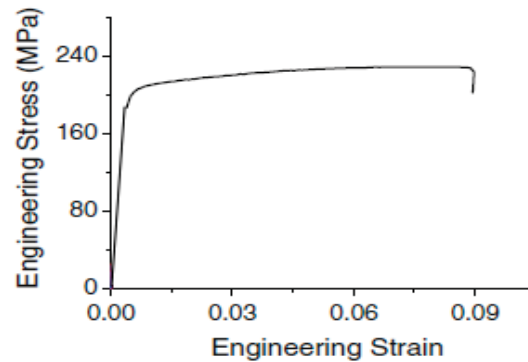


Figure 3. Stress – strain curve of AA 6063 (Guo et al. 2011)

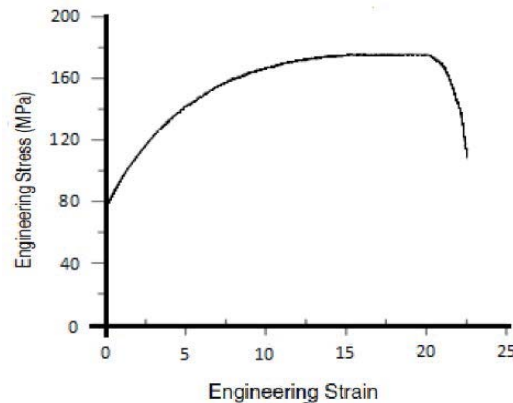


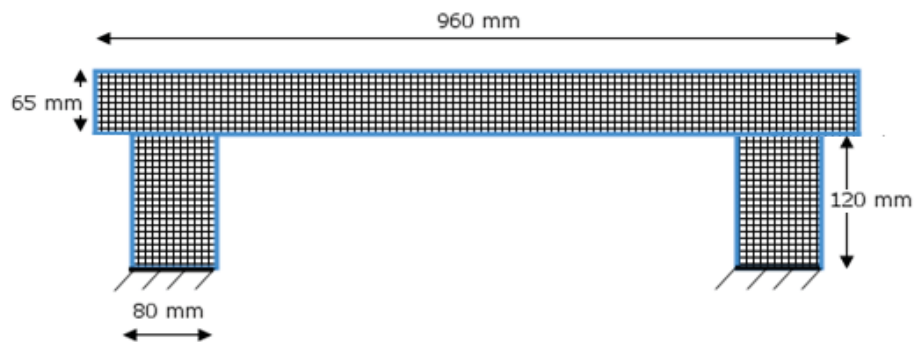
Figure 4. Stress – strain curve of AA 6060 (Reyes et al. 2002)

## Result and Discussion

### *Square column geometries effect of bumper beam side members system*

The geometry of the model can be seen in Fig. 5, where the bumper beam length is 960 mm and cross-sectional area is (80 mm x 65 mm). Side member length is 120 mm and cross-section area is (80 mm x 80 mm). Parameters on the bumper beam are assumed constant.

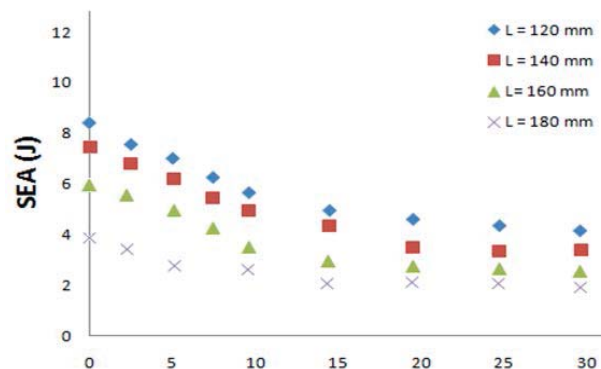
However, the length and thickness of the side member were different. Length varies from 120 mm to 180 mm and the thickness varies from 2.5 mm to 4 mm.



**Figure 5. Geometry of simple bumper beam side member system**

### *Column length effect of side members*

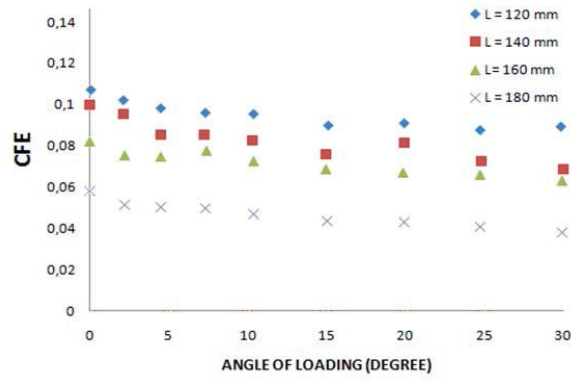
Fig. 6 shows the SEA- angle of loading response of aluminum foam filled square columns of bumper beam side member system with varying lengths.



**Figure 6. SEA versus angle of loading with different length**

The numerical simulation result indicates that shorter columns are more mass efficient in absorbing energy. Loading angle increases, but column SEA decreases. This case suggests that load angle promotes local bending to dominate collapse behavior.

Figure 7 shows the CFE versus angle of loading response of aluminum foam square columns with varying lengths.

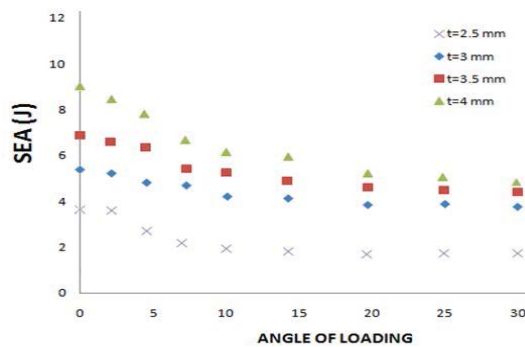


**Figure 7. CFE versus angle of loading with different length**

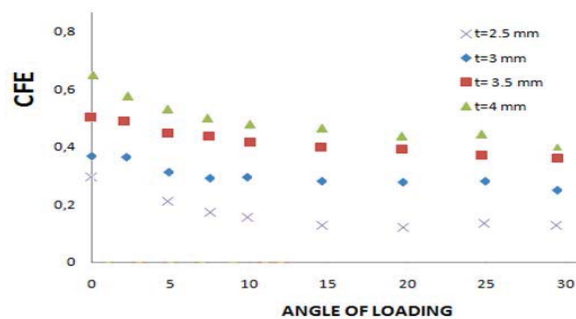
Unlike SEA, CFE increases because of increase in column length. This was caused by a considerably different value between mean crush load and peak crush load. Hence, the value of CFE becomes relatively small. Apart from these, the addition of the load angle decreases CFE.

***Column thickness effect of side member***

Fig. 8 shows the SEA-load angle response of aluminum foam of square columns side members with varying thickness.



**Figure 8. SEA versus angle of loading with different thickness**



**Figure 9. CFE versus angle of loading with different thickness**



The thin walled column was increased from 2.5 mm to 4 mm. SEA increase is caused by increased wall thickness deformation corresponding with additional column thickness. On the other hand, CFE is reduced because of the effect of peak load crash.

Table. 2. SEA and CFE of column under 30° loading angle

Length (mm)	SEA					CFE				
	Thickness (mm)					Thickness (mm)				
	2	2.5	3	3.5	4	2	2.5	3	3.5	4
120	3.23	3.56	4.12	4.45	4.67	0.53	0.40	0.34	0.21	0.18
140	2.32	2.45	2.65	2.87	3.12	0.47	0.38	0.31	0.18	0.15
160	1.65	1.76	1.98	2.09	2.14	0.45	0.36	0.30	0.15	0.12
180	0.56	0.97	1.20	1.32	1.53	0.42	0.34	0.28	0.12	0.10

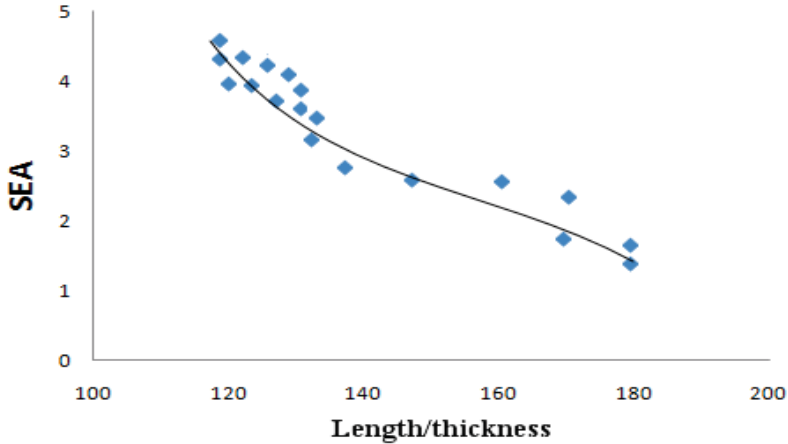


Figure 10. SEA versus length/thickness under 30° loading angle

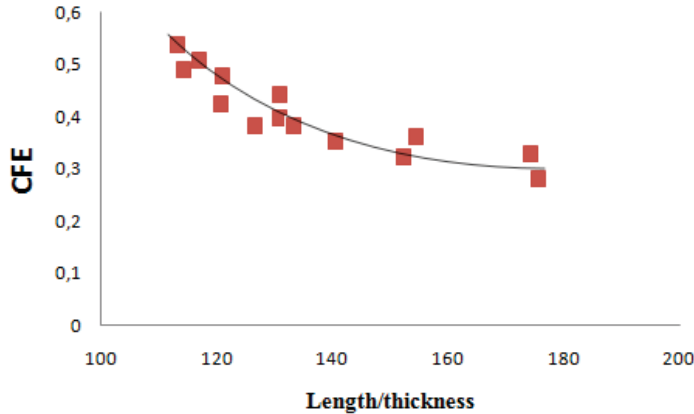


Figure 11. CFE versus length/thickness under 30° loading angle

Table 2 describes the numerical results for SEA and CFE under a load of 30° for the aluminum foam bumper-beam side-member system. The results can be plotted to determine

relationship between the SEA of the aluminum foam column and the length-to-thickness ratio. Based on Figure 10, the equation can be written as

$$SEA = 64.85 \left(\frac{l}{t}\right)^{-0.64} \quad (4)$$

where  $t$  denotes the thickness, and  $l$  denotes the length of the aluminum foam column. Similarly, the CFE versus length-to-thickness ratio is given by

$$CFE = 6.319 \left(\frac{l}{t}\right)^{-0.75} \quad (5)$$

The SEA and CFE of the aluminum foam columns depend on the value of the length-to-thickness ratio. Automotive design parameters must consider both the thickness and length of the column to achieve the optimal weight and stability of the structure.

### Conclusion

This paper facilitated understanding and provided an analysis of column behavior under an oblique impact of  $0^\circ$  to  $30^\circ$ . Different thin-walled column parameters, including length and thickness, induced SEA and CFE effects. Changes in these parameters and the loading angle resulted in the variance of SEA and CFE values.

The SEA and CFE results were plotted to determine the effect of the length-to-thickness ratio of the side member on the properties of the aluminum foam bumper-beam side-member system. The numerical result of CFE and SEA versus the variations of the length-to-thickness ratio can serve as reference for the selection of appropriate parameters for columns made of an aluminum foam bumper-beam side-member system.

### References

- Ahmad Z, Thambiratnam DP, Tan AC C (2010). Dynamic energy absorption characteristics of foam-filled conical tubes under oblique impact loading. *Int. J. Impact Eng.*, 37(5): 475-488.
- Carle D, Blount G (1999). The suitability of aluminium as an alternative material for car bodies. *J. Mater. Design*, 20: 267-272. Davies G (2003a). Future trends in automotive body materials. In *Materials for Automobile Bodies* Oxford:

- Butterworth-Heinemann. pp. 252-269. Davies G (2003b). Materials for consideration and use in automotive body structures. In *Materials for Automobile Bodies* Oxford: Butterworth-Heinemann. pp. 61-98.
- Guo L, Yu J (2011) Dynamic bending response of double cylindrical tubes filled with aluminum foam. *Int J Impact Eng* 2000; 85-94
- Han DC, Park SH (1999). Collapse behavior of square thin-walled columns subjected to oblique loads. *Thin-Walled Structures*. 35(3): 167-184.
- Hanssen AG, Langseth M, Hopperstad OS (2000). Static and dynamic crushing of square aluminium extrusions with aluminium foam filler. *Int J Impact Eng* 2000;24:347-83.
- Hanssen AG, Langseth M, Hopperstad OS (2000). Static and dynamic crushing of circular aluminium extrusions with aluminium foam filler. *Int J Impact Eng* 2000;24:475-507.
- Jensen Ø, Langseth M, Hopperstad OS (2004). Experimental investigations on the behaviour of short to long square aluminium tubes subjected to axial loading. *Int. J. Impact Eng.*, 30(8-9): 973- 1003.
- Nagel GM, Thambiratnam DP (2006). Dynamic simulation and energy absorption of tapered thin-walled tubes under oblique impact loading. *Int. J. Impact Eng.*, 32(10): 1595-1620.
- Reyes A, Hopperstad OS, Langseth M (2004). Aluminum foam-filled extrusions subjected to oblique loading: experimental and numerical study. *Int. J. Solids Struct.*, 41(5-6): 1645-1675.
- Song H-W, Fan Z-J, Yu G, Wang Q-C, Tobota A. (2005) Partition energy absorption of axially crushed aluminum foam-filled hat sections. *Int J Solids Struct* 42:2575-600.

## An SBFEM element for thin-walled beams

\*J.D. Jung<sup>1</sup>, W. Becker<sup>1</sup>

<sup>1</sup>Fachgebiet Strukturmechanik, Technische Universität Darmstadt, Germany.

\*Corresponding author: jung@fsm.tu-darmstadt.de

### Abstract

The scaled boundary finite element method (SBFEM) is a semi-analytical method in which only the boundary is discretized. The results on the boundary are scaled into the domain with respect to a scaling center which must be “visible” from the whole boundary. For beam-like problems the scaling center can be selected at infinity and only the cross-section is discretized.

A new element for thin-walled beams has been developed on the basis of the Reissner-Mindlin plate theory. The beam sections are considered to be multilayered laminate plates with arbitrary layup. The cross-section is discretized with beam elements of Timoshenko type. This leads to a system of differential equations of a gyroscopic type, for which the solution is known.

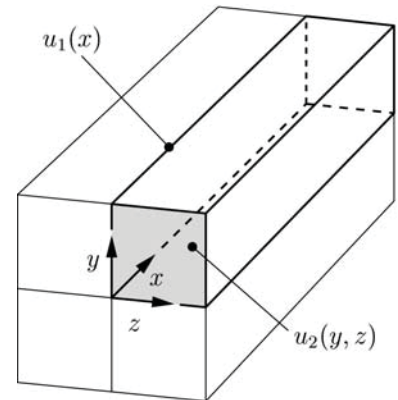
The element has been tested and compared with a finite element model and it gives good results.

**Keywords:** SBFEM, thin-walled beams, semi-analytical, Reissner-Mindlin theory

### Introduction

Beams and beam-like structures are widely used in mechanical and civil engineering. Due to lightweight reasons these beams are often made of thin-walled sections. And recently new materials like fiber-reinforced plastics and other composites are used which are usually made of layers of differently oriented plies. With the number and the orientation of the plies and the order and the thickness of each ply there are many parameters, which can be adjusted during an optimization. Thus an effective and reliable computational method is needed.

The scaled boundary finite element method (SBFEM) is such a method. It is a semi-analytical method for which only a discretization of the boundary is needed and an analytical solution is used within the body. It doesn't need a singular fundamental solution like the boundary element method (BEM) or a discretization of the whole body like the FEM. So it has the benefits of both the FEM and the BEM without adopting the detriments.



**Figure 1: SBFEM for a beam**

Let us start with a beam of arbitrary cross-section. This means that the cross-section does not need to be thin-walled. Then the SBFEM uses a separation approach to solve the differential equations for the displacements  $u$  in the framework of linear elasticity. The function  $u_1$  scales the displacements of the boundary into the body. Or like in this work it scales the displacements of the cross-section along the beam. The boundary or the cross-section, respectively, is described by the function  $u_2$  for which a finite element approach is used.

$$u(x, y, z) = u_1(x) \cdot u_2(y, z) \quad (1)$$

The coordinates  $y$  and  $z$  are on the cross-section (or the boundary) and  $x$  is directed along the beam axis (or into the body) which is depicted for a beam in figure 1.

Inserting this ansatz and the virtual work principle gives a differential equation of Euler-type (scaling center within the body) or of gyroscopic type (beam-like problem). For both differential equations the solution is known.

This method is a discrete Kantorovic method, which has been previously used also by other working groups, which is summarized below.

For an arbitrary 3-dimensional case Dasgupta (1982) published the first work about SBFEM and Wolf and Song (1996) developed this method further. First it was used to calculate the dynamic stiffness of an unbounded domain but body loads, incompressible material and bounded domains can be included in this method. Originally this method was called “consistent infinitesimal finite-element cell method” but using a different way to derive the equations the name “scaled boundary finite element method” (SBFEM) has been introduced (Wolf 2002).

Due to the analytical part of the solution the SBFEM can be used to calculate stress singularities at cracks which is done in (Wolf 2002) and in (Mayland and Becker 2010).

In Dieringer et al. (2011) thin plates are described by using 1D elements for the boundary. Here Kirchhoff's kinematics is used to reduce the dimension by one.

For the case of slender cylindrical bodies like beams several groups developed similar or identical methods. The method developed at the University of Milan is equal to the SBFEM. In (Giavotto et al. 1983) the method is derived by introducing warping functions of the cross-section. These functions are only dependent on  $x$ . In (Morandini et al. 2010) the separation ansatz and a virtual work formulation are used. In contrast to this work, also 2D elements for the discretization of the cross-section are used. The aim is to calculate stiffnesses for the beam which are used in multi-body simulations.

Under the name “semi analytical finite elements” (Dong et al. 2001, Kosmatka et al. 2001, Lin et al. 2001) a method equal to the SBFEM is used to find de-Saint-Venant solutions. In (Alpdogan et al. 2010) this method is employed to examine end effects and transitional effects in prismatic beams. For the discretization 2D elements are used. In (Taweel et al. 2000) this method is extended for the calculation of wave reflections on free ends of cylinders. And in (Gavric 1994) the same is done for thin-walled beams using Kirchhoff-theory. One simplification is, that within an element the membrane and bending components do not interact.

Argyris and Kačianauskas (1996) use the same approach under the name SFE (Semi-analytical Finite Elements). Instead of the Dirichlet-Functional (virtual work principle) they employ the Hellinger-Reissner-Functional. 1D elements are used for the discretization of the cross-section of thin-walled beams. But only shear stresses and normal stresses in the direction of the beam axis are considered. Based on this theory they develop “semi-analytical based finite elements”.

Schardt (1989) developed a “generalized beam theory” for thin-walled beams. 1D elements are used for the discretization of the cross-section. But the Kirchhoff-theory is taken as framework and for sake of simplicity some stresses are neglected. Silvestre and Camotim (2002) extend this method for orthotropic materials where again some stresses are neglected.

In (Altenbach et al. 1994a) and (Altenbach et al. 1994b) a generalized Vlasov theory is developed. 1D elements and Kirchhoff's plate theory are used. Neglecting stresses gives the theory of Schardt or Vlasov.

Artel and Becker (2006) use the SBFEM to calculate free-edge effects in laminates. 2D elements are employed to describe the boundary.

## Theory

The theory is first presented for one element. The assembly of several elements is described later.

New coordinates ( $\xi$ ,  $\eta$  and  $\zeta$ ) are introduced for each element.  $\xi$  is along the beam axis ( $x$ -axis) and  $\eta$  and  $\zeta$  are in the cross-section ( $y,z$  plane).  $\xi$  and  $\eta$  are scaled so that they reach from 0 to 1.

### Kinematics

The kinematics of a Reissner-Mindlin plate is presumed (Yang et al. 1966). One reason is that the Reissner-Mindlin theory is of higher order than the Kirchhoff-theory and includes transversal shear. Another reason is that a finite-element with Reissner-Mindlin theory has less unknown functions than an element based on Kirchhoff's kinematic. The element with Kirchhoff's kinematic has 8 degrees of freedom (dof) but gives an equation of 4th order. After linearization it has  $8*4=32$  unknown functions. The Reissner-Mindlin element (as used here) has 11 dof, but the equation is only of 2nd order. Thus it has  $11*2=22$  unknown functions.

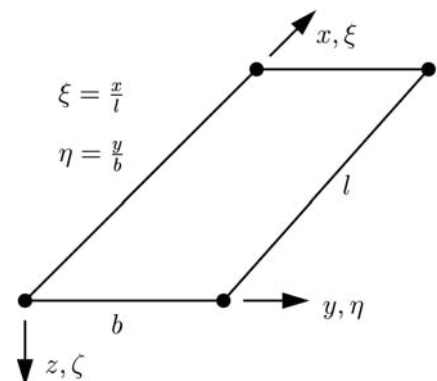


Figure 2: SBFEM Element

The key idea is that the displacements are traced back to the displacements and rotations of the middle plane (index 0)

$$\begin{aligned} u(\xi, \eta, \zeta) &= u^0(\xi, \eta) + \zeta \cdot \psi_\xi(\xi, \eta) \\ v(\xi, \eta, \zeta) &= v^0(\xi, \eta) + \zeta \cdot \psi_\eta(\xi, \eta) \\ w(\xi, \eta, \zeta) &= w^0(\xi, \eta) \end{aligned} \quad (2)$$

where  $\xi$  and  $\eta$  denote the in-plane coordinates and  $\zeta$  the coordinate in the thickness direction of the plate. The in-plane strains are given by

$$(\varepsilon_\xi, \varepsilon_\eta, \gamma_{\xi\eta}) = (\varepsilon_\xi^0, \varepsilon_\eta^0, \gamma_{\xi\eta}^0) + z \cdot (\kappa_\xi, \kappa_\eta, \kappa_{\xi\eta}) \quad (3)$$

and the out-of-plane strains are

$$\gamma_{\eta\zeta} = \gamma_{\eta\zeta}^0 = w_{,\eta}^0 + \psi_\eta \quad \gamma_{\xi\zeta} = \gamma_{\xi\zeta}^0 = w_{,\xi}^0 + \psi_\xi \quad \varepsilon_\zeta = 0 \quad (4)$$

where

$$\varepsilon_\xi^0 = u_{,\xi}^0 \quad \varepsilon_\eta^0 = v_{,\eta}^0 \quad \gamma_{\xi\eta}^0 = u_{,\eta}^0 + v_{,\xi}^0 \quad \kappa_\xi = \psi_{\xi\xi} \quad \kappa_\eta = \psi_{\eta\eta} \quad \kappa_{\xi\eta} = \psi_{\xi\eta} + \psi_{\eta\xi} \quad (5)$$

In total this can be written as a matrix equation

$$\boldsymbol{\varepsilon} = \mathbf{L} \cdot \mathbf{u} \quad (6)$$

where  $\boldsymbol{\varepsilon}$  comprises all strain components,  $\mathbf{u}$  comprises the midplane displacements and rotations and  $\mathbf{L}$  denotes a respective differential operator.

#### Constitutive relations

The constitutive relations are the ones proposed by Yang et al. (1966) where the classical laminate theory (CLT) is extended and the shear strains  $\gamma_{\eta\zeta}$  and  $\gamma_{\xi\zeta}$  and the shear stresses  $\tau_{\eta\zeta}$  and  $\tau_{\xi\zeta}$  are included.

The stresses are integrated over the thickness  $h$  of the plate

$$\begin{aligned} (N_\xi, N_\eta, N_{\xi\eta}) &= \int (\sigma_\xi, \sigma_\eta, \tau_{\xi\eta}) d\zeta, \quad (M_\xi, M_\eta, M_{\xi\eta}) = \int (\sigma_\xi, \sigma_\eta, \tau_{\xi\eta}) \zeta d\zeta, \\ (Q_\xi, Q_\eta) &= \int (\tau_{\xi\zeta}, \tau_{\eta\zeta}) d\zeta \end{aligned} \quad (7)$$

which gives the normal and shear forces  $N_\xi$ ,  $N_\eta$  and  $N_{\xi\eta}$ , the bending and drilling moments  $M_\xi$ ,  $M_\eta$  and  $M_{\xi\eta}$  and the transversal forces  $Q_\xi$  and  $Q_\eta$ .

These cross-sectional forces are related to the strains and curvatures by a corresponding laminate stiffness Matrix  $\mathbf{C}$

$$\begin{pmatrix} N_\xi \\ N_\eta \\ Q_\xi \\ Q_\eta \\ N_{\xi\eta} \\ M_\xi \\ M_\eta \\ M_{\xi\eta} \end{pmatrix} = \begin{pmatrix} A_{11} & A_{12} & 0 & 0 & A_{16} & B_{11} & B_{12} & B_{16} \\ A_{12} & A_{22} & 0 & 0 & A_{26} & B_{12} & B_{22} & B_{26} \\ 0 & 0 & A_{44} & A_{45} & 0 & 0 & 0 & 0 \\ 0 & 0 & A_{45} & A_{55} & 0 & 0 & 0 & 0 \\ A_{16} & A_{26} & 0 & 0 & A_{16} & B_{16} & B_{26} & B_{66} \\ B_{11} & B_{12} & 0 & 0 & B_{16} & D_{11} & D_{12} & D_{16} \\ B_{12} & B_{22} & 0 & 0 & B_{26} & D_{12} & D_{22} & D_{26} \\ B_{16} & B_{26} & 0 & 0 & B_{66} & D_{16} & D_{26} & D_{66} \end{pmatrix} \begin{pmatrix} \varepsilon_\xi^0 \\ \varepsilon_\eta^0 \\ \gamma_{\xi\eta}^0 \\ \gamma_{\xi\zeta}^0 \\ \gamma_{\eta\zeta}^0 \\ \kappa_\xi \\ \kappa_\eta \\ \kappa_{\xi\eta} \end{pmatrix} \quad (8)$$

where the stiffness coefficients for a laminate plate with  $n$  layers are defined by

$$(A_{ij}, B_{ij}, D_{ij}) = \sum \int \overline{Q_{ij}^m} (1, \zeta, \zeta^2) d\zeta \quad (9)$$

Herein the quantities  $\overline{Q_{ij}^m}$  denote the reduced stiffnesses of a single orthotropic layer. See (Yang et al. 1966) for further information.

### Scaled boundary finite element approach

In the present SBFEM approach the degrees of freedom are the displacements  $u$ ,  $v$  and  $w$  and the angles of rotations  $\Psi_\xi$  and  $\Psi_\eta$ . A linear shape function for  $u$ ,  $v$ ,  $\Psi_\xi$  and  $\Psi_\eta$  is chosen. For  $w$  a quadratic function is used to avoid shear locking of the plate. This corresponds to the ‘‘consistent interpolation Timoshenko beam element’’ described in (Reddy 1997). It gives an element which has 11 degrees of freedom, as indicated in figure 3.

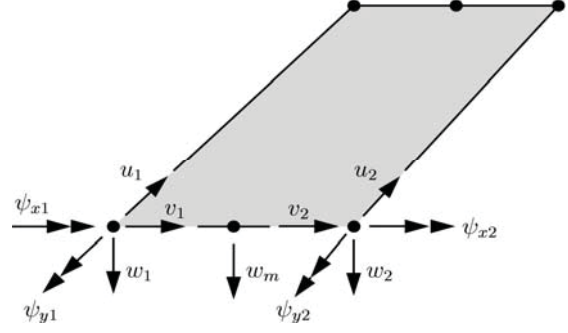


Figure 3: Degrees of freedom of an element

The SBFEM approach can briefly be written as

$$\mathbf{u}(\zeta, \eta) = \mathbf{N}(\eta) \cdot \mathbf{u}_e(\zeta) \quad (10)$$

where  $\mathbf{u}$  are the displacements and rotations,  $\mathbf{N}$  the matrix containing the shape functions and  $\mathbf{u}_e$  the vector with the degrees of freedom of the element.

### Virtual work principle

The virtual work principle is given by

$$\delta \Pi_i = \int \delta \boldsymbol{\varepsilon} \cdot \boldsymbol{\sigma} dV = \int \delta \mathbf{u} \cdot \mathbf{p} dV + \int \delta \mathbf{u} \cdot \mathbf{t} dA = -\delta \Pi_a \quad (11)$$

where  $\delta$  indicates virtual displacements and strains.  $\mathbf{p}$  denotes the volume forces and  $\mathbf{t}$  the forces at the boundary. Using the kinematics and the scaled boundary finite element approach for the displacements gives

$$\boldsymbol{\varepsilon}(\zeta, \eta) = \mathbf{L}\mathbf{u} = \mathbf{L}\mathbf{N}(\eta)\mathbf{u}_e(\zeta) = \mathbf{B}\mathbf{u}_e = \left( \mathbf{B}_2 + \mathbf{B}_1 \frac{\partial}{\partial \zeta} \right) \mathbf{u}_e \quad (12)$$

The matrix  $\mathbf{B}$  can be divided into two parts. The first one contains the derivatives with respect to  $\eta$  and the second one the derivatives with respect to  $\zeta$ .

Inserting these representations into the virtual work principle and using the constitutive equation gives

$$\begin{aligned} \delta \Pi_i &= \int \delta \mathbf{u}_e^T \left( -\frac{1}{l} \mathbf{E}_0 \mathbf{u}_{e,\zeta\zeta} + (\mathbf{E}_1 - \mathbf{E}_1^T) \mathbf{u}_{e,\zeta} + l \mathbf{E}_2 \mathbf{u}_e \right) dx + \delta \mathbf{u}_e^T \left( \frac{1}{l} \mathbf{E}_0 \mathbf{u}_{e,\zeta} + \mathbf{E}_1^T \mathbf{u}_e \right) \Big|_{x=0}^{x=l} = \dots \\ &\dots = \int \delta \mathbf{u}_e^T l \left( \bar{\mathbf{p}} + \mathbf{f}^s(x, b) - \mathbf{f}^s(x, 0) \right) dx + \left( \delta \mathbf{u}_e^T \mathbf{f}(\zeta) \right) \Big|_{x=0}^{x=l} = -\delta \Pi_a \end{aligned} \quad (13)$$

where the matrices  $\mathbf{E}_i$  are

$$\mathbf{E}_0 = \int \mathbf{B}_1^T \mathbf{C} \mathbf{B}_1 b d\eta, \quad \mathbf{E}_1 = \int \mathbf{B}_2^T \mathbf{C} \mathbf{B}_1 b d\eta, \quad \mathbf{E}_2 = \int \mathbf{B}_2^T \mathbf{C} \mathbf{B}_2 b d\eta \quad (14)$$

and the forces at the boundary and the volume forces are given by

$$\mathbf{f}^s(\zeta, \eta) = \mathbf{N}^T(\eta) \begin{pmatrix} N_{\zeta\eta}(\zeta, \eta) \\ N_\eta(\zeta, \eta) \\ Q_\eta(\zeta, \eta) \\ M_{\zeta\eta}(\zeta, \eta) \\ M_\eta(\zeta, \eta) \end{pmatrix}, \quad \mathbf{f}(\zeta) = \int \mathbf{N}^T(\eta) \begin{pmatrix} N_\zeta(\zeta, \eta) \\ N_{\zeta\eta}(\zeta, \eta) \\ Q_\zeta(\zeta, \eta) \\ M_\zeta(\zeta, \eta) \\ M_{\zeta\eta}(\zeta, \eta) \end{pmatrix} b d\eta, \quad \bar{\mathbf{p}} = \int \mathbf{N}^T(\eta) \mathbf{p}(\zeta, \eta) b d\eta \quad (15)$$

Here  $\mathbf{f}^s$  are the forces at the side-faces of the element ( $\eta=0$  and  $\eta=1$ ).  $\mathbf{f}$  are the forces at the ends of the element ( $\zeta=0$  and  $\zeta=1$ ) and  $\bar{\mathbf{p}}$  contains the volume forces. The load vector  $\mathbf{p}$  (Yang et al. 1966) is defined by

$$\mathbf{p} = (p_\zeta \quad p_\eta \quad p_\zeta \quad P_\zeta \quad P_\eta)^T = \left( \int f_\zeta d\zeta \quad \int f_\eta d\zeta \quad \int f_\zeta d\zeta \quad \int f_\zeta \zeta d\zeta \quad \int f_\eta \zeta d\zeta \right)^T \quad (16)$$

The virtual displacement  $\delta \mathbf{u}_e$  is arbitrary and thus the equation

$$-\frac{1}{l} \mathbf{E}_0 \mathbf{u}_{e,\xi\xi} + (\mathbf{E}_1 - \mathbf{E}_1^T) \mathbf{u}_{e,\xi} + l \mathbf{E}_2 \mathbf{u}_e = l (\bar{\mathbf{p}} + \mathbf{f}^s(x,b) - \mathbf{f}^s(x,0)) \quad (17)$$

and the boundary condition

$$\frac{1}{l} \mathbf{E}_0 \mathbf{u}_{e,\xi} + \mathbf{E}_1^T \mathbf{u}_e = \mathbf{f}(\xi) \quad (18)$$

have to be fulfilled.

In the further work only the homogeneous differential equation (17) is considered. The volume forces  $\bar{\mathbf{p}}$  and the forces at the side-faces ( $\mathbf{f}^s$ ) are supposed to vanish.

#### Assembling several elements

Above the equations for one element are given. For each element  $j$  the matrices  $\mathbf{E}_{ij}$  are calculated in the local coordinate system. After that these elements have to be assembled.

Using elements which are oriented differently gives a problem. There are 5 degrees of freedom in the element, but 6 degrees of freedom are needed when joining elements with different normal directions. In figure 4 this problem is depicted. From the point of view of plate 2 the rotation  $\Psi_\zeta$  about the plate normal is missing.

For nodes in edges this additional degree of freedom  $\Psi_{\zeta i}$  is introduced. The vector  $\mathbf{u}_e$  for elements containing this node becomes

$$\mathbf{u}_e = (u_1 \quad v_1 \quad w_1 \quad \psi_{\xi 1} \quad \psi_{\eta 1} \quad \psi_{\zeta 1} \quad u_2 \quad v_2 \quad w_2 \quad \psi_{\xi 2} \quad \psi_{\eta 2} \quad \psi_{\zeta 2} \quad w_m)^T \quad (19)$$

The matrices  $\mathbf{E}_{ij}$  for these elements get additional columns and rows with zero entries. Nodes in the middle of an element and nodes where the elements are in one plane don't need this additional degree of freedom. So for further calculations they are left in local coordinates.

The degrees of freedom for these edge-nodes are transformed into a global coordinate system which is done by a rotation about the  $\xi$ -axis (using the rotation matrix  $\mathbf{T}$ ).

These transformed matrices  $\mathbf{E}_{ij}^g$  can be given by

$$\mathbf{E}_{ij}^g = \mathbf{T} \mathbf{E}_{ij}^l \mathbf{T}^T \quad (20)$$

and they are assembled by adding up the matrices for each element. This gives an SBFEM equation which has the same form like the one for a single element. But the unknowns are  $\mathbf{u}$ , which contains the degrees of freedom of all nodes and the matrices  $\mathbf{E}_i^g$ , which are the assembly of the  $\mathbf{E}_{ij}^g$ .

The resulting SBFEM equation is of a gyroscopic type (see Tisseur and Meerbergen 2001).  $\mathbf{E}_0$  is symmetric and positive definite and  $\mathbf{E}_2$  is positive semidefinite with 4 zero-eigenvalues and  $\mathbf{E}_1 - \mathbf{E}_1^T$  is antisymmetric. Thus the eigenvalues are symmetric to the real and the imaginary axis.

As explained in (Morandini et al. 2010) this problem has 12 zero-eigenvalues and only 4 corresponding eigenvectors. These eigenvectors describe the rigid-body displacements and the rotation around the  $\xi$ -axis. There are two Jordan-Blocks of size 2 which also describe the torsion and the strain of a de-Saint-Venant problem. The two other blocks are of size 4 and describe the rotation about the  $\eta$ - and  $\zeta$ -axis and the bending of a de-Saint-Venant beam due to forces and moments.

The solutions with non-zero eigenvalues describe end-effects which decrease exponentially.

#### Solution process

The SBFEM equation (17) is solved via a matrix exponential as it has been proposed by Song (2004). So first of all it has to be transformed into a linear matrix differential equation. For this purpose new variables  $\tilde{\mathbf{u}}$  are introduced which are defined by

$$\tilde{\mathbf{u}} = l \cdot \mathbf{u}_{,\xi} \quad (21)$$

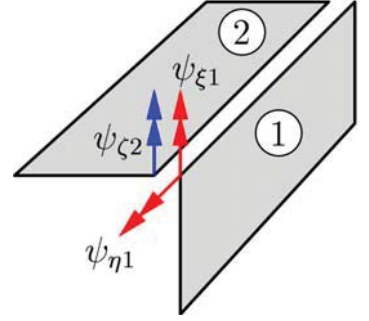


Figure 4: Rotational dof at 2 different elements



Now the SBFEM equation can be written as a matrix differential equation of first order:

$$\begin{pmatrix} \mathbf{u}_{,\xi} \\ \tilde{\mathbf{u}}_{,\xi} \end{pmatrix} = \mathbf{1} \cdot \begin{pmatrix} \mathbf{0} & \mathbf{1} \\ \mathbf{E}_0^{-1} \mathbf{E}_2 & \mathbf{E}_0^{-1} (\mathbf{E}_1 - \mathbf{E}_1^T) \end{pmatrix} \begin{pmatrix} \mathbf{u} \\ \tilde{\mathbf{u}} \end{pmatrix} \quad (22)$$

or simply

$$\boldsymbol{\varphi}_{,\xi} = \mathbf{H} \cdot \boldsymbol{\varphi} \quad (23)$$

The matrix exponential function

$$\boldsymbol{\varphi}(\xi) = e^{\mathbf{H}\xi} \cdot \mathbf{c} = \left( \mathbf{1} + \frac{\mathbf{H}\xi}{1!} + \frac{\mathbf{H}^2 \xi^2}{2!} + \dots \right) \cdot \mathbf{c} \quad (24)$$

solves the differential equation and the vector  $\mathbf{c}$  contains the integration constants, which are determined by the boundary conditions.

For positive eigenvalues and  $\xi \gg 0$  some entries in  $e^{\mathbf{H}\xi}$  become very large which is obvious for an eigenvalue-solution  $\boldsymbol{\varphi}_i = e^{\lambda_i \xi} \mathbf{v}_i$  (where  $\boldsymbol{\varphi}_i$  is the solution made of the  $i$ -th eigenvalue  $\lambda_i$  and the  $i$ -th eigenvector  $\mathbf{v}_i$ ). These solutions are of a significantly larger order of magnitude than the solutions with negative eigenvalues. Due to numerical problems like rounding errors the Jacobian matrix and thus  $e^{\lambda_i \xi}$  then become almost singular.

To avoid this problem a shift is introduced. First positive eigenvalues are separated from zero and negative eigenvalues. Like in (Song 2004) a block-diagonal Schur decomposition

$$\mathbf{S} = \mathbf{T}_s^{-1} \mathbf{H} \mathbf{T}_s \quad (25)$$

is used to obtain the block-diagonal Matrix  $\mathbf{S}$ .

$$\mathbf{S} = \begin{pmatrix} \mathbf{S}_p & \mathbf{0} & \mathbf{0} \\ \mathbf{0} & \mathbf{S}_0 & \mathbf{0} \\ \mathbf{0} & \mathbf{0} & \mathbf{S}_n \end{pmatrix} \quad (26)$$

Each block is an upper triangular matrix and the elements on the diagonal are the eigenvalues of  $\mathbf{H}$ . They are sorted in a way that  $\mathbf{S}_p$  contains the positive eigenvalues,  $\mathbf{S}_0$  the zero eigenvalues and  $\mathbf{S}_n$  the negative eigenvalues.

Then the matrix exponential with the shift  $\xi \rightarrow (\xi - 1)$  is applied, which leads to the solution

$$\boldsymbol{\varphi}(\xi) = \mathbf{T}_s \begin{pmatrix} e^{\mathbf{S}_p(\xi-1)} & \mathbf{0} & \mathbf{0} \\ \mathbf{0} & e^{\mathbf{S}_0 \xi} & \mathbf{0} \\ \mathbf{0} & \mathbf{0} & e^{\mathbf{S}_n \xi} \end{pmatrix} \mathbf{c} = \mathbf{W} \mathbf{c} \quad (27)$$

The integration constants  $\mathbf{c}$  are determined by the boundary conditions. For given displacements the corresponding lines of  $\mathbf{W}$  (for  $\xi=0$  and/or  $\xi=1$ ) are written into a matrix  $\mathbf{K}$ . For given loads the lines of  $(\mathbf{E}_0 \mathbf{E}_1^T) \mathbf{W}$  are written into  $\mathbf{K}$ . And the corresponding displacements and loads are written into a vector  $\mathbf{f}$ .

Solving the equation

$$\mathbf{K} \mathbf{c} = \mathbf{f} \quad (28)$$

gives the integration constants  $\mathbf{c}$  and the SBFEM equation is solved.

## Results

First one single element has been tested. As depicted in figure 5 one end of the element is clamped and at the free end unit-forces and unit-moments are applied. Three different sections are tested. An isotropic section made of steel, a section made of a symmetric

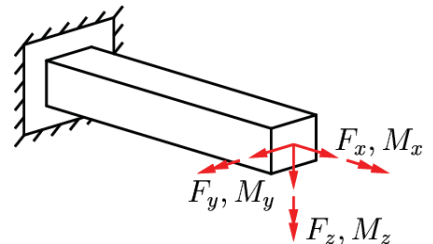
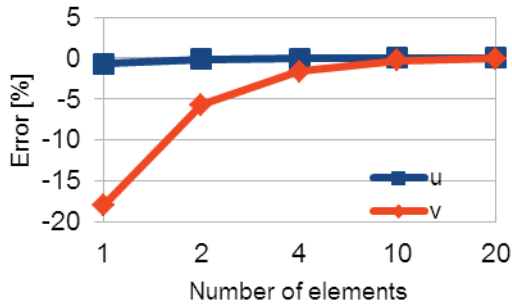


Figure 5: Cantilever beam

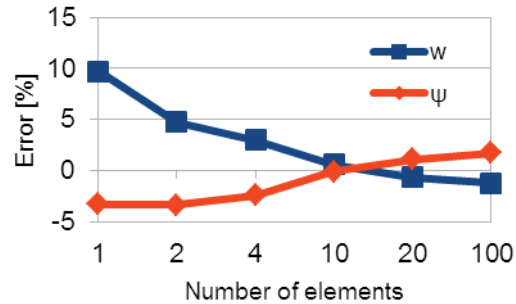
laminate  $[0,90,\pm 45]_s$  and an asymmetric laminate  $[0,90,\pm 45]$ . The comparison of the displacements at the free edges with FE simulations gives good results. The element is only a bit too stiff, which is a characteristic of the displacement method used in this work and thus expected.

Then models of thin-walled beams are built up using these new elements. The calculated displacements are compared with those of a FEM-calculation. Three different cross-sections are considered: a plate, an L-profile and a rectangular box. The same three sections as above are tested. The test-case is again the cantilever beam, which is loaded with forces and moments on its free end (see figure 5). The displacements of nodes at the free end are compared with the FEM solution.

In the FE model the thin-walled beam is modeled with rectangular shell elements in ABAQUS. For both FEM and SBFEM the displacements and rotations at the clamped end are suppressed and the load is distributed over the cross-section.



**Figure 6: Convergence of SBFEM solution (plate made of asymmetric laminate),  $u$  is the displacement into  $x$ -direction due to a unit-force in  $x$ -direction,  $v$  is the displacement into  $y$ -direction due to a unit force in  $y$ -direction**



**Figure 7: Convergence of SBFEM solution (plate made of asymmetric laminate),  $w$  is the displacement into  $z$ -direction due to a unit-moment about the  $x$ -axis,  $\psi$  is the rotation around the  $x$ -axis due to a unit moment around the  $x$ -axis**

In figure 6 and figure 7 the errors of the SBFEM compared to the FEM solution are displayed for the plate with the asymmetric layup. In figure 6 the SBFEM results are seen to converge towards the FEM solution. For the strain of the plate the solution for  $u$  is already very good for one element, because the solution doesn't depend on  $y$ . For the bending about the  $z$ -axis the solution depends on  $y$ . Thus the result for  $v$  is not very good for one element, but converges rapidly. This rapid convergence is the case for all other loads but the torsion. In figure 7 the convergence for the displacement  $w$  of one edge and the rotation angle  $\psi$  about the  $x$ -axis is shown. The case depicted here is the worst case, but also for the other materials (symmetric laminate or steel) the convergence for torsion is not very good. This may result from missing shear correction factors and is still under investigation.

The results for other cross-sections are quite similar. The results converge quickly as long the elements aren't twisted. When a torsion is applied to a closed cross-section like the rectangular box the elements aren't twisted but only sheared. Thus the convergence is good. But for open cross-sections like a L- or a I-profile the elements are twisted and the convergence gets poor.

Another remarkable result is that the agreement between the FEM and the SBFEM is good for the displacements of leading order. Displacements of a smaller order of magnitude don't match very well. It has to be checked whether this is due to numerical results in the SBFEM or due to a FEM solution which isn't fully converged.

## Conclusions and Outlook

In this work a new element for the scaled boundary finite element method has been developed. Its area of application are thin-walled composite beams. Thin-walled sections of a cross-section are modeled with 1 dimensional Timoshenko-like elements which include shear normal to the element. First tests show a quite good convergence.

In further work distributed loads and loads at the side-faces will be included to the method.

An analysis of the strength of the beam is also possible. For that the stresses within each layer have to be calculated, which can be done using the kinematics and the material laws.

Additionally a Hellinger-Reissner functional can be used instead of the Dirichlet functional. Thus shear locking can be avoided and the additional degree of freedom  $w_m$  in the middle of the element is no longer required.

## Acknowledgement

This work has been performed under the financial support of “Deutsche Forschungsgemeinschaft” under BE 1090/33-1, which is gratefully acknowledged.

## References

- Alpdogan, C., Dong, S. and Taciroglu, E. (2010), A method of analysis for end and transitional effects in anisotropic cylinders, *International Journal of Solids and Structures*, 47, pp. 947-956.
- Altenbach, J., Altenbach, H. and Matzdorf, V. (1994a), A generalized Vlasov theory for thin-walled composite beam structures, *Mechanics of Composite Materials*, 30, pp. 43-54.
- Altenbach, J., Kissing, W. and Altenbach, H. (1994b), *Dünnwandige Stab- und Schalenträgerwerke*, Vieweg Verlag Braunschweig
- Argyris, J. and Kačianauskas, R. (1996), Semi-analytical finite elements in the higher-order theory of beams, *Computer Methods in Applied Mechanics and Engineering*, 138, pp. 19-72.
- Artel, J. and Becker, W. (2006), Analysis of free-edge effects by boundary finite element method, *Proceedings in Applied Mathematics and Mechanics*, 6, pp. 205-206.
- Dasgupta, G. (1982), A finite element formulation for unbounded homogeneous continua, *Journal of Applied Mechanics*, 49, pp. 136-140.
- Dieringer, R., Hebel, J. and Becker, W. (2011), The scaled boundary finite element method for plate bending problems, *Proceedings of the 19th International Conference on Computer Methods in Mechanics*, pp. 169-170.
- Dong, S., Kosmatka, J. and Lin, H. (2001), On Saint-Venant's problem for an inhomogeneous anisotropic cylinder: Part I: Methodology for saint-venant solutions, *Journal of Applied Mechanics*, 68, pp. 376-381.
- Gavrić, L. (1994), Finite element computation of dispersion properties of thin-walled waveguides, *Journal of Sound and Vibration*, 173, pp. 113-124.
- Giavotto, V., Borri, M., Mantegazza, P., Ghiringhelli, G., Carmaschi, V., Maffioli, G. and Mussi, F. (1983), Anisotropic beam theory and applications, *Computers & Structures*, 16, pp. 403-413.
- Kosmatka, J., Lin, H. and Dong, S. (2001), On Saint-Venant's problem for an inhomogeneous anisotropic cylinder: Part II: Cross-sectional Properties, *Journal of Applied Mechanics*, 68, pp. 382-391.
- Lin, H., Dong, S. and Kosmatka, J. (2001), On Saint-Venant's problem for an inhomogeneous anisotropic cylinder: Part III: End effects, *Journal of Applied Mechanics*, 68, pp. 392-398.
- Mayland, W. and Becker, W. (2010), Investigation of Stress Singularities due to Geometrical and Material Discontinuities in Piezoelectric Laminates by the Scaled Boundary Finite Element Method, *International Journal of Advances in Mechanics and Applications of Industrial Materials*, 1, pp. 11-17.
- Morandini, M., Chierichetti, M. and Mantegazza, P. (2010), Characteristic behavior of prismatic anisotropic beam via generalized eigenvectors, *International Journal of Solids and Structures*, 47, pp. 1327-1337.
- Reddy, J.N. (1997), On locking-free shear deformable beam finite elements, *Computer Methods in Mechanics and Engineering*, 149, pp. 113-132.
- Schardt, R. (1989), *Verallgemeinerte technische Biegetheorie*, Springer Verlag Berlin.
- Silvestre, N. and Camotim, D. (2002), First-order generalized beam theory for arbitrary orthotropic materials, *Thin-Walled Structures*, 40, pp. 755-789.
- Song, C. (2004), A matrix function solution for the scaled boundary finite-element equations in statics, *Computer Methods in Applied Mechanics and Engineering*, 193, pp. 2325-2356.
- Taweel, H., Dong, S. and Kazic, M. (2000), Wave reflection from the end of a cylinder with an arbitrary cross-section, *International Journal of Solids and Structures*, 37, pp. 1701-1726.
- Tisseur, F. and Meerbergen, K. (2001), The Quadratic Eigenvalue Problem, *SIAM Review*, 43(2), pp.235-286.
- Wolf, J. P. and Song, C (1996), *Finite-element modelling of unbounded media*, Wiley Chichester, England.
- Wolf, J. P. (2002), *The Scaled Boundary Finite Element Method*, Wiley Chichester, England
- Yang, P., Norris, C. and Stavsky, Y. (1966), Elastic wave propagation in heterogeneous plates, *International Journal of Solids and Structures*, 2, pp. 665-684.

**Application of DEM Simulation  
to drum type agitation mill for appropriate comminution  
Yuki Tsunazawa<sup>1</sup>, Kazuki Tahara<sup>1</sup>, Chiharu Tokoro\*<sup>2</sup> and Shuji Owada<sup>2</sup>**

<sup>1</sup>Major in Earth Resources and Environmental Engineering, Graduate School of Science and Engineering,  
Waseda University, Okubo 3-4-1, Shinjuku-ku, Tokyo, 169-8555, Japan

<sup>2</sup>Department of Resources and Environmental Engineering, Faculty of Science and Engineering,  
Waseda University, Okubo 3-4-1, Shinjuku-ku, Tokyo, 169-8555, Japan

\*Corresponding author: tokoro@waseda.jp

## Abstract

A computer simulation using discrete element method (DEM) was applied to a comminution/detachment process of waste printed circuit boards (PCBs). Recycling of PCBs is an important subject not only from the treatment of waste but also from the recovery of valuable metals. However, direct simulation method to investigate a comminution/detachment process of PCBs has not yet been established. We have already published an indirect simulation using the general spherical particle model to discuss the mechanism of parts detachment and board breakage.

This study prepared simulant PCBs on which some capacitors were solder-mounted and used for the comminution test to compare with simulation results. In order to calculate the behavior and comminution/detachment process of PCBs, a PCB was constructed many fine particles and particle based rigid body model was also included to the simulation. This simulation could directly represent the behavior of PCBs in the drum typed agitation mill. Simulation results successfully corresponded to comminution experimental results using drum type mill with agitator.

**Keywords:** DEM, Particle based rigid body, Comminution, Recycling

## Introduction

The amount of electronic waste, commonly known as e-waste, waste electrical and electronic equipment (WEEE) is increasing at a rate of 3-5 % per annum [Herat 2007]. In order to reduce final waste volume and decline environmental burden, it has been expected that the recycling system of e-waste is established. A printed circuit board (PCB) is one of the most important components of e-waste, and contains many electronic components such as resistors, capacitors, relays, semi-conductors and IC chips. These components have not only many valuable metals but also many hazardous chemicals. Although their composition varies slightly depending on the grade, usage and manufacturing year, PCBs represent a useful source of recoverable material values. Efficient recycling and appropriate material treatment will ensure that non-renewable resources are recovered and environmental pollution is prevented.

The computer simulation is an important means of scientific research. The Discrete Element Method (DEM) predicts the behavior of the whole particles from the motion of individual particles (Cundall and Strack 1979). Therefore, in order to analyze the behavior of particle flow and investigate phenomena of powder particles, the DEM is widely used and has been applied to powder simulation such as fluid bed, ball mill, slope failure, and so on. On the other hand, in order to apply DEM to breakage phenomenon, there are some methods which construct an object by bonding many fine particles, analyze contact force of constituent particles, and break the bonds between fine particles if contact forces became over a threshold level. However, it has not been investigated which models are adequate for the grinding process.

The objective of this study was to apply DEM simulation to comminution process in drum type agitation mills and to investigate the mechanism of mechanical detachment to remove electronic components from printed circuit boards (PCBs). In addition to the conventional model, in

this study, two DEM simulation models were constructed. One is the particle breakage model. The other is the particle-based rigid body model. Simulation results were compared with experimental results using test PCBs. And then we investigated whether simulation results successfully corresponded to comminution experimental results or not.

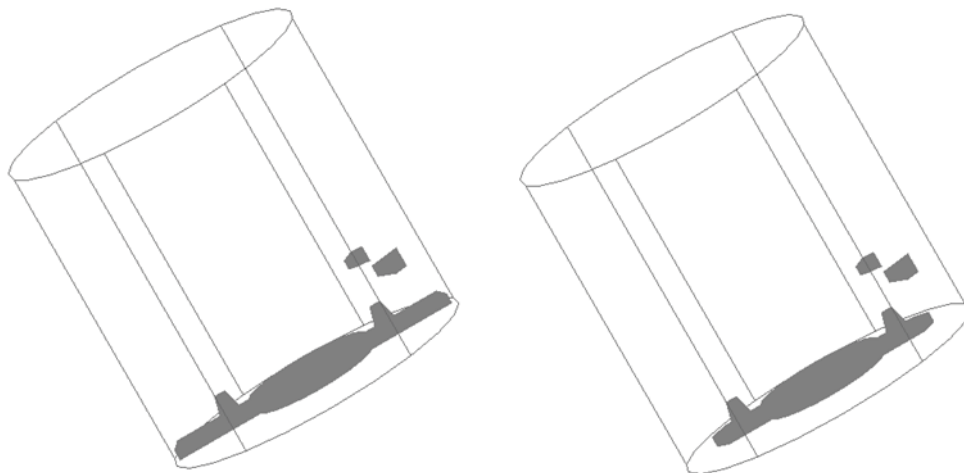
## Comminution experiment

### *Preparation of test PCBs*

A test PCB was prepared to stabilize comminution experimental results. A double side glass epoxy PCB (FR-4, Picotec International, Taiwan) and, 10  $\mu$ F and 35 V of several ceramic condensers (GP075F106Z, Taiyo Yuden, Japan) were used for a test PCB. Nine ceramic condensers were solder-mounted at regular intervals on a PCB. A PCB was 210×155 mm and weighed 92.8 g. A ceramic condenser weighed 0.14 g.

### *Drum-typed impact agitation mill*

Two types of drum-typed impact agitation mill (Parts separator, Hirata corporation, Japan) were used for comminution tests. The mill is a cylinder, 0.86 m diameter and length. The cylinder axis is inclined at 30° from the vertical, and a mechanical stirrer is installed in the bottom of the drum. There are two projections on the surface of the stirrer and the wall. There is a slight difference between two types of agitation mill. Type A has bigger mechanical stirrer than Type B. These simulation models of the agitation mill constructed in DEM simulation are shown in Figure 1.



**Figure 1 Schematic of drum-typed impact agitation mill represented in the DEM simulation (Left : Type A, Right : Type B)**

### *Comminution test*

In the parts detachment test, the grinding time was fixed at 30 s. The rotation speed was changed from 300, 500, 1000, or 1500 rev/min. The mill was charged with 5 – 100 pieces of PCBs. All of comminution products were collected and weight of each PCB and number of remaining parts on PCBs were counted.

## DEM simulation method

### *Spherical particle model*

A spherical particle model is based on the original DEM concept proposed by Cundall and Strack. Contact between particles and between a particle and a wall is modeled using a Voigt model consisting of a spring and a dashpot in normal and tangential directions. A slip model defined by the friction slider is included in the tangential force. Table 1 gives parameter values used in the spherical particle model.

**Table 1 DEM simulation conditions in the spherical particle model**

Spring constant	$5.0 \times 10^6$ N/m
Coefficient of restitution	0.10
Coefficient of friction	0.27
Diameter of a particle	0.1 m
Number of particles	5 - 100
Weight of a particle	92.8 g

### *Particle breakage model*

In the particle breakage model, PCBs and parts geometry were constructed consisting of many fine bonded particles. A phenomena of parts detachment was modeled by breaking the bonds between fine particles if contact forces became over a threshold level. An anchoring concept was developed as a new bonding model to avoid displacement of the bonding point between particles. In this case, torque and bonding force between bonded two particles,  $i$  and  $j$ , were calculated as follows.

$$\mathbf{T}_i = \mathbf{T}_{Di} + \frac{\pi a^4}{4} \mathbf{K}_0 \begin{pmatrix} \Delta\psi_x \\ \Delta\psi_y \\ 2\Delta\psi_z \end{pmatrix} \quad (1)$$

$$\mathbf{T}_j = \mathbf{T}_{Dj} + \frac{\pi a^4}{4} \mathbf{K}_0 \begin{pmatrix} \Delta\psi_x \\ \Delta\psi_y \\ 2\Delta\psi_z \end{pmatrix} \quad (2)$$

$$\mathbf{K} = \pi a^2 \mathbf{K}_0 \quad (3)$$

Where  $\mathbf{T}_i$  and  $\mathbf{T}_j$  were the torque vectors between two bonded particles,  $i$  and  $j$ , and  $\Delta\psi_x$ ,  $\Delta\psi_y$  and  $\Delta\psi_z$  were the difference in rotation angles between two bonded particles around the x, y and z-axis. In this case, the contact point between two bonded particles was set at the origin, the normal direction was set as the z-axis and the tangential direction were set to the x and y axes.  $\mathbf{T}_{Di}$  and  $\mathbf{T}_{Dj}$  were the torques calculated in an original DEM model without particle breakage.  $\mathbf{K}$  was the spring constant vector in the original DEM model without particle breakage.  $a$  was the anchoring area between two bonded particles.

The connection between two particles was considered to be broken if the bonding force calculated from DEM rose above a set threshold level. The threshold level was determined from tensile tests. The DEM parameter used for the particle breakage model are shown in Table 2.

**Table 2 DEM simulation conditions in the particle breakage model**

Diameter of configuration particles per a PCB	0.15 m
Diameter of anchoring area	1.5 mm

### Particle-based rigid body

Since the shape of waste PCBs is complicated, waste PCBs cannot be directly simulated in the original DEM. In order to investigate the behavior of these waste PCBs in the agitation mill, a particle-based rigid model was included into the original DEM.

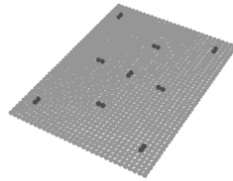
The motion of a rigid body is computed by dividing motion into two parts: translation and rotation. Translation describes the motion of the center of mass, whereas rotation describes how the rigid body rotates around the center of mass. A detailed explanation is reported by Baraff (1997).

In this method, the shape of waste PCBs and the collision detection are based not on the polygons that represent the rigid bodies, but on particles, as done by the authors (Bell, 2005; Tanaka et al., 2006). A waste PCB is represented by a set of fine particles that are spheres of identical size.

The calculation conditions of a waste PCB represented in this model were shown in Table 3. The diameter of constituent particle was set at 5 mm. These particles were aligned in the shape of a lattice. Snapshot of a waste PCB in this model was shown in Figure 2.

**Table 3 Calculation condition of a waste PCB in Particle-based rigid body model**

Particle diameter	5 mm
Number of particles constructed board	$41 \times 32$
Number of particles constructed part	2
Number of parts	9
Mass of a PCB	92.8 g



**Figure 2 Snapshot of PCBs constructed of particle-based rigid body model**

### Collision energy

Breakage of PCBs is caused by collision between PCBs, a PCB and drum wall or agitator. Calculation of the damping energy generated during the collision would be crucial to investigate the mechanism of comminution process. In this study, we counted damping energy during collision of PCBs in order to grasp collision energy of them. Damping energy was calculated from consuming energy in dashpot and friction slider of the Voigt model during collision. This is given by:

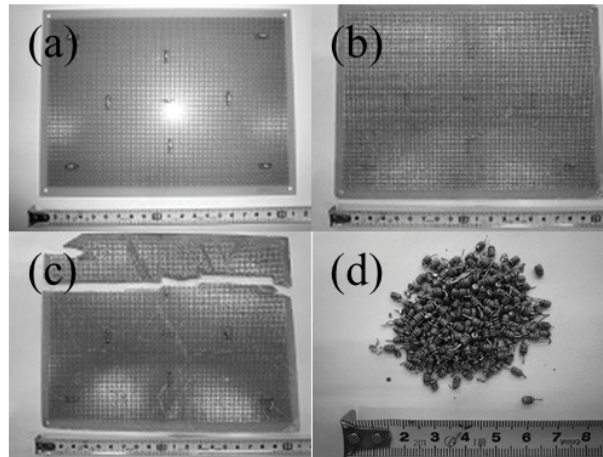
$$E_{loss} = \int P_{dashpot} dt + \int P_{friction} dt \quad (4)$$

where  $E_{loss}$  was damping energy,  $P_{dashpot}$  and  $P_{friction}$  were respectively the rates of energy dissipation in dashpot and friction slider.

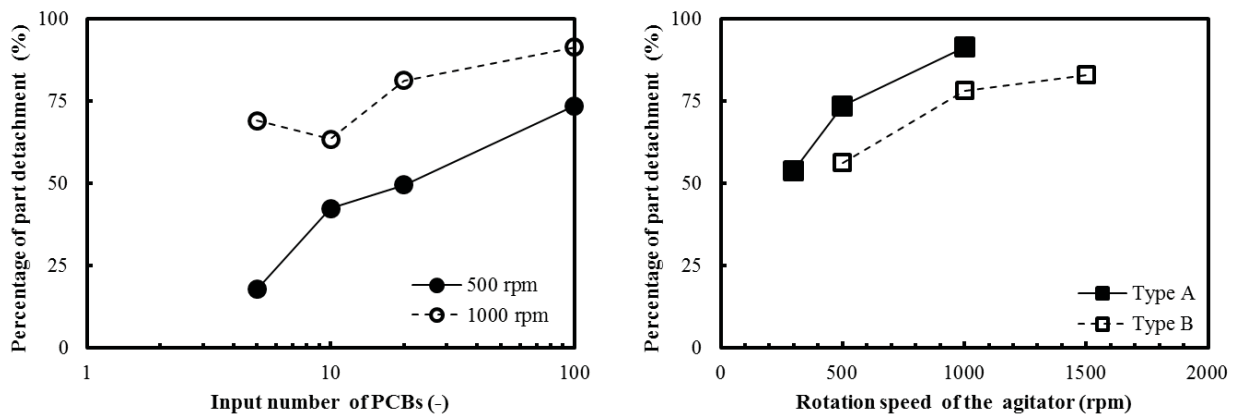
## Results and Discussion

### Experimental results of comminution test

Experimental snapshots of test PCB before/after comminution are presented in Figure 3. After comminution test, most parts were detached from the boards, as shown in snapshots (b) and (c). A part of PCBs was broken like snapshots (c) while most PCBs were unbroken like snapshots (b). Detached parts were unbroken like snapshots (d).



**Figure 3** Result of comminution experiment for test PCB using drum-typed impact agitation mill: (a) test PCB before comminution test, (b) unbroken PCB, (c) broken PCB, (d) detached parts



**Figure 4** Result of comminution experiment for test PCB using drum-typed impact agitation mill: (left : relationship between input number of PCBs and part detachment, right : relationship between rotation speed and part detachment)

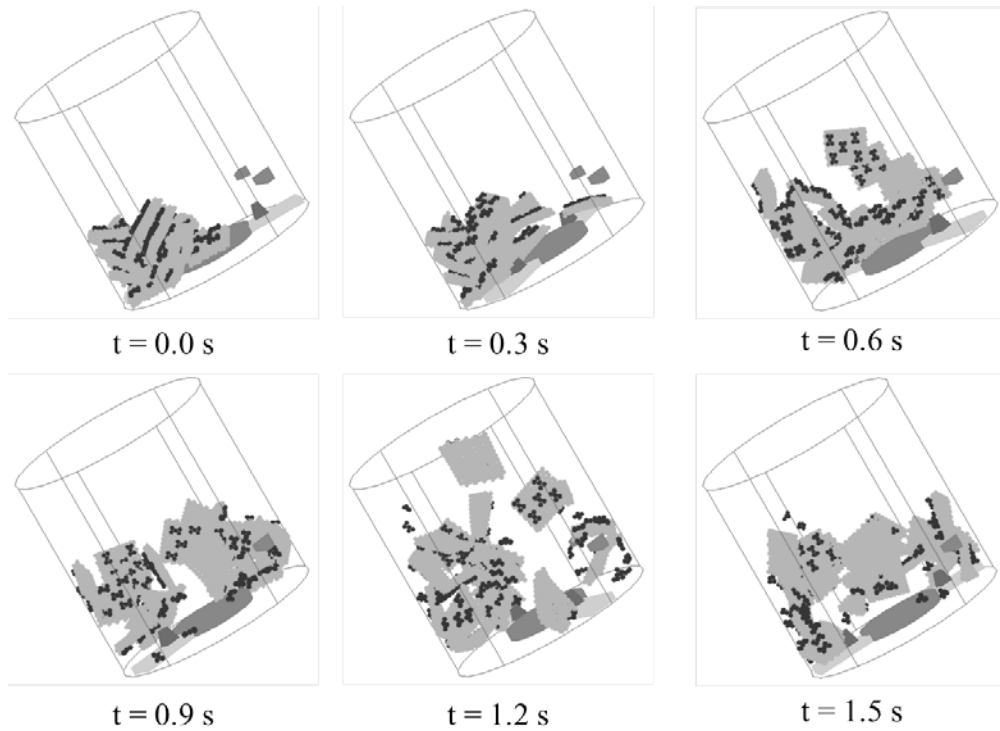
Figure 4 shows the result of comminution experiment for test PCBs. The left graph shows that the relationship between percentage of part detachment and number of PCBs in the mill charge. In this comminution tests, the rotation speed was fixed at 500 or 1000 rpm. As shown in the left graph of Figure 4, the percentage of part detachment was increased with the number of PCBs. These results suggested that interaction between PCBs became more frequent and parts detachment from the board was accelerated. The more input of PCBs is better to achieve parts liberation from the board. On the other hand, the right graph of Figure 4 shows the relationship percentage of part detachment and rotation speed. In these comminution tests, 100 pieces of PCBs were charged in the mill par a batch. As shown in the right graph of Figure 4, the percentage of part detachment increased with rotation speed. The percentage of part detachment in drum type A was larger than that of part detachment in drum type B at each rotation speed. These results indicated that the stress became high when the edge of agitator was narrow, and that the shape of agitation at the bottom of the mill affected the part detachment.

#### *Simulation results of the particle breakage model*

Figure 5 shows a snapshot of DEM simulation using the particle breakage model. In this simulation results, rotational speed was 500 rev/min and the mill was charged with 20 PCBs. The

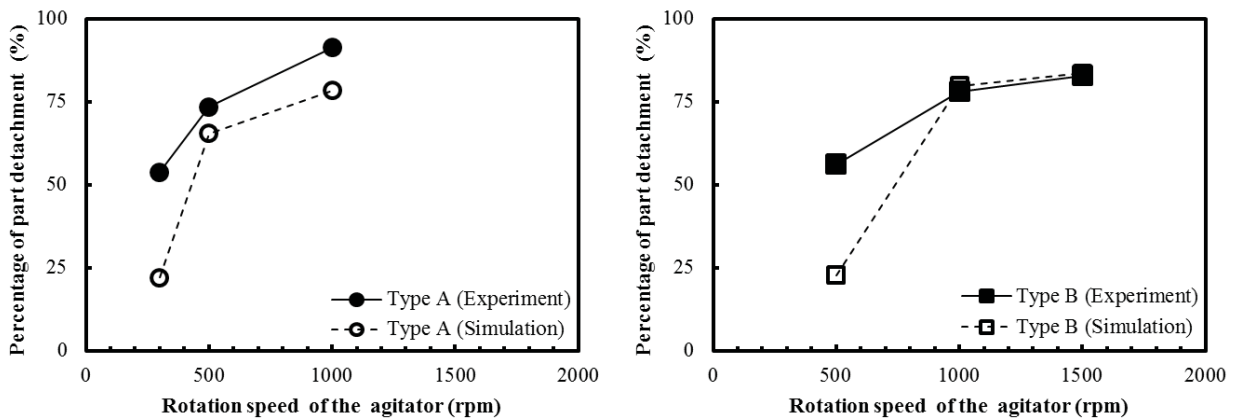


PCBs were agitated by the stirrer, and part detachment process in the mill could be directly represented in this simulation result. In this simulation, the connection between two particles was considered to be broken if the contact force between bonded particles calculated from DEM rose above a set threshold level. The threshold level for the connection between the part particle and the board particle was set as 750 times less than that for the connection between particles inside the board, by reference to experimental results of the breakage energy for parts detachment and board breakage.



**Figure 5 Snapshots of DEM simulation results using the particle breakage model**

Figure 6 shows the percentage of parts detachment of the board calculated from DEM simulation results. When compared with experimental results for parts detachment, upward trend for the percentage of parts detachment to the rotational speed of agitation accorded well with experimental results. These results indicated that this particle breakage model was one of the adequate models to simulate the behavior of PCBs and represent parts detachment of the boards.

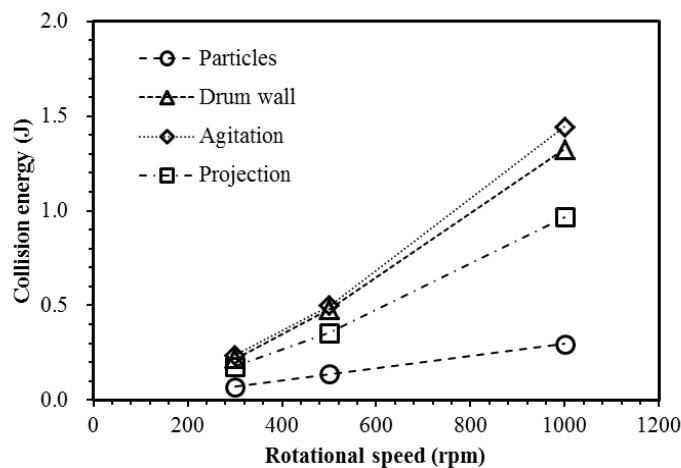


**Figure 6 Comparison of parts detachment between DEM simulation and experiment (Left : Type A, Right : Type B)**

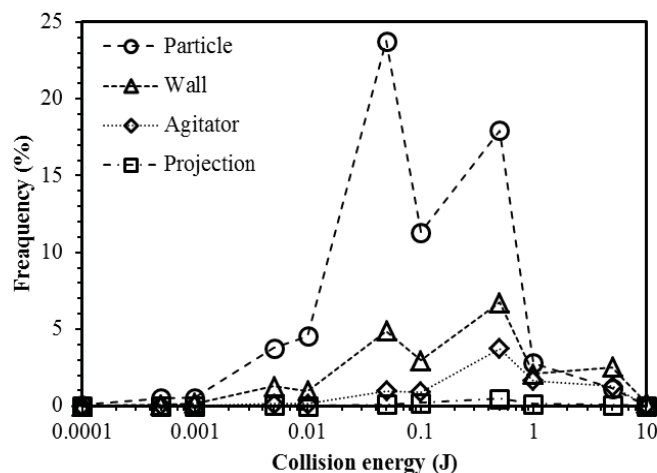
*Simulation results of the particle-based rigid model*

Figure 7 shows the relationship between each rotational speed of the agitator and collision energy calculated from the particle-based rigid model simulation. As the rotational speed of the agitation was increased, collision energy was also increased. The collision energy between the particle and the agitation or the drum wall were much larger than the collision energy between particles. While the collision energy between the particle and the agitation or the drum wall were dramatically changed with rotational speed, the collision energy between particles was gradually increased with rotational speed. These results indicated that the comminution process of PCBs mainly was promoted by the collision of the agitation and the drum wall.

In order to conduct a detailed investigation of the collision energy, Figure 8 shows the collision energy distribution. In this simulation results, rotational speed was 500 rev/min and the mill was charged with 50 PCBs. As shown in Figure 8, the number of collisions between particles was much larger than that of collision between particles and the drum wall, the agitator or the projection. Although the number of collisions between particles was large, the collision energy between particles was smaller.



**Figure 7 Relationship between rotational speed and collision energy in type A simulation**



**Figure 8 Collision energy distribution (Type A, Rotational speed : 500 rpm)**

## Conclusion

Mechanism of part detachment of PCBs by comminution in two drum type agitation mills was investigated from both of the experimental approach and simulation. Comminution experiments using glass-epoxy double side printed circuit boards soldered with nine ceramic condensers were carried out. The comminution process of PCBs was also investigated by two types of DEM simulation.

Experimental results showed that the percentage of parts detachment of the board increased with input number of PCBs and rotation speed. The interaction between PCBs affected parts detachment. Although only an indirect study was possible for part detachment and the behavior of PCBs using an original DEM simulation model, DEM simulation with particle breakage model and particle-based rigid model could directly represent the behavior of PCBs. The relationship between part detachment and rotation speed of the agitation simulated by a DEM model with particle breakage qualitatively corresponded to experimental observations of comminution using test PCBs. The result of DEM simulation with particle-based rigid model showed although the number of the collisions between PCBs was larger than others, the collision energy between PCBs was smaller than others.

## References

- Baraff, D. (1997), An Introduction to Physically Based Modeling: Rigid Body Simulation 1 – Unconstrained Rigid Body Dynamics, *SIGGRAPH '97 Course Notes*, pp. 1 - 68
- Bell, N. (2005), Particle-Based Simulation of Granular Materials, *In Proceedings of the ACM SIGGRAPH / Eurographics Symposium on Computer Animation*, pp. 77 - 86
- Cundall, P. A. and Strack, O. D. L. (1979), A discrete numerical model for granular assemblies, *Geotechnique*, **29** (1), pp. 47-65
- Herat, S. (2007), Sustainable Management of Electronic Waste (e-Waste), *Clean*, **35** (4), pp. 305-310
- Tanaka, M., Sakai, M. and Koshizuka, S. (2006), Rigid Body Simulation Using a Particle Method, *In ACM SIGGRAPH Research Posters*, no. 132

## **Dynamic analysis by a new family of time marching procedures based on numerically computed Green's functions**

**D. Soares Jr.**

Structural Engineering Department, Federal University of Juiz de Fora, CEP 36036-330 Juiz de Fora, MG, Brazil.  
delfim.soares@ufjf.edu.br.

### **Abstract**

In this work, a new family of time marching procedures based on Green's function matrices is presented. The formulation is based on the development of new recurrence relationships, which employ time integral terms to treat initial condition values. These integral terms are numerically evaluated taking into account Newton-Cotes formulas. The Green's matrices of the model are also numerically computed, taking into account the generalized- $\alpha$  method and subcycling techniques. As it is discussed and illustrated along the text, the proposed procedure is efficient and accurate, providing a very attractive time marching technique.

**Keywords:** Dynamics, Time-Marching, Green's Function, Generalized- $\alpha$  Method, Subcycling.

### **Introduction**

Time dependent hyperbolic equations have numerous applications in various branches of science and in practical engineering design. Since it is usually very difficult to obtain analytical transient responses for these equations, numerical techniques must be applied to find approximate solutions, and step-by-step time integration algorithms are routinely employed when dynamic problems are focused, because of their various inherent advantages to solve a great deal of initial value problems.

In this work, time marching algorithms based on numerically computed Green's function matrices are focused. Recently, Tamma et al. (2003) and Zhou and Tamma (2004) derived a new family of unconditionally explicit/implicit algorithms based on analytical solution of first-order ordinary differential equations in which the concept of Green's functions is implicitly present. Other similar approaches have been the subject of some papers discussion, and are usually referred to as "precise time-step integration methods" (Zhong et al., 1994, 1996; Fung, 1997). In Soares (2002, 2004) and Soares and Mansur (2005b), a formulation that implicitly computes Green's function matrices taking into account standard time domain numerical procedures was presented, in order to obtain a new family of time marching schemes. Later on, step response and Green's function matrices were computed explicitly by Mansur et al. (2007), taking into account explicit time marching routines. The methodology was extended to analyse dynamic models discretized by different numerical techniques (Soares, 2002; Soares et al., 2009) and to efficiently analyse coupled problems (Soares, 2008; Soares and Mansur, 2005c; Soares et al., 2007, 2010). The analysis of a variety of coupled problems by the proposed procedure could be carried out very effectively since it allows coupled sub-domains to be treated independently, at each time step (similarly, it also allows a quite efficient analysis of some non-linear models - Soares and Mansur, 2005b; Soares et al., 2009). The direct computation of Green's function matrices in order to develop time marching routines to analyse hyperbolic models has been carried out in transformed domains as well, being the frequency (Soares and Mansur, 2003, 2005a; Correa et al., 2010) and the Laplace (Loureiro and Mansur, 2009b) domain mostly focused. Recently, the methodology has been generalized (Soares, 2011) and also applied to analyse heat conduction models (Loureiro and Mansur, 2009a; Loureiro et al., 2009; Mansur et al. 2009), extrapolating the initially focused context of wave propagation problems and structural dynamic analyses.

### **Time marching procedure based on numerically computed Green's functions**

The governing system of equations describing a linear dynamic model is given by (Clough and Penzien, 1993):

$$\mathbf{M}\ddot{\mathbf{U}}(t) + \mathbf{C}\dot{\mathbf{U}}(t) + \mathbf{K}\mathbf{U}(t) = \mathbf{F}(t) \quad (1)$$

where  $\mathbf{M}$ ,  $\mathbf{C}$  and  $\mathbf{K}$  are mass, damping and stiffness matrices, respectively,  $\mathbf{F}(t)$  stands for the force vector and  $\mathbf{U}(t)$ ,  $\dot{\mathbf{U}}(t)$  and  $\ddot{\mathbf{U}}(t)$  are displacement, velocity and acceleration vectors, respectively.

Supposing that the analysis begins at a time instant  $t$  and that a  $\Delta t$  period of analysis is focused, the following analytical recurrence relationships can be obtained to compute displacements and velocities (Soares, 2011):

$$\mathbf{U}(t + \Delta t) = \mathbf{U}(t) - \int_0^{\Delta t} \mathbf{G}(\Delta t - \tau) d\tau \mathbf{K} \mathbf{U}(t) + \mathbf{G}(\Delta t) \mathbf{M} \dot{\mathbf{U}}(t) + \int_t^{t+\Delta t} \mathbf{G}(t + \Delta t - \tau) \mathbf{F}(\tau) d\tau \quad (2a)$$

$$\dot{\mathbf{U}}(t + \Delta t) = - \int_0^{\Delta t} \dot{\mathbf{G}}(\Delta t - \tau) d\tau \mathbf{K} \mathbf{U}(t) + \dot{\mathbf{G}}(\Delta t) \mathbf{M} \dot{\mathbf{U}}(t) + \int_t^{t+\Delta t} \dot{\mathbf{G}}(t + \Delta t - \tau) \mathbf{F}(\tau) d\tau \quad (2b)$$

where the Green's function matrices that appear in equations (2) can be computed through the solution of the following initial condition problem, within the time period  $\Delta t$ :

$$\mathbf{M} \ddot{\mathbf{G}}(t) + \mathbf{C} \dot{\mathbf{G}}(t) + \mathbf{K} \mathbf{G}(t) = \mathbf{0}; \quad \mathbf{G}(0) = \mathbf{0} \quad \text{and} \quad \dot{\mathbf{G}}(0) = \mathbf{M}^{-1} \quad (3)$$

The solution of the dynamic problem described by equation (3) can be carried out numerically, providing the numerical computation of the Green's functions of the model. The accuracy, stability and efficiency of the recurrence relations (2) are intimately related to the computation of these Green's matrices. Once the Green's function matrices and the time convolution integrals expressed in equations (2) are properly computed, this time marching procedure may become extremely accurate, providing a very attractive methodology (one should observe that recurrence relations (2) are the analytical solutions of the dynamic model, hence, a very accurate procedure is expected, once the terms in relations (2) are properly computed).

In this work, the generalized- $\alpha$  method is employed to compute the Green's matrices of the model (one should observe that several other numerical procedures could be employed, which would result in different time marching techniques). In the generalized- $\alpha$  method, the time discrete equation of motion employed to compute the Green's matrices of the model is written as:

$$\mathbf{M}[\alpha_m \ddot{\mathbf{G}}^\eta + (1 - \alpha_m) \ddot{\mathbf{G}}^{\eta+1}] + \mathbf{C}[\alpha_k \dot{\mathbf{G}}^\eta + (1 - \alpha_k) \dot{\mathbf{G}}^{\eta+1}] + \mathbf{K}[\alpha_k \mathbf{G}^\eta + (1 - \alpha_k) \mathbf{G}^{\eta+1}] = \mathbf{0} \quad (4)$$

and the finite difference formulas of the Newmark method are retained, as described below:

$$\mathbf{G}^{\eta+1} = \mathbf{G}^\eta + \Delta t \dot{\mathbf{G}}^\eta + \Delta t^2 (1/2 - \mu_1) \ddot{\mathbf{G}}^\eta + \Delta t^2 \mu_1 \ddot{\mathbf{G}}^{\eta+1} \quad (5a)$$

$$\dot{\mathbf{G}}^{\eta+1} = \dot{\mathbf{G}}^\eta + \Delta t (1 - \mu_2) \ddot{\mathbf{G}}^\eta + \Delta t \mu_2 \ddot{\mathbf{G}}^{\eta+1} \quad (5b)$$

where  $\mu_1$  and  $\mu_2$  stand for the Newmark's parameters and  $\alpha_m$  and  $\alpha_k$  describe the generalized- $\alpha$  method. By substituting approximations (5) into equation (4), the following time-marching procedure arises, which enables the computation of the Green's function matrix of accelerations:

$$\begin{aligned} & [(1 - \alpha_k) \mu_1 \Delta t^2 \mathbf{K} + (1 - \alpha_k) \mu_2 \Delta t \mathbf{C} + (1 - \alpha_m) \mathbf{M}] \ddot{\mathbf{G}}^{\eta+1} = \\ & = -\mathbf{K} \mathbf{G}^\eta - [\mathbf{C} + (1 - \alpha_k) \Delta t \mathbf{K}] \dot{\mathbf{G}}^\eta - [\alpha_m \mathbf{M} + (1 - \alpha_k)(1 - \mu_2) \Delta t \mathbf{C} + (1 - \alpha_k)(1/2 - \mu_1) \Delta t^2 \mathbf{K}] \ddot{\mathbf{G}}^\eta \end{aligned} \quad (6)$$

In the generalized- $\alpha$  method, second-order accuracy and maximal high-frequency dissipation are achieved if  $\mu_1 = (1 + \alpha_k - \alpha_m)^2 / 4$  and  $\mu_2 = 1/2 + \alpha_k - \alpha_m$  are adopted. For  $\alpha_k = \alpha_m = 0$ , the method reduces to the Newmark method; for  $\alpha_m = 0$ , the method reduces to the HHT method; and for  $\alpha_k = 0$ , the method reduces to the Bossak method.

In order to achieve a more accurate numerical procedure, the Green's matrices of the model can be computed within a time step  $\Delta t$ , taking into account a subcycling technique, i.e.: the system of equations (6) is solved  $n$  times (as well as the actualisations described by equations (5)), considering a time sub-step of  $\Delta t/n$ . As a consequence, the following matrices are computed considering the subcycling technique:  $\mathbf{G}^1, \mathbf{G}^2, \dots, \mathbf{G}^n$  etc; which are the numerical approximations to the following Green's matrices:  $\mathbf{G}(\Delta t/n), \mathbf{G}(2\Delta t/n), \dots, \mathbf{G}(\Delta t)$  etc. To numerically evaluate the time integrals described in equations (2), the trapezoidal rule is considered here, taking into account the  $n$  sub-steps employed to evaluate the Green's function matrices, allowing to obtain the following recurrence relationships:

$$\mathbf{U}^{t+\Delta t} = \mathbf{U}^t - \mathbf{J}^n \mathbf{K} \mathbf{U}^t + \mathbf{G}^n \mathbf{M} \dot{\mathbf{U}}^t + \mathbf{L}_1^n \mathbf{F}^t + \mathbf{L}_2^n \mathbf{F}^{t+\Delta t} \quad (7a)$$

$$\dot{\mathbf{U}}^{t+\Delta t} = -\dot{\mathbf{J}}^n \mathbf{K} \mathbf{U}^t + \dot{\mathbf{G}}^n \mathbf{M} \dot{\mathbf{U}}^t + \dot{\mathbf{L}}_1^n \mathbf{F}^t + \dot{\mathbf{L}}_2^n \mathbf{F}^{t+\Delta t} \quad (7b)$$

where  $\mathbf{L}_1^n = \frac{1}{2} \left(\frac{\Delta t}{n}\right) \mathbf{G}^n + \left(\frac{\Delta t}{n}\right) \sum_{i=1}^{n-1} \left(\frac{i}{n}\right) \mathbf{G}^i$ ,  $\mathbf{L}_2^n = \frac{1}{2} \left(\frac{\Delta t}{n}\right) \mathbf{G}^0 + \left(\frac{\Delta t}{n}\right) \sum_{i=1}^{n-1} \left(1 - \frac{i}{n}\right) \mathbf{G}^i$ ,  $\mathbf{J}^n = \mathbf{L}_1^n + \mathbf{L}_2^n$  and  $\dot{\mathbf{L}}_1^n, \dot{\mathbf{L}}_2^n$

and  $\dot{\mathbf{J}}^n$  can be analogously computed. In equations (7), the  $\mathbf{L}$  terms are evaluated considering a linear behaviour of the acting forces within the time interval  $[t, t+\Delta t]$ , i.e.:  $\mathbf{F}(\tau) = \mathbf{F}^t + (\mathbf{F}^{t+\Delta t} - \mathbf{F}^t)(\tau - t) / \Delta t$ , for  $t < \tau < t + \Delta t$ .

The time marching procedure (7) becomes extremely accurate once high values of  $n$  are selected, allowing considerably large values of  $\Delta t$  to be considered, without damaging the accuracy and the stability of the time marching technique. Once considerably larger time steps  $\Delta t$  are allowed, the time marching procedure (7) may become highly efficient to analyse long period responses. In Figure 1, the spectral radius of the amplification matrix of the new procedure are depicted taking into account several  $\mu_1, \mu_2, \alpha_m$  and  $\alpha_k$  values, as well as  $n = 1, 4$  and  $10$ . Results of the standard generalized- $\alpha$  method are also depicted in the figure, for reference.

## Numerical applications

In this section, two numerical applications are presented to further illustrate some aspects of the proposed methodology. In the first application, a shear-building model is analysed and results are computed taking into account the Newmark's trapezoidal rule and linear acceleration methodologies. In the second application, a more complex physical model is focused. In this case, a clamped beam discretized by finite elements is considered and the Central Difference Method is employed to compute the related results.

### Application 1

A simple four-store shear building is analysed here. A sketch of the model is depicted in Figure 2. The mass and the stiffness values are adopted the same for all floors, they are:  $m = 5 \cdot 10^4 \text{ kg}$  and  $k = 2.5 \cdot 10^7 \text{ N/m}$ . A force, whose time dependence is shown in Figure 2(c), is applied at the fourth floor of the model. Several numerical techniques are considered to analyse the shear building. In the first analyses, the standard Newmark's trapezoidal rule and linear acceleration method are applied to analyse the model considering a small time step ( $\Delta t = 0.0025 \text{ s}$ ), in order to provide reference results for comparisons. Next, the same standard procedures are applied to analyse the model considering a larger time step ( $\Delta t = 0.25 \text{ s}$ ). Taking into account this large time step, the model is finally analysed considering the proposed formulation, adopting  $n = 10$ . The obtained results are depicted in Figure 3.

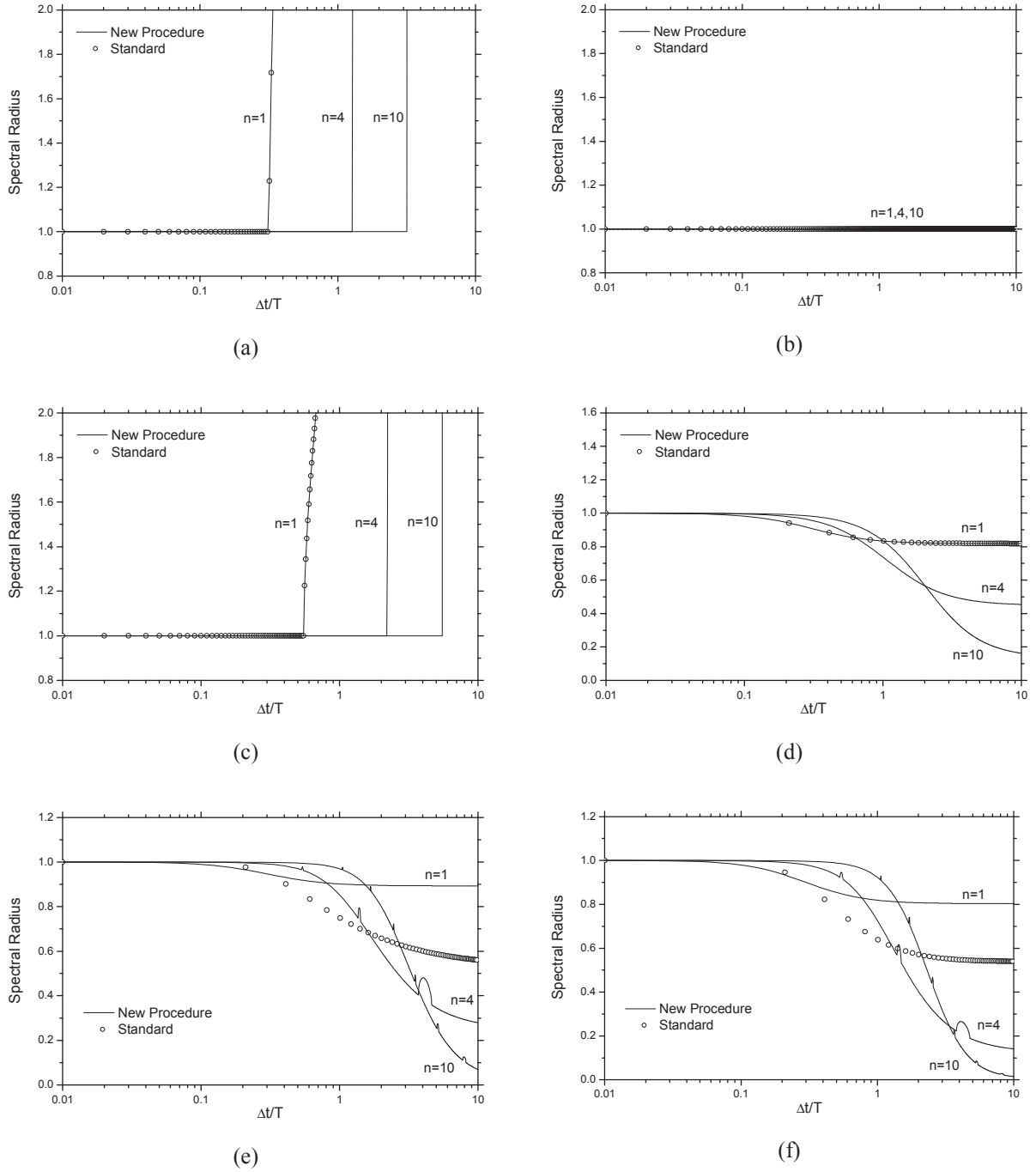


Figure 1. Spectral radius: (a) Central Difference Method ( $\mu_1 = 0$ ,  $\mu_2 = 1/2$ ,  $\alpha_k = \alpha_m = 0$ ); (b) Trapezoidal Rule ( $\mu_1 = 1/4$ ,  $\mu_2 = 1/2$ ,  $\alpha_k = \alpha_m = 0$ ); (c) Linear Acceleration Method ( $\mu_1 = 1/6$ ,  $\mu_2 = 1/2$ ,  $\alpha_k = \alpha_m = 0$ ); (d) Damped Newmark ( $\mu_1 = (\mu_2 + 1/2)^2 / 4$ ,  $\mu_2 = 0.6$ ,  $\alpha_k = \alpha_m = 0$ ); (e) HHT Method ( $\mu_1 = (1 + \alpha_k - \alpha_m)^2 / 4$ ,  $\mu_2 = 1/2 + \alpha_k - \alpha_m$ ,  $\alpha_k = 0.3$ ,  $\alpha_m = 0$ ); (f) Bossak Method ( $\mu_1 = (1 + \alpha_k - \alpha_m)^2 / 4$ ,  $\mu_2 = 1/2 + \alpha_k - \alpha_m$ ,  $\alpha_k = 0$ ,  $\alpha_m = -0.3$ ).

As can be observed in Figure 3, for the larger time step, standard procedures provide very inaccurate results: an expressive period elongation takes place considering the trapezoidal rule, as

depicted in Figure 3(a); and unstable results arise considering the linear acceleration method, as described in Figure 3(b). On the other hand, even for a large time step, stability and accuracy are observed in Figure 3 taking into account the proposed methodology. As a matter of fact, by adopting an appropriate number of sub-steps  $n$ , the proposed methodology can become as accurate as one wishes and critical time steps (above which instabilities arise) can be made as high as it may be desired (as illustrated, for instance, in Figures 1(a) and (c)).

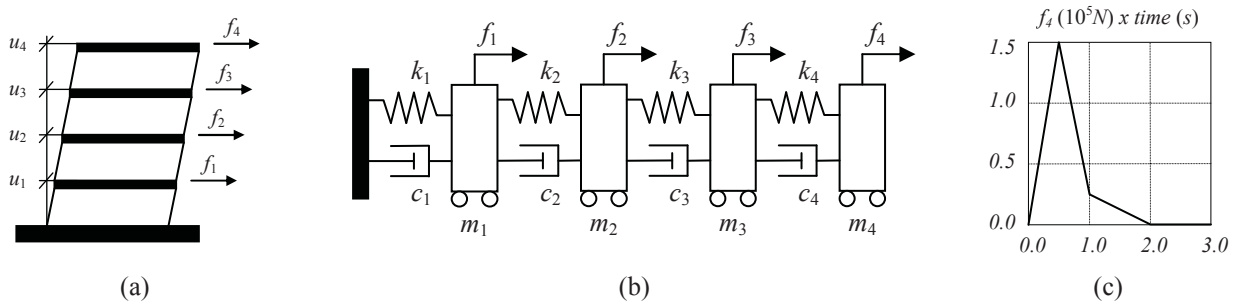


Figure 2. Shear building: (a) four-store shear building model; (b) equivalent spring-dashpot-mass model; (c) load applied at the fourth floor.

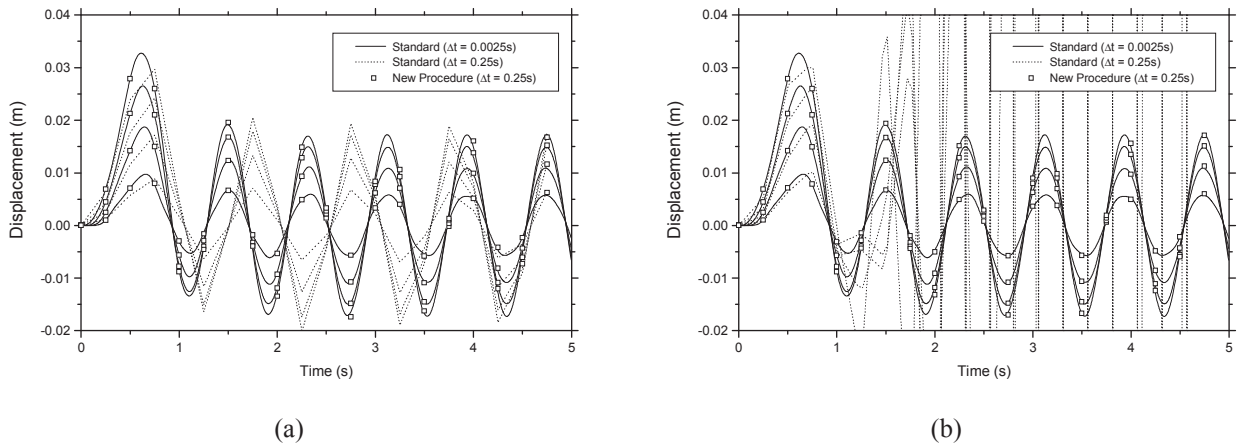


Figure 3. Displacement time history results considering the new ( $n = 10$ ) and the standard time marching procedures: (a) Trapezoidal Rule; (b) Linear Acceleration Method.

### Application 2

In this application a clamped beam is analysed. The geometry, boundary conditions and finite element mesh adopted for the model is depicted in Figure 4(a) e (b) (400 linear triangular finite elements are employed). The geometry of the beam is defined by  $a = 1.0m$  and  $b = 0.5m$ . The model is submitted to a suddenly applied load, which is kept constant along time. The material properties of the beam are:  $\nu = 0.0$  (Poisson's ratio);  $E = 100.0 N/m^2$  (Young modulus);  $\rho = 1.5 kg/m^3$  (mass density).

As before, several numerical approaches are employed to analyse the model. First, in order to provide reference results, the standard Central Difference Method is considered, adopting  $\Delta t = 0.001s$  and  $\Delta t = 0.005s$ . Next, the proposed formulation (associated with the Central Difference Method) is employed to analyse the beam, adopting  $\Delta t = 0.020s$  and  $n = 5$ . The



obtained results are depicted in Figure 4(c). Figure 4(c) shows the vertical displacements obtained at point A (see Figure 4(a)). As can be observed, unstable results arise considering the Central Difference Method with  $\Delta t = 0.005s$ , whereas stable and accurate results are obtained by the proposed methodology with the much larger time step  $\Delta t = 0.020s$ . These results illustrate once again the previously highlighted fact that the proposed methodology can become as accurate as one wishes and critical time steps can be made as high as it may be desired.

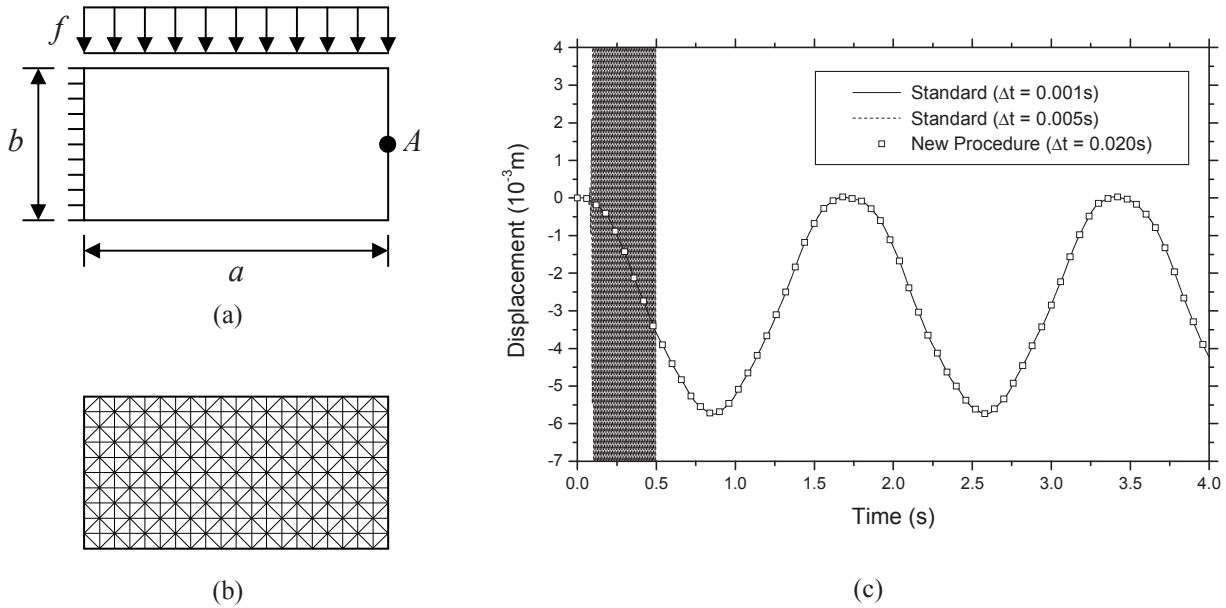


Figure 4. Clamped beam: (a) sketch of the model; (b) finite element mesh; (c) displacement time history results considering the proposed procedure ( $n = 5$ ) and the Central Difference Method (results are plotted just for  $0s \leq t \leq 0.5s$  when  $\Delta t = 0.005s$ ).

## Conclusions

In this work, a time marching procedure based on Green's functions matrices is discussed. It considers the numerical evaluation of the Green's matrices, as well as their time integrations. In the present methodology, time integral terms are employed not only to treat external forces, but also to take into account initial displacement contributions. The generalized- $\alpha$  method is considered to compute the Green's matrices of the model and the 2 points Newton-Cotes quadrature rule (trapezoidal rule) is employed to numerically evaluate the required time integrals. Both procedures take into account a sub-step technique, which is applied in order to improve the accuracy and stability of the methodology.

As it is discussed and illustrated along the text, the proposed formulation is efficient and accurate. It only requires the solution of one initial condition problem to compute the fundamental matrices of the recurrence relationships, rendering more efficient procedures than formulations based on step response matrices (Fung, 1997; Mansur et al., 2007). At the same time, the procedure maintains the good accuracy and stability aspects that are obtained by adopting step response matrices (briefly, it can be said that the procedure inherits the merits of the step response matrices, without inheriting its drawbacks). Moreover, by adopting a sub-step technique, the accuracy and stability of the methodology can be chosen as good as one wishes.

It is important to highlight that several numerical methods and combinations are possible to compute the discussed terms of the recurrence relationships, rendering different time marching techniques. This vast field of possibilities can be explored in future works, allowing more effective time marching procedures to be developed.

### Acknowledgements

The financial support by CNPq (*Conselho Nacional de Desenvolvimento Científico e Tecnológico*) and FAPEMIG (*Fundação de Amparo à Pesquisa do Estado de Minas Gerais*) is greatly acknowledged.

### References

- Clough, R. W. and Penzien, J. (1993), *Dynamics of Structures*, second ed. New York: McGraw-Hill.
- Correa, F. N., Jacob, B. P. and Mansur, W. J. (2010), Formulation of an efficient hybrid time–frequency domain solution procedure for linear structural dynamic problems. *Computers & Structures*, 88, pp.331-346.
- Fung, T. C. (1997), A precise time-step integration method by step-response and impulsive-response matrices for dynamic problems. *International Journal for Numerical Methods in Engineering*, 40, pp.4501–4527.
- Loureiro, F. S. and Mansur, W. J. (2009a), A new family of time integration methods for heat conduction problems using numerical Green’s functions. *Computational Mechanics*, 44, pp.519-531.
- Loureiro, F. S. and Mansur, W. J. (2009b), An efficient hybrid time-Laplace domain method for elastodynamic analysis based on the explicit Green’s approach. *International Journal of Solids and Structures*, 46, pp.3096-3102.
- Loureiro, F. S., Mansur, W. J. and Vasconcellos, C. A. B. (2009), A hybrid time/Laplace integration method based on numerical Green’s functions in conduction heat transfer. *Computer Methods in Applied Mechanics and Engineering*, 198, pp.2662-2672.
- Mansur, W. J., Loureiro, F. S., Soares, D. and Dors, C. (2007), Explicit time domain approaches based on numerical Green’s functions computed by finite differences: the ExGA family. *Journal of Computational Physics*, 227, pp.851-870.
- Mansur, W. J., Vasconcellos, C. A. B., Zambrozuski, N. J. M., Rotunno Filho, O. C. (2009), Numerical solution for the linear transient heat conduction equation using an Explicit Green’s Approach. *International Journal of Heat and Mass Transfer*, 52, pp.694-701.
- Soares, D. (2001), A new family of time marching procedures based on Green’s function matrices. *Computers & Structures*, 89, pp.266-276.
- Soares, D. (2002), *Time and frequency domain dynamic analysis of non-linear models discretized by the finite element method* (in Portuguese). M.Sc. Dissertation, Federal University of Rio de Janeiro, Brazil.
- Soares, D. (2004), *Dynamic analysis of non-linear soil-fluid-structure coupled systems by the finite element method and the boundary element method* (in Portuguese), PhD Thesis, Federal University of Rio de Janeiro, Brazil.
- Soares, D. (2007), A time-marching scheme based on implicit Green’s functions for elastodynamic analysis with the domain boundary element method. *Computational Mechanics*, 40, pp.827-835.
- Soares, D. (2008), A time-domain FEM approach based on implicit Green’s functions for the dynamic analysis of porous media. *Computer Methods in Applied Mechanics and Engineering*, 197, pp.4645-4652.
- Soares, D. (2009), Numerical modelling of electromagnetic waves by explicit multi-level time-step FEM-BEM coupling procedures. *CMES – Computer Modeling in Engineering & Sciences*, 44, pp.157-175.
- Soares, D. and Mansur, W. J. (2003), An efficient time/frequency domain algorithm for modal analysis of non-linear models discretized by the FEM. *Computer Methods in Applied Mechanics and Engineering*, 192, pp.3731-3745.
- Soares, D. and Mansur, W. J. (2005a), A frequency-domain FEM approach based on implicit Green’s functions for non-linear dynamic analysis. *International Journal of Solids and Structures*, 42, pp.6003-6014.
- Soares, D. and Mansur, W. J. (2005b), A time domain FEM approach based on implicit Green’s functions for non-linear dynamic analysis. *International Journal for Numerical Methods in Engineering*, 62, pp.664-681.
- Soares, D. and Mansur, W. J. (2005c), An efficient time-domain BEM/FEM coupling for acoustic-elastodynamic interaction problems. *CMES – Computer Modeling in Engineering & Sciences*, 8, pp. 153-164.
- Soares, D., Mansur, W. J. and von Estorff O. (2007), An efficient time-domain FEM/BEM coupling approach based on FEM implicit Green’s functions and truncation of BEM time convolution process. *Computer Methods in Applied Mechanics and Engineering*, 196, pp.1816-1826.
- Soares, D., Rodrigues, G. G., Gonçalves, K. A. (2010), An efficient multi-time-step implicit-explicit method to analyze solid-fluid coupled systems discretized by unconditionally stable time-domain finite element procedures. *Computers & Structures*, 88, pp.387-394.
- Soares, D., Sladek, J. and Sladek, V. (2009), Dynamic analysis by meshless local Petrov-Galerkin formulations considering a time-marching scheme based on implicit Green’s functions. *CMES – Computer Modeling in Engineering & Sciences*, 50, pp.115-140.

- Tamma, K. K., Sha, D. and Zhou, X. (2003), Time discretized operators. Part1: towards the theoretical design of a new generation of a generalized family of unconditionally stable implicit and explicit representations of arbitrary order for computational dynamics. *Computer Methods in Applied Mechanics and Engineering*, 192, pp.257–290.
- Zhong, W. X. and Williams, F. W. (1994) A precise time step integration method. *Journal of Mechanical Engineering Science*, 208, pp.427–450.
- Zhong, W., Jianing, Z. and Zhong X. X. (1996), On a new time integration method for solving time dependent partial differential equations. *Computer Methods in Applied Mechanics and Engineering*, 130, pp.163–168.
- Zhou, X. and Tamma, K. K. (2004), A new unified theory underlying time dependent linear first-order systems: a prelude to algorithms by design. *International Journal for Numerical Methods in Engineering*, 60, pp.1699–1740.

## High Pressure Zone Capture Wing Configuration for High Speed Air Vehicles

\*K. Cui, G.L. Li, S.C. Hu, Z.P. Qu

State Key Laboratory of High Temperature Gas Dynamics, Institute of Mechanics, CAS, Beijing 100190, China

\*Corresponding author: kcui@imech.ac.cn

### Abstract

To aim at design requirements of large capacity, high lift, low drag, and high lift-to-drag ratio for high air vehicles, a new aerodynamic configuration concept, named high pressure zone capture wing (HCW) configuration is firstly proposed in this paper. By comparison with traditional lift body or waverider configurations, the new feature of the HCW configuration is to introduce a surface wing, which is upon the airframe of the vehicle and paralleled with the free stream. In high speed cruising conditions, the HCW can capture the high pressure zone compressed by the upper surface of the vehicle. Thus the lift of the vehicle can get a considerable compensation due to the large pressure difference between the upper and the lower surface of the HCW. The lift-to-drag ratio can also obtain a large improvement as a result. Besides, the increase of the volume and the weight of the vehicle will lead to higher lift of the HCW. Therefore, a self-compensation effect between the lift and the weight of the vehicle is achieved. The theoretical derivation is made in the two-dimensional condition and some three-dimensional conceptual configurations are designed. Their aerodynamic performances were as well as evaluated by computational fluid dynamics. The results clearly demonstrate the high performance of the HCW configuration. The lift and the lift-to-drag ratio of the HCW configuration are much larger compared with the configuration without HCW. Besides, the larger the volume of the configuration, the effect of the HCW will be more obvious.

**Keywords:** High-speed air vehicles, Aerodynamic configuration, High pressure zone capture wing, Lift-to-drag ratio

### Introduction

Aerodynamic design of new high-speed vehicles is currently a hot topic of research. High-speed vehicles are mainly referred to various types of supersonic or hypersonic vehicles. Such vehicles generally use ramjet/scramjet or rocket engine. High-speed vehicles also include unpowered glider aircraft. Breguet equation<sup>[1]</sup> (Eq. (1)) shows that in cruise flight conditions, the aircraft cruising range can be estimated by the following equation:

$$R = V \cdot (L / D) \cdot I_{sp} \cdot \ln \left( \frac{W_i}{W_f} \right) \quad (1)$$

Where  $R$  is cruising distance,  $V$  is the flying speed,  $L/D$  is lift-to-drag ratio,  $I_{sp}$  is the specific impulse of the engine,  $W_i$  and  $W_f$  is the start and end vehicle loads, respectively. Eq.(1) indicates that the cruising distance is directly proportional to the lift-to-drag ratio of the vehicle. For this reason, the pursuit of high  $L/D$  is always a key issue of concern for aircraft designer. However, the aerodynamic performance of the aircraft results in a sharp decline and meets the so-called “ $L/D$  barrier”<sup>[2]</sup> with the increase of the flight speed, especially in hypersonic flight regime.

The high-speed aerodynamic vehicles can be mainly categorized wing-bodies, blended wing bodies and waveriders. The vehicles listed in reference<sup>[3]</sup> and<sup>[4]</sup> are typical wing-body configurations. These configurations consists of two parts, the body and wing. The wing uses large swept delta wing served as the main lift part and the body uses cone/cylinder combination providing sufficient capacity for the vehicle. The hypersonic test vehicle HTV-2 is a typical representative blended wing body [5]. The main features of this configuration are that the airframe and wing are fully integrated,

and there are no apparent boundaries between the two parts. The upper surface arches upward appropriately to meet the volume requirements. The lower surface compresses the free stream to provide lift required for flight. With respect to the two layouts above, waveriders<sup>[6]</sup> is now recognized as the relatively good configuration whose aerodynamic performance is better. At design conditions, the shock produced at front edge attached to the vehicle. The high pressure region behind the shock wave is completely covered in the lower surface of the aircraft. Therefore, the configuration can get a larger lift-to-drag ratio. This configuration has been a focus research since Bowcutt<sup>[7]</sup> and Corda<sup>[8]</sup> got a series viscous optimized waveriders<sup>[9-16]</sup> in the late eighties. Broadly speaking, waverider can be seen as a special case of blended wing body configuration, but the compression surface (lower surface) has a strict design rule.

However, waveriders are still facing many problems in practice today. First of all, the upper surface of the standard waveriders generally parallel with the free stream or use weak expansive surface design. Its thickness is relatively thin and the volume is small. One approach to increase the volume is to increase its absolute size. Such as the conceptual vehicle proposed in the reference<sup>[9]</sup> and<sup>[10]</sup>, their length are both greater than 60 meters. Obviously, the increase of the size leads to the increase of the flow area and wetted area which result in the significant increase of the drag. There is no power plant can match the drag in the stage of research. Next, one of the basic design principles is that the shock should be attached to its edge, so the leading edge must be sharp. But in the actual high-speed flight, the thermal protection must be considered. The sharp leading edge must be blunted. Recent research results show that the bluntness results in the decline of the aerodynamic performance, particularly of the lift-to-drag ratio, both in a continuous flow condition<sup>[11]</sup> and in the rarefied flow conditions<sup>[12]</sup>, even with a blunted radius or thickness. In addition, waveriders are obtained through the flow stream tracing. The compression surface is so complex and non-ruled that it brings lots of difficulties in the manufacture, stability, control and other aspects.

Another method to increase waveriders volume is to modify its lower surface. As can be generated from any flow field<sup>[13]</sup>, waveriders with different compression surface can be obtained by changing the reference flow field. However, the reference<sup>[14-17]</sup> shows that it can only alleviate the contradiction between lift-to-drag ratio and volume in a small range by changing the reference flow field. In addition, based on waveriders, it is also a kind of scheme to increase the volume by changing the upper surface<sup>[18]</sup> which is free stream surface or weak expansion surface to compression surface. Although this treatment can effectively increase the volume, the compression surface will produce larger drag and negative lift to make the aircraft aerodynamic performance fell sharply. Adjusting the angle of attack for cruise flight can improve aerodynamic performance, but it also make waveriders deviate from its design point which will weak the ability of riding the shock wave.

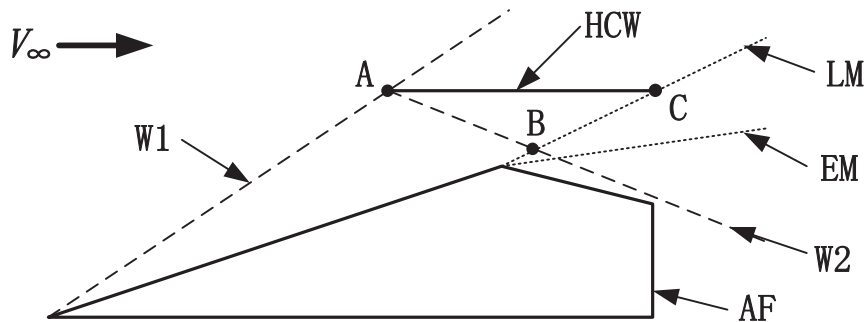
The basic function of high-speed vehicle is to realize the remote rapid transport. So the weight and volume is the two basic constraint parameters. To enhance the aerodynamic performance by adjusting the layout and optimization must be under the condition of satisfying these two indicators. Based on the discussion above, we can see that there is a strong constraint relationship between the volume, lift, drag and lift-to-drag ratio of a vehicle. Currently, the various layout schemes are designed through separating the aerodynamic performance, volume and other properties. Actually, it is a compromise and balance between the indicators or parameters. Namely, it sacrifices one or several properties in exchange for other performance improvement, and obtains a relatively optimal configuration of the overall performance.

One of the main characteristics of high speed is the emergence of shock which leads the drag of aircraft increasing dramatically. Meanwhile, the pressure after the shock rises accordingly, and the pressure is proportional to the flight Mach number. If it can effectively take advantage of this high-pressure zone, the aerodynamic performance of the vehicle would improve, maybe improve greatly. This idea has been put forward in the middle of the last century. But the research focused on the introduction of an additional shock-induced component. As a typical example, Mysliwetz<sup>[18]</sup>

proposed the idea that by the introduction of revolutionary body parts hanging below the wing can induce the shock which produces high pressure acting on the wing to increase the lift. The results suggest that this device can indeed improve the lift of the wing. However, the body itself produces negative lift and drag which make the overall effect weak. Reference<sup>[19]</sup> optimized one kind of hypersonic missiles curved wing. The optimization results show that when the leading edge of the wing forward-swept is appropriate, the part can produce high pressure generated by warhead compression to increase its lift. The lift-to-drag ratio improved about 9%. This provides us a new idea. In process of the aerodynamic layout design, we can introduce some corresponding devices to capture the high pressure zone compressed by the upper surface to increase the lift of the aircraft, so that we can improve its aerodynamic performance under the demand of large volume. Based on this idea, this paper proposes a new aerodynamic concept called high pressure zone capture wing (HCW for short) aerodynamic layout.

### The Principle of the HCW

As described above, in order to meet the volume requirements, the upper surface of the current high-speed vehicles usually adopts arched ways for layout design. In actual flight conditions, the free stream will be compressed by the arched upper surface. It is bound to produce a high pressure zone. The main starting point of the HCW layout design is based on this condition, through reasonable wing to make a substantial increase in lift of the aircraft. Therefore, it is especially suitable for large volume demand for the high-speed vehicles. HCW layout design can be based on shock-expansion theory. To simplify the analysis, here is an example of two-dimensional case. It can be extended to complex three-dimensional shape in practical applications. We will describe them and verify its specific effects in the following paragraphs. In addition, because the main impact of the layout is on the upper surface of the body, we mainly analyze this region. It can be combined with different lower compression surface. This paper validated vehicles combined with waveriders, and the specific results is given in the following paragraphs.



**Figure 1. Diagram of the high pressure zone capture wing (HCW)**

The basic principle of HCW layout is shown in figure 1. In the figure, AF as the body, use compression-expansion design to provide large volume, and volume increases along with the increase of leading compression angle. The principle of HCW producing high lift is given as follows: The high speed stream will be compressed when it flows through the leading edge of the wedge body, resulting in a shock wave W1. The shock wave angle and strength of compression are related to the stream Mach number and the leading edge wedge angle. When the stream flows through the shock wave, the pressure increases, the Mach number decreases, and the flow direction turns upwards. After continuing to flow upwards to HCW, it forms a second shock wave W2. Then the pressure increases further. On the other hand, the flow expands through the inflection point, resulting in the former Mach line and the latter Mach line. The gas pressure drops after expansion area, flowing to the downstream of the vehicle. Through the analysis of the flow process above, we can know that after the introduction of HCW, the triangle area surrounded by ABC points will form

a considerable high pressure zone. At the same time, the pressure of the upper surface of the HCW is almost equal to the flow pressure. So that the pressure of the upper and lower surfaces of HCW will have a large difference which will generate a large lift on the vehicle. In addition, due to the placement of HCW is paralleling to the flow and the structure is very thin, the additional drag generated by HCW is relatively small, so the whole lift-to-drag of the vehicle can be greatly improved.

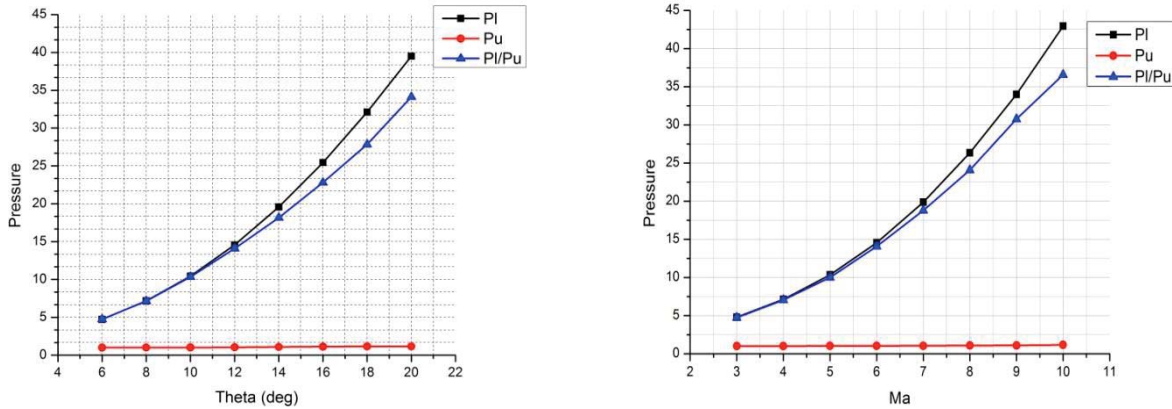
Based on the qualitative analysis above, the pressure ratio of the HCW upper and lower surface can be obtained as follows through the application of oblique shock-expansion wave theory and simple derivation.

$$\frac{P_l}{P_u} = \frac{\left[ 1 + \frac{2\gamma}{\gamma+1} (M_1^2 \sin^2 \beta_2 - 1) \right] \left( 1 + \frac{\gamma-1}{2} M_3^2 \right)^{\frac{\gamma}{\gamma-1}}}{\left( 1 + \frac{\gamma-1}{2} M_1^2 \right)^{\frac{\gamma}{\gamma-1}}} \quad (2)$$

Where,  $P_l$  is the pressure of HCW lower surface,  $P_u$  is the pressure of HCW upper surface,  $\gamma$  is the specific heat ratio,  $M_1$  is the Mach number after the leading edge shock wave,  $\beta_2$  is the shock angle of the secondary shock wave generated by the stream flowing through HCW which can be derived directly by oblique shock wave equation<sup>[20]</sup>,  $M_3$  is the Mach number after the body expansion wave and it can be calculated by the following relationship.

$$\begin{cases} \nu(M) = \sqrt{\frac{\gamma+1}{\gamma-1}} \operatorname{tg}^{-1} \sqrt{\frac{\gamma-1}{\gamma+1} (M^2 - 1)} - \operatorname{tg}^{-1} \sqrt{(M^2 - 1)} \\ \nu(M_3) = \theta + \nu(M_1) \end{cases} \quad (3)$$

Where,  $\theta$  is the expansion angle.



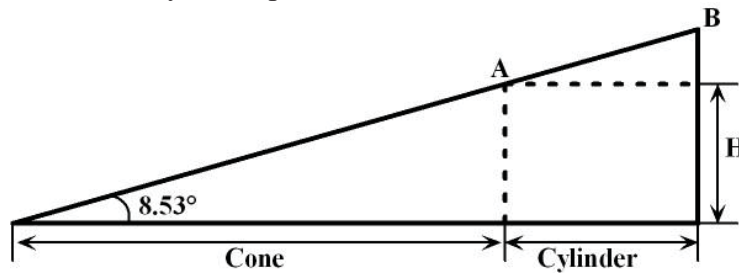
**Figure 2. Pressure difference between the lower and the upper surface of the HCW with different compression angles (left) and Mach numbers (right)**

According to the above formula, we calculated the pressure ratio of the HCW upper and lower surface in different frontal compression Angle (fixed to flow Mach number of 6) and different flow Mach number (fixed front compression Angle of 12 degrees), here the pressure of the upper and lower surface was normalized by the flow pressure. The results shown in figure 2 indicate that after the introduction of HCW, the pressure of its upper and lower surface will generate a big difference. The pressure difference is proportional to the leading edge compression angle and free stream Mach number. The ratio is up to tens of times. This pressure difference is bound to make the vehicle lift increase significantly.

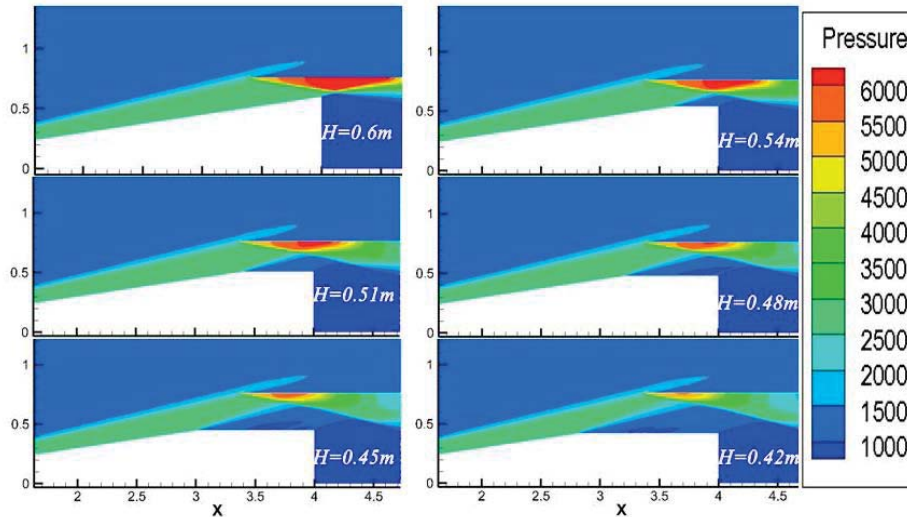
The derivation above is just based on two-dimensional case. To validate the actual effectiveness of HCW in three-dimensional cases, we calculated several two-dimensional axisymmetric model whose body is combination of cone and cylindrical. As shown in figure 3, the body total length is

given 4m and half-cone angle is  $8.53^\circ$ . Here is 6 different shapes as the tail height (cylinder radius) changes. The calculation conditions are as follows: stream Mach number 6, the flight attitude 30km, 0 degrees angle of attack, Euler model. The pressure contours of symmetry plane are shown in figure 4.

As can be seen from figure 4, the different combination of cone and cylinder can all make the lower and upper surface of HCW generating a big pressure difference. Besides, the pressure distribution has a huge difference for these 6 configurations. In the analysis of mutual relations between body and HCW, the volume and aerodynamic performance should be considered.



**Figure 3. The symmetry plane of cone and cylinder combination**



**Figure 4. Pressure contours of symmetry plane in different tail height of cone and cylinder combination**

### Conceptual Design Examples

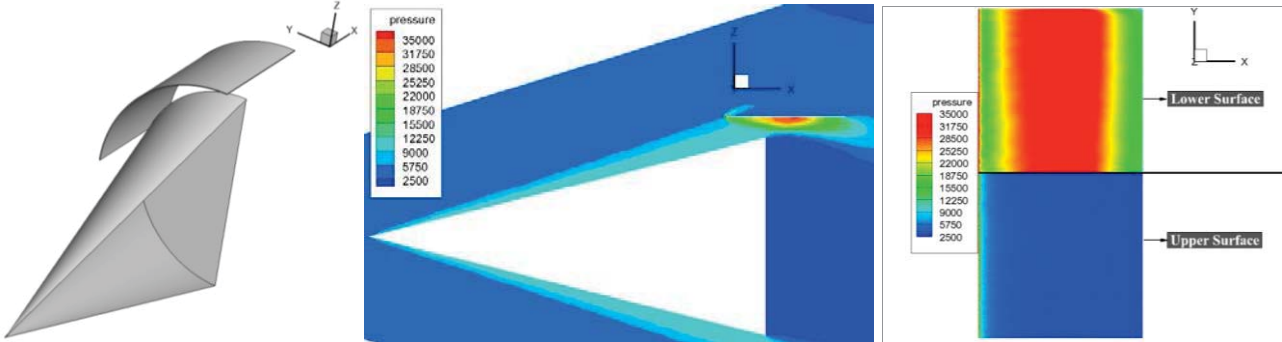
According to the planar two-dimensional and two-dimensional axisymmetric cases above, we popularize this idea to general three-dimensional cases. In order to obtain the leading edge shock wave easily, we firstly studied the relatively simple geometry of the cone and semi-cone configuration combined with HCW in their upper surfaces, and through the comparison with the conventional layout without HCW to verify the performance of the layout. Here, the design and calculation uses the following simplifications: (a) Not considering support connection means between the wing and the body, (b) using the Euler equations or laminar Navier-Stokes equations for performance evaluation, not considering the effect of turbulence, (c) HCW using relatively simple rectangular in shape. These simplified measures can make the layout design relatively simple, less computational consumption, and can seize the main advantages of HCW, namely the lift compensation effect.

#### Case 1: Cone



The body is a cone with the semi-cone angle of  $14^\circ$ , given the length of 1m. HCW is designed as half a torus whose overlooking is rectangular in shape, given the thickness of 2 mm, the length of 0.3m. The configuration is shown in figure 5.

The stream Mach number is 6, flight altitude 25 km, and the calculation model is Euler model. Since the body is axisymmetric, its lift and lift-to-drag ratio is zero with no combination HCW under zero degree angle of attack. After adding HCW, its lift force is 4233.5N, and lift-to-drag ratio increases to 1.81. As can be seen from figure 6 and figure 7, through reasonable design, the pressure distribution of HCW upper and lower surface under the condition of three-dimensional is basically the same as the results of two-dimensional theoretical derivation, and there is no high pressure leakage on both sides of HCW.



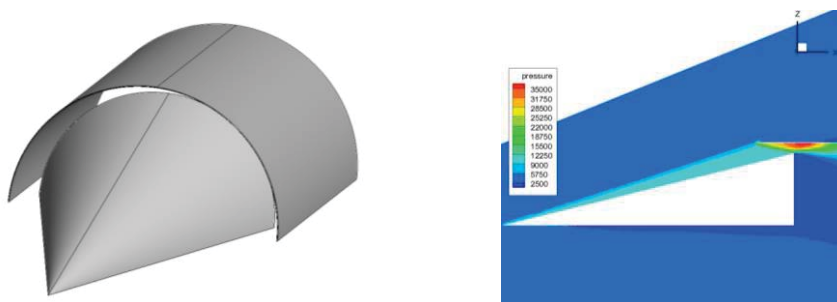
**Figure 5(Left). Combination of cone and HCW configuration (half)**

**Figure 6(Middle). Pressure contours in symmetry plane under combination of cone and HCW**

**Figure 7(Right). Pressure contours comparison between the upper and lower surface of HCW**  
**Case 2: Half cone**

The body is a half cone with half cone angle of  $14^\circ$ , given the length of 1m. This configuration can be regarded as a simplification of HTV-2. As shown in figure in figure 8, the overlooking of HCW is rectangular in shape with a thickness of 2 mm.

The calculation conditions remain Mach number 6, flight altitude 25 km, Euler model. The body is half an axisymmetric body, whose upper surface compresses the stream, and lower surface parallel to the flow. Therefore its lift under zero angle of attack is negative, which is numerically  $-2.82.4\text{N}$ , and the drag is  $1005.6\text{N}$ . The lift-to-drag ratio is  $-2.07$ . After adding HCW, the lift is  $2773.4\text{N}$ , and the drag is  $1081.2\text{N}$ . The lift-to-drag ratio increases to  $2.57$ . The pressure distribution of symmetry plane is shown in figure 9. It is clear that there is a large pressure difference between the upper and the lower surface of HCW.



**Figure 8(Left). Combination of semi-cone and HCW configuration**

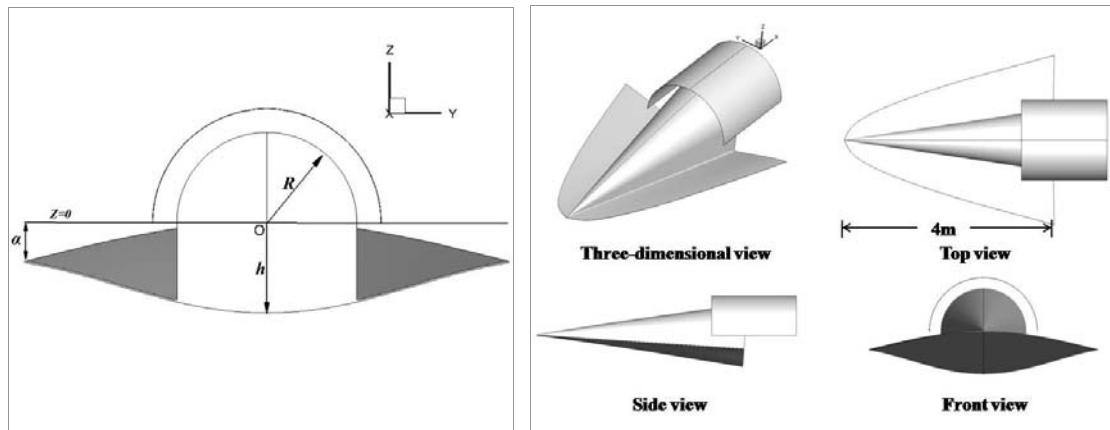
**Figure 9(Right). Pressure contour in symmetry plane of Case 2**

### HCW-Waverider Wing(WW) Combination Configurations

From the simple three-dimensional configuration examples above, the main area of HCW aerodynamic layout is the upper surface. For high-speed aircraft, especially hypersonic vehicles,

waveriders as the lower compression surface have good aerodynamic performance. Therefore, if the upper surface is a half cone, and the lower surface is a waverider. It can not only make the aircraft to have large volume, also can make it get better aerodynamic performance through combining with HCW. For this design idea, we analyzed the influence of HCW on several configurations with different volume.

The upper surface of the body is half cone, and the lower surface of the body is waverider. They are assembled with a certain angle of attack, given the length of 4m. The rear view is shown in figure 10. The half cone is determined by tail radius  $R$ , the assembly angle of attack is determined by the height  $H$  below the horizontal plane. In order to avoid the high pressure generated by half cone compression falling down on the waverider which can produce negative lift, the height  $H$  and tail radius are the same value. Here,  $R$  takes three different values: 0.4m, 0.6m, and 0.7m. When waverider is designed for zero angle of attack state, its front end falls on the plane  $Z=0$ . Therefore, the corresponding assembly angle of attack  $\alpha$  is  $1^\circ$ ,  $4^\circ$ , and  $5.2^\circ$  respectively. The thickness of waverider is 10mm, and the front uses 5mm radius arc bluntness. The overlooking of HCW remains rectangular, given the thickness of 2mm. The three-dimensional shape and three views of the configuration whose half cone tail radius is 0.6m is shown in figure 10. The calculation conditions is given as follows: stream Mach number 6, flight altitude 30km, zero degree angle of attack, the laminar flow model.



**Figure 10(Left). Rear view of HCW-WW configuration**

**Figure 11(Right). View instances of HCW-WW configuration**

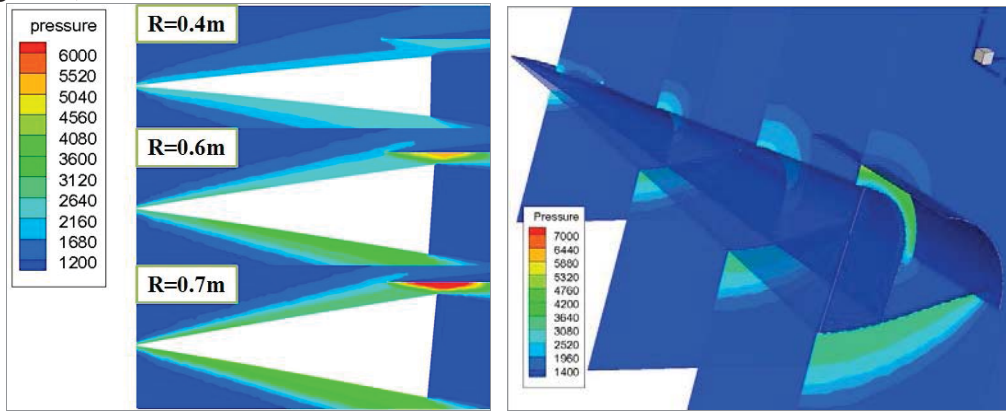
The pressure contours of the three configurations symmetry plane are shown in figure 12. It can be seen that with the increase of the tail radius, the half cone angle of the upper surface and the lower surface of the assembly angle of attack increases. With the compression strengthening, the pressure of the half cone and the waverider increase. The pressure of the lower surface of HCW correspondingly increases, leading to the lift generated by HCW increasing. From the pressure distribution of the configuration section shown in figure 13, we can find that the shock is substantially attached to the leading edge. Taking into consideration the impact of thermal protection, the leading edge is blunted. Some little flow spillage takes place around the leading edge. There exists a considerable pressure difference in the upper and lower surface of the waverider which can produce large lift for the aircraft.

It not hard to find that in this layout design, both the HCW and waverider are wings which forms two-lifting body. In addition, the design idea of HCW and waverider has a strong similarity. They can both effectively utilize the body's own shock. They respectively exploit the compression of the upper and lower surface. Therefore, the configuration of waverider combined with HCW can not only acquire considerable volume performance, also can achieve good aerodynamic performance.

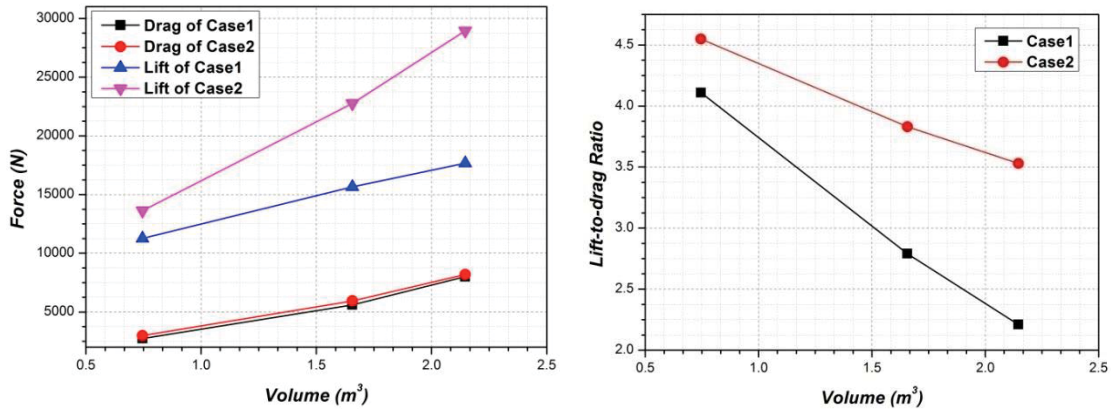
The half cone radius change will result in the change of volume and aerodynamic performance. As shown in figure 14 and 15, the relationship between the volume and lift, drag, and lift-to-drag ratio

was obtained. Here, Case1 and Case2 are respectively the configurations before and after adding HCW. What we can figure out from the figures is followed:

- a) In the same volume, due to the introduction of HCW, the drag increases slightly, while the lift obtains a sharp rise. Therefore, the lift-to-drag ratio improved significantly under the same volume.
- b) For configurations with different volume, with the increase of the volume, the lift generated by waverider and HCW increase dramatically, leading to the overall lift increasing. Besides, because of the increase of flow projection area, the drag also increases with the increase of volume.
- c) The lift-to-drag ratio and volume are inversely related. The lift-to-drag ratio of Case1 decrease sharply with the increase in volume. While the combination of HCW can effectively slow down this trend, it decreases slowly with the increase of volume. Therefore, HCW can not only enhance the lift-to-drag ratio, also can reduce the contradiction between the volume and the lift-to-drag ratio.



**Figure 12(Left). Pressure contours in symmetry plane of different HCW-WW configurations**  
**Figure 13(Right). Pressure contours of the HCW-WW configuration with R=0.6m**

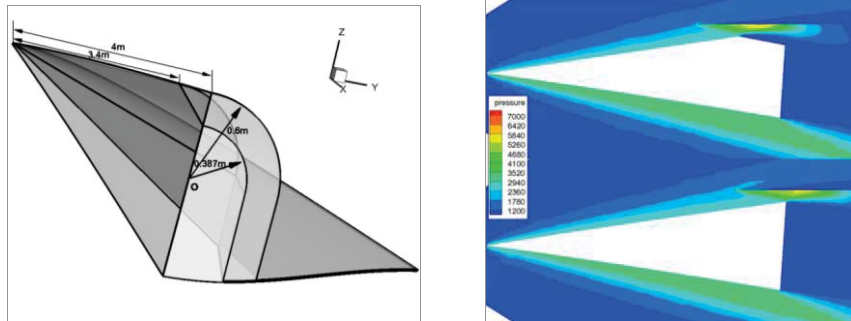


**Figure 14(Left). Lift and drag under different configuration volume**

**Figure 15(Right). L/D under different configuration volume**

The effectiveness of HCW is confirmed from several conceptual configurations above. The aircraft aerodynamic performance can be effectively improved after the introduction of HCW. However, to capture the shock conveniently, the upper surface of the body is given half-cone which can produce large drag due to its huge flow projection area. According to the analysis of axisymmetric shapes, we can find out that if the upper surface of the body takes the connection of half cone and semi-cylindrical or half cone and half truncated cone, the drag and negative lift of the body can be effectively reduced. The position of HCW will be adjusted based on the upper surface. But it can still capture the high pressure effectively. Based on the waverider combined with HCW whose half cone tail radius R is 0.6m, the upper surface take the connection of half cone and half truncated cone substitute for half cone. Then analyze the effect on HCW layout of the body shape through the calculation results.

The body shape before and after modification is shown in figure 16. After modification, at the level of half cone 3.4m combined with half truncated cone, and the total length is still 4m. The tail radius of the half truncated cone is given 0.387m. Then connects to the waverider vertically, other geometric parameters unchanged. The calculation conditions are given as follows: stream Mach number 6, flight altitude 30km, zero degrees angle of attack, laminar flow calculation model.



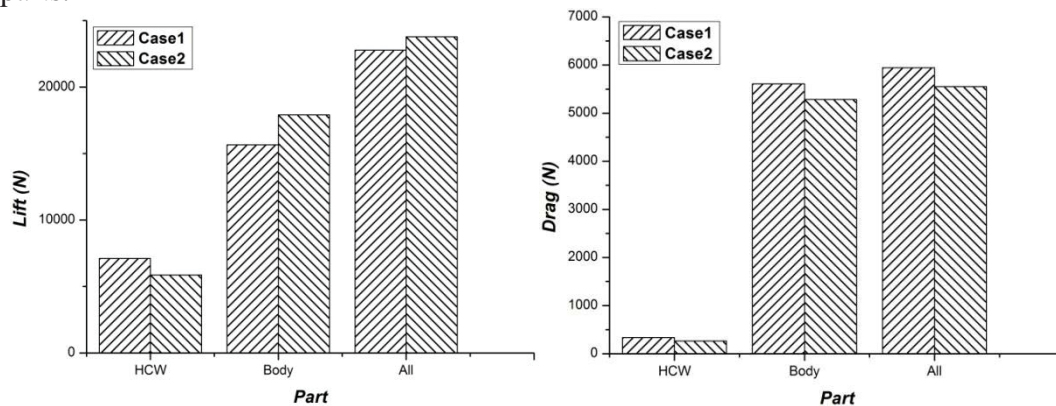
**Figure 16(Left). Body shape comparison before and after modification**

**Figure 17(Right). Pressure contours comparison between before and after modification**

The pressure contours in the symmetry plane is shown in figure 17. It is evident that the high pressure on the half truncated cone dismissed due to the expansion. Meanwhile, the position of the HCW leading edge shifts forward. The area of high pressure in the lower surface of HCW has a weak decrease.

By comparing the lift and drag of all parts of the aircraft before and after modification, as shown in figure 18, it is clear that the lift of HCW is reduced due to the area of high pressure in the lower surface of HCW is decreased after modification. The lift of the body increases sharply with the decrease of negative lift in the upper surface of the body. The overall lift of the aircraft increases by 4.4% from the original configuration (Case1). The drag of HCW is still small relative to the whole drag, and it almost remains unchanged after modification. The drag of the body is significantly reduced due to the decrease of the flow projection area of the body. The whole drag of the aircraft is decreased by 7.1% from the original configuration. On the whole, through the modification of the body, the lift increases and the drag decreases, leading to the lift-to-drag ratio improved obviously. As shown in table 2, the lift-to-drag ratio increases from 3.83 to 4.28, increased by 11.75%. The aerodynamic performance is significantly improved.

As can be seen from the example, the aerodynamic performance of the vehicle can be improved by the shape modification. However, on the other hand, the lift generated by HCW has decreased. There is a strong coupling relationship between the body and HCW. The simple modification of the body may bring the performance of HCW change as a result. Therefore, as one of the next step of work, the optimization design of the body is needed considering the coupling relationship between the two parts.



**Figure 18. Lift and drag of each part before and after modification**

**Table 2 Aerodynamic parameters of the vehicle before and after modification**

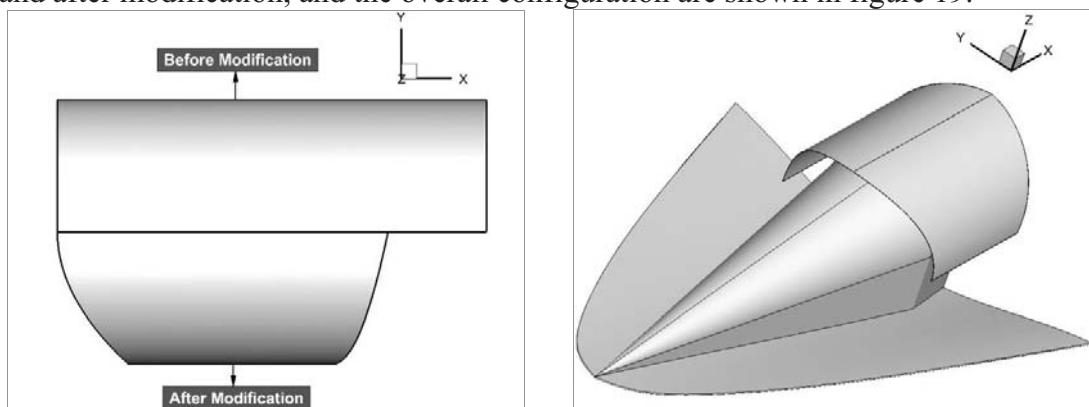
	<i>Lift(N)</i>	<i>Drag(N)</i>	<i>L/D</i>
Case1	22770.0	5944.0	3.83
Case2	23780.3	5552.1	4.28
Percentage Increase	+4.4%	-7.1%	+11.75%

As can be seen from the aircraft configurations above, HCW must be given thin wing structure, torus with parallel to flow, so that we can maximum reduce the drag generated by HCW. Based on the design principle, the shape of HCW can be only determined by the cross section. The cross section shape of HCW should be designed by cross section shape of the shock generated by the upper surface of the body. In the aircraft configurations above, the cross section shape of HCW is all given the semicircular shape. It is because the cross section shape of the shock generated by body is circular.

In the aircraft design above, the overlooking shape of HCW is given rectangular, and the length is given relatively long. In addition, the three dimensional effect of wing is not considered. This is simplified for analysis. The shape of HCW is given cylindrical thin airfoil with parallel to flow. The main drag of HCW is from friction. As the computational analysis mainly uses Euler equations or laminar flow model, the friction drag is relatively small, so the length of HCW we selected has little impact on the performance. Actually, although the length of HCW is long, the high pressure mainly concentrates on its front. The pressure of the latter part decreases gradually because of the expansion wave emerged in the turning point. The contribution to the overall lift of this part is very small. The long HCW may only lead to the friction increasing.

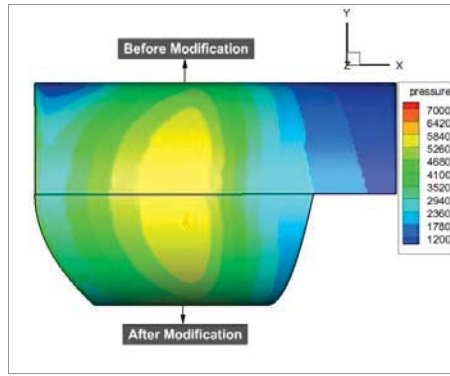
Obviously, the shape and length of HCW exists an optimal state. To validate this conclusion, we made a simple modification of HCW based on the configuration obtained in the last section. Then analyze how the shape and length of HCW influence on aerodynamic performance.

Based on the configuration obtained in the last section, we made a simple modification in HCW, considering the three-dimensional effect and expansion wave emerged in the turning point. We intercepted HCW by quadratic curves in the horizontal plane of vertical projection of the front and rear HCW. The length of HCW in the symmetric plane decreased from 2.2m to 1.7m. The shape before and after modification, and the overall configuration are shown in figure 19.



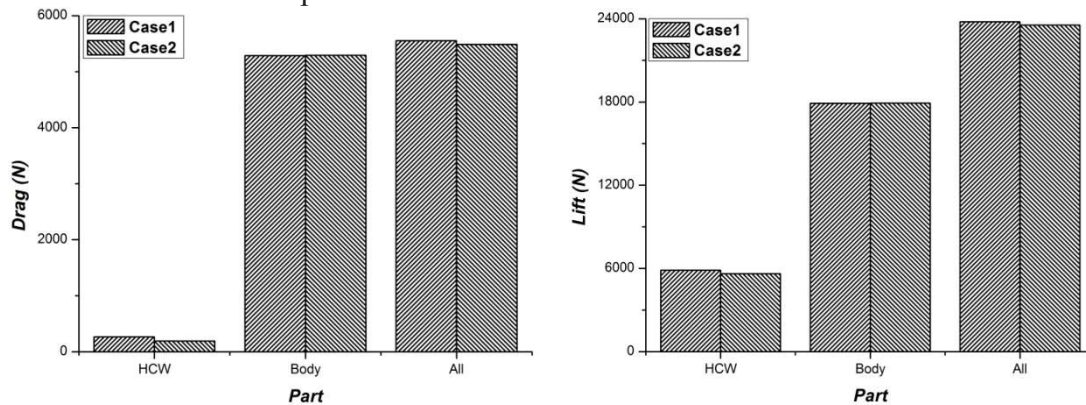
**Figure 19. HCW shapes comparison before and after modification (left) and the whole shape after modification (right)**

Figure 20 shows the pressure contours of the lower surface of HCW before and after modification. We can find out that the lower pressure dismissed after modification. The wet area which is related to friction drag is significantly reduced.



**Figure 20. Pressure contours of the HCW lower surface before and after modification**

The drag of each part before and after modification is shown in figure 21. Case1 and Case2 are respectively the configuration whose HCW is modified and not modified. It is clear that the modification of HCW has no influence on body. Its drag and lift remains unchanged. As shown in table 3, the pressure drag of HCW is basically the same in two configurations. The friction drag decreased significantly because the wet area is sharply reduced, leading to the whole drag of HCW decreasing. The overall drag obtained a certain degree of reduction. The pressure of the part of HCW which is cut off is relatively small, but still larger than the pressure of upper surface. The lift generated by HCW decreased. So the overall lift is also decreased. On the whole, after modification, both the lift and drag is decreased. The lift-to-drag ratio slightly increased from 4.28 to 4.29. It should be noted that the comparison is based on the laminar flow calculation model where the effect of vicious is small. If considering the impact of turbulence, the friction drag will share a large proportion. The effect of HCW modification will be more apparent. From the analysis above, we can learn that the shape of HCW can be optimized under the fixed body. The optimization design of HCW is needed in the next step.



**Figure 21. Drag and lift comparison of HCW, body and the whole vehicle before and after HCW modification**

**Table 3 Pressure drag and friction drag of two cases**

	Case1		Case2	
	$D_p(N)$	$D_f(N)$	$D_p(N)$	$D_f(N)$
HCW	50.14	216.15	50.26	142.04

**Table 4 Lift, drag and lift-to-drag of two cases**

	Case1	Case2
Lift (N)	23780.29	23551.05
Drag (N)	5552.05	5482.38
Lift-to-drag Ratio	4.28	4.29

## Further Analysis

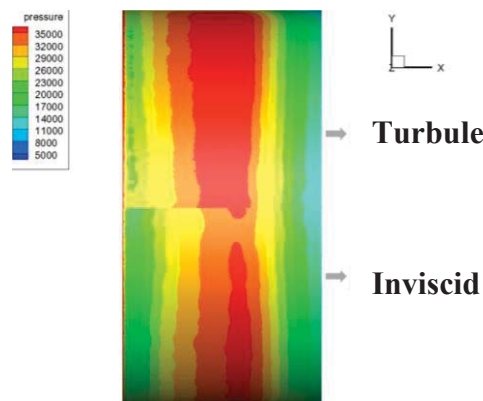
Through the analysis of above several different bodies with HCW, we verified the validity of the HCW aerodynamic layout. In addition, we made some analysis for the shape of body and HCW. The results show that the lift and lift-to-drag ratio can be greatly improved, while the increase of drag is small. It is clear that the aerodynamic performance of aircraft can be greatly improved by introduction of HCW. But the configurations above are mainly to verify the effectiveness of improvement of aerodynamic performance. The shape of HCW and body are greatly simplified. In the actual aircraft design, many other issues will be involved. The following will be some qualitative analysis and discussion about two key problems of them.

In the analysis above, the calculation model is Euler or laminar model. But in the actual calculation, transition and turbulence will lead an increase in friction drag. Based on the analysis above, turbulence will not lead to a dramatic decline of the HCW effect. To verify the conclusion, we calculated the performance of a cone body using the  $k-\varepsilon$  turbulence model. Figure 22 shows the comparison of pressure contours in the lower surface of HCW. Table 5 shows the aerodynamic performance parameters of each part and all in two calculation conditions.

As shown in table 5, under the turbulent conditions, the drag of HCW increased by 213N, the drag of cone body increased by 365N, the drag of base is reduced by almost 30N. However, we can find the pressure of HCW lower surface was higher in turbulent condition, and the lift of this part increased by 360N. On the whole, despite the promotional effect of HCW on lift-to-drag ratio decreased by about 12%, it is still very meaningful. Furthermore, the body is cone with a large cone angle. The volume ratio is big while wet area is small. The wet area of HCW shares a large proportion. For other body shape, the wet area of HCW can be reduced by reasonable optimization. The proportion of HCW friction drag to the total can be reduced.

**Table 5 Comparison of aerodynamic performance between inviscid and turbulent model**

	Inviscid			Turbulent		
	$D(N)$	$L(N)$	$L/D$	$D(N)$	$L(N)$	$L/D$
HCW	280.6	4233.5	15.08	493.6	4593.3	9.30
Body	1584.6	0	0	1949.7	0	0
Base	471.8	0	0	442.6	0	0
All	2337.0	4233.5	1.81	2886.0	4593.0	1.59



**Figure 22. Pressure contours of HCW lower surface in inviscid and turbulent model**

## Conclusion and Discussion

According to the characteristics of high-speed vehicles and demand of high lift-to-drag and large volume, we proposed a new type with high pressure capture wing, and validated the high aerodynamic performance of this layout through some conceptual configurations. From the present

calculation results, it is no hard for us to find that, after the introduction of HCW, both the lift and the lift-to-drag ratio of vehicles can get bigger. Therefore, it is a good aerodynamic layout for high-speed vehicles.

In terms of designing idea, the HCW layout and waverider layout have some similarities. Their purposes are both to fully utilize the high pressure generated by the compression of body, improving the lift and lift-to-drag-ration. Compared to the waverider layout, the HCW layout can ease the contradiction between lift, lift-to-drag ratio with volume of the vehicle. More specifically, the increase of compression angle in upper surface can improve the volume of the vehicle. At the same time, the lift generated by HCW can be bigger. To some extent, HCW can be seen as a lift compensation device. Moreover, it can also be combined with some current good aerodynamic layout to improve the aerodynamic performance dramatically.

This paper is focused on the proposal of new HCW concept, mainly concentrating in the theoretical and conceptual analysis. In the actual design, there will be many other problems in a new aerodynamic layout. For example, the thickness of HCW will be larger along with the increase of stream Mach number considering the limitations of thermal protection and structural strength. The result is that, the effect of HCW will decrease along with the increase of stream Mach number. The main applicable range and conditions of HCW layout will be the next focus research. Besides, many other problems also should be considered, such as the off-design performance analysis, HCW shape optimization, especially when considering the friction, support device between the HCW and body and its effect on the layout, HCW structural design and analysis, and the control and stability after the introduction of HCW. All these problems will be undertaken in our research.

## Acknowledgement

This research was supported by the National Nature Science Foundation of China (Grant No. 90916013).

## References

- 1 Raymer D P. Aircraft design: a conceptual approach [M]. American Institute of Aeronautics and Astronautics, 1999.
- 2 Kuchemann D. The Aerodynamic Design of Aircraft. Oxford: Pergamon Press, 1978
- 3 Matthias T, Rolf J, Marc S, et al. PHOEBUS: A High Lift-over-Drag Vehicle for Earth Reentry. AIAA-2009-7411,2009
- 4 Rodrigo H R, Davide B, Gabriele De Z. High Lift-to-Drag Re-entry Concepts For Space Transportation Missions. AIAA-2009-7412, 2009
- 5 Walker S, Sherk J, Shell D, et al. The DARPA/AF Falcon Program: The Hypersonic Technology Vehicle #2 (HTV-2) Flight Demonstration Phase. AIAA-2008-2539, 2008
- 6 Nonweiler T R F. Delta Wings of Shapes Amenable to Exact Shock-Wave Theory. J of the Royal Aeronautical Society, 1963, 67: 39-40
- 7 Bowcutt K G, Anderson J D, Capriotti D. Viscous Optimized Hypersonic Waveriders. AIAA-87-0272, 1987
- 8 Corda S, Anderson J D. Viscous Optimized Hypersonic Waveriders Designed from Axisymmetric Flow Fields. AIAA-88-0396, 1988
- 9 Takashima M, Lewis M J. Engine-airframe Integration on Osculating Cone Waverider-based Vehicle Designs. AIAA-1996-2551, 1996
- 10 Lobbia M, Suzuki K. Numerical Investigation of Waverider-derived Hypersonic Transport Configurations. AIAA 2003-3804, 2003
- 11 Chen X Q, Hou Z X, Liu J X, et al. Bluntness Impact on Performance of Waverider. Computers & Fluids, 2011, 48: 30-43
- 12 Santos W F N. Leading Edge Thickness Impact on Drag and Lift in Hypersonic Wedge Flow. AIAA 2007-615, 2007
- 13 Cui K, Yang G W. Waverider Configurations Derived from General Conical Flowfields. Acta Mechanica Sinica, 2007, 23(3): 247-255
- 14 Cui K, Yang G W. The Effect of Conical Flowfields on the Performance of Waveriders at Mach 6. Chinese science bulletin, 2007, 52(1): 51-64
- 15 Bauer S X S. Analysis of Two Viscous Optimized Waveriders. In: Proceeding of First International Hypersonic Waverider Symposium, 1990
- 16 Cockrell C E. Interpretation of Waverider Performance Data Using Computational Fluid Dynamics. J of Aircraft, 1994, 31(5): 1095-1100
- 17 Manor D, Johnson D B. Landing the Wave-rider: Challenges and Solutions. AIAA-2005-3201, 2005
- 18 Mysliwetz F. Supersonic Interference Lift. AIAA Journal, 1963, 1(6): 1432-1434
- 19 Cui K, Yang G W. Shape Optimization for Hypersonic Arc-Wing Missiles[J]. Journal of Spacecraft and Rockets, 2010, 47(4): 694-700.
- 20 Anderson J D. Modern compressible flow: with historical perspective[M]. New York: McGraw-Hill, 1990.



## A Method of Weighted Mean for Structural Random Loading Identification

Liao Jun<sup>1</sup>, \*Jiang Bingyan<sup>1</sup>, Xu Dafu<sup>2</sup>, Liao He<sup>2</sup>

<sup>1</sup> College of Mechanical and Electrical Engineering, Central South University, Changsha, China

<sup>2</sup> Institute of Aerospace System Engineering, Shanghai Academy of Spaceflight Technology, Shanghai, China

\*Corresponding author: jby@csu.edu.cn

### Abstract

Multi-input-multi-output stationary random loading identification has been long a difficult problem for its poor identification precision caused by ill-condition problem of transfer function matrix inversion. In this paper, the inverse pseudo-excitation method is used for identification problems. A new condition number weighted average method is developed to improve the accuracy of loading identification. A threshold value is introduced to reduce the computation cost. Simulations and experiments are designed to certify the feasibility of the algorithm and achieve good results. The condition number of FRF is introduced to choose the response measuring point in the experiment to reduce the workload and improves the identification precision.

**Keywords:** condition number, loading identification, inverse pseudo-excitation method, identification experiment, random vibration, method of weighted mean.

### 1. Introduction

Random vibrations exist in process of ground transportation, high-speed flight phase of the aircraft, boost phase of rocket, and so on. It receives increasing attention. For multiple stationary random excitations, the direct problem is the computation of the power spectral densities (PSDs) of the various responses from the given excitation PSD. It has been solved (Robson, 1964; Piersol, 1993) efficiently by many classic method, and pseudo excitation method (PEM) proposed by Lin et al (Lin, J. H. 1992; Lin, J. H. 1994) is a efficient one. There are two types of inverse problems (also called back analysis problems) corresponding to this direct problem. The first is the so called structure identification problem, for which the loadings and response PSD functions are all known and are used to identify the properties of the structure. System identification and modal testing have received much attention and many publications deal with such problems and their successful applications in engineering (Juang, 1994; Ewins, 1986). The second is the so-called loading identification problem, for which the response information and structural properties are known and are used to identify information about the loading.

However, loading identification has received considerably less attention in the technical literature; even some similar works have been done at a high expense, but have rarely yielded satisfactory identification results because of their poor precision, especially for random excitations. In fact, this is a very important field, and many loads in engineering applications need to be identified. For instance, the traffic loads of bridges, the seismic excitations of buildings, the interaction forces between moving machines and their bases, and so on. It is very difficult, or sometimes impossible, to measure such excitations directly, whereas the measurement of some of the responses are relatively easy.

In this paper, the locations of the exciting points are known, and if there is only one excitation acting on the structure, the problem is quite straightforward and is not discussed. For multi-input-multi-output (MIMO) problems, however, its solution is not easy and it is difficult to find papers in this area which demonstrate its difficulty. To the authors' knowledge, some such work has been done at high expense, but has yielded identification results that are unacceptable because of their

very poor precision. The inverse pseudo-excitation method (IPEM)( Lin, J. H.,2001) ,which is a counterpart or an inversion form of PEM, is an efficient approach for the loading identification of a structure subjected to stationary random excitations. IPEM is used in this paper and condition number weighted average method is presented to improve the rank defect of the frequency response function for random loading identification. Simulation process is given to compare the presented method with the common frequency domain approach, the direct inversion method. Experiments are designed to certify the feasibility of the method, and achieved good results. In paper (Papadopoulos, 1998) a method is introduced to select sensors based on the modal kinetic energy (MKE) distribution, which gives a measure of the dynamic contribution of each finite element modal (FEM) physical degree of freedom to each of the target mode shapes. This method is also applied in the paper(Li, D. S.,(2003), and the method is used in the simulation before the experiment, and helps to set sensor in the experiment. However, errors exist in the finite element model and original systems. In this paper the condition number of FRF is used to choose the response measuring point, it reduces the computation workload, and gets a relative accurate result.

## 2. Method of loading identification

In this paper, loading identification is based on some assumptions as follows. The system is linear, the load positions are known and not moving, the measured responses of the structure are caused entirely by the random load to be identified, and does not exist other unknown type of excitation form acting on the system.

### 2.1 Direct inversion method (DIM)

The motion equations of structure can be expressed as

$$M\ddot{y} + C\dot{y} + Ky = F \quad (1)$$

In which,  $M$ ,  $C$  and  $K$  are, respectively, the mass, damping and stiffness matrices, dots denote differentiation with respect to time and  $y$  and  $F$  are, respectively, the displacements and applied force vectors. The order of the system is  $n$ .  $m$  stand for the number of measured responses in  $y$ .  $l$  stand for the number of non-zero excitations in  $F$ .  $m$  and  $l$  are both less than or equal to  $n$ .  $l \leq m$  is the necessary condition for the solvability of the inverse problem. According to the linear system random response power spectrum formula(Paez, T. L.,2008):

$$S_{yy} = H^* S_{FF} H^T \quad (2)$$

In which,  $S_{yy}$  is the PSD matrix of measured response,  $S_{FF}$  is the PSD matrix of the excitation, and  $H$  is the frequency response function matrix.  $H$  is in general not a square matrix, and the number of rows is greater than or equal to the number of columns. The superscripts "\*" and "T" represent complex conjugate and transpose, respectively.  $S_{FF}$  is the matrix to be identified, and it can be obtained by a matrix transformation:

$$S_{FF} = H^{+*} S_{yy} H^{+T} \quad (3)$$

In which, the superscript + represents generalized inversion. The generalized inverse matrix  $H^+$  can be obtained by direct inversion method (Horn,1990):

$$H^+ = (H^T H^*)^{-1} H^T \quad (4)$$

### 2.2 Condition number weighted average method (CNWAM)

The response PSD matrix  $S_{yy}$  can be decomposed as follows(Lin, J. H.,2001;Li, D. S.,2001; Li, D. S.,2003)

$$S_{yy} = \sum_{s=1}^r b_s^* \cdot b_s^T, (s=1, 2 \dots r) \quad (1)$$

$$\mathbf{b}_s = \sqrt{\lambda_s} \cdot \boldsymbol{\psi}_s^* , (s=1, 2 \dots r) \quad (2)$$

In which  $\lambda_s$ ,  $\boldsymbol{\psi}_s$  and  $r$  represent eigenvalue, eigenvector and rank number of matrix  $\mathbf{S}_{yy}$ , respectively. The pseudo-response was defined as  $\tilde{y}_s = \mathbf{b}_s e^{it}$ , where  $i$  is the imaginary unit. Then the pseudo-excitation  $\tilde{x}_s$  can be got by the equation as bellow.

$$\tilde{x}_s = \mathbf{H}^+ \tilde{y}_s = \mathbf{H}^+ \mathbf{b}_s e^{it} (s=1, 2 \dots r) \quad (3)$$

Hence Eq. (5) and (6) enable the excitation PSD matrix  $\mathbf{S}_{xx}$  to be given in terms of the  $\tilde{x}_s$  as

$$\mathbf{S}_{xx} = \sum_{s=1}^r \tilde{x}_s^* \cdot \tilde{x}_s^T = \mathbf{H}^{+*} \cdot \left( \sum_{s=1}^r \mathbf{b}_s^* \cdot \mathbf{b}_s^T \right) \cdot \mathbf{H}^{+T} \quad (4)$$

For large DOFs systems, direct using of Eq. (8) is still computationally very expensive. Therefore, mode-superposition method can be used to reduce the workload. The main error is caused by calculation of generalized inversion  $\mathbf{H}^+$ . The condition number weighted average method (CNWAM) is developed here trying to reduce the impact of ill-conditioning problems of  $\mathbf{H}^+$ . Eq. (7) can be written as:

$$\tilde{x}_s = \mathbf{H}^+ \cdot \tilde{y}_s = \begin{bmatrix} \mathbf{R}_1 \\ \mathbf{R}_2 \\ \mathbf{R}_3 \\ \dots \\ \mathbf{R}_m \end{bmatrix}^T \cdot \begin{bmatrix} \tilde{y}_1 \\ \tilde{y}_2 \\ \tilde{y}_3 \\ \dots \\ \tilde{y}_m \end{bmatrix}_s \quad (5)$$

Where  $\mathbf{R}_i$  ( $i=1,2,\dots,m$ ) is the row vector of  $\mathbf{H}^{m \times l}$ . A square matrix  $\mathbf{H}_j^{l \times l}$  ( $j=1, 2, 3 \dots k$ ) can be made up by choosing number  $l$  of row vectors  $\mathbf{R}_i$  form  $\mathbf{H}$ , and this combination number is  $k = C_n^m$ . Accordingly, number  $l$  of  $\tilde{y}_i$  in the same rows of  $\tilde{y}_s$  are selected to assemble  $\tilde{y}_s^j$  ( $j=1, 2 \dots k, s=1, 2 \dots r$ ). Since  $\mathbf{H}_j$  is a  $l \times l$  square matrix, and generally its inverse matrix  $\mathbf{H}_j^{-1}$  exists and easy to obtain, then,  $\tilde{x}_s^j$  can be obtained by:

$$\tilde{x}_s^j = \mathbf{H}_j^{-1} \cdot \tilde{y}_s^j , (j=1, 2 \dots k, s=1, 2 \dots r) \quad (6)$$

$q_j$  was defined as:

$$q_j = \frac{1}{\text{cond}(\mathbf{H}_j)} , (j=1, 2 \dots k) \quad (7)$$

Where, "cond" is the operation of calculating condition number of matrix:

$$\text{cond}(\mathbf{A}) = \|\mathbf{A}\|_p \cdot \|\mathbf{A}^{-1}\|_p \quad (8)$$

In which,  $\|\cdot\|_p$  is the operation of matrix norm, especially, in this paper, 2–norm is used to obtain  $\text{cond}(\mathbf{A})$

The weights can be defined as follows

$$w_j = \begin{cases} q_j, & q_j \geq q \\ 0, & q_j < q \end{cases} (j=1, 2 \dots k) \quad (9)$$

Where,  $q$  is threshold value:

$$q = \frac{1}{k} \sum_{j=1}^k q_j , (j=1, 2 \dots k) \quad (10)$$

The pseudo-excitation  $\tilde{x}_s$  can be obtained as follows:

$$\tilde{x}_s = \frac{\sum_{j=1}^k w_j \cdot \tilde{x}_s^j}{\sum_{j=1}^k w_j} (s=1, 2 \dots r) \quad (11)$$

Then,  $S_{xx}$  can be obtained by Eq. (8). The weighted average method tries to reduce the impact of the sub matrices with big condition numbers. The threshold  $q$  is used for judging which sub matrices should be selected to compute the pseudo excitation, and which should be discarded.

### 3. Computer simulation example

A 9 DOFs system is given as follows in Fig. 1.  $k_i$  ( $i=1,2,\dots,9$ ) are stiffness coefficients of each floor, and their values are shown in Fig. 1. The first 9 order natural frequencies of the structure are shown in Table 1, and the damping ratio is set as 0.02.

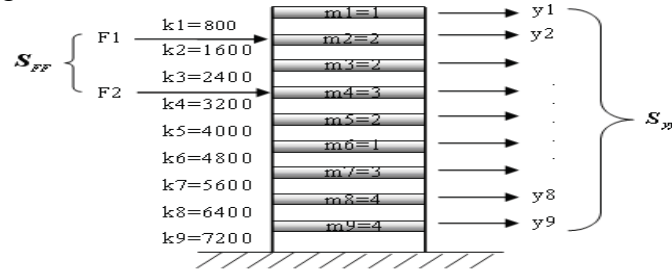


Fig. 1. 9 DOFs shear type model

The stationary random excitations are applied to  $m_2$  and  $m_4$ , where  $\rho$  is the correlation coefficient of the 2 forces  $F_1$  and  $F_2$  as shown in Fig.1, their auto-power spectral density are  $S_1(\omega)$  and  $S_2(\omega)$  as shown in Fig.2 and Fig.4 with solid line, respectively.  $S_{12}$  and  $S_{21}$  are the cross-spectral density of the 2 forces, which are defined by Eq. (17). The excitation PSD matrix then can be given as follows:

$$S(\omega) = \begin{bmatrix} S_1(\omega) & S_{12}(\omega) \\ S_{21}(\omega) & S_2(\omega) \end{bmatrix} \quad (1)$$

$$S_{12} = \sqrt{S_1(\omega)S_2(\omega)}\rho e^{i\omega\Delta t}, \quad S_{21} = \sqrt{S_1(\omega)S_2(\omega)}\rho e^{-i\omega\Delta t} \quad (2)$$

In which,  $\rho = 0.7$ ,  $\Delta t = 0.08$ .

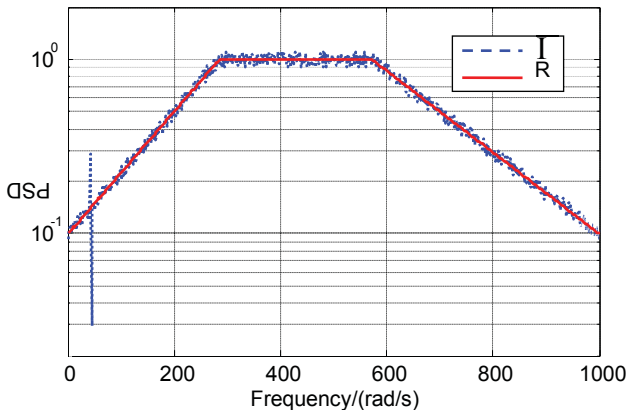
Table 1. First 9 order natural frequencies of the structure (rad/s)

Order	1	2	3	4	5	6	7	8	9
Natural Frequency (rad/s)	19.96	39.85	42.56	45.365	58.70	59.96	93.96	116.71	119.89

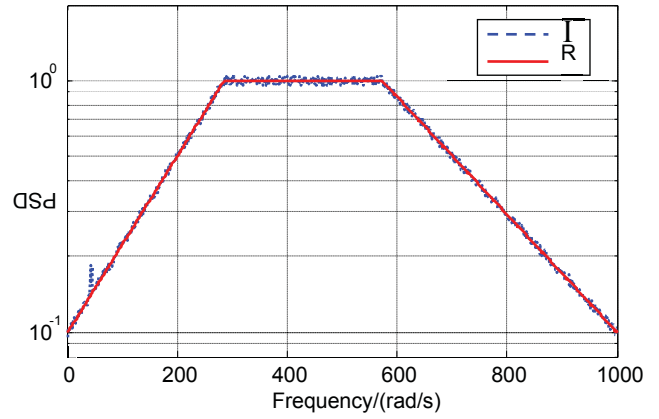
Response nodes combination (3, 5, 7) is used to identify the excitation PSD at (2, 4). The response PSD matrix  $S_{yy}$  can be obtained easily, and it is used to identify the excitation PSD matrix in equation (16) using the direct inversion method (DIM) and the represented method (CNWAM) in this paper. The simulation results are represented in Fig. 2 ~ 9, and the relative errors of the two algorithms are shown in Table 2.

Table 2. Relative errors of two algorithms

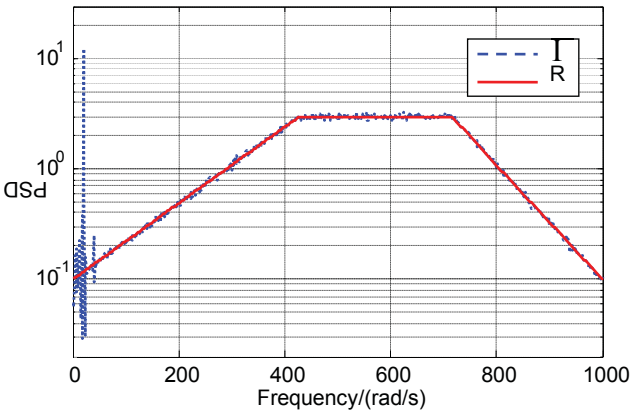
method	Errors by CNWAM	Errors by DIM
Identification error of $S_1$	0.408%	12.02%
Identification error of $S_2$	0.384%	11.94%
Identification error of real part of $S_{12}$	0.284%	6.65%
Identification error of imaginary part of $S_{12}$	0.338%	9.93%



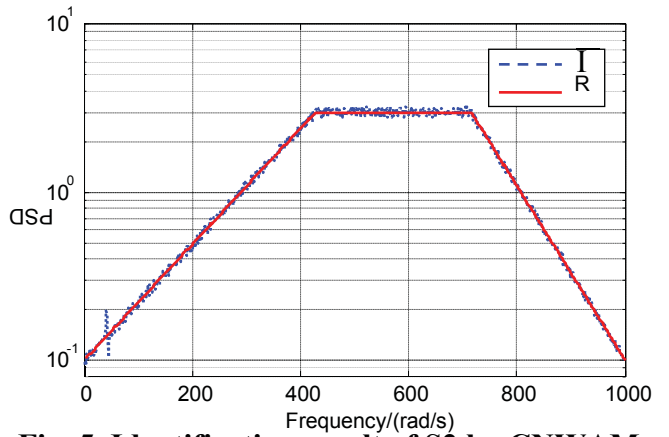
**Fig. 2. Identification result of S1 by DIM**



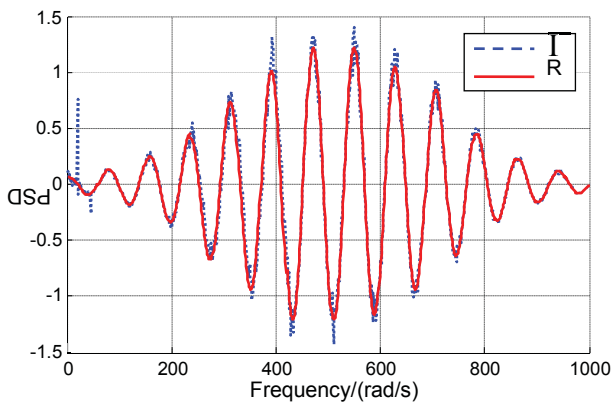
**Fig. 3. Identification result of S1 by CNWAM**



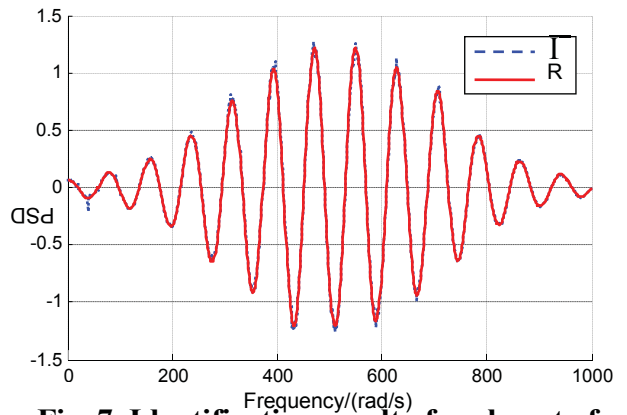
**Fig. 4 Identification result of S2 by DIM**



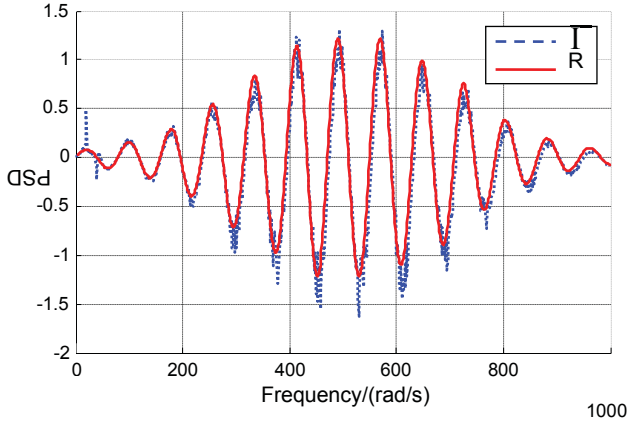
**Fig. 5. Identification result of S2 by CNWAM**



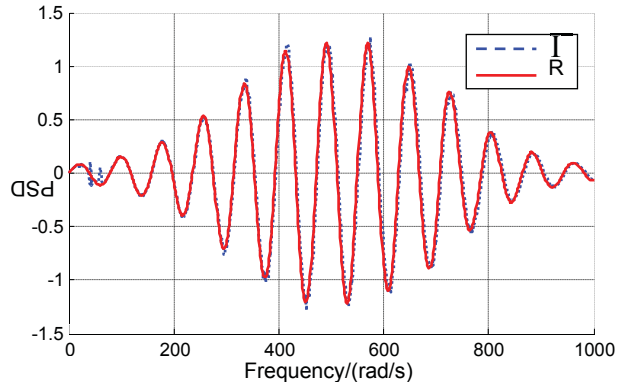
**Fig. 6. Identification result of real part of S12 by DIM**



**Fig. 7. Identification result of real part of S12 by CNWAM**



**Fig. 8. Identification result of imaginary part of S12 by DIM**



**Fig. 9. Identification result of imaginary part of S12 by CNWAM**

In Fig. 2~9, "I" represents result of identification value, and "R" represents theoretical value.

The method of DIM is subject to greater simulation errors than the proposed method as shown in Fig. 2-9 and table 2. Especially, in frequency ranges close-by low nature, the greater calculation errors arise by employing DIM because of inversion of ill-conditioned matrix. The simulation demonstrates the proposed approach is effective to reduce the errors and improve the identification precision. However, Algorithm cannot eliminate the environmental noise and measurement errors, especially, if the measuring point selection is not appropriate. Besides, more matrix inversion need to be done while using CNWAM, it increases the computation load.

#### 4. Identification experiment

Experiment is conducted on the aluminum sheet shown in Fig. 10. The scale of acceleration transducer is shown in Table 3. Two random excitations and two force sensors are applied at T1 and T2. 6 acceleration sensors are applied at A3~A8. Some of the 6 acceleration response measure points are chosen to identify the random excitation and the rule of selecting response points is based on condition number of  $H_{m \times l}$ , and  $H_{m \times l}$  is obtained by the follow equation :

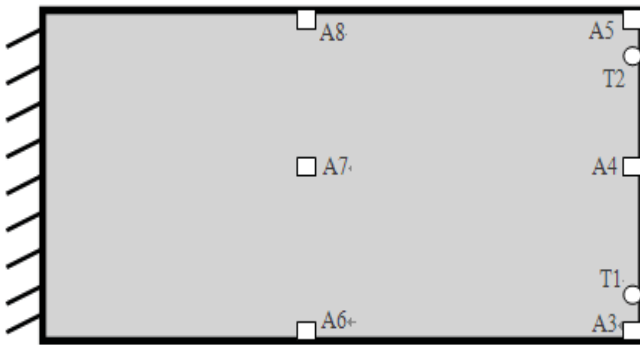
$$\mathbf{H} = G_{YF} G_{FF}^{-1} = YF^* (FF^*)^{-1} \quad (1)$$

In which,  $Y$  is the frequency domain vector obtained by applying Fast Fourier Transform Algorithm(FFT) to their time-domain signals of displacement response,  $F$  is the frequency domain vector of the excitation force, and their time-domain signals are obtained by the experiment measurement.

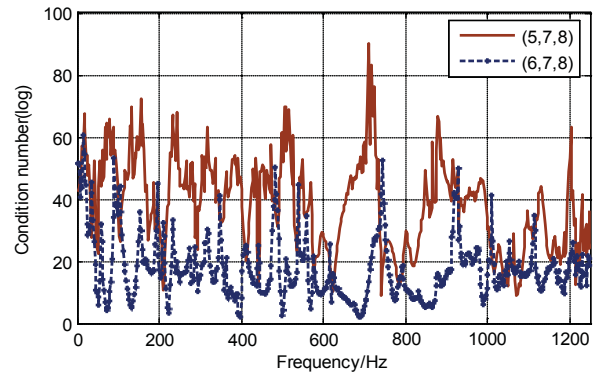
The real force excitations are obtained by force sensors and used to assess the proposed approach. The response combinations, (A5, A7, A8) and (A6, A7, A8), are respectively used to identify the excitation force PSD matrix. The condition number is defined as Eq.(12), and the curves of condition number of frequency response function (FRF)  $H_{m \times l}(f)$  for the 2 combinations are shown in Fig. 11.

**Table 3. Scale of acceleration transducer**

Type	Sensitivity	Frequency Range $\pm 10\%$	Measuring range	Temperature range	Weight
333B30	100mv/g	0.5Hz~3KHz	$\pm 50g$ pk	-18~+66°C	4g
353B32	50mv/g	0.7~8000Hz	$\pm 100g$ pk	-54~121°C	20g



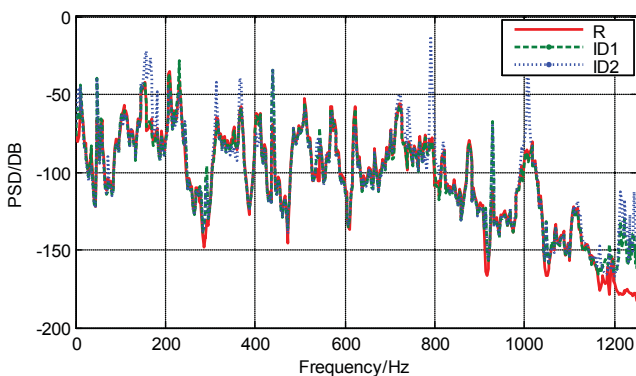
**Fig. 10. Aluminum sheet and the sensor placement**



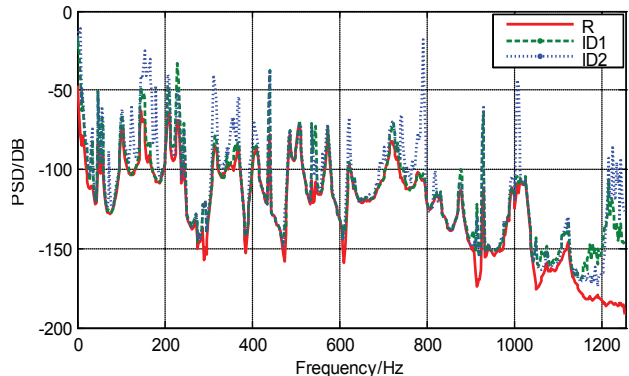
**Fig. 11. Comparison of condition number**

In Fig. 11, "----" represents the condition number of  $H_{m \times l}$  for combination (A6, A7, A8); "\_\_\_" represents the condition number of  $H_{m \times l}$  for combination (A5, A7, A8).

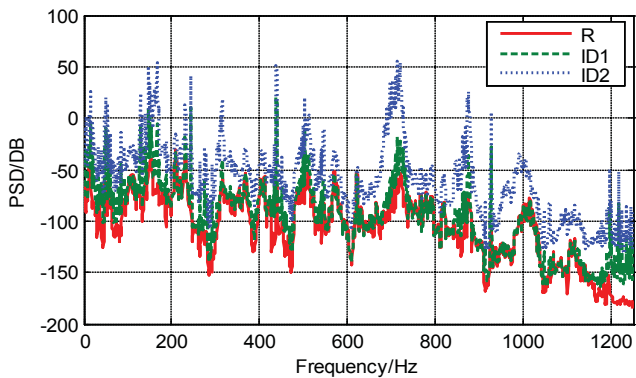
As shown in Fig.11, response combination (A5, A7, A8) has lower condition number than the other one at the concerned frequency range, and the combination (A5, A7, A8) should have a better identification result than the other one. The identification results of the experiment are shown in the Fig. 12 to Fig. 15.



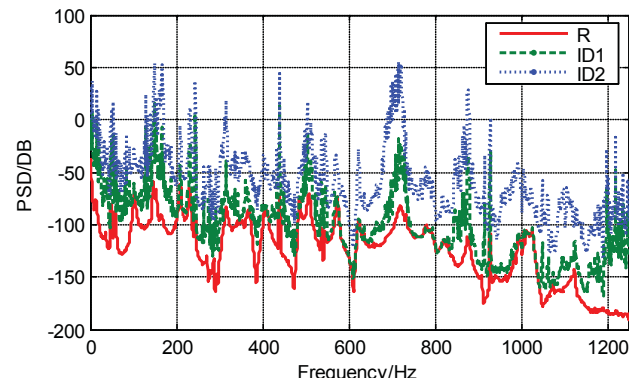
**Fig. 12. Identification of T1 using (A5, A7, A8)**



**Fig. 13. Identification of T2 using (A5, A7, A8)**



**Fig. 14. Identification of T1 using (A6, A7, A8)**



**Fig. 15. Identification of T2 using (A6, A7, A8)**

In Fig. 12~15, "R" represents the real value of the random load; "ID1" represents the identification result by CNWAM; "ID2" represents the identification result by DIM.

As shown in Fig.12-15, the proposed approach can obtain a better identification result when using the same response combination. It proves condition number weighted average method to be effective. A better identification result is obtained by the response combination (A5, A7, A8) than (A6, A7, A8), especially, nearby the natural frequencies. There is only one different measure point between the two combinations, and even a skilled engineer cannot easily to get a clear judgment of which one would be better. These errors are caused by the system, the algorithm cannot remove it completely. While, the selection of appropriate response measure points can change the system frequency response function  $H_{msl}$  and improve the identification precise to some extent. The condition number of FRF can provide reference for experimenter to choose a better response combination. A figure as Fig. 11 can help the engineers to select combination at the frequency range they care about before identification process. This is the effective way to improve the identification precision and to save workload.

On the whole, CNWAM can effectively improve the identification accuracy (Curve ID1 in Fig.12 to Fig. 15) relative to the direct inverse method (Curve ID2 in Fig.12 to Fig. 15). The errors are unacceptable using DIM, especially if the measure point is selected improperly (Curve ID2 in Fig.14 and Fig. 15).

In addition, according to the author's experiences, The measuring point selection should also follow some principles as follows: 1. Response measure points should avoid being set on modal shape node, should as far as possible be set close by the peak or valley of modal shape. 2. The measure points should avoid being set close by each other in the same direction. 3. The measure points should be set on the places where the vibration amplitudes are large enough, so that the signal-to-noise ratio would be improved. 4. If it is possible, greater system damping can improve the identification accuracy.

## 5. Conclusions

For complex engineering structures random loading identifications, direct inverse of FPF gets bad accuracy identification result. The condition number weighted average method is presented in this paper to improve the identification precision. Simulation and experiment are both prove its effectiveness. The selection of the response measure points is one of the key points to improve the loading identification accuracy. Condition number of the FRF is used in the paper to select the appropriate combination of the response measure points. The experimental results demonstrated its effectiveness.

However, more work remains to be done, e.g. the problem of noise disturbance should be extensively investigated in a stricter way and the benefits could be investigated of using Kalman or H1 filtering techniques to further improve the identification precision.

## 6. Acknowledgement

This research is supported by central south university postdoctoral fund.

## References

- [1] Robson, J. D(1964), An introduction to random vibration, Edinburgh University Press, pp.12-99.
- [2] Piersol, A. and Bendat(1993), J. Engineering applications of correlation and spectral analysis, Wiley-Interscience, New York, pp.34-55



- [3] Lin, J. H., Zhang, W. S. and Li, J. J.(1994), Structural responses to arbitrarily coherent stationary random excitations. *Computers and Structures*, 50, pp. 629-633.
- [4] Jiahao, L.(1992), A fast CQC algorithm of PSD matrices for random seismic responses. *Computers & Structures*, 44, pp. 683-687.
- [5] Juang, J. N.(1994), *Applied system identification*, Englewood Cliffs, pp. 34-40
- [6] Ewins, D. J.(1986), *Modal testing: theory and practice*, Research studies press, pp.123-133
- [7] Lin, J. H., Guo, X. L., Zhi, H., Howson, W. P. and Williams, F. W.(2001), Computer simulation of structural random loading identification. *Computers and Structures*, 79, pp. 375-387.
- [8] Papadopoulos, M. and Garcia, E.(1998), Sensor placement methodologies for dynamic testing. *AIAA Journal*, 36, pp. 256-263.
- [9] Li, D. S., Li, H. N. and Guo, X. L.(2003) Computer simulation of optimal sensor locations in loading identification proceedings-spie the international society for optical engineering, 5049, pp. 742-750.
- [10] Paez, T. L.(2006), The history of random vibrations through 1958. *Mechanical Systems and Signal Processing*, 20, pp. 1783-1818.
- [11] Horn, R. A. and Johnson, C. R.(1990), *Matrix analysis*, Cambridge university press, pp.89-93.
- [12] Li, D. S. and Guo, X. I.(2003), Loading identification of structures subjected to random excitations. *Journal of Dalian University of Technology*, 43, pp. 561-566.
- [13] Dongsheng, L., Xinglin, G. and Shibin, X.(2003), Loading identification of random excitations. *IMAC-XXI: A Conference & Exposition on Structural Dynamics*.
- [14] Lin, J. H., Guo, X. L., Zhi, H., Howson, W. P. and Williams, F. W. (2001). Computer simulation of structural random loading identification. *Computers and Structures*. 79, pp. 375-387.

# Application Optimization of Two-Dimensional Nozzle with Alloy Steel Structure in the Supersonic Wind Tunnel

\*Wang Ying<sup>1</sup>, Bu Junhui<sup>2</sup>, Wang Wei<sup>3</sup>, and Chen Ding<sup>4</sup>

<sup>1</sup>China Academy of Aerospace Aerodynamics, 100074, Beijing, China

\* bjhht11@163.com

## Abstract

The two-dimensional nozzle is an important part of supersonic wind tunnels to obtain the flow field with designed Mach number, and the structure of nozzles has direct influence on the uniformity of flow field. Usually, for easy construction and convenience in the two-dimensional nozzle, epoxy resin is adopted in the structural design as the material. However, because of the difference linear expansion coefficient between epoxy resin and the steel framework, often the separation appears due to the reason, and the expansion and contract caused by the heat and cold air flows during the operation of wind tunnel, there often appear some cracks on the edges and body of the nozzle made of epoxy resin; due to the large size of particle contained in the air flow, there often appear some nicks on the nozzle contour. The cracks and nicks will bring about shock waves in the flow field which has disadvantageous effect on the quality of flow field. In order to eliminate the shortcoming caused by the epoxy resin, we have comprehensive consideration of various factors in the two-dimensional nozzle design of 1.2m×1.2m supersonic wind tunnel, making the body structure based on alloy steel for the two-dimensional nozzle design, so a nozzle of steel structure is made with exit size of 1.2m×1.2m and Mach number of 3.5. A great deal of experiments have been conducted on the nozzle, and experimental results show that the flow field of the nozzle is always good. In this paper, the design details of two-dimensional nozzle will be described on the basis of the engineering algorithm, and the stress and deformation analysis is calculated by Ansys, and the calculation results show that two-dimensional nozzle with alloy steel satisfies the design conditions. Some typical experimental results of flow fields of the nozzle steel structure are also presented, the nozzle is reliability and easy to use, and the maintainability is very good, the surface strength of two-dimensional nozzle is greatly increased, extend the service life more than 10 years.

**Keywords:** structure, optimization, two-dimensional nozzle, supersonic, alloy steel

## 1. Determine the scheme

There are two kinds of supersonic nozzle contours, two-dimensional contour and three-dimensional contour. The two-dimensional nozzle has two parallel planar walls and its other two walls are two-dimensional curve surface, while the wall of three-dimensional nozzle, whose cross section is circular, is a three-dimensional curve surface. The supersonic nozzle is an important part of supersonic wind tunnels to obtain the design Mach number of airflow, and it is already known that the Mach number is determined by the area ratio of nozzle throat to test section, meanwhile the quality of flow field is influenced by the nozzle contour. So the design and processing quality of the nozzle have a decisive influence on the quality of the flow field in the test section<sup>[1]</sup>.

A 1.2 meter magnitude supersonic wind tunnel is adopted two-dimensional nozzle structure, the maximum Mach number of this tunnel is M4.0 and two-dimensional nozzle structure is used in it. Now the wind tunnel has now completed the supersonic flow field debugging and this paper focus on M3.5 nozzle structure optimization. The contour of 1.2 meter magnitude supersonic wind tunnel nozzle is 1.2 meter with width and height of outlet dimension. The nozzle length is 4.8m.

According to the design data about supersonic wind tunnel, the structure of solid-block nozzle is usually made of cast aluminum and epoxy coating. When doing the two-dimensional nozzle design in the wind tunnel, the M3.0 and M4.0 nozzles are both made of epoxy resin in the initial stage. 40 millimeter steel plate welding is used to form nozzle's frame, on which is laid. Finally epoxy coating is used to form the surface of nozzle with mould. The advantage of this structure is that the accuracy is easy to ensure, besides its low cost, it is shown in Fig.1. The disadvantage is that the thermal expansion coefficient between epoxy resin and the steel is very different (The epoxy resin is  $56.8 \times 10^{-6} / ^\circ\text{C}$  and the steel is  $11.7 \times 10^{-6} / ^\circ\text{C}$  ). When the wind tunnel is working, the temperature is turn down quickly, causing the appearance of crack when tunnel is working. The crack will propagate if the nozzle is not timely repaired. And also the flow field inevitably contains a large number of foreign particles, which will obtain huge impact and damage when the wind tunnel is working. So the surface of epoxy resin, whose hardness is far lower than steel, may be full of scratch, because of the collision of particles. The cracks and scratches can cause shock wave, bringing adverse effect in the flow field, The nozzle frame and cracks and scratches can be seen in Fig. 2, Fig. 3, Fig. 4.



**Figure 1. The frame foundation of epoxy resin surface**



**Figure 2. The Forming picture of epoxy resin**



**Figure 3. The separation between epoxy resin and the frame of nozzle**



**Figure 4. The scratches on epoxy resin surface**

In order to eliminate the negative factors, we fully analyzed the reason of the above problems during the designing of the M3.5 nozzle. Based on the original structure of nozzles of M3.0 and M4.0, we optimize the design of nozzle. This two-dimensional nozzle scheme is that the whole nozzle structure uses alloy steel, the curve surface is made of alloy steel plate, and is machining by CNC milling machine can reach 0.03mm and the surface roughness can reach more than 1.6, so the stiffness and strength have been greatly improved. Besides the above improvement, the low cost and simple manufacture are also its advantages. This design method by using alloy steel belongs to domestic initiative.

## 2. The engineering algorithm

The material of M3.5 two-dimensional nozzle is made of 16MnR, and the material of it whose allowable stress is  $[\sigma] = 163MPa$ . The pressure of two-dimensional nozzle is  $P_1$  before the throat and  $P_2$  after the throat. The M3.5 nozzle is composed of support ribs intersecting, which is divided into many rectangular plates. Thus each rectangular plate can be seen as fixed edges under uniform load. The structure of M3.5 nozzle is shown in Fig.5.

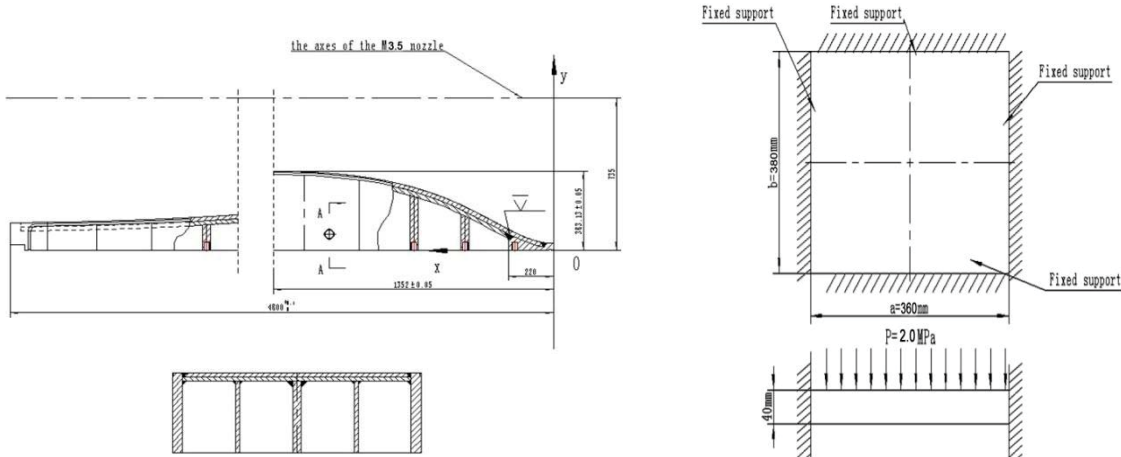


Figure 5. The structure of M3.5 nozzle

Figure 6. The force of M3.5 two-dimensional nozzle

### 2.1 Stiffness calculation

Deformation calculation formula for center part:

$$f = C_3 \frac{qb^4}{Eh^3} \quad (1)$$

$a$  Rectangular plate long edge

$$a = 380mm$$

$b$  Rectangular plate short edge

$$b = 360mm$$

$C_3$  Rectangular plate coefficient

$$C_3 = 0.0165$$

$q$  The uniform load on plate

$$q = 2MPa$$

$E$  Modulus of elasticity

$$E = 206 \times 10^3 MPa$$

$h$  The thickness of rectangular plate

$$h = 40mm$$

The above data into the formula to be  $f = 0.0165 \times \frac{2 \times 360^4}{206 \times 10^3 \times 40^3} = 0.042mm$

According to design requirements of 1.2 meter wind tunnel, the machining tolerance of M3.5 curve surface nozzle by using steel welded need been controlled within  $\pm 0.05mm$ . The curve surface deflection through machining tolerance calculation is  $f < 0.05mm$  which comply with the design requirements.

### 2.2 Strength calculation

The center stress[4] of curve surface panel before throat  $\sigma_E = C_4 P_1 \left(\frac{b}{h}\right)^2$

$$(2)$$

$a$  Rectangular plate long edge

$$a = 380mm$$

$b$  Rectangular plate short edge

$$b = 360mm$$

$C_4$  Rectangular plate coefficient

$$C_4 = 0.1602$$

$q$  The uniform load on plate

$$q = 2MPa$$

$E$  Modulus of elasticity

$$E = 206 \times 10^3 MPa$$

$h$  The thickness of rectangular plate  $h = 40mm$

$$\sigma_E = 0.1602 \times 2 \times \left(\frac{360}{40}\right)^2 = 25.9MPa$$

The center stress of the rectangular plate long edge  $\sigma = -C_6 P_1 \left(\frac{b}{h}\right)^2$  (3)

$C_6$  Rectangular plate coefficient  $C_6 = 0.3324$

The significance of all other symbols are consistent with above symbols

$$\sigma = -0.3324 \times 2 \times \left(\frac{360}{40}\right)^2 = -53.85MPa < 163MPa$$

So the strength is qualified

### 3. The finite element calculation of two-dimensional nozzle

#### 3.1 Processing

(1) Imported model can be seen in Fig.7, Fig.8.

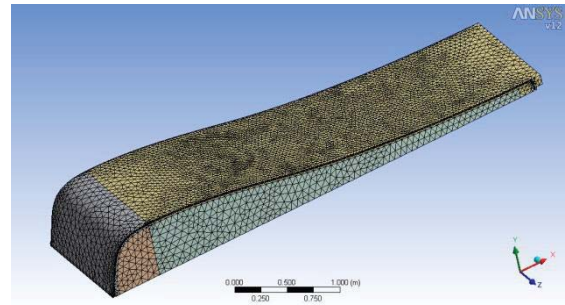
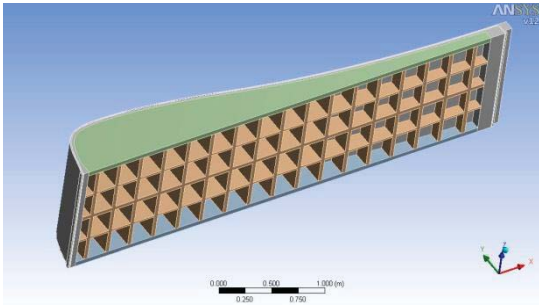


Figure 7. The model of M3.5 two-dimensional nozzle Figure 8. The mesh of M3.5 nozzle

(2) The constraint and load: Considering the actual stress condition on the surface of the nozzle, the bottom of the M3.5 nozzle is received full constraint, the side flange is received Y direction constraint, the surface of entrance and exit is free. The constraint and the load of the structure can be seen in Fig.9, Fig.10.

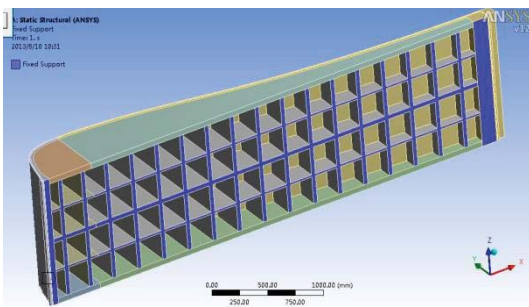


Figure 9. Constraint of M3.5 nozzle

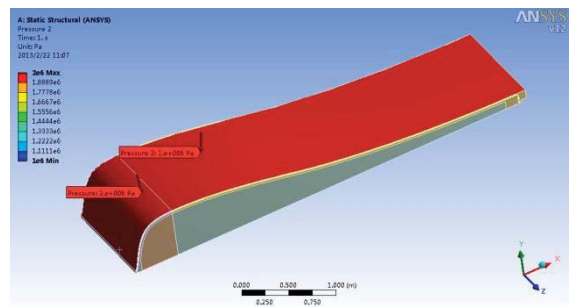


Figure 10. The load of M3.5 nozzle

#### 3.2 Calculation results

The maximum stress value is 44.197MPa which is shown in Fig.11, it appears in the surface panel before the throat which is intersected at the ribs, the whole stress value of M3.5 nozzle is in 0.058 ~ 44.197MPa range, we can see it in Fig.12. The allowable stress value of 16MnR is  $[\sigma] = 163MPa$ .

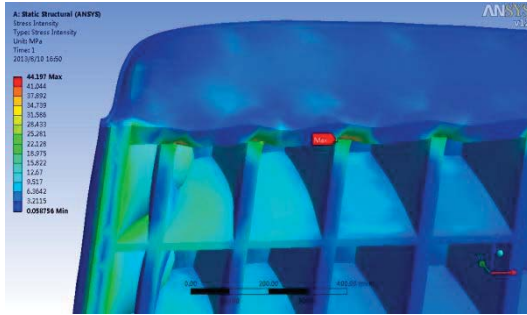


Figure 11. The maximum stress value of M3.5 nozzle

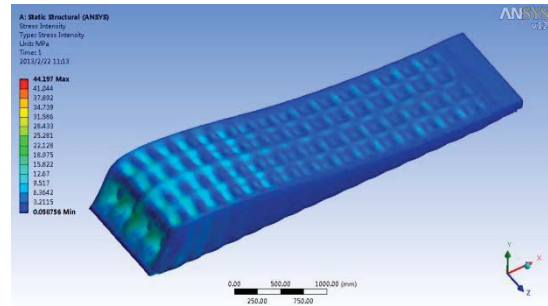


Figure 12. The stress distribution of M3.5 nozzle

Fig.13 shows that the maximum deformation value of the nozzle is 0.05211 mm, the value appears in the curve surface before the throat. The maximum deformation value of the nozzle is less than 0.06mm which accords with design rigidity requirements of the nozzle.

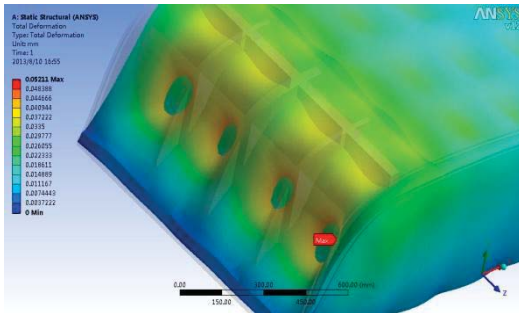


Figure 13. The maximum deformation value of M3.5 nozzle before throat

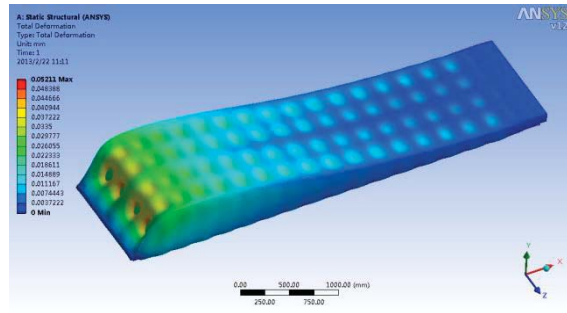


Figure 14. The deformation distribution of M3.5 nozzle

### 3.3 Analysis of the results

The maximum stress value is 53.85MPa and the maximum deformation value is 0.042mm by engineering calculation method, the maximum stress value is 44.197MPa and the maximum deformation value is 0.05211 mm by Ansys calculation method. Comparing one result with another, the difference of the stress value between two methods is 9.653MPa, the difference of the deformation value between two methods is 0.01 mm. According to these results, the result of two methods is similar. Comparing the results and it is shown in Table 1.

Table 1. Comparing the results

Value	Deformation value(mm)	Stress value(MPa)
Calculation method		
The engineering algorithm	0.042	53.85
The finite element calculation	0.05211	44.197
Difference	0.01	9.653

### 4. Flow field calibration

In the process of practical application, the M3.5 two-dimensional nozzle obtains lots of data from field calibration. The analysis of flow field calibration results are completed in strict accordance with the GJB1179-91" high speed and low speed wind tunnel flow quality standard".



Figure 15. Using alloy steel welded for M3.5 nozzle



Figure 16. The picture of M3.5 nozzle



Figure 17. The standard model test of M3.5 nozzle

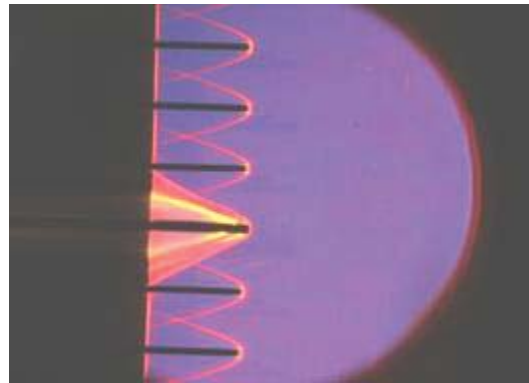


Figure 18. The press testing

## 5. Conclusions

(1) The adoption of alloy steel in the two-dimensional nozzle structure of 1.2 meter supersonic wind tunnel solves the problems of surface cracking, scratches appearing and low surface hardness for the first time. Besides, it can also reduce the manufacturing cost and optimize structure. Comparing the data and it is shown in Table 2.

Table 2. Comparing the data

Name	Manufacturing cost	Surface hardness	Use of time
The nozzle with alloy steel	expensive	hard	long
The nozzle with epoxy resin	expensive	soft	short

(2) M3.5 two-dimensional nozzle is simplifying to the rectangular plate structure, the surface block of supersonic nozzle can be simplified into a flat piece in the engineering calculation for the first time. And the flow field is well, we can see M3.5 nozzle by using alloy steel in Fig.15, Fig.16. Also the test of M3.5 nozzle can be seen in Fig.17, Fig.18. The test result of the two-dimensional nozzle shows that the strength and stiffness of the full steel structure is reasonable and the method of simplifying the surface is feasible.

## 6. References

1. Bu Junhui, Jia Yingsheng, Huang Jingbo and Sun Yongtang. Design Optimization of Supersonic Nozzle Structure The Seventh China-Japan-Korea Joint Symposium on Optimization of Structural and Mechanical Systems

Huangshan. *June, 18-21, 2012, China*

2. Sun Junfang, Sun Bing, Xiang Shenghai. Theoretical calculation of complex nozzle's temperature profile and stress profile in solid rocket motor[J]. *Journal of Propulsion Technology*. 1994, 15(1):23-31.
3. GJB 1179-91. High speed and low speed wind tunnel flow quality standard. Science and technology Committee of National Defense. 1992.6
4. Liu Zhengchong Aerodynamic and structural design of high speed and low wind tunnels. National Defense Industry Press 2003.4
5. Cheng Daxian Manual of mechanical design. Chemical Industry Press 2002.11



## Numerical study of vortex-induced vibration by symmetric Lorentz forces

**\*Hui Zhang, Bao-chun Fan, and Zhi-hua Chen**

Science and Technology on Transient Physics Laboratory, Nanjing University of Science and Technology, China.

\*Corresponding author: zhanghui1902@hotmail.com

**Key Words:** *flow control, vortex-induced vibration, electro-magnetic control, hydrodynamic force*

### Abstract

In this paper, the electro-magnetic control of vortex-induced vibration (VIV) of a circular cylinder is investigated numerically based on the stream function-vorticity equations in the exponential-polar coordinates attached on the moving cylinder for  $Re=150$ . The effects of the instantaneous wake geometries and the corresponding cylinder motion on the hydrodynamic forces of vortex shedding are discussed in the drag-lift phase diagram. The drag-lift diagram is composed of the upper and lower closed curves, due to the contributions of the vortex shedding, but is magnified, translated and turned under the action of the cylinder motion. The symmetric Lorentz force will symmetrize the flow pass over the cylinder, and decrease the lift oscillation, and in turn, suppresses the VIV.

Keywords: flow control, vortex-induced vibration, electro-magnetic control, hydrodynamic force.

### Introduction

Fluid-structure interactions occur in many engineering fields. These interactions give rise to complicated vibrations of the structures and could cause structural damage under certain unfavorable conditions. For a cylinder mounted on flexible supports, the fluctuating forces induced by altering vortex shedding cause the cylinder vibrate. Then, the vibrating cylinder alters the flow field, and in turn changes the flow-induced force. The vibration of the cylinder could increase still further until a limiting behavior has been reached. This vortex-induced vibration (VIV) phenomenon is one of the most basic and revealing problems.

Representative studies carried out experimentally on VIV are the experiments of Feng(1968), Griffin (1980), Griffin & Ramberg (1982), Brika & Laneville (1993), and Hover (1997) et al, in which classic lock-in was observed, while the shedding frequency coincided with the natural structure frequency. The cylinder experiences significant vibration only with lock-in, and the vibration amplitude has a strong relationship with the phase difference between the lift force and the cylinder motion. However, recently experimental results of Gharib et al(1997), Gharib (1999) and Khalak & Williams (1997) exhibited examples of significant flow-induced vibration without lock-in and suggested whether the VIV with or without lock-in is dependent on the values of the cylinder/fluid mass ratio. Recently, Franzini et al(2009), Lam&Zou(2009) and Korkischko&Meneghini(2010) focus on the interaction of multiple cylinders. It was found that the gap or arrangement has significant effect on the response of the VIV system. Moreover, experimental results of flow around a circular cylinder with moving surface boundary layer control (MSBC) are presented which has the advantages of drag reduction and vibration suppression (Korkischko& Meneghini(2012)).

The progress made during the past two decades on VIV have been reviewed (see. e.g. Williamson&Govardhan (2004) and Sarpkaya (2004)). It is clear that the investigation of fluid-structure interactions as a fully coupled problem are far from complete, there still remain some uncertainties, such as added mass, force decomposition and their effects on the characteristics of the fluid-structure system. Therefore more investigations on an in depth analysis are necessary.

In addition, the control of VIV has many practical applications in the engineering point of view, but a little work has been done on it (Gattulli&Ghanem 1999, Owen et al 2001, Korkischko&

Meneghini(2012)). Therefore, the investigations on the control of VIV are also necessary due to the practical and theoretical importance.

The electro-magnetic control is considered as one of the most practical methods to manipulate the flow (Tang&Aubry 1997, Berger et al 2000, Breuer et al 2004, Mutschke et al 2006, Braun et al 2009). Regarding the flow past a fixed circular cylinder, Crawford and Karniadakis (1995) investigated the effects of Lorentz force on the elimination of flow separation numerically. Weier et al (1998) confirmed the suppressing effect of Lorentz force by both experiments and calculations. Kim&Lee(2001) and Posdziech&Grundmann(2001) found that both continuous and pulsed Lorentz forces can suppress the lift oscillation and stabilize the flow. The closed-loop and optimal control methods were developed to improve its control efficiency in our research group(Zhang et al 2010, Zhang et al 2011), and the suppression of VIV by symmetric Lorentz force was also investigated preliminary(Chen et al 2007).

In this paper, the electro-magnetic control of VIV is investigated numerically. The problems discussed are described by the stream function-vorticity equations in coordinates attached on the moving cylinder, coupled with the cylinder motion equation. A VIV of a cylinder started from rest is controlled by symmetric Lorentz forces after reaching a limiting behavior, and then suppressed till the cylinder vibrates steadily with smaller amplitude. The evolutions of VIV undergoing development and suppression are presented.

## Governing equations

For the control of vortex-induced vibration, the cylinder surface consists of two half cylinders mounted with alternating streamwise electrodes and magnets. Obviously, produced Lorentz force is directed parallel to the cylinder surface and decays exponentially in the radial direction, which can be described in dimensionless form (Weier et al 1998, Posdziech et al 2001)

$$\begin{aligned} \mathbf{F}^* &= N\mathbf{F} \\ \text{with } F_r &= 0 \\ F_\theta &= e^{-\alpha(r-1)}g(\theta) \text{ with } g(\theta) = \begin{cases} 1 & \text{covered with actuator on upper surface} \\ -1 & \text{covered with actuator on lower surface} \\ 0 & \text{elsewhere} \end{cases} \end{aligned} \quad (1)$$

where  $r$  and  $\theta$  are polar coordinates, subscripts  $r$  and  $\theta$  represent the components in  $r$  and  $\theta$  directions, respectively.  $\alpha$  is a constant, representing the effective depth of Lorentz force in the fluid. The interaction parameter is defined as  $N = \frac{j_0 B_0 a}{\rho u_\infty^2}$ , giving the ratio of the electromagnetic

forces to the inertia forces,  $j_0$  and  $B_0$  are the applied electric current density and external magnetic field induction,  $a$  is the cylinder radius.

The stream-vorticity equations in the exponential-polar coordinates system  $(\xi, \eta)$ ,  $r = e^{2\pi\xi}$ ,  $\theta = 2\pi\eta$ , attached on the moving cylinder, for an incompressible electrically conducting fluid become

$$H \frac{\partial \Omega}{\partial t} + \frac{\partial(U_r \Omega)}{\partial \xi} + \frac{\partial(U_\theta \Omega)}{\partial \eta} = \frac{2}{\text{Re}} \left( \frac{\partial^2 \Omega}{\partial \xi^2} + \frac{\partial^2 \Omega}{\partial \eta^2} \right) + NH^{\frac{1}{2}} \left( \frac{\partial F_\theta}{\partial \xi} + 2\pi F_\theta - \frac{\partial F_r}{\partial \eta} \right) \quad (2)$$

$$\frac{\partial^2 \psi}{\partial \xi^2} + \frac{\partial^2 \psi}{\partial \eta^2} = -H\Omega \quad (3)$$

where the stream function  $\psi$  is defined as  $\frac{\partial\psi}{\partial\eta} = U_r = H^{\frac{1}{2}}u_r$ ,  $-\frac{\partial\psi}{\partial\xi} = U_\theta = H^{\frac{1}{2}}u_\theta$ , while the vorticity  $\Omega$  is defined as  $\Omega = \frac{1}{H}\left(\frac{\partial U_\theta}{\partial\xi} - \frac{\partial U_r}{\partial\eta}\right)$ , with  $u_r$  and  $u_\theta$  the velocity components in  $r$  and  $\theta$  directions, respectively. Furthermore,  $H = 4\pi^2 e^{4\pi\xi}$ ,  $\text{Re} = \frac{2u_\infty a}{\nu}$ ,  $u_\infty$  is the free-stream velocity,  $\nu$  is the kinematic viscosity,  $a$  is the cylinder radius, the non-dimensional time is  $t = \frac{t^* u_\infty}{a}$ .

The flow is considered to be potential initially and the boundary conditions derived are dependent on the vibrating cylinder. If the cylinder is constrained to move only in cross flow direction, then

$$\begin{aligned} \text{at } t = 0, \quad \psi = 0, \quad \Omega &= -\frac{1}{H} \frac{\partial^2 \psi}{\partial \xi^2} && \text{on } \xi = 0 \\ \psi &= -2sh(2\pi\xi)\sin(2\pi\eta), \quad \Omega = 0 && \text{on } \xi > 0 \\ \text{at } t > 0, \quad \psi = 0, \quad \Omega &= -\frac{1}{H} \frac{\partial^2 \psi}{\partial \xi^2} && \text{on } \xi = 0 \\ \psi &= -\frac{2}{\cos\theta_0} sh(2\pi\xi)\sin(2\pi\eta + \theta_0), \quad \Omega = 0 && \text{on } \xi = \xi_\infty \end{aligned}$$

Where  $\theta_0 = \arctan\left(-\frac{dl(t)}{dt}\right)$ ,  $\frac{dl(t)}{dt}$  is the velocity of cylinder, the non-dimensional cylinder displacement in the cross-flow direction is  $l = l^* / a$ .

The shear stress  $\mathcal{C}_\tau^\theta = \mathcal{C}_{\tau F}^\theta + \mathcal{C}_{\tau V}^\theta$  (4)

where  $\mathcal{C}_{\tau F}^\theta = \frac{4}{\text{Re}} \Omega$ ,  $\mathcal{C}_{\tau V}^\theta = \frac{4}{\text{Re}} \frac{dl}{dt} \cos(2\pi\eta)$

Therefore, the shear stress can be decomposed into  $\mathcal{C}_{\tau F}^\theta$  and  $\mathcal{C}_{\tau V}^\theta$ , where  $\mathcal{C}_{\tau F}^\theta$  is proportional to vorticity at the wall, whereas  $\mathcal{C}_{\tau V}^\theta$  induced by the cylinder motion in viscous flow, is independent of vorticity field.

The pressure  $\mathcal{C}_p^\theta = P_\theta - P_\infty = \mathcal{C}_{pF}^\theta + \mathcal{C}_{pW}^\theta + \mathcal{C}_{pV}^\theta$  (5)

where  $\mathcal{C}_{pF}^\theta = \frac{4}{\text{Re}} \int_0^\eta \frac{\partial \Omega}{\partial \xi} d\eta + \mathcal{C}_p^0$ ,  $\mathcal{C}_p^0 = 1 + 4\pi \int_0^\infty \frac{\partial u_r}{\partial t} e^{2\pi\xi} d\xi + 2 \int_0^\infty u_\theta \frac{\partial u_r}{\partial \eta} d\xi - 4\pi \int_0^\infty u_\theta^2 d\xi + \frac{4}{\text{Re}} \int_0^\infty \frac{\partial \Omega}{\partial \eta} d\xi$

$$\mathcal{C}_{pW}^\theta = 4\pi N \int_0^\eta F_\theta|_{\xi=0} d\eta, \quad \mathcal{C}_{pV}^\theta = -4 \frac{d^2 l(t)}{dt^2} \sin(2\pi\eta)$$

Here, pressure  $\mathcal{C}_p^\theta$  consists of  $\mathcal{C}_{pF}^\theta$  induced by the field Lorentz force,  $\mathcal{C}_{pW}^\theta$  induced by the wall Lorentz force and  $\mathcal{C}_{pV}^\theta$  induced by the inertial force.

Then the drag  $C_d$  can be written as  $C_d = \int_0^{2\pi} \mathcal{C}_d^\theta d\theta = C_{dF} + C_{dW}$  (6)

where  $C_{dF} = \frac{2}{\text{Re}} \int_0^1 \left(2\pi\Omega - \frac{\partial \Omega}{\partial \xi}\right) \sin(2\pi\eta) d\eta$ ,  $C_{dW} = -2\pi N \int_0^1 F_\theta|_{\xi=0} \sin(2\pi\eta) d\eta$

And the lift  $C_l$  is written as  $C_l = \int_0^{2\pi} c_l^\theta d\theta = C_{IF} + C_{IW} + C_{IV}$  (7)

where  $C_{IF} = \frac{2}{\text{Re}} \int_0^1 \left( 2\pi\Omega - \frac{\partial\Omega}{\partial\xi} \right) \cos(2\pi\eta) d\eta$ ,  $C_{IW} = -2\pi N \int_0^1 F_\theta|_{\xi=0} \cos(2\pi\eta) d\eta$

$$C_{IV} = -4\pi \frac{d^2l}{dt^2} - \frac{4\pi}{\text{Re}} \frac{dl}{dt}$$

It is obvious that  $C_{IW}$  is independent of flow field.  $C_{IW} = 0$ , as Lorentz force field symmetric,

hence  $C_l = C_{IF} - 4\pi \frac{d^2l}{dt^2} - \frac{4\pi}{\text{Re}} \frac{dl}{dt}$  (8)

where  $C_{IF}$ , so called vortex-induced force, is only dependent on the vorticity and boundary vorticity flux on the cylinder surface. The second term on the right-hand side of the above equation, called inertial force, is only dependent on cylinder acceleration and the third term, called viscous damping force, is dependent on Reynolds number and cylinder velocity. Therefore both second and third terms are independent of the instantaneous flow field.

Non-dimensional mass  $m = \frac{m^*}{\pi\rho a^2} = \frac{\rho_{cyl}}{\rho}$ ,  $\rho_{cyl}$  and  $\rho$  are the cylinder density and the fluid density respectively; non-dimensional frequency  $f = f^* u_\infty / a$  and non-dimensional structure damping  $\zeta = \frac{D}{\pi\rho a u_\infty}$ . We may write

$$m \frac{d^2l}{dt^2} + \zeta \frac{dl}{dt} + m_{vir} \left( \frac{\omega_n}{\omega} \right)^2 \omega^2 l = F$$
 (9)

where  $F = \frac{C_l}{\pi} = \frac{C_{IF}}{\pi} - \frac{4}{\text{Re}} \frac{dl}{dt} - 4 \frac{d^2l}{dt^2}$ ,  $\omega = 2\pi f$ ,  $f$  is vortex shedding frequency. At vortex lock-in, the vortex shedding frequency and the natural frequency of the cylinder are synchronized,  $f_n / f$  keeps unchanged.

In order to deal with the evolution of the VIV, it is assumed further that the lock-in is kept throughout the developing process of VIV, and then the oscillations of the lift force and the displacement in every motion cycle are represented by a half of peak-to-peak vibration amplitude  $\bar{B}$ , where  $\bar{B}$  is defined by  $(B_{upper} + B_{lower})/2$ ,  $B_{upper}$  and  $B_{lower}$  are the upper and lower peak values respectively in a motion cycle. Clearly, this assumption does not alter the final steady state of the cylinder vibration. Hence,

$$m_{vir} \left( \frac{\omega_n}{\omega} \right)^2 = m + 4 + \frac{1}{\pi\omega^2} \frac{\bar{C}_{IF_0}}{\bar{B}} \sqrt{1 - \left[ \pi\omega \left( \zeta + \frac{4}{\text{Re}} \right) \right]^2 \left( \frac{\bar{B}}{\bar{C}_{IF_0}} \right)^2}$$
 (10)

Clearly,  $m_{vir}$  changes with time.

The calculations have been performed numerically. The equation of vorticity transport is solved by using the Alternative-Direction Implicit (ADI) algorithm, and the equation of stream function is integrated by means of a Fast Fourier Transform (FFT) algorithm. More details about numerical method and validation of the code can be found in Refs (Tang&Aubry 1997, Zhang et al 2010, Zhang et al 2011). The cylinder motion is calculated by solving equation (10) using the Runge-Kutta method.

**Results and discussions**

Time evolutions of displacement of VIV cylinder before and after control are shown in Fig.1. Considering a VIV cylinder started from rest, the confinement is released in the cross-flow direction at time  $t_1$ , the cylinder begins to vibrate under the action of lift force  $F$ , and then tends to reach a limiting behavior. When the symmetric Lorentz force is turned on at time  $t_2$  for a well-developed VIV, the cylinder displacement will decrease with time which is also shown in Fig.1, where the thick solid line and thin dash line represent  $N=1.3$  and  $N=0.8$  respectively. As Lorentz force is strong enough, the separation points disappear completely and the flow becomes symmetric and stable, in turn  $C_{IF}$  vanishes and the cylinder will be fixed finally.

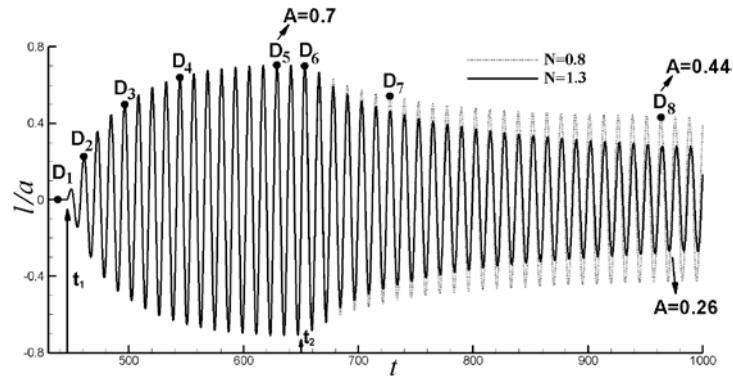


Fig.1 Time evolutions of displacement of VIV cylinder before and after control

Time evolutions of lift  $C_{IF}$  and drag  $C_{dF}$  for VIV development and suppression are shown in Fig.2. As the cylinder begins to vibrate, the closed curve  $A_1B_1C_1D_1A_1$  in Fig.2, representing the stationary cylinder, is turned right with  $180^\circ$  due to the effect of the moving cylinder on the shear layer. Subsequently, the mean energy of the cylinder increases as the increase of the cylinder oscillation and the point A separates from the point C, broking the mirrored symmetry of the curve. In addition, the average drag and the amplitude of oscillating lift increase, which causes the diagram magnify and extend continuously from the left to the right as a twisted curve, till VIV is well-developed, and  $C_{dF} \sim C_{IF}$  phase diagram is represented by a thick solid line. When the symmetric Lorentz force is applied, the drag  $C_{dF}$  induced by the field Lorentz force increases, despite the fact that the total drag  $C_d$  does decrease due to the wall Lorentz force effect (Zhang& Fan 2011). Therefore the phase diagram moves to the right dramatically. The flow around the cylinder tends to be symmetric due to the separation suppression, and the lift force  $C_{IF}$  decreases, which leads to the decay of the cylinder vibration and the decrease of drag. The phase diagram shrinks and moves to the left as a twisted curve, till the cylinder vibrates steadily with an amplitude smaller than that for well-developed VIV and the point A coincides with the point C again.

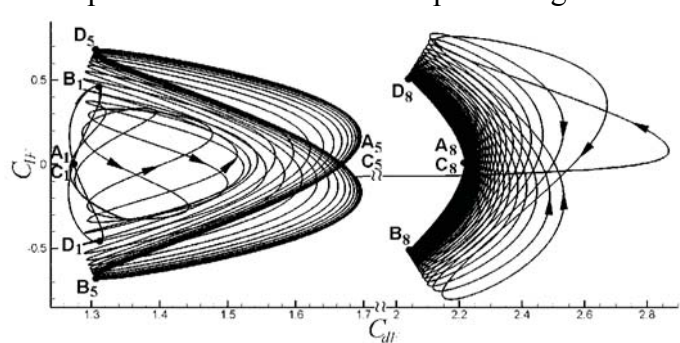


Fig.2 Time evolutions of lift  $C_{IF}$  and drag  $C_{dF}$  for VIV development and suppression ( $N=0.8$ )

The vortex patterns in the wake before and after control by Lorentz force with  $N = 0.8$  are shown in Fig.3. All frames correspond to the uppermost cylinder position. The time  $D_i$  is expressed in the same instants as used in Fig 1. The cylinder begins to vibrate under the action of lift as the confinement is released at time  $t_1 = 446$ . Since the energy transfers from the fluid to the cylinder, the cylinder oscillation increases, the corresponding vortex patterns are indicated by  $D_1 \sim D_4$ . When total energy of cylinder is in the equilibrium state, the cylinder vibrates steadily, the corresponding vortex pattern is indicated by  $D_5$ . The control is applied at time  $t_2 = 650$ , when VIV is well-developed. After control ( $D_6 \sim D_8$ ), the flow in the boundary layer is accelerated under the action of Lorentz force to strengthen the shear layer near the cylinder surface, so that the ability to overcome the adverse pressure gradient is enhanced, which leads to the separation suppression and the wake elongation. Therefore, the separation distance between the upper and lower separation point becomes smaller, and the vortex spaces appear to become wider in stream direction and smaller in the transverse direction.

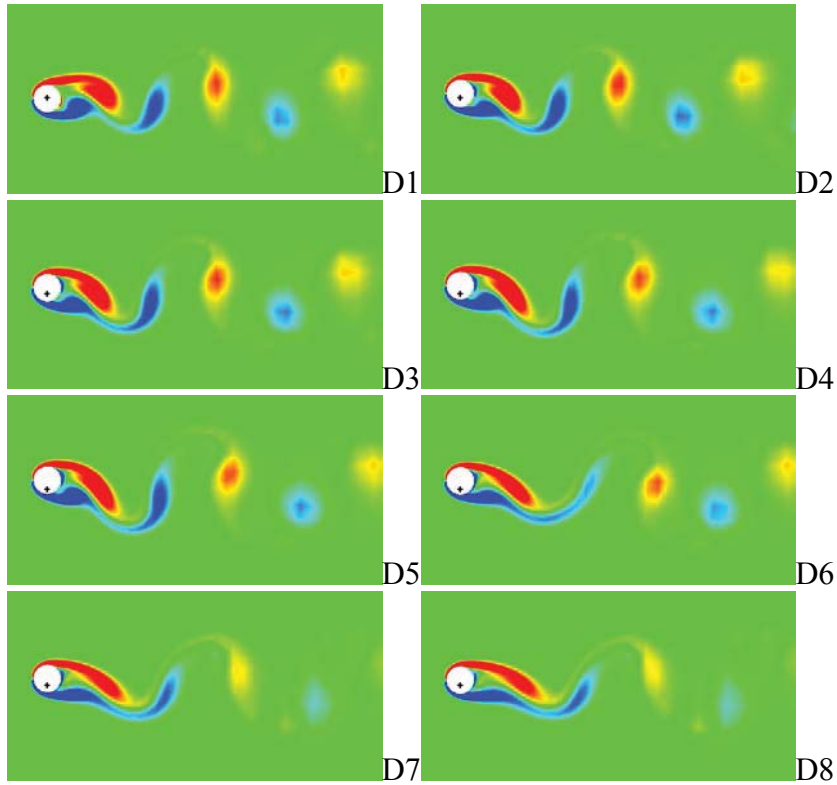


Fig.3 Instantaneous vortex patterns in wake before and after Lorentz force control ( $N=0.8$ )

## Conclusions

The electro-magnetic control of vortex-induced vibration of a cylinder has been investigated numerically based on the stream function-vorticity equations in exponential-polar coordinates attached on the moving cylinder, and the coupled cylinder motion equation. The initial and boundary conditions together with hydrodynamic forces on the cylinder surface are deduced.

The drag-lift diagram is composed of the upper and lower closed curves, due to the contributions of the vortex shedding. As the cylinder begins to vibrate, the diagram magnify and extend continuously from the left to the right as a twisted curve, till VIV is well-developed. When the symmetric Lorentz force is applied, the phase diagram shrinks and moves to the right as a twisted curve, till the cylinder vibrates steadily with an amplitude smaller than that for well-developed VIV.

The symmetric Lorentz forces can be applied to suppress the VIV. The Lorentz force, being independence of the flow field, is classified into the field Lorentz force and the wall Lorentz force. The wall Lorentz force decreases the drag only and has no effect on the lift, whereas the symmetric field Lorentz force will symmetrize the flow pass over the cylinder, and decrease the lift oscillation, and in turn, suppresses the VIV.

## References

- Berger, T., Kim, J., Lee, C., Lim, J., (2000), Turbulence boundary layer control utilizing the Lorentz force. *Physics of Fluids* **12**, pp.631-649.
- Braun, E. M., Lu, F. K., Wilson, D. R., (2009). Experimental research in aerodynamic control with electric and electromagnetic fields. *Progress in Aerospace Sciences* **45**, pp.30-49.
- Breuer, K. Park S. J., Henoch, C., (2004). Actuation and control of a turbulent channel flow using Lorentz forces. *Physics of Fluids*. **16**, pp.897-907.
- Brika, D., Laneville, A., (1993). Vortex-induced vibration of a long flexible circular cylinder. *Journal of Fluid Mechanics* **250**, pp.481-508.
- Chen, Z. H., Fan, B. C., Zhou B. M., Li, H Z., (2007). Open loop control of vortex-induced vibration of a circular cylinder. *Chinese Physics* **16**, pp.1077-1083.
- Crawford, C. H., Karniadakis, G. E. (1995). Control of external flows via electro-magnetic fields. AIAA-952185.
- Franzini, G.R., Fujiarra A.L.C., Meneghini, J.R., Korkischko, I., Franciss, R., (2009). Experimental investigation of Vortex-Induced Vibration on rigid, smooth and inclined cylinders. *Journal of Fluids and Structures* **25**, pp.742-750.
- Gattulli, V., Ghanem, R., (1999). Adaptive control of flow-induced vibrations including vortex effects. *International Journal of non-Linear Mechanics* **34**, pp.853-868.
- Gharib M. R., Shiels, D. Gharib, M. Leonard, A., Roshko, A., (1997). Exploration of flow-induced vibration at low mass and damping. In *Proceedings of Fourth International Symposium on Fluid-Structure Interaction, Aeroelasticity, Flow-Induced Vibration, and Noise, Vol.1*, pp. 75-81. New York: ASME.
- Griffin, O. M., (1980). Vortex-excited cross-flow vibrations of a single cylindrical tube. *ASME Journal of Pressure Vessel Technology* **102**, pp.158-166.
- Griffin, O. M., Ramberg S. E., (1982). Some recent studies of vortex shedding with application to marine tubulars and risers. *ASME Journal of Energy Research and Technology* **104**, pp.2-13.
- Gharib, M.R., (1999). Vortex-induced vibration, absence of lock-in and fluid force deduction. Ph.D dissertation, California Institute of Technology, Pasadena, CA, USA.
- Hover, F. S., Miller, S. N., Triantafyllou M. S., (1997). Vortex-induced vibration of marine cables: experiments using force feedback. *Journal of Fluids and Structures* **11**, pp.307-326.
- Khalak, A., Williamson, C. H. K., (1997). Fluid forces and dynamics of a hydroelastic structure with very low mass and damping. *Journal of Fluids and Structures* **11**, pp.973-982.
- Kim, S., Lee, C. M., (2001). Control of flows around a circular cylinder: suppression of oscillatory lift force. *Fluid Dynamics Research* **29**, pp.47-63.
- Korkischko, I., and Meneghini, J.R., (2010). Experimental Investigation of flow-induced vibrations at low mass-damping, *Journal of Fluids and Structures* **11**, pp.973-982.
- Korkischko, I., Meneghini, J.R., (2012). Suppression of vortex-induced vibration using moving surface boundary-layer control, *Journal of Fluids and Structures* **34**, pp.259-270.
- Lam, K., Zou, L., (2010). Three-dimensional numerical simulation of cross-flow around four cylinders in an in-line square configuration. *Journal of Fluids and Structures* **26**, pp.482-502.
- Mutschke, G., Gerbeth, G., Albrecht, T., Grundmann, R., (2006). Separation control at hydrofoils using Lorentz forces. *European Journal of Mechanics B/Fluids* **25**, pp.137-152.
- Owen, J. C., Bearman, P. W., Szweczyk, A. A., (2001). Passive control of VIV with drag reduction. *Journal of Fluids and Structures* **15**, pp.597-605.
- Posdziech, O., Grundmann, R., (2001). Electromagnetic control of seawater flow around circular cylinders. *European Journal of Mechanics B/Fluids* **20**, pp.255-274.
- Sarpkaya, T., (2004). A critical review of the intrinsic nature of vortex-induced vibrations. *Journal of Fluid and Structures* **19**, pp.389-447.
- Tang, S., Aubry, N., (1997). On the symmetry breaking instability leading to vortex shedding. *Physics of Fluids* **9**, pp.2550-2561.
- Williamson, C.H.K., Govardhan, R., (2004). Vortex-induced vibrations, *Annual Reviews Fluid Mechanics* **36**, pp.413-455.

- Zhang, H. Fan, B. C., Chen, Z. H., (2010). Optimal control of cylinder wake by electromagnetic force based on the adjoint flow field. *European Journal of Mechanics B/Fluids* **29**, pp.53-60.
- Zhang, H., Fan, B. C., Chen, Z. H., (2010). Computations of optimal cylinder flow control in weakly conductive fluids. *Computers & fluids* **39**, pp.1261-1266.
- Zhang, H., Fan, B. C., Chen, Z. H., Li, Y. L., (2011). Effect of the Lorentz force on cylinder drag reduction and its optimal location. *Fluid Dynamics Research* **43**, 015506.



## Fluid-structure coupling analysis and simulation of viscosity effect on Coriolis mass flowmeter

\*Luo Rongmo, and Wu Jian

National Metrology Centre, A\*STAR, 1 Science Park Drive, Singapore 118221.

\*Corresponding author: [luo\\_rongmo@nmc.a-star.edu.sg](mailto:luo_rongmo@nmc.a-star.edu.sg)

### Abstract

Coriolis mass flowmeters (CMFs) are increasingly used in the oil and gas industry with feature of directly measuring mass flow rate. The performance of CMFs influenced by on-line viscosity still needs further study. A computational fluid dynamics model of U-shape CMF was developed. The simulation results were evaluated in terms of the natural frequency of the vibrating system and the corresponding phase difference between the motions of the sensing points symmetrically located on the measuring tube. The simulations were conducted on comparison between water and viscous liquid with flow rates spanning the laminar and turbulent regions. The effects of viscosity on mass flow measurement by CMFs are discussed in details. The findings in the simulations can be used for further compensation of deviation due to viscosity effects.

**Keywords:** Coriolis mass flowmeter, Fluid-structure interaction, High viscosity, Deviation, Mass flow rate

### 1. Introduction

Coriolis mass-flow measurement is used in a huge range of industry sectors, including pharmaceuticals, chemicals and petrochemicals, oil and gas, and food. Although a Coriolis mass flow meter (CMF) is independent of flow profile or installation effects, it may be dependent on the Reynolds number ( $Re$ ) of the mean flow. The measurement deviation at low  $Re$  has significant importance in the metering of highly viscous fluids. Several laboratory and field measurements with certain devices clearly indicate that there can be a shift in the meter calibration factor at viscous liquid (Henry, Tombs et al. 2006, Kumar and Anklin 2011).

The flow measurement industry is one such example where application of these numerical tools is helping to improve product quality and to find innovative solutions. In many flow measurement devices, especially a CMF, fluid-structure interaction (FSI), i.e. where computational structural mechanics (CSM) and computational fluid dynamics (CFD) need to be coupled, related problems are often encountered and a complete understanding of physical phenomena occurring in devices becomes vital (Bobovnik, Mole et al. 2005, Mole, Bobovnik et al. 2008). As far as CMFs are concerned, there are a few attempts to simulate a CMF using coupled FSI approach (Mole, Bobovnik et al. 2008, Kumar and Anklin 2011).

In this paper, a three-dimensional coupled fluid-structure numerical model of a U-shape Coriolis flowmeter is presented. The excitation force has been complemented to address properly the forced vibration conditions of CMF, and then the CFD model is employed for the CMF operating under inflow fluid conditions with different viscosity. Results from coupled fluid-structure numerical simulations mainly for varied viscosity are presented. With the help of these simulations the fluid dynamic effect responsible for the meter deviation at different viscosity can be understood, and better resemblance can be achieved between the numerical model simulation and the true operation of the CMFs.

## 2. MATHEMATICAL MODELS

The fluid-conveying measuring sensor tube in the Coriolis mass flowmeter is maintained to vibrate periodically at its natural frequency under impulsively forced vibration conditions (resonance). Mass flow is usually measured as the time or phase difference between the motion of two sensing points ( $S_1$  and  $S_2$ ) on the tube, which are positioned symmetrically along the tube length. However, the distortion of symmetry of the no-flow drive mode is resulted from the interaction between the motion of the tube and the fluid flow due to the CMF's inertial force field, where the straight measuring tube is clamped at both ends and vibrating at its first natural frequency. This section presents the governing equations and corresponding general boundary/initial conditions which we have used in the present simulations.

### 2.1 Fluid domain

The conservation equations of mass and momentum are written in the integral form for the three-dimensional spatial distribution and time range ( $t > 0$ ) of fluid flow as

$$\frac{\partial}{\partial t} \int_{\Omega_F} \rho_F d\Omega + \int_{\Gamma_F} (\mathbf{V}_F - \mathbf{V}_s) \cdot \mathbf{n} d\Gamma = 0 \quad (1)$$

$$\frac{\partial}{\partial t} \int_{\Omega_F} \rho_F \mathbf{V}_F d\Omega + \int_{\Gamma_F} \rho_F \mathbf{V}_F (\mathbf{V}_F - \mathbf{V}_s) \cdot \mathbf{n} d\Gamma = \int_{\Gamma_F} \boldsymbol{\sigma}_F \cdot \mathbf{n} d\Gamma + \int_{\Omega_F} \mathbf{f}_F d\Omega \quad (2)$$

where movement of fluid flow with the density  $\rho_F(x, t)$  and the velocity  $V_F(x, t)$  in the domain  $\Omega_F (x \in \Omega_F)$  are influenced by the motion of a surrounding boundary velocity  $v_s$ ,  $\Gamma$  denotes the surface-area vector. The vector  $\mathbf{f}_F(x, t)$  in the momentum equation (2) is the volume forces acting inside the domain  $\Omega_F$ , and  $\boldsymbol{\sigma}_F(x, t)$  is the resulting tensor.

The respective boundary conditions can be written as

$$\begin{aligned} \mathbf{V}_F(x, t) &= \mathbf{V}_{\text{inflow}}, \quad x \in \Gamma_{\text{inflow}}, \\ p_F(x, t) &= p_{\text{outflow}}, \quad x \in \Gamma_{\text{outflow}}, \\ \mathbf{V}_F(x, t) &= v_s(x, t), \quad x \in \Gamma_{\text{tube}}^m(t), \\ \mathbf{V}_F(x, t) &= 0, \quad x \in \Gamma_{\text{tube}}^{\text{in}}(t), \quad x \in \Gamma_{\text{tube}}^{\text{out}}(t), \end{aligned} \quad (3)$$

where  $\mathbf{V}_{\text{inflow}}$  is the inflow fluid velocity,  $\Gamma$  is the fluid boundary,  $p_{\text{outflow}}$  is the absolute fluid pressure at fluid outflow, and  $v_s(x, t)$  is the velocity of the measuring tube surface.

### 2.2 Structure domain

The conservation of momentum principles is utilized for the three-dimensional spatial distribution ( $x \in \Omega_s$ ) and time evolution ( $t > 0$ ) of the structural response, where the respective equation of motion can be derived by Hamilton's variation principle,

$$\int_{t_1}^{t_2} \delta(W_p - W_k) dt = 0 \quad (4)$$

where  $W_p$  and  $W_k$  are the total potential energy and the total kinetic energy of the moving solid structure, respectively. The detailed expressions for them are defined as (Mole, Bobovnik et al. 2008),

$$W_p = \frac{1}{2} \int_{\Omega_s} \boldsymbol{\sigma}_s : \boldsymbol{\varepsilon}_s d\Omega - \int_{\Gamma_s} \mathbf{P}_s \cdot \mathbf{u}_s d\Gamma - \mathbf{F} \cdot \mathbf{r}_p \quad (5)$$

$$W_k = \frac{1}{2} \int_{\Omega_s} \rho_s (\mathbf{v}_s \cdot \mathbf{v}_s) d\Omega \quad (6)$$

where the surface tractions  $\mathbf{P}_s(x, t)$  acting upon the moving shell boundary through the respective displacement field  $\mathbf{u}_s(x, t)$ , and the concentrated force  $\mathbf{F}(t)$  at point P, where the forced vibration is generated.  $\varepsilon_s(x, t)$  and  $\sigma_s(x, t)$  are the strain and the stress tensor in the shell structure, and  $\mathbf{r}_p$  is the position vector of point P where the force  $\mathbf{F}$  is applied.  $\rho_s(x, t)$  is the structure material density and  $\mathbf{v}_s(x, t)$  is the structure velocity field.

At  $t = 0$ , the initial velocity and acceleration fields,  $\mathbf{v}_s(x, 0)$  and  $\mathbf{a}_s(x, 0)$  must be given, and  $\sigma_s(x, 0) = \varepsilon_s(x, 0) = 0$ . At  $t > 0$ ,

$$\begin{aligned} \mathbf{u}_s(x, t) &= 0, \quad x \in \Gamma_{\text{tube}}^u, \\ \boldsymbol{\sigma}_s(x, t) \cdot \mathbf{n}(x, t) &= \mathbf{P}_s(x, t), \quad x \in \Gamma_{\text{tube}}^u(t), \\ \mathbf{F}(t) &= (\mathbf{F}(t), 0, 0), \quad x = x_p \end{aligned} \quad (7)$$

For the structural-side boundary conditions, the sensing tube was fixed at both ends. In order to simulate the tube exciter, a periodic or harmonic force was applied at the center of tube point P. The first frequency of the sensing tube (the drive frequency of the meter) is equal to the frequency of the oscillating force. A periodic force was applied at the centre Point P to oscillate the pipe in the x-direction,

$$\mathbf{F}(t) = (F_0 \sin(2\pi n f_d \Delta t), 0, 0) \quad (8)$$

where  $\Delta t$  is the integration time step,  $f_d$  denotes the drive frequency, and  $F_0$  represents the amplitude of the periodic force.

### 2.3 Method of analysis

The present simulation uses the ANSYS Workbench framework employing DesignModeler, SIMULATION, ANSYS, CFX Mesh and CFX solver. The pipe is created in DesignModeler, with the structural and fluid domain representing the tube wall and the fluid inside the tube. SIMULATION and CFX Mesh are used to mesh the solid and fluid domain, respectively.

To determine the investigated tube's natural frequency, a modal analysis of the solid domain is conducted in ANSYS. The determined natural frequency is used to calculate the excitation force at point P. And then a dynamic response analysis for the solid domain is performed based on the linear elastic theory, where the deformations of the sense tube are assumed to be small. And it can determine the time step for FSI analysis.

To obtain the initial conditions for the transient fluid analysis, a steady state analysis is carried out in CFX over the fluid domain.

The two steady state analyses are employed for the transient analysis of the fluid domain. The FSI simulations are carried out within CFX (ANSYS v13.0).

During the information transferring, both the kinematic and dynamic constraints are set for the FSI interface,

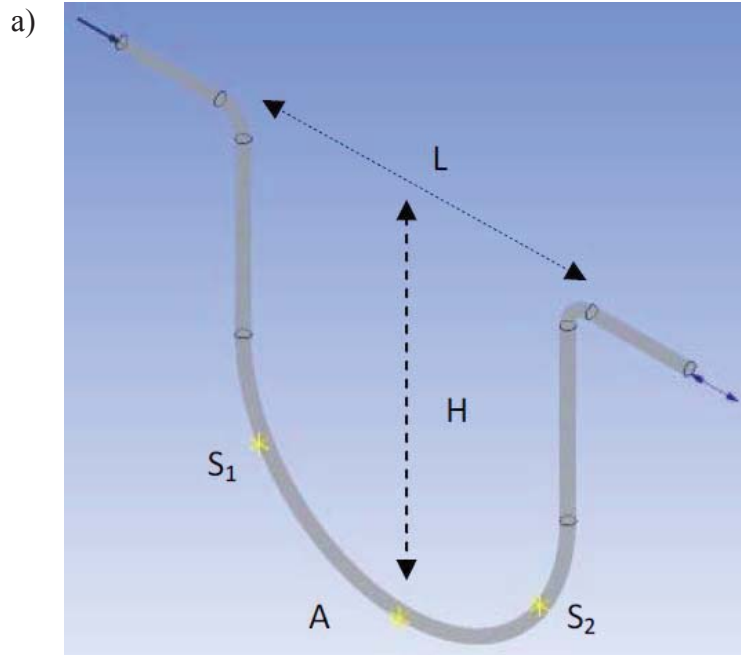
$$\begin{aligned} \mathbf{V}_F(x, t_n)|_F &= \mathbf{V}_F(x, t_n)|_s \\ \mathbf{u}_s(x, t_n)|_s &= \mathbf{u}_s(x, t_n)|_F \\ F_j^{\text{FSI}} &= \int (p\delta_{ij} + \sigma_{ij})d\Gamma_i^{\text{FSI}} \end{aligned} \quad (9)$$

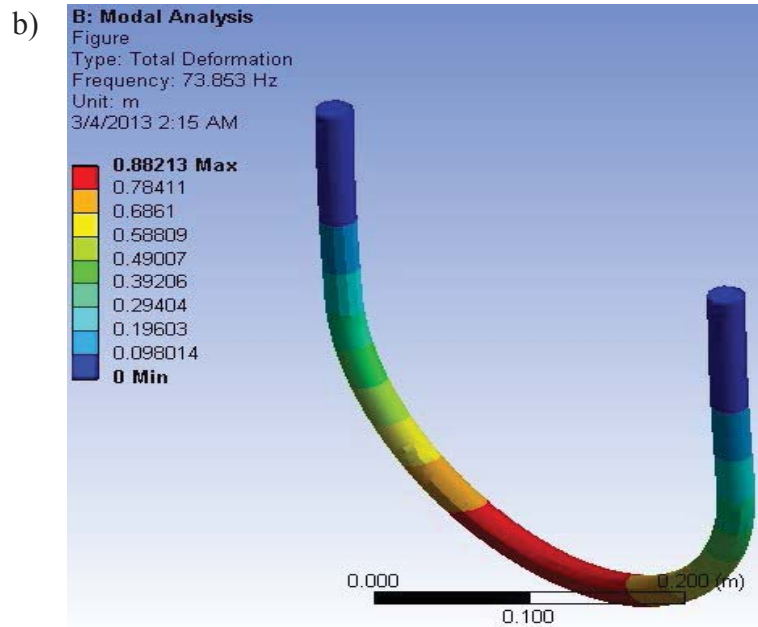
where  $F_j^{\text{FSI}}$  denotes the total force vector from the CFX solver to the structural solver, and  $\sigma_{ij}$  includes the viscous and turbulent part of the momentum tensors. On the other hand, structural displacements  $\mathbf{u}_s(x, t_n)$  are transferred from the structure to the fluid in order to fulfill kinematic constraints.

### 3. RESULTS AND DISCUSSION

The analyzed U-shape CMF, with geometry as presented in Fig. 1(a), is characterized by the length of span  $L=0.4$  m and height of CMF  $H=0.38$  m, and a cross-section geometry which is determined by the internal diameter  $D=0.0254$  m and wall thickness  $\delta=1/40D$ . The distance between the symmetrically positioned sensing points  $S_1$  and  $S_2$  is equal to  $L_s=0.36$  m. The specifications used for the simulations in this work are shown in Table 1.

As the structure has multiple degrees of freedom, the structure will vibrate in a different manner at different natural frequencies without any application of external forces. Looking at all the deformations of the respective frequencies, in order for resonance to occur, the driver has to impose a driving force at the natural frequency  $f_d = 73.853$  Hz, as shown in Fig. 1(b).



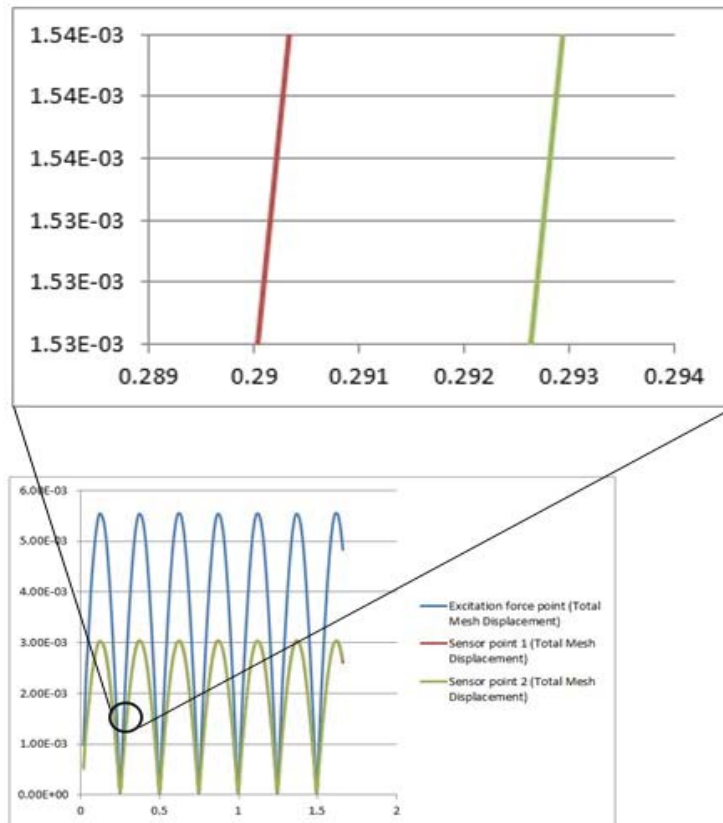


**Figure 1. a) Sensor points, and geometry of the U-shape CMF, and b) modal analysis for natural frequency at 73.853Hz.**

**Table 1. Input parameters for modeling and simulations**

Specifications	Dimensions and Values
Internal diameter of tube (D)	0.0254 m
Thickness of tube	1/40D
Material	Stainless steel 316
Poisson ratio	0.3
Young's modulus	1.93E+11 Pa
Density of stainless steel 316 tube	8000kg/m <sup>3</sup>
Viscosity of liquid fluid	1 - 500 cSt
Density of water	998.2kg/ m <sup>3</sup>
Tested fluid's velocities	2m/s - 20m/s
Number of time steps	100

Through the simulation, the time shift can be gained between the two sensor points  $S_1$  and  $S_2$ , as shown in Fig 2. The blue curve plots the displacement at monitor point 1, where the excitation force is applied. The red curve plots the displacement at the sensor point  $S_1$  which is near the inlet. The green curve plots the mesh displacement at the sensor point 2 which is near the outlet.



**Figure 2. Example result of time difference between sensors  $S_1$  and  $S_2$ .**

The developed FSI model are employed to investigate the effect on fluid viscosity on the performance of the U-shape CMF, including viscosities 50 cSt, 100 cSt, 180 cSt and 500 cSt. The results of time shift  $\delta t$  between sensors  $S_1$  and  $S_2$  for the various viscosities are shown in Fig 3. The time shift increases with the nominal flow velocity, and the drift from the result of water ( $\mu=1$  cSt) of time shift becomes obvious at high velocity.

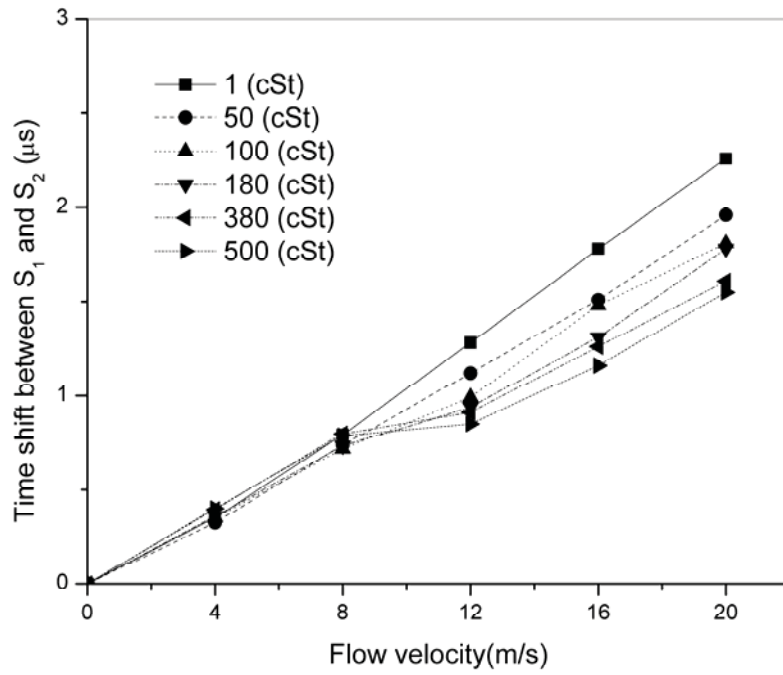


Figure 3. Time shift between sensors S<sub>1</sub> and S<sub>2</sub> against fluid viscosity.

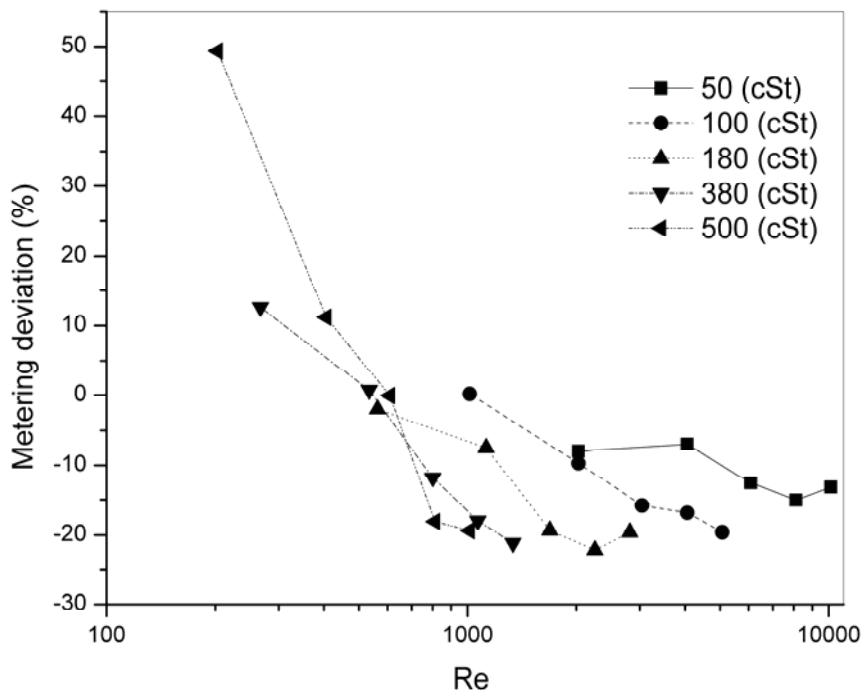


Figure 4. Deviation to water metering of phase difference for different fluid's viscosities.

Since the mass flow rate  $\dot{m}$  of a CMF can be calculated by  $\dot{m} = K_f \delta t$ , where  $K_f$  is the meter factor, and  $\delta t$  is the time shift between the two sensors  $S_1$  and  $S_2$ , the deviation of metering viscous liquid can be calculated based on water a benchmark,

$$Deviation = \frac{K_f \delta t_{viscous\ liquid} - K_f \delta t_{water}}{K_f \delta t_{water}} \times 100\% = \frac{\delta t_{viscous\ liquid} - \delta t_{water}}{\delta t_{water}} \times 100\% \quad (10)$$

The simulation results have been plotted in Fig 4 for the relation between the metering deviation and Reynolds number  $Re = \rho Dv / \mu$ . It is found that when the flow is laminar or transient flow ( $Re \leq 4000$ ), the deviation is fluctuating, while the deviation will be comparably flat when the flow is turbulent.

It is known that fluid with different viscosity may have different damping factor (Kumar and Anklin 2011). When the oscillation of the structure domain experience damping during fluid flow, the driver have to excite additional force to compensate for the amplitude loss caused by the fluid's damping. Since the damping affects the natural frequency of the flow tube, the meter factor  $K_f$  changes, the change directly affects the mass flow rate. The effect of the reduction in natural frequency is caused by the interaction between the fluid and structure dynamics in the CMF. In the future compensation modeling, the damping effect shall be considered.

#### 4. CONCLUSION

In this paper, a computational fluid dynamics model of U-shape CMF was developed to investigate the performance of CMFs influenced by on-line viscosity. The simulation results were evaluated in terms of the natural frequency of the vibrating system and the corresponding time difference between the motions of the sensing points symmetrically located on the measuring tube. The simulations of water and viscous liquid were compared over flow rates spanning the laminar and turbulent regions. The effects of viscosity on CMFs' performance have been discussed in details. The findings in the simulations can be used for further compensation of deviation due to viscosity effects for oil and gas industry.

#### References

- Bobovnik, G., N. Mole, J. Kutin, B. Stok and I. Bajsic (2005). Coupled finite-volume/finite-element modelling of the straight-tube Coriolis flowmeter. *Journal of Fluids and Structures*, 20, pp. 785-800.
- Henry, M., M. Tombs, M. Duta, F. Zhou, R. Mercado, F. Kenyery, J. Shen, M. Morles, C. Garcia and R. Langansan (2006). Two-phase flow metering of heavy oil using a Coriolis mass flow meter: A case study. *Flow Meas. Instrum.*, 17, pp. 399-413.
- Kumar, V. and M. Anklin (2011). Numerical simulations of Coriolis flow meters for low Reynolds number flows. *Mapan*, 26, pp. 225-235.
- Mole, N., G. Bobovnik, J. Kutin, B. Stok and I. Bajsic (2008). An improved three-dimensional coupled fluid-structure model for Coriolis flowmeters. *Journal of Fluids and Structures*, 24, pp. 559-575.



## Uncertainty Modeling and Simulation Highlighting on Tail

### Probability in Biomechanics Study on Pressure Ulcer

**\*Samuel Susanto Slamet<sup>1</sup>, Naoki Takano<sup>1</sup>, and Tomohisa Nagasao<sup>2</sup>**

<sup>1</sup>Keio University, Faculty of Science and Technology, Department of Mechanical Engineering  
3-14-1 Hiyoshi, Kohoku-ku, Yokohama, Kanagawa, Japan

<sup>2</sup>Keio University, School of Medicine, Department of Plastic Surgery  
35 Shinanomachi, Shinjuku-ku, Tokyo, Japan

\*Corresponding author: samuel@z7.keio.jp

#### Abstract

This paper aims at building up a computational procedure to study the bio-mechanism of pressure ulcer using the finite element method. Pressure ulcer is a disease that occurs in the human body after 2 hours of continuous external force. This study assumes that tension and/or shear strain will cause damage to loose fibril tissue between the bone and muscle and that propagation of damaged area will lead to fatal stage. Analysis was performed using the finite element method by modeling the damaged fibril tissue as a cutout. Various uncertainties such as the material properties, loading condition, location of cutout, the length of cutout and configuration of the human buttock were considered in this analysis. By watching both tensile and shear strains, the risk of fibril tissue damage and propagation of the damaged area is discussed and the results may give new insights for careful nursing of patients.

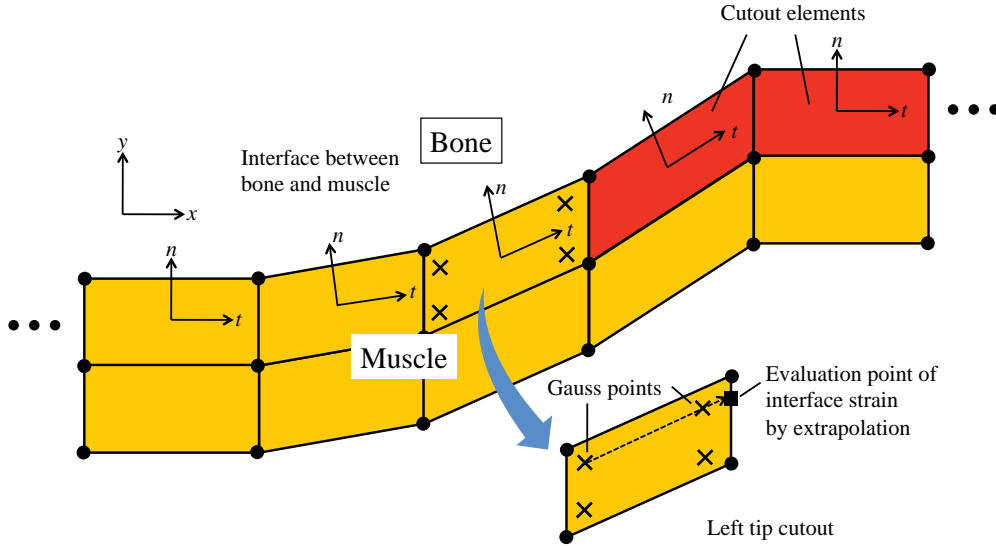
**Keywords:** FEM, Pressure ulcer, Interface strain, Tail probability, Monte Carlo simulation

#### Introduction

The pressure ulcer occurs by sustained pressure and cutoff of blood supply. It has been found that internal damage in deep muscle layers covering bony prominences result in fatal pressure ulcer (Bouten et al., 2003; Maeda, 2006). However, the initial location of that damage is unknown. The final goal of the developed biomechanics simulation is to obtain the set of dangerous material parameters for muscle and fat that can lead to high strain at the bone-muscle interface depending on the load condition under different body positions

The Markov Chain Monte Carlo methods are well known methods to consider any kind of uncertainty (Shenk and Shueller, 2005; Gamerman and Lopez, 2006; Rubinstein and Kroese, 2009). Its demerit is the computational cost required to obtain reliable probability density of the quantity of interest (QoI). Also, the accuracy of Monte Carlo simulation depends on the generation of random numbers algorithm and the number of computational cases.

In this study a practical sampling algorithm named Stepwise Limited Sampling (SLS) is proposed to obtain both accurate enough expected value and the tail probability accurately in the Monte Carlo simulation. It is then applied to a biomechanics problem on the risk prediction of the pressure ulcer.



**Figure 1. Quantity of interest (QoI)**

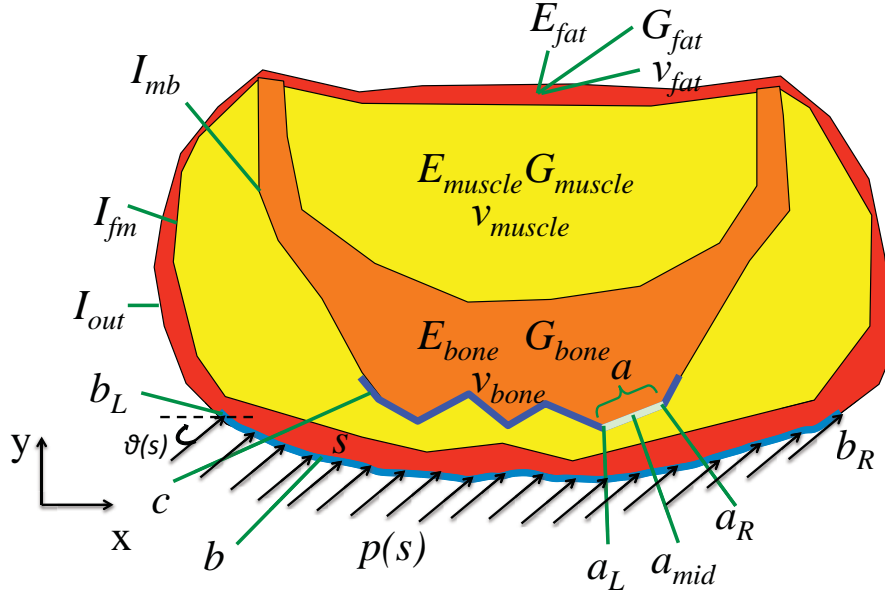
The authors have so far proposed a simplified numerical modeling by assuming that the initial damage occurs at the interface between bone and muscle by the loose fibril tissue damage, in which the risk of reoccurrence of pressure ulcer after surgery was successfully evaluated (Slamet et al. 2012). Also we pointed out that severe shear loading to the patient's buttock might become a trigger of pressure ulcer. The same bio-mechanism assumption is employed in this paper and the interface damage is modeled by a cutout in finite element model.

In the biomechanics analysis of pressure ulcer where the fibril tissue damage at the interface between bone and muscle is modeled by cutout, the strains at the left and right cutout tips are the quantity of interest. The strains are transformed into normal ( $n$ ) and tangential ( $t$ ) coordinate system along the interface as shown in Fig. 1. The cutout tip strain is extrapolated from the values at Gauss points in the neighboring element, so that the extrapolation can be automated. We denote normal strain and shear strain  $\varepsilon_n$  and  $\gamma_m$ . Concerning normal strain  $\varepsilon_n$ , it is assumed that only tensile strain contributes to the breakage of fibril tissue and propagation of damage area.

### Mathematical Parameters and Numerical Models of Pressure Ulcer

In this paper, 2D linear finite element analysis is carried out in the same way with the authors' previous paper (Slamet et al. 2012). Figure 2 shows a typical image of healthy human buttock. Bone, muscle, fat and skin are the main tissues, and the center part is the target region where muscle covering bony prominences is seen. The skin was neglected because Makhsous et al. reported that the deformation of skin was much smaller than that of muscle and fat. So only the Young's modulus, Poisson's ratio and Shear modulus of bone, fat and muscle are considered in this analysis represented by  $E_{fat}$ ,  $E_{muscle}$ , and  $E_{bone}$  for the Young's modulus of fat, muscle and bone,  $\nu_{fat}$ ,  $\nu_{muscle}$  and  $\nu_{bone}$  for Poisson's ratio of fat, muscle and bone and  $G_{fat}$ ,  $G_{muscle}$  and  $G_{bone}$  for the shear modulus of fat, muscle and bone.

The curve of the model is defined as  $I_{out}$ ,  $I_{fm}$ , and  $I_{mb}$  where each represents outline form, curve between fat and muscle, and curve between muscle and bone.



**Figure 2. Mathematical model parameters**

The fibril tissue damage was modeled by a cutout. The location of possible cutout is located in  $c$ , which is an element of  $I_{mb}$ . The location of cutout is then defined as  $a$  as an element of  $c$  with the center location as  $a_{mid}$ , length of cutout as  $L_a$  and left and right edges as  $a_L$  and  $a_R$ .

Contact area or loading area for the model is defined as  $b$ , which is an element of  $I_{out}$ . The left edge and right edge of the loading area is defined as  $b_L$  and  $b_R$ . The loading value itself is defined as  $p(s)$  with  $s$  as the curve along  $b$ . There is also a loading angle of  $\theta$ .

**Table 1. Phenomena identification and ranking table**

Description		Parameter Involved	Importance	
Inter-individual difference	Age	-	High	
	Gender	-	High	
	Geometry	Contour	$I_{out}$	High
		Configuration of fat and muscle	$I_{fm}$	High
		Configuration of bone	$I_{mb}$	High
	Material properties	Skin	-	Low
		Fat	$E_{fat}, G_{fat}$	High
		Muscle	$E_{muscle}$	High
		Bone	-	Low
	Loading area	Area	$b$	High
		Direction	$\theta(s)$	High
Load value		$p(s)$	High	
Cutout	Location	$a_{mid}$	High	
	Length	$L_a$	High	

**Table 2. Material properties**

	Young's modulus, E (MPa)		Shear modulus, G (MPa)		Coefficient of correlation between E and G	Poisson's ratio, $\nu$
	Mean value	Standard deviation (normal distribution)	Mean value	Standard deviation (normal distribution)		
Fat	$8.0 \times 10^{-2}$	$8.0 \times 10^{-3}$	$2.857 \times 10^{-2}$	$2.857 \times 10^{-3}$	0.995	0.4
Muscle	$7.5 \times 10^{-2}$	$7.5 \times 10^{-3}$	$2.517 \times 10^{-2}$	-	-	0.49
Bone	$2.0 \times 10^4$	-	-	-	-	0.3

Uncertainties were considered in 7 areas as seen in Table 1. Location of cutout ( $a_{mid}$ ) with 3 different sampling locations, length of cutout ( $L_a$ ) with 2 different sampling lengths, loading condition ( $b$ ) with 3 different loading sampling and configuration of muscle and fat ( $I_{fm}$ ) with 2 different sampling configurations, and 3 random input parameters in Young's modulus of fat ( $E_{fat}$ ), shear modulus of fat ( $G_{fat}$ ) and Young's modulus of muscle ( $E_{muscle}$ ).

Table 2 shows the material properties based on linear isotropic model. A normal distribution is assumed for simplicity. The coefficient of correlation between Young's modulus and shear modulus for fat was determined so that the Poisson's ratio does not exceed 0.5. For muscle, only the variation of Young's modulus was considered because its Poisson's ratio is close to 0.5. For cutout element,  $10^{-5}$  times smaller value than the mean Young's modulus of muscle was used.

The numerical values for geometry, loading area and cutout can be seen in table 3.

### Stepwise Limited Sampling (SLS) Method

By giving the random distribution with relatively large scattering, the Monte Carlo method provides us the probability density of the quantity of interest, its expected value and standard deviation. It is known that analyses of 10,000 cases are usually required to reach the convergence of both expected value and standard deviation. The accuracy is dependent on the generation scheme of random numbers. The Mersenne Twister is known to give high quality random numbers and it is used in this study too.

The convergence of the expected value is, in general, more easily obtained than standard deviation. One of the reasons is that the quality of random numbers generated in the tail probability is not good enough among 10,000 random numbers even if Mersenne Twister method is adopted. In other words, if one wants to put highlight on the reliability of the tail probability, 10,000 cases are not enough. It is important, for instance, when the prediction of fracture/failure is required even if its probability is very low. Considering that the demerit of Monte Carlo simulation is the high computational cost, a new and cost-effective sampling scheme highlighting on the tail probability would be valuable in vast industries.

Therefore, a Stepwise Limited Sampling (SLS) is proposed in this paper, which stops the iteration when the expected value is converged and spends the computational time for the analyses of the cases in tail probability.

**Table 3. Numerical values for geometry, loading area and cutout.**

Description		Sampling points	Values		
Geometry	$I_{fm}$	$I_{fm1}$	Muscle-rich		
		$I_{fm2}$	Fat-rich		
Loading area	$b$	$b_1$	Supine	$b_L$	(39, 109) mm
				$b_R$	(447, 108) mm
				$p(s)$	$0.8 \times 10^{-2}$ MPa
				$\theta(s)$	$90^\circ$
		$b_2$	Lateral-A	$b_L$	(38, 290) mm
				$b_R$	(28, 120) mm
				$p(s)$	$1.8 \times 10^{-2}$ MPa
				$\theta(s)$	$0^\circ$
		$b_3$	Lateral-B	$b_L$	(470, 133) mm
				$b_R$	(438, 290) mm
				$p(s)$	$1.8 \times 10^{-2}$ MPa
				$\theta(s)$	$180^\circ$
Cutout	$a_{mid}$	$a_{mid-1}$	Left	(186, 100) mm	
		$a_{mid-2}$	Center	(229, 91.9) mm	
		$a_{mid-3}$	Right	(283, 90.5) mm	
	$L_a$	$L_{a-1}$	Left	$L_a$	4 mm
				$a_L$	(184.30, 98.86) mm
				$a_R$	(187.65, 101.10) mm
			Center	$L_a$	4 mm
				$a_L$	(227.70, 92.86) mm
				$a_R$	(230.57, 90.95) mm
		Right	$L_a$	4 mm	
			$a_L$	(281.70, 91.50) mm	
			$a_R$	(285.26, 89.52) mm	
			$L_{a-2}$	Left	$L_a$
		$a_L$			(182.62, 97.74) mm
		$a_R$			(189.33, 102.22) mm
		Center		$L_a$	8 mm
				$a_L$	(226.30, 93.80) mm
				$a_R$	(231.97, 90.02) mm
		Right		$L_a$	8 mm
			$a_L$	(279.96, 92.46) mm	
$a_R$	(287, 88.55) mm				

SLS only assures the moderate accuracy of expected value of quantity of interest. The expected value itself is distributed and therefore the convergence is estimated based on the central limited theorem. Let  $E_{(i)}$  be the expected value and  $\sigma_{(i)}$  be the standard deviation after  $i$  sets of analyses in standard Monte Carlo simulation. The convergence is judged by Eq. (1)

$$E_{(i)} - E_{(i-1)} \leq \frac{\sigma_{(1)}}{E_{(1)} \sqrt{n_{\max}}} \quad (1)$$

where right hand side is normalized by the expected value after the first set of analyses. We recommend to use  $n_{max} = 10,000$ . Let 100 cases be one set of analyses, then Eq. (1) yields as follows.

$$E_{(100j)} - E_{(100(j-1))} \leq \frac{\sigma_{(100)}}{E_{(100)} \sqrt{n_{max}}} \quad (2)$$

If Eq. (2) holds three times continuously, then the expected value is converged. This is because the expected value may oscillate in the Monte Carlo simulation. When the convergence is obtained, the Monte Carlo simulation is suspended.

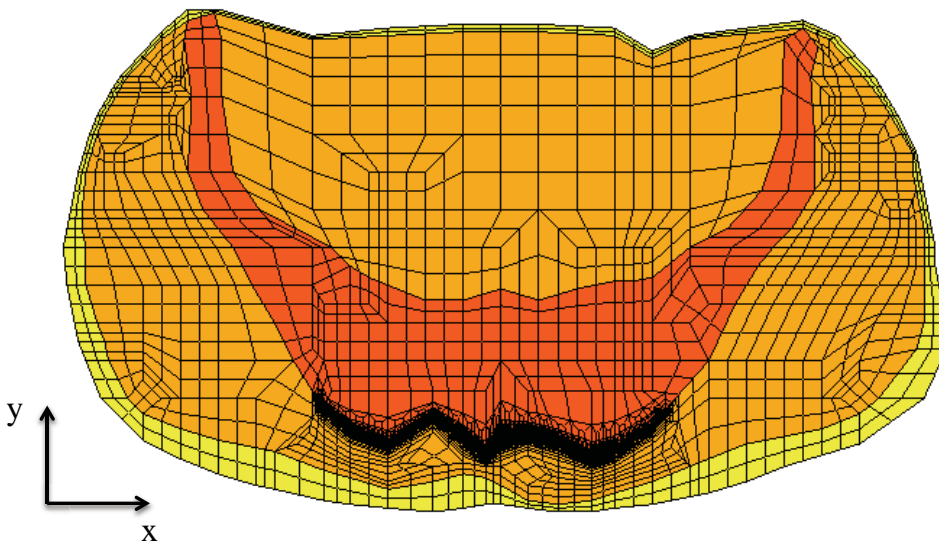
Next, as the post-processing, the correlation between the input parameters sets and the quantity of interest must be investigated. Supposing that the number of parameters is large, sets of two parameters among all parameters are chosen. Then the quantity of interest can be plotted in the two-dimensional space of the parameters. To this end, it is easy to determine the limited zone with specific value of quantity of interest by the following equation.

$$p_i x_i + p_j x_j + q \geq 0 \quad (i \neq j) \quad (3)$$

Here,  $x_i$  and  $x_j$  are the chosen two parameters, and  $p_i$ ,  $p_j$  and  $q$  are scalar factors. By the combination of multiple linear equations, Eq. (3), in the multi-dimensional space of all parameters, the limited zone to be analyzed carefully can be defined. This procedure is automated in the program, because simple linear equations are used.

### Analysis and Discussion

There are a total of 36 models considering by consideration of 4 uncertainties of configuration of fat and muscle, loading area, location of cutout and length of cutout, with each model having 3 random input parameters of  $E_{fat}$ ,  $G_{fat}$  and  $E_{muscle}$ . All uncertainty parameters are modeled using the finite element mesh as shown in Fig. 3. A total of 77,334 four-noded elements were used in the analysis.



**Figure 3. A typical mesh used for 36 data analyses.**

Each model then had a convergence check to decide when the analysis should be stop. The convergence of the models varies between 1,300 analyses to 4,900 analyses. The limited area is then decided for each model from the three-dimensional space of random parameters  $E_{fat}$ ,  $G_{fat}$  and  $E_{muscle}$ .  $\mu + 3\sigma$  was used as the threshold of limited dangerous zone.

The limited zone was originally defined by combinations of  $E_{fat} - G_{fat}$  and  $E_{fat} - E_{muscle}$ , but the results of  $E_{fat} - G_{fat}$  shows the same formula as  $E_{fat} - E_{muscle}$ , so only  $E_{fat} - E_{muscle}$  are then plotted into the limited sampling zone.

After the process of convergence check and deciding the limited area for all 36 models, the results from those six-dimensional space are then put into a two-dimensional space as seen in Fig. 4. The six-dimension space starts from  $L_a$  and in Fig. 4 case is  $L_a = 4$  mm. From there, 2 main axes were considered, one axis is for  $I_{fm}$  and another one is for  $a_{mid}$ . In the  $I_{fm}$  axis, the  $a_{mid}$  (shown in dotted line for  $a_{mid-1}$ , solid line for  $a_{mid-2}$  and dashed line for  $a_{mid-3}$ ) and  $b$  (shown in blue for  $b_1$ , red for  $b_2$  and green for  $b_3$ ) are compacted into 2 figures with one figure for  $I_{fm-1}$  and another for  $I_{fm-2}$ . In the  $a_{mid}$  axis, the  $I_{fm}$  (shown in solid line for  $I_{fm-1}$  and dotted line for  $I_{fm-2}$ ) and  $b$  (shown in blue for  $b_1$ , red for  $b_2$  and green for  $b_3$ ) are compacted into 3 figures with one figure for  $a_{mid-1}$ , another for  $a_{mid-2}$  and  $a_{mid-3}$ . The figures on the axes of  $I_{fm}$  and  $a_{mid}$  itself contain a two-dimensional projection of the limited zone for  $E_{fat} - E_{muscle}$ . Linear interpolation was applied for simplicity to predict the limited zone between  $a_{mid-2}$  and  $a_{mid-3}$ .

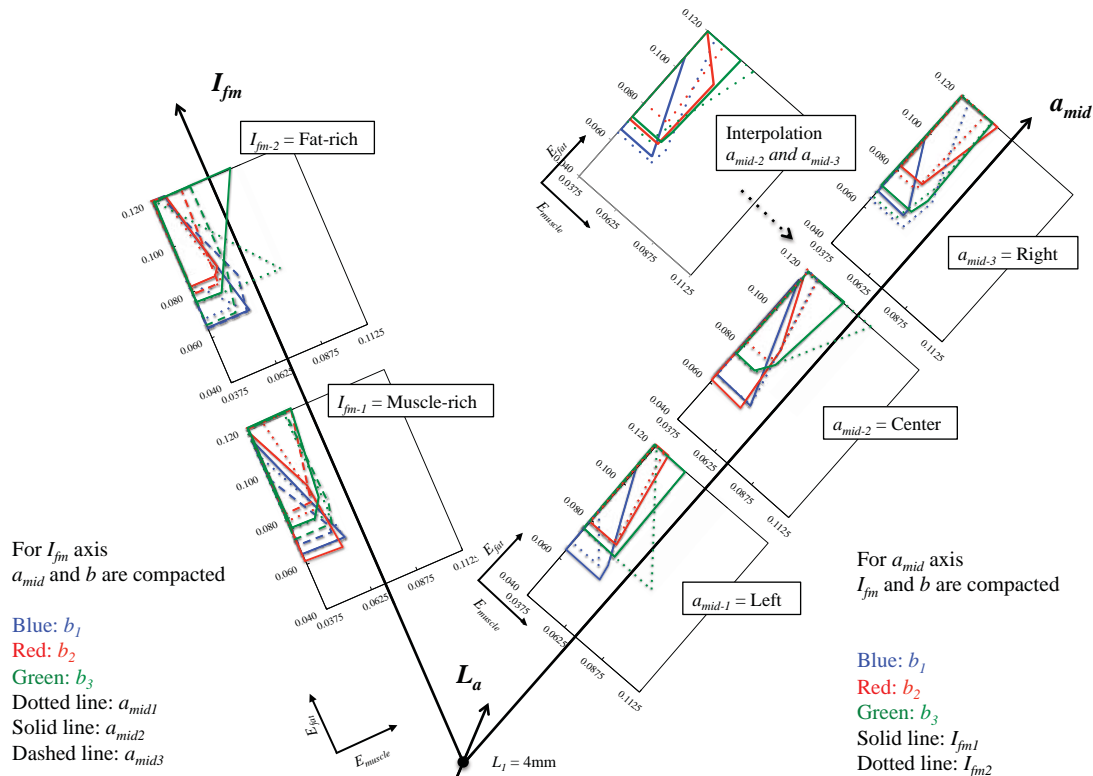


Figure 4. Six-dimensional space of the limited sampling zone on  $L_a = 4$  mm

After determining the limited zone in this way, medical doctors can then predict set of limitation that can lead to pressure ulcers by looking into the corresponding parameters. This will prove useful for nursing patients to prevent the occurrence of pressure ulcer.

## Conclusions

In order to reduce the computational cost of Monte Carlo analysis, a sampling algorithm method was proposed. Seven uncertainty parameters were put into consideration in this analysis with the goal to find a new finding from the clinical viewpoint by predicting the dangerous zone of pressure ulcer. The correlation between geometry, loading area, cutout location, cutout length, and random material parameters at the interface between the bone and muscle was calculated. Medical doctors can find set of parameters that leads to high interface strain in order to prevent the occurrence of pressure ulcer from happening.

The computational time was completely reduced in this analysis compared to the conventional Monte Carlo simulation. The method shown here is cost-effective and practical.

In future works, the biomechanics simulation should contain more random parameters such as age and gender as mentioned in the phenomena identification and ranking table due to its high importance. The SLS algorithm is applicable to a problem with larger input parameters as shown in this paper, and it should be proven to be able to handle more parameter in future simulation. The applied interpolation should also be validated which can lead to finding the response surface along all possible cutout locations and different fat and muscle configurations.

Although 2D linear analyses were carried out as a demonstration in this paper, 3D non-linear analyses should be employed in the future, considering large deformation, contact between body and bed and viscoelasticity.

## References

- Bouten, C. V., Oomens, C. W., Baaijens, F. P. and Bader, D. L., *The Etiology of Pressure Ulcers: Skin Deep or Muscle Bound*, Archives of Physical Medicine and Rehabilitation, 84, 2003, pp. 616-619.
- Maeda, T., *Pressure Ulcers Resulting from Earlier and More Marked Injury in the Deeper Layers - Typical Clinical Cases and an Insight into Pocket Formation*, Japanese Journal of Pressure Ulcers, 8, 2006, pp. 195-202 (in Japanese).
- Shenk, C. A. and Shueller, G. I., *Uncertainty Assessment of Large Finite Element Systems*, Springer, Berlin, 2005.
- Gamerman, D. and Lopez, H. F., *Markov Chain Monte Carlo*, Chapman & Hall, London, 2006.
- Rubinstein, R. Y. and Kroese D. P., *Simulation and the Monte Carlo Method*, John Wiley & Sons, New Jersey, 2009.
- Slamet, S. S., Takano, N., Tanabe, Y., Hatano, A. and Nagasao, T., *Biomechanics Analysis of Pressure Ulcer using Damaged Interface Model between Bone and Muscle in the Human Buttock*, Journal of Computational Science and Technology, 6, 2012, pp. 70-80.
- Makhsous, M., Lim, D., Hendrix, R., Bankard, J., Rymer, W. Z. and Lin, F., *Finite Element Analysis for Evaluation of Pressure Ulcer on the Buttock: Development and Validation*, IEEE Transactions on Neural Systems and Rehabilitation Engineering, 15, 2007, pp. 517-525.



## Application Optimization of Regulating Valve in Wind Tunnel

**\*Shen Feng Jing<sup>1</sup>, Sun Tao<sup>1</sup>, Bu Jun Hui<sup>1</sup>, Sun Yong Tang<sup>1</sup>, and Wang Tie Jing<sup>1</sup>**

<sup>1</sup>1st Lab of Institute of Wind Tunnel Engineer and Technology, China Academy of Aerodynamics, BeiJing, China.

\*Corresponding author: shenfjcas@163.com

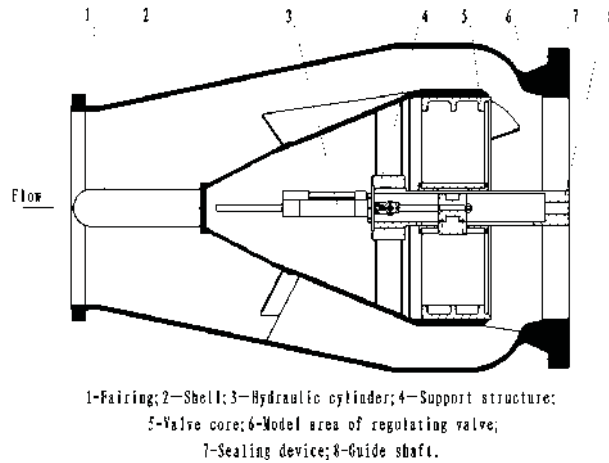
**Key Words:** *S-FEM, CS-FEM, NS-FEM, ES-FEM, FS-FEM*

The regulating valve is a key component in trisonic wind tunnel. Its performance greatly influence the flow field quality. During a wind tunnel test, a crack occurred on the weld line between the support structure and the hydraulic cylinder of a regulating valve. After an analysis on its stress, the reason for the production of crack found. The support structure consists of two parallel steel plates which were welded to the circular support ring on the inner of the shell of the regulating valve. Due to the existence of a closet, one of the steel plates can not be welded completely to the inner of shell, however, the stress reaches its maximum in here, thus the crack occurred. To solve this problem, the support structure was optimized on the basis of stress analysis, and a new structure of cross form was obtained, which eliminate the existence of closet, and all the weld lines are complete. In this paper, the new support structure is described in details, and calculated using the finite element software, and compared with original structure. The analysis results show that at same conditions, the optimization structure has smaller maximum stress less than subduced strength of material. It is also tested in the process that the optimized structure is easy to make and the welding technique becomes quite simpler. In the later application, the support structure is not damaged any more. The design optimization for support structure of the regulating valve is used and its application to wind tunnel test shows the method is efficiency and practicability.

**Keywords:** Design optimization, Support structure, Weld line, Stress analysis, Crack

### Introduction

The regulating valve is an important component of FD-12 wind tunnel used to control air pressure and flow in the settling chamber. One of the most advanced three transonic wind tunnel in our country, different for the general industrial throttle valve, the regulating valve is specially designed to satisfy the strict requirements of FD-12 (Liu, 2003; Jiang, 2001). The structure of the regulating valve is large and complex with entrance diameter of 1.6m, the exit diameter of 1.8m, the length of 3.7m. The regulating valve has inner and outer shell. Its hydraulic cylinder drives the valve core moving on the guide shaft, thus the regulating valve can adjust the air pressure and flow through changing the flow area(Wu, 1985). The hydraulic cylinder and the guide shaft are fixed on the support structure. The support structure was welded on the inner shell. A drawing of the regulating valve is shown in Fig.1.



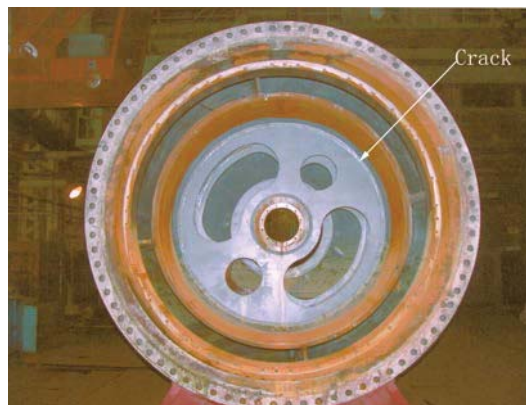
**Figure 1. Structure of regulating valve**

The support structure has a direct impact on the safety and reliability of the regulating valve. The original design of the support structure is of two parallel circular plate. In the wind tunnel test, a crack occurred on the weld line. After an analysis on its stress, the reason for the production of crack is found. In order to solve the problem, it needs an optimization design.

### **Design and Analysis of Parallel Steel Plate Support**

#### *Structure of Parallel Steel Plate Support*

The support structure consists of two parallel steel plates which are welded to the circular support ring on the inner shell of the regulating valve. Two parallel steel plates have open vents. The material of the support structure is 16MnR. The thickness of the parallel steel plates is 30mm. Its picture is shown in Fig.2.



**Figure 2. Picture of parallel steel plate support**

#### *Finite element model of support structure*

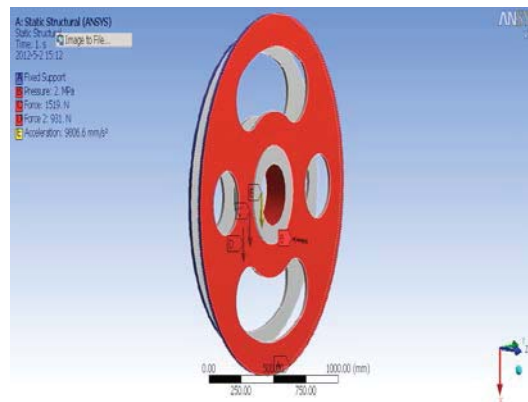
Based on SolidWorks software, the calculation mode of the support structure was built, and was input into the Ansys Workbench through the interface between the SolidWorks and Ansys. The conversion process without data lost ensures the high precision of the finite element analysis.

The precision of the finite element analysis is decided by the geometrical and physical similarity between entity and its calculation model. Usually, in order to increase the calculation feasibility and save the calculation time, the calculation model should be as succinct as possible under the ensurance of calculation precision and reliability of results before meshing the model of the entity(Pu, 2010). For example, before meshing the model of the support structure the bolt connection hole was washed on the hydraulic cylinder and the guide shaft. The finite element model was divided into hexahedral elements, the element size is 5mm. The total number of elements is 606467, node number is 1032959.

### *Constraint and load*

The support structure was constrained by the actual condition during a wind tunnel test. The constraint was fixed on the outer ring of the the parallel steel plate support.

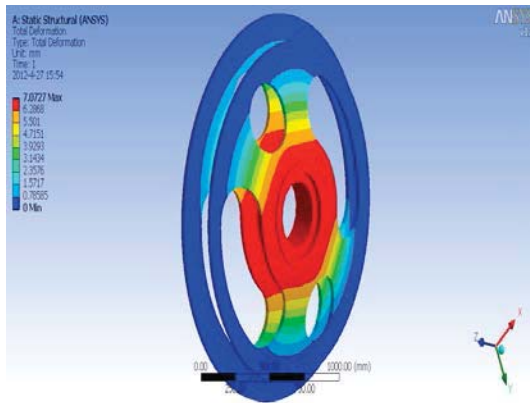
The load of the support structure includes the flow impact and the weights of the hydraulic cylinder, the guide shaft and the support structure. The flow impact is 2MPa, distributed on the upwind side of the support structure; the support of the hydraulic cylinder is cantilever with its all weight of 931N concentrated on the support structure; the guide shaft is fixed beam with half of its weight of 1519N on the support structure; The support structure gravity distribution was decided by the definition of gravity acceleration, as shown in Fig.3.



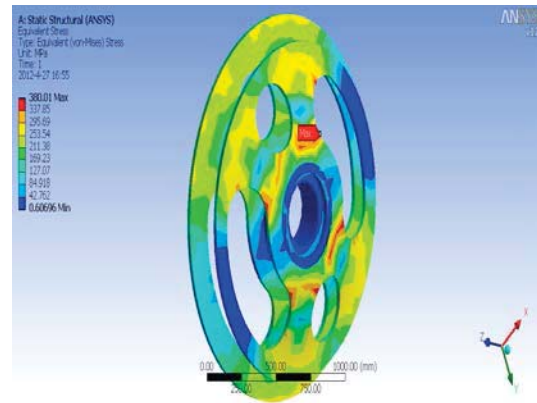
**Figure 3. Constraint and load of parallel plate support**

### *Calculation and result analysis*

During a wind tunnel test, the support structure is the most dangerous working condition. Based on calculation of Ansys software, the maximum strain is 7.0727mm and maximum stress is 380.01MPa. The drawing of the strain and stress of the support structure are shown in figure 4 and figure 5.



**Figure 4. Strain of the support structure**



**Figure 5. Stress of the support structure**

In figure 4, the maximum strain position is on the supporting ring, which accords with the actual deformation of the support structure, but it is larger amount. In figure 5, the maximum stress is 380.01MPa near the inner ring of the smaller steel plate. But a crack on the support structure occurred on the weld line during a wind tunnel test. After an analysis on its reason, it is found that the calculation condition is different from practical processing. Two steel plates and the inner of the shell form a closet cavity, and due to the existence of the closet, one of the steel plates can not be welded completely to the inner of shell, and the crack occurred.

### **Optimization Design of Support structure**

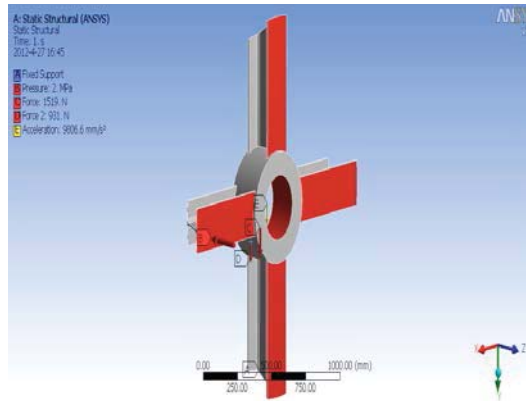
After the analysis of the parallel steel plate support, the key of the optimization design is not only ensurement strength, but also to ensure full penetration welding. The traditional method to this problem simply increasing the thickness and adding more stiffen plates can not solve. Therefore, the support structure is optimized. The design is the cross support structures, which were welded on the inner of the shell as a whole, as shown in figure 6. The material of the cross support structure is Q345, it is open frame, all the weld lines can be penetrated fully.



**Figure 6. Picture of cross support structure**

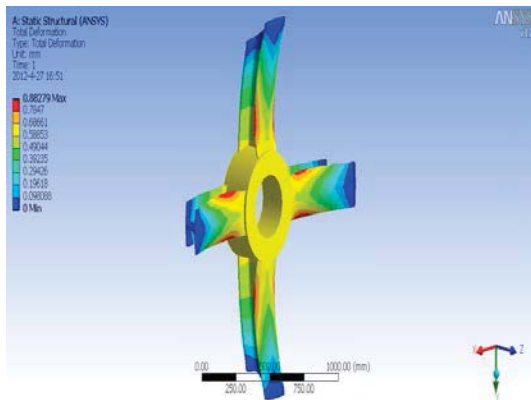
The finite element model using hexahedral element was established by the substantiation of the cross support structure. The element size is 5mm, the ultimately divided element number is 34404,

node number is 589998. The actual stress constraint condition and force load were applied according to the support structure on the operation condition, as shown in figure 7.

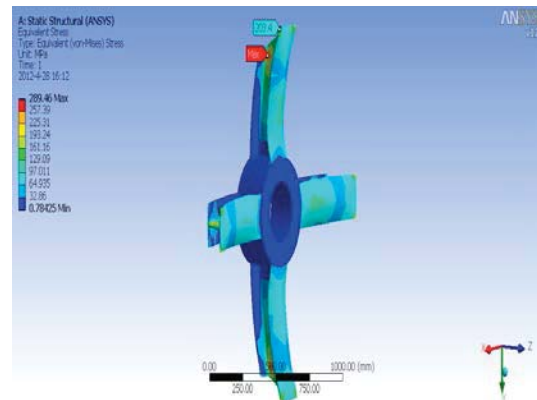


**Figure 7. Constraint and load of cross support structure**

The cross support structure was calculated using the finite element software, the maximum strain is 0.88279mm and maximum stress is 289.46MPa, as shown in figure 8 and figure 9.



**Figure 8. Strain of support structure**



**Figure 9. Stress of support structure**

It is shown that that displacement of the support structure is smaller in figure 8, the maximum strain occurs near the end of the H steel upwind side, it is 289.46MPa. The material yield limit of the support structure is 345MPa, the maximum stress is less than the material yield limit. The maximum stress of the weld connection is 203.4MPa, the stress of the weld line is 235MPa, so the support structure is safe.

**Two Design Comparative Analysis**

Two design are analysed comparatively from the three following aspects:

(1) The strain and stress of two design using the finite element analysis are compared, as shown in Table 1. It can be found in that the optimized design has the maximum strain and stress less than the original design, and the optimized support structure is more reasonable and feasible.

**Table 1. Stress and strain comparison of the two design**

Number	Comparison	Stress(mm)	Strain(MPa)
1	Original structure	7.0727	380.01
2	Optimized structure	0.88279	289.46

(2) The optimized design has four other advantages:

- ① In terms of economy, the optimized design is more simple, the material of H type steel is very common, the optimized saves material, its price is cheaper than the original design;
- ② In the production process, because the cross support structure is in open frame, the workers weld easier than before, and the optimized structure is easy to guarantee the coaxiality of the hydraulic cylinder and the guide shaft;
- ③ The cross support structure need not the induced flow hole, and airflow obstruction area is smaller than the original design, it is favorable for the wind test;
- ④ In the installation process, the optimized design need small space, it provides greater space for other components, it is convenient for people to enter the internal regulating valve, they can easily install and repair and maintain the regulating valve.

(3) In fact, the original structure occurred on weld cracking after dozens of wind tunnel tests. The optimized design has completed safely eight thousands blowdown tests for four years. In the application, the support structure was not damaged any more.

## Conclusion

The paper introduced the optimization design of the support structure of a regulating valve in the FD-12 tunnel wind. Using the finite element software, the reason for the production of crack was found. On this basis, the design of the support structure was optimized, and calculated using the finite element software, and compared with original structure. The analysis results show that the optimized structure has better strength, the design is safe. The optimized structure is more reasonable and feasible in the design and production and installation in the wind tunnel test. In the latter application, the support structure subjected to high frequency and high strength of the wind tunnel test, it was not damaged any more. So it proved the support structure is safe and reliable.

## References

- Liu Zhengchong. (2003), Aerodynamics and construction of high and low speed tunnel. pp. 400–401.
- Jiang Weiben. (2001), Design of hypersonic tunnel facility. National Defence Industrial Press. pp. 37-39.
- Wu Ronglin, Liu Zhenyu. (1985), Theory of wind tunnel. Beijing Institute of Aeronautics Press.
- Pu Guangyi. (2010.10), ANSYS Workbench 12 based tutorial and detailed examples. China WaterPower Press. Pp.120-123.

# Molecular Dynamics Simulation of Shock Wave Propagation in Aluminum Single Crystal

Yuan-Yuan JU, Qing-Ming ZHANG\*

State Key Laboratory of Explosion Science and Technology, Beijing Institute of Technology, Beijing  
100081, People's Republic of China

\*Correspondence author. Email: qmzhang@bit.edu.cn

## Abstract

The characteristics of shock wave propagation in aluminum single crystal are investigated by using molecular dynamics (MD) method based on the embedded atom method (EAM) potential function, including elastic and plastic deformation, Hugoniot relation, width of shock front. The simulated results show that there is a threshold particle velocity value above which an elastic-plastic wave propagates in aluminum single crystal and the velocity of elastic wave increases slightly with the shock loading. Otherwise, only a plastic wave propagates in aluminum single crystal and the width of shock front decreases by exponent with the normal stress.

**Keywords:** molecular dynamics, shock wave propagation, Hugoniot relation, width of shock front, aluminum single crystal

## Introduction

The classical molecular dynamics (MD) simulations have been used increasingly to examine the shock compression response of crystalline materials. The metal materials usually experience elastic-plastic response under one-dimensional shock compression, and finally reach a stable state of stress, temperature and density. The generation and evolution of split shock waves resulting from a dissociative polymorphic phase transition were modeled using MD simulations (*Robertson et al.*, 1991). The particle velocity histories at the interface between an aluminum sample shocked by a 120 fs laser-driven pressure pulse and a fused silica window were first measured by *Evans et al.* (1996). *Dlott et al.* (1998) tried to illustrate how moderate-pressure nanoshocks could be a powerful tool for ultrafast dynamical studies of complex systems of interest to chemists and biochemists, such as crystalline or amorphous molecular solids, glasses, and biomaterials. The massively parallel three-dimensional MD simulations were employed to examine the plasticity induced by shock waves (*Zhou et al.*, 1998; *Holian et al.*, 1998; *Kadau et al.*, 2002). *An et al.* (2012) present MD simulations of shock-induced plasticity and spall damage in single crystal Ta. *Zhao et al.* (2013) investigated shock response of a model Cu nanofoam with cylindrical voids and a high initial porosity by using large-scale MD simulations. It is very important to understand the shock front structure and the detailed broadening mechanisms in response to materials for theoretical treatments and other applications (*Shao et al.*, 2007; *He et al.*, 2009; *Ma et al.*, 2013). However, many macroscopic

properties of materials are not well understood due to the poor knowledge of each physical process in the shock front, particularly at the different length and time scales (Asay *et al.*, 2003). Hence, studying the response of metal materials to the shock compression has a very important significance for the further research of the constitutive relations.

In the current letter, the characteristics of shock wave propagation in aluminum single crystal are investigated by using MD method based on the embedded atom method (EAM) potential function. The shock front structure and the Hugoniot relation are obtained. The results provide useful atomistic knowledge of the characteristics of shock wave propagation in aluminum single crystal.

### Methodology of the simulation

The potential function plays an important role in the MD simulation, and the EAM potential (Mei *et al.*, 1991) is employed in the current study. The functional form of the EAM potentials is given by

$$E_{\text{tot}} = \frac{1}{2} \sum_{i \neq j} V(r_{ij}) + \sum_i F(\rho_i). \quad (1)$$

$$\rho_i = \sum_j \varphi(r_{ij}). \quad (2)$$

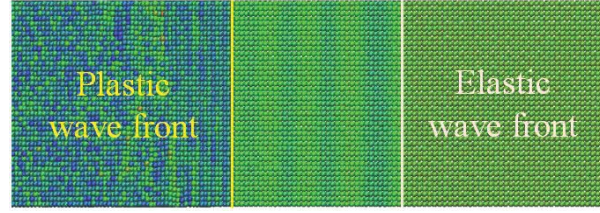
where  $E_{\text{tot}}$  is the total energy,  $V(r_{ij})$  the pair potential, and  $F(\rho_i)$  the embedding function.  $\varphi(r_{ij})$  is the electron density contribution from atom  $j$  to atom  $i$ . The total electron density  $\rho_i$  at an atom position  $i$  is calculated via the linear superposition of electron density contributions from neighboring atoms.

The system is prepared in FCC configuration with about 360000 atoms. The sample size is  $40.5 \times 12.15 \times 12.15$  nm with free surfaces along the shock direction [100]. The periodic boundary conditions (PBC) are imposed to minimize surface and edge effects, simulating a pseudo-infinite lateral dimension in the directions transverse to the shock wave. The system is first minimized using the conjugate gradient method, and equilibrated at 300 K with a time integration step of  $dt = 0.1$  fs, and then applied various shock waves along the direction [100].

### Results and discussion

The MD simulation results can present the micro-structure of the shock front under shock loading. Figure 1 shows the typical two-wave structure in aluminum single crystal in the case of particle velocity  $U_p = 1.25$  km/s. Obviously, the system experiences an elastic-plastic deformation, and two waves of an elastic precursor followed by a slower plastic wave front propagate along the direction of the shock loading.





**Figure 1. Typical two-wave structure in aluminum single crystal in the case of  $U_p = 1.25$  km/s.**

In order to clearly understand the nature of plastic deformation the particle velocity  $U_p$ , normal stress  $\sigma_{xx}$  and shear stress  $\sigma_{VM}$  profiles along the shock wave propagation direction are required to study. The system was divided into 36 bins (each bin contained about 10000 atoms), and then the velocities of atoms in each bin is statistically averaged as the particle velocity at the corresponding position. In the current MD simulation the output stress is the product of the atomic stress and its volume, so the stress in each bin can be defined as

$$\sigma_{\Delta V} = \frac{\sum_i^m \delta_i V_i}{\Delta V}, \quad (3)$$

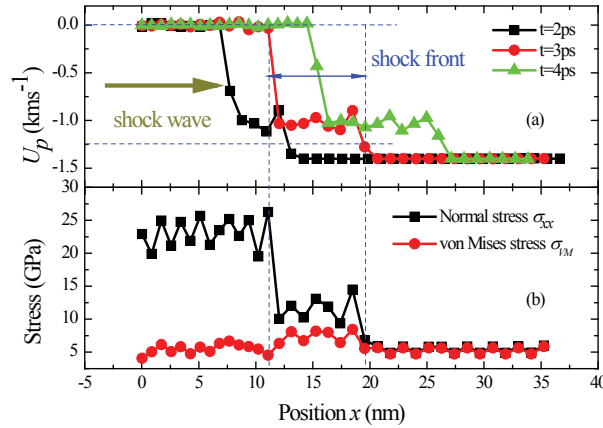
where  $\delta_i$  presents the atomic stress for atom  $i$ ,  $V_i$  the corresponding atomic volume,  $m$  the number of atoms contained within each bin,  $\Delta V$  the volume of each bin.

The normal stress  $\sigma_{xx}$  is the statistical average of stress along the shock direction. The flow stress  $\sigma_{VM}$  is identified as follows

$$\sigma_{VM} = \sqrt{\frac{1}{2}[(\sigma_{xx} - \sigma_{yy})^2 + (\sigma_{yy} - \sigma_{zz})^2 + (\sigma_{zz} - \sigma_{xx})^2]}, \quad (4)$$

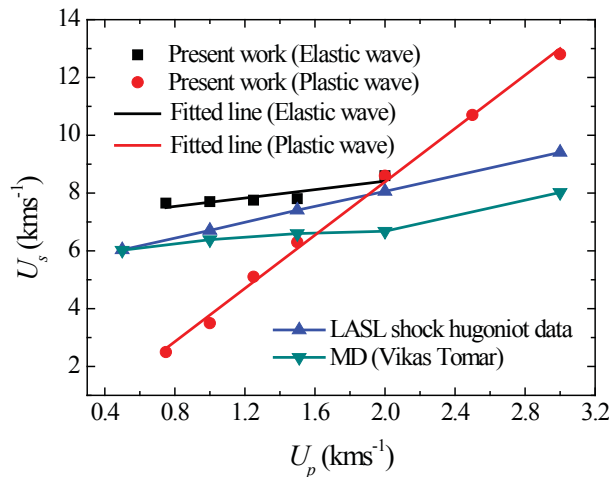
Figure 2(a) shows the particle velocity profiles along the direction of shock wave propagation in the case of  $U_p = 1.25$  km/s. It can be seen that the shock waves consist of an elastic precursor followed by a slower plastic deformation front. The width of the shock front is defined as the profile between the particle velocity  $U_p = 0$  and  $U_p = 1.25$  km/s. The results indicate that the width of the shock front increases gradually with time, so the shock front is unstable. The similar phenomenon was also observed in the shocked aluminum experiment (Gupta *et al.*, 2009). The reason is that the elastic wave propagates faster than the plastic wave for the weaker shock loading, while the propagation of the plastic wave exceeds that of elastic wave and forms stable shock wave if the shock loading is strong enough. Figure 2(b) shows the stress profiles along the direction of shock wave propagation at  $t = 3$  ps in the case of  $U_p = 1.25$  km/s. It can be seen that the variation trend of the stresses is exactly the same as that of the particle velocity. The normal stress gradually increases up to 26 GPa behind the shock front. In the process of dynamic deformation, the decrease of the flow stress indicates the plastic behavior of material. In figure 2(b) the first maximum

value of the flow stress presents the appearance of the plastic behavior in aluminum single crystal and the second one presents the dislocation nucleation and motion.



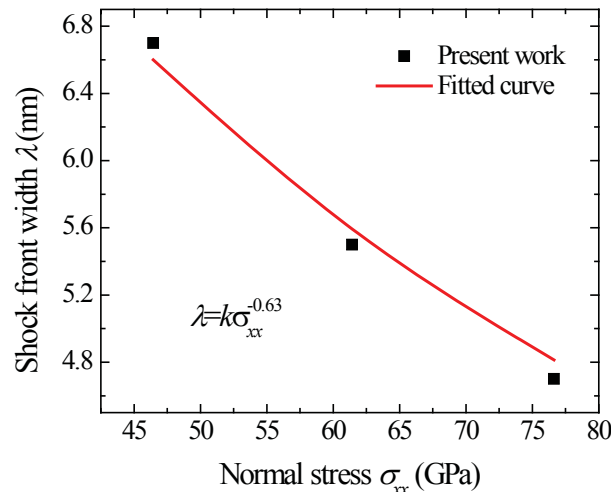
**Figure 2. Wave profiles along the direction of shock wave propagation.**  
**(a) Particle velocity; (b) Normal stress and flow stress.**

Figure 3 shows the Hugoniot relation of aluminum single crystal. The MD simulation results show that an elastic-plastic wave propagates in aluminum single crystal for the particle velocity slower than 2 km/s and the velocity of the elastic wave increases slightly with the shock loading which is consistent with the experimental data (*Yu et al.*, 2006). However, only a plastic wave propagates in aluminum single crystal for the particle velocity faster than 2 km/s. The reason lies in that the propagation of the plastic wave exceeds that of the elastic wave and forming a stable shock wave with the corresponding shock pressure of 45 GPa. The value of the particle velocity corresponding to the transition threshold for observing two-wave structure is  $U_p = 2.0$  km/s which is basically consistent with the critical value of  $U_p = 1.5$  km/s for [100] aluminum single crystal by *Tomar et al.* (2006). The simulated  $U_s$ - $U_p$  relationship differs with the experimental data (*Marsh*, 1980) to a certain degree, as may be related to the orientation dependence of the shocked aluminum single crystal. In addition, the number of the particles contained within the computation system is not enough, as may also enlarge the statistical average error. Overall, the tendency is basically consistent with the experimental data and other MD simulation results.



**Figure 3. Relationship between particle velocity  $U_p$  and shock wave velocity  $U_s$ .**

Figure 4 shows the relationship between the width of shock front and the normal stress along the direction of shock wave propagation. It can be seen that the width of shock front decreases with the normal stress corresponding to the increased particle velocity. By fitting the simulation results, it is found that the width of shock front decreases with the normal stress exponentially, as is consistent with the previous work (Bringa *et al.*, 2005). That is to say, with the increase of shock loading, the time required for aluminum single crystal finishing the plastic deformation is shorter, and the equilibrium state behind the shock front is easier to reach.



**Figure 4. Relationship between width of shock front  $\lambda$  and normal stress  $\sigma_{xx}$ .**

## Conclusion

In summary, the shock wave propagation in aluminum single crystal investigated by MD reveals a distinct threshold particle velocity of 2 km/s beyond which exists a two-wave structure of an elastic precursor followed by a slower plastic wave, and the velocity of elastic wave increases slightly with the shock loading. While only a plastic wave exists for the particle velocity faster than 2 km/s and the width of shock front decreases by exponent with the normal stress.

## Acknowledgments

This work was supported by the National Natural Science Foundation of China (Nos. 11032003 and 11221202), and the State Key Development Program for Basic Research of China (No. 2010CB731600).

## References

- An, Q.; Ravelo, R.; Germann, T. C.; Han, W. Z.; Luo, S. N.; Tonks, D. L. and Goddard, W. A. (2012), Shock compression and spallation of single crystal tantalum. *AIP Conf. Proc.*, **1426**, pp 1259-1262.
- Asay, J. R. and Chhabildas, L. C. in *High-Pressure Shock Compression of Solids VI*, edited by Horie, Y. Davison, L. and Thadhani, N. N. (Springer: New York, 2003), Chap. II.
- Bringa, E. M.; Caro, A.; Victoria, M. and Park, N. (2005), The Atomistic Modeling of Wave

- Propagation in Nanocrystals. *JOM*, **57**, pp 67-70.
- Dlott, D. D.; Hambir, S. and Franken, J. (1998), The New Wave in Shock Waves. *J. Phys. Chem. B*, **102**, pp. 2121-2130.
- Evans, R.; Badger, A. D.; Falliès, F.; Mahdiah, M. and Hall, T. A. (1996), Time- and Space-Resolved Optical Probing of Femtosecond-Laser-Driven Shock Waves in Aluminum. *Phys. Rev. Lett.*, **77**, pp. 3359-3362.
- Gupta, Y. M.; Winey, J. M.; Trivedi, P. B.; LaLone, B. M.; Smith, R. F.; Eggert, J. H. and Collins, G. W. (2009), Large Elastic Wave Amplitude and Attenuation in Shocked Pure Aluminum. *J. Appl. Phys.*, **105**, pp 036107-1-036107-3.
- He, A. M.; Shao, J. L.; Qin, C. S. and Wang, P. (2009), Molecular Dynamics Study on the Plastic Behavior of Monocrystalline Copper Under Shock Loading and Unloading. *Acta Phys. Sin.*, **58**, pp 5667-5672. (in Chinese)
- Holian, B. L. and Lomdahl, P. S. (1998), Plasticity Induced by Shock Waves in Nonequilibrium Molecular Dynamics Simulations. *Science*, **280**, pp 2085-2088.
- Kadau, K. Germann, T. C. Lomdahl, P. S. and Holian, B. L. (2002), Microscopic View of Structural Phase Transitions Induced by Shock Waves. *Science*, **296**, pp 1681-1684.
- Ma, W. and Lu, Y. W. (2013), Molecular Dynamics Investigation of Shock Front in Nanocrystalline Copper. *Acta Phys. Sin.*, **62**, 036201-1-036201-7. (in Chinese)
- Marsh, S. P. *LASL Shock Hugoniot Data* (University of California Press: Berkeley, 1980)
- Mei, J.; Davenport, J. W. and Fernando, G. W. (1991), Analytic Embedded-atom Potentials for fcc Metals: Application to Liquid and Solid Copper. *Phys. Rev. B*, **43**, pp 4653-4658.
- Robertson, D. H.; Brenner, D. W. and White, C. T. (1991), Split Shock Waves From Molecular Dynamics. *Phys. Rev. Lett.*, **67**, pp 3132-3135.
- Shao, J. L.; Wang, P. Q.; Cheng, S. and Zhou, H. Q. (2007), Shock-induced Phase Transformations of Iron Studied with Molecular Dynamics. *Acta Phys. Sin.*, **56**, pp 5389-5393. (in Chinese)
- Tomar, V. and Zhou, M. (2006), Molecular Dynamics Modeling of Shock Wave Propagation in *fcc*-Al,  $\alpha$ -Fe<sub>2</sub>O<sub>3</sub>, and their Interfaces. *AIP Conf. Proc.*, **845**, pp 421-424.
- Yu, Y. Y.; Tan, H.; Hu, J. B.; Dai, C. D. and Chen, D. N. (2006), Measurements of Sound Velocities in Shock Compressed Tantalum and LY12 Al. *Explosion and Shock Waves*, **26**, pp 486-491. (in Chinese)
- Zhao, F. P.; An, Q.; Li, B.; Wu, H. A.; Goddard, W. A. and Luo, S. N. (2013), Shock Response of a Model Structured Nanofoam of Cu. *J. Appl. Phys.*, **113**, pp 063516-1-063516-7.
- Zhou, S. J.; Preston, D. L.; Lomdahl, P. S. and Beazley, D. M. (1998), Large-scale Molecular Dynamics Simulations of Dislocation Intersection in Copper. *Science*, **279**, pp 1525-1527.

# Delamination Damage Propagation Behavior of Composite Laminate Plate Under Low-Velocity Impact Using a New Adhesive Layer Model

Y. ZHAO, \*K. DONG, Y. GAO

School of Naval Architecture and Ocean Engineering, Harbin Institute of Technology AT Weihai,  
Weihai 264209, Shandong P.R. China

\*Corresponding author: dongke213@126.com

## Abstract

Based on interface adhesive theory and delamination damage mechanism, a new adhesive layer model is proposed to analyze the intra-layer delamination damage process of composite laminated plate subjected to low velocity impact. The influences of through-thickness tensile stresses, inter-laminar shear stresses and matrix cracking on delamination damage are taken into consideration in this model. Compared with traditional strength failure criterion model or fracture mechanics energy release rate model, analytical results of this model are in good agreement with experimental data. The damage extension characteristics and the various influence factors on delamination damage are discussed. The results of this research can be applied in composite structure design and life prediction.

**Keywords:** composite laminated plate; delamination damage; adhesive layer model; damage extension characteristics

## 1. Introduction

Composite laminates are being increasingly used in aerospace, automotive, shipbuilding and other industries fields due to their inherently high specific mechanical properties. In those service conditions, transverse impact at low velocity is the normal form of loading which can cause internal damage such as delamination, matrix cracking, local permanent deformation and fiber breakage, leading to a reduction of load carrying capacity of the composite structures. Furthermore, catastrophic failure may occur when the composite laminates are serviced in such damaged state. Hence, understanding the damage involved in the impact of composite targets is important in the effective design of a composite structure.

However, the dynamic behavior of composite laminates is very complex, because there are many concurrent phenomena during composite laminate failure under impact load. The inherent complexity of the structure of composite has brought great difficulties to the experimental or theoretical methods. With the development of numerical techniques, numerical analysis based on finite element method has been widely used in recent years, and many efficient numerical models have been made to analyze the impact problem. Based on continuum damage mechanics, Matzenmiller (1995) first brought up CDM concept which links up the composite material damage and degradation of the elastic properties of materials. This method shows a good prediction of the impulse response of laminates and the damage layer, but can't be predicted the fiber breakage and damage of the matrix damage accurately. Hou(2000), based on strength theory, studied the low speed dynamic response and damage modes

by using explicit finite element algorithm. At the same time the material parameters degradation is replaced by the stress degradation and stiffness degradation. Zerbst(2009) introduced the fracture mechanics methods to predict composite laminates residual compressive strength and delamination damage, but this method can't accurately predict the delamination area.

Considering the disadvantages of present method, this paper proposes a new adhesive layer model is proposed to analyze the intra-layer delamination damage process of composite laminated plate subjected to low velocity impact based on interface adhesive theory and delamination damage mechanism. The influences of through-thickness tensile stresses, inter-laminar shear stress and matrix cracking on delamination damage are taken into consideration in this model. Compared with traditional strength failure criterion model or fracture mechanics energy release rate model, analytical results of this model are in good agreement with experimental data. The damage extension characteristics on delamination damage are discussed. The results of this research can be applied in composite structure design and life prediction..

## 2. Impact damage constitutive model

### 2.1 Three-dimensional rate-dependent constitutive model

Assuming the fiber as the uniform transversely isotropic linear elastic body and the matrix as isotropic viscoelastic, Kairm (2005) derived the expression of the relaxation modulus of this materials under high strain rate:

$$\left. \begin{aligned} E_{11}(t) &= (E_{f1}V_f + E_mV_m) + E_1V_m e^{-\frac{1}{\theta_{e1}t}} + E_2V_m e^{-\frac{1}{\theta_{e2}t}} \\ E_{22}(t) &= \frac{E_{f2}E_m}{E_{f2}V'_m + E_mV'_f} + Qe^{-Mt} + Re^{-Nt} \\ G_{12}(t) &= \frac{G_{f12}G_m}{G_{f12}V'_m + G_mV'_f} + Q_{12}e^{-M_{12}t} + R_{12}e^{-N_{12}t} \\ G_{23}(t) &= \frac{G_{f23}G_m}{G_{f23}V'_m + G_mV'_f} + Q_{23}e^{-M_{23}t} + R_{23}e^{-N_{23}t} \end{aligned} \right\} \quad (1)$$

Based on the Hooke's law, the constitutive model can be expressed as:

$$\varepsilon = S\sigma = EU\sigma \quad (2)$$

Where E is stiffness matrix, S is compliance matrix. The expression of U is

$$U = \begin{bmatrix} 1 & -\mu_{12} & -\mu_{31} & 0 & 0 & 0 \\ -\mu_{12} & 1 & -\mu_{23} & 0 & 0 & 0 \\ -\mu_{31} & -\mu_{23} & 1 & 0 & 0 & 0 \\ 0 & 0 & 0 & 1 & 0 & 0 \\ 0 & 0 & 0 & 0 & 1 & 0 \\ 0 & 0 & 0 & 0 & 0 & 1 \end{bmatrix} \quad (3)$$

Considering the 2 and 3 direction of the unidirectional fiber-reinforced composite

material having the same mechanical properties, so the three-dimensional constitutive relation can be expressed as:

$$\begin{Bmatrix} \sigma_{11} \\ \sigma_{22} \\ \sigma_{33} \\ \sigma_{12} \\ \sigma_{23} \\ \sigma_{31} \end{Bmatrix} = U^{-1} \begin{Bmatrix} \int_0^t E_{11}(t-\tau)\dot{\epsilon}(\tau)d\tau \\ \int_0^t E_{22}(t-\tau)\dot{\epsilon}(\tau)d\tau \\ \int_0^t E_{22}(t-\tau)\dot{\epsilon}(\tau)d\tau \\ \int_0^t E_{12}(t-\tau)\dot{\epsilon}(\tau)d\tau \\ \int_0^t E_{23}(t-\tau)\dot{\epsilon}(\tau)d\tau \\ \int_0^t E_{12}(t-\tau)\dot{\epsilon}(\tau)d\tau \end{Bmatrix} \quad (4)$$

## 2.2 The material failure criterion and the stiffness reduction scheme

The research of the inner-layer damage of composite material mainly includes three parts: the calculation of stress or strain, the criteria of the damage failure and the degradation of material properties. On the failure criteria of composite material, the improved Chang / Chang failure criteria (Hou, 2000) is used as the criteria of the inner-layer damage in this paper:

$$\text{Fiber tensile failure mode: } F_{f i b \bar{e} r} = \left( \frac{\delta_1}{s_1} \right)^2 + \bar{\tau} > 1 \quad (5)$$

$$\text{Matrix cracking failure mode: } F_{matrix} = \left( \frac{\delta_2}{S_2} \right)^2 + \bar{\tau} > 1 \quad (6)$$

Matrix compressive failure mode:

$$F_{comp} = \left( \frac{\delta_2}{2s_{12}} \right)^2 + \left[ \left( \frac{c_2}{2s_{12}} \right)^2 - 1 \right] \frac{\delta_2}{c_2} + \bar{\tau} > 1 \quad (7)$$

$$\bar{\tau} = \frac{\frac{\tau_{12}^2}{2G_{12}} + \frac{3}{4}\alpha\tau_{12}^4}{\frac{S_{12}^2}{2G_{12}} + \frac{3}{4}\alpha S_{12}^4} \quad (8)$$

The mechanical properties must be decreased in damaged areas. In order to make sure the accuracy of the simulation, the stiffness of the laminate is reduced step by step. Different forms of the reduction scheme of material stiffness are applied depending on the form of damage. When the failure happens, the repeated degradation method will be taken (Sebastian, 2008), the degradation scheme is as follows:

**Table 1. Stiffness reduction scheme**

Failure mode	Parameter reduction
Fiber tensile	$E_{11} = E_{22} = G_{12} = \nu_{21} = \nu_{12} = 0$
Matrix cracking	$E_{22} = \nu_{21} = 0, G_{12} = 0$
Matrix compressive	$E_{11} = \nu_{21} = \nu_{12} = 0, G_{12} = 0, X_C = 2Y_C$

### 2.3 Interface cohesive element damage model

The interface cohesive element is introduced into the low speed impact process of composite laminates in this paper. A three-dimensional interface cohesive element (Fig1) is adopted to study the delamination damage. Biphasic constitutive relation of interface element is used to describe the initiation and progression of crack. When the relative displacement of interface element  $\delta$  is less than  $\delta^0$ , no damage occurs. It is shown in the interface strength -relative displacement curve that the slope is the interface element stiffness. When the relative displacement is more than  $\delta^0$ , interface element damage occurs and the interface element stiffness begins to gradually decrease. The new interface stiffness curve is shown in figure 2 with dotted line. With the continual progression damage of the interface element, the relative displacement increases and the interface unit will be completely destroyed. Then the interface element stiffness becomes zero. The area formed by O, A, B three points is energy release rate in the process of damage of the interface element. The initial damage criteria of the model is shown as follows:

$$\left(\frac{T_N}{T}\right)^2 + \left(\frac{S_1}{S}\right)^2 + \left(\frac{S_2}{S}\right)^2 = 1 \quad T_N \geq 0 \quad (9)$$

$$\left(\frac{S_1}{S}\right)^2 + \left(\frac{S_2}{S}\right)^2 = 1 \quad T_N < 0 \quad (10)$$

where:  $\delta^0 = \delta_1^0 \delta_{II}^0 \sqrt{\frac{1+\beta^2}{(\delta_{II}^0)^2 + (\beta\delta_1^0)^2}}$  ;  $\delta_1^0 = \frac{T}{EN}$  ,  $\delta_{II}^0 = \frac{S}{ET}$  ;  $\beta = \frac{\delta_1}{\delta_{II}}$

The formula of final failure displacement of the mixed-mode is:

$$\delta^f = \begin{cases} \frac{2(1+\beta)^2}{\delta^0} \left[ \left(\frac{EN}{GIC}\right)^{XMU} + \left(\frac{ET \cdot \beta^2}{GII C}\right)^{XMU} \right]^{\frac{1}{XMU}} \dots (XMU > 0) \\ \frac{2}{\delta^0 \left( \frac{1}{1+\beta^2} EN + \frac{\beta^2}{1+\beta^2} ET \right)} \left[ GIC + (GII C - GIC) \left( \frac{\beta^2 \cdot ET}{EN + \beta^2 ET} \right)^{|XMU|} \right] \dots (XMU < 0) \end{cases} \quad (11)$$

With the continuous development of damage, a macroscopic crack appears in the interface. It is similar to the crack development in the fracture mechanics. Therefore, the criterion of the rate of strain energy release in fracture mechanics can be used for the analysis of interface crack progression. And the criteria of the damage progression is shown as follows:

$$\left(\frac{G_I}{G_{IC}}\right)^2 + \left(\frac{G_{II}}{G_{IIC}}\right)^2 + \left(\frac{G_{III}}{G_{IIIC}}\right)^2 = 1 \quad (12)$$

where  $G_I$ 、 $G_{II}$ 、 $G_{III}$  respectively mean the rate of strain energy release of the normal



and two tangential of the interface element;  $G_{IC}$ 、 $G_{IIC}$ 、 $G_{IIIC}$  respectively mean the critical energy release rate of I , II , III crack interface models.

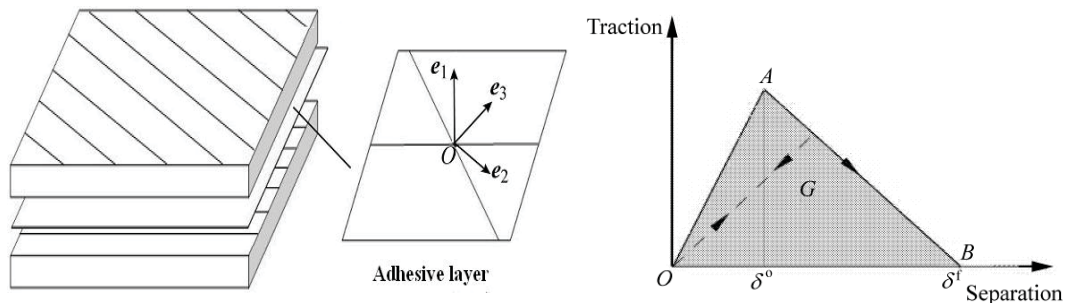


Fig.1 Mechanics model of the laminates Fig.2 Interface force-relative displacements

### 3. The finite element model

#### 3.1 Material model and boundary conditions

Composite material is continuous unidirectional tensile high-strength Carbon fibers (Tenax HTS40 12 K 300). The thickness of composite laminate plate is 2 mm with a ply thickness of 0.25 mm in a stacking sequence  $[0/90]_{2S}$ . The laminate plate is fixed by a rigid fixture and a diameter of 75 mm circular preformed hole is reserved. The material performance of the interface layer has a great impact on delamination damage (Masaaki, 2007). Therefore, its performance parameters are generally measured by the method of experiment. The parameters used in the paper are got from Shi's (2012)

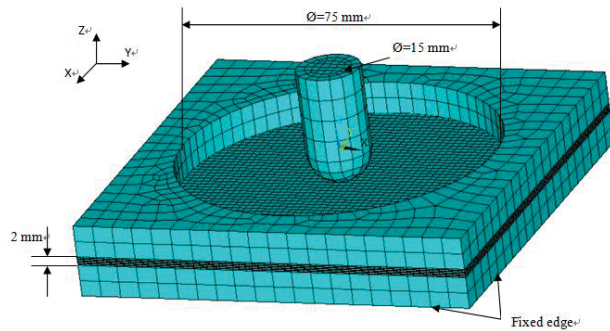


Fig. 3 Finite element model

experimental data. The materials of impactor and fixtures are steel. Material parameters taken as follows:  $E=210$  Gpa;  $\rho=7850$  kg/m<sup>3</sup>;  $\nu=0.3$ . The diameter of impactor is 15 mm. The impact velocity is 3.83 m/s. The impact energy is 7.35 J. Considering that the stiffness of steel is relatively larger than the stiffness of laminate plate, so the impactor and clamp are defined as the rigid body.

#### 3.2 Types of element used in coupled numerical model

Considering the importance of delamination damage under the low velocity impact, two kinds of elements are chosen: Each ply of Laminate plate uses 3D solid elements, which not only can consider the stress in thickness direction of laminate plate, but also can consider the effect of nonlinear shear. At the same time, we introduce a layer of 3D solid shell elements sub-layers between upper layer and lower layer of laminate plate which shown in Fig 1, it makes sure the displacement continuity of the structure. The advantage of 3D solid shell elements is that it can simulate a larger length to thickness ratio of element and has a fast calculation. It also needn't to use the mass

scaling.

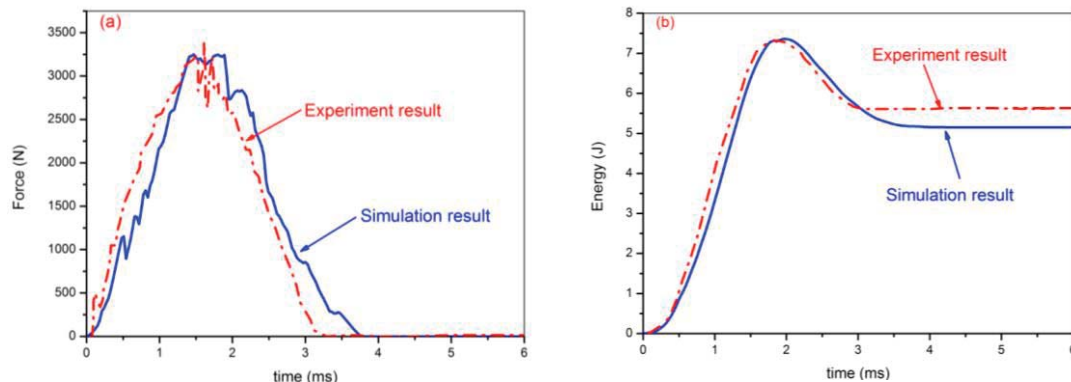
### 3.3 Contact algorithm

The material properties of impactor, fixtures and laminate plate have great different. Between the impactor and the sub-layer, as well as the fixtures and the sub-layer, based on the contact segment, the automatic algorithm is established. This contact algorithm does not depend on the material parameters, but the quality of the node divided by the square of the time step size, which can guarantee the stability and reliability of computation. A kind of tied contact is used between the upper and lower surfaces of interface element contact with adjacent sub-layer respectively. The benefit of tied connect is bounding the slippage of the adhesive layer on upper and lower of sub-layer, which is more in accord with the real structure mechanism of laminated plate. In order to prevent penetration between sub-layer, the automatic contact is established in each ply.

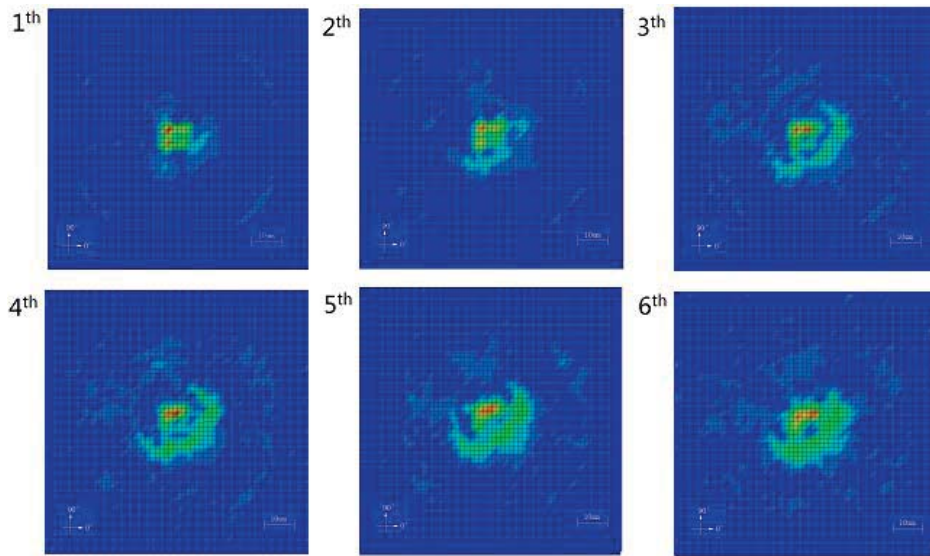
Coefficient of friction between the object depends on the material properties and surface smoothness, coefficient of friction measured experimentally is more accurately. The existing research results of predecessors show that the friction coefficient has a great influence on the impact test, especially on the absorption of impact energy (Schon, 2000). Considering the adhesive effect between the adhesive layer and the sub-layers, the friction coefficient takes a relatively large value of 0.5, at the rest of contact take a value of 0.3.

## 4. Results and discussion

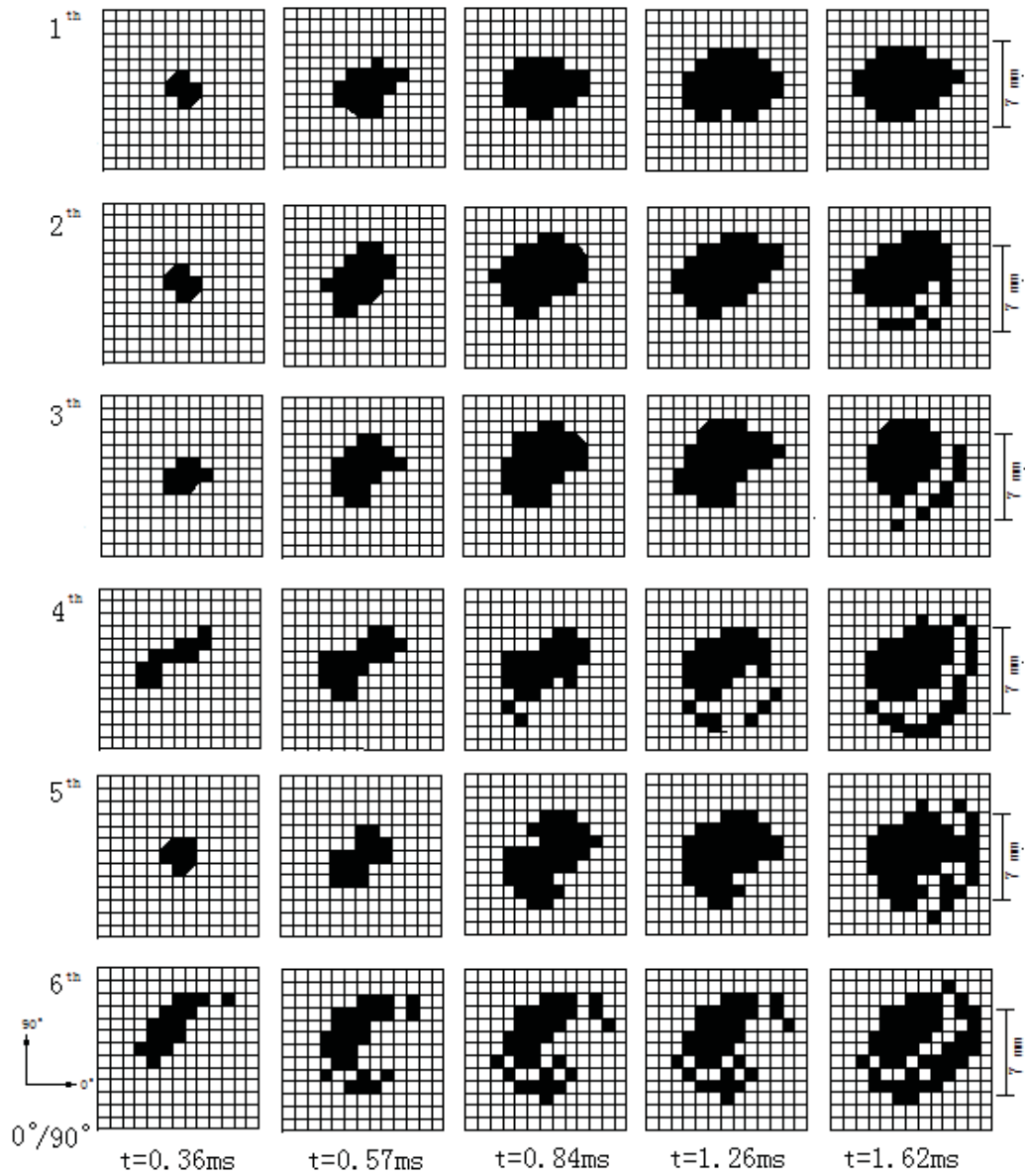
In order to verify the calculated feasibility and accuracy, the simulation results are compared with experimental results which shown in Fig. 4. One can see that the two results from two different solving methods are nearly in agreement. It is also seen from Fig. 4(a) that impact force in the times interval of 0ms to approximate 0.7ms increases approximately linearly, it meanwhile laminated plate material is in the elastic deformation stage, in other word, the damaged does not appear. The damage occurs within laminates when the times form 0.6ms to the peak value1.6ms. After the peak impact force, the impactor begins to rebound until the impact force to zero. Compared to the peak time which shown in Fig. 4a (approximate 1.6ms), the impact energy peak time which shown in Fig. 4b (approximate 2.0ms) appears later. The



**Fig.4 Dispersion curves of low-velocity impact with two different methods**



**Fig.5 The stress clouds in different cohesive layers**



**Fig.6 Delamination damage growth images in adhere layers**

reason causing this kind of phenomenon is the impact energy continue increase when the impact force reaches its maximum value.

Once impactor contacts laminated plate, part of the energy will be absorbed by elastic deformation, the other energy will be dissipated through interlaminar damage and the friction between the sub-layers and adhesive layers. Based on small contact stiffness about laminate plate, impact damage will be smaller than the experimental value, so that the absorbed energy will be smaller about 6.36% than the experimental value.

Figure 5 is stress clouds in different cohesive layers. The red areas indicate complete failure; the green portion represents part of the damaged area which is delamination progression areas; lighter color indicates the smaller degree of damage. It is seen from the figure 5 that the impact damage occur from the upper adhere layer. The delamination damage area of bottom layer is larger than the upper layer. The reason for this is the bottom adhere layer served under the bending stress which caused by the impact. Figure 6 shows the delamination damage growth images in adhere layers. The delamination damage area increased with the increase of time. In different adhere layer, for example the 5<sup>th</sup> layer, the stratified area like peanut shells and damage layered area is approximately 60mm<sup>2</sup>. All those phenomena agree with the experimental data. The method of this research can be applied in composite structure design and life prediction.

### Acknowledgements

The authors thank “Natural Science Foundation of Shandong Province, China” (Grant No. ZR2012EEM003) and “The Fundamental Research Funds for the Central Universities” (Grant No. HIT. NSRIF. 2013128) for the financial support for this project, and the referees for their valuable comments.

### References

- Matzenmiller, A., Lubliner, J. and Taylor, R. L. A. (1995), Constitutive model for anisotropic damage in fiber-composites. *Mechanics of Materials*, 20(2), pp. 125-152.
- Hou, J. P., Petrinic, N., Ruiz, C. and Hallett, S. R. (2000), Prediction of impact damage in composite plates. *Composites Science and Technology*, 60, pp. 273- 281.
- Zerbst, U. and Heinemann, M. (2009), Fracture and damage mechanics modelling of thin-walled structures. *Engineering Fracture Mechanics*, 76, PP. 5-43.
- Karim, M. R. (2005), Constitutive modeling and failure criteria of carbon-fiber reinforced polymers under high strain rate. USA: University of Akron.
- Hou, J. P., Petrinic, N., Ruiz, C. and et al. (2000), Prediction of impact damage in composite plates. *Composite Science and Technology*, 60(2), pp. 273-281.
- Sebastian, Heimbs. And Sven, Heller.(2008), Simulation of Low Velocity Impact on Composite Plates with Compressive Preload. *Material II - Composites*, Copyright by DYNAmore GmbH.
- Masaaki, N. and Tomonaga, O. (2007), Numerical simulation of interlaminar damage propagation In CFRP cross-ply laminates under transverse loading. *Solids And Structures*, 44, pp. 3101-3113.
- Shi, Y., Swait, T. and Soutis, C. (2012), Modelling damage evolution in composite laminates subjected to low velocity impact. *Composite Structures*, 94, pp. 2902-2913.
- Schon, J. (2000), Coefficient of friction of composite delamination surfaces. *Wear*, 237, pp. 77-89.

## Detonation diffraction in combustible high speed flows

\*M.Y. Gui, G. Dong, and B.C. Fan

State Key Laboratory of Transient Physics, Nanjing University of Science and Technology, China

\*Corresponding author: mygui@njust.edu.cn

### Abstract

The detonation propagation in propulsion system is affected by some factors, such as flow before detonation wave front. In this investigation, detonation propagation both upstream and downstream based on T tube were studied numerically for hydrogen/oxygen/nitrogen mixtures using Euler equation with detailed finite-rate chemistry. The fifth-order WENO scheme was adopted to capture the shock wave. Detonation enters the T tube with combustible high speed flows, and diffracts both upstream and downstream. In the downstream direction shock wave decouples from reaction zone due to rarefaction waves, and then couples again by wall reflection. In the upstream direction the detonation wave has some characteristics of oblique detonation due to compression of gas flow. So in the flow system the detonation reinitiation mechanism is categorized into two types: spontaneous reinitiation and reinitiation by reflection.

**Keywords:** Detonation diffraction, high speed flows, reinitiation, WENO scheme

### Introduction

In contrast to the deflagration, the detonation is more efficient thermodynamically. Thus the applications of detonations in propulsion systems have been received more and more interests for many years.

For the transient characteristic of detonation waves, the key point of the detonation engine is how to make the detonation waves stay in the combustor long enough. Currently, there are three approaches to achieving this aim, and so the detonation-based engines are classified as pulse detonation engine (PDE), oblique detonation wave engine (ODWE) and rotating detonation wave engine (RDE) (Lu, 2009).

When these detonation-based engines are stable, the circumstance of detonation propagation in combustor is extremely complex, which is different with that described by the classic CJ theory. But it has been less understood so far. Compared in the quiescent mixture, detonation propagation in the flow mixture is divided into two situations: upwind propagation and downwind propagation. The investigations have been conducted experimentally (Machkenna, 1967; Ishii, 2009). The results reveal that detonation velocity is higher than CJ velocity in upwind direction and lower than CJ velocity in downwind direction. Numerical studies confirm the results again (Yi, et al, 2004; Pan et al, 2010). However, the variation mechanism is not clear. In this article, detonation propagation in flow system is investigated numerically and discussed based on model of T tube.

### Physical and numerical model

*Governing equations and numerical method*

The two-dimensional reactive Euler equations in the non-dimensional form are given as

$$\frac{\partial Q}{\partial t} + \frac{\partial F}{\partial x} + \frac{\partial G}{\partial y} = S \quad (1)$$

where  $Q$  denotes the variable vector,  $F$ ,  $G$ , the convective flux vectors, respectively,  $S$  is the chemical source vector.

To avoid the physical oscillations and excessive numerical dissipations due to the requirements of high resolutions of the fine structures in the flow field, spatial derivatives of inviscid fluxes  $F$  and  $G$  in Eq. (1) are integrated by the fifth-order weighted essentially non-oscillatory (WENO) scheme (Jiang and Shu, 1996). The second-order additive semi-implicit Runge-Kutta method (Zhong, 1996) is employed to discretize the time and treat the stiffness of the chemical source terms.

#### *Physical and computational configurations*

The schematic of the computational model is shown in Fig. 1. In Fig. 1a, the horizontal combustor with length of 310mm and width of 32mm is connected to the vertical detonation tube with length of 18mm and width of 30mm at central location, while in Fig. 1b, at the horizontal location of 96mm. The velocity of combustible mixture is 1200m/s. The grid size is 0.1mm×0.1mm. Slip-boundary condition is given on the wall, and zero gradient condition is on the horizontal combustor exit. The stoichiometric H<sub>2</sub>/O<sub>2</sub>/Ar mixture is used, where the initial pressure and temperature are taken as 10.6KPa and 300K, respectively.

A detailed chemical reaction mechanism with 8 species and 48 elementary reactions (Oran et al, 1982) is employed for the detonation chemistry in a stoichiometric hydrogen/oxygen mixture. The reacting species include H, O, H<sub>2</sub>, OH, H<sub>2</sub>O, O<sub>2</sub>, HO<sub>2</sub> and H<sub>2</sub>O<sub>2</sub>, whose thermodynamic data can be found from the JANAF table.

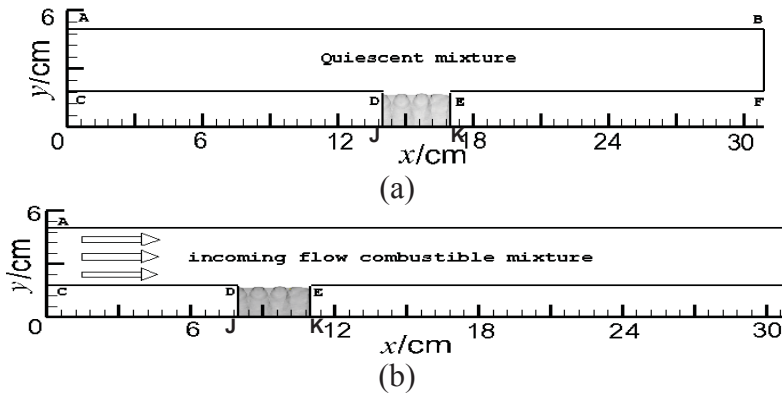


Figure 1. Schematic diagram of computational domain (a) quiescent system; (b) flow system.

## **Results and discussion**

The numerical schlieren about detonation diffraction in the quiescent system are shown in Fig. 2, where the solid line is shock front and the dash line is reaction front. The detonation front doesn't reach the upper wall. The rarefaction wave created

around the corner penetrates into the reaction zone and makes the reaction front decouple from the shock. There are the shocked combustible gas between the leading shock and reaction zone. The undisturbed detonation propagates with CJ velocity.

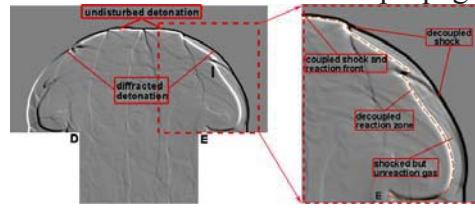


Figure 2.  $t=16.2\mu\text{s}$ , the numerical schlieren of detonation diffraction in the quiescent system.

The numerical schlieren about detonation diffraction in the flow system are shown in Fig. 3. During to the flow in horizontal tube (from left to right) left detonation diffraction is upstream and right detonation diffraction is downstream, which lead to obviously different characteristics. At right detonation diffraction the reaction front decouples from shock with the effect of the disturbance, which is the same as in the quiescent system. At left detonation diffraction the detonation product is compressed by the incoming flow, which is analogous to wedge compression. So the upstream diffraction front has some characteristics of oblique detonation. Steady oblique detonation consists of shock wavelets as show in Fig. 4 (Gui, 2012). The incoming flow compressed by the shock S1 is ignited by the transverse wave, thus leading to the onset of the transverse detonation TS1. As the oblique detonation wavelet D1 gradually curves downstream, its strength decreases. Finally, the decaying wave becomes a non-reactive shock wave S1.

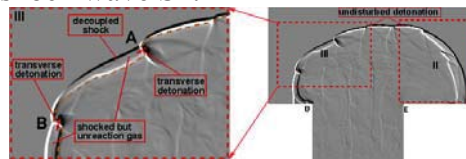


Figure 3.  $t=16.2\mu\text{s}$ , the numerical schlieren of detonation diffraction in the flow system.

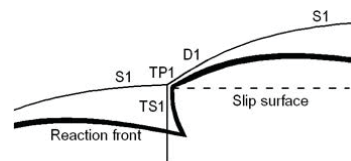


Figure 4. Schematic diagram of oblique detonation wave structure. (Gui, 2012)

So in the flow system detonation diffraction make the reaction zone decoupled from shock downstream, which tend to detonation failure, while make the wave structure similar to oblique detonation wave structure upstream, which tend to detonation self-sustaining.

The detonation wave approaches the upper wall and reflects immediately as shown in Fig. 5 which successively shows numerical schlieren, pressure, temperature and H mass fraction contours from top and bottom. The reflection of diffracted detonation wave from the upper wall is composed of two parts: normal reflection of undisturbed detonation and Mach reflection of curving shock. After reflection there are Mach stem propagating towards two sides and transverse reflection wave propagating towards the bottom wall. The strength of Mach stem is so strong as to the onset of

detonation. Part of transverse reflection wave sweep the layer of pre-shocked combustible gas between the shock wave and reaction zone due to detonation decoupling downstream, which cause to transverse detonation. Therefore the whole reflection wave is the complex wave consisting of detonation wave and inertia shock wave. Through several reflections back and forth between the upper and bottom wall, there is the last formation of planar detonation in horizontal combustor. But at downstream direction there undergoes detonation failure, shock reflection, detonation reinitiation and planar detonation. At upstream direction there undergoes oblique detonation, detonation reflection and planar detonation.

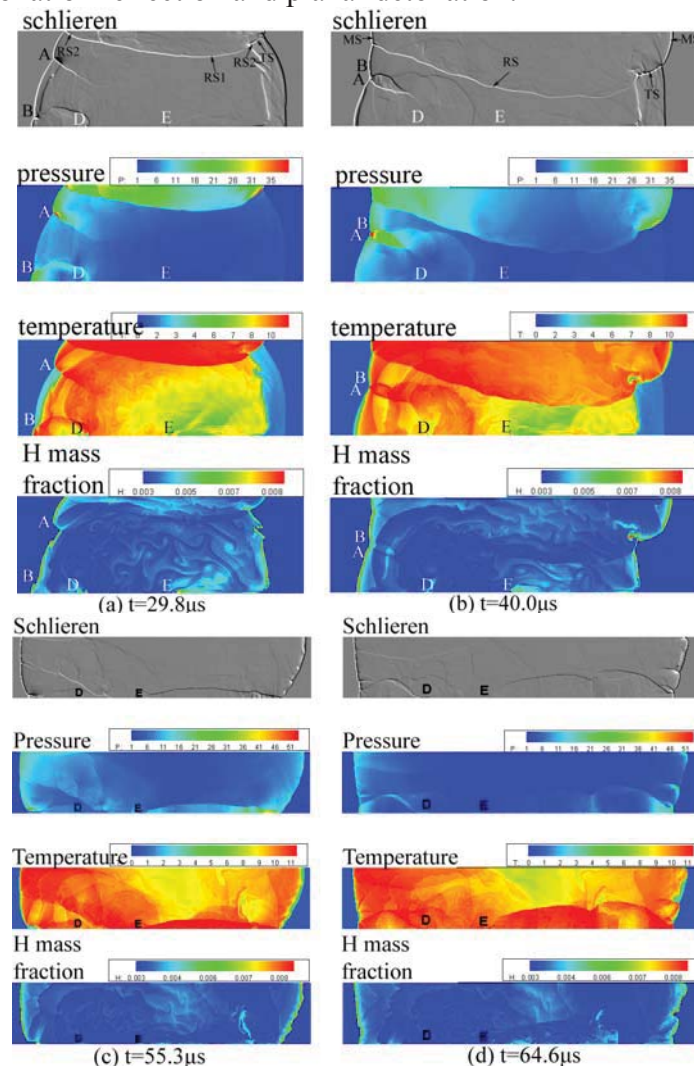


Figure 5. Reinitiation event of detonation in the flow system

## Conclusions

Detonation diffraction in combustible flow mixture was studied numerically based on reactive Euler equation. Detonation fails with the effect of rarefaction wave around the corner downstream. Detonation wave structure has some characteristics of oblique detonation with compression of the incoming flow upstream. Due to restriction of upper and bottom wall there is the last formation of planar detonation both upstream and downstream. But detonation reinitiation is spontaneous reinitiation upstream and reinitiation by reflection downstream.



## Acknowledgments

The work was supported by the National Nature Science Foundation of China (No. 11202104) and the open fund of State Key Laboratory of Explosion Science and Technology, Beijing Institute of Technology (No. KFJJ13-3M).

## References

- Gui, M. Y. and Fan, B. C. (2012), Wavelet structure of wedge-induced oblique detonation waves. *Combust Sci Technol*, 184, pp. 1456-147.
- Ishii, K., Kataoka, H. and Kojima, T. (2009), Initiation and propagation of detonation waves in combustible high speed flows. *Proceed Combust Instit*, 32, pp. 2323-2330.
- Jiang, G. S. and Shu, C. W. (1996), Efficient implementation of weighted ENO schemes. *J Comput Phys*, 126, pp. 202-228.
- Lu, F. K. (2009), Prospects for detonations in propulsion. *Proceedings of the 9th International Symposium on Experimental and Computational Aerothermodynamics of Internal Flows (ISAI9)*. Paper No. IL-2.
- Machkenna W. W. (1967), Interaction between detonation waves and flowfields. *AIAA*, 5, pp. 868-873.
- Oran, E. S., Young, T. R., Boris, J. P., et al. (1982), Weak and strong ignition. I-numerical simulations of shock tube experiments. *Combustion and Flame*, 48, pp. 135-148.
- Pan, Z. H., Fan, B. C., Gui, M. Y., et al. (2010), Numerical study of detonation wave propagation in a flow system. *Explosion Shock Waves*, 30, pp. 593-597 (in Chinese).
- Yi, T. H., Wilson, D. R. and Lu, F. K. (2004), Numerical study of unsteady detonation wave propagation in a supersonic combustion chamber. *25th International Symposium on Shock waves*, Paper No.10041, pp. 17-22.
- Zhong, X. L. (1996), Additive semi-implicit Runge-Kutta methods for computing high-speed nonequilibrium reactive flows. *J Comput Phys*, 128, pp. 19-31.

## Comparison of PIM and RPIM solutions of Elasto-plastic Thick Beams

\*B. Kanber<sup>1</sup>, N. F. Dogan<sup>1</sup>

<sup>1</sup>Mechanical Engineering Department, University of Gaziantep, Turkey.

\*Corresponding author: kanber@gantep.edu.tr

### Abstract

In this study, the point interpolation method (PIM) and radial point interpolation method (RPIM) solutions of elasto-plastic thick beams are compared by using standard Gaussian integration and a nodal integration based on Taylor series expansion. The effects of integration schemes, support domain sizes and RPIM shape parameters on the solution convergence are also investigated after yield point. The global weak form is used to obtain nodal stiffness matrixes. A simply supported beam with constant strength is solved by considering an elasto-plastic hardening material. Its results are compared with finite element solutions in ANSYS.

**Keywords:** PIM, RPIM, Elasto-plastic, Meshfree, Thick Beams.

### Introduction

Beams are mechanical components that are widely used in engineering design. One of the main techniques to analyze beams is the finite element method (FEM) (Owen and Hinton, 1980). Elasto-plastic beams are also analyzed using the finite element method (FEM) (Chebl and Neale, 1984; Lee and McClure, 2005).

Point interpolation method (PIM) is a simple and useful mesh-free technique and originally proposed by Liu and Gu (2001a). In the PIM, the field variables are interpolated using point interpolation shape functions. The main problem in the PIM is the singularity of the moment matrix. The radial point interpolation method (RPIM) is proposed to overcome this problem and based on combining polynomial and radial basis functions (Wang and Liu, 2002a, b; Liu et al., 2005). It becomes a popular technique in the meshfree solution of wide range of problems. It is used in the vibration analysis of 2D solids, shells and beams (Liu and Gu, 2001; Zhao et al., 2009a; Bui et al., 2012), solution of Kirchoff and Mindlin plates (Dinis et al., 2008; Liu et al., 2006; Liew and Chen, 2004; Djeukou and Estorff, 2009), analysis of shell problems (Liu et al., 2006; Zhao et al., 2009b), geometric nonlinear analysis of plates and cylindrical shells (Zhao, 2008), contact analysis of solids (Li et al., 2007), functionally graded materials (Dai et al., 2004) and incompressible flow (Wu and Liu, 2003).

In this study, PIM and RPIM are used to determine the effect of support domain size, RPIM shape parameters and integration schemes on the solution accuracy of elasto-plastic thick beam solutions.

### Elasto-Plastic Thick Beams

Under a distributed load intensity  $q$ , the beam undergoes a set of virtual lateral displacements  $\delta w$ , virtual normal rotations  $\delta \theta$  and associated virtual curvatures  $-z[d(\delta \theta)/dx]$  and virtual shear strains  $\delta \beta$ . Then the global weak form can be expressed as (Owen and Hinton, 1980):

$$\int_0^l \int_{-t/2}^{t/2} \int_{b(-t/2)}^{b(t/2)} \left\{ -z \frac{d(\delta \theta)}{dx} \sigma_x + \delta \beta \tau_{xz} \right\} dy dz dx - \int_0^l \delta w q dx = 0 \quad (1)$$

where  $t$  is depth and  $b$  is breadth of the beam. Eq. (1) can be expressed as:

$$[\mathbf{K}_f + \mathbf{K}_s]\boldsymbol{\varphi} - \mathbf{F} = 0 \quad (2)$$

where  $\mathbf{K}_f$  is the global flexural and  $\mathbf{K}_s$  is the global shear stiffness matrices.  $\mathbf{F}$  is the global force vector. Global matrices and vectors can be obtained by assembling their nodal values. In a field node, the nodal stiffness matrices and nodal force vector can be expressed as follows:

$$\begin{aligned} \mathbf{k}_f &= \int_{x_1}^{x_2} [\mathbf{B}_f]^T (EI) \mathbf{B}_f dx \\ \mathbf{k}_s &= \int_{x_1}^{x_2} [\mathbf{B}_s]^T (GA) \mathbf{B}_s dx \\ \mathbf{f} &= \int_{x_1}^{x_2} [\phi_1 \quad 0 \quad \phi_2 \quad 0]^T q dx \end{aligned} \quad (3)$$

where  $x_1$  and  $x_2$  are integration borders of an integration domain. In a local support domain (Liu, 2002), if  $n$  is considered as number of nodes, the lateral displacement  $w_i$  and slope  $\theta_i$  at a node can be defined in terms of shape functions as follows:

$$\begin{aligned} w_i &= \phi_1 w_1 + \phi_2 w_2 + \dots + \phi_n w_n \\ \theta_i &= \phi_1 \theta_1 + \phi_2 \theta_2 + \dots + \phi_n \theta_n \end{aligned} \quad (4)$$

Using the curvature-displacement relationship,  $\mathbf{B}_f$  can be expressed as:

$$\mathbf{B}_f = \left[ 0 \quad \frac{d\phi_1}{dx} \quad 0 \quad \frac{d\phi_2}{dx} \quad \dots \quad 0 \quad \frac{d\phi_n}{dx} \right] \quad (5)$$

and  $\mathbf{B}_s$  is the shear strain-displacement matrix

$$\mathbf{B}_s = \left[ \frac{d\phi_1}{dx} \quad -\phi_1 \quad \frac{d\phi_2}{dx} \quad -\phi_2 \quad \dots \quad \frac{d\phi_n}{dx} \quad -\phi_n \right] \quad (6)$$

and  $EI$  is the *flexural rigidity* and  $GA$  is the *shear rigidity*,  $\phi$  is the nodal shape function that can be constructed using either PIM or RPIM methods.

Bending moments and shear forces on each support domain can be expressed as (Owen and Hinton, 1980):

$$M = (EI) \mathbf{B}_f \boldsymbol{\varphi} = \left( \frac{EI}{l} \right) (\theta_1 - \theta_2) \quad (7)$$

where  $\theta_1$  and  $\theta_2$  are slopes on the local nodes,  $l$  is integration domain length. Shear force varies linearly over support domain, if we evaluate it on the mid-point of domain and assume that it is constant over the domain:

$$Q = (GA) \mathbf{B}_s \boldsymbol{\varphi} = (GA) \left\{ \left( \frac{w_2 - w_1}{l} \right) - \left( \frac{\theta_1 + \theta_2}{2} \right) \right\} \quad (8)$$

The value of the ultimate moment, in plastic condition can be expressed in terms of yield stress  $\sigma_0$  as:

$$M_0 = \int_{b(-t/2)}^{b(t/2)} \int_{-t/2}^{t/2} z \sigma_0 dz dy \quad (9)$$

where  $M_0 = \sigma_0(bt^2/4)$  for a rectangular beam. After yielding, flexural rigidity  $EI$  becomes elasto-plastic flexural rigidity:

$$(EI)_{ep} = EI \left(1 - \frac{EI}{EI+H}\right) \quad (10)$$

where strain-hardening parameter is  $H' = dM/(d\epsilon_f)_p$ .

### Point Interpolation Method (PIM)

Consider a function  $u(x)$  defined in domain  $\Omega$ , which is represented by field nodes. The  $u(x)$  at the point of interest  $x_Q$  is approximated in the form as presented by Liu (2010):

$$u(x, x_Q) = \sum_{i=1}^n B_i(x) a_i \quad (11)$$

where  $B_i(x)$  is the basis function defined in the Cartesian coordinate,  $a_i$  is the coefficient for the basis function,  $n$  is the number of nodes in a local support domain.

When, the polynomial basis function is used as a basis function Eq. (11) can be written as:

$$u(x, x_Q) = \sum_{i=1}^n p_i(x) a_i(x_Q) = \mathbf{p}^T(x) \mathbf{a}(x_Q) \quad (12)$$

where  $p_i(x)$  is the basis function of monomials,  $a$  is the coefficient of basis function  $p_i(x)$ . A polynomial basis in one dimension is:

$$\mathbf{p}^T(x) = [1, x, x^2, x^3, x^4, \dots, x^{n-1}] \quad (13)$$

At node  $i$ , we have equation in matrix form as:

$$u^{sd} = \mathbf{P}_Q \mathbf{a} \quad (14)$$

where generalized displacement vector  $\mathbf{u}^{sd}$

$$\mathbf{u}^{sd} = \{[w_1, \theta_1, w_2, \theta_2, \dots, w_n, \theta_n]^T\} \quad (15)$$

and  $\mathbf{P}_Q$  is the moment matrix for 1D case is given by

$$\mathbf{P}_Q = \begin{bmatrix} 1 & x_1 & \dots & x_1^{n-1} \\ 1 & x_2 & \dots & x_2^{n-1} \\ \vdots & \vdots & \ddots & \vdots \\ 1 & x_n & \dots & x_n^{n-1} \end{bmatrix} \quad (16)$$

If the inverse of moment matrix exists, using Eq. (16), we have:

$$\mathbf{a} = \mathbf{P}_Q^{-1} \mathbf{u}^{sd} \quad (17)$$

Finally, the Eq. (12) becomes:

$$u(x, x_Q) = \sum_{i=1}^n p_i(x) a_i(x_Q) = \mathbf{p}^T \mathbf{P}_Q^{-1} \mathbf{u}^{sd} \quad (18)$$

where PIM shape function  $\phi$ :

$$\phi = \mathbf{p}^T \mathbf{P}_Q^{-1} = [\phi_1(x) \quad \phi_2(x) \quad \dots \quad \phi_n(x)] \quad (19)$$

### Radial Point Interpolation Method (RPIM)

The field variable is approximated using a radial basis function. Thus, equation Eq. (11) becomes:

$$u(x, x_Q) = \sum_{i=1}^n B_i(x) a_i = \mathbf{R}^T(x) \mathbf{a}(x_Q) \quad (20)$$

where  $\mathbf{a}$  is the unknown constants vector for the radial basis function,  $\mathbf{R}$  is the radial basis function with  $r = x - x_i$ . Although  $\mathbf{R}$  is used itself without powers in the original RPIM, it can be used in the following form to increase its accuracy:

$$\mathbf{R}^T = [R_1(r_1)^0, R_2(r_2)^1, R_3(r_3)^2, \dots, R_n(r_n)^{n-1}] \quad (21)$$

In this study, multiquadric radial basis function (MQ RBF)  $((r_i^2 + (\alpha_c * d_c)^2)^q)$  is used to construct shape functions. In general form of MQ RBF, it has two shape parameters,  $\alpha_c$  and  $q$ , which control the shape of functions and their range of values are proposed by Wang and Liu (2002).  $d_c$  is the nodal spacing in whole problem domain.

$\mathbf{R}_Q$  is the moment matrix of RBFs and can be written as follows:

$$\mathbf{R}_Q = \begin{bmatrix} R_1(r_1)^0 & R_2(r_1)^1 & \dots & R_n(r_1)^{n-1} \\ R_1(r_2)^0 & R_2(r_2)^1 & \dots & R_n(r_2)^{n-1} \\ \vdots & \vdots & \ddots & \vdots \\ R_1(r_n)^0 & R_2(r_n)^1 & \dots & R_n(r_n)^{n-1} \end{bmatrix} \quad (22)$$

It has an inverse, so vector of coefficients  $\mathbf{a}$  can be calculated as:

$$\mathbf{a} = \mathbf{R}_Q^{-1} u^{sd} \quad (23)$$

Substituting Eq. (23) into Eq. (20):

$$u(x, x_Q) = \mathbf{R}^T(x) \mathbf{R}_Q^{-1} u^{sd} \quad (24)$$

RPIM shape functions  $\phi(x)$  are

$$\phi(x) = \mathbf{R}^T(x) \mathbf{R}_Q^{-1} = [\phi_1(x) \quad \phi_2(x) \quad \dots \quad \phi_n(x)] \quad (25)$$

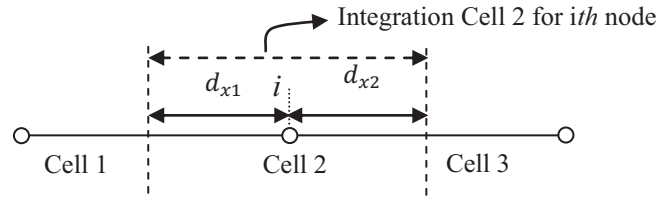
### Integration Schemes

#### Gauss Integration Scheme

To evaluate Eq. (3), two different integration schemes are used. In Gauss integration method, quadrature cells are used to integration. Two sampling points are used to calculate flexural nodal stiffness matrix and one sampling point is used for shear nodal stiffness matrix calculation. Thus,

$$\begin{aligned} \mathbf{k}_f &= EI * (Jac) * \left[ (w_1) \left( [\mathbf{B}_f]^T_{q1} * [\mathbf{B}_f]_{q1} \right) + (w_2) \left( [\mathbf{B}_f]^T_{q2} * [\mathbf{B}_f]_{q2} \right) \right] \\ \mathbf{k}_s &= GA * (Jac) * \left[ (w) \left( [\mathbf{B}_s]^T_q * [\mathbf{B}_s]_q \right) \right] \end{aligned} \quad (26)$$

where  $Jac$  is the Jacobian,  $w$ ,  $w_1$ ,  $w_2$  are weights,  $q$ ,  $q1$ ,  $q2$  are quadrature points and  $\mathbf{B}_f$  and  $\mathbf{B}_s$  are presented in Eq. (5), Eq. (6) respectively.



**Figure.1 Nodal integration scheme.**

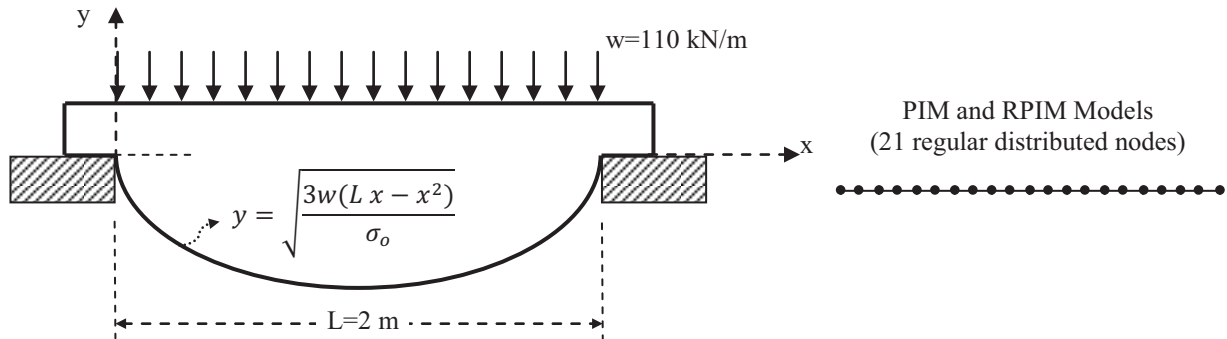
#### 4.2 Nodal Integration Scheme

Second integration scheme is the nodal integration proposed by Liu et al. (2007). In this method, nodal stiffness matrices are introduced by Taylor's expansion. The whole solution domain is divided into non-overlapping cells around each field node as shown in Fig. 1. Thus, the nodal stiffness matrices can be expressed as:

$$\begin{aligned} \mathbf{k}_f &= EI * \left\{ \begin{aligned} & \left( ([\mathbf{B}_f]_{x_0}^T * [\mathbf{B}_f]_{x_0})(d_{x2} - d_{x1}) + \frac{1}{2!} \cdot \frac{\partial}{\partial x} ([\mathbf{B}_f]_{x_0}^T * [\mathbf{B}_f]_{x_0})(d_{x2}^2 - d_{x1}^2) \right) \\ & + \frac{1}{3!} \frac{\partial^2}{\partial x^2} ([\mathbf{B}_f]_{x_0}^T * [\mathbf{B}_f]_{x_0})(d_{x2}^3 - d_{x1}^3) \end{aligned} \right\} \\ \mathbf{k}_s &= GA * \{ ([\mathbf{B}_s]_{x_0}^T * [\mathbf{B}_s]_{x_0})(d_{x2} - d_{x1}) \} \end{aligned} \quad (27)$$

#### Solutions and Discussions

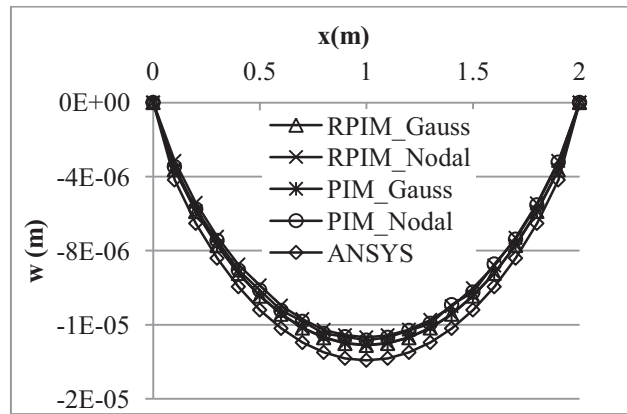
The programs used in this study are developed in Matlab. A constant strength simply supported beam is used to test the developed programs with an elasto-plastic material of  $E=200$  GPa,  $\sigma_y = 50$  MPa and  $H' = 2 * 10^4$  (Fig. 2). A uniformly distributed load of 110 kN/m is applied with ten different increments. In order to compare solution times of methods, a model with 501 regular distributed nodes is developed and solved. All solutions are carried out using a PC with 2.5 GHz CPU and 4 GByte RAM. Although, it is reported that the computational cost of RPIM is higher than PIM and FEM (Liu, 2002), in this study, it is determined that when standard Gauss integration scheme and non-polynomial augmented RPIM are used, there is no significant difference between them in solution times as shown in Table 1. However, when Nodal integration scheme is used, the solution time is nearly reduced 33%. The elastic displacement distributions are all good agreements for all methods as shown in Fig. 3. The support domain size has no a significant effect on the results of PIM and RPIM as shown in Fig. 4-7. Similarly,  $\alpha_c$  has no an important effect in RPIM solutions (Fig. 8 and 9). However,  $q$  only gives acceptable results when its value approaches to 1 as shown in Fig. 10 and 11.



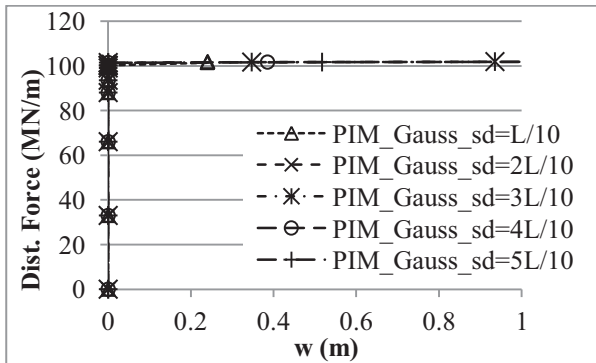
**Figure 2.Constant strenght simply supported beam and its PIM and RPIM models.**

**Table 1. Solution times of Matlab programs for the constant strength simply supported beam (with 501 regular distributed nodes)**

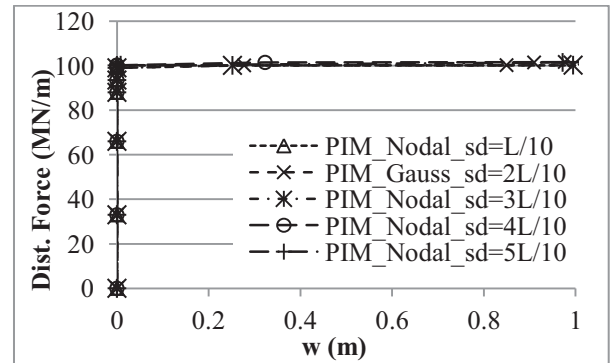
Support Domain Size	Solution times (in Secs)				
	RPIM_Gauss	RPIM_Nodal	PIM_Gauss	PIM_Nodal	FEM
L/10	30.03	20.44	29.96	20.05	
2L/10	30.36	20.61	30.29	20.64	
3L/10	30.41	20.97	30.33	20.98	29.36
4L/10	30.43	21.18	30.38	21.07	
5L/10	30.44	21.52	30.40	21.43	



**Figure 3. Displacement distribution of constant strength simply supported beam along the neutral axis at the last load increment ( $w=100$  kN/m,  $sd=L/10$   $q=1$ ,  $\alpha_c=3$ ).**



**Figure 4. Convergence of the PIM solution of constant strength simply supported beam after yield point for various support domain sizes with  $q=1$ ,  $\alpha_c=3$  and Gauss integration scheme.**



**Figure 5. Convergence of the PIM solution of constant strength simply supported beam after yield point for various support domain sizes with  $q=1$ ,  $\alpha_c=3$  and Nodal integration scheme.**

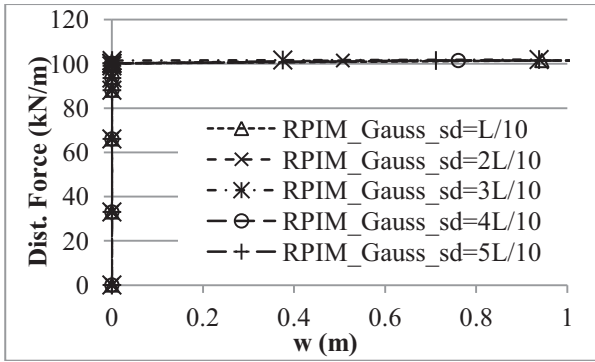


Figure 6. Convergency of the RPIM solution of constant strength simply supported beam after yield point for various support domain sizes with  $q=1$ ,  $\alpha_c=3$  and Gauss integration scheme.

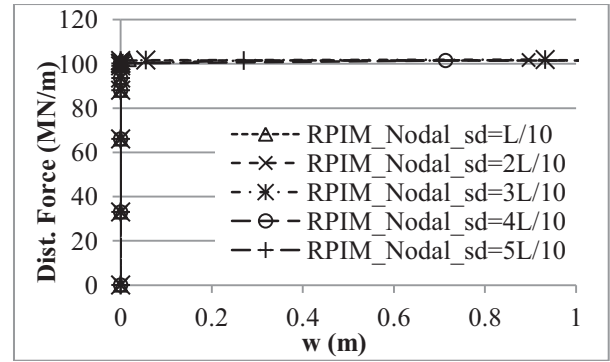


Figure 7. Convergency of the RPIM solution of constant strength simply supported beam after yield point for various support domain sizes with  $q=1$ ,  $\alpha_c=3$  and Nodal integration scheme.

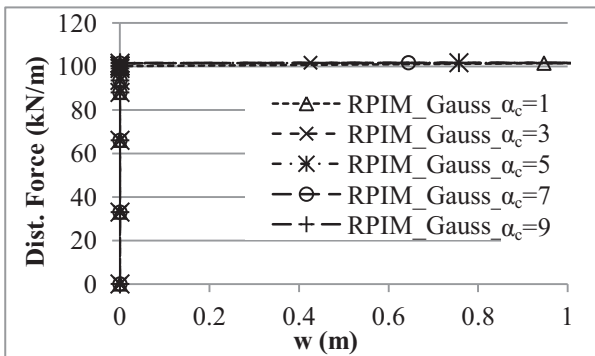


Figure 8. Convergency of the RPIM solution of constant strength simply supported beam after yield point for various  $\alpha_c$  with support domain size  $sd=0.3$ ,  $q=1$  and Gauss integration scheme.

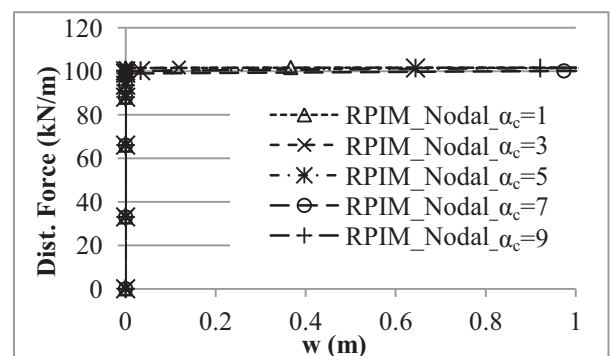


Figure 9. Convergency of the RPIM solution of constant strength simply supported beam after yield point for various  $\alpha_c$  with support domain size  $sd=0.3$ ,  $q=1$  and Nodal integration scheme.

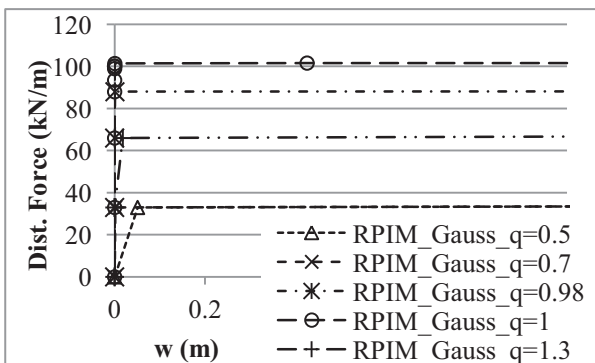


Figure 10. Convergency of the RPIM solution of constant strength simply supported beam after yield point for various  $q$  with support domain size  $sd=0.3$ ,  $\alpha_c=3$  and Gauss integration scheme.

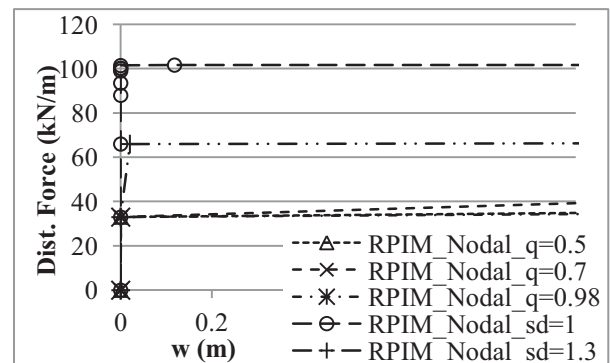


Figure 11. Convergency of the RPIM solution of constant strength simply supported beam after yield point for various  $q$  with support domain size  $sd=0.3$ ,  $\alpha_c=3$  and Nodal integration scheme.



## Conclusions

Although in many studies, it is reported that the computational cost of RPIM is higher than FEM and PIM (Liu, 2002), it is shown that solution times of elasto-plastic thick beams are nearly equal to each other's for PIM, RPIM and FEM when standard Gauss integration scheme and non-polynomial augmented RPIM are used. However, when the nodal integration scheme based on Taylor's series expansion is used, the solution times of PIM and RPIM are reduced 33%. The support domain size and  $\alpha_c$  do not have a significant effect on the results of all methods. However,  $q$  seriously affects the results. It does not give any singular solution when it is equal to 1 and gives best results when it is equal to either 1 or nearly equal to 1.

## References

- Chebl, C. and Neale K.W. (1984), A finite element method for elasto-plastic beams and columns at large deflections, *Computers and Structures*, 18, pp.255-261.
- Dai, K. Y., Liu, G. R., Lim K. M., Han X. and Du S. Y. (2007), A meshfree radial point interpolation method for analysis of functionally graded material (FGM) plates, *Computational Mechanics*, 34, 213–223.
- Dinis, L.M.J.S., Natal Jorgea, R.M. and Belinha, J. (2008), Analysis of plates and laminates using the natural neighbour radial point interpolation method, *Engineering Analysis with Boundary Elements*, 32, 267–279.
- Gu, Y. T. and Liu, G. R. (2000), A local point interpolation method for static and dynamic analysis of thin beams, *Computer Methods in Applied Mechanics and Engineering*, 42, pp. 5515-5528.
- Lee, P.S. and McClure, G. (2005), A general three-dimensional L-section beam finite element for elasto-plastic large deformation analysis, *Computers and Structures*, vol.84, pp. 215-229.
- Li, Y., Liu, G.R., Luan, M.T., Dai, K.Y., Zhong, Z.H., Li, G.Y. and Han, X. (2007), Contact analysis for solids based on linearly conforming radial point interpolation method, *Comput. Mech.* 39, 537–554.
- Liew, K. M. and Chen, X. L. (2004), Mesh-free radial point interpolation method for the buckling analysis of Mindlin plates subjected to in-plane point loads, *Int. J. Numer. Meth. Engng*, 60, 1861–1877.
- Liu, G. R. (2002): *Mesh Free Methods: Moving Beyond the Finite Element Method*. CRC press: USA.
- Liu, G. R. and Gu, Y. T. (2003), *An introduction to Meshfree methods and their programming*, Springer: Berlin, 2005.
- Liu, G. R. and Gu, Y.T. (2001a), A point interpolation method for two-dimensional solids, *Int. J. Numer. Meths. Engrng*, pp. 937-951.
- Liu, G. R. and Gu, Y.T. (2001b), A local radial point interpolation method (LRPIM) for free vibration analyses of 2-d solids, *Journal of Sound and Vibration*, 246, pp. 29–46.
- Liu, G. R., Zhang G. Y., Gu Y. T. and Wang Y. Y. (2005), A meshfree radial point interpolation method (RPIM) for three-dimensional solids, *Comput Mech*, 36, 421–430.
- Liu, G. R., Zhang, G. Y., Wang Y. Y., Zhong, Z. H., Li, G. Y. and Han, X. (2007), A Nodal Integration Technique for Meshfree Radial Point Interpolation Method (NI-RPIM), *Journal of Solid and Structures*, vol. 44.,pp. 3845-3847.
- Liu, L., Chua L.P. and Ghista D.N. (2006), Conforming radial point interpolation method for spatial shell structures on the stress-resultant shell theory, *Arch Appl Mech*, 75, 248–267.
- Liu, Y., Hon Y. C. and Liew K. M. (2006), A meshfree Hermite-type radial point interpolation method for Kirchhoff plate problems, *Int. J. Numer. Meth. Engng*, 66:1153–1178.
- Owen, D.R.J. and Hinton, E. (1980), *Finite Elements in Plasticity: Theory and Practice*, pp. 121-144
- Wang, J. G. and Liu, G. R. (2002a), A point interpolation meshless method based on radial basis functions, *Int. J. Numer. Meth. Engng*, 54, 1623–1648.
- Wang, J. G. and Liu, G. R. (2002b), On the optimal shape parameters of radial basis functions used for 2D meshless methods, *Comput. Methods Appl. Mech. Engrg.*, vol. 191, pp. 2611-2630.
- Wu, Y. L. and Liu, G. R. (2004), A meshfree formulation of local radial point interpolation method (LRPIM) for incompressible flow simulation, *Computational Mechanics*, 30, 355–365.
- Zhao, X., Liu, G. R., Dai K. Y., Zhong Z. H., Li G. Y. and Han X. (2009a), Free-vibration analysis of shells via a linearly conforming radial point interpolation method (LC-RPIM), *Finite Elements in Analysis and Design*, 45, 917–924.
- Zhao, X., Liu, G. R., Dai K. Y., Zhong Z. H., Li G. Y. and Han X. (2009b), A linearly conforming radial point interpolation method (LC-RPIM) for shells, *Comput Mech*, 43, 403–413.
- Zhao, X., Liu, G. R., Dai K. Y., Zhong Z. H., Li G. Y. and Han X. (2008), Geometric nonlinear analysis of plates and cylindrical shells via a linearly conforming radial point interpolation method, *Comput Mech*, 42, 133–144.

## Vibration of Thin Beams by PIM and RPIM methods

\*B. Kanber<sup>1</sup>, and O. M. Tufik<sup>1</sup>

<sup>1</sup>Mechanical Engineering Department, University of Gaziantep, Turkey.

\*Corresponding author: kanber@gantep.edu.tr

### Abstract

In this study, vibration of thin beams are analyzed by using point interpolation (PIM) and radial point interpolation (RPIM) methods with standard Gaussian integration and a nodal integration based on the Taylor series expansion. The effects of integration schemes, support domain sizes and RPIM shape parameters on the vibration modes are investigated. A cantilever beam problem is solved by linear elastic materials with uniform cross-section. The results are compared with finite element and available analytical solutions.

**Keywords:** PIM, RPIM, Vibration, Meshfree, Thin Beams.

### Introduction

The PIM (Liu and Gu, 2001a) and RPIM (Wang and Liu, 2002a, 2002b) are meshfree techniques that are used in the solution of wide range of engineering problems. In addition to these applications, their local versions are used to analyze the vibration of thin beams and 2-D solids (Liu and Gu, 2001b; Gu and Liu, 2000).

In this study, PIM and RPIM solutions of vibration of thin beams are carried out using the standard Gauss integration scheme and a nodal integration scheme based on Taylor Series expansion. The effect of support domain sizes and shape parameters of RPIM are investigated on the natural frequencies and free vibration modes.

### Free Vibrations of Thin Beams

The Lagrangian can be written as follows (Chandrupatla and Belegundu, 1999):

$$L = T - \Pi \quad (1)$$

where  $T$  is the kinetic energy and  $\Pi$  is the potential energy of the beam. Using Eq. (1), Hamilton's principle can be expressed as:

$$\int_{t_1}^{t_2} \delta L = 0 \quad (2)$$

Then, for the free vibration, the equation of motion can be obtained using Eq. 2 as follows:

$$\mathbf{M}\ddot{\mathbf{Q}} + \mathbf{K}\mathbf{Q} = 0 \quad (3)$$

where  $\mathbf{Q}$  is the global displacement vector,  $\mathbf{M}$  is the global mass matrix and  $\mathbf{K}$  is the global stiffness matrix. For the steady state condition, starting from equilibrium state, we set:

$$\mathbf{Q} = \mathbf{U}\sin(\omega t) \quad (4)$$

where  $\mathbf{U}$  is the vector of nodal amplitudes of vibration and  $\omega$  is the circular frequency. Introducing Eq. (4) into Eq. (3), we have:

$$\mathbf{K}\mathbf{U} = \omega^2\mathbf{M}\mathbf{U} \quad (5)$$

where  $\mathbf{U}$  corresponds to the eigenvalue,  $\lambda = \omega^2$ .

The global mass and stiffness matrixes can be obtained assembling their nodal values as in the FEM. Their nodal values are,

$$\mathbf{k} = E I \int_{x_1}^{x_2} \mathbf{N}^T \mathbf{N} dx \quad (6)$$

$$\mathbf{m} = \rho A \int_{x_1}^{x_2} \mathbf{N}^T \mathbf{N} dx \quad (7)$$

where  $E$  is the modulus of elasticity,  $I$  is the second moment of area,  $\rho$  is the material density and  $A$  is the cross-sectional area of the beam. They are assumed constant through an integration cell.  $x_1$  and  $x_2$  are the limits of an integration cell.  $\mathbf{N}$  is the shape function vector that can be replaced with either PIM or RPIM shape functions. They are calculated in terms of real coordinates. So, they must be transformed to natural coordinates of -1 and 1 for Gauss integration scheme. It is not required to transform the limits to the natural limits when the nodal integration scheme is used.

### Point Interpolation Method (PIM)

In the thin beam theory, there are two degrees of freedom at each node: deflection and slope. Therefore,  $u(x)$  at the point of interest  $x_Q$  is approximated by  $2n$  terms as presented by Liu (2010):

$$u(x, x_Q) = \sum_{i=1}^{2n} B_i(x) a_i \quad (8)$$

where  $B_i(x)$  is the basis function defined in the Cartesian coordinate,  $a_i$  is the coefficient for the basis function,  $n$  is the number of nodes in a local support domain.

When, the polynomial basis function is used as a basis function Eq. (8) can be written as:

$$u(x, x_Q) = \sum_{i=1}^{2n} p_i(x) a_i(x_Q) = \mathbf{p}^T(x) \mathbf{a}(x_Q) \quad (9)$$

where  $p_i(x)$  is the basis function of monomials,  $a$  is the coefficient of basis function  $p_i(x)$ . A polynomial basis in one dimension is:

$$\mathbf{p}^T(x) = [1, x, x^2, x^3, \dots, x^{2n-1}] \quad (10)$$

At node  $i$ , we have equation in matrix form as:

$$u^{sd} = \mathbf{P}_Q \mathbf{a} \quad (11)$$

where generalized displacement vector  $\mathbf{u}^{sd}$ :

$$\mathbf{u}^{sd} = \{[w_1, \theta_1, w_2, \theta_2, \dots, w_n, \theta_n]^T\} \quad (12)$$

and  $\mathbf{P}_Q$  is the moment matrix. For 1D case, it is given by:

$$\mathbf{P}_Q = [\mathbf{p}(x_1), \mathbf{p}(x_2), \dots, \mathbf{p}(x_{2n})]^T \quad (13)$$

If the inverse of moment matrix exists, using Eq. (11), we have:

$$\mathbf{a} = \mathbf{P}_Q^{-1} \mathbf{u}^{sd} \quad (14)$$

Finally, the Eq. (9) becomes:

$$u(x, x_Q) = \sum_{i=1}^n p_i(x) a_i(x_Q) = \mathbf{p}^T \mathbf{P}_Q^{-1} \mathbf{u}^{sd} \quad (15)$$

where PIM shape function  $\phi$ :

$$\phi = \mathbf{p}^T \mathbf{P}_Q^{-1} = [\phi_1(x) \quad \phi_2(x) \quad \dots \quad \phi_n(x)] \quad (16)$$

### Radial Point Interpolation Method (RPIM)

Radial basis functions are used in PIM to create shape functions. The field variable is approximated using a radial basis function by considering deflection and slope at each node. Thus, equation Eq. (8) becomes:

$$u(x, x_Q) = \sum_{i=1}^{2n} B_i(x) a_i = \mathbf{R}^T(x) \mathbf{a}(x_Q) \quad (17)$$

where  $\mathbf{a}$  is the unknown constants vector for the radial basis function,  $\mathbf{R}$  is the radial basis function with distance  $r$  between points  $x$  and  $x_i$ . For 1D case,  $r$  can be written as:

$$r = x - x_i \quad (18)$$

As a vector form,  $\mathbf{R}$ :

$$\mathbf{R}^T = [R_1(r_1)^0, R_2(r_2)^1, R_3(r_3)^2, \dots, R_n(r_n)^{2n-1}] \quad (19)$$

In this study, multiquadric radial basis function (MQ RBF)  $((r_i^2 + (\alpha_c * d_c)^2)^q)$  is used to construct shape functions. In general form of MQ RBF, it has two shape parameters,  $\alpha_c$  and  $q$ , which control the shape of functions and their range of values are proposed by Wang and Liu (2002).  $d_c$  is the nodal spacing in whole problem domain. If the nodes are uniformly distributed, it is equal to the distance between two nodes. Else, it is equal to the average nodal spacing. These parameters can be altered to increase the solution accuracy for different type of problems.

The coefficients  $a_i$  in Eq. (17) can be determined by letting Eq. (17) be satisfied at all the  $n$  support nodes as given by Liu (2010). After interpolation at  $k$ th point, we have:

$$u_k = u(x_k) = \sum_{i=1}^{2n} a_i R_i(x_k) \quad k = 1, 2, \dots, n \quad (20)$$

The equation above can be written in matrix form as:

$$u^{sd} = \mathbf{R}_Q \mathbf{a} \quad (21)$$

where  $u^{sd}$  is the generalized displacement vector, and  $\mathbf{R}_Q$  is the moment matrix of RBFs:

$$\mathbf{R}_Q = \begin{bmatrix} R_1(r_1)^0 & R_2(r_1)^1 & \dots & R_n(r_1)^{2n-1} \\ R_1(r_2)^0 & R_2(r_2)^1 & \dots & R_n(r_2)^{2n-1} \\ \vdots & \vdots & \ddots & \vdots \\ R_1(r_n)^0 & R_2(r_n)^1 & \dots & R_n(r_n)^{2n-1} \end{bmatrix} \quad (22)$$

It is the invertible moment matrix and vector of coefficients  $\mathbf{a}$  can be calculated as:

$$\mathbf{a} = \mathbf{R}_Q^{-1} u^{sd} \quad (23)$$

Substituting Eq. (23) into Eq. (17):

$$u(x, x_Q) = \mathbf{R}^T(x) \mathbf{R}_Q^{-1} u^{sd} \quad (24)$$

where RPIM shape functions  $\phi(x)$  are:

$$\phi(x) = \mathbf{R}^T(x) \mathbf{R}_Q^{-1} = [\phi_1(x) \ \phi_2(x) \ \dots \ \phi_n(x)] \quad (25)$$

## Integration Schemes

### Gauss Integration Scheme

To evaluate Eqs. (6) and (7), two different integration schemes are used. The first one is standard Gauss integration. In this method, quadrature cells (background cells) are used to integration. The shape functions are calculated for each node in the support domain.

Two sampling points are used to calculate flexural nodal stiffness matrix and one sampling point is used for shear nodal stiffness matrix calculation. Thus,

$$\mathbf{k} = E I \text{Jac} [w_1(\mathbf{N}_{q1}^T \mathbf{N}_{q1}) + w_2(\mathbf{N}_{q2}^T \mathbf{N}_{q2})] \quad (26)$$

$$\mathbf{m} = \rho A \text{Jac} [w(\mathbf{N}_q^T \mathbf{N}_q)] \quad (27)$$

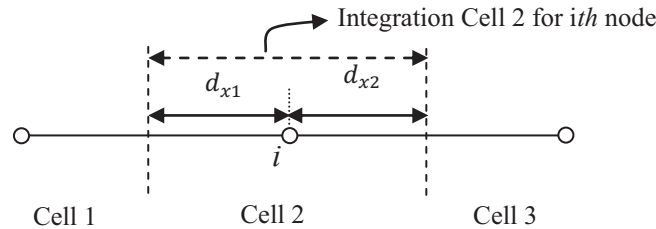
where  $\text{Jac}$  is the Jacobian matrix,  $w$ ,  $w_1$ ,  $w_2$  are weights,  $q$ ,  $q_1$ ,  $q_2$  are quadrature points.

### Nodal Integration Scheme

Second integration scheme is the nodal integration proposed by Liu et al. (2007). In this method, nodal stiffness matrices are introduced by Taylor's expansion. The whole solution domain is divided into non-overlapping cells around each field node (Fig. 1). Thus, the nodal stiffness matrices can be expressed as:

$$\mathbf{k} = E I \left\{ \begin{aligned} &(\mathbf{N}_{x_0}^T \mathbf{N}_{x_0})(d_{x2} - d_{x1}) + \frac{1}{2!} \cdot \frac{\partial}{\partial x} (\mathbf{N}_{x_0}^T \mathbf{N}_{x_0})(d_{x2}^2 - d_{x1}^2) \\ &+ \frac{1}{3!} \frac{\partial^2}{\partial x^2} (\mathbf{N}_{x_0}^T \mathbf{N}_{x_0})(d_{x2}^3 - d_{x1}^3) \end{aligned} \right\} \quad (28)$$

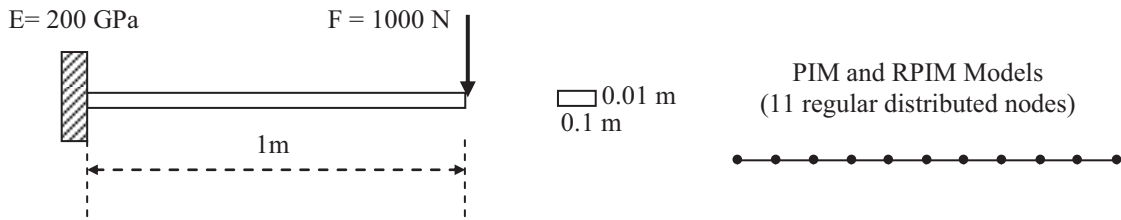
$$\mathbf{m} = \rho A \left\{ \begin{aligned} &(\mathbf{N}_{x_0}^T \mathbf{N}_{x_0})(d_{x2} - d_{x1}) + \frac{1}{2!} \cdot \frac{\partial}{\partial x} (\mathbf{N}_{x_0}^T \mathbf{N}_{x_0})(d_{x2}^2 - d_{x1}^2) \\ &+ \frac{1}{3!} \frac{\partial^2}{\partial x^2} (\mathbf{N}_{x_0}^T \mathbf{N}_{x_0})(d_{x2}^3 - d_{x1}^3) \end{aligned} \right\} \quad (29)$$



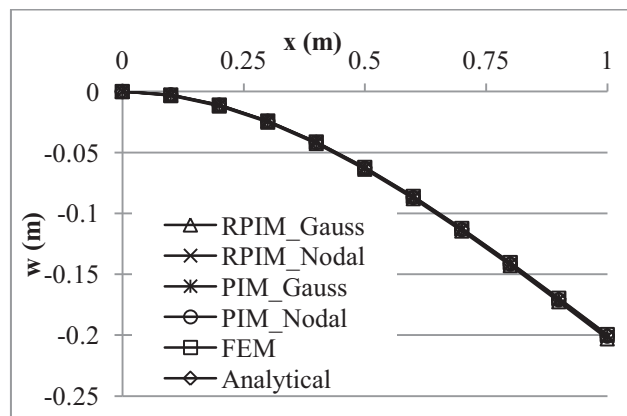
**Figure.1 Nodal integration scheme**

**Solutions and Discussions**

A cantilever beam of uniform rectangular cross section ( $0.1 \times 0.01 \text{ m}^2$ ) is used to test the developed programs as shown in Fig. 2. Structural steel is used with a Young’s modulus of 200 GPa and density of  $7840 \text{ kg/m}^3$ . 1 kN end load is applied. 100 two-node finite elements are used in the FEM solutions. 11 regular distributed nodes are used in the PIM and RPIM solutions. The codes are developed in Matlab and the function “eig” is used to find eigenvalues and eigenvectors. All methods are in excellent agreements with analytical and finite element solutions as shown in Fig. 3 for the vertical deflection of the cantilever beam.

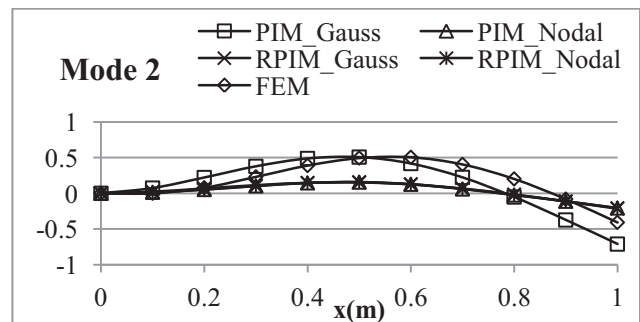
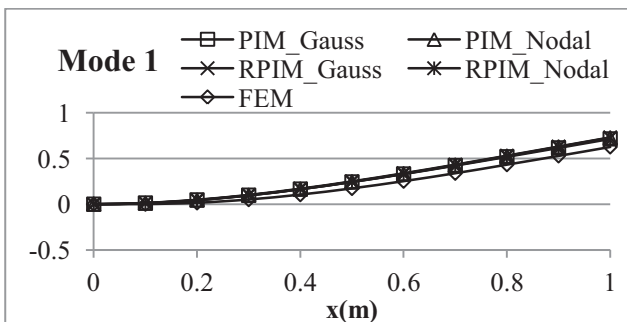


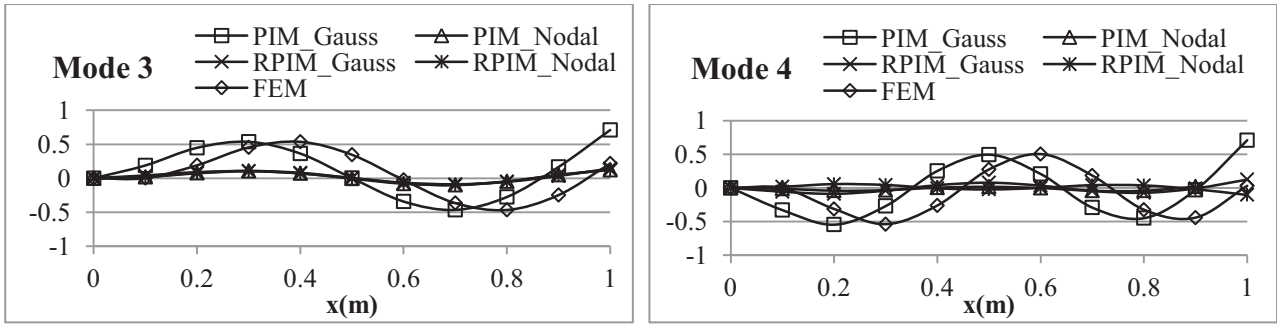
**Figure 2. Cantilever beam and its PIM and RPIM models.**



**Figure 3. Vertical deflections of the cantilever beam under 1kN end load ( $ds=3L/2$  for PIM and RPIM,  $q=1, \alpha_c=3$  for RPIM).**

First four modes of vibration of cantilever beam are given in Fig. 4. In these solutions, support domain size is used as  $3L/10$  for PIM and RPIM.  $q$  and  $\alpha_c$  are used as 1 and 3 respectively for the RPIM. In the first mode, all methods are in good agreements with the FEM solution. However, when the mode number is increased, PIM and RPIM with nodal integration and RPIM with Gauss integration give more stiff results than others.





**Figure 4. First four free vibration modes of the cantilever beam ( $ds=3L/10$  for PIM and RPIM,  $q=1$ ,  $\alpha_c=3$  for RPIM).**

The PIM and RPIM values of frequencies are compared with FEM and exact solutions in Table 1-4 for standard Gauss and nodal integration schemes, for different support domain sizes and shape parameters. Increasing the support domain size (sd) up to  $5L/10$  slightly change the PIM frequencies when the standard Gauss integration scheme is used as shown in Table 1. However, when sd becomes equal to  $5L/10$ , frequencies suddenly drops. When the nodal integration scheme (based on Taylor series expansion) is used, the PIM frequencies in the first mode are slightly improved, but the frequencies in the higher modes get worse. Similar results are also obtained for RPIM frequencies as shown in the Table 2. The best results are obtained when the support domain size is equal to  $L/10$  with Gauss and nodal integration schemes. The change of  $\alpha_c$  and  $q$  values does not significantly change the frequencies as shown in the Table 3 and 4. Although  $q$  causes singular moment matrix problem when it is equal to 1 (Liu and Gu, 2005), it does not cause a singularity problem in this study.

**Table 1. PIM frequencies of the cantilever beam for various support domain (sd) sizes.**

Mode	PIM with Gauss integration (11 nodes)					PIM with Nodal integration (11 nodes)					FEM (100 elements)	Exact (Ferreira, 2009)
	sd					sd						
	L/10	2L/10	3L/10	4L/10	5L/10	L/10	2L/10	3L/10	4L/10	5L/10		
1	3.516	3.516	3.503	3.042	1.117	3.490	3.497	3.501	3.500	3.448	3.516	3.516
2	22.035	22.026	21.870	18.502	12.096	20.183	21.000	22.273	21.623	20.471	22.034	22.035
3	61.707	61.646	60.855	50.439	38.793	38.448	5.560	39.697	57.500	66.965	61.697	-
4	120.966	120.719	117.678	97.908	87.656	45.109	39.276	53.846	39.200	39.713	120.902	-

**Table 2. RPIM frequencies of the cantilever beam for various support domain (sd) sizes ( $\alpha_c=3$ ,  $q=1$ ).**

Mode	RPIM with Gauss integration (11 nodes)					RPIM with Nodal integration (11 nodes)					FEM (100 elements)	Exact (Ferreira, 2009)
	sd					sd						
	L/10	2L/10	3L/10	4L/10	5L/10	L/10	2L/10	3L/10	4L/10	5L/10		
1	3.515	3.512	3.486	2.809	0.944	3.523	3.505	3.502	3.499	3.425	3.516	3.516
2	22.035	21.953	21.626	17.505	13.887	20.471	20.724	22.311	21.097	20.424	22.034	22.035
3	61.656	61.398	59.818	47.277	26.530	39.107	39.353	39.906	39.399	39.614	61.697	-
4	120.598	120.193	114.035	86.843	59.762	45.679	46.415	53.915	45.782	45.786	120.902	-

**Table 3. RPIM frequencies of the cantilever beam for various  $\alpha_c$  (sd=3L/10, q=1).**

Mode	RPIM with Gauss integration (11 nodes)					RPIM with Nodal integration (11 nodes)					FEM (100 elements)	Exact (Ferreira, 2009)
	$\alpha_c$					$\alpha_c$						
	1	3	5	7	9	1	3	5	7	9		
1	3.327	3.486	3.493	3.496	3.498	3.490	3.502	3.502	3.501	3.502	3.516	3.516
2	20.218	21.626	21.703	21.732	21.781	20.792	22.311	22.262	22.107	20.662	22.034	22.035
3	55.492	59.818	60.124	60.224	60.288	66.177	39.906	39.757	39.825	62.947	61.697	-
4	105.393	114.035	114.851	115.089	114.934	40.274	53.915	53.779	54.213	40.348	120.902	-

**Table 4. RPIM frequencies of the cantilever beam for various q (sd=3L/10,  $\alpha_c=3$ ).**

Mode	RPIM with Gauss integration (11 nodes)					RPIM with Nodal integration (11 nodes)					FEM (100 elements)	Exact (Ferreira, 2009)
	q					q						
	0.5	0.7	0.98	1	1.3	0.5	0.7	0.98	1	1.3		
1	3.497	3.494	3.486	3.486	3.475	3.502	3.502	3.502	3.502	3.495	3.516	3.516
2	21.739	21.706	21.634	21.626	21.574	22.190	22.274	22.310	22.311	21.071	22.034	22.035
3	60.273	60.141	59.847	59.818	59.522	39.766	39.769	39.823	39.906	61.715	61.697	-
4	115.278	114.909	114.111	114.035	113.123	53.820	53.728	53.766	53.915	41.293	120.902	-

## Conclusions

All methods are in excellent agreements for the deflection solutions. In the first mode of free vibration of the cantilever beam, all methods are again in good agreements. However, in the higher modes, PIM and RPIM with nodal integration and RPIM with Gauss integration give stiffer results than FEM, analytical results and PIM with Gauss integration. Increasing support domain size generally improve the results. However, when the node numbers in the support domain becomes greater than 10, the beam starts to behave more rigid. The change of  $\alpha_c$  and q values does not significantly change the frequencies.

## References

- Chandrupatla, T.R. and Belegundu, A.D. (1999), Introduction to Finite Elements in Engineering, Prentice-Hall Inc., Upper Saddle River, NJ.
- Ferreira, A. J. M. (2009), MATLAB Codes for Finite Element Analysis-Solids and Structures, Springer, Berlin.
- Gu, Y. T. and Liu, G. R. (2000), A local point interpolation method for static and dynamic analysis of thin beams, Computer Methods in Applied Mechanics and Engineering. 42, pp. 5515-5528.
- Liu, G. R. and Gu, Y. T. (2001a), A point interpolation method for two-dimensional solids. International Journal for Numerical Methods in Engineering. 50,937-951.
- Liu, G. R. and Gu, Y. T. (2001b), A local radial point interpolation method (LRPIM) for free vibration analyses of 2-D solids, Journal of Sound and Vibration. 246, pp. 29-46.
- Liu, G. R. and Gu, Y. T. (2005), An introduction to meshfree methods and their programming, Springer, Berlin.
- Liu, G. R., Zhang, G. Y., Wang Y. Y., Zhong, Z. H., Li, G. Y. and Han, X. (2007), A Nodal Integration Technique for Meshfree Radial Point Interpolation Method (NI-RPIM), Journal of Solid and Structures, vol. 44.,pp. 3845-3847.
- Wang, J. G. and Liu, G. R. (2002a), A point interpolation meshless method based on radial basis functions, Int. J. Numer. Meth. Engng. 54, pp. 1623-1648.
- Wang, J. G. and Liu, G. R. (2002b), On the optimal shape parameters of radial basis functions used for 2-D meshless methods, Comput. Methods Appl. Mech. Engrg. 191, pp. 2611-2630.



# Parameter-free Shape Optimization Method for Natural Vibration Design of Stiffeners on Thin-walled Structures

\*Yang Liu<sup>1</sup>, Masatoshi Shimoda<sup>1</sup>

<sup>1</sup> Department of Advanced Science and Technology, Toyota Technological Institute,  
2-12-1 Hisakata, Tenpaku-ku, Nagoya, 468-8511, Japan

\*Corresponding author: liuyang60212@gmail.com

## Abstract

This paper presents a parameter-free shape optimization method for designing stiffeners on thin-walled structures subject to natural vibration. The design problems deal with natural frequency maximization problem and volume minimization problem, which are subject to a volume constraint and an eigenvalue constraint respectively. The boundary shapes of stiffeners are determined under the condition where the boundary is movable in the in-plane direction to the surface. The both optimization problems are formulated as distributed-parameter shape optimization problems, and the shape gradient functions are derived using the material derivative method and the adjoint variable method. The optimal free-boundary shapes of stiffeners are obtained by applying the derived shape gradient functions to the  $H^1$  gradient method for shells, which is a parameter-free shape optimization method proposed by one of the authors. Several design examples are presented to validate the proposed method and demonstrate its practical utility of the proposed method.

**Keywords:** Shape optimization, Parameter-free, Stiffener, Thin-walled structure, Shell, FEM

## Introduction

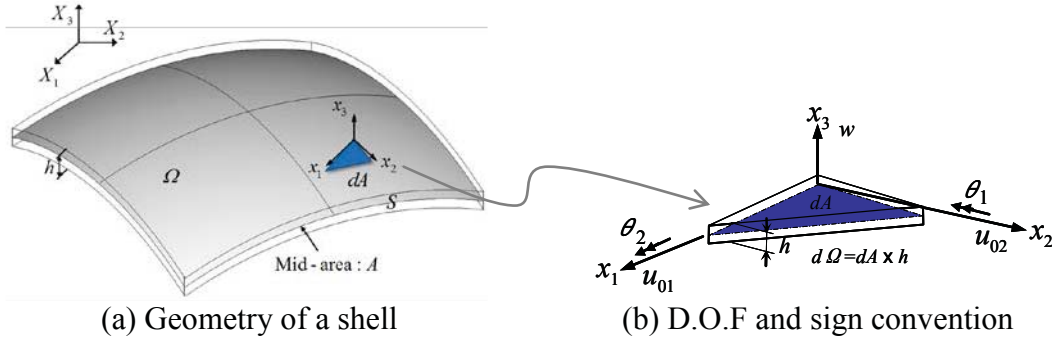
Thin-walled or shell structures are widely used as basic structural components in various industrial products, such as car bodies, aircraft fuselages, and pressure vessels as well as in bridges and buildings. They are commonly stiffened by stiffeners to improve the bending rigidity of the basic structures. With recent enhancements of high speed, high function and weight reduction of thin-walled structures, the vibration design in consideration of the dynamic characteristics has become more important than ever. The natural frequencies (i.e., vibration eigenvalues) usually represent the dynamic characteristics of structures, especially the lower order natural frequencies are considered as an evaluation measure of the dynamic stability. The dynamic response of the structures can be reduced by increasing the lower order natural frequencies (Alejandro and Kikuchi, 1992; Ma *et al.*, 1995). Moreover, the reduction of the dynamic response of a structure generally leads to the minimum weight for the structure design (Zhao *et al.*, 1996).

For the natural vibration problems, this paper presents a shape optimization method for designing the free-boundaries of stiffeners and basic structures of thin-walled or shell structures. This method is based on the parameter-free optimization method for the boundaries of shells as mentioned above. Two kinds of natural vibration design problems are formulated here as distributed parameter shape optimization problems. One is a specified eigenvalue maximization problem subject to a volume constraint, and the other is its reciprocal volume minimization problem subject to a specified eigenvalue constraint. To eliminate difficulties caused by the “mode switching” problem (i.e., frequency crossing) (Eldred *et al.*, 1995), the Modal Assurance Criterion (MAC) (Allemang, 2003) is adopted to track the specified natural mode through changes in the eigenvalue maximization or eigenvalue constraint problem. Sensitivity functions (i.e., shape gradient functions) for the two design problems are theoretically derived using the material derivative method and the adjoint

variable method. The optimal free-boundary shapes of stiffeners and the basic structure are determined by applying the derived shape gradient function to the  $H^1$  gradient method for shells.

### Variational equation for natural vibration of thin-walled structure

As shown in Fig. 1(a), a basic shell structure or stiffener with an initial bounded domain  $\Omega \subset \mathbb{R}^3$  is defined by the mid-area  $A$  and the domain of thickness direction  $(-h/2, h/2)$ , and the side surface  $S$  is defined by the boundary  $\partial A$  of the mid-area  $A$ .



(a) Geometry of a shell

(b) D.O.F and sign convention

Figure 1. Shell geometry consisting of infinitesimal flat surfaces

The weak formed eigenvalue equation for natural vibration in terms of  $r$ th mode  $(\mathbf{u}_0^{(r)}, w^{(r)}, \boldsymbol{\theta}^{(r)}) \in U$  can be expressed as Eq. (1)

$$a((\mathbf{u}_0^{(r)}, w^{(r)}, \boldsymbol{\theta}^{(r)}), (\bar{\mathbf{u}}_0, \bar{w}, \bar{\boldsymbol{\theta}})) = \lambda^{(r)} b((\mathbf{u}_0^{(r)}, w^{(r)}, \boldsymbol{\theta}^{(r)}), (\bar{\mathbf{u}}_0, \bar{w}, \bar{\boldsymbol{\theta}})) \quad , \quad (\mathbf{u}_0^{(r)}, w^{(r)}, \boldsymbol{\theta}^{(r)}) \in U, \forall (\bar{\mathbf{u}}_0, \bar{w}, \bar{\boldsymbol{\theta}}) \in U, \quad (1)$$

where  $u_{0\alpha}$ ,  $w$  and  $\theta_\alpha$  express the in-plane displacement, out-of-plane displacement and rotational angle of the mid-area of the plate as shown in Fig. 1(b), respectively.  $\bar{(\cdot)}$  expresses a variation and  $U$  expresses the admissible space in which the given constraint conditions of  $(\mathbf{u}_0, w, \boldsymbol{\theta})$  is satisfied.  $\lambda^{(r)}$  indicates the eigenvalue of the  $r$ th natural mode. In addition, the bilinear forms  $a(\cdot, \cdot)$  and  $b(\cdot, \cdot)$  are defined respectively as shown below.

$$a((\mathbf{u}_0^{(r)}, w^{(r)}, \boldsymbol{\theta}^{(r)}), (\bar{\mathbf{u}}_0, \bar{w}, \bar{\boldsymbol{\theta}})) = \int_A \{c_{\alpha\beta\gamma\delta}^B \theta_{(\gamma,\delta)}^{(r)} \bar{\theta}_{(\alpha,\beta)} + c_{\alpha\beta\gamma\delta}^M u_{0\gamma,\delta}^{(r)} \bar{u}_{0\alpha,\beta} + kc_{\alpha\beta}^S \gamma_\alpha^{(r)} \bar{\gamma}_\beta\} dA, \quad (2)$$

$$b((\mathbf{u}_0^{(r)}, w^{(r)}, \boldsymbol{\theta}^{(r)}), (\bar{\mathbf{u}}_0, \bar{w}, \bar{\boldsymbol{\theta}})) = \rho \int_A \{h(w^{(r)} \bar{w} + u_{0\alpha}^{(r)} \bar{u}_{0\alpha}) + I \theta_\alpha^{(r)} \bar{\theta}_\alpha\} dA, \quad (3)$$

where  $c_{\alpha\beta\gamma\delta}^B$ ,  $c_{\alpha\beta}^S$  and  $c_{\alpha\beta\gamma\delta}^M$  express an elastic tensor with respect to bending, shearing and membrane stress, respectively.  $\theta_{(\alpha,\beta)} (= \frac{1}{2}(\theta_{\alpha,\beta} + \theta_{\beta,\alpha}))$  expresses the curvatures and  $\gamma_\alpha (= w_{,\alpha} - \theta_\alpha)$  expresses the transverse shear strains. Moreover,  $\rho$  and  $I (= h^3 / 12)$  express a mass density and a second moment of area, respectively. The constant  $k$  denotes a shear correction factor, which can be used as  $k = 5/6$  within Reissner theory of isotropic elastic plates (Reissner, 1945).

### Shape optimization problem of stiffeners on the thin-walled structure

As shown in Fig. 2, the stiffened shell structure consists of a basic shell structure and stiffeners. To determine the optimal free-boundary shapes of stiffeners, the shape variations are considered as in-plane variations  $V$  in the tangential direction to the surfaces.

#### Eigenvalue maximization problem

Letting the eigenvalue equation in Eq. (1) and the volume be the constraint conditions and the eigenvalue of the specified  $r$ th natural mode be the objective functional to be maximized, a

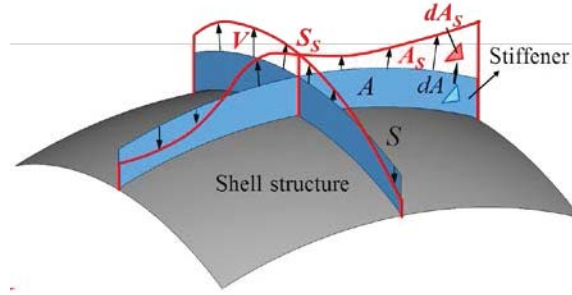


Figure 2. Shape variation of stiffeners and the basic shell by  $V$

distributed-parameter shape optimization problem for finding the optimal design velocity field of the stiffeners  $V$ , or  $A_s (= A + \Delta s V)$  can be formulated as shown below:

$$\text{Given } A, \quad (4)$$

$$\text{find } A_s \text{ (or } V) \quad (5)$$

$$\text{minimize } -\lambda^{(r)} \quad (6)$$

$$\text{subject to Eq.(1) and } M (= \int_A h dA) < \hat{M} \quad (7)$$

where  $M$  and  $\hat{M}$  denote the volume of the thin-walled structure with or without stiffeners and its constraint value, respectively.

For the mode switching problem as mentioned in Section 1, the Modal Assurance Criterion (MAC) [29] is used to track the specified  $r$ th natural mode of the initial shape. The mode with a maximum value of MAC in all natural modes is regarded as the corresponding mode and is tracked.

$$MAC(\phi_0^{(r)}, \phi_s) = \frac{|\{\phi_0^{(r)}\}^T \{\phi_s\}|^2}{(\{\phi_0^{(r)}\}^T \{\phi_0^{(r)}\})(\{\phi_s\}^T \{\phi_s\})} \quad (8)$$

where,  $\phi_0^{(r)}$  and  $\phi_s$  indicate the vectors of the  $r$ th mode of the initial shape and the each mode of the varied shape, respectively.

Letting  $(\bar{u}_0, \bar{w}, \bar{\theta})$  and  $A_M$  denote the Lagrange multipliers for the eigenvalue equation and volume constraints, respectively, the Lagrange functional  $L$  associated with this problem can be expressed as

$$L(A, (\mathbf{u}_0^{(r)}, w^{(r)}, \boldsymbol{\theta}^{(r)}), (\bar{u}_0, \bar{w}, \bar{\theta}), A_M) = -\lambda^{(r)} + \lambda^{(r)} b((\mathbf{u}_0^{(r)}, w^{(r)}, \boldsymbol{\theta}^{(r)}), (\bar{u}_0, \bar{w}, \bar{\theta})) - a((\mathbf{u}_0^{(r)}, w^{(r)}, \boldsymbol{\theta}^{(r)}), (\bar{u}_0, \bar{w}, \bar{\theta})) + A_M (M - \hat{M}) \quad (9)$$

Then, the material derivative  $\dot{L}$  of the Lagrange functional can be derived as shown in Eq. (21) using the formula of material derivative (Choi and Kim, 2005).

$$\begin{aligned} \dot{L} = & -a((\mathbf{u}_0^{(r)}, w^{(r)}, \boldsymbol{\theta}^{(r)}), (\bar{u}_0, \bar{w}, \bar{\theta})) + \lambda^{(r)} b((\mathbf{u}_0^{(r)}, w^{(r)}, \boldsymbol{\theta}^{(r)}), (\bar{u}_0, \bar{w}, \bar{\theta})) \\ & -a((\mathbf{u}_0^{(r)}, w^{(r)}, \boldsymbol{\theta}^{(r)}), (\bar{u}'_0, \bar{w}', \bar{\theta}')) + \lambda^{(r)} b((\mathbf{u}_0^{(r)}, w^{(r)}, \boldsymbol{\theta}^{(r)}), (\bar{u}'_0, \bar{w}', \bar{\theta}')) \\ & + \dot{\lambda}^{(r)} \{b((\mathbf{u}_0^{(r)}, w^{(r)}, \boldsymbol{\theta}^{(r)}), (\bar{u}_0, \bar{w}, \bar{\theta})) - 1\} + \dot{A}_M (M - \hat{M}) + \langle G \mathbf{n}, \mathbf{V} \rangle, \mathbf{V} \in C_{\Theta} \end{aligned} \quad (10)$$

where,

$$\langle G \mathbf{n}, \mathbf{V} \rangle \equiv \int_S G \mathbf{n} \mathbf{V} dS = \int_S [-c_{\alpha\beta\gamma\delta}^B \theta_{(\alpha,\beta)}^{(r)} \bar{\theta}_{(\gamma,\delta)} - kc_{\alpha\beta}^S (\theta_{\beta}^{(r)} - w_{,\beta}^{(r)}) (\bar{\theta}_{\alpha} - \bar{w}_{,\alpha}) - c_{\alpha\beta\gamma\delta}^M u_{0\alpha,\beta}^{(r)} \bar{u}_{0\gamma,\delta}]$$

$$+\lambda^{(r)} \rho \{h(w^{(r)}\bar{w} + u_{0\alpha}^{(r)}\bar{u}_{0\alpha}) + I\theta_{\alpha}^{(r)}\bar{\theta}_{\alpha}\} + A_M] \mathbf{n} \mathbf{V} dS \quad (11)$$

The notation  $\mathbf{n}$  in Eq. (11) is defined as an in-plane outward unit normal vector on boundary  $\partial A$ . Additionally,  $C_{\ominus}$  expresses the admissible function space that satisfies the constraints of domain variation. The notation  $(\cdot)'$  and  $(\cdot)$  are the shape derivative and the material derivative with respect to the domain variation, respectively (Choi and Kim, 2005).

When the optimality conditions with respect to the state variable  $(\mathbf{u}_0^{(r)}, w^{(r)}, \boldsymbol{\theta}^{(r)})$ , the adjoint variable  $(\bar{\mathbf{u}}_0, \bar{w}, \bar{\boldsymbol{\theta}})$  and  $A_M$  are satisfied, Eq. (10) becomes

$$\dot{L} = \langle G\mathbf{n}, \mathbf{V} \rangle, \mathbf{V} \in C_{\ominus}. \quad (12)$$

The sensitivity density function (i.e., the shape gradient density function) for this problem is derived as Eq. (13) by considering the quasi self-adjoint relationship as shown in (14).

$$G = -c_{\alpha\beta\gamma\delta}^B \theta_{(\alpha,\beta)}^{(r)} \bar{\theta}_{(\gamma,\delta)} - kc_{\alpha\beta}^S (\theta_{\beta}^{(r)} - w_{,\beta}^{(r)}) (\bar{\theta}_{\alpha} - \bar{w}_{,\alpha}) - c_{\alpha\beta\gamma\delta}^M u_{0\alpha,\beta}^{(r)} \bar{u}_{0\gamma,\delta} + \lambda^{(r)} \rho \{h(w^{(r)}\bar{w} + u_{0\alpha}^{(r)}\bar{u}_{0\alpha}) + I\theta_{\alpha}^{(r)}\bar{\theta}_{\alpha}\} + A \quad (13)$$

$$(\bar{\mathbf{u}}_0, \bar{w}, \bar{\boldsymbol{\theta}}) = \frac{(\mathbf{u}_0^{(r)}, w^{(r)}, \boldsymbol{\theta}^{(r)})}{b((\mathbf{u}_0^{(r)}, w^{(r)}, \boldsymbol{\theta}^{(r)}), (\mathbf{u}_0^{(r)}, w^{(r)}, \boldsymbol{\theta}^{(r)}))} \quad (14)$$

### Volume minimization problem

With the aim of designing the lightweight of stiffened thin-walled structures, we formulate the reciprocal problem of that treated in the preceding section. Letting the eigenvalue equation in Eq. (1) and the eigenvalue of the specified  $r$ th natural mode be the constraint conditions and the volume be the objective functional to be minimized. A distributed-parameter shape optimization problem is expressed as shown below:

$$\text{Given } A, \quad (15)$$

$$\text{find } A_s \text{ (or } \mathbf{V}) \quad (16)$$

$$\text{minimize } M (= \int_A h dA) \quad (17)$$

$$\text{subject to Eq.(1) and } \lambda^{(r)} = \hat{\lambda}^{(r)} \quad (18)$$

where  $\hat{\lambda}^{(r)}$  is the constraint value of the eigenvalue of the specified  $r$ th natural mode. Letting  $(\bar{\mathbf{u}}_0, \bar{w}, \bar{\boldsymbol{\theta}})$  and  $A_{\lambda}$  denote the Lagrange multipliers for the state equation and eigenvalue constraints, respectively, the Lagrange functional  $L$  associated with this problem can be expressed as

$$L((\mathbf{u}_0^{(r)}, w^{(r)}, \boldsymbol{\theta}^{(r)}), (\bar{\mathbf{u}}_0, \bar{w}, \bar{\boldsymbol{\theta}}), A_{\lambda}) = M + \lambda^{(r)} b((\mathbf{u}_0^{(r)}, w^{(r)}, \boldsymbol{\theta}^{(r)}), (\bar{\mathbf{u}}_0, \bar{w}, \bar{\boldsymbol{\theta}})) - a((\mathbf{u}_0^{(r)}, w^{(r)}, \boldsymbol{\theta}^{(r)}), (\bar{\mathbf{u}}_0, \bar{w}, \bar{\boldsymbol{\theta}})) + A_{\lambda} (\lambda^{(r)} - \hat{\lambda}^{(r)}) . \quad (19)$$

Using the same procedure as in the case of the eigenvalue maximization problem, the shape gradient function of this problem is derived as shown in Eq. (20) by considering the quasi self-adjoint relationship in Eq. (21).

$$G = 1 - A_{\lambda} \{ -c_{\alpha\beta\gamma\delta}^B \theta_{(\alpha,\beta)}^{(r)} \bar{\theta}_{(\gamma,\delta)} - kc_{\alpha\beta}^S (\theta_{\beta}^{(r)} - w_{,\beta}^{(r)}) (\bar{\theta}_{\alpha} - \bar{w}_{,\alpha}) - c_{\alpha\beta\gamma\delta}^M u_{0\alpha,\beta}^{(r)} \bar{u}_{0\gamma,\delta} + \lambda^{(r)} \rho \{h(w^{(r)}\bar{w} + u_{0\alpha}^{(r)}\bar{u}_{0\alpha}) + I\theta_{\alpha}^{(r)}\bar{\theta}_{\alpha}\} \} \quad (20)$$

$$(\bar{\mathbf{u}}_0, \bar{w}, \bar{\boldsymbol{\theta}}) = \frac{A_{\lambda} (\mathbf{u}_0^{(r)}, w^{(r)}, \boldsymbol{\theta}^{(r)})}{b((\mathbf{u}_0^{(r)}, w^{(r)}, \boldsymbol{\theta}^{(r)}), (\mathbf{u}_0^{(r)}, w^{(r)}, \boldsymbol{\theta}^{(r)}))} \quad (21)$$

### Shape optimization method for determining the optimal free boundaries

The non-parametric shape optimization method described here for the design of the stiffened thin-walled structures is based on the  $H^1$  gradient method, which is also called the traction method and is a type of gradient method in a Hilbert space. The original traction method was proposed by Azegami in 1994 (Azegami, 1994; Azegami *et al.*, 1997). One of the authors has developed the optimization method for shell based on the original method (Shimoda and Tsuji, 2007; Shimoda *et al.*, 2009; Shimoda, 2011). It is a node-based shape optimization method that can treat all nodes as design variables and does not require any shape design parametrization. This approach makes it possible to obtain the optimal boundary shapes of stiffened shell structures. The Dirichlet conditions are defined for a pseudo-elastic shell in the case of boundary shape optimization of stiffeners and the basic structure with this method. A distributed force proportional to the shape gradient function  $-Gn$  is applied in the tangential direction to surfaces of the basic structure and stiffeners. The analysis for shape variation is called the velocity analysis. The shape gradient function is not applied directly to the shape variation but rather is replaced by a force, which varies shapes of stiffeners and the basic structure. This makes it possible both to reduce the objective functional and to maintain the smoothness, i.e., mesh regularity, which is the most distinctive feature of this method.

In the design problems of the eigenvalue maximization and the volume minimization, firstly, the eigenvalue analysis is done using a standard commercial FEM code and the outputs of the analysis are utilized to calculate the shape gradient function. After that, the velocity analysis is implemented, where a distributed force proportional to the negative shape gradient function  $-Gn$  is applied to determine the design velocity field  $V$ . Finally the shape is updated iteratively using the design velocity field  $V$ . This process is repeated until the optimal shape of each design problem is obtained.

### Results of numerical analysis

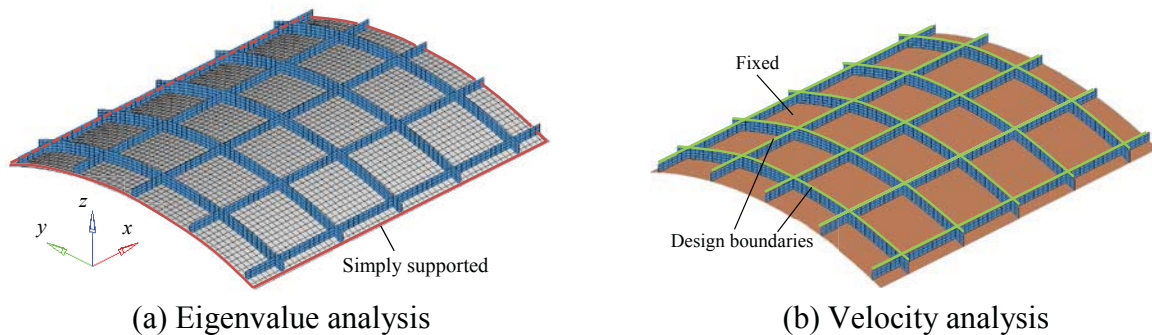


Figure 3. Boundary conditions of stiffened roof shell

The design example considered is a stiffener shape optimization of a roof shell stiffened by latticed stiffeners. Both eigenvalue maximization and volume minimization were carried out by the proposed method. The initial shape is shown in Fig. 3(a) along with the boundary conditions of the eigenvalue analysis, where both the round boundaries and the straight boundaries were simply supported. The constraint conditions for the velocity analysis are shown in Fig. 3(b), where the basic structure was fixed. The 1st natural mode of the initial shape obtained by the eigenvalue analysis is shown in Fig. 4. The specified 1st eigenvalue was maximized subject to the constant volume constraint, and the natural 1st mode was tracked. The optimal stiffener boundaries obtained

in the eigenvalue maximization problem is shown in Fig. 5(a). According to the magnitude of the shape gradient function, the five stiffeners along the straight boundary of the basic structure were reduced, and the reduced volume shifted to the central stiffeners along the round boundary of the basic structure. Iteration histories of the compliance and the volume are shown in Fig. 6(a), in which the values have been normalized to those of the initial shape. The results show that the eigenvalue of the optimized shape increased approximately 40% while satisfying the constant volume constraint. Furthermore, the 1st eigenvalue was set as the constraint and the volume was minimized while tracking the natural 1st mode. Fig. 5(b) shows the optimal stiffener shapes obtained in the volume minimization problem. Fig. 6(b) shows iteration histories of the compliance and the volume for the volume minimization problem. It is confirmed that the volume of stiffeners decreased to 18.2% of the initial shape while satisfying the constant 1st eigenvalue constraint.

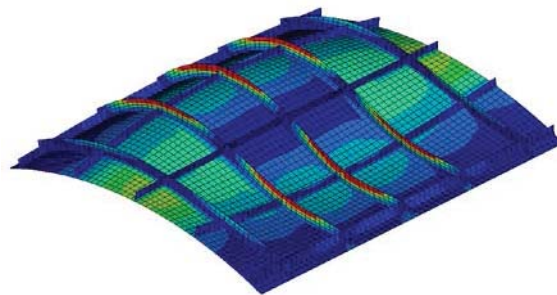
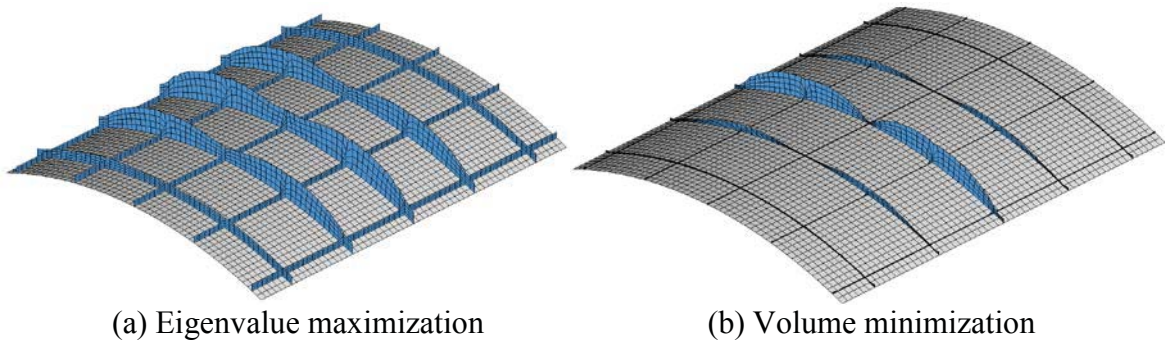


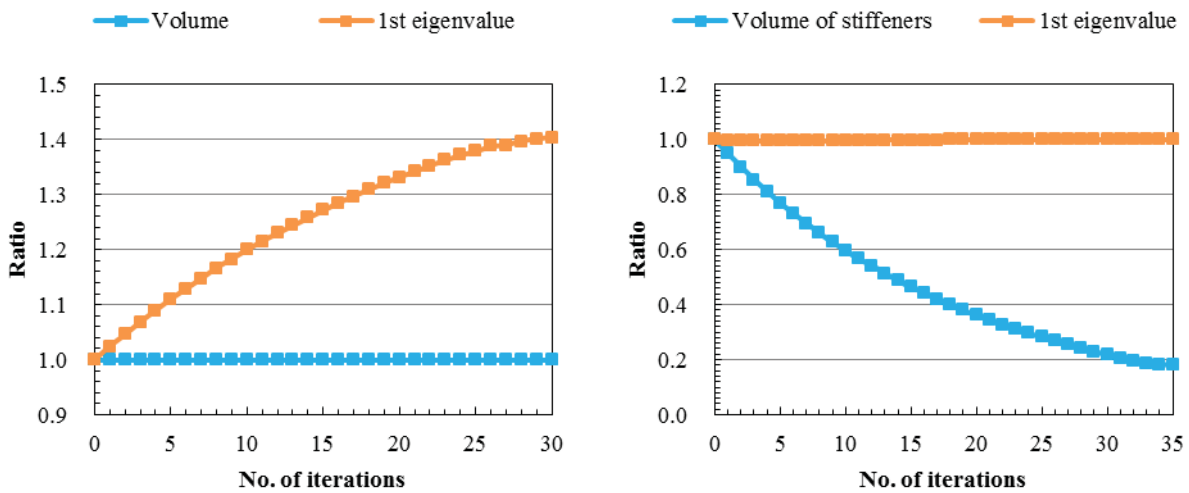
Figure 4. The 1st natural mode of stiffened roof shell



(a) Eigenvalue maximization

(b) Volume minimization

Figure 5. Optimization results of stiffened roof shell



(a) Eigenvalue maximization

(b) Volume minimization

Figure 6. Iteration histories of stiffened roof shell

## Conclusions

This paper has proposed a parameter-free shape optimization method for designing the shapes of stiffened thin-walled or shell structures in the natural vibration problem. The optimal free boundary shapes of stiffeners can be obtained with the proposed method. A specified eigenvalue maximization subject to a volume constraint can be solved along with its reciprocal problem in which volume reduction is the objective. The proposed method has been applied to typical design problems of stiffened thin-walled structures, and the numerical results showed that smooth optimal boundary shapes were obtained in each design problem to achieve the maximum eigenvalue or lightweight structure. It has been demonstrated that the proposed method is an effective tool for designing optimal stiffeners on thin-walled or shell structures.

## References

- Alejandro RD, Kikuchi N. (1992), Solutions to shape and topology eigenvalue optimization problems using a homogenization method. *International Journal for Numerical Methods in Engineering*, 35, pp. 1487–502.
- Ma ZD, Kikuchi N, Cheng HC. (1995), Topological design for vibrating structures. *Computer Methods in Applied Mechanics and Engineering*, 121, pp. 259–80.
- Zhao C, Steven G, Xie Y. (1996), Evolutionary natural frequency optimization of thin plate bending vibration problems. *Structural optimization*, 11(3-4), pp.244–251.
- Eldred MS, Venkayya VB, Anderson WJ. (1995), Mode tracking issues in structural optimization, *AIAA JOURNAL*, 33(10), pp. 1926–33.
- Allemang R. (2003), The modal assurance criterion—twenty years of use and abuse. *Sound and Vibration*, 37, pp. 14–21.
- Reissner E. (1945), The effect of transverse shear deformation on the bending of elastic plates, *Journal of Applied Mechanics*, 67, pp. 69–77.
- Choi KK, Kim NH. (2005), *Structural Sensitivity Analysis and Optimization*. Springer, New York.
- Azegami H. (1994), A solution to domain optimization problems. *Transactions of the Japan Society of Mechanical Engineers*, Series A, 60, pp. 1479–1486.
- Azegami H, Kaizu S, Shimoda M, Katamine E. (1997), Irregularity of shape optimization problems and an improvement technique. *Computer Aided Optimum Design of Structures*, V, pp. 309–326
- Shimoda M, Tsuji J. (2007), Non-parametric shape optimization method for rigidity design of automotive sheet metal structures. *SAE, Journal of Passenger Cars - Mechanical Systems*, 2006-01-0584, pp. 483–492.
- Shimoda M, Iwasa K, Azegami H. (2009), A shape optimization method for the optimal free-form design of shell structures, *proceedings of 8th World Congress on Structural and Multidisciplinary Optimization*.
- Shimoda M. (2011), Free-form optimization method for designing automotive shell structures. *SAE, International Journal of Passenger Cars- Electronic and Electrical Systems*, 4, pp. 42–54.

## Graph grammar based multi-frontal direct solver for isogeometric FEM simulations on GPU

\*M. Paszyński<sup>1</sup>, K. Kuźnik<sup>1</sup>, V.M. Calo<sup>2</sup> and D. Pardo<sup>3</sup>

<sup>1</sup>AGH University of Science and Technology, Krakow, Poland.

<sup>2</sup>King Abdullah University of Science and Technology, Thuwal, Saudi Arabia.

<sup>3</sup>The University of the Basque Country, UPV/EHU and Ikerbasque, Bilbao, Spain.

\*Corresponding author: maciej.paszynski@AGH.EDU.PL

### Abstract

We present a multi-frontal direct solver for two dimensional isogeometric finite element method simulations with NVIDIA CUDA and perform numerical experiments for linear, quadratic and cubic B-splines. We compare the computational cost  $O(Np^2)$  for 2D parallel shared memory implementation with the corresponding estimate  $O(N^{1.5}p^3)$  for a standard 2D sequential implementation. We conclude the presentation with observation that computational cost of the shared memory direct solver scales like  $p^2$  when we increase the global continuity of the isogeometric solution, which is an advantage with respect to sequential isogeometric solver scalability of the order of  $p^3$ .

**Keywords:** Multi-frontal direct solver, isogeometric finite element method, computational cost, shared memory machine

### Introduction

The isogeometric finite element method (Cottrel et al. 2009) is a higher order method providing global  $C^k$  continuity of the solution. It is based on the usage of B-spline basis functions delivering higher order global regularity of the solution. The classical higher order finite element method (Demkowicz 2006, Demkowicz et al. 2007) provides  $C^0$  global continuity only. The isogeometric finite element method generates a sparse system of equations that can be solved by multi-frontal direct solver algorithm (Duff et al. 1984, Duff et al. 1983, Geng et al. 2006).

In this paper we present how isogeometric  $C^k$  finite element method multi-frontal solver differs from  $C^0$  higher order finite element method solver by factor of  $p^3$ . We also show how this  $p^3$  factor can be reduce down to  $p^2$  factor by using shared memory implementation.

### B-spline based isogeometric finite element method

We focus on the 2D model problem, namely the Laplace equation over a square domain

$$\Delta u(x_1, x_2) = 0 \text{ for } (x_1, x_2) \in \Omega = [0,1]^2 \quad (1)$$

$$\text{tr } u(x_1, x_2) = 0 \text{ for } x_1 \in [0,1], x_2 = 0 \quad (2)$$

$$\text{tr } u(x_1, x_2) = 1 \text{ for } x_1 \in [0,1], x_2 = 1 \quad (3)$$

$$\frac{\partial u}{\partial x_1}(x_1, x_2) = 0 \text{ for } x_1 \in \{0,1\}, x_2 \in [0,1] \quad (4)$$

where

$$\Gamma_D = \{(x_1, x_2) : x_1 \in [0,1], x_2 \in \{0,1\}\} \quad (5)$$

$$\Gamma_N = \{(x_1, x_2) : x_1 \in \{0,1\}, x_2 \in (0,1)\} \quad (6)$$



This is a simple model problem, and the solution is  $u(x_1, x_2) = x_2$ . The problem is transformed into weak variational form. We seek  $u \in \tilde{u}_0 + H^1(\Omega)$  where  $\tilde{u}_0 + H^1(\Omega) = \{\tilde{u}_0 + v : v \in H^1(\Omega)\}$  and  $\tilde{u}_0(x_1, x_2) = x_2$  is the lift of the Dirichlet b.c. In other words  $u(x_1, x_2) = w(x_1, x_2) + \tilde{u}_0(x_1, x_2) = w(x_1, x_2) + x_2$  and

$$\int_{\Omega} \sum_{i=1,2} \frac{\partial^2 u(x_1, x_2)}{\partial x_i} v(x_1, x_2) dx_1 dx_2 = 0 \text{ for all } v \in \mathbf{V} = \{v \in H^1(\Omega) : \text{tr}v = 0 \text{ on } \Gamma_D\} \quad (7)$$

we integrate by parts

$$-\int_{\Omega} \sum_{i=1,2} \frac{\partial u(x_1, x_2)}{\partial x_i} \frac{\partial v(x_1, x_2)}{\partial x_i} dx_1 dx_2 + \int_{\Gamma_N} \frac{\partial u(x_1, x_2)}{\partial n} v(x_1, x_2) dS + \int_{\Gamma_D} \frac{\partial u(x_1, x_2)}{\partial n} v(x_1, x_2) dS = 0 \quad (8)$$

$\text{tr}v = 0$  on  $\Gamma_D$  which implies  $\int_{\Gamma_D} \frac{\partial u(x_1, x_2)}{\partial n} v(x_1, x_2) dS = 0$ ,  $\frac{\partial u}{\partial x_1}(x_1, x_2) = 0$  on  $\Gamma_N$  which implies

$\int_{\Gamma_N} \frac{\partial u(x_1, x_2)}{\partial n} v(x_1, x_2) dS = 0$  (since  $\frac{\partial u}{\partial n} = \pm \frac{\partial u}{\partial x_1}$  on  $\Gamma_N$ ) and we get

$$\int_{\Omega} \sum_{i=1,2} \frac{\partial u(x_1, x_2)}{\partial x_i} \frac{\partial v(x_1, x_2)}{\partial x_i} dx_1 dx_2 = 0 \quad (9)$$

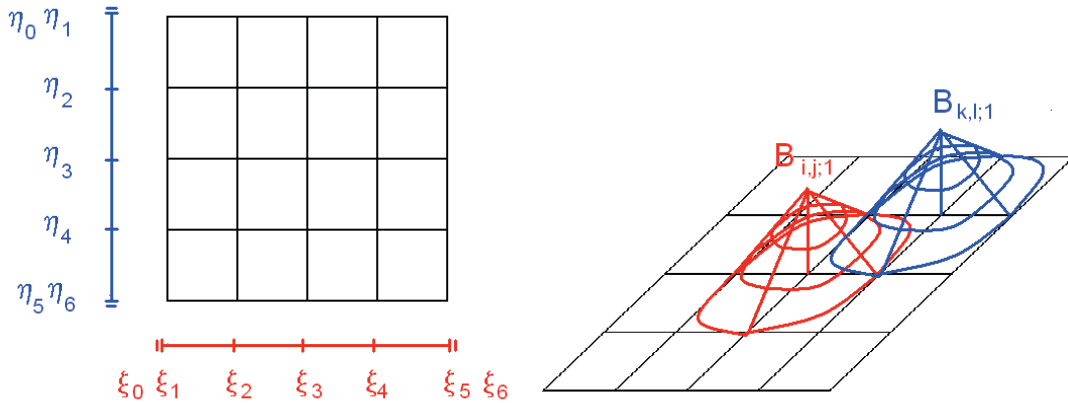
incorporating ‘‘shift’’ of the Dirichlet boundary condition  $u(x_1, x_2) = w(x_1, x_2) + \tilde{u}_0(x_1, x_2) = w(x_1, x_2) + x_2$

$$\int_{\Omega} \sum_{i=1,2} \frac{\partial w(x_1, x_2)}{\partial x_i} \frac{\partial v(x_1, x_2)}{\partial x_i} dx_1 dx_2 = -\int_{\Omega} \sum_{i=1,2} \frac{\partial \tilde{u}_0(x_1, x_2)}{\partial x_i} \frac{\partial v(x_1, x_2)}{\partial x_i} dx_1 dx_2 \text{ and since } \frac{\partial \tilde{u}_0(x_1, x_2)}{\partial x_1} = 0, \frac{\partial \tilde{u}_0(x_1, x_2)}{\partial x_2} = 1$$

we get: Find  $w \in H^1(\Omega)$  such that:

$$\int_{\Omega} \sum_{i=1,2} \frac{\partial w(x_1, x_2)}{\partial x_i} \frac{\partial v(x_1, x_2)}{\partial x_i} dx_1 dx_2 = -\int_{\Omega} \frac{\partial v(x_1, x_2)}{\partial x_2} dx_1 dx_2 \text{ for all } v \in \mathbf{V} = \{v \in H^1(\Omega) : \text{tr}v = 0 \text{ on } \Gamma_D\} \quad (10)$$

If we utilize B-splines for  $p=1$



**Figure 1. Linear B-splines over 2D patch**

our weak variational form

$$b(v, w) = l(v) \quad \forall v \in \mathbf{V}; \quad b(v, w) = \int_{\Omega} \sum_{i=1,2} \frac{\partial w(x_1, x_2)}{\partial x_i} \frac{\partial v(x_1, x_2)}{\partial x_i} dx_1 dx_2; \quad l(v) = -\int_{\Omega} \frac{\partial v(x_1, x_2)}{\partial x_2} dx_1 dx_2 \quad (11)$$

has the following tensor product structure

$$B_{i,j;l}(x_1, x_2) = N_{i;l}(x_1) N_{j;l}(x_2) \quad (12)$$

$$w(x_1, x_2) \approx \sum_{i,j} B_{i,j;l}(x_1, x_2) a_{i,j} = \sum_{i,j} N_{i;l}(x_1) N_{j;l}(x_2) a_{i,j} \quad (13)$$

$$v(x_1, x_2) \leftarrow B_{i,j;l}(x_1, x_2) = N_{i;l}(x_1) N_{j;l}(x_2) \quad (14)$$

$$B_{i,j;l}(x_1, x_2) = N_{i;l}(x_1) N_{j;l}(x_2) \quad (15)$$

$$b(B_{i,j;l}, B_{k,l;l}) = l(B_{k,l;l}) \quad (16)$$

where

$$b(B_{i,j;l}, B_{k,l;l}) = \int_{\Omega} \sum_{m=1,2} \frac{\partial [N_{i;l}(x_1) N_{j;l}(x_2)]}{\partial x_m} \frac{\partial [N_{k;l}(x_1) N_{l;l}(x_2)]}{\partial x_m} dx_1 dx_2 \quad (17)$$

$$l(B_{k,l;l}) = - \int_{\Omega} \frac{\partial [N_{k;l}(x_1) N_{l;l}(x_2)]}{\partial x_2} dx_1 dx_2$$

using Gaussian quadrature the integration over the domain can be substituted by a weighted summation over Gaussian points

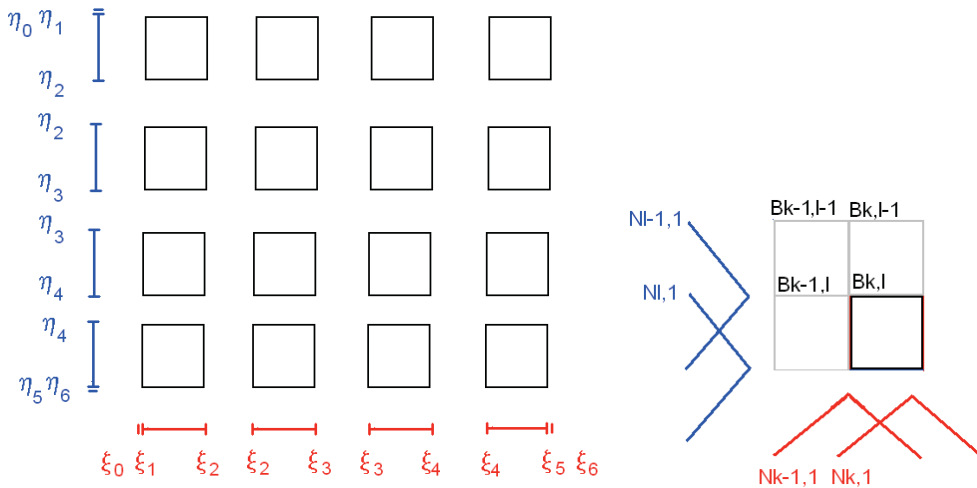
$$b(B_{i,j;l}, B_{k,l;l}) = \int_{\Omega} \sum_{m=1,2} \frac{\partial [N_{i;l}(x_1) N_{j;l}(x_2)]}{\partial x_m} \frac{\partial [N_{k;l}(x_1) N_{l;l}(x_2)]}{\partial x_m} dx_1 dx_2 =$$

$$= \sum_n w_n \sum_{m=1,2} \frac{\partial [N_{i;l}(x_1^n) N_{j;l}(x_2^n)]}{\partial x_m} \frac{\partial [N_{k;l}(x_1^n) N_{l;l}(x_2^n)]}{\partial x_m} \quad (18)$$

$$l(B_{k,l;l}) = - \int_{\Omega} \frac{\partial [N_{k;l}(x_1) N_{l;l}(x_2)]}{\partial x_2} dx_1 dx_2 = - \sum_n w_n \frac{\partial [N_{k;l}(x_1^n) N_{l;l}(x_2^n)]}{\partial x_2}$$

### Multi-frontal solver algorithm for linear B-splines

We partition the mesh into “elements”, compare Figure 2



**Figure 2. Left panel: Partitioning of the 2D patch into elements**  
**Right panel: Linear B-splines over a single element.**  
**The maxim values of B-splines are located at mesh nodes,**  
**thus we identify B-splines with mesh nodes**

We have  $(p+1)(p+1)$  functions of order  $p$  assigned to element  $E_{k,l} = [\xi_K, \xi_{K+1}] \times [\eta_L, \eta_{L+1}]$

$$\{B_{m,n;l}(x_1, x_2)\}_{m=k-p, \dots, k; n=l-p, \dots, l} = \{N_{m;l}(x_1)N_{n;l}(x_2)\}_{m=k-p, \dots, k; n=l-p, \dots, l} \quad (19)$$

We need to perform the integration over a single element

$$\begin{aligned} b(B_{i,j;l}, B_{k,l;l}) &= \sum_n w_n \sum_{m=1,2} \frac{\partial [N_{i;l}(x_1)N_{j;l}(x_2)]}{\partial x_m} \frac{\partial [N_{k;l}(x_1)N_{l;l}(x_2)]}{\partial x_m} = \\ &= \sum_n \left\{ w_n \frac{\partial [N_{i;l}(x_1)N_{j;l}(x_2)]}{\partial x_1} \frac{\partial [N_{k;l}(x_1)N_{l;l}(x_2)]}{\partial x_1} + \frac{\partial [N_{i;l}(x_1)N_{j;l}(x_2)]}{\partial x_2} \frac{\partial [N_{k;l}(x_1)N_{l;l}(x_2)]}{\partial x_2} \right\} = \\ &= \sum_n \left\{ w_n N_{j;l}(x_2) \frac{\partial N_{i;l}(x_1)}{\partial x_1} N_{l;l}(x_2) \frac{\partial N_{k;l}(x_1)}{\partial x_1} + N_{i;l}(x_1) \frac{\partial N_{j;l}(x_2)}{\partial x_2} N_{k;l}(x_1) \frac{\partial N_{l;l}(x_2)}{\partial x_2} \right\} \\ l(B_{k,l;l}) &= - \sum_n w_n \frac{\partial [N_{k;l}(x_1)N_{l;l}(x_2)]}{\partial x_2} = - \sum_n w_n N_{k;l}(x_1) \frac{\partial N_{l;l}(x_2)}{\partial x_2} \end{aligned} \quad (20)$$

For  $p=1$  there are  $2 \times 2 = 4$  two dimensional B-splines (compare Figure 2) so we need to compute  $4 \times 4$  matrix with all four functions talking to each other (see Table 1) so we need to compute  $2 \times 2 = 4$  two dimensional B-splines (see Table 2) so we need to compute  $2 + 2 = 4$  one dimensional B-splines (see Table 3).

$b(B_{k-1,l-1;l}, B_{k-1,l-1;l})$	$b(B_{k,l-1;l}, B_{k-1,l-1;l})$	$b(B_{k-1,l;l}, B_{k-1,l-1;l})$	$b(B_{k,l;l}, B_{k-1,l-1;l})$
$b(B_{k-1,l-1;l}, B_{k,l-1;l})$	$b(B_{k,l-1;l}, B_{k,l-1;l})$	$b(B_{k-1,l;l}, B_{k,l-1;l})$	$b(B_{k,l;l}, B_{k,l-1;l})$
$b(B_{k-1,l-1;l}, B_{k-1,l;l})$	$b(B_{k,l-1;l}, B_{k-1,l;l})$	$b(B_{k-1,l;l}, B_{k-1,l;l})$	$b(B_{k,l;l}, B_{k-1,l;l})$
$b(B_{k-1,l-1;l}, B_{k,l;l})$	$b(B_{k,l-1;l}, B_{k,l;l})$	$b(B_{k-1,l;l}, B_{k,l;l})$	$b(B_{k,l;l}, B_{k,l;l})$

**Table 1. Element matrix for linear B-splines**

$B_{k,l;l}(x_1, x_2) = N_{k;l}(x_1)N_{l;l}(x_2)$	$B_{k,l-1;l}(x_1, x_2) = N_{k;l-1}(x_1)N_{l;l}(x_2)$
$B_{k-1,l;l}(x_1, x_2) = N_{k-1;l}(x_1)N_{l;l}(x_2)$	$B_{k-1,l-1;l}(x_1, x_2) = N_{k-1;l-1}(x_1)N_{l;l}(x_2)$

**Table 2. Contribution to a single entry of linear B-splines based element matrix**

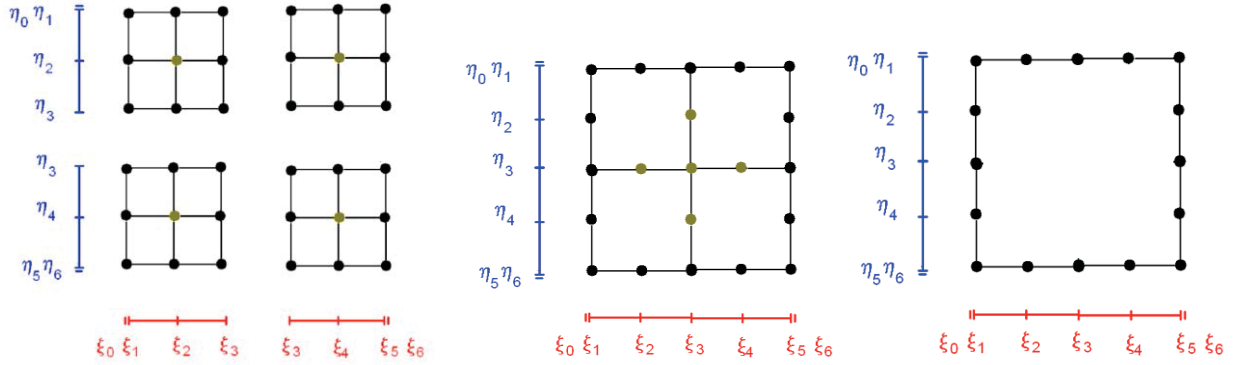
$N_{k;l}(x_1)$	$N_{k-1;l}(x_1)$
$N_{l;l}(x_2)$	$N_{l-1;l}(x_2)$

**Table 3. One dimensional B-splines contributing to linear B-splines based element matrix**

In the second step we merge  $2 \times 2$  elements (actually we merge four  $4 \times 4$  matrices into a single  $9 \times 9$  matrix) as it is presented on left panel in Figure 3. We order the matrices in such a way so the fully assembled B-spline (denoted by dark green color on left panel) is the first row in the matrix so we can eliminate the first row (we can eliminate the single fully assembled B-spline).

In the third step we merge four patches of  $2 \times 2$  element with internal B-splines already eliminated (actually we merge four  $8 \times 8$  matrices into a single  $21 \times 21$  matrix), compare middle panel in Figure 3. We order the matrix in such a way so the 5 fully assembled B-splines (denoted by dark green color on the middle panel) are the first rows in the matrix so we can eliminate the first rows (we can eliminate the internal fully assembled B-splines).

In the last step we eliminate the boundary nodes, see right panel in Figure 3 (we have a single  $16 \times 16$  matrix). We just perform fully forward elimination over the matrix. This is the most expensive step and its computational complexity is  $O(N^{3/2})$  since the boundary has  $O(N^{1/2})$  B-splines.



**Figure 3. Left panel: Second step of the linear B-splines based solver algorithm**

**Middle panel: Third step of the linear B-splines based solver algorithm  
(dark yellow dots denote B-splines to be eliminated)**

**Right panel: We use linear B-splines so the top problem has one layer of B-splines identified with mesh nodes**

### Multi-frontal solver algorithm for quadratic B-splines

In the first step we generate “elements”, with quadratic B-splines as it is presented in in Figure 4. For  $p=2$  there are  $3 \times 3 = 9$  two dimensional B-splines so we need to compute  $9 \times 9$  matrix with all nine functions talking to each other (order in the matrix corresponds to the row by row location of 2D B-splines) (compare Table 4) so we need to compute  $3 \times 3 = 9$  two dimensional B-splines (compare Table 5) so we need to compute  $3 + 3 = 6$  one dimensional B-splines (compare Table 6). We already know how to compute them effectively. Thus, the parallel shared memory implementation of the integration algorithm requires only  $p+1$  steps.

$b(B_{k-2,l-2;1}, B_{k-2,l-2;1})$	...	$b(B_{k,l;1}, B_{k-2,l-2;1})$
...	...	...
$b(B_{k-2,l-2;1}, B_{k,l;1})$	...	$b(B_{k,l;1}, B_{k,l;1})$

**Table 4. Element matrix for quadratic B-splines**

$B_{k,l;1}(x_1, x_2) = N_{k;1}(x_1)N_{l;1}(x_2)$	$B_{k,l-1;1}(x_1, x_2) = N_{k;1-1}(x_1)N_{l;1}(x_2)$	$B_{k,l-2;1}(x_1, x_2) = N_{k;1}(x_1)N_{l-2;1}(x_2)$
$B_{k-1,l;1}(x_1, x_2) = N_{k-1;1}(x_1)N_{l;1}(x_2)$	$B_{k-1,l-1;1}(x_1, x_2) = N_{k-1;1-1}(x_1)N_{l;1}(x_2)$	$B_{k-1,l-2;1}(x_1, x_2) = N_{k-1;1-1}(x_1)N_{l-2;1}(x_2)$
$B_{k-2,l;1}(x_1, x_2) = N_{k-2;1}(x_1)N_{l;1}(x_2)$	$B_{k-2,l-1;1}(x_1, x_2) = N_{k-2;1-1}(x_1)N_{l;1}(x_2)$	$B_{k-2,l-2;1}(x_1, x_2) = N_{k-2;1-1}(x_1)N_{l-2;1}(x_2)$

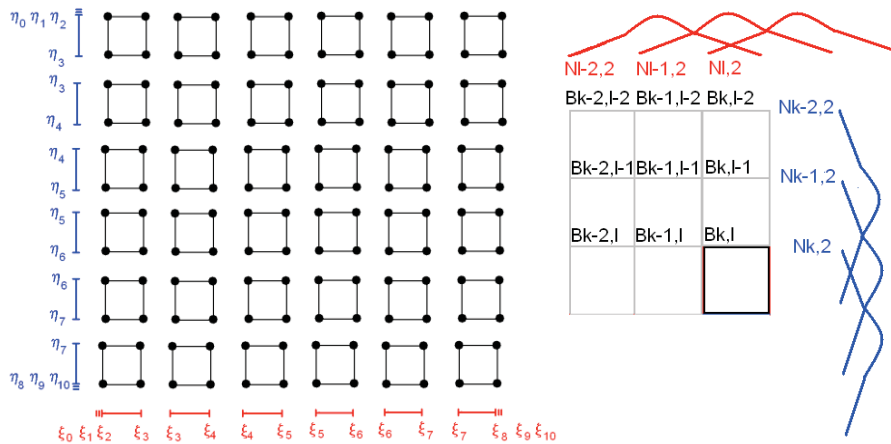
**Table 5. Contribution to a single entry of quadratic B-splines based element matrix**

$N_{k;1}(x_1)$	$N_{k-1;1}(x_1)$	$N_{k-2;1}(x_1)$
$N_{l;1}(x_2)$	$N_{l-1;1}(x_2)$	$N_{l-2;1}(x_2)$

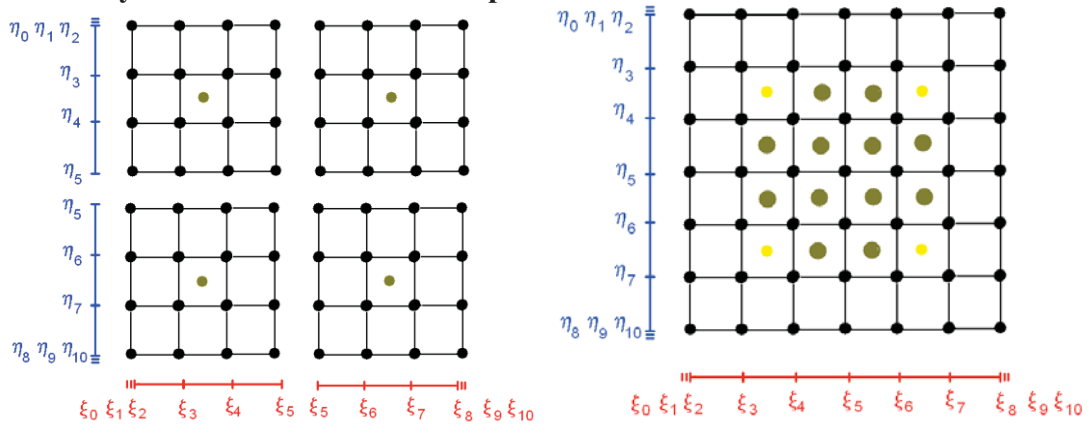
**Table 6. One dimensional B-splines contributing to quadratic B-splines based element matrix**

In the second step we merge  $3 \times 3$  elements (actually we merge nine  $4 \times 4$  matrices into a single  $16 \times 16$  matrix), compare left panel in Figure 5. We order the matrices in such a way so the one fully assembled B-spline (denoted by yellow color on figure) is the first row in the matrix so we can eliminate the first row (we can eliminate the single fully assembled B-spline).

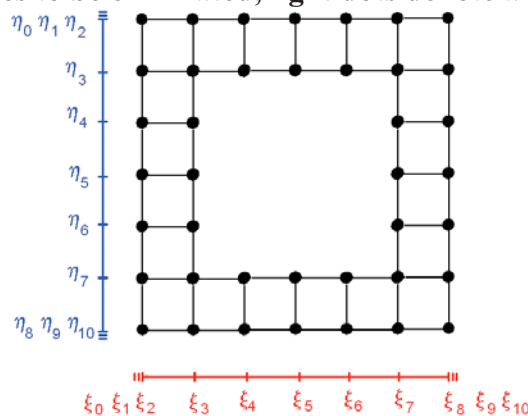
In the third step presented on right panel in Figure 5 we merge four patches of  $3 \times 3$  elements each with one B-spline already eliminated. We get a matrix with  $8 \times 8 - 4 = 60$  rows / columns. We can eliminate 12 fully assembled B-splines.



**Figure 4. Left panel: Partitioning of the 2D patch into elements**  
**Right panel: Quadratic B-splines over a single element. The maximum values of B-splines are located at element centers, thus we identify element centers with B-splines. Additionally, on the boundary elements we have one B-spline with maximum located outside the domain.**



**Figure 5. Left panel: First step of the elimination for quadratic B-splines**  
**Right panel: Second step of the elimination for quadratic B-splines**  
**(dark dots denote B-splines to be eliminated, light dots denote already eliminated B-splines)**



**Figure 6. The top problem for quadratic B-splines finite elements has two layers, since we have one B-spline at each element center, as well as we have boundary B-splines outside the domain, one additional layer of B-splines**

In the last step we end up with the boundary problem, presented in Figure 6. We have a single dense 48x48 matrix here, resulting from one layer of B-splines located at element interiors plus one additional layer of elements located outside the domain.

**Observation 1.** The top problem for the B-splines based direct solver for  $C^k$  isogeometric finite element method has size  $O(N^{1/2} p)$ . The resulting computational cost of the top problem solution is  $O(N^{3/2} p^3)$ . This is the computationally most expensive part of the solution.

**Observation 2.** The top problem for the direct solver for classical  $C^0$  finite element method has size  $O(N^{1/2})$ . The computational cost of the top problem solution is  $O(N^{3/2})$ .

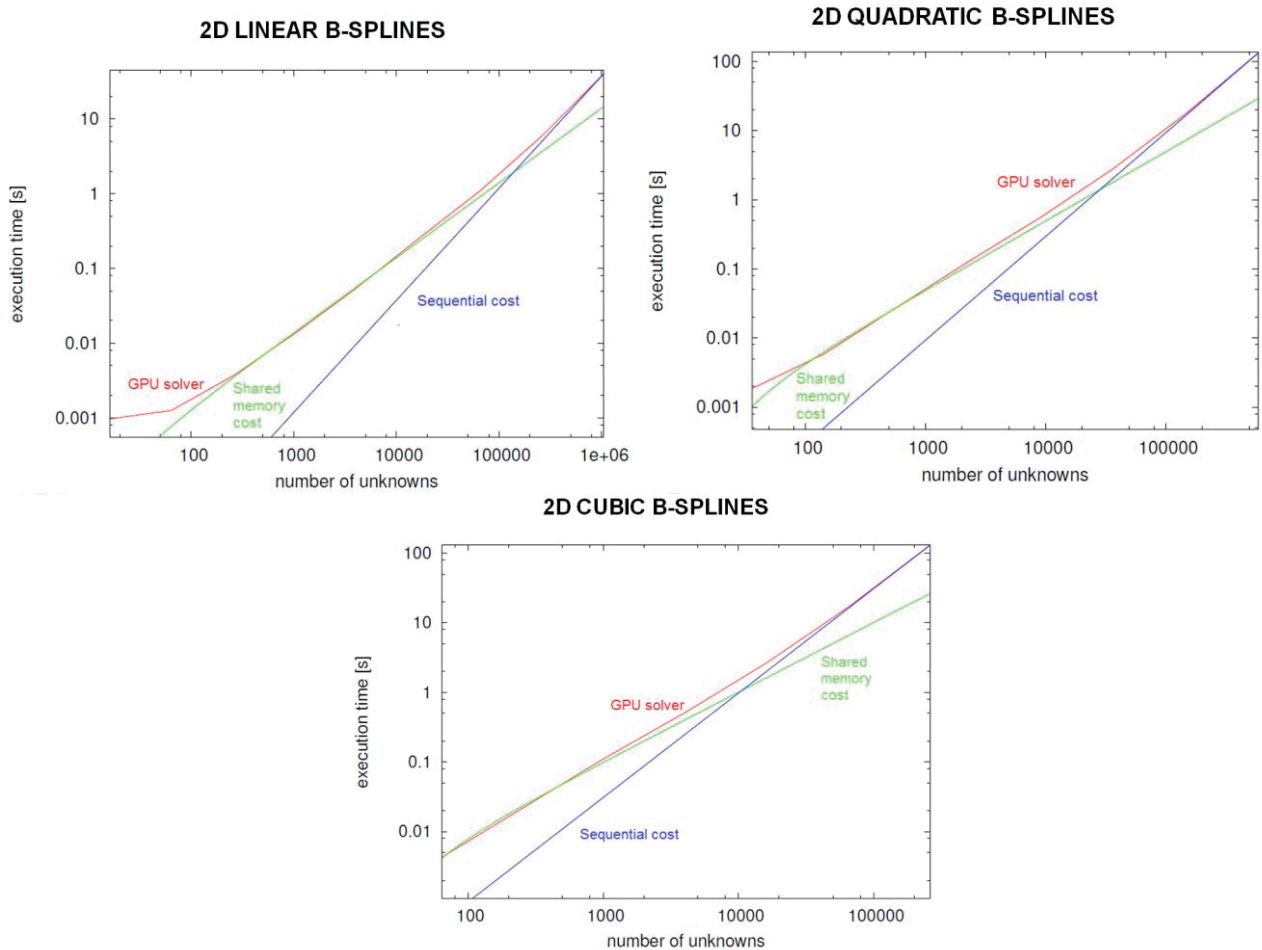


Figure 7. Comparison between theoretical and experimental computational costs

### Graph grammar based multi-frontal solver

The shared memory implementation of the isogeometric direct solver algorithm has been already described in (Kuźnik et al. 2012). The solver algorithm presented there is based on graph grammar concept and implemented in NVIDIA CUDA environment.

The theoretical estimates presented in (Kuźnik et al. 2013, Collier et al. 2012) imply the following computational complexities of the isogeometric as well as classical  $C^0$  higher order FEM (Table 7).

**Observation 3.** In the parallel shared memory implementation of the full Gaussian elimination for the top dense problem it is possible to perform row subtractions at the same time. There are  $O(N^{1/2} p)$  rows to be subtracted at the same time, the size of each row is  $O(N^{1/2} p)$ , and these row subtractions must be performed  $O(N^{1/2} p)$  times. This implies  $O(N p^2)$  computational complexity of the isogeometric  $C^k$  finite element method shared memory direct solver.

The experiments were performed on NVidia Tesla C2070 device, which has 14 multiprocessors with 32 CUDA cores per multiprocessor, which gives us 448 CUDA cores. The total amount of global memory is 5375 megabytes. We used CUDA 4.0 version.

	1D	2D	3D
parallel shared memory IGA	$O(p^2 \log(N/p))$	$O(Np^2)$	$O(N^{1.33} p^2)$
sequential single core IGA	$O(p^3(N/p))$	$O(N^{1.5} p^3)$	$O(N^2 p^3)$
parallel shared memory hp-FEM	$O(\log(N/p))$	$O(N)$	$O(N^{1.33})$
sequential single core hp-FEM	$O(N/p)$	$O(N^{1.5})$	$O(N^2)$

**Figure 7. Comparison between sequential and shared memory computational costs**

The comparison of the theoretical and experimental computational costs are presented in Figure 7. We can observe here how the computational cost of the shared memory solver varies from ideal theoretical cost to sequential cost, when the problem size grows. There are the following reasons for such the behavior. For 2D solver, frontal matrices grow up the elimination tree.

- For the frontal matrices close to the root of the tree, even single row of a matrix cannot fit a shared memory of a single multiprocessor (only one core per multiprocessor is running)
- For the frontal matrices below the root, only a few rows fit into a shared memory of a single multiprocessor (several cores may be idle)
- For the frontal matrices close to leaves several rows fit into a shared memory of a single multiprocessor (all cores over all multiprocessors are running)
- For frontal matrices at the leaves entire frontal matrix fit into a shared memory of a single multiprocessor (all cores over all multiprocessors are running)

## Conclusions

In this paper we presented how the isogeometric finite element method increases the computational cost of the multi-frontal solver by factor  $p^3$ . We also showed how shared memory version of the multi-frontal solver can reduce this factor down to  $p^2$ . The numerical experiments performed on NVIDIA CUDA GPU confirmed the theoretical estimates.

## Acknowledgements

This work was supported by Polish National Science Center grant no. UMO-2012/07/B/ST6/01229.

## References

- Collier N.O., Pardo D., Paszynski M., Dalcin L., Calo V.M. (2012), The cost of continuity: a study of the performance of isogeometric finite elements using direct solvers, *Computer Methods in Applied Mechanics and Engineering*, 213-216, pp.353-361
- Cottrel, J. A., Hughes, T. J. R., Bazilevs, Y. (2009) *Isogeometric Analysis. Towards Integration of CAD and FEA*, Wiley
- Demkowicz, L. (2006) *Computing with hp-Adaptive Finite Element Method. Vol. I. One and Two Dimensional Elliptic and Maxwell Problems*. Chapman & Hall / CRC Applied Mathematics and Nonlinear Science
- Demkowicz L., Kurtz J., Pardo D., Paszynski M., Zdunek A. (2006), *Computing with hp-Adaptive Finite Element Method. Vol. II. Frontiers: Three Dimensional Elliptic and Maxwell Problems*. Chapman & Hall / CRC Applied Mathematics and Nonlinear Science
- Duff I. S., Reid J. K. (1984), The multifrontal solution of unsymmetric sets of linear systems, *SIAM Journal of Scientific and Statistical Computing*, vol. 5, pp.633-641.
- Duff I. S., Reid J. K. (1983) The multifrontal solution of indefinite sparse symmetric linear equations, *ACM Transactions on Mathematical Software*, vol. 9, pp. 302-325
- Geng P., Oden T. J., van de Geijn R. A. (2006) A Parallel Multifrontal Algorithm and Its Implementation, *Computer Methods in Applied Mechanics and Engineering*, vol. 149, pp.289-301.
- Kuznik K., Paszynski M., Calo V. (2012) Graph Grammar-Based Multi-Frontal Parallel Direct Solver for Two-Dimensional Isogeometric Analysis. *Procedia Computer Science* 9, pp.1454-1463.
- Kuznik K., Paszynski M., Calo V., Pardo D. (2013) Multi-Frontal Solvers for IGA Discretization in GPU, *Computers and Mathematics with Applications*, submitted.

## Dual boundary integral equations for three-dimensional rectangular crack problems

Guizhong Xie<sup>1</sup>, \*Jianming Zhang<sup>1</sup>

<sup>1</sup>State Key Laboratory of Advanced Design and Manufacturing for Vehicle Body, College of Mechanical and Vehicle Engineering, Hunan University, Changsha 410082, China

College of Mechanical and Vehicle Engineering, Hunan University, Changsha 410082, China

\*Corresponding author: zhangjm@hnu.edu.cn

### Abstract

An effective numerical implementation of the dual boundary integral equations method (DBIE) for three-dimensional rectangular crack problems is presented in this paper. Accurate evaluation of singular integrals and capture of the crack-tip behavior are important in the implementation of DBIE for crack problems. In our work, all the surfaces are modeled with discontinuous quadratic elements. A novel transformation is introduced to calculate the integrals with weak singularity. Moreover, the integration element is subdivided into several quadrangles and triangles with good shapes, thus high accuracy can be achieved for the singular integrals. Special crack-front elements are introduced to model the distribution of displacements in the vicinity of the crack tips. Furthermore, the stress intensity factors (SIF) are computed by employing a modified distance extrapolation method of the crack opening displacement. Numerical examples of SIFs computation are given for both bounded and unbounded domains. The SIFs obtained by the present method are in very good agreement with existing analytical solutions or numerical results. Results illustrate the accuracy and effectivity of our method.

**Keywords:** boundary face method, boundary element method, boundary integral equation, crack opening displacement, stress intensity factor

### Introduction

SIFs play an important role in characterizing fracture behavior in linear elastic fracture mechanics. Accurate evaluation of SIFs has challenged many numerical modeling techniques. The boundary element method (BEM) is an attractive method for the calculation of SIFs (Cruse, 1988; Aliabadi, 1997). However, the conventional BEM encounters considerable difficulties for crack problems because a singular system of equations is always obtained (Cruse, 1988; Aliabadi, 1997). To circumvent the difficulties, various methods (Pan, 1997) within the scope of BEM including the special Green's method (Telles, 1995), the multi-domain techniques (Blandford et al., 1981), the displacement discontinuity or dislocation method (Crouch, 1983; Pan, 1991), the Galerkin symmetric method (Sirtori et al., 1992) and the dual boundary integral equations method (DBIE) (Mi and Aliabadi 1992; Cisilino and Aliabadi, 1999; Pan, 2000) have been proposed. Among the above methods, DBIE is a promising method (Pan, 1997; Pan, 2000). However, in the DBIE method, the displacements on each side of the crack surface are collocated as unknown variables, which may be unnecessary for the calculation of SIFs. In our method, an improved DBIE method (Cisilino, 1999; Pan, 2000) is employed for crack problems. The improved method is based on a pair of boundary integral equations, namely, the displacement and traction boundary integral equations. The former is collocated exclusively on the uncracked boundary and the latter is discretized only on one of the crack face. The displacement and traction are used as unknown variables on the uncracked boundary and the relative crack opening displacement (COD) is treated



as an unknown quantity on the crack surface. This formulation possesses the advantages of both the traditional displacement boundary element method and the displacement discontinuity (or dislocation) method and thus eliminates the deficiency associated with the conventional DBIE for crack problems.

In our implementation, however, there are some advantages over the improved DBIE. Firstly, all the surfaces are discretized with 9-node discontinuous quadrilateral elements. Then a novel transformation is introduced to evaluating the weakly singular integrals. The Cauchy-type integrals which are involved in the displacement integral equation are calculated directly by the rigid-body motion method. The finite-part integrals associated with the traction boundary integral equation are evaluated by the singular subtraction technique (Guiggiani, 1998; Mi and Aliabadi, 1992). To calculate the singular integrals more accurately, an adaptive element subdivision technique is adopted to improve the conventional singular subtraction technique. In the adaptive subdivision technique, the singular element is subdivided into several triangular and quadrangular patches. The integrals over each quadrangular patch are treated as nearly singular integrals, while the integrals over each triangular patch are computed by the singular subtraction technique based on a Taylor series expansion of kernel function, shape functions, and the transformation Jacobian. Thirdly, two types of special crack-front elements considering the position of the crack fronts are proposed. The special crack-front elements successfully model the distribution of displacements in the vicinity of the crack tips. Finally, SIFs are computed by a modified COD extrapolation method.

The outline of this paper is as follows. In section 2, we introduce the dual boundary integral equations. Section 3 introduces the modeling strategy. In section 4, the treatment of the singular integrals is described. The method for the calculation of SIFs is given in Section 5. Numerical examples are shown in Section 6. The paper ends with conclusions in Section 7.

### The dual boundary integral equations

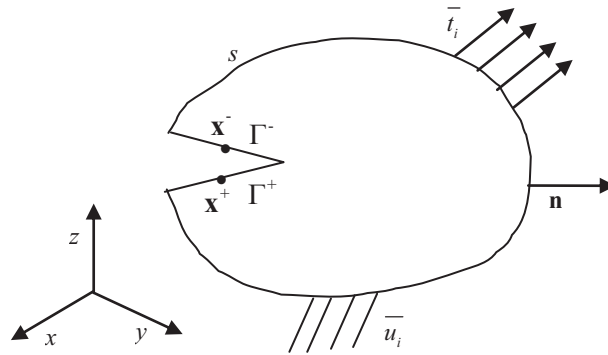


Figure 1. A finite body with a crack

As shown in Fig. 1, a finite body with a crack is considered. The well-known displacement boundary integral equation (the body force is neglected) is as follows :

$$c_{ij}(P_S)u_j(P_S) = \int_{S+\Gamma^++\Gamma^-} u_{ij}^*(P_S, Q)t_j(Q)dS(Q) - \int_{S+\Gamma^++\Gamma^-} t_{ij}^*(P_S, Q)u_j(Q)dS(Q) \quad (1)$$

where  $u_{ij}^*$  and  $t_{ij}^*$  are the Kelvin displacement and traction fundamental solutions, respectively.

$P_S(y_1, y_2, y_3)$  is the source point and  $Q(x_1, x_2, x_3)$  is the field point, and  $c_{ij} = \delta_{ij}/2$ .

The well-known traction boundary integral equation (the body force is neglected) is :

$$c_{ij}t_j(P_S) = n_i(P_S) \int_{S+\Gamma^++\Gamma^-} U_{ijk}^*(P_S, Q)t_k(Q)dS(Q) - n_i(P_S) \int_{S+\Gamma^++\Gamma^-} T_{ijk}^*(P_S, Q)u_k(Q)dS(Q) \quad (2)$$

We assume  $t_k(Q^+) = t_k(Q^-)$  is on the crack faces. From the behaviors of Kelvin's fundamental solutions, we have

$$u_{ij}^*(P_S, Q^+) \Big|_{\Gamma^+} = u_{ij}^*(P_S, Q^-) \Big|_{\Gamma^-}, t_{ij}^*(P_S, Q^+) \Big|_{\Gamma^+} = -t_{ij}^*(P_S, Q^-) \Big|_{\Gamma^-}, U_{ijk}^*(P_S, Q^+) \Big|_{\Gamma^+} = U_{ijk}^*(P_S, Q^-) \Big|_{\Gamma^-},$$

$$T_{ijk}^*(P_S, Q^+) \Big|_{\Gamma^+} = -T_{ijk}^*(P_S, Q^-) \Big|_{\Gamma^-}.$$

So a new pair of boundary integral equations can be obtained as follows :

$$c_{ij}(P_S)u_j(P_S) = \int_S u_{ij}^*(P_S, Q)t_j(Q)dS - \int_S t_{ij}^*(P_S, Q)u_j(Q)dS - \int_{\Gamma^+} t_{ij}^*(P_S, Q^+)\Delta u_j(Q)dS$$

$$(3a) \quad t_j(P_S \Big|_{\Gamma^+}) = n_i(P_S \Big|_{\Gamma^+}) \int_S U_{ijk}^*(P_S \Big|_{\Gamma^+}, Q)t_k(Q)dS - n_i(P_S \Big|_{\Gamma^+}) \int_S T_{ijk}^*(P_S \Big|_{\Gamma^+}, Q)u_k(Q)dS$$

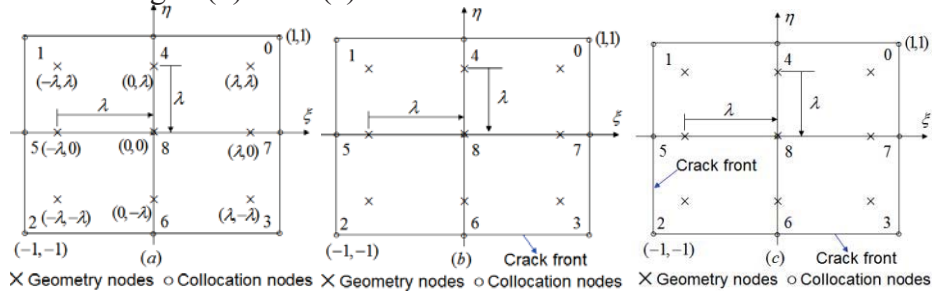
$$(3b) \quad -n_i(P_S \Big|_{\Gamma^+}) \int_{\Gamma^+} T_{ijk}^*(P_S \Big|_{\Gamma^+}, Q)\Delta u_k(Q)dS$$

where  $\Delta u_k(Q)$  represents the COD on the crack surface,  $u_j(Q)$  and  $t_j(Q)$  represent the displacement and traction on the uncracked surfaces. Eqs. (3a) and (3b) are the governing equations to be solved on the uncracked boundary and the relative COD on the crack surface. Eq. (3a) is applied on the uncracked boundary and Eq. (3b) is used on the upper crack surface.

It should be noted that Eqs. (3a) and (3b) can also be employed for the problems containing multiple crack surfaces in a finite space. And for the problems containing multiple crack surfaces in an infinite space, only Eq. (3b) is required. This formulation also has the advantage of a smaller system of equations than the conventional DBIE in Refs. (Mi and Aliabadi, 1992; Mi, 1996) since only one of the crack surface needs to be discretized.

### Modeling strategy

The use of dual boundary integral equations imposes certain restrictions on the choice of element required for the discretization of crack surfaces (Mi and Aliabadi, 1992; Mi and Aliabadi, 1994). These restrictions are due to the continuity requirement of the field variables for the existence of Cauchy and Hadamard principle value integrals. For simplicity, in our method, 9-node discontinuous quadrilateral Lagrangian elements (9DQLE) are employed for uncracked boundary and crack surfaces while special crack-tip elements are used at the crack front. The 9-node discontinuous quadrilateral Lagrangian element is shown in Fig. 2 (a). And the special crack-tip elements are shown in Fig. 2 (b) and 2(c).



**Figure 2. Three types of elements**

**(a) 9-node discontinuous element (b) special crack-tip elements with one edge lying in the crack front (c) special crack-tip elements with two edge lying in the crack front**

For elements of the three types, geometry and functionality are interpolated using different sets of shape functions. Shape functions  $\phi_{geo}^i$  used for the geometry are in Ref. (Mi and Aliabadi, 1994).

The functional shape functions  $\phi_{coll}^i$  for 9DQLE in Fig. 2(a) are in Ref. (Mi and Aliabadi, 1994).

The functional shape functions  $\phi_{coll}^i$  for special crack tip elements are different from these of 9DQLE. Ref. (Mi and Aliabadi, 1994) has presented 8-node discontinuous elements with special shape functions. In our work, 9-node discontinuous quadrilateral Lagrangian elements with special shape functions are proposed. Moreover, special crack tip elements with two edges lying in the

crack fronts are also presented. And we will give a detailed deduction for the two types of special shape functions.

Firstly let us assume that the crack front lies along the local coordinate  $\eta = -1$ , as shown in Fig. 2(b). Ref. (Mi and Aliabadi, 1994) has proposed that the distance  $r = |x(\xi, \eta) - x(\xi, -1)|$  is proportion to  $\eta + 1$  in local coordinate system. The COD ( $\Delta u$ ) over the element adjacent to the crack front can be written as :

$$\Delta u(\xi, \eta) = \Delta u^i M^i(\xi, \eta) = I_2(\xi)r^2 + I_1(\xi)r + I_0 \quad (4)$$

where  $M^i(\xi, \eta)$  are discontinuous quadratic shape functions

The shape functions should be of the form :

$$M^i = a_1^i + a_2^i \xi + a_5^i \xi^2 + a_3^i \sqrt{1+\eta} + a_4^i \xi \sqrt{1+\eta} + a_7^i \xi^2 \sqrt{1+\eta} + a_6^i (1+\eta) + a_8^i \xi (1+\eta) + a_9^i \xi^2 (1+\eta) \quad (5)$$

where  $i=0, \dots, 8$ .

The shape functions in (5) must satisfy the conditions :

$$M^i(\xi_i, \eta_j) = \delta_{ij} \quad i=0, \dots, 8. \quad (6)$$

where  $\delta_{ij}$  is the kronecker delta, and  $(\xi_i, \eta_i)$  are the functional coordinates for the discontinuous element in the  $(\xi, \eta)$  coordinate system, as illustrated in Fig. 2(a). Using Eq. (6), a set of  $9 \times 9$  linear system of equations is obtained. Solving this system of equations by maple will yield the coefficients  $a_j^i$ .

Then let us assume that the crack fronts lie along the local coordinates  $\xi = -1$  and  $\eta = -1$ , as shown in Fig. 2(c). Using the same procedure, the shape functions should be of the form :

$$M^i = a_1^i + a_2^i \xi + a_5^i \eta + a_3^i \sqrt{1+\xi} \sqrt{1+\eta} + a_4^i \xi \sqrt{1+\xi} \sqrt{1+\eta} + a_7^i \eta \sqrt{1+\xi} \sqrt{1+\eta} + a_6^i (1+\xi)(1+\eta) + a_8^i \xi (1+\xi)(1+\eta) + a_9^i \eta (1+\xi)(1+\eta) \quad (7)$$

where  $i=0, \dots, 8$ .

Using Eq. (7), a set of  $9 \times 9$  linear system of equations is obtained. Solving this system of equations by maple will yield the coefficients  $a_j^i$ .

With the shape functions above, Eqs. (3a) and (3b) can be written in a discretized form as :

$$c_{ij}(P_S)u_j(P_S) = \sum_{e=1}^{ne1} \left\{ \sum_{\alpha=0}^8 t_j^\alpha(Q^\alpha) \int_{S_e} u_{ij}^*(P_S, Q(\xi, \eta)) N_\alpha(\xi, \eta) J(\xi, \eta) d\xi d\eta \right\} - \sum_{e=1}^{ne1} \left\{ \sum_{\alpha=0}^8 u_j^\alpha(Q^\alpha) \int_{S_e} t_{ij}^*(P_S, Q(\xi, \eta)) N_\alpha(\xi, \eta) J(\xi, \eta) d\xi d\eta \right\} - \sum_{e=1}^{ne2} \left\{ \sum_{\alpha=0}^8 \Delta u_j^\alpha(Q^\alpha) \int_{\Gamma_e^+} t_{ij}^*(P_S, Q(\xi, \eta)) N_\alpha(\xi, \eta) J(\xi, \eta) d\xi d\eta \right\} \quad (8)$$

$$t_j(P_S |_{\Gamma^+}) = n_i(P_S |_{\Gamma^+}) \sum_{e=1}^{ne1} \left\{ \sum_{\alpha=0}^8 t_k^\alpha(Q^\alpha) \int_{S_e} U_{ijk}^*(P_S |_{\Gamma^+}, Q(\xi, \eta)) N_\alpha(\xi, \eta) J(\xi, \eta) d\xi d\eta \right\} - n_i(P_S |_{\Gamma^+}) \sum_{e=1}^{ne1} \left\{ \sum_{\alpha=0}^8 u_k^\alpha(Q^\alpha) \int_{S_e} T_{ijk}^*(P_S |_{\Gamma^+}, Q(\xi, \eta)) N_\alpha(\xi, \eta) J(\xi, \eta) d\xi d\eta \right\} - n_i(P_S |_{\Gamma^+}) \sum_{e=1}^{ne2} \left\{ \sum_{\alpha=0}^8 \Delta u_k^\alpha(Q^\alpha) \int_{\Gamma_e^+} T_{ijk}^*(P_S |_{\Gamma^+}, Q(\xi, \eta)) N_\alpha(\xi, \eta) J(\xi, \eta) d\xi d\eta \right\} \quad (9)$$

where  $ne1$  represents the total number of elements on the uncracked surfaces,  $ne2$  represents the total number of elements on the upper crack surfaces.  $Q^\alpha$  represents the nodes of each element, and  $Q$  is the inner field points of each element.  $J(\xi, \eta)$  is the Jacobian. When  $P_S$  passes through all the

collocation nodes, Eqs. (8) and (9) give a system of linear equations, which can be expressed in a matrix form as :

$$\mathbf{H}\mathbf{u} = \mathbf{G}\mathbf{t} \quad (10)$$

Where matrix  $\mathbf{H}$  contains integrals involving  $t_{ij}^*$  and  $T_{ijk}^*$ , and matrix  $\mathbf{G}$  contains integrals  $u_{ij}^*$  and  $U_{ijk}^*$ . Vectors  $\mathbf{u}$  and  $\mathbf{t}$  consist of all nodal displacements and traction components on the boundary. Rearranging Eq. (10) according to the boundary conditions results in

$$\mathbf{A}\mathbf{x} = \mathbf{B}\mathbf{y} = \mathbf{f} \quad (11)$$

where  $\mathbf{x}$  is the vector containing the boundary unknowns  $u_i, t_i$  and  $\Delta u_i$ , and  $\mathbf{y}$  is the vector for known components.

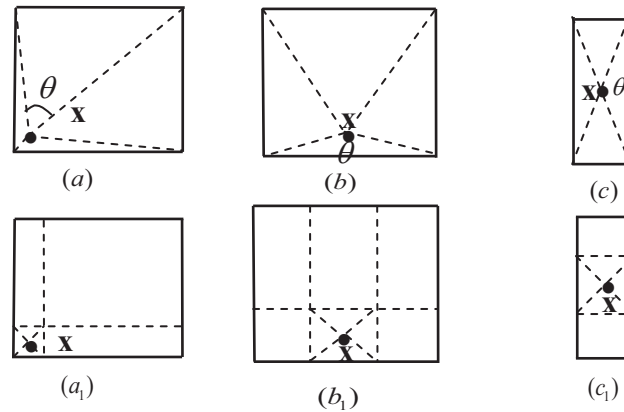
### Treatment of singular integrals

In this section, firstly an element subdivision technique is introduced. Then a new transformation for the weakly singular integrals on the discontinuous elements is introduced. Finally the classic singular subtraction method (Mi and Aliabadi, 1992; Guiggiani, 1998) in combination with the element subdivision techniques is employed for the Cauchy and Hadamard finite part integrals.

#### 4.1 Element subdivision

The element subdivision is indispensable for treating the singular integrals in the 3D cases as in Ref. (Zhang, 2009). In this section, we subdivide an integration element in a suitable pattern considering both element shape and the position of the source point  $\mathbf{x}$  in the element. Adaptive integration based on element subdivisions is employed just as a combination for the singular subtraction method (Mi and Aliabadi, 1992; Guiggiani, 1998).

Note that although the original quadrangle has a fine shape, the four subtriangles may have poor shapes depending on the position of  $\mathbf{x}$  (the source point) (see Fig. 3.(a) and Fig. 3.(b)).



**Figure 3. Subdivisions of quadrilateral element depending on the position of the source point**

Obtaining triangles of fine shape seems more difficult by direct subdivision for irregular initial elements as shown in Fig. 3(c) even  $\mathbf{x}$  is located in the element. If the angle denoted by  $\theta$ , Fig. 3(a) – 3(b) between two lines in common with end point  $\mathbf{x}$  in each triangle is larger by a certain value  $2\pi/3$  and even tends to  $\pi$ , numerical results will become less accurate. To solve the troubles described above, we have developed an adaptive subdivision for an arbitrary quadrilateral element. The original element is divided into several triangles and additional quadrangles, which is different from these as shown in Fig. 3(a<sub>1</sub>)-(c<sub>1</sub>). The adaptive subdivision consists of three main steps described briefly as follows:

First, compute the distances in the real-world-coordinate system from  $\mathbf{x}$  to each edge of the element and obtain the minimum distance  $d$ .

Then, based on  $d$ , we construct a box defined in parametric system, but with square shape in the real-world-coordinate system as can as possible, to well cover  $\mathbf{x}$ .

Finally, triangles are constructed from the box and additional quadrangles are created outside the box in the element.

Applying the strategy above, adaptive subdivisions for the elements in Fig. 3 with suitable patterns are shown in Fig. 3( $a_1$ )-( $c_1$ ). For each triangle, the singular integrals are calculated by the singular subtraction method (Aliabadi et al, 1985; Mi and Aliabadi, 1992; Guiggiani, 1998). However, for each quadrangle, nearly singular integrals will arise but not severe, which can be calculated by adaptive integration scheme based on the element subdivision technique discussed in Ref. (Zhang, 2009).

#### *Evaluation of weakly singular integrals in discontinuous elements*

The term  $\int_{S_e} u_{ij}^*(P_s, Q(\xi, \eta)) N_\alpha(\xi, \eta) J(\xi, \eta) d\xi d\eta$  in Eq. (8) becomes a weakly singular integral when  $P_s$  and  $Q$  belong to a same element, and the element is treated as a singular element. The popular methods for evaluating weakly singular integrals are based on variable transformations. Using variable transformations method in Ref. (Lachat and Watson, 1976) is a promising method, regular Gaussian integration can be used to evaluate the above integral  $\int_{S_e} u_{ij}^*(P_s, Q(\xi, \eta)) N_\alpha(\xi, \eta) J(\xi, \eta) d\xi d\eta$ .

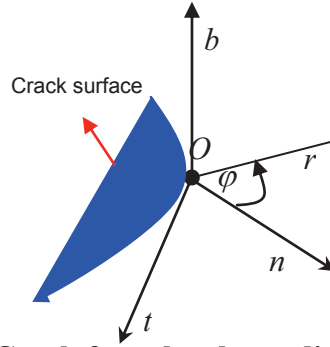
#### *4.3 Evaluation of Cauchy and Hadamard finite part integrals*

Using the rigid-body motion method, the evaluation of singular integrals in the application of DBIE no longer poses any difficulty when the collocation point is not on the crack surface. However, when the collocation point is on the crack surfaces, the integrands are highly singular and required to be treated as Cauchy or Hadamard finite part integrals. The technique employed here for evaluation of these integrals was developed by Guiggiani (Guiggiani 1998) who utilized a singularity subtraction technique pioneered by Aliabadi, Hall & Plemister (Aliabadi et al, 1985).

It should be noted that in our work, firstly, the singular elements are subdivided into several triangle and quadrilateral patches. Then the singularity subtraction technique is employed for the singular integrals on triangle patches while adaptive integration scheme for nearly singular integrals is applied for the regular integrals on quadrilateral patches.

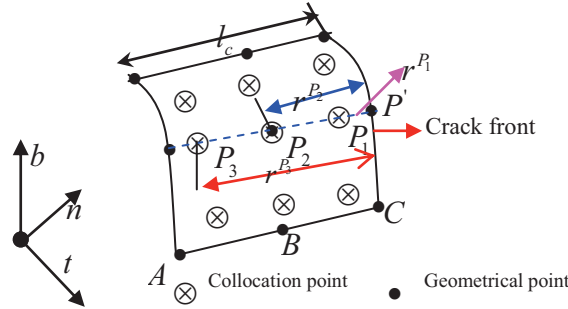
#### **Calculation of stress intensity factors**

Whenever the elasticity solution is available, stress intensity factors can be evaluated at any point on the crack front from the asymptotic behavior of displacement. In our work, the crack opening displacement calculated from boundary element analysis can be directly used to obtain the stress intensity factor. Consider a local coordinate system centered at a point  $O$  along the crack front with coordinate directions :  $\mathbf{t}$  (the tangent unit vector of the front curve),  $\mathbf{b}$  (the unit normal to the crack surface) and  $\mathbf{n} = \mathbf{b} \times \mathbf{t} / |\mathbf{b} \times \mathbf{t}|$  point into the body as shown in Fig. 4.



**Figure 4. Crack front local coordinate system**

As shown in Fig 5, when one point formula is employed, stress intensity factors are evaluated as :



**Figure 5. A crack front element**

$$\begin{aligned}
 K_I^{P'} &= \frac{E}{4(1-\nu^2)} \sqrt{\frac{\pi}{2r}} \Delta u_b^P \\
 K_{II}^{P'} &= \frac{E}{4(1-\nu^2)} \sqrt{\frac{\pi}{2r}} \Delta u_n^P \\
 K_{III}^{P'} &= \frac{E}{4(1+\nu)} \sqrt{\frac{\pi}{2r}} \Delta u_t^P
 \end{aligned} \tag{12}$$

where the CODs  $\Delta \mathbf{u}^P$  are evaluated at point  $P$  (such as  $P_1, P_2, P_3$ ) as shown in Fig. 6,  $\Delta u_b^P, \Delta u_n^P, \Delta u_t^P$  are the projections of  $\Delta \mathbf{u}^P$  on the coordinate directions of the local crack front coordinate system as shown in Fig. 5.

In our work, a COD extrapolation technique is used to calculate the stress intensity factors. Assume points  $P_1, P_2, P_3$  are on line with crack front point  $P'$  as shown in Fig. 6.

$$K^{P'} = \frac{r^{P_3} K^{P_2} - r^{P_2} K^{P_3}}{r^{P_3} - r^{P_2}} \tag{13}$$

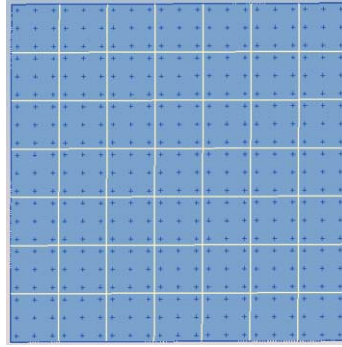
In our work, Eq. (13) is employed, better results can be obtained.

## Numerical examples

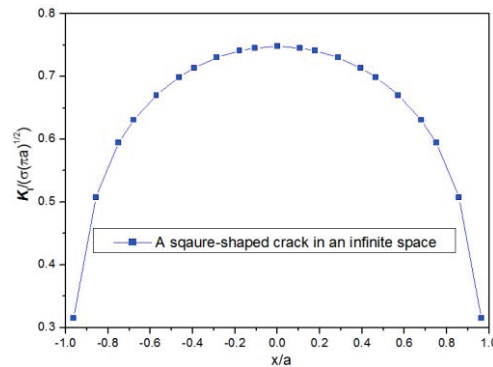
### Example 1: A square-shaped crack in an infinite space

A square-shaped crack in the  $x$ - $y$  plane in an infinite space is considered in this example. The side length of the square is  $2a$  ( $a=1$ ), and a far-field stress  $\sigma$  is applied in the  $z$ -direction. The Young's Modulus ( $E$ ) is 4 Msi and the Poisson's ratio ( $\nu$ ) is 0.3. Forty-nine ( $7 \times 7$ ) discontinuous

quadrilateral elements are used to discretize the square with meshes shown in Fig. 7. The results of SIFs are shown in Fig. 8 and the results compared with other methods are listed in Table 1.



**Figure 7 Discretization of a square-shaped crack (side length  $2a=2$ ) with 49 nine-node discontinuous quadrilateral elements**



**Figure 8. Variation of  $K_I / \sigma\sqrt{\pi a}$  along the square-shaped front**

As shown in Fig. 8, the maximum SIF value occurs at the middle of the square side. And the SIFs decrease to zero at the corners ( $x = \pm a, y = \pm a$ ). We also compare our method with the Xiao's method (Xiao and Yue, 2011), Weaver's method (Weaver, 1977), and Pan's method (Pan and Yuan, 2000). The results are listed in Table 1.

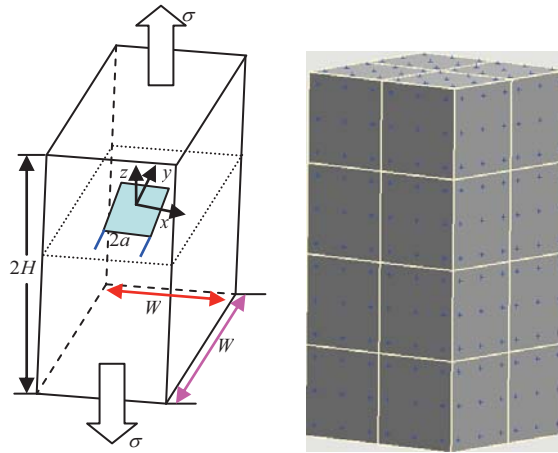
**Table 1 Comparisons with other methods**

<i>methods</i>	<i>Number of nodes</i>	<i>maximum SIF</i>
<i>Our method</i>	225	0.7464
<i>Xiao's method</i>	225	0.7529
<i>Our method</i>	324	0.748
<i>Xiao's method</i>	361	0.7469
<i>Our method</i>	441	0.748
<i>Xiao's method</i>	441	0.7564

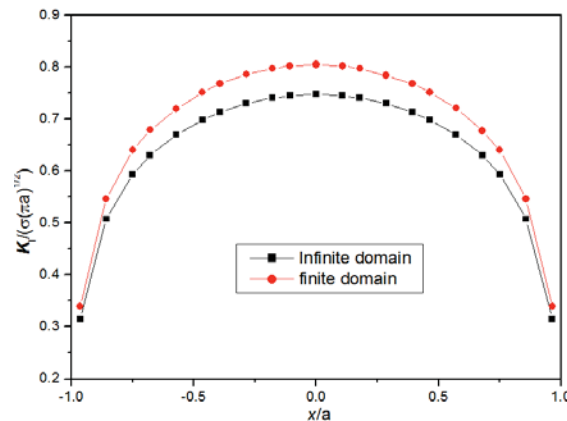
<i>Pan's method</i>	441	0.7626
<i>Weaver's method</i>	<i>unknown</i>	0.74

*Example 2: A square-shaped crack in a finite cube*

To study the effect of finite geometry on the SIFs, a square-shaped crack in a finite cube under a uniform tensile  $\sigma$  applied at the top and bottom faces in the  $z$ -direction is considered. The cube has a height  $2H$  and a width  $W$ . the side length of the square is  $2a$ . In this example,  $2a/W=0.5$ ,  $H/W=1$ . The Young's Modulus ( $E$ ) is 4 Msi and the Poisson's ratio ( $\nu$ ) is 0.3. Forty-four and forty-nine elements are used to discretize the uncracked boundary and the cracked surface as shown in Fig. 9 and Fig. 7. It should be noted that in this example, both Eq. (7a) and Eq. (7b) are required to solve this problem. The normalized model-I SIF along the  $x$ -axis is shown in Fig. 10 and compared with that in the infinite domain. The normalized model-I SIF is larger in a finite cube than that in an infinite domain, with a maximum difference of 7.12 percent occurring at the middle of the square side. The normalized SIF in the finite cube is 0.8053, compared with 0.81 by Wen (Wen and Aliabadi, 1998) and 0.8183 by Pan (Pan and Yuan, 2000) for the same geometry.



**Figure 9. Geometry of a finite cube with a central square-shaped crack under a uniform normal stress  $\sigma$  and meshes of the uncracked boundary**



**Figure 10. Comparisons of  $K_I / \sigma \sqrt{\pi a}$  along the square-shaped crack front in an infinite domain and a finite cube**



## Conclusions

This paper presented an efficient boundary integral equation formulation for three-dimensional rectangular crack problems. The formulation is based on the displacement and traction boundary integral equation. In our numerical implementation, in order to satisfy the existence of the finite part integrals, all the surfaces were discretized with discontinuous quadrilateral quadratic elements. And an element subdivision technique for the singular element was introduced. A novel transformation was proposed to deal with weakly singular integrals. For the Cauchy and Hadamard integrals, the singular subtraction technique in combination with element subdivision was employed. Moreover, two types of special crack-tip elements were proposed and the elements successfully captured the distribution of displacements in the vicinity of the crack tips. Furthermore, a modified COD extrapolation method was adopted for the calculation of SIFs.

Numerical examples of SIFs computation were given for both bounded and unbounded domains. The SIFs obtained by the present method were in very good agreement with previously published results. Results illustrated the accuracy and efficiency of our method.

## References

- Aliabadi, M. H. (1997), Boundary element formulations in fracture mechanics. *Applied Mechanics Reviews* 50, 83.
- Aliabadi, M. H., Hall, W. S., & Phemister, T. G., 1985. Taylor expansions for singular kernels in the boundary element method. *International journal for numerical methods in engineering* 21(12), 2221-2236.
- Blandford, G. E., Ingrassia, A. R., & Liggett, J. A. (1981), Two - dimensional stress intensity factor computations using the boundary element method. *International Journal for Numerical Methods in Engineering* 17(3), 387-404.
- Cruse, T. A. (1988), Boundary element analysis in computational fracture mechanics (Vol. 1). Kluwer Academic Pub.
- Crouch, S. L., & Starfield, A. M. (1983), Boundary element methods in solid mechanics. ALLEN & UNWIN, INC., 9 WINCHESTER TERRACE, WINCHESTER, MA 01890, USA, 1983, 334.
- Cisilino, A. P., & Aliabadi, M. H. (1999), Three-dimensional boundary element analysis of fatigue crack growth in linear and non-linear fracture problems. *Engineering fracture mechanics* 63(6), 713-733.
- Guiggiani, M. (1998), Formulation and numerical treatment of boundary integral equations with hypersingular kernels. *Singular integrals in boundary element methods* 85-124.
- Lachat, J. C., & Watson, J. O. (1976), Effective numerical treatment of boundary integral equations: A formulation for three dimensional elastostatics. *International Journal for Numerical Methods in Engineering* 10(5), 991-1005.
- Mi, Y., & Aliabadi, M. H. (1992), Dual boundary element method for three-dimensional fracture mechanics analysis. *Engineering Analysis with Boundary Elements* 10(2), 161-171.
- Mi, Y., & Aliabadi, M. H. (1994), Discontinuous crack-tip elements: application to 3D boundary element method. *International journal of fracture* 67(3), R67-R71.
- Murakami, Y., & Hasebe, N. (Eds.), (2001). Stress intensity factors handbook. Elsevier Science.
- Mi, Y. (1996). Three-dimensional analysis of crack growth. Computational Mechanics Publications.
- Pan, E. (1997). A general boundary element analysis of 2-D linear elastic fracture mechanics. *International Journal of Fracture* 88(1), 41-59.
- Pan, E. (1991), Dislocation in an infinite poroelastic medium. *Acta mechanica* 87(1-2), 105-115. Pan, E., & Yuan, F. G., 2000. Boundary element analysis of three - dimensional cracks in anisotropic solids. *International Journal for Numerical Methods in Engineering* 48(2), 211-237.
- Raju, I. S., & Newman, J. C. (1977), Three dimensional finite-element analysis of finite-thickness fracture specimens.
- Sih, G. C. (1973). Handbook of stress-intensity factors. Lehigh University, Institute of Fracture and Solid Mechanics.
- Sirtori, S., Maier, G., Novati, G., & Miccoli, S., 1992. A galerkin symmetric boundary - element method in elasticity: Formulation and implementation. *International Journal for Numerical Methods in Engineering* 35(2), 255-282.
- Weaver, J. (1977), Three-dimensional crack analysis. *International Journal of Solids and Structures* 13(4), 321-330.
- Wen, P. H., Aliabadi, M. H., & Rooke, D. P. (1998), Mixed-mode weight functions in three-dimensional fracture mechanics: static. *Engineering fracture mechanics* 59(5), 563-575.
- Xiao H.T., Yue Z.Q. (2011), New Boundary Element Analysis of Fracture Mechanics in Functionally Graded Materials. Higher Education Press. In Chinese. 2011
- Zhang, J., Qin, X., Han, X., & Li, G. (2009), A boundary face method for potential problems in three dimensions. *International journal for numerical methods in engineering* 80(3), 320-337.

## Evaluation of radiative heat transfer effect on fire whirlwind

\*Seigo Sakai

Faculty of Engineering, Yokohama National University,  
79-5, Tokiwadai, Hodogaya-ku, Yokohama 240-8501, Japan

\* Corresponding author: sakai@ynu.ac.jp

### Abstract

Radiative-convective heat transfer analysis with respect to fire whirlwind is performed in consideration of participating media using Radiation Element Method by Ray Emission Model (REM2), in which three dimensional analyses are then performed to investigate the thermal and flow fields by using the Finite Volume Method with introducing divergence of radiative heat flux for gas medium. The SIMPLE method is utilized to solve the discretized equations. Natural convection is caused from a plane source of constant temperature in the flat ground. Fire whirlwind is forcibly generated stably just above the heat source with introducing air currents from four corners. In the analysis, one dimensional radiative exchange analysis above the heat source is compared with three dimensional one to reduce the computational load and time. Then, the composition of participating gases is altered to discuss the effect of radiative heat exchange to the whirlwind flow field.

**Key Words:** *Fire Whirlwind, Radiative Heat Exchange, Participating Media, Natural Convection*

### Introduction

Our Japanese, especially the residents in east area of Japan, have experienced a large earthquake on March 11, 2011, i.e. East Japan great earthquake disaster (Takewaki et al., 2011). There were a lot of fires in the northeast area of Japan, for example in Kesen-numa City. Despite of a number of town area fires, a fire whirlwind was never observed in this disaster. However, fire whirlwind is still one of the concerned accidents in the earthquake (Hough & Bilham; 2005).

When a large-scale wide area fire such as a town area fire or a forest fire occurs, there can be a strong rotating flow to be called fire whirlwind. Fire whirlwind is a tornado that includes flames, hot winds and sparks. Fire whirlwind is regarded as one of the worst cases which we should avoid at the time of a large-scale fire, because the whirlwind itself is critical and scatters sparks widely to promote spread of a fire.

As a fire occurs, a flame makes an ascending current of air and uses up neighboring oxygen. Furthermore, to collect oxygen from a wide area, there is a current of air against the flame, resulting in big natural convection in the fire current of air. When the wind from a certain specified direction blows in this fire current of air, homogeneity of suction of air with an ascending current of air collapses. Then, a vortex is easy to come to occur, the fire current of air becomes a fire whirlwind that is an ascending current of air accompanied with rotating. Fire whirlwind may be pushed away by wind downstream, or may move in search of oxygen.

Aiming at a property and elucidation of an outbreak factor of fire whirlwind as examples of the pasts for a lesson, investigation and a reproduction experiment of the outbreak situation (Graham, 1955; Emmons & Ying, 1967; Byram & Martin, 1970; Haines & Updike, 1971; Martin et al., 1976; Muraszew et al., 1979; Emori & Saito, 1982; Satoh & Yang, 1996; Hayashi et al., 2003; Liu, 2005; Kuwana et al., 2007; Liu et al., 2007; Kuwana et al., 2008; Chuah et al., 2011), numerical analysis are performed till now (Satoh & Yang, 1997; Battaglia et al., 2000; Snegirev et al., 2004; Hassan et al., 2005; Chuah et al., 2007; Grishin et al., 2009). Though various factors are thought about outbreak of a fire whirlwind, such as climatic condition or existence of underground flammable gas, it is hard to say that property and outbreak mechanism of a fire whirlwind are to be elucidated enough.

Convective and radiative-convective heat transfer analyses with respect to fire whirlwind were also performed in our laboratory on former studies (Sakai and Watanabe, 2007; Sakai and Miyagi, 2010; Sakai, 2012), just radiative exchange between solid surfaces was carried out. Therefore, in this study, radiative heat exchange is dealt in consideration of radiative gas using Radiation Element Method by

Ray Emission Model (REM2) (Maruyama & Aihara, 1997). Radiative heat transfer effect on fire whirlwind is discussed.

Then, three dimensional analyses are performed to investigate the thermal and flow fields by using the Finite Volume Method (Patankar, 1980) with introducing divergence of radiative heat flux for gas medium. The SIMPLE method is utilized to solve the discretized equations. Natural convection is caused from a plane source of constant temperature in the flat ground. Fire whirlwind is forcibly generated stably just above the heat source with introducing air currents from four corners. For making of analysis models, a representative example of the fire whirlwind that occurred at Tokyo in the Great Kanto Earthquake (1923) is referred.

In the analysis, one dimensional radiative exchange analysis above the heat source is compared with three dimensional one to reduce the computational load and time. Then, the composition of participating gases is altered to discuss the effect of radiative heat exchange to the whirlwind flow field.

## Analysis and Modelling

**Radiative Exchange** We consider the radiation element of participating medium, which is comprised of a polyhedron surrounded by polygons as shown in Fig. 1. The spectral radiation intensity,  $I_\lambda$ , at  $\vec{r}$  in the direction  $\hat{s}$  can be expressed in terms of the radiation energy balance by

$$\frac{dI_\lambda(\vec{r}, \hat{s})}{dS} = -(\kappa_\lambda + \sigma_{s,\lambda})I_\lambda(\vec{r}, \hat{s}) + \kappa_\lambda I_{b,\lambda}(T) + \frac{\sigma_{s,\lambda}}{4\pi} \int_{4\pi} I_\lambda(\vec{r}, \hat{s}') \Phi_\lambda(\hat{s}' \rightarrow \hat{s}) d\omega, \quad (1)$$

where  $\kappa_\lambda$  and  $\sigma_{s,\lambda}$  are spectral absorption and scattering coefficients, respectively.  $I_{b,\lambda}$  is spectral black-body radiation intensity. Here,  $S$  is the path length in the direction  $\hat{s}$  and  $\Phi_\lambda(\hat{s}' \rightarrow \hat{s})$  is the phase function from the direction  $\hat{s}'$  to  $\hat{s}$ .

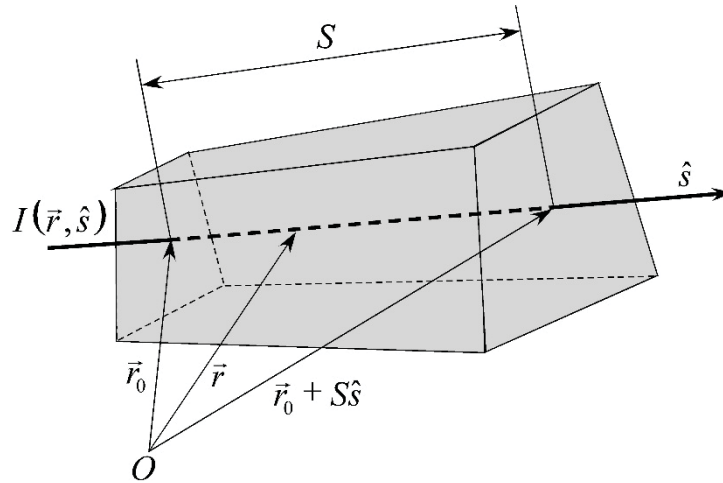


Fig. 1. Radiation element

Considering the  $i$ -th participating radiation element, we assume that each radiation element is at a constant uniform temperature of  $T_i$  and its refractive index and heat generation rate per unit volume,  $q_{\lambda,i}$ , are also constant and uniform throughout the element. A ray passing through the radiation elements attenuates by absorption, and a part of the ray is scattered. The ray is separated into absorbed, scattered and transmitted fractions. Moreover, it is assumed that the scattered radiation is distributed uniformly over the element.

For anisotropic scattering media, we introduced an apparent extinction coefficient  $\beta_\lambda^*$  and thus, a corrected scattering albedo  $\Omega_\lambda^*$  by introducing the delta function approximation (Maruyama, 1998). Thus, an anisotropic scattering medium can be treated as an isotropic scattering one. The third term on the right hand side of equation (1) can be approximated by

$$\frac{\Omega_\lambda}{2} \int_{-1}^1 I_\lambda(x, \mu') \Phi_\lambda(\mu') d\mu' \approx \frac{\Omega_\lambda^*}{2} \int_{-1}^1 I_\lambda(x, \mu') d\mu' \approx \Omega_\lambda^* I_\lambda^D, \quad (2)$$

where  $I_\lambda^D$  is the average scattered radiant intensity and  $\mu'$  is directional cosine.

A radiation element  $i$  can be regarded as either a volume element or a surface boundary. Equation (1) is integrated along the path length  $\bar{S}_i(\hat{s}) = V_i/A_i(\hat{s})$  and over all discretized solid angles, in which  $V_i$  and  $A_i(\hat{s})$  are the volume and area projected onto the surface normal to  $\hat{s}$ , respectively. The spectral radiation energy,  $Q_{j,i,\lambda}$ , from the radiation element  $i$ , is given by

$$Q_{j,i,\lambda} = \pi(\varepsilon_{i,\lambda} I_{b,i,\lambda} + \Omega_{i,\lambda}^D I_{i,\lambda}^D) A_{i,\lambda}^R, \quad (3)$$

where  $\varepsilon_{i,\lambda} = 1 - \Omega_{i,\lambda}^D - \Omega_{i,\lambda}^S$ , in which  $\varepsilon_{i,\lambda}$ ,  $\Omega_{i,\lambda}^D$  and  $\Omega_{i,\lambda}^S$  are emissivity, diffuse reflectivity and specular reflectivity, respectively.  $A_{i,\lambda}^R$  is the effective radiation area (Maruyama & Aihara, 1997) which is defined as follows,

$$A_{i,\lambda}^R \equiv \frac{1}{\pi} \int_{4\pi} A_i(\hat{s}) [1 - \exp(-\beta_{i,\lambda}^* \bar{S}_i(\hat{s}))] d\omega. \quad (4)$$

By introducing the absorption view factors  $F_{ij}^A$  and the diffuse scattering view factors  $F_{ij}^D$  defined by Maruyama (Maruyama, 1998) and equation (3), we can obtain the following equations:

$$Q_{T,i,\lambda} = \pi \varepsilon_{i,\lambda} I_{b,i,\lambda} A_{i,\lambda}^R, \quad (5)$$

$$Q_{j,i,\lambda} = Q_{T,i,\lambda} + \sum_{j=1}^N F_{ji}^D Q_{j,i,\lambda}, \quad (6)$$

$$Q_{X,i,\lambda} = Q_{T,i,\lambda} - \sum_{j=1}^N F_{ji}^A Q_{j,i,\lambda}. \quad (7)$$

The heat transfer rate of the emissive power,  $Q_{T,i,\lambda}$ , or the net rate of heat generation,  $Q_{X,i,\lambda}$  for each radiation element is given arbitrarily as a boundary condition. The unknown  $Q_{X,i,\lambda}$  or  $Q_{T,i,\lambda}$  can be obtained by solving equations (6) and (7) using the method previously described by Maruyama and Aihara (Maruyama & Aihara, 1997). The relationship between  $q_{X,i}$  and  $Q_{X,i,\lambda}$  is obtained by

$$q_{X,i} = \frac{Q_{X,i}}{V_i} = \frac{1}{V_i} \int_0^\infty Q_{X,i,\lambda} d\lambda. \quad (8)$$

An analytical method for radiative heat transfer, i.e. the radiation element method by ray emission model, REM2, is used in radiative heat transfer analysis, and the Statistical Narrow Band (SNB) model is combined to the REM2 to consider the spectral dependence of the radiative properties.

**Thermal and Fluid Flow Fields** The governing equations of thermal and flow fields are the continuum equation, the Navier-Stokes equation, and the energy equation. The thermal and flow fields are assumed to be unsteady state and three dimensional. These equations are normalized and transformed to the following generalized conservation equation.

$$\frac{\partial \phi}{\partial t} + \frac{\partial}{\partial x}(u\phi) + \frac{\partial}{\partial y}(v\phi) + \frac{\partial}{\partial z}(w\phi) = \Gamma \left( \frac{\partial^2 \phi}{\partial x^2} + \frac{\partial^2 \phi}{\partial y^2} + \frac{\partial^2 \phi}{\partial z^2} \right) + S, \quad (9)$$

where  $u$ ,  $v$  and  $w$  are the normalized velocity components for  $x$ ,  $y$  and  $z$  directions, respectively. Variable  $\phi$  takes 1 for the continuum equation,  $u$ ,  $v$  and  $w$  for the Navier-Stokes equation, and normalized temperature  $T$  for the energy equation. Generalized diffusion coefficient  $\Gamma$  takes 0 for the continuum equation,  $1/Re$  for the Navier-Stokes equation and  $1/(Re \cdot Pr)$  for the energy equation. Normalized source term  $S$  takes 0 for the continuum equation, the summation of the normalized pressure term and the normalized buoyancy term by Boussinesq approximation, and the normalized source term from radiative exchange mentioned in the previous section (equation(8)). Turbulent flow is treated by using high Reynolds number turbulence model.

In the thermal and fluid flow analysis, equation (9) is discretized by using the Finite Volume Method (Patankar, 1980). The SIMPLE method is utilized to solve the discretized equations. Physical properties of the mixture are altered depending on the change of temperature.

**Analysis Procedure** Fig. 2 shows an analysis procedure in this study. Temporal temperature distribution is initially given to analyze nongray radiative heat transfer by REM2. Then, the derived heat generation rate is introduced to the energy equation, and the thermal and flow field is analyzed by FVM using the SIMPLE method. The derived temperature is introduced to the REM2 again as an initial temperature distribution, and iteration is repeated until the derived distribution is converged to the initial distribution. Steady state solution is obtained through this iteration loop.

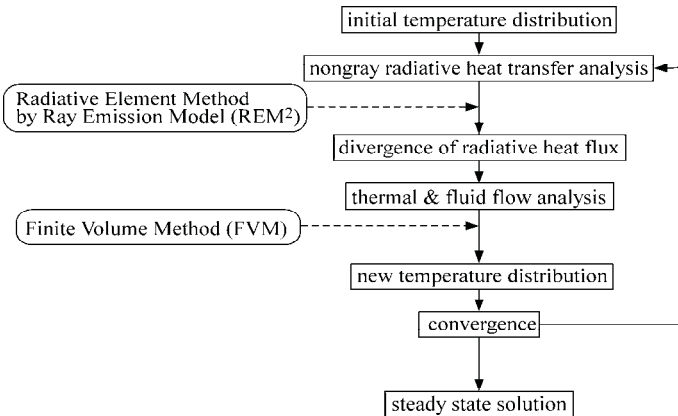


Fig. 2. Flow chart of numerical simulation procedure

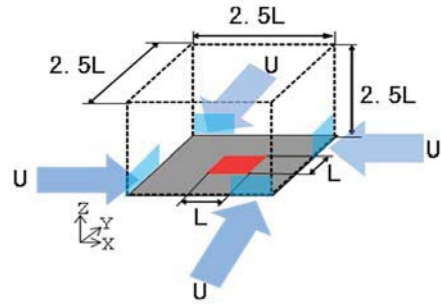


Fig.3. Analytical domain

**Analytical Model** Fig. 3 shows analytical domain for calculation, which scale is based on the Great Kanto Earthquake (1923) in Japan. Heat source on the bottom center has 800m in width and depth, and this value is representative length  $L$ . Therefore, the analytical domain is a cubic of 2,000m in width, depth and height. Heat source is applied uniform temperature of 2,000K, and the domain is assumed to be surrounded by circumstance of 293.15K. Initial temperature of the domain is also set to 293.15K. Mixture gas is constituted by water vapor,  $CO_2$  and Nitrogen. All the domain surfaces are assumed to be black for radiative exchange, and the surfaces except the bottom are opened. Fire whirlwind is forcibly generated stably just above the heat source with introducing air currents from four corners. The currents velocities  $U$  are constant of 5m/s at the inlet surfaces of 600m in width and 200m in height. Combustion nor chemical reaction is not considered in the calculation.

Table 1 shows concentration of participating gases in mixture for radiative heat exchange. Carbon dioxide has three values; no concentration, concentration in general atmosphere and the maximum concentration in case of fire. Water vapor also has three values; no concentration, concentration of saturated water vapor at the initial temperature and the concentration of saturated water vapor at boiling point.

Table 1 Concentration of participating gases

	Concentration of $CO_2$ (ppm)	Concentration of $H_2O$ (ppm)
Case A	0	0
Case B	0	$3.56 \times 10^4$
Case C	$3.60 \times 10^2$	$3.56 \times 10^4$
Case D	$8.00 \times 10^4$	$3.56 \times 10^4$
Case E	$8.00 \times 10^4$	$1.02 \times 10^6$

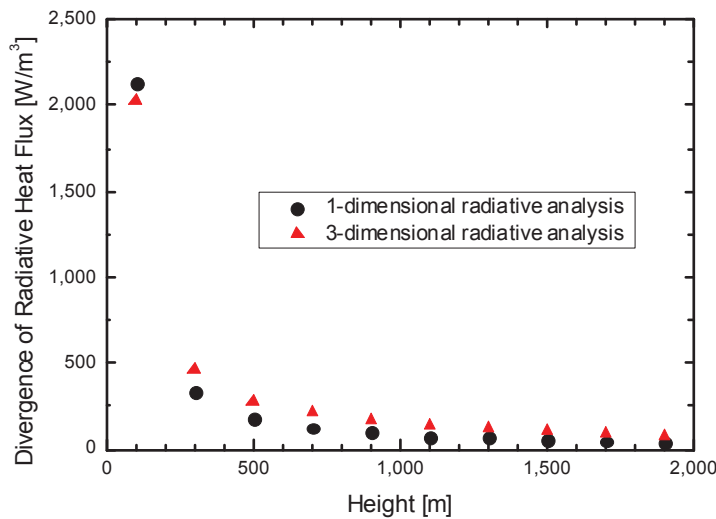
**Results and discussions**

In our previous study, performing the numerical analysis of fire whirlwind with respect to scale effect, it was examined whether a relationship exists between a real phenomenon and the phenomenon in the reduction model with taking into account radiative heat transfer (Sakai & Miyagi, 2010). The P-1 model was utilized to simulate the radiative heat transfer from the heat source at high temperature.

It was found that radiative heat exchange played an important role in the heat transfer at the higher temperature field, whereas just radiative exchange between solid surfaces was carried out.

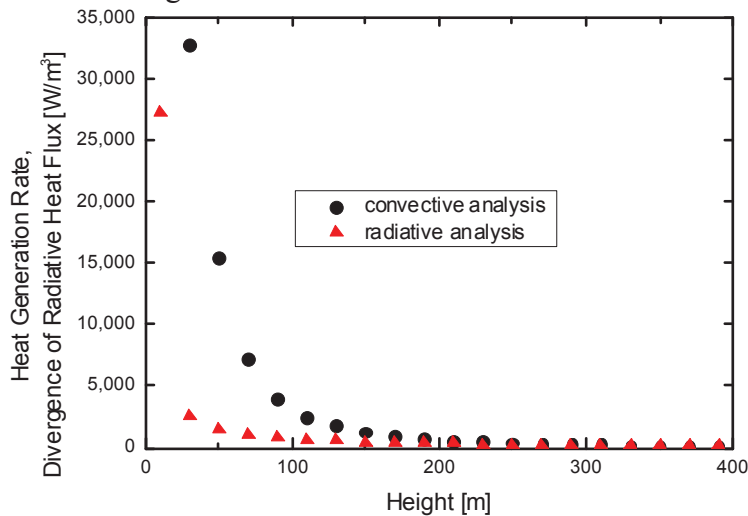
In this study, radiative heat exchange is dealt in consideration of radiative gas using Radiation Element Method by Ray Emission Model (REM2) (Maruyama & Aihara, 1997). Radiative heat transfer effect on fire whirlwind is discussed.

**Comparison of 1-d and 3-d radiative heat exchange** One dimensional radiative exchange analysis above the heat source is compared with three dimensional one to reduce the computational load and time. Fig. 4 shows the comparison of divergence of radiative heat flux above the heat source between one dimensional parallel analysis model and three dimensional analysis model. Even though the one dimensional analysis model omitted the effect of surrounding boundaries, these two results coincide comparable. Therefore, further analysis employs one dimensional model for radiative heat exchange.



**Fig. 4. Comparison of 1-d and 3-d radiative analysis (Distribution of divergence of radiative heat flux above the heat source)**

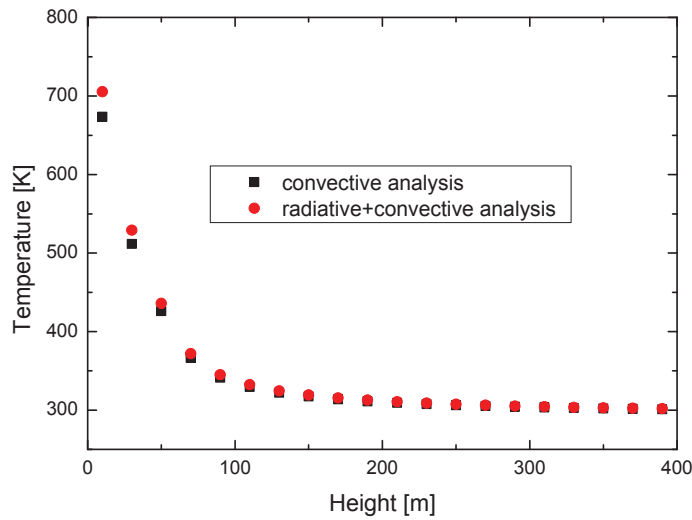
**Comparison of convective flow analysis and radiative-convective flow analysis** Fig. 5 shows heat generation rate for convective flow analysis and divergence of radiative heat flux for radiative heat exchange above the heat source. Though values of divergence of heat flux are smaller than those of heat generation rate, just convective flow analysis ignores these amounts to simulate. It is easily expected that the radiative heat exchange due to participating media plays an important role more than the radiative heat exchange between surfaces.



**Fig.5. Comparison of heat generation rate and divergence of heat flux above the heat source**

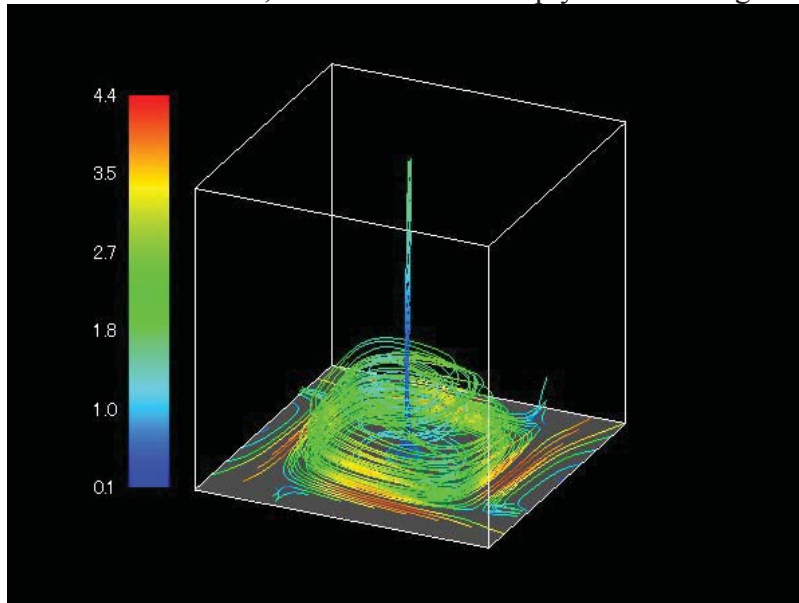
Fig. 6 shows comparison of temperature distribution above the heat source after 30 minutes from air current induction between convective flow analysis and combined radiative-convective flow analysis.

As expected from the distribution of heat generation and divergence of radiative heat flux, temperature distribution is different, especially until lower height 100m. Participating media have much influence to the temperature distribution, and play an important role.



**Fig.6. Comparison of temperature distribution above the heat source after 30 minutes from air current induction between convective flow analysis and combined radiative-convective flow analysis**

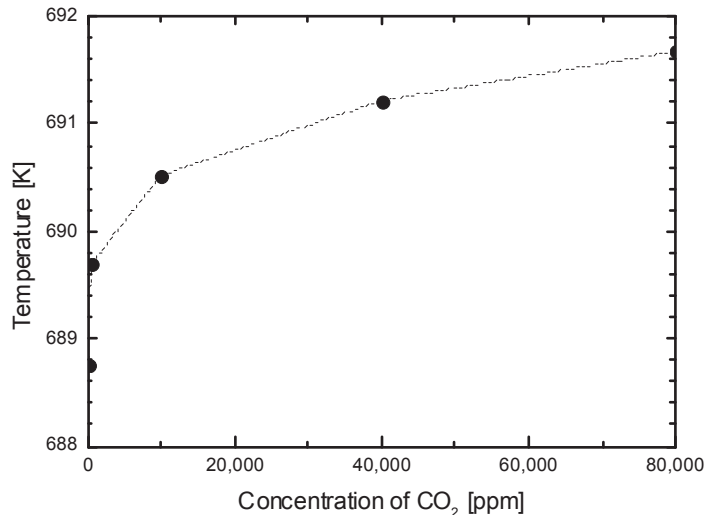
Fig. 7 shows streamlines of the flow field. Lines are colored by velocity magnitude. Whirlwind is stably generated above the heat source, and is shrunk sharply with the height from the heat source.



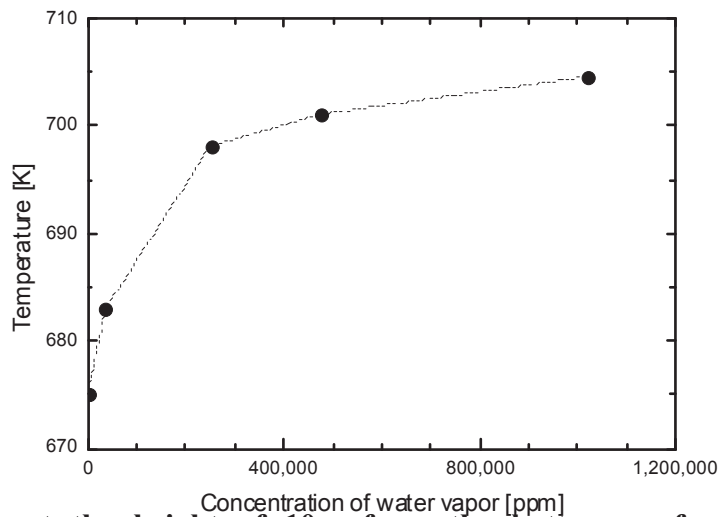
**Fig.7. Streamlines of whirlwind**

**Influence of Participating Media Concentration on Heat Exchange and Flow Distribution** In practical fire whirlwind, combustion and chemical reaction release some participating media. In this section, representative participating media, i.e. carbon dioxide and water vapor is considered, and the concentration of these participating media is altered to evaluate the influence on heat exchange and flow distribution.

Figs.8 and 9 shows temperature at the height of 10m from the bottom surface with changing the concentration of carbon dioxide and that of water vapor, respectively. Some values of both participating media concentration are added from the Table 1 for the combined analysis to observe the tendency between temperature and concentration. Water vapor plays more important role to the thermal field than carbon dioxide.



**Fig.8. Temperature at the height of 10m from the bottom surface with changing the concentration of carbon dioxide**



**Fig.9. Temperature at the height of 10m from the bottom surface with changing the concentration of water vapor**

## Conclusions

In this study, three dimensional analyses are performed to investigate the thermal and flow fields by using the Finite Volume Method with introducing divergence of radiative heat flux for gas medium. Fire whirlwind is forcibly generated stably just above the heat source with introducing air currents from four corners. One dimensional radiative exchange analysis above the heat source is compared with three dimensional one to reduce the computational load and time. Then, the composition of participating gases is altered to discuss the effect of radiative heat exchange to the whirlwind flow field. The following concluding remarks are gotten from the combined heat transfer analysis.

- From the comparison of thermal and flow field between convective flow analysis and combined radiative-convective flow analysis, radiative heat exchange has a great influence to the thermal field and a less influence to the flow field. Flow field is much characterized by turbulent.
- Increase of participating media concentration gives raise of temperature due to absorption and re-emission, and water vapor influences thermal field more than carbon dioxide. However, these calculations employ uniform concentration over the analytical domain. Release and diffusion of participating media have to be considered for more practical evaluation of the whirlwind.



## References

- Takewaki, I.; Murakami, S.; Fujita, K.; Yoshitomi, S. & Tsuji, M. (2011). The 2011 off the Pacific coast of Tohoku earthquake and response of high-rise buildings under long-period ground motions, *Soil Dynamics and Earthquake Engineering*, in press
- Hough, S. E. & Bilham, R. G. (2005). *After the Earth Quakes: Elastic Rebound on an Urban Planet*, Oxford University Press USA
- Graham, H. E. (1955). Fire whirlwinds, *Bulletin American Meteorological Society*, Vol.36, pp. 99–103
- Emmons, H. W. & Ying, S. J. (1967) The fire whirl, *Proceedings of the Combustion Institute*, Vol.11, pp. 475–488
- Byram, G. M. & Martin, R. E. (1970). The Modeling of Fire Whirlwinds, *Forest Science*, Vol.16, No.4, pp.386-399
- Haines, D. A. & Updike, G. H. (1971). Fire Whirlwind Formation over Flat Terrain, USDA Forest Service Research Paper, NC-71
- Martin, R. E.; Pendleton, D. W. & Burgess, W. (1976). Effect of Fire Whirlwind Formation on Solid Fuel Burning Rates, *Fire Technology*, Vol.12, No.1, pp.33-40
- Muraszew, A.; Fedele, J. B. & Kuby W.C. (1979). The fire whirl phenomenon, *Combustion and Flame*, Vol. 34, pp.29-45
- Emori, R. I. & Saito, K. (1982). Model experiment of hazardous forest fire whirl, *Fire Technology*, Vol.18, No.4, pp.319-327
- Satoh, K. & Yang, K. T. (1996). Experimental Observations of Swirling Fires, *Proceedings of ASME Heat Transfer Division*, HTD-Vol.335, No.4, pp.393-400
- Hayashi, Y.; Ohmiya, Y.; Iwami, T. & Saga, T. (2003). Experimental Study on Fire and Plume Properties Using BRI's Fire Wind Tunnel Facility, *International Journal for Fire Science and Technology*, Vol.22, pp.17-35
- Liu, N. A. (2005). Experimental and Theoretical Investigation on Fire Interactions and the Induced Firewhirls in Square Fire Arrays, *Proceedings of Fifth NRIFD International Symposium on Forest Fires*, Tokyo, pp.293-301
- Kuwana, K.; Sekimoto, K.; Saito, K. & Williams, F. A. (2007). Can We Predict the Occurrence of Extreme Fire Whirls?, *AIAA JOURNAL*, Vol.45, pp.16-19
- Liu, N. A.; Liu, Q.; Deng, Z. H.; Satoh, K. & Zhu, J. P. (2007). Burn-out Time Data Analysis on Interaction Effects among Multiple Fires in Fire Arrays, *Proceedings of the Combustion Institute*, Vol.31, pp.2589-2597
- Kuwana, K.; Sekimoto, K.; Saito, K. & Williams, F. A. (2008). Scaling fire whirls, *Fire Safety Journal*, Vol.43, No.4, pp.252-257
- Chuah, K. H.; Kuwana, K.; Saito, K. & Williams, F. A. (2011). Inclined fire whirls, *Proceedings of the Combustion Institute*, Vol.33, pp.2417-2424
- Satoh, K. & Yang, K. T. (1997). Simulations of swirling fires controlled by channeled self-generated entrainment flows [A], *Fire Safety Sci.*, *Proceedings of the 5th International Symposium*[C], pp.201-212
- Battaglia, F.; Rehm, R. G. & Baum, H. R. (2000a). Fluid Mechanics of Fire Whirls: An Inviscid Model, *Physics of Fluids*, Vol.12, No.11, pp.2859-2867
- Snegirev, A. Y.; Marsden, J. A.; Francis, J. & Makhviladze, G. M. (2004). Numerical studies and experimental observations of whirling flames, *International Journal of Heat and Mass Transfer*, Vol.47, pp.2523–2539
- Hassan, M. I.; Kuwana, K.; Saito, K. & Wang, F. (2005). Flow Structure Of A Fixed-frame Type Firewhirl, *Proceedings of the Eighth International Symposium*, International Association for Fire Safety Science, Beijing, China, September 18-23, pp.951-962
- Chuah, K. H. & Kushida, G. (2007). The prediction of flame heights and flame shapes of small fire whirls, *Proceedings of the Combustion Institute*, Vol. 31, pp.2599–2606
- Grishin, A. M.; Matvienko, O. V. & Rudi, Y. A. (2009). Mathematical Modeling of Gas Combustion in A Twisted Jet and of The Formation of A Fiery Whirlwind, *Journal of Engineering Physics and Thermophysics*, Vol.82, No.5, pp.906-913
- Sakai, S. & Watanabe, Y. (2007). Numerical Study of Interaction between Natural Convection Flow and horizontal wind, *Proceedings of the FEDSM2007, 5th Joint ASME/JSME Fluids Engineering Conference*, FEDSM2007-37212, San Diego, California, USA, July 30-August 2, 2007
- Sakai, S. & Miyagi, N. (2010). Numerical Study of Fire Whirlwind Taking into Account Radiative Heat Transfer, *IOP Conference Series: Materials Science and Engineering*, Vol.10, 012031
- Sakai, S. (2012). Numerical Prediction of Fire Whirlwind Outbreak and Scale Effect of Whirlwind Behavior, *Advances in Geotechnical Earthquake Engineering – Soil Liquefaction and Seismic Safety of Dams and Monuments*, Chapter 15, pp.383-404
- Maruyama, S. & Aihara, T. (1997). Radiation Heat Transfer of Arbitrary Three-Dimensional Absorbing, Emitting and Scattering Media and Specular and Diffuse Surfaces, *Trans. ASME, Journal of Heat Transfer*, Vol.119, pp.129-136
- Patankar, S. V. (1980). *Numerical heat transfer and fluid flow*, edited by M. A. Phillips and E. M. Millman, Hemisphere Publishing Corporation, USA
- Maruyama, S. (1998). Radiative heat transfer in anisotropic scattering media with specular boundary subjected to collimated irradiation, *International Journal of Heat and Mass Transfer*, Vol.41, pp.2847-2856

---

## Vibration of Double-walled Carbon Nanotubes Predicted by Timoshenko Beam Models and Molecular Dynamics

Rumeng Liu<sup>1</sup>, \*Lifeng Wang<sup>1</sup>

<sup>1</sup>State Key Laboratory of Mechanics and Control of Mechanical Structures, Nanjing University  
Aeronautics and Astronautics, 210016 Nanjing, PR China

\*Corresponding author: Tel/Fax: +86 25 8489 2003-8004. E-mail address: walfe@nuaa.edu.cn (Lifeng Wang)

### Abstract

Vibration of double-walled carbon nanotubes (DWCNTs) are studied by using different beam models of continuum mechanics and the molecular dynamics (MD) simulations. The models of the double Euler beam (DEB) and the double Timoshenko beam (DTB), with the energy of van der Waals interaction between layers taken into consideration are applied to predict the natural frequencies of DWCNTs with one ends fixed. For the relatively long DWCNTs, the results obtained by the DEB model and the DTB model are very close, and the MD simulations show that these two models can predict the natural frequencies well. However, for the vibration of the relatively short DWCNTs, the difference between the DEB model and the DTB model becomes obvious, and the DTB model offers much better predictions than the DEB model.

**Keywords:** double-walled carbon nanotubes, double-Timoshenko beam, molecular dynamics simulation, van der Waals, natural frequency

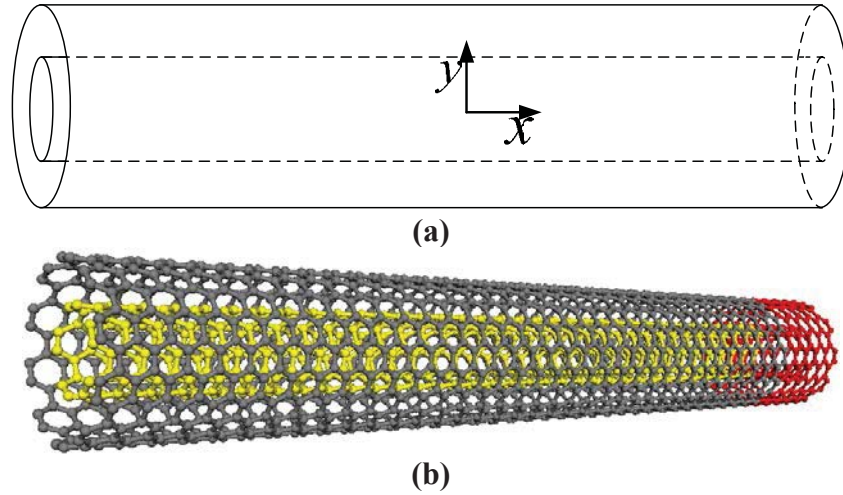
### 1. Introduction

Carbon nanotubes (CNTs) have attracted lots of researches for their novel electronic properties and superior mechanical strength (Ahlskog et al. 2001; Cumings & Zettl 2000; Postma et al. 2001; Roschier et al. 2001; Rueckes et al. 2000). Experiments and MD simulations have been effectively used to study mechanical behavior, including vibrational behavior, of CNTs. Treacy et al. (1996) estimated Young's modulus of isolated CNTs by measuring, in the transmission electron microscope, the amplitude of their intrinsic thermal vibration. Hsiesh et al. (2006) investigated the intrinsic thermal vibration of a CNT using MD simulations. There are some difficulties encountered in experiments study on the mechanical behavior of CNTs, and MD simulations remain expensive for large scale systems. Continuum mechanics models, including the Euler beam model are widely used in vibration and buckling analyses and in sound wave propagation problems (Yoon et al. 2003a; Yoon et al. 2003b). Besides, the Timoshenko beam model with the rotary inertia and the shear deformation taken into account has been used to analyze the vibration and wave propagation of short CNTs which may be used widely as nanoelectronic materials (Ahlskog et al. 2001; Roschier et al. 2001) and AFM tip (Ishikawa et al. 2002; Snow et al. 2002). Yoon et al. (2005) studied vibration of short DWCNTs with supported-supported boundary condition and they found that the Timoshenko-beam model, rather than the Euler-beam model, is relevant for terahertz vibration of short DWCNTs. For more boundary conditions, Wang et al. (2006) solved the governing Timoshenko equations for DWCNTs by using the differential quadrature method. They show that the frequencies are significantly over predicted by the Euler beam theory when the

length-to-diameter ratios are small. Wang et al. (2010) studied the thermal vibration of single-walled CNTs based on the model of Timoshenko beam, together with the law of energy equipartition and MD simulations. Wang & Hu (2012) analyzed the difference in natural frequencies predicted by using the DEB model and the MD simulation, they found that the difference is obvious for high-order frequencies and more accurate models, such as Timoshenko beam model, are needed to predict the natural frequencies of a DWCNT.

The primary objective of this study is to derive theoretical solutions of DTB model and check the validity of it, in studying the vibration, simulated via the MD simulations, of a DWCNT with one end fixed and the other end free. For this purpose, Section 2 presents the natural frequency of a model of DTB to be used to model the vibration of a DWCNT. Section 3 gives the MD simulation for the free vibration of DWCNTs based on the Brenner potential and Lennard-Jones pair potential. Section 4 outlines a comparison, which is verified by using results of MD simulations in Section 3, between the DTB model and DEB model. Finally, the paper ends with Section 5 with some conclusions.

## 2. Double-Timoshenko-beams model



**Figure 1. Models for DWCNT (a) Continuum mechanics model (b) Molecular structure model**

This section starts with the dynamic equation of a DTB of infinite length and uniform cross section placed along direction  $x$  in the frame of coordinates  $(x, y, z)$ , the dynamic equations of the inner and outer tubes for a DWCNT are (Huang 1961; Ru 2000)

$$\rho A_1 \frac{\partial^2 w_1}{\partial t^2} + \beta A_1 G \left( \frac{\partial \varphi_1}{\partial x} - \frac{\partial^2 w_1}{\partial x^2} \right) = C_{12} (w_2 - w_1), \quad (1a)$$

$$\rho I_1 \frac{\partial^2 \varphi_1}{\partial t^2} + \beta A_1 G_1 \left( \varphi_1 - \frac{\partial w_1}{\partial x} \right) - E_1 I_1 \frac{\partial^2 \varphi_1}{\partial x^2} = 0, \quad (1b)$$

$$\rho A_2 \frac{\partial^2 w_2}{\partial t^2} + \beta A_2 G_2 \left( \frac{\partial \varphi_2}{\partial x} - \frac{\partial^2 w_2}{\partial x^2} \right) = C_{12} (w_1 - w_2), \quad (1c)$$

$$\rho I_2 \frac{\partial^2 \varphi_2}{\partial t^2} + \beta A_2 G_2 \left( \varphi_2 - \frac{\partial w_2}{\partial x} \right) - E_2 I_2 \frac{\partial^2 \varphi_2}{\partial x^2} = 0, \quad (1d)$$

where  $w_k(x, t)$  ( $k=1, 2$ ) is the displacement of section  $x$  of the  $k$ th tube in direction  $y$  at the moment  $t$ ,  $\varphi_k$  is the slope of the deflection curve of the  $k$ th tube when the shearing force is neglected,  $A_k$  is the cross section area of the  $k$ th tube,  $I_k = \int y^2 dA_k$  is the moment of inertia for the cross section of the  $k$ th tube,  $\beta$  is the form factor of shear depending on the shape of the cross section, and  $\beta=0.5$  holds for the circular tube of the thin wall (Timoshenko et al. 1972).  $C_{jk}$  is the coefficient of the van der Waals (vdW) interaction for the interaction pressure per unit axial length and estimated based on an effective interaction width (He et al. 2005).  $E_k$ ,  $\rho_k$ ,  $G_k$  are Young's modulus, mass density and shear modulus of the  $k$ th tube respectively. The boundary conditions of a cantilever beam are

$$w_k(0, t) = 0, \quad \varphi_k(0, t) = 0, \quad \frac{\partial^2 w_k(L, t)}{\partial x^2} = 0, \quad \frac{\partial^2 \varphi_k(L, t)}{\partial x^2} = 0. \quad (2)$$

Both nested tubes with the same boundary conditions have the same vibrational modes,  $\hat{w}(x)$ ,  $\hat{\varphi}(x)$ . The dynamic deflection and slope can be given by

$$w_k = a_k \hat{w}_n(x) e^{j\omega t}, \quad \varphi_k = a_k \hat{\varphi}_n(x) e^{j\omega t}, \quad (3)$$

where  $\hat{w}$  represents the deflection amplitude of the beam,  $\hat{\varphi}$  the slope amplitude of the beam due to bending deformation alone, and  $j \equiv \sqrt{-1}$ . Let

$$\xi = x/L. \quad (4)$$

Substituting Equation (3), (4) into Equation (1), one obtains

$$a_1 \frac{\partial^2 \hat{w}_n}{\partial \xi^2} - a_1 L \frac{\partial \hat{\varphi}_n}{\partial \xi} + a_1 b_1^2 s_1^2 \hat{w}_n = \frac{C_{12} L^2}{\beta A_1 G_1} (a_1 \hat{w}_n - a_2 \hat{w}_n), \quad (5a)$$

$$s_1^2 \frac{\partial^2 \hat{\varphi}_n}{\partial \xi^2} + \frac{1}{L} \frac{\partial \hat{w}_n}{\partial \xi} - (1 - b_1^2 r_1^2 s_1^2) \hat{\varphi}_n = 0, \quad (5b)$$

$$a_2 \frac{\partial^2 \hat{w}_n}{\partial \xi^2} - a_2 L \frac{\partial \hat{\varphi}_n}{\partial \xi} + a_2 b_2^2 s_2^2 \hat{w}_n = \frac{C_{12} L^2}{\beta A_2 G_2} (a_2 \hat{w}_n - a_1 \hat{w}_n), \quad (5c)$$

$$s_2^2 \frac{\partial^2 \hat{\varphi}_n}{\partial \xi^2} + \frac{1}{L} \frac{\partial \hat{w}_n}{\partial \xi} - (1 - b_2^2 r_2^2 s_2^2) \hat{\varphi}_n = 0, \quad (5d)$$

where

$$b_k^2 = \frac{\rho A_k L^4 \omega^2}{E_k I_k}, \quad r_k^2 = \frac{I_k}{A_k L^2}, \quad s_k^2 = \frac{E_k I_k}{\beta A_k G_k L^2}. \quad (6)$$

So

$$\frac{\partial^4 \hat{w}_n}{\partial \xi^4} + B \frac{\partial^2 \hat{w}_n}{\partial \xi^2} - C \hat{w}_n = 0, \quad (7)$$

$$\text{where } B = b_1^2 s_1^2 + b_1^2 r_1^2 - \frac{C_{12} L^2}{\beta A_1 G_1} \left(1 - \frac{a_2}{a_1}\right), \quad C = \frac{(1 - b_1^2 r_1^2 s_1^2) \left[ b_1^2 s_1^2 - \frac{C_{12} L^2}{\beta A_1 G_1} \left(1 - \frac{a_2}{a_1}\right) \right]}{s_1^2}.$$

The solutions  $\hat{w}_n, \hat{\varphi}_n$  of Equation(7) reads

$$\hat{w}_n = C_1 \cosh \alpha_1 \xi + C_2 \sinh \alpha_1 \xi + C_3 \cos \alpha_2 \xi + C_4 \sin \alpha_2 \xi, \quad (8a)$$

$$\hat{\varphi}_n = C'_1 \sinh \alpha_1 \xi + C'_2 \cosh \alpha_1 \xi + C'_3 \sin \alpha_2 \xi + C'_4 \cos \alpha_2 \xi, \quad (8b)$$

where

$$\alpha_1 = \left( \frac{\mp B + \sqrt{B^2 + 4C}}{2} \right)^{1/2} \quad (9)$$

And  $\sqrt{B^2 + 4C} > B$  is assumed.

In the case of  $\sqrt{B^2 + 4C} < B$ , then Equation (7) should be replaced by (Huang 1961)

$$\hat{w}_n = C_1 \cos \alpha_1' \xi + j C_2 \sin \alpha_1' \xi + C_3 \cos \alpha_2 \xi + C_4 \sin \alpha_2 \xi, \quad (10a)$$

$$\hat{\phi}_n = j C_1' \sin \alpha_1' \xi + C_2' \cos \alpha_1' \xi + C_3' \sin \alpha_2 \xi + C_4' \cos \alpha_2 \xi, \quad (10b)$$

where  $\alpha_1 = j \alpha_1'$ .

In Equations (8) and (10), only one half of the constants are independent since they are related by Equations (5) as following

$$C_1 = \frac{L}{b_1 \alpha_1} [1 - b_1^2 s_1^2 (\alpha_1^2 + r_1^2)] C_1' = \Lambda_1 C_1', \quad (11a)$$

$$C_2 = \frac{L}{b_1 \alpha_1} [1 - b_1^2 s_1^2 (\alpha_1^2 + r_1^2)] C_2' = \Lambda_2 C_2', \quad (11b)$$

$$C_3 = -\frac{L}{b_1 \alpha_2} [1 + b_1^2 s_1^2 (\alpha_2^2 - r_1^2)] C_3' = \Lambda_3 C_3', \quad (11c)$$

$$C_4 = \frac{L}{b_1 \alpha_2} [1 + b_1^2 s_1^2 (\alpha_2^2 - r_1^2)] C_4' = \Lambda_4 C_4'. \quad (11d)$$

The natural frequency  $\omega$  of the cantilever Timoshenko beam can be determined from the determinant of the follow matrix

$$\begin{vmatrix} \Lambda_1 & 0 & \Lambda_3 & 0 \\ 0 & 1 & 0 & 1 \\ \Lambda_1 \alpha_1^2 \cosh \alpha_1 & \Lambda_2 \alpha_1^2 \sinh \alpha_1 & -\Lambda_3 \alpha_2^2 \cos \alpha_2 & -\Lambda_4 \alpha_2^2 \sin \alpha_2 \\ \alpha_1^2 \sinh \alpha_1 & \alpha_1^2 \cosh \alpha_1 & -\alpha_2^2 \sin \alpha_2 & -\alpha_2^2 \cos \alpha_2 \end{vmatrix} = 0. \quad (12)$$

$$\begin{vmatrix} \Lambda_1 & 0 & \Lambda_3 & 0 \\ 0 & 1 & 0 & 1 \\ -\Lambda_1 \alpha_1'^2 \cos \alpha_1' & -\Lambda_2 j \alpha_1'^2 \sin \alpha_1' & -\Lambda_3 \alpha_2^2 \cos \alpha_2 & -\Lambda_4 \alpha_2^2 \sin \alpha_2 \\ -j \alpha_1'^2 \sin \alpha_1' & -\alpha_1'^2 \cos \alpha_1' & -\alpha_2^2 \sin \alpha_2 & -\alpha_2^2 \cos \alpha_2 \end{vmatrix} = 0. \quad (13)$$

Solving Equation (12) and (13), one can obtain the natural frequency of the double Timoshenko beam with one end fixed.

### 3. Molecular dynamics model

The MD simulations are carried out using Brenner's second generation reactive empirical bond order (REBO) potential (Brenner et al. 2002) which has been widely used in a great number of studies on the mechanical behavior of carbon materials. In the REBO potential, the chemical binding energy  $E_b$  can be simply written as a sum over nearest neighbors in the form

$$E_b = \sum_i \sum_{j(>i)} [V^R(r_{ij}) - b_{ij} V^A(r_{ij})], \quad (14)$$

where  $r_{ij}$  is the distance between pairs of nearest-neighbour atoms  $i$  and  $j$ ,  $b_{ij}$  is a many-body empirical bond-order function. The functions  $V^R(r_{ij})$  and  $V^A(r_{ij})$  are interatomic repulsion and attraction terms, which represent bonding from valence

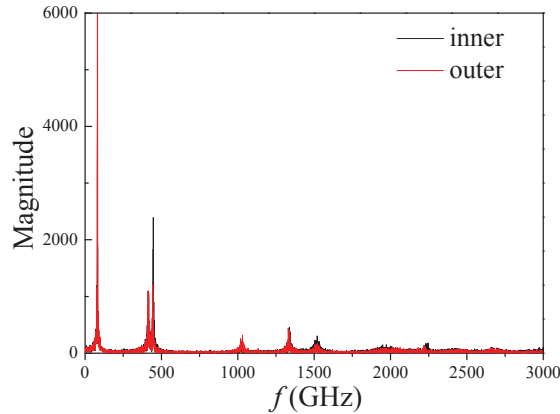
electrons, respectively.

The long range vdW interaction is calculated by Lennard-Jones 12-6 potential, given by

$$E = 4\varepsilon \left[ \left( \frac{\sigma}{r} \right)^{12} - \left( \frac{\sigma}{r} \right)^6 \right], \quad (15)$$

with well-depth energy of  $\varepsilon=4.7483 \times 10^{-22}$  J and equilibrium distance of  $\sigma=0.34$  nm.

The atoms in the red region shown in Figure 1(b) are fixed in order to simulate the cantilever boundary condition. The DWCNT is allowed vibrating freely for  $2 \times 10^6$  steps with time step 1fs at a room temperature (300K) using Nose-Hoover thermostat (Hoover 1985; Nose 1984a; Nose 1984b; Nose 1991) after the system is fully relaxed for 2ns. The coordinates histories in y direction of one random of the free atoms are recorded for certain duration, and the natural frequencies are computed by using the fast Fourier transform (FFT) method. The frequencies of a (9, 0)/(18, 0) zigzag DWCNT with 7.614nm length are shown in Figure 2, in which every peak represents one natural frequency of the DWCNT. It shows that although the diameters of the inner and outer tubes are different, the atoms oscillate in the same frequencies due to the effect of vdW force between these two tubes.



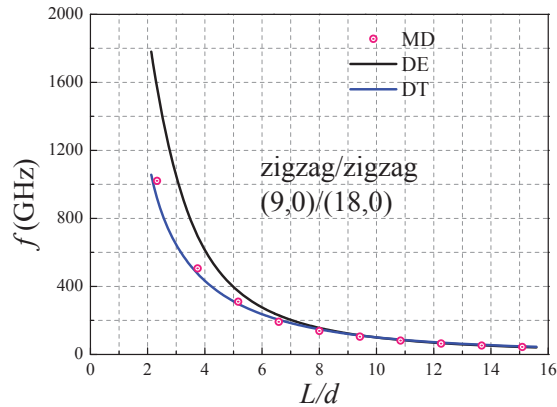
**Figure 2. Magnitude-frequency curves of atoms on inner tube and outer tube with the same 7.614nm length**

#### 4. Results and Discussions

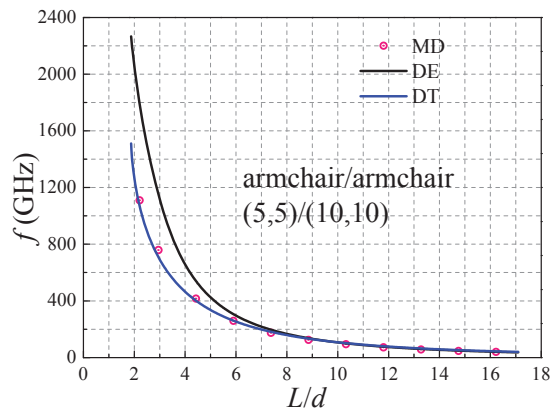
To predict the free vibration of a DWCNT, it is necessary to know Young's modulus  $E$  and the shear modulus  $G$  or Poisson's ratio  $\mu$ . The previous studies based on the REBO potential gave a great variety of Young's modulus and Poisson's ratio of single-walled CNTs. For our calculations, the inner and outer tubes of DWCNT is assumed to have the same geometrical and material parameters where  $E=0.87$  TPa and  $\mu=0.41$  are given by MD tensile method introduced in (Liu & Wang 2012) when the thickness of the wall was chosen as 0.34nm.

Vibration of (5, 5)/(10, 10) DWCNTs and (9, 0)/(18, 0) DWCNTs with one end fixed are simulated by MD method. Figure 3 and Figure 4 show the first-order natural frequencies of these two kinds of DWCNTs with different lengths calculated by MD

and beam models. From Figure 3 and Figure 4, it can be found that the DTB model and DEB model which is introduced by Yoon et al.(2003b) give very similar frequencies if the aspect ratio  $L/d$  is about bigger than 8. However, the difference between these two beam models becomes obvious along with the aspect ratio getting small, and the DEB model gives the higher frequencies. From the comparison with results of MD simulations, the DTB beam model offers much better predictions than the DEB beam model. It suggests rotary inertia and shear deformation are significant for the vibration of short DWCNTs. And the DTB model is relevant for vibration of short DWCNTs.

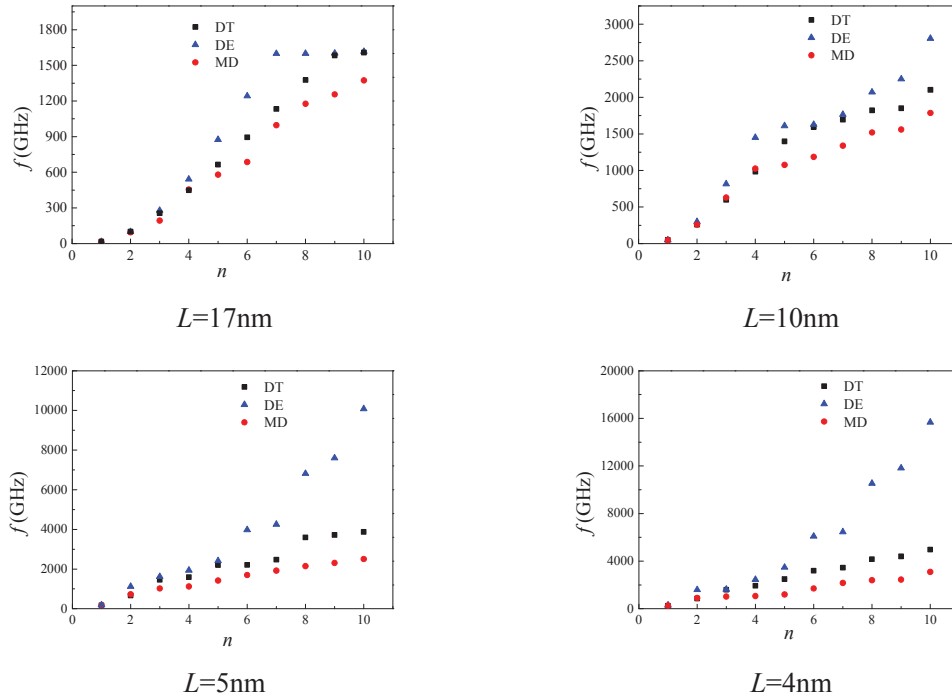


**Figure 3. (9, 0)/(18, 0) DWCNT frequencies calculated by beam models and MD**



**Figure 4. (5, 5)/(10, 10) DWCNT frequencies calculated by beam models and MD**

High-order frequencies can be obtained according to the magnitude-frequency curves as shown in Figure 2. Note that some peaks response frequencies of the longitudinal vibration not the transverse vibration of the DWCNT. And frequencies responded by these peaks should be ignored in the statistical process. Figure 5 shows the first ten frequencies of (5, 5)/(10, 10) DWCNTs in different lengths. One can see that the natural frequencies predicted by the DTB model are better than those based on the DEB model, especially when the DWCNT getting very short. That's because the shorter of the DWCNT, the greater the impacts of rotary inertia and shear deformation on the free vibration of DWCNT. However, the differences in natural frequencies, mainly high-order frequencies, predicted by DTB model and the MD simulation still looks obvious. More accurate models, such as shell model, may give a better prediction for the natural frequencies of such a DWCNT.



**Figure 5. The first ten natural frequencies of (5, 5)/(10, 10) DWCNTs in different lengths**

## 5. Conclusions

Free vibration of cantilever DWCNTs is studied using MD simulation and a DTB model which considers vdW force between the inner and outer tubes and treats the inner and outer tubes as two individual Timoshenko beams. A theoretical solution of cantilever DTB model has been obtained to predict the resonant frequency of DWCNTs with one end fixed. A comparison for the first-order frequencies between DTB model and DEB model shows that for the relatively long DWCNTs, the results obtained by the DTB model and the DEB model are very close, and the MD simulations show that both of these two models can predict the natural frequencies well. However, for the vibration of the relatively short DWCNTs, the difference between the DTB model and the DEB model becomes obvious, and the DTB model offers much better predictions than the DEB model. For high-order frequencies of DWCNTs, DTB model gives much better predictions than DEB model, especially when the length of DWCNTs is very short.

## Acknowledgements:

This work was supported in part by the National Natural Science Foundation of China under Grants 11072108, the Foundation for the Author of National Excellent Doctoral Dissertation of China under Grants 201028, Program for New Century Excellent Talents in University under Grants NCET-11-0832, the Funding for Outstanding Doctoral Dissertation in NUAU under Grants BCXJ13-03 and in part by Fundamental Research Funds for the Central Universities of China.



## References:

- Ahlskog, M., Hakonen, P., Paalanen, M., Roschier, L. and Tarkiainen, R. (2001), Multiwalled carbon nanotubes as building blocks in nanoelectronics. *Journal of Low Temperature Physics* 124, pp. 335-352.
- Brenner, D. W., Shenderova, O. A., Harrison, J. A., Stuart, S. J., Ni, B. and Sinnott, S. B. (2002), A second-generation reactive empirical bond order (REBO) potential energy expression for hydrocarbons. *Journal of Physics-Condensed Matter* 14, pp. 783-802.
- Cummings, J. and Zettl, A. (2000), Low-friction nanoscale linear bearing realized from multiwall carbon nanotubes. *Science* 289, pp. 602-604.
- He, X. Q., Kitipornchai, S. and Liew, K. M. (2005), Buckling analysis of multi-walled carbon nanotubes: a continuum model accounting for van der Waals interaction. *Journal of the Mechanics and Physics of Solids* 53, pp. 303-326.
- Hoover, W. G. (1985), Canonical dynamics: equilibrium phase-space distributions. *Physical Review A (General Physics)* 31, pp. 1695-1697.
- Hsieh, J. Y., Lu, J. M., Huang, M. Y. and Hwang, C. C. (2006), Theoretical variations in the Young's modulus of single-walled carbon nanotubes with tube radius and temperature: a molecular dynamics study. *Nanotechnology* 17, pp. 3920-3924.
- Huang, T. C. (1961), The effect of rotatory inertia and of shear deformation on frequency and normal mode equations of uniform beams with simple end conditions. *Journal of Applied Mechanics* 28, pp. 579-584.
- Ishikawa, M., Yoshimura, M. and Ueda, K. (2002), A study of friction by carbon nanotube tip. *Applied Surface Science* 188, pp. 456-459.
- Liu, R. M. and Wang, L. F. (2012), Stochastically driven vibrations of single-layered graphene sheets. *Science China Physics, Mechanics and Astronomy* 55, pp. 1103-1110.
- Nose, S. (1984a), A molecular dynamics method for simulations in the canonical ensemble. *Molecular Physics* 52, pp. 255-268.
- Nose, S. (1984b), A unified formulation of the constant temperature molecular dynamics methods. *Journal of Chemical Physics* 81, pp. 511-519.
- Nose, S. (1991), Constant temperature molecular dynamics methods. *Progress of Theoretical Physics Supplement*, pp. 1-46.
- Postma, H., Teepen, T., Yao, Z., Grifoni, M. and Dekker, C. (2001), Carbon nanotube single-electron transistors at room temperature. *Science* 293, pp. 76-79.
- Roschier, L., Tarkiainen, R., Ahlskog, M., Paalanen, M. and Hakonen, P. (2001), Multiwalled carbon nanotubes as ultrasensitive electrometers. *Applied Physics Letters* 78, pp. 3295-3297.
- Ru, C. Q., (2000), Column buckling of multiwalled carbon nanotubes with interlayer radial displacements. *Physical Review B* 62, pp. 16962-67.
- Rueckes, T., Kim, K., Joselevich, E., Tseng, G. Y., Cheung, C. L. and Lieber, C. M. (2000), Carbon nanotube-based nonvolatile random access memory for molecular computing. *Science* 289, pp. 94-97.
- Snow, E. S., Campbell, P. M. and Novak, J. P. (2002), Single-wall carbon nanotube atomic force microscope probes. *Applied Physics Letters* 80, pp. 2002-2004.
- Timoshenko, S., Gere, J. (1972), Mechanics of materials. *New York, NY: Van Nostrand Reinhold Company*.
- Treacy, M. M. J., Ebbesen, T. W. and Gibson, J. M. (1996), Exceptionally high Young's modulus observed for individual carbon nanotubes. *Nature* 381, pp. 678-680.
- Wang, C. M., Tan, V. and Zhang, Y. Y. (2006), Timoshenko beam model for vibration analysis of multi-walled carbon nanotubes. *Journal of Sound and Vibration* 294, pp. 1060-1072.
- Wang, L. F. and Hu H.Y. (2012), Thermal vibration of double-walled carbon nanotubes predicted via double-Euler-beam model and molecular dynamics. *Acta Mechanica* 223, pp. 2107-2115.
- Wang, L. F., Hu, H.Y., and Guo, W.L., (2010), Thermal vibration of carbon nanotubes predicted by beam models and molecular dynamics. *Proceedings of the Royal Society of London, Series A (Mathematical, Physical and Engineering Sciences)* 466, pp. 2325-2340.
- Yoon, J., Ru, C. Q. and Mioduchowski, A. (2003a), Sound wave propagation in multiwall carbon nanotubes. *Journal of Applied Physics* 93, pp. 4801-4806.
- Yoon, J., Ru, C. Q. and Mioduchowski, A. (2003b), Vibration of an embedded multiwall carbon nanotube. *Composites Science and Technology* 63, pp. 1533-1542.
- Yoon, J., Ru, C. Q. and Mioduchowski, A. (2005), Terahertz vibration of short carbon nanotubes modeled as Timoshenko beams. *Journal of Applied Mechanics-transactions of the Asme* 72, pp. 10-17.

## Numerical Simulation of Drag and Flow Noise Property on Structure for Carrier of Multi-loads AUV

\*Guang Pan, Yao shi, Baowei Song, Xiaoxu Du, Zhidong Yang, Jun Jiang

School of Marine Science and Technology, Northwestern Polytechnical University, China

\*Corresponding author: panguang601@163.com

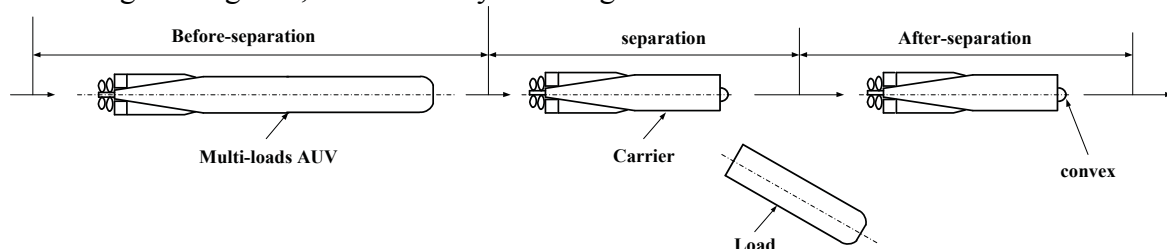
### Abstract

The LES with Smagorinsky model and the FW-H equation based on Lighthill acoustic theory were adopted to simulate the sound and flow field with different kinds of structures. Based on the analysis of field, drag and flow noise reduction mechanism of the structures with different shapes and sizes was gotten. The result demonstrate preliminarily that the match between the length and diameter of the cylindrical structure has different effect on the drag and flow noise reduction. The drag and noise reduction of the model studied in the paper with a length ratio of 0.1 and a diameter ratio of 0.55 is best. The relationship between hemispherical structure diameter and its drag and flow noise reduction effect is monotonic positive.

**Keywords:** Structure, Drag and flow noise reduction, Separation of flow field, Numerical simulation, Multi-loads AUV.

### Introduction

Autonomous Underwater Vehicle (AUV) serves as the mobile node of underwater autonomous navigation, performs such tasks as surveillance and reconnaissance, marine environmental monitoring, navigation nodes, anti-mine warfare, anti-submarine warfare, detection and identification, load drop, time-sensitive target, and so on. No matter in civil field or in the military field, it plays an important role, especially in deep sea confrontation in the future (UUV Master Plan, 2000, UUV Master Plan, 2004 and FY2011–2036, 2011). But with the progress of science and technology and the actual needs of military and civilian, considering the factors such as long distance, long term, and the aircraft technology developing a multiple load has become the development direction of the future. This aircraft is a multi-body system which made up of a load and delivery. When the load carries to the designated area, load separates step by step from the top which shown in Figure1. The idea for a new vehicle technology research has important realistic meaning and reference value, multiple sonar cloth, large gap sensor placement, one carrier segment carries more loads at a same time to complete the task which can greatly shorten the work time, reduce the engineering cost, and has many advantages.



**Figure.1 Diagram of separation**

After the separation of multi-load AUV, AUV becomes into two parts-loads and carry, it destroys a good shape of the original AUV hydrodynamic characteristics, thus appears the bluff body structure. The emergence of bluff body structure makes the interference between the carrier

segment and flow field enhanced, greatly increases the resistance and flow noise of carry segment, reduces the sail distance of carry segment, destroys the sound concealed of carry segment and let segment not be able to reach the predetermined position to lay, finally impacts on the separation process. Therefore, how to reduce the flow resistance and noise of carry segment on the separation of multi- load AUV deployment is important.

Studies have shown that many scholars(LIOW Y S, 2006 and SHAO C P, 2008 ) reduces the cycle alternating force on blunt object by arranging disturbed object to control the vortex shedding on the upstream or downstream of bluff body, thus achieves the purpose of vibration and noise reduction. Inspired by this, the paper controlled the separation of the flow field around carry segment by increasing the convex structure, used the finite volume method to solve Navier-Stokes equations, calculated the convex with different cross-sectional shapes (square, round) and got the influences of the convex on the carrier flow hydrodynamic performance, explored the results which the cross-sectional shapes and scales of convex controlled the separation of carrier flow field. All done above is provided for multi-load AUV design as the technical support.

## Governing equation

### 1 LES basic idea and equation

The basic idea of LES can be summarized as follows: the instantaneous N-S equation directly simulates the large scale turbulent vortex, not the small scale eddy, while the effects of small vortex on large eddy can simulate by approximate model. To get the achievement of LES, two parts are needed to do:

(1) build mathematical filtering function, filter out the vortex whose scale is smaller than filtering function from the turbulent transient equation of motion, break down the description of field equation of motion of large vortex, and filter out the motion effects of small vortex on large vortex, it can be reflected by adding the stress which is grid dimension stress into the motion equation of large eddy field;

(2) Sub Grid-Scale model was built can be seen in the authors (Smagorinsky J, 1963).

By using the filtering function to filter the N-S equation, LES control equation is obtained. The filtering function determines the solution of the vortex's scale. The continuity equation after filtering and the N-S equation is the same as the form of the general control equation, i.e.:

$$\begin{cases} \frac{\partial}{\partial x_i}(\bar{u}_i) = 0 \\ \frac{\partial}{\partial t}(\bar{u}_i) + \frac{\partial}{\partial x_j}(\bar{u}_i \bar{u}_j) = -\frac{1}{\rho} \frac{\partial p}{\partial x_i} + \nu \frac{\partial^2 \bar{u}_i}{\partial x_j \partial x_j} - \frac{\partial \tau_{ij}}{\partial x_j} \end{cases} \quad (1)$$

### 2 Acoustic equation

The noise module used in FLUENT code that based on the acoustic analogy of Lighthill, its basic principle is based on the simulation of time-varying flow. Ffowcs-Williams and Hawkings(1969) used the powerful theory of generalized function to develop the Lighthill equation, established FW-H equation which named with their name:

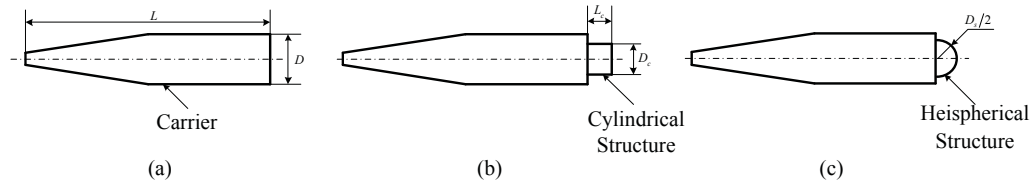
$$\frac{1}{a_0^2} \frac{\partial^2 p}{\partial t^2} - \nabla^2 p' = \frac{\partial}{\partial t} [\rho_0 u_n \delta(f)] + \frac{\partial^2}{\partial x_i \partial x_j} T_{ij} - \frac{\partial}{\partial x_i} [P_{ij} n_j \delta(f)] \quad (2)$$

## Physical model and calculation method

### 1 Physical model

The physical model for the numerical simulation is shown in Figure.2. Where, (a) is the original model, which is a cylinder, length is 3500mm, maximum diameter is 534.4mm;(b) is a

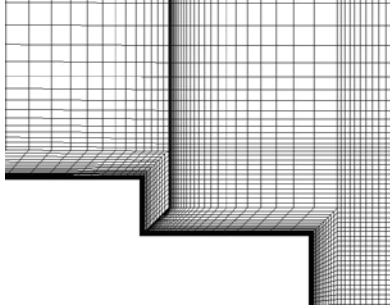
model with a cylindrical structure,  $L_c$  is the cylindrical structure's length,  $D_c$  is the diameter; (c) is a model with a hemispherical structure, the diameter of the hemisphere is  $D_s$ .



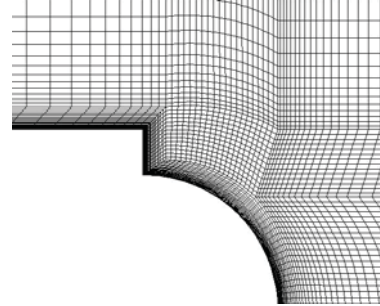
**Figure.2 Model of simulation**

## 2 Calculation method

Considering the symmetry properties of carrier structure and low computational expand, the paper used 2D axisymmetric calculation method. Structured grid is used in the numerical simulation (Figures.3 and 4), the total number of grid was about 20 million. Computational domain was a rectangle, the width direction was 10 times of the model radius, the longitudinal direction, to ensure the full development of the wakes, and this paper decided the front end to the flow section was 1.5 times of the model's length, the rear end to the flow section was 2.5 times of the model's length. To describe the flow field accurately, according to the flow conditions and geometry,  $y^+$  of the grid's bottom took 10 to fully capture the information about the near-wall flow.



**Figure.3 Grid of cylindrical structure**



**Figure.4 Grid of hemispherical structure**

In the process of the whole calculation, the flow control equations, turbulence kinetic energy equation and turbulent dissipation equation coupled solution, and had achieved second-order accuracy format. A velocity inlet and pressure-outlet boundary condition was respectively used for imports and exports; wall was under a condition of adiabatic heating and no slip boundary condition. With the residual coefficient reached the following changes and no longer as the convergence criteria. The convergence criteria took the situation as a standard, which the correlation residual coefficient reached  $1e-06$  low and almost changed no more.

The SST turbulence model based on  $k-\omega$  model was used for the steady-state's numerical simulation; the results would serve as the initial value of unsteady calculation. The sound field was simulated by the Smagorinsky model which used large eddy simulation after the unsteady calculation was stable. In the flow area of the sound field calculation, the pressure fluctuation on the surface of the model would be used as the sound source of FW-H equation. Discrete control equations used the finite volume method, the time term and non-conservative part of convective term both were second order upwind format, the conservative part and diffusion term both were second-order central difference format, and the pressure and velocity coupling calculation used the algorithm of SIMPLEC. The time steps of unsteady calculation took 0.00005s to capture the high frequency noise and fulfilled the CFL condition.

## Result of simulation

### 1 Result of Flow field

In order to study the effects of the convex section dimensions and cross section shape on the carrier segment's flow resistance and noise, this paper carried out a series of carrier flow field simulation research with different  $L_c$ ,  $D_c$  and  $D_s$  values, the specific working condition is shown in table 1.

**Table.1 Simulation model in paper**

Cylindrical structure	Hemispherical structure	
	$L_c/L = 0.05$	
$D_c/D = 0.4 \sim 0.8$ (per 0.05)	$L_c/L = 0.1$	$D_s/D = 0.4, 0.45, 0.5, 0.55, 0.6, 0.65, 0.7, 0.75, 0.8, 0.9, 1$
	$L_c/L = 0.15$	

The total drags which the object suffered are pressure drag and frictional drag. Pressure drag is mainly determined by the shape of the object, and friction drag is mainly determined by the object's surface area. The total Drag coefficient is defined as (Zhang Yuwen, 1998):

$$C_d = \frac{F}{0.5\rho sv^2} \quad (3)$$

In the Eq. (3),  $F$  acts as the resistance on the object,  $\rho$  acts as medium density,  $s$  acts as the reference area (the maximum cross-sectional area of this model is  $0.224m^2$ ),  $v$  acts as the velocity.

By comparing the different shapes of convex model and original model, the paper got the results about the drag reduction. Drag reduction factor is defined as

$$\varepsilon = \frac{F - F_1}{F} \times 100\% \quad (4)$$

In the Eq. (4),  $F$  is the resistance of the original model,  $F_1$  is the resistance of the convex model.

#### 1.1 Cylindrical convex drag reduction effect

Table2 shows the drag coefficients of the original model and convex model with different  $L_c/L$  ( $D_c/D = 0.5 - 0.6$ ).

**Table.2 Calculation results with different  $L_c/L$**

$D_c/D$	$L_c/L$	Pressure drag coefficient	Frictional drag coefficient	Total drag coefficient
	Original	0.8169	0.0096	0.8265
0.50	0.05	0.3866	0.0230	0.4096
	0.10	0.2350	0.0319	0.2669
	0.15	0.2512	0.0349	0.2861
0.55	0.05	0.3287	0.0253	0.354
	0.10	0.2037	0.0363	0.2400
	0.15	0.2446	0.0361	0.2807
0.60	0.05	0.2660	0.0280	0.294
	0.10	0.2260	0.0335	0.2595
	0.15	0.2768	0.0345	0.3113

From Table.2, when  $D_c/D$  kept the same value, the drag reduction of cylindrical convex platform showed a trend of increase firstly and then decrease with the increase of  $L_c/L$ . It didn't show that the cylinder's length was longer, the drag reduction effect was better; but there was a suitable value that made the drag reduction effect was best.

Table.3 shows the drag coefficients of the original model and convex model with different  $D_c/D$  ( $L_c/L = 0.1$ ).

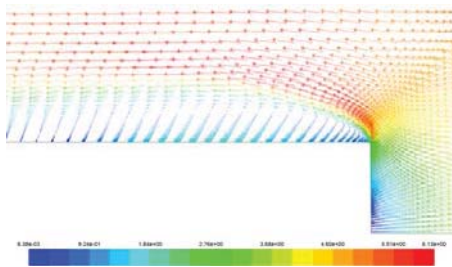
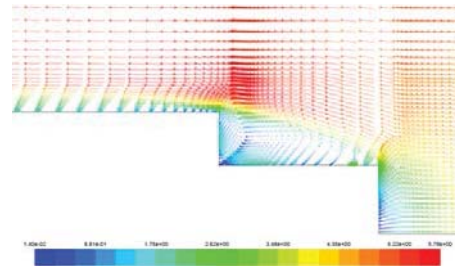
**Table.3 Calculation results with different  $D_c/D$** 

$D_c/D$	Pressure drag coefficient	Frictional drag coefficient	Total drag coefficient
Original	0.8169	0.0096	0.8265
0.40	0.3411	0.0258	0.3669
0.45	0.2881	0.0289	0.3170
0.50	0.2350	0.0319	0.2669
0.55	0.2037	0.0363	0.2400
0.60	0.2260	0.0335	0.2595
0.65	0.2583	0.0315	0.2898
0.70	0.2906	0.0296	0.3202
0.75	0.3229	0.0276	0.3505
0.80	0.3931	0.0252	0.4183

From Table.3, when  $L_c/L$  kept the same value, the drag reduction of cylindrical convex showed a trend of increase firstly and then decrease with the increase of  $D_c/D$ . It didn't show that the cylinder diameter was longer, the drag reduction effect was better; but there was a suitable diameter that made the drag reduction effect was best.

As can be seen from the above results, compared to the original model, the model with cylindrical convex suffered slightly increased frictional resistance, but the pressure drag which was more than 90% of the total drag was significantly reduced, thus formed the drag reduction effect. What can be found at the same time, the length and diameter of cylindrical convex had a certain relationship with the drag reduction effect, its length and diameter of the cylinder should reach a certain value, then achieved a good drag reduction effect. Analysis suggested that, to the flow around of original model, the boundary layer separation occurred ahead of time because of the existence of blunt body structure, produced bigger pressure in the original model, and then formed the most parts resistance of original model. However, the existence of the cylindrical convex delayed the separation of boundary layer and reduced the pressure drag of the model, thus achieved the goal of drag reduction.

Figure 5 is a velocity vector diagram of the original model; Figure 6 is a velocity vector diagram of the cylindrical convex. As can be seen from the figure, after the fluid came across the front face of carrier section, formed a large-scale and non-stable vortex, existed obvious adverse pressure gradient; while the connection of the convex and carrier formed a small-scale vortex, reduced the separation of the fluid, and lowed the resistance of the model. The model in this paper, When  $L_c/L = 0.1$  and  $D_c/D = 0.55$ , the drag reduction was best.

**Figure.5 Velocity of the original model****Figure.6 Velocity of the cylindrical convex**

### 1.2 Hemispherical convex drag reduction effect

Table4 shows the drag coefficients of the original model and convex model with different  $D_s/D$ .

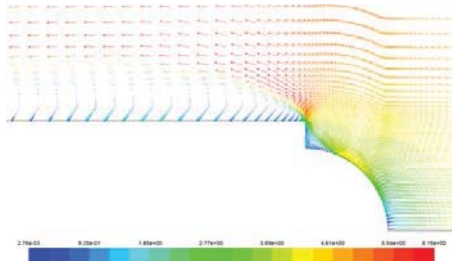
**Table.4 Calculation results with different  $D_c/D$** 

$D_s/D$	Pressure drag coefficient	Frictional drag coefficient	Total drag coefficient
Original	0.8169	0.0096	0.8265

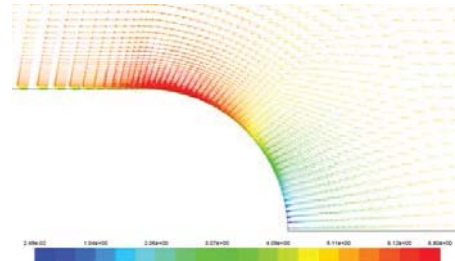
0.40	0.8019	0.0115	0.8134
0.45	0.7912	0.0119	0.8031
0.50	0.7805	0.0123	0.7928
0.55	0.7655	0.0125	0.7780
0.60	0.7454	0.0131	0.7585
0.65	0.7127	0.0139	0.7266
0.70	0.6800	0.0147	0.6947
0.75	0.6473	0.0155	0.6628
0.80	0.6144	0.0165	0.6309
0.85	0.4050	0.0263	0.4313
0.90	0.1956	0.0361	0.2317
1.00	0.0087	0.0635	0.0722

From Table.4, with the increasing of  $D_s/D$  value, the drag reduction effect of hemispherical convex increased. When  $D_s/D < 0.8$ , the drag reduction effect was below 20%; when  $D_s/D > 0.8$ , the drag reduction effect had increased dramatically. When  $D_s/D = 1$ , the drag reduction effect achieved more than 90%. The drag reduction effect of cylindrical convex was not exactly same the same result. Analyzing its reason, the existence of the hemispherical convex delay the separation of boundary layer, in addition, the “Streamline” of hemispherical convex reduced the resistance of the model. Due to the smaller side of hemispherical convex, smaller  $D_s$  made the boundary layer delay effect wasn’t obvious, so the drag reduction effect was not enormous.

Figure.7 is a velocity vector diagram of  $D_s/D = 0.75$ , Figure 8 is a velocity vector diagram of  $D_s/D = 1$ . The two figures were good enough to reflect the above characteristics. From the diagrams, when  $D_s/D = 0.75$ , the convex in a certain extent reduced the scale of the vortex but not obvious; when  $D_s/D = 1$ , the fluid flowed along the surface and didn’t exist the whorl, it validated the calculation results of the above indirectly.



**Figure.7 velocity vector of  $D_s/D = 0.75$**



**Figure.8 velocity vector of  $D_s/D = 1$**

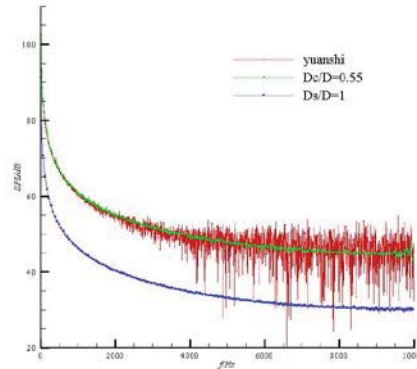
## 2 Sound field result analysis

As we all know, the flow field noise is mainly composed of the various scales of the vortex and turbulence (Lu Yuntao, 2008). Predictably, the separation region of flow boundary layer is the main vocal position. By comparing the flow noise of feature point, studied the influence of the cross-sectional shape and size of the convex to the carrier flow noise.

By convention (Wang Zhicheng, 2004), choose the vertical upper part 0.5L point (3.5,1.75,0) of original model as the feature point. According to the calculation result of flow, when the size of the cylindrical projection was  $L_c/L = 0.1$  and  $D_c/D = 0.55$ , the effect of drag reduction was best, in order to reduce the uncertainty of the variables and increase the reliability of the comparative study, the paper used the fixed size  $L_c/L = 0.1$  and changed the value of  $D_c/D$  to study the influence characteristics of flow noise.

Table5 is the calculation results of the average sound pressure level of different feature points of convex structures. Figure 9 is the average sound pressure level of feature points under a situation of the original model, cylindrical convex with  $D_c/D = 0.55$ , hemispherical convex with  $D_s/D = 1$ .

Model	SPL/dB	Noise Reduction/dB
Original	120.69	—
Cylindrical structure	$D_c/D = 0.5$	119.07
	$D_c/D = 0.55$	117.88
	$D_c/D = 0.6$	118.25
	$D_c/D = 0.65$	118.89
Hemispherical structure	$D_s/D = 0.4$	109.96
	$D_s/D = 0.6$	108.49
	$D_s/D = 0.8$	106.97
	$D_s/D = 1$	94.45



**Figure.9 SPL curves of different convex structures**

As can be seen from Table5, the existence of cylindrical convex made the sound pressure level amplitude of feature spot lower about 2db, and the noise reduction showed a trend of increase firstly and then decrease with the changes of  $D_c/D$ . The existence of hemispherical convex made the sound pressure level amplitude of feature spot lower about 10 ~ 15db which was very obvious, and the noise reduction monotonically increased with the increasing of  $D_s/D$ .

From Figure 9, in the low frequency area ( $f < 2kHz$ ) the sound pressure level of different structure model changed smoothly without sharp fluctuation; in the high frequency area ( $f = 4kHz \sim 10kHz$ ), the sound pressure level of original model had a tremendous change, the sound pressure level with a convex model changed gently. Preliminary analysis suggested that the flow noise of flow field, the pressure distribution on the surface of the object and change are closely related. For the original model, there existed a large scale vortex in the surface of model, fluid in the whirlpool area appearance unsteady phenomenon such as transition, separation, reattachment and some other sharp changes (Fig 5), and the existence of convex structure reduced the scale of the eddy and the degree of the change (Fig 6 and 8), thus reduced the flow noise caused by the unsteady pressure change.

## Conclusion

In this article, by analyzing the flow field numerical simulation results of original model, cylindrical convex model with different sizes and hemispherical convex model with different sizes,



the law of drag reduction noise reduction with the convex cross-section shape and size of the model was found. In-depth analysis of these results was done and the following conclusions were gotten:

(1)The around blunt body structure of fluid flow tended to cause turbulent flow, initiate boundary layer and form a large scale vortex in the surface, thus created a larger pressure drag and caused a unsteady pressure fluctuation noise. The existence of convex structure changed the flow separation, inhibited the vortex and significantly reduced the pressure drag, thus achieved a drag reduction and noise reduction effect.

(2)The numerical calculations of the cylindrical convex model showed that the length and diameter of cylindrical convex had a certain match relationship with the drag reduction and noise reduction effect, the length and diameter of the cylinder should reach a certain quantity so as to play a good drag reduction noise reduction effect. The paper believed that when the length ratio was 10% and the diameter ratio was 55%, the drag reduction and noise reduction result was best.

(3)The numerical calculations of the hemispheric convex model showed that the drag reduction and noise reduction effect monotonically increased with the increasing of hemispheric diameter. When the diameter ratio was close to 1, the drag reduction and noise reduction result was best.

The conclusion of this paper provided a reference for the matching design research about the drag and noise reduction of the vehicle sail after the separation of convex structure and multi-load AUV, the next problems needed to be solved was the experimental verification to the flow field characteristics of convex structure.

## Acknowledgment

This study was undertaken an part of a project supported by Ministry of education " program for New Century Excellent talents "(NCET-09-0074) , National Natural Science Foundation of China Projects(51279165), and National Defense Basic Research Project(B2720132014), China, which is gratefully acknowledged by the authors.

## References:

- The Navy Unmanned Undersea Vehicle (UUV) Master Plan, *Assistant Secretary of the Navy for Research Development & Acquisition*, April 20, 2000.
- The Navy Unmanned Undersea Vehicle (UUV) Master Plan. *Assistant Secretary of the Navy for Research Development & Acquisition*, November 9, 2004.
- FY2011–2036 Unmanned Systems Integrated Roadmap. *Department of defense*, United States of America. 2011.
- LIOW Y S K.TAN B T. THOMPSON M C, HOURIGANK. Sound generated in laminar flow past a two-dimensional rectangular cylinder[J]. *Journal of Sound and Vibration*, 2006, 295(1-2): pp. 407-427.
- SHAO C P, WEI Q D. Control of vortex shedding from a square cylinder[J]. *AIAA Journal*, 2008, 46(2): pp. 397-407.
- Smagorinsky J. General circulation experiments with the primitive equations [J]. *Monthly Weather Review*, 1963, 91(3): pp. 99-164.
- Ffowcs-Williams J E, Hawkings D L. Sound generation by turbulence and surface in arbitrary motion [C]// *Proc Roy Soc, London: Roy Soc*, 1969, 264A: pp. 321- 342.
- Zhang Yuwen. Shape Design of Torpedo. *Xi'an: Northwestern Polytechnical University Press*, 1998. (in Chinese).
- Lu Yuntao. Numerical Simulation of the Flow-Field and Flow-Noise of Fully Appendage Submarine. Master Degree Dissertation. *Shanghai: Shanghai Jiao Tong University*, 2008. (in Chinese).
- Wang Zhicheng, Chen Zongqi, Yu Feng, Liu Wenshui. Warship Noise Measuring and Analyzing. *Beijing: National Defence Industry Press*, 2004. (in Chinese).

## A Framework for Auto-segmentation of Left Ventricle from Magnetic Resonance Images

\*Xulei Yang<sup>1</sup>, Si Yong Yeo<sup>1</sup>, Calvin Lim<sup>1</sup>, Yi Su<sup>1</sup>, Min Wan<sup>2</sup>, Liang Zhong<sup>2</sup>, and Ru San Tan<sup>2</sup>

<sup>1</sup>Computing Science Department, Institute of High Performance Computing, A\*STAR, 1 Fusionopolis Way #16-16 Connexis, Singapore 138632.

<sup>2</sup>National Heart Centre Singapore, 17 Third Hospital Avenue, Mistri Wing, Singapore 168752.

\*Corresponding author: yangx@ihpc.a-star.edu.sg

### Abstract

A practical framework is proposed for the auto-segmentation of the left ventricle (LV) endocardium boundary in cardiac magnetic resonance (CMR) images. The segmentation method is based on the random walk (RW) algorithm, which requires user-selected background and foreground seeds. In this paper, the seeds are initialized automatically. The first image frame of a short-axis slice is first partitioned into different regions using the fuzzy clustering algorithm, and the LV region is identified using a heuristic method. Two circular region of interests (ROIs) are then defined based on the estimated centre of the partitioned LV region, which are used as the RW seeds initialization to segment the LV of the first image frame. The centre pixel of the adjacent image frame is then computed using the segmented LV of the previous frame. The foreground and background circular ROIs can then be defined and used as initialization of the RW algorithm to segment the adjacent image. The effectiveness of the proposed framework is verified by the experimental results on real CMR images.

**Keywords:** Cardiac Magnetic Resonance, Image Segmentation, Random Walk, Left Ventricle, Fuzzy Clustering.

### 1. Introduction

Cardiac image segmentation plays a crucial role and allows for a wide range of applications, including quantification of volume, computer-aided diagnosis, localization of pathology, and image-guided interventions. However, manual delineation is tedious, time-consuming, and is limited by inter- and intra- observer variability. In addition, many segmentation algorithms are sensitive to the initialization and therefore the results are not always reproducible, which is also limited by inter algorithm variability. Furthermore, the amount and quality of imaging data that needs to be routinely acquired in one or more subjects has increased significantly. Therefore, it is crucial to develop automated, precise, and reproducible segmentation methods.

Cardiac Magnetic Resonance (CMR) is a well established and rapidly advancing imaging modality in analyzing heart disease. It is considered by some authors to be the reference standard. CMR has proved to be more accurate than echo-cardiology in the calculation of the ejection fraction and also shown superior results in endo-cardium border segmentation. It has a wide topographical field of view and high contrast between soft tissues without the need for a contrast agent. This means there is a high discrimination between the flowing blood and the myocardium muscle. It is non-invasive with high spatial resolution and can be gated using an elec-trocardiogram (ECG) at different phases during the hearts pulse. In this study, the proposed framework aims to segment the left ventricle (LV) endo-cardium border in CMR images.

Segmentation and tracking of LV in CMR data has been extensively addressed for the last decades (Petitjean, 2011; Kang, 2012). Basically, the LV segmentation task can be approached by four major approaches: image-based methods (e.g., Weng, 1997), deformable model-based (e.g., Jolly,

2006) methods, registration-based methods (e.g., Lorenzo-Valdés, 2004), and graph-based methods (e.g., Kedenburg, 2006): The first approach utilizes the basic image analysis operators like thresholding, region-growing, image morphology, edge detection, pixel classification, etc, to delineate the LV boundaries from the image. The second approach trains a shape/curve model of the LV, and lets the curve model evolve in new subjects until it converges to the LV boundaries. The basic idea of the third approach is to transfer those expert-segmentations in training images (i.e., atlases) onto target image through image registration, and then fuse the transferred segmentations to derive an ultimate segmentation. The last approach has also been employed in LV segmentation without heavy reliance on explicitly learned or encoded priors, but the user has to initialize the set of foreground and background seeds.

Graph-based methods have been successfully employed in image segmentation without heavy reliance on explicitly learned or encoded priors. However, graph cuts algorithm proposed in (Boykov, 2000) is a fundamentally two-label algorithm, and susceptible to the “small cuts” problem in the presence of weak boundaries. The random walk (RW) algorithm proposed in (Grady, 2004 & 2006) does not suffer from the “small cut” problem and extends naturally to an arbitrary number of labels. As the good performance of weak boundary detection, noise robustness, and the assignment of ambiguous regions, RW segmentation has been applied in cardiac data, MR brain images (Grady, 2004 & 2006, Eslami, 2013, Dakua, 2011). However, manual selection of the seeds is a hard task in slow intensity varying medical images, and limits its application for real problems.

In this study, a new framework is proposed for the auto-segmentation of the LV endo-cardium boundary in CMR images. The segmentation method is based on the RW algorithm, and the seeds are initialized automatically. The first image frame of a short-axis slice is first partitioned into different regions using the fuzzy c-means (FCM) algorithm (Bezdek, 1981), and the LV region is identified using a heuristic method. Two circular region of interests (ROIs) are then defined based on the estimated centre of the partitioned LV region, which are used as the RW seeds initialization to segment the LV of the first image frame. The centre pixel of the adjacent image frame is then computed using the segmented LV of the previous frame. The foreground and background circular ROIs can then be defined and used as initialization of the RW algorithm to segment the adjacent image. The effectiveness of the proposed framework is verified by the experimental results on real CMR images from RV challenge website (<http://www.litislabs.eu/rvsc>).

The rest of this paper is organized as follows: Section 2 reviews the related techniques and presents the proposed framework. The experimental results of the proposed framework are reported in Section 3. Finally, the conclusion is given in Section 4.

## 2. Methodology

In this section, we first brief review the FCM and RW algorithms, then present the proposed cardiac image segmentation framework, which is specifically for LV endo-cardium boundary delineation in CMR images.

### 2.1 Fuzzy C-Means (FCM)

Mathematically, FCM algorithm is formulated to minimize the following objective function with respect to the membership function  $u_{k|ij}$  and the cluster centre  $v_k$  as given by

$$J_{fcm} = \sum_{x_{ij} \in I} \sum_{k=1}^c (u_{k|ij})^m \cdot (x_{ij} - v_k)^2 \quad \text{subject to} \quad \sum_{k=1}^c u_{k|ij} = 1, \forall x_{ij} \in I \quad (1)$$

Where  $c$  is the cluster number,  $m$  is the weighing exponent on fuzzy memberships, and a value of  $m = 2$  is known to give good results with the FCM algorithm. Note if  $m = 1$ , then the FCM becomes the hard K-means algorithm (Macqueen, 1967) with each point uniquely belonging to its nearest cluster. The  $u_{k|ij}$  is the membership of the point  $x_{ij}$  in the  $k$ th cluster. The minimization of (1) gives the updating equations for membership  $u_{k|ij}$  and cluster centre  $v_k$ , which are given by

$$u_{k|ij} = \frac{(x_{ij} - v_k)^{-2/(m-1)}}{\sum_{k=1}^K (x_{ij} - v_k)^{-2/(m-1)}} \quad \text{and} \quad v_k = \frac{\sum_{x_{ij} \in I} u_{k|ij}^m x_{ij}}{\sum_{x_{ij} \in I} u_{k|ij}^m} \quad (2)$$

The FCM algorithm is summarized as follows,

- 1) Fix the cluster number  $c$ , initialize the cluster centres  $v_k$  ( $k=1,2,\dots,c$ ), and set the threshold  $\varepsilon$  be a small positive value, e.g.,  $\varepsilon=0.001$ .
- 2) Alternatively update the membership function and cluster centre by using (2) until the changes between two iterations smaller than the threshold  $\varepsilon$

## 2.2 Random Walk (RW)

RW algorithm was first proposed by Leo Grady (2004 & 2006) for performing multi-label, interactive image segmentation. User predefines a series of pixels as the labels, then the probability that a random walker starting at each unlabeled pixel (a pixel can be considered as a node) will first reach one of the prelabeled pixels on different labels is calculated. A high-quality segmentation image can be obtained by assigning to each node the label corresponding to the greatest probability.

The summary of the RW algorithm is described as follows:

- 1) Obtain a set of marked (or labeled) pixels with  $K$  labels (wher  $K$  is the number of the labels), either interactively or automatically.
- 2) Build the lattice, which is composed of nodes and edges. RW treats an image as a purely discrete object -- a graph with a fixed number of vertices and edges.
- 3) Choose a weighting function, which maps a change in image intensities to edge weights. The typical Gaussian weighting function is given by

$$w_{ij} = \exp(-\beta(g_i - g_j)^2) \quad (3)$$

Where  $g_i$  indicates the image intensity at pixel  $i$ , and  $\beta$  is the weighting parameter.

- 4) Solve each label by

$$L_U x^s = -B^T m^s \quad (4)$$

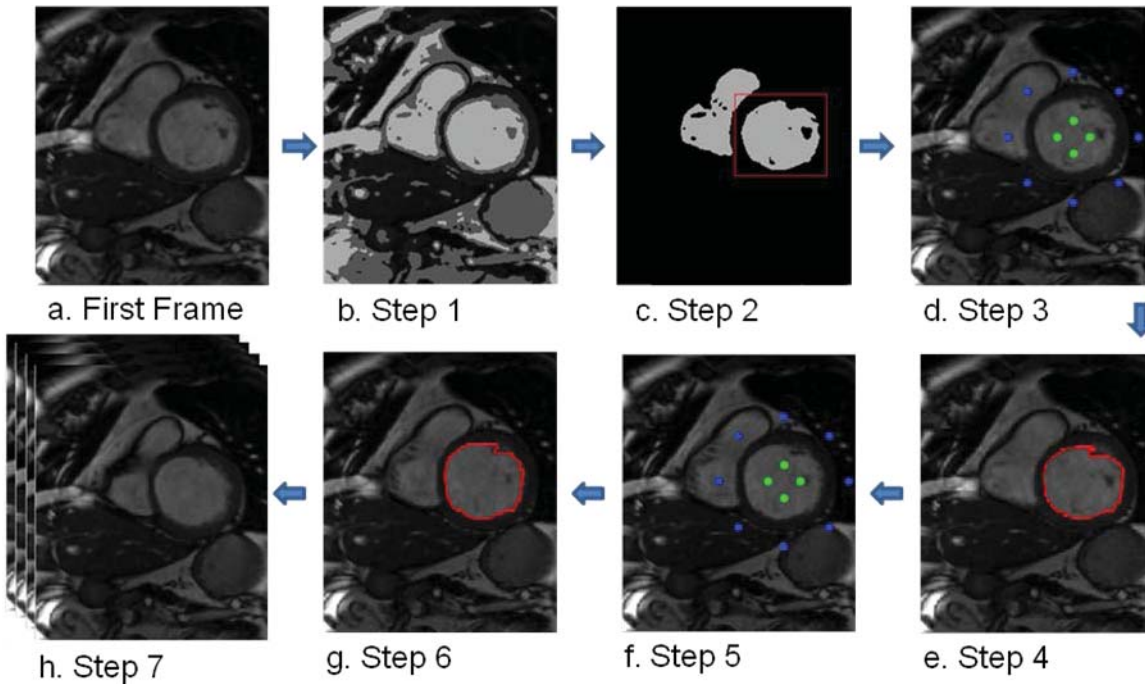
Where  $x_s$  ( $0 < s \leq K$ ) represents a vector of probabilities for each node to reach to the seeds with label  $s$ . Please refer to (Grady, 2006) for the definition of  $L_U$ ,  $B^T$  and  $m^s$ .

- 5) Assign to each node the label according to the maximum probability  $\max_s(x_i^s)$ , and the final segmentation can be obtained.

The detailed discussion of RW algorithm for image segmentation can be found in (Grady, 2004 & 2006). It is noted that the seeds selection is the key step for RW implementation. Segmentation result is extremely sensitive to the position of seeds, and any improper position of seeds will lead to the false results.

### 2.3 The proposed framework

This study aims to propose a fully automated framework for cardiac image segmentation with the auto initialization of the background and foreground seeds for RW algorithm. The FCM algorithm and heuristic method are used to locate the LV region in the first image frame of a short-axis slice, then the seeds are initialized based on the centre of the located LV region, after that, the RW algorithm is used to segment the first frame. In sequence, the centre of the segmented LV region of the current frame is then propagated to the adjacent frame to initialize the seeds and RW is used to segment the LV boundary in the frame.



**Fig.1 Illustration of the proposed framework for segmentation of a sequence of CMR images, refer to the main text for the details.**

The proposed framework for the LV segmentation on a sequence of frames can be summarized as follows,

- 1) Given the first frame in Fig.1-a, set cluster number  $c=3$ , using the FCM algorithm to partition the first frame into different regions with three intensity levels, low, middle and high, as shown in Fig.1-b.
- 2) Among the regions with high intensity level, choose two big regions whose centres have similar  $y$  coordinate, and identify LV as the right one (the left one is right ventricle (RV)), as shown in Fig.1-c. The LV region is indicated by red-colour rectangle.
- 3) Calculate the centre of LV region, and initialize foreground and background seeds for the first frame, as shown in Fig.1-d. The green-colour and blue-colour dots indicate the foreground and background seeds, respectively.
- 4) Segment the first frame by using RW algorithm with the initialized seeds from step 3, the segmented LV boundary is shown in Fig.1-e. The Segmented LV boundary is indicated by red-colour curve.
- 5) Calculate the centre of LV boundary, propagate it to the adjacent frame, and initialize foreground and background seeds for the adjacent frame, as shown in Fig.1-f. The green-colour and blue-colour dots indicate the foreground and background seeds, respectively.

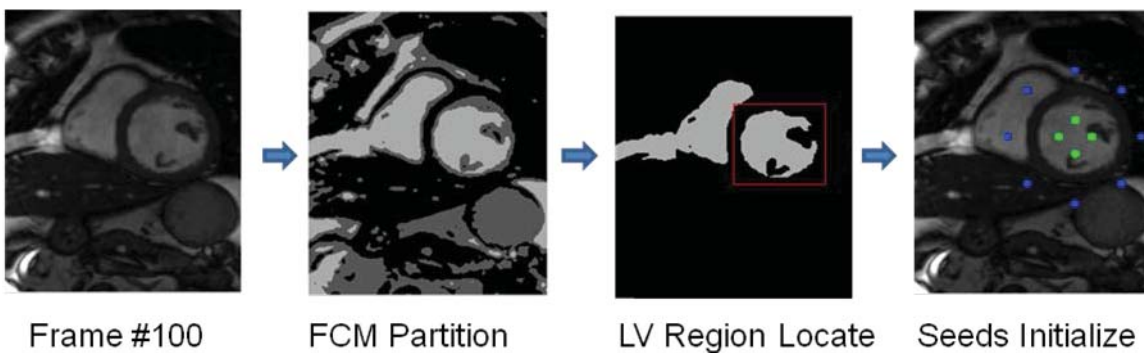
6) Segment the adjacent frame by using RW algorithm with the initialized seeds from step 5, the segmented LV boundary is shown in Fig.1-g. The Segmented LV boundary is indicated by red-colour curve.

7) Repeat steps 5 and 6 to segment the next adjacent frame until it is done on all the frames in the sequence, as shown in Fig.1-h.

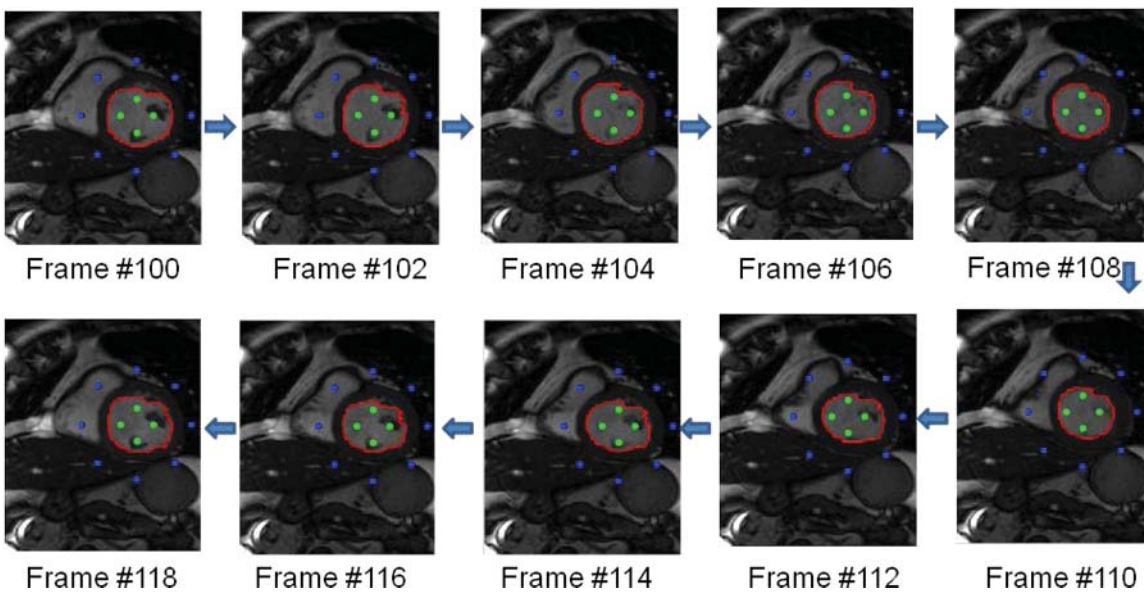
The location of LV region in the first frame in step 2 is based on the LV and RV intensity distributions and their overall relevant locations in the CMR images.

### 3. Experimentation

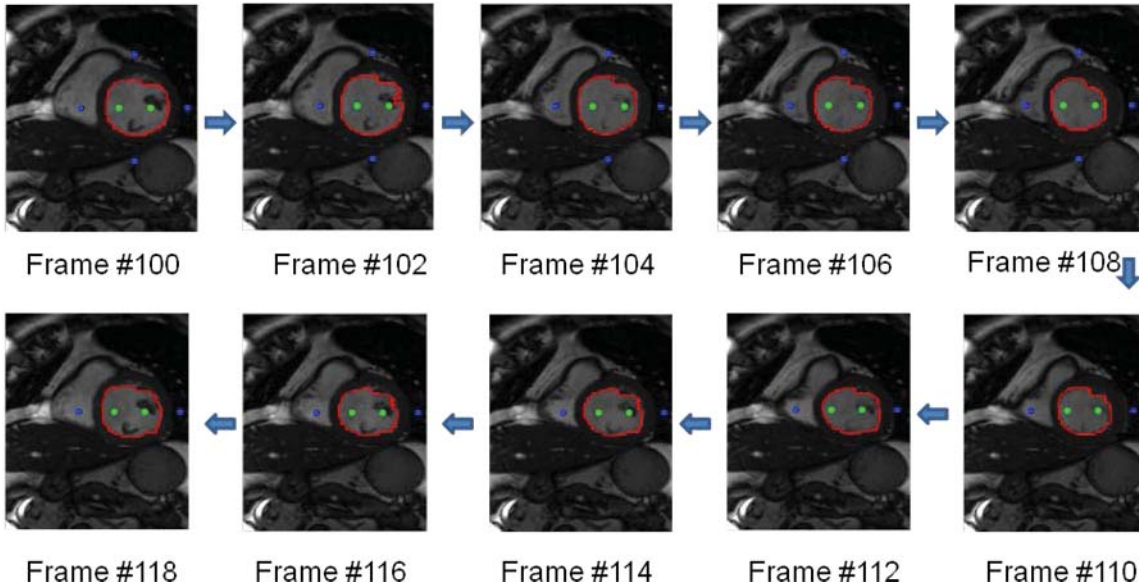
To evaluate the performance of the proposed framework on cardiac LV segmentation, we apply it to the real CMR images from RV challenge website (<http://www.litislabs.eu/rvsc>). In all examples, we fix the cluster number  $c=3$  for FCM clustering algorithm and the weighting parameter  $\beta=90$  for RW segmentation algorithm. The software used in this study is modified based on the MATLAB source code from L. Grady's homepage ([www.cns.bu.edu/~lgrady](http://www.cns.bu.edu/~lgrady)). In all examples, the green dots indicate the foreground seeds, blue dots indicate the background seeds, and red curves indicate the segmented LV boundaries.



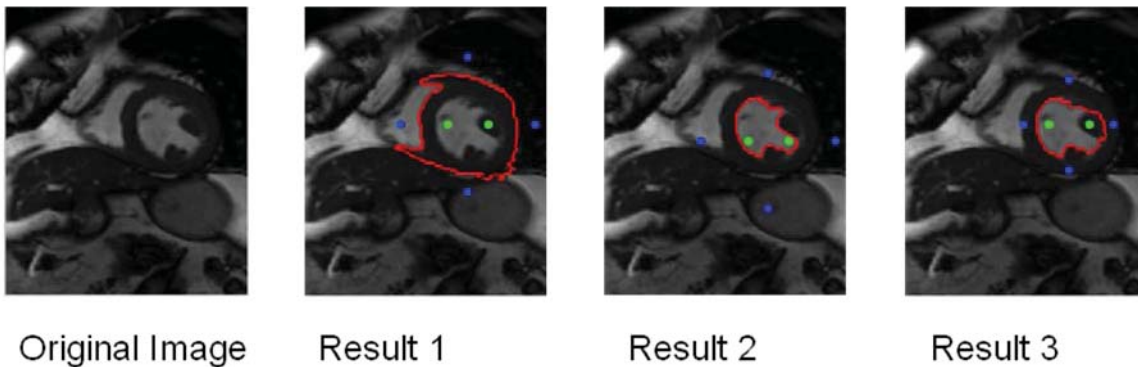
**Fig.2 The seeds initialization for the first frame, i.e., frame #100.**



**Fig.3 The segmentation results of the proposed framework on the frames #100 to #109 (only show the frames with even number). Here the number of background seeds and foreground seeds are 8 and 4, respectively.**



**Fig.4** The segmentation results of the proposed framework on the frames #100 to #109 (only show the frames with even number). First row, the number of background seeds and foreground seeds are reduced to 4 and 2, respectively. Second row, the number of background seeds and foreground seeds are reduced to 2 and 2, respectively.



**Fig.5** The segmentation results of different seed locations on the same original image. Note the locations of the background and foreground seeds are changed, which affect the segmentation results.

The image size is 256x216, 20 images per cardiac cycle. The testing is performed on the patient #1, frame #100 to frame #119 (one cardiac cycle). We select frame #100 as the first frame, and locate the LV region by using FCM and heuristic method, as shown in Fig.2. The segmented result of the first frame is then propagated to initialize the seeds and segment all the frames in the sequence, as shown in Fig.3. It can be observed from the figure that the segmented LV boundaries are quite reasonable even though papillary muscles are adjacent to or fall inside the LV region in some frames. We need to highlight that whole segmentation procedure is fully automatic processed, which is desirable for practical clinic applications. It is noted that the segmentation results are not sensitive to the number of the seeds, if we reduce the number of background and foreground seeds from 8 and 4 to 4 and 2, or even 2 and 2, respectively, the segmentation results are quite similar, as shown in Fig.4. However, the locations of the background and foreground seeds may affect the segmentation results, as shown in Fig.5, the segmentation may fail if the seeds are not properly located.

#### 4. Conclusion

Accurate and robust extraction of the LV cavity is the key step for analyzing heart functions quantitatively. In this study, we propose a framework for fully automated segmentation of the LV boundary in CMR images in terms of fuzzy clustering and graph segmentation techniques. The effectiveness of the proposed framework has been verified by the experimental results of LV segmentation on real CMR images. This study focuses on LV endocardial delineation only, to extend the proposed framework for LV epicardial delineation is one of the future research topics.

#### References

- Petitjean, C. and Dacher, J.N. (2011), A review of segmentation methods in short axis cardiac MR images, *Medical Image Analysis*, 15, pp. 169-184.
- Kang, D., Woo, J., Slomka, P.J., Dey, D., Germano, G. and Jay-Kuo, C. (2012), Heart chambers and whole heart segmentation techniques: review, *SPIE Journal of Electronic Imaging*, 21, pp. 131-139.
- Weng, J., Singh, A., and Chiu, M. (1997). Learning-based ventricle detection from cardiac MR and CT images. *IEEE Trans. on Medical Imaging*, 16, pp. 378–391.
- Jolly, M.-P. (2006), Automatic segmentation of the left ventricle in cardiac MR and CT images. *International Journal of Computer Vision*, 70, pp. 151–163.
- Lorenzo-Valdés, M., Sanchez-Ortiz, G., Elkington, A., Mohiaddin, R., and Rueckert, D. (2004). Segmentation of 4D cardiac MR images using a probabilistic atlas and the EM algorithm. *Medical Image Analysis*. 8, pp. 255–265.
- Kedenburg, G., Cocosco, C., Kothe, U., Niessen, W., Vonken, E., and Viergever, M. (2006). Automatic cardiac MRI myocardium segmentation using graphcut. *Proceedings of SPIE, Medical Imaging*, 6144.
- Boykov, Y. and Jolly, M. P. (2000), Interactive Organ Segmentation Using Graph Cuts, in *Medical Image Computing and Computer-Assisted Intervention*, pp. 276-286.
- Grady, L. and Funka-Lea, G. (2004), Multi-Label Image Segmentation for Medical Applications Based on Graph-Theoretic Electrical Potentials, *ECCV04*, pp. 230-245.
- Grady, L. (2006), Random Walks for Image Segmentation, *IEEE Trans. on Pattern Analysis and Machine Intelligence*, 28, pp. 1-17.
- Eslami, A., Karamalis, A., Katouzian, A. and Navab, N. (2013), Segmentation by retrieval with guided random walks: application to left ventricle segmentation in MRI. *Medical Image Analysis*, 17, pp. 236–253.
- Dakua, S.P. and Sahambi, J.S. (2011), Modified active contour model and random walk approach for left ventricular cardiac MR image segmentation, *International Journal for Numerical Methods in Biomedical Engineering*, 27, pp.1350–1361.
- Bezdek, J.C. (1981), *Pattern Recognition with Fuzzy Objective Function Algorithms*, Plenum Press, New York.
- Macqueen, J.B. (1967), Some methods for classification and analysis of multivariate observations, *proceedings of 5<sup>th</sup> Berkeley Symposium on Mathematical Statistics and Probability*, pp. 281-297.



## Application of Digital Image Correlation for strain measurements of large masonry walls

A.H. Salmanpour<sup>1</sup> and \*N. Mojsilović<sup>1</sup>

<sup>1</sup>Institute of Structural Engineering, ETH Zurich, Switzerland.

\*Corresponding author: mojsilovic@ibk.baug.ethz.ch

### Abstract

Full-scale testing of large unreinforced masonry walls subjected to in-plane static-cyclic loading is underway at ETH Zurich. During testing the measurements included all applied forces together with an overall and a local picture of the deformation state of the specimens. In order to achieve this, in addition to the traditional hard-wired instruments, i.e. LVDTs, a 2D Digital Image Correlation (DIC) measurement system was used. DIC is a cutting-edge, non-contact, optical measurement technique that provides full-field displacements and strains by comparing the digital images of the test object's surface obtained before and after deformation. The present paper reports on the measurement procedure and discusses the results obtained and the applicability of DIC for strain measurements when testing large masonry walls at full-scale. A set of conclusions and recommendations for the practical application are also given.

**Keywords:** Full-scale testing, unreinforced masonry, digital image correlation, static-cyclic loading, strain measurement.

### Introduction

A research project on the deformation capacity of unreinforced masonry structures has been initiated at the Institute of Structural Engineering of ETH Zurich. The objective of the research project, which should be seen as the first step of an initiative to investigate the limits of the deformation capacity of structural masonry, is the development of the basic building blocks for the displacement-based design of masonry structures. Before our own experimental program started, a thorough survey and assessment of existing experimental and analytical research in the area of the deformation capacity of structural masonry was carried out (Salmanpour et al., 2012a,b). The experimental work is divided into two phases, i.e. the preliminary and main phases, and consists of a total of 11 cyclic-static tests on full-scale unreinforced masonry walls in order to investigate the effects of the various factors, i.e. unit type, vertical pre-compression level, aspect ratio, size effect and boundary conditions on the deformation capacity of structural masonry. A novel approach will be developed and utilized for the purpose of applying experimental evidence collected from our own tests for the development of reliable mechanical models for structural masonry. The abovementioned experimental data, i.e. full-field information on displacements, deformation and strains of the specimens has been acquired using the Digital Image Correlation (DIC) method.

From early in the 1950's until recent years, various non-contact optical methods, e.g. electronic speckle pattern interferometry, shearography, Moiré interferometry, holographic interferometry and digital image correlation have been developed to extract full-field shape, deformation and motion information. Amongst the abovementioned methods, DIC is the most widely used because of its low requirements on equipment, easy application, wide range of measurement resolution and, above all, high accuracy. In principle, DIC is optical metrology based on digital image processing and numerical computing. It directly provides full-field displacements and strains by comparing the digital images of the specimen surface obtained before and after deformation. The DIC measurement system was first developed by a group of researchers at the University of South Carolina in the 1980s when digital image processing and numerical computing were still in their

infancy (Bing et al., 2009). Although DIC has been widely accepted and used in the field of experimental mechanics, its application has been limited to rather small specimens. However, in recent applications also tests on larger specimens, e.g. concrete and masonry walls, and even in-situ tests on large-scale structures, e.g. bridges and towers, have been considered (Salmanpour et al., 2013 and McCormick and Lord, 2010). Such applications have been made possible by recent developments in computational technology and the availability of high-resolution digital cameras. Recently, tests on full-scale masonry shear walls were performed at ETH Zurich applying DIC to measure full-field displacements and strains. The present paper reports on the measurement procedure and discusses the results obtained and the applicability of DIC for strain measurements when testing large masonry shear walls at full-scale.

### Testing Program

In order to investigate the deformation capacity of structural masonry, a total of 11 static-cyclic tests were performed in two phases. Table 1 summarizes the details of the performed tests, where  $l_w$ ,  $h_w$  and  $t_w$  are the length, the height and the thickness of the specimens,  $\sigma_0$  is the pre-compression stress, and  $f_x$  is the mean compressive strength of the masonry (perpendicular to the bed joints). The first phase (preliminary phase) of the experimental program included tests P1 to P4, and the second phase (main phase) of the experiments included tests T1 to T7.

**Table 1. Test program**

Phase	Test	Units	Specimen Dimensions $l_w \times h_w \times t_w$ [mm]	Boundary Conditions	$\sigma_0/f_x$
Preliminary	P1	Clay	1500x1600x150	Fixed Ends	0.10
Preliminary	P2	Clay	1500x1600x150	Fixed Ends	0.15
Preliminary	P3	Calcium-Silicate	1550x1600x150	Fixed Ends	0.10
Preliminary	P4	Calcium-Silicate	1550x1600x150	Fixed Ends	0.15
Main	T1	Clay	2700x2600x150	Fixed Ends	0.10
Main	T2	Clay	2700x2600x150	Fixed Ends	0.05
Main	T3	Clay	2700x2600x150	Fixed Ends	0.15
Main	T4	Clay	900x2600x150	Fixed Ends	0.10
Main	T5	Clay	1800x2600x150	Fixed Ends	0.10
Main	T6	Clay	3600x2600x150	Fixed Ends	0.10
Main	T7	Clay	2700x2600x150	Cantilever	0.10

Figure 1 shows a picture of the test set-up. The specimens are built on 350 mm thick reinforced concrete foundations, which can be clamped to the strong floor by means of post-tensioned steel bars. The horizontal servo-hydraulic actuator reacting on the strong wall of the laboratory applies a shear force to the top of the walls through a stiff steel beam (loading beam). The loading beam is connected to the walls by a layer of mortar. The vertical load is applied by means of two servo-hydraulic actuators reacting on the reaction frame. A more detailed description of the testing procedure can be found in Salmanpour et al. (2013).



**Figure 1. Test set-up with tested wall T2**

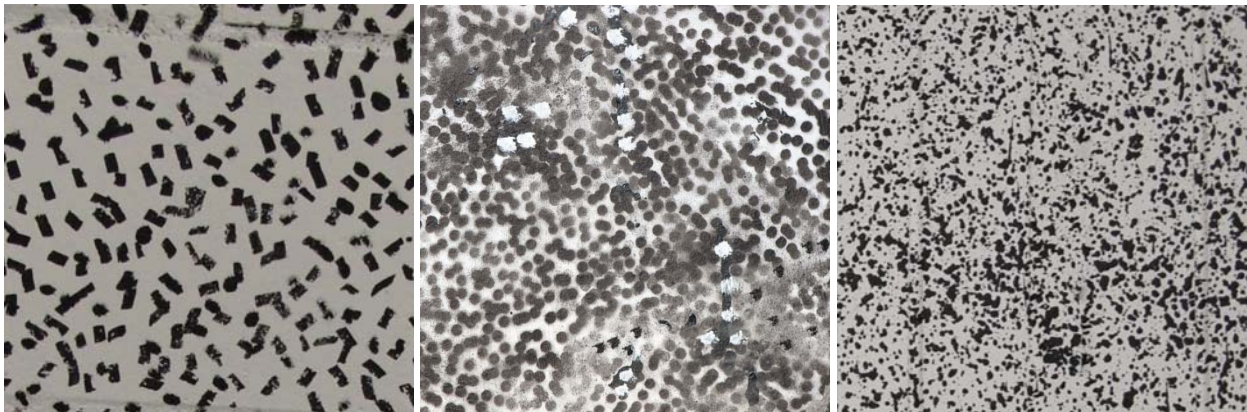
### **DIC instrumentation and measurement procedure**

During the tests, measurements included all applied forces together with an overall and a local picture of the deformation state of the specimens. In order to achieve this, in addition to the traditional hard-wired instruments, i.e. LVDTs, a two-dimensional DIC measurement system was used. DIC is a non-contact, optical measurement technique that provides full-field displacements and strains by comparing digital images of the test object's surface obtained before and after deformation. In general, the implementation of the 2D DIC method comprises the following three steps: (1) specimen preparation; (2) recording images of the specimen's surface before and after deformation; (3) processing the acquired images. This section reports and discusses issues on these three steps.

#### *Specimen preparation*

The digital image correlation technique relies on a contrasting speckle pattern on the surface of the test specimen. This pattern can be the natural texture of the surface or artificially made. The pattern quality has a dominant influence on the spatial resolution and accuracy of DIC results. In general, to achieve effective correlation, the pattern must be random, isotropic, i.e. must not exhibit a bias to one orientation, and highly contrasting, i.e. must show dark blacks and bright whites (Correlated Solutions, 2011). In addition to the above requirements, speckles should be neither too small nor too large. In DIC, a small subset of the image is tracked as the specimen moves and deforms. To perform the tracking, the subset is shifted until the pattern in the deformed image matches the pattern in the reference image as closely as possible; this match is calculated as the total difference in gray levels at each point. If the pattern is too large, we may find that certain subsets may be entirely on a black field or entirely on a white field. This does not allow us to make a good match. We can compensate for this by increasing the subset size, but at the cost of spatial resolution. Conversely, too small speckles can cause the aliasing effect resulting in images that often show a pronounced Moiré pattern in the measurement results (Correlated Solutions, 2011). As a rule, speckles should be 3-8 pixels in size to achieve effective correlation.

Applying the pattern is the most important and challenging step in the implementation of 2D DIC method. There are several techniques for applying different pattern sizes on the specimen surface, e.g. spraying paint, printing, lithography, using toner powder and stencils. For our own tests, the surface of the specimen was first coated with a white paint and then random black speckles were applied. Figure 2 shows the detail of the applied patterns on an area of 150×150 mm of the wall surface. Three different techniques were tried out for application of the speckles. In the first preliminary test (P3), the pattern was obtained by means of a marker pen, see Figure 2. A pattern of adequate density could not be obtained using this method. Although the compensation of the low-density pattern was made possible, it came at the cost of spatial resolution. Hence, for the other preliminary tests, the pattern was applied using a stencil with randomly distributed openings produced using a laser printer. The stencil was made of acrylic glass and had the dimensions 900×600 mm. The latter method appeared better and was less labor intensive. However, the material used for stencil degraded continuously during the pattern application and the stencil had to be re-printed. For the main tests, in order to increase the spatial resolution of DIC results, smaller speckles were created using a paint gun. Speckles of the right size could be achieved by adjusting the air pressure, paint flow and also paint viscosity. However, this technique was found to be prone to some too small speckles which can sometimes cause aliasing.



**Figure 2. Random pattern applied using: marker pen (left), stencil (middle) and paint gun (right)**

#### *Recording images of the specimen's surface*

Two different conventional DSLR cameras were used during the testing. For the preliminary tests (P1 to P4), a Nikon D3 camera that utilizes a full-frame size CMOS sensor of 12.1 MP was used. The camera was positioned at a distance of 5 m from the specimen and recorded the specimen surface area with a spatial resolution of 0.68 mm. For the main tests, T1 to T7, a somewhat better camera, namely the Nikon D800E, was engaged. This camera includes a 36.3 MP full-frame size CMOS sensor. While almost all digital cameras employ an optical low-pass filter over their sensors, this filter has been removed in the Nikon D800E. Removing the effect of the low-pass filter should, theoretically, result in higher resolution and sharpness but at the expense of being more prone to the Moiré patterning. The camera was located at a distance of 6 m from the specimen and recorded the specimen surface area with a spatial resolution of 0.58 mm. Since accurate 2D DIC depends on the specimen being planar and parallel to the camera sensor, special attention was given to the alignment of the cameras. A professional flash lightning set, i.e. Elinchrom Style RX 1200 (see Figure 1), was used to ensure that the specimen surface was brightly and also evenly illuminated to maintain the maximum range possible.

Before applying the load, the reference image was taken and later compared to the subsequently taken images of the deformed states of the specimen. A custom-made device interacting with the DAQ system triggered the camera at pre-specified vertical forces (while applying the pre-compression force) and horizontal displacements (while applying the cyclic displacement). On average, about 500 images per test were taken.

### *Processing the acquired images*

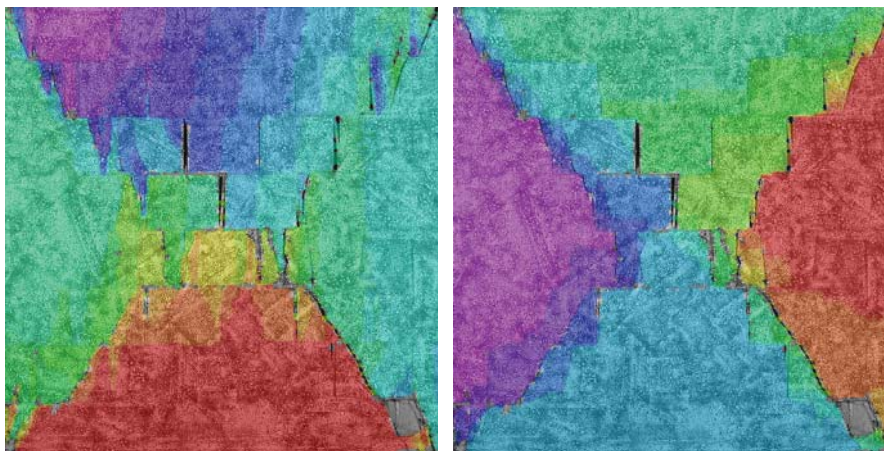
The recorded digital images were first corrected to remove the lens distortion influence and then processed using licensed Vic2D commercial code to obtain full-field displacements and strains. The normalized squared differences criterion was chosen as the correlation criterion and to achieve sub-pixel accuracy, the optimized 8-tap splines were used for gray value interpolation. The size of the subsets was determined based on minimization of the confidence interval. For the description of the principles and concepts of DIC, see Bing et al. (2009) and Sutton et al. (2009). It is worth mentioning that currently, in addition to commercial codes, several free university codes are also available for the application of DIC, see Table 2.

**Table 2. Commercial and free university DIC codes**

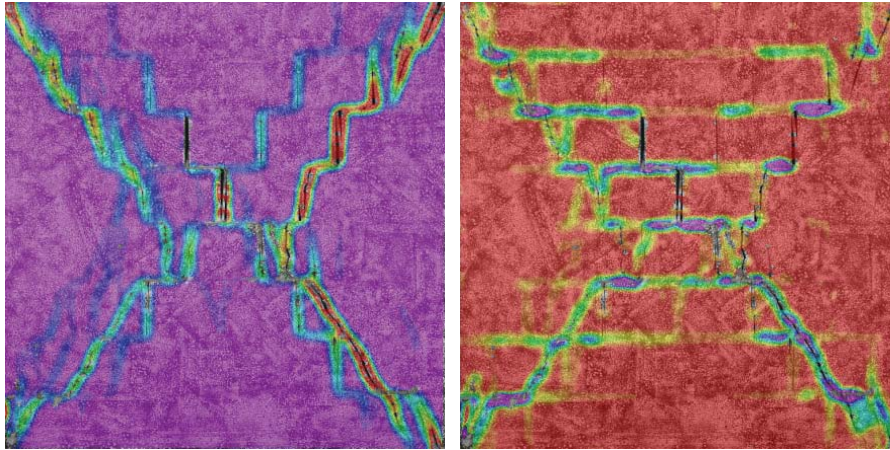
Commercial Codes		Free University Codes	
Code	Company	Code	University
Vic2D and Vic3D	Correlated Solutions	MatchID	Catholic University College Ghent, KULeuven
StrainMaster	LaVision Inc.	Opticist	The Catholic University of America
ISTRA 4D	Dantec Dynamics	Matlab Code	Karlsruhe Institute of Technology
ARAMIS	GOM Gbmh		(KIT) and Johns Hopkins University

### **DIC measurement results**

Using analyzed data the deformation of the specimen during static-cyclic loading can be tracked in detail. Figures 3 and 4 show the displacement and principal strain fields in specimen P4 just before the collapse of the specimen.

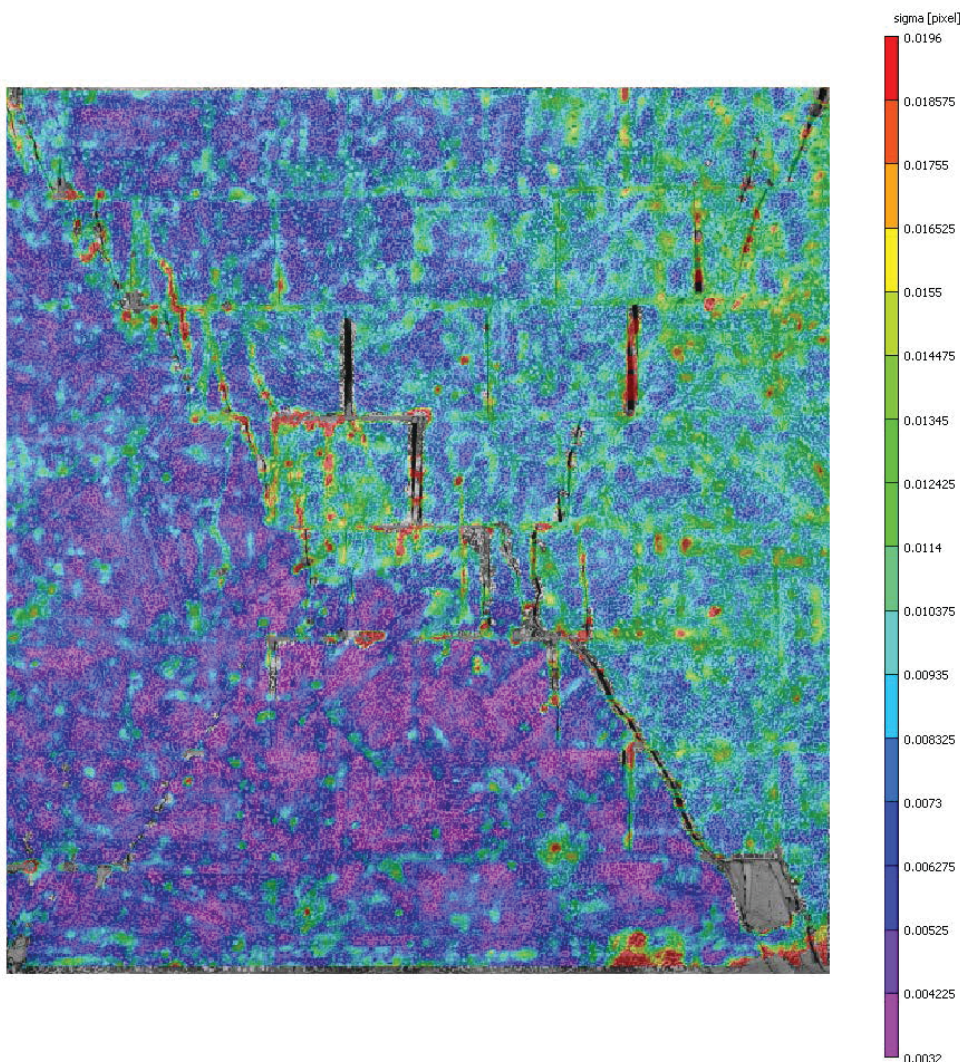


**Figure 3. Vertical (left) and longitudinal (right) displacement fields in wall P4**



**Figure 4. Major (left) and minor (right) principal strain fields in wall P4**

Accuracy of DIC measurement is a controversial issue because it is very difficult, if not impossible, to exactly determine the measurement errors. The accuracy of DIC measurement is influenced by several factors. Table 3 presents a short list of error sources of 2D DIC measurement (Bing et al., 2009).



**Figure 5. Confidence interval, in pixels, in wall P4**

**Table 3. Error sources of 2D DIC (Bing et al., 2009)**

Errors related to specimen, loading and imaging	Speckle pattern Non-parallelism between sensor and the object surface Out-of-plane displacement Imaging distortion Noise during image acquisition and digitization
Errors related to the correlation algorithm	Subset size Correlation function Sub-pixel algorithm Shape function Interpolation scheme

However, as shown by several studies, a displacement accuracy of 0.01 pixel can be achieved with typical setups. Hence, the displacement accuracies of 0.0068 and 0.0058 mm are expected in the preliminary and main tests. Figure 5 shows the confidence interval (in pixels) for specimen P4 just before the collapse of the specimen. The confidence interval is calculated using the covariance matrix of the correlation equation. Although it does not reflect bias, e.g. aliasing, it is an accurate noise estimate and can be used to estimate the accuracy of the measurements. A statistical analysis of the confidence interval values for specimen P4 showed that the spatial mean value of the confidence interval was 0.0082 pixel (just before the collapse of the specimen), which somehow confirms the expected displacement accuracy of 0.01 pixel.

## Conclusions

A successful implementation of the 2D DIC measurement technique using conventional DSLR cameras for cyclic-static tests on full-scale large masonry shear walls was reported. The obtained results proved that 2D DIC may be considered to be an effective technique to measure full-field displacements and strains with high level of accuracy and spatial resolution even in the case of large specimens and complicated deformation fields. Furthermore, using low-cost conventional DSLR cameras (compared to special industrial cameras) make this technique affordable in most of structural engineering laboratories.

## References

- Correlated Solutions (2009), Vic-2D Testing Guide, available at <http://correlatedsolutions.com>.
- McCormick, N. J. and Lord J. D. (2010), Practical in-situ applications of DIC for large structures, *Applied Mechanics and Materials*, 24-25, pp. 161-166.
- Pan, B., Qian, K., Xie, H. and Asundi A. (2009), Two-dimensional digital image correlation for in-plane displacement and strain measurement: a review, *Measurement Science and Technology*, 20 062001.
- Salmanpour, A. H., Mojsilović, N. and Schwartz, J. (2012a), Deformation Capacity of Structural Masonry: A Review of Experimental Research, *Proceedings, 15th International Brick/Block Masonry Conference, Florianopolis, June 3-6, 2012, CD-ROM, Paper No. 4C2*.
- Salmanpour, A. H., Mojsilović, N. and Schwartz, J. (2012b), Deformation Capacity of Structural Masonry: A Review of Theoretical Research, *Proceedings, 15th World Conference on Earthquake Engineering, Lisbon, September 24-28, 2012, Paper No. WCEE2012-2145*.
- Salmanpour, A. H., Mojsilović, N. and Schwartz, J. (2013), Experimental Study of the Deformation Capacity of Structural Masonry, *Proceedings, 12th Canadian Masonry Symposium, Vancouver, British Columbia, June 2-5, 2013, Paper No. 161*.
- Sutton, M. A., Orteu, J. J. and Schreier, H. W. (2009), *Image Correlation for Shape, Motion and Deformation Measurements Basic Concepts, Theory and Applications*, Springer.

## Discrete crack modeling of RC structure using hybrid-type penalty method

\*Y. Fujiwara<sup>1</sup>, N. Takeuchi<sup>1</sup>, T. Shiomi<sup>2</sup>, and A. Kambayashi<sup>3</sup>

<sup>1</sup>Graduate School of Engineering and Design, Hosei University, 2-33 Ichigaya Tamachi, Shinjuku, Tokyo, Japan.

<sup>2</sup>Mind Inc., 7-17-19 Maebara-nishi Funabashi Chiba, Japan.

<sup>3</sup> Research & Development Institute, Takenaka Corporation, 1-5-1 Ohtsuka, Inzai, Chiba, Japan.

\*Corresponding author: fujiwara.yoshihiro@3d-lab.jp

### Abstract

The hybrid-type penalty method (HPM) is suitable for representing failure phenomena that occur during the transition from continua to discontinua in materials such as concrete. The initiation and propagation of dominant cracks and the branching of cracks can easily be modeled as discrete cracks. The HPM represents a discrete crack by eliminating the penalty that represents the separation of elements at the intersection boundary. This treatment is easy because no change is required in the degrees of freedom for the discrete crack. In addition, it is important to correctly evaluate the deformation of continua before crack formation is initiated. To achieve this, we implemented a constitutive model of reinforced concrete for the HPM. In this paper, we present the implemented constitutive model and describe the simulation of a deep beam test using the HPM to demonstrate its capability for evaluating progressive failure.

**Keywords:** Hybrid-type penalty method, Discrete crack, Reinforced concrete

### Introduction

Recent large earthquakes caused significant damage to concrete structures. Therefore, understanding the failure mechanism of concrete structures is important. A dominant crack is initiated in a concrete structure because of tensile stress. The crack subsequently grows, propagates, and branches until the structure finally collapses. To predict the progressive failure of a concrete structure, accurate computation of a discrete crack is essential. Computer simulations can predict the crack growth, propagation, and branching that lead to failure of the concrete structure.

The rigid body spring model (RBSM) developed by Kawai (1977) is a good method for modeling a discrete crack. The advantage of this method lies in its simplicity; there is no need to track the crack path. Initially, the model obtained good results when solving the problem of the strong nonlinearity of steel. It was then applied to discrete limit analysis of soils and concrete structures (Takeuchi et al., 2005). Unfortunately, the elastic deformation in continua obtained by the RBSM is not accurate because it models a continuum that connects the spring elements between the edges of rigid bodies. However, the RBSM is still used to model the realistic behavior of concrete structures, which includes cracking and failure (Gedik et al., 2011).

The hybrid-type penalty method (HPM) developed by Takeuchi et al. (2009) refined the RBSM method for calculating the elastic deformations of elements using the finite element method; a Lagrange multiplier was also introduced to satisfy the subsidiary condition of continuous displacement in the hybrid-type virtual work formulation. The HPM is suitable for analyzing the progressive failure of concrete structures; this method offers the following features:

- Accurate deformation can be calculated before crack initiation because an elastic element (called a subdomain in the HPM) is used. Even after crack initiation, accurately calculating the deformation within the elastic area between cracks is important.
- The HPM models a discrete crack by eliminating the penalty caused by separation of the elements at the intersection boundary. This treatment is easy because no change is required in the degrees of freedom for a discrete crack.
- The concentrated stress at the crack tip can be calculated without the use of the J-integral, which was originally developed by Rice (1968). The HPM can easily and accurately obtain



concentrated stresses around the crack by directly using the correct relationship between the tensile stress and displacement of the crack mouth opening. It can calculate not only the growth of the existing cracks but also the formation of new cracks.

We simulated an anchor bolt pullout test in plain concrete, and the results matched well with the experimental results (Fujiwara *et al.*, 2012). As a next step, we implemented a constitutive model of a reinforcing bar in the HPM to allow for computation of the progressive failure phenomena of a reinforced concrete structure.

In the present paper, we introduce the basic formulation of the HPM and describe an implemented constitutive model of reinforced concrete. We validated the accuracy of the constitutive model by simulating a deep beam test.

## Theory of HPM

### Governing Equation

The basic equations of the elastic problem are as follows:

$$\operatorname{div} \boldsymbol{\sigma} + \mathbf{f} = 0 \quad \text{in } \Omega, \quad (1)$$

$$\boldsymbol{\sigma} = \mathbf{D} : \boldsymbol{\varepsilon}, \quad (2)$$

$$\boldsymbol{\varepsilon} = \nabla^s \mathbf{u} \stackrel{\text{def.}}{=} \frac{1}{2} [\nabla \mathbf{u} + (\nabla \mathbf{u})^t], \quad (3)$$

where  $\boldsymbol{\sigma}$  is the Cauchy stress tensor;  $\mathbf{f}$  is the body force per unit volume;  $\boldsymbol{\varepsilon}$  is the infinitesimal strain tensor;  $\mathbf{D}$  is the constitutive tensor;  $\nabla := (\partial/\partial x_i) \mathbf{e}_i$  is the differential operator;  $\nabla^s$  is the symmetric part of  $\nabla$ ; and  $\mathbf{u}$  is the displacement field in  $\mathbf{x} \in \Omega$ , where  $\Omega$  is the reference configuration of the continuum body with a smooth boundary  $\Gamma = \Gamma_u \cup \Gamma_\sigma$ . Here,  $\Gamma_u := \partial_u \Omega \subset \partial \Omega$  is the geometric boundary, and  $\Gamma_\sigma := \partial_\sigma \Omega \subset \partial \Omega$  is the stress boundary. At the boundaries, the following conditions are satisfied:

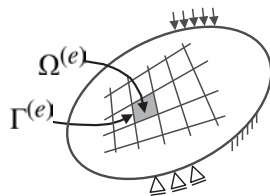
$$\mathbf{u}|_{\Gamma_u} = \hat{\mathbf{u}} \quad (\text{given}), \quad (4)$$

$$\boldsymbol{\sigma}|_{\Gamma_\sigma} \mathbf{n} = \hat{\mathbf{t}} \quad (\text{given}), \quad (5)$$

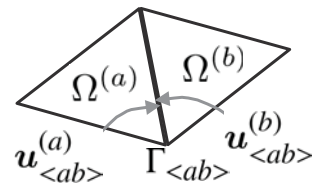
where  $\mathbf{t}$  is the traction and  $\mathbf{n}$  is the field normal to the boundary  $\Gamma_\sigma$ .

Let  $\Omega$  consist of  $M$  subdomains  $\Omega^{(e)} \subset \Omega$  with the closed boundary  $\Gamma^{(e)} := \partial \Omega^{(e)}$ , as shown in Fig. 1, that is,

$$\Omega = \bigcup_{e=1}^M \Omega^{(e)} \quad \text{where } \Omega^{(r)} \cap \Omega^{(q)} = \emptyset \quad (r \neq q). \quad (6)$$



**Figure 1.** Subdomain  $\Omega^{(e)}$  and its common boundary  $\Gamma^{(e)}$



**Figure 2.** Boundary  $\Gamma_{\langle ab \rangle}$  between subdomains  $\Omega^{(a)}$  and  $\Omega^{(b)}$

We denote  $\Gamma_{\langle ab \rangle}$  as the common boundary between two subdomains  $\Omega^{(a)}$  and  $\Omega^{(b)}$ , which are adjoined, as shown in Fig. 2;  $\Gamma_{\langle ab \rangle}$  is defined as follows:

$$\Gamma_{\langle ab \rangle} \stackrel{\text{def.}}{=} \Gamma^{(a)} \cap \Gamma^{(b)}. \quad (7)$$

The relation for the displacement of  $\Gamma_{\langle ab \rangle}$ , which is the intersection boundary between  $\Omega^{(a)}$  and  $\Omega^{(b)}$ , is as follows:

$$\mathbf{u}_{\langle ab \rangle}^{(a)} = \mathbf{u}_{\langle ab \rangle}^{(b)} \quad \text{on } \Gamma_{\langle ab \rangle}. \quad (8)$$

Equation (8) introduces a subsidiary condition into the framework of the virtual work equation with the Lagrange multiplier  $\lambda$  as follows:

$$H_{ab} \stackrel{\text{def.}}{=} \delta \int_{\Gamma_{\langle ab \rangle}} \lambda \cdot (\mathbf{u}_{\langle ab \rangle}^{(a)} - \mathbf{u}_{\langle ab \rangle}^{(b)}) dS, \quad (9)$$

where  $\delta(\bullet)$  represents the variation in  $(\bullet)$ . From Eqs. (1) and (9), the following hybrid-type virtual work equation is obtained (Mihara and Takeuchi, 2008):

$$\begin{aligned} & \sum_{e=1}^M \left( \int_{\Omega^{(e)}} \boldsymbol{\sigma} : \text{grad}(\delta \mathbf{u}) dV - \int_{\Omega^{(e)}} \mathbf{f} \cdot \delta \mathbf{u} dV \right) \\ & - \sum_{s=1}^N \left( \delta \int_{\Gamma_{\langle s \rangle}} \lambda \cdot (\mathbf{u}_{\langle s \rangle}^{(s_a)} - \mathbf{u}_{\langle s \rangle}^{(s_b)}) dS \right) - \int_{\Gamma_{\sigma}} \hat{\mathbf{t}} \cdot \delta \mathbf{u} dS = 0 \quad \forall \delta \mathbf{u}. \end{aligned} \quad (10)$$

Here,  $N$  represents the number of common boundaries of the subdomain, and  $\delta \mathbf{u}$  represents the virtual displacement. The superscripts  $(s_a)$  and  $(s_b)$  represent the subdomains  $\Omega^{(s_a)}$  and  $\Omega^{(s_b)}$ , respectively, related to the common boundary  $\Gamma_{\langle s \rangle}$ .

The physical interpretation of the Lagrange multiplier  $\lambda$  is that of a surface force at the boundary  $\Gamma_{\langle s \rangle}$ . In this paper, the Lagrange multiplier  $\lambda_{\langle ab \rangle}$  on the boundary  $\Gamma_{\langle ab \rangle}$  is defined as follows:

$$\lambda_{\langle ab \rangle} = \mathbf{k} \cdot \boldsymbol{\delta}_{\langle ab \rangle}. \quad (11)$$

Here,  $\boldsymbol{\delta}_{\langle ab \rangle}$  represents the relative displacement on the boundary  $\Gamma_{\langle ab \rangle}$ , and  $\mathbf{k}$  is the penalty function.

#### Discretized Equation in Matrix Form

The independent linear displacement field  $\mathbf{u}^{(e)}$  in each subdomain  $\Omega^{(e)}$  is assumed to be as follows:

$$\mathbf{u}^{(e)} = \mathbf{N}_d^{(e)} \mathbf{d}^{(e)} + \mathbf{N}_{\varepsilon}^{(e)} \boldsymbol{\varepsilon}^{(e)}. \quad (12)$$

Here,  $\mathbf{d}^{(e)}$  is the rigid displacement and rigid rotation at point  $\mathbf{x}^p = (x_p, y_p) \in \Omega^{(e)}$ , and  $\boldsymbol{\varepsilon}^{(e)}$  is a constant strain in the subdomain  $\Omega^{(e)}$ .

In the case of a two-dimensional problem, the coefficients in Eq. (12) are as follows:

$$\mathbf{d}^{(e)} = [u^p, v^p, \theta^p]^t, \quad \boldsymbol{\varepsilon}^{(e)} = [\varepsilon_x, \varepsilon_y, \gamma_{xy}]^t, \quad (13)$$

$$\mathbf{N}_d^{(e)} = \begin{bmatrix} 1 & 0 & -(y - y_p) \\ 0 & 1 & (x - x_p) \end{bmatrix}, \quad (14)$$

$$\mathbf{N}_{\varepsilon}^{(e)} = \begin{bmatrix} x - x_p & 0 & (y - y_p)/2 \\ 0 & y - y_p & (x - x_p)/2 \end{bmatrix}. \quad (15)$$

Here,  $u^p$  and  $v^p$  represent rigid displacements at point  $\mathbf{x}^p$  in a subdomain;  $\theta^p$  represents rigid rotation; and  $\varepsilon_x$ ,  $\varepsilon_y$ , and  $\gamma_{xy}$  represent the constant strains in the subdomain.

We obtain the following discretized equation:

$$\mathbf{K} \mathbf{U} = \mathbf{P}, \quad (16)$$

where

$$\mathbf{K} = \sum_{e=1}^M \mathbf{K}^{(e)} + \sum_{s=1}^N \mathbf{K}_{\langle s \rangle}, \quad \mathbf{P} = \sum_{e=1}^M \mathbf{P}^{(e)}. \quad (17)$$

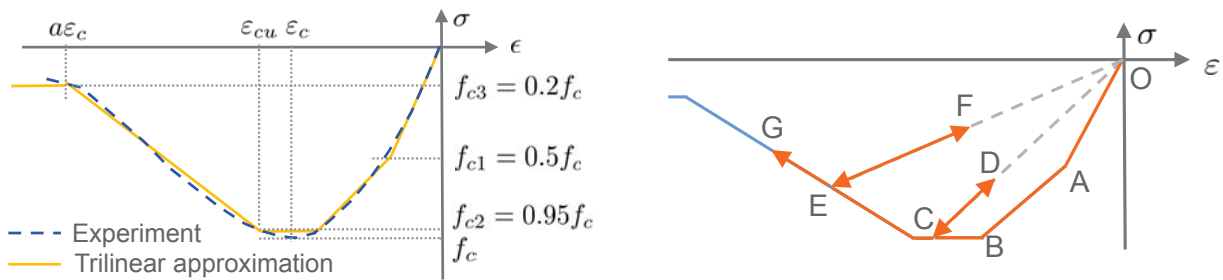
The discretized equation of the HPM is thus transformed into the simultaneous linear equation of Eq. (16) (Mihara and Takeuchi, 2008). The coefficient matrix of  $\mathbf{K}$  on the left-hand side can be obtained to assemble each stiffness matrix of the subdomain  $\mathbf{K}^{(e)}$  and the subsidiary condition on the boundary  $\mathbf{K}_{\langle s \rangle}$ . Discontinuous phenomena such as opening can be expressed without changing the degrees of freedom by setting the right-hand side of Eq. (11) to zero.

**Implementation of Constitutive Model of Reinforced Concrete**

*Constitutive Law for Compressive Stress of Concrete Material*

A typical compressive stress–strain relationship for concrete is shown by the dashed line in Fig. 3. The stiffness gradually degrades with increasing stress up to the compressive strength  $f_c$ . After the stress exceeds  $f_c$ , softening occurs. The solid line in Fig. 3 represents a trilinear approximation for the skeleton curve, which was also adopted in the RBSM by Takeuchi *et al.* (2005).

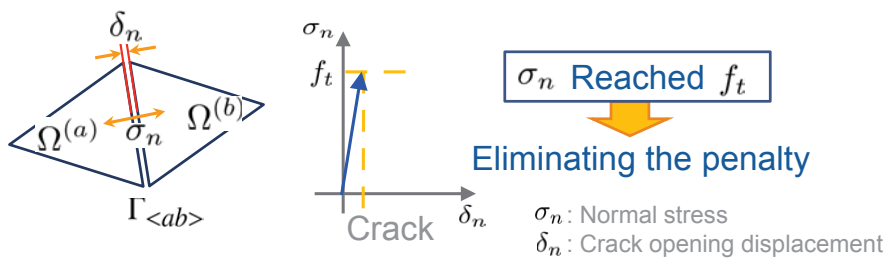
An origin-oriented model was adopted for the unloading path, as shown in Fig. 4.



**Figure 3. Skeleton curve of compressive stress** **Figure 4. Hysteresis rule in compressive stress**

*Constitutive Law for Tensile Stress of Concrete Material*

The HPM can separate two subdomains by simply eliminating the penalty. This feature is suitable for representing a discrete crack in concrete. When the surface force  $\sigma_n$  at boundary  $\Gamma_{\langle ab \rangle}$  reaches tensile failure strength  $f_t$ , the penalty can then be eliminated, and the discrete crack can be computed as shown in Fig. 5.

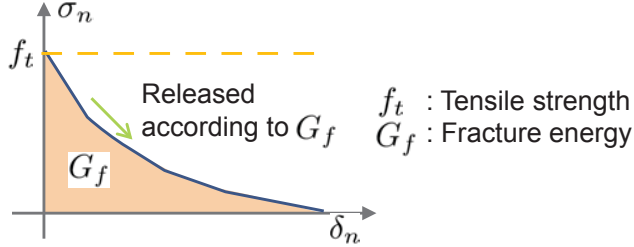


**Figure 5. Surface force and tensile strength**

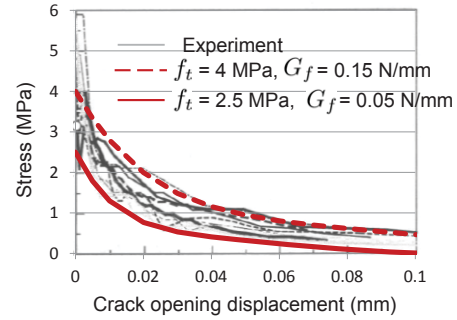
The stress in the concrete gradually decreases as the crack opening displacement increases once the tensile failure is exceeded. This behavior is called tension softening. Hilerborg *et al.* (1976) introduced the fracture energy for this tension softening behavior in a fictitious (or cohesive) crack model. The fracture energy  $G_f$  is the area enclosed by the tension softening curve, and it has a unique value that represents the strength of a concrete material with tensile strength  $f_t$ . In the HPM, the tension softening curve is defined as the relation between the normal stress  $\sigma_n$  and the crack opening displacement  $\delta_n$ , as shown in Fig. 6.

Many institutes and universities have conducted numerous tests in an effort to obtain the tension softening curve and fracture energy  $G_f$ . In a Technical Committee Report, published by the Japan Concrete Institute (JCI) (2001), on a test method for the fracture property of concrete, several

institutes and universities reported the round-robin results of a three-point bending test on a notched beam. The thin lines in Fig. 7 indicate the results of these tests. For the HPM, we applied a tension-softening curve that corresponds to these test results.



**Figure 6. Tension-softening curve for concrete**



**Figure 7. Test results of tension-softening curve (after JCI 2001)**

Nakamura *et al.* (1999) compared many empirical derivations of the tension-softening curve and determined that the empirical expression given by Hordijk *et al.* (1986) (Eq. (18)) matched well with past experiments; they used the following expression as a standard for comparison:

$$\frac{\sigma}{f_t} = \left(1 + 27 \left(\frac{w}{w_c}\right)^3\right) \exp\left(-6.93 \frac{w}{w_c}\right) - 28 \frac{w}{w_c} \exp(-6.93), \quad (18)$$

where  $w$  is the crack opening displacement (mm), and  $w_c$  is the limit virtual crack opening displacement (mm) when the tensile stress is zero; this is given by

$$w_c = 5.14 G_f / f_t, \quad (19)$$

where  $f_t$  is the tensile strength (MPa) and  $G_f$  is the fracture energy (N/mm).

Equation (18) was adopted to obtain the tension-softening curve in the present study because it corresponded better to the test results than the other proposed empirical expressions.

The thick lines in Fig. 7 are examples of tension-softening curves obtained from Eq. (18). The thick dashed line represents the curve for tensile strength  $f_t = 4.0$  MPa and fracture energy  $G_f = 0.15$  N/mm, and the thick solid line corresponds to  $f_t = 2.5$  MPa and  $G_f = 0.05$  N/mm. Almost all test results fell in the region between these two curves. Therefore, we can conclude that Eq. (18) can represent various materials in concrete.

The origin-oriented model was used for the unloading paths of tensile and compressive stresses.

Thus, stresses and displacements that occur after crack initiation can be calculated accurately because the fracture energy is determined directly.

#### *Constitutive Law for Reinforcing Bar*

The reinforcing bar was implemented using layered elements. Fig. 8 shows a schematic image of the layered element for reinforced concrete. The element consists of a concrete layer and arbitrary reinforced bar layers. The layer of a reinforced bar was modeled using a spring element identical to that used in the RBSM. The stiffness matrix for the penalty at the intersection boundary  $\Gamma_{\langle ab \rangle}$  is obtained as follows:

$$\mathbf{k}_{\langle ab \rangle} = p \mathbf{k}_{c\langle ab \rangle} + \sum_{i=1}^n \mathbf{k}_{si\langle ab \rangle}, \quad (20)$$

where  $P$  is the penalty value,  $\mathbf{k}_{c\langle ab \rangle}$  is the stiffness matrix of the concrete material,  $\mathbf{k}_{si\langle ab \rangle}$  is the stiffness matrix of the  $i$ -th layer of the reinforced bar, and  $n$  is the number of reinforced layers.

$k_{si<ab>}$  is obtained from the following relationship between traction and relative displacement at the intersection boundary:

$$\begin{Bmatrix} \sigma_n \\ \tau_s \end{Bmatrix} = \frac{E_s}{h} \begin{bmatrix} \cos^2 \theta + \beta \sin^2 \theta & (\beta - 1) \cos \theta \sin \theta \\ (\beta - 1) \cos \theta \sin \theta & \sin^2 \theta + \beta \cos^2 \theta \end{bmatrix} \begin{Bmatrix} \delta_n \\ \delta_s \end{Bmatrix}, \quad (21)$$

where  $\sigma_n$  and  $\tau_s$  are normal stress and tangential stress, respectively, at the surface  $\Gamma_{<ab>}$ ;  $\delta_n$  and  $\delta_s$  are the relative displacements at the  $\Gamma_{<ab>}$ ;  $E_s$  is the Young's modulus of the steel;  $\beta$  is the coefficient of the Dowel effect;  $h$  is the length between two adjacent subdomains; and  $\theta$  is the angle to the normal direction of the surface from the axial reinforcement steel (Fig. 9).

A bilinear model was used to solve for the nonlinearity of the reinforcing bar.

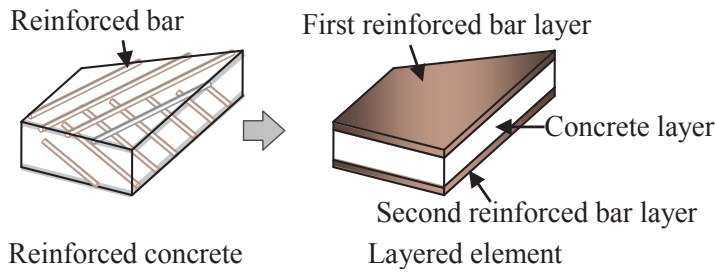


Figure 8. Modeling of reinforced concrete

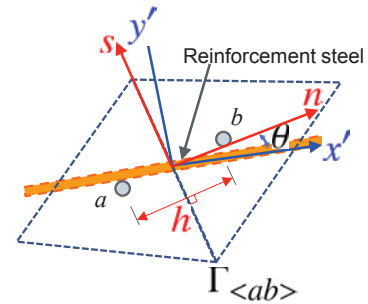


Figure 9. Direction of the steel

**Validation**

To validate the HPM with a newly implemented reinforced concrete constitutive model, a deep beam test that shows typical progressive failure was simulated.

*Description of Deep Beam Test*

The crack model was implemented in the HPM to solve a progressive failure problem. This was validated through a simulation of the deep beam test. Details on this experiment were reported by the JCI (1993).

The test model is schematically shown in Fig. 10. The deep beam was placed on steel plates, and a vertical load was applied to the loading plates. The specimen was 900 mm wide, 400 mm high, and 100 mm thick. The specimen was reinforced with six bars.

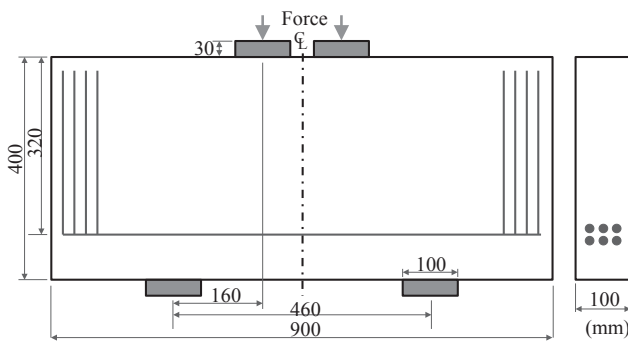


Figure 10. Schematic of test model

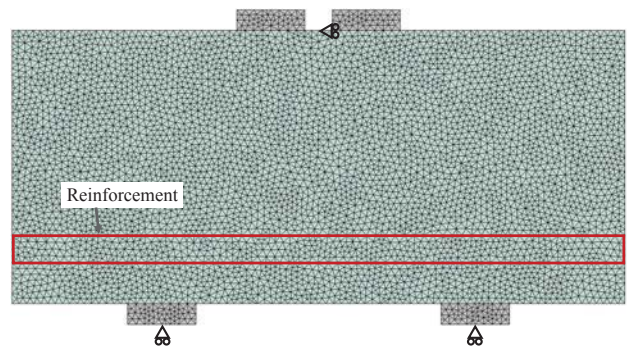


Figure 11. Simulation model

*Simulation Model*

The simulation model is shown in Fig. 11. The supported point is indicated by a triangular marker. Only the vertical direction was fixed because the concrete block could be rotated during the test. A static load was applied to the top of the plate.

The material properties of the concrete, reinforced layer and steel plates are listed in Table 1. These values were set according to the JCI report (1993).

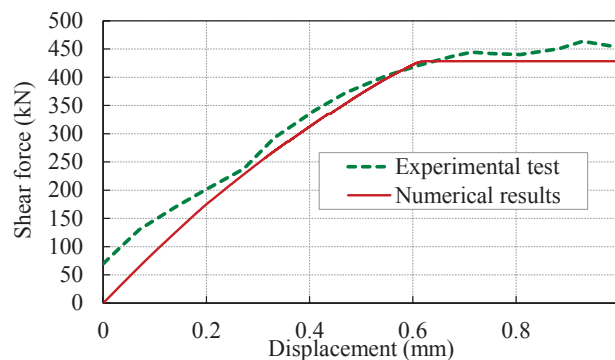
Yamada's  $r_{min}$  method (1968) extended Takeuchi *et al.*'s (2005) method. In the RBSM, this method is used as a nonlinear algorithm that can accurately represent the tensile cracking and compressive failure problems in concrete. This extended  $r_{min}$  method was used for the nonlinear algorithm in the present study.

**Table 1. Material properties.**

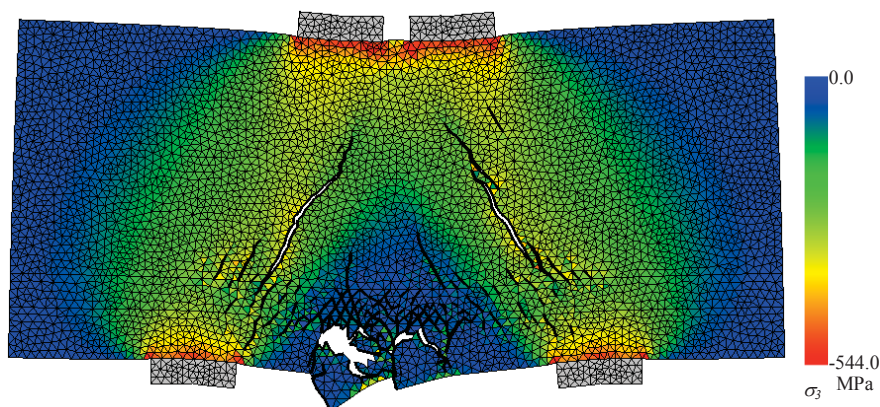
(a) Concrete		(b) Reinforcement		(c) Steel plate	
Parameter	Value	Parameter	Value	Parameter	Value
Compressive strength $f_c$ (MPa)	54.4	Young's modulus $E$ (GPa)	210.0	Young's modulus $E$ (GPa)	210.0
Tensile strength $f_t$ (MPa)	3.3	Thickness (mm)	29.79	Thickness (mm)	100.0
Young's modulus $E$ (GPa)	33.3	Angle to the horizontal ( $^\circ$ )	0.0	Poisson's ratio $\nu$	0.3
Poisson's ratio $\nu$	0.167	Tensile strength $f_t$ (MPa)	375.3		
Thickness (mm)	100.0	Coefficient of Dowel effect $\beta$	0.005		
Fracture energy $G_f$ (N/mm)	0.13				

### Numerical Results

Figure 12 shows the relationship between the shear force and vertical displacement. The dashed line represents the experimental results, and the solid line represents the numerical results. The numerical results matched well with the experimental results. In the numerical results, a large vertical displacement occurred after the concrete compressive stress under the loading plates reached the compressive strength.



**Figure 12. Relationship between shear force and vertical displacement**



**Figure 13. Deformation and contour of minimum principal stress  $\sigma_3$**

Figure 13 shows the numerical deformation (amplification factor 40.0) with a contour of the minimum principal stress  $\sigma_3$ . Multiple progressive cracks propagated from the bottom support steel plate toward the upper loading steel plate in the concrete.

## Conclusions

A method to simulate progressive concrete failure was presented and verified using experimental test results. The presented method is an extension of the HPM, in which a constitutive model (discrete crack model) for reinforced concrete is implemented. The discrete crack was evaluated at the intersection boundary between subdomains of the HPM. Simulating the tensile stress behavior and crack displacement is easy; these were directly related to the fracture energy through empirical expressions that were introduced by Hordijk *et al.* (1986). The nonlinearity of the compressive behavior is considered in the compressive stress–strain components of the subdomain of the HPM on the basis of the trilinear approximation function of the empirical stress–strain relationship.

Reinforcing bars were implemented using a layered spring element that is similar to that used in the RBSM. A bilinear model was used to solve for the nonlinearity of the reinforcing bar.

To confirm the validity of the new HPM, we carried out a simulation of a deep beam test. The numerical results were compared with the experimental observations, and we obtained good agreement in the relationship between the shear force and vertical displacement.

## Acknowledgments

The experimental results in Figs. 7 and 12 were published in the Committee Report of Japan Concrete Institute (JCI) (2001, 1993).

We extend special thanks to Dr. Ueda for sharing his knowledge of discrete limit analysis and the constitutive model of reinforced concrete.

## References

- Cornelissen, H. A. W., Hordijk, D. A., and Reinhardt, H. W. (1986), Experiments and theory for the application of fracture mechanics to normal and lightweight concrete. *International Conference on Fracture Mechanics of Concrete*. (Edited by Wittmann, F. H.), Elsevier, Amsterdam.
- Fujiwara, Y., Takeuchi, N., Shiomi, T., and Kambayashi, A. (2012), Discrete crack analysis in concrete structure using hybrid-type penalty method. *Proceedings of the 2nd International Conference on Computational Design in Engineering*, 249.
- Gedik, Y. H., Nakamura, H., Yamamoto, Y., and Kunieda, M. (2011), Evaluation of three-dimensional effects in short deep beams using a rigid-body-spring-model. *Cement and Concrete Composites*, 33(9–10), pp. 978–91.
- Hillerborg, A., Modéer, M., and Petersson, P.-E., (1976), Analysis of crack formation and crack growth in concrete by means of fracture mechanics and finite elements. *Cement and Concrete Research*, 6, pp. 773–782.
- JCI (1993), *Application of fracture mechanics to concrete structures*. Japan Concrete Institute, Tokyo.
- JCI (2001), Committee report on test method for fracture property of concrete. *Proceedings of the Japan Concrete Institute*, 23, pp. 19–28, (in Japanese).
- Kawai, T. (1977), New element models in discrete structural analysis. *Journal of the Society of Naval Architects of Japan*, 141, pp. 187–193.
- Mihara, R. and Takeuchi, N. (2008), Nonlinear analysis of Riedel shearing test by using mesh dividing method in HPM. *Proceedings of the 8th International Conference on Analysis of Discontinuous Deformation: Fundamentals and Applications to Mining and Civil Engineering*, pp. 201–206.
- Nakamura, S., Kitsutake, Y., Mihashi, H., and Uchida, Y. (1999), Discussion on standard evaluation method for tension softening properties of concrete. *Concrete Research and Technology*, 10(1), pp. 151–164 (in Japanese).
- Rice, J. R. (1968), Path independent integral and the approximate analysis of strain consideration by notches and cracks. *Journal of Applied Mechanics*, 35, pp. 379–386.
- Takeuchi, N., Ueda, M., Kambayashi, A., and Kito, H. (2005), *Discrete limit analysis of reinforced concrete structure*, Maruzen, Tokyo (in Japanese).
- Takeuchi, N., Tajiri, Y., and Hamasaki, E. (2009), Development of modified RBSM for rock mechanics using principle of hybrid-type virtual work. *Analysis of Discontinuous Deformation: New Developments and Applications*, (Ma, G. and Zhou, Y.), pp. 395–403, Research Publishing Service, Singapore.
- Yamada, Y., Yoshimura, N., and Sakurai, T. (1968), Plastic stress–strain matrix and its application for the solution of elasto-plastic problem by a finite element method. *International Journal of Mechanical Sciences*, 10, pp. 343–354.

## Numerical Simulations of Particle Deposition in Metal Foam Heat Exchangers

\*E. Sauret<sup>1</sup>, S. C. Saha<sup>1</sup>, and Y. T. Gu<sup>1</sup>

<sup>1</sup>School of Chemistry, Physics and Mechanical Engineering, Queensland University of Technology, Brisbane, Australia.

\*Corresponding author: [Emilie.sauret@qut.edu.au](mailto:Emilie.sauret@qut.edu.au)

**Key Words:** *CFD Modeling, Metal Foam Heat Exchangers, Particle Tracking, Particle Deposition*

### Abstract

Australia is a high-potential country for geothermal power with reserves currently estimated in the tens of millions of petajoules, enough to power the nation for at least 1000 years at current usage. However, these resources are mainly located in isolated arid regions where water is scarce. Therefore, wet cooling systems for geothermal plants in Australia are the least attractive solution and thus air-cooled heat exchangers are preferred. In order to increase the efficiency of such heat exchangers, metal foams have been used. One issue raised by this solution is the fouling caused by dust deposition. In this case, the heat transfer characteristics of the metal foam heat exchanger can dramatically deteriorate. Exploring the particle deposition property in the metal foam exchanger becomes crucial. This paper is a numerical investigation aimed to address this issue. Two dimensional (2D) numerical simulations of a standard one-row tube bundle wrapped with metal foam in cross-flow are performed and highlight preferential particle deposition areas.

### Introduction

Increasing the electricity production while reducing the carbon emissions is a priority for many countries. Australia has a high-potential to produce geothermal power thanks to hot rocks reaching 300 degrees Celsius at approximately 5km under the surface (Hooman, 2010). However, these resources are mainly located in isolated arid areas. In such places, water is rare and precious and wet cooling systems for geothermal power plants are not the most appropriate solution. Instead, air-cooled heat exchangers appear a more suitable choice (Hooman & Gurgenci, 2010; Odabae & Hooman, 2011).

For many thermal applications such as air conditioning or refrigeration, tube-bundles heat exchangers have been used and studied for many years (Kays & London, 1955). Their main advantages include: compactness, light weight and high efficiency. Fins were added to the tubes in order to improve the heat transfer thanks to a surface area increase. New developments led to further improve the efficiency of heat exchangers by replacing the fins by metal foams (Boomsma, Poulikakos, & Zwick, 2003). It has been recently suggested to replace finned tubes by metal foams in air-cooled heat exchangers for geothermal applications (Ejlali, Eljali, Hooman, & Gurgenci, 2009). Metal foams are fibrous materials which are becoming increasingly popular thanks to their attractive thermophysical properties such as high surface-to-volume ratio, low density, thermal and corrosion resistance and high mechanical strength and rigidity (Mahjoob & Vafai, 2008; T'Joel, De Jaeger, Huisseune, Van Herzeele, Vorst, & De Paepe, 2010). Heat transfer is enhanced by increasing the turbulence and mixing and dispersion induced by the ligaments of the foam as well as by high heat conductivity through the metallic ligaments. These properties lead to smaller, lighter and more efficient heat exchangers which become more attractive than conventional heat exchangers (Calmidi & Mahajan, 2000; Odabae & Hooman, 2012; Obadaee, De Paepe, De Jaeger, T'Joel, & Hooman, 2013). Finally, the reduction in production cost also makes them more and more competitive.

For geothermal power plants, the use of binary cycle with a very low thermal efficiency requires high heat transfer rates. Hence, it is vital to make the technology highly efficient. To achieve this in



arid areas, air-cooled systems enhanced with metal foams are required. However, this technology still presents issues that need to be solved in order to achieve high efficiencies. Indeed, one issue raised by this enhancement technique is the fouling caused by the deposition of particles inside the pores of the metal foam. This deposition reduces the heat transfer rate between the flow and the metallic ligaments. The flow can be blocked causing an increase of pressure drop through the heat exchanger and reducing its permeability. All this affects negatively the efficient of the heat exchanger. As underlined by Obadaee et al. (Obadaee, De Paepe, De Jaeger, T'Joen, & Hooman, 2013), this issue has not been extensively studied in the current literature and needs further investigation especially numerical models capable of predicting the dust deposition and its effects on the heat exchanger performance.

Hooman et al. (Hooman, Tamayol, & Malayeri, 2012) investigated theoretically the impact of particle deposition in metal foam exchangers. Their findings outline the high pressure drop that can be reached due to blocked pores and the negative effect of particle deposition especially with high velocity flows. However, they assume a uniform layer distribution of dust on the foam surfaces, then noticing the importance of the challenges to model accurately such complex configurations.

Recently, Odabae and Hooman (Odabae & Hooman, 2012) performed simulations on a four-row tube bundle in cross-flow. The presented results showed that metal foam heat exchangers improve the heat transfer performance compared to conventional finned-tube heat exchangers at the expense of a slightly higher pressure drop. However, this study doesn't include any particles and the geometry of the metal foam is simply modelled as a porous media. In another study, Odabae et al. (Obadaee, De Paepe, De Jaeger, T'Joen, & Hooman, 2013) numerically simulate the effects of particle deposition in a single-row metal foam-wrapped tube bundle. They compare cases with different fouling to clean metal foam and validate their simulations against some experiments (T'Joen, De Jaeger, Huisseune, Van Herzeele, Vorst, & De Paepe, 2010). However, the dust layer is assumed to be uniform with no particle modelling and the foam is considered as a simple porous media.

In order to extend the understanding of fouling in metal foam heat exchangers, this paper will look at the particle transport in a single-row tube bundle wrapped with metal foam and will give insights of the preferential particle deposition areas.

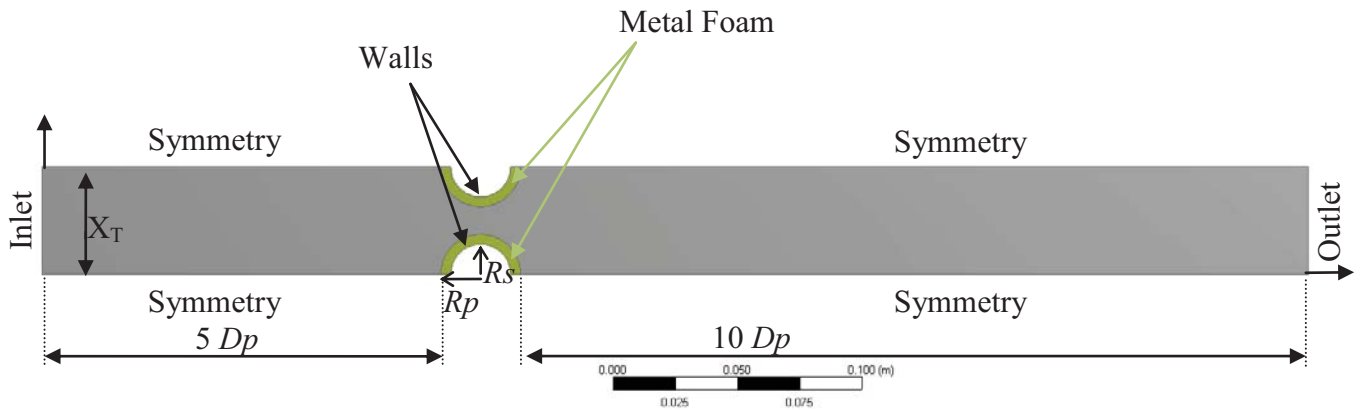
## **Approach**

### *Geometry and Boundary Conditions*

The geometry, as shown in Figure 1, is the same as the one presented in (T'Joen, De Jaeger, Huisseune, Van Herzeele, Vorst, & De Paepe, 2010) of a single-row tube bundle wrapped with an aluminium foam.

To reduce the cost of the simulations, a 2D case is chosen with symmetry conditions applied at the top and the bottom of the configuration. Symmetries are also applied at the front and back. The walls of the tubes have a fixed temperature of  $T_w=353\text{K}$  and we set a no slip condition. At the inlet, the flow temperature and velocity are set to respectively  $T_\infty=298\text{K}$  and  $U_\infty=3\text{ m/s}$ . At the outlet, the atmospheric pressure is specified.

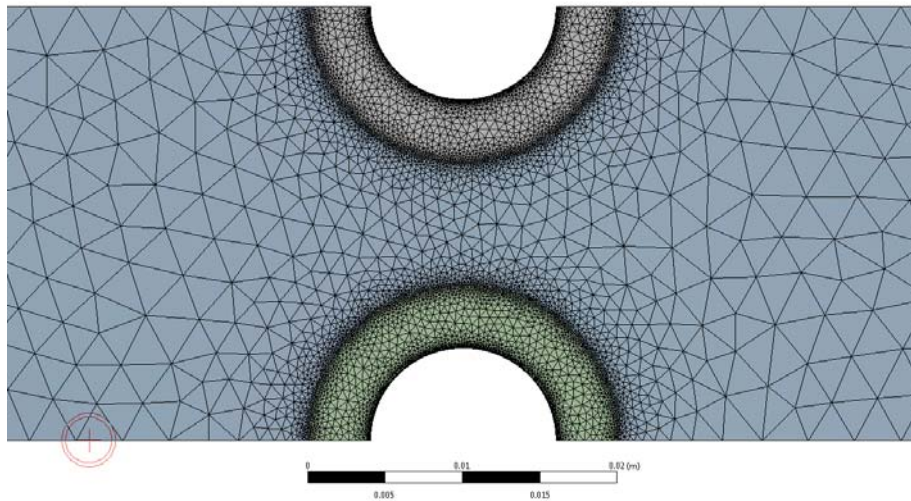
The tube radius  $R_s$  is 0.006 m while the thickness of the foam is 0.004 m and the transversal tube pitch  $X_T$  is 0.028 m.



**Figure 1: Single-row tube bundle wrapped with aluminum foam with boundary conditions**

### *Mesh*

An unstructured grid was obtained using ANSYS. The grid independency was performed and the selected mesh presented consisting of 86728 nodes is presented in Figure 2. An inflation layer was applied on the walls of the tubes with 5 layers and a growth rate of 1.3. At the interface between the foam and the main flow, the grid is refined with a growth rate of 1.3.



**Figure 2: Mesh used for the present simulations**

### *Numerical modeling*

The particles injected at the inlet have the same velocity as the main flow through a zero slip velocity applied to them and a mass flow rate of  $10^{-3}$  kg/s. We consider soot particles of density  $2000 \text{ kg}\cdot\text{m}^{-3}$ . In our simulations, 5000 particles are introduced which was proved to be largely enough for a preliminary investigation. A normal distribution of particles was set with a minimum particle diameter of  $10 \text{ }\mu\text{m}$ , a maximum diameter of  $250 \text{ }\mu\text{m}$ , mean diameter of  $50 \text{ }\mu\text{m}$  and a standard deviation of  $50 \text{ }\mu\text{m}$ .

Our approach is to model the foam wrapped around the tubes as a porous media for which the experimental permeability and porosity are set as follows:  $K=5.3\text{e-}7 \text{ m}^2$  and  $\varepsilon=0.913$ . Because of the

complexity of the real foam geometry, the ligaments are not modeled inside the porous media. However, the aluminum properties of the ligaments are taken into account through an interfacial area density calculated from Calmidi and Mahajan (Calmidi & Mahajan, 2000) and an interfacial heat transfer coefficient from T'Joen, et al., 2010, respectively set to  $a_{sf}=1239.4\text{m}^{-1}$  and  $h_{sf}=200\text{W}\cdot\text{m}^{-2}\cdot\text{K}^{-1}$ . At the interface between the porous domain and the main flow, a conservative flux is applied.

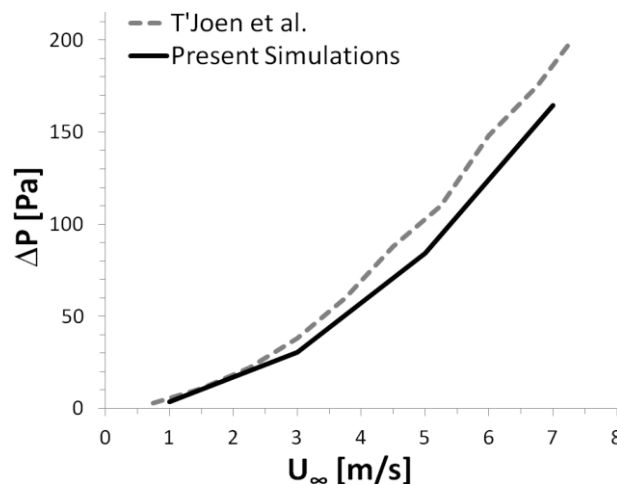
ANSYS-CFX is used to perform the simulations. An Eulerian-Lagrangian approach was chosen for which the Eulerian models the continuous phase while the particle transport is modeled with a Lagrangian particle tracking model. In this study, the particulate phase is assumed to have negligible effects on the continuous phase thanks to a reduced volume fraction of particles entering the heat exchangers. As a consequence, a one-way coupling method is employed. This means that the continuous phase can influence the particles' trajectories but the particles have no impact on the flow pattern.

The standard k- $\epsilon$  model with scalable wall function is used to model the continuous phase.

We first assume a restitution coefficient at the wall to get the particles bouncing at the wall. We also run a case with a zero restitution coefficient. In that case, the particles reaching the wall stick to it and then disappear from the system.

## Results and Discussion

First, the evolution of the pressure drop with the inlet velocity in Figure 3 was validated against the experiments from T'Joen et al. (T'Joen, De Jaeger, Huisseune, Van Herzeele, Vorst, & De Paepe, 2010).



**Figure 3: Comparison between the experiments (T'Joen, De Jaeger, Huisseune, Van Herzeele, Vorst, & De Paepe, 2010) and the present simulations of the evolution of the pressure drop with the inlet velocity.**

The non-dimensional temperature distribution and the axial velocity are plotted in Figure 4. As this is a one-way coupling between the particles and the flow, the flow pattern is not affected by the particles and the particles mainly follow the same path as the flow. The high temperature areas near the tube wall correspond to the recirculation zone behind the cylinder. In this region, the backward velocity is really small (-0.6 m/s) compared to the main jet (around 10 m/s). As a consequence, the heat transfer is smaller at the rear of the tube than at the front. Indeed, the heat transfer coefficient at the wall behind the tube is around  $3\text{W}\cdot\text{m}^{-2}\cdot\text{K}^{-1}$  while it reaches  $15\text{W}\cdot\text{m}^{-2}\cdot\text{K}^{-1}$  at the front of the tube as shown in Figure 5.

As recently observed numerically by Nagendra et al.(Nagendra, Tafty, & Viswanathan, 2011), the regions of higher heat transfer correspond to the zones of preferential particle deposition. In our case, this is also observed in Figure 5 as when switching to the zero restitution coefficient, the particles deposition rate is mainly represented at the front of the tube (Figure 6) In addition, the case with a non-zero restitution coefficient also shows a larger volume fraction of particles at the front of the tube as shown in Figure 7. The transient simulation of this configuration was performed validating our conclusions (Figure 8).

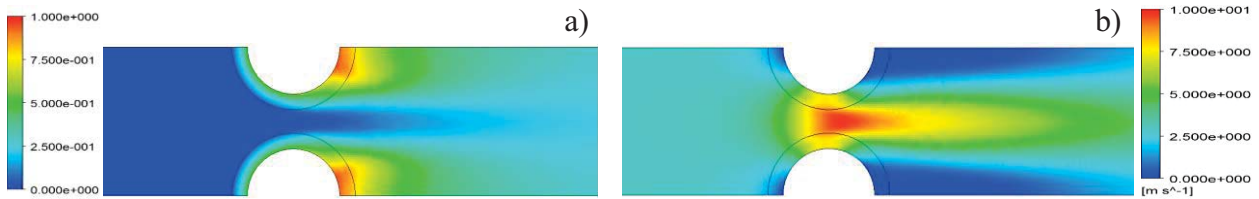


Figure 4: a) Non-dimensional temperature distribution and b) axial velocity distribution at  $U_{\infty}=3$  m/s

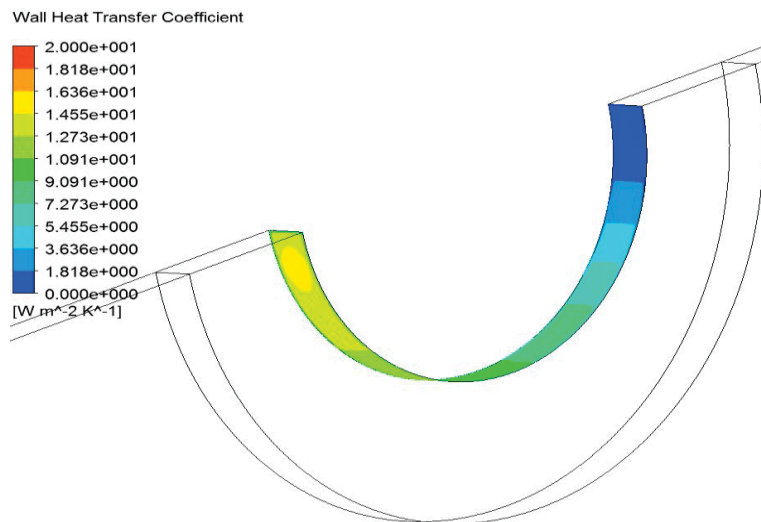


Figure 5: Wall Tube Heat Transfer Coefficient at  $U_{\infty}=3$ m/s

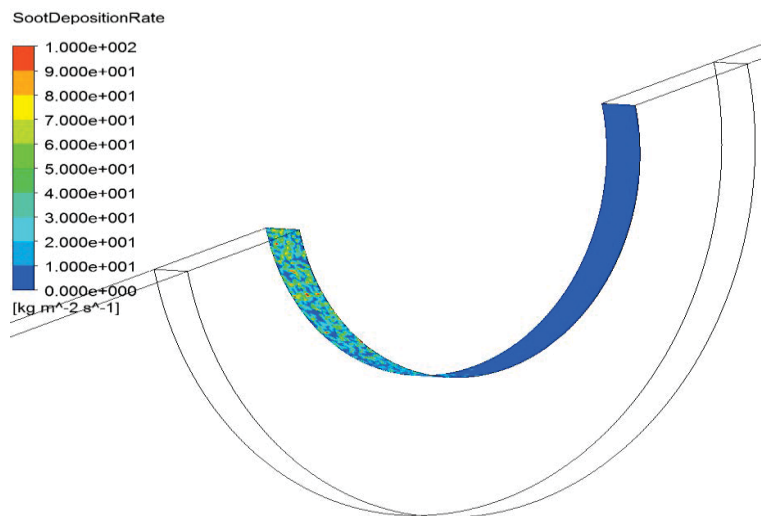


Figure 6: Wall mass flow density of particles at the tube wall in the case with a zero restitution coefficient at  $U_{\infty}=3$  m/s



Figure 7: Averaged Volume Fraction of Particles for the steady simulation at  $U_{\infty}=3$  m/s

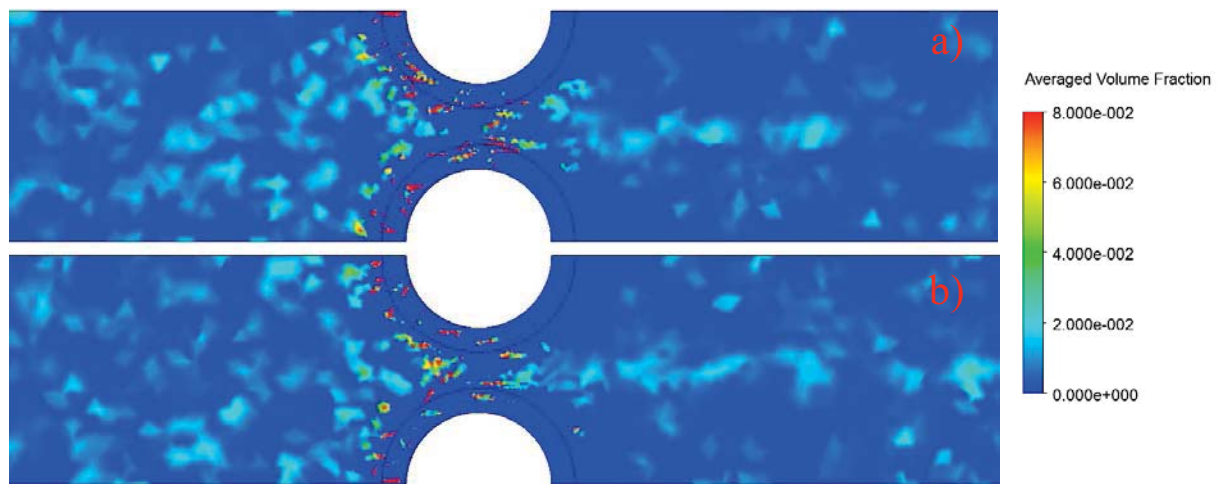


Figure 8: Averaged Volume Fraction of Particles for the transient simulation at  $U_{\infty}=3$  m/s a)  $t=0.5$ s b)  $t=1$ s

## Conclusions

This work is one of the first CFD studies carried out for the particle transport and deposition in metal foam heat exchangers. This preliminary study looked at the particle movements in a one-row tube bundle wrapped with metal foam and identified preferential deposition areas. It is shown that the front of the tubes is more exposed to particle deposition than the rear because of a higher velocity and a higher heat transfer in this region. The rear of the tube is subject to a large zone of recirculation which could lead to some particles moving back to the wall. However, due to the weak backward velocity and the low volume fraction of particles, this doesn't seem to happen.

Further investigations will be conducted including the effect of the wall temperature, the particle size distribution and other tube arrangements for which more experimental data will be available to extend the validation of our CFD.

Finally, new numerical models will be also developed in order to accurately model the particle deposition and re-entrainment process in metal foam heat exchangers.

## Nomenclature

$R_p, D_p$  Tube+Foam radius and diameter, [m]  
 $R_s$  Tube Radius, [m]

$X_T$	Transversal Tube Pitch, [m]
$T$	Temperature, [K]
$K$	Permeability, [m <sup>2</sup> ]
$\varepsilon$	Porosity
$a_{sf}$	Interfacial area density, [m <sup>-1</sup> ]
$h_{sf}$	Interfacial heat transfer coefficient, [W.m <sup>-2</sup> .K <sup>-1</sup> ]
$t$	Time, [s]

### Subscripts

$w$	wall
$\infty$	inlet

### References

- Boomsma, K., Poulidakos, D., & Ventikos, Y. (2003). Simulations of flow through open cell metal foams using an idealized periodic cell structure. *International Journal of Heat and Fluid Flow*, 34, pp. 825-834.
- Boomsma, K., Poulidakos, D., & Zwick, F. (2003). Metal foams as compact high performance heat exchangers. *Mechanics of Materials*, 35, pp. 1161-1176.
- Calmidi, V. V., & Mahajan, R. L. (2000). Forced Convection in High Porosity Metal Foams. *Journal of Heat Transfer*, 122, pp.557-565.
- Ejlali, A., Eljali, A., Hooman, K., & Gurgenci, H. (2009). Application of high porosity metal foams as air-cooled heat exchangers to high heat load removal systems. *International Communication in Heat and Mass Transfer*, 36, pp. 674-679.
- Ghosh, I. (2009). How Good Is Open-Cell Metal Foam as Heat Transfer Surface? *Journal of Heat Transfer*, 131, pp. 1-8.
- Hooman, K. (2010). Dry Cooling Towers as Condensers for Geothermal Power Plants. *International Communication in Heat and Mass Transfer*, 37, pp. 1215-1220.
- Hooman, K., & Gurgenci, H. (2010). Porous Medium Modeling of Air-Cooled Condensers. *Transp. Porous Med.*, 84, pp. 257-273.
- Hooman, K., Tamayol, A., & Malayeri, M. (2012). Impact of Particulate Deposition on the Thermohydraulic Performance of Metal Foam Heat Exchangers: A Simplified Theoretical Model. *Journal of Heat Transfer*, 134 (9), pp.1-7.
- Kays, W. M., & London, A. L. (1955). *Compact Heat Exchangers: A Summary of Basic Heat Transfer and Flow Friction Design Data*. Palo Alto, California: National Press.
- Mahjoob, S., & Vafai, K. (2008). A synthesis of fluid and thermal transport models for metal foam heat exchangers. *International Journal of Heat and Mass Transfer*, 51, pp. 3701-3711.
- Nagendra, K., Taftý, D. K., & Viswanathan, A. K. (2011). Modeling of soot deposition in wavy-fin exhaust gas recirculator coolers. *International Journal of Heat and Mass transfer*, Vol. 54, pp. 1671-1681.
- Odabae, M., De Paepe, M., De Jaeger, P., T'Joel, C., & Hooman, K. (2013). Particle Deposition Effects on Heat Transfer from a Metal Foam-Wrapped Tube Bundle. *International Journal of Numerical Methods for Heat and Fluid Flows*, 23 (1), pp. 74-87.
- Odabae, M., & Hooman, K. (2011). Application of metal foams in air-cooled condensers for geothermal power plants: An optimization study. *International Communication in Heat and Mass Transfer*, 38, pp. 838-843.
- Odabae, M., & Hooman, K. (2012). Metal foam heat exchangers for heat transfer augmentation from a tube bank. *Applied Thermal Engineering*, 36, pp.456-463.
- Odabae, M., Hooman, K., & Gurgenci, H. (2011). Metal Foam Heat Exchangers for Heat Transfer Augmentation from a Cylinder in Cross-Flow. *Transp. Porous Media*, 86, pp. 911-923.
- T'Joel, C., De Jaeger, P., Huisseune, H., Van Herzeele, S., Vorst, N., & De Paepe, M. (2010). Thermo-hydraulic study of a single row heat exchanger consisting of metal foam covered round tubes. *International Journal of Heat and Mass Transfer*, 53, 3262-3274.

## Seismic response of a concrete gravity dam considering hydrodynamic effects

\*A. Dey<sup>1</sup> and M. B. Sawant<sup>2</sup>

<sup>1</sup> Department of Civil Engineering, Indian Institute of Technology Guwahati, Assam-781039, India.

<sup>2</sup> Department of Civil Engineering, Northern India Engineering College, New Delhi-110053, India.

\*Corresponding author: [arindam.dey@iitg.ernet.in](mailto:arindam.dey@iitg.ernet.in)

### Abstract

Massive concrete gravity dams supporting huge water reservoir are subjected to hydrodynamic forces resulting from the time-dependent stresses generated at the reservoir water-dam interface. Indian Standard Code (IS 1893-2003) suggests considering hydrodynamic pressure that varies with depth of reservoir and shape of the dam, similar to a pseudo-static analysis. Such an assumption leads to largely conservative analysis and over-safe design. This article reports the response of the Pine Flat Dam under seismic conditions considering hydrodynamic stresses on the upstream face, varying both spatially and temporally. The Kern County seismic ground motion has been chosen for the analysis, for which both S69E and vertical component of accelerations have been considered along with their combined action. GeoStudio 2007 modules of Sigma/W and Quake/W have been used in unison to achieve the modeling. The study illustrates a significant variation in the estimated seismic response when the hydrodynamic forces are included in the design.

**Keywords:** Concrete gravity dam, Seismic response, Hydrodynamic effect, Geo-Studio 2007.

### Introduction

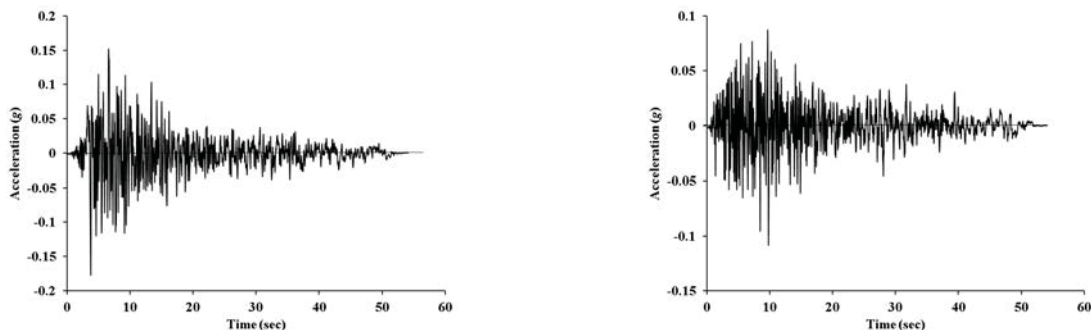
Dams are barriers that impound water or underground streams for various purposes such as hydropower and hydroelectricity, water storage and irrigations, water flow stabilization, flood prevention, land reclamation, navigation, water channel diversion as well as recreation and aquatic beautification. Dams can be natural, anthropogenic, or animal-made. Based upon their construction materials, shape and purpose, dams can be classified structurally as arch dams, gravity dams, arch-gravity dams, barrages, embankment dams, rock-fill dam, concrete faced-rock fill dam, and earth – and-rock fill dams. In terms of usability, they can be categorized as saddle dams, weirs, check dams, dry dams, diversionary dams, underground dams and tailing dams. The importance of these structures convey the idea of the catastrophic disaster which can occur due to its failure, the main causes of which may include inadequate spillway capacity, piping through the embankment, foundation or abutments, spillway design error, geological instability caused by the water level fluctuation in the upstream, poor maintenance, extreme rainfall and seismic shocks and earthquakes. Failure of dams occurs quite rapidly without adequate prior warning with a potential of causing excessive calamity.

During the earthquakes, the additional pressure exerted by the moving water on the upstream face of the dam is termed as hydrodynamic force. A similar situation arises when a wave impacts on the offshore jetties. The hydrodynamic forces are spatially and temporally variable, and in contrary, significantly different to the pseudo-static analysis conventions. According to the Indian Standards (IS 1893-2003), due to horizontal acceleration, instantaneous hydrodynamic pressure is produced on the dam face, opposite to the direction of the earthquake, which results in alternate cycles of compression and tension forces (extreme tension may lead to cavitations). The methodology detailed in the IS code to determine this hydrodynamic force is based on pseudo-static analysis, with no temporal variation of the same. This may lead to significant over-safe design.

Pseudo-static method of analysis has been one of the earliest methods of estimating the hydrodynamic pressure distribution. ‘Added-mass’ effect of an incompressible reservoir fluid (Westergaard, 1933), linear momentum balance principle to investigate earthquake forces (Chwang and Housner, 1978), potential-flow theory (Chwang, 1978, 1979), and the application of Laplace’s equation (Zee and Zee, 2006) are the examples of the applicability of the pseudo-static analysis in such problems. It is worth mentioning that such analyses considers the worst condition of the earthquake force acting through a special location of the structure, and hence, avoids the temporal

effect of the earthquake motions on the developed hydrodynamic pressure and its time-dependent variation on the upstream face of the dam. The pseudo-static analyses reveals that the hydrodynamic pressure distribution is mostly parabolic and the maximum pressure occurs at the base (or near the base) of the dam. However, it is well understandable that the variation of hydrodynamic pressure is time-dependent, which varies during the event of an earthquake. To-and-fro motion of the dam, reservoir and dam-reservoir foundation results in an alternate build-up and release of reservoir water-dam face interaction stresses, which are representations of the hydrodynamic pressures itself. Hence, the hydrodynamic pressure may be significantly different in comparison to that estimated from a worst-case scenario pseudo-static analysis. Both the distribution and magnitude of the forces along the upstream face of the dam are different, and at time might exceed the magnitudes as observed in the pseudo-static analysis. Hence, it is necessary to have a proper dynamic analysis of the dam-reservoir systems to understand the hydrodynamic pressure variation. Limited studies in this respect have been carried out, and hence, this aspect needs further investigation.

Most of the earlier researches have been focused on to determine the hydrodynamic pressure variation on the upstream face of the dam, without delving deeper into finding what would be the consequence of the same on the response of the dam. This paper reports the findings of the dynamic analysis carried out on Pine Flat Dam to determine the effect of hydrodynamic stresses on the response of the dam. Chopra and Gupta (1981) reported the findings of a similar study on behavior of Pine Flat Dam considering the horizontal and vertical components of the Kern County Earthquake (Taft ground motion). The study reported the utilization of the first 20 sec duration of the motion with the PGA as 0.15g for horizontal (S69E) component and 0.083g for the vertical component of the motion. Since the entire duration of the strong motion was 54.14 sec (Fig. 1), the above segment with the corresponding PGA is not believed to provide proper representation of the effect of the earthquake in the generation of the hydrodynamic pressure. Based on the approach by Trifunac and Brady (1975), this article reports a more realistic application of the earthquake strong motions in the determination of effect of hydrodynamic pressure distribution on the response of the dam. Comparative data have also been reported herein to portray the differences in the results of the present study with that of the earlier one by Chopra and Gupta (1981). In order to achieve the dynamic analysis of the concerned dam and determine its response, a geotechnical finite element package, GEOSTUDIO 2007 has been used in the present study.



**Figure 1. (a) Horizontal S69E and (b) Vertical component of the Kern County ground motion (Taft Lincoln station)**

### GeoStudio Modeling of Pine Flat Dam

Pine Flat Dam is a concrete gravity dam on the Kings River of central California in United States. The dam is 122 m high supporting the Pine Flat Lake, one of the largest reservoirs in California. The freeboard of reservoir is at level of 116 m. The upstream face of the dam is nearly vertical having a slope 0.05H:1V, while the inclined downstream side has slope of 0.78H:1V. The dam material (i.e. concrete) is a brittle material with no yield point and does not show any plastic deformation. Hence, linear elastic model has been used represent the behavior of unreinforced concrete gravity dam. The model comprises of two parts namely the concrete dam and the foundation rock. The presence of water in the reservoir is simulated through hydrostatic and hydrodynamic stresses. The modeling and subsequent analysis of the dam has been carried out on the basis of the following assumption: (i) Reservoir water is incompressible and inviscid, (ii)



Concrete gravity dam is perfectly rigid, and (iii) Hydrodynamic pressure at the surface of water is zero. The dam has been modeled and analyzed using the FEM package GEOSTUDIO 2007 and its various modules namely SIGMA/W (Load-deformation for hydrostatic stresses) and QUAKE/W (Generation of initial static stress conditions and equivalent linear dynamic analysis for dynamic and hydrodynamic stresses).

### **Analysis of Pine Flat Dam**

The hydrodynamic analysis of the Pine Flat Dam has been carried out under the action of 1952 Kern County strong motion recorded at Taft Lincoln station. For the analysis, the horizontal component of the motion (S69E) and the combined horizontal-vertical motion have been used; the motions were so chosen that a comparative study can be provided with the results reported by Chopra and Gupta (1981). The analysis has been carried out for both empty and full reservoir conditions to comprehend the effect of reservoir water on the seismic response of the dam. The hydrodynamic force have been determined using the methodology provided by Chwang and Housner (1978) and used on the upstream face of the dam (for a full-reservoir condition) in several segments to compromise on the variation of the continuous variation of the hydrodynamic pressure on the dam face. The entire analysis has been carried out in three stages which are described in the subsequent sections.

#### *Stage I: Empty Reservoir Condition*

Initial Static Condition under Geostatic Stress: This sub-stage has been modeled using the QUAKE/W 'in-situ stress' module and is used to simulate the development of geostatic stresses in the dam in an empty reservoir condition (hence, just after the construction of the dam). The dam rests on a 30m thick foundation rock. Both the dam and foundation has been considered to be perfectly rigid, and has been represented by a linear elastic model. The unit weight of the dam and foundation has been considered as 25 and 26 kN/m<sup>3</sup> respectively, the Young's modulus of the material are 22.5 and 68.94 GPa respectively, while the Poisson's ratio has been considered to be 0.2 and 0.33 respectively. The bottom of the foundation rock has been restrained from both horizontal and vertical movements, while the far-off lateral boundaries have been restricted from only horizontal displacements. Fig.2 depicts the GeoStudio model used.

Dynamic Condition: In order to simulate the dynamic response of the dam after construction, the QUAKE/W 'equivalent linear elastic dynamic' model has been used. Apart from the material parameters defined for the in-situ condition, the Damping ratio for both the material has been chosen to be 0.1, and the shear stiffness ( $G_{max}$ ) for the dam and foundation has been chosen as 9.33 and 25.92 GPa respectively (Chopra and Gupta, 1981).

#### *Stage II: Full Reservoir Condition*

Initial Static Condition under Geostatic Stress: This sub-stage has been modeled as has been mentioned for Stage I.

Hydrostatic Stress Condition: The hydrostatic pressure has been applied on the upstream face of the dam using the 'Load-deformation analysis' unit of the SIGMA/W module. Based on the full reservoir level, the hydrostatic pressure is calculated for a triangular variation towards the base of the reservoir (Hydrostatic pressure,  $P=\gamma h$ , where  $\gamma$  is the unit weight of water and  $h$  is the depth from the reservoir water level), with a zero value at the reservoir water level. The hydrostatic pressure is applied through stress boundary conditions, which require the stress value to be provided either as a constant or temporally varying. Unlike as stated, since the hydrostatic pressure varies continuously along the depth of the dam face below reservoir water level, which is not possible to be applied directly through stress boundary conditions. Hence, the upstream face of the dam has been divided into several segments (each segment being marked by two nodes of the finite element discretization), and the average of the hydrostatic pressures on those particular segments has been applied as the average constant hydrostatic pressure on the corresponding segment. Hence, the continuous hydrostatic pressure is applied as stepped incremental pressure on the segmented upstream face of the dam. The hydrostatic pressure boundary condition is shown in Fig. 3.

Dynamic Condition: This sub-stage has been modeled as has been mentioned for Stage I.

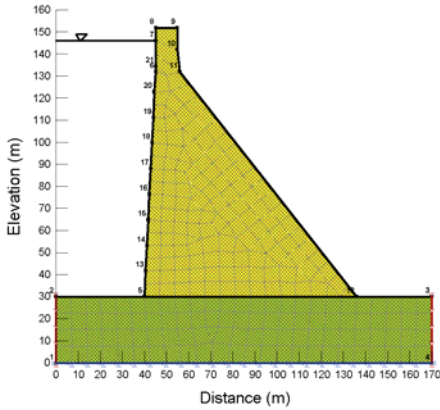


Figure 2 Geostatic stress condition

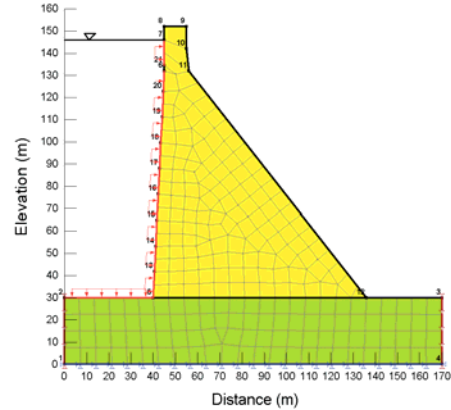


Figure 3 Hydrostatic stress condition

### Stage III: Full Reservoir Condition

**Hydrodynamic Stress:** Hydrodynamic stress, generated due to colliding reservoir water with the dam face, is a coupled phenomenon, and requires a fluid-structure interaction module for its proper modeling and analysis. However, GEOSTUDIO 2007 does not have the same facility and cannot differentiate the reservoir water to be compressible/incompressible or viscid/inviscid. Hence, an uncoupled analysis have been attempted and reported to take into account the hydrodynamic stress analysis. Similar to the hydrostatic stress application, the hydrodynamic stress has also been applied on the segmented upstream face of the dam. Initially, following the Momentum method (Chwang and Housner, 1978) and based on the degree of inclination of the upstream face with the horizontal ( $\theta$ ), the variation of the hydrodynamic pressure coefficient ( $C_p$ ) with the normalized depth below freeboard ( $y/h$ ) has been determined (Fig. 4). Based on the peak ground acceleration coefficient of the strong motion ( $a_0$ ), the hydrodynamic pressure is subsequently calculated as

$$p = C_p \gamma a_0 h \quad (1)$$

The estimated pressure corresponds to a pseudo-static condition, which has been subsequently modified to a temporal scale,  $p(t)$ . The dam and foundation material have been considered as infinitely rigid (owing to its high modulus of elasticity) and hence, does not affect the propagation of the strong motion (i.e. does not result in significant augmentation or attenuation) through the body of the dam and foundation. Hence, the estimated pseudo-static hydrodynamic pressures are multiplied with the corresponding strong motion temporal acceleration factor ( $\alpha(t)$ ) as obtained from the strong motion data modified for the PGA). The modified hydrodynamic pressure is then algebraically added to the estimated pseudo-static pressure (computed earlier) so as to maintain the latter as the mean of the temporal variation of the hydrodynamic stress. The procedure can be represented as:

$$p(t) = p \pm \alpha(t) \cdot p = p [1 \pm \alpha(t)] \quad (1)$$

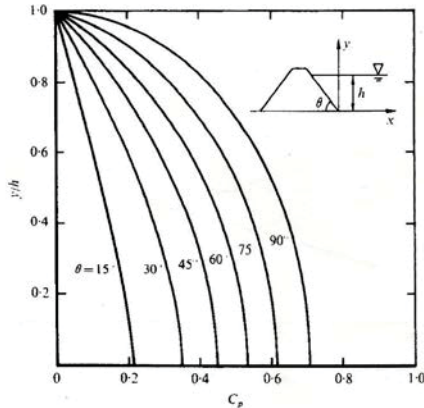
Similar to the application of hydrostatic pressure, the temporal hydrodynamic stress as estimated above is applied over different segments on the upstream face of the dam (Fig. 5). Fig. 6 depicts a typical variation of the hydrodynamic stress on one of the segments of the upstream face of the dam.

## Results and Discussions

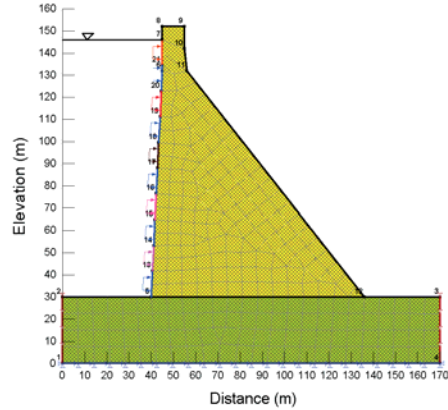
### Static Analysis of the Pine Flat Dam

Under both empty and full reservoir conditions, the static analysis of the dam has been carried out to determine the in-situ and geostatic stresses generated in Pine Flat dam due to the material properties and geometry of the structure. The empty reservoir condition simulates the immediate post-construction behavior of the dam; while the full reservoir condition represents the situation when the reservoir has been filled completely up to the desired level (i.e. the hydrostatic pressure of water is active). Fig. 7 shows the distribution of mean total stress on the upstream face of the dam

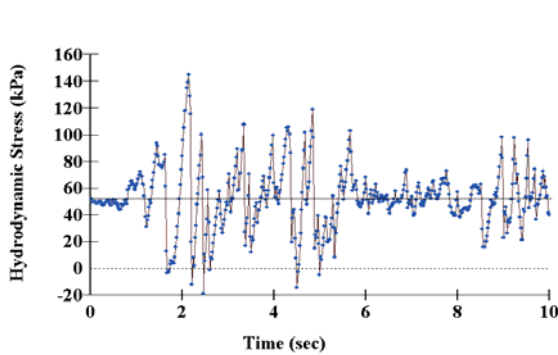
for the above two conditions. For the empty reservoir condition, the variation is nearly linear since the stresses are affected only by the geometry and weight of the structure. Upon the application of hydrostatic pressure on the upstream face, the crest of the dam suffers a displacement away from the reservoir (~ 20 mm), which results in a significant stress reduction in the upstream face (as evident from Fig. 7) especially near the toe of the dam.



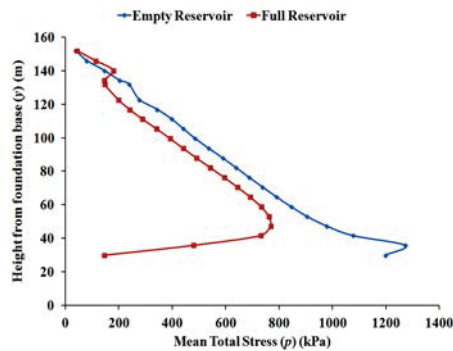
**Figure 4** Variation of  $C_p$  (Chwang and Housner, 1978)



**Figure 5** Hydrodynamic stress condition



**Figure 6** Typical temporal hydrodynamic pressures



**Figure 7** Variation of mean total stress under in upstream dam-face under static conditions

*Dynamic Analysis of the Pine Flat Dam: 20 sec Kern County Motions*

Pine Flat Dam had been subjected to the Kern County Earthquake in 1952, and hence the same strong motion recorded with the Taft Lincoln Station has been used for the dynamic analysis of the same. In order to validate the present FE model, as used by Chopra and Gupta (1981) in a coupled hydrodynamic analysis, the first 20 sec of the motion (only horizontal and combined components) have been used in the present preliminary study with the corresponding PGAs as mentioned earlier. Fig. 8(a) depicts the variation of mean total stress in the upstream face under empty reservoir condition when only the horizontal S69E component has been used in analysis. It has been observed that although the PGA of the 20sec motion occurs at 6.6 sec, the maximum mean total stress occurs at a time step (6.7 sec) beyond the occurrence of PGA. The stresses at these two time-steps are significantly different from each other and are attributed to the accumulation of stresses during the earthquake motion. The dam also experiences tensile stresses towards the end of the seismic motion as evidenced from the negative stresses experienced. Similar exercise has been carried out considering the full reservoir condition (i.e. in the presence of hydrostatic pressure). As depicted in Fig. 8(b), the outcome has been similar to Fig. 8(a). The attempt has been repeated with the combined use of S69E and the vertical component of the Kern County motion, and the results have been compared with that reported by Chopra and Gupta (1981). Table 1 enlists the comparative for the full reservoir condition which shows a reasonable agreement between the results.

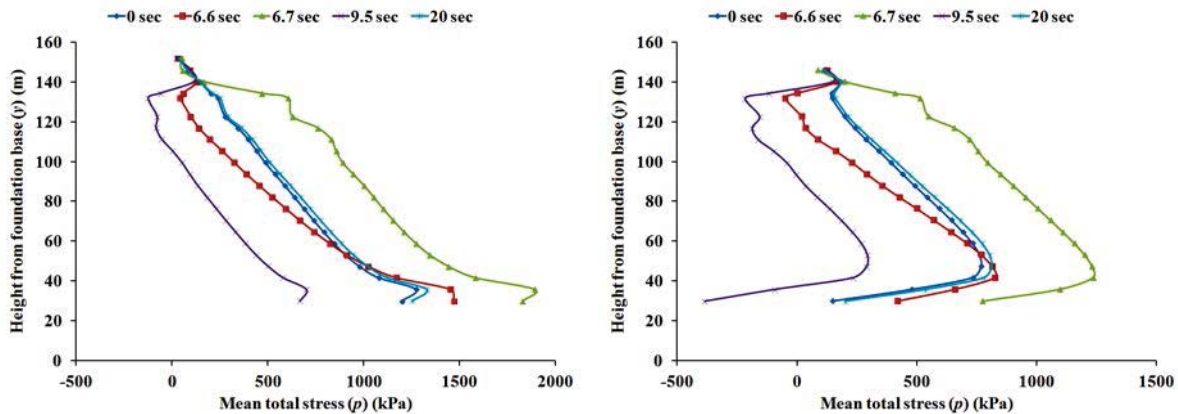


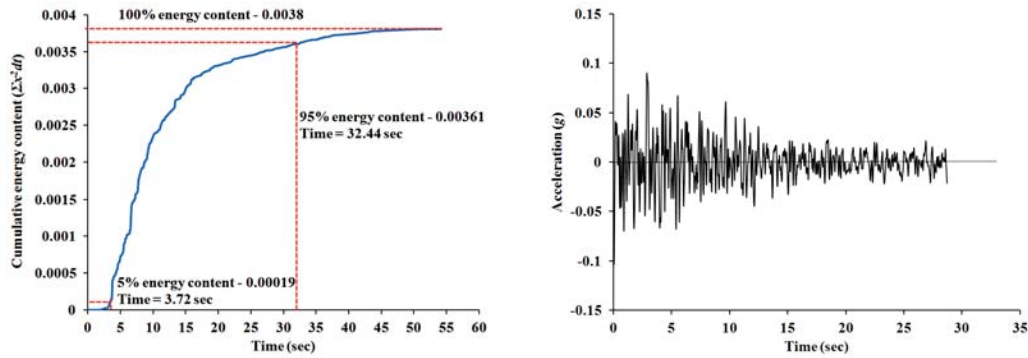
Figure 8 Variation of mean total stress for S69E component with (a) empty and (b) full reservoir conditions

Table 1 Comparative study of mean total stresses under full reservoir condition

Full Reservoir Condition	S69E component		S69E and Vertical components	
	GeoStudio modeling	Chopra and Gupta (1981)	GeoStudio modeling	Chopra and Gupta (1981)
Max. mean total stress on the u/s face (kPa)	1235.38	1055.7	1271.93	1221.3
Max. mean total stress on the d/s face (kPa)	1156.89	1435.2	1178.24	1552.5
Relative crest displacement (mm)	21	35	21	37

#### Dynamic Analysis of the Pine Flat Dam: Modified Kern County Motions

Chopra and Gupta (1981) considered the first 20 sec motion for the dynamic analysis using PGAs as 0.15g and 0.083g for the horizontal and vertical component respectively. However, this motion includes a rising part of significant time duration (~5 sec) beyond which the prominent intensity of the earthquake is experienced. Moreover, the actual Kern County motion is of significantly higher duration (54.14 sec) having a very long decaying tail as well. Hence, a 20 sec segment of the complete motion [as adopted by Chopra and Gupta (1981)] will not be a precise complete representation of the input motion. In order to assess the complete dynamic response of the dam, it is necessary to use the entire input motion. However, in this consideration, it is not advisable to use the PGA for the estimation of the mean temporal hydrodynamic pressure at a particular point on the upstream face of the dam. The PGA occurs momentarily, while the mean hydrodynamic stress is evaluated for the entire time duration, and is liable to be overestimated if the afore-mentioned procedure is used. In order to tackle such overestimation, the methodology proposed by Trifunac and Brady (1975) has been used. Instead of utilizing the entire strong motion history, the technique suggests to use only the effective duration that accommodates the stationary content of the signal (that part of the signal containing the significant maximum energy of the entire strong motion). This method is well suited for the signals having large anterior transition and posterior decay. The postulate suggests using the central 90% of the motion having the significant energy content. The same has been used to estimate the effective time duration for the Kern County motion components. Fig. 9(a) depicts the determination of the stationary content of the horizontal S69E component, pertaining to time duration of 3.72 sec to 32.44 sec. The root mean square (RMS) acceleration computed for this duration is obtained as 0.034g, and the maximum probable acceleration (MPA) is estimated to be three times the RMS acceleration (= 0.103g). The estimated MPA is considered to be the PGA of the modified motion (of time duration 2.73 sec). Fig. 9(b) shows the modified S69E component of the strong motion, which is further used for the present study. Similar exercise for the vertical component modified the time duration to 31.37 sec, and the MPA is obtained as 0.063g.



**Figure 9 (a) Significant energy content of a strong motion as per Trifunac and Brady (1975)  
(b) Stationary content of strong motion signal and estimation of MPA**

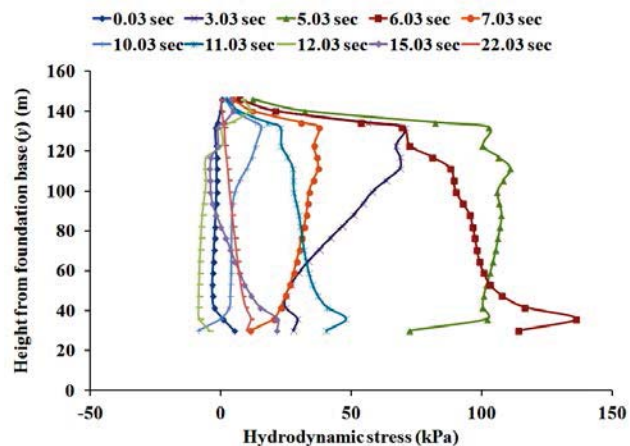
The modified Kern County horizontal and vertical components are utilized as the input motions in the GeoStudio FE model and the dynamic response of the dam are inspected. It is observed that the magnitudes of mean total stress for various conditions reduces as compared to the 20sec motion as has been used earlier, the latter exercise yielding more realistic results in terms of reducing the degree of overestimation. Table 2 provides a comparative of the results as reported by Chopra and Gupta (1981) to those obtained in the present study using the 20 sec S69E motion and 28.73 sec of the modified S69E motion. Apart from the maximum mean stresses, the maximum crest displacement is also significantly reduced which definitely leads to a more engineered and economic design of the dam geometry and configuration.

**Table 2 Comparative study of mean total stresses for Kern County S69E motion**

Full Reservoir Condition	GeoStudio modeling		Chopra and Gupta (1981)
	20 sec S69E	28.73 sec modified S69E	
Max. mean total stress on the u/s face (kPa)	1235.38	1034.57	1055.7
Max. mean total stress on the d/s face (kPa)	1156.89	783.25	1435.2
Relative crest displacement (mm)	21	12	35

*Hydrodynamic Analysis of the Pine Flat Dam: Modified Kern County Motions*

Using the mean hydrodynamic stress obtained from the stationary content of the Kern County strong motion components, the temporal and spatial variation of the hydrodynamic stresses on the upstream face of the dam is determined. As enlisted in Table 3, the magnitudes of the stresses reveal that in comparison to the results obtained by Chopra and Gupta (1981), utilization of the stationary content of the signal results in the reduced hydrodynamic stresses on the dam face. It is also noticed that the hydrodynamic stresses and the relative crest displacement does not change with the inclusion of the vertical component in the excitation motion. This is attributed to the fact that in the present study, the temporal variation of the applied hydrodynamic stress at specified locations on the upstream dam-face has been determined solely on the basis of horizontal component, and hence the effect of the vertical component is not portrayed in the estimated hydrodynamic stresses. However, it is worth mentioning that a dam of irregular structure shows the non-coincidence of the centre of stiffness and centre of application of vertical seismic force, and hence, the effect of vertical



**Figure 10 Typical hydrodynamic stress variation**

component of the strong motion should also be used for the estimation of the applied hydrodynamic stresses.

Fig. 10 shows a typical variation of the temporal and spatial variation of the hydrodynamic stresses on the upstream face of the dam as obtained from the present study. The figure reveals that hydrodynamic pressure significantly varies with time, as well as along the height of the dam, during the occurrence of an earthquake. Due to the stress accumulations during seismic motions, the maximum hydrodynamic pressure, in most cases, had been observed to occur beyond the PGA time-step. The observed variation is substantially different than that defined by the 'exact theory' or the 'momentum method', as shown in Fig. 4 (Chwang and Housner, 1978). It can be well noted that the maximum hydrodynamic pressure need not always occur near the toe of the dam (which is portrayed by the pseudo-static analysis), rather can occur anywhere along the height of the dam during the occurrence of strong motion.

**Table 3 Comparative study of hydrodynamic stresses and relative crest displacement**

Full Reservoir Condition	GeoStudio modeling		Chopra and Gupta (1981)	
	S69E (modified)	S69E+ Vertical (modified)	S69E	S69E+ Vertical
Max. mean total stress on u/s face (kPa)	156.8	156.8	483	420.9
Max. mean total stress on d/s face (kPa)	126.9	126.9	317.4	55.2
Relative crest displacement (mm)	2.2	2.2	11	6.6

## Conclusions

The article reports the response of a concrete gravity dam subjected to seismic motions considering hydrodynamic effects. Stage-wise analysis has been carried simulating various conditions of geostatic, hydrostatic, seismic and hydrodynamic stress developments. Geostatic stresses, as expected, are found to vary linearly with the depth of the dam, while the presence of hydrostatic stresses lowered the stresses developed at the upstream dam face. In case of seismic motions, the maximum stress accumulated in the dam is observed at a time-step beyond the occurrence of the PGA. Strong motions have been found to generate tensile force in the dam face as well. Hydrodynamic stresses have been applied on the upstream dam face at specified locations and its overall effect on the upstream face of the dam has been investigated. Instead of using the entire strong motion, the stationary content of the strong motion with modified PGA has been applied to have a realistic assessment of the dynamic and hydrodynamic response of the dam. Comparison with the earlier literature shows a significant reduction in the generated stresses. The hydrodynamic stress is found to significant temporal and spatial variation in case of a seismic event, which is substantially different as conventionally treated by the pseudo-static methods, and should be accounted in the design and analysis of such dams.

## References

- Chopra, A. K. and Gupta, S. (1981), Hydrodynamic and foundation interaction effects in earthquake response of a concrete gravity dam. *J. of Structural Engineering, ASCE*, 107, pp.1399-1412.
- Chwang, A. T. (1978), Hydrodynamic pressures on sloping dams during earthquakes. Part 2- Exact theory. *J. of Fluid Mechanics, ASCE*, 87, pp.343-348.
- Chwang, A. T. (1979), Hydrodynamic pressures on an accelerating dam and criteria for cavitation. *J. of Engineering Mathematics*, 13, pp.143-152.
- Chwang, A. T. and Housner, G.W. (1978), Hydrodynamic pressures on sloping dams during earthquakes. Part 1- Momentum method. *J. of Fluid Mechanics, ASCE*, 87, pp.335-341.
- IS 1893:1984(Reaffirmed in 2003) *Criteria for Earthquake resistant design of structures*, B.I.S.
- Trifunac, M. D. and Brady, A. G. (1975), A study on the duration of strong earthquake ground motion. *Bulletin of the Seismological Society of America*, 65, pp. 581-626.
- Westergaard, H. M. (1933), Water pressures on dams during earthquake. *Transactions, ASCE*, 98, pp.418-472.
- Zee, C. and Zee, R. (2006), Earthquake Hydrodynamic pressure on dams. *J. of Hydraulic Engineering, ASCE*, 132, pp. 1128-1133.

## Development of multi-phase-field crack model to express crack propagation in polycrystal

Kento Oshima<sup>1</sup>, \*Tomohiro Takaki<sup>1</sup>, and Mayu Muramatsu<sup>2</sup>

<sup>1</sup>Mechanical and System Engineering, Kyoto Institute of Technology,  
Matsugasaki, Sakyo, Kyoto 606-8585, Japan

<sup>2</sup>Functional and Structural Damage Verification Group,  
Advanced Manufacturing Research Institute,  
National Institute of Advanced Industrial Science and Technology,  
1-1-1 Higashi, Tsukuba 305-8561, Japan

\*Corresponding author: takaki@kit.ac.jp

### Abstract

It is vitally important to ensure the safety of brittle materials. Therefore, it is essential to deeply understand the interaction of the material's microstructure and crack propagation. In this study, we constructed a multi-phase-field crack model which can express both, grain growth and crack propagation. To evaluate the basic characteristics of the developed model, we performed two-dimensional crack propagation simulations in a bicrystal when a crack enters a grain boundary by changing the ratio of the grain boundary energy to the crack surface energy and a threshold value of elastic strain energy for crack propagation. As a result, it is confirmed that the model can reasonably determine the crack path, depending on those conditions. Furthermore, by performing crack propagation simulations in a polycrystal, it is concluded that the model can properly express transgranular and intergranular cracks.

**Keywords:** Multi-phase-field method, Crack propagation, Polycrystal, Fracture mechanics

### Introduction

Ferroelectric ceramics are widely used for ceramic condensers due to their superior properties in terms of dielectricity and insulation. In order to ensure the safety of brittle ferroelectric ceramics, it is important that microcrack propagation leading to fracture is evaluated accurately. However, the details of fracture have not yet been understood because fracture phenomena in microstructure are very complicated (Abdollahi and Arias, 2012). It is essential to deeply understand the interaction of the material's microstructure and crack propagation, because these two factors are closely interrelated (Guo, Chang and Chen, 2012). There are many studies on the fracture behavior of ferroelectric ceramics (Landis, 2003; Sheng and Landis, 2007; Zhu and Yang, 1999). However, since a fixed crack is assumed in most of these studies, investigations to understand the interaction of the material's microstructure and crack propagation are required as soon as possible.

The finite element method is the most famous numerical approach to evaluate crack propagation. However, it needs complex remeshing operations around the crack tip (Nagashima, Omoto and Tani, 2003; Kim, Wakayama and Kawahara, 1995). In addition, it is difficult to track the crack tip in complex microstructures. Recently, phase-field crack models have been developed (Henry, 2008; Song, Soh and Ni, 2007). Because the phase-field method does not need to track the crack tip position, it is thought that it can show its strength in crack propagation simulations in complex microstructures. However, such a phase-field crack model has not yet been proposed.

In this study, we develop a multi-phase-field crack model which can express crack propagation in those parts of the microstructure where grain growth takes place. To evaluate the validity of this model, we performed two-dimensional crack propagation simulations in a bi- and a polycrystal.

### Multi-phase-field crack model

In the framework of the general multi-phase-field method applied to problems like grain growth, we construct a multi-phase-field crack model that can simulate crack propagation and grain growth simultaneously. Here, we use the multi-phase-field model proposed by Steinbach and Pezzolla (Steinbach and Pezzolla, 1999).

### Phase-field variable

We use multiple phase-field variables  $\phi_1, \phi_2, \dots, \phi_n$ . Here,  $n$  is the number of grains and cracks and the phase-field variable  $\phi_i$  is defined as  $\phi_i = 1$  inside of grain or crack  $i$  and  $\phi_i = 0$  in all other grains or cracks.  $\phi_i$  changes smoothly and rapidly at the grain boundary and crack surface regions. The phase-field variable  $\phi_i$  must satisfy the condition  $\sum_{i=1}^n \phi_i = 1$  at a grid point.

### Free energy functional

The free energy functional can be described as

$$F = \int_V f dV = F = \int_V (f = f_{doub} + f_{grad} + f_{elast}) dV, \quad (1)$$

where the double well potential  $f_{doub}$  and the gradient energy density  $f_{grad}$  are expressed as

$$f_{doub} = \sum_{i=1}^n \sum_{j=i+1}^n (W_{ij} \phi_i \phi_j), \quad (2)$$

$$f_{grad} = \sum_{i=1}^n \sum_{j=i+1}^n \left( -\frac{a_{ij}^2}{2} \nabla \phi_i \cdot \nabla \phi_j \right), \quad (3)$$

with  $W_{ij}$  and  $a_{ij}$  being the energy barrier height and the gradient coefficient, respectively, in the grain boundary between grain  $i$  and  $j$ .  $f_{elast}$  is the elastic strain energy density.

### Time evolution equation

Substituting Eq. (1) into the Allen-Cahn equation yields the time evolution equation of the phase-field variable  $\phi_i$ :

$$\frac{\partial \phi_i}{\partial t} = -\frac{2}{n} \sum_{j=1}^n M_{ij}^{\phi} \left[ \sum_{k=1}^n \left\{ (W_{ik} - W_{jk}) \phi_k + \frac{1}{2} (a_{ik}^2 - a_{jk}^2) \nabla^2 \phi_k \right\} + \left( \frac{\partial f_{elast}}{\partial \phi_i} - \frac{\partial f_{elast}}{\partial \phi_j} \right) \right], \quad (4)$$

where  $M_{ij}^{\phi}$  is the phase-field mobility. The derivative of the elastic strain energy density is expressed as

$$\frac{\partial f_{elast}}{\partial \phi_i} - \frac{\partial f_{elast}}{\partial \phi_j} = \mp \frac{8}{\pi} \sqrt{\phi_i \phi_j} (f_e - f_c), \quad (5)$$

with

$$f_e = \frac{1}{2} C_{ijkl} \varepsilon_{ij} \varepsilon_{kl}. \quad (6)$$

Here,  $C_{ijkl}$  is the elastic coefficient tensor of a material;  $\varepsilon_{ij}$  is the strain tensor; and  $f_c$  represents the threshold value of the elastic strain energy for crack propagation. The subscripts only in Eq. (6) indicate tensor components. Here, Eq. (5) only works at the crack surface between a crack and the surrounding material. The sign of the right side becomes negative when  $i$  represents a crack and it becomes positive when  $i$  indicates bulk material. As a result, by substituting Eq. (5) into Eq. (4), the following final time evolution equation for  $\phi_i$  can be obtained:



$$\frac{\partial \phi_i}{\partial t} = -\frac{2}{n} \sum_{j=1}^n M_{ij}^{\phi} \left[ \sum_{k=1}^n \left\{ (W_{ik} - W_{jk}) \phi_k + \frac{1}{2} (a_{ik}^2 - a_{jk}^2) \nabla^2 \phi_k \right\} \mp \frac{8}{\pi} \sqrt{\phi_i \phi_j} (f_e - f_c) \right]. \quad (7)$$

Here, the gradient coefficient  $a_{ij}$ , the energy barrier height  $W_{ij}$ , and the phase-field mobility  $M_{ij}^{\phi}$  can be related to material parameters by the following equations:

$$a_{ij} = \frac{2}{\pi} \sqrt{2\delta\gamma_{ij}}, \quad W_{ij} = \frac{4\gamma_{ij}}{\delta}, \quad \text{and} \quad M_{ij}^{\phi} = \frac{\pi^2}{8\delta} M_{ij}, \quad (8)$$

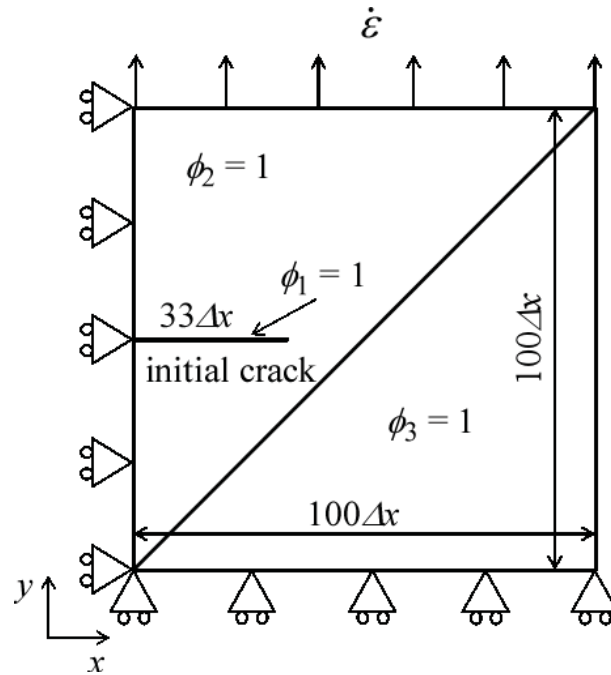
where  $\delta$  is the grain boundary or crack surface thickness (both are assumed to be identical),  $\gamma_{ij}$  is the grain boundary energy, and  $M_{ij}$  is the grain boundary mobility.

### Simulations of crack propagation in a bicrystal

The basic characteristics of the multi-phase-field crack model derived in the previous section are investigated by performing crack propagation simulations in a bicrystal. Here, we evaluate the effects of the grain boundary energy and the threshold value of elastic strain energy on crack propagation into a grain boundary. The computational model and the boundary conditions used in the present simulations are shown in Fig. 1. Here, we set  $\phi_1 = 1$  in the crack,  $\phi_2 = 1$  in grain 1 and  $\phi_3 = 1$  in grain 2. The displacements of the left and bottom sides of the model are constrained to the  $x$ - and  $y$ -directions, respectively. The lattice size is set to  $\Delta x = \Delta y = 1 \mu\text{m}$ , and an initial crack has a length of  $1/3$  of the width of the computational domain. The constant strain rate of  $\dot{\varepsilon} = 1 \times 10^{-2} / \text{s}$  is applied to the top surface. For  $\phi_i$ , we set the zero Neumann condition in all boundaries. Moreover, the following parameters are used: grain boundary thickness of  $\delta = 4\Delta x$ , surface energy of the crack of  $\gamma = 1 \text{ J/m}^2$ , and crack mobility of  $M = 1 \times 10^{-5} \text{ m}^4/\text{Js}$ . In case of the conditions illustrated in Fig. 1, the gradient coefficient  $a_{ij}$ , energy barrier height  $W_{ij}$ , and phase-field mobility  $M_{ij}^{\phi}$  in Eq. (8) are expressed as

$$a_{ij} = \begin{bmatrix} 0 & a & a \\ a & 0 & a_{gb} \\ a & a_{gb} & 0 \end{bmatrix}, \quad W_{ij} = \begin{bmatrix} 0 & W & W \\ W & 0 & W_{gb} \\ W & W_{gb} & 0 \end{bmatrix}, \quad \text{and} \quad M_{ij}^{\phi} = \begin{bmatrix} 0 & M^{\phi} & M^{\phi} \\ M^{\phi} & 0 & 0 \\ M^{\phi} & 0 & 0 \end{bmatrix}, \quad (9)$$

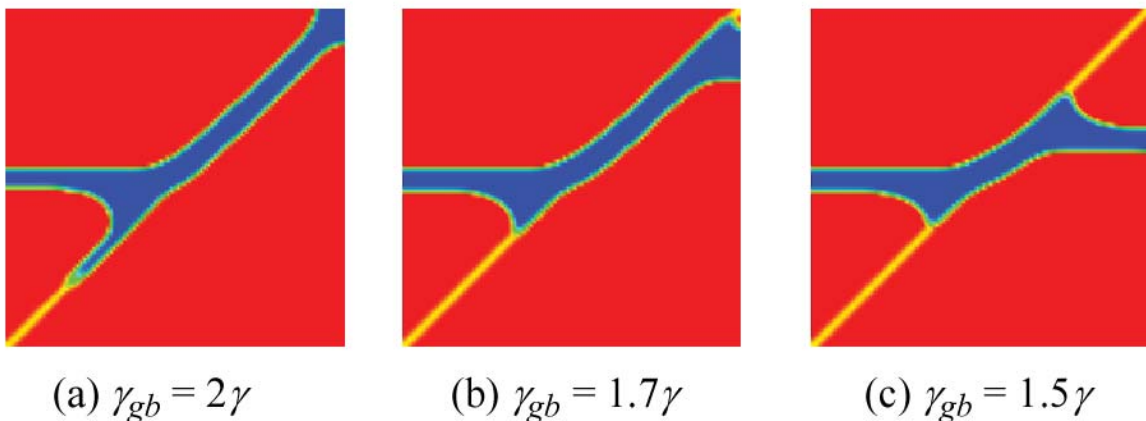
where  $a$  with and without subscript stands for the grain boundary and crack surface, respectively. In the present simulations, we assumed that the grain boundaries have zero mobility, though the present model can simulate the crack propagation in microstructure where the grains grow.



**Figure 1. Computational model and boundary conditions for a bicrystal**

#### *Effect of grain boundary energy*

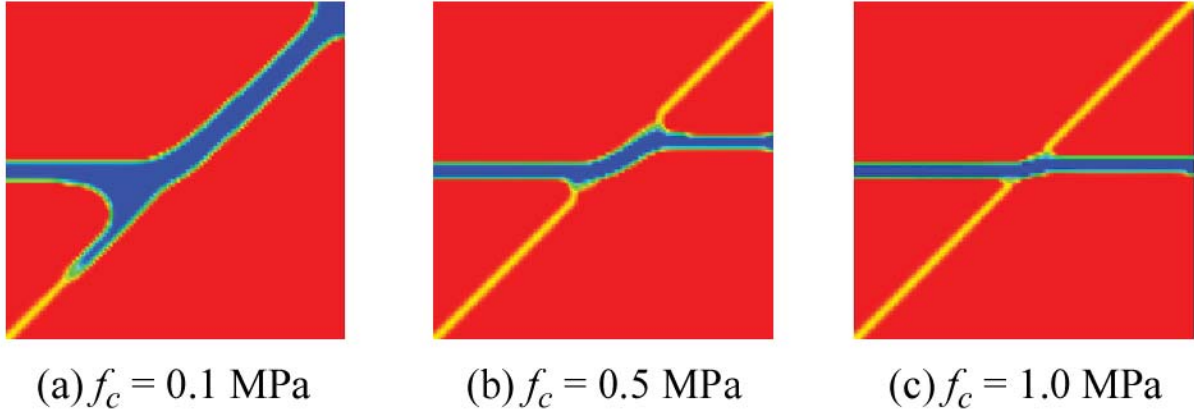
The grain boundary energies  $\gamma_{gb}$  are set to  $2.0\gamma$ ,  $1.7\gamma$  and  $1.5\gamma$ . Figure 2 shows the calculated crack paths after crack propagation for three different grain boundary energies. In Fig. 2, the blue area represents the crack, the red areas represent grains 1 and 2 and the yellow line represents the grain boundary. As a result, we confirmed that the crack develops along the grain boundary for all grain boundary energies. In Fig. 2 (b) and (c), the crack propagates into grain 2 from the grain boundary. Because the crack path is determined in such a way as to reduce the total energy of the system, in case of small grain boundary energy, a larger energy benefit is obtained if the crack runs into the grain. We can also see that the crack progresses toward the lower left direction. The tendency is remarkable in case of larger grain boundary energy with larger tension. From the above, it is confirmed that the multi-phase-field crack model can represent the crack path in dependence of the grain boundary energy.



**Figure 2. Crack propagation paths depending on the grain boundary energy**

### *Effect of a threshold value of the elastic strain energy*

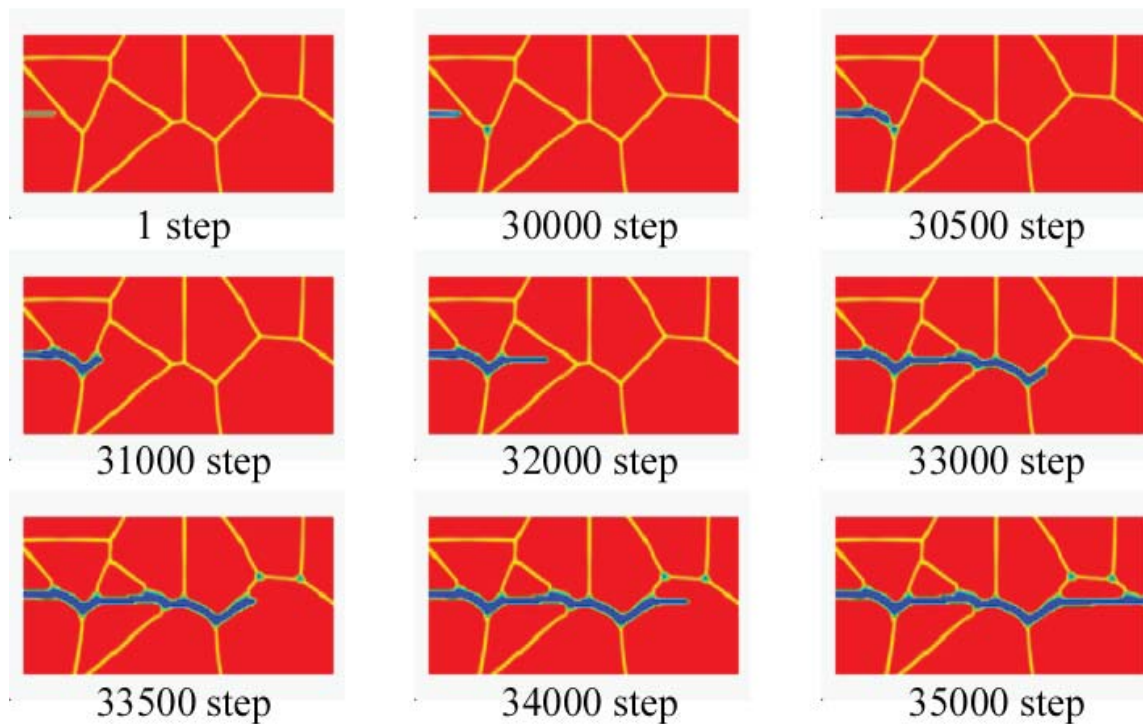
The variable threshold values of the elastic strain energy used for crack propagation are 0.1 MPa, 0.5 MPa, and 1.0 MPa. Figure 3 shows the calculated crack path for three different threshold values. Here, we use  $\gamma_{gb} = 2\gamma$ . As evident from Fig. 3, it is observed that the crack propagation length in the grain boundary decreases with an increase of the threshold value. Moreover, the start time of crack propagation was delayed by increasing the threshold value. Therefore, it is confirmed that the threshold value of the elastic strain energy is appropriately incorporated into the model.



**Figure 3. Crack propagation paths depending on the threshold value of the elastic strain energy**

### **Simulation of crack propagation in a polycrystal**

In this section, we perform a crack propagation simulation in a polycrystal by applying the multi-phase-field crack model. Figure 4 shows the time slices during crack propagation for a model size of  $200\Delta x \times 100\Delta y$ . In the numerical model, an initial crack of length  $20\Delta x$  is placed at the center of the left side and 10 crystal grains are prepared. The other conditions are identical to those described in the previous section. Here, we use  $\gamma_{gb} = 2\gamma$  and  $f_c = 0.5$  MPa. From Fig. 4, we can see blue regions at some triple points in front of the crack tip. This phenomenon should not be considered strictly, because it is caused by the particular choice of the selected parameters. Nevertheless, it is observed that transgranular and intergranular cracks can be automatically represented in a polycrystal by the developed multi-phase-field crack model.



**Figure 4. Time slices during crack propagation in a polycrystal**

## Conclusions

We developed a multi-phase-field crack model that can represent crack propagation and grain growth simultaneously. By performing two-dimensional crack propagation simulations in a bicrystal, the basic characteristics of the multi-phase-field crack model were evaluated by changing the ratio of the grain boundary energy to the surface energy of the crack surface and including a threshold value of the elastic strain energy. Furthermore, by performing crack propagation simulations in a polycrystal, it is concluded that the multi-phase-field crack model can appropriately represent transgranular and intergranular cracks.

## References

- Abdollahi, A. and Arias, I. (2012), Numerical simulation of intergranular and transgranular crack propagation in ferroelectric polycrystals. *International Journal of Fracture*. 174, pp.3-15.
- Guo, X., Chang, K. and Chen, L. Q. (2012), Determination of fracture toughness of AZ31 Mg alloy using the cohesive finite element method. *Engineering Fracture Mechanics*. 96, pp.401-415.
- Landis, C. M. (2003), On the fracture toughness of ferroelastic materials. *J Mech Phys Solids*. 51, pp.1347-1369.
- Sheng, J. S. and Landis, C. M. (2007), Toughening due to domain switching in single crystal ferroelectric materials. *Int J Fract*. 143, pp.161-175.
- Zhu, T. and Yang, W. (1999), Fatigue crack growth in ferroelectrics driven by cyclic loading. *J Mech Phys Solids*. 47, pp.81-97.
- Nagashima, T., Omoto, Y. and Tani, S. (2003), Stress intensity factor analysis of interface cracks using X-FEM. *International Journal for Numerical Methods in Engineering*. 56, pp.1151-11773.
- Kim, B., Wakayama, S. and Kawahara, M. (1995), Simulation of transgranular/intergranular crack propagation process in 2-dimensional polycrystals. *The Japan Society of Mechanical Engineers*. 61, pp.1241-1247.
- Henry, H. (2008), Study of the branching instability using a phase field model of inplane crack propagation. *Europhysics Letters*. 83, pp.1-6.
- Song, Y. C., Soh, A. K. and Ni, Y. (2007), Phase field simulation of crack tip domain switching in ferroelectrics. *J Phys D Appl Phys*. 40, pp. 1175-1182.
- Steinbach, I. and Pezzolla, F. (1999), A generalized field method for multiphase transformations using interface fields. *Physica D*. 134, pp.385-393.

## Low-dispersion sampling-based parameter importance measure analysis for anti-ice piccolo structure of anti-resonance design

\*ZHANG Feng, HE Xindang, NAN Hua, YAO Huiju

School of Mechanics, Civil Engineering and Architecture, Northwestern Polytechnical University, China

\*Corresponding author: yifengzhang@163.com

### Abstract

In this paper, low-dispersion sampling-based importance measure analysis method is carried out for the anti-ice piccolo structure of anti-resonance design. First, the finite element model of anti-ice piccolo structure is established and the modal analysis is performed. Then based on the deterministic analysis, the importance measure model between structural size parameters and the natural frequency response is established. The proposed method uses the quadratic response surface methodology to fit the fundamental function between the natural frequency and variables, and a low dispersion sampling method is used to perform the structural parameter importance measure analysis. The analysis results can provide guidance for the anti-ice piccolo structural anti-resonance design.

**Keywords:** anti-ice piccolo structure, natural frequency, importance measure, low-dispersion sampling, response surface

### Introduction

When an aircraft flies through clouds with low temperature or high humidity, the unexpected icing phenomenon may occur. Icing at wings will increase the aircraft weight, thus affect the maneuverability and stability of the aircraft. Light icing may trigger flight failures, and severe cases can lead to plane crash [1, 2]. Therefore, anti-ice design is needed for the civil and transport aircrafts, especially at the wing leading edge and other key parts.

Anti-ice piccolo structure is the core part of a wing anti-ice system. Its location is close to aircraft engines, and it is subject to random excitations generated by the engines. Therefore, there exists the possibility of structural resonances. Once the resonance happens, it may result in structural fatigue failures [3, 4]. Therefore, anti-resonance design is needed for anti-ice piccolo structure. Importance measure analysis can find out those design parameters which significantly affect the structural dynamics performance. This can provide guidance for the anti-resonance design of anti-ice piccolo structure [5].

Among importance measure analysis methods, the Monte Carlo method has been studied extensively. The most important advantage of Monte Carlo method is that it is unrestricted by the number of random variables, the type of probability distributions and response function etc [6,7]. However, the traditional Monte Carlo method firstly draws random samples using the uniformly distributed random number generator, and then obtains the needed samples by the conversion according to the real distributions. It is pointed out that at the case of small sample size, the distribution characteristics of sample points obtained in this way are not evenly distributed. In order to improve the quality of sampling points, Hua and Wang[8] proposed low dispersion sampling method based on number theory. It is proved that the convergence rate of this method is faster and the computing cost is smaller than the random sampling methods[9]. Therefore, we adopt the low dispersion sampling method to perform parameter importance measure analysis for the anti-ice piccolo structure.

In this paper, the anti-ice piccolo structure is taken as the research target, and the low-dispersion sampling-based importance measure analysis method is applied to perform importance measure

analysis for the anti-ice piccolo structure. First, the anti-ice piccolo structure finite element model is established and the modal analysis is performed. Then, considering the structural size dispersion and based on the deterministic analysis, the importance measure model between structural size parameters and the natural frequency response is established. The proposed method uses the quadratic response surface methodology to fit the fundamental function between natural frequency and variables, and a low dispersion sampling method is used to perform the structural parameter importance measure analysis. The analysis results can provide guidance for the anti-ice piccolo structural anti-resonance design.

**1. The importance measure analysis model for the anti-ice piccolo structure**

**1.1 Modal analysis pipeline**

An aircraft wing anti-ice cavity structure is shown in Fig.1. Anti-ice piccolo is in the middle of the ice chamber. Its role is to assign the hot air coming from the engine to the wing leading edge. By heating the wing surface, we can achieve the purpose of anti-ice.

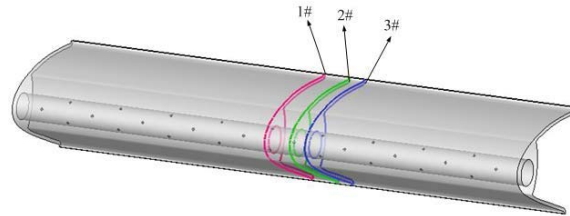


Fig.1 Geometrical model of anti-ice cavity structure

In this paper, we take one of the components of the anti-ice piccolo structure to perform the parameter importance measure analysis. The geometric dimension model of anti-ice piccolo structure is shown in Fig.2.

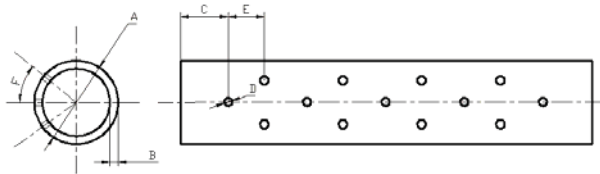


Fig.2 Geometrical model of piccolo structure

The finite element model (FEM) of anti-ice piccolo structure is shown in Fig.3, which is built with ANSYS software. The local mesh model is shown in Fig.4.

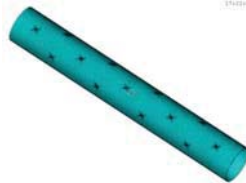


Fig.3 FEM model of piccolo structure

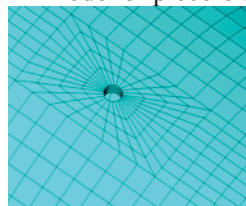


Fig.4 Local mesh model

By the modal analysis, the first four steps of nature frequencies of anti-ice piccolo structure can be obtained. The analysis results of nature frequencies are shown in Table 1 and the first four steps of natural mode shapes are shown in Fig.5.

Table 1 First four steps of nature frequencies of piccolo structure

mode step	1	2	3	4
nature frequency(Hz)	1538.4	1613.8	1819.0	1827.5

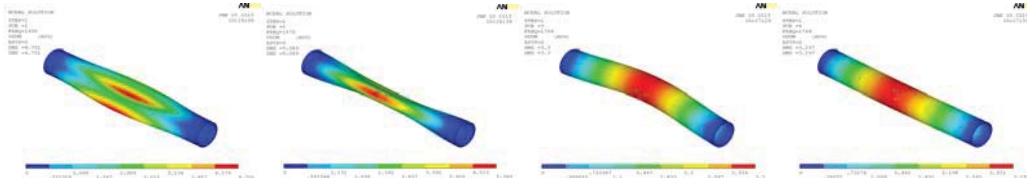


Fig.5 First four steps of natural mode shapes of piccolo structure

## 1.2 Importance measure analysis model of anti-ice piccolo structure

Randomness exists in the dimension parameters of piccolo structure, and these random variables are independent. The distribution types and distribution parameters are shown in table 2.

Table 2 Distribution type and parameter of the random variables

inputs	Identifier	the type of distribution	mean	standard deviation
Pipe diameter A(m)	$x_1$	Normal distribution	0.0558	0.001
Pipe wall thickness B(m)	$x_2$	Normal distribution	0.001	0.00004
Hole Side C(m)	$x_3$	Normal distribution	0.04	0.0008
Diameter D(m)	$x_4$	Normal distribution	0.0018	0.00007
Hole spacing E(m)	$x_5$	Normal distribution	0.04	0.0008
Hole angle F(°)	$x_6$	Normal distribution	45	1

Assume that the probability density functions of the variables  $x_k (k=1,2,\dots,6)$  are marked with  $f_k(x_k) (k=1,2,\dots,6)$ . Then the joint probability density function of the structural parameters is

$$f_x(\mathbf{x}) = \prod_{k=1}^6 f_k(x_k).$$

In the anti-ice cavity structure, the piccolo structure is subject to random excitations. As can be seen in Table 1, the external excitation frequency  $\lambda$  is close to the first natural frequency  $\eta$  of the structure. According to the stress-strength interference model, performance function of structure resonance failure can be calculated by Eq.(1):

$$g(\eta, \lambda) = |\eta - \lambda| \quad (1)$$

In engineering, a value  $\delta$  is first given according to the requirement of anti-resonance design. When  $g(\eta, \lambda) \leq \delta$ , the resonance structure fails; when  $g(\eta, \lambda) > \delta$ , the structure is safe. This shows that the natural frequency  $\eta$  is important for the anti-resonance design. The natural frequency  $\eta$  is a function of the basic variables  $(x_1, x_2, \dots, x_6)$ . Therefore, performing importance measure analysis for the natural frequency is meaningful for anti-resonance design of the piccolo structure.

According to Refs.[10, 11], the importance measures of the structural parameters for the natural frequency are defined below

$$S_k = \frac{Var[E(\eta(\mathbf{x}) | x_k)]}{Var[\eta(\mathbf{x})]} \quad (k=1,2,\dots,6) \quad (2)$$

where  $Var[\eta(\mathbf{x})]$  is the variance of  $\eta(\mathbf{x})$ ,  $E(\eta(\mathbf{x}) | x_k)$  is the mean value of  $\eta(\mathbf{x})$ .

In Eq.(2), the value of  $Var[\eta(\mathbf{x})]$  can be estimated by the Monte Carlo method. The estimated value  $\hat{Var}[\eta(\mathbf{x})]$  of  $Var[\eta(\mathbf{x})]$  is formulated as

$$\hat{Var}[\eta(\mathbf{x})] = \frac{1}{N} \sum_{j=1}^N [\eta(\mathbf{x}_j)]^2 - \left[ \frac{1}{N} \sum_{j=1}^N \eta(\mathbf{x}_j) \right]^2 \quad (3)$$

Similarly,  $Var[E(\eta(\mathbf{x}) | x_k)]$  can be calculated by Monte Carlo method. Then substitute it into Eq.(2), the importance measures of the structural parameters can be obtained. The importance measure indicator  $S_k$  of the input parameter  $x_k$  characterizes the uncertainty of random variables  $x_k$  acting alone on the variability of the natural frequency  $\eta(\mathbf{x})$ . This variance-based importance measure can reflect the impact of input parameters variability on the variability of the natural

frequency. So it can provide guidance for engineers to adjust the input design parameters for the purpose of improving the anti-resonance capability.

### 1.3 First natural frequency approximation based on quadratic response surface

In the process of importance measure analysis, structural natural frequency is an implicit function of input parameters, so it needs to perform the mode analysis with ANSYS software to obtain the natural frequency of anti-ice piccolo structure. If we directly use Monte Carlo method to repeatedly call the ANSYS software to implement random sample analysis, the computation cost will be very high. Therefore, in this paper, we use high-precision fitting method to fit the relationship between the natural frequency and input parameters so as to reduce the computation cost [12]. Among the response surface models, the fitting error of first-order response surface model is too large to reflect the true performance of structure. Although higher-order polynomial has higher fitting accuracy, it needs a high computational cost because a large number of items are involved. Especially in the case of multi-variable problem, the computational cost of fitting response surface will be unacceptable. For piccolo structure analysis, computational cost of second-order response surface is relatively small, and its fitting accuracy can meet the engineering application requirements [13, 14]. Therefore, this work uses quadratic response surface method to fit explicit functional relationship between the structure natural frequency and size parameters, and the formula is expressed as

$$\hat{\eta}(\mathbf{x})=F(x_1, \dots, x_6) + \varepsilon \quad (4)$$

where  $\varepsilon$  is the statistical error.

The quadratic polynomial response surface model contains 28 coefficients, and  $\hat{\eta}(\mathbf{x})$  can be calculated by Eq.(5).

$$\hat{\eta}^{(p)}(\mathbf{x}) = c_0 + \sum_k c_k x_k^{(p)} + \sum_{i=1}^6 \sum_{j=i}^6 c_{ij} x_i^{(p)} x_j^{(p)} \quad (p = 1, 2, \dots, n_s) \quad (5)$$

where  $n_s$  is the number of sample, and  $\mathbf{c} = [c_0 \quad c_1 \quad \dots \quad c_{27}]^T$  is the regression coefficient matrix.

Eq.(5) can be written in the form of matrices, as shown in Eq.(6)

$$\hat{\boldsymbol{\eta}} = \mathbf{X}\mathbf{c} + \boldsymbol{\varepsilon} \quad (6)$$

The regression coefficient matrix can be obtained by the least squares method.

$$\mathbf{c} = (\mathbf{x}^T \mathbf{x})^{-1} \mathbf{x}^T \hat{\boldsymbol{\eta}} \quad (7)$$

After the response surface model is obtained, we use  $R^2$  (multiple correlation coefficient),  $R_a^2$  (corrected multiple correlation coefficient) and %RMSE (root mean square deviation) to assess the adaptability of the model, which are calculated as follows

$$R^2 = 1 - \frac{SS_E}{SS_T} \quad (8)$$

$$R_a^2 = 1 - \frac{SS_E / (n_s - 20)}{SS_T / (n_s - 1)} \quad (9)$$

$$\%RMSE = 100 \sqrt{\frac{1}{n_s} \sum_{p=1}^{n_s} (\eta^{(p)} - \hat{\eta}^{(p)})^2} \bigg/ \left( \frac{1}{n_s} \sum_{p=1}^{n_s} \eta^{(p)} \right)} \quad (10)$$

where  $SS_E = \sum_{p=1}^{n_s} (\eta^{(p)} - \hat{\eta}^{(p)})^2$  is squares sum of error,  $SS_T = \sum_{p=1}^{n_s} (\eta^{(p)})^2 - (\sum_{p=1}^{n_s} \eta^{(p)})^2 / n_s$  is the total squares sum.

## 2 Methods for solving importance measures of the anti-ice piccolo structural parameters

### 2.1 The existent method-random sampling method

The Monte Carlo-based parameter importance measure analysis method needs to produce samples following the distributions of the basic variables, which are transformed from samples of uniform distribution [0,1]. Currently, there are many methods to generate samples that follow the [0,1] uniform distribution, and the simplest method is the random sampling. The samples generating recurrence formula can be expressed as



$$\begin{cases} y_j \equiv (\lambda y_{j-1} + b) \pmod{M} \\ r_j = y_j / M \end{cases} \quad j = 1, 2, \dots \quad (11)$$

where  $\lambda$  is multiplier,  $M$  is modulus,  $b$  is incremental, and  $y_0$  is random source. All of them are pre-selected non-negative integers.

## 2.2 The proposed method-low dispersion sampling method

Low dispersion sampling method excludes the randomness of samples by the number theory. Thus, it can be more specific and exact to give the evenly distributed sample points. There are three low dispersion point sets. They are good lattice points set, good points set, and best uniform points set. Among these three points sets, the good lattice points set and best uniform points set are finite sets, and their sample sizes are imposed, so they are not able to add additional sample on the basis of existing sample size [9]. When using Monte Carlo method to perform importance measure analysis, the required sample size cannot be known in advance, which restricts the application of the good lattice point set and the best consistent points set on the importance measure analysis. Nevertheless, the sample size of good point set is not limited, and its computation process is simple, which makes it possible for us to use it into importance measure analysis. Hua and Wang[8] give the construction method of good points set based on low-dispersion sample. The analysis process of this method is as follows.

A six dimension good point  $\mathbf{r} = (r_1, r_2, \dots, r_6)$  iteration formats can be expressed as

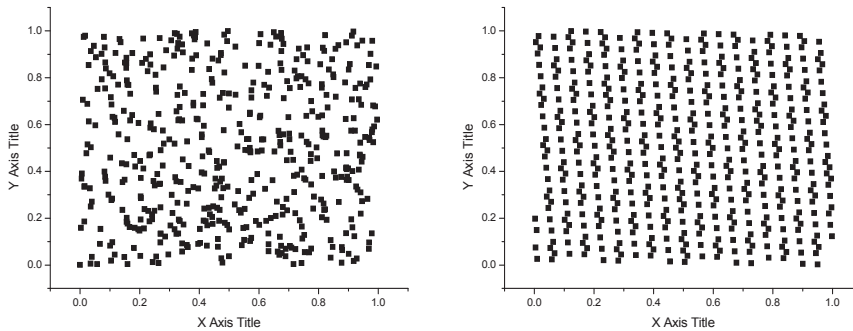
$$r_k^{(j)} = q_k j - \text{int}(q_k j) \quad (j = 1, 2, \dots, N; k = 1, 2, \dots, 6) \quad (12)$$

where  $\text{int}(\cdot)$  denotes the tail section rounding operation, and  $q_k$  can be generated through the sub-domain method, such as

$$q_k = 2 \cos \frac{2k\pi}{s} \quad (k = 1, 2, \dots, 6) \quad (13)$$

where  $s$  is a prime number, and  $s \geq 13$ .

Fig.6 shows the distribution characteristics -of 500 two-dimensional [0,1] uniformly distributed random samples that are generated by random sampling and low dispersion sampling respectively. Fig.6 clearly shows that low-dispersion sampling method under small sample size is better than random sampling method in terms of sample uniformity.



(a) random sampling

(b) low dispersion sample

Fig.6 500 Group 2D [0,1] uniformly distributed sample points

## 3 Importance measure analysis of the structural parameters

Based on the above analysis, we can get the process of parameter importance measure analysis for anti-ice piccolo structure, which is shown in Fig.7.

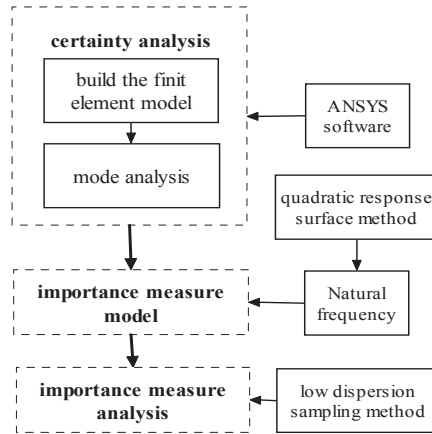


Fig 7. Flowchart of importance measure analysis for anti-icing cavity structural parameter

By using the quadratic response surface method, we obtain the relationship function  $\hat{\eta}(x)$  between the first natural frequency and size parameters. After the response surface model is obtained, we use the  $R^2$  (multiple correlation coefficient),  $R_a^2$  (corrected multiple correlation coefficient) and % RMSE (root mean square deviation) to assess the adaptability of the model with Eqs.(8)-(10). The result shows that the multiple correlation coefficient  $R^2$  is 3.158%, the corrected multiple correlation coefficient  $R_a^2$  is 2.49%, and the root mean square deviation (%RMSE) is 0.98573%, which can meet the requirements of analysis accuracy.

Then low dispersion sampling method is used to perform the parameter importance measure analysis. The analysis results are shown in Table 3 and Fig.8.

Table 3 Results of importance measure analysis

variable	$x_1$	$x_2$	$x_3$	$x_4$	$x_5$	$x_6$
measure	0.566144	0.296415	0.002300	0.029427	0.070208	0.000254

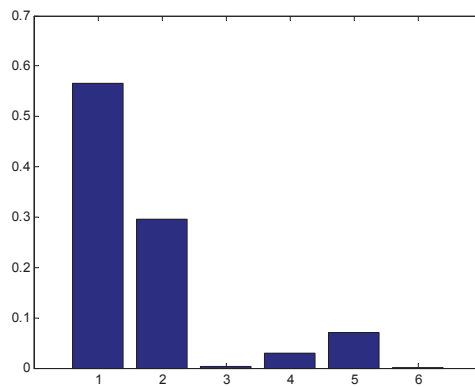


Fig.8 Diagram of random variables importance measure analysis results

As can be seen from Fig.8, pipe diameter and pipe wall thickness of the structure have greater impacts. Therefore, in optimization design they should be especially focused on.

#### 4 Conclusions

- (1) Based on mode analysis with ANSYS software, the importance measure model between structural size parameters and the natural frequency response is established. The fitting process of structural natural frequency based on quadratic response surface method is proposed.
- (2) The flowchart of low-dispersion sampling-based importance measure analysis for the anti-ice piccolo structure is established.

(3) By the parameter importance measure analysis, we find that the pipe diameter and pipe wall thickness of the structure have important influences on the variability of the natural frequency. Hereby these parameters need to be paid more attention to in the anti-ice piccolo design.

### Acknowledgements

This work was financially supported by the foundation of the NPU-FFR-JC20100232 and 111 project (NO: B0750).

### Reference

- [1] Thomas R, Guido SB, Cristhian A, Martin SA. FENSAP- ICE: Application of unsteady CHT to De-icing simulations on a wing with inter-cycle ice formation[R]. AIAA 2010-7835.
- [2] Bragg MB, Hutchison T, Merret J. Effect of ice accretion on aircraft flight dynamics [R], AIAA 2000-0360.
- [3] Zhai HB, Wu ZY, Liu YS. Analysis of resonance reliability for a simply supported pipe conveying fluid. *Journal of Vibration and Shock*. 2012,31(12):160-164
- [4] Wang YR, Tian AM. Research on reliability design method of structural vibration [J]. *Journal of Aerospace Power* 2003,18(2):197-200.
- [5] Lu ZZ. Structural mechanism reliability and reliability sensitivity analysis [M]. Beijing: Science Press, 2009.
- [6] Harald N. Random number generation and quasi-monte carlo methods[M]. Pennsylvania: Capital City Press, Montpelier, Vermont, 1992.
- [7] Dai HZ, Wei W. Application of low-discrepancy sampling method in structural reliability analysis[J]. *Structural Safety*, 2009,31(1):55-64.
- [8] Hua LG, Wang Y. Applications of number theory to numerical analysis[M]. Beijing: Science Press, 1981.
- [9] Dai HZ, Wang W. Low discrepancy sampling method for structural reliability sensitivity analysis [J]. *Engineering Mechanics*, 2010,27(1):104-108.
- [10] Saltelli A. Sensitivity analysis for importance assessment [J]. *Risk Analysis*. 2002,22(3):579-590
- [11] Borgonovo E. A new uncertainty importance measure[J]. *Reliability Engineering and System Safety*, 2007,92(6):771-784.
- [12] Kaymaz I, McMahon CA. A response surface method based on weighted regression for structural reliability analysis [J]. *Probabilistic Engineering Mechanics*, 2005,20(1):11-17.
- [13] Gupta S, Manohar CS. An improved response surface method for the determination of failure probability and importance measures[J]. *Structural Safety*, 2004,26(2):123-139.
- [14] Lv ZZ, Zhao J, Yue ZF. An advanced response surface method for mechanical reliability analysis[J]. *Applied Mathematics and Mechanics*. 2007,28(1):19-26.

## A facade design idea generation support system through evolutionary computing

\*Hiroki Matsuda<sup>1</sup> and Kazutoshi Tsutsumi<sup>2</sup>

<sup>1,2</sup>College of Systems Engineering and Science, Shibaura Institute of Technology, JPN  
\*me13078@shibaura-it.ac.jp

### Abstract

In recent years, design methods using algorithms have been incorporated into the designs positively. Creativity support systems can be expected to eliminate the problem of design ruts. In particular, geometric shapes have infinite design pattern, therefore creativity support system will lead to the possibility of greater designs.

In this study, facade design is generated by dividing areas using straight lines. The various product designs will be possible by devising the setting of the parameters.

Keywords: façade design, idea generation support system, evolutionary computing, IDES,

### Introduction

The person's way of thinking has limitations, for it is dependent on the person's own experience or environment. For this reason, we are concerned about the problem of design ruts. A geometric form, such as that shown in Figure. 1, can have infinite design patterns, and thus a more wonderful design may exist in patterns that surpass our own imaginations.

Even if we are able to imagine beautiful architectural designs, these must be realized within an actual structure. In response to this problem, the use of an idea generation support system which proposes a design might be an effective solution, and we have been carrying out various studies for that purpose.

In recent years, complicated structural analysis has become possible through improvements in computer performance.



Figure. 1 Reference examples of building

## System summary

### 1. The design creation technique

Arbitrary points are placed at circumference freely, and then random lines which connect arbitrary two points are set up. These lines divide the surface of a wall and opening design is generated.

#### 1) Cell division and placement of the free points.( Figure.2)

Set the points freely to vertical and horizontal circumference. Facade is divided to cells, and is able to handle with each cell.

#### 2) Placement of random lines. (Figure.3)

Designate the lower and upper limits of the number of lines connecting points. The cells on the lines are the wall. Set whether multiple lines from the same point are permitted. Figure 3 shows an example in which it was not permitted to set multiple lines. The following are conditions for the lines:

- The lines do not overlap with each other.
- The line you have set does not overlap with lines of the circumference.

#### 3) Making the opening and wall. (Figure.4)

Calculate the area of each compartment (number of cells) that is divided by the lines. Set as the opening in order from the small compartment until opening ratio reaches the designated value. In this case, the user sets the minimum area of the opening by consideration of construction process and design evaluation. No compartments below the minimum area can be set as the opening.

#### 4) Setting openings not adjacent to each other. (Figure.5)

As shown in Figure 4, a design with openings born in succession gives a poor design impression. Therefore, in order to prevent continuous openings, the centroid of each compartment must be calculated at first. If the number of intersection of the boundary line and the centroid between each compartment is one, the opening processing does not perform as adjacent compartments.

#### 5) Structural analysis and study

Structural analysis performs two cases, one is a frame structure in which the structure is only a portion of the line, and the other is wall structure as whole facade. The analysis is performed with FEM analysis by applying a uniform load to the mesh nodes of the floor of each layer. Consider the structure performance by indicating analytical results such as the danger figure and the stress contour figure. Danger figure is diagram showing a cell stress equal to or greater than the specified value has occurred.

#### 6) Link with the IDES.

Incorporate the parameters as gene locus to the IDES (Interactive Differential Evolution with Score). A new design which matches the sensitivity of the user and satisfies the opening ratio is proposed by the IDES.

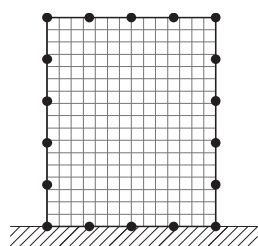


Figure.2

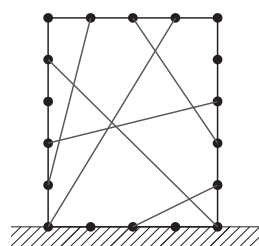


Figure.3

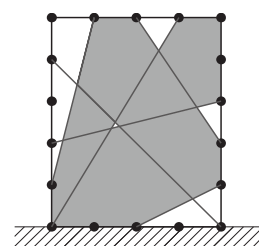


Figure.4

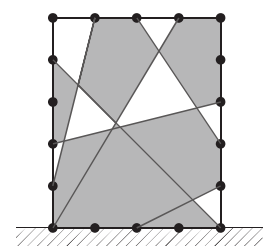


Figure.5 Final image

## 2. System Flow

There are two methods for the form creation, one is evolutionary computation technique which is determined by subjective evaluation by interaction with users and computers, and the other is the method of obtaining the optimal form numerically analytically.

The forms that stimulate the ideas of the user and the forms that have the functions desired by the user can be gained efficiently from the many forms to be presented, by using evolutionary computation techniques.

Our laboratory proposed IDES, and adopted IDES as evolutionary computation technique of design in this system. In IDES, it is necessary to impart a score according to the preference of the user in the paired comparison. Therefore, to reflect the selection of the parent individual of the next generation, a score is given to each individual according to the preference of the evaluator.

In this occasion, this system displays a dangerous figure and stress contour figure of analysis results so that user can take into account the mechanical properties.

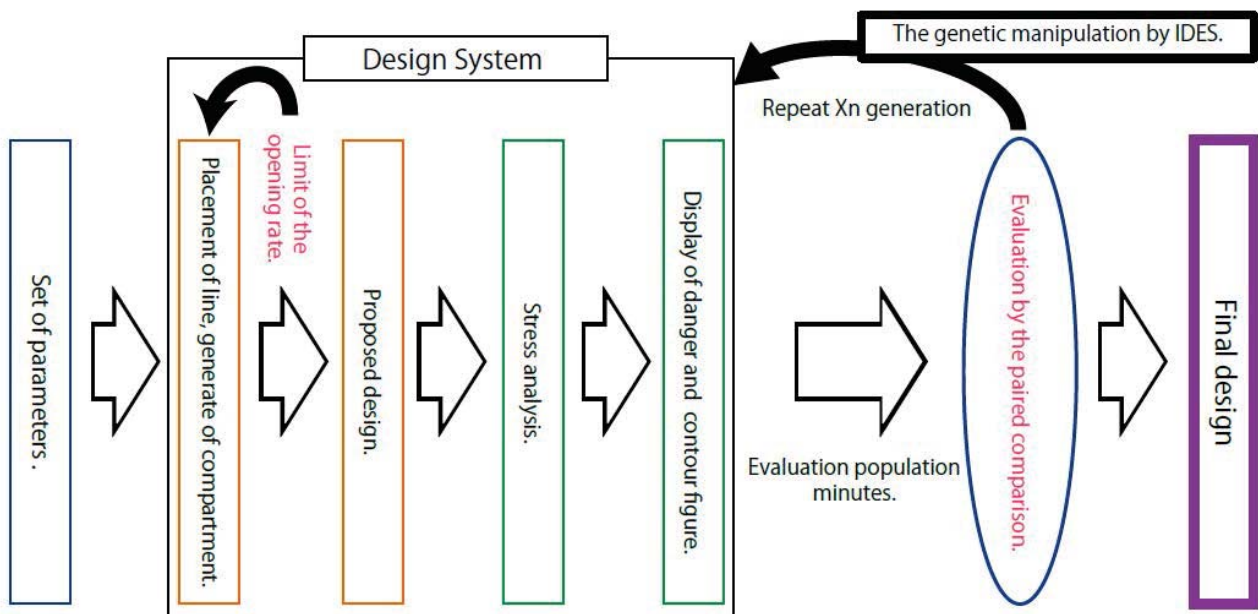


Figure.6 System flow

**The example of execution, and validity**

Figure 7 shows the program execution screen. Figure 8 shows various examples for changing the number of layers, nodes and lines.

The validity of this system was examined by the possibility of generating designs similar to the facade design of the building of Fig. 1. (Figure.9)

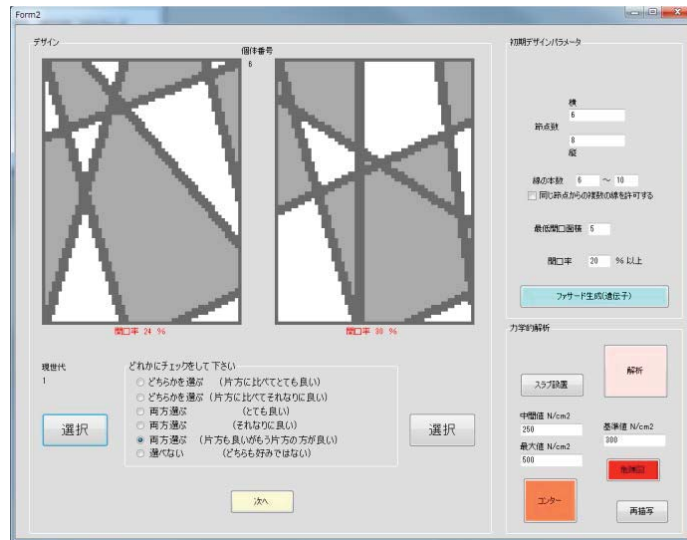


Figure.7 System screen

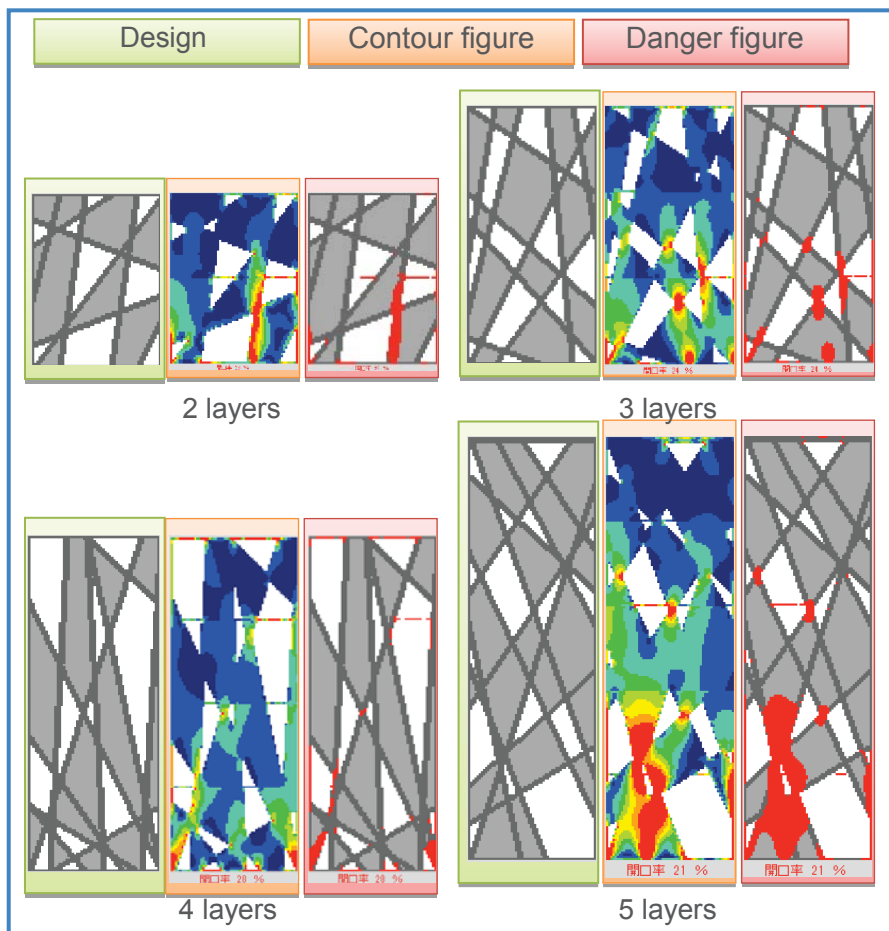


Figure.8 Various examples

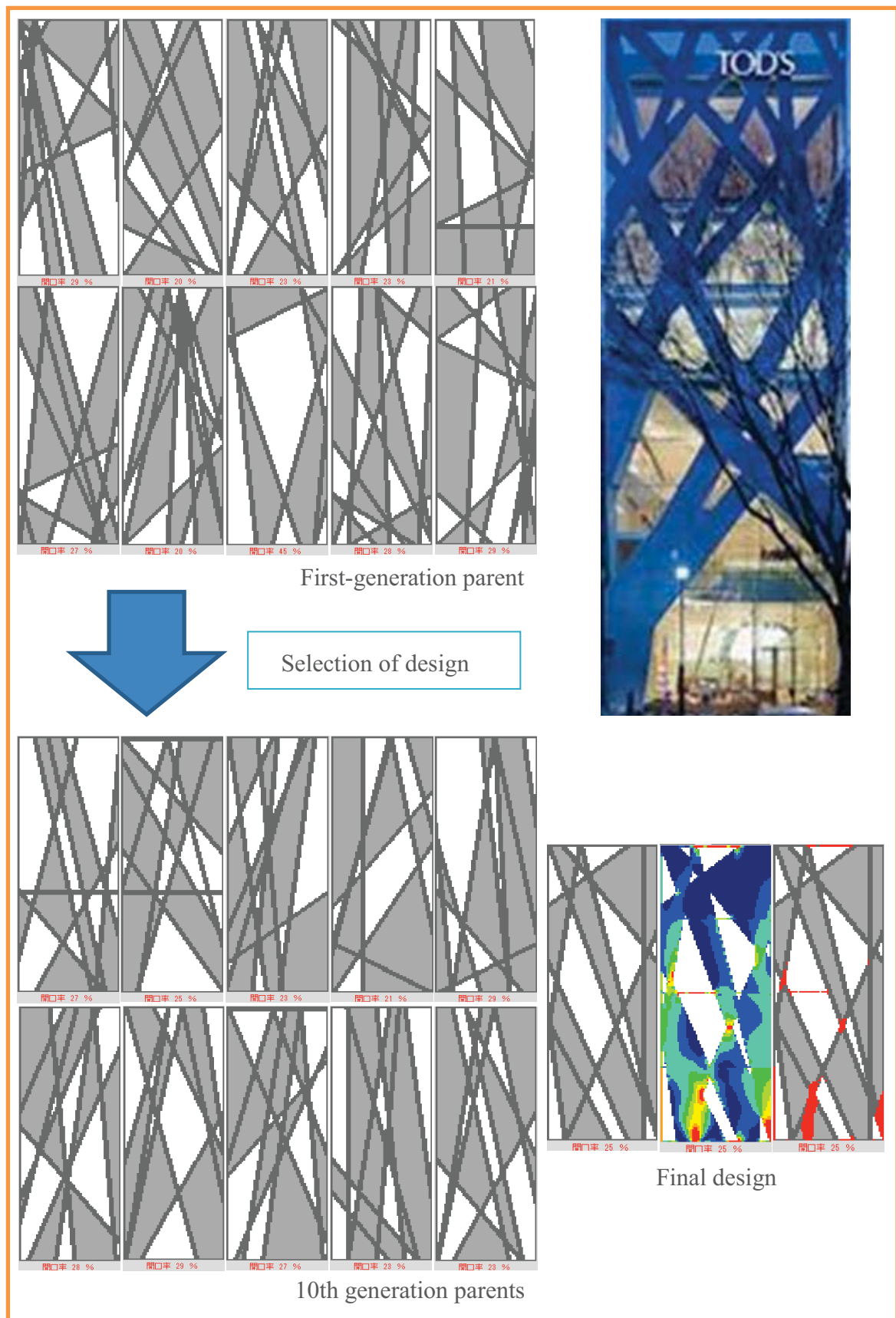


Figure.9 Verification of validity.



## **Conclusions**

Generating various designs is possible by changing the parameters. This system could not create design in complete agreement with the building in Figure 1, but the generation of facade design was approximately similar. It is possible to generate designs considered with the sensibility of the user using this system.

## **Future issue**

In the future, we aim to generate designs not only on a planar dimension but also in 3D. Facade design is considered a crucial factor in the indoor environment and surrounding environment, such as heat or light. Therefore, it is necessary to aim at facade design incorporated environmental factors.

## **References**

Yuya Takeda, Tsutsumi Kazutoshi, (2012), "The way of thinking of the facade design made into the structure Research on a supporting system. Generation and mechanical assessment of the opening design using the lifegame as 3." Analysis and creation 2012 of a Colloquium structure form. , 23-26.

# Effect of Shear Deformation on Convergability of Simple Contact Analysis with Large Displacement

\*Z.M. Nizam<sup>1</sup>, H. Obiya<sup>2</sup>, K. Ijima<sup>3</sup>, R. Tokubuchi<sup>4</sup>, and K. Ishibashi<sup>5</sup>

<sup>1,4</sup> School of Environmental Science and Engineering, Saga University, Japan.

<sup>2,3,5</sup> Department of Civil Engineering and Architecture, Saga University, Japan.  
Saga University, Honjo 1, Saga City, Saga Prefecture, 840-8502, Japan.

\*Corresponding author: mnizam@uthm.edu.my

**Key Words:** *Frictionless Contact Problem, Node-Element Contact, Critical Area, Shear Deformation, Tangent Stiffness Method, Pass-Through*

## Abstract

A common problem encountered in the study of frictionless contact is the failure to obtain stable and accurate convergence result when the contact node is close to the element edge, which is referred as “critical area”. In previous studies, we modified the element force equation to apply it to frictionless node-element contact problem using the Euler-Bernoulli beam theory (Tsutsui, Obiya and Ijima, 2009). A simple single-element consists two edges and a contact point was used to simulate contact phenomenon of a plane frame. The modification was proven to be effective by the convergability of the unbalanced force at the tip of element edge, which enabled the contact node to “pass-through”, resulting in precise results. However, in another recent study, we discovered that, if the shear deformation based on Timoshenko beam theory is taken into consideration, a basic simply supported beam coordinate afforded a much simpler and more efficient technique for avoiding the divergence of the unbalanced force in the “critical area”. Using our unique and robust Tangent Stiffness Method, the improved equation can be used to overcome any geometrically nonlinear analyses, including those involving extremely large displacements.

## 1 Introduction

The various methods and definitions that have been used to study contact problems in recent times have contributed numerous and interesting computation procedures. Previously studied contact phenomena involving large displacements analyses can be classified into four categories, namely contact between surfaces (Aliabadi and Martin, 2000; Rebel, Park and Felippa, 2002; Ayyad, Barboteu and Fernandez, 2009), contact between a node and a surface (Klarbing, 2002), contact between a node and an element (Chen, Nakamura, Mori and Hisada, 1998), and contact between elements (Konyukhov and Schweizrhof, 2010).

In this study, we developed a simple but effective method for studying the basic phenomenon of a node–element contact involving large displacements, and introduce a beam element comprising two edges and a contact point. We elaborate on the development of the method in Section 3. The idealization of the contact element produces a feasible contact phenomenon, which can be realistically computerized. This is illustrated by some numerical examples presented in this paper, in which accurate equilibrium of all nodes within the structure was achieved and the convergence of the unbalanced force was stable during each load increment.

To simulate extremely large deformation analyses, we used the tangent stiffness method (TSM), which produces very accurate and robust results for geometrically nonlinear analyses. Using this method, we formulated a simple but precise contact element without additional parameters or any complex derivation of the tangent geometrical stiffness and the element stiffness equation. Yet the method better satisfied the perfect equilibrium state than a common finite element method (FEM). The robustness is specifically shown in Section 4 as the numerical example 4.2 (Accuracy comparison of FEM to TSM), where a comparison of TSM to the study done by Konyukhov and Schweizrhof, 2010 using solid element by FEM. The study simulated the analysis of a large-deformation frictionless node–element contact of a cantilever beam, densely partitioned into 50 divisions. The comparison showed that the creation of such a large number of divisions is not necessary to obtain accurate results in TSM. Considering the discontinuity of the element boundary discussed by Chen and Nakamura (1998), an equilibrium state can hardly be achieved when the number of element increases. Conversely, TSM can be used to achieve stable convergence result without any concern with the density of mesh division.

In a node–element contact, it is difficult to achieve equilibrium when the contact node approaches the element edge owing to the nonconvergence of the unbalanced force. The sliding of the contact point toward element edges may reduce the  $l_i$  or  $l_j$  in Eqs. (5)-(8) to zero. This is due to a “division by zero” of the force equation matrices of the element given in Eq. (5), and it leads to the divergence of the unbalanced force. It should also be noted that the distance between the edges and the contact node are also the denominator of the matrices. To solve this problem, we used a shear deformation in Timoshenko beam as a countermeasure, including for slender beams. Furthermore, by introducing the shear deformation to the element force equation, the “critical area” where the unbalanced force hardly converges can be made significantly less than those of the Euler–Bernoulli beam, as shown in several examples.

We also studied the “pass-through” of a contact node using a simple algorithm for the inner and outer vector product, which produced stable convergence results, including at the tip of the element. In addition, the algorithm for the “pass-through” of the contact node to the next element was easier to implement and much more accurate at all the edges of the elements. In their work on frictionless node–element contact, Nizam, Obiya, and Burhaida (2008) proposed an algorithm that combines a contact element with the next noncontact element that the contact node is about to “pass-through”. The equilibrium state was successfully achieved by this technique, although its reliability is low due to the change of mesh configuration, which affects the entire scheme. In another study (Tsutsui, Obiya and Ijima, 2009), an element force equation based on the cantilever beam coordinate was used to improve the “pass-through”. The introduced equation enabled the convergence of the unbalanced force when the contact node was relatively close to the edge of the element—a configuration that had not been previously achieved. Furthermore, the findings of this study would facilitate further studies on node–element contact because its definitions and analytical results are precise, reliable, and very robust.

## 2 Tangent Stiffness Method

The TSM was solely idealized to overcome numerical cases exhibiting significant nonlinearity. The superiority of this method is that it converges the unbalanced force with high accuracy by defining element behavior using a simple form of the element

force equation. This theory requires the element edge forces to be treated separately and independently of each other. In addition, strict compatibility and an equilibrium equation are disseminated in the iteration configuration to converge the unbalanced force. This is equivalent to the Newton–Raphson method, which has an extremely high convergence performance.

### 2.1 General formulation

Here, an element has two edges and the force vector of both edges is assumed to be  $\mathbf{S}$ . Considering a plane coordinate system, if the external force vector is denoted by  $\mathbf{U}$ , and the equilibrium matrix by  $\mathbf{J}$ , the equilibrium condition can be expressed by the following equation:

$$\mathbf{U} = \mathbf{J}\mathbf{S} \quad (1)$$

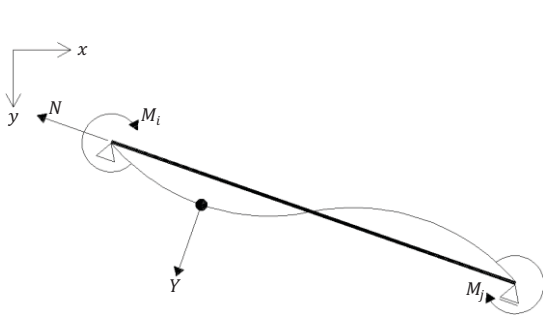
By differentiating Eq. (1), the tangent stiffness equation can be expressed as

$$\delta\mathbf{U} = \mathbf{J}\delta\mathbf{S} + \delta\mathbf{J}\mathbf{S} = (\mathbf{K}_O + \mathbf{K}_G)\delta\mathbf{d} \quad (2)$$

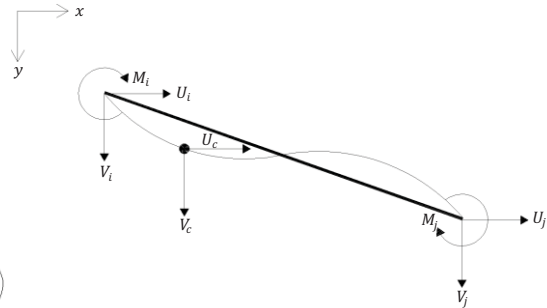
Here, the differentiation of Eq. (1) simultaneously extracts  $\delta\mathbf{S}$  and  $\delta\mathbf{J}$ , which enables the expression of a linear function of the displacement vector  $\delta\mathbf{d}$  in the local coordinate system. Meanwhile,  $\mathbf{K}_O$  represents the element stiffness matrix, which also simulates the element behavior corresponding to the element stiffness.  $\mathbf{K}_G$  is the tangent geometrical stiffness.

Furthermore, a strict tangential stiffness equation can be obtained by a concise induction process without the use of a nonlinear stiffness equation. The induction process using a Lagrangian finite element is more complicated than the TSM.

## 3 Contact Problem



**Figure 1: Element edge forces for contact element**



**Figure 2: Nodal forces for contact element**

A direct approach to frictionless contact between a node and an element using the Euler–Bernoulli and Timoshenko beams was developed and is presented in detail in this paper. A common equilibrium condition can be expressed for both theories as illustrated by means of a contact element in Figs. 1 and 2.

Fig. 1 shows the element edge forces for a single contact element, whereas Fig. 2 shows the nodal forces. The rotation of the contact node is neglected, which reduces the degree of freedom of the node to two. The vectors of the element edge force are independent of each other and are defined by the following equation:

$$\mathbf{S} = [N \quad M_i \quad M_j \quad Y]^T \quad (3)$$

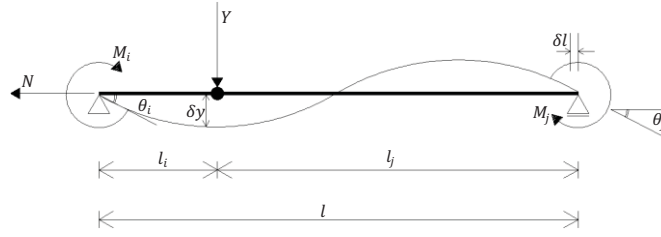
Furthermore, the vector  $\mathbf{U}$  can be expressed as follows:

$$\mathbf{U} = [U_i \quad V_i \quad Z_i \quad U_j \quad V_j \quad Z_j \quad U_c \quad V_c]^T \quad (4)$$

By differentiating Eqs. (3) and (4), the tangent geometrical stiffness can be obtained from the equilibrium between  $\mathbf{S}$  and  $\mathbf{U}$ .

### 3.1 Euler-Bernoulli beam theory using simply supported coordinate

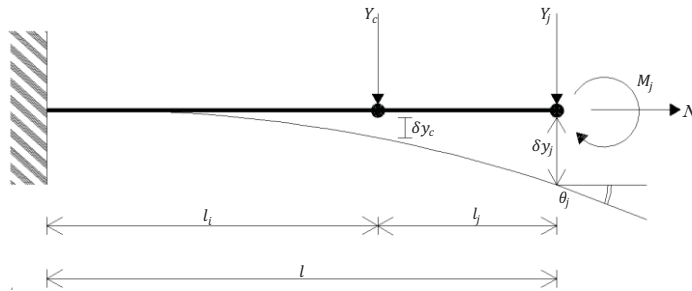
Fig. 3 shows the equilibrium condition of an elastic and homogeneous simply supported beam under the action of the axial force  $N$ , edge moments  $M_i$  and  $M_j$ , and contact force  $Y_c$ . Using the Euler–Bernoulli beam coordinate, it is assumed that the contact force  $Y_c$  is within the range of the beam, and that it produces the geometric and kinematic variables expressed in detail in the figure. This coordinate is a simple but accurate idealization of the frictionless node–element contact problem. The element force equations of this case are given as Eqs. (5) and (6).



**Figure 3: Contact problem in simply supported beam coordinate**

$$\begin{bmatrix} N \\ M_i \\ M_j \\ Y_c \end{bmatrix} = \begin{bmatrix} \frac{EA}{l} & 0 & 0 & 0 \\ 0 & \frac{4l_{ic} + 3l_{jc}}{l_{ic}} k_a & \frac{9l_0^2 - l_{ic}^2 l_{jc}^2}{l_{ic}^2 l_{jc}^2} k_a & -\frac{3l_{jc} l_0^2}{l_{ic}^2 l_{jc}^2} k_a \\ 0 & \frac{9l_0^2 - l_{ic}^2 l_{jc}^2}{l_{ic}^2 l_{jc}^2} k_a & \frac{4l_{jc} + 3l_{ic}}{l_{jc}} k_a & \frac{3l_{ic} l_0^2}{l_{ic}^2 l_{jc}^2} k_a \\ 0 & -\frac{3l_{jc} l_0^2}{l_{ic}^2 l_{jc}^2} k_a & \frac{3l_{ic} l_0^2}{l_{ic}^2 l_{jc}^2} k_a & \frac{3l_0^4}{l_{ic}^3 l_{jc}^3} k_a \end{bmatrix} \begin{bmatrix} \delta l \\ \theta_i \\ \theta_j \\ \delta y_c \end{bmatrix} \quad k_a = \frac{EI}{l_0} \quad (5), (6)$$

### 3.2 Euler-Bernoulli beam theory using cantilever coordinate



**Figure 4: Contact problem in cantilever beam coordinate**

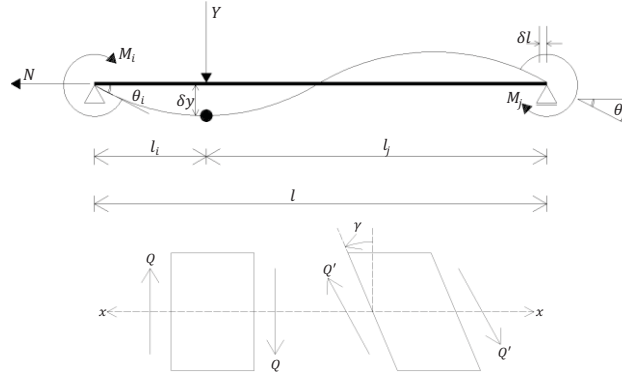
$$\begin{bmatrix} N \\ Y_j \\ Y_c \\ M_j \end{bmatrix} = \begin{bmatrix} \frac{EA}{l} & 0 & 0 & 0 \\ 0 & l_i^3(l_i + 4l_j)k_b & -l_i^2(l_i + 3l_j)k_b & -l_i^3 l_j(l_i + 2l_j)k_b \\ 0 & -l_i^2(l_i + 3l_j)k_b & l_i^4 k_b & -l_i^2 l_j k_b \\ 0 & -l_i^3 l_j(l_i + 2l_j)k_b & -l_i^2 l_j k_b & \frac{l_i^3 l_j^2(3l_i + 4l_j)}{3} k_b \end{bmatrix} \begin{bmatrix} \delta l \\ \delta y_j \\ \delta y_c \\ \theta_j \end{bmatrix} \quad k_b = \frac{3EI}{l_i^3 l_j^3} \quad (7), (8)$$

The same Euler–Bernoulli beam is used in a cantilever coordinate system for a node–element contact. In this case, the existence of two concentrated forces; the contact force  $Y_c$  and the edge shear force act at the beam edge  $Y_j$ , should be noted. In this coordinate, it is more likely to overcome the problem of “critical area” when the

distance between the contact node and the element edge is small, compared to the previous simply supported coordinate (Nizam, Obiya, and Burhaida (2008)). The element force equations (Eqs. (7) and (8)) can be easily used to execute a “pass-through” of the contact node to the next element. The equation for this coordinate system consists of the axial force  $N$ , edge moment  $M_j$ , contact force  $Y_c$ , and the edge shear force  $Y_j$  which are independent to each other.

### 3.3 Timoshenko Beam Theory using simply supported coordinate

The fundamental assumption of the Euler–Bernoulli and the Timoshenko beam are the plane cross section remains plane. In Timoshenko beam, the cross section rotates due to the effect of shear deformation and no longer normal to the neutral axis. Furthermore, it is also assumed that the beam deformation is produced by two components, namely the bending and shear deformations (Fig. 5).



**Figure 5: Effect of shear deformation in a beam**

To simulate a contact phenomenon using the Timoshenko beam, a simply supported coordinate system can be used. The figure also reveals the existence of kinematic components, which were used in the previous Euler–Bernoulli beam (subsection 3.1).

$$\begin{bmatrix} N \\ M_i \\ M_j \\ Y_c \end{bmatrix} = \begin{bmatrix} \frac{EA}{l} & 0 & 0 & 0 \\ 0 & (4\Omega + 3l_{ic}l_{jc}^3 - 108\Psi^2)k_c & \{9(l_0^2 - l_{jc}\Psi) - \Omega\}k_c & -3l_0(l_{jc}l_0 + 6\Psi)k_c \\ 0 & \{9(l_0^2 - l_{jc}\Psi) - \Omega\}k_c & (4\Omega + 3l_{ic}^3l_{jc} - 108\Psi^2)k_c & 3l_0(l_{ic}l_0 + 6\Psi)k_c \\ 0 & -3l_0(l_{jc}l_0 + 6\Psi)k_c & 3l_0(l_{ic}l_0 + 6\Psi)k_c & \frac{3l_0(l_0^3 + 12l_0\Psi)}{l_{ic}l_{jc}}k_c \end{bmatrix} \begin{bmatrix} \delta l \\ \theta_i \\ \theta_j \\ \delta y_c \end{bmatrix} \quad (9)$$

$$k_c = \frac{EI}{l_0\Omega}, \quad \Psi = \frac{EI}{GA_e}, \quad \Omega = (l_{ic}l_{jc})^2 + 3\Psi(l_0^2 + l_{ic}l_{jc}) + 36\Psi^2 \quad (10), (11), (12)$$

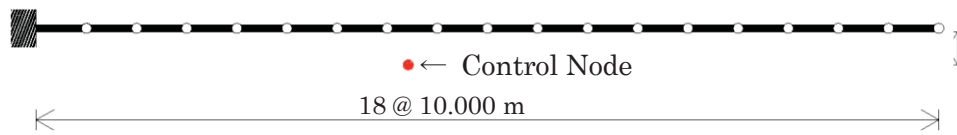
In this subsection, the element force equation of node-element contact for the Timoshenko beam is expressed as Eqs. (9)-(12). These equations are developed to overcome the “division by zero” discussed in section 1, to encounter the problem when the contact node approaches element edge into the “critical area” and leads to the divergence of unbalanced force. Furthermore, owing to the reduction of “critical area” enhanced by these equations, “pass-through” could be executed smoothly for the contact node to shift to the next noncontact element with stable convergence result. The effectiveness of these equations are demonstrated in details in each numerical examples in the following section.

## 4 Numerical Examples

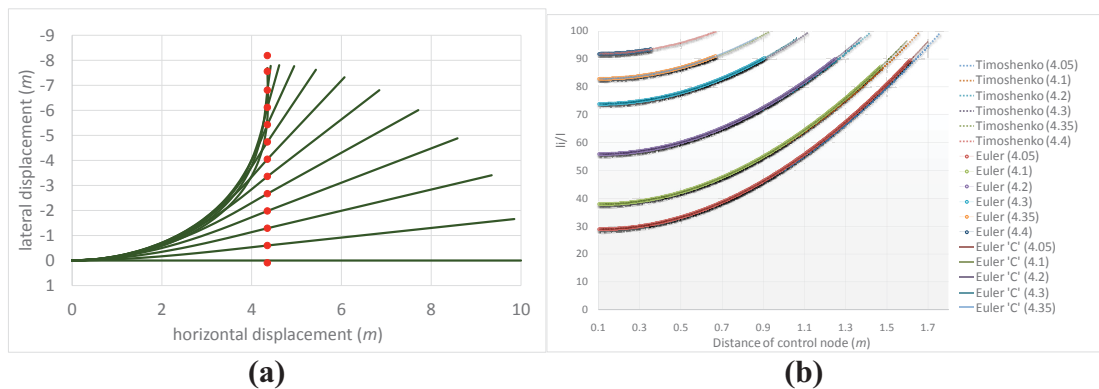
### 4.1 Frictionless contact analysis of a cantilever beam

The main objective of this analysis is to investigate the range of the “critical area”, by comparing the application of the Timoshenko beam in the element force equation (see Eqs. (9)–(12)) to the previous equations developed by Tsutsui, Obiya, and Ijima (2009). As shown in Fig. 5, the distances between the contact point and the two edges are  $l_i$  and  $l_j$ , respectively. In this case, if  $l_i \rightarrow 0$  or  $l_j \rightarrow 0$  in Eqs. (5) and (7), the matrices become singular. Therefore, if  $l_i$  or  $l_j$  is close to zero, the unbalanced force would hardly converge. This implies that there is a particular space close to the element edge in which the approach of the contact node is prohibited from achieving convergence result. We refer to this space as the “critical area”.

As shown in Fig. 6, a cantilever beam configuration is used in this analysis, and the beam consists of 18 elements and 19 nodes. A compulsory displacement in the lateral upward direction is applied to the control node, which is independent and unconnected to any element in the primary position. The material parameters are  $E = 2.1 \times 10^{11}$  [N/m<sup>2</sup>],  $A = 0.005$  [m<sup>2</sup>],  $I = 0.001$  [m<sup>4</sup>],  $G = 7.5 \times 10^{10}$  [N/m<sup>2</sup>], and  $\nu = 0.4$ .



**Figure 6: Cantilever beam model**



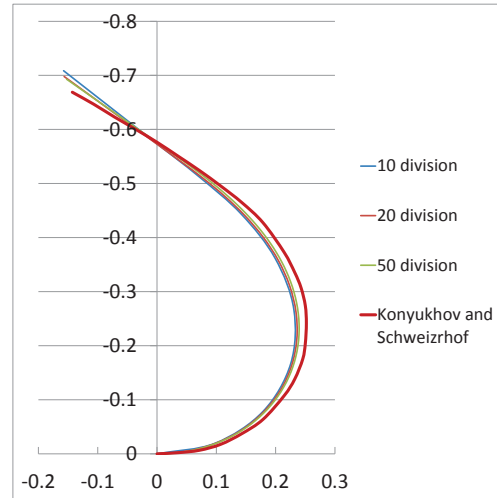
**Figure 7: (a) Beam deformation, (b) Comparison of “critical area” by three different element force equations**

Fig. 7(a) shows the beam deformation due to the displacement of the control node, whereas Fig. 7(b) shows the relationship between the ratio  $l_i/l$  of a contact element and the displacement of the control node after contact. In this analysis, the control node was set at six primary positions, namely 4.05, 4.1, 4.2, 4.3, 4.35, and 4.4 m in the horizontal direction. The results of the analysis showed that the “critical area” of the Euler–Bernoulli beam in the simply supported coordinate system of Nizam, Obiya, and Burhaida (2008) ranged between 7.749% and 12.952%, whereas that of the cantilever coordinate system of Tsutsui, Obiya, and Ijima (2009) ranged between 2.164% and 3.865%. An idealization of the cantilever coordinate system by comparison of the two results can be used to reduce the range of the “critical area”. However, using the Timoshenko beam, the “critical area” can be significantly reduced from 0.067% to 0.501%. The reduction of the “critical area” makes it easier

for the contact node to smoothly “pass-through” the element edge to the next element, producing a strict equilibrium solution.

#### 4.2 Accuracy comparison of FEM to TSM

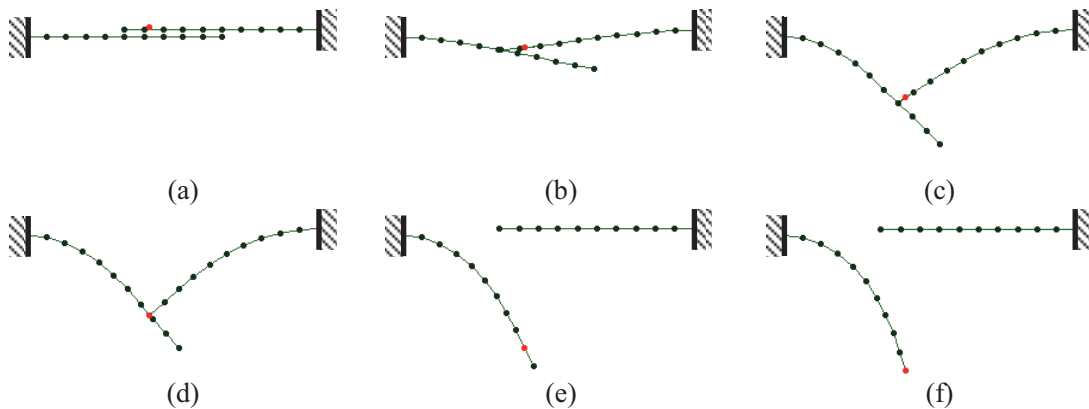
In this analysis, we compare the FEM of Konyukhov and Schweizrhof (2010) with the TSM for contact simulation. A cantilever beam with solid elements and 50 divisions was used for the FEM study, whereas simple linear elements are used for our TSM study. To demonstrate the accuracy of TSM, 10, 20, and 50 divisions of the beam are used in this study. The control node is displaced in the upper left direction by the vector  $[1, 0.6366]$ , and the material parameters are  $E = 2.1 \times 10^4$   $[\text{N/m}^2]$ ,  $b \times h = 0.02 \times 0.02$   $[\text{m}]$ ,  $L = 1.00$   $[\text{m}]$ ,  $G = 7.5 \times 10^{10}$   $[\text{N/m}^2]$ , and  $\nu = 0.3$ .



**Figure 8: Beam deformation**

Fig. 8 shows the beam deformation for both methods. The figure reveals that the beam deformations for TSM and FEM are not significantly different. The TSM solution for the larger 10 and 20 divisions is similar to that of FEM using densely partitioned solid elements. Furthermore, a simple definition of the contact element is sufficient to simulate the TSM contact analysis, while also avoiding the complex settings of the nonlinearity between the strain and the displacement.

#### 4.3 Contact of double beams



**Figure 9(a)-(f): Control node displacement quantity and beams deformation**

Two independent cantilever beams are used in this analysis, and the control node is displaced laterally and downward until it exceeds those of the two beams. The objective of this analysis is to perform multiple contacts using the Timoshenko beam, taking into consideration the “critical area”, the “pass-through” phenomenon, and the deformation behavior of both structures. Both beams have 10 equal divisions, and the material parameters in this case are  $E = 2.0 \times 10^7$   $[\text{N/m}^2]$ ,  $A = 3.0 \times 10^{-4}$   $[\text{m}^2]$ ,  $I = 2.2 \times 10^{-8}$   $[\text{m}^4]$ ,  $G = 7.142 \times 10^6$   $[\text{N/m}^2]$ , and  $\nu = 0.4$ .

Contact is about to occur when the displacement of the control node is at stage (a). At stage (b), multiple contacts initially occur between the control node and an element of the upper beam, and between the tip of the upper beam and an element of the lower



beam. The control node is displaced until stage (d), at which time the control node is about to shift from the upper beam and make contact with an element of the lower beam. The analysis is continued until the control node displacement is at stage (f), when the node is about to exceed the lower beam. By applying the Timoshenko beam, the significant reduction of the “critical area” discussed in Subsection 4.1 enables the contact nodes to smoothly and simultaneously “pass-through” every element edge.

## 5 Conclusion

The application of proposed contact element enables feasible node-element contact with large displacement. Based on the findings of this study, we make the following conclusions:

- 1) The convergence of the solution observed in the numerical analyses shows the effectiveness of the idealization of applying shear deformation of Timoshenko beam. Smooth “pass-through” solves the problem associated with discontinuous element boundaries. In addition, the reduction of “critical area” at every element edges to 0.067% facilitated the converged solutions.
- 2) The proposed contact element shows a very high performance with the usage of less element division and adequate if compared to the application of solid element. Furthermore, this is a significant merit in order to reduce the cost of calculation thus, it is practical to be deal with.
- 3) Regarding to the decrement of the range of “critical area”, the provided numerical example 4.3 shows multiple contact phenomena could be executed at the same time. All of the contact nodes were able to “pass-through” smoothly without any divergence of the unbalanced force.

## References:

- Aliabadi, M. H.; Martin, D.** (2000): Boundary element hyper-singular formulation for elastoplastic contact problems. *International Journal for Numerical Methods in Engineering*, vol. 48, pp. 995–1014.
- Rebel, G.; Park, K. C.; Felippa, C. A.** (2002): A contact formulation based on localized Lagrange multipliers: formulation and application to two-dimensional problems. *International Journal for Numerical Methods in Engineering*, vol. 54, pp. 263–297.
- Ayyad, Y.; Barbotou, M.; Fernandez, J. R.** (2009): A frictionless viscoelastodynamic contact problem with energy consistent properties: Numerical analysis and computational aspects. *Computer Methods in Applied Mechanics and Engineering*, vol. 198, pp. 669–679.
- Klarbring, A.** (2002): Stability and Critical Points in Large Displacement Frictionless Contact Problems. *J.A.C. Martins and M. Raous (Eds.) Friction and Instabilities*, Springer 2002, no. 457, pp. 39–64.
- Chen, X.; Nakamura, K.; Mori, M.; Hisada, T.** (1998): Finite Element Analysis for Large Deformation Frictional Contact Problems with Finite Sliding. *The Japan Society of Mechanical Engineers*, vol. 64, pp. 50–57.
- Z. M. Nizam; H. Obiya; B. Burhaida.** (2008): A study on non-friction contact problem with large deformational analyses. *Malaysian Technical Universities Conference on Engineering and Technology*.
- T. Tsutsui; H. Obiya; K. Ijima.** (2009): An algorithm for contact problem with large deformation of plane frame structures. *Advances in Computational Engineering & Sciences*.
- Konyukhov, A.; Schweizerhof, K.** (2010): Geometrically exact covariant approach for contact between curves. *Computer Methods in Applied Mechanics and ENgineering*, vol. 199, pp. 2510–2531.
- Alexander, T., Marco, S., Marco, G.,** (2007): *Refinement of Timoshenko Beam Theory for Composite and Sandwich Beam using Zigzag Kinematics*. National Aeronautics and Space Administration (NASA).

## The robustness of Timoshenko beam in geometrically non-linear frame analysis

\*Ryota Tokubuchi<sup>1</sup>, Hiroyuki Obiya<sup>2</sup>, Katsushi Ijima<sup>3</sup>, Noriaki Kawasaki<sup>4</sup>,  
Z.M.Nizam<sup>5</sup>

<sup>1,5</sup>School of Environmental Science and Engineering, Saga University, Japan

<sup>2,3,4</sup>Department of Civil Engineering and Architecture, Saga University, Japan  
Saga University, 1 Honjo-machi, Saga, 840-8502, Japan

\*Corresponding author: suzuta1128@gmail.com

**Keywords:** The robustness of Timoshenko, Tangent Stiffness Method, The huge load, finite rotation

### Abstract

Tangent Stiffness Method using strict geometrical stiffness gives perfect equilibrium solutions with convergence of unbalanced forces at all nodes. In case of deep beam or dense mesh division, Timoshenko beam elements show better convergence against to the huge load which causes extremely large displacement than Euler-Bernoulli beam elements. In this study, a numerical example of large displacement analyses for 3-D frame structure with finite rotation is shown, and the performance of Timoshenko beam elements is discussed when the flat rectangular cross section is applied.

### 1 Introduction

The tangent stiffness method (TSM), which defines the element behavior in the element coordinate, gives a useful algorithm for large deformational analysis of 2-D and 3-D frame structures. The superiority of this method is that strict equilibrium solutions can be obtained by convergence of unbalanced solution using strict geometrical compatibility. We applied this method to 3-D analysis considering the finite rotations and obtained an equilibrium path with extremely large displacement (H.Obiya, K.Ijima, N.Kawasaki, 2000; K.Abe, H.Obiya, K.Ijima, 2007).

However, we defined the element force equation, which is a stiffness equation between the element edge forces and the element edge deformation, as linear based on Euler-Bernoulli beam. Therefore, in particular cases such as follows, we had problem of divergence of unbalanced forces when some elements have large deformations.

- 1) Cross section has extremely thin shape.
- 2) Number of mesh division exceeds a limit.

For example, in the case of the simulation of folding a ring into a third size, the cross section should be thin to observe stable behavior, but the problem of 1) was a bottleneck. Furthermore, the linear element force equations would require dense mesh division for realization of accuracy, against to the problem of 2).

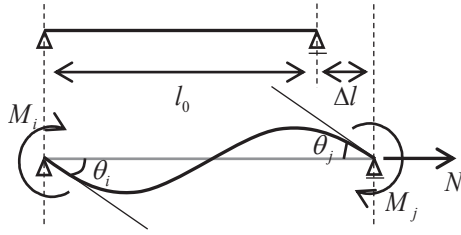
In this study, we try two modifications of the element force equations as follows.

- 1) To the direction around the strong axis, Timoshenko beam theory that consider shear deformation would be applied. This modification would ensure the stable convergence, even if in case that the element length becomes short and/or that cross section becomes deep.

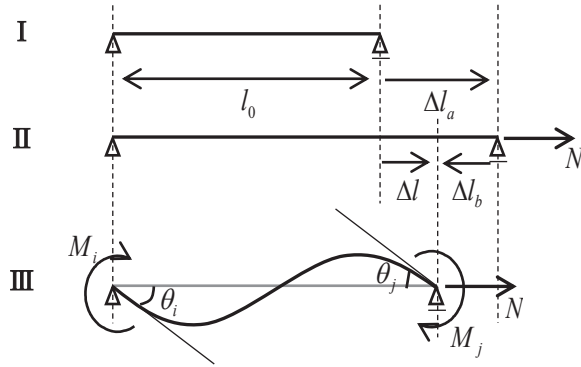
- 2) To the direction around the weak axis, the non-linear theory that consider the movement of the distance between both ends caused by bending.

This modification can give more accurate solutions than the linear element force equation, so we can expect the reduction of the number of mesh division. The numerical example in this paper shows the application of above two modifications can contribute the expansion of the coverage of TSM, thus a strict and robust algorithm for geometrical non-linear analysis can be realized.

**2 Element edge force**



**Fig.1 Element edge force and beam deformation in small deformation theory**



**Fig.2 Element force edge and beam deformation in large deformation theory**

*2.1 Euler-Bernoulli beam and Timoshenko beam theory in small deformation*

Let an element constituted by a stable and statically determinate support condition as shown in Fig.1. Element edge forces consist of axial force  $N$ , edge moments  $M_i$  and  $M_j$  are independent to each other. The element force equation for Euler-Bernoulli is shown in Eq. (1) and Timoshenko beam is shown in Eq. (2) could be expressed as a linear equation.

$$\begin{bmatrix} N \\ M_i \\ M_j \end{bmatrix} = \begin{bmatrix} F_0 & 0 & 0 \\ 0 & 4k & 2k \\ 0 & 2k & 4k \end{bmatrix} \begin{bmatrix} \Delta l \\ \theta_i \\ \theta_j \end{bmatrix} \tag{1}$$

$$\begin{bmatrix} N \\ M_i \\ M_j \end{bmatrix} = \begin{bmatrix} F_0 & 0 & 0 \\ 0 & \frac{k}{(1+q)}(4+q) & \frac{k}{(1+q)}(2-q) \\ 0 & \frac{k}{(1+q)}(2-q) & \frac{k}{(1+q)}(4+q) \end{bmatrix} \begin{bmatrix} \Delta l \\ \theta_i \\ \theta_j \end{bmatrix} \tag{2}$$

$$F_0 = \frac{EA}{l_0}, k = \frac{EI}{l_0}, q = \frac{12EI}{GA l_0^2} \tag{3), (4), (5)}$$

*2.2 Nonlinear Element force equation considering movement of string length*

When setting up the element forces and the element deformations in a line element whose area of cross section and moment of inertia are  $A$  and  $I$ , respectively, the bending moments at the edges are written as

$$\begin{bmatrix} M_i \\ M_j \end{bmatrix} = k \begin{bmatrix} a & b \\ b & a \end{bmatrix} \begin{bmatrix} \theta_i \\ \theta_j \end{bmatrix} \quad (6)$$

$N > 0$

$$a = \frac{\omega^2 \cosh \omega - \omega \sinh \omega}{\omega \sinh \omega + 2(1 - \cosh \omega)}, \quad b = \frac{\omega \sinh \omega - \omega^2}{\omega \sinh \omega + 2(1 - \cosh \omega)} \quad (7), (8)$$

$N < 0$

$$a = \frac{\omega^2 \cos \omega - \omega \sin \omega}{\omega \sin \omega - 2(1 - \cos \omega)}, \quad b = \frac{\omega \sin \omega - \omega^2}{\omega \sin \omega - 2(1 - \cos \omega)} \quad (9), (10)$$

$$\omega = l_0 \sqrt{\frac{N}{EI}} \quad (11)$$

in which,  $E$  is Young's modulus. Rewriting Eq. (6) into simple form, its differential calculus is the following.

$$\mathbf{M} = \mathbf{B}\boldsymbol{\theta} \quad (12)$$

$$\delta \mathbf{M} = \mathbf{B}\delta \boldsymbol{\theta} + \delta \mathbf{B}\boldsymbol{\theta} = \mathbf{B}\delta \boldsymbol{\theta} + \frac{d\mathbf{B}}{dN} \boldsymbol{\theta} \delta N = \mathbf{B}\delta \boldsymbol{\theta} + u \delta N \quad (13)$$

The axial force is proportionate to the difference between the curve length of the element and the nonstressed length.

$$N = \frac{EA}{l_0} (\Delta l + \Delta l_b) \quad (14)$$

in which  $\Delta l_b$  is the movement of string length which is distance between both element ends, caused by bending.

$$\Delta l_b = \frac{1}{2} \boldsymbol{\theta}^T \frac{d\mathbf{B}}{dN} \boldsymbol{\theta} = \frac{l_0}{4} \{p(\theta_i^2 + \theta_j^2) + 2\bar{p}\theta_i\theta_j\} \quad (15)$$

Therefore, the axial force depends on the bending deformations, so Eq. (13) becomes

$$\begin{bmatrix} \delta N \\ \delta M_i \\ \delta M_j \end{bmatrix} = \begin{bmatrix} F & Fu_1 & Fu_2 \\ Fu_1 & Fu_1^2 + ak & Fu_1u_2 + bk \\ Fu_2 & Fu_1u_2 + bk & Fu_2^2 + ak \end{bmatrix} \quad (16)$$

in which;

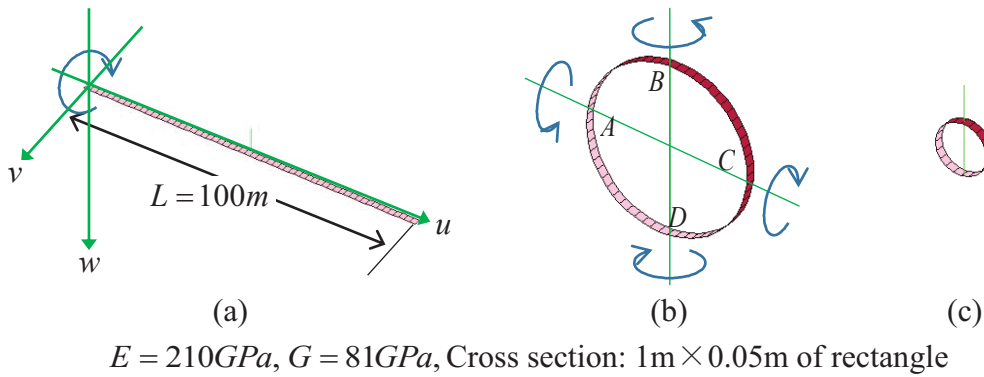
$$u_1 = \frac{l_0}{2} (p\theta_i - \bar{p}\theta_j), \quad u_2 = \frac{l_0}{2} (p\theta_j - \bar{p}\theta_i) \quad (17), (18)$$

$$p = \frac{a - b^2}{\omega^2}, \quad \bar{p} = \frac{ab - a - 2b}{\omega^2} \quad (19), (20)$$

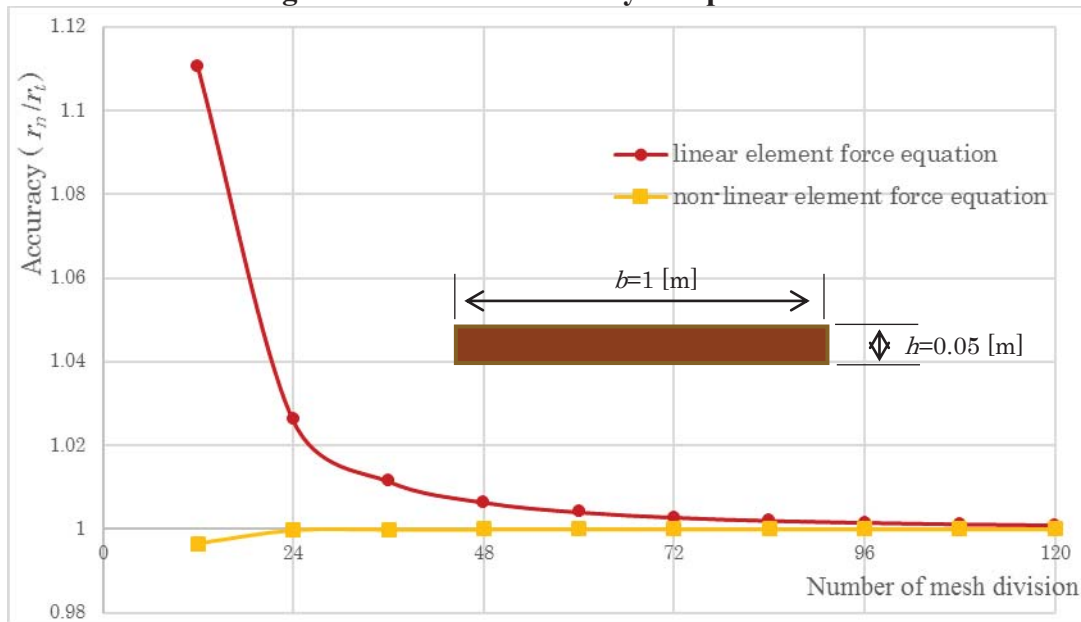
$$F = \frac{F_0}{1 + WF_0}, \quad W = \frac{l_0^2}{4k} \{s(\theta_i^2 + \theta_j^2) - 2\bar{s}\theta_i\theta_j\} \quad (21), (22)$$

$$s = \frac{1}{2\omega^4} \{a + 3b^2 - 2ab(b-1)\}, \quad \bar{s} = \frac{1}{2\omega^4} \{[(a+b)^2 - a](b-1) - 2ab^2\} \quad (23), (24)$$

### 3 Numerical Example

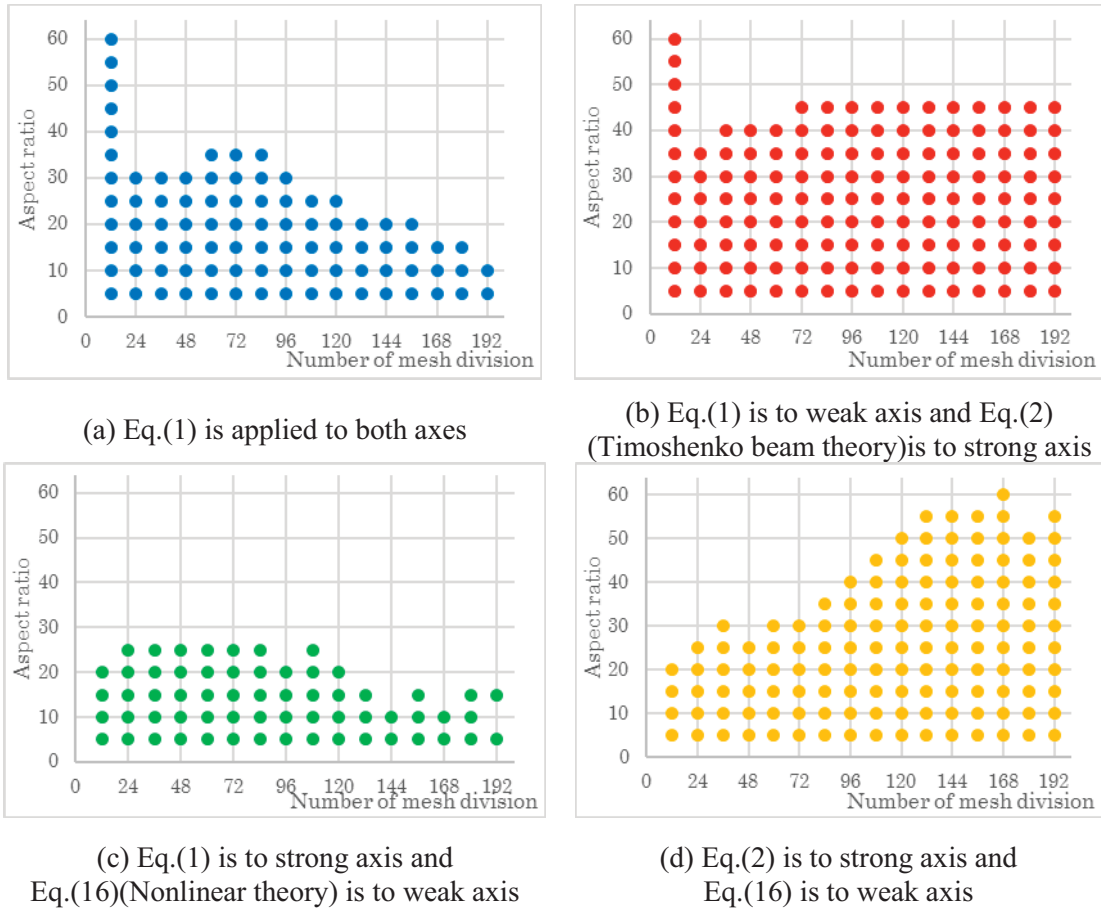


**Fig.3 Initial form and analytical procedure**



**Fig.4 Accuracy of numerical solutions (Section aspect ratio:20)**

Fig.3 (a) shows the primary configuration of a cantilever beam, while Fig.3 (b) and (c) are the deformed sketch. In Fig.3 (a), compulsory rotational displacement around the  $v$ -direction is applied on the free edge of the cantilever beam. When  $2\pi$  of rotational displacement is applied, the beam was deformed as Fig.3 (b) which results as a perfect circular shape. Further, when  $\pi$  of rotational displacement is applied on node of A-D to directions illustrated in Fig.3 (b), the beam deforms as Fig.3 (c), which exhibits a 3-layer circular shape with a third radius of primary. Fig.4 shows the ratio of  $r_n/r_t$  in which  $r_n$  is radius of numerical solutions and  $r_t$  is theoretical radius ( $r_t = L / 6\pi$ ), in case of linear (Eq.(1), (2)) and nonlinear element force equations (Eq.(16)). Section aspect ratio in this paper is  $b/h$  shown in Fig.4. When using Eq. (16) as the element force equation, highly accurate result was obtained with small number of mesh division. Further, the error of accuracy is almost equal to 0.1 percent with 24 mesh when applying nonlinear element force equation to the direction around weak axis. On the other hand, if the linear element force equation to the direction around weak axis is applied, it is unable to satisfy 0.1 percent of error even with 120 mesh. Therefore, it is clear that nonlinear element force equation of Eq. (16) ensures high accuracy with less mesh division and significantly more efficient than the linear element force equation of Eq. (1).



**Fig.5 Section aspect ratio and number of mesh division when a folding solution was obtained**

In Fig.5, in order to evaluate the performance of the element force equations defined in this study, we examined the influence of section aspect ratio and number of mesh division to convergence of unbalanced forces. Every dot is indicated when the “folded solution” in Fig.3 (c) had been obtained corresponding to the conditions of the section aspect ratio and the number of mesh division. Namely, the conditions where no dot is indicated could not achieve convergence. If Euler-Bernoulli beam theory (Eq. (1)) is applied to the direction around strong axis (Fig.5 (a), (c)), thin and flat cross section is not available especially in case of dense mesh division. Fig.5 (b) shows that application of Timoshenko beam theory (Eq. (2)) to the direction around strong axis is effective to thin and flat cross section. On the other hand, when the nonlinear element force equation considering the movement of string length (Eq. (16)) is applied, even rough mesh division can provide strict solutions, but thin and flat cross section seems to disturb convergence.

#### 4 Conclusion

Based on the findings of this study, application of Timoshenko beam theory is effective to avoid divergence of unbalanced force in case of dense mesh division and/or thin rectangular cross section. Furthermore, to ensure highly accurate result when dealing with a large displacement analysis which consumes huge calculation cost, we can use the nonlinear element force equation considering the movement of string length on the weak axis. Consequently, the combination of the Timoshenko

beam theory and the nonlinear element force equation considering the movement of string length supplement the versatility and robustness of TSM.

#### References

**K.Abe, H.Obiya, K.Ijima** (2007): A Study on Multi-bifurcation Equilibrium Paths using the Tangent Stiffness Method, *Third Asian-Pacific Congress on Computational Mechanics in conjunction with Eleventh International Conference on the Enhancement and Promotion of Computational Methods in Engineering and Science*, in CD-ROM.

**H.Obiya, K.Ijima, N.Kawasaki** (2000): A Strict Compatibility in 3-D Large Deformational Analysis for Shell and/or Frame Structures, *Advances in Computational Engineering and Sciences*, TECH SCIENCE PRESS, Vol.1, pp. 843-848.

**H. Obiya, S. Goto, K. Ijima, K. Koga** (1995): Equilibrium analysis of plane frame structures by the tangent stiffness method, *Stability of steel structures Volume2*, pp. 305-312.

## Interval identification of thermal parameters for convection-diffusion heat transfer problems

Xue Yanni, \*Yang Haitian

State Key Lab of Structural analysis for industrial Equipment Dept. of Engineering Mechanics,  
Dalian University of Technology  
Dalian, 116024, Dalian, P.R. China

\*Corresponding author: Haitian@dlut.edu.cn

### Abstract

This paper presents a numerical method to identify the intervals of thermal parameters for steady state convection-diffusion heat transfer problems when uncertainty of measurement is characterized by the interval. A two step strategy is suggested to estimate the lower and upper bounds of thermal parameters in the terms of central value and radius. A 2D numerical example is provided to verify the proposed approach.

**Keywords:** interval; identification; uncertainty; estimate; thermal parameters.

### 1. Introduction

Thermal parameter estimation is an important issue related with many engineering aspects (Rodriguez and Nicolau,2012;Liu and Xu,2000;Reverberi and Fabiano,2013), and is usually based on an assumption that measurement is deterministic. Unfortunately all measurements are indeterministic, and contain various uncertainties(Hugh and Steele,1999). Such uncertainties may result in fault results in the analysis process, and necessitate to take into account(Wang and Qiu,2010;Shome,1999).The point is how to estimate the uncertainty of thermal parameter caused by the measurement uncertainty.

There are mainly three mathematical means to describe the uncertainty, including probabilistic method, fuzzy theory, and interval analysis(Rao and Berke,1997; Elishakoff,1998;Muhanna and Mullen,2001). The interval analysis does not require any prior knowledge or assumption of the uncertainty distribution inside their definition ranges as probability and fuzziness do, only the bounds of changes of the uncertain quantities are necessary(Jiang, Liu and Han,2008). As matter of fact, there were some previous reports concerned with the interval analysis in forward heat transfer problems. C.P. Sebastiao(pereiar,2004) presented an interval uncertainty assessment in 1-D thermal basin modeling via an Element-By-Element(EBE) technique, and provided good results in accordance with those given by the Mento Carlo and combinatorial methods. J.P. Li(Li and Chen,2009)employed a perturbation technique to acquire the lower and upper bounds of temperatures for the transient heat conduction problem with interval parameters. H.T. Yang(Xue and Yang,2013)developed two methods to estimate the bounds of temperatures by utilizing Taylor and Neumann expansion skills for convection-diffusion heat transfer problems when thermal parameters are uncertain and described by intervals. However by authors best knowledge, there seems no any report directly related to the interval estimation of thermal parameters for uncertain convection-diffusion heat transfer problems so far, although great achievement has been gained for the interval estimation of physical parameters in structural engineering(Wang and Qiu,2010;Jiang, Liu and Han,2008) and other aspects(Braems and Berthier,2000;Jorge,2004; Sergey and Nazin,2005).



This paper focuses on the interval estimation of thermal parameters for the steady state conduction-diffusion heat transfer problem when the uncertainty of temperature measurements is characterized by intervals. Section 2 gives a brief description of numerical modeling of forward convection-diffusion heat transfer problems with interval parameters; Section 3 presents a two step strategy to estimate interval bounds of thermal parameters when measurement temperature is characterized by interval; Section 4 provides 2D numerical tests to verify the proposed approach; Section 5 reaches the conclusion.

## 2. Numerical modeling of forward convection-diffusion heat transfer problems with interval parameters

The governing equation of steady state convection-diffusion heat transfer problems is(Platten and Legos,1984)

$$cu_i T_{,i} = [k_{ij} T_{,j}]_{,i} + Q \quad \mathbf{x}_i \in \Omega \quad (1)$$

where  $T$  stands for the temperature,  $c$  and  $k_{ij}$  are heat capacity and thermal conductivity respectively,  $u_i$  refers to the vector of the fluid velocity,  $Q$  is a volumetric heat source term,  $\mathbf{x}_i$  is the vector of the coordinates,  $\Omega$  represents the space domain of the problem and subscript  $i, j$  refers to a summation index( $i, j = 1, 2$  for the 2D problem,  $i, j = 1, 2, 3$  for the 3D problem).

The boundary condition is given by

$$T = T_B \quad \mathbf{x}_i \in \Gamma_1 \quad (2)$$

$$n_i k_{ij} T_{,j} = q \quad \mathbf{x}_i \in \Gamma_2 \quad (3)$$

where  $T_B$  and  $q$  are prescribed functions,  $\Gamma = \Gamma_1 + \Gamma_2$  represents the whole boundary of  $\Omega$ , and  $n_i$  refers to the outward unit normal along  $\Gamma_2$ .

Eqs. (1-3) can be formulated in a FEM form(Huebner and Thornton,1995)

$$\mathbf{KT} = \mathbf{P} \quad (4)$$

where  $\mathbf{T}$  refers to the general nodal vector of temperature.

$$\mathbf{K} = \sum_e \int_{\Omega^e} \mathbf{N}_{,i}^T k_{ij} \mathbf{N}_{,i} d\Omega^e + \sum_e \int_{\Omega^e} \mathbf{N}^T c u_i \mathbf{N}_{,i} d\Omega^e \quad (5)$$

$$\mathbf{P} = \sum_e \int_{\Omega^e} \mathbf{N}^T Q d\Omega^e + \sum_e \int_{\Gamma^e} \mathbf{N}^T q d\Gamma^e \quad (6)$$

$\mathbf{N}$  stands for a matrix of shape functions.

Assume the thermal parameter vector  $\mathbf{b} = [k_{ij}, u_i, c, Q, q]^T$  is an interval vector and is described by (Alefeid and Herzberger, 1983; Moore, 1979).

$$\mathbf{b}^I = [\underline{\mathbf{b}}, \bar{\mathbf{b}}] = \mathbf{b}^c + \Delta\mathbf{b} \cdot \mathbf{e}_\Delta \quad (7)$$

$$\mathbf{b}^c = (\bar{\mathbf{b}} + \underline{\mathbf{b}}) / 2 \quad \Delta\mathbf{b} = (\bar{\mathbf{b}} - \underline{\mathbf{b}}) / 2 \quad \mathbf{e}_\Delta = [-1, 1] \quad (8)$$

where  $\mathbf{b}^c$  and  $\Delta\mathbf{b}$  represent the vectors of central value and radius of  $\mathbf{b}^I$ ,  $\underline{\mathbf{b}}$  and  $\bar{\mathbf{b}}$  refer to the lower and upper bounds vectors of  $\mathbf{b}^I$ .

Near the neighbor of  $\mathbf{b}^c$ ,  $\mathbf{b}$  can be described by

$$\mathbf{b} = \mathbf{b}^c + \delta\mathbf{b}, \quad \delta\mathbf{b} \in \Delta\mathbf{b}^I = [-\Delta\mathbf{b}, \Delta\mathbf{b}] \quad (9)$$

Utilizing the Taylor series expansion, the first order approximation of the solution of Eq. (4) can be written as (Qiu and Wang, 2004)

$$\mathbf{T}(\mathbf{b}) = \mathbf{T}(\mathbf{b}^c + \delta\mathbf{b}) = \mathbf{T}^c + \sum_{j=1}^m \frac{\partial \mathbf{T}(\mathbf{b}^c)}{\partial b_j} \delta b_j \quad (10)$$

where

$$\mathbf{T}^c = \mathbf{T}(\mathbf{b}^c) \quad (11)$$

$$\frac{\partial \mathbf{T}(\mathbf{b}^c)}{\partial b_j} = [\mathbf{K}(\mathbf{b}^c)]^{-1} \left[ \frac{\partial \mathbf{P}(\mathbf{b}^c)}{\partial b_j} - \frac{\partial \mathbf{K}(\mathbf{b}^c)}{\partial b_j} \mathbf{T}^c \right] \quad (12)$$

The lower and upper bounds of  $\mathbf{T}^I$  are estimated by

$$\underline{\mathbf{T}}(\mathbf{b}) = \mathbf{T}^c - \Delta\mathbf{T} = \mathbf{T}(\mathbf{b}^c) - \sum_{j=1}^m \left[ [\mathbf{K}(\mathbf{b}^c)]^{-1} \left[ \frac{\partial \mathbf{P}(\mathbf{b}^c)}{\partial b_j} - \frac{\partial \mathbf{K}(\mathbf{b}^c)}{\partial b_j} \mathbf{T}^c \right] \right] \Delta b_j \quad (13)$$

$$\bar{\mathbf{T}}(\mathbf{b}) = \mathbf{T}^c + \Delta\mathbf{T} = \mathbf{T}(\mathbf{b}^c) + \sum_{j=1}^m \left[ [\mathbf{K}(\mathbf{b}^c)]^{-1} \left[ \frac{\partial \mathbf{P}(\mathbf{b}^c)}{\partial b_j} - \frac{\partial \mathbf{K}(\mathbf{b}^c)}{\partial b_j} \mathbf{T}^c \right] \right] \Delta b_j \quad (14)$$

where

$$\Delta\mathbf{T} = \sum_{j=1}^m \left[ [\mathbf{K}(\mathbf{b}^c)]^{-1} \left[ \frac{\partial \mathbf{P}(\mathbf{b}^c)}{\partial b_j} - \frac{\partial \mathbf{K}(\mathbf{b}^c)}{\partial b_j} \mathbf{T}^c \right] \right] \Delta b_j \quad (15)$$

utilizing Eqs. (11) and (15), lower and upper bounds of temperatures can be estimated for the convection-diffusion heat conduction problem with interval parameters.

### 3. Interval identification of thermal parameters

Assume that the measurement temperature  $T^*$  is characterized by the interval via  $[\underline{T}^*, \bar{T}^*]$  where  $\underline{T}^*$  and  $\bar{T}^*$  stand for lower and upper bounds of  $T^*$ . The central value and radius of  $T^*$  are given by

$$T^{c*} = \frac{\bar{T}^* + \underline{T}^*}{2}, \quad \Delta T^* = \frac{\bar{T}^* - \underline{T}^*}{2} \quad (16)$$

Using  $\underline{T}^*$  and  $\bar{T}^*$ , the interval estimation of thermal parameters can be realized via the identification of  $\mathbf{b}^c$  and  $\Delta \mathbf{b}$ .

The identification of  $\mathbf{b}^c$  and  $\Delta \mathbf{b}$  is conducted by minimizing two  $L_2$  norms defined by

$$[\mathbf{L}T^c(\mathbf{b}^c) - T^{c*}]^2 \quad (17)$$

$$[\mathbf{L}\Delta T(\Delta \mathbf{b}) - \Delta T^*]^2 \quad (18)$$

where  $T^c$  and  $\Delta T$  is given by Eqs. (11) and (15),  $\mathbf{L}$  is a matrix mapping the relationship of  $\mathbf{T}$  and the vector of measurement points.

The above minimizations can be realized by the L-M (Levenberg—Marquardt) algorithm(Levenberg,1994). For a problem defined by

$$\text{Min } \prod = \frac{1}{2} \mathbf{F}^T(\boldsymbol{\varphi}) \mathbf{F}(\boldsymbol{\varphi}) \quad (19)$$

the major procedure of L-M algorithm includes

$$\boldsymbol{\varphi}^{m+1} = \boldsymbol{\varphi}^m + \Delta \boldsymbol{\varphi} \quad (20)$$

$$(\mathbf{G}^T \mathbf{G} + \mu^n \mathbf{I}) \Delta \boldsymbol{\varphi} = -\mathbf{G}^T \mathbf{F} \quad (21)$$

where  $\mathbf{G}^T$  stands for the gradient matrix of  $\mathbf{F}$  with respect to  $\boldsymbol{\varphi}$ ,  $\mu$  is a non-negative damping factor, and  $\mathbf{I}$  refers to an identity matrix.

When  $\|\Delta \boldsymbol{\varphi}\| \leq \beta$ , the above iteration stops,  $\beta$  refers to an error tolerance.

For Eq. (17)

$$\boldsymbol{\varphi} = \mathbf{b}^c \quad (22)$$

$$\mathbf{G} = \mathbf{L} \frac{\partial \mathbf{T}^c}{\partial \mathbf{b}^c} = \mathbf{L} \sum_{j=1}^m \mathbf{K}^{-1} \left( \frac{\partial \mathbf{P}}{\partial b_j} - \frac{\partial \mathbf{K}}{\partial b_j} \mathbf{T}^c \right) \quad (23)$$

$$\mathbf{F} = \mathbf{L} \mathbf{T}^c - \mathbf{T}^{c*} \quad (24)$$

For Eq.(18)

$$\boldsymbol{\varphi} = \Delta \mathbf{b} \quad (25)$$

$$\mathbf{G} = \mathbf{L} \frac{\partial \Delta \mathbf{T}}{\partial \Delta \mathbf{b}} = \mathbf{L} \sum_{j=1}^m \left[ \mathbf{K}^{-1} \left[ \frac{\partial \mathbf{P}}{\partial b_j} - \frac{\partial \mathbf{K}}{\partial b_j} \mathbf{T}^c \right] \right] \quad (26)$$

$$\mathbf{F} = \mathbf{L} \Delta \mathbf{T} - \Delta \mathbf{T}^* \quad (27)$$

Therefore the lower and upper bounds of thermal parameters are given by

$$\underline{\mathbf{b}} = \mathbf{b}^c - \Delta \mathbf{b} \quad (28)$$

$$\bar{\mathbf{b}} = \mathbf{b}^c + \Delta \mathbf{b} \quad (29)$$

#### 4. Numerical verification

For the simplicity, all the computing parameters are assumed dimensionless.

Consider an inverse 2D steady state convection-diffusion heat transfer problem in a  $10 \times 10$  rectangular domain which is meshed by  $10 \times 10$  finite elements, as shown in Fig.1.

The boundary condition is defined by

$$\begin{aligned} T(x, y = 0) &= 1, \quad T(x, y = 10) = 0, \\ T(x = 0, y) \Big|_{y \in [0, 4]} &= 1, \quad T(x = 0, y) \Big|_{y \in (4, 10]} = 0, \quad T(x = 10, y) = 0 \end{aligned}$$

The effect of noisy data is taken into account in the form

$$\underline{\mathbf{T}}_n^* = (1 + \sigma_\zeta) \underline{\mathbf{T}}^* \quad (30)$$

$$\bar{\mathbf{T}}_n^* = (1 + \sigma_\zeta) \bar{\mathbf{T}}^* \quad (31)$$

where  $\underline{T}_n^*$  and  $\overline{T}_n^*$  represents the vectors of lower and upper bounds of measured or stimulated temperature containing the noisy data,  $\zeta$  is a random variable between -0.5~0.5,  $\sigma$  refers to a noisy level.

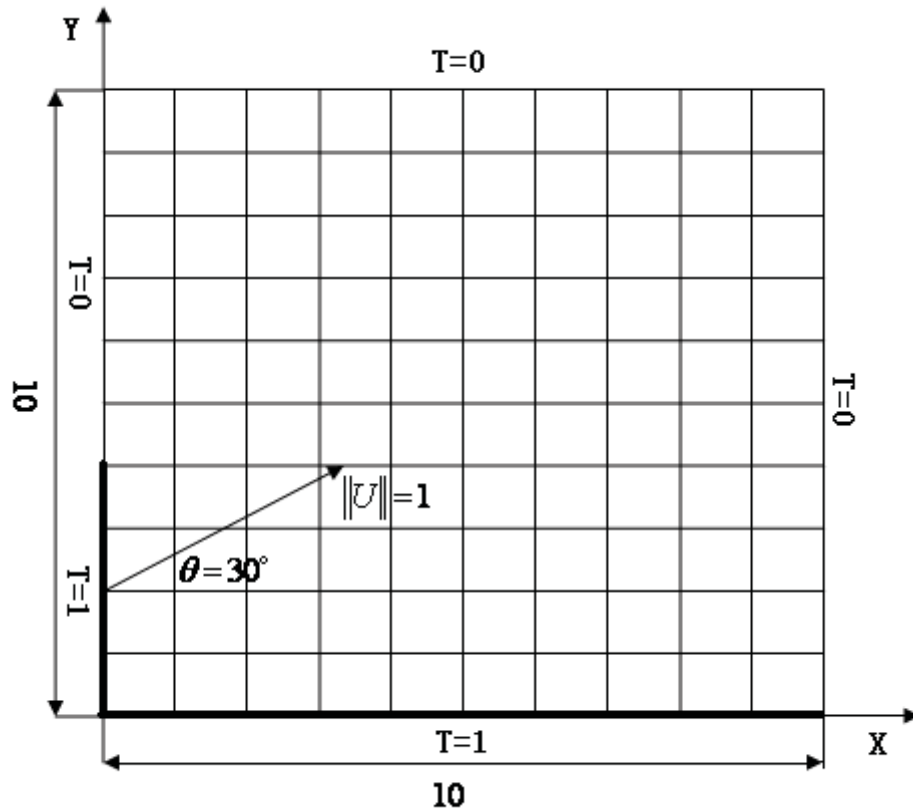


Figure 1 The FE mesh of the rectangular plate

Case 1

$c^c = 1$ ,  $\Delta c = \alpha \cdot c^c$ ,  $u_x^c = \cos 30^\circ$ ,  $\Delta u_x = \alpha \cdot u_x^c$ ,  $u_y^c = \sin 30^\circ$ ,  $\Delta u_y = \alpha \cdot u_y^c$ ,  $\alpha$  is defined as the degree of uncertainty. The intervals of  $k_{xx}$  and  $k_{yy}$  are to be identified.

Tab. 1 exhibits the solutions with different initial guesses; Tab. 2 presents solutions with different arrangement of measuring points as shown in Fig2; Tab. 3 gives solutions at different noisy levels.

Tab. 1. The effects of initial guesses on the results

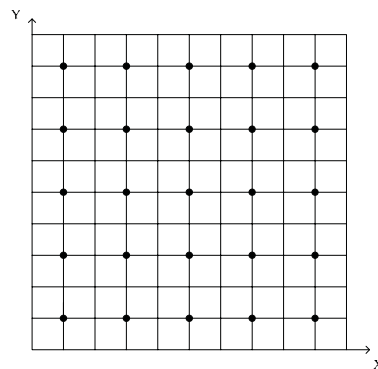
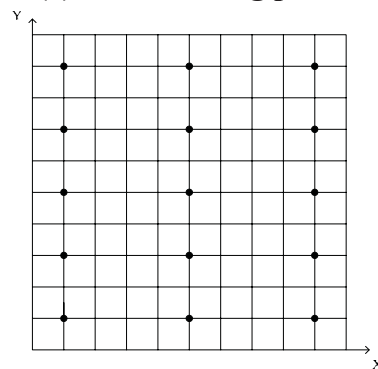
Identified parameters	1			2			Actual values
	Initial guesses	Results of identification	Iterative steps	Initial guesses	Results of identification	Iterative steps	
$k_{xx}^c$	0.1	0.6	6	5	0.6	9	0.6
$\Delta k_{xx}$	0.1	0.06	4	5	0.06	4	0.06
$k_{yy}^c$	0.1	0.5	6	5	0.5	9	0.5
$\Delta k_{yy}$	0.1	0.05	4	5	0.05	4	0.05

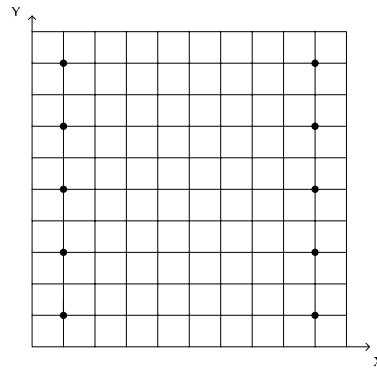
**Tab. 2 The effect of different distribution of measuring points on the results**

Identified parameters	Results of identification			Actual values
	25 measuring points	15 measuring points	10 measuring points	
$k_{xx}^c$	0.6	0.6	0.6	0.6
$\Delta k_{xx}$	0.06	0.06	0.06	0.06
$k_{yy}^c$	0.5	0.5	0.5	0.5
$\Delta k_{yy}$	0.05	0.05	0.05	0.05

**Tab. 3. The effects of noisy data on the results**

Identified parameters	$\sigma=1\%$		$\sigma=5\%$		Actual values
	Result	Error(%)	Result	Error(%)	
$k_{xx}^c$	0.6041	0.68	0.5913	1.45	0.6
$\Delta k_{xx}$	0.0603	0.50	0.0593	1.17	0.06
$k_{yy}^c$	0.5078	1.56	0.4833	3.34	0.5
$\Delta k_{yy}$	0.0498	0.40	0.0504	0.80	0.05

**(a) 25 measuring points****(b) 15 measuring points**



(c) 10 measuring points

**Fig 2 Distribution of measuring points**

Case 2:

$c^c = 1$ ,  $\Delta c = \alpha \cdot c^c$ ,  $k_{xx}^c = 0.6$ ,  $\Delta k_{xx} = \alpha \cdot k_{xx}^c$ ,  $k_{yy}^c = 0.6$ ,  $\Delta k_{yy} = \alpha \cdot k_{yy}^c$ . The intervals of  $u_x$  and  $u_y$  are to be identified.

Tab. 4 and 5 exhibit solutions with different initial guesses and different arrangement of measuring points, Tab. 6 gives solutions at different noisy levels.

Numerical tests indicate

1. Initial guesses seems no impact on the solution, as shown in Tab. 1 and Tab. 4 where the largest ratio between initial guesses and true values is 10. The accurate intervals were identified with few iterative steps which shows the high efficiency of the presented method.
2. Since the problem defined in the numerical test is homogeneous the variation of number and location of measuring points gives no impact on the solution, as shown in Tab. 2 and Tab.5, respectively.
3. The proposed algorithm is not sensitive to noisy data when  $\sigma \leq 5\%$ , the maximum relative error is 3.34% when  $\sigma = 5\%$ .
4. Only few iterations are required to obtain satisfactory results, as shown in Tab. 1 and Tab.4.

**Tab. 4. The effects of initial guesses on the results**

Identified parameters	1			2			Actual values
	Initial guesses	Results of identification	Iterative steps	Initial guesses	Results of identification	Iterative steps	
$u_x^c$	0.1	0.866	12	5	0.866	6	0.866
$\Delta u_x$	0.1	0.086	4	5	0.086	4	0.086
$u_y^c$	0.1	0.5	12	5	0.5	6	0.5
$\Delta u_y$	0.1	0.05	4	5	0.05	4	0.05

**Tab. 5 The effect of different distribution of measuring points on the results**

Identified parameters	Results of identification			Actual values
	25 measuring points	15 measuring points	10 measuring points	
$u_x^c$	0.866	0.866	0.866	0.866
$\Delta u_x$	0.086	0.086	0.086	0.086
$u_y^c$	0.5	0.5	0.5	0.5

$\Delta u_y$	0.05	0.05	0.05	0.05
--------------	------	------	------	------

**Tab. 6. The effects of noisy data on the results**

Identified parameters	$\sigma = 1\%$		$\sigma = 5\%$		Actual values
	Result	Error(%)	Result	Error(%)	
$u_x^c$	0.8714	0.54	0.8517	1.65	0.866
$\Delta u_x$	0.0869	1.05	0.0856	0.47	0.086
$u_y^c$	0.5041	0.82	0.4892	2.16	0.5
$\Delta u_y$	0.0504	0.80	0.0489	2.2	0.05

## Conclusions

Since there seems no direct report concerned with the inverse convection-diffusion heat transfer problems when the uncertainty of temperature measurements is characterized by the interval, this paper attempts to present a numerical model to solve this kind of problem. In terms of central value and radius of interval, a two step strategy is suggested to estimate the lower and upper bounds of thermal parameters and fluid velocity. The L-M method is employed in the estimation procedure, and a numerical test is given to illustrate the advantages of the proposed algorithm with the consideration of initial guess, arrangement of measurement points, and data noise.

The presented model is verified via some numerical tests, however due to the lack of actual uncertainty information either from experiment or industry (some of parameter is based on assumption) more efforts for the further model V&V are required. For the model application of industry, in addition to the numerical verification similar to this paper, the experiment based verification is particularly required. On the other hand we need collect sufficient message on the interval uncertainty from industry, such as the width of interval, noisy level, etc., and validate/verify the proposed model via some industry cases to secure the validity of identification results.

## References

- [1] Fernando López Rodríguez, Vicente de Paulo Nicolau.(2012) Inverse heat transfer approach for IR image reconstruction: Application to thermal non-destructive evaluation. *Applied thermal engineering*, 33-34,pp:109-118
- [2] Liu jing, Xu Lisa.(2000) Boundary information based diagnostics on the thermal states of biological bodies. *International Journal of Heat and Mass Transfer*, 34(12)pp:2827-2839.
- [3] A.P. Reverberi, B. Fabiano, V.G. Dovi.(2013) Use of inverse modelling techniques for the estimation of heat transfer coefficients to fluids in cylindrical conduits. *International Communication in Heat and Mass Transfer*, 42pp:25-31.
- [4] Hugh W. Coleman, W. Glenn Steele. (1999)*Experimentation and Uncertainty Analysis for Engineers* second edition. John Wiley&Sons. Newyork.
- [5] Wang X.J., Qiu, Z.P.(2010). Interval Analysis Method for Damage Identification of Structures. *AIAA Journal*, 48(6), pp.1108-1116.
- [6] Biswadip Shome.(1999) Effect of uncertainties in fluid properties on mixed convection laminar flow and heat transfer in a uniformly heated smooth tube. *Numerical Heat transfer, Part A, Applications*, 35:875-889.
- [7] S.S. Rao, L. Berke.(1997) Analysis of uncertain structural systems using interval anlysis. *AIAA Journal*, 35(4):727-735
- [8] I. Elishakoff. (1998)Three versions of the finite element method based on concepts of either stochasticity, fuzziness or anti-optimization. *Applied Mechanics Review*, 51(3):209-218.
- [9] R. L. Muhanna, R. L. Mullen.(2001) Uncertainty In Mechanics Problems-Interval-Based. Approach. *Journal of Engineering Mechanics*, 127 (6)
- [10]C. Jiang, G.R. Liu, X. Han.(2008) A novel method for uncertainty inverse problems and application to material characterization of composites. *Experimental Mechanics*48:539-548.



- [11] Pereira, S.C., (2004) Uncertainty in Thermal Basin Modeling: An Interval Element Finite Element Approach, *Reliable Computing*, Vol. 12 No. 6 p. 451-470.
- [12] Li, J.P., Chen, J.J., Liu, G.L. and Li, J.S., (2009) Numerical Analysis of Transit Temperature Field with Interval Parameters, *Journal of University of Electronic Science and Technology of China*, Vol. 38 No. 3 pp. 463-466.
- [13] Y.N. Xue, H.T. Yang. (2013) Interval estimation of convection-diffusion heat transfer problems. *Numerical Heat Transfer, Part B: Fundamentals*, 64(03):263-273.
- [14] I Braems, F Berthier, L Jaulin, M Kieffer, E Walter. (2000) Guaranteed estimation of electrochemical parameters by set inversion using interval analysis. *Journal of Electroanalytical Chemistry*, 495:1-9.
- [15] Laurent Granvilliers, Jorge Cruz, Pedro Barahona. (2004) Parameter estimation using interval computations. *Society for Industrial and Applied Mathematics*, 26(2):591-612.
- [16] Sergey A., Nazin, Boris T., Polyak. (2005) Interval Parameter Estimation under Model Uncertainty. *Mathematical and Computer Modelling of Dynamical Systems*, 11(2):225-237.
- [17] Platten, J. K. and Legros, J.C., (1984) *Convection in Liquids*, Springer-Verlag, New York.
- [18] Huebner, K. H. and Thornton, E. A., (1995) *The Finite Element Method for Engineers*, John Wiley & Sons.
- [19] Alefeld, G. and Herzberger, J. (1983) *Introduction to Interval Computations*, Academic Press, New York, 1983.
- [20] Moore, R E., (1979) *Methods and Applications of Interval Analysis*, Prentice-Hall, London.
- [21] Qiu, Z.P. and Wang, X.J., (2004) Comparison between non-probabilistic interval analysis method and probabilistic approach in static response problem of structures with uncertain-but-bounded parameters, *Communications in Numerical Methods in Engineering*, 20 pp. 279-290.
- [22] Levenberg K. (1944) A method for the solution of certain nonlinear problems in least squares. *Quarterly Applied Mathematics*, 2:164-166.

## Hybrid algorithm for inverse DC/AC resistivity logging measurement simulations

\*M. Paszyński<sup>1</sup>, E. Gajda-Zagórska<sup>1</sup>, M. Smółka<sup>1</sup>, R. Schaefer<sup>1</sup>, D. Pardo<sup>2</sup>

<sup>1</sup>AGH University of Science and Technology, Krakow, Poland.

<sup>2</sup>The University of the Basque Country, UPV/EHU and Ikerbasque, Bilbao, Spain.

\*Corresponding author: maciej.paszynski@AGH.EDU.PL

### Abstract

We present a hybrid algorithm for solving inverse 3D resistivity logging measurement simulation problem with DC and AC tools in deviated wells. The term “simulation of measurements” is widely used by the geophysical community. A quantity of interest, voltage, is measured at a receiver electrode located in the logging instrument. Computer simulations are used to explain obtained measurements. We solve the inverse problem with goal-oriented *hp* adaptive finite element method interfaced with Hierarchic Genetic Strategy (HGS) algorithm during a global phase and Conjugated Gradient (CG) algorithm in a local phase. The global search HGS algorithm generates starting points for local search CG algorithm. We conclude the presentation with numerical experiments for DC/AC problems.

**Keywords:** inverse algorithms, resistivity logging measurement simulations, goal-oriented *hp* adaptive finite element method, hierarchic genetic search

### Introduction

In this paper, we solve a forward and inverse problem of 3D direct and alternate current (DC/AC) borehole resistivity measurement simulations in a deviated well.

The expression “simulation of measurements” is widely used within the geophysical community. A quantity of interest, voltage in this case, is measured at a receiver electrode located in the logging instrument. Actual logging instruments are equipped with several transmitter and receiver electrodes. These instruments move along the axis of the borehole, and measure the voltage induced at the receiver electrodes at different positions. The voltage measured at the receivers is expected to be related to the electrical conductivity of the nearby formation. Thus, logging instruments are used to estimate the properties (in this case, the electrical conductivity) of the sub-surface material, with the ultimate objective of describing hydrocarbon (oil and gas) bearing formations.

In the forward problem, the behavior of a resistivity logging instrument is simulated by performing computer-based simulations of resistivity logging instruments in a borehole environment. The resulting simulator is utilized as a core part of an inverse problem infrastructure. The inverse infrastructure allows to determine unknown conductivities of formation layers, based on actual measurements recorded by logging instruments.

The resistivity logging tool with receiver and transmitter electrodes is moving along the trajectory of the well. The electromagnetic waves generated by the transmitter electrode are reflected from formation layers and recorded by the receiver electrodes. Of particular interest to the oil industry are 3D simulations of resistivity measurements in deviated wells, where the angle between the borehole and the formation layers is not equal to 90 degrees ( $\theta_0 \neq 90^\circ$ ).

### Formulation of 3D DC/AC problem in deviated well with Fourier series expansions

A forward DC problem is formulated in the following way, by the conductive media equation:

Find  $u: R^3 \supset \Omega \ni x \rightarrow u(x) \in R$  the electrostatic scalar potential such that

$$-\sum_{i=1}^3 \sigma \frac{\partial^2 u}{\partial x_i^2} = \nabla \circ J \text{ in } \Omega \quad (1)$$

where  $\nabla \circ J$  is the load (divergence of the impressed current, Pardo et al. 2006) and  $\sigma$  represents the conductivity of the media.

To solve the above 3D problem (1), a new quasi-cylindrical non-orthogonal system of coordinates shown in Figure 1 is introduced. This chapter presents a summary of the derivation presented in details in (Pardo et al. 2008a and Pardo et al. 2008b). The notation from the papers is utilized here. The variational formulation, with respect to the electric potential  $u$  in this new system of coordinates, can be expressed in the following way:

Find  $u \in V$  such that:

$$\int_{\Omega} \sum_{n=1}^3 \frac{\partial u}{\partial \zeta_n} \hat{\sigma} \frac{\partial v}{\partial \zeta_n} d\zeta = \int_{\Omega} v \nabla \circ \hat{J} d\zeta \quad \forall v \in V \quad (2)$$

where

$$V = \left\{ v \in L^2(\Omega) : \int_{\Omega} \|v\|^2 + \|\nabla v\|^2 dx < \infty : \text{tr}(v) = 0 \text{ on } \Gamma_D \right\} \quad (3)$$

The electric conductivity of media in the new system of coordinates is equal to  $\hat{\sigma} := \text{Jac}^{-1} \sigma \text{Jac}^{-T} |\text{Jac}|$ , and  $\nabla \circ \hat{J} := \nabla \circ J |\text{Jac}|$  with  $\text{Jac}$  being the Jacobian matrix of the change of coordinates with respect to the Cartesian reference system of coordinates  $(x_1, x_2, x_3)$ , namely,

$$\text{Jac} = \frac{\partial(x_1, x_2, x_3)}{\partial(\zeta_1, \zeta_2, \zeta_3)} \quad (4)$$

Then, we take a Fourier series expansion of the solution, material and  $\zeta_2$  direction

$$u(\zeta_1, \zeta_2, \zeta_3) = \sum_{l=-\infty}^{l=+\infty} u_l(\zeta_1, \zeta_3) e^{jl\zeta_2} \quad (5)$$

$$\sigma(\zeta_1, \zeta_2, \zeta_3) = \sum_{m=-\infty}^{m=+\infty} \sigma_m(\zeta_1, \zeta_3) e^{jm\zeta_2} \quad (6)$$

$$\nabla \circ J(\zeta_1, \zeta_2, \zeta_3) = \sum_{l=-\infty}^{l=+\infty} \nabla \circ J_l(\zeta_1, \zeta_3) e^{jl\zeta_2} \quad (7)$$

where

$$u_l = \frac{1}{2\Pi} \int_0^{2\Pi} u e^{-jl\zeta_2} d\zeta_2, \quad \sigma_m = \frac{1}{2\Pi} \int_0^{2\Pi} \sigma e^{-jm\zeta_2} d\zeta_2, \quad \nabla \circ J_l = \frac{1}{2\Pi} \int_0^{2\Pi} \nabla \circ J e^{-jl\zeta_2} d\zeta_2 \text{ and } j \text{ is the imaginary unit.}$$

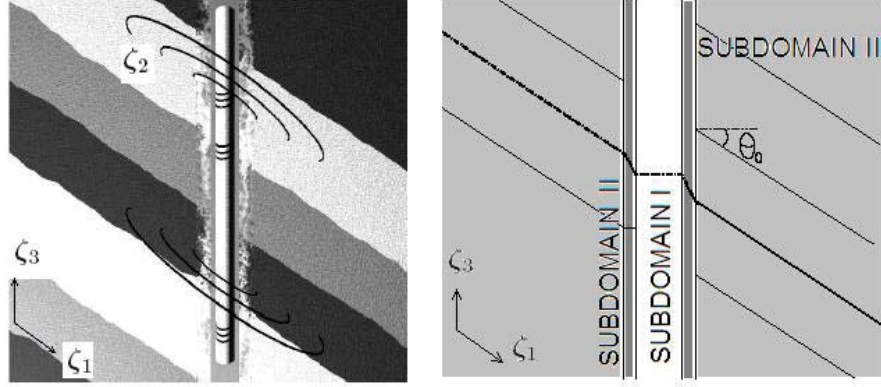
We introduce symbol  $F_l$  such that applied to a scalar function  $u$  it produces the  $l^{\text{th}}$  Fourier modal coefficient  $u_l$ , and when applied to a vector or matrix, it produces a vector or matrix of the components being  $l^{\text{th}}$  Fourier modal coefficients of the original vector or matrix components.

Using the Fourier series expansions we get the following variational formulation:

Find  $F_l(u) \in V$  such that:

$$\int_{\Omega} \sum_{l,m=-\infty}^{+\infty} F_l \left( \frac{\partial u}{\partial \xi} \right) F_m(\hat{\sigma}) \frac{\partial v}{\partial \xi} e^{j(l+m)\zeta_2} d\zeta = \int_{\Omega} v F_l(\hat{J}) e^{jl\zeta_2} d\zeta \quad \forall v \in V \quad (8)$$

The summation is applied with respect to  $-\infty \leq l, m \leq \infty$ . We select a mono-modal test function  $v = v_k e^{jk\zeta_2}$ .



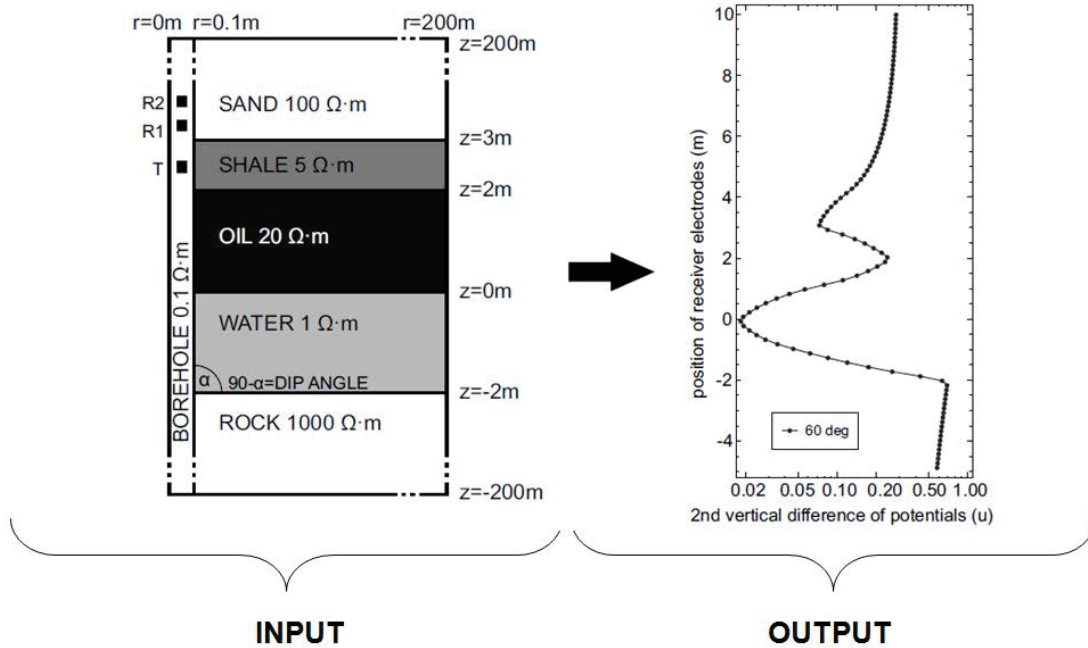
**Fig. 1. Three non-orthogonal systems of coordinates in the borehole and formation layers**

Thanks to the orthogonality of the Fourier modes in  $L^2(\Omega)$  the problem (8) reduces to:  
 Find  $F_l(u) \in V$  such that:

$$\int_{\Omega_{2D}} \sum_{n=k-2}^{n=k+2} F_l \left( \frac{\partial u}{\partial \xi} \right) F_{k-1}(\hat{\sigma}) F_l \left( \frac{\partial v}{\partial \xi} \right) d\zeta_1 d\zeta_3 = \int_{\Omega_{2D}} F_k(v) F_k(\hat{f}) d\zeta_1 d\zeta_3 \quad \forall F_k(v) \in V \quad (9)$$

since five Fourier modes are enough to represent exactly the new material coefficients. We refer to Pardo et al. 2008a for more details.

In the similar (however more algebraically complicated) manner, the variational formulation for the AC problem can be derived, which is presented in Pardo et al. 2008b. The forward problem is solved with self-adaptive, goal-oriented  $hp$  finite element method ( $hp$ -FEM) (Demkowicz 2006). The algorithm starts with an initial mesh, called the *coarse mesh* and solves the weak problem. The mesh is then globally  $hp$ -refined, each element is broken into four elements and the polynomial order of approximation is increased by one. The resulting mesh is called the *fine mesh*. The weak problem is solved again over the fine mesh. The algorithm considers different refinement strategies for each finite element from the coarse mesh.



**Fig. 2. The summary of the formulation of the forward problem**

### Forward and inverse problems

In the forward problem the behavior of resistivity logging instrument is analyzed by performing computer-based simulations for borehole environment. In particular, given the resistivities of the formation layers, the voltage at certain positions of transmitter and receiver electrodes is sought according to (9). A series of forward problems for these positions forms a *logging curve* (Figure 2). In the inverse problem (Figure 3), we are given a reference logging curve and aim to find the best approximation of the unknown resistivities that result in a curve closest to the reference one.

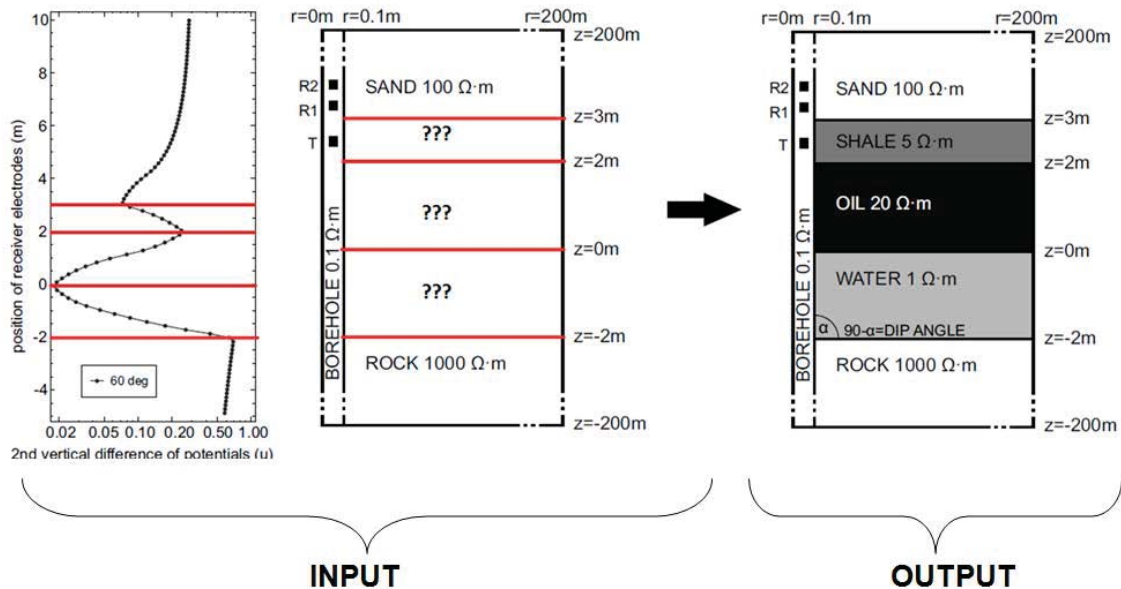


Fig. 3. The summary of the formulation of the inverse problem

### Hierarchic genetic strategy interfaced with self-adaptive hp-FEM

The *hp*-HGS strategy is based on HGS (see e.g. Schaefer and Kołodziej 2004), which is dedicated to solving multimodal, global optimization problems. It creates a tree of demes, in which the encoding accuracy grows with the distance from the root. We start with most coarse, chaotic solutions (which, as a result, can be computed quickly) and as we progress down the tree, we obtain more accurate solutions, with the final ones reached in the tree leaves. In the left part of Figure 4, the individuals of the root-node deme are marked by red points. In the left and central parts, green points denote second-level (branch) individuals. For evaluation of individuals from particular levels of the tree of populations the self-adaptive *hp*-FEM code is used. The accuracy of the *hp*-FEM solver grows with the depth of the tree of populations. In other words, close to the root we evaluate individuals by using cheap low accuracy solver, while at the leaves of the tree of populations we utilize high accuracy expensive estimates.

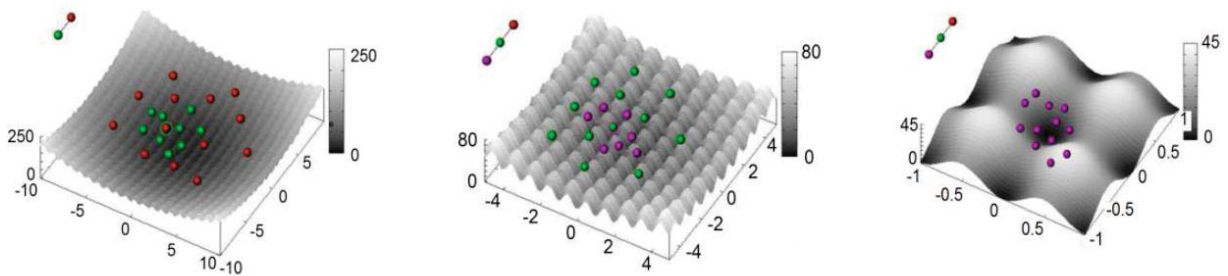


Fig. 4: Red color – root individuals, green – branch individuals, violet – leaf individuals.

The following pseudocode shows main ideas of *hp*-HGS (including scaling errors):

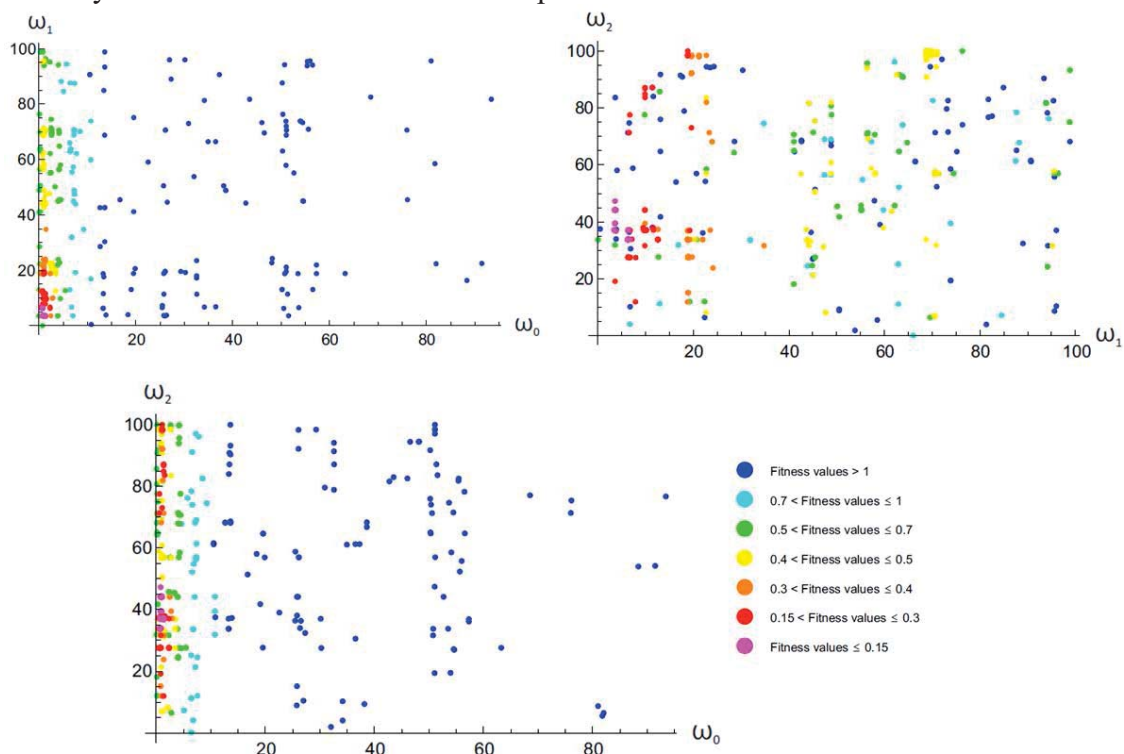
```

1 Inverse analysis loop
2   do
3     Solve the problem on the current coarse and fine FE mesh
4     Compute FE error
5     Compute goal function error on the coarse mesh
6     if goal function error on the coarse mesh <
7       < rate * relative FE error then
8       Execute one step of (parallel) hp adaptivity
9     else break endif
10  enddo
11  Compute goal function error on the fine mesh
12  if goal function error on the fine mesh <
13    < required accuracy then
14    stop
15  endif
16  Propose new values for inverse problem parameters
17 endloop

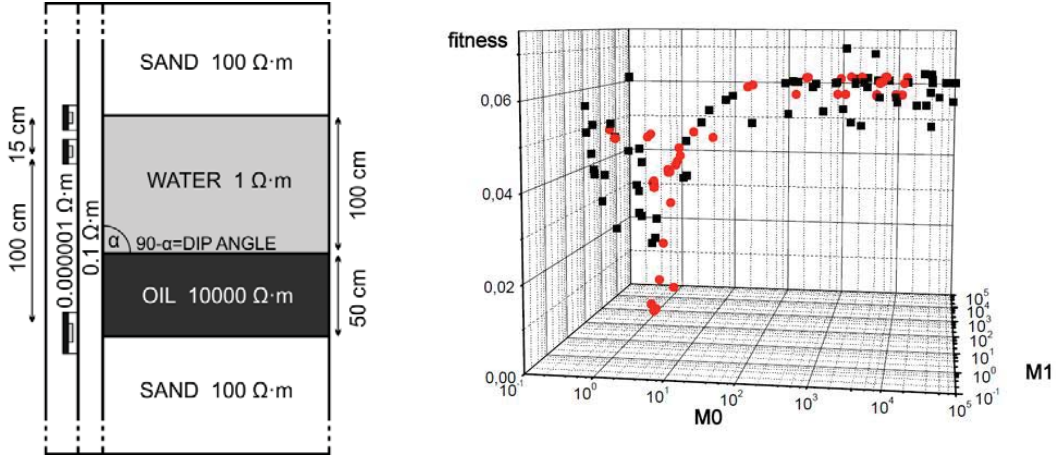
```

### Numerical results for pure *hp*-HGS algorithm

The *hp*-HGS algorithm has been executed for DC and AC cases. For the DC case, the algorithm has been looking for the resistivities (1,5,20) (compare Figures 2 and 3) of the three formation layers. The algorithm has found  $\omega_0 \approx 1$  (correct result) and  $\omega_1 \approx 5$  (correct result), however  $\omega_2$  had different values varying from 10 up to 100. The results are summarized in Figure 5; they suggest the insensitivity of the measurements to the third parameter.



**Fig. 5.** The DC results of the *hp*-HGS algorithm



**Fig. 6. The AC forward problem and inverse results of the hp-HGS algorithm**

For the AC case, we solved a much more computationally difficult problem where the borehole is equipped with steel casing with high contrast resistivity (compare left panel in Figure 6). The inverse algorithm has been looking for the two central resistivities (1,10000). The algorithm has found  $\omega_o \approx 1$  (correct result), however  $\omega_1$  had different values varying from 40 up to 40000. The results are summarized on the right panel in Figure 6; they suggest the insensitivity of the measurements to the second parameter.

The pure hp-HGS algorithm is suitable for recognizing the landscape of the solved problems, in particular for finding the basins of attraction of global and local minimizers in case of multimodal problems (see Schaefer and Telega 2007 and references therein). It is also capable of finding the solutions (its asymptotic properties has been formally proven), but has to be synchronized at the end of each metaepoch to determine, in which regions new branches and leaves should be sprouted. One should also notice that with increasing depth in the HGS tree, the accuracy and computation time of each candidate solution also increases, which makes the leaves the most heavy parts of the computations, even if leaf populations are very small. Summing the above facts with the stochastic nature of HGS opens the area for improvement by limiting the depth of the HGS tree and by applying local methods in the interesting regions found by hp-HGS.

### Numerical results for the hybrid computations

In order to reduce the computational cost of the inverse algorithm we have interfaced the hp-HGS algorithm with conjugated gradient (CG) type of iterative method. Once the inverse algorithm finds areas with local minima, we to switch to local gradient search methods with higher accuracy.

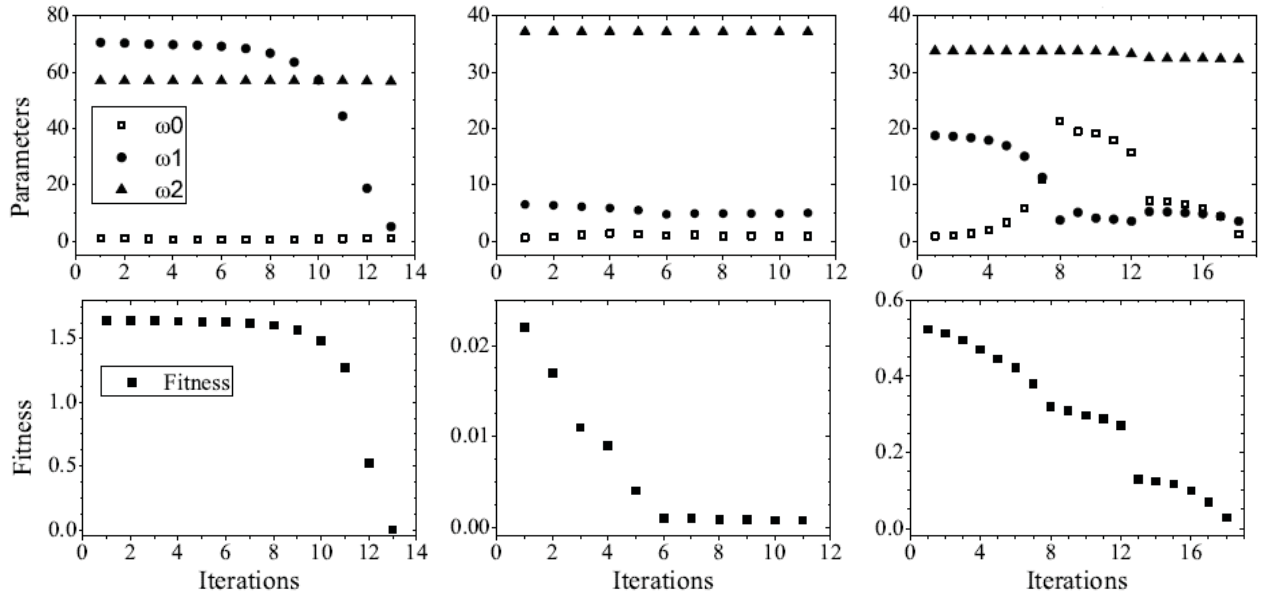
In the DC case, we stopped the first phase hp-HGS genetic search after 6 metaepochs, when we could select six starting points for the second gradient phase from the leaves of the tree of populations. We have executed the CG algorithm from these points, with the following results:

- The CG algorithm starting from the first point and the fourth point converges to the border of the domain and gets stuck there.
- The CG algorithm starting from the second, third and the fifth point converged to local minima
- The computations started from the sixth starting point require much more iterations, and has been stopped.

The convergence history for the second, third and fifth points is presented in Figure 7.

We obtained similar results to those obtained from the global genetic search, namely  $\omega_o \approx 1$  (correct result) and  $\omega_1 \approx 5$  (correct result), however  $\omega_2$  had different values varying from 30 up to 60. This confirmed our thesis that these measurements are insensitive to the third layer.

In the AC case, we stopped the first phase hp-HGS genetic search after eight metaepochs and selected 10 starting points to the second phase of gradient search. All the points converged to local minima (summarized in Figure 8). We obtained similar results as those of the global genetic search, namely the algorithm has found  $\omega_o \approx 1$  (correct result), however  $\omega_1$  had different values varying from 6 up to 52000. This confirmed our thesis that these measurements are insensitive to the second layer.



**Fig. 7. The local gradient search for the DC problem**

	number of solver calls	final value $\omega_0$	final value $\omega_1$	final fitness
1	4	1.077	542.599	0.000008582
2	61	1.234	47541.290	0.000067900
3	28	1.015	1309.719	0.000000366
4	4	1.122	74.889	0.000018307
5	8	1.038	10.406	0.000024504
6	4	0.784	769.435	0.000096289
7	4	0.798	51924.700	0.000082576
8	4	1.427	5536.764	0.000185538
9	4	0.731	124.052	0.000163327
10	24	1.242	6.815	0.000079457

**Fig. 8. The local gradient search for the AC problem**

### Computational cost

In the DC case, the HGS algorithm finds six starting points for gradient algorithm with 5-11 genetic steps, and the gradient algorithm converges to local minima between 12-14 iterations (compare Figure 7). Thus, the local minima can be found with 17-25 direct problem evaluations.



In the AC case, the HGS algorithm finds ten starting points for gradient algorithm with 8 genetic steps, and the gradient algorithm converges to local minima with 4-28 solver calls (compare Figure 8, with the assumption that we skip the expensive second point). Thus, the local minima can be found with 12-36 direct problem evaluations.

The hybrid algorithm can be parallelized on the level of these meta-steps. Thus, the sequential execution time is equal to 17-25 or 12-36 consecutive direct solver calls, for DC or AC case, respectively.

## Conclusions

In this paper we presented *hp*-HGS hierarchic genetic strategy using the self-adaptive *hp* finite element as direct solver. The *hp*-HGS was interfaced with local gradient search, which is more efficient once the genetic algorithm reaches the local minima. The strategy was utilized for solution of the inverse problem related to the identification of the formation layers based on the borehole resistivity logging measurement for direct current as well as alternate current (DC/AC) cases. In both cases the numerical results converged to a local valley, where one of the formation layers had different values. These results imply that, in some cases, the resistivity measurements are insensitive to some formation layers, and for better results they might be combined with other methods of measurements, using e.g. sonic or nuclear tools.

## Acknowledgements

This work was supported by Polish National Science Center grant no. DEC-2012/05/N/ST6/03433.

## References

- Demkowicz, L. (2006) *Computing with hp-Adaptive Finite Element Method. Vol. I. One and Two Dimensional Elliptic and Maxwell Problems*. Chapman & Hall / CRC Applied Mathematics and Nonlinear Science
- Pardo, D. Demkowicz, L. Torres-Verdin, C. Paszyński M. (2006) Simulation of Resistivity Logging-While-Drilling (LWD) Measurements Using a Self-Adaptive Goal-Oriented *hp*-Finite Element Method. *SIAM Journal on Applied Mathematics*, 66, pp. 2085-2106
- Pardo, D. Calo, V. M. Torres-Verdin, C. Nam, M. J. (2008a) Fourier Series Expansion in a Non-Orthogonal System of Coordinates for Simulation of 3D DC Borehole Resistivity Measurements. *Computer Methods in Applied Mechanics and Engineering*, 197, 1-3, pp. 1906-1925
- Pardo, D. Torres-Verdin, C. Nam, M. J. Paszyński, M., Calo, V. (2008b) Fourier Series Expansion in a Non-Orthogonal System of Coordinates for the Simulation of 3D Alternating Current Borehole Resistivity Measurements. *Computer Methods in Applied Mechanics and Engineering*, 197, 45-48, pp. 3836-3849
- Kołodziej, J. Schaefer, R. Paszynska, A. (2004) Hierarchical genetic computation in optimal design, *Journal of Theoretical and Applied Mechanics*, 42 (3) pp.519–539
- Schaefer, R., Kołodziej, J. (2003) Genetic search reinforced by the population hierarchy. In: *Foundations of Genetic Algorithms 7*, Morgan Kaufman Publisher, pp. 383–399.
- Schaefer, R., Telega, H. (2007). *Foundations of global genetic optimization*. Heidelberg: Springer.

## Characteristics of MFS analysis for finite plate problems with a hole

\*Wataru Fujisaki, T.Suetugu, and M. Takashima

Department of Mechanical Engineering, Faculty of Technology, Kyusyu Sangyo University,  
2-3-1 Matsukadai, Higashi-ku, Fukuoka City, Japan

\*Corresponding author: fujisaki@ip.kyusan-u.ac.jp

### Abstract

By using the method of fundamental solutions (MFS), an accurate stress field can be obtained in infinite problems. One of the authors has been improving the source loads of the MFS program based on the collocation method to be able to calculate the maximum stress of the notch problem correctly. It is found that the improved MFS, which uses the equally dispersed point loads (EDPL), gives the good accuracy for some infinite problems with high stress concentration factor. To confirm the accuracy, the index of the balanced forces was also proposed. Although, in case of the finite plate with a hole, the stability of accuracy mainly depends on the allocation of the collocation points and the source points. Therefore, in this study, we examine and clarify the proper allocation of the source loads in some finite plates including a center hole with internal pressure.

**Keywords:** method of fundamental solutions, MFS, source load, B.F-error, stress field

### Introduction

It is an important matter for the mechanical engineers to evaluate failure loads of some products including a hole. The linear notch mechanics (LNM) as shown in the work by Nisitani(1995), is a useful method to calculate the failure tensile stress and the LNM needs an accurate stress field. In this paper, the effects of source point dispositions to the accuracy of maximum stress on the finite problems are investigated using the method of fundamental solutions with the equally dispersed point load (EDPL). In this study, we calculate the stress around the hole with internal pressure of the rectangle plate as shown in Figure1. We consider a linear elastic problem, governed by the Navier equation. The fundamental solution for surface tractions on the fictitious boundary is

$$p_{lm}^{j*}(x) = \frac{-1}{4\pi(1-\nu)r^j(x)} \left\{ \left[ (1-2\nu)\delta_{lm} + 2r^j(x)_{,l} r^j(x)_{,m} \right] \frac{\partial r}{\partial n} - (1-2\nu) \left( r^j(x)_{,l} n_m(x) - r^j(x)_{,m} n_l(x) \right) \right\} \quad (1)$$

where  $r^j(x) = \left[ (x_1^j - x_1)^2 + (x_2^j - x_2)^2 \right]^{1/2}$ ,  $r_{,m}^j = \partial r^j / \partial x_m$ , and  $\delta_{lm}$  is the Kronecker delta. Equations (1) is written for the plane strain problem. In the homogeneous problem, we can obtain the known value of the variable by the sum of a series of fundamental solutions with unknown source loads  $f(j), j=1, 2N$ . For point loads, following equation (2) can be expressed.

$$\sum_{j=1}^N \left[ p_{1m}^{j*}(x^i) \cdot f(j) + p_{2m}^{j*}(x^i) \cdot f(j+N) \right] = \bar{p}_m^{-i} \quad (2)$$

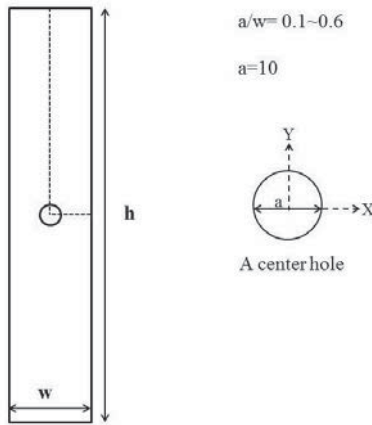
where  $p_{1m}^{j*}$  and  $p_{2m}^{j*}$  are fundamental solutions for surface tractions. For equally dispersed point loads (EDPL) by the author (Fujisaki 2005), we obtain the following equation (3). Here,  $M$  is a number of EDPL, and in this study, we put  $M=10$

$$\sum_{j=1}^N \left[ \sum_{k=1}^M p_{1m}^{j*}(x_k^i) \cdot \frac{f(j)}{M} + \sum_{k=1}^M p_{2m}^{j*}(x_k^i) \cdot \frac{f(j+N)}{M} \right] = \bar{p}_m^{-i} \quad (3)$$

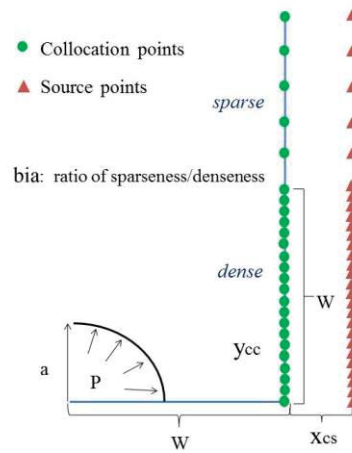
**Stress around a circle hole in a finite plate**

We have calculated the accurate stress fields in the finite plate problem by varying the two dispositions of source loads, namely, inside the hole or outside the plate end (Fujisaki and Fujisawa 2012). Following two conclusions were obtained. (1) the index on the balanced forces is effective tool to obtain good accuracy. (2) In case of the finite plate problem, we find less good allocations to obtain good accuracy than the infinite plate problem in case of no bias ( $bia=1.0$ ).

The stress concentration mainly occurs in a square area ( $h < W$ ) including a hole. In this study, in order to increase the height of the plate, we divided the fictitious boundary line into the dense part and the sparse part as shown in Figure2. Here,  $x_{cs}$  is the distance between collocation point and source point, and  $y_{cc}$  is the distance between collocation points. The number of collocation points on the plate end  $N_e=100$ , and source loads inside hole are located on a fictitious arc of a circle (radius= $0.7a$ ), the number of collocation points on circle hole  $N_c=40$ .



**Figure 1. Calculation model**



**Figure 2. Discretization of plate end**

We illustrate the free body diagram of a plate with a hole problem in Figure3. Here, the total external force ( $pa$ ) is the summation of longitudinal force by the pressure of a quarter hole. On the other hand, the total internal force is obtained by the integral of  $\sigma(x) dx$  at the ligament(unit thickness). Here if we define the index of B.F (balanced forces) as the ratio of the internal force and the external force, we can calculate the index of B.F. correctly by using some integral formula. Therefore if the index of B.F. is 1, then we can assure that the correct stress distribution is obtained. In the MFS, each point source load essentially yields a smooth curve of  $\sigma_{22}$ . Therefore the total superimposed curve of  $\sigma_{22}$  also becomes a smooth curve. If we obtain  $B.F\text{-error}(\%) > 0.0$ , then the calculated distribution curve exceeds the correct curve. If we obtain  $B.F\text{-error}(\%) < 0.0$ , the calculated curve is lower than the correct curve. This is an advantage of the MFS, and by using  $B.F\text{-error}(\%)$ , we can ensure the accuracy of maximum stress as shown in the work by the author (Fujisaki 2010).

In Figure4, we show the proper combinations of  $x_{cs}$  and  $y_{cc}$  to obtain  $B.F\text{-error}(\%) < 1.0$  with  $a/w=0.6$ . In case of equal division ( $bia=1.0$ ), the number  $N_{pc}$  of proper combinations is 30, but when we apply  $bia=2.0$ , we obtain  $N_{pc} = 69$ . When we put  $bia=3.0$ , we can obtain  $N_{pc} = 92$ , therefore  $bia=3.0$  is recommended to use. In Figure5, we summarize the results of proper combinations to obtain  $B.F\text{-error}(\%) < 0.1$ . In case of  $bia=1.0$ ,  $N_{pc}$  is only 1, but when  $bia=2.0$  or

3.0, we obtain  $Npc = 9$ . In Figure6, we show the circumferential stress around the hole by the two conditions (A) (B) in Figure5, namely (A)  $x_{cs}=3.5, y_{cc}=5.2$ , and (B)  $x_{cs}=14.0, y_{cc}=2.2$ . We compare

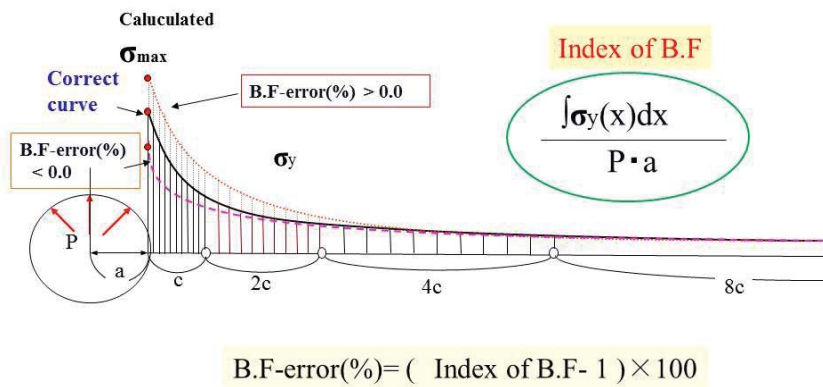


Figure 3. Comparison of circumferential stress

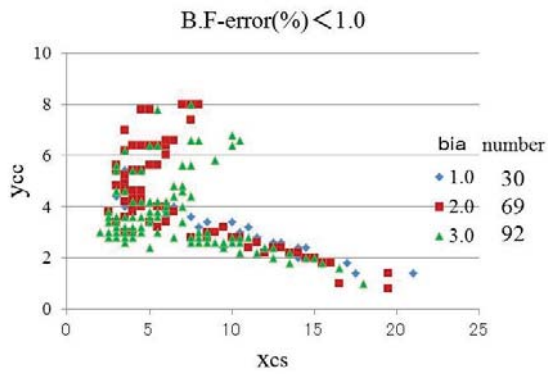


Figure4. Proper combinations- 1

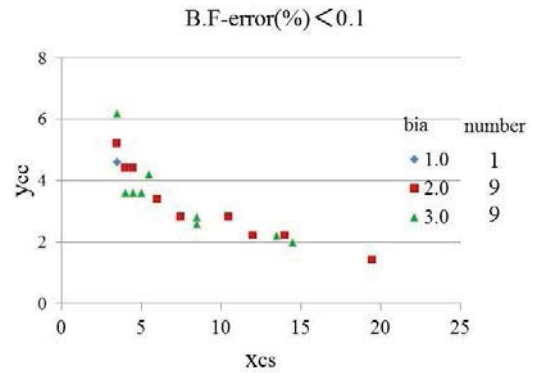


Figure 5. Proper combinations- 2

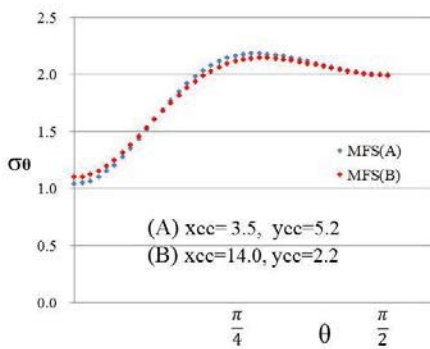


Figure 6. Comparison of circumferential stress

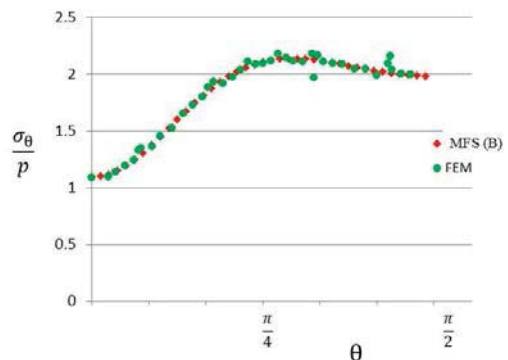


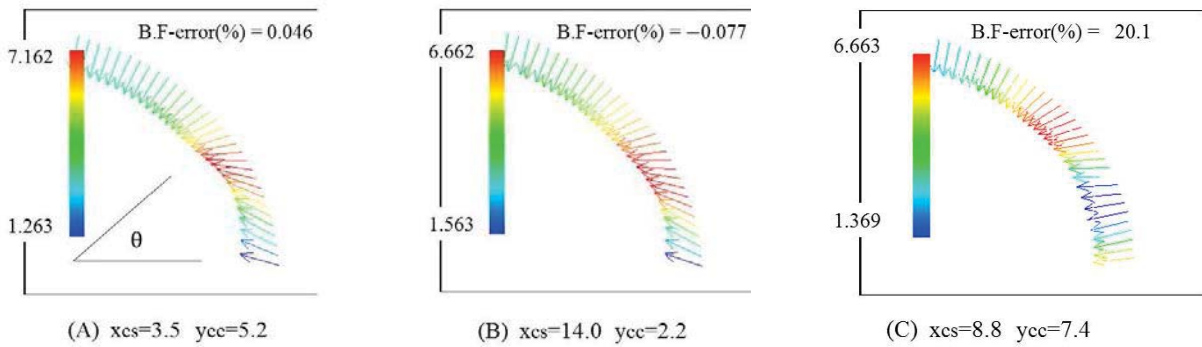
Figure 7. Comparison of MFS/FEM

those two cases with FEM (MS-Marc,8-nodes element, 2190 elements) ,and it is found that the case (B) is very consistent with FEM as shown in Figure7.

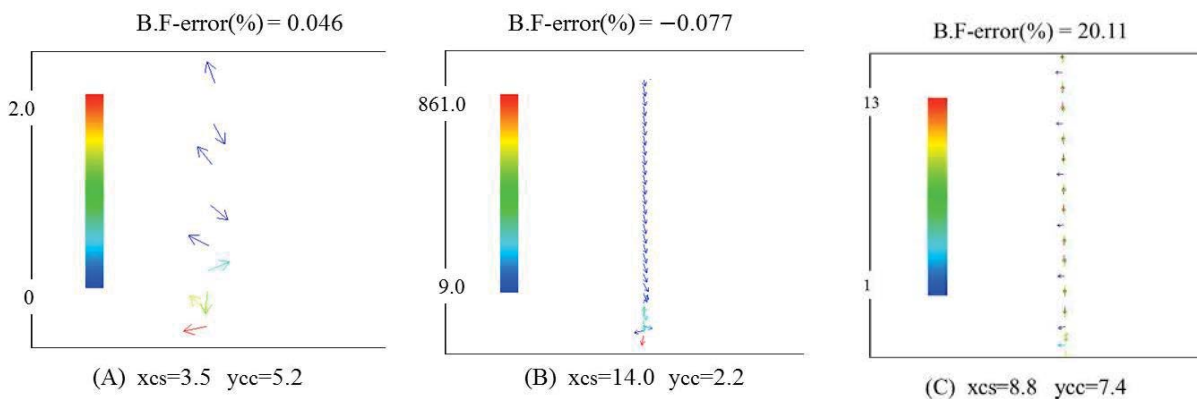
**Characteristics of source loads**

In Figure8, we compare the shape of source loads inside the hole in case of small width ( $a/w=0.6$ ) with the three combinations ((A);  $x_{cs}=3.5, y_{cc}=5.2$ , B.F-error(%)=0.046, (B);  $x_{cs}=14.0, y_{cc}=2.2$ , B.F-error(%)= -0.077, (C);  $x_{cs}=8.8, y_{cc}=7.4$ , B.F-error(%)=20.1). In cases of (A),(B),we obtain good B.F-errors and the shapes of the source loads are similar. High source loads appear from  $\Theta=0.1\pi$  to  $0.25\pi$ . In case of (C), we obtain a bad B.F-error and the shape of the source loads is not so similar. High source loads appear from  $\Theta=0.2\pi$  to  $0.35\pi$ .

We show the three shapes of source loads outside the plate end ( $a/w=0.6$ ) in Figure9. In case of (A), because of low  $x_{cs}$ , the maximum source load is small and appears near the ligament ( $h < w$ ).



**Figure 8. Comparison of source load shape inside hole**



**Figure 9. Comparison of source load shape outside plate end**

In case of (B), because of large  $x_{cs}$ , the maximum source load is high and appears near the ligament ( $h < w$ ) to satisfy the boundary conditions. And also because of small  $y_{cc}$ , we can see that monotonous pattern occurs in  $h > w$ . These source loads create the accurate stress field in the square area ( $h < w$ ) and the remote area ( $h > w$ ). In case of (C), B.F-error is very high, the directions of source load are horizontal or vertical and the large source loads appear everywhere not only near the ligament.

## Conclusions

In order to obtain an accurate stress field of notched plate problem by the MFS, we applied the B.F-error and the sparse/dense allocation area to the plate end. Finally, the following results are mainly obtained.

- (1) An accurate stress field can be obtained by minimizing B.F-error based on balanced forces.
- (2) Combination of  $x_{cs}$  and  $y_{cc}$  is important to make an accurate stress field near and far the ligament. The most proper  $x_{cs}$  is nearly  $0.8w$ , and  $y_{cc}$  is around  $0.2w$  in case of  $a/w=0.6$ .
- (3) We can allocate the collocation points and the source points sufficiently in longitudinal direction by using the sparse /dense allocation technique.

## References

- Nisitani, H. (1995), Linear Crack Mechanics and Linear Notch Mechanics in Fracture Problems, *Acta Mechanica Solida Sinica*, 8, pp. 114-117.
- Fujisaki,W.(2005), Characteristics of Source Loads and Accuracy on Elliptical Hole by the MFS, *Advances in Computational & Experimental Engineering & Science 2005*, Tech Science Press, pp. 332-337,.
- Fujisaki,W. (2010) ,Assurance of Accuracy on High SCF of Double Holes Problems by the Method of Fundamental Solutions, *Recent Studies in Meshless & Other Novel Computational Methods*, Tech Science Press, pp. 57-69.
- Fujisaki,W. and Fujisawa,T. (2012) ,Stress around a center hole in a finite Plate Subjected to Internal Pressure, *European Congress on Computational Methods in Applied Science and Engineering*, Vienna, No.875,pp. 1-7.

## A Non-parametric Form-Finding Method for Designing Membrane Structure

\* Masatoshi Shimoda<sup>1</sup> and Koichi Yamane<sup>2</sup>

<sup>1</sup>Department of Advanced Science and Technology, Toyota Technological Institute, 2-12-1 Hisakata, Tenpaku-ku, Nagoya, Japan.

<sup>2</sup>Graduate School of Toyota Technological Institute, Japan

\*Corresponding author: shimoda@toyota-ti.ac.jp

### Abstract

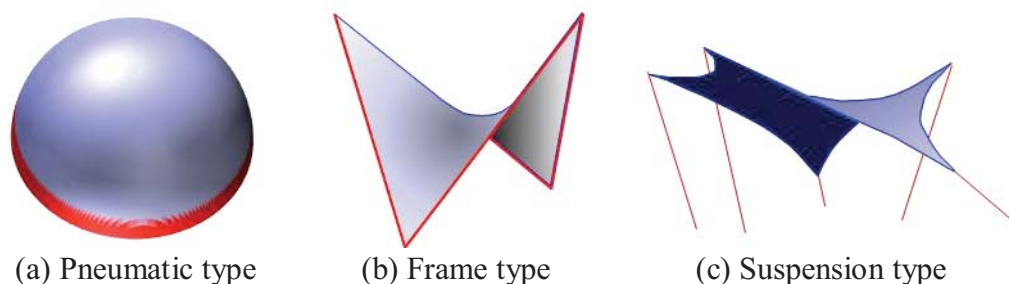
In this paper, we present a non-parametric form-finding method for designing the minimal surface, or the uniformly tensioned surface of membrane structures with arbitrary specified boundaries. The area minimization problems are formulated as distributed-parameter shape optimization problems, and solved numerically. The internal volume or the perimeter is added as the constraints according to the type of a structure such as pneumatic or suspended membranes. It is assumed that the membrane is varied in the out-of-plane and/or the in-plane direction to the surface. The shape gradient function for each problem is derived using the material derivative method. The minimal surface is numerically determined without the shape parameterization by the free-form optimization method, a gradient method in a Hilbert space, where the shape is varied by the traction force in proportion to the sensitivity function. The calculated results show the effectiveness of the proposed method for finding the optimal form of membrane structures.

**Keywords:** Membrane structure, Form finding, Shape optimization, Minimal surface, Free form

### Introduction

Membrane structures have many advantages: they contribute to safety and economy, they are lightweight and not bulky, and they have good aesthetic aspects due to their curved surface and translucency. By taking advantage of these characteristics, various membrane structures have been developed and widely used for industrial products such as roofs, yacht sails, balloons and air-bags. Membranes must maintain their shapes by mainly in-plane tension due to their negligible bending stiffness, which makes it difficult for designers to create the required shapes. In addition, in order to maintain the designed shape and to secure sufficient stiffness and strength against self-weight and external force, initial tensions must be appropriately applied to membranes. Therefore, form-finding is vitally important in the design process.

Membrane structures are classified into the pneumatic (air-support) membrane type in which tensions are generated by differential pressure and the non-pneumatic membrane type to which tensions are applied by mechanical force. Non-pneumatic structures are also classified into the frame membrane type and the suspension membrane type. Non-pneumatic structures must have non-positive Gaussian curvature over the whole surface to maintain the shape. Fig. 1 shows the classification of membrane structures. Regardless of the structure type, membranes cannot be expected to have much bearing capacity due to their thinness even if they are made of strong materials. Therefore, designers need to determine the membrane shape so that there is a uniform stress field across the entire surface.



**Figure 1. Classification of membrane structures**

It is well known that a shape with a uniform stress field conforms to the minimal surface which has zero mean curvature across the surface if the deformation due to the self-weight is negligible. If a constraint condition is given, it has a certain amount of curvature. Such a surface with a constant curvature is also regarded as the minimal surface under the constraint condition. Physical experiments using a soap film or a hanging cloth can easily find minimal surfaces (Otto, 1973). It was also mathematically studied as a variational problem and many minimal surface functions were found (Gray, 1998). However, it is difficult to find minimal surfaces taking account of complicated boundary conditions or mechanical characteristics. In order to solve these disadvantages, many versatile numerical solutions have been studied (e.g., Monterde, 2004, Bletzinger *et al.*, 2005, Pan and Xu, 2011). The solutions can be classified into node-based and parametric surface-based methods, or geometry-based and experiment simulation-based methods.

The authors also have proposed a numerical solution for finding a minimal surface, i.e., an equally tensioned surface, with an arbitrarily specified boundary (Shimoda and Yamane, 2013). This is a node-based and geometry-based method. In this paper we introduce the method and present application examples by the method. This method finds a minimal surface by formulating the form-finding problem as a distributed-parameter shape optimization problem, and applying the sensitivity function derived by the material derivative method to the proposed method, which was based the free-form optimization methods for shells (Shimoda and Tsuji, 2006, Shimoda *et al.*, 2009). The advantages of this method include efficiency for treating large-scale problems and the ability to obtain a smooth shape without any shape parameterization. With this method, numerical form-finding can be performed for a pneumatic membrane structure, a frame membrane structure and a suspension membrane structure, where the shape could vary in the in-plane direction and/or out-of-plane direction according to the type of membrane structures to be solved.

In the following sections, we will first show the formulations of minimal surface problems as distributed-parameter optimization problems and derive each sensitivity function, which is called the shape gradient function. Then, the free-form optimization method for membrane structures will be introduced. Finally, we will show examples of each type of membrane structure.

## Domain variation of membrane structure

### Definition of shape variation for free-form design

As shown in Fig. 2, consider that a membrane having an initial domain  $A$  with the boundary  $\partial A$  is varied into one having domain  $A_s$  with the boundary  $\partial A_s$  by the shape variation (the design velocity field)  $\mathbf{V}$  distributed across the surface. It is assumed that the boundary  $\partial A$  is included in the domain  $A$  ( $\partial A \subset A$ ) and that the thickness  $h$  is constant during the deformation. The shape variation  $\mathbf{V}$  consists of the out-of-plane variation  $V_n$  which deforms in the normal direction to the surface and the in-plane variation  $V_t$  which deforms in the tangential direction to the surface. The membrane shape is varied by  $V_n(A)$  distributed on  $A$  and  $V_t(\partial A)$  distributed on  $\partial A$  since  $V_t(A)$  does not affect the shape variation except on  $\partial A$ . The shape variation is expressed by the piecewise smooth mapping  $T_s : \mathbf{X} \in A \mapsto \mathbf{X}_s(\mathbf{X}) \in A_s$ ,  $0 \leq s \leq \varepsilon$ , where  $\varepsilon$  and  $(\cdot)_s$  indicate a small integer and the iteration history of the shape variation equivalent to time. Using the relations  $\mathbf{X}_s = T_s(\mathbf{X})$ ,  $A_s = T_s(A)$ , the small shape variation around the  $s$ -th variation is expressed as

$$T_{s+\Delta s}(\mathbf{X}) = T_s(\mathbf{X}) + \Delta s \mathbf{V} + O(|\Delta s|^2), \quad (1)$$

where the design velocity field  $\mathbf{V}(\mathbf{X}_s) = \partial T_s(\mathbf{X}) / \partial s$  is given as the Euler derivative of the mapping  $T_s(\mathbf{X})$ , and  $O(|\Delta s|^2)$  is assumed to be neglected as a high-order term. The optimal design velocity

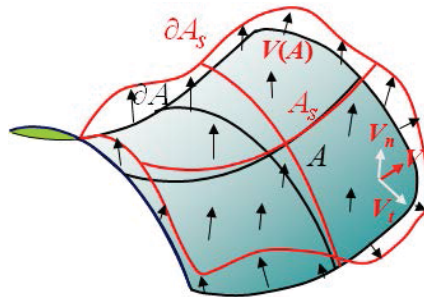


Figure 2. Shape variation of membrane by  $\mathbf{V}$



field  $\mathbf{V}(\mathbf{X}_s)$  is determined by the free-form optimization method proposed, which will be explained later.

### Form-finding problems of membrane structures and derivation of shape gradient function

In order to find the minimal surface, the area of a membrane is defined as an objective functional. In addition to the boundary shape, the internal volume or perimeter is set as another constraint condition according to the structure type. In this section, we will formulate a distributed-parameter shape optimization problem for each type of membrane structure, so as to determine the design velocity field that leads to the minimal surface, and then the shape gradient function will be derived.

#### Frame membrane structure problem

Consider a shape optimization problem for minimizing the area of a frame membrane structure like that shown in Fig. 1(b). When an initial membrane shape  $A_0$  and a specified boundary shape formed by the frame, which may be an open boundary, are given, this problem is expressed as

$$\text{Given } A_0, \quad (2)$$

$$\text{find } \mathbf{V} \text{ (or } A_s), \quad (3)$$

$$\text{that minimizes } A (= \int_A dA). \quad (4)$$

The Lagrange functional  $L$  for this problem is expressed as

$$L(A) = \int_A dA. \quad (5)$$

The material derivative (Choi and Kim, 2005)  $\dot{L}$  of the Lagrange functional  $L$  with respect to shape variation is expressed as

$$\dot{L} = \langle G_A \mathbf{n}, \mathbf{V} \rangle_A + \langle G_{\partial A} \mathbf{t}, \mathbf{V} \rangle_{\partial A}, \quad \mathbf{V} \in C_{\odot}, \quad (6)$$

where the notations of  $\langle G_A \mathbf{n}, \mathbf{V} \rangle_A$  and  $\langle G_{\partial A} \mathbf{t}, \mathbf{V} \rangle_{\partial A}$  are defined as

$$\langle G_A \mathbf{n}, \mathbf{V} \rangle_A \equiv \int_A G_A \mathbf{n} \cdot \mathbf{V} dA = \int_A G_A V_n dA, \quad (7)$$

$$\langle G_{\partial A} \mathbf{t}, \mathbf{V} \rangle_{\partial A} \equiv \int_{\partial A} G_{\partial A} \mathbf{t} \cdot \mathbf{V} d\Gamma = \int_{\partial A} G_{\partial A} V_t d\Gamma, \quad (8)$$

$$G_A = H_A, \quad (9)$$

$$G_{\partial A} = H_{\partial A}, \quad (10)$$

where  $C_{\odot}$  indicates the admissible function space that satisfies the specified geometric boundary condition. The coefficient functions  $G_A$  and  $G_{\partial A}$  are called the shape gradient function and are distributed on the surface and on the boundary, respectively. The notation  $V_n (\equiv \mathbf{n} \cdot \mathbf{V})$  is the normal component of  $\mathbf{V}$  and the vector  $\mathbf{n}$  is an outward unit normal vector to the surface.  $V_t (\equiv \mathbf{t} \cdot \mathbf{V})$  is the tangential component of  $\mathbf{V}$  and the vector  $\mathbf{t}$  is a unit tangential vector to the surface.  $H_A$  and  $H_{\partial A}$  indicate twice the mean curvature on the surface  $A$  and the curvature on the boundary  $\partial A$ .

If the arbitrary boundary is closed, the second term on the right-hand side in Eq. (6) is omitted.

#### Pneumatic membrane structure problem

Consider a problem for minimizing the area of a pneumatic membrane structure subjected to differential pressure, which is shown in Fig. 1(a). Defining a specified boundary as the geometric constraint condition and an internal volume  $\Omega$  (i.e., a space bounded by the membrane) as the equality constraint condition (the constraint value is represented as  $\Omega$ ), this problem is expressed as

$$\text{Given } A_0, \quad (11)$$

$$\text{find } \mathbf{V} \text{ (or } A_s), \quad (12)$$

$$\text{that minimizes } A (= \int_A dA), \quad (13)$$

$$\text{subject to } \Omega (= \int_{\Omega} d\Omega) = \hat{\Omega}. \quad (14)$$

The Lagrange functional  $L$  for this problem is expressed as

$$L(A, \Omega) = \int_A dA + \Lambda_{\Omega} (\int_{\Omega} d\Omega - \hat{\Omega}). \quad (15)$$

The material derivative  $\dot{L}$  of the Lagrange functional  $L$  with respect to shape variation is expressed as

$$\dot{L} = \langle G_A \mathbf{n}, \mathbf{V} \rangle_A + \Lambda'_{\Omega} (\int_{\Omega} d\Omega - \hat{\Omega}), \quad \mathbf{V} \in C_{\Theta}, \quad (16)$$

$$G_A = H_A + \Lambda_{\Omega}. \quad (17)$$

When the constraint condition with regard to the internal volume is met, Eq. (16) can be written as

$$\dot{L} = \langle G_A \mathbf{n}, \mathbf{V} \rangle_A, \quad \mathbf{V} \in C_{\Theta}. \quad (18)$$

### *Suspension membrane structure problem*

Consider the problem for minimizing the area of a suspension membrane structure like that shown in Fig. 1(c). Defining specified fixed points on the boundary as the geometric constraint condition and a perimeter  $\Gamma$  of the boundary as the equality constraint condition (the constraint value is represented as  $\hat{\Gamma}$ ), this problem is expressed as

$$\text{Given } A_0, \quad (19)$$

$$\text{find } \mathbf{V} \text{ (or } A_s), \quad (20)$$

$$\text{that minimizes } A (= \int_A dA), \quad (21)$$

$$\text{subject to } \Gamma (= \int_{\partial A} d\Gamma) = \hat{\Gamma}. \quad (22)$$

The Lagrange functional  $L$  for this problem is represented as

$$L(A, \Gamma) = \int_A dA + \Lambda_{\Gamma} (\int_{\partial A} d\Gamma - \hat{\Gamma}). \quad (23)$$

If the constrained perimeter condition is met, the material derivative  $\dot{L}$  of the Lagrange functional  $L$  with respect to shape variation is represented as

$$\dot{L} = \langle G_A \mathbf{n}, \mathbf{V} \rangle_A + \langle G_{\partial A} \mathbf{t}, \mathbf{V} \rangle_{\partial A}, \quad \mathbf{V} \in C_{\Theta}, \quad (24)$$

$$G_A = H_A, \quad (25)$$

$$G_{\partial A} = 1 + \Lambda_{\Gamma} H_{\partial A}. \quad (26)$$

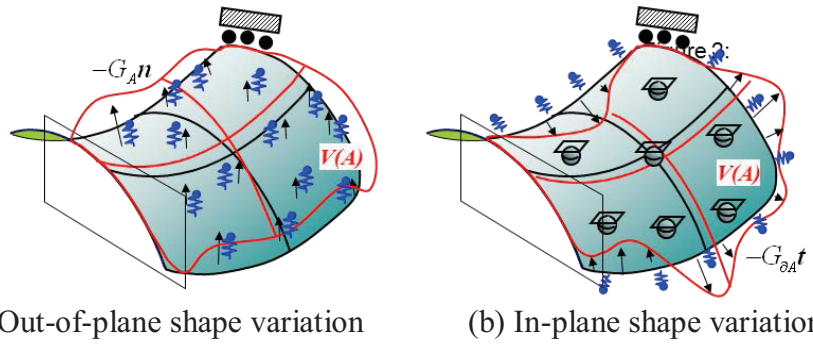
The shape gradient functions derived here are used for determining the minimal surface (or the optimal design velocity field or the optimal shape variation). We will explain the method in the next section.

### **Free-form optimization method for form-finding of membranes**

The free-form optimization method for form-finding, i.e., minimal surface of membrane structures, were developed by combining the free-form optimization methods for shells with respect to the in-plane variation (Shimoda and Tuji, 2006) and the out-of-plane variation (Shimoda *et al*, 2009). The free-form optimization method is a node-based shape optimization method based on the traction method (Azegami, 1994, Shimoda *et al*, 1998) which is a gradient method in a Hilbert space, and can treat all nodes as design variables without parameterization.

In order to determine the optimal design velocity field that minimizes the objective functional using both the derived shape gradient functions and the gradient method in a Hilbert space, a tensor with

positive definitiveness must be introduced. A unit tensor cannot maintain the smoothness of the shape since it leads to a jagged shape problem. A stiffness tensor of an elastic shell under the Robin boundary condition similar in shape to a membrane is used in this method to make the computation simple and linear. This stiffness tensor serves not only to reduce the objective functional, but also to maintain the mesh smoothness. The Robin condition is employed to stabilize the convergence. The reference shape is updated with the optimal design velocity field  $\mathbf{V}$  obtained by applying the distributed external forces in proportion to the negative shape gradient function to this pseudo-elastic shell. Consider the design velocity field  $\mathbf{V} = \{V_i\}_{i=1,2,3}$  divided between the in-plane component  $\mathbf{V}_0 = \{V_{0\beta}\}_{\beta=1,2}$  and the out-of-plane component  $V_3$  on the local coordinate systems. Using Kirchhoff's theorem as a plate bending theory, each governing equation of the design velocity field is explained as Eq. (27) and Eq. (29), respectively. In the case of the in-plane variation, the out-of-plane velocity field needs to be constrained (i.e.,  $V_3 = 0$ ). Therefore, after each design field is determined separately, they are synthesized as required with the relation  $\mathbf{V} = \mathbf{V}_n + \mathbf{V}_t$ . We call this analysis for  $\mathbf{V}$  "velocity analysis". Fig. 3 shows schematics of the velocity analysis for (a) out-of-plane shape variation and (b) in-plane shape variation.



**Figure 3. Schematics of the free-form optimization method for membranes**

$$a((\mathbf{V}_{0\beta}, V_3, \boldsymbol{\theta}), (\bar{\mathbf{u}}_0, \bar{w}, \bar{\boldsymbol{\theta}})) + \alpha \langle (\mathbf{V} \cdot \mathbf{n}) \mathbf{n}, (\bar{\mathbf{u}}_0, \bar{w}, \bar{\boldsymbol{\theta}}) \rangle_A = - \langle G_A \mathbf{n}, (\bar{\mathbf{u}}_0, \bar{w}, \bar{\boldsymbol{\theta}}) \rangle_A, \quad (\mathbf{V}_{0\beta}, V_3, \boldsymbol{\theta}) \in C_\Theta, \quad \forall (\bar{\mathbf{u}}_0, \bar{w}, \bar{\boldsymbol{\theta}}) \in C_\Theta, \quad (27)$$

$$C_\Theta = \{(V_0, V_2, V_3, \theta_1, \theta_2) \in (H^1(A))^5 \mid (\mathbf{V}_0, V_3, \boldsymbol{\theta}) \text{ satisfy the constraints of shape variation on } A\}. \quad (28)$$

$$a((\mathbf{V}_{0\beta}, V_3, \boldsymbol{\theta}), (\bar{\mathbf{u}}_0, \bar{w}, \bar{\boldsymbol{\theta}})) + \alpha \langle (\mathbf{V} \cdot \mathbf{t}) \mathbf{t}, (\bar{\mathbf{u}}_0, \bar{w}, \bar{\boldsymbol{\theta}}) \rangle_{\partial A} = - \langle G_{\partial A} \mathbf{t}, (\bar{\mathbf{u}}_0, \bar{w}, \bar{\boldsymbol{\theta}}) \rangle_{\partial A}, \quad (\mathbf{V}_{0\beta}, V_3, \boldsymbol{\theta}) \in C_\Theta, \quad \forall (\bar{\mathbf{u}}_0, \bar{w}, \bar{\boldsymbol{\theta}}) \in C_\Theta, \quad (29)$$

$$C_\Theta = \{(V_0, V_2, V_3, \theta_1, \theta_2) \in (H^1(A))^5 \mid (\mathbf{V}_0, V_3, \boldsymbol{\theta}) \text{ satisfy the constraints of shape variation on } S \text{ and } V_3 = 0 \text{ on } A\}. \quad (30)$$

Here, the bilinear form  $a(\cdot, \cdot)$ , which represents virtual work related to internal force, and the linear forms  $\langle \cdot, \cdot \rangle_A$ ,  $\langle \cdot, \cdot \rangle_{\partial A}$  are expressed as Eq. (31), Eq. (32) and Eq. (33), respectively.  $(\cdot)$  expresses the variation. The tensor subscript notation uses Einstein's summation convention and a partial differential notation for the spatial coordinates  $(\cdot)_{,i} = \partial(\cdot) / \partial x_i$ .

$$a((\mathbf{u}_0, w, \boldsymbol{\theta}), (\bar{\mathbf{u}}_0, \bar{w}, \bar{\boldsymbol{\theta}})) = \int_A \{c_{\alpha\beta\gamma\delta}^B \kappa_{\gamma\delta} \bar{\kappa}_{\alpha\beta} + c_{\alpha\beta\gamma\delta}^M \varepsilon_{0\gamma,\delta} \bar{\varepsilon}_{0\alpha,\beta}\} dA, \quad (31)$$

$$\langle G_A \mathbf{n}, (\bar{\mathbf{u}}_0, \bar{w}, \bar{\boldsymbol{\theta}}) \rangle_A = \int_A G_A \bar{w} dA, \quad (32)$$

$$\langle G_{\partial A} \mathbf{t}, (\bar{\mathbf{u}}_0, \bar{w}, \bar{\boldsymbol{\theta}}) \rangle_{\partial A} = \int_{\partial A} (G_{\partial A\beta} \bar{u}_{0\beta}) d\Gamma, \quad (33)$$

where  $w$  and  $\mathbf{u}_0 = \{u_{0\alpha}\}_{\alpha=1,2}$  represent the out-of-plane displacement and the in-plane displacement vector at the mid-plane, respectively.  $\{\kappa_{\alpha\beta}\}_{\alpha,\beta=1,2}$  and  $\{\varepsilon_{0\alpha\beta}\}_{\alpha,\beta=1,2}$  represent the curvature tensor and the strain tensor at the mid-plane, respectively, which are defined as

$$\kappa_{\alpha\beta} \equiv \frac{1}{2} (w_{,\alpha\beta} + w_{,\beta\alpha}), \quad (34)$$

$$\varepsilon_{0\alpha\beta} \equiv \frac{1}{2}(u_{0\alpha,\beta} + u_{0\beta,\alpha}). \quad (35)$$

$H_A$  and  $H_{cA}$  in the shape gradient functions are approximately calculated at all points of a finite element model by a discrete method proposed by Meyer *et al.*, (2002).

The fact that the shape variation due to the design velocity field  $\mathbf{V}$  obtained in the velocity analysis, i.e., Eq. (27) and/or Eq. (29) decreases the objective functional was verified in the previous papers (Shimoda and Yamane, 2013, Shimoda *et al.*, 2009).

The minimal surface can be obtained by repeating the three processes: (i) computation of the shape gradient function, (ii) velocity analysis and (iii) shape updating. In this study, a general-purpose FEM code was used in the velocity analysis.

## Calculated results for three types of membrane structures

### Frame membrane structure problem

The initial shape of a frame membrane structure is shown in Fig. 4(a). The red lines show the fixed frames, or the specified boundaries. In the velocity analysis their boundaries were simply supported. The minimal surface obtained is shown in Fig. 4(b), which was determined by the out-of-plane variation according to the shape gradient function, i.e., Eq. (9). Fig. 4(c) shows the result of soap-film experiment by Otto (1973).

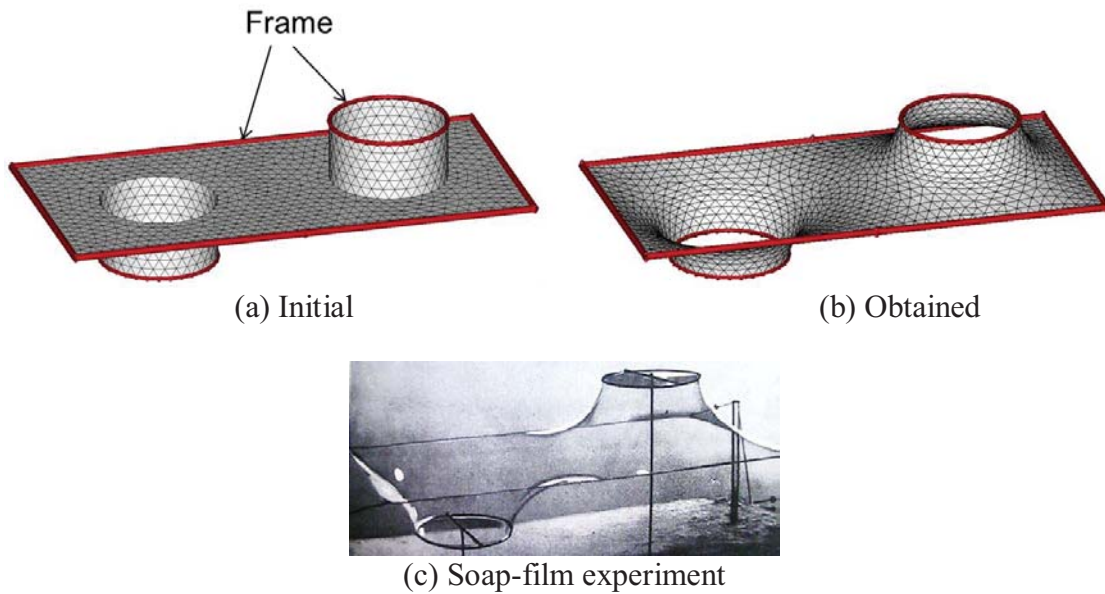


Figure 4. Optimization result of frame membrane structure

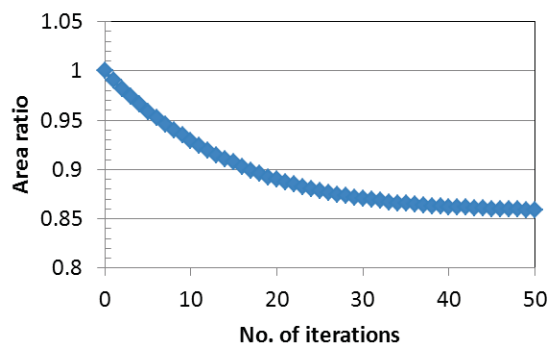
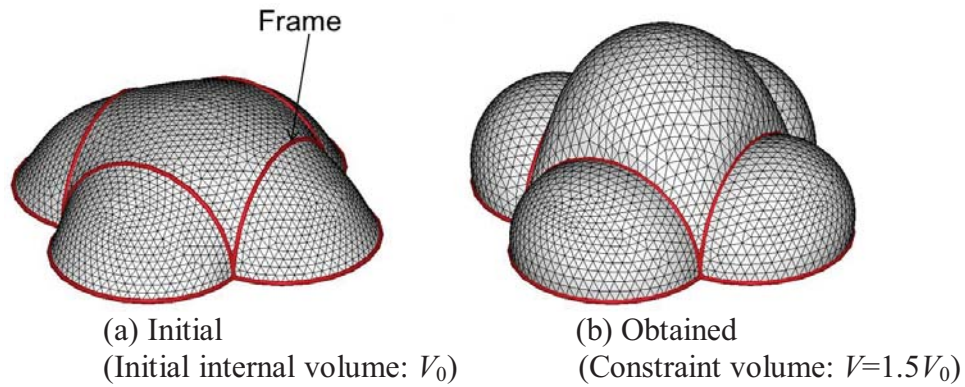


Figure 5. Iteration histories for frame membrane structure

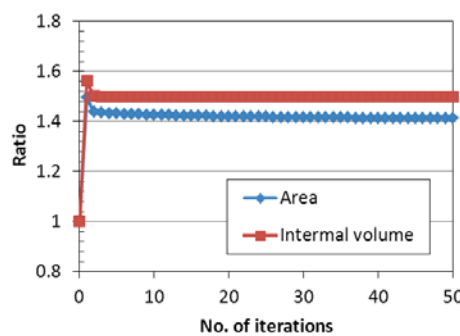
Fig. 5 shows the iteration convergence histories of the area. The results show that the shape obtained is smooth and well-approximated to the soap-film experiment. The area was decreased by about 14% and converged steadily.

*Pneumatic membrane structure problem*

The initial shape having internal volume, i.e., the space bounded by the membrane with frames, was designed as shown in Fig. 6(a). Under the internal volume constraint condition (i.e., 150% of the initial shape), analysis of the minimal surface was conducted. In the velocity analysis, the specified boundaries by the frames were simply supported. The minimal shapes were determined by the out-of-plane variation according to the shape gradient function, i.e., Eq. (17). The internal volume was computed by space discretization using tetra elements. Fig. 6(b) shows the minimal surface obtained, and Fig. 7 shows the iteration convergence histories of the area and the internal volume. The graph shows that the area was increased by about 40%, while satisfying the internal volume constraint.



**Figure 6. Optimization result of pneumatic membrane structure**

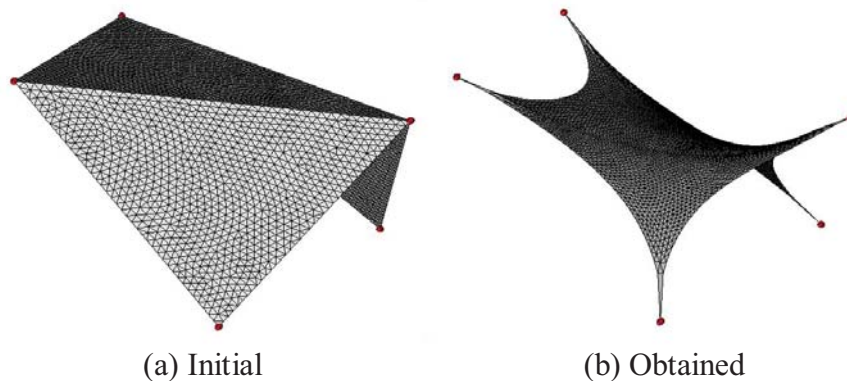


**Figure 7. Iteration histories for pneumatic membrane structure**

*Suspension membrane structure problem*

As a problem of suspension membrane structures, an area minimization analysis was conducted under a perimeter constraint condition. The initial shape of a tarpaulin-like structure, the five vertices of which were fixed, is shown in Fig. 8(a). In the velocity analysis, the vertices were simply supported. The perimeter constraint was set as 102% of the initial shape. The minimal surface was determined by the out-of-plane and in-plane variations according to the shape gradient functions, i.e., Eq. (25) and Eq. (26). Fig. 8 (b) shows the minimal surface obtained. The area was minimized

and reduced by around 58%, while the perimeter constraint was satisfied.



**Figure 8. Optimization result of 5-points spatial suspension membrane structure**

## Conclusion

In this paper, we presented a numerical non-parametric form-finding method for designing the minimal surface of a membrane structure. Design problems according to the type of membrane structure (i.e., frame, pneumatic and suspension type) are formulated as distributed-parameter shape optimization problems, and the shape gradient functions are derived, where the in-plane shape variation and/or the out-of-plane shape variation was defined as the variable for form-finding. By applying the derived sensitivity function to the gradient method in a Hilbert space, the minimal surfaces were determined by iterative computations. With this method, the optimal and smooth free-form of membranes can be found without any shape parameterization. Design examples were illustrated for each type of membrane structure.

## References

- Azegami, H. (1994), A Solution to Domain Optimization Problems, *Transactions of Japan Society of Mechanical Engineers.*, 60, pp. 1479-1486, (in Japanese).
- Bletzinger, K. U., Wuchner, R., Daoud, F., and Camprubi, N. (2005), Computational Methods for Form Finding and Optimization of Shells and Membranes, *Computer Methods in Applied Mechanics and Engineering*, 194(30-33), pp. 3438-3452.
- Choi, K. K. and Kim, N. H. (2005), *Structural Sensitivity Analysis and Optimization 1*, Springer.
- Gray, A. (1998), *Modern Differential Geometry of Curves and Surfaces with MATHEMATICA*, CRC Press.
- Meyer, M., Desbrun, M., Schroder, P. and Barr, A. H. (2002), Discrete Differential-Geometry Operators for Triangulated 2-Manifolds, *Visualization and Mathematics III*, pp. 35-57.
- Monterde, J. (2004), Bézier Surfaces of Minimal Area: The Dirichlet Approach, *Computer Aided Geometric Design*, 21(2), pp. 117-136.
- Otto, F. (1973), *Tensile Structures*, MIT Press.
- Pan, Q. and Xu, G. (2011), Construction of minimal subdivision surface with a given boundary, *Computer-Aided Design*, 43, pp. 374-380.
- Shimoda, M, Azegami, H. and Sakurai, T. (1998), Numerical Solution for Min-Max Shape Optimization Problems (Minimum Design of Maximum Stress and Displacement), *JSME International Journal*, Series A, Vol. 41, No. 1, pp.1-9.
- Shimoda, M. and Tsuji, J. (2006), Non-parametric Shape Optimization Method for Rigidity Design of Automotive Sheet Metal Structure, *SAE 2006 Transactions, Journal of Passenger Cars - Mechanical Systems*, Paper No. 2006-01-0584, pp.483-492.
- Shimoda, M., Iwasa, K. and Azegami, H. (2009), A Shape Optimization Method for the Optimal Free-form Design of Shell Structure, *CD-proceedings of 8th World Congress on Structural and Multidisciplinary Optimization*.
- Shimoda, M. and Yamane, K. (2013), A Numerical Form-finding Method for Minimal Surface of Membrane Structures, *Structural and Multidisciplinary Optimization*, (submitted).

# Ultra-Accurate Isogeometric Structural Vibration Analysis with Novel Higher Order Mass Formulations

**\*Dongdong Wang, Xiwei Li, Wei Liu, and Hanjie Zhang**

Department of Civil Engineering, Xiamen University, Xiamen, Fujian 361005, China

\*Corresponding author: ddwang@xmu.edu.cn

## Abstract

An ultra-accurate isogeometric structural vibration analysis is presented. The key ingredient of the proposed methodology is the development of novel higher order mass matrices which are realized through a new two-step mass construction method. Firstly by using the standard consistent mass matrix a special reduced bandwidth mass matrix with equal order of accuracy is designed under the mass conservation constraint. A mixed mass matrix follows through a linear combination of the consistent mass matrix and the reduced bandwidth matrix. Subsequently the desired higher order mass matrix is then rationally deduced from the mixed mass matrix by optimizing the linear combination parameter in order to minimizing the frequency error. It turns out that for the semi-discrete free vibration analysis, the orders of accuracy associated with the proposed higher order mass matrices are two orders higher than those of their corresponding consistent mass formulations. Meanwhile, a detailed analysis of the full-discrete formulation with Newmark temporal integration demonstrates that the accuracy of the full-discrete frequency associated with the higher order mass matrices is superior compared with that of the standard consistent matrix matrices. The ultra-accurate performance of the proposed method is illustrated through several examples.

**Keywords:** isogeometric analysis, structural vibration, semi- and full-discretization, frequency accuracy, higher order mass matrix.

## Introduction

To seamlessly integrate the computer aided geometry design (CAGD) and the finite element analysis (FEA), Hughes et al. [1] proposed the isogeometric analysis where the CAGD data, i.e., the non-uniform rational B-splines (NURBS) and control points, is directly employed as the shape functions and geometry input for the finite element analysis. Thus exact geometry is preserved in the isogeometric analysis regardless of the model refinement. Meanwhile, high order smoothing convex approximation can be readily constructed for the NURBS basis functions, which makes isogeometric analysis ideal for the solution of problems with high order governing differential equations.

The excellent performance of isogeometric analysis has been demonstrated in many important problems [1-4], one of which is the structural vibration analysis. It has been shown by Cottrell et al. [5] and Reali [6] that the frequency spectra by isogeometric analysis are much more accurate than those by the typical higher order finite elements. Later Shojaee et al. [7] employed the isogeometric approach for free vibration analysis of thin plates. Thai et al. [8] investigated the static, free vibration, and buckling behaviors of laminated composite shear deformable plate with the isogeometric method. Very recently, Wang et al. [9] developed a set of novel higher order mass matrices for structural vibration analysis with ultra-accurate frequency accuracy. These higher order mass matrices are constructed by a two-step rational method. In the first stage, a reduced bandwidth mass matrix with the same order accuracy as the consistent mass matrix is developed, where the

mass conservation is maintained. Then an optimal linear combination of the reduced bandwidth mass matrix and the consistent mass matrix yields the desired higher order mass matrix. An elevation of two orders of frequency accuracy is observed for the higher order mass matrix.

In this work the higher order mass matrix formulations for isogeometric analysis are first summarized, whose accuracy is demonstrated via classical free vibration examples. Thereafter a fully discrete formulation is introduced for the higher order mass isogeometric analysis to examine its discrete properties. The temporal discretization is completed by the widely used Newmark method. The full-discrete frequency is then derived with the aid of the semi-discrete frequency. Comparison between the full-discrete frequency and the continuum frequency is presented in detail. It turns out the higher order mass isogeometric analysis produces more favorable full-discrete frequency compared with the consistent mass formulation. Finally transient analysis results are also given to illustrate the proposed methodology.

## Isogeometric Higher Order Mass Matrix

### Isogeometric Basis Functions

The isogeometric analysis often employs B-Spline and NURBS as the basis function for geometric description and finite element analysis. A set of  $n$   $p$ -th order B-spline basis functions  $N_{ap}(\xi)$ 's are recursively defined as follows [1]:

$$N_{ap}(\xi) = N_{a(p-1)}(\xi)(\xi - \xi_a) / (\xi_{a+p} - \xi_a) + N_{(a+1)(p-1)}(\xi)(\xi_{a+p+1} - \xi) / (\xi_{a+p+1} - \xi_{a+1}) \text{ for } p \geq 1 \quad (1)$$

where in case of  $p = 0$ ,  $N_{a0}(\xi) = 1$  for  $\xi_a \leq \xi < \xi_{a+1}$  and otherwise  $N_{a0}(\xi) = 0$ .  $\xi$  is the parametric coordinate,  $\xi_a$  is the  $a$ -th knot of the knot vector  $\mathbf{k}_\xi = \{\xi_1 = 0, \dots, \xi_a, \dots, \xi_{n+p+1} = 1\}^T$ . A NURBS basis function  $R_a^p(\xi)$  is given by assigning a weight  $w_a$  to each B-spline basis function  $N_{ap}(\xi)$ :

$$R_a^p(\xi) = N_{ap}(\xi)w_a / \sum_{b=1}^n N_{bp}(\xi)w_b \quad (2)$$

Through tensor product operation, 2D NURBS basis function  $R_{ab}^{pq}(\xi, \eta)$  takes the following form:

$$R_{ab}^{pq}(\xi, \eta) = N_{ap}(\xi)N_{bq}(\eta)w_{ab} / \sum_{c=1}^n \sum_{d=1}^m N_{cp}(\xi)N_{dq}(\eta)w_{cd} \quad (3)$$

where  $w_{ab}$  is the 2D weight for geometry description.  $N_{bq}(\eta)$  is the  $q$ -th order basis function and  $m$  is the number of basis functions in the  $\eta$  direction, respectively.

### Construction of Higher Order Mass Matrices

Here we consider the quadratic isogeometric approximation of an elastic rod with cross section area  $A$  and density  $\rho$ . In this case the element consistent mass matrix  $\mathbf{M}^e$  and stiffness matrix  $\mathbf{K}^e$  are given by [9]:

$$\mathbf{M}^{ec} = \frac{\rho Ah}{120} \begin{bmatrix} 6 & 13 & 1 \\ 13 & 54 & 13 \\ 1 & 13 & 6 \end{bmatrix}, \quad \mathbf{K}^e = \frac{EA}{6h} \begin{bmatrix} 2 & -1 & -1 \\ -1 & 2 & -1 \\ -1 & -1 & 2 \end{bmatrix} \quad (4)$$



where  $h$  is the element length. Consider the classical semi-discrete vibration model problem:

$$\mathbf{M}\ddot{\mathbf{d}} + \mathbf{K}\mathbf{d} = \mathbf{0} \quad (5)$$

in which  $\mathbf{d}$  contains the coefficients associated with the control points, the overhead dots represent time differentiation. It is noted that since NURBS basis functions are not interpolatory functions in general,  $\mathbf{d}$  does not represent physical values of the control points and thus proper treatment of essential boundary conditions is required [10, 11]. Based on Eqs. (4) and (5), it is shown that the frequency error associated with the consistent mass matrix is [9]:

$$\omega^h / \omega \approx 1 + (kh)^4 / 1440 \quad (6)$$

where  $k$  is the wave number.  $\omega$  and  $\omega^h$  are the exact continuum frequency and the semi-discrete (spatially discrete) frequency. In [9], an equal order accurate reduced bandwidth mass matrix  $\mathbf{M}^{er}$  can be postulated as follows:

$$\mathbf{M}^{er} = \frac{\rho h}{120} \begin{bmatrix} 7 - \beta/2 & 13 + r/2 & 0 \\ 13 + \beta/2 & 54 - r & 13 + r/2 \\ 0 & 13 + r/2 & 7 - r/2 \end{bmatrix}, \quad \omega^h / \omega \approx 1 - (4 - r)(kh)^2 / 240 + (18 - r)(kh)^4 / 2880 \quad (7)$$

with  $r$  being an adjustable coefficient. Clearly selecting  $r = 4$  gives us a 4<sup>th</sup> order accurate mass matrix that reduces the half-bandwidth of the consistent mass matrix by 1.

To establish a higher order mass matrix, we further consider the following mixed mass matrix  $\mathbf{M}^{em}$  through linear combination of  $\mathbf{M}^{ec}$  and  $\mathbf{M}^{er}$ :

$$\left\{ \begin{array}{l} \mathbf{M}^{em} = (1 - s)\mathbf{M}^{er} + s\mathbf{M}^e = \frac{\rho h}{120} \begin{bmatrix} 5 + s & 15 - 2s & s \\ 15 - 2s & 50 + 4s & 15 - 2s \\ s & 15 - 2s & 5 + s \end{bmatrix} \\ \omega^h / \omega \approx 1 - (7 - 6s)(kh)^4 / 1440 + (29 - 28s)(kh)^6 / 40320 \end{array} \right. \quad (8)$$

where  $s$  is a parameter. Thus we can choose  $s = 7/6$  to achieve a 6<sup>th</sup> order accurate higher order mass matrix:  $\mathbf{M}^{eho} = (7\mathbf{M}^e - \mathbf{M}^{er}) / 6$ .

Though the tensor product formulation, the previous algorithm can be extended to construct multidimensional higher order mass matrix. In 2D case, we have the following quadratic higher order mass matrix [9]:

$$\mathbf{M}^{eho} = (13\mathbf{M}^{ec} - \mathbf{M}^{er}) / 12, \quad \omega^h / \omega \approx 1 + 11(kh)^6 / 120960 \quad (9)$$

where  $\mathbf{M}^{ec}$  and  $\mathbf{M}^{er}$  are the 2D consistent and reduced bandwidth mass matrix whose explicit expressions can be found in [9].

### Analysis of Fully Discrete Algorithm with Higher Order Mass Matrices

The analysis of the fully discrete algorithm can be completed for the following model problem through the standard modal reduction technique for Eq. (5):

$$\ddot{q} + (\omega^h)^2 q = 0 \quad (10)$$

where  $q$  is the generalized displacement. As for the temporal discretization, we consider the Newmark method. According to this method, the advancement of the variables such as

displacement, velocity and acceleration at time  $t_n$ , i.e.,  $\{\mathbf{d}_n, \mathbf{v}_n, \mathbf{a}_n\}$ , to their corresponding counterparts at  $t_{n+1}$ , say,  $\{\mathbf{d}_{n+1}, \mathbf{v}_{n+1}, \mathbf{a}_{n+1}\}$ , follows the following formula:

$$\mathbf{d}_{n+1} = \mathbf{d}_n + \Delta t \mathbf{v}_n + \frac{\Delta t^2}{2} \{(1-2\beta)\mathbf{a}_n + 2\beta\mathbf{a}_{n+1}\}, \quad \mathbf{v}_{n+1} = \mathbf{v}_n + \Delta t \{(1-\gamma)\mathbf{a}_n + \gamma\mathbf{a}_{n+1}\} \quad (11)$$

where  $\Delta t = t_{n+1} - t_n$ ,  $\beta$  and  $\gamma$  are parameters. Introducing Eq. (11) into Eq. (10) gives [12]:

$$\mathbf{y}_{n+1} = \mathbf{A}\mathbf{y}_n, \quad \mathbf{y} = \{q, \dot{q}\}^T, \quad \mathbf{A} = \begin{bmatrix} \frac{2-(1-2\beta)(\omega^h \Delta t)^2}{2[1+\beta(\omega^h \Delta t)^2]} & \frac{\Delta t}{1+\beta(\omega^h \Delta t)^2} \\ (\gamma-1)(\omega^h)^2 \Delta t & 1 \end{bmatrix} \quad (12)$$

with  $\mathbf{A}$  being the amplification matrix. In the following discussion,  $\gamma = 1/2$  is employed. The characteristic equation of  $\mathbf{A}$  is:

$$\det(\mathbf{A} - \lambda \mathbf{I}) = \lambda^2 - 2A_1\lambda + A_2 = 0, \quad A_1 = 1 - (\omega^h \Delta t)^2 / [21 + \beta(\omega^h \Delta t)^2], \quad A_2 = 1 \quad (13)$$

where  $\mathbf{I}$  is the 2 by 2 identity matrix,  $\lambda$  is the eigenvalue of  $\mathbf{A}$  that has the following form:

$$\lambda = e^{i\alpha}, \quad i = \sqrt{-1}, \quad \alpha = \bar{\omega}^h \Delta t \quad (14)$$

with  $\bar{\omega}^h$  being the full-discrete frequency that is different to semi-discrete frequency. The comparison of  $\bar{\omega}^h$  and the exact continuum frequency  $\omega$  is a useful index to measure the accuracy of the discrete algorithm. Substituting Eq. (14) into Eq. (13) leads to:

$$\sin^2(\bar{\omega}^h \Delta t / 2) = 1 / [4\beta + (2 / \omega^h \Delta t)^2] \quad (15)$$

For the 1D quadratic isogeometric higher order mass matrix we have [9]

$$\omega^h = \frac{c}{h} \sqrt{\frac{20[6-2\cos(2kh)-4\cos(kh)]}{2s\cos(2kh)+2(30-4s)\cos(kh)+60+6s}}, \quad s = 7/6 \quad (16)$$

where  $c$  is the wave speed. While in 2D case,  $\omega^h$  is given by [9]:

$$\omega^h = \frac{c}{h} \sqrt{\frac{40[-\cos(4kh)-28\cos(3kh)-112\cos(2kh)-4\cos(kh)+145]}{[s\cos(4kh)+52s\cos(3kh)+(900-92s)\cos(2kh)] + (3600-116s)\cos(kh)+2700+155s}}, \quad s = 13/12 \quad (17)$$

Further substituting Eqs. (16) and (17) into (15) gives the respective fully discrete frequencies:  
1D rod model problem:

$$\sin^2 \frac{\bar{\omega}^h \Delta t}{2} = \frac{20\Delta t^2 [6-2\cos(2kh)-4\cos(kh)]}{\left\{ \begin{array}{l} 480\beta\Delta t^2 + 4h^2(60+6s) + (8sh^2 - 160\beta\Delta t^2)\cos(2kh) \\ + [8h^2(30-4s) - 320\beta\Delta t^2]\cos(kh) \end{array} \right\}} \quad (18)$$

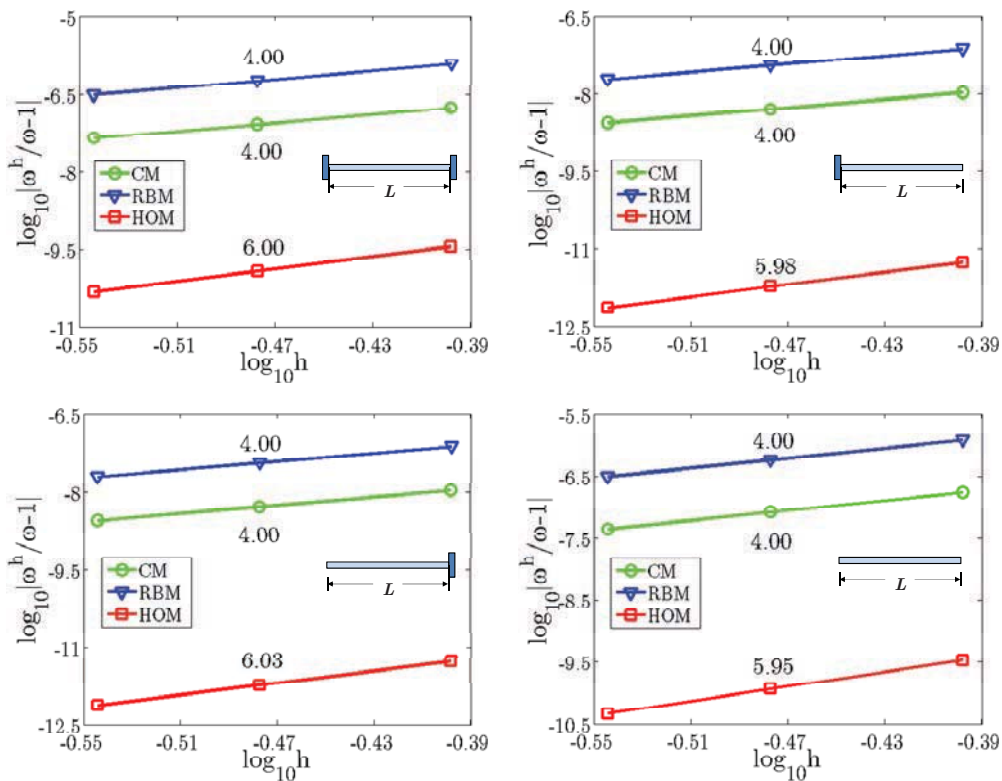
2D membrane model problem:

$$\left\{ \sin^2 \frac{\bar{\omega}^h \Delta t}{2} \right\}^{-1} = 4\beta + \frac{h^2 \left[ \begin{array}{l} s\cos(4kh) + 52s\cos(3kh) + (900-92s)\cos(2kh) \\ + (3600-116s)\cos(kh) + 2700 + 155s \end{array} \right]}{10c^2(\Delta t)^2 [145 - \cos(4kh) - 28\cos(3kh) - 112\cos(2kh) - 4\cos(kh)]} \quad (19)$$

## Results and Discussions

### *Accuracy of Semi-discrete Frequency*

First we consider a free vibration elastic rod problem, the geometry and material properties for the elastic rod are: length  $L=10$ , cross section area  $A=1$ , material density  $\rho=1$ , and Young's modulus  $E=1$ . Figure 1 list the fundamental frequency results for the vibrations of fixed-fixed, fix-free, free-fixed, free-free elastic rods using quadratic basis functions, where three types of mass formulations are compared, i.e., the consistent mass matrix "CM", the reduced bandwidth mass matrix "RBM", and the higher order mass matrix "HOM". The periodic basis functions are used to eliminate the boundary effect. The numerical results in Fig. 1 apparently demonstrate that the proposed higher order mass matrix has a 6<sup>th</sup> order of accuracy, while both the accuracy orders for the reduced bandwidth matrix and the standard consistent mass matrix are 4.



**Figure 1. Comparison of  $\omega^h$  and  $\omega$  for 1D rod vibration problem**

### *Accuracy of Full-discrete Frequency*

The accuracy for the fully discrete algorithm with the proposed higher order mass matrix formulations is shown in Figs. 2-5. For convenience of presentation, the Courant number  $C = c\Delta t / h$  is employed in the discussion. In Fig. 2 and 3, the 1D comparisons of the full-discrete and continuum frequency are plotted with respect to the element size and Courant number, four typical Newmark methods, i.e., central difference method ( $\beta=0$ ), Fox-Goodwin method ( $\beta=1/12$ ), linear acceleration method ( $\beta=1/6$ ) and average acceleration method ( $\beta=1/4$ ). The results reveal that in general the higher order mass formulation gives the most favorable full-discrete frequency accuracy. Similar conclusions are also observed for the frequency comparison for the 2D membrane model problem results as shown in Fig. 4. The transient analysis results of 2D fixed square membrane under the initial velocity  $v_0 = \sin(\pi x)\sin(\pi y)$  in Fig. 5 once again demonstrate that the higher order mass formulation yields the superior solution accuracy, where unit geometric and material properties are adopted.

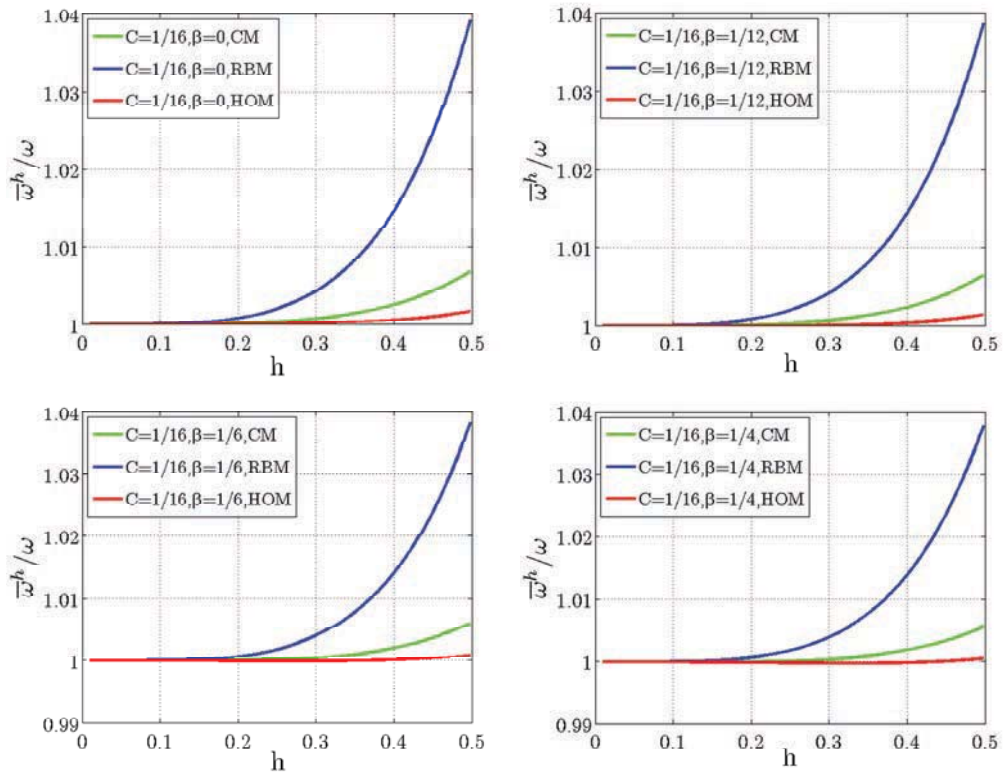


Figure 2. Comparison of  $\bar{\omega}^h$  and  $\omega$  with varying element size for 1D rod problem

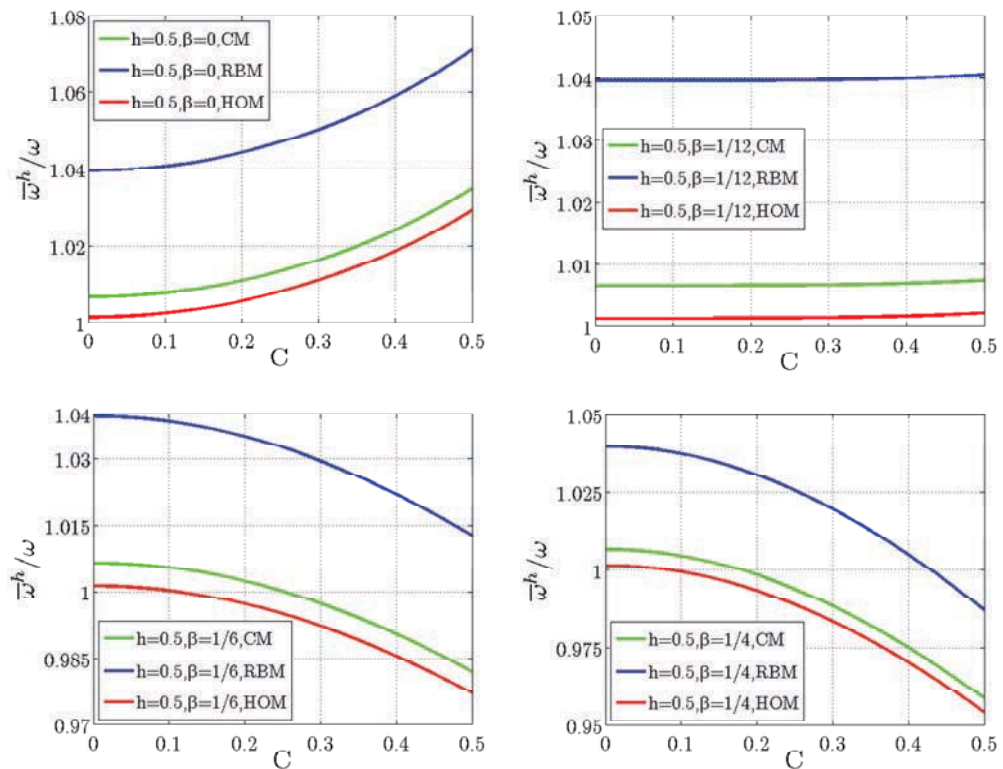


Figure 3. Comparison of  $\bar{\omega}^h$  and  $\omega$  with varying Courant number for 1D rod problem

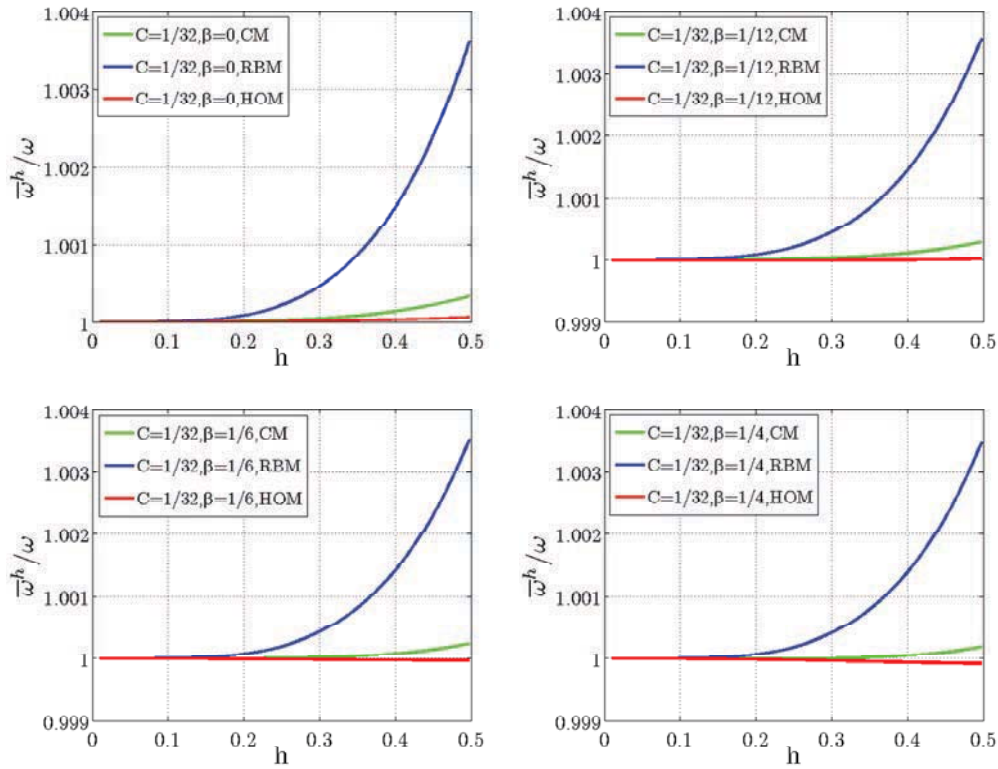


Figure 4. Comparison of  $\bar{\omega}^h$  and  $\omega$  with varying element size for 2D membrane problem

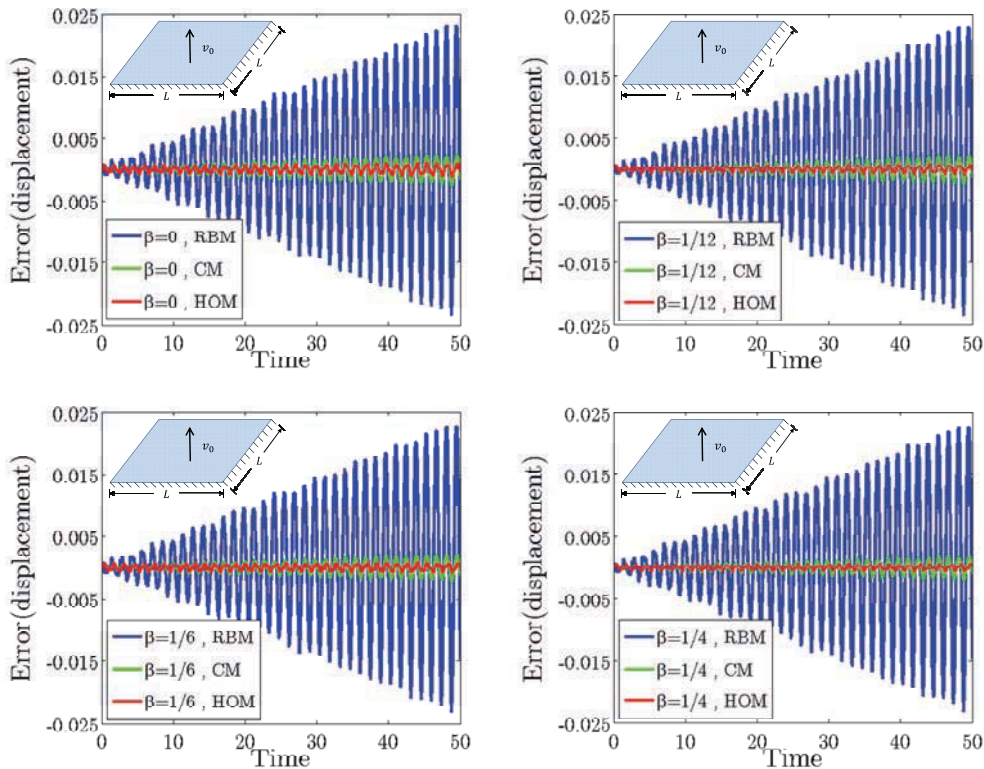


Figure 5. Comparison of the center deflection errors for a fixed square membrane under given initial velocity

## Conclusions

An ultra-accurate isogeometric method was presented for structural vibration analysis. This method is featured by the novel higher order mass formulations. The higher order mass matrix was rationally formulated by optimally combining the consistent mass matrix and the so-called reduced bandwidth mass matrix that has an equal order of frequency accuracy with its consistent counterpart. For free vibration analysis, two orders of extra accuracy were gained by the higher order mass matrix. Furthermore, by introducing the Newmark time integration method, the accuracy of the fully discrete algorithm with the present higher order mass isogeometric approach is studied in detail. The full-discrete frequencies for four typical Newmark time integration methods, i.e., central difference method, Fox-Goodwin method, linear acceleration method and average acceleration method were compared with the continuum frequency with respect to the element size and the Courant number, respectively. Moreover, a 2D transient membrane example was also presented to investigate the dynamic response of the proposed method. All the numerical results universally demonstrated that the most favorable solution accuracy is attached with the proposed higher order mass isogeometric method.

## Acknowledgements

The support of this work by the National Natural Science Foundation of China (11222221) is gratefully acknowledged.

## References

1. Hughes, T. J. R., Cottrell, J. A. and Bazilevs, Y. (2005), Isogeometric analysis: CAD, finite elements, NURBS, exact geometry and mesh refinement, *Computer Methods in Applied Mechanics and Engineering*, 194, pp. 4135-4195.
2. Verhoosel, C. V., Scott, M.A., and Hughes, T. J. R. (2011), An isogeometric analysis approach to gradient damage models, *International Journal for Numerical Methods in Engineering*, 86, pp. 115–134.
3. Lu, J. (2011), Isogeometric Contact analysis: geometric basis and formulation for frictionless contact, *Computer Methods in Applied Mechanics and Engineering*, 200, pp. 726-741.
4. Koo B., Yoon, M. and Cho, S. (2013), Isogeometric shape design sensitivity analysis using transformed basis functions for kronecker delta property, *Computer Methods in Applied Mechanics and Engineering*, 253, pp. 505-516.
5. Cottrell, J. A., Reali, A., Bazilevs, Y. and Hughes, T. J. R. (2006), Isogeometric analysis of structural vibrations, *Computer Methods in Applied Mechanics and Engineering*, 195, pp. 5257-5296.
6. Reali, A. (2006), An isogeometric analysis approach for the study of structural vibrations, *Journal of Earthquake Engineering*, 10, pp. 1–30.
7. Shojaee, S., Izadpanah, E., Valizadeh, N., and Kiendl, J. (2012), Free vibration analysis of thin plates by using a NURBS-based isogeometric approach, *Finite Elements in Analysis and Design*, 61, pp. 23–34.
8. Thai, C. H., Nguyen-Xuan, H., Nguyen-Thanh, N., Le, T. H., Nguyen-Thoi, T., and Rabczuk, T. (2012), Static, free vibration, and buckling analysis of laminated composite Reissner-Mindlin plates using NURBS-based isogeometric approach, *International Journal for Numerical Methods in Engineering*, 91, pp. 571–603.
9. Wang, D., Liu, W. and Zhang H. (2013), Novel higher order mass matrices for isogeometric structural vibration analysis. *Computer Methods in Applied Mechanics and Engineering*, 260, pp. 92-108.
10. Wang, D. and Xuan, J. (2010), An improved NURBS-based isogeometric analysis with enhanced treatment of essential boundary conditions, *Computer Methods in Applied Mechanics and Engineering*, 199, pp. 2425-2436.
11. Wang, D., Xuan J., and Zhang, C. (2012), A three dimensional computational investigation on the influence of essential boundary condition imposition in NURBS isogeometric finite element analysis, *Chinese Journal of Computational Mechanics*, 29, pp. 31-37.
12. Hughes, T. J. R. (1983), Analysis of Transient Algorithms with Particular Reference to Stability Behavior, *Computational Methods for Transient Analysis*, eds. Belytschko, T. and Hughes, T. J. R., Amsterdam: North-Holland, pp. 67-155.

## Numerical modeling on concrete debris ricocheting off sand ground

\*J. Xu, C.K. Lee, and S.C. Fan

School of Civil & Environmental Engineering, Nanyang Technological University, Singapore.

\*Corresponding author: xu0003in@e.ntu.edu.sg

### Abstract

A numerical study on concrete debris ricocheting off sand ground is presented in this paper. The numerical package ANSYS LS-DYNA is used to model the whole process of the impact of concrete debris on sand ground. A set of formulation is retrieved from the numerical results to predict the ricochet angle and the ricochet velocity in terms of the incident angle and the incident velocity. The debris size effect on the ricochet phenomenon is studied. It is found that for the range of the debris size studied in this paper, the debris size only has very minor influence on the ricochet.

**Keywords:** Ricochet, Concrete debris, sand, debris size, LS-DYNA.

### Introduction

Ricochet phenomenon appears when a hard projectile impacting on a relatively soft target medium with a certain impact condition. In general, the ricochet process could be controlled by the shape, the size, the strength, the launching velocity and the incident angle of the debris as well as the mechanical properties of the target medium (i.e. ground conditions). In the past, most research work has focused on the ricochet of projectiles off water surface and debris with different materials against soft ground. Soliman et al. (1976) studied the impact of steel and duralumin balls on water and dry, fine sand surfaces analytically and experimentally. It was found that for a given medium (e.g. water or sand), there exists a limiting incident angle beyond which ricochet does not occur, regardless of the incident velocity. On the other hand, when the incident angle is less than the limiting angle, there is an upper bound for the incident velocity beyond which ricochet does not occur. This upper bound is usually named as the (upper) critical incident velocity (for that angle). Knock et al. (2004) studied the impact of masonry debris against hard and soft grounds and concluded that the shape of masonry debris is not a major factor affecting the ricochet phenomenon.

Since experiments are costly, time-consuming and limited in obtaining data, numerical simulation is an attractive alternative for studying the high speed impact and ricochet phenomenon. In this paper, a numerical study on concrete debris impact on sand surface is presented. In the current study, numerical simulations were performed by using Arbitrary Lagrangian Eulerian (ALE) formulation with multi-material (MM) models. A total of six types of concrete debris are employed, namely 20mm, 50mm and 80mm  $\varnothing$  spheres and 40mm, 60mm and 100mm chamfered cubes.

Ricochet of projectiles against water is defined as an impact or a rebound such that at no time was the projectile fully below the water surface (Johnson 1998). However, when using sand as the target medium, it is found that concrete debris is more likely to come out of the sand after an impact (Xu et al. 2013). Furthermore, it is obvious that concrete debris is able to stand on a sand surface, while it sinks when it is placed on a water surface. Hence, the definition of ricochet against water may not be

applicable for the present study and a new criterion should be employed to define the ricochet of concrete debris against sand.

### Numerical model of impact

All numerical simulation works in this study are carried out by using the commercial software ANSYS LS-DYNA. The Arbitrary Lagrangian Eulerian (ALE) algorithm embedded in ANSYS LS-DYNA is adopted to model the impact process of concrete debris on sand surface. The concrete debris is meshed by a Lagrangian grid as solid, whereas the air and the sand are meshed by an Eulerian grid as fluid. An advance fluid structure interaction algorithm (FSI) is used to model the interaction between the debris and the sand/air.

The material type Mat\_Null (Mat 9) in ANSYS LS-DYNA (LSTC 2007) is employed for air. This material type has no shear stiffness or yield strength and behaves as a fluid. The cut-off pressure is set as 0, so that only positive pressure is considered. The equation of state (EOS) for air is expressed as  $p=0.4E(\rho/\rho_0)$ , where  $p$  is the pressure,  $\rho$  is the current density,  $\rho_0$  is the reference density which is taken as  $\rho_0=1.29\text{kg/m}^3$  (density of air) and  $E$  is the initial internal energy which is taken as  $E=2.5\times 10^5\text{Pa}$ .

The Material Type 16 (Mat 16) in ANSYS LS-DYNA (Livermore Software Technology Corporation 2007) is used to model the concrete behavior. The Mat 16 Mode II provides an automatic internal generation of a simple model for concrete. The material property for concrete debris is taken as: density  $\rho_c = 2400\text{kg/m}^3$ , shear modulus  $G = 3.414\times 10^{10}\text{Pa}$  and Poisson's ratio  $\nu = 0.18$ . By using Mat 16 Mode II model, a two-curve model with damage and failure, namely the maximum yield strength curve and the failure model curve, can be defined. The maximum yield strength  $\sigma_{\max}$  and the failed strength  $\sigma_{\text{failed}}$  are expressed as

$$\sigma_{\max} = a_0 + \frac{p}{a_1 + a_2 p}, \quad \sigma_{\text{failed}} = a_{0f} + \frac{p}{a_{1f} + a_2 p} \quad (1)$$

In Eq. (1),  $a_0$ ,  $a_1$ ,  $a_2$ ,  $a_{0f}$  and  $a_{1f}$  are coefficients which can be determined by  $a_0=f_c'/4$ ,  $a_1=1/3$ ,  $a_2=1/(3f_c')$ ,  $a_{0f}=0$  and  $a_{1f}=0.385$ , where  $f_c'$  is the concrete compressive strength. In the present numerical simulation, the compressive strength of the concrete is set as  $f_c' = 45\text{MPa}$ . The two curves are shown in Fig. 1(a). The change in yield strength with respect to plastic strain is taken into account. The relationship is given in the form:

$$\lambda = \int_0^{\varepsilon^p} \left( 1 + \frac{p}{\sigma_{\text{cut}}} \right)^{-b_1} d\varepsilon^p \quad (2)$$

where coefficient  $b_1$  is set as 1.25,  $p$  is the pressure,  $\varepsilon_p$  is the plastic strain and  $\sigma_{\text{cut}}$  is obtained by the expression:

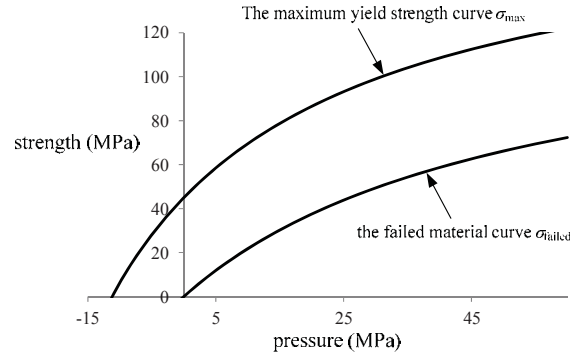
$$\sigma_{\text{cut}} = 1.7 \left( \frac{f_c'^2}{-A_0} \right)^{\frac{1}{3}} \quad (3)$$



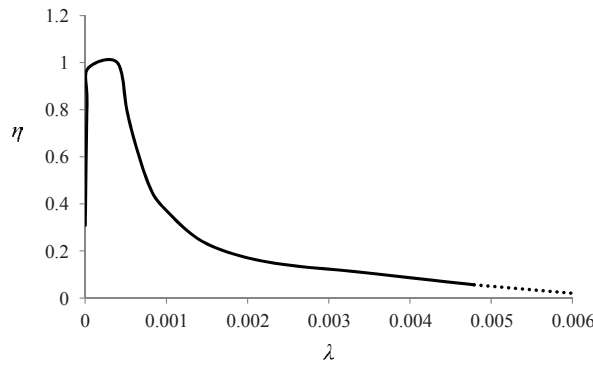
In Eq. (3),  $A_0 = -145$ . The yield strength of concrete is given by

$$\sigma_{\text{yield}} = \sigma_{\text{failed}} + \eta(\sigma_{\text{max}} - \sigma_{\text{failed}}) \quad (4)$$

The relation between  $\eta$  and  $\lambda$  is shown in Fig. 1(b). As the concrete strength is much higher than that of the sand, the EOS is not set for concrete material. A tri-linear polynomial function is automatically generated from the unconfined compressive strength and Poisson's ratio by ANSYS LS-DYNA.



(a) The strength curves for concrete



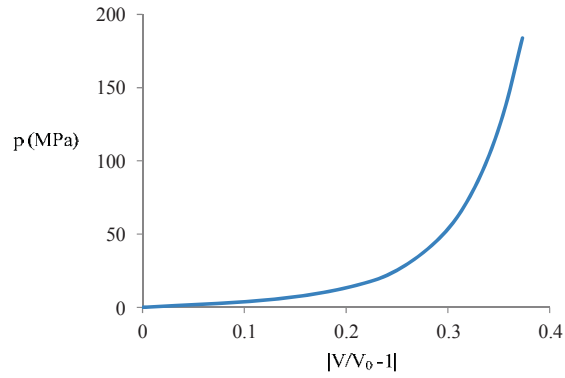
(b) The relation between scaled yield strength and effective plastic strain

Figure 1. Model for concrete material

The strength equation of the sand is modeled by the Mohr-Coulomb criterion, in which tension strength is set as 0 and cohesion effect is excluded. The Tresca criterion is used as the cut of limit for the shear strength. The shear strength curve for sand can be expressed as

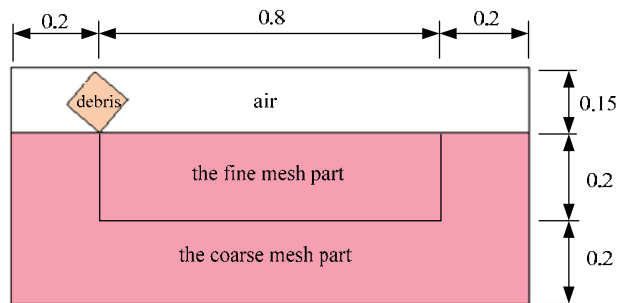
$$\sigma_{\text{ys}} = \frac{\sigma_1 - \sigma_3}{2} = \begin{cases} P \tan 30^\circ & 0 < P < P_{\text{mc}} \\ P_{\text{mc}} \tan 30^\circ & P \geq P_{\text{mc}} \end{cases} \quad (5)$$

where  $\sigma_1$  and  $\sigma_3$  are the maximum and minimum principal stresses,  $P$  is the pressure and  $P_{\text{mc}}$  is the Mohr-Coulomb pressure ( $=0.186\text{GPa}$ ), beyond which yield strength is pressure insensitive (Grujicic et al. 2008). Hence, the tension cut-off value ( $\sigma_1 - \sigma_3$ ) is  $0.258\text{GPa}$ .

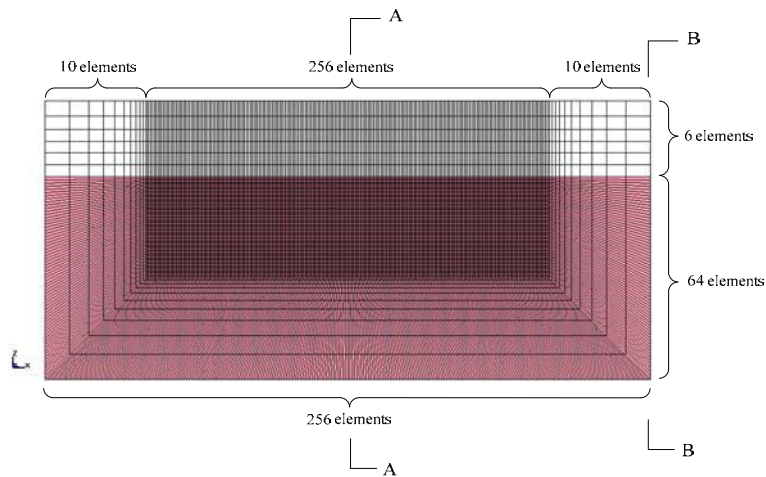


**Figure 2. The EOS of sands**

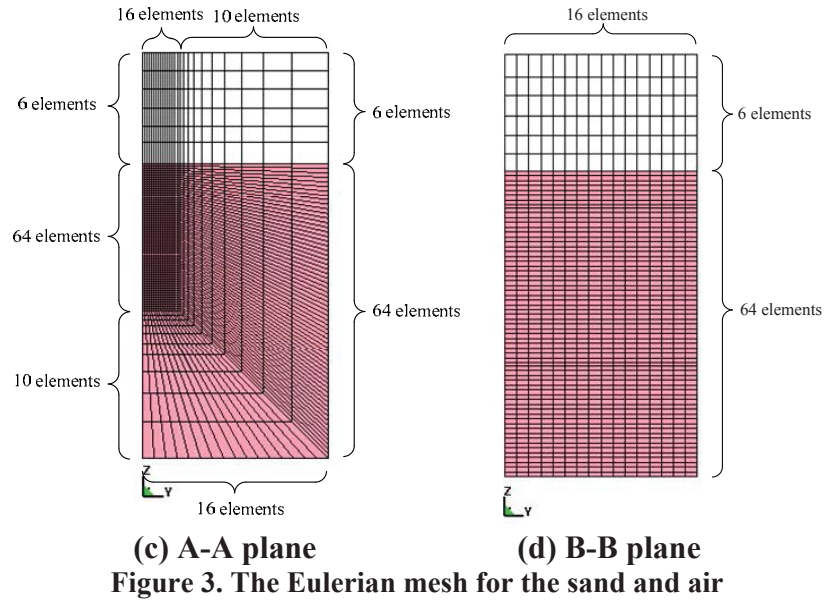
The EOS used for sand is shown in Fig. 2. The initial and the reference densities of sand are both set as  $1700\text{kg/m}^3$ . The friction coefficient between the concrete debris and the sands is set as 0.6 (Leonards 1965) in the numerical simulation.



**(a) Configuration (X-Z plane)**



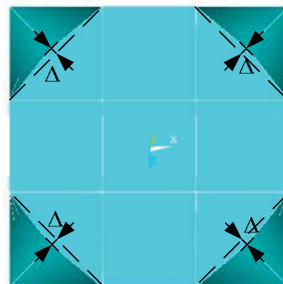
**(b) X-Y plane**



For the ALE mesh used, after introducing symmetric condition, only half model is considered as shown in Fig. 3, where the X-Z plane ( $Y=0$ ) is the symmetric plane. In Fig. 3a, the red part is the impact target (sand) with dimensions of 1.2m (X)  $\times$  0.25m (Y)  $\times$  0.4m (Z), and the upper part is air with the dimensions of 1.2m (X)  $\times$  0.25m (Y)  $\times$  0.15m (Z). The meshing scheme of the sand medium and the air is shown in Figs. 3b to 3d. In order to mesh the chamfered cube by hexahedral elements, the half cube is first divided into  $3 \times 3 \times 2 = 18$  hexahedrons (Fig. 4a). The four chamfered corners are modeled by collapsed hexahedron. The middle point of the chamfered edge is shifted by  $\Delta = 0.0033\text{mm}$ ,  $0.005\text{mm}$  and  $0.0083\text{mm}$  for the 40mm, 60mm and 100mm cube, respectively, as shown in Fig. 4b. Each hexahedron is then further meshed by  $3 \times 3 \times 3$  hexahedral linear elements.



(a) The half model of the chamfered cube



(b) The shift of the middle point of the chamfered edge  
**Figure 4: Model of the chamfered cube**

### The methodology employed for analysis

In each simulation, a set of given vertical and horizontal incident velocities,  $v_{ix}$  and  $v_{iz}$ , are assigned to all the nodes affiliated to concrete debris so that the debris has *no* rotation before it touches the sand surface. At the end of a simulation, the vertical and horizontal rigid body velocities,  $v_{ox}$  and  $v_{oz}$ , when the concrete debris emerges above the surface level entirely are recorded. The out-going velocity  $v_o$  is calculated by  $v_o = (v_{ox}^2 + v_{oz}^2)^{1/2}$ . The out-going angle  $\theta_o$  is calculated by  $\theta_o = \arctan(v_{oz}/v_{ox})$ .

The impact outcome parameters, namely the angle change of debris path  $\Delta\theta = \theta_i + \theta_o$  and the ratio  $v_o/v_i$  are employed in the numerical study to find out the relationship between the impact responses ( $\theta_o$  and  $v_o$ ) and the incident conditions ( $\theta_i$  and  $v_i$ ). As it is found in (Xu et al. 2013) that the two impact features are almost independent of the impact velocity  $v_i$ , only the plot of  $\Delta\theta$  against  $\theta_i$  and  $v_o/v_i$  against  $\theta_i$  are illustrated in this paper.

As shown in the authors' previous work (Xu et al. 2013), a parameter  $\varepsilon = (v_o/v_i)^2 = 5\%$  is adopted to distinguish ricochet. This ricochet criterion is also employed in the present study. It is noted that although the total kinetic energy after impact can be obtained in numerical simulations, only the kinetic energy corresponding to translation is considered.

### The numerical results

In this section, the numerical results are presented. The 20mm, 50mm and 80mm spherical debris and the 40mm, 60mm and 100mm chamfered cubic debris are employed. It is noted that the numerical modeling was calibrated by comparing the numerical and the experimental results from 50mm  $\varnothing$  spheres, 60mm and 100mm cubes in (Xu et al. 2013).

The plot of  $\Delta\theta$  against  $\theta_i$  is shown in Fig. 5. It can be found from Fig. 5 that a linear function can be retrieved to evaluate the outgoing angle  $v_o$  based on the incident angle  $v_i$  as:

$$\theta_o = 0.37\theta_i + 5.5 \quad (6)$$

The plot of  $v_o/v_i$  against  $\theta_i$  is shown in Fig. 6. The scatters in Fig. 6 show a strong linear relationship and the outgoing velocity  $v_o$  can be expressed as:

$$v_o = (0.8 - 0.018\theta_i)v_i \quad (7)$$

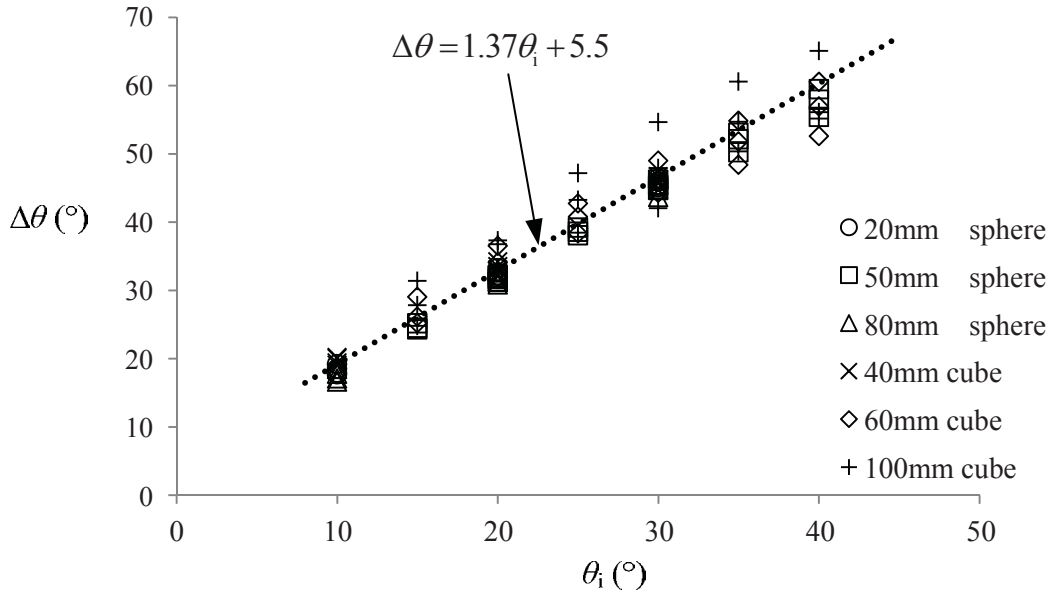


Figure 5. The plot of  $\Delta\theta$  against  $\theta_i$

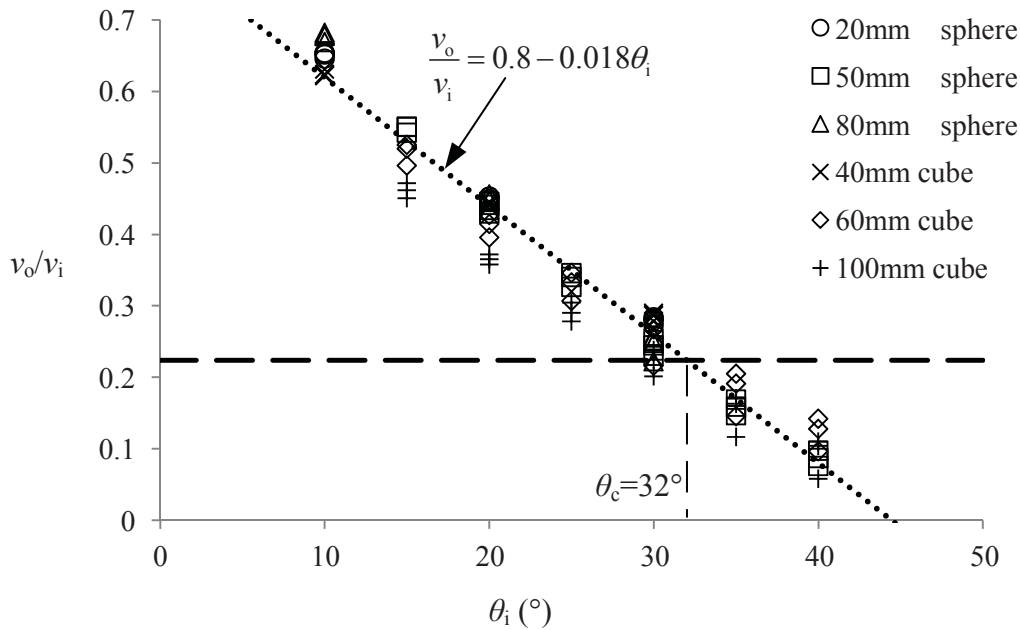


Figure 6. The plot of  $v_o/v_i$  against  $\theta_i$

Applying  $v_o/v_i = 0.224$ , which implies  $\varepsilon=5\%$ , into Eq. (7), it can be found that the critical ricochet angle for the concrete debris against sand surface is  $\theta_c=32^\circ$ .

**Conclusions**

In this paper, the numerical modeling to simulate concrete debris impacting on sand surface is presented. A total of six types of concrete debris are employed in the numerical simulation. It is found that the concrete debris impact response is independent of the debris size and shape. A unique set of formulations are provided for concrete debris to predict the outgoing angle and the outgoing velocity based on the incident angle and the incident velocity.

## Acknowledgements

This research was supported by a research grant provided by the Defence Science & Technology Agency (DSTA), Singapore, under the Protective Technology Research Centre, Nanyang Technological University, Singapore. Any opinions, findings and conclusions expressed in this paper are those of the writers and do not necessarily reflect the view of DSTA, Singapore.

## References

- Grujicic, M., B. Pandurangan, J. D. Summers, B. A. Cheeseman, W. N. Roy and R. R. Skaggs (2008), Application of the modified compaction material model to the analysis of landmine detonation in soil with various degrees of water saturation. *Shock & Vibration*, 15(1), pp. 79-99.
- Johnson, W. (1998), Ricochet of non-spinning projectiles, mainly from water Part I: Some historical contributions. *International Journal of Impact Engineering*, 21(1-2), pp. 15-24.
- Knock, C., I. Horsfall, S. M. Champion and I. C. Harrod (2004), The bounce and roll of masonry debris. *International Journal of Impact Engineering*, 30(1), pp. 1-16.
- Leonards, G. A. (1965), Experimental study of static and dynamic friction between soil and typical construction materials, School of Civil Engineering, Purdue University.
- Livermore Software Technology Corporation (2007), LS-DYNA keyword user's manual.
- Soliman, A. S., S. R. Reid and W. Johnson (1976), The effect of spherical projectile speed in ricochet off water and sand. *International Journal of Mechanical Sciences*, 18(6), pp. 279-284.
- Xu, J., C. K. Lee, S. C. Fan and K. W. Kang, A study on the ricochet of concrete debris against sand. Submitted to *International Journal of Impact Engineering*.

## Molecular simulation of the influence of nickel coating on the interfacial bonding strength of carbon nanotube/magnesium composites

\*X. Zhou, S. Y. Song, L. Li, and J. Y. Wu

State Key Laboratory of Structural Analysis for Industrial Equipment, Department of Engineering Mechanics, Faculty of Vehicle Engineering and Mechanics, Dalian University of Technology, Dalian 116024, China.

\*Corresponding author: zhouxia@dlut.edu.cn

### Abstract

The mechanical behaviors of Ni-coated single-walled carbon nanotubes (SWCNTs) reinforced magnesium matrix composites are investigated using molecular dynamics (MD) simulation method. The results show that the Young's modulus of the Ni-coated SWCNT/Mg composite is obviously larger than that of the uncoated SWCNT/Mg composite. The results also show that the interfacial bonding of SWCNT/Mg composite can be drastically increased by addition of Ni coating to provide an effective channel for load transfer between the nanotube and Mg matrix. Furthermore, the influences of Ni coating number on the interfacial bonding characteristics of SWCNT/Mg composites also are studied. For three types of Ni coating number, i.e., without Ni coating, with one layer of Ni and two-layer of Ni, the final pullout interfacial bonding strength of the Ni-coated SWCNT from Mg matrix about are 3.9 and 11.9 times larger, respectively, than that of the uncoated SWCNT.

**Keywords:** Magnesium matrix composites, Mechanical properties, Molecular dynamics simulation, Carbon nanotube.

### Introduction

Metal matrix nanocomposites reinforced with carbon nanotubes have good mechanical properties, high shear strength, high temperature resistance and excellent abrasion resistance, so they are widely used in automobile, aerospace and other high-tech areas. Usually studies on carbon nanotube reinforced metal matrix composite are focused on its macro-mechanical properties; however, it is less involved in the microscopic behavior caused by heterogeneity.

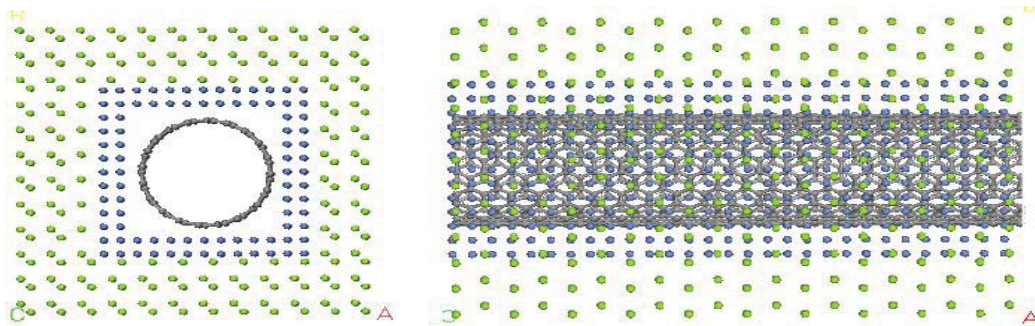
Accurate methods of interface tests are difficult to be conducted and the description theory is not yet complete, so molecular dynamics simulation has been widely used in the study of interfacial behavior. The tensile properties of nickel-coated armchair single-walled carbon nanotube reinforced gold matrix composite were studied by Song (2010) with molecular dynamics. A modified embedded atom method was used by Uddin (2010) to predict mechanical properties of single-walled and multi-walled nanotubes reinforced nickel monocrystal composites. They found that large volume fraction and large diameter carbon nanotubes with modified coating can be effective in improving mechanical properties of the composites.

Carbon nanotubes reinforced magnesium alloy composites have excellent mechanical properties than other metal alloys, so it had become a research focus in the field of nano-composite mechanics. Some scholars studied effects of the volume fraction, distribution, interface characteristics and fabrication process of carbon nanotube on its mechanical properties. The interfacial bonding problem of carbon nanotube and matrix is still a challenge and carbon nanotubes reinforced magnesium matrix composite's interfacial behavior studied by molecular dynamics have not been reported. In this paper, using self-compiled molecular dynamics simulation program, we studied the tensile properties of carbon nanotubes reinforced nano-crystal magnesium composites without Ni

coating, with one-layer of Ni and with two-layer of Ni, respectively, and found some laws of Ni-coated carbon nanotubes affecting the mechanical properties of the composite. These laws provided some references in the design of nanotubes reinforced magnesium matrix composite.

### Potential Function and Calculation Model

In order to simulate the single-walled carbon nanotubes (SWCNTs) reinforced nano-monocrystal magnesium composite accurately, we chose EAM/FS potential proposed by Finnis and Sinclair (1984) and EAM potential shown in the work by Daw and Baskes (1984) to describe the interaction of HCP magnesium atoms and nickel atoms, respectively. According to the rule of mixture, we chose Lennard-Jone potential to describe the interaction of magnesium, nickel and carbon atoms as well as magnesium and nickel metal. Describing the interaction of carbon atoms in SWCNTs, we chose AIREBO potential used in the work by Stuart and Tutein (2000).



**Figure 1. Top and side view of composite model embedded by SWCNT with two-layer of Ni**

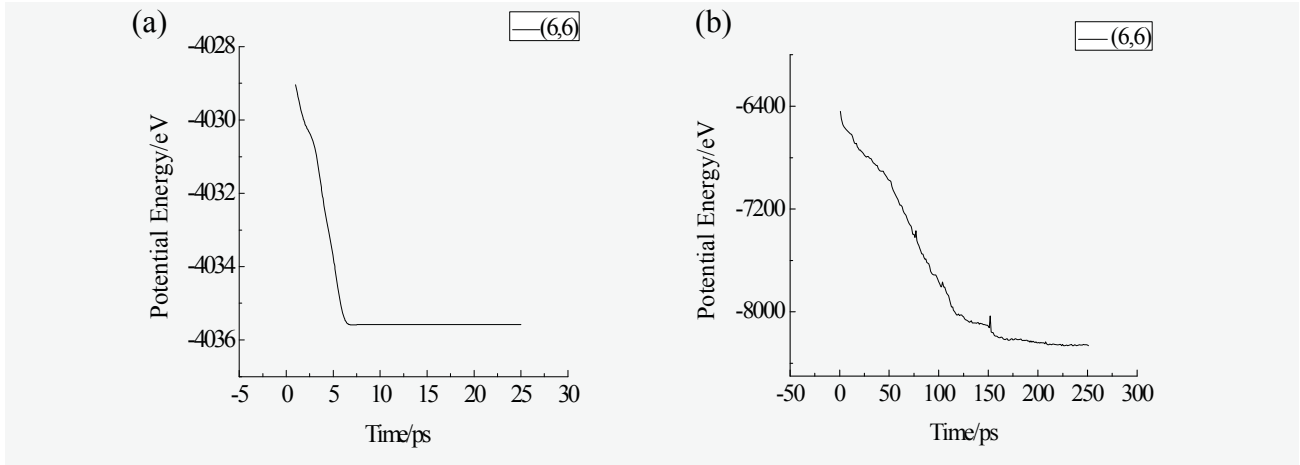
Composite models with two-layer of Ni-coated interface are shown in Fig.1. The model's actual size is  $3.851 \times 3.851 \times 5.211$  nm. In the simulation, displacement loading was applied along the Z-axis direction. The simulation process was as follows: the unconstrained relaxation was conducted on the initial configuration so that the system reached a steady free state; fixed one end of the model and applied 0.001 tensile strain along the Z-direction on the atom of the other end. Then did a relaxation of 2400~3000 steps in 10~170ps so that system returned to equilibrium state. Added the same displacement load and repeated the above-mentioned process.

### Simulation Results and Analysis

#### *Relaxation Process*

Before molecular dynamics simulation, we balanced the simulation system. At 0.01 K, we minimized the energy of nano-monocrystal magnesium composite with carbon nanotubes without Ni coating and with one layer of Ni embedded in. The step-length of simulation is 5fs with a relaxation of 30000 steps. Fig. 2 (a) and (b) respectively show the potential energy variation curves of magnesium composites reinforced by (6, 6) SWCNTs without Ni coating and with two-layer of Ni during the balance process. As can be seen from Fig.2, the system without Ni coating reached equilibrium substantially at 7ps, but for that with tow-layer of Ni, the time of equilibrium was more than 150ps.



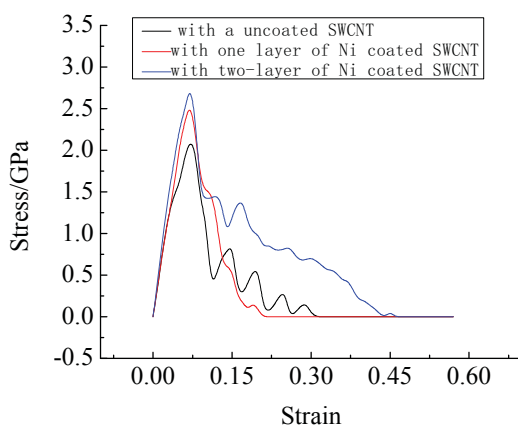


**Figure 2. Potential energy variation curves of magnesium composites reinforced by (6, 6) SWCNT: (a) without Ni and (b) with two-layer of Ni**

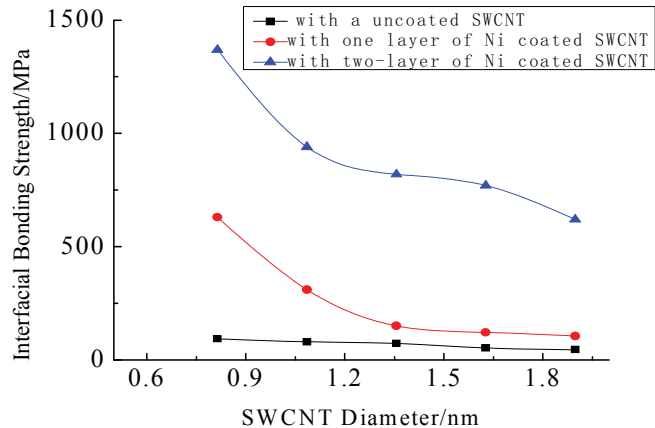
Before molecular dynamics simulation, we balanced the simulation system. At 0.01 K, we minimized the energy of nano-monocrystal magnesium composite with carbon nanotubes without Ni coating and with one layer of Ni embedded in. The step-length of simulation is 5fs with a relaxation of 30000 steps. Fig. 2 (a) and (b) respectively show the potential energy variation curves of magnesium composites reinforced by (6, 6) SWCNTs without Ni coating and with two-layer of Ni during the balance process. As can be seen from Fig.2, the system without Ni coating reached equilibrium substantially at 7ps, but for that with tow-layer of Ni, the time of equilibrium was more than 150ps.

#### *Mechanical Properties of CNT/Mg composite*

The stress-strain curves of (6, 6) CNTs reinforced magnesium matrix composite are shown in Fig.3. It can be seen that the strength of the interface with Ni coating is higher than that without Ni coating and the strength of the two-layer is higher than the one-layer.



**Figure 3. The stress and strain curve of SWCNT/Mg composites with different Ni atom layers**



**Figure 4. The influence of SWCNT diameter and Ni layer number on interface bonding strength**

#### *Interface Bonding Strength of CNTs/Mg composite*

Diameters and interfacial characteristics of single-walled carbon nanotubes have an important impact on the interface strength of the CNTs / Mg composite. The change trend of interface

bonding strength is shown in Fig.4. It can be seen that CNT's diameter and Ni layer greatly influenced the interfacial strength of composite. Whether there existed Ni layer on the interface or not, the interface bonding strength between carbon nanotubes and magnesium decreased as CNT's diameter increased. Ni layer on the interface improved the strength of carbon nanotubes reinforced composite greatly and the more the nickel atom was, the higher the interfacial strength was. The interfacial strength of the CNTs reinforced composite increased more than 200 percent with every increase of Ni layer. Fig.5 shows the morphology of the carbon nanotube pulled out from the magnesium matrix completely. It can be seen that there existed a strong interaction between Ni and Mg atoms.

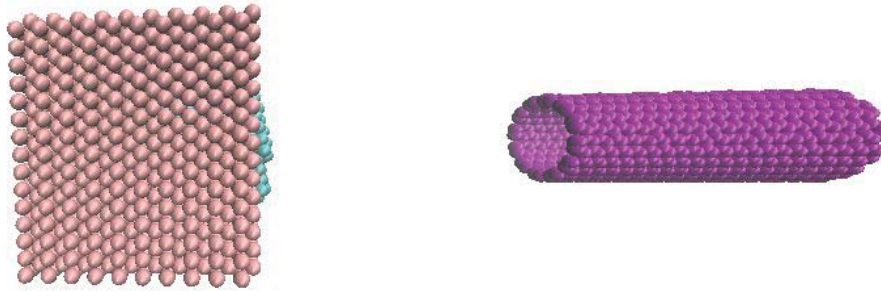


Fig. 5 The model of SWCNT after being pulled-out

## Conclusions

This study investigated effects of Ni layer on mechanical properties of the modified SWCNT reinforced magnesium matrix composite. The calculation results indicate that with a fixed diameter of CNTs, the Ni-coated CNT/Mg composite had a higher elastic modulus, yield strength and interfacial strength than that without Ni layer. And the more the Ni layer was, the higher the elastic modulus, yield strength and interfacial strength was. Besides, when the diameter of CNTs was smaller, its coupling with interfacial Ni layer was better. CNTs/Mg composites with smaller diameters and more nickel layers had better mechanical properties. This conclusion has an important guiding significance for the design of high-performance CNTs / Mg composite.

## Acknowledgments

The authors gratefully acknowledge the financial support from the National Natural Science Foundation of China (Grant No. 11272072) and the Natural Science Foundation Project of Liaoning Province of China (Grant No. 201102040).

## References

- Song, H. Y. and Zha, X. W. (2010), Mechanical properties of nickel-coated single-walled carbon nanotubes and their embedded gold matrix composites. *Phys Lett A*. 374, pp. 1068–1072.
- Uddin, J. and Baskes, M. I. (2010), Modified embedded atom method study of the mechanical properties of carbon nanotube reinforced nickel composites. *Phys Rev B*. 81, pp. 104103.
- Finnis, M. W. and Sinclair, J. E. (1984), A simple empirical N-body potential for transition metals. *Phil Mag A*. 50, pp. 45-55.
- Daw, M. S. and Baskes, M. I. (1984), Embedded-atom method: derivation and application to impurities, surfaces, and other defects in metals. *Phys Rev B*. 29, pp. 6443-6453.
- Stuart, S. J., Tutein, A. B. and Harrison, J. A. (2000), A reactive potential for hydrocarbons with intermolecular interactions. *J Chem Phys*. 112, pp. 6472–6486.

## A hybrid approach to structural topology optimization of vehicle for crashworthiness

\*Kun Yan<sup>1</sup>, Gengdong Cheng<sup>2</sup>

<sup>1</sup>State Key Laboratory for Structural Analysis of Industrial Equipments Dalian University of Technology, Dalian, 116024, P. R. China

\*Corresponding author: [yankun@mail.dlut.edu.cn](mailto:yankun@mail.dlut.edu.cn)

### Abstract

Structural topology optimization of vehicle for crashworthiness is a challenging subject because it involves geometric and material nonlinearity as well as transit dynamic analysis. The difficulty of gradient calculation in crashworthiness design problem constitutes a major obstacle to apply the existing topology optimization methods such as homogenization method and SIMP method. HCA (hybrid cellular automata) approach is one of heuristic approaches and does not need gradient information to get a crashworthiness topology optimum design. Each execution of HCA iteration needs a complete crashworthiness analysis to obtain the yield parameters for the update rule of design variables, which renders the method high computational cost. The well-known inertia relief method replaces the transit dynamic analysis by approximate static analysis under the impact load and inertia load. However, in car collision event the magnitude and spatial distribution of the impact load is unknown in prior and depends on the structure being crashed. The present study proposes a hybrid approach by integrating the improved inertia relief method with HCA. The structural topology optimization is obtained iteratively under the given impact load with the inertia relief method, nonlinear static analysis and HCA approach. A simplified car model example is tested to show the effectiveness and efficiency of the hybrid approach.

**Keywords:** Crashworthiness, Energy absorption, Inertia relief, Topology Optimization

### Introduction

Crashworthiness design is an important and challenging subject for vehicle design. The performance of vehicle in a crash event has a direct impact on the safety of drivers, passengers and pedestrians. The difficulty of crashworthiness analysis is widely recognized, because it involves highly nonlinear and dynamic effects of the vehicle structure, such as large deformation, large strain, material nonlinearity, contact, structural and material damage and even non-linear wave propagation. The formulation of crashworthiness optimization problem should both concern the criterion of auto industry and the product cost, so energy absorption and mass cost should both be reflected in the optimization formulation.

Over the decades, many contributions have been done to enhance the vehicle crashworthiness and prevent the passenger and driver from injuries. While most works optimize one vehicle component, a few works study topology optimization (Bendsøe, M.P., 2003) of the whole car body (Mayer et al., 1996; Pedersen, 2003; Soto, 2004). Mayer et al. In structural topology optimization, there are two methods most widely used, homogenization method and SIMP (Solid Isotropic Material with Penalization) method. But both of them are gradient-based approach, they can't be used in nonlinear problem directly. The HCA method does not use mathematical programming techniques, but makes use of the cellular automata paradigm to drive the design synthesis. This approach is inspired by the biological process of bone remodeling and was first presented by Tovar (2004). Patel and Tovar (2009) have applied the HCA method to the crashworthiness topology optimization problem, which considered both material and geometrically nonlinear behavior. In HCA method, each step in optimization process requires a complete transit nonlinear analysis, which is computationally very

expensive. The inertia relief method (Nelson et al., 1977; Lin liao, 2011) is an approximate analytical technique for transit analysis. It has been applied by the aerospace industry in structural analysis and optimization of free-free vehicle for many years.

In this paper, a new hybrid approach, which integrates the improved inertia relief method with HCA method, is developed to vehicle energy absorption optimization. The results show that the hybrid approach could reduce the computational cost of the optimization significantly and get a better design of the crashworthiness design problem.

## 1 Modified Inertia relief method and its accuracy analysis

The basic idea of inertia relief assumes that a free-free structure under impact load moves as a rigid body. In order to use the inertia relief method, the impact load should be first determined and applied on a totally unconstraint structure, and the accelerations is calculated by rigid body moving laws.



Figure 1. The simple spring-mass model

A simple spring-mass model in Figure 1 illustrates the process that using inertia relief to get an approximate result. The mass-spring system consists of two masses  $M_1$  and  $M_2$  connected by a spring of stiffness  $K$  and is subject to a dynamic external force  $F(t)$  on mass  $M_1$ . First, the model is treated as a rigid body of total mass  $M_1+M_2$ . The acceleration of the system can be obtained as:

$$a_{sys}(t) = F(t)/(M_1 + M_2) \quad (1)$$

Accelerations of  $M_1$  and  $M_2$  are equal to the system acceleration and the inertia forces  $-M_1 a_{sys}$ ,  $-M_2 a_{sys}$  act on two masses, respectively. Static analysis under the external load  $F(t)$  and the inertia forces  $-M_1 a_{sys}$ ,  $-M_2 a_{sys}$  results the internal force of the spring  $K$ :

$$F_K(t) = F(t)M_2/(M_1 + M_2) \quad (2)$$

But this model is not fully suitable for a crash event because the magnitude and its spatial distribution of the impact load form is not known in prior and is dependent on the structure being crashed. In this paper, to improve the inertia relief method and study its accuracy, we propose an improved simple dynamic analysis model which was presented by Wu and Yu (2001). The improved model is shown in figure 2. Since in car crash event, there exists often a lower stiffness part in the front part of the structural body, we assume the stiffness of  $K_1$  is less than  $K_2$ .



Figure 2. The simple dynamic model presented by Wu and Yu

In comparison with former model, the new model is built by adding one moving mass and one spring in the original model, the latter of which simulates the structural behavior of the local impact area or the lower stiffness part. As the moving mass  $M_1$  with initial velocity  $V_0$  impacts the mass  $M_2$ , the spring  $K_1$  is compressed and the whole mass-spring system moves as an integrated one. At

certain stage, the moving mass  $M_1$  will be rebounded. However, here we are only interested in their behavior before rebound happens. By transit dynamic analysis of this model, the analytical forms of the internal forces of the two springs can be expressed as:

$$\begin{cases} F_1(t) \\ F_2(t) \end{cases} = \begin{cases} k_1 \\ k_2 r_1 \end{cases} \frac{V_0 r_2}{\omega_1^* (r_1 - r_2)} \sin(\omega_1^* t) - \begin{cases} k_1 \\ k_2 r_2 \end{cases} \frac{V_0 r_1}{\omega_2^* (r_1 - r_2)} \sin(\omega_2^* t) \quad (3)$$

Where

$$\begin{aligned} \omega_1^2 &= \frac{k_1(M_1 + M_2)}{M_1 M_2} & \omega_2^2 &= \frac{k_2(M_2 + M_3)}{M_2 M_3} \\ \alpha_1 &= \frac{M_1}{M_1 + M_2} & \alpha_2 &= \frac{M_3}{M_2 + M_3} \\ r_1 &= \frac{\omega_1^2 - \omega_1^{*2}}{\alpha_2 \omega_2^2} = \frac{\alpha_1 \omega_1^2}{\omega_2^2 - \omega_1^{*2}} & r_2 &= \frac{\omega_1^2 - \omega_2^{*2}}{\alpha_2 \omega_2^2} = \frac{\alpha_1 \omega_1^2}{\omega_2^2 - \omega_2^{*2}} \end{aligned}$$

And the first and second frequency of the mass-spring system is given by

$$\omega_{1,2}^{*2} = \frac{\omega_1^2 + \omega_2^2}{2} \pm \frac{1}{2} \sqrt{(\omega_1^2 - \omega_2^2)^2 + 4\alpha_1 \alpha_2 \omega_1^2 \omega_2^2}$$

Through the analytical forms, we find that when  $\omega_1 \ll \omega_2$  the analytical forms could be simplified, and the peak load could be express as:

$$F_1(t) = -k_1 \frac{V_0}{\alpha_2 \omega_1^* (r_1 - r_2)} \sin(\omega_1^* t) \quad (4)$$

$$F_2(t) = -k_2 \frac{\alpha_1 \omega_1^2 V_0}{\alpha_2 \omega_1^* (r_1 - r_2) \omega_2^2} \sin(\omega_1^* t) - k_2 \frac{\alpha_1 V_0 \omega_1^2}{\alpha_2 \omega_2^* (r_1 - r_2) \omega_2^2} \sin(\omega_2^* t) \quad (5)$$

When  $\sin(\omega_1^* t) = 1$ , the internal force of spring  $K_1$  reaches its maximum, the internal force of the spring  $K_2$  by the inertia relief method at the same time could be expressed as:

$$F_2^{ir} = \alpha_2 F_1' \quad (6)$$

And the analytical form of the internal forces of spring  $K_2$  could be further simplified as following:

$$F_2' = -k_2 \frac{\alpha_1 \omega_1^2 V_0}{\alpha_2 \omega_1^* (r_1 - r_2) \omega_2^2} - k_2 \frac{\alpha_1 V_0 \omega_1^2}{\alpha_2 \omega_2^* (r_1 - r_2) \omega_2^2} \sin\left(\frac{\omega_2^* \pi}{\omega_1^* 2}\right) \quad (7)$$

Then we could get:

$$F_2' = \alpha_2 \left( 1 + \frac{\omega_1^*}{\omega_2^*} \sin\left(\frac{\omega_2^* \pi}{\omega_1^* 2}\right) \right) F_1' \quad (8)$$

$$\left| \frac{F_2' - F_2^{ir}}{F_2^{ir}} \right| = \frac{\omega_1^*}{\omega_2^*} \left| \sin\left(\frac{\omega_2^* \pi}{\omega_1^* 2}\right) \right| \leq \frac{\omega_1^*}{\omega_2^*} \quad (9)$$

The error of maximum force of the inertia relief’s result and the analytical result could be estimated by the ratio of the first order and second order frequencies.

### 2 Numerical examples of the modified inertia relief method

A numerical example has been carried out to verify the above conclusion obtained from the new mass-spring model. We choose seven parameter sets of the spring-mass model for comparison. The first model has parameters  $M_1=50\text{Kg}$ ,  $M_2=50\text{Kg}$ ,  $M_3=50\text{Kg}$ ,  $K_1=2000\text{N/m}$ ,  $K_2=2000\text{N/m}$ , and the other six sets just changes the stiffness of spring  $K_2$  by 5times, 10 times, 50 times, 100times, 500times and 1000 times, respectively. The results of the seven models are listed in table 1. Here, the internal force results are chosen at the time when the internal force of spring  $K_1$  reaches its maximum.

**Table 1. The results of inertia relief method and dynamic analysis**

	$K_2$	$F_2^{ls}$	$F_2^{ir}$	$\frac{F_2^{ls} - F_2^{ir}}{F_2^{ir}}$	$\frac{\omega_1^*}{\omega_2}$
First model	2.00E+03	-304.10	-569.07	0.466	0.577
K2*5	1.00E+04	-954.75	-608.00	0.570	0.366
K2*10	2.00E+04	-739.27	-633.99	0.166	0.267
K2*50	1.00E+05	-625.12	-643.94	0.029	0.122
K2*100	2.00E+05	-683.79	-644.57	0.061	0.086
K2*500	1.00E+06	-635.87	-645.32	0.015	0.038
K2*1000	2.00E+06	-638.23	-645.40	0.011	0.027

The results showed in table 1 improve that the difference between the results of two methods will be smaller when the ratio between the first and second order frequencies decreasing. And the difference is smaller than the ratio of frequencies when spring  $K_2$ ’s stiffness larger than 10 times of spring  $K_1$ ’s stiffness which verify the previous conclusion. We can also change the other parameters to decrease the difference, and this part will be showed in further work.

### 3 Hybrid Cellular Automaton Algorithm

The information of each element contains two parts of parameters, one is the design variable  $x_i$ , and the other is the yield parameter  $S_i$  gained by FEM. In HCA method, the yield parameters in its neighborhood are used to modify the yield parameter in the concerned cell. There are a variety of neighborhood forms, the form used in this paper is the right one shown in figure 3, and the yield parameter can be expressed as:

$$S^{(k)} + \nabla S^{(k)} \tag{10}$$

### Figure 3. Three neighborhood forms

Due to the consideration of both requirement of industry criterion and product cost, we set the energy absorption maximization as the objective and the uniform strain energy distribution as the criterion. The structural mass factor is constrained, as Patel al did in his work. The mathematical formulation is

$$\begin{aligned}
 & \min_x && \sum_{i=1}^N |\bar{S}_i - S^*| \\
 & \text{Such that} && \sum_{i=1}^N x_i \rho v_i = M_f^* \sum_{i=1}^N \rho v_i \\
 & && \mathbf{KU}=\mathbf{P} \\
 & && \mathbf{x}_{\min} \leq \mathbf{x}_i \leq \mathbf{1}
 \end{aligned} \tag{11}$$

In this paper, the update rules and yield parameter of HCA method are same as Patel did.  $S_i$  is equal to  $U_i$ , the strain energy of the  $i$ th element. The  $S^{*(k)}$  is the global set point value of the  $k$ th iteration, by adjusting  $S^{*(k)}$  from iteration to iteration the mass fraction constraint  $M_f^*$  is gradually imposed. The update rule of the design parameter  $x_i$  to make the strain energy uniform can be expressed as:

$$\Delta x_i = \max\{-0.1, \min\{K_p(\bar{S}_i^{(k)} - S^{*(k)}), 0.1\}\} \tag{12}$$

The  $K_p$  is a problem-dependent constant, and the  $S^{*(k)}$  is a global set point. The material follows the bilinear form, and parameterization of the material is expressed as:

$$E_i(x_i) = x_i^3 E_0 \quad \sigma_{yi}(x_i) = x_i^3 \sigma_{y0} \quad E_{hi}(x_i) = x_i^3 E_{h0} \tag{13}$$

## 4 A new hybrid method of HCA and IRM

The new integrated approach is described as follows:

Step 1. Define the design domain, materials properties, initial velocity  $v_0$ , and assume the initial design  $x^{(0)}$  variables distribution, and specify the convergence condition the tolerance of the peak load change  $\Delta P_i$ .

Step 2. Do a complete transient dynamic analysis, and find the peak value and its spatial distribution of the impact load of the design area.

Step 3. Apply the peak load to the design and carry out a static inertia relief analysis, which is a static nonlinear analysis under the peak load and inertia loads. The error of the results between inertia relief and dynamic analysis at the first execution of step 3 could be used to check the error of inertia relief.

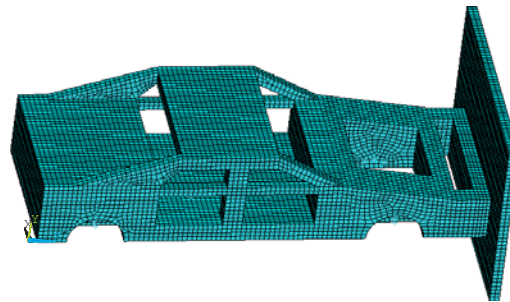
Step 4. Update the design variables and the global set point based on HCA update rule, obtain an improved design and check its convergence. If the convergence criterion is reached go to step 5. If not, go back to step 3.

Step 5. Carry out transient dynamic analysis of the improved design with the same initial conditions and find the new peak load. If the change of the peak load is small enough, the optimization process is finished.

## 5 Numerical example of new hybrid method

### 5.1 A simplified car model

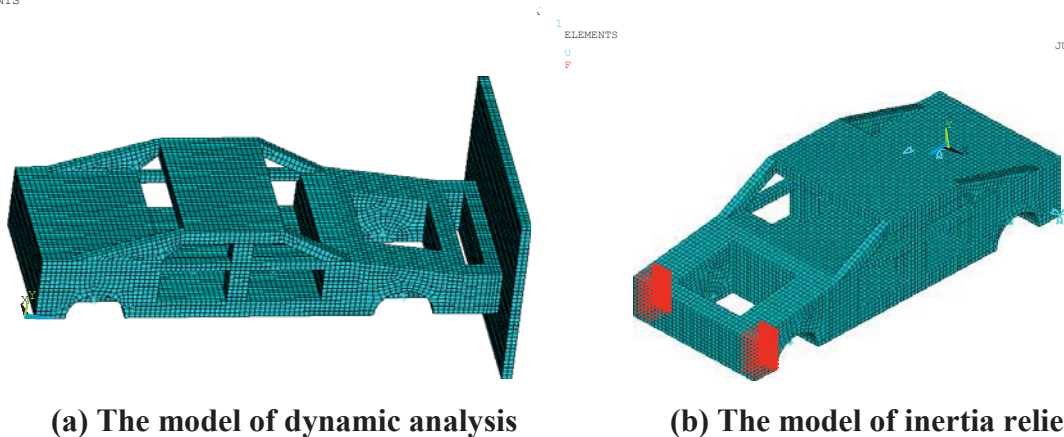
A complex car model is simplified to two parts, one is the car body with concentrated masses, and the other is the bumper part to protect the car, shown in figure 4. The total mass of the concentrated masses at the front are 600Kg, and the mass of the masses in the rear are 300Kg. There are four masses placed on the location of the passengers in the car body, each of them is 100Kg. At last, four masses on the location of the tires, and each of them is 50 Kg. We use fully integrated selectively-reduced 8-node brick hexahedral element to divide design domain in order to use the HCA method. The material's parameters of the design area are, density is  $785\text{Kg/m}^3$ , elastic modulus is  $2.1\text{e}10\text{Pa}$ , yield stress is  $2.1\text{e}5\text{Pa}$ , and tangent modulus is  $1\text{e}9\text{Pa}$ . For the material's parameters of the bumper, material density is  $785\text{Kg/m}^3$ , elastic modulus  $E$  is  $2.1\text{e}9\text{Pa}$ , yield stress is  $2.1\text{e}4\text{Pa}$ , and tangent modulus is  $1\text{e}8\text{Pa}$ . The simplified car model contains 26961 elements, 34662 nodes, and the design domain contains 25076 elements. The impact load is 5% of the peak load of previous peak load.



**Figure 4. Car model of topology optimization**

### 5.2 Optimization process of the new hybrid method

In this example, the impact load of the body part is transformed from the bumper part, which leads to uniform stress distributions of the impact load's areas. Thus, the static load on different nodes of inertia relief analysis model has same magnitude. The structural models for transient dynamic analysis and inertia relief analysis are shown in figure 5. The dynamic analysis uses Ls-dyna program, and the model is meshed by fully integrated selectively-reduced 8-node brick hexahedral element, and the model is meshed by Full



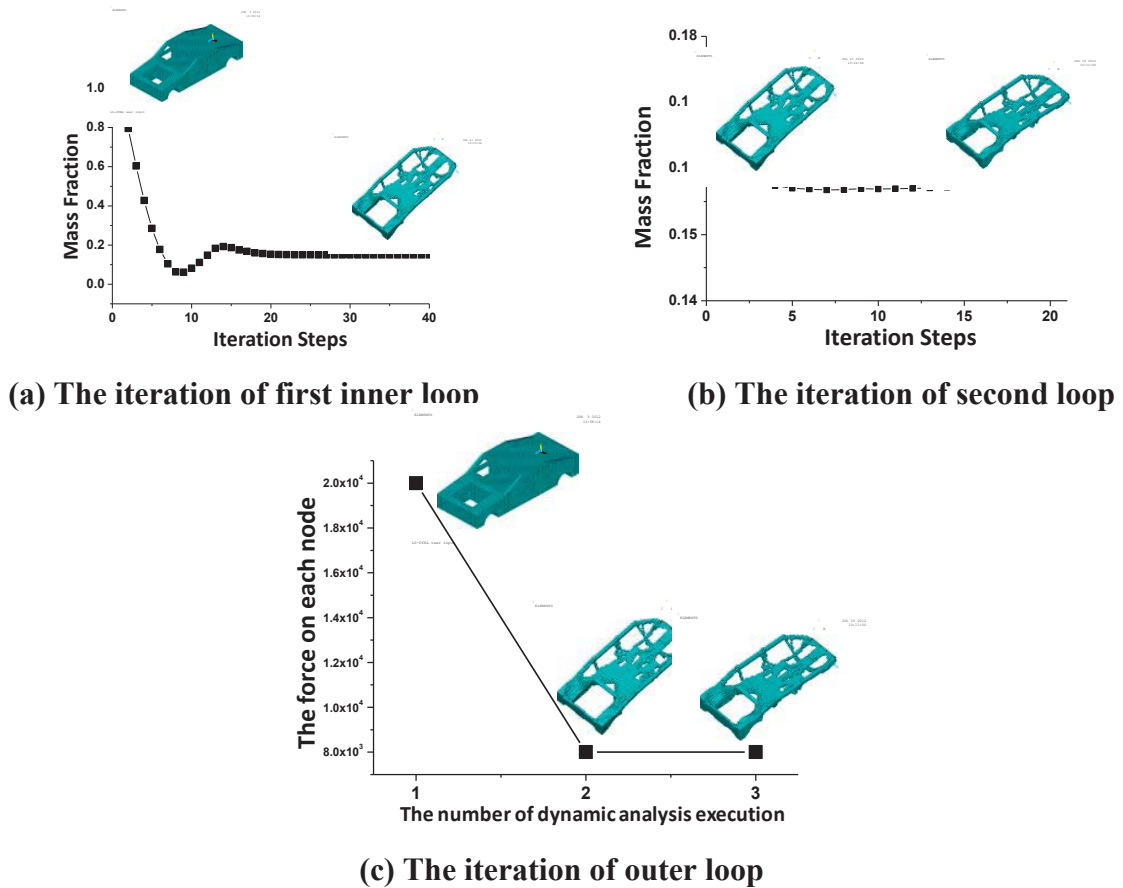
**(a) The model of dynamic analysis**

**(b) The model of inertia relief**

**Figure 5. The analysis models and stress distributions of two methods**



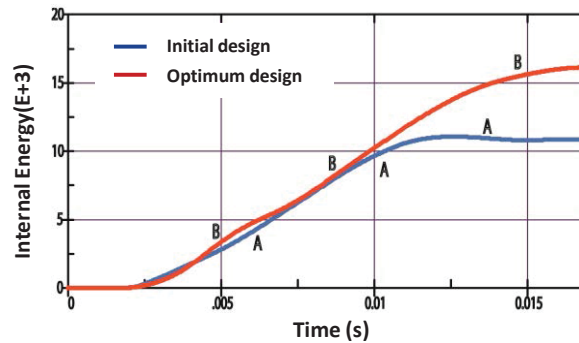
The iteration process of the new hybrid method for the mass fraction constraint  $M_j^*=0.16$  is shown in figure 6. Three dynamic analyses totally execute and the inner loop executes twice. The first dynamic analysis is to find the peak impact load of the initial design, which is  $2.0e4N$  on each node in the crash area. The second dynamic analysis changes the peak load of the optimized design, and the peak load of each node reduced to  $0.8e4N$ . After the third dynamic analysis, the peak load is still  $0.8e4N$ , and then the optimization is finished because of reaching the convergence condition. There are 40 iterations in first inner loop and 20 iterations in second inner loop. The inner loop is the optimization process of the HCA method. By our computer, the time cost of the dynamic analysis is about 20 minutes, but the inertia relief method just cost 2 or 3 minutes for this model. Though extra 20 iterations needed, the new hybrid method still reduces the time cost of the optimization significantly. In this problem, the structural nonlinearity is not significant, and the optimized design after first inner loop is almost the same as the optimized design after second inner loop. So for the similar problem, maybe we just need two inner loops to find the optimized design and the time cost could be further reduced.



**Fig. 6 The optimization process of the new hybrid method (mass fraction is 0.16)**

Now let us compare the optimum design under the mass fraction constraint  $M_j^*=0.16$  with the initial full design. However, the kinetic energy will be different for these two models because the initial full design is more heavy than the optimum design under the mass fraction constraint  $M_j^*=0.16$ . In order to compare the designs, we reduce the density of the full design to make the kinetic energy equal with the optimized design. The following comparison is based on the model of reduced density.

First we compare the energy absorption ability. The energy absorption history curves are shown in figure 7, the curve of the optimized design is the red one, the maximum energy absorption is 16.58KJ, and the blue one is for the initial design, the maximum energy absorption is 11.44KJ. The energy absorption ability of the optimized design is enhanced about 45% than the initial design.



**Figure 7. Energy absorption-time curve of initial and optimized design**

## Conclusions

The presented new hybrid method takes advantage of HCA and inertia relief method and provides an alternative approach to structural topology optimization of vehicle for crashworthiness design. However, it needs further improvement, more elaborated investigation and more complicated test examples.

In this paper, we propose a new hybrid method to vehicle energy absorption optimization problem. Then we construct a simplified car body model and test the hybrid method. The results show that the hybrid method could reduce the computational cost of the optimization significantly and get a better design of the crashworthiness concept design. And the proposed approach converges very fast.

## Acknowledgements

The present study is supported by Ford Company and NSF of China (90816026). We are grateful to Dr.R.J.Yang and C.H.Chuang for their suggestion of the research topics and stimulating discussion.

## References

- Bendsoe, M. P. (2003). *Topology optimization: theory, methods and applications*. Springer.
- Lin L (2011) A Study of Inertia Relief Analysis. 52nd AIAA/ASME/ASCE/AHS/ASC Structures, Structural Dynamics and Materials Conference<BR> 19th 4 - 7 April 2011, Denver, Colorado
- Mayer RR, Kikuchi N, Scott RA (1996) Applications of Topology Optimization Techniques to Structural Crashworthiness. *Int. J. Numer. Methods Eng.*, 39: 1383–1403.
- Nelson MF, Wolf JA (1977) Use of Inertia Relief to Estimate Impact Loads. *Proceeding of International Conference on Vehicle Structural Mechanics*, April, 1977: 149-155.
- Patel NM, Kang BS, Renaud JE, Tovar A (2009) Crashworthiness Design Using Topology Optimization, JUNE 2009, Vol. 131 / 061013-1.
- Pedersen CBW (2003) Topology Optimization Design of Crushed 2d-Frames for Desired Energy Absorption. *Struct. Multidiscip. Optim.*, 25: 368–382.
- Soto CA (2004) Structural Topology Optimization for Crashworthiness. *Int. J. Numer. Methods Eng.*, 9.3.: 277–283.
- Tovar A (2004) Bone Remodeling as a Hybrid Cellular Automaton Optimization Process. Ph.D. thesis, University of Notre Dame, Notre Dame, IN.
- Wu KQ, Yu TX (2001) Simple dynamic models of elastic–plastic structures under Impac. *International Journal of Impact Engineering* 25: 735–754.

## Damage Identification of Beams based on Element Modal Strain Energy and Data Fusion with Reconstructed Modal Rotations

H Cao\*, T Liu

College of Civil Engineering, Chongqing University; Key Laboratory of New Technology for Construction of Cities in Mountain Area (Chongqing University), Ministry of Education, P R China

\*Corresponding author: caohui@cqu.edu.cn

### Abstract

Damage identification of structures is always attractive to researchers because it plays an important role in the health monitoring in many civil engineering structures. When carrying out a health monitoring, sensors are usually laid on a beam to record acceleration signals, in which the modes of the beam can be extracted to construct indicators for detecting damages of the investigated beam. It should be noted that it is difficult to measure rotational signals of the beam at a position where sensors are laid, thus only the modal translations can be available. Although the pure modal translations can still be used to construct indicators and often it is the case, an indicator taking into account modal rotations is suggested in application to consider the effect of signal noise on the accuracy of measurement. In this paper, modal rotations were reconstructed by modal translations using the principle of static condensation. Then both modal translations and rotations were used to build an indicator based on an idea regarding element modal strain energy together with the theory of data fusion. The modal translations were extracted from accelerations recorded on a beam using stochastic subspace identification (SSI). Studies were carried out on choosing values of parameters in SSI in order to eliminate the effect of noise as nearly as possible. The simulation given by a FEM model and analyses of real accelerations recorded on a reinforced concrete beam show that this proposed damage indicator with elimination of noise effects is able to determine the locations of damage in the investigated beams.

**Key Words:** Damage identification, Element modal strain energy, Data fusion, Reconstructed modal rotations

### Introduction

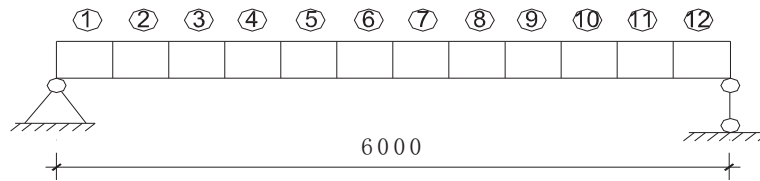
The initial defects of materials, improper construction methods and the combination of effects by long time load and environment, as well as sudden hazard may lead to damage in civil engineering structures. Structural health monitoring (SHM) can help to prevent significant damage and so to improve structural reliability and durability. Damage identification in early stage using recorded structural dynamic responses is an important branch of SHM. In practice, some dynamic responses are difficult to measure, such as rotations of a structure. So many damage identification methods utilize only structural translations, i.e. shear-type structural model (Hjelmstad et al, 1995). Damage indicators based on element modal strain energy were proved by researchers to be sensitive to damage and able to resist noise (Shi et al, 2002; Liu et al, 2004). Such indicators need structural rotational information and consequently researchers often used only simulations to verify them. In this paper, modal rotations were reconstructed by modal translations using the principle of static condensation (Guyan, 1965; Zhao and Li, 2003). Then both modal translations and rotations were used to construct a damage indicator based on element modal strain energy together with the theory of data fusion. The modal translations were extracted from accelerations recorded on a concrete beam using stochastic subspace identification (SSI). In order to eliminate the effect of noise as nearly as possible, studies were carried out on choosing values of parameters in SSI prior to constructing the indicator. The constructed damage indicator was applied to damage identification

of both simulated simple beams and a test simple beam. The results show that the indicator with elimination of noise effects is able to locate the damaged parts in the investigated beams.

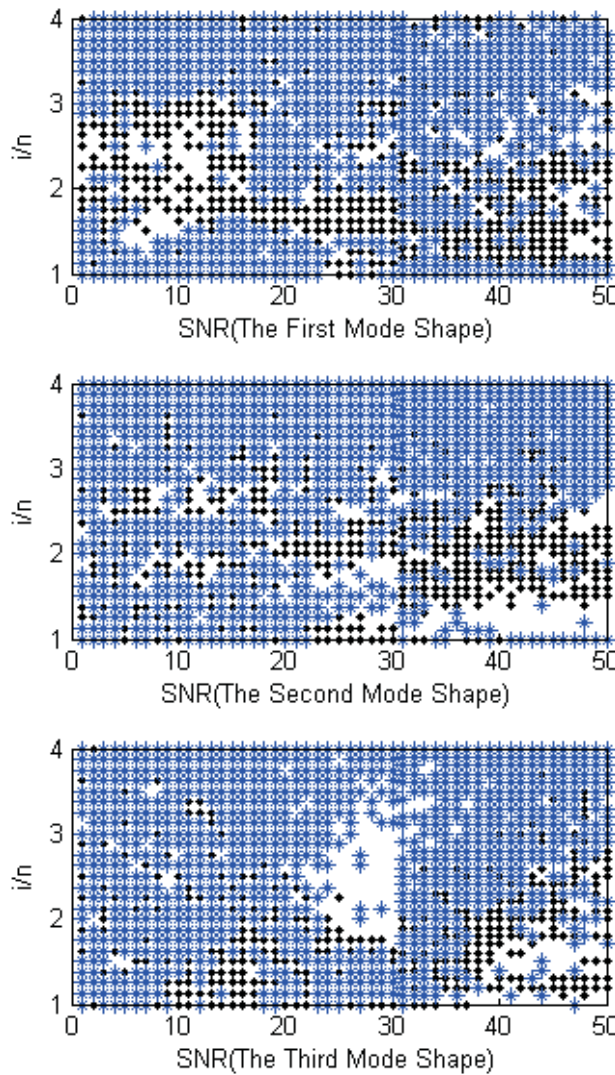
**Value choosing of parameters in stochastic subspace identification**

There have been many papers related to stochastic subspace identification (SSI). The principle of SSI can be referred to reference (Peeters, 2000).

Determination of the order of system is usually regarded as most important in the modal parameter identification using SSI. However, it was found by simulations of simple beams that there were relations among the row block number  $i$  of Hankel matrix, the order of system  $n$  and the signal noise ratio (SNR). So the value of  $i$  is also important to the modal parameter identification. But there has been no reported work to prove it so far. Analyses on choosing values of  $i$  and  $n$  will be carried out as follows.



**Figure 1. The finite element model of a simple beam**



**Figure 2. The relation between  $i/n$  and SNR**

A simple beam model was built in ANSYS, of which the configuration is shown in Figure 1. The cross section dimension was  $0.25 \times 0.20 \text{ m}^2$ , the span length was 6m. The Young's modulus was 32Gpa and the density was  $2500 \text{ kg/m}^3$ . The beam was divided into 12 elements uniformly and the nodes were numbered from the left to the right.

The vibration modes of the beam were obtained by modal analysis in ANSYS and by SSI respectively. The former is called exact modes. As for the latter, the following steps are adopted.

- 1) Accelerations at each node were calculated by dynamic analysis in ANSYS.
- 2) The accelerations were added with white noise of different amplitude (Cao and Lin, 2010).
- 3) The noise-polluted accelerations were used as signals to identify structural modes with SSI. In the process,  $i$  was taken as different values with signals of different SNR to get different modes.
- 4) Comparing the modes identified with different values of  $i$  with the corresponding exact modes, the values of  $i$  of the modes the most related and the least related to the exact mode were called TM and TL respectively.
- 5) Using SNR as the abscissa, the value of  $i/n$  as the ordinate, the values of  $i/n$  corresponding to TM and TL were plot with black dots and blue asterisks respectively.

The above steps were repeated 10 times considering the random property of noise.

As shown in Figure 2, it is easy to find the relations of  $i/n$  and SNR by the distribution of the blue asterisks and the black dots. For the first three modes, with SNR being around 40dB, when  $i/n$  is taken as 1.2~2.2, 1.4~2.2 and 1.2~2.0 respectively, the modes related to the corresponding exact modes well. So it is suggested that, when SNR is about 40dB,  $i/n$  is taken as 1.5~2.0 to get the best results.

### Reconstruction of structural modal rotations

The dynamic equilibrium equation of a bending-type structure is expressed as

$$\begin{bmatrix} M & \\ & J \end{bmatrix} \begin{Bmatrix} x \\ \varphi \end{Bmatrix} + \begin{bmatrix} C_{xx} & C_{x\varphi} \\ C_{\varphi x} & C_{\varphi\varphi} \end{bmatrix} \begin{Bmatrix} x \\ \varphi \end{Bmatrix} + \begin{bmatrix} K_{xx} & K_{x\varphi} \\ K_{\varphi x} & K_{\varphi\varphi} \end{bmatrix} \begin{Bmatrix} x \\ \varphi \end{Bmatrix} = \begin{Bmatrix} f(t) \\ 0 \end{Bmatrix} \quad (1)$$

The relation of rotational vector and translational vector can be easily obtained by eq.1

$$\varphi = -K_{\varphi\varphi}^{-1} K_{\varphi x} x \quad (2)$$

The global stiffness matrix is expressed as

$$K_i = \sum_{i=1}^n b_i \bar{K}_i \quad (3)$$

Where,  $b_i$  is the parameter of the  $i^{\text{th}}$  element to be identified.  $\bar{K}_i$  is the elemental stiffness matrix with the parameter  $b_i$  being extracted.

Similarly, for the respective block matrix, the following holds,

$$K_{\varphi x} = \sum_{i=1}^n b_i \bar{K}_{\varphi x}^{(i)} \quad (4)$$

$$K_{\varphi\varphi} = \sum_{i=1}^n b_i \bar{K}_{\varphi\varphi}^{(i)} \quad (5)$$

in which,

$$B = (b_1 I_n, b_2 I_n, \dots, b_n I_n) \quad (6)$$

$n$  is the number of elements,  $I_n$  is  $n \times n$  unit matrix.

$$\bar{K}_{\varphi x} = (\bar{K}_{\varphi x}^{(1)}, \bar{K}_{\varphi x}^{(2)}, \dots, \bar{K}_{\varphi x}^{(n)})^T \quad (7)$$

$$\bar{K}_{\varphi\varphi} = (\bar{K}_{\varphi\varphi}^{(1)}, \bar{K}_{\varphi\varphi}^{(2)}, \dots, \bar{K}_{\varphi\varphi}^{(n)})^T \quad (8)$$

So we have

$$K_{\varphi x} = B \bar{K}_{\varphi x} \quad (9)$$

$$K_{\varphi\varphi} = B \bar{K}_{\varphi\varphi} \quad (10)$$

Eq.2 can be rewritten as,

$$\varphi = -(B\bar{K}_{\varphi\varphi})^{-1}\bar{K}_{\varphi x}x \quad (11)$$

By the above steps, the modal rotations can be evaluated by modal translations.

### Damage indicator based on element modal strain energy and data fusion theory

#### Element damage variable

Liu et al (2004) constructed a damage indicator based on element modal strain energy (EMSE), called element damage variable. The element damage variable of the  $j^{\text{th}}$  element is expressed as

$$D_j = \frac{|EMSE_j^d - EMSE_j^u|}{|EMSE_j^d - EMSE_j^u| + EMSE_j^u} \quad (12)$$

Where  $EMSE_{ij}^u$  and  $EMSE_{ij}^d$  are EMSEs of the  $j^{\text{th}}$  element in intact and damaged state respectively.

And are expressed as,

$$EMSE_j^u = \sum_{i=1}^m \varphi_i^T K_j \varphi_i \quad (13)$$

$$EMSE_j^d = \sum_{i=1}^m \tilde{\varphi}_i^T K_j \tilde{\varphi}_i \quad (14)$$

In which,  $K_j$  is the stiffness matrix of the  $j^{\text{th}}$  element,  $\varphi_i$  and  $\tilde{\varphi}_i$  are the  $i^{\text{th}}$  mode under intact and damaged state respectively.

Since damage leads to reduction of structural stiffness, the value of EMSE of damaged state should be larger than that of intact state calculated by Eq.13 and Eq.14 respectively. If the numerator in Eq.12 is not taken the absolute value, as in Eq.15, the damaged element will always give positive D while those intact elements will often do reversely. So by both the value and sign of D, it is much easier to identify the damaged elements, which has been verified by the authors (Cao et al, 2008).

$$D_j = \frac{EMSE_j^d - EMSE_j^u}{|EMSE_j^d - EMSE_j^u| + EMSE_j^u} \quad (15)$$

#### Multi-source information fusion

Multi-source information fusion or multi-sensor information fusion is a new technology which has been developed since 70s in the last century (Waltz 1990; Linn et al, 1991; Hall, 1992; Kang, 1997; Yang, 2004; Wan et al, 2005; Han et al, 2006; Liu et al, 2008). The principle is that information obtained by data fusion from several sensors is more useful than that from only one sensor. The main techniques involved include classic derivation and statistics, Byes derivation, Dempster-Shafer evidence theory, fuzzy theory, etc. In this paper, Dempster-Shafer evidence theory (D-S theory in short) (Shafer, 1976; Han et al, 2006) is used to improve the indicator based on EMSE.

The basic idea of D-S theory is as follows.

Assume that  $A_1, A_2, \dots, A_n$  are  $n$  incompatible events,  $D_1, D_2, \dots, D_m$  are  $m$  sensors. The occurrence probability of the  $j^{\text{th}}$  event by the  $i^{\text{th}}$  sensor is  $M_i(A_j)$ , then the occurrence probability of event P is,

$$M(P) = C^{-1} \sum_{\cap A_j = P} \prod_{1 \leq i \leq m} M_i(A_j) \quad (16)$$

in which,

$$C = 1 - \sum_{\cap A_j = \emptyset} \prod_{1 \leq i \leq m} M_i(A_j) = \sum_{\cap A_j \neq \emptyset} \prod_{1 \leq i \leq m} M_i(A_j) \quad (17)$$

#### Damage indicator

Previously, the value of number  $i$  of Hankel matrix row block was suggested to ensure exact extraction of modes by SSI. However, the extracted modes are still influenced by noise. So the D-S evidence theory will be used to carry out data fusion for results obtained by different values of  $i$  to eliminate noise as nearly as possible.

Firstly, the change of EMSE is defined as,

$$LEMSE_{ij} = \frac{D_j}{\sum_j D_j} \quad (18)$$

in which,  $D_j$  is calculated by Eq. 15.

That  $n$  elements being damaged is thought as  $n$  events. The values of LEMSE corresponding to  $m$  values of  $i$  are regarded as information given by  $m$  sensors. By eq.16, the damage indicator based on EMSE and data fusion theory is,

$$LEMSE_p = C^{-1} \sum_{\cap j=p} \prod_{1 \leq i \leq m} LEMSE_{ij} \quad (19)$$

in which

$$C = 1 - \left| \sum_{\cap j=\emptyset} \prod_{1 \leq i \leq m} LEMSE_{ij} \right| = \left| \sum_{\cap j \neq \emptyset} \prod_{1 \leq i \leq m} LEMSE_{ij} \right| \quad (20)$$

$P$  means the  $p^{\text{th}}$  element.

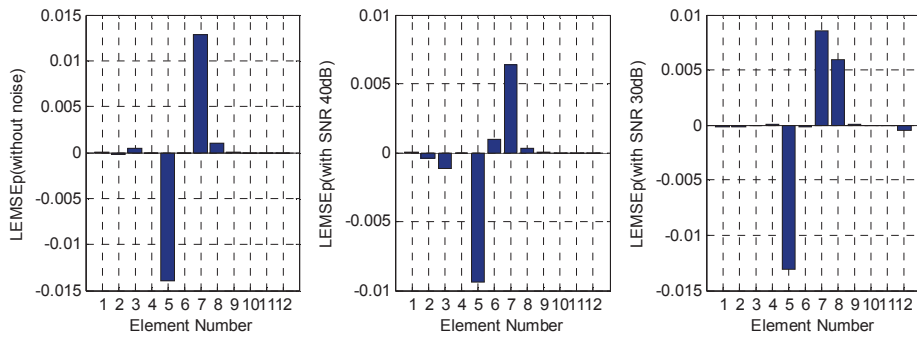
### Simple beam simulations

A simple beam simulation was used to verify the suggested damage indicator. The simple beam was the same as that in Figure 1. Damage of element was simulated by the reduction of element stiffness. The cases of damage see table 1. With white noise excitations being applied at the 4<sup>th</sup> node, acceleration responses at each node of intact and damaged state were calculated respectively. Noise was added into the responses with two SNR correspondingly, i.e. 40dB and 30dB. SSI was used to extract the first three modes of the beam under intact and damaged state respectively from the noised responses. Then the modal rotations were estimated by eq.11. Both the modal translations and rotations were utilized to construct the damage indicator by eq.19. The results are shown in (a) to (e) of Figure 3.

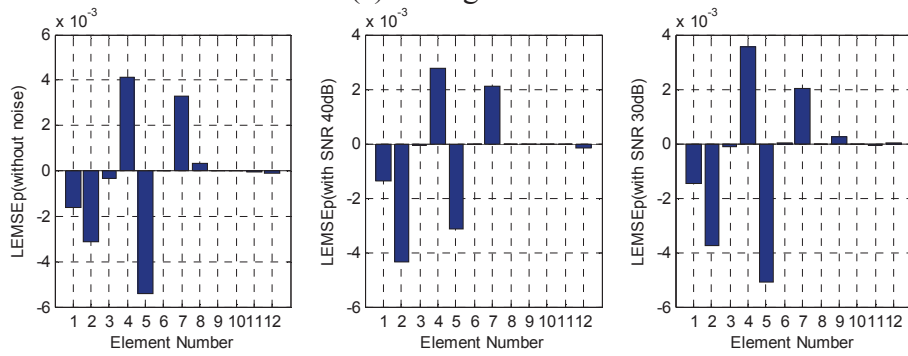
In single damage cases, the suggested damage indicator can locate the damaged elements even under 30dB noise. However, the adjacent elements are wrongly identified as damaged. In two damage cases, the element with less damage can be identified, but the value of damage indicator is close to those of wrongly identified elements. If the two elements have damage of the same degree, the results are better. So it is possible to identify damage of a simple beam with the suggested damage indicator. Even under heavy noise with SNR being 30dB, the damage elements can still be located.

**Table 1. Damage cases of the simple beam**

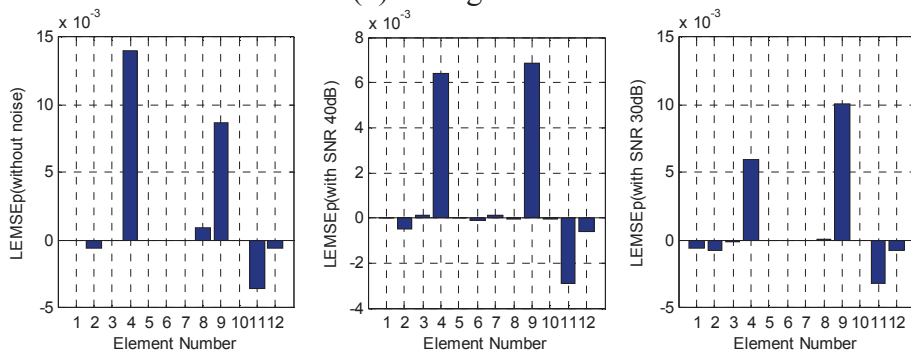
Damage case	Damaged elements	Damaged extent
1	7	7-10%
2	4、7 (non-symmetric)	4-10%、7-10%
3	4、9 (symmetric)	4-10%、9-10%
4	4、7 (non-symmetric)	4-10%、7-20%
5	4、7、9	4-10%、7-10%、9-10%



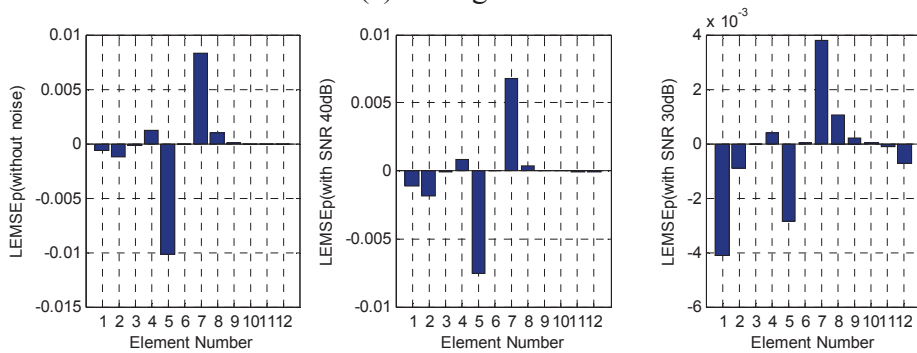
(a) damage case 1



(b) damage case 2

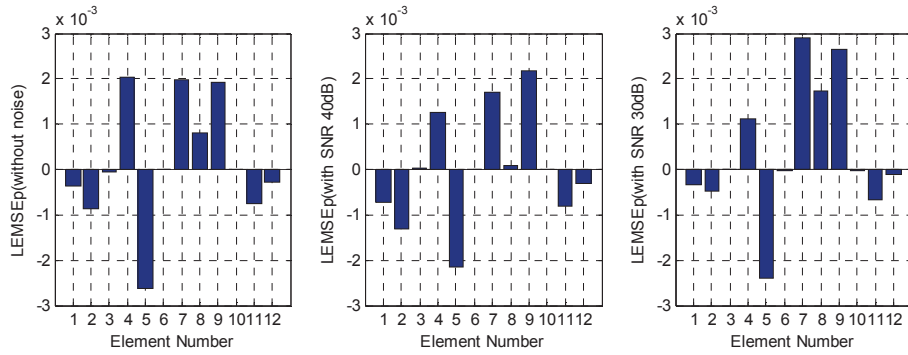


(c) damage case 3



(d) damage case 4





(e) damage case 5

Figure 3. Damage detection of the simple beam under different noise levels

**The test simple beam**

The test beam was a simple reinforced concrete beam, with section dimension being 210x190mm, and span length being 4.5m. Three steel bars and two steel bars, with diameter being 12mm, were uniformly distributed in the tension side and compression side respectively. The confined steel was Φ8@225. The thickness of concrete cover was 20mm. Nine acceleration sensors were evenly distributed on the top of the beam, dividing the beam into ten segments, see Figure 4.

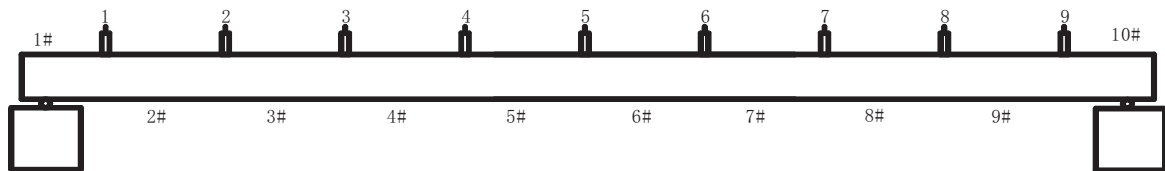
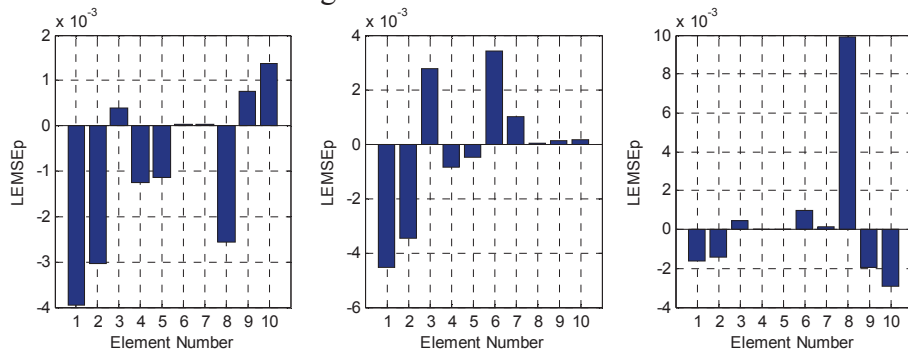


Figure 4. The layout of acceleration sensors on the test beam

Firstly, the beam was excited by a wood hammer. The accelerations of free vibration were recorded by the nine sensors. Then damage in the beam were made by cutting a slot. The slot was of U shape, on both sides and the bottom of the beam, 20mm wide and 20mm deep. After the first slot was cut in the middle of the 3<sup>rd</sup> segment, the beam was excited and accelerations were recorded. And then the second slot was cut in the middle of the 6<sup>th</sup> segment and accelerations of free vibration of the beam were also recorded. At last, in the middle of the 8<sup>th</sup> segment the last slot was cut and accelerations were recorded.

With the recorded accelerations, damage indicators were constructed by the procedure suggested previously. The results are shown in Figure 5.



(a) damage in the 3<sup>rd</sup> element (the first cut) (b) damage in the 3<sup>rd</sup> and 6<sup>th</sup> elements (the second cut) (c) damage in the 3<sup>rd</sup>, 6<sup>th</sup> and 8<sup>th</sup> elements (the third cut)

Figure 5. Damage detection of the test beam

From Figure 5, after the first cutting was made, the suggested damage indicator could locate the damaged segment, i.e. the 3<sup>rd</sup> segment. However, the 9<sup>th</sup> and 10<sup>th</sup> segment were wrongly identified

as damaged. By checking the original signals recorded by the 8<sup>th</sup> and 9<sup>th</sup> sensors, the signals were found with heavier noise than the others. It is estimated that the two sensor were not adhesive tightly to the top of the beam when the first dynamic test was made. And maybe they were not as tight as should be in the second dynamic test. When the 6<sup>th</sup> segment and 8<sup>th</sup> segment were damaged, the damage indicator could also locate them, although the 7<sup>th</sup> segment was wrongly recognized as damaged.

## Conclusions

Structural modal translations were extracted from accelerations by stochastic subspace identification. Modal rotations were reconstructed by modal translations using the principle of static condensation. Both modal translations and rotations were used to calculate the change of element modal strain energy, which was then utilized to construct a damage indicator based on the theory of data fusion. Analyses were also carried out on choosing values of parameters in SSI for eliminating the effect of noise. The constructed damage indicator was applied to damage identification of both simulated simple beams and a test simple beam.

The results of simulations show that the suggested damage indicator could locate the damaged elements of simple beams even under heavy noise in one damaged element cases, although the adjacent elements were wrongly recognized as damaged. In multi-damage cases, the less damaged element could not be detected when the difference of damaged level between any two elements is higher than the damaged level of the less damaged element.

As for the test simple beam, the damage indicator could identify the damaged segments after the slots were cut sequentially. The adjacent segment was wrongly identified, but its value of damage indicator was smaller than that of damaged segments.

It can be seen from the results from simulation and test that the suggested damage indicator can locate the position of damage of beam-type structures. It is sensitive to small damage. Moreover, it is able to resist noise at a considerable level.

## References

- Cao H, Zhang X L, Cao Y H, Li Y M (2008), Damage identification based on improved elemental stiffness reduction factor [J]. *Journal of Vibration and Shock*. 27(6), pp.132-135. (in Chinese)
- Cao H, Lin X P (2010), Noise simulation in structural damage identification[J]. *Journal of Vibration and Shock*. 29(5), pp.106-109. (in Chinese)
- Guyan R J (1965), Reduction of stiffness and mass matrices[J]. *AIAA Journal*. 3(2), pp.380-381.
- Hall D L (1992), *Mathematical techniques in multi-sensor data fusion* [M]. Norwood: Artech House.
- Hjelmstad K D, Banan Mo R, Banan Ma R (1995), Time-domain parameter estimation algorithm for structures I: computational aspects [J]. *Journal of Engineering Mechanics*. 121(3), pp.424-434.
- Han C Z, Zhu H Y, Duan Z S (2006), *Multi-resource information fusion* [M]. Beijing: Tsinghua University Press. (in Chinese)
- Kang Y H (1997), *Theory and application of data fusion* [M]. Xi'an: Xidian University Press. (in Chinese)
- Linn R J, Hall D L, Llinas J (1991), A survey of multi-sensor data fusion systems [J]. *Data Structures and Target Classification of SPIE*. 1470, pp.13-29.
- Liu H, Qu W L, Yuan R Z (2004), Structural damage detection method based on the theory of dissipation-ratio of modal strain energy[J]. *Journal of Vibration and Shock*. 23(2), pp.118-121. (in Chinese)
- Liu T, Li A Q, Miao C Q (2008), Study of structural damage identification methods based on data fusion[M]. *Engineering Mechanics*. 25(1), pp.16-21. (in Chinese)
- Peeters B (2000), *System identification and damage detection in civil engineering*[D]. Ph.D. Thesis, Katholieke Universiteit Leuven.
- Shafer G A (1976), *A mathematical theory of evidence* [M]. New Jersey: Princeton University Press.
- Shi Z Y, Law S S, Zhang L M (2002), Improved damage quantification from elemental modal strain energy change [J]. *Journal of Engineering Mechanics*. 128(5), pp.521-529
- Waltz L (1990). *Multi-sensor data fusion* [M]. Norwood: ArtechHouse.
- Wan X P, Shi X L, Zhao M Y (2005), Damage detection of composite wing by using modal strain energy[J]. *Journal of Mechanical Strength*. 27(5), pp.691-695. (in Chinese)
- Yang W H (2004), *Multi-sensor data fusion and its application*[M]. Xi'an: Xidian University Press. (in Chinese)

Zhao X, Li J (2003), Structural parameter estimation with unknown rotational response. *Engineering Mechanics*. 20(4), pp.55-59. (in Chinese)

## Continued fraction formulation for infinite acoustic fluid with uniform cross section

\*S.M. Li<sup>1</sup>

<sup>1</sup>Institute of Systems Engineering, CAEP, Mianyang City, Sichuan Province 621999, China.

\*Corresponding author: hustmingsl@126.com

### Abstract

Based on the continued fraction theory and the diagonalization procedure of the scaled boundary finite element method (SBFEM) for infinite acoustic fluid with uniform cross section, the high-frequency and the doubly asymptotic continued fraction formulations were derived. These formulations were applied to analyze a transient response of infinite acoustic fluid with uniform cross section under upstream excitations. Based on the transient response, the stability and convergence of the continued fraction formulations were discussed. Numerical results showed the doubly asymptotic continued formulation converged much faster than the high-frequency continued fraction formulation to analytical solutions. Comparison of computational efficiency between the continued formulation and the dynamic mass matrix was made. Computational costs of the continued fraction formulation were much less than that of the dynamic mass matrix.

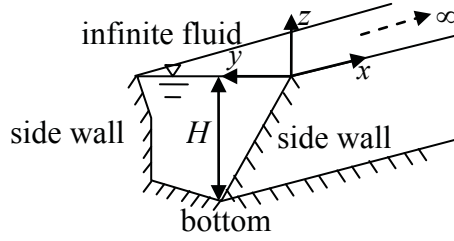
**Keywords:** SBFEM, Continued fraction formulation, Infinite acoustic fluid, Transient analysis.

### Introduction

The infinite acoustic fluid with uniform cross section is often encountered in dam-reservoir interaction problems. To obtain the dam-reservoir interaction response, the infinite acoustic fluid was truncated into a near-field with arbitrary geometry in the vicinity of dam and a far-field with uniform cross section which extends to infinity. The near-field can be easily modeled by FEM or BEM et al, while the far-field with uniform cross section can be modeled by transmitting boundary conditions (Gogoi and Maity (2006)), BEM (Czygan and Estorff Von (2002)) and so on. An alternative to model a far field, the scaled boundary finite element method (SBFEM), was verified to model accurately and effectively unbounded medium problems (Wolf and Song (1996)).

Based on the SBFEM formulation in displacement, Lin and his co-authors developed and applied the SBFEM to solve the semi-infinite acoustic fluid with uniform cross section problems in the frequency domain (Lin et al. (2007), Lin et al. (2010)), while Li and his co-authors improved the SBFEM for frequency problems of the semi-infinite acoustic fluid with uniform cross section (Fan and Li (2008), Li et al. (2008)), based on the SBFEM formulation in dynamic stiffness. In addition, based on the dynamic mass matrix, Li (2011) also applied the SBFEM to solve the transient analysis of the semi-infinite acoustic fluid with uniform cross section. Its results were very similar to solutions from other methods, but in the author's experience, its computational efficiency was affected greatly by convolution integrals in the SBFEM. In order to improve the computational efficiency of SBFEM, a diagonalization formulation of SBFEM and a Bessel function to evaluate the dynamic stiffness of SBFEM were proposed by Li (2009) and Li (2012), respectively. Although these methods improved the SBFEM efficiency, they still need a convolution integral evaluation which results in the nonlinear increase of computational cost with analysis step number increasing. An alternative, a continued fraction formulation, was proposed by Prempramote et al. (2009), which can avoid the evaluation of convolution integral. Based on the continued fraction formulation and the SBFEM diagonalization formulation, this research derived the continued fraction formulation in matrix form of infinite acoustic fluid with uniform cross section.

## SBFEM Formulation for Infinite Acoustic Fluid with Uniform Cross Section



**Figure 1. Infinite acoustic fluid with uniform cross section**

For an infinite acoustic fluid with uniform cross section of arbitrary geometry as shown in Figure 1 only subjected to upstream excitations in  $x$  direction, the whole infinite acoustic fluid can be modeled by the SBFEM, which only needs the discretization of cross section of the infinite fluid. Its boundary conditions can refer to the reference (Li et al. (2008)). Ignoring effects of surface waves and absorption of side walls and bottom, its SBFEM formulation satisfies (Li (2009)) on the cross section

$$\mathbf{V}_n = \sqrt{(\mathbf{E}^2 - \omega^2 \mathbf{M}^0) \mathbf{E}^{0-1} \mathbf{E}^0} \boldsymbol{\Phi} = \mathbf{S}^\infty(\omega) \boldsymbol{\Phi} \quad (1)$$

The symbols  $\mathbf{S}^\infty(\omega)$ ,  $\boldsymbol{\Phi}$ ,  $\mathbf{V}_n$  are the dynamic stiffness matrix of infinite fluid after SBFEM discretization, velocity potential vector and equivalent normal velocity vector caused by upstream excitations, respectively.  $\omega$  is the excitation frequency.  $\mathbf{E}^0$ ,  $\mathbf{E}^2$ ,  $\mathbf{M}^0$  are SBFEM coefficient matrices, which were defined by Wolf and Song (1996).  $\mathbf{V}_n$  is expressed as

$$\mathbf{V}_n = \int_A \mathbf{N}_f^T v_n dA \quad (2)$$

The symbol  $A$  denotes the cross section.  $\mathbf{N}_f$  is the shape function of acoustic fluid finite element.  $v_n$  is normal velocity. Using the diagonalization technique (Li (2009)), one has

$$\mathbf{S}_d^\infty(\omega) = \mathbf{X}^T \mathbf{S}^\infty(\omega) \mathbf{X} = \sqrt{\boldsymbol{\Lambda} - \left(\frac{\omega}{c}\right)^2 \mathbf{I}} \quad (3)$$

with

$$\frac{\mathbf{E}^2}{H} \mathbf{X} = H \mathbf{E}^0 \mathbf{X} \boldsymbol{\Lambda} \quad (4)$$

$$\mathbf{X}^T \frac{\mathbf{E}^2}{H} \mathbf{X} = \boldsymbol{\Lambda} \quad (5)$$

$$\mathbf{X}^T H \mathbf{E}^0 \mathbf{X} = \mathbf{I} \quad (6)$$

where the square matrix  $\mathbf{X}$  is the eigenvector matrix and the matrix  $\boldsymbol{\Lambda}$  is the eigenvalue matrix of the eigenvalue equation (4);  $\mathbf{I}$ ,  $c$ ,  $H$  are the identity matrix, the sound speed in fluid and the height of cross section, respectively.

### Continued Fraction Formulation of Dynamic Stiffness Matrix

According to the continued fraction theory (Prempramote et al. (2009)) based on the dynamic stiffness of semi-infinite layer with constant depth, the order  $M_H$  high-frequency continued fraction solution of Equation (3) is equivalent to

$$\mathbf{S}_d^\infty(\omega) = i \frac{\omega}{c} \mathbf{C}_\infty^d - (\mathbf{Y}_d^{(1)}(\omega))^{-1} \boldsymbol{\Lambda} = i \frac{\omega}{c} \mathbf{I} - (\mathbf{Y}_d^{(1)}(\omega))^{-1} \boldsymbol{\Lambda} \quad (7)$$

$$\mathbf{Y}_d^{(j)}(\omega) = i \frac{\omega}{c} \mathbf{Y}_1^{(j)} - \boldsymbol{\Lambda} (\mathbf{Y}_d^{(j+1)}(\omega))^{-1} \quad (j = 1, 2, \dots, M_H) \quad (8)$$

Substituting Equations (7, 8) into Equation (3) yields

$$\Lambda - i \frac{\omega}{c} 2\mathbf{b}_1^{(j)} \mathbf{Y}_d^{(j)}(\omega) - (\mathbf{Y}_d^{(j)}(\omega))^2 = 0 \quad (j=1,2,\dots,M_H) \quad (9)$$

$$\mathbf{b}_1^{(j)} = (-1)^{j+1} \mathbf{b}_1^{(1)} = (-1)^{j+1} \mathbf{I} \quad (j=1,2,\dots,M_H) \quad (10)$$

$$\mathbf{Y}_1^{(j)}(\omega) = (-1)^j 2\mathbf{b}_1^{(1)} = (-1)^j 2\mathbf{I} \quad (j=1,2,\dots,M_H) \quad (11)$$

In order to improve the accuracy of Equations (7, 8) in low frequency range, the residual term  $\mathbf{Y}_d^{(M_H+1)}(\omega)$  of Equation (8) is denoted as

$$\mathbf{Y}_L(\omega) = \mathbf{Y}_d^{(M_H+1)}(\omega) \quad (12)$$

$$\mathbf{Y}_L(\omega) = \mathbf{Y}_{L0}^{(0)} + i \frac{\omega}{c} \mathbf{Y}_{L1}^{(0)} - \left( i \frac{\omega}{c} \right)^2 (\mathbf{Y}_L^{(1)}(\omega))^{-1} \quad (13)$$

$$\mathbf{Y}_L^{(j)}(\omega) = \mathbf{Y}_{L0}^{(j)} - \left( i \frac{\omega}{c} \right)^2 (\mathbf{Y}_L^{(j+1)}(\omega))^{-1} \quad (j=1,2,\dots,M_L) \quad (14)$$

$$\mathbf{Y}_{L0}^{(0)} = (-1)^{M_H+1} \sqrt{\Lambda} \quad (15)$$

$$\mathbf{Y}_{L1}^{(0)} = (-1)^{M_H+1} \mathbf{I} \quad (16)$$

$$\mathbf{Y}_{L0}^{(j)} = (-1)^{M_H+j+1} 2\sqrt{\Lambda} \quad (j=1,2,\dots,M_L) \quad (17)$$

Note that continued fraction formulations of Equations (7-17) are expressed in a matrix form. The formulations with  $M_L = 0$  and  $M_L \neq 0$  are called a high-frequency and a doubly asymptotic continued fraction formulation, respectively.

## Time-Domain Formulation Based on Continued Fraction Formulation

Re-writing Equation (1) yields

$$\mathbf{V}_n^d = \mathbf{X}^T \mathbf{V}_n = \mathbf{S}_d^\infty(\omega) \mathbf{X}^{-1} \Phi = \mathbf{S}_d^\infty(\omega) \Phi^d \quad (18)$$

Substituting Equations (7, 8) into Equation (18) yields

$$\mathbf{V}_n^d = i \frac{\omega}{c} \mathbf{C}_\infty^d \Phi^d - \sqrt{\Lambda} \Phi_d^{(1)} \quad (19)$$

$$\sqrt{\Lambda} \Phi_d^{(j)} = \mathbf{Y}_d^{(j+1)}(\omega) \Phi_d^{(j+1)} \quad (j=0,1,2,\dots,M_H) \quad (20)$$

$$\sqrt{\Lambda} \Phi_d^{(j-1)} = i \frac{\omega}{c} \mathbf{Y}_1^{(j)} \Phi_d^{(j)} - \sqrt{\Lambda} \Phi_d^{(j+1)} \quad (j=1,2,\dots,M_H) \quad (21)$$

where  $\Phi_d^{(0)} = \Phi^d$  and  $\Phi_d^{(j)}$  is an auxiliary variable. Substituting Equations (12, 13) into Equation (21), one has

$$\sqrt{\Lambda} \Phi_d^{(M_H)} = \mathbf{Y}_{L0}^{(0)} \Phi_d^{(M_H+1)} + i \frac{\omega}{c} \mathbf{Y}_{L1}^{(0)} \Phi_d^{(M_H+1)} - i \frac{\omega}{c} \Phi_{dL}^{(1)} \quad (22)$$

where  $\Phi_{dL}^{(1)}$  is an auxiliary variable and satisfies

$$i \frac{\omega}{c} \Phi_{dL}^{(M_H+1)} = i \frac{\omega}{c} \Phi_{dL}^{(0)} = \mathbf{Y}_L^{(1)}(\omega) \Phi_{dL}^{(1)} \quad (23)$$

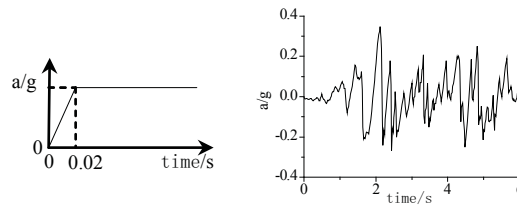
Substituting Equation (14) into Equation (23) leads to

$$i \frac{\omega}{c} \Phi_{dL}^{(j)} = \mathbf{Y}_L^{(j+1)}(\omega) \Phi_{dL}^{(j+1)} \quad (j=0,1,2,\dots,M_L) \quad (24)$$

$$i \frac{\omega}{c} \Phi_{dL}^{(j-1)} = \mathbf{Y}_{L0}^{(j)} \Phi_{dL}^{(j)} - i \frac{\omega}{c} \Phi_{dL}^{(j+1)} \quad (j=1,2,\dots,M_L) \quad (25)$$

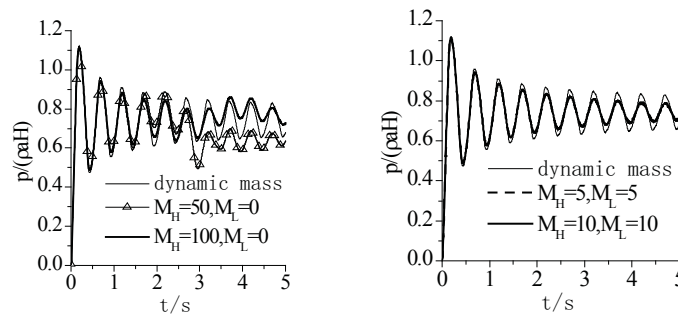
$$\Phi_{dL}^{(0)} = \Phi_d^{(M_H+1)} \quad (26)$$



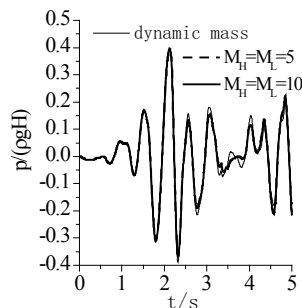


**Figure 3. Horizontal accelerations (Left: Ramped; Right: El Centro)**

Figure 4 shows the pressure at the heel of dam obtained by different order  $M_H$  and  $M_L$  continued fraction formulations under horizontal ramped acceleration shown in Figure 3. Time step increment is 0.005s. Results from high-frequency continued fraction formulation with  $M_H = 50, 100$  were different with that obtained from dynamic mass matrix after the time 2.5s, while results from doubly asymptotic continued fraction formulation with  $M_H = M_L = 5$  and  $M_H = M_L = 10$  were much more accurate, especially at late time, which showed that the doubly asymptotic continued formulation can obtain more accurate results than high-frequency continued fraction formulation. Figure 5 plots the pressure of dam's heel from the doubly asymptotic continued fraction formulation under horizontal El Centro acceleration shown in Figure 3. With the order increasing, results gradually tend to those from dynamic mass matrix. Results from dynamic mass matrix were almost similar to analytical solutions (Li (2009)). Figure 6 plots results from the doubly asymptotic continued fraction formulation with  $M_H = M_L = 10$  using different time step increments 0.0002s and 0.005s. Results from 0.0002s are more accurate than those from 0.005s. Figures 4-6 show that results from the continued fraction formulation become more and more similar to exact solution when time step increment becomes smaller and smaller and the order of doubly asymptotic continued fraction formulation becomes higher and higher, which validates the convergence of Equation 27.

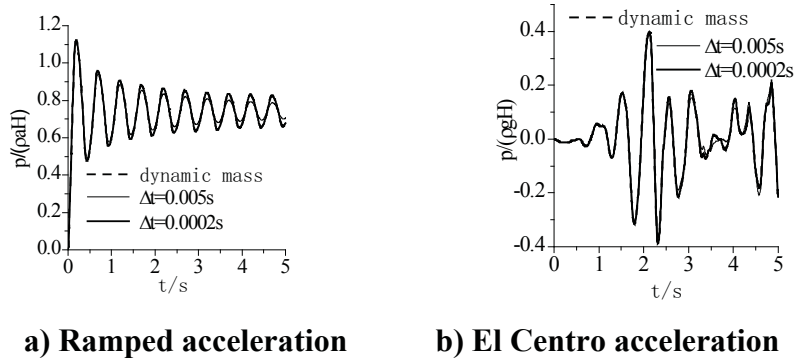


**Figure 4. Pressure at the heel of rigid vertical dam under ramped acceleration**



**Figure 5. Pressure at the heel of rigid vertical dam under El Centro acceleration**





**Figure 6. Pressure at the heel of rigid vertical dam under different time increment**

Through solving eigenvalues of Equation (27), it can be found that real parts of eigenvalues are positive when  $M_H$  and  $M_L$  are greater than zero, which ensure Equation (27) is stable. When  $M_L$  is equal to zero, real parts of eigenvalues of Equation (27) are zeros, which ensure Equation (27) is not divergent. Maybe that is why results from high-frequency continued fraction formulation are not convergent to analytical solutions.

**Table 1. Response computational time comparison**

Time step	1000	2000	5000
Dynamic mass matrix, matrix dimension $20 \times 20$	0.35s	2.17s	25.25s
Continued fraction formulation with $M_L=M_h=5$ , matrix dimension $240 \times 240$	0.07s	0.14s	0.34s
Continued fraction formulation with $M_L=M_h=10$ , matrix dimension $440 \times 440$	0.28s	0.58s	1.38s

Table 1 lists the response computational cost based on the dynamic mass matrix and the continued fraction formulation. Response computational time of dynamic mass matrix is only the time cost to evaluate the response based on convolution integral, not including the dynamic mass matrix evaluation time. The response computational cost of the continued fraction formulation is the time to solve Equation (27). Table 1 shows the efficiency of the continued fraction formulation is much higher than that of the dynamic mass matrix, although the continued fraction formulation increase the dimension  $N \times N$  of response solving matrix equation up to  $(M_H + M_L + 2)N \times (M_H + M_L + 2)N$ .

## Conclusions

The continued fraction formulation of infinite acoustic fluid with uniform cross section was derived, which is applicable to two- and three-dimensional problems. The formulation can accurately model the infinite acoustic fluid and its calculation efficiency is much higher than the convolution integral efficiency of SBFEM based on dynamic mass matrix.

## Acknowledgments

This work is supported by the National Natural Science Foundation of China (10902060, 11272299) and the Science Foundation of China Academy of Engineering Physics (2011B0201036), for which the author is grateful.

**References**

- Czygan, O., Estorff von, O. (2002), Fluid-structure interaction by coupling BEM and nonlinear FEM. *Engineering Analysis with Boundary Elements* 26, pp.773–779.
- Fan, S.C., Li, S.M. (2008), Boundary finite element method coupling finite element method for steady-state analyses of dam-reservoir systems. *Journal of Engineering Mechanics* 134, pp.133-142.
- Gogoi, I., Maity, D. (2006), A non-reflecting boundary condition for the finite element modeling of infinite reservoir with layered sediment. *Advances in Water Resources* 29, pp.1515–1527.
- Li, S.M. (2012), Transient Analysis of Dam-Reservoir Interaction Based on Dynamic Stiffness of SBFEM. *Advanced Materials Research* 378, pp.213-217.
- Li, S.M.(2011), Coupled Finite Element - Scaled Boundary Finite Element Method for Transient Analysis of Dam-Reservoir Interaction. *ICCSA 2011, Part IV, LNCS 6785*, pp.26-34.
- Li, S.M. (2009), Diagonalization procedure for scaled boundary finite element method in modelling semi-infinite reservoir with uniform cross section. *International Journal for Numerical Methods in Engineering* 2009, 80, pp.596–608.
- Li, S.M., Liang, H., Li, A.M. (2008), A semi-analytical solution for characteristics of a dam-reservoir system with absorptive reservoir bottom. *Journal of Hydrodynamics* 20, pp.727-734.
- Lin, G., Du, J.G., Hu, Z.Q. (2007), Dynamic dam-reservoir interaction analysis including effect of reservoir boundary absorption. *Science in China Series E: Technological Sciences* 50, pp.1-10.
- Lin, G., Wang, Y., Hu, Z.Q. (2010), Hydrodynamic pressure on arch dam and gravity dam including absorption effect of reservoir sediments. *Material Science and Engineering* 10, pp.012234.
- Prempramote, S., Song C.M., Francis, T.L., Lin, G. (2009), High-order doubly asymptotic open boundaries for scalar wave equation. *International Journal for Numerical Methods in Engineering* 79, pp.340-374.
- Wolf, J.P., Song, C. (1996), *Finite-Element Modelling of Unbounded Media*, Wiley, New York.

## Mechanisms of strain rate effect of metal foams with numerical simulations of 3D Voronoi foams during SHPB tests

B. Yang<sup>1</sup>, Z.J. Liu<sup>1</sup>, \*L.Q. Tang<sup>1</sup>, Z.Y. Jiang<sup>1</sup> and Y.P. Liu<sup>1</sup>

<sup>1</sup>School of Civil Engineering and Transportation, State Key Laboratory of Subtropical Building Science, South China University of Technology, Guangzhou 510640, China

\*Corresponding author: lqtang@scut.edu.cn

### Abstract

Metal foams were usually prepared and tested as light-weight and efficient energy absorption materials. Controversial results among different tests and numerical simulations show that the mechanisms of strain rate effect of metal foams are not clear yet. To study the main mechanisms of strain rate effect of metal foams during split Hopkinson pressure bar (SHPB) tests, numerical simulations were carried out by FEM, in which metal foams were simulated with 3D Voronoi models. In these simulations, the matrix material of metal foams is assumed to have no strain rate sensitivity, which helps to determine the strain rate effect of metal foams clearly. The numerical simulations show that metal foams' specimens still exhibit some strain rate sensitivity even the matrix material without strain rate sensitivity. Further quantitative analysis reveals that effects of inertia and localized deformation of metal foams are two main causes to induce the strain rate sensitivity of metal foams.

Keywords: Metal foams, Strain rate effect, Inertia, Localized deformation, 3D Voronoi model

### Introduction

Metal foams, as light-weight and highly effective energy absorption materials, are widely employed as protective materials to resist impact loading (Gibson1997). With the development and application of metal foams, an accurate measurement of its dynamic properties become especially important. A split Hopkinson pressure bar (SHPB) (Kolsky1949) is the most common device to measure dynamic properties, with which the characteristic of compression deformation, energy absorption and strain rate sensitivity of metal foams have been intensively investigated. However, the experimental results showed that strain rate effect of metal foams were inconsistent and divided into two categories: the apparent strain rate sensitivity (Mukai1999, Dannemann2000, Paul2000 and Mukai2006) and the independent strain rate sensitivity (Deshpande2000 and Hall2000). Under dynamic conditions, strain rate effect of metal foams have attributed to the effect of strain rate sensitivity of cell wall's materials (Deshpande2000), micro-inertial effects (Paul2000, Deshpande2000 and Paul2000) and the effect of compressed air pressure in closed-cell foams (Gibson1997 and Deshpande2000). For these factors are too difficult and complex to be quantitatively measured in tests, which factor plays a vital role in strain rate sensitivity also is not clear yet.

A series of SHPB tests indicated the compressed deformation of metal foams were observed to be non-uniform (Tan2005, Cady2009, Edwin Raj2009 and Shen2010), especially in high speed impact tests. The strain distribution of aluminum foams were quantitatively analyzed and showed the maximum localized strain can be more than 100% greater than the average values, specially the maximum strain occurred on the front end of specimens under middle and high speed impact tests (Yang2013). SHPB technique is based on the assumption of one-dimensional wave propagation and stress equilibrium in the bars, which is simply assumed that uniform deformation occurred on specimens. However, the tests results showed that the deformation of metal foams were not well satisfied the assumptions of SHPB under dynamic conditions. The obviously localized deformation will likely affect the results.

For complexity of dynamic tests and micro-structure of metal foams, analysis of mechanisms of strain rate effect, especially quantitatively analysis, will be a challenge and significance. In present work, we have carried out numerical simulation by FEM, in which metal foams were simulated

with 3D Voronoi models, to analyze the mechanisms of strain rate effect of metal foams during split Hopkinson pressure bar tests.

### Numerical simulation

Meso-structures of metal foams, as shown Figure.1, with the characteristic of random spatial distribution, are very complex. For an excess of units and complex contact properties, it is too difficult to build the finite element model of metal foams according to the real meso-structure, especially in 3D FE models. In order to retain the main characteristic of random porous structure with controlled porosity, meso-structures of metal foams were constructed using Voronoi models, shown in Figure.2. The macro-scale dimension of both Voronoi specimen and solid specimen in simulation were set as diameter of 35 mm and length of 17.5 mm. There are about 1200 pores in the Voronoi model, which was constructed using the method as Yang (Yang2013), with the average pore diameter of 3mm and porosity of 80%. For purpose of comparison, a solid specimen with the same size as Voronoi model was constructed. SHPB models were carried out according to real device to keep the characteristic of stress wave propagation in bars. The striker bar, incident bar and transmission bar included in SHPB were set as diameter of 37 mm, length of 1600 mm, 8000 mm and 4000 mm, respectively.

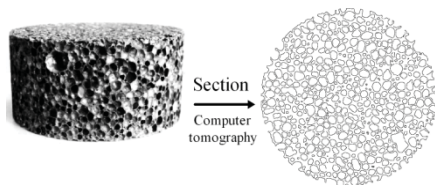


Figure.1 Section of Aluminum foams

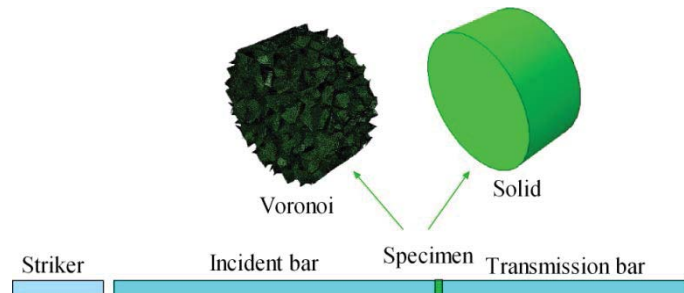


Figure.2 SHPB model and specimens model

The FE analysis was performed on ABAQUS explicit. Figure. 2 shows the FE models for the whole testing system. The cell walls of Voronoi specimen were modeled using general-purpose shell element (S4R) with edge length less than 0.4 mm. Eight nodes solid element with edge length of 4 mm was used for the strike, incident bar and transmission bar. A general-contact interaction was set among the parts. In order to learn the mechanism of strain rate of the metal foam clearly, the material of cell walls is assumed to be no sensitive to the strain rate. Table 1 lists the mechanical properties of Voronoi foams and Hopkinson bars. The material is considered as an elastic-plastic material with little hardening.

Table 1. Material properties in simulation

Material	Elastic modulus	Density [kg/m <sup>3</sup> ]	Poisson's ratio	Yield stress	Hardening modulus
Bulks (bars)	70 GPa	2.7e3	0.	-	
Cell walls (foams)	70 GPa	2.7e3	0.33	50MPa	40MPa

### Results and discussion

Five different compressed speeds of specimens were carried out to study strain rate effect of metal foams. The impact speed of striker bar is from 10m/s to 70m/s, corresponding strain rate range 514/s to 3744/s in Voronoi specimen. When radial deformation overflowed the section of bars, the test results would be invalid. Hence, the impact speed of striker bar was restricted in a narrow range from 10m/s to 50m/s, corresponding strain rate range 300/s to 2439/s, on the solid specimen tests. Simulation results, as shown in Figure.3, indicated that there are some strain rate sensitivity occurred on Voronoi specimens and absence on solid specimens.

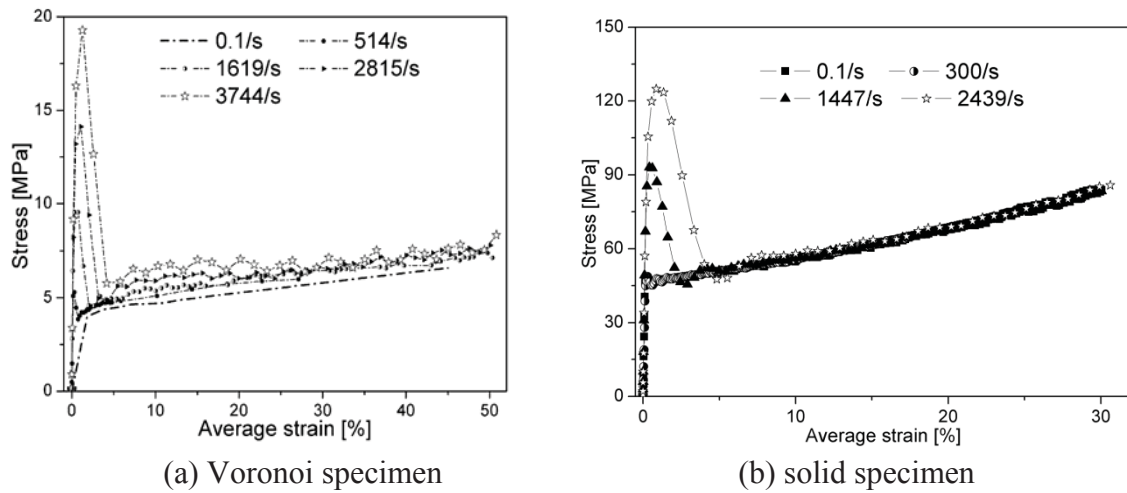


Figure.3 Stress-strain curve of specimens under different impact speed

Four factors as strain rate sensitivity of cell walls' material, micro inertia, air compressed pressure and localized deformation would affect the strain rate sensitivity of specimen. In these models, there is no strain rate sensitivity on matrix and no air compressed pressure. Hence, it just needs to consider the effect of inertia and localized deformation. With the observation of deformation of both Voronoi and solid specimens, it is found there are non-uniform deformation on Voronoi specimen, the concentration of strain occurred on one end or both ends and substantially uniform deformation on solid specimen. For the effect of inertia, there are some peaks on the initial stage of curves as shown Figure.3. The strain-stress curves of solid specimen aligned with each other after the peaks, while the curves of Voronoi specimen are different and still showed some strain rate sensitivity. For the existence of pores, localized deformation of Voronoi specimen is much different to that of solid specimen, which also led to different performance of strain rate sensitivity. In this work, we can extract stress of bar ends directly and then analyzed the relationship between stress of bar ends and average strain of Voronoi specimen, as shown in Figure.4. The performance of strain rate sensitivity on the incident bar end is obvious, while that of transmission bar end is absence. For the obviously different performance of strain rate sensitivity on bar ends, the effect of inertia of cell wall and localized deformation on the ends of Voronoi specimens were further analyzed.

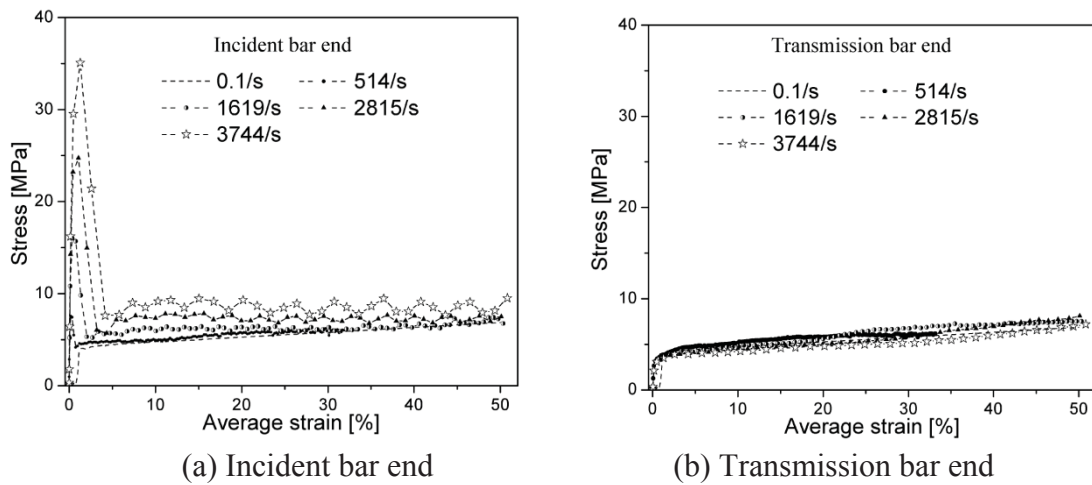


Figure.4 Stress-strain curves of Voronoi specimen

The performance of inertia which is resistance of changes specimen momentum or particle motion state, can be expressed as the acceleration of cell walls:

$$\sigma_a = \frac{F_a}{A_0} = \frac{\sum m_i a_i}{A_0} \quad (1)$$

where,  $m_i$  represents basic unit quality of Voronoi specimen,  $a_i$  represents corresponding axial acceleration,  $A_0$  represents the initial area of specimen. Voronoi specimen was divided into eight equal parts to analyze the effect of inertia and localized deformation. The effect of inertia on the front part and the back part were assumed to represent the effect of inertia to incident bar end and transmission bar end, respectively.

Figure.5 shows the effect of inertia on both incident bar end and transmission bar end. The effect of inertia on incident bar end is great and that on transmission bar end can be neglect, which agree with the experimental observation by high-speed photography(Yang2013) : there is no obvious movement occurred in the transmission bar under first impact in SHPB tests.

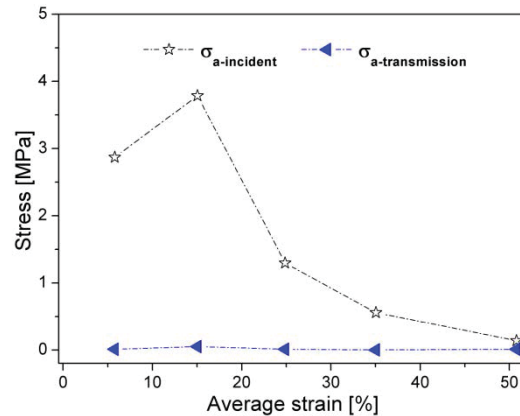


Figure.5 Effect of inertia on bar ends (3744/s)

The spatial distribution of strain of Voronoi specimen under impact is non-uniform, especially on the end of specimen, as shown in Figure.6 (a). Localized strain of the front end of specimen is always much greater than average strain of specimen under high -speed impact tests. While the localized strain of the back end of specimen is little lower than average strain at the first stage of curves (shown in Figure.6(a)) and become greater than average strain when average strain is more than 25%. With the increasing of impact speed, lower localized strain occurs on the back of specimen at the first stage of curves, which is consistent with the finding of Yang (Yang2013). Localized strain is much different from average strain of specimen, which may means that the stress is also non-uniform. Unfortunately, strain rate sensitivity was discussed only according to the relationship between stress and average strain of specimens. Figure.6(b) shows the stress-strain curve under quasi-static test (0.1/s). Under SHPB impact tests, when localized strain B is greater than average strain of specimen, corresponding stress B is greater, it will show "positive strain rate sensitivity", on the other hand, localized strain A is lower than average strain, it will show "negative strain rate sensitivity". This can explain some confusing relationship between stress and average strain, the stress under greater impact speed is little lower, under different impact speed test on the transmission bar end.

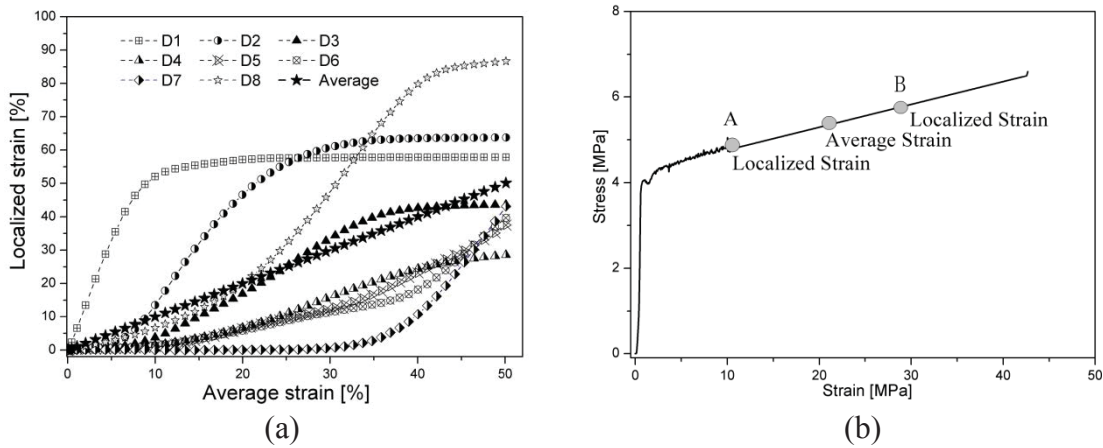


Figure.6 Relationship between localized strain and average strain

To quantitatively analyze the performance of strain rate sensitivity, it can be described as the difference of stress corresponding to the same strain under different strain rates (set benchmark as quasi-static (0.1/s) result). Based on numerical simulation, the effect of inertia and localized deformation on the performance of strain rate sensitivity could be quantitatively measure. Table.1 illustrates the relationship between strain rate sensitivity and the effect of inertia and localized deformation on the ends of specimen under different strain rates. The quantitatively results shows that the performance of strain rate sensitivity is approximately equal to the sum of the effect of inertia and localized deformation. It means that effect of inertia and localized deformation are the primary cause of the strain rate sensitivity under the condition of cell wall material with no strain rate sensitivity.

Table.1 Relationship between strain rate sensitivity and effect of inertia and localized deformation

Imposed strain rate [ $s^{-1}$ ]	Incident bar end							
	2815				3744			
Average strain [%]	5.4	15.6	25.3	35.8	5.8	15	24.8	35
Localized strain [%]	35.5	59.6	63.5	64.2	36.6	67.9	71.8	72.5
Effect of inertia [MPa]	1.1	0.2	0	0	2.9	1.3	0.3	0
Effect of localized deformation [MPa]	1.5	2.3	2	1.3	1.6	2.7	2.4	2
Performance of strain rate sensitivity [MPa]	2.6	2.8	1.9	1.2	4.4	4.1	3	1.8
Imposed strain rate [ $s^{-1}$ ]	Transmission bar end							
	2815				3744			
Average strain [%]	5.4	15.6	25.3	35.8	5.8	15	24.8	35
Localized strain [%]	1	10.7	26	50	1.6	6.2	14.9	29.5
Effect of inertia [MPa]	-	-	-	-	-	-	-	-
Effect of localized deformation [MPa]	-0.5	-0.3	0	0.6	-0.5	-0.5	-0.5	-0.4
Performance of strain rate sensitivity [MPa]	-0.4	-0.2	-0.1	0.5	-0.5	-0.4	-0.6	-0.5

### Conclusions

In the present paper, the FE model, using 3D Voronoi model simulated meso-structure of metal foams, was built to study the performance of strain rate sensitivity under different impact speeds (or strain rates). The numerical results indicated that metal foams show some strain rate sensitivity even under the condition of cell walls' material with no strain rate sensitivity, which was attributed to the effect of inertia and localized deformation. The performance of strain rate sensitivity on incident bar

end and that on transmission bar end are very different: obvious strain rate sensitivity on incident bar end and absence of strain rate sensitivity on transmission bar end. Therefore, different data processing method during SHPB tests may be a cause of controversy on the existing literature.

## Acknowledgements

This work was financially supported by the National Natural Science Foundation of China (Grant No. 90916026, 11202081, 11272124) and State Key Laboratory of Subtropical Building Science (2012ZC24).

## References

- Cady, C. M., Gray, G. T. and Liu, C. (2009), Compressive properties of a closed-cell aluminum foam as a function of strain rate and temperature. *Materials Science and Engineering a-Structural Materials Properties Microstructure and Processing*, 525, pp.1-6.
- Dannemann, K. A. and Lankford, J.(2000), High strain rate compression of closed-cell aluminium foams. *Materials Science and Engineering a-Structural Materials Properties Microstructure and Processing*, 293(1-2), pp. 157-164.
- Deshpande, V. S. and Fleck, N. A.(2000), High strain rate compressive behaviour of aluminium alloy foams. *International Journal of Impact Engineering*, 24(3), pp. 277-298.
- Edwin Raj, R., Venkitanarayanan Parameswaran and Daniel, B.S.S. (2009), *Comparison of quasi-static and dynamic compression behavior of closed-cell aluminum foam*. *Materials Science and Engineering a-Structural Materials Properties Microstructure and Processing*, 2009. 526(1-2): p. 11-15.
- Gibson, L. J. , Ashby, M. F. (1997), *Cellular solids: structure and properties*, second ed. *Cambridge University Press, Cambridge*.
- Hall, I. W., Guden, W. and Yu, C. J. (2000), Crushing of aluminium closed cell foams: density and strain rate effect. *Scripta Materialia*, 43, pp.515-521.
- Kolsky, H.(1949), An investigation of the mechanical peoperties of materials at very high rates of loading. *Proceedings of the Physical Society. Section B*, 62, pp. 676.
- Mukai, T., Miyoshi, T., Nakano, S., Somekawa, H., and Higashi, K.(2006), Compressive response of a closed - cell aluminum foam at high strain rate.*Scripta Materialia*, 54(4), pp. 533-537.
- Mukai, T., Kanahashi, H., Miyoshi, T., Mabuchi, M., Nieh, T.G., and Higashi, K.(1999), Experimental study of energy absorption in a close-celled aluminum foam under dynamic loading. *Scripta Materialia*, 40(8), pp. 921-927.
- Paul, A. and Ramamurty, U.(2000), Strain rate sensitivity of a closed-cell aluminum foam. *Materials Science and Engineering a-Structural Materials Properties Microstructure and Processing*, 281(1-2), pp. 1-7.
- Shen, J. H., Lu, G. X. and Ruan, D. (2010), Compressive behaviour of closed-cell aluminium foams at high strain rates. *Composites part B: Engineering*, 528(6), pp.2326-2330.
- Tan, P.J., Reid, S.R., Harrigan, J.J., Zou, Z. and Li, S. (2005), Dynamic compressive strength properties of aluminum foams. Part II- ‘shock’ theory and comparison with experimental data and numerical models. *Journal of the Mechanics and Physics of Solids*,53(10), pp.2206-2230.
- Yang, B., Tang, L.Q., Liu, Y.P., Liu, Z.J., Jiang, Z.Y. and Fang, D.N. (2013), Localized deformation in aluminium foam during middle speed Hopkinson bar impact tests. *Materials Science and Engineering a-Structural Materials Properties Microstructure and Processing*,560, pp.734-743



## Experimental Study on High Damping Polymer Concrete

\*HUA Jianmin<sup>1,2</sup>, HU Zhimao<sup>1</sup>, CAO Hui<sup>1,2</sup>, ZHENG Xing<sup>1</sup>

<sup>1</sup>College of Civil Engineering, Chongqing University, Chongqing 400045, China;

<sup>2</sup>Key Laboratory of New Technology for Construction of Cities in Mountain Area (Chongqing University), Ministry of Education, Chongqing 400045, China.

\*Corresponding author: huajianmin@cqu.edu.cn

### Abstract

The damping performance of concrete can be improved when mixed with polymer. In this paper, the standard test methods were used to compare mechanical properties and durability between polymer concrete and ordinary concrete. Vibration tests and fatigue experiments were carried out with two prestressed simple beams respectively made by polymer concrete and ordinary concrete. The loss factors of ordinary cement mortar and polymer cement mortar were measured by using dynamic viscoelastometer, and they were also analyzed by scanning electron microscope. The experimental results show that the flexural strength, splitting tensile strength and durability of the polymer concrete are higher than those of ordinary concrete. The elastic modulus and compressive strength of the former decrease slightly but yet meet the requirement of code. The loss factor of polymer cement mortar is higher than that of the ordinary cement mortar, due to the reticular formation of the polymer. The damping ratio of the polymer concrete beam is significantly greater than that of ordinary concrete beam, and their fatigue performance are similar.

**Key words:** polymer concrete, high damping, mechanical properties, durability, fatigue performance

### Introduction

At present, high-speed railway is playing an increasingly important role in the fast-growing Chinese economy. The technology involved, however, has been proven to be challenging. Trains travelling in high-speed cause more bridge vibration than those in normal speed. Consequently, enhancing structural resistance to vibration has become the focus of recent studies. Since 1990s, researchers around the globe have been dedicating themselves to improve the property of concrete by means of adding macromolecular material, for instance: a series of studies have been conducted by Prof. Chung and his team to improve the damping property and stiffness of cement paste (Fu and Chung, 1996; Li and Chung, 1998; Wen and Chung, 2000). Reference (Amick and Monteiro, 2005) reviewed the application of polymer concrete for vibration mitigation in mechanical and optical engineering. Reference (Cao et al, 2011) provided a means of increasing the damping ratio of concrete by adding carboxylic styrene butadiene latex (CSBL). Reference (Liu and Ou, 2003a; Liu and Ou, 2003b; Liu and Zhou, 2008) improved the loss factor of cement mortar and analyzed its microscopic mechanism by using scanning electron microscopy (SEM). Reference (Yao et al, 2005) pointed out that the mechanical performance and wearing resistance of concrete modified by CSBL are much better. Wan (2005) succeeded in improving the crush resistance of concrete by adding CSBL.

On the basis of previous work (Cao et al, 2011), the authors prepared polymer concrete in line with both construction and mechanical requirement by using materials of different origin, and conducted analysis that follow: comparison of damping and fatigue properties between normal and polymer concrete; durability tests, such as the property of polymer concrete to resist permeability,

carbonization, shrinkage and early cracking; micro-structure analysis by using SEM.

### Raw material and mix ratio adopted in the experiment

Ordinary Portland cement manufactured by YA DONG CEMENT CORPORATION LIMITED; Water consumption of standard consistency: 25.6%; 28d compressive strength: 43.2 MPa; Coal ash: manufactured by YONG SHUN in Jiangyou, (water requirement ratio: 88%); Gravel: machine-made coarse gravel (maximum diameter: 30mm), continuous grading; Water reducing agent: catalytic high efficiency water reducing agent; Polymer emulsion: CSBL (SD622S) manufactured by BASF in Gaoqiao, Shanghai (solid content: 47%; film-forming temperature: 11°C); Cement mix ratio is in line with the standard of C60: 1:2.52:2.82:0.36. Workability is shown in Table 1. Cement-mortar proportion is shown in Table 2. SD00: cement without any polymer; SD15: cement with 15% polymer; SJ00: cement mortar without any polymer; SJ15: cement mortar with 15% polymer;

**Table 1 Workability of the specimen**

Indicators of workability	Slump (mm)	Expansion (mm)
SD00	195	600
SD15	240	590

**Table 2 Cement-mortar proportion**

NO.	Water-cement ratio	Polymer-cement ratio	Fluidity
SJ00	0.42	0	243
SJ15	0.32	15	242

### Mechanical property experiments

Mechanical properties including cube strength (CS), static compressive strength elasticity modulus (SC), bending strength (BS) and splitting tensile strength (SS) were tested in accordance with the standards regulated in reference (National Standard of the People's Republic of China, 2002). Trial cube sizes for each test are as follow: CS: 150mm×150mm×150mm ; SC: 150mm×150mm×300mm; BS: 100mm×100mm×400mm; SS: 150mm×150mm×150mm. Results are shown in Table 3:

**Table 3 Mechanical properties**

NO.	CS (MPa)	SC (GPa)	BS (MPa)	SS (MPa)
S00	68.4	38.49	6.13	4.51
S15	61.5	37.01	7.2	4.65

As indicated in Table 3, the presence of polymer results in a slight decrease in both cube strength and elasticity modulus, which still meets the requirement of C60 concrete. Table 3 also indicates an improvement in bending and splitting tensile strength.

## Durability experiments

Durability properties including permeability, chloride ion permeation, carbonization, shrinkage and early cracking were tested in accordance with the standards regulated in reference (National Standard of the People's Republic of China, 2009).

### *Water permeability resistance test*

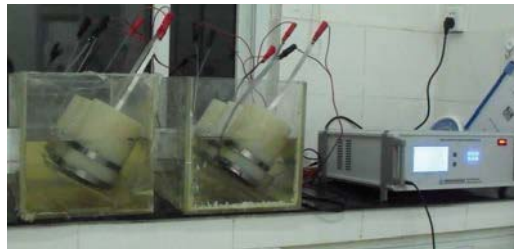
The test was conducted by using concrete permeability automatic recording instrument and graduated compression method. Specimens were prepared in the shape of truncated cone (top diameter: 175mm; bottom diameter: 185mm; height: 150mm). At the end of compression process, neither SD00 nor SD15 shows any signs of leakage.



**Fig 1 Concrete permeability automatic recording instrument**

### *Chloride ion permeation resistance test*

The test was conducted by using RCM method and chlorine ion diffusion coefficient meter (see Fig 2). Specimens were prepared in cylinder shape (height: 50mm; diameter: 100mm). Test results after maintenance 28d in standard conditions are shown in Table 4.



**Fig 2 Test device**

**Table 4 Chloride ion diffusion coefficient**

NO.	SD00	SD15
$D_{RCM}$ ( $\times 10^{-12}$ $m^2/s$ )	4.2316	2.3707

### *Carbonization test*

The test was conducted by using carbonization chamber ( $CO_2$  concentration:  $20\pm 3\%$ ; humidity:  $70\pm 5\%$ ; temperature:  $20\pm 5^\circ C$ ). Test results are shown in Table 5.

**Table 5 Carbonization depth (mm)**

NO.	3d	7d	14d	28d
SD00	2.2	3	3.7	6.8
SD15	0	0	0	0

### Early cracking resistance test

This test was designed to find out the property of concrete to resist early cracking under restrains. Test mold is made 800mm×600mm×100mm with all four sides welded with channel steels and fixed on a bottom slab with bolts. 7 stress-triggered risers made of angle bars (50mm×50mm, 40mm×40mm) and steel slabs (5mm×50mm) are fixed on the bottom slab and parallel with the short side of mold.

According to observation, reference concrete shows two visible penetrating cracks and a number of minute cracks on the surface. Polymer concrete shows two visible penetrating cracks and two smaller crack on the surface. Test results are shown in Table 6.

**Table 6 Plate anti-cracking test results**

NO.	Average cracking area (mm <sup>2</sup> /crack)	Number of cracks on unit area (crack/m <sup>2</sup> )	Total cracking area on unit area (mm <sup>2</sup> /m <sup>2</sup> )
S00	10.2	12.5	127.5
S15	9.4	8.3	77.9

### Shrinkage test

Shrinkage tests include contact and non-contact approaches. The latter is mainly adopted for free shrinkage of early age concrete, whereas the former is for long term shrinkage. Non-contact test was done by using concrete shrinkage measuring instrument developed by China Academy of Building Research, which is capable of yielding accurate value of early shrinkage. Contact test was done by using horizontal concrete shrinkage device with an accuracy of 0.001mm. The trial cubes were prepared in 100mm×100mm×515mm. Test environment: constant temperature (room temperature: 20±2°C) and humidity (relative humidity: 60±5%);

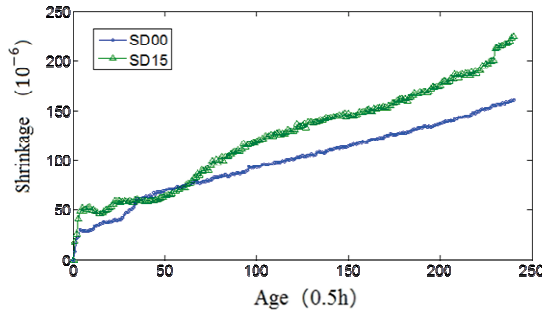


**Fig 3 Non-contact concrete shrinkage test**

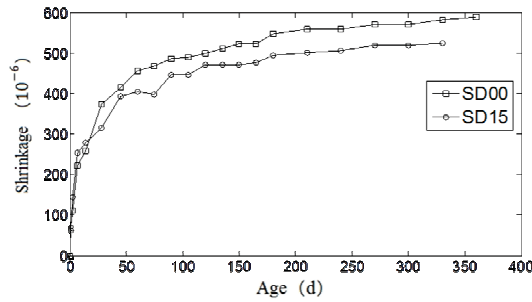


**Fig 4 Contact concrete shrinkage test**

Early shrinkage test collected data of 120 hours. Shrinkage rates are shown in Fig 5. Polymer concrete shows higher rate of early shrinkage but kept within  $225 \times 10^{-6}$  at the scale of 120 hours. Shrinkage rate at age 1d, 3d, 7d, 14d, 28d, 45d, 60d till 330d. Results are shown in Fig 6.



**Fig 5 Early shrinkage**



**Fig 6 Long time shrinkage**

According to the test results, conclusions can be drawn that polymer concrete shows: better properties in terms of permeability and early cracking resistance; better chloride ion permeation resistance (78% higher than regular concrete); no signs of carbonization 28 days after the test which indicates a strong property of resistance; slightly higher early shrinkage rate than regular concrete but lower rate after 45d.

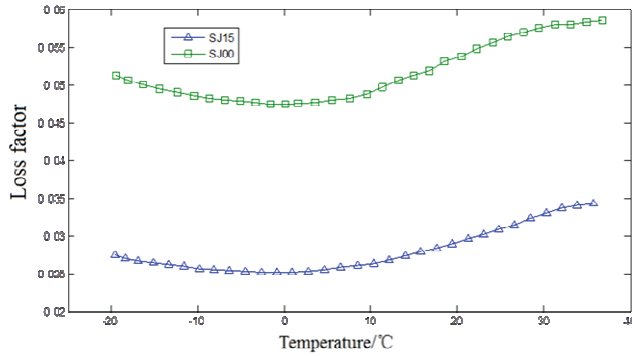
**Cement mortar damping test**

CSBL is a polymer material, the most significant feature of which is viscoelasticity. The damping mechanism of polymeric material is directly related to its dynamic mechanical relaxation properties. The mechanical part of vibrational energy absorbed by polymeric material is dissipated in the form of heat, through which damping is achieved. Damping property of a material can be expressed with loss factor as shown in Equation (1):

$$\eta = D / 2\pi W = E'' / E' 10^{-6} \mu\mu\epsilon \tag{1}$$

In Equation (1),  $E''$  =loss modulus,  $E'$  =storage modulus.

By using dynamic mechanical analyzer (DMA-Q800) and dual cantilever beam method, motar cubes (40mm×10mm×5mm) were tested for its loss factor (temperature: -20<sup>0</sup>C-40<sup>0</sup>C; frequency: 1HZ-10HZ ). Comparison indicates that the loss factor of SJ00 and SJ15 exhibit similar trend on 1HZ, 3HZ, 5HZ, 10HZ and decreases in order (10HZ: the lowest; 1HZ: the highest ). Loss factor comparison on 10HZ is shown in Fig 7.

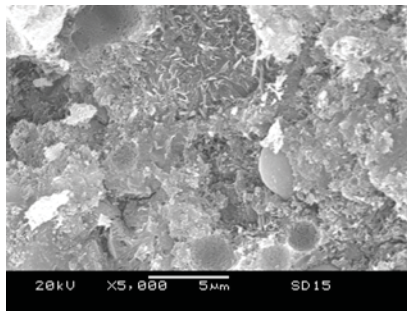


**Fig 7 Dissipation modulus on 10 HZ of SJ00 and SJ15**

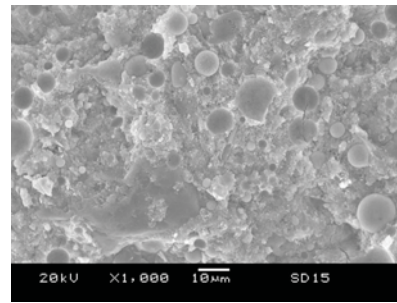
As indicated in Fig 7, the presence of polymer doubled cement mortar’s loss factor which means a great increase of damping property.

**SEM test**

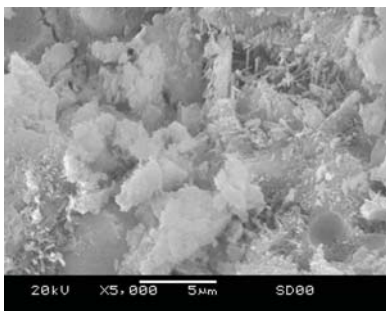
The test was done by using JSM-5900LV. A small gilded section of 28d cement mortar was chosen for SEM analysis. Results are shown in Fig 8.



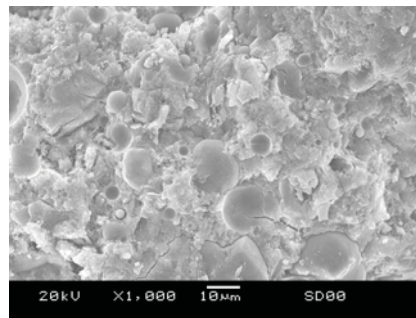
**(a) SJ15 5,000x magnification SEM**



**(b) SJ15 1,000x magnification SEM**



**(c) SJ00 5,000x magnification SEM**



**(d) SJ00 1,000x magnification SEM**

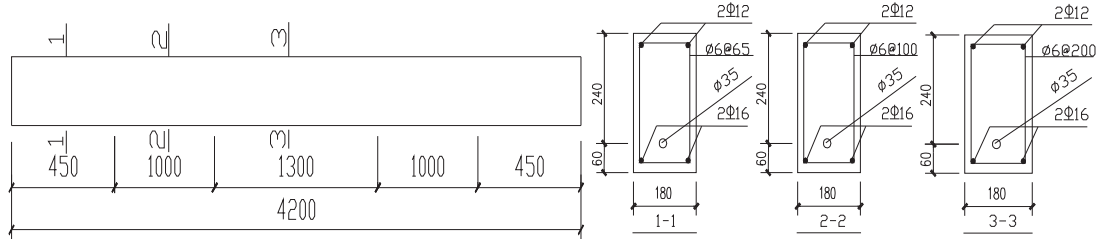
**Fig 8 SEM results**

As indicated in both 1,000x and 5,000x magnification SEM: fibrous C-S-H of regular cement mortar crosslinks with acicular ettringite crystal, forming discontinuous and reticulated porous skeletal framework; cement mortar with polymer material is producing polymeric membrane, mingling with hydration products of cement and forming densely filled fluffy networks. Such structure is capable of dissipating part of the effects caused by vibrational load in the form of heat, which increases the damping property of cement.

**Fatigue test**

Test beam specifications are as follow, cross section: 300mm×180mm;length: 4200mm;actual span: 3900.

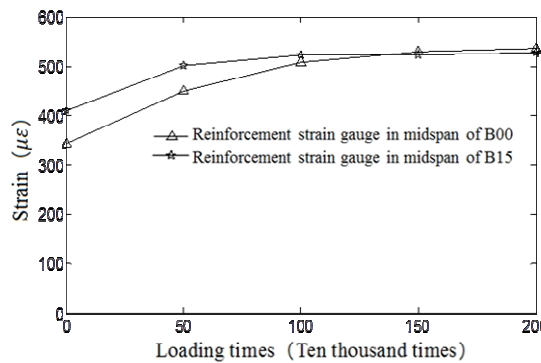
Beside regular reinforcement, lower part of the beam is equipped with linear prestressed tendons. The cross section and reinforcement are shown in Fig 9.



**Fig. 9 Experimental beam and cross section**

Fatigue test is conducted through third point loading. Upper loading limit equals to the cracking load of the beam, approximately 37kN; lower limit is 6kN ; loading frequency = 6.9Hz.

After 2,000,000 fatigue loading, neither B15 nor B00 were damaged. Cracking trend of both beams are similar: developing fast before 500,000 times loading cycles and stabled afterwards.



**Fig 10 Comparison of steel-strain of B00 and B15**

Fig 10 shows the strain pattern of regular steel reinforcements in reaction to fatigue loading. The strain of B00 and B15 increases fast before 500,000 loading cycles and slows down afterwards; very small strains are detected after 1,000,000 cycles; strains become very close to each other after 1,500,000 cycles. It is in line with the patter of cracking development: grows fast before 500,000 cycles and slows down afterwards. Accordingly, adding polymeric material has no impacts on strain development, and the fatigue property of polymer concrete is equal to regular concrete in normal application.

**Dynamic test**

The test was conducted by applying exciting hammer on the top of beam and 5 acceleration transducers (to record acceleration signals) were evenly distributed in the direction of length. The signals were analyzed by using stochastic subspace identification (SSI). SSI is a widely adopted technique, by which the recorded signals can be analyzed to obtain the structural dynamic characteristics, such as frequencies, mode shapes and damping. Comparing to other signal processing methods, SSI can use only the structural outputs to get useful dynamic information. SSI used here is one featuring reference-based data-driven. The details are referred to (Peeters and Roeck, 1999).

**Table 7 Damping ratio of B00 and B15**

Test beam	B00	B15
Damping Ration (%)	0.87	1.31

Table 7 shows the damping ratio of BD00 and BD15 (both intact) in the first vibration mode. Results indicate that the damping ratio of polymer concrete beam is 50% higher than regular concrete beam.

## Conclusions

Compared to regular concrete:

- 1) polymer concrete shows slightly lower property in terms of compressive strength and elasticity modulus, but higher rupture strength and tensile splitting strength.
- 2) Polymer concrete exhibits great improvement in terms of carbonization, chloride ion permeation and early cracking resistance. Its shrinkage is slightly higher in early age than regular cement, but lower after 45d.
- 3) The loss factor of cement mortar nearly doubled after adding polymeric materials. The dynamic test of prestressed rectangle simple beam indicates that polymeric materials are capable of greatly increase the damping ration of concrete.
- 4) SEM analysis shows that the compact reticular formation of polymer enfoldes cement hydrates, increasing its resistance to environmental erosion and damping property.
- 5) The fatigue test of prestressed rectangle simple beam shows that the fatigue property of polymer concrete is equal to regular concrete in normal application.

## References

- Amick H, Monteiro P J M (2005), Modification of concrete damping properties for vibration control in technology facilities. *Proceedings of the SPIE-The International Society for Optical Engineering*, 5933, pp.1-12.
- Cao H, Chen X H, Hua J M, Hu Z M (2011), Tests of Polymer Concrete Used for Structural Vibration Mitigation. *Journal of Vibration and Shock*, 5, pp.188-191. (in Chinese)
- Fu X, Chung D D L (1996), Vibration damping admixtures for cement. *Cement and Concrete Research*, 26(1), pp. 69-71.
- Li X, Chung D D L (1998), Improving silica fume for concrete by surface treatment. *Cement and Concrete Research*, 28(4), pp. 493-498.
- Liu P, Zhou W M (2008), Experimental Study on Damping Property of Polymer Cement. *Building Technique Development*, 35(7), pp. 26-28. (in Chinese)
- Liu T J, Ou J P (2003a), Study on Polymer Cement Mortar Damping Property. *New Building Materials*, (4), pp. 7-9. (in Chinese)
- Liu T J, Ou J P, L J H (2003b), Effects of Silane-treated Silica Fume on Damping Property of Cement Mortar. *Journal of the Chinese Ceramic Society*, 31(11), pp. 1125-1129. (in Chinese)
- National Standard of the People's Republic of China. (2002), Standard for Test Methods of Mechanical Properties of Ordinary Concrete (GB/T 50081-2002). Beijing: China Architecture & Building Press. (in Chinese)
- National Standard of the People's Republic of China. (2009), Standard for Test Methods of Long-term Performance and Durability of Ordinary Concrete (GB/T 50082-2009). Beijing: China Architecture & Building Press. (in Chinese)
- Peeters B, Roeck G D (1999), Reference-based stochastic subspace identification for output-only modal analysis [J]. *Mechanical Systems and Signal Processing*, 13(6), pp.855-878



- Wen S H, Chung D D L (2000), Enhancing the vibration reduction ability of concrete by using steel reinforcement and steel surface treatments, *Cement and Concrete Research*,30(2), pp. 327-330.
- Wan Z Q (2005), Experimental Research and Application of High Damping Concrete in Structural Energy Dissipation and Vibration Mitigation. Master's thesis of Yangzhou University. (in Chinese)
- Yao H Y, Liang N X, Sun L J, et al. (2005),Property Study of SD622S Polymer Modified Concrete and the Analysis of Modification Mechanism. *Journal of Building Materials*, 8(1), pp. 30-36. (in Chinese)

## A new assumed strain beam element based on a sixth-order beam theory for static and dynamic analysis of composite beams

Xiaodan Wang<sup>1</sup>, \*Guangyu Shi<sup>1</sup>

<sup>1</sup> Department of Mechanics, Tianjin University, Tianjin 300072, China

\*Corresponding author: shi\_guangyu@163.com

### Abstract

An accurate, efficient and reliable two-noded beam element is presented in this paper for the static and dynamic analysis of laminated composite beams. The element formulation is based on the quasi-conforming element technique and a new sixth-order beam theory proposed by the second author in which the average rotation of beam cross-section is employed as the independent field variable instead of the rotation at the beam midplane used in other higher-order beam theories. The element stiffness matrix of the resulting beam element is given explicitly; consequently it is very computationally efficient. Furthermore, this new shear flexible beam element exhibits higher accuracy than the conventional shear flexible beam elements, as it possesses a linear bending strain field although there are only three nodal parameters associated with bending deformation at each node. Both static and dynamic analyses of laminated composite beams with different aspect ratios and boundary conditions are solved. The numerical results clearly demonstrate that the present composite beam element is not only efficient and locking free but also very accurate. The free vibration analysis of composite beams also indicates that the use of the average rotation of the beam cross-section improves the prediction accuracy of the higher-mode flexural frequencies.

**Keywords:** Shear flexible beam element, Sixth-order beam theory, Quasi-conforming element technique, Composite beam, Higher-mode flexural vibration

### Introduction

Laminated composite beams are widely used in various engineering structures because of the high specific stiffness and high strength. The transverse shear deformations play an important role in the analysis of composite beams. Various shear deformable beam theories and shear flexible beam elements have been proposed for the static and dynamic analyses of composite beams in the past few decades (Kapania and Raciti, 1989; Chandrashekhara and Bangera, 1993; Shi *et al.*, 1998, 1999; among others). The theoretical and numerical modeling of composite beams is still attracting many researchers' attention even today (Carrera and Giunta, 2010; Feng *et al.*, 2012). Among all the refined beam theories, the simple third-order shear deformation beam theory presented by Bickford (1982) or reduced from Reddy plate theory (1984) is very attractive in the finite element modeling of composite beams, as it does not need the shear correction factors and the warping of the cross-section can be accounted for to a certain extent.

Shi and Voyiadjis (1991) demonstrated that the assumed strained method what is based on the quasi-conforming element technique (Tang *et al.*, 1980) is a very efficient approach to formulate the shear flexible arch/beam elements and shell elements, since the resulting elements are not only free from shear locking, but also free from the time consuming numerical integration. Shi *et al.* (1998, 1999) presented efficient and accurate two-noded composite beam elements based on the third-order shear deformation beam theory. The composite beam elements developed by Shi *et al.* (1998, 1999) yield accurate results for the static analysis and the lower-mode frequencies of flexural

vibration of composite beams. However, the accuracy of the predicted higher-mode frequencies, e.g. the fourth and fifth-mode frequencies, is not good enough (Shi and Lam, 1999).

Hutchinson (1986) studied the influence of the different definition of the rotation variable used in plate theories on the accuracy of higher-mode frequencies of the clamped plates. Hutchinson showed that the plate theory in which average rotation across the plate thickness is used can correctly predict both the fundamental natural frequency and the higher-mode frequencies of the clamped plates, but the theory in which the midplane rotation is used can only give the correct solutions of the first and second natural frequencies, but predicts physically impossible results for the third and fourth natural frequencies. Shi and Voyiadjis (2011) proposed a beam theory with the sixth-order differential equations (for bending only) based on a refined third-order transverse shear function which is similar to that used in Bickford beam theory. However, one major difference of this new beam theory from other higher-order beam theories is that the averaged rotation of the beam cross-section is defined as a displacement variable as opposed to the rotation measured at the beam midplane used in other higher-order beam theories. Wang and Shi (2012) demonstrated that this new sixth-order beam theory is not only accurate but also capable of predicting correct boundary layer solutions at the locations with displacement boundary conditions.

The objective of this paper is to present a new composite beam element with the averaged rotation of beam cross-section as one of the nodal degrees of freedom by using the sixth-order beam theory proposed by Shi and Voyiadjis (2011) and the quasi-conforming element technique. The resulting two-noded beam element is not only free from the shear locking, but also free from the numerical integration. Both static and dynamic analyses of composite beams with various aspect ratios and boundary conditions are solved here to evaluate the accuracy and reliability of the new composite beam element. The results of numerical examples show that the sixth-order beam theory proposed by Shi and Voyiadjis (2011) can yield more accurate results, especially the higher-mode flexural frequencies of composite beams than Bickford beam theory.

### **The static analysis of finite element formulation of composite beams based on the sixth-order beam theory**

The new finite element formulation of composite beams is based on the sixth-order beam theory proposed by Shi and Voyiadjis (2011), which has been proved a high efficiency and accuracy sixth-order theory in both static and dynamic analysis.

#### *Displacement fields and strains of shear deformable beams*

The displacement field in the sixth-order beam theory proposed by Shi and Voyiadjis (2011) is of the form

$$u(x, z, t) = u_0(x, t) - z\left(\frac{\partial w_0}{\partial x} - \gamma\right) + (\alpha z - \beta z^3)\gamma, \quad w(x, z, t) = w_0(x, t) \quad (1)$$

where  $u_0$  and  $w_0$  are the axial displacement and the deflection of a point on the beam reference plane respectively;  $\bar{\phi}_x$  is the averaged rotation of the beam cross-section through the beam thickness;  $\gamma$  is the transverse shear strain of the beam cross-section;  $h$  is the beam thickness;  $\alpha = 1/4$  and  $\beta = 5/(3h^2)$ . The transverse shear strain  $\gamma$  takes the form

$$\gamma = \frac{\partial w_0}{\partial x} + \bar{\phi}_x \quad (2)$$

It follows from Eq. (1) that the normal strain and the transverse shear strain under consideration take the form

$$e_x = e_m - ze_b + (\alpha z - \beta z^3)e_{hs}, \quad 2e_{xz} = \left(\frac{5}{4} - \frac{5z^2}{h^2}\right)e_s \quad (3)$$

with

$$e_m = \frac{\partial u_0}{\partial x}, \quad e_b = \frac{\partial^2 w_0}{\partial x^2} - \frac{\partial \gamma}{\partial x}, \quad e_{hs} = \frac{\partial \gamma}{\partial x}, \quad e_s = \gamma \quad (4)$$

The expression of strains above results in a  $C^1$ -continuity element under the displacement-based formulation. The strains in Eq. (4) are the functions of the deflection and transverse shear deformation. Corresponding to the strains defined in Eq. (4), the simplest nodal degrees of freedom at node  $i$ ,  $\mathbf{q}_i$  can be chosen as

$$\mathbf{q}_i = [u_{0i}, w_{0i}, \left(\frac{\partial w_0}{\partial x}\right)_i, \gamma_i]^T, \quad i = 1, 2 \quad (5)$$

The nodal variables in Eq. (5) result in a cubic approximation for deflection  $w_0$  and a linear transverse shear strain  $\gamma$ . Then Eq. (4) can give a linear element bending strain. Because the bending strain is the dominant term in bending problems, then in finite element analysis, the strain expressions derived from the displacement defined in Eq. (1) should lead to a more accurate solution than those higher-order beam theories which give a constant bending strain over an element, even though they have the same number of degrees of freedom at each node (Shi *et al.*, 1998).

#### Stiffness matrix of the sixth-order composite beam element

Now consider a straight beam of length  $l$  and rectangular cross-section with thickness  $h$  and width  $b$ . The strain energy density of the beam,  $U$  is of the form

$$U_e = \frac{b}{2} \int_l \int_{-h/2}^{h/2} (e_x Q_{xx} e_x + 4e_{xz} Q_{xz} e_{xz}) dz dx \quad (6)$$

where  $Q_{xx}$  and  $Q_{xz}$  are the longitudinal Young's modulus and transverse shear modulus respectively, and they are functions of  $z$ . Substituting Eqs. (3, 4) into Eq. (6) leads to

$$U_e = \frac{1}{2} \int_l [e_m A_{xx} e_m + e_b D_{xx} e_b + e_{hs} (\alpha^2 D_{xx} - 2\alpha\beta F_{xx} + \beta^2 H_{xx}) e_{hs} + \gamma S_{xx} \gamma - B_{xx} (e_b e_m + e_m e_b) + (\alpha B_{xx} - \beta E_{xx}) (e_m e_{hs} + e_{hs} e_m) + (\beta F_{xx} - \alpha D_{xx}) (e_b e_{hs} + e_{hs} e_b)] dx \quad (7)$$

in which

$$A_{xx}, B_{xx}, D_{xx}, E_{xx}, F_{xx}, H_{xx} = b \int_{-h/2}^{h/2} (1, z, z^2, z^3, z^4, z^6) Q_{xx} dz, \quad S_{xx} = b \int_{-h/2}^{h/2} \left(\frac{5}{4} - \frac{5z^2}{h^2}\right)^2 Q_{xz} dz \quad (8)$$

The element strains in Eq. (7) can be expressed in terms of the element nodal displacement  $\mathbf{q}$  and the element strain matrices as follows

$$e_m = \mathbf{B}_m \mathbf{q}_e, \quad e_b = \mathbf{B}_b \mathbf{q}_e, \quad e_{hs} = \mathbf{B}_{hs} \mathbf{q}_e, \quad \gamma = \mathbf{B}_s \mathbf{q}_e \quad (9)$$

Consequently, the strain energy in an element of length  $l$ ,  $\Pi_e$  takes the form

$$\begin{aligned} \Pi_e = & \frac{1}{2} \mathbf{q}_e^T \int_l [\mathbf{B}_m^T A_{xx} \mathbf{B}_m + \mathbf{B}_b^T D_{xx} \mathbf{B}_b + \mathbf{B}_{hs}^T (\alpha^2 D_{xx} - 2\alpha\beta F_{xx} + \beta^2 H_{xx}) \mathbf{B}_{hs} \\ & + \mathbf{B}_s^T S_{xx} \mathbf{B}_s - B_{xx} (\mathbf{B}_m^T \mathbf{B}_b + \mathbf{B}_b^T \mathbf{B}_m) + (\alpha B_{xx} - \beta E_{xx}) (\mathbf{B}_m^T \mathbf{B}_{hs} + \mathbf{B}_{hs}^T \mathbf{B}_m) \\ & + (\beta F_{xx} - \alpha D_{xx}) (\mathbf{B}_b^T \mathbf{B}_{hs} + \mathbf{B}_{hs}^T \mathbf{B}_b)] dx \mathbf{q}_e \end{aligned} \quad (10)$$

If we define element bending, membrane, transverse shear, higher-order shear and coupling stiffness matrix, respectively, as

$$\mathbf{K}_b = \int_l \mathbf{B}_b^T D_{xx} \mathbf{B}_b dx, \quad \mathbf{K}_m = \int_l \mathbf{B}_m^T A_{xx} \mathbf{B}_m dx, \quad \mathbf{K}_s = \int_l \mathbf{B}_s^T S_{xx} \mathbf{B}_s dx \quad (11a)$$

$$\mathbf{K}_{hs} = \int_l \mathbf{B}_{hs}^T (\alpha^2 D_{xx} - 2\alpha\beta F_{xx} + \beta^2 H_{xx}) \mathbf{B}_{hs} dx \quad (11b)$$

$$\mathbf{K}_c = \int_l -B_{xx} (\mathbf{B}_m^T \mathbf{B}_b + \mathbf{B}_b^T \mathbf{B}_m) + (\alpha B_{xx} - \beta E_{xx}) (\mathbf{B}_m^T \mathbf{B}_{hs} + \mathbf{B}_{hs}^T \mathbf{B}_m) + (\beta F_{xx} - \alpha D_{xx}) (\mathbf{B}_b^T \mathbf{B}_{hs} + \mathbf{B}_{hs}^T \mathbf{B}_b) dx \quad (11c)$$

Then the element stiffness matrix  $\mathbf{K}$  is of the form

$$\mathbf{K}_e = \mathbf{K}_b + \mathbf{K}_m + \mathbf{K}_s + \mathbf{K}_{hs} + \mathbf{K}_c \quad (12)$$

*Element strain matrix obtained from the quasi-conforming element technique*

In conventional displacement-based finite element formulation, the element strain matrices in Eq. (9) are obtained from the interpolated displacement function in the element. However, these matrices will be evaluated by the quasi-conforming element technique (Tang *et al.*, 1980) in this work. For a quasi-conforming element, the element strain field is interpolated directly over the element domain rather than differentiated from the assumed displacement field, and the compatibility in an element domain is satisfied in a weak form. Let a *prime* signify the assumed element strain field, then the element strain energy in Eq. (10) can be modified as

$$\Pi_e^* = \Pi_e + \int_l \tilde{M}(e_b - e_b') dx + \int_l \tilde{N}(e_m - e_m') dx + \int_l \tilde{Q}(e_s - e_s') dx + \int_l \tilde{P}(e_{hs} - e_{hs}') dx \quad (13)$$

where  $\tilde{M}$ ,  $\tilde{N}$ ,  $\tilde{Q}$  and  $\tilde{P}$  are the test functions corresponding to their relevant strains. A cubic displacement  $w_0$ , a linear transverse shear strain  $\gamma$  and a linear displacement  $u_0$  can be interpolated over the element from the element nodal variables. Then a suitable element strain field for the strains defined in Eq. (4) can be approximated as

$$e_b = \frac{d^2 w_0}{dx^2} - \frac{d\gamma}{dx} \approx e_b' = \alpha_{b1} + x\alpha_{b2}, \quad e_m = \frac{du_0}{dx} \approx e_m' = \alpha_m, \quad 2e_s = \gamma \approx 2e_s' = \alpha_s, \quad e_{hs} = \frac{d\gamma}{dx} \approx e_{hs}' = \alpha_{hs} \quad (14)$$

where  $\alpha_{bi}$  ( $i=1, 2$ ),  $\alpha_m$ ,  $\alpha_s$  and  $\alpha_{hs}$  are the assumed element strain parameters which can be determined from the weak form of compatibility given in Eq. (13) at element level. A linear bending strain is assumed here which is corresponding to the cubic deflection  $w_0$  given by the element nodal displacements. The assumed constant transverse shear strain in Eq. (14) is one order lower than the interpolation given by the two nodal shear strain variables, which is equivalent to the reduced integration in the displacement-based formulation. In the quasi-conforming element formulation,  $2e_s$  and  $e_{hs}$  can be approximated independently. It should be pointed out that the bending strain defined in this way optimally utilizes the given nodal variables since the bending strain is the dominant term in the beam analysis. The shear locking can be avoided by the quasi-conforming element technique (Shi *et al.*, 1991, 1998). By substituting the matrices  $\mathbf{B}$  into Eqs. (11) and (12), the element stiffness matrix can be obtained. Therefore, the resulting element stiffness matrix can be evaluated explicitly, i.e. no numerical integration is needed, which makes the resulting beam element very computationally efficient.

## The dynamic analysis of finite element modeling of composite beams based on Shi's sixth-order beam theory

### *Velocities of shear deformable beams*

It follows from the Eq. (1) that the velocities in the  $x$ -direction and  $z$ -direction respectively take the form

$$v_x = \frac{\partial u}{\partial t} = \frac{\partial u_0}{\partial t} - \frac{\partial}{\partial t} \left( \frac{\partial w_0}{\partial x} - \gamma \right) z + (\alpha z - \beta z^3) \frac{\partial \gamma}{\partial t}, \quad v_z = \frac{\partial w_0}{\partial t} \quad (15)$$

### Equation of motion of composite beam element

In dynamic analysis, the equation of motion is derived in terms of the element stiffness matrix and the mass matrix from Hamilton's Principle.  $U_e$  and  $K_{ke}$  are the element strain energy and kinetic energy respectively, and then the Hamilton's Principle states that

$$\delta \sum_{elem} \int_{t_0}^t (U_e - K_{ke}) dt = 0 \quad (16)$$

In dynamic analysis of natural frequency of system, the work done by external forces is neglected and the damping is not considered. And Eq. (16) leads to the equilibrium equations of a system as

$$\mathbf{M}\ddot{\mathbf{q}} + \mathbf{K}\mathbf{q} = \mathbf{0} \quad (17)$$

where  $\mathbf{M}$  and  $\ddot{\mathbf{q}}$  are the global mass matrix and acceleration vector of the system. Consequently, the frequency  $\omega$  can be evaluated by

$$(\mathbf{K} - \omega^2 \mathbf{M})\mathbf{q} = \mathbf{0} \quad (18)$$

The mass matrix based on the sixth-order beam theory will be presented in next section.

### Consistent mass matrix for sixth-order beam theory

The kinetic energy of an element  $K_{ke}$  corresponding to the sixth-order theory takes the form

$$\begin{aligned} K_{ke} &= \frac{b}{2} \int_I \int_{-h/2}^{h/2} (v_x^2 + v_z^2) \rho(z) dz dx = \frac{b}{2} \int_I \int_{-h/2}^{h/2} \left[ \left( \frac{\partial w}{\partial t} \right)^2 + \left( \frac{\partial u}{\partial t} \right)^2 \right] \rho(z) dz dx \\ &= \frac{b}{2} \int_I \int_{-h/2}^{h/2} \left[ \left( \frac{\partial w_0}{\partial t} \right)^2 + \left( \frac{\partial u_0}{\partial t} \right)^2 + z^2 \left( \frac{\partial^2 w_0}{\partial t \partial x} \right)^2 + ((1 + 2\alpha + \alpha^2)z^2 - 2(\beta + \alpha\beta)z^4 + \beta^2 z^6) \left( \frac{\partial \gamma}{\partial t} \right)^2 \right. \\ &\quad \left. - 2z \frac{\partial u_0}{\partial t} \frac{\partial^2 w_0}{\partial t \partial x} + 2((\alpha + 1)z - \beta z^3) \frac{\partial u_0}{\partial t} \frac{\partial \gamma}{\partial t} + 2((-1 - \alpha)z^2 + \beta z^4) \frac{\partial \gamma}{\partial t} \frac{\partial^2 w_0}{\partial t \partial x} \right] \rho dz dx \end{aligned} \quad (19)$$

where  $\rho(z)$  is the density across the beam thickness. By defining

$$J_A, J_B, J_D, J_E, J_F, J_H = b \int_{-h/2}^{h/2} (1, z, z^2, z^3, z^4, z^6) \rho dz \quad (20)$$

The element kinetic energy  $K_{ke}$  can be written as

$$\begin{aligned} K_{ke} &= \frac{1}{2} \int_I J_A \left( \frac{\partial w_0}{\partial t} \right)^2 + J_A \left( \frac{\partial u_0}{\partial t} \right)^2 + J_D \left( \frac{\partial^2 w_0}{\partial t \partial x} \right)^2 + ((1 + 2\alpha + \alpha^2)J_D - 2(\beta + \alpha\beta)J_F + \beta^2 J_H) \left( \frac{\partial \gamma}{\partial t} \right)^2 \\ &\quad - 2J_B \frac{\partial u_0}{\partial t} \frac{\partial^2 w_0}{\partial t \partial x} + 2((\alpha + 1)J_B - \beta J_E) \frac{\partial u_0}{\partial t} \frac{\partial \gamma}{\partial t} + 2((-1 - \alpha)J_D + \beta J_F) \frac{\partial \gamma}{\partial t} \frac{\partial^2 w_0}{\partial t \partial x} dx \end{aligned} \quad (21)$$

The equation above shows that similar to the stretching and bending coupling in the stiffness matrix there is also an axial and rotary velocity coupling in the mass matrix when the density is not symmetric about the reference plane of the composite beams. The coupling of the transverse shear velocity and the deflection slope velocity is always non-zero as long as the transverse shear deformation is not zero. In the finite element analysis, the element displacement can be interpolated in terms of the element nodal displacement vector  $\mathbf{q}_e$  as

$$u_0 = \mathbf{N}_u \mathbf{q}_e, \quad w_0 = \mathbf{N}_w \mathbf{q}_e, \quad \frac{\partial w_0}{\partial x} = \mathbf{N}_{wx} \mathbf{q}_e, \quad \gamma = \mathbf{N}_\gamma \mathbf{q}_e \quad (22)$$

where  $\mathbf{N}_j$  ( $j=u, w$  and  $\gamma$ ) are the interpolation matrices. By substituting Eq. (21) and (22) into (16), one obtains the consistent element mass matrix  $\mathbf{M}_e$  as

$$\mathbf{M}_e = \mathbf{M}_w + \mathbf{M}_u + \mathbf{M}_{wx} + \mathbf{M}_\gamma + \mathbf{M}_{uw} + \mathbf{M}_{w\gamma} + \mathbf{M}_{w\gamma} \quad (23)$$

with

$$\begin{aligned}
\mathbf{M}_w &= \int_l \mathbf{N}_w^T J_A \mathbf{N}_w dx, \quad \mathbf{M}_{wx} = \int_l \mathbf{N}_{wx}^T J_D \mathbf{N}_{wx} dx, \quad \mathbf{M}_u = \int_l \mathbf{N}_u^T J_A \mathbf{N}_u dx \\
\mathbf{M}_\gamma &= \int_l \mathbf{N}_\gamma^T [(1+\alpha)^2 J_D - 2\beta(1+\alpha)J_F + \beta^2 J_H] \mathbf{N}_\gamma dx, \quad \mathbf{M}_{uw} = -\int_l [\mathbf{N}_u^T J_B \mathbf{N}_w + \mathbf{N}_w^T J_B \mathbf{N}_u] dx \\
\mathbf{M}_{u\gamma} &= \int_l [\mathbf{N}_u^T ((\alpha+1)J_B - \beta J_E) \mathbf{N}_\gamma + \mathbf{N}_\gamma^T ((\alpha+1)J_B - \beta J_E) \mathbf{N}_u] dx \\
\mathbf{M}_{w\gamma} &= \int_l [\mathbf{N}_{wx}^T ((-\alpha-1)J_D + \beta J_F) \mathbf{N}_\gamma + \mathbf{N}_\gamma^T ((-\alpha-1)J_D + \beta J_F) \mathbf{N}_{wx}] dx
\end{aligned} \tag{24}$$

$\mathbf{M}_w$ ,  $\mathbf{M}_{u0}$  and  $\mathbf{M}_{wx}$  are, respectively, the usual transverse, axial and rotary inertia matrices;  $\mathbf{M}_\gamma$  is the mass matrix resulting from the higher-order displacement; and  $\mathbf{M}_{u0w}$ ,  $\mathbf{M}_{u0\gamma}$  and  $\mathbf{M}_{w\gamma}$  are the coupling terms of different components of the axial displacement. The variational consistent mass matrix above can account for the contribution of the higher-order displacement to the mass matrix and the results show that the consistent mass matrix can provide more accurate results than those given by lump mass matrix (Shi and Lam, 1999).

### Numerical examples

The accuracy of new finite element formulation based on Shi and Voyiadjis' sixth-order beam theory is evaluated by three examples of statics and dynamics of composite beams with different aspect ratios boundary conditions in this section.

#### Example 1 simply supported composite beam under uniformed load

A four layered composite beam of rectangular cross-section is considered in this example. Its length to thickness ratio is 100, and its mechanical and geometrical properties are shown bellow.

$$E_1 = 144.8GPa, \quad E_2 = 9.65GPa, \quad G_{12} = G_{13} = 4.14GPa, \quad G_{23} = 3.45GPa, \quad \nu_{12} = 0.3, \quad L/h=100, \quad h/b=1$$

Table 1. Non-dimensional\* deflections of simply supported composite beam

Lamination schemes	Element formulations	No. of elements		
		4	8	16
[0]	HQCB-8A (Shi <i>et al.</i> , 1998)	0.08267	0.08597	0.08677
	Chandrashekhara <i>et al.</i> (1993)	0.06282	0.07519	0.08155
	Present	0.08273	0.08598	0.08679
[0/90/90/0]	HQCB-8A (Shi <i>et al.</i> , 1998)	0.09369	0.09738	0.09827
	Chandrashekhara <i>et al.</i> (1993)	0.07107	0.08551	0.09225
	Present	0.09364	0.09733	0.09825

\*the non-dimensional deflection is defined in Shi *et al.* (1998)

The beam element of HQCB-8A in the table is a  $C^1$  composite beam element presented by Shi *et al.* (1998) which is based on Bickford beam theory (1982) and the quasi-conforming element technique. The results of Chandrashekhara *et al.* (1993) in Table 1 were given by a beam element based on the same type beam theory and the conventional displacement-based element formulation. It can be seen from the results in the table that the new beam element based on the sixth-order beam theory of Shi and Voyiadjis yield almost the same results as HQCB-8A in this numerical example; and the present beam element gives much better results than the conventional beam element.

#### Example 2 Laminated composite beams with different aspect ratios and different boundary conditions under the action of uniformed distributed load

Four equal thickness laminated composite beams with different boundary conditions and different length to height ratios are considered in this example. The material properties of the laminated composite beams are the same as the previous example. The lamination scheme of this example is [0/90/90/0]. The boundary conditions here include the clamped-clamped ends (denoted by CC); the clamped-free ends (CF); the clamped-simply supported ends (CS) and the simply supported ends

(SS). The non-dimensional maximum deflections of the beams given by various methods are listed in Table 2. Eight elements are used in the present analysis. The results in the table show that the beam element presented in this paper is not only free from shear locking but also very accurate.

Table 2 Influence of boundary conditions and aspect ratios on the accuracy of solutions

Boundary conditions	Element types	Aspect ratio $L/h$			Analytical Solution of thin beams (Timoshenko <i>et al.</i> , 1972)
		15	100	1000	
CC	HQCB-8A (Shi <i>et al.</i> , 1999)	0.03344	0.01998	0.01966	0.01967
	Kadoli <i>et al.</i> (2008)	0.02993	-	-	
	Present	0.03344	0.01997	0.01965	
CF	HQCB-8A (Shi <i>et al.</i> , 1999)	1.0038	0.9497	0.9481	0.9439
	Kadoli <i>et al.</i> (2008)	0.9108	-	-	
	Present	1.0034	0.9503	0.9485	
CS	HQCB-8A (Shi <i>et al.</i> , 1999)	0.05657	0.04113	0.04078	0.04090
	Kadoli <i>et al.</i> (2008)	0.0517	-	-	
	Present	0.05600	0.04088	0.04052	
SS	HQCB-8A (Shi <i>et al.</i> , 1999)	0.1112	0.09738	0.09706	0.09831
	Kadoli <i>et al.</i> (2008)	0.1035	-	-	
	Present	0.1111	0.09733	0.09702	

*Example 3 Laminated composite beam under uniformed load with different boundary conditions and different aspect ratios*

The four layered laminated composite beams considered in Example 2 with the density of  $1389.23 \text{ kg/m}^3$  are taken in this example for free vibration analysis. Twenty elements are used for the whole beam. The first five non-dimensional flexural frequencies (designated by  $f(1)$ - $f(5)$ ) of thick composite beams ( $L/h=15$ ) are tabulated in Table 3. The nondimensional frequency is defined by  $\bar{\omega}_i = \omega_i L^2 \sqrt{J_A / (E_1 b h^3)}$ . Some other numerical results and analytical solutions are also listed in Table 3 for comparison. The numerical solutions of ABAQUS are obtained by the 8-noded solid elements, and two-layers of solid elements are used for each lamina of the laminated beam.

Table 3. Nondimensional frequencies of symmetric  $[0/90/90/0]$  cross-ply beams with  $L/h = 15$

Formulation	BCs	Nondimensional frequency at various vibration modes					
		$f(1)$	$f(2)$	$f(3)$	$a(1)$	$f(4)$	$f(5)$
Present (20 elements)	SS	2.4952	8.4551	15.7208	17.2113	23.2552	30.7395
	CC	4.6228	10.4438	17.2895	-	24.4919	31.7930
	CS	3.5313	9.4970	16.5073	17.2110	23.8354	31.1695
	CF	0.9163	4.9085	11.5193	17.2110	18.8428	26.3646
HQCB-8A (Shi <i>et al.</i> 1998)	SS	2.4979	8.4364	15.5932	-	22.8974	30.0061
	CC	4.6194	10.4162	17.1724	-	24.2001	31.2144
	CS	3.5264	9.4736	16.4201	-	23.5591	30.6107
Chandrashekhara <i>et al.</i> (1993)	CF	0.9199	4.9054	11.4886	-	18.6886	25.9931
	SS	2.5023	8.4812	15.7558	-	23.3089	30.8386
	CC	4.5940	10.2906	16.9559	-	24.1410	31.2874
	CS	3.5254	9.4423	16.3839	-	23.6850	31.0569
Analytical solutions	CF	0.9241	4.8925	11.4400	-	18.6972	26.2118
	SS	2.4862	8.4415	15.7185	-	23.3170	30.9390
	CC	4.5866	10.3185	17.0647	-	24.2398	31.6197
	CS	3.5108	9.4336	16.4144	17.1934	23.7902	31.2835
ABAQUS (80x8 mesh)	CF	0.9181	4.8749	11.4333	17.1920	18.7360	26.3304

The frequencies of the axial vibration, denoted by  $a(1)$ , of the beams with boundaries of SS, CS and CF predicted by the present beam element are also listed in the table. The  $a(1)$  of 3D composite beams are given by ABAQUS for the beams with the boundary  $u(0, y, z) = 0$ . One can see from the



results in Table 3 that the present element which is based on the sixth-order beam theory of Shi and Voyiadjis (2011) yields more accurate results especially for the higher-mode frequencies than the beam element HQCB-8A which is based on the third-order shear beam theory of Bickford (1982). The major difference between the sixth-order beam theory of Shi and Voyiadjis and the third-order shear beam theory of Bickford lies on the different definitions of the rotation of the cross-section; the former employs an averaged rotation across the beam cross-section and the later uses the rotation measured at the beam midplane. As matter a fact, Hutchinson (1986) showed that the third-order shear plate theory yielded the incorrect results of the higher-mode frequencies of a clamped circular plate when the rotation along the clamped boundary was fixed at the plate midplane.

### Acknowledgements

The financial support provided by the grant of NSFC-91230113 is thankfully acknowledged.

### Conclusions

This paper presents a new beam element which is based on the quasi-conforming element technique and a new beam theory with the averaged rotation of beam cross-section as one of the field variable proposed by Shi and Voyiadjis. There are two conclusions can be made from the result comparisons conducted in the paper.

1. The present assumed strain beam element is not only free from shear-locking as well as free from the time consuming numerical integration, but also very accurate.
2. The averaged rotation across the beam cross-section used in the sixth-order beam theory of Shi and Voyiadjis yield more accurate higher-mode frequencies than the high-order beam theories with the rotation of the cross-section measured at the beam midplane.

### References

- Bickford, W.B. (1982), A consistent higher-order beam theory. *In Developments in Theoretical and Applied Mechanics, Vol. XI, University of Alabama, Huntsville, AL*, pp. 137-150.
- Carrera, E. and Giunta, G. (2010), Refined beam theories based on a unified formulation. *Int. J. Appl. Mech.*, **2**(1), pp. 117-143.
- Chandrashekhara, K. and Bangera, K.M. (1993), Linear and geometrically nonlinear analysis of composite beams under transverse loading. *Compos. Sci. Technol.*, **47**, pp. 339-347.
- Feng, H., Cui, X.Y. and Li, G.Y. (2012), Static and dynamic analysis of Timoshenko beam using nodal integration technique. *Int. J. Appl. Mech.*, **4**(4), 1250045:1-20.
- Hutchinson, J. (1986), On the axisymmetric vibrations of thick clamped plates. *Proc. Int. Conf. on Vibration Problems in Engineering, Xi'an, China*, pp. 75-81.
- Kadoli, R., Akhtar, K. and Ganesan, N. (2008) Static analysis of functionally graded beams using higher order shear deformation theory. *Appl. Math. Modeling*, **32**, pp. 2509-2525.
- Kapania, R.K. and Raciti, S. (1989), Recent advances in analysis of laminated beams and plates. Part I, shear effect and buckling. *AIAA J*, **27**, pp. 923-934.
- Reddy, J.N. (1984), A simple higher-order theory for laminated composite plates. *J. Appl. Mech.*, **51**, pp. 745-752.
- Shi, G. and Voyiadjis, G.Z (1991), Simple and efficient shear flexible two-node arch/beam and four-node cylindrical shell/plate finite elements. *Int. J. Num. Meth. Eng.*, **31**, pp.759-776.
- Shi, G., Lam, K.Y. and Tay, T.E. (1998), On efficient finite element modelling of composite beams and plates using higher-order theories and an accurate composite beam element. *Compos. Struct.*, **41**, pp. 159-165.
- Shi, G. and Lam, K.Y. (1999), Finite element vibration analysis of composite beams based on higher-order beam theory. *J. Sound. Vib.*, **219**(4), pp. 707-721.
- Shi, G. and Voyiadjis, G.Z. (2011), A sixth-order theory of shear deformable beams with variational consistent boundary conditions. *J. Appl. Mech. ASME.*, **78**, pp. 021019:1-11.
- Tang, L., Chen, W. and Liu, Y. (1980), Quasi-conforming element for finite element analysis (in Chinese). *J. Dalian Inst. Tech.*, **19**(2), pp. 19-35.
- Timoshenko, S. and Gere, J. (1972), *Mechanics of Materials*. New York: Van Nostrand Reinhold Co.
- Wang, X. and Shi, G. (2012), The boundary layer solutions induced by displacement boundary conditions of shear deformable beams and accuracy study of higher-order beam theories. *J. Eng. Mech. ASCE*, **138**, pp. 1388-1399.

# Computation of Hydrodynamic Coefficients of Portable Autonomous Underwater Vehicle

\* J. Jiang, Y. Shi, and G. Pan

School of Marine Science and Technology, Northwestern Polytechnical University, China  
127 Youyi west St, Beilin Dist, Xi'an City, China

\*Corresponding author: jiangjun@nwpu.edu.cn

## Abstract

Hydrodynamic coefficients in the motion equations of any underwater vehicle are inherent characteristics of the body geometry, the geometry and location of control surfaces and other appendages and separation of centers of gravity and buoyancy. This paper reports the prediction of values of straight-line hydrodynamic coefficients for a portable autonomous underwater vehicle (PAUV) by using empirical methods and Computational Fluid Dynamics (CFD), which is being developed by Northwestern Polytechnical University for ocean reconnaissance. At the same time, hydrodynamic coefficients test results in wind tunnel are shown in this paper. And computational results by empirical methods and CFD are compared with experimental results from wind tunnel tests of the same PAUV. It is proved that the trends in variation of forces and moments are captured well by CFD.

**Keywords:** PAUV, Hydrodynamic coefficient, CFD, Wind tunnel

## Introduction

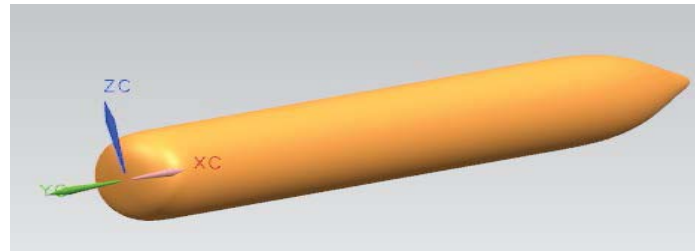
As a new generation of Autonomous Underwater Vehicles, a kind of low cost, small and portable vehicles have been developed, such as REMUS (Remote Environmental Measuring UnitS), which could provide an affordable means of performing scientific researches, including coastal ocean survey, pollution identification and source tracking, in the coastal ocean, bays and estuaries, etc.( Allen, B. Stokey, R. etc.). In recent years, Chinese researchers in universities or institutes began to study the portable autonomous underwater vehicle (PAUV) and to design and fabricate PAUV, which is small, low-speed and accessible AUV. As well known, the controllability and motion stability characteristics of underwater vehicles are commonly evaluated in terms of hydrodynamic coefficients (HDCs) or hydrodynamic derivatives, which are used in the rigid body equations of motion to express the external forces acting on the vehicle due to its motion in the fluid (Abkowitz M. A.). And coefficients in non-dimensional form are considered to be inherent characteristics of the body geometry, the geometry and location of control surfaces and other appendages of AUV.

Shape and hydrodynamic layout design of a PAUV, which is being developed by Northwestern Polytechnical University (NWPU), are described in this paper. In order to ensure optimized maneuvering characteristics for the vehicle to meet its designated roles, the hydrodynamic coefficients need to be gotten during initial design phase. In this paper, methods of computing these parameters are described, including empirical methods, numeric simulation method, and full-scale model wind tunnel tests.

## System Description of Hydrodynamic Layout

### *Hull shape*

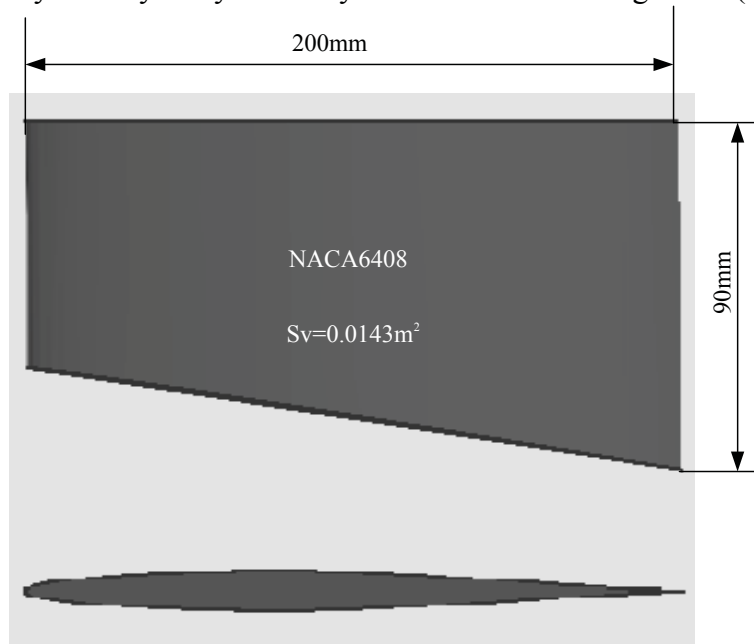
The Shape of NWPU PAUV was designed according to minimize drag based on torpedo shape. Fig.1 shows the vehicle bare body shape. The bare vehicle is 1850mm long with a columniform body diameter of 200mm. The head section shape and tail section shape are all designed based on Granville series. The axial length of head section ( $L_h$ ) is 150mm and the length of tail section ( $L_A$ ) is 450mm.



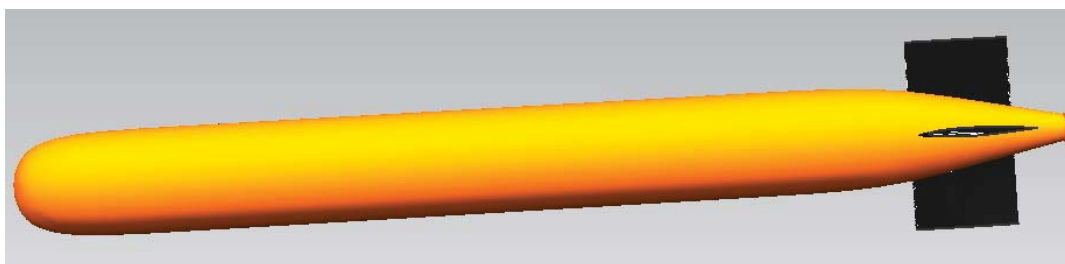
**Figure 1. Bare body shape of NWPU PAUV**

### *Layout of Rudders*

The rudder (Fig. 2) was designed based on aerofoil form for two reasons: one is low speed and the other is motion stability. The hydrodynamic layout is cruciform arrangement (Fig. 3).



**Figure 2. Rudder**



**Figure 3. Hydrodynamic layout of NWPU PAUV**

So the vehicle's specifications are given in Table 1.

**Table 1. Specifications and characteristics of NWPU PAUV**

Items	Specifications and characteristics
Dimension	$\Phi 200\text{mm}(D) \times 1850\text{mm}(L)$
Weight	50kg
Displacement	$0.051\text{m}^3$
Maximum depth	150m

Operation time	40h
Speed	3-5knots
Main thruster	single screw propeller

### Empirical Calculation of Main Linear Hydrodynamic Coefficients

The controllability and motion stability characteristics of UUV are commonly evaluated in terms of hydrodynamic coefficients or hydrodynamic derivatives, which are used in the rigid body equations of motion to express the external forces acting on the vehicle due to its motion in the fluid (W. S. Richardson, P. B. Stimson, etc.). So, in initial design phase, it is important to evaluate main hydrodynamic coefficients by using empirical methods. It is well known that main hydrodynamic coefficients include drag coefficient, lift coefficient, lateral force coefficient, pitch moment coefficient, yaw moment coefficient and roll moment coefficient. The forces and moments are nondimensionalized by  $0.5\rho v^2 S$  and  $0.5\rho v^2 SL$  respectively, where  $\rho$  is the density of water,  $v$  is velocity of wind,  $S$  is max transect area, and  $L$  is the length of the PAUV.

For PAUV with torpedo shape, empirical calculation of main hydrodynamic coefficients is shown as follows (Y. W. Zhang, etc):

#### A. Drag Coefficient

$$C_{d(\Omega)} = K * (2.07 - 18.44T_A - 4.15l_r + 73.25T_A l_r + 3.26l_r^2 + 10.81T_A T_F - 56.96T_A l_r^2 - 38.34T_A T_F l_r + 37.75T_A T_F l_r^2) C_{fb} \quad (1)$$

$$T_A = \frac{4V_A}{\pi D L_A L'_A}$$

$$l_r = 1 - \frac{L_c}{L}$$

$$T_F = \frac{2V_h}{\pi D L_h^2}$$

$$C_{fb} = 1.328\sqrt{R_e}, R_e < 5 \times 10^5$$

$$C_{fb} = \frac{0.455}{(\lg R_e)^{2.58}} - \frac{1700}{R_e}, 5 \times 10^5 < R_e < 5 \times 10^7$$

$$C_{fb} = \frac{0.455}{(\lg R_e)^{2.58}}, 5 \times 10^7 < R_e$$

where,  $K$  is correctional coefficient,  $[1.1, 1.15]$ ,  $V_A$  is volume of tail section of bare body,  $L_A$  is length of tail section,  $L'_A$  is nominal axial length of tail section,  $L_c$  is length of columniform section.  $V_h$  is volume of head section of bare body,  $L_h$  is length of head section,  $C_{fb}$  is friction drag coefficient of plate in fluid.

#### B. Lift Coefficient

$$C_y = C_{yb} + C_{yfh} + C_{yrh} \quad (2)$$

where,  $C_{yb}$  is lift coefficient of bare body,  $C_{yfh}$  is lift coefficient of horizontal fins,  $C_{yrh}$  is lift coefficient of elevators.

$$C_{yb} = [2 - 2\zeta_k(1 - \eta_k^2) - C_{d0}] \alpha \quad (3)$$

$$\zeta_k = 0.15 \sim 0.2$$

$$\eta_k = \sqrt{S_A / S}$$

where,  $C_{d0}$  is drag coefficient of bare body when attack angle ( $\alpha$ ) is zero,  $S_A$  is area of tail end section,  $S = \frac{\pi}{4}D^2$  is max transect area of body.

$$C_{yfh} = 5.6 \frac{5.5\lambda}{5.5\lambda + 5.6} \frac{2A_f}{S} \alpha \quad (4)$$

where,  $\lambda$  is ratio of span to chord of fin,  $A_f$  is area of fin.

$$C_{yrh} = 2\pi \frac{\lambda_r}{2 + \lambda_r} (0.5 + 0.734\bar{a} + 0.6\sqrt{A_r/A_f}) \frac{2A_r}{S} \delta_h \quad (5)$$

where,  $\lambda_r$  is ratio of span to chord of rudder,  $\bar{a} = \frac{a}{D}$ ,  $a$  is span of rudder,  $A_r$  is area of rudder,  $\delta_h$  is the deflection angle of rudder .

### C. Lateral Force Coefficient

As the symmetry of shape, the calculation methods of lateral force coefficient are similar with lift coefficient.

### D. Pitch Moment Coefficient

$$M_Z = M_{zb} + M_{zfh} + M_{zrh} \quad (6)$$

where,  $M_{zb}$  is pitch moment coefficient of body,  $M_{zfh}$  is pitch moment coefficient of horizontal fins,  $M_{zrh}$  is pitch moment coefficient of elevators.

$$M_{zb} = 2(0.62 + 0.013 \frac{L}{D}) \frac{V}{\frac{\pi}{4} D^2 L} \quad (7)$$

where,  $V$  is the volume of body.

$$M_{zfh} = -C_{yfh} \frac{L_{fh}}{L} \quad (8)$$

where,  $L_{fh}$  is distance of lift point of horizontal fins from origin of body coordinate.

$$M_{zrh} = -C_{yrh} \frac{L_{rh}}{L} \quad (9)$$

where,  $L_{rh}$  is distance of lift point of elevators from origin of body coordinate.

### E. Yaw Moment Coefficient

As the symmetry of shape, the calculation methods of yaw moment coefficient are similar with pitch moment coefficient.

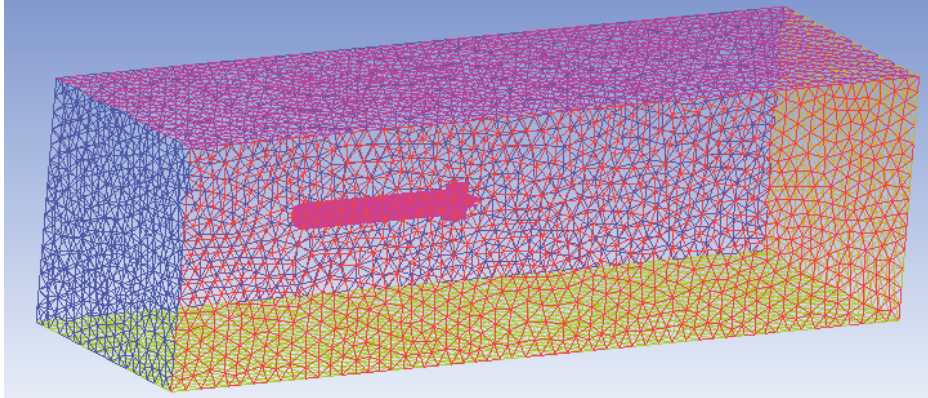
It is noticeable that the origin of coordinate is at the buoyancy center of PAUV.

## Numeric Simulation

### Grid Generation

Quality of grid generation in numerical simulation takes an important role to gain accurate simulation results of hydrodynamic coefficients. So, most of the human time and effort required in numerical simulation analysis (for example CFD) studies is spent in grid generation.

For studying rectilinear flow past the PAUV, the intermediate volume was meshed using tetrahedral elements, creating an unstructured mesh around the PAUV in a rectangular domain. The length of rectangular is 5L with width is 5D and height is 5D, which can be seen in Fig. 4.



**Figure 4. Rectilinear flows at various angles of attack**

To evaluate the rectilinear hydrodynamic coefficients, the PAUV was to be placed at various angles of attack. This was efficiently implemented by rotating the enclosing rectangular domain of the specified angle, and then re-meshing (unstructured mesh) the intermediate volume.

#### *Governing Equations*

Since the velocity of PAUV changed from 3 to 5 knots, the Reynolds number is not high for the flow to be simulated. Also the Reynolds-averaged Navier-Stokes (RANS) equations were used in this paper.

#### *Solver Settings*

The 3-dimensional double precision segregated solver was used for steady flow and the SIMPLE algorithm was selected for pressure-velocity coupling. First order upwinding was adopted initially, followed by second order upwinding after the solution residuals had dropped by about 3 orders of magnitude. Residuals of continuity, velocities and turbulence parameters were monitored and convergence criteria were set as  $10^{-6}$  for all residuals.

#### *Turbulence Model*

Renormalization Gradient  $k - \varepsilon$  model was adopted as turbulence model in this paper.

#### **Model Wind Tunnel tests**

According to the shape and hydrodynamic layout of the PAUV, full-scale model wind tunnel test at the same Reynolds number with numerical simulation was accomplished.

For the symmetry of shape and hydrodynamic layout, side slip angle (Fig. 5) and elevators deflection angle (Fig. 6) change tests are accomplished, and the wind velocity is 26.5m/s.



**Figure 5. Side slip angle change test**



**Figure 6. Elevators deflection angle change test**

#### **Results**

For the NWPU PAUV, based on test data processing, the main hydrodynamic coefficients or derivative are listed in Tab. 2 by empirical method, numeric simulation and wind tunnel tests.

**Table 2. Results of main hydrodynamic coefficients or derivatives**

Parameters	Empirical method	Numeric simulation	Wind tunnel test
$C_d$	0.1650	0.1673	0.1726
$C_y^\alpha$	2.8631	2.7512	2.6896
$m_z^\alpha$	0.5621	0.5532	0.5608
$C_z^\beta$	-2.8631	-2.7512	-2.6896
$m_y^\beta$	0.5621	0.5532	0.5608
$m_x^\beta$	0.0025	0.0022	0.0031

According to Tab. 2, the results of empirical method, numeric simulation and wind tunnel test are almost consistent.

### Conclusions

For initial design of UUV, quick answers are sought to question like effects of variation in size and location of control surfaces, adequacy of dynamic stability and maneuverability. So computation of hydrodynamic coefficients is important in initial design phase of UUV's design.

The computational results in this paper aim at maneuvering analysis of the NWPU PAUV. The max error for main hydrodynamic coefficients or derivatives comparing wind tunnel test is less than 10%. For accurately evaluating NWPU PAUV motion characters, rotary hydrodynamic coefficients computational methods are due to further study.

### Acknowledgements

The authors gratefully acknowledge the Northwestern Polytechnical University, the Institute of Underwater Vehicle for their technical, intellectual and financial support of this research.

This study was undertaken an part of a project supported by National Natural Science Foundation of China Projects(51279165), and National Defense Basic Research Project(B2720132014), China, which is gratefully acknowledged by the authors.

### References

- Allen, B. Stokey, R. Austin, T. and Forrester, N, REMUS: A small, low cost AUV; system description, field trials and performance results. pp. 994–1000.
- Abkowitz, M.A. (1969) .Stability and Motion Control of Ocean Vehicles, MIT Press, Massachusetts.
- W. S. Richardson, P. B. Stimson and C. H. Wilkins (1963), Current measurements from moored buoys. *Deep-Sea Research*, Vol.10,3,pp.369-388
- A. Ray, S. N. Singh, V. Seshadri (2009), Evaluation of linear and nonlinear hydrodynamic coefficients of underwater vehicles using CFD. 28th International Conference on Ocean, Offshore and Arctic Engineering.
- Y. W. Zhang (1998), Shape design of torpedo, NWPU Press, Xi'an.

# Experimental and numerical evaluation of fatigue behavior of foam core sandwich structure

\*Peiyan Wang<sup>1</sup>, Xiaoyu Li<sup>2</sup>, Zhufeng Yue<sup>1</sup>

<sup>1</sup>School of Mechanics, Civil Engineering and Architecture, Northwestern Polytechnical University, Xi'an 710129, P.R.China

<sup>2</sup>Baotou North Chuangye Limited Company, Inner Mongolia First Machinery Group, Baotou 014032, China

\*Corresponding author: pywang@nwpu.edu.cn

## Abstract

Fatigue crack growths of foam core sandwich structure loaded in three-point bending under room temperature, low temperature and hygrothermal environment have been investigated. The fatigue life and S-N curve are given, and the results of flexural fatigue test confirm the obvious effect of low temperature and hygrothermal environment on the fatigue life of foam core sandwich structure. Core shear was found to be the dominant failure mode under fatigue loading condition at all of three environments. Three-dimensional numerical simulation of the progressive collapse of foam core sandwich structure was conducted using user subroutine USDFLD in FEM software ABAQUS/Standard. The maximum stress failure criterion and Hashin failure criterion were used to judge the failure of foam core and skin, respectively. Finite element analysis explains the crack initiation and propagation under flexural load, and progressive damage method can be used to simulate the failure of foam core sandwich structure.

**Keywords:** Foam core sandwich, Flexural fatigue property, Crack propagation, Failure criterion

## 1. Introduction

Sandwich structures are widely employed in aerospace, civil and mechanical industries due to their excellent performances, such as stiffness/weight ratio, and acoustic insulation properties. Over the last decade, various improvements have been made in manufacturing of sandwich structure, and different combinations of core materials and face sheet materials have been developed. Compared with honeycomb sandwich, foam core sandwich structures have the advantage of lighter quality and better waterproof. Therefore, foam core sandwich structures are being widely replacing with honeycomb sandwich structures and other stiffened structures (Yi Ming Jen, 2009). Recently, a lot of research has been focused on the static strength and fatigue behavior of foam core sandwich structure. Basir (2006) investigated the quasi-static and flexural fatigue failure mode of sandwich structure through AE analysis. Kulkarni (2003) studied the fatigue crack growth of foam core sandwich beams loaded in flexural load. Abderrezak (2007) discussed the use of an artificial neural network (ANN) to estimate fatigue lifetime of a sandwich composite material structure subjected to cyclic three-point bending loads. However, almost the study is based on experimental method, and rare on the numerical method (Ivanez, 2010). In this paper, the fatigue behaviors of foam core sandwich structure under room temperature, cold temperature and hygrothermal environments are investigated, and the failure mode will be simulated by numerical method.



## 2. Experimental procedure

Core material was foam of ROHCELL PMI71S which was homogeneous and isotropic. Both upper and lower skins were made of composite laminate T700/3234, and the symmetrical layup was  $[45^\circ/-45^\circ/0^\circ/0^\circ/90^\circ/0^\circ]_s$ . Mechanical properties of foam core are listed in Table 1. The sandwich structure specimens studied in this paper were made by Vacuum Assisted Resin Infusion molding technology (shorted as VARI). The thickness of foam core sandwich structure was 15mm, and the core thickness was 12mm. All the specimens were 340mm in length, and 60mm in width.

The 3-point static bending tests were conducted according to GB/T1456 (2005). The experimental setup is presented in Fig.1, and the geometry of the specimen is listed in Table.2 .The diameter of the upper roller was the same as that of the lower rollers for fixture used for three-point bending. Load and support rollers had a radius of 5mm. The lower supports were placed on a rail which allowed the variation of span length, and the support span used in this test was 300mm.

Experimental tests were carried out on a material testing machine (INSTRON 8801). Static test was performed under displacement control at a constant crosshead speed of 0.5mm/min. The specimen was loaded until a load maximum was reached and load had dropped off about 30% from the maximum. The load maximum was defined as ultimate load of bending,  $P_{ul}$ .

By using the ultimate bending load acquired from the static bending tests, the maximum flexural load applied per cycle was determined at different load levels,  $L$ , as defined by

$$L = \frac{P_{\max}}{P_{ul}} \quad (1)$$

Where  $P_{\max}$  is the maximum load applied per fatigue cycle. The minimum flexural load applied per cycle  $P_{\min}$  was defined by stress ratio  $R = \frac{P_{\min}}{P_{\max}}$  and maximum load.

Fatigue testing was conducted at a stress ratio  $R=0.06$  using a sinusoidal wave form and a frequency of 4HZ. Three-point flexural fatigue test was performed at different load levels ranging from 0.5 to 0.7.

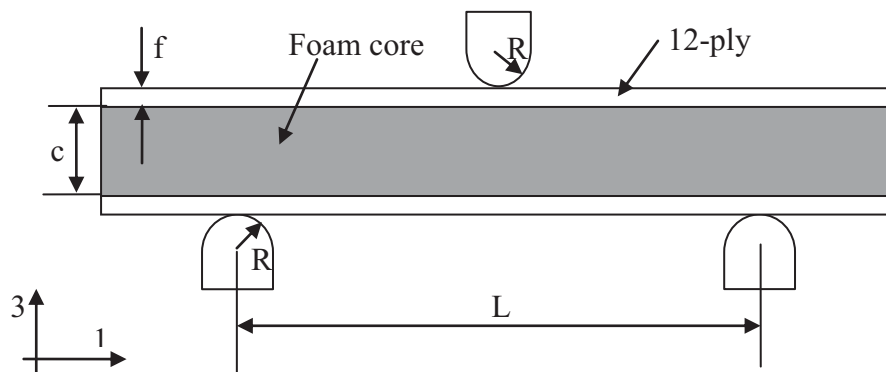


Fig.1 Three-point bending of sandwich beam with indenter and supports

Table 1 Mechanical properties of foam core material

Property	PMI71S
Nominal density (kg/m <sup>3</sup> )	75
Modulus (MPa)	92.0
Poisson's ratio (MPa)	0.37
Tension strength (MPa)	2.3
Compressive strength (MPa)	1.5
Shear strength (MPa)	1.3

Table 2 Test configurations for 3-point bending tests

$f$ (mm)	$c$ (mm)	$L$ (mm)	$R$ (mm)
1.5	12	300	10

### 3. Experimental result

#### 3.1 The effect of temperature

Flexural fatigue tests were performed at different load levels (from  $r=0.5$  to  $r=0.7$ ), but the test environment is always room temperature. Then flexural fatigue tests were performed at low temperature ( $-55^{\circ}\text{C}$ ) and hygrothermal environments ( $70^{\circ}\text{C}, 85\%$ ), at load level of 55%. Five replicate specimens of sandwich structure beams were used for the flexural fatigue tests at each temperature.

The experimental results of flexural fatigue tests performed on sandwich structure beams at different test environments are presented in Table 3. The number of cycles to failure  $N_f$  was recorded just before final failure. The retention percentage is based on the fatigue life at room temperature. The coefficient of variation (short for COV) reflects the discrete degree of fatigue life. All the COVs of fatigue life at three test environments are less than 30%, and it represents that the experimental data are in creditable range. From Table 3, it can be seen that the number of cycles to failure  $N_f$  is the greatest in cold temperature, and smallest in hygrothermal environment.

From the results of flexural fatigue test, it can be seen that the cold temperature can improve the property of sandwich structure. However, hygrothermal environment greatly reduces the fatigue property. The failure mode of foam core sandwich structure under room temperature, cold temperature and hygrothermal environment is almost the same to each other, and all the specimens failed suddenly due to core shear, as seen in Fig.2. The entire crack formation and growth sequence occurred in a fraction of a second, and the final crack pattern observed under static loading appeared to be quite similar to that of fatigue loading. The crack initially occurred at the interface under the loading point, then propagated along the interface between the upper skin and foam core, but after a short distance crack propagating path deflected, and the crack propagated along the interface between the lower skin and foam core until final failed.

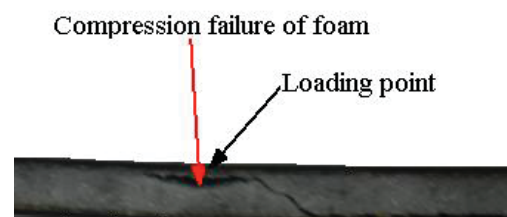


Fig.2 Failure modes of foam core sandwich beams

Table 3 Fatigue life of glass/PEI sandwich beam at different temperature

Test environment	Experimental data		
	$N_f$	Retention percentage	COV
Room	131708	100%	28.7%
Cold	164964	↑ 25.25%	22.5%
Hygrothermal	73822	↓ 43.04%	29.7%

### 3.2 S-N curve

Summarized, fatigue models can be generally classified into three categories: S-N curves; the residual stiffness/strength model; and the progressive damage model. All the three categories of fatigue models are aimed to determine final failure and the fatigue life of composite or metal material. S-N curves do not take into account damage accumulation, but they predict the number of cycles to failure under fixed loading conditions (Hashin Z, 1973 and Fawaz, 1994). Therefore, S-N curve is widely used in the prediction of the number of cycles to failure.

For convenience, the modified S-N curve was plotted with maximum applied load/ultimate load,  $P_{max}/P_{ul}$ , (which is also defined as the load level  $L$ ) on the Y-axis, and the number of cycles to failure on the X-axis. The modified S-N curve data at room temperature is shown in Fig.3. Modified S-N curve shows that the number of cycles to failure of foam core sandwich structure increases with reductions in the load level,  $L$ . The fatigue life at load level of 50% is nearly one hundred million times, so the fatigue limit strength of the foam core sandwich structure is about 50% of the ultimate strength. The S-N equation as shown in Eq.(3) can be used to evaluate the fatigue life of foam core sandwich structure.

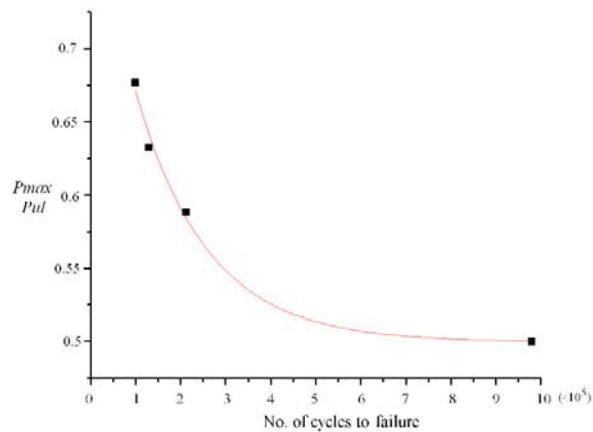


Fig.3 Modified S-N curve data for foam core sandwich structure on fatigue life

$$L = 0.21 \exp\left(\frac{-N}{179943}\right) + 0.50 \quad (2)$$

There are many proposed experimental results charactering the damage evolution of composite laminates by stiffness degradation, but rare on foam core sandwich structure. In this study, the shear stiffness of foam core sandwich structure was obtained through the load of displacement. The curve is demonstrated in Fig.4, showing the shear stiffness degradation under load level of 55% at room temperature. The fitting equation is shown in Eq.(3) which can be used in the evaluation of fatigue life.

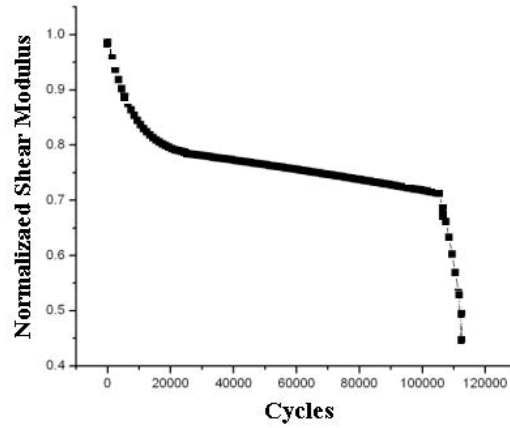


Fig.4 Shear stiffness under room temperature at load level of 55%

$$\Delta G = 0.218 \exp\left(\frac{-N}{8303.9}\right) + 0.775$$

$$\Delta G = 1 - 0.217 \exp\left((N - 24415) \times 3.67 \times 10^{-6}\right) \quad (3)$$

$$\Delta G = 1 - 0.285 \exp\left[(N - 105322) \times 8 \times 10^{-5}\right]$$

#### 4 Finite Element Analysis

To simulate damage initiation and propagation until the final damage occurs, progressive damage models have been developed and implemented by finite element method. The commercial package ABAQUS was used to develop the finite element (FE) model of foam core sandwich structure and carry out the progressive damage analysis through the user subroutine USDFLD. In the present analysis, the material properties of composite skin and foam core both depend on three field variables based on failure criterion. The procedure is as below: firstly perform a stress analysis, then check for failure at each integration point by using a set of failure criterion, and thirdly, if failure occurred, degrade the material properties. This procedure must be repeated at every increasing load level until the analysis is not convergence because so many integration points fail (ABAQUS V6.10).

##### 4.1 Finite Element Model

Two dimensional (2D) four-node quadrangle elements (S4R) were used for face sheets and three dimensional (3D) eight-node brick elements (C3D8R) were used for foam core. The foam core was modeled as homogenous and isotropic, and the cell structure was not considered. The skin and foam core were joined together through 'tie' interaction in ABAQUS, and the FE model is shown in Fig.4.

The lower rollers, upper roller and foam core sandwich structure were modeled, respectively. In order to prevent the contact surfaces from penetrating into each other, contact pairs were defined between the surfaces that contact with each other. The surfaces of lower and upper roller were modeled as master surfaces, while the ones of specimen were modeled as deformable surfaces.

The displacement load along through-thickness direction of foam core sandwich structure was loaded on the indenter. The lower rollers were restrained in all the translational and rotational degrees, while the upper indenter was restrained in all the six degrees except the load direction.

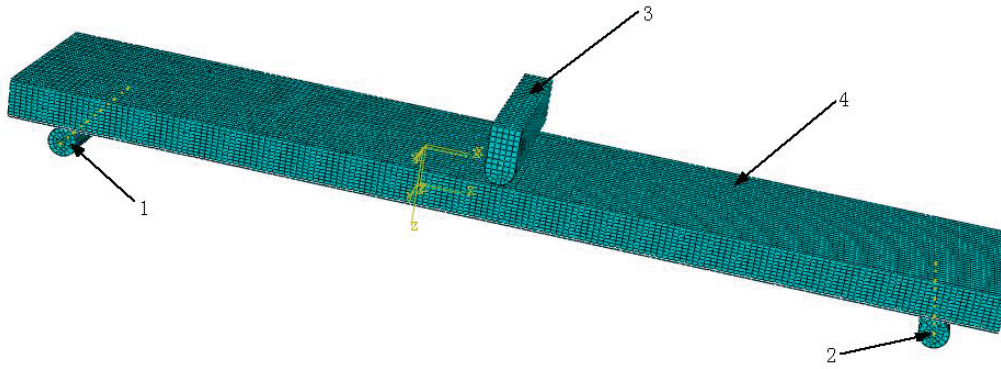


Fig.4 FE model of three-point bending

#### 4.2 Failure criterion

In this study, research was focused on the failure of foam core and skins. Hashin failure criterion is used to assess the severity of the stress state and decide which regions of the laminates skins will fail (Hashin Z, 1980 and Marie-laure Dano, 2000). The maximum stress failure criterion is used to judge the foam core element failure. According to the maximum stress failure criterion, failure occurs when one stress component along the principal material axes exceeds the corresponding strength in that direction.

$$\begin{cases} \sigma_t > [\sigma_t] \\ \sigma_c > [\sigma_c] \\ S > [S] \end{cases}$$

where  $[\sigma_t]$ ,  $[\sigma_c]$  and  $[S]$  are the tensile strength, compression strength and shear strength, respectively. All the strength values are listed in Table 1.

### 5 Results and Discussion

From the experiment, the failure mode is directly viewing, but the reason that causes the failure mode was still unknown. In this section, the bearing strength, failure mode and propagation of failure are investigated numerically, and the reason will be revealed. The three-point bending load of foam core sandwich structure at room temperature was simulated by the method in section 4, and the result will be compared with the experiment data.

Table 4 The static strength and fatigue life of foam core sandwich structure

	Experimental data	Simulations	Error
Strength /N	1600	1701	6.31%
Fatigue life /time	106829	82152	23.10%

Table 4 gives the experimental and numerical results. The bending load predicted is 1.701KN, and the experimental result is 1.6KN. The difference between simulation and experiment is 6.31%. It is approved that the numerical method can be used to evaluate the failure load of foam core sandwich structure under three-point bending load.

The simulation result shows that the stress S13 and S33 of foam core is bigger than other components, and the stress S13 plays a main role in the process of damage progression. Therefore, the stress S13 is used to evaluate the fatigue life of foam core

sandwich structure. The distribution of stress S13 is given in Fig.5. The maximum S13 is 0.7517MPa, and the stress ratio is 57.82%. Based on the S-N curve in Eq.(2), the fatigue life was calculated, and the result is listed in Tab.4. From the Tab.4, the difference of predicted result and experimental data is less than 23.1%, which is in the tolerance design. So the stress S13 is the appropriate parameter to evaluate the fatigue life of foam core.

Fig.6 shows that damage progressive of foam core structure. The main failure mode of foam core sandwich structure is compressive failure and shear failure. When the load is 1432.6N, compressive damage firstly occurred at the middle of foam core under the upper skin, and then extend to the bottom and span size of the foam. And shear damage occurred at the load of 1701N, later than compressive damage, as the compressive stress is bigger than shear stress. Shear damage extend mainly along the interface of foam core and the lower surface.

From damage progression analysis, it can be seen that the foam core sandwich structure firstly fail in compression at the middle of foam core, then the damage extend along the interface of upper skin and foam core. In the second stage, the failure mode is the combination of compression and shear, but the compression damage predominate the failure mode. In the next stage, the shear failure becomes the main failure mode, the damage changes direction, and extends along the interface between the lower skin and foam core. The progression procedure obtained numerical analysis is coincided with experimental result. Therefore, progressive damage method can be used to simulate the failure of foam core sandwich structure.

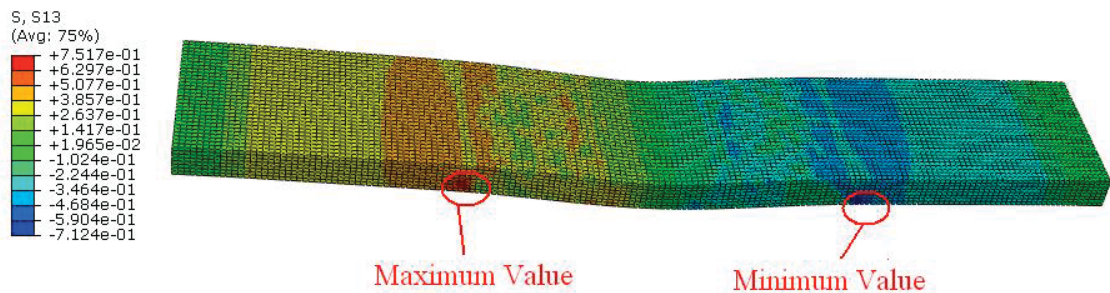


Fig.5 Stress (S13) contour of foam core

Fig.6 Damage progression of foam core

Load /N	Compressive damage	Shear damage
1432.6		--
1701		
1229		

## 6. Conclusions

The static and fatigue properties of foam core sandwich structure loaded in flexural load under room temperature, low temperature and hygrothermal environment were investigated by experimental method. Besides, the maximum stress failure criterion and Hashin failure criterion were used to judge the foam core and skin, and damage initiation and propagation of sandwich structure were simulated by finite element method. On the basis of the above work, some useful conclusion can be drawn.

(1) The flexural fatigue tests under different environments shows that the number of cycles to failure  $N_f$  is the greatest in cold temperature, and smallest in hygrothermal environment.

(2) The main failure mode of foam core sandwich structure is compressive failure and shear failure. Compression failure results in the damage initiation, but shear failure is the reason for damage progressive.

(3) The progression procedure obtained by numerical analysis is coincided with experimental result. Therefore, progressive damage method can be used to simulate the failure of foam core sandwich structure.

## Acknowledgements

This study is supported by Fundamental Research Fund (JC201237, JC20120231) at Northwestern Polytechnical University and National Science Foundation(No:51205315).

## References

- Yi Ming Jen, Li Yen Chang. Effect of thickness of face sheet on the bending fatigue strength of aluminum honeycomb sandwich beams. *Engineering Failure Analysis*, 16 (2009), pp. 1282-1293
- Basir Shafiq, Amilcar Quispitupa. Fatigue characteristics of foam core sandwich composites. *International Journal of fatigue*, 28(2006), pp. 96-102.
- Nitin Kulkarni, Hassan Mahfuz, Shaik Jeelani, Leif A. Carlsson. Fatigue crack growth and life prediction of foam core sandwich composites under flexural loading. *Composite Structures* 59 (2003), pp. 499-505.
- Abderrezak Bezazi, S. Gareth Pierce, Keith Worden, El Hadi Harkati. Fatigue life prediction of sandwich composite materials under flexural tests using a Bayesian trained artificial neural network. *International Journal of Fatigue* 29 (2007), pp. 738-747.
- Inés Ivanez, Carlos Santiuste, Sonia Sanchez-Saez. FEM analysis of dynamic flexural behaviour of composite sandwich beams with foam core. *Composite Structures* 92 (2010), pp. 2285-2291
- GBT1456-2005. Test method for flexural properties of sandwich constructions.
- Hashin Z and Rotem A (1973), A fatigue criterion for fibre reinforced composite materials, *J. Compos. Mater.* 7, pp. 448-464
- Fawaz Z and Ellyin F (1994), Fatigue failure model for fibre reinforced materials under general loading conditions, *J. Compos.Mater.* 28, pp. 1432-1451.
- ABAQUS V6.10 User Subroutines Reference Manual, Dassault Systèmes Simulia Corp.; 2010.
- Hashin Z. Failure criteria for unidirectional fibre composites[J]. *J Appl Mech*, 1980, 47, pp. 329-334.
- Marie-laure Dano, Guy Gendron, Andre Picard. Stress and failure analysis of mechanically fastened joints in composite laminates. *Composite structures*, 50(2000), pp. 287-296.

# Non-Parametric Shape Optimization of 3-D Frame Structures for Maximizing a Natural Frequency

\*Takashi Morimoto<sup>1</sup> and Masatoshi Shimoda<sup>2</sup>

<sup>1</sup> Department of Advanced Science and Technology, Graduate School of Engineering, Toyota Technological Institute,

<sup>2</sup> Department of Advanced Science and Technology, Toyota Technological Institute,  
2-12-1 Hisakata, Tenpaku-ku, Nagoya, 468-8511, Japan

\*Corresponding author: sd12443@toyota-ti.ac.jp

## Abstract

This paper presents a non-parametric, or a node-based, shape optimization method for designing the optimal geometry of a 3-D frame structure composed of arbitrarily curved linear elastic members. A design problem dealt with maximizing the natural frequency of a specified mode is formulated as a distributed-parameter shape optimization problem. Under the assumption of that each member varies in the normal direction to its centroidal axis, the shape gradient function and the optimality conditions are theoretically derived by the Lagrange multiplier method and the material derivative method. The optimal free-form geometry is determined by applying the derived shape gradient function as the fictitious external forces to the members to minimize the objective functional, which is referred as the free-form optimization method for frame structures, a gradient method in a Hilbert space, proposed by the authors. The effectiveness and validity of the proposed method is verified through several design problems.

Keywords: Shape Optimization, Parameter-Free, Free-Form, Frame Structure, Space Frame

## Introduction

Structures composed of thin straight or curved members are classified as frame structures, which are widely utilized in the fields of engineering. Large stadiums, bridges, and radio towers are the typical examples in urban architecture and civil engineering. The lightness and slenderness are the favorable features as they are resource saving and eco-friendly; however, these features are apt to result in a lack of stiffness, which may be a cause of noise or vibration. To avoid undesirable vibration modes to be dominant and incur noise or fatigue of the composing members when a frame structure is excited, it is important to optimize the natural frequency, or the eigenvalue, for designing a frame structure. In the early stages of the design process, the shape can often be treated as the design variables, and in that case, the mechanical characteristics can be dramatically improved rather than optimizing the cross sectional shapes or sizes. Up to today, various numerical shape optimization methods for frame structures have been proposed. For instance, Wang, *et al.* (2004) reported simultaneous shape and sizing optimization to minimize the weight under multiple frequency constraints by calculating the integrated discrete sensitivity numbers. Ohsaki and Fujita (2011) applied the SQP method to multi-objective shape optimization of latticed shells parameterized by a Bezier surface. Numbers of heuristic approaches have also been reported; Hashemian *et al.* (2011) applied the genetic algorithm (GA) method for a squared lattice cylindrical shell under a compressive axial load to achieve a maximum buckling load. Kaveh and Bakhshpoori (2013) reported optimum design of space trusses for achieving minimum weight subjected to the stress limitations using the Cuckoo search algorithm (CS) with Levy flights. These are categorized in the parametric methods; however, few non-parametric methods have been reported, and considering the possible number of members and degrees of freedom of a frame structure, a shape



optimization method that can efficiently solve a large scale problem has much utility value. The authors proposed the free-form optimization method for frame structures taking up the stiffness maximization problems (Shimoda, *et al.*, 2013). It is a node-based, gradient method in a Hilbert space, and it can treat all nodes as design variables and provide a smoothly curved optimal free-form shape. In this study, we applied this method to natural vibration problems that aim to maximize a specified vibration eigenvalue while tracking its natural vibration mode. In the following sections, we will describe a non-parametric shape optimization problem for frame structures, a formulation of the problem and the shape gradient function, the free-form optimization method for frame structures, and calculated design examples.

## Non-parametric shape optimization problem of frame structures

### Governing equation of frame structure

As shown in Fig.1, a frame structure is defined as an assembly of arbitrarily curved members  $\{\Omega^j\}_{j=2,\dots,N}$ , and each member is consisted of piecewise straight Timoshenko beams, which is used for applicability to a wide range of problems by considering shear deformation. The frame structure occupies a bounded domain ( $\Omega \subset \mathbb{R}^3, \Omega = \bigcup_{j=1}^N \Omega^j$ ),  $N$  representing the number of members. The notation  $(x_1^j, x_2^j, x_3^j)$  and  $(X_1, X_2, X_3)$  indicates the local coordinate system with respect to the  $j$ th member and the global coordinate system, respectively,

$$\Omega^j = \left\{ (x_1^j, x_2^j, x_3^j) \in \mathbb{R}^3 \mid (x_1^j, x_2^j) \in A^j \subset \mathbb{R}^2, x_3^j \in S^j \subset \mathbb{R} \right\}, \quad \Gamma^j = \partial A^j \times S^j, \quad \Omega^j = A^j \times S^j, \quad (1)$$

where  $S^j$ ,  $A^j$  and  $\Gamma^j$  express the  $j$ th member's centroidal axis, cross section, and circumference surface except the end faces, respectively. Note that, for the sake of avoiding complex notations, the superscript  $j$  will often be omitted in the following sections unless necessary. The weak form of the governing equation of natural vibration is expressed as Eq. (2), where  $\mathbf{w} = \{w_i\}_{i=1,2,3}$  denotes the transverse displacement vector in  $x_1, x_2, x_3$  direction, and  $\boldsymbol{\theta} = \{\theta_i\}_{i=1,2,3}$  denotes the rotation vector related to the  $x_1, x_2, x_3$  axis.

$$a\left(\left(\mathbf{w}^{(r)}, \boldsymbol{\theta}^{(r)}\right), \left(\bar{\mathbf{w}}, \bar{\boldsymbol{\theta}}\right)\right) = \lambda^{(r)} b\left(\left(\mathbf{w}^{(r)}, \boldsymbol{\theta}^{(r)}\right), \left(\bar{\mathbf{w}}, \bar{\boldsymbol{\theta}}\right)\right), \quad \forall \left(\bar{\mathbf{w}}, \bar{\boldsymbol{\theta}}\right) \in U, \quad \left(\mathbf{w}, \boldsymbol{\theta}\right) \in U, \quad (2)$$

where  $(\cdot)^{(r)}$  denotes the eigenvector of  $r$ th natural mode and  $\lambda^{(r)}$  denotes its eigenvalue. Moreover, the notation  $(\bar{\cdot})$  expresses a variation, and  $U$  expresses the admissible function space in which the given constraint conditions of  $(\mathbf{w}, \boldsymbol{\theta})$  are satisfied. The bilinear form  $a(\cdot, \cdot)$  and  $b(\cdot, \cdot)$  are defined respectively, as shown below:

$$\begin{aligned} a\left(\left(\mathbf{w}^{(r)}, \boldsymbol{\theta}^{(r)}\right), \left(\bar{\mathbf{w}}, \bar{\boldsymbol{\theta}}\right)\right) &= \sum_{j=1}^N \int_{\Omega^j} \left\{ \left( w_{1,3}^{(r)} - x_2 \theta_{3,3}^{(r)} - \theta_2^{(r)} \right) \mu \left( \bar{w}_{1,3} - x_2 \bar{\theta}_{3,3} - \bar{\theta}_2 \right) \right. \\ &\quad + \left( w_{2,3}^{(r)} + x_1 \theta_{3,3}^{(r)} + \theta_1^{(r)} \right) \mu \left( \bar{w}_{2,3} + x_1 \bar{\theta}_{3,3} + \bar{\theta}_1 \right) \\ &\quad \left. + \left( w_{3,3}^{(r)} - x_1 \theta_{2,3}^{(r)} + x_2 \theta_{1,3}^{(r)} \right) E \left( \bar{w}_{3,3} - x_1 \bar{\theta}_{2,3} + x_2 \bar{\theta}_{1,3} \right) \right\} d\Omega, \end{aligned} \quad (3)$$

$$\begin{aligned} b\left(\left(\mathbf{w}^{(r)}, \boldsymbol{\theta}^{(r)}\right), \left(\bar{\mathbf{w}}, \bar{\boldsymbol{\theta}}\right)\right) &= \sum_{j=1}^N \int_{\Omega^j} \rho \left\{ \left( w_1^{(r)} - x_2 \theta_3^{(r)} \right) \left( \bar{w}_1 - x_2 \bar{\theta}_3 \right) + \left( w_2^{(r)} + x_1 \theta_3^{(r)} \right) \left( \bar{w}_2 + x_1 \bar{\theta}_3 \right) \right. \\ &\quad \left. + \left( w_3^{(r)} - x_1 \theta_2^{(r)} + x_2 \theta_1^{(r)} \right) \left( \bar{w}_3 - x_1 \bar{\theta}_2 + x_2 \bar{\theta}_1 \right) \right\} d\Omega, \end{aligned} \quad (4)$$

where  $\mu$ ,  $E$ ,  $\rho$  denote the Lamé parameters, the Young's modulus, and the material density, respectively. Moreover, the tensor subscript notation uses Einstein's summation convention and a partial differential notation for the spatial coordinates  $(\cdot)_{,i} = \partial(\cdot) / \partial x_i$ .

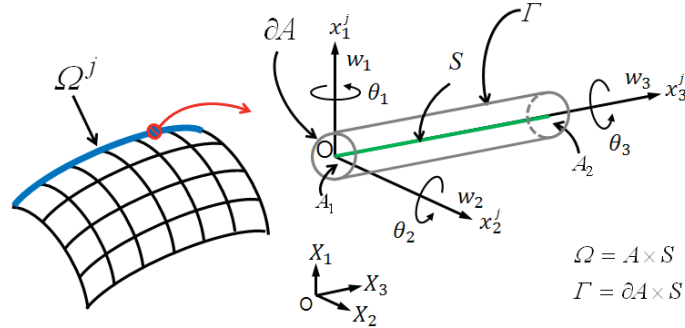


Figure 1. Frame structure composed of members consisting of Timoshenko beams

*Domain variation*

In the frame structure shown in Fig. 2, we consider that member  $j$  having an initial domain  $\Omega^j$  and the centroidal axis  $S^j$  undergoes the domain variation  $V^j$  (design velocity field) in the normal direction to the axis such that its domain and axis become  $\Omega_s^j$  and  $S_s^j$ , respectively. The subscript  $s$  expresses the iteration histories of the domain variation. Defining the notation  $\mathbf{n}_1$  and  $\mathbf{n}_2$  as outward unit normal vectors of the centroidal axis in the  $\mathbf{x}_1$  and  $\mathbf{x}_2$  directions,  $V^j$  can be expressed by:

$$V^j = (V^j \cdot \mathbf{n}_1) \mathbf{n}_1^j + (V^j \cdot \mathbf{n}_2) \mathbf{n}_2^j. \tag{5}$$

In this study, a beam of a uniform rectangular cross section with height  $h_1$  and width  $h_2$  is considered as shown in Fig. 3. The relationships of  $(V \cdot \mathbf{n}^t) \mathbf{n}^t = (-V \cdot \mathbf{n}^b) \mathbf{n}^b$  and  $(V \cdot \mathbf{n}^r) \mathbf{n}^r = (-V \cdot \mathbf{n}^l) \mathbf{n}^l$  are assumed by using the notations  $\mathbf{n}^t$ ,  $\mathbf{n}^b$ ,  $\mathbf{n}^r$  and  $\mathbf{n}^l$ , which denote the unit outward normal vector at the top, bottom, right and left edges of the cross section, respectively. Moreover,  $\mathbf{n}_1$ ,  $\mathbf{n}_2$  denote unit vectors of the centroid in the directions of axis  $\mathbf{x}_1$  and  $\mathbf{x}_2$ , and then they have the relationships of  $\mathbf{n}_1 = \mathbf{n}^t = -\mathbf{n}^b$ ,  $\mathbf{n}_2 = \mathbf{n}^r = -\mathbf{n}^l$ , respectively.

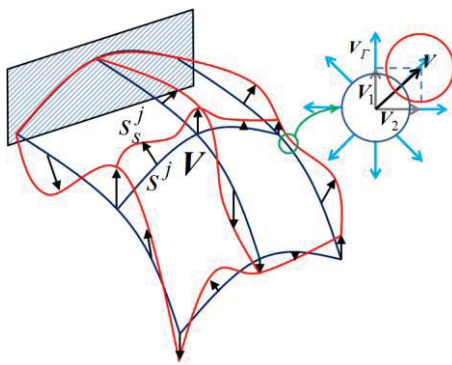


Figure 2. Shape variation

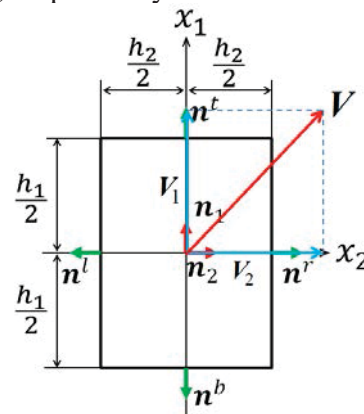


Figure 3. Sign notation of cross section

*Eigenvalue maximization problem and the shape gradient function*

With the aim of maximizing the specified order  $r$  th vibration eigenvalue  $\lambda^{(r)}$ , or minimizing  $-\lambda^{(r)}$ , introducing the natural vibration equation stated in Eq.(2) and the maximum allowable volume as the constraint conditions, the shape optimization problems for finding  $V$  can be formulated as:

$$\text{Given } \Omega, \quad (6)$$

$$\text{find } V \text{ or } \Omega_s, \quad (7)$$

$$\text{that minimizes } -\lambda^{(r)}, \quad (8)$$

$$\text{subject to Eq. (2) and } M\left(=\sum_{j=1}^N \int_{S^j} AdS\right) \leq \hat{M}, \quad (9)$$

where  $M$  and  $\hat{M}$  denote the volume and its constraint value, respectively.

As the order of the specified mode may differ from the one at the initial shape after the shape is updated, MAC (Modal Assurance Criterion) is introduced for tracking the specified mode. MAC value is calculated by the following equation,

$$MAC(\phi_0^{(r)}, \phi_s^{(i)}) = \frac{|\phi_0^{(r)T} \phi_s^{(i)}|^2}{(\phi_0^{(r)T} \phi_0^{(r)})(\phi_s^{(i)T} \phi_s^{(i)})}. \quad (10)$$

The notation  $\phi_0^{(r)}$  denotes the specified  $r$  th eigenvector of the initial shape.  $\phi_s^{(i)}$  denotes the  $i$  th eigenvector ( $i=1$  to the maximum analysis order) of the shape after  $s$  number of times updated, and the superscript T denotes the transpose of a vector. The mode that has the maximum MAC value in all modes is regarded as the corresponding mode to be tracked.

Allowing  $(\bar{w}, \bar{\theta})$  and  $\Lambda$  denote the Lagrange multipliers for the specified natural vibration equation and the volume constraint, respectively, the Lagrange functional  $L$  associated with this problem can be expressed as

$$L(\Omega, (\mathbf{w}^{(r)}, \boldsymbol{\theta}^{(r)}), (\bar{w}, \bar{\theta}), \Lambda) = -\lambda^{(r)} + \lambda^{(r)} b((\mathbf{w}^{(r)}, \boldsymbol{\theta}^{(r)}), (\bar{w}, \bar{\theta})) - a((\mathbf{w}^{(r)}, \boldsymbol{\theta}^{(r)}), (\bar{w}, \bar{\theta})) + \Lambda(M - \hat{M}). \quad (11)$$

The material derivative  $\dot{L}$  of the Lagrange functional can be derived as shown in Eq. (12) using the design velocity field of the centroidal axis  $V$ , the design velocity field on the circumference surface  $V_\Gamma$ , and an outward unit normal vector  $\mathbf{n}$  on the centroidal axis or the virtual cross section.

$$\begin{aligned} \dot{L} = & \dot{\lambda}^{(r)} \left\{ b((\mathbf{w}^{(r)}, \boldsymbol{\theta}^{(r)}), (\bar{w}, \bar{\theta})) - 1 \right\} + \lambda^{(r)} b\left( (\mathbf{w}^{(r)'}, \boldsymbol{\theta}^{(r)'}) , (\bar{w}, \bar{\theta}) \right) + \lambda^{(r)} b\left( (\mathbf{w}^{(r)}, \boldsymbol{\theta}^{(r)}) , (\bar{w}', \bar{\theta}') \right) \\ & - a\left( (\mathbf{w}^{(r)'}, \boldsymbol{\theta}^{(r)'}) , (\bar{w}, \bar{\theta}) \right) - a\left( (\mathbf{w}^{(r)}, \boldsymbol{\theta}^{(r)}) , (\bar{w}', \bar{\theta}') \right) + \dot{\Lambda}(M - \hat{M}) + \langle G\mathbf{n}, V \rangle, \quad V \in C_\Theta \end{aligned} \quad (12)$$

$$\begin{aligned} \langle G\mathbf{n}, V \rangle \equiv & \sum_{j=1}^N \left\{ \int_{\Gamma^j} G V_\Gamma \cdot \mathbf{n} d\Gamma + \int_{S^j} G_0 V \cdot \mathbf{n} dS \right\} \\ = & \sum_{j=1}^N \left[ - \int_{\Gamma^j} \left\{ (w_{1,3}^{(r)} - x_2 \theta_{3,3}^{(r)} - \theta_2^{(r)}) \mu (\bar{w}_{1,3} - x_2 \bar{\theta}_{3,3} - \bar{\theta}_2) + (w_{2,3}^{(r)} - x_1 \theta_{3,3}^{(r)} + \theta_1^{(r)}) \mu (\bar{w}_{2,3} + x_1 \bar{\theta}_{3,3} + \bar{\theta}_1) \right\} \right. \end{aligned}$$

$$\begin{aligned}
& + \left( w_{3,3}^{(r)} - x_1 \theta_{2,3}^{(r)} + x_2 \theta_{1,3}^{(r)} \right) E \left( \bar{w}_{3,3} - x_1 \bar{\theta}_{2,3} + x_2 \bar{\theta}_{1,3} \right) \left\{ \mathbf{V}_r \cdot \mathbf{n} \, d\Gamma \right. \\
& + \int_{\Gamma^j} \lambda^{(r)} \rho \left\{ \left( w_1^{(r)} - x_2 \theta_3^{(r)} \right) \left( \bar{w}_1 - x_2 \bar{\theta}_3 \right) + \left( w_2^{(r)} + x_1 \theta_3^{(r)} \right) \left( \bar{w}_2 + x_1 \bar{\theta}_3 \right) \right. \\
& + \left. \left. \left( w_3^{(r)} - x_1 \theta_2^{(r)} + x_2 \theta_1^{(r)} \right) \left( \bar{w}_3 - x_1 \bar{\theta}_2 + x_2 \bar{\theta}_1 \right) \right\} \mathbf{V}_r \cdot \mathbf{n} \, d\Gamma \right. \\
& \left. + \int_{S^i} \Lambda AHV \cdot \mathbf{n} dS \right], \tag{13}
\end{aligned}$$

where  $G\mathbf{n}$  ( $\equiv \mathbf{G}$ ) expresses the shape gradient function (i.e., sensitivity function), which is a coefficient function in terms of  $\mathbf{V}_r$  or  $\mathbf{V}$ , and the notation  $H$  denotes the curvature of the centroidal axis. The notations  $(\cdot)'$  and  $(\dot{\cdot})$  are the shape derivative and the material derivative with respect to the domain variation, respectively (Choi and Kim, 2005).

The optimality conditions of the Lagrange functional  $L$  with respect to  $(\mathbf{w}^{(r)}, \boldsymbol{\theta}^{(r)})$ ,  $(\bar{\mathbf{w}}, \bar{\boldsymbol{\theta}})$  and  $\Lambda$  are expressed as:

$$a\left(\left(\mathbf{w}^{(r)}, \boldsymbol{\theta}^{(r)}\right), \left(\bar{\mathbf{w}}', \bar{\boldsymbol{\theta}}'\right)\right) = \lambda^{(r)} b\left(\left(\mathbf{w}^{(r)}, \boldsymbol{\theta}^{(r)}\right), \left(\bar{\mathbf{w}}', \bar{\boldsymbol{\theta}}'\right)\right), \quad \forall \left(\bar{\mathbf{w}}', \bar{\boldsymbol{\theta}}'\right) \in U, \tag{14}$$

$$a\left(\left(\mathbf{w}^{(r)'}, \boldsymbol{\theta}^{(r)'}\right), \left(\bar{\mathbf{w}}, \bar{\boldsymbol{\theta}}\right)\right) = \lambda^{(r)} b\left(\left(\mathbf{w}^{(r)'}, \boldsymbol{\theta}^{(r)'}\right), \left(\bar{\mathbf{w}}, \bar{\boldsymbol{\theta}}\right)\right), \quad \forall \left(\mathbf{w}^{(r)'}, \boldsymbol{\theta}^{(r)'}\right) \in U, \tag{15}$$

$$b\left(\left(\mathbf{w}^{(r)}, \boldsymbol{\theta}^{(r)}\right), \left(\bar{\mathbf{w}}, \bar{\boldsymbol{\theta}}\right)\right) = 1, \tag{16}$$

$$\dot{\Lambda} (M - \bar{M}) = 0, \quad M - \bar{M} \leq 0, \quad \Lambda \geq 0. \tag{17}(18)(19)$$

When the optimality conditions are satisfied,  $\dot{L}$  becomes:

$$\dot{L} = \langle G\mathbf{n}, \mathbf{V} \rangle. \tag{20}$$

Considering the self-adjoint relationship,  $(\mathbf{w}^{(r)}, \boldsymbol{\theta}^{(r)}) = (\bar{\mathbf{w}}, \bar{\boldsymbol{\theta}})$  obtained by Eq.(14) and Eq.(15) and  $\int_{\Gamma^j} (\dot{\cdot}) d\Gamma = \int_{S^i} \int_{\partial A} (\dot{\cdot}) dAdS$ , the shape gradient density functions,  $G_1, G_2, G_0$ , are derived in the following equations.

$$\langle G\mathbf{n}, \mathbf{V} \rangle = \sum_{j=1}^N \int_{S^j} \{G_1 \mathbf{V} \cdot \mathbf{n}_1 + G_2 \mathbf{V} \cdot \mathbf{n}_2 + G_0 \mathbf{V} \cdot \mathbf{n}_1\} dS, \tag{21}$$

$$G_1 = 2h_1 h_2 \left\{ E w_{3,3}^{(r)} \theta_{2,3}^{(r)} - \mu \theta_{3,3}^{(r)} \left( w_{2,3}^{(r)} + \theta_1^{(r)} \right) + \lambda^{(r)} \rho \left( w_2^{(r)} \theta_3^{(r)} - w_3^{(r)} \theta_2^{(r)} \right) \right\}, \tag{22}$$

$$G_2 = 2h_1 h_2 \left\{ \mu \theta_{3,3}^{(r)} \left( w_{1,3}^{(r)} - \theta_2^{(r)} \right) - E w_{3,3}^{(r)} \theta_{1,3}^{(r)} + \lambda^{(r)} \rho \left( w_3^{(r)} \theta_1^{(r)} - w_1^{(r)} \theta_3^{(r)} \right) \right\}, \tag{23}$$

$$G_0 = \Lambda AH. \tag{24}$$

The derived shape gradient function is utilized for obtaining the optimal shape by using the free-form optimization method for frame structures which will be explained in the next section.

### Free-form optimization method for frame structures

The free-form optimization method for frame structures was developed by the authors for finding an optimal free-form shape of a frame structure (Shimoda, et al, 2013). It is a node-based shape optimization method based on the  $H^1$  gradient method, which is a gradient method in a Hilbert space, and it can treat all nodes as design variables without shape parameterizations (Azegami and

Takeuchi, 2006, Shimoda, 2011). In this study, we applied this method to the natural vibration problem. In this method, the negative shape gradient function  $-G(=-Gn)$  is applied as a distributed force to a fictitious-elastic frame structure in the normal direction to the centroidal axis under a Robin boundary condition, i.e., an elastic support condition with a distributed spring constant  $\alpha > 0$  as shown in Fig. 4. The stiffness matrix is used for the positive definite matrix required for a gradient method in a Hilbert space, and it also takes the role of a smoother to maintain the mesh regularity while reducing the objective functional. The shape variation  $V=(V_1, V_2, V_3)$  is determined in the fictitious-elastic frame analysis, which is called velocity analysis, and the obtained  $V$  is used to update the shape. The governing equation of the velocity analysis for  $V$  is expressed as Eq. (25). The constraint conditions for velocity analysis are arbitrarily set by considering each individual shape design conditions.

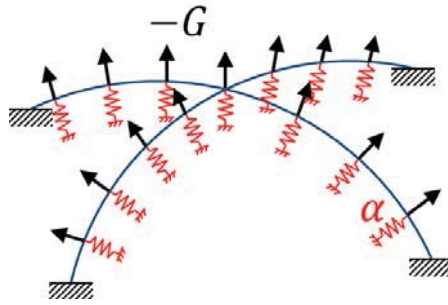


Figure 4. Schematic of the free-form optimization method for frame structures

$$a((V, \theta), (\bar{w}, \bar{\theta})) + \alpha \langle (V \cdot n) n, (\bar{w}, \bar{\theta}) \rangle = -\langle Gn, (\bar{w}, \bar{\theta}) \rangle, \quad \forall (\bar{w}, \bar{\theta}) \in C_\theta, \quad (V, \theta) \in C_\theta, \quad (25)$$

$$C_\theta = \left\{ (V_1, V_2, V_3, \theta_1, \theta_2, \theta_3) \in (H^1(S))^6 \mid \text{satisfy Dirichlet condition for shape variation} \right\}. \quad (26)$$

In problems where convexity is assured, this gradient method reduces the Lagrange functional in the process of updating the frame shape using the design velocity field  $V$  determined by Eq. (25). The optimal free-form frame structure is obtained by iterating a process consisting of (1) eigenvalue analysis, (2) sensitivity analysis for calculating the shape gradient functions, (3) velocity analysis and (4) shape updating. The analyses in (1) and (3) are conducted using a general FEM code.

### Calculated design examples

To verify the effectiveness and validity of the proposing optimization method for the natural vibration problems, two design problems are solved by using the developed system based on the method. Although the eigenvalue analyses were performed up to the 10th mode, the result graphs shows only the modes related to the specified mode, and those modal orders at the initial shape are tracked through the plots.

#### Square frame model

The first design example is a square frame model having two cross members inside (size: 1000  $\times$  1000). For all members, the cross sections are a square 20 on a side. Each of the circumference members and the cross members are meshed into 2 and 20 two-node elements, respectively, for a total of 48 elements. For this problem, the 1st eigenvalue is maximized and the design object is the cross members. The volume constraint was set as 1.05 times the initial value. Fig. 5(a) shows the initial shape and the boundary conditions for eigenvalue analysis and Fig. 5(b) shows the conditions

for velocity analysis. The numbers with a triangle in the figures express the single point constraint (SPC), and 1, 2, 3 express the  $X_1, X_2, X_3$  translational degrees of freedom, respectively. Fig. 6(a) shows the initial 1st modal shape and Fig. 6(b) shows the obtained optimal shape, in which the cross members became smooth arches. The iteration convergence histories of the eigenvalue and the volume are shown in Fig. 6(c), where the values were normalized to those of the initial shape. Without switching to the higher modes, the eigenvalue was maximized at 1.26 times the value of the initial while satisfying the volume constraint.

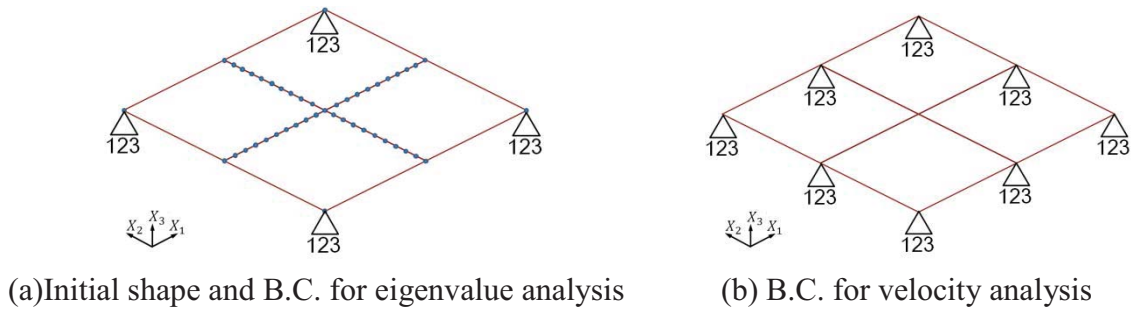


Figure 5. Initial shape and boundary conditions of square frame model

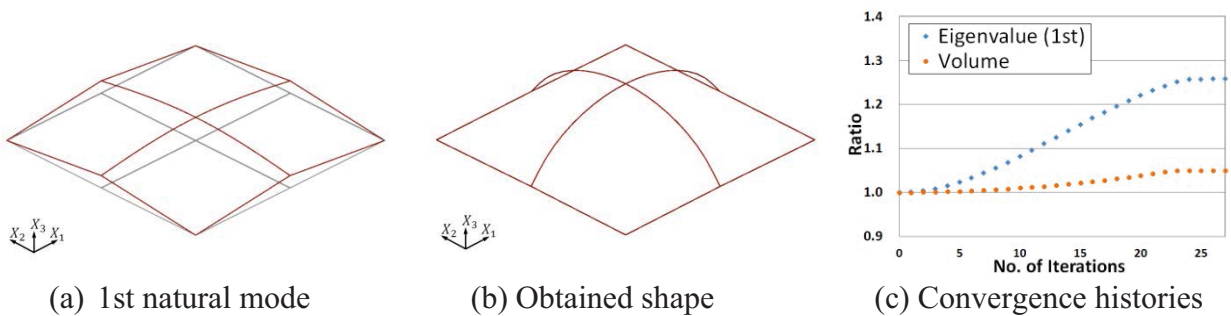


Figure 6. Calculated results of square frame model

*Portal frame model*

The second design problem is concerned with a portal frame model (size:  $3000 \times 2800 \times 600$ ) as shown in Fig. 7(a). The cross sections are a square 10 on a side for the members that compose the sine-curved top lattice and a square 20 on a side for the side support members, respectively. All the members were meshed with two-node elements at the intersections of square grids, for a total of 398 elements. For this problem, the 2nd eigenvalue was maximized and the volume constraint was set as 1.01 times the initial value. Fig.7(a) shows the initial shape and the boundary conditions for eigenvalue analysis and Fig. 7(b) shows the conditions for velocity analysis. Fig. 8(a) shows the initial 2nd modal shape and Fig. 8(b) shows the obtained optimal shape, in which two beads were created along with the free edges and the side support members became slightly recurved. The iteration convergence histories of the eigenvalue and the volume are shown in Fig. 8(c), where the values were normalized to those of the initial shape. Without switching to the lower or higher modes, the eigenvalue was maximized at 6.40 times the value of the initial while satisfying the volume constraint.

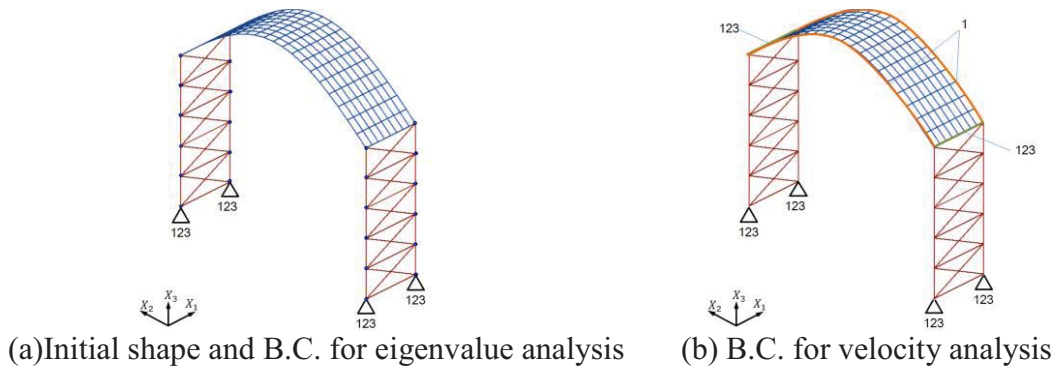


Figure 7. Initial shape and boundary conditions of portal frame model

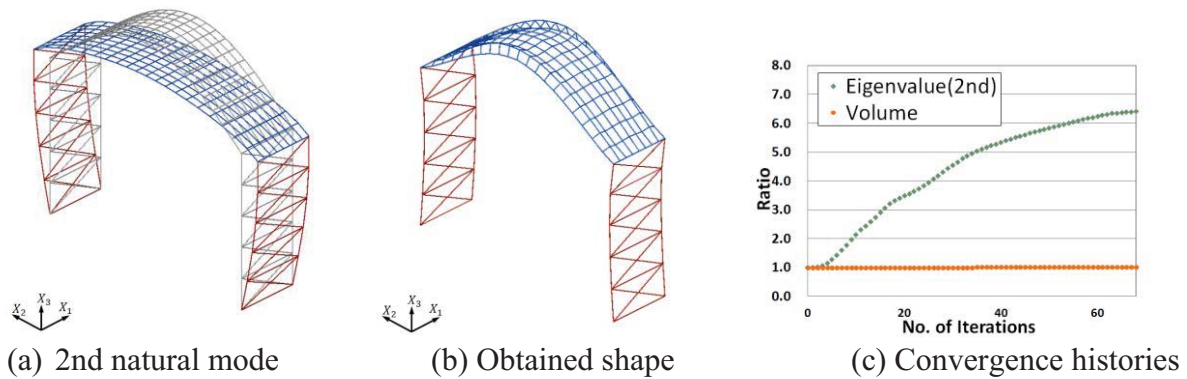


Figure 8. Calculated results of portal frame model

## Conclusions

The free-form optimization method for frame structures was applied to the natural vibration problems that aim to maximize a specified eigenvalue. It is a node-based method that does not require any shape parameterization and it can efficiently find the smooth optimal shape for large scale problems under arbitrary shape design conditions. With the developed optimization system based on the proposing method, two design problems were solved and the validity and the effectiveness were confirmed.

## References

- Azegami, H. and Takeuchi, K.(2006), A smoothing method for shape optimization: Traction method using the Robin condition. *International Journal of Computational Methods*, 3, 21–33
- Ohsaki, M. and Fujita, S. (2011), Multiobjective shape optimization of latticed shells for elastic stiffness and uniform member lengths, *Proceedings of International Symposium on Algorithmic Design for Architecture and Urban Design 2011, Tokyo*.
- Choi, K. K. and Kim, N. H.(2005), Structural Sensitivity Analysis and Optimization, 1, *Springer, New York*
- Hashemian, AH., Kargarnovin, MH. and Jam, JE. (2011), Optimization of geometric parameters of latticed structures using genetic algorithm, *Aircraft Engineering and Aerospace Technology*, 83, 59–68.
- Kaveh, A. and Bakhshpoori, T. (2013), OPTIMUM DESIGN OF SPACE TRUSSES USING CUCKOO SEARCH ALGORITHM WITH LÉVY FLIGHTS, *Transactions of Civil Engineering*, Vol. 37, No. C1, pp 1-15
- Shimoda, M.(2011), Free-form optimization method for designing automotive shell structures. *SAE, International Journal of Passenger Cars- Electronic and Electrical Systems*, 4, 42–54,
- Shimoda, M., LIU, Y., and Morimoto, T. (2013\*), Free-form Optimization Method for Frame Structures, *Structural and Multidisciplinary Optimization*, \*submitted in 2013
- Wang, D., Zhang, W. H., and Jiang, J. S. (2004), Truss Optimization on Shape and Sizing with Frequency Constraints, *AIAA Journal*, Vol. 42, No. 3, pp. 622-630.

## Analysis of Exterior Acoustics using the Edge-based Smoothed Finite Element Method (ES-FEM)

Wei Li <sup>1</sup>, Ming Lei <sup>1\*</sup>, Yingbin Chai <sup>1</sup> and G.R. Liu <sup>2</sup>

<sup>1</sup>Department of Naval Architecture and Ocean Engineering, Huazhong University of Science and Technology, Wuhan City, P. R. China 430074

<sup>2</sup> School of Aerospace Systems, University of Cincinnati, Cincinnati Ohio, 45221

\*Corresponding author: hustleiming@163.com

### Abstract

Solving acoustic problems governed by Helmholtz equation by standard finite method (FEM), the numerical dispersion error is not negligible when the wave increases due to the “overly-stiff” character of FEM. To overcome this numerical dispersion error, this paper uses the edge-based smoothed finite method (ES\_FEM) to analyze the 2D exterior scattering problems. Linear triangle elements and is employed separately to mesh the 2D computational domain. Using gradient smoothing technology to build a relatively soft stiffness thus the numerical dispersion error can significantly decreased. In addition, the gradient smoothing technology transfers domain integrals involving gradient of shape function to simple boundary integrals involving only shape function, which can reduce computing cost. In order to model exterior acoustic problems defined in unbounded domains, the unbounded domain is truncated by an artificial boundary on which the non-reflecting boundary condition is imposed to replace the Sommerfeld condition at infinite. Examples for exterior scattering problems with known exact solutions are calculated to demonstrate the ES-FEM realization, result shows that the ES-FEM is also very accurate. Compared FEM calculation process and results, ES-FEM is more effective and could achieve much more accurate result in solving exterior acoustic problems, especially when number is large.

**Keywords:** Smoothed Finite Element Method, Acoustic Scattering, Unbounded Domain, non-reflecting boundary

### 1. Introduction

Seeking for the numerical solution of acoustic problems governed by Helmholtz equation has been a widely concerned issue in numerical research which aims to improve the computational accuracy and efficiency and applicability of the algorithm. The analytical solution can be derived for simple acoustic problems, but it's difficult to derive analytical solution when acoustic model is relatively complex. Thus it cannot avoid using numerical methods to solve engineering problems. In the past few decades, many numerical methods are extensively used to get approximate solution of acoustic problems (Abboud, 1990; Avorinde, 1990; Dokumaci, 1991; Givoli, 1989 and Gerdes, 2000), especially the standard finite element method (FEM) (Lonny, 2006 and Harari, 2004) and boundary element method (BEM) (Burton, 1971; Colton, 1983 and Walsh, 2004). A known issue is that numerical method including FEM usually generate “numerical dispersion” error which cannot be neglected in high frequency range (the wave number  $k$  is large) (Suleau, 2000).

In order to eliminate the numerical dispersion error, researchers has proposed a series of methods. In recent years, element-free technique has been widely used and developed. Belytschko et al., 1994 proposed the element-free Galerkin method (EFGM), but this method is also sensitive to dispersion error. Bouillard et al., 1998 improved EFGM and obtained higher accuracy and better convergence. Petersen et al.



used high-order spectral element shape function to analyze acoustic problems, and it showed that this method lead to higher accuracy and stability as well as good computational efficiency (Petersen, 2006). Harari et al., 2004 applied stabilized finite element method to basic Galerkin form for Helmholtz equation and improved its stability. Although FEM has been widely used to solve acoustic problems, FEM solution shows the lower bound property due to the character of overly-stiff, and on the contrary, NS-FEM solution presents the upper bound property duo to its overly-soft character. In order to artificially control the character of the stiffness,  $\alpha$ -FEM (Liu, 2008, 2009a) was proposed with a controlling factor ( $\alpha$ ) whose value varies between 0 and 1.

In recent several years, smoothed finite element method (ES-FEM) was introduced by Liu et al., 2009b which combines FEM with strain smoothing techniques and it showed that ES-FEM can provide better accuracy and stability because ES-FEM settled the “overly stiff” issue that standard FEM may face. At first, ES-FEM was mainly used to solve solid mechanics problems like free and forced vibration (Dai, 2007; Cui, 2010 and Nguyen, 2010). Result showed that ES-FEM obtained more accurate natural frequency than FEM and thus obtained more accurate stress and strain. Later, ES-FEM was applied to solve acoustic problems and still behaves better than FEM. Z.C.He et al., 2010 studied the coupled problems of structural-acoustic by ES-FEM and successfully alleviated the shear locking phenomenon. Z.CHe et al., 2009 also studied pure acoustic problems governed by Helmholtz equation and demonstrated that ES-FEM achieved better result than FEM.

Since analysis of interior acoustic problems has been researched by SFEM, this paper pays attention on exterior acoustic problems and investigates if SFEM still behaves better than FEM. To solve acoustic problems in unbounded domain, an artificial boundary is usually introduced to make the computational domain finite and impose certain condition on it. Keller and Givoili, 1988 derived an exact non-reflecting boundary condition (the Dirichlet-to-Neumann condition) in case that the artificial boundary is a sphere. Berengers, 1994 proposed perfectly matched layer (PLM) method to solve Maxwell equation in unbounded domain. Local absorbing boundary condition (Wilcox, 1956) and infinite elements (Bettess, 1992) can also be applied to treat the artificial boundary. In this paper DtN boundary condition is used to deal with the artificial boundary.

In this paper, exterior acoustic problems are investigated by ES-FEM, and we further study the efficiency and accuracy of ES-FEM. The organization of this paper is as follows: section 2 is a briefly description of the computational model and a detailed introduction of ES-FEM formulation; section 3 is a comparison of ES-FEM to FEM in three aspects: the computing efficiency, the accuracy and the sensitivity to irregular mesh; section 4 is a demonstration of ES-FEM in practical application; section 5 shows the conclusions derived from the numerical results.

## 2. Basic theory of ES-FEM for acoustic problem

### 2.1 Governing equation

For ideal homogeneous fluid, the acoustic wave equation can be described as:

$$\nabla^2 p = \frac{1}{c^2} \frac{\partial^2 p}{\partial t^2} \quad (1)$$

where  $\nabla^2$  represents the Laplace operator,  $c$  is the speed of acoustic wave and  $p$  is the acoustic pressure. If the acoustic wave is further time-harmonic, Eq. (1) can be simplified as:

$$\nabla^2 p + k^2 p = 0 \quad (2)$$

where  $k$  represents the wave number.

Consider the situation that a scattering object outlined by boundary  $\Gamma_1$  is located in an infinite domain  $\Omega$ , solve the scattering field when an incident wave passes by. The problem can be stated as: given boundary condition (such as particle vibration velocity or a description about the velocity) on  $\Gamma_1$ , find acoustic pressure  $p$  in domain  $\Omega$  such that:

$$\nabla^2 p + k^2 p = 0 \quad \text{in } \Omega \quad (3)$$

$$\nabla p \cdot n = -j\rho\omega v_n \quad \text{On } \Gamma_1 \quad (4)$$

$$\lim_{r \rightarrow \infty} r \left( \frac{\partial p}{\partial r} - jkp \right) = 0 \quad \text{At infinity} \quad (5)$$

where  $v_n$ ,  $\omega$  and  $\rho$  represent the normal velocity on boundary  $\Gamma_1$ , the angle frequency and the density of the fluid, respectively. Eq. (5) is the Sommerfeld radiation condition which guarantees the positive energy flux at infinity so that the solution is unique. However Eq. (5) is not practicable for numerical method because it requires the mesh to be infinitely vast. An alternative is to introduce an artificial boundary  $\Gamma_2$  on which impose the following condition:

$$\nabla p \cdot n = -M \cdot p \quad \text{On } \Gamma_2 \quad (6)$$

In Eq. (6),  $M$  is the Dirichlet to Neumann (DtN) map which describes the relationship between pressure  $p$  and its derivative. In 2-D problems when the artificial boundary is a circle, Givoli derived that  $M$  could be expressed as:

$$M_n = -\frac{k \dot{H}_n^{(1)}(kR)}{\pi H_n^{(1)}(kR)} \cos n(\theta - \theta') \quad (7)$$

## 2.2 Formulation of standard FEM

To get the weak formulation of Helmholtz equation, firstly multiply test function  $w$  to Eq. (1):

$$\int_{\Omega} w (\Delta p + k^2 p) d\Omega = 0 \quad (8)$$

Then use Green's theorem to integrate Eq. (8) by parts to obtain:

$$-\int_{\Omega} \nabla w \cdot \nabla p d\Omega + k^2 \int_{\Omega} w \cdot p d\Omega + \int_{\Gamma} w (\nabla p \cdot n) d\Gamma = 0 \quad (9)$$

Adding the boundary condition Eq. (4) and Eq. (6) to Eq. (9):

$$\int_{\Omega} \nabla w \cdot \nabla p d\Omega - k^2 \int_{\Omega} w \cdot p d\Omega + \int_{\Gamma_2} w \cdot M \cdot p d\Gamma_2 = -j\rho\omega \int_{\Gamma_1} w \cdot v_n d\Gamma_1 \quad (10)$$

Assuming both the acoustic pressure  $p$  and the test function  $w$  can be expressed approximately as

$$p = \sum_{i=1}^m N_i p_i = NP \quad (11)$$

where  $p_i$  and  $N_i$  represent the unknown nodal pressure and FEM shape function, respectively. Applying Eq. (11) to Eq. (10), the discretized system equation is finally obtained as the following matrix form:

$$\{K - k^2 M + K_{AB}^b\} = \{F\} \quad (12)$$

where  $K$  is the FEM stiffness matrix:

$$K = \int_{\Omega} (\nabla N)^T \cdot \nabla N d\Omega \quad (13)$$

$M$  is the mass matrix:

$$M = \int_{\Omega} N^T \cdot N d\Omega \quad (14)$$

$K_{AB}^b$  is the boundary matrix:

$$K_{AB}^b = \sum_{n=0}^{\infty} -\frac{k}{\pi} \frac{\dot{H}_n^{(1)}(kR)}{H_n^{(1)}(kR)} \left( \int_{\Gamma_2} N_A [\cos n\theta \quad \sin n\theta] d\Gamma_2 \right) \left( \int_{\Gamma_2} N_B \begin{bmatrix} \cos n\theta' \\ \sin n\theta' \end{bmatrix} d\Gamma_2 \right) \quad (15)$$

and  $F$  is the force matrix:

$$F = -j\rho\omega \int_{\Gamma_1} N^T v_n d\Gamma_1 \quad (16)$$

Solving scattering problems, it is common to make the particle vibration velocity of the incident and scattered wave to meet certain conditions on surface of scatters, thus scattering problems is replaced by radiation problems. If the scattering object is rigid, it is granted that particle vibration velocity of the scattered wave  $V_s$  is negative to

that of the incident wave  $V_i$ , namely  $V_s = -V_i$ . When velocity is complex,

$V_s = -conj(V_i)$ , which means if the velocity angle phase of the incident wave at point

A advances that at point B, so it is the same with the scattered wave.

### 2.3 Creation of Edge-Based smoothing domain and ES-FEM stiffness matrix

To solve the same acoustic problem, ES-FEM and FEM have exactly the same mass matrix、boundary matrix and force matrix, the only difference between them lies in the stiffness matrix .ES-FEM introduces the gradient smoothing technique which

replaces the gradient component  $\nabla N$  with the smoothed item  $\overline{\nabla N}$ , thus the ES-FEM stiffness matrix can be written as:

$$\overline{K} = \int_{\Omega} (\overline{\nabla N})^T \overline{\nabla N} d\Omega \quad (17)$$

Assuming the 2-D acoustic domain  $\Omega$  has been divided into  $N_e$  “no-overlap” and “no-gap” triangle elements  $\Omega_i$  with  $N_n$  nodes and  $N_{eg}$  edges, such that:

$\Omega = \bigcup_{i=1}^{N_e} \Omega_i$  and  $\Omega_i \cap \Omega_j = 0, (i \neq j)$ . Find the central point of each element and

connect it with its neighbor nodes, therefore the sub-smoothing domain  $\Omega_k^s$  for edge

$k$  is created. Thus the problem domain  $\Omega$  can further be divided into  $N_{eg}$

“no-overlap” and “no-gap” smoothing domains, such that:

$\Omega = \bigcup_{k=1}^{N_{eg}} \Omega_k^s$  and  $\Omega_i^s \cap \Omega_j^s = 0 (i \neq j)$ . The inner character of smoothing technique for

acoustic pressure is smoothing the velocity. For the  $k^{th}$  smoothing domain  $\Omega_k^s$ , the smoothing velocity can be expressed as:

$$\overline{v}(x_k) = \int_{\Omega_k^s} v(x_k) W(x - x_k) d\Omega \quad (18)$$

In which  $W(x - x_k)$  is the smoothing function by:

$$W(x - x_k) = \begin{cases} 1/V_k & (x \in \Omega_k^s) \\ 0 & (x \notin \Omega_k^s) \end{cases} \quad (19)$$

where  $V_k = \int_{\Omega_k^s} d\Omega$  is the area of smoothing domain of edge  $k$ . Substituting Eq. (18)

into Eq. (17), the domain integration of velocity is transformed into the boundary integration of acoustic pressure:

$$\overline{v}(x_k) = -\frac{1}{j\rho\omega V_k} \int_{\Omega_k^s} \nabla p d\Omega = -\frac{1}{j\rho\omega V_k} \int_{\Gamma_k} p n d\Gamma \quad (20)$$

The gradient smoothing acoustic pressure can be written as:

$$\overline{\nabla} p = \sum_{l=1}^N \overline{B}_l p_l \quad (21)$$

where  $N$  is the total number of element surrounding the smoothing edge (for boundary edge  $N=1$ , for inner edge  $N=2$ ) and  $\overline{B}_l$  is the gradient smoothing

matrix with  $\overline{B}_I = [b_{I1} \quad b_{I2}]$ . Substituting shape function into Eq. (20) and using one point Gauss integration method to get

$$b_{Id} = \frac{1}{V_k} \int_{\Gamma_k} N_I n_d d\Gamma = \sum_{i=1}^{N_b} \frac{1}{V_k} N_I(x_i^{GP}) n_{id} l_i \quad d=1,2 \quad (22)$$

In which,  $\Gamma_k$  is the boundary of smoothing domain  $\Omega_k^s$ ,  $N_I$  the shape function,  $N_b$  the segment number of boundary  $\Gamma_k$ ,  $x_i^{GP}$  the midpoint of boundary segment,  $n_{id}$  the unit outward vector,  $l_i$  the length of boundary segment.

Finally Eq. (17) can be written as:

$$\overline{K} = \sum_{k=1}^{N_{eg}} \int_{\Omega_k} \overline{B}_I^T \overline{B}_I d\Omega \quad (23)$$

From above it can be found that: for FEM stiffness each node interacts only with the node belonging to the same element, which means the stiffness of each element is only distributed to the nodes belonging to it. In terms of ES-FEM stiffness, each node interacts not only with the node belonging to the same element, but also with the node belonging to its neighbor elements, which indicates that the stiffness of each element is distributed not only to the nodes belonging to it, but also to the nodes belonging to its neighbor elements. This special distribution increases the bandwidth of the stiffness matrix and seems to take more computation cost, but on the contrary ES-FEM introduces smoothing function to the domain integration and transfers it into simple boundary integration which greatly reduces the computation time. Besides that distribution is the way how ES-FEM softens the FEM stiffness and reduce numerical dispersion error caused by overly-rigid stiffness.

### 3. Numerical solution for 2D problems

In this section, an example with known exact solution is studied to analyze the computing efficiency, accuracy and mesh sensitivity of ES-FEM. Assume a rigid cylinder of infinite length is located in an unbounded domain, use both ES-FEM and FEM to solve the scattering pressure field when a plane wave passes by. The computation domain is the area surrounded by two circular boundary, one is the outline of the cylinder with radius  $a=0.2\text{m}$  and the other is the artificial boundary with radius  $R=1\text{m}$ . Assume the plane wave is propagating along the x-axis with the following formulation:

$$P_i = \exp(-jkx) \quad (23)$$

The exact solution of this scattering problem can be expressed by the following formulation:

$$P_s = \sum_{n=0}^{\infty} \left[ \begin{array}{c} \frac{d}{d(ka)} J_n(ka) \\ -(-j)^n \varepsilon_n \frac{d}{d(ka)} H_n^{(2)}(ka) \end{array} \right] H_n^{(2)}(kr) \cos(n\theta) \quad (24)$$

In Eq. (24), when  $n=0$ ,  $\varepsilon_n = 1$  otherwise  $\varepsilon_n = 2$ ,  $J_n(x)$  and  $H_n(x)$  are Bessel function of the first and third (Hankel function) kind.

### 3.1 Computing efficiency comparison

The main and the only difference of ES-FEM and FEM in solving the same problem is the global stiffness matrix. Therefore to evaluate the computing efficiency of ES-FEM and FEM is to compare their computing time on calculating the global stiffness matrix. It is common sense that differentiation and integration operator is much more time-costing than basic arithmetic operator such as addition and multiplication. Comparing to FEM, ES-FEM prevails in that ES-FEM does not need to perform differentiation even though the formulation has an item of  $\nabla N$ , because the smoothing technology is introduced to transform the domain integration of  $\nabla N$  into boundary integration of  $N$  as shown in Eq. (19). Thus the integration of ES-FEM is one-dimensional while the integration of FEM is two-dimensional which also reveals the advantage of ES-FEM in computing cost.

Use ANSYS mesh generator to mesh the computation domain, and set the mesh size to get five different models with 576, 1196, 1620, 2176 and 2660 nodes, each model being meshed by both T3 and Q4 element. The global stiffness matrix of both ES-FEM and FEM are programmed and computed by MATLAB whose version is MATLAB 2010 and the computing time result are listed in Table 1. Note that the main hardware equipment of the computer is as follows: Intel(R) Xeon(R) CPU E3-1230 V2 @ 3.30GHz, Intel(R) 7series /C 216 Chipset Family USB Enhanced Host Controller and ACPI x64-based PC.

It can be obviously observed from Table 1 that: (1) regardless of the element type, computing of both ES-FEM and FEM are linearly increasing with the total number of nodes; (2) for model of the same nodes, computing speed of ES-FEM is approximately 40 times faster than that of FEM in terms of T3 element, and 1400 times faster in terms of Q4 element; (3) the computing time of ES-FEM is less effected by element type than that of FEM. The detailed reason why ES-FEM computes faster than FEM lies in that: (1) ES-FEM does not need to perform differentiation or integration for both T3 and Q4 element; (2) for T3 element, FEM does not need to perform integration because  $\nabla N$  is constant; (3) for Q4 element, FEM needs to perform both differentiation and integration, and the integration is numerically solved by Gaussian integral with two Gauss points in each dimension. It can be concluded from above that ES-FEM behaves much better than FEM does in computing efficiency.

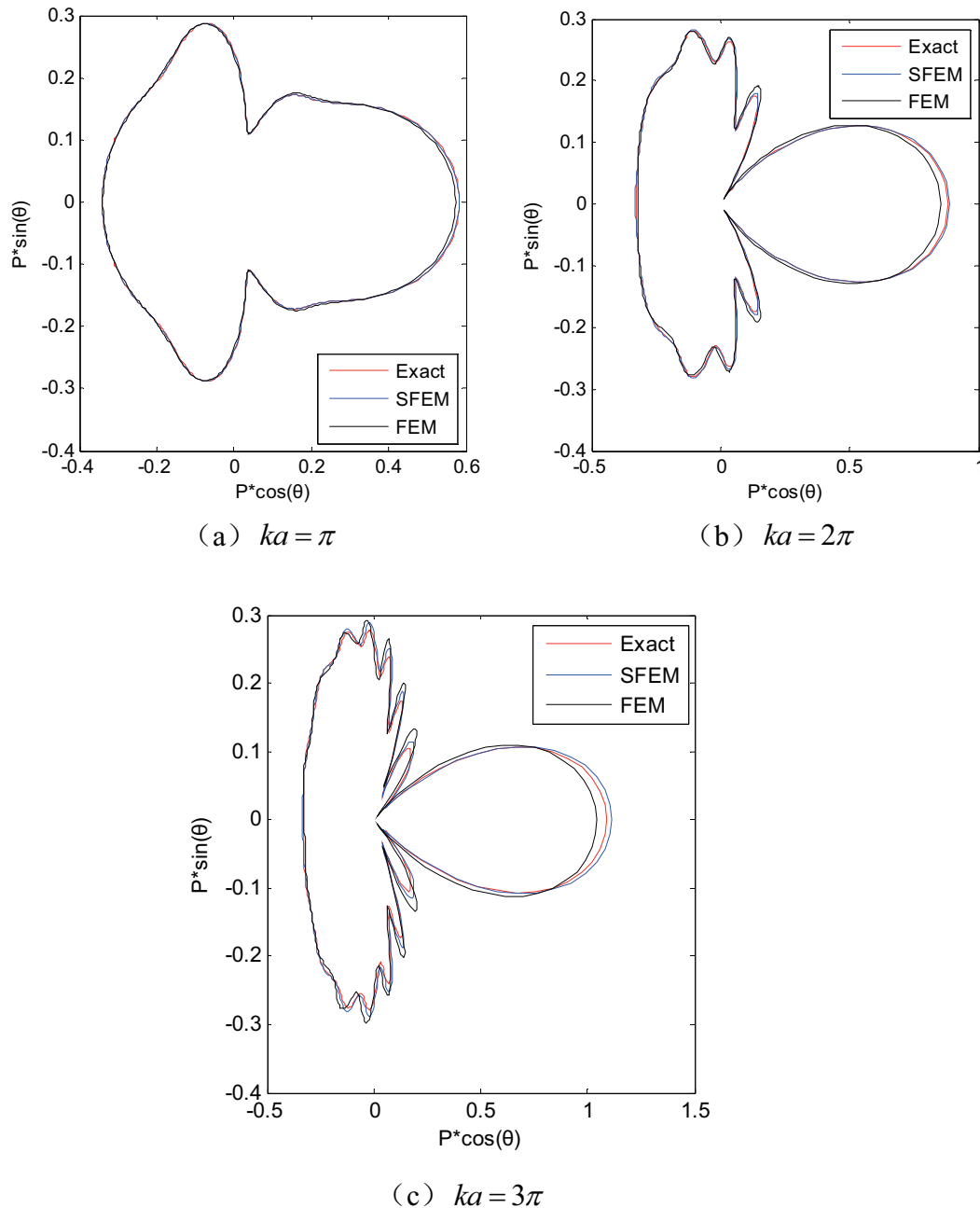
**Table 1. Computing time of the global stiffness matrix using ES-FEM and FEM, T3 means triangular element and Q4 means quadrilateral element**

Total node number	ES-FEM(T3) (s)	FEM(T3) (s)	ES-FEM(Q4) (s)	FEM(Q4) (s)
576	0.17	57.01	0.75	1034.28
1196	0.30	126.14	1.66	2254.13
1620	0.41	180.24	2.33	3325.81
2176	0.57	205.50	3.60	4955.62
2660	0.71	270.33	4.48	5250.75

### 3.2 Accuracy comparison

From last section it concludes that ES-FEM is more efficiency than FEM, this section focuses on the accuracy of ES-FEM. The accuracy of ES-FEM is investigated and the result comparison with FEM is mainly conducted in the following three aspects:

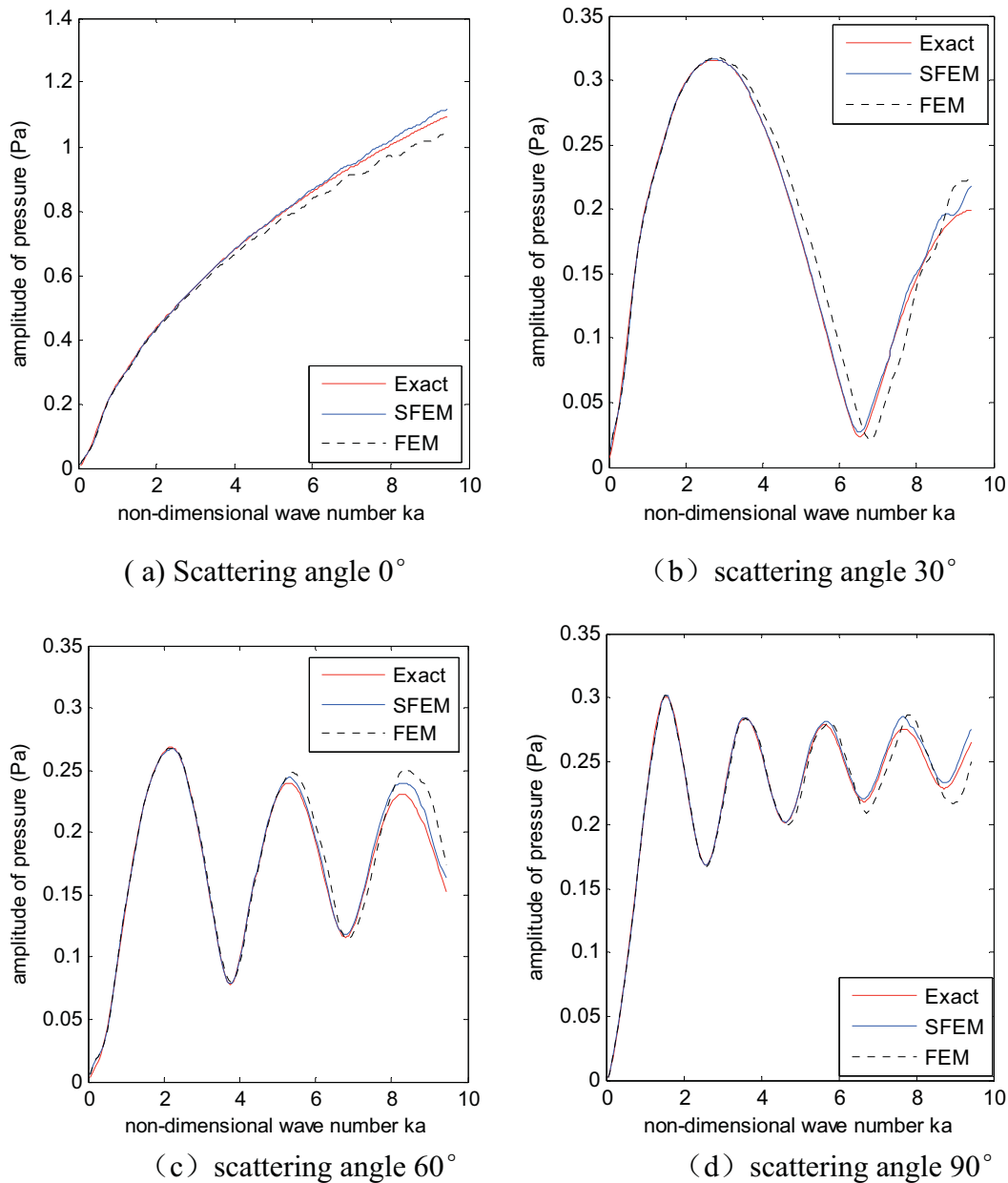
Firstly, for certain wave number, compare the numerical result of ES-FEM and FEM with the exact solution. To demonstrate scattering properties, pressures of nodes on artificial boundary are picked to be plotted in Fig.1, where (a), (b) and (c) are corresponding to low frequency ( $ka = \pi$ ), medium frequency ( $ka = 2\pi$ ) and high frequency ( $ka = 3\pi$ ). It is shown that both ES-FEM and FEM could achieve acceptable result on the whole and ES-FEM result is as same accurate as FEM result in terms of backward scattering. Besides, ES-FEM obtains more accurate result than FEM in terms of forward scattering, especially at petal-like corner. In order to demonstrate the accuracy of ES-FEM, special attention will be paid on forward scattering.



**Figure 1. Pressure distribution on artificial boundary at different wave number**  
 Secondly, for certain scattering angle, how the scattering pressure varies with non-dimensional number is investigated and behavior of ES-FEM and FEM is observed. Nodes on artificial boundary at angle of  $0^\circ$ ,  $30^\circ$ ,  $60^\circ$  and  $90^\circ$  are picked to demonstrate the comparison which are plotted in Fig.2. It is shown that: (1)

at low frequency band, numerical results of both ES-FEM and FEM are exactly the same as the exact solution; (2) at high frequency band, ES-FEM result is more close to exact solution than FEM result although error of both ES-FEM and FEM becomes larger as frequency increases.

Finally, separately observe the real part and the image part of the pressure result since the scattering field is complex. Pressures of nodes on artificial boundary at several scattering angles are picked for the comparison and the results are listed in Table 2, Table 3 and Table 4.



**Figure 2. Pressure variation with wave number at certain scattering angle**

It can be observed that both the real part and the image part of ES-FEM result pressure are very close to that of the exact solution in case of low frequency, medium frequency and even high frequency. In terms of FEM result, the amplitude of pressure is close to the exact solution, but neither the real part nor the image part of the pressure is very close to the exact solution. It can be concluded that: (1) for ES-FEM, the real part, the image part and the amplitude of the result pressure are all very



approximate to the exact solution; (2) for FEM, only the amplitude of the pressure is approximate to the exact solution while the real part and the image part of the pressure is less accurate than ES-FEM at low frequency and not stable at high frequency; (3) ES-FEM has better convergence and accuracy than FEM.

**Table 2. Pressures of nodes on artificial boundary at different scattering angle when non-dimensional wave number  $ka = \pi$ .**

Scattering angle	Exact (Pa)	ES-FEM result (Pa)	FEM result (Pa)
<b>0.00°</b>	0.3265 + 0.4839i	0.3262 + 0.4861i	0.3036 + 0.4901i
<b>10.25°</b>	0.3222 + 0.4289i	0.3220 + 0.4306i	0.3023 + 0.4360i
<b>20.51°</b>	0.3093 + 0.2875i	0.3094 + 0.2881i	0.2974 + 0.2970i
<b>30.75°</b>	0.2505 - 0.0197i	0.2512 - 0.0214i	0.2562 - 0.0073i
<b>39.87°</b>	0.2589 + 0.0008i	0.2597 - 0.0008i	0.2636 + 0.0133i
<b>50.13°</b>	0.2162 - 0.0566i	0.2170 - 0.0585i	0.2236 - 0.0454i
<b>60.38°</b>	0.1616 - 0.0268i	0.1622 - 0.0282i	0.1664 - 0.0193i
<b>70.63°</b>	0.0971 + 0.0630i	0.0973 + 0.0625i	0.0963 + 0.0655i
<b>79.75°</b>	0.0350 + 0.1565i	0.0349 + 0.1568i	0.0287 + 0.1551i
<b>90.00°</b>	-0.0352 + 0.2384i	-0.0356 + 0.2392i	-0.0459 + 0.2340i

**Table 3. Pressures of nodes on artificial boundary at different scattering angle when non-dimensional wave number  $ka = 2\pi$ .**

Scattering angle	Exact (Pa)	ES-FEM (Pa)	FEM (Pa)
<b>0.00°</b>	-0.6371 - 0.6103i	-0.6361 - 0.6247i	-0.4119 - 0.7495i
<b>10.25°</b>	-0.5159 - 0.4272i	-0.5151 - 0.4350i	-0.3708 - 0.5489i
<b>20.51°</b>	-0.2512 - 0.0955i	-0.2504 - 0.0925i	-0.2442 - 0.1727i
<b>30.75°</b>	0.1055 - 0.1056i	0.1081 - 0.1078i	0.1413 - 0.0632i
<b>39.87°</b>	0.0895 - 0.0718i	0.0918 - 0.0723i	0.1061 - 0.0380i
<b>50.13°</b>	0.1388 - 0.1727i	0.1419 - 0.1788i	0.2142 - 0.1125i
<b>60.38°</b>	0.1427 - 0.0627i	0.1448 - 0.0665i	0.1735 - 0.0152i
<b>70.63°</b>	0.0854 + 0.1619i	0.0854 + 0.1646i	0.0259 + 0.1732i
<b>79.75°</b>	-0.0255 + 0.2620i	-0.0272 + 0.2676i	-0.1186 + 0.2405i
<b>90.00°</b>	-0.1693 + 0.1676i	-0.1718 + 0.1703i	-0.2166 + 0.1170i

**Table 4. Pressures of nodes on artificial boundary at different scattering angle when non-dimensional wave number  $ka = 3\pi$ .**

Scattering angle	Exact (Pa)	ES-FEM (Pa)	FEM (Pa)
<b>0.00°</b>	0.8957 + 0.6257i	0.8940 + 0.6713i	0.0210 + 1.0468i
<b>10.25°</b>	0.4843 + 0.3266i	0.4766 + 0.3394i	0.0655 + 0.6087i
<b>20.51°</b>	-0.0811 + 0.0316i	-0.0972 + 0.0187i	0.0161 + 0.0076i
<b>30.75°</b>	-0.0506 + 0.0036i	-0.0518 + 0.0077i	-0.0674 - 0.0604i
<b>39.87°</b>	-0.0654 + 0.0632i	-0.0693 + 0.0723i	-0.1392 - 0.0521i
<b>50.13°</b>	0.0042 - 0.1933i	0.0138 - 0.2064i	0.2010 - 0.0575i
<b>60.38°</b>	0.1262 - 0.0857i	0.1374 - 0.0888i	0.1582 + 0.0755i

<b>70.63°</b>	0.0996 + 0.2164i	0.0997 + 0.2303i	-0.1640 + 0.1747i
<b>79.75°</b>	-0.1198 + 0.1812i	-0.1278 + 0.1877i	-0.2392 + 0.0023i
<b>90.00°</b>	-0.2345 - 0.1232i	-0.2412 - 0.1349i	0.03 - 0.2509i

### 3.3 Sensibility to irregular mesh

Since the computation domain boundary is curved, no mesh generator can produce 100% equilateral triangle elements. Use element quality statistics to evaluate the irregularity of the whole mesh, and the quality of each element is evaluated by the following expression:

$$Q = \frac{3\alpha_{\min}}{\pi} \quad (25)$$

where  $\alpha_{\min}$  is the minimum inner angle of the triangle and  $Q$  is a number between 0 and 1, 1 stands for equilateral triangle and 0 the worst element.

The original mesh data is automatically obtained by ANSYS mesh generator and the irregular mesh data is generated programmatically by the following expression:

$$x' = x + \Delta x \cdot r_c \cdot \beta_{ir} \quad (26)$$

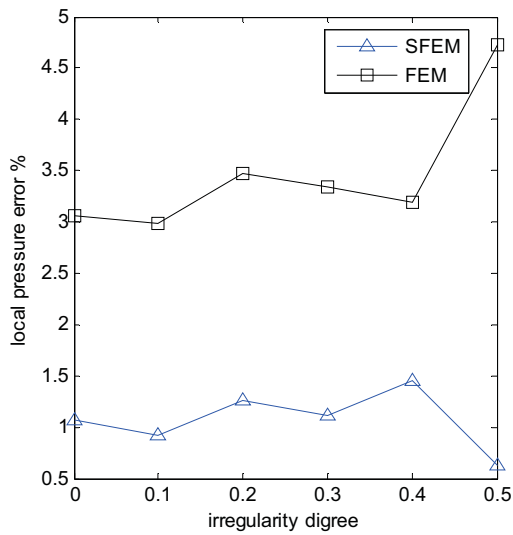
$$y' = y + \Delta y \cdot r_c \cdot \beta_{ir} \quad (27)$$

where  $r_c$  is a random number between -1.0 and 1.0 and  $\beta_{ir}$  is the irregularity degree whose value varies between 0 and 0.5. The larger value of  $\beta_{ir}$  brings about more irregular element distribution. Table 1 shows the element quality statistics of both original mesh data and the irregular mesh data varying with  $\beta_{ir}$ . Element quality statistics of original mesh and irregular mesh is listed in Table 5 from and it can be found that the percentage of worst element increases with irregularity degree while the percentage of best element decreases as expected.

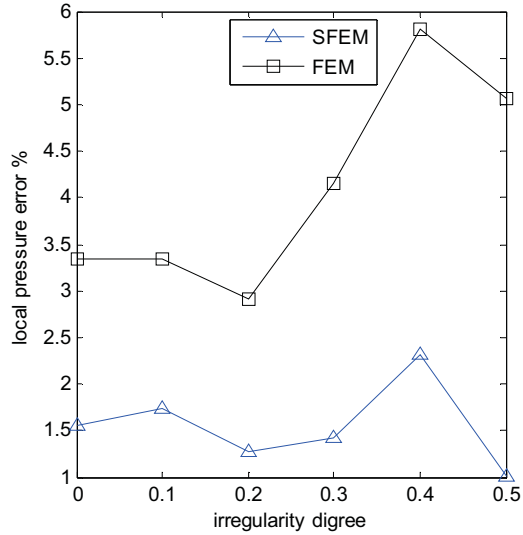
**Table 5. Element quality statistics with different irregularity degree  $\beta_{ir}$**

Q	Percentage of worst element ←-----→ percentage of best element									
	0~0.1	0.1~0.2	0.2~0.3	0.3~0.4	0.4~0.5	0.5~0.6	0.6~0.7	0.7~0.8	0.8~0.9	0.9~1.0
Original mesh	—	—	—	—	—	0.01%	6.88%	20.36%	35.38%	37.37%
$\beta_{ir}=0.1$	—	—	—	—	—	0.43%	10.77%	23.38%	34.78%	30.64%
$\beta_{ir}=0.2$	—	—	—	0.01%	0.51%	4.82%	15.31%	27.97%	33.02%	18.35%
$\beta_{ir}=0.3$	—	—	0.01%	0.54%	3.64%	10.72%	20.17%	27.11%	26.54%	11.28%

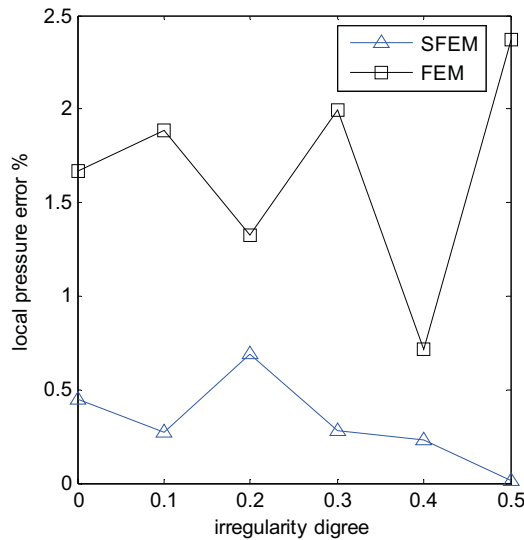
$\beta_{ir}=0.4$	0.02%	0.10%	0.69%	2.94%	7.95%	15.34%	21.09%	24.20%	19.90%	7.77%
$\beta_{ir}=0.5$	0.19%	0.79%	2.88%	6.64%	10.79%	16.40%	20.31%	19.80%	16.28%	5.92%



(a) Scattering angle is 0°



(b) scattering angle is 90°



(c) Scattering angle is 180°

**Figure 3. Local pressure error varies with the irregularity degree of mesh at certain scattering angle**

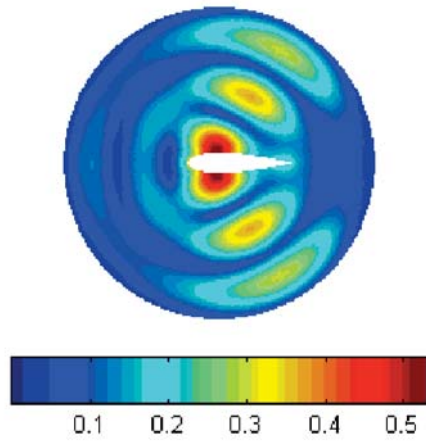
In order to investigate the sensibility of ES-FEM, five models with irregularity varies between 0.1 and 0.5 are generated for computation and for each model both ES-FEM solution and FEM solution are computed for purpose of comparison. The study is performed at medium frequency when non-dimensional wave  $ka=2\pi$ , and local pressure error of node on artificial boundary at scattering angle of 0°, 90° and 180° are calculated which are plotted in Fig.3. The pictures shows that: (1) ES-FEM has lower local pressure error than FEM on the whole; (2) local pressure error of

ES-FEM changes only a little as irregularity degree increases, and achieves even less error when irregularity is 0.5 compared with result from original mesh;(3) local pressure error of FEM has more visible change than ES-FEM as irregularity degree increases, and in general local pressure error becomes larger as irregularity degree increases.

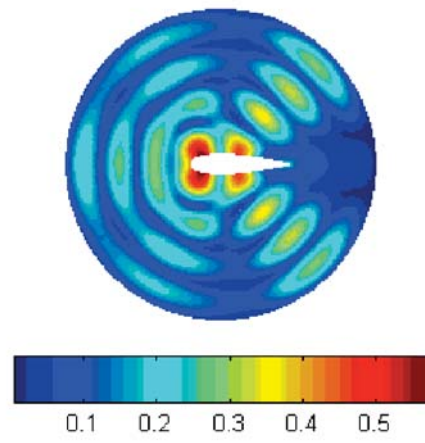
#### 4. Exterior acoustic problem for 2D rudder

Form above it can be found that ES-FEM has more efficiency and accuracy than FEM in solving scattering problem by a circular object. In this section, pressure distribution of a scattering field is studied by ES-FEM and FEM solution. The scattering field is formed by the outline of a 2D rudder and a circular artificial boundary with radius  $R=3\text{m}$ . It is difficult to derivate the exact solution for this problem since the curve of the 2D rudder is complicated, and the FEM solution of a very fine mesh is taken as the reference solution. For sake of simplicity, assume the density of the fluid media is  $1000 \text{ kg/m}^3$  and the wave velocity is  $1500 \text{ m/s}$ . The computation domain is meshed by linear triangular element with average mesh size  $h$  of  $0.05$  and  $0.2\text{m}$ . The former mesh size generates  $12970$  nodes and  $25451$  elements, being used to compute reference solution. The latter mesh size generates  $1575$  nodes and  $3007$  elements, being used to compute ES-FEM solution and FEM solution for comparison.

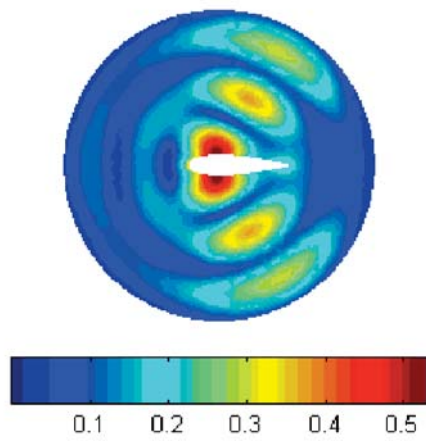
The acoustic pressure distribution of the problem domain is plotted in Figure 4 when wave number  $k = \pi$ , where (a), (b) and (c) are respectively obtained by FEM ( $12970$  nodes), ES-FEM ( $1575$  nodes) and FEM ( $1575$  nodes). Similarly, the acoustic pressure distribution in case of wave number  $k = 2\pi$  and  $k = 3\pi$  are plotted in Figure 5 and Figure 6. From figure 4 it is found that both ES-FEM and FEM solution are very approximate to the reference solution when wave number satisfying “the rule of thumb”, which requires  $kh < 1$  guaranteeing the accuracy. From Figure 5 it is found that ES-FEM solution is obviously more close to the reference solution than FEM solution when wave number is approaching the limit value according to “the rule of thumb”. Figure 6 shows that ES-FEM solution is still acceptable comparing to reference solution even though the wave number breaks “the rule of thumb”, while FEM solution departs a lot from the reference solution. This numerical example illustrates that ES-FEM could achieve more accurate result than FEM using the same mesh and calculate higher frequency.



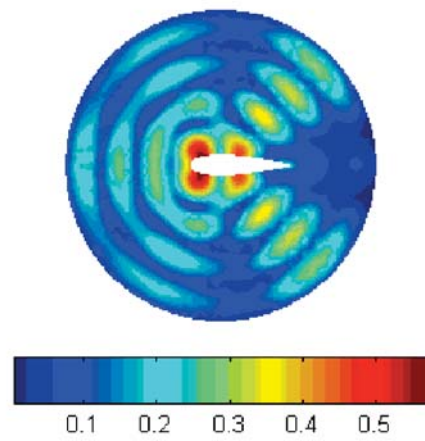
(a) Reference solution



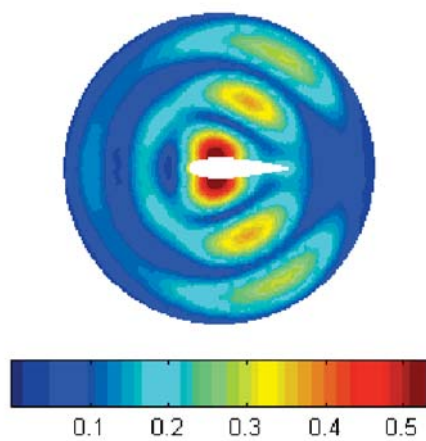
(a) Reference solution



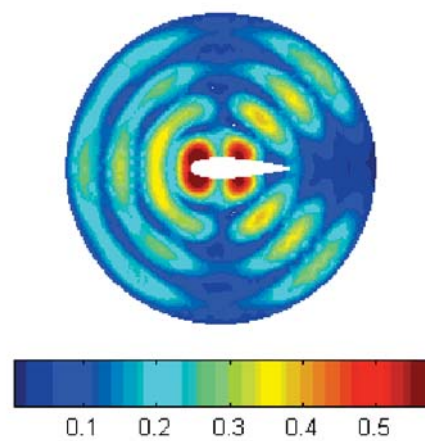
(b) ES-FEM solution



(b) ES-FEM solution

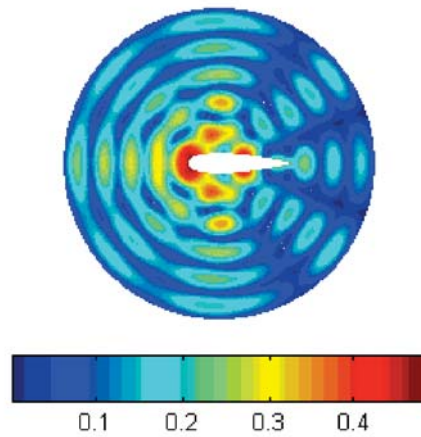


(c) FEM solution

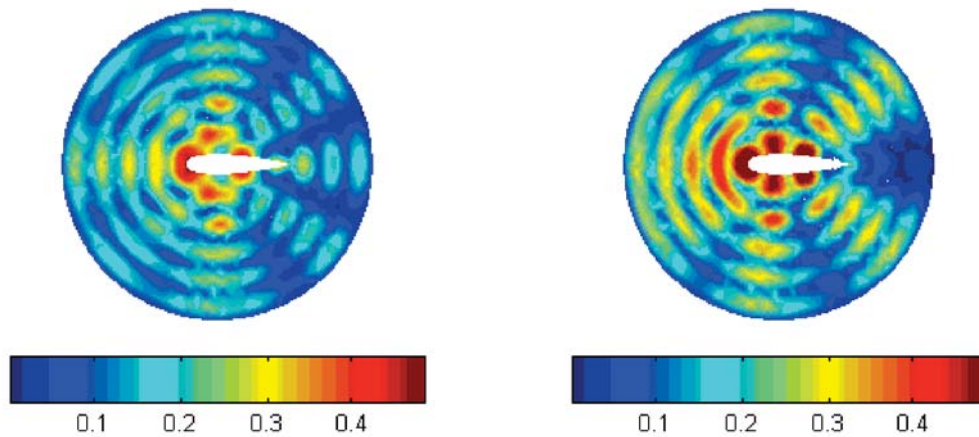
**Figure 4. Pressure distribution when wave number  $k = \pi$** 

(c) FEM solution

**Figure 5. Pressure distribution when wave number  $k = 1.5\pi$**



(a) Reference solution



(b) ES-FEM solution

(c) FEM solution

**Figure 6. Pressure distribution when wave number  $k = 2\pi$ .**

## 5. Conclusions and discussions

In this paper, T3 element is used to investigate 2D exterior scattering problem. MATLAB program code for FEM and ES-FEM is written to calculate the scattering field generated by an infinitely-long cylinder and a 2D rudder. The computation efficiency, accuracy and sensibility to irregular mesh of ES-FEM are studied and its comparison to FEM is also made. Conclusions could be derived as follows:

- (a) Solving 2D exterior acoustic problems, ES-FEM is more efficient than FEM in that ES-FEM creates no extra degrees of freedoms and transfers differentiation and integration into simple arithmetic operator when computing global stiffness matrix.
- (b) Comparing to analytical solution, both the global and local pressure results of ES-FEM is more accurate than that of FEM. Especially in high wave number, FEM result departs a lot from analytical solution while ES-FEM result is still accurate.

- (c) ES-FEM is less sensitive to the mesh irregularity than FEM.
- (d) For practical scattering problems, ES-FEM result is more accurate FEM result with the same mesh which suggests that ES-FEM is of great practical value for the future.

## References

- Abboud, N.N. and P.M. Pinsky (1990), Finite element solution and dispersion analysis for transient structural acoustics problem. *Appl. Mech. Rev.* 43 (5), pp. 381-388.
- Avorinde, E.O. (1990), Cylinder structural acoustic vibration by finite element method. *Struct. Compos.: Design. Process. Technol.*, pp. 507-514.
- Dokumacl, E. (1991), An integral equation formulation for boundary element analysis of acoustic radiation problems in viscous fluids. *J. Sound Vib.* 147 (2), pp. 335-348.
- Givoli, J.B.Keller (1989), A finite element method for large domains. *Comput Meth Appl Mech Engrg.*
- Gerdes, K. (2000), A review of infinite element methods for exterior Helmholtz problems. *J. Comput. Acoust.*
- Lonny, L. Thompson (2006), A review of finite-element methods for time-harmonic acoustics. *Acoustical Society of America*, pp. 1315-1330.
- Harari, I., Magoules, F. (2004), Numerical investigations of stabilized finite element computations for acoustics. *Wave Motion*, pp. 339-349.
- Burton, A. and Miller, G. (1971), The application of integral equation methods to the numerical solution of some exterior boundary-value problems. *Proc. R. Soc. London, Ser.* 323, pp. 201-210.
- Colton, D. and Kreiss, R. (1983), Integral equation methods in scattering theory. *Wiley-Interscience, New York.*
- Walsh, T., Demkowicz and Charles, R. (2004), Boundary element modeling of external human auditory system. *J. Acoust Soc Am*, 115(3), pp. 1033-1043.
- Suleau, S., Deraemaeker, A. (2000), Dispersion and pollution of meshless solution for the Helmholtz equation. *Comput Meth Appl Mech Engrg*, 190, pp. 639-657.
- Petersen, S., Dreyer, D. and Estorff, O.V. (2006), Assessment of finite and spectral element shape function or efficient iterative simulation of interior acoustics. *Comput. Meth. Appl. Mech Engrg*, 195, pp. 6463-6478.
- Harari, I., Magoules, F. (2004), Numerical investigations of stabilized finite element computations for acoustics. *Wave Motion*, 39, pp. 339-349.
- Belytschko, T., Lu, Y.Y. and Gu, L. (1994), Element-free Galerkin methods, *Nune Meth Engrg*, 37, pp. 229-256.
- Bouillard, Ph. and Suleau, S. (1998), Element-free Galerkin solutions for Helmholtz problems: formulation and numerical assessment of the pollution effect. *Comput Meth Appl Mech Engrg*, 162, pp. 317-335.
- Liu, G.R., Nguyen T.T. and Lam K.Y. (2008), A novel alpha finite element method ( $\alpha$ FEM) for exact solution to mechanics problems using triangular and tetrahedral elements. *Comput Meth Appl Mech Engrg*, pp. 3883-3896.
- Liu, G. R., Nguyen-Xuan, H. and Nguyen-Thoi, T. (2009a), A novel Galerkin-like weak form and a super convergent alpha finite element method (S alpha FEM) for mechanics problems using triangular meshes. *Journal of Computational Physics*, 228, pp. 4055-4087.

- Liu, G.R., Nguyen T.T. and Lam, K. Y. (2009b), An edge-based smoothed finite element method (ES-FEM) for static free, and forced vibration analysis. *J. Sound Vib*, 320, pp. 1100-1130.
- Cui, X.Y., Liu, G.R., Li, G.Y. and Zhao, X. (2010), Analysis of plates and shells using edge-based smoothed finite element method. *Comput Mech*, 45, pp. 141-156.
- Dai, K.Y., Liu, G.R. (2007), Free and forced vibration analysis using the smoothed finite element method (SFEM). *J. Sound Vib*, 301, pp. 803-820.
- Nguyen-Xuan, H., Liu, G.R., Thai-hoang, C. and Nguyen-Thoi, T. (2010), An edge-based smoothed finite element method (ES-FEM) with stabilized discrete shear gap technique for analysis of Reissner-Mindlin plates, *Comput Meth Appl Mech Engrg*, 199, pp. 471-489.
- He, Z.C., Liu, G.R., Zhong, Z.H., Zhang, G.Y., Cheng, A.G. (2010), Coupled analysis of 3D structural-acoustic problems using the edge-based smoothed finite element method/finite element method. *Finite Elements in Analysis and Design*, 46, pp. 1114-1121.
- He, Z.C., Liu, G.R., Zhong, Z.H., Wu, S.C., Zhang, G.Y. and Cheng, A.G. (2009), An edge-based smoothed finite element method (ES-FEM) for analyzing three-dimensional acoustic problems. *Comput Meth Appl Mech Engrg*, 199, pp. 20-23.
- Keller, B. and Givoli, D. (1988), Exact non-reflecting boundary conditions. *J. Comput. Phys*, 82, pp. 172-192.
- Berenger, J.P. (1994), A perfectly matched layer for the absorption of electromagnetic waves. *J. Comput. Phys*, 114(2), pp. 195-200.
- Wilcox, C.H. (1956), An expansion theorem for electromagnetic fields. *Commun. Pure Appl. Math*, 9, pp. 115-134.
- Bettess, P. (1992), Infinite elements, *Int. J. Numer. Methods Eng*, 11(1), pp. 53-64.



# Simulation of Nonlinear Magnetorheological Particle-filled Elastomers

Shulei Sun<sup>1</sup>, \*Xiongqi Peng<sup>2</sup>, Zaoyang Guo<sup>3</sup>

<sup>1</sup> School of Mechanical Engineering, Northwestern Polytechnical University, Xi'an, China

<sup>2</sup> School of Materials Science and Engineering, Shanghai Jiao Tong University, Shanghai, China

<sup>3</sup> Department of Engineering Mechanics, Chongqing University, 400044, China

\*Corresponding author: xqpeng@sjtu.edu.cn

Polymer matrix filled with ferromagnetic particles is a class of smart materials whose mechanical properties can be changed under different magnetic field. They are usually referred to as magnetorheological elastomers (MREs). A finite element simulation was presented to describe the mechanical behavior of MREs with the nonlinearity of the particle magnetization being incorporated. By introducing the Maxwell stress tensor, a representative volume element (RVE) was proposed to calculate the Young's modulus and shear modulus of MREs due to the applied magnetic field. The influences of the applied magnetic field and the particle volume fractions in the shear modulus and Young's modulus were studied. Results show that the shear modulus increases with the magnitude of the applied magnetic field, while the Young's modulus decreases.

**Keywords:** Magnetorheological elastomers; Mechanical properties; Maxwell stress tensor; Representative volume element

## Introduction

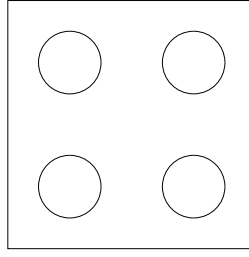
Magnetorheological elastomers (MREs) are a new material, whose structure is that micro-sized ferrous particles disperse in a polymer matrix. The materials have rheological properties that can be changed by an applied magnetic field continuously, rapidly and reversibly. The increasing interest in MREs has heightened the need for potential applications in vales, dumpers,brakes and sensor constructions. Some theoretical models were established to simulate MREs. The widely used one now is the dipole model (Davis,1999; Jolly,1996; Shiga and Okada,1995). However, it puts the dipole as the center of the sphere thus being limited to the case of larger particle spacing. The dipole theory indicates that the ferromagnetic particles are linear magnetization. In fact, the particles are nonlinear. The distribution of magnetic field in MREs can be calculated by the magnetic finite element method. The shear modulus, the particle volume fraction and the relationship between the size of the magnetic field were obtained by considering the nonlinear magnetization of particles. This work can provide guidance for the optimized material and device design.

## Modeling procedure

### Representative volume element

As shown in Fig. 1, a representative volume element was used to simulate MREs. Two dimension square RVE was regarded as the rubber matrix, which includes

several circles representing carbonyl iron particles CIPs.



**Fig. 1 RVE model**

### Governing equations

Cauchy's equation of continuum mechanics reads

$$\rho \frac{d^2 \mathbf{r}}{dt^2} = \nabla \cdot \mathbf{T} + \mathbf{f}_{ext} \quad (1)$$

where  $\rho$  is the density,  $\mathbf{r}$  is the coordinates of a material point,  $\mathbf{T}$  is the stress tensor, and  $\mathbf{f}_{ext}$  is an external volume force such as gravity ( $\mathbf{f}_{ext} = \rho \mathbf{g}$ ). It is an equation solved in the structural mechanics physics interfaces in the special case of a linear elastic material, which neglects the electromagnetic contributions. In the stationary case, there is no acceleration, and the equation representing the force balance is

$$\mathbf{0} = \nabla \cdot \mathbf{T} + \mathbf{f}_{ext} \quad (2)$$

In certain cases, the stress tensor  $\mathbf{T}$  can be divided into two parts. One depends on the electromagnetic field quantities and another is the mechanical stress tensor,

$$\mathbf{T} = \mathbf{T}_{EM} + \boldsymbol{\sigma}_M \quad (3)$$

It is sometimes convenient to use a volume force instead of the stress tensor. This force is obtained from the relation

$$\mathbf{f}_{em} = \nabla \cdot \mathbf{T}_{EM} \quad (4)$$

as stated in the structural mechanics physics interfaces

$$\mathbf{0} = \nabla \cdot \boldsymbol{\sigma}_M + \mathbf{f}_{em} + \mathbf{f}_{ext} \quad (5)$$

### Magnetic equations

In a current free region, where  $\nabla \times \mathbf{H} = 0$ . It is possible to define the scalar magnetic potential,  $V_m$  from the relation  $\mathbf{H} = \nabla V_m$ . Using the constitutive relation between the magnetic flux density and magnetic field

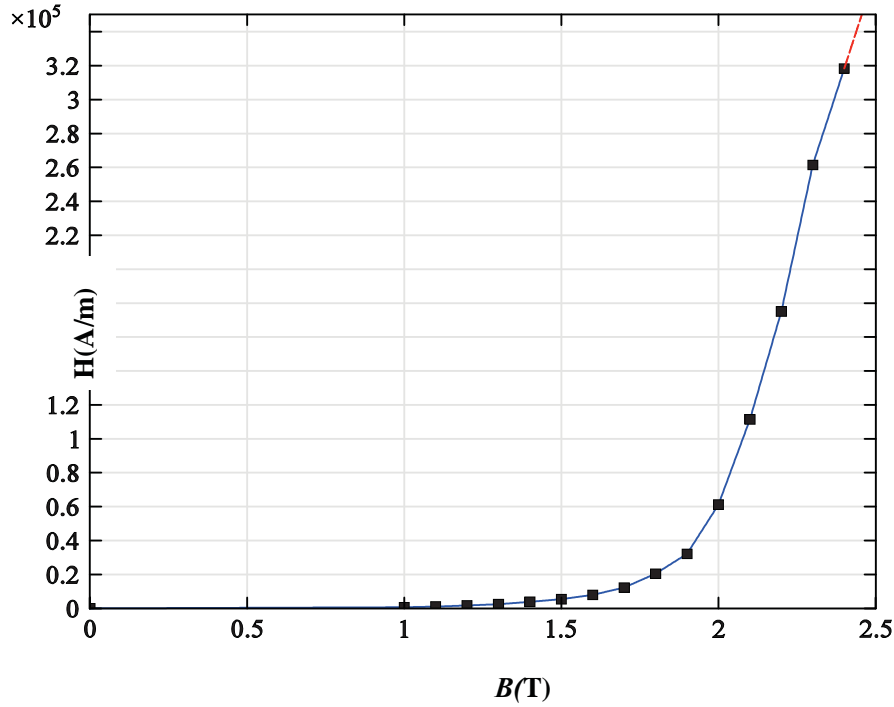
$$\mathbf{B} = \mu_0 (\mathbf{H} + \mathbf{M}) \quad (6)$$

together with the equation

$$\nabla \cdot \mathbf{B} = 0 \quad (7)$$

then  $V_m$  can be obtained from the equation

$$-\nabla \cdot (\mu_0 \nabla V_m - \mu_0 \mathbf{M}_0) = 0 \quad (8)$$



**Fig. 2 HB curve**

The nonlinear magnetic behavior of the steel particles is modeled by using a HB curve to specify the magnetic constitutive relation. (Fig. 2)

### Mechanical equations

The expressions for the stress tensor in a general electromagnetic context stem from a fusion of material theory, thermodynamics, continuum mechanics, and electromagnetic field theory. With the introduction of thermodynamic potentials of mechanical, thermal, and electromagnetic effects, explicit expressions for the stress tensor can be derived in a convenient way by forming the formal derivatives with respect to the different physical fields (Kovetz,1990;Wilson,1988). Alternative derivations can be made for a vacuum (Wangsness,1986) but it is difficult to polarize and magnetize materials. In general, an elastic solid material of that is dielectric and magnetic (nonzero  $\mathbf{M}$ ), the stress tensor is given by the expression

$$\mathbf{T} = \boldsymbol{\sigma}(\mathbf{B}) + \frac{1}{\mu_0} \mathbf{B} \cdot \mathbf{B}^T - \mathbf{M} \mathbf{B}^T - \frac{1}{2\mu_0} (\mathbf{B} \cdot \mathbf{B} - \mathbf{M} \cdot \mathbf{B}) \mathbf{I} \quad (9)$$

where in  $\boldsymbol{\sigma}(\mathbf{B})$ , the dependence of  $\mathbf{B}$  has not been separated out. Thus  $\boldsymbol{\sigma}$  is not a purely mechanical stress tensor in this case. Different material models give different appearances of  $\boldsymbol{\sigma}(\mathbf{B})$ . The electromagnetic contributions to  $\boldsymbol{\sigma}(\mathbf{B})$ , which represent piezoelectric, dielectric, and magnetization effects. The expression for the stress

tensor in vacuum, air, and pure conductors can be derived from this general expression by setting  $M=0$ . The Maxwell stress on CIPs causes the deformation of the RVE.

### Simulations procedures

A test of the MREs was simulated to investigate the changes of shear modulus and Young's modulus with different magnetic field and radius of CIPs. The values of magnetic field are  $0.5e-5$ wb/m,  $1e-5$ wb/m,  $1.5e-5$ wb/m, and  $2e-5$ wb/m (Fig.3 and Fig.4), respectively. The radius of CIPs is  $1.5 \mu\text{m}$ ,  $2 \mu\text{m}$ ,  $2.5 \mu\text{m}$ ,  $3 \mu\text{m}$ ,  $3.5 \mu\text{m}$ ,  $4 \mu\text{m}$ ,  $4.5 \mu\text{m}$  (Fig.5), respectively.

### Results and discussions

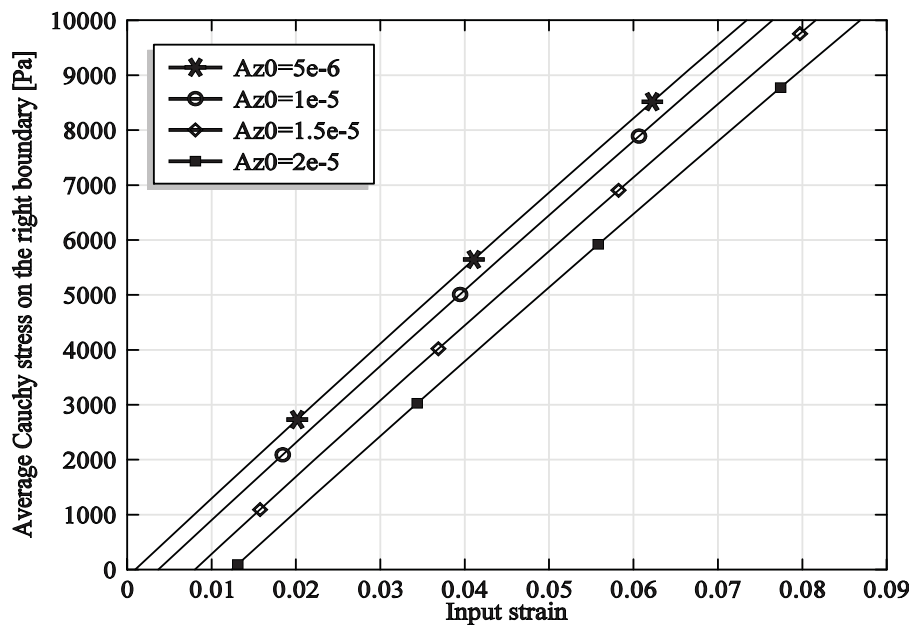
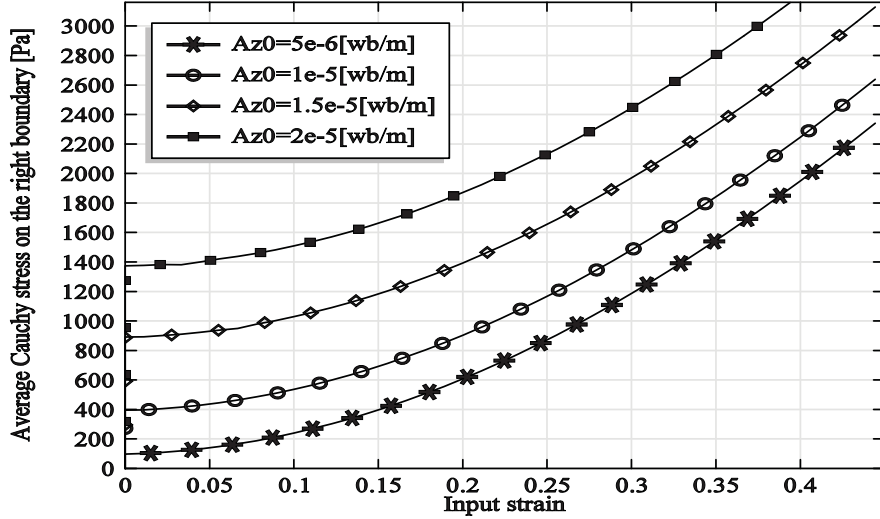


Fig. 3 different magnetic fields for tension deformation



**Fig. 4 different magnetic fields for shear deformation**

When no shear deformation occurs,  $\gamma = 0$ , the magnetic field contribution to the normal stress and shear strain is equal to the magnetic energy density function of the first derivative of strain,

$$\sigma_B = \frac{\varphi M^2 d_p^3 \mu_0}{4r^3} - \frac{\varphi M^2 d_p^3 \mu_0}{r_0^3} \varepsilon \quad (10)$$

Young's modulus is:

$$\Delta E(B) = \frac{\varphi M^2 d_p^3 \mu_0}{r_0^3} \quad (11)$$

As stated in the above equation, the magnetic field will cause magnetic force and the load will result in compression of the matrix (rubber), which is actually magnetic pre-stressed. This is because that the CIPs attract each other, which increases the reliability of material in some ways. But in the contact force between the particles and the rubber, the rubber is easy to be torn. The MREs working in the compressed state are unreasonable (the compressed state becomes the extrusion of the two rigid iron balls). Young's modulus induced by the magnetic field is negative. Its physical meaning is the magnetic energy and a matrix strain energy conversion. With increasing the magnetic field (Fig.3). MREs will become softer. The results of the simulation show that the shear modulus increases with the magnitude of the applied magnetic field, while the Young's modulus decreases (Fig.4).

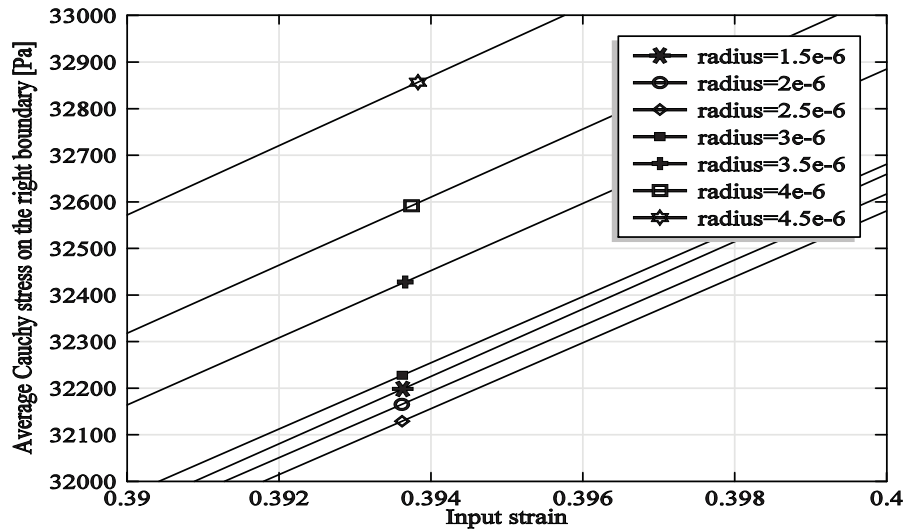


Fig. 5 different radius of CIPs

## Conclusions

The study focuses on the mechanical behavior of MREs. A two-dimension RVE was introduced with CIPs and pure rubber. Mechanical behavior of the RVE was simulated under magnetic field. It is demonstrated that the shear modulus increases with the magnitude of the applied magnetic field, while the Young's modulus decreases. Additional research should focus not only upon the applied magnetic field, but also considering the magnetostriction of MREs.

## References

- Davis, LC. "Model of Magnetorheological Elastomers." *Journal of Applied Physics* 85, no. 6 (1999): 3348-51.
- Jolly, Mark R, J David Carlson, Beth C Muñoz, and Todd A Bullions. "The Magnetoviscoelastic Response of Elastomer Composites Consisting of Ferrous Particles Embedded in a Polymer Matrix." *Journal of Intelligent Material Systems and Structures* 7, no. 6 (1996): 613-22.
- Kovetz, Attay. *The Principles of Electromagnetic Theory*. CUP Archive, 1990.
- Shiga, Tohru, Akane Okada, and Toshio Kurauchi. "Magnetoviscoelastic Behavior of Composite Gels." *Journal of Applied Polymer Science* 58, no. 4 (1995): 787-92.
- Wangsness, Roald K. "Electromagnetic Fields." *Electromagnetic Fields, 2nd Edition*, by Roald K. Wangsness, pp. 608. ISBN 0-471-81186-6. Wiley-VCH, July 1986. 1 (1986).
- Wilson, Oscar Bryan. *Introduction to Theory and Design of Sonar Transducers*. Peninsula publishing Los Altos, CA, 1988.

## An Improved Genetic Algorithm with Two-level Approximation for

### Truss Topology and Size Optimization

Dongfang Li<sup>1</sup>, \*Shenyan Chen<sup>1</sup>, and Hai Huang<sup>1</sup>

<sup>1</sup>School of Astronautics, BeiHang University, China  
BeiHang University, 37 Xueyuan Rd, Dist. Haidian, Beijing City, China

\*Corresponding author: chenshenyan@buaa.edu.cn

#### Abstract

Truss topology optimization with Genetic Algorithm usually requires very large computational cost, especially for large-scale problems. To decrease the structural analyses, Genetic Algorithm with Two-level Approximation (GATA) was proposed in previous work which showed good efficiency. However, the optimization process sometimes converges to sub-optimum points for its low capability in global optimum searching. The present paper proposes an Improved Genetic Algorithm with Two-level Approximation (IGATA) which includes several changes to the basic genetic algorithm developed previously. A modified Lemonge penalty function is adopted for fitness calculation, and an Elite selection strategy is proposed to improve the quality of initial points. Example demonstrates reduced computational cost and increased reliability of the algorithm due to these changes.

**Keywords:** Truss, Topology optimization, Genetic algorithm, Two-level approximation

#### Introduction

The two-level multi-point approximation algorithm, proposed by Huang and Xia (1995), combines a mathematical programming method and approximation concepts. This algorithm is very efficient when performing size optimization of a structure. To improve the efficiency of truss topology optimization, Dong and Huang (2004) proposed a GA with a Two-level Approximation (GATA), which combines a simple GA with the efficient Two-level Approximation method. GATA obtains an optimal solution by alternating topology optimization and size optimization. Because there are no structural analyses during the execution of the GA, the computational efficiency is greatly improved and the structural analyses can be reduced to the order of tens. Later, Xian and Huang (2008; 2009) modified the multi-point approximation function in the form of a branched function for application in the field of optimal actuator/sensor location in a piezoelectric truss. However, owing to the weak exploitation capabilities and premature convergence of the simple GA, the algorithm often reaches a local optimum, and not global optimal solution.

In this paper, with the aim of solving the shortcomings mentioned above, an Improved GA with a Two-level Approximation (IGATA) is proposed. IGATA inherits the optimization strategy from GATA, but certain improvements are applied to the approximation function and GA to strengthen the capability of seeking an optimum solution. These improvements address two aspects. First, the original static exterior penalty function is replaced by an improved Lemonge penalty function, which is adaptive and can address various problems without artificially setting any parameters. Second, faced with the difficulty of convergence, an Elite Selection Strategy (ESS) is adopted, which improves the quality of initial points and allows searching in more domains. The effectiveness and efficiency of the proposed IGATA is demonstrated using two numerical examples.

#### Problem descriptions

The truss topology optimization problem in GATA is formulated in (1). Here,  $X = \{x_1, x_2, \dots, x_n\}^T$  is the size variable vector, with  $x_i$  ( $i=1, 2, \dots, n$ ) denoting the cross-sectional area of bar members in the  $i$ -th group and  $n$  denoting the number of groups.  $\alpha = \{\alpha_1, \alpha_2, \dots, \alpha_n\}$  is the topology variable vector: if  $\alpha_i=0$ , members in the  $i$ -th group are removed, and  $x_i$  is set to a very small value  $x_i^b$ , which is generally calculated as  $10^{-4}$  multiplied by the initial value of  $x_i$ ; if  $\alpha_i=1$ , members in the  $i$ -th group are retained, and  $x_i$  is optimized between the upper bound  $x_i^U$  and the lower bound  $x_i^L$ .

$$\left\{ \begin{array}{l}
\text{Find} \quad X = \{x_1, x_2, \dots, x_n\}^T \\
\quad \quad \alpha = \{\alpha_1, \alpha_2, \dots, \alpha_n\}^T \\
\text{Min} \quad W^{(p)} = \sum_{i=1}^n \alpha_i f_i^{(p)}(X) \\
\text{s.t.} \quad \beta_j g_j^{(p)}(X) \leq 0 \quad j = 1, \dots, J_1 \\
\quad \quad \alpha_i x_{i(p)}^L + (1 - \alpha_i) x_i^b \leq x_i \quad i = 1, \dots, n \\
\quad \quad x_i \leq \alpha_i x_{i(p)}^U + (1 - \alpha_i) x_i^b \\
\quad \quad \alpha_i = 0 \quad \text{or} \quad \alpha_i = 1 \\
x_{i(p)}^U = \min\{x_i^U, \Delta x_{i(p)}^U\} \\
x_{i(p)}^L = \max\{x_i^L, \Delta x_{i(p)}^L\}
\end{array} \right. \quad (1)$$

If some bar members are removed, the corresponding constraints are eliminated, such as the stress constraints of the removed members. Thus,  $\beta_j$  indicates whether the respective constraint is eliminated; if  $\beta_j=0$ , the  $j$ -th constraint is eliminated, otherwise if  $\beta_j=1$ , the  $j$ -th constraint is retained. Here,  $f_i^{(p)}(X)$  and  $g_j^{(p)}(X)$  are the approximation functions of objective function  $f_i(X)$  and normalized constraints  $g_j(X)$ , respectively, in the  $p$ -th iteration, and  $J_1$  is the number of considered constraints.  $\Delta x_{i(p)}^U, \Delta x_{i(p)}^L$  are the moving limits of  $x_i$ , and  $x_{i(p)}^U, x_{i(p)}^L$  are the upper and lower bounds of  $x_i$  in the  $p$ -th iteration.

#### Optimization strategy of GATA

GATA is an optimization method which can perform truss topology and size optimization simultaneously. In the  $p$ -th iteration process, GATA is implemented as follows: First, structural and sensitivity analysis is implemented on a truss structure with  $X_p = \{x_{1p}, x_{2p}, \dots, x_{np}\}^T$ . Second, the results of the structural and sensitivity analysis at  $X_p$  are used to construct a first-level approximation problem using the multi-point approximation function. For further details, please see the works by Dong (2004). Third, an optimization strategy is implemented. In this strategy, the GA generates sequences of 0/1 variable vectors,  $\alpha_{l,k,p} = \{\alpha_{l,k,p,1}, \dots, \alpha_{l,k,p,n}\}^T$ . Each sequence is the genotype of one individual in the population, representing a topology configuration. For the  $l$ -th individual in the initial generation, GATA seeks the optimum  $X_{l,k,p}^*$  ( $k=1$ ) by means of an efficient dual method. Then the fitness,  $fitness(X_{l,k,p}^*)$ , is obtained using  $W^{(p)}(X_{l,k,p}^*)$  and  $g_j^{(p)}(X_{l,k,p}^*)$  ( $k=1$ ) by means of the penalty function method. After the fitness values of all the individuals in the initial generation have been calculated, the genetic operator works on the sequences of  $\alpha$  and generates the next generation ( $k+1 \rightarrow k$ ). The dual method is then repeated. This optimization strategy terminates when the maximum generation of the GA,  $maxG$ , is reached. Finally,  $X_{p+1}$  is selected by (2) and (3) signaling the start of the  $(p+1)$ -th iteration, the  $p$ -th iteration terminates, and  $p+1 \rightarrow p$ .

$$X_{p+1} \in \{X_{l,k,p}^* \mid l = 1, \dots, Popsiz; k = 1, \dots, \max G\} \quad (2)$$

$$fitness(X_{p+1}) = \max\{fitness(X_{l,k,p}^*) \mid l = 1, \dots, Popsiz; k = 1, \dots, \max G\} \quad (3)$$

If the convergence criteria are satisfied before iteration  $p$  reaches the artificial threshold, say 100, a convergence solution is obtained; if not, a non-convergence solution is reached. GATA terminates under both conditions.

The computational cost of GATA is low because it requires only a few structural analyses. However, numerical tests have shown that results of GATA are not always perfect, because it can easily be trapped in a sub-optimum design or even get infeasible design if the initial design of  $p$ -th iteration  $X_p$  is infeasible and far from the optimal design. Conversely, it may be difficult for GATA to reach convergence with a long iteration process if an optimum is obtained. These problems are solved by IGATA.



### Validity of topology configuration check

Under some circumstances, the topology configuration may not be valid, e.g., if load nodes are removed, part of the structure can move, or the structure is not a geometrically stable one. In GATA, the validity of the topology configuration is checked before calculating the fitness of each individual, which means that invalid individuals cannot to be considered by the GA.

## Improvements to GATA

### Modified penalty function

The penalty function, which penalizes an infeasible solution depending on its violation of constraints, is essential for a GA to deal with the constrained optimization problem (Su et al., 2009). One kind of exterior penalty function is used by GATA to cope with the constraints, which can be considered as static penalty function (see (4)). The method for calculating fitness is given in (4)-(6). Here  $a$  and  $b$ , which are used to control the number of copied individuals in the new population, are functions that include  $F_2$  as an argument. Therefore,  $a$  and  $b$  retard the premature convergence of the GA.

$$F_1 = f(X_{l,k,p}^*) + R \sum_{j=1}^{J_2} \left[ \max(0, g_j(X_{l,k,p}^*)) \right]^q \quad (4)$$

$$F_2 = \left( 1 - \frac{F_1 - \min(F_1)}{\max(F_1) - \min(F_1)} \right)^s \quad (5)$$

$$AdaptValue = aF_2 + b \quad (6)$$

Values of penalty factor  $R$ , penalty exponent  $q$ , and normalized exponent  $s$  are obtained by trial and error depending on the specific optimization problems. Always bad or even infeasible solutions are obtained if these values are not correctly initialized, which is an intrinsic defect of the static penalty function. One approach to solve this problem is to make the penalty function adaptive.

The Lemonge penalty function is an adaptive penalty function that can automatically adjust the level of penalty depending on the constraints. This penalty function was originally applied in size optimization of trusses (Barbosa and Lemonge, 2003; 2004). After various improvements, the penalty function has been applied in topology optimization of skeletal structures under frequency constraints (Liu, 2011; 2012). Based on the topology optimization model given in (1), the Lemonge penalty function and corresponding fitness function are shown in (7) and (11), respectively.

$$penal(X_l) = \overline{W}(X) \sum_{j=1}^{J_1} \frac{\overline{v}_j}{\sum_{j=1}^{J_1} \overline{v}_j} v_j(X_l) \quad (7)$$

$$\overline{W}(X) = \frac{1}{Popsize} \sum_{l=1}^{Popsize} W^{(p)}(X_l) \quad (8)$$

$$v_j(X_l) = \max \{ 0, g_j^{(p)}(X_l) \} \quad (9)$$

$$\overline{v}_j = \frac{1}{Popsize} \sum_{l=1}^{Popsize} v_j(X_l) \quad (10)$$

$$fitness(X_l) = f_{\max}^p - (W^{(p)}(X_l) + penal(X_l)) \quad (11)$$

$$f_{\max}^p = \max_{l=1,2,\dots,Popsize} \{ W^{(p)}(X_l) + penal(X_l) \} \quad (12)$$

$\overline{W}(X)$  is the average of the objective function of all the individuals in the population, which is calculated by (8);  $v_j(X_l)$  denotes the violation level of the  $j$ -th constraint of  $l$ -th individual, which is calculated by (9);  $\overline{v}_j$  is the average of  $v_j(X_l)$  in the population;  $J_l$  is the number of considered constraints; and  $Popsiz$ e is the population size.

Compared with the exterior penalty function used by GATA, the Lemonge penalty function has the ability to create an adaptive penalty without using other parameters, thereby avoiding any adjustment of parameters. As such, it can tackle various problems and its versatility is good. To better align the method for calculating fitness using the Lemonge penalty function to deal with truss topology optimization, some improvements have been incorporated.

#### 1) The treatment of eliminated constraints and invalid individuals

The Lemonge penalty function includes all the constraints. In fact, some eliminated constraints need to be dealt with flexibly as shown in (13).  $X_l^*$  is the optimum of the size optimization of the  $l$ -th valid individual, and  $g_j^{(p)}(X_l^*)$  is the multi-point approximation value of the  $j$ -th constraint  $g_j(X^*)$ .

$$g_j^{(p)}(X_l^*) = \begin{cases} g_j^{(p)}(X_l^*) & \beta_j = 1 \\ -0.01 & \beta_j = 0 \end{cases} \quad (j=1, \dots, J_l) \quad (13)$$

To ensure that genetic operators do not operate on invalid individuals, their fitness should be set to zero. Moreover, invalid individuals should be excluded from the method for calculating fitness (see (14) and (45)).  $N_s$  is the number of valid individuals in the population,  $W^{(p)}(X_l^*)$  is the weight of the  $l$ -th valid individual,  $\overline{W'}$  is the average of  $W^{(p)}(X_l^*)$  in the population, and  $\overline{g_j}$  is the average of  $g_j^{(p)}(X_l^*)$  of valid individuals in the population.

$$\overline{W'} = \frac{1}{N_s} \sum_{l=1}^{N_s} W^{(p)}(X_l^*) \quad (14)$$

$$\overline{g_j} = \frac{1}{N_s} \sum_{l=1}^{N_s} g_j^{(p)}(X_l^*) \quad (15)$$

The violation level of the  $j$ -th constraint of the  $l$ -th individual and its average are given in (16) and (17). Based on (7), the penalty function is shown in (18), where  $J_l$  is the number of considered constraints.

$$v_j(X_l^*) = \max \{ 0, g_j^{(p)}(X_l^*) \} \quad (16)$$

$$\overline{v}_j = \frac{1}{N_s} \sum_{l=1}^{N_s} v_j(X_l^*) \quad (17)$$

$$penal(X_l^*) = \overline{W'} \sum_{j=1}^{J_l} \frac{\overline{v}_j}{\sum_{j=1}^{J_l} \overline{v}_j^2} v_j(X_l^*) \quad (18)$$

Here,  $g_j^{(p)}(X_l^*)$  ( $j=1, \dots, J_l$ ) is not the result of structural analysis, but the multi-point approximation value. It is usually a positive value close to zero or a negative one. Thus,  $penal(X_l^*)$  may be singular; see (18). By modifying (17) and (18) as shown in (19) and (20), this problem can be solved and the penalty function retains its adaptivity.

$$\overline{g_j} = \frac{1}{N_s} \sum_{l=1}^{N_s} g_j^{(p)}(X_l^*) \quad (19)$$

$$penal(X_i^*) = \overline{W'} \sum_{j=1}^{J_1} \frac{|\overline{g_j}|}{\sum_{j=1}^{J_1} \overline{g_j}^2} v_j(X_i^*) \quad (20)$$

### 2) Slight amplification of fitness

If the stochastically generated valid individuals satisfy (12), their fitness values will be zero according to (11). Such individuals will not be available to the genetic operator, thus limiting the diversity of the population. Hence, we multiply the fitness values by a factor  $R$  equal to  $1.01$  to make all the fitness values of valid individuals positive (see (21)). After this transformation, the fitness of all valid individuals is slightly larger than before.

$$f_{max}^p = R \times \max_{i=1,2,\dots,N_s} \{ W'(X_i^*) + penal(X_i^*) \} \quad (21)$$

### 3) Critical constraint scale factor

The optimal structure always contains several critical constraints. Consequently, an individual with more critical constraints should have better adaptability. Thus, we add the value  $M_{crit}/J_1$  to (11) to ensure that individuals with more critical constraints have better fitness; see (22).  $M_{crit}$  is the number of critical constraints, while  $M_{crit}/J_1$  is the critical constraint scale factor, which denotes the number of critical constraints relative to the total number of considered constraints. If  $g_j^{(p)}(X_i^*) \in (-10^{-2}, 10^{-3})$ , it is treated as a critical constraint. The upper bound of the critical constraints' determination interval ( $10^{-3}$ ) is positive, and therefore, an individual that violates a constraint slightly has good fitness, which is helpful for maintaining population diversity and avoiding premature convergence of the GA.

$$fitness(X_i^*) = \{ f_{max}^p - (W^{(p)}(X_i^*) + penal(X_i^*)) \} \times (1 + \frac{M_{crit}}{J_1}) \quad (22)$$

### Elite Selection Strategy

Different topology configurations map one-to-one onto different degenerate sub-regions of the design variables' space. In the  $p$ -th iteration of IGATA, after the GA terminates, an elite individual must be selected to proceed to the  $(p+1)$ -th iteration. In other words, the "best"  $\alpha_{p+1}$  and  $X_{p+1}$  need to be determined. If  $X_{p+1}$  is selected according to (23) and (24), it may take more iterations for IGATA to converge. This difficult-convergence phenomenon can be ascribed to the poor quality of  $X_{p+1}$ .

$$X_{p+1} \in \{X_{l,k,p}^* | l=1, \dots, Popsiz; k=\max G\} \quad (23)$$

$$fitness(X_{p+1}) = \max \{ fitness(X_{l,k,p}^*) | l=1, \dots, Popsiz; k=\max G \} \quad (24)$$

Multi-point approximation is not global approximation. If  $X_{p+1}$  is an infeasible design and far from the boundary of the feasible region, then  $X_{p+1}$  seriously violates the constraints; see (25) and (26).  $\varepsilon \geq 0$ , e.g.,  $\varepsilon = 1.0$ . Under this condition, the size optimization optimum may vary greatly from the real optimum, which will probably give rise to slow convergence or even an infeasible solution. Thus, ESS is proposed to overcome the difficulty of convergence.

$$g_{max}(X_{p+1}) \geq \varepsilon \quad (25)$$

$$g_{max}(X_{p+1}) = \max \{ \beta_1 g_1(X_{p+1}), \dots, \beta_m g_m(X_{p+1}) \} \quad (26)$$

The ESS is a method that aims for excellent individual selection. In the  $p$ -th iteration, it is implemented after the GA terminates. Before it is implemented, a parameter called the maximum constraint value control threshold ( $MVCCT$ ) is set in the range of 0.01-1.0. The ESS is given in the  $p$ -th iteration as follows.

1) Select an individual with the maximum fitness from the  $\max G$ -th generation and label the individual as  $SEL(I)$ .

2) Order the objective function values of all the valid individuals from the *first* to the *maxG*-th generation in ascending order; select four individuals labeled as  $SEL(2), SEL(3), SEL(4)$ , and  $SEL(5)$  from the front. It should be noted that the five individuals ( $SEL(s), s=1, \dots, 5$ ) must each have a different topology configuration. In other words,  $\alpha_{SEL(1)}, \dots, \alpha_{SEL(5)}$  differ from each other, and  $W^{(p)}(X_{SEL(2)}^*) \leq \dots \leq W^{(p)}(X_{SEL(5)}^*)$ .

3) Carry out structural and sensitivity analysis at  $X_{SEL(1)}^*$ . If  $g_{\max}(X_{SEL(1)}^*) \leq MCVCT$ , then the ESS terminates. If  $g_{\max}(X_{SEL(1)}^*) > MCVCT$ , carry out structural and sensitivity analysis at  $X_{SEL(2)}^*$  and compare  $g_{\max}(X_{SEL(2)}^*)$  and  $MCVCT$ . This process terminates only when  $g_{\max}(X_{SEL(w)}^*) \leq MCVCT$  ( $g_{\max}(X_{SEL(1)}^*), \dots, g_{\max}(X_{SEL(w-1)}^*) > MCVCT, w=1, 2, 3, 4, 5$ ) or  $g_{\max}(X_{SEL(5)}^*) > MCVCT$  ( $g_{\max}(X_{SEL(1)}^*), \dots, g_{\max}(X_{SEL(5)}^*) > MCVCT$ ). Then, the selected individual that will move into the  $(p+1)$ -th iteration is labeled as  $SEL$ ; see (27).  $SEL$  is defined as in (28), while  $min$  should satisfy (29) and (30).

$$X_{p+1} = X_{SEL}^* \quad (27)$$

$$SEL = \begin{cases} \min & g_{\max}(X_{SEL(1)}^*), \dots, g_{\max}(X_{SEL(5)}^*) > MCVCT \\ w & g_{\max}(X_{SEL(1)}^*), \dots, g_{\max}(X_{SEL(w-1)}^*) > MCVCT, g_{\max}(X_{SEL(w)}^*) \leq MCVCT \end{cases} \quad (28)$$

$$g_{\max}(X_{min}^*) = \min(g_{\max}(X_{SEL(1)}^*), \dots, g_{\max}(X_{SEL(5)}^*)) \quad (29)$$

$$w, \min \in \{1, 2, 3, 4, 5\} \quad (30)$$

If  $X_{SEL}^*$  is an infeasible solution, its violation is controlled by the ESS, which accelerates the rate of convergence. For small-scale problems, IGATA may need only a few structural analyses to obtain the optimum. Meanwhile, the ESS helps search in more degenerate sub-regions, which extends the search region and improves the capacity for finding a better feasible solution.

Figure1 gives a flowchart of the procedure for IGATA.

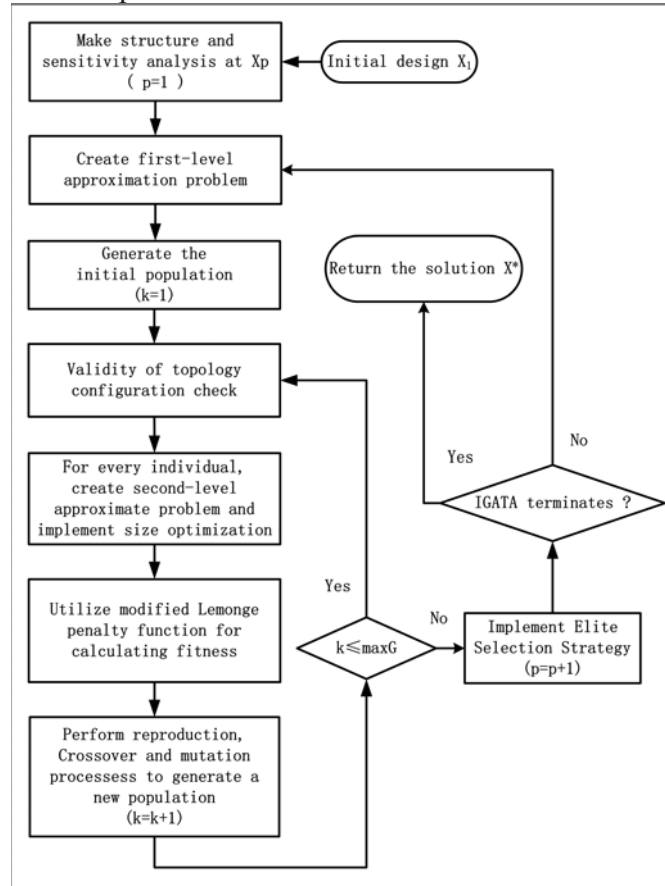
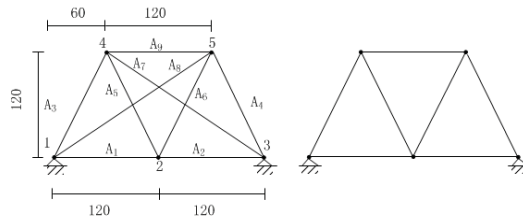


Figure1. A flowchart of IGATA

**Numerical examples**

This example is explained in detail in works by Huang and Wang (2008). The IGATA and GATA parameters are set as follows:  $Popsiz$ =30,  $maxG$ =30,  $P_c$ =0.90,  $P_m$ =0.05. In addition, for IGATA,  $MCVCT$ =1.0. Figure 2 shows the topology configuration of IGATA, Figure 3 illustrates the iteration process of IGATA, and Table 1 gives the optima reported by various studies in the literature.



**Figure 2. Original structure and topology configuration of 9-bar planar truss**



**Figure 3. Iteration process**

**Table 1. Results obtained by different studies for the 9-bar planar truss**

Var	Optimization results					
	GA (Huang and Wang, 2008)		GATA		IGATA (proposed)	
	Cons 1	Cons 2	Cons 1	Cons 2	Cons 1	Cons 2
$A_1=A_2$	1.4081	1.6770	0	0	1.3881	1.7224
$A_3=A_4$	9.3185	9.3190	2.3312	2.3313	9.3153	9.3147
$A_5=A_6$	5.6003	5.6195	2.7955	3.0061	5.5888	5.5885
$A_7=A_8$	0.0	0.0	11.264	11.2643	0	0
$A_9$	5.5556	5.6449	0	0	5.5548	5.5564
No. of analyses	—	—	4	4	9	4
Weight	1417.19	1439.99	1768.521	1784.557	1414.691	1437.383
Feasibility	Feasible	Feasible	$3.0 \times 10^{-4}$	$2.7 \times 10^{-4}$	$5.68 \times 10^{-4}$	$3.17 \times 10^{-4}$

Note: Cons- Constraint set No.

Comparing the results of GATA and IGATA, we can see that their corresponding topology configurations are different, with IGATA being lighter, which means that IGATA can better confirm degenerate sub-regions and improve the capability of finding optimum. Although the number of structural analyses is not given in works of Huang (2008), it is substantial (possibly thousands to tens of thousands). In contrast, the computational cost of IGATA is greatly reduced.

## Conclusion

An improved topology optimization method for truss structures was presented in this paper. This method inherits the optimization frame of the GA with a Two-level Approximation. The discrete variables (0/1 variables representing the existence of each bar member) are optimized by means of a GA, while the continuous size variables are optimized through a series of second-level approximation problems. Various modifications, including a modified Lemonge penalty function, and the Elite Selection Strategy have been implemented to improve the global optimum searching capability and convergence rate. The modified Lemonge penalty function works without any adjustment to arguments and includes a critical constraint scale factor, which means that individuals with more critical constraints have better fitness. The Elite Selection Strategy controls the violation of  $X_{SEL}^*$ , which improves the quality of the initial points and extends the search domain. Sometimes, the Elite Selection Strategy results in the fact that the structural analyses are more than iterations. However, the improved method has a lower computational cost. Numerical experiments have shown that Improved GA with a Two-level Approximation can rapidly and in a stable manner obtain a solution. The effectiveness of IGATA is comparable to GATA and other methods.

## References

- Barbosa, H.J.C. and Lemonge A.C.C., (2003), A new adaptive penalty scheme for genetic algorithms. *Inform Sciences J.* 156, pp.215-251.
- Dong, Y. and Huang H., (2004), Truss topology optimization by using multi-point approximation and GA. *Chinese Journal of Computational Mechanics J.* 21, pp.746-751.
- Huang, H. and Xia R.W., (1995), Two-level multipoint constraint approximation concept for structural optimization. *Structural Optimization J.* 9, pp.38-45.
- Huang, J. and Wang Z., (2008), Topology optimization design for discrete structures using genetic algorithm. *Engineering Mechanics J.* 25, pp.32-38.
- Lemonge, A.C.C. and Barbosa H.J.C., (2004), An adaptive penalty scheme for genetic algorithms in structural optimization. *International Journal for Numerical Methods in Engineering J.* 59, pp.703-736.
- Liu, X. (2011), The improvement of automatic grouping genetic algorithms and its application in structural engineering. Dalian University of Technology, Dalian
- Liu, X.F. and Cheng G.D. and Yan J. et al., (2012), Singular optimum topology of skeletal structures with frequency constraints by AGGA. *Structural and Multidisciplinary Optimization J.* 45, pp.451-466.
- Su, R. and Gui L. and Fan Z. Topology and sizing optimization of truss structures using adaptive genetic algorithm with node matrix encoding. In: Fifth International Conference on Natural Computation, Tianjin, China, 2009. IEEE, pp 485-491
- Xian, K.-c. (2009), Optimal Actuators Locations for adaptive structures and structure optimization including discrete variables. BeiHang University, Beijing
- Xian, K.-c. and Huang H., (2008), Research on algorithm of optimal actuator/sensor location for piezoelectric truss. *Chinese Journal of Computational Mechanics J.* 25, pp.827-832.

## Free vibration analysis of 2D FG plates by a meshfree boundary-domain integral equation method

\*Y. Yang<sup>1,2</sup>, K.P. Kou<sup>2</sup>, V.P. Iu<sup>2</sup>, C.C. Lam<sup>2</sup>, Ch. Zhang<sup>1</sup>

<sup>1</sup>Department of Civil Engineering, Faculty of Science and Technology, University of Siegen, Germany

<sup>2</sup>Department of Civil Engineering, Faculty of Science and Technology, University of Macau, Macau, China

\*Corresponding author: yangyang.lijun@hotmail.com

### Abstract

Free vibration of two-dimensional functionally graded plates with an exponential material gradation is analyzed in this paper by a meshfree boundary-domain integral equation method. Based on two-dimensional elasticity theory, boundary-domain integral equations are derived by using elastostatic fundamental solutions. Due to the material inhomogeneity and the inertial effect, two domain integrals emerge in the boundary-domain integral equation formulation. Radial integration method is employed to convert the domain integrals into boundary integrals. A meshfree scheme is achieved through approximating the normalized displacements in the domain integrals by a combination of the radial basis functions and polynomials. Thus, the free vibration problem is reduced to a generalized eigenvalue problem, which involves system matrices with boundary integrals only. By using the present meshfree boundary-domain integral equation method, free vibration of two-dimensional exponentially graded plates with various material gradients, boundary conditions and aspect ratios are investigated, which demonstrates the high convergence, efficiency and accuracy of the present method.

**Keywords:** free vibration, functionally graded plates, exponential material gradation, boundary element method, meshfree method, boundary-domain integral equations.

### Introduction

Functionally graded materials (FGMs) are heterogeneous advanced composite materials, in which the volume fractions of the constituents vary gradually and functionally. It has drawn the attentions of the engineering and scientific communities of various disciplines since the concept was first introduced in 1984. Meanwhile, FGMs bring extraordinary merits of high resistance of temperature gradients, high wear resistance and an increase in strength to weight ratio, which make FGMs having motivated the world-wide research activities.

The determination of the natural frequencies and the mode shapes of a functionally graded (FG) structure is an important and necessary process during the engineering design and development. Thus dynamic analysis of the FG plates plays an indispensable role in the engineering practice. Due to the mathematical complexity, most practical problems of FG plates can be solved only with numerical scheme. Among many numerical methods, the boundary element method (BEM) with its superior efficiency and accuracy has been well established as a powerful method. The dual reciprocity method (DRM) proposed by Nardini and Brebbia (1983) is recognized as one efficient method to treat the dynamic analyses of structures (Wilson et al. 1990) and FGMs (Masataka et al. 2000) in BEM. However, the application of DRM to deal with the domain integrals in the boundary-domain

integral equations requires particular solutions, whose construction is restricted to the approximation functions chosen. Another efficient alternative technique to handle the domain integrals in BEM is the radial integration method (RIM) proposed by Gao (2002). The RIM is based on pure mathematical treatments, and the main advantage of the RIM over the DRM is that the radial basis functions (RBF) can be freely chosen. The RIM has been successfully implemented and applied to elastodynamic problems in anisotropic materials by Albuquerque et al (2003, 2007). A meshless boundary-domain integral equation method for transient thermoelastic analysis has been developed and applied by Ekhlakov et al (2010, 2012), where the Laplace-transform technique is used and the domain integrals are handled by the RIM. In contrast to the above mentioned investigations, few works can be found in literature on the vibration problems of FG plates by using these methods.

In this paper a meshfree boundary-domain integral equation method is presented to analyze the free vibration behaviours of two-dimensional (2D) FG plates. The material properties are assumed to vary continuously according to the exponential law either in longitudinal or in transverse directions. The boundary-domain integral equations are derived based on 2D elastodynamic theory, while the elastostatic fundamental solutions for homogeneous materials are applied. The RIM is applied to transform the domain integrals into boundary integrals. A meshfree scheme is achieved by approximating the normalized displacements in the domain integrals by a combination of the radial basis functions and polynomials in term of the global coordinates. Internal nodes are necessary to increase the accuracy of the solution due to the fact that the correct function approximation requires a rather uniform distribution of nodal points. Then the eigenvalues and eigenvectors can be obtained by solving the generalized eigensystem with only boundary discretization. Numerical examples demonstrate that the present method has high efficiency and accuracy. The main advantages of the present method can be summarized as:

- (1) The present method is based on a boundary-domain integral equation formulation. It requires the discretization of the global boundary of the problem domain and some internal nodes, but no domain-like elements.
- (2) The present method uses elastostatic fundamental solutions and avoids the complicated complex frequency-domain dynamic fundamental solutions.
- (3) The present method for computing the eigensolutions is quite robust. No instability and spurious eigenvalues are observed by using the method, which is a critical issue in real valued BEM to analyze eigenvalue problems.
- (4) Numerical examples for free vibration analyses of 2D FG plates with various material gradation directions, gradient parameters, aspect ratios, and boundary conditions show the fast convergence, high efficiency and accuracy of the present method. In addition, the present method is easy to implement and very flexible for free vibration analyses of 2D FG structures.

### Exponential Material Properties

A two-phase steel/aluminum FG plate is considered in this paper. The corresponding material parameters are:  $E_S=210\text{GPa}$ ,  $\rho_S=7806\text{ kg/m}^3$ ,  $E_{Al}=70\text{GPa}$ ,  $\rho_{Al}=2707\text{kg/m}^3$ , and  $\nu=0.3$ . The schematic sketch of the plate and its dimensions are illustrated in Fig. 1. The material properties of the FG plates are assumed to vary continuously along spatial coordinates in longitudinal or transverse directions according to an exponential law. In particular, the Poisson's ratio  $\nu$  is taken as constant, while the Young's



modulus  $E$  and the mass density  $\rho$  are assumed to vary according to the following exponential functions

$$E(x_d) = E_0 e^{\beta x_d}, \quad \beta = \frac{1}{L_d} \ln\left(\frac{E_1}{E_0}\right), \quad \rho(x_d) = \rho_0 e^{\gamma x_d}, \quad \gamma = \frac{1}{L_d} \ln\left(\frac{\rho_1}{\rho_0}\right), \quad (1)$$

where  $E_0$  and  $\rho_0$  denote the Young's modulus and the mass density for the starting face constituent,  $E_1$  and  $\rho_1$  are for the ending face constituent,  $\beta$  and  $\gamma$  represent the material gradient parameters for the Young's modulus and the mass density respectively,  $x_d$  ( $d=1,2$ ) stands for the Cartesian coordinates, and  $L_d$  is the length parameter of the considered plate.

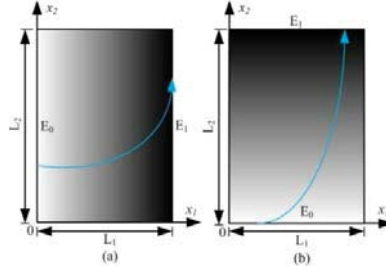


Figure 1. Coordinates and geometry of FG plates: (a) material gradation in  $x_1$ -direction; (b) material gradation in  $x_2$ -direction

### Problem Formulation and Numerical Solution Method

Based on the 2D elasticity theory, the governing partial differential equations of the steady-state elastodynamics without damping are given by

$$\sigma_{ij,j}(\mathbf{x}) + \omega^2 \rho u_i(\mathbf{x}) = 0, \quad (2)$$

where  $\omega$  is the natural frequency,  $\rho$  is the mass density,  $u_i$  is the amplitude of the displacement vector, and  $\sigma_{ij}$  is the stress tensor. A comma after a quantity represents spatial derivatives and repeated indices denote summation.

Since the Young's modulus varies with the Cartesian coordinates while the Poisson's ratio is constant, the elasticity tensor can be described by the shear modulus  $\mu(\mathbf{x})$  varying with the coordinates and the elasticity tensor  $c_{ijkl}^0$  for the reference homogeneous material in the form of

$$c_{ijkl}(\mathbf{x}) = \mu(\mathbf{x}) c_{ijkl}^0, \quad \mu(\mathbf{x}) = \frac{E(\mathbf{x})}{2(1+\nu)}, \quad c_{ijkl}^0 = \frac{2\nu}{1-2\nu} \delta_{ij} \delta_{kl} + \delta_{ik} \delta_{jl} + \delta_{il} \delta_{jk}, \quad (3)$$

in which  $\delta_{ij}$  is the Kronecker delta. By taking the elastostatic displacement fundamental solutions  $U_{ij}(\mathbf{x}, \mathbf{y})$  as the weight function, the weak-form of the equations of motion Eq. (2) can be obtained as

$$\int_{\Omega} [\sigma_{jk,k} + \rho \omega^2 u_j] \cdot U_{ij} d\Omega = 0. \quad (4)$$

Application of the generalized Hooke's law  $\sigma_{ij} = c_{ijkl} u_{k,l} = \mu(\mathbf{x}) c_{ijkl}^0 u_{k,l}$  and Gauss's divergence theorem yields the following boundary-domain integral equations

$$\begin{aligned} \tilde{u}_i(\mathbf{y}) &= \int_{\Gamma} U_{ij}(\mathbf{x}, \mathbf{y}) t_j(\mathbf{x}) d\Gamma - \int_{\Gamma} T_{ij}(\mathbf{x}, \mathbf{y}) \tilde{u}_j(\mathbf{x}) d\Gamma + \int_{\Omega} V_{ij}(\mathbf{x}, \mathbf{y}) \tilde{u}_j(\mathbf{x}) d\Omega \\ &+ \omega^2 \int_{\Omega} \frac{\rho(\mathbf{x})}{\mu(\mathbf{x})} U_{ij}(\mathbf{x}, \mathbf{y}) \tilde{u}_j(\mathbf{x}) d\Omega. \end{aligned} \quad (5)$$

In Eq. (5),  $t_i = \sigma_{ij} n_j$  is the traction vector with  $n_j$  being the components of the outward unit normal to the boundary  $\Gamma$  of the considered domain  $\Omega$ .  $\tilde{u}_i(\mathbf{x}) = \mu(\mathbf{x}) u_i(\mathbf{x})$  is the

normalized displacement vector and  $\tilde{\mu}(\mathbf{x}) = \ln[\mu(\mathbf{x})]$  is the normalized shear modulus (Gao et al. 2008). The fundamental solutions  $U_{ij}(\mathbf{x}, \mathbf{y})$ ,  $T_{ij}(\mathbf{x}, \mathbf{y})$ , and  $V_{ij}(\mathbf{x}, \mathbf{y})$  are chosen as the elastostatic displacement fundamental solutions for homogeneous, isotropic and linear elastic solids with  $\mu=1$ , which can be expressed as (Gao 2002b)

$$U_{ij} = \frac{-1}{8\pi(1-\nu)}[(3-4\nu)\delta_{ij} \ln(r) - r_{,i}r_{,j}], \quad (6)$$

$$\Sigma_{ijl} = c_{rsjl}^0 U_{ir,s} = \frac{-1}{4\pi(1-\nu)r}[(1-2\nu)(\delta_{il}r_{,j} + \delta_{ij}r_{,l} - \delta_{jl}r_{,i}) + 2r_{,i}r_{,j}r_{,l}], \quad (7)$$

$$T_{ij} = \Sigma_{ijl}n_l = \frac{-1}{4\pi(1-\nu)r}[(1-2\nu)(n_i r_{,j} - n_j r_{,i}) + ((1-2\nu)\delta_{ij} + 2r_{,i}r_{,j})r_{,l}n_l], \quad (8)$$

$$V_{ij} = \Sigma_{ijl}\tilde{\mu}_{,l} = \frac{-1}{4\pi(1-\nu)r}[(1-2\nu)(\tilde{\mu}_{,i}r_{,j} - \tilde{\mu}_{,j}r_{,i}) + ((1-2\nu)\delta_{ij} + 2r_{,i}r_{,j})r_{,l}\tilde{\mu}_{,l}], \quad (9)$$

where  $r=|\mathbf{x}-\mathbf{y}|$  is the distance from the field point  $\mathbf{x}$  to the source point  $\mathbf{y}$ . Boundary-domain integral equations for boundary points can be obtained by letting  $\mathbf{y}$  to the boundary  $\Gamma$  in Eq. (5).

There are two domain integrals emerged in Eq. (5), the first one is due to the gradation of the material properties and the other arises from the inertial effect. The radial integration method (RIM) of Gao (2002a) is employed to transform the domain integrals into boundary integrals over the global boundary. In the RIM, the normalized displacements in the domain integrals of Eq. (5) are approximated by a combination of the radial basis functions and the polynomials of the global coordinates, which has been demonstrated as the most promising one (Şimşek, and Kocatürk 2009). Then the normalized displacements  $\tilde{u}_i(\mathbf{x})$  can be expressed as

$$\tilde{u}_i(\mathbf{x}) = \sum_A \alpha_i^A \phi^A(R) + \alpha_i^k x_k + \alpha_i^0, \quad \sum_A \alpha_i^A = 0, \quad \sum_A \alpha_i^A x_j^A = 0, \quad (10a, b, c)$$

where  $\phi^A(R)$  is the radial basis function,  $\alpha_i^A$ ,  $\alpha_i^k$  and  $\alpha_i^0$  are unknown coefficients to be determined,  $x_k$  and  $x_j^A$  denote the coordinates of the field point  $\mathbf{x}$  and the application point  $A$  respectively. In this analysis, the following 4th order spline-type radial basis function is applied

$$\phi^A(R) = \begin{cases} 1 - 6\left(\frac{R}{d_A}\right)^2 + 8\left(\frac{R}{d_A}\right)^3 - 3\left(\frac{R}{d_A}\right)^4, & 0 \leq R \leq d_A, \\ 0, & R \geq d_A, \end{cases} \quad (11)$$

where  $R=|\mathbf{x}-\mathbf{x}^A|$  is the distance from the application point  $A$  to the field point  $\mathbf{x}$ , and  $d_A$  is the support size for the application point  $A$ . The total number of the application points  $A$  is given by  $N_t=N_b+N_i$  with  $N_b$  and  $N_i$  being the number of the boundary nodes and internal nodes, respectively. By choosing  $N_t$  application points  $A$  in Eqs. (10) and avoiding two coincident nodes,  $\alpha$  can be calculated by a set of linear algebraic equations as

$$\tilde{\mathbf{u}} = \boldsymbol{\phi} \cdot \boldsymbol{\alpha}, \quad \boldsymbol{\alpha} = \boldsymbol{\phi}^{-1} \cdot \tilde{\mathbf{u}}. \quad (12)$$

Then substitution of Eq. (10a) into the domain integrals of Eq. (5) and application of RIM, the domain integrals can be transformed into boundary integrals as

$$\int_{\Omega} V_{ij} \tilde{u}_j d\Omega = \alpha_j^A \int_{\Gamma} \frac{1}{r} \frac{\partial r}{\partial n} F_{ij}^A d\Gamma + \alpha_j^k \int_{\Gamma} \frac{r_{,k}}{r} \frac{\partial r}{\partial n} F_{ij}^1 d\Gamma + (\alpha_j^k y_k + \alpha_j^0) \int_{\Gamma} \frac{1}{r} \frac{\partial r}{\partial n} F_{ij}^0 d\Gamma, \quad (13)$$

$$\begin{aligned} \omega^2 \int_{\Omega} \frac{\rho}{\mu} U_{ij} \tilde{u}_j d\Omega &= \omega^2 \frac{\rho_0}{\mu_0} e^{(\gamma-\beta)y_d} [\alpha_j^A \int_{\Gamma} \frac{1}{r} \frac{\partial r}{\partial n} P_{ij}^{Ad} d\Gamma + a_j^k \int_{\Gamma} \frac{r_{,k}}{r} \frac{\partial r}{\partial n} P_{ij}^{1d} d\Gamma \\ &+ (a_j^k y_k + a_j^0) \int_{\Gamma} \frac{1}{r} \frac{\partial r}{\partial n} P_{ij}^{0d} d\Gamma], \end{aligned} \quad (14)$$

where the relation  $x_i = y_i + r_{,i} r$  is used to relate  $\mathbf{x}$  with  $r$ . By rewriting Eq. (9) with  $V_{ij} = \bar{V}_{ij}/r$ , the integral functions in Eqs. (13) and (14) can be expressed as

$$F_{ij}^A = \int_0^r r V_{ij} \phi^A dr = \bar{V}_{ij} \int_0^r \phi^A dr, \quad F_{ij}^1 = \int_0^r r^2 V_{ij} dr = \frac{1}{2} r^2 \bar{V}_{ij}, \quad F_{ij}^0 = \int_0^r r V_{ij} dr = r \bar{V}_{ij}, \quad (15a,b,c)$$

$$P_{ij}^{Ad} = \int_0^r r U_{ij} \phi^A e^{(\gamma-\beta)r_{,d}r} dr, \quad P_{ij}^{1d} = \int_0^r r^2 U_{ij} e^{(\gamma-\beta)r_{,d}r} dr, \quad P_{ij}^{0d} = \int_0^r r U_{ij} e^{(\gamma-\beta)r_{,d}r} dr. \quad (16a,b,c)$$

Since  $r_{,i}$  in the above radial integrals is constant, then Eqs. (15b-c) can be evaluated analytically and other integrals are calculated by standard Gaussian quadrature formula. The function  $\phi^A(R)$  can be expressed as a function of  $r$ , which can be done by using the following relation

$$R = \sqrt{r^2 + sr + \bar{R}^2}, \quad s = 2r_{,i} \bar{R}_i, \quad \bar{R} = |\mathbf{y} - \mathbf{x}^A| = \sqrt{\bar{R} \cdot \bar{R}}, \quad \bar{R}_i = y_i - x_i^A. \quad (17)$$

After the spatial discretization of the global boundary into quadratic boundary elements with  $N_b$  nodes, and collocating the resulting boundary integral equations at the  $N_t = N_b + N_i$  boundary and internal nodes, two sets of discretized boundary integral equations are obtained, which can be expressed in matrix form as

$$\mathbf{H}_b \cdot \tilde{\mathbf{u}}_b = \mathbf{G}_b \cdot \mathbf{t}_b + \mathbf{V}_b \cdot \tilde{\mathbf{u}} + \omega^2 \cdot \mathbf{P}_b \cdot \tilde{\mathbf{u}} \quad \text{for boundary nodes,} \quad (18)$$

$$\tilde{\mathbf{u}}_i = \mathbf{G}_i \cdot \mathbf{t}_b - \mathbf{H}_i \cdot \tilde{\mathbf{u}}_b + \mathbf{V}_i \cdot \tilde{\mathbf{u}} + \omega^2 \cdot \mathbf{P}_i \cdot \tilde{\mathbf{u}} \quad \text{for internal nodes.} \quad (19)$$

The system matrices in the above equations involve boundary integrals only. The normalized displacement vector  $\tilde{\mathbf{u}}_b$  and the corresponding traction vector  $\mathbf{t}_b$  of the boundary nodes have the size of  $2N_b \times 1$ , while the normalized displacement vector of the internal nodes  $\tilde{\mathbf{u}}_i$  has the size of  $2N_i \times 1$ . The normalized displacement vector  $\tilde{\mathbf{u}}$  at all nodes has the size of  $2N_t \times 1$ . In Eq. (18), the matrices  $\mathbf{V}_b$  and  $\mathbf{P}_b$  have the dimension of  $2N_b \times 2N_t$ , and in Eq. (19) the matrices  $\mathbf{V}_i$  and  $\mathbf{P}_i$  have the size of  $2N_i \times 2N_t$ . By considering the boundary conditions, Eqs. (18) and (19) can also be written in terms of known and unknown vectors and in a more compact form as

$$\left( \begin{bmatrix} \mathbf{A}_b & \mathbf{0} \\ -\mathbf{A}_i & \mathbf{I} \end{bmatrix} - \begin{bmatrix} \mathbf{V}_b \\ \mathbf{V}_i \end{bmatrix} \right) \begin{Bmatrix} \bar{\mathbf{x}}_b \\ \tilde{\mathbf{u}}_i \end{Bmatrix} = \omega^2 \begin{bmatrix} \mathbf{P}_b \\ \mathbf{P}_i \end{bmatrix} \begin{Bmatrix} \bar{\mathbf{x}}_b \\ \tilde{\mathbf{u}}_i \end{Bmatrix}, \quad (20)$$

where  $\mathbf{I}$  is the identity matrix with the size of  $2N_i \times 2N_i$ . The vector  $\bar{\mathbf{x}}_b$  contains the unknown normalized displacements and unknown boundary tractions for boundary nodes, and the corresponding matrices  $\mathbf{A}_b$  and  $\mathbf{A}_i$ , have the dimensions  $2N_b \times 2N_b$ , and  $2N_i \times 2N_b$ , respectively. It should be noted that the sub-columns of the matrices  $\mathbf{V}_b$ ,  $\mathbf{P}_b$  and  $\mathbf{V}_i$ ,  $\mathbf{P}_i$  corresponding to the known boundary displacement nodes should be taken as zero. In free vibration analysis, only the homogeneous system of the linear algebraic equations is needed, thus the vectors containing the known normalized boundary displacements as well as the known boundary tractions should be taken as zero. By resolving this general eigenvalue equation, the eigenvalues  $\omega$  and the eigenvectors can be obtained numerically.

## Numerical Examples and Discussion

The boundary conditions of the rectangular FG plates are determined by the combination of the boundary conditions on the four edges moving counter clockwise

starting from the edge  $x_2=0$ . As boundary conditions, simply supported (S), fixed (C) and free (F) boundary conditions are imposed as S:  $t_{x1}=0, v=0$ , on  $x1=0$ ; C:  $u=v=0$ , on  $x1=0$ ; F:  $t_{x1}=t_{x2}=0$ , on  $x1=0$  and shown in Fig. 2. The natural frequencies are all normalized by  $\varpi = \omega L_2 \sqrt{\rho_{Al}/E_{Al}}$ , where  $L_2$  is the length of the analyzed plate in the  $x_2$ -direction.

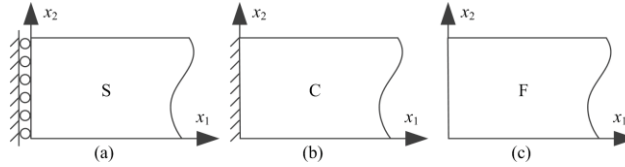


Figure 2. Different supports for FG plates (a) simply supported; (b) fixed; (c) free

To verify the accuracy of the present method, SSSS supported FG plates with aspect ratios  $L_1/L_2=1, 2$  and  $5$  are studied. The first ten normalized natural frequencies are given in Table 1 and the results are compared with the FEM results by using COMSOL. The comparison shows an excellent agreement. For the FG plate with  $L_1/L_2=1$ , 20 boundary elements ( $N_b=40$ ) and 81 internal nodes ( $N_i=81$ ) are used and the results are compared with that of the FEM with 11081 quadratic elements. For  $L_1/L_2=2$ ,  $N_b=60$  and  $N_i=36$  in the BEM and 20000 quadratic elements in the FEM are used. For  $L_1/L_2=5$ ,  $N_b=120$  and  $N_i=96$  in the BEM and 13873 quadratic elements in the FEM are used. The comparison demonstrates that the present method has high accuracy even for high frequencies.

Table 1. Comparison for SSSS supported FG plates with aspect ratios  $L_1/L_2=1, 2, 5$

Mode	$L_1/L_2=1$			$L_1/L_2=2$			$L_1/L_2=5$		
	$N_b=40$ $N_i=81$	FEM (11081*)	diff. %	$N_b=60$ $N_i=36$	FEM (20000*)	diff. %	$N_b=120$ $N_i=96$	FEM (13873*)	diff. %
1	1.9185	1.9207	0.11	0.9987	0.9988	0.01	0.3995	0.3995	0.01
2	1.9980	1.9975	0.03	1.9504	1.9513	0.05	0.7900	0.7901	0.01
3	2.8638	2.8637	0.01	1.9736	1.9752	0.08	1.1822	1.1826	0.03
4	3.8901	3.9026	0.32	2.2292	2.2290	0.01	1.5753	1.5756	0.02
5	3.9502	3.9503	0.00	2.7992	2.7966	0.09	1.9666	1.9689	0.11
6	4.4183	4.4118	0.15	2.9519	2.9565	0.16	1.9686	1.9690	0.02
7	4.4576	4.4579	0.01	3.5570	3.5544	0.07	2.0085	2.0083	0.01
8	5.2336	5.2355	0.04	3.9242	3.9342	0.25	2.1237	2.1225	0.05
9	5.6107	5.5932	0.31	3.9298	3.9391	0.24	2.2988	2.2976	0.05
10	5.8631	5.8875	0.41	4.0654	4.0650	0.01	2.3587	2.3622	0.15

\*Number of quadratic elements

Free vibration of 2D exponential FG plates with different gradient parameters  $\kappa=0.33$  and  $3$ , where  $\kappa=E_1/E_0$ , gradation directions, boundary conditions (SSSS, CCCC, CFFF, FFSS, SSCC, CCFF) and aspect ratios  $L_1/L_2=1, 2$  and  $5$  is then investigated. The first five normalized natural frequencies are shown in Table 2. For SSSS and CCCC supported FG plates, the frequencies for  $\kappa=0.33$  and  $\kappa=3$  are the same due to the double symmetry of the problem with respect to the central lines of the FG plates. For CFFF supported FG plates, the frequencies for  $\kappa=0.33$  and  $\kappa=3$  are the same only for the material gradation in the  $x_1$ -direction. The first five vibration modes of SSSS, CFFF and SSCC supported FG plates are presented in Fig. 3.

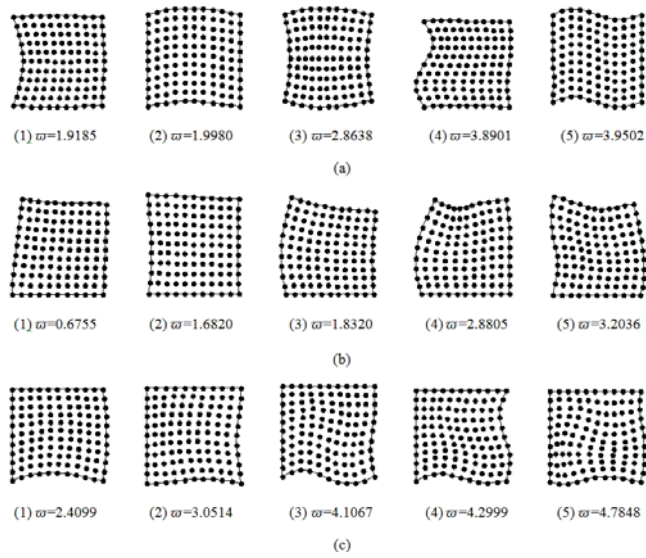


Figure 3. First five vibration modes of the FG plates with material gradation in  $x_1$ -direction,  $L_1/L_2=1$  and  $\kappa=0.33$  (a) SSSS; (b) CFFF; (c) SSCC

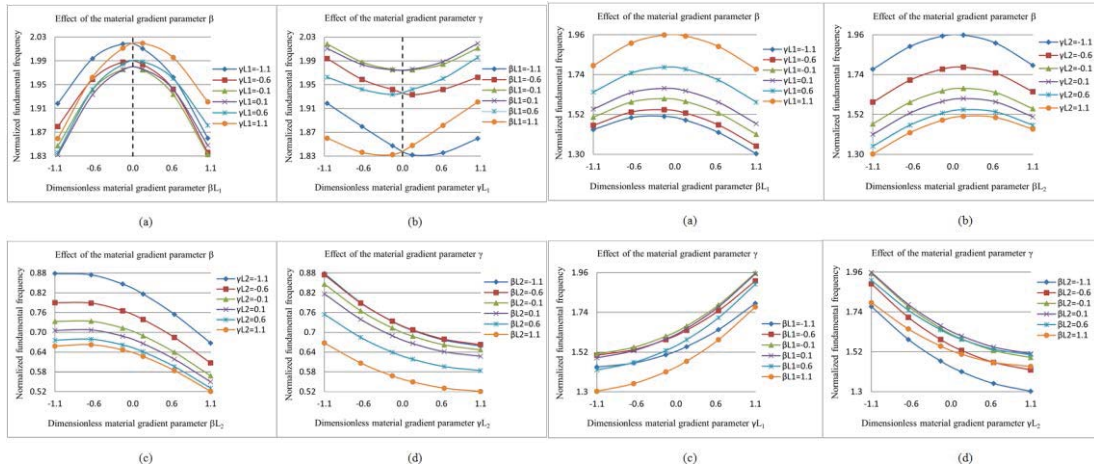


Figure 4. Effect of the material gradient parameters for FG plates with  $L_1/L_2=1$  (a) effect of  $\beta L_1$  for SSSS supported FG plates; (b) effect of  $\gamma L_1$  for SSSS supported FG plates; (c) effect of  $\beta L_2$  for CFFF supported FG plates; (d) effect of  $\gamma L_2$  for CFFF supported FG plates

Figure 5. Effect of the material gradient parameter for CFFF supported FG plates with  $L_1/L_2=1$  (a) effect of  $\beta L_1$ ; (b) effect of  $\beta L_2$ ; (c) effect of  $\gamma L_1$ ; (d) effect of  $\gamma L_2$

Fig. 4 shows the effects of the material gradient parameters  $\beta$  and  $\gamma$  on the free vibration of the FG plates. For each of both parameters six dimensionless material gradient parameters  $\beta L_d$  and  $\gamma L_d$   $d=1, 2$  are considered. SSSS supported FG plates with an aspect ratio  $L_1/L_2=1$  and a material gradation in the  $x_1$ -direction are taken as an example of doubly symmetrical FG plates with respect to their mid-lines. The normalized fundamental frequencies change with the dimensionless material gradient parameters obeying a parabolic tendency as shown in Fig. 4(a). For a fixed material gradient parameter  $\beta L_1$ , each pair of  $\gamma L_1$  intersects at the value for homogeneous case and achieves the highest frequency. A decreasing absolute value of  $\gamma L_1$  decreases the

fundamental frequencies. However, the material gradient parameter  $\gamma L_1$  has a totally opposite effect on the natural frequencies which can be observed from Fig. 4(b). For CFFF supported FG plates with a material gradation in the  $x_1$ -direction, the influences of the material gradient parameters on the free vibration are the same as that of the doubly symmetrical (with respect to the mid-lines) FG plates. For a material gradation in the  $x_2$ -direction as shown in Fig. 4(c), an increasing dimensionless parameter  $\beta L_2$  decreases the fundamental frequencies, while the normalized natural frequencies decrease with the increase of the dimensionless material gradient parameter  $\gamma L_2$ . The influence of the material gradient parameter  $\gamma L_2$  is similar to that of  $\beta L_2$  but with an opposite slope.

Fig. 5 presents the normalized fundamental frequencies versus the dimensionless material gradient parameters for asymmetrical CFFF supported FG plates with an aspect ratio  $L_1/L_2=1$ . To investigate the effect of the aspect ratio on the free vibration of FG plates, the normalized natural frequencies versus the dimensionless material gradient parameters with aspect ratios  $L_1/L_2=1, 2$  and  $5$  are shown in Fig. 6. Generally, an increasing aspect ratio decreases the normalized natural frequencies, as shown in Fig. 6(a) for the SSSS supported FG plates with a material gradation in the  $x_1$ -direction. However, for CFFF supported FG plates, an opposite tendency is observed. As an example, the corresponding results for CFFF supported FG plates with a material gradation in the  $x_2$ -direction are shown in Fig. 6(b).

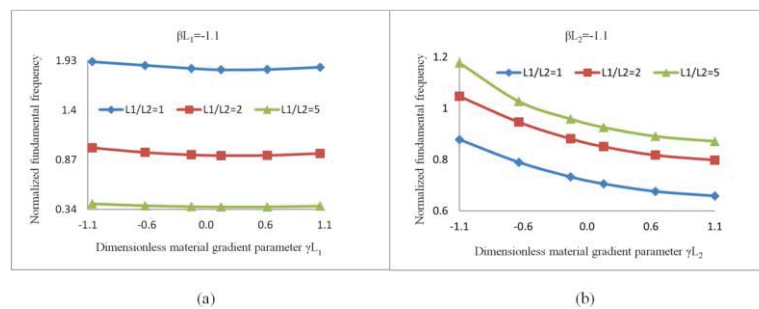


Figure 6. Effect of the aspect ratios  $L_1/L_2=1, 2, 5$  on the normalized fundamental frequencies of (a) SSSS supported FGM plates with material gradation in  $x_1$ -direction; (b) CFFF supported FG plates with material gradation in  $x_2$ -direction

## Conclusions

In this paper, a meshfree boundary-domain integral equation method for free vibration analysis of two-dimensional FG plates is presented. An exponential law is used to describe the continuous material gradation either in longitudinal or transverse directions. The effects of the material gradient parameters, gradation directions, aspect ratios and boundary conditions on the free vibration of the FG plates are investigated in details by numerical examples. The numerical examples demonstrate that the present method has fast convergence, high efficiency and accuracy.

**References**

- Nardini, D., Brebbia C. A. (1983), A new approach to free vibration analysis using boundary elements. *Applied Mathematical Modelling*, 7(3), pp. 157-162.
- Gao, X. W. (2002), The radial integration method for evaluation of domain integrals with boundary-only discretization. *Engineering Analysis with Boundary Elements*, 26(10), pp. 905-916.
- Albuquerque, E. L., Sollero, P., Fedelinski, P. (2003), Free vibration analysis of anisotropic material structures using the boundary element method. *Engineering Analysis with Boundary Elements*, 27(10), pp. 977-985.
- Albuquerque, E.L., Sollero, P., Portilho de Paiva W. (2006), The radial integration method applied to dynamic problems of anisotropic plates. *Communications in Numerical Methods in Engineering*, 23(9), pp. 805-818.
- Ekhlakov, A., Khay, O., Zhang, Ch. (2010), Effects of the material gradation on the SIFs of a crack in a 2-D FGM plate under thermal shock. *Proceedings in Applied Mathematics and Mechanics*, 10(1), pp. 111-112.
- Ekhlakov, A. V., Khay, O. M., Zhang, Ch., Sladek, J., Sladek, V. (2012), A BDEM for transient thermoelastic crack problems in functionally graded materials under thermal shock. *Computational Materials Science*, 57, pp. 30-37.
- Gao, X. W., Zhang, Ch., Sladek, J., Sladek, V. (2008), Fracture analysis of functionally graded materials by a BEM. *Composites Science and Technology*, 68, pp. 1209-1215.
- Gao, X. W., Davies, T. G. (2002), *Boundary Element Programming in Mechanics*. Cambridge University Press.
- Golberg, M. A., Chen, C. S., Bowman H. (1999), Some recent results and proposals for the use of radial basis functions in the BEM. *Engineering Analysis with Boundary Elements*, 23, pp. 285-296.
- Şimşek, M., Kocatürk, T. (2009), Free and forced vibration of a functionally graded beam subjected to a concentrated moving harmonic load. *Composite Structures*, 90, pp. 465-473.

Table 2. First five normalized natural frequencies of SSSS, CCCC, CFFF, FFSS, SSCC and CCFF supported FG plates

BC	GD	$\kappa$	$L_1/L_2=1$					$L_1/L_2=2$					$L_1/L_2=5$				
			1st	2nd	3rd	4th	5th	1st	2nd	3rd	4th	5th	1st	2nd	3rd	4th	5th
SSSS	$x_1$	0.33	1.9185	1.9980	2.8638	3.8901	3.9502	0.9987	1.9504	1.9736	2.2292	2.7992	0.3995	0.7900	1.1822	1.5753	1.9666
		3	1.9210	1.9986	2.8644	3.9020	3.9451	0.9987	1.9504	1.9736	2.2292	2.7992	0.3995	0.7900	1.1822	1.5753	1.9666
	$x_2$	0.33	1.9213	1.9973	2.8641	3.8997	3.9464	0.9462	1.9185	1.9968	2.2599	2.8659	0.3758	0.7549	1.1387	1.5278	1.9184
		3	1.9213	1.9973	2.8641	3.8997	3.9464	0.9462	1.9185	1.9968	2.2599	2.8659	0.3758	0.7549	1.1387	1.5278	1.9184
CCCC	$x_1$	0.33	4.0353	4.0712	4.5259	5.8049	6.3136	2.6543	3.6359	3.6661	3.9935	4.1453	2.0916	2.4151	2.8717	3.3908	3.4700
		3	4.0367	4.0747	4.5251	5.8077	6.3019	2.6543	3.6359	3.6661	3.9935	4.1453	2.0916	2.4151	2.8717	3.3908	3.4700
	$x_2$	0.33	4.0381	4.0713	4.5257	5.8067	6.3011	2.6569	3.6805	3.6991	3.9968	4.1827	2.1154	2.4354	2.8881	3.4016	3.5159
		3	4.0381	4.0713	4.5257	5.8067	6.3011	2.6569	3.6805	3.6991	3.9968	4.1827	2.1154	2.4354	2.8881	3.4016	3.5159
CFFF	$x_1$	0.33	0.6755	1.6820	1.8320	2.8805	3.2036	0.8326	1.5934	1.7656	1.8556	2.1765	0.9178	1.0904	1.5290	1.7364	1.7956
		3	0.6753	1.6824	1.8328	2.8844	3.1974	0.8326	1.5934	1.7656	1.8556	2.1765	0.9178	1.0904	1.5290	1.7364	1.7956
	$x_2$	0.33	0.8782	2.0385	2.1389	3.0845	3.2308	1.0468	1.7526	2.1232	2.1783	2.4654	1.1336	1.2565	1.6857	1.8286	1.9649
		3	0.5208	1.3455	1.5414	2.8038	3.0062	0.6565	1.3411	1.4365	1.5979	1.9382	0.7291	0.9418	1.3367	1.4113	1.4440
FFSS	$x_1$	0.33	1.4112	2.4668	2.7163	2.9319	3.6889	1.0305	1.2060	1.8981	2.1627	2.7168	0.3046	0.6738	0.9972	1.0731	1.2833
		3	1.0375	2.1785	2.7945	2.9075	3.7173	0.7315	1.3365	1.8173	2.1102	2.6000	0.2554	0.6386	0.9571	1.1028	1.2608
	$x_2$	0.33	1.0373	2.1783	2.7933	2.9074	3.7170	0.7630	1.1495	1.7493	1.9655	2.6416	0.2918	0.6346	0.8182	0.9842	1.1337
		3	1.4118	2.4670	2.7181	2.9320	3.6896	0.9299	1.3978	1.9427	2.3003	2.6278	0.0002	0.2597	0.6381	1.0249	1.2475
SSCC	$x_1$	0.33	2.4099	3.0514	4.1067	4.2999	4.7848	1.8686	2.2288	2.4994	3.1320	3.4424	1.7363	1.7862	1.8858	2.0292	2.1114
		3	2.0816	2.8309	3.9397	4.1037	4.6979	1.7956	2.1908	2.4108	3.1268	3.3633	1.7344	1.7853	1.8755	2.0238	2.0933
	$x_2$	0.33	2.0816	2.8310	3.9375	4.1062	4.6984	1.5432	2.0756	2.3047	2.9699	3.3633	1.4124	1.4557	1.5877	1.8128	2.0401
		3	2.4102	3.0517	4.1070	4.2998	4.7849	2.0485	2.3943	2.7059	3.2819	3.5138	1.9923	2.0226	2.1330	2.2827	2.3887
CCFF	$x_1$	0.33	1.4373	1.9425	2.2423	3.5871	4.0334	1.0574	1.7672	1.8869	2.3545	2.6623	0.9503	1.3496	1.7264	1.8013	1.8315
		3	1.7702	2.4659	2.6311	3.8513	4.2927	1.2823	1.8594	1.9299	2.4445	2.7816	1.0063	1.3726	1.7251	1.7993	1.8358
	$x_2$	0.33	1.7701	2.4656	2.6287	3.8545	4.2840	1.3241	2.1588	2.2398	2.6790	2.8262	1.1772	1.5222	1.9647	2.1653	2.2181
		3	1.4394	1.9431	2.2459	3.5852	4.0440	1.0390	1.4625	1.6019	2.1521	2.6256	0.7998	1.2200	1.4207	1.4435	1.4728

BD: boundary condition; GD: gradation direction



# Direct determination of critical load combinations for elastoplastic structures subject to multiple load cases

**\*S. Tangaramvong, and F. Tin-Loi**

School of Civil and Environmental Engineering, The University of New South Wales, NSW 2052, Australia

\*Corresponding author: sawekchai@unsw.edu.au

**Key Words:** *Structural design, Multiple load cases, Elastoplasticity, Integer program*

## Abstract

The paper presents a mathematical programming based approach for the safety assessment of nonlinear structures that can be subject to a number of predefined load combinations. The objective is to determine in a single step the critical load combination, for which the chosen maximum (or minimum) response (e.g. stress or displacement) occurs. Assuming elastoplastic material properties, the governing formulation takes the form of challenging nonconvex and nonsmooth optimization problem, known as a 0-1 mathematical program with equilibrium constraints or 0-1 MPEC. The numerical algorithm proposed to solve the 0-1 MPEC is a regularization technique that involves iteratively processing a series of reformulated mixed integer nonlinear programming problems (MINLP) using a penalty function. Optimal solutions to each MINLP subproblem are obtained by the proposed novel space search formulation or FSS scheme.

Keywords: Structural design, Multiple load cases, Elastoplasticity, Integer program

## Introduction

The safety assessment of structures under multiple load cases provides a well-accepted numerical approximation for the critical structural responses, such as the extreme maximum and minimum bound values to some specified variables of interest, e.g. member forces, nodal displacement, etc. Various papers in this area (see e.g. Mullen and Muhanna, 1999; Suarjana and Law, 1994) have established reliable theoretical and numerical treatments, albeit solely for elastic material related problems. It is useful, and often mandatory, to incorporate the influence of material nonlinear properties for the realistic assessment of practical engineering mechanics applications.

The present study proposes a pair of novel mathematical programming based approaches to directly identify the maximum bound value in one case and the minimum bound value in the other case to some selected set of response variables of an elastoplastic structure subjected to various pattern load cases. The governing problem takes the “nonstandard” and difficult form known in the nonconvex and/or nonsmooth optimization theory as a 0-1 mathematical program with equilibrium constraints or 0-1 MPEC (Kocis and Grossmann, 1989; Luo et al., 1996). The specific equilibrium constraints are characterized by complementarity conditions (representing plastic behavior). We propose a penalty regularization technique to transform the challenging original 0-1 MPEC to a standard mixed integer nonlinear programming or MINLP problem, and then successively solve a series of MINLP subproblems to iteratively enforce the complementarity. A novel formulation space search or FSS algorithm (López and Beasley, 2013) is adopted to capture the best (optimal) solution for each of the MINLP subproblems. We illustrate the application and robustness of the proposed method through one of the many examples we have solved.

### Critical Load Combinations as a 0-1 MPEC

Our work adopts a standard “line” finite element framework, where the structure is suitably discretized into  $n$  elements,  $m$  basic stresses/strains,  $d$  degrees of freedom and  $y$  yield functions. The nonlinear material properties are accommodated through the classical plastic hinge concept. Plasticity is confined solely at fixed critical zones, namely the two ends for each generic element, whilst the rest of the member between these ends remains elastic. A computationally advantageous piecewise linear plastic concept (Maier, 1970) is adopted to provide a close approximation to the actual nonlinear yield surfaces, as a number of linear hyperplanes.

The generic formulations describing the path-independent or holonomic elastoplastic response of the structure under a single load case are written as follows (see e.g. Maier, 1970; Tangaramvong and Tin-Loi, 2007, 2008):

$$\mathbf{C}^T \mathbf{Q} = \mathbf{F}, \quad (1)$$

$$\mathbf{C} \mathbf{u} = \mathbf{e} + \mathbf{p}, \quad (2)$$

$$\mathbf{Q} = \mathbf{E} \mathbf{e}, \quad (3)$$

$$\mathbf{p} = \mathbf{N} \boldsymbol{\lambda}, \quad (4)$$

$$\mathbf{w} = -\mathbf{N}^T \mathbf{Q} + \mathbf{r} \geq \mathbf{0}, \quad \boldsymbol{\lambda} \geq \mathbf{0}, \quad \mathbf{w}^T \boldsymbol{\lambda} = 0. \quad (5)$$

More explicitly, equilibrium between basic stresses  $\mathbf{Q} \in \mathfrak{R}^m$  and externally applied forces  $\mathbf{F} \in \mathfrak{R}^d$  is given in Eq. (1) through a (constant) compatibility matrix  $\mathbf{C} \in \mathfrak{R}^{m \times d}$ . The linear compatibility relation between nodal displacements  $\mathbf{u} \in \mathfrak{R}^d$  and basic strains, written as a summation of elastic  $\mathbf{e} \in \mathfrak{R}^m$  and plastic  $\mathbf{p} \in \mathfrak{R}^m$  strains, is described in Eq. (2). The elastic constitutive behaviors are expressed in Eq. (3) using a positive definite stiffness matrix  $\mathbf{E} \in \mathfrak{R}^{m \times m}$ .

The associative flow rule in Eq. (4) defines the plastic strains  $\mathbf{p}$  as functions of plastic multipliers  $\boldsymbol{\lambda} \in \mathfrak{R}^y$  through a constant normality matrix  $\mathbf{N} \in \mathfrak{R}^{m \times y}$ , which collects unit normal directions to all piecewise linear yield hyperplanes. Finally, the complementarity condition (viz.  $\mathbf{w}^T \boldsymbol{\lambda} = 0$ ) in Eq. (5) between the two sign-constrained variables, namely the yield functions  $\mathbf{w} \geq \mathbf{0} \in \mathfrak{R}^y$  and the plastic multipliers  $\boldsymbol{\lambda} \geq \mathbf{0}$  describes the inherent holonomic structural behavior that permits reversal of plastic strains at the potential plastic hinges, where  $\mathbf{r} \in \mathfrak{R}^y$  is a vector of yield limits.

Simply collecting and manipulating the governing holonomic Eqs (1) to (5) provides the following state problem in mixed static-kinematic variables  $(\mathbf{Q}, \mathbf{u}, \boldsymbol{\lambda})$ :

$$\begin{aligned} \mathbf{C}^T \mathbf{Q} - \mathbf{F} &= \mathbf{0}, \\ \mathbf{Q} - \mathbf{E} \mathbf{C} \mathbf{u} + \mathbf{E} \mathbf{N} \boldsymbol{\lambda} &= \mathbf{0}, \end{aligned} \quad (6)$$

$$\mathbf{w} = -\mathbf{N}^T \mathbf{Q} + \mathbf{r} \geq \mathbf{0}, \quad \boldsymbol{\lambda} \geq \mathbf{0}, \quad \mathbf{w}^T \boldsymbol{\lambda} = 0.$$

The state problem given in Eq. (6) is a mixed complementarity problem or MCP (Dirkse and Ferris, 1995a). For any predefined force vector  $\mathbf{F}$ , the key response variables  $(\mathbf{Q}, \mathbf{u}, \boldsymbol{\lambda})$  can be obtained by solving the MCP (6) using, for instance, the state-of-the-art complementarity solver, namely PATH (Dirkse and Ferris, 1995b), that is available from within the general algebraic modeling system or GAMS (Brooke et al., 1998), that we adopted for this work.

When pattern load cases, as for practical design instances, are considered, it is essential that the critical load combination leading to the worst value to some response variables of interest is determined. An attempt to achieve this typically involves exhaustive trial-and-error and often requires excessive computing and designer-time resources, especially when a large number of load cases are concerned. To circumvent this, the present method develops a robust optimization technique that determines, within a single step, the critical load case associated with the maximum (or minimum) response variable of the structure under all possible load combinations.

We first replace the known force vector  $\mathbf{F}$  in Eq. (6) with the set of all  $s$  possible predefined load cases  $\mathbf{f} \in \mathfrak{R}^{d \times s}$  and additional unknown binary (0 or 1) variables  $\boldsymbol{\alpha} \in \mathfrak{R}^s$ :

$$\mathbf{F} = \mathbf{f}\boldsymbol{\alpha}. \quad (7)$$

The variables  $\boldsymbol{\alpha}$  play the crucial role in automatically selecting which particular load case  $\mathbf{f}^i \in \mathfrak{R}^d$  for  $i = 1$  to  $s$  is retained (viz.  $\alpha^i = 1$ ) or eliminated ( $\alpha^i = 0$ ) from the structural system. A direct determination is then enabled by forming an optimization problem, in variables  $(\boldsymbol{\alpha}, \mathbf{Q}, \mathbf{u}, \boldsymbol{\lambda})$ , that maximizes (or minimizes) an objective function representing the specific response variable  $Y$  (i.e. some basic stress  $Q^i$ , nodal displacement  $u^i$ , etc.), subject to the constraints describing the holonomic elastoplastic relations in Eq. (6) and the multiple load cases in Eq. (7):

$$\begin{aligned} & \max \text{ (or } \min) Y \\ & \text{subject to} \quad \mathbf{C}^T \mathbf{Q} - \boldsymbol{\alpha} \mathbf{f} = \mathbf{0}, \\ & \quad \mathbf{Q} - \mathbf{E} \mathbf{C} \mathbf{u} + \mathbf{E} \mathbf{N} \boldsymbol{\lambda} = \mathbf{0}, \\ & \quad \mathbf{w} = -\mathbf{N}^T \mathbf{Q} + \mathbf{r} \geq \mathbf{0}, \boldsymbol{\lambda} \geq \mathbf{0}, \mathbf{w}^T \boldsymbol{\lambda} = 0. \end{aligned} \quad (8)$$

The problem in Eq. (8) belongs to the challenging class of “nonstandard” optimization programs, known as a 0-1 MPEC (Kocis and Grossmann, 1989; Luo et al., 1996). In addition to the difficulties associated with the presence of complementarity constraints making the problem severely nonconvex and/or nonsmooth, the binary variables  $\boldsymbol{\alpha}$  impart computationally nasty disjunctive and combinatorial conditions to the 0-1 MPEC (8). To date, there are no known algorithms that can guarantee the (global) optimality to the solutions of MPECs, let alone of 0-1 MPECs. The best method is often dependent on the nature of the specific problem.

### Penalty-FSS Algorithm

In this section, we propose a combined penalty regularization (Tangaramvong and Tin-Loi, 2007, 2008) and FSS (López and Beasley, 2013) technique as a scheme to obtain the optimal solutions of the 0-1 MPEC (8). The 0-1 MPEC (8) is first reformulated as a standard MINLP problem by replacing the complementarity condition with the penalized term (viz.  $\mu \mathbf{w}^T \boldsymbol{\lambda}$  or  $-\mu \mathbf{w}^T \boldsymbol{\lambda}$ ) added directly to the objective function, where  $\mu$  denotes a (positive scalar) penalty parameter. We attempt to enforce the complementarity condition by iteratively increasing the parameter  $\mu$ . Thus, the penalty algorithm we use processes a series of MINLP subproblems, each represented by

$$\begin{aligned} & \max \text{ (or } \min) Y - \mu \mathbf{w}^T \boldsymbol{\lambda} \text{ (or } Y + \mu \mathbf{w}^T \boldsymbol{\lambda}) \\ & \text{subject to} \quad \mathbf{C}^T \mathbf{Q} - \boldsymbol{\alpha} \mathbf{f} = \mathbf{0}, \\ & \quad \mathbf{Q} - \mathbf{E} \mathbf{C} \mathbf{u} + \mathbf{E} \mathbf{N} \boldsymbol{\lambda} = \mathbf{0}, \\ & \quad \mathbf{w} = -\mathbf{N}^T \mathbf{Q} + \mathbf{r} \geq \mathbf{0}, \boldsymbol{\lambda} \geq \mathbf{0}, \end{aligned} \quad (9)$$

with increasing  $\mu$  (e.g.  $\mu = 10\mu$ ) until the preset tolerance on the original complementarity condition (e.g.  $\mathbf{w}^T \boldsymbol{\lambda} \leq 10^{-6}$ ) is satisfied.

The success of the penalty method relies on the ability to capture the optimal solutions for each of the MINLP subproblems (9). Unfortunately, directly processing such a problem entails severe combinatorial difficulties and is likely to fail in generating optimal results. A better numerical (albeit heuristic) method, namely FSS (López and Beasley, 2013), is proposed to circumvent these challenges, by simply adding the following additional nonlinear constraint to increase the “tightness” of the original MINLP (9):

$$\boldsymbol{\alpha}^T(\mathbf{1} - \boldsymbol{\alpha}) \leq \gamma, \quad (10)$$

where  $\gamma$  is a (positive) relaxation parameter to FSS and  $\mathbf{1}$  a unit vector. Therefore, the original MINLP subproblem (9) can be rewritten as:

$$\begin{aligned} & \max \text{ (or } \min) \ Y - \mu \mathbf{w}^T \boldsymbol{\lambda} \text{ (or } Y + \mu \mathbf{w}^T \boldsymbol{\lambda}) \\ & \text{subject to} \quad \mathbf{C}^T \mathbf{Q} - \boldsymbol{\alpha} \mathbf{f} = \mathbf{0}, \\ & \quad \mathbf{Q} - \mathbf{E} \mathbf{C} \mathbf{u} + \mathbf{E} \mathbf{N} \boldsymbol{\lambda} = \mathbf{0}, \\ & \quad \mathbf{w} = -\mathbf{N}^T \mathbf{Q} + \mathbf{r} \geq \mathbf{0}, \ \boldsymbol{\lambda} \geq \mathbf{0}, \\ & \quad \boldsymbol{\alpha}^T(\mathbf{1} - \boldsymbol{\alpha}) \leq \gamma. \end{aligned} \quad (11)$$

The algorithm attempts to explore, at inner-level iterations, various different sets of MINLP solutions by initially setting  $\gamma$  to some suitable value and subsequently decreasing  $\gamma$  to tighten the binary constraints. After obtaining the multiple sets of MINLP solutions, the best value is selected as the “optimum” to the original MINLP (9).

The proposed penalty-FSS algorithm can be summarized in the pseudocode as follows:

#### Step (a) – Initialization

- Set: initial  $\gamma$ ,  $\mu$ , maximum penalty iterations ( $maxplt$ ), maximum FSS iterations ( $maxfss$ ),  $\mathbf{w}^T \boldsymbol{\lambda} = 100$ ,  $Y_{best} = 0$  for maximization (or  $Y_{best} = 1000$  for minimization),  $rpt = 0$

#### Step (b) – Penalization

- For  $j = 1$  to  $maxplt$ 
  - if  $\mathbf{w}^T \boldsymbol{\lambda} \leq 10^{-6}$ , terminate, end
  - go to FSS Step (c) to obtain the solutions of MINLP (9)
  - increase  $\mu = 10\mu$

#### Step (c) – FSS

- For  $k = 1$  to  $maxfss$ 
  - if  $rpt > 3$  or  $\gamma \leq 10^{-5}$ , terminate, end
  - solve MINLP (11)
  - if  $Y = Y_{best}$ 
    - count  $rpt = rpt + 1$
  - elseif  $Y > Y_{best}$  for maximization (or  $Y < Y_{best}$  for minimization)
    - update:  $Y_{best} = Y$  and variables  $(\boldsymbol{\alpha}_{best}, \mathbf{Q}_{best}, \mathbf{u}_{best}, \boldsymbol{\lambda}_{best})$
    - reset  $rpt = 0$
- end
- decrease  $\gamma = 0.1\gamma$
- end
- Update:  $Y = Y_{best}$ ,  $\boldsymbol{\alpha} = \boldsymbol{\alpha}_{best}$ , and so on. Return to Step (b)

In Step (a), we initialize the penalty parameter to  $\mu = 1$ , and the FSS relaxation parameter  $\gamma$  by processing the following relaxed (continuous but bounded) system to the original MINLP problem (9) in noninteger variables  $(\alpha, \mathbf{Q}, \mathbf{u}, \lambda)$ :

$$\begin{aligned} & \max (\text{or } \min) \quad Y - \mu \mathbf{w}^T \lambda \quad (\text{or } Y + \mu \mathbf{w}^T \lambda) \\ & \text{subject to} \quad \mathbf{C}^T \mathbf{Q} - \alpha \mathbf{f} = \mathbf{0}, \\ & \quad \quad \quad \mathbf{Q} - \mathbf{E} \mathbf{C} \mathbf{u} + \mathbf{E} \mathbf{N} \lambda = \mathbf{0}, \\ & \quad \quad \quad \mathbf{w} = -\mathbf{N}^T \mathbf{Q} + \mathbf{r} \geq \mathbf{0}, \quad \lambda \geq \mathbf{0}, \\ & \quad \quad \quad \mathbf{0} \leq \alpha \leq \mathbf{1}, \end{aligned} \quad (12)$$

and hence from the solutions obtained in Eq. (12)

$$\gamma = \alpha^T (\mathbf{1} - \alpha). \quad (13)$$

It is clear that the optimization given in Eq. (12) is a standard nonlinear programming or NLP problem that can be easily solved by any available NLP code, such as GAMS/CONOPT (Drud, 1994). Furthermore, the solutions obtained from the relaxed NLP (12) provide a good approximation to the initial variables of MINLP (11).

In Step (b), each MINLP (9) subproblem is processed using the FSS scheme in Step (c), where a series of increasingly “tighter” MINLPs (11) is solved by systematically reducing the value of  $\gamma$ . Thus, different sets of solutions to MINLP (11) are generated, and the best optima are updated. The FSS Step (c) terminates when either the MINLP (11) solve finds more than three consecutive identical solutions or the FSS parameter  $\gamma$  is sufficiently small, namely  $\gamma \leq 10^{-5}$ .

We process the MINLP solve using the GAMS/DICOPT solver (Kocis and Grossmann, 1989). The proposed penalty-FSS algorithm is coded within a MATLAB framework that is linked directly to the GAMS environment through a MATLAB-GAMS interface software (Ferris, 1998).

### Illustrative Example

The three-span continuous beam in Fig. 1 with three identical vertical point loads of 80 kN, each independently applied at midspan, is considered. This structure was previously investigated by Mullen and Muhanna (1999) to illustrate applications of the fuzzy finite element method to obtain the maximum and minimum bounds to the bending moments under multiple load combinations, where only elastic material properties were assumed.

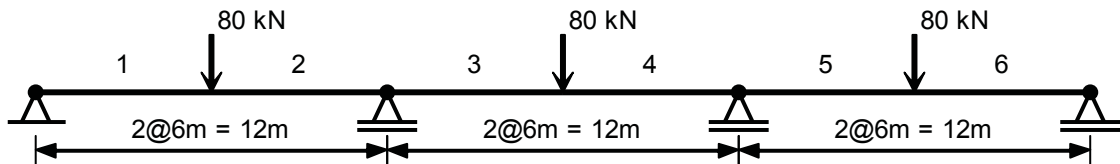


Figure 1. Three-span continuous beams under multiple load cases.

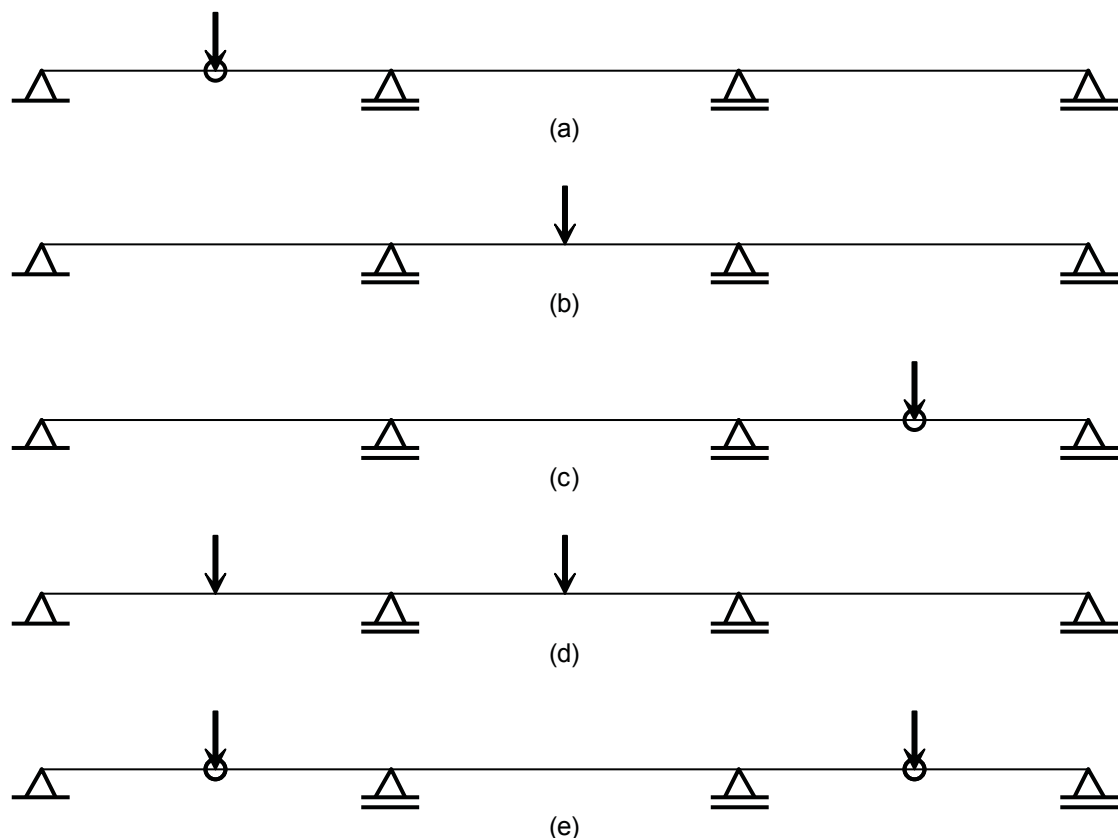
In the present study, we further incorporate the influences of elastic perfectly plastic material (steel) properties: modulus of elasticity of  $E = 2 \times 10^8 \text{ kNm}^{-2}$ ; cross sectional area of  $A = 6000 \times 10^{-6} \text{ m}^2$ ; second moment of area of  $I = 30 \times 10^{-6} \text{ m}^4$ ; and flexural force plastic capacity of  $Q_{2u} = 175 \text{ kNm}$ .

As is practical for the beam structure, a pure bending yield model is adopted for each of the potential plastic hinges, namely at member ends.

The beam discretization consists of 6 elements, 18 basic stresses/strains, 16 degrees of freedom and 24 yield functions. The pattern loads generated by the three point loads (Fig. 1) lead to 8 possible combinations (e.g. one point load at each span, two point loads at two adjacent spans, etc.).

**Table 1. Critical bending moments and associated load patterns by penalty-FSS method.**

	Element 1		Element 2		Element 3	
	$Q_2^1$	$Q_3^1$	$Q_2^2$	$Q_3^2$	$Q_2^3$	$Q_3^3$
Maximum $Y$	–	175 {A}	36 {B}	32.5 {C}	168 {D}	168 {B}
Minimum $Y$	–	–36 {B}	–175 {A}	–168 {D}	–32.5 {C}	–130 {E}



**Figure 2. Critical load combinations (a) pattern A, (b) pattern B, (c) pattern C, (d) pattern D and (e) pattern E, where o denotes plastic hinge.**

The proposed penalty-FSS algorithm successfully computed the critical (viz. the most maximum and the least minimum) bounds to flexural forces (unit kNm) at the two start  $Q_2^i$  and end  $Q_3^i$  nodes

for each of the members 1 to 6. In view of symmetry of the structural system, the obtained results of a half beam, namely members 1 to 3, are summarized in Table 1, where positive and negative signs define clockwise and anticlockwise flexural directions, respectively. The critical load patterns (also indicated in brackets in Table 1) corresponding to each of the 0-1 MPEC solutions are displayed in Fig. 2. The CPU times are not reported as each of the 0-1 MPEC (8) solves only took few seconds to furnish the results for the modest 2.7-GHz Pentium personal computer with 3-GB RAM running WinXP.

The accuracy of these optimal solutions is validated through a comparison with the results found from the complete (exhaustive) MCP (6) solves involving 8 possible load combinations.

## Conclusions

A mathematical programming based penalty-FSS method has been proposed for the direct determination of the critical bound to some response variables of structures under multiple load cases. The present study incorporates the influences of material (elastic perfectly plastic) nonlinearity, as is necessary for the realistic safety assessment of the structures. The key feature of the proposed scheme is to compute, within a single step, the most maximum in one case and the least minimum in the other case response values of interest for the structure subjected to known design multiple load combinations. The specific pattern load corresponding to each of the critical bounds is obtained as a by-product.

The governing problem takes the form of a challenging optimization problem, known in the nonconvex and/or nonsmooth optimization literature as a 0-1 MPEC. To circumvent the difficulties associated with nonconvexity and disjunctiveness, a penalty-FSS algorithm has been proposed. Such a scheme enforces the complementarity condition by iteratively processing a series of penalized MINLP subproblems with successively increasing penalty parameter. The solutions of are searched at an inner-level enumeration using the FSS technique by introducing an additional “tightness” constraint to the MINLP subproblem. By suitably decreasing the FSS relaxation parameter, various different sets of optimal solutions to the original MINLP subproblem can be identified, and the algorithm then selects the best optimum.

A number of numerical examples, a simple one of which has been provided herein, indicate the robustness and efficiency of the proposed penalty-FSS method. The scheme can accurately capture the desired optimal bound solutions, as validated by computationally expensive exhaustive MCP solves representing all possible load cases.

A straightforward extension to the present scheme is to incorporate various other nonlinear behaviors found in practical engineering mechanics applications, such as nonlinear geometry and physically instabilizing softening materials.

## References

- Brooke, A., Kendrick, D., Meeraus, A. and Raman, R. (1998), *GAMS: A User's Guide*. GAMS Development Corporation, Washington, DC.
- Dirkse, S. P. and Ferris, M. C. (1995a), MCPLIB: a collection of nonlinear mixed complementarity problems. *Optimization Methods and Software* 5, pp. 319-345.
- Dirkse, S. P. and Ferris, M. C. (1995b), PATH solver: a nonmonotone stabilization scheme for mixed complementarity problems. *Optimization Methods and Software* 5, pp. 123-156.
- Drud, A. S. (1994), CONOPT-a large-scale GRG code. *ORSA Journal on Computing* 6, pp. 207-216.
- Ferris, M. C. (1998), MATLAB and GAMS: interfacing optimization and visualization software, *Technical Report TR98-19*. Computer Sciences Department, University of Wisconsin, Madison, Wisconsin.

- Kocis, G. R. and Grossmann, I. E. (1989), Computational experience with DICOPT solving MINLP problems in process systems engineering. *Computers & Chemical Engineering* 13, pp. 307-315.
- López, C. O. and Beasley, J. E. (2013), A note on solving MINLP's using formulation space search. *Optimization Letters*, DOI10.1007/s11590-013-0623-8.
- Luo, Z. Q., Pang, J. S. and Ralph, D. (1996), *Mathematical Programs with Equilibrium Constraints*. Cambridge University Press, Cambridge.
- Maier, G. (1970), A matrix structural theory of piecewise linear elastoplasticity with interacting yield planes. *Meccanica* 5, pp. 54-66.
- Mullen, R. L. and Muhanna, R. L. (1999), Bounds of structural response for all possible loading combinations. *ASCE Journal of Structural Engineering* 125, pp. 98-106.
- Suarjana, M. and Law, K. H. (1994), Successive conjugate gradient methods for structural analysis with multiple load cases. *International Journal for Numerical Methods in Engineering* 37, pp. 4185-4203.
- Tangaramvong, S. and Tin-Loi, F. (2007), Limit analysis of strain softening steel frames under pure bending. *Journal of Constructional Steel Research* 63, pp. 1151-1159.
- Tangaramvong, S. and Tin-Loi, F. (2008), Simultaneous ultimate load and deformation analysis of strain softening frames under combined stresses. *Engineering Structures* 30, pp. 664-674.



## Computational Method for Thermal Interactions between Compressible Fluids and Complicated-Shaped Structures with Multiphase Modeling

\*D.Toriu<sup>1</sup>, S.Ushijima<sup>2</sup> and K.Aoki<sup>1</sup>

<sup>1</sup>Civil and Earth Resources Eng., Kyoto University, Japan.

<sup>2</sup>Academic Center for Computing and Media Studies, Kyoto University, Japan.

\*toriu.daisuke.57x@st.kyoto-u.ac.jp

### Abstract

In this paper, a new computational method based on multiphase model was presented to deal with the thermal interactions between compressible fluids and complicated-shaped structures with thermal conductivities as well as its mechanical interactions. The numerical procedures of our method are divided into three stages, advection, diffusion and acoustic stages, and the phase averaged governing equations are discretized with a finite volume method (FVM). The present method was applied to the natural convection flows in a rectangular cavity and the calculated results were compared with the reference computational results for temperature and velocity distributions. As a result, it was shown that the natural convection flows could be reasonably simulated by our method. In addition, the natural convections arising in the porous media were calculated with the present method. Through the numerical experiments, its applicability to complicated-shaped structures was discussed.

**Keywords:** Compressible fluid, Complicated-shaped structure, Multiphase model, Natural convection.

### Introduction

In many engineering subjects, it is important to predict accurately heat transfers in the domain, which contains compressible fluids and complicated-shaped structures. In the management of spent fuel storage system of nuclear power plants with the concrete cask for extended periods, the temperature distributions in the canister, which stores spent fuels and helium gas, need to be predicted accurately for the development of the helium leak detection system (Takeda et al., 2008). The canister has complicated-shaped internal structures and the temperature and pressure differences are large when the helium leakage from the canister occurs. Thus, it is essential to estimate the thermal interactions compressible helium gas and the influence of internal structures. For example, a finite element method (FEM) using unstructured grids has been used with thermal coupled problem between fluids and complex geometries (Goung et al., 1990). Such methods using unstructured grids can accurately predict the phenomena. However, the generations of grids become difficult as the shapes of geometries become complex.

The multiphase model (Ushijima et al., 2007 and 2009) enables us to predict thermal and mechanical interactions between incompressible fluids and complicated-shaped structures easily with simple structured grids. In this paper, a new computational method based on multiphase model was proposed to deal with the interactions between compressible fluids and complicated-shaped structures. The present method was applied to the natural convection flows in a rectangular cavity. As a result, it was shown that the natural convection flows could be reasonably simulated by our method. In addition, the natural convections arising in the porous media were calculated with the present method. Through the numerical experiment, its applicability to complicated-shaped structures was discussed.

## Computational Method

### Governing Equations

The multiphase field consisting of fluids and solids is considered, where fluids are compressible and each phase is immiscible. In this study, solids are taken as fluids which do not move.

Averaged governing equations for the multiphase field, which contain compressible fluids, consist of mass conservation equation in Eulerian description, momentum equations and energy equation given by

$$\frac{\partial \rho}{\partial t} + \frac{\partial(\rho u_i)}{\partial x_i} = 0 \quad (1)$$

$$\frac{\partial(\rho u_i)}{\partial t} + \frac{\partial(\rho u_i u_j)}{\partial x_j} = -\frac{\partial p}{\partial x_i} + \frac{\partial \tau_{ij}}{\partial x_j} + \rho g_i \quad (2)$$

$$\frac{\partial(\rho e)}{\partial t} + \frac{\partial(\rho e u_j)}{\partial x_j} = -p \frac{\partial u_i}{\partial x_i} + \tau_{ij} \frac{\partial u_i}{\partial x_j} - \frac{\partial q_j}{\partial x_j} \quad (3)$$

where  $t$  is time,  $x_i$  is the  $i$ -th component of two-dimensional orthogonal coordinates and  $g_i$  is the acceleration of external force in  $x_i$  direction. While velocity component  $u_i$  and internal energy  $e$  are the mass-averaged value in the mixture of phases, volume-averaged variables are defined for density  $\rho$ , pressure  $p$ , viscous stress  $\tau_{ij}$ , heat flux  $q_j$ . For example,  $e$  and  $p$  are defined as

$$e = \frac{\sum_k \rho_k V_k e_k}{\sum_k \rho_k V_k} \quad \text{and} \quad p = \frac{\sum_k V_k p_k}{V} \quad (4)$$

Furthermore,  $e$ ,  $\tau_{ij}$ ,  $q_j$  and the state equation are given by

$$e = C_V T \quad (5)$$

$$\tau_{ij} = \mu \left( \frac{\partial u_i}{\partial x_j} + \frac{\partial u_j}{\partial x_i} \right) - \frac{2}{3} \mu \frac{\partial u_m}{\partial x_m} \delta_{ij} \quad (6)$$

$$q_j = -\lambda \frac{\partial T}{\partial x_j} \quad (7)$$

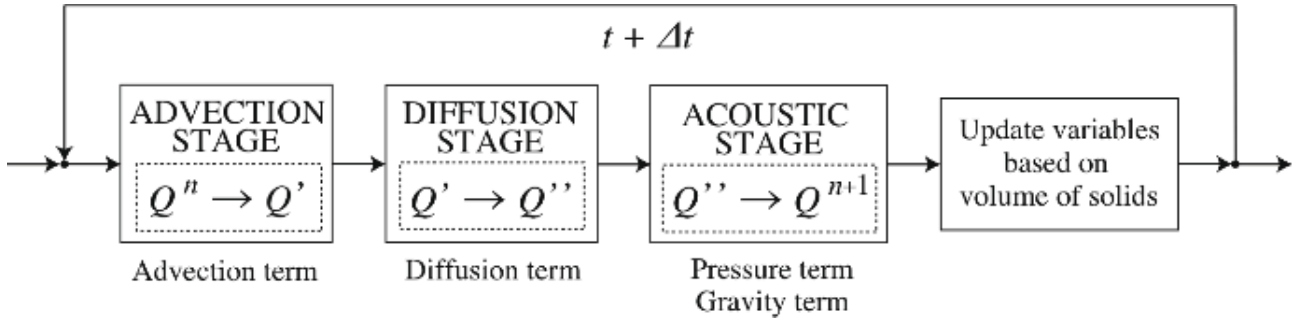
$$p = (\gamma - 1) \rho e \quad (8)$$

where  $C_V$ ,  $T$ ,  $\mu$ ,  $\lambda$  and  $\gamma$  are specific heat at constant volume, temperature, viscosity, thermal conductivity and specific heat ratio respectively. These are volume-averaged variables and coefficients same as  $\rho$ ,  $p$ ,  $\tau_{ij}$  and  $q_j$ .

### Numerical Procedures

In our method, the numerical procedures are divided into three stages, advection, diffusion and acoustic stages, like CCUP (Yabe et al., 2004) and TCUP method (Himeno et al., 2003). The governing equations are written by conservation forms and the multiphase model is applied. The governing equations of each stage are discretized with a finite volume method (FVM) and variables,  $\rho$ ,  $\mathbf{u}$ ,  $T$  and  $p$ , are updated in all stages. Thus, the mass conservation law is sufficiently satisfied in a calculation area. On the other hand, in CCUP and TCUP method, the governing equations are written by non-conservation forms. Therefore, the conservation of mass in the calculation area is not necessarily satisfied.

Figure 1 shows the flow chart of numerical procedures. In the advection and diffusion stages, advection and diffusion terms are calculated respectively. Pressure and gravity terms are calculated in the acoustic stage. After that, phase averaged variables are updated based on volume of solids. These calculations are performed iteratively and numerical solutions are calculated in time evolution. In what follows, variables after advection and diffusion stages will be expressed as  $Q'$  and  $Q''$  respectively. In addition, variables after acoustic stage are  $Q^{n+1}$ .



**Figure 1. Flow chart of numerical procedures**

### Advection Stage

Governing equations of advection stage are given by

$$\frac{\partial \rho}{\partial t} + \frac{\partial(\rho u_i)}{\partial x_i} = 0 \quad (9)$$

$$\frac{\partial(\rho u_i)}{\partial t} + \frac{\partial(\rho u_i u_j)}{\partial x_j} = 0 \quad (10)$$

$$\frac{\partial(\rho e)}{\partial t} + \frac{\partial(\rho e u_j)}{\partial x_j} = 0 \quad (11)$$

Equations (9), (10) and (11) express advection equations of  $\rho$ ,  $\rho \mathbf{u}$ ,  $\rho e$  respectively. The advection terms are calculated with a fifth-order TVD scheme (Harten, 1984). After that,  $T'$  and  $p'$  are updated from  $\rho'$ ,  $\mathbf{u}'$ ,  $e'$  with Eqs.(5) and (8).

### Diffusion Stage

Governing equations of diffusion stage are indicated as follows :

$$\frac{\partial \rho}{\partial t} = 0 \quad (12)$$

$$\frac{\partial(\rho u_i)}{\partial t} = \frac{\partial \tau_{ij}}{\partial x_j} \quad (13)$$

$$\frac{\partial(\rho e)}{\partial t} = \tau_{ij} \frac{\partial u_i}{\partial x_j} - \frac{\partial q_j}{\partial x_j} \quad (14)$$

In this stage, right-hand sides of Eqs.(13) and (14) are calculated and variables are updated with the following equations :

$$\rho'' \frac{u_i'' - u_i'}{\Delta t} = \frac{\partial \tau_{ij}'}{\partial x_j} \quad (15)$$

$$\frac{\rho'' C_p (T'' - T')}{\gamma \Delta t} = - \frac{\partial (\rho' C_v T' u_j')}{\partial x_j} + \frac{\partial (\tau_{ij}' u_j')}{\partial x_j} - \frac{\partial q_j'}{\partial x_j} - \frac{\rho'}{2} \frac{\partial u_j'^2}{\partial t} \quad (16)$$

$$p'' - p' = \frac{\gamma - 1}{\gamma} \frac{\rho'' C_p}{\rho'' C_p \mu_J + 1} (T'' - T') \quad (17)$$

where  $\mu_J$  is Joule-Thomson coefficient.

### Acoustic Stage

Governing equations of acoustic stage are given by

$$\frac{\partial \rho}{\partial t} + \frac{\partial (\rho u_i)}{\partial x_i} = 0 \quad (18)$$

$$\frac{\partial (\rho u_i)}{\partial t} = - \frac{\partial p}{\partial x_i} + \rho g_i \quad (19)$$

$$\frac{\partial (\rho e)}{\partial t} = - p \frac{\partial u_i}{\partial x_i} \quad (20)$$

Equations (18), (19) and (8) applied to Eq.(20), we can obtain the equation of  $p^{n+1}$  as follows :

$$\frac{1}{\rho'' C_s^2} \frac{p^{n+1} - p''}{\Delta t} = - \frac{\partial}{\partial x_i} \left( - \frac{1}{\rho''} \frac{\partial p^{n+1}}{\partial x_i} \Delta t + u_i'' \right) \quad (21)$$

where  $C_s$  is the sound speed. Equation (21) is discretized and solved with the SOR method (Young, 1954). The variables,  $u^{n+1}$ ,  $e^{n+1}$  and  $\rho^{n+1}$ , are calculated with the following equations :

$$u_i^{n+1} = u_i'' + \left( - \frac{1}{\rho''} \frac{\partial p^{n+1}}{\partial x_i} + g_i \right) \Delta t \quad (22)$$

$$\rho'' \frac{e^{n+1} - e''}{\Delta t} = p^{n+1} \frac{\partial u_i^{n+1}}{\partial x_i} \quad (23)$$

$$\frac{\rho^{n+1} - \rho''}{\Delta t} = - \frac{\partial \rho'' u_i^{n+1}}{\partial x_i} \quad (24)$$

## Application

### Natural Convection in a Rectangular Cavity

In order to confirm the validity of the present method, it was applied to the 2D natural convection flows in a rectangular cavity as shown in Fig.2. The lengths  $l_1$  and  $l_2$  are 0.04 [m], while the left-hand side wall is heated at  $T_h$  and the right-hand side wall is cooled at  $T_c$ , the temperature difference  $\Delta T = T_h - T_c$  is 1.465 [K] in Fig.2. Adiabatic conditions are imposed on the top and bottom walls. On the wall boundaries, non-slip conditions are imposed.

Fluids are taken as air, which satisfy the equation of state. The initial spatially averaged temperature  $T_0$  and pressure  $P_0$  are 283.15 [K] and 1.0 [atm]. Regarding physical properties of fluids, viscosity  $\mu$ , thermal conductivity  $\lambda$ , specific heat at constant pressure and volume  $C_p$ ,  $C_v$ , are  $\mu = 1.82 \times 10^{-5}$  [kg/(m•s)],  $\lambda = 2.587 \times 10^{-2}$  [W/(m•K)],  $C_p = 1.007 \times 10^3$  [J/(kg•K)] and  $C_v = 7.17 \times 10^2$  [J/(kg•K)] respectively. The number of fluid cells is  $100 \times 100$ .

Figures 3, 4 and 5 show comparisons of calculated results in the steady states by the present method and reference results by TCUP method (Himeno et al., 2003). As shown in these figures, the predicted results are almost in good agreement with the results by TCUP method. From these results, it was shown that the present method enables us to predict a natural convection appropriately.

In addition,  $err^*$ , which made dimensionless the total change of the mass of air in a calculation area, is defined as  $err^* = |M - M_0|/M_0$ . Here  $M$  and  $M_0$  are the total mass of air in the calculation area at each time step and in the initial state. The maximum value of  $err^*$  obtained in the calculation was  $5.713 \times 10^{-15}$ . From this result, it was shown that the mass conservation law is sufficiently satisfied in the calculation area.

In the following cases, the temperature difference was set to  $\Delta T = 100$  [K] and density variations were compared with the result in  $\Delta T = 1.465$  [K]. The density variations are estimated with Lagrangian derivative of non-dimensional density  $D\rho^*/Dt$ . Here  $\rho^*$  is given by  $\rho^* = \rho / \rho_0$  and  $\rho_0$  is the spatial averaged density in the initial state. It is noted that  $D\rho^*/Dt = 0$  in incompressible fluids. Figure 6 shows the distributions of  $D\rho^*/Dt$  in the steady state and Table 1 shows maximum and minimum values of  $D\rho^*/Dt$  in each case. In Figure 6 and Table1, the densities change near the heated and cooled wall and absolute values of variations increase as  $\Delta T$  increases. In general, compressibility effects become large as  $\Delta T$  increases. Thus, it can be said that calculated results are appropriate and the present method enable us to estimate the compressibility effects of fluids.

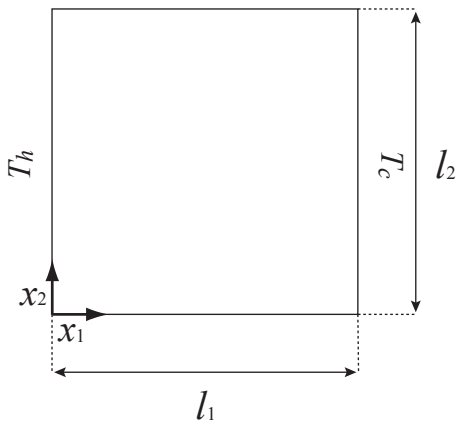


Figure 2. Calculation area

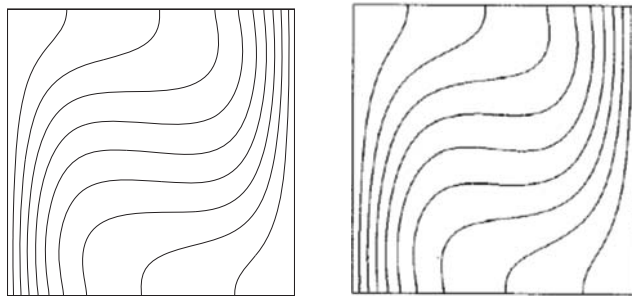


Figure 3. Comparison of temperature distributions (Left : present results, Right : TCUP (Himeno et al., 2003))

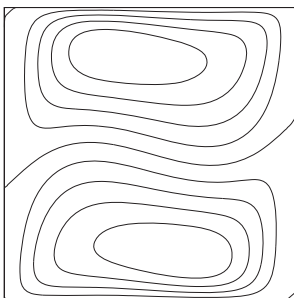


Figure 4. Comparison of  $u_1$  distributions (Left : present calculations, Right : TCUP (Himeno et al., 2003))

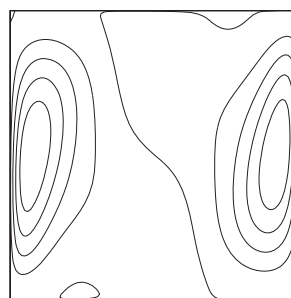
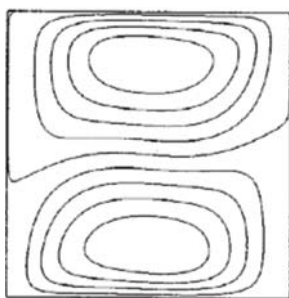
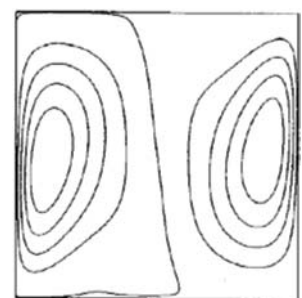
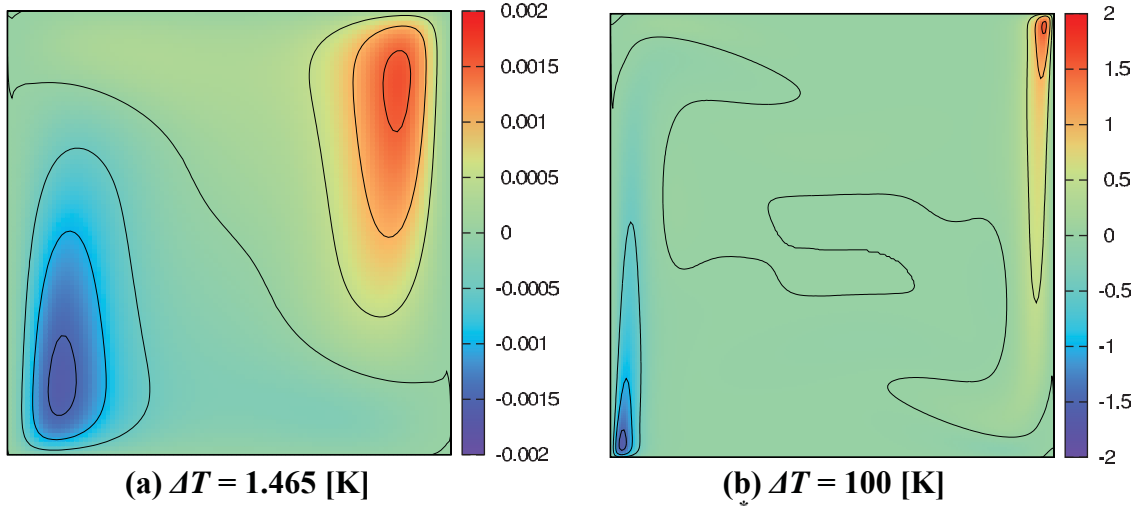


Figure 5. Comparison of  $u_2$  distributions (Left : present calculations, Right : TCUP (Himeno et al., 2003))





**Figure 6. Distributions of  $D\rho^*/Dt$**

**Table 1. Maximum and minimum values of  $D\rho^*/Dt$**

$\Delta T$ [K]	Max [1/s]	Min [1/s]
1.465	$1.615 \times 10^{-3}$	$-1.618 \times 10^{-3}$
100	1.576	-1.663

### *Natural Convection in Porous Media with Thermal Conductivity*

To confirm the applicability of the present method to complicated-shaped structures, natural convections in porous media with thermal conductivity were calculated.

As shown in Figure 7, 32 cylinders are located in a calculation area. The lengths  $l_1$  and  $l_2$  are 0.17 and 0.33 [m], while the diameter of the cylinders  $d$  is 0.03 [m] and the interval between each cylinder  $s$  is 0.01 [m] respectively. The left-hand side wall is heated at  $T_h = 310$  [K] and the right-hand side wall is cooled at  $T_c = 300$  [K], the temperature difference  $\Delta T = T_h - T_c$  is 10 [K] in Fig 7. Adiabatic conditions are imposed on the top and bottom walls. On the wall boundaries, non-slip conditions are imposed. The physical properties of fluids (air) were set same values as the preceding section and physical properties of the solids (cylinders) were same as that of fluids. In addition, the number of fluid cells is  $51 \times 99$ .

Figure 8 shows temperature distributions ((a)  $t = 1.0$  [s], (b) steady state). First, heats transferred by convections in the fluids area. After that, the temperatures of solids changed by heat conductions in the solids. Thus, the temperature differences between the fluids and the solids occurred at  $t = 1.0$  [s] in Fig 8 (a). In the steady state, the temperatures of solids became equal to that of fluids as shown in Fig 8 (b). Figure 9 is the vertical distribution of  $T$  at  $x_1^* = 0.5$  in the steady state. Here,  $x_1^*$  and  $T^*$  are defined as follows :

$$x_i^* = \frac{x_i}{l_i} \quad \text{and} \quad T^* = \frac{T - T_m}{T_h - T_m} \quad (25)$$

where,  $l_i$  is the length of the calculation area,  $T_h$  is the temperature of the heated wall and  $T_m$  is the temperature at  $x_1^* = 0.5$  and  $x_2^* = 0.5$ . In the calculated result, the top area is high temperature and the bottom area is low temperature. This is the typical temperature distribution of the natural convection in the closed cavity.

Predicted the horizontal velocities  $u_1$  at  $x_1^* = 0.5$  and the vertical velocities  $u_2$  at  $x_2^* = 0.5$  are shown in Fig 10 and 11 respectively. Here,  $u_i^*$  is defined as follows :

$$u_i^* = \frac{u_i}{U_i} \quad (26)$$

where,  $U_i$  is the maximum value of  $|u_i|$  in the calculation area. As shown in these figures, buoyancy-driven flows occurred near the heated and cooled walls and cyclic flows were predicted in the fluids area. Thus, it can be said that the present method enables us to predict the natural convections in porous media with thermal conductivity reasonably.

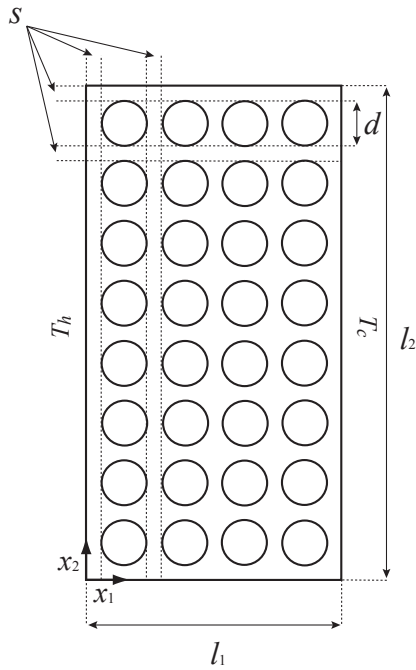
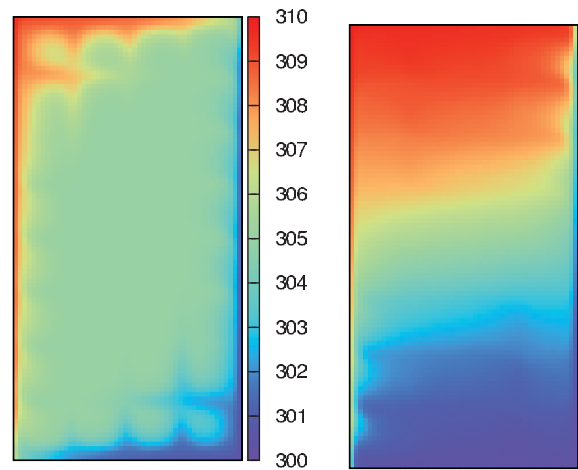


Figure 7. Calculation area



(a)  $t = 1.0$  [s]

(b) Steady state  
( $t = 10.0$  [s])

Figure 8. Temperature distributions

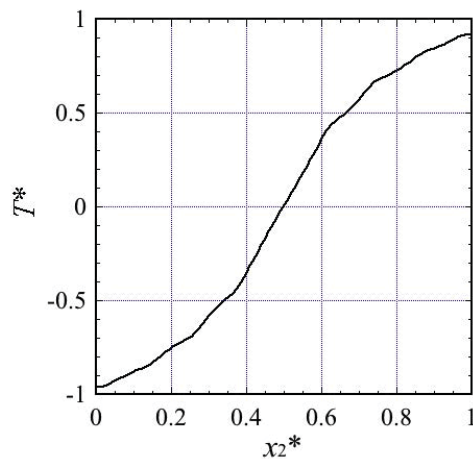
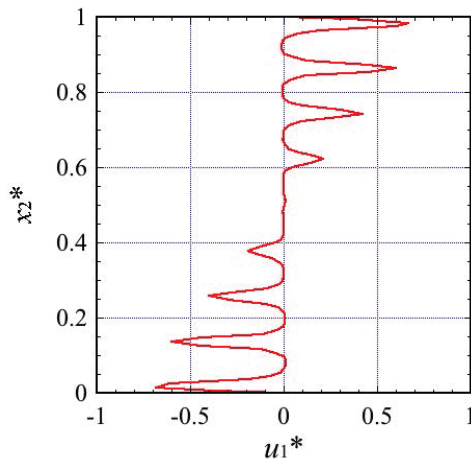
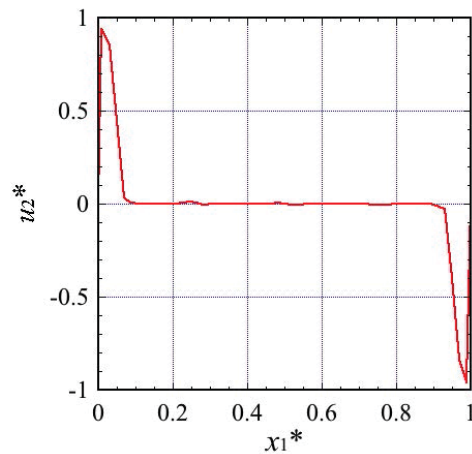


Figure 9. Vertical distribution of  $T$  ( $x_1^* = 0.5$ )



**Figure 10. Vertical distribution of  $u_1^*$  ( $x_1^* = 0.5$ )**



**Figure 11. Horizontal distribution of  $u_2^*$  ( $x_2^* = 0.5$ )**

## Conclusions

In this paper, a new computational method based on multiphase model was proposed to deal with the thermal and mechanical interactions between compressible fluids and complicated-shaped structures with thermal conductivities. The numerical procedures of our method are divided into three processes, advection, diffusion and acoustic stages, and the phase averaged governing equations are discretized with a finite volume method (FVM). Thus, the mass conservation law is sufficiently satisfied in a calculation area in our method.

The present method was applied to the natural convection flows in a rectangular cavity and the calculated results were compared with the reference computational results for temperature and velocity distributions. As a result, it was shown that the natural convection flows can be reasonably simulated by our method. It was also confirmed that the mass conservation law is satisfied sufficiently in the calculation area, and the present method enables us to estimate the compressibility effects of fluids by the temperature difference. In addition, the natural convections arising in the porous media were calculated with the present method. Through the numerical experiment, its applicability to complicated-shaped structures was verified.

## References

- Young, D. M. (1954), Iterative Methods for Solving Partial Differential Equations of Elliptic Type, *Transactions of the American Mathematical Society*, Vol.76, pp.92-111.
- Harten, A. (1984), On a Class of High Resolution Total-Variation-Stable Finite-Difference Schemes, *SIAM Journal on Numerical Analysis*, Vol.21.
- Goung, J. L. and Soon H. C. (1990), Development of the finite element method of body fit nodalization for mixed convection analysis in rod bundles, *Nuclear Engineering and Design*, 122, pp.195-208.
- Yabe, T., Xiao, F. and Utsumi, T. (2001), The Constrained Interpolation profile Method for Multiphase Analysis. *Journal of Computational Physics*, 43, pp. 531-545.
- Himeno, T. and Watanabe, T. (2003), Thermo-Fluid Management under Low-Gravity Conditions (1st Report: TCUP Method for the Analysis of Thermo-Fluid Phenomena) (in Japanese), *Trans. JSME, Ser. B*, Vol.69, No.678, pp.266-273.
- Ushijima, S. (2007), Multiphase-model approach to predict arbitrarily-shaped objects moving in free surface flows. *Proc of APCOM'07-EPME SC XI*, MS41-3-1.
- Takeda, H., Wataru, K. Shirai, K. and Saegusa, T. (2008), Development of the detecting method of helium gas leak from canister. *Nuclear Engineering and Design*, Vol.238, pp.1220-1226.
- Ushijima, S. and Kuroda, N. (2009), Multiphase modeling to predict finite deformations of elastic objects in free surface flows. *Fluid Structure Interaction V*, WIT Press, pp.34-45.



## Effects of Continuum Breakdown on Aerodynamics

Fei Huang<sup>1</sup>, Liang Zhang<sup>1</sup>, \*Wen-bo Miao<sup>1</sup> and Xiao-li Cheng<sup>1</sup>

<sup>1</sup> China Academy of Aerospace Aerodynamics, China.

YunGang West Road No.17,FengTai District,Bei Jing City,In China,100074

\*Corresponding author: Tingles@126.com

### Abstract

Attempt was made to analyse aerodynamics of hypersonic vehicle near space with slip NS methods. The applicability of several different slip boundary conditions was investigated. The difference between continuum and rarefied predictions for surface properties of cylinder and trapezoid wing was shown. The results show that present code was valid for predicting slip regime flow by comparing with results in reference. Type-2 slip model proposed by Gokcen had more extensive rarefied limit, and could give a best agreement with DSMC results in higher Knudsen numbers comparing with other slip models. Peak transfer rate differences range from over 1.6% for 50KM to almost 14.5% for 80KM. Pressure coefficient on the surface is little affected by rarefied gas effect, while heat transfer rate is most influenced by that.

**Keywords:** near space; hypersonic vehicle; aerodynamics; rarefied gas effect; slip model

### 0.Introduction

Future hypersonic flight vehicles<sup>[1]</sup> have many specific performance features, such as long distance and accurate attack, and maneuvering flight. Therefore, these vehicles in atmosphere must have the ability of large passage maneuvering flight, the characteristics of long-time flight and high lift-to-drag ratio aerodynamic configurations, and specific trajectories. A typical configuration property is the sharp leading edges. The flight passage suffering transitional flow effect is much larger due to the smaller characteristic length scale, and hence in flight at high altitude, the vehicles can globally or locally suffer transitional flow effect. So, it is a key and important problem that the transitional flow effects on aerodynamic force and heating for flight vehicle design. Aerodynamic force and heating for these type vehicles in rarefied flow regime are very different from that in continuum flow regime. These difference are never been paid much attention for traditional blunted vehicles due to more redundancy design used. However, future hypersonic flight vehicles allow only to taking less redundancy, and thus aerodynamics in the near space need to be investigated in detail.

At low altitude, traditional CFD method is generally used in continuum flow regime. As increasing of altitude, flow changes gradually from continuum flow regime to near free molecule flow regime. In that processing, it need to be answered that when continuum breakdown is starting, and how much error that will result in. The continuum breakdown criteria was investigated by many researchers<sup>[2-6]</sup>. The rarefied gas effect on aerodynamics of hypersonic vehicles near space have been investigated little<sup>[7-9]</sup>.

The applicability of different slip models will be investigated around cylinder, and then The comparison of the aerodynamics of hypersonic vehicle near space using slip method and noslip method in transitional flow regime will be made.

## 1. Computational approach

### A. N-S equation

3-D laminar N-S equation can be written as 
$$\frac{\partial \vec{Q}}{\partial t} + \frac{\partial \vec{F}}{\partial x} + \frac{\partial \vec{G}}{\partial y} + \frac{\partial \vec{H}}{\partial z} = \frac{\partial \vec{F}_v}{\partial x} + \frac{\partial \vec{G}_v}{\partial y} + \frac{\partial \vec{H}_v}{\partial z}$$

Here,  $\vec{Q}$  is a conservative vector.  $\vec{F}$ ,  $\vec{G}$ ,  $\vec{H}$  are convection vector flux in three direction respectively, and  $\vec{F}_v$ ,  $\vec{G}_v$ ,  $\vec{H}_v$  are viscous vector flux in corresponding direction.

Roe scheme is used for space discretization under the finite volume frame, minmod limiter is adopted. The center-difference method is used for viscous numerical flux. LU-SGS implicit time integration method is introduced.

### B. Slip boundary models

Four type models are investigated in this paper. Type1 is defined by Maxwell model. Type2 is Gokcen<sup>[10]</sup> slip model. Lockerby<sup>[11]</sup> model is defined as Type3. HS model is Maxwell slip model modified by hard sphere model.

Type1 (Corresponding to CFD(1) in reference [9]) is given by

$$U_s = \frac{2-\sigma}{\sigma} \lambda \frac{\partial U}{\partial n} \Big|_0, \quad T_s - T_w = \frac{2-\alpha}{\alpha} \frac{2\gamma}{(\gamma+1)P_r} \lambda \frac{\partial T}{\partial n} \Big|_0, \quad \lambda = \frac{\mu}{\rho} \sqrt{\frac{\pi}{2RT}}$$

Type2 (Corresponding to CFD(2) in reference [9]) is given by

$$\sigma U_\lambda = 2\lambda \frac{\partial U}{\partial n} \Big|_0, \quad \alpha(T_\lambda - T_w) = 2 \frac{2\gamma}{(\gamma+1)P_r} \lambda \frac{\partial T}{\partial n} \Big|_0, \quad \lambda = \frac{\mu}{\rho} \sqrt{\frac{\pi}{2RT}}$$

Type3 (Corresponding to CFD(3) in reference [9]) is given by

$$U_s = A \frac{2-\sigma}{\sigma} \lambda \frac{\partial U}{\partial n} \Big|_0, \quad T_s - T_w = \frac{2-\alpha}{\alpha} \frac{2\gamma}{(\gamma+1)P_r} \lambda \frac{\partial T}{\partial n} \Big|_0, \quad \lambda = \frac{\mu}{\rho} \sqrt{\frac{\pi}{2RT}}, \quad \mu = \mu \psi^{-1}$$

$$\text{Here, } \psi\left(\frac{n}{\lambda}\right) = 1 + \frac{7}{10} \left(1 + \frac{n}{\lambda}\right)^{-3}, \quad A = \sqrt{2/\pi}$$

HS is given by

$$U_s = \frac{2-\sigma}{\sigma} \lambda \frac{\partial U}{\partial n} \Big|_0, \quad T_s - T_w = \frac{2-\alpha}{\alpha} \frac{2\gamma}{(\gamma+1)P_r} \lambda \frac{\partial T}{\partial n} \Big|_0, \quad \text{Here, } \lambda = \frac{m}{\sqrt{2\pi d^2 \rho}}, \quad m \text{ is molecule mass.}$$

### C. Main dimensionless parameters

$$\text{Wall pressure coefficient } C_p = \frac{(p_w - p_\infty)}{0.5 \rho_\infty U_\infty^2}$$

$$\text{Wall heat flux coefficient } C_H = \frac{q}{0.5 \rho_\infty U_\infty^3}$$

$$\text{Wall friction coefficient } C_F = \frac{\tau}{0.5 \rho_\infty U_\infty^2}$$

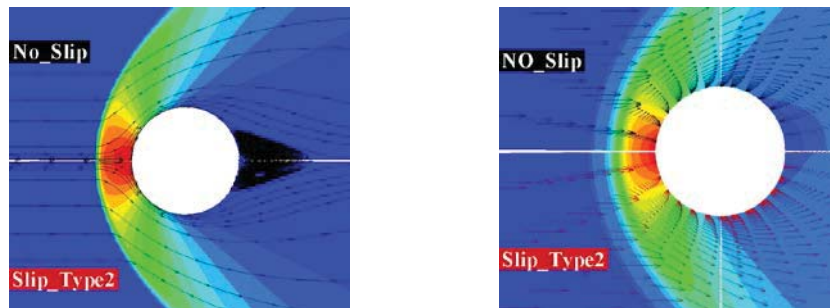
Error can be written as 
$$Error = \frac{q_{noslip} - q_{slip2}}{q_{slip2}} \times 100\%$$

Here,  $q_{noslip}$  is no\_slip results,  $q_{slip2}$  is slip results with Type2 model.

**2.Code validation and applicability analysis of different slip models**

The flow over cylinder is simulated to analyse applicability of above several slip models at Mach number of 10, 25. Cylinder diameter is 304.8mm. The argon flow is considered in this work<sup>[9]</sup>. Knudsen number based on diameter is 0.002、0.05、0.25, respectively. Free steam temperature is 300K.

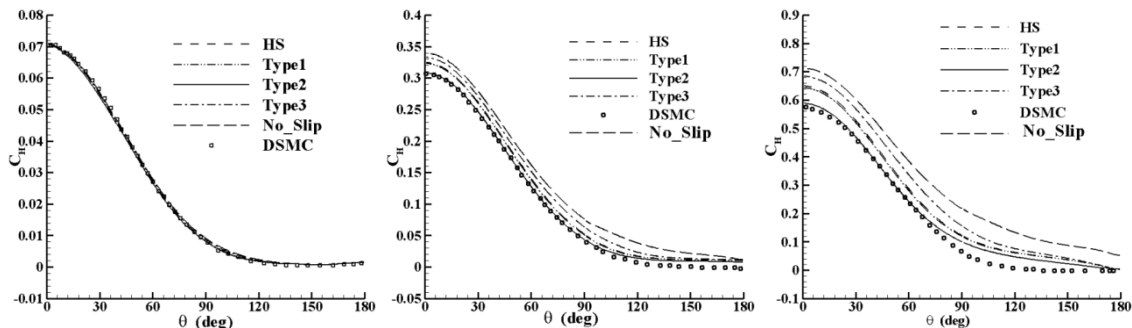
**A. M=10, U=2624m/s, T<sub>w</sub>=500K**



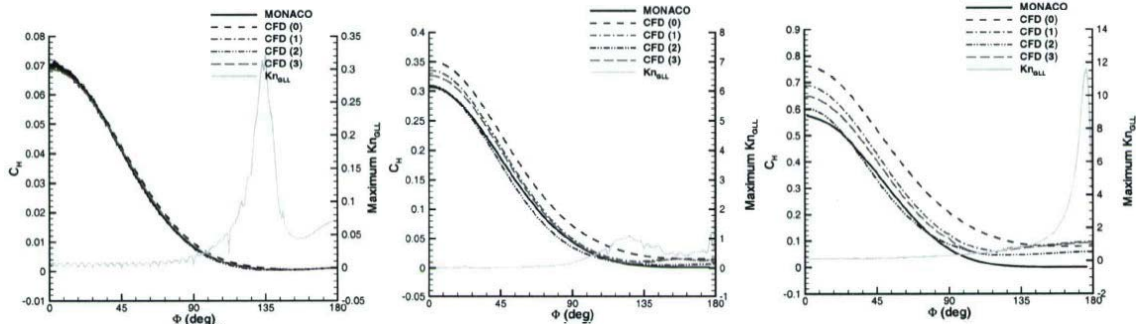
**(a)Pressure contours and streamline (b)Pressure contours and vector  
(Kn=0.002) (Kn=0.05)**

**Fig.1Flow field with different methods(Ma=10)**

Fig1(a) show pressure contours at Knudsen number 0.002, and Fig.1(b) show pressure contours and vector. It can be concluded from Fig.1(a) that at the continuum regime, the agreement of flow between slip boundary conditions and no slip boundary conditions is very good. Present slip method can capture the shock structure and wake eddy. As Knudsen number increases to 0.05, the flow is well within the slip regime. The flow demonstrates breakdown in a larger area of the flow in each of the three regions(shock, boundary layer and wake). The slip CFD shock is much thicker than the no\_slip CFD shock. Velocity-slip at the wall can be seen clearly with slip boundary conditions. The difference of pressure contours at the wake can be found evidently. It can be predicted from previous several flow difference that wall pressure, heat flux may be very different.



**(a)Present results**



(b)Computational results in reference [9]

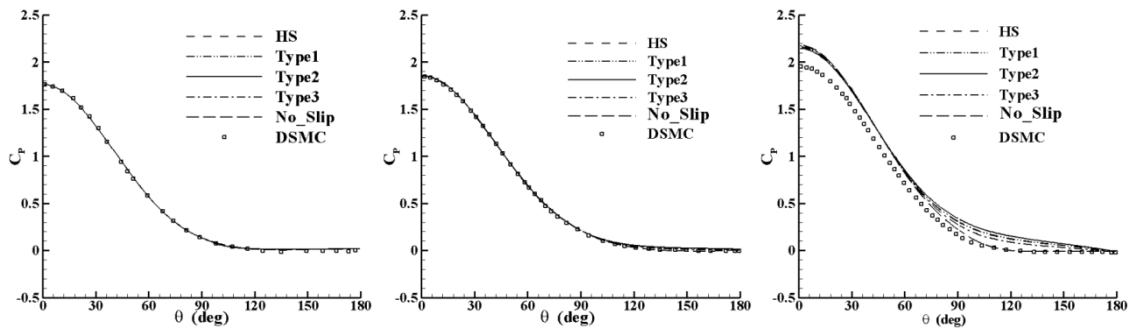
Kn=0.002

Kn=0.05

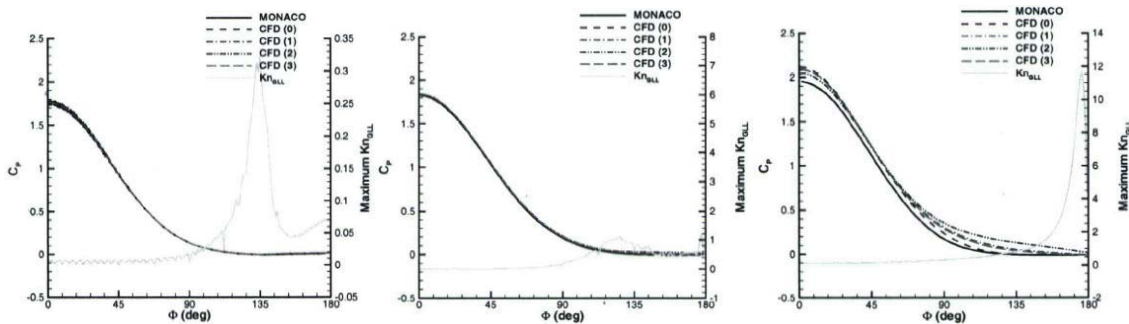
Kn=0.25

**Fig.2 Heat transfer rate on the surface at different Knudsen numbers (Ma=10)**

Figure 2 quantify the differences in the surface properties by comparing CFD and DSMC predictions for heat flux coefficient at Mach number 10. Where Fig.2(a) shows present results, and Fig.2(b) shows computational results in reference [9]. At a Knudsen number of 0.002, the flow is within the continuum regime, and the results predicted by CFD and DSMC are in excellent agreement. As Knudsen increasing to 0.05, 0.25, the results predicted by different slip models keeps no longer in agreement. It can be found the heat flux coefficient shows surprisingly good agreement between the type-2 case and DSMC even at the higher Knudsen number of 0.05,0.25. The surface properties predicted by DSMC tended to be lower than those predicted by CFD, even for the CFD cases implementing slip conditions. From comparison among several different types of slip boundary conditions, the best agreement appeared to be obtained using Type-2 slip model. It can be concluded that present results are consistent with computational results in reference [9].



(a)Present results



(b)Computational results in reference [9]

**Kn=0.002****Kn=0.05****Kn=0.25****Fig.3 Pressure coefficient on the surface at different Kn numbers( Ma=10)**

Pressure coefficient on the surface at different Kn numbers are shown in Fig.3, and Fig.3(a) is present results, Fig.3(b) is reference's results. At Knudsen number of 0.002,0.05, the results predicted by slip NS keep a good agreement with those by DSMC. Pressure coefficient by DSMC tend to be lower than those by CFD at Kn=0.25. The main reason can be explained by that shock thickness predicted by DSMC is bigger than that by CFD, and compressibility predicted by DSMC is more weakly than that predicted by CFD. Above all will result in a bigger pressure after shock wave. It can be concluded from Figs.(2-3) that pressure coefficient variation is more sensitive to rarefied gas effect than heat flux coefficient, and present results keep an excellent agreement with computational results in reference [9].

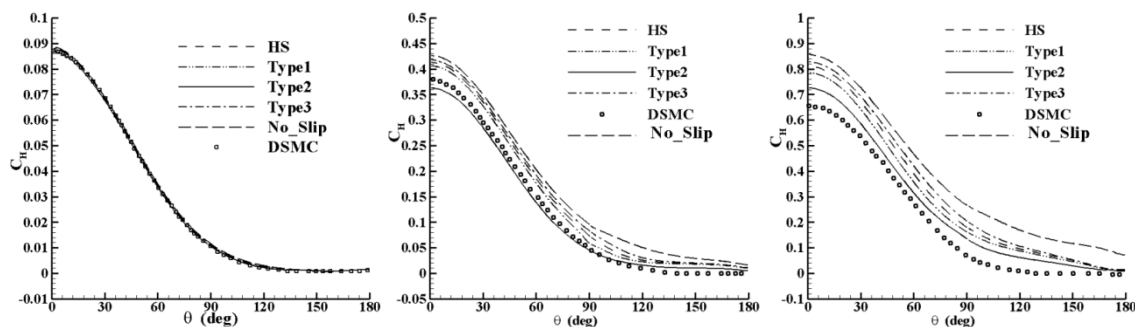
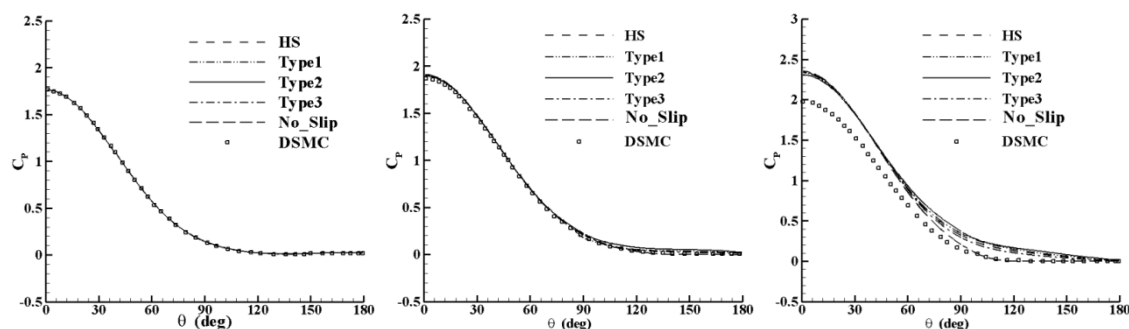
**B. M=25, U=6585m/s, T<sub>w</sub>=1500K****Kn=0.002****Kn=0.05****Kn=0.25****Fig.4 Heat transfer rate on the surface at different Kn numbers( Ma=25)****Kn=0.002****Kn=0.05****Kn=0.25****Fig.5 Pressure coefficient on the surface at different Kn numbers( Ma=25)**

Fig.4 shows heat flux coefficient on the surface at different Kn numbers with mach number of 25. Fig.5 shows corresponding pressure coefficient distribution. They are computed by different slip models, and compared with DSMC results in reference [9]. The surface properties at mach number of 25 is similar to that at mach number of 10. Even at Mach-25 case, type-2 CFD solution also keeps a less error than others.

It can found from above all that present code is valid for predicting slip regime flow by comparing with results in reference[9]. Type-2 slip model can be adopted in more extensive rarefied limit. At a bigger Knudsen number, surface properties predicted by DSMC tend to be lower than those by slip CFD. Comparing with heat flux rate, pressure is more sensitive to rarefied gas effect. Like conclusion in reference[9], all of the slip boundary conditions increases

the computational expense of the CFD simulations, with the Type-2 being the most expensive. If possible for designing, other slip boundary conditions may be a good choice.

### 3. Aerodynamics of trapezoid wing in near space

Aerodynamics of trapezoid wing in near space is investigated with Type-2 slip model at mach number of 15. The altitude range is from 50km to 80km, and the angle of attack is 10°. Wall temperature is 500K. Wing head diameter is 30mm. Wing is with 1.96m root chord length, 0.63m tip chord length, 0.5m span length. Swept back angle is 20°. Fig.6 shows grid in the computation region. Fig.7 shows slice station of trapezoid wing.

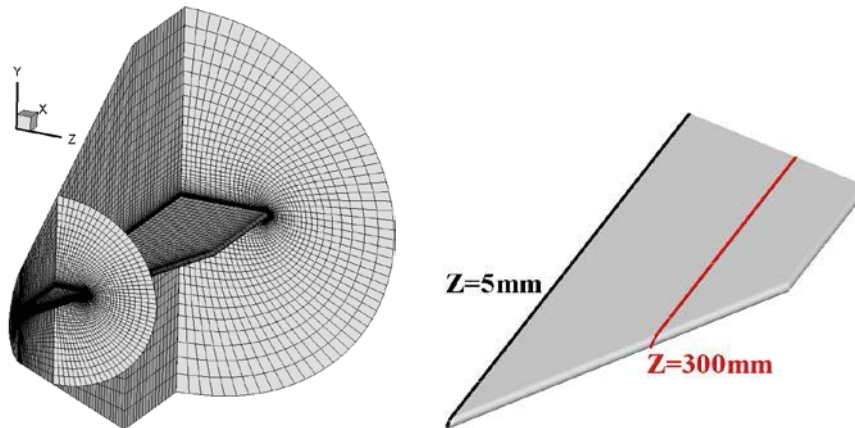


Fig.6 Grid in the computation region      Fig.7 Slice at different stations

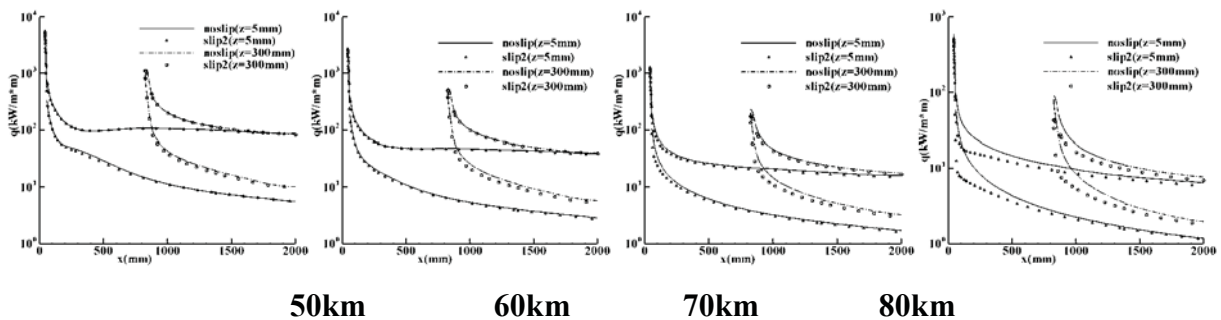


Fig.8 heat flux at different stations

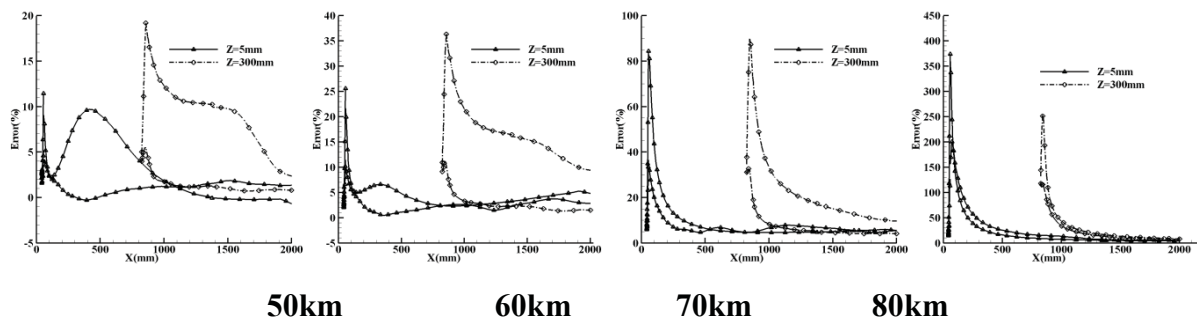


Fig.9 Error at different stations

Figs.(8-9) show respectively heat flux and its error along both the slice stations. At a lower altitude, the heat transfer rate along slice station shows surprising agreement between slip case and no\_slip case. As altitude increasing, the difference of results predicted by different methods tends to be evident. With windward compressed and leeward expanded, rarefied gas effect firstly appear on the windward, and so the difference of results predicted by different methods

is smaller on the windward than on the leeward. It can be seen from Fig.9 that the maximum error is at the expanding region of wing leading edge, and error of heat transfer on the surface of the wing range from 5% for 50km altitude to almost 15% for 80km altitude.

**Table1 Aerodynamics with different methods**

H (km)		$C_{Af}$ ( $\times 100$ )	$C_A$ ( $\times 100$ )	$C_N$ ( $\times 100$ )	L/D
50	No_slip	0.4496	0.7410	5.339	3.096
	Slip	0.4493	0.7410	5.334	3.094
	Error	0.07%	0.00%	0.09%	0.06%
60	No_slip	0.8509	1.150	5.473	2.492
	Slip	0.8454	1.145	5.423	2.485
	Error	0.65%	0.44%	0.92%	0.28%
70	No_slip	1.770	2.083	5.757	1.740
	Slip	1.738	2.051	5.448	1.689
	Error	1.84%	1.56%	5.67%	3.02%
80	No_slip	4.245	4.593	6.342	0.676
	Slip	4.083	4.422	5.382	0.591
	Error	3.97%	3.87%	17.84%	14.38%

Table1 shows comparison of aerodynamics by different methods. It can be concluded that as flight altitude increases, friction coefficient, axial force coefficient and normal force coefficient increase, and the ratio of Lift-to-Drag decrease. It can be seen from the error results that rarefied gas effect enhance much as flight altitude increasing, traditional CFD method is invalid in continuum breakdown region and cannot give an accurate velocity jump boundary condition. So error tends to be increasing as rarefied gas effect enhancing.

**Table2 Peak heat flux with different methods**

H (km)	50	60	70	80
Q (kW/m <sup>2</sup> *m)				
No_slip	5701.9	2816.6	1348.4	594.1
Slip	5614.9	2755.7	1272.1	518.8
Error	1.55 %	2.21%	5.99%	14.52%

Table 2 shows variation of peak heat transfer rate as flight altitude. The density increases, and peak heat transfer rate decreases sharply as flight altitude increases. Like aerodynamics, the error of peak heat transfer rate also increases as flight altitude increases with continuum breakdown.

#### 4. Conclusions

Different slip model validation was investigated by comparing cylinder flow. Hypersonic aerodynamics of trapezoid wing in near space flying near continuum flow regime was analyzed with slip CFD method in this paper. The difference between slip CFD and no\_slip CFD simulations was quantified lastly. The main contents and achievements are concluded as follows:

- (1) Present code was valid for predicting slip regime flow by comparing with results in reference.
- (2) Type-2 slip model proposed by Gokcen had more extensive rarefied limit, and could give a best agreement with DSMC results in higher Knudsen numbers comparing with other slip models.
- (3) The surface properties predicted by DSMC tended to be lower than those by CFD, so CFD solutions could give much redundancy for thermal protection designing.
- (4) The surface pressure was less affected by continuum breakdown than heat transfer rate.
- (5) For present trapezoid wing, as flight altitude ranged from 50km to 80km, error of heat transfer on the surface of the wing is from 5% to 15%, with peak heat transfer rate ranging from 1.6% to 14.5% at stagnation, and the error of the ratio of Lift-to-Drag is from 0.06% to 14.38%.

#### References

- [1] Li Yi-yong, Shen Huai-rong. Key Technologies of Developing Near Space Aircraft Systems[J]. Journal of the Academy of Equipment Command and Technology. Vol.17 No.5,2006(in Chinese)
- [2] Bird, G.A. Breakdown of Translational and Rotational Equilibrium in Gaseous Expansions[J]. AIAA Journal, Vol.8, No.11, 1970, pp.1998-2003.
- [3] Tiwari, S. Coupling of the Boltzmann and Euler Equations with Automatic Domain Decomposition[J]. Journal of Computational Physics, Vol.144, Aug. 1998, pp.710-726
- [4] Camberos, J.A., Schrock, C.R., McMullan, R.J. Development of Continuum onset Criteria with Direct Simulation Monte-Carlo Using Boltzmann's H-Theorem: Review and Vision[R]. Proceedings of the 9th AIAA/ASME Joint Thermophysics and Heat Transfer Conference, San Francisco, California, June 2006.
- [5] Boyd, I.D., Chen, G., and Xandler, G.V. Predicting Failure of the Continuum Fluid Equations in Transitional Hypersonic Flows[J]. Physics of Fluids, Vol.7, No.1, Jan. 1995, pp.210-219
- [6] Wand, W.-L. A Hybrid Particle/Continuum Approach for Nonequilibrium Hypersonic Flows[D], Phd thesis, The University of Michigan, 2004.
- [7] Boyd, I.D. and Padilla, J.F., Simulation of Sharp Leading Edge Aerothermodynamics[R]. AIAA Paper 2003-7062.
- [8] Andrew J. Lofthouse and Iain D. Boyd etc. Effects of Continuum Breakdown on Hypersonic Aerothermodynamics[R]. AIAA Paper 2006-993, 2006
- [9] Andrew J. Lofthouse, Leonard C. Scalabrin and Iain D. Boyd. Velocity Slip and Temperature Jump in Hypersonic Aerothermodynamics[R]. AIAA Paper 2007-0208, 2007.
- [10] Gokcen, T. and MacCormack, R.W., "Nonequilibrium Effects for Hypersonic Transitional Flows Using Continuum Approach"[R]. AIAA Paper 1989-0461, 1989.
- [11] Lockerby, D.A., Reese, J.M., and Gallis, M.A., Capturing the Knudsen Layer in Continuum-Fluid Models of Nonequilibrium Gas Flows[J]. AIAA Journal, Vol.43, No.6, June 2005, pp.1391-1393.



## Optimization of stiffened shell structures with stability objective/constraint based on kriging surrogate model and the explicit FEM

\*Bin Wang<sup>1</sup>, Jiandong Tian<sup>1</sup>, Cheng Huang<sup>1</sup>

<sup>1</sup> Beijing Institute of Astronautical Systems Engineering, Beijing, 100076, P. R. China,

\*Corresponding author: [b\\_wang@189.cn](mailto:b_wang@189.cn)

### Abstract

In this paper, a parametric model of a stiffened shell is built with Python language in Abaqus. The explicit FEM is used as an analysis tool in the optimal design of stiffened shell structures. The skin thickness and stiffener size are designed and optimized. The optimization contains two strategies: one is to obtain the minimum mass subjected to the structural performance, and the other is to obtain the high structural performance subject to the mass. In spite of the advantages of computer capacity and speed, the enormous computational cost of complex simulations makes it impractical to rely exclusively on simulation codes for the purpose of design optimization. To solve this problem, a surrogate model is built employing the experimental design and Kriging model, constructing the relationship between variables and standard deviation of the objective, reduced the computing time of uncertainty analysis in optimization to improve computing efficiency.

**Keywords:** Stiffened shell structures, Post-buckling, Explicit FEM, Optimization, Kriging surrogate model.

### Introduction

Stiffened shell structures are by far the most consumed structural components in the aerospace industry due to good stability, design ability and low cost. Buckling of such structures is often of mayor concern to designers. However, it is still a difficult task to perform a stability analysis of stiffened shells when the post-buckling behavior is considered. In fact the post-buckling analysis is quite necessary for completely describing the stability characteristics of stiffened shells. In this situation, the optimization problem with stability objective/constraints of these structures becomes difficult to evaluate.

Literature [1,2] pointed out that the explicit finite element method is an effective way to analysis the post-buckling behavior. However, because of explicit finite element analysis aims to simulate structural response under impact loads, an appropriate loading rate is important to quasi-static loading process simulation. Before optimization performing, the appropriate loading rate is determined firstly by comparing the effect of loading rate on numerical results. We set skin thickness, rib height, width and quantity as design parameters, using the Python language to build a parametric model for optimization. This procedure uses the commercial finite element software Abaqus as working platform. Because of discrete design parameters existing, Kriging surrogate model method and multi-island genetic algorithm are employed firstly to get a preliminary design, and then applying sequential linear programming algorithm to obtain the optimized design of other continuous variables' optimization problem based on the preliminary design.

In this paper, the optimization contains two strategies: one is to obtain the minimum mass subjected to the structural performance, and the other is to obtain the high structural performance subject to

the mass. The numerical results show that the mass decreases 14.2% or the loading capacity increases 19.3% through the above optimal processes, respectively. The proposed optimization procedure provides an effective tool for the safe exploitation of stiffened shell structures.

## 1 Model introduction

The parametric model (skin thickness, the number of ribs, height, width) built by Python language is shown in Figure 1. The stiffened shell's height is 1200.0mm, diameter is 2000.0mm, and the skin thickness is 2.0mm. There are nine hoop ribs and fifty longitudinal ribs in the stiffened shell. The rib's height is 10.0mm, width is 4.0mm. The material of the structure is aluminum alloy, which elastic modulus is 70GPa, Poisson's ratio is 0.3, yield strength is 350MPa, ultimate strength is 450MPa, elongation is 10%, and the material density is  $2.7 \times 10^9 \text{ ton/mm}^3$ . Full integration 4-node shell element is employed to mesh the structure, and one skin cell between ribs has  $5 \times 5$  elements. To ensure accuracy, the height direction along the rib is meshed by two elements.

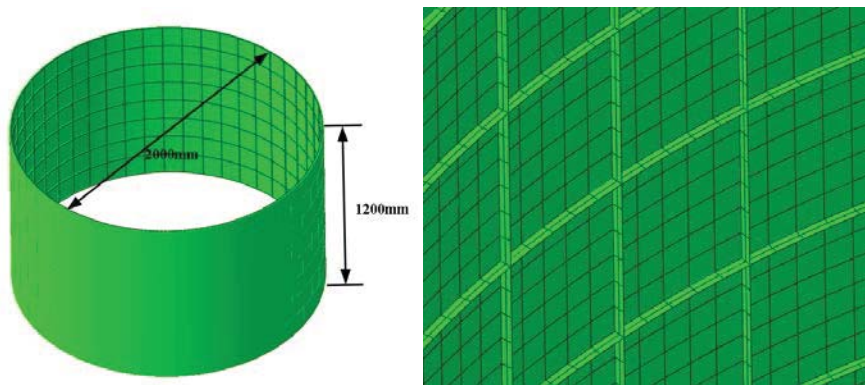
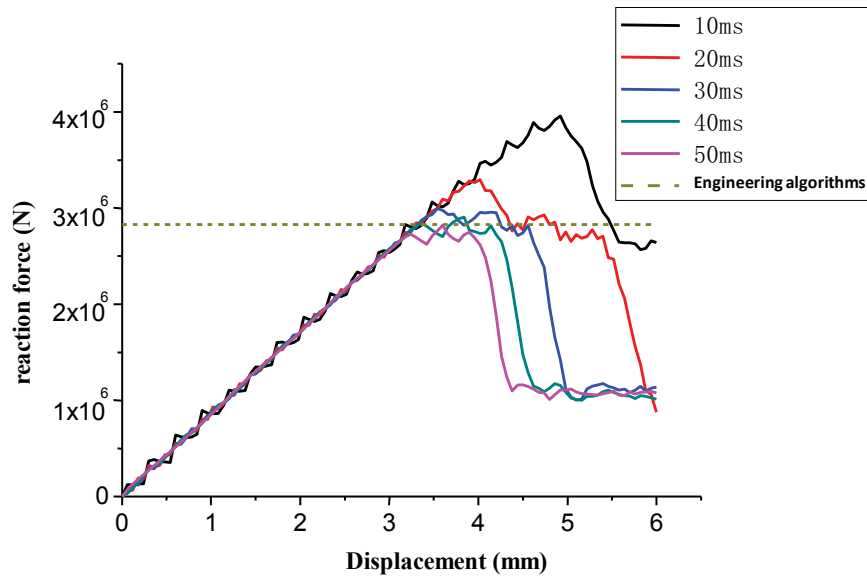


Figure 1. Finite element model

## 2 Loading rate selection

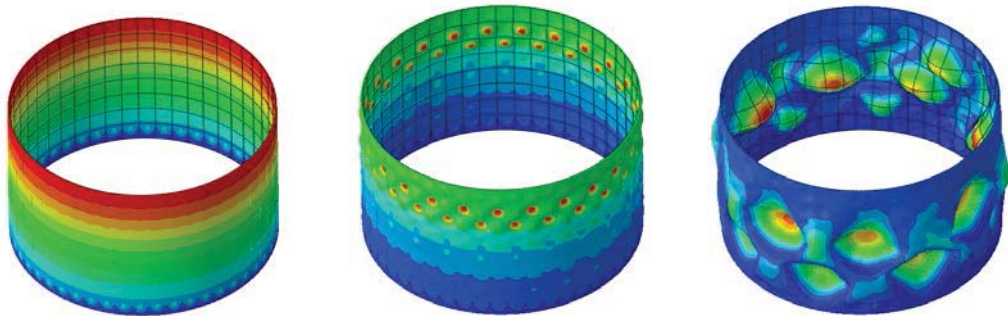
For the structure shown in Figure 1, post-buckling load of the structure is 282.81 ton though the engineering algorithms [3]. To apply explicit finite element algorithm to obtain the post-buckling load, the boundary and loading condition are clamping the lower end and applying a displacement on vertical downward face of the structure, the load size is 6mm.

Because of explicit finite element analysis aims to analysis structural response under impact loads, we need to select the appropriate loading speed in order to simulate quasi-static loading process firstly. Solving 5 load time conditions (10ms, 20ms, 30ms, 40ms, 50ms) respectively, and the support reaction force - displacement curves are shown in Figure 2. One can observe from the results, when the loading speed relatively faster, the support reaction force - displacement curve becomes unstable, and the post-buckling load of the structure is also higher. When load time is 10ms, the post-buckling load obtained from explicit finite element analysis is 395.87 ton higher than the engineering algorithm's result. And when the loading time increases, the calculated post-buckling load gradually decreases. If load time is chosen as 50ms, the analysis result is 281.93ton agreeing well with the engineering algorithm.

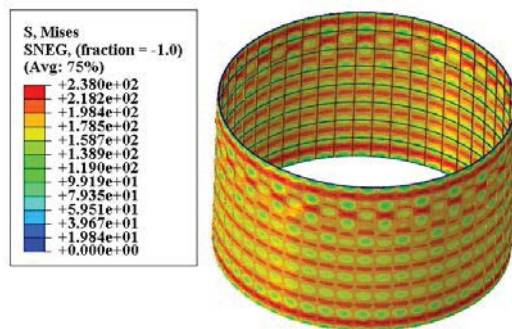


**Figure 2. Support reaction force - displacement curves**

From the comparison of the results of different loading rates, we can also find that the post-buckling load getting smaller when loading time over 30ms and the result of loading time is 50ms can be treated as a convergence solution. Because the computing time is proportional to the loading time, we choose 50ms as the loading time in the following calculations but not a longer loading time.



**Figure 3. Instability process**



**Figure 4. Stress distribution when post-buckling load reaching**

Figure 3 and Figure 4 shows steps of instability process of the structure when loading time is 50ms and the stress distribution when post-buckling load reaching. Though observation of the figures, one can find that the skin local buckled firstly, and then whole structure buckled. During this process,

the maximum stress in the structure is 230MPa lower than the yield stress. So the structure not makes use of the material because of instability.

### 3 Parameter Optimization

#### 3.1 Optimal column type and solution strategy

The two optimization formulations are showed following, the (a) formulation is the minimize structure weight optimization, and the (b) formulation is for maximize the structure performance optimization:

$$\begin{array}{ll}
 \text{find} & mpt, zjn, hjn, jg, jk \\
 \text{min} & mass \\
 \text{s.t.} & 40 \leq zjn \leq 60 \\
 & 6 \leq hjn \leq 10 \\
 & 1.5 \leq mpt \leq 2.5 \\
 & 7.5 \leq jg \leq 12.5 \\
 & 3.0 \leq jk \leq 5.0 \\
 & RF \geq 282ton \\
 \end{array} \quad \dots(a)
 \qquad
 \begin{array}{ll}
 \text{find} & mpt, zjn, hjn, jg, jk \\
 \text{max} & RF \\
 \text{s.t.} & 40 \leq zjn \leq 60 \\
 & 6 \leq hjn \leq 10 \\
 & 1.5 \leq mpt \leq 2.5 \\
 & 7.5 \leq jg \leq 12.5 \\
 & 3.0 \leq jk \leq 5.0 \\
 & mass \leq 53.2kg \\
 \end{array} \quad \dots(b) \quad (1)$$

The *mpt* is the thickness of skin, and the *zjn* and *hjn* are respective the number of longitudinal ribs and ring ribs, which are integer variables. It should be noted that the actual number of ring ribs is *hjn*+1. *jg* and *jk* are respective the height and width of the ribs. *mass* is the total mass of the structure. *Rf* is the maximum post-buckling load of the structure. As to the structure in the figure, the parameters are, *mpt*=2.0, *zjn*=50, *hjn*=8, *jg*=10.0, *jk*=4.0, and the total mass and the post-buckling load are 53.22Kg and 281.93ton, respective.

Because of the integer variables, the optimization problem could not use the sequential linear programming algorithm directly. So the Kriging surrogate model method is first use to get an approximate model, and then the multi-island genetic algorithm is used to obtain a preliminary design based on the approximate model. At last, applying sequential linear programming algorithm to get the optimized design of continuous variables' optimization problem based on the preliminary design.

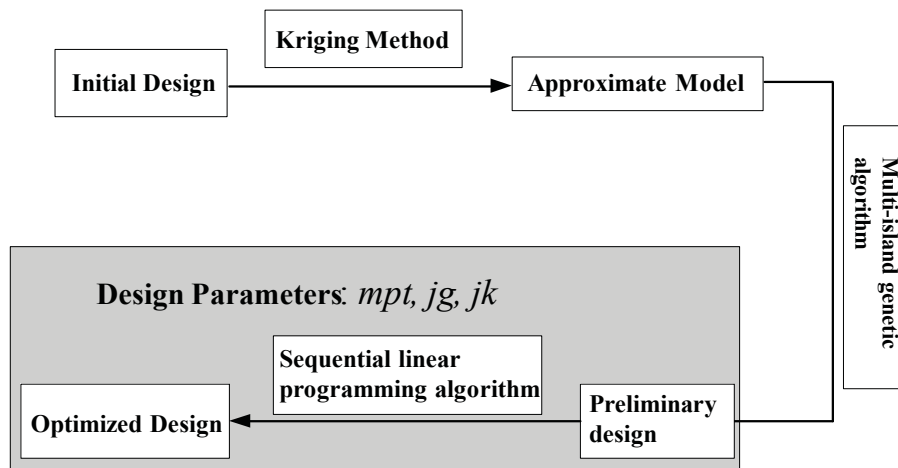


Figure 5. Optimization Process

### 3.2 Numerical examples

As mentioned in the previous content, the initial parameters are  $mpt=2.0$ ,  $zjn=50$ ,  $hjn=8$ ,  $kg=10.0$ ,  $jk=4.0$ . Firstly, establish an approximate model using Kriging surrogate model (in this paper, we randomly select 100 design points to build an approximate mode). The two optimization formulations have same design parameters and the needed structure response, so one approximation model is sufficient. The parameters and objective values of final optimized designs under these two optimization formulations are both showed in table 1. The results show that the optimized designs reduce the 14.2% weight of the structure or increase 19.3% of the post-buckling load, respectively.

**Table 1. Optimization Results Summary**

	Initial Design	minimize structure weight		maximize the structure post-buckling load	
$mpt(mm)$	2.00	1.51	1.52	1.77	1.79
$zjn$	50	46	46	41	41
$hjn$	8	10	10	9	9
$kg(mm)$	10.00	11.94	12.50	11.14	11.25
$jk(mm)$	4.00	3.32	3.53	4.93	4.93
$mass$ ( $kg$ )	Approximate model		43.94		52.58
	Finite element model	53.22	43.97	45.67	52.55
$RF$ ( $ton$ )	Approximate model		283.26		368.55
	Finite element model	281.93	266.55	282.50	332.16

Figure 6 shows support reaction force - displacement curves of two optimized designs. Figure 7 and Figure 8 show the buckling modes and stress distributions when total structure buckled (the left figure is optimized design got by minimizing the total structure weight). Compare with the initial design, the stress when total structure buckled of the two optimized designs both reaching the yield stress, which means that the material are fully utilized. And because of it, the support reaction force - displacement curves are stable without any flutter.

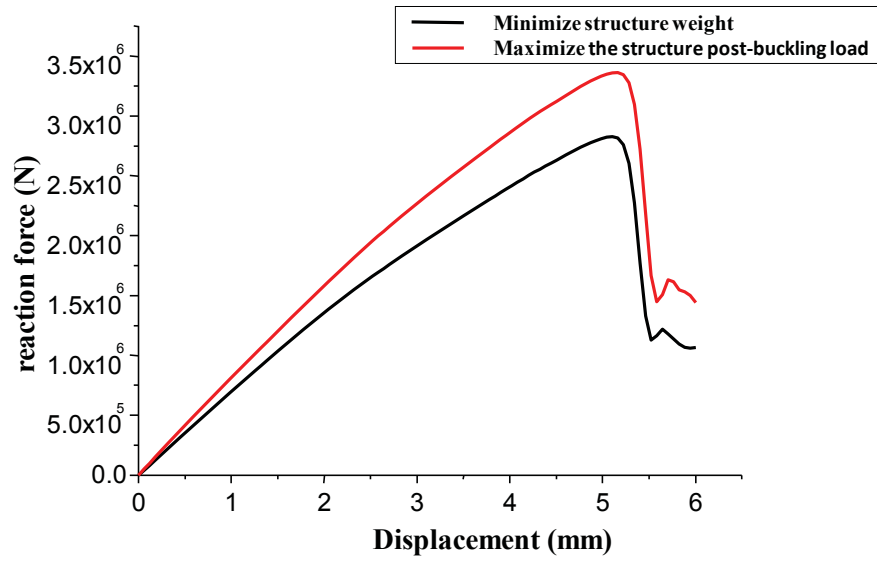


Figure 6. Support reaction force - displacement curves of two optimized designs

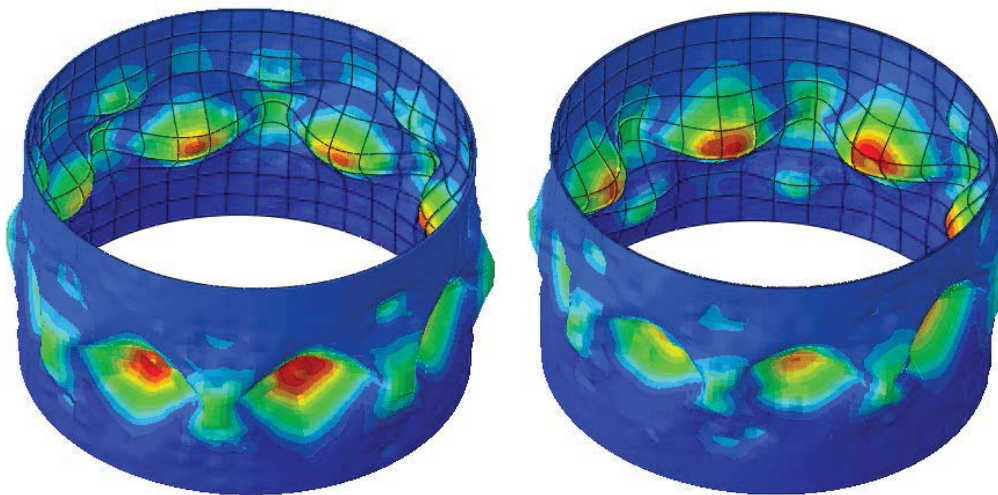


Figure 7. Buckling modes of optimized designs

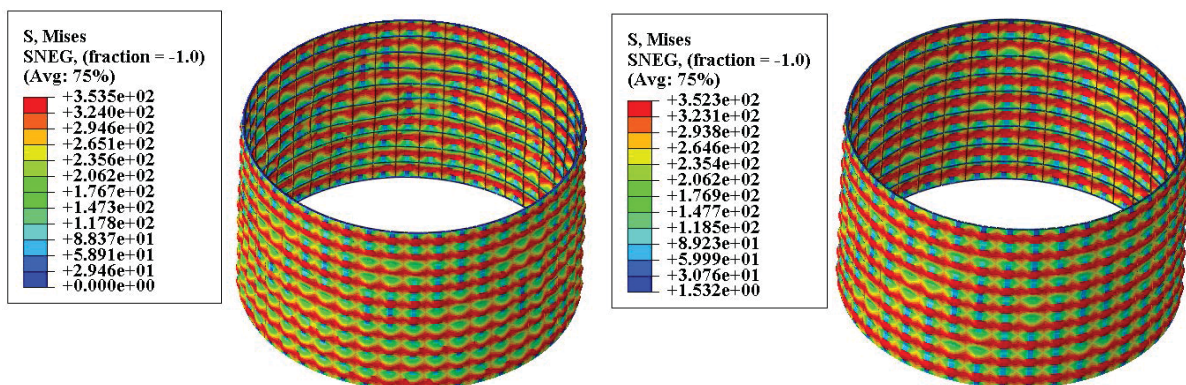


Figure 8. Stress distributions when total structure buckled

#### 4 Conclusions

In this paper, explicit finite element algorithm is used to solve the grid stiffened cylindrical shell post-buckling load. The skin thickness, rib height, width and quantity are set as the design parameters, and two optimized designs under two optimization formulations are obtained. Because of there are integer variables, the Kriging surrogate model method and the multi-island genetic algorithm are firstly used to get a preliminary design based on the approximate model, and then using sequential linear programming algorithm to get the optimized design of other continuous variables' optimization problem based on the preliminary design. The results show that the method used in this paper can get a reasonable and effective design for an optimization problem which contains both integer variables and continuums variables.

#### References

- Bin Wang, (2010)Multi-performance Optimization of Structures and Its Application in Aerospace Structural Design, Dalian, Dalian university of technology.
- Cheng Huang, Xi Zhang, Bin Wang, Bo Wang,(2010) Optimization of an axially compressed ring and stringer stiffened cylinder structure with the explicit FEM. The 6th China-Japan-Korea Joint Symposium on Optimization of Structural and Mechanical Systems, 2010, Kyoto, Japan.
- Missile structural strength calculation manual. (1978) Beijing: national defence industrial press.

## A STUDY OF THE OPTIMAL DESIGN AND MECHANICS SENSIBILITY IN THREE HINGE TRUSS

### “For two asymmetrical truss with different or equal component section sizes”

\*Toru Katori<sup>1</sup>, Kazutoshi Tsutsumi<sup>2</sup>

<sup>1</sup> Graduate student, <sup>2</sup> professor, Shibaura institute of Technology

\*me12022@sic.shibaura-it.ac.jp

#### • ABSTRACT

In carrying out a structural design, mechanics sensibility is important. However not all registered architects have sufficient mechanics sensibility. The purpose of this research is to offer the design know-how by analysis of the optimal solution in order to cultivate mechanics sensibility. This research formulates the form height and the section depth size, with the minimum weight for the load and span length, for a three hinge H-beam truss, using the admissible stress formula of compression. Analysis and verification of the form are performed by parameter analysis after formulation, and then the differences between both patterns are considered.

This research compared 2 patterns for an asymmetric three hinge truss. The conclusions gained are as follows:

- 1) In terms of form height, a truss with a same section size will be higher than that with a different section size.
- 2) In terms of section size, for a section size of short span, a pattern with same component section size is larger than that with different component section sizes. On the other hand, for section size of long span, a pattern with different component section size is larger than that with same component section sizes.

The above-mentioned conclusions contribute to design know-how for three hinge trusses, with such know-how being effective to cultivate mechanics sensibility.

#### • KEYWORDS

Mechanics sensibility, Mechanics rationality, Design know-how, Optimal design

### 1. INTRODUCTION

In carrying out a structural design, mechanics sensibility is important. However not all registered architects have sufficient mechanics sensibility. In order to cultivate sensibility generally, it is important to experience a "genuine article". What is the "genuine article" for mechanics sensibility? In this research, the minimum weight solution is treated as the "genuine article". It is thought that by analyzing the mechanics rational forms which become minimum weight, under the structure form to which the domain for a design, the loading condition, and the boundary condition were set, it is possible to gain design knowhow. The objects of this paper are as follows:

- The asymmetrical truss with different component section sizes and with compression force
- The asymmetrical truss with equal component section sizes and with compression force

The purpose of this research is to determine the form height and the section depth size with the minimum weight for the load and span length and height position, and it is to provide design know-how by comparing both patterns in order to cultivate mechanics sensibility.

### 2. The asymmetrical truss with different component section sizes and with compression force

This model is shown in Figure 1. Although section shape does not need to be considered for a tension member, the section shape does need to be considered for a compression member with buckling phenomenon. The section shape parameters of a component are shown in Figure 2.



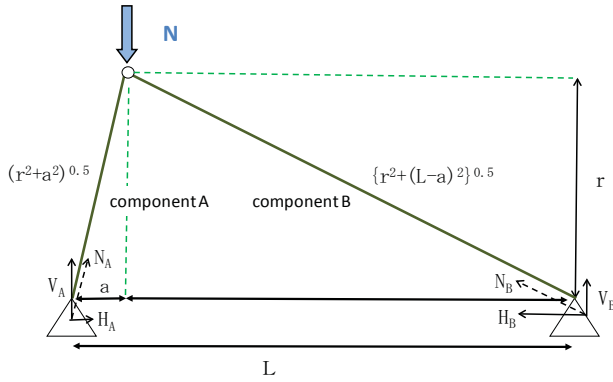


Figure 1. Model

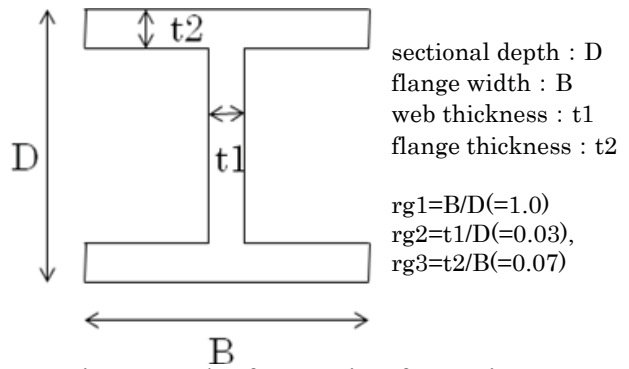


Figure 2. The form ratio of a section

2-1. Analysis method

This research formulates the form height with the minimum weight for the load and span, using the admissible stress formula of tension and compression. The optimal form with mechanics rationality is searched using the created formula. Analysis and verification of the form are performed by parameter analysis.

2-2. Formulization

For the formulization, refer to the last paper. (Toru Katori, 2012)

2-3. Analysis result

When the values of N were from 100 to 200 [kN] at 20 [kN] intervals, the values of L were from 300 to 600 [cm] at 50 [cm] intervals, the values of section depth size of the component A of assumption 2 and 3 and the section depth size of the component B of assumption 3 were from 1 to 20 [cm] at 0.01 [cm] intervals, and the values of a1 were from 0.1 to 0.5 at 0.1 intervals, the form height and the sectional depth size with the minimum weight were computed. The sectional depth size ratio and the height ratio are shown from Figure 3 to Figure 5. Here, the value of compressive force, span length, and material strength are normalized as a formula (1) in order to give general versatility.

$$N1 = \frac{N}{F \cdot L^2}, r1 = \frac{r}{L}, a1 = \frac{a}{L}, D_{A1} = \frac{D_A}{L}, \frac{a}{L}, D_{B1} = \frac{D_B}{L}, \frac{a}{L} \tag{1}$$

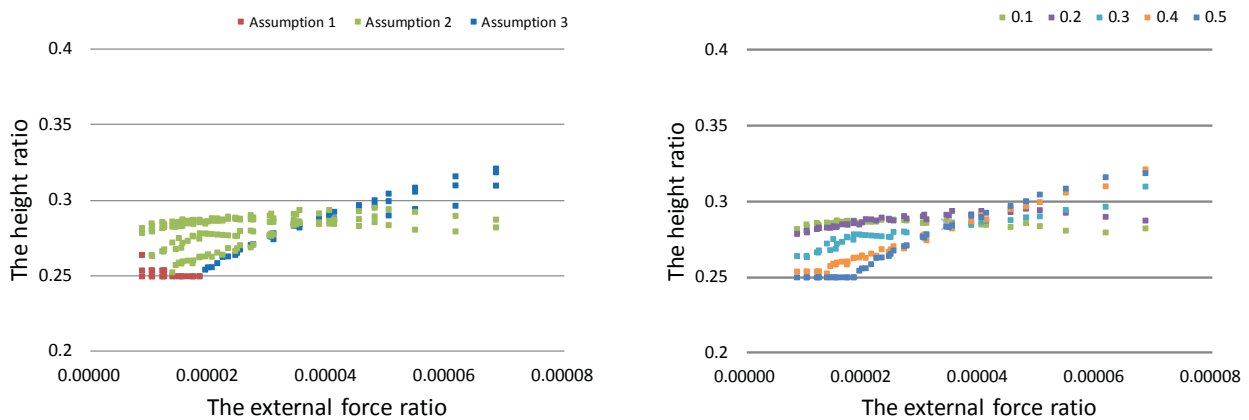


Figure 3. The height ratio for different component section size

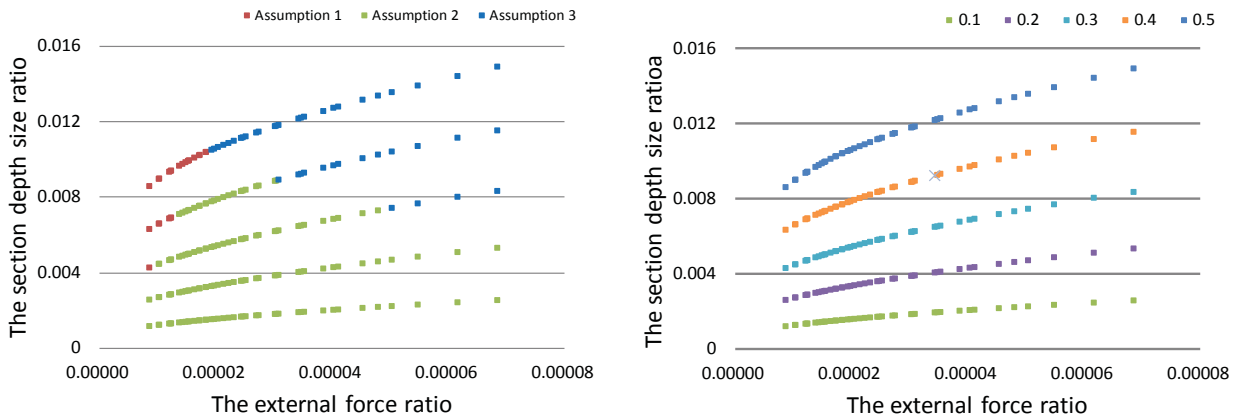


Figure 4. The section depth size ratio of the component A for different component section size

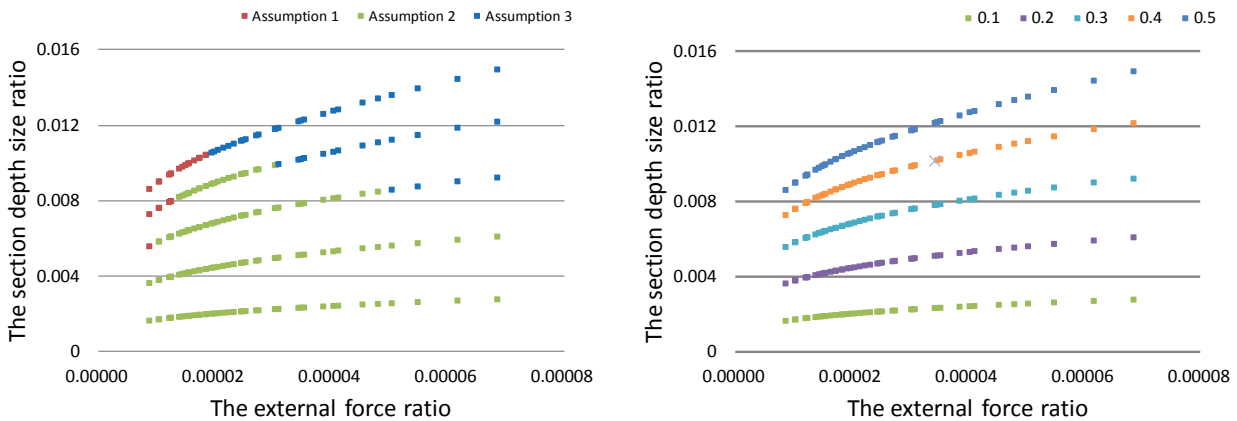


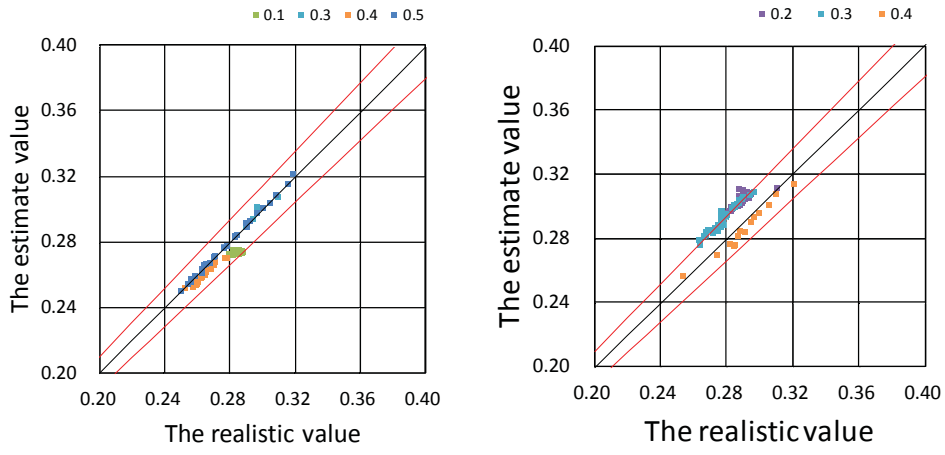
Figure 5. The section depth size ratio of the component B for different component section size

2-4. Verification and the approximate expressions of exponential functions

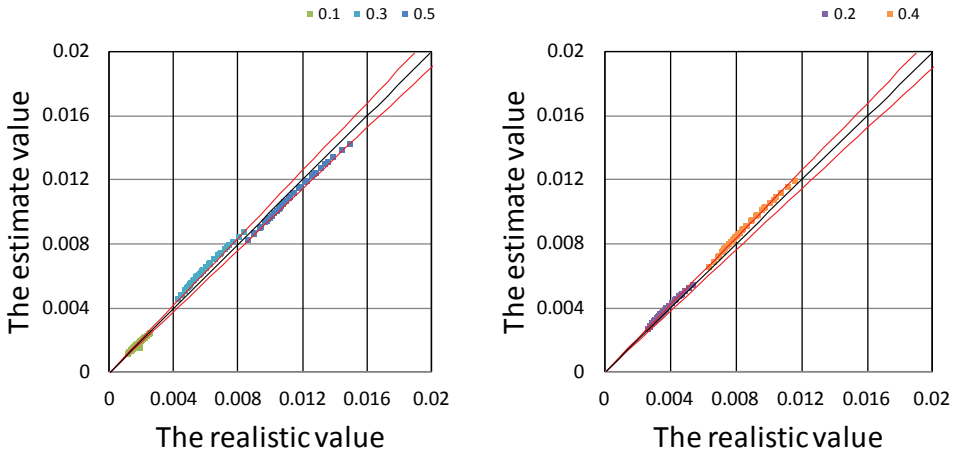
Figure 3 to 5 show that the height ratio of assumption 1 can be approximated as a straight line. The height ratio of assumption 2 and 3 and the section depth size ratio can be approximated as the exponential functions. The approximate expressions of assumption 1 and 3 of the height ratio were determined by using the values of  $a_1=0.3, 0.5$ . The approximate expressions of assumption 2 of the height ratio were determined by using the values of  $a_1=0.1, 0.4$ . The approximate expressions of the section depth size ratio were determined by using the values of  $a_1=0.1, 0.3, 0.5$ . The approximate expressions are expressed from a formula (2) to (6).

- The height ratio for the external force ratio and height position ratio
  - Assumption 1:  $r_1' = -0.0706a_1 + 0.2853$  (2)
  - Assumption 2:  $r_1' = (1.4115a_1 + 0.1168)N_1^{(0.315a_1 - 0.037)}$  (3)
  - Assumption 3:  $r_1' = (-0.749a_1 + 2.243)N_1^{(-0.0635a_1 + 0.2154)}$  (4)
- The section depth size ratio for the external force ratio and height position ratio
  - The component A:  $D1A' = (-1.2162a_1^2 + 0.9635a_1 - 0.0023) N_1^{(-0.2603a_1 + 0.3921)}$  (5)
  - The component B:  $D1B' = (0.3615a_1 - 0.0083) N_1^{(0.0198a_1 + 0.2445)}$  (6)

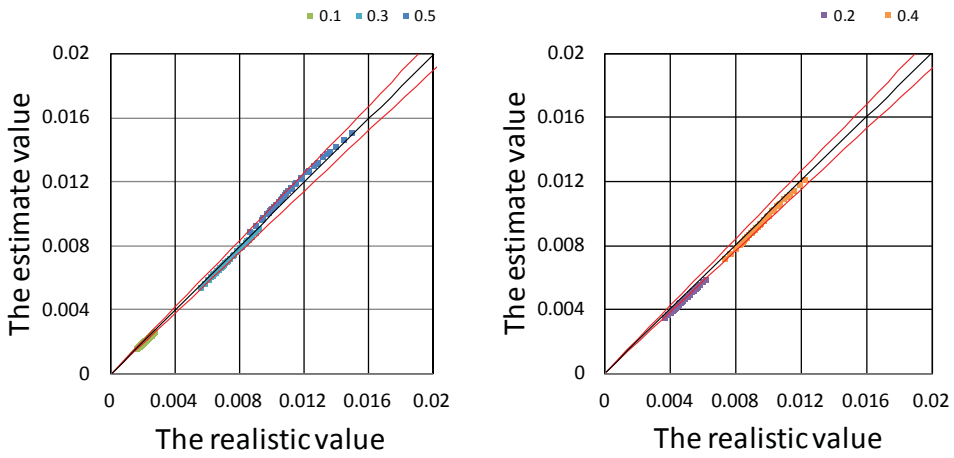
We carried out numerical experiments in order to check the validity from formula (2) to (6). The validity of the height ratio of assumption 1 and 3 was verified for  $a_1=0.4$ , the validity of the height ratio of assumption 2 was verified for  $a_1=0.2, 0.3$ , and the validity of the section depth size ratio was verified for  $a_1=0.2, 0.4$ . The form height and the sectional depth size with the minimum weight were computed. The relation between the assumed height ratio and an actual height ratio is shown in Figure 6. The relation between the assumed section depth size ratio and the actual section depth size ratio is shown in Figure 7 and Figure 8.



(a) Learning data (b) Verification data  
 Figure 6. The height ratio for different component section size



(a) Learning data (b) Verification data  
 Figure 7. The section depth size ratio of the component A for different section component size



(a) Learning data (b) Verification data  
 Figure 8. The section depth size ratio of the component B for different section component size

2-5.Consideration

The following results were found:

1. Assumption 1 is dependent on the height position and the span length regardless of external force or material strength. However, assumption 2 and assumption 3 are dependent on external force, material strength, the span length, and the height position.
2. In terms of height ratio, from Figure 3 to 5 show that in the range from  $a_1=0.1$  to  $0.2$  only assumption 2 is present. In the range from  $a_1=0.3$  to  $0.4$ , all from assumption 1 to 3 are present. And at  $a_1=0.5$ , assumption 1 and 3 are present.
3. As the value of  $a_1$  increases, the actual section depth size ratio becomes larger. Furthermore, the increment of the actual section depth size ratio for the vertex position ratio is the same degree.
4. The approximation formula of height ratio in assumption 1 can be expressed by a straight line. The approximation formula of height ratio in assumption 2, 3, and the approximation formula of actual section depth size ratio can be expressed by an exponential function of the force ratio. Figure 6 to 8 show that the accuracy of the approximate expression is good.
5. In terms of the height ratio, Figure 3 to 5 show that an inversion phenomenon occurred for the vertex position ratio. On the other hand, this did not occur for the actual section depth size ratio. In regards to this too, further investigations will be carried out.

3. The asymmetrical truss with same component section sizes and with compression force

This model and the section shape parameters of a component are shown in Figure 1 and Figure 2.

3-1. Analysis method

When the span length and height form, height position ratio, and the form height were set, the sectional depth sizes with the minimum weight were computed. When determining the member section, the stress ratio of the two components was compared, and the section size of member component whose stress ratio is close to the 1 is adopted.

3-2. Analysis result

When the values of  $N$  were from 100 to 200 [kN] at 20 [kN] intervals, the values of  $L$  were from 300 to 600 [cm] at 50 [cm] intervals, the values of the form height were from 50 to 200 [cm] at 0.05 [cm] intervals, the values of section depth size were from 1 to 20 [cm] at 0.01 [cm] intervals, and the values of  $a_1$  were from 0.1 to 0.5 at 0.1 intervals, the form height and the sectional depth size with the minimum weight were computed. The sectional depth size ratio and the height ratio is shown in Figure 9 and Figure 10. Here, the value of compressive force, span length, and material strength are normalized as a formula (1) in order to give general versatility.

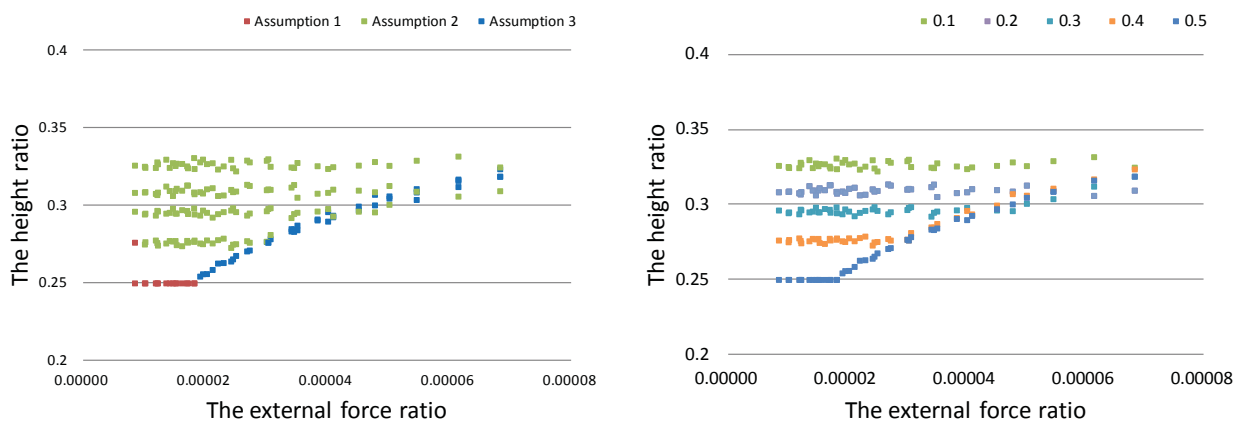


Figure 9. The height ratio for same component section size :

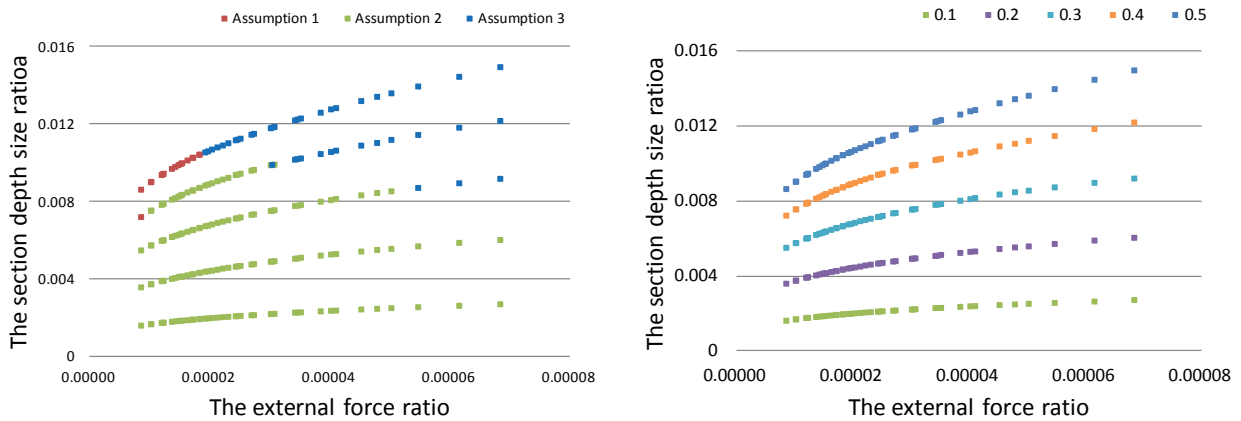


Figure 10. The section depth size ratio for same component section size

3-3. The approximate expressions of exponential functions, and Verification

Figure 9, 10 shows that the height ratio of assumption 1 and 2 can be expressed by straight lines. The height ratio of assumption 3 and the section depth size ratio can be expressed by exponential functions. The approximate expressions of assumption 1 and 2 of the height ratio were determined by using the values of a1=0.1, 0.3, 0.5. The approximate expressions of assumption 3 of the height ratio were determined by using the values of a1=0.3, 0.5. The approximate expressions of the section depth size ratio were determined by using the values of a1=0.1, 0.3, 0.5. The approximate expressions are expressed from formulas (7) to (9).

- The height ratio relation with the external force ratio and height position ratio

$$\text{Assumption 1, 2: } r1' = -0.1916a1 + 0.3483 \tag{7}$$

$$\text{Assumption 3: } r1' = (-3.345a1 + 3.541)N1^{(-0.163a1 + 0.2651)} \tag{8}$$

- The section depth size ratio relation with the external force ratio and height position ratio

$$D1' = (0.364a1 - 0.0074)N1^{(0.022a1 + 0.2457)} \tag{9}$$

We carried out numerical experiments in order to check the validity from formulas (7) to (9). The validity of the height ratio of assumption 1 and 2 was verified for a1=0.2, 0.4, the validity of the height ratio of assumption 3 was verified for a1=0.4, and the validity of the section depth size ratio was verified for a1=0.2, 0.4. The form height and the sectional depth size with the minimum weight were computed. The relation between the assumed height ratio and an actual height ratio is shown in Figure 11. The relation between the assumed section depth size ratio and the actual section depth size ratio is shown in Figure 12.

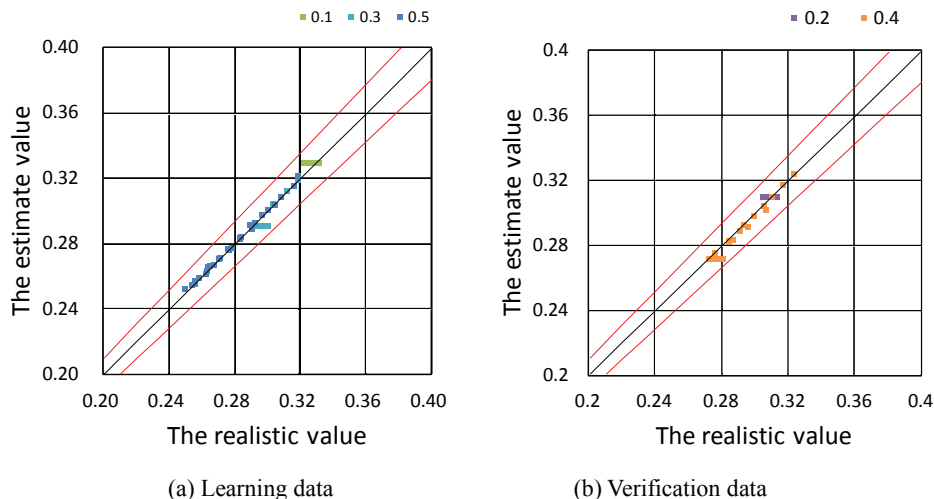


Figure 11. The height ratio for same component section size

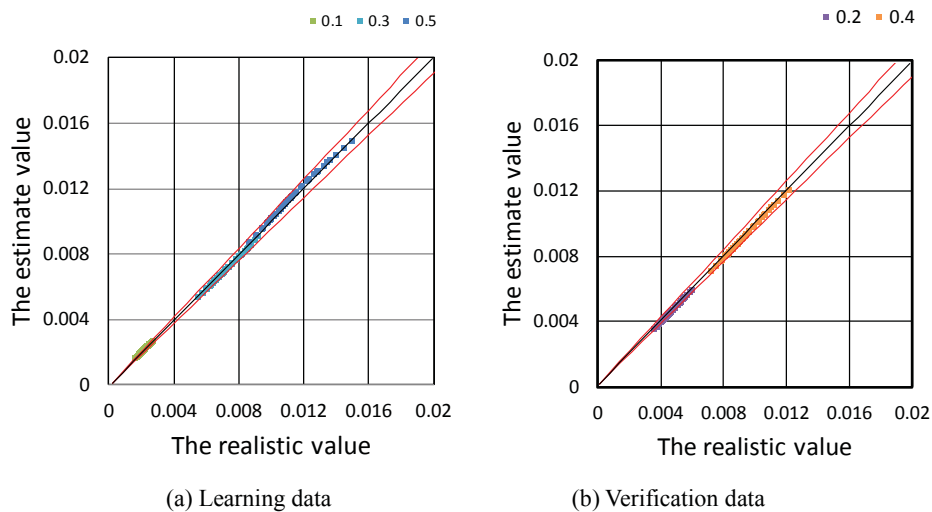


Figure 12. The section depth size ratio for same component section size :

### 3-4. Consideration

The results gained are as follows:

1. Assumption 1 and assumption 2 are dependent on the height position and the span length regardless of external force or material strength. However, assumption 3 is dependent on external force, material strength, the span length, and the height position.
2. With regard to the height ratio, in the range from  $a_1=0.1$  to 0.3, only assumption 2 is present. At  $a_1=0.4$ , all assumptions 1 to 3 are present. At  $a_1=0.5$ , only assumptions 1 and 3 are present.
3. As the value of  $a_1$  increases, the actual section depth size ratio becomes larger. Furthermore, the increment of the actual section depth size ratio for the vertex position ratio is the same degree.
4. Assumption 1, 2 for the height ratio can be expressed by straight lines. Assumption 3 for the height ratio, and the actual section depth size ratio can be expressed by exponential functions of the force ratio. Figure 9 to 10 show that the accuracy of the approximate expression is good.
5. In terms of the height ratio, an inversion phenomenon occurred for the range of  $a_1=0.3$  to 0.5 when the external force ratio increases. On the other hand, in terms of the section depth size ratio, inversion phenomenon did not occur for the vertex position ratio. In regards to this too, further investigations will be carried out.

### 4. Conclusions

This research compared 2 patterns for an asymmetric three hinge truss, that is, their two component member sizes are same or different. The conclusions gained are as follows:

1. From Figure 3 and Figure 9, the approximate expressions of assumption 2 are expressed by curve in case of the different component section sizes, but are constant in case of the same component section sizes.
2. From Figures 6 to 8 and Figure 11, 12, the approximate expressions of the actual section depth size ratio and the height ratio are effective.
3. In terms of the height ratio, an inversion phenomenon occurred for the vertex position ratio, for 2 patterns together. On the other hand, for the actual section depth size ratio, an inversion phenomenon did not occur.
4. A form height of truss with same component section size is higher than that with a different component section size.
5. For component member of short span, member section size of same component member pattern is larger than that of different component member pattern. On the other hand, for component member of long span, member section size of different component pattern is larger than that of same component member pattern.

The above-mentioned conclusions contribute to an element of design know-how for three hinge trusses, and it is thought that such know-how will be effective for the cultivation of mechanics sensibility. Hereafter, it is necessary that the design know-how is learned by analyzing the mechanics rational forms which become minimum weight, under various structure forms.

#### References

Toru Katori, Kazutoshi Tsutsumi (2012), A study on mechanics sensibility and the optimal design ~In case of three hinge truss~, The Seventh China-Japan-Korea Joint Symposium on Optimization of Structural and Mechanics Systems Huangshan.

## Porohyperelastic Analysis of Single Chondrocyte Using AFM and inverse FEA

Trung Dung Nguyen, Yuantong Gu\*

School of Chemistry, Physics and Mechanical Engineering, Science and Engineering Faculty, Queensland University of Technology, Brisbane, Queensland, Australia

\*Corresponding author: yuantong.gu@qut.edu.au

### Abstract

The aim of this paper is to determine the creep and relaxation responses of single chondrocytes *in vitro*. Firstly, Atomic Force Microscopy (AFM) was used to obtain the force-indentation curves of single chondrocytes at the strain-rate of  $7.05 \text{ s}^{-1}$ . This result was then employed in inverse finite element analysis (FEA) using porohyperelastic (PHE) idealization of the cells to determine their mechanical properties. The PHE model results agreed well with AFM experimental data. This PHE model was then utilized to study chondrocyte's creep and relaxation behaviors. The results revealed that the effect of fluid was predominant for cell's mechanical behaviors and that the PHE is a good model for biomechanics studies of chondrocytes.

**Keywords:** Biomechanics, Chondrocytes, Finite Element Analysis, Porohyperelastic, AFM.

### Introduction

Chondrocytes are cytoskeleton (CSK)-rich eukaryotic cells which are the mature cells in cartilage tissues performing a number of functions within the cartilage. The deterioration of the mechanical properties of these cells is believed to be one of the main factors in the development and progression of osteoarthritis (Jones et al. 1997, Trickey, Lee and Guilak 2000). Cellular behaviour in response to external stimuli such as shear stress, fluid flow, osmotic pressure and mechanical loading have been investigated recently (Guilak, Erickson and Ting-Beall 2002, Ofek et al. 2010, Wu and Herzog 2006).

There are several continuum mechanical models that have been developed for the single cell as well as other biological tissues (Lim, Zhou and Quek 2006). One of them is porohyperelastic (PHE) model which can account for the non-linear behavior, fluid-solid interaction and rate-dependent drag effects is potentially a good candidate for investigating the responses of a cell to external loading and other load- induce stimuli. This PHE model considers soft tissues as porous materials consisting of a pore fluid that saturates the tissue and percolates and exudes transiently relative to the deformable porous elastic solid skeleton. Although the PHE model has been widely and effectively utilized in biomechanics, e.g. articular cartilage modeling (Oloyede and Broom 1991, Oloyede and Broom 1996), its application in the modeling of the single living cell has been quite limited.

Because of recent advances in nanotechnology, a number of new experimental techniques for characterizing and studying the mechanical behavior of living cells have been developed. One such technique is based on Atomic Force Microscopy (AFM) which is a state-of-the-art experimental facility for high resolution imaging of tissues, cells and artificial surfaces, including probing the mechanical properties of samples both qualitatively and quantitatively (Touhami, Nysten and Dufrene 2003, Rico et al. 2005, Zhang and Zhang 2007, Lin, Dimitriadis and Horkay 2007, Kuznetsova et al. 2007, Faria et al. 2008, Yusuf et al. 2012). Its principle is to indent the material/sample with a tip of microscopic dimension which is attached to a very flexible cantilever and the force is measured from the deflection of the cantilever to obtain the force-indentation ( $F-\delta$ ) curve (Darling, Zauscher and Guilak 2006, Faria et al. 2008, Ladjal et al. 2009). This powerful tool



is increasingly applied in the study of cell responses to external stimuli such as mechanical and chemical loading. This tool is ideal for bridging the research gap in the understanding of microscale responses of biological organisms.

The aim of this study is to utilize the PHE model to explore the creep and relaxation responses of non-living chondrocytes using Atomic Force Microscopy (AFM) and inverse finite element analysis (FEA).

## Methodology

### 1. Sample preparation and AFM set-up

The chondrocytes were cultured using Dulbecco's Modified Eagle's Medium (low glucose) (GIBCO, Invitrogen Corporation, Melbourne, Australia) supplemented with 10% fetal bovine serum (FBS) (HyClone, Logan, UT) and 1% penicillin and streptomycin (P/S) (GIBCO, Invitrogen Corporation, Melbourne, Australia). After culturing for a week until the cells were confluent, they were detached using 0.5% Trysin (Sigma-Aldrich). They were seeded onto poly-D-lysine (PDL, Sigma-Aldrich) coated cultured petri dish for 1-2h. Chondrocytes were placed on the PDL surface to form a strong attachment while keeping their morphology round. Then the chondrocytes were fixed using 4% Paraformaldehyde (Sigma-Aldrich) for 20 minutes before changing it to Phosphate Buffered Saline (PBS, Sigma-Aldrich). All the samples were stored at  $-4^{\circ}\text{C}$  until required for experiments. Biomechanical testing was conducted at room temperature. Atomic Force Microscopy (AFM) (NT-MDT SOLVER P47-PRO SPM) was used in this study. A triangular colloidal probe CP-PNPL-BSG-A-5 (NanoAndMore GMBH) cantilever attached to a crystal cantilever holder was used in the experiment. This allows the scanning and force spectroscopy of samples in liquid. The colloidal probe is of diameter  $5\ \mu\text{m}$  and its spring constant is  $0.08\ \text{N/m}$ .

The force-indentation curves of single chondrocytes were first obtained with the AFM. The porohyperelastic (PHE) FEA model of the chondrocyte was then developed and used to determine its mechanical properties by inverse analysis, where the experimental data was used as input. Following this, the model was extended to study the creep and relaxation responses of the cell.

### 2. Porohyperelastic (PHE) field theory

It has been applied in many engineering fields including Soil Mechanics (Sherwood 1993) and Biomechanics (Simon 1992, Meroi, Natali and Schrefler 1999, Nguyen 2005, Olsen and Oloyede 2002); with the theoretical details extensively presented by several authors (Simon 1992, Simon et al. 1996, Simon et al. 1998b, Simon et al. 1998a, Kaufmann 1996). The field equations for the isotropic form of this theory are summarized below:

Conservation of linear momentum:

$$\frac{\partial T_{ij}}{\partial x_j} = 0 \quad (1)$$

Conservation of fluid mass (Darcy's law):

$$\tilde{k}_{ij} \frac{\partial \pi^f}{\partial x_i} = \dot{\tilde{w}}_j \quad (2)$$

Conservation of (incompressible) solid and (incompressible) fluid mass:

$$\frac{\partial \tilde{w}_i}{\partial x_k} + J H_{kl} \dot{E}_{kl} = 0 \quad (3)$$

The constitutive law:

$$\sigma_{ij} = \sigma_{ij}^e + \pi^f \delta_{ij}, \quad \sigma_{ij}^e = J^{-1} F_{im} S_{mn}^e F_{jn} \quad (4)$$

$$S_{ij} = S_{ij}^e + J\pi^f H_{ij}, \quad H_{ij} = F_{im}^{-1} F_{jm}^{-1}, \quad S_{ij}^e = \frac{\partial W^e}{\partial E_{ij}} \quad (5)$$

where  $T_{ij}$ ,  $\pi^f$ ,  $\tilde{k}_{ij}$ ,  $\tilde{w}_j$ ,  $H_{ij}$ ,  $S_{ij}^e$  and  $W^e$  are first Piola-Kirchhoff total stress, fluid stress, symmetric permeability tensor, Lagrangian fluid velocity, Finger's strain, second Piola-Kirchhoff stress and effective strain energy density function, respectively. Neo-Hookean strain energy density function shown below would be used in this study (Brown et al. 2009, ABAQUS 1996):

$$W^e = C_1(\bar{I}_1 - 3) + \frac{1}{D_1}(J - 1)^2 \quad (6)$$

where  $J$  is the volume strain of the material,  $\bar{I}_1 = J^{-2/3} I_1$  is the first deviatoric strain invariant, and  $C_1$  and  $D_1$  are material constants.

The hydraulic permeability of the chondrocyte was assumed to be deformation-dependent in this study. The constitutive law of deformation-dependent permeability proposed by (Holmes and Mow 1990) was adopted. In order to adopt this to finite element simulations, the permeability was employed as a function of void ratio which is the ratio of the volume of fluid to the volume of solid component as proposed by (Wu and Herzog 2000):

$$k = k_0 \left(\frac{e}{e_0}\right)^\kappa \exp\left\{\frac{M}{2} \left[\left(\frac{1+e}{1+e_0}\right)^2 - 1\right]\right\} \quad (7)$$

where  $k_0$  is the initial permeability,  $e_0$  is the initial void ratio, and  $\kappa$  and  $M$  are non-dimensional material parameters.

Note that void ratio  $e$  relates to porosity  $n$  e.g. the volume of the matrix occupied by fluid by:  $e = n/(1 - n)$ . The chondrocyte's water content was determined to be around 60% of total volume (Oswald et al. 2008). Thus, the initial void ratio  $e_0$  was calculated to be  $e_0 = 1.5$ . The material parameters  $\kappa$  and  $M$  have been determined to be 0.0848 and 4.638, respectively in (Holmes 1986), and used in (Wu and Herzog 2000, Holmes and Mow 1990, Moo et al. 2012). Figure 1 presents the strain-dependent permeability used in ABAQUS model in this study.

The volume strain of the cell is given by:

$$J = \frac{dV}{dV_0} = \frac{1+e}{1+e_0} \quad (8)$$

where  $V$  and  $V_0$  are deformed and undeformed volume of material, respectively.

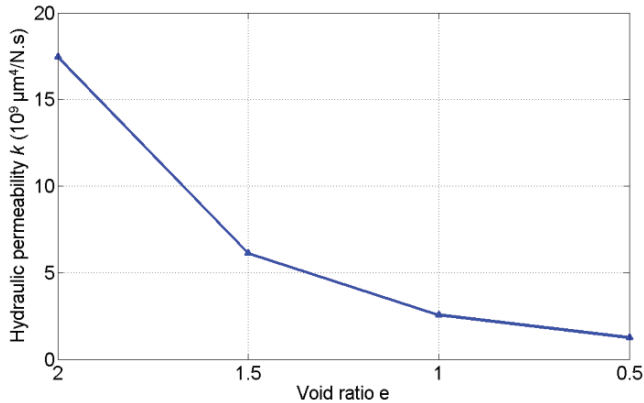
### 3. Chondrocytes diameter

In order to develop a FEA model, there are several important parameters required. One of these is the chondrocytes diameter. It was measured with a Leica Light Microscope M125 (Leica Microsystems). Note that only the round chondrocytes were picked for measurement and the diameter is the average of the horizontal and vertical diameters, leading to  $16.99 \pm 2.041 \mu\text{m}$  ( $n = 50$ ) (Figure 2). This average diameter was used in the FEM modeling of the single chondrocyte.

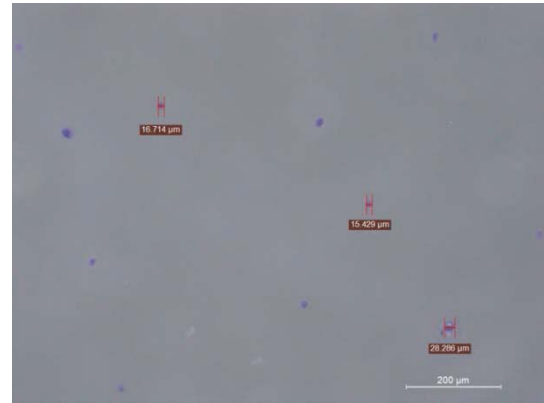
### 4. Finite Element Analysis (FEA) model

A finite element analysis (FEA) model of a single chondrocyte was developed (Figure 3) to study its micro-deformation response, using the commercial software ABAQUS version 6.9-1 (ABAQUS Inc., USA). The atomic force microscopy (AFM) nano-indentation experiment was simulated with this model. Because both the chondrocyte and AFM tip are spherical, axisymmetric geometry and element-approximation was assumed, thereby saving computational cost (ABAQUS 1996). The model consists of a chondrocyte cell of diameter  $17 \mu\text{m}$  which was indented with a colloidal probe of diameter  $5 \mu\text{m}$ . At first, the chondrocyte was indented to a maximum strain of around 15% of cell's diameter (corresponding to a displacement of approximately  $2.5 \mu\text{m}$ ). The reaction forces were then extracted and compared to the experimental data to determine cell's mechanical

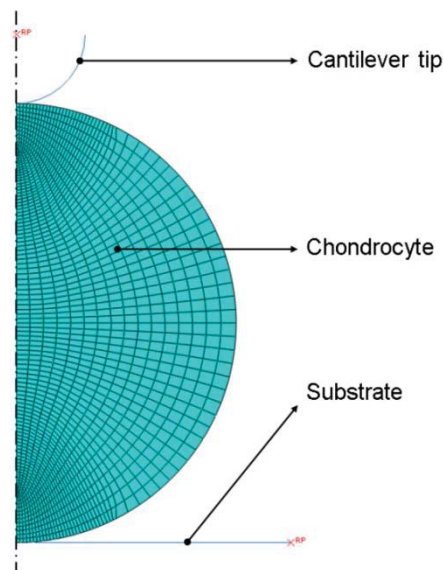
properties which are  $C_I$ ,  $D_I$  and  $k_0$  in Eq. (6) and (7) using inverse FEA procedure. This model was also used to study the relaxation of chondrocytes by keeping the displacement of the tip constant. Secondly, the force of 27.7 nN was applied on the spherical tip and kept constant to study chondrocyte's creep response. This force value was the maximum force obtained from previous model.



**Figure 1 Deformation dependent hydraulic permeability**



**Figure 2 Chondrocytes diameter measurement**



**Figure 3 FEM model of single chondrocyte**

## RESULTS AND DISCUSSION

### 1. AFM experiment

Before conducting force spectroscopy to probe the mechanical properties of chondrocytes, scanning was done to locate the position of single chondrocytes using the contact mode scanning method. Figure 4 presents the height scanned image of chondrocytes. Using this image, the cantilever was adjusted so that the colloidal tip was placed centrally at the top of the chondrocyte to apply a load. Following this, the cell was indented to approximately 15% of its diameter at strain-rate of  $7.05 \text{ s}^{-1}$ , and the force-indentation curves were recorded.

### 2. FEM results

In the first model, the chondrocyte was indented to 15% strain of cell's diameter. The PHE model using Neo-Hookean strain energy density function was developed and analyzed using inverse FEA

modeling methodology in order to capture the behavior of the cell. The software ABAQUS was utilized with pore fluid/stress axisymmetric elements with the PHE constitutive material law presented earlier. The material parameters which were determined using inverse FEA procedure mentioned above are presented in table 1.

**Table 1 PHE model material parameters (Oswald et al. 2008)**

$C_1$	$D_1$	Initial permeability $k_0$ ( $\mu\text{m}^4/\text{N.s}$ )	Initial void ratio $e_0$
0.00105	3060	$6.14 \times 10^9$	1.5

Figure 5 presents the AFM experimental data and PHE simulation results. It is observed that the PHE model agreed well with AFM experiment demonstrated that this model can be used to capture cells' mechanical behavior. The relaxation of the cell was then studied by keeping the displacement of spherical tip constant for around 70 s. It can be observed that the PHE can capture the relaxation of chondrocyte very well (Figure 6). Note that the relaxation response was fast because of the effect of pore fluid pressure developed during indentation. This pressure gradient caused the fluid to exude out from the cell fast enough in the relaxation state. The volume strain of the chondrocyte at the end of transient and relaxation states were determined to be 0.969797 and 0.829007, respectively using Eq. (8). It demonstrated that there was loss of fluid during relaxation state. This response will be considered clearer in the next model.

In the second model, the chondrocyte was applied a force of 27.7 nN on cantilever tip instead of displacement in the first model. This force was then kept constant for around 70 s to study the creep response of the cell. When the force was kept constant, the chondrocytes continued to deform until its deformation reached an asymptotic value (Figure 7). This is when the cell is in its equilibrium condition. In order to have a clearer understanding, the von Mises or solid skeleton stress and fluid pore pressure at the closest node to the cantilever tip was shown in Figure 8. It is observed that the Mises or solid stress increased significantly in the transient state and gradually reached its maximum value in the steady state e.g. when the applied force was kept constant. Also, in this steady state, the pore pressure dropped to its asymptotic/limiting low value. It demonstrated that the solid skeleton provided load bearing stiffness in this state where the pore pressure is practically zero.

It is worthy to note that pore fluid pressure reached its maximum value earlier compared to the applied load (Figure 8). It demonstrated that the effect of fluid is superior only in the beginning of the indentation. In brief, in the transient state, all of applied load was taken by the pore fluid pressure. The load was then transferred from fluid to solid skeleton when the pore pressure dropped and all of load was taken by solid skeleton after all. These results reveal the predominant role of the fluid in determining the responses of a chondrocyte to mechanical stimuli.

## CONCLUSIONS

Both creep and relaxation responses of single chondrocytes were investigated in this study using AFM and inverse FEA modeling methodology. The results revealed that PHE model can capture these responses very well and that the effect of fluid was predominant for cell's mechanical behaviors. This model can also be improved to account for other behaviors i.e. swelling effect. Thus, PHE is a very good candidate for exploration of mechanical deformation responses of chondrocyte cells.

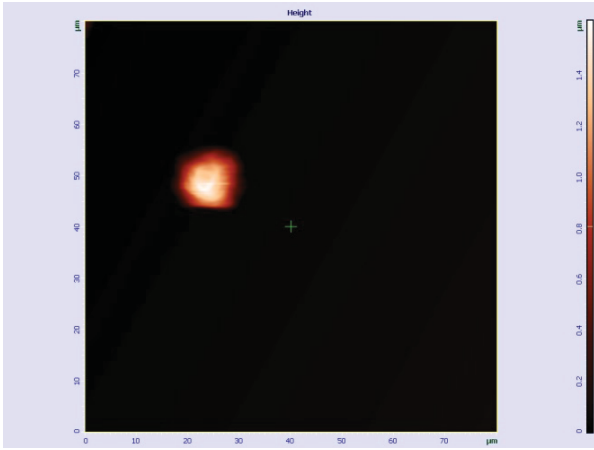


Figure 4 Height image of chondrocyte

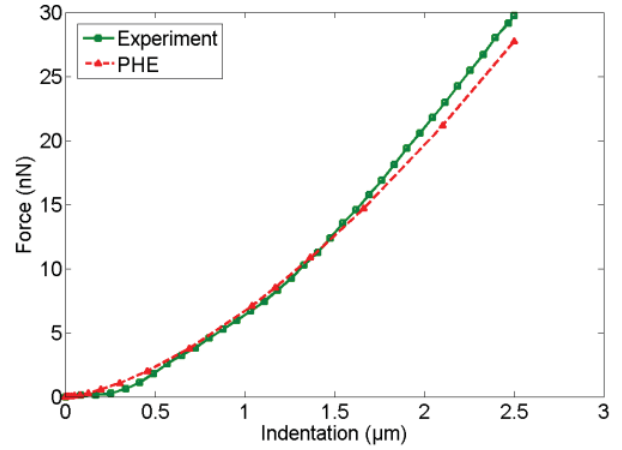


Figure 5 Force-indentation curves of AFM and FEM-PHE model with Neo-Hookean density function

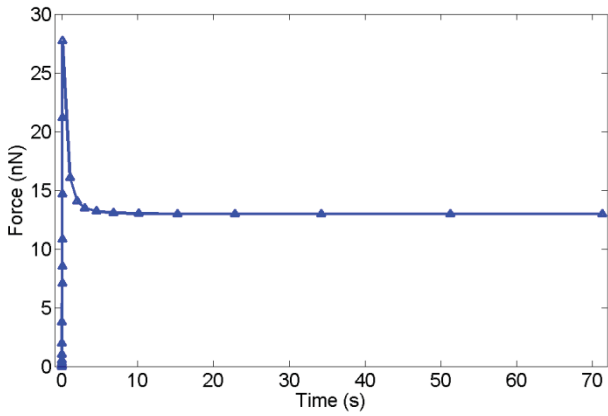


Figure 6 Relaxation behavior of chondrocyte

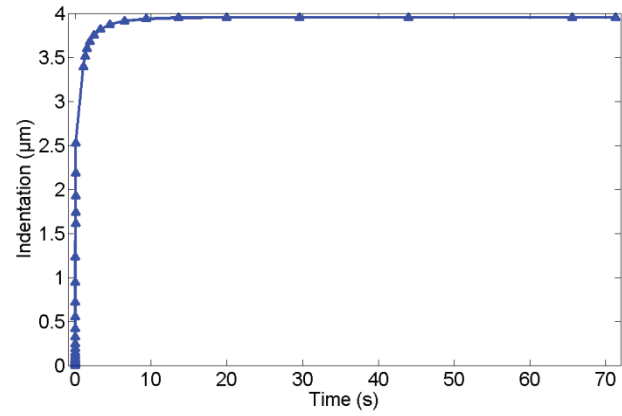


Figure 7 Creep responses of chondrocytes

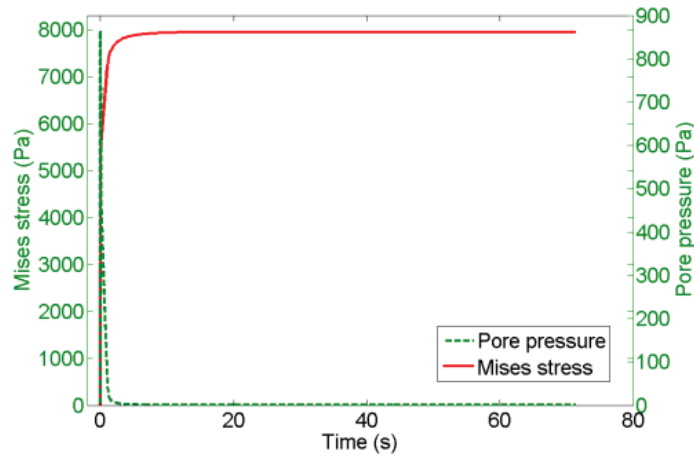


Figure 8 The von Mises or solid skeleton stress and pore pressure versus time curves

## REFERENCES

- Darling, E. M., S. Zauscher & F. Guilak (2006) Viscoelastic properties of zonal articular chondrocytes measured by atomic force microscopy. *Osteoarthritis and Cartilage*, 14, 571-579.
- Faria, E. C., N. Ma, E. Gazi, P. Gardner, M. Brown, N. W. Clarke & R. D. Snook (2008) Measurement of elastic properties of prostate cancer cells using AFM. *Analyst*, 133, 1498-1500.
- Guilak, F., G. R. Erickson & H. P. Ting-Beall (2002) The Effects of Osmotic Stress on the Viscoelastic and Physical Properties of Articular Chondrocytes. *Biophysical Journal*, 82, 720-727.
- Jones, W. R., H. P. Ting-Beall, G. M. Lee, S. S. Kelley, R. M. Hochmuth & F. Guilak. 1997. Mechanical Properties of Human Chondrocytes and Chondrons from Normal and Osteoarthritic Cartilage. In *43rd Annual Meeting, Orthopaedic Research Society*. San Francisco, California.
- Kuznetsova, T. G., M. N. Starodubtseva, N. I. Yegorenkov, S. A. Chizhik & R. I. Zhanov (2007) Atomic force microscopy probing of cell elasticity. *Micron*, 38, 824-833.
- Ladjal, H., J. L. Hanus, A. Pillarisetti, C. Keefer, A. Ferreira & J. P. Desai. 2009. Atomic Force Microscopy-Based Single-Cell Indentation: Experimentation and Finite Element Simulation. In *IEEE/RSJ International Conference on Intelligent Robots and Systems*. St. Louis, MO: Univited States.
- Lim, C. T., E. H. Zhou & S. T. Quek (2006) Mechanical models for living cells--a review. *Journal of Biomechanics*, 39, 195-216.
- Lin, D. C., E. K. Dimitriadis & F. Horkay (2007) Elasticity of rubber-like materials measured by AFM nanoindentation. *eXPRESS Polymer Letters*, 1, 576-584.
- Ofek, G., E. Dowling, R. Raphael, J. McGarry & K. Athanasiou (2010) Biomechanics of single chondrocytes under direct shear. *Biomechanics and Modeling in Mechanobiology*, 9, 153-162.
- Oloyede, A. & N. D. Broom (1991) Is classical consolidation theory applicable to articular cartilage deformation? *Clinical Biomechanics*, 6, 206-212.
- (1996) The Biomechanics of Cartilage Load-Carriage. *Connective Tissue Research*, 34, 119-143.
- Rico, F., P. Roca-Cusachs, N. Gavara, R. Farre, M. Rotger & D. Navajas (2005) Probing mechanical properties of living cells by atomic force microscopy with blunted pyramidal cantilever tips. *Physical Review*, 72, 1-10.
- Touhami, A., B. Nysten & Y. F. Dufrene (2003) Nanoscale mapping of the elasticity of microbial cells by atomic force microscopy. *Langmuir*, 19, 4539-4543.
- Trickey, W. R., G. M. Lee & F. Guilak (2000) Viscoelastic Properties of Chondrocytes from Normal and Osteoarthritic Human Cartilage. *Journal of Orthopaedic Research*, 18, 891-898.
- Wu, J. Z. & W. Herzog (2006) Analysis of the mechanical behavior of chondrocytes in unconfined compression tests for cyclic loading. *Journal of Biomechanics*, 39, 603-616.
- Yusuf, K. Q., N. Motta, Z. Pawlak & A. Oloyede (2012) A microanalytical study of the surfaces of normal, delipidized, and artificially "resurfaced" articular cartilage. *Connective Tissue Research*, 53, 236-245.
- Zhang, C. Y. & Y. W. Zhang (2007) Effects of membrane pre-stress and intrinsic viscoelasticity on nanoindentation of cells using AFM. *Philosophical Magazine*, 87, 3415-3435.

## **Fundamental study for seawall collapse simulation during Tsunami by using a particle method**

**\*Toshihiro Morimoto<sup>1</sup>, Mitsuteru Asai<sup>2</sup>, and Yoshimi Sonoda<sup>2</sup>**

<sup>1</sup>Department of Civil and Structural Engineering, Graduate School of Engineering, Kyushu University, Japan.

<sup>2</sup>Department of Civil and Structural Engineering, Kyushu University, Japan.

\*Corresponding author: asai@doc.kyushu-u.ac.jp

### **Abstract**

In 2011, Tohoku-Kanto earthquake tsunami caused serious damage on the infrastructures. Soil scour and erosion behind the seawall had occurred during the overflow, and it may become one of the main reasons for the collapse of seawall. Fluid-Structure-Soil coupling simulation is desired for a systematic comprehension of seawall collapse mechanism, and it may help to develop next disaster prevention method. In this study, a new numerical simulation tool for the Fluid-Soil interactions problem is developed as a fundamental study related to the soil scour and erosion.

SPH Method has been selected as a basic numerical simulation method for Fluid-Soil interactions. In this research, soil is modeled by a Bingham flow model which is one of the Non-Newtonian fluids, and the Mohr-Coulomb criterion is utilized in the plastic yield judgment.

Finally, efficiency and adequacy of the proposed simulation technique has been validated through an application to one of experimental test.

**Keywords:** SPH, Soil erosion, Particle Method, Tsunami

### **Introduction**

The interaction between water, soil and structures causes various problems to different areas of marine, geomechanics and hydraulic engineering. As an example of these problems, Tohoku-Kanto earthquake tsunami in 2011 is impressive incident. This tsunami hit the bridges and flowed away. On the other hand, tsunami overflowed seawalls and scoured behind the seawall. Soil scour and erosion may become one of the main reasons for the collapse of seawall.

Under these circumstances, Fluid-Structure-Soil coupling numerical simulation is desired for a systematic comprehension of multi-physics problems such as seawall collapse mechanism, and it may help to develop next disaster prevention method. There are some traditional numerical methods for deformation and failure of geomaterials in the framework of continuum mechanics, such as finite element method (FEM), finite difference method (FDM), and boundary element method (BEM). These methods have been successfully implemented. On the other hand, in the case of large deformation problems, several numerical methods have been introduced. SPH method and other Particle method have been developed for solving large deformation, crack propagation and post flow failure phenomenon of soil. In this study, focusing on the Fluid-Soil interaction, soil scouring simulation was carried out by using SPH method.

In the water-soil problem, many researchers have been proposed various soil models from different perspective. In this study, the fluid is modeled as a Newtonian fluid, and the soil model considers the granular material as a fluid with a variable viscosity, where a Bingham type constitutive model is proposed based on the Mohr-Coulomb yield-stress criterion.

Finally, efficiency and adequacy of the proposed simulation technique has been validated through an application to one of experimental test done by Yamamoto. These numerical results show a reasonable soil erosion behavior.

### Smoothed particle hydrodynamics (SPH) formulation

In this paper, smoothed particle hydrodynamics (SPH) method<sup>1),2)</sup> was adopted. A basic concept in SPH method is that any function  $\phi$  attached to particle “ $i$ ” at a position  $r_i$  is written as a summation of contributions from neighbor particles

$$\phi(r_i) \approx \langle \phi_i \rangle = \sum_j \frac{m_j}{\rho_j} \phi_j W(r_{ij}, h) \quad (1)$$

Note that, the triangle bracket  $\langle \phi_i \rangle$  means SPH approximation of a function  $\phi$ . The divergence of a vector function can be assumed by using the above defined SPH approximation as follows

$$\nabla \cdot \bar{\phi}(r_i) \approx \langle \nabla \cdot \bar{\phi}_i \rangle = \frac{1}{\rho_i} \sum_j m_j (\bar{\phi}_j - \bar{\phi}) \cdot \nabla W(r_{ij}, h) \quad (2)$$

and the expression for the gradient can be represented by

$$\nabla \phi(r_i) \approx \langle \nabla \phi_i \rangle = \rho_i \sum_j m_j \left( \frac{\phi_j}{\rho_j^2} + \frac{\phi_i}{\rho_i^2} \right) \nabla W(r_{ij}, h) \quad (3)$$

In this study, Incompressible SPH (ISPH) method<sup>3)</sup> developed in the incompressible fluid analysis was adopted. In this method, the pressure is calculated implicitly and the velocity is calculated explicitly.

### The Governing equation

In natural phenomenon, there is regularity and it is organized as continuum mechanics or discontinuity mechanics. Here, fluid and soil are written as the following equation by using Lagrange description.

$$\frac{D\mathbf{v}}{Dt} = \frac{1}{\rho} \nabla \cdot \boldsymbol{\sigma} + \mathbf{g} \quad (4)$$

In the case of solid mechanics, total stress tensor  $\boldsymbol{\sigma}$  is evaluated following equation.

$$\sigma_{ij} = D_{ijkl} \varepsilon_{kl} \quad (5)$$

On the other hand, in the case of viscous fluid, total stress tensor  $\boldsymbol{\sigma}$  is evaluated following equation.

$$\sigma_{ij} = -p\delta_{ij} + \tau_{ij} \quad (6)$$

Here,  $\tau_{ij}$  is shear stress tensor. In the continuum mechanics, the difference between solid and fluid is only way to evaluate the total stress tensor.

#### Modeling of fluid

Fluid is generally modeled as Newtonian fluid. This fluid has a feature that shear stress and strain rate are linear relationship, and described below equation.

$$\tau_{ij} = \mu^* \left( \frac{\partial u_i}{\partial x_j} + \frac{\partial u_j}{\partial x_i} \right) \quad (7)$$



Where,  $\mu^*$  is the effective dynamic viscosity and composed from a viscosity  $\mu$  and an eddy viscosity  $\mu_T$  as.

$$\mu^* = \mu + \mu_T \quad (8)$$

Substituting Eq.(6) and Eq.(7) to Eq.(4), Navier-Stokes equation can be derived.

$$\frac{D\mathbf{v}}{Dt} = -\frac{1}{\rho}\nabla P + \nabla^2\mathbf{u} + \mathbf{g} \quad (9)$$

In addition to the above equation, law of conservation of mass equation was also used as governing equation.

$$\frac{D\rho}{Dt} + \rho\nabla \cdot \mathbf{v} = 0 \quad (10)$$

### Modeling of soil

At the field of soil mechanics, behavior of various type of soil is very complicated and its organized constitutive law is difficult to be derived. In the present circumstances, it is modeled in accordance with each types and phenomenon. In general, soil is modeled as solid and nonlinear elastic-plastic material. However, in this study, soil was modeled as Bingham fluid<sup>4),5)</sup> which is one of Non-Newtonian fluid because of expressing flow failure of ground. Bingham fluid has shear strength and can be written as following equation

$$\boldsymbol{\tau} = \mu_s^0 \dot{\boldsymbol{\gamma}} + \boldsymbol{\tau}_y \quad (11)$$

Here,  $\tau_y$  is yield shear stress and  $\mu_s^0$  is viscosity after yield. Note, a Bingham fluid has behavior such as a rigid body and dose not deform but when the shear stress surpasses the yield stress, flow failure occurs resulting in large deformations. The Mohr-Coulomb criterion is introduced for the yield shear strength in the Bingham model for a given soil as

$$\tau_y = c + P \tan \varphi \quad (12)$$

Where,  $c$  is the cohesion, and  $\varphi$  is the internal friction angle. Then, the soil viscosity should be expressed in Bingham model<sup>6)</sup> as

$$\mu_s = \frac{\boldsymbol{\tau}}{\dot{\boldsymbol{\gamma}}} = \begin{cases} \frac{c + p \tan \varphi}{\dot{\boldsymbol{\gamma}}} (= \mu_E) & \dot{\boldsymbol{\gamma}} \leq \dot{\boldsymbol{\gamma}}_y \\ \mu_s^0 (= \mu_P) + \frac{c + p \tan \varphi}{\dot{\boldsymbol{\gamma}}} & \dot{\boldsymbol{\gamma}} > \dot{\boldsymbol{\gamma}}_y \end{cases} \quad (13)$$

Here, drawing the graph of above Eq.(12), relationship  $\boldsymbol{\tau}$  and  $\dot{\boldsymbol{\gamma}}$  is expressed as

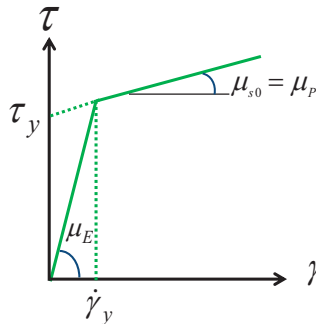
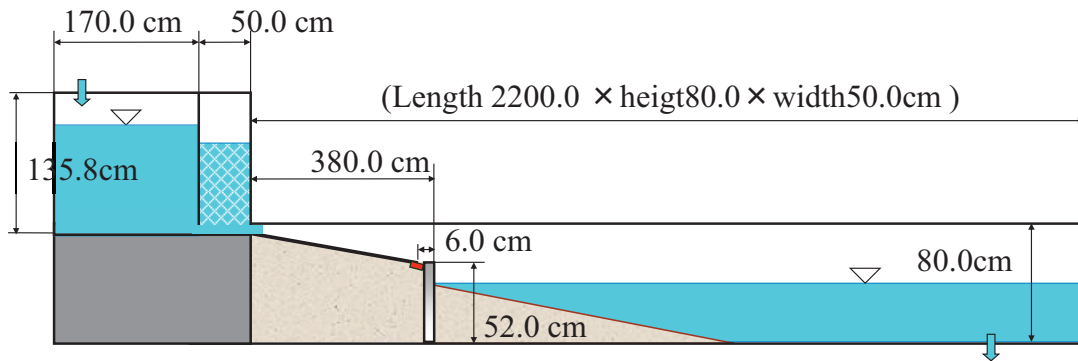


Figure1. Relationship  $\boldsymbol{\tau}$  and  $\dot{\boldsymbol{\gamma}}$

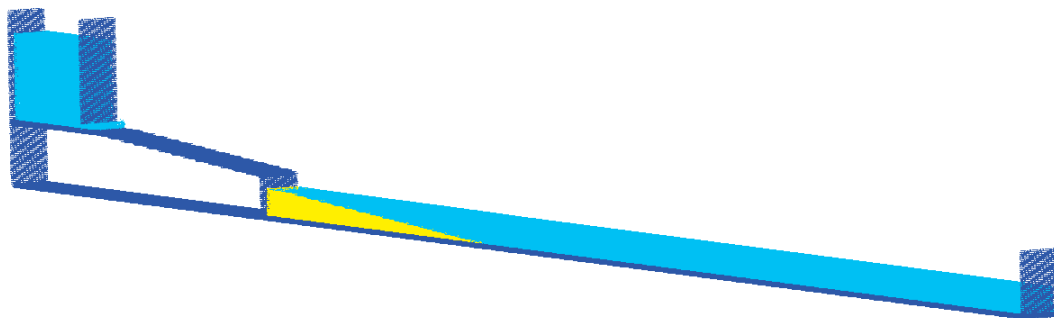
**Numerical validation test**

In the following section, the numerical examples have been conducted to validate the current scheme. The hydraulic experiment<sup>7)</sup> done by Yamamoto was adopted. Fig.2. presents the schematic diagram for the experiment. This experiment is return flow scouring experiment and its scale is showing below. As for soil parameters, the density ratio between soil density  $\rho_s$  and water density  $\rho_w$  is taken as  $\rho_s / \rho_w = 1.6$ . The soil viscosity after yield is set to  $\mu_s^0 = 5\text{Pa}\cdot\text{s}$ . The internal angle and cohesion are taken as  $\varphi = 3^\circ$  and  $c = 30\text{kPa}$ .



**Figure2. Initial schematic diagram for hydraulic experiment**

Here, gradient of sandy beach and slope is one-fifteenth, and there is a seawall at the front of sandy beach. There is a velocity meter away from the seawall by 6cm. Arrows in left side and right side are respectively water supply pipe and drainage pipe, and tank in right hand side is rectification tank. From above diagram, making a particle model as

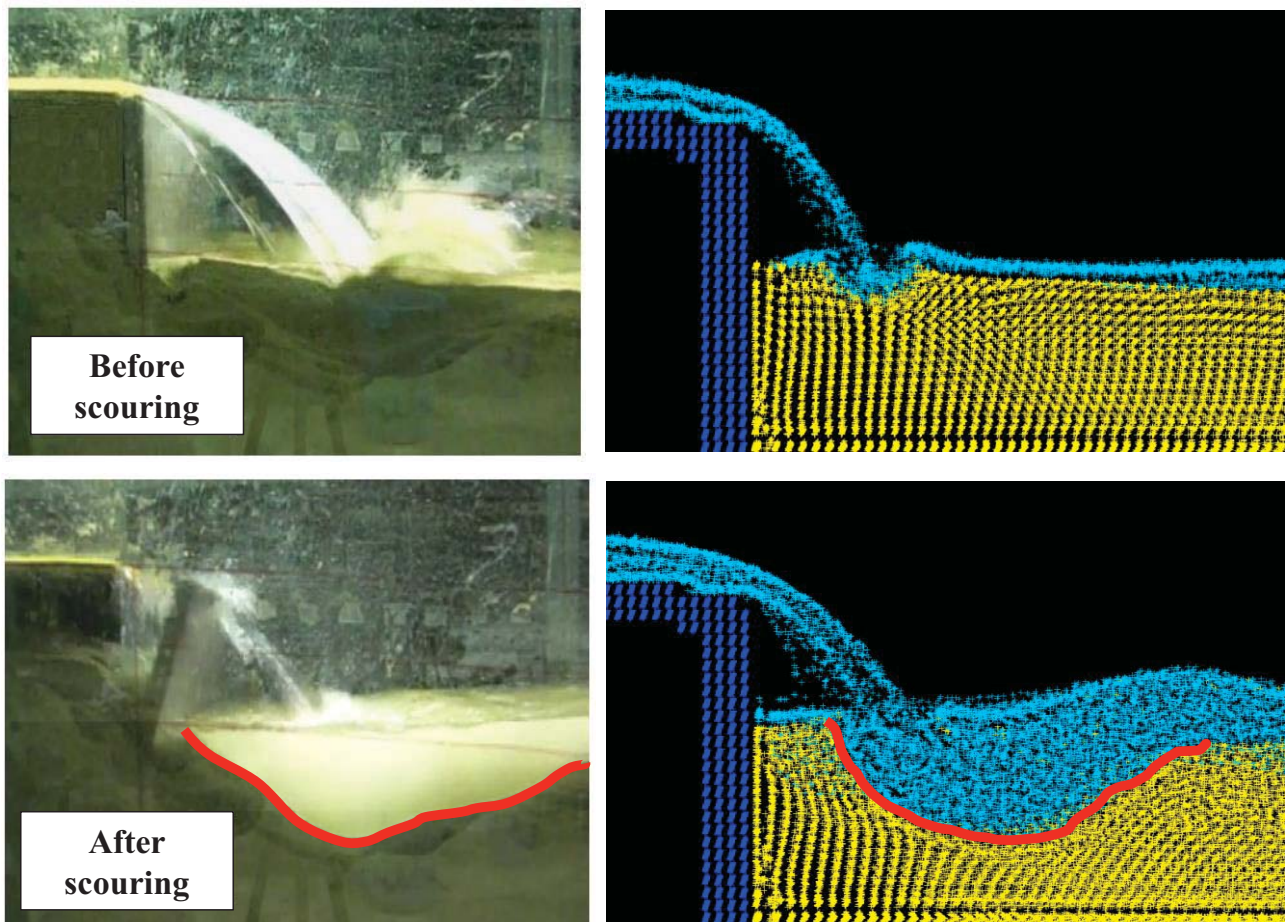


**Figure3. Complete view of the particle model**

**Table1. Analysis option**

Initial particle distance	Total particles	Time step	Real time	Analysis time
2cm	1371475	0.001s	25s	24h(16odes×16cores)

Table1 shows the analysis parameters. This numerical experiment was carried out by using super computer in Kyushu University, Fujitsu PRIMERGY CX400. Under these conditions, numerical experiment was carried out. It is shown that analysis result on the next page.



**Figure4. Comparison between experiment and analysis result**

Fig.4. shows the analysis result compared to experimental result. Left hand side pictures are before and after scouring snap shot of hydraulic experiment and right hand side pictures are those of numerical experiment. In the right hand side pictures, the soil particles are transported by the flow. From these pictures, the predicted express soil erosion and scouring behaviors shows a good agreement with the hydraulic experiment test. However, the shape of soil erosion is slightly different. As for the reason, various factors are taken into account. One of them is not considering permeability of soil.

### **Conclusions**

In this study, an improved ISPH algorithm has been used to simulate water and soil interactions. All of them are modeled by SPH method. The fluid is modeled as a Newtonian fluid, and the soil is modeled as a Bingham model. In this approach, the soil model considers the granular materials as a fluid, where a Bingham type constitutive model is proposed based on Mohr-Coulomb yield-stress criterion, and the viscosity is derived from the cohesion and friction angle. And in order to validate above scheme and modeling, numerical experiment was carried out. Through this experiment, it was confirmed that ISPH method and modeling soil as a Bingham flow can express soil erosion and scouring. However, its analysis result is good from qualitative perspective, but not so good from quantitative one.

Finally, as a future work, obtaining validated result from quantitative perspective is our goal, in order to achieve this goal, considering permeability of soil is important.

## Acknowledgements

This work is partially supported by JSPS Grant-in-Aid for Young Scientists (B); Grant Number 24760365.

## References

- [1] S.J. Cummins and M. Rudman(1999), An SPH projection method, *Journal Computational Physics*, Vol.152(2), pp.584-607.
- [2] E. S. Lee, C. Moulinec, R. Xu, D. Violeau, D. Laurence and P. Stansby(2008), Comparisons of weakly compressible and truly incompressible algorithms for the SPH mesh free particle method, *Journal of Computational Physics*, Vol.227(18), pp.8417-8436.
- [3] A. Khayyer, H. Gotoh and S. Shao(2008), Corrected incompressible SPH method for accurate water-surface tracking in breaking waves, *Coastal Engineering*, Vol.55,pp. 236-250.
- [4] S. Shao, E.Y.M. Lo(2003), Incompressible SPH method for simulating Newtonian and non-Newtonian flows with a free surface, *Advances in Water Resources*, Vol.26, pp.787-800.
- [5] X.Y. Hu and N.A. Adams(2007), An incompressible multi-phase SPH method, *Journal of Computational Physics*, Vol.227, pp. 264-278.
- [6] Christian Ulrich and Thomas Rung.( 2010), Multiphysics SPH for harbor and ocean engineering hydrodynamics., V European Conference on Computational Fluid Dynamics ECCOMAS CFD 2010.
- [7] Yoshimichi Yamamoto, Nunthawath CHARUSROJTHANADECH, Kenji NARIYOSHI(2011), Proposal of rational evaluation methods of structure damage by tsunami, *Journal of Japan Society of Civil Engineers, Ser. B2(Coastal Engineering)*, Vol. 67, No.1 P72-91

## Subjective Evaluation of Crash Behavior of Muscle at Subsonic Level for Simulation of Bird Strike

\* Naoki Torii <sup>1</sup>, Atsushi Sakuma <sup>2</sup>, and Hirokazu Shoji <sup>3</sup>

<sup>1</sup> Graduate School of Engineering, Tokyo University of Agriculture and Technology,  
2-24-16 Naka-cho, Koganei-shi, Tokyo 184-8588, Japan

<sup>2</sup> Institute of Technology, Tokyo University of Agriculture and Technology,  
2-24-16 Naka-cho, Koganei-shi, Tokyo 184-8588, Japan

<sup>3</sup> Japan Aerospace Exploration Agency (JAXA),  
6-13-1 Osawa, Mitaka-shi, Tokyo 181-0015, Japan

\*Corresponding author: asakuma@cc.tuat.ac.jp

### Abstract

Because any impact test method for materials at the subsonic level has not been developed so far, numerical simulations of crash problems at this level have been inaccurate. This inaccuracy causes serious problems, especially in the analysis of bird collisions with airplanes. Therefore, a shock impact test system using an airsoft gun is developed to evaluate material behavior at the subsonic level that will support technological design of anti-bird-strike structures of airplanes. The viscoelastic characteristics of specimens are evaluated by analyzing the stress response using the extended Hertzian contact theory and wave equation at the moment when a simple ball bullet is shot at the specimen using the airsoft gun. In the experimental results of the test, an obvious relationship between quasi-static and impact responses of the specimen is observed subjectively. The evaluated viscoelastic relationship is applied to simulate the impact test by using LS-DYNA with the fundamental viscoelastic constitutive equation and the material parameters derived from the impact test, and the simulation of the crash is completed using the identified parameters.

**Keywords:** Bird Strike, Airplane, Viscoelastic, Biomechanics, Dynamic Stress, SPH Method

### Introduction

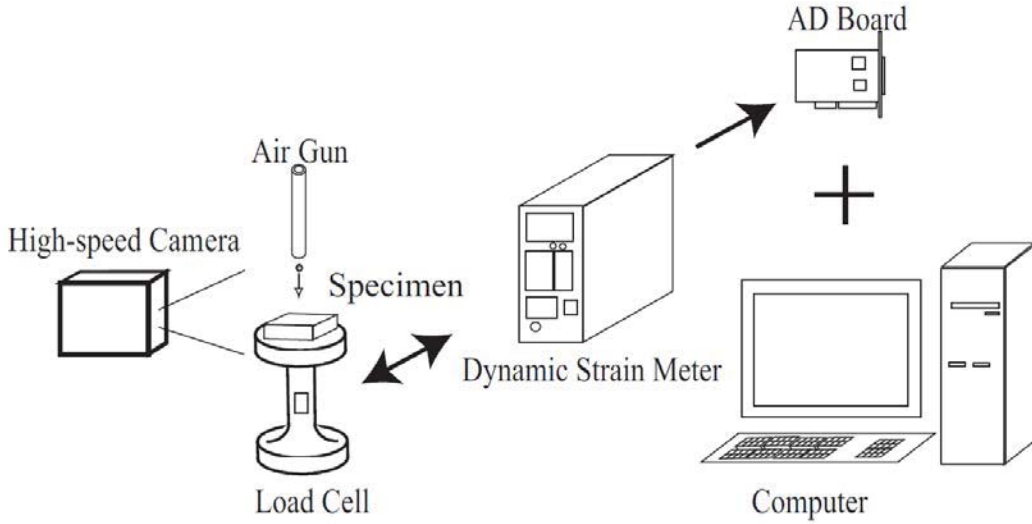
While the number of aviation accidents caused by bird strikes increases each year [1], aircraft miniaturization and lightening are being advanced to improve economic efficiency; consequently, safety design technology for airplanes becomes difficult to develop. Therefore, a shock impact test system using an airsoft gun is developed in this study to evaluate the design technology of anti-bird-strike structures of airplanes. A simple ball bullet is shot at the test specimen using an airsoft gun and the stress response in the load cell of the test system is evaluated by the extended Hertzian contact theory and the wave equation, which are used to analyze the viscoelastic characteristics of the specimen. In the experimental results, an obvious relationship between quasi-static and impact responses of the specimen is observed subjectively, and the hardening effect caused by the impact is clearly observed in the results of muscles of chicken. The evaluated viscoelastic relationship is applied to simulate the impact test by using LS-DYNA with the fundamental viscoelastic constitutive equation and the material parameters derived from the impact test, and a phantom imitating a real bird will be developed as a standard specimen for an anti-bird-strike test using the shock impact test system.

### Experimental System

#### *Shock Impact Test by Ball Collision*

To evaluate the deformation behavior of materials at the subsonic level, an impact system using a ball bullet is adopted for the development of an impact test using an airsoft gun. The bullet used is the product made of polystyrene resin containing lime. The system developed is shown in Figure 1

with other measurement instruments used in the evaluation. The airsoft gun used in this system is an airsoft gun (toy gun) made by Tokyo Marui Co., Ltd., Japan. The M14 model of the airsoft gun is adopted because it has the capability to shoot a ball bullet at almost 100 m/s. The shot bullet collides with the specimen on a load cell vertically, causing stress waves in the cell. Furthermore, the wave in load cell is measured using a strain gauge pasted onto the side of the cell and logged through the dynamic strain meter CDV-700A (Kyowa Electronic Instruments Co., Ltd.) and the AD board LPC-320724 (sample frequency: 1.556 MHz; Interface Corp.) using a MS-Windows PC. The collision is also observed with a high-speed camera.



**Figure 1. System of impact test**

*Evaluation Procedure for Deformation Characteristics of Materials*

The famous Hertzian contact stress theory [2] is extended to evaluate the collision behavior of the impact test system. The fundamental form of the theory can be written in the following form as the relationship between contact force  $F$  and indentation depth  $\delta$  for the contact problem of a rigid ball and elastic body with a planar surface:

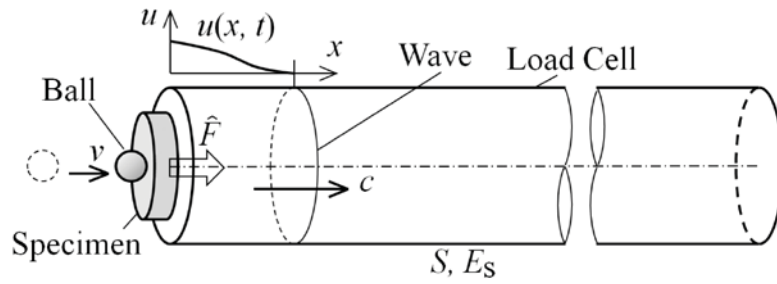
$$F = \frac{4}{3} \frac{E}{1 - \nu^2} \left( \frac{\phi}{2} \right)^{\frac{1}{2}} \delta^{\frac{3}{2}} = A\delta^{\frac{3}{2}} \quad (1)$$

Here, variables  $E$ ,  $\nu$ , and  $\phi$  indicate Young's modulus, Poisson's ratio, and the diameter of the ball indenter, respectively.

Equation (1) is the theoretical solution for a semi-infinite elastic body, but the specimen on the load cell in Figure 1 should have a finite body because of the measurement of the stress wave in the load cell. The extended relationship [3]-[4] of the Hertzian contact stress theory is then adopted to analyze the contact problem of the finite elastic body. The extended Hertzian contact stress theory has the following form with thickness coefficient  $B$ :

$$\hat{F} = \frac{4}{3} \frac{E}{1 - \nu^2} \left( \frac{\phi}{2} \right)^{\frac{1}{2}} \{ \delta(1 + B\delta) \}^{\frac{3}{2}} = A\{(1 + B\delta)\delta\}^{\frac{3}{2}} \quad (2)$$

As for the ball collision problem illustrated in Figure 2, the contact force  $\hat{F}$  at the specimen on the load cell causes a stress wave to propagate through the cell to the bottom. The propagation can be represented by wave equation (3) with constant  $c$  as a function of time  $t$  and position  $x$  as follows:



**Figure 2. Wave analysis model of ball impact on specimen at the bar end of load cell**

$$\frac{\partial^2 u}{\partial t^2} = c^2 \frac{\partial^2 u}{\partial x^2} \quad (3)$$

By using equation (2) as a boundary condition for the wave equation (3), the solution  $u(x, t)$  can be derived with constants  $a$ ,  $b$ , and  $c$  as follows:

$$\begin{aligned} u(x, t) = & a \{ 3 \log \{ \sqrt{1 + b(ct - x)} + \sqrt{b(ct - x)} \} \\ & + \sqrt{b(ct - x)} \{ 1 + b(ct - x) \} \\ & \{ 16b^3(ct - x)^3 + 24b^2(ct - x)^2 + 2b(ct - x) - 3 \} \} \end{aligned} \quad (4)$$

Equation (4) can be used to analyze the wave profile in the cell for the mechanical evaluation of the specimen on the cell. Then, coefficients  $A$  and  $B$  can be derived with the following relationship using  $a$ ,  $b$ , and  $c$ , which were identified by using the above procedure.

$$A = - \frac{64ab^{\frac{5}{2}}c^{\frac{3}{2}}E_s S}{v^{\frac{3}{2}}} \quad (6)$$

$$B = \frac{bc}{v} \quad (7)$$

Here, variables  $E_s$  and  $S$  indicate Young's modulus and the section area of the load cell, respectively.

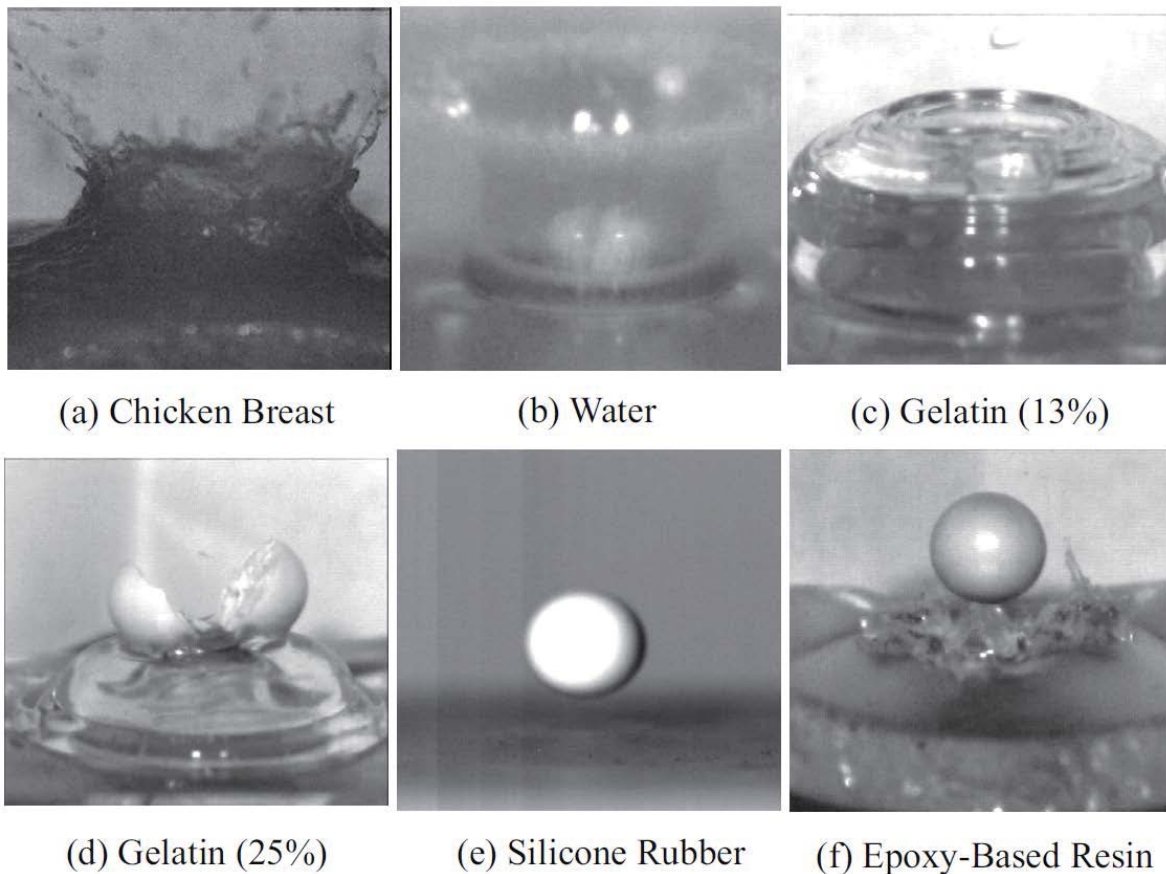
From coefficient  $A$ , Young's modulus  $E$  is derived by using equation (1). However, the effect of viscosity is included in the deformation behavior that is observed in the shock impact test. Coefficient  $D$  is then used to represent the deformation behavior of the specimen in this paper. Coefficient  $D$  is defined as follows by Hooke's law with the consideration of the viscous effect, and is referred to as the deformation-resistant modulus in this paper:

$$D = \frac{3}{4} A (1 - \nu^2) \left( \frac{\phi}{2} \right)^{-\frac{1}{2}} \quad (5)$$

## Experimental Results and Numerical Simulation

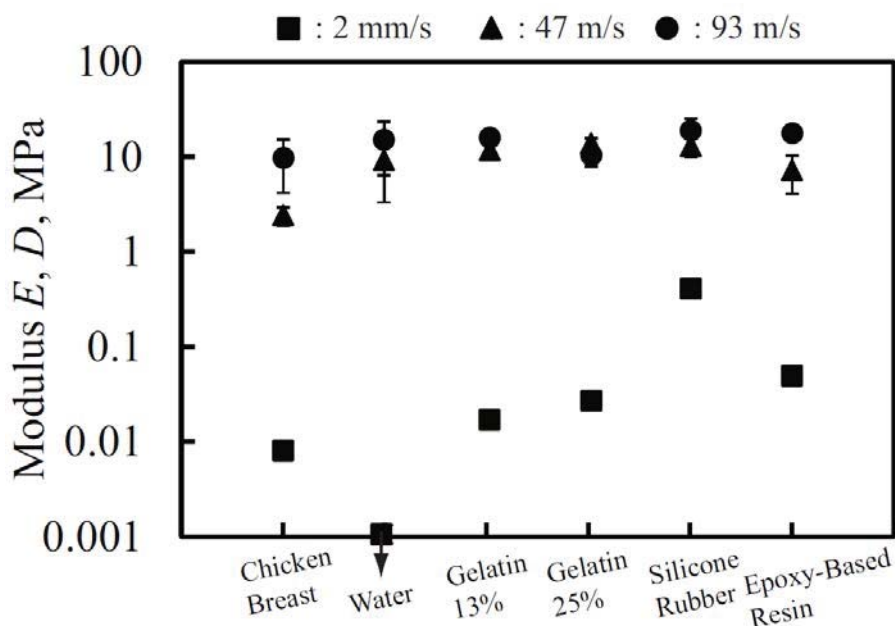
### Experimental Result

In Figure 3, the experimental results measured by the system shown in Figure 1 are shown as examples of ball collisions. Here, six materials are shown: chicken breast, water, 13% gelatin, 25% gelatin, silicone rubber, and epoxy-based resin. The impact crown at the moment of the collision is shown for each material, but their shapes are different, indicating that the deformation characteristics of the materials are also different.



**Figure 3. Moment of ball collision**

These experimental results are evaluated by Young's modulus  $E$  and  $D$  shown in Figure 4. Here, Young's modulus  $E$  is measured using a fundamental material indentation tester SoftMeasure HS-3001 (Horiuchi Electronics Co., Ltd.) [5] for all materials except water. Young's modulus of water, which is a liquid, could not be measured because of its characteristic lack of elasticity. In these results, it is shown that every material becomes hard at the subsonic level.



**Figure 4. Effect of deformation velocity**

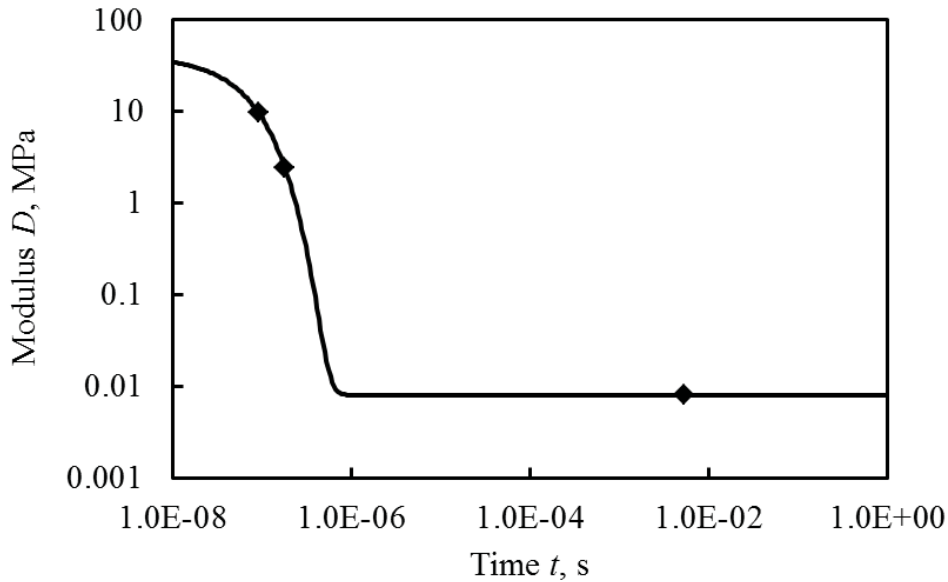


### Numerical Simulation

The differences observed in each material are analyzed by the relationship shown in the following section. The analyzed result is applied to deformation analysis using LS-DYNA (Livermore Software Technology Corp.), which uses the evaluated results of the materials. In this analysis, the constitutive equation of Hermann and Peterson [6] is adopted to represent the viscous effect of the materials. The equation defines shear elasticity  $G(t)$  in terms of the relationship among short-run shear elasticity  $G_0$ , long-run shear elasticity  $G_\infty$ , and coefficient  $\beta$  (equation (6)). Furthermore, normal elasticity  $D(t)$  is defined for applying equation (5) in terms of short-run normal elasticity  $D_0$  and long-run normal elasticity  $D_\infty$  in this paper:

$$G(t) = G_\infty + (G_0 - G_\infty) e^{-\beta t} \quad (6)$$

$$D(t) = D_\infty + (D_0 - D_\infty) e^{-\beta t} \quad (7)$$

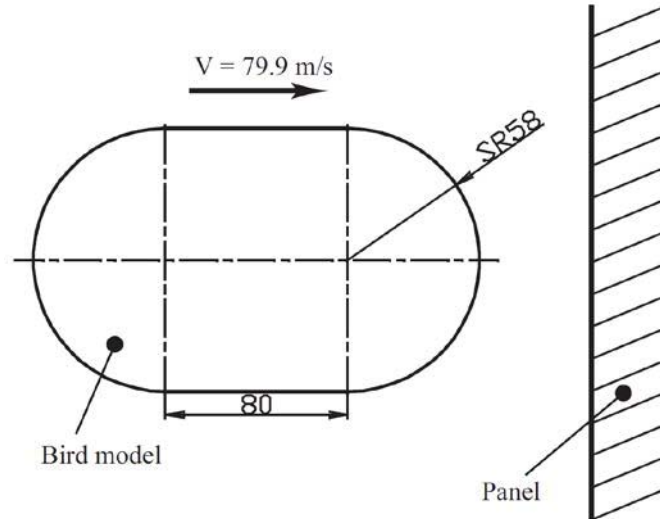


**Figure 5. Identified viscoelastic property**

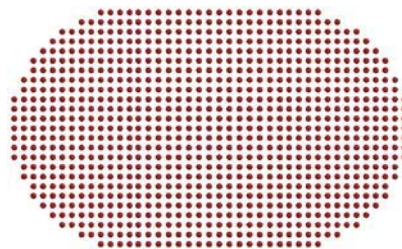
If the experimental result shown in Figure 4 is used, the relationship between the equations of Hermann and Peterson in the form of equation (7) can be defined as shown by the example in Fig. 5. The relationship defined in this manner can be applied to various simulations by using LS-DYNA. As an application of the defined relationship, a simulated collision imitating a bird strike is shown in Figure 6. This simulated result is calculated by the SPH method. In this simulated result, the situation representing the deformation of the viscoelastic body, which imitated a real bird finely deformed by the collision, is captured well. Thus, it is possible to analyze various problems related to bird collisions using the simulation procedure shown here.

**Table 1. Material properties of bird-strike model**

$G_0$ [MPa]	$G_\infty$ [MPa]	$\beta$
$1.34 \times 10$	$2.67 \times 10^{-3}$	$1.58 \times 10^7$

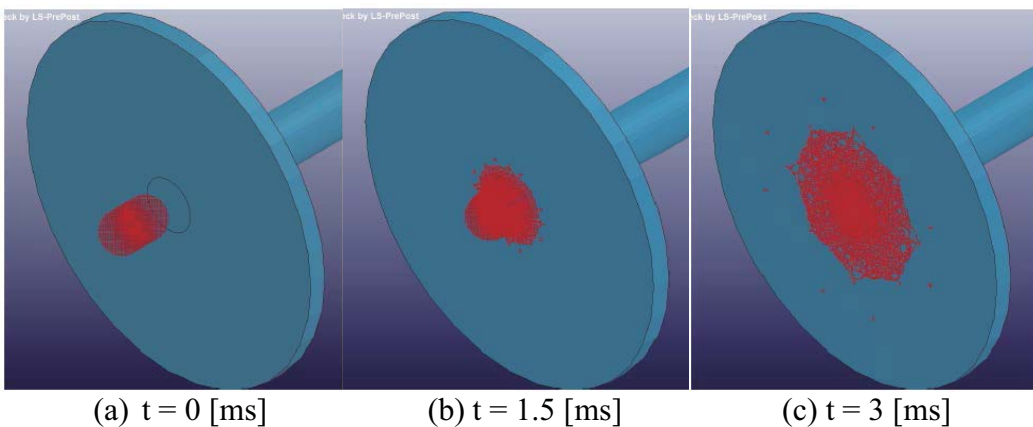


(a) Schematic showing bird-strike model for flat panel impact



(b) SPH bird model with 16041 particles

**Figure 6. Numerical model of bird strike**



(a)  $t = 0$  [ms]      (b)  $t = 1.5$  [ms]      (c)  $t = 3$  [ms]

**Figure 7. Simulated bird strike ( $M = 1.81$  kg,  $V = 79.9$  m/s)**

**Conclusion**

The ball collision impact test system introduced in this paper can be used to quantitatively evaluate material deformation at the subsonic level. Dynamic evaluation of the impact of bird strike on the airplane can be realized in more detail by numerical analysis using the results presented this paper. Many problems related to bird strike will be analyzed by using this method in the future.

## Acknowledgement

This research was supported by General Invitation Joint Research of Japan Aerospace Exploration Agency (JAXA).

## References

- [1] FAA-USDA report, Wildlife Strikes to Civil Aircraft in USA, 1990-2011, *Report of the Associate Administrator of Airports Office of Airports Safety and Standards, Airport Safety and Certification*, (2012), 6:8-13.
- [2] Hertz, H., Ueber die Berührung fester elastischer Körper, *Journal für die reine und angewandte Mathematik (Crelle's Journal)*, (1882), 92: 156-171.
- [3] Tani, M. Sakuma, A. and Shinomiya, M., Evaluation of Thickness and Young's Modulus of Soft Materials by using Spherical Indentation Testing, *Transactions of the Japan Society of Mechanical Engineers, Series A*, (2009), 75-755:901-908 (in Japanese).
- [4] Tani, M. and Sakuma, A., Applicability Evaluation of Young's Modulus Measurement using Equivalent Indentation Strain in spherical Indentation Testing for Soft Materials, *Transactions of the Japan Society of Mechanical Engineers, Series A*, (2010), 76-761:102-108 (in Japanese).
- [5] Sakuma, A., Desktop Robot to Measure the Elasticity of Any Objects by Palpation Mechanics, *Journal of the Japan Society of Mechanical Engineers*, (2013), 116-1134:355 (in Japanese).
- [6] Gladman, B., *LS-DYNA® Keyword User's Manual (Version 971) - Volumes II*, (2013), 2-61.

## Random vibration analysis of structures with uncertain-but-bounded parameters

**\*Duy Minh Do<sup>1</sup>, Wei Gao<sup>1</sup>, and Chongmin Song<sup>1</sup>**

<sup>1</sup>School of Civil and Environment Engineering, The University of New South Wales, Sydney, NSW  
2052, Australia

\*Corresponding author: duy.m.do@student.unsw.edu.au

### Abstract

Random vibration response of structures with uncertain-but-bounded parameters under random process excitation is investigated in this paper. The interval natural frequencies, interval mean square displacements and stresses are analysed under the framework formed by the theories of structural dynamics and interval analysis. The lower and upper bounds of structural dynamic characteristics and random responses are determined by solving optimization problems. An improved particle swarm optimization algorithm, namely lower sequence initialized high-order nonlinear particle swarm optimization algorithm, is adopted to find their exact change ranges. Three numerical examples are provided to demonstrate the feasibility of the presented method. Quasi-Monte Carlo and Monte Carlo methods are also used to assess the effectiveness of the method.

**Keywords:** Interval analysis, random excitation, random vibration response, improved particle swarm optimization algorithm.

### Introduction

Dynamic behavior of structures with uncertainty has been increasingly investigated as structural systems do have uncertainties in loads, geometric and material properties. The traditional technique to address these uncertainties is the probability theory. However, this technique is not available for most cases as there is not enough information to model probabilistic features. This situation requires other models of uncertainty which can be accessible for incomplete data. Taken interval analysis (Moore, 1966) into account, it can be employed to describe imprecision with known lower and upper bounds of altered features. The representation of interval analysis in structural engineering, first, was introduced to consider uncertainty in statics problems (Köylüoğlu et al., 1995). Many studies regarding interval analysis for static and dynamic problems of structures was developed by some authors (Moens and Vandepitte, 2001; Muhanna and Mullen, 2001; Qiu et al., 2005; Gao, 2007). The task of interval analysis is to achieve enclosures of system outputs which can be converted to optimization problems. Although there are various algorithms for treatment of optimization problems, PSO presented by Kennedy and Eberhart (1995) is more effective with fewer number of iteration to target the same or better results in comparison with others algorithms. (Hu et al., 2003; Elbeltagi et al., 2005). The effective application of PSO into different engineering problems including structural optimization has been recently shown and developed in the work of some authors. The improvement of PSO by means of using randomized low discrepancy sequences for initialized particles has been recently considered. Liu et al., (2013) employed the

low-discrepancy sequences initialized high-order nonlinear particle swarm optimization algorithm (LHNPSO) for interval analysis of vehicle-bridge interaction system with simple model of structure. Meanwhile, there are still potential problems such as investigation of this method with multi-dimension particles for complex structures. In this paper, random vibration response of structures with uncertain-but-bounded parameters under random process excitation of space truss is studied with adoption of LHNPSO. This paper is organized as follows. The next section provides a brief introduction of interval dynamic analysis. Then, application of LHNPSO for interval analysis and the numerical example are presented in following sections. Conclusions are stated in the last section.

### Interval dynamic analysis of structures under random process excitation

An interval variable  $\mathbf{x}^I$  can also be denoted in as the following (Moore, 1966):

$$\mathbf{x}^I = [\underline{\mathbf{x}}, \bar{\mathbf{x}}] = \mathbf{x}^c + \Delta\mathbf{x}^I \quad (1)$$

where  $\mathbf{x}^c = (\underline{\mathbf{x}} + \bar{\mathbf{x}}) / 2$  and  $\Delta\mathbf{x}^I = [-\Delta\mathbf{x}, +\Delta\mathbf{x}]$

Interval analysis is considered as design variables of structures are modeled as uncertainty- but-bounded values. Thus, structural parameters and responses are also interval values. The dynamic equation of structures under stationary process excitation can be expressed as the following:

$$\mathbf{M}^I \ddot{\mathbf{u}}^I(t) + \mathbf{C}^I \dot{\mathbf{u}}^I(t) + \mathbf{K}^I \mathbf{u}^I(t) = -\mathbf{M}^I \{\mathbf{1}\} \ddot{a}(t) \quad (2)$$

where  $\mathbf{M}^I$ ,  $\mathbf{C}^I$  and  $\mathbf{K}^I$  are the interval matrices with respect to mass, damping and stiffness of structures respectively.  $\mathbf{u}^I(t)$ ,  $\dot{\mathbf{u}}^I(t)$  and  $\ddot{\mathbf{u}}^I(t)$  are interval vectors defining structural displacement, velocity and acceleration in that order.  $\{\mathbf{1}\}$  is a column vector with all components 1 and  $\ddot{a}(t)$  is the random ground acceleration. By employing Rayleigh's quotient in the form of modal analysis with normalization of modes and spectral matrices, frequency equation is expressed as:

$$\mathbf{W} = \text{diag}\left(\left(\omega^I\right)^2\right) = \left(\boldsymbol{\varphi}^I\right)^T \mathbf{K}^I \boldsymbol{\varphi}^I \quad (3)$$

where  $\mathbf{W}$ ,  $\boldsymbol{\varphi}^I$  and  $\mathbf{K}^I$  are the interval matrices of natural frequencies, normalized-natural modes and global matrices of stiffness.

The solution of coupled equations presented by Eq. (2) can be achieved by using Duhamel integral:

$$\mathbf{u}^I(t) = \int_0^t \boldsymbol{\varphi}^I \mathbf{h}^I(t-\tau) \left(\boldsymbol{\varphi}^I\right)^T \mathbf{M}^I \{\mathbf{1}\} \ddot{a}(\tau) d\tau \quad (4)$$

In this case,  $\tau$  is assigned as 0. The interval matrix of response function is defined as:

$$\mathbf{h}^I(t) = \text{diag}(h_j^I(t))$$

$$h_j^I(t) = \begin{cases} \frac{1}{\omega_{jD}^I} \exp(-\xi_j \omega_{jD}^I t) \sin \omega_{jD}^I t & t \geq 0 \\ 0 & t < 0 \end{cases} \quad (5)$$

By performing a Fourier transformation for the correlation function matrix and integrating Eq. (4) step by step, the mean square value matrix of the structural displacement  $(\psi_u^I(t))^2$  can be obtained as (Gao and Kessissoglou, 2007):

$$(\psi_u^I(t))^2 = \int_0^\infty \boldsymbol{\phi}^I \mathbf{H}^I(\omega) (\boldsymbol{\phi}^I)^T \mathbf{M}^I \{\mathbf{1}\} \{\mathbf{1}\}^T (\mathbf{M}^I)^T \mathbf{S}_p(\omega) \boldsymbol{\phi}^I \mathbf{H}_*^I(\omega) (\boldsymbol{\phi}^I)^T d\omega \quad (6)$$

where  $\mathbf{S}_p(\omega) = \text{diag}(S_{pi}(\omega))$  is the equivalent one-side power spectral density matrix of  $\ddot{\mathbf{a}}(t)$ . In this paper, model of Kanai-Tajimi designated by (Lin and Yong, 1987) is employed to define random ground level accelerations as:

$$S_{pi}(\omega) = \frac{(1 + 4(\xi_g \omega / \omega_g)^2) S_0}{(1 - \omega^2 / \omega_g^2)^2 + 4(\xi_g \omega / \omega_g)^2} \quad (7)$$

The modal damping in this paper is given by  $\xi_j = 0.01 (j = 1, 2, \dots, n)$ . Parameters for the equivalent one-side power spectral density are defined as the following:  $\omega_g = 16.5 \text{ (rad/s)}$ ,  $\xi_g = 0.7$ ,  $S_0 = 15.6 \text{ (cm}^2 / \text{s}^3)$ .

$\mathbf{H}^I(\omega)$  is the interval matrix with respect to the frequency response function matrix of the structures expressed as:

$$\mathbf{H}^I(\omega) = \text{diag}(H_j^I(\omega))$$

$$H_j^I(\omega) = \frac{1}{(\omega_j^I)^2 - \omega^2 + i2\xi_j \omega_j^I \omega}, \quad j = 1, 2, \dots, n \quad (8)$$

where  $i = \sqrt{-1}$  is the complex number.  $\mathbf{H}_*^I(\omega)$  is interval matrix termed as complex conjugate matrix of  $\mathbf{H}^I(\omega)$ .

The mean square value of the kth degree of freedom of structural displacement:

$$(\psi_{uk}^I(t))^2 = \int_0^\infty \boldsymbol{\phi}_k^{-I} \mathbf{H}^I(\omega) (\boldsymbol{\phi}^I)^T \mathbf{M}^I \{\mathbf{1}\} \{\mathbf{1}\}^T (\mathbf{M}^I)^T \mathbf{S}_p^I(\omega) \boldsymbol{\phi}^I \mathbf{H}_*^I(\omega) (\boldsymbol{\phi}_k^{-I})^T d\omega \quad (9)$$

$$k = 1, 2, \dots, n$$

where  $\boldsymbol{\phi}_k^{-I}$  is the kth line vector of the matrix  $\boldsymbol{\phi}^I$ . Similarly, the interval variable of the eth element stress response of 3D trusses can be determined as:

$$(\psi_{\sigma e}^I(t))^2 = E_e^I \mathbf{B} \mathbf{T} (\psi_{ue}^I(t))^2 \mathbf{T}^T \mathbf{B}^T E_e^I \quad (10)$$

where  $(\psi_{ue}^I(t))^2$  is the interval matrix of mean square value of  $\mathbf{u}_e(t)$

### Random vibration response of structures using the low-discrepancy sequences initialized high-order nonlinear particle swarm optimization algorithm

Random vibration response with uncertain-but-bounded parameters is difficult to attain because of its complexity. The methodology of interval analysis is to determine the band for structural response based on structural parameters varying within a fixed range. In other words, lower and upper bounds are the minimum and maximum values of system outputs respectively. Practically, interval analysis problems are converted to optimization problems. In this paper, an improved particle swarm optimization algorithm is employed to solve presented problems.

The traditional technique of particle swarm optimization, known as PSO algorithm was proposed by Kennedy and Eberhart (1995). This algorithm is initialized with a population of random solutions called particles. Each particle moves through the multidimensional design space corresponding to fitness problem to search its optimal position via adjusting its position and velocity simultaneously as the following expression:

$$v_{ik}(t+1) = w(t+1)v_{ik}(t) + c_1r_1(x_{ik}^{Pb}(t+1) - x_{ik}(t)) + c_2r_2(x_{ik}^{Gb}(t+1) - x_{ik}(t)) \quad (11)$$

$$x_{ik}(t+1) = x_{ik}(t) + v_{ik}(t+1) \quad (12)$$

where  $k$  denotes any individual of particle.  $x_{ik}^{Pb}$  and  $x_{ik}^{Gb}$  denote the local best ever position and global best position of each individual of particle at iteration  $t$  respectively.  $c_1$  and  $c_2$  are the coefficients indicating the degree of directing to the better positions of particles.  $c_1$  and  $c_2$  are specified as  $0 < c_1 + c_2 < 4$ , regularly  $c_1 = c_2 = 2$  (Perez and Behdinan, 2007).  $r_1$  and  $r_2$  indicate random numbers ranging between 0 and 1.

In recent studies, initialization of particle swarms by low-discrepancy sequences have been considering to obtain the better results (Liu et al., 2013). For LHNPSO, the constant acceleration coefficients are assigned as  $c_1 = c_2 = 2$  and the nonlinearly decreasing inertial weight is varied as the following:

$$w(t+1) = w_{\max} - (w_{\max} - w_{\min}) \left( \frac{k}{k_{\max}} \right)^{1/\pi^2} \quad (13)$$

This improved technique of PSO algorithm, known as LHNPSO shows efficiency in interval analysis. This technique is employed to capture sharp bounds for structural responses for complex structures in the work of this paper where  $w_{\max} = 0.95$  and  $w_{\min} = 0.5$  in this paper. The interval structural responses  $\mathbf{R}(x,t)$  such as natural frequency, displacement and stress are used as the fitness functions in the LHNPSO and the lower and upper bounds of these functions are respectively the minimum and maximum values of investigated variables.

$$\begin{cases} \bar{R}(x,t) = \max(\mathbf{R}(x,t)) \\ \underline{R}(x,t) = \min(\mathbf{R}(x,t)) \end{cases} \quad (14)$$

### Numerical Example

The performance of work is examined by a space truss with 108 members, shown in Figure 1, in which structural responses are investigated by different methods, namely, LHNPSO with 100 iterations, Monte Carlo Simulation and Quasi-Monte Carlo Simulation with 5000 iterations simultaneously. The comparison of results among methods is shown by Table 3, Table 4, and Table 5 while the convergence history of selected responses is depicted in Figure 2, Figure 3, and Figure 4 with lower and upper bounds. The varied variables for structural design are described as  $\mathbf{X}^I = \{A_1^I, A_2^I, A_3^I, E^I, \rho^I\}$  where their middle values are defined as the following:

**Table 1. Middle values of varied parameters**

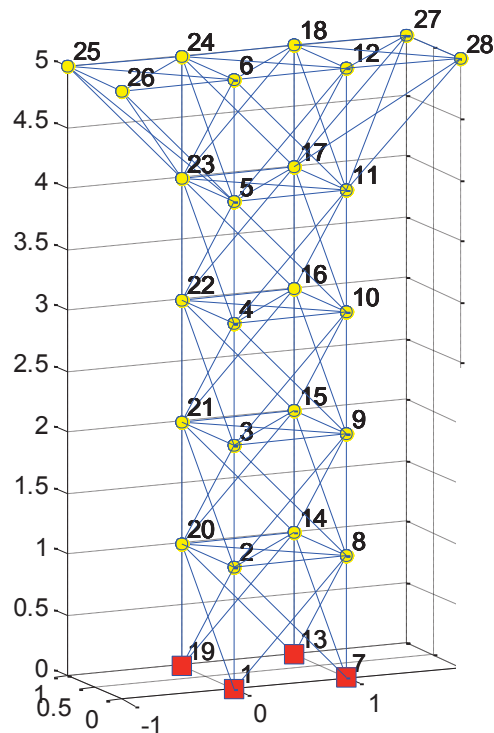
$A_1^c (m^2)$	$A_2^c (m^2)$	$A_3^c (m^2)$	$E^c (GPA)$	$\rho^c (kg / m^3)$
0.007	0.0084	0.014	200	7850

All varied parameters are restricted by the variance within  $\alpha_1 = 10\%$ . The structural members are divided into three groups as:

**Table 2. Groups of structural members**

Group	Area	Elastic Modulus	Density
1	$A_1^I$	$E^I$	$\rho^I$
2	$A_2^I$	$E^I$	$\rho^I$
3	$A_3^I$	$E^I$	$\rho^I$

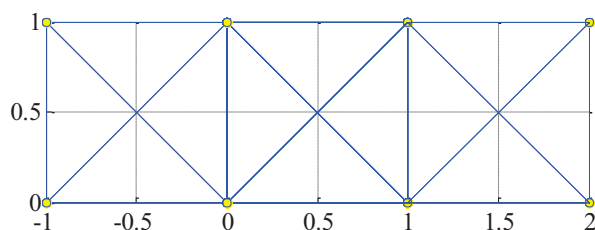
Each group is defined by members as the following:



Group 1: 1-2, 2-3, 3-4, 4-5, 5-6, 7-8, 8-9, 9-10, 10-11, 11-12, 13-14, 14-15, 15-16, 16-17, 17-18, 19-20, 20-21, 21-22, 22-23, 23-24, 12-28, 18-27, 12-27, 18-28, 11-27, 17-28, 11-28, 17-27, 27-28, 24-25, 6-26, 25-26, 24-26, 25-6, 26-5, 25-23, 26-23, 25-5.

Group 2: 14-20, 20-2, 2-8, 8-14, 2-14, 20-8, 15-21, 21-3, 3-9, 9-15, 15-3, 21-9, 16-22, 22-4, 4-10, 10-16, 16-4, 22-10, 17-23, 23-5, 5-11, 11-17, 17-5, 23-11.

Group 3: Other members.

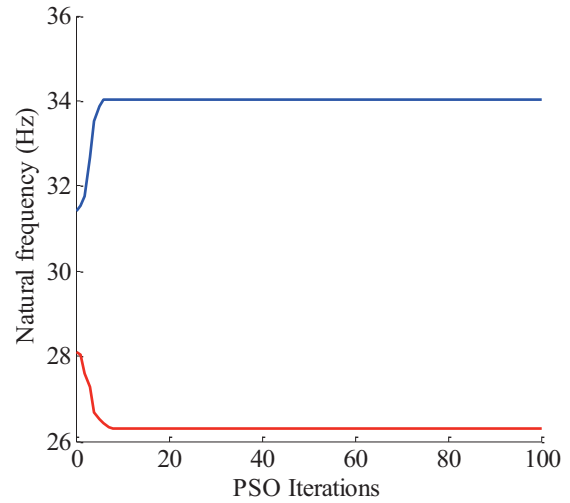


**Figure 1. 3-D view and top view of the model**



**Table 3. Natural frequency**

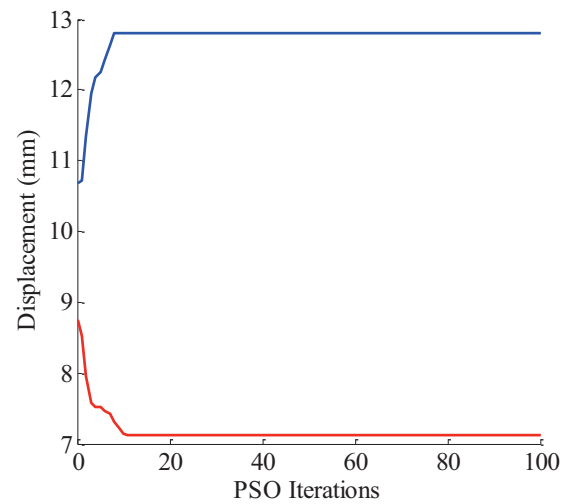
Natural frequency		
1 <sup>st</sup> natural frequency $f_1$ (Hz)		
Method	Upper bound	Lower bound
LHNPSO	34.027	26.294
QMCS	33.590	26.586
MCS	33.576	26.665
2 <sup>nd</sup> natural frequency $f_2$ (Hz)		
Method	Upper bound	Lower bound
LHNPSO	35.879	27.378
QMCS	35.224	27.963
MCS	35.182	27.791



**Figure 2.** LHNPSO for  $f_1$  (Hz)

**Table 4. Mean square root of displacement**

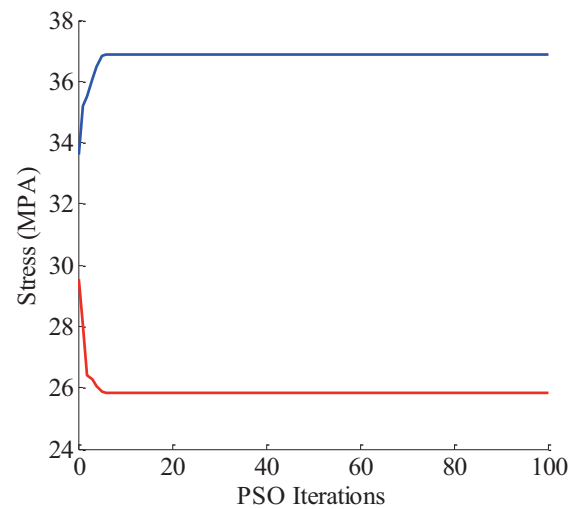
Mean square root of displacement		
$\Psi_{u12X}$ (mm)		
Method	Upper bound	Lower bound
LHNPSO	14.080	8.054
QMCS	13.483	8.300
MCS	13.542	8.350
$\Psi_{u27Y}$ (mm)		
Method	Upper bound	Lower bound
LHNPSO	12.802	7.115
QMCS	12.141	7.347
MCS	12.501	7.336



**Figure 3.** LHNPSO for  $\Psi_{u27Y}$  (mm)

**Table 5. Mean square root of structural stress**

Mean square root of structural stress		
$\Psi_{\sigma(5-6)}$ (MPa)		
Method	Upper bound	Lower bound
LHNPSO	36.853	25.849
QMCS	36.124	26.366
MCS	36.053	26.330
$\Psi_{\sigma(3-10)}$ (MPa)		
Method	Upper bound	Lower bound
LHNPSO	29.057	20.079
QMCS	28.707	20.390
MCS	28.676	20.430



**Figure 4.** LHNPSO for  $\Psi_{\sigma(5-6)}$  (MPa)

The selected responses are the first natural frequency,  $f_1$ , the second natural frequency,  $f_2$ , displacements at node 12 in direction X,  $\psi_{u12X}$ , and at node 27 in direction Y,  $\psi_{u27Y}$ , stresses of element 5-6,  $\psi_{\sigma(5-6)}$ , and element 3-10,  $\psi_{\sigma(3-10)}$ .

## Conclusion

It is observed that bounded range of target solutions of LHNPSO embraces that of QMCS or MCS, as shown as Table 3, Table 4, Table 5. In other words, LHNPSO provide a sharp enclosure, namely close upper bound and close lower bound with reliable precision of convergence. In addition, it takes less time for LHNPSO to achieve the target solutions much more than those of QMCS or MCS, namely smaller iterations. It is shown that LHNPSO is suitable for dynamic analysis for structures.

## References

- Elbeltagi, E., Hegazy, T., Grierson, D. (2005), Comparison among five evolutionary-based optimization algorithms. *Advanced Engineering Informatics*, 19, pp. 43-53.
- Gao, W. (2007), Random seismic response analysis of truss structures with uncertain parameters. *Engineering Structures*, 29, pp. 1487-1498.
- Gao, W. and Kessissoglou, N. J. (2007), Dynamic response analysis of stochastic truss structures under non-stationary random excitation using the random factor method. *Computer Methods in Applied Mechanics and Engineering*, 196, pp. 2765-2773.
- Hu, X. H., Eberhart, R. C., Shi, Y. H. (2003), Engineering optimization with particle swarm. *Proceedings of the 2003 Ieee Swarm Intelligence Symposium (Sis 03)*, pp. 53-57.
- Kennedy, J. and Eberhart, R. (1995), Particle swarm optimization, *Proceedings, IEEE International Conference on Neural Networks*.
- Köylüoğlu, H., Ş. Çakmak, A., Nielsen, S. (1995), Interval Algebra to Deal with Pattern Loading and Structural Uncertainties. *Journal of Engineering Mechanics*, 121(11), pp. 1149-1157.
- Lin, Y. K. and Yong, Y. (1987), Evolutionary Kanai-Tajimi Type Earthquake Models. *Stochastic Approaches in Earthquake Engineering*. Y. K. Lin and R. Minai, Springer Berlin Heidelberg, 32, pp. 174-203.
- Liu, N., Gao, W., Song, C., Zhang, N., Pi, Y.L. (2013), Interval dynamic response analysis of vehicle-bridge interaction system with uncertainty. *Journal of Sound and Vibration*, 332, pp. 3218-3231.
- Moens, D. and Vandepitte, D. (2001), Envelope frequency response function calculation of uncertain structures. *Proceedings on Noise and Vibration Engineering*, 1 - 3, pp. 395-402.
- Moore, R. E. (1966), *Interval Analysis*. Prentice-Hall, Englewood Cliffs, N.J., 1966. *Science*, 158, pp. 365.
- Muhanna, R. L. and Mullen, R. L. (2001), Uncertainty in mechanics problems interval-based approach. *Engineering Mechanics*, 127, pp. 557-566.
- Perez, R. E. and Behdinan, K. (2007), Particle swarm approach for structural design optimization. *Computers & Structures*, 85, pp. 1579-1588.
- Qiu, Z. P., Wang, X. J., Friswell, M. I. (2005), Eigenvalue bounds of structures with uncertain-but-bounded parameters. *Journal of Sound and Vibration*, 282, pp. 297-312.

## Implementation of fundamental-solution based hybrid finite element model for elastic circular inclusions

H. Wang<sup>1</sup> and Qing H. Qin<sup>2,\*</sup>

<sup>1</sup>Department of Mechanics, Henan University of Technology, Zhengzhou 450001, China

<sup>2</sup>Research School of Engineering, Australian National University, ACT 0200, Australia

\*Corresponding author: qinghua.qin@anu.edu.au

### Abstract

In this paper, a doubly periodic array of inclusions in infinite plane matrix is studied for analyzing its effective elastic properties. A representative rectangular cell containing single inclusion is taken from the composites and then is investigated using the present hybrid finite element model to obtain numerical results of boundary tractions under the applied displacement boundary conditions. In the present numerical model, a general polygonal hybrid finite element with arbitrary number of sides is constructed by coupling the independent element interior and frame displacement fields. The element interior fields are approximated by the combination of fundamental solutions to prior satisfy the governing equation of the problem, so that the domain integral appeared in the weak-form functional is converted into boundary integrals. Independently the element frame fields are approximated by the conventional shape functions to guarantee the continuity conditions across inter-element boundaries. Following this, the polygonal inclusion elements are designed to reduce mesh effort in the inclusion domain. Numerical tests are conducted for assessing the performance of the element model and it is found that the present method gives good accuracy as compared with the conventional finite element.

**Keywords:** Representative volume element; Effective elastic properties; Fundamental solutions; Polygonal inclusion element.

### Introduction

In the context of composite with reinforced inclusions, the simplified model with periodic distribution of multiple inclusions is usually taken as an example for determining the corresponding effective properties of composites. However, the analytical methods (Yu and Qin, 1996; Feng et al., 2003; 2004; Bonnet, 2007; Nemat-Nasser and Hori, 1999; Qin and Yang, 2009; To et al, 2013) like fast Fourier transforms and so on are usually difficult to deal with composites containing the inclusion with complicated geometric shapes or distributions. As alternatives to the analytical methods, numerical methods were developed for solving composite problems involving various periodic inclusions (Dong, 2006; Kaminski, 1999; Michel et al., 1999; Qin, 2004; Yang and Qin, 2003; 2004; Wang and Qin, 2011a; Würkner et al., 2011). For example, Würkner et al. (2011) evaluated the effective material properties for composite structures with rhombic fiber arrangements by the finite element method (FEM). Michel et al. (1999) compared the two numerical methods including the finite element method and the fast Fourier transform-based numerical method in determining effective properties of composite materials with periodic microstructure. Yang and Qin (2003) studied the effect of fiber bundling on the effective transverse properties of unidirectional fiber composites by way of finite element method. Dong (2006) employed the boundary element method (BEM) to predict the effective elastic properties of composites including doubly periodic array of inclusions. Yang and Qin (2004) extended the boundary element formulation to the micro-mechanical analysis of composite materials. Kaminski (1999) employed the boundary element method based homogenization to deal with the periodic transversely isotropic linear elastic fiber-reinforced composites. Besides the FEM and the BEM, Wang and Qin (2011a) developed the hybrid finite element formulation for analyzing the effective thermal conductivity of fiber-reinforced composites, in which the fiber can be regularly, or randomly distributed.

Among the numerical methods mentioned above, the hybrid finite element method based on fundamental solutions has shown its advantages over the others (Qin, 2005; Qin and Wang, 2008; Wang and Qin, 2010). One feature of the method is the use of special elements. Within the developed special elements (Wang and Qin, 2011b), special fundamental solutions analytically satisfying the governing equations and certain boundary conditions are employed to approximate the internal displacement and stress fields. Besides the development of special elements based on the special fundamental solutions, another feature of the hybrid model is to construct arbitrarily shaped elements with more nodes and edges, because all integrals appearing in the hybrid model are boundary integrals along the element frame.

In the paper, large polygonal elements or super elements with many edges and nodes are developed for solving such problems as composites with doubly periodic circular inclusions, and the corresponding hybrid finite element formulation for calculating effective properties of the composite is presented.

### Computational model and effective elastic properties

Consider a composite with doubly periodic inclusions of arbitrary shape in an infinite plane matrix subject to remote tension  $\sigma_{11}^\infty$ ,  $\sigma_{22}^\infty$  and in-plane shear forces  $\sigma_{12}^\infty$  (see Fig. 1). The elastic parameters of inclusion and matrix are respectively denoted by  $E^{(I)}$  and  $\nu^{(I)}$ , and  $E^{(M)}$  and  $\nu^{(M)}$ .

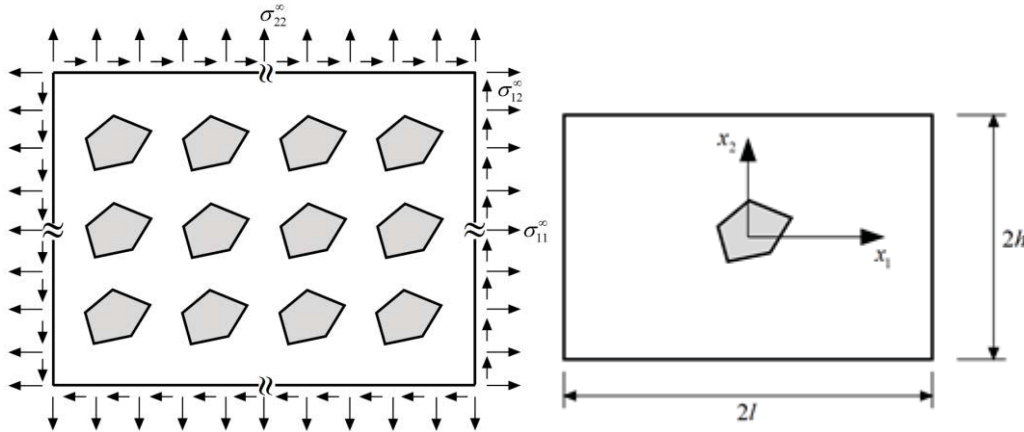


Fig. 1 Sketch of doubly periodic inclusions with arbitrary shape in the infinite plane matrix and a rectangular cell containing single inclusion of arbitrary shape

For such periodic structure, a representative rectangular cell shown in Fig. 1 with edge length  $2l$  and  $2h$  along the coordinate directions  $x_1$  and  $x_2$  are chosen as an example. On the outer boundary of the cell, the suitable periodic boundary conditions corresponding to remote tension and shear forces, respectively are given by (Dong, 2006).

Because a solid containing doubly periodic array of inclusions with arbitrary shape considered in the paper is usually considered as a homogeneous orthotropic solid, the corresponding constitutive relationship associated to average stresses  $\bar{\sigma}_{ij}$  and strains  $\bar{\varepsilon}_{ij}$  can be written as (Kaw, 2006; Nemat-Nasser and Hori, 1999)

$$\bar{\varepsilon}_{11} = \bar{\sigma}_{11} / \bar{E}_1 - \bar{\nu}_{21} \bar{\sigma}_{22} / \bar{E}_2, \quad \bar{\varepsilon}_{22} = \bar{\sigma}_{22} / \bar{E}_2 - \bar{\nu}_{12} \bar{\sigma}_{11} / \bar{E}_1, \quad \bar{\gamma}_{12} = \bar{\sigma}_{12} / \bar{G}_{12} \quad (1)$$

where  $\bar{E}_1$ ,  $\bar{E}_2$ ,  $\bar{\nu}_{21}$ ,  $\bar{\nu}_{12}$  and  $\bar{G}_{12}$  are effective orthotropic elastic parameters, respectively.

In order to determine the effective elastic properties  $\bar{E}_2$  and  $\bar{\nu}_{21}$ , the remote loading conditions can be given by

$$\sigma_{11}^\infty = 0, \quad \sigma_{22}^\infty = p, \quad \sigma_{12}^\infty = 0 \quad (2)$$

Thus, in the effective homogeneous orthotropic solid, the average stress and strain states are separately written by

$$\bar{\sigma}_{11} = 0, \bar{\sigma}_{22} = p, \bar{\sigma}_{12} = 0, \bar{\varepsilon}_{11} = u_{11}/l, \bar{\varepsilon}_{22} = u_{h2}/h \quad (3)$$

Substituting Eq. (3) into Eq. (1) yields

$$\begin{cases} \bar{\varepsilon}_{11} = -\bar{v}_{21}p/\bar{E}_2 = u_{11}/l \\ \bar{\varepsilon}_{22} = p/\bar{E}_2 = u_{h2}/h \end{cases} \Rightarrow \begin{cases} \bar{E}_2 = ph/u_{h2} \\ \bar{v}_{21} = -u_{11}h/(u_{h2}l) \end{cases} \quad (4)$$

where  $u_{11}$ ,  $u_{12}$ ,  $u_{h1}$  and  $u_{h2}$  are the unknown displacements to be determined.

Similarly, in order to determine the effective elastic properties  $\bar{E}_1$  and  $\bar{v}_{12}$ , the remote loading conditions can be given by

$$\sigma_{11}^\infty = p, \sigma_{22}^\infty = 0, \sigma_{12}^\infty = 0 \quad (5)$$

To find the effective shear modulus, one needs to apply the remote shear loading, i.e.

$$\sigma_{11}^\infty = 0, \sigma_{22}^\infty = 0, \sigma_{12}^\infty = p \quad (6)$$

The corresponding average stress and strain states can be written as

$$\bar{\sigma}_{11} = 0, \bar{\sigma}_{22} = 0, \bar{\sigma}_{12} = p, \bar{\gamma}_{12} = u_{12}/h + u_{h1}/l \quad (7)$$

Substituting Eq. (7) into Eq. (1), one obtains

$$\bar{G}_{12} = p/\bar{\gamma}_{12} \quad (8)$$

From the procedure above, it can be seen that for three cases including single tension along the  $x_1$  direction, single tension along the  $x_2$  direction and in-plane shear, the relation of the remote stresses and the displacement boundary conditions should be established to determine the effective properties of the composite. According to the formulations in the literature (Dong, 2006), the traction variation along the outer boundary of the cell taken from the composite must be evaluated under the applied unit displacement boundary conditions, and this procedure can be performed by using the present super element below.

## Basic formulations and polygonal inclusion elements

### Basic formulations

For the matrix and inclusion under consideration, the integral formulation of hybrid finite element in a particular hybrid element  $e$  can be written as follows (Wang and Qin, 2010; Wang and Qin, 2011b)

$$\Pi_{me} = \frac{1}{2} \int_{\Omega_e} \boldsymbol{\sigma}^T \boldsymbol{\varepsilon} d\Omega - \int_{\Gamma_e^s} \bar{\mathbf{s}}^T \tilde{\mathbf{u}} d\Gamma + \int_{\Gamma_e} \mathbf{s}^T (\tilde{\mathbf{u}} - \mathbf{u}) d\Gamma \quad (9)$$

where  $\boldsymbol{\sigma} = \{\sigma_{11} \quad \sigma_{22} \quad \sigma_{12}\}^T$ ,  $\boldsymbol{\varepsilon} = \{\varepsilon_{11} \quad \varepsilon_{22} \quad \gamma_{12}\}^T$  and  $\mathbf{u} = \{u_1 \quad u_2\}^T$  are respectively stress, strain and displacement fields in the element domain  $\Omega_e$ ,  $\tilde{\mathbf{u}} = \{\tilde{u}_1 \quad \tilde{u}_2\}^T$  is the compatible displacement field defined on the boundary  $\partial\Omega_e = \Gamma_e$  with an outward normal  $\mathbf{n} = \{n_1 \quad n_2\}^T$ ,  $\mathbf{s} = \mathbf{A}\boldsymbol{\sigma}$  is the traction field and  $\bar{\mathbf{s}}$  denotes the specified traction on the boundary  $\Gamma_e^s$ .

Provided that the internal displacement and stress fields satisfy the governing equation in the element domain, applying the Gaussian divergence theorem to the functional  $\Pi_{me}$  yields

$$\Pi_{me} = -\frac{1}{2} \int_{\Gamma_e} \mathbf{u}^T \mathbf{s} d\Gamma - \int_{\Gamma_e^s} \bar{\mathbf{s}}^T \tilde{\mathbf{u}} d\Gamma + \int_{\Gamma_e} \mathbf{s}^T \tilde{\mathbf{u}} d\Gamma \quad (10)$$

In the application of variational principle, the displacement field in the interior of the element is approximated by a linear combination of fundamental solutions centered at series of source points  $\mathbf{x}^s$  locating on the pseudo boundary similar to the element boundary  $\Gamma_e$ , that is,

$$\mathbf{u} = \mathbf{Nc}_e \quad (11)$$

Subsequently, according to the strain-displacement equations and the stress-strain relationship, the corresponding stress components and tract components are expressed as

$$\boldsymbol{\sigma} = \mathbf{T}\mathbf{c}_e \quad \text{and} \quad \mathbf{s} = \mathbf{Q}\mathbf{c}_e \quad (12)$$

In order to enforce the conformity of the displacement field on the common interface of adjacent elements, the element boundary displacement field  $\tilde{\mathbf{u}}$  can be interpolated from the generalized nodal displacement  $\mathbf{d}_e$  in the form

$$\tilde{\mathbf{u}} = \tilde{\mathbf{N}}\mathbf{d}_e \quad (13)$$

where  $\tilde{\mathbf{N}}$  denotes the matrix consisting of shape functions widely used in the standard FEM and BEM.

The substitution of Eqs. (11) and (13) into the functional **Error! Reference source not found.** including boundary integrals only gives

$$\Pi_{me} = -\frac{1}{2}\mathbf{c}_e^T \mathbf{H}_e \mathbf{c}_e - \mathbf{d}_e^T \mathbf{g}_e + \mathbf{c}_e^T \mathbf{G}_e \mathbf{d}_e \quad (14)$$

where

$$\mathbf{H}_e = \int_{\Gamma_e} \mathbf{Q}^T \mathbf{N} \mathbf{d}\Gamma, \quad \mathbf{G}_e = \int_{\Gamma_e} \mathbf{Q}^T \tilde{\mathbf{N}} \mathbf{d}\Gamma, \quad \mathbf{g}_e = \int_{\Gamma_e^s} \tilde{\mathbf{N}}^T \bar{\mathbf{s}} \mathbf{d}\Gamma \quad (15)$$

The stationary of  $\Pi_{me}$  with respect to the displacement coefficient  $\mathbf{c}_e$  and nodal displacement  $\mathbf{d}_e$  yields the following optional relationship between  $\mathbf{c}_e$  and  $\mathbf{d}_e$

$$\mathbf{c}_e = \mathbf{H}_e^{-1} \mathbf{G}_e \mathbf{d}_e \quad (16)$$

and the element displacement-load equation given by

$$\mathbf{K}_e \mathbf{d}_e = \mathbf{g}_e \quad (17)$$

where  $\mathbf{K}_e = \mathbf{G}_e^T \mathbf{H}_e^{-1} \mathbf{G}_e$  is the symmetric element stiffness matrix, like the one in the conventional FEM.

### *Polygonal inclusion elements*

It's known that the conventional displacement finite element method with polynomial representations is difficult to construct an element with arbitrary number of sides. However, from the hybrid formulation described above we can see that it is appropriate for constructing  $n$ -sided polygonal elements more nodes and edges than the conventional finite elements, due to the fact of the independence of interior displacement fields and boundary displacements. More importantly, because the interior approximation displacement and stress fields analytically satisfy the elastic governing equations within the element domain, all integrals are evaluated along the element boundary. Thus, it's possible to design the super elements with multiple element edges to achieve the effort of mesh reduction in the inclusion region.

Although arbitrarily shaped inclusions such as circular, triangular or square inclusions can be studied theoretically using the present hybrid finite element formulation, in the paper, just the circular inclusion is studied for the sake of simplicity. Then, the hybrid super elements with multi-edges shown in Fig. 1 can be used to model the inclusion. In Fig. 1, the solid line represents the inclusion element boundary, while the dash line is the *pseudo* boundary which is similar to the element boundary from the point of geometry. The triangle symbol is the center of the inclusion of interest. Source points are preassigned on the pseudo boundary and can be generated by means of the relation

$$\mathbf{x}^s = \mathbf{x}_c + \gamma \mathbf{x}_b \quad (18)$$

where  $\mathbf{x}^s$  and  $\mathbf{x}_b$  are respectively the source point and boundary node, and  $\mathbf{x}_c$  denotes the element centroid. The dimensionless parameter  $\gamma$  scales the distance of the pseudo boundary and the element boundary (Wang et al, 2005; Wang and Qin, 2008).

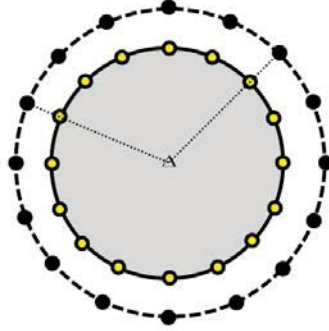


Fig. 1 Configuration of hybrid element with multi-edges for circular inclusion

### Numerical examples

The matrix in the composite with doubly period circular inclusions is considered to be isotropic and homogeneous, and the elastic modulus and Poisson's ratio of the medium are respectively taken as  $E^M=1$ ,  $\nu^M=0.3$ . The isotropic and homogeneous elastic inclusion is assumed to have same Poisson's ratio as that of matrix, and its elastic modulus is assumed to be  $E^I/E^M=10$ . For the sake of convenience, the geometry size of the RVE is taken as  $h/l=1$  with the assumption of  $h=0.5$ .

In order to investigate the effect of inclusion on the mechanical properties of composites, the effective elastic properties are compared for the circular inclusion under same volume fraction. For example, if the value of volume fraction is supposed to be  $\alpha$ , the corresponding geometrical characteristic parameter for the circular inclusion can be determined, i.e. radius of the circular inclusion  $=\sqrt{4hl\alpha/\pi}$ .

#### Inversion of $\mathbf{H}$ matrix

From the hybrid finite element formulation given above, one observes that the mechanical properties of the present hybrid element with multiple edges are associated with the inverse operation of matrix  $\mathbf{H}$ . In order to investigate the accuracy of the inverse operation of matrix  $\mathbf{H}$ , the following problem involving the circular inclusion only is firstly considered. The radius of the circle is taken to be unit. The boundary of the circle is discretized by one super element with  $k$  edges including three nodes each, thus the total number of nodes for the super element is  $2k$ .

To reveal the ill-conditioning of the matrix  $\mathbf{H}$ , the singular value decomposition is employed herein. Let  $\mathbf{H}$  be a square matrix with  $n$  by  $n$  entries. Then the SVD of  $\mathbf{H}$  is a decomposition of the form

$$\mathbf{H} = \mathbf{U}\mathbf{S}\mathbf{V}^T = \sum_{i=1}^n \mathbf{u}_i \sigma_i \mathbf{v}_i^T \quad (19)$$

where  $\mathbf{U} = (\mathbf{u}_1, \mathbf{u}_2, \dots, \mathbf{u}_n)$  and  $\mathbf{V} = (\mathbf{v}_1, \mathbf{v}_2, \dots, \mathbf{v}_n)$  are matrices with orthonormal columns, that is,  $\mathbf{U}^T \mathbf{U} = \mathbf{V}^T \mathbf{V} = \mathbf{I}$ , and  $\mathbf{S} = \text{diag}(\sigma_1, \sigma_2, \dots, \sigma_n)$  has non-negative diagonal elements appearing in non-increasing order such that

$$\sigma_1 \geq \sigma_2 \geq \dots \geq \sigma_n$$

As a result, the matrix condition number of  $\mathbf{H}$  can be given by the ratio  $\sigma_1 / \sigma_n$ , and the inverse of  $\mathbf{H}$  is evaluated by

$$\mathbf{H}^{-1} = \mathbf{V}\mathbf{S}^{-1}\mathbf{U}^T \quad (20)$$

In the following test, a super-element with  $k=8$  and 20 edges is considered and the size of  $\mathbf{H}$  matrix is  $4k$  by  $4k$ . To investigate the accuracy of the matrix inversion of  $\mathbf{H}$ , we evaluate the norm of the residue matrix  $\mathbf{H}\mathbf{H}^{-1} - \mathbf{I}$  for various values of  $\gamma$ .

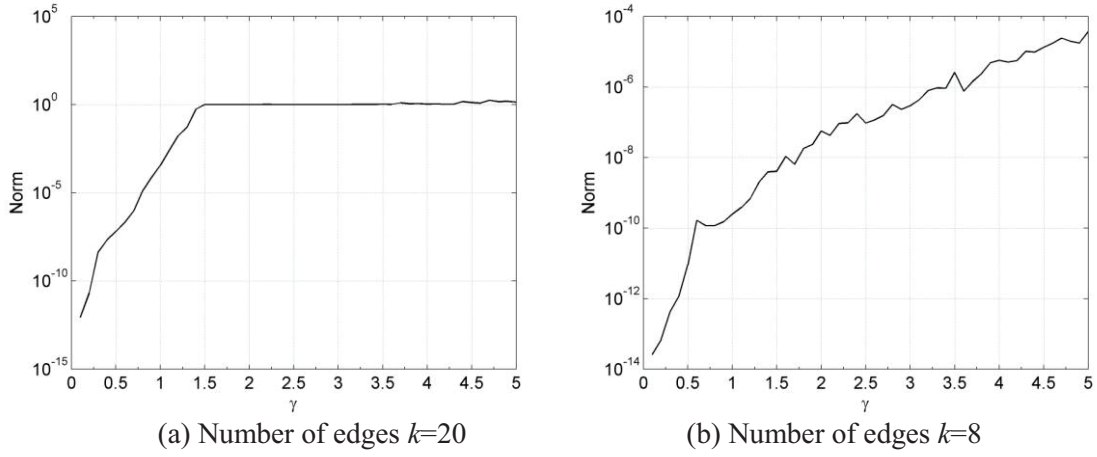


Fig. 3 The norm for various number of element edges

From the numerical results shown in Fig. 3, we can conclude that the total number of element nodes affects the choice of the parameter  $\gamma$ , which is important to keep the inversion of  $\mathbf{H}$  stable and accurate. To establish a proper rule to determine the value of  $\gamma$  according to the specified element type, the maximum value of  $\gamma$  is in proper value when the corresponding norm of inversion is less than  $10^{-6}$ . In Fig. 4, the maximum proper value of  $\gamma$  is plotted as the change of number of degrees of freedom (DOFs) of the element. Subsequently, the curve fitting technology is employed to give an approximated expression of the maximum proper value of  $\gamma$  in terms of number of DOFs of the element, which is denoted by the symbol  $x$ . Here, we employ the 6<sup>th</sup> degree polynomial to perform the curve fitting

$$\gamma = p_1x^6 + p_2x^5 + p_3x^4 + p_4x^3 + p_5x^2 + p_6x + p_7 \quad (21)$$

with

$$p_1 = -2.782 \times 10^{-10}, p_2 = 5.274 \times 10^{-8}, p_3 = 1.033 \times 10^{-7}$$

$$p_4 = -7.219 \times 10^{-4}, p_5 = 6.869 \times 10^{-2}, p_6 = -2.690, p_7 = 41.92$$

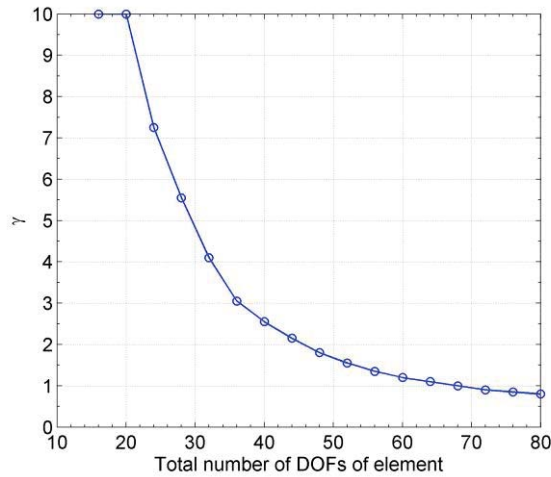


Fig. 4 The maximum proper value of  $\gamma$  for different number of DOFs of the element



### Circular inclusion

Next, in this section, the mechanical response of the composite with circular inclusion is taken into consideration for the purpose of estimating the effective properties of the composite in the future. For convenience, the RVE is assumed to be subjected to a unit uniform tension along the vertical direction.

For a moderate volume fraction of the inclusion, i.e.  $\alpha=10\%$ , the typical mesh division is shown in Fig. 5. To make comparison, we keep the mesh same in the matrix for both ABAQUS and HFS-FEM, while in the inclusion, the mesh strategy is different. For the mesh discretization generated by ABAQUS, some typical quadratic isoparametric elements are produced to discretize the inclusion domain. The total number of elements in the ABAQUS is 124 elements with 405 nodes. In contrast, a super element with 20 edges is employed in the developed HFS-FEM to model the inclusion and no any nodes are put inside the inclusion. Thus, the total number of elements in the present HFS-FEM is just 81 elements and the number of nodes reduces to 292. It's clear that the effect on mesh reduction is achieved by the present super hybrid element.

Besides, the variation of traction components along the outer boundary of the RVE is displayed in Fig. 6, from which we observe that there is a good agreement between the numerical results of HFS-FEM and those of ABAQUS. So, the accuracy and efficiency of the present super hybrid element is demonstrated for the analysis of composite embedded with circular inclusions.

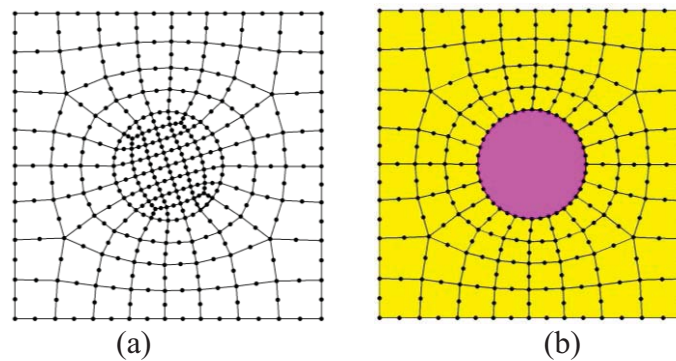


Fig. 5 Illustration of mesh division in: (a) ABAQUS (b) HFS-FEM for the case of  $\alpha=10\%$

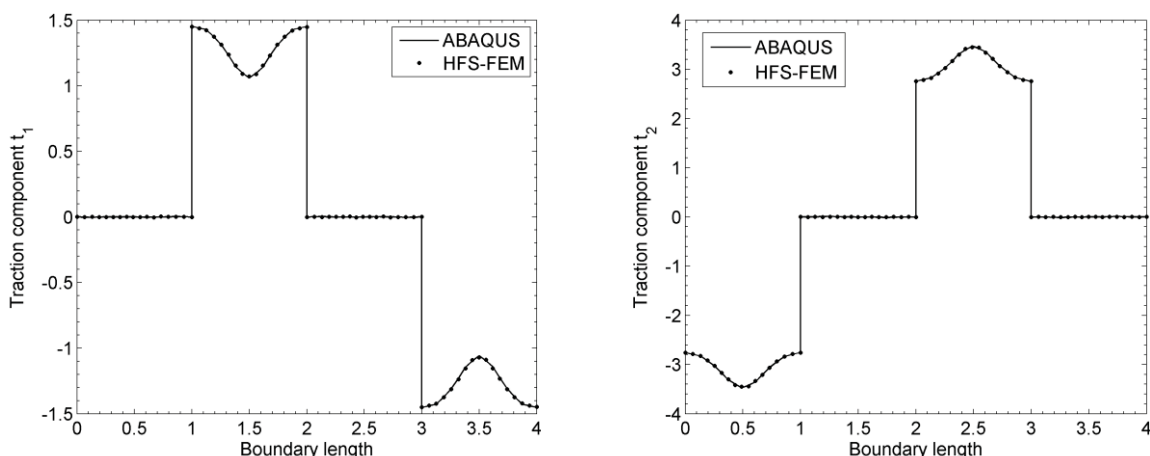


Fig. 6 Traction distribution along the outer boundary of RVE for the case of  $\alpha=10\%$

## 5. Conclusions

The present study proposes a fundamental-solution-based hybrid finite element formulation for the analysis of unidirectional fiber reinforced composites. The fiber is with circular cross section. By

virtue of the property of the present hybrid element, we can construct a super inclusion element with multiple edges and nodes for the purpose of mesh reduction and don't need to make any mesh discretization inside the inclusion. The numerical results from the proposed element model are in good agreement with those from ABAQUS, which indicates that the present hybrid finite element is effective and convenient for determining effective properties of composites with doubly periodic array of circular inclusions. In the future, elements for modeling composites containing other shaped inclusions including triangular, square and elliptic inclusions will be studied to investigate the shape effect of the inclusions on the elastic properties of the composite.

**Acknowledgements** The work described in this paper was partially supported by the National Natural Science Foundation of China (No. 11102059), and the Program for Innovation Talents of Science and Technology in Universities in Henan Province (No. 13HASTIT019).

## References

- Bonnet G. (2007), Effective properties of elastic periodic composite media with fibers. *J Mech Phys Solids*, 55, pp. 881-899.
- Dong, C.Y. (2006), Effective elastic properties of doubly periodic array of inclusions of various shapes by the boundary element method. *Int J Solid Struct*, 43, pp. 7919-7938.
- Feng, X.Q., Mai, Y.W. and Qin, Q.H. (2003), A micromechanical model for interpenetrating multiphase composites. *Comput Mater Sci*, 28, pp. 486-493.
- Feng, X.Q., Qin, Q.H. and Yu, S.W. (2004), Quasi-micromechanical damage model for brittle solids with interacting microcracks. *Mech Mater*, 36, pp. 261-273.
- Kaminski M. (1999), Boundary element method homogenization of the periodic linear elastic fiber composites. *Eng Anal Bound Elem*, 23, pp. 815-824.
- Kaw A.K. (2006), *Mechanics of Composite Materials*. CRC Press.
- Michel J., Moulinec H., Suquet P. (1999), Effective properties of composite materials with periodic microstructure: a computational approach. *Comput Method Appl M*, 172, pp. 109-143.
- Nemat-Nasser, S. and Hori, M. (1999), *Micromechanics: Overall properties of heterogeneous materials*. Elsevier.
- Qin, Q.H. (2004), Micromechanics-BE solution for properties of piezoelectric materials with defects. *Eng Anal Bound Elem*, 28, pp. 809-814.
- Qin, Q.H. (2005), Trefftz finite element method and its applications. *Appl Mech Reviews*, 58, pp.316-337.
- Qin, Q.H. and Wang, H. (2008), *Matlab and C programming for Trefftz finite element methods*. CRC Press.
- Qin, Q.H. and Yang, Q.S. (2009), *Macro-micro theory on multifield coupling behavior of heterogeneous materials*. Higher Education Press and Springer.
- To, Q.D., Bonnet G., To V.T. (2013), Closed-form solutions for the effective conductivity of two-phase periodic composites with spherical inclusions. *P Roy Soc A-Math Phy*, 469, pp. 20120339
- Wang, H. and Qin, Q.H. (2008), Meshless approach for thermo-mechanical analysis of functionally graded materials. *Eng Anal Bound Elem*, 32, pp. 704-712.
- Wang, H. and Qin, Q.H. (2010), Fundamental-solution-based finite element model for plane orthotropic elastic bodies. *Eur J Mech A-Solid*, 29, pp. 801-809.
- Wang, H. and Qin QH. (2011a), Special fiber elements for thermal analysis of fiber-reinforced composites. *Eng Comput*, 28, pp. 1079-1097.
- Wang, H. and Qin, Q.H.(2011b), Fundamental-solution-based hybrid FEM for plane elasticity with special elements. *Comput Mech*, 48, pp. 515-528.
- Wang, H., Qin, Q.H. and Kang, Y.L. (2005), A new meshless method for steady-state heat conduction problems in anisotropic and inhomogeneous media. *Arch Appl Mech*, 74, pp. 563-579.
- Würkner M., Berger H., Gabbert U. (2011), On numerical evaluation of effective material properties for composite structures with rhombic fiber arrangements. *Int J Eng Sci*, 49, pp. 322-332.
- Yang, Q.S. and Qin, Q.H. (2003), Modelling the effective elasto-plastic properties of unidirectional composites reinforced by fibre bundles under transverse tension and shear loading. *Mat Sci Eng A-Struct*, 344, pp.140-145.
- Yang, Q.S. and Qin, Q.H. (2004), Micro-mechanical analysis of composite materials by BEM. *Eng Anal Bound Elem*, 28, pp. 919-926.
- Yu, S.W. and Qin, Q.H. (1996), Damage analysis of thermopiezoelectric properties: Part II. Effective crack model. *Theor Appl Fract Mech*, 25, pp. 279-288.

# Direct numerical simulation of unsteady natural convection boundary layers on an evenly heated plate with time-varying heating flux

\*Wenxian Lin<sup>1,2</sup> and S.W. Armfield<sup>3</sup>

<sup>1</sup>School of Engineering, James Cook University, Townsville, QLD 4811, Australia.

<sup>2</sup>Solar Energy Research Institute, Yunnan Normal University, Kunming, Yunnan 650092, China.

<sup>3</sup>School of Aerospace, Mechanical and Mechatronic Engineering, University of Sydney, NSW 2006, Australia.

\*Corresponding author: Wenxian.lin@jcu.edu.au

## Abstract

It is of fundamental significance and application importance to fully understand the flow behavior of unsteady natural convection boundary layers under time-dependent heating conditions. Such an understanding is currently scarce. In this paper, a series of scalings developed for the major parameters representing the flow behavior of the unsteady natural convection boundary layer of a homogeneous Newtonian fluid with  $Pr > 1$  adjacent to a vertical plate evenly heated with a time-varying sinusoidal heat flux were validated by comparison to ten direct numerical simulations. These scaling provide relations between these parameters with the governing parameters of the flow, i.e., the Rayleigh number ( $Ra$ ), the Prandtl number ( $Pr$ ), and the dimensionless natural frequency ( $f_n$ ) of the time-varying sinusoidal heat flux, at the start-up stage, at the critical time, and at the quasi-steady state. The results show that in general these scalings provide an accurate description of the flow at different development stages.

**Keywords:** Natural convection, boundary layer, scaling, direct numerical simulation, heat flux, time-dependent heating.

## Introduction

As a classic fluid mechanics problem, owing to its fundamental and practical significance, natural convection boundary layer flow has been the subject of numerous studies. Earlier studies have focused on experimental and analytical investigations of the steady-state behavior of the flow, in particular that on a heated semi-infinite vertical wall and in a rectangular cavity with differentially heated sidewalls (see, e.g., Hyun (1994)). More recent studies have focused on the transient flow behavior. In particular, scaling analysis has proven to be a very effective tool to reveal the transient behavior of such a flow and it has been employed to develop scalings to represent the transient behavior of natural convection boundary layers under various configurations and flow conditions (see, e.g., Patterson and Imberger (1980), Lin and Armfield (1999, 2001, 2005, 2012), Lin et al. (2007)).

Unsteady natural convection boundary layers on a vertical plate heated by a time-dependent heat flux are found in many applications, such as in the Trombe wall system of a passive solar house and in a solar chimney. In the Trombe wall case, the wall, which is usually painted in black or with a solar selective coating, absorbs solar radiation and converts it into heat which is then transported to the dwelling by the heated air via natural convection boundary layer flow in the channel formed by the glazing and the wall. A solar chimney operates in a similar manner. For both cases, the time-dependent solar radiation, which varies sinusoidally under a clear sky condition (only in the first half of the sinusoidal cycle), serves as the heat flux for the natural convection boundary-layer flows.

Although there have been numerous studies on natural convection boundary layers on a vertical plate heated by a heat flux, the majority of these studies have been on the cases where the applied heat flux is either uniformly constant or spatially varied but not time dependent (see, e.g., Armfield et al. (2007), Lin et al. (2009), Patterson et al. (2009), Bednarz et al. (2009), Saha et al. (2012), Capobianchi and Aziz (2012)). The studies on unsteady natural convection boundary layers on a vertical plate heated by a time-dependent heat flux are currently lacking, which motivates this study.

### Governing equations and scalings

Under consideration is the unsteady natural convection boundary layer of a homogeneous Newtonian fluid with  $Pr > 1$  adjacent to a vertical plate evenly heated with a time-varying sinusoidal heat flux in the form of

$$\frac{dT}{dX} = -\Gamma_w(t) = -\Gamma_{wm} \sin(2\pi ft), \quad (1)$$

where  $T$  is temperature,  $X$  is the horizontal coordinate,  $\Gamma_w(t)$  is the transient temperature gradient across at the plate at time instant  $t$ ,  $\Gamma_{wm}$  is the maximum temperature gradient across at the plate, and  $f$  is the natural frequency of the time-varying flux applied to the plate. The flow is assumed to be two-dimensional and the fluid is initially at rest. The plate lies at  $X=0$  with the origin at  $Y=0$  ( $Y$  is the vertical coordinate), with the plate boundary conditions,

$$U = V = 0, \quad \frac{dT}{dX} = -\Gamma_{wm} \sin(2\pi ft) \text{ at } x = 0 \text{ for } Y > 0, t \geq 0, \quad (2)$$

where  $\Gamma_{wm}$  and  $f$  are assumed to be constant for a specific time-varying flux condition.

### Governing equations

The governing equations of motion are the Navier-Stokes equations with the Boussinesq approximation for buoyancy, which together with the temperature equation can be written in the following dimensionless, two-dimensional forms,

$$\frac{\partial u}{\partial x} + \frac{\partial v}{\partial y} = 0, \quad (3)$$

$$\frac{\partial u}{\partial \tau} + u \frac{\partial u}{\partial x} + v \frac{\partial u}{\partial y} = -\frac{\partial p}{\partial x} + \frac{Pr}{Ra^{2/5}} \left( \frac{\partial^2 u}{\partial x^2} + \frac{\partial^2 u}{\partial y^2} \right), \quad (4)$$

$$\frac{\partial v}{\partial \tau} + u \frac{\partial v}{\partial x} + v \frac{\partial v}{\partial y} = -\frac{\partial p}{\partial y} + \frac{Pr}{Ra^{2/5}} \left( \frac{\partial^2 v}{\partial x^2} + \frac{\partial^2 v}{\partial y^2} \right) + Pr Ra^{1/5} \theta, \quad (5)$$

$$\frac{\partial \theta}{\partial \tau} + u \frac{\partial \theta}{\partial x} + v \frac{\partial \theta}{\partial y} = \frac{1}{Ra^{2/5}} \left( \frac{\partial^2 \theta}{\partial x^2} + \frac{\partial^2 \theta}{\partial y^2} \right), \quad (6)$$

where  $Ra$  and  $Pr$  are the Rayleigh number and the Prandtl number, defined as

$$Ra = \frac{g\beta\bar{\Gamma}_w H^4}{\nu\kappa}, \quad Pr = \frac{\nu}{\kappa}, \quad (7)$$

in which  $g$  is the acceleration due to gravity which acts in the negative  $y$ -direction,  $\beta$ ,  $\nu$  and  $\kappa$  are the thermal expansion coefficient, kinematic viscosity and thermal diffusivity of the fluid,  $H$  is the height of the plate, and  $\bar{\Gamma}_w$  is the time-averaged temperature gradient across the plate thickness calculated by

$$\bar{\Gamma}_w = \frac{1}{t_{total}} \int_0^{t_{total}} \Gamma_{wm} \sin(2\pi ft) dt = \frac{2}{\pi} \Gamma_{wm}, \quad (8)$$

where  $t_{total}$  is the total heating time of the time-varying flux applied. In this paper, it is assumed that  $2\pi ft_{total} = \pi$ , i.e.,  $f = 0.5/t_{total}$  (hence only the first half heating cycle is considered, which is in line with the time-dependent solar radiation model under a clear sky condition, although the results obtained here are not limited to only the cases driven by time-dependent solar radiation). Apparently,  $Ra$  defined above is the time-averaged global Rayleigh number for the unsteady natural convection boundary layer over the duration of heating under the time-varying flux applied to the plate.

In the above governing equations,  $x$ ,  $y$ ,  $u$ ,  $v$ ,  $\tau$ ,  $p$ , and  $\theta$  are respectively the dimensionless forms of  $X$ ,  $Y$ ,  $U$ ,  $V$ ,  $t$ ,  $P$ , and  $T$ , which are the horizontal and vertical coordinates, horizontal and vertical

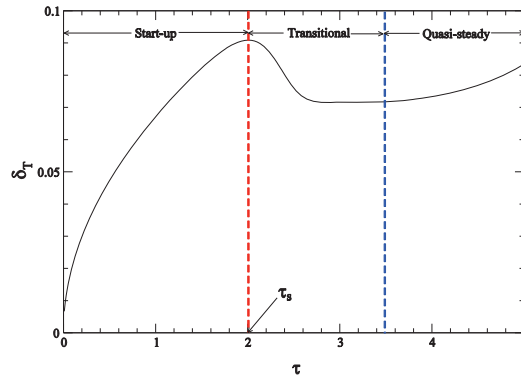
velocity components, time, pressure, and temperature.  $x$ ,  $y$ ,  $u$ ,  $v$ ,  $\tau$ ,  $p$ , and  $\theta$  are made dimensionless by their respective characteristic scales as follows,

$$x = \frac{X}{H}, y = \frac{Y}{H}, u = \frac{U}{V_0}, v = \frac{V}{V_0}, \tau = \frac{t}{(H/V_0)}, p = \frac{P}{\rho V_0^2}, \theta = \frac{T - T_a}{\bar{T}_w}, \quad (9)$$

in which  $H$  is the characteristic length scale,  $T_a$  is the initial temperature of the ambient fluid,  $V_0 = \kappa Ra^{2/5} / H$  is the characteristic velocity scale,  $\bar{T}_w = \bar{\Gamma}_w H = 2\Gamma_{wm} H / \pi$  is the characteristic temperature difference scale, respectively.

### Scalings

With the initiation of the flow, a vertical boundary layer will be developed adjacent to the plate, experiencing a start-up stage dominated by one-dimensional conduction, followed by a transitional stage during which a transition to two-dimensional convection occurs, before eventually attaining a quasi-steady state, with the transition time scale  $\tau_s$  to separate the start-up stage and the transitional stage, as illustrated in Fig. 1, where a typical numerically simulated time series of the dimensionless thermal boundary-layer thickness  $\delta_T$  at height  $y=0.5$  for the specific case of  $Ra=10^8$ ,  $Pr=7$  and  $f_n=0.1$  ( $f_n=f/(V_0/H)$  is the dimensionless natural frequency of the time-varying flux applied) is shown. Similar behavior is also observed for the other parameters to represent the transient behavior of an unsteady natural convection boundary layer on a vertical plate evenly heated with a time-varying heat flux, i.e., the plate temperature,  $\theta_w$ , the maximum vertical velocity within the boundary layer,  $v_m$ , and the inner viscous boundary-layer thickness,  $\delta_{vi}$ , as shown in Fig. 2.



**Figure 1. The three development stages of an unsteady natural convection boundary layer.**

We have developed the following dimensionless scalings for the unsteady natural convection boundary layer of a homogeneous Newtonian fluid with  $Pr > 1$  adjacent to a vertical plate evenly heated with a time-varying sinusoidal heat flux:

1. *At the start-up stage:*

$$\delta_T \sim \frac{\tau^{1/2}}{Ra^{1/5}}, \quad (10)$$

$$\delta_{vi} \sim \frac{\tau^{1/2}}{(1 + Pr^{-1/2})Ra^{1/5}}, \quad (11)$$

$$\theta_w \sim \left( \frac{\pi}{2} \right) \frac{\sin(2\pi f_n \tau) \tau^{1/2}}{Ra^{1/5}}, \quad (12)$$

$$v_m \sim \left( \frac{\pi}{2} \right) \frac{\sin(2\pi f_n \tau) \tau^{3/2}}{(1 + Pr^{-1/2})^2}. \quad (13)$$

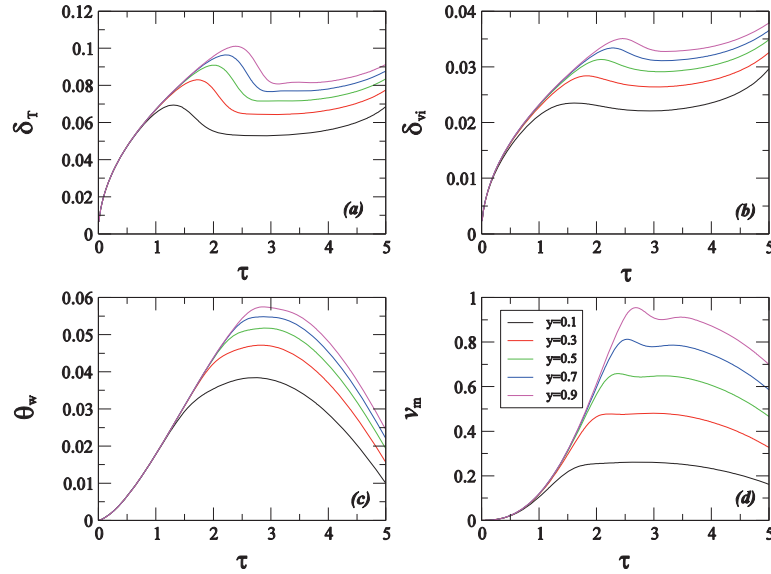


Figure 2. Time series of  $\delta_T$ ,  $\delta_{vi}$ ,  $\theta_w$ , and  $v_m$  at  $y=0.1, 0.3, 0.5, 0.7$  and  $0.9$  for the case of  $Ra=10^8$ ,  $Pr=7$  and  $f_n=0.1$ .

2. At the dimensionless transition time scale  $\tau_s$ :

$$\delta_{T,s} \sim \left(\frac{2}{\pi}\right)^{1/5} \frac{(1+Pr^{-1/2})^{2/5} y^{1/5}}{[\sin(2\pi f_n \tau_s)]^{1/5} Ra^{1/5}}, \quad (14)$$

$$\delta_{vi,s} \sim \left(\frac{2}{\pi}\right)^{1/5} \frac{y^{1/5}}{(1+Pr^{-1/2})^{3/5} [\sin(2\pi f_n \tau_s)]^{1/5} Ra^{1/5}}, \quad (15)$$

$$\theta_{w,s} \sim \left(\frac{\pi}{2}\right)^{4/5} \frac{(1+Pr^{-1/2})^{2/5} [\sin(2\pi f_n \tau_s)]^{4/5} y^{1/5}}{Ra^{1/5}}, \quad (16)$$

$$v_{m,s} \sim \left(\frac{\pi}{2}\right)^{2/5} \frac{[\sin(2\pi f_n \tau_s)]^{2/5} y^{3/5}}{(1+Pr^{-1/2})^{4/5}}. \quad (17)$$

3. At the quasi-steady state:

$$\delta_{T,qs} \sim \left(\frac{2}{\pi}\right)^{1/5} \frac{(1+Pr^{-1/2})^{2/5} y^{1/5}}{[\sin(2\pi f_n \tau)]^{1/5} Ra^{1/5}}, \quad (18)$$

$$\delta_{vi,qs} \sim \left(\frac{2}{\pi}\right)^{1/5} \frac{y^{1/5}}{(1+Pr^{-1/2})^{3/5} [\sin(2\pi f_n \tau)]^{1/5} Ra^{1/5}}, \quad (19)$$

$$\theta_{w,qs} \sim \left(\frac{\pi}{2}\right)^{4/5} \frac{(1+Pr^{-1/2})^{2/5} [\sin(2\pi f_n \tau)]^{4/5} y^{1/5}}{Ra^{1/5}}, \quad (20)$$

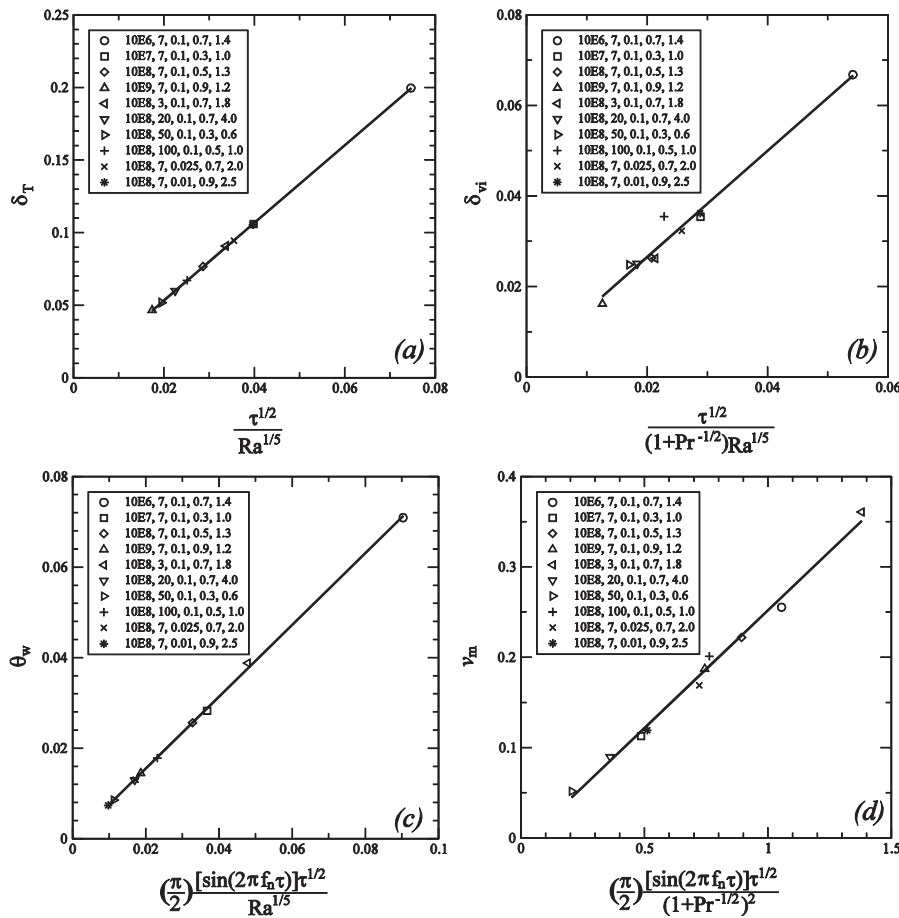
$$v_{m,qs} \sim \left(\frac{\pi}{2}\right)^{2/5} \frac{[\sin(2\pi f_n \tau)]^{2/5} y^{3/5}}{(1+Pr^{-1/2})^{4/5}}. \quad (21)$$

### Validation and quantification of scalings with numerical results

From the scalings, it is clear that the major parameters that govern the behavior of the unsteady natural convection boundary layer studied in this work are  $Ra$ ,  $Pr$ , and  $f_n$ . To examine the effects of these three parameters on the scalings ten direct numerical simulation runs were performed; four

runs are at varying  $Ra$  ( $10^6$ ,  $10^7$ ,  $10^8$ , and  $10^9$ , respectively) with fixed  $Pr=7$  and  $f_n=0.1$  for the  $Ra$  dependence; five runs are at varying  $Pr$  (3, 7, 20, 50, and 100, respectively) with fixed  $Ra=10^8$  and  $f_n=0.1$  for the  $Pr$  dependence; and three runs are at varying  $f_n$  (0.1, 0.025, and 0.01, respectively) with fixed  $Ra=10^8$  and  $Pr=7$  for the  $f_n$  dependence. All simulations were conducted in a dimensionless  $2 \times 2$  computational domain with a mesh of  $399 \times 396$  nodes. This mesh was chosen after a detailed mesh dependence test which ensures the simulation results obtained with it are mesh independent. The same code used in Lin and Armfield (1999, 2001, 2005, 2012) was used for these simulations. As the numerical methods, the construction and dependence test of the computational meshes, and the benchmarking of the code against the known theoretical results were well detailed in these references, these will not be repeated here.

### 1. At the start-up stage



**Figure 3.** Validation and quantification of the scalings at the start-up stage with the numerical results.

The validation results for the scalings at the start-up stage are presented in Fig. 3, which clearly shows that all scalings are in good agreement with the numerical results as each scaling collapses the corresponding numerical results well onto a single straight line. The scalings are also quantified by the numerical results with a linear regression technique, giving the following quantified relations:

$$\delta_T = 2.676 \frac{\tau^{1/2}}{Ra^{1/5}}, \quad (22)$$

$$\delta_{vi} = 1.251 \frac{\tau^{1/2}}{(1 + Pr^{-1/2}) Ra^{1/5}}, \quad (23)$$

$$\theta_w = 0.767 \left( \frac{\pi}{2} \right) \frac{\sin(2\pi f_n \tau)^{1/2}}{Ra^{1/5}}, \quad (24)$$

$$v_m = 0.261 \left( \frac{\pi}{2} \right) \frac{\sin(2\pi f_n \tau)^{3/2}}{(1 + Pr^{-1/2})^2}. \quad (25)$$

## 2. At the dimensionless transition time scale $\tau_s$

The validation results for the scalings at the dimensionless transition time scale  $\tau_s$  are presented in Fig. 4, which clearly shows that all scalings are also in good agreement with the numerical results as each scaling collapses the corresponding numerical results well onto a single straight line. The scalings are also quantified by the numerical results with the following quantified relations:

$$\delta_{T,s} = 3.906 \left( \frac{2}{\pi} \right)^{1/5} \frac{(1 + Pr^{-1/2})^{2/5} y^{1/5}}{[\sin(2\pi f_n \tau_s)]^{1/5} Ra^{1/5}}, \quad (26)$$

$$\delta_{v_i,s} = 1.775 \left( \frac{2}{\pi} \right)^{1/5} \frac{y^{1/5}}{(1 + Pr^{-1/2})^{3/5} [\sin(2\pi f_n \tau_s)]^{1/5} Ra^{1/5}}, \quad (27)$$

$$\theta_{w,s} = 1.291 \left( \frac{\pi}{2} \right)^{4/5} \frac{(1 + Pr^{-1/2})^{2/5} [\sin(2\pi f_n \tau_s)]^{4/5} y^{1/5}}{Ra^{1/5}}, \quad (28)$$

$$v_{m,s} = 1.053 \left( \frac{\pi}{2} \right)^{2/5} \frac{[\sin(2\pi f_n \tau_s)]^{2/5} y^{3/5}}{(1 + Pr^{-1/2})^{4/5}}. \quad (29)$$

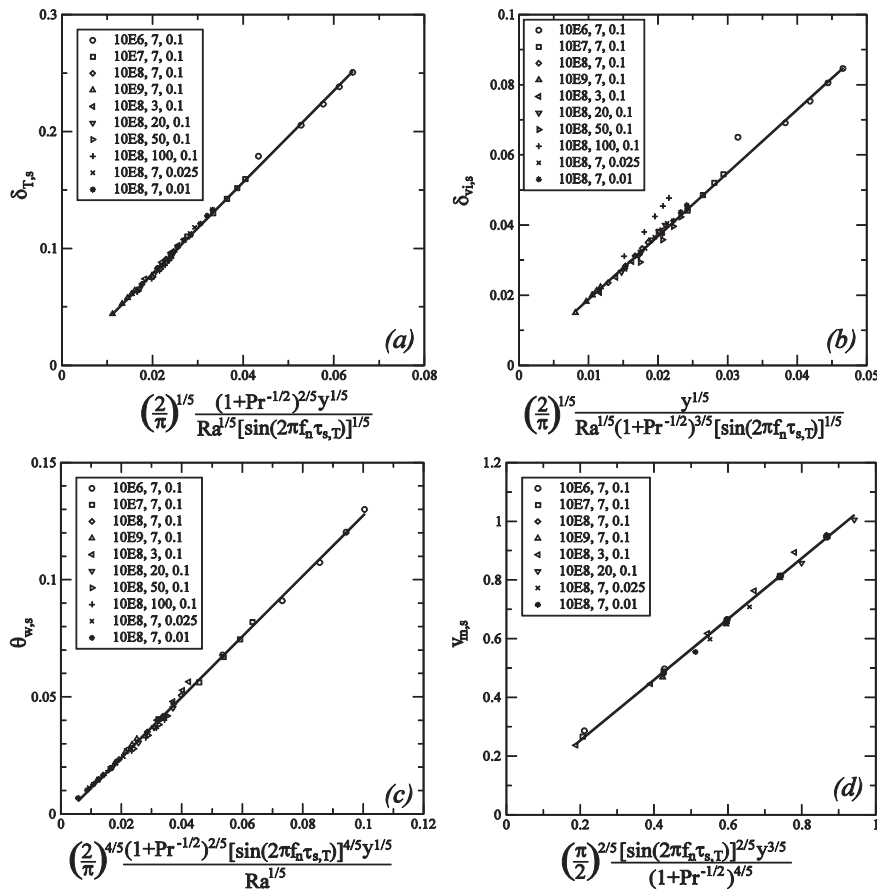


Figure 4. Validation and quantification of the scalings at the dimensionless transition time scale  $\tau_s$  with the numerical results.



### 3. At the quasi-steady state

The validation results for the scalings at the quasi-steady state are presented in Fig. 5, which clearly shows that all scalings are again in good agreement with the numerical results as each scaling collapses the corresponding numerical results well onto a single straight line. The scalings are again quantified by the numerical results with the following quantified relations:

$$\delta_{T,qs} = 2.988 \left( \frac{2}{\pi} \right)^{1/5} \frac{(1 + Pr^{-1/2})^{2/5} y^{1/5}}{[\sin(2\pi f_n \tau)]^{1/5} Ra^{1/5}}, \quad (30)$$

$$\delta_{vi,qs} = 1.640 \left( \frac{2}{\pi} \right)^{1/5} \frac{y^{1/5}}{(1 + Pr^{-1/2})^{3/5} [\sin(2\pi f_n \tau)]^{1/5} Ra^{1/5}}, \quad (31)$$

$$\theta_{w,qs} = 1.684 \left( \frac{\pi}{2} \right)^{4/5} \frac{(1 + Pr^{-1/2})^{2/5} [\sin(2\pi f_n \tau)]^{4/5} y^{1/5}}{Ra^{1/5}}, \quad (32)$$

$$v_{m,qs} = 0.1136 + 1.039 \left( \frac{\pi}{2} \right)^{2/5} \frac{[\sin(2\pi f_n \tau)]^{2/5} y^{3/5}}{(1 + Pr^{-1/2})^{4/5}}. \quad (33)$$

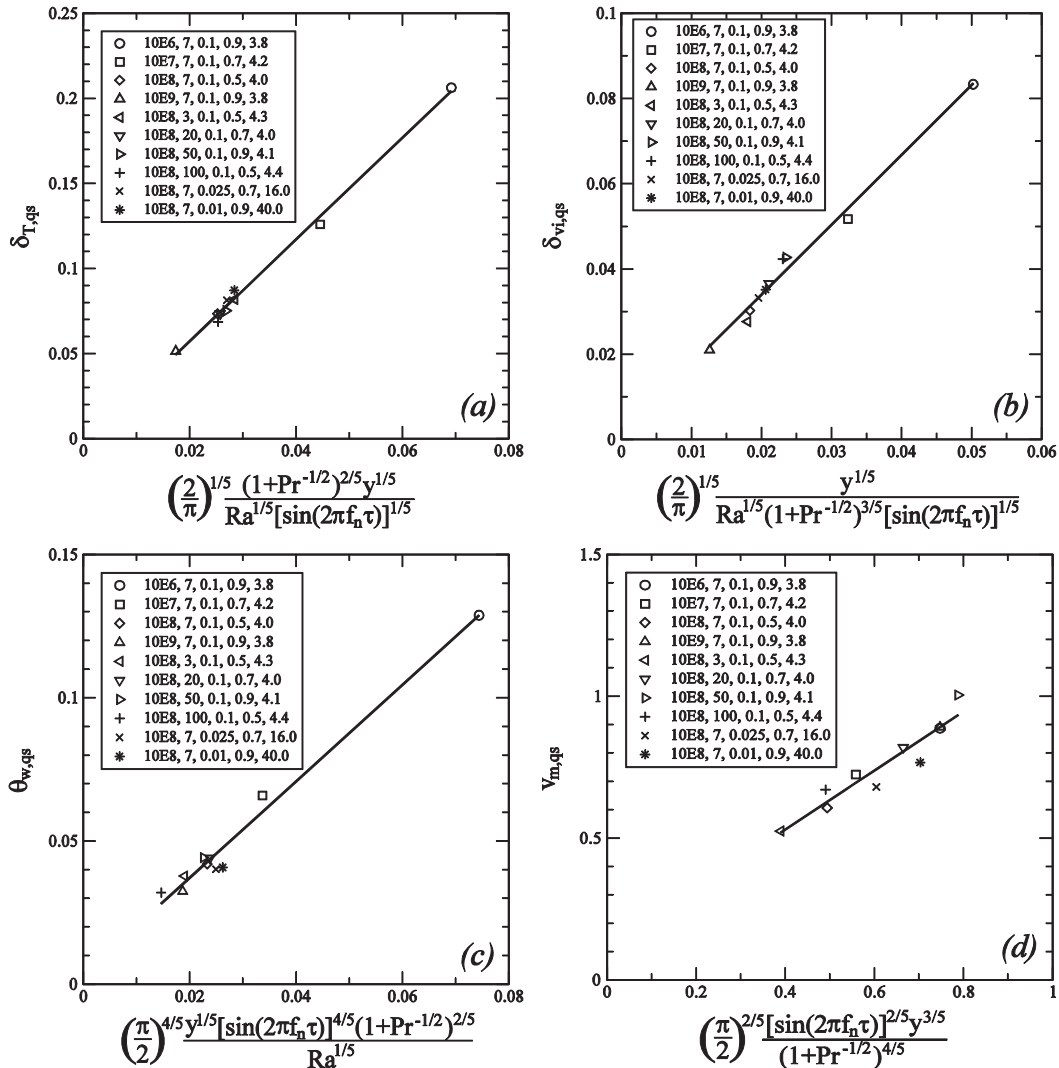


Figure 5. Validation and quantification of the scalings at the quasi-steady state with the numerical results.

## Conclusions

In this paper, it was found that the transient and quasi-steady flow behavior of the unsteady natural convection boundary layer of a homogeneous Newtonian fluid with  $Pr > 1$  adjacent to a vertical plate evenly heated with a time-varying sinusoidal heat flux is controlled by the Rayleigh number, the Prandtl number, and the dimensionless natural frequency of the sinusoidal heat flux and is well represented by parameters such as the thermal boundary-layer thickness, the plate temperature, the viscous boundary-layer thickness, and the maximum vertical velocity within the boundary layer. The scalings developed for these parameters were compared with a series of direct numerical simulation, which clearly shows that these scalings in general predict the flow behavior very well, no matter at the start-up stage, or at the transition time scale which represents the end of the start-up stage and the beginning of the transitional stage of the boundary-layer development, or at the quasi-steady state.

## Acknowledgments

The support from the National Natural Science Foundation of China (Grant No. 11072211), the Natural Science Foundation of Yunnan Province (2011FA017), the Program for Changjiang Scholars and Innovative Research Team in University of Ministry of Education of China, and the Australian Research Council is gratefully acknowledged.

## References

- Armfield, S. W., Patterson, J. C. and Lin, W. (2007), Scaling investigation of the natural convection boundary layer on an evenly heated plate. *Int. J. Heat Mass Transfer*, 50, pp. 1592–1602.
- Bednarz, T. P., Lei, C. and Patterson, J. C. (2009), A numerical study of unsteady natural convection induced by iso-flux surface cooling in a reservoir model. *Int. J. Heat Mass Transfer*, 52, pp. 56–66.
- Capobianchi, M. and Aziz, A. (2012), A scale analysis for natural convective flows over vertical surfaces. *Int. J. Thermal Sciences*, 54, 82–88.
- Hyun, J. M. (1994), Unsteady buoyant convection in an enclosure. *Adv. Heat Transfer*, 24, pp. 277–320.
- Lin, W. and Armfield, S. W. (1999), Direct simulation of natural convection cooling in a vertical circular cylinder. *Int. J. Heat Mass Transfer*, 42, pp. 4117–4130.
- Lin, W. and Armfield, S. W. (2001), Natural convection cooling of rectangular and cylindrical containers. *Int. J. Heat Fluid Flow*, 22, pp. 72–81.
- Lin, W. and Armfield, S. W. (2005), Scaling laws for unsteady natural convection cooling of fluid with Prandtl number less than one in a vertical cylinder. *Phys. Rev. E*, 72, article no. 016306.
- Lin, W. and Armfield, S. W. (2012), Unified Prandtl number scaling for start-up and fully developed natural-convection boundary layers for both  $Pr > 1$  and  $Pr < 1$  fluids with isothermal heating. *Phys. Rev. E*, 86, article no. 066312.
- Lin, W., Armfield, S. W. and Patterson, J. C. (2007), Cooling of a  $Pr < 1$  fluid in a rectangular container. *J. Fluid Mech.*, 574, 85–108.
- Lin, W., Armfield, S. W., Patterson, J. C. and Lei, C. (2009), Prandtl number scaling of unsteady natural convection boundary layers for  $Pr > 1$  fluids under isothermal heating. *Phys. Rev. E*, 79, article no. 066313.
- Patterson, J. C. and Imberger, J. (1980), Unsteady natural convection in a rectangular cavity. *J. Fluid Mech.*, 100, pp. 65–86.
- Patterson, J. C., Lei, C., Armfield, S. W. and Lin, W. (2009), Scaling of unsteady natural convection boundary layers with a non-instantaneous initiation. *Int. J. Thermal Science*, 48, pp. 1843–1852.
- Saha, S. C., Brown, R. J. and Gu, Y. T. (2012), Scaling for the Prandtl number of the natural convection boundary layer of an inclined flat plate under uniform surface heat flux. *Int. J. Heat Mass Transfer*, 55, 2394–2401.

## Numerical Simulation of Nonlinear Acoustic Waves in Two-Phase Fluid

\* Yoshiaki Tamura<sup>1</sup>, Nobuo Tsurumi<sup>2</sup>, and Yoichiro Matsumoto<sup>3</sup>

<sup>1</sup> School of Information Sciences and Arts / Center for Computational Mechanics Research, Toyo University, Kujirai 2100, Kawagoe, Saitama 350-8585, Japan.

<sup>2</sup> ANSYS Japan K.K., 6-10-1 Nishishinjuku, Shinjuku-ku, Tokyo 160-0023, Japan.

<sup>3</sup> School of Engineering, The University of Tokyo, Hongo 7-3-1, Bunkyo-ku, Tokyo 113-8656, Japan.

\*Corresponding author: tamura@toyo.jp

### Abstract

Nonlinear acoustic wave propagation equation with void fraction (volume fraction of gas phase) is derived and numerically solved for the simulation of HIFU (High Intensity Focused Ultrasound) with micorbubbles in the present paper. HIFU is one of promising treatments for cancer. The focused pressure waves generate heat and necrose cancer cells. It has been lately reported that the existence of micorbubbles enhances heating at the focal area and the present paper is intended to clarify this mechanism with numerical approach. After describing the derivation of the governing equations and the detail of the numerical method, computed results with varying initial void fractions and bubble sizes are presented to show the propagation of ultrasound and the bubble motions in the focal area. Additionally heat generation by microbubbles are also simulated and evaluated.

**Keywords:** Ultrasound, Bubble, CFD, Multiphase, HIFU (High Intensity Focused Ultrasound)

### Introduction

HIFU (High Intensity Focused Ultrasound) is a promising treatment for cancer because of its low invasiveness, high controllability and low cost compared with other existing methods. On the other hand, HIFU has a problem when it is applied to deep body such as liver cancer. Ultrasound may reflect and refract due to non-uniformity of body tissue and the focal area then shifts or diffuses. At the same time, attenuation of ultrasound during the propagation is not also negligible. As a result, insufficient energy reaches the lesion. To overcome this problem, utilization of microbubbles is proposed (Bailey et al., 2001; Holt and Roy, 2001). Bubbles exposed in ultrasound oscillate volumetrically and convert kinetic energy of ultrasound into heat energy. This phenomenon has been experimentally observed but the detailed mechanism has not yet been clear. In this paper, ultrasound wave propagation in fluid with microbubbles is numerically simulated. First, nonlinear acoustic wave propagation equation with void fraction (volume fraction of gas phase) is derived. Second, the above equation is solved with Keller equation that describes the volumetric motion of a bubble, varying initial bubble size and void fraction. Finally heat generation by bubbles is numerically simulated solving the heat conduction equation to evaluate the effect of bubbles.

### Derivation of Equations

Nonlinear acoustic wave propagation equation with void fraction is derived from the following two conservation equations and one constraint.

- *Conservation of mass*

$$\frac{\partial(f_L \rho_L)}{\partial t} + \frac{\partial(f_L \rho_L u_{Lj})}{\partial x_j} = 0 \quad (1)$$

- *Conservation of momentum*

$$\frac{\partial(f_L \rho_L u_{Li})}{\partial t} + \frac{\partial(f_L \rho_L u_{Li} u_{Lj})}{\partial x_j} = -\nabla_i P \quad (2)$$

- *Volume constraint*

$$f_G + f_L = \frac{4}{3} \pi r_G^3 n_G + f_L = 1 \quad (3)$$

Suffix  $L$  denotes liquid and  $G$  denotes gas.  $f$  the volume fraction,  $\rho$  the density,  $u$  the velocity,  $P$  the pressure and  $r$  the radius. Here bubbles are assumed to be all spherical and to keep number density  $n_G$  be constant. Following the derivation of KZK (Khokhlov – Zabolotskaya – Kuznetsov) equation (Zabolotskaya and Khokhlov, 1969; Kuznetsov, 1970) to introduce small perturbation up to the second order terms and Aubry et al.'s idea of ultrasound propagation in inhomogeneous medium (Aubry et al., 2003), the following equation is obtained finally.

$$\begin{aligned} \frac{\partial^2(f_L p)}{\partial t^2} = & c_{L0}^2 \left( 2 \frac{\partial^2 p}{\partial x_j^2} - \frac{\partial}{\partial x_j} \left( f_L \frac{\partial p}{\partial x_j} \right) \right) + \frac{\beta}{\rho_{L0} c_{L0}^2} \frac{\partial^2}{\partial t^2} (f_L p^2) \\ & + \frac{\lambda_L}{\rho_{L0} c_{L0}^2} \left( \frac{1}{c_{vL}} - \frac{1}{c_{pL}} \right) \frac{\partial^2}{\partial t^2} \left( f_L \frac{\partial p}{\partial t} \right) + \frac{\partial}{\partial t} \left( p \frac{\partial f_L}{\partial t} \right) - \rho_{L0} c_{L0}^2 \frac{\partial^2 f_L}{\partial t^2} \end{aligned} \quad (4)$$

where  $\lambda$  is heat conductivity,  $c$  is speed of sound,  $p$  is perturbation pressure,  $c_v$  and  $c_p$  are specific heat at constant volume or pressure, respectively and suffix 0 denotes the equilibrium state.  $\beta$  is called nonlinear coefficient and is a material property. For volumetric oscillation of bubbles, the Keller's equation (Keller and Kolodner, 1956) is solved together with eq. (4).

$$\begin{aligned} r_G \left( 1 - \frac{1}{c_{L0}} \frac{dr_G}{dt} \right) \frac{d^2 r_G}{dt^2} + \frac{3}{2} \left( 1 - \frac{1}{3c_{L0}} \frac{dr_G}{dt} \right) \left( \frac{dr_G}{dt} \right)^2 \\ = \frac{1}{\rho_{L0}} \left( 1 + \frac{1}{c_{L0}} \frac{dr_G}{dt} + \frac{1}{c_{L0}} r_G \frac{d}{dt} \right) \left( P_G - \frac{2\sigma}{r_G} - \frac{4\mu_L}{r_G} \frac{dr_G}{dt} - P_L \right) \end{aligned} \quad (5)$$

where  $r_G$  is bubble radius,  $\sigma$  is the surface tension,  $\mu$  is viscosity coefficient.  $P_G$ , the pressure inside of the bubble, is obtained with a reduced-order model (Preston and et al., 2002; Sugiyama et al., 2005). Lastly the heat conduction equation (6) is used for estimating the temperature rise around the focal area.

$$\rho_L c_{pL} \frac{\partial T}{\partial \tau} = \frac{\partial}{\partial x} \left( \lambda_L \frac{\partial T}{\partial x} \right) + \frac{\partial}{\partial r} \left( \lambda_L \frac{\partial T}{\partial r} \right) + \frac{1}{r} \left( \lambda_L \frac{\partial T}{\partial x} \right) + \bar{W}_{th} + \bar{W}_{vis} \quad (6)$$

where  $\bar{W}_{th}$  and  $\bar{W}_{vis}$  are time-averaged heat source terms of

$$\begin{aligned} W_{th} = & -\lambda_G \frac{\partial T}{\partial r} \Big|_{r=R} \cdot 4\pi r_G^2 \\ W_{vis} = & 4\mu_L \frac{1}{r_G} \frac{dr_G}{dt} \frac{dr_G}{dt} \cdot 4\pi r_G^2 \end{aligned} \quad (7)$$

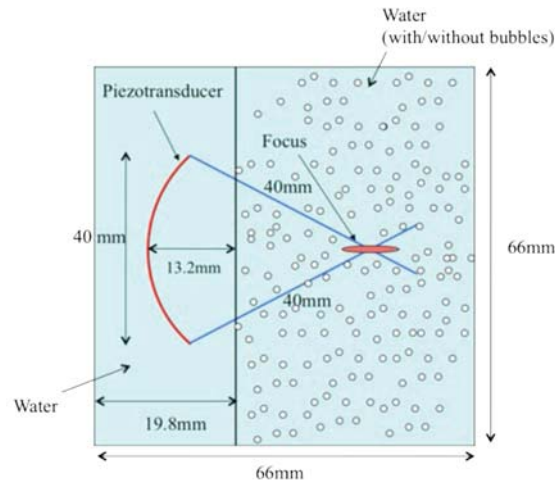
and they are the thermal conduction from a bubble and the viscous dissipation of surrounding liquid, respectively.

## Numerical Methods

Equations (4) and (6) are solved by a finite difference method. The spatial terms are discretized with second order central difference and the temporal terms are discretized with second order backward difference, resulting the second order accuracy scheme. The Keller's equation (5) is integrated with 2nd order Runge-Kutta method.

## Results and Discussions

The present problem setup is illustrated in Fig. 1. The right hand side of area is assumed to be human body and bubbles are uniformly distributed. The outside of the body is filled with water. Thus reflection and fraction are expected to occur at the interface. Typical conditions are summarized in Table 1.

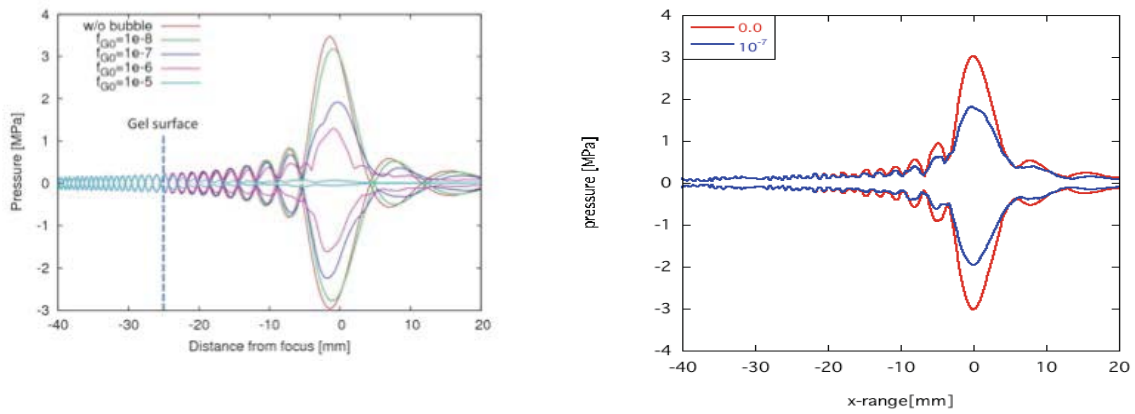


**Figure 1. Problem Setup**

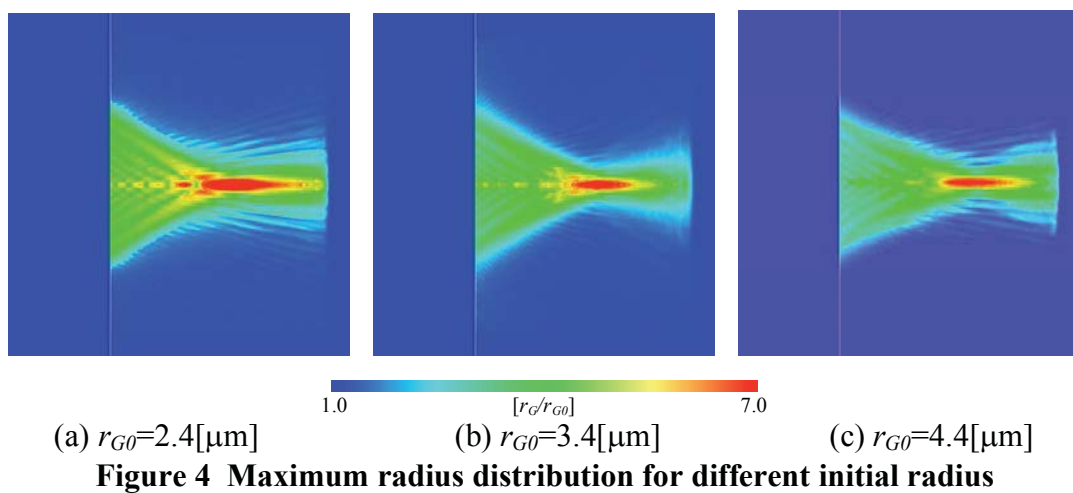
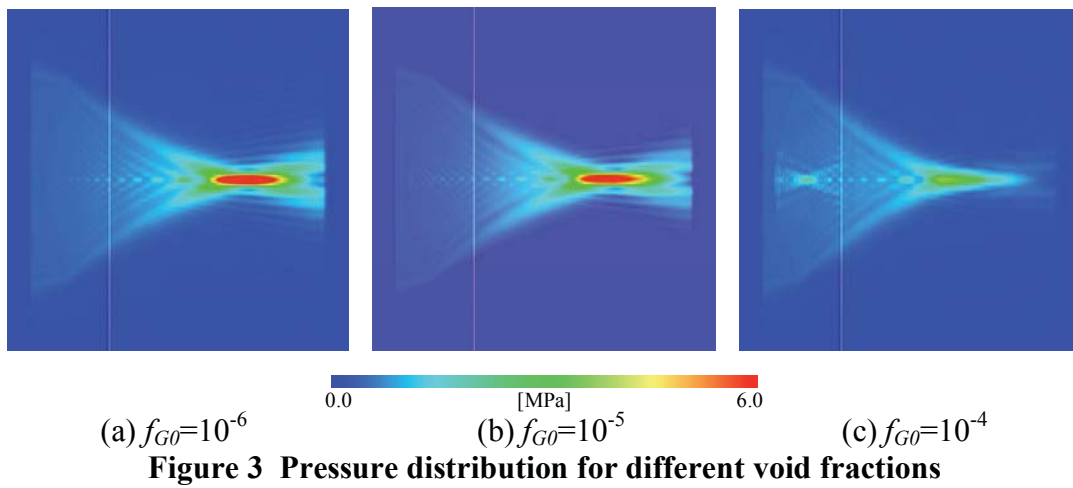
**Table 1. Summary of conditions**

Liquid phase, Gas phase	Water, Air
Liquid density	1,000 kg/m <sup>3</sup>
Sound speed of liquid	1,500 m/s
Liquid viscosity	$8.64 \times 10^{-4}$ Pa·s
Liquid specific heat at constant pressure	4.179 J/kg K
Liquid specific heat ratio	1.012
Liquid thermal conductivity	$6.1 \times 10^{-1}$ W/m K
Coefficient of nonlinearity	3.5
Initial pressure	101.3 kPa
Input frequency	1.0 MHz
Wave cycle	Continuous wave
Void fraction	0.0, $1.0 \times 10^{-6}$ , $10^{-5}$ , $10^{-4}$
Bubble radius	2.4, 3.4, 4.4, 10.0 $\mu$ m
Surface tension	$7.2 \times 10^{-2}$ N/m
Gas specific heat ratio	1.4

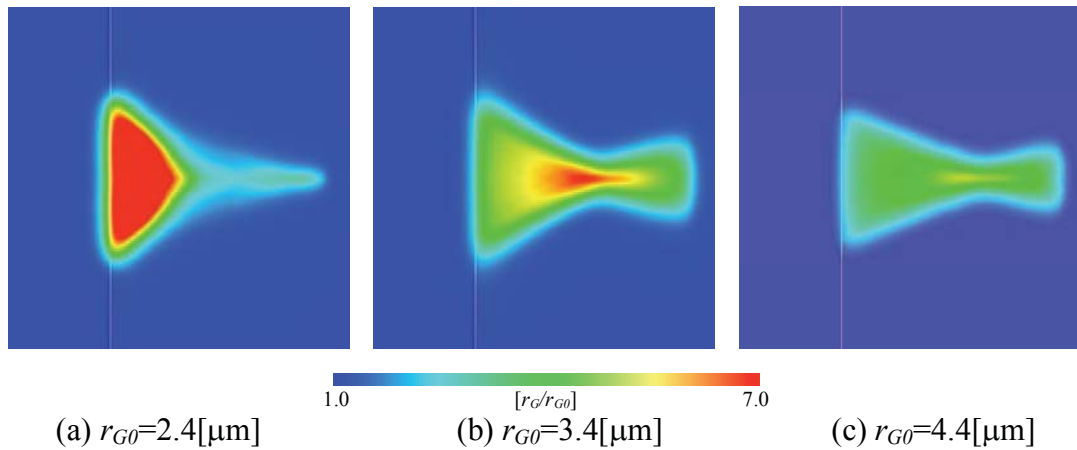
First, Figure 2 shows a comparison with the other research result (Okita et al., 2012) of similar problem setting, solved with a stricter but more time consuming method. The maximum pressure distribution on the axis of symmetry shows good agreement, especially the pressure drop at the focal area with higher void fraction case. Figures 3 show maximum absolute pressure distribution under the continuous wave radiation with two void fractions. High void fraction prevents ultrasound to penetrate and the pressure in focal area is much lower. Figures 4 compare the effect of bubble size with initial void fraction of  $10^{-6}$ . The radius of 3.4 $\mu$ m is the resonance radius of 1MHz for the linear theory. However the result suggests that 2.4 $\mu$ m is closer to the resonance due to the nonlinear effect, because the bubbles react more violently.



**Figure 2 Validation of the present method; maximum pressure distribution on the axis of symmetry. left: Okita et al. (2012), right: present**



Finally, Figures 5 give temperature rise due to the bubbles after 30 second in cases of Fig. 3. In the case of  $2.4\mu\text{m}$  radius, bubbles oscillate close to the interface and thus the temperature at the focal area does not rise.



**Figure 5 Temperature rise for different initial radius**

## Conclusions

In order to be applied for HIFU simulation, nonlinear acoustic wave propagation equation with void fraction was derived and numerically solved with Keller's equation. A simple setup of focused ultrasound field with microbubbles gave reasonable results and revealed the effect of void fraction and bubble size. Heat conduction equation was also solved to demonstrate the heat generation of bubbles.

## Acknowledgments

A part of the present research is supported by MEXT Japan of Supported Program for the Strategic Research Foundation at Private Universities.

## References

- Bailey, M. R. et al. (2001), Use of overpressure to assess the role of bubbles in focused ultrasound lesion shape in vitro, *Ultrasound in Medicine & Biology*, 27, 5, pp. 695-708.
- Holt, R. G. and Roy, R. A. (2001), Measurements of bubble-enhanced heating from focused, MHz-frequency ultrasound in a tissue-mimicking material, *Ultrasound in Medicine & Biology*, 27, 10, pp. 1399-1412.
- Zabolotskaya, E.A. and Khokhlov, R. V. (1969), Quasi-plane waves in the nonlinear acoustics of confined beams, *Soviet Physics Acoustics*, 15, pp. 35-40.
- Kuznetsov, V. P. (1970), Equation of nonlinear acoustics, *Soviet Physics Acoustics*, 16, pp.467-470.
- Aubry, J. F. et al. (2003), Experimental demonstration of non invasive transskull adaptive focusing based on prior CT scans, *Journal of the Acoustical Society of America*, 113, 1, pp. 84-93.
- Keller, J.B. and Kolodner, I. I. (1956), Damping of underwater explosion bubble oscillations, *Journal of Applied Physics*, 27, 10, pp. 1152-1161.
- Preston, A. and et al. (2002), A reduce-order model of heat transfer effects on the dynamics of bubbles, *proceedings of ASME FEDSM'02*, Montreal, Canada.
- Sugiyama, K. et al. (2005), A New Reduced-Order Model for the Thermal Damping Effect on Radial Motion of a Bubble : 2nd Report, Validation of the Model by Numerical Simulation, *JSME ser. B*. 71, 2, pp. 1239-1246 (in Japanese).
- Okita, K. et al. (2012), Numerical study on focusing of ultrasounds in microbubble-enhanced high intensity focused ultrasound therapy, *proceeding of ECCOMAS 2012*, Vienna, Austria.

## Finite element modeling of a tunnel affected by dislocation of faults

\*Xingwen Luo<sup>1,2</sup>, Zhenjun Yang<sup>2,3</sup>

<sup>1</sup> State Key Laboratory of Geomechanics and Geotechnical Engineering, Institute of Rock and Soil Mechanics, Chinese Academy of Sciences, Wuhan, Hubei 430071, China

<sup>2</sup> School of Mechanical, Aerospace and Civil Engineering, The University of Manchester, Manchester, M13 9PL, UK

<sup>3</sup> College of Civil Engineering and Architecture, Zhejiang University, Hangzhou 310058, China

\*Corresponding author: luoxw2005@hotmail.com

### Abstract

Many tunnels built in mountainous areas go through active faults whose dislocation can severely affect the stability, strength and serviceability of the tunnels. In this study, finite element method was used to simulate the dislocation of the faults, and we investigated the effects of main factors such as fault dip angle and tunnel lining segment length on the internal stress and deformation of lining structures of the tunnels. Failure mechanism of the lining structures was studied, and the sensitivity of the main factors was analyzed. It is found that the optimal lining segment length of the tunnel was 5m.

**Keywords:** Finite element method, Tunnels through faults, Lining structures, Dislocation of faults, Internal stress, Deformation.

### Introduction

Faults are often encountered in highway tunnel constructions. It is a normal way to avoid faults in highway tunnel constructions in existing design standards<sup>[1]</sup>. But with the rapid development of Chinese national economy and the exploitation of land resources, a number of tunnels constructions projects inevitably encounter faults problems, Especially, in strong earthquake areas. In these areas the faults which the tunnels go through are often active faults. The tunnels go through active faults are hugely impacted by the dislocation of the faults, which have direct impacts on the constructions and operation safety of the tunnels.

The impacts of the faults fracture zone on the tunnel structures are mainly manifested in below two aspects. The first is that the faults fracture zone take place dislocation along the faults surfaces which are often called dislocation problems. The second is that dynamic response characteristics of tunnels in the faults fracture zone under the earthquake which are often called vibration problems. After investigating the designs and studies on tunnels engineering which go through active faults, a lot of studies are concentrated on the anti-seismic of tunnels. Appropriate engineering measures of anti-seismic are relatively mature, but the measure of anti-relatively dislocation is very little.

John Caulfield, et al (2004) designed the tunnel in southern California Claremont water pressure tunnel by expanding its section size and reducing the length of the lining segments. A lot of shear seams in the lining of the tunnel were set in southern California Claremont water pressure tunnel projects<sup>[2,3]</sup>.



Russo M, et al (2002) proposed to build relatively flexible connections in Turkey Bolu highway tunnel projects.<sup>[4-6]</sup>

In China in the construction of WuXiaoLing tunnel (2004) also met the same problem. The tunnel go through an activities fault. The design of the tunnel taken a way of expanding section size and set aside shear displacement seams in the lining of the tunnel<sup>[7]</sup>.

A R Shahidi, et al (2005), in Greece Koohrang-III water pressure tunnels project also adopted a relatively flexible connection design. Numerical calculations was used to certificate that the tunnel was safe when the fault take place dislocation<sup>[8]</sup>.

Jiang Shuping, et al (2008), respectively discussed both of the methods of overexcavation design and hinged design of the tunnels<sup>[9]</sup>.

Hinge design is a way which minimize the length of lining segments. A certain range of the lining segments structures besides the faults become relatively independent after the tunnels which adopted hinge design. The rigid linings of the tunnels are connected by flexible connectors. When the fault take place dislocation the mechanical behavior are concentrated on the flexible connectors or part of the structures, which will cause localized structural damage and not lead to an overall destruction of the whole tunnel structures.

In order to fully reveal the mechanics, deformation and failure characteristics of the lining structures of the tunnels under the dislocation of faults. Numerical simulation of finite element method was adopted to analyze the mechanical and deformation behavior of the tunnel structures under the activity of the dislocation of the faults. Horseshoe-shaped section tunnels are the most widely used in tunnels engineering, so horseshoe-shaped section tunnels were chosen in numerical simulation of the tunnels which go through the faults. In order to reveal better the deformation and failure mechanisms of the dislocation of the faults on the lining structures of the tunnels, we carried out study on the mechanical behavior of the faults.

### **Engineering geology and tectonic**

According to the regional geological data, geological survey and geophysical drilling results, the engineering geology of tunnel zones were below successively: Quaternary Holocene strata colluvium (Q4c+dl), Quaternary Holocene alluvial (Q4al+pl), Fourth Department of Holocene debris accumulation layer (Q4sef) and the Triassic Feixianguan group (Tf), Permian Yangxin group (Py), Liangshan group (Pl) and Carboniferous Zongchanggou (Cz)<sup>[10]</sup>.

Folds traces were not obvious in this tunnel area. The occurrence of the rock in the entrance of the tunnel was  $121^{\circ} \angle 49^{\circ}$ . The occurrence of the rock in the exit of the tunnel was  $321^{\circ} \angle 71^{\circ}$ . The inclination and incidence were subject to effects of the tectonic, and they change quickly in the tunnel area. There were two kinds of faults respectively named F22 and F22-1 going through the tunnel area. Fault F22 go through the tunnel near the entrance of the tunnel, and Fault F22-1 go through the tunnel at the middle of tunnel area. Fault F22-1 and Fault F22 were secondary faults in Longmen Central Fault in China. The two faults active in the 5·12 Earthquake in China and formed cracks in the body of the mountain. A 3-8m width fracture can be seen in Fault F22, and this fracture formed a groove ground subsidence. The large sinking height was approximately 2m. The fracture extends continuously.

## Finite element model establishment and parameters selection

### *Modeling and model size*

The study on the stress and deformation of tunnels structures were strict and complex three dimensional problems in condition of faults taking place dislocation. The longitudinal of tunnels was the largest impacted by the activity of the dislocation of the fault. Therefore, the fault and the tunnel structures could be set orthogonal relation in space when establishing a 3d finite element model. In order to fully reveal the longitudinal deformation and mechanical behavior of the tunnel lining structures under the dislocation of the tunnel and reduce the impact of the boundary of the tunnel, the finite element model size was below: Length×Width ×Height = 120 m ×80 m × 80 m, namely vertical length of the tunnel was 200 m, the lateral width of the tunnel was 60 m, the depth of the tunnel was 40 m and the depth of the top of tunnel was 100 m.

### *Boundary conditions and fault activity simulation implementation*

On the left and the right sides of the finite element calculation model, X direction and Y direction horizontal displacement were restricted respectively. Z direction displacement of the lower plate of the fault was restricted, while its upper plate could active. The fault was a thrust fault. The active pattern was the upper plate of the fault move up while its lower plate kept stable. In the model a displacement was added on the upper plate to simulate the vertical dislocation of the fault. The average dislocation on the fault was 0.5m. The basic conditions of the model were below:

A. The model was composed of bedrock, concrete lining of the tunnel and fault fractured zones.

B. The tunnel went through the faults fractured zones in the model. The left part of the fault was called the lower plate, and the right part of the faults was called the upper plate. The two parts could dislocate along the fault surface. The dislocation pattern was reverse faulting.

### *Material constitutive and calculations parameters*

As geotechnical materials have heterogeneity, anisotropy, strength-difference effect and other characters. Any one model can not fully accurately represent these characteristics of geological materials. There are three categories of constitutive models which are respectively elastic model, plastic model and elastic-plastic model currently in rock and soil. In this analysis model soil and tunnel lining were assumed to be ideal elastic-plastic material. D-P yield criterion and the associated flow rule were adopted because D-P yield criterion could take into account the effects of principal stress and hydrostatic pressure on yield and destruction of the tunnel. Its yield surface smooth and non-angular. It help to determine the direction of the increment of plastic strain and numerical calculations. The material parameters are less and easy to be test or conversed by the Mohr-Coulomb criterion and its material constant. D-P parameters can be conversed as follow formulas.

$$\sigma_y = \frac{9c \cos \varphi}{\sqrt{9 + 3 \sin^2 \varphi}} \quad \alpha = \frac{\sin \varphi}{\sqrt{9 + 3 \sin^2 \varphi}}$$

Contact surface was set between the upper plate and the lower plate of the fault. Between soil and the lining structure a contact surface was also set. Contact analysis was made on these surfaces in the model. Friction coefficient of the contact surface

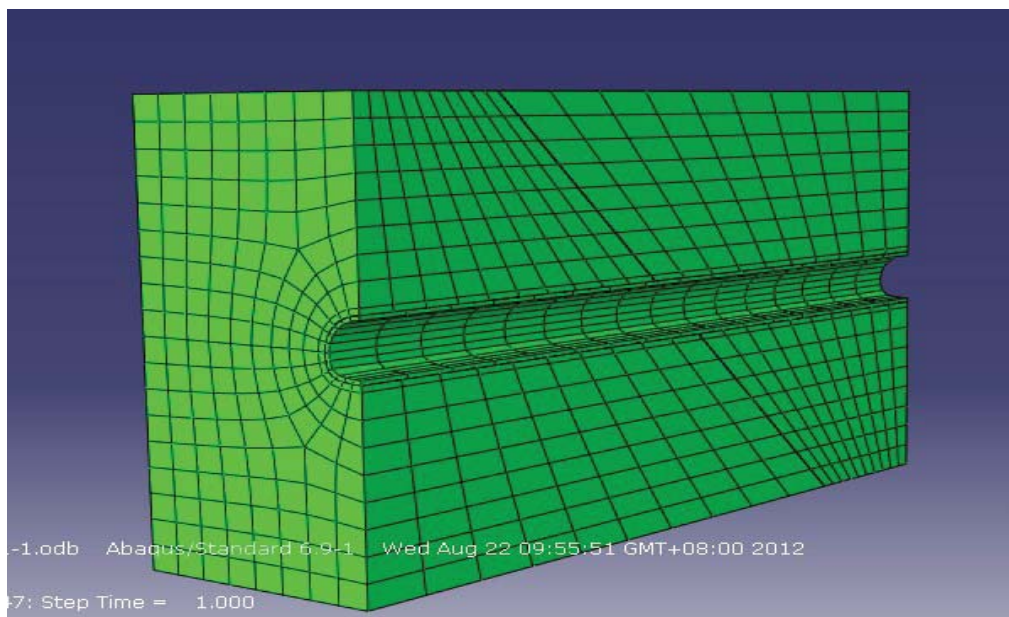
between the upper plate and the lower plate was 0.3. Friction coefficient between strata and tunnel lining structures was 0.7. Coulomb friction model was adopted in the numerical analysis. The inter force and deformation laws of the lining of the tunnel were analyzed under different amount of dislocation in this model. The average calculation dislocations amount was 50cm.

Rock, lining and fracture zones were simulated by solid element. The material of initial support and secondary lining of the tunnel adopted elastic-plastic constitutive. Rock adopted D-P yield criterion and incremental elastic-plastic constitutive. Calculation parameters and calculation model are shown in Table 1 and Figure 1.

**Table 1 Calculation parameters of rock, fracture zone and lining of the tunnel**

Material's name	Modulus /GPa	Poisson's ratio	G /kN.m <sup>-3</sup>	Friction angle /°	Cohesion /MPa
Rock	0.5	0.38	22	34	0.3
Fracture zone	0.05	0.4	18	30	0.1
Lining	28	0.20	25	58	3

Finite element numerical model of cross-fault tunnel under the dislocation of fault is shown in Figure 1.

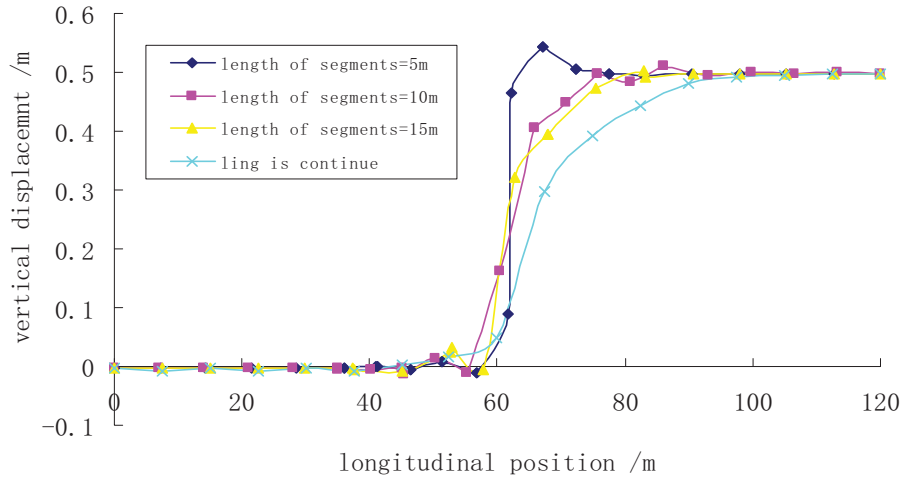


**Figure 1 Finite element numerical model of cross-fault tunnel under the dislocation of the fault**

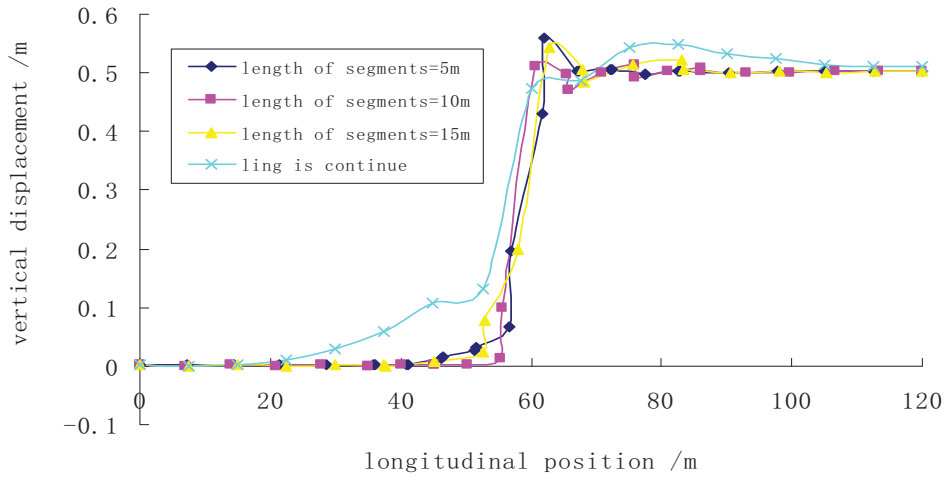
### FEM numerical results

Four kinds of lining segment lengths of the tunnel were taken into account in FME calculation model. They were respectively 15m, 10m, 5m and no shear seam in tunnel which was mean the tunnel was continue. Tunnel lining segment length could be optimized according to FEM calculation.

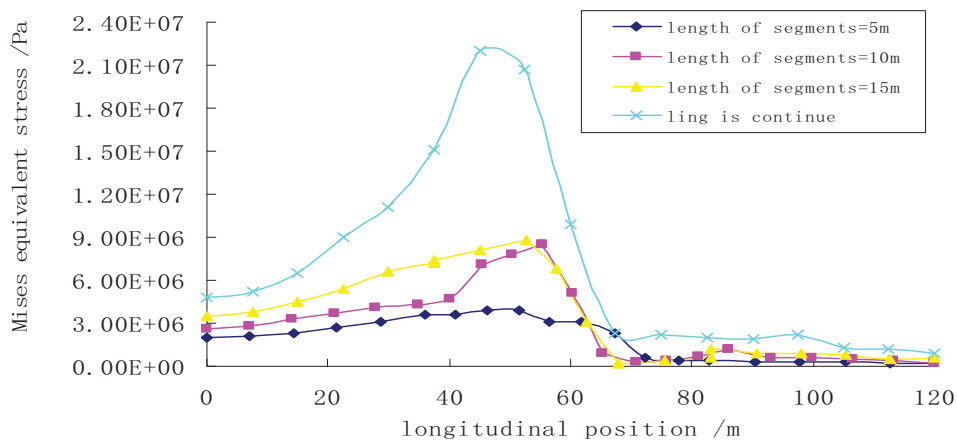
Response results contrast of different lining segments lengths of the tunnel are shown in Fig.2- Fig.6.



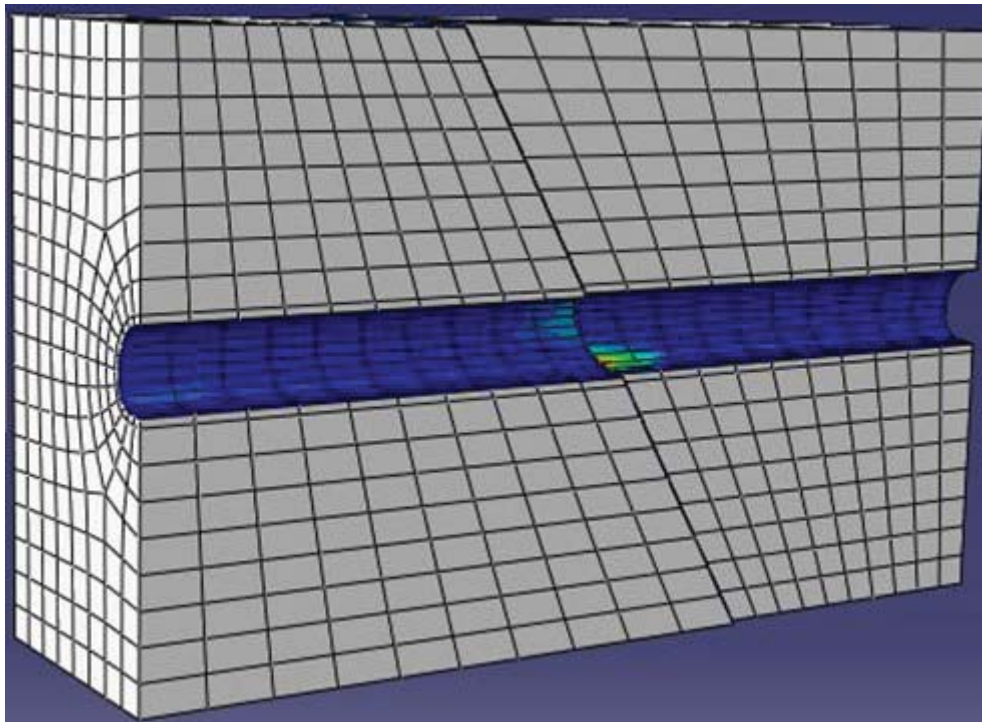
**Figure 2 Vertical displacement of the arch top of the tunnel for different lining segment lengths along longitudinal**



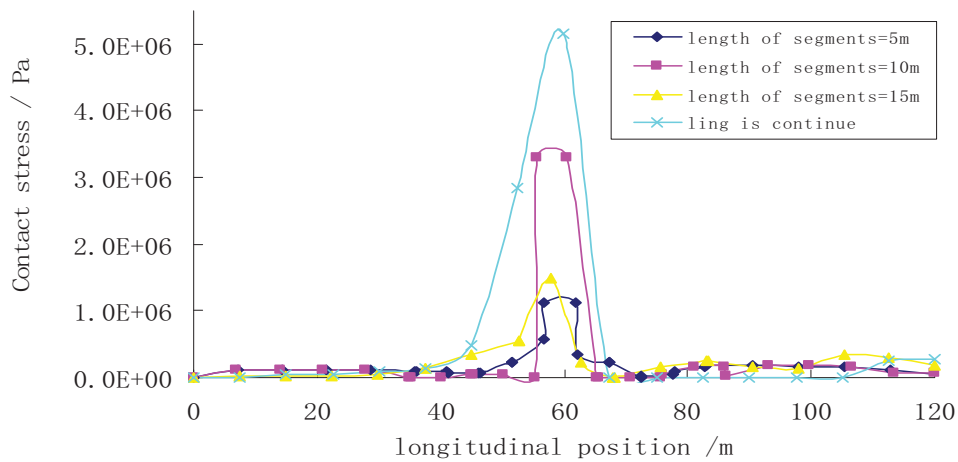
**Figure 3 Vertical displacement of the arch bottom of the tunnel for different lining segment lengths along longitudinal**



**Figure 4 Mises equivalent stress of the arch top of the tunnel for different lining segment lengths along longitudinal**



**Figure 5 Contact stress of the tunnel which the length of segment is 10m under the dislocation of the fault**



**Figure 6 Contact stress of the arch bottom of the tunnel for different lining segment lengths along longitudinal**

**Table 2 Maximum Mises stress of the tunnel for different lining segment lengthss**

Lining segment length	Maximum Mises stress /MPa
No shear seam in tunnel	21.91
15m	20.98
10m	17.5
5m	13.12

## Conclusions

According to dynamic response calculations and the comparison charts of the tunnel structures for different lining segment lengths below conclusions can be get.

(1) It is better to adopt chain segmented structures than non-segmented structures in tunnel engineering. Chain segmented structures tunnel can reduce the influence of the dislocation of the fault on the tunnel structures.

Although vertical displacement along tunnel longitudinal increase with the lining segment length of the tunnel decrease, but the affect zone of the displacement mutation was significantly reduced. The affected zone of dislocation of the fault on the tunnel was 40m when there was no shear seam in the ling structures. When the lining segment length was 5m, the affected zone was the minimum, and the affected length along tunnel longitudinal was shorter than the lining segment length.

(2) After adopting chain segmented structures, the maximum Mises stress of the tunnel lining reduced and the stress reduced more quickly when the lining segment length become shorter. The maximum Mises stress was 13.12MPa when the lining segment length was 5m, and it was 59.88% of the Mises stress of the tunnel with no shear seam . While the maximum Mises were almost the same between the tunnel which the lining segment length was 15m and the tunnel with no shear seam.

The distribution of Mises stress was more uniform with the lining segment length decrease. The maximum stress was mainly concentrated on the lining arch waist of the tunnel near the fault. Contact stress in the tunnel lining reaches maximum near the surface of the fault. With the lining segment length decreases, contact stress of the tunnel lining decrease. Contact stress of the tunnel changed abruptly from the tunnel with no shear seam to the tunnel which the lining segments length was 15m.

(3) The plastic zone significantly reduced when the tunnel adopt chain segmented structures than no-chain segmented structures. When the lining segment length was 15m, the plastic zone of the lining was mainly distributed in one lining segment length range near the fault surface. When the lining segment length was 10 m, the plastic zone of the lining was mainly distributed in one-two lining segment length range near the fault surface. It can be seen the plastic zone of chain segmented structures significantly reduced with the lining segment length decreases. The maximum equivalent plastic strain decreased with the decrease of the lining segment length.

Based on the above analysis, when chain segment structures were adopted in tunnel engineering, the maximum stress, the distribution of the plastic zone and the maximum equivalent plastic strain of the lining significantly reduced. With the decrease of section length, the stress significantly reduced, and it become more uniform. The plastic zone and the maximum equivalent plastic strain were also significantly reduced. When the lining segment length was 5m, the tunnel could adapt to the dislocation of the better than that of the lining segment length was more than 5m. The tunnel which segment length was 5m give full play to the lining of carrying capacity and had good resistance. If the segment length is too short the project costs will increase and it will cause no necessary waste. Also it will increase the construction process and increase the difficulty of construction control when the lining segment length is too short. Therefore the lining segment length of chain segment structures tunnel was recommended 5m.

## References

- [1] WangWei, Ren Qingwen(2006), Research on the effects of active faults of deep buried tunnel

- outline. Earthquake engineering and engineering vibration, 26 (1), pp.175-180
- [2] R. John Caulfield, D. Scott Kieffer, David F. Tsztsoo, Bill Cain (2005), Seismic design measures for the retrofit of the Claremont. RETC PROCEEDINGS, Chapter 89
  - [3] D. Scoa Kieffe, R. John Caulfield, Bill Cain (2001), Seismic upgrades of the Claremont tunnel. RETC PROCEEDINGS, Chapter 68
  - [4] Russo M, Germani G Amberg W(2002), Design and construction of large tunnel through active faults: a recent application, International Conference of Tunnelling & Underground Space Use, pp.16-18
  - [5] Walter AMBERG, Marco RUSSO(2001), Seismic design of underground structures-the Bolu Tunnel. AITES-ITA World Tunnel Congress, ISBN 88-555-2594-8
  - [6] Suleyman Dalglc7(2002), Tunneling in squeezing rock, the Bolu tunnel, Anatolian Motorway, Turkey, Engineering Geology, 6, pp.73-96
  - [7] Wenhao Liang, Guoliang Li (2004), WuXiaoLing tunnel design, Modern tunnel technology, 4(2), pp.1-7
  - [8] Feng Qimin, Shao Guangbiao(2004), Near-fault ground motion attenuation rule of velocity and displacement peak research . Earthquake engineering and engineering vibration, 24 (4), pp.13-19
  - [9] Lipeng(2009), Active fault zone fault structure design of highway tunnel, ChongQing JiaoTong University
  - [10] Sichuan Province Geological Engineering Investigation Institute(2011), MianMao road highway engineering geological investigation report, pp.13-14

# Multi-objective optimization design of coronary stent based on kriging surrogate model

H.X. Li<sup>1</sup>, B. Zhu<sup>2</sup> and \*X.C. Wang<sup>1</sup>

<sup>1</sup>State Key Laboratory of Structural Analysis for Industrial Equipment, Department of Engineering Mechanics, Dalian University of Technology, Dalian 116024, China

<sup>2</sup>Surface Engineering Laboratory, School of Materials Science and Engineering, Dalian University of Technology, Dalian 116024, China

\*Corresponding author: guixum@dlut.edu.cn

## Abstract

To improve the performance of stent expansion for reducing a risk of vascular restenosis injuries, an adaptive optimization method based on the kriging surrogate model is proposed to decrease the dogboning effect (i.e. the ends of a stent opening first during expansion) and the radial recoil of stent dilation. Integrating design of experiment (DOE) methods with the kriging surrogate model can build an approximate functional relationship between the objective function and the design parameters, replacing the expensive reanalysis of the stent dogboning rate and the radial recoil during the optimization process. In this adaptive process, an infilling sampling criterion termed expected improvement (EI) is used to balance local and global search and tends to find the global optimal design. Finite element method is used to analyze stent expansion. As an example, a typical diamond-shaped coronary balloon-stent system is investigated, where six key geometries of stent and the length of balloon are selected to be the design variables. Numerical results demonstrate that the proposed adaptive optimization method can effectively improve the performance of stent dilation.

**Keywords:** Coronary stent, Dogboning, Elastic recoil, Multi-objective optimization, Kriging surrogate model

## 1 Introduction

Cardiovascular diseases are one of the principal causes of mortality, often related to atherosclerosis which may lead to the progressive formation of plaque and eventually cause an obstruction (stenosis) for blood flow through the artery (Beule, 2006). Currently, three of the most common treatments for a narrowed or weakened coronary artery disease are coronary artery bypass grafting, percutaneous transluminal coronary balloon angioplasty, and percutaneous transluminal coronary stenting with the aid of coronary balloon angioplasty. Of these, the coronary stent market increased rapidly because of their high initial success rate, minimal invasive nature, and improved long-term effectiveness compared to coronary artery bypass grafting or coronary balloon angioplasty. A stent is a wire metal mesh tube used to overcome the acute elastic recoil during coronary balloon angioplasty offering radial strength. Coronary balloon angioplasty restores blood flow through narrowed or blocked arteries. Once the balloon removed, the stent remains the shape to act as a scaffold and help prevent arteries from becoming narrowed or blocked again. Although intravascular stents are nowadays routinely and successfully used, this endovascular intervention still remains suboptimal, as the success rate is limited by mechanical failure and restenosis. This phenomenon is related to both arterial injury and inflammatory response of the wall against the stent struts. Therefore, efforts aiming at reducing the injury caused by stent implantations are continuously being researched into.

Previous studies indicate that the dogboning phenomenon (i.e. the ends of a stent opening first during expansion), which is due to non-uniform balloon-stent expansion,



and radial elastic recoil have a significant impact on thrombosis and hyperplasia development (Lim, 2008; Mortier, 2008). This mechanical injury that is caused by the struts of stent is often thought to induce an inflammatory response, which results in thrombosis and affects artery restenosis (McClellan, 2002; Rogers, 1995; Rogers, 1999 and Schulz, 2000). It is believed that the stent design may affect stent expansion performance, including the dogboning phenomenon and radial elastic recoil. Thus, it is important in stenting to predict and optimize the dogboning effect and radial elastic recoil before manufacturing the stent.

Computer simulation (e.g., finite element analysis (FEA)) can be a very useful tool to study the stent expansion (Dumoulin, 2000; Tan, 2001; Lally, 2005 and Holzapfel, 2005). Dumoulin and Cochelin (2000) evaluated and characterized the mechanical properties and behaviors of a balloon expandable stent. Etave (2001) compared the performance of two types of stents. In terms of stent design, Migliavacca (2002; 2004 and 2005) and Beule (2006) assessed the mechanical properties and behavior of balloon-expandable stents to determine how the FEA method could be used to optimize stent designs. It is easy to perform and analyze the effective factors, but the obtained 'optimal stents' in the literature mentioned above are only the best combinations of given geometric parameter levels and are not the optimal solution in the design space. In addition, design modifications with enough comparisons are usually time-consuming and costly because they require too much structural reanalysis or experimentation for a nonlinear system. In the previous approaches, an optimization scheme was developed using Lagrangian interpolation elements (Lucas, 2007).

The dogboning and radial recoil are two important issues for assessing the quality of stent expansion (Lim, 2008 and Wang, 2006). But, as the most of the problems in reality, it is a nonlinear, implicit function of the geometrical parameters and internal pressure loads for the stent. Depending on the fidelity of simulation for stent dilation, it can become computationally expensive, limiting structural optimization of the stent. Therefore, it is challenging to reduce the computational cost of predicting the dogboning rate during the optimization process. Consequently, some approximation models are widely used during engineering to construct simplified approximations for the analysis codes, providing a surrogate model of the original code. In the present paper, we use kriging models as alternatives to traditional second-order polynomial response surfaces for constructing global approximations for stent optimization. The kriging model (Lophaven, 2002 and Jones, 1998), a semi-parametric approach that does not rely on any specific model structure, is much more flexible than approaches based on parametric behavioral models (Costa, 1999).

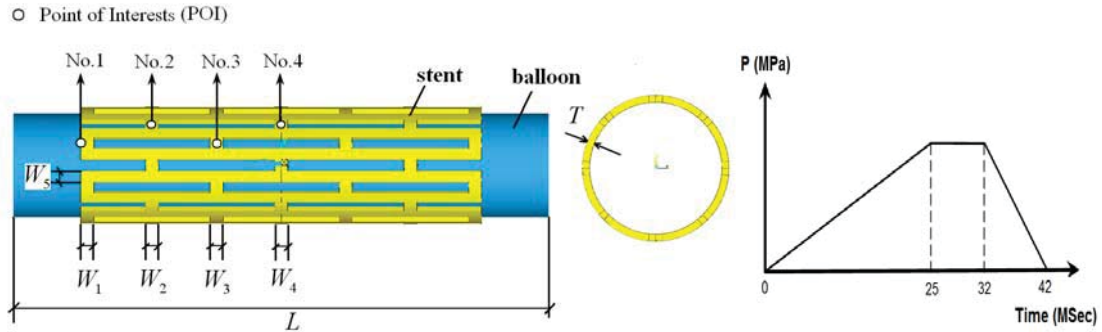
Keeping the consideration above in mind, in the present paper, the kriging model was used to build an approximate function relationship between the objective function and the design parameters, replacing the expensive reanalysis of the stent dogboning rate and the radial elastic recoil during the optimization process. The optimization iterations are based on the approximate relationship for reducing the high computational cost. An adaptive optimization method based on the kriging surrogate model with a Latin Hypercube Sampling strategy was proposed to minimize the radial recoil and the absolute value of the stent dogboning rate during the expansion process. The adaptive process was implemented by the EI function (Jones, 1998), which can balance local and global searches and tends to find the global optimal design, even with a small sample size. The ANSYS program was used to analyze the deformations and dogboning rates of the stents.

## 2 Methods

### 2.1 Finite element model

A typical diamond-shaped coronary stent (shown in Fig. 1) was investigated in this study. All data on the geometries and loading case for the investigated stent were also assumed as in Chua (2004). A balloon with an 11.4 mm length and a 0.12 mm thickness was placed inside the stent. Its outside diameter was equal to the inside

diameter of the stent. Geometric dimensions of the stent are shown in Fig. 1. A time-related pressure (shown in Fig. 2) was loaded on the inner surface of balloon.



**Fig. 1 Balloon-stent system model and design variables:  $W_i$ ,  $i = 1, \dots, 5$ ,  $T$  and  $L$ . Four POIs used to validate the FEA simulation for radial recoil calculation.**

**Fig. 2 Time-related pressure**

Bi-linear elastic-plastic and hyper-elastic (Mooney-Rivlin) materials were assumed for slotted tube stents and balloon. All material properties used were based on the data available from previous studies (Chua, 2002 and 2004).

The stent's dilatation involves nonlinearities such as elasto-plasticity and large deformation. Therefore, a three-dimensional representation solid 185 in ANSYS was utilized to model the stent. The element has plasticity, large deflection, and large strain capabilities. It also has mixed formulation capability for simulating deformations of nearly incompressible elastoplastic materials. Shell 181 which is well-suited for large strain nonlinear applications was employed to model the balloon. Due to the symmetry of the entire structure, only 1/16 of the model (1/8 in circumferential direction and 1/2 in axis direction) was needed to predict the dogboning rate and radial recoil.

### 2.1 Optimization problem

Generally, the dogboning effect exists throughout the expanding process. It usually reaches its maximum in the beginning of loading (Kiousis, 2009 and Zahedmanesh, 2010), but the struts do not reach to the vessel wall. While, from 25ms-32ms, the dogboning observed during this period was relatively large (Li, 2013) and it can cause serious transient mechanical injury. The dogboning rate of the stent was defined as:

$$\text{Dogboning Rate (DR)} = \frac{d_{\text{radial}}^{\text{distal}} - d_{\text{radial}}^{\text{proximal}}}{d_{\text{radial}}^{\text{proximal}}} \quad (1)$$

where  $d_{\text{radial}}^{\text{distal}}$  and  $d_{\text{radial}}^{\text{proximal}}$  are the distal and proximal radial displacements of the stent at 32ms, respectively. It is easy to be found that if the distal of stent was over-expanded  $DR$  is larger than 0, while is the proximal of stent was over-expanded  $DR$  is less than 0. Therefore, in order to expand the stent uniformity along the longitudinal direction, we need to minimize  $|DR|$ .

The following equation was used to define radial recoil:

$$\text{Radial Recoil (RR)} = \frac{1}{4} \sum_{i=1}^4 \frac{R_{\text{POI(No.i)}}^{\text{loading}} - R_{\text{POI(No.i)}}^{\text{unloading}}}{R_{\text{POI(No.i)}}^{\text{loading}}} \quad (2)$$

where  $R_{POI(No.i)}^{loading}$  and  $R_{POI(No.i)}^{unloading}$  are the radius at the POI of the stent (shown in Fig.1) at 32ms and 42ms, respectively. Obviously,  $RR$  is the average of the radial recoil at the POIs.

Our objective is to find a set of design variables that both  $DR$  and  $RR$  are all minimized. A common approach in multi-objective optimization is to optimize a weighted average of all the objective functions. Therefore consider the objective function

$$\omega_1 |DR| + \omega_2 RR \quad (3)$$

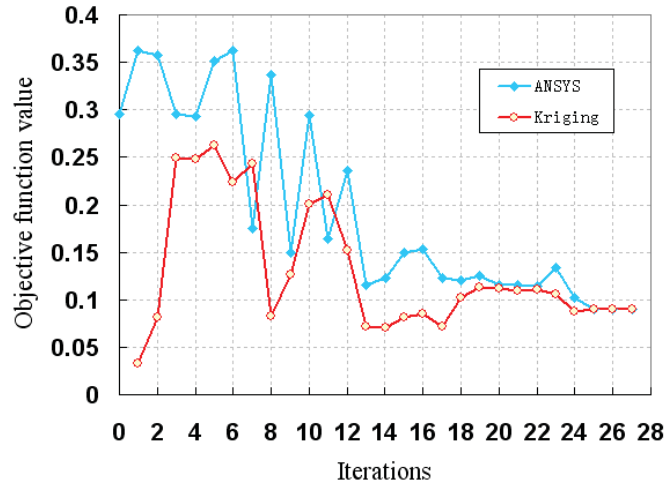
Because the two objectives are mutually incompatible, it is not easy to choose appropriate weights  $\omega_1$  and  $\omega_2$ . Moreover, the two objectives have different scales. If we scale both  $|DR|$  and  $RR$  to a same range  $[0, 1]$ , then we might be able to assign some reasonable weights. We need to improve the objective function in order to do this. And the optimization problem for the coronary stent during the expanding process can be defined as follows:

$$\begin{aligned} \text{Min} \quad & f(\mathbf{x}) = \omega_1 \frac{|DR| - |DR|_{\min}}{|DR|_{\max} - |DR|_{\min}} + \omega_2 \frac{RR - RR_{\min}}{RR_{\max} - RR_{\min}} \\ \text{S.t.} \quad & 0.22 \leq W_i \leq 0.34, \quad i = 1, \dots, 4 \\ & 0.2 \leq W_5 \leq 0.3 \\ & 0.1 \leq T \leq 0.14 \\ & 4.5 \leq L \leq 6.5 \end{aligned} \quad (4)$$

where  $|DR|_{\min}$  and  $|DR|_{\max}$  are the minimum and maximum of  $|DR|$  in the samples,  $RR_{\min}$  and  $RR_{\max}$  are the minimum and maximum of  $RR$  in the samples,  $\mathbf{x}$  is a vector of design variables, which consists of the geometrical parameters  $W_i, i = 1, \dots, 5$  and  $T$  of stent and  $L$  which is the length of balloon, as shown in Fig. 1. In this study,  $\omega_1 = \omega_2 = 0.5$ .

### 3 Results and Discussion

The dogboning rate and radial recoil of a typical diamond-shaped coronary stent were minimized by the proposed method. The initial trial samples were selected for building kriging surrogate model, which include a initial experience design and another 30 samples selected by the LHS. The dogboning rate and radial recoil of stents for all trial samples are simulated by ANSYS software, EI function was employed to balance local and global search for design space. The optimization process started from the initial point with the minimum value of optimization function in all the sample points. The optimization process stops when the Euclidean norm between real value  $f(\mathbf{x}_k)$  from FEM simulation and predictive value  $\hat{y}_k$  from kriging predictor falls below a given tolerance  $\varepsilon_1$  and the Euclidean norm between current and previous iterates falls below a given tolerance  $\varepsilon_2$ . 27 iterations were needed to obtain the optimal solution shown in Fig.3.



**Fig. 3 Optimization iteration process**

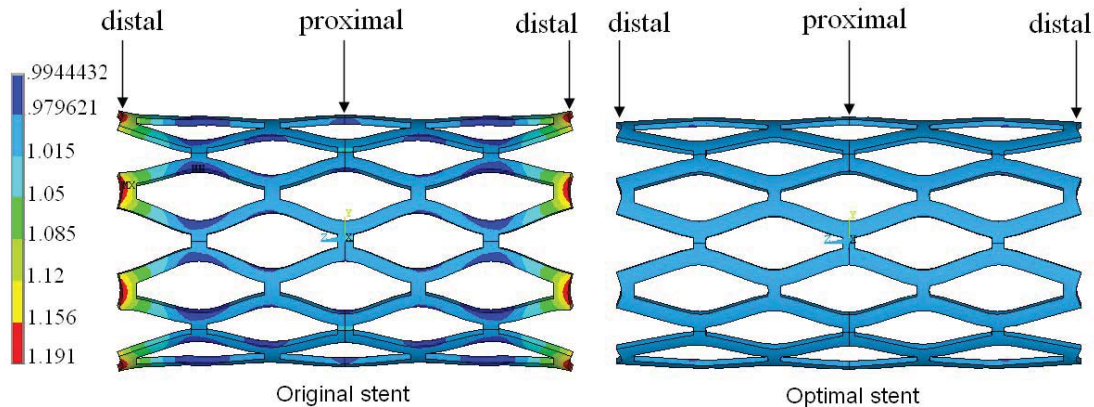
The optimization result was shown in Table 1 by comparing to the original design. The absolute value of the dogboning rate at 32 ms was reduced by 94.21%. It indicates that the dogboning effect was almost eliminated. Furthermore, the absolute value of dogboning rate after unloading at 42 ms was reduced by 89.43%, although it was not considered in the optimization objective. The average of radial recoil was reduced by 15.17%. Because the radial recoil is not only related to the structure, but also related to the materials and the expansion process, it is hard to eliminate the radial recoil completely. Both the dogboning and radial recoil are two important features to evaluate the stent expansion performance, but they have same contradictory factors. From the optimal result, the optimal stent with the greater  $W_5$  resulted in higher radial force, which means that the optimal stent have a better support capacity to artery wall. This is the reason for the decrease of radial recoil of optimal stent. But the stent with a higher radial force is hard to be expanded. Generally, if the stent with a higher radial force and it is hard to be dilated, the ends of it will open first during expansion, that is the dogboning effect. However, the smaller  $W_2, W_3, W_4$  and  $T$  and appropriate  $W_1$  and  $L$  resulted in lower dogboning, although they can result higher radial recoil. Our proposed adaptive optimization method can effectively find a set of design variables that minimizes both dogboning and radial recoil.

**Table 1 Optimization results**

	$W_1$ (mm)	$W_2$ (mm)	$W_3$ (mm)	$W_4$ (mm)	$W_5$ (mm)	$T$ (mm)	$L$ (mm)	$P$ (MPa)	$DR$ (t=32ms)	$DR$ (t=42ms)	$RR$
Original stent	0.28	0.28	0.28	0.28	0.249	0.12	5.8	1.8654	0.0622	0.0634	0.0178
Optimal stent	0.235	0.22	0.22	0.22	0.3	0.1	5.63	1.9077	0.0036	0.0067	0.0151

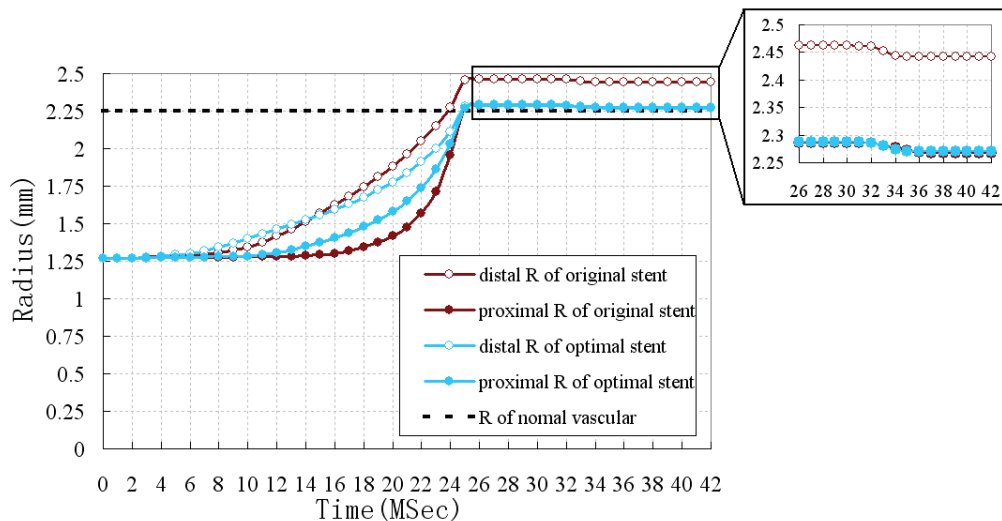
The radial displacement distributions of the original and optimal stents at 32 ms are shown in Fig. 4. The diameters of both the original and optimal stents at the proximal (marked in Fig. 4) ends are dilated from 2.54mm to 4.54mm. The radial displacement of the original stent at the distal ends was much larger than that at the proximal ends. In contrast, the proximal and distal radial expansions of the optimal stent are similar

and the dogboning effect is nearly absent. The smaller absolute value of dogboning rate indicates more uniform expansion along the length of stent.



**Fig. 4** The radial displacement distributions of the original and optimal stents

The proximal and distal radius of both the original and optimal stents during the dilation process are shown in Fig. 5. The proximal radius of all the stents in the sample points were dilated to the same nominal radius (2.27mm) after unloading. The smaller distance between the curves of the proximal and distal radials of stent indicated a more uniform dilation of stent along its length. Fig. 5, shows that the distance between the curves of the proximal and distal radials of the optimal stent was smaller than that of original one, particularly in the period from 25 ms to 32 ms, where this distance was almost zero. This indicates a uniform dilation of the optimal stent along its length, and the dogboning effect was almost completely eliminated. The reduction of the radius during the period from 25ms to 42ms demonstrated radial recoil of stent. Because the radial recoil is not only related to the structure, but also related to the materials and the expansion process, it wasn't decreased completely in this study.



**Fig. 5** The proximal and distal radius of original and optimal stent in the dilation process

## Conclusions

This paper presents an adaptive optimization method based on the kriging surrogate model to minimize both the dogboning and radial recoil. The kriging surrogate model integrating design of experiment (DOE) methods was applied to construct an approximate relationship between the objective function and geometries of the balloon-stent system. The EI function was employed to balance local and global searches and tended to find the global optimal design. As an example, a typical diamond stent was investigated. The results showed that the proposed optimization method effectively decreased both the dogboning and radial recoil of stent.

In addition to dogboning and radial recoil, there are some other issues with respect to the design of coronary stents: (1) radial force, (2) flexibility, (3) minimal foreshortening, (4) minimal longitudinal recoil, (5) minimal coverage area, and (6) fatigue durability. These issues have mutual restriction relationship and mutual influence between them. Therefore, multi-objective optimization considering more issues mentioned above should be taken into account in our future studies.

## Acknowledgements

The authors gratefully acknowledge financial support for this work from the National Natural Science Foundation (No.11072048) of China.

## References

- Beule M. De, Impe R. Van, Verhegghe B., Segers P. and Verdonck P. (2006), Finite element analysis and stent design: Reduction of dogboning, *Technology and Health Care*, 14, pp. 233-241
- Lim D., Cho S. K., Park W. P., Kristensson A., Ko J. Y., Hassani S. T. S., Kim H. S., Al-Hassani STS and Kim H. S. (2008), Suggestion of Potential Stent Design Parameters to Reduce Restenosis Risk driven by Foreshortening or Dogboning due to Non-uniform Balloon-Stent Expansion. *Annals of Biomedical Engineering*, 36, pp. 1118 - 1129.
- Mortier P., Beule M. De, Carlier S. G., Impe R. Van, Verhegghe B., Verdonck P. (2008), Numerical Study of the Uniformity of Balloon-Expandable Stent Deployment. *Journal of Biomechanical Engineering*, 130, pp. 210-218.
- McClellan D. R., Eigler N. L. (2002), Stent design: implications for restenosis. *Rev Cardiovasc Med*, 3, pp. 16-22
- Rogers C., Edelman E.R. (1995), Endovascular stent design dictates experimental restenosis and thrombosis. *Circulation*, 91, pp. 2995- 3001
- Rogers C., Tseng D. Y., Squire J. C. and Edelman E. R. (1999), Balloon-artery interactions during stent placement: a finite element analysis approach to pressure, compliance, and stent design as contributors to vascular injury. *Circulation*, 84, pp. 378-383
- Schulz C., Herrmann R. A., Beihzrz C., Pasquantonio J. and Ait E. (2000), Coronary stent symmetry and vascular injury determine experimental restenosis. *Heart*, 83, pp. 462-467
- Dumoulin, C., and Cochelin, B. (2000), "Mechanical Behaviour Modelling of Balloon-Expandable Stents," *J. Biomech.*, 33, pp. 1461-1470.
- Tan, L. B., Webb, D. C., Kormi, K., and Al-Hassani, S. T. S. (2001), "A Method for Investigating the Mechanical Properties of Intracoronary Stents Using Finite Element Numerical Simulation," *Int. J. Cardiol.*, 78, pp. 51-67.
- Lally, C., Dolan, F., and Prendergast, P. J. (2005), "Cardiovascular Stent Design and Vessel Stresses: A Finite Element Analysis," *J. Biomech.*, 38, pp. 1574-1581.
- Holzapfel, G. A., Stadler, M., and Gasser, T. C. (2005), *Mechanics of Biological Tissue*, Springer-Verlag, Heidelberg, pp. 207-220.
- Dumoulin, C., and Cochelin B. (2000), Mechanical behavior modeling of balloon-expandable stents. *J. Biomech*, 33, pp. 1461 - 1470

- Etave, F., Finet G., Boivin M., Boyer J. C., Rioufol G. and Thollet G. (2001), Mechanical properties of coronary stents determined by using finite element analysis. *J. Biomech*, 34, pp. 1065 - 1075
- Migliavacca, F., Petrini L., Colombo M., Auricchio F. and Pictrabissa R. (2002), Mechanical behavior of coronary stents investigated through the finite element method. *J. Biomech*, 35, pp. 803 - 811
- Migliavacca, F., Petrini L., Massarotti P., Schievano S., Auricchio F. and Dubini G. (2004), Stainless and shape memory alloy coronary stents: a computational study on the interaction with the vascular wall. *Biomech. Model. Mechanobiol*, 2, pp. 205 - 217
- Migliavacca, F., Petrini L., Massarotti V., Quagliana I., Auricchio F. and Dubini G. (2005), A predictive study of the mechanical behaviour of coronary stents by computer modelling. *Med. Eng. Phys*, 27, pp. 13 - 18
- De Beule M., Vam Impe R., Verheghe B., Segers P. and Verdonck, P. (2006), Finite element analysis and stent design: Reduction of dogboning. *Technology and Health Care*, 14, pp. 233-241.
- Lucas H. T., Michael R. M., Clark A. M., John C. C., Alexander R., James E. M. J. (2007), Stented artery biomechanics and device design optimization. *Med Bio Eng Comput*, 45, pp. 505-513.
- Wang W. Q., Liang D. K., Yang D. Z., Qi M. (2006), Analysis of the transient expansion behavior and design optimization of coronary stents by finite element method. *Journal of Biomechanics*, 39, pp. 21-32.
- Lophaven S. N., Nielsen H. B., Sondergaard J. (2002), 'DACE—a Matlab Kriging toolbox'; version 2; Informatics and mathematical modelling, Technical University of Denmark
- Jones D. R., Schonlau M. and Welch W. J. (1998), Efficient global optimization of expensive black-box functions. *Journal of Global Optimization*, 13, pp. 445-492.
- Costa J. P., Pronzato L. and Thierry E. (June 20-23, 1999), A comparison between kriging and radial basis function networks for nonlinear prediction. Paper presented at: NSIP 1999. Proceedings of the IEEE-EURASIP Workshop on Nonlinear Signal and Image Processing 1999, Antalya, Turkey.
- Chua S. N. D., Donald B. J. M. and Hashmi M. S. J. (2004), Effects of varying slotted tube (stent) geometry on its expansion behaviour using finite element method. *Journal of Materials Processing Technology*, 155-156, pp. 1764-1771.
- Chua S. N. D. and Donald B. J. M. (2002), Hashmi MSJ. Finite-element simulation of stent expansion. *Journal of Materials Processing Technology*, 120, pp. 335-340.
- Kiousis D. E., Wulff A. R. and Holzapfel G. A. (2009), Experimental studies and numerical analysis of the inflation and interaction of vascular balloon catheter-stent systems. *Annals of Biomedical Engineering*, 37, pp. 315-330.
- Zahedmanesh H., Kelly D. J. and Lally C. (2010), Simulation of a balloon expandable stent in a realistic coronary artery Determination of the optimum modelling strategy. *Journal of Biomechanics*, 43, pp. 2126-2132.
- Hongxia Li, Xicheng Wang, Design Optimization of Balloon-expandable Coronary Stent, Structural and Multidisciplinary Optimization, 2013, DOI 10.1007/s00158-013-0926-5

# A time-domain BEM for dynamic crack analysis of magnetoelastic composites

M. Wünsche<sup>1</sup>, \*Ch.Zhang<sup>1</sup>, J. Sladek<sup>2</sup>, V. Sladek<sup>2</sup>

<sup>1</sup>Chair of Structural Mechanics, Faculty of Science and Technology, University of Siegen, 57068 Siegen, Germany

<sup>2</sup>Institute of Construction and Architecture, Slovak Academy of Sciences, 84503 Bratislava, Slovakia

\*Corresponding author: c.zhang@uni-siegen.de

## Abstract

Transient dynamic crack analysis in two-dimensional, layered, anisotropic and linear magnetoelastic solids is presented in this paper. A time-domain boundary element method (BEM) is developed for this purpose. The layered magnetoelastic solids are modeled by the multi-domain formulation and the time-domain dynamic fundamental solutions for homogeneous linear magnetoelastic solids are applied in the present BEM. A Galerkin-method is used for the spatial discretization of the boundary integral equations and a collocation method is implemented for the temporal discretization of the arising convolution integrals. An explicit time-stepping scheme is obtained to compute the discrete boundary data including the generalized crack-opening-displacements (CODs). Numerical examples are presented and discussed to show the effects of the interface, the material combinations and the dynamic loading on the intensity factors.

**Keywords:** time-domain BEM, magnetoelastic composites, interior and interface cracks, dynamic intensity factors, impact loading.

## Introduction

Due to their inherent coupling effects between mechanical, electrical and magnetic fields magnetoelastic materials offer many possibilities for advanced smart structures (Nan, 1994). Layered or laminated composites are important applications of magnetoelastic materials because they can be optimized to satisfy the high-performance requirements according to different in-service conditions. Interface cracks, may be induced by the mismatch of the mechanical, electric, magnetic and thermal properties of the material constituents during the manufacturing process and the in-service loading conditions, are one of the most dominant failure mechanisms in layered or laminated composites. Although the dynamic crack analysis in homogeneous magnetoelastic solids have been presented in several works (e.g., Sladek et al., 2008, Sladek et al., 2011, Wünsche et al., 2012) the analysis of interface cracks in layered magnetoelastic solids is rather limited due to the problem complexity.

In this paper, the dynamic analysis of interface crack in two-dimensional, layered and linear magnetoelastic solids under impact loading is presented. A time-domain boundary element method (TDBEM) is developed. The homogeneous magnetoelastic layers are modeled by the multi-domain BEM formulation. The time-domain dynamic fundamental solutions for homogeneous and linear magnetoelastic solids are applied in the present BEM. The spatial discretization of the boundary integral equations is performed by a Galerkin-method, while a collocation method is implemented for the temporal discretization of the arising convolution integrals. An explicit time-stepping scheme is applied to compute the discrete boundary data including the generalized crack-opening-displacements (CODs). In contrast to a crack inside a homogeneous material the asymptotic crack-tip field for an interface crack between two dissimilar linear magnetoelastic materials shows different kinds of oscillating and non-oscillating singularities. This makes an implementation of a special crack-tip element very difficult and therefore only standard elements are used at the crack-tips. A displacement-based extrapolation technique is applied to minimize the error in the computation of the dynamic intensity factors. To investigate the effects of the interface, the material combinations and the dynamic loading on the dynamic intensity factors, numerical examples are presented and discussed.



## 2 Problem formulation

Let us consider a piecewise homogeneous, layered and linear magneto-electroelastic solid with an interface crack. In the absence of body forces, free electric charges, magnetic induction sources and applying the quasi-static assumption for the electric and magnetic fields, the cracked solid satisfies the generalized equations of motion

$$\sigma_{i,j,i}(\mathbf{x}, t) = \rho^s \delta_{JK}^* \ddot{u}_K(\mathbf{x}, t), \quad \delta_{JK}^* = \begin{cases} \delta_{JK}, & J, K = 1, 2 \\ 0, & \text{otherwise} \end{cases} \quad (1)$$

and the constitutive equations

$$\sigma_{i,j}(\mathbf{x}, t) = C_{i,jkl}^s u_{k,l}(\mathbf{x}, t). \quad (2)$$

The generalized displacements  $u_i$ , the generalized stresses  $\sigma_{i,j}$  and the generalized elasticity matrix  $C_{i,jkl}$  for a homogenous domains  $\Omega^\zeta$  ( $\zeta=1, 2, \dots, N$ ) are defined by

$$u_i = \begin{cases} u_i, & I = 1, 2 \\ \varphi, & I = 4 \\ \phi, & I = 5 \end{cases}, \quad \sigma_{i,j} = \begin{cases} \sigma_{i,j}, & J = 1, 2 \\ D_i, & J = 4 \\ B_i, & J = 5 \end{cases}, \quad C_{i,jkl} = \begin{cases} c_{ijkl}, & J, K = 1, 2 \\ e_{lij}, & J = 1, 2, \quad K = 4 \\ h_{lij}, & J = 1, 2, \quad K = 5 \\ e_{ikl}, & J = 4, \quad K = 1, 2 \\ -\varepsilon_{il}, & J, K = 4 \\ -\beta_{il}, & J = 4, \quad K = 5 \\ h_{ikl}, & J = 5, \quad K = 1, 2 \\ -\beta_{il}, & J = 5, \quad K = 4 \\ -\gamma_{il}, & J, K = 5 \end{cases}. \quad (3)$$

Further, the initial conditions

$$u_i(\mathbf{x}, t = 0) = \dot{u}_i(\mathbf{x}, t = 0) = 0, \quad (4)$$

the boundary conditions

$$t_i(\mathbf{x}, t) = \bar{t}_i(\mathbf{x}, t), \quad \mathbf{x} \in \Gamma_t, \quad (5)$$

$$u_i(\mathbf{x}, t) = \bar{u}_i(\mathbf{x}, t), \quad \mathbf{x} \in \Gamma_u, \quad (6)$$

with  $t_i$  being the traction vector defined by

$$t_i(\mathbf{x}, t) = \sigma_{ji}(\mathbf{x}, t) e_j(\mathbf{x}), \quad (7)$$

and the continuity conditions on the interface except the crack-faces

$$u_i^I(\mathbf{x}, t) = u_i^{II}(\mathbf{x}, t), \quad \mathbf{x} \in \Gamma_{if}, \quad (8)$$

$$t_i^I(\mathbf{x}, t) = -t_i^{II}(\mathbf{x}, t), \quad \mathbf{x} \in \Gamma_{if} \quad (9)$$

are applied. In Eqs. (1)-(9),  $u_i$ ,  $\varphi$ ,  $\phi$ ,  $\sigma_{i,j}$ ,  $D_i$ ,  $B_i$  are the mechanical displacements, the electric potential, the magnetic potential, the mechanical stresses, the electric displacements and the magnetic inductions;  $\rho$ ,  $c_{ijkl}$ ,  $\varepsilon_{ij}$ ,  $\gamma_{ij}$ ,  $e_{ijk}$ ,  $h_{ijk}$  and  $\beta_{ij}$  denote the mass density, the elasticity tensor, the dielectric permittivity tensor, the magnetic permittivity tensor, the piezoelectric tensor, the piezomagnetic tensor and the magneto-electric tensor.  $\Gamma_t$  and  $\Gamma_u$  are the external boundaries where

the generalized tractions  $t_i$  and the generalized displacements  $u_i$  are known and  $\Gamma_{if}$  is the interface between the homogenous domains  $\Omega^\zeta$  ( $\zeta=1,2,\dots,N$ ). In the present work, the interface cracks are considered as free of mechanical stresses, electric displacements and magnetic inductions with

$$\sigma_{ij}(\mathbf{x} \in \Gamma_{c^+}, t) = \sigma_{ij}(\mathbf{x} \in \Gamma_{c^-}, t) = 0, \quad (10)$$

where  $\Gamma_{c\pm}$  are the two crack-faces. The generalized crack-opening-displacements (CODs) are defined by

$$\Delta u_i(\mathbf{x}, t) = u_i(\mathbf{x} \in \Gamma_{c^+}, t) - u_i(\mathbf{x} \in \Gamma_{c^-}, t) \quad (11)$$

A comma after a quantity represents spatial derivatives while a dot over the quantity denotes time differentiation. Lower case Latin indices take the values 1 and 2 (elastic), while capital Latin indices take the values 1, 2 (elastic), 4 (electric) and 5 (magnetic).

### 3 Time-domain boundary integral equations

The initial-boundary value problem is solved with a spatial Galerkin-method. The time-domain BIEs for the generalized displacements and the generalized tractions can be written in a weighted residual sense as

$$\int_{\Gamma} \psi(\mathbf{x}) u_j(\mathbf{x}, t) d\Gamma_x = \int_{\Gamma} \psi(\mathbf{x}) \int_{\Gamma} \left[ u_{ij}^G(\mathbf{x}, \mathbf{y}, t) * t_j(\mathbf{y}, t) - t_{ij}^G(\mathbf{x}, \mathbf{y}, t) * u_j(\mathbf{y}, t) \right] d\Gamma_y d\Gamma_x, \quad (12)$$

$$\int_{\Gamma} \psi(\mathbf{x}) t_j(\mathbf{x}, t) d\Gamma_x = \int_{\Gamma} \psi(\mathbf{x}) \int_{\Gamma} \left[ v_{ij}^G(\mathbf{x}, \mathbf{y}, t) * t_j(\mathbf{y}, t) - w_{ij}^G(\mathbf{x}, \mathbf{y}, t) * u_j(\mathbf{y}, t) \right] d\Gamma_y d\Gamma_x, \quad (13)$$

where  $\psi$  is the weighting function, an asterisk “\*” denotes the Riemann convolution,  $u_{ij}^G(\mathbf{x}, \mathbf{y}, t)$ ,  $t_{ij}^G(\mathbf{x}, \mathbf{y}, t)$ ,  $v_{ij}^G(\mathbf{x}, \mathbf{y}, t)$  and  $w_{ij}^G(\mathbf{x}, \mathbf{y}, t)$  are the generalized displacement, traction and higher-order traction fundamental solutions. The dynamic time-domain fundamental solutions for homogeneous, anisotropic and linear magnetoelastic solids are not available in explicit form (Rojas-Díaz et al., 2008, Wünsche et al., 2012). Using the Radon transform technique the fundamental solutions in the 2D case can be defined by a line integral over a unit circle as

$$u_{ij}^G(\mathbf{x}, \mathbf{y}, t) = \frac{H(t)}{4\pi^2} \int_{|\mathbf{n}|=1} \sum_{m=1}^M \frac{P_{ij}^m}{\rho c_m} \frac{1}{c_m t + \mathbf{n} \cdot (\mathbf{y} - \mathbf{x})} d\mathbf{n}, \quad (14)$$

where  $H(t)$ ,  $\mathbf{n}$ ,  $c_m$  and  $P_{ij}^m$  are the Heaviside step function, the wave propagation vector, the phase velocities of the elastic waves and the projector (Wünsche et al., 2012). By integration by parts and applying the properties of the time convolution the time-domain generalized displacement fundamental solutions can be divided into a singular static and a regular dynamic part as

$$u_{ij}^G(\mathbf{x}, \mathbf{y}, t) * f(t) = u_{ij}^S(\mathbf{x}, \mathbf{y}) f(t) + u_{ij}^D(\mathbf{x}, \mathbf{y}, t) * \dot{f}(t). \quad (15)$$

Like the displacement fundamental solutions, the traction and the higher-order traction fundamental solutions can also be divided into their singular static and regular dynamic parts.

### 4 Dynamic intensity factors for an interface crack

The intensity factors for an interface crack between two dissimilar linear magnetoelastic materials can be computed from the generalized crack-opening-displacements (CODs)

$$\Delta \mathbf{u}(r, t) = (\mathbf{H} + \bar{\mathbf{H}}) \sqrt{\frac{r}{2\pi}} \left[ \frac{K_1 r^{i\epsilon_1} \mathbf{w}}{(1 + 2i\epsilon_1) \cosh(\pi\epsilon_1)} + \frac{\bar{K}_1 r^{-i\epsilon_1} \bar{\mathbf{w}}}{(1 - 2i\epsilon_1) \cosh(\pi\epsilon_1)} + \frac{K_4 r^{-\epsilon_2} \mathbf{w}_4}{(1 - 2\epsilon_2) \cos(\pi\epsilon_2)} + K_5 \mathbf{w}_5 \right], \quad (16)$$

where  $K=K_1+iK_2$  is the complex stress intensity factor,  $K_4$  is the electric displacement intensity factor and  $K_5$  is the magnetic induction intensity factor,  $\varepsilon_1$  and  $\varepsilon_2$  are the bimaterial constants, an overbar denotes the complex conjugate and  $i$  stands for the imaginary unit. The complex Hermitian matrix  $\mathbf{H}$  as well as the eigenvectors  $\mathbf{w}$ ,  $\mathbf{w}_4$  and  $\mathbf{w}_5$  are defined by the material properties and can be computed similar to an interface crack between two piezoelectric materials (Suo et al., 1992).

## 5 Numerical solution algorithm

To solve the time-domain BIEs (12) and (13) numerically a solution procedure is presented in this section. The layered piecewise homogeneous and magneto-electroelastic solids with interface cracks are dealt with by the multi-domain technique. A collocation method is used for the temporal discretization while the Galerkin-method is applied for the spatial discretization. For the spatial discretization, the crack-faces, the external boundary of each homogeneous sub-domain and the interfaces of the cracked magneto-electroelastic solid are discretized by linear elements. All boundary integrations can be computed analytically by special techniques. Linear shape functions are used for the temporal discretization and all time integrations can also be performed analytically. Only the line integrals over the unit circle arising in the dynamic parts of the time-domain fundamental solutions need to be computed numerically by the standard Gaussian quadrature.

The asymptotic crack-tip field for an interface crack between two dissimilar magneto-electroelastic materials shows different oscillating and non-oscillating singularities in the generalized stress field (Gao and Tong, 2003, Fan et al., 2009). This makes an implementation of special crack-tip elements rather difficult. For this reason, only standard elements are applied at the crack-tips for interface cracks. This is in contrast to crack-tips inside a homogeneous sub-domain. In this case special crack-tip elements can be implemented to describe the local square-root behavior of the generalized CODs near the crack-tips properly. This makes an accurate and a direct calculation of the intensity factors from the numerically computed CODs possible.

After temporal and spatial discretizations and considering the initial conditions the following systems of linear algebraic equations can be obtained for each sub-domain  $\Omega^\zeta$  ( $\zeta=1,2,\dots,N$ )

$$\mathbf{C}_\zeta \mathbf{u}_\zeta^K = \mathbf{U}_\zeta^S \mathbf{t}_\zeta^K - \mathbf{T}_\zeta^S \mathbf{u}_\zeta^K + \mathbf{T}_\zeta^S \Delta \mathbf{u}_\zeta^K + \sum_{k=1}^K [\mathbf{U}_\zeta^{D;K-k+1} \mathbf{t}_\zeta^k - \mathbf{T}_\zeta^{D;K-k+1} \mathbf{u}_\zeta^k], \quad (17)$$

$$\mathbf{D}_\zeta \mathbf{t}_\zeta^K = \mathbf{V}_\zeta^S \mathbf{t}_\zeta^K - \mathbf{W}_\zeta^S \mathbf{u}_\zeta^K + \mathbf{W}_\zeta^S \Delta \mathbf{u}_\zeta^K + \sum_{k=1}^K [\mathbf{V}_\zeta^{D;K-k+1} \mathbf{t}_\zeta^k - \mathbf{W}_\zeta^{D;K-k+1} \mathbf{u}_\zeta^k]. \quad (18)$$

By invoking the continuity conditions (8) and (9) on the interface  $\Gamma_{if}$  and by considering the boundary conditions (5) and (6) as well as the crack-face boundary conditions (10), Eqs. (17) and (18) can be summarized and recast into a common system of linear algebraic equations

$$\mathbf{x}^K = (\mathbf{C}^1)^{-1} \left[ \mathbf{D}^1 \mathbf{y}^K + \sum_{k=1}^{K-1} (\mathbf{B}^{K-k+1} \mathbf{t}^k - \mathbf{A}^{K-k+1} \mathbf{u}^k) \right], \quad (19)$$

where  $\mathbf{x}^K$  is the vector of the unknown boundary data,  $\mathbf{y}^K$  represents the vector of the prescribed boundary data,  $\mathbf{A}^k$ ,  $\mathbf{B}^k$ ,  $\mathbf{C}^1$  and  $\mathbf{D}^1$  are the system matrices. Eq. (19) is an explicit time-stepping scheme and the unknown boundary data can be computed time-step by time-step.

## 6 Numerical examples

In the following, numerical examples are presented and discussed to show the effects of the interface, the mismatch of the material properties, the coupled fields and the dynamic loading on the intensity factors (IFs). To measure the intensity of the electric and magnetic loading the following loading parameters are introduced

$$\chi^e = \frac{e_{22}^I D_0}{\varepsilon_{22}^I \sigma_0}, \quad \chi^m = \frac{h_{22}^I D_0}{\gamma_{22}^I \sigma_0}, \quad (20)$$

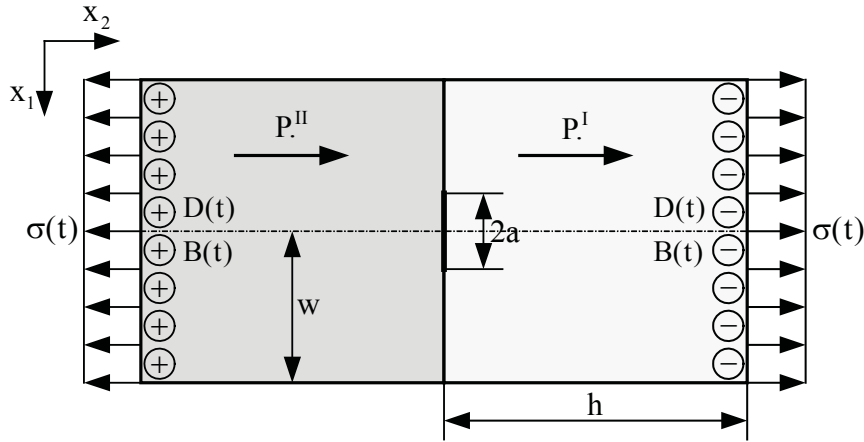
where  $\sigma_0$ ,  $D_0$  and  $B_0$  are the mechanical, electrical and magnetic loading amplitudes. For convenience of the presentation, the real part  $K_1$  and the imaginary part  $K_2$  of the complex dynamic stress intensity factors as well as the electric displacement intensity factor  $K_4$  and the magnetic induction intensity factor  $K_5$  of the interface crack are normalized by

$$K_1^*(t) = \frac{K_1(t)}{K_0}, \quad K_2^*(t) = \frac{K_2(t)}{K_0}, \quad K_4^*(t) = \frac{e_{22}^I K_4(t)}{\varepsilon_{22}^I K_0}, \quad K_5^*(t) = \frac{h_{22}^I K_5(t)}{\gamma_{22}^I K_0}, \quad (21)$$

where  $K_0 = \sigma_0 \sqrt{\pi a}$  with  $a$  being the half-length of an internal interface crack. In the same sense the dynamic intensity factors for a crack inside a homogenous layer, as defined in (Wünsche et al., 2012), are normalized by

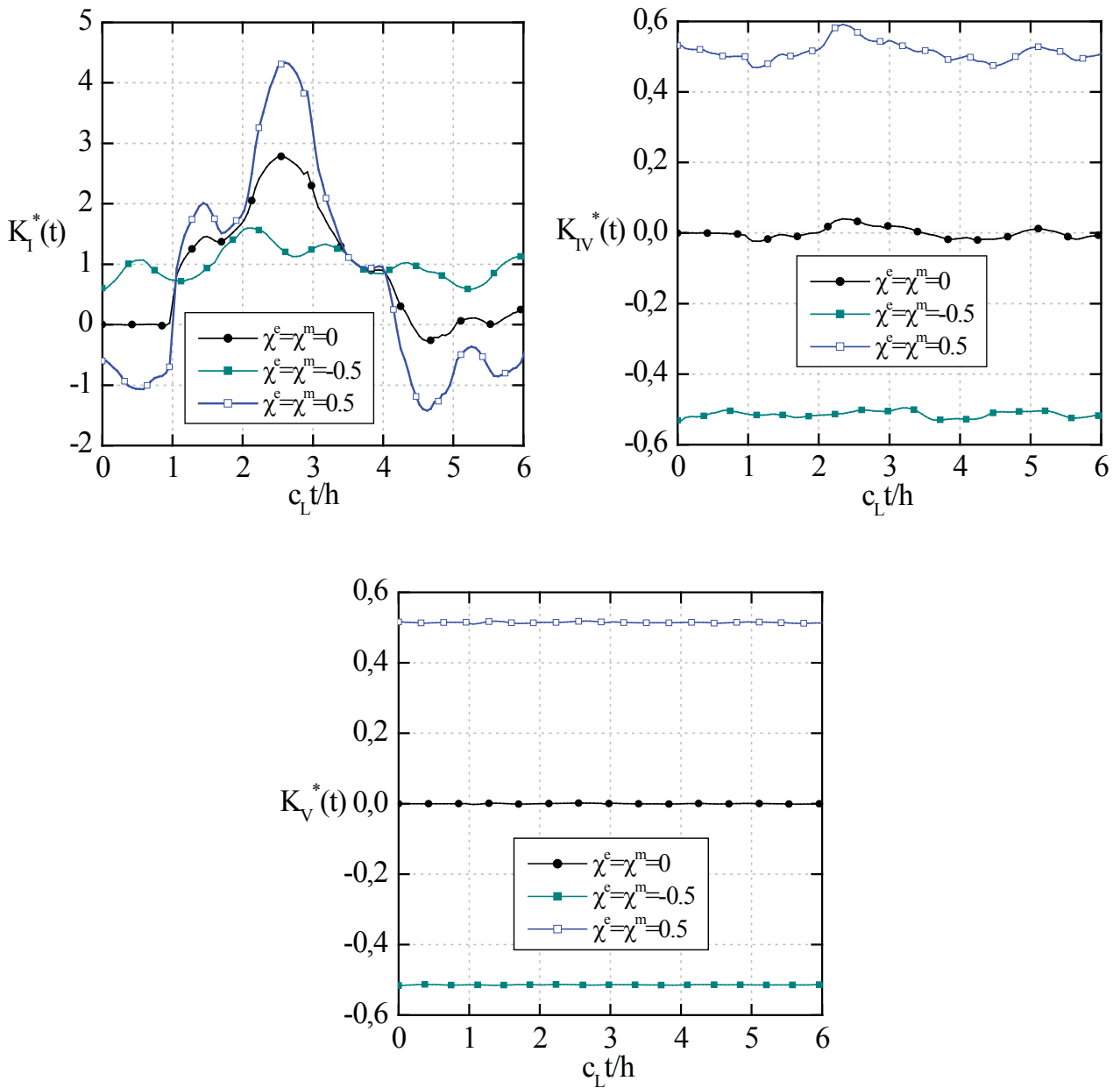
$$K_{I}^*(t) = \frac{K_I(t)}{K_0}, \quad K_{II}^*(t) = \frac{K_{II}(t)}{K_0}, \quad K_{IV}^*(t) = \frac{e_{22}^I K_{IV}(t)}{\varepsilon_{22}^I K_0}, \quad K_V^*(t) = \frac{h_{22}^I K_V(t)}{\gamma_{22}^I K_0}. \quad (22)$$

As example a rectangular, layered and linear magneto-electroelastic plate with a central interface crack of length  $2a$  as shown in Figure 1 is considered. The poling directions are normal to the interface crack. The geometrical data are  $h=20.0\text{mm}$ ,  $w=10.0\text{mm}$  and  $2a=4.8\text{mm}$ .



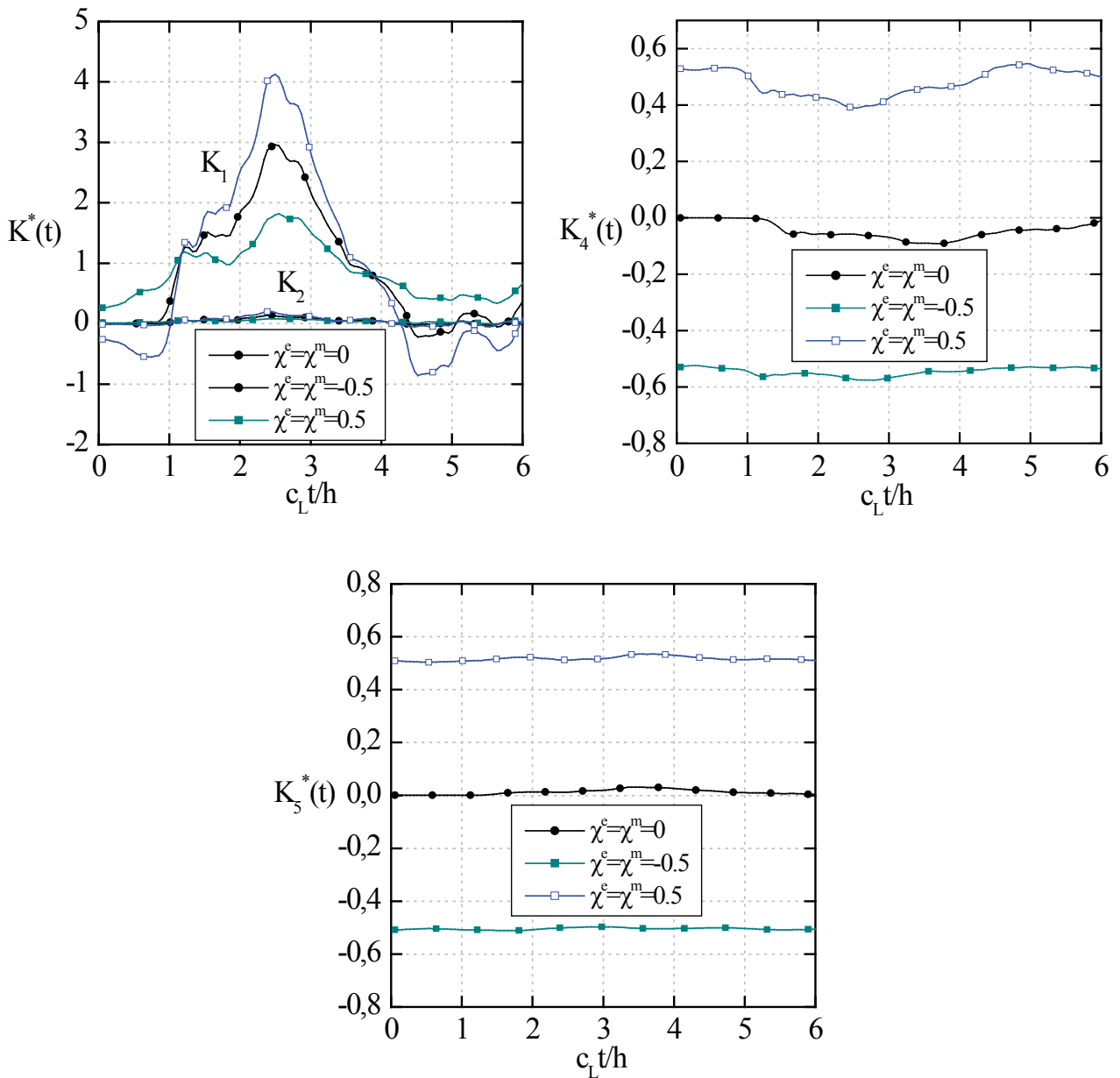
**Figure 1. An interface crack in a rectangular layered magneto-electroelastic plate**

On the left and the right boundary of the cracked plate an impact tensile loading  $\sigma(t)=\sigma_0H(t)$ , an impact electric loading  $D(t)=D_0H(t)$  and an impact magnetic loading  $B(t)=B_0H(t)$  is applied. The external boundary and the interface are discretized by an element-length of 1.0mm and each crack-face is approximated by 20 elements. A normalized time-step of  $c_L\Delta t/h=0.05$  is chosen, where  $c_L$  is the quasi-longitudinal wave velocity. As material a  $\text{BaTiO}_3\text{-CoFe}_2\text{O}_4$  composite, with  $\text{BaTiO}_3$  being the piezoelectric phase and  $\text{CoFe}_2\text{O}_4$  the piezomagnetic phase, is used (Nan, 1994). Figure 2 shows the numerical results of the present time-domain BEM obtained for different loadings and  $\text{BaTiO}_3\text{-CoFe}_2\text{O}_4$  with a volume fraction  $v_f=0.5$  for both layers. This special case is equal to an interior crack inside a homogenous magneto-electroelastic plate. The normalized dynamic intensity factors for an interface crack between to magneto-electroelastic layers with volume fractions of  $v_f=0.5$  for domain I and  $v_f=0.2$  for domain II are presented in Figure 3.



**Figure 2. Normalized dynamic intensity factors for an interior crack subjected to different loadings**

Figures 2 indicate that, if an electric and magnetic impact is applied, the normalized dynamic mode-I stress intensity factor starts from a non-zero value at  $t=0$ . This is due to the quasi-static assumption on the electromagnetic fields, which implies that the cracked magneto-electroelastic plate is immediately subjected to an electromagnetic wave and as a consequence the crack opens at  $t=0$ . In contrast, the elastic waves induced by the mechanical impact need some time to reach the crack, as clearly observed for the case  $\chi^e = \chi^m = 0$ . The peak values of the normalized dynamic intensity factors decrease with increasing electric and magnetic loading amplitudes. The dynamic mode-II intensity factors vanish, since no shear stress components are induced for all applied loadings normal to the crack-faces in the case of a transversely isotropic material behavior.



**Figure 3. Normalized dynamic intensity factors for an interface crack subjected to different loadings**

The real part of the complex intensity factor, the electrical displacement intensity factor and the magnetic induction intensity factor for the interface crack, as shown in Figure 3, have a similar global behavior than the dynamic mode-I, mode-IV and mode-V intensity factors for an interior crack in a homogenous magnetoelastostatic plate. In contrast to the homogenous case, the crack opening and sliding modes I and II are coupled each other for the interface crack and therefore the imaginary part of the complex intensity factor is unequal zero. It can be observed, that the applied electric and magnetic loading may lead to a physically meaningless crack-face intersection in different time ranges for the case  $\chi^e = \chi^m = 0.5$ . This requires an advanced iterative solution procedure for the crack-face contact analysis which is not considered in this work.

## Conclusions

Transient dynamic crack analysis in layered and linear magneto-electroelastic solids is presented in this work. For this purpose, a time-domain BEM is developed which uses a Galerkin-method for the spatial discretization and a collocation method for the temporal discretization. Both temporal and spatial integrations are carried out analytically. Only the line integrals over the unit circle in the dynamic fundamental solutions are computed numerically. An explicit time-stepping scheme is obtained for computing the unknown boundary data. Since the generalized displacement field for a crack in the interface between two dissimilar magneto-electroelastic materials shows different oscillating and non-oscillating singularities the intensity factors are computed by a displacement extrapolation technique. The presented numerical examples indicate a significant influence of the interface, the material combination and the dynamic loading condition on the dynamic intensity factors.

## Acknowledgements

This work is supported by the German Research Foundation (DFG) under the project number ZH 15/14-1 and by the Slovak Science and Technology Assistance Agency registered under the number APVV-0014-10. The financial support is gratefully acknowledged.

## References

- Gao, C.-F., Tong, P. (2003), Zhang, Interfacial crack problems in magneto-electroelastic solids. *International Journal of Engineering Science*, 41, pp. 2105-2121.
- Fan, C., Zhou, Y., Wang, H., Zhao M. (2009), Singular behaviors of interfacial cracks in 2D magneto-electroelastic bimaterials. *Acta Mechanica Solida Sinica*, 22, pp. 232-239.
- Nan, C.W. (1994), Magneto-electric effect in composite of piezoelectric and piezomagnetic phases. *Phys. Rev. B*, 50, pp. 6082-6088.
- Rojas-Díaz, R., Sáez, A., García-Sánchez, F., Zhang, Ch. (2008), Time-harmonic Green's functions for anisotropic magneto-electroelasticity. *International Journal of Solids and Structures*, 45, pp. 144-158.
- Sladek, J., Sladek, V., Sölek, P., Pan E. (2008), Fracture analysis of cracks in magneto-electro-elastic solids by the MLPG. *Computational Mechanics*, 42, pp. 697-714.
- Sladek, J., Sladek, V., Stanak, P., Zhang, Ch., Wünsche, M. (2011), An interaction integral method for computing fracture parameters in functionally graded magneto-electroelastic composites. *Computer, Materials and Continua*, 23, pp. 35-68.
- Suo, Z., Kuo, C.M., Barnett, D.M., Willis, J.R. (1992), Fracture mechanics for piezoelectric ceramics. *Journal of the Mechanics and Physics of Solids*, 40, pp. 739-765.
- Wünsche, M., Sáez, A., García-Sánchez, F., Zhang, Ch. (2012), Transient dynamic analysis of cracked magneto-electroelastic solids by a time-domain BEM. *European Journal of Mechanics - A/Solids*, 32, pp. 118-130.

# Application of Surface Mapping to Visualize Wall Shear Stress and Particles deposition in a Realistic Human Nasal Cavity

**\*Yidan Shang, Kiao Inthavong, and Jiyuan Tu**

School of Aerospace, Mechanical & Manufacturing Engineering, RMIT University, Australia.

\*Corresponding author: s3395646@student.rmit.edu.au

## Abstract

Nasal cavity is an important component of respiration system for the various physiological functions (Elad et al., 2008; Lee, 2010). By using a commercial CFD software Ansys-Fluent and a surface mapping software Unfold3D, wall shear stress (WSS) distribution and particle deposition patterns on the nasal cavity wall were simulated and transformed into a normalized UV domain (where U and V denote coordinate axes of a 2D space) to present a complete view of an entire wrapped surface, therefore to be analyzed with better precision and to allow direct comparisons between left and right cavities. In this paper, applications of surface mapping methods on a nasal cavity are demonstrated, and results for WSS distribution and time dependent particle deposition on UV domain during steady inhalation are analyzed.

**Keywords:** nasal cavity, UV-mapping, CFD

## Introduction

The interactions between the nasal cavity surface wall, inhaled air and inhaled particles all occur simultaneously during inhalation. Intra-individual differences is found between left and right nasal chambers, and temporal variations caused by nasal cycling (Eccles, 1996). Moving air passing over the nasal cavity walls creates a wall shear stress (WSS) (Elad et al., 2006). Recent WSS mapping on surface walls in hemodynamic studies have helped establish risk assessments of aneurysms (Goubergrits et al., 2012; Reneman et al., 2006). Displaying the WSS contour over the 3D domain allows a qualitative result that can reveal local concentrated stresses. However the representation of 3D model results is limited to digital media and typically software to view and rotate the model. Doorly (2008) analysed the effect of flow instability on WSS, by mapping out the WSS occurring along the perimeter of one cross-sectional slice. Using this method it would be ineffective to display all possible WSS profiles along the perimeter of cross-section slices to map out the entire cavity wall.

An alternative is to transform the 3D model into a 2D domain by the UV-mapping method widely used in the computer graphics industry. The letters U and V denote the coordinate axes of the 2D domain while X, Y, Z are retained in the 3D coordinate axes. This is highly effective for reporting results of nasal cavities in 2D format since both septal and lateral wall surfaces can be displayed simultaneously. The 3D model is then transformed into a 2D space representation by ‘unwrapping’ the model along a cut edge and the WSS data is then mapped along the entire surface wall of the 2D domain, to highlight localized regions. Furthermore, transient particles can also be mapped onto a UV domain to highlight localized concentration regions.

## Method

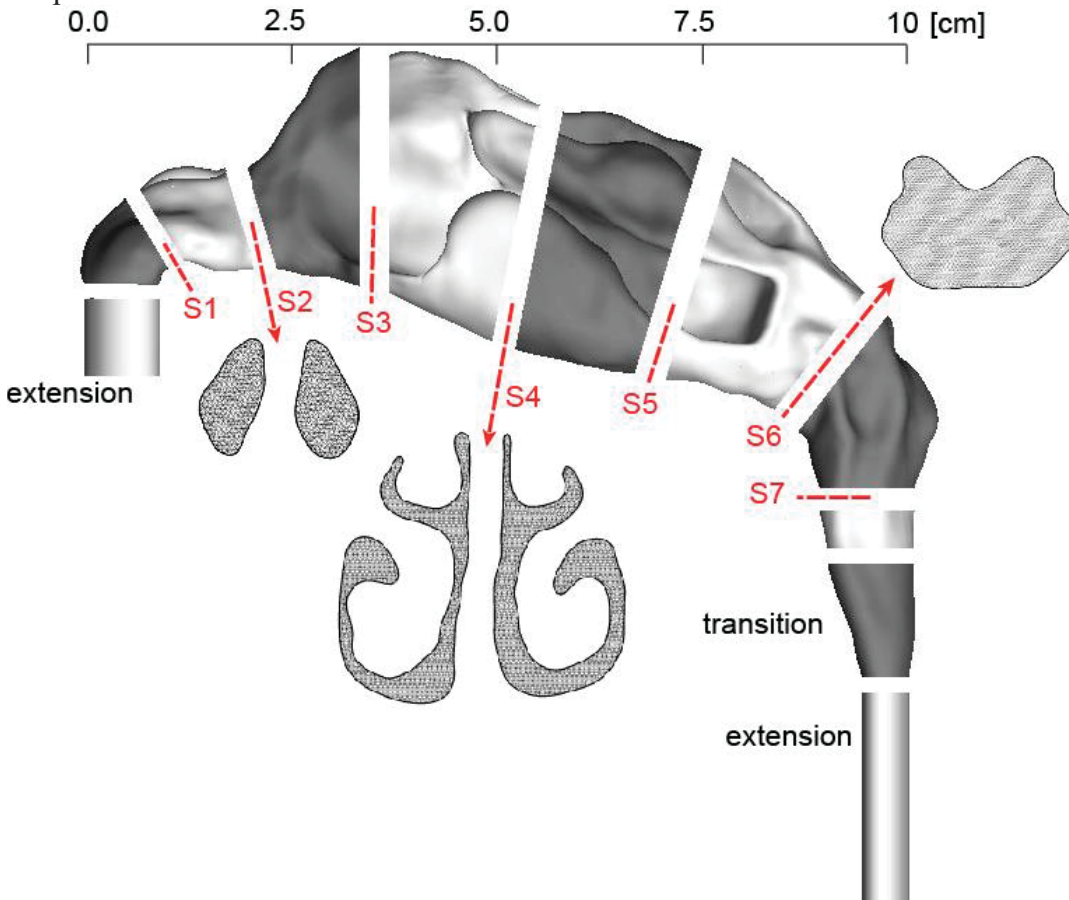
### *Model description*

The CFD model of human nasal cavity obtained through CT scans from a healthy 25-year old, Asia male (170 cm height, 75 kg mass) (Inthavong et al. 2011) has been created. Grid independence was



tested and the mesh was refined in the near wall and regions of high curvature. The computational model was divided into eight sections, by seven slices and labelled as S1 to S7 (Figure 1). Cross sectional slices showing the internal mesh is taken at S2, S4, and S6 which lay approximately in the nasal valve, turbinate near posterior choanae region. Two straight extension pipes, one at the inlet, and one at the outlet were created into the geometry to satisfy a fully developed flow assumption. Since the cross-sectional area decreases sharply behind the nasal pharynx, a transition section was created from the original model to connect nasal cavity with the extension of outlet.

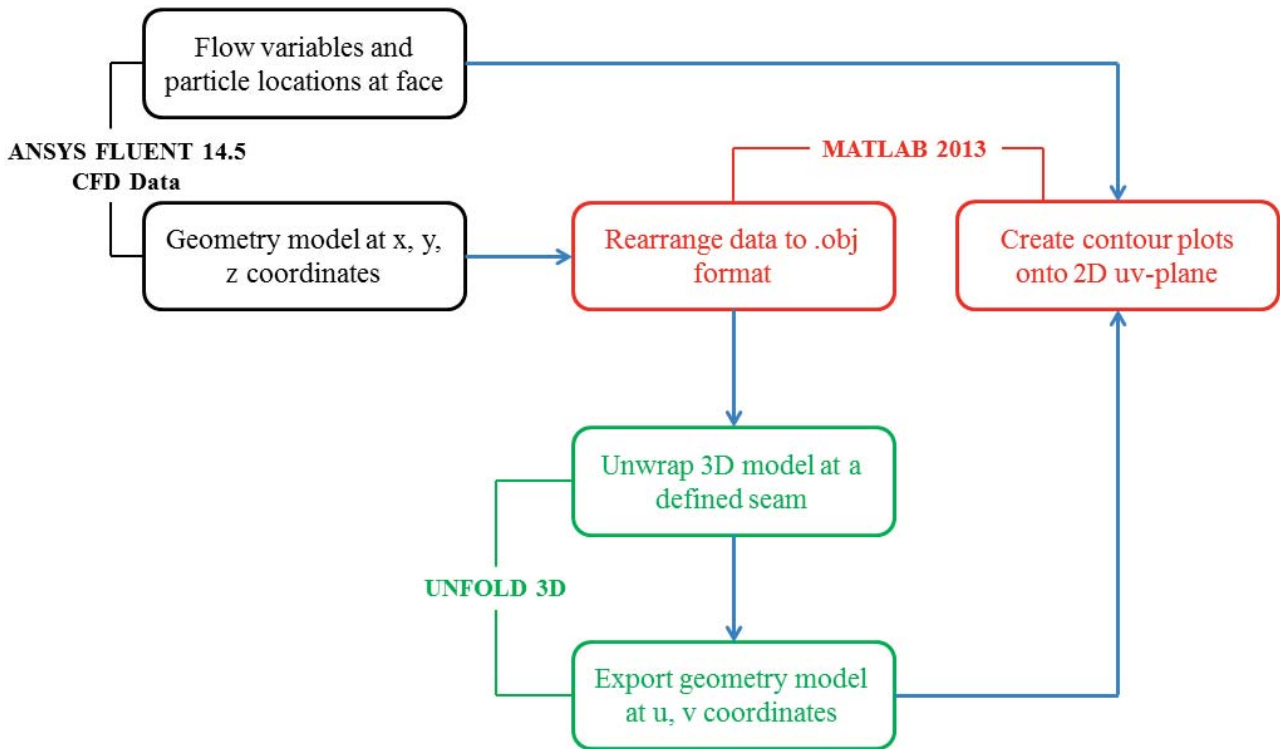
The inlet extension has a pressure boundary condition set to zero gauge pressure to mimic the ambient surrounding environment. To simulate flow patterns of different flow rates, the extension of outlet was set as velocity outlet with the required negative velocity. A laminar flow field was adopted for the flow rates 10 L/min



**Figure 1. Nasal cavity geometry with sectioned slices, labelled S1 to S7.**

#### *UV-Mapping*

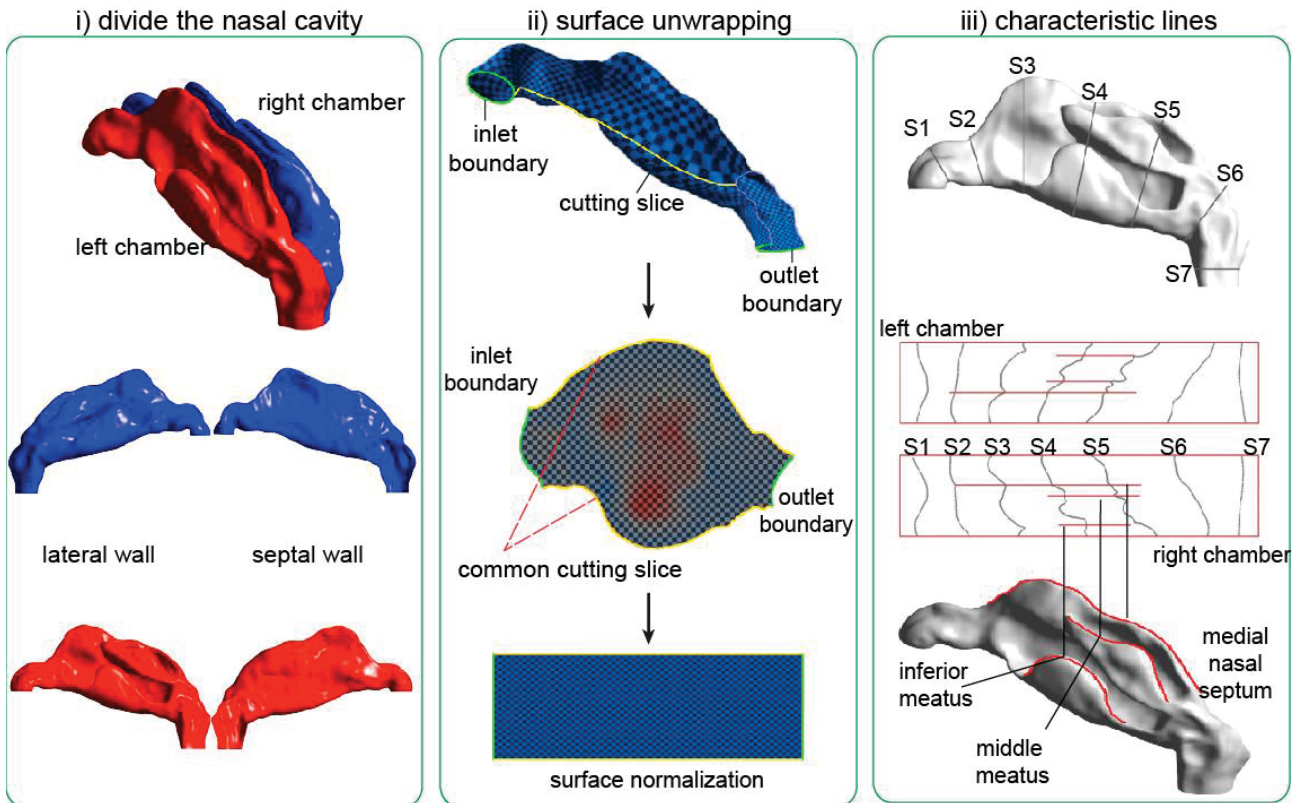
Figure 2 shows Matlab connecting CFD software Ansys-Fluent and UV-Mapping software Unfold 3D to convert a 3D model to a 2D domain. The data containing information regarding the 3D nasal cavity geometry from Ansys-Fluent is outputted and accessed through Matlab. The data is rearranged so that it conforms to the .obj file format which can be imported into Unfold 3D. Within the software, the 3D model is unwrapped at a defined seam based on the ISOMAP algorithm (Tenenbaum et al., 2000). The converted 2D geometry with new coordinates in the UV domain is exported back into Matlab and is coupled with solution data obtained from CFD in the form of the flow variables WSS and particles location.



**Figure 2. Flow chart showing the transformation from a cavity geometry in 3D domain into a 2D domain.**

Graphically Figure 3 presents the flow process. Firstly the nasal cavity is divided into the left and right chambers. Each chamber is then unwrapped by creating a cutting slice along the bottom of the geometry to create a common reference boundary in which the surface coordinates can be related to. This common boundary edge is separated by the inlet and outlet of the nasal chamber. Furthermore the selection of the nasal floor ensures correct topology in the UV domain for regions of overlapping geometry such as that found in the meatus airway.

A further mapping normalizes the UV domain into a dimensionless rectangular space to provide better visualization. Direct comparisons between individual nasal cavity geometries can be made in normalized 2D form. This will provide a means for determining persistent flow features among all different geometries during nasal cavity inhalation. Finally projection of characteristic lines, serving as visual markers, are created based on the slices S1 to S7 (see Figure 1) and the ceiling of the inferior meatus, middle meatus and the medial nasal septum.

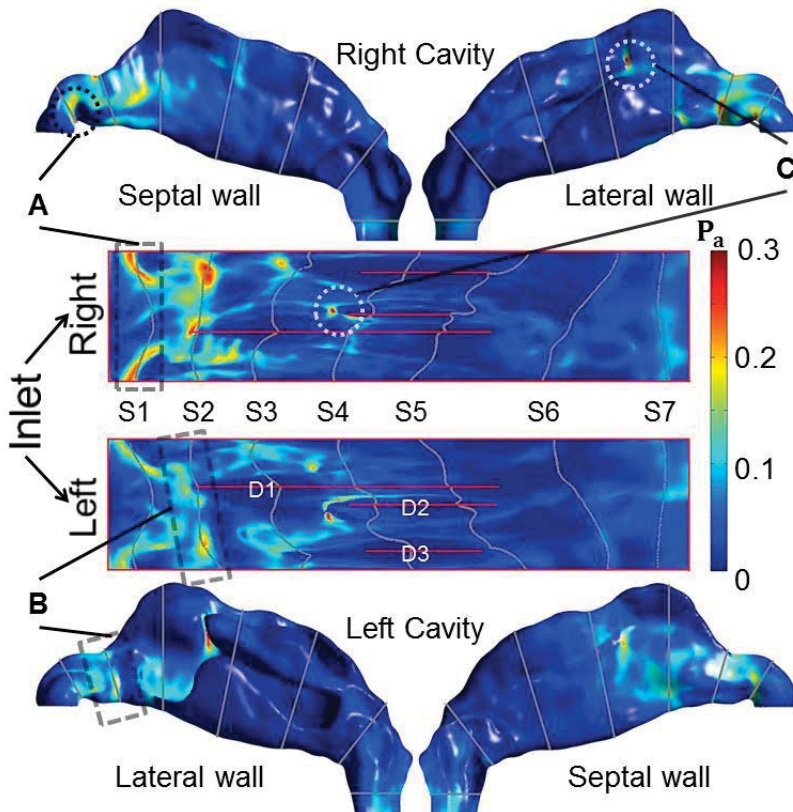


**Figure 3.** Flow process in unwrapping the surface of a 3D model into a 2D domain. Characteristic lines are defined at the apex of the septum wall, middle meatus, and inferior meatus.

## Results

### *WSS Distribution Mapping*

In 3D domain the nasal cavity can be displayed from one perspective view only. Figure 4 demonstrates the advantages of UV-Mapping. Under a flow rate of 10L/min, the high WSS region A and region B on both lateral and septal slides, which are hidden at the bottom of the nasal model in the 3D view, are clearly displayed in the UV domain. This suggests the inhaled air disperses laterally and shears across the side walls of each chamber as it enters the nasal vestibule. Local peaks C of approximately 0.3Pa are found in the region between the middle meatus and lateral wall in both chambers. As shear stresses are linearly related to the local velocity, these values significantly increase as breathing efforts increase. High shear stresses that are concentrated locally may also cause irritation of the blood vessels within that area.

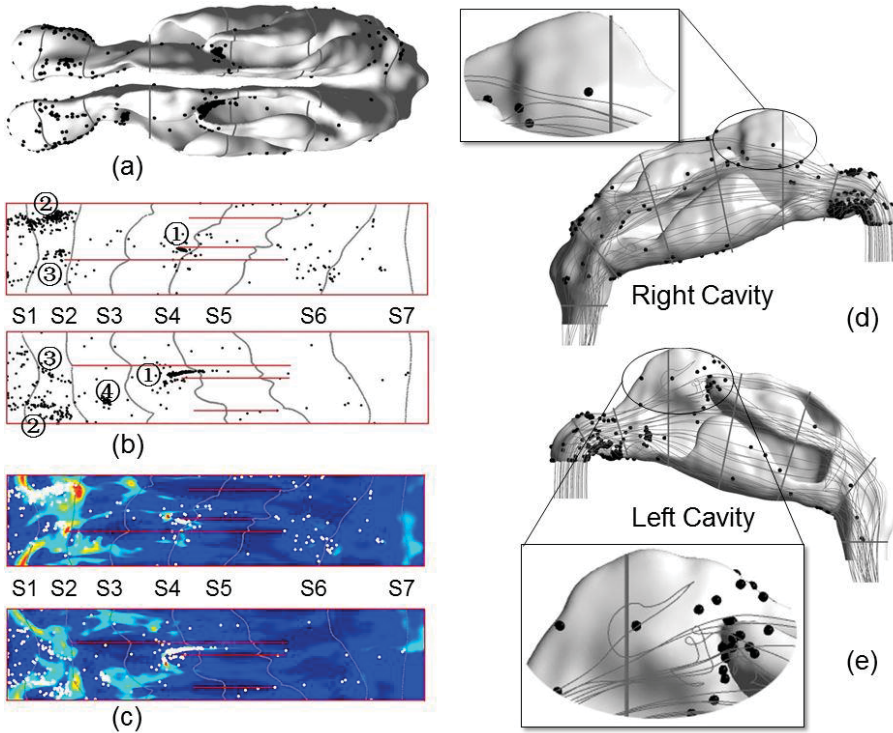


**Figure 4. Local peaks, identified with the red arrows, are found near slice S4. The three red lines running in the axial direction are the characteristic lines defined in Figure 3.**

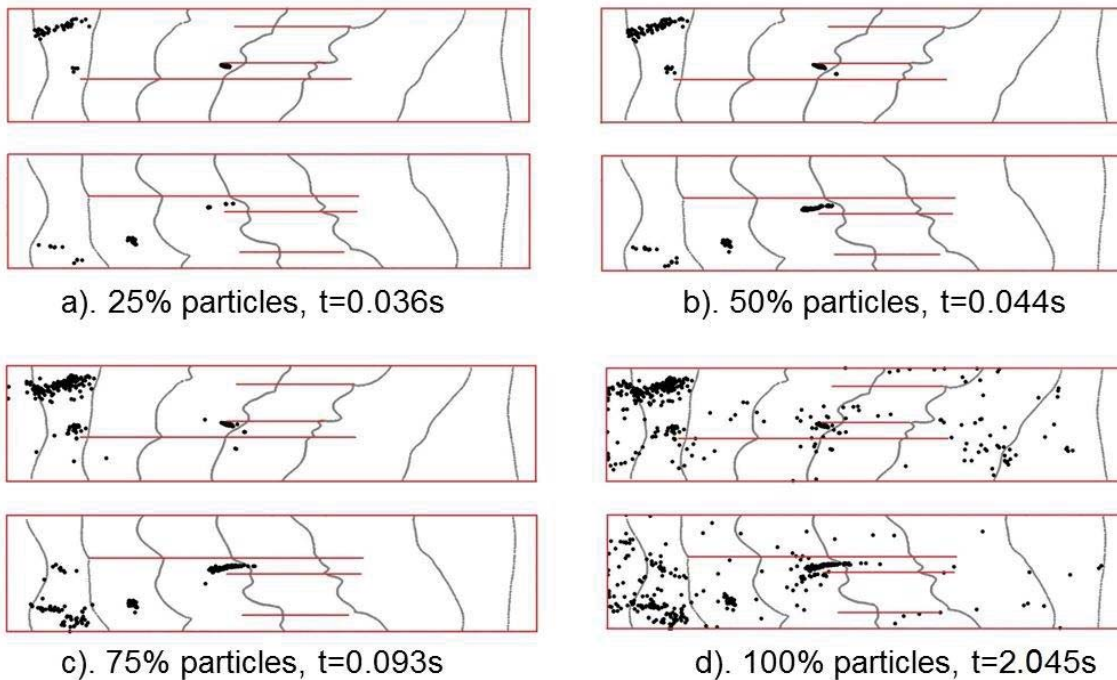
#### *10 $\mu$ m Particle Deposition*

The total deposition efficiency of 10 $\mu$ m particles is shown in Figure 5 where there is higher deposition in the left chamber (21.9% deposition) and lower value in the right chamber (18.8% deposition) which is attributed to the different flow patterns caused by the differences in geometry. The greater resistance in the left airway shown in Figure 5(c) suggests a more intricate and narrow passageway that enhances the particle deposition.

Figure 6 shows the different deposition fractions (25%, 50%, 75%, and 100%) of all deposited particles patterns and its corresponding residence time in the UV domain. Deposition in preferential local regions are established early where 25% of deposited particles occur within  $t = 0.036$  seconds and this pattern continues for up to 75% of the deposited particles by  $t = 0.093$  seconds. The remaining 25% of particles take longer to settle, up to  $t = 2.045$ s. This may be caused by the particles being caught in recirculating regions shown in Figure 5(d)(e) and therefore producing a scatter pattern. Interestingly an unsteady inhalation cycle takes approximately 2s before exhalation occurs, and therefore it is expected that nearly all deposited particles have sufficient time to impact onto the airway surface before exhalation occurs, given that there will be decelerated flow during the end of the inhalation cycle.



**Figure 5. Nasal deposition patterns for 10µm particles in 3D and UV domains. (a). Top view of 3D particles deposition pattern. (b). Particles deposition pattern in UV domain. (c). Deposition pattern with background of WSS. (d)(e). Deposition patterns with flow streamlines showing the influence from the inhaled air.**



**Figure 6. Time dependent deposition patterns for 10µm particles in the UV domain. Each image represents the total fraction of all deposited particles.**

## Conclusions

UV-Mapping method, which transforms the nasal cavity wall in 3D domain into 2D domain, provides a deeper insight into the physiological mechanisms involved with respiratory airflow. The pressure distribution was mapped onto the UV domain which showed a higher resistance in the anterior regions of the left nasal chamber, suggesting that the geometry is susceptible to impediment to flow. This may be in the form of a more narrowed geometry, high curvatures or regions leading to flow separation. Wall shear stresses, which lead to mechano-physical responses in the epithelium surfaces, are mapped which revealed the most vulnerable regions in the form of peaks occurring in the anterior nasal chambers and at the entrance of the middle meatus passageway. This mapping technique allows precise predictions of local regions that are disposed to high shearing which is not possible in 3D mode. The visualization technique presented can be used to make direct comparisons between left and right nasal chambers by normalizing UV mapped geometries. The predictions of particle deposition provided insight into likely deposition regions which were in the anterior nasal regions and middle meatus. These regions corresponded with the local WSS peaks and high resistance regions, however there needs further studies to quantify this correlation. Time dependent particle deposition was also mapped which showed that most of the particle deposition occurred within the 1.0secs of residence time in the nasal cavity. In this study, a visualization technique is presented that takes a 3D wrapped surface and maps it onto a UV domain, which extends the current CFD technology and capability in visualizing the fluid flow dynamics.

## References

- Elad, D., Wolf, M., Keck, T., 2008. Air-conditioning in the human nasal cavity. *Respiratory Physiology & Neurobiology* 163, 121-127.
- Lee, J.-H., Na, Y., Kim, S.-K., Chung, S.-K., 2010. Unsteady flow characteristics through a human nasal airway. *Respiratory Physiology & Neurobiology* 172.
- Eccles, R., 1996. A role for the nasal cycle in respiratory defence. *Eur Respir J* 9, 371-376.
- Elad, D., Naftali, S., Rosenfeld, M., Wolf, M., 2006. Physical stresses at the air-wall interface of the human nasal cavity during breathing. *Journal of Applied Physiology* 100, 1003-1010.
- Goubergrits, L., Schaller, J., Kertzsch, U., van den Bruck, N., Poethkow, K., Petz, C., Hege, H.C., Spuler, A., 2012. Statistical wall shear stress maps of ruptured and unruptured middle cerebral artery aneurysms. *J R Soc Interface* 9, 677-688.
- Reneman, R.S., Arts, T., Hoeks, A.P., 2006. Wall shear stress--an important determinant of endothelial cell function and structure--in the arterial system in vivo. Discrepancies with theory. *J Vasc Res* 43, 251-269.
- Doorly, D.J., Taylor, D.J., Schroter, R.C., 2008. Mechanics of airflow in the human nasal airways. *Respiratory Physiology & Neurobiology* 163, 100-110.
- Inthavong, K., Ge, Q., Se, C.M.K., Yang, W., Tu, J.Y., 2011. Simulation of sprayed particle deposition in a human nasal cavity including a nasal spray device. *Journal of Aerosol Science* 42, 100-113.
- Tenenbaum, J.B., Silva, V.d., Langford, J.C., 2000. A Global Geometric Framework for Nonlinear Dimensionality Reduction. *Science* 290, 2319-2323.

11-14th December, 2013, Singapore

## Time-Implicit Gas-Kinetic Scheme

S. Tan, Q.B. Li \*, and S. Fu

Department of Engineering Mechanics, Tsinghua University, Beijing 100084, China

\*Corresponding author: lqb@tsinghua.edu.cn

### Abstract

In order to improve the computational efficiency of newly developed gas-kinetic scheme in engineering simulations, the time-implicit GKS is constructed in combination with several common-used time-implicit methods, such as LU-SGS, Point-Relaxation, GMRES and LU-SGS based on the numerical Jacobian matrix. Besides, the Crank-Nicholson method is adopted to achieve second-order accuracy in time. Numerical tests show that implicit schemes based on the numerical Jacobian matrix constructed by gas-kinetic fluxes are better than that based on macroscopic eigen decomposition, due to the distinctive characteristics of GKS, which describes particle movement at the microscopic level. The results also show that the time-implicit technique leads to a significant improvement of computational efficiency.

**Keywords:** Gas-kinetic scheme, time-implicit, computational efficiency

### Introduction

The gas-kinetic scheme (GKS) has shown good performance in various fluid problems, including high speed flows, turbulent flows, etc. When solving engineering problems, besides accuracy, computational efficiency is also an important issue. Therefore in order to improve the computational efficiency, it is worthy to extend GKS to time-implicit.

In researches on time-implicit technique, approximate factorization (AF) has achieved great success. Based on AF, lower-upper symmetric Gauss-Seidel (LU-SGS), point-relaxation (PR), liner-relaxation and etc. have been proposed. In these methods, fluxes are decomposed according to the eigenvalues of Jacobian matrix. Because of simple structure and good stability, these methods, especially LU-SGS, have been widely used in many CFD schemes including GKS (Xu, Mao & Tang, 2005; Li & Fu, 2006). However it is not difficult to notice the shortcomings. First, the approximation decomposition of inviscid fluxes introduces errors, which leads to the spatial accuracy loss of the left side of Eq. (5). Second, the decomposition is based on Euler equations.

11-14th December, 2013, Singapore

When solving viscous problems with Navier-Stokes (NS) equations, the viscous spectral radius is added on diagonal terms directly. This introduces too many approximations to viscosity fluxes. Third, in GKS, the evolution of fluxes is computed by the microscopic distribution function, which is the integral solution of BGK equation,

$$f(\mathbf{x}, t, \mathbf{u}, \xi) = \frac{1}{\tau} \int_0^t g(\mathbf{x} - \mathbf{u}(t-t'), t', \mathbf{u}, \xi) e^{-(t-t')/\tau} dt' + e^{-t/\tau} [H[x-ut]f_0^l(\mathbf{x}-ut) + (1-H[x-ut])f_0^r(\mathbf{x}-ut)]. \quad (1)$$

Here  $f_0^l$  and  $f_0^r$  are the initial distribution function,  $g$  the equilibrium state,  $H$  Heaviside function and  $\tau$  the collision time. Consequently, the mismatch between fluxes and matrix decomposition affects the performances of the implicit methods in GKS. Thus more accurate matrix decomposition is needed. Sun, Wang & Liu (2009) and Zhang & Wang (2004) have proposed implicit method (marked as JA) with the idea of numerical Jacobian matrix, in which the Jacobian is calculated and decomposed from the fluxes only. The method is expected to be more suitable for GKS.

In recent years, generalized minimum residual (GMRES) (Luo, Bauma & Lohner, 2001) has been widely studied. In GMRES, numerical differential is applied in generating the orthogonal basis of Krylov subspace. So the mathematical and physical properties of GKS fluxes can be maintained. It is worth mentioning that the inviscid and viscous fluxes are coupled in GKS. So the numerical Jacobian contains the effect of viscosity naturally. No special treatments on viscosity terms are required. In addition, the numerical Jacobian doesn't lose space accuracy, which keeps the same as the right-side residual items in Eq. (5).

In this paper, the performances of the common-used time-implicit methods are tested in GKS. The second part is an introduction of the numerical schemes. The third part is numerical experiments, which is followed by conclusions.

### Time-implicit methods

The time schemes can be written as,

$$\frac{Q^{n+1} - Q^n}{\Delta t} = \varepsilon R(Q^n) + (1-\varepsilon)R(Q^{n+1}). \quad (2)$$

When  $\varepsilon = 1$ , the scheme is time-explicit. When  $\varepsilon = 0$ , the scheme is backward-Euler (BE), which is of first-order accuracy in time. When  $\varepsilon = 0.5$ , the scheme is CN, which is second-order accurate.



11-14th December, 2013, Singapore

The implicit scheme can also be written as,

$$\frac{(1+\phi)(Q^{n+1}-Q^n)-\phi(Q^n-Q^{n-1})}{\Delta t}=R(Q^{n+1}). \quad (3)$$

When  $\phi=0.5$ , the scheme is second-order accurate, but additional storage for  $Q^{n-1}$  is required.

When solving equation (2) or (3),  $R(Q^{n+1})$  is linearized as,

$$R(Q^{n+1})=R(Q^n)+\left(\frac{\partial R}{\partial Q}\right)^n \Delta Q^n, \quad \Delta Q^n=Q^{n+1}-Q^n. \quad (4)$$

The uniform expression of implicit schemes can be obtained,

$$\left[\frac{I}{\Delta \tau'}-\left(\frac{\partial R}{\partial Q}\right)^n\right] \Delta Q=R^n+S^n. \quad (5)$$

Here  $S^n$  is the source term and  $\Delta \tau'$  the pseudo-time step. Different implicit schemes focus on different treatments of the left side of Eq. (5). For LU-SGS, the fluxes of the left side are decomposed by maximum eigenvalue. For PR, they are decomposed by positive and negative eigenvalues. For JA, the Jacobian and decomposed fluxes are calculated by numerical differential.

For GMRES, the convergence of solution is related to the condition number of the left-side matrix, which can be reduced by the preconditioner. In the present study, LU-SGS is adopted as the preconditioner.

Among the implicit schemes considered in this paper, LU-SGS is the simplest one, and requires minimal computation and storage cost for a single-step. In PR and JA, the left-side matrix can't be completely diagonalized, so a  $5 \times 5$  system of equations should be solved at each grid point. Besides, in order to store the numerical Jacobian, JA requires much more storage. In GMRES, the extra storage is little due to the matrix-free approach, and the computational cost for a single-step is determined by the number of orthogonal basis.

## Numerical experiments

### *Case 1: Advection of Density Perturbation*

When combined with GKS, the time-implicit schemes are all second-order accurate in

11-14th December, 2013, Singapore

time, which can be tested with this one-dimensional case. The computational domain is chosen as  $[-1,1]$ . The case is inviscid and the initial condition is set to be (Li, Xu & Fu, 2010),

$$\rho(x) = 1 + 0.2 \sin(\pi x), U(x) = 1, p(x) = 1. \quad (6)$$

For this case, the exact solution is,

$$\rho(x,t) = 1 + 0.2 \sin(\pi(x-t)), U(x,t) = 1, p(x,t) = 1. \quad (7)$$

The computed accuracy of different time-implicit schemes is shown in Fig. 1. JA and GMRES show second-order accuracy, while LU-SGS couldn't achieve second-order. As mentioned before, the approximation reduces the accuracy of the matrix in LU-SGS. Although it's nominally second-order accurate in time, the final accuracy couldn't be maintained.

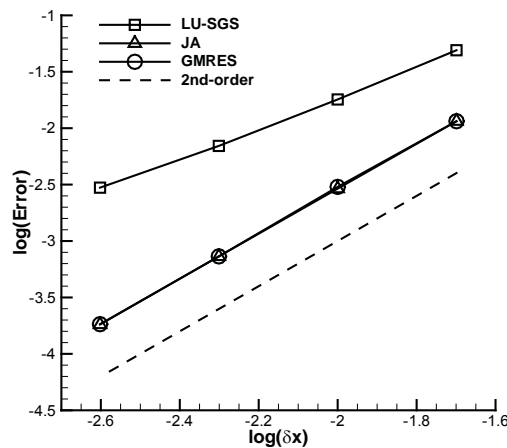


Figure 1 Errors in density vs. cell size of different time-implicit schemes.

### Case 2: Sod Shock Tube

The shock tube problem is a typical unsteady case, which can be used to test the performance of the time-implicit scheme in flow field containing shock. The computational domain is chosen as  $[-0.5,0.5]$ . The initial condition is set to be (Luo, Bauma & Lohner, 2001),

$$\begin{aligned} \rho = 1, U = 0, p = 1.0 & \quad -0.5 \leq x \leq 0 \\ \rho = 0.125, U = 0, p = 0.1 & \quad 0 \leq x \leq 0.5. \end{aligned} \quad (8)$$

The final computation time is  $t=0.2$ . Time steps are set to be 0.004, 0.008 and 0.012. GMRES with BE and CN are used in this case.

Figure 2 shows the distribution of physical quantities computed with different time steps. In the case with shock wave, although the temporal accuracy of CN can't achieve second-order, the solution still shows lower dissipation than the first order. Besides, it can be observed that the time step has little effect on the results, which is important for time-implicit scheme.

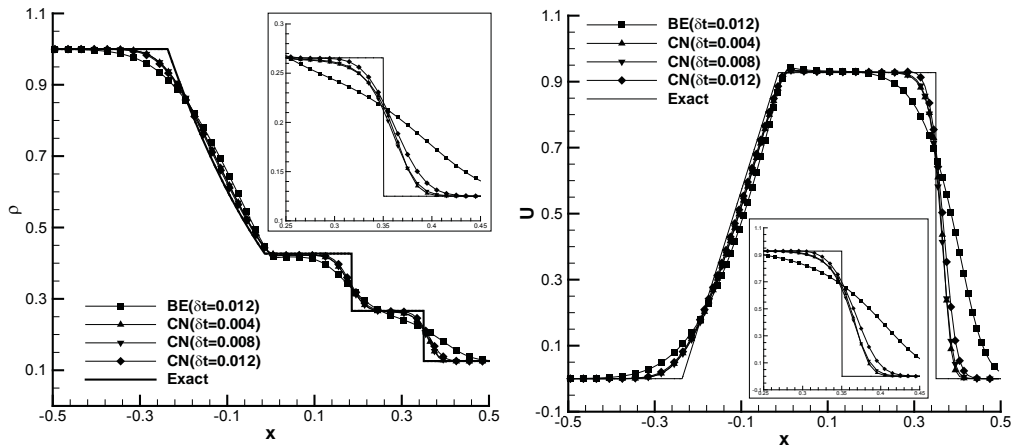


Figure 2 Density and velocity distributions predicted by GMRES.

Case 3: Cavity Flow

This case is chosen to test the computational efficiency of time-implicit schemes when dealing with steady flow problems. A grid with 128x128 cells is used. The computation condition is set to be (Su, Xu & Ghidaoui, 1999),

$$Ma = 0.15, Re = 100. \tag{9}$$

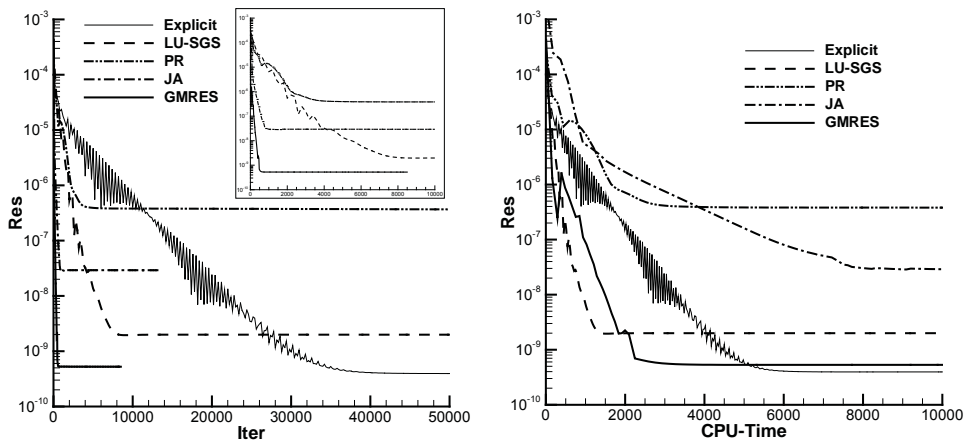


Figure 3 Computational efficiency (Left: iterations, Right: CPU-time).

As shown in Fig. 3, the iteration number for implicit schemes to achieve steady state is dramatically reduced when compared with the explicit method, especially for

11-14th December, 2013, Singapore

GMRES and JA. However, in respect of CPU time, LU-SGS still has superiority, while JA is the most time-consuming one among these schemes.

Figure 4 presents the velocity distributions along the central lines calculated by different time-implicit schemes. The results agree well with each other, which confirm the reliability of the implicit schemes. However it can be found that there is some difference between the present calculations and Ghia's data. This comes from the flux construction, not the time-implicit techniques, where the quasi-one-dimensional extension is adopted for the sake of computational cost, which can introduce large dissipation (Li & Fu, 2006a). In order to illustrate this, the multidimensional flux, where the tangential slopes are included at a cell interface, is tried in the same test case. As shown in Fig. 5, with the help of multidimensional flux, GKS-GMRES, as well as the explicit scheme, yields much better results.

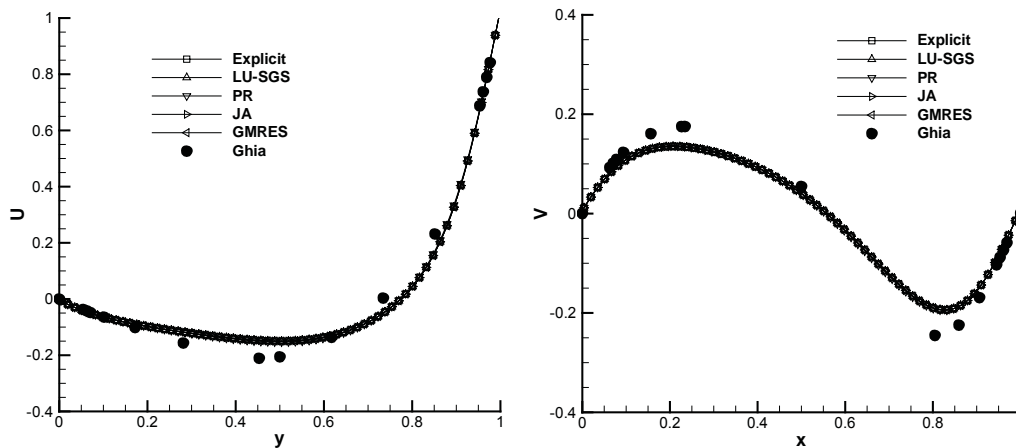


Figure 4 Velocity distributions along vertical and horizontal lines.

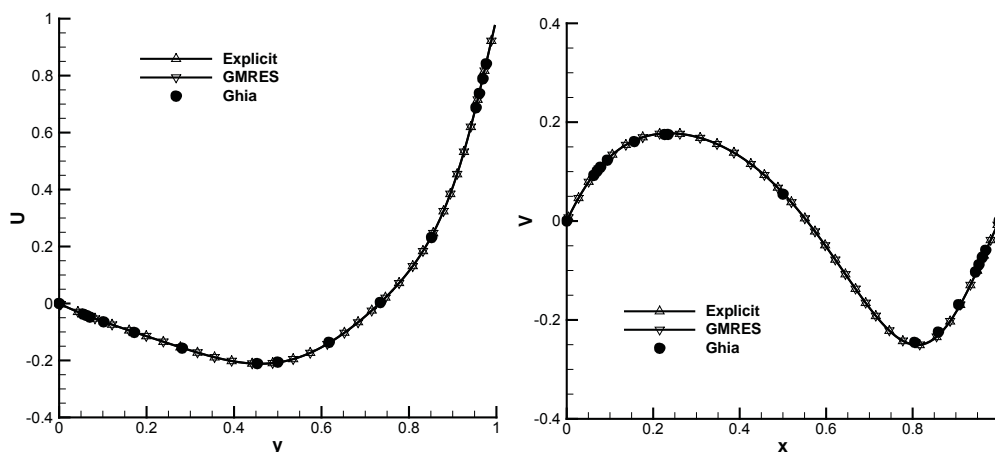


Figure 5 Velocity distributions along vertical and horizontal lines computed with multidimensional schemes.

11-14th December, 2013, Singapore

*Case 4: Rotating Flow inside 3D Cavity*

A cubic box rotates along an axis in the z-direction and drive the internal fluid. The computational condition is set as (Jin, Xu & Chen, 2010),

$$\begin{aligned} \omega_z &= 1, \quad Ma = 0.15, \quad Re = 1000 \\ N_x \times N_y \times N_z &= 64 \times 64 \times 64. \end{aligned} \quad (10)$$

In order to keep the rotating speed of the cavity and simplify the boundary conditions, moving mesh technique is applied in this simulation.

Figure 6 shows the velocity profile in the symmetry plane along the vertical centerline after one cycle ( $t = 2\pi$ ). When the explicit scheme is adopted, about 10000 iterations are required in one cycle. With GMRES, 128 iterations are satisfactory, which can give acceptable results compared with the explicit computation. With 1024 iterations, the difference can hardly be observed. So it can be concluded that the time-implicit technique has effectively improved the computational efficiency of GKS in three-dimensional unsteady flow.

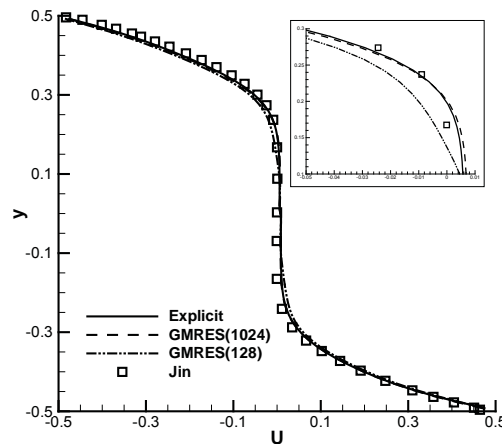


Figure 6 Velocity distributions along vertical central lines in the symmetry plane.

## Conclusions

In this paper, the time-implicit GKS is constructed in combination with common-used time-implicit techniques and validated by several typical test cases. The results show a remarkable improvement of the time-implicit GKS in computational efficiency while preserving second-order accuracy. For flow with discontinuities, such as shocks, the scheme can still keep high accuracy.

11-14th December, 2013, Singapore

## Acknowledgements

This work was supported by National Natural Science Foundation of China (Project No. 11172154, 10932005).

## References

- Jin C.Q., Xu K. & Chen S.Z. (2010), A three dimensional gas-kinetic scheme with moving mesh for low-speed viscous flow computations. *Adv. Appl. Math. Mech.* 2(6), pp. 746-762.
- Li Q.B. & Fu S. (2006), Application of implicit BGK scheme in near-continuum flow. *Int. J. Comput. Fluid Dyn.* 20(6), pp. 453-461.
- Li Q.B. & Fu S. (2006a), On the multidimensional gas-kinetic BGK scheme, *J. Comput. Phys.*, 220, pp.532-548.
- Li Q.B., Xu K. & Fu S. (2010), A high-order gas-kinetic Navier–Stokes flow solver. *J. Comput. Phys.* 229, pp. 6715-6731.
- Luo H., Bauma J.D. & Lohner R. (2001), An accurate, fast, matrix-free implicit method for computing unsteady flows on unstructured grids. *Comput. Fluids.* 30, pp. 137-159.
- Su M.D., Xu K. & Ghidaoui M.S. (1999), Low-speed flow simulation by the gas-kinetic scheme. *J. Comput. Phys.* 150, pp. 17-39.
- Sun Y.Z., Wang Z.J. & Liu Y. (2009), Efficient implicit non-linear LU-SGS approach for compressible flow computation using high-order spectral difference method. *Commun. Comput. Phys.* 5(2-4), pp. 760-778.
- Xu K. (2001), A gas-kinetic BGK scheme for the Navier–Stokes equations and its connection with artificial dissipation and Godunov method. *J. Comput. Phys.* 171, pp.289-335.
- Xu K., Mao M. & Tang L. (2005), A multidimensional gas-kinetic BGK scheme for hypersonic viscous flow. *J. Comput. Phys.* 203, pp. 405-421.
- Zhang L.P. & Wang Z.J. (2004), A block LU-SGS implicit dual time-stepping algorithm for hybrid dynamic meshes. *Comput. Fluids.* 33, pp. 891-916.

## Influence of boundary slip effect on thermal environment in thermo-chemical non-equilibrium flow

Wenbo Miao, \*Junming Lv, Fei Huang and Xiaoli Cheng

China Academy of Aerospace Aerodynamics, P.O.Box 7201-16, Beijing 100074, China

\*Corresponding author: junminglv@gmail.com

### Abstract

A kind of new hypersonic vehicle makes long-time flight in transitional flow regime where boundary slip effect caused by low gas density will have an important influence on the thermal environment around the vehicles. Numerical studies on the boundary slip effect as hypersonic vehicles fly in high Mach number has been carried out. The method for solving non-equilibrium flows considering slip boundary, surface catalysis and chemical reactions has been built up, and been validated by comparing the thermal environment results with STS-2 flight test data. The mechanism and rules of impact on surface heat flux by different boundary slip level (Knudsen number from 0.01 to 0.5) has been investigated in typical hypersonic flow conditions. The results show that the influence mechanisms of boundary slip effect are different on component diffusion heat flux and convective heat flux; slip boundary increases the near wall temperature which diminish the convective heat; whereas enhances the near wall gas diffusion heat because of the internal energy's growing. Component diffusion heat flux takes a smaller portion of the total heat flux, so the slip boundary condition reduces the total wall heat flux. As Knudsen number goes up, the degree of rarefaction increases, the influences of slip boundary on convective and component diffusion heat flux are both enhanced, total heat flux grows by a small margin, and boundary slip effect is more distinct.

**Keywords:** Non-equilibrium, thermal environment, boundary slip, surface catalysis

### Nomenclature

#### Symbols

$C_i$	mass fraction of species $i$
$D_i$	diffusion coefficient of species $i$
$h_i$	enthalpy of species $i$
$K_n$	Knudsen number
$Ma$	Mach number
$P$	Pressure
$P_r$	Prandtl number
$q$	heat flux
$R$	universal gas constant
$T$	temperature
$U$	velocity
$\alpha$	accommodation coefficient for energy
$\rho$	density
$\mu$	molecule viscosity

$\eta$	conductivity
$\lambda$	mean free path
$\gamma$	ratio of specific heat
$\sigma$	accommodation coefficient for moment
Subscripts	
$i$	species $i$
$w$	wall
$s$	slip boundary

## Introduction

Continuum hypothesis will break down at high altitude where energy exchange between molecule and molecule, molecule and surface is inadequate. Scott (Scott, 1973) first presented the surface slip boundary conditions for a multi-component mixture with diffusion and surface recombination. In obtaining these boundary conditions, he used a first order velocity distribution function at the edge of the Knudsen layer next to the wall where velocity slips and temperature jumps. Gupta (Gupta, 1985) suggested that for an accurate prediction of the aerothermal environment of a hypersonic vehicle entering the Earth's atmosphere in low Reynolds number, or flight in high altitude regime, the multi-component, non-equilibrium gas chemistry, as well as the wall slip and catalysis effects, must be evaluated.

In the last three decades, a great deal of researches were undertaken to understand these surface slip effects. Based on STS-2 flight data, Zoby (Zoby, 1982), Scott (Scott, 1982), Daiß (Daiß, 1997) studied windward aero-heating of space shuttle with high angle of attack, when the flow condition is near rarefaction, Knudsen number from 0.001 to 0.03. Results show that besides the multi-component mixtures, non-equilibrium reactions and surface recombination, surface slip condition must be considered to obtain reasonable numerical results. Another typical research is validation of sharp and blunt 25° double cones. Several numerical methods were compared with a series of test data. Mesh distribution, difference schemes and surface slip conditions were analyzed. Results show that the pressure and heat transfer rate match well on the cone forebody, through the separation zone, and on the second cone, except that the heat transfer rate on the cone forebody is over predicted by about 20%.

In this paper, aeroheating mechanism of surface recombination with slip surface conditions was focused on. First of all, the numerical method applied in double cone and STS -2 flight mentioned above was evaluated. The validation showed good agreement with test data and flight data. Then aeroheating of a cone was studied with different surface catalytic conditions and different Knudsen number.

## CFD methods

The CFD codes have been applied for several hypersonic researches. Basic equations are 3-D full Navier-Stokes equations with 7 species of air using Park's chemical reaction model<sup>2</sup>. For the time integration, Lower-Upper Symmetric Gauss-Seidel (LU-SGS) scheme is applied. Convective terms are discrete by AUSM+ scheme (Liou, 2003).



Surface slip boundary condition follows Davis's slip model (Davis, 1970), where velocity, temperature and mass fraction at the Knudsen layer are described with equations below. Local mean free path is decided by molecule viscosity and gas density.  $\alpha$  and  $\sigma$  is respectively the accommodation coefficient for moment and energy, and the value is between 0 and 1.

$$U_s = \frac{2-\sigma}{\sigma} \lambda \frac{\partial U}{\partial n} \Big|_0$$

$$T_s - T_w = \frac{2-\alpha}{\alpha} \frac{2-\gamma}{(\gamma+1)P_r} \lambda \frac{\partial T}{\partial n} \Big|_0$$

$$C_{i,s} - C_{i,w} = \frac{2-\alpha}{\alpha} \sqrt{\frac{\pi}{2RT}} (D_i \frac{\partial C_i}{\partial n}) \Big|_0$$

$$\lambda = \frac{\mu}{\rho} \sqrt{\frac{\pi}{2RT}}$$

Full catalytic and non catalytic surface conditions are involved to describe surface recombination. Considering low surface temperature, mass fraction of species on surface is set equal to that of free stream for full catalytic condition. Heat transfer rate are solved by equations below, where first term is convective heat flux and the second term is mass diffusion heat flux.

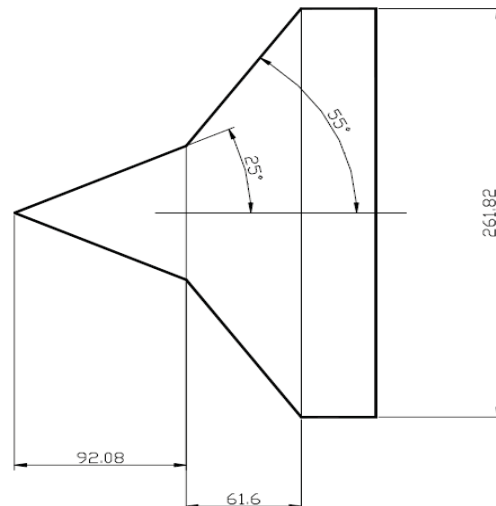
$$q_{flux} = \eta \frac{\partial T}{\partial n} \Big|_s + \sum_i \rho D_i h_i \frac{\partial C_i}{\partial n} \Big|_s$$

### Sharp Double Cone Test Validation (Candler, 2002)

Data from Runs 35 of the Holden's experiment (Harvey, Holden and Wadhams, 2001) is compared at Mach number equals 11.3. The test was performed in an impulse shock tunnel with nitrogen as the test gas. Calibration runs were made ahead to verify the uniformity of the flow in test section. The tests were carried out at the same nominal conditions as in calibration test. Because of the high temperature and pressure, a kind of molecule vibrational excitation would occur, so thermal non-equilibrium may be considered. In the simulation thermal equilibrium and chemical reactions are assumed, both no-slip boundary and slip boundary are employed. The flow condition at the nozzle outlet is shown in Table 1. Outline of the double cone is shown in Figure 1, with a 25° first sharp cone and a 55° second cone. The diameter of the base is 261.02 mm. Grid condition of these simulations is set as a symmetric structural form, grid number of streamwise, normal direction and circular direction is 281×161×33.

**Table 1. Flow condition at the nozzle outlet**

<i>Ma</i>	<i>Radius /m<sup>-1</sup></i>	<i>U/m•s<sup>-1</sup></i>	<i>T/K</i>	<i>T<sub>w</sub>/K</i>	<i>P/Pa</i>
11.3	1.33×10 <sup>5</sup>	2.71×10 <sup>3</sup>	138.9	297	22.05

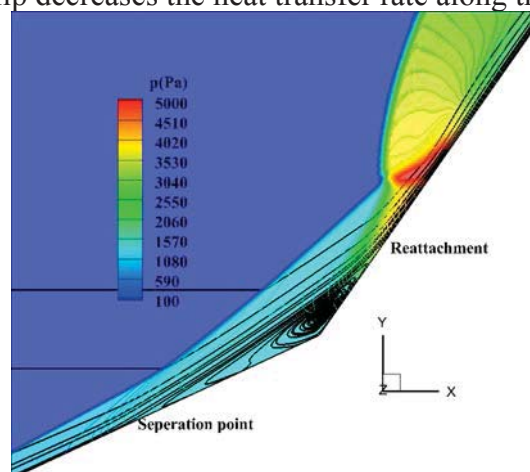


**Figure 1. Outline of the sharp double cone (unit: mm)**

Figure 2 shows the computed pressure distribution and streamlines in the axisymmetric plane. An evident separate swirl can be seen in the corner. The pressure increases suddenly at the reattachment point.

Figure 3 shows the temperature profile with two different surface conditions. Flow structure is almost the same, but the separation area of slip wall is somewhat bigger than that of nonslip wall. Surface velocity slip makes more gas stay in the separation corner that causes a bigger vortex. A depressed region on the separation bow shock is observed where free stream forces separation shock moving towards the wall, pressure and heat transfer rate enhanced at streamwise  $x=0.13\text{m}$  as presented in Figure 4.

Figure 4 plots total heat transfer rate with two slip conditions along  $x$  direction, agreement between calculation and experiment is obtained. Note that the length of separation zone and the peak heat rate match the test data well, except that 10% over prediction at the first cone. The difference between slip wall and nonslip wall is not significant. Surface slip decreases the heat transfer rate along the full cone.



**Figure 2. Pressure distribution and streamlines in the separation area**

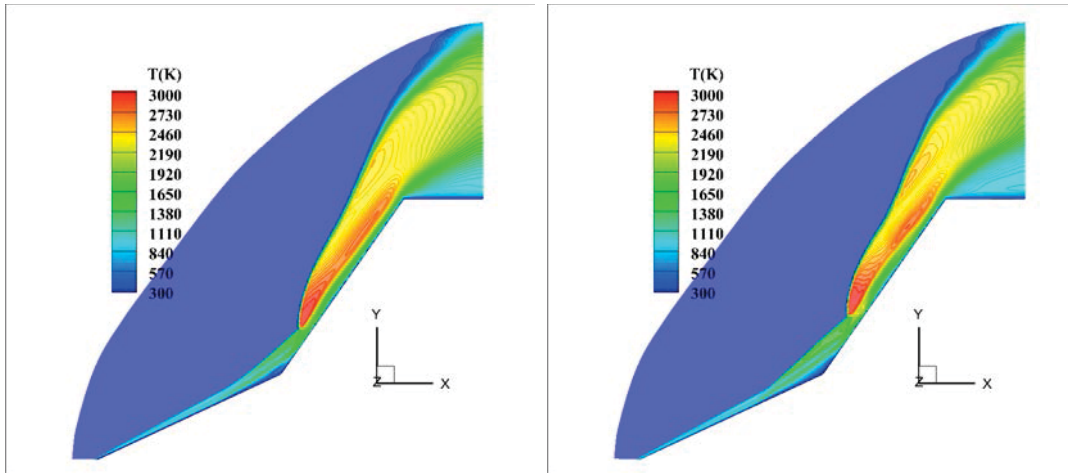


Figure 3. Temperature distribution in the flow field

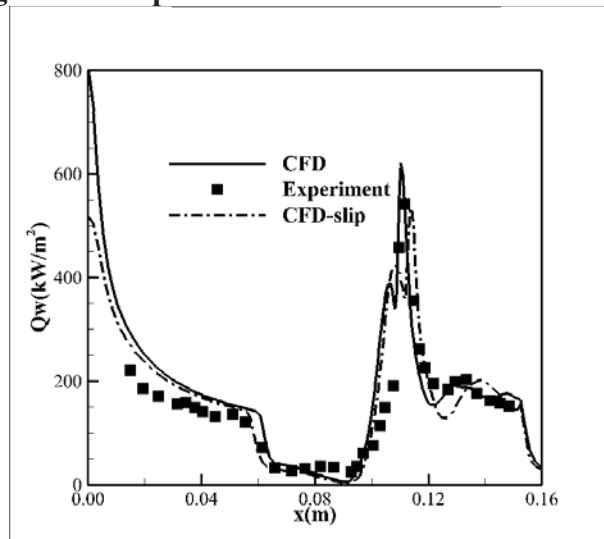


Figure 4. Heat transfer rate of double cone

## Results and Discussion

### *STS-2 Flight Data Analysis*

According to the trajectory of space shuttle, simulations are taken at  $H=92.35\text{km}$  and  $H=79.11\text{km}$ , where Knudsen number are 0.028 and 0.0023. Accommodation coefficients of 0.5 and 1 are considered with both full catalytic and non catalytic conditions. The flow at the trajectory point of Knudsen number equals 0.028 can be considered as a typical slip flow case.

Figure 5 plots the heat transfer rate of the calculation and flight data. Recombination coefficient of STS-2's TPS material is near zero, so the heat flux calculated with non catalytic condition is rational and close to the flight data. The agreement between the calculated and measured heat flux is poor when accommodation coefficient is set to 1. A possible reason for the discrepancies might be that the reasonable accommodation coefficient should be smaller than 1. Figure 5 shows that the agreement becomes better when accommodation coefficient is set to 0.5. Difference between two accommodation coefficients is large than 20%. When Knudsen number equals 0.0023, difference caused by accommodation coefficient is reduced to about 10%. It is guessed that the actual accommodation coefficient is close to 0 when flow is near free molecule flow.

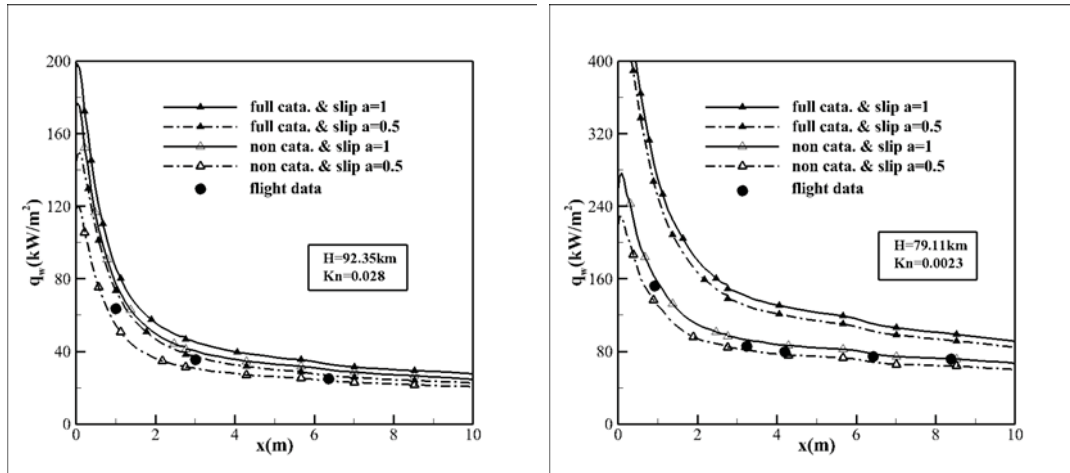


Figure 5. Comparison of heat transfer rate of STS-2 flight

#### Cone with Catalytic Conditions

Surface catalytic conditions with slip effect were studied. Based on a blunt cone, calculations were done with Knudsen number, which is the ratio of the mean free path to the cone diameter, equal 0.05, 0.01 and 0.00185. Both full catalytic and non catalytic condition was considered. For wall slip effect, accommodation coefficient was set to 1. Flow at  $Ma$  equals 20 involves intense chemical reactions behind the shock and increases the capability of atoms recombination near the wall. Table 2 shows the test configurations. Because the configuration is very simple grid number of streamwise, normal direction and circular direction is set as  $61 \times 161 \times 33$ .

Table 2. Test configurations for catalytic and slip effects

Cases	Radius/m	Ma	Kn	$T_w$ /K	Surface catalytic	Wall Slip
1	0.175	20	0.00185	300	Full catalytic/Non catalytic	Slip/Nonslip
2	0.175	20	0.01	300	Full catalytic/Non catalytic	Slip/Nonslip
3	0.025	20	0.05	300	Full catalytic/Non catalytic	Slip/Nonslip

Figure 6 shows comparison of slip and nonslip condition when Knudsen number is 0.05. Shock layer of slip wall is a little thicker than nonslip. The temperature behind the shock is higher. In contrast with the isothermal wall of 300K, slip temperature at the Knudsen layer is almost 2000K, which makes gas behind the shock dissociate more.

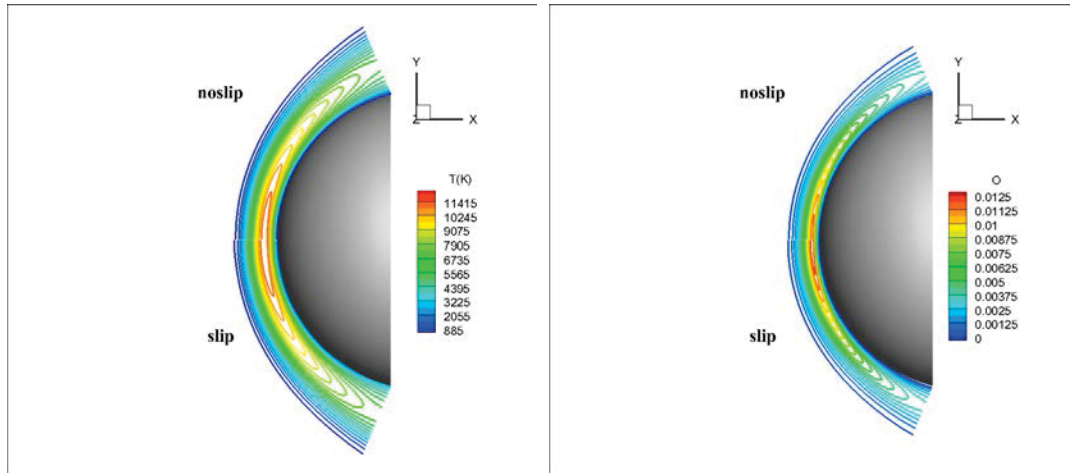


Figure 6. Comparison of temperature and O between slip and nonslip wall

Figure 7 shows surface pressure of different Knudsen number. Pressure with different slip conditions is almost the same at any Knudsen number. Considering slip surface effect is enhanced as Knudsen number goes up, the case of  $Kn$  equal 0.05 is chosen to analyze the mechanism.

Figure 8 shows the distribution of the heat transfer rate. Both differences between the mass diffusion heat flux and the convective heat flux are evident. Surface slip lead to higher surface temperature and better thermal conductivity which increases the mass diffusion heat transfer rate. On the other hand, the gradient of the temperature on the wall decreases when the surface slip temperature increases, which decreases the convective heat transfer rate.

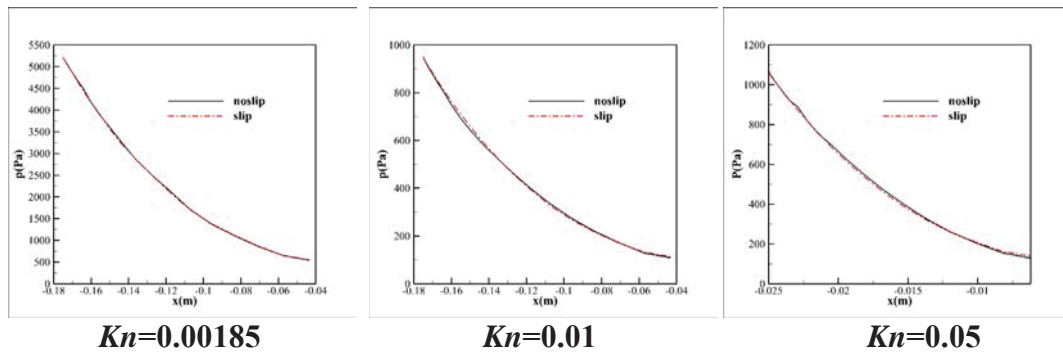


Figure 7. Comparison of surface pressure

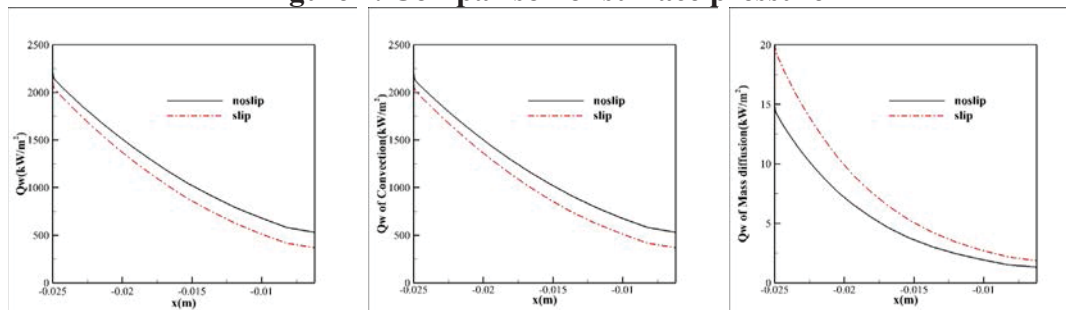


Figure 8. Heat transfer rate of  $Kn=0.05$

Despite two mechanisms are widely divergent, total heat transfer rate keeps decreasing with slip wall condition. Figure 9 and Figure 10 show discrepancy between slip wall and nonslip wall with different catalytic surface. When Knudsen number is below 0.01, the difference of the total heat flux between two slip conditions

is less than 5%. The difference increases to almost 20% when Knudsen number rises to 0.05. Meanwhile it can be found that the mass diffusion part of the heat flux decreases quickly as Knudsen number goes up. The reason is that low density reduces the chemical reaction rate and decreases the gas recombination on the wall.

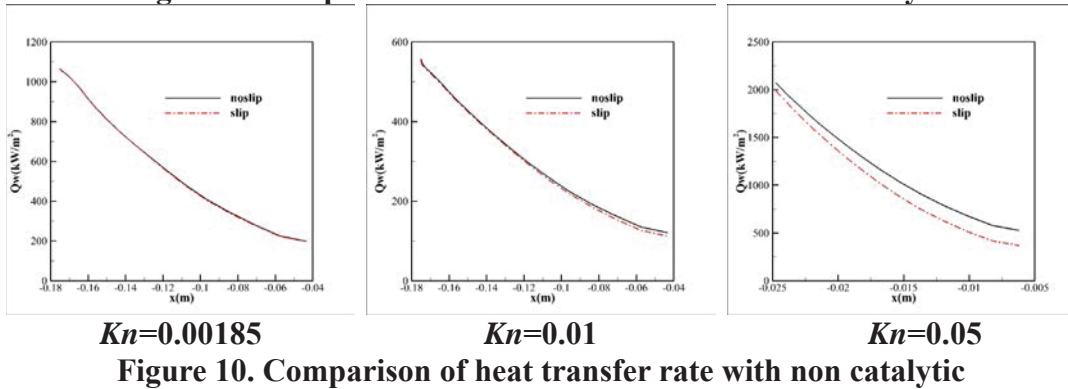
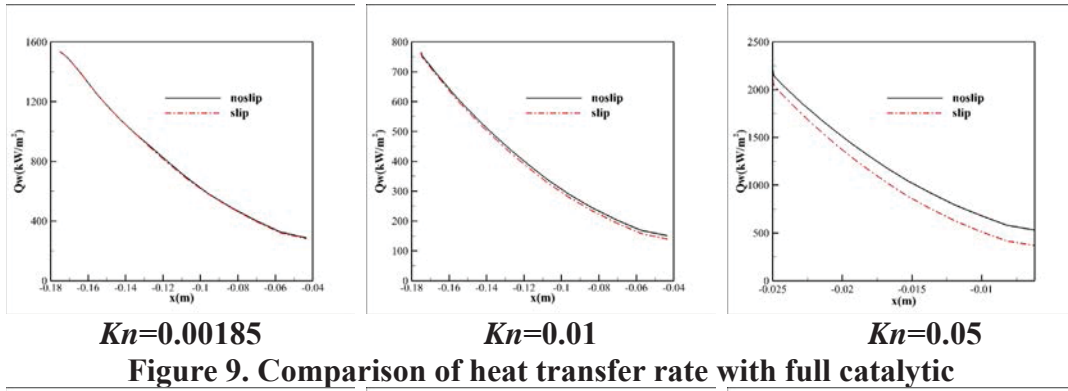
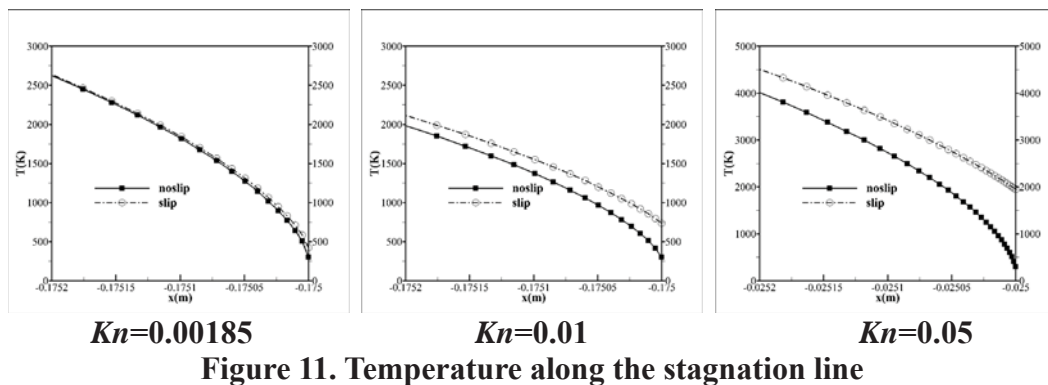


Figure 11 plots the temperature profile along the stagnation line. In despite of Knudsen number and chemical reaction, the temperature increases anyway. The discrepancy of temperature between slip wall and nonslip wall increases as Knudsen number rises.



## Conclusions

Surface slip effect in hypersonic flow with chemical reactions was studied. Two cases were simulated and compared with test data to verify the numerical method. Slip and nonslip flow of a blunt cone were calculated to understand the mechanism of slip effect with different catalytic conditions. Some specific conclusions are:

1. Numerical method employed characterizes the double cone detail flow. The prediction of the heat transfer rate agrees well with the test data. Slip surface may somewhat enlarge the separation area and reduce the peak heat flux.
2. Accommodation coefficient in slip boundary model plays a key role in predicting the heat transfer rate. It functions importantly when Knudsen number get larger.
3. Surface slip leads to larger mass diffusion heat flux and smaller convective heat flux. When Knudsen number goes up, discrepancy between slip and nonslip wall get larger. Bigger Knudsen number which means smaller gas density slows down atoms recombination in chemical reactions.

## References

- Scott, C.D. (1973), Wall Boundary Equations With Slip and Catalysis for Multicomponent Nonequilibrium Gas Flows. NASA TM X-58111, 1973.
- Gupta, R.N. (1985), Slip Boundary Equations for multicomponent Nonequilibrium Airflow. NASA Technique paper 1985-2452.
- Zoby, E.V. (1982), Analysis of STS-2 Experimental Heating Rates and Transition Data. Journal of Spacecraft, Vol. 20, No.3, 1982, pp. 232-237.
- Scott, C.D. (1982), Space Shuttle Laminar Heating with Finite Rate Catalytic Recombination Thermophysics of Atmospheric Entry. Progress in Astronautics and Aeronautics, Vol. 82, 1982, pp. 273-289.
- Daiß, A. (1997), Modeling of Catalytic Reactions on Silica Surfaces with Consideration of Slip Effects. Journal of Thermophysics and Heat Transfer, Vol.11, No.3, 1997, pp. 346-352.
- Meng-Sing Liou (2003), A Further Development of the AUSM+ Scheme Towards Robust and Accurate Solutions for All Speeds. AIAA Paper 2003-4116.
- Davis, R. T. (1970), Numerical Solution of the Hypersonic Viscous Shock-Layer Equations. AIAA Journal, Vol. 8, No. 5, 1970, pp. 843-851.
- Candler, G.V. (2002), CFD Validation for Hypersonic Flight: Hypersonic Double-Cone Flow Simulations. AIAA Paper 2002-0581.
- Harvey, J.K., M.S. Holden, and T.P. Wadhams (2001), Code Validation Study of Laminar Shock/Boundary Layer and Shock/Shock Interactions in Hypersonic Flow, Part B: Comparison with Navier-Stokes and DSMC Solutions. AIAA Paper 2001-1031.

## Parameter Optimization of the Transition Zone of Large Thin-walled Tank Structure

\* Ling Zhang<sup>1</sup>, Xi Zhang<sup>1</sup>, Cheng Huang<sup>1</sup>

<sup>1</sup> Beijing Institute of Astronautical Systems Engineering, Beijing, 100076, P. R. China,

\*Corresponding author: [mr.zhangling@gmail.com](mailto:mr.zhangling@gmail.com)

### Abstract

When a large thin-walled tank structure is subjected to internal pressure, large local bending moment and stress gradient is formed in the transition zone between the cylinder shell and the semi-spherical shell. It is known that it is difficult to realize the constant strength design through the traditional method. Also, the topological optimization is relatively difficult due to the existence of internal pressure on the design region. In this paper, firstly finite element method is conducted to analyze the conventional design of the transition zone; it is discovered that there is a change of force transmission path from the inner wall to the outer wall, which produces a high stress gradient in the transition zone. Secondly, based on the concept of force transmission path control, two weakened zones are constructed respectively in the transition ring and the thick section of cylinder shell; then a parameter optimization model is formed. Finally, sub-model approach is introduced and Non-dominated Sorting Genetic Algorithm (NSGA) is adopted for the parameter optimization. Then, more uniform stress distribution of the welding zone is obtained, and the maximum stress value is decreased from 227.3 MPa to 137.5 MPa.

**Key words:** Large thin-walled tank structure; Transition zone; Welding zone; Force transmission path; Parameter optimization.

### Introduction

The propellant tank is critical for a space launch vehicle in liquid propellant: the quality and mass of the tank structure play an important role in the product use, and can even affect the range or carrying capacity of the launch vehicle [1]. The propellant container is a typical aluminum alloy thin-walled structure. The tank can be divided into three main parts: the cylinder shell, the semi-spherical shell and the short cylinder shell. Different parts are welded together with transition rings to form a closed propellant container, and the tank can be connected with other sections through the short cylinder shell.

The internal pressure of large thin-walled tank structure is often high, and also there is strict weight requirement in the design process. It is resulted that the load carrying capacity of the structure is approaching to its limit. Therefore, it is of high difficulty to design the structure. Besides, on the one hand, the weld seams in the transition zone are intensive and its strength is low. On the other hand, both analytical method and finite element method (FEM) show that: large local bending moment is formed in the transition zone under the action of internal pressure, and there exists large axial stress gradient from the inner wall to the outer wall, which make the carrying capacity further reduced. So the design of transition zone is the critical factor in the design of the tank.

The conventional design method, using engineering algorithm, mainly takes into account the geometric smoothness and production process. However, the effect of transition zone local topography on the carrying capacity of the structure cannot be considered in detail. Also, the



topological optimization is relatively difficult due to the existence of internal pressure on the design region. The parameter optimization method can be applied to the design of transition region, to reduce the local moment near the weld seam and obtain more uniform stress field in the welding zone, so as to improve the bearing capacity and reliability of the structure. Currently, the method has been widely applied to the structural design of space vehicles. With regard to the post-buckling problem of grid-stiffened tank under axial compression, Hao et al. [2] proposed a hybrid optimization approach based on surrogate model and smeared stiffener model. The surrogate model was built for optimization using multi-island genetic algorithm to obtain the minimum mass solution under buckling constraints, with significant weight reduction achieved.

In this paper, firstly, finite element analysis is conducted for the conventional design of large thin-walled tank subjected to internal pressure, to obtain the stress distribution; then, based on the idea of controlling force transmission path, the morphology of the transition zone was constructed as a parameter optimization model; finally, with the maximum axial stress in the welding zone as the optimization objective, and the maximum Mises stress in the transition zone as a constraint, the sub-model method was introduced to conduct parameter optimization[3], so as to obtain a more uniform stress distribution in the welding area.

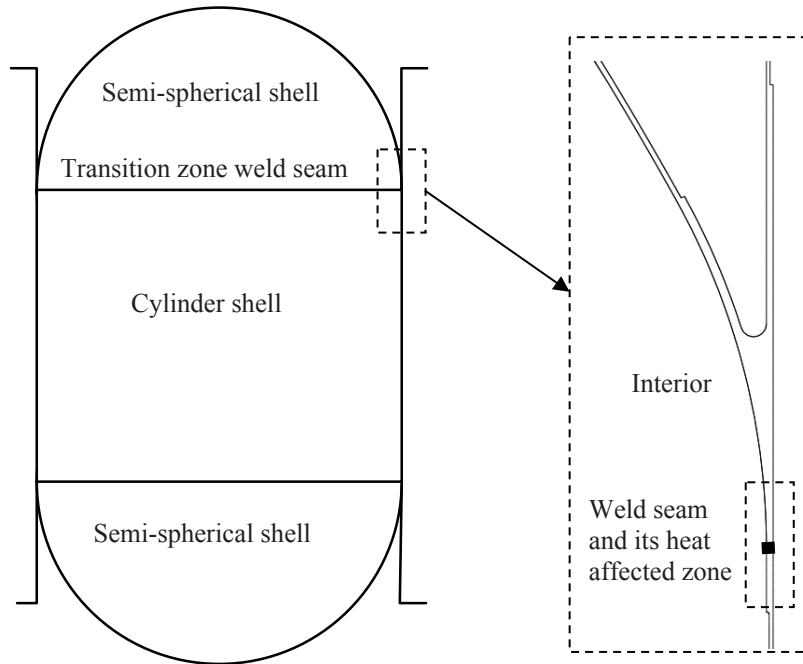
## 1 Analysis of the conventional design approach

Generally, the transition zone refers to the transition ring and the welded edges with adjacent structure of the tank; the welding zone refers to the weld seam and its heat affected zone. The strength of the welding zone is relatively low, and its stress distribution is affected by the topography of the transition zone. The stress distribution can be calculated by analytic method for the transition zone between the cylindrical section and semi-spherical shell with uniform thickness [4]. But the transition zone of tank structure is much more complicated, so the stress field cannot be obtained by analytic method. Therefore, the conventional design method mainly takes the geometric smoothness and production process into consideration. The conventional design of large thin-walled tank and the transition zone refers to Fig.1.

Stress analysis shows that: for large diameter thin-walled tank structure, the stress caused by internal pressure is much larger than that caused by bending moment, axial force, shear load, etc. Therefore, the high stress in the transition zone caused by internal pressure is the main concern of tank structural design. Hereinto: the stress field in the welding zone between the transition ring and semi-spherical shell is relatively uniform, thus the design can be accomplished with engineering algorithm; while the stress field in the welding zone between the transition ring and cylinder is more complicated, and thus higher stress gradient is produced under the action of local bending moment.

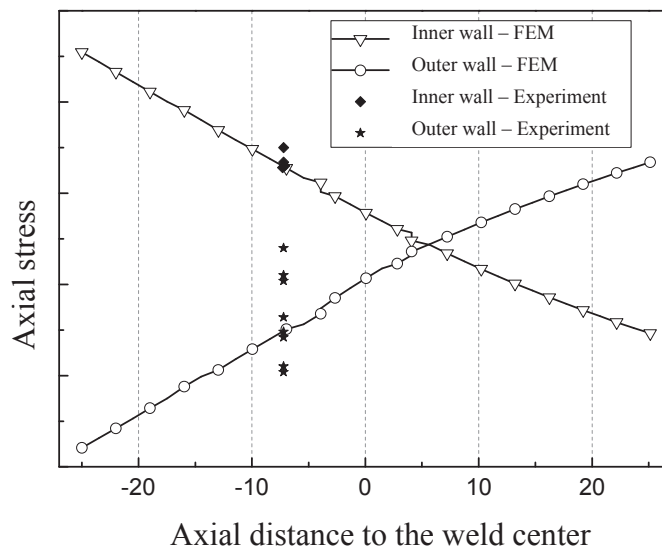
The Axial stress distribution of the welding zone between the transition ring and cylinder is shown Fig.2: the experimental result is obtained by internal pressure test of the tank; the axial position of the strain gauges is in the weld center, close to the transition ring with a distance of about 7.2 mm, and there was a uniform circumferential distribution; also there were four strain gauges on the inner wall and eight strain gauges on the outer wall. From the figure it can be seen that: the experimentally measured stresses on the inner wall have good consistency, and are close to the FEM result; while the experimental stresses on the outer wall have large dispersion, almost uniformly distributing around the finite element result. This is because the local welding deformation causes a deviation of the stress from the theoretical value, which cannot be considered in the finite element method. But the FEM result still reflects the average stress to some extent. In addition, the FEM result also indicates that: in the welding zone there is high stress gradient and in the transition ring the inner wall stress is higher than the outer wall stress; yet in the cylindrical

section the outer wall stress is higher than the inner wall stress instead and there exists a point in the middle where the inner wall stress equals the outer wall stress. This is because the inner walls of the semi-spherical shell and the transition ring are aligned, while the outer walls of the thick section and thin section of the cylinder are aligned. Thus the transmission path of axial stress can be concluded as: semi-spherical shell → inner wall of transition ring → outer wall of thick section of cylinder → thin section of cylinder.



**Figure 1 Design of large thin-walled tank and the transition zone**

A preliminary improvement about the conventional design method is: making the equal stress point right in the weld center by using the finite element method. However, there exists a problem that as the strength of the welding zone is relatively lower and the weakest position of strength is in the fusion line, equal capacity design cannot be achieved by this method.

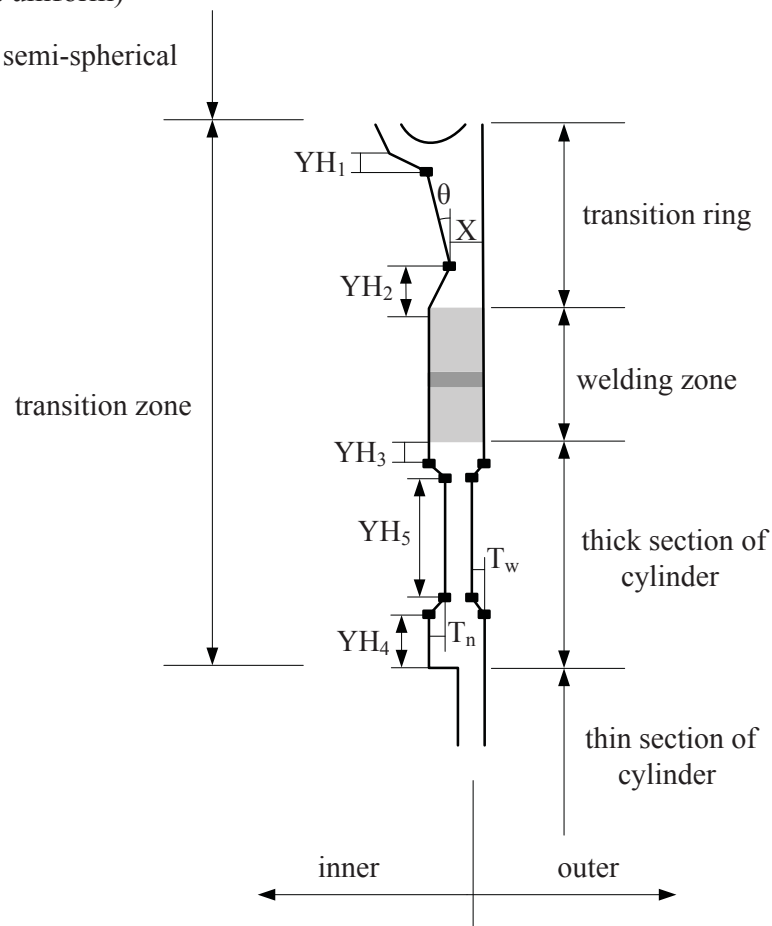


**Figure 2 Axial stress of the welding zone (positive horizontal coordinate corresponds to the cylinder)**

## 2 Construction of parameter optimization model

The conventional design method cannot be used for equal strength design, and topology optimization can not be conducted due to the existence of internal pressure on the design zone. In this section, according to the stress distribution feature of the transition zone and based on the concept of force transmission path control, the morphology of the transition zone is constructed and then a parameter optimization model is formed.

The FEM result of the conventional design has shown that the transmission path of axial stress is: semi-spherical shell  $\rightarrow$  inner wall of transition ring  $\rightarrow$  outer wall of thick section of cylinder  $\rightarrow$  thin section of cylinder. It has a change from the inner wall to the outer wall in the transition zone, which produces a high stress gradient in the welding zone. To avoid this high stress gradient, one solution is to control the force transmission path by constructing weakened zones at both sides of the welding zone. In detail, some material in the inner wall of the transition ring is removed so that the axial stress of the semi-spherical shell can transfer from the middle of the transition ring; and meanwhile double-sided milling is employed in the thick section of the cylinder so that the axial stress can also transfer from the middle. Based on these, the basic morphology of the transition zone is constructed, and the parameter optimization model is established, as shown in Fig.3. (The scale in the schematic is not uniform)



**Figure 3 Schematic of the parameter optimization model of the transition zone**

The two geometrical points in the weakened zone of the transition ring are described by four parameters, i.e.,  $YH_1$ 、 $YH_2$ 、 $\theta$ 、 $X$ ; and the morphology of the thick section of cylinder is depicted by five parameters:  $YH_3$ 、 $YH_4$ 、 $YH_5$ 、 $T_n$ 、 $T_w$ . The meanings of these parameters are explained in Table 1.

**Table 1 Meanings of the optimization parameters**

Described region	Parameter	Geometrical description
Transitional ring	X	Minimal thickness of the transition ring
	$\theta$	Inclination of the weakened zone
	YH <sub>1</sub>	Distance from the weakened zone to the edge of semi-spherical shell
	YH <sub>2</sub>	Distance from the minimal thickness point to the heat affected zone
Thick section of cylinder	YH <sub>3</sub>	Distance from the weakened zone to the heat affected zone
	YH <sub>4</sub>	Distance from the weakened zone to the thin section of cylinder
	YH <sub>5</sub>	Axial size of the weakened zone
	T <sub>n</sub>	Depth of the inner wall weakened zone
	T <sub>w</sub>	Depth of the outer wall weakened zone

### 3 Local optimization based on sub-model method

The aim of this section is as follows: to optimize the force transmission path without regard to the material nonlinearity; according to the structure feature of large thin-walled tank, axisymmetric model is employed and also geometrical nonlinearity is taken into consideration. Besides, in order to reduce the computation work, the sub-model method is introduced in the parameter optimization process.

By using the sub-model technology, the degrees of freedom of the model have been reduced by half and the computation time has been reduced to only 1/8. Moreover, as there exists proper distance from the boundary of the sub-model to the optimization zone, trial computation has shown that the change of optimization variables has little effect on the stress and displacement fields on the boundary of the sub-model. Thus there is only weak coupling between the optimization variables and the boundary of the sub-model, and the convergency of the optimization can be guaranteed.

#### 3.1 Update rule of sub-model boundary

After the introduction of sub-model method in the optimization process, iterative optimization is conducted to the sub-model, in which the boundary conditions remain unchanged. However, the change of sub-model parameters has certain influence on the computational result of the global model, which accordingly has influence on the sub-model boundary conditions. Therefore, the more the step number of sub-model optimization iteration, the more its boundary conditions deviate from the true situation. For this reason, the update rule of sub-model boundary should be determined during the optimization process.

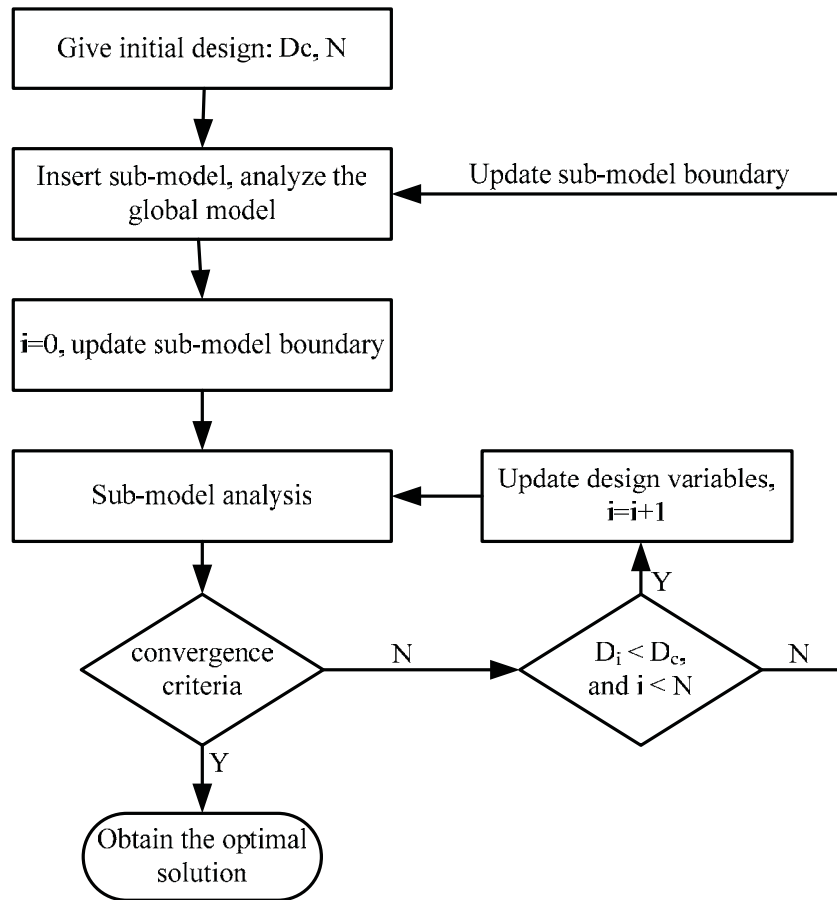
The indicator of the maximum displacement variation in the sub-model is defined as following:

$$D_i = \left| \frac{u_{\max}^i - u_{\max}^0}{u_{\max}^0} \right| \quad (1)$$

Hereinto:  $u_{\max}^0$  is the maximum displacement of the sub-model region in the computational result of global model,  $u_{\max}^i$  is the maximum displacement of the sub-model in the  $i^{\text{th}}$  optimization applied to the sub-model.

The update rule of sub-model boundary is given as follows: when  $D_i$  is greater than the set value  $D_c$ , or  $i$  is greater than the set value  $N$ , the sub-model boundary conditions should be updated. In this

rule,  $D_c$  and  $N$  are related with the optimization scale and optimization algorithm. Generally,  $D_c$  should be less than 50%, and  $N$  should be less than 50. The update procedure of sub-model boundary conditions is illustrated in Fig.4.



**Figure 4 Optimization procedure after introducing sub-model**

### 3.2 Parameter optimization of tank transition zone

The two optimization formulations are showed following:

$$\begin{aligned}
 &\text{find} && YH_1, YH_2, x, \theta, YH_3, YH_4, YH_5, T_n, T_w \\
 &\text{min} && \max(HF\_S_{22}) \\
 &\text{s.t.} && 3.2 \leq YH_1 \leq 32 \\
 &&& 3.2 \leq YH_2 \leq 32 \\
 &&& 2.5 \leq x \leq 5 \\
 &&& 0 \leq \theta \leq 3.8 \\
 &&& 0 \leq YH_3 \leq 12.7 \\
 &&& 5.0 \leq YH_4 \leq 12.7 \\
 &&& 5.0 \leq YH_5 \leq 95.0 \\
 &&& 0 \leq T_n \leq 2.0 \\
 &&& 0 \leq T_w \leq 2.0 \\
 &&& S \leq \sigma_b \\
 &&& HF\_S_{22} \leq \sigma_b/3
 \end{aligned}$$

(2)

Hereinto:  $HF_{S_{22}}$  is the maximum axial stress in the welding zone,  $S$  is the maximum Mises stress in the transition zone,  $\sigma_b$  is the tensile strength of the material, the meaning of other parameters is listed in table 1.

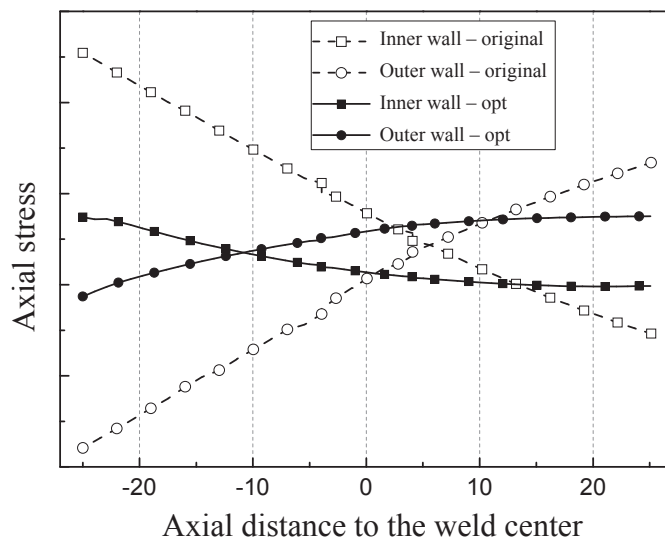
After several trials, it was found that this optimization problem has the features of non-convex and multi-peak, so the global optimal solution cannot be obtained solely by the mathematical programming method. Thus the genetic algorithm is used for the parameter optimization. The non-dominated sorting genetic algorithm is chosen for the optimal solution: 28 populations are set; the crossover probability is 0.9; the crossover distribution index and mutation distribution index are 10.0 and 20.0 respectively.

The results of parameter optimization are listed in Table 2: the objective function, i.e., the maximum stress is decreased from 227.3 MPa to 137.5 MPa. It shows an obvious optimization effect.

**Table 2 The optimization parameters and constraint conditions**

	Optimization parameters									Objective		Constraint
	YH <sub>1</sub>	YH <sub>2</sub>	$\theta$	X	YH <sub>3</sub>	YH <sub>4</sub>	YH <sub>5</sub>	T <sub>n</sub>	T <sub>w</sub>	HF	S <sub>22</sub>	S
Initial value	16.3	24.3	3.2	4.6	6.3	9.5	31.7	0.6	0.6	227.3		462.3
Optimal value	5.24	17.60	3.79	3.68	4.36	12.59	63.56	0.09	0.63	137.5		434.5

The axial stress distribution of the transition zone near the weld seam is shown in Fig.5: the trend of stress distribution is unchanged: in the transition ring the inner wall stress is still higher than the outer wall stress; and in the cylindrical section, the outer wall stress is still higher than the inner wall stress. However, the stress gradient is reduced a great deal, with the stress difference between the inner wall and outer wall being reduced to 20% of the conventional design. After parameter optimization, more uniform stress distribution is achieved in the welding zone.



**Figure 5 Axial stress in the transition zone (positive horizontal coordinate corresponds to the cylindrical section)**

#### 4 Conclusions

The conventional design can not achieve the equal stress design of the welding zone of large thin-walled tank structure. This paper adopts the finite element method to make an analysis about the existing problem and it is discovered that the reason causing high stress gradient in the welding zone is a change of the force transmission path from the inner wall to the outer wall. Then, based on the concept of force transmission path control, the weaken zone is constructed in the transition zone and then a parameter optimization model is formed. Finally, sub-model approach is introduced and non-dominated sorting genetic algorithm is used for the parameter optimization in the transition zone. After optimization, more uniform stress distribution is obtained, with the maximum stress of the welding zone being decreased from 227.3 MPa to 137.5 MPa.

#### References

- [1] ZHOU Guangwen. Optimal structure design for launch vehicle tank [J]. Missiles and space vehicles, 2011, 1: 26-28
- [2] HAO Peng, WANG Bo, LI Gang, WANG Xiao-jun. Hybrid optimization of grid-stiffened cylinder based on surrogate model and smeared stiffener model [J]. Chinese Journal of Computational Mechanics, 2012, 29(4): 481-486
- [3] CHENG Gengdong. Introduction to optimum design of engineering structures [M]. Dalian University of Technology Press
- [4] S. Timoshenko. Theory of plates and shells [M]. Beijing: Science Press, 1977

## State Estimation Problem for the Action Potential Modeling in Purkinje Fibers

**\*D. C. Estumano<sup>1</sup>, H. R. B.Orlande<sup>1</sup> and M. J.Colaço<sup>1</sup>**

<sup>1</sup>Federal University of Rio de Janeiro – UFRJ, Department of Mechanical Engineering – PEM/COPPE, Brazil

\*Corresponding author: diegoestumano@ufrj.br

### Abstract

In this work we use the Particle Filter Method to solve a state estimation problem resulting from the application of Hodgkin-Huxley's model to Purkinje fibers, by applying Liu and West's Auxiliary Sampling Importance Resampling (ASIR) algorithm. This algorithm allows the simultaneous estimation of state variables and parameters. The estimation of the action potential in Purkinje fibers can be related to the identification of heart anomalies. The use of Bayesian particle filters is of great interest for such specific application, since they take into account uncertainties in the mathematical models for the evolution of the state variables and the measurements. Simulated measurements are used in this work to examine the accuracy of the Particle Filter Method under analysis.

**Keywords:** Particle Filters, Bayesian estimate, Hodgkin-Huxley's model, Purkinje fibers.

### Introduction

Hodgkin and Huxley (1952) proposed a model for the action potential in an axon, in terms of an electric circuit with capacitance and ionic currents. Sodium and potassium ions are the most important in the action potential and are distinguished in terms of their own proper currents, in comparison to the other ions. The model involves a non-linear system of four ordinary differential equations, whose coefficients are given in terms of functions of the applied potential. Although Hodgkin-Huxley's model has been originally proposed for the experimental data involving an axon, it has also been used to model the action potential in heart cells, like Purkinje fibers (Noble, 1962).

State estimation problems are dynamically solved within the Bayesian framework (Kaipio and Somersalo, 2004; Arulampalam et al., 2001). In this framework, an attempt is made to utilize all available information in order to reduce the amount of uncertainty present in inferential or decision-making problems. As new information is obtained, it is combined with previous information to form the basis for statistical procedures. The formal mechanism that combines the new information with the previously available information is known Bayes' theorem (Kaipio and Somersalo, 2004). Monte Carlo methods have been developed in order to represent the posterior density in terms of random samples and associated weights and can be applied to non-linear models with non-Gaussian errors (Kaipio and Somersalo, 2004; Arulampalam et al., 2001; Ristic et al., 2004; Doucet et al., 2001; Orlande et al., 2012), such as the one under analysis in this work.

In this paper we extend our previous work (Estumano et al., 2013) in order to compare the results obtained with the Sampling Importance Resampling (SIR) algorithm and the Auxiliary Sampling Importance Resampling (ASIR) algorithm (Kaipio and Somersalo, 2004; Arulampalam et al., 2001; Ristic et al., 2004; Doucet et al., 2001), to results obtained with the algorithm proposed by Liu and West (2001). This paper is focused on the use of Hodgkin-Huxley's models for the action potential in Purkinje Fibers (Noble, 1962). The three algorithms are compared in terms of their computational times and RMS errors. We note, beforehand, that Liu and West's algorithm is the most general of the three algorithms listed above, since uncertainties in the model parameters are taken into account through Gaussian kernel smoothing (Liu and West, 2001). Other recent applications of inverse



problems to Hodgkin-Huxley's model include the works of Dokos and Lovell (2004) and Meng et al. (2011).

### Hodgkin-Huxley's Model

Hodgkin and Huxley, in their classical paper of 1952, examined the behavior of an axon under the effects of an imposed electric current across the cell membrane. The cell electric potential was assumed to be independent of the position within the cell, that is, the intracellular electric resistance was neglected. In their experiments, Hodgkin and Huxley (1952) observed that the conductance of some ions across the cell membrane, like sodium and potassium, varied with changes in the axon's potential. The imposed electric current across the cell membrane was then modeled in terms of capacitive and ionic currents. Being the sodium and potassium ions recognized as the most important ones in this process, their currents were treated separately from those corresponding to the other ions, which were quantified in a global manner and referred to as leakage current. For the model, an inflow of ions was assumed as positive.

A basic difference between axons and Purkinje fibers results from the fact that in the last ones the potassium flow is governed by both a fast and a slow channel dynamics. In addition, the flow of ions other than sodium and potassium through the cell membrane can be neglected, so that the analogous electric circuit for the problem is presented in Figure 1. The imposed electric current is null for the case involving Purkinje fibers because these cells are auto-excitable (Noble, 1962). Therefore, the equation for the action potential in Purkinje fibers is given by (Noble, 1962):

$$C_m \frac{dV_m}{dt} + G_{Na} (V_m - V_{Na}) + G_K (V_m - V_K) = 0 \quad (1)$$

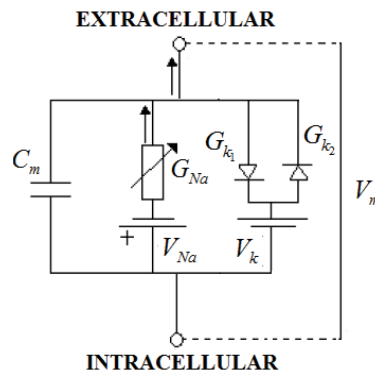


Figure 1. – Electric circuit for a Purkinje fibers (Noble, 1962)

The equations given by Noble (1962) for sodium and potassium conductances of a Purkinje fiber are given, respectively, by:

$$G_{Na} = G_{Na}^{max} m^3 h + G_{Na,l} \quad (2)$$

$$G_K = 1.2 \exp\left(-\frac{V_m + 90}{50}\right) + 0.015 \exp\left(\frac{V_m + 90}{60}\right) + 1.2n^4 \quad (3)$$

where  $m$  and  $n$  represent the open fraction, or probability of the channels being open, for sodium and potassium, respectively, while  $h$  is the probability of the channel being closed for the sodium ions. The variables  $m$  and  $n$  are also referred to as the *activations* of the ion transfer through the

cell membrane, while  $h$  is referred to as the *inactivation* for the sodium ion transfer. In equation (2),  $G_{Na}^{max}$  refers to the maximum sodium conductance.

Hodgkin and Huxley (1952) proposed the following ordinary differential equations to describe the ion channels opening/closing dynamics:

$$\frac{dm}{dt} = \alpha_m(1-m) + \beta_m m \quad \frac{dh}{dt} = \alpha_h(1-h) + \beta_h h \quad \frac{dn}{dt} = \alpha_n(1-n) + \beta_n n \quad (4-6)$$

The parameters for the computation of the activations  $m$  and  $n$  and inactivation  $h$  in Eq. (4)-(6) are given as (Noble, 1962):

$$\alpha_m = -0.1 \frac{V_m + 48}{\exp\left[-\frac{V_m + 48}{15}\right] - 1} \quad \beta_m = \frac{0.12(V_m + 8)}{\exp\left[\frac{V_m + 8}{5}\right] - 1} \quad \alpha_h = 0.17 \exp\left[-\frac{V_m + 90}{20}\right] \quad (7-9)$$

$$\beta_h = \left[ \exp\left(-\frac{V_m + 42}{10}\right) + 1 \right]^{-1} \quad \alpha_n = -\frac{10^{-4}(V_m + 50)}{\exp\left(-\frac{V_m + 50}{10}\right) - 1} \quad \beta_n = 0.002 \exp\left[-\frac{V_m + 90}{80}\right] \quad (10-12)$$

Other parameters for the application of Hodgkin-Huxley's model for a Purkinje fiber are presented in Table 1 (Estumano et al., 2013).

**Table 1. Parameters for Hodgkin-Huxley's model for Purkinje fiber**

Parameter	Values	Parameter	Values	Parameter	Values
$C_m (\mu F cm^{-2})$	12	$V_{Na} (mV)$	40	$G_{Na,l} (mS)$	0.14
$G_{Na}^{max} (mS)$	400	$V_k (mV)$	-100		

### State Estimation Problem

In order to define the state estimation problem, consider a model for the evolution of the vector  $\mathbf{x}$  in the form (Kaipio and Somersalo, 2004; Arulampalam et al., 2001; Ristic et al., 2004; Doucet et al., 2001; Orlande et al., 2012):

$$\mathbf{x}_k = \mathbf{f}_k(\mathbf{x}_{k-1}, \mathbf{v}_{k-1}) \quad (13)$$

where the subscript  $k = 1, 2, \dots$ , denotes a time instant  $t_k$  in a dynamic problem. The vector  $\mathbf{x} \in R^{n_x}$  is called the *state vector* and contains the variables to be dynamically estimated. This vector advances in accordance with the *state evolution model* given by Eq. (13), as a non-linear function of the state variables  $\mathbf{x}$  and of the *state noise* vector  $\mathbf{v} \in R^{n_v}$ . Consider also that measurements  $\mathbf{z}_k \in R^{n_z}$  are available at  $t_k$ ,  $k = 1, 2, \dots$ . The measurements are related to the state variables  $\mathbf{x}$  through the general function  $\mathbf{h}$  in the form

$$\mathbf{z}_k = \mathbf{h}_k(\mathbf{x}_k, \mathbf{n}_k) \quad (14)$$

where  $\mathbf{n} \in R^n$  is the *measurement noise*. Equation (14) is referred to as the *observation (measurement) model*.

The state estimation problem aims at obtaining information about  $\mathbf{x}_k$  based on the state evolution model (13) and on the measurements  $\mathbf{z}_{1:k} = \{\mathbf{z}_i, i = 1, K, k\}$  given by the observation model (14). The state estimation problem addressed in this work deals with Hodgkin-Huxley's model applied to Purkinje fibers. Therefore, the state variables are given by

$$\mathbf{x}^T = [V_m, m, h, n] \quad (15)$$

with state evolution models given by Eqs. (1) to (12). Measurements of the cell potential,  $V_m$ , are supposed available for the estimation of the state variables.

Due to its nonlinear character, the Particle Filter Method was used for the solution of the present state estimation problem (Kaipio and Somersalo, 2004; Arulampalam et al., 2001; Ristic et al., 2004; Doucet et al., 2001; Orlande et al., 2012). In this method, the required posterior density function is represented by a set of random samples (particles) with associated weights, which are then used for the sequential computation of its associated statistics. The particle filter algorithms generally make use of an *importance density*, which is proposed to represent another density that cannot be exactly computed, that is, the sought posterior density in the present case. Then, samples are drawn from the importance density instead of the actual density (Kaipio and Somersalo, 2004; Arulampalam et al., 2001; Ristic et al., 2004; Doucet et al., 2001; Orlande et al., 2012).

The set of particles from time  $t_0$  to time  $t_k$  is denoted as  $\{\mathbf{x}_{0:k}^i, i = 0, K, N\}$  and their associated weights as  $\{w_k^i, i = 0, K, N\}$ , where  $N$  is the number of particles. The weights are normalized, so

that  $\sum_{i=1}^N w_k^i = 1$ . The sequential application of the particle filter might result in the *degeneracy*

*phenomenon*, where after a few states very few particles have negligible weight (Kaipio and Somersalo, 2004; Arulampalam et al., 2001; Ristic et al., 2004; Doucet et al., 2001; Orlande et al., 2012). An attempt to overcome this difficulty is to use a resampling step in the application of the particle filter, where particles with small weights are discarded and particles with large weights are replicated. In the *Sampling Importance Resampling* (SIR) algorithm, resampling is applied every time step (Arulampalam et al., 2001; Ristic et al., 2004). Although the resampling step reduces the effects of the degeneracy problem, it may lead to a loss of diversity and the resultant sample may contain many repeated particles, which is more likely to occur in the case of small state evolution noise (Kaipio and Somersalo, 2004; Arulampalam et al., 2001; Ristic et al., 2004; Doucet et al., 2001; Orlande et al., 2012). In addition, in the SIR algorithm the state space is explored without the information conveyed by the measurements at the specific instant that the state variables are sought. With the *Auxiliary Sampling Importance Resampling* (ASIR) algorithm an attempt is made to overcome these limitations, by performing the resampling step at time  $t_{k-1}$ , with the available measurement at time  $t_k$  (Arulampalam et al., 2001; Ristic et al., 2004). The resampling is based on some point estimate  $\mu_k^i$  that characterizes  $\pi(\mathbf{x}_k|\mathbf{x}_{k-1}^i)$ , which can be the mean of  $\pi(\mathbf{x}_k|\mathbf{x}_{k-1}^i)$  or simply a sample of  $\pi(\mathbf{x}_k|\mathbf{x}_{k-1}^i)$ . If the state evolution model noise is small,  $\pi(\mathbf{x}_k|\mathbf{x}_{k-1}^i)$  is generally well characterized by  $\mu_k^i$ , so that the weights  $w_k^i$  are more even and the ASIR algorithm is less sensitive to outliers than the SIR algorithm. On the other hand, if the state evolution model noise is large, the single point estimate  $\mu_k^i$  in the state space may not characterize well  $\pi(\mathbf{x}_k|\mathbf{x}_{k-1}^i)$  and the ASIR algorithm may not be as effective as the SIR algorithm.

We note that the functions  $\mathbf{f}_k(\cdot)$  and  $\mathbf{h}_k(\cdot)$ , in the evolution and observation models, respectively, contain several constant parameters, here denoted as the vector  $\boldsymbol{\theta}$ . However, in general, such parameters are not deterministic or might not be deterministically known. Therefore, the samples need to be extended to  $\{\mathbf{x}_k^i, \boldsymbol{\theta}_k^i : i = 0, K, N\}$  with associated weights  $\{w_k^i : i = 0, K, N\}$ . In this work, the algorithm developed by Liu and West (2001), and based on the ASIR algorithm, is used for the solution of the state estimation problem, with the vector of state variables given by equation (15) and the vector of parameters given by:

$$\boldsymbol{\theta}^T = [C_m, G_{Na}^{max}, G_{Na,l}] \quad (17)$$

Such parameters were selected for the present analysis because they are the ones with larger variabilities in the open literature.

The algorithms of the SIR and ASIR filters, as well as the one due to Liu and West, can be found in Kaipio and Somersalo (2004), Arulampalam et al. (2001), Ristic et al. (2004), Liu and West (2001), Orlande et al. (2012), Colaço et al. (2012) and are not repeated here for the sake of brevity.

## Results and Discussion

In this paper, the three algorithms described above are compared in terms of their RMS errors and computational times, for cases dealing with axons and Purkinje fibers. The CPU times correspond to a computational code running under the Matlab platform, in an Intel i5 CPU with 6 Gb of RAM memory. The RMS error is computed as

$$RMS = \sqrt{\frac{1}{M} \sum_{i=1}^M [x_{est}(t_i) - x_{exa}(t_i)]^2} \quad (18)$$

where the subscripts *est* and *exa* denote the estimated and exact values of the state variable  $x(t_i)$  at time  $t_i$ , while  $M$  is the number of time steps. A similar definition was used to compute the RMS errors for each parameter  $\boldsymbol{\theta}$ . The RMS errors were compared in terms of the means of 100 repetitions of the particle filter estimates, in order to avoid any bias resulting from different sets of simulated measurements used in the analysis (Hamilton et al., 2013).

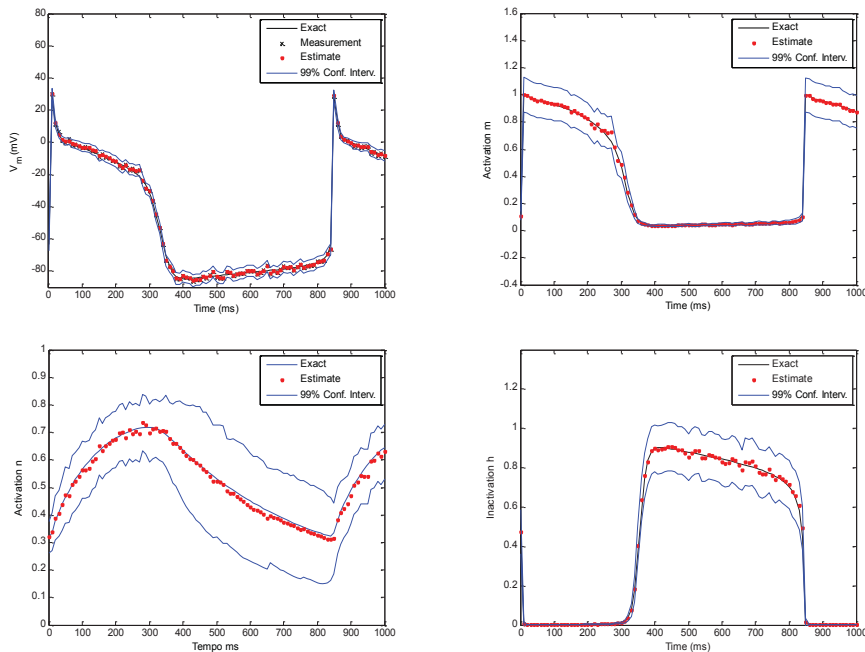
Simulated measurements of the cell potential,  $V_m$ , were utilized in the present work. Such measurements were generated from a numerical simulation of the deterministic dynamic problem for the Purkinje fibers. Errors in the simulated measurements were additive, uncorrelated, with a Gaussian distribution, zero mean and a constant standard deviation  $\sigma$ , so that the likelihood function at time  $t_k$  is given by

$$\pi(\mathbf{z}_k | \mathbf{x}_k) = \frac{1}{\sqrt{2\pi\sigma^2}} \exp \left\{ -\frac{1}{2\sigma^2} [V_m^{mod}(t_k) - V_m(t_k)]^2 \right\} \quad (19)$$

where the superscript *mod* refers to the measurement variable computed with the observation model given by Eq. (14). Simulated measurements were considered available in time intervals of 10 ms. For the results presented below, the parameters given by Eqs. (1) to (12) and Table 1 were used in the analysis. The initial conditions for these cases were taken as  $V_m(0) = -70mV$ ,  $m(0) = 0.079$ ,  $n(0) = 0.323$  and  $h(0) = 0.602$  (Estumano et al., 2013). The

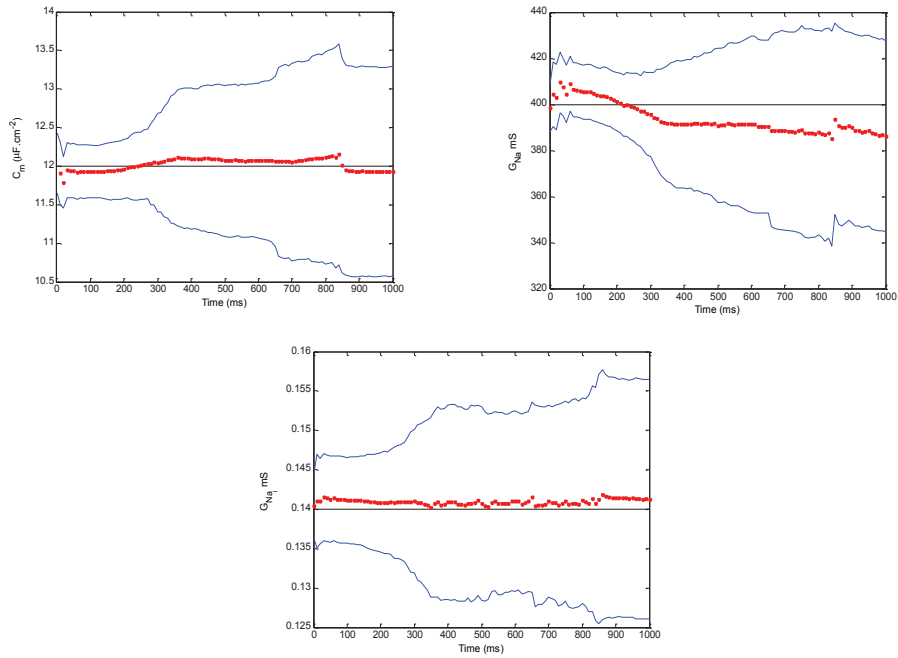
errors in the evolution model were additive, uncorrelated, with Gaussian distribution, zero mean and a constant standard deviation of 5% of the absolute value of the state variables at the initial time. The standard deviations of the measurements were taken as 5% of the maximum absolute value of the measured variable, that is,  $\sigma = 0.05|V_{m,max}|$ .

The results obtained for the estimation of the state variables and the model parameters with Liu and West's algorithm are presented in figures 2 and 3, respectively. Such results were obtained with 500 particles. Figure 2 shows an excellent agreement between exact and estimated state variables, even for those for which measurements are not available, such as  $m$ ,  $n$  and  $h$ . Similarly, uncertainties in the model parameters are appropriately taken into account as depicted from figure 3. Note in this figure that the exact values of the parameters fall within the confidence intervals of the estimates. Figures 2 and 3 reveals the robustness of Liu and West's algorithm as applied to the present problem, which was capable of accurately estimating state variables and model parameters, despite the large uncertainties in the evolution and measurement models, as well as in the model parameters.



**Figure 2: Estimation of the state variables**

Tables 2-4 present the RMS errors and the computational times for the three Particle filter algorithms examined in this work, for various numbers of particles ( $N_p$ ). Let us first examine tables 2 and 3, which present the results obtained with the SIR and the ASIR algorithms, respectively. Such algorithms deal only with the estimation of the state variables. These tables show, as expected, a reduction on the RMS errors, followed by an increase in the computational time, as the number of particles is increased. In addition, we notice in tables 2 and 3 that the RMS errors tend to approach a constant value as the number of particles is increased. According to tables 2 and 3, similar RMS errors were obtained with the ASIR algorithm by using less particles than those of the SIR algorithm. Although the ASIR algorithm is more expensive than the SIR algorithm in terms of computational time for the same number of particles, the ASIR algorithm is capable of providing accurate results with a much smaller number of particles. As a result, the computational times are smaller with the ASIR algorithm than with the SIR algorithm, for results of comparable accuracy.



**Figure 3: Estimation of the model parameters**

**Table 2: RMS errors and computational times for the SIR algorithm**

$N_p$	CPU Time (s)	$V_m$ (mV)	$m$	$n$	$h$
20	3.12	2.8126	0.0945	0.0806	0.0289
50	7.35	1.6984	0.0889	0.0743	0.0240
100	15.01	1.5899	0.0884	0.0698	0.0231
500	72.07	1.5811	0.0883	0.0669	0.0221
1000	140.08	1.5778	0.0882	0.0662	0.0221
2000	247.73	1.5769	0.0882	0.0662	0.0220

**Table 3: RMS errors and computational times for the ASIR algorithm**

$N_p$	CPU Time (s)	$V_m$ (mV)	$m$	$n$	$h$
50	15.91	1.4275	0.0902	0.0757	0.0191
100	48.00	1.4195	0.0901	0.0732	0.0182
200	111.03	1.4118	0.0900	0.0711	0.0174
300	205.77	1.4069	0.0900	0.0706	0.0173
400	332.19	1.4043	0.0900	0.0692	0.0170
500	485.80	1.4021	0.0900	0.0685	0.0170

The results obtained with Liu and West's algorithm (2001) are presented in table 4. A comparison of tables 3 and 4 reveal an increase on the computational time, for the same number of particles, when Liu and West's algorithm was used, caused by the simultaneous estimation of parameters and state variables. Anyhow, both state variables and parameters can be accurately estimated (see also figures 2 and 3) with this algorithm. In addition, the RMS error was reduced when the uncertainties on the parameters was taken into account, as compared to the original ASIR algorithm.

**Table 4: RMS errors and computational times for Liu and West's algorithm**

$N_p$	CPU Time (s)	$V_m$ (mV)	$m$	$n$	$h$	$C_m$ ( $\mu F cm^{-2}$ )	$G_{Na}$ (mS)	$G_{Na,l}$ (mS)
50	96.76	1.1360	0.0109	0.0133	0.0109	0.0621	5.2964	0.0003
100	191.55	1.1417	0.0111	0.0133	0.0129	0.0734	7.0376	0.0008
200	383.40	1.1373	0.0108	0.0132	0.0138	0.0662	8.6214	0.0007
300	574.81	1.2897	0.0108	0.0134	0.0173	0.0885	8.5989	0.0007
400	765.37	1.1356	0.0108	0.0133	0.0126	0.1613	9.3856	0.0009
500	957.93	1.1402	0.0109	0.0135	0.0135	0.0782	8.9281	0.0009

## Conclusions

Particle filter methods are the most general techniques for the solution of state estimation problems involving nonlinear and non-Gaussian models. In this paper, three different particle filter algorithms were applied to the estimation of state variables of the model proposed by Hodgkin and Huxley to describe the action potential in excitable cells. Cases involving Purkinje fiber are examined in the paper, by using simulated measurements of the action potential. Although the SIR and the ASIR algorithms are capable of accurately estimating the state variables, we notice that the more general algorithm by Liu and West allows the simultaneous estimation of the state variables and model parameters. Furthermore, such quantities can be estimated with better accuracy than those related to the estimation of only the state variables.

## Acknowledgements

The support provided CNPq, ANP/PRH37, CAPES and FAPERJ, Brazilian agencies for the fostering of science, is greatly appreciated.

## References

- A. Hodgkin and A. Huxley (1952), A Quantitative Description of Membrane Current and Its Application to Conduction and Excitation in Nerve, *Journal of Physiology*, 117, pp. 500-544.
- B. Ristic, S. Arulampalam and N. Gordon (2004), *Beyond the Kalman Filter*, Artech House, Boston.
- D. Noble (1962), Modification of Hodgkin- Huxley Equations Applicable to Purkinje Fiber Action and Pace – Maker Potentials, *Journal of Physiology*, 160, pp. 317 – 352.
- D. Estumano, H. Orlande and M. Colaço (2013), State Estimation Problem For Hodgkin-Huxley'S Model: A Comparison of Particle Filter Algorithms, *4th Inverse Problems, Design and Optimization Symposium (IPDO-2013)*, Albi, France, June 26-28.
- F. Hamilton, M. Colaço, R. Carvalho and A. Leiroz (2013), Heat Transfer Coefficient Estimation of an Internal Combustion Engine Using Particle Filters, *Inverse Problems in Science and Engineering*, DOI:10.1080/17415977.2013.797411.
- H. Orlande, M. Colaço, G. Dulikravich, F. Vianna, W. Silva, H. Fonseca and O. Fudym (2012), State Estimation Problems in Heat transfer, *International Journal for Uncertainty Quantification*, 2, pp. 239–258.
- J. Kaipio and E. Somersalo (2004), Statistical and Computational Inverse Problems, *Applied Mathematical Sciences 160*, Springer-Verlag.
- J. Liu and M. West (2001), Combined Parameter and State Estimation in Simulation-Based Filtering, *Chapter 10 in Sequential Monte Carlo Methods in Practice*, A. Doucet, N. Freitas, N. Gordon (editors), Springer, New York.
- L. Meng, M. A. Kramer and U. T. Eden (2011), A sequential Monte Carlo approach to estimate biophysical neural models from spikes, *Journal of Neural Engineering*, 8(6), DOI: 10.1088/1741-2560/8/6/065006.
- M. Colaço, H. Orlande, W. Silva and G. Dulikravich (2012), Application of Two Bayesian Filters to Estimate Unknown Heat Fluxes in a Natural Convection Problem, *Journal of Heat Transfer*, 134, pp. 092501-092511.
- S. Arulampalam, S. Maskell, N. Gordon and T. Clapp (2001), A Tutorial on Particle Filters for On-Line Non-linear/Non-Gaussian Bayesian Tracking, *IEEE Trans. Signal Processing*, 50, pp. 174-188.
- S. Dokos and N. H. Lovell (2004), Parameter estimation in cardiac ionic models, *Progress in Biophysics & Molecular Biology*, 85, pp.407–431.

# An iterative truly meshless coupling to solve embedded crack problems

E.F. Fontes Jr<sup>1</sup>, J.A.F. Santiago<sup>1</sup>, and \*J.C.F. Telles<sup>1</sup>

<sup>1</sup>Civil Engineering Programme, COPPE/UFRJ, Caixa Postal 68506, CEP21941-972, Rio de Janeiro, Brazil.

\*Corresponding author: telles@coc.ufrj.br

## Abstract

A meshless iterative domain decomposition approach is presented to solve linear elastic fracture mechanic (LEFM) problems. The global domain of the problem is decomposed into sub-domains, where each one is addressed using an appropriate meshless method. The sub-domain which has embedded cracks is modeled by the method of fundamental solutions (MFS) with the help of the numerical Green's function (NGF) approach and the sub-domain without cracks is modeled by the meshless local Petrov-Galerkin (MLPG) procedure. The specific computations of each method are performed separately, coupled with a successive update of variables procedure, restricted to interface unknowns, to achieve the final convergence. The iterative solution procedure presented yields good results as compared with the boundary element method and analytical solutions for stress intensity factor computations.

**Keywords:** Iterative coupling, MLPG, MFS, Green's function, Crack, Meshless.

## Introduction

Meshless methods have been increasingly applied to obtain solutions of partial differential equations as an alternative to mesh type methods like the boundary element method (BEM) and the finite element method (FEM). Previous references on the development of alternative meshless methods can be found in the works by Belytschko et al. 1996 and Atluri 2002. However, like in any numerical approach, meshless methods can present inherent drawbacks depending on the engineering problem to be solved. To circumvent this, coupling procedures using the appropriate meshless method for each typical problem region can be adopted, improving not only efficiency, but also solution accuracy for different coupled engineering problems as shown in the works by Godinho and Soares, 2013.

A meshless method that has been applied to a large range of problems is the local Petrov-Galerkin (MLPG) method presented by Atluri and Zhu 1998. The MLPG is a truly meshless method, not requiring any type of mesh discretization. However, this flexibility in solving engineering problems can be computationally expensive in some cases. By using the MLPG to solve linear elastic fracture mechanics (LEFM) problems one needs to introduce several points near the crack tips, what may lead to a computationally expensive procedure.

The method of fundamental solutions (MFS), developed by Kupradze and Aleksidze in 1964 is a simple meshless boundary-type method. In order to build the solution, MFS uses a linear combination of fundamental solutions associated with the problem.



This is done without using any integrals, greatly simplifying its implementation. This particularity actually exposes the great drawback of the MFS, which is the necessity of defining the location of the virtual sources to generate a good solution. For LEFM problems a regularized version of the MFS employing the numerical Green's function procedure MFS-NGF has been developed, which greatly facilitates the positioning of the virtual sources, as shown in the work by Fontes, Santiago and Telles, 2013.

The purpose of the present paper is to use an efficient iterative coupling procedure to solve LEFM. The problem domain is divided in sub-domains. Here, the NGF procedure is adopted for embedding a precise crack representation within the MFS idea while for standard elastic regular sub-domains the MLPG is adopted. This strategy permits to solve the principal problem in a decoupled manner without the necessity to introduce several near crack tip points to capture accurate stress intensity factors (SIF), as in the standard MLPG approach for fracture mechanics applications found in the works by Ching and Batra 2001 and Miers and Telles 2011. The adoption of MFS with the NGF approach to selectively represent the cracks of the problem alleviates the computer time burden found in traditional MLPG.

### Governing equations

For a two-dimensional linear elastic body  $\Omega$ , bounded by the boundary  $\Gamma$ , the Navier equation in terms of displacements  $u_i$  can be written in the form:

$$Gu_{j,kk} + \frac{G}{1-2\nu}u_{k,kj} + b_j = 0. \quad (1)$$

where  $G$  is the shear modulus,  $\nu$  is the Poisson's ratio and  $b_j$  is the body force component. The displacement  $u_i$  is solved from Eq. (1) satisfying the boundary conditions:

$$u_i = \bar{u}_i, \quad \text{on } \Gamma_u \quad \text{and} \quad p_i = \sigma_{ji}n_j = \bar{p}_i, \quad \text{on } \Gamma_p. \quad (2)$$

In the above equation,  $\bar{u}_i$  and  $\bar{p}_i$  are the prescribed displacements and tractions on the boundary  $\Gamma_u$  and  $\Gamma_p$ , respectively. The external boundary of the body is  $\Gamma = \Gamma_u \cup \Gamma_p$ .

Due to the presence of cracks in the elastic medium, there will be opposite surfaces sharing the same geometric position, this creates difficulties in the implementation of numerical methods, like singularity of the system matrix or degeneration of the boundary integral equation as discussed by Telles, Castor and Guimaraes, 1995. So, to circumvent such a limitation, the MFS formulation using the alternative NGF procedure as a Green's function is proposed in what as follows.

### Numerical Green's Function (NGF)

The fundamental solution used in this work is the numerical Green's function as presented in the work by Telles, Castor and Guimaraes, 1995. The NGF is written in terms of a superposition of the Kelvin fundamental solution and a complementary part, which ensures that the final result is equivalent to an embedded crack unloaded within the infinite elastic medium subject to a unit applied load, given by

$$u_{ij}^*(\xi, x) = u_{ij}^k(\xi, x) + u_{ij}^c(\xi, x) \quad (3)$$

where  $u_{ij}^*(\xi, x)$  is the fundamental displacements in  $j$  direction at the field point  $x$  due to a unit point load applied at the source point  $\xi$  in  $i$  direction. The kernel  $u_{ij}^k(\xi, x)$  represent the known Kelvin's fundamental solution for the uncracked body (see Brebbia, Telles and Wrobel, 1984). Here,  $u_{ij}^c(\xi, x)$  stands for complementary components of the problem defined as an infinite space containing crack(s) of arbitrary geometry. An analogous superposition can be made for tractions where  $p_{ij}^c(\xi, x)$  is added to its Kelvin counterpart.

The NGF procedure presents a suitable feature for mesh-free methods, it introduces the existing crack surfaces without need to include boundary condition points there for the problem representation. This is guaranteed by the traction-free crack representation simulated by the addition of the complementary solutions  $u_{ij}^c(\xi, x)$  and  $p_{ij}^c(\xi, x)$ . A general alternative to obtain the complementary solutions in a real variable numerical approach can be found in the work by Telles et al., 1995. Consider  $x \notin \Gamma^f$  and using the Somigliana's identity, the complementary solutions can be defined in terms of the following boundary integral equations

$$u_{ij}^c(\xi, x) = \int_{\Gamma^-} p_{jk}^k(x, \zeta) c_{ik}(\xi, \zeta) d\Gamma(\zeta) \quad (4)$$

$$p_{ij}^c(\xi, x) = \int_{\Gamma^-} P_{jk}^k(x, \zeta) c_{ik}(\xi, \zeta) d\Gamma(\zeta) \quad (5)$$

where  $c_{ik}(\xi, \zeta) = u_{ik}^c(\xi, \zeta^+) - u_{ik}^c(\xi, \zeta^-)$  is the crack opening displacements of the Green's function. Here,  $\Gamma^+$  and  $\Gamma^-$  stand for superior and inferior surfaces of the crack  $\Gamma^f$ , with  $\zeta \in \Gamma^-$ . Also,  $P_{jk}^k(x, \zeta)$  originates from the hyper-singular formulation.

Prescribing traction boundary conditions  $p_{ij}^c(\xi, \zeta) = -p_{ij}^k(\xi, \zeta)$  along the crack surface and evaluating the limit of Eq. (5) as  $x \mapsto \Gamma^-$ , the following hyper-singular boundary integral equation for unknowns  $c_{ik}(\xi, \zeta)$  can be written

$$\oint_{\Gamma^-} P_{ij}^k(\bar{\zeta}, \zeta) c_{ik}(\xi, \zeta) d\Gamma(\zeta) = -p_{ij}^k(\xi, \bar{\zeta}) \quad (6)$$

where, the symbol "=" indicates Hadamard's finite part integral and  $\bar{\zeta} \in \Gamma^-$ . The point collocation technique is adopted to solve Eq. (6); hence the following square system of equations, in matrix notation, is generated as

$$\mathbf{S} \mathbf{c}_i(\xi) = -\mathbf{p}_i^k(\xi) \quad (7)$$

where  $\mathbf{S}$  is a square matrix with dimension  $2BNpi \times 2BNpi$  ( $B$  is the number of subdivisions of the surface crack) dependent only on the crack geometry and vectors  $\mathbf{c}_i(\xi)$  and  $\mathbf{p}_i^k(\xi)$  contain the unknown fundamental crack openings and the independent traction values, respectively, in normal and transversal directions, due to the unit point load at source point  $\xi$  in  $i$  direction. Finally, Eq. (3) and its traction counterpart are used to numerically compute the Green's function.

### The method of fundamental solutions

Consider the boundary value problem of an elastic solid of domain  $\Omega$  enclosed by a boundary  $\Gamma$  governed by the Navier Equation (1), subjected to mixed boundary conditions given in Eq. (2) in the absence of body forces. The method of fundamental solutions (MFS) establish that the approximate solution can be constructed by a summation of similar problems solutions given by the following matrix notation

$$\mathbf{u}^M(x) = \mathbf{u}^*(\xi, x) \mathbf{d}(\xi) \quad (8)$$

$$\mathbf{p}^M(x) = \mathbf{p}^*(\xi, x) \mathbf{d}(\xi) \quad (9)$$

where  $\mathbf{u}^M$  and  $\mathbf{p}^M$  are approximations for displacements and the tractions corresponding to a point  $x \in \Omega \cup \Gamma$ , respectively,  $\mathbf{u}^*$  and  $\mathbf{p}^*$  are matrices of NGF coefficients, usually  $\xi \notin \Omega \cup \Gamma$  are the virtual sources and  $\mathbf{d}(\xi)$  is the unknown intensity factor vector. The superscript M represents the MFS variables.

First, an indirect problem must be solved to compute the intensity factors  $\mathbf{d}(\xi)$ . The boundary  $\Gamma$  is represented by  $M$  field points  $x_m$ , then  $N$  source points  $\xi_n$  are chosen and distributed forming a fictitious boundary surrounding  $\Gamma$ . In order to enforce the boundary conditions (2) in Eqs. (8-9) one obtains a linear system of equations:

$$\mathbf{A} \mathbf{d}(\xi) = \mathbf{b} \quad (10)$$

where  $\mathbf{A}$  is a dense matrix of NGF coefficients either  $u_{ij}^*$  or  $p_{ij}^*$  and  $\mathbf{b}$  is the right-hand side vector of boundary conditions. Finally, once all the values of  $\mathbf{d}(\xi)$  are determined, the displacements and tractions at any point on the boundary can be evaluated using Eqs. (8-9).

An important result for LEFM problems is the stress intensity factor (SIF). As we are using the NGF procedure, it can be calculated by a natural superposition of the fundamental generalized crack openings  $c_{ij}$  obtained as the solution of Eq. (7) and the intensity factors  $d_i$ , written as

$$\tilde{c}_j(\zeta) = \sum_{n=1}^N c_{ij}(\xi_n, \zeta) d_i(\xi_n) \quad (11)$$

where  $\tilde{c}_1$  and  $\tilde{c}_2$  are the generalized openings of the crack calculated over the crack line. Details can be found in the work by Fontes, Santiago and Telles, 2013.

### The meshless local Petrov-Galerkin method

Among the several formulations of the MLPG, here we use the version known by MLPG-1, as described in the work by Atluri and Shen, 2002, based on the moving least square (MLS) approximation for the displacement field  $\mathbf{u}$ . In the MLPG-1, the weight function in the MLS approximation is taken to be the test function in each sub-domain over which integrals are calculated. Details about the MLS can be seen in the work by Lancaster and Salkauskas, 1981. As shown in Atluri and Zhu, 2002 one can obtain a generalized local weak form of the Eq. (1) and boundary conditions (2) over a local sub-domain  $\Omega_s$  covering the whole global domain  $\Omega$  given by each point  $x$  and local boundary  $\Gamma_s = L_s \cup \Gamma_{su} \cup \Gamma_{st}$ . Taking into account the stress-strain

relation and the strain-displacement relation, a system of linear equations can be written:

$$\mathbf{K}\mathbf{u}^{\text{PG}} = \mathbf{f} \quad (12)$$

where, for  $i, j = 1, \dots, n$

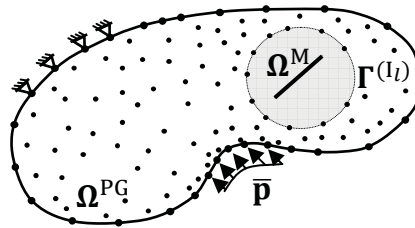
$$\mathbf{K}_{ij} = \int_{\Omega_s} \boldsymbol{\varepsilon}_{\mathbf{w}_i} \mathbf{D}\mathbf{B}_j \, d\Omega + \alpha \int_{\Gamma_{su}} \mathbf{w}_i(x) \boldsymbol{\Phi}_j \, d\Gamma - \int_{\Gamma_{su}} \mathbf{w}_i(x) \mathbf{N}\mathbf{D}\mathbf{B}_j \, d\Gamma \quad (13)$$

$$\mathbf{f}_i = \int_{\Gamma_{st}} \mathbf{w}_i(x) \bar{\mathbf{p}} \, d\Gamma + \alpha \int_{\Gamma_{su}} \mathbf{w}_i(x) \bar{\mathbf{u}} \, d\Gamma + \int_{\Omega_s} \mathbf{w}_i(x) \mathbf{b} \, d\Omega \quad (14)$$

where  $\mathbf{w}_i(x)$  is the same MLS weight function associated with a point  $\mathbf{i}$ ,  $\mathbf{D}$  is a matrix that depends on whether the problem is one of plane stress or plane strain,  $\boldsymbol{\Phi}_j$  is the shape function from the MLS approximation,  $\boldsymbol{\varepsilon}_{\mathbf{w}_i}$  and  $\mathbf{B}_j$  represent partial derivatives of the weight function  $\mathbf{w}_i(x)$  and of the shape function  $\boldsymbol{\Phi}_j$ , respectively,  $\mathbf{N}$  is a matrix composed of terms related to the outward normal direction to the boundary and  $\alpha$  is a penalty factor employed to enforce satisfaction of the essential boundary conditions. The superscript PG represents the MLPG method variables.

### Iterative coupling of the MFS with the NGF approach and the MLPG

The iterative coupling is a technique that consists of partitioning the global domain of the problem in subdomains and solving the coupling iteratively until the satisfaction of an established convergence criteria. Such an iterative coupling technique has the advantage permitting the solution for each subdomain region separately. The MFS is employed for embedded cracks with the help of the NGF and the MLPG can be employed for alternative geometries, leading to a truly meshless coupling.



**Figure 1. Subdomains and common interface for the coupling procedure.**

There are several types of iterative coupling procedures as shown in the work by Elleithy and Al-Gahtani, 2000. Here a sequential iterative algorithm proposed in the work by Lin et al., 1996 with the same optimal relaxation parameter is employed. To illustrate the algorithm, consider Eqs. (10) and (12) and Fig. 1. The main problem was subdivided in two problems. Subdomain  $\Omega^M$  comprehends a crack embedded and is to be solved by the MFS-NGF procedure, whereas subdomain  $\Omega^{\text{PG}}$  is to be solved by the MLPG method.

In order to solve the coupled problem, compatibility and equilibrium conditions at the interface  $\Gamma^{(I_l)}$ , between the subdomains  $\Omega^M$  and  $\Omega^{\text{PG}}$ , can be written:

$$\mathbf{u}_{I_l}^M = \mathbf{u}_{I_l}^{\text{PG}} \quad \text{and} \quad \mathbf{p}_{I_l}^M + \mathbf{p}_{I_l}^{\text{PG}} = \mathbf{0} \quad (15)$$

where the subscript  $I_l$  represents the common interface  $l$  and vectors  $\mathbf{u}^M = [\mathbf{u}_M^M \ \mathbf{u}_{I_l}^M]^T$ ,  $\mathbf{u}^{PG} = [\mathbf{u}_{PG}^{PG} \ \mathbf{u}_{I_l}^{PG}]^T$ ,  $\mathbf{p}^M = [\mathbf{p}_M^M \ \mathbf{p}_{I_l}^M]^T$  and  $\mathbf{p}^{PG} = [\mathbf{p}_{PG}^{PG} \ \mathbf{p}_{I_l}^{PG}]^T$  represent the decomposed displacement and tractions for each meshless method. The iterative coupling algorithm comes from a successive renewal of the interface variables defined in Eq. (15) as follows:

1. The principal problem is decomposed in two or more sub-problems and each one is modeled by either the MLPG method or the MFS for cracks;
2. Choose over the common interface  $\mathbf{u}_{I_l}^M = \mathbf{0}$  for the MFS;
3. Solve Eq. (10) and obtain the tractions  $\mathbf{p}_{I_l}^M$  using Eq. (9) for subdomain  $\Omega^M$ ;
4. Assemble matrix and nodal force vector Eqs. (13-14) using  $\mathbf{p}^{PG} = [\mathbf{p}_{PG}^{PG} \ -\mathbf{p}_{I_l}^M]^T$ ;
5. Solve Eq. (12) for displacements  $\mathbf{u}_{I_l}^{PG}$ ;
6. Check convergence at the interface values, i.e.:  $\frac{\|\mathbf{u}_{I_l,n+1}^M - \mathbf{u}_{I_l,n}^M\|}{\|\mathbf{u}_{I_l,n+1}^M\|} \leq 10^{-6}$   
if yes then stop; otherwise set  $\mathbf{u}_{I_l,n+1}^M = (1 - \alpha)\mathbf{u}_{I_l,n}^M + \alpha\mathbf{u}_{I_l,n}^{PG}$  and return to step 3 until convergence at step 6.

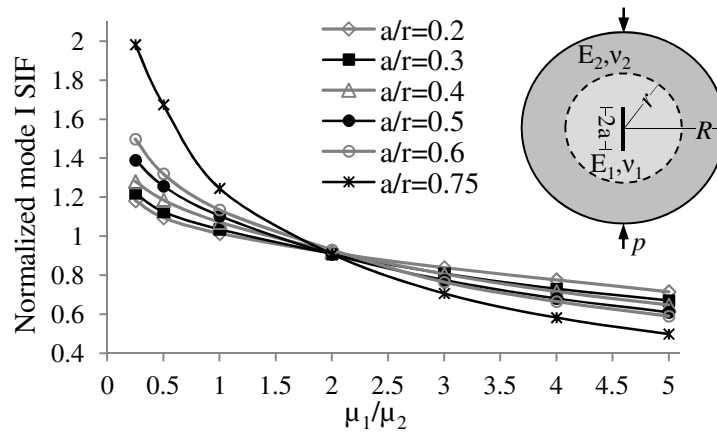
In all examples an optimal choice for the relaxation parameter  $\alpha$  as presented in the work by Lin et al., 1996 has been used. Considering the square error functional:

$$\|\mathbf{u}_{I_l,n+1}^M(\alpha) - \mathbf{u}_{I_l,n}^M(\alpha)\|^2 \quad (16)$$

Minimizing the Eq. (16) with respect to the relaxation parameter  $\alpha$  one can obtain an optimal dynamic value for the next iteration as:

$$\alpha = \frac{\langle \mathbf{e}_n^M, \mathbf{e}_n^M - \mathbf{e}_n^{PG} \rangle}{\|\mathbf{e}_n^M - \mathbf{e}_n^{PG}\|^2}, \quad \text{with } n > 1 \text{ and } 0 < \alpha \leq 1. \quad (17)$$

where  $\mathbf{e}_n^M = \mathbf{u}_{I_l,n}^M - \mathbf{u}_{I_l,n-1}^M$  and  $\mathbf{e}_n^{PG} = \mathbf{u}_{I_l,n}^{PG} - \mathbf{u}_{I_l,n-1}^{PG}$ .



**Figure 2. SIF for the Brazilian bi-material case.**

## Numerical results

Consider the Brazilian disk test developed by professor Carneiro (Carneiro, 1943), which is an useful method for determining the tensile strength of concrete materials. Here, a Bi-material disk specimen, with a central crack of length  $2a$ , is subjected to a compression load in plane stress. The dimensions are shown in Fig. 2. The problem is modeled by MFS with the NGF procedure in the interior circle using 52 boundary points and the outer circle is modeled by the MLPG method using 1000 points (no symmetry). The problem was solved for various values of crack length  $a$  with fixed radius  $r = 40$  and  $R = 75$ . The SIF is normalized with respect to  $K_0 = p\sqrt{\pi a}$ , calculated for several ratios of  $\mu_1/\mu_2$  and  $\nu_1 = \nu_2 = 0.1$ .

Fig. 2 shows the SIF versus the ratio of the shear modulus  $\mu_1/\mu_2$  for several values of  $a/r$ . It is noted that as the crack distance ratio  $a/r$  increases the SIF increases. The result for  $\mu_1/\mu_2 = 1$  and some values of  $a/R$  exhibits less than 2% of relative error, as presented in Table 1 comparing with close form solutions presented in the work by Yarema et al., 1984. The authors could not find results of SIF for other  $\mu_1/\mu_2$  ratios on the literature to compare with.

**Table 1. Normalized SIF for the Brazilian test with  $\mu_1 = \mu_2$ .**

$a/R$	$K_I/K_0$ (current paper)	$K_I/K_0$ (ref.)	error (%)
0.1	<b>1.0227</b>	<b>1.01500</b>	<b>0.76</b>
0.2	<b>1.0645</b>	<b>1.06004</b>	<b>0.42</b>
0.3	<b>1.1257</b>	<b>1.13555</b>	<b>0.87</b>
0.4	<b>1.2565</b>	<b>1.24310</b>	<b>1.08</b>
0.5	<b>1.3852</b>	<b>1.38690</b>	<b>0.12</b>

Another example is an isotropic plate with one horizontal crack and one inclined crack, both of length  $2a = 1.0$  subjected to uniform stress (see Fig. 3). This example was chosen to show an interesting capability of the iterative coupling procedure when using the NGF procedure to represent cracks. In Fig. 4 the circular subdomains are modeled by the MFS-NGF procedure. The circular subdomains for crack AB and crack CD have 18 and 14 points, respectively. Each crack is divided in 10 segments and each segment has 12 integration points. In this case, matrix  $\mathbf{S}$  defined in Eq. (7), for each crack, has the dimension of  $240 \times 240$ . So the iterative coupling technique can be used to decoupling the matrix  $\mathbf{S}$  and solve two MFS+NGF problems separately.

For the MLPG subdomain, 513 points are used, the dimensions are  $W=h=10$ ,  $2a/d=0.1$ ,  $\theta = 30^\circ$  and  $\sigma = 1.0$ . Normalized SIF results are compared with the BEM+NGF for an infinite plate in Table 2. These numerical results indicate that the iterative coupling approach is quite effective for decoupling problems with multiple cracks.

**Table 2. Normalized SIF for a the MFS+NGF/MLPG and the BEM+NGF**

	MFS+NGF/MLPG				BEM+NGF			
	Tip A	Tip B	Tip C	Tip D	Tip A	Tip B	Tip C	Tip D
$K_I/K_0$	<b>1.0112</b>	<b>1.0112</b>	<b>0.759</b>	<b>0.759</b>	<b>1.0071</b>	<b>1.0072</b>	<b>0.754</b>	<b>0.755</b>
$K_{II}/K_0$	<b>-0.0007</b>	<b>-0.0008</b>	<b>0.436</b>	<b>0.436</b>	<b>-0.0005</b>	<b>-0.0006</b>	<b>0.435</b>	<b>0.435</b>

### Concluding remarks

In this paper an iterative coupling between two meshless methods is presented to solve LEM problems. The use of NGF in the MFS subdomains allows for accurately solving crack problems saving computational cost. Another advantage is that matrix  $\mathbf{S}$  for the crack geometry can now be decoupled, improving the computational potential of the NGF procedure. Good results for SIF computations were obtained in the two examples presented. Further improvements can be obtained if one takes advantage of parallel computing, a natural procedure for the coupling routine presented here.

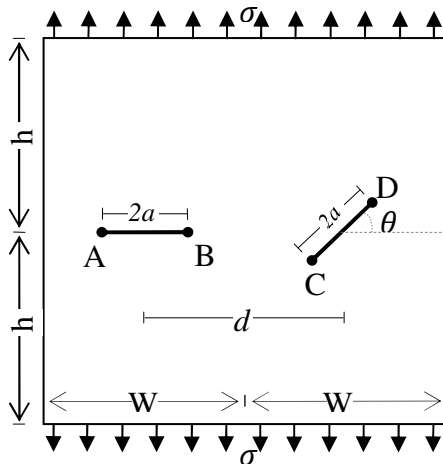


Figure 3. Problem representation

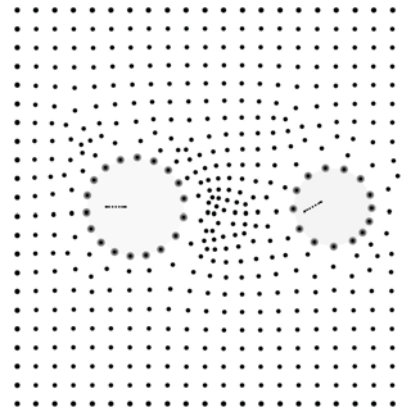


Figure 4. Problem representation by the MFS+NGF/MLPG Proposed coupling procedure

### References

- Carneiro F. L. L. B. (1943), A new method to determine the tensile strength of concrete. In: proceedings of the fifth meeting of the Brazilian association for technical rules; pp. 126–129.
- Kupradze V. D. and Aleksidze M. A. (1964), The method of functional equations for the approximate solution of certain boundary value problems. U.S.S.R. Comp Mats and Math Phis, 4: pp.82–126.
- Lancaster P. and Salkauskas K. (1981), Surfaces generated by moving least squares methods, *Mathematics of Computation*, 37:pp. 141–158.
- Brebbia C. A. and Telles, J. C. F. and Wrobel, L. C. (1984), *Boundary Elements Techniques: Theory and Applications in Engineering*. Springer-Verlag, Berlin Heidelberg New York.
- Yarema S. Ya. and Ivanitskaya G. S. and Maistrenko A. L. and Zboromirskii A. I. (1984), Crack development in a sintered carbide in combined deformation of types I and II. *Strength of Materials*, 16(8):pp. 1121–1128.
- Telles J. C. F. and Castor G. S. and Guimaraes S. (1995), A numerical Green's function approach for boundary elements applied to fracture mechanics. *Int J Num Methods Eng*, 38:pp. 3259–74.
- Belytschko T and Krongauz Y. and Organ D. and Fleming M. and Krysl P. (1996), Meshless methods: An overview and recent developments, *Comput Methods Appl Mech Eng*, 139: pp.3–47.
- Lin C. C. and Lawton E. C. and Caliendo J. A. and Anderson L. R. (1996), An iterative finite element-boundary element algorithm, *Computers & Structures*, 59(5): pp.899–909.
- Atluri S. N. and Zhu T. (1998), A new meshless local Petrov-Galerkin (MLPG) approach in computational mechanics. *Comput. Mech.*, 22: pp.117–127.
- Elleithy W. M. and Al-Gahtani H. J. (2000), An overlapping domain decomposition approach for coupling finite and boundary element methods. *Eng Anal Boundary Elem*, 24: pp.391–398.
- Ching H. -K. and Batra R. C. (2001), Determination of crack tip field in linear elastostatics by the meshless local Petrov-Galerkin (MLPG) method. *CMES*, 2: pp.273–289.
- Atluri S. N. and Shen S. (2002), The meshless local Petrov-Galerkin (MLPG) method. *Tech. Science*.
- Miers L. S. and Telles J. C. F. (2011). On NGF Applications to LBIE Potential and Displacement Discontinuity Analyses. *Key Engineering Materials*, 454: p. 127–135.

- Fontes Jr., E. F. and Santiago, J. A. F. and Telles, J. C. F. (2013), On a regularized method of fundamental solutions coupled with the numerical Green's function procedure to solve embedded crack problems, *Eng Anal Boundary Elem*, 37(1): pp.1–7.
- Godinho L. and Soares Jr. D. (2013), Frequency domain analysis of interacting acoustic-elastodynamic models taking into account optimized iterative coupling of different numerical methods. *Eng Anal Boundary Elem*, 32: pp.1074–1088.



## Computations of Compound Droplet Formation in a Flow Focusing Device

**\*S. Homma**

Division of Materials Science, Graduate School of Science and Engineering, Saitama University,  
255 Shimo-Okubo, Sakura-ku, Saitama 338-8570, Japan

\*Corresponding author: honma@apc.saitama-u.ac.jp

### Abstract

The formation of compound droplets in a flow focusing device is simulated numerically by a three-fluid front-tracking method. The geometry of the device and the flow rates of core, shell, and external fluids are changed to examine the effects of those on the formation of compound droplets. Several modes of the formation were observed: simple droplets (no core droplets) formation, regular compound droplets formation in jetting and dripping. They are mapped on the diagram of non-dimensional numbers, the viscosity ratio and the Capillary number. It was observed that the size of the compound droplets abruptly increased as the flow rate of the shell fluid was increased. It suggests that the mode changes suddenly due to the balance of the flow rates among core, shell, and external fluids.

**Keywords:** Compound droplets, Front-tracking, Flow focusing device

### Introduction

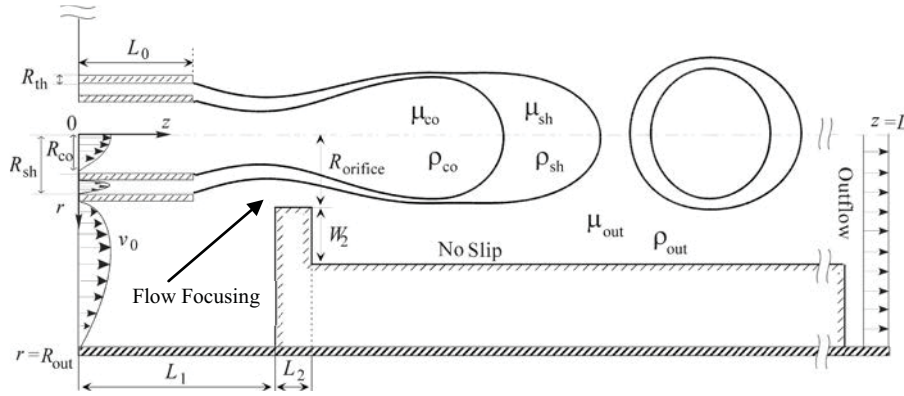
Compound droplets, which consist of two immiscible phases (core and shell) in yet another immiscible continuous phase, have attracted considerable attention, because of its potential to manufacture highly structural materials such as micro capsules for drug delivery vehicle (Prankerd and Stella, 1990). If mono-dispersed compound droplets are obtained without any separation or classification, high-quality products are yielded inexpensively.

Utada *et al.* (2005) successfully fabricated mono-dispersed tiny compound droplets using the micro-fluidic device, which had co-axial dual nozzle with an outlet of an external flow outside of the nozzle. They controlled the flow of external fluid to form a thin compound jet breaking up at the tip, where tiny compound droplets are produced. This is the so-called flow focusing device, where strong external flow through a constriction draws a thin jet of the second immiscible liquid from the nozzle. Even though they have experimentally quantified to determine the size of the resulting droplets, full examination in large parameter space including physical properties and flow ratios, has not been done yet.

Homma *et al.* (2013) carried out numerical simulations for a flow focusing device by changing flow rates and physical properties. They obtained several modes of compound droplet formation and the modes were mapped on the diagram of non-dimensional numbers, as done by Zhou *et al.* (2006). In this paper, we will review this work and show recent results changing the flow rate of a shell fluid.

### Problem Definition and Numerical Methods

**Figure 1** shows a schematic of the problem, formation of compound droplets by a flow focusing device. In the flow focusing device, core and shell fluids of compound droplets are injected from an inner nozzle of  $R_{co}$  and an outer one of  $R_{sh}$ , respectively. An external flow is imposed to enhance the droplet formation. The radius of the cylindrical tube is  $R_{out}$ . The length and the thickness of the nozzles are  $L_0$  and  $R_{th}$ , respectively. In order to focus the external flow toward the core and shell fluids, an obstacle is set apart from the nozzle exit. The radius of the hole of the obstacle is  $R_{orifice}$  and the thickness of the obstacle is  $L_2$ .



**Figure 1. Schematic diagram of the simulation of compound droplet formation by flow focusing device**

All three fluids are assumed to be Newtonian, incompressible, and immiscible. When this situation is described with one fluid model, the governing equations are as follows:

$$\nabla \cdot \mathbf{u} = 0, \quad (1)$$

$$\frac{\partial}{\partial t} \rho \mathbf{u} + \nabla \cdot \rho \mathbf{u} \mathbf{u} = -\nabla P + \nabla \cdot \mu (\nabla \mathbf{u} + \nabla \mathbf{u}^T) + \int_f \sigma \kappa \mathbf{n}_f \delta(\mathbf{x} - \mathbf{x}_f) dA_f, \quad (2)$$

$$\frac{D}{Dt} \rho = \frac{D}{Dt} \mu = 0, \quad (3)$$

Here,  $\mathbf{u}$  is the velocity vector and  $P$  the pressure. The surface tension is found using twice the mean curvature,  $\kappa$ , the unit normal of the interface,  $\mathbf{n}_f$ , and a delta function,  $\delta(\mathbf{x} - \mathbf{x}_f)$ , which is zero everywhere except at the interface,  $\mathbf{x}_f$ .

Eqs. (1) and (2) are discretized on the axisymmetric cylindrical coordinate by finite difference approximations with second order. The boundary conditions of  $z$ -axis are symmetry, and those of the tube wall ( $r = R_{out}$ ) are no-slip. The boundary conditions of the exit of the tube are out flow. At the inlet of the tube, inflow boundary conditions, which are fully developed velocity distributions for cylinders and annular pipes, are applied as follows (Bird *et al.*, 2006):

$$v_0(r) = 2v_{0,co} \left[ 1 - \left( \frac{r}{R_{co}} \right)^2 \right] \quad \text{at } 0 \leq r \leq R_{co}, \quad (4)$$

$$v_0(r) = 2v_{0,sh} \left[ \frac{\ln(1/\alpha)}{\ln(1/\alpha) \cdot (1 + \alpha^2) - (1 - \alpha^2)} \right] \left[ 1 - \left( \frac{r}{R_{sh}} \right)^2 - \frac{1 - \alpha^2}{\ln(1/\alpha)} \cdot \ln \left( \frac{R_{sh}}{r} \right) \right] \quad \text{at } R_{co} + R_{th} \leq r \leq R_{sh}, \quad (5)$$

$$v_0(r) = 2v_{0,out} \left[ \frac{\ln(1/\gamma)}{\ln(1/\gamma) \cdot (1 + \gamma^2) - (1 - \gamma^2)} \right] \left[ 1 - \left( \frac{r}{R_{out}} \right)^2 - \frac{1 - \gamma^2}{\ln(1/\gamma)} \cdot \ln \left( \frac{R_{out}}{r} \right) \right] \quad \text{at } R_{sh} + R_{th} \leq r \leq R_{out}. \quad (6)$$

Here,  $\alpha = (R_{co} + R_{th})/R_{out}$  and  $\gamma = (R_{sh} + R_{th})/R_{out}$ . The symbols  $v_{0,co}$ ,  $v_{0,sh}$ , and  $v_{0,out}$  are the average injection velocities for core, shell, and external fluids, respectively.

The motion of interfaces was traced by a front-tracking method (Unverdi and Tryggvason, 1992). The detailed description of the front-tracking method was given by Tryggvason *et al.* (2001) and an axisymmetric version for jet breakup into droplets was explained by Homma, *et al.* (2006 and 2010). The extension of the front-tracking method for three-fluid was described by Homma, *et al.* (2011) and its validation for compound jets and droplets was found in Vu *et al.* (2012).

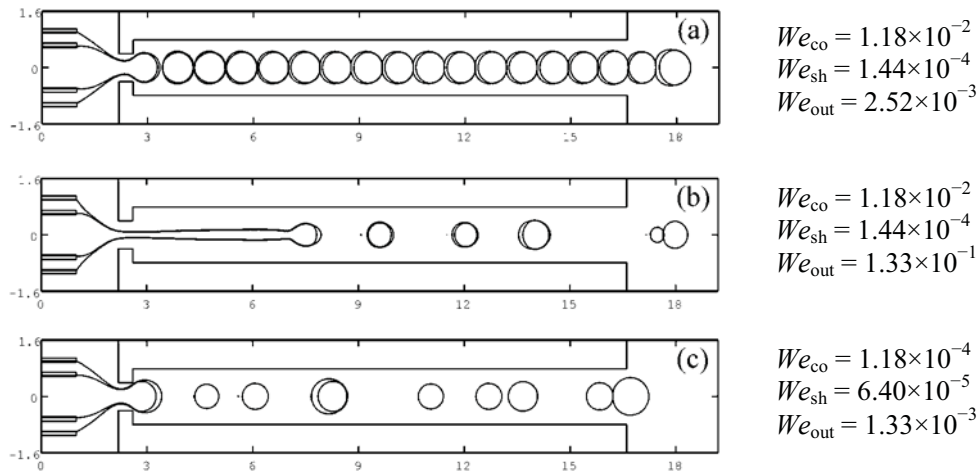
## Results and Discussion

The geometries of the flow focusing device were set based on the numerical study by Zhou *et al.* (2006). The sizes have been normalized by the inner radius of the outer nozzle  $R_{sh}$  and fixed as follows:  $R_{co}/R_{sh} = 0.6$ ,  $R_{out}/R_{sh} = 1.6$ ,  $R_{th}/R_{sh} = 0.08$ ,  $L/R_{sh} = 19.6$ ,  $L_0/R_{sh} = 1.0$ ,  $L_1/R_{sh} = 2.2$ ,  $L_2/R_{sh} = 0.4$ ,  $R_{orifice}/R_{sh} = 0.4$ , and  $W_2/R_{sh} = 0.4$ . In order to increase accuracy, denser grid meshes in  $r$  direction were arranged near the dual nozzle. By preliminary grid refinement tests, the grid resolution was determined as 128x2048.

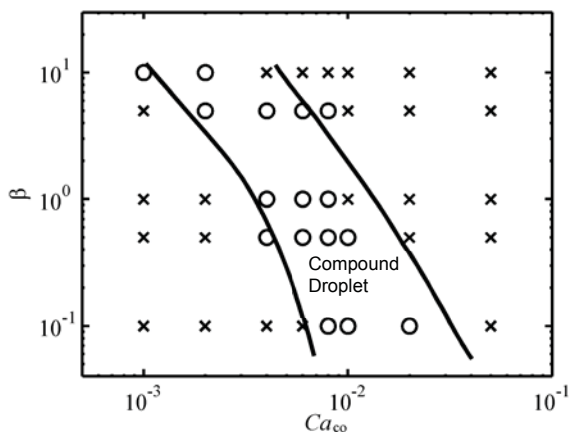
Physical properties were set referring to the study by Utada *et al.* (2005) and Zhou *et al.* (2006). Density ratios were fixed as follows:  $\rho_{sh}/\rho_{co} = 1.25$  and  $\rho_{out}/\rho_{co} = 1.22$ . The viscosity ratio between core and shell fluids ( $\mu_{sh}/\mu_{co}$ ) was fixed at unity. The viscosity ratio between core and ambient fluids was changed as a parameter ( $\beta = \mu_{out}/\mu_{co}$ ). Interfacial tension coefficient between core and shell fluids and that between shell and ambient fluids were set to be the same.

The definition of non-dimensional numbers and their ranges are as follows:  $Re_{co} = D_{co}v_{0,co}\rho_{co}/\mu_{co}$  ( $9.72 \times 10^{-3} < Re_{co} < 1.18$ ),  $Re_{sh} = D_{sh}v_{0,sh}\rho_{sh}/\mu_{sh}$  ( $1.06 \times 10^{-2} < Re_{sh} < 0.960$ ),  $Re_{out} = D_{out}v_{0,out}\rho_{out}/\mu_{out}$  ( $9.17 \times 10^{-3} < Re_{out} < 36.7$ ),  $We_{co} = D_{co}v_{0,co}^2\rho_{co}/\sigma$  ( $1.18 \times 10^{-4} < We_{co} < 1.18 \times 10^{-2}$ ),  $We_{sh} = D_{sh}v_{0,sh}^2\rho_{sh}/\sigma$  ( $6.40 \times 10^{-5} < We_{sh} < 8.47 \times 10^{-3}$ ),  $We_{out} = D_{out}v_{0,out}^2\rho_{out}/\sigma$  ( $1.33 \times 10^{-3} < We_{out} < 4.89 \times 10^{-1}$ ), and  $Ca_{co} = We_{co}/Re_{co}$ , where  $D$  is the hydraulic diameter defined by  $D_{co} = 2R_{co}$ ,  $D_{sh} = 2(R_{sh} - R_{th} - R_{co})$ , or  $D_{out} = 2(R_{out} - R_{th} - R_{sh})$ . The viscosity ratio  $\beta$  was chosen one from among 0.1, 0.5, 1, 5, and 10.

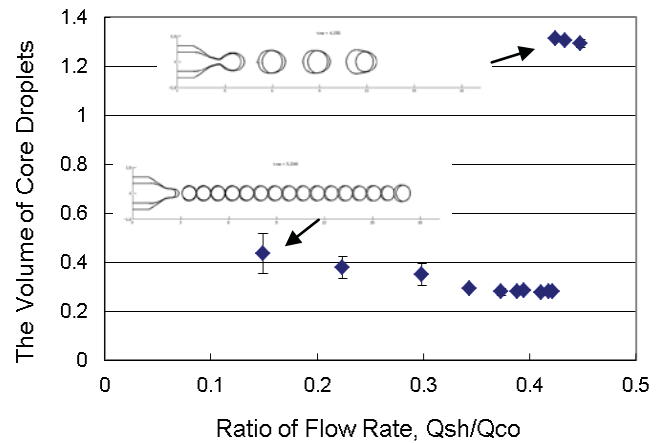
**Figure 2** shows instantaneous interfacial shapes for three different cases ( $\beta = 1$ ). In case (a), uniform compound droplets are successfully produced in a fairly regular manner. This is a dripping mode (Homma, *et al.*, 2006 and 2010) and the orifice acts as a nozzle. In case (b), only  $We_{out}$  is different ( $1.33 \times 10^{-1}$ ) from case (a), where the external flow is much faster than that of case (a). A compound jet is produced and breaks up into compound droplets. This is a typical jetting mode (Homma, *et al.*, 2006 and 2010). The external flow accelerates at the orifice and the dispersed core and shell fluids are dragged by the external flow and a compound jet forms. Capillary waves are growing on the jet surface and compound droplets break off. In case (c), just one compound droplet is observed in the middle of the domain. All others are simple droplets of shell fluid. In this case, the supply of core fluid is not sufficient and no-core simple droplets are mainly produced.



**Figure 2. Instantaneous shapes of jets and droplets**



**Figure 3. Map of compound droplet formation ( $We_{co} = 3.89 \times 10^{-4}$ ); ○: successful formation, ×: unsuccessful formation**



**Figure 4. Volume of core droplet vs. ratio of flow rate between core and shell fluids**

**Figure 3** shows a map of compound droplet formation on the diagram of  $\beta$  vs.  $Ca_{co}$  for  $We_{co} = 3.89 \times 10^{-4}$ . This map is identical with Fig. 16 of Zhou *et al.* (2006). All plots are obtained from our computations and the solid lines are the border between success and failure of compound droplet formation determined by Zhou *et al.* (2006). The range of the success formation of compound droplets is almost exactly the same between Zhou *et al.* (2006) and this study.

**Figure 4** shows the relationship between the volume of core droplet and the ratio of the flow rate between core and shell fluids. The viscosity ratio  $\beta$  is 1. As the ratio of the flow rate increases, where the flow rate of the shell fluid increases, the volume of core droplets as well as compound droplet itself slightly decreases. Around the ratio 4.2, however, the volume of core droplet abruptly increases. Embedded figures show instantaneous shapes of jet and droplets. The droplets observed after the critical ratio were about 4 times larger before the critical one. It suggests that the increasing flow of the shell fluid slows the growth of capillary waves at the interface between core and shell fluids and a series of 4 waves may become one compound droplet. The similar phenomenon was observed in other viscosity ratio but the critical flow rate is different. Although the detailed investigation is underway, the flow rate of shell fluid can be one of the control parameters for the size of compound droplets.

## Conclusions

The formation of compound droplets in a flow focusing device is simulated numerically by a three-fluid front-tracking method. The modes of droplet formation, simple droplets with no core and compound droplets were observed and they were mapped on the diagram, the viscosity ratio vs. Capillary number in terms of core fluid. The volume of core droplet as well as compound droplet itself suddenly increases as the flow rate of shell fluid increases beyond a critical value. The flow rate of shell fluid can be one of the control parameters for the size of compound droplets.

## Acknowledgement

I am grateful to Professor Gretar Tryggvason for providing an original front-tracking code, and Professor Jiro Koga for useful discussion of this problem. I want to thank Mr. Kouta Moriguchi and Mr. Taeseon Kim for their assistance in computations. This research is supported in part by Japan Society for the Promotion of Science, Grant-in-Aid for Scientific Research (C) 24560917.

**References**

- Bird, R. B., Stewart, W. E. and Lightfoot, E. N. (2006), *Transport Phenomena*, 2nd Ed., John Wiley & Sons, New York, U.S.A.
- Homma, S., Koga, J., Matsumoto, S., Song, M. and Tryggvason, G. (2006), Breakup mode of an axisymmetric liquid jet injected into another immiscible liquid, *Chemical Engineering Science*, 61, pp. 3986–3996.
- Homma, S., Yokotsuka, M. and Koga, J. (2010), Numerical simulation of the formation of jets and drops in co-flowing ambient fluid, *Journal of Chemical Engineering of Japan*, 43, pp. 7–12.
- Homma, S., Yokotsuka, M., Tanaka, T., Moriguchi, K., Koga, J. and Tryggvason, G. (2011), Numerical simulation of a compound droplet by three-fluid front-tracking method,” *Fluid Dynamics & Materials Processing*, 7, 231–240.
- Homma, S., Moriguchi, K., Kim, T. and Koga, J. (2013), Computations of compound droplet formation from a co-axial dual nozzle by three-fluid front tracking method, *Journal of Chemical Engineering of Japan*, *in press*.
- Pranker, R. J. and Stella, V. J. (1990), The use of oil-in-water emulsions as a vehicle for parenteral drug administration,” *J. Parenteral Sci. Technol.*, 44, pp. 139–149.
- Vu, T. V., Homma, S., Tryggvason, G., Wells, J. C. and Takakura, H. (2012), Computations of breakup modes in laminar compound liquid jets in a coflowing fluid, *International Journal of Multiphase Flow*, 49, pp. 58–69.
- Tryggvason, G., Bunner, B., Esmaeeli, A., Juric, D., Al-Rawahi, N., Tauber, T., Han, J., Nas, S. and Jan, Y. (2001), A front-tracking method for the computations of multiphase flow,” *Journal of Computational Physics*, 169, pp. 708–759.
- Unverdi, S. O. and Tryggvason, G. (1992), A front tracking method for viscous, incompressible, multi-fluid flows, *Journal of Computational Physics*, 100, pp. 25–37.
- Utada, A. S., Lorenceau, E., Link, D. R., Kaplan, P. D., Stone, H. A. and Weitz, D. A. (2005), Monodispersed double emulsions generated from a microcapillary device, *Science*, 308, pp. 537–541.
- Zhou, C., Yue, P. and Feng, J. J. (2006), Formation of simple and compound drops in microfluidic devices, *Physics of Fluids*, 18, 092105–092105–14.

## Hybrid probabilistic interval dynamic analysis of vehicle-bridge interaction system with uncertainties

Ningguang Liu<sup>1</sup>, \*Wei Gao<sup>1</sup>, Chongmin Song<sup>1</sup> and Nong Zhang<sup>2</sup>

<sup>1</sup> School of Civil and Environmental Engineering, The University of New South Wales, Sydney, NSW 2052, Australia

<sup>2</sup> School of Electrical, Mechanical and Mechatronic Systems, Faculty of Engineering and IT, University of Technology, Sydney, NSW 2007, Australia

\*Corresponding author: w.gao@unsw.edu.au

### Abstract

Hybrid probabilistic interval dynamic analysis of vehicle-bridge interaction system with a mixture of random and interval properties is studied in this paper. The vehicle's parameters are considered as interval variables and the bridge's parameters are treated as random variables. By introducing the random interval moment method into the dynamic analysis of vehicle-bridge interaction system, the expressions for the mean value and standard deviation of the random interval bridge dynamic response are developed. Examples are used to illustrate the effectiveness of the presented method. A hybrid simulation method combining direct simulations for interval variables and Monte-Carlo simulations for random variables is implemented to validate the computational results.

**Keywords:** Vehicle-bridge interaction system, probabilistic interval analysis, random interval moment method, random interval dynamic response.

### Introduction

The coupled vehicle-bridge dynamic system has attracted considerable attentions over the past two decades (Yang and Lin, 2005; Ju and Lin, 2007; Zhang et al., 2008). The values of system parameters are given precisely in most of studies. Actually, vehicles moving on a bridge have nondeterministic characteristics because the system parameters are not constant.

Probabilistic methods are preferred when information of uncertain parameters in the form of preference probability function is provided. And these have been widely used to predict the response and in the implementation of structural system reliability evaluation of uncertainty (Liu et al., 2011). In probabilistic methods, uncertain parameters are modeled as random variables/fields and uncertainties of loads are described by random processes/variables. However, sometimes it is hard to get the enough probabilistic information for structural parameters as their values are affected by a lot of non-deterministic factors. Meanwhile, loads of many scenarios can hardly be modeled as random variables due to large changes in their magnitudes. The interval methods can be used when the probability function is unavailable but the range of the uncertain parameter is known. In the past decade, significant progress in analysis and optimal design of structures with bounded parameters has been achieved (Qiu et al., 2009; Jiang et al., 2008; Impollonia and Muscolino, 2011).

It is desirable to model structural parameters/loads as random variables if sufficient information can be obtained to form the probability density functions. Meanwhile,

some structural parameters/loads might be best considered as interval variables if the information/data are not enough to model uncertain structural parameters and loadings as random variables, especially in the early design stages. Consequently, hybrid probabilistic interval analysis and reliability assessment of structures with a mixture of random and interval properties has been conducted (Gao, 2010). The random interval moment method has been developed by the authors to determine the mean value and standard deviation of random interval responses of structures under static forces (Gao, 2010).

As aforementioned, some parameters of vehicle-bridge interaction system could be considered as random variables and some of them might be assumed as interval variables. For example, the change range of vehicle's mass is large due to the different loading conditions; therefore, these can be taken as interval variables. In contrast, the change ranges of bridge's parameters are small because of the strict manufacturing standards, which can be considered as random variables. Therefore, a hybrid probabilistic interval analysis model for vehicle-bridge coupled systems needs to be developed.

### Random interval moment method

Let  $X(R)$  be the set of all real random variables on a probability space  $(\Omega, A, P)$ ,  $x^R$  is a random variable of  $X(R)$ .  $R$  denotes the set of all real numbers.  $\mu_x$  (or  $\bar{x}$ ) and  $\sigma_x$  are the mean (deterministic) value and standard deviation of  $x^R$ , respectively.  $y^I = [\underline{y}, \bar{y}] = \{t, \underline{y} \leq t \leq \bar{y} | \underline{y}, \bar{y} \in R\}$  is an interval variable of  $I(R)$  which denotes the set of all the closed real intervals.  $\underline{y}$  and  $\bar{y}$  are the lower and upper bounds of interval variable  $y^I$ , respectively. Interval variable  $y^I$  can also be written as

$$y^I = y^c + \Delta y^I; \Delta y^I = [-\Delta y, +\Delta y]; y^c = \frac{y + \bar{y}}{2}; \Delta y = \frac{\bar{y} - y}{2} \quad \Delta y_F = \frac{\Delta y}{y^c} \quad (1)$$

where  $y^c$ ,  $\Delta y$ ,  $\Delta y^I$  and  $\Delta y_F$  represent the midpoint value, maximum width (interval width), uncertain interval and interval change ratio of the interval variable  $y^I$ .

Without loss of generality, random interval variable  $Z^{RI}$  is the function of multiple random and interval variables, which are respectively represented by random vector  $\bar{X}^R = (x_1^R, x_2^R, \dots, x_n^R)$  and interval vector  $\bar{Y}^I = (y_1^I, y_2^I, \dots, y_m^I)$ . The deterministic values of  $\bar{X}^R$  and  $\bar{Y}^I$  are  $\bar{\bar{X}} = (\bar{x}_1, \bar{x}_2, \dots, \bar{x}_n)$  and  $\bar{\bar{Y}}^c = (y_1^c, y_2^c, \dots, y_m^c)$ .

The Taylor series to the first-order of the random interval variable  $Z^{RI} = f(\bar{X}^R, \bar{Y}^I)$  about  $(\bar{\bar{X}}^R, \bar{\bar{Y}}^I)$  is expressed as

$$Z^{RI} = f(\bar{X}^R, \bar{Y}^I) = f(\bar{\bar{X}}, \bar{\bar{Y}}^I) + \sum_{i=1}^n \left\{ \frac{\partial f}{\partial x_i^R} \Big|_{\bar{\bar{X}}, \bar{\bar{Y}}^I} \right\} \cdot (x_i^R - \bar{x}_i) + R$$

$$\begin{aligned}
&= f(\bar{X}, \bar{Y}^c) + \sum_{j=1}^m \left\{ \frac{\partial f}{\partial y_j^I} \Big|_{\bar{X}, \bar{Y}^c} \right\} \cdot \Delta y_j^I \\
&\quad + \sum_{i=1}^n \left\{ \frac{\partial f}{\partial x_i^R} \Big|_{\bar{X}, \bar{Y}^c} + \sum_{j=1}^m \left\{ \frac{\partial^2 f}{\partial x_i^R \partial y_j^I} \Big|_{\bar{X}, \bar{Y}^c} \right\} \cdot \Delta y_j^I \right\} \cdot (x_i^R - \bar{x}_i) + R \quad (2)
\end{aligned}$$

where  $R$  is the remainder term.

From this equation, and the higher order terms  $R$  is ignored, the expectation and variance of random interval variables  $Z^{RI} = f(\bar{X}^R, \bar{Y}^I)$  can be calculated as (Gao et al., 2010)

$$\begin{aligned}
\mu_{Z^{RI}} &= E(Z^{RI}) = f(\bar{X}, \bar{Y}^c) + \sum_{j=1}^m \left\{ \frac{\partial f}{\partial y_j^I} \Big|_{\bar{X}, \bar{Y}^c} \right\} \Delta y_j^I \quad (3) \\
\sigma_{Z^{RI}}^2 &= E(Z^{RI} - E(Z^{RI}))^2 = \sum_{i=1}^n \sum_{k=1}^n \left\{ \frac{\partial f}{\partial x_i^R} \Big|_{\bar{X}, \bar{Y}^c} + \sum_{j=1}^m \left\{ \frac{\partial^2 f}{\partial x_i^R \partial y_j^I} \Big|_{\bar{X}, \bar{Y}^c} \right\} \Delta y_j^I \right\} \\
&\quad \cdot \left\{ \frac{\partial f}{\partial x_k^R} \Big|_{\bar{X}, \bar{Y}^c} + \sum_{j=1}^m \left\{ \frac{\partial^2 f}{\partial x_k^R \partial y_j^I} \Big|_{\bar{X}, \bar{Y}^c} \right\} \Delta y_j^I \right\} \text{Cov}(x_i^R, x_k^R) \\
&= \sum_{i=1}^n \left\{ \frac{\partial f}{\partial x_i^R} \Big|_{\bar{X}, \bar{Y}^c} + \sum_{j=1}^m \left\{ \frac{\partial^2 f}{\partial x_i^R \partial y_j^I} \Big|_{\bar{X}, \bar{Y}^c} \right\} \Delta y_j^I \right\}^2 \cdot \text{Var}(x_i^R) \\
&\quad + \sum_{i(\neq k)=1}^n \sum_{k=1}^n \left\{ \frac{\partial f}{\partial x_i^R} \Big|_{\bar{X}, \bar{Y}^c} + \sum_{j=1}^m \left\{ \frac{\partial^2 f}{\partial x_i^R \partial y_j^I} \Big|_{\bar{X}, \bar{Y}^c} \right\} \Delta y_j^I \right\} \cdot \left\{ \frac{\partial f}{\partial x_k^R} \Big|_{\bar{X}, \bar{Y}^c} + \sum_{j=1}^m \left\{ \frac{\partial^2 f}{\partial x_k^R \partial y_j^I} \Big|_{\bar{X}, \bar{Y}^c} \right\} \Delta y_j^I \right\} \cdot \text{Cov}(x_i^R, x_k^R) \quad (4)
\end{aligned}$$

### Vehicle-bridge interaction model

In the vehicle-bridge interaction system, the bridge is modeled as a simply supported beam (Yang, 2005) and the vehicle is represented by a half-car model as shown in Figure 1. Here,  $m_v$ ,  $m_1$  and  $m_2$  denote the sprung and unsprung masses respectively; the suspension system is represented by two linear springs of stiffness  $k_{s1}$ ,  $k_{s2}$  and two linear dampers with damping rates  $C_{s1}$ ,  $C_{s2}$ ; the tires are also modeled by two linear springs of stiffness  $k_{t1}$ ,  $k_{t2}$  and two linear dampers with damping rates  $C_{t1}$ ,  $C_{t2}$ ;  $\rho$ ,  $E$ ,  $I$  and  $L$  are the mass per unit length, elastic modulus, moment of inertia and length of the beam respectively.

In this study, parameters of the vehicle  $m_1^I$ ,  $m_2^I$ , and  $m_v^I$ , are considered as interval variables, meanwhile, bridge's parameters,  $\rho^R$ ,  $E^R$  and  $I^R$ , are treated as random variables. The equation of motion governing the transverse vibration of the bridge under the moving vehicle with uncertain parameters can be written as



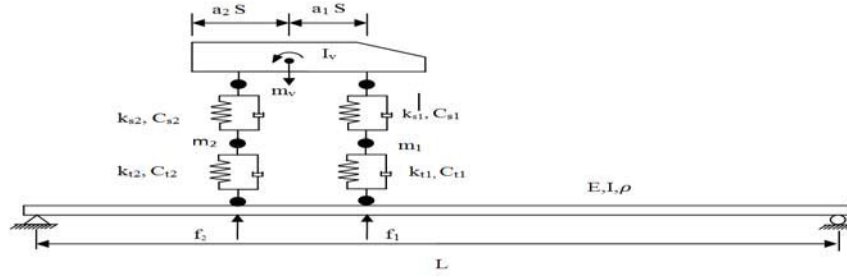


Figure 1. Model of vehicle-bridge interaction system

$$\rho^R \frac{\partial^2 W^{RI}(x,t)}{\partial t^2} + C \frac{\partial W^{RI}(x,t)}{\partial t} + E^R I^R \frac{\partial^4 W^{RI}(x,t)}{\partial x^4} = (f_1^{RI}(x,t) + f_2^{RI}(x,t)) \delta(x-vt) \quad (5)$$

$$\begin{cases} f_1^{RI}(x,t) = -(m_1^I + a_2 m_v^I)g - k_{t1}^R(x_v(t)^{RI} - W^{RI}(x,t))\Big|_{x=vt} - C_{t1}^R(\dot{x}_v(t) - \dot{W}^{RI}(x,t))\Big|_{x=vt} \\ f_2^{RI}(x,t) = -(m_2^I + a_1 m_v^I)g - k_{t2}^R(x_v(t)^{RI} - W^{RI}(x,t))\Big|_{x=vt} - C_{t2}^R(\dot{x}_v(t) - \dot{W}^{RI}(x,t))\Big|_{x=vt} \end{cases} \quad (6)$$

where  $C$  is the damping of the bridge,  $W^{IR}(x,t)$  is the random interval vertical displacement of the bridge,  $x_v(t)^{RI}$  is the random interval vertical displacement of the moving vehicle,  $f_1^{RI}(x,t)$  and  $f_2^{RI}(x,t)$  are the random interval contact forces,  $\delta(x-vt)$  is the Dirac delta function evaluated at the contact point at position  $x=vt$ , and  $v$  is the speed of the moving vehicle. Using the modal superposition method, the solution to Eq. (5) can be expressed as in terms of the mode shapes  $\varphi_j(x)$ .

In this paper, the Wilson's damping hypothesis is adopted. As vehicle mass is much less than the bridge mass and the tires' damping is quite small. Using the Duhamel integral solution, the displacement response of the bridge can be calculated by

$$W^{RI}(x,t) = -\sum_{j=1}^{\infty} \sin \frac{j\pi x}{L} \cdot \frac{2(m_1^I + m_2^I + m_v^I)g}{L\sqrt{1-\zeta_{bj}^2} \frac{j^2\pi^2}{L^2} \sqrt{\rho^R E^R I^R}} \cdot \int_0^t e^{-\zeta_{bj} \frac{j^2\pi^2}{L^2} \sqrt{\frac{E^R I^R}{\rho^R}}(t-\tau)} \sin \left( \sqrt{1-\zeta_{bj}^2} \frac{j^2\pi^2}{L^2} \sqrt{\frac{E^R I^R}{\rho^R}}(t-\tau) \right) \sin \frac{j\pi vt}{L} d\tau \quad (7)$$

In this study, the contribution of tires' stiffness to bridge vertical displacement response is omitted due to the assumption that the bridge mass is much greater than that of the vehicle (Yang, 2005). Additionally, bridge damping is treated as deterministic because the existing research outcomes show that the mechanism of structural damping is still not clear enough.

Furthermore, the lower and upper bounds of the mean value of the bridge's displacement  $\mu(W^{RI})$  are given by

$$\begin{aligned} \overline{\mu(W^{RI}(x,t))} &= \frac{-2}{S_1\sqrt{\rho EI}} \sum_{j=1}^{\infty} \sin \frac{j\pi x}{L} \cdot \int_0^t ((m_1^c + m_2^c + m_v^c)g) \cdot \bar{S}_2 \sin(\bar{S}_3) \sin \frac{j\pi v\tau}{L} d\tau \\ &- \left| \frac{-2g}{S_1\sqrt{\rho EI}} \sum_{j=1}^{\infty} \sin \frac{j\pi x}{L} \cdot \int_0^t \bar{S}_2 \sin(\bar{S}_3) \sin \frac{j\pi v\tau}{L} d\tau \cdot (\Delta m_1 + \Delta m_2 + \Delta m_v) \right| \end{aligned} \quad (8)$$

$$\begin{aligned} \overline{\mu(W^{RI}(x,t))} &= \frac{-2}{S_1\sqrt{\rho EI}} \sum_{j=1}^{\infty} \sin \frac{j\pi x}{L} \cdot \int_0^t ((m_1^c + m_2^c + m_v^c)g) \cdot \bar{S}_2 \sin(\bar{S}_3) \sin \frac{j\pi v\tau}{L} d\tau \\ &+ \left| \frac{-2g}{S_1\sqrt{\rho EI}} \sum_{j=1}^{\infty} \sin \frac{j\pi x}{L} \cdot \int_0^t \bar{S}_2 \sin(\bar{S}_3) \sin \frac{j\pi v\tau}{L} d\tau \cdot (\Delta m_1 + \Delta m_2 + \Delta m_v) \right| \end{aligned} \quad (9)$$

The lower and upper bounds of the variance of the bridge's displacements  $\sigma^2(W^{RI}(x,t))$  are

$$\begin{aligned} \overline{\sigma^2(W^{RI}(x,t))} &= \left\{ \frac{\partial W^{RI}(x,t)}{\partial E^R} - \left( \frac{\partial^2 W^{RI}(x,t)}{\partial E^R \partial m_1^I} \cdot \Delta m_1 + \frac{\partial^2 W^{RI}(x,t)}{\partial E^R \partial m_2^I} \cdot \Delta m_2 + \frac{\partial^2 W^{RI}(x,t)}{\partial E^R \partial m_v^I} \cdot \Delta m_v \right) \right\}^2 \cdot \sigma_E^2 \\ &+ \left\{ \frac{\partial W^{RI}(x,t)}{\partial I^R} - \left( \frac{\partial^2 W^{RI}(x,t)}{\partial I^R \partial m_1^I} \cdot \Delta m_1 + \frac{\partial^2 W^{RI}(x,t)}{\partial I^R \partial m_2^I} \cdot \Delta m_2 + \frac{\partial^2 W^{RI}(x,t)}{\partial I^R \partial m_v^I} \cdot \Delta m_v \right) \right\}^2 \cdot \sigma_I^2 \\ &+ \left\{ \frac{\partial W^{RI}(x,t)}{\partial \rho^R} - \left( \frac{\partial^2 W^{RI}(x,t)}{\partial \rho^R \partial m_1^I} \cdot \Delta m_1 + \frac{\partial^2 W^{RI}(x,t)}{\partial \rho^R \partial m_2^I} \cdot \Delta m_2 + \frac{\partial^2 W^{RI}(x,t)}{\partial \rho^R \partial m_v^I} \cdot \Delta m_v \right) \right\}^2 \cdot \sigma_\rho^2 \end{aligned} \quad (10)$$

$$\begin{aligned} \overline{\sigma^2(W^{RI}(x,t))} &= \left\{ \frac{\partial W^{RI}(x,t)}{\partial E^R} + \left( \frac{\partial^2 W^{RI}(x,t)}{\partial E^R \partial m_1^I} \cdot \Delta m_1 + \frac{\partial^2 W^{RI}(x,t)}{\partial E^R \partial m_2^I} \cdot \Delta m_2 + \frac{\partial^2 W^{RI}(x,t)}{\partial E^R \partial m_v^I} \cdot \Delta m_v \right) \right\}^2 \cdot \sigma_E^2 \\ &+ \left\{ \frac{\partial W^{RI}(x,t)}{\partial I^R} + \left( \frac{\partial^2 W^{RI}(x,t)}{\partial I^R \partial m_1^I} \cdot \Delta m_1 + \frac{\partial^2 W^{RI}(x,t)}{\partial I^R \partial m_2^I} \cdot \Delta m_2 + \frac{\partial^2 W^{RI}(x,t)}{\partial I^R \partial m_v^I} \cdot \Delta m_v \right) \right\}^2 \cdot \sigma_I^2 \\ &+ \left\{ \frac{\partial W^{RI}(x,t)}{\partial \rho^R} + \left( \frac{\partial^2 W^{RI}(x,t)}{\partial \rho^R \partial m_1^I} \cdot \Delta m_1 + \frac{\partial^2 W^{RI}(x,t)}{\partial \rho^R \partial m_2^I} \cdot \Delta m_2 + \frac{\partial^2 W^{RI}(x,t)}{\partial \rho^R \partial m_v^I} \cdot \Delta m_v \right) \right\}^2 \cdot \sigma_\rho^2 \end{aligned} \quad (11)$$

## Numerical Simulations

In this paper, the vehicle-bridge interaction model is demonstrated as the Figure 1. The bridge's parameters are considered as Gaussian random variables. The parameters of vehicle are treated as interval variables. The nominal values (mean/midpoint values) of system parameters taken in the numerical simulation are listed in Table 1. The unit of the bridge displacement response is meter in this paper.

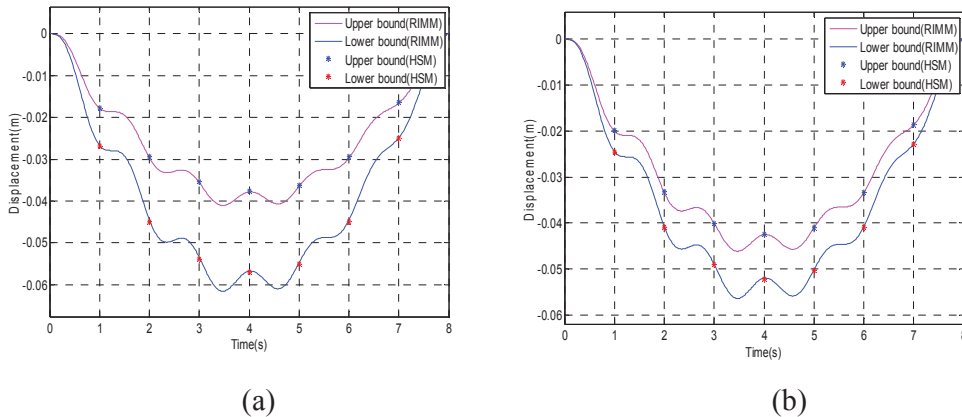
In this study, the bridge damping ratios  $\zeta_{bj}$  for all modes are taken as 0.05. For the sake of simplicity, the coefficient of variation (COV) of  $\rho^R$ ,  $E^R$  and  $I^R$  is adopted to represent the dispersal degree of random variables. Meanwhile, the interval change ratio (ICR) of  $m_1^I$ ,  $m_2^I$ , and  $m_v^I$  is used to describe the scatter level of interval variables. vehicle speed,  $v = 5m/s$  is taken into account to investigate the influence of vehicle velocity on the bridge response.

**Table 1. Data of the vehicle-bridge model**

Data of the bridge (mean value)	Data of the vehicle (midpoint)	
$L = 40m$	$m_1^c = 1000kg$	$m_2^c = 1500kg$
$E = 33 GN/m^2$	$m_v^c = 17800kg$	$I_v = 1.5 \times 10^5 kg \cdot m^2$
$I = 0.16m^4$	$k_{s1} = 2.5 \times 10^6 N/m$	$k_{s2} = 4.2 \times 10^6 N/m$
$\rho = 7800kg/m$	$k_{t1} = 5.2 \times 10^6 N/m$	$k_{t2} = 7.2 \times 10^6 N/m$
	$a_1 = 0.52$	$a_2 = 0.48$
	$C_{s1} = 9000N/m$	$C_{s2} = 9600N/m$
	$C_{t1} = 920N/m$	$C_{t2} = 960N/m$
	$S = 4.27m$	

The mean value of the random interval bridge displacement response at its mid-span is given in Figures 2(a) ( $COV(\rho^R, E^R, I^R) = 0.05$ ,  $ICR(m_1^I, m_2^I, m_v^I) = 0.2$ ) and (b) ( $COV(\rho^R, E^R, I^R) = 0.05$ ,  $ICR(m_1^I, m_2^I, m_v^I) = 0.1$ ), when different combinations of uncertain parameters are taken. Figure 2 shows the mean bridge displacement response when the randomness of all random parameters and all interval parameters are considered. From Figure 2, it can be observed that the interval width of bridge response increases when the interval changes of interval variables become larger.

In summary, the mean value of the random interval bridge response is independent of the dispersal degrees of random system parameters as expected. The interval width of the mean value of bridge response is directly proportional to the uncertainties of interval variables and vehicle speed.



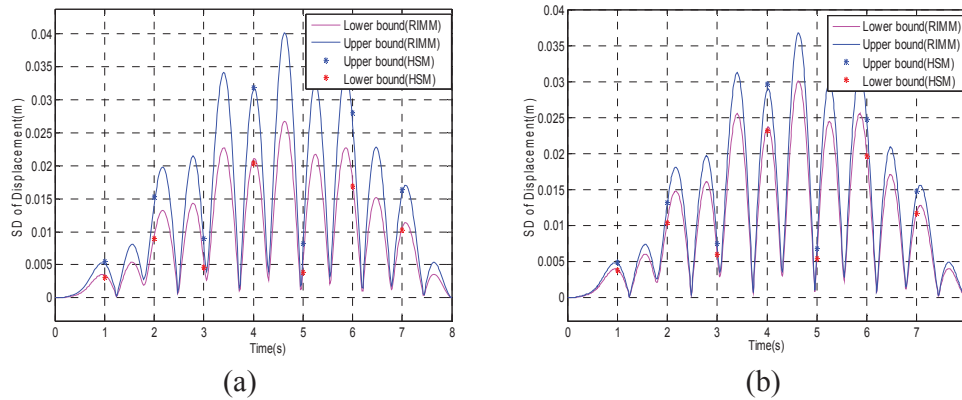
**Figure 2. Mean value of random interval bridge displacement response**

The standard deviation (SD) of the random interval bridge displacement response at its mid-span is shown in Figures 3(a) and (b). It can also be observed that the interval

width of the standard deviation of the random interval bridge response is directly proportional to the uncertainties of random and interval variables from Figures 3.

To validate the accuracy of the random interval moment method (RIMM) presented in this paper, a hybrid simulation method (HSM) is employed. This hybrid simulation method (HSM) combines direct simulation for interval variables and Monte-Carlo simulations for random variables.

To show the differences between the results generated by the RIMM and HSM in detail, the relative errors of mean value and standard deviation of bridge displacement are listed in Tables 2 and 3. Given the maximum relative error is 1.10% , while the coefficients of variation for all random parameters are 0.05 and the interval change ratios of all interval parameters are 0.2, the mean values calculated by the two methods are very closed to each other. For the standard deviation, the maximum relative error is 6.45%, which can be accepted because the hybrid simulation times used in this study are not enough to provide convergent results. 10,000 simulations used in the two rounds of HSM cannot yield convergent and reliable results although the total simulations are  $10^6$ . The accuracy of the results obtained by the HSM can be improved if more simulations are implemented.



**Figure 3. Standard deviation of random interval bridge displacement**

Generally, the accuracy of these results is satisfactory in practice. The presented random interval moment method has much less computational work than the simulation method. It should be noted that the accuracy of the results of random interval moment method can be further improved if second or higher order Taylor expansions are used.

**Table 2. Comparison of mean values**

Time (s)	Upper bound			Lower bound		
	RIMM	HSM	Error	RIMM	HSM	Error
1	0.02663	0.02671	0.29%	0.01793	0.01790	0.17%
2	0.04437	0.04461	0.55%	0.02958	0.02947	0.36%
3	0.05327	0.05353	0.49%	0.03550	0.03549	0.02%
4	0.05671	0.05680	0.16%	0.03781	0.03768	0.35%
5	0.05459	0.05467	0.14%	0.03639	0.03610	0.81%
6	0.04420	0.04436	0.37%	0.02961	0.02929	1.10%
7	0.02482	0.02506	0.97%	0.01636	0.01625	0.68%

**Table 3. Comparison of standard deviations**

Time	Upper bound			Lower bound		
	RIMM	HSM	Error	RIMM	HSM	Error
1	0.00521	0.00547	4.72%	0.00347	0.00339	2.33%
2	0.01394	0.01415	1.50%	0.00923	0.00894	3.22%
3	0.00886	0.00894	0.91%	0.00589	0.00577	2.14%
4	0.03162	0.03182	0.62%	0.02108	0.02095	0.63%
5	0.00852	0.00854	0.19%	0.00568	0.00549	3.54%
6	0.02617	0.02797	6.45%	0.01744	0.01713	1.83%
7	0.01596	0.01638	2.57%	0.01064	0.01024	3.87%

### Conclusions

In this paper, stochastic dynamic response of vehicle-bridge interaction system with uncertainties is investigated by extending the random interval moment method to the dynamic coupling system. The uncertainties of system are modeled as random and interval variables. The expressions for calculating the bounds of expectation and variance of the random interval bridge response are derived. Using these formulations, the upper and lower bounds of mean value and standard deviation of bridge response can be very easily obtained. The results obtained by the presented random interval moment method are in very good agreement with those determined by Monte-Carlo simulation method. The relative errors of these two methods are quite small when the change ranges of system parameters are not large.

### Acknowledgements

The work reported in this paper was supported by the Australian Research Council through Discovery Projects.

### References

- Gao, W., Song, C., and Tin-Loi, F. (2010), Probabilistic interval analysis for structures with uncertainty. *Structural Safety*, 32, pp. 191-199.
- Impollonia, N. and Muscolino, G. (2011), Interval analysis of structures with uncertain-but-bounded axial stiffness. *Computer Methods in Applied Mechanics and Engineering*, 200, pp. 1945-1962.
- Jiang, C., Han, X. and Liu, G. P. (2008). Uncertain optimization of composite laminated plates using a nonlinear interval number programming method. *Computers & Structures*, 86, pp. 1696-1703.
- Jiang, C., Han, X., Li, W. X., Liu, J. and Zhang, Z. (2012), A hybrid reliability approach based on probability and interval for uncertain structures. *Journal of Mechanical Design*, 134, 031001.
- Ju, S. H. and Lin, H. T. (2007), A finite element model of vehicle-bridge interaction considering braking and acceleration. *Journal of sound and vibration*, 303, pp. 46-57.
- Liu, N., Gao, W., Song, C. M. and Zhang, N. (2011), Probabilistic dynamic analysis of vehicle-bridge interaction system with uncertain parameters. *CMES-Computer Modeling in Engineering & Sciences*, 72(2), pp. 79-102.
- Qiu, Z., Ma, L. and Wang, X. (2009), Non-probabilistic interval analysis method for dynamic response analysis of nonlinear systems with uncertainty. *Journal of Sound and Vibration*, 319, pp. 531-540.
- Yang, Y. B. and Lin, C. W. (2005), Vehicle-bridge interaction dynamics and potential applications. *Journal of sound and vibration*, 284, pp. 205-226.
- Zhang, N., Xia, H. and Guo, W. (2008), Vehicle-bridge interaction analysis under high-speed trains. *Journal of Sound and Vibration*, 309, pp. 407-425.

## Dynamic reliability based structural optimization

\*W. Gao<sup>1</sup>, J. Ma<sup>2</sup>, C.M. Song<sup>1</sup> and F. Tin-Loi<sup>1</sup>

<sup>1</sup>School of Civil and Environmental Engineering, The University of New South Wales, Sydney, NSW 2052, Australia

<sup>2</sup>School of Electromechanical Engineering, Xidian University, Xi'an, 710071, P. R. China

\*Corresponding author: w.gao@unsw.edu.au

### Abstract

Structural dimension and shape optimization based on the structural dynamic reliability is investigated in this paper. Structural gross mass is taken as the objective function and the structural dynamic reliability is incorporated into the constraints. The dynamic reliability constraints are transferred and simplified, and the normalization of design variables is discussed to avoid some variables being drowned by others during optimization due to their different dimensions and orders of magnitude. The optimal models of dimension and shape with dynamic reliability constraints are then presented. Numerical examples are used to illustrate the results of different optimal designs, which demonstrate that the efficiency to solve the structural optimization with dynamic reliability constraints can be significantly improved if the design variables and their initial values are selected properly.

**Keywords:** Dimension and shape optimization, normalization of design variables, dynamic reliability constraints, random process excitation.

### Introduction

Structural reliability optimization conducted from 1960s and has been extensively investigated (Chen et al., 1997; Gao et al., 2003; Kang and Luo, 2010; Li et al., 2011; Jiang et al., 2010). Probabilistic approaches have been developed to account for the uncertainties in structural parameters, such as stochastic finite element method, perturbation method, response surface method and Monte-Carlo simulation based methods. First-order and second-order reliability methods have been proposed and improved to assess the reliability/safety of structures with uncertain properties. The randomness of forces has been also considered in the reliability assessments. Structural optimization with the reliability constraints accounting for the uncertainties in structural parameters and inputs has been investigated by many researchers and has been widely applied to the design of different types of structures (Gao, 2006). However, dynamic reliabilities or random process excitations were rarely adopted in the structural optimal design. In reality, the external loads are often random process excitations such as winds, earthquake motions, waves and explosions.

In this paper, a framework is presented to optimize the dimension or shape of the truss structures in the context of the element or system dynamic reliability constraints. Central to the construction of this framework is the reasonable mathematic models of dimension and shape optimization of truss structures where the minimization of structural gross mass is taken to be the optimization goal, with a particular emphasis on the discussion of the simplification of element and system dynamic reliability constraints, as well as on the normalization of design variables in order to facilitate the optimization. Finally, the feasibility and rationality of models and method given are demonstrated by the implementation of examples and some important conclusions are obtained.

### Construction of general optimization models with implicit dynamic reliability constraints

Due to the different optimization aims, choices of the optimal design variables are different too. In

the topology optimization, topology variables are design variables whether structural elements with topology variables exist or not; in the shape optimization, the coordinates of structural nodes are design variables; in the dimensions optimization, cross-section areas of structural elements are design variables. Generally, optimization with only one kind of design variables is presented, but sometimes it is necessary to consider the optimization including several kinds of design variables simultaneously. For this purpose, both shape and dimension optimizations are considered at the same time in the following deduction.

Because external loads are random process excitations, all constraints like structural displacement and stress are then functions of random process in the dynamic optimization and they are given in the form of dynamic reliability. For the two-side boundary constraints (Ma et al., 2010), the optimal model of structural dimensions and shape for the minimal gross mass is constructed in Eq. (1) where design variables are bars' cross-section areas and nodal coordinates and the dynamic reliability constraints are nodal displacement and element's stress

$$\begin{aligned}
& \text{find} : \{\bar{A}\} = (A_1, A_2, \dots, A_n)^T, \{\bar{Z}\} = (Z_1, Z_2, \dots, Z_m)^T \\
& \text{min} : W(\bar{A}) = \sum_{i=1}^{ne} \rho_i A_i L_i \\
& \text{s.t.} : R_{x_j}^* - P_r \{ (\max_{t \in T} x_j(t) \leq \lambda_{xju}) \cap (\min_{t \in T} x_j(t) \geq -\lambda_{xjl}) \} \leq 0 \quad (j = 1, 2, \dots, N) \\
& \quad R_{s_e}^* - P_r \{ (\max_{t \in T} S_e(t) \leq \lambda_{seu}) \cap (\min_{t \in T} S_e(t) \geq -\lambda_{sel}) \} \leq 0 \quad (e = 1, 2, \dots, M) \\
& \quad A_{li} \leq A_i \leq A_{ui} \quad (i = 1, 2, \dots, ne) \\
& \quad Z_{li} \leq Z_i \leq Z_{ui} \quad (i = 1, 2, \dots, me)
\end{aligned} \tag{1}$$

where elemental cross-section areas  $\bar{A}$  and nodal coordinates  $\bar{Z}$  are design vectors;  $\rho$  is mass density of bars;  $A_i$  and  $L_i$  are cross-section area and bar's length corresponding to the  $i$ th type of design variables;  $W(\bar{A})$  is the gross mass;  $x_j$  and  $S_e$  are the displacement response of the  $j$ th degree of freedom and the stress response of the  $e$ th element under random process excitation respectively;  $\lambda_{xju}$ ,  $\lambda_{xjl}$ ,  $\lambda_{seu}$  and  $\lambda_{sel}$  are the upper and lower transcending bounds of displacement of the  $j$ th degree of freedom and stress of  $e$ th element respectively;  $R_{x_j}^*$  and  $R_{s_e}^*$  are dynamic reliabilities required by design;  $P_r(\cdot)$  is the dynamic reliability solved;  $A_{ui}$  and  $A_{li}$  are upper and lower bounds of the  $i$ th type of cross-section area design variables;  $Z_{ui}$  and  $Z_{li}$  are upper and lower bounds of the  $i$ th type of nodal coordinate design variables;  $ne$  and  $me$  are dimensions of cross-section area design vector and nodal coordinate design vector;  $N$  is the number of displacement constraints and  $M$  is the number of structural elements.

If the dynamic reliability is one-side transcending bound (Ma et al., 2010), constraints in Eq. (1) can then be replaced by

$$\begin{aligned}
& \text{s.t.} : R_{x_j}^* - P_r \{ x_j(t) \leq \lambda_{xj}, 0 \leq t \leq T \} \leq 0 \quad (j = 1, 2, \dots, N) \\
& \quad R_{s_e}^* - P_r \{ S_e(t) \leq \lambda_{se}, 0 \leq t \leq T \} \leq 0 \quad (e = 1, 2, \dots, M) \\
& \quad A_{li} \leq A_i \leq A_{ui} \quad (i = 1, 2, \dots, ne) \\
& \quad Z_{li} \leq Z_i \leq Z_{ui} \quad (i = 1, 2, \dots, me)
\end{aligned} \tag{2}$$

where  $\lambda_{xj}$  and  $\lambda_{se}$  are transcending bounds of displacement of the  $j$ th degree of freedom and stress of  $e$ th element respectively.

### Optimization models of truss structures under stationary stochastic process excitation

Considering the structural determinate parameters, structural dynamic responses are stationary stochastic process too when external excitation is a stationary random process. From the first-passage failure theory, Poisson equations to compute the dynamic reliability of single degree of freedom with two-side boundary, symmetric boundary and one-side boundary are respectively

$$R_i(t) = \exp\left\{-\frac{1}{2\pi} \frac{\dot{\psi}_{Y_i(t)}}{\psi_{Y_i(t)}} T \left[ \exp\left(-\frac{\lambda_{Yiu}^2}{2\psi_{Y_i(t)}^2}\right) + \exp\left(-\frac{\lambda_{Yil}^2}{2\psi_{Y_i(t)}^2}\right) \right]\right\} \quad (3)$$

$$R_i(t) = \exp\left\{-\frac{1}{\pi} \frac{\dot{\psi}_{Y_i(t)}}{\psi_{Y_i(t)}} T \exp\left(-\frac{\lambda_{Yi}^2}{2\psi_{Y_i(t)}^2}\right)\right\} \quad (4)$$

$$R_i(t) = \exp\left\{-\frac{1}{2\pi} \frac{\dot{\psi}_{Y_i(t)}}{\psi_{Y_i(t)}} T \exp\left(-\frac{\lambda_{Yi}^2}{2\psi_{Y_i(t)}^2}\right)\right\} \quad (5)$$

In Eq. (3),  $\psi_{Y_i(t)}$  and  $\dot{\psi}_{Y_i(t)}$  are roots of mean square values of stationary response  $Y_i(t)$  (displacement, stress or strain) and its derivation response  $\dot{Y}_i(t)$ , respectively.  $\lambda_{Yil}$  and  $\lambda_{Yiu}$  are lower and upper safe bounds of  $Y_i(t)$ , and  $\lambda_{Yi}$  is the safe bound too. The two-side boundary dynamic reliability is most common among Eqs. (3)-(5).

Then the structural displacement and stress dynamic reliability constraints with the two-side boundary are

$$R_{x_j}^* - \exp\left\{-\frac{1}{2\pi} \frac{\dot{\psi}_{x_j}}{\psi_{x_j}} T \left[ \exp\left(-\frac{\lambda_{xju}^2}{2\psi_{x_j}^2}\right) + \exp\left(-\frac{\lambda_{xjl}^2}{2\psi_{x_j}^2}\right) \right]\right\} \leq 0 \quad (6)$$

$$R_{s_e}^* - \exp\left\{-\frac{1}{2\pi} \frac{\dot{\psi}_{s_e}}{\psi_{s_e}} T \left[ \exp\left(-\frac{\lambda_{Seu}^2}{2\psi_{s_e}^2}\right) + \exp\left(-\frac{\lambda_{Sel}^2}{2\psi_{s_e}^2}\right) \right]\right\} \leq 0 \quad (7)$$

where  $\psi_{x_j}$ ,  $\psi_{s_e}$ ,  $\dot{\psi}_{x_j}$  and  $\dot{\psi}_{s_e}$  are roots of mean square values of the  $j$ th nodal displacement response  $x_j(t)$  and the  $e$ th-element's stress response  $S_e(t)$  and their corresponding derivation response respectively.  $\lambda_{xju}$ ,  $\lambda_{xjl}$ ,  $\lambda_{Seu}$ ,  $\lambda_{Sel}$ ,  $R_{x_j}^*$  and  $R_{s_e}^*$  are the same as those in Eq. (1).

The structural dimension optimization model with dynamic reliability constraints of the two-side boundary is

$$\begin{aligned} \text{find : } & \bar{A} = (A_1, A_2, \dots, A_n)^T \\ \text{min : } & W(\bar{A}) = \sum_{i=1}^{ne} \rho_i A_i l_i \\ \text{s.t. : } & R_{x_j}^* - \exp\left\{-\frac{1}{2\pi} \frac{\dot{\psi}_{x_j}}{\psi_{x_j}} T \left[ \exp\left(-\frac{\lambda_{xju}^2}{2\psi_{x_j}^2}\right) + \exp\left(-\frac{\lambda_{xjl}^2}{2\psi_{x_j}^2}\right) \right]\right\} \leq 0 \quad (j = 1, 2, \dots, N) \\ & R_{s_e}^* - \exp\left\{-\frac{1}{2\pi} \frac{\dot{\psi}_{s_e}}{\psi_{s_e}} T \left[ \exp\left(-\frac{\lambda_{Seu}^2}{2\psi_{s_e}^2}\right) + \exp\left(-\frac{\lambda_{Sel}^2}{2\psi_{s_e}^2}\right) \right]\right\} \leq 0 \quad (e = 1, 2, \dots, M) \\ & A^l \leq A_i \leq A^u \quad (i = 1, 2, \dots, ne) \end{aligned} \quad (8)$$

Similarly, optimization models with symmetric boundary dynamic reliability constraints and one-side boundary dynamic reliability constraints can also be obtained. Here only dynamic reliability





$\min_{i=1, n-(m-1)} \{P_{ri}(t)\} \longrightarrow$  seek for the  $(m-1)th$  weakest among the left  $n - (m - 1)$  elements

Taking the lower bound  $\prod_i^n P_{fi}(t)$  of  $P_r(t)$  as system dynamic reliability, the constraints of the new optimization model with the same design variables and objective function same as those in Eq. (10) are

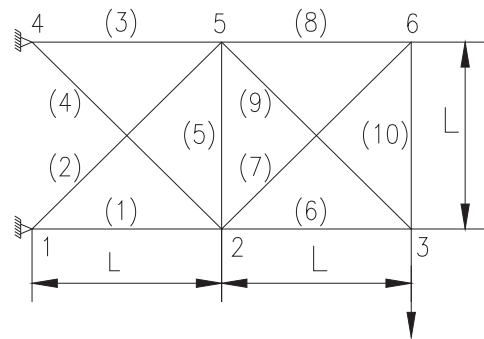
$$s.t.: \quad P_j(\bar{A}) \leq P_j^* \quad (j = 1, 2, \dots, m)$$

$$\prod_i^n P_{fi}(t) \leq P_f^* \quad (12)$$

Because the lower bound of system dynamic reliability is smaller than practical system dynamic reliability, the optimal results under the constraints in Eq. (12) tend to conservative, which is acceptable in the practical engineering.

**Example**

In Figure 1, elastic module  $E = 210Gpa$ , mass density  $\rho = 7800kg/m^3$ . A random load  $P$  acts on the node 3 in the vertical direction, excitation source is the Gaussian white noise process with zero mean value and its power spectrum density is  $S_p = 100N^2s$ , the load's durative time  $t = 1000s$ . The two-side symmetric boundary is  $\lambda = 100Mpa$ , the stress dynamic reliability of every bar is 0.99. The objective function is the structural gross mass  $W$ . When the design variables are bars' cross-section areas with initial values  $0.005m^2$ , the dimension optimal results are listed in Table 1.



**Figure 1. 10-bar truss**

**Table 1. Dimensions optimal results under dynamic reliability constraint**

parameters	$A1(cm^2)$	$A2(cm^2)$	$A3(cm^2)$	$A4(cm^2)$	$A5(cm^2)$	$A6(cm^2)$
initial	50	50	50	50	50	50
optimum	23.7908	20.9263	30.1170	11.4981	2.0000	10.5384
parameters	$A7(cm^2)$	$A8(cm^2)$	$A9(cm^2)$	$A10(cm^2)$	$W(kg)$	$R_{min}$
initial	50	50	50	50	909.2346	1
optimum	5.9143	4.8669	13.7567	20.4613	258.0997	0.9900

From results of Table 1, the structural gross mass reduces to 28.4 percent of the original mass on the basis of ensuring the stress reliability. Moreover, among optimal results of  $Ai(i = 1, 2, \dots, 10)$ ,  $A3$  is the greatest and  $A5$  is the smallest, this is because bar 3 is the an important workload bearing element while bar 5 is the less important one according to the analysis of theoretical mechanics.

In the following, structural shape and dimension are optimized simultaneously under dynamic reliability constraint. Taking  $Ai(i = 1, 2, \dots, 10)$  and ordinates of node 4, 5 and 6 as design variables simultaneously, initial values of  $Ai$  are  $0.005m^2$ , initial values of three ordinates are  $2m$ . The optimal results are given in Table 2.

**Table 2. Shape and dimension optimum results under dynamic reliability constraint**

parameters	$A1(cm^2)$	$A2(cm^2)$	$A3(cm^2)$	$A4(cm^2)$	$A5(cm^2)$
initial design	50	50	50	50	50
optimum	14.1104	14.8950	16.6942	3.3414	3.6604
parameters	$A6(cm^2)$	$A7(cm^2)$	$A8(cm^2)$	$A9(cm^2)$	$A10(cm^2)$
initial design	50	50	50	50	50
optimum	7.8812	3.4494	4.9532	13.5123	65.7645
parameters	$Y4(m)$	$Y5(m)$	$Y6(m)$	$W(kg)$	$R_{min}$
initial design	2	2	2	909.2346	1
optimum	4.94243	3.38567	0.22864	209.5853	0.9900

From Table 2, it can be observed that

1) the gross mass reduces further under the premise of dynamic reliability satisfying the constraint condition.

2) the optimal results of dimension variables are different from those in Tab.11, and  $A10$  is the greatest while  $A8$  is the smallest,  $A3$  and  $A1$  are still comparatively greater as the connection elements of structural root, which is similar to the conclusion of Tab.11.

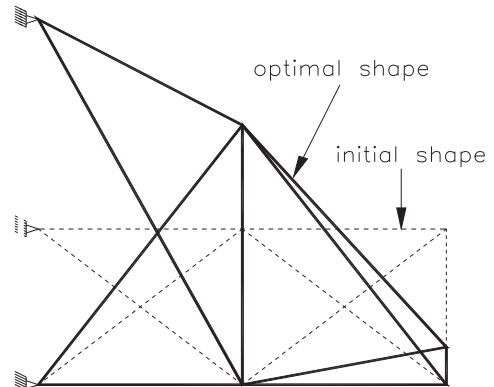
The structural shape after optimization is showed in Figure 5, and it tends to a triangle as a whole which enables structure to be more stable and is a better load-carrying shape.

## Conclusion

The structural optimal design based on dynamic reliability is more complicated than conventional structural static optimal design, and optimal design with system dynamic reliability constraint is more complicated than that with element dynamic reliability constraint. How to quickly finish structural dynamic analysis and further improve optimization methods are critical to the widespread application of dynamic optimal design based on the dynamic reliability.

Because it's very hard to obtain system dynamic reliability according to Eq. (10) and sometimes it is impossible at all. So one can only consider two extreme cases to approximately evaluate it. Moreover, its solution is based on the simplified dynamic reliability which is suitable for many engineering structures because their responses are often narrow band processes. The dynamic reliability obtained by the simplified method does not greatly differ from its true value because the upper bound of the integral interval of power spectral density is not much greater than the intermediate value, thus the lower bound of system dynamic reliability will not much smaller than its true value. Hence the optimization results are just comparatively conservative and still applicable in practical engineering when lower bound of system dynamic reliability is used

Some measures such as reasonably choosing design variables (dimensions or shape parameters) or evaluating initial values of the design variables can effectively enhance the efficiency of dynamic optimal design based on dynamic reliability.



**Figure 2. shape optimal result**

**References**

- Chen, J. J., Duan, B.Y. and Zen, Y. G. (1997), Study on dynamic reliability analysis of the structures with multidegree-of-freedom system. *Computers and Structures*, 62, pp. 877-881.
- Gao W, Chen JJ, Ma HB and Ma XS (2003) Optimal placement of active bars in active vibration control for piezoelectric intelligent truss structures with random parameters, *Computers & Structures* 81(1): 53-60.
- Kang, Z. and Luo, Y. J. (2010), Reliability-based structural optimization with probability and convex set hybrid models. *Structural and Multidisciplinary Optimization*, 42, pp. 89-102.
- Li, F. Y., Luo, Z. and Sun, G. Y. (2011), Reliability-based multiobjective design optimization under interval uncertainty. *CMES-Computer Modeling in Engineering & Sciences*, 74, pp. 39-64.
- Jiang, C., Bai, Y. C., Han, X. and Ning, H. M. (2010), An efficient reliability-based optimization method for uncertain structures based on non-probability interval model. *CMC-Computers Materials & Continua*, 18, pp. 21-42.
- Gao, W. (2006), Stochastically optimal active control of a truss structure under stationary random excitation. *Journal of Sound and Vibration*, 290, pp. 1256-1268.
- Ma, J., Gao, W., Wriggers, P., Wu, T. and Sahraee, S. (2010), The analyses of dynamic response and reliability of fuzzy-random truss under stationary stochastic excitation. *Computational Mechanics*, 45, pp. 443-455.

# Research on structural optimization design for shield beam of hydraulic support based on response surface method

**\*Dongchen Qin, Huiyu Li, Zhuli Liu, and Jiangyi Chen**

School of Mechanical Engineering, Zhengzhou University, China

\*Corresponding author: dcqin@zzu.edu.cn

## Abstract

The shield beam is the main load-bearing component of the hydraulic support. The structural optimization design of one shield beam is fulfilled by the response surface method. Using the weight as the objective function, the structural optimization mathematical models of shield beam is set up. The experimental design is performed in the ANSYS software and uniform design. The maximum stresses of shield beam are gotten in the different sizes. The response surface models of design parameters and maximum stresses are fitted by the least squares method. The structural optimization design of shield beam is completed by the random direction method. This research implements the structural optimization design of hydraulic support shield beam in a modern design method, and provides a valuable guidance for the hydraulic support research and development.

**Keywords:** hydraulic support, shield beam, structural optimization design, response surface method.

## Introduction

The shield beam is one of the main components of the hydraulic support to bear load. Optimizing the design of the shield beam structure can reduce its weight, which plays an important role for the sustainable development of coal machinery enterprises.

Traditional structural optimization of the shield beam structure can be roughly divided into two types. One is that, according to the theory of material mechanics or mechanical formula, the response of the structure can be computed and the design variables and objective functions can be chosen, then to optimize the design using efficient optimization algorithm (Liu, 2007). For numerous simplifications to models, this method would yield the optimization results more-conservative outcome. While the other is that, the response of the structure is obtained by using finite element software and is chosen as the constraint condition, then to select the suitable optimization strategy for more accurate structure optimization design (Yao, 2011a). This approach, where each iteration will be made during the optimization process with finite element calculations, is running slowly.

To overcome the insufficiency of above traditional optimal design methods, by using the response surface methodology, this research has realized the structure optimization of shield beam for a certain type hydraulic support. With section dimensions of the shield beam as variables, ANSYS is used to calculate the stress of the shield beam under partial loads, and the response surface method of uniform design experiment is applied to obtain the functional relationship between stress values and section dimensions of the shield beam. For the weight reduction purpose, the structure optimization design of shield beam is performed under the constraints of structure strength and geometrical dimension. It is proved that the optimization method is feasible and effective by finite element analysis and validation results.

## Optimization Based on Response Surface Method

The optimization based on response surface method generally includes such certain steps as, experiment design, response surface model, and searching for the optimal point (Liang, etc., 2010).

Experiment design is for the sake of scientific and reasonable arrangement of test schemes with fewer experiments to get more properties of design space (Kleijnen, 2005a). A scientific experiment design can arrange various experimental factors reasonably and analyse test data effectively, thus

realizing more rich and reliable data obtained with using less resources. Commonly used experimental design methods are full factorials, orthogonal design of experiment and uniform design experimentation, etc.

The uniform design experimentation, which will distribute design points evenly within the design space, is chosen in this research. Compared with other methods, the uniform design experimentation can require less experiment times, and improve the precision of response surface to a certain extent (Li, etc.,2005b). Using this approach, several numerical simulation tests are carried out to obtain a series of design points, whose number and locations are determined. On this basis, the function relationship between control variables and target variables is established with regression method, namely, response surface model. The response surface model reflects the function relationship between target variables (dependent variable) and several control variables (independent variables). As this function relationship is generally curve or curved surface, which is called as response surface model.

Because the response surface model is based on series of regression of test data, the quality of regression analysis directly determines the accuracy of response surface model (Todoroki, A. and Ishikawa, T., 2004). In the field of structural mechanics, the response surface function model often adopts the quadratic polynomial forms, such as

$$Y(X) = a_0 + \sum_{i=1}^n a_i x_i + \sum_{i=1}^n \sum_{j=1}^n a_{ij} x_i x_j \quad (1)$$

where,  $a_0$ ,  $a_i$  and  $a_{ij}$  are undetermined coefficients,  $x_i$  ( $i=1,2,\dots,n$ ) are basic variables. In order to simplify the calculation and avoid application range restrictions for the response surface, the constant term, first-order term and second-order squared are remained, and the second-order cross term is neglected, namely, the simplified form is

$$Y(X) = a_0 + \sum_{i=1}^n a_i x_i + \sum_{i=1}^n a_{ii} x_i^2 \quad (2)$$

Searching for the optimal point in the generated response surface model typically includes to select the design objectives, constraints and the optimal algorithm. For different situations, the mathematical constraints are appended to the model, the design objectives and a series of the search algorithms for the optimal point are provided, such as gradient algorithm, random direction method, penalty function method, etc. The random direction method, which possesses the easy procedures and fast convergent rate, is adopted here.

## The Response Surface Model Establishment

### Shield Beam Statics Analysis

The shield beam of a certain type hydraulic support is taken as the research object. Finite element model for the shield beam is established under ANSYS environment, then the shield beam is meshed freely with SOLID187 element. According to the technical specifications and load-bearing situation of hydraulic support under partial loads (Qin, etc.,2011b), the corresponding boundary conditions and loads are applied, and ANSYS structural statics analysis is performed to obtain the stress distribution and deformation conditions for the shield beam, as shown in Figs. 1 and 2. The figures show the shield beam's stress situation and deformation under partial loads, where the maximum stress value of the shield beam is 359.61 MPa, and the maximum deformation is 8.96 mm.

To verify the reliability of the finite element analysis, the real physical prototype stress test for the shield beam is also made. According to the characteristics of stress distribution of the shield beam, paste positions of the foil strain gauge are determined for the physical stress tests, and the stress values of the test points are obtained. The locations of the testing points are shown in Fig. 3. At the same time, the corresponding 6 positions at finite element model of shield beam are selected too, where the average stress results are recorded. A comparison of finite element calculation results and measured values is shown in Table 1.

The finite element results and the experimental results are not consistent to a certain degree, which is caused by the test error and calculation error. The long-time experiment results in unstable

working environment of the strain gauge, possible different characteristics of each strain gauge, and angular deviation and position deviation for the gauge patch, all these factors will lead to test errors. When finite element model is being simulated, parameter settings, grid division and the differences among the constraint boundary conditions will cause calculation errors. Therefore, it is possible to cause larger relative error of some individual points.

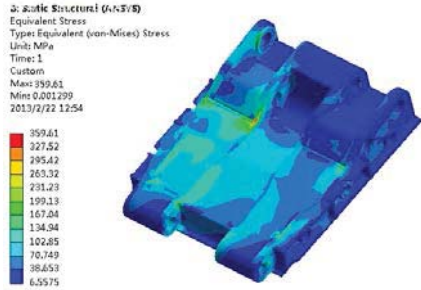


Figure 1. Shield beam's stress distribution

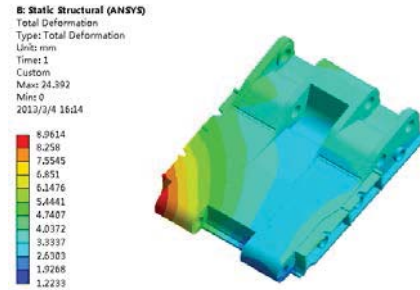


Figure 2. Shield beam's deformation

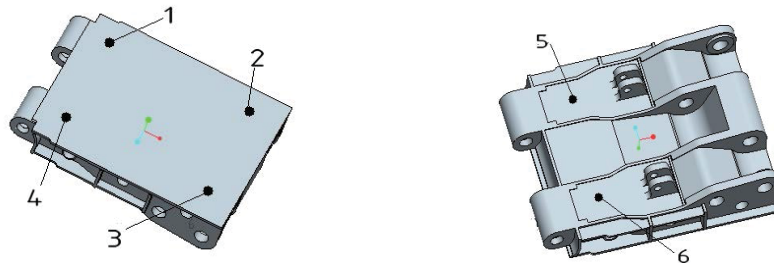


Figure 3. Locations of test points

Table 1. Experimental verification

Number of measuring points	Finite element results/MPa	Measured results/MPa	Relative error/%
1	129.96	120.37	7.97
2	56.36	53.73	4.89
3	42.52	46.96	-9.46
4	164.05	138.04	18.84
5	322.84	305.35	5.72
6	113.24	120.28	-5.85

### Uniform Design Experimental Analysis

As shield beam's structure is complex, there are more parameters affecting the component strength. Since the distance between the shield beam's front and back hinged points is already determined during overall design of hydraulic support, the lightest weight will be treated as the optimization objective of shield beam. In other words, the minimum sectional area will be regarded as optimization objective (Zhu, etc., 2012). The shield beam, made up of upper and lower cover plates and vertical ribs, is a box welded structure with a cross section of 5 cavities, which is shown in Fig. 4.

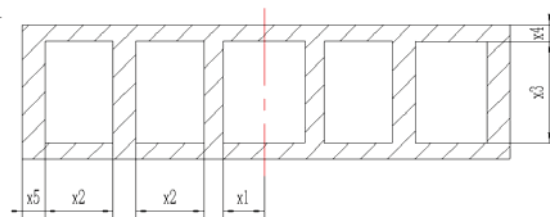


Figure4. The shield beam's cross section

Where,  $x_1$  is the distance between the first cavity and middle plane,  $x_2$  is the width of the second and third cavities,  $x_3$  is the height of the cavity,  $x_4$  and  $x_5$  are the thickness of upper and lower cover plates and the thickness of the vertical rib, separately.

In this paper, the uniform design experimentation is used to carry out response surface experiments. Through the parameterized modeling to realize the change of size of thickness, and the finite element analysis of each group of dimensional data, we can obtain the maximum stress value of the shield beam. The quadratic polynomial without cross terms is taken as the response surface equation which contains 5 parameters and 11 unknown coefficients (that is equal to  $2n+1$ ,  $n$  is the number of parameter). So, 16 times orthogonal tests, namely including 16 levels 5 parameters, can be determined and performed. The test results are shown in Table 2.

**Table 2. Uniform test table**

Times	$x_1$ /mm	$x_2$ /mm	$x_3$ /mm	$x_4$ /mm	$x_5$ /mm	$\sigma_{\max}$ /MPa
1	190.00	128.00	160.00	24.33	21.20	340.51
2	193.33	138.00	172.00	27.00	20.13	334.67
3	196.67	148.00	150.00	24.00	19.07	356.14
4	200.00	124.00	162.00	26.67	18.00	364.59
5	203.33	134.00	174.00	23.67	21.47	327.02
6	206.67	144.00	152.00	26.33	20.40	350.47
7	210.00	120.00	164.00	23.33	19.33	346.41
8	213.36	130.00	176.00	26.00	18.27	352.32
9	216.67	140.00	154.00	23.00	21.73	340.67
10	220.00	150.00	166.00	25.67	20.67	346.29
11	223.33	126.00	178.00	22.67	19.60	325.40
12	226.67	136.00	156.00	25.33	18.53	351.94
13	230.00	146.00	168.00	22.33	22.00	350.93
14	233.33	122.00	180.00	25.00	20.93	336.66
15	236.67	132.00	158.00	22.00	19.87	335.18
16	240.00	142.00	170.00	24.67	18.80	347.15

Using the least-square method to fit the response surface function,

$$y_e = 3849.4835 - 2.5428x_1 - 16.7542x_2 - 1.3887x_3 - 12.6922x_4 - 181.4884x_5 + 0.0061x_1^2 + 0.0625x_2^2 + 0.0026x_3^2 + 0.3031x_4^2 + 4.4595x_5^2 \quad (3)$$

where  $y_e$  is a response value of the maximum stress.

According to the evaluation formula of multiple correlation coefficient (equation (4)), we can evaluate the fitting degree and get  $R^2$  for every response surface function. The relative high evaluation index ( $R^2=0.9664$ ) for equation (3) proves that the fitted response surface function is suitable, which means that the response surface experiment is well with respect to practical simulation, and it will provide a good foundation for the next step of structure optimization.

$$R^2 = 1 - \frac{SSE}{SST} = 1 - \frac{\sum_{i=1}^n (y_i - \hat{y}_i)^2}{\sum_{i=1}^n (y_i - \bar{y})^2} \quad (4)$$

## The Optimization Design

### Optimal Design Mathematic Model



The lightest weight of the shield beam, is equivalent to the minimum cover of cross section area of the shield beam. From the Fig.2, the objective function can be made as

$$F(X) = 2x_4(2x_1 + 4x_2 + 6x_5) + 6x_3x_5 \quad (5)$$

The constraint conditions of the structural optimization on shield beam are divided into the following kinds:

Strength conditions: It is ensured that the the maximum stress value of the shield beam under partial loads must not exceed the allowable stress. There is

$$y_e \leq \sigma_s / n_s \quad (6)$$

$\sigma_s$ —the material's yield limit (MPa);  $n_s$ —allowable safety factor.

The thickness restrictions of the shield beam: Considering the factors such as the ventilation section, the gas emission, pedestrians and the overall effect of the support, a thickness range of shield beam is often specified in the design. There is

$$T_{\min} \leq x_3 + 2x_4 \leq T_{\max} \quad (7)$$

$T_{\min}$ —the minimum thickness of the shield beam;  $T_{\max}$ —the maximum thickness of the shield beam (mm).

The overall thickness restrictions of the abdomen: Considering that the shield beam of hydraulic support has certain stiffness, the abdomen design should define a minimum thickness. There is

$$-2(x_1 + 2x_2 + 3x_5) \leq -c_{\min} \quad (8)$$

$c_{\min}$ —lower bound of the total thickness of the abdomen (mm).

Boundary conditions: The value of the parameter is restricted by various specification of the plate, also by the overall or partial stiffness and deformation. Therefore, the design variables are within a certain range. There is

$$l_i \leq x_i \leq u_i \quad i = 1, 2, \dots, 5 \quad (9)$$

$l_i$ —the lower bound of the variable (mm);  $u_i$ —the upper bound of the variable (mm).

So the mathematical model can be summarized as follows:

$$\begin{aligned} & \text{Min } F(X) = 2x_4(2x_1 + 4x_2 + 6x_5) + 6x_3x_5 \\ & X = [x_1, x_2, x_3, x_4, x_5] \\ & \text{s.t. } \begin{cases} y_e \leq \sigma_s / n_s \\ T_{\min} \leq x_3 + 2x_4 \leq T_{\max} \\ -2(x_1 + 2x_2 + 3x_5) \leq -c_{\min} \\ l_i \leq x_i \leq u_i \quad i = 1, 2, \dots, 5 \end{cases} \end{aligned}$$

## Optimization and Validation Results

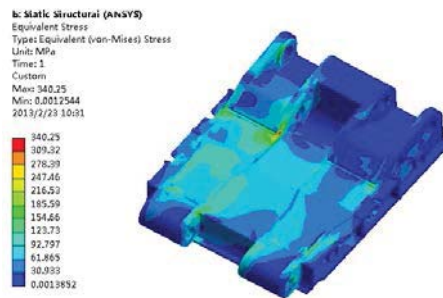
In this paper, the random direction method is programmed with MATLAB to solve optimization model. Combining with actual production requirements, the optimal results of design variables for engineering process can be obtained as shown in Table 3.

Before optimization, the cross sectional area of the shield beam is 0.0769 m<sup>2</sup>, and through optimization, the cross sectional area of the shield beam decreases to 0.0678 m<sup>2</sup>. That means, the shield beam themselves in weight will be reduced by 11.8%.

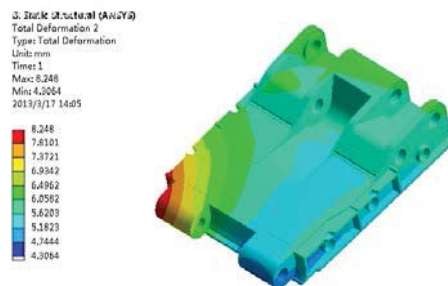
According to the above optimization, the shield beam has to be modeled again. Under the unilateral loading conditions of top beam, the finite element analysis for the shield beam is performed again. The contours of stress and displacement of the optimized shield beam are shown in Figs. 5 and 6.

**Table3. Design variables optimization results**

Parameters	Upper limit value/mm	Lower limit value/mm	Original value/mm	Optimal value/mm
$x_1$	190	240	225	221
$x_2$	120	150	140	135
$x_3$	150	180	170	172
$x_4$	20	28	25	22
$x_5$	15	22	20	19



**Figure 5. Optimized stress distribution of the shield beam**



**Figure 6. Optimized deformation of the shield beam**

**Conclusions**

(1) Based on the response surface method, the structural optimization on shield beam is proposed. And the response surface method and the finite element analysis are applied for shield beam structure optimization. The shield beam sectional dimension of a certain type Hydraulic Support is optimized to verify the practicality of the method.

(2) The independent variables of response surface function are chosen according to sectional dimensions of shield beam, and the experiment design is carried out by using uniform experimental methods. The least-square is used to fit the response surface function, which can approximately reflect the relation between the sectional dimension and the maximum stress.

(3) Since the response surface function fitting is independent of the specific structure shape, the method has a certain universality and can be applied to other structures optimization for hydraulic support.

### References

- Liu, W.W. (2007), A mechanical analysis and the design of the main structural on the main top coal hydraulic powered support. *The master thesis of Liaoning Technical University*.
- Yao, X.Y. (2011a), An reeseach for structural optimization design of hydraulic support's shield beam. *The master thesis of Zhengzhou University*.
- Liang, J., Xu, J.S., Xie, J. etc. (2010), Hull lines automatic optimization based on design space exploration. *Journal of Ship Mechanics*, 7, pp. 50-64.
- Kleijnen, P.C. (2005a), An overview of the design and analysis of simulation experiments for sensitivity analysis. *European Journal of Operational Research*, 164, pp. 287-300.
- Li, X., Li, W.J. and Peng, C.Y. (2005b), Response surface methodology based on uniform design and its application to complex engineering system optimization. *Mechanical Science and Technology*, 24, pp. 575-616.
- Akira Todoroki and Tetsuya Ishikawa. (2004), Design of experiments for stacking sequence optimizations with genetic algorithm using response surface approximation. *Composite Structures*, 64, pp. 349-357.
- Qin, D.C., Yao, X.Y., Wu, H.X., etc. (2011b), Finite element analysis of hydraulic support caving shield based on Pro/E and ANSYS. *Coal Mine Machinery*, 32, pp. 94-96.
- Zhu, Q., Qin, D.C. and Yao, X.Y. (2012), Study on structural optimization of hydraulic support caving shield using ANSYS. *Coal Mine Machinery*, 33, pp. 2-4.

## An Effective Level Set-based Method for the Design of Extrudable Structures

H. Li<sup>1</sup>, \*L. Gao<sup>1</sup>, P.G. Li<sup>1</sup> and T. Wu<sup>2</sup>

<sup>1</sup> School of Mechanical Science & Engineering, Huazhong University of Science and Technology, China

<sup>2</sup> School of Software Engineering, Huazhong University of Science and Technology, China

\*Corresponding author: gaoliang@mail.hust.edu.cn

### Abstract

Extrusion is a manufacturing technique that creates products with constant cross sections. The extrusion process is widely employed to reduce cost. The conventional structure optimization approaches are typically failed to deal with this particular manufacture constraint. Therefore, this paper presents an effective level set method for the optimal design of structures with extrusion constraint. The free boundary of the structure is embedded into a higher-dimensional level set function, which can be used to implement the structural shape and topology optimization simultaneously. The compactly supported radial basis functions (CS-RBFs) are introduced to convert the conventional level set method to an easier parameterization form. Discrete wavelets transform (DWT) approximation is utilized to produce a sparser linear system to accelerate the fitting and evaluation operations arise from the parametric formulation. Furthermore, a cross section projection strategy is applied to reduce the design variables and satisfy the extrusion constraint. Several numerical examples are provided.

**Keywords:** Level set method, Radial basis functions, Parameterization, Discrete wavelets transform, Extrusion constraint purposes.

### Introduction

Manufacturing significantly influences the cost in a product. The extrusion process is introduced to be an effective technique to reduce the cost of production. In the extrusion manufacturing process, materials are squeezed through an orifice of the required shape in a die by using the pressure from a ram. The primary fact of enforcing this process is to keep the same cross-sections along the extrusion path. It is suggested that one should take care of the manufacturing issues in the early stage of the design cycle, in order to save the development costs and shorten the research time.

Structural topology optimization is identified as one of the most effective tools for improving the performance of structures. This topic has experienced remarkable progress in various engineering areas during the past decades (Bendsøe and Kikuchi, 1988; Rozvany, 2008). Nevertheless, these research works are mainly focused on optimizing the structural performance, and only a few amounts of them consider the other aspect in the design of structures – manufacturing. For an extrudable product, it means that we must simultaneously optimize the performance of a structure and guarantee the structure has the constant geometries along the fixed path to satisfy the extrusion constraint.

Several studies have been made for solving the optimization problems with extrusion constraints. Kim and Kim (2000) were among the earliest researchers who studied the topology optimization of beam cross-section. Zhou et al. (2002) proposed the mathematical formulation for the topology optimization with extrusion constraint, which is embedded in the software Optistruct. Ishii and Aomura (2004) utilized the homogenization method to solve the extrusion-based structural optimization problem. Liu et al. (2007) solved the beam cross-sectional optimization problems considering warping of sections and coupling among deformations by using the SIMP-based approach. Patel et al. (2009) proposed a methodology by using the hybrid cellular automaton method to handle the extrusion-based nonlinear transient design problems. Zuberi et al. (2009) investigated the influence of different configuration and location of the boundary conditions on the optimal results for the extrudable designs.

In this study, we present an effective parametric level set method for the design of extrudable structures. The DWT is incorporated into the CSRBF-based level set formulation to achieve an extremely sparse linear system for the interpolation. It transforms the collection matrix into a wavelet basis, and then compresses this matrix with very few nonzero elements via thresholding. The extrusion constraint is satisfied by an elaborated strategy called cross section projection.

### Implicit free boundary representation

The level set method implicitly models the motion of free boundary of a structure via the Lipschitz-continuous scalar function, and the structural boundary can be interpreted by the zero iso-surface of the one-higher dimensional level set function. Assume that  $\Omega \subset R^d$  ( $d = 2 \text{ or } 3$ ) is the space occupied by a structure, each part of the domain can be defined with the level set function as:

$$\begin{cases} \Phi(\mathbf{x}) > 0 \Leftrightarrow \forall \mathbf{x} \in \Omega \setminus \partial\Omega & \text{(solid)} \\ \Phi(\mathbf{x}) = 0 \Leftrightarrow \forall \mathbf{x} \in \partial\Omega \cap D & \text{(boundary)} \\ \Phi(\mathbf{x}) < 0 \Leftrightarrow \forall \mathbf{x} \in D \setminus \Omega & \text{(hole)} \end{cases} \quad (1)$$

where  $D$  is a pre-defined design domain where all admissible shapes  $\Omega$  are included, i.e.  $\Omega \subseteq D$ .

In order to dynamically drive the free boundary, introducing the pseudo-time  $t$  into the level set function leads to following first-order Hamilton-Jacobi PDE:

$$\frac{\partial \Phi(\mathbf{x}, t)}{\partial t} + \mathbf{v}_n(\mathbf{x}) |\nabla \Phi(\mathbf{x}, t)| = 0, \quad \Phi(\mathbf{x}, 0) = \Phi_0(\mathbf{x}) \quad (2)$$

where  $\mathbf{v}_n(\mathbf{x})$  is the normal velocity associated with the sensitivity of the objective function with respect to the boundary variation. Moving the structural boundary  $\Phi(\mathbf{x}, 0)$  along the normal direction  $\mathbf{n}$  is equivalent to update the values of level set function via solving the Hamilton-Jacobi PDE with proper numerical schemes.

An important issue of the conventional level set method is that the explicit analytical form of the level set function is unknown. As a result, to solve the Hamilton-Jacobi PDE on the fixed Eulerian grids and obtain the discrete level set values, one should conquer the numerical difficulties in handling the complicated PDEs, including the CFL condition, re-initializations of level-set surface and velocity extensions (Wang, Wang et al., 2003; Allaire, Jouve et al., 2004).

### Level set parameterization

To overcome the unfavorable numerical features in the standard level set method, the parametric level set formulation has been developed as an alternative. In this paper, the CSRBFs are used to parameterize the level set-based optimization model. The CSRBF is a kind of radial symmetrically function centered at a particular knot with compact support (Wendland, 2006), which is widely applied to interpolate massive scatter data. Comparing with the globally supported kernels or the piecewise polynomials, the CSRBFs have several attractive features, such as strictly definiteness, sparseness of interpolant matrix, desirable smoothness of the partial derivatives and so on.

Here, we adopt the CSRBF with C2 continuity of Wendland' series, in that it can be utilized to interpolate the level set function with favorable smoothness and desired completeness when the knots are dense enough (Luo, Wang et al., 2008). The Wendland function with C2 continuity, whose shapes are plotted in Fig. 1, is given as follows:

$$\psi(r) = \max\{0, (1-r)^4\} (4r+1) \quad (3)$$

and its derivatives in the X and Y direction are stated respectively as:

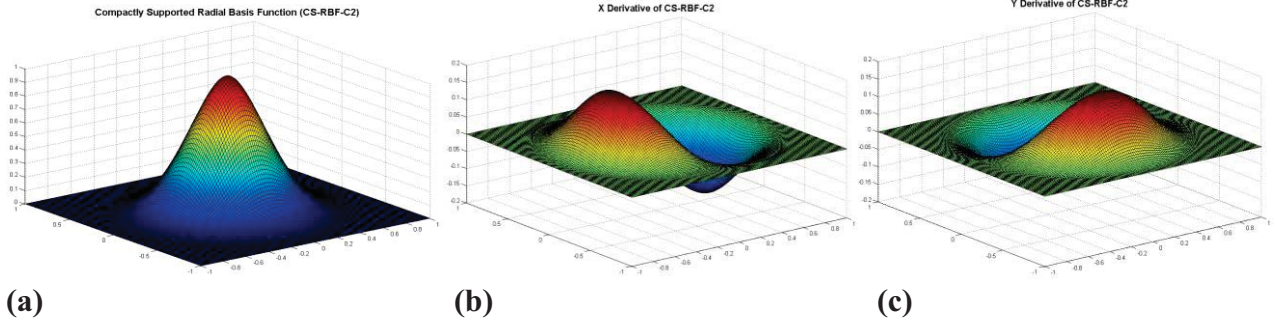
$$\frac{\partial \psi}{\partial x} = \frac{\partial \psi}{\partial r} \frac{\partial r}{\partial x} = \max\left\{0, (1-r)^3 (-20r) \frac{\partial r}{\partial x}\right\} \quad (4)$$

$$\frac{\partial \psi}{\partial y} = \frac{\partial \psi}{\partial r} \frac{\partial r}{\partial y} = \max\left\{0, (1-r)^3 (-20r) \frac{\partial r}{\partial y}\right\} \quad (5)$$

where  $r$  is the radius of support, which is defined in a 2D Euclidean space as:

$$r = \frac{d_I}{R} = \frac{\sqrt{(x-x_i)^2 + (y-y_i)^2}}{R} \quad (6)$$

The parameter  $R$  is introduced to determine the compact support size at each knot. It is suggested that a too small radius may lead to singular stiffness matrix, and a too large radius would obviously increase the computation time. Therefore, an experiential criterion in selecting a radius of support is used (Luo, Tong et al., 2009).



**Figure 1. CSRBF with C2 continuity and its derivatives: (a) shape of CSRBF; (b) X derivative of CSRBF; (c) Y derivative of CSRBF.**

Now, we aim at interpolating the level set function with the CSRBFs. For simplicity, the level set grids are assumed to be identical with the meshes for finite element analysis, which are consisting of  $N$  individual nodes or knots. For the CSRBF kernels, we rewrite them in the vector form as:

$$\boldsymbol{\psi}(\mathbf{x}) = [\psi_1(\mathbf{x}), \psi_2(\mathbf{x}), \dots, \psi_N(\mathbf{x})]^T \in \mathbb{R}^N \quad (7)$$

and the expansion coefficients served as the design variables are given as:

$$\boldsymbol{\alpha}(\mathbf{t}) = [\alpha_1(t), \alpha_2(t), \dots, \alpha_N(t)]^T \in \mathbb{R}^N \quad (8)$$

It is obviously that the coefficients  $\boldsymbol{\alpha}$  are time-dependent, and the CSRBFs are only space-dependent. The originally coupled level set function can be separated of time and space by the product of a matrix and a vector:

$$\boldsymbol{\Phi} = \mathbf{A}\boldsymbol{\alpha}, \text{ where } \boldsymbol{\Phi} = [\Phi_1, \Phi_2, \dots, \Phi_N]^T \quad (9)$$

In Equation (8), the matrix  $\mathbf{A}$  is theoretically invertible, and can be expressed as:

$$\mathbf{A} = \begin{bmatrix} \boldsymbol{\psi}^T(x_1) \\ \boldsymbol{\psi}^T(x_2) \\ \dots \\ \boldsymbol{\psi}^T(x_N) \end{bmatrix} = \begin{bmatrix} \psi_1(x_1) & \psi_2(x_1) & \dots & \psi_N(x_1) \\ \psi_1(x_2) & \psi_2(x_2) & \dots & \psi_N(x_2) \\ \dots & \dots & \dots & \dots \\ \psi_1(x_N) & \psi_2(x_N) & \dots & \psi_N(x_N) \end{bmatrix} \quad (10)$$

It should be pointed out that for the initialization of the optimization, one must, firstly, solve the following system to obtain the initial value of expansion coefficients:

$$\boldsymbol{\alpha} = \mathbf{A}^{-1}\boldsymbol{\Phi}_0 \quad (11)$$

where  $\boldsymbol{\Phi}_0$  are the pre-determined discrete level set values before the iteration.

With regard to the Hamilton-Jacobi PDE, it can be rewritten with the CSRBF approximation as:

$$\boldsymbol{\psi}^T(\mathbf{x}) \frac{d\boldsymbol{\alpha}(t)}{dt} + \mathbf{v}_n \cdot |\nabla \boldsymbol{\psi}^T(\mathbf{x})\boldsymbol{\alpha}(t)| = 0 \quad (12)$$

Hereto, the conventional level set method has been converted into a parametric one without losing any of its favorable characteristics, and the well-established gradient-based approaches can be conveniently applied to deal with the parameterization formulation.

### Matrix compression

In this section, we discuss the large-scale linear system arisen from the RBF interpolant. Let us consider the Eq. (9) and (11). It is easy to notice that for the large system, especially with the 3D structural optimization problems, more zeros in the matrix  $\mathbf{A}$  means less computational cost as well

as less computer storage for solving the system. We can expect that CSRBFs will somewhat reduce the impediments caused by the fully dense matrix, but it is not satisfied. Here, a DWT-based matrix compression technique is introduced to produce much sparser linear system.

DWT is worked as fast linear operation acting on a data vector or matrix, and transforms it into a numerically disparate vector or matrix with the wavelet basis. The new vector or matrix is always of the same size with the original one. This technique has been successfully implemented in the field of image/video processing, signal analysis, computer vision and so on (Mallat, 1989). In recent years, its application has been extended into solving the fully populated linear system (Chen, 1999; Ravnik, Škerget et al., 2004).

In this paper, the Haar wavelet is adopted due to its non-overlapping support and constant scaling function (Ravnik, Škerget et al., 2004). To facilitate the discussion, we introduce the  $\mathbf{W}$  matrix that is defined in previous work by the authors (Chen, 1999; Ford and Tyrtshnikov, 2003). The orthogonal matrix  $\mathbf{W}$  can be used to convert the vector from the standard basis to the wavelet basis. Considering the three components within the system defined in Eq. (9), we can transform the vectors into wavelet forms as:

$$\bar{\alpha} = \mathbf{W} \cdot \alpha \quad (13)$$

$$\bar{\Phi} = \mathbf{W} \cdot \Phi \quad (14)$$

and the matrix can be given as:

$$\bar{\mathbf{A}} = \mathbf{W} \cdot \mathbf{A} \cdot \mathbf{W}^T \quad (15)$$

From Eq. (9) we get

$$\mathbf{W} \cdot \mathbf{A} \cdot (\mathbf{W}^T \cdot \mathbf{W}) \cdot \alpha = \mathbf{W} \cdot \Phi \quad (16)$$

Substituting Eq. (13)-(15) into Eq. (16), it yields:

$$\bar{\mathbf{A}} \cdot \bar{\alpha} = \bar{\Phi} \quad (17)$$

Since the elements in original matrix  $\mathbf{A}$  have smoothly variational values, there are only a few important coefficients in the wavelet representation  $\bar{\mathbf{A}}$ . In other words, we can zero out the elements with redundant information in  $\bar{\mathbf{A}}$  by means of hard thresholding. In this study, we determine the adaptive threshold using the scheme described in the work by Ravnik et al. (2004), and eliminate the non-zero elements with the absolute values less than the threshold.

Therefore, an extremely sparse system consisting of matrix  $\bar{\mathbf{A}}^*$  is obtained after denoising:

$$\bar{\mathbf{A}}^* \cdot \bar{\alpha} = \bar{\Phi} \quad (18)$$

Eventually, the value of level set function and expansion coefficients can be determined by the reconstruction operator as:

$$\alpha = \mathbf{W}^T \cdot \bar{\alpha} \text{ or } \Phi = \mathbf{W}^T \cdot \bar{\Phi} \quad (19)$$

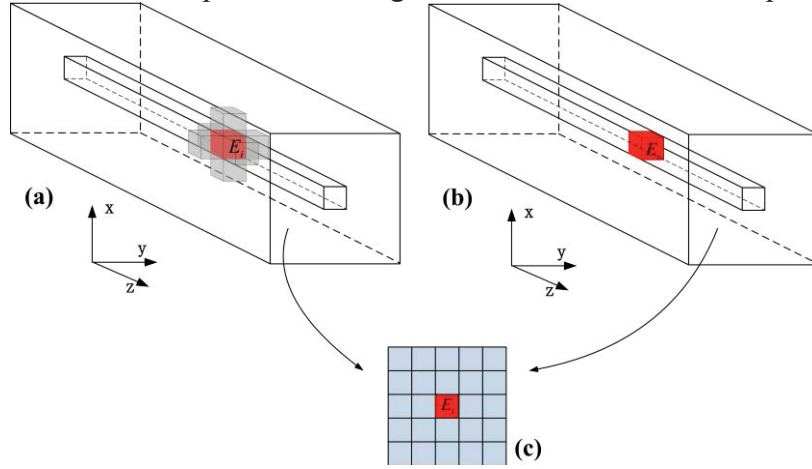
It is expected that incorporating DWT-based scheme into CSRBF interpolation can produce an easily-solved linear system with much less computational cost and computer storage.

### Extrusion based optimization design

In this section, we take the minimum strain energy problem considering the extrusion constraint as an example. Generally, if an extrudable design is required, one must ensure that the cross-sections along a specified path are kept constant. Regarding the level set-based approach, it means the discrete level set values at the corresponding knots within the structural cross sections must be identical to maintain the same level set surface along the extrusion path. Thus, the extrusion-based compliance optimization problem is established as:

$$\begin{aligned}
& \underset{(u, \Phi)}{\text{Minimize}} : J(u, \Phi) = \int_D f(u) H(\Phi) d\Omega \\
& \text{Subject to} : a(u, v, \Phi) = l(v, \Phi), \forall v \in U, u|_{\partial\Omega} = u_0 \\
& G(u, \Phi) = \int_D H(\Phi) d\Omega - V_{\max} \leq 0 \\
& (\Phi_i = \Phi_j = \dots = \Phi_{ne})_k, \quad k = 1, 2, \dots, K
\end{aligned} \tag{20}$$

where  $J$  is the objective function and  $G$  is the global volume constraint with an upper bound of  $V_{\max}$ , respectively.  $H$  is the Heaviside function associated with the implicit level set  $\Phi$ .  $K$  denotes the number of elements in a single cross section, and  $ne$  represents the number of elements along the path of the extrusion. The main problem in this formulation is that too many extra constraints are introduced, which will cause complicated solving scheme and exorbitant computational effort.



**Figure 2. The cross section projection strategy: (a) the adjacent elements; (b) the parallel elements; (c) the projection plane.**

As a result, we propose the cross section projection strategy to model the structural optimization problem with extrusion constraint. In the presented method, we aim at mapping the elements in 3D space to a relative 2D projected plane shown in Fig. 2. Generally, we consider two types of elements in the 3D FE model, i.e. the adjacent elements and the parallel elements. The adjacent elements are defined as the elements in a fixed neighborhood of individual element  $E_i$ , and the parallel elements are considered as the elements along the same extrusion axis of element  $E_i$ . To implement the cross section projection strategy, we must aggregate the influences from the above-mentioned two types of elements to  $E_i$  via two specified operation.

For the bilinear functional, we firstly handle the influence from adjacent elements:

$$\bar{a}(u, v, \Phi)_i = \frac{1}{\sum_{j=1}^{nae} w(i, j)} \sum_{j=1}^{nae} \left[ w(i, j) \left( \int_{D_{E_i}} (\varepsilon(v_j))^T C(E_i) \varepsilon(u_i) H(\Phi_i) d\Omega_{E_i} \right) \right], \tag{21}$$

$$w(i, j) = rd - dist(i, j)$$

and then the influence from the parallel elements:

$$a_p(u, v, \Phi) = \sum_{k=1}^K \left\{ \sum_{i=1}^{ne} \bar{a}(u, v, \Phi)_i / ne \right\}_k \tag{22}$$

In Equation (21) and (22),  $\Omega_{E_i}$  is the sub-domain occupied by element  $E_i$ .  $w(i, j)$  is the weight coefficient determined by the radius of neighborhood and the distance between the relatively adjacent elements, i.e.  $rd$  and  $dist(i, j)$ .  $nae$  represents the number of adjacent elements within radius  $rd$ .

Similarly, the loading functional is given by the aforementioned two steps:



$$\bar{l}(v, \Phi)_i = \frac{1}{\sum_{j=1}^{nae} w(i, j)} \sum_{j=1}^{nae} w(i, j) \left[ \int_{D_{Ei}} pvH(\Phi_i) d\Omega_{Ei} + \int_{\Gamma_{Ei}} \tau v H d\Gamma_{Ei} \right] \quad (23)$$

$$l_p(v, \Phi) = \sum_{k=1}^K \left\{ \sum_{i=1}^{ne} \bar{l}(v, \Phi)_i / ne \right\}_k \quad (24)$$

Hereto, the new model for extrusion-based topology optimization can be stated as:

$$\begin{aligned} \text{Minimize : } J_p(u, \Phi) &= \int_{D_p} f(u)H(\Phi) d\Omega_p \\ \text{Subject to : } a_p(u, v, \Phi) &= l_p(v, \Phi), \forall v \in U_p, u|_{\partial\Omega_p} = u_0 \end{aligned} \quad (25)$$

$$G_p(u, \Phi) = \int_{D_p} H(\Phi) d\Omega_p - V_{\max} \leq 0$$

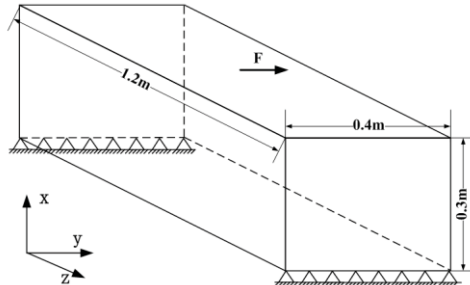
We remark that in Eq. (25), there are no manufacturing constraints explicitly existing. Further, since that the search space of the optimization is within a 2D domain, we only need to update a reduced set of design variables with the global volume constraint. However, a 3D finite element analysis is still needed to measure the performance of the entire structure.

### Numerical examples

In this section, the proposed method is applied to two 3D examples. The well-established optimality criteria (OC) method (Luo, Tong et al., 2009) is utilized as a numerical solution for these structural compliance optimization problems. The iteration is terminated when the prescribed tolerance  $TOL=10^{-2}$  for the difference of two successive objective values is achieved, or the maximum iteration  $T=200$  is reached. It is noted that all the computations are done with MATLAB, and are processed in a computer configured with a CPU 2.67 GHz processor as well as a 4 GB RAM.

We assume that the Young's modulus for solid material is 180GPa and for void material is 0.001Pa. The Possion's ratio for the elastic material is 0.3. The 'ersatz material' model is adopted to evaluate the strain energies on the discontinued boundary without remeshing.

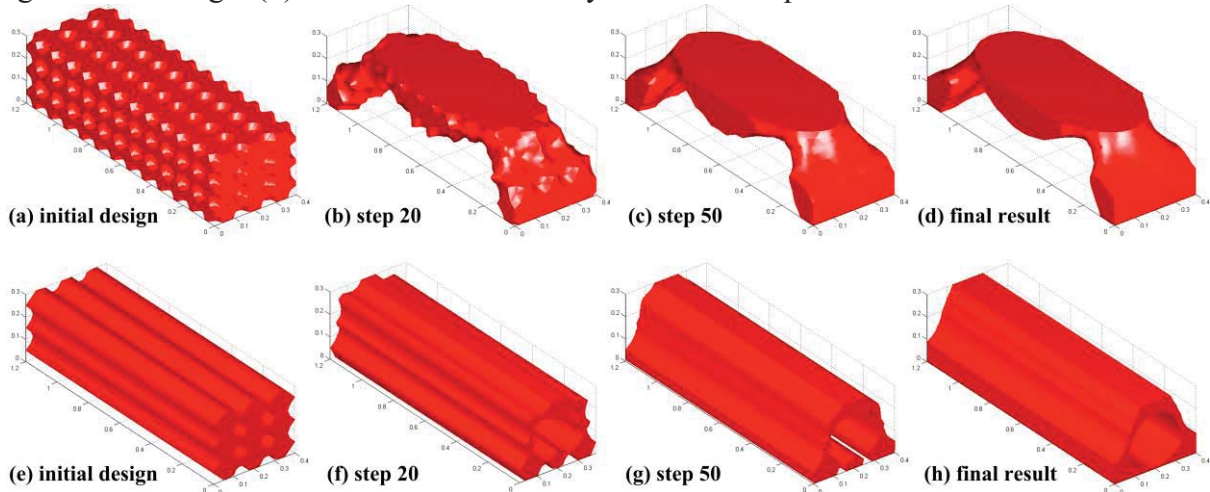
We consider the minimum compliance problem for a 3D structure, shown in Fig. 3. The design domain is a beam of size  $0.3m \times 0.4m \times 1.2m$  with the two edges at the bottom face being fixed as the Dirichlet boundary. An external force  $F=400kN$  loaded at the center of the top face along the y axis is defined as the non-homogeneous Neumann boundary. The limit of material usage is set to 35% in volume fraction. The radius of support for CSRBF is 3.5. For the finite element analysis, we discretize the entire structure with  $12 \times 16 \times 48$  tri-linear 8-node cube elements.



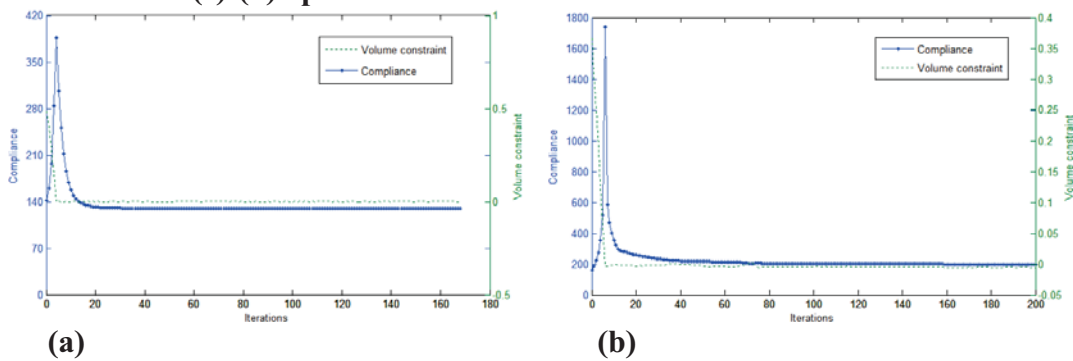
**Figure 3. The 3D design domain**

In the first example, the optimization problem is solved without considering extrusion constraint. We use the improved parametric level set method to model the 3D structure design problem. The percentage of zero elements in above-mentioned matrix  $\mathbf{A}$ , whose size is  $10829 \times 10829$ , is 98.86%. In other words, only a few nonzero elements are needed to give a good enough approximation of the entire level set surface. Fig. 4(a)-(d) show the evolution of structural boundary. It should be noticed

that several regular holes are added factitiously into the rectangular solid in order to speed up the optimization process, and the optimal design achieved by shape fidelity and topological changes via deleting the voids and adding new voids inside the design domain. It is obviously that the final design shown in Fig. 4(d) cannot be fabricated by the extrusion process.



**Figure 4. Process of the optimization: (a)-(d) optimization without the extrusion constraint; (e)-(h) optimization with the extrusion constraint.**



**Figure 5. Convergence histories: (a) without extrusion constraint; (b) with extrusion constraint.**

In the second example, we consider the design problem with extrusion constraint. We assume that the extrusion path is along the Z axis, and the process of optimization can be seen in Fig. 4(e)-(h). We remark that the initial design (shown in Fig. 4(e)) is quite different from that in the first example, which contains several holes penetrating the entire structure along the extrusion direction to maintain the uniform cross section from the very beginning. Comparing to the first example, the cross-sections in this example are always kept constant during iteration, due to that the optimization is only applied to a 2D projected domain. The optimal design shown in Fig. 4(h) can be manufactured by the extrusion technique along the Z axis.

The iterative histories for the two examples are given in Fig. 5. It takes 167 steps to complete the optimization for the first example, and 200 steps to achieve the optimal design for the second example. The optimal results for the two examples are 129.65 and 197.79, respectively. The compliance in the case without extrusion constraint is smaller than that of the extrusion-based case, in that the manufacturing constraint will reduce the flexibility in the distribution of materials. Moreover, the CPU time of the problem with extrusion constraint is approximately 175.48s per step, which is much less than that of the first example (230.51s per step). It is because that the proposed cross section projection strategy reduces the numbers of design variables to a great extent.

## Conclusions

In this study, an effective level set-based parameterization method has been proposed for 3D structures with extrusion constraint. The DWT scheme is incorporated into the CSRBF-based parametric level set model to produce an extremely sparse system. The numerical stability and volume conservative prove its effectiveness. A cross section projection strategy is developed to convert the extrusion-based 3D structure optimization to the 2D issue with fewer numbers of design variables. Two numerical examples in 3D are provided. The numerical results show that the final design can be manufactured by the extrusion process.

## Acknowledgments

This work is supported by the National Natural Science Foundation of China (Grant No. 51175197) and the Open Research Fund Program (No. 31115020) of the State Key Laboratory of Advanced Design and Manufacturing for Vehicle Body, Hunan University, China.

## References

- Allaire, G., Jouve, F. and Toader, A. M. (2004), Structural optimization using sensitivity analysis and a level-set method. *Journal of Computational Physics*, 194(1), pp. 363-393.
- Bendsøe, M. P. and Kikuchi, N. (1988), Generating optimal topology in structural design using a homogenization method. *Computer Methods in Applied Mechanics and Engineering*, 71, pp. 197-224.
- Chen, K. (1999), Discrete wavelet transforms accelerated sparse preconditioners for dense boundary element systems. *Electronic Transaction Numerical Analysis*, 8, pp. 138-153.
- Ford, J. M. and Tyrtshnikov, E. E. (2003), Combining Kronecker product approximation with discrete wavelet transforms to solve dense, function-related linear systems. *SIAM Journal on Scientific Computing*, 25(3), pp. 961-981.
- Ishii, K. and Aomura, S. (2004), Topology optimization for the extruded three dimensional structure with constant cross section. *JSME International Journal Series A Solid Mechanics and Material Engineering*, 47(2), pp. 198-206.
- Kim, Y. Y. and Kim, T. S. (2000), Topology optimization of beam cross sections. *International Journal of Solids and Structures*, 37, pp. 477-493.
- Liu, S. T., An, X. M. and Jia, H. P. (2007), Topology optimization of beam cross-section considering warping deformation. *Structural and Multidisciplinary Optimization*, 35(5), pp. 403-411.
- Luo, Z., Tong, L. Y. and Kang, Z. (2009), A level set method for structural shape and topology optimization using radial basis functions. *Computers & Structures*, 87(7-8), pp. 425-434.
- Luo, Z., Wang, M. Y., Wang, S. and Wei, P. (2008), A level set-based parameterization method for structural shape and topology optimization. *International Journal for Numerical Methods in Engineering*, 76(1), pp. 1-26.
- Mallat, S. G. (1989), A theory for multiresolution signal decomposition: the wavelet representation. *IEEE Transactions on Pattern Analysis and Machine Intelligence*, 11(7), pp. 674-693.
- Patel, N. M., Penninger, C. L. and Renaud, J. E. (2009), Topology optimization for synthesizing extrusion based nonlinear transient designs. *Journal of Mechanical Design*, 131(6), pp. 061003.
- Ravnik, J., Škerget, L. and Hriberšek, M. (2004), The wavelet transform for BEM computational fluid dynamics. *Engineering Analysis with Boundary Elements*, 28(11), pp. 1303-1314.
- Rozvany, G. I. N. (2008), A critical review of established methods of structural topology optimization. *Structural and Multidisciplinary Optimization*, 37(3), pp. 217-237.
- Wang, M. Y., Wang, X. and Guo, D. (2003), A level set method for structural topology optimization. *Computer Methods in Applied Mechanics and Engineering*, 192, pp. 227-246.
- Wendland, H. (2006), Computational aspects of radial basis function approximation, Topics in Multivariate Approximation and Interpolation. *Studies in Computational Mathematics*, 12, pp. 231-256.
- Zhou, M., Fleury, R., Shyy, Y. K., Thomas, H. L. and Brennan J. M. (2002), Progress in topology optimization with manufacturing constraints. *9th AIAA/ISSMO Symposium on Multidisciplinary Analysis and Optimization*, Atlanta.
- Zuberi, R. H., Zuo, Z. X. and Long, K. (2009). Topological optimization of beam cross section by employing extrusion constraint. *ISCMII and EPMESCXII*, Hong Kong-Macau.

## Substructure dual reciprocity boundary element method for prediction of acoustic attenuation performance of silencers with potential flow

X. H. Miao, \*X. R. Wang, D. Jia, D. J. Qian, and F. Z. Pang

Naval Academy of Armament  
Liuliqiao of FengTai District, Beijing, 100161, China,  
\*Corresponding author: wangxueren@aliyun.com

### Abstract

The complex flow and sound fields inside silencers require a three-dimensional numerical method for the accurate prediction of acoustic attenuation performance of silencers. In the present study, the dual reciprocity boundary element method (DRBEM) is developed to predict and analyze the acoustic characteristics of the ducts and silencers with complex three-dimensional potential flow. Compared to the conventional boundary element method (CBEM), the DRBEM takes into account the second order terms of flow Mach number in the acoustic governing equation, which is suitable for the acoustic analysis of ducts and silencers with higher Mach number subsonic flow. In order to overcome the singularity in the single domain BEM for complex silencer analysis, the substructure approach is used. Predictions of four-pole parameters and transmission loss of a conical duct and a single expansion chamber silencer are compared with experimental results to verify the validity of the present method. The effects of complex three-dimensional potential flow on the acoustic attenuation performance of double expansion chamber silencers are examined.

**Keywords:** DRBEM, Silencer, Acoustic attenuation performance, Potential flow.

### Introduction

In the engine exhaust silencing systems, the presence of exhaust gas flow will influence the sound propagation inside the systems, and therefore may affect the acoustic attenuation performance of the silencers [1]. In view of the complex flow and sound fields inside the silencers, a three-dimensional numerical method is needed for the accurate prediction of the acoustic attenuation performance of silencers. The boundary element method (BEM) is an effective and powerful numerical tool, and has been developed to predict the acoustic attenuation performance of silencers without flow [2], with uniform flow [3] and low Mach number non-uniform flow [4]. However, the CBEM is not suitable for solving the acoustic problems of silencers with higher Mach number subsonic flow, due to the presence of domain integral.

The dual reciprocity method (DRM) [5] is an effective technique to convert the domain integral into the boundary integral. Applying the DRM to BEM forms the so-called dual reciprocity boundary element method. This method was initially developed by Nardini and Brebbia [5] and applied to the two-dimensional elasto-dynamics. A comprehensive description of its application in problems governed by Poisson equation was given by Partridge et al [6]. Now the DRBEM has been applied successfully to linear and nonlinear problems including structure vibration, elasto-dynamics, heat transfer and etc. The governing equations of those problems have to be transformed into Poisson equations when applying the DRBEM to them. Helmholtz equation can also be transformed into Poisson equation. However, it is necessary to deal with Helmholtz equation directly to meet special boundary conditions in some cases. Chen et al [7] and Golberg et al [8] developed the DRBEM to deal with the practical problems governed by Helmholtz equations by finding their particular solutions.

Lee, et al [9] applied the DRBEM to calculate the acoustic radiation in a subsonic non-uniform flow field, and indicated that the Sommerfeld-radiation condition at infinite is satisfied when DRBEM is used to deal with this problem. They supposed that non-uniform flow only existed partially and uniform flow existed in the other area. The flow field inside the silencers is full non-uniform usually and the application of DRBEM to predict acoustic attenuation performance of silencers with complex three-dimensional potential flow has not been reported in the literature.

The objective of the present study is to develop the DRBEM to compute and analyze problems of sound propagation and attenuation in the three-dimensional potential flow.

## GOVERNING EQUATIONS

### *DRBEM for Acoustic Governing Equation*

The acoustic governing equation in the three-dimensional potential flow field [10]

$$\nabla^2 \Phi + k^2 \Phi - j2k(\mathbf{M} \cdot \nabla \Phi) - (\mathbf{M} \cdot \nabla)(\mathbf{M} \cdot \nabla \Phi) = 0 \quad (1)$$

The particle velocity  $\mathbf{u}$  and the sound pressure  $p$  may be expressed in terms of the acoustic velocity potential  $\Phi$  as:

$$p = \rho_0(j\omega\Phi + \mathbf{V}_0 \cdot \nabla \Phi) \quad (2)$$

$$\mathbf{u} = -\nabla \Phi \quad (3)$$

where  $\rho_0$  is the density of medium.

Moving all terms involving the flow in Eq. (1) to the right-hand side yields

$$\nabla^2 \Phi + k^2 \Phi = b(\Phi) \quad (4)$$

where

$$b(\Phi) = j2k(\mathbf{M} \cdot \nabla \Phi) + (\mathbf{M} \cdot \nabla)(\mathbf{M} \cdot \nabla \Phi) \quad (5)$$

The integral formulation of Eq. (4) may be expressed as [9]

$$C(P)\Phi(P) = \int_s (G \frac{\partial \Phi}{\partial n} - \Phi \frac{\partial G}{\partial n}) dS - \int_v G b(\Phi) dV \quad (6)$$

where

$$C(P) = \int_s \frac{\partial G_L}{\partial n} dS \quad (7)$$

$G_L$  is the fundamental solution of Laplace equation, and  $G$  is the fundamental solution of Helmholtz equation.

Eq. (6) contains volume integral, which may be converted to the boundary integral by using DRM.  $b(\Phi)$  may be approximated by the following expression

$$b(\Phi) = \sum_{i=1}^{N+L} \alpha_i f_i \quad (8)$$

where  $\alpha_i$  are the undetermined coefficients,  $f_i$  are the simple source (approximate) functions. For each point on the boundary and in the volume,  $N$  is the number of collocation points on the boundary, and  $L$  is the number of collocation points in the volume. Reconstructing Eq. (8) leads the following matrix

$$\mathbf{b} = \mathbf{F}\boldsymbol{\alpha} \quad (9)$$

where  $\mathbf{b}$  is an  $(N+L) \times 1$  vector that contains the function values of  $b$  at the collocation points,  $\mathbf{F}$  is an  $(N+L) \times (N+L)$  matrix, and  $\boldsymbol{\alpha}$  is an  $(N+L) \times 1$  coefficient vector. For each simple source function  $f_i$ , a particular solution  $\varphi_i$  needs to be found and satisfied

$$\nabla^2 \varphi_i + k^2 \varphi_i = f_i \quad (10)$$

One of the key ingredients of the dual reciprocity method is the expansion introduced in Eq. (8). There are virtually an infinite number of ways to choose  $f_i$  for use in the expansion. The trouble is that we have to find the associated particular solution  $\varphi_i$  for each choice of  $f_i$ . The usual practice is to construct  $\varphi_i$  first and then find  $f_i$  from Eq. (10).

In the dual reciprocity method,  $f_i$  is chosen usually as [6]

$$f_i = 1 + r_i \quad (11)$$

For the problem in the present study, the following particular solution  $\varphi_i$  [7, 11] is chosen

$$\varphi_i = \begin{cases} -\frac{2}{k^4 r_i} + \frac{1+r_i}{k^2} + \frac{2 \cos(kr_i)}{k^4 r_i} & r_i \neq 0 \\ \frac{1}{k^2} & r_i = 0 \end{cases} \quad (12)$$

where  $r_i = \sqrt{(x-x_i)^2 + (y-y_i)^2 + (z-z_i)^2}$ .

Substituting Eqs. (8) and (10) into Eq. (6) yields:

$$\begin{aligned} C(P)\Phi(P) &= \int_S (G \frac{\partial \Phi}{\partial n} - \Phi \frac{\partial G}{\partial n}) dS - \sum_{i=1}^{N+L} \alpha_i \int_V G (\nabla^2 \varphi_i + k^2 \varphi_i) dV \\ &= \int_S (G \frac{\partial \Phi}{\partial n} - \Phi \frac{\partial G}{\partial n}) dS - \sum_{i=1}^{N+L} \alpha_i \left\{ C(P)\varphi_i(P) - \int_S (G \frac{\partial \varphi_i}{\partial n} - \varphi_i \frac{\partial G}{\partial n}) dS \right\} \end{aligned} \quad (13)$$

By using discretization and numerical integration for Eq. (13), and combining Eq. (9), the following algebraic system of equations in matrix form may be obtained

$$\mathbf{H}\Phi - \mathbf{G} \frac{\partial \Phi}{\partial n} = \mathbf{R}\alpha = \mathbf{R}\mathbf{F}^{-1}\mathbf{b} \quad (14)$$

where  $\mathbf{H}$  and  $\mathbf{G}$  are the BEM coefficient matrices,  $\mathbf{R}$  is a matrix obtained by integrating the known particular integral contained in  $\{ \}$  of Eq. (13). From Eq. (5), it may be seen that  $b$  is a function of the first- and second-order derivatives of  $\Phi$ . The derivatives of  $\Phi$  can be obtained by first introducing a set of global interpolating functions for  $\Phi$  and then differentiating the interpolating functions, therefore the values of  $b$  at each point may be determined. We choose

$$\Phi = \mathbf{E}\beta \quad (15)$$

where  $\mathbf{E} = [f_{1ij}]_{(N+L) \times (N+L)}$  is the coefficient matrix formed by the global interpolating functions  $f_{1ij}$ ,  $\beta$  is the undetermined coefficients for each collocation points. Eventually, the nodal values of  $b(\Phi)$  at the collocation points can be written as:

$$\mathbf{b} = \mathbf{B}\Phi \quad (16)$$

where  $\mathbf{B}$  is a coefficient matrix that depends on the choice of  $\mathbf{E}$ . Substituting Eq. (16) into Eq. (10) gives:

$$\mathbf{H}\Phi - \mathbf{G} \frac{\partial \Phi}{\partial n} = \mathbf{R}\alpha = \mathbf{R}\mathbf{F}^{-1}\mathbf{B}\Phi \quad (17)$$

Combining the boundary conditions, Eq. (17) may be solved and the unknown variables are obtained.

The accuracy of the dual reciprocity method will also depend on the choice of  $f_1$  used in the interpolating and differentiating  $\Phi$ . The global interpolating functions contained in  $\mathbf{E}$  should be as simple as possible because differentiation of complicated functions may result in peculiar behaviors. Here we choose

$$f_{1ij} = 1 + r_{ij}^2 + r_{ij}^3 \quad (18)$$

which is suitable for the problems contained derivatives in the source term  $b(\Phi)$  [12], and

$$r_{ij} = \sqrt{(x_i - x_j)^2 + (y_i - y_j)^2 + (z_i - z_j)^2}.$$

### Determination of Acoustic Performance

After the impedance matrix for the silencer is obtained, the four-pole parameters can be evaluated as

$$A = \frac{m \bar{Z}_{11}}{n \bar{Z}_{21}} \quad (19)$$

$$B = \frac{\bar{Z}_{12} - \bar{Z}_{11} \bar{Z}_{22} / \bar{Z}_{21}}{n \rho_0 c_0} \quad (20)$$

$$C = \frac{m \rho_0 c_0}{\bar{Z}_{21}} \quad (21)$$

$$D = -\bar{Z}_{22} / \bar{Z}_{21} \quad (22)$$

where  $\bar{Z}_{11}$ ,  $\bar{Z}_{12}$ ,  $\bar{Z}_{21}$  and  $\bar{Z}_{22}$  are the average values of all coefficients in  $\mathbf{Z}_{11}$ ,  $\mathbf{Z}_{12}$ ,  $\mathbf{Z}_{21}$  and  $\mathbf{Z}_{22}$ , respectively,  $n$  and  $m$  are the number of elements on the inlet and outlet, respectively.

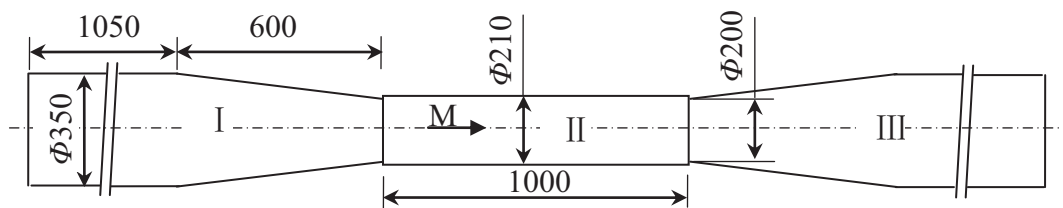
Therefore, transmission loss of the silencer may be determined by using the following expression

$$TL = 20 \log \left| \frac{(A+B+C+D)}{2} \right| + 10 \log \frac{S_i}{S_o} \quad (23)$$

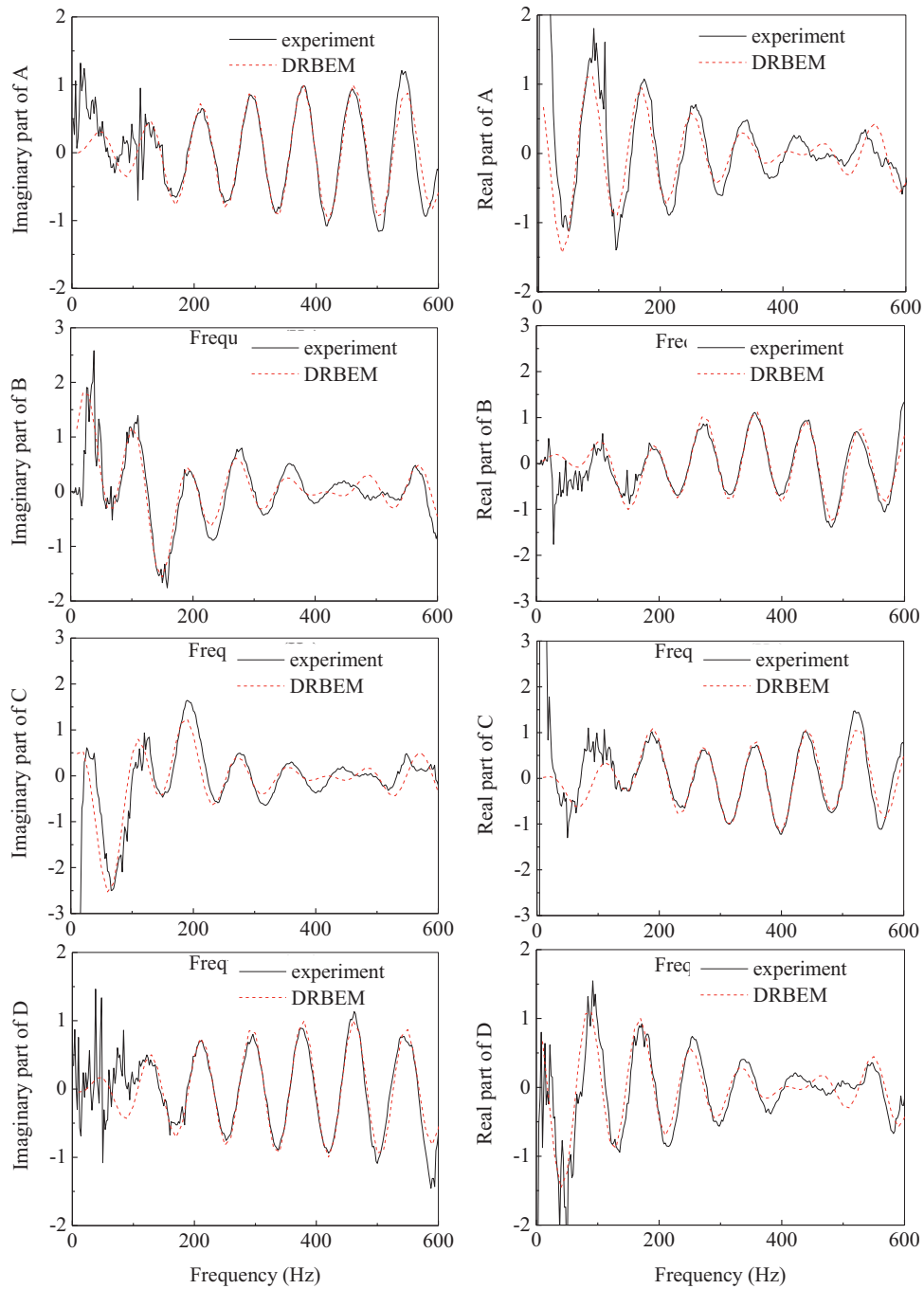
where,  $S_i$  and  $S_o$  are the cross-sectional areas of the inlet and outlet, respectively.

## RESULTS AND DISCUSSION

A conical duct as shown in Fig. 1 is examined first. In order to use the substructure DRBEM, the conical duct is divided into 3 sections denoted by I, II and III. Comparisons of the four-pole parameters are shown in Figs. 2 and 3 when the highest Mach numbers of air flow in the section II are 0.1 and 0.3, respectively. It can be seen that the predictions and experimental results agree well. One reason for the difference between them may be the measurement errors of pressure and temperature. Experimental results under 100Hz are different from the DRBEM predictions obviously. The reasons may be attributed that the distance between a pair of microphones is too short compared with the wavelength at lower frequencies, so that the difference between the pressure signals of the two microphones is not obvious. As the Mach number increases, errors of the experimental results become bigger. The main reason is that regenerated noise and structure vibration caused by the air flow, which can not be ignored.

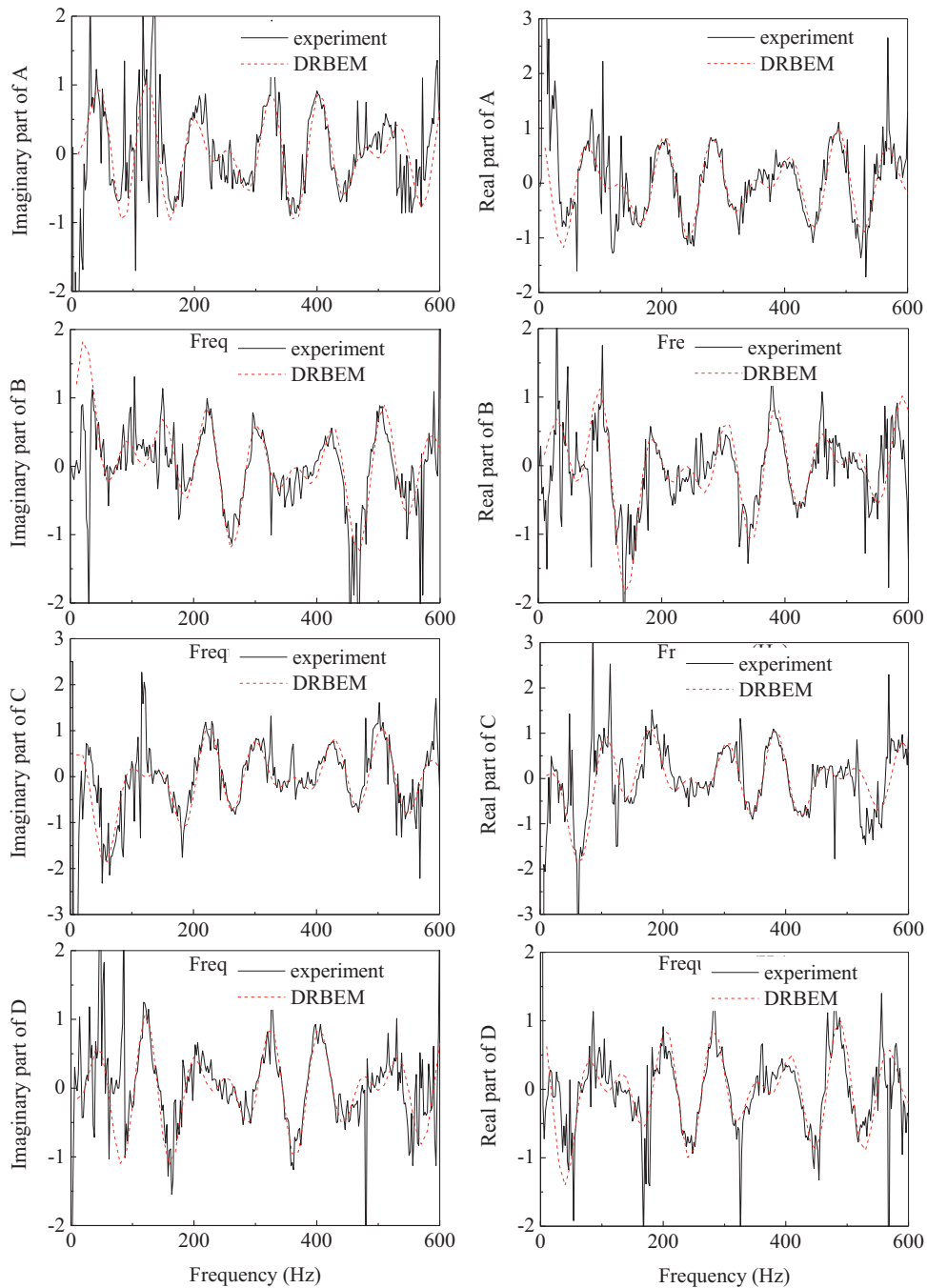


**Figure 1 Structure and dimension of conical duct (Dimensions in mm)**



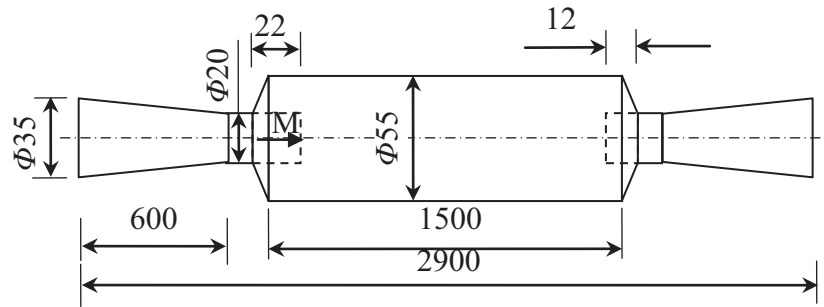
**Figure 2 Comparison of the four-pole parameters of conical duct ( $M=0.1$ )**



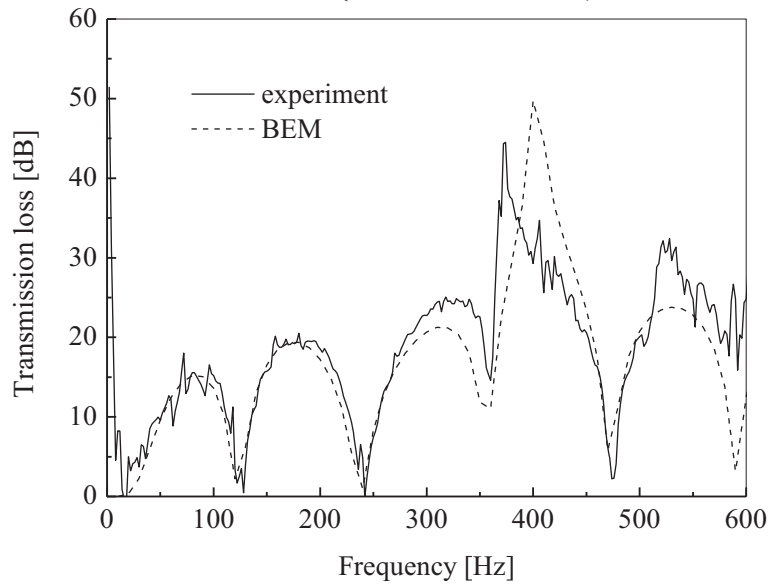


**Figure 3 Comparison of the four-pole parameters of conical duct ( $M=0.3$ )**

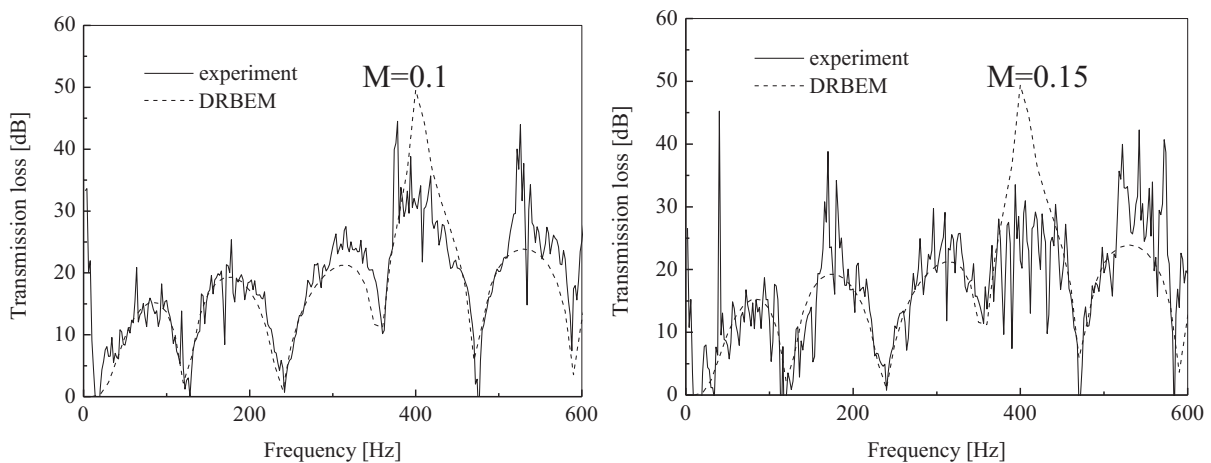
A single expansion chamber with extended inlet and outlet as shown in Fig.4 is considered to verify the present DRBEM by comparing the transmission loss predictions and the experimental results. In order to apply the substructure DRBEM, the silencer is divided into three substructures: inlet tube I, expansion chamber II and outlet tube III. Figs. 5-7 compare the predicted and measured transmission loss results of the silencer without and with flow. It can be seen that the agreement is reasonable well in the frequency range from 100Hz to 600Hz. Errors are also caused by same reasons as that in the conical duct. The regenerated noise and structure vibration caused by the air flow are more obvious and even lead to invalidity of the measurement as Mach number becomes higher.



**Figure 4** A single expansion chamber silencer with extended inlet and outlet and its dimensions (dimensions in mm)



**Figure 5** Transmission loss comparison for the single expansion chamber silencer without flow ( $M=0$ )



**Figure 6** Transmission loss comparison for the single expansion chamber silencer with flow

## Conclusions

The substructure DRBEM is applied successfully to predict the four-pole parameters and transmission loss of ducts and silencers with three-dimensional potential flow, and the basic

principle and numerical procedure of the DRBEM are introduced. Compared to the CBEM, the DRBEM takes into account the second order terms of flow Mach number in the acoustic governing equation, so it is suitable for the situations with higher Mach number subsonic flow. Comparison of predictions and experimental results for a conical duct and a single expansion chamber silencer showed that the present method is valid for prediction of the acoustic characteristics of ducts and silencers.

Numerical results also showed that the choice of approximation function  $f_i$  and particular solution  $\varphi_i$  is suitable for prediction of acoustic characteristics of ducts and silencers.

### Acknowledgement

The authors acknowledge the support of the research grant 10474016 from National Natural Science Foundation of China.

### References

- M.L. Munjal, *Acoustics of ducts and mufflers*, Wiley-interscience publication, New York, 1987.
- A.F. Seybert and C.Y.R. Cheng, Application of the boundary element method to acoustic cavity response and muffler analysis. *Journal of Vibration, Acoustics, Stress, and Reliability in Design* 109 (1987) 15-21.
- Z.L. Ji, Q. Ma, Z.H. Zhang, Application of the boundary element method to predicting acoustic performance of expansion chamber mufflers with mean flow. *Journal of Sound and Vibration* 173(1) (1994) 57-71.
- Z.L. Ji, Q. Ma, Z.H. Zhang, A boundary element scheme for evaluation of the four-pole parameters of ducts and mufflers with low Mach number non-uniform flow. *Journal of Sound and Vibration* 185(1) (1995) 107-117.
- D. Nardini and C.A. Brebbia, A new approach to free vibration analysis using boundary elements, In: C. A. Brebbia (Ed.), *Boundary Element Methods in Engineering*, Proceedings 4th International Conference on BEM, Berlin and New York: Springer-Verlag, (1982) 312–326.
- P.W. Partridge, C.A. Brebbia, L.C. Wrobel, *The dual reciprocity boundary element method*, Computational Mechanics Publications, London & New York, 1992.
- C.S. Chen, Y.F. Rashed, Evolution of thin plate spline based particular solutions for Helmholtz-type equation for the DRM. *Mechanical and Research Communication* 25(2) (1998) 195–201.
- M.A. Golberg, C.S. Chen, M. Ganesh, Particular solutions of 3D Helmholtz-type equations using compactly supported radial basis functions. *Engineering Analysis with Boundary Elements* 24 (2000) 539–547.
- L. Lee, T.W. Wu, P. Zhang, A dual-reciprocity method for acoustic radiation in a subsonic non-uniform flow. *Engineering Analysis with Boundary Elements* 13 (1994) 365-370.
- Astley R J. A finite element, wave envelope formulation for acoustical radiation in moving flows. *Journal of Sound and Vibration*, 1985; 103(1): 471-485
- E. Perrey-Debain, Analysis of convergence and accuracy of the DRBEM for axisymmetric Helmholtz-type equation. *Engineering Analysis with Boundary Elements* 23 (1999) 703–711
- Yinglong Zhang, Songping Zhu, On the choice of interpolation functions used in the dual reciprocity boundary element method. *Engineering Analysis with Boundary Elements* 13 (1994) 387–396.

## Simulations of Droplets falling on a solid surface Using Phase-Field Method

T. Sakakiabara<sup>1</sup>, \*T.Takaki<sup>1,2</sup>, and M.Kurata<sup>2</sup>

<sup>1</sup>Graduate School of Science and Technology, Kyoto Institute of Technology, Matsugasaki, Sakyo, Kyoto, 606-8585, Japan.

<sup>2</sup>Nuclear Science and Engineering Directorate, Japan Atomic Energy Agency, Shirakata, Tokai-mura, Ibaraki, 319-1195, Japan.

\*Corresponding author: takaki@kit.ac.jp

### Abstract

Due to the accident involving the Fukushima-Daiichi nuclear power plants, it becomes necessary to construct a numerical scheme to precisely evaluate the process of meltdown, including phase transformation among solid, liquid and gas phases. In this study, we constructed a model for gas-liquid two-phase flow with a high density ratio. We used the phase-field method to express a droplet of molten nuclear fuel flowing down a wall. By performing a dam break simulation using the developed model, we confirmed the model's validity. We also performed a numerical simulation of a droplet falling down a solid surface with wettability. The wettability was modeled by setting the boundary condition of the phase-field variable. As a result, we confirmed that the developed model can express the typical characteristics of a falling droplet on a wall.

**Keywords:** Two-phase flow, Phase-field method, Navier-Stokes equation, Contact angle, Droplet

### Introduction

The development of a simulation model able to accurately evaluate the meltdown process was made urgent by the accident at the Fukushima-Daiichi nuclear power plants. This process includes phase changes, such as melting and solidification, as well as the falling down of molten material. In order to simulate gas-liquid two-phase flow including phase change, we needed to choose an interface tracking method. The volume of fluid (VOF) method (Tomiyama, Sou, Minamigawa and Sakagushi, 1991; Minato, Ishida and Takamori, 2000; Tan, Aoki, Inoue and Yoshitani, 2011) and the level-set method (Olsson and Kreiss, 2005; Tan, Aoki, Inoue and Yoshitani, 2011) are widely used as interface tracking methods for gas-liquid two-phase flow. Since the VOF method uses a sharp interface, applying it to treat complicated morphologies is difficult. The level-set method requires re-initialization of the advection equation, leading to large calculation costs. Therefore, in this study we used the phase-field method as an interface tracking method. The phase-field method has multiple advantages; it can automatically construct an interface of complex shape and express interface migration simply by solving a time evolution equation. The biggest reason for applying the phase-field method in this study is that it enabled the expression of phase changes among gas, liquid and solid states using the multi-phase-field method. The purpose of this study was to construct the gas-liquid two-phase flow model which can express a falling droplet on a wall using the single phase-field method.

### Numerical model and calculation technique

#### *Governing equations of the two-phase flow model*

In this study, we constructed a model to simulate gas-liquid two-phase flow with a high density ratio in order to express droplets falling on a solid surface. The phase-field method was used as an interface tracking method and was coupled with the Navier-Stokes equation for incompressible flows. In phase-field method, we used the Cahn-Hilliard equation with an advection term of conservation form, where the phase-field variable  $\phi$  was regarded as a conserved quantity to keep a constant liquid volume. The phase-field variable  $\phi$  was defined as 0 in the gas phase and 1 in the liquid phase, and it continuously and sharply changed from 0 to 1 in the interface region. The Navier-Stokes equation includes surface tension force and gravity force terms, considered body

force in previous work (Anderson, McFadden, and Wheeler, 1998; Inamuro, Ogata, Tajima and Konishi, 2004; Takada, Matsumoto, Matsumoto and Ichikawa, 2008; Borcia, Borcia and Bestehorn, 2006; Borcia and Bestehorn, 2007). The governing equations of the gas-liquid two-phase flow model are

$$\frac{\partial \phi}{\partial t} + \nabla \cdot (\phi \bar{u}) = -M_\phi \nabla^2 \eta \quad (1)$$

$$\eta = a^2 \nabla^2 \phi + W \phi (1 - \phi) \left( \phi - \frac{1}{2} \right)$$

$$\nabla \cdot \bar{u} = 0 \quad (2)$$

$$\rho \left( \frac{\partial \bar{u}}{\partial t} + \bar{u} \cdot \nabla \bar{u} \right) = -\nabla p + \mu \nabla^2 \bar{u} + \phi a^2 \nabla \nabla^2 \phi + (\rho_v - \rho) \bar{g}, \quad (3)$$

where  $\bar{u}$  denotes the velocity vector;  $M_\phi$ , phase-field mobility;  $\eta$ , chemical potential;  $a$ , the gradient coefficient;  $W$ , the energy barrier;  $\rho$ , density;  $p$ , pressure;  $\mu$ , viscosity; and  $\bar{g}$ , the gravitational acceleration vector. The gradient coefficient  $a$  and energy barrier  $W$  are related to physical properties by the following equations.

$$a = \sqrt{\frac{3\delta\gamma}{b}} \quad (4)$$

$$W = \frac{6\gamma b}{\delta} \quad (5)$$

Here,  $\delta$  denotes interface width;  $\gamma$ , the interface energy between gas and liquid; and  $b$ , the coefficient to be related to the interface ( $b \approx 2.2$ ). We assumed that the density  $\rho$  and viscosity  $\mu$  continuously changed in the interface region, with a change in the phase-field variable, according to following equations.

$$\rho = \rho_l \phi + \rho_v (1 - \phi) \quad (6)$$

$$\mu = \mu_l \phi + \mu_v (1 - \phi) \quad (7)$$

The subscripts  $v$  and  $l$  represent the gas and liquid phases, respectively.

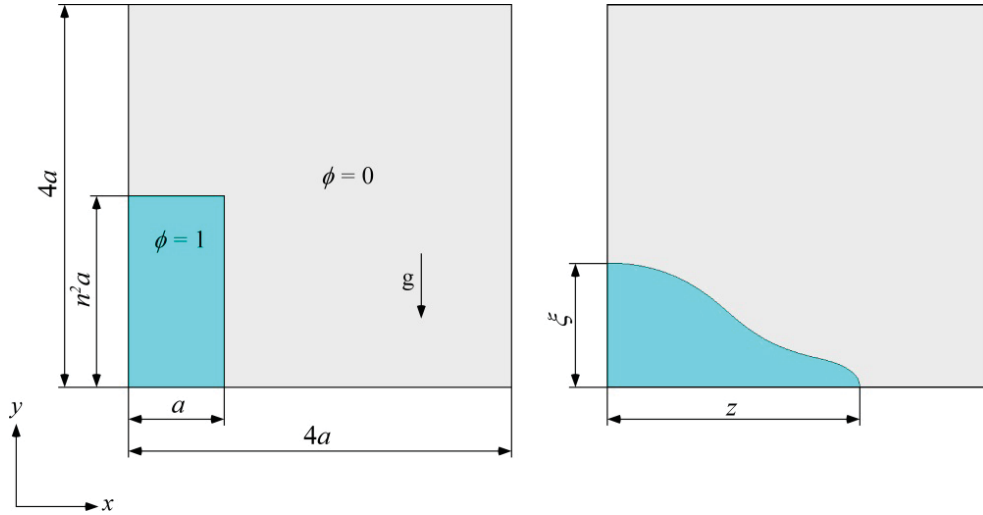
### Numerical scheme

The Cahn-Hilliard equation was solved by a perfectly explicit method. The Laplacian discretization of the phase-field variable and chemical potential was evaluated with a fourth-order central difference scheme. The advection term was evaluated with a third-order upwind scheme. Time integration was evaluated with a first-order forward difference scheme. The solution of the flow field was obtained using the SMAC method. The Poisson equation for pressure was discretized by a second-order scheme and the sparse matrix was solved using the SOR method. The diffusion term was evaluated with a second-order central difference scheme. The advection term and the time integration were calculated with the same scheme as the Cahn-Hilliard equation.

### Dam break problem

The dam break problem is well-known for validity verification of gas-liquid two-phase flow calculation code. Therefore, in this study we confirmed the reliability of our calculation code using a two-dimensional calculation of this problem. The computational model of a water-air system is shown in Figure 1. The initial water column width  $a$  and height  $n^2 a$  were  $a = 57.15 \times 10^{-3}$  m and  $n^2 a = 114.3 \times 10^{-3}$  m (aspect ratio  $n^2 = 2$ ); the same values were used in a previous experiment by Martine and Moyce (Martine and Moyce, 1952). The physical properties were as follows  $\rho_l = 1000$  kg/m<sup>3</sup>,  $\mu_l = 1.137 \times 10^{-3}$  Pa·s,  $\rho_v = 1.226$  kg/m<sup>3</sup>,  $\mu_v = 1.78 \times 10^{-5}$  Pa·s,  $\gamma = 72.8 \times 10^{-3}$  J/m<sup>2</sup>,  $\delta = 4\Delta x$  and

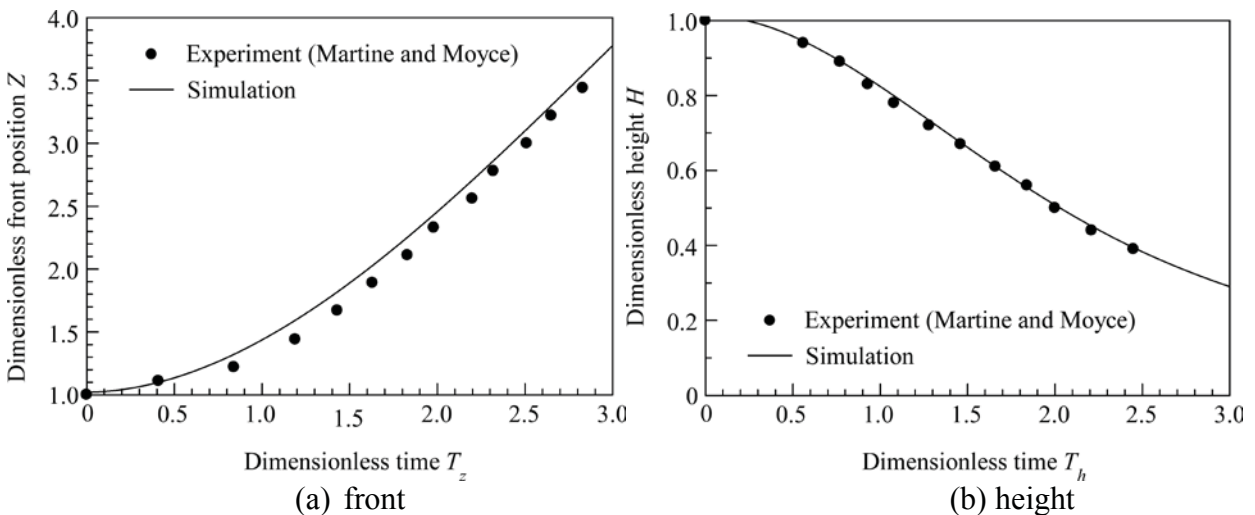
$M_\phi = 1.0 \times 10^{-4} \text{ m}^5/(\text{J}\cdot\text{s})$ . The lattice number was set to  $160 \times 160$ . The lattice sizes,  $\Delta x$  and  $\Delta y$ , and the time increment  $\Delta t$  were  $\Delta x = \Delta y = 1.43 \times 10^{-3} \text{ m}$  and  $\Delta t = 1.05 \times 10^{-6} \text{ s}$ . In all boundaries, we set the following conditions:  $\vec{n} \cdot \nabla \phi = 0$ ,  $\vec{n} \cdot \nabla \eta = 0$ ,  $\vec{n} \cdot \vec{u} = 0$  and  $\vec{n} \cdot \nabla p = 0$ , where  $\vec{n}$  denotes the normal vector. Equation (8) represents a static contact angle of 90 degrees and Equation (9) represents the fact that fluids cannot pass through the wall boundaries.



**Figure 1. Computational model for the dam break problem.**

Time variations of the front coordinate  $z$  and height  $\xi$  when the water column is broken by the gravity force are shown in Figure 2. Here,  $z$ ,  $\xi$  and respective times are nondimensionalized by  $Z = z/a$ ,  $T_z = nt\sqrt{g/a}$ ,  $H = \xi/(n^2 a)$  and  $T_h = t\sqrt{g/a}$ .

As shown in Figure 2(a), the front position moved more rapidly in the simulation than in the experiment. This is because the experiment was not perfectly two-dimensional even though it was performed in a thin region of the thickness dimension. In addition, the initial rectangular water column and its sudden breaking were difficult to express in the experiment. In Figure 2(b), the time variation of the height corresponds faithfully. Although there are some discrepancies between the numerical and experimental results, we see reasonable agreement between them and can thus confirm the reliability of our calculation code.



**Figure 2. Time variations of front and altitudinal contact lines in the dam break problem.**

## Droplet falling on a solid surface with wettability

### Boundary conditions for wettability

In order to give wettability to the boundary, we introduced an idea which implements the geometry shown in Figure 3. This model is different from that used in previous work (Briant, Papatzacos and Teomans, 2002); it directly gives wettability to the boundary. The contact angle  $\theta$  formed by the interface energy between solid and liquid and between liquid and gas (black vectors in Figure 3) is geometrically identical to the angle formed by the normal vector  $\vec{n}$  of the wall and the outward interfacial normal vector  $-\nabla\phi$  (red vectors in Figure 3). Then, by calculating the inner product of the two red vectors, the boundary condition giving wettability to the left boundary is given by the following equation.

$$\frac{\partial\phi}{\partial x} = \pm \sqrt{\frac{\cos^2\theta}{1-\cos^2\theta}} \left| \frac{\partial\phi}{\partial y} \right| \quad \begin{cases} \text{if } \cos\theta < 0 \text{ then sign is } + \\ \text{otherwise, sign is } - \end{cases} \quad (16)$$

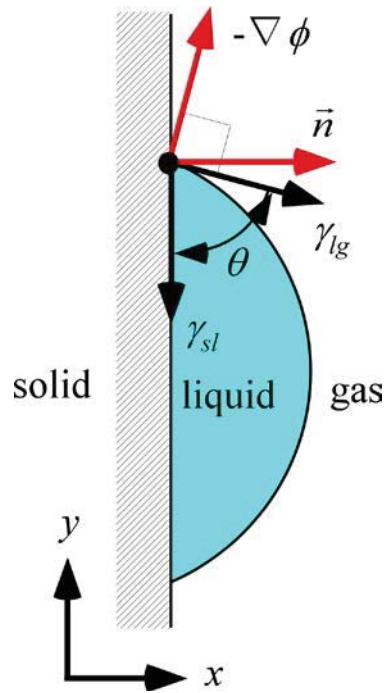
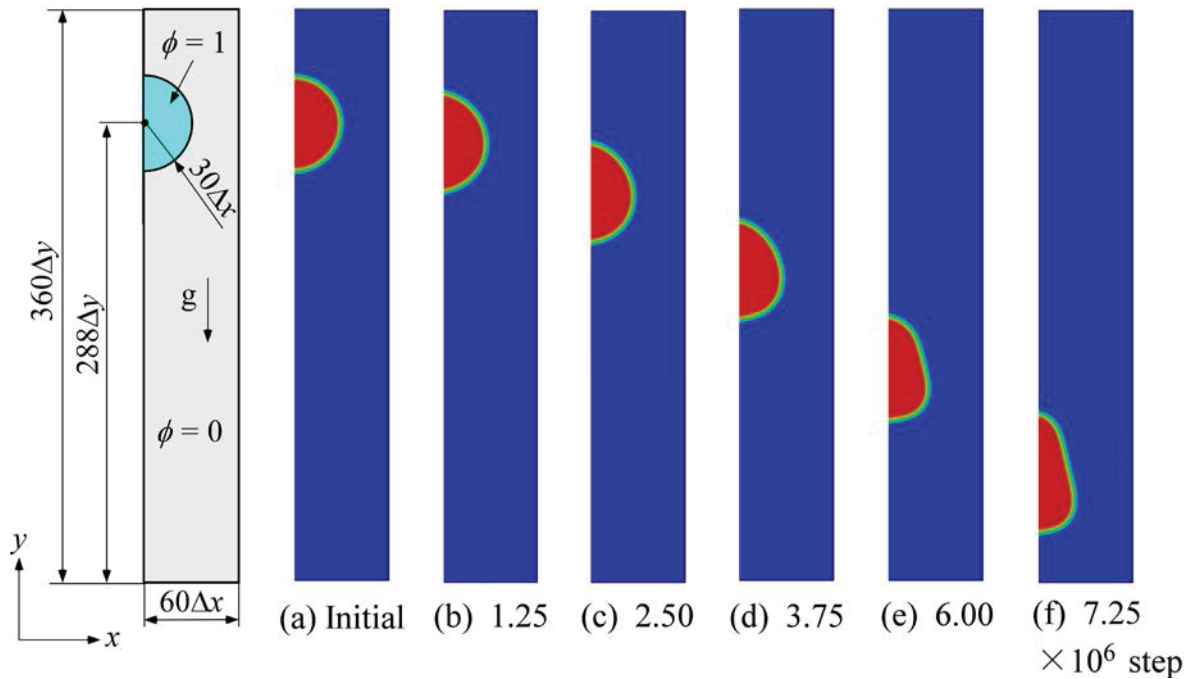


Figure 3. Boundary condition of wettability.

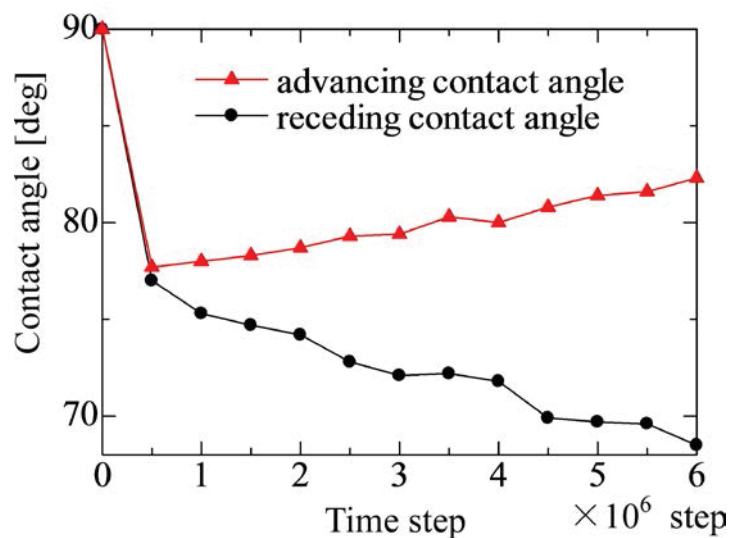
### Numerical conditions and results

We conducted the numerical simulation of a droplet falling down a solid surface with wettability. The leftmost part of Figure 4 shows the computational domain and initial condition. The velocity of the initial semicircular droplet was set to zero. The boundary condition of the phase-field variable on the left wall was set to the Neumann condition considered wettability given by Equation (16). We set the contact angle to  $\theta = 70^\circ$ . The other boundary conditions were identical to those used for the simulation of the dam break problem in the previous section. The other parameters were also unchanged from the previous simulation, with the following exceptions:  $M_\phi = 5.0 \times 10^{-7} \text{ m}^5/(\text{J}\cdot\text{s})$ ,  $\Delta x = \Delta y = 5.0 \times 10^{-5} \text{ m}$  and  $\Delta t = 8.99 \times 10^{-9} \text{ s}$ .

Figure 4 shows the morphological changes of a droplet on a solid surface with wettability. The upper part of the droplet becomes thin and the lower part expands as time progress. The bottom and side of the droplet become flat. In the simulation, we assumed phase-field mobility. If we used a larger value, the droplet shape would tend to be round due to the influence of curvature. To perform quantitative simulation, we needed to accurately identify the value of phase-field mobility. Time variations of advancing and receding contact angles are shown in Figure 5. In the early stage of falling, the contribution from the boundary condition is larger than that from the gravity force. Therefore, the advancing and receding contact angles approached the static contact angle  $\theta = 70^\circ$ . With time, because the contribution from the gravity force became larger, the advancing contact angle increased and the receding contact angle decreased to minimize the system energy.



**Figure 4. Computational domain and morphological changes of droplet on a wall surface with wettability.**



**Figure 5. Time variations of advancing and receding contact angles.**



## Conclusions

We constructed a model for gas-liquid two-phase flow with a high density ratio by using the phase-field method. Using the two-dimensional dam break problem, we confirmed that our calculation code can reasonably simulate gas-liquid two-phase flow with a high density ratio. Next, we conducted a simulation of a droplet falling down a solid surface with wettability, where the wettability was modeled by setting the boundary condition of the phase field variable. It was observed that advancing and receding contact angles are changed by the contributions of the boundary condition and the external force.

## References

- Hirt, C. W. and Nichols, B. W. (1981), Volume of Fluid (VOF) Method for the Dynamics of Free Boundaries. *Journal of Computational Physics* 39, pp. 201–225.
- Tomiyama, A., Sou, A., Minamigawa, H. and Sakaguchi, T. (1991), Numerical Analysis of a Single Bubble with VOF Method. *Transactions of the Japan Society of Mechanical Engineers, Series (B)* 57, pp. 2167–2173.
- Takada, N., Misawa, M., Tomiyama, A. and Hosokawa, S. (2001), Simulation of Bubble Motion under Gravity by Lattice Boltzmann Method. *Journal of Nuclear Science and Technology* 38, pp. 330–341.
- Tan, N., Aoki, T., Inoue, K. and Yoshitani, K. (2011), Numerical Simulation of Two-Phase Flow Driven by Rotating Object. *Transactions of the Japan Society of Mechanical Engineers, Series (B)* 77, pp. 1699–1714.
- Olsson, E. and Kreiss, G. (2005), A conservative level set method for two phase flow. *Journal of Computational Physics* 210, pp. 225–246.
- Anderson, D.M., McFadden, G.B., Wheeler, A.A. (1998), DIFFUSE-INTERFACE METHODS IN FLUID MECHANICS. *Annual Review of Fluid Mechanics* 30, pp. 139–165.
- Inamuro, T., Ogata, T., Tajima, S. and Konishi, N. (2004), A lattice Boltzmann method for incompressible two-phase flows with large density differences. *Journal of Computational Physics* 198, pp. 628–644.
- Takada, N., Matsumoto, J., Matsumoto and N., Ichikawa, N. (2008), Application of a Phase-Field Method to the Numerical Analysis of Motions of a Two-phase Fluid with High Density Ratio on a Solid Surface. *Journal of Computational Science and Technology* 2, pp. 318–329.
- Borcia, R., Borcia, I.D. and Bestehorn, M. (2006), Drops on an arbitrarily wetting substrate: A phase field description. *Physical review E* 78, 066307
- Borcia, R. and Bestehorn, M. (2007), Phase-field simulations for drops and bubbles. *Physical review E* 75, 056309
- Martine, J.C. and Moyce, W.J. (1952), An experimental study of the collapse of liquid columns on a rigid horizontal plane. *Philosophical Transactions of the Royal Society of London Series A* 244, pp.312-324.
- Briant, A.J., Papatzacos, P. and Yeomans, J.M. (2002), Lattice Boltzmann simulations of contact line motion in a liquid-gas system. *Philosophical Transactions of the Royal Society of London Series A* 360, pp.485-495.

## Uncertainty in long-term behavior and buckling of concrete-filled steel tubular columns

\* Xue Shi, Wei Gao, Yong-Lin Pi, Mark A. Bradford<sup>1</sup>

<sup>1</sup>School of civil and environment engineering, University of New South Wales, Australia.

### Abstract

This paper presents a long-term and buckling analysis of concrete-filled steel tubular (CFST) columns under sustained axial compression by accounting for the uncertainties of creep and shrinkage of the concrete core. The intervals of the final shrinkage strain and final creep coefficient of concrete core are derived from test results. An interval analytical model based on the algebraically tractable age-adjusted effective modulus method is proposed for the uncertain long-term and buckling analysis of CFST columns. An interval finite element model was developed in this paper for long-term behavior and buckling analysis. Perturbation method was employed to determine the two bounds of the solution. The results of the proposed analytical model and finite element model were compared with experimental results and analyzed.

**Keywords:** creep, shrinkage, interval analysis, interval finite element analysis, perturbation method

### 1. Introduction

Concrete-filled steel tubular (CFST) columns have been used in construction since the mid-1980s (Schneider, 1998) and become increasingly popular in both high-rise buildings and bridges (Shams and Saadeghvaziri, 1997). A CFST section consists of a steel tube and a concrete core (Fig. 1). Creep and shrinkage of the concrete core occur with an increase of time, which influence the long-term behavior of CFST columns significantly. It is of great importance to correctly predict effects of creep and shrinkage of the concrete core on the long-term behavior of CFST columns.

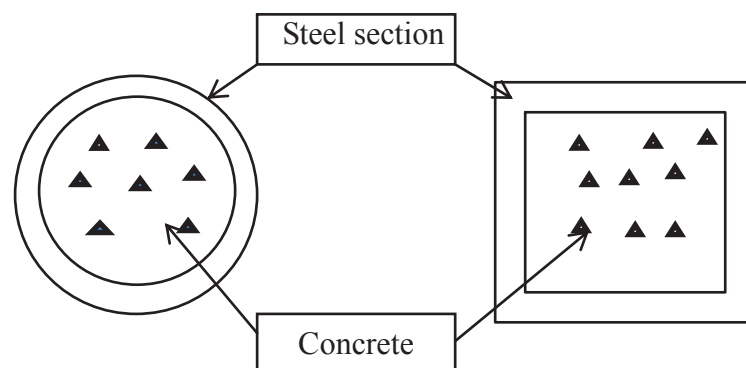


Figure 1. Cross-sections of CFST columns

Experimental and analytical studies have been performed by pioneers over the past three decades. Terrey et al. (1994) conducted similar experiments on circular CFST columns axially loaded at an earlier age of the concrete core. The first test on square CFST columns was carried out by Morino et al. (1996) and six concentrically loaded columns, two eccentrically loaded columns and one flexural member were tested. Experiments for similar cross-sections were implemented by Uy (2001)

applying axial loading to the CFST columns at 14 and 28 days of age of the concrete core respectively. Square CFST columns subjected to higher sustained loads were investigated by Han et al. (2004). Terry et al. (1994), Uy (2001) and Han et al. (2001) predicted the concrete time-dependent behavior by using the age-adjusted effective modulus (AAEM) method proposed by ACI-209. Cheng et al. (2005) introduced a three-dimensional nonlinear laminated element into the long-term modeling and assumed the creep behavior to be described by the Kelvin model. All of these experimental and analytical investigations treated the creep and shrinkage behaviors of the concrete core as deterministic phenomena.

However, it is noted that the creep coefficient obtained from tests vary significantly from one experiment to another. Very different predictions of the time-dependent behavior of CFST columns have been reported in different studies. This shows that the uncertainties of creep and shrinkage of the concrete core do exist. To predict the long-term behavior of CFST columns reasonably, these uncertainties have to be considered. Uncertain analysis of engineering structures has been developed in the last two decades and probabilistic methods are usually used if sufficient probabilistic information is available to validate the distributions or probability density functions of random variables. Other non-probabilistic approaches such as interval arithmetic and fuzzy sets theory are excellent alternatives when the statistical data of variables are not enough. For the long-term analysis of CFST columns considering the creep and shrinkage of the concrete core, probabilistic methods require probabilistic distributions of the final creep coefficient and final shrinkage strain to be determined first. Unfortunately, the available test data for creep and shrinkage of the concrete core of CFST sections are quite limited. Hence, it is impossible to derive correct probabilistic distributions of the final creep coefficient and final shrinkage strain.

In this paper, intervals are adopted to represent the uncertainties. In interval model, only the lower and upper bounds are required, which will be determined from the currently available experiment results for the final creep coefficient and final shrinkage strain. The age-adjusted effective modulus method (AEMM) (Bažant, 1972) is used to describe the creep of the concrete core and a virtual work method is used to establish the differential equation for the long-term-analysis of CFST columns that are subjected to a sustained axial uniform compression. Interval analyses are then implemented to predict the uncertain long-term behavior of CFST columns and buckling loads caused by the variations of the creep and shrinkage of the concrete core. Finally, an extensive parametric study is carried out to evaluate the influence of time, load level, steel ratio for CFST columns.

## 2. Interval analytical analysis

### 2.1 Interval linear elastic analysis of long-term behavior of CFST column

To predict the long-term performance, interval constitutive model considering creep and shrinkage of the CFST column needs to be established. The basic assumptions adopted for the interval long-term linear elastic analysis of CFST columns in this paper are: (1) deformations of the CFST columns are elastic and satisfy the Euler–Bernoulli hypothesis; and (2) the steel tube is fully bonded with the concrete core. Then, the linear strain of the CFST column can be expressed as

$$\varepsilon = u' \quad (1)$$

where  $u$  is the vertical displacement along the longitudinal direction of the CFST column. Based on the age-adjusted effective modulus method (AEMM), the stress in concrete can be expressed as

$$\sigma_c = E_{ec}(\varepsilon + \varepsilon_{sh}) = E_{ec}(u' + \varepsilon_{sh}) \quad (2)$$

where  $E_{ec}$  is the age-adjusted effective modulus of concrete,  $\varepsilon_{sh}$  is the shrinkage strain of concrete and can be given by AS3600 (2001)

$$\varepsilon_{sh}(t) = \frac{\varepsilon_{shfinal}}{35+t} \cdot t \quad (3)$$

where  $t$  is the loading time,  $\varepsilon_{shfinal}$  is the final shrinkage strain of concrete when  $t \rightarrow \infty$ .  $E_{ec}$  can be calculated by

$$E_{ec}(t, \tau_0) = \frac{E_c}{1 + \chi(t, \tau_0)\varphi(t, \tau_0)} \quad (4)$$

where  $\tau_0$  is the age at loading,  $\chi(t, \tau_0)$  is the aging coefficient and  $\varphi(t, \tau_0)$  is the creep coefficient that can be expressed as

$$\varphi(t, \tau_0) = \left[ \frac{(t - \tau_0)^{0.6}}{10 + (t - \tau_0)^{0.6}} \right] \cdot \varphi_{final} \quad (5)$$

where  $\varphi_{final}$  is the final creep coefficient when  $t \rightarrow \infty$ . The aging coefficient  $\chi(t, \tau_0)$  can be expressed as (Gilbert, 1988)

$$\chi(t, \tau_0) = 1 - \frac{(1 - \chi^*)(t - \tau_0)}{20 + (t - \tau_0)} \quad (6)$$

where

$$\chi^* = \frac{k_1 \tau_0}{k_2 + \tau_0} \quad (7)$$

with

$$k_1 = 0.78 + 0.4e^{-1.33\varphi_{\infty,7}} \quad (8)$$

$$k_2 = 0.16 + 0.8e^{-1.33\varphi_{\infty,7}} \quad (9)$$

$$\varphi_{\infty,7} = \varphi_{final} t_0^{0.118} / 1.25 \quad (10)$$

As the concrete core is assumed to be fully bonded with the steel tube, the deformations of the steel and concrete must be compatible with each other. Consequently, their mechanical membrane strains are equal to each other and the mechanical strains at the interface between the steel tube and concrete core are the same. Therefore, the stress  $\sigma_s$  in the steel tube can be written as

$$\sigma_s = E_s \varepsilon = E_s u' \quad (11)$$

where  $E_s$  is the Young's modulus of steel.

The differential equations for the long-term analysis of the CFST column can be obtained using the virtual work method. When the virtual work principle is used for the long-term equilibrium of the CFST column, it can be stated as

$$\delta W = \int_{V_s} \sigma_s \delta \varepsilon dV + \int_{V_c} \sigma_c \delta \varepsilon dV - Pu = 0 \quad (12)$$

where  $V_s$  is the volume of the steel tube,  $V_c$  is the volume of the concrete core,  $\delta(\ )$  denotes the Lagrange operator of simultaneous variations. By substituting Eqs. (1), (2) and (4), the statement of the principle of virtual work given by Eq. (12) can be written as

$$\delta W = \int_0^L (A_s E_s + A_c E_{ec}) u'' \delta u dy + (A_s \sigma_s + A_c \sigma_c - P) \delta u \Big|_0^L = 0 \quad (13)$$

Integrating Eq. (13) by parts leads to the differential equation of equilibrium for the long-term behavior of CFST column

$$u'' = 0 \quad (14)$$

and leads to the static boundary condition for CFST column as

$$A_s \sigma_s + A_c \sigma_c - P = 0 \text{ at } x=L \quad (15)$$

where  $L$  is the length of the CFST column. The essential geometric boundary condition is

$$u = 0 \text{ at } x = 0 \quad (16)$$

The long-term displacement of the CFST column can be obtained from Eq. (14) - (16) as

$$u = \frac{P + A_c E_c \varepsilon_{sh}}{A_s E_s + A_c E_c} x \quad (17)$$

and the strain of the steel tube and concrete core can be obtained from Eq. (17) as

$$\varepsilon = u' = \frac{P + A_c E_c \varepsilon_{sh} / [1 + \chi(t, \tau_0) \varphi(t, \tau_0)]}{A_s E_s + A_c E_c / [1 + \chi(t, \tau_0) \varphi(t, \tau_0)]} \quad (18)$$

In this paper, the final creep coefficient  $\varphi_{final}$  and the final shrinkage strain  $\varepsilon_{shfinal}$  can be described in terms of interval variables as

$$\varphi^I_{final} = [\underline{\varphi}_{final}, \overline{\varphi}_{final}] \quad (19)$$

$$\varepsilon^I_{shfinal} = [\underline{\varepsilon}_{shfinal}, \overline{\varepsilon}_{shfinal}] \quad (20)$$

Based on the interval arithmetic and the deterministic solutions of long-term displacement, the interval long-term displacement of CFST column can be obtained from Eq. (17) as

$$\underline{u} = \frac{P + A_c E_c \underline{\varepsilon}_{sh} / [1 + \underline{\chi}(t, \tau_0) \cdot \underline{\varphi}(t, \tau_0)]}{A_s E_s + A_c E_c / [1 + \underline{\chi}(t, \tau_0) \cdot \underline{\varphi}(t, \tau_0)]} x \quad (21)$$

$$\overline{u} = \frac{P + A_c E_c \overline{\varepsilon}_{sh} / [1 + \overline{\chi}(t, \tau_0) \cdot \overline{\varphi}(t, \tau_0)]}{A_s E_s + A_c E_c / [1 + \overline{\chi}(t, \tau_0) \cdot \overline{\varphi}(t, \tau_0)]} x \quad (22)$$

and the interval strain of the steel tube and concrete core can be obtained from Eq. (18) as

$$\underline{\varepsilon} = \frac{P + A_c E_c \underline{\varepsilon}_{sh} / [1 + \underline{\chi}(t, \tau_0) \cdot \underline{\varphi}(t, \tau_0)]}{A_s E_s + A_c E_c / [1 + \underline{\chi}(t, \tau_0) \cdot \underline{\varphi}(t, \tau_0)]} \quad (23)$$

$$\overline{\varepsilon} = \frac{P + A_c E_c \overline{\varepsilon}_{sh} / [1 + \overline{\chi}(t, \tau_0) \cdot \overline{\varphi}(t, \tau_0)]}{A_s E_s + A_c E_c / [1 + \overline{\chi}(t, \tau_0) \cdot \overline{\varphi}(t, \tau_0)]} \quad (24)$$

## 2.2 Interval buckling analysis

The classic equilibrium equation for column can be expressed as

$$EI \frac{d^4 v}{dx^4} + P \frac{d^2 v}{dx^2} = 0 \quad (25)$$

where  $x$  denotes the axial coordinate,  $v$  is the transverse deflection,  $P$  is the applied axial force,  $E$  is the Young's modulus and  $I$  is the second moment of area. By using the kinematic boundary conditions that  $v=0$  at  $x=0, L$  and the static boundary conditions, the solution of Eq. (25) can be obtained as

$$v = C_1 \sin \mu x \quad (26)$$

where  $\mu$  is a time-dependent dimensionless axial force parameter defined by

$$\mu^2 = \frac{P}{E_s I_s + E_c I_c} \quad (27)$$

where  $P$  can be express as

$$P = A_s E_s \varepsilon + A_c E_{ec} \varepsilon - A_c E_{ec} \varepsilon_{sh} \quad (28)$$

Considering the  $E_{ec}$  is an interval variable, Eq. (26) becomes

$$v = C_1 \sin \sqrt{\frac{A_s E_s \varepsilon_s + A_c E_{ec}^I \varepsilon_c - A_c E_{ec} \varepsilon_{sh}^I}{E_s I_s + E_{ec}^I I_c}} x \quad (29)$$

and the critical load can be obtain as when  $\sqrt{\frac{A_s E_s \varepsilon_s + A_c E_{ec}^I \varepsilon_c - A_c E_{ec} \varepsilon_{sh}^I}{E_s I_s + E_{ec}^I I_c}} = n\pi$ .

The interval critical load  $P_{cr}^I$  can be expressed as

$$P_{cr}^I = \frac{n^2 \pi^2 (E_s I_s + E_{ec}^I I_c)}{L^2} \quad (30)$$

when

$$\varepsilon^I = \left[ \frac{n^2 \pi^2 (E_s I_s + \overline{E_{ec} I_c}) + A_c \overline{E_{ec} \varepsilon_{sh}} L^2}{L^2 (A_s E_s + A_c \underline{E_{ec}})}, \frac{n^2 \pi^2 (E_s I_s + \underline{E_{ec} I_c}) + A_c \underline{E_{ec} \varepsilon_{sh}} L^2}{L^2 (A_s E_s + A_c \underline{E_{ec}})} \right] \quad (31)$$

### 3. Interval finite element analysis

The equilibrium equations of the CFST column can be derived from the principle of virtual work that requires

$$dU = \int_{V_s} \{d\varepsilon^I\}^T \{\sigma_s^I\} dV + \int_{V_c} \{d\varepsilon^I\} \{\sigma_c^I\} dV - \{du^I\}^T \{p\} = 0 \quad (32)$$

The relationship between the stress and strain of concrete core can be expressed as

$$\{\sigma_c^I\} = [D_{ec}^I] \{\varepsilon^I + \varepsilon_{sh}^I\} \quad (33)$$

where  $[D_{ec}^I]$  is the interval stress-strain matrix for concrete core. Similarly, the relationship between the stress and strain of the steel tube is

$$\{\sigma_s^I\} = [D_s^I] \{\varepsilon^I\} \quad (34)$$

Strains are determined from displacements, that is

$$\{\varepsilon^I\} = [B] \{u^I\} \quad (35)$$

where  $[B]$  is the strain-displacement matrix.

Substituting Eqs. (33) to (35) into Eq. (32) yields

$$dU = \{du^I\}^T \left\{ \int_{V_s} [B]^T [D_s^I] [B] \{u^I\} dV + \int_{V_c} [B]^T [D_{ec}^I] [B] \{u^I\} \left(1 + \frac{\varepsilon_{sh}^I}{\varepsilon^I}\right) dV - \{P\} \right\} = 0 \quad (36)$$

The CFST member is assumed to deform from the previous equilibrium state defined by  $\{P\}$  and  $\{u\}$  to an incremental equilibrium state defined by  $\{P + \Delta P\}$  and  $\{u + \Delta u\}$ . Applying principle of virtual work, we can obtain

$$dU(u^I + \Delta u^I) = 0 \quad (37)$$

By using Taylor's series expansion, Eq. (40) becomes

$$\left\{ \frac{\partial(dU)}{\partial u^I} \right\}^T \{\Delta u^I\} + \left\{ \frac{\partial(dU)}{\partial p} \right\}^T \{\Delta p\} = 0 \quad (38)$$

Substituting Eq. (36) to Eq. (38), we have

$$\{du^I\}^T K(u)_T^I \Delta u^I = \{du^I\}^T \Delta P(u^I) \quad (39)$$

where  $\Delta u^I$  is the increment of interval displacement of the structure,  $\Delta P(u^I)$  is the increment of load.  $K(u)_T^I$  is the interval tangent stiffness matrix of the structure and can be expressed as

$$\begin{aligned}
K_T^I(u) &= \int_{V_s} [B]^T [D_s^I] [B] dV + \int_{V_c} [B]^T [D_{ec}^I] [B] dV + \int_{V_c} [B]^T \left( \frac{\varepsilon_{sh}^I}{\varepsilon^I} [D_{ec}^I] \right) [B] dV \\
&= K_s^I + K_{ec}^I + K_{sh}^I
\end{aligned} \tag{40}$$

of which  $K_s^I$  is the linear interval elastic stiffness matrix for steel tubular,  $K_{ec}^I$  is the interval effective stiffness matrix for concrete core, and  $K_{sh}^I$  is the interval strain stiffness caused by shrinkage.  $K_{ec}^I$  and  $K_{sh}^I$  are both dependent on time. The tangent stiffness matrix is updated after each increment of load or each increment of displacement due to creep and shrinkage.

#### 4. Model validation and discussions

##### 4.1 Determination of intervals for the final shrinkage strain and creep coefficient

The empirical values of the final shrinkage strain  $\varepsilon_{shfinal}^I$  and creep coefficient  $\varphi_{final}^I$  are proposed in several experimental studies. The value of the final shrinkage strain given by Han et al. (2004), Morino et al. (1996), Terrey et al. (1994) and Uy (2001) is 43.5, 83.6, 50 and 160, respectively. Correspondingly, the final creep coefficient is 0.5, 0.83, 1.0 and 1.5 respectively. These values vary considerably. To account for these variations in the long-term analysis of CFST columns, the interval of the final shrinkage strain and creep coefficient of their concrete cores can be derived from these test results as  $\varepsilon_{shfinal} = [43.5, 340]$  and  $\varphi_{final} = [0.5, 1.7]$  respectively, which are used in this study. It can be expected that the results obtained by the interval models proposed in this paper will contain these experimental results, in other words, the experimental results will fall into the interval bounds produced by the proposed models.

##### 4.2 Long-term behavior of CFST column by interval analytical analysis

Han et al. (2004) carried out long-term tests on CFST square section columns. The dimensions of the square section are 100 mm and the thickness of the square section is 2.93 mm. The length of the CFST columns is  $L = 600$  mm. Young's modulus of the steel tube  $E_s = 202 \times 10^3$  MPa and Young's modulus of the concrete core  $E_c = 29200$  MPa. The first loading time is 28 days after concrete core casting. A central axial load of 360 kN was applied to the CFST columns.

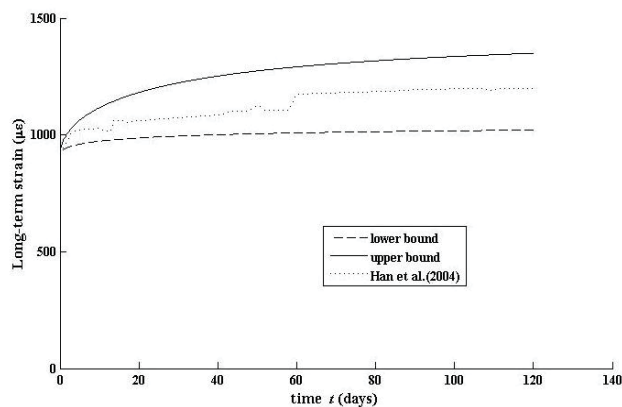


Figure 2. Comparison of creep and shrinkage strains

The analytical interval solution for the strain of CFST columns is compared with the test results in Figure 2. It can be observed that the interval uncertainty analysis can provide good upper and lower bounds for test results.

##### 4.3 Interval numerical buckling analysis

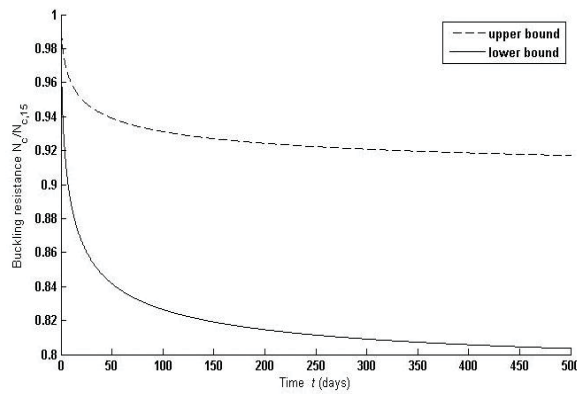


Figure 3. Interval critical buckling load on long-term sustained loading

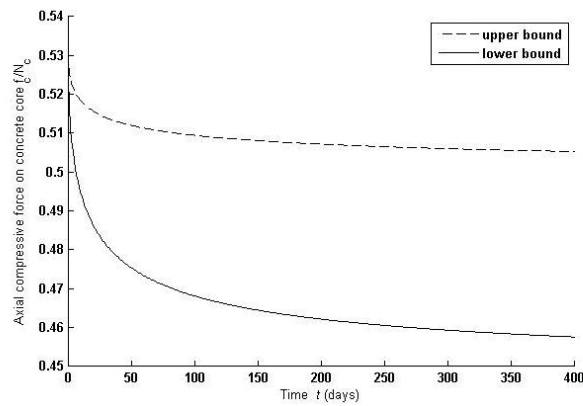


Figure 4. Compression force on concrete core when buckling

Fig. 3 shows the interval critical buckling load under long-term sustained load obtained by the interval finite element analysis method. Figs.4 shows the compression force on concrete core  $f_c / N_{cr}$  with time  $t$ , respectively. Young’s modules of the steel and concrete are  $E_s = 200GPa$  and  $E_c = 30GPa$ . The size of section is  $100mm \times 100mm \times 3mm$ . The length is 1000 mm.

It can be seen from Fig. 3 that when time  $t$  increases, the critical buckling load decreases significantly due to the effects of the creep and shrinkage. The decrease range is [7%, 20%] at  $t=300$ days. Fig. 4 shows that, along the time  $t$ , the “buckling resistance contribution” from the concrete is decreasing while from the steel tubular is increasing.

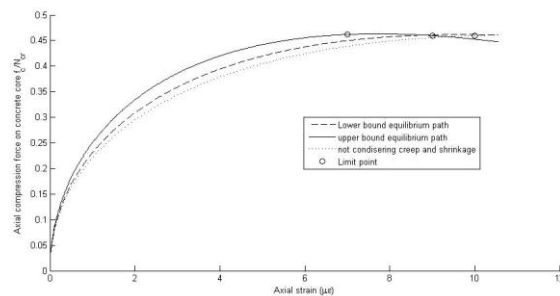


Figure 5. Axial strain for limit point buckling



Fig. 5 shows the compression force on the concrete core with axial strain. Buckling is investigated in a way that the column under an incremental load and the load criterion applies (Zhou, 2010). When creep buckling tends to happen, increment of the load becomes very small. From these figures, it can be seen that the axial strain is becoming smaller when buckling happens, in other words, the buckling resistance of the column is decreased due to the creep and shrinkage.

## 5. Conclusions

This paper presents a theoretical study on the uncertain long-term and buckling analysis of concrete-filled steel tubular columns. An interval analytical model based on the algebraically tractable age-adjusted effective modulus method is proposed to describe the time-dependent behavior of concrete in CFST columns. The solution of this model is compared with the experimental results reported by other researchers, which show the good agreements. Based on the energy method, the formulations for elastic buckling of the steel plate in rectangular CFT columns under axial compression are derived. An interval finite element was developed to describe the long-term behavior and analysis buckling. The buckling load or buckling time can be evaluated using this model.

In the future, the proposed models will be further developed to analyze other types of CFST structures accounting for the uncertainties in their material and geometric properties.

## Reference

1. Schneider, S. P. (1998), "Axially loaded concrete-filled steel tubes." *J. Struct. Eng.*, 124(10), pp.1125–1138
2. Shams M, Saadeghvaziri MA.( 1997), State of the art of concrete-filled steel tubular columns. *ACI Struct J*; 94(5), pp.558–71.
3. Terrey, P. J., Bradford, M. A., & Gilbert, R. I. (1994), Creep and shrinkage of concrete in concrete-filled circular steel tubes. *Proc.,6th Int. Symposium on Tubular Structures*, Melbourne, Australia, pp.293–298.
4. Morino, S.; Kawaguchi, J.; & Cao, Z. S. (1996), Creep Behavior of Concrete-Filled Steel Tubular Members. *Composite Construction in Steel and Concrete III*. Proceedings of an Engineering Foundation Conference, Irsee, Germany, pp.514-525.
5. Uy, B. (2001), Static long-term effects in short concrete-filled steel box columns under sustained loading. *ACI Structural Journal* 98(1), pp. 96–104.
6. Han, L. H., Tao, Z. & Liu, W. (2004), Effects of Sustained Load on Concrete-Filled Hollow Structural Steel Columns. *J. Struct. Eng* 130(9), pp.1392–1404.
7. Cheng, X.D., Li, G.Y. & Ye, G.R. (2005), Three-dimensional nonlinear analysis of creep in concrete filled steel tube columns. *Journal of Zhejiang University (Science)* 6A(8), pp. 826–835.
8. Bažant, Z.P. (1972), Prediction of concrete creep effects using age-adjusted effective modulus method. *ACI Structural Journal* 69(4), pp.212–217.
9. AS3600,(2001), Australian Standard: Concrete Structures, Standard Association of Australia, Sydney.
10. R.I. Gilbert, (1988), Time Effects in Concrete Structures, Elsevier Applied Science, Amsterdam.
11. H.Z. Zhou. (2010), Buckling of reticulated laminated veneer lumber shells in consideration of the creep *Engineering Structures* 32, pp. 2912-2918

## Direct Numeric Simulation of Sheared Convective Boundary Layer Entrainment with GPUs

\*Nicholas J. Stewart<sup>1</sup>, David W. Holmes<sup>1</sup>, Wenxian Lin<sup>1</sup>, Steven W. Armfield<sup>2</sup>  
and Michael P. Kirkpatrick<sup>2</sup>

<sup>1</sup>School of Engineering and Physical Sciences, James Cook University, QLD 4811, Australia

<sup>2</sup>School of Aerospace, Mechanical and Mechatronic Engineering, The University of Sydney, NSW 2006, Australia

\*Corresponding author: [nicholas.stewart@my.jcu.edu.au](mailto:nicholas.stewart@my.jcu.edu.au)

### Abstract

Sheared convective boundary layers (SCBL) are a frequently observed boundary layer in nature and industry. This paper presents work conducted to validate a numerical fluid model of sheared convective boundary layers implemented in Nvidia's CUDA programming language for graphical processing units. The code is based on finite difference implementation of the SIMPLE algorithm using the Boussinesq approximation to couple the energy equation through the buoyancy term. Work presented shows validation of the model on simpler test cases that are more thoroughly understood, and the model shows agreement with physical phenomena.

**Keywords:** high performance computing, GPGPU, CUDA, boundary layer

### Introduction

Sheared convective boundary layers (SCBL) are turbulent boundary layers that are prevalent in environmental systems such as the Earth's atmosphere and engineered systems including air-conditioning and natural ventilation of building spaces. As the name suggests, a SCBL is a boundary layer that is driven by both shear and convective motion of the fluid. Currently the flow behaviours of SCBLs are not well understood and parameterising entrainment and other flow characteristics is unresolved. Numerical modelling and laboratory scale experiments are required to give a better understanding of SCBLs [1]. Both techniques have been employed previously to develop understanding of a similar problem, convective boundary layers. The work presented in this paper will focus on validating the numerical model against simplified cases including a lid driven cavity, a Blasius flat plate and a stratified shear layer.

Due to the turbulent nature of SCBLs, high resolution numerical meshes are required to resolve the smallest scales possible. This requires significant computational power that is typically derived from either distributed (cluster) computing or through multi-core processing. In recent years, GPUs, or more commonly known as graphics cards, have been developed to perform general purpose processing tasks and are now similar in capabilities to CPUs, but offer significantly higher performance due to GPU's massively parallel architecture. To unlock this performance, heavy modification of traditional algorithms is usually required, leading to the field of programming known as GPGPU, or General Purpose computing on GPUs.

This paper will validate the numerical model developed on Nvidia's GPGPU programming language, CUDA, using several simplified cases of SCBLs. The numerical model

is based on the semi-implicit SIMPLE [2] algorithm and solves the incompressible Navier-Stokes equations while using a buoyancy term to couple the energy equation through the Boussinesq approximation.

### Numerical Model

The Navier-Stokes and energy equations are needed to be solved to model a SCBL system. The model was simplified by assuming that the system is incompressible and the Boussinesq approximation is valid for the buoyancy force. The incompressible form of the governing equations can be written as follows

$$\nabla \cdot \mathbf{u} = 0, \quad (1)$$

$$\frac{\partial \mathbf{u}}{\partial t} + \mathbf{u} \cdot \nabla \mathbf{u} = -\frac{1}{\rho} \nabla P + \nu \nabla^2 \mathbf{u} - \frac{\rho}{\rho_0} \mathbf{g}, \quad (2)$$

$$\frac{\partial T}{\partial t} + \mathbf{u} \cdot \nabla T = \sigma \nabla^2 T, \quad (3)$$

where  $\mathbf{u}$  is the velocity vector,  $t$  is time,  $\rho$  is density of fluid at temperature  $T$ ,  $\rho_0$  is the density of fluid at a reference temperature  $T_0$ ,  $P$  is pressure,  $\mathbf{g}$  is acceleration due to gravity, and  $\nu$  and  $\sigma$  are the kinematic viscosity and thermal diffusivity of fluid, respectively. The Navier-Stokes equation (2) is coupled with the energy equation (3) through the buoyancy term  $\frac{\rho}{\rho_0} \mathbf{g}$ .

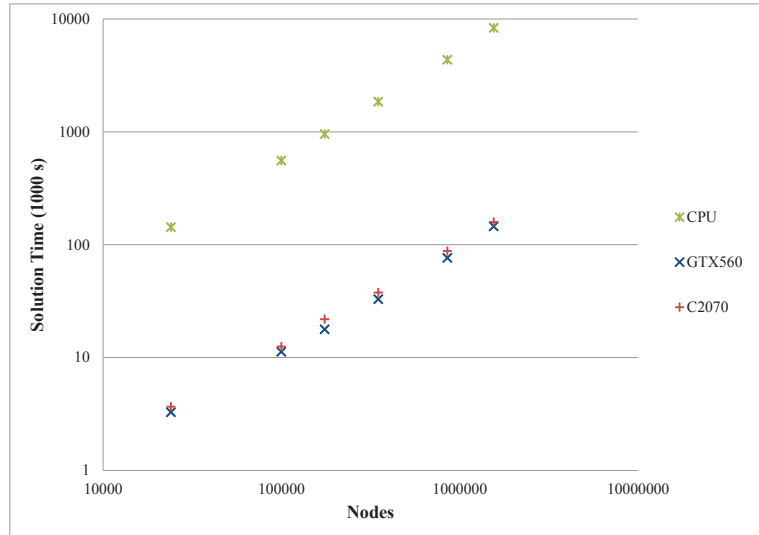
The SIMPLE algorithm is used to solve the governing equations by using a cyclic system of guess and correct steps. The velocity components are first determined by solving the momentum equations using an approximated pressure field, coupled with the energy equation, then the pressure and velocity fields are corrected to satisfy continuity. This process continues until the system converges. The accuracy of the model is largely based on how the individual terms are discretised. The model was implemented with first order upwind advection terms and second order central diffusion terms.

### GPGPU Implementation

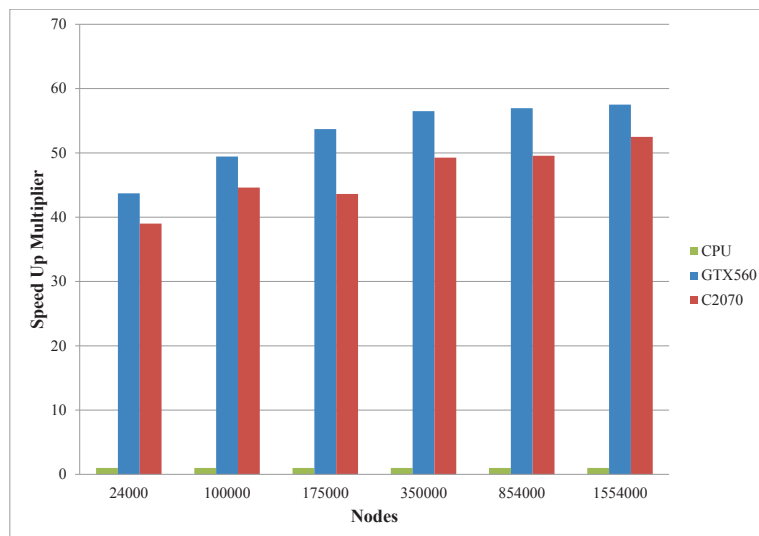
The numerical algorithms were implemented in Nvidia's CUDA programming language. The development process started with modifying an existing code and implementing it in a naive way on GPU (unrolling loop structures into GPU kernels) and followed with optimizing the algorithm for GPU. The code was benchmarked during all stages of development to determine how much performance is gained by which stages of implementation. This is helpful to gauge the viability of projects such as OpenACC, which provide compiler directives for automatic generation of GPU kernels, when applied to non-trivial parallel problems.

The performance of the algorithm was submitted as another conference paper [10], however a brief of those results are shown here which demonstrate that the implementation on GPU significantly improved the performance, as shown in Fig. 1, which shows the solution time of different processing units as the model node count is increase. Both the CPU and GPU solution time increases linearly as node number increases, but the GPU model performs consistently much better than the CPU model. Fig. 2 shows the speed

up obtained with the semi-implicit algorithm (as a multiplier of the CPU performance), demonstrating it steadily growing as the model size increases. The performance difference between the two GPUs is largely explained by the different clock speed on the units.



**Fig. 1: Semi-implicit model performance as node number is increased.**



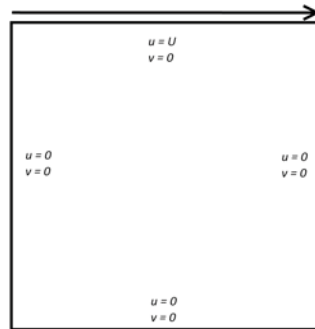
**Fig. 2: Semi-implicit model performance improving when implemented on GPU.**

### Validation

Simplified test cases were used to ensure the correctness of the numerical model. Three main cases were investigated: a lid driven cavity flow, uniform flow over a flat plate, and a stratified shear layer. These cases were compared with literature to ensure consistent results.

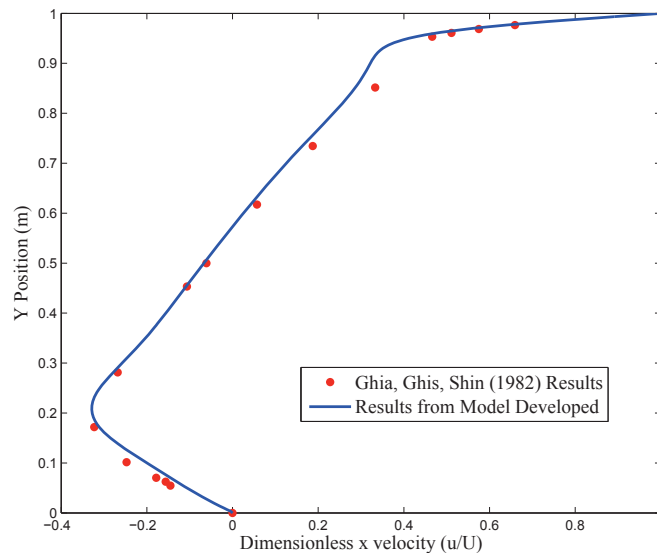
#### *Lid Driven Cavity.*

The lid driven cavity is a common validation case with simple geometry and boundary conditions. The case is set up by having a square field of fluid, with non-slip conditions on the sides and floor, and a constant velocity boundary on the lid of the cavity as shown in Fig. 3.



**Fig. 3: Numerical setup of lid driven cavity flow.**

The work performed by Ghia, Ghis and Shin [7] is frequently used as a benchmark, as it provides both images to compare, and tables of values. Fig. 4 shows an agreement of velocity profiles between the developed model and results of previous work. Fig. 5 shows the streamlines of the lid driven cavity, similar to those shown in other work.



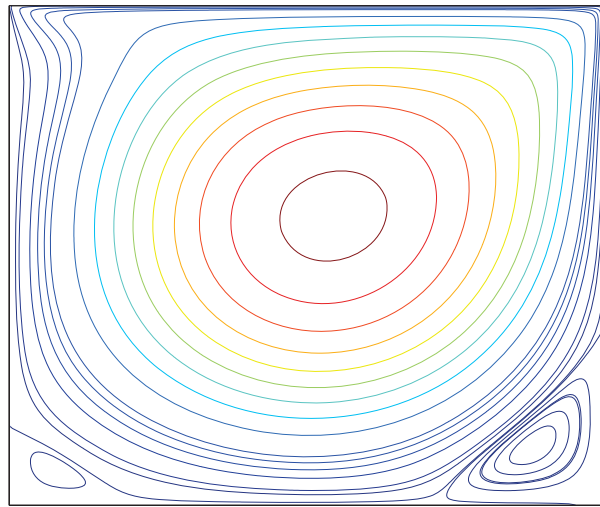
**Fig. 4: Horizontal velocity profile over the midline of lid driven cavity with a Reynolds number of 1000**

#### *Flat Plate.*

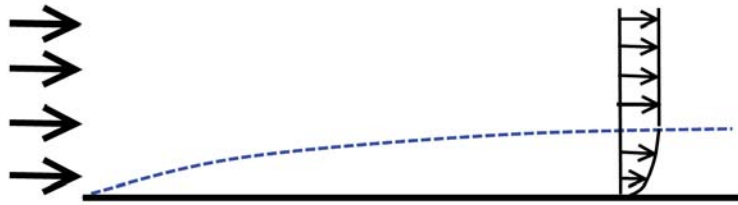
In the flat plate example a uniform velocity field is applied over a non-slip flat plate, on which a boundary layer develops. Fig. 6 shows a uniform flow field being applied to a flat plate, with the dashed line showing the boundary layer thickness (defined as where the velocity is less than 99% of the free field velocity).

The Blasius solution [8] gives the expected velocity profile and thickness of the boundary layer developed over a flat plate. Fig. 7 shows the profile determined by the CUDA algorithm matches closely with the Blasius solution. The main difference between the solutions is the bump occurring at the edge of the boundary layer, caused by the uniform inlet being applied at the start of the non-slip plate.

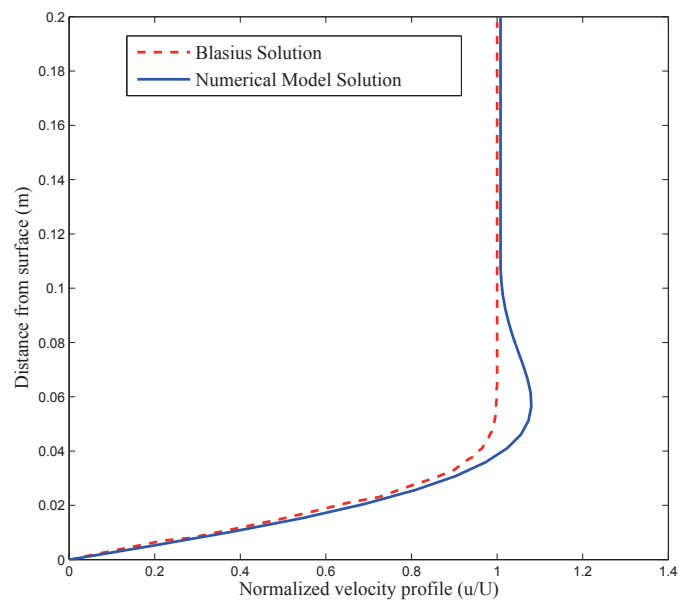
#### *Stratified Shear Layer.*



**Fig. 5: Streamlines of lid driven cavity with a Reynolds number of 1000**



**Fig. 6: The flat plate example showing the development of the boundary layer and the resultant velocity profile.**



**Fig. 7: Comparison of velocity profile calculated by the Blasius solution and the developed model.**

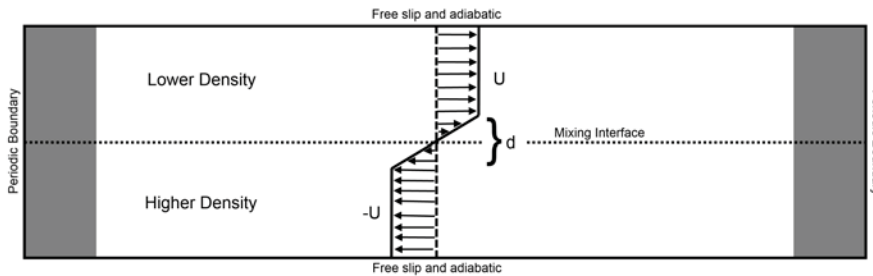
In the stratified shear layer case two statically stable layers of fluid are moving at different velocities causing a shearing effect at the interface. A model can be set up as shown in Fig. 8 to investigate the effects of shear and buoyancy forces on the system. Characteristics of the system are largely determined by the Reynolds number and the Richardson number. The Reynolds number is given by

$$Re = \frac{\Delta U d}{\nu}, \quad (4)$$

where  $\Delta U$  is the velocity difference between the two layers, and  $d$  is the interface thickness. The Richardson number is given by

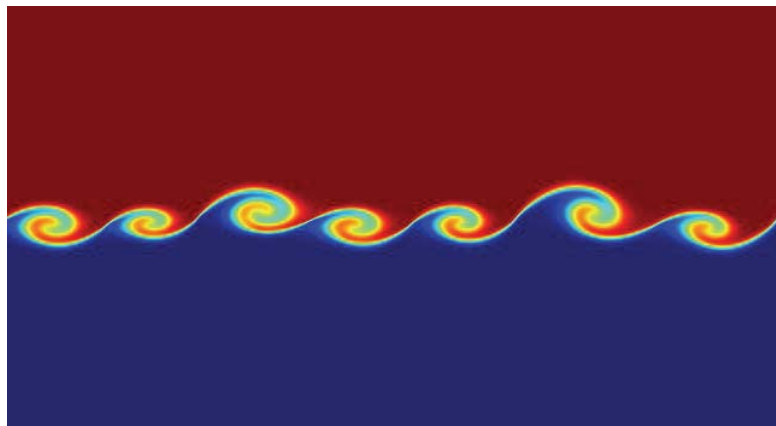
$$Ri_g = \frac{N^2}{\left(\frac{\partial u}{\partial z}\right)^2}, \quad (5)$$

where  $N^2 = \frac{-g}{\rho_1} \frac{\partial \rho_0}{\partial z}$  is the buoyancy frequency,  $\frac{\partial u}{\partial z}$  is the rate of change of velocity in the vertical direction,  $g$  is gravity,  $\rho_1$  is the upper layer density and  $\rho_0$  is the reference density. The Richardson number gives the ratio of buoyancy forces to shear forces.



**Fig. 8: The numerical model setup for stratified shear flow.**

When the value for Richardson number is below 0.25, shear forces overwhelm the buoyancy forces to the extent that Kelvin-Helmholtz instabilities begin to occur [9]. The code developed reliably shows the development of K-H instabilities at low values of Richardson number as shown in figure 9, where  $Ri = 0.2$  and  $Re = 5000$ . In this case the density gradient is generated by a change in temperature of  $0.5^\circ\text{C}$ .



**Fig. 9: Kelvin-Helmholtz instabilities in a stratified shear layer at  $Ri = 0.2$  and  $Re = 5000$ .**

## Conclusion

The developed code was tested against several simplified cases of SCBLs, i.e. a lid driven cavity, a flat plate boundary layer and a stratified shear layer. In all cases it

was shown the numerical model agrees with previous works to within reasonable expectations. This work is to be extended to investigating the case of sheared convective boundary layers.

### Acknowledgements

This work has been supported by an Australian Research Council Discovery Project Grant DP110102343.

### References

- [1] J.R. Conzemius, E. Fedorovich, Dynamics of shear convective boundary layer entrainment, *J. Atmospheric Sci.*, 66, (2006) 1151-1178.
- [2] L.S. Caretto, A.D. Gosman, S.V. Patankar, Two calculation procedures for steady, three-dimensional flows with recirculation, *Proc. of the 3rd Int. Conf. on Numerical Methods in Fluid Mechanics, Lecture Notes in Physics, Vol. 19, 1972, Pages 60-68.*
- [3] R.W. MacCormack: The effect of viscosity in hypervelocity impact cratering, *AIAA Paper*, 1969, Pages 69-354.
- [4] Nvidia: CUDA Programming Guide on <http://www.nvidia.com/cuda/>.
- [5] R.S. Bernard, A MacCormack scheme for incompressible flow, *Computers & Mathematics with Applications*, 24, (Issues 5–6), (1992) 151-168.
- [6] R.H. Pletcher, J.C. Tannehill, D.A. Anderson: *Computational Fluid Mechanics and Heat Transfer*, third ed., CRC Press, Boca Raton, 2012.
- [7] U. Ghia, K.N. Ghis, C.T. Shin: High-Re Solutions for Incompressible Flow Using the Navier-Stokes Equations and a Multigrid Method, *J. Computational Physics*, 48, (1982) 387-411.
- [8] F.M. White: *Fluid Mechanics*, fifth ed., McGraw-Hill, 2003.
- [9] E.J. String, H.J.S Fernando: Entrainment and mixing in stratified shear flows, *J. Fluid Mechanics*, 428, (2001) 349-386
- [10] N.J. Stewart, D.W. Holmes, W. Lin, et al: Comparison of Semi-Implicit and Explicit Finite Difference Algorithms on Highly Parallel Processing Architectures, submitted to Australasian Conference on Computational Mechanics 2013, Sydney, AU



## Non-linear elastic in-plane buckling of crown-pinned arches with rotational end restraints

\*K. Luo<sup>1</sup>, Y. L. Pi<sup>1</sup>, W. Gao<sup>1</sup> and M. A. Bradford<sup>1</sup>

<sup>1</sup> The School of Civil and Environmental Engineering, The University of New South Wales,  
Sydney, NSW 2052, AUSTRALIA.

\*Corresponding author: kai.luo@unsw.edu.au

### Abstract

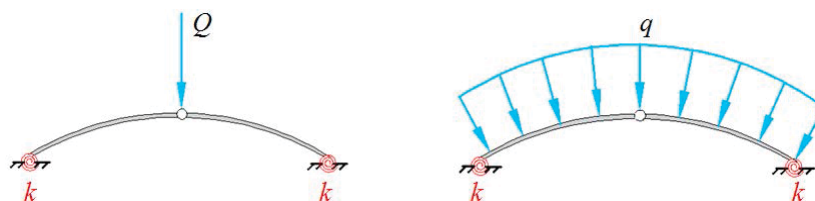
This paper investigates the non-linear elastic in-plane buckling behaviour of a crown-pinned shallow circular arch with rotational end restraints under a uniform radial load or under a central concentrated load. A finite element method and an analytical method are used for the investigation. It is shown that the finite element results agree well with the analytical solutions. It is found that the stiffness of the rotational end restraints has significant effects on the buckling behaviour of arches and that the buckling loads increase with an increase of the stiffness. It is also found that the crown-pin plays an important role in the buckling behaviour of arches. The crown-pinned arches can buckle in a limit point instability mode, but not in a bifurcation mode.

**Keywords:** Crown-pinned arch, finite element, in-plane buckling, limit point, rotational restraint

### Introduction

Studies of the buckling behaviour have been focused on pin-ended and fixed arches (Pi et al. 2002, Bradford et al. 2002). In addition to pin-ended and fixed arches, in engineering structures, an arch is often supported on the elastic foundations or by other structures which provide elastic restraints to the arch ends. Pi et al. (2008) investigated the non-linear in-plane buckling of shallow circular arches with elastic rotational end restraints under a central concentrated load, while Pi and Bradford (2009) reported studies on the non-linear in-plane postbuckling behaviour of shallow circular arches with elastic rotational end restraints under a uniform radial load. In these studies, the arch is assumed to be continuous without any pins between its ends. It is known that in many cases, arches are built by joining two separate curvilinear segments together at the crown, thereby reducing the arch size to meet transport requirements and to create a pin at the arch crown. Because of the crown-pin, the structural responses and buckling behaviour of the arch are different from those of arches without the crown-pin. However, investigations on crown-pinned shallow circular arches with elastic rotational end restraints do not appear to be reported in the open literature.

This paper, therefore, uses both an analytical method and a finite element method to investigate the non-linear in-plane buckling behaviour of crown-pinned shallow circular arches with rotational end restraints subjected to a central point load or to a uniform radial load (Fig. 1).



**Figure 1. Crown-pinned arches subjected to different loading cases**

### Non-linear in-plane equilibrium

Assumptions adopted in this investigation are: 1. The Euler-Bernoulli hypothesis is applied. 2. The dimension of the cross-section is much smaller than the length and radius of the arch to ensure sufficient slenderness. Because the arch and load system is symmetric, equilibrium of a half arch ( $0 \leq \theta \leq \Theta$  and  $\Theta$  is half of the included angle of the arch) is considered (Fig. 2). Based on the assumptions, differential equations of equilibrium for a crown-pinned circular arch with equal rotational end restraints can be derived from the principle of virtual work as

$$N' = 0 \quad \text{and} \quad \frac{\tilde{v}^{iv}}{\mu^2} + \tilde{v}'' = -1 \quad (1)$$

for arches that are subjected to a central concentrated load  $Q$  (Pi et al. 2008), and as

$$N' = 0 \quad \text{and} \quad \frac{\tilde{v}^{iv}}{\mu^2} + \tilde{v}'' = P \quad \text{with} \quad P = \frac{qR}{N} - 1 \quad (2)$$

for arches that are subjected to a uniform radial load  $q$  (Pi and Bradford 2009), where  $(\ )' \equiv d(\ )/d\theta$ ,  $\theta$  denotes the angular coordinates,  $\tilde{v} = v/R$  and  $\tilde{w} = w/R$ ,  $v$  and  $w$  are the radial and axial displacements with  $R$  being the radius of the arch,  $\mu$  is the dimensionless axial force parameter defined by  $\mu = NR^2/EI$  with  $E$  being Young's modulus and  $I$  being the second moment of area of the cross-section, and the axial compressive force  $N$  is defined by

$$N = -AE \int_{-\Theta}^{\Theta} (\tilde{w}' - \tilde{v} + \frac{1}{2}\tilde{v}'^2) dA \quad (3)$$

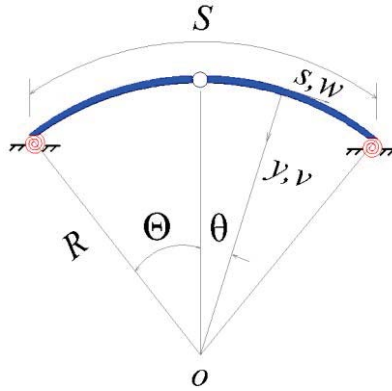


Figure 2. Arch geometry

The static boundary conditions can also be derived as

$$\tilde{v}'' + \frac{\tilde{v}'}{2\Theta\alpha} = 0 \quad \text{at} \quad \theta = \Theta \quad \text{and} \quad \frac{EI}{R} \tilde{v}''' + \frac{\mu^2 EI}{R} \tilde{v}' = \frac{QR}{2} \quad \text{at} \quad \theta = 0 \quad (4)$$

for arches subjected to a central concentrated load  $Q$ , and

$$\tilde{v}'' + \frac{\tilde{v}'}{2\Theta\alpha} = 0 \quad \text{at} \quad \theta = \Theta \quad \text{and} \quad \frac{EI}{R} \tilde{v}''' + \frac{\mu^2 EI}{R} \tilde{v}' = 0 \quad \text{at} \quad \theta = 0 \quad (5)$$

for arches subjected to a uniform radial load, where  $\alpha$  is the dimensionless restraint flexibility defined by  $\alpha = EI/kS$  with  $k$  being the stiffness of rotational end restraints and  $S$  being the length of the arch.

In addition, the kinematic boundary conditions are

$$\tilde{w} = 0 \quad \text{at} \quad \theta = 0 \quad \text{and} \quad \theta = \Theta \quad \text{and} \quad \tilde{v} = 0 \quad \text{at} \quad \theta = \Theta \quad (6)$$

for both loading cases.

Solving the three equations given by Eqs. (1) and (3) or by Eqs. (2) and (3) simultaneously leads to the solution of the radial displacement as

$$\begin{aligned} \tilde{v} = & -\frac{1}{2\mu^3 EI (2\alpha\beta \sin \beta - \cos \beta)} (-2\mu EI \cos \beta \cos \mu\theta + 4\mu\alpha\beta EI \sin \beta \cos \mu\theta - \mu^3 \theta^2 EI \cos \beta \\ & + 2\mu^3 \theta^2 \alpha\beta EI \sin \beta + 2\mu EI - 4\mu\alpha\beta EI \sin \beta - 2\mu\beta EI \sin \beta + \mu\beta^2 EI \cos \beta - 2\mu\alpha\beta^3 EI \sin \beta \\ & + QR^2 \sin \beta - QR^2 \beta \cos \beta + 2QR^2 \alpha\beta^2 \sin \beta) + \frac{H(\theta)}{2\mu^3 EI (2\alpha\beta \sin \beta - \cos \beta)} (2\mu EI \sin \beta \sin \mu\theta \\ & + 4\mu\alpha\beta EI \cos \beta \sin \mu\theta - 4\mu\alpha\beta EI \sin \mu\theta - 2\mu\beta EI \sin \mu\theta + QR^2 \sin \mu\theta - QR^2 \mu\theta \cos \beta \\ & + 2QR^2 \mu\theta \alpha\beta \sin \beta) \end{aligned} \quad (7)$$

for crown-pinned arches subjected to a central concentrated load, and

$$\begin{aligned} \tilde{v} = & \frac{P}{2\mu^2 (\cos \beta - 2\alpha\beta \sin \beta)} (2\cos \beta \cos \mu\theta - 4\alpha\beta \sin \beta \cos \mu\theta + \mu^2 \theta^2 \cos \beta - 2\mu^2 \theta^2 \alpha\beta \sin \beta \\ & + 2\beta \sin \beta - 2 + 4\alpha\beta \sin \beta - \beta^2 \cos \beta + 2\alpha\beta^3 \sin \beta) + \frac{H(\theta)P \sin \mu\theta}{\mu^2 (\cos \beta - 2\alpha\beta \sin \beta)} (\sin \beta - \beta \\ & + 2\alpha\beta \cos \beta - 2\alpha\beta) \end{aligned} \quad (8)$$

for crown-pinned arches subjected to a uniform radial load ( $\beta = \mu\Theta$ ), and leads to the non-linear equilibrium equation between the internal force parameter  $\mu$  and external force  $Q$  or  $q$  as

$$A_1 \tilde{Q}^2 + A_2 \tilde{Q} + A_3 = 0 \quad \text{and} \quad B_1 P^2 + B_2 P + B_3 = 0 \quad (9)$$

for the arches subjected to a central concentrated load and to a uniform radial load respectively, where  $\tilde{Q}$  is the dimensionless load defined by  $\tilde{Q} = R^2 \Theta Q / 2EI$ , and the expressions for coefficients for  $A_1, A_2, A_3, B_1, B_2$  and  $B_3$  are given in Appendix.

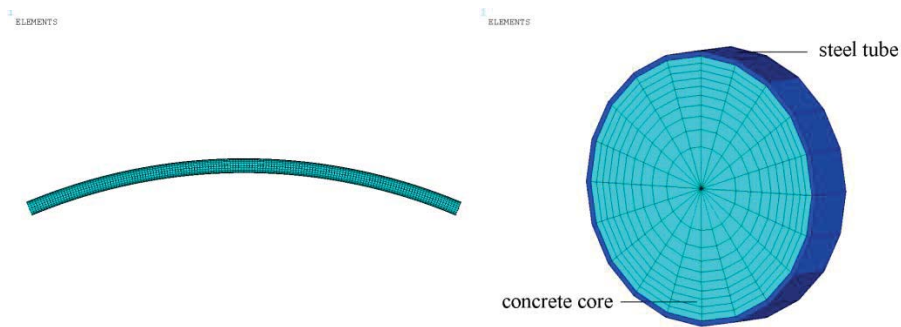
The non-linear equilibrium equation between internal force parameter  $\mu$  and external force  $Q$  (or  $q$ ) given by Eq. (9) has limit points. To determine the limit point, Eq. (9) can be considered as an implicit function of  $Q$  (or  $q$ ) with  $\mu$ . Hence, the load corresponding to the limit points needs to satisfy

$$\frac{dQ}{d\mu} = -\frac{\partial F(Q, \mu) / \partial \mu}{\partial F(Q, \mu) / \partial Q} = 0 \quad \text{or} \quad \frac{dq}{d\mu} = -\frac{\partial F(q, \mu) / \partial \mu}{\partial F(q, \mu) / \partial q} = 0 \quad (10)$$

### Finite element model

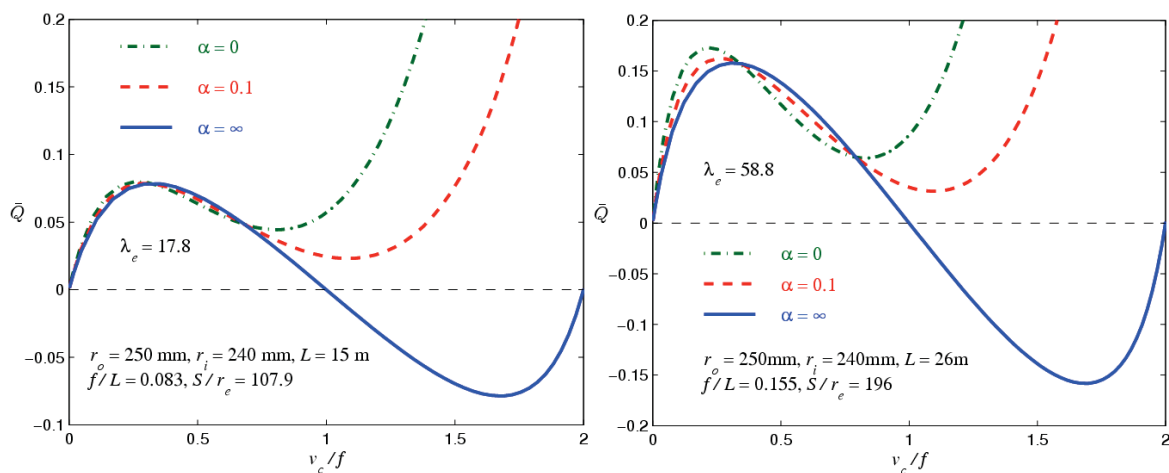
The non-linear behaviour of crown-pinned arches is also investigated using the commercial finite

element package ANSYS (2011). The beam element beam188 of ANSYS is herein used to model crown-pinned concrete-filled steel tubular (CFST) arches because the beam188 provides stress stiffness terms, which enable the element to analyse buckling problems. As shown in Figure 3, CFST section is modelled by using two independent subsections which are fully bonded together. To model an arch, 161 nodes connected in sequence lead to 320 elements through the entire arch. It is noted that in ANSYS, the steel tube and the concrete core are generated into separate but fully-bonded elements. To form the pin connection at the crown of the arch, the rotational degree at the crown about  $z$  axis is released at which the bending moment vanishes. The combined element combin14 of ANSYS is adopted to model the rotational end restraints at two ends where only rotational movement is allowed so that, to some extent, the bending moment can be transmitted but there are no translational movements. In the element combin14, the stiffness  $k$  can be assigned through the relation between load and displacement.



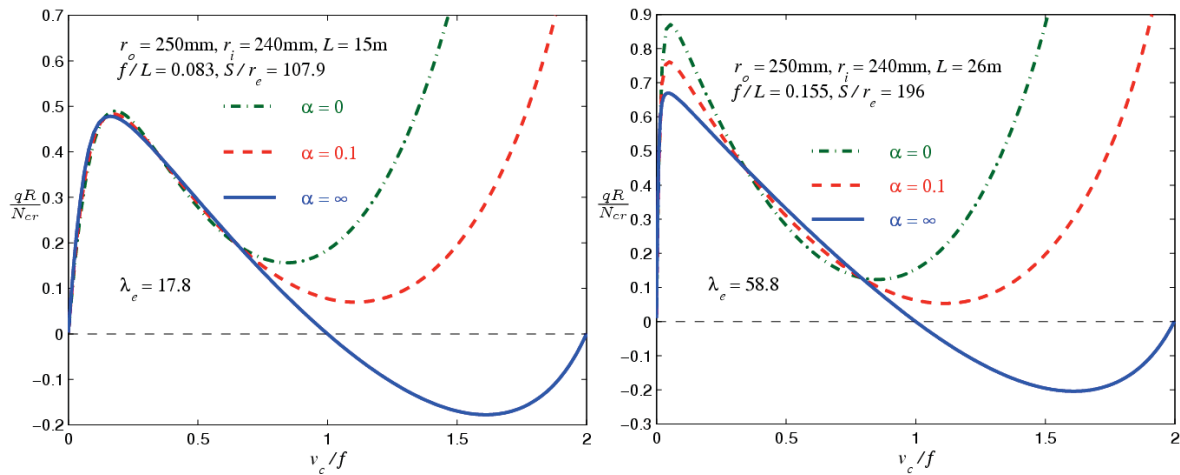
**Figure 3. Finite element model of a crown-pinned CFST arch**

In non-linear analysis, the switch for the geometric nonlinearity is turned on. The Newton-Raphson method is applied in equilibrium iterations to overcome convergence difficulties. To investigate the buckling behaviour of a crown-pinned arch subjected to different loading cases, the arc-length method is used to ensure numerical stable solutions for the static analysis when external load increases in a step-by-step fashion. Based on the computational results, the buckling behaviour of the crown-pinned arch can be characterized by the load-displacement curve as shown in Figs. 4 and 5, which show the buckling behaviour of a crown-pinned CFST arch under different loading cases along with different boundary conditions: pinned ends, fixed ends and rotationally restrained ends.



**Figure 4. Limit point buckling of rotationally restrained crown-pinned arches under a central concentrated load**

The geometry of the arch used in the analyses is shown in Figs. 4 and 5 where  $\lambda_e$  is the modified slenderness of the CFST arch defined by  $\lambda_e = S\Theta/2r_e$  and  $r_e$  is the radius of gyration of the CFST cross-section defined by  $r_e = \sqrt{(E_s I_s + E_c I_c)/(A_s E_s + A_c E_c)}$  where  $E_s$  and  $E_c$  are Young's modulus of the steel tube and core concrete,  $A_s$  and  $A_c$  are the area of the steel tube and concrete core, and  $I_s$  and  $I_c$  are the second moment of the area of the steel tube and concrete core, respectively. Also in Figs 4 and 5,  $\bar{Q} = Q/N_{cr}$  is the dimensionless central concentrated and  $N_{cr}$  is the second mode buckling load of a pinned CFST column about its major axis under uniform axial compression (Pi et al., 2011). When the modified slenderness  $\lambda_e$  is 17.8, the span of the arch is  $L = 15$  m with the rise to span ratio  $f/L = 0.083$  and the ratio of the arch length to the radius of gyration  $S/r_e = 107.9$  which reflects the slenderness of the arch. The stiffness of each rotational end restraint is  $k = 1.12 \times 10^8$  Nm/rad when the dimensionless flexibility of the restraint  $\alpha = 0.1$ . When  $\lambda_e = 58.8$ ,  $L = 26$  m,  $f/L = 0.155$  and  $S/r_e = 196$ , the corresponding stiffness is  $k = 6.15 \times 10^7$  Nm/rad if the dimensionless flexibility  $\alpha = 0.1$ .



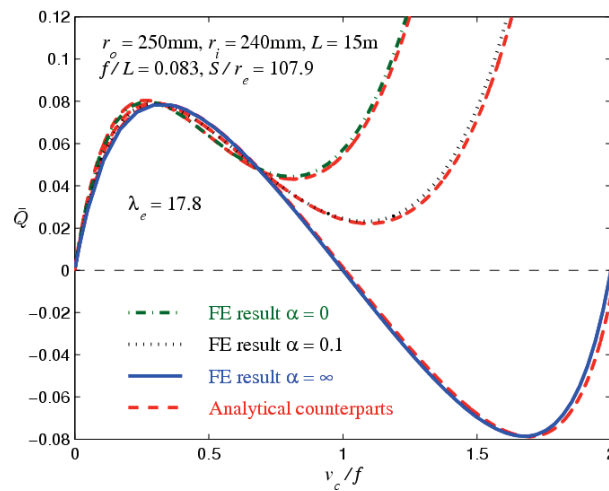
**Figure 5. Limit point buckling of rotationally restrained crown-pinned arches under a uniform radial load**

It can be seen from Figs. 4 and 5 that when the stiffness vanishes, the arch becomes pin-ended, while when the stiffness approaches infinite, the arch ends are fully fixed. When the stiffness is neither zero nor infinite, the buckling behaviour falls in between these two extreme cases. When  $\lambda_e$  equals 17.8, the limit point buckling load increases slightly with a decrease of the dimensionless flexibility  $\alpha$  of rotational end restraints (i.e. with an increase of the corresponding stiffness  $k$ ). When  $\lambda_e = 58.8$ , the increase of the buckling load appears to be more substantial. This shows that effects of the stiffness of the rotational end restraints on the buckling behaviour are more significant for deep and slender crown-pinned arches than for their shallow and stocky counterparts. The finite element results show that the crown-pinned arches can buckle in a limit point instability mode, but cannot buckle in a bifurcation mode, which is quite different from arches without the crown-pin that may buckle in a limit point instability mode or in a bifurcation mode.

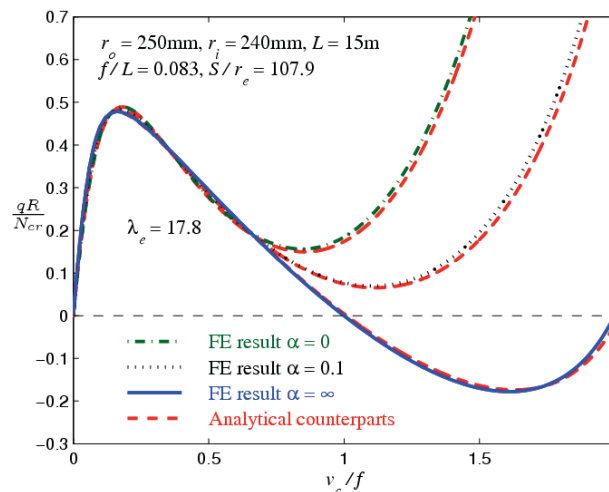
### Comparison of finite element results with analytical solutions

The finite element results are compared with the analytical solutions in Figs. 6 and 7 for the crown-pinned arches with  $\lambda_e = 17.8$ . It can be seen that the discrepancies between finite element result and their analytical counterparts are extremely small and thus can be neglected. They agree very well with each other. This demonstrates that the finite element model is capable of providing accurate

results for predicting the non-linear in-plane buckling loads of crown-pinned shallow circular arches with rotational end restraints.



**Figure 6. Comparison between analytical and finite element results of limit point buckling of a crown-pinned CFST arch under a central concentrated load**



**Figure 7. Comparison between analytical and finite element results of limit point buckling of a crown-pinned CFST arch under a uniform radial load**

## Conclusions

This paper studied the non-linear buckling behaviour of a crown-pinned shallow circular arch with rotational end restraints under a central concentrated load or under a uniform radial load. It was found that the boundary conditions at both ends influence the buckling load of the arch significantly. It was also found that the crown-pin plays an important role in the buckling behaviour of arches. The crown-pinned arches can buckle in a limit point instability mode, but not in a bifurcation mode, which is quite different from arches without the crown-pin that may buckle in a limit point instability mode or in a bifurcation mode. Comparisons of the finite element results with the analytical solutions have shown that the finite element model is capable of providing accurate results for the non-linear buckling behaviour of crown-pinned arches with rotational end restraints.

## References

- Pi, Y. L., Bradford, M. A. and Uy, B. (2002), In-plane stability of arches. *International Journal of Solids and Structures*, 39(1), pp. 105–125.
- Bradford, M. A., Uy, B. and Pi, Y. L. (2002), In-plane stability of arches under a central concentrated load. *Journal of Engineering Mechanics*, 128(7), pp. 710–719.
- Pi, Y. L., Bradford, M. A. and Francis, T. L. (2008), Non-linear in-plane buckling of rotationally restrained shallow arches under a central concentrated load. *International Journal of Non-Linear Mechanics*, 43, pp. 1–17.
- Pi, Y. L., Bradford, M. A. (2009), Non-linear in-plane postbuckling of arches with rotational end restraints under uniform radial loading. *International Journal of Non-Linear Mechanics*, 44(9), pp. 975–989.
- Pi, Y. L., Bradford, M. A. and Qu, W. L. (2011), Long-term non-linear behaviour and buckling of shallow concrete-filled steel tubular arches. *International Journal of Non-Linear Mechanics*, 46, pp. 1155–1166.
- ANSYS, Release 13.0. ANSYS, Inc. Southpointe, 275 Technology Drive, Canonsburg, PA 15317.

## Appendix

$A_1$ ,  $A_2$  and  $A_3$  for the arch subjected to a central concentrated load are given by

$$A_1 = -\frac{1}{12\psi} (24\alpha^2\beta^3 \sin^2 \beta - 24\alpha\beta^2 \cos \beta \sin \beta - 9\cos \beta \sin \beta + 9\beta + 24\alpha\beta \sin^2 \beta - 6\beta \sin^2 \beta) \quad (11)$$

$$A_2 = -\frac{1}{24\psi} [-12\beta^3 + 24\alpha\beta^3 \cos^2 \beta - 72\alpha\beta^3 + (72\alpha\beta^2 \sin \beta - 24\beta \cos \beta)(1 - \cos \beta) + (12\beta^2 \sin \beta + 24\alpha\beta^3 \cos \beta)(1 + \cos \beta)] \quad (12)$$

$$A_3 = \frac{\beta^2}{\lambda^2} - \frac{1}{48\psi} [(48\alpha\beta^5 + 96\alpha^2\beta^5 - 96\alpha^2\beta^4 \sin \beta - 12\beta^4 \sin \beta - 96\alpha\beta^4 \sin \beta)(1 - \cos \beta) - 12\beta^2 \sin \beta \cos \beta + 12\beta^3 - 12\beta^4 \sin \beta + 4\beta^5 + 8\beta^5 \sin^2 \beta + 48\alpha\beta^3 \sin^2 \beta - 48\alpha\beta^4 \sin \beta \cos \beta + 32\alpha\beta^6 \sin \beta \cos \beta - 32\alpha^2\beta^7 \sin^2 \beta] \quad (13)$$

with  $\psi$  and  $\lambda$  defined by

$$\psi = \beta^5 (-\cos^2 \beta + 4\alpha\beta \sin \beta \cos \beta - 4\alpha^2\beta^2 \sin^2 \beta) \quad (14)$$

$$\lambda = \frac{S\Theta}{2r_e} \quad (15)$$

and  $B_1$ ,  $B_2$  and  $B_3$  for for crown-pinned arches subjected to a uniform radial load are given by

$$B_1 = \frac{1}{12\zeta} (-24\beta \cos \beta - 36\alpha\beta^3 - 3\beta - 36\alpha\beta + 6\beta^2 \sin \beta + 15\cos \beta \sin \beta - 48\alpha\beta \cos \beta + 84\alpha\beta \cos^2 \beta - 3\beta^3 - 8\alpha^2\beta^5 + 72\alpha\beta^2 \sin \beta + 24\alpha^2\beta^3 \cos \beta + 120\alpha^2\beta^2 \sin \beta + 12\alpha\beta^3 \cos \beta - 12\alpha\beta^2 \cos \beta \sin \beta + 48\alpha^2\beta^3 \cos^2 \beta - 120\alpha^2\beta^2 \cos \beta \sin \beta - 72\alpha^2\beta^3 + 9\beta^2 \sin \beta \cos \beta + 8\alpha\beta^4 \cos \beta \sin \beta + 24\alpha\beta^3 \cos^2 \beta + 8\alpha^2\beta^5 \cos^2 \beta + 12\beta \cos^2 \beta - 2\beta^3 \cos^2 \beta) \quad (16)$$

$$\begin{aligned}
B_2 = \frac{1}{12\zeta} & (-16\alpha^2\beta^5 + 12\cos\beta\sin\beta + 48\alpha\beta^2\sin\beta + 72\alpha\beta\cos^2\beta - 24\alpha\beta - 24\alpha\beta^3 \\
& - 48\alpha\beta\cos\beta - 24\beta\cos\beta - 48\alpha^2\beta^3 + 96\alpha^2\beta^2\sin\beta + 16\alpha\beta^4\cos\beta\sin\beta - 4\beta^3\cos^2\beta \\
& + 12\beta\cos^2\beta + 12\beta^2\cos\beta\sin\beta + 48\alpha^2\beta^3\cos^2\beta - 96\alpha^2\beta^2\cos\beta\sin\beta + 16\alpha^2\beta^5\cos^2\beta \\
& + 24\alpha\beta^3\cos^2\beta)
\end{aligned} \tag{17}$$

$$B_3 = \frac{\beta^2}{\lambda^2} \tag{18}$$

with  $\zeta$  defined by

$$\zeta = \beta^3(-\cos^2\beta + 4\alpha\beta\cos\beta\sin\beta - 4\alpha^2\beta^2\sin^2\beta) \tag{19}$$



## Deformation Properties of Single Red Blood Cell in a Stenosed Microchannel

P.G.H. Nayanajith<sup>1</sup>, S. C. Saha<sup>1</sup>, and Y.T. Gu<sup>1\*</sup>

<sup>1</sup>School of Chemistry, Physics and Mechanical Engineering  
Queensland University of Technology, Brisbane, Queensland, Australia

\*Corresponding author: yuantong.gu@qut.edu.au

### Abstract

Red Blood Cells (RBCs) exhibit different types of motions and different deformed shapes, when they move through capillaries. RBCs can travel through capillaries having smaller diameters than RBCs' diameter, due to the capacity of high deformability of the viscoelastic RBC membrane. The motion and the steady state shape of the RBCs depend on many factors, such as the geometrical parameters of the microvessel through which blood flows, the RBC membrane bending stiffness and the flow velocity. In this study, the effect of the RBC's membrane stiffness on the deformation of a single RBC in a stenosed capillary is comprehensively examined. Smoothed Particle Hydrodynamics (SPH) in combination with the two-dimensional spring network membrane model is used to investigate the motion and the deformation property of the RBC. The simulation results demonstrate that the membrane bending stiffness of the RBC has a significant impact on the RBCs' deformability.

**Keywords:** Red Blood Cell (RBC), Smoothed Particle Hydrodynamics (SPH), Stenosed Capillary, Meshfree Methods, Microcirculation, Numerical Simulations.

### Introduction

RBCs are the most common type of the blood cell in the human blood and they occupy about 45% of total blood volume (Skalak et al. 1989, Tsubota et al. 2006a). Human RBCs consist of a thin viscoelastic membrane and they do not contain nuclei inside of the cell. Due to the existence of the viscoelastic membrane, RBCs exhibit different types of motions and deformed shapes, when the blood flows within the cardiovascular network (Fedosov et al. 2010, Pozrikidis 2003). The motion and the deformation mechanism of a RBC highly depend on the maximum velocity of the plasma flow, bending stiffness of the RBC and the diameter of the microchannel, through which the RBC flows (Shi et al. 2012). Over the last few decades, a number of numerical studies were conducted to understand the RBCs' behaviour in the microchannels.

It is important to study the RBCs' motion and deformation accurately, when they are squeezing through capillaries. Since, some diseases such as malaria, cancer, and sickle cell anemia can alter

the ability of deformability of the RBCs (Jiang et al. 2013), they might not be able to deform enough to pass through the narrow capillaries. Further, if the blood vessel is stenosed, there is a high risk of micro vascular blockage (Cooke et al. 2001). In the past, most of the studies were carried out to investigate the RBCs' behaviour in the microchannels with uniform cross sectional areas and few studies have been done to explore the RBCs' motion and deformation mechanism in stenosed microchannels. Hosseini and Feng (2009) have presented the RBCs' ability of squeezing through a tiny capillary, whose diameter is smaller than the mean diameter of the RBCs. They used the SPH method and modelled the microchannel, such that it has a larger uniform diameter at the inlet and a smaller uniform diameter at the outlet. Vahidkhah and Fatourae (2012) proposed a immersed boundary–lattice Boltzmann method to investigate the RBCs' behaviour in a stenosed arteriole. However, they presented more qualitative results of the RBCs' deformation in a stenosed arteriole.

The purpose of this paper is to present an advanced numerical modelling technique using SPH to analyse motion and deformation of a single RBC through a stenosed capillary. The RBC membrane is modelled by a spring network and the forces acting on the RBC membrane is determined based on the minimum energy principle (Gallage et al. 2012a, Pan and Wang 2009, Tsubota et al. 2006b). First, we present the motion and deformation of a RBC, when it passes through a stenosed capillary. Then, we compare the effect of the RBC's membrane stiffness on the deformation and the motion of the RBC.

## Model and Method

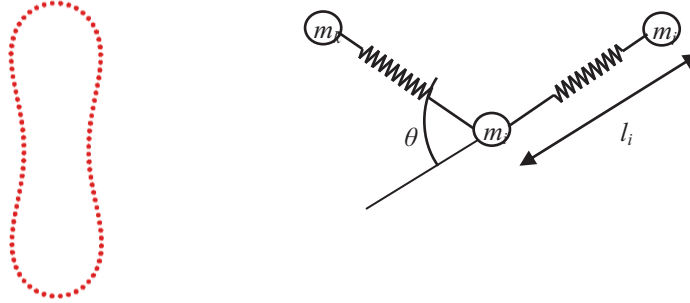
In this study, the RBC membrane is modelled by a two-dimensional spring network as used in the previous studies (Gallage et al. 2012b, Shi et al. 2012). The membrane of the RBC is constructed by 88 membrane particles, which are interconnected by elastic springs. Initially, it is assumed that the shape of the RBC membrane is a circle with radius of  $2.8 \mu\text{m}$ .

$$E_l = \frac{1}{2} K_l \sum_{i=1}^N \left( \frac{l_i - l_0}{l_0} \right)^2 \quad (1)$$

$$E_b = \frac{1}{2} K_b \sum_{i=1}^N \tan^2 \left( \frac{\theta_i}{2} \right) \quad (2)$$

$$E_s = \frac{1}{2} K_s \left( \frac{s - s_e}{s_e} \right)^2 \quad (3)$$

$$\mathbf{F}_i = -\frac{\partial(E_l + E_b + E_s)}{\partial \mathbf{r}_i} \quad (4)$$



**Fig. 1:** Spring network model of the RBC

The elastic energy ( $E_l$ ) stored in the springs due to the stretch/ compression is given by **Eq. (1)** and the elastic bending energy ( $E_b$ ) stored in the springs due to the bending is given by **Eq. (2)**. In order to maintain a constant membrane area, a penalty function ( $E_s$ ) is introduced as in **Eq. (3)**. The total force ( $\mathbf{F}_i$ ) acting on the  $i^{\text{th}}$  membrane particle is calculated, using the principal of virtual work as in **Eq. (4)**, where  $\mathbf{r}_i$  is the Position vector of the  $i^{\text{th}}$  Particle.  $l_i$ ,  $\theta_i$ , and  $s$  are length of the  $i^{\text{th}}$  spring, angle between two consecutive springs and area of the RBC respectively. Spring constant for stretching/compression ( $K_l$ ), spring constant for bending ( $K_b$ ) and penalty coefficient ( $K_s$ ) are set to  $5 \times 10^{-8}$  N.m,  $5 \times 10^{-10}$  N.m and  $1 \times 10^{-5}$  N.m respectively as used by Shi et al. (2012). The reference length ( $l_0$ ) is taken as  $0.2 \mu\text{m}$ , while the Equivalent area of the RBC ( $s_e$ ) is set to  $\pi \times (2.8 \times 10^{-6})^2 \times 0.55 \text{ m}^2$  as used in the work by Pan and Wang (2009). When the forces acting on the RBC membrane particles are minimised, the initial circular shape gives a biconcave shape as shown in **Fig. 1**.

RBC internal fluid (cytoplasm) and external fluid (plasma) are modelled by a set of particles and Navier-Stokes equations (**Eq. (5)** and **Eq. (6)**) in Lagrangian form are used to model the whole flow field, with the assumption of the system is isothermal.

$$\frac{D\rho}{Dt} = -\rho \nabla \cdot \mathbf{v} \quad (5)$$

$$\frac{D\mathbf{v}}{Dt} = -\frac{1}{\rho} \nabla p + \frac{\mu}{\rho} \nabla^2 \mathbf{v} + \mathbf{f} \quad (6)$$

where  $\rho$  and  $\mu$  are the density and the dynamic viscosity of the fluid,  $\mathbf{v}$  is the velocity vector and  $p$  is the pressure while  $\mathbf{f}$  is the vectorial external force.

In SPH methodology, any field function value ( $f$ ) of a particle can be approximated from the same field function value of surrounding neighbouring particles using a kernel function ( $W$ ) as shown in

**Eq. (7).** For this study, popular cubic spline smoothing function is used as used by Gallage et al. (2012b).

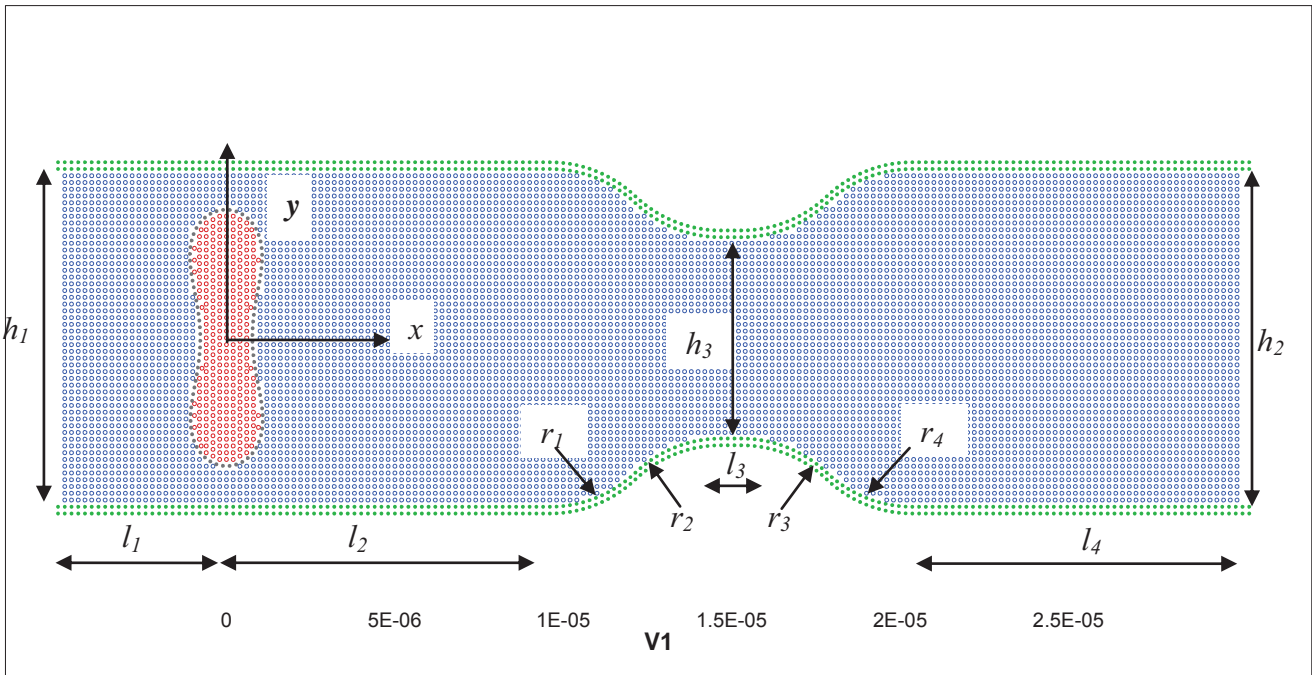
$$f_i = \sum_{j=1}^N \frac{m_j}{\rho_j} f_j W_{ij} \quad (7)$$

The Navier-Stokes equations are modified according to the SPH methodology (Liu and Liu 2003) and are used to determine the particle positions and velocities. The capillary wall is modelled by a set of boundary particles and pair-wisely repulsive forces are introduced to avoid any penetration of fluid particles through the capillary wall (Gallage et al. 2012b).

The problem domain is discretised into SPH particles, as shown in **Fig. 2**, such that the particle spacing is equal to  $0.2 \mu\text{m}$ . Geometrical parameters of the problem domain is shown in the **Table 1**.

**Table 1:** Geometrical parameters of the stenosed capillary

Parameter	$h_1$	$h_2$	$l_1$	$l_2$	$l_3$	$l_4$	$r_1$	$r_2$	$r_3$	$r_4$
Value ( $\mu\text{m}$ )	9.8	9.8	4.9	19.6	0.6	9.7	3.7	3.7	3.7	3.7



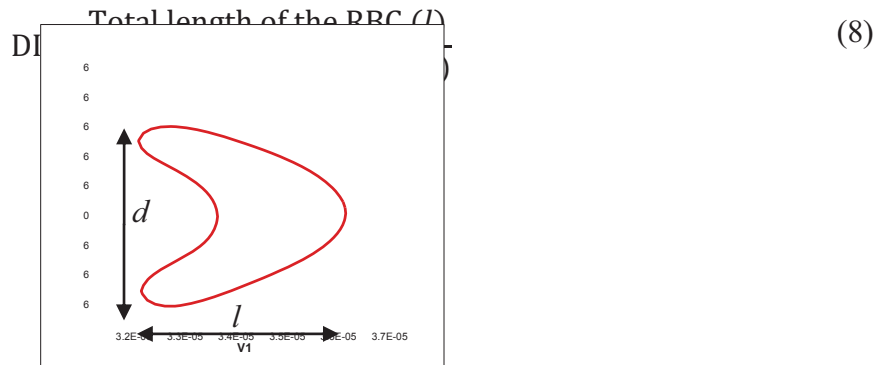
## Results and discussions

### Deformation Index of the RBC in the stenosed capillary

A constant pressure ( $P_I=450 \text{ Pa}$ ) is applied at the inlet, and the outlet pressure is set to zero. Those boundary conditions give a constant pressure gradient of  $1 \times 10^7 \text{ Pa/m}$ . The pressure of each particle is calculated based on the  $x$ -directional distance and the pressure gradient, and then it is applied to the particles. The pressure gradient used for this study is quiet high. If this pressure gradient was applied to a capillary having a uniform diameter of  $9.8 \mu\text{m}$  and no RBCs, then the peak velocity of

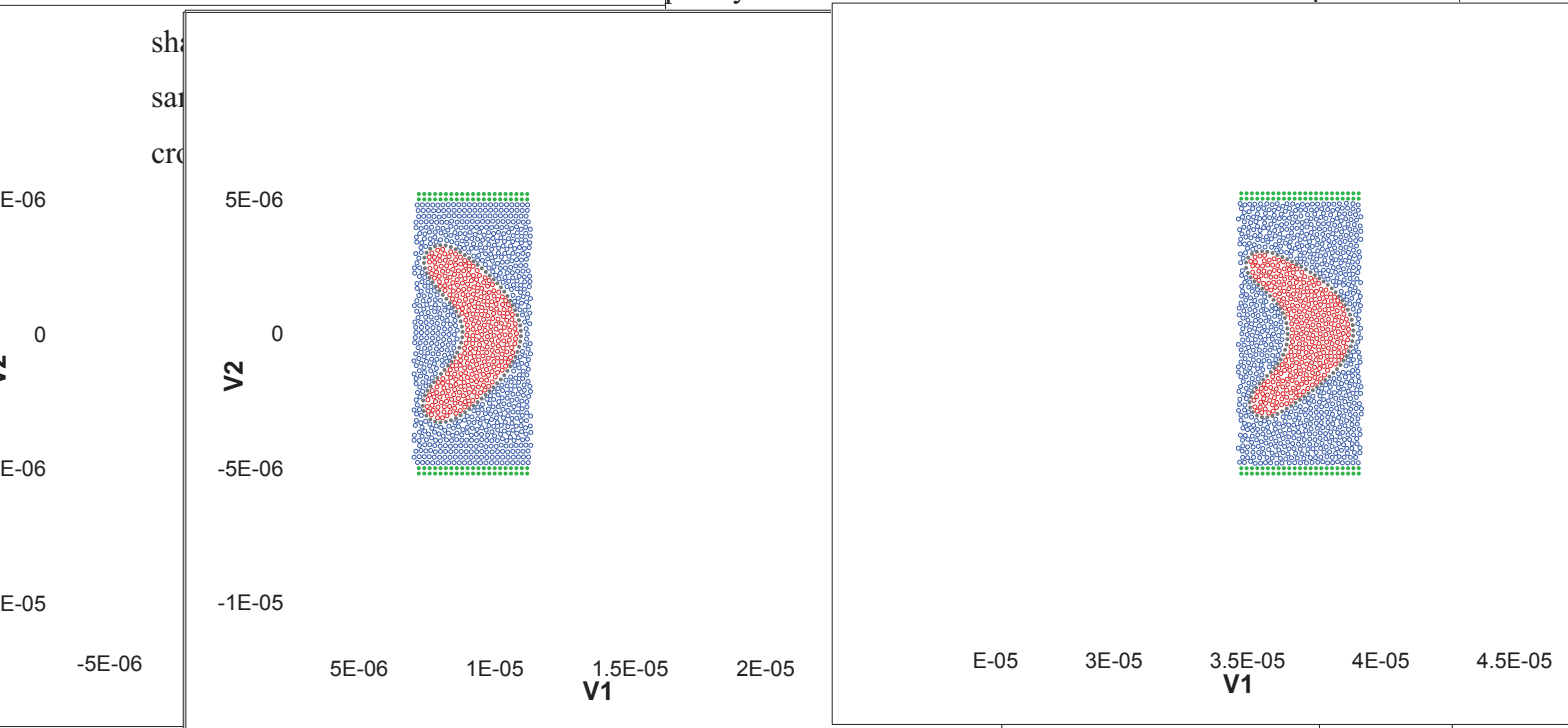
the plasma flow would be 0.12005 m/s. It corresponds to Reynolds number,  $Re=1.17649$ . Due to the applied pressure in the inlet, the RBC begins to move with plasma flow. While RBC is moving it deforms and the initial biconcave shape of the RBC is changed to the parachute shape. **Fig. 3** shows that the deformation of the RBC is quite significant, when it is flowing through the stenosed area.

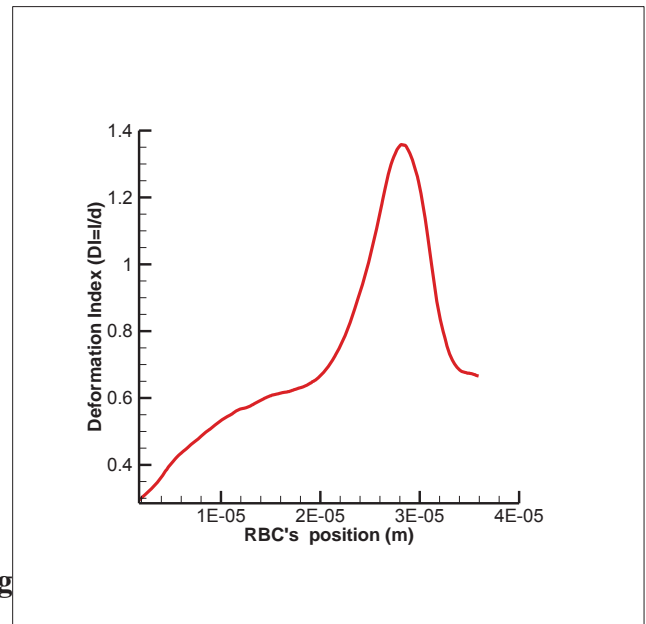
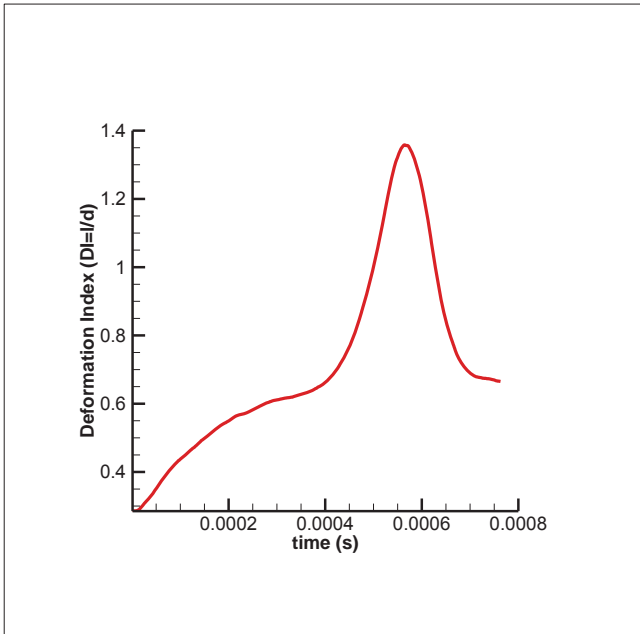
The Deformation Index of the RBC can be defined as in **Eq. (8)**



**Fig. 3:** Deformed RBC;  $DI= l/d$

Initially, RBC flows through a section where capillary diameter is uniform and during that period of time DI of the RBC increases gradually (see **Fig. 4**). When  $t=0.4$  ms, the DI reaches almost a steady value of 0.65. But after  $t=0.4$  ms RBC enters to a narrow passage, where cross sectional area of the capillary is suddenly reduced. Then the DI of the RBC increases drastically with time and variation of the DI with the RBC's position shows a similar pattern (see **Fig. 5** and **Fig. 6**). However, it can be seen that from **Fig. 7** the RBC's position does not have a linear relationship with time. The DI reaches a peak value about 1.39 when the RBC squeezes through the stenosed area. This happens at  $t=0.6$  ms and a significant difference in the deformed RBC's shape can be observed when it passes through the narrowest area of the capillary (see **Fig 4**). Then the RBC's DI decreases with the time, as it leaves the stenosed area of the capillary and the RBC starts to recover its normal parachute





Fig

When the RBC squeezes through the stenosed area, it flows at a maximum velocity of about 0.06 m/s. However, the mean velocity of the RBC takes a lower value just after the stenosed area, compared with its velocity just before the stenosed area (see Fig. 7). At  $t=0.84$  ms, all the RBC membrane particles and cytoplasm particles have almost reached a unique velocity (see Fig. 8). But, the mean RBC velocity is still subjected to some minor fluctuation, as seen in Fig. 7. Fig. 8 shows that the plasma particles located close to the capillary wall have a lower velocity, while the plasma

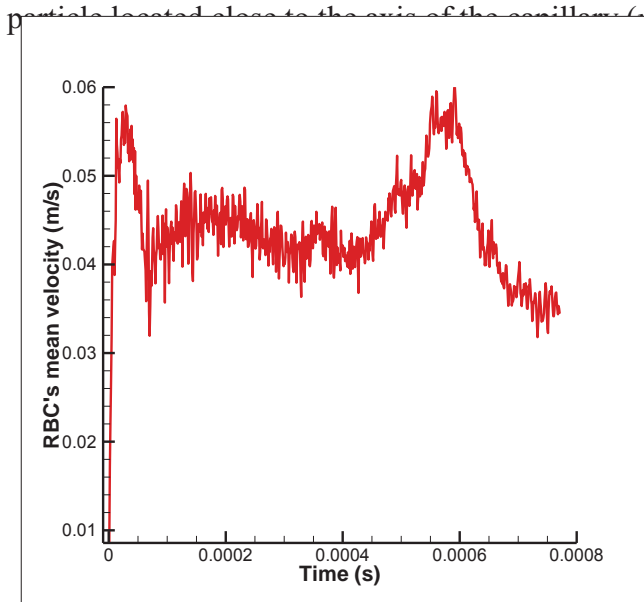


Fig. 7: Variation of RBC's mean velocity

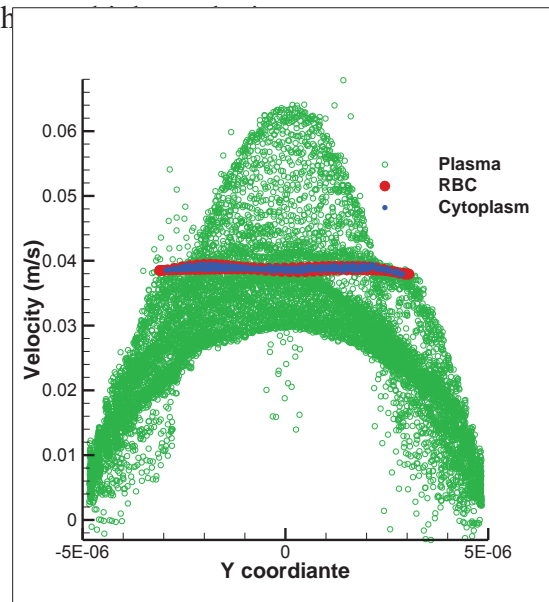


Fig. 8: Velocity profile at  $t=0.84$  ms

*Effect of the RBC's membrane stiffness*

Deformation Indices of three RBC with different membrane stiffness are compared. For this simulation,  $l_2$  is set to  $9.6 \mu\text{m}$ . Therefore, the total length of the stenosed capillary in  $x$ -direction is  $35 \mu\text{m}$  and the minimum height ( $h_3$ ) at the stenotic area is not changed.  $P_1$  is set to 350 Pa, to

maintain a constant pressure gradient of  $1 \times 10^7$  Pa/m. Spring constant for bending ( $K_b$ ) is changed from  $5 \times 10^{-10}$  N.m to  $5 \times 10^{-9}$  N.m and  $5 \times 10^{-11}$  N.m. All the other simulation parameters are kept same as previous. The RBC having higher  $K_b$  value exhibits a lower deformation and the RBC with a less  $K_b$  value shows a greater deformation. When the RBC with  $K_b = 5 \times 10^{-9}$  N.m flows the stenosed area, the thickness of the plasma layer exist between RBC membrane and the capillary wall is very narrow (see Fig. 9). Further increase in bending constant would lead to blockage of the RBC, since RBC deforms less for higher bending constant values. Fig. 10 shows that three RBCs exhibit similar deformation pattern with respect to their positions. Further, DI of the RBC with  $K_b = 5 \times 10^{-9}$  has been reduced drastically. While, there is no significant change in the deformation indices of the RBCs with  $K_b = 5 \times 10^{-11}$  and  $K_b = 5 \times 10^{-10}$ .

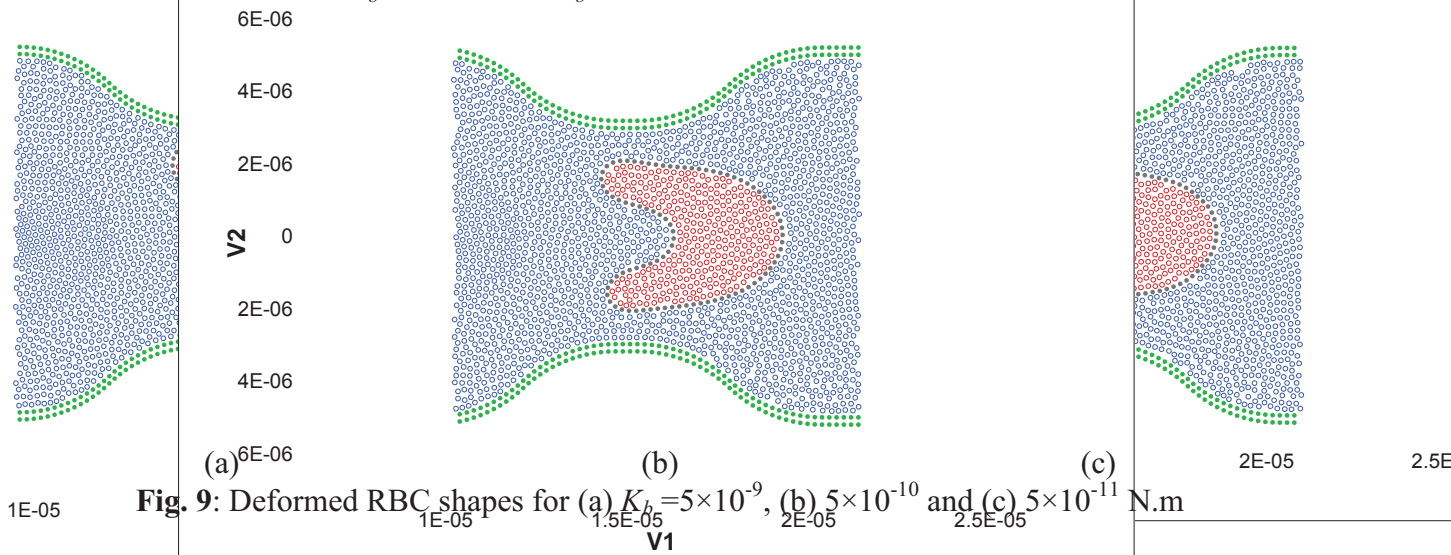


Fig. 9: Deformed RBC shapes for (a)  $K_b = 5 \times 10^{-9}$ , (b)  $5 \times 10^{-10}$  and (c)  $5 \times 10^{-11}$  N.m

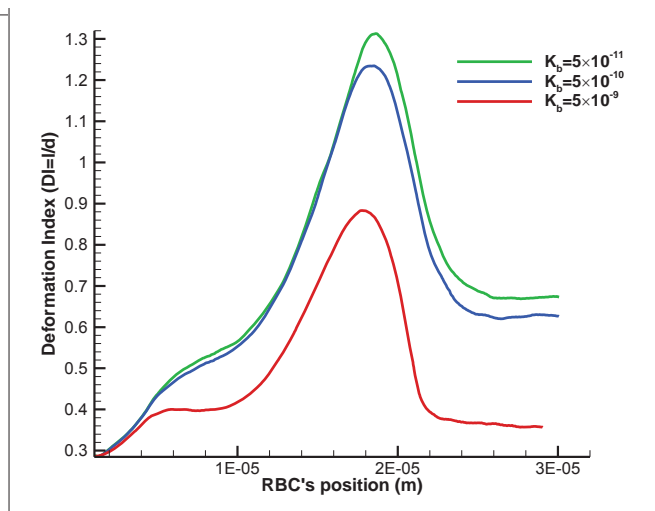


Fig. 10: The variation of the DI with time for different  $K_b$  values

## Conclusions

The SPH model in combined with the spring network model is used to investigate the RBCs deformation behaviour through a stenosed capillary. We observed that, the geometrical shape of the capillary, through which RBCs move, makes a significant effect on the deformation index of the RBC. When there is a stenosed part in the capillary, the flow field changes and the RBCs are subjected to larger deformation. Further, results revealed that the deformability of the RBCs highly depends on the RBCs bending stiffness. The RBC having a higher bending stiffness shows a less Deformation Index and the thickness of the plasma layer exist between RBC membrane and the capillary wall is very narrow, when the RBC moves through a stenosed capillary. However, to get more accurate results, the deformation property of the RBCs should be studied, when they are interacted with other RBCs. In our future's work, we aim to study the effect of multiple RBCs, when blood is flowing through a stenosed capillary in the near future.

## Acknowledgements

Support from the ARC Future Fellowship grant (FT100100172) is gratefully acknowledged.

## References

- Cooke BM, Mohandas N, Coppel RL. 2001. The malaria-infected red blood cell: structural and functional changes. *Advances in parasitology* 50: 1-86.
- Fedosov DA, Caswell B, Karniadakis GE. 2010. A multiscale red blood cell model with accurate mechanics, rheology, and dynamics. *Biophysical journal* 98: 2215-2225.
- Gallage P, Nayanajith H, Gu Y, Saha SC, Senadeera W, Oloyede A. 2012a. Numerical simulation of red blood cells' motion: a review.
- Gallage P, Nayanajith H, Gu Y, Saha SC, Senadeera W, Oloyede A. 2012b. Numerical simulation of red blood cells' deformation using SPH method.
- Hosseini SM, Feng JJ. 2009. A particle-based model for the transport of erythrocytes in capillaries. *Chemical Engineering Science* 64: 4488-4497.
- Jiang XM, Wang T, Xing ZW. 2013. Simulation Study of Hemodynamics of Red Blood Cells in Stenotic Microvessels. *Advanced Materials Research* 647: 321-324.
- Liu G-R, Liu M. 2003. *Smoothed particle hydrodynamics: a meshfree particle method*: World Scientific Publishing Company Incorporated.
- Pan TW, Wang T. 2009. Dynamical simulation of red blood cell rheology in microvessels. *International Journal of Numerical Analysis & Modeling* 6: 455-473.
- Pozrikidis C. 2003. Numerical simulation of the flow-induced deformation of red blood cells. *Annals of biomedical engineering* 31: 1194-1205.
- Shi L, Pan TW, Glowinski R. 2012. Deformation of a single red blood cell in bounded Poiseuille flows. *Physical Review E* 85: 016307.
- Skalak R, Ozkaya N, Skalak TC. 1989. Biofluid mechanics. *Annual review of fluid mechanics* 21: 167-200.
- Tsubota K-i, Wada S, Yamaguchi T. 2006a. Particle method for computer simulation of red blood cell motion in blood flow. *Computer methods and programs in biomedicine* 83: 139-146.
- Tsubota K-i, Wada S, Yamaguchi T. 2006b. Simulation study on effects of hematocrit on blood flow properties using particle method. *Journal of Biomechanical Science and Engineering* 1: 159-170.
- Vahidkhah K, Fatourae N. 2012. Numerical simulation of red blood cell behavior in a stenosed arteriole using the immersed boundary–lattice Boltzmann method. *International journal for numerical methods in biomedical engineering* 28: 239-256.



# Natural convection in a reservoir induced by periodic thermal forcing at the water surface

\*Yadan Mao

State Key Laboratory of Geological Processes and Mineral Resources, Institute of Geophysics and Geomatics, China  
University of Geosciences, Wuhan 430074, China

\*Corresponding author: yadan\_mao@cug.edu.cn

## Abstract

Natural convection in nearshore waters induced by differential heating has significant biological and environmental impact. The present investigation is concerned with natural convection in a reservoir model induced by periodic thermal forcing at the water surface. A semi-analytical approach coupled with scaling analysis and numerical simulation is adopted to resolve the problem. The scales for temperature and flow velocity, as well as the time lag of flow response to the thermal forcing have been derived. These derived scales have been verified by results from numerical simulations. Flow response at different stages of the periodic forcing has been illustrated through snapshots of isotherms and streamlines. The phase delay of the flow response to the thermal forcing decreases as the length of period increases.

**Keywords:** Natural convection, Buoyant boundary layers, Scaling analysis, Semi-analytical solution, Numerical simulation, Periodic thermal forcing,

## Introduction

As the depth of water increases in the offshore direction, when subject to the same rate of daytime heating or nighttime cooling, the shallow water near shore experiences larger temperature variations than that in offshore regions. This generates a horizontal temperature gradient that drives a circulation across shore, often referred to as a ‘thermal siphon’. Field observations (Adams and Wells, 1984; Monismith *et al.* 1990; 2006) have demonstrated the significance of this buoyancy driven flow in promoting water exchanges across shore. It is revealed that this thermal siphon plays the dominant role in driving cross-shore circulation in calm nearshore regions with limited wind-driven or tidal circulation, substantially reducing the residence of nearshore water bodies.

This convective circulation plays an important role in the transport of nearshore nutrients or pollutants (James and Barko, 1991; Niemann *et al.*, 2004), and therefore has significant biological and environmental implications. These have motivated a series of theoretical investigations to quantify it. For the daytime heating case, the asymptotic solutions (Farrow & Patterson 1994) and scaling analysis (Lei and Patterson, 2002; Mao *et al.*, 2009) provide important insight into natural convection induced by absorption of radiation. For the nighttime surface cooling case, Horsch and Stefan (1988) established an approximate relation between the flow rate and the Rayleigh number through numerical simulations and laboratory experiments. Later, through scaling analysis, detailed scaling has been derived for the cooling case (Lei and Patterson, 2005; Mao *et al.*, 2010).

All the above theoretical investigations have been conducted for constant thermal forcing. For the case of diurnally varying thermal forcing, the asymptotic solution (Farrow 2004) has been derived under the assumption that the daytime radiation energy and nighttime heat loss is uniformly distributed over the local water depth. A diurnal thermal forcing model more relevant to field situations was realized in the numerical simulations of Lei and Patterson (2006). However, no

scaling analysis is yet available for natural convection generated by diurnal thermal forcing. This has motivated the present study, which focuses on natural convection generated by periodic thermal forcing at the water surface.

### Model formulation

A two-dimensional (2D) model with water depth varying with offshore distance is adopted to capture the basic mechanism of the cross-shore exchange flow. A 2D reservoir consisting of one section with a sloping bottom with a slope of  $A$  and the other section with a uniform depth is considered (Figure 1). With the Boussinesq assumption, the normalized 2D Navier-Stokes and energy equations governing the flow and temperature evolution are written as:



Figure 1 Sketch of the flow domain and the coordinate system.

$$\frac{\partial u}{\partial x} + \frac{\partial v}{\partial y} = 0, \quad (1)$$

$$\frac{\partial u}{\partial t} + u \frac{\partial u}{\partial x} + v \frac{\partial u}{\partial y} = -PrRa \frac{\partial p}{\partial x} + Pr \nabla^2 u, \quad (2)$$

$$\frac{\partial v}{\partial t} + u \frac{\partial v}{\partial x} + v \frac{\partial v}{\partial y} = -PrRa \frac{\partial p}{\partial y} + Pr \nabla^2 v + PrRa\tau, \quad (3)$$

$$\frac{\partial \tau}{\partial t} + u \frac{\partial \tau}{\partial x} + v \frac{\partial \tau}{\partial y} = \nabla^2 \tau. \quad (4)$$

where  $Pr$  and  $Ra$  are Prandtl number and Rayleigh number respectively, defined as:

$$Pr = \nu/\kappa, \quad Ra = g\beta\Delta T h^3 / (\nu k) \quad (5)$$

The parameters  $g$ ,  $\kappa$ ,  $\nu$ ,  $\beta$  are the acceleration due to gravity, thermal diffusivity, kinematic viscosity and thermal expansion coefficient of the fluid at a reference temperature  $T_0$ , respectively. The respective scales for the normalization are: the length scale  $x, y \sim h$ ; the time scale  $t \sim h^2/\kappa$ ; the velocity scale  $u, v \sim \kappa/h$ ; and the pressure gradient scale  $p_x, p_y \sim \rho_0 g \beta \Delta T$ . The non-dimensional temperature  $\tau$  is defined as  $(T - T_0)/\Delta T$ . Temperature at the water surface  $T_{y=0}$  is varying periodically:

$$T_{y=0} = T_0 + \Delta T \sin(2\pi t/P) \quad (6)$$

The water surface is assumed to stress free ( $\partial u/\partial y = 0$ ,  $v=0$ ), whereas, the bottom is assumed adiabatic ( $\partial \tau/\partial \hat{n} = 0$ ) and no-slip ( $u=0$ ,  $v=0$ ). An open boundary condition is considered for the endwall ( $\partial u/\partial x = 0$ ,  $v=0$ ,  $\partial \tau/\partial x = 0$ ) with a backflow at the reference temperature  $T_0$ . The water body is initially set to be stationary and isothermal.

### Theoretical analysis

Under an isothermal water surface, the vertical temperature gradient is much larger than the horizontal temperature gradient, and therefore vertical conduction dominates over horizontal conduction. Initially, the flow velocity is small and, thus, convection is also small. If convection and

horizontal conduction are neglected, the problem can be simplified as a one-dimensional conduction problem with a variable local water depth of  $Ax$ :

$$\frac{\partial \tau}{\partial t} = \frac{\partial^2 \tau}{\partial y^2} \quad (7)$$

$$\tau = \sin(2\pi t / P) \quad (y=0), \quad (8)$$

$$\frac{\partial \tau}{\partial y} = 0 \quad (y=-Ax), \quad (9)$$

$$\tau = 0 \quad (t=0). \quad (10)$$

An isothermal water surface and an adiabatic bottom are specified by (8) and (9), respectively. Equation (9) is the leading order approximation of  $\partial \tau / \partial \hat{n} = 0$  under the assumption of small bottom slope  $A$ . An isothermal initial condition is embodied in (10). The above equations can be solved through separation of variables, and the solution of (7-10) is

$$\tau = \sin\left(\frac{2\pi}{P}t\right) + \sum_{n=0}^{\infty} \frac{32A^2x^2 \cos(2\pi t/P)}{(2n+1)^3 P \pi^2} \left(1 - e^{-\frac{(n+1/2)^2 \pi^2 t}{A^2 x^2}}\right) \sin\left(\frac{(n+1/2)\pi}{Ax}y\right). \quad (11)$$

Given sufficient length of time, the exponential term approaches zero.  $n = 0$  is the dominant term. Therefore the temperature can be simplified as:

$$\tau = \sin\left(\frac{2\pi}{P}t\right) + \frac{32A^2x^2}{\pi^2 P} \sin\left(\frac{\pi y}{2Ax}\right) \cos\left(\frac{2\pi}{P}t\right), \quad (12)$$

The non-dimensional temperature  $\tau$  averaged over the local depth can be obtained from equation (12):

$$\bar{\tau} = \frac{1}{Ax} \int_{-Ax}^0 \tau dy \approx \sin\left(\frac{2\pi}{P}t\right) - \frac{64A^2x^2}{P\pi^3} \cos\left(\frac{2\pi}{P}t\right) \approx \sqrt{1 + \left(\frac{64A^2x^2}{P\pi^3}\right)^2} \sin\left(\frac{2\pi}{P}t - \theta\right) \quad (13)$$

where  $\theta$  is the phase delay of the vertically-averaged temperature,

$$\theta \sim \arctan\left(\frac{64A^2x^2}{\pi^3 P}\right), \quad (14)$$

Following the same procedure described in Mao *et al.* (2012), a balance between buoyancy induced pressure gradient and viscous terms in the momentum equations yields the following scaling for velocity:

$$u \sim \frac{128RaA^5x^4}{\pi^3 P} \cos\left(\frac{2\pi t}{P} - \theta\right). \quad (15)$$

The above derivation is conducted under the assumption that convection is negligible and therefore applies only to the conductive region. As revealed by Mao *et al.* (2009, 2010), even for high  $Ra$  number flow regime, there is a nearshore conductive subregion, and the scope of this subregion shrinks landward as  $Ra$  increases. In the following verification of the above scaling results, the data is selected within the nearshore conductive region.

### Numerical simulations

The normalized equation (1)-(4) are solved numerically using a finite-volume method. The SIMPLE (semi-implicit method for pressure-linked equations) scheme is adopted for pressure-velocity coupling; and the QUICK (quadratic upstream interpolation for convective kinematics)

scheme is applied for spatial derivatives. A second-order implicit scheme is applied for time discretization in calculating the transient flow.

The simulation is conducted with a non-dimensional depth of 1, a bottom slope of  $A=0.1$ , a horizontal length of  $L = 20$ , and a fixed Prandtl number of  $Pr = 7$ . The section with a uniform depth is set to be of the same length as the sloping section. The numerical simulation is conducted for ten full thermal forcing cycles to minimize the start-up effect.

### Verification for scaling

The verification of scaling results is conducted with respect to both the magnitude and the phase delay. The maximum velocity  $u_{max}$  over the local depth is obtained for each  $x$ . Time series of  $u_{max}$  is plotted in Figure 2(a, c) for different horizontal positions and different periods respectively. It is clear that the start-up effect is only noticeable within the first cycle. If there were no phase delay  $\theta$ , the velocity would reach a maximum at the start of a cycle as indicated by the cosine sign in scaling (15). However, this maximum is delayed due to the phase lag. Phase lag obtained from simulation is plotted against the scaling result in figure 2(b, d), where a clear linear relation is identified, and therefore the dependency of phase lag on  $x$  and  $P$  predicted by scaling (15) is verified.

Figure 2(a, c) shows that the maximum horizontal velocity within the cooling phase is smaller than that within the heating phase. During the heating phase, the circulation is clockwise with the surface layer flowing horizontally offshore and the bottom layer flowing up long the slope, and thus the maximum horizontal velocity  $u_{max}$  is obtained within the surface layer (Mao *et al.* 2009). During the cooling phase, the circulation is anticlockwise and the surface layer flows landward and bottom layer flows down the slope (Mao *et al.* 2010), and therefore,  $u_{max}$  is obtained within the bottom layer. As the intensity of thermal forcing during the cooling phase is the same as the heating phase, the absolute value of velocity is the same, but the direction is opposite. This reveals that the absolute value of  $u$  in the bottom layer is smaller than that in the surface layer.

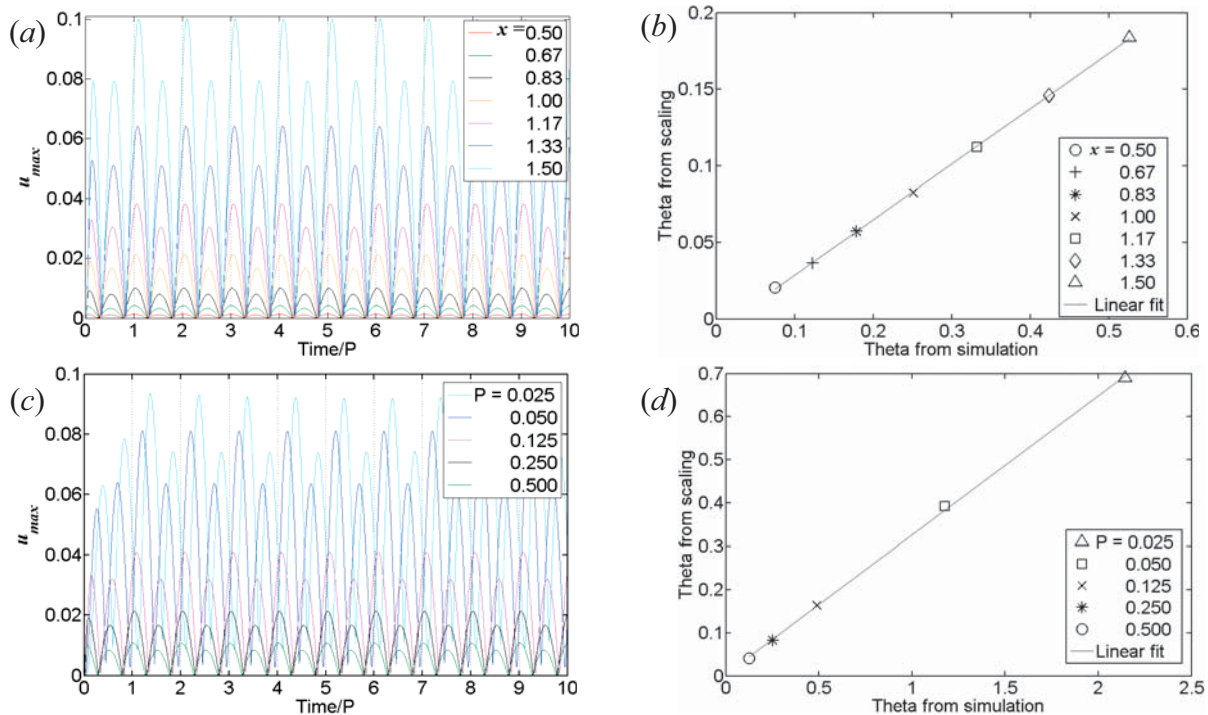


Figure 2 Verification of the phase delay  $\theta$  in scaling (14),  $Ra = 10^4$ . (a) Time series of  $u_{max}$  at different  $x$  with  $P=0.25$  (b)  $\theta$  at different  $x$  from simulation versus scaling. (c) Time series of  $u_{max}$  under different  $P$  with  $x = 1.0$ . (d)  $\theta$  under different  $P$  from simulation versus scaling.

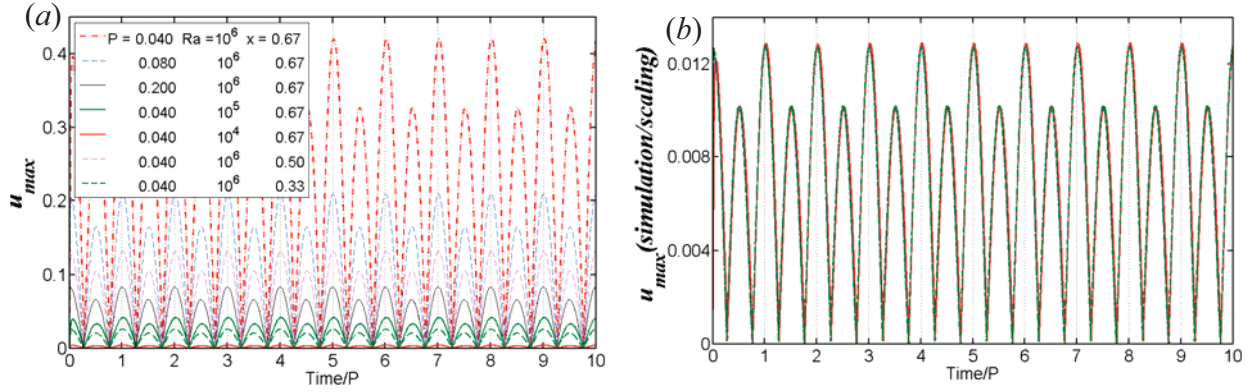


Figure 3 Verification of the dependency of  $u_{max}$  on  $x$ ,  $P$  and  $Ra$ , (a) Time series of  $u_{max}$  at various  $P$ ,  $Ra$  and  $x$  obtained from simulation. (b) Simulation results normalized by scaling.

The dependency of the magnitude of  $u_{max}$  on the period  $P$ ,  $Ra$  and the horizontal position  $x$  predicted by scaling (15) is verified by the results of numerical simulations (Figure 3). Since the focus is on the magnitude, the effect of phase delay is minimized by selecting relatively large  $P$  and small  $x$  as scaling (14) suggests. Figure 3(a) shows the time series of the maximum horizontal velocity  $u_{max}$  for various  $P$ ,  $Ra$  and  $x$ . It is clear that the amplitude of  $u_{max}$  increases with  $Ra$  and  $x$ , and decreases with  $P$ . After normalization by scaling (15), simulation results collapse together (Figure 3b), confirming the dependency of the magnitude of  $u_{max}$  on  $P$ ,  $Ra$  and  $x$ .

#### Flow response from simulation

To illustrate the overall flow response over the entire domain, isotherms and streamlines obtained from simulation for  $Ra = 10^5$ ,  $P = 0.04$  are plotted in figure 4 over a cycle. The times shown in this figure are relative to the beginning of the cycle. Details of flow response are described below.

Before the start of the cycle ( $t = 0.00P$ ), temperature at the water surface has been increasing for the last quarter of a cycle. Therefore, at the beginning of the cycle, a water surface layer is formed below the water surface (figure 4a). The isotherms in figure 4a suggest that a cool gravity current is expected to flow down the sloping bottom, which is confirmed in the streamlines in figure 4a, an anticlockwise flows is formed within the domain. The wavy feature in the streamlines is caused by the instability in the last quarter of a cycle. This effect of instability is counteracted by stratification caused by warm surface water at  $t = 0.10P$  as shown by the streamline in figure 4b. The isotherms of 4b suggest that the warm surface layer grows thicker. Compared to figure 4a, the horizontal temperature gradient which drives the flow is smaller in figure 4b and therefore flow velocity decreases as confirmed by the streamlines. At time  $t = 0.25P$ , the warm surface layer becomes even thicker, and the flow becomes even more stratified, as a result, the velocity continue to decrease as shown by the streamlines in figure 4c. Near the tip of flow domain, a conductive subregion is observed where the warm surface layer reaches the sloping bottom as shown by the isotherms. The negative horizontal temperature gradient near shore leads to a clockwise circulation as shown in the streamlines (figure 4c).

From time  $t = 0.25P$ , temperature at the water surface starts to decrease, as a results, the warm surface layer disappears at  $t = 0.50P$  (Figure 4d). The surface layer becomes cooler than the layer below, which is potentially unstable. The clockwise flow expands to a larger scope as shown by the streamlines (figure 4d). After time  $t = 0.50P$ , temperature at the water surface continues to decrease, eventually lead to instabilities with cold thermal plumes plunging down the water surface at time  $t = 0.75P$  (Figure 4e).

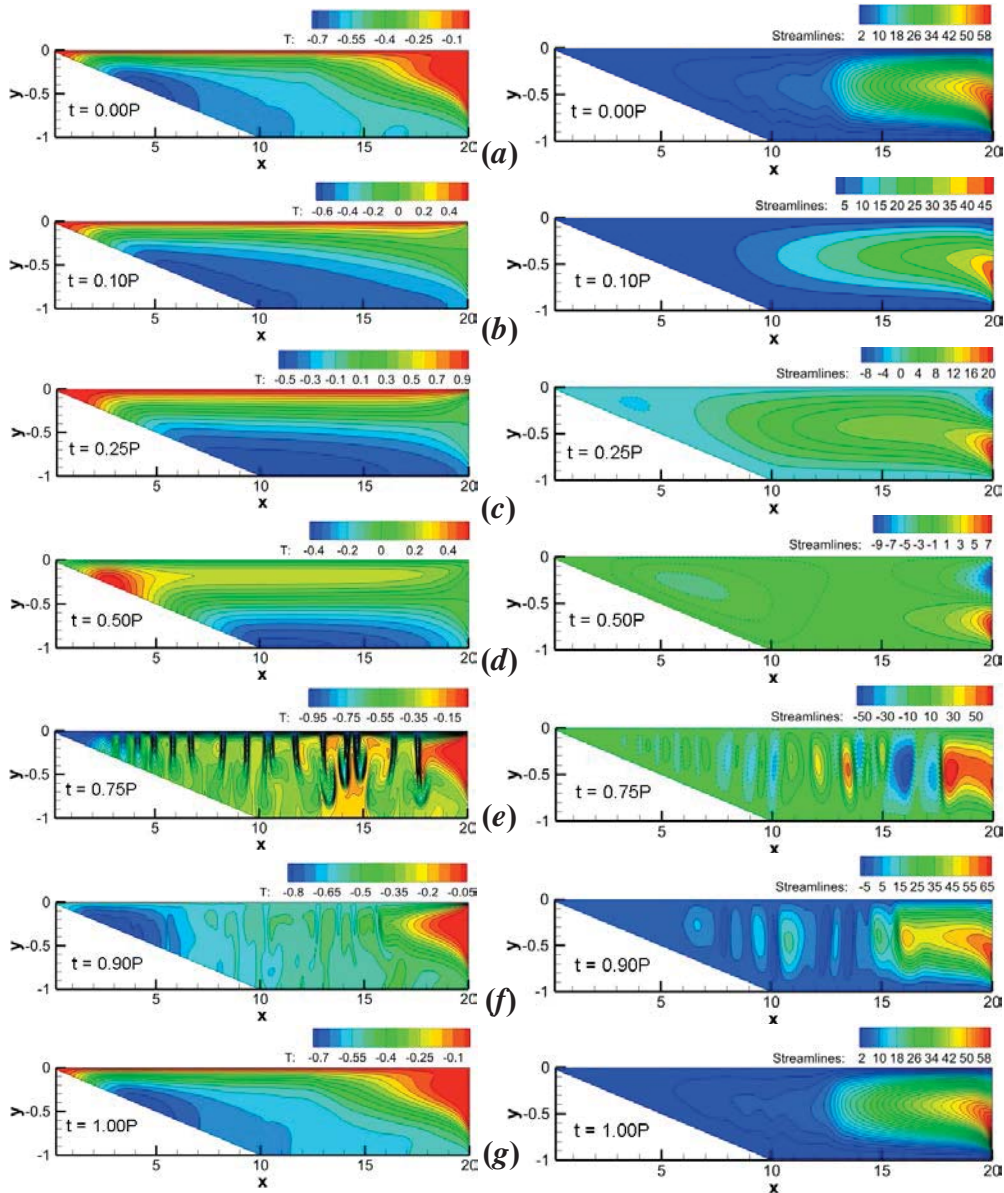


Figure 4 Flow responses to periodic thermal forcing at the water surface ( $Ra = 10^5$ ,  $P = 0.04$ ). Left: temperature contours. Right: streamlines. Dashed streamlines indicates clockwise flow.

After  $t = 0.75P$ , temperature at the water surface starts to increase, as a results, the circulation at time  $t = 0.90P$  is less unstable with decreased intensity of plumes (figure 4f). When the cycle finishes at  $t = 1.00P$ , the plunging plumes disappear and flow becomes less unstable. The end of the cycle at  $t = 1.00P$  is also the start of the next cycle. Since simulation is conducted over 10 full thermal forcing cycles, the effect of start-up flow is minimized. Therefore, features of the isotherms and streamlines at the end of the cycle  $t = 1.00P$  (figure 4g) is the same as at the beginning of the cycle  $t = 0.00P$  (figure 4a).

To quantify the intensity of horizontal exchange flow rate at a specified location  $x$ , the horizontal exchange rate  $Q(x)$  at position  $x$  is calculated for the 2D domain as:

$$Q(x) = \frac{1}{2} \int_{-h_x}^0 |u| dy, \quad (16)$$

where  $h_x$  is the local water depth at the horizontal position  $x$ . The average volumetric horizontal flow rate  $Q$  is obtained by integrating  $Q(x)$  horizontally over a length of  $L$ :

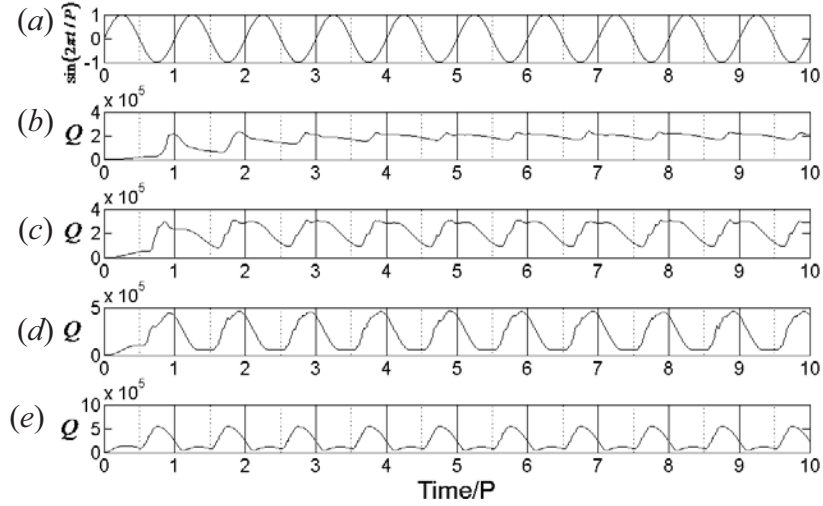


Figure 5 Flow response to periodic thermal forcing represented by the time series of  $Q$  for different period,  $Ra=10^6$ . Plotted are (a) time series of thermal forcing. (b-e) are time series of  $Q$ . (b)  $P = 0.004$  (c)  $P = 0.008$  (d)  $P = 0.020$  (e)  $P = 0.080$

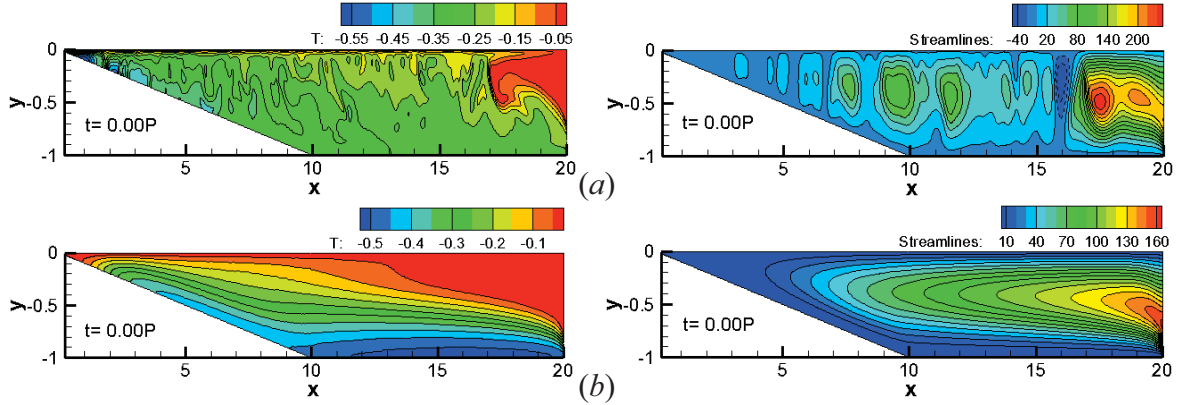


Figure 6 Isotherms and streamlines at the beginning of the cycle,  $Ra = 10^6$ . (a)  $P = 0.004$  (b)  $P = 0.08$ . Left: temperature contours. Right: streamlines.

$$Q = \frac{1}{L} \int_0^L Q(x) dy \quad (17)$$

Figure 5 plots the time series of  $Q$  for different periods with  $Ra = 10^6$ . Time series of thermal forcing is shown in figure 5(a). The corresponding  $Q$  shown in figure 5(b-e) reveals that the length of period significantly affects the flow response. Given an isothermal domain,  $Q$  induced by surface heating (positive value in figure 5a) is expected to be much smaller than by surface cooling (negative value in figure 5a). During heating time, horizontal exchange is only induced by the horizontal temperature gradient near shore (figure 4c). During the cooling time, the thermal plumes induced by instability enhance the horizontal exchange rate significantly (figure 4e). Therefore, if there is no inertia and the flow responds instantly to the thermal forcing, a low value of  $Q$  is expected for the heating phase and a high value for the cooling phase. However, the flow response is delayed due to inertia as shown in figure 5. For short period, the delay of response is most evident. As shown in figure 6 (a), at the start of heating phase ( $t = 0.00 P$ ), the flow is still unstable for the short period ( $P = 0.004$ ), whereas it becomes stable for the long period ( $P = 0.080$ ) which has sufficient time to respond to the varying thermal forcing. As a result, the delay is minimized for the largest period ( $P = 0.08$ ) in figure 5(e), where the low and the high value of  $Q$  correspond well with the heating and the cooling phase with only a slight time delay.

## Conclusions

The present investigation focuses on natural convection induced by periodic thermal forcing at the water surface in a reservoir model. Through coupled analytical solutions and scaling analysis, temperature and velocity scales for the near shore conductive region have been derived and verified by numerical simulations. The scaling quantifies the dependency of velocity on  $Ra$ ,  $A$ ,  $x$ , and  $P$ , and the dependency of phase delay on  $A$ ,  $x$  and  $P$ .

The flow response over the entire domain is revealed by isotherms and streamlines at different stages of the thermal forcing cycle. An effect of phase delay is observed and the details of flow response are analyzed. Time series of horizontal exchange rate  $Q$  for different lengths of period  $P$  reveals that the length of period affects flow response significantly. The phase delay of flow response resulting from inertia is most evident in the result of the shortest period. As the length of period increases, this delaying effect becomes less obvious. For sufficiently large period, the heating and cooling phase of the thermal forcing is characterized by low and high values of  $Q$  respectively.

## Acknowledgement

This research was supported by National Science Foundation of China (grant number 11002127) and the Fundamental Research Fund for National University, China University of Geosciences (Wuhan).

## References

- Adams, E. E. and Wells, S. A. (1984), Field Measurements on Side Arms of Lake. *J of Hydraul. Engng. ASLE* 110, pp. 773-793.
- Farrow D. E. and Patterson J. C. (1993), On the response of a reservoir sidearm to diurnal heating and cooling, *J. Fluid Mech.* 246, pp. 143-161.
- Farrow D. E. (2004), Periodically forced natural convection over slowly varying topography, *J. Fluid Mech.* 508, pp. 1-21.
- Horsch G. M. and Stefan H. G. (1988), Convective circulation in littoral water due to surface cooling, *Limnol. Oceanogr.*, 33, pp. 1068-1083.
- James W. F. and Barko J. W. (1991), Estimation of phosphorus exchange between littoral and pelagic zones during nighttime convective circulation, *Limnol. Oceanogr.*, 36, pp. 179-187.
- Lei C. and Patterson J. C. (2002), Unsteady natural convection in a triangular enclosure induced by absorption of radiation, *J. Fluid Mech.*, 460, pp. 181-209.
- Lei C. and Patterson J. C. (2005), Unsteady natural convection in a triangular enclosure induced by surface cooling, *Int. J. of Heat Fluid Fl.*, 26, pp. 307-321.
- Lei C. and Patterson J. C. (2006), Natural convection induced by diurnal heating and cooling in a reservoir with slowly varying topography, *JSME Int. J. B-Fluid T.*, 49, pp. 605-615.
- Mao Y., Lei C. and Patterson J. C. (2009), Unsteady natural convection in a triangular enclosure induced by absorption of radiation – a revisit by improved scaling analysis, *J. Fluid Mech.*, 622, pp. 75-102.
- Mao Y., Lei C. and Patterson J. C. (2010), Unsteady near-shore natural convection induced by surface cooling, *J. Fluid Mech.*, 642, pp. 213-233.
- Monismith S. G., Imberger J. and Morison M. L. (1990), Convective motions in the sidearm of a small reservoir, *Limnol. Oceanogr.*, 35, pp. 1676-1702.
- Monismith S. G., Genin A., Reidenbach M. A., Yahel G. and Koseff J. R. (2006), Thermally driven exchanges between a coral reef and the adjoining ocean, *J. Phys. Oceanogr.*, 36, pp. 1332-1347.
- Niemann H., Richter C., Jonkers H. M. and Badran M. I. (2004), Red sea gravity currents cascade near-reef phytoplankton to the twilight zone, *Mar. Ecol.-Prog. Ser.*, 269, pp. 91-99.



## Development of a Steam Distribution Network Simulator for Enhanced Oil Recovery Systems

\*Tatsuro Yashiki<sup>1</sup>, Yukinori Katagiri<sup>1</sup>, Yoshikazu Ishii<sup>1</sup>,  
Shunichi Kuba<sup>2</sup>, Takayuki Mitadera<sup>3</sup>, and Tomohiko Yoshida<sup>2</sup>

<sup>1</sup>Hitachi, Ltd., Hitachi Research Laboratory, 7-2-1, Omika-cho, Hitachi-shi, Ibaraki, Japan

<sup>2</sup>Hitachi, Ltd., Hitachi Power Systems Company, 3-1-1 Saiwai-cho, Hitachi-shi, Ibaraki, Japan

<sup>3</sup>Hitachi Power Solutions Co., Ltd., 3-1-1, Saiwai-cho, Hitachi-shi, Ibaraki, Japan

\*Corresponding author: tatsuro.yashiki.zn@hitachi.com

### Abstract

Enhanced oil recovery (EOR) by injecting steam into oil wells is widely used to make the oil less viscous, thereby improving its mobility and recovery. Steam is generated by steam generators and supplied to oil wells through a steam distribution network. In order to optimize the effects of EOR, it is necessary to predict steam properties in the distribution network with high accuracy. In this paper, a newly developed steam distribution network simulator for EOR systems is introduced. The features of the simulator are providing: (1) a highly accurate prediction of steam properties including phase change (steam to drain) in a complex steam distribution network by adopting a pipe flow model using the finite volume method and the Newton-Raphson method and a steam distribution network flow model according to graph theory and (2) a dedicated interface for operators to build the steam distribution network model easily by referring to a topographic map. The simulation results show that the developed simulator is useful to evaluate and modify an existing steam distribution network and to design a new one.

**Keywords:** Steam Distribution Network, Simulator, Two-phase Flow, EOR.

### Introduction

Enhanced oil recovery (EOR) by injecting steam into oil wells has been the most widely used recovery method for heavy and extra-heavy oil production in sandstone reservoirs. For the steam injection, several steam generators are located throughout the oil field to produce the steam that is fed into a distribution network. As the distribution network becomes more complex and larger, the steam flow becomes more complicated and the steam properties along the pipes vary greatly. Additionally the heat loss from the pipe to the surrounding air makes the steam condense into a drain and these condensations also complicate the steam flow. Thus, the effective operation of the EOR systems requires an understanding of the steam flow in the distribution network that may be done using numerical simulation.

The requirements for the steam distribution network simulation of EOR systems are: (1) providing highly accurate prediction of steam properties including phase change (steam to drain); (2) having applicability to complex and large distribution networks with multiple loops, steam generators and oil wells; and (3) realizing easy building of a distribution network model for the simulation. Many studies on the fluid and heat flow in a distribution network have been reported. However most of the mathematical models or computer programs that were developed in these studies do not satisfy the above-mentioned requirements simultaneously. Majumdar et al. (1997) developed a computer program for analyzing steady compressible flow with phase change and heat transfer in a complex distribution network. This program involves complicated procedures for operators to build a distribution network model with long distance pipes, since the operators must divide each of the pipes into many partial pipes to predict steam properties with high accuracy. This paper describes a

newly developed steam distribution network simulator for EOR systems. The simulation results are a highly accurate prediction of steam properties including the phase change. The results also show that the developed simulator is useful to evaluate and modify an existing steam distribution network and to design a new steam distribution network.

### Mathematical model of pipe flow

The following three sections describe the mathematical model and the user interface developed to satisfy the above-mentioned requirements for the steam distribution network simulation of EOR.

#### Governing equations

In this paper, the pipe flow is assumed to be one-dimensional steady compressible flow with phase change and heat transfer. Additionally the pipe geometry is assumed to be straight with a constant diameter and surrounded by thermal insulation. The governing equations for the pipe flow are the mass conservation, the momentum conservation and the energy conservation equations which are given by

$$\partial \dot{m} / \partial z = 0 \quad (1)$$

$$\partial \left\{ (v \cdot \dot{m}^2) / A \right\} / \partial z + \partial (A \cdot p) / \partial z - A \cdot F_w = 0 \quad (2)$$

$$\partial (\dot{m} \cdot h) / \partial z - P \cdot q_w = 0 \quad (3)$$

where  $F_w$  denotes wall friction force and  $q_w$  wall heat flux that flows from the pipe to the surrounding air. For the two-phase flow, the slip flow model (JSME, 2006) is chosen. In the slip flow model, the specific volume  $v$  in Eq. (2) and the specific enthalpy  $h$  in Eq. (3) are given by

$$v = \left\{ (1-x)^2 / (1-\alpha) \right\} v_L + (x^2 / \alpha) v_G \quad (4)$$

$$h = (1-x)h_L + xh_G \quad (5)$$

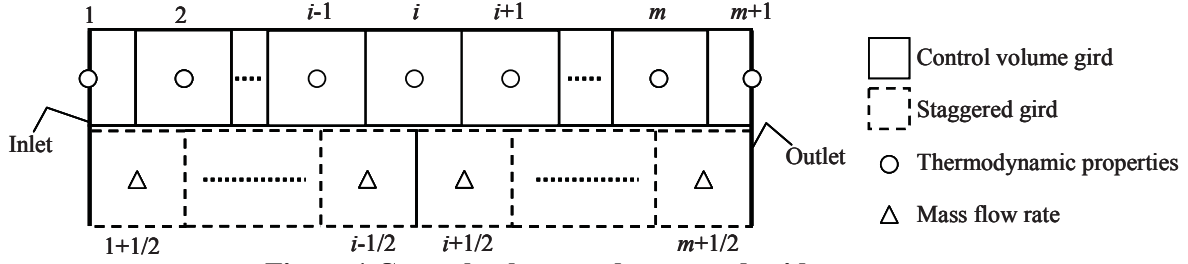
where the void fraction  $\alpha$  is defined using Thom's void fraction correlation (Thom, 1964). To deal with one-phase flow and two-phase flow, the equations for calculating  $F_w$  and  $q_w$  are switched depending on the phase status of the pipe flow. Details of the equations appear in Appendix A. The independent variables in Eqs. (1), (2) and (3) are mass flow rate, pressure and specific enthalpy. Other thermodynamic properties of steam and water are calculated using the equation of IF97 (IAPWS, 1997)

#### Discretization of governing equations according to the finite volume method

In order to predict the steam properties with high accuracy, Eqs. (1), (2) and (3) are discretized according to the finite volume method, where the number of control volumes is set to be high enough to resolve the spatial distribution of the properties. The proposed method uses the staggered grid approach (Patankar, 1980) in order to preventing pressure oscillations. In this approach, the mass and energy conservation equations are solved on a control volume grid and the momentum conservation equation is solved on a staggered grid as shown in Fig. 1. The mass flow rate is defined at the staggered grid center and all of the thermodynamic properties are defined at the control volume grid center.

Integrating Eqs. (1) and (3) over the control volume grid gives

$$\dot{m}_{i-1/2} - \dot{m}_{i+1/2} = 0 \quad (6)$$



**Figure 1 Control volume and staggered grid structure**

$$\dot{m}_{i-1/2} \hat{h}_{i-1/2} - \dot{m}_{i+1/2} \hat{h}_{i+1/2} - P_i \Delta z \cdot q_{w,i} = 0 \quad (7)$$

where  $\hat{h}_{i-1/2}$  is defined at the control volume grid face. The first order upwind scheme is used to obtain the value of  $\hat{h}_{i-1/2}$ , thus

$$\dot{m}_{i-1/2} \hat{h}_{i-1/2} = \left\{ (\dot{m}_{i-1/2} + |\dot{m}_{i-1/2}|) / 2 \right\} h_{i-1} + \left\{ (\dot{m}_{i-1/2} - |\dot{m}_{i-1/2}|) / 2 \right\} h_i \quad (8)$$

The value of  $\hat{h}_{i+1/2}$  can be obtained in the same way as  $\hat{h}_{i-1/2}$ . Integrating Eq. (2) over a staggered grid gives

$$v_i \left( \dot{m}_{i+1/2} / A \right)^2 - v_{i+1} \left( \dot{m}_{i+1/2} / A \right)^2 + p_i - p_{i+1} - \Delta z \cdot K_{i+1/2} \left( |\dot{m}_{i+1/2}| + \dot{m}_\varepsilon \right) \dot{m}_{i+1/2} = 0 \quad (9)$$

#### Computational scheme using the Newton-Raphson method

The discretized equations (Eqs. (6), (7) and (9)) are non-linear and require iterative calculation. The proposed method applies the Newton-Raphson method (NRM) (Shamir and Howard, 1968), where pressure is corrected so that it satisfies the mass conservation equation (Eq. (6)). The pressure correction equation is given by

$$-\beta_{i-1/2} dp_{i-1} + (\beta_{i-1/2} + \beta_{i+1/2}) dp_i - \beta_{i+1/2} dp_{i+1} = \dot{m}_{i+1/2}^{n-1} - \dot{m}_{i-1/2}^{n-1} \quad (10)$$

$$\beta_{i+1/2} \equiv 1 / \left[ 2(v_{i+1}^{n-1} - v_i^{n-1}) \dot{m}_{i+1/2}^{n-1} / A^2 + 2K_{i+1/2}^{n-1} (|\dot{m}_{i+1/2}^{n-1}| + \dot{m}_\varepsilon) \right] \quad (11)$$

where the superscript  $n-1$  denotes the previous iteration number. Eq. (10) forms a set of linear equations in terms of  $dp_i$ . Once solved, the current iteration pressure  $p_i^n$  is updated by

$$p_i^n = p_i^{n-1} + dp_i \quad (12)$$

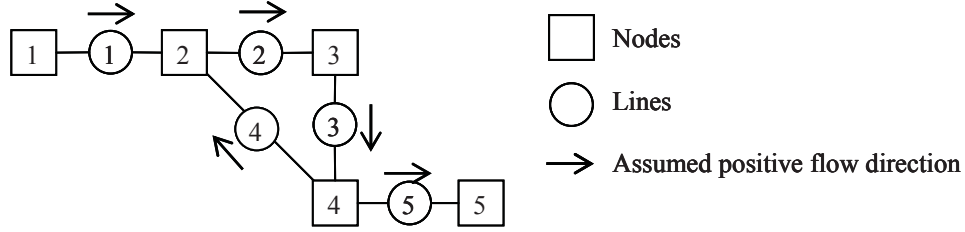
The current iteration mass flow rate  $\dot{m}_{i+1/2}^n$  and specific enthalpy  $h_i^n$  are calculated by substituting  $p_i^n$  into Eqs. (7) and (9). The calculation process of  $p_i^n$ ,  $\dot{m}_{i+1/2}^n$  and  $h_i^n$  is repeated until convergence.

### Mathematical model of the steam distribution network flow

#### Representation of the steam distribution network according to graph theory

According to graph theory, an arbitrary steam distribution network can be represented as a directed linear graph. The network consists of a number of oriented lines connected to nodes as shown in Fig. 2. Lines contain pipes and nodes contain branches, steam sources (steam generators) and steam sinks (oil wells). Lines are connected to one another by nodes and each line is associated with an upstream and a downstream node. The topology of a directed linear graph of  $N_l$  lines and  $N_n$  nodes can be described by a  $N_l \times N_n$  node incidence matrix  $\mathbf{B}$  with the typical element:

$$b_{jk} = \begin{cases} +1, & \text{if line } j \text{ is directed away from node } k \\ -1, & \text{if line } j \text{ is directed toward node } k \\ 0, & \text{if line } j \text{ is not connected to node } k \end{cases} \quad (13)$$



**Figure 2 Representation of a network**

The node incidence matrix  $\mathbf{B}$  for the network shown in Fig. 2 is as follows:

$$\mathbf{B} = \begin{bmatrix} 1 & -1 & 0 & 0 & 0 \\ 0 & 1 & -1 & 0 & 0 \\ 0 & 0 & 1 & -1 & 0 \\ 0 & -1 & 0 & 1 & 0 \\ 0 & 0 & 0 & 1 & -1 \end{bmatrix} \quad (14)$$

### Computational scheme

The governing equations for the steam distribution network flow are the mass and the energy conservation equations at nodes and the momentum conservation equation at lines. The proposed method uses the NRM to solve the network flow. In the same way as the pipe flow calculation, the pressure at nodes is calculated by the following pressure correction equation:

$$\mathbf{B} \cdot \begin{bmatrix} y_1 & & 0 \\ & \ddots & \\ 0 & & y_{N_l} \end{bmatrix} \cdot \mathbf{B}^T \cdot \begin{bmatrix} dp_{node,1} \\ \vdots \\ dp_{node,N_n} \end{bmatrix} = \mathbf{B}^T \cdot \begin{bmatrix} \dot{m}_{line,1}^{n-1} \\ \vdots \\ \dot{m}_{line,N_l}^{n-1} \end{bmatrix} \quad (15)$$

$$y_j \equiv \sum_{i=1}^{m_j} \beta_{j,i+1/2} \quad (16)$$

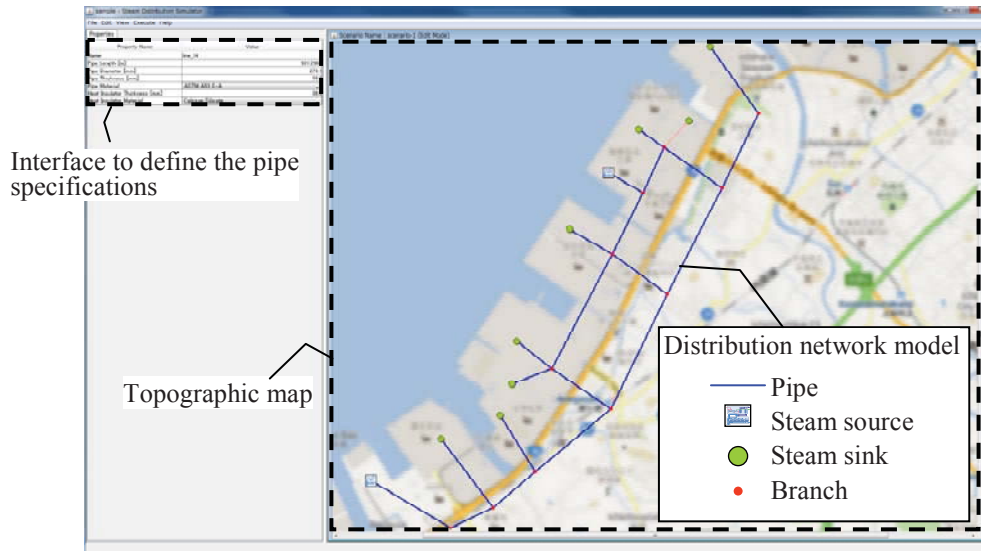
Once  $dp_{node,j}$  is solved, the current iteration pressure at nodes  $p_{node,j}^n$  is updated by

$$p_{node,k}^n = p_{node,k}^{n-1} + dp_{node,k} \quad (17)$$

Current iteration mass flow rate at lines  $\dot{m}_{line,j}^n$  can be computed from the above-mentioned pipe flow model and current iteration specific enthalpy at nodes  $h_{node,j}^n$  can be computed from the energy conservation. The calculation process of  $p_{node,k}^n$ ,  $\dot{m}_{line,j}^n$  and  $h_{node,k}^n$  is repeated until convergence.

### User interface of the simulator

The simulator provides a dedicated user interface (Fig. 3) for operators to build the distribution network model easily and to visualize the simulation results. The simulator first takes in a topographic map where the actual distance is associated. Then the operators can build the distribution network model by referring to the map. The pipe length can be calculated automatically using the actual distance associated with the map and the other pipe specifications such as diameter, thickness etc. are defined by the operator inputs. At the beginning of the simulation, each of the pipes is automatically divided into control volumes whose number is set to be high enough to resolve the spatial distribution of the steam properties. In this paper, the pipe is divided into control volumes of 10 meters in length. On the completion of the simulation, the results can be visualized



**Figure 3 User interface of the developed simulator**

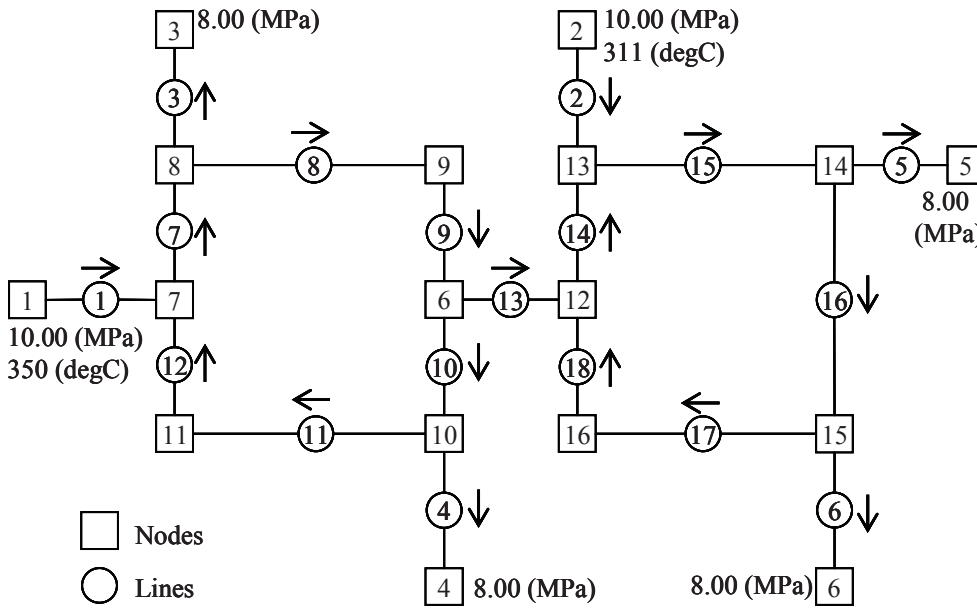
as a numeric form or a graphical form. In the provided user interface, the operators can build the distribution network model and calculate the network flow without special knowledge of numerical simulation.

### Results and discussion

An example steam distribution network flow was calculated to demonstrate the functionality of the developed simulator. Fig.4 shows the layout of the network that included two loops, two steam sources (nodes 1 and 2) and four steam sinks (nodes 3, 4, 5 and 6). The boundary conditions of the steam sources and steam sinks are given in Fig. 4 and the pipes data are given in Table 1. The pipe thickness and the thermal insulation thickness of all the pipes was 0.03 m. Node 1 supplied superheated steam and node 2 supplied saturated steam.

The results for the example network are shown in Table 2. Because the flow direction for line 13 was left-to-right (from node 6 to node 12), node 1 supplied the steam to nodes 3, 4, 5 and 6, while node 2 supplied the steam to nodes 5 and 6. The steam flowing into nodes 3 and 4 was superheated steam. In contrast, the steam flowing into nodes 5 and 6 was partially condensed into the drain, since the distance from node 1 to node 5 or 6 was far and the heat loss of the steam supplied by node 1 was large. Fig. 5 shows the spatial distribution along lines 17 and 18 flow for five steam properties: pressure, temperature, quality, flow resistance coefficient, and heat transfer coefficient between steam and pipe. The phase status of the pipe flow changed from one-phase flow to two-phase flow at the pipe length of 1230 m. The flow resistance coefficient and heat transfer coefficient were constant over the one-phase region, while they increased throughout the two-phase region due to the steam condensation. Because the developed simulator divides each of the pipes into control volumes automatically and switches the equations of wall friction force and wall heat flux depending on phase status of the pipe flow, it can predict steam properties including phase change with high accuracy.

In order to estimate the effect from degradation of heat insulation, the thermal insulation thickness of lines 17 and 18 was changed from 0.03 m to 0.005 m. The results around lines 17 and 18 for this condition are compared in Table 3 with the original condition (*Italic font*). Because heat loss of lines 17 and 18 increased and large quantities of the steam were condensed, the quality at nodes 6 and 15 decreased. In order to increase the quality at nodes 6 and 15, a mobile steam source that supplied saturated steam was connected to node 15. The steam pressure and temperature supplied



**Figure 4** Layout of the example steam distribution network

**Table 1 Pipes data**

Line number	Length (m)	Diameter (m)
1	500	0.2731
2	1000	0.1682
3	500	
4	1000	
5	500	
6	500	
7	750	0.2731
8	2000	
9	750	
10	750	
11	2000	
12	750	
13	1000	
14	750	
15	2000	
16	1500	
17	2000	
18	750	

**Table 2 Results for the example network**

Line number	Mass flow rate (kg/s)	Node number	Pressure (MPa)	Temperature (°C)	Quality (-)
1	31.92	1	10.00	350	1.00
2	5.61	2	10.00	311	1.00
3	11.74	3	8.00	325	1.00
4	8.31	4	8.00	308	1.00
5	8.63	5	8.00	295	0.92
6	8.85	6	8.00	295	0.93
7	19.38	7	9.70	346	1.00
8	7.64	8	9.53	341	1.00
9	7.64	9	9.46	324	1.00
10	-4.23	10	9.44	328	1.00
11	-12.54	11	9.63	341	1.00
12	-12.54	12	9.36	313	1.00
13	11.87	13	9.35	306	0.98
14	3.51	14	9.25	305	0.93
15	9.12	15	9.25	305	0.95
16	0.48	16	9.33	308	1.00
17	-8.36				
18	-8.36				

**Table 3 Results for estimating the effect from degradation of heat insulation**

Node number	Pressure (MPa)		Temperature (°C)		Quality (-)	
6	8.00	8.00	295	295	0.67	0.93
12	9.38	9.36	312	313	1.00	1.00
13	9.37	9.35	306	306	0.98	0.98
14	9.28	9.25	306	305	0.93	0.93
15	9.28	9.25	306	305	0.67	0.95
16	9.35	9.33	306	308	0.93	1.00

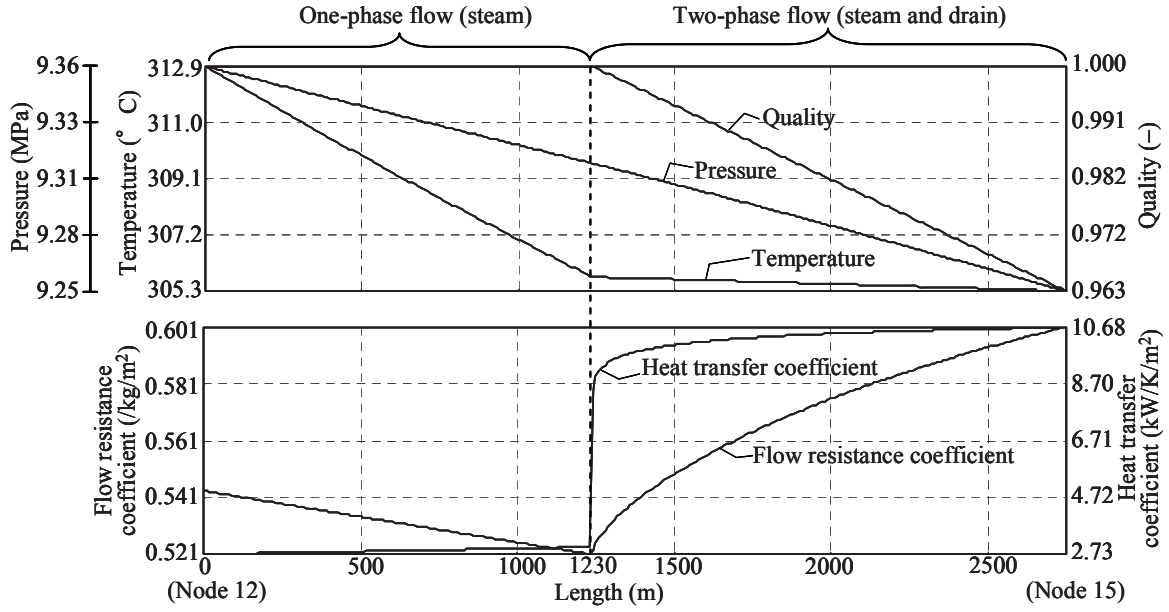
**Table 4 Results for connecting the mobile steam source**

Node number	Pressure (MPa)	Temperature (°C)	Quality (-)
6	8.00	295	0.74
15	9.48	307	0.74

by the mobile steam source were 9.5 MPa and 307 °C. The results of nodes 6 and 15 for this condition are shown in Table 4. Owing to the saturated steam supplied by the mobile steam source, the quality at nodes 6 and 15 increased. By using the developed simulator, it is possible to evaluate and modify an existing steam distribution network and to design a new one.

**Conclusions**

A steam distribution network simulator for EOR systems was developed. The simulator provides: (1) highly accurate prediction of steam properties including phase change (steam to drain) in a complex steam distribution network by adopting the pipe flow model using the finite volume



**Figure 5 Steam properties along lines 17 and 18 flow**

method and the Newton-Raphson method and the steam distribution network flow model according to graph theory and (2) a dedicated interface for operators to build the steam distribution network easily by referring to a topographic map. The simulation results showed that the developed simulator is useful to evaluate and modify an existing steam distribution network and to design a new one. The developed simulator is also applicable to the steam distribution network in petrochemical complexes or district heating facilities.

### Acknowledgment

A part of this work was supported by the subsidies program of the Ministry of Economy, Trade and Industry, Japan.

### Appendix A. Equations for wall friction force and wall heat flux

#### Wall friction force

The wall friction force is modeled as the product of the flow resistance coefficient  $K$  and the square of the mass flow rate which is given by

$$F_w = K(\dot{m} + \dot{m}_\varepsilon)^2 \quad (\text{A-1})$$

where  $\dot{m}_\varepsilon$  is the small mass flow rate for stabilization of pipe flow calculation. For the one-phase flow,  $K$  is expressed with the Darcy-Weisbach equation and the Swamee-Jain equation (Swamee and Jain, 1976). For the two-phase flow,  $K$  is expressed with the Nozu equation (Nozu et al., 1998).

#### Wall heat flux

The wall heat flux is given by the following equation

$$q_w = (T - T_{am}) / (\pi \cdot d \cdot L \cdot R) \quad (\text{A-2})$$

where

$$R = \frac{1}{2\pi \cdot L} \left( \frac{1}{r1 \cdot hi} + \frac{1}{k_m} \ln \frac{r2}{r1} + \frac{1}{k_{ins}} \ln \frac{r3}{r2} + \frac{1}{r3 \cdot ho} \right) \quad (\text{A-3})$$

The equation for the heat transfer coefficient between steam and pipe  $hi$  is switched depending on the phase status of the pipe flow.  $hi$  for the one-phase flow is expressed with the Gnielinski equation (Gnielinski, 1976) and  $hi$  for the two-phase flow is expressed with the Shah equation (Shah, 1979).

### References for Appendix A

- Gnielinski, V. (1976), New equations for heat and mass transfer in turbulent pipe and channel flow, *Int. Chemical Engineering*, 16-2, pp. 359–368.
- Nozu, S., Katayama, H., Nakata, H. and Honda, H. (1998), Condensation of a refrigerant CFC11 in horizontal microfin tubes (Proposal of a correlation equation for frictional pressure gradient), *Experimental Thermal and Fluid Science*, 18, pp. 82-96.
- Shah, M. M. (1979), A general correlation for heat transfer during film condensation inside pipes, *Int. J. Heat Mass Transfer*, 22-4, pp. 547-556.
- Swamee, P. K. and Jain, A. K. (1976), Explicit equations for pipe-flow problems, *J. Hydraulics Division (ASCE: American Society of Civil Engineers)*, 102-5, pp. 657-664.

### Appendix B. Nomenclature

$A$	Cross-sectional area (m <sup>2</sup> )	$r3$	Pipe outer radius with heat insulator (m)
$\mathbf{B}$	Incidence matrix (-)	$T$	Temperature (°C)
$b$	Incidence matrix element (-)	$v$	Relative volume (m <sup>3</sup> /kg)
$d$	Pipe inner diameter (m)	$x$	Vapor quality (-)
$dp$	Correction of pressure (Pa)	$z$	Space coordinate (m)
$F_w$	Wall friction force (N/m <sup>3</sup> )	$\Delta z$	Control volume gird size (m)
$h$	Specific enthalpy (J/kg)		
$hi$	Heat transfer coefficient between steam and metal of pipe (W/K/m <sup>2</sup> )	<b>Greek</b>	
$ho$	Heat transfer coefficient between thermal insulator and atmosphere (W/K/m <sup>2</sup> )	$\alpha$	Void fraction (-)
$K$	Flow resistance coefficient (1/kg/m)	<b>Subscripts</b>	
$k$	Thermal conductivity (W/m/K)	$atm$	Atmosphere
$L$	Pipe length (m)	$G$	Saturated steam
$\dot{m}$	Mass flow rate (kg/s)	$i$	Control volume gird index
$\dot{m}_e$	Small mass flow rate for stabilization (kg/s)	$ins$	Thermal insulation
$m$	Number of staggered grids (-)	$j$	Line index
$N_l$	Number of lines (-)	$k$	Node index
$N_n$	Number of nodes (-)	$L$	Saturated water
$P$	Wetted perimeter (m <sup>2</sup> )	$m$	Metal of pipe
$p$	Pressure (Pa)	$line$	Value at line
$q_w$	Wall heat flux (W/m <sup>2</sup> )	$node$	Value at node
$R$	Thermal resistance (K/W)	<b>Superscripts</b>	
$r1$	Pipe inner radius (m)	$n$	New iteration step
$r2$	Pipe outer radius without heat insulator (m)	$n-1$	Previous iteration step

### References

- IAPWS (The International Association for the Properties of Water and Steam) (1997), Release on the IAPWS industrial formulation 1997 for the thermodynamic properties of water and steam, *IAPWS*, pp. 48.
- JSME (The Japan Society of Mechanical Engineers) (2006), Handbook of gas-liquid two-phase flow technology - second edition. *Corona Publishing*, pp. 70–71.
- Majumdar, A. K., Bailey, J. W. and Sarkar, B. (1997), A generalized fluid system simulation program to model flow distribution in fluid networks, 33<sup>rd</sup> *AIAA/ASME/SAE/ASEE Joint Propulsion Conference*, AIAA 97-3225.
- Patankar, S. V. (1980), Numerical heat transfer and fluid flow, *Hemisphere*, pp. 118-126.
- Shamir, U., and Howard, C. D. (1968), Water distribution system analysis, *J. Hydraulics Div., Proc. Amer. Soc. Civil Engineers*, 94, pp. 219-234.
- Thom, J. R. S. (1964), Prediction of pressure drop during forced circulation boiling of water. *Int. J. Heat Mass Transfer*, 7-7, pp. 709–724.



## CIVA-Stabilized Finite Element Method for Tsunami Simulations

\*Yusuke Takahashi<sup>1</sup>, Masaaki Sakuraba<sup>2</sup>, and Kazuo Kashiwama<sup>1</sup>

<sup>1</sup> Department of Civil and Environmental Engineering, Chuo University, Kasuga 1-13-27, Bunkyo-ku, Tokyo, Japan

<sup>2</sup> Disaster Prevention Hydraulics Group, Nippon Koei Co., Ltd., 2304 Inarihara, Tsukuba-shi, Ibaraki 300-1259, Japan

\*Corresponding author: takahashi@civil.chuo-u.ac.jp

### Abstract

This paper presents a numerical method using the CIVA-stabilized finite element method based on SUPG (CIVA-SUPG) for tsunami simulations. The Boussinesq equation is employed for the governing equation in order to treat both the wave nonlinearity and dispersion effects. The equation is divided into two phases, an advection phase and a non-advection phase. The CIVA method is employed to the advection phase and the stabilized finite element method based on SUPG is employed to the discretization for non-advection phase. The present method is applied to several benchmark examples to show the validity and efficiency of the method. For the application example, the present method is employed to the tsunami simulation generated by Great East-Japan earthquake.

**Keywords:** CIVA-SUPG finite element method, Tsunami, Boussinesq equation, Wave run-up

### Introduction

A number of flood disasters by tsunami occur in various parts of the world. The flood disasters by tsunami waves cause the enormous damage to the human life and economic activities. In order to estimate the extent of the disaster quantitatively, it is important to use accurate numerical method for tsunami waves. The two-dimensional shallow water equation and the Boussinesq equation are normally used for the governing equation for tsunami waves. The shallow water equation can describe the wave nonlinearity, however, the wave dispersion effect is not considered in the shallow water equation. On the other hand, Boussinesq equation can treat both the wave nonlinearity and dispersion effects, the equation is suitable for the governing equation for tsunami simulation.

For the tsunami numerical simulation, a number of numerical methods have been proposed. The finite difference is well used. However, it is necessary to use the nesting techniques in order to use the fine grid at the nearshore area since the regular grid is employed in the finite difference method. On the other hand, the finite element method does not need the nesting techniques since the unstructured grid is employed. Therefore, the finite element method is suitable for tsunami simulation since that can treat the complicated geometry easily.

This paper presents a numerical method using the CIVA-stabilized finite element method based on SUPG (CIVA-SUPG) for tsunami simulations. The Boussinesq equation is employed for the governing equation. The governing equation is divided into two phases, an advection phase and a non-advection phase. The CIVA method (Tanaka, 1999) is employed to the advection phase and the stabilized finite element method based on SUPG (Takase et al, 2010) is employed to the discretization for non-advection phase. The moving boundary technique based on fixed grid is employed. The present method is applied to several numerical examples to show the validity and efficiency of the method. For the application example, the present method is applied to the tsunami simulation generated by Great East-Japan earthquake using an unstructured triangular grid with the element Courant number constant.

### Governing Equations

For the governing equation, the Boussinesq equation is employed. This equation can treat the wave nonlinearity and dispersion effects. The governing equation can be described as follows:

$$\frac{\partial H}{\partial t} + \frac{\partial(u_i H)}{\partial x_i} = 0 \tag{1}$$

$$\frac{\partial(u_i H)}{\partial t} + \frac{\partial(u_j u_i H)}{\partial x_j} + gH \frac{\partial(H+z)}{\partial x_i} + \frac{gn^2 u_i \sqrt{u_j u_j}}{\partial x_i} + \frac{\partial}{\partial x_i} \left( \frac{h^2}{3} \frac{\partial(u_j H)}{\partial t \partial x_j} \right) = 0 \tag{2}$$

Where  $H$ ,  $u_i$ ,  $g$ ,  $z$  and  $n$  are total water depth, depth averaged velocity, acceleration of gravity, still water depth, bed slope and Manning’s coefficient, respectively.

The governing equation can be divided into two phases as below:

$$\frac{\partial(u_i H)}{\partial t} + u_j \frac{\partial(u_i H)}{\partial x_j} = 0 \tag{3}$$

$$\frac{\partial H}{\partial t} + \frac{\partial(u_i H)}{\partial x_i} = 0 \tag{4}$$

$$\frac{\partial(u_i H)}{\partial t} + (u_i H) \frac{\partial u_j}{\partial x_j} + gH \frac{\partial(H+z)}{\partial x_i} + \frac{gn^2 u_i \sqrt{u_j u_j}}{\partial x_i} + \frac{\partial}{\partial x_i} \left( \frac{h^2}{3} \frac{\partial(u_j H)}{\partial t \partial x_j} \right) = 0 \tag{5}$$

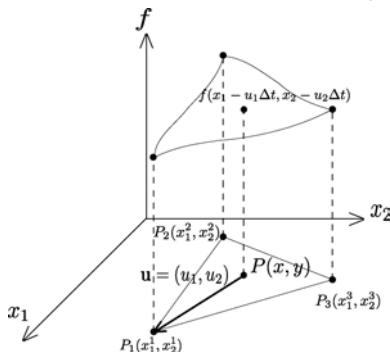
Eq. (3) is equation of advection phase (advection equation), the Eq. (4) and (5) are equations of non-advection phase.

**Numerical methods**

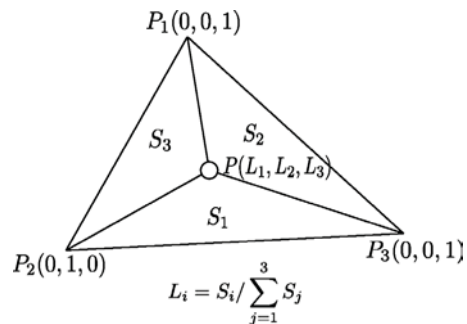
*Advection Phase*

The solution of Eq. (3) for advection phase is computed by the CIVA method (Cubic Interpolation with Volume/Area co-ordinates) proposed by Tanaka (1999). The method is an extended method of CIP for unstructured-grid, and the solution for advection equation is solved by the cubic interpolation as:

$$f(L_1, L_2, L_3) = \sum_{i=1}^3 \alpha_i L_i + d \sum_{i=1}^3 \beta_{jk} \left( L_j^2 L_k + \frac{1}{2} L_1 L_2 L_3 \right) \tag{6}$$



**Figure 1. CIVA method**



**Figure 2. Area coordinate**

Where,  $f$  is the discharge fluxes  $u_i H$  for  $x_i$  directions and  $L_i$  is the area coordinates (see Fig. 2). In order to compute the nodal value at P1 at time level n+1, the position of node P1 at time level n

(Point P) is determined by using the velocity at time level n. Then, the value at point P is obtained by Eq. (3) using three nodal values at time level n. The computed value is transported to point P at time level n+1. (see Fig.1)

### Non-advection Phase

After the advection phase, Eqs. (4), (5) are discretized by the stabilized finite element method based on SUPG method (Streamline-Upwind Petrov Galerkin) using the results of the advection phase. Eqs. (4), (5) can be expressed by the vector form as follows:

$$\frac{\partial \mathbf{U}}{\partial t} + \mathbf{A}_i \frac{\partial \mathbf{U}}{\partial x_i} - \mathbf{R} + \mathbf{G}\mathbf{U} + \frac{\partial^2}{\partial t \partial x_i} (\mathbf{K}) = 0 \quad (7)$$

$$\mathbf{U} = \begin{bmatrix} H \\ u_1 H \\ u_2 H \end{bmatrix}, \quad \mathbf{R} = \begin{bmatrix} 0 \\ -c^2 \frac{\partial z}{\partial x_1} \\ -c^2 \frac{\partial z}{\partial x_2} \end{bmatrix}, \quad \mathbf{K} = \begin{bmatrix} 0 \\ -\frac{h^2}{3} \left( \frac{\partial(\overline{u_1 H})}{\partial x_1} + \frac{\partial(\overline{u_2 H})}{\partial x_2} \right) \\ -\frac{h^2}{3} \left( \frac{\partial(\overline{u_1 H})}{\partial x_1} + \frac{\partial(\overline{u_2 H})}{\partial x_2} \right) \end{bmatrix},$$

$$\mathbf{A}_1 = \begin{bmatrix} 0 & 1 & 0 \\ c^2 - \overline{u_1^2} & \overline{u_1} & 0 \\ -\overline{u_1} \overline{u_2} & \overline{u_2} & 0 \end{bmatrix}, \quad \mathbf{A}_2 = \begin{bmatrix} 0 & 0 & 1 \\ -\overline{u_1} \overline{u_2} & 0 & \overline{u_1} \\ c^2 - \overline{u_2^2} & 0 & \overline{u_2} \end{bmatrix}, \quad \mathbf{G} = \begin{bmatrix} 0 & 0 & 0 \\ 0 & \frac{u_*}{H} & 0 \\ 0 & 0 & \frac{u_*}{H} \end{bmatrix}, \quad u_* = \frac{gn^2}{H^{1/3}} \sqrt{\overline{u_1^2} + \overline{u_2^2}}$$

Here  $\mathbf{U}$ ,  $\mathbf{R}$ ,  $\mathbf{K}$ ,  $\mathbf{A}_i$  and  $\mathbf{G}$  are unknown vector, bed slope term, dispersion term, nonlinear term and friction term respectively. The valuables with overline are the computed results by the advection phase. Applying the stabilized finite element method to Eq. (7), the weighted residuals equation is given as follows:

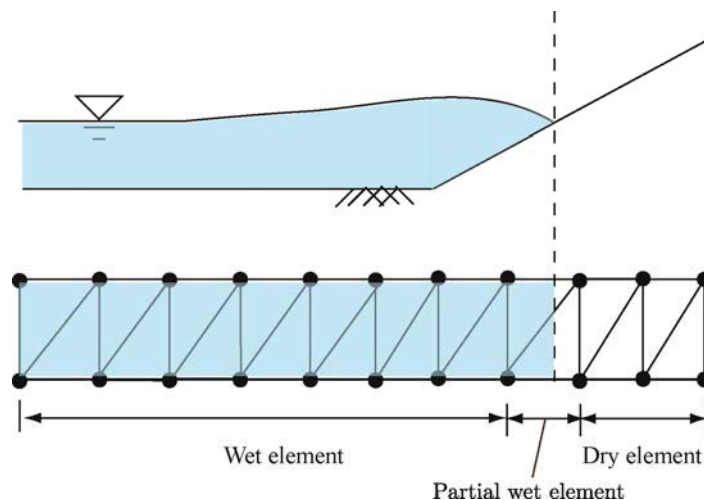
$$\begin{aligned} & \int_{\Omega} \mathbf{U}^* \cdot \left( \frac{\partial \mathbf{U}}{\partial t} + \mathbf{A}_i \frac{\partial \mathbf{U}}{\partial x_i} - \mathbf{R} + \mathbf{G}\mathbf{U} \right) d\Omega + \int_{\Omega} \left( \frac{\partial \mathbf{U}^*}{\partial x_i} \right) \cdot \left( \frac{\partial}{\partial t} (\mathbf{K}) \right) d\Omega \\ & + \sum_{e=1}^{n_{el}} \int_{\Omega} \tau(\mathbf{A}_i) \left( \frac{\partial \mathbf{U}^*}{\partial x_i} \right) \cdot \left( \frac{\partial \mathbf{U}}{\partial t} + \mathbf{A}_i \frac{\partial \mathbf{U}}{\partial x_i} - \mathbf{R} + \mathbf{G}\mathbf{U} \right) d\Omega \\ & + \sum_{e=1}^{n_{el}} \int_{\Omega} \delta \left( \frac{\partial \mathbf{U}^*}{\partial x_i} \right) \cdot \left( \frac{\partial \mathbf{U}}{\partial x_i} \right) d\Omega = \int_{\Gamma} \mathbf{U}^* \cdot \mathbf{T} d\Gamma \end{aligned} \quad (8)$$

Here  $\tau$  is the SUPG stabilization parameter,  $\delta$  is the shock-capturing parameter. In Eq. (8), the first term, second term and right hand side term are Galerkin terms, the third term are SUPG stabilization terms, the fourth terms are shock-capturing term. For the spatial discretization, the continuous linear interpolation element is employed. For the discretization in time, the implicit method based on Crank-Nicolson method is employed.

### *Moving Boundary Techniques*

In order to describe the behavior of the tsunami run-up and run-off, the Eulerian approach using fixed grid is employed for the moving boundary condition. Fig. 3 shows the definition sketch for the treatment of moving boundary. Every nodal water depth is compared with the small water depth  $\varepsilon$  at every time step. Each element is classified into three types; wet, dry or partial wet element (Kawahara and Umetsu (1986)).

- Wet element : The water depth for all three nodes are greater than  $\varepsilon$ . The element is included in the computational area.
- Dry element : The water depth for all three nodes are smaller than  $\varepsilon$ . The element is omitted from the computational area. The nodal velocity is assumed to be zero.
- Partial wet element : The water depth for one or two nodes are greater than  $\varepsilon$ . The element is included in the computational area. The nodal velocity is assumed to be zero and the water depth is assumed to be  $\varepsilon$  for the node located on dry bed.



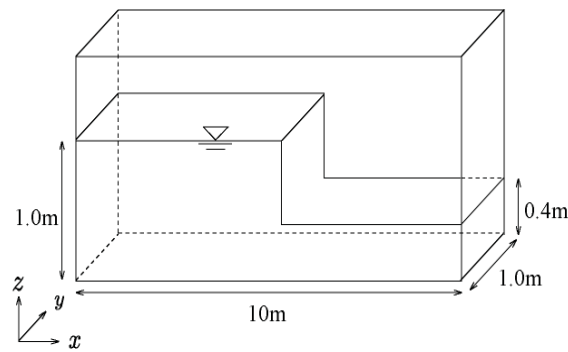
**Figure 3. Moving boundary technique**

### **Numerical Examples**

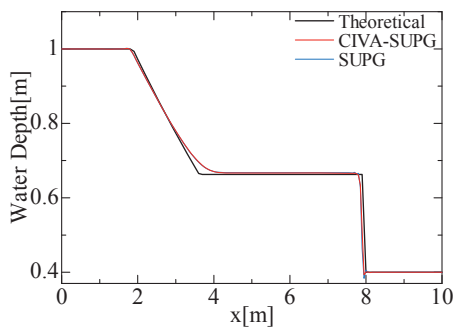
The present method is applied to several numerical examples to investigate the validity and efficiency.

#### *Dam-break Problem*

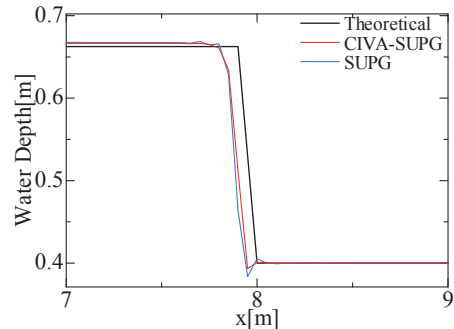
The present method is applied to dam-break problem in the rectangular tank. The computational model and initial water depth are shown in Fig. 4. The dam is broken instantaneously at time  $t = 0s$ . In this problem, the shallow water equation is employed for the governing equation in order to investigate the numerical accuracy comparing with the theoretical result. For the numerical condition, the time increment is assumed to be 0.001sec. For the boundary condition, the slip boundary condition is set to the wall.



**Figure 4. Computational model**



**Figure 5. Computed water depth**

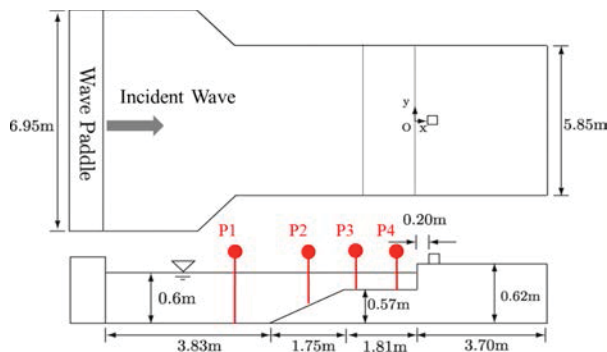


**Figure 6. Zoom up around x=8.0m**

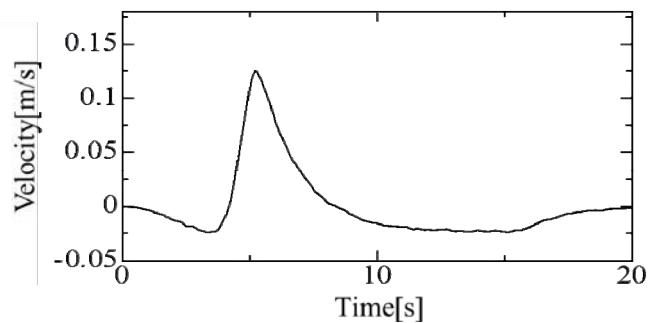
Fig. 5 shows the comparison with the theoretical solution for water depth at time  $t = 1s$ . Fig. 6 shows the zoom-up around  $x = 8.0m$ . The computed results obtained by the present method are in good agreement with the results obtained by the SUPG method (Takase et al, 2010).

*Tsunami Run-up Problem*

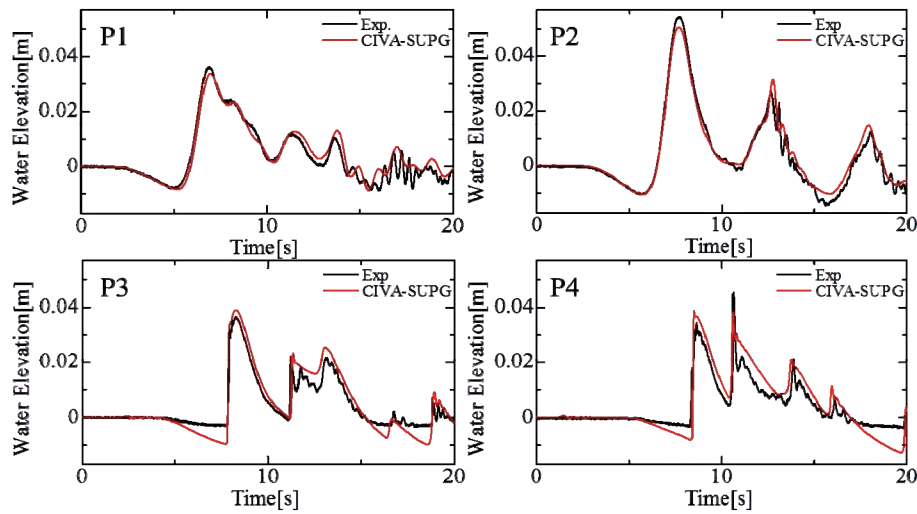
The present method is applied to a tsunami run-up problem in the tank. Fig.7 shows the computational model which is used by the experiment by National Defence Academy of Japan (Fujima et al, 2009). The wave paddle moves to make the incident wave. Fig. 8 shows the time history of velocity of paddle which is applied to the boundary condition for the velocity for  $x_1$  direction at the paddle. The slip boundary condition is set to other walls. For the numerical condition, the time increment is assumed to be 0.005s and the Manning’s coefficient is assumed  $0.01 m/s^{1/3}$ . The computed results were compared with the experimental data at the observation points of P1, P2, P3 and P4 (see Fig. 7).



**Figure 7. Computational model**



**Figure 8. Velocity of wave paddle**



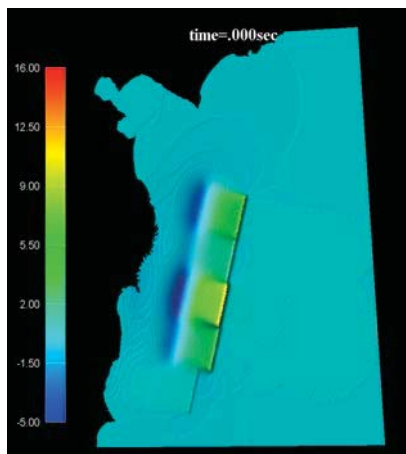
**Figure 9. Comparison with the experimental results at the observation points**

Fig. 9 shows the comparison of water elevation with the experimental results at the observation points P1-P4. From this figure, the computed results by the present method are in good agreement with the experimental results at all observation points.

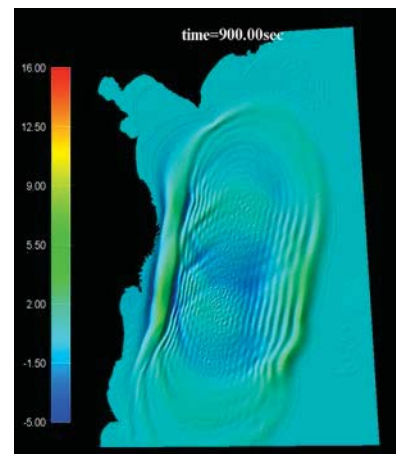
#### *Tsunami Simulation by the Great East Japan Earthquake*

The present method is applied to tsunami run-up simulation by the Great East-Japan Earthquake as the application example. The unstructured triangular mesh with the element Courant number constant is employed. The initial water surface displacement is given by the faults model proposed by Mansinha and Smylie (1971). The fault data proposed by Tohoku University Ver. 1.0 ([http://www.tsunami.civil.tohoku.ac.jp/hokusai3/J/events/tohoku\\_2011/model/](http://www.tsunami.civil.tohoku.ac.jp/hokusai3/J/events/tohoku_2011/model/)), is employed. Fig. 10 shows the computational domain and the initial condition for water elevation. Time increment is assumed to be 0.1s. The non-slip boundary condition is employed at the coastline and the open boundary condition is employed at the open boundary. The treatment method for moving boundary is employed at the land area. In this simulation, we focus on the Onagawa area because the area had big damage by tsunami.

Fig. 11 shows the computed results at time = 900s. The wave dispersive effect is clearly shown in the results.



**Figure 10. Initial condition**



**Figure 11. Wave propagation (time=900sec)**

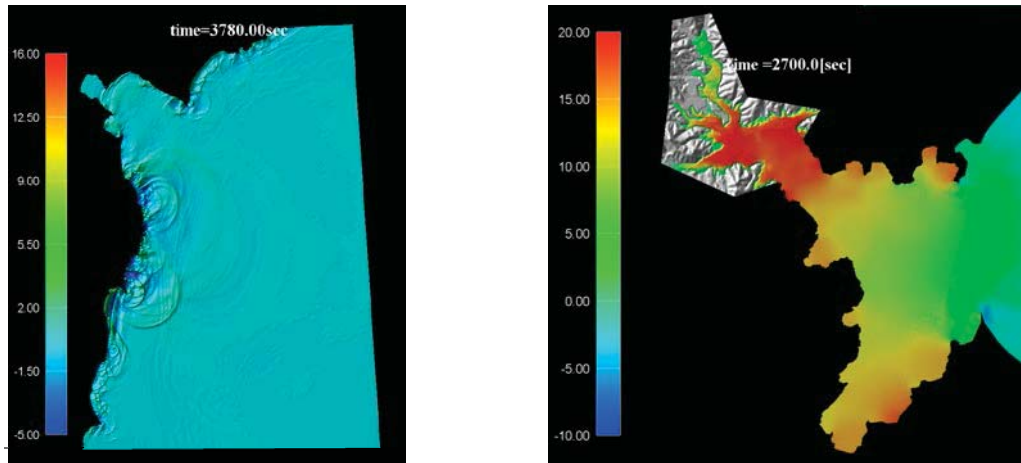


Figure 12. Wave propagation and run-up at Onagawa (time=2700s)

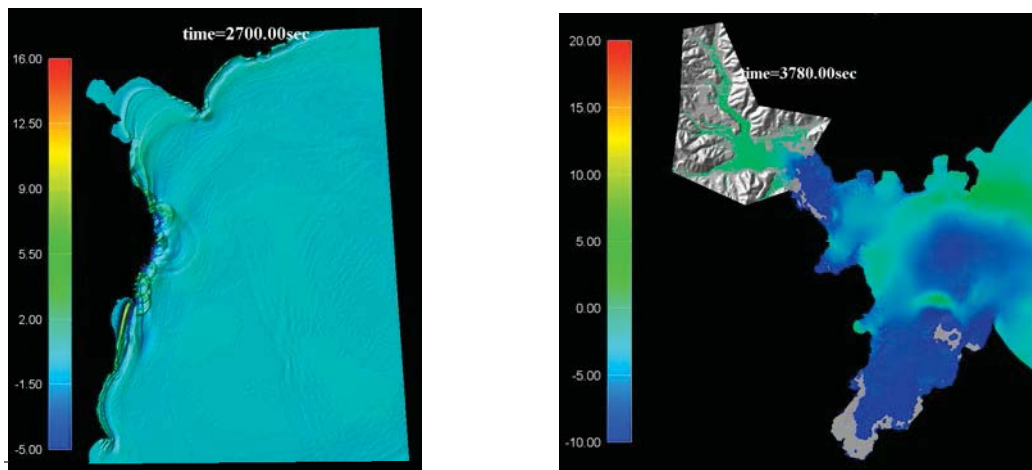


Figure 13. Wave propagation and run-off at Onagawa (time=3780s)

Fig. 12 shows the computed wave propagation (left) and the run-up at Onagawa area (right) at time =2700s, which is the state that the maximum water elevation is observed at Onagawa by first tsunami wave. Fig. 13 shows the computed wave propagation (left) and the run-off at Onagawa area (right) at time =3780s, which is the state that the minimum water elevation is observed at Onagawa by first tsunami.

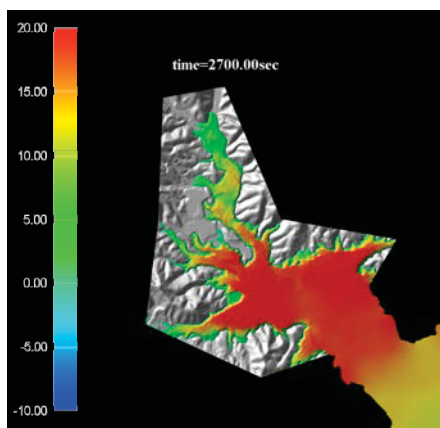


Figure 14. Computed inundation area

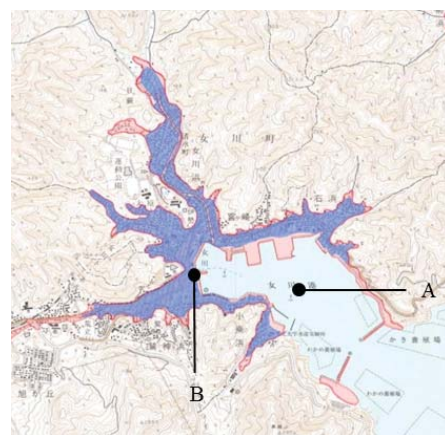
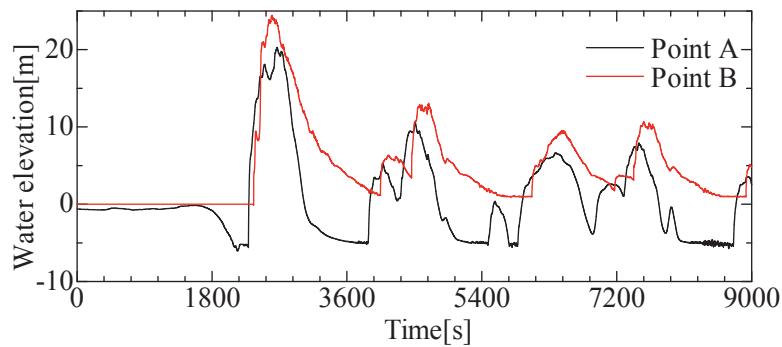


Figure 15. Tsunami damaged area



**Figure 16. Time history of water elevation at point A and B**

Fig.14 shows the computed inundation area by the first wave in Onagawa. Fig. 15 shows the investigation map of tsunami damaged area at Onagawa. The red area shows the inundation area and the blue area shows the building damaged area. The computational result is good agreement with the observed data. Fig.16 shows the time history of water elevation at the observation points A and B in Fig. 15. From the figure, the maximum water elevation over 20m is obtained at time = 2700s.

## Conclusions

The CIVA-stabilized finite element method has been presented for tsunami simulation. The Boussinesq equation is employed for governing equation. In order to show the validity and efficiency, the present method is applied to several numerical examples. From the results, the following conclusions are obtained.

For the dam break problem, the computed results by CIVA-SUPG finite element method are good agreement with the theoretical results comparing with the stabilized finite element method based on SUPG. For the tsunami run-up problem, the computed results by present method are good agreement with the experimental results.

For the application example by the Great East Japan Earthquake, the computed inundation area is good agreement with the observed data.

From the results in this paper, it can be concluded that the present method is useful for tsunami simulation.

We plan to consider the effect of collapse of building in future works.

## References

- Tanaka, N. (1999), Development of a highly accurate interpolation method for mesh-free flow simulations I. Integration of gridless, particle and CIP methods, *International Journal for Numerical methods in Fluids*, 30, pp. 957-976.
- Takase, S., Kashiyama, K., Tanaka and S. Tezduyar, T. E. (2010), Space-time SUPG formulation of the shallow-water equations, *International Journal for Numerical methods in Fluids*, 64, pp. 1379-1394.
- Fujima, K., Achmad, F., Shigihara, Y. and Mizutani, N. (2009), Estimation of tsunami force acting on rectangular structures, *Journal of Disaster Research*, 4, pp. 404-409.
- Mansinha, L. and Smylie D. E. (1971), The displacement fields of inclined faults, *Bullet of the Seismological Society of America*, 61, pp.1433-1440.
- Kawahara, M. and Umetsu, T. (1986), Finite element method for moving boundary problems in river flow, *International Journal of Numerical Methods in Fluids*, pp.163-186.



## Large-Scale Tsunami Simulation Based on Three-Dimensional Parallel SUPG-VOF Method

\*Taiki Fumuro<sup>1</sup>, Seizo Tanaka<sup>2</sup>, and Kazuo Kashiya<sup>1</sup>

<sup>1</sup>Department of Civil and Environmental Engineering, Chuo University, Japan

<sup>2</sup>Earthquake Research Institute, University of Tokyo, Japan

\*Corresponding author: fumuro@civil.chuo-u.ac.jp

### Abstract

This paper presents a large-scale tsunami simulation based on the three-dimensional parallel SUPG-VOF method. The three-dimensional Navier-Stokes equation and continuity equation are employed for solving velocity and pressure. The advection equation is employed for solving interface function between air and water. The stabilized finite element method based on unstructured grid is employed for the discretization for governing equations. In order to handle the large-scale tsunami simulations, several parallel implementations are designed by using MPI, OpenMP and hybrid method with MPI/OpenMP. The presented method is applied to several tsunami wave problems to show the validity and efficiency.

**Keywords:** Tsunami simulation, Stabilized finite element method, SUPG-VOF method, Parallel computing, Three-dimensional Navier-Stokes equation

### Introduction

The huge tsunami wave generated by the Great East Japan Earthquake (March 11, 2011) damaged the coastal area, and it is recognized that the tsunami cause the enormous damage to the human life and economic activities. There have been presented a number of numerical methods for tsunami simulation. The shallow water equation and Boussinesq equation are normally used for the governing equations. However, in order to predict the damage of structures, the three-dimensional simulation based on Navier-Stokes equation is required. There have been presented a number of numerical methods for Navier-Stokes equation with free surface. Based on the frame of reference used, these approaches can be classified into two categories: interface-capturing method using Eulerian stationary mesh and interface-tracking method using Lagrangian moving mesh. The interface-capturing method generally utilizes the VOF method (Hirt and Nichols (1981)) and level set method (Sussman et al. (1994)). On the other hand, the interface-tracking method generally utilizes the ALE method (Hughes et al. (1981)) and space-time method (Behr and Tezduyar (1993)). In the case of the three-dimensional Navier-Stokes equation, the simulation becomes quite large-scale and it is essential to use the parallel computing techniques. Parallel computing techniques are classified into three methods (Pacheco (1997), Changra et al. (2001)): process parallelism using MPI, thread parallelism using OpenMP, and hybrid parallelism combined these two methods.

This paper investigates three types of parallel computing methods for three-dimensional tsunami simulation. Each of the method is executed on a supercomputer CRAY XE6. Three-dimensional Navier-Stokes equation with the incompressibility condition is employed as the governing equation. The interface-capturing approach based on VOF method is employed because the method is robust in the applicability: for example, the method can be usefully applied to the complicated phenomena involving breaking waves. The stabilized finite element method based on SUPG/PSPG (Tezduyar (1992)) using P1/P1 element is employed for the spatial discretization. The full implicit scheme based on Crank-Nicolson method is used for the temporal discretization.

In Section 2, we describe the governing equations. The stabilized formulations are described in Section 3. Parallel implementation is described in Section 4. The present method is applied to numerical examples in Section 5. The conclusions are stated in Section 6.

## Governing Equations

To model a free surface flow, we consider two immiscible fluids, A and B, with densities  $\rho_A$  and  $\rho_B$  and viscosities  $\mu_A$  and  $\mu_B$ . An interface function  $\phi$  serves a marker identifying fluids A and B with the definition  $\phi = \{1$  for fluid A, 0 for fluid B and 0.5 for two-fluid interfaces}, as shown in Fig. 1. In this context, the density and viscosity,  $\rho$  and  $\mu$ , are defined as

$$\rho = \phi\rho_A + (1-\phi)\rho_B \quad (1)$$

$$\mu = \phi\mu_A + (1-\phi)\mu_B \quad (2)$$

The evolution of the interface function is governed by a time-dependent advection equation as

$$\frac{\partial\phi}{\partial t} + u_i \frac{\partial\phi}{\partial x_i} = 0 \quad \text{on } \Omega \quad (3)$$

where  $\Omega$  denotes the space domain. The velocity,  $u_i$ , is obtained from the solution of the unsteady Navier-Stokes equations under the incompressibility condition as

$$\rho \left( \frac{\partial u_i}{\partial t} + u_j \frac{\partial u_i}{\partial x_j} - f_i \right) + \frac{\partial p}{\partial x_i} - \mu \frac{\partial}{\partial x_j} \left( \frac{\partial u_i}{\partial x_j} + \frac{\partial u_j}{\partial x_i} \right) = 0 \quad \text{on } \Omega \quad (4)$$

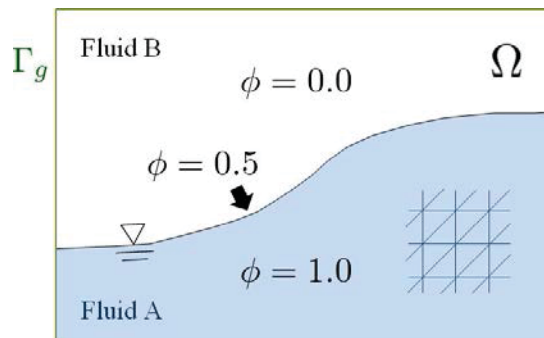
$$\frac{\partial u_i}{\partial x_i} = 0 \quad \text{on } \Omega \quad (5)$$

where  $p$  is the pressure and  $f_i$  is the external force. The following conditions are imposed at the boundary.

$$u_i = g_i \quad \text{on } \Gamma_g \quad (6)$$

$$\left\{ -p\delta_{ij} + \mu \left( \frac{\partial u_i}{\partial x_j} + \frac{\partial u_j}{\partial x_i} \right) \right\} n_j = h_i \quad \text{on } \Gamma_h \quad (7)$$

where  $\Gamma_g$  and  $\Gamma_h$  denote the Dirichlet and Neumann boundaries.  $\delta_{ij}$  is the Kronecker delta.



**Figure. 1** Distribution of interface function

### Finite Element Formulations

The stabilized finite element method based on the SUPG/PSPG method with shock capturing is employed for the governing equations. The stabilized formulation of Eqs. (4) and (5) can be written as follows.

$$\begin{aligned}
& \int_{\Omega} w_i \rho \left( \frac{\partial u_i}{\partial t} + u_j \frac{\partial u_i}{\partial x_j} - f_i \right) d\Omega - \int_{\Omega} \frac{\partial w_i}{\partial x_i} p d\Omega + \int_{\Omega} \mu \frac{\partial w_i}{\partial x_j} \left( \frac{\partial u_i}{\partial x_j} + \frac{\partial u_j}{\partial x_i} \right) d\Omega + \int_{\Omega} q \frac{\partial w_i}{\partial x_i} d\Omega \\
& + \sum_{e=1}^{n_{el}} \int_{\Omega_e} \left( \tau_s u_k \frac{\partial w_i}{\partial x_k} + \tau_p \frac{1}{\rho} \frac{\partial q}{\partial x_k} \right) \left\{ \rho \left( \frac{\partial u_i}{\partial t} + u_j \frac{\partial u_i}{\partial x_j} - f_i \right) + \frac{\partial p}{\partial x_i} \right\} d\Omega_e \\
& + \sum_{e=1}^{n_{el}} \int_{\Omega_e} \tau_c \frac{\partial w_i}{\partial x_i} \rho \frac{\partial u_j}{\partial x_j} d\Omega_e = \int_{\Gamma} w_i h_i d\Gamma
\end{aligned} \tag{8}$$

where  $w_i$  and  $q$  denote weighting functions,  $\tau_s$ ,  $\tau_p$  and  $\tau_c$  are stabilization parameters given by

$$\tau_s = \left\{ \left( \frac{2}{\Delta t} \right)^2 + \left( \frac{2 \|u_i^e\|}{h_e} \right)^2 + \left( \frac{4\nu}{h_e^2} \right)^2 \right\}^{\frac{1}{2}} \tag{9}$$

$$\tau_p = \tau_s \tag{10}$$

$$\tau_c = \frac{h_e}{2} \|u_i^e\| \xi(\text{Re}_e) \tag{11}$$

where

$$\xi(\text{Re}_e) = \begin{cases} (\text{Re}_e/3), & \text{Re}_e \leq 3 \\ 1, & \text{Re}_e > 3 \end{cases} \tag{12}$$

$\nu = \mu/\rho$ ,  $\Delta t$  is the time increment,  $h_e$  is the element length and  $\text{Re}_e$  is the element Reynolds number.

In Eq. (8), the first four integrals, together with the right-hand side, represent the Galerkin formulation of Eq. (4) and Eq. (5). The first series of element-level integrals in the formulation are the SUPG and PSPG stabilization terms. The second series of element-level integrals are the shock capturing terms.

The stabilized formulation of Eq. (3) can be written as follows.

$$\int_{\Omega} w \left( \frac{\partial \phi}{\partial t} + u_i \frac{\partial \phi}{\partial x_i} \right) d\Omega + \sum_{e=1}^{n_{el}} \int_{\Omega_e} \left( \tau_s u_j \frac{\partial w}{\partial x_j} \right) \left( \frac{\partial \phi}{\partial t} + u_i \frac{\partial \phi}{\partial x_i} \right) d\Omega_e + \sum_{e=1}^{n_{el}} \int_{\Omega_e} \tau_{\phi} \frac{\partial w}{\partial x_i} \frac{\partial \phi}{\partial x_j} d\Omega_e = 0 \tag{13}$$

where  $\tau_s$  and  $\tau_{\phi}$  are the stabilization parameters given by

$$\tau_s = \left\{ \left( \frac{2}{\Delta t} \right)^2 + \left( \frac{2 \|u_i^e\|}{h_e} \right)^2 \right\}^{-\frac{1}{2}} \quad (14)$$

$$\tau_\phi = \frac{h_e}{2} \|u_i^e\| \quad (15)$$

In Eq. (13), the first integral represents the Galerkin formulation of Eq. (3). The first series of element-level integrals in the formulation are the SUPG stabilization terms. The second series of element-level integrals are the discontinuity capturing terms.

The linear tetrahedral element is employed for the discretization in space and the Crank-Nicolson method is employed for the discretization in time. The advection speed is approximated on the basis of the second-order Adams-Bashforth method. The GPBi-CG method is employed for solving the simultaneous linear equations. Also, the interface-sharpening/mass-conservation algorithm (Aliabadi and Tezduyar (2000)) is employed in order to express the interface clearly and conserve the mass for each fluid. In this approach, the interface function  $\phi$  which is calculated from the simultaneous linear equations is replaced by  $\hat{\phi}$  as follows.

$$\hat{\phi} = c^{1-a} \phi^a, \quad 0 \leq \phi \leq c \quad (16)$$

$$\hat{\phi} = 1 - (1-c)^{1-a} (1-\phi)^a, \quad c \leq \phi \leq 1 \quad (17)$$

$$\phi \leftarrow \hat{\phi} \quad (18)$$

where  $a$  is a sharpening parameter, and  $0 \leq c \leq 1$  is a mass conservation level.

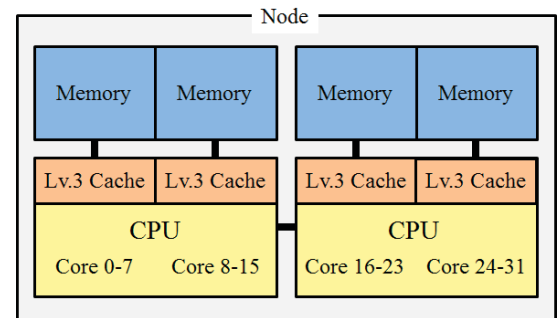
### Parallel Implementation

Parallel implementation is a technique for fast computation and realization of large-scale computing. Parallel computing techniques are classified into three methods of program parallelism: process parallelism, thread parallelism, and hybrid parallelism combined these two methods. MPI is used for the process parallelism and OpenMP is used for the thread parallelism. To minimize the amount of interprocessor communication, the automatic mesh decomposer, METIS, is employed.

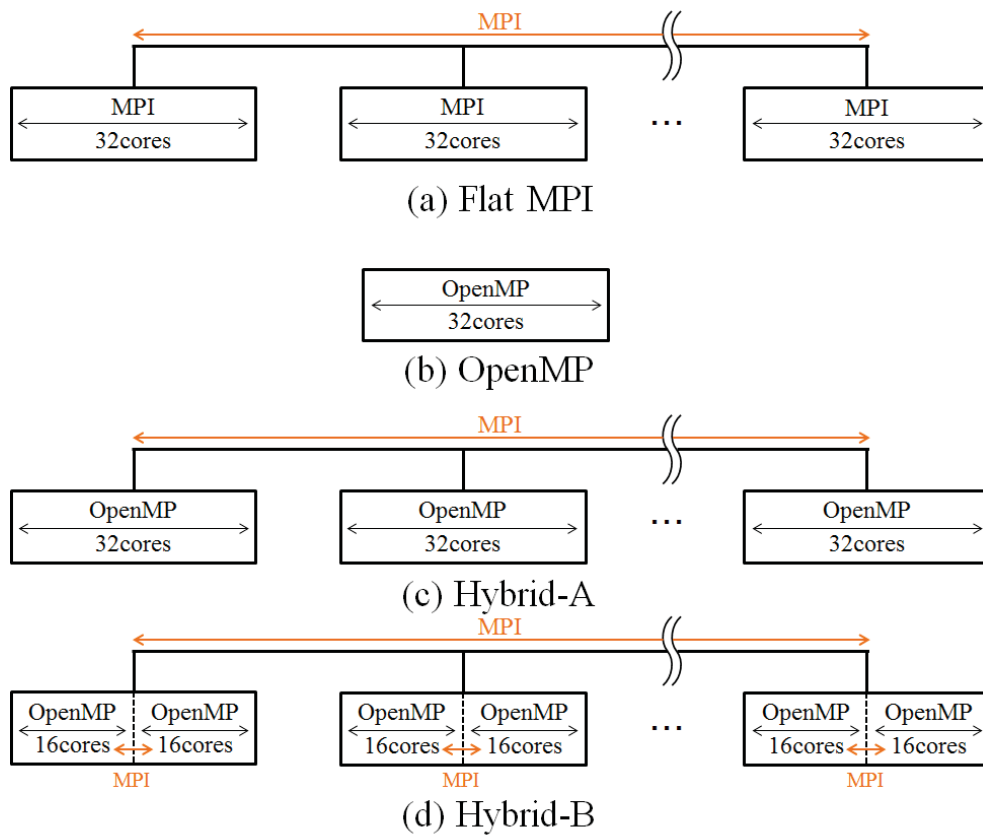
Table 1 shows the specifications of the parallel supercomputer. Fig. 2 shows the architecture of the CPUs and memories in a node for CRAY XE6. In this paper, four type of parallel computing methods are investigated, as shown in Fig. 3.

**Table 1. Specifications of the parallel supercomputer used to calculate**

	CRAY XE6
CPU	AMD Opteron 6238 (2.9GHz)
Memory size (1 Node)	64GB
Number of cores	16cores $\times$ 2CPUs $\times$ 940nodes
O.S.	SUSE Linux Enterprise Server 11
Compiler	Intel Composer XE2011



**Figure 2. Architecture of the CPUs and memories in a node**



**Figure 3. The four type of parallel computing methods**

### Numerical Examples

The four type of parallel computing methods are applied to two numerical examples: the dam-break problem and large-scale tsunami simulation.

#### *Dam-Break Problem*

The parallel computing methods are applied to the dam-break problem, as shown in Fig. 4. The computational domain was discretized by a uniform finite element mesh with  $233 \times 40 \times 190$  elements ( $x \times y \times z$  direction). The total number of nodes and elements are 1,832,454 and 10,624,800, respectively. The density/viscosity of water and air are assumed as  $1000.0\text{kg/m}^3 / 1.0 \times 10^{-3}\text{Pa} \cdot \text{s}$  and  $1.293\text{kg/m}^3 / 1.8 \times 10^{-5}\text{Pa} \cdot \text{s}$ . The slip condition is employed at the wall boundary condition. The time increment  $\Delta t$  is assumed to be 0.0001 s.

Fig. 5 shows the time history of the waterfront line. The computed result obtained by the present method is good agreement with the experimental results (Koshizuka et al. (1995) and Martin, Moyce (1952)). Fig. 6(a) and 6(b) show the speed-up ratio and parallel efficiency versus the total number of cores/nodes. In this figures the normalization are performed using the flat MPI using 1 node. From the results of parallel performance, it can be seen that the good parallel efficiency are obtained in all approaches and the significant difference is not appeared.

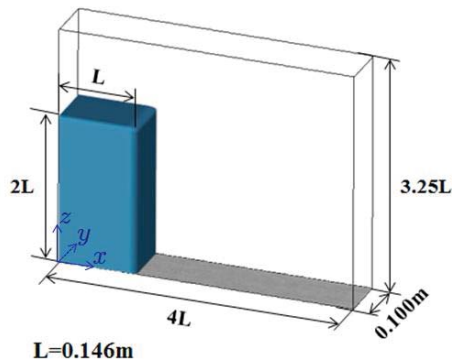


Figure 4. Computational domain and initial condition

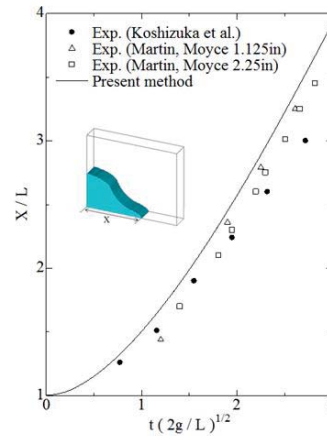


Figure 5. The time history of the waterfront line

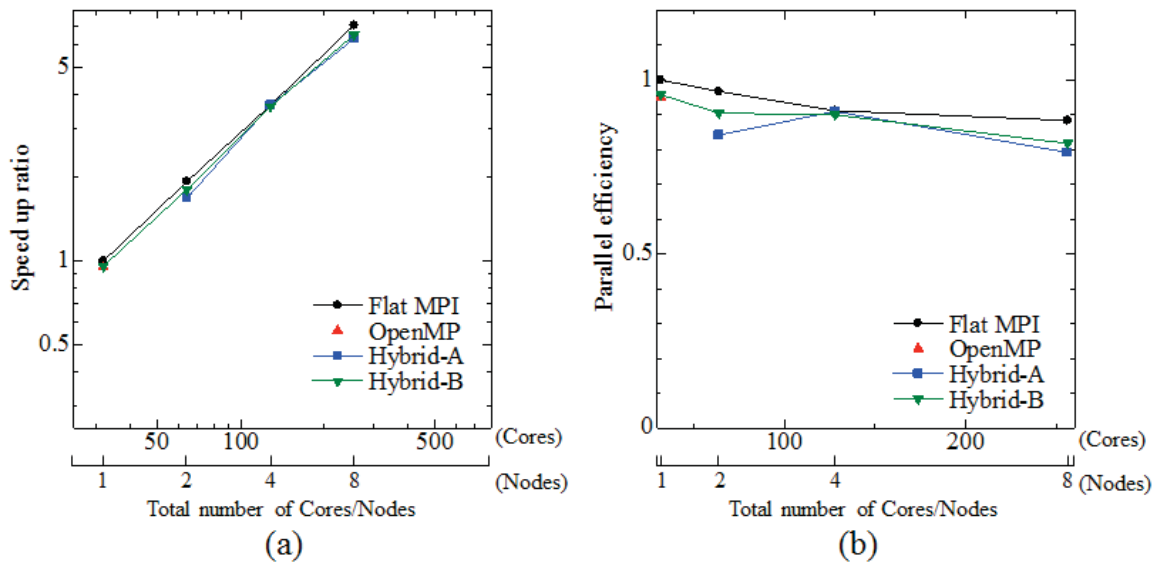


Figure 6. Comparison of speed-up and efficiency

*Large-scale Tsunami Simulation*

The parallel computing methods are applied to the large-scale tsunami simulation. Fig. 7 shows the initial condition and the finite element mesh. The total number of nodes and elements are 6,738,732 and 37,560,556, respectively. The minimum mesh size is assumed to be 0.50m around the water surface and structures. The density and viscosity of water and air are same as the dam-break problem. The slip boundary condition is employed at solid boundary. The time increment  $\Delta t$  is set to be 0.050 s.

Fig. 8 shows the computed results at  $t = 30.0s$  and  $45.0s$ . Fig. 9(a) and 9(b) show the speed-up ratio and parallel efficiency versus the total number of cores/nodes. In this figures, the normalization are performed using the flat MPI using 2 nodes. From the result of parallel performance, it can be seen that the result by flat MPI shows a better parallel efficiency compared with those using Hybrid A and Hybrid B, and the result by Hybrid-B is better than that by Hybrid-A by the effect of the conflict of memory access. Fig. 10 shows the mass conservation ratio versus the time. From this figure, it can be seen that the mass of each fluid is conserved.

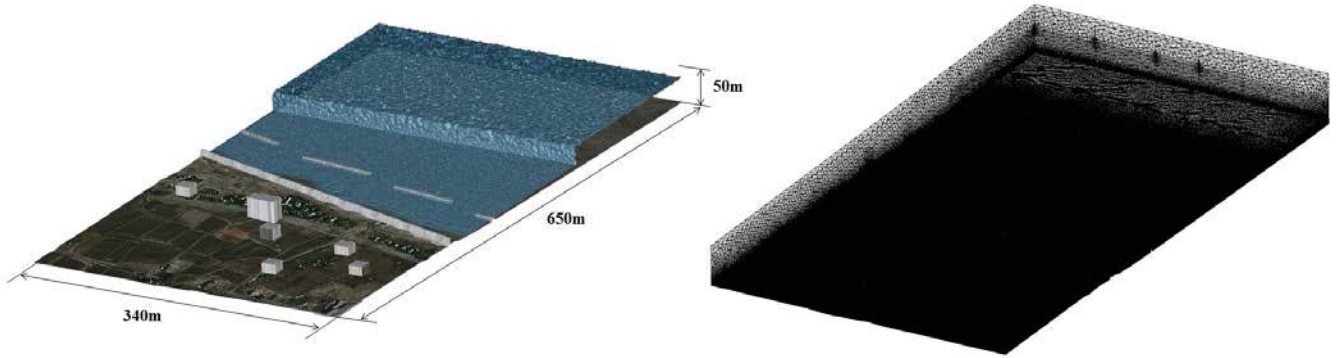


Figure 7. Initial condition and the finite element mesh

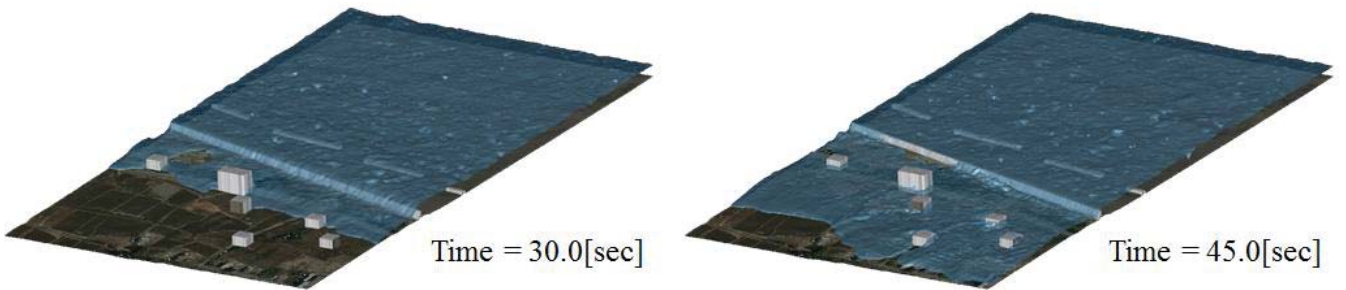


Figure 8. Computed results

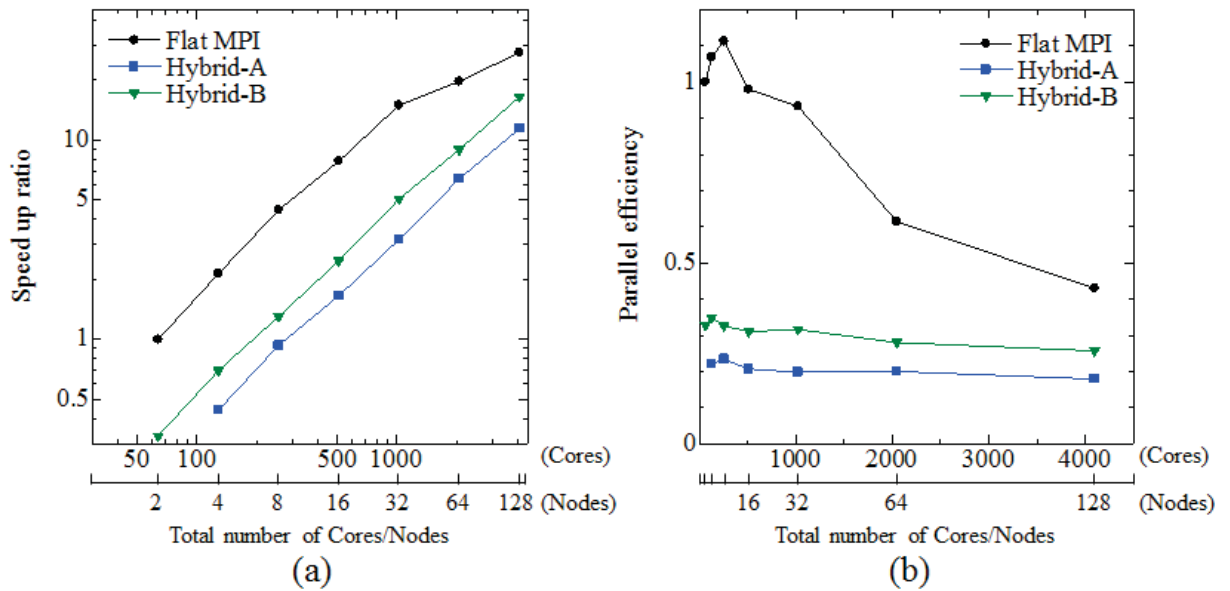
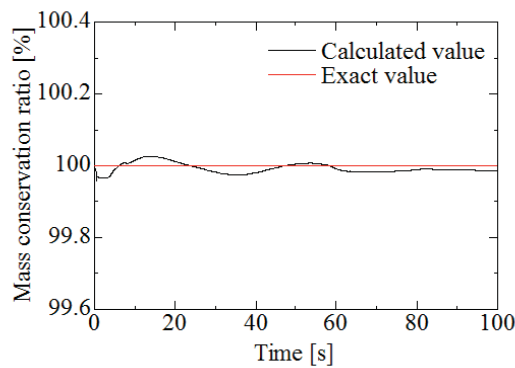


Figure 9. Comparison of speed-up and efficiency



**Figure 10. Mass conservation ratio**

## Conclusions

A parallel computational methods using MPI, OpenMP and hybrid method with MPI/OpenMP are investigated for three dimensional tsunami simulation based on SUPG/VOF method. The following conclusions can be made:

- The good parallel efficiency is obtained in all approaches and the significant difference is not appeared in the small-scale simulation example.
- The good parallel efficiency is obtained in flat MPI compared with those using Hybrid-A and Hybrid-B in the large-scale simulation example, and the result by Hybrid-B is better than that by Hybrid-A by the effect of the conflict of memory access.

From the results obtained in this paper, it can be concluded that the proposed computational method with MPI parallelization is a useful and powerful tool for the large-scale tsunami simulation.

## References

- Hirt, C. W. and Nichols, B. D. (1981), Volume of fluid (VOF) method for the dynamics of free boundaries. *Journal of Computational Physics*, 39, pp. 201-225.
- Sussman, M., Smereca, P. and Osher, S. (1994), A level set approach for computing solutions for incompressible two-phase flow. *Journal of Computational Physics*, 144, pp. 146-159.
- Hughes, T. J. R., Liu, W. K., Zimmermann, T. K. (1981), Lagrangian-Eulerian finite-element formulation for incompressible viscous flows. *Computer Methods in Applied Mechanics and Engineering*, 29, pp. 329-349.
- Behr, M. and Tezduyar, T. E. (1993), Finite element solution strategies for large-scale flow simulations, *Computer Methods in Applied Mechanics and Engineering*, 112, pp. 3-24.
- Pacheco, P. S. (1997), *Parallel Programming with MPI*, Morgan Kaufmann
- Chandra, R., Dagum, L., Kohr, D., Maydan, D., McDonald, J., Menon, R. (2001), *Parallel Programming in OpenMP*, Morgan Kaufmann.
- Tezduyar, T. E. (1992), Stabilized finite element formulations for incompressible flow computations. *Advance in Applied Mechanics*, 28, pp. 1-44.
- Aliabadi, S. and Tezduyar, T. E. (2000), Stabilized-finite-element/interface-capturing technique for parallel computation of unsteady flows with interface. *Computer Methods in Applied Mechanics and Engineering*, 190, pp. 243-261.
- Koshizuka, S., Tamako, H. and Oka, Y. (1995), A particle method for incompressible viscous flow with fluid fragmentation. *Computational Fluid Dynamics Journal*, 4, No. 1, pp. 29-46.
- Martin, J. C. and Moyce, W. J. (1952), An experimental study of the collapse of liquid columns on a rigid horizontal plane. *Philosophical Transactions of the Royal Society of London, Series A*, vol. 244, p. 312.
- Hord, R. M. (1999), *Understanding Parallel Supercomputing*, p. 356, IEEE Press.
- Kumar, V., Grama, A., Gupta, A. and Karypis, G. (1994), Introduction to Parallel Computing, *Design and Analysis of Algorithms*, p. 597, The Benjamin/Cummings Publishing Company, Inc.
- Karypis, G. and Kumar, V. (1998), Multilevel k-way partitioning scheme for irregular graphs, *Journal of Parallel and Distributed Computing*, 48, No. 1, pp. 96-129.



## Effect of Temperature Gradient within Solid Particles for Dispersed Two-Phase Flow and Heat Transfer

\*Takaaki TSUTSUMI<sup>1</sup>, Shintaro TAKEUCHI<sup>2</sup>, and Takeo KAJISHIMA<sup>2</sup>

<sup>1</sup>Graduate School of Osaka University, Osaka University, Japan

<sup>2</sup>Department of Mechanical Engineering, Osaka University, 2-1 Yamada-oka, Suita-city, Osaka 565-0871, Japan

\*Corresponding author: tsutsumi@fluid.mech.eng.osaka-u.ac.jp

### Abstract

Liquid-solid two-phase flow with heat transfer is directly simulated to investigate the effect of temperature gradient within the solid objects. The interaction between fluid and particles is solved by our original immersed solid approach on a rectangular grid system. And a discrete element model with soft-sphere collision is applied for particle-particle interaction. A new heat conduction model is proposed for the heat conduction at the solid-liquid interface by considering the interface direction. The method is applied to liquid-solid two-phase flows in a confined square domain with a hot bottom plate and a cold top plane under a relatively low Rayleigh number. In dense condition, the particles of high heat conductivity induce strong convection and promote the heat transfer, while the particles of low heat conductivity depress the incoming heat flux from the bottom wall, resulting in low Nusselt number. The above simulation results highlight the importance of temperature distributions within the particles and liquid.

**Keywords:** Multiphase flow, Solid dispersion, Immersed solid object, Thermal flow, Heat conductivity

### Introduction

Solid-dispersed two phase flows often involve heat (and mass) transfer through the interface. Temperature distributions in both fluid and solid phases play important roles on the fluid-solid interaction.

For numerical simulation of heat transfer problem in a flow including multiple solid objects, an immersed boundary method has an advantage. Kim et al. (2001) and Kim and Choi (2004) proposed a heat source/sink method for imposing iso-thermal and iso-heat-flux boundary conditions at the immersed boundary of a fixed particle. Similar approaches were proposed by Pacheco and co-workers (Pacheco, Pacheco-Vega, Rodić and Peck, 2005; Pacheco-Vega, Pacheco, Rodić, 2007) with a successive determination algorithm of the temperatures inside the body to match the iso-thermal and iso-heat-flux conditions at the immersed boundary. Ren et al. (2012) proposed an implicit formulation of the momentum and heat source/sink approach. The boundary force and heat flux are solved implicitly so that the no-slip and fixed temperature conditions are enforced on the immersed boundary.

The above researchers simplify the problem by imposing a boundary condition of either constant temperature or constant flux. And, there are few previous studies that deal with a conjugate heat transfer problem (convective and conductive heat transfers) in a two-phase flow including freely-moving particles (Yu, Shao and Wachs, 2006; Ueyama, Moriya, Nakamura and Kajishima, 2011).

In the present work, we study a heat transfer problem in a multiphase flow of dispersed solid particles including the effect of local heat flux at the liquid-solid surface (and therefore temperature gradient within the solid object). To facilitate the treatment of interaction problem between the fluid and a large number of relatively moving particles, a fixed grid approach is adopted.

The interaction between fluid and particles is solved with our original immersed solid approach (Kajishima, Takiguchi, Hamasaki and Miyake, 2001; Yuki, Takeuchi and Kajishima, 2007) on a rectangular grid system. The method employs a simple procedure for the momentum-exchange by imposing a volume force (as an interaction force) on both solid and fluid phases. The method has been applied for studying a clustering process with a total of 1000 spherical particles in a turbulent flow (Kajishima, Takiguchi, Hamasaki and Miyake, 2001; Kajishima and Takiguchi, 2002; Kajishima, 2004). Also the usefulness of our method has been demonstrated by Nishiura et al. (Nishiura Shimosaka, Shirakawa, and Hidaka, 2006) through the analysis of sedimentation process employing a total of  $10^5$  spherical particles. In the present study, to include the effect of conjugate heat transfer in a liquid-solid interaction problem, a heat flux decomposition model is proposed for the heat conduction at the liquid-solid interface. The model employs a procedure for solving the temperature field in an Eulerian frame by considering the interface direction.

The present method is applied to a direct numerical simulation of laminar natural convection of relatively low Rayleigh number in a confined square domain including multiple particles of round shape. By including the particles of different ratios of heat conductivity (solid to liquid), we look into the effect of the solid temperature distribution on the behaviour of the particles, and the heat transfer mechanism is studied in the solid-dispersed two-phase flow field.

## Governing Equations and numerical Methods

### Governing equations

The governing equations for fluid are the equations of continuity, momentum and energy:

$$\nabla \cdot \mathbf{u}_f = 0, \quad (1)$$

$$\rho_f \frac{\partial \mathbf{u}_f}{\partial t} + \rho_f \mathbf{u}_f \cdot \nabla \mathbf{u}_f = -\nabla p + \mu_f \nabla^2 \mathbf{u}_f + \rho_f \beta (T - T_0) \mathbf{g}, \quad (2)$$

$$\frac{\partial \rho_f c_f T_f}{\partial t} + \mathbf{u}_f \cdot \nabla (\rho_f c_f T_f) = \nabla \cdot (\lambda_f \nabla T_f). \quad (3)$$

Here, an incompressible fluid is assumed and Boussinesq approximation is employed to include the effect of density fluctuation. In the following, viscous coefficient ( $\mu_f$ ), heat capacity per unit volume ( $\rho_f c_f$ ) and thermal conductivity ( $\lambda_f$ ) are assumed to be constant.

### Fluid-solid interaction model: Immersed solid approach

Momentum exchange at the fluid-solid interface is solved by an immersed solid approach developed by Kajishima and the co-workers (Kajishima, Takiguchi, Hamasaki and Miyake, 2001; Kajishima and Takiguchi, 2002; Kajishima, 2004), on a uniformly distributed fixed grid system. This is briefly described below.

A velocity field  $\mathbf{u}$  is established through volume-averaging the local fluid velocity  $\mathbf{u}_f$  and the local particle velocity  $\mathbf{u}_p$  in a cell:

$$\mathbf{u} = (1 - \alpha) \mathbf{u}_f + \alpha \mathbf{u}_p, \quad (4)$$

where  $\alpha$  ( $0 \leq \alpha \leq 1$ ) is the local solid volume fraction in the cell. The particle velocity  $\mathbf{u}_p$  is decomposed into translating and rotating components as  $\mathbf{u}_p = \mathbf{v}_p + \boldsymbol{\omega}_p \times \mathbf{r}$ . This mixture velocity field  $\mathbf{u}$  is assumed to obey the following equation:

$$\frac{\partial \mathbf{u}}{\partial t} = -\frac{\nabla p}{\rho_f} + \mathbf{H}_u + \beta (T - T_0) \mathbf{g} + \mathbf{f}_p. \quad (5)$$

Interaction term  $\mathbf{f}_p$  works to assign the mixture velocity that satisfies the non-slip boundary condition at the interface (Kajishima, Takiguchi, Hamasaki and Miyake, 2001; Kajishima and Takiguchi, 2002; Kajishima, 2004). For time-update, the 2nd-order Adams-Bashforth and Crank-Nicolson methods are employed for the convective and viscous terms, respectively. The pressure gradient term in Eq. (5) is treated implicitly by a fractional step method. With the corrected velocity field  $\tilde{\mathbf{u}}$ , the fluid-solid interaction term  $\mathbf{f}_p$  is modelled as:

$$\mathbf{f}_p = \alpha \frac{(u_p - \tilde{u})}{\Delta t}, \quad (6)$$

where  $\Delta t$  is the time increment.

For motion of the particles, Newton's equations for momentum and angular momentum are solved. The same force as Eq. (6) applies to the fraction of the solid in the cell with the opposite sign. The surface integration of the hydrodynamic forces is changed to the integration of  $\mathbf{f}_p$  over the volume of the particle  $V_p$ :

$$m_p \frac{v_p^{n+1} - v_p^n}{\Delta t} = \int_{V_p} (-\rho_f \mathbf{f}_p) dV + \mathbf{G}_p, \quad (7)$$

$$\mathbf{I}_p \frac{\omega_p^{n+1} - \omega_p^n}{\Delta t} = \int_{V_p} \mathbf{r} \times (-\rho_f \mathbf{f}_p) dV + \mathbf{N}_p. \quad (8)$$

The above replacement from surface to volume integrations considerably facilitates the computation of the solid motion, and also the use of the same body force  $\mathbf{f}_p$  for both (fluid and particle) phases in a shared Cartesian cell ensures no leakage of momentum between the phases. Eqs. (7) and (8) are solved with a predictor-corrector method (Ueyama, Moriya, Nakamura and Kajishima, 2011).

#### *Temperature field and interfacial heat conduction*

Temperature field is treated in an Eulerian way irrespective of the substance occupying the cell. The numerical simulation are conducted under  $\rho_s = \rho_f (= \rho)$  and  $c_s = c_f (= c)$ . The following equation is solved with heat flux  $\mathbf{q}$ :

$$\frac{\partial \rho c T}{\partial t} + \mathbf{u} \cdot \nabla (\rho c T) = -\nabla \cdot \mathbf{q}. \quad (9)$$

In the present work,  $\mathbf{q}$  is given by a single equation that covers both phases as well as the interface. The discretised temperature gradient  $\nabla T|_{ij}$  at  $(i, j)$  cell is decomposed into surface-normal component  $(\mathbf{nn}) \cdot \nabla T|_{ij}$  and tangential component  $(\mathbf{I} - \mathbf{nn}) \cdot \nabla T|_{ij}$ . In an interfacial cell partially occupied by the solid object (local solid volume fraction  $\alpha$ ), the following mean heat conductivities are defined in the surface normal and tangential directions, respectively:

$$\frac{1}{\lambda_n} = \frac{1-\alpha}{\lambda_f} + \frac{\alpha}{\lambda_p}, \quad (10)$$

$$\lambda_a = (1 - \alpha)\lambda_f + \alpha\lambda_p. \quad (11)$$

Assuming that the solid and fluid temperatures match with each other at the interface, the heat flux (covering the interfacial cell)  $\mathbf{q}$  is given by the following formula:

$$\mathbf{q} = -\lambda_n (\mathbf{nn}) \cdot \nabla T|_{ij} - \lambda_a (\mathbf{I} - \mathbf{nn}) \cdot \nabla T|_{ij}. \quad (12)$$

Eq. (9) is time-updated with the Crank-Nicolson method for diffusion term with the treatment of Eq. (12). This semi-implicit scheme stabilises the computation and enables simulation with particles of very high/low heat conductivities.

#### *Interparticle and particle-wall collision model*

A soft-sphere model is used to allow multiple-body collisions for interparticle and particle-wall collisions. A spring and dashpot model is employed to calculate the contact forces. In the present study, the same parameter values as Tsuji et al. (1993) are used for the spring constant, restitution coefficient and friction coefficient.

Tsuji et al. (1993) suggested the following condition for determining the time increment to sufficiently resolve the eigen oscillation of the mass-spring system:

$$\Delta t \leq \frac{\pi}{n} \sqrt{\frac{m_p}{k}} \quad (n \geq 10). \quad (13)$$

In the present study, the smallest value of the right hand side of the above equation is found to be  $1.47 \times 10^{-3}$  for the smallest  $m_p$  employed in the following section. Considering the numerical accuracy of the momentum and energy equations from our preliminary study, the time increment is fixed to  $\Delta t = 5.0 \times 10^{-4}$ , hereafter.

In the present study, no heat exchange or heat source is modelled in the interparticle collisions.

## **Results and discussion**

Solid-dispersed two-phase flow under natural convection is studied for different heat conductivity ratios (solid to fluid). The non-dimensional numbers used are Rayleigh number ( $Ra$ ) and Prandtl number ( $Pr$ ).

In the present work, the computational domain is a square shape of side length  $L$ , and the particles are initially arranged regularly in the domain. Temperature difference between the top and bottom wall is kept constant ( $\Delta T = 1$ ), and no heat flux is given at the lateral walls. The non-slip condition and the Neumann condition are applied for the velocity and pressure, respectively, on the solid walls. The equations are non-dimensionalised with the reference length  $L$ , the reference velocity  $U = \sqrt{g\beta\Delta TL}$ , the reference pressure  $\rho_f U^2$  and the characteristic temperature difference  $\Delta T$ . To investigate the natural convection on the particles behaviour and heat transfer, Prandtl number, density ratio, and specific heat ratio are set to unity.

In the following, interaction between the fluid and particles is simulated with different ratios of heat conductivity.

#### *Dense case with bulk solid volume fraction 38.5% (2-D)*

Table1: Simulation parameters.

Number of grids	$N_x \times N_y$	$200 \times 200$
Spatial resolution	$D_p/\Delta$	10
Number of particles	$N_p$	$14^2$
Diameter of particles	$D_p$	$0.05L$
Rayleigh number	$Ra$	$1.0 \times 10^5$
Heat conductivity ratio	$\lambda_s/\lambda_f$	$10^{-3}, 10^0, 10^1, 10^2, 10^3$

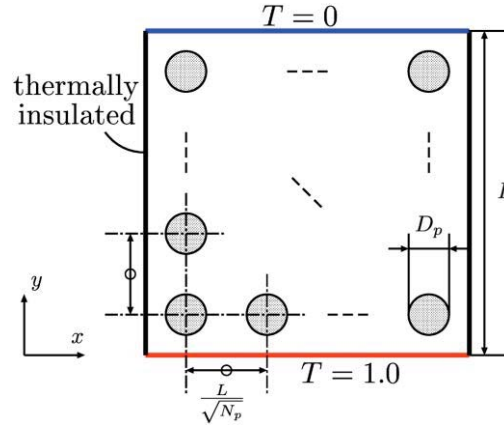


Figure 1: Schematic of arrangement of particles.

We look into the effect of the heat conductivity ratio on the particle motion in a natural convection of Rayleigh number  $10^5$ . The particles are initially arranged regularly in the domain as illustrated in Figure 1. The other parameters are summarised in Table 1. The bulk solid volume fraction is 38.5%. Figure 2 shows instantaneous flow and temperature fields at  $t = 1000$  by employing the particles of  $\lambda_s/\lambda_f = 10^{-3}$  and  $10^3$ . In both cases, the particles and fluid are found to constantly circulate in one direction around the domain centre after the initial developing stage. However, the local concentrations of the particles and time-averaged flow fields are different for the two cases. Figure 3 and 4 compare the time-averaged temperature and velocity fields and the time-averaged local solid volume fraction in each cell, respectively, for the two heat conductivity ratios.

For the particles of  $\lambda_s/\lambda_f = 10^{-3}$ , as shown in Figure 2(a), temperature gradient within the particle hardly re-distributes within the particle or to the fluid. From Figures 3(a) and 4(a), the concentrated isothermal lines and a region of high number density of the particles is found near the top and bottom walls. These suggest that, once a layer of particles is formed in those regions, the particles of poor-conductivity intercept the heat exchange with the walls. Therefore, low heat conduction in the particle could cause weak fluid convection and low Nusselt number.

On the other hand, for the case of  $\lambda_s/\lambda_f = 10^3$ , the particles efficiently transfer the heat to ambient fluid and generate temperature gradient in the fluid phase, resulting in strong fluid convection as observed in Figure 3(b). It is also characteristic, from Figure 4(b), that a region of low number density of the particles is found near the domain centre due to high rotating speed of the particulate flow and number density of the particles is distributed evenly except for the domain centre.

The heat transfer rate in two-phase natural convection system is compared for different particle conductivities. For evaluating heat transfer rate, the following Nusselt number is used with the heat flux at the hot (bottom) wall:

$$\text{Nu} = \frac{1}{\Delta T} \int_0^L \left( -\frac{\partial T}{\partial y} \right)_{y=0} dx . \quad (14)$$

Figure 5 compares the time evolutions of Nusselt number for five different  $\lambda_s/\lambda_f$  cases. The average level of the Nusselt number is found to increase as the heat conductivity ratio increases.

The above results show that the solid heat conductivity largely influences the flow pattern in solid dispersed two-phase flows and that the circulation of the particles enhances the heat transfer rate by transporting the heat from bottom to top.

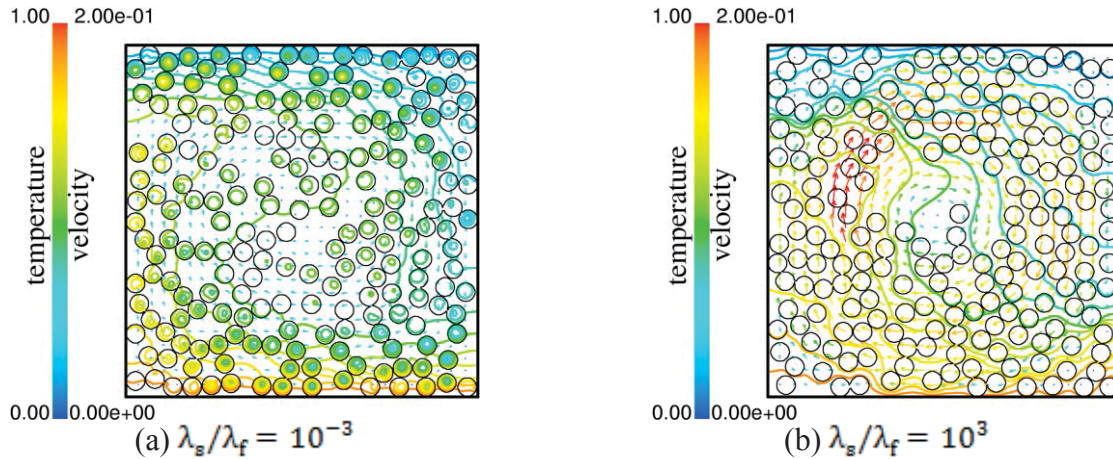


Figure 2: Instantaneous flow field and contours of temperature for different heat conductivities. Rayleigh number is  $10^5$  and bulk solid volume fraction is 38.5%. Colour shows the magnitude of the fluid velocity and iso-contour of temperature.

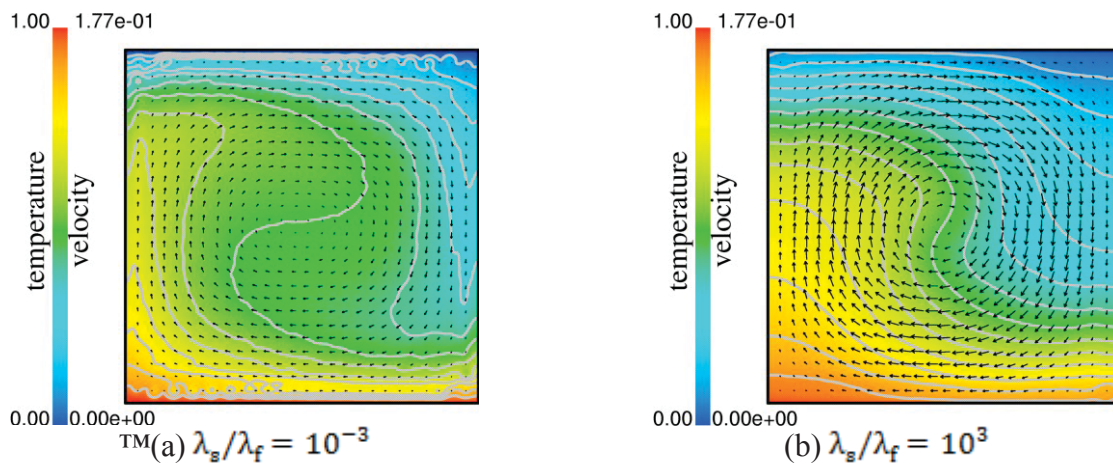


Figure 3: Time-averaged temperature and velocity fields for different heat conductivities. Rayleigh number is  $10^5$ . Average is taken between  $t = 500$  and  $1500$ . Magnitude the fluid velocity are levelled by colour, and iso-contours of temperature are plotted at constant intervals.

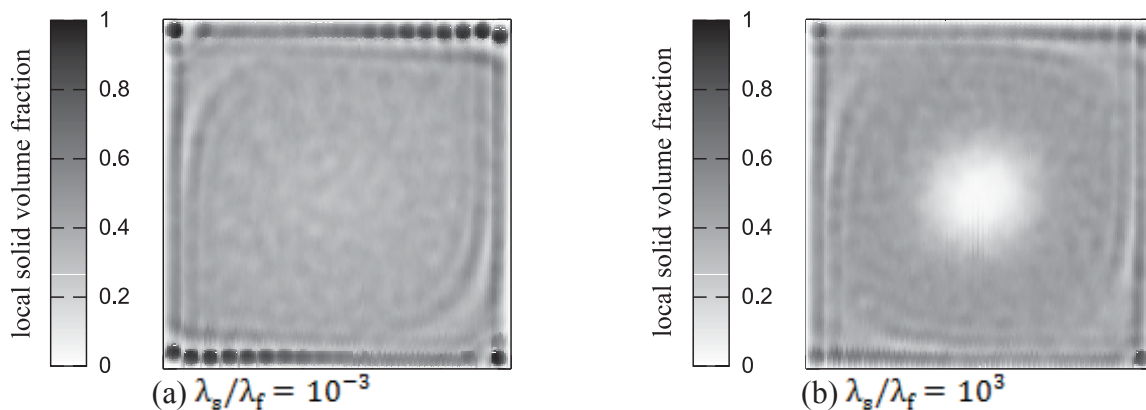


Figure 4: Time-average local solid volume fraction in a cell for different heat conductivities. Average is taken between  $t = 500$  and  $1500$ .

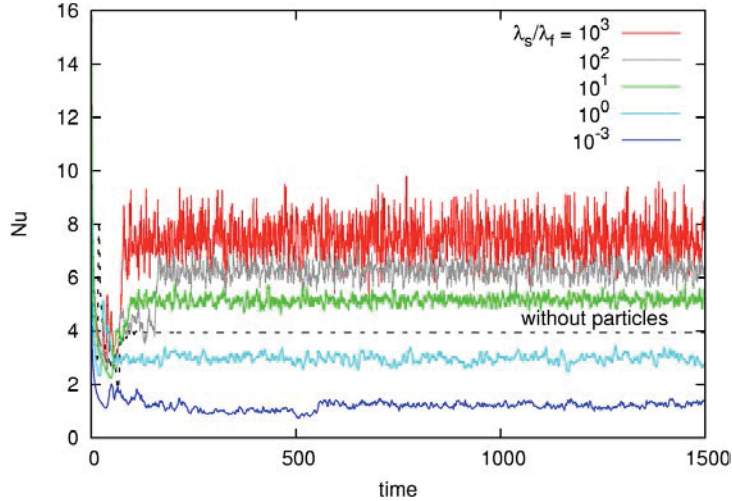


Figure 5: Comparison of time evolutions of Nusselt number for different ratios of heat conductivity. Solid volume fraction is 38.5%.

*Dilute case with bulk solid volume fraction 6.54% (3-D)*

Our method is extended to 3-D liquid-solid two-phase flow of Rayleigh number  $10^5$ . Figure 6 is an example of an instantaneous flow field including  $5^3$  spherical particles of  $\lambda_g/\lambda_f = 10^2$  in a cubic domain. The other parameters are summarised in Table 2. The bulk solid volume fraction is 6.54%. The particles and fluid move randomly in the initial developing stage. After that, the particles and fluid are found to constantly circulate in one direction around the domain centre. Our preliminary study shows that, for different  $\lambda_g/\lambda_f$  and Rayleigh numbers, characteristic flow behaviours (such as circulating mode and weak oscillating mode) are observed.

Table2: Simulation parameters.

Number of grids	$N_x \times N_y \times N_z$	$100 \times 100 \times 100$
Spatial resolution	$D_p/\Delta$	10
Number of particles	$N_p$	$5^3$
Rayleigh number	$Ra$	$1.0 \times 10^5$
Diameter of particles	$D_p$	$0.1L$

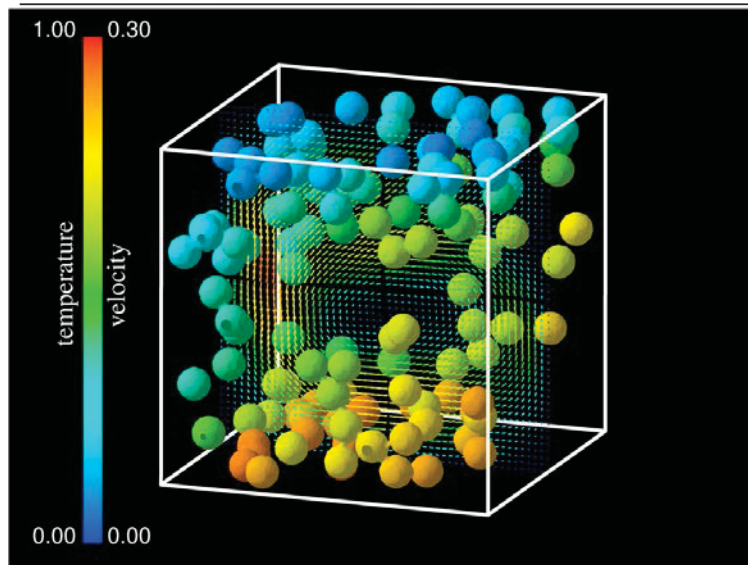


Figure 6: Instantaneous flow field and contours of temperature for different heat conductivities. Rayleigh number is  $10^5$  and bulk solid volume fraction is 6.54%. Temperature distribution on the surface of each particle and velocity vectors in a vertical cross section.

## Conclusions

To simulate solid-dispersed two-phase flow with heat transfer, a method considering the effects of temperature distribution within a particle was developed based on our original immersed solid and a discrete-element methods.

The method is applied to 2-D and 3-D liquid-solid two-phase flow under a relatively low Rayleigh number. In the dense condition (2-D), the particles of a high heat conductivity induce the heat convection of the fluid, and promote the heat transfer of the system. On the other hand, for the low heat conductivity case, the particles concentrate in the near-wall regions and intercept the heat transfer from the hot wall to the fluid, resulting in low Nusselt number.

These results highlight the effect of temperature distributions within the particles as well as liquid on the overall heat transfer performance in the multiphase flow.

## References

- Kajishima, T., Takiguchi, S., Hamasaki, H. and Miyake, Y. (2001), Turbulence structure of particle-laden flow in a vertical plane channel due to vortex shedding. *JSME International Journal, Series B* 44-4, pp. 526-535.
- Kajishima, T. and Takiguchi, S. (2002), Interaction between particle clusters and fluid turbulence. *International Journal of Heat and Fluid Flow*, 23-5, pp. 639-646.
- Kajishima, T. (2004), Influence of particle rotation on the interaction between particle clusters and particle-induced turbulence. *International Journal of Heat and Fluid Flow*, 25-5, pp. 721-728.
- Kim, J., Kim, D. and Choi, H. (2001), An immersed-boundary finite-volume method for simulation of flow in complex geometries. *Journal of Computational Physics*, 171, pp. 132-150.
- Kim, J. and Choi, H. (2004), An immersed-boundary finite-volume method for simulation of heat transfer in complex geometries. *KSME International Journal*, 18, pp. 1026-1035.
- Nishiura, D., Shimosaka, A., Shirakawa, Y. and Hidaka, J. (2006), Hybrid Simulation of Hindered Settling Behaviour of Particles Using Discrete Element Method and Direct Numerical Simulation (in Japanese). *Kagaku Kogaku Ronbunshu*, 32-4, pp. 331-340.
- Pacheco, J.R., Pacheco-Vega, A., Rodić, T. and Peck, R.E. (2005), Numerical Simulations of Heat Transfer and Fluid Flow Problems Using an Immersed-Boundary Finite-Volume Method on Nonstaggered Grids. *Numerical Heat transfer, Part B* 48, pp. 1-24.
- Pacheco-Vega, A., Pacheco, J. R. and Rodić, T. (2007), A general scheme for the boundary conditions in convective and diffusive heat transfer with immersed boundary methods. *Journal of Heat Transfer*, 129, Issue 11, pp. 1506-1516.
- Ren, W.W., Shu, C., Wu, J. and Yang, W.M. (2012), Boundary condition-enforced immersed boundary method for thermal flow problems with Dirichlet temperature condition and its applications. *Computers & Fluids*, 57, pp. 40-51.
- Tsuji, Y., Kawaguchi, T. and Tanaka, T. (1993), Discrete particle simulation of two-dimensional fluidized bed. *Powder Technology*, 77, pp. 79-87.
- Ueyama, A., Moriya, S., Nakamura, M. and Kajishima, T. (2011), Immersed Boundary Method for Liquid-Solid Two-Phase Flow with Heat Transfer. *Transaction of JSME, Series B* 77-775, pp. 803-814.
- Yu, Z., Shao, X. and Wachs, A. (2006), A fictitious domain method for particulate flows with heat transfer. *Journal of Computational Physics*, 217, pp. 424-452.
- Yuki, Y., Takeuchi, S. and Kajishima, T. (2007), Efficient immersed boundary method for strong interaction problem of arbitrary shape object with the self-induced flow. *Journal of Fluid Science and Technology*, 2-1, pp. 1-11.



## Mesh Modification System for Three Dimensional Unstructured Mesh Using VR Technology

\*Satoshi Tanaka<sup>1</sup>, Kazuo Kashiya<sup>1</sup>, and Akira Kageyama<sup>2</sup>

<sup>1</sup>Department of Civil and Environmental Engineering, Chuo University, Japan

<sup>2</sup>Department of Computer Science and Systems Engineering, Kobe University, Japan

\*Corresponding author: tanaka@civil.chuo-u.ac.jp

### Abstract

This paper presents an interactive mesh modification system for three dimensional unstructured mesh using virtual reality (VR) technology. The present system is developed by the VR programming languages, OpenGL and CAVE library. Users can check the details of three dimensional mesh structures and can modify the shape of mesh idealization in VR space interactively. For the mesh modification methods, the node relocation method and the mesh refinement methods are implemented. The linear and 2-nd order tetrahedron elements are available in this system. Users can change the nodal position of the bad quality element in case of the node relocation method, and can refine the bad quality element in case of the mesh refinement method interactively. The present system is applied to the mesh modification for the simulation of 3D solid analysis and is shown to be a useful tool to assist the high quality computing.

**Keywords:** Virtual reality, Mesh modification, Node relocation, Mesh refinement.

### Introduction

The three dimensional finite element simulations are becoming more powerful and popular tool for various CAE (Computational Aided Engineering) problems in accordance with the development of hard- and software of computers. Especially, the theory of automatic mesh generation is remarkable and a number of automatic mesh generator has been presented (Lo(2013), Cheng et al.(2013)). However, in some cases bad quality elements are created by the automatic mesh generator when the shape of computational domain is complicated. Users will try to modify the quality of mesh using the mesh idealization show on 2D display with perspective drawing. However, it is difficult to understand the position information for the depth direction cleanly.

This paper presents an interactive mesh modification system for three dimensional unstructured mesh using virtual reality technology in order to overcome the problem. Authors focused on immersive virtual reality device such as CAVE. Users can check the details of three dimensional mesh structures and can modify the shape of mesh idealization in VR space interactively by using the controller. Generally, the mesh modification method can be classified into three methods; the node relocation method, the mesh refinement method and the replacement method using higher order element. In this system, the node relocation method and the mesh refinement method are implemented. Users can change the nodal position of the element in the node relocation method, and can refine the element in the mesh refinement method. The present system is available for the unstructured tetrahedron elements based on linear and 2-nd order elements. The system is developed by the VR programming languages, Open GL and CAVE library.

The present system is applied to several mesh modification examples for the 3D finite element simulation and is shown to be a useful tool to assist the high quality computing.

### CAVE Environment

The present system is designed for the use of virtual reality system based on IPT (Immersive Projection Technology) such as CAVE (Cruz-Neira et al. 1993). The stereoscopic view is realized in VR space by creating the images that corresponds to binocular retinal images. The mesh modification system is developed by using VR device "Holostage" of Chuo University. The "Holostage" consists of a PC cluster (one master-PC and four-slave-PC), three projectors, three

large screens and a position tracking system. The stereoscopic image from the arbitrary viewpoint of user is displayed in VR space by the position tracking system. Users can move in VR space freely like the real space. Therefore, users can check the three-dimensional structure of the mesh clearly and it can be expected to modify the mesh accurately and easily. Users can see the stereoscopic image by using the liquid shutter glasses in Fig. 1. The silver balls which are mounted to the controller and liquid shutter glasses are marker (see Fig. 1) to track the position information by the tracking device. Fig. 2 shows the scene the user modifies the mesh idealization manually using the present system. The red color virtual beam is generated from the controller shown in the figure. User can specify the target node or mesh by moving the tip of the virtual beam.

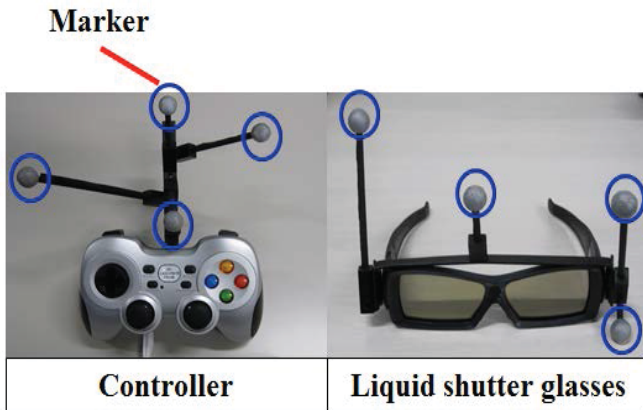


Figure 1. Device for VR system

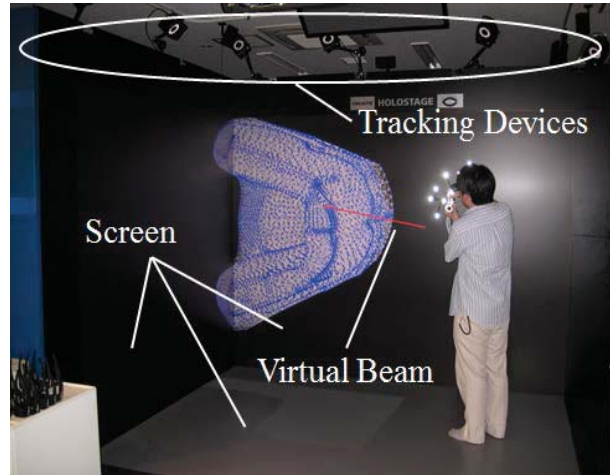


Figure 2. CAVE environment

### The three-dimensional mesh modification system

Users can check the details of three dimensional mesh structures and modify the mesh quality interactively in VR space by the present system. The present system is developed by the VR programming languages, Open GL and CAVE library. The system is available for the unstructured tetrahedron elements based on linear and 2-nd order elements as shown in Fig. 3.

Fig. 4 shows the flow chart of the present system. First, the mesh quality is computed, and then the mesh quality is improved by the mesh modification by both node relocation and mesh refinement methods. Users can select the modification method from the menu which is displayed in the VR space. Users can change the nodal position of the bad quality element in the node relocation method, and can refine the bad quality element in the mesh refinement method.

The mesh quality  $Q_m$  can be evaluated by the following equation (Freitag and Knupp ,2002).

$$Q_m = \frac{\left( \frac{1}{6} \sum_{i=1}^6 L_i^2 \right)^{\frac{3}{2}}}{8.4796 V} \quad (1)$$

Where  $L_i$  denotes the length of the edge of the element,  $V$  is the volume of the element. The mesh quality is to be 1 if the element is to be a regular tetrahedron and the value is to be big value if the element becomes a bent element. In this system, the elements which exceed the setting value for mesh quality are displayed by the red color in VR space.

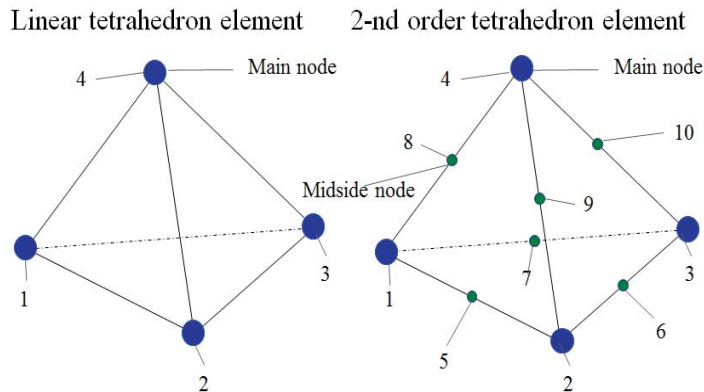


Figure 3. Tetrahedron elements

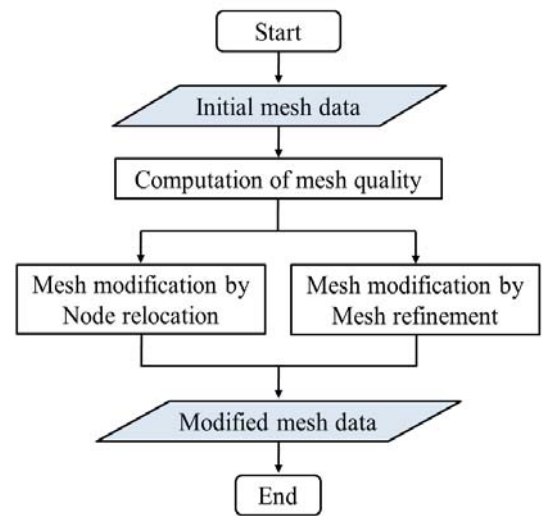


Figure 4. Flow chart of the system

**Modification Method by node relocation method**

Users can select functions from the menu interface as shown in Fig. 5. In the modification method by node relocation, if users move the tip of beam generated from the controller to the main node and click the button of controller, then the node can be specified and users can modify the element by the movement of tip of beam, as shown in Fig. 6.

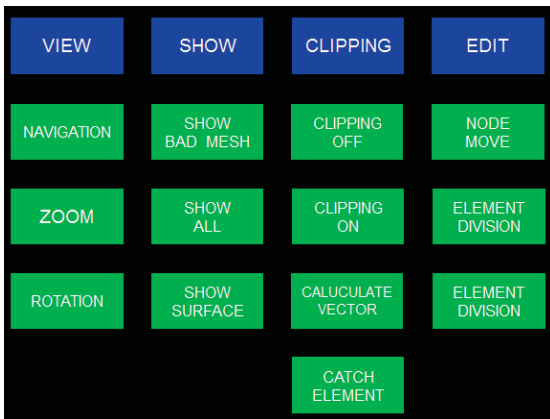


Figure 5. Menu interface

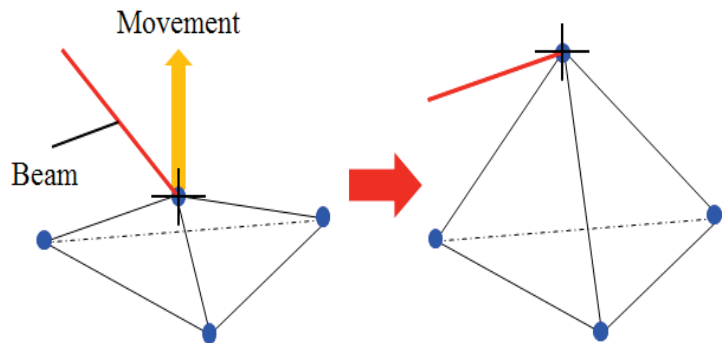
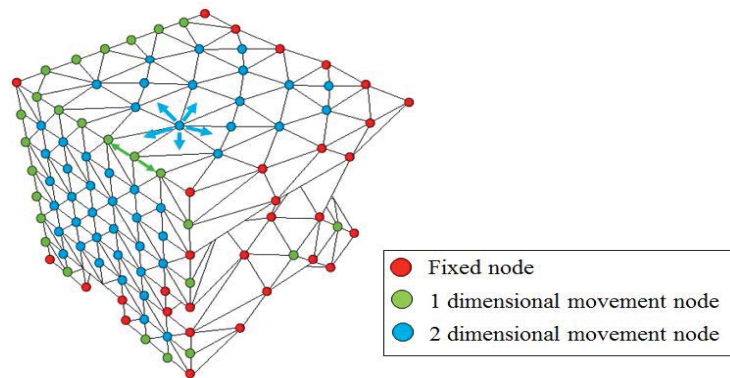


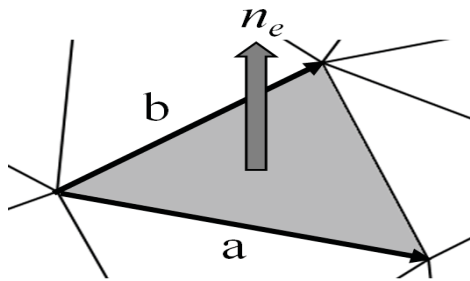
Figure 6. Modification of node relocation

In case of the 2-nd order tetrahedron elements, users move only the main nodes of the top of the element, and the position of the midside node on the edge is interpolated automatically.

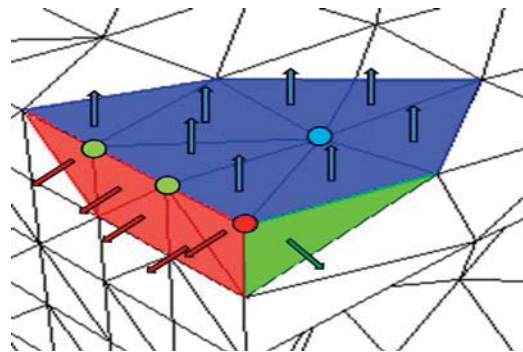
In order to avoid the violation of the geometrical shape of the computational domain by the node relocation, the node movement condition must be specified for the nodes on the boundary surface. The condition is prepared by the geographical information, which is obtained by the mesh data. The nodes on the boundary surface can be classified into three types as follows; (a) Fixed node: The nodes on the uneven edge-line or surface (red nodes in Fig. 7) are assumed to be fixed point, (b) 1D movement node: The nodes on the even edge-line of the structure (green nodes) can move on the edge-line only, (c) 2D movement node: The nodes on the even surface of the structure (light blue nodes) can move on the surface only. In this system, the control of the movement of nodes is performed by the node movement condition which is generated by the information of unit normal vector as shown in Fig. 8 and Fig. 9.



**Figure 7. Node movement condition**



**Figure 8. Normal unit vectors**



**Figure 9. Classification of node movement condition**

The normal unit vector of each triangles  $n_e$  can be evaluated by the following equation.

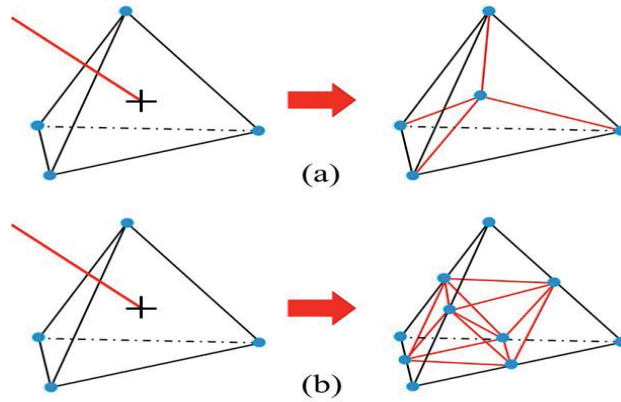
$$n_e = \frac{\mathbf{a} \times \mathbf{b}}{\|\mathbf{a} \times \mathbf{b}\|} \quad (2)$$

Where, vector  $\mathbf{a}$  and  $\mathbf{b}$  is shown in Fig. 8. If the values of normal unit vectors for the triangles connected to the node have only one value, the node can be specified as the 2D movement node. If the values of normal unit vectors for the triangles connected to the node have two different values, the node can be specified as the 1D movement node. On the other hand, if the values have more than three different values, the node can be specified as the fixed node. Users can recognize the node movement condition using the nodal color information same as Fig. 7 in VR space.

### Modification Method by Mesh Refinement Method

In the modification method by mesh refinement, the elements which exceed the setting value for mesh quality are refined.

Users can specify the element and decide the position by using the controller. If users move the tip of beam generated from the controller to the inside of the element and click the button, then the element can be specified. At this time, in order to investigate the judgment that the element includes the tip of beam or not for all elements of the mesh, the mapping method (Shirayama, 2002) using a generalized coordinate system is employed. The mapping method can be applied to the 2-nd order tetrahedron element.



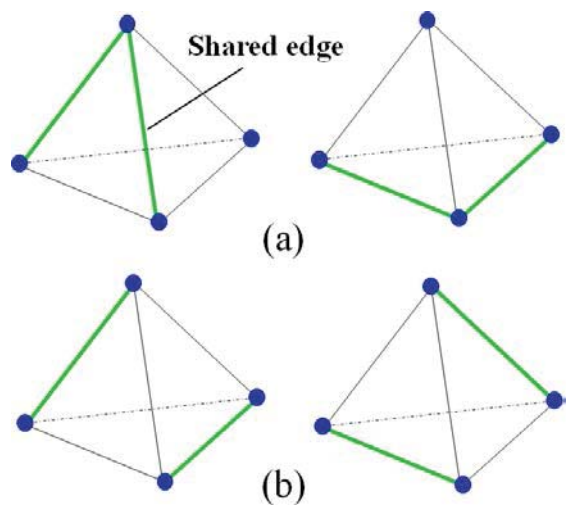
**Figure 10. Mesh refinement methods**

Fig. 10 shows mesh refinement patterns in this system. In the case of (a), a new node is generated at the centroid of the element. The connectivity of the element except the refined element does not change. However, the shape of the element becomes bent in this case. On the other hand, in the case of (b), a new node generated at the middle point on the each edges of the element. Therefore the shape of subdivided mesh is resemblance. However, the connectivity of the neighboring elements around the subdivide element changes and we have to manage the change of the connectivity.

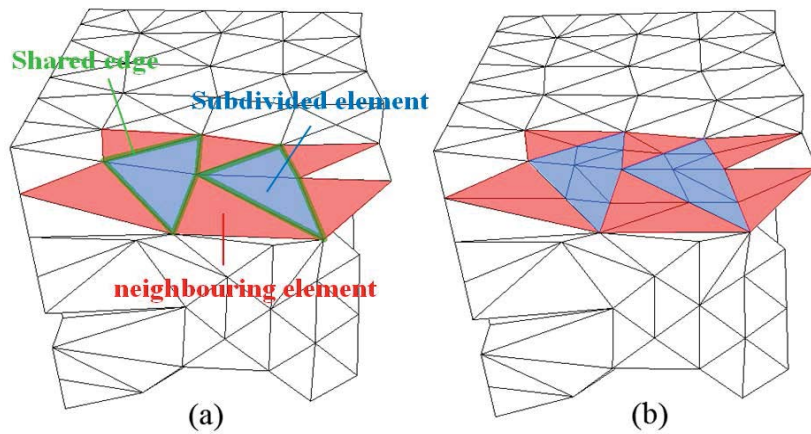
The refinement patterns of neighboring elements can be classified into 64 patterns as shown in Table 1 since the tetrahedral element is constituted by 6 edges ( $2^6=64$ ) where the possibility of the generation of a new node. Fig. 11 shows an example that the number of shared edge is two. Considering the rotational property of the element in (a) and (b), the left and right patterns are one and the same. The refinement patterns are reduced to 11 patterns if the rotational property of the elements is considered. Consequently, the mesh refinement is performed by using the 11 patterns. Fig. 12 shows the example for mesh refinements, where (a) shows the initial mesh and (b) shows the refined mesh, in which the blue elements show the subdivided element and the red elements show the neighboring elements for the subdivided elements. The validity of the algorithm of mesh refinements is shown in this figure.

**Table 1. The refinement patterns of neighboring elements**

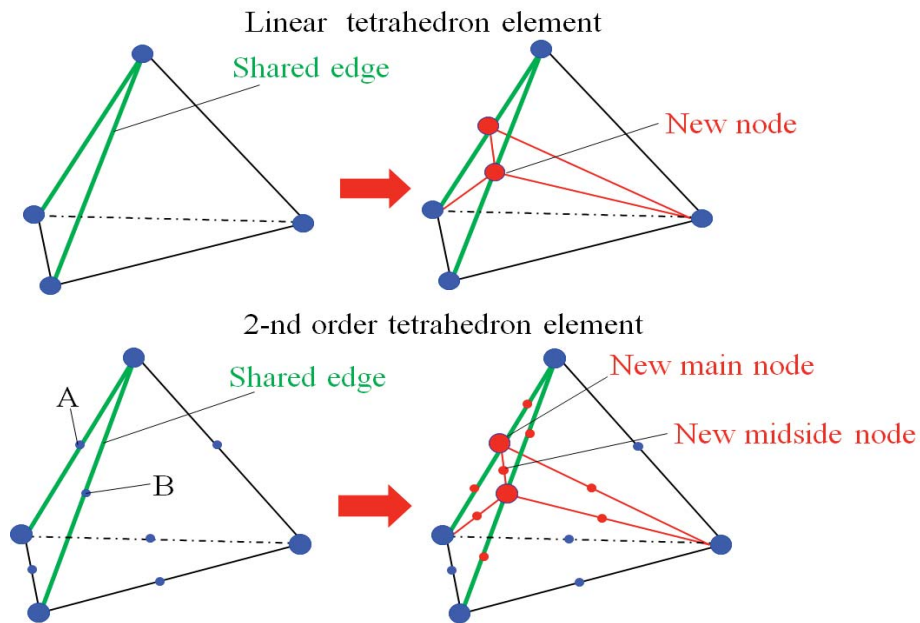
The number of shared edges	The number of refinement pattern of neighbouring elements	The number of refinement pattern (Considering the rotation)
0	1	1
1	6	1
2	15	2
3	20	3
4	15	2
5	6	1
6	1	1
	Total:64	Total:11



**Figure 11. Example that the number of shared edge is two edges**



**Figure 12. An example of the element refinement**



**Figure 13. The generated node**

Fig. 13 shows the mesh refinement for the neighboring element in case of Fig.11 (a) for linear (top) and 2-nd order (bottom) tetrahedron elements. In case of the 2-nd order (bottom) tetrahedron element, the midside nodes A and B are changed to the main nodes and a new midside node is generated at the center of each new edge (totally 8 nodes)

**Application Examples**

In order to investigate the validity and efficiency of the present system, the system is applied several mesh modification examples.

*Dental Implants mesh*

The system is applied to the mesh for stress analysis of dental implants which uses the 2-nd order tetrahedron elements. (Hirano et al. 2008). Fig. 14 shows the mesh idealization in VR space using display functions; node color ON/OFF and midside node ON/OFF. In this system, fixed node is displayed in red, 1D movement node is displayed in green, 2D movement node is displayed in light blue (as shown in Fig. 7) and the node inside the domain and midside node is displayed in blue.

The mesh modification by node relocation is employed and the modification time by using the node color ON/OFF function is compared. Fig. 15 shows the comparison of the distribution of mesh quality before and after the mesh modification by node relocation. In this case, the bad shaped elements which exceed the mesh quality values “10” (29 elements) are modified. From the Figure, it can be seen that the bad shaped elements which exceed the mesh quality values are erased perfectly.

The operation time for mesh modification are compared using the node color ON/OFF function and the results are 7m55s (ON) and 8m50s (OFF) respectively. From, this the operation time is reduced more than 10% by using the node color function.

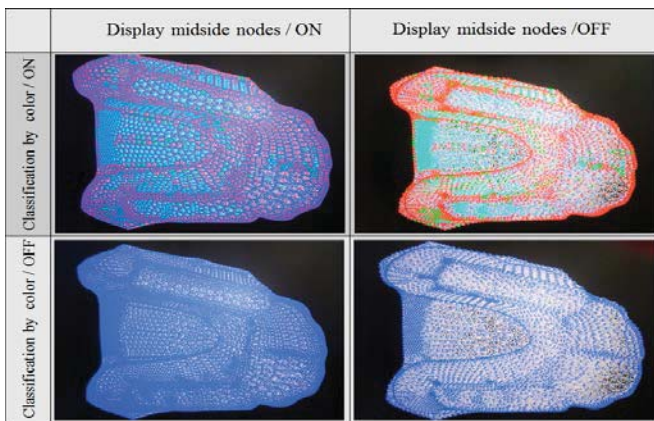


Figure 14. Dental implants mesh

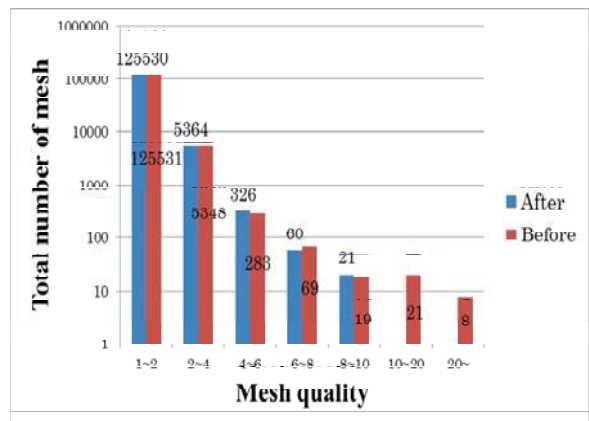


Figure 15. Distribution of mesh quality

*City Model Mesh*

The present system is applied to the mesh modification for wind flow simulation in urban area as shown in Fig. 16. Fig. 17 (left) shows the zoom-up surface idealization around the base of building. From this figure, it can be seen that the mesh located on the junction with the building base and the ground surface, do not reproduce the proper shape. In order to modify the nodal position on the surface boundary, the node movement condition must be released for this type of problem. So, the node movement condition is released for the node where users change the position of node. Fig. 17 (right) shows the mesh idealization after the mesh modification. From this figure, the proper shape of building and ground surface can be reproduced by the mesh modification.

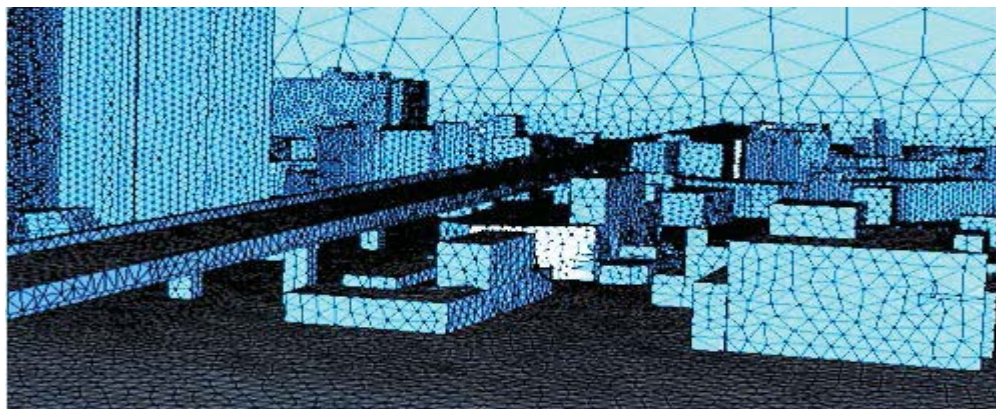
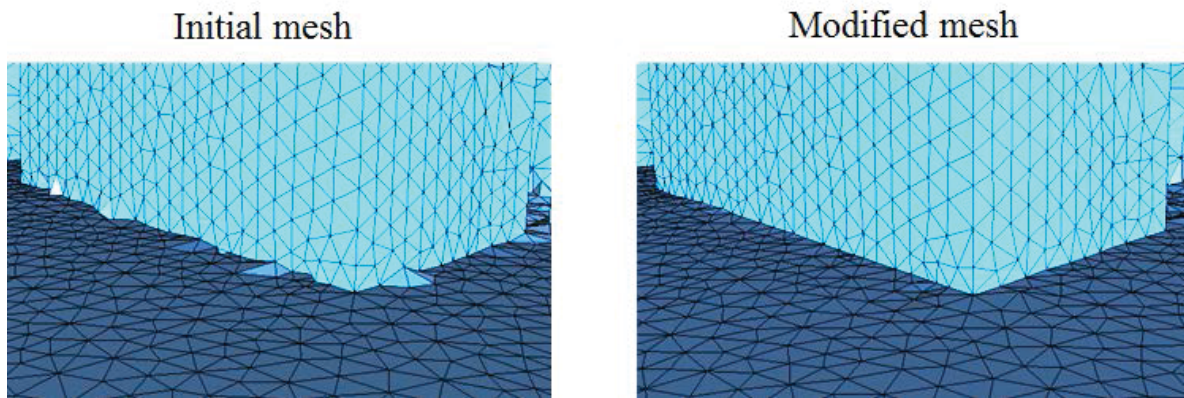


Figure 16. City model mesh



**Figure 17. Comparison of before and after modification**

## Conclusions

An interactive mesh modification system for three dimensional unstructured mesh using VR technology has been developed in this paper. And, we got the following conclusions.

- Users can check and modify the mesh idealization interactively and easily by using the controller in VR space. From this, users can understand the three dimensional unstructured mesh structures by using the present system.
- The mesh modification system based on the node relocation method and mesh refinement method has been successfully developed. For the finite element, the four nodes linear and the ten nodes 2-nd order elements are available.

From the results obtained in this paper, it can be concluded that the present system provide useful tool to realize the high quality computing simulations. In the future, we plan to do to confirm the effectiveness of the system by application to actual problems.

## References

- Cheng S-W, Dey, T.K. and Shewchuk, J. (2013), Delaunay Mesh Generation, 394p., *CRC Press*.
- Lo, D. (2013), Finite Element Mesh Generation, 448p., *CRC Press*.
- Cruz-Neira, C., Sandin, D. J. and DeFanti, T. A.(1993), Surround screen projection based virtual reality The design and implementation of the CAVE, *Proc. of SIGGRAPH'93*, pp.135-142.
- Freitag, L.A. and Knupp, P.M.(2002), Tetrahedral mesh improvement via optimization of the element condition number, *Int. J. Numer. Meth. Eng.*, Vol.53, pp.1377-1391.
- Shirayama, S.(2002), Intellectual visualization, Computational mechanics lecture series, *Maruzen*.
- Hirano, K., Nagashima, T., Matsushita, Y. and Todo, M. (2008)., Three-dimensional finite element analysis of overdentures using dental implants, *JSME 21st Computational Mechanics Division Conference*, pp.624-625,.
- Kashiyama, K., Yamazaki, T., Miyawaki, T., Hayashida, K., Ohno, N., Kageyama, A. and Terada, K.(2010), Application of virtual reality technology to pre-processing for 3-D finite element simulation", *Proc. 10th Int. Conf. on Construction Applications of Virtual Reality*, pp.367-374.
- Tanaka, S., Kashiyama, K., Kageyama, A. and Ohno, N. (2012)., Development of mesh modification system for finite element simulations using CAVE Environments, *Japan Society for Simulation Technology 2012*.



## Development of Simulation System for Tsunami Evacuation Using Virtual Reality Technology

\*Takeshi Kawabe<sup>1</sup>, Kazuo Kashiya<sup>1</sup>, Hiroshi Okawa<sup>2</sup> and Hideo Miyachi<sup>3</sup>

<sup>1</sup> Department of Civil and Environmental Engineering, Chuo University, Japan

<sup>2</sup> Eight-Japan Engineering Consultants Inc.

<sup>3</sup> Advanced Solution Division, CYBERNET Inc.

\*Corresponding author: kawabe@civil.chuo-u.ac.jp

### Abstract

This paper presents a simulation system for tsunami evacuation using virtual reality technology. The system can be classified into two parts: simulation part and visualization part. For the simulation part, the simulation of tsunami wave considering the collapse of building is carried by the Boussinesq equation using finite element method. Then the simulation of evacuation based on multi-agent model is performed. For the visualization part, the simulation results are visualized by the stereoscopic view using virtual reality technology. The present system is applied to the evacuation analysis by the tsunami waves at studied area is shown to be a useful tool to investigate the damage of building and human being by tsunami waves.

**Keywords:** Virtual Reality, Evacuation analysis, Multi-Agent, Tsunami Simulation

### Introduction

A number of tsunami disasters occur annually in various part of the world. In order to estimate the extent of a disaster quantitatively, it is necessary to estimate the behavior of natural phenomena which causes the natural disaster. There have been presented a number of numerical methods to evaluate the damage by the tsunami waves, such as the methods based on the finite difference method, finite volume method and finite element method. The finite element method is one of the powerful tool to investigate the damage by tsunami wave since the finite element method can treat the arbitrary land and building shape.

Recently, the numerical evacuation analysis is becoming popular to estimate the extent of the damage of human being. In the evacuation analysis, it is very important to evaluate the evacuation behavior of the human being in the time during the disaster accurately. The evacuation behavior is strongly related to the circumstance, age and sex of the refugees. The multi-agent model is one of the techniques which can evaluate the evacuation behavior accurately (Uno and Kashiya (2008)).

This paper presents a simulation system for Tsunami evacuation using virtual reality technology. The present system can be classified into two parts: simulation part and visualization part. For the simulation part, the simulation of tsunami wave considering the collapse of building is carried by the Boussinesq equation using finite element method (Tonegawa and Kashiya (2009)). Then the simulation of tsunami evacuation based on multi-agent model. For the visualization part, the simulation results are visualized by the stereoscopic view using virtual reality technology. From this, users can understand the simulation results easily. Also, as the view from the refugee's eye can be created in the VR space, the user can understand the feeling of refugee easily. The present system is applied to the evacuation analysis by the tsunami waves at studied area is shown to be a useful tool to investigate the damage of building and human being by tsunami waves.

### Tsunami Numerical Simulation

#### *Governing Equation*

The Boussinesq equation is employed for the governing equation in order to consider the effect of the wave and dispersion. The governing equations can be described as:

$$\frac{\partial \mathbf{U}}{\partial t} + \mathbf{A}_i \frac{\partial \mathbf{U}}{\partial x_i} - \frac{\partial}{\partial x_i} \left( \mathbf{N}_{ij} \frac{\partial \mathbf{U}}{\partial x_i} \right) = \frac{\partial^2}{\partial t \partial x_i} (\mathbf{K}) + \mathbf{R} - \mathbf{G}\mathbf{U} \quad (1)$$

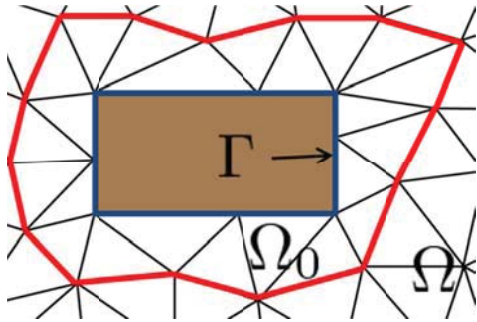
where  $H(=h+\xi)$ ,  $u_i$ ,  $c$ ,  $n$ , and  $\nu_e$  denote the total water depth, mean current velocity, wave velocity, Manning's coefficient and kinematic viscosity respectively,  $\mathbf{U}$ ,  $\mathbf{K}$ ,  $\mathbf{R}$ ,  $\mathbf{A}_i$ ,  $\mathbf{N}_{ij}$  and  $\mathbf{G}$  are unknown matrix, dispersive matrix, gradient vector, advection matrix, diffusion matrix, friction matrix respectively. The SUPG finite element method is employed for the discretization in space and the Crank-Nicolson method for the discretization in time.

#### Evaluation Method of Fluid Force

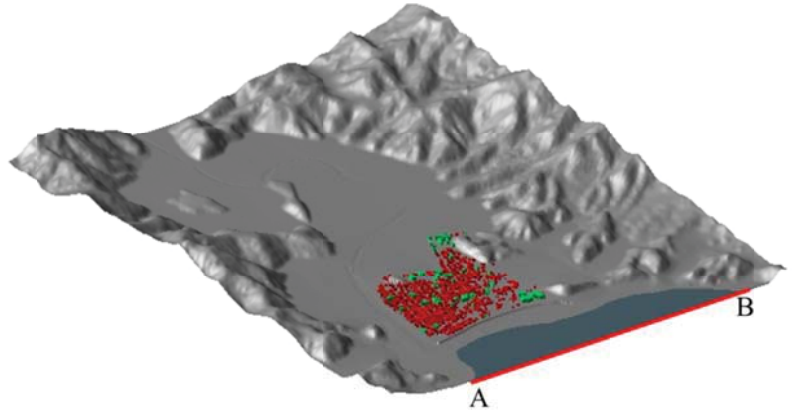
The fluid force acting to building is evaluated by the weak form of the governing equation using the computational results at every time step. The weak form for the governing equation can be written as follows.

$$\int_{\Omega_0} \mathbf{U}^* \left( \frac{\partial \mathbf{U}}{\partial t} + \mathbf{A}_i \frac{\partial \mathbf{U}}{\partial x_i} - \mathbf{R} + \mathbf{G}\mathbf{U} \right) d\Omega + \int_{\Omega_0} \left( \frac{\partial \mathbf{U}^*}{\partial x_i} \right) \left( -\mathbf{L}_i \mathbf{U} + \mathbf{N}_{ij} \frac{\partial \mathbf{U}}{\partial x_i} + \frac{\partial}{\partial t} (\mathbf{K}) \right) d\Omega = \int_{\Gamma} \mathbf{U}^* \mathbf{T} d\Gamma \quad (2)$$

where  $\Omega$ ,  $\Omega_0$  and  $\Gamma$  denotes the analytical area, area using by evaluation method of fluid force and boundary of building. The right side of Eq. (2) shows the fluid force acting on building.



**Figure 1. Evaluation Method of Fluid Force**

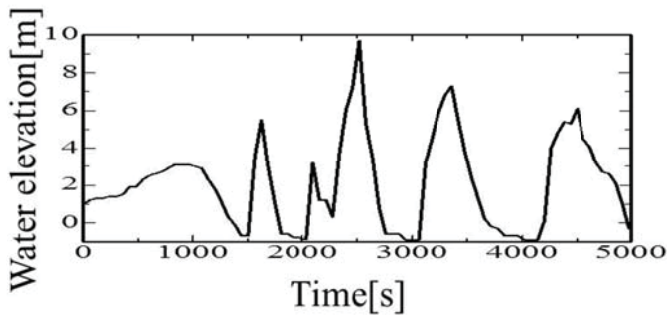


**Figure 2. Initial geometry for tsunami simulation**

The details of evaluation method of fluid force are described in the references (Tonegawa, Kashiya, (2009)).

#### Simulation Condition

The tsunami simulation system is applied to the studied area shown in Fig. 2. In this figure, the red building denote the wooden building and the green building denote the concrete building. Fig. 3 shows the time history of the incident wave which is applied at the boundary AB (Fig. 2). Table. 1 shows the critical yield strength for the concrete and wooden buildings (Izuka and Matsutomi). The building will be collapsed when the fluid force exceed the critical strength value. The unstructured grid based on the linear triangular element is employed (total number of elements: 261,171, total number of nodes: 130,794). The time increment is assumed to be 0.05sec. The Manning's coefficient is assumed to be  $0.04 s/m^{1/3}$  on dry bed area and  $0.025 s/m^{1/3}$  in water area.



**Figure 3. Condition of incident wave**

**Table 1. Critical strength**

	Concrete building	Wooden building
Case A	332kN/m	27.4kN/m
Case B	603kN/m	49.0kN/m

*Simulation Results*

Fig. 4 and Fig. 5 show the largest tsunami run-up area in case A and B respectively. From the figures, it can be seen that the number of collapsed building and the wave run-up area are related to the strength of building.



**Figure 4. Tsunami run-up area in case A**



**Figure 5. Tsunami run-up area in case B**

**Tsunami Evacuation Simulation**

The evacuation simulation system based on multi-agent model is developed using the multi-agent simulator “Net Logo”. Users can set the simulation condition and parameter (walking speed of refugees, traffic speed of car leading refuge and the time to start the refuge action) using the panel on the screen as shown in Fig. 6.

*Input data*

The initial positions of refugees are set to the center of gravity of the building as shown in Fig. 7. In order to prepare the data, the data of the road centerlines and the connecting points, which is referred as intersection nodes are prepared by the GIS data. For the evacuation analysis, the data for land elevation, distance from refuge is prepared at every intersection node. The distance from refuge is obtained by the computation of the distance between intersection nodes and refuge points along the road. The shortest route is obtained by the Dijkstra algorithm (Dijkstra (1959)). The new nodes are generated on the land at constant interval as shown in Fig. 8. The unsteady water depth and velocity are evaluated and stored at every new node using the tsunami simulation data. As the tsunami simulation is performed by the triangular mesh (Fig.9), the water depth and velocity are evaluated at new nodes by the linear interpolation using the triangular mesh as shown in Fig. 8.

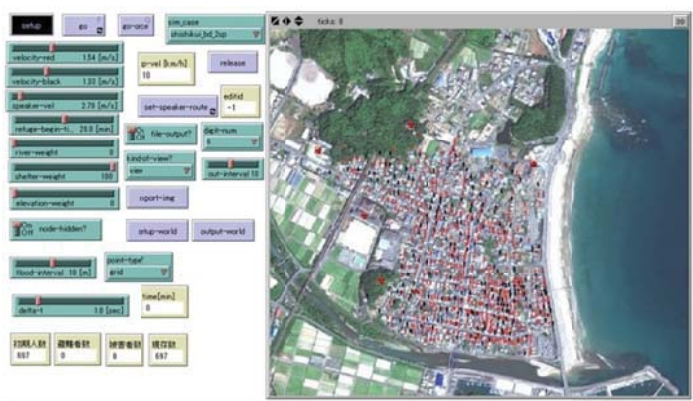


Figure 6. Screen of evacuation simulation

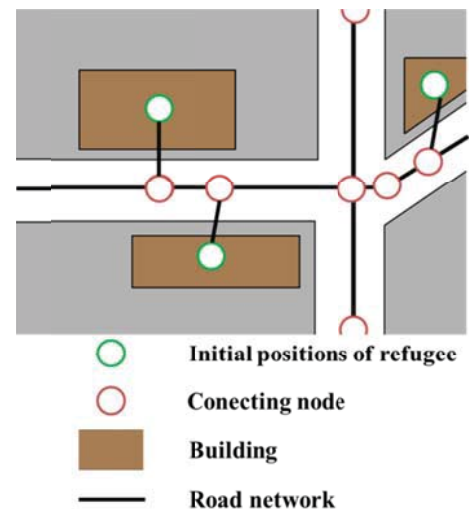


Figure 7. Evacuation route

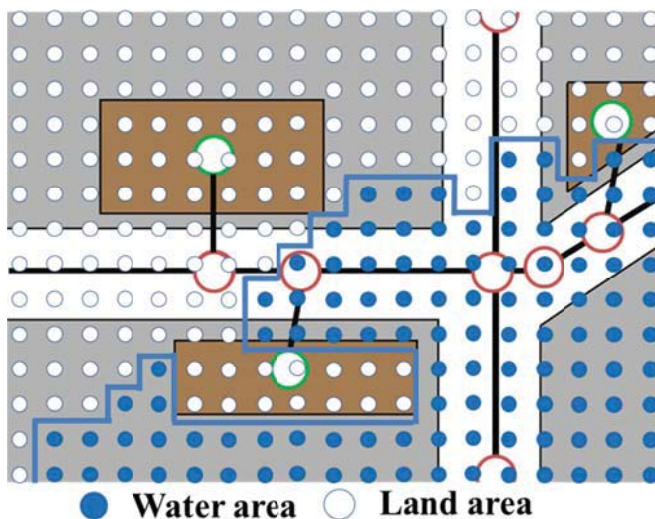


Figure 8. Generation of new nodes

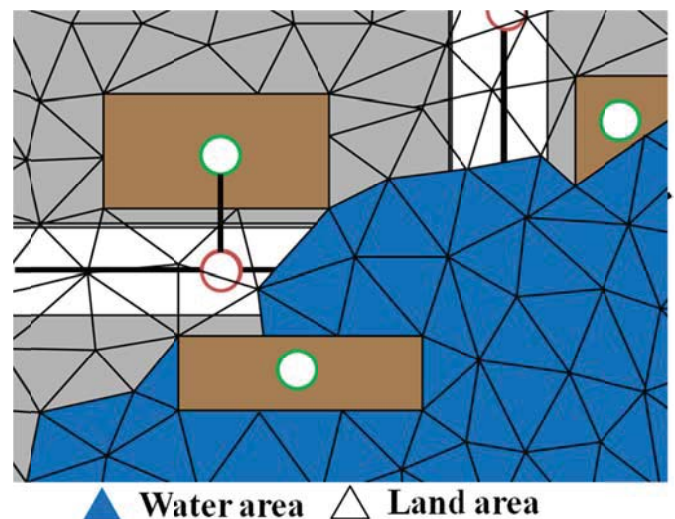


Figure 9. Triangular mesh

*Judgment of refugee's route*

The selection of refugee's route performs when the refugee arrives at the intersection node as shown in Fig. 10, and refugee compares the potential value of the neighbor intersection nodes on the evacuation route. The potential values are evaluated by the gravity model as:

$$S = \frac{a}{s^\alpha} - \frac{b}{z^\beta} \tag{3}$$

where  $s$  [m] is the distance from refuge,  $z$  [m] is the elevation of intersection node,  $\alpha$  and  $\beta$  are the weighting coefficients for  $s$  and  $z$ , respectively. The evacuation route is decided to the direction of intersection node which has the highest value of  $S$  by Eq. (3).

*Evacuation speed*

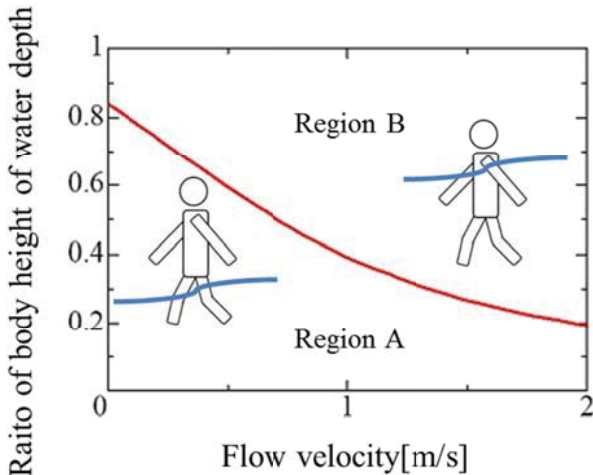
The evacuation speed is related to sex and age. However the speed is changed by the refugee's status which is related to the flood status and the density of refugee.

The flood status can be classified into three patterns as shown in Tab. 2 according to the water depth and flow velocity. Fig. 11 shows the relationship between flood status and refugee's status. In this figure, the region A denotes the status that the refugee can evacuate safely (class 2 in Table. 2) but the evacuation speed is reduced by half, and region B denotes the status that the refugee can not evacuate safely (class 3 in Table .2) and evacuation speed is assumed to be zero.

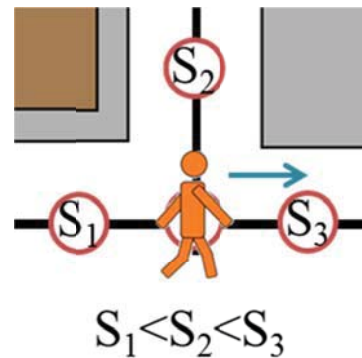
The evacuation speed of refugee is also related to the density of refugee. The evacuation speed is changed by number of refugee in this area.

$$V = v - 0.17\rho \tag{4}$$

where  $V$  [m/s] is evacuation speed considered density,  $v$  [m/s] is evacuation speed decided and  $\rho$  [number of refugee /  $m^2$ ].



**Figure 11. Relationship between flood and refugee's status**



**Figure 10. Judgment of refugee's route**

**Table 2. Categories of refugee's status according to flood status**

Class	Flood status	Refugee's status
1	Water depth is 0[m]	No influence
2	Region A in Fig. 8	Speed reduced by half
3	Region B in Fig. 8	Victim

### Simulation Condition

The present method is applied to the evacuation simulation by tsunami disaster in studied area. The number of refugees is assumed to be 697 which involve 210 refugees over 65 years old. Table 3 show the height and evacuation speed for refugee. The traffic speed of public information car is assumed to be 2.78m/s, the effective area of the public information car is assumed to be a circle with a radius of 150 m. It is assumed that refugees do not know the refuge place, the time to start the car moving  $T$  [time] is changed from 20 min to 40 min with 1 min interval (42 cases simulated in all). The time means that the evacuation action starts after the occurrence of tsunami. The present method is applied to the following two cases, case 1: comparison of the consideration of refugee's year or not, case 2: comparison between case A and case B (Table 1) with the consideration of age.

**Table 3. Refugee's data**

		number	Height	Evacuation speed
<b>Over</b>	<b>65</b>	210	1.6m	1.33m/s
<b>Under</b>	<b>65</b>	487	1.7m	1.54m/s

### Simulation Results

Fig.12 shows the results of tsunami evacuation simulation when the wave run-up area is the largest. The simulation results of case 1 and case 2 are shown in Fig. 13 and fig. 14. From this figure, it can be seen that the number of victims are increased in accordance with the time delay to start the evacuation action. Fig.13 shows that number of victim considering refugee over 65 years old is larger than that without the consideration, because the evacuation speed of refugee over 65 years old is slow. The victim appears at 25 minutes, because the first tsunami waves flow over the breakwater at that time. On the other hand, Fig.14 shows the number of victim in the case A is larger than the number of victim in the case B, because the flood area is larger than the case B. Fig.12 shows that result of tsunami evacuation simulation in case A (left) and case B (right) when the time to start the refuge action is 36 minutes and the wave run-up area is the largest.



**Figure 12. Tsunami evacuation simulation (left case A, right case B)**

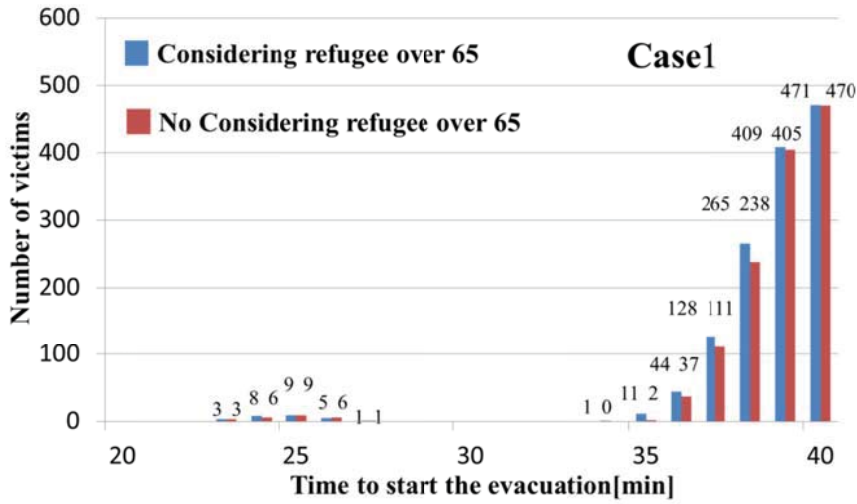


Figure 13. Simulation result (case 1)

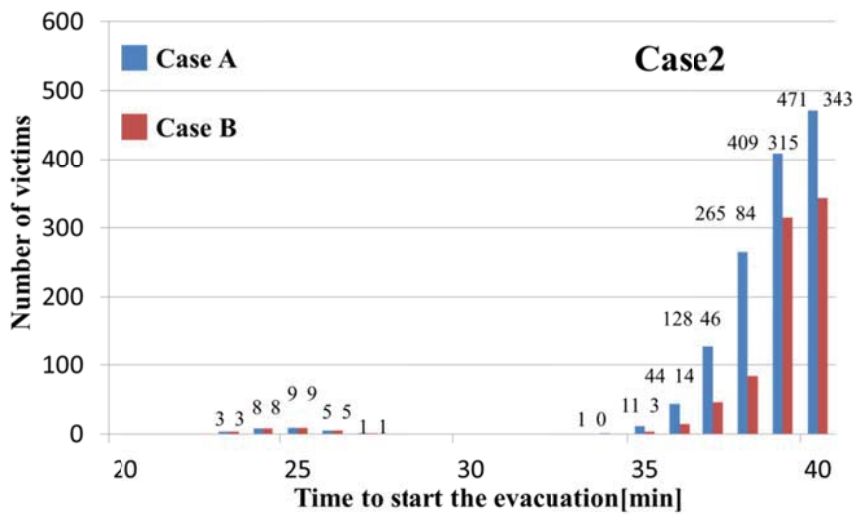


Figure 14. Simulation result (case 2)

**Visualization Using VR technology**

The simulation results are visualized by the stereoscopic view using virtual reality technology. Fig. 15 and Fig. 16 show the VR system “Holostage” and the shutter glasses and controller for users. The results of tsunami and evacuation simulation are visualized by different visualization software. In this paper, the attempt to combine the different CG images created by different visualization



Figure 15. VR system



Figure 16. Device for VR system

software is performed. Fig.17 shows the visualization process of the software, Fusion VR (Miyachi et al. 2005). Fig.18 shows the scene the user check the visualization result in VR space. The users can understand the simulation results easily. Also, as the view from the refugee's eye can be created in the VR space, the user can understand the feeling of refugee easily.

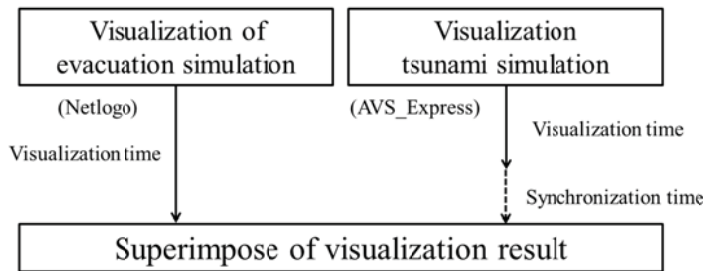


Figure 17. Controlling display time

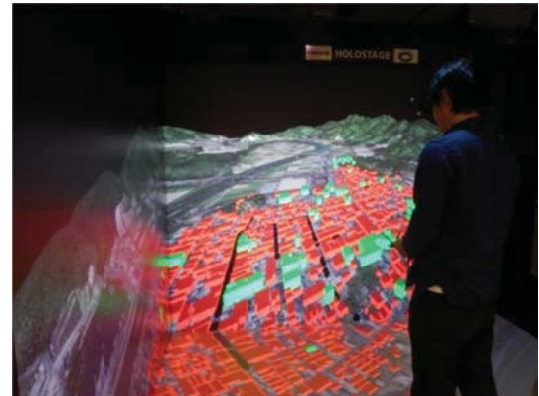


Figure 18. Visualization Using VR technology

## Conclusions

The simulation method for the tsunami evacuation using virtual reality technology has been presented. The present system can be classified into two parts: simulation part and visualization part. For the simulation part, the simulation of tsunami wave considering the collapse of building is carried by the Boussinesq equation using finite element method. Then the simulation of tsunami evacuation based on multi-agent model. For the visualization part, the simulation results are visualized by the stereoscopic view using virtual reality technology. The present system is applied to the studied area and is shown to be a useful tool to investigate the damage of building and human being by tsunami waves.

The verification and modification of evacuation model is left for the future work.

## References

- Uno, K. and Kashiyama, K. (2008), Development of simulation system for the disaster evacuation based on multi-agent model using GIS. *Tsinghua science and technology*, 13, pp. 348-353.
- Kashiyama, K. Takada, T. and Miyachi, H. (2008), Large scale finite element modeling, simulation and visualization for wind flows in urban area using virtual reality. *Tsinghua science and technology*, 13, pp. 84-89.
- Tonegawa, D. Kashiyama, K. (2009), Development of a numerical method for tsunami runup and fluid force based on stabilized finite element method. *Journal of applied mechanics*, 12, pp. 127-134.
- Katada, T. Asada, J. and Kuwazawa, T. (2000), Simulation analysis on disaster information transmission using GIS. *Engineering works information system thesis collection*, 9, pp. 45-58.
- Ishida, T. Nakajima, Y. Murakami, Y. and Nakanishi, H. (2007), Augmented Experiment: Participatory Design with Multiagent Simulation. *International Joint Conference on Artificial Intelligence*, pp. 1341-1346.
- Murakami, Y, Sugimoto, Y. and Ishida, T. (2005), Human Behavior for Visual Training System. *AAAI-05*, pp. 127-132.
- Haklay, M. O'Sullivan, Thurstain-Goodwin, D. and Schelhorn, T. (2001), "So go down town": simulating pedestrian movement in town centres. *Environment and Planning B: Planning Design*, 28, pp. 343-359.
- Dijkstra, W, E. (1959), A note on two problems in connexion with graphs. *Numerische Mathematik*, 1, pp. 269-271.
- Suga, K. (1995), Flood of Tonegawa, *Sankaido* (in Japanese).
- Miyachi, H., Oshima, M., Ohyoshi, Y., Matsuo, T., Tanimae, T. and Oshima, N. (2005), Visualization PSE for multi-physics analysis by using OpenGL API fusion technique, *Proceedings of the First International Conference on e-Science and Grid*, pp.530-535.
- Izuka, H, H and Matsutomi. (2000), Assessment of damage of a tsunami ascension style, *Proceedings of Coastal Engineering*, 46, pp.381-385 (in Japanese).



## A Road Traffic Noise Evaluation System Considering A Stereoscopic Sound Field Using Virtual Reality Technology

\*Kou Ejima<sup>1</sup>, Kazuo Kashiyama<sup>1</sup>, Masaki Tanigawa<sup>2</sup> and Masayuki Shimura<sup>3</sup>

<sup>1</sup>Department of Civil and Environmental Engineering, Chuo University, Japan

<sup>2</sup>Deputy Senior Research Engineer, Shimizu Corporation, Japan

<sup>3</sup>General Engineer, Civil Engineering and Eco-Technology Consultants, Japan

\*Corresponding author: ejima@civil.chuo-u.ac.jp

### Abstract

This paper presents a road traffic noise evaluation system based on spatialization of sound using virtual reality technology. The key feature of the system is that the road traffic noise is provided for users by both audio and visual information under various road and vehicle conditions. The geometric acoustic theory is employed for the simulation of traffic noise to realize the real-time simulation. In order to improve the reality, the sound source data for the auralization in VR space are generated from the various car driving tests. This system is applied to several examples in order to investigate the validity of the method.

**Keywords:** Geometric acoustic theory, Road traffic noise, Stereoscopic sound field, Virtual reality

### Introduction

The evaluation of road traffic noise is very important for planning and designing of road environment, because the road traffic noise infect the human body such as disruption of sleep and psychological malaise and so on. There have been presented a number of numerical simulation methods in accordance with the development of computer. The theory for numerical simulation can be classified into two approaches; wave acoustic theory and geometric acoustic theory. The geometric acoustic theory is very useful for the development of the real time simulation system because the computational time is much shorter than the wave acoustic theory.

Generally, the numerical results are visualized using computer graphics (CG). However it is difficult to understand the noise level intuitively with CG, because the visualization is not auditory information. In order to overcome the problem, several systems that expose road traffic noise as the auditory information have been presented in the past studies (Nagano et al. (1999), Makaanae et al. (2004)). However, there have not been presented a system that presents auditory and visual information simultaneously under the various road environments. The present author developed a system to expose the numerical results both with auditory and visual information using virtual reality (VR) technology (Tajika et al. (2010), Shibata et al. (2011)). The ASJ RTN-Model 2008, which is the Japanese standard model for road traffic noise, was employed for the model based on the geometric acoustic theory. The system was designed as an interactive system which realizes the real time simulation. However, the following problems are pointed out from the point of the reality of our system; 1) The effects of directivity of the sound wave and delay of the arrival time are not considered. 2) The sound source of the vehicle in the system is not related to the vehicle type and speed.

This paper presents an advanced road traffic noise evaluation system that can overcome above mentioned problems. In order to consider the effects of directivity of the sound wave and delay of the arrival time, we realize stereoscopic sound field in VR space. Furthermore, the sound source data for the auralization in VR space is generated from the various vehicle driving test.

### VR Environments

The IPT (Immersive Projection Technology) is employed for VR technology. Fig.1 shows the VR system "HoloStage" of Chuo University, Japan. This system is composed of three large and flat screens and three high-performance projectors corresponding to the screen. The front and side screens are transmissive ones and the bottom screen is reflective one. The projector shows the CG

image for left and right eyes alternatively with 120Hz. Users wears the shutter glasses ( Fig.2 (a)), which will open and close the shutter with the synchronization to the CG image through infrared emitters . Users can move the arbitrary position using the controller (Fig.2 (b)). This system has 7.1ch sound speakers (Fig.2 (c)) and the VR space is created by the auditory information and the visual information. Observer’s motion is captured by a system called VICON Tracking system (Fig.2 (d)), which is the optics type motion tracking system. The positions of markers fitted to shutter glasses and controller are tracked by the tracking system.



Figure 1. VR system (Holostage)

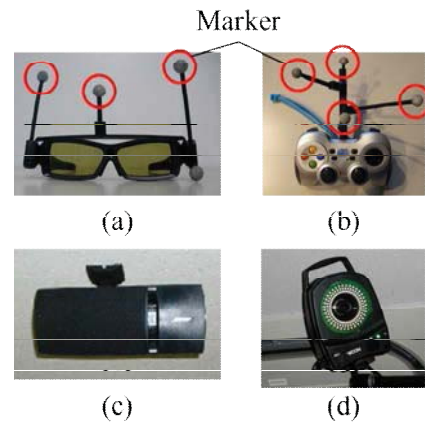


Figure 2. The device of VR system

**A Road Traffic Noise Evaluation System Using VR Technology**

The interactive road traffic noise evaluation method is designed for the use of CAVE environments based on the immersive projection technology (IPT). The auditory information of road traffic noise is created using the MAX (Cycling’74). Fig.3 shows the concept of the system. This system provides two presentation methods for computed road traffic noise level, a) auralization function, which presents the auditory information of the road traffic noise based on numerical results with the stereoscopic animation of vehicle run (Fig.3 left), and b) visualization function, which presents the stereoscopic iso-surface of the road traffic noise level by CG image with the road environment’s CG (Fig.3 right). Users can easily understand how big the noise of the simulation results using the auralization function. On the other hand, users can easily understand the spatial distribution on the noise level using the visualization function.

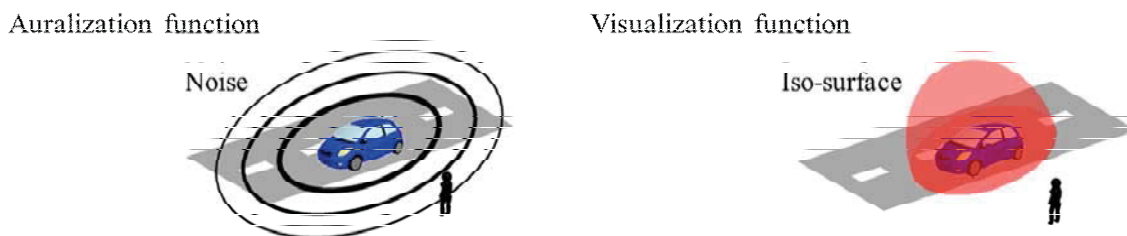


Figure 3. The concept of the system

The present system provides following three characteristics. First, users can move to arbitrary position and can hear the road traffic noise that correspond with the position, since the road traffic noise level is computed in real time using the position of user (Fig.4 (a)). Second, users can change the road environment; height of noise barrier, pavement type (drainage pavement and dense

pavement) and passage years after pavement (Fig.4 (b)). Third, users can change the vehicle conditions; vehicle type, vehicle speed and running distance of vehicle (Fig.4 (c)). Fig.5 shows the available road environments for the simulation in this system. Table 1 shows the input data in case of the road environment with noise barrier and users can set the data using the interface function which is displayed on the front screen as shown in Fig.6. Fig.7 shows computational result when building is set.

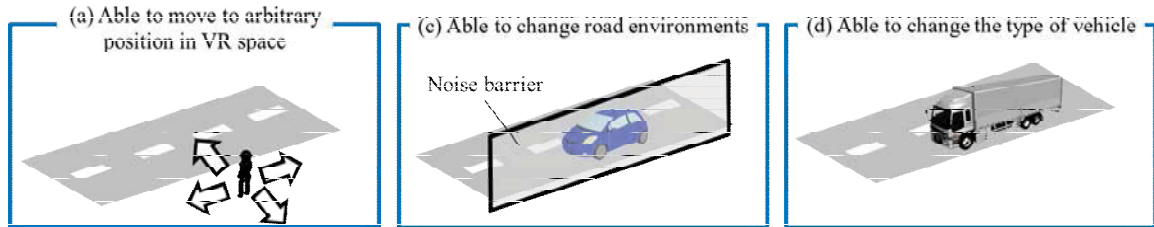


Figure 4. The overview of the system

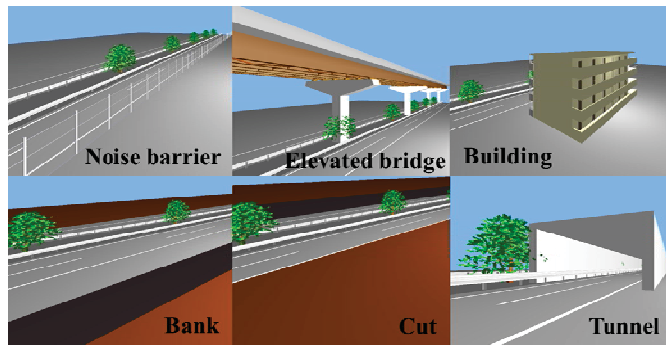


Figure 5. Surrounding road environments

Table 1. Input data

The height of sound barrier	0 ~ 5m
Type of vehicle	Standard, Subcompact, Middle, Large car and Bike
Vehicle velocity	50 ~ 100km/h (interval :10km/h)
Type of the pavement	Drainage and dense-graded pavement
The passage years of pavement	0 ~ 15years (interval:5years)

sound barrier	0m	1m	2m	3m	4m	5m
distance	100m	200m	400m	800m		
car	standard	subcompact	medium	large	bike	
passage years of pavement	0	5	10	15		
type of pavement	dense	drainage				
car speed	50km/h	60km/h	70km/h	80km/h	90km/h	100km/h

Figure 6. Interface function

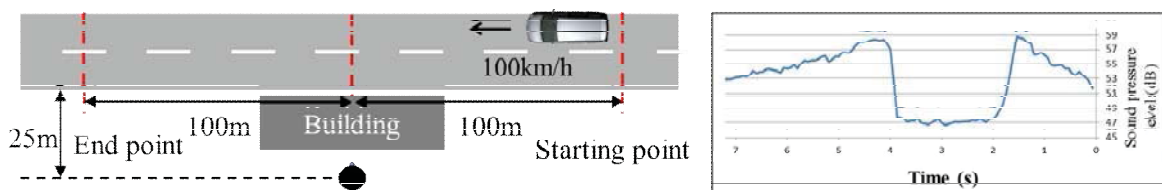


Figure 7. Computational result

### Computation of road traffic noise level

The road traffic noise level is computed by using the ASJ RTN-Model 2008 (The Acoustic Society of Japan (2009)). The sound pressure level is evaluated in real time by the model, since the model is based on the geometric acoustic theory.

The computation is performed using the position data of the vehicle, the observer, and the surrounding environment in real time using a motion tracking system. Fig.8 shows the sound propagation with sound barriers. The A-weighted sound power level of vehicle noise  $L_{WA}$  can be expressed as:

$$L_{WA} = a + b \log_{10} V + C \quad (1)$$

where  $a$  is the factor related to the types of vehicle (the values for standard car, bike, subcompact car, middle car and large car are assumed to be 46.7, 47.6, 51.5, 44.4, 49.6, respectively),  $b$  is the coefficient relate to the vehicle speed,  $V$  is the vehicle speed,  $C$  is the correction term (the noise reduction with drainage pavement etc, the change of road vehicle noise by the vertical slope, the directivity of vehicle noise).

The A-weighted sound pressure level  $L_A$  of direct sound which is propagation from vehicles is evaluated as:

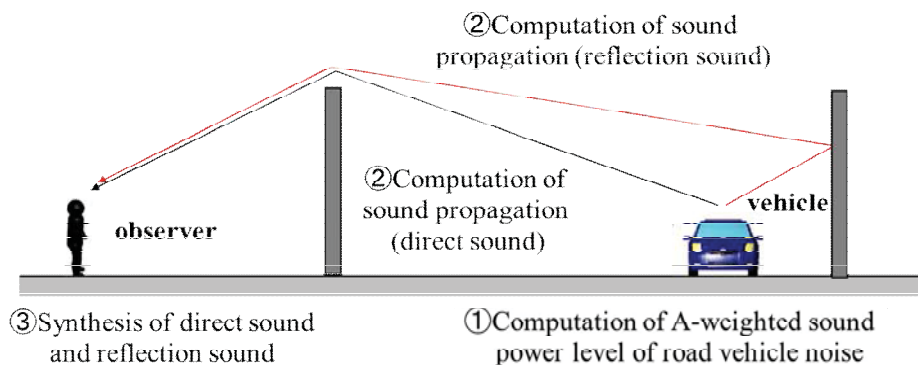
$$L_A = L_{WA} - 8 - 20 \log_{10} r + \Delta L_{cor} \quad (2)$$

where  $r$  is the distance in a straight line between observer and vehicle,  $\Delta L_{cor}$  is the correction concerning with attenuation factors (attenuation caused by diffraction, ground effect and atmospheric absorption).

When it is necessary to consider about the plural propagations such as direct sound, reflection and diffraction sounds, the A-weighted sound pressure level is computed as:

$$L_A = 10 \log \left( \sum_{i=0}^{i_{max}} 10^{\frac{L_{A,i}}{10}} \right) \quad (3)$$

where  $i_{max}$  is the number of the sound propagations,  $L_{A,i}$  is the sound pressure level corresponding the sound propagation. The Doppler effect is also considered in this system.

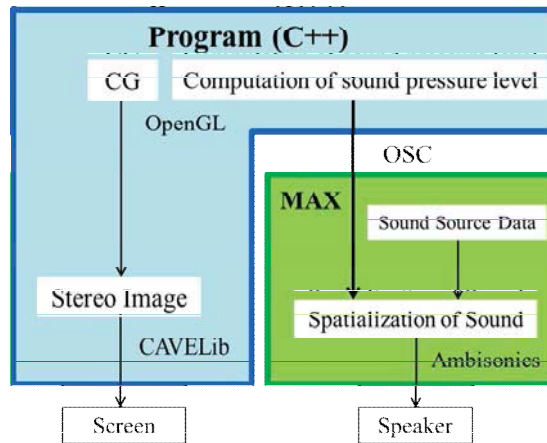


**Figure 8. Sound Propagation by ASJ RTN-Model 2008**

### Development of Stereoscopic Sound System

In order to improve the presence of auralization function, the spacialization of sound field is

achieved. The system consists of two parts; visualization and auralization parts as shown in Fig.9. The sound source data is obtained from the various vehicle driving test which is explained in the next section. The Open Sound Control (OSC) which is UDP/IP protocol is used for the data communication. The spatialization of sound is achieved by the method named “ambisonics” (Ward, 2001, Tanigawa et al. (2013)), which is based on the spherical surface function expansion, using computational results and sound source data. For the preparation of CG image, the Open GL and CAVE library are employed and the Max is employed for the specialization of sound.



**Figure 9. Flowchart of the stereoscopic sound system**

## Implementation of the Sound Source Data

### *Observation of road traffic noise*

In order to obtain the sound source data for the road traffic noise, the observation of driving sound for various type of vehicle is performed at The National Institute for Land and Infrastructure Management, Tsukuba, Japan. Fig.10 shows the type of vehicles which are used for the observation. The sound is observed by the noise level meter which is set to the fixed point as shown in Fig.11. The vehicle speed is changed from 50km/h to 100km/h with the constant interval 10km/h. The sampling frequency of the noise level meter is assumed to be 20kHz.

Fig.12 (a) shows the observed waveform in case for the standard car 90km/h. In this figure, the maximum sound pressure is normalized as 1.0 and the time when the vehicle pass through the front of the noise level meter is assumed to be 0 sec. From this figure, it can be seen that the sound pressure involves the distance attenuation clearly.



**Figure 10. Type of vehicle in driving tests**

Generation of sound source data for auralization

In order to generate the sound source data for auralization from the measured data, it is necessary to remove the effects of the distance attenuation using the geometrical relation as shown in Fig.10. In this figure,  $T_1$  is the actual elapsed time,  $T_1'$  is the elapsed time considering the sound speed (time at observation point),  $S$  is the sound pressure at vehicle and  $S'$  is the sound pressure at observation point. The sound pressure  $S'(T_1')$  can be expressed by the following equation considering the distance attenuation.

$$S'(T_1') = \frac{1}{R(T_1)} \cdot S(T_1) + \alpha \tag{4}$$

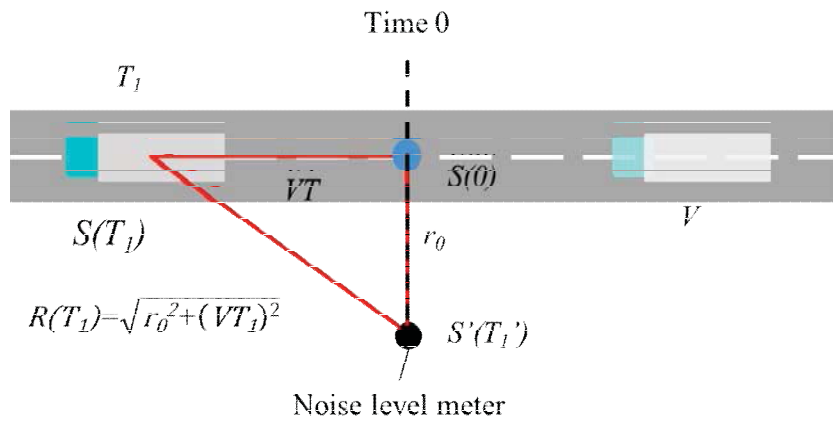


Figure 11. Measurement of vehicle noise

where  $R(T_1) (= \sqrt{r_0^2 + (VT_1)^2})$  denotes the horizontal distance between observer and vehicle, and  $\alpha$  denotes other sounds such as reflected sound and background noise, and which is assumed to be 0.

Time  $T_1'$  is expressed by the following equation.

$$T_1' = T_1 + \frac{R(T_1)}{c_0} \tag{5}$$

where,  $c_0$  is acoustic velocity. From Eq. (4) and (5), the time  $T_1$  can be expressed as:

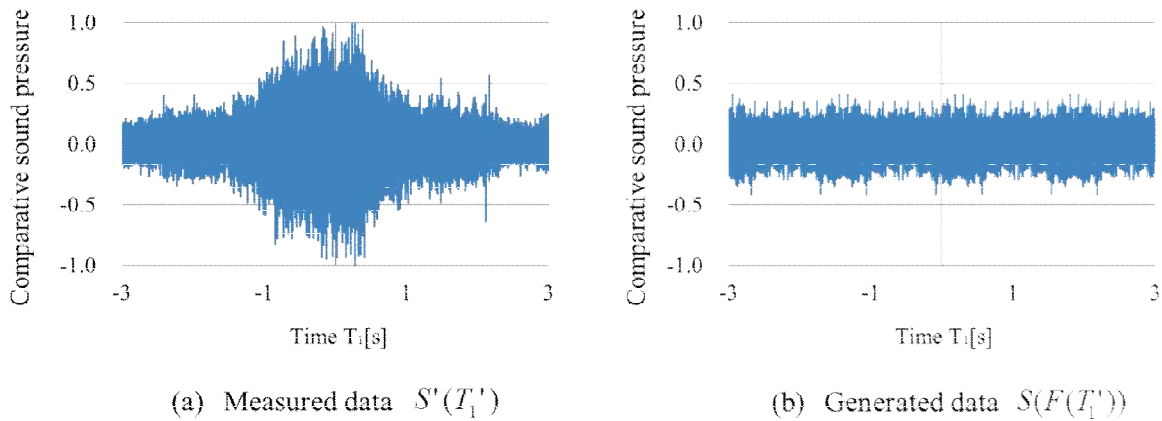
$$T_1 = \frac{2T_1' + \sqrt{4T_1'^2 - 4(1 - M_0^2)(T_1'^2 - Q_0^2)}}{2(1 - M_0^2)} = F(T_1') \tag{6}$$

where, variable of  $M_0$  and  $Q_0$  is  $V/c_0$  and  $r_0/c_0$ . Therefore, the sound pressure at the vehicle  $S(T_1)$  can be evaluated by following equation as the function of  $T_1'$ .

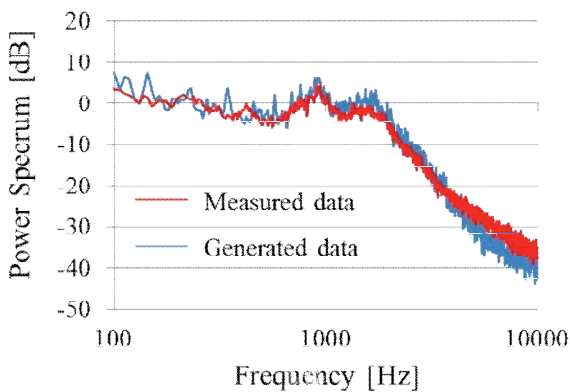
$$S(F(T_1')) = \beta(T_1')S'(T_1') \tag{7}$$

where  $\beta(T_1')$  is the correction coefficient which can be written as  $R(F(T_1'))$ . Fig.12 (b) shows the sound source data which is used for the auralization of the road traffic noise system. From this figure, it can be seen that the effects of the distance attenuation is removed. Fig.13 shows the

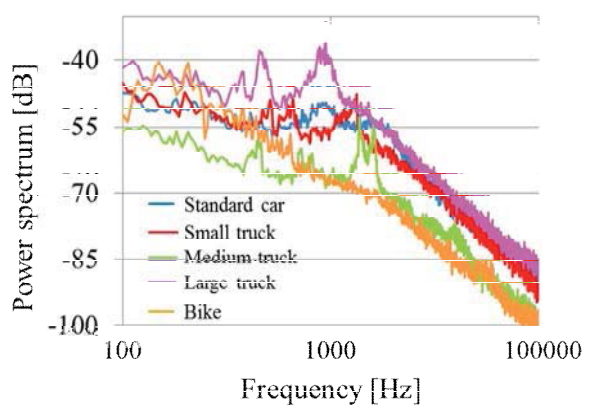
comparison of power spectrum in case that the both sound at 1000Hz are assumed as 0dB. It can be seen that both power spectrums coincide with each other. Fig.14 shows the comparison of power spectrum for various type of vehicle in case that the speed of vehicle is 100km/h. From this figure, the power spectrum of large truck and bike are big in the range of low frequency comparing with others.



**Figure 12. Generation of sound source data**



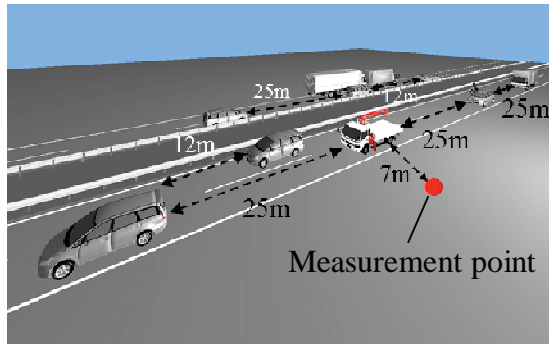
**Figure 13. Comparison of power spectrum**



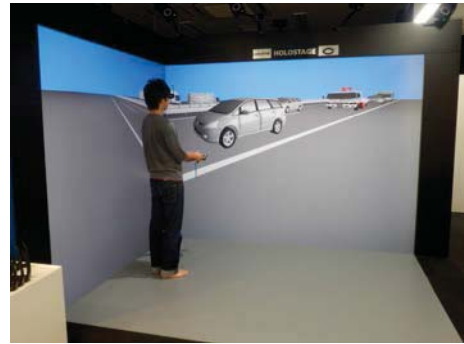
**Figure 14. Comparison of power spectrum**

**Application example**

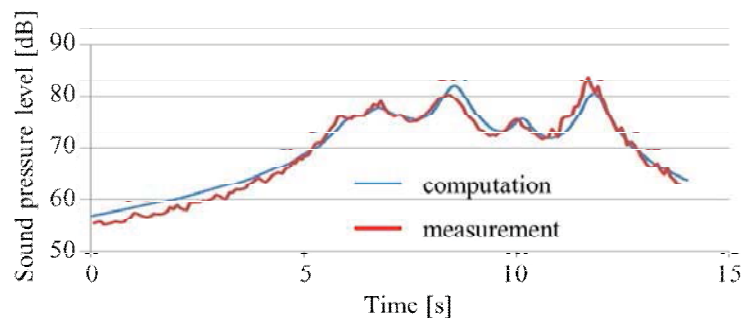
The present system is applied the traffic simulation with various type of vehicle as shown in Fig.15. The sound source data generated from the various car driving tests is implemented to the simulation. Fig.16 shows the scene that the observer uses the system. The computed results are compared with the measured results by the noise level meter (vehicle velocity:100km/h, pavement of road:drainage pavement, passage years of pavement:0year) as shown in Fig.17. From this figure, it can be seen that the computational results are good agreement with the measurement.



**Figure 15. Computational condition**



**Figure 16. Scene that the observer uses the system**



**Figure 17. Comparison of computational and measured results**

## Conclusion

A road traffic noise evaluation system based on spatialization of sound using virtual reality technology has been presented. In order to consider the effects of directivity of the sound wave and delay of the arrival time, a stereoscopic sound field has been developed in VR space. Furthermore, the sound source data for the auralization in VR space has been generated from the various vehicle driving tests. The following conclusions can be obtained.

- The reality and presence of the system has been improved by the spatialization of sound field in VR space.
- The power spectrum of generated sound source data for auralization is good agreement with the observed data, and the high quality sound source data has been obtained.

The verification of the present system to the complicated road environment is left in the future work.

## References

- Nagano T. Yasuda Y. Turihata K. and Yanagisawa T. (1999). "The examination of virtual reality system for noise experience", The Technical Report of The Proceeding of The IEIC, EA99-56, pp.33-40.
- Makane K. and Takahashi K. (2004). "3D Traffic Noise Simulator for VR Environment ." CONVR 2004: 4<sup>th</sup> Conference of Construction Applications of Virtual Reality, Lisbon, Portugal, Sept. 14-15, 183-186.
- The Acoustical Society of Japan. (2009), "Road traffic noise prediction model "ASJ RTN-Model 2008" proposed by the Acoustical Society of Japan", Journal of Japan Acoustical Society of Japan, Vol.65.
- Tajika S. Kashiyama K. and Shimura M. (2009)," Development of a road traffic noise estimation system using virtual reality technology", Construction Virtual Technology 2009,pp305-314.
- Shibata, K. Tajika S. Kashiyama K. and Shimura M. (2010), "Development of an experienced-based road traffic noise evaluation system using VR technology", Construction Virtual Technology, pp.513-522.
- Tanigawa M. Moriya Y. Ejima K. Kashiyama K. Shimura M. (2013) , A study on three dimensional spatialization of sound with more reality for road traffic noise evaluation system based on virtual reality technology, Journal of Applied Mechanics, JSCE, Vol.16. (in Japanese) (in press)
- Ward, D.B. and Abhayapala, T.D. (2001), Reproduction of aplane-wave sound field using an array of loudspeakers, Speech and Au-dio Processing, IEEE Transactions on, Vol.9, pp.697-707.



## Interval method for solving the dynamics problems of multibody system with uncertain parameters

Jinglai. Wu<sup>1</sup>, Zhen. Luo<sup>1\*</sup>, and Nong. Zhang<sup>1</sup>

<sup>1</sup> School of Electrical, Mechanical and Mechatronic Systems  
The University of Technology, Sydney, NSW 2007, Australia

\*Corresponding author: zhen.luo@uts.edu.au

The theoretical and computational aspects of interval methodology based on Chebyshev polynomials for modeling complex nonlinear multi-body dynamic systems in the presence of parametric and external excitation uncertainties is formulated, implemented, and validated. Both the parameters uncertainties and external excitation uncertainties are modeled by uncertain-but-bounded interval variables, where the bounds on the magnitude of uncertain parameters or external force are only required, not necessarily knowing the probabilistic distribution densities. The Chebyshev inclusion function which employs the truncated Chebyshev series expansion to approximate the original nonlinear calculates sharper range than the traditional Taylor inclusion function. The coefficients of the Chebyshev polynomials are calculated through the Mehler numerical integral method. The multi-body systems dynamics are governed by differential algebraic equations (DAEs) which are transformed to nonlinear equations with interval parameters at each integral step by HHT-I3 methods, and then the proposed method for nonlinear systems with interval parameters can be employed to find the interval region of the system responses. The numerical example results show that the novel methodology can reduce the overestimation largely and is computationally faster than the scanning method.

**Keywords:** interval method; Chebyshev polynomials; uncertain analysis; DAEs

### Introduction

Modern multibody systems containing such as mechanisms, robotics, vehicles, and machines etc. are often very complex and consist of many components interconnected by mechanical joints and force elements. The governing equations of such systems are often governed by index-3 differential algebraic equations (DAEs). Although mathematical modeling tools for multibody dynamics simulation have experienced a tremendous growth, most researches were based on the assumption that all parameters of multibody systems are deterministic. However, the realistic engineering multibody systems often operate under some degree of uncertainty which may be resulted from variability in their geometric or material parameters, or caused by the assembly process and manufacturing tolerances and/or wear, ageing and so on. Hence, the multibody dynamics models must account for these uncertainties for achieving the realistic predictions of the system responses.

Interval arithmetic has appeared several decades, but interval theory was not mainly concentrated until the appearance of Moore's work (Revol, Makino et al. 2005). Interval arithmetic can obtain the system response bounds quickly, because it is not a type of optimization algorithm which needs a large amount of iterations. However, interval arithmetic has its own drawback that is the calculation results may be overestimated too much caused by the wrapping effect. How to reduce the overestimation is the key for interval arithmetic. Many interval methods have been proposed to solve the static problems (Zingales and Elishakoff 2000; Chen, Lian et al. 2002; Gao 2006; Muhanna, Zhang et al. 2007; Wang, Elishakoff et al. 2009; Gao, Song et al. 2010). However, the interval methods for solving the dynamics problems which are expressed as differential equations including ODEs and DAEs are presented not much. The numerical methods for solving differential

equations contain much iteration which aggravates the overestimation, so besides using the interval set theory, many other particular algorithms are introduced to reduce the overestimation. Interval Taylor series method (Nedialkov, Jackson et al. 1999; Alefeld and Mayer 2000; Jackson and Nedialkov 2002) and Taylor model method (Berz and Makino 1999) are the two important methods. The Taylor model uses higher order Taylor series to approximate the system responses and adds a remainder interval to guarantee the interval ranges contain all the possible results, which reduces the wrapping effect induced by the dependency of interval variables. Lin's VSPODE (Lin and Stadtherr 2007) combined the two methods to solve the ODEs with interval parameters, which made the interval results sharper. The mechanical dynamics problems are generally governed by DAEs, especially by the index-3 DAEs. The numerical solution of DAEs has a comparatively short history related to ODEs, still, numerically solving DAEs poses fundamental difficulties not encountered when solving ODEs (Negrut, Jay et al. 2009).

To reduce the overestimation of interval inclusion function, the Chebyshev inclusion function using the truncated Chebyshev series to calculate the bounds of function with interval parameters is proposed. The Chebyshev inclusion function can reduce the overestimation effectively, because it can be expressed as cosine functions which make the interval range sharper for non-monotonic functions. Utilizing the Chebyshev inclusion function on DAEs with interval parameters, the overestimation can be controlled effectively. For Mehler integral is an interpolation quadrature formula, the solutions at each interpolation point are needed, and the traditional HHT-I3 numerical method is used to produce the solutions at each interpolation point. At last, the interval arithmetic can be employed to calculate the bounds of solutions of DAEs based on the obtained Chebyshev inclusion function.

### Modeling and Solving the Multibody Dynamics System

The constrained equations of the dynamics of multibody systems can be expressed as (Negrut, Jay et al. 2009)

$$\begin{aligned}\dot{\mathbf{q}} &= \mathbf{v} \\ \mathbf{M}(\mathbf{q})\dot{\mathbf{v}} &= \mathbf{Q}(t, \mathbf{q}, \mathbf{v}, \boldsymbol{\lambda}, \mathbf{u}(t)) - \boldsymbol{\Phi}_q^T(\mathbf{q}, t)\boldsymbol{\lambda}, \\ \boldsymbol{\Phi}(\mathbf{q}, t) &= \mathbf{0}\end{aligned}\quad (1)$$

where  $\mathbf{q} \in R^n$  are the generalized coordinates,  $\mathbf{v} \in R^n$  are the generalized velocities,  $\boldsymbol{\lambda} \in R^m$  are the Lagrange multipliers, and  $\mathbf{u}: R \rightarrow R^c$  represent time dependent external dynamics, e.g. control variables. The matrix  $\mathbf{M}(\mathbf{q})$  is the generalized mass matrix,  $\mathbf{Q}(t, \mathbf{q}, \mathbf{v}, \boldsymbol{\lambda}, \mathbf{u}(t))$  represents the vector of generalized applied forces, and  $\boldsymbol{\Phi}(\mathbf{q}, t)$  is the set of  $m$  holonomic constraints. The notation in bold denotes vector, while the notation in italic denotes scalar.

The classical numerical techniques for DAEs contain two classes: state-space methods and direct methods (Bauchau and Laulusa 2008). The major intrinsic drawback associated with state-space methods remains the expensive DAE to ODE reduction process that is further exacerbated in the context of implicit integration (Negrut, Jay et al. 2009). Direct methods discretize the constrained equations and transform the DAEs to algebraic equations at each integral step. Many direct methods have been proposed to solve the index-3 DAEs, such as the Newmark method (Newmark 1959), HHT-I3 (Negrut, Rampalli et al. 2007), and generalized  $\alpha$ -method (Chung and Hulbert 1993) and so on. In this paper, we use the HHT-I3 method which would be described as follows.

Discretize the Eq. (1) with respect to time leads to the following equations (Negrut, Jay et al. 2009)

$$\begin{aligned}\mathbf{q}_{n+1} &= \mathbf{q}_n + h\dot{\mathbf{q}}_n + \frac{h^2}{2}[(1+2\beta)\mathbf{a}_n + 2\beta\mathbf{a}_{n+1}] \\ \dot{\mathbf{q}}_{n+1} &= \dot{\mathbf{q}}_n + h[(1-\gamma)\mathbf{a}_n + \gamma\mathbf{a}_{n+1}] \\ \frac{1}{1+\alpha}(\mathbf{M}(\mathbf{q})\mathbf{a})_{n+1} - (\boldsymbol{\Phi}_q^T\boldsymbol{\lambda} - \mathbf{Q})_{n+1} - \frac{\alpha}{1+\alpha}(\boldsymbol{\Phi}_q^T\boldsymbol{\lambda} - \mathbf{Q})_n &= \mathbf{0} \\ \frac{1}{\beta h^2}\boldsymbol{\Phi}(\mathbf{q}_{n+1}, t_{n+1}) &= \mathbf{0}\end{aligned}\quad (2)$$

where  $h$  is the integration step-size,  $\mathbf{a}_{n+1}$  is the approximation of  $\ddot{\mathbf{q}}(t_n + (1 + \alpha)h)$ , and the initial value  $\mathbf{a}_0$  can be set as  $\mathbf{a}_0 = \ddot{\mathbf{q}}_0$ , subscript  $n$  denotes the  $n$ th integral step, and subscript  $\mathbf{q}$  denotes the derivative of  $\mathbf{q}$ .  $\alpha, \beta$ , and  $\gamma$  are the parameters of HHT-I3 method that confirm the conditions as follow:

$$\alpha \in [-1/3, 0], \beta = (1 - \alpha^2)/4, \gamma = 1/2 - \alpha. \tag{3}$$

The smaller value of  $\alpha$  leads larger numerical dissipation for HHT-I3 method, but it makes the solution more stability. The last two equations of Eq. (2) are the nonlinear system of  $\mathbf{w}_{n+1} = [\mathbf{a}_{n+1} \ \lambda_{n+1}]^T$ , so the Newton method can be used to solve the system. The Newton method does not consider the uncertain parameters in the equations, and the method treating for uncertainties will be presented in following sections.

**Interval Arithmetic**

Let us define a real interval  $[x]$  is a connected nonempty subset of real set  $R$ . It can be expressed as

$$[x] = [\underline{x}, \bar{x}] = \{x \in R : \underline{x} \leq x \leq \bar{x}\}, \tag{4}$$

where  $\underline{x}$  is the lower bound of interval  $[x]$  which also can be noted as  $\inf([x])$ ;  $\bar{x}$  is the upper bound of interval  $[x]$  which also can be noted as  $\sup([x])$ . The set of all intervals over  $R$  is denoted by  $IR$  where

$$IR = \left\{ [\underline{x}, \bar{x}] : \underline{x}, \bar{x} \in R : \underline{x} \leq \bar{x} \right\}. \tag{5}$$

Interval arithmetic operations are defined on the real set  $R$  such that the interval result closes all possible real result. Given the two real interval  $[x]$  and  $[y]$ ,

$$[x] * [y] = \{x * y : x \in [x], y \in [y]\} \text{ for } * \in \{+, -, \times, \div\}. \tag{6}$$

Consider a function  $f$  from  $R^n$  to  $R^m$ . The interval function  $[f]$  from  $IR^n$  to  $IR^m$  is an inclusion function for  $f$  if

$$\forall [x] \in IR^n, f([x]) \subset [f]([x]). \tag{7}$$

The direct calculation of an enclosure for a function using interval arithmetic will often lead to large overestimation. To make the result sharper, the higher order Taylor series expansion can be used. If the function  $f$  is  $n+1$  times differentiable on the interval  $[x]$ , the  $n$ th-order Taylor inclusion function (Jaulin 2001) can be obtained as follows:

$$[f_{T_n}]( [x] ) = f(x_c) + f'(x_c)[\Delta x] + \dots + \frac{1}{n!} f^{(n)}(x_c)[\Delta x]^n + \frac{1}{(n+1)!} [f^{(n+1)}([x])][\Delta x]^{n+1}, \tag{8}$$

where  $x_c$  denotes the midpoint of  $[x]$

$$x_c = mid([x]) = \frac{1}{2}(\underline{x} + \bar{x}). \tag{9}$$

And  $[\Delta x]$  is a symmetry interval of  $[x]$ , which is expressed by

$$[\Delta x] = \left[ \frac{x - \bar{x}}{2}, \frac{\bar{x} - x}{2} \right]. \tag{10}$$

In the above, the Eq. (8) calculates the rigorous enclosure for the function  $f(x)$ . The last term in the right hand side of Eq. (8) is usually neglected to obtain the approximate enclosure of  $f(x)$  in engineering. Some specific interval function can be calculated through some special algorithms, e.g. the trigonometric function (Jaulin 2001) and so on..

## Chebyshev Method for Multibody Dynamics System with Interval Parameters

### Chebyshev inclusion function

If the function  $f(x)$  is contained in  $C[a, b]$ , which means  $f(x)$  is continuous on  $[a, b]$ , then it can be approximated as truncated Chebyshev series with degree  $n$  (Li, Wang et al. 2003), shown as follow

$$f(x) \approx p_n(x) = \frac{1}{2} f_0 + \sum_{i=1}^n f_i C_i(x), \quad (11)$$

where  $f_i$  are the constant coefficients, and  $C_i(x)$  denotes the Chebyshev polynomial. The Chebyshev polynomial for  $x \in [-1, 1]$  of degree  $n$  is denoted by  $C_n$  and is defined by (Rivlin 1981)

$$C_n(x) = \cos n\theta, \quad (12)$$

where  $\theta = \arccos(x) \in [0, \pi]$ ,  $n$  denotes the nonnegative integer. The Chebyshev polynomial on  $[a, b]$  of degree  $n$  is also defined by Eq. (12), but here  $\theta = \arccos\left(\frac{2x-(b+a)}{b-a}\right)$ . For multi-dimension problem,

the polynomials are the tensor product of each one-dimension polynomial. For example, the  $k$  dimensions Chebyshev polynomials of  $x_i \in [-1, 1]$ ,  $i=1, 2, \dots, k$  can be expressed as

$$C_{n_1, n_2, \dots, n_k}(x_1, \dots, x_k) = \cos(n_1\theta_1) \dots \cos(n_k\theta_k), \quad (13)$$

where  $\theta_i = \arccos(x_i)$ . The corresponding multi-dimension function  $f(\mathbf{x})$  can be approximated as

$$\mathbf{f}(\mathbf{x}) \approx \sum_{i_1=0}^n \dots \sum_{i_k=0}^n \left(\frac{1}{2}\right)^p \mathbf{f}_{i_1, \dots, i_k} C_{i_1, \dots, i_k}(\mathbf{x}), \quad (14)$$

where  $p$  denotes the total number of zero(s) to be occurred in the subscripts  $i_1, \dots, i_k$ ,  $C_{i_1, \dots, i_k}(\mathbf{x})$  is the  $k$ -dimensional Chebyshev polynomials given in Eq. (13), and  $\mathbf{f}_{i_1, \dots, i_k}$  denotes the vector including the coefficients of Chebyshev polynomials which can be calculated by Eq. (15)

$$\mathbf{f}_{i_1, \dots, i_k} = \left(\frac{2}{\pi}\right)^k \int_0^\pi \dots \int_0^\pi \mathbf{f}(\cos\theta_1, \dots, \cos\theta_k) \cos i_1\theta_1 \dots \cos i_k\theta_k d\theta_1 \dots d\theta_k, \quad (15)$$

where  $k$  denotes the number of dimension, and subscript  $i_1, \dots, i_k = 0, 1, \dots, n$ . The numerical integral methods should be used to calculate the Eq. (15), and the Mehler integral method is suitable. The Mehler integral is a type of interpolation integral which can be expressed as

$$\mathbf{f}_{i_1, \dots, i_k} \approx \left(\frac{2}{m}\right)^k \sum_{j_1=1}^m \dots \sum_{j_k=1}^m \mathbf{f}(\cos\theta_{j_1}, \dots, \cos\theta_{j_k}) \cos i_1\theta_{j_1} \dots \cos i_k\theta_{j_k}, \quad (16)$$

where  $m$  denotes the number of interpolation points,  $\theta_j$  denotes the interpolation points

$$\theta_j = \frac{2j-1}{m} \frac{\pi}{2}, j = 1, 2, \dots, m. \quad (17)$$

Similar to Taylor inclusion function, we define the Chebyshev inclusion function of  $f(x)$  which can be expressed as

$$[\mathbf{f}_{C_n}][[\mathbf{x}]] = \sum_{j_1=0}^n \dots \sum_{j_k=0}^n \left(\frac{1}{2}\right)^p \mathbf{f}_{j_1, \dots, j_k} \cos(j_1[\theta_1]) \dots \cos(j_k[\theta_k]), \quad (18)$$

where  $[\theta] = [0, \pi]$ . Eq. (18) can be calculated through the algorithm of interval trigonometric function shown in section 3.

### Chebyshev method for solving multibody systems containing interval parameters

From section 2, we know that the numerical method for solving the multibody dynamics system transform the DAEs to nonlinear equations at each integral step. When consider the uncertain parameters and uncertain external excitation are contained in the multibody system, such as the length tolerance of components inducing the mass and center of mass uncertain, the density uncertainty leading the mass and the moment of inertia uncertain, and the fluctuated driving force, the DAEs can be transformed to nonlinear equations containing uncertain parameters.

Since the DAEs are transformed to nonlinear equations at each iteration step, the nonlinear equations with interval parameters will be researched. Consider the  $q$  dimensions function group  $\mathbf{F} = [f_1, f_2, \dots, f_q]^T$ , where  $f_i : x \in \mathbf{X} \subset R^q \rightarrow R, i = 1, 2, \dots, q$ . If the uncertain parameters which are expressed as interval parameters  $\xi \subset [\mathbf{a}, \mathbf{b}]^k$  exist in the nonlinear system, the nonlinear system can be described as

$$\mathbf{F}(\mathbf{X}, \xi) = \mathbf{0}. \tag{19}$$

The solution set of Eq. (19) is a function with respect to uncertain parameters  $\xi$ , and its interval solution is  $[\mathbf{X}([\xi])]$

$$\mathbf{X}(\xi) = \mathbf{F}^{-1}(\mathbf{Y}, \xi)|_{\mathbf{Y}=\mathbf{0}} \subset [\mathbf{X}([\xi])]. \tag{20}$$

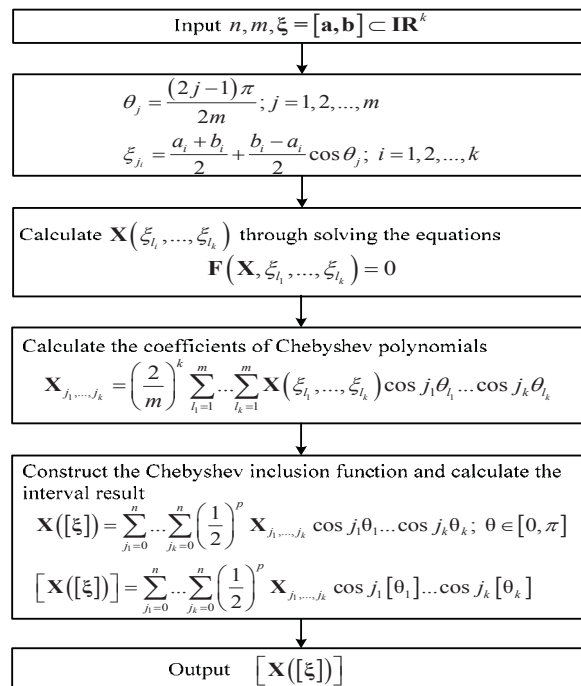
Considering the Chebyshev inclusion function Eq. (19), the interval solution  $[\mathbf{X}([\xi])]$  can be calculated as

$$[\mathbf{X}([\xi])] = \sum_{j_1=0}^n \dots \sum_{j_k=0}^n \left(\frac{1}{2}\right)^p \mathbf{X}_{j_1, \dots, j_k} \cos(j_1[\theta_1]) \dots \cos(j_k[\theta_k]), \tag{21}$$

where  $\theta \subset [0, \pi]^k$ , and the coefficients vector  $\mathbf{X}_{j_1, \dots, j_k}$  can be obtained through Eq. (16)

$$\mathbf{X}_{j_1, \dots, j_k} = \left(\frac{2}{m}\right)^k \sum_{l_1=1}^m \dots \sum_{l_k=1}^m \mathbf{X}(\theta_{l_1}, \dots, \theta_{l_k}) \cos j_1 \theta_{l_1} \dots \cos j_k \theta_{l_k}, \tag{22}$$

where  $\theta_i$  denotes the interpolation points expressed by Eq. (17), and  $\mathbf{X}(\theta_{l_1}, \dots, \theta_{l_k})$  denotes the solution of nonlinear system shown in Eq. (19) when the values of uncertain parameters are set as  $\xi = [\cos \theta_{l_1}, \dots, \cos \theta_{l_k}]^T$ . The detail algorithm for solving multibody systems with uncertain parameters can be described as **Algorithm 1**.

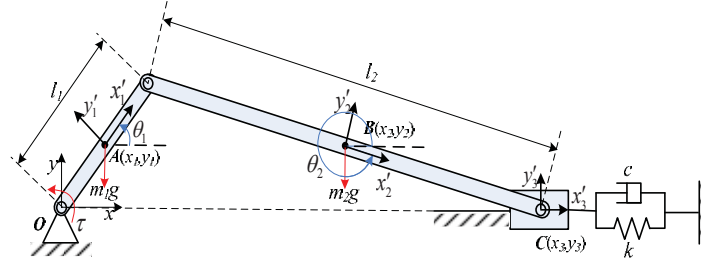


**Algorithm 1**

From the calculation flow, we find that the algorithm solving the uncertain problem is similar to a type of sampling method, but its pre-processing and post-processing are particular. Thus, the proposed method can be used in black box problems even, but the accuracy and efficiency should be researched further.

**Numerical Application**

In this section, the numerical example which is slider crank mechanism containing interval parameters is presented. In the slider crank mechanism, the length of crank is firstly considered as an interval parameter, we hope to obtain the range of slider displacement in the whole calculation period. The schematic of slider crank is shown in Fig. 1, and the parameters are shown in Table 1.



**Figure. 1 The schematic of slider crank**

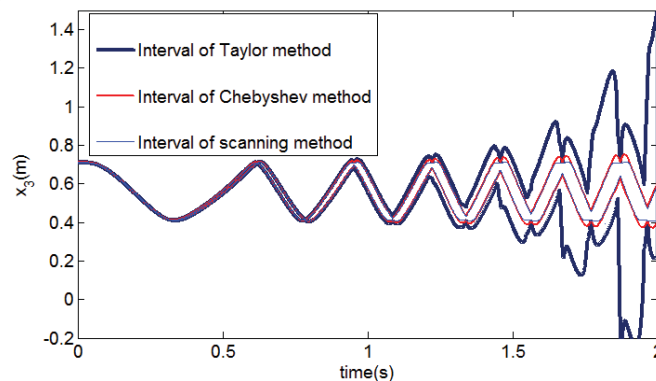
**Table 1. The parameters of slider crank**

parameters	$l_1(m)$	$l_2(m)$	$m_1(kg)$	$m_2(kg)$	$m_3(kg)$	$c(N/(m/s))$	$k(N/m)$	$\tau(Nm)$
value	0.15	0.56	0.37	0.77	0.45	1	5	-0.5

As shown in Fig. 1, point A, B, and C is the gravity center of crank, connecting rod, and slider respectively.  $\theta_1$  and  $\theta_2$  denotes the angle between the global coordinate and the local coordinate of crank and connecting rod respectively. The slider is connected with a spring damper, and the spring force is zero when the angle  $\theta_1$  and  $\theta_2$  equal to zero.  $l_1$  and  $l_2$  denotes the length of crank and connecting rod;  $m_1$ ,  $m_2$ , and  $m_3$  denotes the mass of crank, connecting rod, and slider respectively;  $c$  is the damp coefficient of spring damper,  $k$  is the stiffness of spring damper, and  $\tau$  denotes the external torque applied on the crank. Choose the seven generalized coordinates which are  $\mathbf{q} = [x_1, y_1, \theta_1, x_2, y_2, \theta_2, x_3]^T$ , where the subscript 1, 2, and 3 denotes the crank, connecting rod, and slider, respectively. Suppose the length of crank  $l_1$  containing uncertainty with 1% of its nominal value, noting it as

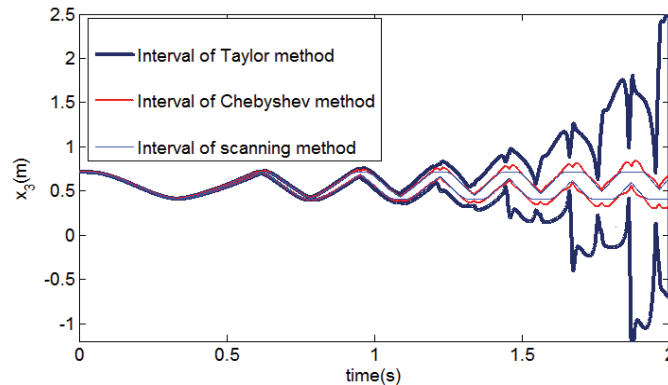
$$\hat{l}_1 = l_1(1 + 0.01\xi_1), \quad \xi_1 \in [-1, 1]. \tag{23}$$

The system is solved for a period of 2s by using the Chebyshev method with 5th-order polynomials and the second-order Taylor method, respectively. To ensure the precise ranges of results, the scanning method (Buras, Jamin et al. 1996) is employed with symmetrical 30 sampling points. The results are shown in Fig. 2.



**Figure. 2 The displacement of piston with uncertain crank length**

The results obtained by Chebyshev method enclose the range of scanning method tightly in the initial period, compared with the Taylor inclusion function method.



**Figure. 3 The displacement of piston with uncertain crank length and torque**

Secondly, we also consider the external torque  $\tau$  under interval uncertainty with 1% of its nominal value, and the uncertain external torque is then expressed as

$$\hat{\tau} = \tau(1 + 0.01\xi_2), \quad \xi_2 \in [-1, 1] \quad (24)$$

The initial conditions keep unchanged. Solve the system for a period of 2s using the Chebyshev method with the 5th-order polynomials and the second-order Taylor method. The results are shown as Fig. 3. For the computational time, the proposed Chebyshev method requires 422s, while the Taylor method and scanning method needs 1392s and 10584s, respectively.

## Conclusions

A new interval numerical method using Chebyshev series to solve the multibody dynamics system with uncertainties is presented. Interval method is mainly used in the cases that only the bounds of uncertain parameters are known. To weaken the drawback of interval method, overestimated too much, the Chebyshev inclusion function which employs the truncated Chebyshev series to approximate the original function is proposed. The Chebyshev polynomials approximation theory is also used in solving the nonlinear system with interval parameters. To solve the multibody system dynamics problems containing uncertain parameters, the classical HHT-I3 method is used to transform the DAEs to nonlinear systems at each integral step, so the proposed algorithm for solving nonlinear system with interval parameters can be utilized. The numerical example of slider crank mechanism is presented, where the length of crank and torque forced on crank are considered as interval parameters. The numerical results show that the results of Chebyshev method enclose the results of scanning method tighter than the Taylor method, also the Chebyshev method is higher efficient than both scanning method and Taylor method. The proposed method is similar to the sampling method which may even settle the black box problems.

## References

- Alefeld, G. and G. Mayer (2000). "Interval analysis: theory and applications." *Journal of Computational and Applied Mathematics* **121**: 421-464.
- Bauchau, O. A. and A. Laulusa (2008). "Review of Contemporary Approaches for Constraint Enforcement in Multibody Systems." *Journal of Computational and Nonlinear Dynamics* **3**(1): 011005.
- Berz, M. and K. Makino (1999). "Efficient Control of the Dependency Problem Based on Taylor Model Methods." *Reliable Computing* **5**: 3-12.
- Buras, A. J., M. Jamin, et al. (1996). "A 1996 Analysis of the CP. Violating Ratio  $\varepsilon' / \varepsilon$ ." *Physics Letters B* **389**(4): 749-756.
- Chen, S., H. Lian, et al. (2002). "Interval static displacement analysis for structures with interval parameters." *International Journal for Numerical Methods in Engineering* **53**(2): 393-407.
- Chung, J. and G. Hulbert (1993). "A time integration algorithm for structural dynamics with improved numerical dissipation: The generalized- $\alpha$  method." *Journal of Applied Mechanics* **60**: 371-375.

- Gao, W. (2006). "Interval Finite Element Analysis using Interval Factor Method." *Computational Mechanics* **39**(6): 709-717.
- Gao, W., C. Song, et al. (2010). "Static response and reliability analysis of structural systems with random and interval properties." *IOP Conference Series: Materials Science and Engineering* **10**: 012200.
- Jackson, K. R. and N. S. Nedialkov (2002). "Some recent advances in validated methods for IVPs for ODEs." *Applied Mathematics and Computation* **42**: 269-284.
- Jaulin, L. (2001). *Applied interval analysis: with examples in parameter and state estimation, robust control and robotics*. New York, Springer.
- Li, Q., N. Wang, et al. (2003). *Numerical Analysis*. Wuhan, Huazhong University of Science and Technology Press.
- Lin, Y. and M. A. Stadtherr (2007). "Validated solutions of initial value problems for parametric ODEs." *Applied Numerical Mathematics* **57**(10): 1145-1162.
- Muhanna, R. L., H. Zhang, et al. (2007). "Combined axial and bending stiffness in interval finite-element methods." *Journal of Structural Engineering* **133**(12): 1700-1709.
- Nedialkov, N. S., K. R. Jackson, et al. (1999). "Validated solutions of initial value problems for ordinary differential equations." *Applied Mathematics and Computation* **105**: 21-68.
- Negrut, D., L. O. Jay, et al. (2009). "A Discussion of Low-Order Numerical Integration Formulas for Rigid and Flexible Multibody Dynamics." *Journal of Computational and Nonlinear Dynamics* **4**(2): 021008.
- Negrut, D., R. Rampalli, et al. (2007). "On an implementation of the Hilber–Hughes–Taylor method in the context of index 3 differential-algebraic equations of multibody dynamics." *Journal of Computational and Nonlinear Dynamics* **2**: 73-85.
- Newmark, N. M. (1959). "A method of computation for structural dynamics." *Journal of Engineering Mechanics Division*: 67-94.
- Revol, N., K. Makino, et al. (2005). "Taylor models and floating-point arithmetic: proof that arithmetic operations are validated in COSY☆." *Journal of Logic and Algebraic Programming* **64**(1): 135-154.
- Rivlin, T. J. (1981). *An Introduction to the Approximation of Functions*. New York, Dover.
- Wang, X., I. Elishakoff, et al. (2009). "Comparisons of Probabilistic and Two Nonprobabilistic Methods for Uncertain Imperfection Sensitivity of a Column on a Nonlinear Mixed Quadratic-Cubic Foundation." *Journal of Applied Mechanics* **76**(1): 011007.
- Zingales, M. and I. Elishakoff (2000). "Anti-optimization versus probability in applied mechanics problem: vector uncertainty." *Journal of Applied Mechanics* **67**: 472-484.



# Numerical evaluation of fluid force acted on bridge girders during tsunami by using particle method

\* Shoichi Tanabe<sup>1</sup>, Mitsuteru Asai<sup>2</sup>, and Yoshimi Sonoda<sup>2</sup>

<sup>1</sup>Department of Civil Engineering, University of Kyushu, JAPAN.

<sup>2</sup>Department of Civil Engineering, University of Kyushu, JAPAN.

\*Corresponding author: asai@doc.kyushu-u.ac.jp

## Abstract

On March 11, 2011, the huge tsunami caused by the great east Japan earthquake devastated the Pacific coast of north-eastern Japan. Many infrastructures including bridges were collapsed by the tsunami. New generation of tsunami disaster prevention and mitigation method should be reconsidered toward the next millennium Tsunami. In this study, a stabilized Smoothed Particle Hydrodynamics (SPH) has been utilized for an evaluation of fluid force acted on bridge girders. In addition, a new boundary treatment using the fixed ghost boundary method is developed in the model having step-shaped incompatible boundary surface. Finally, the accuracy and efficiencies of our proposed method are validated by comparison between a numerical solution and experimental results.

**Keywords:** *SPH, Fluid Force, Boundary Condition, Tsunami.*

## Introduction

On March 11, 2011, the huge tsunami caused by the great east Japan earthquake devastated the Pacific coast of north-eastern Japan. Many infrastructures including bridges and other tsunami prevention facilities were collapsed by the tsunami. In order to construct safe and secure coastal structures, present tsunami disaster prevention and mitigation methods are necessary to reconsider and to develop an accurate prediction tool toward the next millennium Tsunami. At present, numerical evaluation of the fluid force during tsunami is strongly desired for generating the new regulation of tsunami disaster prevention, because real size experimental tests for this purpose are almost impossible and too costly. In this study, focusing on the numerical evaluation of fluid forces acted on bridge girders, a reasonable numerical simulation technique based on the Incompressible Smoothed Particle Hydrodynamics (ISPH) has been selected. The features of our proposed simulation technique are stabilization of ISPH with a modified source term in pressure Poisson equation and a new boundary treatment using the fixed ghost boundary method.

The source term in pressure Poisson equation (PPE) for ISPH is not unique. It has several formulations in the literature as Lee *et al.* (2008) and Khayyer *et al.* (2008,2009). The source term is derived from a function of density variation and velocity divergence condition. Both source terms are not complete the density invariant and divergence free condition, so modified schemes have been proposed to satisfy the above conditions. Relaxation coefficient is multiplied in term of density invariant for smoothing the resultant pressure. Recently, in the framework of MPS, there is a trend to introduce a higher order source term in the PPE, Kondo and Koshizuka (2010) and Tanaka and Masunaga (2010). In this paper, the similar approach is implemented with the ISPH for their stabilization and for smoothed pressure evaluation.

Generally, particle methods in fluid dynamics are not so easy to treat boundary conditions like pressure Neumann condition and slip or no-slip conditions on the solid surface. This is one of

typical difficulties in mesh-less method. Recently, pressure Neumann condition in SPH is re-focused with fixed ghost boundary method using a virtual marker. A new boundary treatment using the fixed ghost boundary method is proposed to satisfy the slip and no-slip boundary conditions on the solid boundary surface, which is modeled by step-shaped incompatible boundary surface. The accuracy and efficiencies of our proposed method are validated by comparison between a numerical solution and experimental results.

After the validation, an ISPH method with a modified source term and a new boundary treatment are utilized to estimate the fluid force acted on bridge girders in a real scale model, which has a complicated shape. The estimation value is discussed in a couple of cases by differences as to the position of the girders.

### Improved ISPH

In this section, a stabilized ISPH (Asai *et al.* 2012), which includes a modified source term in the pressure Poisson equation, for incompressible flow is summarized.

#### Governing equation

The governing equations are the continuum equation and the Navier-Stokes equation. These equations for the flow are represented as

$$\frac{D\rho}{Dt} + \rho \nabla \cdot \mathbf{u} = 0 \quad (1)$$

$$\frac{D\mathbf{u}}{Dt} = -\frac{1}{\rho} \nabla p + \nu \nabla^2 \mathbf{u} + \frac{1}{\rho} \nabla \cdot \boldsymbol{\tau} + \mathbf{F} = \mathbf{0} \quad (2)$$

where  $\rho$  and  $\nu$  are density and kinematic viscosity of fluid,  $\mathbf{u}$  and  $p$  are the velocity and pressure vectors of fluid respectively.  $\mathbf{F}$  is external force, and  $t$  indicates time. The turbulence stress  $\boldsymbol{\tau}$  is necessary to represent the effects of turbulence with coarse spatial grids. In the most general incompressible flow approach, the density is assumed by a constant value with its initial value.

#### Modification in the source term of pressure Poisson equation

The main concept in an incompressible SPH method is to solve a discretized pressure Poisson equation at every time step to get the pressure value. In a sense of physical observation, physical density should keep its initial value for incompressible flow. However, during numerical simulation, the ‘particle’ density may change slightly from the initial value because the particle density is strongly dependent on particle locations in the SPH method. If the particle distribution can keep almost uniformity, the difference between ‘physical’ and ‘particle’ density may be vanishingly small. That is, the density invariant condition is not satisfied only if the number of nearest neighboring particles is fixed and the uniform distribution of the particles is kept perfectly. Therefore, developing the scheme like that the errors don’t occur in the long term is needed by allowing some density errors in a moment. For this purpose, the different source term in pressure Poisson equation can be derived using the ‘particle’ density. The SPH interpolations are introduced into the original mass conservation law before the perfect compressibility condition is applied.

$$\langle \nabla \cdot \mathbf{u}_i^{n+1} \rangle = -\frac{1}{\rho^0} \frac{\langle \rho_i^{n+1} \rangle - \langle \rho_i^* \rangle}{\Delta t} \quad (3)$$

Then, the pressure Poisson equation reformulated as:

$$\langle \nabla^2 p_i^{n+1} \rangle = \frac{\rho^0}{\Delta t} \langle \nabla \cdot \mathbf{u}_i^* \rangle + \alpha \frac{\rho^0 - \langle \rho_i^* \rangle}{\Delta t^2} \quad (4)$$

where  $\alpha$  is relaxation coefficient,  $\mathbf{u}_i^*$  is temporal velocity and triangle bracket  $\langle \rangle$  means SPH approximation. Note that this relaxation coefficient is strongly dependent on the time increment and the particle resolution. Then, the reasonable value can be estimated by the simple hydrostatic pressure test using the same settings on its time increment and the resolution.

### Boundary treatment

In this section, a new boundary treatment using a virtual marker in incompatible step shaped boundary model is proposed here. The concept of this treatment is to give a wall particle accurate physical properties, velocity and pressure. The procedure is summarized briefly.

#### *Procedure of proposed boundary Treatment*

Wall particle is placed on a grid-like structure with equally spaced in a solid boundary. Virtual marker is put in a position which is symmetrical to the wall particle across its solid boundary. Velocity and pressure on the marker are interpolated based on the concept of weighted average of neighboring particles, which is the fundamental equation of SPH.

$$\phi(\mathbf{x}_i, t) \approx \langle \phi_i \rangle = \sum_j \frac{m_j}{\rho_j} W(r_{ij}, h) \phi_j(\mathbf{x}_j, t) \quad (5)$$

However, the portion of the particles within the compact support may be in wall domain or vacant domain such as an air layer, in that case, interpolation using the modified weight function ( $\tilde{W}$ ) as below is performed.

$$\phi(\mathbf{x}_i, t) \approx \langle \phi_i \rangle = \sum_j \frac{m_j}{\rho_j} \tilde{W}(r_{ij}, h) \phi_j(\mathbf{x}_j, t) \quad (6)$$

$$\tilde{W} = \frac{W(r_{ij}, h)}{\sum_j \frac{m_j}{\rho_j} W(r_{ij}, h)} \quad (7)$$

The most important point is that the marker is not directly related to the SPH approximation but uses just a computational point to give the wall particle accurate physical properties. Therefore, the density of the marker does not have a bad influence on accuracies in SPH and hence, it is possible to give the boundary condition more robustly. Moreover, computational cost can reduce compared to the ghost particle method because the marker is created only once at the preprocess assuming that the wall particle is fixed.

In order to satisfy the slip condition, the wall particle needs to be given the velocity, which is mirror-symmetric to the one on the virtual marker. This mirroring processing ( $\mathbf{v}_v \rightarrow \mathbf{v}'_w$ ) is given by the following equation.

$$\mathbf{v}'_w = \mathbf{M} \mathbf{v}_v \quad (8)$$

where  $\mathbf{M}$  is a second order tensor to implement the mirroring processing, and it is represented by the use of inward normal vector of the wall ( $\mathbf{n} = (n_1, n_2, n_3)^T$ ) and the kronecker delta  $\delta$ .

$$M_{ij} = \delta_{ij} - 2n_i n_j \quad (9)$$

On the other hand, in order to satisfy the non-slip condition, the wall particle needs to be given the velocity, which is point-symmetrical to the one on the virtual marker.  $\mathbf{R}$  is a mirror-symmetric tensor and the velocity is given the same way as the Eq.(8).

$$\mathbf{v}'_w = \mathbf{R}\mathbf{v}_v, \quad R_{ij} = -\delta_{ij} \quad (10)$$

Fig.1 shows the examples of velocity vectors, which should be given the wall particles to satisfy slip or no-slip conditions.

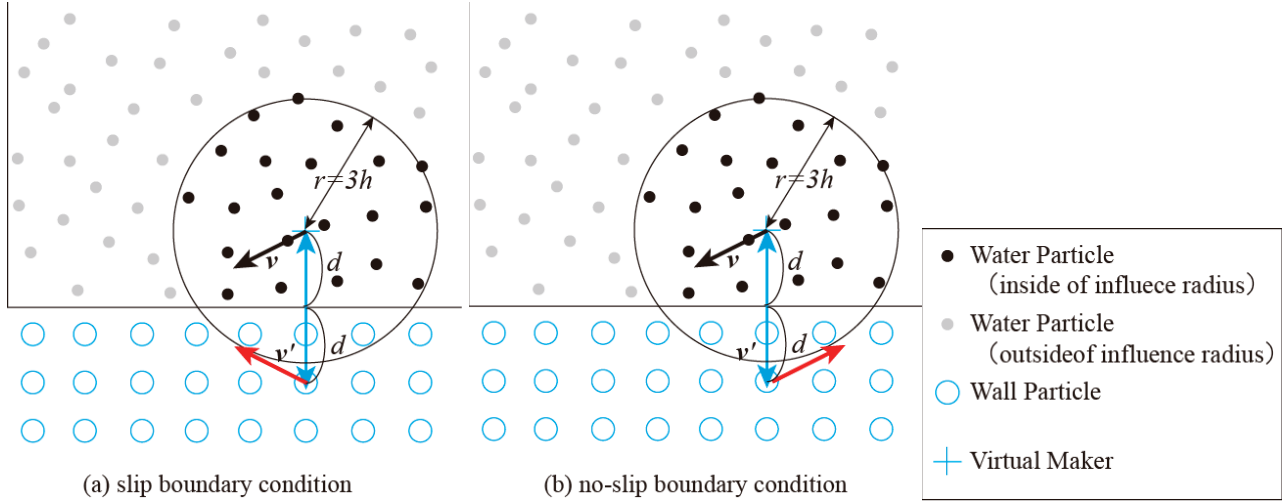


Fig.1 Virtual marker for the slip and no-slip boundary conditions

For the purpose of satisfying the pressure Neumann condition, giving the wall particle accurate pressure is necessary by referring to the one on the marker. Since normal component of the velocity on the solid boundary is equal to zero, the following equation needs to be satisfied.

$$\mathbf{v}_{w0} \cdot \mathbf{n} = 0 \quad (11)$$

where  $\mathbf{v}_{w0}$  is the velocity of the solid boundary. Referring to the Navier-Stokes equation (Eq.(12)), which describes the same one as Eq. (2), the next non-uniform pressure Neumann condition needs to be satisfied to complete Eq. (11).

$$\frac{D\mathbf{u}}{Dt} = -\frac{1}{\rho^0} \nabla P + \underbrace{\nu \nabla^2 \mathbf{u} + \mathbf{g}}_f \quad (12)$$

$$\frac{\partial p}{\partial \mathbf{n}} = \rho \mathbf{f} \cdot \mathbf{n} \quad (13)$$

In order to satisfy the non-uniform pressure Neumann condition in SPH method, it is necessary to give the wall particle the pressure, which is evaluated by the following equation.

$$p'_w = \langle p_v \rangle + 2d\rho \langle \mathbf{f}_v \rangle \cdot \mathbf{n} \quad (14)$$

where  $p_v$  and  $\mathbf{f}_v$  are the pressure and external force on the marker evaluated by SPH approximation.  $d$  represents the distance from a solid boundary to the targeting wall particle and  $\rho$  describes a water density respectively. Triangle bracket  $\langle \rangle$  means SPH approximation.

## Results and discussion

In the following section, the comparison between a numerical solution and experimental results has been introduced to validate the proposed scheme. The relation between the difference of the boundary conditions and evaluation of fluid impact force are also investigated. Next, the degree of the fluid impact force acted on a real size and shape of bridge girder is estimated.

### Analysis model

The analysis model and the detail of the girder model are shown in Fig.2. This experiment was carried out by Nakao *et al.* (2011), and the fluid impact force is evaluated while the wave acts on the girder model. The shape of the girder model is upside down trapezoid. In this study, the numerical simulation is conducted by using the proposed boundary treatment described in section 3 and the particle distance  $d_0 = 0.5\text{cm}$ , time increment  $\Delta t = 0.001\text{s}$  and the total number of particles is about 8millions.

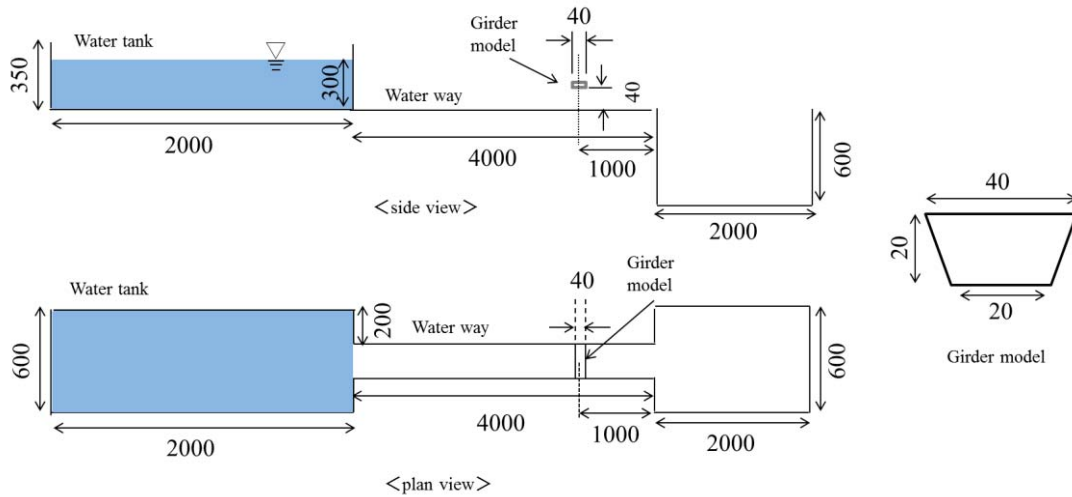


Fig.2 Analysis model (unit: mm)

### Analysis results

Fig.3 shows the result of horizontal and vertical force in upside down trapezoid girder model by filtering to cut a component of more than 15 Hz as with the experiment. The chart (a) is given the slip condition and (b) is given the no-slip condition respectively. So far, in the conventional method, the fluid force in the model having complicated boundaries could not be validated sufficiently because the evaluation has been only 2 dimensional or quasi-2 dimensional. Also, the decline of the force which originates from the penetration of water particle into the solid boundary is occurred. However, according to the result shown in Fig.3, this simulation applying our proposed method is confirmed to be useful and this simulation result matches the experimental one at the practical level. In short, the application of our proposed method to the model having incompatible step-shaped boundary is utilized with high accuracy for the purpose of evaluating the fluid impact force. As how to give the boundary conditions, it is not concluded which condition is the best for the simulation, but it seems to be middle or somewhere close to the middle of the two conditions. Further discussion is required in this verification.

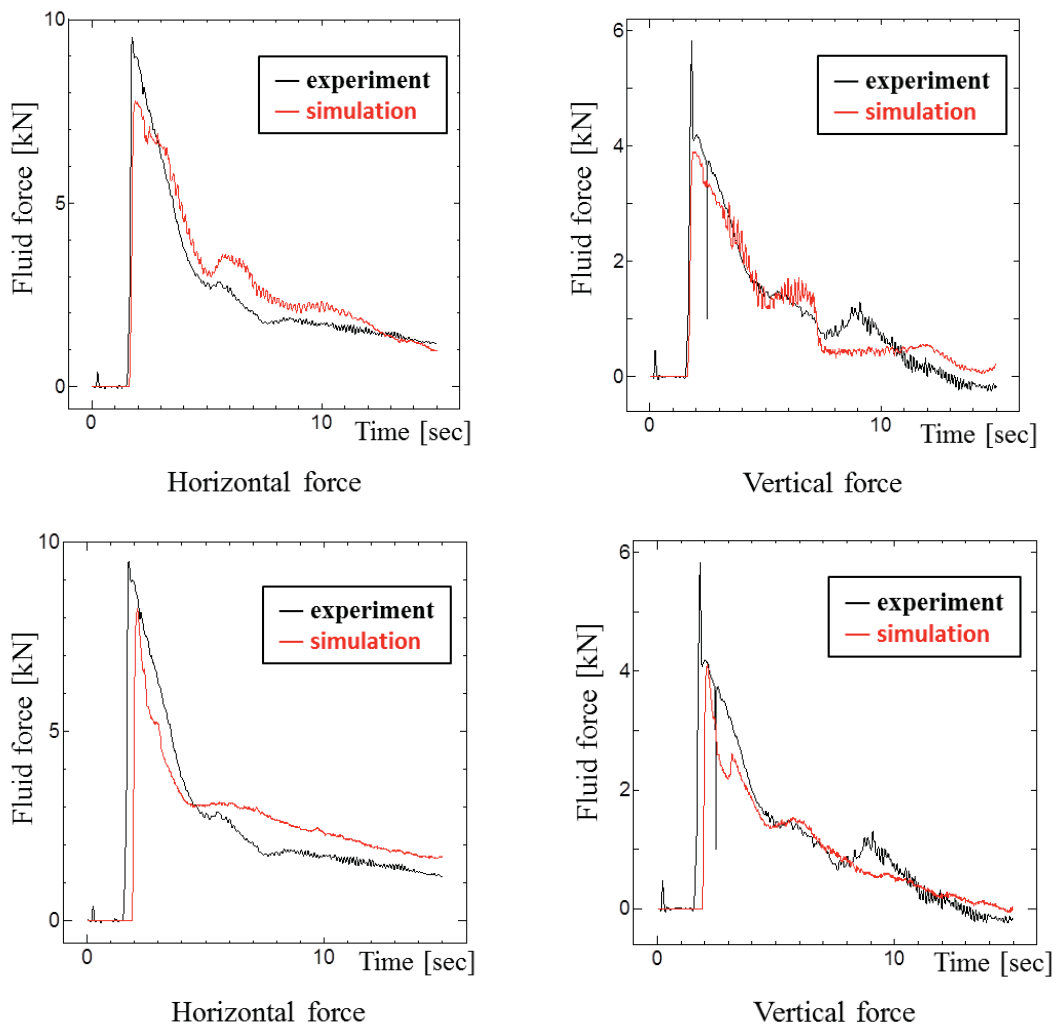


Fig.5 Horizontal and vertical force in upside down trapezoid model

### *Application for real sized and shape of girders*

In this chapter, the fluid impact force acting on a real scale and shape girder model is estimated. The wave is modeled for a gentle stream, and the girders are modeled to three patterns to investigate the change of the value of the fluid force on the assumption that the girders are pushed away with rotating by tsunami. One is horizontal and the others are 10 or 30 degree tilted to the ground respectively. Initial water level is set to be 10m referring to the report that water levels in many disaster cites reached over 10m in the huge tsunami caused by the great east Japan earthquake. The initial velocity of the wave is set 10m/s referring to shallow water long-wave equation assuming that the water level is 10m. Fig.4 shows the analysis model and the detail of the girder models are shown in Fig.5. The depth in the model is 4m. The particle distance  $d_0 = 12.5\text{cm}$ , time increment  $\Delta t = 0.001\text{s}$  and the total number of particles is about 10 millions.

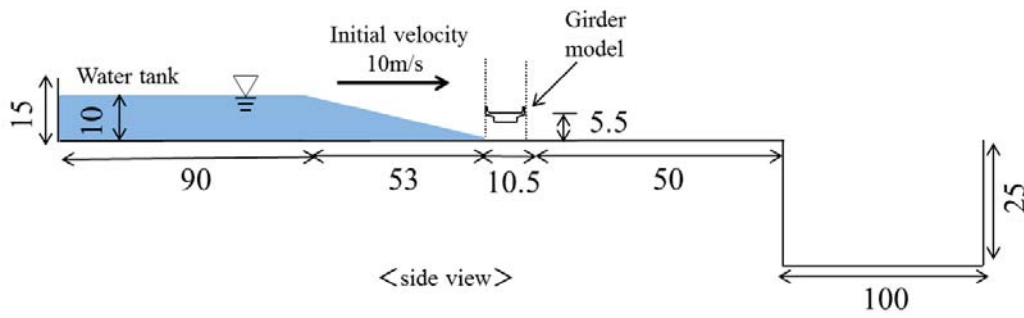


Fig.4 real size and shape of girder model

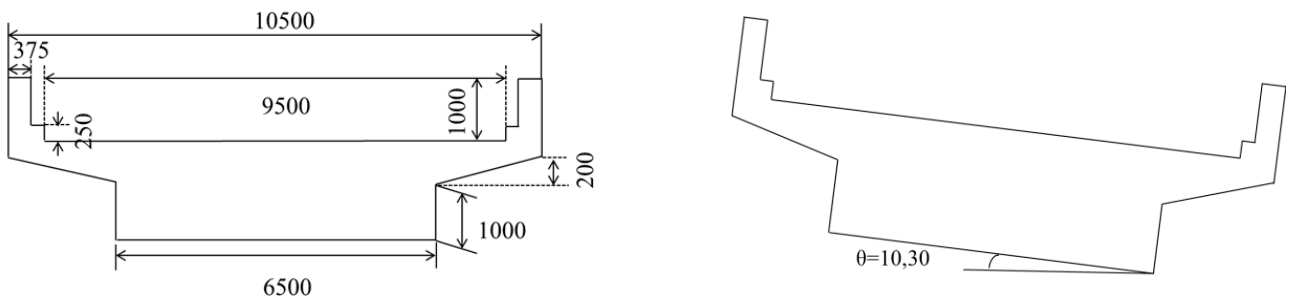


Fig.5 girder models

**Result and discussion**

Fig.6 shows the results for horizontal and vertical forces acting on the bridge girder model in this simulation. The predicted horizontal force shows a trend that the fluid force increases as the girder is more tilted. On the other hand, the vertical force shows the largest value in 10 degree tilted model. According to these results, it shows that the girder is lifted by the first vertical impact force and then pushed away by the horizontal force. From this result, it can be shown that the lift force is important factor to prevent bridges from tsunami. During the past tsunami disasters, many bridge girders may be pushed away mainly because of the lift force (vertical force) acted on the girders.

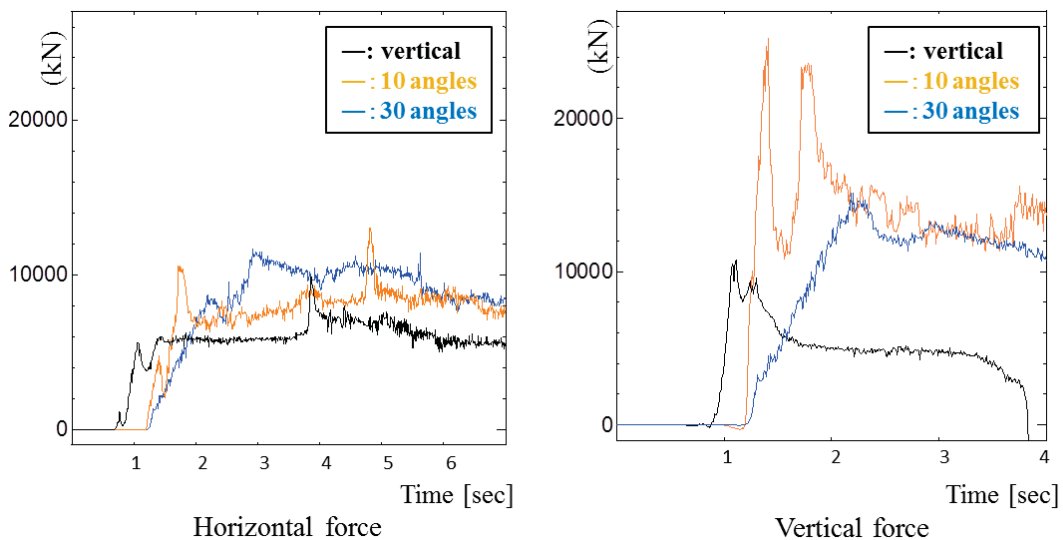


Fig.6 Horizontal and Vertical force in real and shape of girder model

## Conclusion

A stabilized incompressible smoothed particle hydrodynamics is proposed to simulate free surface flow. The modification is appeared in the source term of pressure Poisson equation, and the idea is similar to the recent development in Moving Particle Semi-implicit method (MPS). In addition, a new boundary treatment using a virtual marker is proposed to solve an incompatible step-shaped boundary model. The accuracy and efficiency of our proposed method are validated by comparison between a numerical solution and experimental results. From our numerical test, the proposed method can handle the model having a complicated boundary with high accuracy. Finally, the estimation of fluid impact force in a real size and shape girder model is performed by applying the proposed method. This simulation results can show the trend of change of the fluid force value in this model, and also show that the lift force acted on girders is important factor to prevent them from tsunami.

In the future work, a movable girder model as a rigid body should be developed to investigate the process that girder is pushed away, and it may need to discuss the relation between the fluid force and the shape of the girders and waves.

## Acknowledgements

Part of the results in obtained by using the K computer at RIKEN Advanced Institute for Computational Science (Proposal number hp130015), and this work is partially supported by JSPS Grant-in-Aid for Young Scientists (B); Grant Number 24760365.

## References

- Lee E-S, Moulinec C, Xu R, Violeau D, Laurence D, Stansby P. Comparisons of weakly compressible and truly incompressible algorithms for the SPH mesh free particle method. *Journal of Computational Physics* 2008; 18: 8417–8436.
- Khayyer A, Gotoh H, Shao S. Corrected incompressible SPH method for accurate water-surface tracking in breaking waves. *Coastal Engineering* 2008; 55: 236–250.
- Khayyer A, Gotoh H, Shao S. Enhanced predictions of wave impact pressure by improved incompressible SPH methods. *Applied Ocean Research* 2009; 31: 111-131.
- Kondo M, Koshizuka S. Improvement of stability in moving particle semi-implicit method. *Int. J. Numer. Meth. Fluids* 2010 (in press).
- Tanaka M, Masunaga T. Stabilization and smoothing of pressure in MPS method by Quasi-Compressibility. *Journal of Computational Physics* 2010; 229: 4279-4290.
- Asai M, Aly Abdelraheem M., Sonoda Y and Sakai Y. A stabilized incompressible SPH method by relaxing the density invariance condition. *Journal of Applied Mathematics*, Vol. 2012, Article ID 139583.



## Statistical Independence, Measures and Testing

\*Y. Unnisa<sup>1</sup>, D. Tran<sup>1</sup> and F. Huang<sup>1</sup>

<sup>1</sup> College of Engineering and Science, Victoria University, FP Campus, PO Box 14428, MCMC 8001, Australia.

\*Corresponding author: Danh.Tran@vu.edu.au

### Abstract

Independent Component Analysis has recently been employed in structural damage detection and blind source separation to extract source signals and the unmixing matrix of the system from response signals. This novel method relies on the assumption that source signals are statistically independent. This paper looks at statistical independence, its measures and testing procedures. First the concepts of kurtosis, negentropy and mutual information are reviewed, followed by Bakirov's measures of coefficient of statistical independence and distance correlation between two signals coupled with Hypothesis testing to avoid Type I and Type II error. Bakirov's tests are nonparametric, simple to implement and do not require any approximation. Algorithms developed by Bakirov and associates to test the statistical independence of two arbitrary signals are reviewed. A case study using signals commonly found in vibration testing showed that Bakirov's tests are both reliable and rigorous. They are then applied to investigate the effects of corrupted signals by various forms on the statistical independence and performance of fastICA, a popular independent component analysis algorithm.

**Keywords:** Statistical independence, Bakirov's dCov test, Independent component analysis, Structural damage detection, Multivariate statistics, Package "energy", fastICA.

### Introduction

Independent Component Analysis (ICA) is fundamentally a blind source separation method that seeks to separate underlying components from available data whether the data are in the form of sounds, images, vibration responses or financial share prices. Since 1990s, Independent Component Analysis has been of great interest to researchers in diversified areas of statistics, medical imaging, telecommunication and structural damage detection( Comon and Jutten, 2010, Hastie et al, 2008, Hyvärinen et al, 2001, Zang et al 2004). Essentially, ICA relies on response data collected by sensors, called *mixture signals*, and the assumption that the independent component sources, called *source signals*, are statistically independent, to extract the unknown source signals. Most of the studies require that there are as many sensors as there are independent components and that the system behaves linearly, but non-linear behavior and both under-determined and over-determined cases have also been solved. A well known case study is the so called cocktail party problem: identify speech by two speakers in a room by using sounds recorded by two microphones. A demonstration is given on [http://research.ics.aalto.fi/ica/cocktail/cocktail\\_en.cgi](http://research.ics.aalto.fi/ica/cocktail/cocktail_en.cgi).

ICA assumes that there is a relationship between  $\mathbf{S}$ , the vector represents *source signals*, or underlying components and  $\mathbf{X}$ , the vector represents *mixture or response signals* of the system to the source signals. In the simplest form, the relationship is linear and can be expressed as:  $\mathbf{X} = \mathbf{A}\mathbf{S}$ , where  $\mathbf{X}$  is available from sensors output,  $\mathbf{A}$  is called the *mixing matrix*.  $\mathbf{W}$ , the inverse of  $\mathbf{A}$  is called the *unmixing matrix*. While both  $\mathbf{A}$  or  $\mathbf{W}$  and  $\mathbf{S}$  have to be determined, ICA seeks the optimum solution out of all possible  $\mathbf{W}$  such that the statistical independence of  $\mathbf{S}$  is maximized. Naturally the product of  $\mathbf{A}$  and  $\mathbf{W}$  must be the identity matrix. In statistics, ICA is considered as

supervised learning which includes principal component analysis and factor analysis. It is also connected to the technique of projection pursuit in multivariate statistics (Hastie et al, 2008). This has led to many novel methods of medical diagnosis of neurology and image processing. The restriction that has been stated by Hyvärinen et al (2001) is that not both variables are normal or Gaussian random signals. First, let us look at the concept of statistical independence (SI) and different measures and tests to evaluate statistical independence (SI).

### Statistical Independence

Consider two scalar variables  $X$  and  $Y$ ,  $X$  is said to be independent of  $Y$  if knowing the value of  $Y$  does not give any information on the value of  $X$ . This conceptual definition leads to the use of probability density function (pdf), a normalized histogram, of an event. When two events are studied, conditional probability,  $P(B|A)$ , is defined as the probability that event  $B$  occurs given that event  $A$  occurs; and joint probability,  $P(A\&B)$  is defined as the probability of both  $A$  and  $B$  occur. They are related by the rule  $P(B|A) = P(A\&B)/P(A)$ .

Two events are statistically independent if  $P(B|A) = P(B)$ . It then follows that if  $A$  and  $B$  are independent:  $P(A\&B) = P(A).P(B)$ . The joint probability can be found by constructing a contingency table, however it should be noted that marginal probabilities can be found from joint probability but the reverse is not true except in the case of statistical independence. This leads to the notion that two scalar variables  $X$  and  $Y$  are statistically independent if and only if their jpdf is a product of their individual pdf which are also called marginal pdf:

$$p_{XY}(x,y) = p_X(x) \cdot p_Y(y) \quad (1)$$

In Eq. 1,  $x$  and  $y$  are particular values of variable  $X$ ,  $Y$  respectively.

Note that in Eq.1, cumulative distribution functions can replace the respective probability density functions, as so do expected values of absolutely integrable functions of variables, including positive powers of  $x$  and  $y$ :

$$E\{g(x).h(y)\} = E\{g(x)\} \cdot E\{h(y)\} \quad (2)$$

$$E\{x^p y^q\} = E\{x^p\} \cdot E\{y^q\} \quad (3)$$

Where operator  $E$  stands for expected value,  $p$  and  $q$  are positive integers. It follows from Eq. 3 that SI is more stringent requirement than un-correlatedness, as un-correlatedness requires only  $E\{x.y\} = E\{x\} \cdot E\{y\}$ , i.e only for the case that both  $p$  and  $q$  equal 1. Thus statistical independence implies un-correlatedness but the reverse is not true, except for normal or Gaussian random variable. A simple example is given by Stone (2004), in which two simple pendulums swinging  $90^\circ$  out of phase,  $x = \cos(t)$ ,  $y = \sin(t)$ , giving correlation coefficient of zero, hence  $x$  and  $y$  are uncorrelated but they are statistically identical. At the same time, variables describing physically independent phenomena are intuitively thought to be statistically independent but it is not generally true.

Statistical Independence can also be defined in terms of characteristic functions of  $X$  and  $Y$  and their joint characteristic functions, where characteristic function of  $X$  is the inverse Fourier transform of its pdf and jpdf respectively, i.e.  $f_X(t) = E\{e^{itX}\}$  and  $f_{XY}(t,s) = E\{e^{i(Xt+Ys)}\}$ . Note that characteristic functions are complex. In a similar fashion as using pdf and jpdf:  $X$  and  $Y$  are statistically independent if:

$$f_{XY}(t,s) = f_X(t) \cdot f_Y(s) \quad (4)$$

In most engineering applications variables are obtained from random process without further knowledge of the joint distribution, hence the jpdf cannot be determined from marginal pdfs, unless statistical independence is assumed or implied.

It must be noted that testing of the equality of the two sides of either of Eq. 1-4 highlights the basic concept of statistical hypothesis testing: a test must have hypotheses, the null and alternative hypothesis, a corresponding statistic and a measure of the reliability of the test. In other words the testing of Eq. 1 itself must be perceived in a probabilistic sense, not in a deterministic sense. This is to ensure not to commit Type I (rejecting true null hypothesis) and Type II error (accepting false null hypothesis).

Probably the first paper on statistical independence was due to Wilks (1935). Most researchers of ICA argue that the mixtures, as a consequence of Central Limit Theorem, would be more gaussian than the sources. As a consequence, a heuristic assumption is that the sources would be more non-Gaussian, hence the objective is seeking sources as variables of maximum non-Gaussianity, effectively using non-Gaussianity as a measure of statistical independence (Hyvärinen et al, 2001). Non-Gaussianity of a variable can be measured by kurtosis and negentropy. Kurtosis is defined as  $kurt(x) = E\{x^4\} - 3(E\{x^2\})^2$  i.e. a normalized version of fourth moment of statistical distribution to make kurtosis of a normal or Gaussian random variable to be zero. Although simple to calculate, kurtosis is sensitive to outliers. The concept of entropy in Thermodynamics, representing the degree of being unstructured, unorganized, unpredictability, is also popular in Theory of Information. For a distribution Y, entropy of a variable is defined in terms of probability density function (pdf) as  $H(y) = -\int p(y) \log p(y) dy$ . Negentropy J is then defined as  $J(y) = H(y_{Gauss}) - H(y)$ , where  $y_{Gauss}$  is a Gaussian random variable of the same covariance matrix as y, which is shown by Information Theory to have the largest entropy among all random variables of equal variance. Thus negentropy is always non-negative. It is more involved to compute negentropy than kurtosis, and like kurtosis, it refers to only one variable and would fail as a measure of independence when one variable is a multiple of the other.

In most engineering applications, the variable has a finite number of values, as a consequence kurtosis of variables, even of the same distribution model, would depend heavily on how many elements are taken into account. As an example a variable was obtained by the Gaussian random generator in Matlab to yield a variable X of 1,000 elements, kurtosis was then found for varying number of elements from 100 to 1000. A typical result is shown in Table 1.

**Table 1: Kurtosis of variables of varying number of elements from a normal (Gaussian) random variable**

Element no	100	200	300	400	500	600	700	800	900	1000
kurtosis	-.3049	-.1041	-.1139	.0774	.0048	.2558	.2273	.1708	.2210	.1999

A more rigorous concept is mutual information of two variables X and Y defined as:

$$I(X, Y) = \sum_{y \in Y} \sum_{x \in X} p_{XY}(x, y) \log \left( \frac{p_{XY}(x, y)}{p(x)p(y)} \right) \quad (5)$$

It can be seen that mutual information is zero when the two variables are independent and ICA aims to minimize the mutual information among candidates of the source signals. Hyvärinen et al (2001) argued that this approach gives rigour to the more heuristic approach of using kurtosis and negentropy and is equivalent to method based on maximum likelihood estimation. However this measure of statistical independence also requires the knowledge of jpdf. Mutual information can be defined in terms of Shannon entropy, which can be further estimated (Comon and Jutten, 2010).

### Bakirov's measures of statistical independence

Bakirov and his associates published two papers, Bakirov et al (2006), Szekely et al (2007) addressing the needs to have measure of statistical independence that are non-parametric, that is independent of the statistical model that one has to assume otherwise. Such a measure has to be practical to implement and conform to requirements of statistical hypothesis testing: null and alternative hypothesis, a test statistic and a confidence indicator of the test.

#### 1. Coefficient of independence

Bakirov, Rizzo and Szekely proposed a statistic  $I_n$  based on the idea of independence coefficient  $I$ , defined in terms of characteristic functions:

$$I = \frac{\|f_{XY}(t, s) - f_X(t)f_Y(s)\|}{\|\sqrt{(1 - |f_X(t)|^2)(1 - |f_Y(s)|^2)}\|} \quad (6)$$

$I_n$  itself is defined for a finite subset of variable of  $n$  elements, based on various Euclidean norms, or "distances" of distributions of  $X$ ,  $Y$  and of their joint distribution  $Z$ , hence does not require the joint characteristic function as  $I$ . However, the authors proved that in the limit,  $I_n$  tends to  $I$  and  $0 \leq I_n \leq 1$ , where the sublimit 0 corresponds to statistical independence.

Further, it is shown that for all confidence level  $\alpha$  below 0.215, the null hypothesis  $H_0$  that  $X$  and  $Y$  are independent is rejected when  $\sqrt{n}I_n \geq \phi^{-1}(1 - \alpha/2)$  where  $\phi^{-1}$  is the inverse function of the cumulative distribution function of the standard normal distribution. This assertion would yield a parameter indicating the strength of the hypothesis testing, normally given by the p-value of the hypothesis testing. It is normally accepted that p-value less than 0.05,  $H_0$  would be rejected. The calculation of  $I_n$  is computing extensive for large  $n$ .

#### 2. Distance of covariance

Szekely, Rizzo and Bakirov (2007) proposed the concept of distance covariance,  $dCov(X, Y)$  and distance correlation,  $dCor R(X, Y)$ , defined respectively as:

$$v^2(X, Y) = \|f_{XY} - f_X f_Y\|^2 \quad (7)$$

$$R^2(X, Y) = \frac{v^2(X, Y)}{\sqrt{v^2(X)v^2(Y)}} \quad (8)$$

It can be seen from Eq. 7 that  $dCov$  is directly related to the definition of statistical independence. Further, the authors proved that the right hand side of Eq. 7 does not need information on the joint characteristic function and can be calculated as the limit of:

$$v_n^2(X, Y) = S_1 + S_2 - 2S_3 \quad (9)$$

Where  $S_1$ ,  $S_2$  and  $S_3$  can be calculated in terms of Euclidean norms related to distributions of  $X$ ,  $Y$ . Similar hypothesis testing with statistic  $nv_n^2(X, Y)$  and p-value are also proposed.

#### 3. Implementation in R language

The authors proposed two tests called *mvI.test* and *dcov.test*. Both tests use the null and alternative hypotheses  $H_0: p(x, y) = p(x).p(y)$ ,  $H_1: p(x, y) \neq p(x).p(y)$ . They are implemented as options in the

module *indep.test* of the package “energy” developed by Rizzo and Szekely in R language. The *mvI.test* corresponds to the coefficient of independence and takes longer than the *dCov.test*, as many times as the number of elements which can be in thousands or more. These tests yield the *p-value* of the null hypothesis test and it is widely accepted that  $H_0$  should be rejected if  $p\text{-value} < 0.05$ . It should be noted that in statistical hypothesis test, *p-value* is viewed as a measure of the strength of the hypothesis test.

In this paper, Bakirov’s *dCov* test is used to evaluate the statistical independence of source signals, measured by *p-value* of the test, before sending them to evaluate performance of ICA or to act as excitation signals in vibration testing or finite element simulation.

### Statistical independence testing of common signals used in vibration

In this test, the interest is statistical independence of various excitation signals commonly used in vibration testing. Source signals of 1,000 elements were generated in Matlab, except that impact force signals were obtained in a vibration impact hammer test. These signals were then paired and tested for statistical independence by Bakirov’s *dCov* test. Certainly if one signal is an exact copy or a multiple of the other, no matter what kind of signal, they would be tested dependent. The results are reported in Table 2. Typical plots of two signals for the case of sine-sawtooth pair and sinusoidal function of different frequencies (and also amplitude and phase) are shown in Figure 1 and 2.

**Table 2: Statistical Independence of pairs of signals of 1,000 elements**

Name of signal pair	dCov p-value
Unirandom, Unirandom (generated at different times)	0.660
Unirandom, Sine	0.415
Unirandom, Impact	0.635
Impact, Sine	0.5
Sine, Sine of different frequency	0.76
Sine, periodic Sawtooth of different frequency	0.965
Gaussian random, Gaussian random	0.815
Impact, Impact sampled at different points of structures	0.015
Unirandom (u), $5*u$	0.005

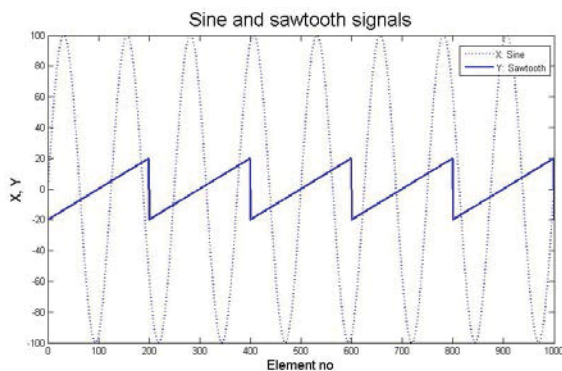


Figure 1: Sine and sawtooth signals

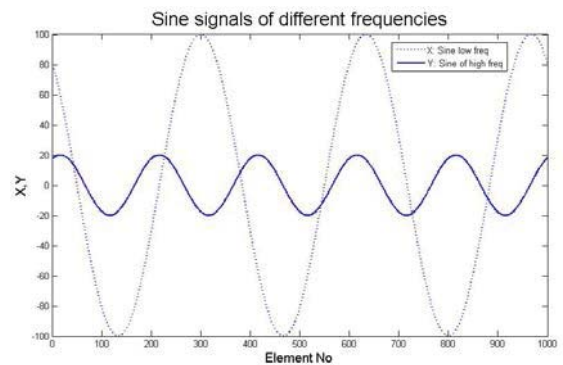


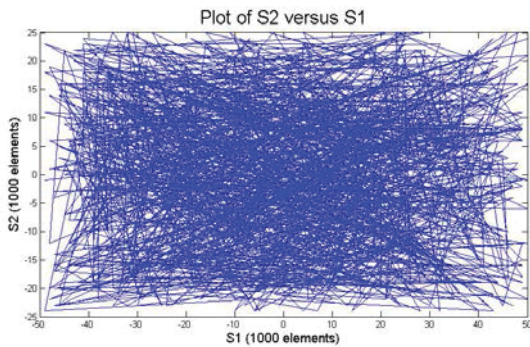
Figure 2: Sine signals of different frequencies

Inspection of Table 2 indicates that there is a variety of combination of different signals that would be statistical independent, except when one is a multiple of the other, or both are impact signals obtained from the same hammer tip-structure impact tests even if they were sampled at different points of the structure. It should be noted that as far as statistical independence is concerned, for sinusoidal signals, difference in frequencies is important whereas difference in amplitude or phase are not.

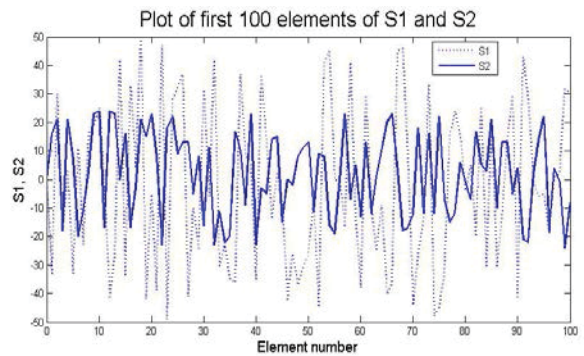
**Statistical independence testing of corrupted signals**

*1. One signal partially corrupted by the other signal:*

Two uniform random signals were generated in Matlab, called S1 and S2, of different ranges, each of 1000 elements. They are plotted against each other in Figure 3, showing the random nature of these two sources and their fast changing. The statistical independence of these signals was tested, giving p-value of 0.425, indicating that they are statistically independent. To avoid crowding, only the first 100 elements of S1 and S2 are plotted versus element number, as shown in Figure 4.



**Figure 3: Uniform random source S2 versus S1**



**Figure 4: Plot of first 100 elements of S1 and S2**

Next S1 was kept unchanged, S2 was changed by a varying percentage  $e\%$  of the source signal S1. The new S2 is designated S2\*, i.e.  $S2^* = S2 + e\% \cdot S1$ . These new sets of signals S1 and S2\* were then tested for statistical independence by Bakirov’s dCov test. The following values of  $e\%$  were investigated: 1, 2, 3, 4, and 10. The results are reported in Table 3,

**Table 3: Effect of  $e\%$  corruption of one signal on the other**

$e\%$	0	1	2	3	4	5	10
<b>p-value of dCov test</b>	0.425	0.555	0.43	0.185	0.045	0.005	0.005

It can be seen from Table 3 that in this case, Bakirov’s dCov test of SI is very stringent: an addition of only 4% of S1 to S2 would make them not independent,

*2. Effect of random noise on statistical independence*

In this test, S1 was in the form of a sine wave and S2 was a sawtooth wave of equal amplitude of 1.00, as shown in Figure 5. They were then corrupted by Gaussian random noise of increasing amplitude of 0.05, 0.10, 0.15, 0.20. A plot of corrupted signals at amplitude of 0.10 is shown in Figure 6. The signals are tested for statistical independence in a similar fashion. The results are shown in Table 4.

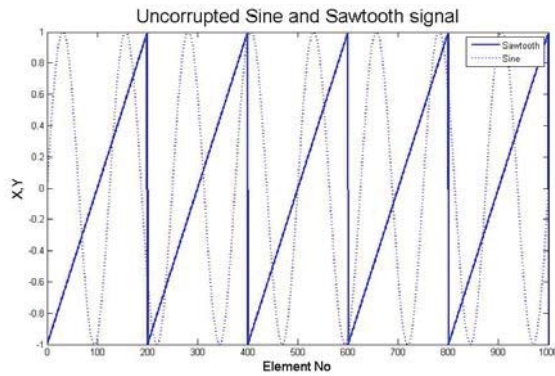


Figure 5: Sine and sawtooth signals

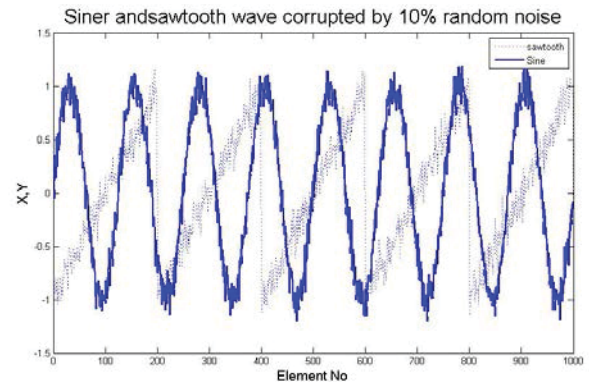


Figure 6; Corrupted sine and sawtooth signals by 10% gaussian random noise

Table 4: Effect of corruption of both signals by gaussian random noise

e% random noise	0	5	10	15	20
p-value dCov test	1.00	1.00	0.965	0.855	0.510

It was found that for the case of similar amplitude signals, Gaussian random noise, commonly exhibited by equipment used in vibration testing, does decrease the p-value of dCov test, but signals were still independent at 20% noise.

### 3. Evaluation the performance of Independent Component Analysis

As previously mentioned, Independent Component Analysis uses statistical independence as the objective function in searching for the blind sources from measured mixture signals. One popular algorithm is *fastICA*. Available in R, Matlab, C++ and Python programming, *fastICA* was developed by Marchini, Heaton and Ripley and can be downloaded from <http://research.ics.aalto.fi/ica/fastica/>. Basically it employs an approximation of negentropy as the objective function in searching of the unmixing matrix  $\mathbf{W}$  under the constraints that  $\mathbf{W}$  is an orthonormal matrix after the data has been centered, normalized and whitened. As the name implies it is a very fast algorithm, using fixed point iteration scheme for maximizing negentropy. It should be noted that the output of *fastICA* (source signals  $\mathbf{S}$ , matrices  $\mathbf{A}$  and  $\mathbf{W}$ ) are ambiguous as far as sign, scale and order are concerned. Here, the performance of *fastICA* was judged by the equality of  $\mathbf{A} \cdot \mathbf{W}$  with the identity matrix of the same order. The signals used are S1 and S2\* in Table 3. They were multiplied by a chosen  $\mathbf{A}$  to yield the mixture signals which were then passed to *fastICA* for processing. The results are reported in Table 5, where  $\mathbf{A}_0$  is the mixing matrix corresponding to zero e%. It can be seen from Table 5 that up to adding 3% of S1 to S2, *fastICA* performed satisfactorily as far as the criterion of  $\mathbf{A} \cdot \mathbf{W} = \mathbf{I}$  is concerned, as expected. This equality is still satisfied at 4% but the mixing matrix obtained at this p% value is very different from the previous ones. This is further highlighted by inspecting the values of the ratio of the determinants of  $\mathbf{A}$  at e% cases to that of the 0% case which was designated as  $\mathbf{A}_0$ . At 4% the ratio was 0.0048 instead of 1. At 10%, p-value was 0.005, *fastICA* failed to give the complete solution and no results reported.

## Conclusions

The notion of statistical independence is very important in the area of blind source separation, including independent component analysis. It is shown that the non-parametric tests developed by Bakirov and associates, especially dCov test, provide a good measure of statistical independence. It was found that many signals commonly used as excitation sources in vibration testing are statistically independent, except when one is a multiple of the other, sinusoidal functions of the

same frequency and impact signals sampled between the same hammer tip-structures in impact tests. The test was used to investigate effects of various sources of corruption on statistical independence: corruption of one signal by a small percentage of the other can affect enormously the statistical independence while corruption by random noise on both signals can be tolerated to a high level. It was also found that the statistical independence measured by p-value in dCov test is related to performance of fastICA, a popular package of ICA. It is recommended that Bakirov' measures of statistical independence should be incorporated in an independent component analysis algorithm.

**Table 5: Results of effects of statistical independence on performance of *fastICA***

e%	dCov value	p-	Mixing matrix A	Unmixing matrix W	A*W	detA/detA0
0	0.425		-8.33133    -7.69348 -18.4173    7.9057	-0.03809    -0.03707 -0.08873    0.04014	1.0000    0.0000 0.0000    1.0001	1
1	0.555		7.865551    -8.01238 -7.50953    -18.7385	0.090281    -0.0386 -0.03618    -0.0379	1.0000    0.0001 -0.0001    1.0000	1
2	0.43		8.023941    7.693739 18.73223    -7.90597	0.03809    0.037068 0.090251    -0.03866	1.0000    0.0000 -0.0000    1.0000	1
3	0.185		-7.87029    -7.69384 -18.8896    7.906206	-0.03809    -0.03707 -0.09101    0.037919	1.0000    0.0000 -0.0000    1.0000	1
4	0.045		0.006301    0.99998 0.99998    -0.0063	0.006301    0.99998 0.99998    -0.0063	1.0000    0.0000 0.0000    1.0000	0.0048

## References

- Bakirov, N. K., Rizzo, M. L. and Szekely, G. J. (2006), A multivariate non-parametric test of independence, *Journal of Multivariate Analysis*, 97 pp.1742-1756.
- Comon, P. and C. Jutten, C. (2010), Handbook of Blind Source Separation, Independent Component analysis and Applications, Academic Press, Amsterdam.
- Hastie, T., Tibshirani, R. and Friedman, J. (2008), The elements of statistical learning, data mining, inference and prediction, Second Edition, Springer.
- Hyvärinen, A., Karhunen, J. and Oja, E. (2001), Independent Component Analysis, Wiley, New York.
- Stone, J. V. (2004), Independent Component Analysis, a tutorial introduction, The MIT Press, Massachusetts.
- Szekely, G. J., Rizzo, M. L. and Bakirov, N. K. (2007), Measuring and testing dependence by correlation of distances, *Journal of The Annals of Statistics*, 35, 6 pp. 2769–2794.
- Zang, C., Friswell, M. I., and Imregun, M. (2004), Structural Damage Detection using Independent Component Analysis, *Structural Health Monitoring*, 3(1) pp. 69-83.
- Wilks, S. S. (1935), On the independence of k sets of normally distributed statistical variable, *Econometrica*, Vol. 3, No. 3 pp. 309-326.



## A Linear Response Surface based on SVM for Structural Reliability Analysis

\*U. Alibrandi, C.Y. Ma, and C.G. Koh

<sup>1</sup>Department of Civil and Environmental Engineering, National University of Singapore, 117576 Singapore

\*Corresponding author: [umberto.alibrandi@nus.edu.sg](mailto:umberto.alibrandi@nus.edu.sg)

**Key Words:** *Structural Reliability Analysis, FORM, design point, Response Surface, Support Vector Method, Monte Carlo Simulation*

### Abstract

The Structural Reliability theory allows the rational treatment of the uncertainties and gives the methods for the evaluation of the safety of structures in presence of uncertain parameters. The main challenge is the computational cost, since the failure probability with respect to an assigned limit state is given as the solution of a very complicated multidimensional integral. The most robust procedure is the Monte Carlo Simulation (MCS), but especially in its crude form is very demanding. For this reason, wide popularity has been gained by the First Order Reliability Method (FORM) by its simplicity and computational efficiency. However, for strongly nonlinear systems the FORM approximation is not very close to the exact one. To this aim, in this paper we introduce a novel Linear approximation of the limit state, based on the Support Vector Method (SVM), and which allows to improve the FORM solution, starting from the knowledge of the design point.

### Introduction

Recently it has been largely recognized that a realistic analysis of the structural systems should take into account all the unavoidable uncertainties appearing in the problem at hand. In this context a powerful tool is represented from the structural reliability theory (Madsen et al. 1986, Ditlevsen & Madsen 1999, Melchers, 1999) which gives a rational treatment of the uncertainties and which allows the assessment of the evaluation of the safety of structures in presence of uncertain parameters.

The failure probability  $P_f$  with respect to an assigned limit state is defined as

$$P_f = \int_{g(\mathbf{x}) \leq 0} f_{\mathbf{x}}(\mathbf{x}) d\mathbf{x} \quad (1)$$

where  $\mathbf{x}$  is an  $n$ -vector collecting the basic random variables,  $y = g(\mathbf{x})$  is the Limit State Function (LSF),  $g(\mathbf{x}) = 0$  is the Limit State Surface (LSS) separating the failure set  $g(\mathbf{x}) \leq 0$  from the safe set  $g(\mathbf{x}) > 0$ ,  $f_{\mathbf{x}}(\mathbf{x})$  is the joint probability density function of the random variables  $x_1, x_2, \dots, x_n$ . The evaluation of the failure probability  $P_f$  is known in closed form only for a very restricted number of cases, in the most general case it is necessary to solve numerically a multidimensional integral, which is computationally demanding.

The most robust procedure for the evaluation of the failure probability is represented by the Monte Carlo Simulation (MCS), which however, especially in its crude form, requires an excessive computational effort for the evaluation of the very small failure probabilities.

For this reason, wide popularity has been gained by the First Order Reliability Method (FORM) by its simplicity and computational efficiency, moreover extensive numerical experimentation has

shown that it gives good approximations of the failure probability for most practical problems. However, it is known that the FORM approximation is not adequate for limit state surfaces which depart significantly from linearity around the design point.

In this paper we overcome this shortcoming with a particular type of Response Surface Methodology (RSM) based on the Support Vector Method (SVM) and the theory of the statistical learning (Vapnik 1995, Burges 1998).

The basic idea of the RSM is the building of a surrogate model of the target limit state function, defined in a simple and explicit mathematical form; once the Response Surface (RS) is built, it is possible to substitute the RS with the target LSF, and then it is no longer necessary to run demanding finite element analyses; starting from this definition, FORM itself is a particular kind of RS, which approximates the LSS with the hyperplane passing through the design point  $\mathbf{u}^*$  and normal to the design point direction, the latter being the ray joining the origin of the standard normal space with the design point.

The RS models can be built to find the design point with reduced computational cost (Bucher & Burgound 1990, Alibrandi & Der Kiureghian 2012); recently, many alternative response surface methodologies have been proposed, whose aim is the improvement of the FORM approximation (Bucher & Most, 2008; Alibrandi & Ricciardi 2005, Alibrandi & Ricciardi 2008, Alibrandi, Impollonia & Ricciardi 2010).

To the latter category belong the RS approaches based on the SVM (Hurtado 2004; Alibrandi & Ricciardi 2011). Using the SVM the reliability problem is treated as a classification approach (Hurtado & Alvarez 2003), since we are not interested to the exact value of the LSF, but only to its sign. Therefore the samples are labelled with the value “+1” (safe sample) and “-1” (unsafe sample) and this requisite is less strong than approximating the exact value of the LSF.

In the existing approaches based on SVM, the improvement of the FORM solution is obtained by choosing non-linear models for approximating the limit state; conversely, in this paper, we adopt a simple linear model, where the constraints of correct classification are relaxed, accepting therefore that some points may be misclassified (Alibrandi 2012)

The starting model is built choosing a set of sample points along the design point direction, the latter being the direction of probabilistic interest. In this way, starting from the knowledge of the design point, it is possible to approximate the limit state with an hyperplane close to FORM but secant to the limit state, giving rise to an alternative Linear response surface based on SVM (LSVM), and giving a better approximation than FORM.

### Structural Reliability Analysis as a classification approach

Usually the multidimensional integral (1) is very difficult to be evaluated, and then some approximate techniques are used. As a first step, a probabilistic coordinate transformation is done toward the standard normal space and the failure probability is given as

$$P_f = \int_{g(\mathbf{u}) \leq 0} f_v(\mathbf{u}) d\mathbf{u} \quad (2)$$

In (2) the integrand function is the multivariate normal standard probability density function (pdf), while the integration domain is the region failure  $g(\mathbf{u}) \leq 0$ . According to (2), the failure probability can be obtained using the Monte Carlo Simulation (MCS), considering a set of  $N$  samples  $\mathbf{u}_1, \mathbf{u}_2, \dots, \mathbf{u}_N$  and evaluating the ratio between the number  $N_f$  of samples belonging to the failure region  $g(\mathbf{u}) \leq 0$  and the total number of simulated samples  $N$ :

$$P_{f,MCS} = \frac{N_f}{N} = \frac{1}{N} \sum_{j=1}^N I[g(\mathbf{u}_j) \leq 0] \quad (3)$$

where  $I[\cdot]$  is an indicator function, equal to 1 if  $g(\mathbf{u}_j) \leq 0$  and zero otherwise. The quality of the obtained approximation is determined evaluating the coefficient of variation of  $P_{f,MCS}$ ; it is however well known that the MCS, especially in its crude form, requires an excessive computational effort.

Alternatively, a good estimate of (2) is obtained by approximating the target Limit State Function (LSF)  $y = g(\mathbf{u})$ , usually complicated and implicit, with an approximate model  $\tilde{y} = \tilde{g}(\mathbf{u})$ , called Response Surface (RS). Once the RS is built, it is no longer necessary to run demanding Finite Element Analyses, but we can use the surrogate model. In the following we will consider only problems where the limit state surface has neither peak or valleys, nor multiple design points.

From (3) it is seen that we are not interested to the value  $y = g(\mathbf{u})$  of the LSF, but to its sign  $z = \text{sign}[g(\mathbf{u})]$ , so that the points  $\mathbf{u}_i$  belonging to the safe region have the value  $z_i = +1$ , and the points  $\mathbf{u}_i$  belonging to the failure region have the value  $z_i = -1$ . It is easy to see that the building of a surrogate model  $\tilde{y} = \tilde{g}(\mathbf{u})$  such that it satisfies only the sign constraints  $z = \text{sign}[g(\mathbf{u})]$ , is equivalent to the building of a RS which models directly the LSS. Then, according to the RS Methodology, the estimated failure probability can be evaluated using (3), by substituting the indicator function  $I[g(\mathbf{u}_j) \leq 0]$  with  $I[\tilde{g}(\mathbf{u}_j) \leq 0]$ .

A function which separates the points belonging to the safe set from the ones belonging to the failure set, is named classifier, since attributes a class (“safe” or “failure”) to each point. The LSS  $g(\mathbf{u}) = 0$  is the target classifier, while a RS which approximates the LSS, is able to classify correctly only a limited number of points. Clearly, because the RS works well, it is necessary that it classifies correctly the points at least in the region of probabilistic interest.

### A Linear Response Surface based on SVM

Let be known a set of  $m$  sampling points  $\mathbf{u}_1, \mathbf{u}_2, \dots, \mathbf{u}_m$ , while  $y_1, y_2, \dots, y_m$  and  $z_1, z_2, \dots, z_m$  be the corresponding values of the LSF  $y_i = g(\mathbf{u}_i)$  and signs  $z_i = \text{sign}[g(\mathbf{u}_i)]$ , respectively.

Suppose that the target LSS is linear,  $g(\mathbf{u}) = \mathbf{a} \cdot \mathbf{u} - c$ , then the sampling points  $\mathbf{u}_i$  are linearly separable. Consider now the approximated LSS  $\hat{g}(\mathbf{u}) = \mathbf{w} \cdot \mathbf{u} - b$ , where  $\mathbf{w}$  determines the orientation of the plane, while the scalar  $b$  determines the offset of the plane from the origin. Clearly, when the number of support points converges toward infinity  $m \rightarrow \infty$ , then the linear classification function becomes coinciding with the target LSS, i.e.  $\mathbf{w} \rightarrow \mathbf{a}$ ,  $b \rightarrow c$ . Conversely, for a limited number of support points, there are infinite possible planes that classify the points correctly. Intuitively, a hyperplane that passes too close to the sampling points will be less likely to generalize well for the unseen data, while it seems reasonable to expect that a hyperplane that is farthest from all points will have better generalization capabilities. Given a set of  $m$  sampling points, the *margin* is defined as the minimum distance between points belonging to different classes. Therefore, the optimal separating hyperplane is the one maximizing the margin.

Recall from the elementary geometry that the distance  $\delta_i$  of a point  $\mathbf{u}_i$  from the hyperplane  $\hat{g}(\mathbf{u}) = 0$  reads as  $\delta_i = |\mathbf{w} \cdot \mathbf{u}_i - b| / \|\mathbf{w}\|$ ; noticing that  $\hat{g}(\mathbf{u}) = \mathbf{w} \cdot \mathbf{u} - b = 0$  is invariant under a positive rescaling, we choose the solution for which the function  $\hat{y} = \hat{g}(\mathbf{u})$  becomes one for the points

closest to the boundary, i.e.  $|\mathbf{w} \cdot \mathbf{u}_i - b| = 1$ . The couple of hyperplanes  $\hat{g}_s(\mathbf{u}) = \mathbf{w} \cdot \mathbf{u} - b = 1$ ,  $\forall \mathbf{u} \in g(\mathbf{u}) > 0$  and  $\hat{g}_f(\mathbf{u}) = \mathbf{w} \cdot \mathbf{u} - b = -1$ ,  $\forall \mathbf{u} \in g(\mathbf{u}) \leq 0$ , are called *canonical hyperplanes* (or *support hyperplanes*). The distance from the closest points to the boundary  $\hat{g}(\mathbf{u}) = 0$  is  $\delta = 1/\|\mathbf{w}\|$ , and the margin becomes  $M = 2/\|\mathbf{w}\|$ , as shown in Figure 1(a).

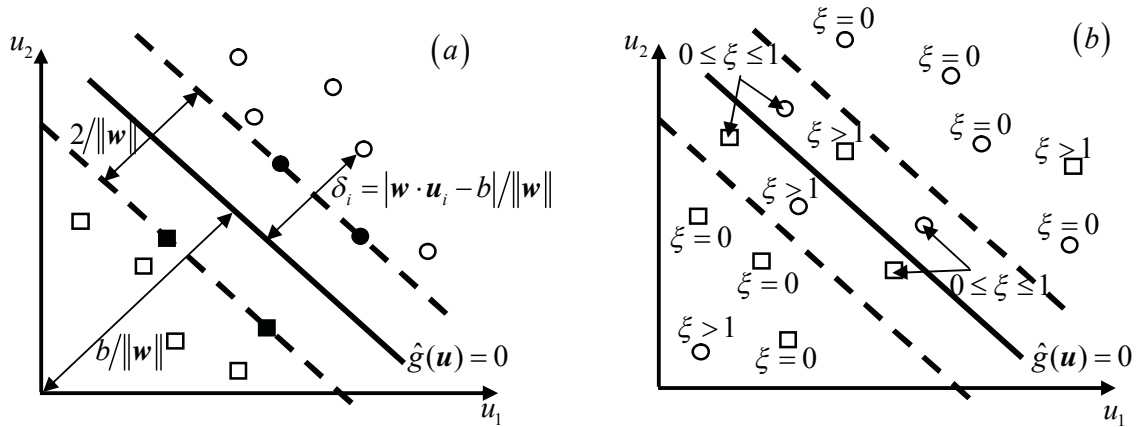


Figure 1. (a) Linear SVM, (b) Non-linearly separable SVM

Maximizing the margin is equivalent to minimize  $\|\mathbf{w}\|/2$ , giving rise to the following Quadratic Programming (QP) problem

$$\begin{cases} \min_{\mathbf{w}, b} \frac{1}{2} \|\mathbf{w}\|^2 \\ \text{s.t. } z_i (\mathbf{w} \cdot \mathbf{u}_i - b) \geq 1, \quad i = 1, 2, \dots, m \end{cases} \quad (4)$$

where the inequality constraints are equivalent to  $\mathbf{w} \cdot \mathbf{u}_i - b \geq 1$ ,  $\forall \mathbf{u}_i \in g(\mathbf{u}_i) > 0$ , and  $\mathbf{w} \cdot \mathbf{u}_i - b \leq -1$ ,  $\forall \mathbf{u}_i \in g(\mathbf{u}_i) \leq 0$ . It is here noted that (4) is a standard convex optimization problem, so the uniqueness of the solution is guaranteed and moreover there are many robust algorithms that can effectively solve it.

Among the  $m$  sampling points, the *support vectors* are the  $m_{SV}$  points lying on the support hyperplanes  $\mathbf{w} \cdot \mathbf{u}_i - b = \pm 1$ ; in Figure 1(a) the support vectors are represented from the filled markers. It is seen that only the support vectors contribute to defining the optimal hyperplane, thus, the complete sampling set could be replaced by only the  $m_{SV}$  support vectors, and the separating hyperplane would be the same.

Suppose now that the LSS is non-linear, so that it is not possible to identify an hyperplane which correctly classifies all the sampling points. To this aim, we relax the constraints of (4) by introducing the slack variables  $\xi_i \geq 0$ , giving rise to  $\mathbf{w} \cdot \mathbf{u}_i - b \geq 1 - \xi_i$ ,  $\forall \mathbf{u}_i \in g(\mathbf{u}_i) > 0$  and  $\mathbf{w} \cdot \mathbf{u}_i - b \leq -1 + \xi_i$ ,  $\forall \mathbf{u}_i \in g(\mathbf{u}_i) \leq 0$ . The variables  $\xi_i$  give a measure of the departure from the condition of correct classification. In particular, when  $0 < \xi_i \leq 1$  the point is well classified but falls inside the margin, while when  $\xi_i > 1$  the point is not well classified. Finally, if  $\xi_i = 0$  the point is

correctly classified, see Figure 1(b). Under this hypothesis, the optimal separating hyperplane has maximum margin with minimum classification error. The optimization problem (4) becomes

$$\begin{cases} \min_{\mathbf{w}, b, \xi} & \frac{1}{2} \|\mathbf{w}\|^2 + \sum_{i=1}^m \xi_i \\ \text{s.t.} & z_i (\mathbf{w} \cdot \mathbf{u}_i - b) \geq 1 - \xi_i, \quad i = 1, 2, \dots, m \\ & \xi_i \geq 0 \quad i = 1, 2, \dots, m \end{cases} \quad (5)$$

### Outline of the procedure

It will be used the following iterative procedure:

- 1 Probabilistic transformation toward the  $n$ -dimensional standard normal space, as it is usually done in reliability analysis;
- 2 Evaluation of the design point  $\mathbf{u}^*$  and of the corresponding reliability index  $\beta = \|\mathbf{u}^*\|$ , together with the FORM approximation  $P_{f,FORM} = \Phi(-\beta)$ , see Figure 2.
- 3 Choice of a set of sampling points  $\mathbf{u}_k$ ,  $k = 1, 2, \dots$  along the design point direction  $\mathbf{u}^*/\|\mathbf{u}^*\|$ . Classification of failure and safe points belonging to the direction through  $z_k = \text{sign}[g(\mathbf{u}_k)]$ ;
- 4 Building of a first LSVM model through (5), together with its margins;
- 5 Choice of a new point  $\mathbf{u}_k$  inside the margin and its classification;
- 6 Building of the SVM model through (5) and evaluation of the estimated failure probability. Since the LSVM is a linear response surface we have  $P_{f,LSVM} = \Phi(-\beta_{LSVM})$ ,  $\beta_{LSVM}$  being the distance of the LSVM from the origin of the standard normal space.
- 7 If the convergence on  $P_f$  is achieved stop, else go to step 5.

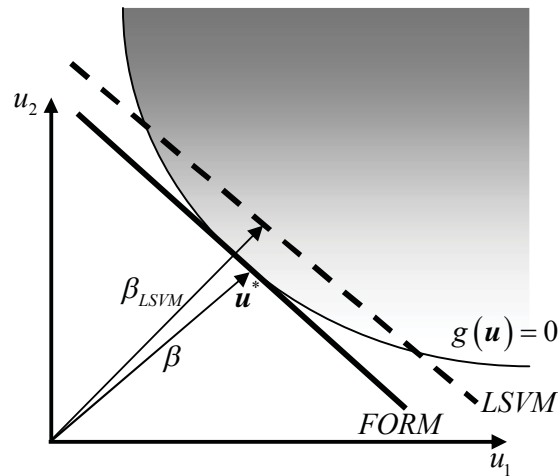


Figure 2. FORM and LSVM

### Example 1 – Static Analysis of a 2-dof frame

As a first example, we applied the proposed approach to a shear type frame with two-stories, subjected to two deterministic concentrated loads,  $F_1 = F_2 = \bar{F}$  with random stiffnesses  $k_1 = \bar{k}_1(1 + x_1)$  and  $k_2 = \bar{k}_2(1 + x_2)$ , being  $\bar{F} = 1$ ,  $\bar{k}_1 = \bar{k}_2 = 1$  and the fluctuations  $x_1, x_2$  modelled as two independent Gaussian random variables with zero mean and standard deviation  $\sigma = 0.20$  (Figure 3a). Be  $X_2(x_1, x_2)$  the horizontal displacement of the second storey, and the considered limit state is  $g(x_1, x_2) = X_2(x_1, x_2) - X_{2,\text{lim}}$ , with  $X_{2,\text{lim}} = 2.25$ . The failure probability is  $P_f = 9.427 \times 10^{-3}$  obtained using MCS, with an estimated coefficient of variation equal to  $v_{P_f} = 1\%$ , and required 1,050,848 analyses. The corresponding generalized reliability index is  $\beta_G = \Phi^{-1}(1 - P_f) = 2.348$ .

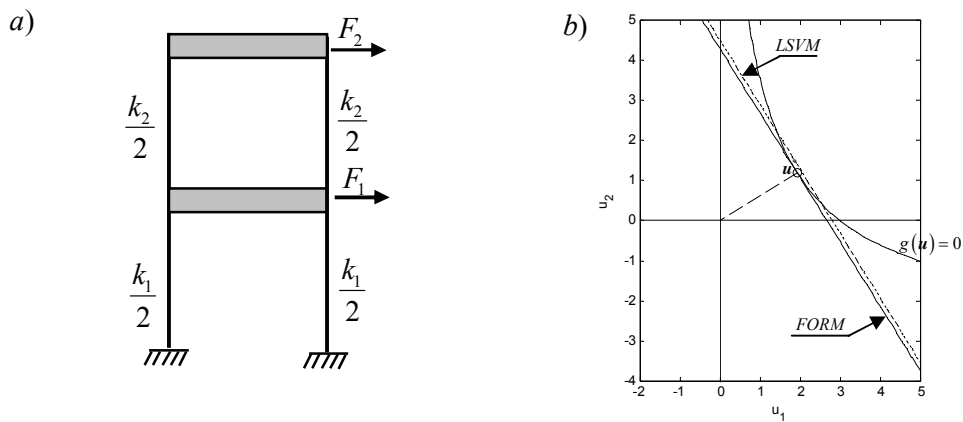


Figure 3. Example 1: (a) 2-dof shear-type frame, (b) LSS, FORM and LSVM

As shown in Figure 3(b), the LSS is nonlinear, and The FORM solution gives a failure probability  $P_{f,FORM} = 11.593 \times 10^{-3}$ , with a relative error  $e_{FORM} = 22.97\%$ . The LSVM achieves the convergence after 328 samples, obtaining  $\beta = 2.344$  and corresponding failure probability  $P_{f,LSVM} = 9.471 \times 10^{-3}$  (relative error  $e_{LSVM} = 0.46\%$ ). In Figure 4(a) we represent the obtained failure probabilities in terms of the number of samples, while in Figure 4(b) the corresponding relative errors are shown.

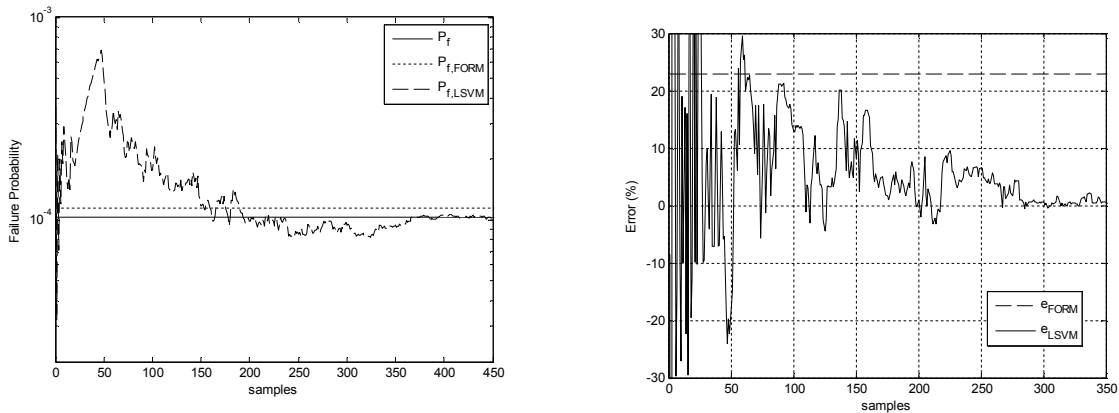


Figure 4. Example 1: (a) Failure Probability, (b) Relative error, in terms of the number of samples

### Example 2 – Nonlinear random waves

Let  $S_{xx}(\omega)$  a wave spectrum partitioned into  $N$  components of equal interval  $\Delta\omega$ . The second-order wave elevation is represented as (Longuet-Higgins 1963, Moarefzadeh & Melchers 2006)

$$\eta = \eta_1 + \eta_2 = \sum_{n=1}^{2N} \alpha_n u_n + \sum_{n=1}^{2N} \sum_{m=1}^{2N} \gamma_{nm} u_n u_m \quad (6)$$

where  $u_1, u_2, \dots, u_{2N}$  are normal standard random variables, while  $\eta_1$  and  $\eta_2$  are the first and second order terms of the nonlinear sea elevation,

$$\begin{aligned} \alpha_n &= \sigma_n, \quad \alpha_{n+N} = 0, \\ \gamma_{nm} &= \frac{1}{2g} \min(\omega_n^2, \omega_m^2) \sigma_n \sigma_m, \quad \gamma_{n+N, m+N} = -\frac{1}{2g} \max(\omega_n^2, \omega_m^2) \sigma_n \sigma_m, \quad \gamma_{n+N, m} = \gamma_{n, m+N} = 0 \end{aligned} \quad (7)$$

$$n, m = 1, 2, \dots, N$$

being  $\sigma_n = \sqrt{G_{\eta\eta}(\omega_n) \Delta\omega}$ , with  $G_{\eta\eta}(\omega)$  the spectral density function of the sea elevation. As a case study, we considered the JONSWAP spectrum with a shape factor of unity  $G_{\eta\eta}(\omega) = a\omega^{-5} \exp[-1.25(\omega/\omega_p)^{-4}]$ , where  $\omega_p = 0.4$  rad/sec is the peak frequency,  $a$  is a scaling factor that is selected so that the area under the spectrum is  $15 \text{ m}^2$  (Low 2013). The spectrum is divided into  $N = 40$  harmonic components from 0.2 to 1.2 rad/sec. It is required to evaluate the probability that the wave elevation is greater than  $15 \text{ m}$ , that is  $P_f = \text{Prob}[\eta \geq 15]$ ; the Limit State Function is  $G(\mathbf{u}) = 15 - \eta(\mathbf{u})$ , while the number of basic random variables is  $n = 2N = 80$ . It is here noted that  $\eta(\mathbf{u})$  is a quadratic function of the normal standard random variables, from which it follows the nonlinearity of the Limit State Surface.

The “exact” solution obtained with a MCS is  $P_f = 1.035 \times 10^{-4}$  with a coefficient of variation  $v_{P_f} = 5\%$  and it required 3,863,373 samples. The FORM approximation is  $P_{f,FORM} = 1.15 \times 10^{-4}$  with a relative error  $e_{FORM} = 11.11\%$ , while the LSVM, after 355 samples, gives  $P_{f,LSVM} = 1.021 \times 10^{-4}$  ( $e_{LSVM} = 1.28\%$ ). In Figure 5 we represent the obtained failure probabilities and the corresponding relative errors in terms of the number of samples.

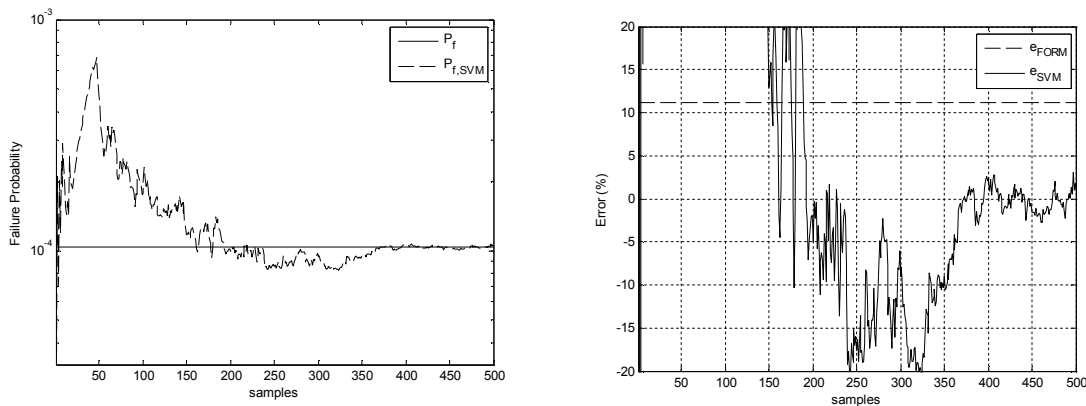


Figure 5. Example 2: (a) Failure Probability, (b) Relative error, in terms of the number of samples

## Conclusions

FORM is a powerful tool for Structural Reliability Analysis, and in most cases of practical interest it gives a good approximation of the failure probability. However, for limit state surfaces which depart significantly from linearity around the design point, the FORM solution may be inadequate. In this paper we presented a Linear response surface based on SVM, called LSVM, which starting from the design point direction, allows an improvement of FORM, requiring a reduced number of sampling points. Two simple numerical examples showed the accuracy and effectiveness of the presented procedure.

## Acknowledgements

The authors would like to acknowledge the research grants (R-302-501-009-305) funded by the Agency for Science, Technology and Research of Singapore.

## References

- Alibrandi U. An alternative linear response surface improving FORM solution for stochastic dynamic analysis, *Reliability and Optimization of Structural Systems, IFIP WG 7.5 Working conference*, 24-27 June 2012, Yerevan, Armenia
- Alibrandi U. & Der Kiureghian A. (2012), A Gradient-Free Method for Determining the Design Point in Nonlinear Stochastic Dynamic Analysis, *Probabilistic Engineering Mechanics*, 28, 2-10.
- Alibrandi U., Impollonia N. & Ricciardi G. (2010). Probabilistic Eigenvalue Buckling Analysis solved through the Ratio of Polynomial Response Surface, *Computer Methods in Applied Mechanics and Engineering*, 199(9-12), 450-464.
- Alibrandi U. & Ricciardi G. (2005), Bounds of the probability of collapse of rigid-plastic structures by means of Stochastic Limit Analysis, *9th International Conference on Structural Safety and Reliability*, Rome, Italy, 19-23 June 2005
- Alibrandi U. & Ricciardi G. (2008), The use of stochastic stresses in the static approach of probabilistic limit analysis. *International Journal for Numerical Methods in Engineering*, 73(6), 747-782.
- Alibrandi U. & Ricciardi G. (2011). Structural Reliability Analysis solved through a SVM-based Response Surface, *ICASP 2011, The 11th International Conference on applications of Statistics and Probability in Civil Engineering*, 1-4 August 2011, Zurich, Switzerland
- Bucher C. & Burgound U. (1990), A fast and efficient response surface approach for structural reliability problems, *Structural Safety*, 7, 57-66.
- Bucher, C. & Most, T. (2008), A comparison of approximate response functions in structural reliability analysis, *Probabilistic Engineering Mechanics*, 23, 154-163.
- Burges, C.J.C. (1998), A tutorial on Support Vector Machines for Pattern Recognition. *Data Mining and Knowledge Discovery 2*: 121-167
- Ditlevsen O., Madsen H.O. (1999), *Structural Reliability Methods*, Wiley
- Hurtado, J.E. & Alvarez, D.A. (2003). A classification approach for reliability analysis with stochastic finite element modelling, *Journal of Structural Engineering*, 129, 1141-1149.
- Hurtado, J.E. (2004), An examination of methods for approximating implicit limit state functions from the viewpoint of statistical learning theory, *Structural Safety*, 26, 271-293.
- Longuet-Higgins MS (1963). The effect of nonlinearities on statistical distributions in the theory of sea wave, *J Fluid Mech*, 17(3): 459-480.
- Low Y.M. (2013). A new distribution for fitting four moments and its applications to reliability analysis, *Structural Safety*, 42, 12-25
- Madsen H.O., Krenk S. & Lind, N.C. (1986). *Methods of Structural Safety*, Prentice-Hall.
- Melchers R.E. (1999), *Structural Reliability, analysis and prediction*, New York: Wiley & Sons.
- Moarefzadeh MR & Melchers RE (2006). Nonlinear wave theory in reliability analysis of offshore structures, *Probabilistic Engineering Mechanics*, 21(2), 99-111.
- Vapnik, V. (1995), *The Nature of Statistical Learning Theory*, New York: Springer-Verlag.



## A novel MR device with variable stiffness and damping capability

Shiyu Zhao<sup>1</sup>, Huaxia Deng<sup>1\*</sup>, Jin Zhang<sup>1</sup>, Shuaishuai Sun<sup>1,2</sup>, Weihua Li<sup>2\*</sup>, Laijun Zhou<sup>1</sup>

<sup>1</sup>School of Instrument Science and Opto-electronics Engineering, HeFei University of Technology, Hefei, China.

<sup>2</sup>School of Mechanical, Materials & Mechatronic Engineering, University of Wollongong, Wollongong, Australia

\*Corresponding author: [hxdeng@hfut.edu.cn](mailto:hxdeng@hfut.edu.cn) and [weihuali@uow.edu.au](mailto:weihuali@uow.edu.au)

### Abstract

- This paper proposes a novel device based on the Magnetorheological (MR) fluid which has the capability to change stiffness and damping under control. MR fluid is a type of smart material whose properties could be controlled by the external magnetic field. Most of MR devices are MR dampers, which normally are used as variable damping devices. The presented device consists of two hydro-cylinder-spring structures and one MR valve linking these two structures. The rheological characteristics of MR fluid in the fluid flow channels of MR valve are controlled by the strength of magnetic fields, which directly affect the link conditions. The equivalent stiffness and damping coefficients of the device thus varies with the rheological characteristics of MR fluid simultaneously. A mathematical model is established to describe the properties of the proposed device based on the Bouc-wen model. The mathematical model the simulation results indicate that the proposed device can control both the stiffness and damping which has potential to be applied for restrain vibration mitigation efficiently.

**Keywords:** Variable stiffness and damping, MR damper, effective stiffness and damping coefficients

### Introduction

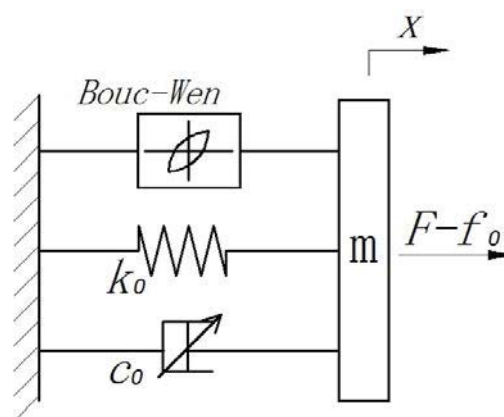
In the engineering circle or daily life, there exists a great deal of vibration and most of them are harmful which may result in financial loss or endanger lives. Numerous researchers from various fields investigate the methods to reducing and controlling the vibration. The traditional passive vibration control method <sup>[1]</sup> is widely used, but the effect of controlling vibration is not well at certain working conditions especially in the changing conditions. Because of the fixed stiffness and damping, the passive control devices normally are designed for a certain stable working condition. This kind of vibration control methods can not adjust for the changing conditions, which may even induce the vibration worse at some conditions. The active vibration control methods are proposed for providing extra energy to mitigate the vibration. This method needs more power and the control strategies of the control system are complicated, the requirement of active vibration control methods limits their applications in practice. Semi-active vibration control method is a method which balance the advantages of the two methods mentioned above. By changing the parameters itself with less energy to adjust the changing conditions, the semi-active control method achieve improved performances over a wide operating range and has long been receiving people's attention.

The damper based on magnetorheological fluids (MRF) is a typical semi-active device. MR fluid is one kind of smart materials, which is similar to the electrorheological (ER) fluid. Because of many merits, such as quick response, easy control, low energy, changing reversely etc. , the MR damper become one of the most potential vibration control device. The rheological properties of MRF is highly related to the external magnetic field induced by control current and the parameters of MR damper can be easier changed by controlling the current<sup>[2]</sup>. Researchers do a lot of study on the theory and application of the MR device. In order to analyze the ER damping mechanism, Stanway

et al proposed a Bingham model<sup>[3]</sup>. Due to similar behavior<sup>[4]</sup>, the Bingham model is also widely used to describe the MR damper. Spencer build a model containing a Bouc-Wen hysteretic operator and this model can describe the characteristics of MRF very well, especially for the hysteretic performance<sup>[5]</sup>. Xu proposed the temperature phenomenological model with mass element<sup>[6]</sup> and do some research on house anti-seismic capability by using MR damper. Laura M. Jansen studied various algorithms used to control multiple MR dampers and analyze the performance of the algorithms by making comparisons<sup>[7]</sup>. Lord Corporation did a lot of researches on development and application of MR damper and their products were used in the cable-stayed Dongting Lake Bridge to reducing the rain-wind induced vibration. Seung-Bok Choi applied the MR damper to a full-car model and derived the governing equations of motions based on the skyhook controller<sup>[8]</sup>. The result of the experiment indicated that MR damper can improve the security and comfort. Beside, MR damper is widely used in the aerospace, military machine, electrical appliances, etc. The simple MR device is MR damper and MR damper only can change the damping. Deng developed a series of adaptive tuned vibration absorbers<sup>[9-11]</sup> based on MR elastomer(MRE) which has changeable and controllable stiffness. It will be better for restraining vibration if the damping and stiffness are both variable. W.H. Li proposed a MR bladder can change the damping and stiffness simultaneously<sup>[12]</sup>. The model is composed by two air springs and the two springs were connected by a MR valve. The equivalent stiffness of the device is controlled by MR valve. However, the device is very large and requires extra equipment to provide air pressure. Liu propose a model which may have variable stiffness and damping capability<sup>[13-14]</sup>. The model is consisted of two elements in series and every element contain a variable damping and a spring in parallel<sup>[15]</sup>.

The purpose of this paper is to present a novel vibration control device with controllable damping and stiffness. This device is based on the MRF and it is consisted of two MR dampers in series. A model is build to describe the device and simulated by Simulink. In the model, Bouc-Wen model is used to describe the characteristics of the MR damper. The force versus displacement figures and force versus velocity figures are got through simulation and used to discuss the parameters on the capability of changing equivalent damping and stiffness.

### Model of the MR damper



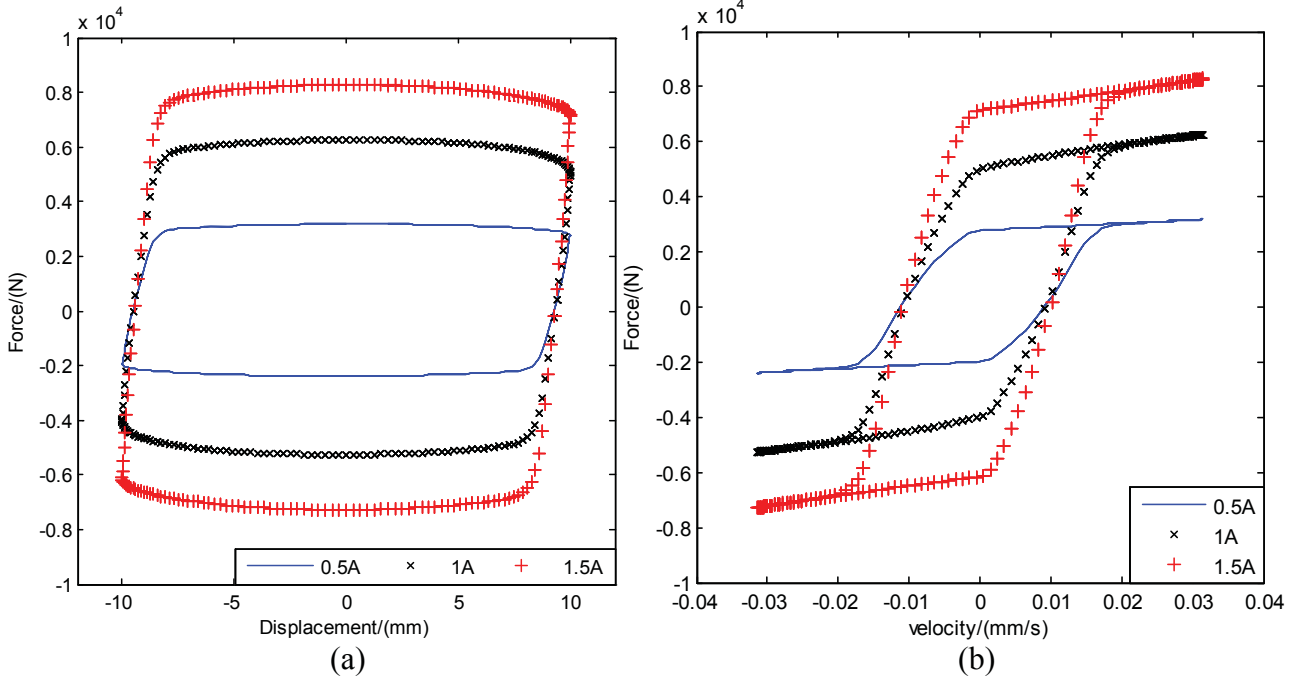
**Fig.1 Bouc-Wen model**

MR damper is based on the MRF and the characteristics of MR damper is complex. Bouc-Wen model is one of the most widely used models to describe the characteristics of MR damper. As shown in Fig.1, the Bouc-Wen model is consisted by three part: a spring with constant stiffness, a damper related to the magnetic field and a Bouc-Wen winding<sup>[2]</sup> which can represent the hysteresis. The equation of Bouc-Wen are as follows:

$$F - f_0 = \alpha z + k_0 x + c_0 \dot{x} + m \ddot{x} \quad (1)$$

$$\dot{z} = -\gamma |\dot{x}| |z|^{n-1} z - \beta \dot{x} |z|^n + A \dot{x} \quad (2)$$

The characteristic curve of the MR damper is obtained through the Eq.(1) to Eq.(2) shown in Fig.2.



**Fig.2 Simulated damping forces of the MR damper under a 1.00 Hz sinusoidal excitation with amplitude of 10.00 mm for three current levels: (a)the force versus displacement, (c) the force versus velocity**

Fig.2.(a) shows the relation between force and displacement and x-axis and y-axis are the force and displacement respectively. The area of the loop showed in Fig.2.(a) represents work of the damper force which indicate the damping and the ratio of the curve reflect the stiffness. Fig.2.(b) shows the relation between force and displacement and x-axis and y-axis are the force and velocity respectively. The ratio of the curve reflects the damping. Through these two figures, the damping is increased with the increasing current and the stiffness neatly has no change.

### Model of the novel variable stiffness and damping device

A model of the novel vibration control device is shown in Fig.3.(a) and the equivalent model is shown in Fig.3.(b). The model is composed of two MR dampers in series. The damping and hysteretic loop is changed with the variable current and the stiffness is fixed. The initial values of all the parameters is fixed when the MR damper is designed. The model of the device is equivalent to the model shown in Fig.3.(b). and Eq.(1) is expressed as Eq.(3):

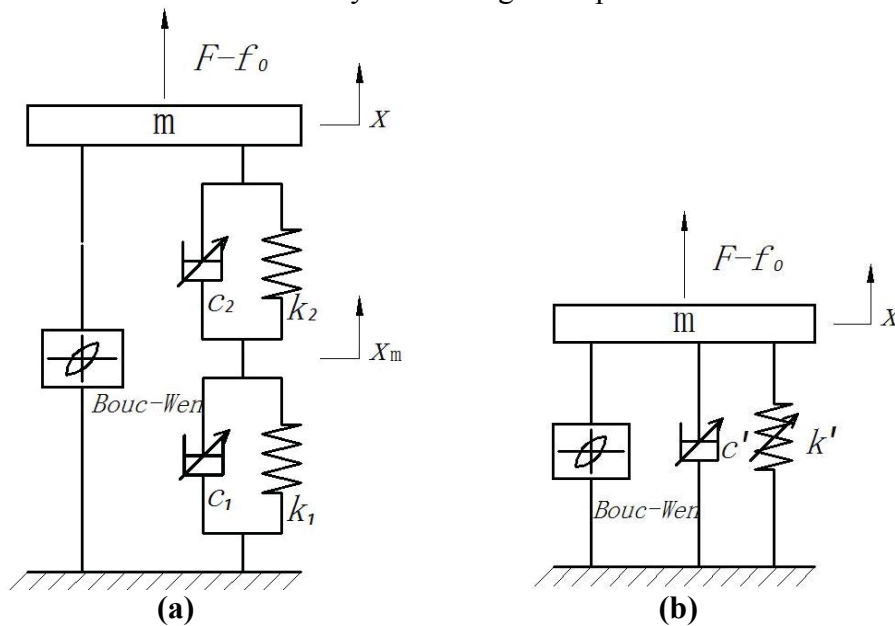
$$F - f_0 = \alpha z + k'x + c' \dot{x} + m \ddot{x} \quad (3)$$

The equivalent damping  $c'$  and the equivalent stiffness  $k'$  are as followings<sup>[11]</sup>

$$k' = \frac{(k_1 k_2 - c_1 c_2 \omega^2)(k_1 + k_2) + (k_1 c_2 + k_2 c_1)(c_1 + c_2) \omega^2}{(k_1 + k_2)^2 - (c_1 - c_2)^2 \omega^2}, \tag{4}$$

$$c' = \frac{(k_1 c_2 + k_2 c_1)(k_1 + k_2) - (k_1 k_2 - c_1 c_2 \omega^2)(c_1 + c_2)}{(k_1 + k_2)^2 - (c_1 - c_2)^2 \omega^2}, \tag{5}$$

Eq.(1) and Eq.(2) show that  $k'$  is related with the parameters  $k_1, k_2, c_1, c_2, \omega$ .  $k_1, k_2$  are determined by the design of MR damper.  $c_1, c_2$  are determined by the magnetic induction intensity generated by controllable current.  $\omega$  is determined by the input excitation. The stiffness and damping of the device can be controlled by controlling these parameters.



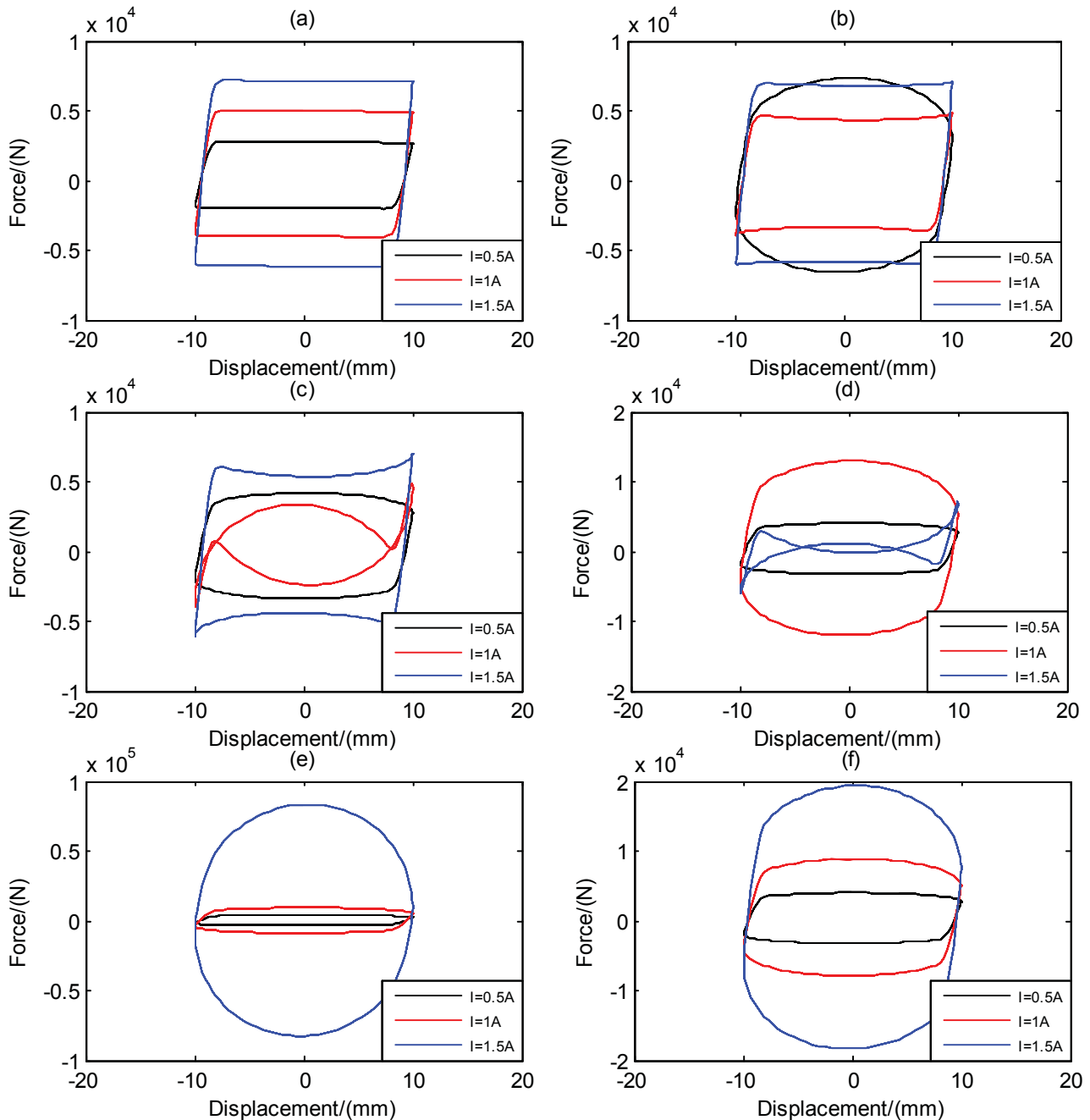
**Fig.3 The structure of the vibration control system**  
**(a)Original model and (b) Equivalent model**

**Discussion of the characteristics of the device**

As shown in the above analysis, the equivalent damping and stiffness of the proposed structure has the relationship with the parameters. In order to analyze the influence induced by the changing parameters on the equivalent stiffness and damping of system. The force versus displacement diagrams are showed in the Fig.4 and Fig.6. The force versus velocity diagrams are showed in the Fig.5 and Fig.7. In each figure, there are six subplots and the stiffness ratio of two springs is different. In each subplot, there are three curves corresponding three different control currents: 0.5A, 1A, 1.5A. Comparing the same curve in different subplots of one figure can be used to analysis influence of the stiffness ratio between two springs. Comparing the different subplots in one figure can be used to analysis influence of the changing of the ratio between two different springs to the change of the damping. Comparing the two figures can be used to analysis the influence of the different MR damper in the control current. In figures, the unit of  $k$  is  $N \cdot m^{-1}$  and the unit of  $c$  is  $N \cdot s \cdot m^{-1}$ .

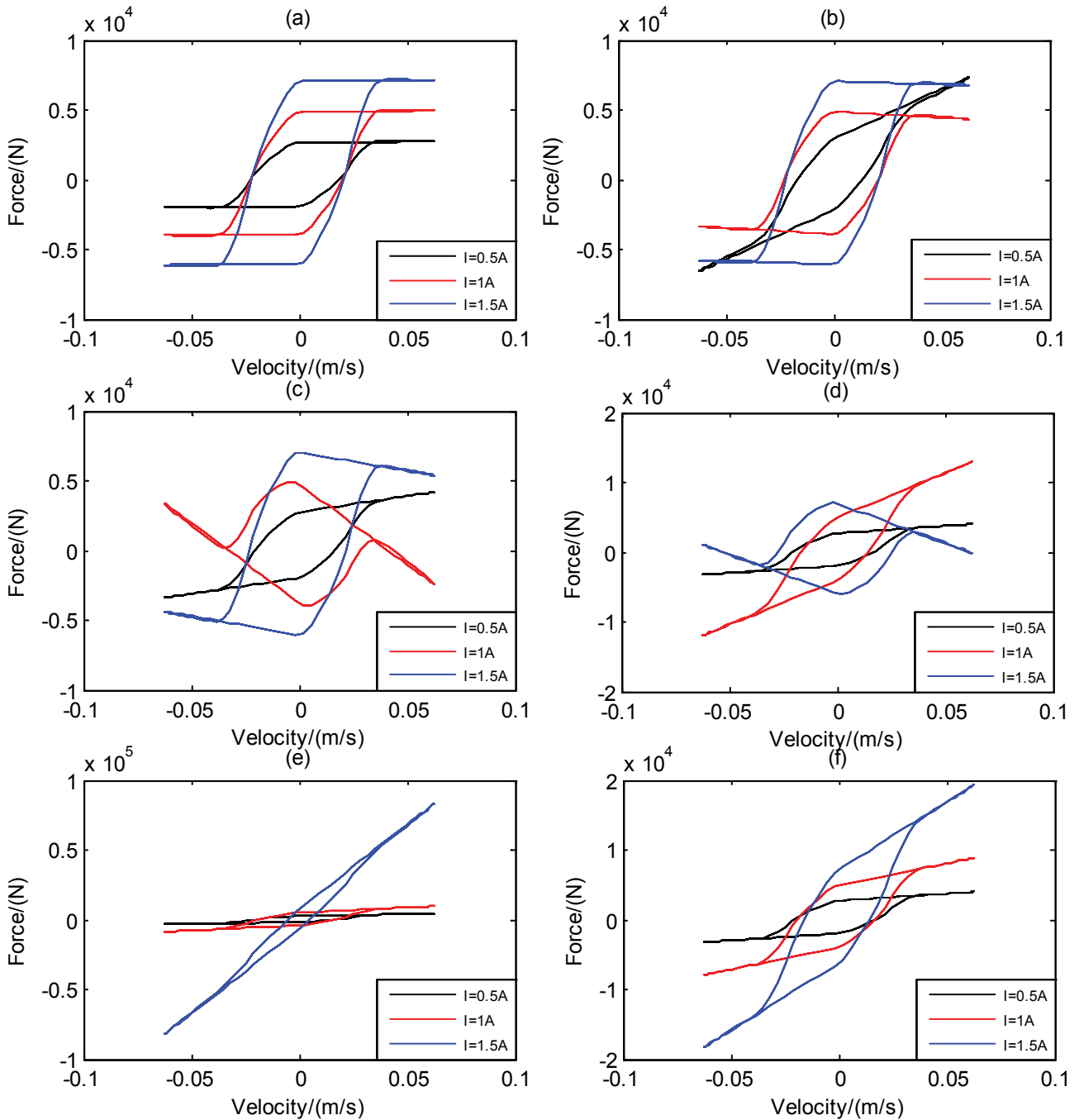
Fig.4 shows the relation between force and displacement in six different stiffness ratios. In each subplot, the control currents of MR damper 1 are varied and the currents of MR damper 2 are fixed.

In each subplot of Fig.4, the area of loop under the curve is varied with the change of current, but the changes of slope of the curves are inconspicuously. When the current achieved at 1.5 A, a strong nonlinearity behavior is encountered for  $k_1$  at 40000 N/m and 6000 N/m. It can be conclude that the damping of system is varied with the increasing current and the stiffness of system neatly has no change.



**Fig.4 damping forces versus displacement with varying current on MR damper 1 in different parameter: (a)  $k_1=2500N/m$ ,  $k_2=2500N/m$ , (b)  $k_1=20000N/m$ ,  $k_2=2500N/m$ , (c)  $k_1=40000N/m$ ,  $k_2=2500N/m$ , (d)  $k_1=60000N/m$ ,  $k_2=2500N/m$ , (e)  $k_1=80000N/m$ ,  $k_2=2500N/m$ , (f)  $k_1=100000N/m$ ,  $k_2=2500N/m$**

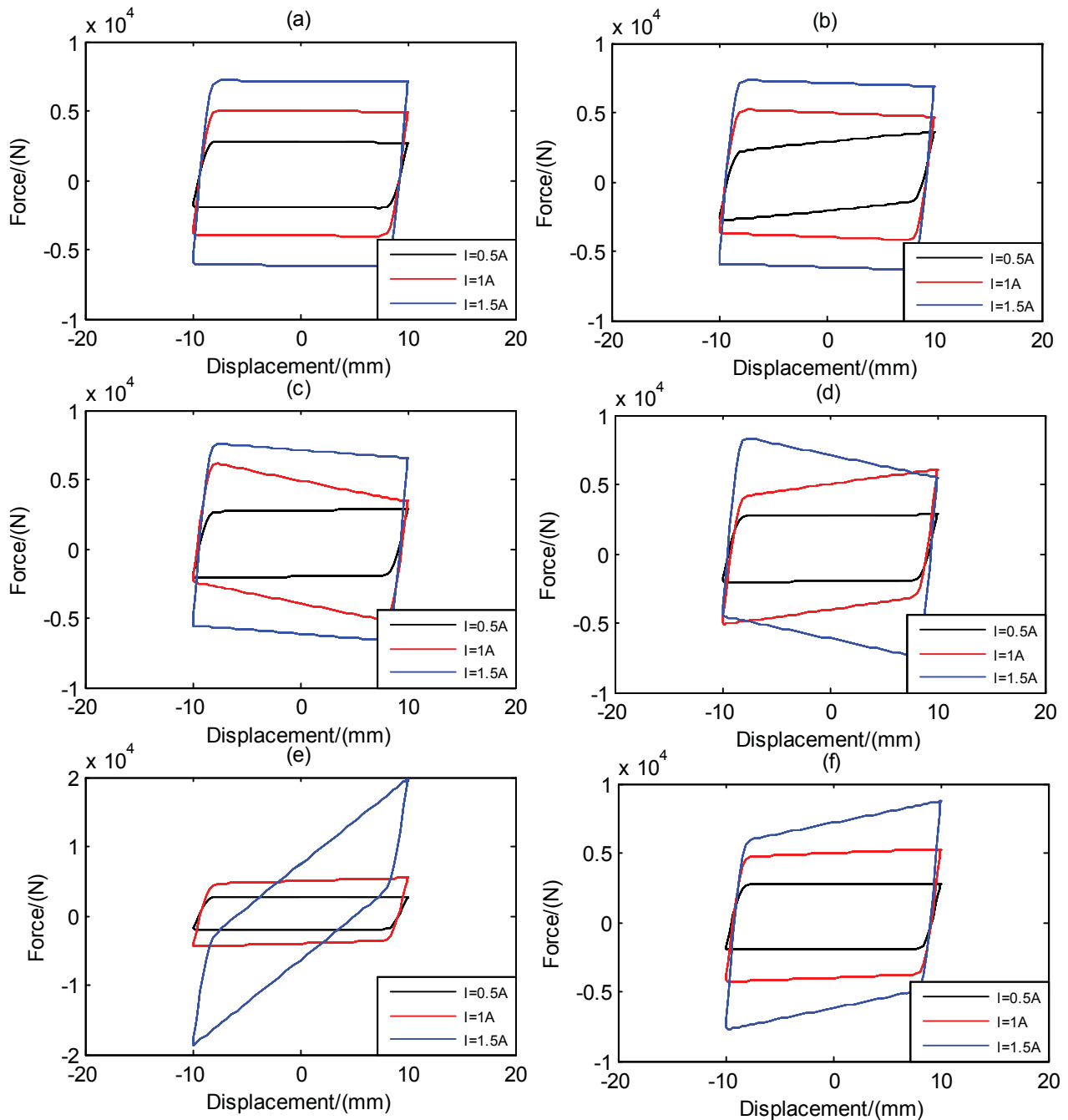
Fig.5 shows the relation between force and velocity in six different stiffness ratios and the parameters are in the same with Fig.4. In each subplot, the slope of curves are varied which also indicate that the damping is varied with the increasing current.



**Fig.5 Simulinked damping forces versus velocity with varying current on MR damper1 in different parameter: (a)  $k_1=2500\text{N/m}, k_2=2500\text{N/m}$ , (b)  $k_1=20000\text{N/m}, k_2=2500\text{N/m}$ , (c)  $k_1=40000\text{N/m}, k_2=2500\text{N/m}$ , (d)  $k_1=60000\text{N/m}, k_2=2500\text{N/m}$ , (e)  $k_1=80000\text{N/m}, k_2=2500\text{N/m}$ , (d)  $k_1=100000\text{N/m}, k_2=2500\text{N/m}$**

Fig.6 shows in the same with Fig.4, the difference is that the control currents of MR damper1 is fixed and the current of MR damper2 is varied. The area of loop under the curve is varied with the increasing current which indicate that the damping is varied and the change of slope of the curves is

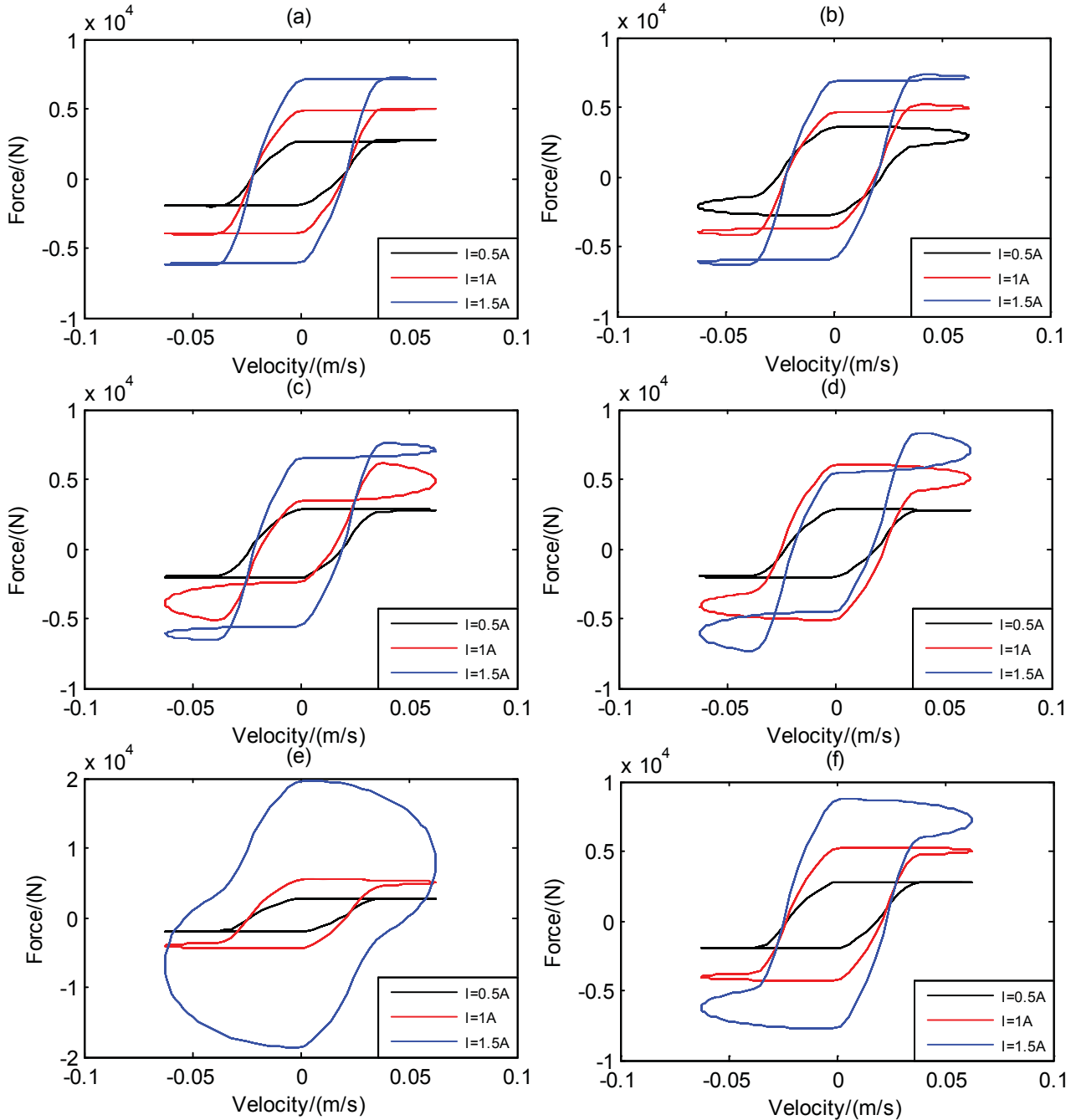
inconspicuously which indicated that the stiffness neatly have no change. The area of loop under the curve and the slope of the curves both are varied which indicated that the stiffness and damping both change dramatically with the increasing current. The stiffness changing capability is largely influenced by the parameters especially for the ratio of two spring elements. At last, the stiffness will maintain a constant with increasing current when the current is larger than a limited value.



**Fig.6 damping forces versus displacement with varying current on MR damper2 in different parameter: (a)  $k_1=2500N/m, k_2=2500N/m$ , (b)  $k_1=20000N/m, k_2=2500N/m$ , (c)  $k_1=40000N/m, k_2=2500N/m$ , (d)  $k_1=60000N/m, k_2=2500N/m$ , (e)  $k_1=80000N/m, k_2=2500N/m$ , (f)  $k_1=100000N/m, k_2=2500N/m$**

Fig.7 shows in the same with Fig.5, the difference is that the control currents of MR damper1 is fixed and the current of MR damper2 is varied. Comparing among the subplots of Fig.5, it clearly shows that the area of loop changed with the increasing current which indicate that the damping is

varied. Comparing the four figures, the MR damper2 has more influence on the change of the stiffness and damping of the system and these two equivalent damping and stiffness will be increased with the increase of the stiffness ratio of two spring elements.



**Fig.7 damping forces versus velocity with varying current on MR damper2 in different parameter: (a)  $k_1=2500\text{N/m}, k_2=2500\text{N/m}$ , (b)  $k_1=20000\text{N/m}, k_2=2500\text{N/m}$ , (c)  $k_1=40000\text{N/m}, k_2=2500\text{N/m}$ , (d)  $k_1=60000\text{N/m}, k_2=2500\text{N/m}$ , (e)  $k_1=80000\text{N/m}, k_2=2500\text{N/m}$ , (f)  $k_1=100000\text{N/m}, k_2=2500\text{N/m}$**



## Conclusion

In this paper, a novel vibration device with variable stiffness and damping is proposed on the basis of MR fluids. A Bouc-Wen model is used to describe the characteristics of MR device. An equivalent model is built to analyze the equivalent damping and stiffness of the system. Through analyzing the characteristics of MR damper, it is clear that simply MR damper has no capability of changing stiffness. Comparing the original model with the equivalent model, it will be found that the stiffness and damping of the system is related with stiffness and damping of MR damper constituting the device. The results of simulation show that the stiffness and damping of the device both are varied with the variable current simultaneously at certain parameters.

## Acknowledgement

The authors would like to appreciate for the supports of 111 project (No. B12019), National Natural Science Foundation of China (No.51305121, No. 51205100, No. 51328502), Higher Specialized Research Fund for the Doctoral Program (No. 20120111120020) and the Fundamental Research Funds for the Central Universities.

## References

- [1] G. Yang, B.F. Spencer Jr., J.D. Carlson, M.K. Sain. (2002), Large-scale MR fluid dampers: modeling and dynamic performance considerations. *Engineering Structures*, 24, 309–323.
- [2] D H Wang and W H Liao. (2011), Magnetorheological fluid dampers: a review of parametric modelling. *Smart Mater. Struct.*, 20, 1-34.
- [3] R Stanway, J L Sproston and N G. Stevens (1987), Non-linear modelling of an electro-rheological vibration damper. *J. Electrostat.*, 20, 167–84.
- [4] N D Sims, D J Peel, R Stanway, A R Jonhson, and W A Bullough, (2000) The ER long-stroke damper: a new modelling technique with experimental validation. *J Sound Vib.*, 229(2), 207–227
- [5] B F Spencer, S J Dyke, M K Sain and J D Carlson (1997), Phenomenological model for magnetorheological dampers. *J. Eng. Mech. ASCE*, 123, 230–8.
- [6] Z D Xu, A Q Li, W R Cheng, J H Ye (2005), A temperature phenomenological model with mass element of MR damper. *Engineering Mechanics*, 22(2), 144-145.
- [7] M J Laura and J D Shirley (2000), Semiactive control strategies for MR dampers: comparative study. *J. Eng. Mech.*, 126, 795-803.
- [8] S B Choi, H S Lee and R H Sung, et al. (2000), Control and Response Characteristics of a Magneto-Rheological Fluid Damper for Passenger Vehicles. *SPIE*, 11, 80-87,
- [9] H X Deng , X L Gong. (2007), Adaptive Tuned Vibration Absorber based on Magnetorheological Elastomer. *Journal of Intelligent Material Systems and Structures*, 18, 1205-1210.
- [10] H X Deng , X L Gong. (2008), Application of magnetorheological elastomer to vibration absorber. *Communications in Nonlinear Science and Numerical Simulation*, 13, 1938 - 1947.
- [11] H X Deng , X L Gong and L H Wang. (2006), Development of an adaptive tuned vibration absorber with magnetorheological elastomer. *Smart Mater. Struct.* 15, 111–116
- [12] W H Li, X Y Wang, X Z Zhang and Y Zhou. (2009), Development and analysis of a variable stiffness damper using an MR bladder. *Smart Mater. Struct.* 18, 1–8..
- [13] Y Q Liu, Hiroshi Matsuhisa, Hideo Utsuno, Jeong Gyu Park. (2005), Vibration isolation by a variable stiffness and damping system. *JSME International Journal*, 48(2), 1036-1041.
- [14] Y Q Liu, Hiroshi Matsuhisa, Hideo Utsuno, (2008), Semi-active vibration isolation system with variable stiffness and damping control. *Journal of sound and vibration*, 313, 16-28..
- [15] M Ismail, F Ikhouane, J Rodellar. (2009), The Hysteresis Bouc-Wen Model, a Survey. *Arch Comput Methods Eng*, 16: 161–188.

## Error Analysis of Dynamical Measurement System Based on Binocular Vision

Yue Wang, Jin Zhang\*, and Huaxia Deng\*

<sup>1</sup> School of Instrument Science and Opto-electronics Engineering, Hefei University of Technology, China

\*Corresponding author: [zhangjinhi\\_2005@china.com.cn](mailto:zhangjinhi_2005@china.com.cn) and [hxdeng@hfut.edu.cn](mailto:hxdeng@hfut.edu.cn)

### Abstract

With the rapid development of industrial cameras, binocular stereo vision is widely used in the field of manufacturing. Using two or more image points of one point in space to restore space depth information is called stereo vision, which process is three-dimensional reconstruction. Nowadays binocular vision which applied for vibration test is widely used. While binocular stereo vision is normally used in static test and has been rarely reported for the dynamical measurement. So it is important to establish this dynamic error model and analyze error sources to improve measurement accuracy. In this paper, an error analysis of binocular vision for dynamical test is presented. For this measurement system of binocular vision, errors of results are generated by the deviation between the calculated world coordinate values and the actual world coordinate values. On the assumption that the calibration result is correct, an error model of dynamic measurement is established in the article which the deviation of Z coordinate value between the ideal point and the reconstructed point is mainly studied. This deviation is so-called reconstruction error. In this model, two cameras are non-synchronized. And the effects of motion parameters, such as amplitude, frequency, phase when double cameras take photos of one point respectively with simple harmonic motion or sinusoidal movements are analyzed. The proposed model is close to the actual situation and can be used to set up cameras and control cameras' non-synchronized time to improve measurement accuracy when performing dynamic measurement.

**Keywords:** Binocular vision, Error model, Dynamic measurement, 3D reconstruction.

### Introduction

In the field of measurement, vibration test is widely studied. Now two common methods can be used to achieve vibration test. One can be achieved indirectly by sensors and the other method is to use a laser. The former requires the sheet sensor to attach on the target point, so the structure of this method is complicated with lower precision; although the latter method is simple, it can't be applied to long distance test and the intensity is susceptible to be affected by external environment. These two methods are single-point measurement method. Currently, visual technology is developing rapidly. And vibration test that achieved by the use of visual measurement technology has been proposed. Especially binocular vision technology is widely used. This emerging measurement method is a full field type which has various advantages, such as experimental convenience, high precision, quick access to large amounts of information, automatic processing <sup>[1]</sup>.

According to what are mentioned above, understanding and learning binocular vision technology has great significance. The basic model of binocular vision is pinhole model, which theoretically requires at least two photos to be realized 3D information of one scene point. This process is called 3D reconstruction <sup>[2]</sup>. Theory of binocular vision in practical application has a high practical value, for example, in the industrial field binocular vision technology can be used to identify and positioning some parts of the shape of quite different shape and colors and make them separated; in the field of public security, binocular vision can be used to reproduce the scene of the accident scene and determine responsibility <sup>[3-4]</sup>. In view of that, binocular vision has gradually improved and

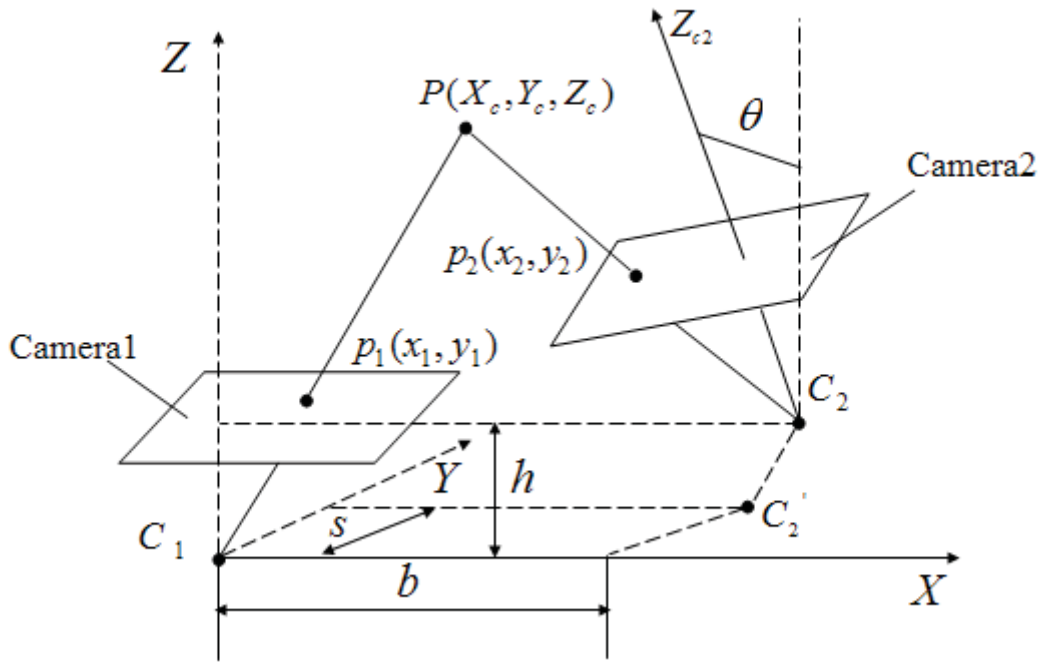
affects our lives. In order to improve the measurement accuracy, the establishment and analysis of 3D reconstruction error model based on binocular vision is very important. And error models based on binocular vision are involved in many papers. H.J.Yu analyzed the relationship between structural parameters of binocular vision and measurement results. Theoretically, the relationship between coordinate measurement precision and angle of two cameras' optical axis or the baseline distance are analyzed<sup>[5]</sup>. In order to improve the measurement precision for visual measure system, research on the influence of stereovision structure based on binocular vision is presented by A.X.Guo. A structure parameter model of binocular visual measure system is investigated with the trigonometric method<sup>[6]</sup>. Q.j.Li once proposed a measurement system of parallel-axes binocular stereoscopic. The Monte-Carlo method was used in simulating and analyzing the errors which caused by the calibrated parameters<sup>[7]</sup>. L.F.Cai analyzed image recognition errors' influence on the measurement accuracy of the visual system. And the relationship between structural parameters of visual system and measurement errors is introduced<sup>[8]</sup>. S.F performed left-right consistency checks and compared matching error between the corresponding pixels in binocular disparity calculation, and classified the stereoscopic images into non-corresponding, binocular fusion, and binocular suppression regions<sup>[9]</sup>. Gal'Pem derived some basic relations analytically for the determination of the degree of distortion and the connection between coordinates of object and image for stereoscopic vision are derived. The degree of distortion is calculated and its effect on stereo-vision is discussed<sup>[10]</sup>. Derek Bradley proposed an error correction algorithm which can solve the mismatch problem of multi-cameras' polar constraint. And this error correction method error algorithm is more effective in reducing camera calibration errors in the same scene than error algorithm of reprojection<sup>[11]</sup>.

In the previous paragraph, error models mostly belong to model of static measurement. This static theory has been quite mature because the measurement error in this stationary case is easier to control. While error theory of dynamic test based on binocular vision is very rare. Because this dynamic measurement should consider not only the factors that must be considered in static measurement, such as calibration error, matching error, pixel positioning error of camera's CCD, etc, but also asynchronous error and the movement of moving objects. X.L.Zhang built a system of binocular vision measurement which the two optic axes are parallel. That was adopted to measure the attitude of measured missile which is moving<sup>[12]</sup>. This model of binocular vision is not realistic and does not take into account the motion form of measured object that has effect on the measurement results. The motion parameters such as amplitude, frequency and phase will have a certain impact on measurement accuracy. Today achieving vibration test by binocular vision is an irresistible trend which belongs to the category of dynamic test. Therefore, the establishment of error model based on binocular vision in dynamic measurement and reconstructed error analysis on various cameras' parameters and motion parameters of measured object is the key.

In this paper, a dynamic measurement model base on binocular vision which relatively closes to the reality is mainly established. The double cameras has a certain distance between front and rear, left and right, up and down and there is a tiny angle between cameras' optical axes. This article focuses on the analysis on the deviation of 3D coordinate values that caused by these two non-synchronized cameras between original point and reconstructed point under the premise there is no calibration error. First, the deviation is calculated when a spatial point does uniform motion respectively on each axis based on that established model. Second, assuming that the measured point respectively does simple harmonic motion on each axis or propagates forward as a form of a sine wave on a plane, the error equals to precious deviation which affected by motion parameters is discussed.

**One Dynamic Error Model Based on Binocular Vision**

For actual measurement, one system of binocular visual is not a standard system, for example, two cameras has a certain distance between front and rear, left and right, up and down, and two optical axes of cameras are not necessarily parallel . Theoretically parameters of camera system will affect the measurement accuracy such as focal length, the baseline distance of two cameras, the angle between the two optical axes of cameras and so on. In order to close to the actual situation and consider these parameters, a model based on binocular vision as shown below is built.



**Figure1. A model of 3D reconstruction based on binocular vision**

The system parameters are reflected in fig1 and  $C_1, C_2$  are the optical centers of the two cameras. The right optical axis revolved around Z-axis which has an extremely angle  $\theta$  between the two optical axes. This system puts the coordinate system of the left camera as the world coordinate system. Spatial point P has two projection points on the two cameras, respectively  $p_1(x_1, y_1)$  and  $p_2(x_2, y_2)$ . And some formulas can be obtained by the principle of similar triangle.

$$x_1 = f \frac{X_c}{Z_c} \quad y_1 = f \frac{Y_c}{Z_c} \quad x_2 = f \frac{X'_c}{Z'_c} \quad y_2 = f \frac{Y'_c}{Z'_c} \tag{1}$$

Coordinate systems of the two cameras can be interchangeable, so

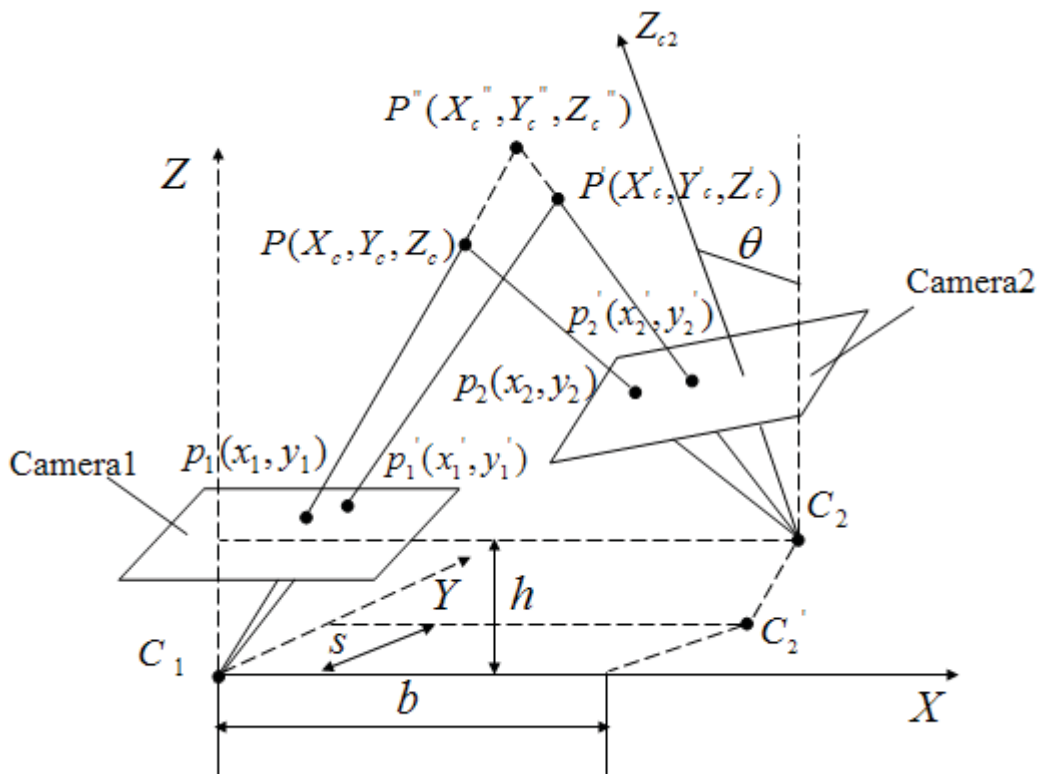
$$\begin{bmatrix} \cos \theta & \sin \theta & 0 & b \\ -\sin \theta & \cos \theta & 0 & s \\ 0 & 0 & 1 & h \\ 0 & 0 & 0 & 1 \end{bmatrix} \times \begin{bmatrix} X_c \\ Y_c \\ Z_c \\ 1 \end{bmatrix} = \begin{bmatrix} X'_c \\ Y'_c \\ Z'_c \\ 1 \end{bmatrix} \tag{2}$$

Then coordinate values of point  $P(X_c, Y_c, Z_c)$  can be obtained according to (1) (2)

$$X_c = \frac{x_1 Z_c}{f} \qquad Y_c = \frac{y_1 Z_c}{f}$$

$$Z_c = \frac{(x_2 - y_2)h - f(b - s)}{(\cos\theta + \sin\theta)x_1 + (\sin\theta - \cos\theta)y_1 - (x_2 - y_2)} \approx \frac{(x_2 - y_2)h - f(b - s)}{(x_1 - y_1) + \theta(x_1 + y_1) - (x_2 - y_2)} \quad (3)$$

The above formulas are obtained in the static case which reflects the 3D information of one spatial point by the use of binocular vision. While theory of dynamic testing based on binocular vision is not yet ripe. So the following dynamic system in fig.2 based on binocular vision is established which the double cameras are non-synchronized in order to analyze the deviation of the 3D coordinate values between actual reconstructed point  $P''$  and original point  $P$ .



**Figure2. Schematic of 3D reconstruction in dynamic measurement**

The schematic of dynamic test is shown in figure2. The left camera exposures earlier than the right one and point  $P$  moves to point  $P'$  when the right camera starts to take pictures. Point  $P'$  also has the two projection points in imaging planes, respectively  $p_1'(x_1', y_1')$ ,  $p_2'(x_2', y_2')$ . In the actual process of reconstruction, projection point  $p_1$  and  $p_2'$  are used to restore 3D coordinate information.

Here assuming that the point  $P$  does uniform linear motion respectively along X-axis, Y-axis, Z-axis and corresponding displacement are  $\Delta X$ ,  $\Delta Y$ ,  $\Delta Z$ . And the deviation between  $P$  and  $P''$  will be calculated in the latter.

1) When Point  $P$  does uniform motion along X-axis, reconstructed 3D coordinate values are

$$X_c'' = \frac{x_1 Z_c''}{f} \quad Y_c'' = \frac{y_1 Z_c''}{f}$$

$$Z_c'' = \frac{(x_2' - y_2')h - f(b-s)}{(x_1 - y_1) + \theta(x_1 + y_1) - (x_2' - y_2')} = \frac{(X_c + \Delta X)(1 + \theta)h + h(\theta - 1)Y_c - (b-s)Z_c}{Z_c(1 + \theta)(h - \Delta X) + (\theta - 1)Y_ch - (b-s)Z_c} Z_c \quad (4)$$

$$\Delta Z_c = Z_c'' - Z_c = \frac{(1 + \theta)(Z_c + h)\Delta X}{Z_c(1 + \theta)(h - \Delta X) + (\theta - 1)Y_ch - (b-s)Z_c} Z_c \quad (5)$$

2) Similarly when Point  $P$  does uniform motion along Y-axis, reconstructed 3D coordinate values are

$$X_c'' = \frac{x_1 Z_c''}{f} \quad Y_c'' = \frac{y_1 Z_c''}{f} \quad Z_c'' = \frac{hX_c(1 + \theta) + h(\theta - 1)(Y_c + \Delta Y) - (b-s)Z_c}{X_c(1 + \theta)h + (\theta - 1)(Y_ch - \Delta Y Z_c) - (b-s)Z_c} Z_c \quad (6)$$

$$\Delta Z_c = Z_c'' - Z_c = \frac{(\theta - 1)(h + Z_c)\Delta Y}{X_c(1 + \theta)h + (\theta - 1)(Y_ch - \Delta Y Z_c) - (b-s)Z_c} Z_c \quad (7)$$

3) When Point  $P$  does uniform motion along Z-axis, reconstructed 3D coordinate values are

$$X_c'' = \frac{x_1 Z_c''}{f} \quad Y_c'' = \frac{y_1 Z_c''}{f} \quad Z_c'' = \frac{hX_c(1 + \theta) + h(\theta - 1)Y_c - (b-s)(Z_c + \Delta Z)}{(1 + \theta)X_c(\Delta Z + h) + (\theta - 1)(\Delta Z + h)Y_c - (b-s)Z_c} Z_c \quad (8)$$

$$\Delta Z_c = Z_c'' - Z_c = \frac{[s - b + Y_c - X_c - \theta(X_c + Y_c)]\Delta Z}{(1 + \theta)X_c(\Delta Z + h) + (\theta - 1)(\Delta Z + h)Y_c - (b-s)Z_c} Z_c \quad (9)$$

4) Assuming that point  $P$  moves to  $P'$  ( $X_c + \Delta X, Y_c + \Delta Y, Z_c + \Delta Z$ ) when the right camera starts to take pictures, the actual reconstructed 3D coordinate values are obtained as follows.

$$X_c'' = \frac{x_1 Z_c''}{f} \quad Y_c'' = \frac{y_1 Z_c''}{f} \quad Z_c'' = \frac{[(X_c + \Delta X)(1 + \theta) + (\theta - 1)(Y_c + \Delta Y)]h - (Z_c + \Delta Z)(b-s)}{(1 + \theta)(X_ch + X_c\Delta Z - Z_c\Delta X) + (\theta - 1)(hY_c + Y_c\Delta Z - Z_c\Delta Y) - (b-s)Z_c} Z_c \quad (10)$$

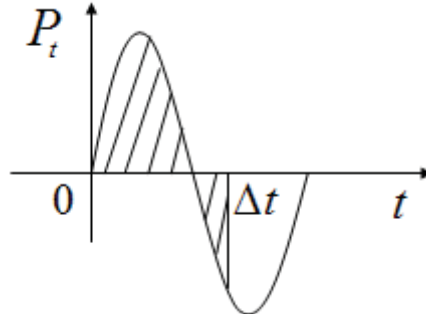
$$\Delta Z_c = Z_c'' - Z_c = \frac{(1 + \theta)(h\Delta X - X_c\Delta Z + Z_c\Delta X) + (\theta - 1)(h\Delta Y - Y_c\Delta Z + Z_c\Delta Y) - (b-s)\Delta Z}{(1 + \theta)(X_ch + X_c\Delta Z - Z_c\Delta X) + (\theta - 1)(hY_c + Y_c\Delta Z - Z_c\Delta Y) - (b-s)Z_c} Z_c \quad (11)$$

### Error Analysis of Dynamic Measurement

For this dynamic testing model based on binocular vision in fig.2, point  $P$  can moves with different ways, such as harmonic motion, sinusoidal motion, etc. The motion parameters, such as amplitude, frequency and phase, of point  $P$  which has effect on 3D coordinate values will be analyzed when point  $P$  respectively does these two motions.

#### A. Error Analysis of Z Coordinate of Point $P$ with Harmonic Motion

In the following, point  $P$  does harmonic motion on each axis. Fig.3 reflects characteristics of harmonic motion which  $P_t = A\sin(2\pi ft + \varphi)$ . The area of shaded portion represents the distance  $\Delta S$  that point  $P$  has traveled during the unsynchronized time  $\Delta t$  of the two cameras.



**Figure3. Characteristics of harmonic motion**

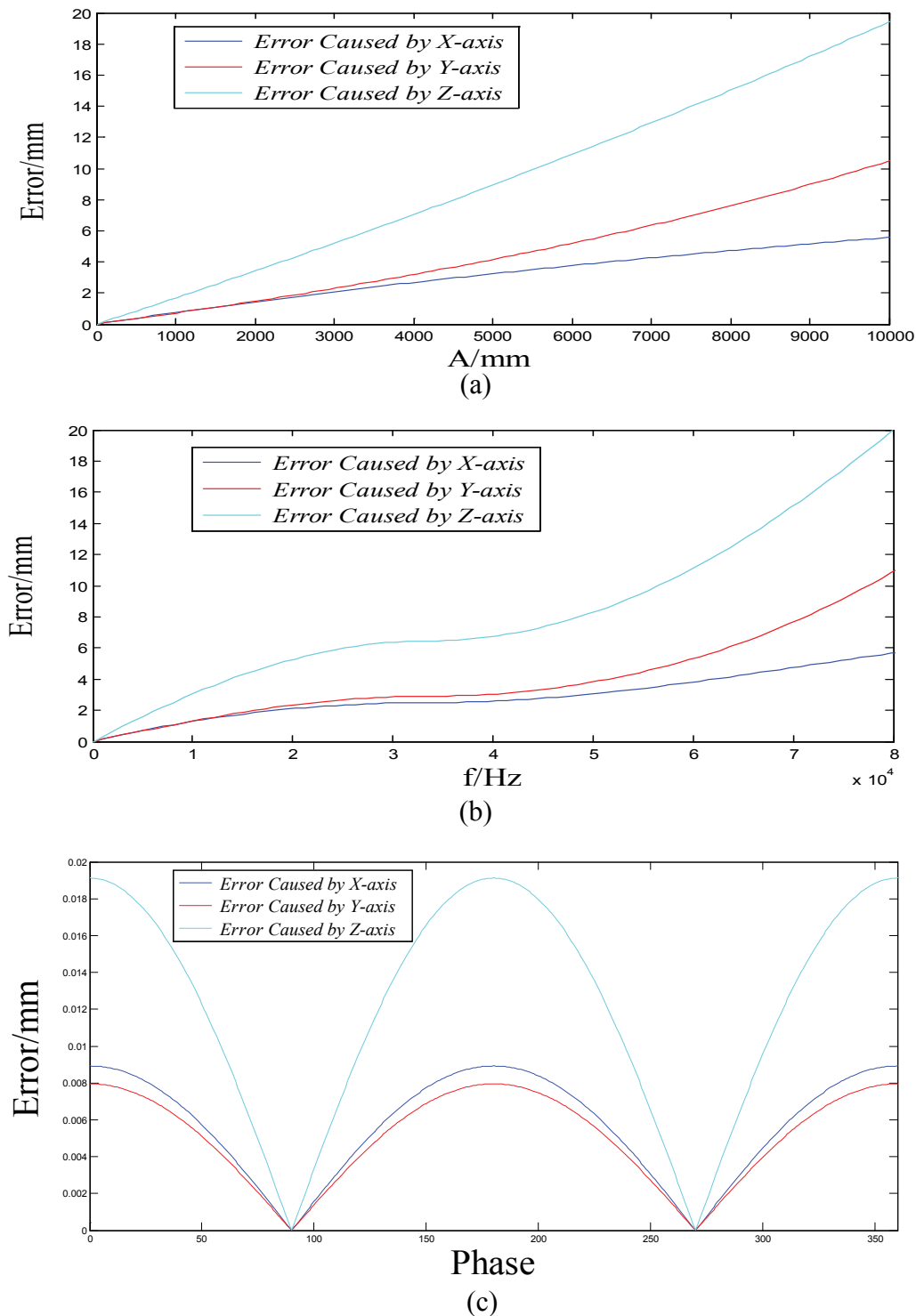
$$\Delta S = \int_0^{\Delta t} \left| \frac{dx}{dt} \right| dt = \int_0^{\Delta t} 2\pi Af |\cos(2\pi ft + \varphi)| dt \quad (12)$$

1) When point  $P$  does harmonic motion on X-axis, the distance  $\Delta X$  which point  $P$  has traveled on X-axis is equal to  $\Delta S$ . Put  $\Delta S$  into the above equation (5), then the error of Z coordinate between origin point  $P$  and reconstructed point  $P''$  in this occasion can be got. In order to discuss the measurement error here, supposing that  $\theta = 5^\circ$ ,  $X_c = 12 \text{ mm}$ ,  $Y_c = 10 \text{ mm}$ ,  $Z_c = 10 \text{ mm}$ ,  $b = 50 \text{ mm}$ ,  $s = h = 10 \text{ mm}$ ,  $t_0 = 0 \text{ s}$ ,  $\Delta t = 5 \mu\text{s}$ . Look at figure 4(a), if given  $f = 50 \text{ Hz}$ ,  $\varphi = \frac{\pi}{6}$ , the relationship between error and amplitude can be obtained. And the

greater amplitude, the greater error; if given  $A = 10 \text{ mm}$ ,  $\varphi = \frac{\pi}{6}$ , the relationship in figure 4(b) between error and frequency can be obtained. And the higher frequency, the greater error; if given  $A = 10 \text{ mm}$ ,  $f = 50 \text{ Hz}$ , the relationship in figure 4(c) between error and phase can be obtained, the relationship curve is a cycle curve with a period of  $\pi$ . According to this picture, phase has little effect on the error.

2) When point  $P$  does harmonic motion on Y-axis, the distance  $\Delta Y$  which point  $P$  has traveled on Y-axis also equals to  $\Delta S$ . If  $\Delta S$  was put into the above equation (7), the error of Z coordinate can also be obtained. Error analysis of Z coordinate is similar to the upper part. Here given the same parameter values like the upper part, respectively relation formulas between error and amplitude or frequency or phase can be obtained. The following cures reflect the relationships between the error which caused by Y-axis and these three parameters.

3) When point  $P$  does harmonic motion on Z-axis, the distance  $\Delta Z$  that point P has traveled on Z-axis also equals to  $\Delta S$ . If  $\Delta S$  was put into the above equation (9), the error of Z coordinate can be obtained. The process of error analysis is the same as the previous two cases. And the relationships between error and various parameters are shown below in figure4.



**Figure 4. The relationships between motion parameters and errors of Z coordinate of point P with harmonic motion on each axis (a) Relationship between error and amplitude. (b) Relationship between error and frequency. (c) Relationship between error and phase.**

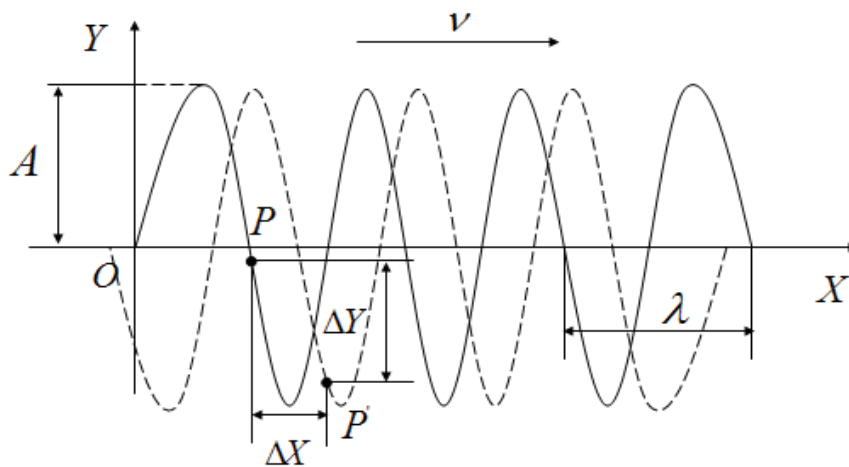
Figure 4 (a), (b), (c) respectively reflects the relationships between error of Z coordinate and amplitude, frequency or phase when point P does harmonic motion on the each axis. Error increases with the larger amplitude or greater frequency. And when frequency varies in the range of



30 – 40KHz , the error stays in a flat stage. At last, the relation curves between error and phase are cycle curves with a period of  $\pi$  which reflect phase has little effect on the error.

*B. Error Analysis of Z Coordinate of Point P with Sinusoidal Motion*

Here the second motion of point  $P$  which point  $P$  propagates forward as a sine wave on  $XOY$  plane will be discussed. The characteristics of sinusoidal motion are reflected below in fig.5 .And this wave equation is formula (13). Assuming velocity  $v$  is one constant and equals to  $3.4 \times 10^4 \text{ mm/s}$  , then displacements including  $\Delta X$  and  $\Delta Y$  respectively on the horizontal direction and the vertical direction can be calculated when the point  $P$  moves to  $P'$  during the time  $\Delta t$  in this case.



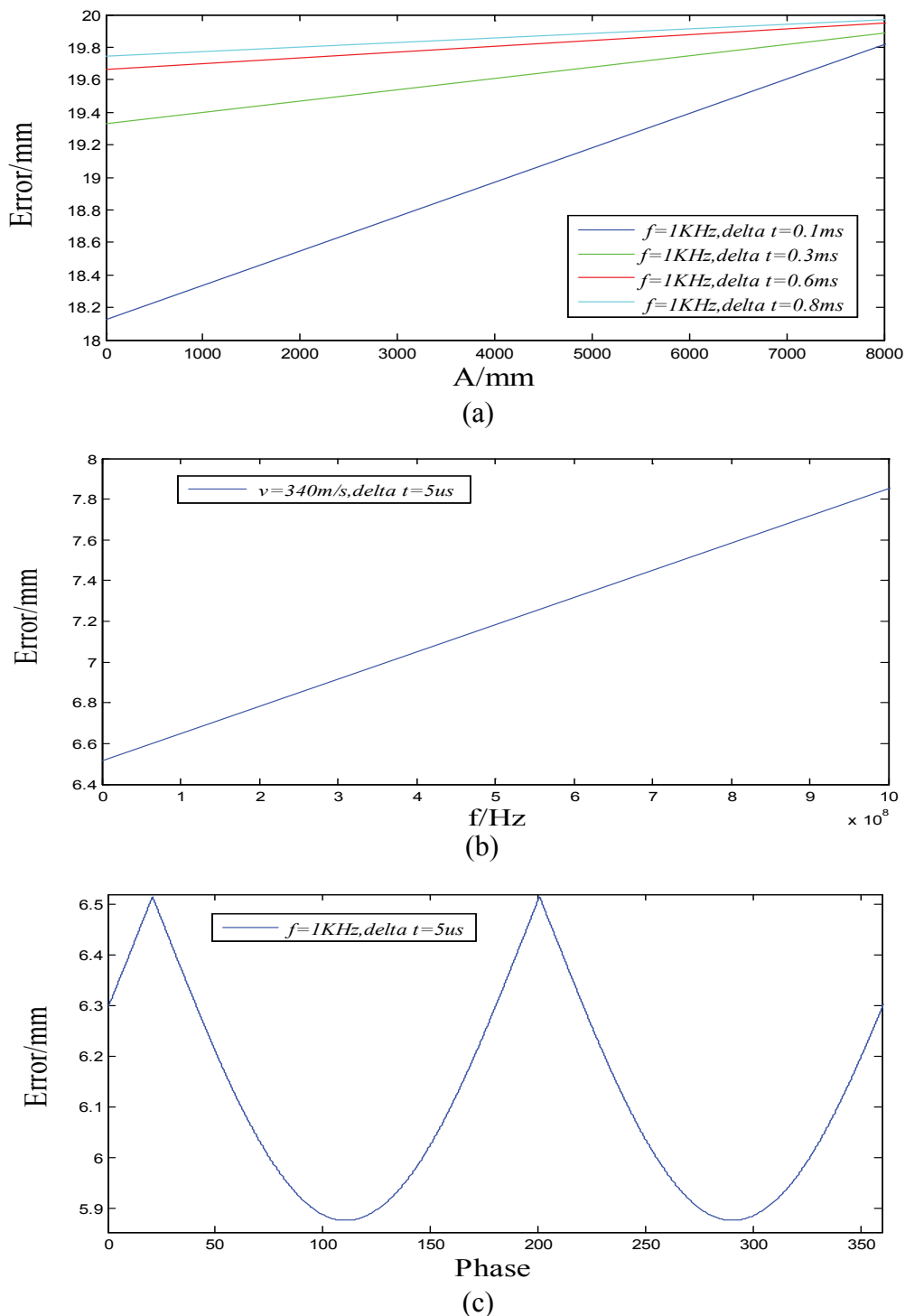
**Figure5. Characteristics of sinusoidal motion**

$$y = A \cos\left[2\pi f \left(t - \frac{x}{v}\right) + \varphi\right] \tag{13}$$

$$\Delta X = v\Delta t \tag{14}$$

$$\Delta Y = 4\|\Delta t f\| \left| A + A \cos\left[2\pi f \left(t_0 + \Delta t - \frac{X_c + \Delta X}{v}\right) + \varphi\right] - \cos\left[2\pi f \left(t_0 - \frac{X_c}{v}\right) + \varphi\right] \right| \tag{15}$$

Here  $\theta = 5^\circ$  ,  $X_c = 12 \text{ mm}$  ,  $Y_c = 10 \text{ mm}$  ,  $Z_c = 10 \text{ mm}$  ,  $b = 50 \text{ mm}$  ,  $s = h = 10 \text{ mm}$  ,  $t_0 = 0 \text{ s}$  and substituting  $\Delta X$  ,  $\Delta Y$  ,  $\Delta Z = 0$  into equation(11), then the relationship between error and amplitude, phase, wavelength or frequency can be obtained. Figs of the results will be given.



**Figure 6.** The relationships between motion parameters and error of Z coordinate of point P with sinusoidal motion on XOY plane. (a) Relationship between error and amplitude. (b) Relationship between error and frequency. (c) Relationship between error and phase.

Figure 4 (a) is the curve which reflects the relationship between frequency and error of Z coordinate. When the frequency of this sine wave is a constant which  $f = 1\text{KHz}$ , the relationships between the amplitude and error of Z coordinate are analyzed when to take special value of the non-synchronization time  $\Delta t$  in the range of  $0-1/4 T$ ,  $1/4 T -2/4T$ ,  $2/4T- 3/4T$  and  $3/4T-4/4T$ . From the four curves in fig.4 (a), this error increases with the increasing amplitude. And every error curve

does not pass through the origin point, because the error will be produced which results in a lateral displacement on X-axis because of velocity, through amplitude is zero. Comparing these four curves in figure 4(a), the greater the asynchronous time  $\Delta t$ , the larger the error of Z coordinate. Figure 4 (b) reflects the relationship between this error and frequency. When velocity is certain and a value of frequency is determined, then the wavelength can be obtained. In this case, the error increases as the frequency increases. This error curve involved with frequency does not pass through the origin point either due to the vibration on longitudinal direction which produces the displacement on Y direction. The diagram (c) is a cycle curve with a period of  $\pi$  and this error influence on the phase can not be neglected.

## Conclusions

In this paper, a dynamic error model based on binocular vision is mainly established. This model is not a standard system. Specific camera settings are reflected in the above fig1. The deviation of Z-coordinate between the origin point  $P$  and the reconstructed point is analyzed when two cameras are not synchronized and the spatial point  $P$  respectively does uniform motion, harmonic motion on each axis or sinusoidal motion on a plane. When point  $P$  does uniform motion on each axis, this deviation can be calculated. When point  $P$  does harmonic motion on each axis, that deviation of results that affected by the motion parameters are analyzed. Error equals to that deviation increases with the greater amplitude or larger frequency. The relationship between phase and error is a cycle curve which has litter effect on accuracy. When point  $P$  propagates forward as a form of sine wave on  $XOY$  plane which velocity is a constant, firstly the greater frequency, then the smaller wavelength and greater error; secondly obviously error increases with the increasing amplitude; thirdly the curve involved with phase and error is also a periodic curve and the effect caused by phase can not be neglected. Thus, for the dynamic measurement systems, not only the structure of binocular vision system, but also the movement pattern and parameters of one target point will have impact on measurement accuracy. This proposed model can be helpful to set up cameras and can reduce measurement error caused by asynchronous cameras when it comes to dynamic vibration test based on binocular vision.

## Acknowledgement

The authors would like to appreciate for the supports of 111 project (No. B12019), National Natural Science Foundation of China (No.51305121, No. 51205100, No. 51328502), Higher Specialized Research Fund for the Doctoral Program (No. 20120111120020) and the Fundamental Research Funds for the Central Universities.

## References

- [1]H.W. Gao, Y. Yu , X.Y .Liu . Research of 3D reconstruction experiment platform based on binocular vision .Computer Engineering and Applications, 2009, 45(33), 149-152
- [2]X.J. Zou, H. Zou, J. Lu.Virtual manipulator-based binocular stereo vision positioning system and errors modeling. Machine Vision and Applications, 2012, 23(1), 43-63.
- [3]Bradley D, Heidrich W. Binocular Camera Calibration Using Rectification Error. Proceedings of the 2010 Seventh Canadian Conference on Computer and Robot Vision, 2010, 183-190.
- [4]Q. Liu, X.S. Qin, S.S. Yin, F. He .Structural parameters optimal design and accuracy analysis for binocular vision measure system .International Conference on Advanced Intelligent Mechatronics, 2008, 156-161
- [5] H.J. Yu, P.T. Han. Measurement error analysis based on binocular stereo vision system. Optical Technology, 2007, 33 (1):157-159.
- [6]A.X. Guo, J.T. Xiong.Error analysis on camera calibration in binocular stereo vision. International Conference on Information Engineering and Computer Science, 2009, 4pp.

- [7]Q.J .Li, T.Q. Chang, X.J. Jiao.Error analysis in parallel-axes binocular stereoscopic measurement system caused by the calibrated parameters. IEEE International Conference on Virtual Environments Human-Computer Interfaces and Measurement Systems, 2012, 163-166.
- [8]F.C. Liu, M.H. Xie, G.L. Yan. Accuracy Analysis of Binocular Stereo Vision System. Computer Engineering, 2011, 37(19):280-285.
- [9]F.Shao,W.S.Lin,S.B.Gu,G.Y.Jiang,Srikanthan T.Perceptual Full-Reference Quality Assessment of Stereoscopic Images by Considering Binocular Visual Characteristics. IEEE Transactions on Image Processing, 2013, 22(5):1940-1953.
- [10]Gal'pern,D.Yu, Golovanova, L.N. The effect of distortion on binocular space perception. Soviet Journal of Optical Technology, 1974, 41(10):466-469.
- [11]Bradley D, Heidrich W, Binocular Camera Calibration Using Rectification Error. Computer and Robot Vision, Vancouver, 2010, 183-190.
- [12] X.L .Zhang , B.F .Zhang Lin,Y.C .Lin ,X.F .Li .Study on Attitude of Dynamic Missile in Long Distance Based on Parallel Optic Axes Binocular Vision System. 7Th International Symposium on Test and Measurement, 2007, 1351-1354.

## Large-deformation plasticity analysis using the edge-based smoothed finite element method

\*J. Liu<sup>1</sup>, Z.Q. Zhang<sup>2</sup>

<sup>1</sup>Department of Mechanical Engineering, National University of Singapore, 117576, Singapore.

<sup>2</sup>Institute of High Performance Computing, Singapore.

\*Corresponding author: nickliujun@gmail.com

### Abstract

An edge-based smoothed finite element method (ES-FEM) using 3-node triangular element was recently proposed to improve the accuracy and convergence rate of the standard finite element method (FEM) for 2D elastic solid mechanics problems. In this research, ES-FEM is extended to the large-deformation plasticity analysis, and a selective edge-based / node-based smoothed finite element (selective ES/NS-FEM) method using 3-node triangular element is adopted to address the volumetric locking problem. Validity of ES-FEM for large-deformation plasticity problem is proved by benchmarks, and numerical examples demonstrate that, the proposed ES-FEM and selective ES/NS-FEM method possess (1) superior accuracy and convergence properties for strain energy solutions comparing to the standard FEM using 3-node triangular element (FEM-T3), (2) better computational efficiency than FEM-T3 and similar computational efficiency as FEM using 4-node quadrilateral element and 6-node quadratic triangular element, (3) a selective ES/NS-FEM method can successfully simulating severe element distortion problem, and address volumetric locking problem in large-deformation plasticity analysis.

**Keywords:** Large-deformation plasticity, Finite element method (FEM), Edge-based smoothed finite element method (ES-FEM), Volumetric locking, Gradient smoothing.

### Introduction

Numerical simulation of finite-deformed material has attracted numerous research efforts. The finite element method (FEM) has been developed during last decades to deal with material and geometric nonlinear problem. Usually, lower order elements, especially 3-node linear triangular element (T3) for 2-D problem and 4-node linear tetrahedron element (T4) for 3-D problem, are attractive in practical engineering problems because of their intrinsic simplicity, easy preprocessing, and lower requirement on solution regularity. However, the use of T3 or T4 element is highly limited in the large deformation plasticity analysis, because of disadvantages such as convergence problem, element distortion and volumetric locking. Therefore, developing techniques to optimize the linear triangular element is a significant job, and lower order elements with superior accuracy and convergence properties are powerful tools for the simulations of contact-impact, crack propagations, material fracturing progressing, large scale multi-physics etc.

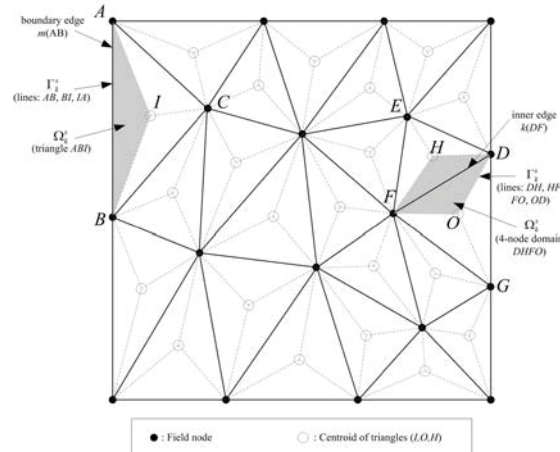
In order to overcome the limitations of FEM, various technologies have been proposed. The strain smoothing technique was used for stabilizing the nodal integrated meshfree method (Chen JS, Wu CT et al. 2001) and then applied in the natural element method (Yoo JW, Moran B et al. 2004). Liu et al. has generalized a gradient (strain) smoothing technique (Liu GR 2008) and applied it in general meshfree settings to accommodate discontinuous shape functions (Liu GR 2009). Applying the same technique to the finite element method, an edge-based smoothed finite element method (ES-FEM)(Liu GR, Nguyen-Thoi T et al. 2009) has been formulated based on the gradient (strain) smoothing technique for static, free and forced vibration analyses in 2D plane strain and plane stress problems. The system stiffness matrix of this method is computed using the gradient smoothing technique over the smoothing domains associated with the edges of the element, which endows its superior convergence properties, computational accuracy and efficiency, spatial and temporal stability.

In this paper, the edge-based smoothed finite element (ES-FEM) is extended to be applied for large strain plasticity analysis, and a selective ES/NS-FEM approach is used to address the volumetric locking problem. Compared to standard FEM, this smoothed technique could be able to use fewer elements to get more precise and stable results, and better convergence property; these properties can decrease the computational cost significantly.

## 2. Edge-based smoothed finite element method for finite strain plasticity

### 2.1 Basic ES-FEM theory and formulation

In ES-FEM, the domain discretization is still based on T3 element in standard FEM, but the integration required in the virtual principle is performed based on the smoothing domains associated with the edges instead of on the triangular element in standard FEM. In this method, the closed problem domain  $\Omega$  is divided into  $N_s$  smoothing domains with  $\overline{\Omega} = \bigcup_{k=1}^{N_s} \overline{\Omega}_k^s$  and  $\Omega_i^s \cap \Omega_j^s = 0$  when  $i \neq j$ , where  $N_s$  is the number of smoothing domains equal to the total number of element edges located in the entire problem domain. For triangular elements, the smoothing domain  $\Omega_k^s$  associated with the element edge  $k$  can be created by connecting two endpoints of the edge to centroids of adjacent elements as shown in Fig. 1.



**Fig.1** Triangular elements and the smoothing domains (shaded areas) associated with edges in ES-FEM(Liu GR, Nguyen-Thoi T et al. 2009)

In edge-based smoothing domains, the smoothed gradient of displacement field  $u_i$  can be obtained by

$$\overline{\nabla} u_i = \int_{\Omega_k^s} \nabla u_i(\mathbf{x}) \Phi_k(\mathbf{x}) d\Omega \quad (1)$$

where  $\nabla u_i(\mathbf{x})$  is the gradient of the displacement field  $u_i$ , and  $\overline{\nabla}$  is defined as a *smoothed gradient operator*.  $\Omega_k^s$  is the smoothing domain associated with the edge  $k$ .  $\Phi_k(\mathbf{x})$  is a given smoothing function that satisfies at least unity property

$$\int_{\Omega_k^s} \Phi_k(\mathbf{x}) d\Omega = 1 \quad (2)$$

In ES-FEM, a simple local constant smoothing function can be used in the calculation (Liu GR, Nguyen-Thoi T et al. 2009)

$$\Phi_k(\mathbf{x}) = \begin{cases} 1/A_k^s, & x \in \Omega_k^s \\ 0, & x \notin \Omega_k^s \end{cases} \quad (3)$$

where  $A_k^s$  is the area of the smoothing domain  $\Omega_k^s$ , and is calculated by

$$A_k^s = \int_{\Omega_k^s} d\Omega = \frac{1}{3} \sum_{i=1}^{n_{sd}} A_i^e \quad (4)$$

where  $n_{sd}$  is the number of elements around the edge  $k$  and  $A_k^s$  is the area of the  $j^{th}$  element around the edge  $k$ . Fig.1 shows that  $n_{sd} = 1$  when edge  $k$  is a boundary edge, and  $n_{sd} = 2$  when edge  $k$  is an inside edge.

Using divergence theorem on Eq. (1), it can be obtained that

$$\bar{\nabla} u_i = \frac{1}{A_k^s} \int_{\Gamma_k^s} u_i(\mathbf{x}) \mathbf{n} d\Gamma \quad (5)$$

where  $\mathbf{n}$  is the outward normal vector of the smoothing domain boundary  $\Gamma_k^s$ .

In the ES-FEM-T3, the displacement field is interpolated by the linear FEM shape function, and can be written in the following form

$$u_i = \sum_{I \in G_L} N_I u_{li} \quad (6)$$

where  $N_I$  is the shape function of node  $I$  at reference configuration,  $u_{li}$  is the displacement component of node  $I$ .  $G_L$  is the set of the so-called *supporting nodes* of the smoothing domain  $\Omega_k^s$ . Therefore, the smoothed gradient of displacement field can be formulated by substituting Eq. (6) into (5)

$$\bar{\nabla} u_i = \frac{1}{A_k^s} \int_{\Gamma_k^s} \left( \sum_{I \in G_L} N_I u_{li} \right) \mathbf{n} d\Gamma = \sum_{I \in G_L} \left( \frac{1}{A_k^s} \int_{\Gamma_k^s} N_I \mathbf{n} d\Gamma \right) u_{li} = \sum_{I \in G_L} \bar{b}_{li} u_{li} \quad (7)$$

where  $\bar{b}_{li}$  is the *smoothed derivatives of shape function* as

$$\bar{b}_{li} = \frac{1}{A_k^s} \int_{\Gamma_k^s} N_I n_i d\Gamma \quad (8)$$

Naturally, the smoothed strain  $\bar{\boldsymbol{\varepsilon}}$  in the domain  $\Omega^{(k)}$  associated with edge  $k$  can now be obtained using  $\bar{b}_{li}$

$$\bar{\boldsymbol{\varepsilon}} = \begin{bmatrix} \bar{b}_{lx} & 0 \\ 0 & \bar{b}_{ly} \\ \bar{b}_{ly} & \bar{b}_{lx} \end{bmatrix} \mathbf{u}_I = \bar{\mathbf{B}}_I \mathbf{u}_I \quad (9)$$

## 2.2 Formulating the large deformation plasticity model

In continuum mechanics, the deformation gradient has the form of

$$\mathbf{F} = \nabla \mathbf{u} + \mathbf{I} \quad (10)$$

where  $\mathbf{u}$  is the displacement field tensor,  $\nabla$  is the gradient operator, and  $\mathbf{I}$  is the identity matrix. The *smoothed deformation gradient* associated with edge  $k$  based on the smoothed domain can be defined as:

$$\bar{\mathbf{F}} = \int_{\Omega^{(k)}} \mathbf{F}(X) \Phi_k(X) d\Omega = \frac{1}{A^{(k)}} \int_{\Omega^{(k)}} \mathbf{F}(X) d\Omega = \frac{1}{A^{(k)}} \int_{\Omega^{(k)}} \nabla \mathbf{u} d\Omega + \mathbf{I} \quad (11)$$

Applying divergence theorem to Eq. (11) in the current configuration yields

$$\bar{\mathbf{F}} = \frac{1}{A_k^s} \int_{\Gamma_k^s} \mathbf{u} \otimes \mathbf{n} d\Gamma + \mathbf{I} = \bar{\mathbf{e}} + \mathbf{I} \quad (12)$$

where  $\bar{\mathbf{e}}$  represents the smoothed gradient field of displacement, i.e.  $\bar{\nabla}u_i$  given in Eq. (5).  $\mathbf{n}$  is the outward normal vector. Also, the *smoothed rate of deformation* tensor could be calculated as

$$\bar{\mathbf{L}} = \dot{\bar{\mathbf{F}}}\bar{\mathbf{F}}^{-1} \quad (13)$$

The *smoothed deformation rate* and *smoothed continuum spin* can be additively decomposed as

$$\bar{\mathbf{D}} = \bar{\mathbf{D}}^e + \bar{\mathbf{D}}^p \quad (14)$$

$$\bar{\mathbf{W}} = \bar{\mathbf{W}}^e + \bar{\mathbf{W}}^p = \bar{\mathbf{W}}^e \quad (15)$$

The *smoothed Jaumann stress rate* could be obtained by

$$\bar{\mathbf{T}}^{\nabla} = \kappa \text{tr}(\bar{\mathbf{D}}^e)\mathbf{I} + 2\mu\bar{\mathbf{D}}^e \quad (16)$$

where  $\kappa$  and  $\mu$  are conventional Lamé elastic constants. The  $J_2$  associated flow theory has the form of

$$\bar{\mathbf{D}}^p = \dot{\lambda} \frac{\partial \bar{\mathbf{F}}}{\partial \bar{\mathbf{T}}} \quad (17)$$

where  $\dot{\lambda}$  is the plasticity multiplier. The consistent tangent matrix can be solved by (Zienkiewicz OC and Taylor RL 2000)

$$\mathbf{C}^{ep} = \kappa \mathbf{m} \mathbf{m}^T + 2\mu \left[ \left( 1 - \frac{2\mu\Delta\lambda}{|\bar{\mathbf{T}}^{tr}|} \right) \mathbf{I}_0 - \left( \frac{3\mu}{3\mu + H_i} - \frac{2\mu\Delta\lambda}{|\bar{\mathbf{T}}^{tr}|} \right) \bar{\mathbf{n}} \bar{\mathbf{n}}^T \right] \quad (18)$$

The meaning of parameters mentioned in Eq. (18) can be found in reference (Zienkiewicz OC and Taylor RL 2000).

### 2.3 A smoothing-domain-based selective ES/NS-FEM model for the volume locking problem

In large plasticity deformation problem, the elastic strain could be negligible compared to the plastic strain which does not change the volume of material. Therefore, incompressible deformation may occur in plane strain, axisymmetric, or three dimension problem, and this could probably result in volumetric locking phenomenon in FEM analysis. Traditional ( $u/p$ ) mixed formulations could solve the problem, with increasing of computational cost. Reduced integration is the most common method used in commercial FEM software, however, the developer should be careful about the zero energy modes and it may yield inaccurate result.

Based on these considerations, a combined ES/NS-FEM approach was proposed (Liu GR, Nguyen-Thoi T et al. 2009), which was mainly used to solve the volumetric locking problem when Poisson's ratio approaches to 0.5. In this paper, this method will be extended to the incompressible large deformation plasticity analysis to overcome volumetric locking. For plasticity deformation, the consistent tangent matrix  $\mathbf{C}^{ep}$  in Eq. (18) can be decomposed into two portions - i.e. volumetric and deviatoric parts respectively, as

$$\mathbf{C}^{ep} = \mathbf{C}_{vol}^{ep} + \mathbf{C}_{dev}^{ep} \quad (19)$$

where  $\mathbf{C}_{vol}^{ep}$  is related to the material volume change, and  $\mathbf{C}_{dev}^{ep}$  is corresponding to shape change.

These two matrix can be obtained by

$$\begin{aligned} \mathbf{C}_{vol}^{ep} &= K \mathbf{m} \mathbf{m}^T \\ \mathbf{C}_{dev}^{ep} &= 2\mu \left[ \left( 1 - \frac{2\mu\Delta\lambda}{|\bar{\mathbf{T}}^{tr}|} \right) \mathbf{I}_0 - \left( \frac{3\mu}{3\mu + H_i} - \frac{2\mu\Delta\lambda}{|\bar{\mathbf{T}}^{tr}|} \right) \bar{\mathbf{n}} \bar{\mathbf{n}}^T \right] \end{aligned} \quad (20)$$

In large deformation plasticity,  $\mathbf{C}_{vol}^{ep}$  is significant in FEM simulation. However, it contributes little for the displacement results, because the volume change only occurs in elasticity deformation; this



may result in volume locking. Since node-based smoothing domain used in NS-FEM is effective in overcoming volumetric locking (Liu GR, Nguyen-Thoi T et al. 2009), it is proper to use NS-FEM to calculate the volumetric portion of the stiffness matrix, and ES-FEM to calculate the deviatoric portion of the stiffness matrix. This approach is so-called *selective ES/NS-FEM*.

### 3. Numerical examples

#### 3.1 Plane strain beam bending

A  $0.02\text{m} \times 0.2\text{m}$  beam is fixed on the left side and subjected to a constant downward velocity on the bottom point of the right side as shown in Fig.2. A total displacement of  $0.05\text{m}$  is performed in this problem. The material properties are given as: Young's modulus  $E=120\text{MPa}$ , Poisson's ratio  $\nu=0.3$ , yield stress  $\sigma_y=1\text{MPa}$ . Isotropic hardening with the plasticity modulus  $H_i=1\text{MPa}$ , and plane strain condition is assumed.

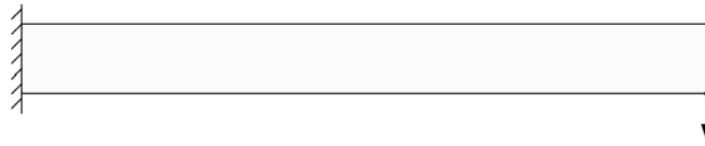


Fig.2 The beam bending problem

Four different methods are used in this case for comparison, i.e. FEM-T3, FEM-Q4, FEM-T6 and ES-FEM. 200 time steps are used in all solutions. Reference solutions are calculated using Abaqus with very fine meshes.

The elastic strain energies are calculated using FEM-T3, FEM-Q4, FEM-T6 and ES-FEM respectively, with different mesh densities and time steps. And the comparison of strain energy convergence with the number of degrees of freedom (DOFs) is plotted in Fig.3. It shows that for the same number of DOFs, the ES-FEM can get result much closer to the reference solution than FEM-T3, i.e. ES-FEM-T3 is much more accurate than FEM-T3. Furthermore, with the increasing of number of DOFs, ES-FEM converges to the reference result much faster than FEM-T3. The FEM-T3 is hardly to converge because it is very stiff. Moreover, ES-FEM-T3 can get similar accurate result compared with FEM using 4-node quadrilateral element and 6-node quadratic triangular element; this is a big advantage for the ES-FEM-T3 technique.

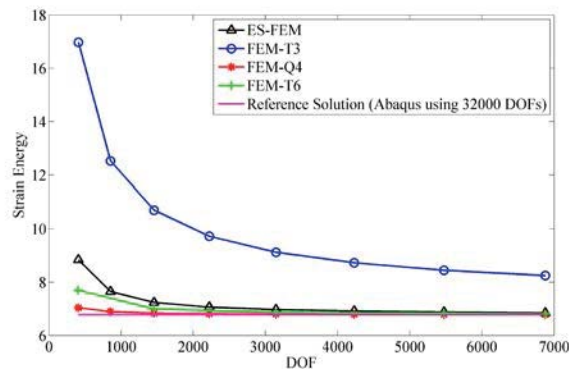
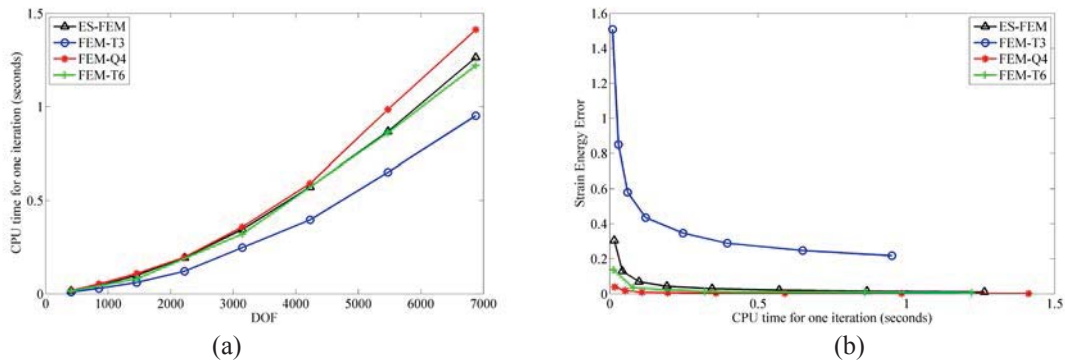


Fig.3 Convergence of the elastic strain energy versus the number of degrees of freedom

Fig.4 compares the computational cost and efficiency of the four different methods for different mesh densities. The CPU time shown in the figure represents the average computational cost for one iteration; this include the time of assembling stiffness matrix and solving linear equations, and it can be calculated by

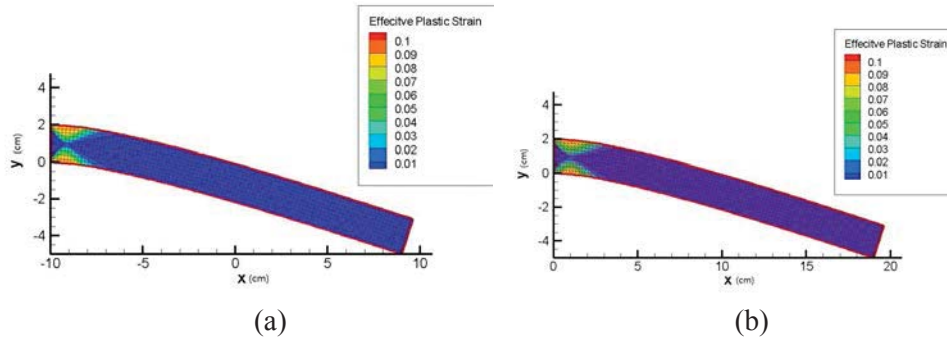
$$t = \frac{t_{total}}{N_{ite}} \tag{21}$$

where  $t_{total}$  is the total CPU time and  $N_{ite}$  is the number of iterations. Fig.4(a) shows that with the same mesh density, the computational cost of ES-FEM is larger than FEM-T3 and similar as FEM-Q4 and FEM-T6. However, when the computational efficiency (computation time for the same accuracy) is considered, ES-FEM is much more effective than FEM-T3, and could get similar computational efficiency compared to FEM-Q4 and FEM-T6.



**Fig.4** Comparison of the computational cost and efficiency of three different methods  
 (a) Computational cost; (b) Computational efficiency

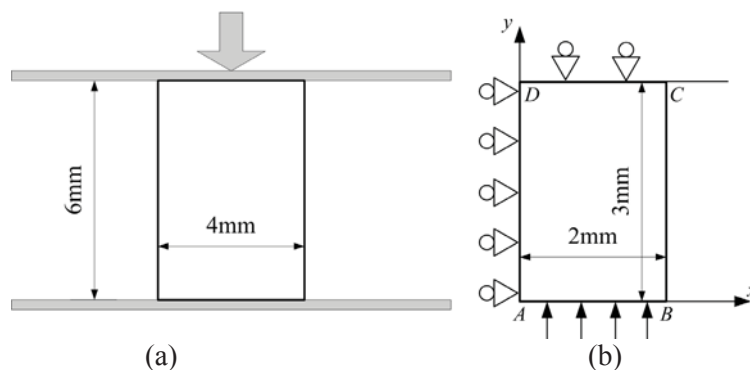
The deformation configurations with effective plastic strain contours for ES-FEM and FEM-Q4 (Abaqus) are plotted in Fig.5, and similar contour profiles are obtained. Fig.5 illustrates that ES-FEM is a valid and effective method in large deformation plasticity analysis.



**Fig.5** Effective plastic strain contour using 2222 DOFs (a) FEM-Q4 (Abaqus) and (b) ES-FEM

### 3.2 Downward forging of a billet

A billet is subjected to a constant downward velocity on the top surface as shown in Fig.6(a). The material properties are given as: Young's modulus  $E=200\text{GPa}$ , Poisson's ratio  $\nu=0.49$ , yield stress  $\sigma_Y=500\text{MPa}$ . Isotropic hardening with the plasticity modulus  $H_i=1000\text{MPa}$  and plane strain condition is assumed.



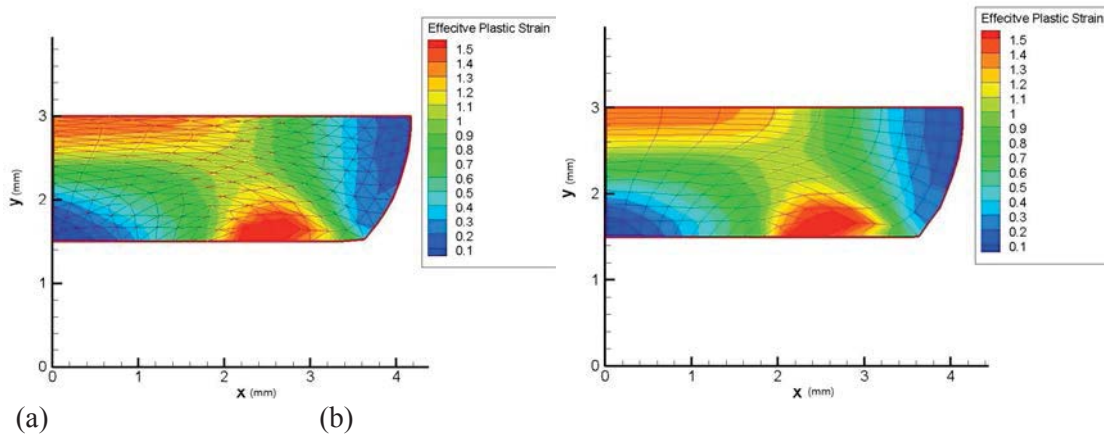
**Fig.6** (a) Compression forging of a billet (b) A quarter symmetrical model for the forging of a billet

A quarter symmetrical model and boundary conditions imposed are shown in Fig.6(b). The dies were modeled as being rigid, and no sliding is assumed between the billet and die during contact. Because the material is nearly incompressible ( $\nu = 0.49$ ) and the deformation is very large, the volumetric locking must be considered. Hence the selective ES/NS-FEM technique is used in this simulation. The problem domain is discretized by ES-FEM-T3, ES/NS-FEM-T3, Q4 and T6 elements, as illustrated in Tab.1.

**Tab. 1** Mesh discretization schemes for different methods

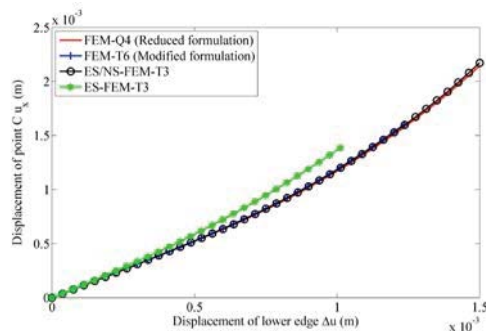
	Number of elements	Number of nodes
ES-FEM-T3/ES/NS-FEM-T3	332	192
Q4	150	176
T6	332	715

The solution of FEM-Q4 is given by Abaqus using  $\bar{\beta}$  method, and FEM-T6 is solved using modified formulation provided in Abaqus (Abaqus 2009). At the end of this simulation, ES/NS-FEM and FEM-Q4 are capable to achieve 50% compression, i.e. the displacement of lower edge  $\Delta u = 0.0015\text{m}$ . However, FEM-T6 can only achieve 42% compression, i.e. the displacement of lower edge  $\Delta u = 0.00126\text{m}$  before the element distorted. ES-FEM-T3 cannot get an accurate result because of volumetric locking. The contours of effective plastic strain for different schemes are plotted in Fig.7.



**Fig.7** Solution of forging of billet: deformation configurations  $\Delta u = 1.5\text{mm}$  (50% Compression) solved by (a) Selective ES/NS-FEM-T3, (b) FEM-Q4

Fig.8 plotted the displacement of point C in  $x$  direction by different schemes. It illustrates that the result calculated by ES/NS-FEM-T3 using linear 3-node triangular element agrees very well with FEM-Q4 and FEM-T6, and could bear larger element distortion than FEM-T6. ES-FEM-T3 cannot get a correct result because of volumetric locking, and no locking problem is observed in ES/NS-FEM-T3 approach.



**Fig.8** Displacement solutions of forging of billet at point C

#### 4. Conclusion

In order to utilize 3-node linear triangular element for analyzing large strain plasticity problem, an edge-based gradient smoothing technique has been formulated in large deformation plasticity theory. A selective ES/NS-FEM method is also adopted to solve the volumetric locking problem. In this method, the deviatoric portion of tangent modulus is calculated by edge-based smoothed gradient method, and the volumetric portion is solved by node-based smoothed gradient method. Two numerical examples are simulated to show the validity and advantages of ES-FEM compared to standard FEM method. Conclusions could be drawn as follows:

- (1) With the same displacement control, the ES-FEM-T3 can get lower strain energy than the standard FEM with T3 element. This indicates that ES-FEM-T3 is softer than FEM-T3. This property can perfectly alleviate the “over-stiff behavior” of the linear triangular element, and greatly improve the performance of linear triangular element.
- (2) The edge-based smoothing gradient technique can get much more accurate results and faster convergence rate than standard FEM with T3 element. Furthermore, the convergence rate and computing efficiency of ES-FEM using just 3-node element is similar as the standard FEM using 4-node quadrilateral element and 6-node quadratic triangular element.
- (3) Even though only linear triangular element is used, ES/NS-FEM possesses strong capability of handling element distortion. It can sustain larger plastic distortion than FEM-T6 in large strain plasticity analysis.
- (4) No volumetric locking is observed when ES/NS-FEM technique is adopted.

#### Reference

- Abaqus (2009). "ABAQUS 6.9-1 Theory manual."
- Chen JS, Wu CT, et al. (2001). "A stabilized conforming nodal integration for Galerkin mesh-free methods." *Int J Numer Methods Eng* **50**(2): 435–466.
- Liu GR (2008). "A generalized gradient smoothing technique and the smoothed bilinear form for Galerkin formulation of a wide class of computational methods." *Int J Comput Methods* **5**(2): 199-236.
- Liu GR (2009). *Mesh free methods: moving beyond the finite element method*. Boca Taton, USA, CRC press.
- Liu GR, Nguyen-Thoi T, et al. (2009). "An edge-based smoothed finite element method (ES-FEM) for static, free and forced vibration analyses of solids." *J Sound Vib* **320**(4-5): 1100-1130.
- Liu GR, Nguyen-Thoi T, et al. (2009). "A node-based smoothed finite element method (NS-FEM) for upper bound solutions to solid mechanics problems." *Comput Struct* **87**(1-2): 14-26.
- Yoo JW, Moran B, et al. (2004). "Stabilized conforming nodal integration in the natural-element method." *Int J Numer Methods Eng* **60**: 861-890.
- Zienkiewicz OC and Taylor RL (2000). *The Finite Element Method: Solid mechanics*, Butterworth-Heinemann.

## Numerical simulation of cross-flow around four cylinders by Local Domain Free Discretization-Immersed Boundary Method

\*Y.L.Wu<sup>1</sup>, C.Shu<sup>2</sup>, and H.Ding<sup>3</sup>

<sup>1</sup>Lord's Register Global Technology Centre, 1 Bukit Batok Street 22 #03-02, Singapore 659592.

<sup>2</sup>Department of Mechanical Engineering, National University of Singapore, 10 Kent Ridge Crescent, Singapore 119260

<sup>3</sup>Department of Modern Mechanics, University of Science and Technology of China, Hefei, China

\*Corresponding author: yanling.wu@LR.ORG

### Abstract

In this paper, a hybrid of Local Domain Free Discretization and Immersed Boundary Method (termed as LDFD-IBM), is applied to simulate the incompressible flow over four circular cylinders in an in-line square configuration. LDFD-IBM belongs to the family of "Cartesian mesh methods", which means the complication of mesh generation is avoided for the problems with complex geometries. A Stencil Adaptive Mesh Refinement (SAMR) is also adopted to improve the computational efficiency. Instantaneous flow patterns and other quantitative information from the numerical simulation agree well with the available data from literatures.

**Keywords:** Flow over cylinders, Cartesian mesh method, LDFD-IBM, Local Domain-Free Discretization, Immersed Boundary Method, Stencil Adaptive Mesh Refinement

### Introduction

Cross-flow of fluid around a group of cylinders has practical importance in engineering applications, such as offshore oil and gas pipelines. From the viewpoint of traditional numerical method (such as Finite Difference Method, FDM) in Computational Fluid Dynamics (CFD), the mesh generation in the flow domain for this kind of problem is obviously not a trivial task.

To solve this kind of problems involving with complex geometries, non-conforming mesh methods seem to be a good choice. Local Domain-Free Discretization (LDFD) (Shu and Wu, 2006) and Immersed Boundary Method (IBM) (Peskin, 1977) are among of them.

LDFD is inspired from the analytical method. Consider a partial differential equation (PDE) on an irregular domain. The PDE is discretized at all mesh points inside the solution domain (referred here as to *interior points*), but the spatial discretization at an interior mesh point may involve some points outside the solution domain (referred here as to *exterior points*). The functional values at those exterior points can be approximated using the values at the interior points nearby by a local extrapolation scheme. However, it is found that the extrapolation in LDFD can cause errors and bring in numerical instabilities.

The basic idea of IBM is that the enforcement of the boundary to the surrounding fluids is through a body force appeared in the governing equation. The major advantage of IBM is its simplicity and easy implementation in dealing with flows with complex geometries. However, it should be indicated that the conventional IBM suffers two major drawbacks: one is to allow for the penetration of fluid flows into the immersed bodies; the other is the low order accuracy of presenting the immersed boundary.

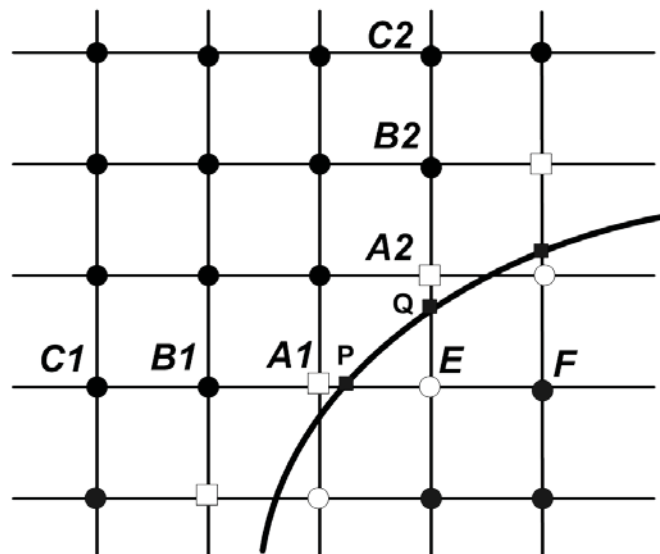
Recently, Wu et al (2012) proposed LDFD-IBM, which is a delicate combination of LDFD method and IBM, and enjoys the merits of both methods. For example, the penetration of streamlines into

solid objects in the conventional IBM, due to inaccurate satisfaction of no-slip boundary conditions, can be avoided by using the LDFD method. On the other hand, the treatment of boundary condition for pressure at the solid boundary in the LDFD method, is no longer necessary after introducing IBM.

In general, LDFD-IBM can be applied to any kind of mesh configuration. When the LDFD-IBM is applied on the Cartesian mesh, it can also be considered as a kind of Cartesian mesh solver. It is well known that solving these flow problems on a uniform Cartesian mesh usually needs very expensive computation. Therefore, from the viewpoint of computational efficiency, adaptive mesh refinement (AMR) is a desirable technique for Cartesian mesh solvers. In this paper, the recently proposed stencil mesh refinement (Ding and Shu, 2006) technique is introduced into LDFD-IBM.

### Solution of Incompressible N-S Equations by LDFD-IBM

In this work, LDFD-IBM is used to simulate incompressible N-S equations. The governing equations are solved at all the mesh nodes (referred as the Eulerian points in conventional IBM) in the computational domain, regardless they are inside the solid bodies or inside the fluid field. The velocity boundary conditions are accurately enforced at the intersection points of the mesh lines and the boundary (referred as the Lagrangian points in the conventional IBM). The functional values at the intersection points are used to determine the solution at the interior dependent points via an interpolation scheme with second- or higher order of accuracy.



**Figure 1 Classification of points in LDFD-IBM**

For the application of LDFD-IBM to problems with complex geometry, let us consider a solid boundary immersed in a fixed Cartesian mesh as shown in Fig. 1. The mesh points take one of the following three statuses:

- 1) interior dependent points (the mesh nodes which are inside the fluid domain just adjacent to the immersed boundary, represented by symbol “ $\square$ ” in Figure 1);
- 2) exterior dependent points (the mesh nodes which are inside the solid domain just adjacent to the immersed boundary, represented by symbol “ $\circ$ ” in Figure 1);
- 3) all other mesh nodes (represented by symbol “ $\bullet$ ” in Figure 1).

Obviously, A1 and A2 are interior dependent points. In present LDFD-IBM method, the functional values at interior dependent points are approximated by interpolation. For example, the velocity at A1 can be evaluated by a second order polynomial along the x direction, which involves three points P, B1, C1 as shown in Fig. 1. Here, B1 and C1 are the interior mesh points, and point P is the intersection point of the horizontal mesh line with the immersed boundary (represented by symbol “■”), where the velocity of immersed boundary is assigned. Point E is the exterior dependent node. In the original LDFD method, the functional values at exterior dependent points are obtained by extrapolation. However, in this work, since E is inside the solid body (outside flow domain), its velocity is simply assigned to the wall velocity

Clearly, the present approach combines the advantages of conventional IBM and LDFD method in the sense that:

- (1) Since the pressure on all the Eulerian nodes is obtained by solving the pressure Poisson equation, the treatment of Neumann boundary condition at the Lagrangian points for pressure is no longer needed;
- (2) There is no need to calculate the restoration force  $F$  on the Lagrangian points, and thus no need to distribute the restoring force  $F$  to the Eulerian nodes. The boundary effect is considered by updating the velocity at interior and exterior dependent points. Velocity boundary conditions are enforced accurately; As a consequence, the flow penetration is avoided.
- (3) An interpolation scheme rather than extrapolation scheme is adopted to obtain the approximate solution at the dependent points, which makes the computation more stable.

#### **Application of LDFD-IBM to Simulate Flow over Four Circular Cylinders**

Flow past cylinder arrays can be found in many engineering applications, such as offshore structures, heat exchangers. The complexity of flow separation and free shear layer interference generated by the cylinder arrays have been studied by many researchers (Farrant et al, 2000; Lam et al, 2010). Flows over four equally spaced cylinders of equal diameter are computed by LDFD-IBM in this section. The configuration is shown in Figure 2, in which  $G$  is denoted as the minimum distance between the centers of 4 cylinders.

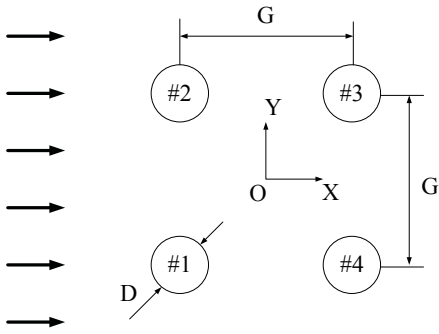
##### *1) Two-dimensional study*

The computation was performed at  $Re=200$ , based on one cylinder diameter and the spacing of cylinders  $G/D=3.0$ .

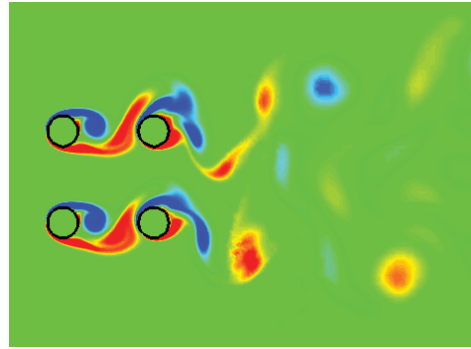
The computational domain is taken as  $50D \times 40D$ . Uniform Cartesian mesh of  $201 \times 161$  is taken as the initial mesh. 8 levels of mesh refinement by stencil mesh refinement technique (Ding and Shu, 2006) are performed around the cylinders, and the final mesh contains 97121 nodes.

Figure 3 shows the instantaneous vorticity contours. According to Farrant et al (2000), the vortices formed in between the cylinders are weaker than those on the outside. This is confirmed by our results as shown in Figure 3.

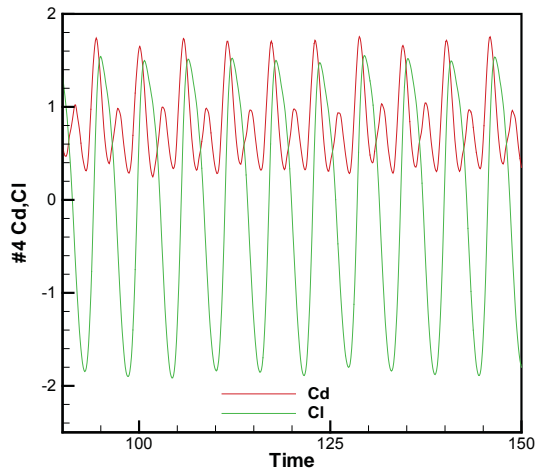
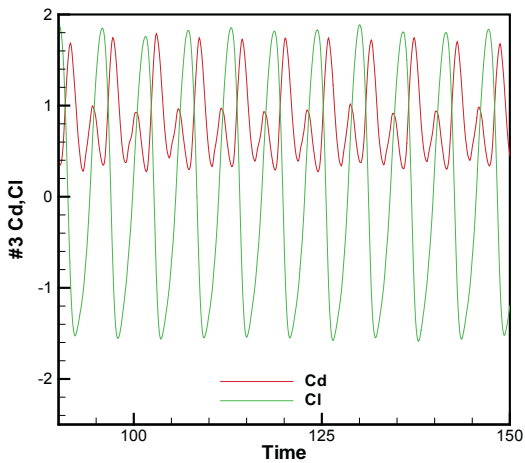
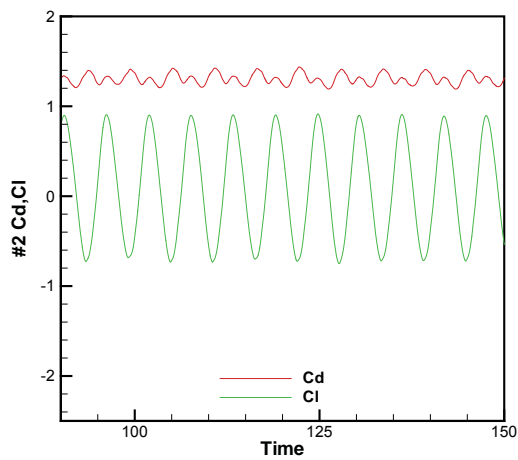
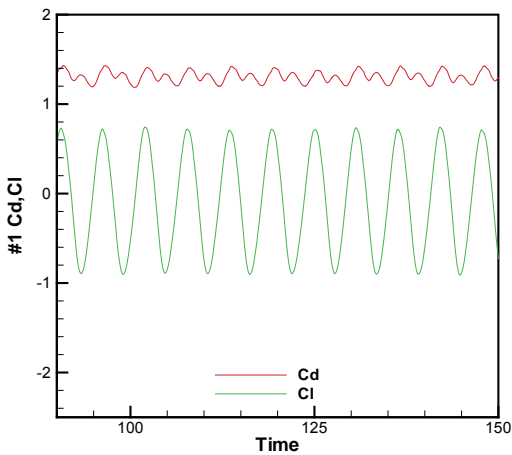
Figure 4 shows the lift and drag coefficients history. From Fig. 4, it is found that the flow patterns around all cylinders are periodic with same frequencies, which suggests that the shedding is synchronized. It has been found that the present results have a good agreement with those of Farrant et al (2000).



**Figure 2. Configuration of flow past four equi-spaced cylinders**



**Figure 3. Instantaneous vorticity contours for 2D flow at  $Re=200$  and  $G/D=3.0$**



**Figure 4 Drag and lift coefficients  $C_D$  and  $C_L$ : the curves correspond to cylinders #1 to #4,**

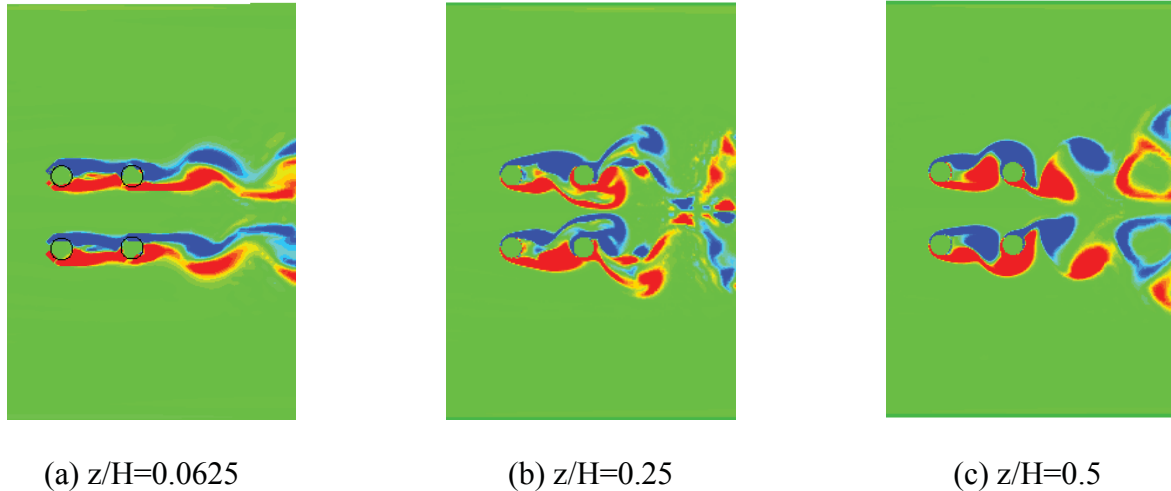
2) *Three-dimensional study*

The LDFD-IBM can be easily extended to three-dimensional simulation of flows with curved geometry. The numerical discretization and the treatment of boundary condition are very similar to the two-dimensional case, except that one additional coordinate  $Z$  needs to be considered.

The computations were performed at  $Re=200$ , based on one cylinder diameter and the spacing of cylinders  $G/D=3.5$ ,  $H/D=12$ . The two end wall is taken as the boundary condition along  $z$  direction.



The computational domain is a rectangular box with  $32D \times 20D \times 11D$  in  $x$ ,  $y$ ,  $z$  directions, respectively. The mesh strategy in 3D is to use the two-dimensional stencil AMR technique to refine the mesh in the  $X$ - $Y$  plane, and use a uniform mesh in the  $Z$ -direction. The initial mesh on the  $x$ - $y$  plane is  $161 \times 101$ , after refined around cylinder by 8 levels, final mesh on the  $x$ - $y$  plane has 46791 nodes. There are 41 nodes uniformly distributed along the  $z$  direction.



**Figure 5 Instantaneous vorticity contours for 3D flow at  $Re=200$  and  $G/D=3.5$ ,  $H/D=12$ .**

Figure 5 shows the instantaneous spanwise vorticity component  $\omega_z$  at three different spanwise positions ( $z/H=0.0625$  (near end wall),  $z/H=0.25, z/H=0.5$  (mid-span of the cylinders)) for  $G/D=3.5$  with cylinder length  $H=12D$ . In general, due to the end wall effect, with additional stronger streamwise vorticity and transverse vorticity generated along the spanwise direction of the cylinders, the 3-D vortex structure distributions are complex. It is found that the change of flow pattern at different spanwise positions of the cylinders is successfully captured by LDFD-IBM.

## Conclusions

LDFD-IBM is the combination of LDFD and Immersed Boundary method (IBM), as well as their merits. In this paper, LDFD-IBM is applied to predict the 2D and 3D cross-flow over four cylinders in an in-line square configuration. Numerical results show that LDFD-IBM is a promising method to simulate flow problems with complex geometries accurately and easily.

## References

- Ding H. and Shu C. (2006): A Stencil Adaptive Algorithm for Finite Difference Solution of Incompressible Viscous Flows, *J. Comput. Phys.*, 214, pp.397-420.
- Farrant T., Tan M., and Price W.G. (2000): A cell boundary element method applied to laminar vortex-shedding from arrays of cylinders in various arrangements, *J. of Fluids and Structures*, 14, pp 375-402.
- Lam K, Zou L. (2010), Three-dimensional numerical simulations of cross-flow around four cylinders in an in-line square configuration, *Journal of Fluids and Structures*, 26, pp.482-502.
- Peskin C.S. (1977): Numerical analysis of blood flow in the heart, *J.Comput.Phys.*25, pp 220
- Wu Y.L., Shu C, and Ding H. (2012): Simulation of Incompressible Viscous Flows by Local DFD-Immersed Boundary Method, *Advances in Applied Mathematics and Mechanics*, 4 (3), pp. 311-324.

## Solid-Fluid Interaction Analysis in Fixed Mesh and its Application to Functional Design of Component

\*Yuta Tamura<sup>1</sup>, Atsushi Kawaguchi<sup>2</sup>, Toru Hamasaki<sup>2</sup>, \*Shigenobu Okazawa<sup>1</sup> and Satoyuki Tanaka<sup>2</sup>

<sup>1</sup>Department of Transportation and Environmental System, Graduate School of Engineering,  
Hiroshima University, Higashi-Hiroshima 739-8527, Japan

<sup>2</sup>Toyota Central R & D Labs, 41-1 Yokomichi, Nagakute, Aichi 480-1192, Japan

\*okazawa@hiroshima-u.ac.jp

### Abstract

This paper describes computational method with finite element method in fixed mesh for flexible solid-fluid interaction problems. Finite element method in fixed mesh can treat large deformation without mesh failure and contact between different materials. This paper describes governing equation in strong form with mixture theory and capturing method of free-moving material interfaces. In addition, after verification of the above computational method in simple example, we apply the proposed procedure to practical solid-fluid interaction behavior such as functional design of component.

**Keywords:** Solid-Fluid Interaction, Fixed Mesh, Functional Design

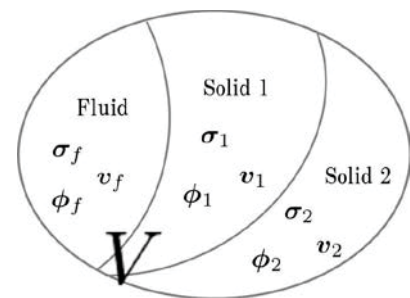
### Introduction

Recent years, high performance computing is developed dramatically. Various simulations can be performed by the high performance computing. A dynamics phenomenon has few phenomena to occur by the motion of single solid and fluid. There is more solid-fluid interaction phenomenon. Therefore, not only solid analysis and fluid analysis, but also solid-fluid interaction analysis is essential. Various studies have been performed about solid-fluid interaction analysis. The present approach establishes one governing equation for both solid and fluid models using mixture theory assuming incompressibility in the full Eulerian framework. Hyperelasticity for solid and Newtonian fluid are employed in the constitutive equations. A discretization of the proposed formulation for solid-fluid interaction dynamics is based on an explicit finite element method. The explicit finite element method reduces computational cost, except that the finite different method instead of the finite element method is used to solve Poisson and advective equations.

In this study, we focus on solid-fluid interaction analysis for automotive rubber bush. In the analyses, the strain velocity affects the stiffness. It is one of a characteristic of rubber bush so-called the velocity dependence. Our final goal is to simulate the rubber bush considering the mechanical characteristic.

### Mixture government equations

The present formulation treats interaction problem of shaft, rubber and viscous fluid for the rubber bush analysis. Fig. 1 is a representative volume with solid and fluid. In the Eulerian formulation, the one computational mesh contains different plural materials. In this section, we formulate the Eulerian mixture governing equations using volume fraction (Drew and Passman 1998).



**Figure 1. Representative volume with solid and fluid**

For the following discussion, the subscripts  $I$ ,  $2$  and  $f$  indicate quantities of solid1, solid2 and fluid respectively. The equations of motion for three materials are as follows,

$$\rho_I \left( \frac{\partial \mathbf{v}_I}{\partial t} + (\mathbf{v}_I \cdot \nabla) \mathbf{v}_I \right) = \nabla \cdot \boldsymbol{\sigma}_I + \rho_I \mathbf{b} \quad (1)$$

$$\rho_2 \left( \frac{\partial \mathbf{v}_2}{\partial t} + (\mathbf{v}_2 \cdot \nabla) \mathbf{v}_2 \right) = \nabla \cdot \boldsymbol{\sigma}_2 + \rho_2 \mathbf{b} \quad (2)$$

$$\rho_f \left( \frac{\partial \mathbf{v}_f}{\partial t} + (\mathbf{v}_f \cdot \nabla) \mathbf{v}_f \right) = \nabla \cdot \boldsymbol{\sigma}_f + \rho_f \mathbf{b} \quad (3)$$

Where  $\rho$  is density,  $\mathbf{v}$  is velocity and  $\boldsymbol{\sigma}$  is Cauchy stress. We assume that body force  $\mathbf{b}$  is identical for volume. The equations of continuity for incompressibility are as follow,

$$\nabla \cdot \mathbf{v}_I = 0 \quad (4)$$

$$\nabla \cdot \mathbf{v}_2 = 0 \quad (5)$$

$$\nabla \cdot \mathbf{v}_f = 0 \quad (6)$$

We make the equation of motion and continuity volume average. The mixture equation of motion and continuity are as follow,

$$\rho_{mix} \left( \frac{\partial \mathbf{v}_{mix}}{\partial t} + (\mathbf{v}_{mix} \cdot \nabla) \mathbf{v}_{mix} \right) = \nabla \cdot \boldsymbol{\sigma}_{mix} + \rho_{mix} \mathbf{b} \quad (7)$$

$$\nabla \cdot \mathbf{v}_{mix} = 0 \quad (8)$$

The index mix is meant mixture, and mixture physical quantity is satisfied with follow equation.

$$\mathbf{v}_{mix} = \phi_1 \mathbf{v}_1 + \phi_2 \mathbf{v}_2 + \phi_3 \mathbf{v}_3 \quad (9)$$

$$\rho_{mix} = \phi_1 \rho_1 + \phi_2 \rho_2 + \phi_3 \rho_3 \quad (10)$$

$$\boldsymbol{\sigma}_{mix} = \phi_1 \boldsymbol{\sigma}_1 + \phi_2 \boldsymbol{\sigma}_2 + \phi_3 \boldsymbol{\sigma}_3 \quad (11)$$

$\phi_i$  is volume rate function of materials. Total of volume rate function are always 1 shown in the following.

$$\phi_1 + \phi_2 + \phi_3 = 1 \quad (12)$$

By solving the mixture equation, it is possible to be analyzed a unified way without solving to discriminate equations for each material.

### Computational flow

The mixture stress  $\boldsymbol{\sigma}_{mix}$  in Eq. (7) is divided into deviatoric stress and pressure. Where  $I$  is the second order unit tensor.

$$\boldsymbol{\sigma}_{mix} = \boldsymbol{\sigma}'_1 - p_{mix} \mathbf{I} \quad (13)$$

The mixture deviatoric stress  $\boldsymbol{\sigma}'_{mix}$  is evaluated with respective volume fractions. On the other hand, the mixture pressure  $p_{mix}$  can be calculated with SMAC method. The following subsections review computational flow. For details, see references (Okazawa, Terasawa, Kurumatani, Terada and Kashiyama, 2010; Okazawa, Kashiyama and Kaneko, 2007; Benson and Okazawa, 2004).

### Intermediate velocity

We discretize spatially the mixture governing Eq. (7) by finite element method without advection term (Chorin, 1980). The present study employs 8-node isoparametric element for 3-dimensional analysis. For numerical integration, we use selective reduced integration to avoid volumetric locking. The explicit method with the central difference method is used to advance time. The discretized equation is as follows

$$\mathbf{v}^* = \mathbf{v} + \Delta t \mathbf{M}^{-1} (\mathbf{F}_{ext} - \mathbf{F}_{int}) \quad (14)$$

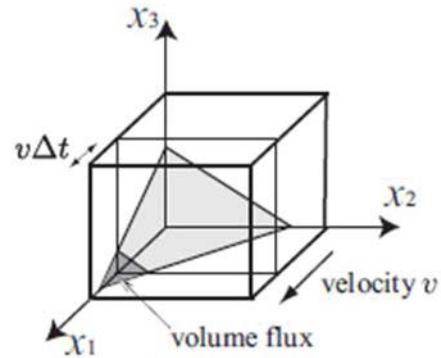
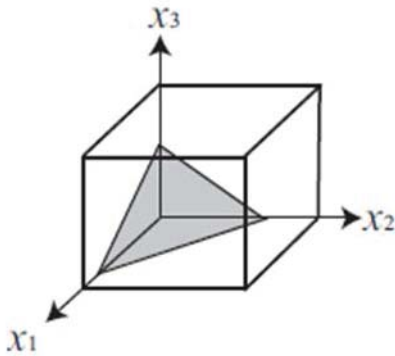
$\mathbf{M}$  is mass matrix,  $\mathbf{v}$  is velocity vector at current time and  $\mathbf{v}^*$  is intermediate velocity vector.  $\mathbf{F}_{int}$  is internal force and  $\mathbf{F}_{ext}$  is external force. We adopt the lumped mass matrix.  $\Delta t$  is time increment.

### Pressure and Modification of Velocity

After calculating pressure with conventional SMAC method, the intermediate velocity is modified (A. Amsden and F. Harlow, 2007). The corrective pressure is calculated in center of all computational mesh. By using the corrective pressure, we modify velocity to satisfy Eq. (8).

### Advective calculation and interface capturing

Because the above calculation for the intermediate velocity excludes advective term, we advect the physical quantities with the 1st order upwind difference method. The advected quantities are velocity and left Cauchy-Green deformation tensor. Also regarding accurate mass advection, we employ PLIC (Piecewise Linear Interface Calculation) method (D.L. Youngs, 1982; Rider, and Kothe 1998). The PLIC method linearly approximates to the interface of the mesh from the volume rate as Fig. 2. We calculate a volume flux using the interfacial information like Fig. 3. By using the PLIC method, it is possible to capture of free-moving material interfaces.



**Figure 2. Material interface in PLIC method**      **Figure 3. Volume flux with PLIC method**

### Numerical simulation

We apply the described Eulerian formulation using mixture theory to rubber bush analysis. Fig. 4, Fig. 5 is computational models. We treat three materials, shaft, rubber and viscous fluid. As for computational model 2, the duct of fluid is narrow. Therefore, the influence of fluid becomes strong. We give a frequency 200Hz~400Hz and a displacement  $\pm 5$ mm to the shaft. The shaft is rigid body. We calculate the internal force of x-direction component of the rubber and fluid part.

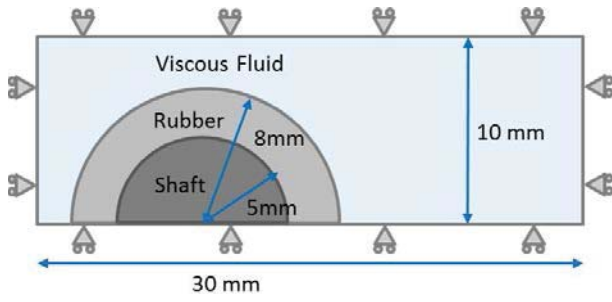


Figure 4. Computational model 1

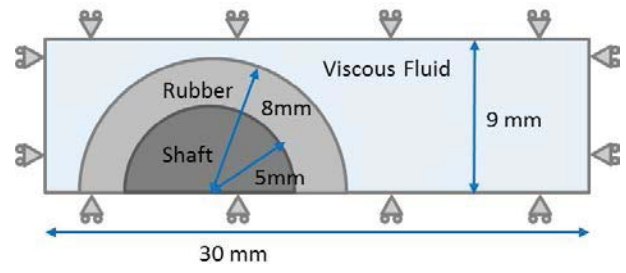
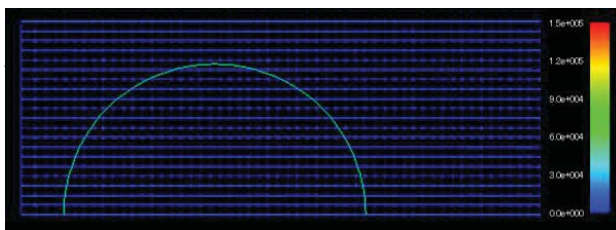
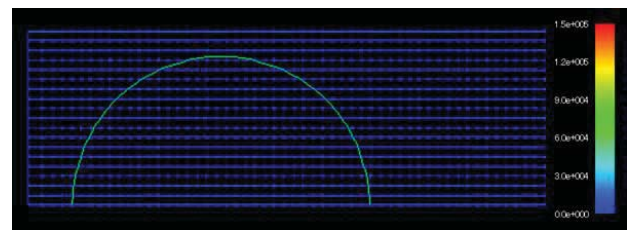


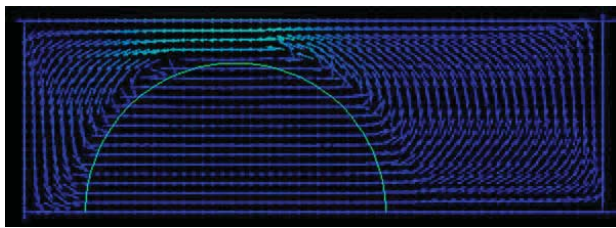
Figure 5. Computational model 2



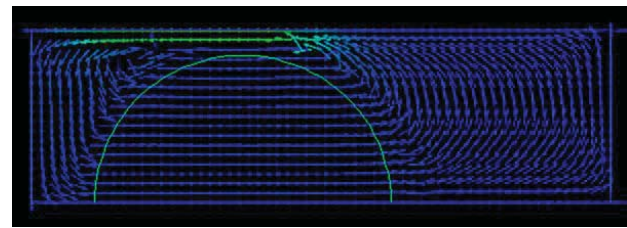
t=0.0 (model1)



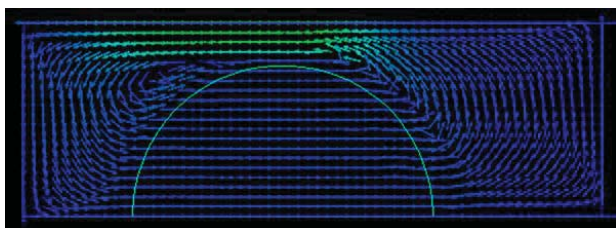
t=0.0 (model2)



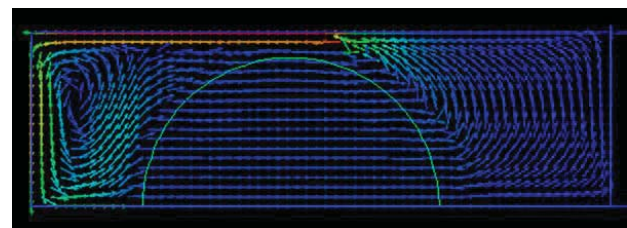
t=0.025 (model1)



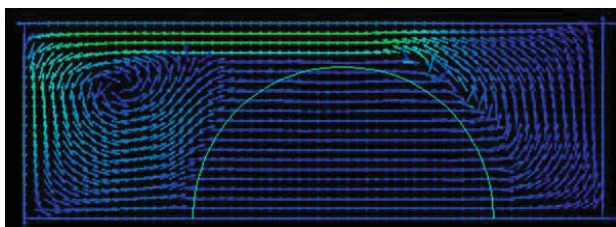
t=0.025 (model2)



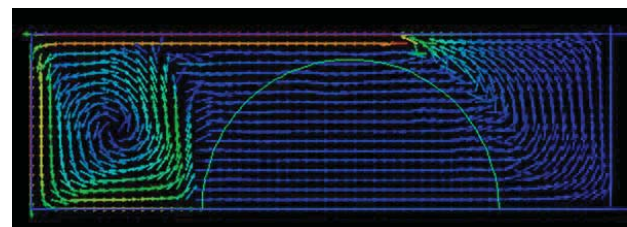
t=0.05 (model1)



t=0.025 (model2)



t=0.075 (model1)



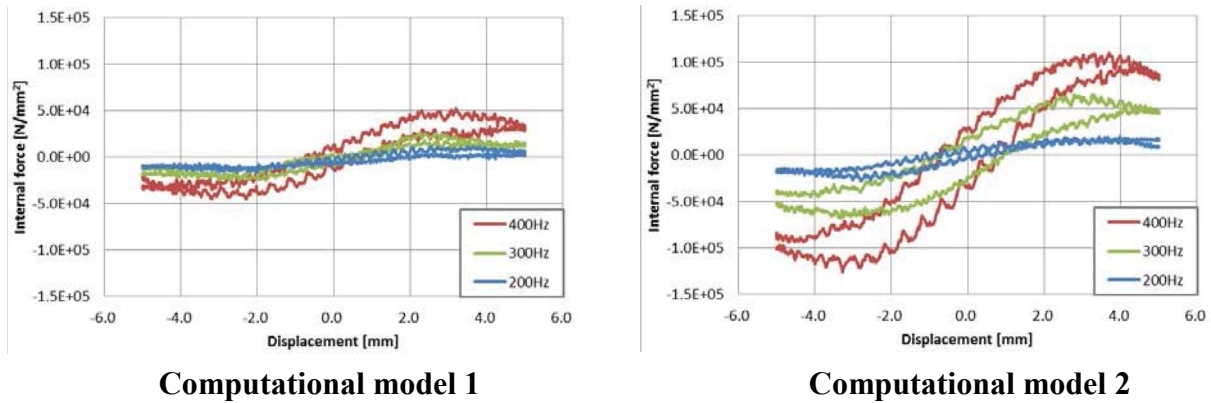
t=0.075 (model2)

Figure 6. Velocity line of each model

**Table 1. Material Parameters**

	Shaft	Rubber	Fluid
Young’s Modulus (MPa)	300	300	-
Poisson Ratio (-)	0.5	0.5	-
Density ( $10^{-6}$ kg/mm <sup>3</sup> )	5.0	1.0	0.5
Viscosity ( $10^{-3}$ Pa · s)	-	-	7.7

Fig.6 shows velocity line. We confirm that velocity line changes with solid movement. We compare the result of analysis computational model 1 and computational model 2. In computational model 2, the duct of fluid is narrow. Flow velocity of computational model 2 is faster than computational model 1. Therefore, it is thought that the influence of fluid is strong with computational model 2.



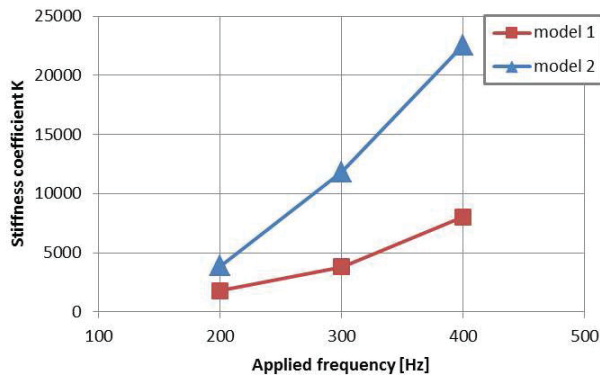
**Figure 7. Internal force of rubber and viscous fluid**

Fig.7 shows the internal force of rubber and viscous fluid. We confirm that the gradient of graph is increasing both computational model 1 and computational model 2. In addition, the path of graph is different in the forward and return. The graph of computational model 2 is the large oval. Therefore, we think that viscous fluid is affects the path of graph.

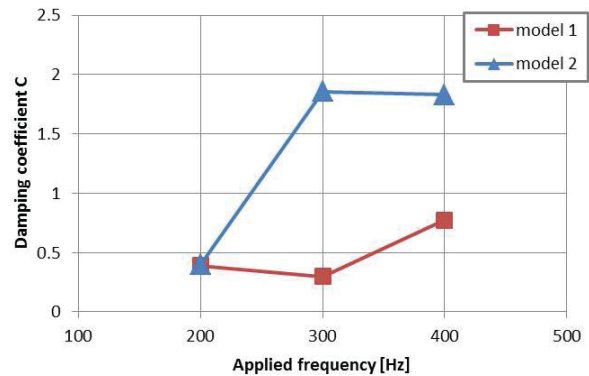
Next, we perform a parameter identification of stiffness coefficient ‘K’ and damping coefficient ‘C’ using a least squares method. The equations of approximation are as follows,

$$F = Kx + Cv \tag{15}$$

Where  $x$  is displacement of the shaft and  $v$  is applied velocity.



**Figure 8. Stiffness coefficient 'K'**



**Figure 9. Damping coefficient 'C'**

We confirm that the stiffness coefficient 'K' has increased by the vibration frequency. The computational model 2 indicates a large value. The stiffness coefficient 'K' depends on the gradient of graph of Fig.7. Fig.9 shows the damping coefficient 'C'. The computational model 2 indicates a larger value than the computational model 1. The computational model 2 is strongly influenced by the viscous fluid. Therefore, we consider the damping coefficient 'C' is larger in the computational model 2. As a result, the stiffness coefficient is dependent on the gradient of graph of Fig.7. The damping coefficient is dependent on the area of graph of Fig.7.

## Conclusions

The present paper have described the mixture Eulerian formulation and the vibration simulation of the automotive rubber bush. We performed a parameter identification of stiffness coefficient 'K' and damping coefficient 'C' using a least squares method. The future study, we improve the computational model. We apply the digital data such as voxel data to the computational model. Therefore, it is possible to simulate the rubber bush analysis with high accuracy.

## References

- D.A. Drew and S.L. Passman (1998), Theory of Multicomponent Fluids, *Springer*.
- S. Okazawa, H. Terasawa, M. Kurumatani, K. Terada and K. Kashiya (2010), Eulerian finite cover method for solid dynamics, *International Journal of Computational Methods*, **7**, pp.33-54.
- S. Okazawa, K. Kashiya and Y. Kaneko (2007), Eulerian formulation using stabilized finite element method for large deformation solid dynamics, *International Journal for Numerical Methods in Engineering*, **72**, pp.1544-1559.
- D.J. Benson and S. Okazawa (2004), Contact in a multi-material Eulerian finite element formulation, *Computer Methods in Applied Mechanics and Engineering*, **193**, pp.4277-4295.
- A. Amsden and F. Harlow (2007), The SMAC method: *A numerical technique for calculating incompressible fluid flows*, Technical Report LA-4370 , Los Alamos National Laboratory , pp.1286-1305.
- A.J Chorin (1980), Flame advection and propagation algorithm, *Journal of Computational Physics*, **35**, pp.1-31
- D.L. Youngs (1982) , Time-dependent multi-material flow with large fluid distortion, in K.W. Morton and M.J. Baines (eds), *Numerical Methods for Fluid Dynamics*, , Academic, New York, pp.273-285.
- W.j. Rider, and D.B. Kothe (1998), Reconstructing volume tracking, *Journal of Computational Physics*, **114**, pp.112-152.

## FTMP-based Simulation and Continuum Description of Discrete Dislocation System

\*Motoki Uematsu<sup>1</sup> and Tadashi Hasebe<sup>2</sup>

Graduate School of Engineering, Kobe University, 1-1 Rokkodai, Nada, Kobe 657-8501, Japan.

<sup>2</sup>Department of Mechanical Engineering, Faculty of Engineering, Kobe University,  
1-1 Rokkodai, Nada, Kobe 657-8501, Japan.

\*Corresponding author: 138t310t@stu.kobe-u.ac.jp

### Abstract

This study proposes a method for a continuum description of discrete dislocation systems based on Field Theory of Multiscale Plasticity (FTMP). Dislocations are linear defects generally extended in 3D space in complex manners: They can be bent (or curved), mutually tangle, multiply, annihilate and even yield topological changes (e.g., junction formations). Those pieces of information are discrete in nature and, at the same time, include complicated spatial details. FTMP-based incompatibility representation of the 3D dislocation system enables us to express not only the density-related information (i.e., change in the total length) but also those about the configurational changes such as rigid-body translations, local bowing-out and pinning-unpinning behaviors, including their directionalities, which are absent in the conventional dislocation density-based representation. The associated energy flow is also examined in detail based on the flow-evolutionary perspectives that relates the spatio-temporal fluctuation in the elastic strain energy with the incompatibility field.

**Keywords:** Field theory, Dislocation, Discrete dislocation dynamics, Incompatibility tensor, Continuum mechanics, crystalline plasticity

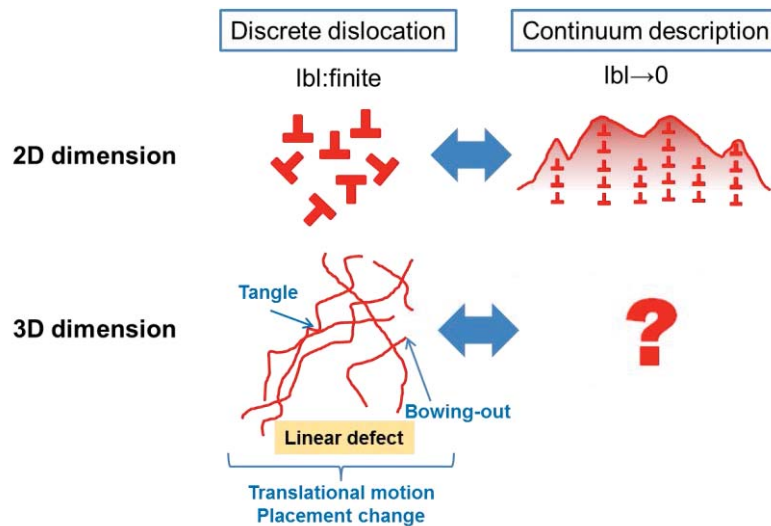
### Introduction

Dislocation is a major carrier of plasticity in crystalline solids, which is often compared to “wrinkle” of a wide-spreading carpet as a tangible simile. Although dominant roles of dislocations have been well-recognized and well-documented to date, still there seem to be many mysteries remain unfolded, e.g., with respect to their critical roles in controlling micro/macroscale properties of the targeted crystalline materials. One of the reasons is that dislocations do not always determine the system response individually but frequently do as groups, like as substructures evolving during the course of elasto-plastic deformation. One of such eloquent examples is “dislocation cells” that are universally observed in plastically-deformed crystals [Kubin (1996), Raj and Phar (1986)], in the sense that they substantially controls the overall mechanical properties notwithstanding we do not essentially know why and how they are formed. Since the dislocation cells are composed of extremely large number of dislocations having roughly a periodic structure with wavelengths commensurate with submicron to micron, which is much larger than the magnitude of Burgers vector (characteristic (intrinsic) length of dislocation), it may safely be said that this dilemma is a critical “missing link” against achieving multiscale modeling of plasticity in terms of “transcending” scales.



To solve the above dilemma, we ought to establish, above all, how to view dislocation aggregates in coarse-grained manner, maintaining their linear nature including the configurational complexities when necessary. Figure 1 shows a schematic drawing for “discrete vs. continuum” dislocations in 2D and 3D. One can notice exclusive difficulties in expressing 3D discrete dislocations based on a continuum picture, whereas relatively easy method may be found for 2D counterparts such as using distribution functions like for aggregate of particles. We must admit almost nothing has been done in this respect since Kröner suggested a use of statistical mechanics in his approach based on multi-point dislocation correlation function for expressing distributed dislocations [Kröner (1970)].

This study extensively discusses a method for describing complex dislocation systems based on Field Theory of Multiscale Plasticity (FTMP) [Hasebe (2004), (2006), (2011)], taking an example of simplified dislocation arrangements, after briefly showing the FTMP-based 3D evaluation scheme. The example to be taken is about damping motions of dislocation segments, leading practically, e.g., to the apparent reduction in elastic moduli as a macroscopic mechanical response.



**Figure 1. Discrete vs. continuum representations of dislocation aggregates.**

### About “Apparent” Reduction in Elastic Modulus

Experimentalists might have noticed decreasing elastic modulus observable in loading and reloading stress-strain curves [e.g., Yang, et al. (2004)], implying the elastic modulus (e.g., Young’s modulus) is not always be constant at least apparently during elasto-plastic deformation. This phenomenon causes many engineering problems, greatly affecting the predicting precisions of practically-important mechanical properties of metallic materials such as springback and the amount of ratcheting. Few studies, however, seem to have been carried out (this phenomenon seem to have not been taken so seriously by analytical researchers) probably and partially because of lack of such practical experiences.

The simplest mechanism yielding the “apparent” reduction in the elastic modulus is damping motions of pinned dislocation segments. During loading and unloading, pinned dislocation segments bow out and subsequently come back to the original configurations if there is no internal stress. This “reversible” plastic response consequently contributes to the “apparent softening” in the elastic stress-strain response, which appears as the apparent “reduction in the shear modulus.”

Let  $\Delta\gamma_p$  be the recovered plastic strain and  $\Delta\mu$  be the apparent decrement of the shear modulus caused by  $\Delta\gamma_p$ , we have,

$$\gamma^e + \Delta\gamma^p = [\mu^{-1} + \Delta\mu^{-1}] \tau = \mu^{-1} [1 + (\mu / \Delta\mu)] \tau \quad (1)$$

What we resultantly observe as the shear modulus from the given stress-strain response is  $\mu [1 + (\mu / \Delta\mu)]^{-1}$  instead of  $\mu$ . Therefore, the ‘‘apparent’’ reduction ratio of the shear modulus is given by,

$$\mu' / \mu \equiv [1 + (\mu / \Delta\mu)]^{-1} \quad (2)$$

where  $\mu'$  denotes the shear modulus to be observed. Theoretically,  $\mu' / \mu$  can be evaluated as,

$$\mu' / \mu \equiv [1 + \ell^3 N / (6 \times L^3)]^{-1} \quad (3)$$

with  $N$  is the number of dislocation segments, while  $L$  and  $\ell$  are the simulation cell size and the segment length, respectively.

## Analytical Model and Procedure

### *FTMP-based Incompatibility Model and Duality Diagram Representation*

Given 3D dislocation configurations, the dislocation density tensor  $\alpha_{ij}$  is firstly evaluated for each sub-cell, where the simulation cell is divided into  $10 \times 10 \times 10$  sub-cells in the present study. Here, a coarse-grained line vector is introduced for the dislocations contained in each sub-cell, without which all the details about the segment-wise geometrical fluctuations affect the distinction between edge and screw components. The definition of  $\alpha_{ij}$  in this context is given as,

$$B_i = \alpha_{ji} dS_j \quad (4)$$

where  $B_i$  is the Burgers vector corresponding to the coarse-grained line vector and  $dS_j$  is the area through which the dislocations penetrate. Note the total length of the dislocations within the sub-cell is renormalized into the coarse-grained counterpart to conserve the density.

Based on the thus evaluated dislocation density tensor, the incompatibility tensor is further evaluated as,

$$\eta_{ij} = -(\epsilon_{ikl} \partial_k \alpha_{jl})_{SYM} \quad (5)$$

where the spatial derivative is evaluated for a given arbitrary coarse-grained region by utilizing the least-square method [Yoon (2011)].

According to the flow-evolutionary hypothesis [Hasebe (2013)] in FTMP, the incompatibility tensor is equated with the fluctuation part of the energy-momentum tensor, where both the tensors are defined in the four-dimensional space-time. The temporal components provides the following specific relationship (assuming static conditions),

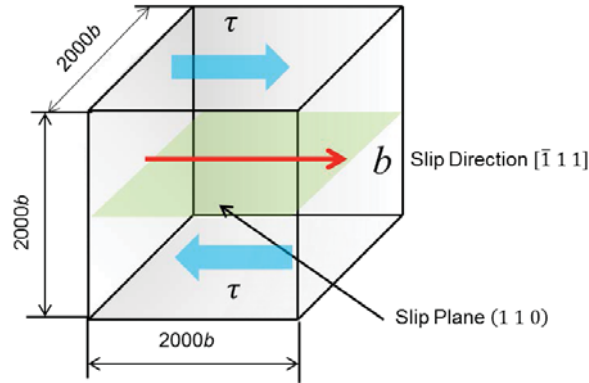
$$\eta_{KK} = \kappa \delta U^e \quad (6)$$

where  $\kappa$  is named duality coefficient. Based on Eq.(6), we can draw duality diagrams, i.e., the relationship between the trace of the incompatibility tensor and (the fluctuation part of) the elastic strain energy. The duality diagram representation allows us to ‘‘visualize’’ the energy conversion process or ‘‘energy flow’’ in terms of dislocation movements within the system.

### *Analytical Conditions and Simulation Models*

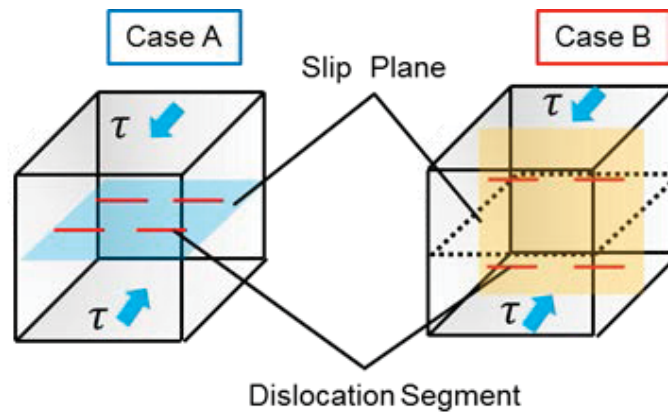
We perform a series of dislocation dynamics simulations [Zbib (2002)] for obtaining dislocation systems to be examined. Figure 2 shows the simulation cell with  $(2000b)^3$  edges, together with a prescribed slip plane and Burgers vector. We assume  $\alpha$ -Fe (BCC), with the density  $7.88 \times 10^3 \text{ kg/m}^3$ ,

the shear modulus 80.0GPa, Poisson's ratio  $\nu=0.324$ , and the magnitude of Burgers vector  $b=2.483\times 10^{-10}$ m. The external shear stress  $\tau$  is applied as shown in Fig.2 until 500 steps (loading) and is then reversed until 1,000 steps (unloading), with the increment of the simulation time step being  $1.8\times 10^{-12}$  sec.



**Figure 2. Schematic drawing of simulation cell.**

Pinned dislocation segments are placed in the simulated cell as schematically shown in Fig.3, where the initial length of each segment is set to be  $200b$  ( $b$  is the magnitude of Burgers vector). We consider roughly two arrangements of the dislocation segments, as shown in the figure, i.e. horizontal (Case A) and vertical (Case B) arrangements with respect to the slip plane. Note the Case B (vertical arrangement) may be regarded as a simplified model for dislocation walls.



**Figure 3. Schematics of simulation models with two representative dislocation arrangements, Case A (horizontal arrangement) and Case B (vertical arrangement).**

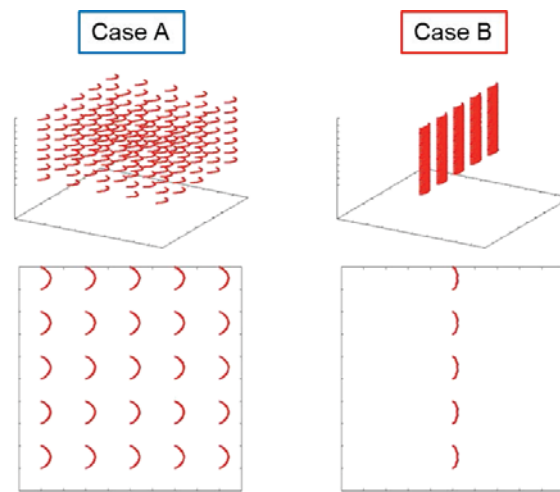
## Results and Discussions

### *Stress-strain response and apparent reduction in shear modulus*

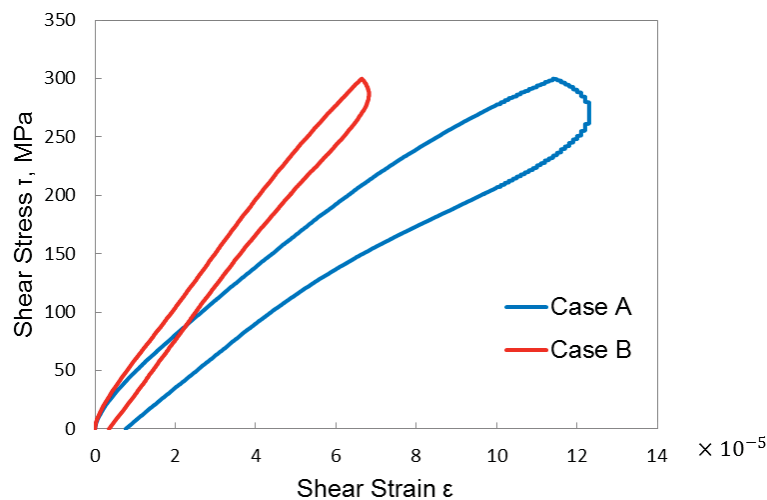
Figure 4 shows examples of simulation results for Case A and B with  $N=175$ , showing bowing-out dislocation segments. As observed in these snapshots, we immediately learn that the bowing-out motions are greatly restricted in Case B compared with Case A, probably due to the induced back stress field.

The corresponding shear stress-shear strain curves to the results in Fig.4 are presented in Fig.5. The restricted bowing-out motions of the dislocation segments for Case B results in much smaller slope of the diagram than those in Case A. Both the cases, however, exhibit nearly “reversible” stress-strain responses; the plastic shear strain caused by the bowing-out motions of dislocation segments is roughly recovered to zero when the bowed-out segments come back to the original configuration (i.e., straight line).

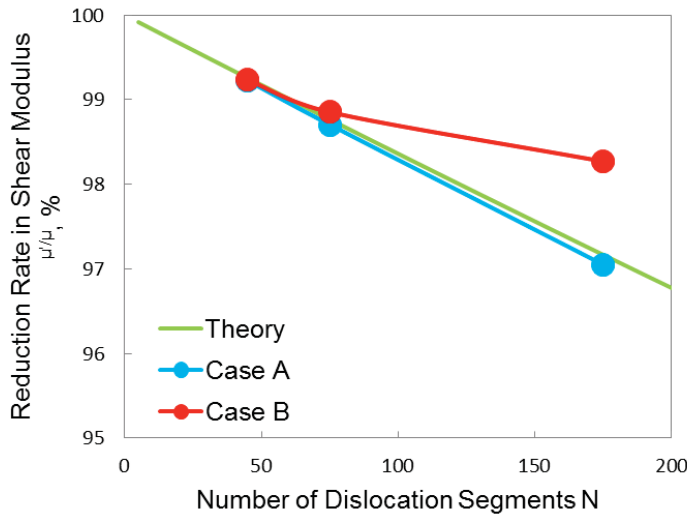
The corresponding “apparent” reduction ratios of the shear modulus to the results in Fig.5 are calculated by using Eq.(2) substituting  $L = 2000b$  and  $\ell = 200b$ . Figure 6 shows variations of the “apparent” reduction rate of the shear modulus with increasing number of dislocation segments  $N$ , comparing Cases A, B and the theory given by Eq.(3). The results for Case A agree well with the theory, whereas Case B exhibits deviation from the theory as  $N$  increases. The deviation corresponds to the greatly-restricted bowing-out motions of dislocation segments seen in Fig.4.



**Figure 4. 3D and 2D snap shots of bowing-out dislocation segments for Case A and Case B (The number of dislocations is 175).**



**Figure 5. Shear stress-plastic shear strain responses for Cases A and B.**



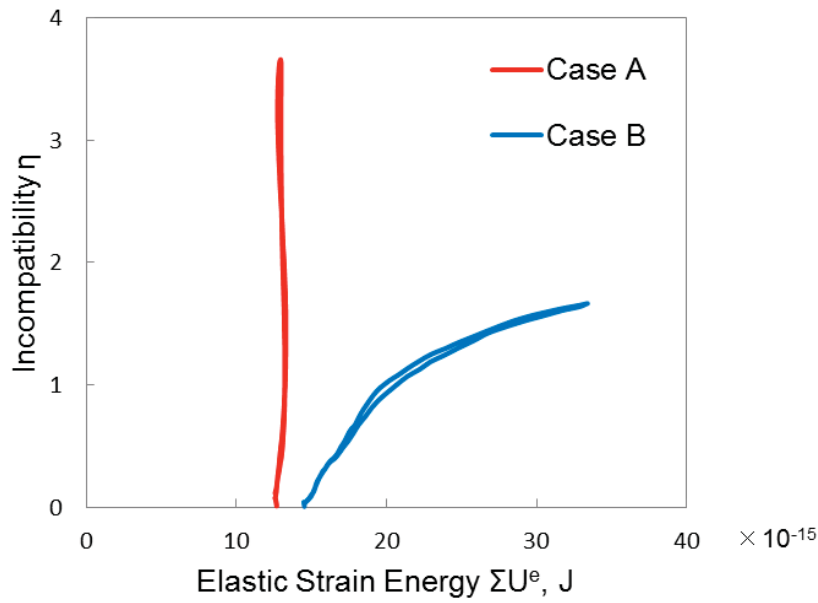
**Figure 6. Relationship between “apparent” reduction rate in shear modulus and number of dislocation segments.**

#### *Duality diagram representation*

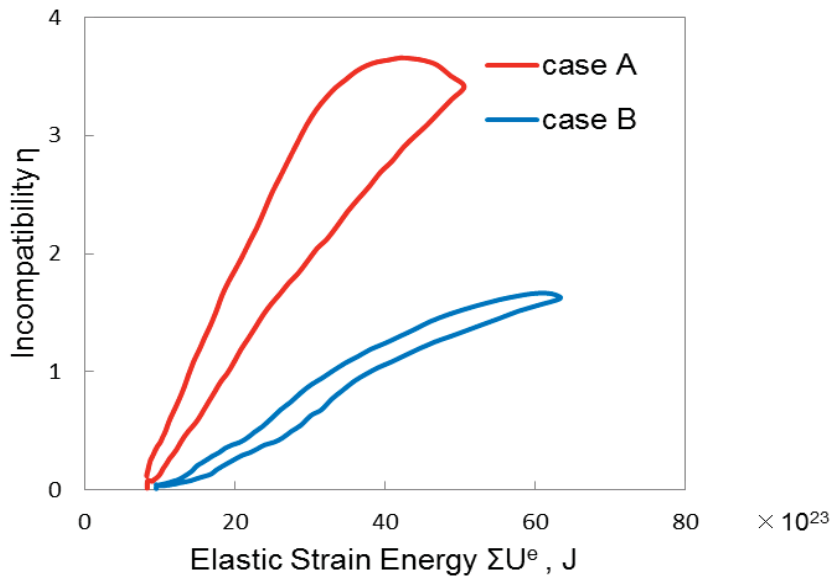
We examine the above bowing-out responses of the dislocation segments based on the duality diagram representation based on the flow-evolutionary hypothesis [Hasebe (2013)]. Figure 7 displays a duality diagram for  $N=175$ , comparing between Cases A and B. One can observe a large difference between the two cases. As demonstrated, Case A exhibits a sharp increase in  $\eta$  almost vertically in the diagram, meaning most of the externally-applied work is consumed as the growth of the incompatibility, without being stored in the dislocations. In sharp contrast to this, in Case B, the incompatibility grows but the growth rate tends to saturate as the elastic strain energy increases. This indicates that the external energy is effectively stored in the bowing-out dislocation segments until the critical configuration is reached.

The above distinct trends between Case A and B well correspond to those in the bowing-out configurations of dislocation segments in Fig.4. Thus way, the energy flow associated with the configurational changes of the dislocations can be visualized via the duality diagram.

Let us discuss further the duality diagram in terms of the interrelationship with the system response, i.e., the apparent reduction in the shear modulus discussed above associated with Fig.6. it should be noted that the duality diagram displayed in Fig.7 does not take into account the contribution of the external work done by the applied stress in the abscissa, meaning the indicated energy flow is limited to the internal one solely associated with the configurational change of the dislocation segments, thus not directly representing the stress-strain response as a system. If we consider the contribution of the external work, the duality diagram can be redrawn as Fig.8, which is regarded as being reflected the response of the system. From this re-drawn diagram, we evaluate the duality coefficient via  $\kappa \equiv \sum \eta / \sum U^e$ , which measures how much strain energy is converted to (or dissipated into) local plasticity (the bowing-out motions of dislocation segments, in this case) that manifests itself as the growth of the incompatibility tensor.

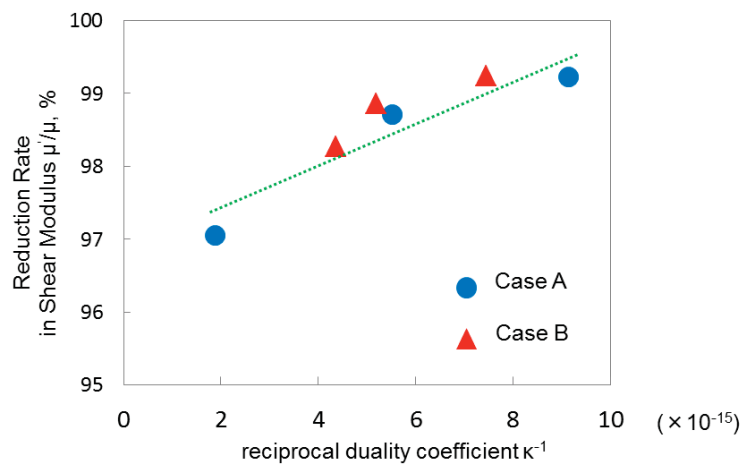


**Figure 7. Duality diagram: relationship between  $\eta$  and  $\Sigma U^e$  (The number of dislocations is 175).**



**Figure 8. System-wise duality diagram: relationship between  $\eta$  and  $\Sigma U^e$  (The number of dislocations is 175).**

Figure 9 correlates the apparent reduction rate of the shear modulus with the above-obtained duality coefficient. There observed a good correlation between the two regardless of the arrangements (Cases A and B) and the number of dislocation segments, implying the duality coefficient can be a parameter measuring the system response for the present dislocation systems.



**Figure 10. Relationship between reciprocal of duality coefficient and apparent reduction rate in shear modulus.**

## Conclusion

This study discusses FTMP-based continuum description of discrete dislocation systems, together with the duality diagram representation based on the flow-evolutionary hypothesis. Two typical dislocation arrangements yielding distinct bowing-out configurations of dislocation segments are examined in connection with the system response leading to the “apparent” reduction in the shear modulus. The configurational changes of the dislocation segments are demonstrated to be rationally expressed by the incompatibility tensor. The associated energy flow is shown to be successfully visualized by the duality diagram, while the duality coefficient provides a quantitative measures of the system response, i.e., apparent reduction rate of the shear modulus.

## References

- Hasebe, T., (2004), “Field Theoretical Multiscale Modeling of Polycrystal Plasticity,” *Trans. MRS-J*, Vol.29, pp.3619-3624.
- Hasebe, T., (2006), “Multiscale Crystal Plasticity Modeling based on Field Theory,” *Comp. Mech. Eng. Sci. (CMES)*, **11-3**, 145-155.
- Hasebe, T., (2013), “Flow-Evolutionary Hypothesis based on Field Theory of Multiscale Plasticity (FTMP) and Its Applications,” Proc. APCOM2013.
- Kröner, E., (1970), “Initial Studies of a Plastic Theory based upon Statistical Mechanics,” in “Inelastic Behavior of Solids,” (Eds. Kanninen, M. F., et al.), p.137, McGraw-Hill.
- Kubin, L. P., “Dislocation Patterns: Experiment, Theory and Simulation,” in “Stability of Materials” (eds: Gonis, A., Turchi, P. E. A. and Kurdrnovsky, J.), *Procs. NATO Advanced Study Institute on Stability of Materials, 1994, Greece*, (1996), 99-133, Plenum Press.
- Raj, S. V. and Pharr, G. M., (1986), “Compilation and Analysis of Data for the Stress Dependence of the Subgrain Size, Mater. Sci. Eng., **81**, 217-237.
- Yang, M., et al. (2004) , “Materials Processing Technology” 151,232-236
- Yoon, I., (2012), “FTMP based Development of Continuous Field Evaluation Method for Three-Dimensional Discrete Dislocation System,” Undergraduate Thesis, Kobe University.
- Zbib, H. M. (2002), “Multiscale Dislocation Dynamics Plasticity For FCC and BCC Single Crystals Version 02”.

## DEM Simulation of a Screw Feeder Using the Adhesion Powder

\*M. Kimata, S. Kikai, T. Kagami and M. Hasegawa

Department of Chemistry and Chemical Engineering, Yamagata University, 4-3-16 Jonan, Yonezawa, Japan

\*Corresponding author: kimata@yz.yamagata-u.ac.jp

### Abstract

The simulation of the screw feeder was carried out by a disintegration element method (DEM). This simulation model was compared with the feed rate of the small screw feeder at 45 mm diameter and 215 mm length with potato starch powder of 45  $\mu\text{m}$  average particle size. The potato starch could change the adhesion force between the particles by controlling quantity of water. Therefore, it was used as adhesion powder. Each parameters of the DEM simulation determine the value of the angle of repose by comparing actual measurement value with simulation. In addition, the angle of repose was measured using potato starch containing the different moisture. As a result, the repose angle of the powder and the porosity increased by increasing quantity of moisture, and the flowability of the powder got worse. In the screw feeder of the actual machine, it was found that powder is hardly fed at 25% of moisture. Because a value of the adhesion was chosen properly, in simulation, we were able to reproduce flowability and feed rate of the powder well.

**Keywords:** DEM simulation, Screw feeder, Angle of repose, Moisture, Feed rate, Flowability

### Introduction

Unit operation such as feeding and handling is always necessary in the process to treat powder. Screw feeder is shown as the device which can convey powder in the constant flow and the constant speed (Hayashi, 1998). The design of this device is difficult because such feeder depends on particle size, size distribution and flowability greatly. If the particle size becomes small, powder adhesive power increases, and feeding accuracy will decrease. A powder kinetic property can be measured by the angle of repose and the bulk density. However, it is difficult to measure a powder bulk density in the feeder (Kimata, et al. 2001). Furthermore, it seems that the feed rate of the powder is affected by the screw shape of the feeder and the roughness of the cylinder surface. It is hard to make the devices for every experiment condition. In the feed process of powders, the trouble such as blocks by the adhesion of powders is easy to happen, and it is necessary to predict the behavior (Sakashita, 1998).

On the other hand, for speedup of the computer processing, computer simulation about the powder flow is carried out widely. And the understanding of the phenomena in various powder processes is progressing. Discrete element method (DEM) is used as simulation to handle the powder flow well (SPTJ, 1998 and Hidaka, Katsura 2003). This dissolves a motion equation of individual particles discretely, and kinetic properties of the particle bed are explained, because the interaction of those particles is calculated. Therefore, in this study, we handled the adhesion change of powders "it is one of the causes of the block in the screw feeder" as its moisture change. About the kinetic property of those powders and a change of the feed speed with the actual machine, it was aimed at analyzing it by DEM simulation using numerical analysis software "RFLOW". The parameter to show the interaction between particles in the DEM simulation cannot just use the value to be different from a physical properties value of the real particle. Therefore it is necessary to make a physical properties value and the particle parameter of powders provide when we carry out DEM simulation. And we compared an actual value and the simulation value in the cheap angle of repose which was a representative physical properties value of powders. Then, the dynamic property of moisture controlled powders was measured, and relations between the powder moisture and the adhesion force were investigated. Furthermore, influence of the powders moisture was investigated by carrying out the DEM simulation that adhesion force was given between particles.



## Experimental

### Sample Powder

Potato starch (Hokkaido, Japan product, an average particle diameter: 45.4  $\mu\text{m}$ ) was used. The moisture of the powder was controlled by 3.6 - 25.4 % by using a sprayer and a drying machine kept at 60 degrees Celsius.

### Dynamic Measurement of Powders

Powder tester PE-T (Hosokawa Micron Corp.) was used for the measurement of the repose angle, and that porosity and the bulk density of the sample powders controlled for water. The tensile test and the shear test were conducted by a powder bed tester (Sankyo Piotech Co., Ltd.). A Mohrs circle was drawn by a obtained result, and flow index  $FI$  [m] was calculated.

$$FI = f_c / (\rho_b \cdot g) \quad (1)$$

Where,  $f_c$  is uniaxial collapse stress,  $\rho_b$  is bulk density of the powder and  $g$  is acceleration of gravity.

### Feed Experiment

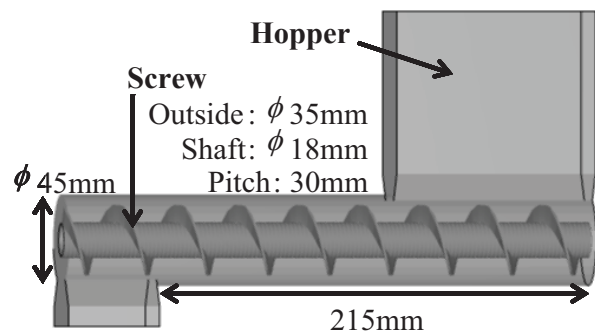
Two screw feeders (Akatake engineering Co., Ltd.) of an inside diameter: 45 mm, a screw diameter: 35 mm, a shaft diameter: 18 mm, pitch: 28 - 32 mm, the distance from hopper to an outlet: 215 mm (short type) and 1155 mm (long type) were used. After sample powders were put in Hopper, with screw number of revolutions set in 0.4 - 0.82 rps, a measurement of the powders mass from an outlet was started with a turn by a road cell. The feed speed was calculated from the mean of a feed provided every five seconds.

### DEM Simulation

Typical analysis conditions were shown in **Table 1**. And the short screw feeder model was shown in **Figure 1**. Using the screw feeder model of dimensions same as an actual machine, the analysis that changed adhesion from  $10^{-8}$  N to  $5 \times 10^{-6}$  N was carried out. The analysis results were compared with the actual values, respectively.

**Table 1. Simulation conditions of the short screw feeder**

RPM scale ratio [ - ]	33
Density [ $\text{kg}/\text{m}^3$ ]	1521
Num. of particle [ - ]	90040
Adhesion force [ $\times 10^{-6}$ N]	0, 0.01 - 5
Spring const. [N/m]	7000
Restitution coef. [ - ]	0.1
Friction coef. (Particle-Particle) [ - ]	0.36
Friction coef. (Particle-Wall) [ - ]	0.7
Rotational speed [rps]	0.8



**Figure 1. Schematic diagram of short screw feeder**

## Results and Discussion

An angle of repose of potato starch controlled to 3.6 - 21.0 % of moisture was shown in **Figure 2**. And the porosity when an angle of repose was measured was shown in addition. The red plot shows an angle of repose, and the blue plot shows porosity. In this figure, it was found that the angle of repose and the porosity increased with increase of the moisture. In the case of 10-15% of moisture, the angle of repose was increased greatly. Therefore, it is thought that flowability of the sample powder rapidly gets worse at this time.

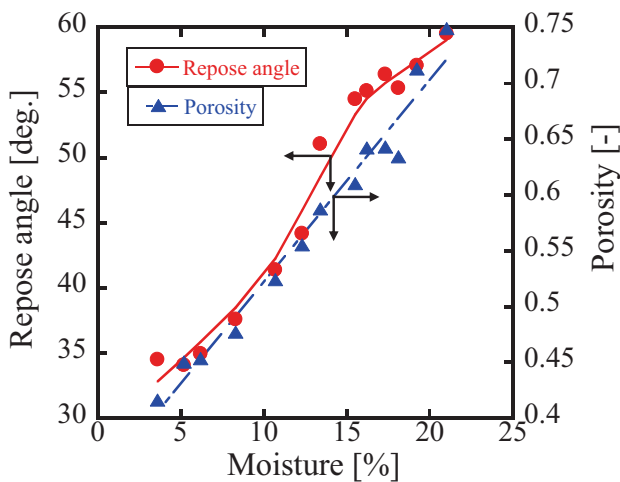
In two screw feeders which the sample powder of 5.5 - 25.4 % of moisture was used for, the relations between supply speed  $X$  and number of revolutions  $N$  were shown in **Figure 3**. In this figure, straight line relations were provided between supply speed and number of revolutions with all moisture. And these relations were arranged in the next equation.

$$X = \alpha \cdot N \quad (2)$$

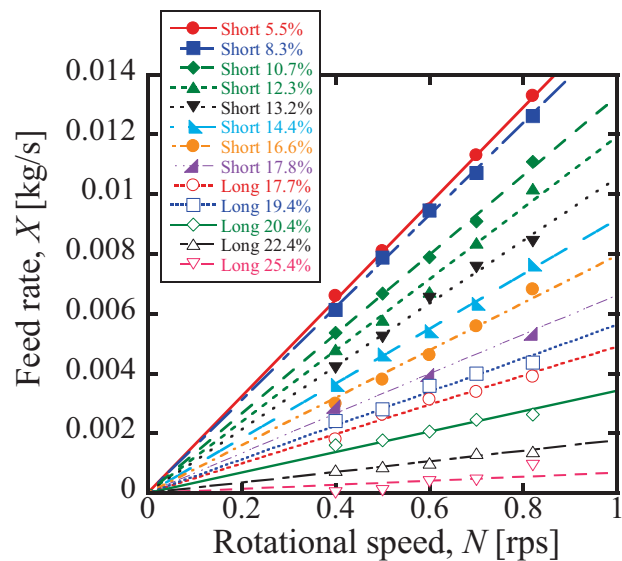
Where,  $\alpha$  is experimental constant about the feed speed. In addition, the feed speed decreased with increase of the moisture. Furthermore, it was stopped up in the trough inside when we exceeded 25.4% of moisture. And the phenomenon that it could hardly feed was confirmed.

A powder yield locus and a Mohrs circle were drawn on powder of the different moisture by the measurement of the powder bed tester. From those results, calculated flow index  $FI$  and the feed rate constant  $\alpha$  by the feed experiment of the actual machine were shown in Figure 4. In this figure, it was found that the rate constant  $\alpha$  decreased with increase of  $FI$  namely flowability got worse. Therefore, it was confirmed that a good correlation was provided between the dynamic property and feed rate of the powders having different moisture.

Angles of repose by the real potato starch with different moisture and by the DEM simulation in consideration of adhesion force were shown in Figure 5. A red plot shows an actual value by the potato starch, and a blue plot shows a simulation value. In this figure, there is unevenness in those values. However, a tendency to increase greatly was seen in the angle of repose (35 - 67 degree) of the actual value by the potato starch with the increase of the adhesion force (0 -  $10^{-6}$  N). Therefore, it was found that the flowability of model particles got worse by considering an adhesion force. The possibility that could reproduce adhesive powders by setting an appropriate adhesion force was suggested.



**Figure 2. Repose angle and porosity as a function of sample moisture**



**Figure 3. Relationships between  $X$  and  $N$**

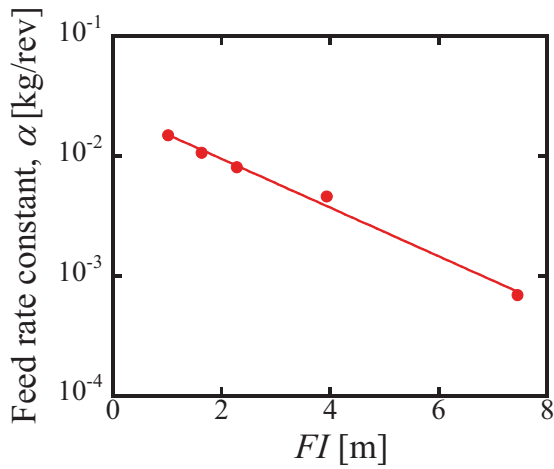


Figure 4. Relationship between  $\alpha$  and  $FI$

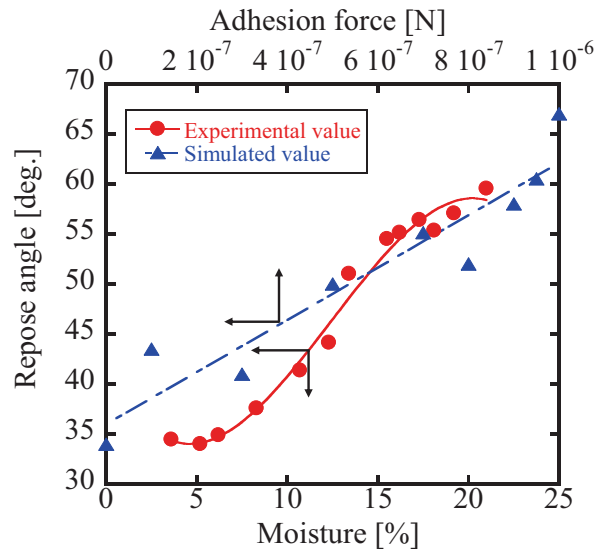


Figure 5. Repose Angle as a function of moisture and adhesion force

The values of feed rate constant  $\alpha$  by the screw feeder with the actual machine by the DEM simulation that adhesion was considered were shown in Figure 6. In this figure, feed rate tested with an actual machine with increase of the moisture decreased. As a similar tendency, the feed rate decreased by the simulation by giving adhesion. In addition, it was found that the feed rate of the model powders to approximately 8% of moisture could reproduce in the range of an adhesion force set by this simulation.

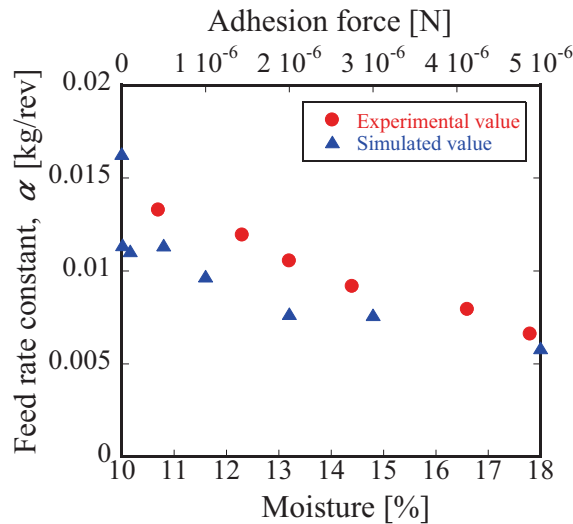


Figure 6. Feed rate constant  $\alpha$  as a function of the moisture and the adhesion force

### Conclusions

It was found that feed rate changed by a difference of the moisture. In addition, in the comparison between the dynamic property and supply rate of the powder in moisture different, it was confirmed that they were satisfactory correlations. It understood that we could control behavior and the feed

rate of the particles by an appropriate adhesion force being considered. From these results, the possibility that could reproduce the occlude behavior in the screw feeder was suggested.

### References

- Hayashi, T. (1998) Powder Thechnology Pocket Book. Kogyo Chosakai, pp.282-288.
- Kimata, M., Tsujikawa, H. and Matsumoto, K. (2001) Effect of Bulk Density and Flowability of Powders on the Feed Rate of Screw Feeder. *J. Soc. Powder Technol., Japan*, 38, pp.18-24
- Sakashita, S. (1998) Introduction powders trouble engineering.
- Society of Powder Technology, Japan (1998) Introduction of powder simulation. Sangyo Tosho
- Hidaka, J. and Katsura, N. (2003) Particle Model in Powder Mechanics. *J. Soc. Powder Technol., Japan*, 40, pp.25-28

## FTMP-based Simulation of Twin Nucleation and Substructure Evolution under Hypervelocity Impact

\*Tatsuya Okuda<sup>1</sup>, Kazuhiro Imiya<sup>2</sup>, and Tadashi Hasebe<sup>3</sup>

<sup>1</sup>Graduate School of Engineering, Kobe University, 1-1 Rokkodai, Nada, Kobe 657-8501, Japan.

<sup>2</sup>Iga Campus, Mori Seiki Co. Ltd, 201 Midai, Iga City, Mie 519-1414, Japan.

<sup>3</sup>Department of Mechanical Engineering, Faculty of Engineering, Kobe University,  
1-1 Rokkodai, Nada, Kobe 657-8501, Japan.

\*Corresponding author: 137t316t@stu.kobe-u.ac.jp

### Abstract

The deformation twinning model based on Field Theory of Multiscale Plasticity (FTMP) utilizes the twin degrees of freedom via an incompatibility tensor, incorporating it into the hardening law of the FTMP-based crystalline plasticity framework, which is then further implemented into a finite element code. The FTMP-based model is adapted to a single slip-oriented FCC single crystal sample, and preliminary simulations are conducted under static conditions to confirm the model's basic capabilities. The simulation results exhibit nucleation and growth of twinned regions, accompanied by serrated stress response with softening. Simulations under hypervelocity impact conditions are also conducted to investigate the model's descriptive capabilities of induced complex substructures composing of both twins and dislocations. The simulated nucleation of twins is examined in detail by using duality diagrams in terms of the flow-evolutionary hypothesis.

**Keywords:** Deformation twinning, Twin nucleation, Hypervelocity impact, Crystalline plasticity, Multiscale modeling, Field theory

### Introduction

Twinning, which is a predominant deformation mechanism in hexagonal close-packed (HCP) metals, is also observed in deformation of body-centered cubic (BCC) metals as well as deformation of face-centered cubic (FCC) metals under impact. In polycrystalline metals, twinning is known to act as an accommodation to redundant deformation attributed to geometrical constraints. Since the earliest evidence of deformation twinning, several efforts have been undertaken to incorporate twinning, mainly for the purpose of predicting textures and stress-strain responses. However, there is no established twinning model with the capability of simulating the nucleation and growth of twinned regions, together with the resulting lattice rotation altogether.

The conventional crystal plasticity-based FEM is capable of simulating slip-induced deformation, though it is incapable of taking into account the formation of dislocation substructures, which form via additional microscopic degrees of freedom. Since dislocation substructures are known to effectively alter the mechanical properties of materials, it is crucial to consider the formation of dislocation substructures via dislocation interaction as well as other phenomenon occurring in the microscopic scale, in order to sufficiently measure plastic deformation.

The Field Theory of Multiscale Plasticity (FTMP) (Hasebe, 2008a,b) is a comprehensive approach that enables direct treatments of the evolutions of "inhomogeneity," instead of merely linking microscopic events to macro-plasticity. Inhomogeneity within a particular field can be expressed completely with "torsion" and "curvature"; in continuum mechanics, torsion (or dislocation density tensor) is given as the first derivative of distortion, and curvature (or incompatibility tensor) is given as the second derivative of strain. These notions are applied to metallic materials as non-

Riemannian plasticity (Kondo, 1955), and form the foundation of the differential geometry-based field theory incorporated in FTMP. The past results imply that locally-stored strain is transformed to incompatibility, which is released in various size scales, and that the resulted evolution of the inhomogeneity field follows; this process is proposed as the Flow-Evolutionary Hypothesis in FTMP. In FTMP-based modeling, the incompatibility tensor model, which corresponds to the degree of freedom (DOF) of deformation modes, is implemented in the hardening law of the crystalline plasticity framework, and this makes it possible for the present model to explicitly analyze multiscale evolution of inhomogeneity as well as interactions between scales.

The FTMP-based deformation twinning model to be proposed here incorporates the twin DOF via the incompatibility tensor, which is implemented in a hardening law independent from that of slip, is capable of simulating concurring slip and twin deformations. The present model qualitatively simulates the formation of a lenticular twin nucleus and its growth, together with the resulting lattice rotation, softening and serrated stress response in analyses conducted in low temperatures under static condition. The results demonstrate that twinning can be associated to the evolution of the inhomogeneity field, though further examination of the basic capabilities of the model and assessment on the evolution of inhomogeneity based on incompatibility is necessary.

Deformation twinning is also observed under impact and hypervelocity impact conditions. When stressed under such extremely high strain rates, FCC metals such as Nickel exclusively form diverse substructures composing of mixed twins and dislocations, which vary according to the applied pressure and pulse durations. Associated with the morphology of the induced substructure, the mechanical properties of materials can be significantly altered.

In this work, the basic capabilities of the FTMP-based deformation twinning model are demonstrated by adaptation to FCC metals, and the simulated nucleation of twins is examined in detail by using duality diagrams in terms of the flow-evolutionary hypothesis (Hasebe, 2013). Simulations under impact conditions are also conducted to investigate the model's descriptive capabilities for reproducing induced complex substructures.

### Modeling Deformation Twinning – Kinematics and Constitutive Model

In the present study, the elasto-plastic decomposition by Lee is extended to that including the twin deformation by introducing an intermediate configuration,

$$\mathbf{F} = \mathbf{F}^e \cdot \mathbf{F}^{tw} \cdot \mathbf{F}^p \quad (1)$$

where the deformation gradient tensor for the twinning is represented by  $\mathbf{F}^{tw}$ . Correspondingly, the Jaumann rate of the Kirchhoff stress tensor is given by,

$$\boldsymbol{\tau}_{(J)} = \mathbf{C}^e : \mathbf{d} - \sum_{\alpha=1}^N \mathbf{R}^{(\alpha)} \dot{\gamma}^{(\alpha)} + \sum_{\bar{\alpha}=1}^N \mathbf{R}^{tw(\bar{\alpha})} \dot{\gamma}^{tw(\bar{\alpha})} \quad (2)$$

with

$$\begin{cases} \mathbf{R}^{(\alpha)} = \mathbf{C}^e : \mathbf{P}^{(\alpha)} + \boldsymbol{\beta}^{(\alpha)} \\ \boldsymbol{\beta}^{(\alpha)} = \mathbf{W}^{(\alpha)} \cdot \boldsymbol{\sigma} - \boldsymbol{\sigma} \cdot \mathbf{W}^{(\alpha)} \end{cases} \text{ and } \begin{cases} \mathbf{R}^{tw(\bar{\alpha})} = \mathbf{C}^e : \mathbf{P}^{tw(\bar{\alpha})} + \boldsymbol{\beta}^{tw(\bar{\alpha})} \\ \boldsymbol{\beta}^{tw(\bar{\alpha})} = \mathbf{W}^{tw(\bar{\alpha})} \cdot \boldsymbol{\sigma} - \boldsymbol{\sigma} \cdot \mathbf{W}^{tw(\bar{\alpha})} \end{cases} \quad (3)$$

The strain rate due to deformation twin is assumed to be driven by the evolution of the incompatibility tensor field for the twinning mode,  $\eta_{tw}^{(\bar{\beta})} \equiv (\mathbf{t}^{tw(\bar{\beta})} \otimes \mathbf{s}^{tw(\bar{\beta})}) : \boldsymbol{\eta}$ , i.e.,

$$\dot{\gamma}^{tw(\bar{\alpha})} = Q_{\bar{\alpha}\bar{\beta}}^{tw} \left| \dot{\gamma}_{prev}^{tw(\bar{\beta})} \right| \quad (4)$$

$$Q_{\bar{\alpha}\bar{\beta}}^{tw} = \delta_{\bar{\alpha}\bar{\beta}} \cdot F(\eta_{tw}^{(\bar{\beta})}) \cdot \left\langle 1 - \frac{|F(\eta_{tw}^{(\bar{\beta})})|}{F_{sat}^{tw}} \right\rangle \quad (0 \leq a \leq 1) \quad (5)$$

Thus, the activation of twinning in the present model depends solely on the evolution of  $F(\eta_{tw}^{(\bar{\beta})})$ , which denotes the FTMP-based incompatibility term defined as,

$$F(\eta_{tw}^{(\bar{\alpha})}) = \text{sgn}(\eta_{tw}^{(\bar{\alpha})}) \frac{\bar{k}}{p_\eta} \left( \frac{l_{tw}}{b} |\eta_{tw}^{(\bar{\alpha})}| \right)^{1/2} \quad (6)$$

### *Flow-Evolutionary Hypothesis in FTMP*

The “flow-evolutionary” hypothesis asserts a generalized law for the evolutions of the inhomogeneous fields and the attendant local plastic flow accompanied by the energy dissipation. The notion “duality” between fluctuating hydrostatic stress and deviatoric strain fields introduced in FTMP (Hasebe, 2006) can be embodied by this law, although it still is a “working hypothesis,” deserving further verifications and validations. Specifically, it represents an interrelationship between the locally-stored strain energy (fluctuation part) and the local plastic flow (in the form of incompatibility tensor field  $\eta_{ij}$ ) as has been discussed in the context of polycrystalline plasticity (Aoyagi and Hasebe, 2007). The hypothesis is given by Eq. (7). The details of “flow-evolutionary” hypothesis is found in the work by Hasebe (2013). A brief derivation process is described below.

$$\eta_{ij} = \kappa \delta T_{ij} \quad (7)$$

Here,  $\eta_{ij}$  and  $\delta T_{ij}$  are the incompatibility tensor, which represents inhomogeneity within a particular field, and the fluctuation of the energy-momentum tensor, which represents locally-stored internal energy, respectively. Let  $\kappa$  be the transport coefficient which represents the energy flow between strain and locally-stored energy. Four-dimensional representation of the incompatibility tensor is given as the derivation of local elastic strain  $\varepsilon^e$

$$\eta_{ab} = -\varepsilon_{aklp} \varepsilon_{bmnq} \partial_k \partial_m \varepsilon_{ln}^e \quad (8)$$

where the indices  $a, b$  denote spatio-temporal components, i.e.,  $a, b = 1, 2, 3, 4$ , with 4 being time. In this study, we focus on the duality relation based on the temporal components of  $\eta_{ij}$  and  $\delta T_{ij}$ , i.e.,  $\eta_{44}$  and  $T_{44}$ , given by Eq. (9).

$$\eta_{44} = \kappa \delta T_{44} = \kappa \delta (K + U^e) \quad (9)$$

In Eq. (9),  $T_{44}$  on the right-hand side coincides with the Hamiltonian of the system, i.e., the total energy, consisting of the kinetic energy  $K$  and the local strain  $U^e$ . For the left-hand side, on the other hand, by utilizing the generalized definition of the cross product for 4D (McDavid and McMullen, 2006), we have,

$$\eta_{44} = \varepsilon_{4klp} \varepsilon_{4mnp} \partial_k \partial_m \varepsilon_{ln}^p = \eta_{KK} \quad (10)$$

In this study, in order to investigate the energy flow in twinning, we examine the local strain  $U^e$  in addition to the fluctuation of the local strain  $\delta U^e$ .

### *Hardening Law and Field Theoretical Strain Gradient terms*

As mentioned above, the present constitutive model incorporates the contributions of  $\alpha^{(\alpha)}$  and  $\eta^{(\alpha)}$  through the hardening ratio  $Q_{\alpha\beta}$  as,

$$Q_{\alpha\beta} = f_{\alpha k} S_{\beta k} + \delta_{\alpha\beta} \{1 + F(\alpha^{(\alpha)}; \eta^{(\alpha)})\} \quad (11)$$

where  $f_{\alpha k}$  represents the dislocation interaction matrix, and  $S_{\beta k}$  expresses history matrix further given as an increasing function of plastic work done by the effective stress that responsible for dislocation processes, e.g.,

$$S_{\alpha\beta} = \tanh \left[ \frac{(W_p)_{\alpha\beta}^*}{(W_p)_{sat}^*} \right] \text{ with } (W_p)_{\alpha\beta}^* = \delta_{\alpha\beta} (W_p)_{(\beta)}^* \quad (12)$$

where  $(W_p)_{(\beta)}^*$  defines the plastic work done by the effective stress for dislocation processes only (excluding other contributions), e.g.,

$$(W_p)_{(\beta)}^* = \int (\dot{W}_p)_{(\beta)}^* dt \text{ with } (\dot{W}_p)_{(\alpha)}^* = \langle \tau^{(\alpha)} - \tau_{Peierls}^{*(\alpha)} \rangle \cdot \dot{\gamma}^{(\alpha)} \quad (13)$$

Here,  $F_k(\alpha_k^{(\beta)}; n_k^{(\beta)}) \equiv F_k(\alpha_k^{(\beta)}) + F_k(n_k^{(\beta)})$  expresses the field theoretical “strain gradient terms” given respectively as (Aoyagi and Hasebe, 2007),

$$\begin{cases} F(\alpha_{slip}^{(\alpha)}) = \frac{\bar{k}}{p_\alpha} \left( \frac{|\alpha^{(\alpha)}|}{b} \right)^{1/2} \\ F(\eta_{slip}^{(\alpha)}) = \text{sgn}(\eta^{(\alpha)}) \frac{\bar{k}}{p_\eta} \left( \frac{l_{defect}}{b} |\eta^{(\alpha)}| \right)^{1/2} \end{cases} \quad (14)$$

where  $p_\alpha, p_\eta$  are coefficients related with the contributions of the  $\alpha_k^{(\beta)}$  and  $\eta_k^{(\beta)}$ , the resolved components of  $\alpha_{ij}$  and  $\eta_{ij}$  respectively, to the change in the effective cell size  $d_{cell}$ , while  $l_{defect}$  represents the characteristic length of the defect field considered, e.g.,  $l_{defect} = b$  for dislocation dipoles and  $l_{defect} = 10^{-6}$  m for dislocation substructures like cells. In Eq. (11), the hardening law can be obtained without the effect of the strain gradient terms, which take into account the slip-induced inhomogeneity which occurs with deformation.

## Results and Discussion

### Basic Capability of FTMP-based Twinning Model

Here we incorporate a  $24 \times 24 \mu\text{m}^2$  finite element model with  $24 \times 24$  crossed-triangle elements, assuming single crystal Cu. The nodes at the top end are given a total displacement of  $7.2 \mu\text{m}$ , corresponding to 30% tensile strain of the model, at the strain rate of  $1.0 \times 10^{-3} \text{ s}^{-1}$  in plane strain condition. The model surface is set to be in parallel to (1 2 1), while the loading axis is oriented in  $[1 \ 2 \ \bar{5}]$ .

Firstly, simulations are conducted incorporating precursor inhomogeneity due to slip by implementing the FTMP- $\eta$  model, i.e.,  $F(\alpha)$  and  $F(\eta)$ , into the hardening law of the model. The simulated contour diagrams for frequency of twinning in the primary twinning plane ( $\bar{1} \ 1 \ 0$ ) are shown in the upper part of Fig.1. The results exhibit nucleation and the subsequent evolution of lenticular twinned regions at the center of the sample, accompanied by serrated stress response and softening. The frequency of twinning is given as the total number of simulation time steps in which the twinning plane meets a critical resolved shear stress condition, the point at which the twin model becomes operative. In the present model, the activation of twins at nucleation sites is essentially controlled by the evolution of precursor inhomogeneities driven by slip, and this implies that the twinning behavior of materials is greatly affected by slip and strain history.

To investigate this implication, simulations are repeated under conditions without precursor inhomogeneity, i.e.,  $F_1(\alpha), F_2(\eta) \rightarrow 0$ . The simulation results are shown in the bottom part of Fig. 1. In this case, nucleation is delayed until  $\varepsilon = 0.163$ , and growth is ultimately initiated around  $\varepsilon = 0.170$ , not from the center, but from the upper/lower edges. There is also a decrease in the overall flow stress, though this is attributed mainly to the absence of  $F(\alpha)$ , which associates the



slip-induced formation of dislocation substructures and its effect on hardening, and not to the difference in twinning behavior.

Figure 2 compares evolving contours for twinned regions, together with the incompatibility term  $F(\eta_{twin})$ , between the two cases: with and without precursor inhomogeneity. When there is no precursor inhomogeneity, we can see that weak evolution of slip-induced inhomogeneity, which is displayed as the mild modulation in  $F(\eta_{twin})$ , tends to inhibit the twin nucleation within the sample. Twinning in this case occurs from non-uniformity associated with boundary conditions. Twinning in this case occurs from non-uniformity associated with boundary conditions.

The results eloquently demonstrate some of the prominent capabilities of the proposed twinning model, where (1) natural representations of twin nucleation (in the sense that it requires no artificial imperfections that promote the activation of twins), (2) the nucleated twins grow while forming a lenticular shape, and (3) the attendant stress-strain response was accompanied by serration and softening. In addition, the nucleation of twinning was obtained exclusively by incorporating precursor inhomogeneity, and thus our theory implies that the formation of twin nuclei within metallic crystals is largely influenced by the strain history.

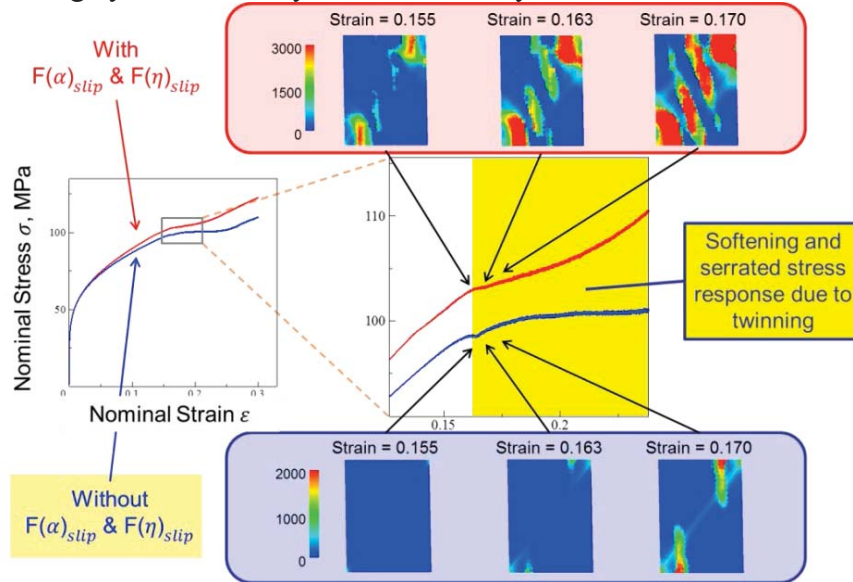


Figure 1. Stress-strain responses comparing effect of precursor inhomogeneity on twin evolution.

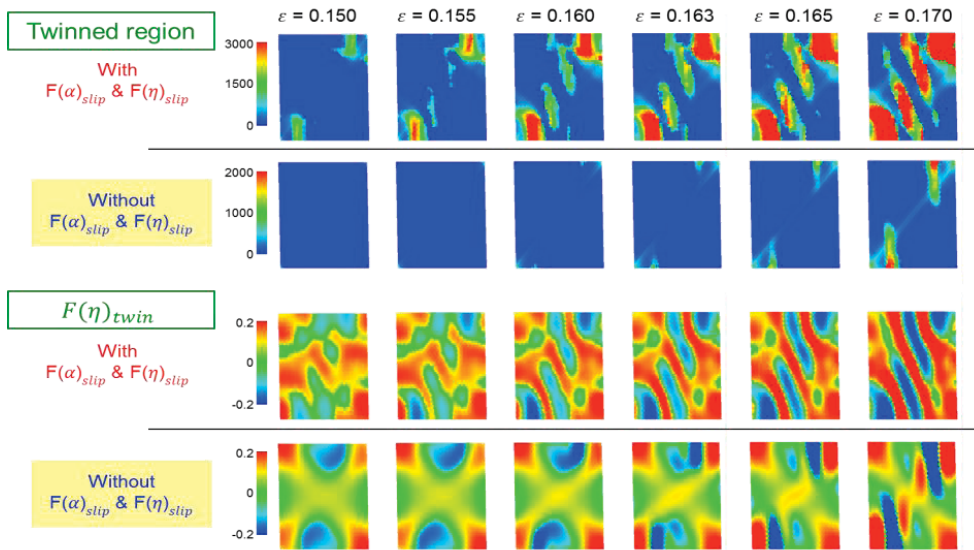
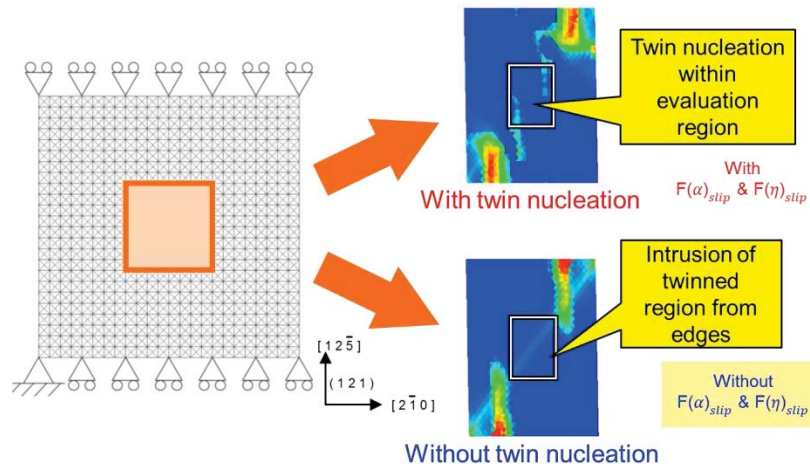


Figure 2. Comparison of twin domains (top) and incompatibility (bottom) for simulations with and without dislocation- and incompatibility-induced hardening.

### Examination of Twin Nucleation via Duality Diagram

In this section, we investigate the simulated nucleation and growth of the twinned region in detail via the duality diagram in terms of the flow-evolutionary hypothesis. As explained previously, the duality diagram represents an interrelationship between the local plastic flow (energy dissipation) in the form of incompatibility tensor  $\eta_{KK}$  and the locally-stored elastic strain energy  $U^e$ . Since the present model incorporates the twin DOF as an alternative mode for releasing locally-stored strain energy, it is assumed that the differences in the evolution, e.g. nucleation and the subsequent growth of the twinned regions is reflected in the process of converting local strain energy to incompatibility.

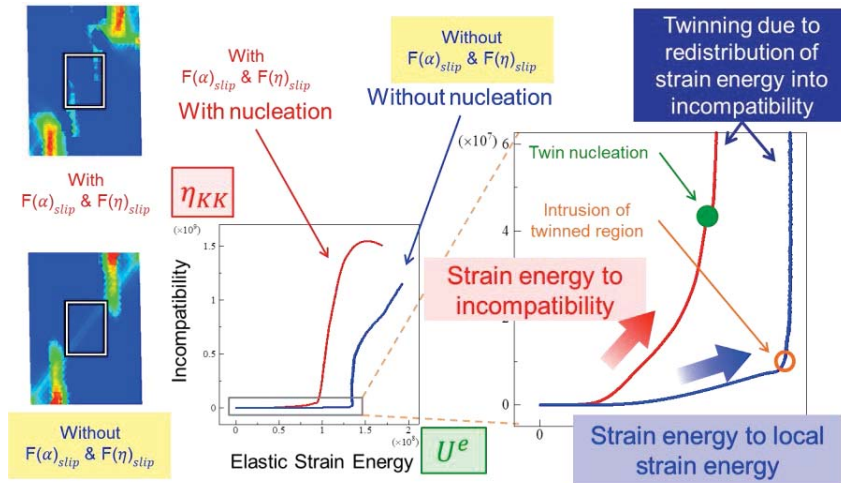
In order focus on the twin nucleation phenomena, we limit the area of examination to the center of the model to exclude the influence of intruding twinning from the upper/lower edges. Here we compare the two cases: with and without twin nucleation. Figure 3 illustrates the targeted area together with the simulation results.



**Figure 3. Observation area for duality diagram comparing cases with and without nucleation.**

Figure 4 shows the duality diagram, i.e. the duality relation between incompatibility tensor  $\eta_{KK}$  and elastic strain energy  $U^e$ . The red line represents the case with twin nucleation, whereas the blue line represents the case without twin nucleation. When we compare the two cases, both cases show a sharp rise in  $\eta_{KK}$  as the strain energy  $U^e$  increases, and the case with nucleation shows a much earlier onset of rise in  $\eta_{KK}$  than that without nucleation. To examine this difference more in detail, we enlarge the portion in the duality diagram where the sharp rises occur, where we can clearly confirm marked differences between the two cases. For the case with nucleation, we observe a relatively gradual rise in  $\eta_{KK}$ , followed by a sharp rise occurring at the point of nucleation, indicated with the solid circle. The pre-growth of  $\eta_{KK}$  corresponds to the evolution of the precursor inhomogeneity, as discussed earlier. The case without nucleation, on the other hand, yields a much smaller growth rate of  $\eta_{KK}$ , which is followed by a sharp increase not by twin nucleation, but by the intrusion of twinned regions into the targeted area, the point of which is indicated with the open circle.

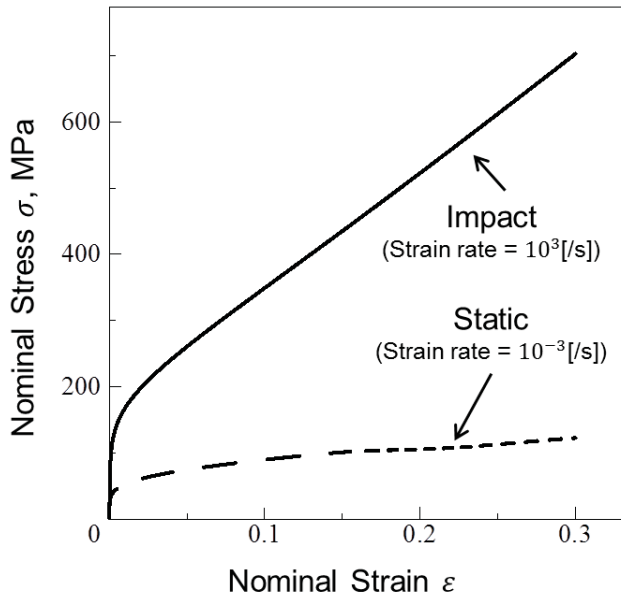
From the energetic point of view, the duality diagram provides the following insight; in the case with twin nucleation, a rapid release of energy that has been stored elastically into the twin degrees of freedom results in twin nucleation and subsequent growth. By using the duality diagram, we are able to visualize the twinning evolution (nucleation and growth) in terms of associated energy flow (how elastically-stored strain energy is converted to localized plastic flow in the form of twinning). Our results demonstrate the effectiveness of the duality diagram as a quantitative approach to twinning behavior.



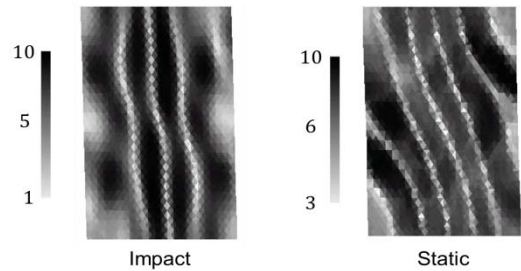
**Figure 4. Duality diagram for FCC copper simulation results comparing cases with and without nucleation.**

*Application of FTMP-based Twin Model to Impact Conditions*

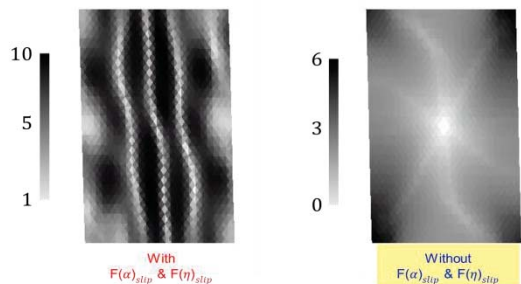
Here we conduct simulations that investigate the model’s descriptive capabilities under impact conditions. The analyses are carried out as a preliminary step to the model’s application to hypervelocity impact conditions, which is to be conducted in future works. When stressed under hypervelocity impact conditions, a wide variety of complex substructures composing both of twins and dislocations, whose morphology varies according to imparted pressure and pulse duration, form within materials. The present model aims to simulate the formation of such substructures, together with their significant effects on the mechanical properties. The simulations in this section are carried out statically, and the dynamic effect is not considered. The analytical model employed in the analysis is the same as that in the previous sections, except that the strain rate is set to  $\dot{\epsilon} = 1.0 \times 10^3$  /s, which corresponds to impact condition.



**Figure 5. Simulated stress-strain curves comparing results for impact and static conditions.**



**Figure 6. Contour diagrams for dislocation density comparing results under impact and static conditions.**



**Figure 7. Contour diagrams for dislocation density comparing effect of precursor inhomogeneity.**

Firstly, we examine the simulation results by comparing with those obtained in static conditions. Figures 5 and 6 show simulated stress-strain responses and contour diagrams of dislocation density, respectively, for both impact and static conditions. It is apparent that by increasing the strain rate, the flow stress is greatly raised, and the resulting pattern in dislocation density is also altered.

Secondly, the simulations are repeated without precursor inhomogeneity, in order to examine the characteristics of the present model under impact conditions. Figure 7 compares contour diagrams of dislocation density for the two typical cases: with and without precursor inhomogeneity. The result-with precursor inhomogeneity exhibits a banded pattern clearly, notwithstanding the absence of the precursor inhomogeneity results in no notable patterns. The simulation results imply that even under impact loading conditions, the deformation behavior is greatly influenced by the strain history, i.e., slip-induced inhomogeneity.

## Conclusions

In this work, we demonstrate the basic capabilities of the FTMP-based deformation twinning model, investigate the twin nucleation process by using duality diagrams, and apply the present model to analyses carried out under impact conditions. The foregoing results demonstrate some prominent capabilities of the proposed twinning model:

- Natural representations of twin nucleation are possible in the sense that no artificial imperfections which promote the onset of twinning are required.
- Nucleation and subsequent growth into lenticular shapes of twinned regions is realistically captured.
- Stress-strain responses accompanied by overall softening and serration are predicted.

Also, by examining the nucleation process in detail based on the duality diagram representation, we can readily visualize the energy flow associated with the nucleation and the subsequent growth of the twinning. With the application of the present model to impact conditions, we obtain dislocation density contour with different morphology from those attained in static conditions, implying that the present model has a potential of simulating twinning-induced complex substructures under a wide variety of loading conditions.

## Acknowledgements

A support from Army Research Laboratory (ARL) under Contract No. FA5029-13-P-0043 is greatly acknowledged.

## References

- Aoyagi, Y. and Hasebe, T. (2007), New Physical Interpretation of Incompatibility and Application to Dislocation Substructure Evolution., *Key Engineering Materials*, 340-341, pp. 217-222.
- Hasebe, T. (2013), FTMP-based Flow-Evolutionary Hypothesis and Its Applications., Proc. APCOM2013 (this issue).
- Hasebe, T. (2008a), Interaction Fields Based on Incompatibility Tensor in Field Theory of Plasticity-Part I: Theory-. *Interaction and Multiscale Mechanics*, 2-1, pp. 1-14.
- Hasebe, T. (2008b), Interaction Fields Based on Incompatibility Tensor in Field Theory of Plasticity-Part II: Application-. *Interaction and Multiscale Mechanics*, 2-1, pp. 15-30.
- Hasebe, T. (2006), Multiscale Crystal Plasticity Modeling based on Field Theory., *CMES*, 11-3, pp. 145-155.
- Imiya, K. (2011), Modeling of Twin Deformation based on Field Theory of Multiscale Plasticity., Graduation thesis, Kobe University.
- Kondo, K. (1955), Non-Riemannian Geometry of Imperfect Crystals from a Macroscopic Viewpoint., *RRAG Memoirs*, 1D-1, pp. 458-469.
- McDavid, A.W. and McMullen, C.D. (2006), Generalizing Cross Products and Maxwell's Equations to Universal Extra Dimensions., arXiv:hep-ph/0609260.

## Inverse scattering analysis of an elastic half space by means of volume integral equation method

\*Terumi Touhei<sup>1</sup> and Takuya Hinago<sup>2</sup>

<sup>1</sup>Professor, Department of Civil Engineering, Tokyo University of Science, Japan

<sup>2</sup>Graduate student, Department of Civil Engineering, Tokyo University of Science, Japan

\*Corresponding author: touhei@rs.noda.tus.ac.jp

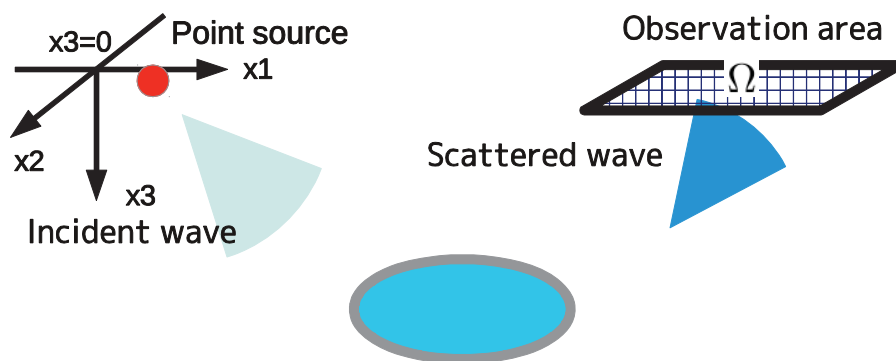
### Abstract

Inverse scattering analysis is dealt in this article by means of the fast volume integral equation method (Touhei, 2011). The purpose of this research is to reconstruct a fluctuation of the wave field in an elastic half space. Incident waves due to a point source and scattered waves observed at the free surface are used for reconstructing fluctuations of the wave field. The formulation uses the direct representation of the relationship between scattered waves and fluctuation of the wave field by the volume integral equation. The Tikhonov regularization method is also employed to improve the convergence properties of the solution. Several numerical examples are carried out to examine the effects of regularization parameter on the convergence properties of the iterative method.

**Keywords:** Volume integral equation, Elastic half space, Generalized Fourier transform, Tikhonov regularization method

### Introduction

Inverse scattering analysis of an elastic half space is an important issue in the fields of earthquake engineering, site characterization and among others. This article presents a method for the inverse scattering analysis based on the fast volume integral equation method (Touhei, 2011). The proposed method in this article reconstructs the fluctuation of the wave field from the observed scattered waves at the free surface. The method is due to the advantage of the volume integral equation is in that it clarifies the relationship fluctuation of the medium and scattered wave field. During the formulation, the Tikhonov regularization method is also employed to the equation for the inverse scattering analysis to improve the convergence properties of the solution. Numerical calculations are carried out to examine the accuracy of the inverse scattering analysis as well as the effects of the regularization.



Fluctuation of the medium  
Figure 1 Concept of the inverse scattering analysis

## Formulation

Figure 1 shows a concept of analyzed model dealt in this article. Fluctuations of the medium are embedded in an elastic half space. A point source is applied to a surface of an elastic half space to generate the incident wave. Scattered waves are caused due to the interaction between the incident wave and the fluctuations. Scattered waves are observed in a restricted area, which is denoted by  $\Omega$ . The formulation in this article is carried out to reconstruct fluctuation of wave field from observed scattered wave. The wave field is characterized by Lamé constants as well as mass density as can be seen in the following equations

$$\lambda(x) = \lambda_0 + \tilde{\lambda}(x) \quad (1)$$

$$\mu(x) = \mu_0 + \tilde{\mu}(x) \quad (2)$$

$$\rho(x) = \rho_0 + \tilde{\rho}(x) \quad (3)$$

where  $\lambda_0$ ,  $\mu_0$  and  $\rho_0$  are the background Lamé constants and mass density, and  $\tilde{\lambda}$ ,  $\tilde{\mu}$  and  $\tilde{\rho}$  are their fluctuations, respectively. Let the time factor of the wave field is  $e^{-i\omega t}$ , where  $\omega$  is the circular frequency and  $t$  is the time.

The equation of wave propagation is defined by

$$L_{ij}(\partial_1, \partial_2, \partial_3)u_j(x) = N_{ij}(\partial_1, \partial_2, \partial_3, x)u_j(x) - F_i \quad (4)$$

$$P_{ij}(\partial_1, \partial_2, \partial_3, x)u_j(x) = 0, \quad (\text{at } x_3 = 0) \quad (5)$$

where  $\delta_{ij}$  is Kronecker's delta,  $F$  is the amplitude of a point source, and  $L_{ij}$ ,  $N_{ij}$  and  $P_{ij}$  are differential operators constructed by Lamé constants as well as mass density. The explicit forms of the operators  $L_{ij}$ ,  $N_{ij}$  and  $P_{ij}$  are expressed as

$$L_{ij}(\partial_1, \partial_2, \partial_3) = (\lambda_0 + \mu_0)\partial_i\partial_j + \delta_{ij}\mu_0\partial_k^2 + \delta_{ij}\rho_0\omega^2 \quad (6)$$

$$N_{ij}(\partial_1, \partial_2, \partial_3, x) = -\left(\tilde{\lambda}(x) + \tilde{\mu}(x)\right)\partial_i\partial_j - \delta_{ij}\tilde{\mu}(x)\partial_k^2 - \partial_i\tilde{\lambda}(x)\partial_j - \delta_{ij}\partial_k\tilde{\mu}(x)\partial_k - \partial_j\tilde{\mu}(x)\partial_i - \delta_{ij}\tilde{\rho}(x)\omega^2 \quad (7)$$

$$P_{ij}(\partial_1, \partial_2, \partial_3, x) = \begin{bmatrix} \mu(x)\partial_3 & 0 & \mu(x)\partial_1 \\ 0 & \mu(x)\partial_3 & \mu(x)\partial_2 \\ \lambda(x)\partial_1 & \lambda(x)\partial_2 & (\lambda(x) + 2\mu(x))\partial_3 \end{bmatrix} \quad (8)$$

The Green's function of the equation of wave propagation is defined as

$$L_{ij}(\partial_1, \partial_2, \partial_3)G_{jk}(x, y) = -\delta_{ik}\delta(x - y) \quad (9)$$

$$P_{ij}^{(0)}(\partial_1, \partial_2, \partial_3, x)G_{jk}(x, y) = 0, \quad (\text{at } x_3 = 0) \quad (10)$$

where  $G_{jk}$  is the Green's function,  $\delta(\cdot)$  is the Dirac delta function, and  $P_{ij}^{(0)}$  is as follows

$$P_{ij}^{(0)}(\partial_1, \partial_2, \partial_3, x) = \begin{bmatrix} \mu_0\partial_3 & 0 & \mu_0\partial_1 \\ 0 & \mu_0\partial_3 & \mu_0\partial_2 \\ \lambda_0\partial_1 & \lambda_0\partial_2 & (\lambda_0 + 2\mu_0)\partial_3 \end{bmatrix} \quad (11)$$

The volume integral equation for the present problem is defined by

$$u_i^S(x) = - \int_{\mathbb{R}_+^3} G_{ij}(x, y) N_{jk}(\partial_1, \partial_2, \partial_3, y) u_k^I(y) dy - \int_{\mathbb{R}_+^3} G_{ij}(x, y) N_{jk}(\partial_1, \partial_2, \partial_3, y) u_k^S(y) dy \quad (12)$$

where  $u_i^S$  and  $u_k^I$  are the scattered and incident wave field, respectively. In order to carry out the inverse scattering analysis, let Eq. (12) be modified into

$$u_i^S(x) = - \int_{\mathbb{R}_+^3} G_{ij}(x, y) M_{jk}(\partial_1, \partial_2, \partial_3, y) q_k(y) dy \quad (13)$$

where  $q_k$  is the states vector of the fluctuation whose components are

$$q_k(x) = (\tilde{\lambda}(x), \tilde{\mu}(x), \tilde{\rho}(x))^T \quad (14)$$

and  $M_{jk}$  is the differential operator constructed by incident wave field. Note that the Born approximation is applied to Eq. (12) to obtain Eq. (13) for linearizing equation. In addition, the generalized Fourier transform and inverse transforms (Touhei, 2011) are employed to Eq. (13) such as

$$u_i^S(x) = -U_{ij}^{-1} \hat{h}(\xi) U_{jk} M_{kl}(\partial_1, \partial_2, \partial_3, y) q_l(y) \quad (15)$$

where  $U$ ,  $U^{-1}$  are the operators of the generalized Fourier transform and inverse transforms, respectively, and  $\hat{h}$  is the Green's function in wavenumber domain. Equation (15) shows the relationship between the scattered wave field  $u_i^S(x)$ , ( $x \in \mathbb{R}_+^3$ ) and the fluctuation of the medium. We have to, however, restrict the range of  $x \in \mathbb{R}_+^3$  for  $u_i^S(x)$ , because we observe the scattered waves at the restricted area of  $\Omega$  at the free surface. To restrict the range, let us introduce the definition function as follows

$$\chi_\Omega(x) = \begin{cases} 1 & (x \in \Omega) \\ 0 & (otherwise) \end{cases} \quad (16)$$

and apply it to Eq. (15) such that

$$\chi_\Omega(x) u_i^S(x) = -\chi_\Omega(x) U_{ij}^{-1} \hat{h}(\xi) U_{jk} M_{kl}(\partial_1, \partial_2, \partial_3, y) q_l(y) \quad (17)$$

The Tikhonov regularization method is also employed to stabilize the convergence property of solution. The result of the application of the Tikhonov regularization method is

$$A_{li}^* u_i^S(x) = [\alpha \delta_{il} + A_{ji}^* A_{jl}] q_l(y) \quad (18)$$

where  $A_{li}^*$  is the adjoint operator for  $A_{jl}$ , and  $\alpha$  is the regularization parameter.

## Numerical examples

Several numerical examples are shown in this section to examine the effects of regularization parameter on convergence properties of the solution. Setting an adequate Tikhonov parameter is very important to have accurate result of the inverse scattering analysis. In general, a larger Tikhonov parameter is known to improve the convergence properties of iterative procedures, while that makes the accuracy of the reconstructed results worse. There are two cases for numerical examples, one is that the analysis is carried out without regularization, namely  $\alpha = 0.0$ , and the other is that the regularization parameter is set at  $\alpha = 1.0 \times 10^{-8}$ . Figure 2 shows the target model of the inverse scattering analysis for numerical examples. The fluctuation of the wave field is embedded in the form of a cube at depth 5km from the free surface whose size is 3km on a side. The amplitude and excitation frequency of the point source are  $10^7$  kN and 1.0Hz, respectively, and direction of the force is vertical. Figure 3 shows the observed data of the scattered waves which are obtained from the forward analysis. The background and fluctuation Lamé constants are  $(\lambda_0, \mu_0) = (4.0, 2.0)$  [GPa] and  $(\tilde{\lambda}, \tilde{\mu}) = (0.1, 0.1)$  [GPa], and their mass density  $\rho = 2.0$  [g/cm<sup>3</sup>] and  $\tilde{\rho} = 0.0$  [g/cm<sup>3</sup>], respectively. Figure 4 shows the target of the fluctuation of the wave field.

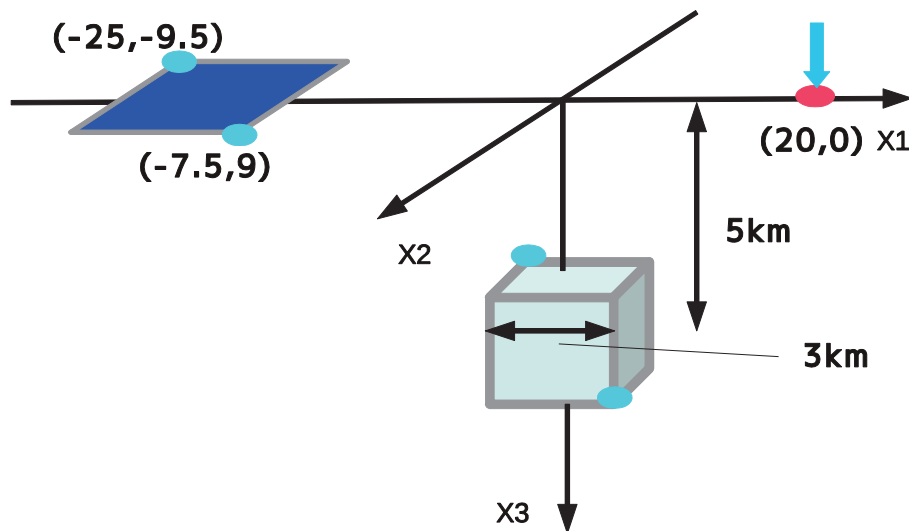


Figure 2 Target model

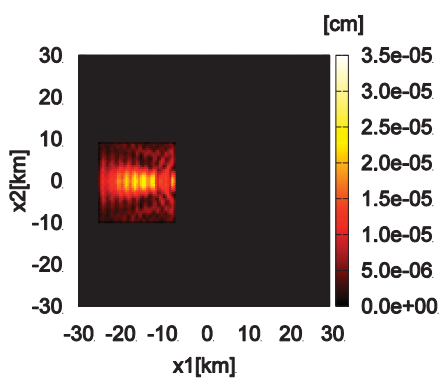


Figure 3 Observed data

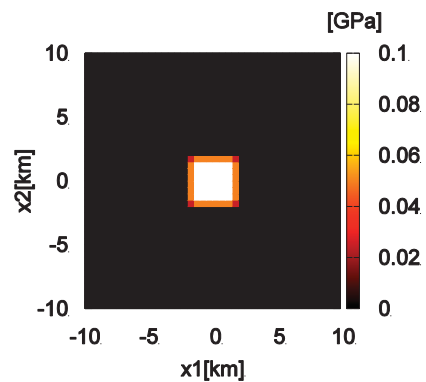


Figure 4 Target of the fluctuation of the wave field



Figures 5 and 6 show the convergence properties of the solution in case that Bi-CGSTAB method is employed for the solver. In the figures, horizontal axis denotes the number of iterations and vertical axis denotes the relative errors. According to Fig. 5, relative errors don't decrease even if the numbers of iterations increase. On the other hand, according to Fig. 6, the relative errors decrease as the numbers of the iterations increase. Therefore, the Tikhonov regularization method is effective for improving the convergence of the solution. Figures 7 and 8 show the results of the reconstruction of  $\tilde{\mu}$  at depth  $x_3 = 5.0$ [km]. It is found from Fig. 7 that the reconstruction results overestimate the target model of the fluctuation shown in Fig. 4. However, comparing between the target model and Fig. 8, the fluctuation is found to be close to that of the target model. From the above results, the convergence properties are improved by the Tikhonov regularization method. Future tasks for inverse scattering analysis are to improve the accuracy of the estimation of the spatial spreads of the fluctuation.

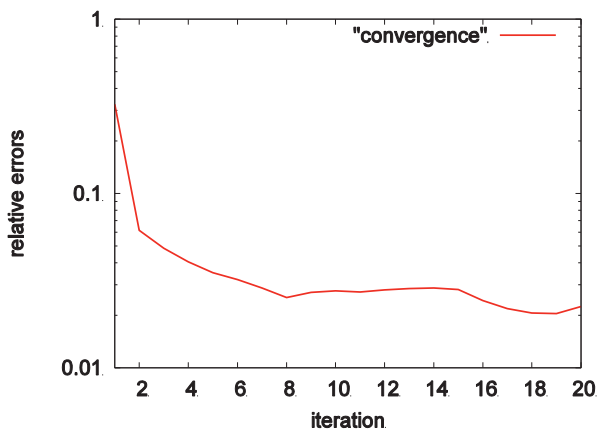


Figure 5 Convergence ( $\alpha = 0.0$ )

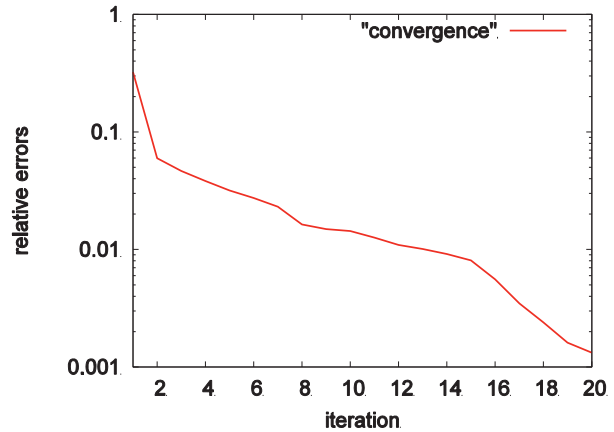


Figure 6 Convergence ( $\alpha = 1.0 \times 10^{-8}$ )

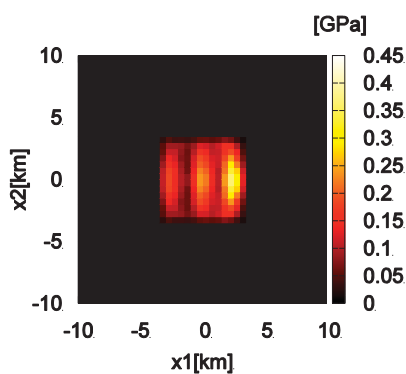


Figure 7 Reconstruction of the fluctuation  $\tilde{\mu}$   
( $\alpha=0.0$ )

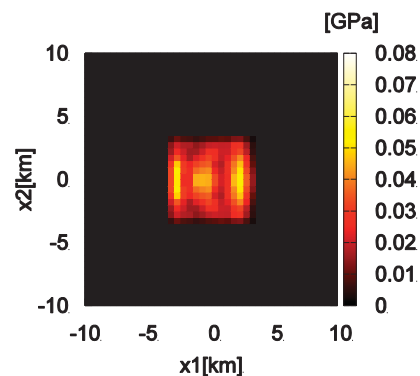


Figure 8 Reconstruction of the fluctuation  $\tilde{\mu}$   
( $\alpha = 1.0 \times 10^{-8}$ )

## Conclusion

Inverse scattering analysis was carried out based on the fast volume integral equation method in this article. The Tikhonov regularization method was employed to examine the convergence properties of the solution of the inverse scattering analysis. According to the numerical examples, the Tikhonov regularization method was effective to improve the convergence properties. For the future, however, accuracy of the reconstruction of the results has to be improved.

## References

- Touhei, T. (2011), A fast volume integral equation method for elastic wave propagation in a half space, *International Journal of Solids and Structures* 48, 3149-3208
- Colton, D. and Kress, R (1998), *Inverse Acoustic and Electromagnetic Scattering Theory*, Springer-Verlag, Berlin, Heidelberg

## Development of a triple-scale analysis method for plain-woven laminates based on a homogenization theory for time-dependent composites

Kohei Oide<sup>1</sup>, \*Tetsuya Matsuda<sup>1</sup>, and Fumiya Kawasaki<sup>2</sup>

<sup>1</sup>Department of Engineering Mechanics and Energy, University of Tsukuba  
1-1-1 Tennoudai, Tsukuba, 305-8573, Japan

<sup>2</sup>All Nippon Airways Co. Ltd., Tokyo, 105-7133, Japan

\*Corresponding author: matsuda@kz.tsukuba.ac.jp

### Abstract

In this study, a triple-scale elastic-viscoplastic analysis method for plain-woven laminates is newly developed based on a homogenization theory for time-dependent composites. For this, triple-scale modeling of plain-woven laminates is performed by considering a plain-woven laminate as a macrostructure, plain fabrics and a matrix in the laminate as a mesostructure, and fibers and a matrix in the plain fabrics as a microstructure. Then, the boundary value problems for macro/meso and meso/micro scales are derived based on the homogenization theory for time-dependent composites, and the relationship between these problems are discussed. Using the relationship, a triple-scale elastic-viscoplastic analysis method for plain-woven laminates and its computational procedure are developed. It is shown that the present method is successful in taking into account the effects of elastoviscoplasticity of an epoxy matrix in plain fabrics on the elastic-viscoplastic behavior of plain-woven GFRP laminates.

**Keywords:** Plain-woven laminate, Triple-scale analysis, Homogenization, Viscoplasticity

### Introduction

Plain-woven laminates made of plain fabrics and polymer materials are now regarded as some of the most important engineering materials, because of their high specific strength, high specific stiffness and good formability. Thus, they are used in major industrial fields such as aerospace, transportation and energy-related industries. It is therefore of great importance to clarify their mechanical properties.

The mathematical homogenization theory (Sanchez-Palencia, 1980) is one of the most useful theories for inelastic analysis such as damage analysis and elastic-viscoplastic analysis of plain-woven laminates. Thus, some researchers have already applied this theory to such analysis, and shown its usefulness. Takano et al. (1995) conducted a microscopic damage analysis of plain-woven glass fiber-reinforced plastic (GFRP) laminates. The authors (Matsuda et al., 2007; Matsuda et al., 2011) have performed the elastic-viscoplastic analysis of plain-woven GFRP laminates using

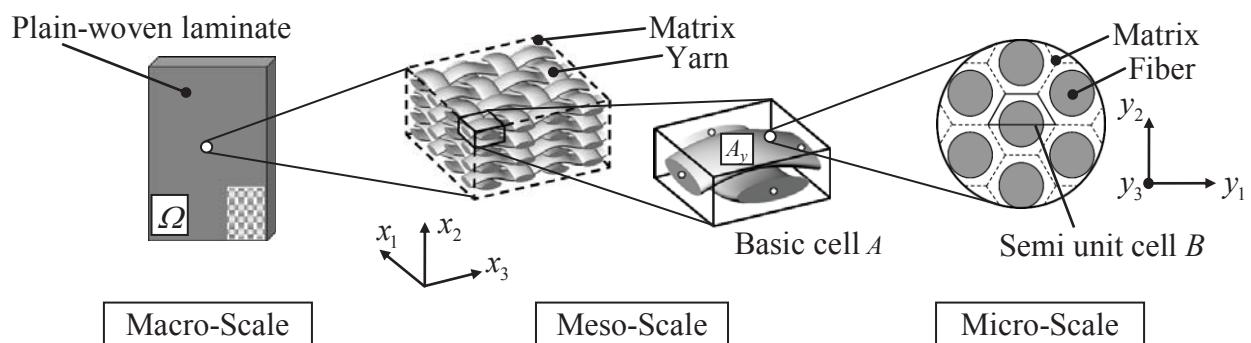


Figure 1. Triple-scale model of plain-woven laminates

the homogenization theory for nonlinear time-dependent composites (Wu and Ohno, 1991; Ohno et al., 2000). However, these studies regarded fiber bundles (yarns) in plain-woven laminates as homogeneous elastic materials, neglecting their microstructures consisting of fibers and matrix materials. In reality, yarns should exhibit not only elastic but also viscoplastic behavior due to the viscoplasticity of matrix materials. Therefore, to perform more advanced analysis of plain-woven laminates, it is necessary to develop a novel analysis method that is able to consider microstructures in yarns.

In this study, a triple-scale analysis method for plain-woven laminates which can consider viscoplasticity in yarns is newly developed based on the homogenization theory for time-dependent composites (Wu and Ohno, 1991; Ohno et al., 2000). First, plain-woven laminates are modeled in three scales as illustrated in Figure 1. Then, the homogenization theory for time-dependent composites is dually applied to the macro/meso and meso/micro problems, deriving an elastic-viscoplastic constitutive equation of the plain-woven laminates incorporating the microscopic information in yarns. Using the present theory, the elastic-viscoplastic analysis of plain-woven glass fiber/epoxy laminates is performed. Moreover, the results of analysis are compared with experimental data (Matsuda et al., 2007) to validate the analysis method.

### Triple-Scale modeling of plain-woven laminates

Let us consider a plain-woven laminate  $\Omega$  with microscopic periodic structure subjected to a macroscopic uniform load as illustrated in Figure 1. Then, a basic cell  $A$  consisting of yarns and a matrix is defined as a smallest unit in the meso-scale. Cartesian coordinates  $x_i (i=1,2,3)$  are provided for the meso-scale. Next, in the micro-scale, a semiunit cell  $B$  consisting of a fiber and a matrix is defined as a smallest unit for the yarn region  $A_y$  in the basic cell  $A$ . Cartesian coordinates  $y_i (i=1,2,3)$  are provided for the micro-scale. It is noted that the superscripts 0, 1 and 2 respectively indicate macro, meso and micro variables hereafter.

### Micro/meso problem

Microscopic stress rate and strain rate fields in the semiunit cell  $B$  are denoted as  ${}^2\dot{\sigma}_{ij}(\mathbf{y}, t)$  and  ${}^2\dot{\epsilon}_{ij}(\mathbf{y}, t)$ , respectively, where  $t$  represents time and  $(\cdot)$  indicates differentiation with respect to  $t$ . Then, denoting partial differentiation with respect to  $y_i$  as  $(\cdot)_{,y_i}$ , the equilibrium of microscopic stress is expressed as

$${}^2\dot{\sigma}_{ij,y_j} = 0. \quad (1)$$

The microscopic constitutive equation of each constituent in yarns is defined as

$${}^2\dot{\sigma}_{ij} = {}^2c_{ijkl}({}^2\dot{\epsilon}_{kl} - {}^2\beta_{kl}), \quad (2)$$

where  ${}^2c_{ijkl}$  and  ${}^2\beta_{kl}$  respectively represent the elastic stiffness and viscoplastic strain rate of fibers and a matrix, i.e.

$$\begin{aligned} {}^2c_{ijkl} &= c_{ijkl}^f \text{ or } c_{ijkl}^m & (f : \text{fiber}, m : \text{matrix}). \\ {}^2\beta_{kl} &= \beta_{kl}^f \text{ or } \beta_{kl}^m \end{aligned} \quad (3)$$

The microscopic velocity field  ${}^2\dot{u}_i(\mathbf{y}, t)$  in  $B$  has the following expression:

$${}^2\dot{u}_i(\mathbf{y}, t) = {}^1\dot{F}_{y_j}(\mathbf{x}, t)y_j + {}^2\dot{u}_i^\#(\mathbf{y}, t), \quad (4)$$

where  ${}^1\dot{F}_{ij}(\mathbf{x}, t)$  denotes the mesoscopic deformation gradient, and  ${}^2\dot{u}_i^\#(\mathbf{y}, t)$  denotes the microscopic perturbed velocity.

Now, let  ${}^2v_i(\mathbf{y}, t)$  be an arbitrary variation of  ${}^2\dot{u}_i^\#$  defined in  $B$  at  $t$ . Then, integration by parts and the divergence theorem allow Eq. (1) to be transformed to

$$\int_B {}^2\dot{\sigma}_{ij} {}^2v_{i,y_j} dB - \int_{\Gamma_B} {}^2\dot{\sigma}_{ij} n_j {}^2v_i d\Gamma_B = 0, \quad (5)$$

where  $\Gamma_B$  denotes the boundary of  $B$ , and  $n_j$  indicates the unit vector outward normal to  $\Gamma_B$ . In the above equation, the second term of the left-hand side, i.e. the boundary integral term, vanishes by considering the  $Y$ -periodicity and point-symmetry (Ohno et al., 2001) of  ${}^2\dot{\sigma}_{ij}$  and  ${}^2v_i$  on  $\Gamma_B$ . Consequently, the second term of left-hand side in Eq. (5) vanishes, resulting in

$$\int_B {}^2\dot{\sigma}_{ij} {}^2v_{i,y_j} dB = 0. \quad (6)$$

By substituting Eq. (2) into Eq. (6), the following boundary value problems are derived:

$$\int_B {}^2c_{ijpq} {}^2\chi_{p,y_q}^{kl} {}^2v_{i,y_j} dB = - \int_B {}^2c_{ijkl} {}^2v_{i,y_j} dB, \quad (7)$$

$$\int_B {}^2c_{ijpq} {}^2\varphi_{p,y_q} {}^2v_{i,y_j} dB = \int_B {}^2c_{ijkl} {}^2\beta_{kl} {}^2v_{i,y_j} dB, \quad (8)$$

where  ${}^2\chi_i^{kl}$  and  ${}^2\varphi_i$  are characteristic functions obtained by solving the boundary value problems Eqs. (7) and (8). Then, the evolution equation of microscopic stress rate  ${}^2\dot{\sigma}_{ij}$  is expressed as

$${}^2\dot{\sigma}_{ij} = \left[ {}^2c_{ijkl} (\delta_{pk} \delta_{ql} + {}^2\chi_{p,y_q}^{kl}) \right] {}^1\dot{\varepsilon}_{kl} - \left[ {}^2c_{ijkl} ({}^2\beta_{kl} - {}^2\varphi_{k,y_l}) \right], \quad (9)$$

where  $\delta_{ij}$  indicates Kronecker's delta. Then, the relation between mesoscopic stress rate and strain rate is derived as follow:

$$\begin{aligned} {}^1\dot{\sigma}_{ij} &= {}^1c_{ijkl} ({}^1\dot{\varepsilon}_{kl} - {}^1\beta_{kl}) \\ &= \left\langle {}^2c_{ijkl} (\delta_{ik} \delta_{jl} + {}^2\chi_{i,y_j}^{kl}) \right\rangle_B {}^1\dot{\varepsilon}_{kl} - \left\langle {}^2c_{ijkl} ({}^2\beta_{kl} - {}^2\varphi_{k,y_l}) \right\rangle_B, \end{aligned} \quad (10)$$

where  $\langle \cdot \rangle_B$  designates the volume average in  $B$  defined as  $\langle \# \rangle_B = |B|^{-1} \int_B \# dB$ , in which  $|B|$  signifies the volume of  $B$ .

### Meso/macro problem

Mesoscopic stress rate and strain rate fields in the basic cell  $A$  are denoted as  ${}^1\dot{\sigma}_{ij}(\mathbf{x}, t)$  and  ${}^1\dot{\varepsilon}_{ij}(\mathbf{x}, t)$ , respectively. Then, denoting partial differentiation with respect to  $x_i$  as  $(\cdot)_{,x_i}$ , the equilibrium of mesoscopic stress is expressed as

$${}^1\dot{\sigma}_{ij,x_j} = 0. \quad (11)$$

The mesoscopic constitutive equation of each constituent in the plain-woven laminate is defined as

$${}^1\dot{\sigma}_{ij} = {}^1c_{ijkl} ({}^1\dot{\varepsilon}_{kl} - {}^1\beta_{kl}) = {}^1c_{ijkl} {}^1\dot{\varepsilon}_{kl} - {}^1c_{ijkl} {}^1\beta_{kl}, \quad (12)$$

where  ${}^1c_{ijkl}$  and  ${}^1\beta_{kl}$  respectively represent the elastic stiffness and viscoplastic strain rate of yarns and a matrix in the plain-woven laminate, i.e.

$$\begin{aligned} {}^1c_{ijkl} &= c_{ijkl}^y \text{ or } c_{ijkl}^m \\ {}^1\beta_{kl} &= \beta_{kl}^y \text{ or } \beta_{kl}^m \end{aligned} \quad (y: \text{yarn}, m: \text{matrix}). \quad (13)$$

Here, comparing Eq. (10) with Eq. (12), the following relationships can be obtained:

$${}^1c_{ijkl} = c_{ijkl}^y = \left\langle {}^2c_{ijkl} \left( \delta_{ik} \delta_{jl} + {}^2\chi_{i,y_j}^{kl} \right) \right\rangle_B, \quad (14)$$

$${}^1c_{ijkl} {}^1\beta_{kl} = c_{ijkl}^y \beta_{kl}^y = \left\langle {}^2c_{ijkl} \left( {}^2\beta_{kl} - {}^2\varphi_{k,y_l} \right) \right\rangle_B. \quad (15)$$

The mesoscopic velocity field  ${}^1\dot{u}_i(\mathbf{x}, t)$  in  $A$  has the following expression:

$${}^1\dot{u}_i(\mathbf{x}, t) = {}^0\dot{F}_{ij}(t) x_j + {}^1\dot{u}_i^\#(\mathbf{x}, t), \quad (16)$$

where  ${}^0\dot{F}_{ij}(t)$  denotes the macroscopic deformation gradient, and  ${}^1\dot{u}_i^\#(\mathbf{x}, t)$  denotes the mesoscopic perturbed velocity, respectively.

Now, let  ${}^1v_i(\mathbf{x}, t)$  be an arbitrary variation of  ${}^1\dot{u}_i^\#$  defined in  $A$  at  $t$ . Then, considering  $Y$ -periodicity and point-symmetry (Ohno et al., 2001) of  ${}^1\dot{\sigma}_{ij}$  and  ${}^1v_i$  on the boundary of basic cell  $A$ ,  $\Gamma_A$ , the following equation is derived in the same manner as in the preceding section:

$$\int_A {}^1\dot{\sigma}_{ij} {}^1v_{i,x_j} dA = 0. \quad (17)$$

By substituting Eq. (12) into Eq. (17), the following boundary value problems are derived:

$$\int_A {}^1c_{ijpq} {}^1\chi_{p,x_q}^{kl} {}^1v_{i,x_j} dA = - \int_A {}^1c_{ijkl} {}^1v_{i,x_j} dA, \quad (18)$$

$$\int_A {}^1c_{ijpq} {}^1\varphi_{p,x_q} {}^1v_{i,x_j} dA = \int_A {}^1c_{ijkl} {}^1\beta_{kl} {}^1v_{i,x_j} dA, \quad (19)$$

where  ${}^1\chi_i^{kl}$  and  ${}^1\varphi_i$  are characteristic functions obtained by solving the boundary value problems Eqs. (18) and (19). Then, the evolution equation of mesoscopic stress rate  ${}^1\dot{\sigma}_{ij}$  is expressed as

$${}^1\dot{\sigma}_{ij} = \left[ {}^1c_{ijkl} \left( \delta_{pk} \delta_{ql} + {}^1\chi_{p,x_q}^{kl} \right) \right] {}^0\dot{\epsilon}_{kl} - \left[ {}^1c_{ijkl} \left( {}^1\beta_{kl} - {}^1\varphi_{k,x_l} \right) \right]. \quad (20)$$

Then, the relation between macroscopic stress rate and strain rate is derived as follows:

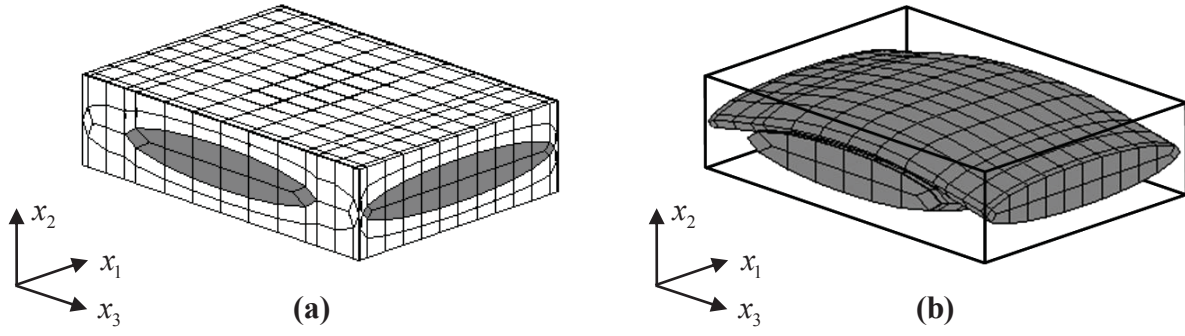
$$\begin{aligned} {}^0\dot{\sigma}_{ij} &= {}^0c_{ijkl} ({}^0\dot{\epsilon}_{kl} - {}^0\beta_{kl}) \\ &= \left\langle {}^1c_{ijkl} \left( \delta_{ik} \delta_{jl} + {}^1\chi_{i,x_j}^{kl} \right) \right\rangle_A {}^0\dot{\epsilon}_{kl} - \left\langle {}^1c_{ijkl} \left( {}^1\beta_{kl} - {}^1\varphi_{k,x_l} \right) \right\rangle_A, \end{aligned} \quad (21)$$

where  $\langle \cdot \rangle_A$  designates the volume average in  $A$  defined as  $\langle \# \rangle_A = |A|^{-1} \int_A \# dA$ , in which  $|A|$  signifies the volume of  $A$ .

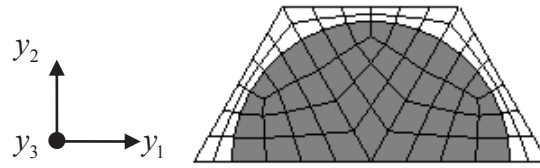
Using the Eqs. (20) and (21) accompanied by Eqs. (14) and (15), the elastic-viscoplastic behavior of plain-woven laminates can be analyzed through the triple scales.

### Analysis conditions

In the present analysis, elastic-viscoplastic behavior of a plain-woven glass fiber/epoxy composite laminate manufactured by Nitto Shinko Corporation (10 plain fabrics stacked) was analyzed using the theory developed. A basic cell  $A$  was defined as shown in Figure 2 in accordance with the microscope observation (Matsuda et al., 2007) of the plain-woven GFRP laminate, and was divided into eight-node isoparametric elements (1624 elements, 1995 nodes). On the other hand, a semiunit cell  $B$  of yarns was defined as depicted in Figure 3, and was divided into four-node isoparametric elements assuming the generalized plain strain condition (81 elements, 97 nodes). For  $B$ , the fiber volume fraction was set to be 75% (Matsuda et al., 2007).



**Figure 2. Basic cell A of the plain-woven laminate in meso-scale and finite element mesh: (a) full view and (b) yarns in basic cell**



**Figure 3. Semiunit cell B of the yarns in micro-scale and finite element mesh**

**Table 1. Material constants**

Glass fiber	$E_f = 80.0$	$\nu_f = 0.30$
Epoxy	$E_m = 5.0$	$\nu_m = 0.35$
	$\dot{\epsilon}_0^p = 1.0 \times 10^{-5}$	
	$n = 25$	$g(\bar{\epsilon}^p) = 105.0(\bar{\epsilon}^p)^{0.20} + 24.5$
GPa(stress),mm/mm(strain),s(time)		

The plain-woven laminate was subjected to macroscopic uniaxial tension at a constant strain rate  ${}^0\dot{\epsilon}_\theta = 10^{-5} [\text{s}^{-1}]$  at room temperature. The loading directions were  $0^\circ, 15^\circ, 30^\circ$  and  $45^\circ$ -directions rotated from the  $x_3$ -direction in the  $x_1 - x_3$  plane.

The material constants of fibers and an epoxy matrix are listed in Table 1. The glass fibers were regarded as isotropic elastic materials. The epoxy matrix, on the other hands, was regarded as an isotropic elastic-viscoplastic material which obeyed the following constitutive equation:

$$\dot{\epsilon}_{ij} = \frac{1+\nu_m}{E_m} \dot{\sigma}_{ij} - \frac{\nu_m}{E_m} \dot{\sigma}_{kk} \delta_{ij} + \frac{3}{2} \dot{\epsilon}_0^p \left[ \frac{\sigma_{eq}}{g(\bar{\epsilon}^p)} \right]^n \frac{s_{ij}}{\sigma_{eq}}, \quad (22)$$

where  $E_m, \nu_m, n$  signify the material constants,  $g(\bar{\epsilon}^p)$  stands for a hardening function depending on equivalent viscoplastic strain  $\bar{\epsilon}^p$ ,  $\dot{\epsilon}_0^p$  indicates reference strain rate,  $s_{ij}$  denotes the deviatoric part of  $\sigma_{ij}$ , and  $\sigma_{eq} = [(3/2)s_{ij}s_{ij}]^{1/2}$ . Incidentally, no failure was assumed to occur in the glass fibers and an epoxy.

## Results of analysis

Figure 4 shows the macroscopic stress-strain relations of the plain-woven GFRP laminate subjected to the uniaxial tension in the  $0^\circ, 15^\circ, 30^\circ$  and  $45^\circ$ -directions. As seen from the experimental data,

the macroscopic stress-strain relations markedly vary depending on the loading direction. Thus, it can be said that the plain-woven GFRP laminate has remarkable elastic-viscoplastic anisotropy. Comparing such experimental data with the results of the present analysis indicated by the lines in Figure 4, it is found that the present method is successful in predicting the macroscopic behavior of the plain-woven GFRP laminate.

Figures 5-8 show the distributions of mesoscopic equivalent plastic strain in the basic cell  $A$ . As seen from Figure 5, very small plastic strain is observed in the yarns with the on-axis loading. In contrast, high plastic strain can be found with the off-axis loading as shown in Figures 6-8. It is emphasized that such plastic strain in yarns was not able to be considered in the previous studies.

Finally, Figure 9 shows the microscopic equivalent plastic strain distribution at the points ( i ) and ( ii ) in the yarn when  $\theta = 45^\circ$ . As seen from the figure, considerably large plastic strain occurs at the interface of the fiber and epoxy matrix in the semiunit cell  $B$ . This also cannot be dealt with in the previous studies.

## Conclusions

In the present study, a triple-scale analysis method for plain-woven laminates was developed based on the homogenization theory for nonlinear time-dependent composites. Then, the elastic-viscoplastic behavior of a plain-woven glass fiber/epoxy laminate was analyzed using the present method. Moreover, the analysis results were compared with experimental data. The stress-strain curves in the macro-scale showed remarkable anisotropy, and the analysis results were in good agreement with the experimental data. From the equivalent plastic strain distribution in the meso-scale, considerable plastic strain was observed in yarns when the plain-woven GFRP laminate was subjected to off-axis tensile loading. It was also observed that, in the micro-scale, large equivalent plastic strain was accumulated at the epoxy matrix in yarns. It should be noted that these results cannot be obtained using the previous methods which completely neglected the viscoplasticity of yarns.

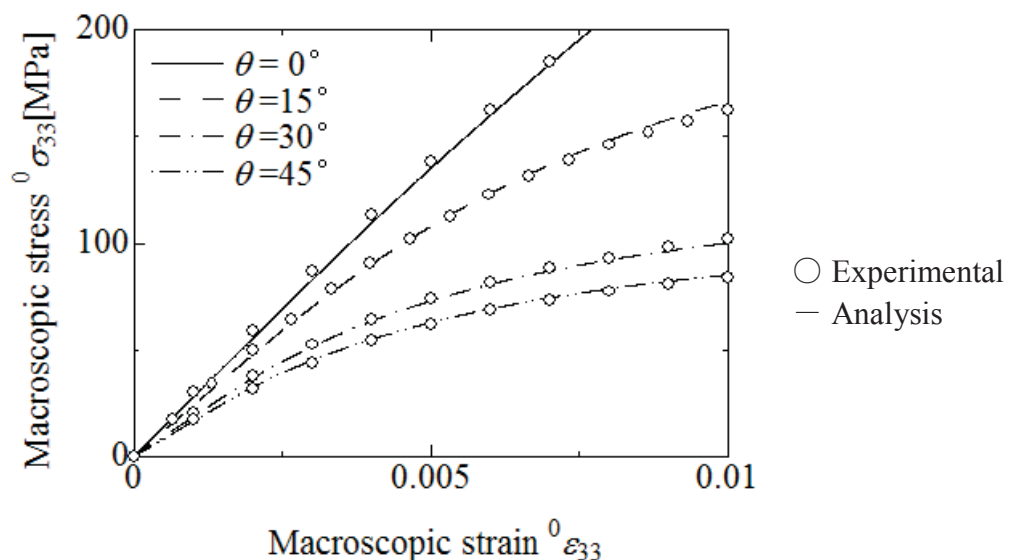


Figure 4. Macroscopic stress-strain relations



**Reference**

- Matsuda. T, Nimiya. Y, Ohno. N, and Tokuda. M (2007), Elastic-viscoplastic behavior of plain-woven GFRP laminates Homogenization using reduced domain of analysis, *Compos. Struct.*, 79, pp. 493-500.
- Matsuda. T, Kanamaru. S, Yamamoto. N, and Fukuda. Y (2011), A homogenization theory for elastic-viscoplastic materials with misaligned internal structures, *Int. J. Plast.*, 27, pp. 2056-2067.
- Ohno. N, Wu. X, Matsuda. T (2000), Homogenized properties of elastic-viscoplastic composites with periodic integral structures, *Int. J. Mech. Sci.*, pp. 1519-1536.
- Ohno. N, Matsuda. T, Wu. X (2001), A homogenization theory for elastic-viscoplastic composites with point symmetry of internal distributions, *Int. J. Solids Struct.*, 38, pp. 2867-2878.
- Sanchez-Palencia. E (1980), *Non-Homogeneous Media and Vibration Theory*, Lecture Notes in Physics, No. 127, Springer-Verlag, Berlin.
- Takano. N, Zako. M, Sakaki. S (1995), Three-dimensional microstructural design of woven fabric composite materials by the homogenization method: 1st report, effect of mismatched lay-up of woven fabrics on the strength, *Trens. Jpn Soc. Mech. Eng. Ser. A*, 61, pp.1038-1043.
- Wu. X, Ohno. N (1999), A homogenization theory for time-dependent nonlinear composites with periodic internal structures, *Int. J. Solids Struct.*, 36, pp.4991-5012.

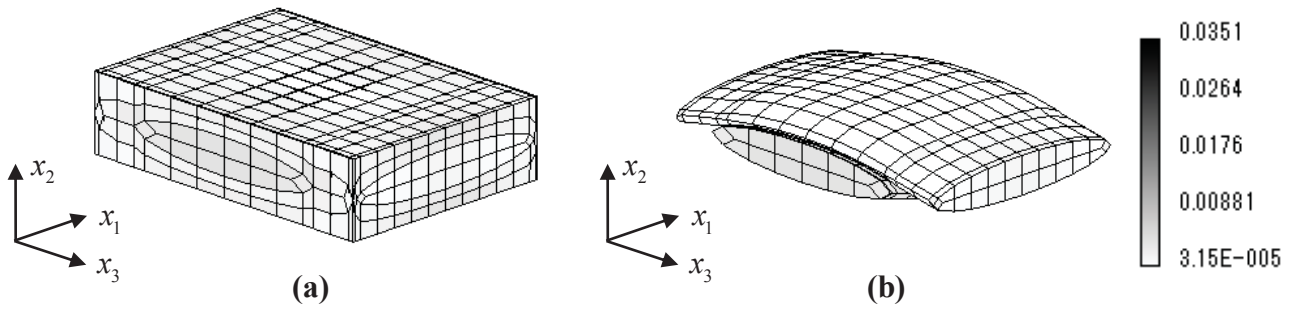


Figure 5. Mesoscopic equivalent plastic strain distribution ( $\theta = 0^\circ$ ): (a) full view and (b) yarns

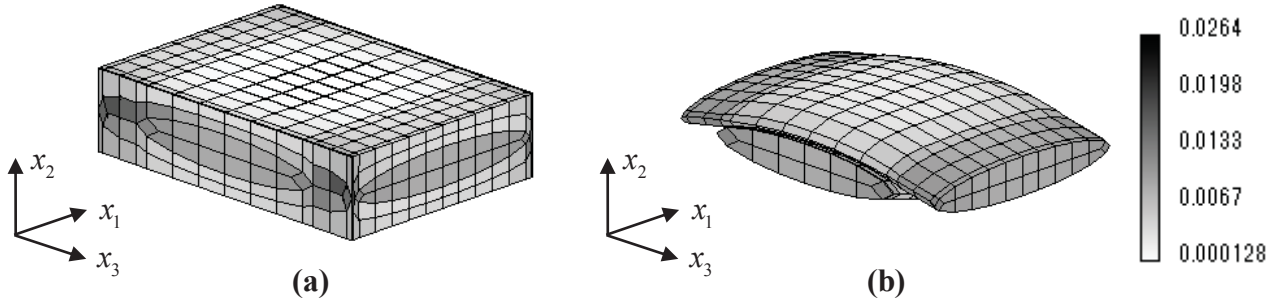


Figure 6. Mesoscopic equivalent plastic strain distribution ( $\theta = 15^\circ$ ): (a) full view and (b) yarns

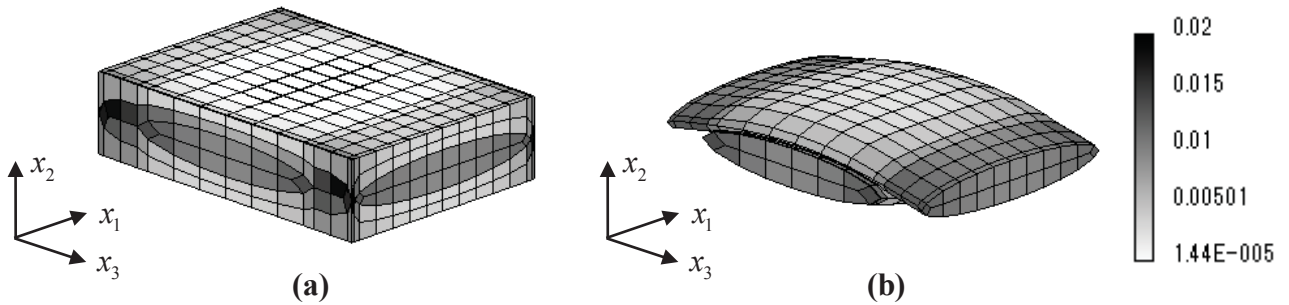


Figure 7. Mesoscopic equivalent plastic strain distribution ( $\theta = 30^\circ$ ): (a) full view and (b) yarns

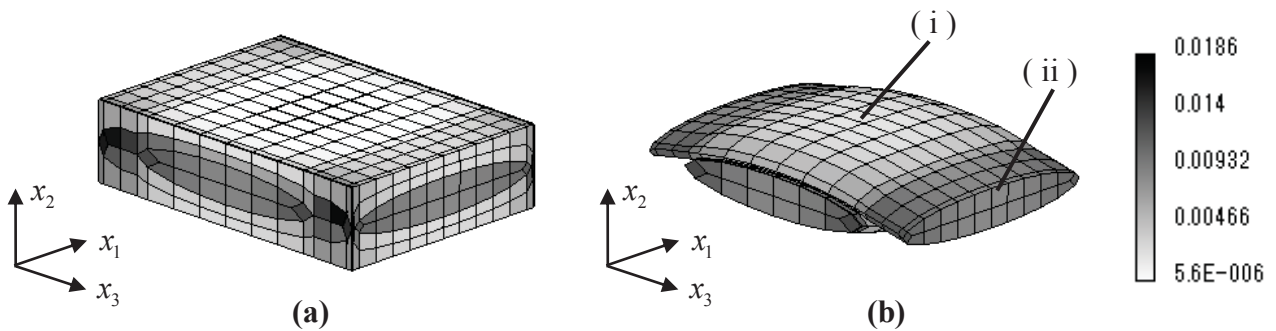


Figure 8. Mesoscopic equivalent plastic strain distribution ( $\theta = 45^\circ$ ): (a) full view and (b) yarns

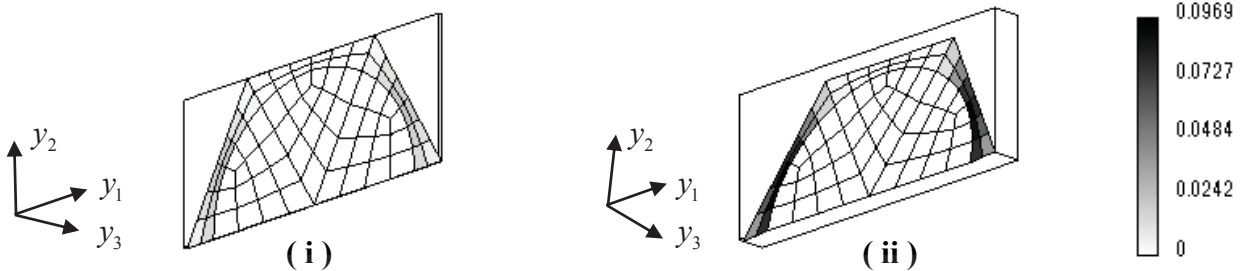


Figure 9. Microscopic equivalent plastic strain distribution at (i) and (ii)

## FTMP-based Modeling and Simulation of Magnesium

\*Naoki Kajiwara<sup>1</sup>, Kazuhiro Imiya<sup>2</sup> and Tadashi Hasebe<sup>3</sup>

<sup>1</sup>Graduate School of Engineering, Kobe University, 1-1 Rokkodai, Nada, Kobe 657-8501, Japan

<sup>2</sup>Iga Campus, Mori Seiki Co. Ltd, 201 Midai, Iga City, Mie 519-1414, Japan

<sup>3</sup>Department of Mechanical Engineering, Faculty of Engineering, Kobe University,  
1-1 Rokkodai, Nada, Kobe 657-8501, Japan.

\*Corresponding author: 133t318t@stu.kobe-u.ac.jp

### Abstract

The present study proposes a constitutive model for deformation twinning which taking account of the twin degrees of freedom via incompatibility tensor model based on Field Theory of Multiscale Plasticity (FTMP). The model is introduced in the hardening law in the FTMP-based crystalline plasticity framework, which is further implemented into a finite element code. Deformation analyses are made for pure single crystal magnesium with HCP structure, and the descriptive capabilities of the proposed model are confirmed based on critical comparisons with experimental data under plain-strain compression in multiple orientations, available in the literature. The simulated results are demonstrated to successfully reproduce the unique stress-strain responses induced by twinning. The evolution of the relative activities of the various slips, and twin mechanisms for each orientation are extensively examined.

**Keywords:** Deformation twinning, Crystalline plasticity, Multiscale modeling, Field theory, Magnesium

### Introduction

The extensive use of Mg in industry has attracted many attentions in recent years mainly because of its superior properties such as light-weight, high strength, and workability. Specifically, unfavorable textures inevitably introduced during rolling processes tend to inhibit both deformability and formability of the material. Therefore, intensive studies have been conducted by many researchers aiming at appropriately controlling the textures. Moreover, complicated fracture modes are observed such as cracking along twin boundaries where twin-slip/twin-twin interactions take place. Accordingly, subtle balances among the different degrees of freedom result in distinct stress-strain responses. A tangible of example of making positive use of such feature is the addition of Yttrium (Nagao, 2012): Yttrium tends to inhibit the twin boundary cracking that leads effectively to the enhancement of the ductility (elongation), thereby relaxing the stress concentration, which is consumed via sub-grain formations or else rotations about the c-axis. What we learn from such observed facts is not only the twin degrees of freedom but also the others associated with all the possible mechanisms ought to be appropriately taken into account in the proposed model.

A key to establish a successful model for Mg is undoubtedly the rational modeling of the deformation twinning in the above-mentioned respect. Major difficulties of the twin modeling come down to how to express the twinning degrees of freedom as an alternative to the slip-based deformation in rational as well as sophisticated manners. A simple but robust model proposed by van-Houtte (van-Houtte, 1978) has been widely used in simulating twin-related phenomena, partially because of its conciseness in the implementation into the conventional crystal plasticity framework. The descriptive capabilities of the model, however, are evidently limited, in the sense that the model will unable to simulate, e.g., the above-mentioned experimental observation.

Hasebe have advocated a comprehensive theoretical framework and model named Field Theory of Multiscale Plasticity (FTMP) (Hasebe, 2004, 2006) that is effective for tackling the above issues. In FTMP, differential geometric quantities, i.e., curvature and torsion, are utilized to rationally describe the generalized “inhomogeneity.” The theory provides us with general views concerning not only how we should recognize the elasto-plastic hierarchy in terms of “evolving” inhomogeneities but also how we can model the targeted phenomena in terms of underlying microscopic degrees of freedom within, e.g., crystal plasticity-based continuum mechanics framework. Geometrically-necessary types of dislocation substructures, as examples of slip-induced inhomogeneities, have demonstrated to be successfully reproduced based on the model (Aoyagi and Hasebe, 2007; Tsunemi and Hasebe, 2009; Imiya and Hasebe, 2013). The model is also applied to the twin modeling and simulations (Okuda and Hasebe, 2013).

In this paper, we apply the FTMP-based model for deformation twinning to Magnesium (Mg, hereafter) with HCP (hexagonal close-packed) structure. Based on the kinematic descriptions for HCP metals, i.e., with the three slip systems (basal, pyramidal and prismatic) and two twin systems (tensile/compression twins), the proposed model will be applied to Mg. The basic capabilities for pure Mg (with mechanical properties available in the literature) will be examined.

## Theoretical Background and Model for Deformation Twin

### *Differential Geometrical Pictures of Dislocation/Defect Fields*

The theory (FTMP) partially puts its basis on the differential geometrical descriptions of dislocations and defects. The major concepts have been established as non-Riemannian plasticity by Kondo (Kondo, 1955). Here, some basics are outlined.

Torsion and curvature tensors are defined, as shown above, respectively as,

$$\begin{cases} S_{kl}^{\cdot j} = \Gamma_{[kl]}^j \\ R_{klm}^{\cdot \cdot n} = 2 \left[ \partial_{[k} \Gamma_{l]m}^n + \Gamma_{[k|p}^n \Gamma_{l]m}^p \right] \end{cases} \quad (1)$$

where  $\Gamma_{kl}^j$  represents the coefficients of connection  $\Gamma_{kl}^j$  in the non-Riemannian space.

Contractions of these higher order tensors considering the symmetry result in well-known second rank tensors. They are respectively called “dislocation density tensor” and “incompatibility tensor” given respectively by a curl of distortion tensor and double curl of strain tensor, i.e.,

$$\begin{cases} \alpha_{ij} = -\epsilon_{ikl} \partial_k \beta_{ij}^p = \frac{1}{2} \epsilon_{ikl} S_{kl}^{\cdot j} \\ \eta_{ij} = \epsilon_{ikl} \epsilon_{jmn} \partial_k \partial_m \epsilon_{ln}^p = \frac{1}{4g} \epsilon_{ikl} \epsilon_{jmn} R_{klm}^{\cdot \cdot n} \quad (g = \det(g_{ij})) \end{cases} \quad (2)$$

To be noted that these quantities are expressed as gradients of distortion or strain tensor in the context of continuum mechanics, meaning the theory intrinsically requires “strain gradients” at least up to the second order.

### *Modeling Deformation Twin – Kinematics and Constitutive Model*

The constitutive models both for slip and deformation twinning employed in the present study are overviewed. Here, the elasto-plastic decomposition by Lee is extended to that including the twin deformation by introducing an intermediate configuration,

$$\mathbf{F} = \mathbf{F}^e \cdot \mathbf{F}^{tw} \cdot \mathbf{F}^p \quad (3)$$

where the deformation gradient tensor for the twinning is represented by  $\mathbf{F}^{tw}$ . Correspondingly, the Jaumann rate of the Kirchhoff stress tensor is given by,

$$\boldsymbol{\tau}_{(J)} = \mathbf{C}^e : \mathbf{d} - \sum_{\alpha=1}^N \mathbf{R}^{(\alpha)} \dot{\gamma}^{(\alpha)} + \sum_{\bar{\alpha}=1}^N \mathbf{R}^{tw(\bar{\alpha})} \dot{\gamma}^{tw(\bar{\alpha})} \quad (4)_1$$

with

$$\begin{cases} \mathbf{R}^{(\alpha)} = \mathbf{C}^e : \mathbf{P}^{(\alpha)} + \boldsymbol{\beta}^{(\alpha)} \\ \boldsymbol{\beta}^{(\alpha)} = \mathbf{W}^{(\alpha)} \cdot \boldsymbol{\sigma} - \boldsymbol{\sigma} \cdot \mathbf{W}^{(\alpha)} \end{cases} \text{ and } \begin{cases} \mathbf{R}^{tw(\bar{\alpha})} = \mathbf{C}^e : \mathbf{P}^{tw(\bar{\alpha})} + \boldsymbol{\beta}^{tw(\bar{\alpha})} \\ \boldsymbol{\beta}^{tw(\bar{\alpha})} = \mathbf{W}^{tw(\bar{\alpha})} \cdot \boldsymbol{\sigma} - \boldsymbol{\sigma} \cdot \mathbf{W}^{tw(\bar{\alpha})} \end{cases} \quad (4)_2$$

The slip rate is given by,

$$\begin{cases} \dot{\gamma}^{(\alpha)} = \dot{A}_{SR} \text{sgn}(\tau^{(\alpha)}) \left\{ \exp B_{SR} \left( 1.0 - \left| \frac{\tau^{(\alpha)}}{K^{(\alpha)}} \right|^p \right)^q + C_{SR} \right\}^{-1} \\ \dot{A}_{SR} = \rho_m b L v_0, \quad B_{SR} = \frac{\Delta G_0}{kT}, \quad C_{SR} = \frac{v_0 B L}{K^{(\alpha)}} \end{cases} \quad (5)$$

where  $K^{(\alpha)}$  is drag stress, responsible for isotropic type of hardening. The above constitutive equation can express stress-strain responses for FCC, HCP and BCC metals over a wide range of strain rate and temperature including impact loading conditions.

The evolution models for drag stress  $K^{(\alpha)}$  and back stress  $\Omega^{(\alpha)}$  given respectively by [Hasebe, Kumai and Imaida (1998b)],

$$\dot{K}^{(\alpha)} = Q_{\alpha\beta} H(\gamma) |\dot{\gamma}^{(\beta)}| \text{ and } \dot{\Omega}^{(\alpha)} = -A_{cell} \left\{ \left\langle d_{cell}^* - \bar{x}_N^{(\alpha)} \right\rangle + \alpha \right\}^{-2} \quad (6)$$

where  $H(\gamma)$  represents hardening modulus for a referential stress-strain curve. The hardening ratio  $Q_{\alpha\beta}$ , through which the contributions of  $\tilde{\alpha}^{(\alpha)}$  and  $\tilde{\eta}^{(\alpha)}$  are accounted for, is given by,

$$Q_{\alpha\beta} = f_{\alpha\kappa} S_{\kappa\beta} + \delta_{\alpha\beta} \left\{ 1 + F(\tilde{\alpha}^{(\alpha)}; \tilde{\eta}^{(\alpha)}) \right\} \quad (7)$$

The strain gradient terms are given as,

$$F(\alpha^{(\alpha)}) = \frac{\bar{k}}{p_\alpha} \sqrt{\frac{|\alpha^{(\alpha)}|}{b}}, \quad F(\eta^{(\alpha)}) = \text{sgn}(\eta^{(\alpha)}) \frac{\bar{k}}{p_\eta} \sqrt{\frac{l_{defect}}{b} |\eta^{(\alpha)}|} \quad (8)$$

where  $b$  denotes the Burgers vector and  $\bar{k}$ ,  $p_\alpha$  and  $p_\eta$  are the material constants.  $\alpha^{(\alpha)}$  and  $\eta^{(\alpha)}$  are respectively written in the forms as mappings of  $\alpha_{ij}$  and  $\eta_{ij}$  into a  $\alpha$  slip system.

The strain rate due to deformation twin is assumed to be an additional degree of freedom to that due to the slip, driven by the evolution of the incompatibility tensor field for the twinning mode,  $\eta_{tw}^{(\bar{\beta})} \equiv (\mathbf{t}^{tw(\bar{\beta})} \otimes \mathbf{s}^{tw(\bar{\beta})}) : \boldsymbol{\eta}$ , i.e.,

$$\dot{\gamma}^{tw(\bar{\alpha})} = Q_{\bar{\alpha}\bar{\beta}}^{tw} |\dot{\gamma}_{prev}^{tw(\bar{\beta})}|, \quad Q_{\bar{\alpha}\bar{\beta}}^{tw} = \delta_{\bar{\alpha}\bar{\beta}} \cdot F(\eta_{tw}^{(\bar{\beta})}) \cdot \left\{ 1 - \frac{|F(\eta_{tw}^{(\bar{\beta})})|}{F_{sat}^{tw}} \right\} \quad (9)$$

Here,  $F(\eta_{twin}^{(\bar{\beta})})$  denotes the FTMP-based incompatibility term defined as,

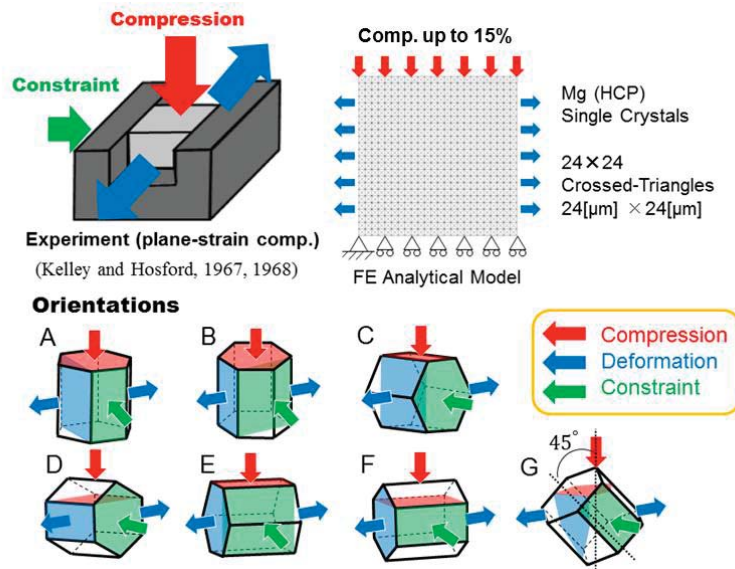
$$F(\eta_{twin}^{(\bar{\alpha})}) \equiv \text{sgn}(\tilde{\eta}^{(\alpha)}) \cdot \frac{k}{p_\eta} \left( \frac{l_{twin}}{b} |\eta_{twin}^{(\bar{\alpha})}| \right)^{1/2} \quad (10)$$

The above twinning model becomes operative when the critical condition for the resolved shear stress is met, i.e.,  $\tau^{\chi} \geq \tau_{cr}^t$ .

### Analytical Model and Procedure

Deformation analyses are made for pure single crystal magnesium (Mg) with HCP structure, and the descriptive capabilities of the proposed model are confirmed based on critical comparisons with experimental data under plain-strain compression in multiple orientations, available in the literature (Kelley and Hosford, 1967, 1968).

Kelley-Hosford conducted a systematic series of plane-strain compression experiments on Mg single crystals, as schematically illustrated in Fig.1. In the present simulations, the die-constraint condition is realistically mimicked by using plane strain assumption. The orientations E and F are reported to exhibit peculiar stress responses showing plateau-like work hardening stagnation followed by a rapid stress increase. The plateau-like stress response observed for the two orientations is supposed to be an indication of the twin activity as the dominant deformation mode, while the latter (rapid stress increase) is driven by the outset of slip modes.

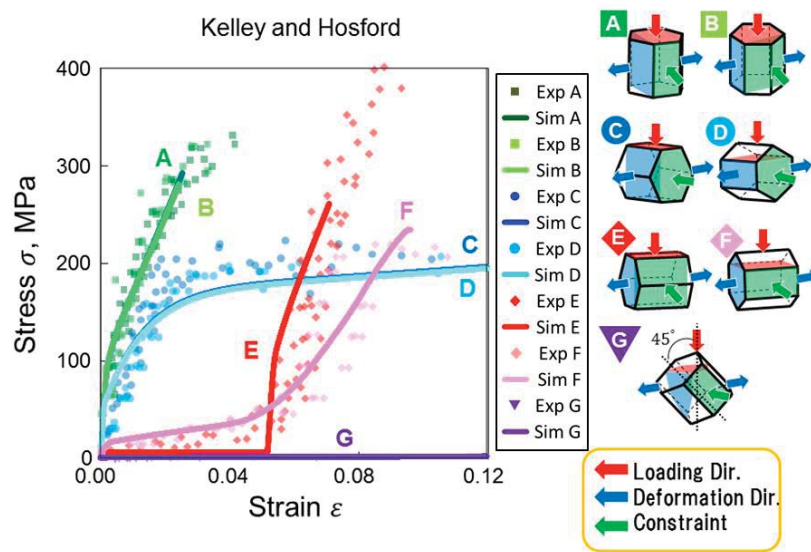


**Figure 1. Simulation set-ups for plane-strain compressions of single crystal magnesium in various crystallographic orientations, where original experiments are conducted by Kelly-Hosford (1967, 1968). Twinning mode is reported to be dominantly activated in orientations E and F.**

### Results and Discussion

#### *Orientation-dependent stress-strain responses*

Figure 2 shows the simulated stress-strain curves for the A-G orientations, comparing with the experimental data (plots). We find excellent agreements between the two for all the orientations. In particular, the simulated results for orientations E and F are demonstrated to successfully reproduce the unique stress-strain responses induced by twinning.



**Figure 2. Simulated stress-strain curves for orientations A to G. Corresponding experimental data by Kelly-Hosford are overplotted for comparison.**

#### *Sample size dependence and Mesh size dependence*

One of the noteworthy features of the present model is the ability to represent absolute scale that is conveyed through the evaluation range of spatial derivative for obtaining the incompatibility tensor field. For the orientations E and F where the twinning mode is dominant, we expect that the stress response is sensitively affected by the sample dimensions. Figure 3 (a) shows the variation of the stress-strain diagram with the sample size for the orientation E, while Fig.3 (b) displays the same result but for the orientation F. What can be clearly confirmed is that the emerging patterns obviously depend on the sample size both for the two orientations. The peculiar stress responses, i.e., plateau-like stress response due to the dominant twinning mode followed by the slip-induced rapid stress rise, are basically unaltered regardless of the sample size. Roughly, larger sample size tends to yield earlier onset of the stress rise, except orientation F with  $12 \times 12 \mu\text{m}^2$ . The variation of the stress-strain curves roughly covers the scatter range of the data in the experiment both for the orientations E and F, implying a possible reason for causing the scatter in the real situations.

To examine the mode-wise contributions, we evaluate the activity ratio of the slip/twin modes for the two cases. Here, activity ratios among two twinning modes and three slip modes are considered, where the total contribution of all the modes is normalized to 1.

Figure 4 compares the variations of slip/twin activity ratio with strain among the three sample sizes for (a) orientation E and (b) orientation F. Orientation E yields 100% activity of the tensile twin mode until the pyramidal and prismatic slip modes are abruptly activated, when the twin activity is stagnated. This corresponds to the stress rise in Fig.3 (a). For orientation F, on the other hand, the prismatic slip is also active in addition to the tensile twin from the early stage of deformation, which lasts (or slightly increases) even after the twin activity is declined. When the activity of the tensile twin starts to be declined, the pyramidal slip is activated, similar to the trend in orientation E. An intriguing point to be noted here is the activity of the basal slip is found in the smallest sample size,  $12 \times 12 \mu\text{m}^2$ , which is absent in all the other cases. The smaller the sample size is, the more the boundary condition becomes influential on the subtle slip/twin activities within. The basal slip, in this case, tends to restrict the activities of the others, i.e., prismatic and the pyramidal slip modes.

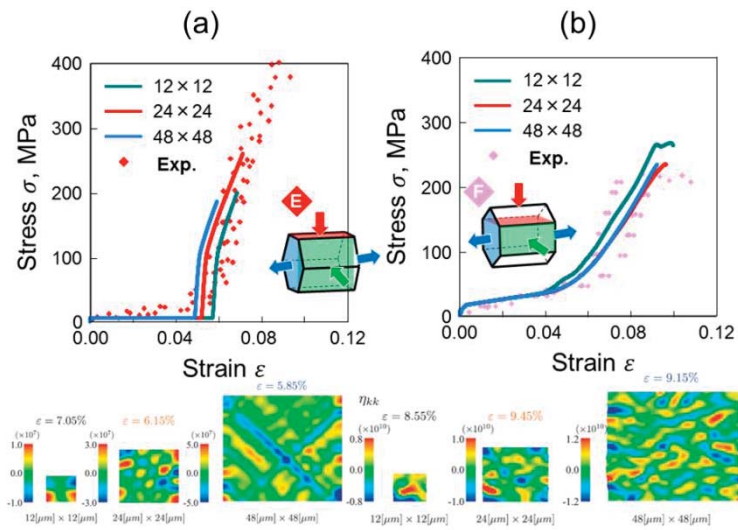


Figure 3. Sample size effect on emerging twinning pattern (strain contour) and stress-strain responses for orientations E and F, comparing  $12 \times 12$ ,  $24 \times 24$  and  $48 \times 48 \mu\text{m}^2$ .

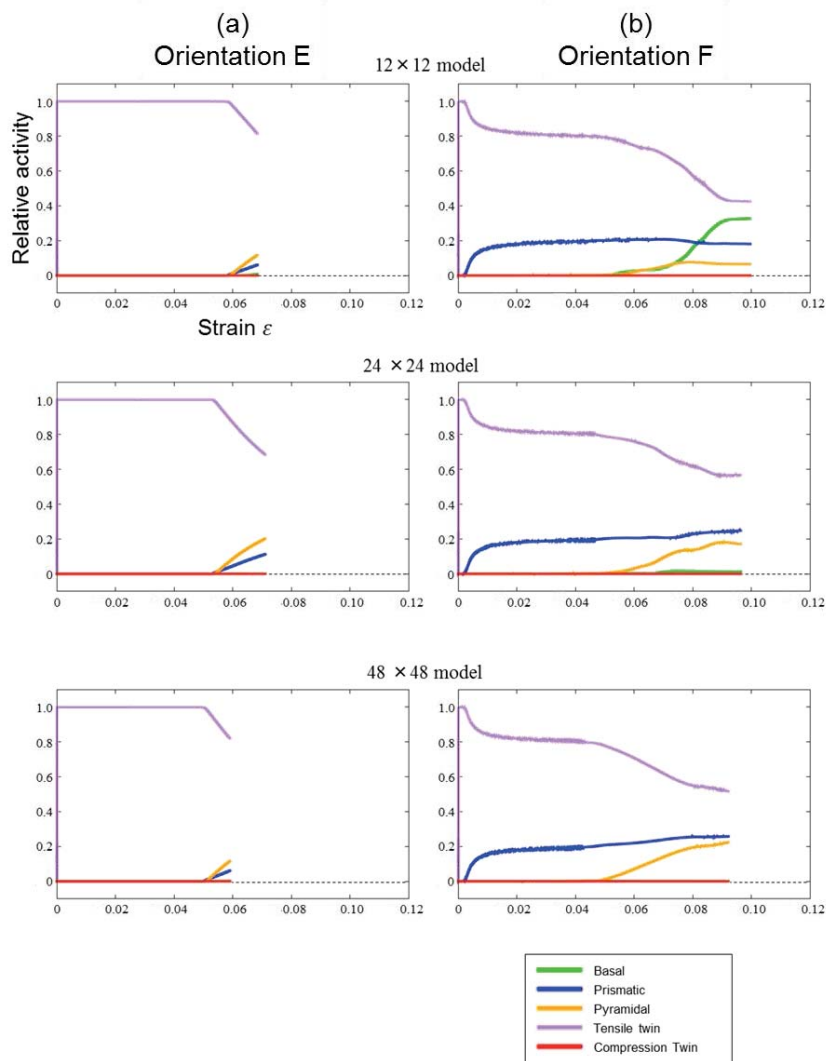


Figure 4. Relative activities of slip and twin modes depended orientation and analysis conditions, comparing three model sizes, i.e.,  $12 \times 12$ ,  $24 \times 24$  and  $48 \times 48 \mu\text{m}^2$ .



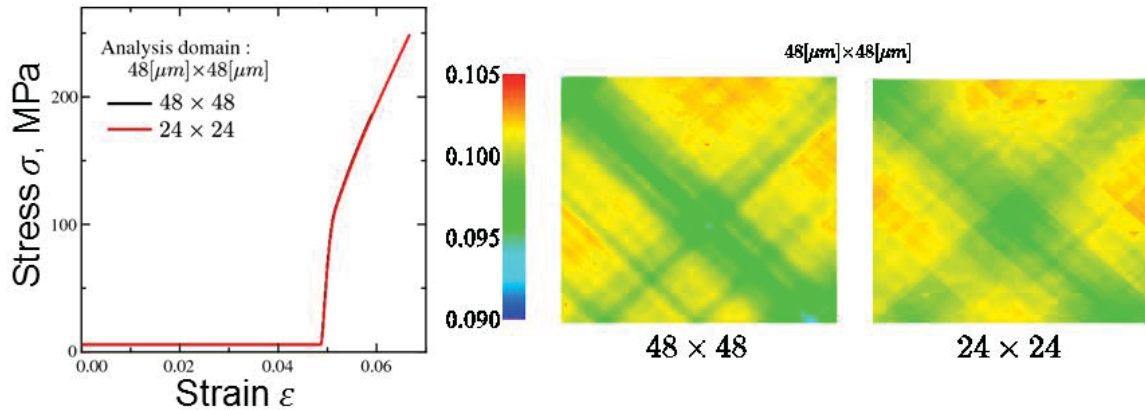
Another feature to be noted of the current modeling scheme is its mesh independency of the simulation results. To demonstrate this, simulations using two mesh divisions, 24x24 and 48x48 cross triangle elements, with a common evaluation size of the derivative for the incompatibility tensor calculation, are compared. Figure 5 shows two twinning strain contours with different mesh divisions. One can confirm basically the same patterns regardless the mesh size. The corresponding stress-strain curves are displayed in the inset, showing almost identical response.

As leverage, let us briefly review conventionally-proposed models, pointing out their drawbacks. They in common introduced a sort of mode transition condition from twin to slip in artificial manners (e.g. Graff, Steglich and Brocks, 2007; Zhang and Josh, 2012). For example, Graff, et al. assumed two functions in their hardening law as,

$$h(\gamma) = \begin{cases} h_0 & \text{for } \gamma \leq \gamma_{ref} \\ h_0 \left( \frac{\gamma}{\gamma_{ref}} \right)^{m-1} & \text{for } \gamma \geq \gamma_{ref} \end{cases} \quad (8)$$

As can be easily imagined, such models always behave similarly regardless of the sample geometry and dimensions, which is obviously unrealistic.

The phase field (PF) model, on the other hand, seems to be powerful even considering the above respect at first glance. We ought to notice, however, it requires us to introduce initial fluctuations in the phase field (twined region, in this case) that critically controls the nucleation site and number of the twined regions. Since where and when the twinning should take place varies strongly depend on the precursor inhomogeneities and other boundary conditions, the PF approach needs some rational reasoning for introducing the initial field fluctuations.



**Figure 5. Supplementary results demonstrating mesh independency of proposed model-based simulations. Strain contours for twinning and corresponding stress-strain diagrams almost coincide regardless the mesh division.**

## Conclusion

A new rational model for deformation twinning has been developed, extending the original FTMP theory of Hasebe for dislocation-based crystal plasticity. Twinning degrees of freedom are taken into account via the FTMP-based incompatibility model, which is further implemented into a crystalline plasticity constitutive framework via the hardening law. Numerical simulations have been performed for pure single-crystal magnesium with HCP structure, and descriptive capabilities of the model have been confirmed by critical comparisons with experimental data for plane-strain

compression of crystals of multiple orientations available in the literature. Results successfully reproduce the unique stress-strain responses induced by twinning. Activities of the various slip systems and twinning mechanisms for each orientation have been predicted. Other noteworthy features addressed here, but not captured by conventional continuum plasticity models, are sample size dependence and mesh size independence.

### Acknowledgement

A support from Army Research Laboratory (ARL) under Contract No. FA5029-13-P-0043 is greatly acknowledged.

### References

- Aoyagi, Y. and Hasebe, T., (2007), New Physical Interpretation of Incompatibility Tensor and Its Application to Dislocation Substructure Evolution. *Key Materials Engineering*, 340-341, 217-222.
- Graff, S., Steglich, D. and Brocks, W., (2007), Forming of Magnesium-Crystal Plasticity and Plastic Potentials. *Adv. Eng. Mater.*, 9-9, 803-806.
- Hasebe, T., (2006), Multiscale Crystal Plasticity Modeling based on Field Theory. *Comp. Mech. Eng. Sci. (CMES)*, 11-3, 145-155.
- Hasebe, T., (2004), Continuum Description of Inhomogeneously Deforming Polycrystalline Aggregate based on Field Theory. *Meso-Scale Simulation and Modeling of Strength and Fracture of Materials, IUTAM Symp. Mesoscopic Dynamics of Fracture Process and Materials Strength* (Eds. H. Kitagawa and Y. Shibutani), Kluwer, pp.381-390.
- Hasebe, T., (2004), Field Theoretical Multiscale Modeling of Polycrystal Plasticity. *Trans. MRS-J*, Vol.29, pp.3619-3624.
- Hasebe, T., (2011), Field Theory of Multiscale Plasticity. Cambridge (to be published).
- Kelly, E. W. and Hosford, W. F. Jr., (1968), The Deformation Characteristics of Textured Magnesium. *Trans. Metall. Soc. AIME*, 242, 5; *ibid.* 242, 654.
- Kondo, K. (1955), Non-Riemannian Geometry of Imperfect Crystals from a Macroscopic Viewpoint. *RAAG Memoirs of Unifying Study of Basic Problems in Engineering and Physical Science by Means of Geometry*, 1 D-I, 458-469.
- Nagao, M., Mukai, T. and Somegawa, H., (2012), Ductility of Mg-Y binary alloy under dynamic compression loading. The 123rd Conference of Japan Institute of Light Metals, pp. 335-336.
- van Houtte, P., (1978), Simulation of the Rolling and Shear Texture of Brass by the Taylor Theory Adapted for Mechanical Twinning. *Acta Metall.*, 26, 591-601.
- Zhang, J. and Josh, S. P., (2012), Phenomenological Crystal Plasticity Modeling and Detailed Micromechanical Investigations of Pure Magnesium. *J. Mech. Phys. Solids*, 60-5, 945-972.
- Okuda, T., Imiya, K. and Hasebe, T., FTMP-based Simulation of Twin Nucleation and Substructure Evolution under Hypervelocity Impact. Graduation thesis, Kobe University.
- Tsunemi, Y. and Hasebe, T., (2009), Simulation of the Heterogeneous Grain Development based on a Distortion Incline Model. Graduation thesis, Kobe University.
- Imiya, K. and Hasebe, T., (2013), Modeling of Twin Deformation based on Field Theory of Multiscale Plasticity. Master's thesis, Kobe University.
- Hasebe, T., Kumai, S. and Imaida, Y., (1998), Impact Compression Behavior of FCC Metals with Pre-Torsion Technique. *J. Mater. Process. Technol.*, 85, 194-197.

## DEM simulation of agglomerated particle behavior in pan-type pelletizer using liquid bridge model

Daiki Fujihashi<sup>1</sup>, Yuki Tsunazawa<sup>1</sup>, Kazuki Tahara<sup>1</sup>, Chiharu Tokoro\*<sup>2</sup> and Shuji Owada<sup>2</sup>

<sup>1</sup> Major in Earth, Resources and Environmental Engineering, Graduate School of Science and Engineering, Waseda University, Okubo 3-4-1, Shinjuku-ku, Tokyo, 169-8555, Japan.

<sup>2</sup> Department of Resources and Environmental Engineering, Faculty of Science and Engineering, Waseda University, Okubo 3-4-1, Shinjuku-ku, Tokyo, 169-8555, Japan

\*Corresponding author: tokoro@waseda.jp

### Abstract

Particle behavior in a pan-type pelletizer was simulated by Discrete Element Method (DEM). In order to represent the effect of added water to adhesive force, liquid bridge model was also included in the simulation. In this study, to investigate detailed behavior of various sizes of particles in pan-type pelletizer, agglomerated particles in five representative particle sizes were simulated by DEM. Velocity and trajectory of several size of particles were compared with experimental results obtained from image processing using high speed camera and their results were consistent each other. In particular, simulation results showed that large particles tend to be located in bottom side of pan and upper side of particles layer, which coincided with the trend obtained from the experiment.

**Keywords:** DEM, Agglomeration, Liquid Bridge, Pan Type Pelletizer.

### Introduction

A pan type pelletizer or a drum type mixer has been generally used for agglomeration of particle mixture by adding binding liquid, because this agglomeration process is productive and low cost. The formation of particle agglomeration is due to adhesion forces between particles, which are attributed to several kinds of inter-particle forces such as Van der Waals' force, electrostatic force or liquid bridge force.

It is well-known that even a small amount of liquid has a significant effect on particulate flow. The adhesion force due to liquid bridges between particles is one of those factors which have long been attracting attention in the field of powder technology. Theories of the liquid bridge between two particles have been developed by several researchers [Fisher, 1926; Lian, Thornton and Adams 1993]. However, since the agglomeration process is very complicated, agglomeration phenomenon has not been revealed fully. Additionally, effective methods to observe particle flows in a pan type pelletizer have not been established. In order to control this agglomeration process properly in a pan type pelletizer, it is necessary and important to understand the motion of particle flows in a pan more particularly and directly.

Computer simulation is one of the effective tools for scientific research. The discrete element method (DEM) simulation can predict behavior of the particle flows from the motion of individual particles. Therefore DEM has been applied to particle simulation such as fluid bed, ball mill, slope failure, and so on. Several researchers have also been proposed DEM simulation taking into account the liquid bridge force.

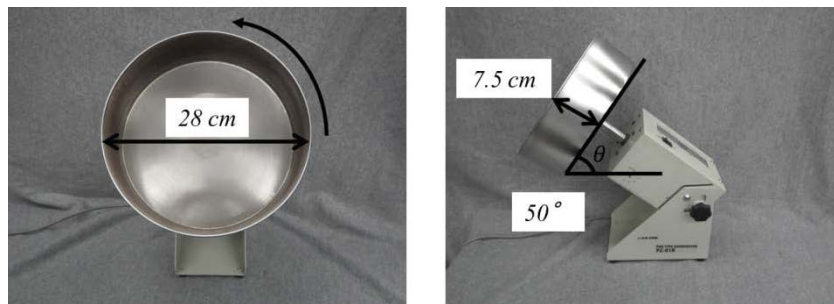
The objective of this study is to predict several particle sizes of particle flows in a pan type pelletizer by using DEM simulation. In this study, the motion of different sizes of particles was calculated by DEM simulation taking into account a static model of liquid bridge. In order to compare with simulation results, agglomeration experiment using a laboratory scale pan type

pelletizer was also conducted. Trajectory and moving velocity of coarse particle in a pan were measured by using a high speed camera and compared with DEM simulation results.

## Materials and Methods

### Agglomeration Experiment

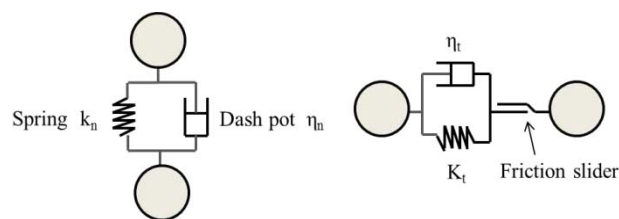
Agglomeration experiment was carried out in order to validate and compare the DEM simulation results. A pan type pelletizer (ASONE, Japan, PZ-01R) was used for the experiment. The inner diameter and length of the pelletizer were 280 and 730 mm respectively. Figure 1 shows the schematic diagram of a pan type pelletizer used in the experiment. The granulating time was set 5 minutes and the rotation speed was set at 39.0 rpm. Water was added to powder with a spray bottle. Calcium carbonate particles were used in the agglomeration experiment.



**Figure 1. Snapshots of a pan type pelletizer**

### Discrete Element Method (DEM)

The DEM model used in this study is based on the original DEM concept proposed by Cundall and Strack (1979). As shown in Figure 2, contact between particles and between a particle and a wall is modeled using a Voigt model consisting of a linear spring and dashpot in normal and tangential directions. A slip model defined by the friction coefficient is included in the tangential force. A linear contact model is adopted to reduce the computation load. In this study, the particles are considered to be spherical.



**(a) Normal direction    (b) Tangential direction**

**Figure 2. Principle of Voigt model**

### Inter-particle forces

The liquid bridges cause various effects on the particles, such as the adhesion force exerted by the static forces, the dynamic forces exerted by the viscosity of the liquid and relative displacement of the particles. Static strength forces as surface tension and capillary forces are conservative forces in the sense that they always act to pull particles together in wetted systems. In this study, only static strength forces between the particles were considered. Both of the contact force and the

adhesion force of a liquid bridge were taken into account for contacting particles. In the case that a liquid bridge was formed between separated particles, only the adhesion force was considered.

### Modeling of liquid bridge

The static strength of liquid bridge consists of two components. One is suction pressure caused by the curvature of the liquid interface. The other is force due to the interfacial surface tension acting around the perimeter of the bridge cross-section. In the case that gravitational effects arising from bridge distortion and buoyancy can be neglected, the total force  $F$  acting between two equal-sized spherical particles, whose radius is  $r_0$ , is given by the sum of two components; one is the axial component of the surface tension acting on the three-phase (solid / liquid / air) contact line and the other is the hydrostatic pressure acting on the projected area of the liquid contact to each particle. This leads to the following expression,

$$F = \pi \cdot \Delta P \cdot r_0^2 \cdot \sin^2(\varphi) + 2\pi \cdot \gamma \cdot r_0 \cdot \sin(\varphi) \cdot \sin(\varphi + \theta) \quad (1)$$

where  $\varphi$  is the half-filling angle,  $\theta$  is the contact angle and  $\gamma$  is the liquid surface tension. Schematic representation of a liquid bridge between two equal-sized spherical particles, particle  $i$  and particle  $j$ , with definition of these parameters is shown in Figure 3. In this figure,  $2h$  is the surface distance between particles.

$\Delta P$  in equation (1) is the pressure difference across the curvature of the air-liquid interface. Assuming that the liquid surface has constant mean curvature  $\Delta P$  is given by the Laplace-Young equation as follows.

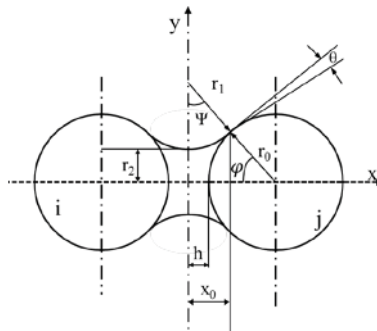
$$\Delta P = \gamma \left[ \frac{1}{r_1} - \frac{1}{r_2} \right] \quad (2)$$

where  $r_1$  and  $r_2$  are the radius of curvatures of the liquid bridge surface.

There is a general lack of reliable theoretical formulas for the calculation of the liquid bridge force between two unequal-sized spheres. In this case, following approximation is generally used. That is, the radius term  $r_0$  in equation (1) is replaced by an effective particle radius  $r_{eff}$  according to the following equation.

$$r_{eff} = \frac{2r_i r_j}{r_i + r_j} \quad (3)$$

where  $r_i$  and  $r_j$  are radius of particle  $i$  and  $j$ , respectively.



**Figure 3. Schematic diagram of liquid bridge**

### *Restriction on liquid bridge formation*

Liquid bridges are formed not only between contacting particles, but also between separating particles with a small gap. It is necessary to determine the limit length of the gap in which the liquid bridge is formed.

The liquid bridge can be sustained when the capillary pressure is larger than zero. The limit length of gap  $H_{\max}$  can be derived by solving the Laplace's equations under the condition of the capillary pressure equal to zero.  $H_{\max}$  of neighboring particles is given by the following formula.

$$H_{\max} = r_2 \cdot \ln\left(\frac{1 + \sqrt{1 - r_2}}{\sqrt{r_2}}\right) + \sqrt{1 - r_2} - 1 \quad (4)$$

### *Determination of Parameters*

The DEM parameters used in this study are shown in Table 1. These simulation parameters were determined from experimental results. In particular, the frictional coefficient was determined carefully since it strongly affects granules behavior. Dashpot coefficient was calculated from spring constant and coefficient of restitution. The particle diameter was determined from sieve mesh used in sieving of particles before/after agglomeration test. The number of particles was determined from weight balanced particle size distribution measurement.

**Table 1. Calculation condition**

Simulation	Time step (s)	$1.0 \times 10^{-6}$
	Gradient angle (°)	50.0
	Spring constant (N/m)	1000
	Reflection coefficient (-)	0.1
	Friction coefficient (-)	0.484
	Surface tension of liquid (J/m <sup>2</sup> )	0.0725
	Water content (-)	0.00, 0.08
Particles	Particle diameter (mm)	16, 8, 4, 2, 1
	Number of particle (-)	2, 43, 1466, 11868, 41823
	Density of particles (g/cm <sup>3</sup> )	2.60

## Results and Discussion

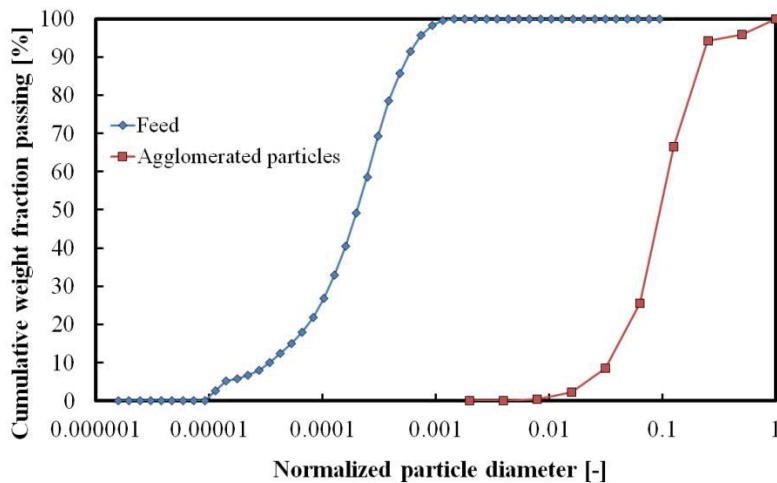
### *Behavior of particles in pan type pelletizer*

Figure 4 shows the particle size distribution of the feed particles and the agglomerated particles; particle size is normalized by maximum particle size.

The particle size of the agglomerated particles was larger than that of the feed particles, which showed that effective agglomeration was achieved in the experiment.

In order to compare the behavior of particles in an experiment with the behavior calculated from DEM simulation, the behavior of particles in the experiment was taken by a high speed camera. In this study, the behavior of coarse particles was especially focused on. Figure 5 shows the state of calcium carbonate particles after the agglomeration experiment.

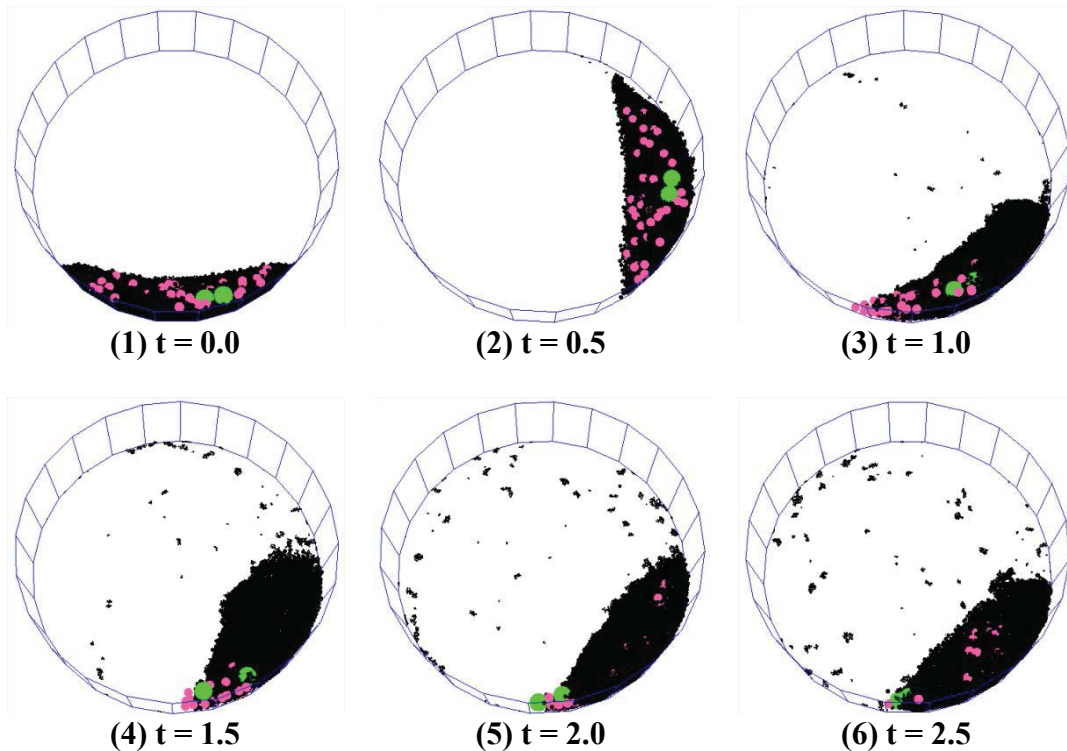
Figure 6 shows snapshots of particle motion calculated by DEM simulation. Coarse particles whose diameter were 8 mm, were painted pink color, and coarse particles whose diameter were 16 mm, were painted green color. That is, the particles rose along the pan wall and then fell down on the surface layer of the granules toward the downside. At this time, the particles cascaded on the surface layer of other granules in the pan. This cascading motion of granules would be important for the agglomeration behavior. Additionally, some particles adhered to the bottom wall of the pan by the force of liquid bridge.



**Figure 4. Particle size distribution of feed and agglomerated particles**



**Figure 5. Snapshots of particle behavior (Experiment)**



**Figure 6. Snapshots of particle behavior (Simulation)**

#### *Trajectory and Velocity of Coarse particles*

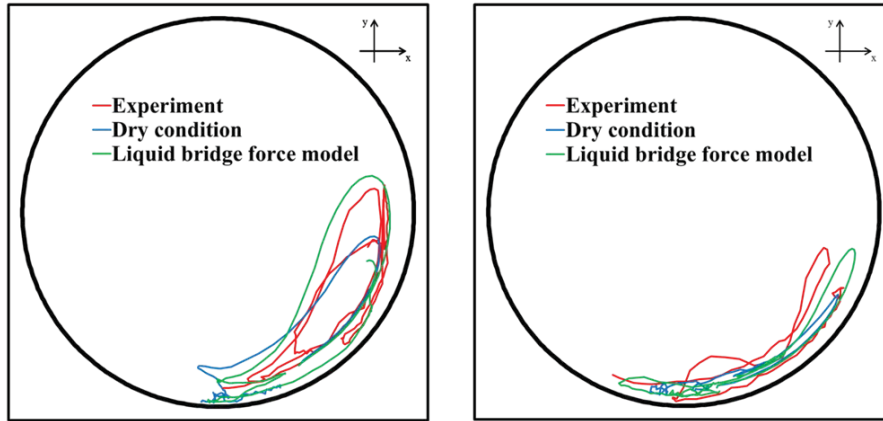
In order to validate simulation results, we focused trajectory and velocity distribution of coarse particles, whose diameters were 8 mm or 16 mm. As shown in Table 1, two different situations in the simulation were compared with experimental results. One was wet condition which was calculated with the liquid bridge model. The other was dry condition which was calculated without the liquid bridge model.

Figure 7 shows the trajectory of coarse particles. Experimental results and simulation results with the liquid bridge model had similarities of the trajectory of coarse particles. In particular, when we focused the maximum height which coarse particle rose up on the surface of particulate bed, simulation results considering the liquid bridge force had almost the same height with experimental results. On the other hand, the maximum height of particles obtained from calculation without the liquid bridge model was much lower than that of experimental results.

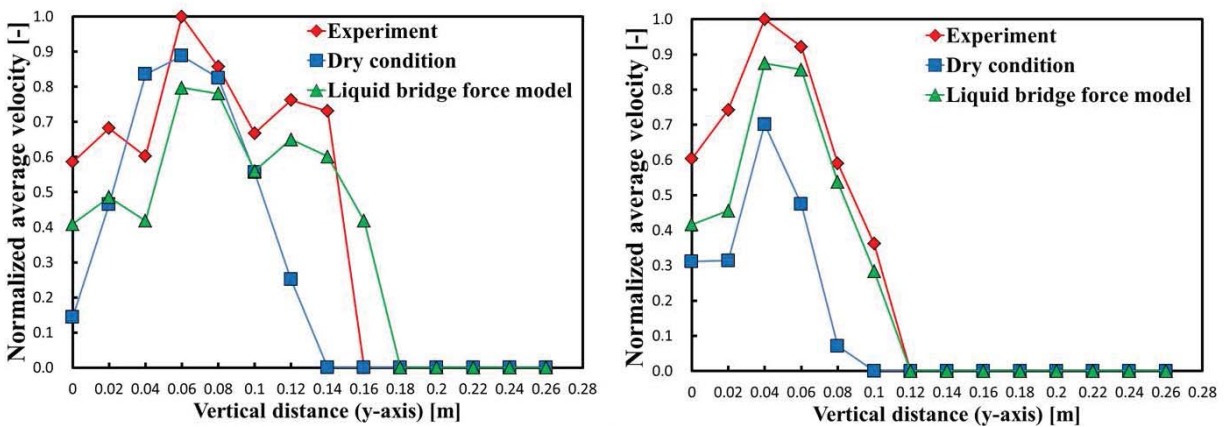
Figure 8 shows the velocity distribution of coarse particles; velocity is normalized by maximum velocity. In the experiment, coarse particles whose diameter were 8 mm, were painted pink color, and coarse particles whose diameter were 16 mm, were painted green color. The velocity of coarse particles was measured by the behavior of particles which was recorded on a high speed camera.

As shown in the figure 9, in the simulation, the x-y plane of the pan was split by square cells, 2 cm on a side, and the velocity was calculated from the average of particle velocity in each cell. Both experimental results and simulation results with the liquid bridge model had similar trend and peak position. Especially velocity distribution of 8 mm coarse particles had unique trend, which could not be represented in the result calculated by the model of dry conditions. These results suggested that the effect of the liquid bridge force was strong for particulate flow in the pan type pelletizer. Comparing between simulation results and experimental ones in Figures 7 and 8, liquid bridge model should be included to DEM simulation in order to represent experimental results exactly.

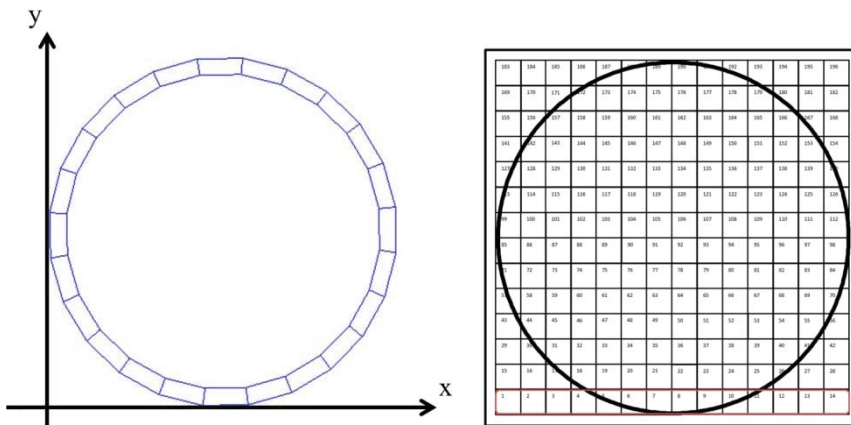




(a) 8 mm (b) 16 mm  
**Figure 7. Trajectory of coarse particles**



(a) 8 mm (b) 16 mm  
**Figure 8. Velocity distribution of vertical direction**



(a) Coordinate axes (b) Grid pattern  
**Figure 9. Schematic diagram of particle velocity measurement**

## Conclusion

The behavior of agglomerated particles in the pan type pelletizer with small amount of water was simulated by using the DEM taking account of the adhesion force due to water. The adhesion force acting on two particles was formulated by using the theory of the liquid bridge. The simulation results indicated that the adhesion force due to liquid bridges largely affects particle flows. Concerning the trajectory of coarse particles, both experimental and simulation results with the liquid bridge model had similar trends. Additionally, the velocity distribution also agreed well between both experimental and simulation results when the liquid bridge model was included. These results suggested that the DEM simulation with the liquid bridge model could apply to the determination of appropriate operating condition, such as water content, gradient angle, number of rotations, in the pan type pelletizer.

## Reference

- Cundall P.A., Stack O.D.L., (1979), *Geotechnique*, 29(1), pp. 47-65.  
Fisher R.A., (1926), *J. Agric.Sci.*, 16, pp. 492-505.  
Lian G., Thornton C., Adams M.J., (1993), *J. Colloid Interface Sci.*, 161, pp. 138-147.

## Fast multi-scale simulations of a Step-and-Flash Imprint Lithography

\*M. Sieniek<sup>1</sup>, P. Gurgul<sup>1</sup> and M. Paszyński<sup>1</sup>

<sup>1</sup>AGH University of Science and Technology, Krakow, Poland

\*Corresponding author: msieniek@GMAIL.COM

### Abstract

In this paper we present a graph grammar based multi-frontal direct solvers resulting in 90 percent speedup in a multi-scale simulations of the Step and Flash Imprint Lithography (SFIL) a modern patterning process. The multi-scale simulation involves nano-scale Molecular Statics model coupled with macro-scale linear elasticity with thermal expansion coefficient. The simulations involves the densification of the liquied polymer inside the feature resulting from the photopolimerization, as well as shrinkage of the feature after removal of the template. The macro-scale domain is solved with a new version of multi-frontal direct solver with the graph grammar based mechanism for the reuse of the sub-domains with similar geometries and similar material properties. The graph grammar model enables for automatic localization of the sub-domain that can be reuse in our solver algorithm. We show that the new solver enables for 90 percent speedup of the numerical solution.

**Keywords:** Multi-frontal solver, nanolithography, molecular statics, linear elasticity with thermal expansion coefficient, multi-scale modeling

### Introduction

The paper presents the multi-scale modeling of the Step-and-Flash Imprint Lithography (SFIL), a modern patterning process utilizing photopolymerization in order to replicate a template onto a substrate (Colburn et al. 2001). The SFIL process can be simulated by macro-scale model as linear elasticity with thermal expansion coefficient (Hughes 2000), however in some areas of the domain e.g. on the interface between the feature and the template, the nano-scale model, namely the molecular statics model must be included (Paszynski et al. 2005). The three dimensional finite element method simulations are expensive (Demkowicz et al. 2007), and thus we propose a multi-frontal solver algorithm with the reuse technique. The multi-frontal solvers are most advanced direct solvers used to solve the linear systems of equations (Duff and Reid 1983, Duff and Reid 1984, Geng et al. 2006). In our previous works we already modeled the mesh generation and multi-frontal solvers by graph grammar (Paszynska et al. 2012a, Paszynska et al. 2012b, Paszynska et al. 2008, Paszynski et al. 2009a, Paszynski et al. 2009b, Paszynski et al. 2010, Paszynski and Schaefer 2010). However in this work we introduce a new graph grammar model allowing for efficient reuse of identical sub-branches of the elimination tree.

### Step-and-Flash Imprint Lithography

The major processing steps of SFIL include (compare Figure 1): depositing a low viscosity, silicon containing, photocurable etch barrier on to a substrate; bringing the template into contact with the etch barrier; curing the etch barrier solution through UV exposure; releasing the template, while leaving high-resolution features behind; a short, halogen break-through etch; and finally an anisotropic oxygen reactive ion etch to yield high aspect ratio, high resolution features. Photopolymerization, however, is often accompanied by densification (see Fig. 1a). The average distance between molecules decreases and causes volumetric contraction. Densification of the SFIL photopolymer (the etch barrier) may affect both the cross sectional shape of the feature and the placement of relief patterns.

### Macro scale model

The macro-scale model is based on the adaptive Finite Element Method (FEM) discretization of linear elasticity with thermal expansion coefficient. The FEM model can be summarized as follows: Find  $\mathbf{u} \in \mathbf{V}$  such that

$$\int_{\Omega} w_{(i,j)} c_{ijkl} u_{(k,l)} d\Omega = -\theta \int_{\Omega} w_{(i,j)} c_{ijkl} \alpha_{kl} d\Omega - \int_{\Omega} w_{(i,j)} \sigma_{ij}^0 d\Omega \quad \forall \mathbf{w} \in \mathbf{V} \quad (1)$$

where  $c_{ijkl}$  are elastic coefficients,  $\alpha_{kl}$  thermal expansion coefficients,  $\sigma_{ij}^0$  initial stress.  $\theta$  temperature, and  $u_{(i,j)} = \frac{u_{i,j} + u_{j,i}}{2}$  is the strain tensor.

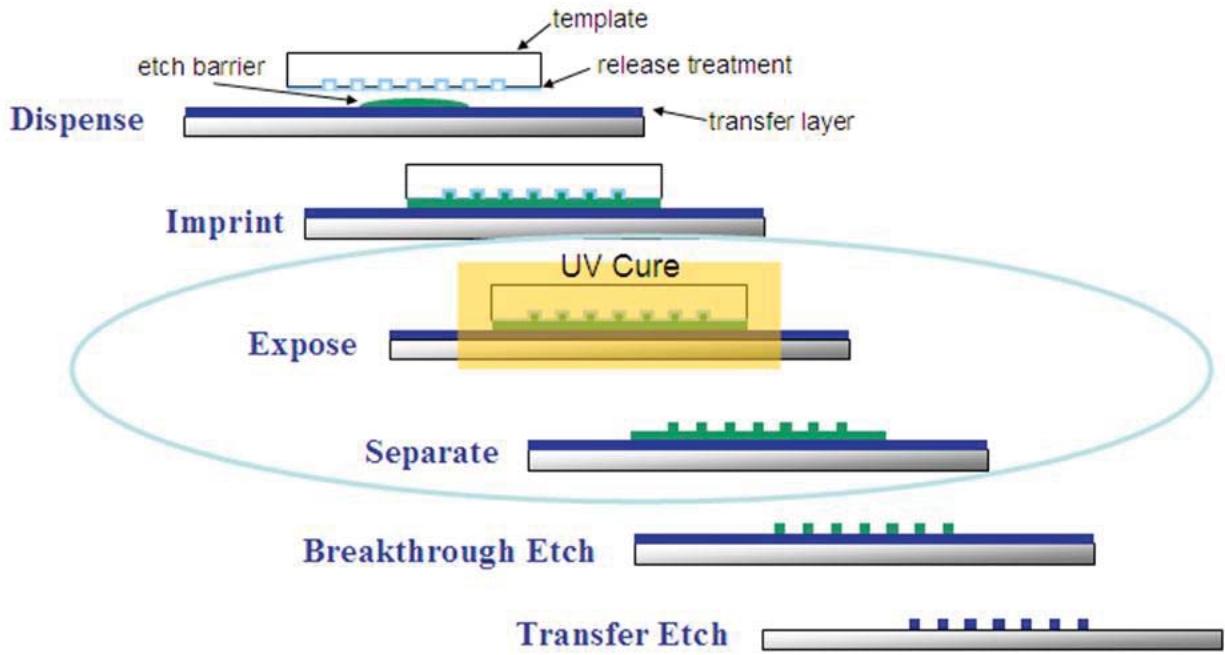


Figure 1. Step and Flash Imprint Lithography

### Molecular statics model

The molecular statics nano-scale model can be summarized as follows:

Find the equilibrium configuration of particles satisfying

$$\sum_{\beta} \mathbf{F}_{\alpha\beta} = \mathbf{0} \quad (2)$$

where

$$\mathbf{F}_{\alpha\beta} = k_{\alpha\beta} \left( r_{\alpha\beta} + \Delta r_{\alpha\beta} - r_{\alpha\beta}^0 \right) \frac{(\mathbf{x}_{\beta} - \mathbf{x}_{\alpha})}{\|\mathbf{x}_{\beta} - \mathbf{x}_{\alpha}\|} \quad (3)$$

is the force between interacting particles  $\alpha$  and  $\beta$ ,  $k_{\alpha\beta}$  is the spring stiffness coefficient,  $r_{\alpha\beta} + \Delta r_{\alpha\beta} = \|\mathbf{x}_{\beta} - \mathbf{x}_{\alpha}\|$  is the length of the spring in the equilibrium configuration,  $\mathbf{x}_{\alpha}, \mathbf{x}_{\beta}$  represents the (unknown) equilibrium configuration of particles,  $r_{\alpha\beta}^0$  is the length of the unstretched spring. The spring stiffness coefficients are obtained from Monte Carlo simulations concerning the photopolymerization of the feature (Colburn et. al. 2001)

**Coupling between the models**

The coupling between the macro-scale and non-scale model is done through identification of particles located on the interface of the nano-scale domain with nodes of the finite element mesh. In such the case over the nano-scale model we solve the molecular statics equations, over the macro-scale model we solve discretized variational formulation for finite element method for linear elasticity with thermal expansion coefficient, however the interface between domains we treat in a special way. The variables from the interface are treated by the nano-scale model as particles represented by their relative change of location  $\Delta\tilde{p}_\alpha = \tilde{x}_\alpha - \tilde{p}_\alpha$ , but from the macro-scale FEM model the variables are treated as degrees of freedom of finite element mesh  $\tilde{u}_\alpha$ . This is equivalent to identification of these two variables

$$\Delta\tilde{p}_\alpha = \tilde{u}_\alpha \tag{4}$$

for each particles (or finite element degrees of freedom)  $\alpha$  located on the interface. In practice it is not necessary to add these new equations to the system, we can just aggregate the nano-scale and macro-scale entries to the same row of the global matrix.

**Graph grammar based solver with reuse technique**

In this section we describe a graph grammar based multi-frontal solver with reuse technique. The first step of the solver algorithm is to generate the computational mesh. It is done by executing a sequence of graph grammar productions, generating a graph structure representing computational mesh. The first graph grammar production is presented on left panel in Figure 2. The productions replaces the starting graph containing only a single vertex **S** with a graph representing a single hexahedral element with eight nodes. The following graph grammar productions replaces some nodes by sub-graphs representing smaller elements. The graph nodes as well as graph grammar productions are attributed by the location over the rectangular domain. The graph grammar production  $(P)^{TNW}$  from right panel in Figure 2 is actually replicated for different locations, for  $\{TNW, TNE, TSW, TSE, BNW, BNE, BSW, BSE\}$  where **T** and **B** stands for top and bottom, and **N**, **S**, **W**, **E** stand for north, south, west, east.

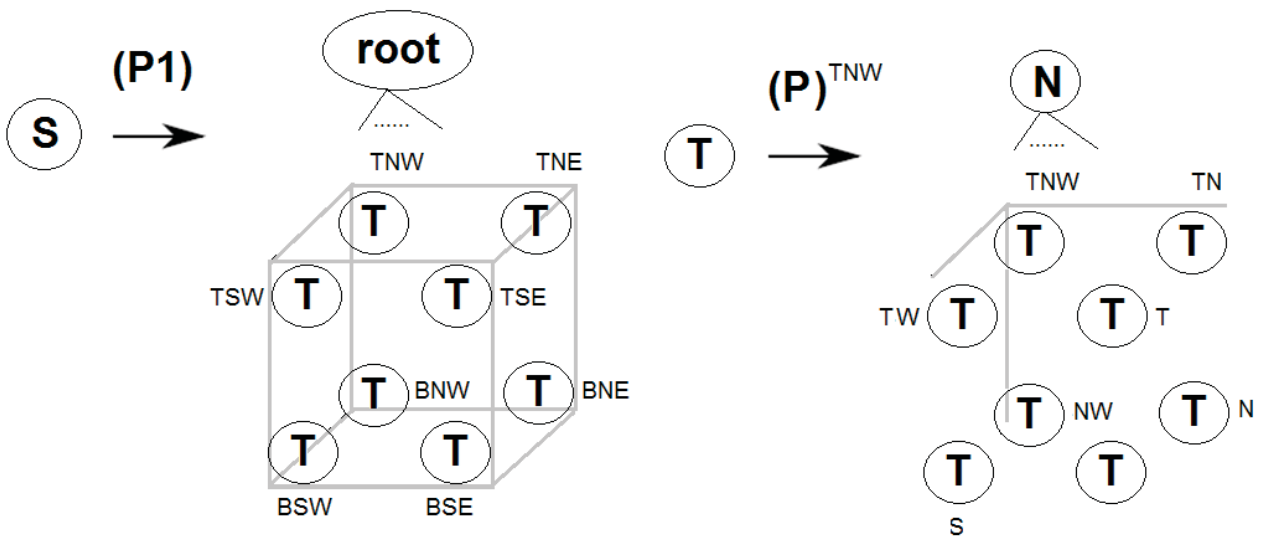


Figure 2. Exemplary graph grammar productions for generating of the structure of the mesh

The exemplary derivation of eight finite element mesh is presented in Figure 3. In the first step of the derivation, production (P1) is executed, in the second step, productions (P)<sup>TNW</sup> - (P)<sup>TNE</sup> - (P)<sup>TSW</sup> - (P)<sup>TSE</sup> - (P)<sup>BNW</sup> - (P)<sup>BNE</sup> - (P)<sup>BSW</sup> - (P)<sup>BSE</sup> are executed to obtain the eight finite element mesh. The graph representing the mesh has hierarchical tree-like structure storing the history of graph grammar productions derivation. To obtain larger meshes, it is necessary to add graph grammar productions for locations like {T,B,N,S,W,E,TN,TS,TW,TE,BN,BS,BW,BE,NE,NW,SE,SW}, compare labels of the left bottom sub-graph at Figure 3.

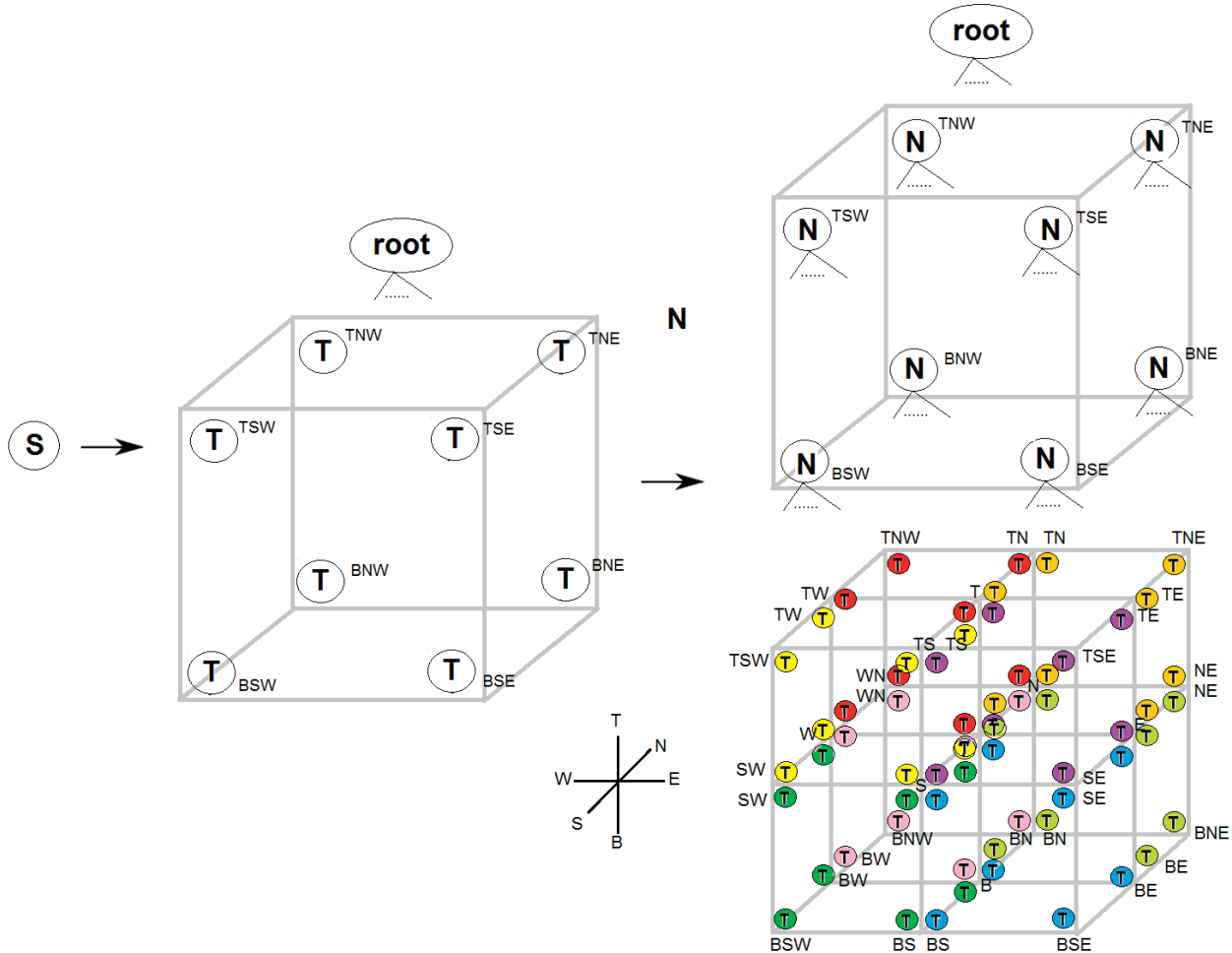


Figure 3. Derivation of eight finite element mesh

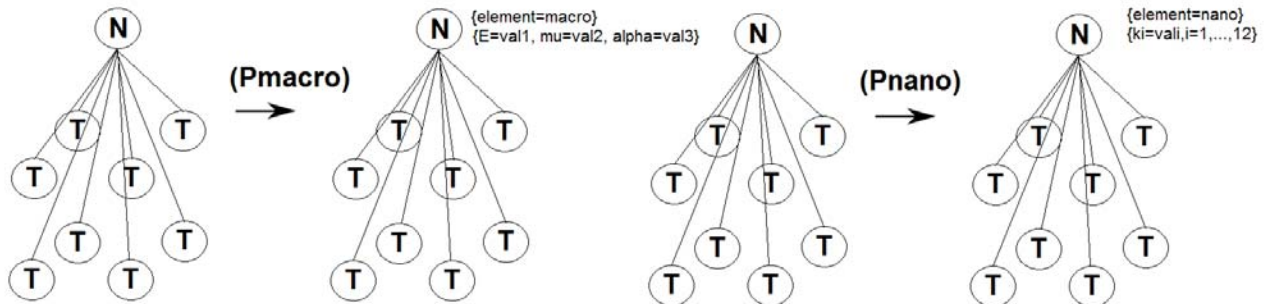
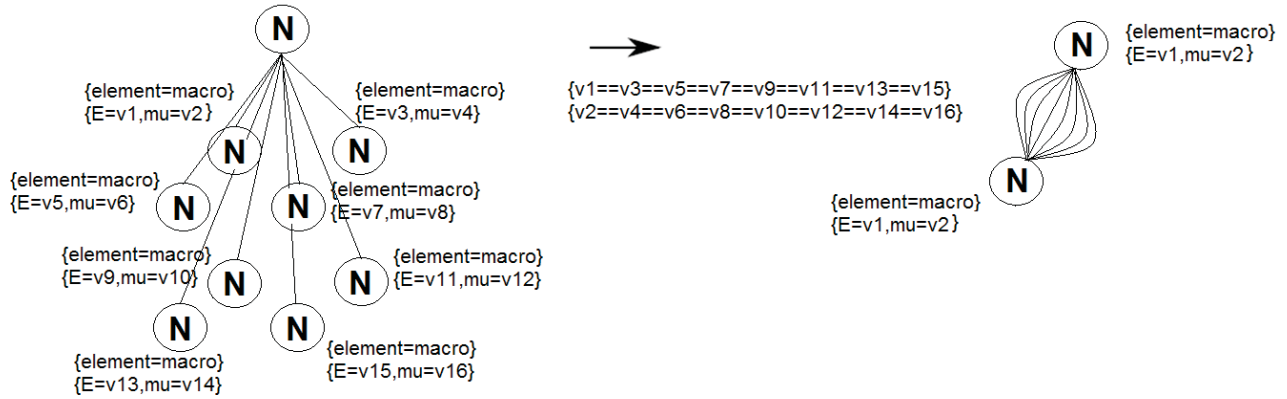


Figure 4. Graph grammar productions for identification of macro- and nano-scale elements

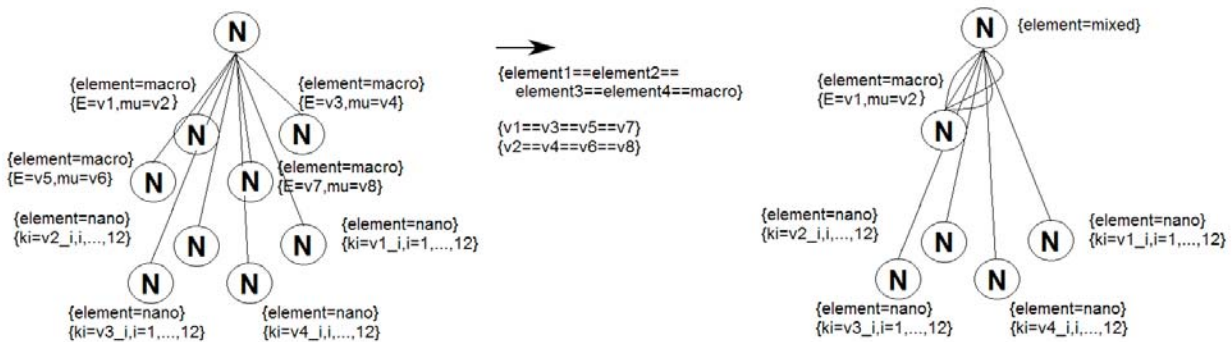
The next step of the solver algorithm is the identification of macro-scale and nano-scale elements. Notice that graph nodes labeled with N actually represents particles (over nano-scale elements) or finite element method nodes (over macro-scale elements). Thus, the elements are represented by

patches of eight nodes. In our exemplary mesh presented in Figure 3 we have eight elements denoted by different colors.

This identification is performed by graph grammar production presented in Figure 4. The macro-scale elements are attributed by Young modulus and Poisson ratio values. The nano-scale elements are attributed by parameters of the spring force parameters  $k_{\alpha\beta}$ .



**Figure 5. Exemplary graph grammar production for identification of macro-scale elements with identical material data**



**Figure 6. Exemplary graph grammar production for partial identification of macro-scale elements with identical material data**

The resulting tree structure can be directly utilized by the multi-frontal solver algorithm (Paszynski et al. 2010, Paszynski and Schaefer 2010)

The third step of the solver algorithm is the identification of identical sub-branches of the elimination tree, for the reuse of partially LU factorized matrices. The exemplary graph grammar production for such the identification is presented in Figure 5. Such the graph grammar production checks if all eight son elements are macro-scale elements and if corresponding Young modulus and Poisson ratios are identical. If this is the case, the eight son element nodes are reduced to one representative node, so the LU factorization can be performed only once and father node can merge eight identical matrices from the same representative son node.

Another more complicated case for the identification is presented in Figure 6. In this example only four son elements are macro-scale elements with identical Young modulus and Poisson ratio values. The four identical macro-scale elements are reduced to one representative elements, however the nano-scale elements are stochastic in their nature and cannot be reduce to one representative element.

Finally, on the modified elimination tree we can execute the multi-frontal solver algorithm – namely the forward elimination

```

1 function forward_elimination(node)
2 if new_schur_matrix already computed for the node then
3 return schur_matrix
4 if node is a leaf then
5     generate local system assigned to node
6     excluding boundary conditions
7 else
8     loop through son_nodes
9         schur_matrix = forward_elimination(son_node)
10        merge schur_matrix into new_system
11    end loop
12 end if
13 find fully assembled nodes and eliminate them
14 return new_schur_matrix
15 end function

```

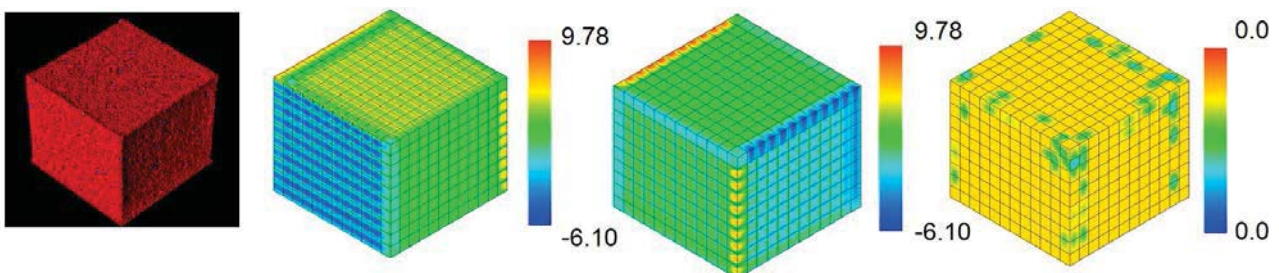
Notice that in case of representative nodes in line 9 we actually call the same node of the elimination tree many times and line 2 prevents from recomputing the identical Schur complement matrices many times. The forward elimination algorithm is followed by analogous backward substitution.

### Numerical results

In this paper we consider two simulations. The first simulation concerns the multi-scale simulations of the feature inside the template, where the interior of the domain is modeled by the macro-scale model, but the boundary layers where the interactions between the feature and the template must be well captured the nano-scale model is utilized, compare Figure 7.

The second simulation concerns the macro-scale model for the feature outside the template, compare Figure 8.

In both cases the graph grammar based reuse technique can be utilized. In the second example we are able to reuse all of the matrices at each level of the elimination tree. In the first case, we are also able to reuse all the matrices from the macro-scale domain, however the boundary nano-scale layers must be process at the very end.



**Figure 7. Nano-scale simulations of the feature inside the template**  
**Left panel: Boundary layers modeled by molecular statics**  
**Other panels: X, Y and Z components of the displacement vector field for the interior modeled by linear elasticity with thermal expansion coefficient**



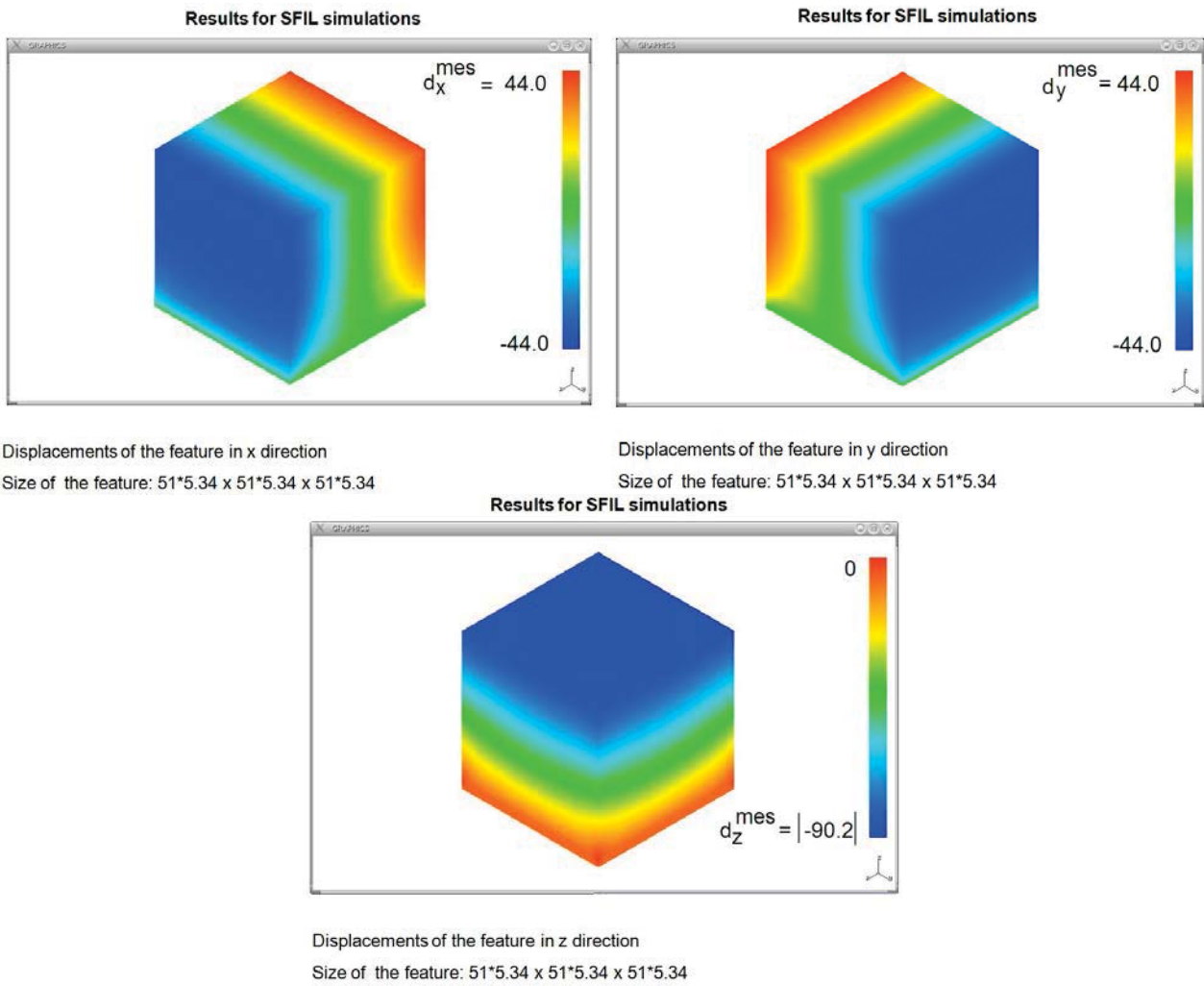


Figure 8. Macro-scale simulations of the feature outside the template.

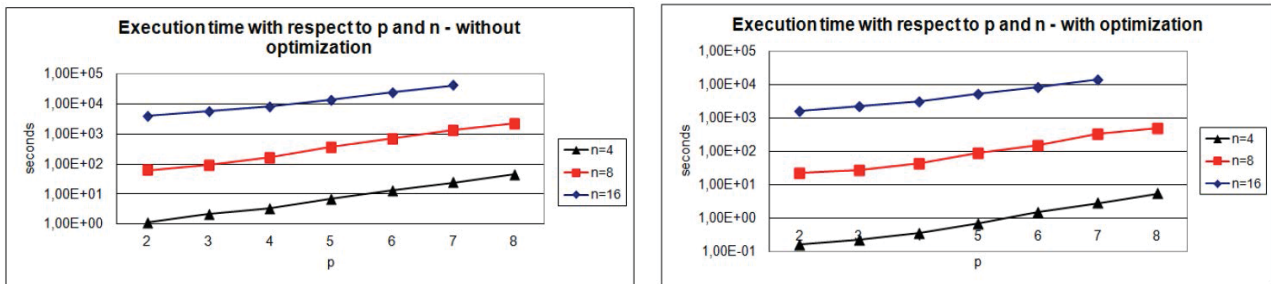


Figure 9. Left panel: Execution time of the solver without reuse  
Right panel: Execution time of the solver with reuse

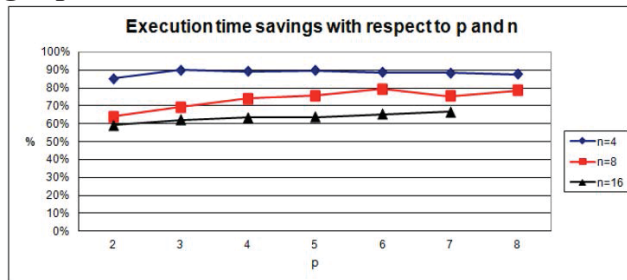


Figure 10. Speedup of the reuse solver

We conclude the numerical results section with comparison of the execution times of the graph grammar based multi-frontal solver with and without the reuse technique. The results presented in Figure 9 concerns computational grids with different number of elements in each direction ( $n$  parameter) as well as different polynomial orders of approximations utilized over the macro-scale domain ( $p$  parameter). The resulting speedup of the reuse solver algorithm is presented in Figure 10.

## Conclusions

In this paper we presented a fast multi-frontal solver algorithm enabling for speed-up up to 90% of the solution over the macro-scale domain in the multi-scale nanolithography simulations. The direct solver algorithm utilized the graph grammar model and the efficient reuse of identical sub-branches of the elimination tree.

## Acknowledgements

The work of MS was supported by Polish National Science Center grant no. DEC-2011/03/N/ST6/01397. The work of MP was supported by Polish National Science Center grant no. DEC-2012/06/M/ST1/00363.

- Demkowicz L., Kurtz J., Pardo D., Paszynski M., Zdunek A. (2007), Computing with *hp*-Adaptive Finite Element Method. Vol. II. Frontiers: Three Dimensional Elliptic and Maxwell Problems. Chapman & Hall / CRC Applied Mathematics and Nonlinear Science
- Duff I. S., Reid J. K. (1984), The multifrontal solution of unsymmetric sets of linear systems, *SIAM Journal of Scientific and Statistical Computing*, vol. 5, pp.633-641.
- Duff I. S., Reid J. K. (1983) The multifrontal solution of indefinite sparse symmetric linear equations, *ACM Transactions on Mathematical Software*, vol. 9, pp. 302-325
- Geng P., Oden T. J., van de Geijn R. A. (2006) A Parallel Multifrontal Algorithm and Its Implementation, *Computer Methods in Applied Mechanics and Engineering*, vol. 149, pp.289-301.
- Paszynska, A., Grabska, E. and Paszynski, M. (2012a). A graph grammar model of the hp adaptive three dimensional finite element method. part I, *Fundamenta Informaticae*, vol. 114 no., pp. 149–182.
- Paszynska, A., Grabska, E. and Paszynski, M. (2012b). A graph grammar model of the hp adaptive three dimensional finite element method. part II, *Fundamenta Informaticae* vol. 114 np. 2, 183–201.
- Paszynska, A., Paszynski, M. and Grabska, E. (2008). Graph transformations for modeling hp-adaptive finite element method with triangular elements, *Lecture Notes in Computer Science*, vol. 5103 pp. 604–613.
- Paszynski, M. (2009a). On the parallelization of self adaptive hp-finite element methods part I. composite programmable graph grammar model, *Fundamenta Informaticae*, vol. 93 no. 4, pp. 411–434.
- Paszynski, M. (2009b). On the parallelization of self-adaptive hp-finite element methods part ii. partitioning communication agglomeration mapping (PCAM) analysis, *Fundamenta Informaticae*, vol. 93 no. 4, pp. 435–457.
- Paszynski, M. Pardo, D., Paszynska, A. (2010) Parallel multi-frontal solver for p adaptive finite element modeling of multi-physics computational problems, *Journal of Computational Science*, vol. 1, no. 1, pp. 48-54.
- Paszynski, M. Schaefer R., (2010) Graph grammar driven partial differential equations solver, *Concurrency and Computations: Practise and Experience*, vol. 22, no. 9, pp.1063-1097.
- Colbum, M. E.Suez, I. Choi, B. J.Meissi, I.Bailey, T.Sreenivasan, S. V.Ekerdt, J. E.Willson, C. G. (2001) Characterization and modeling of volumetric and mechanical properties for SFIL photopolymers. *Journal of Vacuum Science and Technology B*, vol. 19, pp. 6-20.
- Paszynski, M.Romkes, A.Collister, E.Meiring, J.Demkowicz, L. F.Willson, C. G (2005) On the modeling of Step-and-Flash Imprint Lithography using molecular statics models. *ICES Report*, vol. 05-38
- Hughes T. J. R. (2000) *The Finite Element Method. Linear Statics and Dynamics Finite Element Method Analysis*, Dover, 2000.

## Thermal stress simulation of ultrafine plate-fin structures using a homogenization theory

Hiromu Kobori<sup>1</sup>, \*Tetsuya Matsuda<sup>1</sup>, and Masahiro Arai<sup>2</sup>

<sup>1</sup> Department of Engineering Mechanics and Energy, University of Tsukuba  
1-1-1 Tennodai, Tsukuba, 305-8573, Japan.

<sup>2</sup> Department of Mechanical Systems Engineering, Shinshu University  
4-17-1 Wakasato, Nagano, 380-8553, Japan

\*Corresponding author: matsuda@kz.tsukuba.ac.jp

**Key Words:** *Homogenization, Ultrafine plate-fin structure, Thermal stress, Thermal expansion*

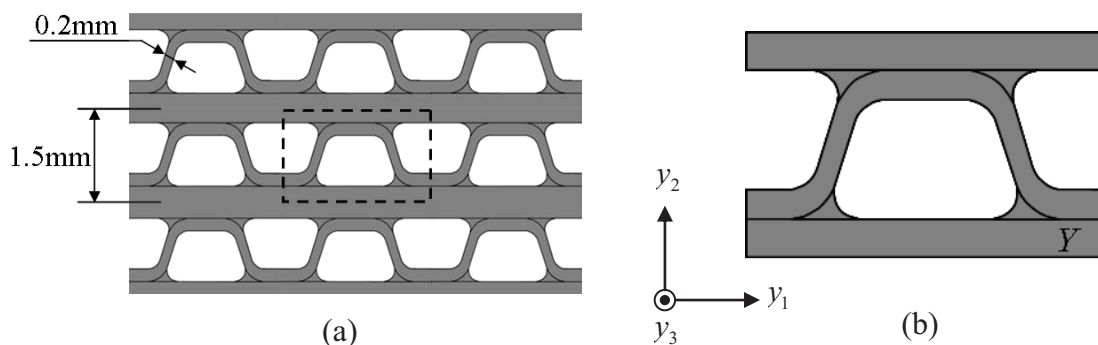
### Abstract

In this work, the thermal stress in ultrafine plate-fin structures made of a Ni-based alloy subjected to a macroscopic temperature increment is simulated macroscopically and microscopically, using a homogenization theory for thermoelastoviscoplasticity. For this purpose, the homogenization theory for thermoelastoviscoplasticity is constructed by introducing the effects of thermal expansion into the homogenization theory for time-dependent materials. The present theory is then applied to the thermal stress simulation of ultrafine plate-fin structures, in which three cases of macroscopic temperature rates are considered. The results show that the higher the macroscopic temperature rate is, the higher the thermal stress is. Moreover, it is shown that the stress concentration occurs at joint regions between plates and brazing parts, and at some parts of fins, indicating the importance of thermal stress analysis of ultrafine plate-fin structures.

### Introduction

High temperature gas-cooled reactor gas-turbine (HTGR-GT) systems have been regarded as some of the most promising power generating systems. The HTGR produces much higher outlet temperature than conventional reactors. Using the thermal energy, the total efficiency of the systems can be increased (Po-Jui et al, 2008). In the systems, helium is employed as a working fluid, and can reach 850~950°C in heat exchangers. In such a high temperature condition, the heat exchangers encounter severer thermal loads. Especially when a reactor scram happens, they may become even severer due to the steep change of helium temperature. In fact, a lot of studies as to structural integrity of heat exchangers in scram events have been performed at the high temperature engineering test reactor (HTTR) built in Japan, which is an experimental reactor of HTGR (Tachibana et al, 2003).

Ultrafine plate-fin structures for heat exchangers manufactured by stacking thin metallic plates and fins alternately (Fig. 1) offer high heat-exchange efficiency, because their small structures provide large heat-transfer areas. Thus, they are expected to be used in the heat exchangers of HTGR-GT systems (Kawashima et al, 2007). It is therefore important to estimate high temperature structural



**Figure 1. Ultrafine plate-fin structures: (a) whole structure. (b) its unit cell  $Y$**

integrity of ultrafine plate-fin structures. In particular, analyzing their inelastic thermal behavior in scram events is indispensable for designing heat exchangers.

In general, ultrafine plate-fin structures have such complicated microstructures that it is difficult to analyze their mechanical properties, although there have been some reports on elastic/inelastic analysis of plate-fin structures. For example, Tsuda et al. (2010) analyzed the macroscopic elastic-viscoplastic behavior of ultrafine plate-fin structures based on a homogenization technique (Sanchez-Palencia, 1980) using the FEM, and succeeded in developing a macroscopic constitutive model which can reproduce the homogenized elastic-viscoplastic behavior of plate-fin structures. In their study, however, they did not take thermal stress into consideration. On the other hand, Shabana and Noda. (2008) analyzed the elastic thermal stress of unidirectional fiber-reinforced plastic composites using a homogenization theory for thermoelasticity, and showed the accuracy of the theory by comparing the results with experimental ones. However, elastic thermal stress analysis is not sufficient for ultrafine plate-fin structures because inelastic thermal stress can occur in them during scram events.

In the present study, therefore, the thermal stress in ultrafine plate-fin structures subjected to a macroscopic temperature increment is simulated macroscopically and microscopically, using a homogenization theory for thermoelastoviscoplasticity. For this purpose, the homogenization theory for thermoelastoviscoplasticity is constructed by introducing the effects of thermal expansion into the homogenization theory for time-dependent materials (Ohno et al., 2000). The present theory is then applied to the thermal stress simulation of ultrafine plate-fin structures, in which three cases of macroscopic temperature rates are considered.

### Homogenization Theory for thermoelastoviscoplasticity

In this section, the homogenization theory for thermoelastoviscoplasticity is constructed by introducing the effects of thermal expansion into the homogenization theory for time-dependent materials (Ohno et al., 2000).

Let us consider an ultrafine plate-fin structures shown in Fig. 1(a), its unit cell having been defined as  $Y$  (Fig. 1(b)). For this  $Y$ , the Cartesian coordinates  $y_i$  ( $i=1, 2, 3$ ) are defined, and microscopic stress and strain fields are denoted by  $\sigma_{ij}$  and  $\varepsilon_{ij}$ , respectively. Then, the equilibrium of  $\sigma_{ij}$  can be expressed in a rate form as

$$\dot{\sigma}_{ij,j} = 0, \quad (1)$$

where  $(\dot{\quad})$  and  $(\quad)_{,j}$  indicate the differentiation regarding  $t$  and  $y_j$ , respectively. The base material of the plate-fin structure is assumed to exhibit linear elasticity and non-linear viscoplasticity as characterized by

$$\dot{\sigma}_{ij} = c_{ijkl} (\dot{\varepsilon}_{kl} - \beta_{kl} - \Delta\dot{T}\alpha_{kl}), \quad (2)$$

where  $c_{ijkl}$ ,  $\beta_{kl}$ ,  $\Delta\dot{T}$  and  $\alpha_{kl}$  stand for the elastic stiffness, viscoplastic strain rate, macroscopic temperature increment and the coefficient of thermal expansion of the base material, respectively.

Let  $v_i(\mathbf{y}, t)$  be an arbitrary variation of the perturbed velocity field defined in  $Y$  at  $t$ . Then, the integration by parts and the divergence theorem allow Eq. (1) to be transformed to

$$\int_Y \dot{\sigma}_{ij} v_{i,j} dY - \int_{\Gamma} \dot{\sigma}_{ij} n_j v_i d\Gamma = 0, \quad (3)$$

where  $\Gamma$  denotes the boundary of  $Y$ , and  $n_j$  indicates the unit vector outward normal to  $\Gamma$ . In Eq. (3), the second term of the left-hand side, i.e. the boundary integral term, vanishes because of the following reason: on the boundaries,  $\dot{\sigma}_{ij}$  and  $v_i$  satisfy the  $Y$ -periodicity, while  $n_i$  takes an opposite direction on an opposite boundary facet. Thus, the boundary integral term becomes zero. Consequently, Eq. (3) results in

$$\int_Y \dot{\sigma}_{ij} v_{i,j} dY = 0. \quad (4)$$

The above equation and Eq. (2) derive

$$\int_Y c_{ijpq} \dot{u}_{p,q}^{\#} v_{i,j} dY = -\dot{E}_{kl} \int_Y c_{ijkl} v_{i,j} dY + \int_Y c_{ijkl} \beta_{kl} v_{i,j} dY + \Delta\dot{T} \int_Y c_{ijkl} \alpha_{kl} v_{i,j} dY, \quad (5)$$

where  $u_i^\#$  and  $\dot{E}_{ij}$  denote the perturbed displacement and macroscopic strain, respectively. They are related as follows:

$$\dot{u}_i^\# = \chi_i^{kl} \dot{E}_{kl} + \varphi_i + \Delta T \dot{\psi}_i. \quad (6)$$

The functions  $\chi_i^{kl}$ ,  $\varphi_i$  and  $\psi_i$  in the above equation are called the characteristic functions, and can be obtained by solving the following boundary value problems:

$$\int_Y c_{ijpq} \chi_{p,q}^{kl} v_{i,j} dY = - \int_Y c_{ijkl} v_{i,j} dY, \quad (7)$$

$$\int_Y c_{ijpq} \varphi_{p,q} v_{i,j} dY = \int_Y c_{ijkl} \beta_{kl} v_{i,j} dY, \quad (8)$$

$$\int_Y c_{ijpq} \psi_{p,q} v_{i,j} dY = \int_Y c_{ijkl} \alpha_{kl} v_{i,j} dY. \quad (9)$$

The microscopic relation and the macroscopic constitutive equation are as follows:

$$\dot{\sigma}_{ij} = c_{ijpq} (\delta_{pk} \delta_{ql} + \chi_{p,q}^{kl}) \dot{E}_{kl} - c_{ijkl} (\beta_{kl} - \varphi_{k,l}) - \Delta T \dot{c}_{ijkl} (\alpha_{kl} - \psi_{k,l}), \quad (10)$$

$$\dot{\Sigma}_{ij} = \langle c_{ijpq} (\delta_{pk} \delta_{ql} + \chi_{p,q}^{kl}) \rangle \dot{E}_{kl} - \langle c_{ijkl} (\beta_{kl} - \varphi_{k,l}) \rangle - \Delta T \langle c_{ijkl} (\alpha_{kl} - \psi_{k,l}) \rangle, \quad (11)$$

where  $\delta_{ij}$  indicates Kronecker's delta, and

$$\langle \# \rangle = \frac{1}{|Y|} \int_Y \# dY. \quad (12)$$

Here,  $\langle \ \rangle$  designates the volume average in  $Y$ , and  $|Y|$  signifies the volume of  $Y$ .

### Analysis Conditions

In the present analysis, macroscopic stress-temperature relations and microscopic thermal stress of ultrafine plate-fin structures were analyzed using the theory mentioned above. Table 1 shows the temperature conditions. Assuming that a reactor scram occurs, the macroscopic temperature change from  $950^\circ\text{C}$  to  $360^\circ\text{C}$  was given to the plate-fin structures. Three cases of macroscopic temperature rate, i.e.  $\Delta T = -0.05, -0.25$  and  $-0.5^\circ\text{C/s}$ , were considered. These temperature conditions were determined by referring to the data obtained by a reactor scram experiment done at HTTR. The macroscopic strain was set to zero ( $\dot{E}_{ij} = 0$ ).

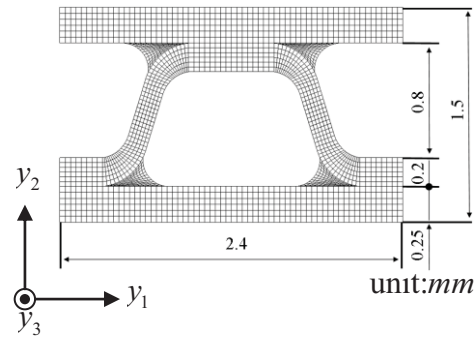
A unit cell  $Y$  was defined and divided into four-node isoparametric elements as illustrated in Fig. 2. This  $Y$  was two-dimensional rather than three-dimensional, and the generalized plane strain condition was assumed, because the plate-fin structures were assumed to have uniform and infinite

**Table 1. Temperature conditions**

Macroscopic temperature increment	$\Delta T [^\circ\text{C}]$	-590
		1. -0.05
Macroscopic temperature increment per second	$\Delta \dot{T} [^\circ\text{C/s}]$	2. -0.25
		3. -0.5

**Table 2. Material properties(HastelloyX)**

Poisson's ratio	$\nu$	0.32
Reference strain rate	$\epsilon_0 [s^{-1}]$	$10^{-3}$
Stress power index	$n$	$-0.0295T + 33.075$
Young's modulus	$E [\text{GPa}]$	$-0.0684T + 212.22$
Coefficient of thermal expansion	$\alpha [10^{-6}/\text{K}]$	$0.0031T + 13.548$



**Figure 2. Unit cell  $Y$  and its finite element mesh**

material distribution in the  $y_3$ -direction. A base metal for the plate-fin structures was Hastelloy X, which was a Ni-based alloy with excellent heat resistance. The Hastelloy X was regarded as an isotropic elastic-viscoplastic material characterized by the following constitutive equation:

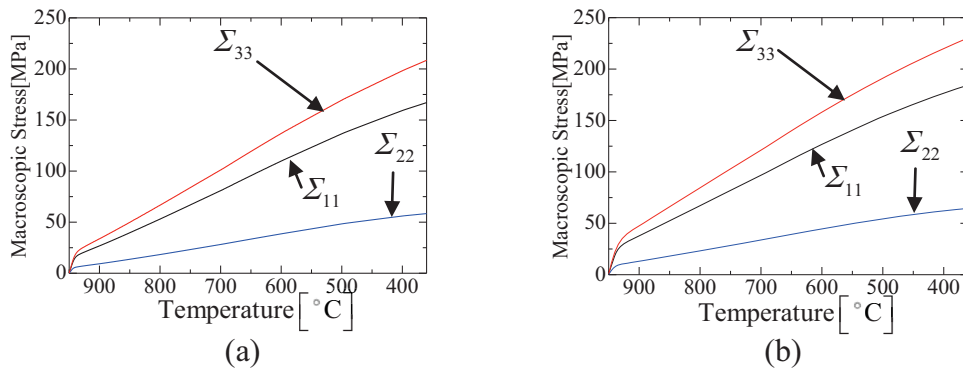
$$\dot{\epsilon}_{ij} = \frac{1+\nu}{E} \dot{\sigma}_{ij} - \frac{\nu}{E} \dot{\sigma}_{kk} \delta_{ij} + \frac{3}{2} \dot{\epsilon}_0^p \left( \frac{\sigma_{eq}}{\sigma_0} \right)^{n-1} \frac{s_{ij}}{\sigma_0}, \quad (13)$$

where,  $E$  and  $\nu$  indicate elastic constants,  $\dot{\epsilon}_0$  and  $\sigma_0$  represent reference strain rate and reference stress, respectively,  $n$  is a material parameter of viscoplasticity,  $s_{ij}$  stands for the deviatoric part of  $\sigma_{ij}$ , and  $\sigma_{eq} = [(3/2)s_{ij}s_{ij}]^{1/2}$ . Here,  $n$ ,  $E$  and  $\alpha$  were the parameters dependent on the current temperature  $T$ . Material constants used are listed in Table 2.

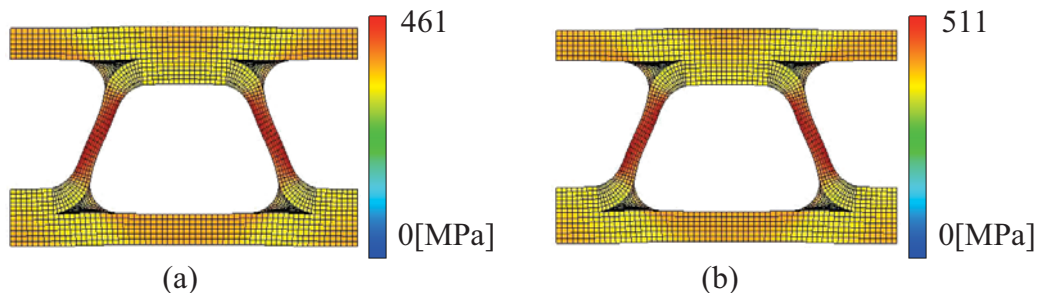
**Results**

Figures 3 (a) and (b) respectively show the macroscopic stress-temperature relations of the plate-fin structures at  $\Delta T = -0.05^\circ\text{C/s}$  and  $-0.5^\circ\text{C/s}$ . Due to the lack of space, the stress-temperature curves when  $\Delta T = -0.25^\circ\text{C/s}$  are omitted. From Figs. 3(a) and (b), stress-temperature relations in the  $y_1$ ,  $y_2$  and  $y_3$  directions are markedly different from one another, indicating the thermoelastoviscoplastic anisotropy resulting from the complicated microstructures of plate-fin structures. Moreover, it can be seen that, comparing Fig. 3(a) with (b), the maximum tensile stress of Fig. 3(b) is higher than that of (a) on each direction: the maximum increase is about 10%. This means that the higher the macroscopic temperature rate is, the higher the macroscopic thermal stress is. Incidentally, macroscopic shear stress did not occur.

Next, Figs. 4(a) and (b) show the deformed unit cells and the microscopic Mises's equivalent stress distributions at  $360^\circ\text{C}$  when  $\Delta T = -0.05^\circ\text{C/s}$  and  $-0.5^\circ\text{C/s}$ , respectively. The displacement is magnified five times. As seen from these figures, high stress concentration occurs in the middle of the fins, and moreover, the stress concentration also occurs at joint regions between plates and brazing parts. Comparing Fig. 4(a) with (b), the maximum tensile stress of Fig. 4(b) is about 10%



**Figure 3. Macroscopic Stress-Temperature curves on different macroscopic temperature increment per second; (a)  $-0.05^\circ\text{C/s}$ , (b)  $-0.5^\circ\text{C/s}$**



**Figure 4. Microscopic Mises's equivalent stress distribution at  $360^\circ\text{C}$  on different macroscopic temperature increment; (a)  $-0.05^\circ\text{C/s}$ , (b)  $-0.5^\circ\text{C/s}$**

higher than that of (a). This indicates that the higher the macroscopic temperature rate is, the higher the microscopic thermal stress is, too.

## Conclusions

In this study, the homogenization theory for thermoelastoviscoplasticity was proposed and the thermal stress simulation of ultrafine plate-fin structures was performed. In the analysis, the plate-fin structures experienced macroscopic temperature change from 950°C to 360°C assuming a reactor scram. Three patterns of macroscopic temperature rates are considered. The results are as follows.

- (1) The stress-temperature relations of ultrafine plate-fin structures in the  $y_1$ ,  $y_2$  and  $y_3$  directions are markedly different from one another, indicating the thermoelastoviscoplastic anisotropy of plate-fin structures.
- (2) The stress concentration occurs at joint regions between plates and brazing parts, and at some parts of fins.
- (3) The higher the macroscopic temperature rate is, the higher both the macroscopic and microscopic thermal stresses are.

These results show that high thermal stress can occur in the case of the scram events, indicating the importance of inelastic thermal stress analysis of ultrafine plate-fin structures.

## References

- Kawashima, F., Igari, T., Miyoshi, Y., Kamito, Y. and Tanihira, M. (2007), High temperature strength and inelastic behavior of plate-fin structures for HTGR. *Nuclear Engineering and Design*, 237, pp. 591–599.
- Ohno, N., Wu, X. and Matsuda, T. (2000), Homogenized properties of elastic-viscoplastic composites with periodic internal structures. *International Journal of Mechanical Sciences*, 42, pp. 1519-1536.
- Po-Jui, L., Tzu-Chen, H., Bau-Shei, P., Jaw-Ren, L., Ching-Chang, C. and Ge-Ping, Y. (2012), A thermodynamic analysis of high temperature gas-cooled reactors for optimal waste heat recovery and hydrogen production. *Applied Energy*, pp. 183-191.
- Sanchez-Palencia, E. (1980), Non-homogeneous Media and Vibration Theory. Lecture Notes in Physics 127, Springer-Verlag.
- Shabana, Y. M. and Noda, N. (2008), *International Journal of Solids and Structures*, 45, pp. 3494-3506.
- Tachibana, Y., Nakagawa, S., Takeda, T., Saikusa, A., Furusawa, T., Takamatsu, K., Sawa, K. and Iyoku, T. (2003), Plan for first phase of safety demonstration tests of the High Temperature Engineering Test Reactor (HTTR). *Nuclear Engineering and Design*, pp. 179-197
- Tsuda, M., Takemura, E., Asada, T., Ohno, N. and Igari, T. (2010), Homogenized elastic-viscoplastic behavior of plate-fin structures at high temperatures: Numerical analysis and macroscopic constitutive modeling. *International Journal of Mechanical Sciences*, 52, pp. 648-656.

## Combined Method for Rigid Bodies-Spring Model and Discrete Element Method

\* T.Yagi and N.Takeuchi<sup>1</sup>, K.Yamamura<sup>2</sup>, E.Hamasaki<sup>3</sup>

<sup>1</sup> Graduate School of Engineering and Design, Hosei University, Tokyo, Japan.

<sup>2</sup> Nippon Steel & Sumitomo Metal Corporation, Chiba, Japan

<sup>3</sup> Advantech Co., Ltd., Miyagi, Japan

\*Corresponding author: takeuchi@hosei.ac.jp

### Abstract

This paper presents a new method for a dynamic explicit scheme called as a combined RBSM-DEM. RBSM was developed as a numerical model for generalizing limit analysis in plasticity, in which a structure to be analyzed is idealized as an assemblage of rigid bodies connected by normal and tangential springs. Although the contact surfaces are handled differently by RBSM and DEM, the degree of freedom is the same. If the formulization using an explicit method for each element is used, the algorithms for dynamic analyses are identical. In this paper, we illustrate the formulization of RBSM that is expanded to include DEM. In addition, we examine the accuracy of the solutions obtained from some examples of numerical computations by the present method.

**Keywords:** RBSM, DEM, Combined model, Explicit method

### 1. Introduction

The implicit method is widely used for time integration in the numerical analysis of dynamic problems using the finite element method (FEM). On the other hand, the explicit method (Belytschko 1984), which involves the fracture problem, has also been extensively used. In this case, the time integration technique is represented by the central difference method, which calculates a solution sequentially. Recently, discontinuous analyses using the distinct element method (DEM) (Cundall 1971) and a combined DEM/FEM (Munjiza et al. 1995) have attracted considerable attention, and the use of the explicit scheme has increased. Therefore, a combined analysis technique is useful in the explicit method, and the same also applies to other numerical algorithms in a discontinuous problem.

The rigid bodies-spring model (RBSM) (Kawai 1977) was developed as a numerical model for generalizing the limit analysis in plasticity, in which a structure to be analyzed is idealized as an assemblage of rigid bodies connected by normal and tangential springs. Although contact surfaces are handled differently in RBSM and DEM, the degree of freedom is the same. If formulization by the explicit method for each element is used, the algorithms for dynamic analyses are identical.

This paper illustrates the formulization of RBSM for each element using the principle of hybrid virtual work. The same discussion is expanded to include DEM, and a method that combines RBSM and DEM is expressed. In addition, we numerically verify the stability and accuracy of the solutions obtained by a method that combines RBSM and DEM from some examples.

### 2. Discretization of equation of motion by using principle of hybrid virtual work

The basic equation of the elastic problem is as follows:

$$\operatorname{div} \boldsymbol{\sigma} + \boldsymbol{f} + \boldsymbol{f}_\alpha = 0 \quad \text{in } \Omega \quad (1)$$

$$\boldsymbol{\sigma} = \boldsymbol{D} : \boldsymbol{\varepsilon} \quad \boldsymbol{\varepsilon} = \nabla^s \boldsymbol{u} \stackrel{\text{def.}}{=} \frac{1}{2} [\nabla \boldsymbol{u} + (\nabla \boldsymbol{u})^t]$$

$$\boldsymbol{u}|_{\Gamma_u} = \hat{\boldsymbol{u}} \quad (\text{given}) \quad \boldsymbol{\sigma}|_{\Gamma_\sigma} \cdot \hat{\boldsymbol{n}} = \hat{\boldsymbol{t}} \quad (\text{given})$$

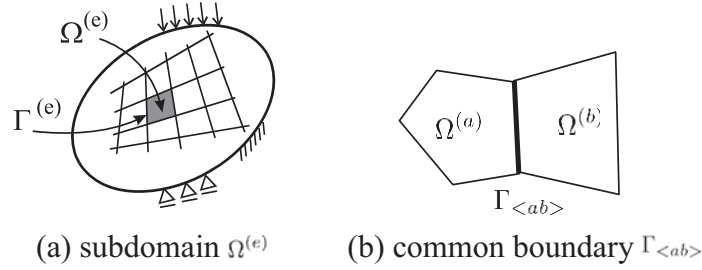
where  $\Omega$  is the reference configuration of a continuum body with smooth boundary  $\Gamma := \partial\Omega$ ;  $\Gamma_u := \partial_u\Omega \subset \partial\Omega$ , the geometrical boundary;  $\Gamma_\sigma := \partial_\sigma\Omega \subset \partial\Omega$ , the kinetic boundary;  $\boldsymbol{\sigma}$ , the Cauchy stress tensor;  $\boldsymbol{\varepsilon}$ , the infinitesimal strain tensor;  $\boldsymbol{f}$ , the body force per unit volume;  $\nabla$ , the differential vector



operator; and  $\nabla^s$ , the symmetric part of  $\nabla$ . When the displacement field in  $x \in \Omega$  is expressed as  $\mathbf{u}$  and the density, as  $\rho$ , the inertia force  $\mathbf{f}_\alpha$  of equation (1) is expressed as follows:

$$\mathbf{f}_\alpha = -\rho \frac{\partial^2 \mathbf{u}}{\partial t^2} \quad (2)$$

Let  $\Omega$  consist of  $M$  subdomains  $\Omega^{(e)} \subset \Omega$  with the closed boundary  $\Gamma^{(e)} := \partial\Omega^{(e)}$ , as shown in Figure 1(a). In other words,  $\Omega = \bigcup_{e=1}^M \Omega^{(e)}$ ; here,  $\Omega^{(r)} \cap \Omega^{(q)} = 0$  ( $r \neq q$ ).



**Figure 1. Subdomain and its common boundary**

We use  $\Gamma_{\langle ab \rangle}$ , defined as  $\Gamma_{\langle ab \rangle} \stackrel{\text{def.}}{=} \Gamma^{(a)} \cap \Gamma^{(b)}$ , as the common boundary for two subdomains  $\Omega^{(a)}$  and  $\Omega^{(b)}$  adjoined as shown in Figure 1(b). The relation for the displacement  $\tilde{\mathbf{u}}^{(e)}$  on  $\Gamma_{\langle ab \rangle}$ , which is the intersection boundary between  $\Omega^{(a)}$  and  $\Omega^{(b)}$ , is as follows:

$$\tilde{\mathbf{u}}^{(a)} = \tilde{\mathbf{u}}^{(b)} \quad \text{on } \Gamma_{\langle ab \rangle} \quad (3)$$

The following hybrid-type virtual work equation is obtained by introducing this subsidiary condition into a virtual work equation using Lagrange multipliers  $\lambda$ :

$$\sum_{e=1}^M \left( \int_{\Omega^{(e)}} \boldsymbol{\sigma} : \text{grad}(\delta \mathbf{u}) dV - \int_{\Omega^{(e)}} \mathbf{f} \cdot \delta \mathbf{u} dV - \int_{\Omega^{(e)}} \mathbf{f}_\alpha \cdot \delta \mathbf{u} dV \right) - \sum_{s=1}^N \left( \delta \int_{\Gamma_{\langle s \rangle}} \lambda \cdot (\tilde{\mathbf{u}}^{(a)} - \tilde{\mathbf{u}}^{(b)}) dS \right) - \int_{\Gamma_\sigma} \hat{\mathbf{t}} \cdot \delta \mathbf{u} dS = 0 \quad \forall \delta \mathbf{u} \in \mathbb{V} \quad (4)$$

Here,  $N$  denotes the number of common boundaries of the subdomain, and  $\delta \mathbf{u}$  shows the virtual displacement. An independent displacement field in each subdomain is assumed as follows:

$$\mathbf{u}^{(e)} = \mathbf{N}^{(e)} \mathbf{U}^{(e)} \quad (5)$$

$$\mathbf{U}^{(e)} = [\mathbf{d}^{(e)}, \boldsymbol{\varepsilon}^{(e)}]^t, \quad \mathbf{N}^{(e)} = [\mathbf{N}_d^{(e)}, \mathbf{N}_\varepsilon^{(e)}]$$

Here,  $\mathbf{d}^{(e)}$  denotes the rigid displacement and the rigid rotation in point P in the subdomain  $(e)$ , and  $\boldsymbol{\varepsilon}^{(e)}$  denotes a constant strain in the subdomain  $(e)$ . Equation (4) implies that the Lagrange multiplier  $\lambda$  is the surface force on the boundary  $\Gamma_{\langle ab \rangle}$  in subdomain  $\Omega^{(a)}$  and  $\Omega^{(b)}$ ; hence, the surface force is defined as follows:

$$\lambda_{\langle ab \rangle} = \mathbf{k} \cdot \boldsymbol{\delta}_{\langle ab \rangle} \quad (6)$$

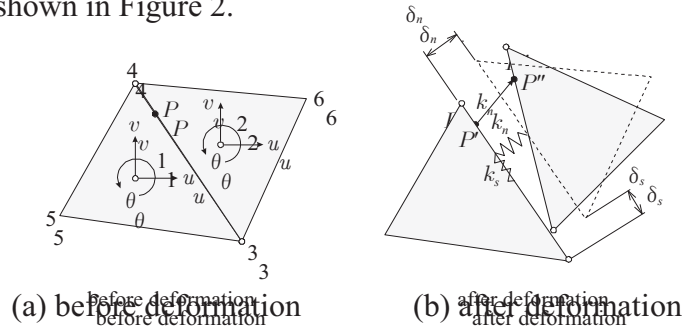
Here,  $\boldsymbol{\delta}_{\langle ab \rangle}$  shows the relative displacement on the boundary  $\Gamma_{\langle ab \rangle}$ , and  $\mathbf{k}$  shows the penalty function. The equation of motion discretized about space by substituting the abovementioned relations in equation (4) is obtained as follows:

$$M\ddot{\mathbf{U}} + \mathbf{K}\mathbf{U} = \mathbf{P} \quad (7)$$

$$\mathbf{M} = \sum_{e=1}^M \mathbf{M}^{(e)} \quad \mathbf{K} = \sum_{e=1}^M \mathbf{K}^{(e)} + \sum_{s=1}^N \mathbf{K}_{\langle s \rangle}$$

### 3. Method for combining RBSM and DEM

The formulization of RBSM is advanced by evaluating the energy stored in the spring between the adjoining elements as shown in Figure 2.



**Figure 2. Rigid bodies-spring model**

The equation of motion (7) is simplified by  $d$  and  $\varepsilon$ . Moreover, it is expressed in the global coordinate system as

$$\begin{bmatrix} M_{dd} & M_{d\varepsilon} \\ M_{\varepsilon d} & K_{\varepsilon\varepsilon} \end{bmatrix} \begin{Bmatrix} \ddot{d} \\ \ddot{\varepsilon} \end{Bmatrix} + \begin{bmatrix} K_{dd} & K_{d\varepsilon} \\ K_{\varepsilon d} & K_{\varepsilon\varepsilon} + D \end{bmatrix} \begin{Bmatrix} d \\ \varepsilon \end{Bmatrix} = \begin{Bmatrix} P_d \\ P_\varepsilon \end{Bmatrix} \quad (8)$$

Here, the linear displacement field of equation (5), assuming a rigid displacement field and a mass matrix that contains only diagonal elements, is given as follows:

$$M_{dd} = \rho \begin{bmatrix} A & 0 & 0 \\ 0 & A & 0 \\ 0 & 0 & I_p \end{bmatrix} \quad (9)$$

The substitution of the abovementioned relations into equation (8) gives

$$M_{dd}\ddot{d} = P_d - K_{dd}d \quad (10)$$

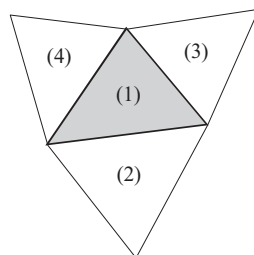
In equation (6),  $k$  is the spring constant, and it is assumed as follows:

$$\begin{Bmatrix} \lambda_n \\ \lambda_s \end{Bmatrix} = \begin{bmatrix} k_n & 0 \\ 0 & k_s \end{bmatrix} \begin{Bmatrix} \delta_n \\ \delta_s \end{Bmatrix} \quad (11)$$

Here, under a plane stress condition,  $k_n$  and  $k_s$  are expressed as follows:

$$\left. \begin{aligned} k_n &= \frac{E}{(1-\nu^2)(h_1+h_2)} \\ k_s &= \frac{E}{(1+\nu)(h_1+h_2)} \end{aligned} \right\} \quad (12)$$

where  $E$  is Young's modulus;  $\nu$ , Poisson's ratio; and  $h$ , the length of the vertical line to the boundary edge from the centroid of each subdomain.



**Figure 3. Element (1) and adjoining element**

Here, as shown in Figure 3, we expand equation (11) as an example to element (1) and the adjoining element. In this case, the integration on the boundary edge, with a focus on element (1), is only relevant to elements (2)–(4). Therefore, the other elements are not relevant simultaneous equations. We represent a portion of equation (10) for this example as follows:

$$\begin{Bmatrix} \vdots \\ M^{(1)} \\ M^{(2)} \\ M^{(3)} \\ M^{(4)} \\ \vdots \end{Bmatrix} \begin{Bmatrix} \vdots \\ \mathbf{d}^{(1)} \\ \mathbf{d}^{(2)} \\ \mathbf{d}^{(3)} \\ \mathbf{d}^{(4)} \\ \vdots \end{Bmatrix} = \begin{Bmatrix} \vdots \\ \mathbf{P}_d^{(1)} \\ \mathbf{P}_d^{(2)} \\ \mathbf{P}_d^{(3)} \\ \mathbf{P}_d^{(4)} \\ \vdots \end{Bmatrix} - \begin{bmatrix} \ddots & & & & & \\ & 0 & 3k_{dd}^{(1,1)} & k_{dd}^{(1,2)} & k_{dd}^{(1,3)} & k_{dd}^{(1,4)} & 0 \\ & & k_{dd}^{(1,2)} & k_{dd}^{(2,2)} & & & \\ & & k_{dd}^{(1,3)} & & k_{dd}^{(3,3)} & & \\ & & k_{dd}^{(1,4)} & & & k_{dd}^{(4,4)} & \\ & & & & & & \ddots \end{bmatrix} \begin{Bmatrix} \vdots \\ \mathbf{d}^{(1)} \\ \mathbf{d}^{(2)} \\ \mathbf{d}^{(3)} \\ \mathbf{d}^{(4)} \\ \vdots \end{Bmatrix} \quad (13)$$

Because  $M^{(e)}$  is independent of each element, when focusing on element (1), the following relations are obtained.

$$M^{(1)} \mathbf{d}^{(1)} = \mathbf{P}_d^{(1)} - (3k_{dd}^{(1,1)} \mathbf{d}^{(1)} + k_{dd}^{(1,2)} \mathbf{d}^{(2)} + k_{dd}^{(1,3)} \mathbf{d}^{(3)} + k_{dd}^{(1,4)} \mathbf{d}^{(4)}) \quad (14)$$

From the above relationship, the stress element is obtained using the surface forces of the element boundary, which can be expressed as follows:

$$M^{(e)} \ddot{U}^{(e)} = \mathbf{P}_d^{(e)} - \oint_{\Gamma^{(e)}} \mathbf{N}_d^{(e)} \mathbf{t}^{(e)} d\Gamma \quad (15)$$

Thus, the equation of motion becomes computable for each element. As shown in Figure 4, the element acceleration is obtained by the resultant of the contact forces in the case of discontinuous bodies.

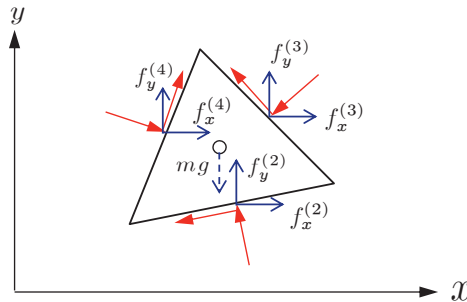


Figure 4. Resultant of contact forces

$$\begin{aligned} \ddot{u}^{(e)} &= \sum_{e=1}^3 f_x^{(e)} / m^{(e)} \\ \ddot{v}^{(e)} &= \sum_{e=1}^3 f_y^{(e)} / m^{(e)} \\ \ddot{\theta}^{(e)} &= \sum_{e=1}^3 -(y - y_G) f_x^{(e)} + (x - x_G) f_y^{(e)} / I^{(e)} \end{aligned} \quad (16)$$

The equation of motion (7) for the present time  $n$  is expressed as follows:

$$M \ddot{U}^n + K U^n = P^n \quad (17)$$

Now, this formula is rewritten as follows:

$$M \ddot{U}^n = \tilde{P}^n \quad (18)$$

This is a simplified form of equation (16) using the global coordinate system. Here,

$$\tilde{\mathbf{P}}^n = \mathbf{P}^n - \mathbf{F}^n \quad (19)$$

$$\mathbf{F}^n = \mathbf{K}\mathbf{U}^n \quad (20)$$

Equation (18) contains unknown acceleration parameters that can be obtained as follows:

$$\ddot{\mathbf{U}}^{n+1} = \mathbf{M}^{-1}\tilde{\mathbf{P}}^n \quad (21)$$

Therefore, the following relations are obtained:

$$\dot{\mathbf{U}}^{n+1} = \dot{\mathbf{U}}^n + \ddot{\mathbf{U}}^{n+1}\Delta t \quad (22)$$

$$\mathbf{U}^{n+1} = \mathbf{U}^n + \dot{\mathbf{U}}^{n+1}\Delta t \quad (23)$$

The approach of equation (21), in a manner similar to DEM, is effective in solving collision problems. Thus, we can update the position of each element by looping  $\Delta t$  in these calculations.

#### 4. Numerical examples

As a numerical example, we present some simple problems.

First, we consider a laminated structure with a point load, as shown in Figure 5(a). In this example, we consider a brick block.

The material constants of this block are as follows: Young's modulus, 5127 N/mm<sup>2</sup>; Poisson's ratio, 0.112; and density, 1850 kg/m<sup>3</sup>. The incremental time is assumed to be  $\Delta t = 5.0 \times 10^{-8}$  s. In addition, the load condition is constant.

The results for the displacement response on point A are shown in Figure 5(b). The blue solid line shows the results obtained by FEM, and the red dotted line shows those obtained by the present method. The results are almost identical.

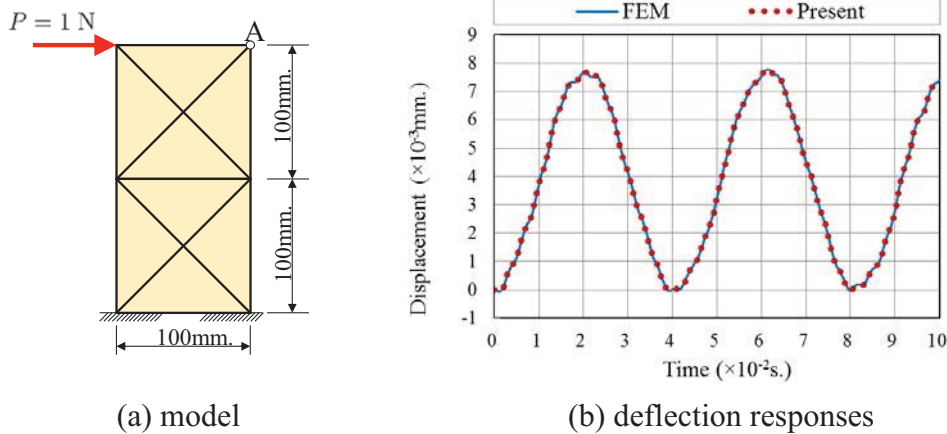
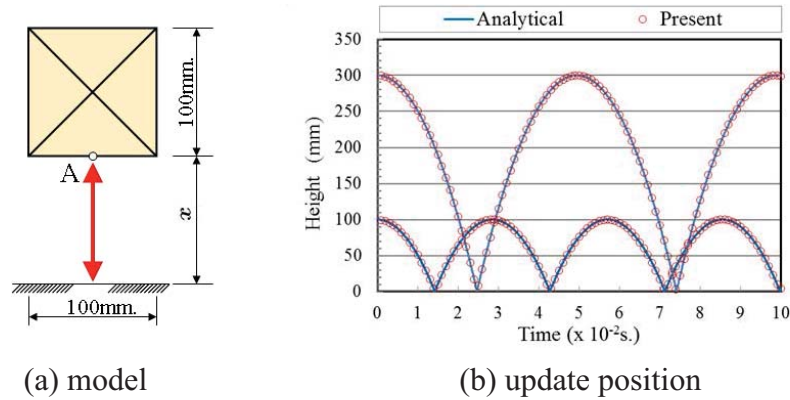


Figure 5. Case of elastic problem

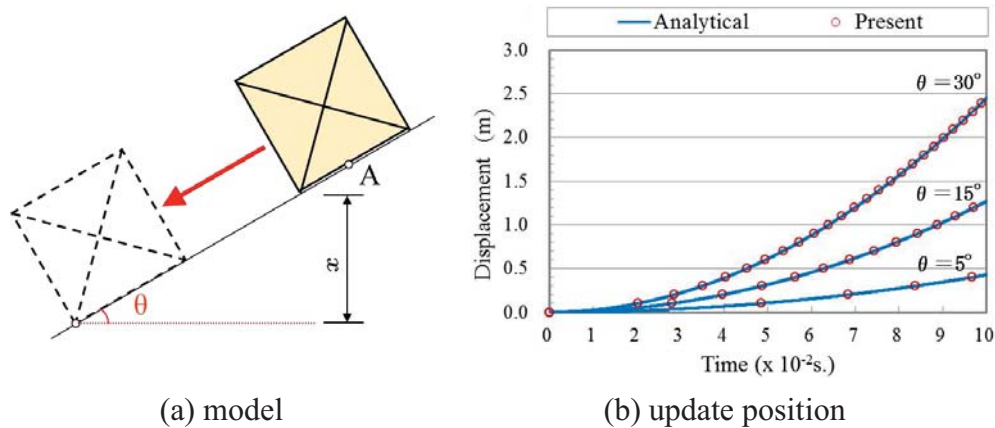
The next example is a problem involving hopping movement when a block is allowed to freely fall and collide with the ground, as shown in Figure 6(a). The gravitational acceleration is 9.80665 m/s<sup>2</sup>. The material constants of this block are the same as those listed in the previous example. In this case, we assumed that no energy loss occurred from the block as a result of rebounding from the ground after the collision.

Figure 6(b) shows the status of contact point A when a brick block falls and hits the ground. The position was updated by repeated calculations when the length of ground penetration on the boundary side was larger than the allowable spring stiffness length, which verified the effect of the contact force. This result showed good agreement with the theoretical solution obtained by the equation of motion.



**Figure 6. Case of hopping movement**

The last example is a problem involving the sliding movement of a block on a slope in a gravitational field, as shown in Figure 7(a). We place a square block on slopes inclined at angles of  $\theta = 5^\circ$ ,  $15^\circ$ , and  $30^\circ$  and let it slide down as shown in Figure 7(b). Again, the results of the present method are almost identical to those of the theoretical solution obtained by the equation of motion.



**Figure 7. Case of sliding movement**

## 5. Conclusions

This paper illustrated the formulization of RBSM for each element using the principle of hybrid virtual work. The same solution was also applied to DEM, and we developed a method that combined RBSM and DEM. As numerical examples, we first considered an elastic solution by using the present method, which had accuracy similar to that of FEM. Then, in a collision problem involving a falling block, we used the combined method for RBSM and DEM and expressed the effectiveness of the handling of the contact surface. Finally, from the behavior of a block sliding on a slope, we confirmed the applicability of the slip analysis.

## References

- Belytschko, T., Lin, J.I. & Tsay, C.S. (1984), Explicit algorithms for the nonlinear dynamics of shells, *Computer Methods in Applied Mechanics and Engineering*, 42, pp.225–251.
- Cundall, P.A. (1971), A computer model for simulating progressive, large scale movements in blocky rock systems, *Proceedings of the Symposium of International Society of Rock Mechanics*, 1(II-1), pp.129–136.
- Munjiza, A., Owen, D.R.J. & Bicanic, N. (1995), A combined finite/discrete element method in transient dynamics of fracturing solids, *Engineering Computations*, 12, pp.145–174.
- Kawai, T. (1977), New element models in discrete structural analysis, *Journal of the Society of Naval Architects of Japan*, 114, pp.1867–193.

## Effects of laminate misalignment on thermoelastoviscoplastic properties of ultrafine plate-fin structures

Yuki Yamanaka<sup>1</sup>, \*Tetsuya Matsuda<sup>1</sup>

<sup>1</sup>Department of Engineering Mechanics and Energy, University of Tsukuba  
1-1-1 Tennodai, Tsukuba, 305-8573, Japan

\*Corresponding author: [matsuda@kz.tsukuba.ac.jp](mailto:matsuda@kz.tsukuba.ac.jp)

### Abstract

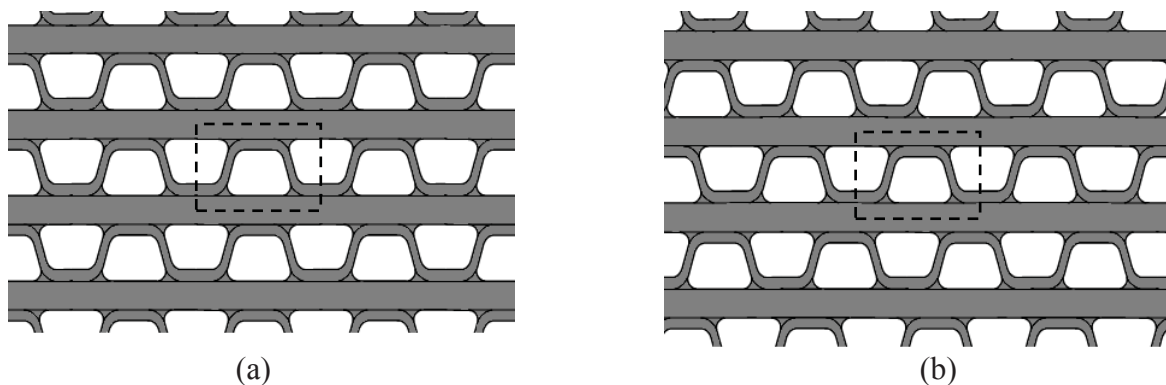
In this study, effects of laminate misalignment on the thermoelastoviscoplastic properties of ultrafine plate-fin structures are investigated using a homogenization theory for thermoelastoviscoplasticity. For this, the homogenization theory for time-dependent materials is combined with the homogenization theory for thermoelasticity. Moreover, the substructure method is introduced into the theory to deal with the randomness of laminate misalignment in ultrafine plate-fin structures. The present method is then applied to the analysis of thermoelastoviscoplastic behavior of ultrafine plate-fin structures made of a Ni-based alloy with laminate misalignment subjected to a macroscopic temperature increment. The results reveal the effects of the laminate misalignment on the macroscopic and microscopic thermoelastoviscoplastic properties of ultrafine plate-fin structures.

**Keywords:** Plate-fin structure, Laminate misalignment, Randomness, Thermal stress, Thermoelastoviscoplasticity, Homogenization

### Introduction

Ultrafine plate-fin structures for heat exchangers, which are manufactured by stacking thin metallic plates and fins alternately, offer high heat exchanger efficiency, because their small structures provide large heat-transfer areas. Hence, they are expected to be used in the heat exchangers of high temperature gas-cooled reactor gas-turbine (HTGR-GT) systems. The HTGR-GT systems are regarded as some of the most promising power generating systems because of their excellent balance between power generation and economic efficiency. In the systems, helium is employed as a working fluid, which becomes extremely hot and can reach 950 °C. It is therefore important to analyze thermoelastoviscoplastic behavior of ultrafine plate-fin structures.

In general, fins in an ultrafine plate-fin structure are not necessarily stacked in precise alignment as illustrated in Fig. 1(a), but can have misalignment as shown in Fig. 1(b). Hence, when analyzing the



**Figure 1. Ultrafine plate-fin structures (a) without laminate misalignment, (b) with random laminate misalignment**

thermoelastoviscoplastic behavior of ultrafine plate-fin structures, such laminate misalignment should be taken into account. In the previous study (Yamamoto et al., 2011), the effects of laminate misalignment on the elastic-viscoplastic behavior of plate-fin structures have been revealed based on the homogenization theory for nonlinear time-dependent materials (Ohno et al., 2000). However, the effects of laminate misalignment on the thermoelastoviscoplastic behavior of plate-fin structures have not been revealed yet.

In this study, therefore, the effects of laminate misalignment on the thermoelastoviscoplastic properties of ultrafine plate-fin structures are investigated based on a homogenization theory. For this, the homogenization theory for thermoelastoviscoplasticity combined with the substructure method (Zienkiewicz and Taylor, 2000) is proposed to analyze the thermoelastoviscoplastic properties of ultrafine plate-fin structures with random laminate misalignment. The present method is then applied to the analysis of thermoelastoviscoplastic behavior of ultrafine plate-fin structures made of Ni-based alloy with random laminate misalignment subjected to a macroscopic temperature increment. The results reveal the effects of laminate misalignment on the macroscopic and microscopic thermoelastoviscoplastic properties of ultrafine plate-fin structures.

### Homogenization theory for thermoelastoviscoplastic behavior of plate-fin structures with random laminate misalignment

Let us consider an ultrafine plate-fin structure with random laminate misalignment, and its unit cell  $Y$  (Fig. 2). It is assumed that  $Y$  has  $N$  fin layers with random laminate misalignment, and that  $Y$  is periodically stacked with laminate misalignment in the  $y_2$  -direction. For this  $Y$ , the Cartesian coordinates  $y_i$  are defined, and microscopic stress and strain are denoted as  $\sigma_{ij}(\mathbf{y}, t, T)$  and  $\varepsilon_{ij}(\mathbf{y}, t, T)$ , respectively, Where  $t$  is time and  $T$  is current temperature. The equilibrium of  $\sigma_{ij}$  can be expressed in a rate form as

$$\dot{\sigma}_{ij} = 0, \quad (1)$$

where  $(\cdot)_{,i}$  and  $(\dot{\cdot})$  indicate differentiation regarding  $y_i$  and  $t$ , respectively. The base material of the plate-fin structure is assumed to exhibit linear elasticity, nonlinear viscoplasticity and thermal expansion as characterized by

$$\dot{\sigma}_{ij} = c_{ijkl}(\dot{\varepsilon}_{kl} - \beta_{kl} - \Delta T \alpha_{kl}), \quad (2)$$

where  $c_{ijkl}$  and  $\beta_{kl}$  indicate the elastic stiffness tensor and viscoplastic strain rate of the base material, respectively, and  $\Delta T$  and  $\alpha_{kl}$  indicate the temperature increment and coefficient of linear expansion of the base material, respectively. Then, the integration by parts and the divergence theorem allow Eq. (1) to be transformed to

$$\int_Y \dot{\sigma}_{ij} v_{i,j} dY - \int_{\Gamma} \dot{\sigma}_{ij} n_j v_i d\Gamma = 0, \quad (3)$$

where  $\Gamma$  indicate the boundary of  $Y$ , and  $v_i$  and  $n_j$  indicate the arbitrary variation and the unit vector outward normal to  $\Gamma$ , respectively. Now, to examine boundary integral term in the above equation, let us divide  $\Gamma$  into six parts,  $\Gamma_{AB}$ ,  $\Gamma_{BC}$ ,  $\Gamma_{CD}$ ,  $\Gamma_{ED}$ ,  $\Gamma_{FE}$  and  $\Gamma_{AF}$ , as shown in Fig. 2(b), and consider three axes  $\alpha$ ,  $\beta$  and  $\gamma$ . Then, the boundary integral term in Eq. (3) can be expressed as

$$\begin{aligned} \int_{\Gamma} \dot{\sigma}_{ij} n_j v_i d\Gamma = & \int_{\Gamma_{AB}} \dot{\sigma}_{ij} n_j v_i d\Gamma_{AB} + \int_{\Gamma_{BC}} \dot{\sigma}_{ij} n_j v_i d\Gamma_{BC} + \int_{\Gamma_{CD}} \dot{\sigma}_{ij} n_j v_i d\Gamma_{CD} \\ & + \int_{\Gamma_{ED}} \dot{\sigma}_{ij} n_j v_i d\Gamma_{ED} + \int_{\Gamma_{FE}} \dot{\sigma}_{ij} n_j v_i d\Gamma_{FE} + \int_{\Gamma_{AF}} \dot{\sigma}_{ij} n_j v_i d\Gamma_{AF} \end{aligned} \quad (4)$$

First, let us focus on  $\Gamma_{AF}$  and  $\Gamma_{CD}$ . Figure 2 shows that the distribution of  $\dot{\sigma}_{ij}$  and  $v_i$  on AF and CD are identical, respectively, because the internal structure of the plate-fin structure has the periodicity in the  $\alpha$ -direction. Whereas,  $n_j$  takes opposite directions on AF and CD. As a result, the following equation can be obtained:

$$\int_{\Gamma_{AF}} \dot{\sigma}_{ij} n_j v_i d\Gamma_{AF} + \int_{\Gamma_{CD}} \dot{\sigma}_{ij} n_j v_i d\Gamma_{CD} = 0. \quad (5)$$

Second, let us focus on  $\Gamma_{FE}$  and  $\Gamma_{BC}$ . Figure 2 shows that the same situation exists on FE and BC in the  $\beta$ -direction, resulting in the following equation:

$$\int_{\Gamma_{FE}} \dot{\sigma}_{ij} n_j v_i d\Gamma_{FE} + \int_{\Gamma_{BC}} \dot{\sigma}_{ij} n_j v_i d\Gamma_{BC} = 0. \quad (6)$$

Finally, on  $\Gamma_{AB}$  and  $\Gamma_{ED}$ , the usual  $Y$ -periodicity is satisfied in the  $\gamma$ -direction as seen from Fig. 2. Thus, we have

$$\int_{\Gamma_{AB}} \dot{\sigma}_{ij} n_j v_i d\Gamma_{AB} + \int_{\Gamma_{ED}} \dot{\sigma}_{ij} n_j v_i d\Gamma_{ED} = 0. \quad (7)$$

Substituting Eq. (5), (6) and (7) into Eq. (4), Eq. (4) vanishes, and Eq. (3) results in

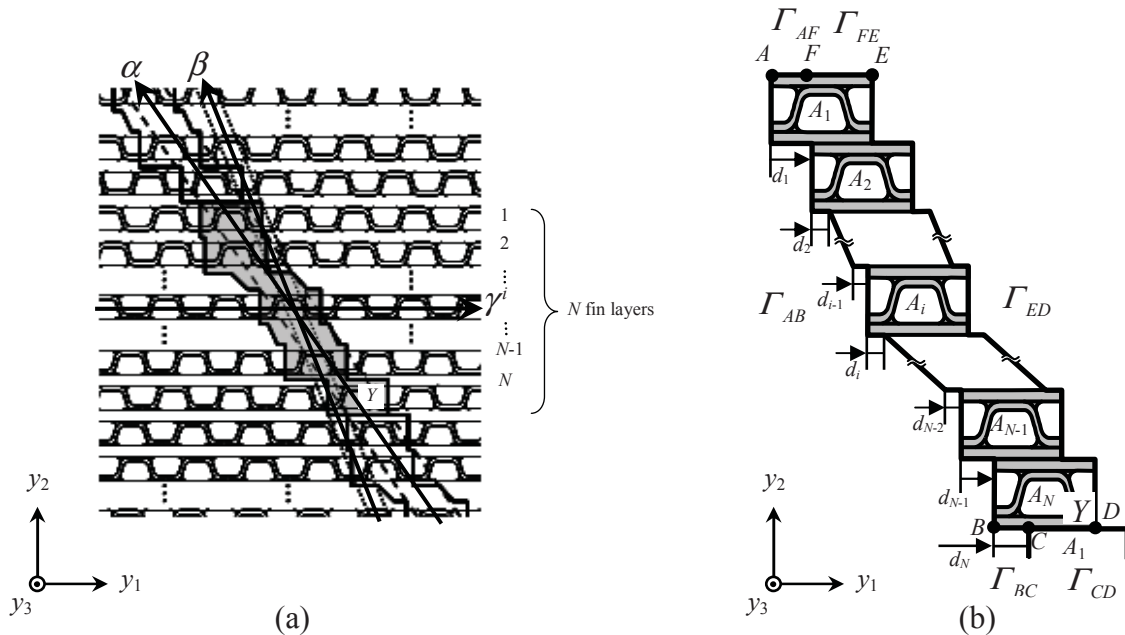
$$\int_Y \dot{\sigma}_{ij} n_j v_i dY = 0. \quad (8)$$

Using Eqs. (2) and (8), we obtain the following equation

$$\int_Y c_{ijkl} \dot{u}_{p,q}^{\#} v_{i,j} dY = -\dot{E}_{kl} \int_Y c_{ijkl} v_{i,j} dY + \int_Y c_{ijkl} \beta_{kl} v_{i,j} dY + \Delta \dot{T} \int_Y c_{ijkl} \alpha_{kl} v_{i,j} dY, \quad (9)$$

where  $\dot{u}_i^{\#}(\mathbf{y}, t, T)$  and  $\dot{E}_{ij}$  indicate of the perturbed velocity field defined in  $Y$  and macroscopic strain rate, respectively. In this case,  $\dot{u}_i^{\#}$  can be expressed as

$$\dot{u}_i^{\#}(\mathbf{y}, t, T) = \chi_i^{kl}(\mathbf{y}, T) \dot{E}_{kl}(t) + \varphi_i(\mathbf{y}, t, T) + \Delta \dot{T}(t) \psi_i(\mathbf{y}, T), \quad (10)$$



**Figure 2. Ultrafine plate-fin structures with random laminate misalignmet, (a) whole structure and its unit cell  $Y$ , (b) unit cell  $Y$  and substructures  $A_i$**



where  $\chi_i^{kl}$ ,  $\varphi_i$  and  $\psi_i$  in the above equation denote the characteristic functions determined by solving the following boundary value problems in  $Y$  using the finite element method (FEM):

$$\int_Y c_{ijpq} \chi_{p,q}^{kl} v_{i,j} dY = - \int_Y c_{ijkl} v_{i,j} dY, \quad (11)$$

$$\int_Y c_{ijpq} \varphi_{p,q} v_{i,j} dY = \int_Y c_{ijkl} \beta_{kl} v_{i,j} dY, \quad (12)$$

$$\int_Y c_{ijpq} \psi_{p,q} v_{i,j} dY = \int_Y c_{ijkl} \alpha_{kl} v_{i,j} dY. \quad (13)$$

Then, the evolution equation of microscopic stress rate and the relation between macroscopic stress rate and strain rate are derived as follows:

$$\dot{\sigma}_{ij}(\mathbf{y}, t, T) = c_{ijpq} (\delta_{pk} \delta_{ql} + \chi_{p,q}^{kl}) \dot{E}_{kl} - c_{ijkl} (\beta_{kl} - \varphi_{k,l}) - \Delta \dot{T} c_{ijkl} (\alpha_{kl} - \psi_{k,l}), \quad (14)$$

$$\dot{\Sigma}_{ij}(\mathbf{y}, t, T) = \langle c_{ijpq} (\delta_{pk} \delta_{ql} + \chi_{p,q}^{kl}) \dot{E}_{kl} - c_{ijkl} (\beta_{kl} - \varphi_{k,l}) - \Delta \dot{T} \langle c_{ijkl} (\alpha_{kl} - \psi_{k,l}) \rangle \rangle, \quad (15)$$

where  $\delta_{ij}$  indicates Kronecker's delta, and  $\langle \# \rangle$  denote the volume average in  $Y$  defined as

$$\langle \# \rangle = \frac{1}{|Y|} \int_Y \# dY. \quad (16)$$

Here,  $|Y|$  signifies the volume of  $Y$ .

### Substructure Method

First, the unit cell  $Y$  is divided into substructures  $A_i$  ( $i=1,2,\dots,N$ ) as shown in Fig. 2(b). In addition, the amount of laminate misalignment between the substructures is defined as  $d_i$  ( $i=1,2,\dots,N$ ) illustrated in Fig. 2(b). Then, the boundary value problems for the individual substructure in a finite element discretized from are derived as follows:

$$\mathbf{k} \chi_i^{kl} = \mathbf{f}^{kl}, \quad (i=1,2,\dots,N), \quad (17)$$

$$\mathbf{k} \varphi_i = \mathbf{g}_i, \quad (i=1,2,\dots,N), \quad (18)$$

$$\mathbf{k} \psi_i = \mathbf{h}_i, \quad (i=1,2,\dots,N). \quad (19)$$

Next, the components of  $\chi_i^{kl}$ ,  $\varphi_i$  and  $\psi_i$  are respectively divided into two parts,  $\chi_i^{kl(\Omega)}$  and  $\chi_i^{kl(\Gamma)}$ ,  $\varphi_i^{(\Omega)}$  and  $\varphi_i^{(\Gamma)}$ , and  $\psi_i^{(\Omega)}$  and  $\psi_i^{(\Gamma)}$ , where  $(\ )^{(\Omega)}$  and  $(\ )^{(\Gamma)}$  represent vectors or matrices for the internal and the boundary nodes of  $A_i$ , respectively. Then, the boundary value problems for  $A_i$ , Eqs. (17), (18) and (19), are rewritten into the following equations:

$$\begin{bmatrix} \mathbf{k}^{(\Omega)} & \mathbf{k}^{(\Omega\Gamma)} \\ \mathbf{k}^{(\Gamma\Omega)} & \mathbf{k}^{(\Gamma)} \end{bmatrix} \begin{Bmatrix} \chi_i^{kl(\Omega)} \\ \chi_i^{kl(\Gamma)} \end{Bmatrix} = \begin{Bmatrix} \mathbf{f}^{kl(\Omega)} \\ \mathbf{f}^{kl(\Gamma)} \end{Bmatrix}, \quad (20)$$

$$\begin{bmatrix} \mathbf{k}^{(\Omega)} & \mathbf{k}^{(\Omega\Gamma)} \\ \mathbf{k}^{(\Gamma\Omega)} & \mathbf{k}^{(\Gamma)} \end{bmatrix} \begin{Bmatrix} \varphi_i^{(\Omega)} \\ \varphi_i^{(\Gamma)} \end{Bmatrix} = \begin{Bmatrix} \mathbf{g}_i^{(\Omega)} \\ \mathbf{g}_i^{(\Gamma)} \end{Bmatrix}, \quad (21)$$

$$\begin{bmatrix} \mathbf{k}^{(\Omega)} & \mathbf{k}^{(\Omega\Gamma)} \\ \mathbf{k}^{(\Gamma\Omega)} & \mathbf{k}^{(\Gamma)} \end{bmatrix} \begin{Bmatrix} \boldsymbol{\psi}_i^{(\Omega)} \\ \boldsymbol{\psi}_i^{(\Gamma)} \end{Bmatrix} = \begin{Bmatrix} \mathbf{h}_i^{(\Omega)} \\ \mathbf{h}_i^{(\Gamma)} \end{Bmatrix}, \quad (22)$$

where  $\boldsymbol{\chi}_i^{kl(\Omega)}$ ,  $\boldsymbol{\varphi}_i^{(\Omega)}$  and  $\boldsymbol{\psi}_i^{(\Omega)}$  can be expressed as

$$\boldsymbol{\chi}_i^{kl(\Omega)} = (\mathbf{k}^{(\Omega)})^{-1} (\mathbf{f}^{kl(\Omega)} - \mathbf{k}^{(\Omega\Gamma)} \boldsymbol{\chi}_i^{kl(\Gamma)}), \quad (23)$$

$$\boldsymbol{\varphi}_i^{(\Omega)} = (\mathbf{k}^{(\Omega)})^{-1} (\mathbf{g}_i^{(\Omega)} - \mathbf{k}^{(\Omega\Gamma)} \boldsymbol{\varphi}_i^{(\Gamma)}), \quad (24)$$

$$\boldsymbol{\psi}_i^{(\Omega)} = (\mathbf{k}^{(\Omega)})^{-1} (\mathbf{h}_i^{(\Omega)} - \mathbf{k}^{(\Omega\Gamma)} \boldsymbol{\psi}_i^{(\Gamma)}). \quad (25)$$

The eliminations of  $\boldsymbol{\chi}_i^{kl(\Omega)}$ ,  $\boldsymbol{\varphi}_i^{(\Omega)}$  and  $\boldsymbol{\psi}_i^{(\Omega)}$  from Eqs. (20), (21) and (22) using the above equations respectively yields

$$\bar{\mathbf{k}}^{(\Gamma)} \boldsymbol{\chi}_i^{kl(\Gamma)} = \bar{\mathbf{f}}^{kl(\Gamma)}, \quad (i=1,2,\dots,N), \quad (26)$$

$$\bar{\mathbf{k}}^{(\Gamma)} \boldsymbol{\varphi}_i^{(\Gamma)} = \bar{\mathbf{g}}_i^{(\Gamma)}, \quad (i=1,2,\dots,N), \quad (27)$$

$$\bar{\mathbf{k}}^{(\Gamma)} \boldsymbol{\psi}_i^{(\Gamma)} = \bar{\mathbf{h}}_i^{(\Gamma)}, \quad (i=1,2,\dots,N), \quad (28)$$

where  $\bar{\mathbf{k}}^{(\Gamma)}$ ,  $\bar{\mathbf{f}}^{kl(\Gamma)}$ ,  $\bar{\mathbf{g}}_i^{(\Gamma)}$  and  $\bar{\mathbf{h}}_i^{(\Gamma)}$  are expressed as follows:

$$\bar{\mathbf{k}}^{(\Gamma)} = \mathbf{k}^{(\Gamma)} - \mathbf{k}^{(\Gamma\Omega)} (\mathbf{k}^{(\Omega)})^{-1} \mathbf{k}^{(\Omega\Gamma)}, \quad (29)$$

$$\bar{\mathbf{f}}^{kl(\Gamma)} = \mathbf{f}^{kl(\Gamma)} - \mathbf{k}^{(\Gamma\Omega)} (\mathbf{k}^{(\Omega)})^{-1} \mathbf{f}^{kl(\Omega\Gamma)}, \quad (30)$$

$$\bar{\mathbf{g}}_i^{(\Gamma)} = \mathbf{g}_i^{(\Gamma)} - \mathbf{k}^{(\Gamma\Omega)} (\mathbf{k}^{(\Omega)})^{-1} \mathbf{g}_i^{(\Omega)}, \quad (31)$$

$$\bar{\mathbf{h}}_i^{(\Gamma)} = \mathbf{h}_i^{(\Gamma)} - \mathbf{k}^{(\Gamma\Omega)} (\mathbf{k}^{(\Omega)})^{-1} \mathbf{h}_i^{(\Omega)}. \quad (32)$$

Finally, Eqs. (26), (27) and (28) are respectively assembled into the following equations, which are boundary value problems with respect to just the boundary nodes of all substructures:

$$\mathbf{K}^{(\Gamma)} \boldsymbol{\chi}^{kl(\Gamma)} = \mathbf{F}^{kl(\Gamma)}, \quad (33)$$

$$\mathbf{K}^{(\Gamma)} \boldsymbol{\varphi}^{(\Gamma)} = \mathbf{G}^{(\Gamma)}, \quad (34)$$

$$\mathbf{K}^{(\Gamma)} \boldsymbol{\psi}^{(\Gamma)} = \mathbf{H}^{(\Gamma)}, \quad (35)$$

where  $\mathbf{K}^{(\Gamma)}$  stands for the matrix consisting of  $\bar{\mathbf{k}}^{(\Gamma)}$ ,  $\mathbf{F}^{kl(\Gamma)}$ ,  $\mathbf{G}^{(\Gamma)}$  and  $\mathbf{H}^{(\Gamma)}$  indicates the vector consisting of  $\bar{\mathbf{f}}^{kl(\Gamma)}$ ,  $\bar{\mathbf{g}}_i^{(\Gamma)}$  and  $\bar{\mathbf{h}}_i^{(\Gamma)}$ . Moreover,  $\boldsymbol{\chi}^{kl(\Gamma)}$ ,  $\boldsymbol{\varphi}^{(\Gamma)}$  and  $\boldsymbol{\psi}^{(\Gamma)}$  denote the nodal vectors of the characteristic functions at the boundary nodes of substructures. The characteristic functions  $\boldsymbol{\chi}^{kl(\Gamma)}$ ,  $\boldsymbol{\varphi}^{(\Gamma)}$  and  $\boldsymbol{\psi}^{(\Gamma)}$  are determined by solving Eqs. (33), (34) and (35) with appropriate boundary conditions. Then, the characteristic functions at the internal nodes,  $\boldsymbol{\chi}_i^{kl(\Omega)}$ ,  $\boldsymbol{\varphi}_i^{(\Omega)}$  and  $\boldsymbol{\psi}_i^{(\Omega)}$ , are calculated using Eqs. (23), (24) and (25).

### Analysis conditions

In the present analysis, thermoelastoviscoplastic properties of ultrafine plate-fin structures with random laminate misalignment under temperature change  $\Delta T$  were analyzed using the above method. A base metal for the plate-fin structures was Hastelloy X, which was a Ni-based alloy with

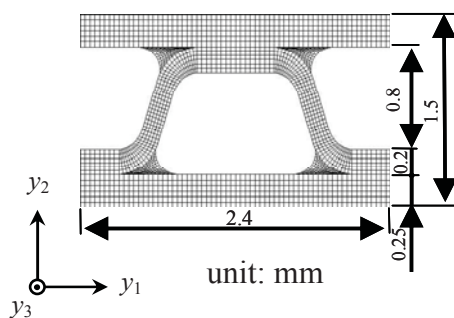
excellent heat resistance. The material constants used are listed in Table 1, which depend on temperature. The substructure  $A_i$  was defined and divided into four-node isoparametric elements as shown in Fig.3. This substructure  $A_i$  was two-dimensional rather than three-dimensional, and the generalized plane strain condition was assumed, because the plate-fin structures were assumed to have uniform and infinite material distribution in the  $y_3$ -direction.

The number of layers of unit cell  $Y$  was five kinds that include  $N = 10, 20, 30, 40$  and  $50$ . Twenty patterns of random laminate misalignment were given to  $N = 10, 20, 30$ , and ten patterns to  $N = 40, 50$ . In addition, five case of periodic laminate misalignment, i.e.  $d = 0, d = l/8, d = l/4, d = 3l/8$  and  $d = l/2$  where  $l$  indicates the width of substructure  $A_i$ , were also considered to compare with random laminate misalignment. Macroscopic temperature increment was from  $20^\circ\text{C}$  (room temperature) to  $200^\circ\text{C}$ , and temperature rate  $\Delta T = 1\text{K/s}$  was applied to the plate-fin structures. No macroscopic strain (Macroscopic strain rate) was assumed to occur ( $E_{ij} = 0$ ).

### Results of analysis

First, Figs. 4(a) and (b) respectively show the macroscopic stress-temperature relations in the  $y_1$ -direction in case of  $N = 10$  and  $N = 50$  with macroscopic temperature increment from  $20^\circ\text{C}$  to  $200^\circ\text{C}$ . These figures show the results of all random laminate misalignment patterns when  $N = 10$  and  $N = 50$ . In addition, the macroscopic stress-temperature relations of periodic laminate misalignment for  $d = l/8$  and  $d = 3l/8$  are also shown in the figure, which exhibited the maximum and minimum stress, respectively. It is seen from the figure that the results of all random laminate misalignment patterns exist between two results of periodic laminate misalignment. Furthermore, as the number of layers  $N$  increases, the dispersion of macroscopic stress-temperature relations decreases, and they converges to an intermediate value of  $d = l/8$  and  $d = 3l/8$ .

Next, Figs. 5(a) and (b) respectively show the maximum microscopic compressive stresses in the  $y_1$  and  $y_2$ -directions for all the random laminate misalignment patterns at  $N = 10, 20, 30, 40$  and  $50$ . Also, the maximum microscopic compressive stresses for the periodic laminate misalignment are shown in the figure as the results for  $N = 1$ . As seen from Figs. 5(a) and (b), the maximum microscopic compressive stresses of random laminate misalignment tend to be higher than those of periodic laminate misalignment. In addition, as the number of layers  $N$  increases, the dispersion of microscopic stresses decreases, which is similar tendency to the macroscopic stress-temperature relations. However, the maximum microscopic stresses converge to not an intermediate but higher value, meaning that elastic-viscoplastic properties of plate-fin structures have to be investigated both macroscopically and microscopically.



**Figure 3. Substructures  $A_i$  and finite element mesh**

**Table 1. Material properties of Hastelloy X**

Poisson's ratio	$\nu$	0.32
Reference strain rate	$\epsilon_0[\text{s}^{-1}]$	$10^3$
Stress power index	$n$	$-0.0295T+33.075$
Young's modulus	$E[\text{GPa}]$	$-0.0684T+212.22$
Coefficient of thermal expansion	$\alpha[10^{-6}/\text{K}]$	$0.0031T+13.548$
Yielding stress	$\sigma_0[\text{MPa}]$	$-8 \times 10^{-7} \times T^3 + 0.0013T^2 - 0.6826T + 391.51$

HASTELLOY®X ALLOY, HAYNES International(1997)

## Conclusions

In this study, the homogenization theory for thermoelastoviscoplasticity combined with the substructure method was proposed to investigate the effects of laminate misalignment on thermoelastoviscoplastic behavior of ultrafine plate-fin structures. The present method was applied to the analysis of thermoelastoviscoplastic behavior and thermal stress of ultrafine plate-fin structures with laminate misalignment subjected to macroscopic temperature increment from 20 °C to 200 °C. It was shown that laminate misalignment affects the thermoelastoviscoplastic behavior and thermal stress of plate-fin structures both macroscopically and microscopically.

## References

- Yamamoto, N. and Matsuda, T. (2011), Effects of Laminate Misalignment on Elastic-Viscoplastic Properties of Ultra-Fine Plate-Fin structures: Analysis Using Time-Dependent Homogenization Theory. *Materials Research Innovations*, 15, pp. 147–150.
- Ohno, N., Wu, X. and Matsuda, T. (2000), Homogenized properties of elastic-viscoplastic composites with periodic internal structures. *International Journal of Mechanical Sciences*, 42, pp. 1519-1536.
- Zienkiewicz, O. C. and Taylor, R. L. (2000), The Finite Element Method. *Butterworth-Heinemann*, 5, pp. 177-179.

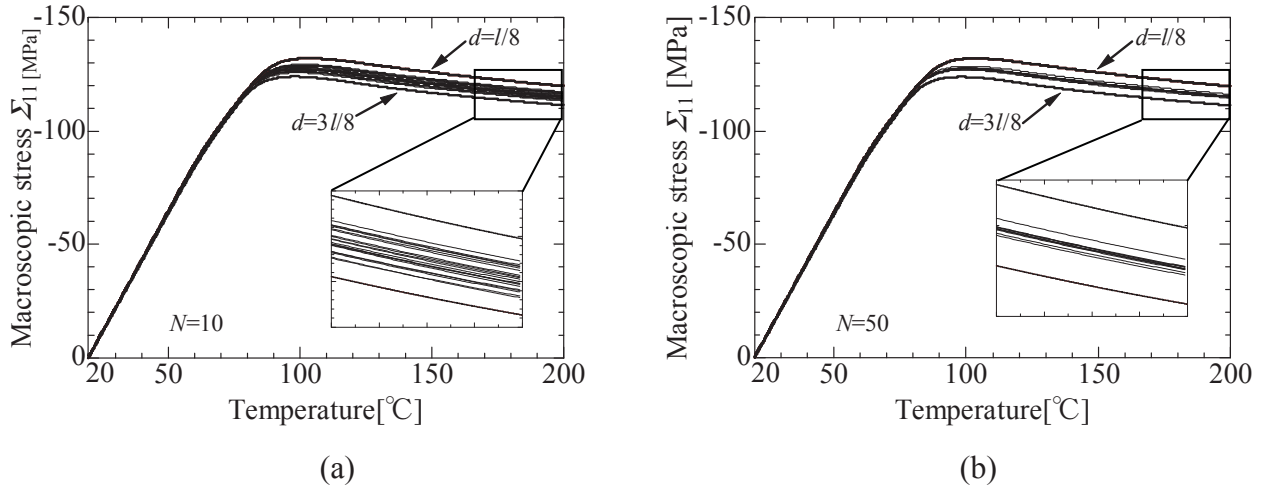


Figure 4. Macroscopic stress-temperature relations of ultrafine plate-fin structures with random laminate misalignment in  $y_1$ -directions , (a)  $N=10$ , (b)  $N=50$

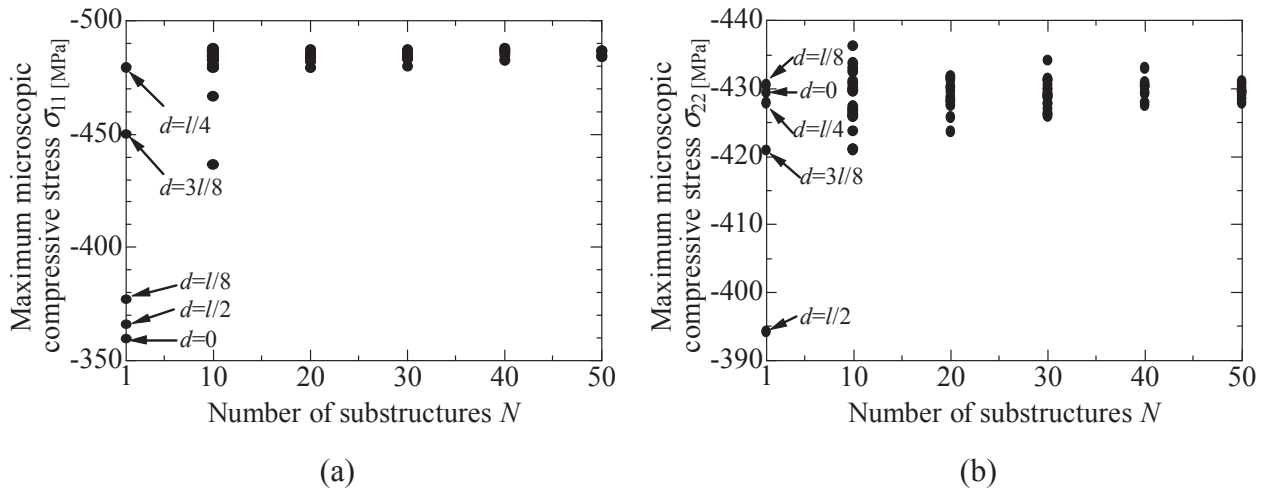


Figure 5. Effects of number of substructures  $N$  on maximum microscopic compressive stress , (a)  $y_1$ -direction, (b)  $y_2$ -direction

## Computational Study of Reynolds Number Effect on Owl-like Wing Aerodynamics at Low Reynolds Numbers

\*K. Kondo<sup>1</sup>, H. Aono<sup>2</sup>, T. Nonomura<sup>2</sup>, A. Oyama<sup>2</sup>, K. Fujii<sup>2</sup>, M. Yamamoto<sup>1</sup>

<sup>1</sup> Department of Mechanical Engineering, Tokyo University of Science, 6-3-1, Niijuku, Katsushika-ku, Tokyo, Japan.

<sup>2</sup>Institute of Space and Astronautical Science/JAXA, 3-1-1, Yoshinodai, Chuo-ku, Sagami-hara, Kanagawa, Japan.

\*Corresponding author: kondo@flab.isas.jaxa.jp

### Abstract

Present study highlights the effects of Reynolds number on aerodynamic characteristics and flow-fields around a rigid stationary cross-sectional owl wing (owl-like wing model) at the Reynolds numbers of 10,000, 23,000 and 46,000. In these Reynolds number regime, the flow-field includes laminar separation, laminar-to-turbulent transition, and reattachment. Therefore, this work employs three-dimensional implicit large-eddy simulation approach that is capable of accurate capturing three-dimensional breakdown of coherent vortices and reattachment physics. Results show that maximum lift-to-drag ratios gently increase comparing with conventional smooth airfoils, while variation of lift-to-drag ratio against the angle of attack appears with increasing Reynolds number. Furthermore, the locations of separation, laminar-to-turbulent transition, and reattachment points on the upper side move to the leading edge side with increasing Reynolds number. These movements have impact on steady and unsteady aerodynamics.

**Keywords:** Low Reynolds number flow, Aerodynamics, Reynolds number effect, Large eddy simulations.

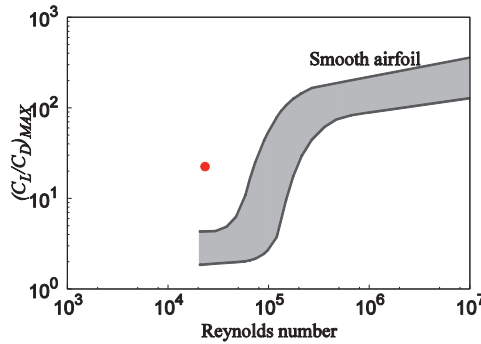
### Introduction

Development of Unmanned Air Vehicles (UAVs) has been an active research area. From the requirement of size, flight speed, and so forth, flight Reynolds number of the UAV becomes the order of  $10^4$ - $10^5$ . Under such low Reynolds number conditions, laminar separation, laminar-to-turbulent transition, sometimes reattachment, subsequently laminar separation bubble is generated so that aerodynamic performance of smooth airfoils, which are generally utilized under high Reynolds number conditions, drastically degrade as shown in Figure 1 (Lissaman, 1983). The behavior of such laminar separation bubble has been investigated by various researchers; the laminar separation bubble affects stalling behavior (Mueller and Batill, 1980) and the response of  $C_L$ - $\alpha$  curve (Okamoto, 2005). Therefore, it is important to understand the aerodynamic characteristics associated with the fixed-wing and to study design for high aerodynamic performance UAV wing under such low Reynolds number conditions.

Several researchers have been investigated how to design the airfoil shape in low Reynolds number, and recommended following features (Schmitz, 1980; Laitone, 2005); thin airfoil is better than thick one: the airfoil with camber is better than symmetric airfoil: the sharp leading edge and flat upper surface can improve the aerodynamic ability. Then, we have been interested in the aerodynamic characteristics associated with the avian wings, especially, an owl wing which consists of aforementioned several geometrical features. Additionally, Owl approaches its prey at a moderate speed of 2.5 m/s to 7.0 m/s (Bachmann et al., 2012), so that flight Reynolds numbers based on a mean chord length of approximately 150 mm becomes 25,000 to 70,000. These Reynolds number regimes correspond to UAV flight conditions. Liu et al. (2006) have experimentally measured the owl wing shape and provided mathematical formulation of its shape.

In our previous study, fundamental aerodynamic characteristics and flow-fields around the cross-sectional owl wing based on the experiment data of Liu et al. (2006) are investigated at the

Reynolds number of 23,000 using three-dimensional large-eddy simulations (Kondo et al., 2013). This study focuses on effects of the angle of attack on aerodynamic characteristics and flow-fields at fixed Reynolds number. The results show that the owl-like wing model possesses higher aerodynamic performance than conventional smooth airfoils as plotted in Figure 1. However, it is important to understand the effects of Reynolds number on aerodynamic characteristics of an airfoil when a wing of UAV is designed. Then, present study focuses on effects of Reynolds number on the aerodynamic characteristics and flow-fields around the owl-like wing model. Current work is continuous of the previous study associated with the owl-like wing aerodynamics.



**Figure 1.** The diagram of Reynolds number effect on maximum  $C_L/C_D$  (Lissaman, 1983).

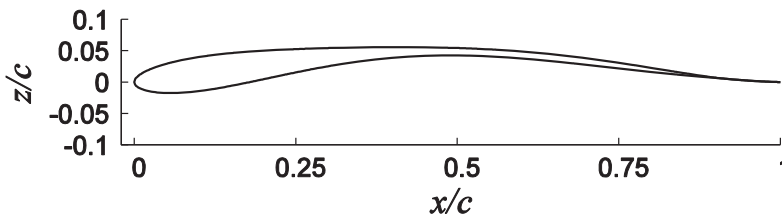
## Computational Set-up

### *Flow Conditions and Model Description*

Present study performs numerical simulations for an owl-like wing model at chord-based Reynolds numbers ( $Re_c$ ) of 10,000, 23,000, and 46,000, a Mach number of 0.2, and the angles of attack ( $\alpha$ ) of  $0.0^\circ$ ,  $1.5^\circ$ ,  $3.0^\circ$ ,  $4.5^\circ$ ,  $6.0^\circ$ ,  $7.5^\circ$ , and  $9.0^\circ$ .

The owl-like wing model is the rigid, stationary, and cross-sectional owl wing at 40% span length as shown in Figure 2. This airfoil geometry is constructed based on experiment data by Liu et al. (2006). The owl-like airfoil has a maximum thickness and camber of 5.4% at  $x/c=0.11$  and 4.9% at  $x/c=0.47$ , respectively.

Three dimensional implicit large-eddy simulations (3D-iLES) are carried out at the all angles of attack for Reynolds numbers of 23,000 and 46,000. For the Reynolds number of 10,000 where the flow is basically laminar flow regime, two-dimensional laminar simulations (2D-Laminar) are carried out at the all angles of attack as well as 3D-iLES are also performed at selected angles of attack (e.g.  $3.0^\circ$ ,  $6.0^\circ$  and  $9.0^\circ$ ).



**Figure 2.** The owl-like wing model.

### *Computational Methods*

Present computations utilize a flow solver LANS3D developed in ISAS/JAXA (Fujii and Obayashi, 1989). The LANS3D solves the compressible Navier-Stokes equations that are normalized by a chord length ( $c$ ) and the sound speed at a free-stream and generalized in curvilinear coordinates. The spatial derivatives of convective and viscous terms, metrics, and Jacobians are evaluated by the sixth-order compact difference scheme (Lele, 1992) with tenth-order filtering,  $\alpha_f=0.495$ , (Gaitonde and Visbal, 2000) for the numerical stability. For time-integration, the second-order backward

difference scheme is converged by the alternating directional symmetric Gauss-Seidel implicit method (Nishida and Nonomura, 2009) with five sub-iterations (Chakravarthy, 1984) in each time step. All computations are performed with a non-dimensional time step of  $dt=0.00025$  so that maximum Courant-Friedrichs-Lewy number becomes approximately 1.9. For turbulent modeling, implicit Large-Eddy Simulation (Boris et al., 1992) approach is adopted. In an iLES, unlike the traditional LES approach, no additional subgrid-scale terms are appended to the governing Navier-Stokes equations. Instead, a high-order low-pass filter selectively damping only the poorly resolved high-frequency waves are employed.

#### Computational Mesh and Boundary Conditions

Computational mesh around the owl-like wing model is illustrated in Figure 3. C-type structure mesh is utilized for the computational mesh. Grid coordinates are oriented such that  $\xi$  traverses clockwise around the airfoil,  $\eta$  follows spanwise direction, and  $\zeta$  is normal to the surface. Computational mesh consists of  $615 \times 201 \times 101$  points in  $\xi$ ,  $\eta$ , and  $\zeta$  directions, respectively, which is approximately 12 million grid points in total. The first grid points away from the airfoil surface are fixed for all grids and set to be  $0.03c/\sqrt{Re}$ . The farfield boundary is positioned  $30c$  away from the airfoil in order to reduce its influence on the solution near the airfoil. For the spanwise direction, 20% chord length are computed

At the outflow boundary, all variables are extrapolated from one point inside of the outflow boundary. On the airfoil surface, no-slip adiabatic wall boundary condition is adopted. For the spanwise, 20% chord length are computed with periodic boundary condition to simulate an infinite wing. This boundary condition is imposed using ten points overlap.

Figure 4 shows the grid spacings are evaluated by the wall unit for the current model at Reynolds number of 46,000 and angle of attack of  $6.0^\circ$ . Computational grid in terms of the wall unit satisfies the following inequality in range of turbulence flow region;  $\Delta\xi^+ < 25$ ,  $\Delta\eta^+ < 15$ ,  $\Delta\zeta_{min}^+ < 1$  where,  $\Delta\xi$  is the clockwise around airfoil,  $\Delta\eta$  is the spanwise direction, and  $\Delta\zeta$  is normal to the surface minimum grid spacing, and superscript plus donates the normalized value based on the wall unit. With these criteria, the turbulent analysis including near wall flow structure is sufficiently resolved for the present computations. It should be noted that the number of grid points and grid distribution used in current study are determined by grid sensitive analysis. Moreover, grid generation tools and LANS3D have been tested and validated through in a series of previous studies with regard to low Reynolds number flow simulations.

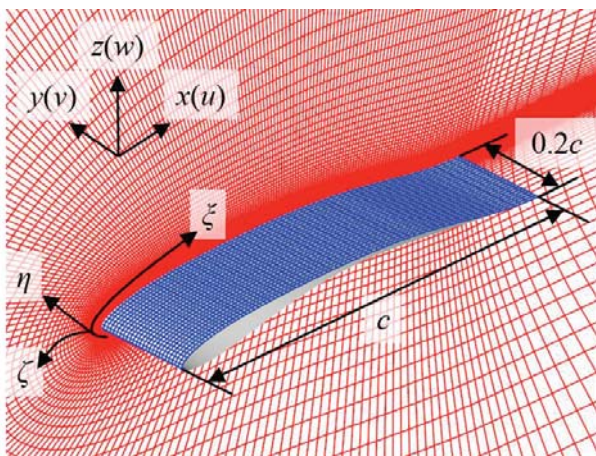


Figure 3. Computational mesh. Grid resolution of  $615 \times 201 \times 101$ .

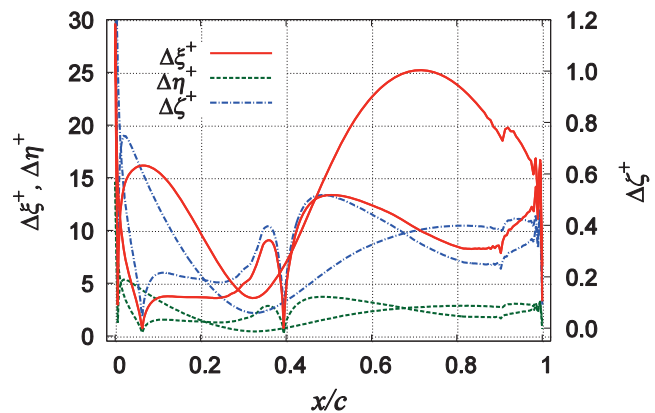


Figure 4. Grid-size distribution in the chord direction at  $Re=46,000$  and  $\alpha=6.0^\circ$ .



## Results and discussion

Present study highlights the Reynolds number effects of aerodynamic characteristics and flow-fields around the owl-like wing model. To this end, time-averaged aerodynamic force coefficients which are lift and drag coefficients and lift-to-drag ratio are discussed. In addition, surface pressure and skin friction coefficient, locations of separation and reattachment points, time-averaged flow-fields, Reynolds stress, instantaneous flow-fields and time history of the lift coefficients are compared at selected angles of attack of  $6.0^\circ$  to discuss the effects of Reynolds number on flow-fields. The reason that the angle of attack of  $6.0^\circ$  is selected for comparison is that the owl-like wing model attains maximum lift-to-drag ratio at the angle of attack of  $6.0^\circ$  for the Reynolds number of 23,000, and our group has investigated the aerodynamic characteristics at the Reynolds number of 23,000 in previous studies (Kondo, 2013).

### *Effects of Reynolds Number on Aerodynamic Coefficients*

Time- and span-averaged lift-to-drag ratios as a function of the angle of attack and maximum lift-to-drag ratios as a function of the Reynolds number are plotted in Figures 5 and 6, respectively. In addition, time- and span-averaged lift and drag coefficients are given in Figure 7. Before starting discussion of Reynolds number effects, it can be seen that there are differences between the results of 2D-Laminar simulations and 3D-iLES at the Reynolds number of 10,000 and higher angles of attack. It is difficult to estimate the locations of the reattachment points due to limited predictability of laminar-to-turbulent transition by 2D-Laminar.

As the Reynolds number increases, the lift-to-drag ratios increase for all the angles of attack. Moreover, variation of the lift-to-drag ratios against the angle of attack is also large with increasing the angle of attack. Especially, remarkable increment of the lift-to-drag ratio can be seen at the Reynolds number of 46,000 and the angle of attack from  $1.5^\circ$  to  $3.0^\circ$ . Maximum lift-to-drag ratios at the Reynolds number of 10,000, 23,000, and 46,000 are approximately 12 at the angle of attack of  $4.5^\circ$ , 23 at  $6.0^\circ$ , and 33 at  $3.0^\circ$ , respectively. These maximum lift-to-drag ratios of the owl-like wing model are higher than those of smooth airfoils and almost same value with rough airfoils as shown in Figure 6. This figure displays that the owl-like wing model possesses high aerodynamic performance under the low Reynolds number conditions in spite of the smooth airfoil.

Lift coefficients gently increase for almost all of the angle of attack with increasing Reynolds number. Most notably, nonlinearity of lift curves appears at lower angle of attack with increasing Reynolds number. Generally, nonlinearity of the lift curve is related to generation of the laminar separation bubble (Okamoto, 2005). Therefore, it is considered that formation of the laminar separation bubble is promoted as the Reynolds number increases.

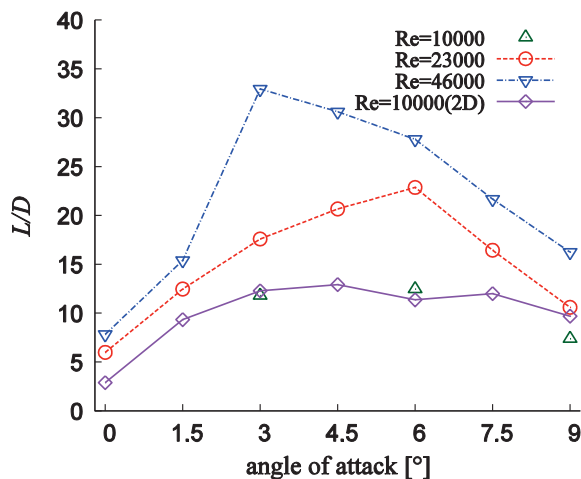


Figure 5. Lift-to-drag ratio as a function of the angle of attack.

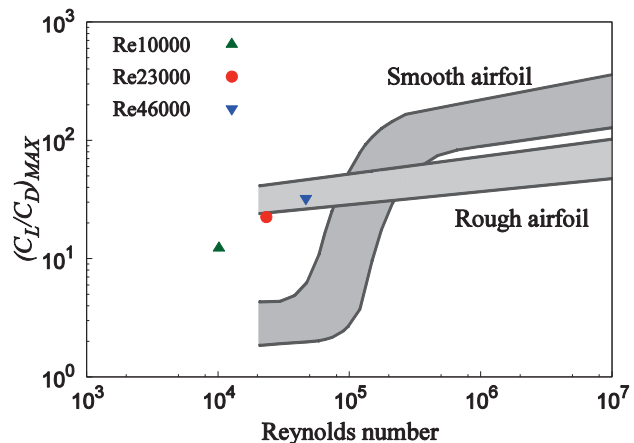
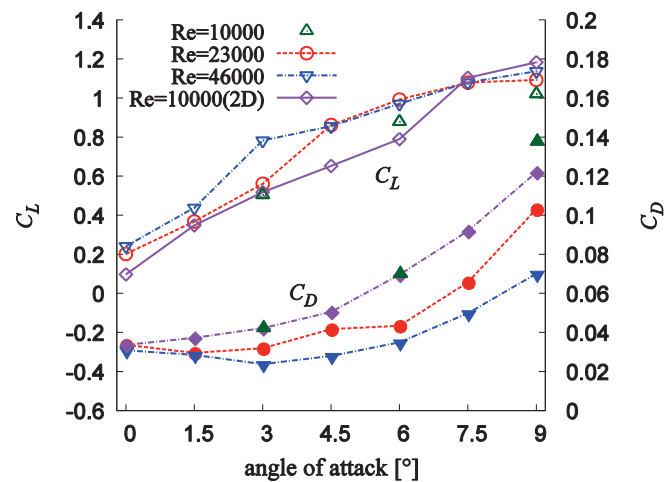


Figure 6. Lift-to-drag ratio as a function of the Reynolds number.



**Figure 7. Lift and drag coefficients as a function of the angle of attack.**

Increasing Reynolds number leads to decrease of drag coefficient for all the angles of attack. Furthermore, it can be seen that there is small variation in the drag coefficient to change of angle of attack. It is interesting that the angle of attack of minimum drag moves toward higher angle of attack with increasing Reynolds number. For instance, the angles of attack of minimum drag at Reynolds number of 10,000, 23,000, and 46,000 correspond to  $0.0^\circ$ ,  $1.5^\circ$ , and  $3.0^\circ$ , respectively. This fact implies that flow structure on upper and lower side may or may not have drastic change. In short, from above discussion, changing the Reynolds number significantly affects the aerodynamic characteristics of the owl-like wing model. The lift coefficient increases, drag coefficient decreases, and, subsequently lift-to-drag ratio is enhanced with increasing Reynolds number. Furthermore, change of the Reynolds number affects nonlinearity of the lift curve and variation of the lift-to-drag ratio against the angle of attack.

#### *Effects of Reynolds Number on Flow Characteristics at Fixed Angle of Attack*

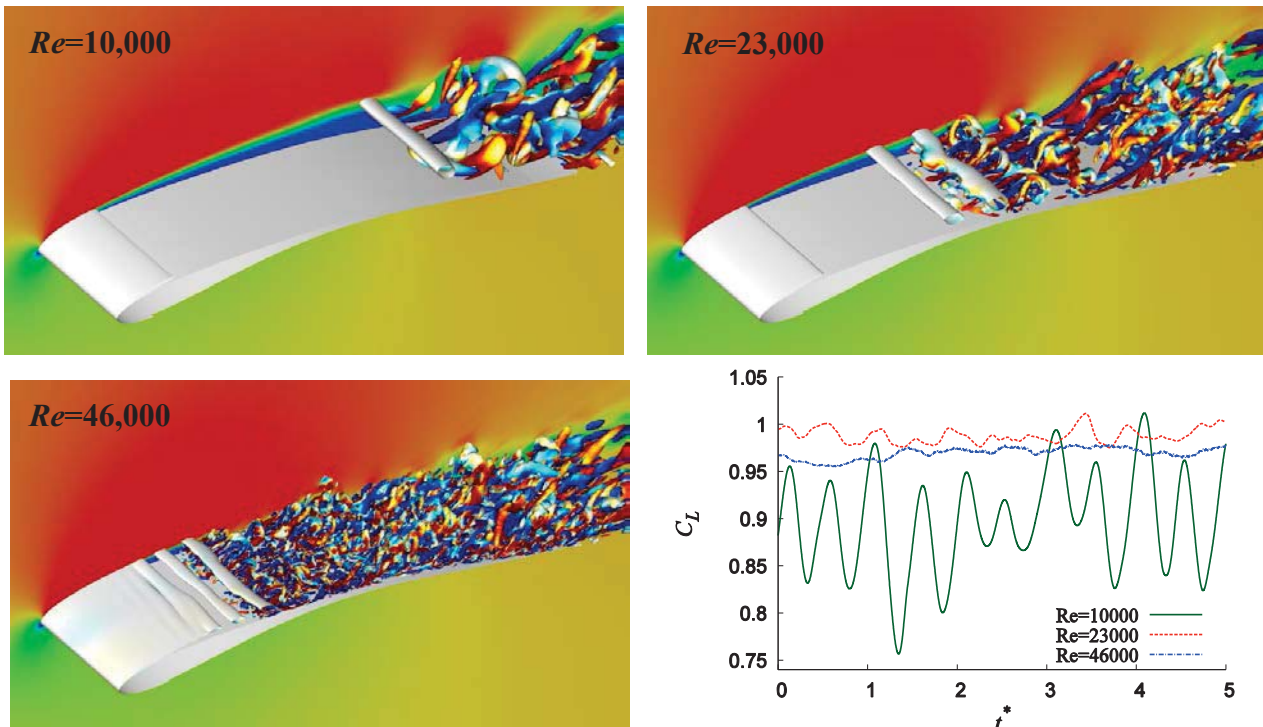
Instantaneous iso-surfaces of second invariant of the velocity gradient tensor ( $Q$ -criterion) with the comparison of time history of the lift coefficients are shown in Figure 8. It is found in all the Reynolds numbers that shear layer separates near the leading edge, develops as going down stream, subsequently generate the dead fluid region in the separated shear layer. Significant differences among three Reynolds numbers are location at which coherent vortices are formed and size of the vortices including three-dimensional vortices structure. Time-history and fluctuation of lift coefficient show influence of location and size of vortices due to change of the Reynolds number. Time- and span-averaged surface pressure and skin friction coefficients at the angle of attack of  $6.0^\circ$  are given in Figures 9 and 10. There is no difference in the surface pressure coefficients on the lower side for all the Reynolds numbers. On the other hand, the surface pressure coefficients on the upper side display suction peak and relatively flat distribution associated with laminar separation for all the Reynolds numbers. Rapid pressure recovery following the transition and reattachment can be observed except the Reynolds numbers of 10,000. These characteristics of the surface pressure coefficient have been shown in the study of SD7003 airfoil by Uranga et al. (2011). In addition, magnitude of the suction peak and pressure plateau are enhanced, and the location and length of the pressure plateau and pressure recovery move toward the leading edge side as Reynolds number increases. Magnitude of the pressure coefficients near the trailing edge is significantly related to drag generation. As shown in Figure 7, larger drag is generated at the lowest Reynolds number. This is because of difference in the magnitude of pressure coefficient near the trailing edge. There are sudden drops of the skin friction coefficient at certain location of the airfoil in all the Reynolds numbers as shown in Figure 10. This is related to the flow physics such as the separated

shear layer rolling up and shedding the coherent vortex from the separated shear layer. The locations of the sudden drop move toward leading edge side with increasing Reynolds number. Furthermore, at Reynolds number of 10,000, downstream of the sudden drop, the skin friction coefficient remains negative. Consequently, it is likely that the flow at the Reynolds number of 10,000 does not reattach unlike the Reynolds numbers of 23,000 and 46,000.

Contours of time-averaged chordwise velocity and Reynolds stress are shown in Figures 11 and 12. Time-averaged flow-fields clearly demonstrate that length of the shear layer becomes shorter and thickness of that also becomes thinner with increasing Reynolds number. In addition increasing Reynolds number leads to reduce the separated region corresponding to blue area in the figures. From these flow-fields, movement of the location of separation and reattachment points to leading edge side is clearly visualized. As shown in Figure 12, small values of Reynolds stress are observed near the trailing edge region for the lowest Reynolds number of 10,000. For Reynolds numbers of 23,000 and 46,000, relatively large values of Reynolds stress are observed near the center of the airfoil. Generally, the location of higher Reynolds stress corresponds to the location where coherent vortex structure that shed from shear layer collapses (see Figure 8). In other words, the increasing magnitude of Reynolds stress is indicative of a more intense laminar-to-turbulent transition process causing the reattachment location. As a result, the locations of reattachment point are located at the just downstream of the highest Reynolds stress for Reynolds number of 23,000 and 46,000.

#### *Effect of Reynolds Number on Separation and Reattachment Characteristics*

In previous section, flow characteristics at fixed angle of attack are discussed. It has been clarified that the locations of separation and reattachment point are significantly affected by the change of the Reynolds number. In this section, effects of changing Reynolds number and the angle of attack on separation and reattachment points are discussed.



**Figure 8. Instantaneous  $Q$ -criterion ( $Q=5$ ) colored by chordwise vorticity (-5 - 5) with background contours indicating magnitude of chordwise velocity (0 - 1.25), and time history of lift coefficients.**

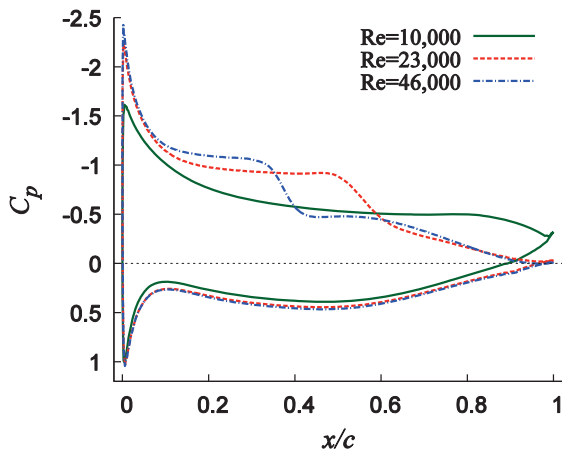


Figure 9. Effects of Reynolds number on surface pressure coefficients for  $\alpha=6.0^\circ$ .

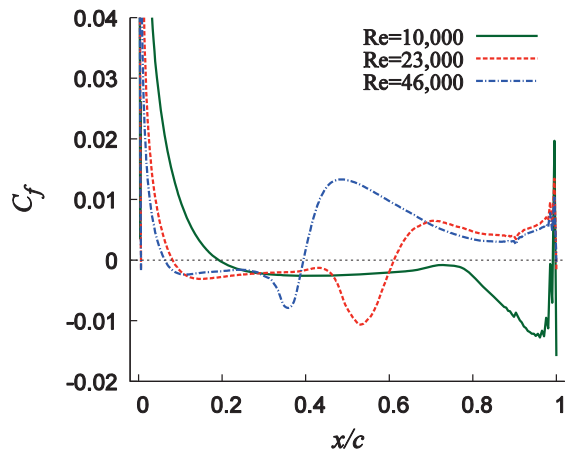


Figure 10. Effects of Reynolds number on skin friction coefficients at  $\alpha=6.0^\circ$ .

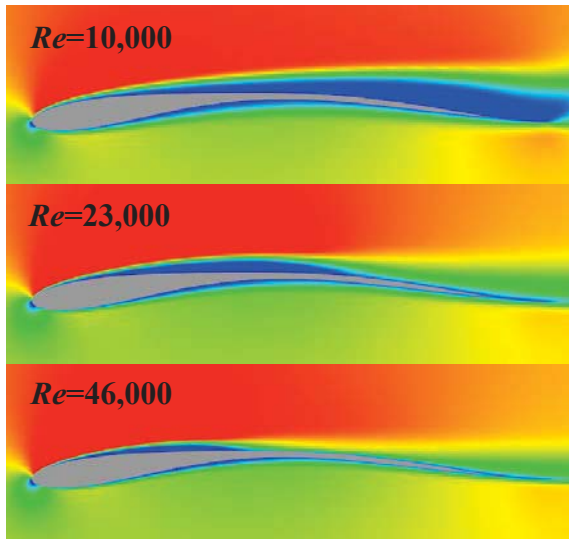


Figure 11. Contours of time-averaged chordwise velocity at  $\alpha=6.0^\circ$ .

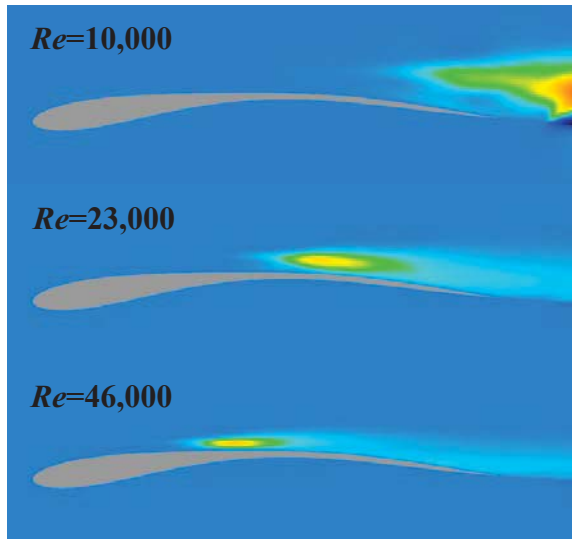
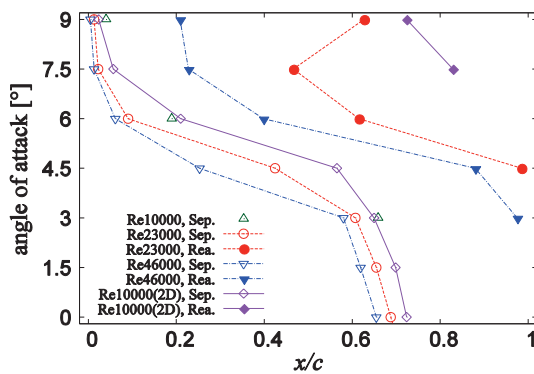
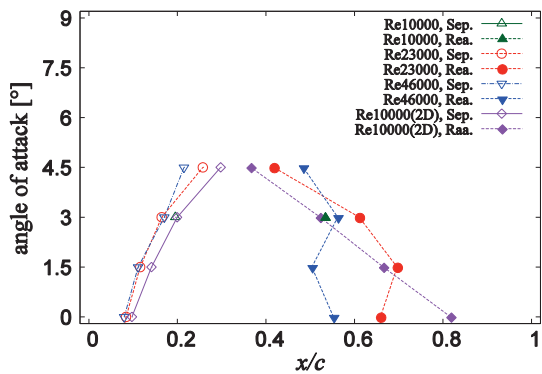


Figure 12. Contours of Reynolds stress  $(\overline{u'w'})$  at  $\alpha=6.0^\circ$ .



Upper surface



Lower surface

Figure 13. Location of the separation and reattachment points for upper and lower side.

Figure 13 shows the locations of separation and reattachment point as a function of the angle of attack. The locations of separation points on the upper side gently move to leading edge side. A more significant difference in reattachment location is observed among three Reynolds numbers. At Reynolds number of 10,000, the results of 3D-iLES show that the flow does not reattach at all the

angles of attack. It is noteworthy that the length of laminar separation bubble between separation and reattachment points becomes shorter and that location moves toward leading edge side with rising Reynolds number. It is noted that the results of 2D-Laminar overestimate in terms of reattachment points at the high angles of attack. This difference between the results of 2D-Laminar and 3D-iLES is currently under investigation. The phenomena of separation and reattachment can be also seen in the lower surface. The locations of the separation points slightly move to the leading edge side with increasing Reynolds number as similar to upper side. However, common features cannot be identified in the behavior of the reattachment points without the angle of attack at which the flow fully attaches. Therefore it is expected that flow-fields on the lower surface are complicated.

## Conclusions

Effects of Reynolds number change on the aerodynamic characteristics and the flow-fields around the owl-like wing model are discussed at chord based Reynolds numbers of 10,000, 23,000, and 46,000 and at the angle of attack ranging from  $0.0^\circ$  to  $9.0^\circ$  using three-dimensional implicit large-eddy simulations. Results show that response of maximum lift-to-drag ratio is less sensitive to change of Reynolds number. However, variation of lift-to-drag ratio to change of the angle of attack shows Reynolds number dependency. The locations of separation, laminar-to-turbulent transition, and reattachment point on the upper side move to the leading edge side with increasing the Reynolds number at angle of attack of  $6.0^\circ$ . Noticeable variation of location of separation and reattachment points appears with increasing Reynolds number. Therefore, sensitivity of lift-to-drag ratio to change of the angle of attack is varied due to change of Reynolds number.

## Reference

- Bachmann, T., Blazek, S., Erlinghagen, T., Baumgartner, W., and Wagner, H. (2012), Barn Owl Flight, *Nature-Inspired Fluid Mechanics*, volume 119, pp. 101-117.
- Boris, J. P., Grinstein, F. F., Oran, E., Kolbe, R. J., (1992), New insights into large eddy simulation, *Fluid Dynamics Research*, 10, pp. 199-228.
- Chakravarthy, S. R. (1984), Relaxation Methods for Unfactored Implicit Upwind Schemes, AIAA Paper 84-0165.
- Fujii, K., Obayashi, S. (1989), High-resolution upwind scheme for vertical-flow simulations, *Journal of Aircraft*, 26(12), pp. 1123-1129.
- Gaitonde, D. V., Visbal, R. M. (2000), Pade-type high-order boundary filters for the navier-stokes equations, *AIAA Journal*, 38, pp. 2103-2112.
- Kondo, K., Aono, H., Nonomura, T., Oyama, A., Fujii, K., Yamamoto, M. (2013), Large-Eddy Simulations of Owl-like Wing under Low Reynolds Number Conditions, FEDSM2013-16377.
- Laitone, E. V. (2005), Wind tunnel tests of wings at Reynolds numbers below 70,000, *Experiments in Fluids*.
- Lele, S. K. (1992), Compact Finite Difference Scheme with Spectral-Like Resolution, *Journal of Computational Physics*, Vol.103, pp. 16-42.
- Lissaman, P. B. S. (1983), Low-Reynolds-number airfoils. *Annual Review of Fluid Mechanics*, Vol. 15, pp. 223-239.
- Liu, T., Kuykendoll, K., Rhew, R., Jones, S. (2006), Avian Wing Geometry and Kinematics, *AIAA Journal*, vol.44, No.5.
- Mueller, T. J. and Batill, S. M. (1980), Experimental Studies of Separation on a Two Dimensional Airfoil at Low Reynolds Numbers, AIAA Paper, pp. 80-1440.
- Nishida, H., Nonomura, T. (2009), Adi-sgs scheme on ideal magnetohydrodynamics, *Journal of Computational Physics*, 228, pp. 3182-3188.
- Okamoto, M. (2005), An experimental study in aerodynamic characteristics of steady and unsteady airfoils at low Reynolds number, Ph.D. thesis, Nihon University.
- Schmitz, F. W. (1980), The aerodynamics of small Reynolds numbers, NASA technical memorandum, pp. 51
- Uranga, A., Persson, P.-O., Drela, M. and Peraire, J. (2011), Implicit Large Eddy Simulation of transition to turbulence at low Reynolds numbers using a Discontinuous Galerkin method, *International Journal for Numerical Methods in Engineering*, Vol.87, pp. 232-261.

# M-integral and configurational forces for Mode-I crack growth based on Gurson-Tvergaard model in elastoplasticity materials

B.H. Zhang<sup>a,\*</sup>, Q. Li<sup>a</sup>, Y.H. Chen<sup>a</sup>, H.L. Wang<sup>b</sup>

<sup>a</sup>State Key Laboratory for Mechanical Structural Strength and Vibration, School of Aerospace, Xian Jiaotong University, 710049, P.R. China

<sup>b</sup>Northwest Nuclear Technology Institute, Xian, Shannxi, 710024, P.R. China

---

## Abstract

A configurational force method is proposed for evaluating the crack driving force for material damage and fracture in elastoplasticity materials. By using Helmholtz free energy characterized by internal variable and deformation gradient decomposition, nodal configurational forces due to the material degradation and damage are derived based on G-T model in finite strain setting. The G-T Plasticity theory developed by Gurson and Tvergaard and Needleman offers an insight to analysis and solve the degradation and damage behavior of ductile porous metals at an applied overload. This model allows you to incorporate microscopic material behaviors, such as void dilatancy, void nucleation, and void coalescence into macroscopic plasticity models. Based on this model, M-integral concept is extended to study the degradation of a microvoid dilation and nucleation for a plane strain ductile porous metal under Mode-I tensile loading. Attention is focused on the change in the M-integral before, during, and after coalescence of many microvoids. Using finite element analyses, the influences of different G-T model parameter on M-integral are discussed in detail.

**Keywords:** Configurational forces; M-integral; G-T model; Elastoplasticity

---

## 1. Introduction

The notion of force is central to all of continuum mechanics. There are two force systems in physics space and in material space which are standard (Newtonian) forces and configurational forces respectively. Configurational forces in material space have been playing a significant role in the description of material discontinuous and inhomogeneities (e.g., voids, cracks, inclusion, bimaterial interfaces) as they move relatively to the material. Gurtin (1995, 2000) elaborates this quantity based on the motion ideas of material and spatial observers within a classical context. The framework of several fundamental issues such as bulk, inner interface, and coherent phase interface configurational forces are established. Moreover, He believes that configurational forces should be viewed as basic objects consistent with their own force balance. Eshelby tensor may be a natural result of those framework. So-called Eshelby tensor (also referred to as the Maxwell tensor, or the energy momentum tensor, or the material momentum tensor) is introduced and developed by Eshelby (1951, 1956, 1970, 1975) in studying forces on elastic singularities and defects in his series of papers, making clear that the integrand of J-integral presented by Rice (1968) is just the Eshelby tensor contracted with the unit outward-normal vector. Due to the seminal contributions of Eshelby, Maugin (1992, 1993, 1994, 2002) introduced even the concept of Eshelbian mechanics whose main ingredient is the Eshelby tensor. Kienzler and Herrmann (1997, 2000) have also performed a rather detailed discussion of the properties such as Invariants, principal values, principal directions and extremal values associated with this tensor and give physics interpretation of its components. As an application of local properties of the Eshelby tensor, fracture criteria is presented to plane crack under mixed-mode loading conditions in Kienzler and Herrmann (2002). Epstein (2002) reaffirm the fact that there exists a natural connection between Noll's theory of inhomogeneities and Eshelby tensor by using of the local form of the Clausius-Duhem inequality. Additionally the application of the concept of configurational forces in the

---

\*Corresponding author now at Northwest Nuclear Technology Institute, Xian, Shannxi, 710024, P.R. China

Email addresses: bai.hua.cool1@stu.xjtu.edu.cn (B.H. Zhang), liqun@mailst.xjtu.edu.cn (Q. Li), yhchen2@xjtu.edu.cn (Y.H. Chen), Wanghongliang1984@163.com (H.L. Wang)

context of Finite Element (FE) discretizations is a relatively new application which is discussed by Braun (1995). For more details of configurational forces and Eshelby tensor reader is also referred to Gross (2003), Mueller and Maugin (2002), Mueller, Kolling and Gross (2002), Steinmann (2000), Steinmann, Ackermann and Barth (2001), Naser (2007). Thus a whole edifice of a mechanics in material space have been established.

Theory and method based on the configurational forces and Eshelby tensor afford a novel tool to characterize the crack driving force and dissipation for crack growth in elastoplastic materials under finite deformation considering general yielding and local hardening conditions. Due to Eshelby tensor related to J-integral, we briefly mention J-integral and its property firstly. J-integral approach can evaluate the crack driving force on a contour around crack tip in elastoplastic materials by Rice (1978), but this has to be limited to be an assumption that the material behavior keeps to deformation plasticity, i.e. all loading paths should remain radial direction in stress space. Consequently, both of the realistic behavior of cracks in elastoplastic finite deformation conditions are concealed: one is that stress state of moving crack because of unloading behind the crack tip is not able to comply proportional loading assumption, the other is that plastic work at applied stress should not be included in stored energy density but should be dissipated. Path-independence utility of J-integral is satisfied in quasi-static problems for elastic materials, the property exists for inelastic materials only under certain conditions, such as deformation materials and elastoplastic materials that can be treated as non-linear elastic. However, in the more general elastoplastic materials J-integral becomes path-dependent, e.g. in Carka (1995). In fact, This instance may be extended to the other conservative integrals such as M-integral in N. Y. Yu (2007). Hence, some physical explanation difficulties what J-integral is up against may be suspicious of its using as a crack driving force in general elastoplastic materials.

In contrast, configurational force methods for elastoplastic material fracture mechanics is proposed and developed gradually recently. The theory of configurational forces is presented within the non-linear dynamic framework by Gross (2003). The occurrence of configurational forces in the FE is illustrated, but only limited to a quasistatic case and neglect other dissipative mechanism like for example hardening. Nguyen (2005) proposes a material force method, i.e. configurational force, to solve viscoelastic and elastoplastic fracture problem at small deformations, moreover, expressions for dissipation forces are obtained. But his derivatives about dissipation forces doesn't appeal to the second law of thermodynamics, so this effects its generality. Simha (2003) elaborates the relationship between J-integral and configurational forces in elastic-plastic materials based on the second law of thermodynamics without making any assumptions about the constitutive nature of the body, but the crack growth isn't considered. Fiscer (2007) extends the application of configurational forces to fracture of bimaterial materials as illustrative examples.

In this paper, we extend the configurational force method to analysis more complex material behaviors in fracture mechanics. Several material behaviors such as crack growth, plastic flow and hardening phenomenon are discussed in configurational force framework. Helmholtz free energy density as part of the Eshelby tensor is introduced as a fundamental quantity associated with the field of configurational forces and material dissipation. The free energy density is expressed in terms of the elastic, plastic and internal variable. Moreover, configurational forces and material dissipation formulation is also related to material gradient of plastic strain and internal variable. Based on the relationship, we show that the path-independence property of J-integral is not able to agreement with this case and has to be modified due to bulk and crack tip dissipation. This yields a formulation about global configurational forces balance associated with far field J-integral, near crack tip J-integral and configurational body forces. At a steady state crack growth condition, configurational body forces are related to bulk dissipation due to the effect of plastic deformation. Given these conditions, several quantities are evaluated such as the distribution of nodal configurational forces, bulk dissipation against crack growth distance.

The goal of this paper is to determine how the theories based on the configurational forces and Eshelby tensor in material space are applied in the context of incremental plasticity considering crack growth. The first section, nodal configurational forces and total dissipation in the body including crack tip due to the crack tip moving are derived based on the theories of Eshelbian mechanics in finite strain setting by using Helmholtz free energy characterized by internal variable and deformation gradient decomposition. The base of theoretical derivations is configurational forces method presented by Gurtin (1995, 2000). Specifically, Maugin (1992, 1993, 1994, 1995, 2002) and coworkers Cleja-Tigolu (2000) elaborate the Eshelby stress tensors in the finite and small-strain setting and a series of formulations, e.g., the standard variational energy and plastic dissipation are established. In section 2, for numerical evaluation, an equivalent domain integral expression are obtained from the sum of weights nodal configurational force of per element. Consideration is given to the central differential method, particularly to computing quantities involving effective plastic strain gradients. Therefore, this paper is focused on issues of physics interpretation and numerical

implementation that are unique to plasticity.

In the final section, the configurational force method is applied to evaluate crack driving force and dissipation for steady state crack growth in a C(T)-specimen for elastoplasticity materials. Specializations to isotropic hardening condition and homogeneous materials. Several quantities are obtained by a separate postprocessing step after a standard finite element simulation is performed. The variation of nodal configurational forces and total dissipation in the body in the process of crack growth are discussed in a cracked body.

## 2. Configurational forces for elastoplasticity

There are two force systems in physics space and in material space which are standard (Newtonian) forces and configurational forces respectively. Accordingly, in two spaces there are separate balance laws for the standard and configurational forces. In configurational force framework, crack growth is treated formally as a change in the reference configuration. Configurational forces and Eshelby stress tensors have been derived in papers by Gurtin (1995, 2000); Simha (2003); Fiscer (2007); Maugin (1995). Hence detailed deductions are omitted here and a briefly review are showed. For simplicity we ignore inertia and external body force.

### 2.1. Balance of configurational forces

We consider a cracked elastic plastic body in the two-dimensional setting identified with the region  $\Omega$  as shown in Fig. 1. Let  $(X_1, X_2)$  and  $(\xi_1, \xi_2)$  denote fixed and moving Cartesian coordinate with fixed origin and moving origin with at crack tip respectively. A contour  $\Gamma_{far}$  surrounding the volume  $\Omega$  with outward unit normal  $\mathbf{N}$  is defined in outer boundary, likewise, a similarly directed contour  $\Gamma_\delta(t)$  surrounding the infinitesimal volume  $\Omega_\delta(t)$  containing the crack tip is defined. Two line segments identified with  $\Gamma_+$  and  $\Gamma_-$  on the crack plane join  $\Gamma_{far}$  and  $\Gamma_\delta$  respectively. Then a closed path made of  $\Gamma_{far} + \Gamma_+ + \Gamma_\delta(t) + \Gamma_-$  is obtained and the area surrounded by the closed path is referred to  $\Omega - \Omega_\delta(t)$ .

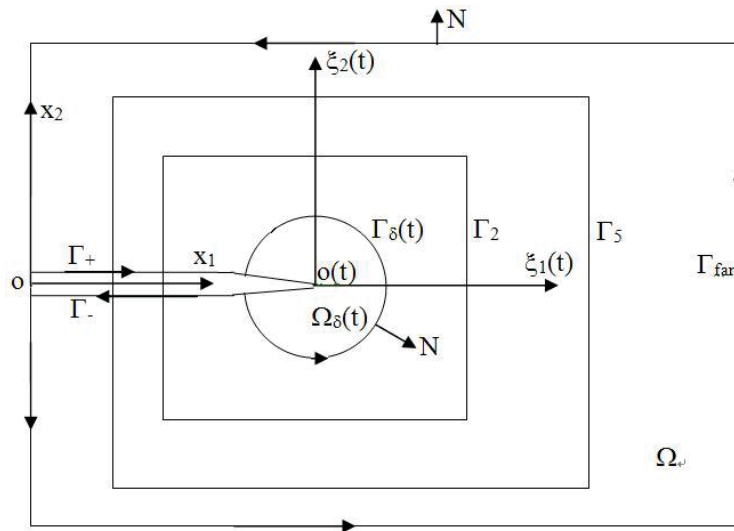


Figure 1: A crack in a two dimensional body  $\Omega$  in its reference configuration

Firstly, we assume that the physical motion problem has been solved so that the yield of displacement and physics stress are known. And then the material motion is described using configurational force method. The configurational force system consists of two fields:

- C** Eshelby stress tensor defined in the whole region
- g** internal configurational body force in the bulk  $\Omega_0$



As with standard forces, configurational tractions  $\mathbf{CN}$  and body forces  $\mathbf{g}$  are measured in the reference body.  $\mathbf{C}(\mathbf{X}, t)$  is a linear transformation of material vectors into material vectors, while  $\mathbf{g}(\mathbf{X}, t)$  is material vectors. The net working of the reference body is attributed to 1st Piola-Kirchhoff stress  $\mathbf{S}$  and Eshelby stress  $\mathbf{C}$  in (1).

$$W(\Omega_t) = \int_{\partial\Omega_t} \mathbf{CN} \cdot \mathbf{q} dl + \int_{\partial\Omega_t} \mathbf{SN} \cdot \dot{\mathbf{y}} dl \quad (1)$$

with  $\mathbf{q}$  represents a velocity field for the boundary of undeformed body  $\partial\Omega_0$ .  $\dot{\mathbf{y}}$  represents a velocity field for the boundary of deformed body  $\partial\Omega_t$ .

Applying invariance of net working under changes in material observer, local configurational force balance formulation (2) is obtained in bulk.

$$\nabla \cdot \mathbf{C} + \mathbf{g} = 0 \quad (2)$$

Furthermore, by using mechanical version of the thermodynamical second law (3),

$$\frac{d}{dt} \left\{ \int_{\Omega_t} \psi dA \right\} \leq W(\Omega_t) \quad (3)$$

with  $\psi$  the (Helmholtz) free energy potential. Eshelby stress tensor and internal configurational body force relation are achieved in (4) and (5).

$$\mathbf{C} = \psi \mathbf{I} - \mathbf{F}^T \mathbf{S} \quad (4)$$

$$\mathbf{g} = -\nabla \cdot \mathbf{C} = -\nabla \cdot (\psi \mathbf{I} - \mathbf{F}^T \mathbf{S}) \quad (5)$$

with  $\mathbf{F}$  deformation gradient tensor.

If we restrict attention to stationary  $\Omega_t$ , by (1) and (3), the local dissipation inequality is obtained in (6).

$$\mathbf{S} \cdot \dot{\mathbf{F}} \geq \dot{\psi} \quad (6)$$

Secondly, we has to define another configurational force at the internal interface of a cracked body. The internal interface is made of  $\Gamma_+ - \Gamma_\delta(t) + \Gamma_-$  and the internal interface is referred to  $\Gamma$ .

$\mathbf{g}^\Gamma$  internal configurational force at the interface  $\Gamma$

Here,  $\mathbf{g}^\Gamma$  is concentrated at the interface.  $\mathbf{g}^\Gamma$  is related to the rearrangement of material at the interface during its evolution. Similarly in the above context, we summarize the working performed by standard force and configurational force (due to movement of bulk and interface), and consider the change in material and spatial observers, then a series of important formulations are obtained as follows:

$$[\mathbf{S}]\mathbf{N} = \mathbf{0} \quad (7)$$

$$[\mathbf{C}]\mathbf{N} + \mathbf{g}^\Gamma = \mathbf{0} \quad (8)$$

with formulation (7) saying that crack faces are traction free, while formulation (8) saying that internal configurational force at interface is related to the Eshelby stress tensor at interface. Moreover, the local configurational force balance formulation similar to eq. (2) is obtained. In fact, stress is free at crack plane  $\Gamma_+$  or  $\Gamma_-$  and the free energy is not considered at crack plane. As  $\delta \rightarrow 0$ ,  $\Gamma_\delta(t)$  converges the crack tip, consequently,  $\mathbf{g}^{\Gamma_\delta(t)}$  implies it is a limit value of  $\mathbf{g}^\Gamma$  at crack tip. Additionally, the second law requires that the rate of change of free energy isn't more than the rate of working, hence it yields the internal dissipation inequality for the bulk and the interface in (9).

$$\mathbf{D} = \int_{\Omega} (\mathbf{S} \cdot \dot{\mathbf{F}} - \dot{\psi}) dA - \int_{\Gamma_\delta} \mathbf{g}^{\Gamma_\delta} V dl \geq 0 \quad (9)$$

with  $V$  interface growth velocity.

The right second item of eq. (9),  $-\mathbf{g}^{\Gamma_\delta} V$  is the energy dissipation by the interface per unit length. In fact, shrinking  $\mathbf{X}$  to the interface yields the local interfacial dissipation inequality (10).

$$-\mathbf{g}^{\Gamma_\delta} V \geq 0 \quad (10)$$

Eq. (9) states total dissipation of a cracked body is equal to bulk dissipation and crack dissipation due to crack growth with a velocity  $V$ . Eq. (10) explicitly states  $\mathbf{g}^{\Gamma_\delta}$  may be identified as the crack driving force because it is the force term conjugate to the crack growth velocity. Substituting (4) and (8) into (9) yields total dissipation including bulk and crack by (11).

$$\mathbf{D} = \int_{\Omega} (\mathbf{S} \cdot \dot{\mathbf{F}} - \dot{\psi}) dA + V \cdot \int_{\Gamma_\delta} (\psi \mathbf{I} - \mathbf{F}^T \mathbf{S}) \mathbf{N} dl \geq 0 \quad (11)$$

Now we consider the region between a circle close to the tip  $\Omega_\delta$  and another contour  $\Gamma_{far}$  that encloses the tip contour (Fig. 1): this region does not include the crack tip or the region inside  $\Gamma_\delta$ . We referred to this region by  $\Omega - \Omega_\delta$ . Clearly, only the configurational forces act on this region, hence the formulation (12) of configurational force balance is obtained by integrating eq. (2) on the region  $\Omega - \Omega_\delta$ .

$$\int_{\Omega_0 - \Omega_\delta} \mathbf{g} dA + \int_{\Gamma_{far}} (\psi \mathbf{I} - \mathbf{F}^T \mathbf{S}) \mathbf{N} dl - \int_{\Gamma_\delta} (\psi \mathbf{I} - \mathbf{F}^T \mathbf{S}) \mathbf{N} dl = 0 \quad (12)$$

This derivation of the balance of configurational forces and dissipation in bulk and crack plane is accomplished without using constitutive equations or a variational principle. The derivations are based on a mechanical version of the thermodynamical second law appropriate to control volumes whose boundaries migrate with time. This observation is fit for solving the plastic problem. In the following, we elucidate the application of configurational forces in homogeneous isotropic plastic materials.

## 2.2. Material description

A deformation of the reference configuration  $\Omega_0$  is a mapping of points  $\mathbf{X}$  in  $\Omega_0$  and time  $\mathbf{t}$  into points  $\mathbf{x}(\mathbf{X}, \mathbf{t})$  of space. It occupies in a current configuration  $\Omega_t$ . Conventionally, the total deformation is expressed via an intermediate configuration identified with the region  $\tilde{\Omega}$  by assuming that the elastic deformation follows plastic deformation. The multiplicative decomposition of deformation gradient is given by

$$\mathbf{F} = \mathbf{F}^e \mathbf{F}^p \quad (13)$$

For finite elastoplasticity, the plastic deformations are often assumed to be volume conserving, i.e.  $J^i = \det \mathbf{F}^p = 1$ . The deformation gradient  $\mathbf{F}$  is a gradient of a vector field. Its rate of time is given by

$$\dot{\mathbf{F}} = \dot{\mathbf{F}}^e \mathbf{F}^p + \mathbf{F}^e \dot{\mathbf{F}}^p \quad (14)$$

Now let's pay attention to the (Helmholtz) free energy potential  $\psi(\mathbf{F}^e, \alpha)$  for elastoplastic materials where  $\alpha$  is an internal variable introduced to account for isotropic hardening effects. Its rate of time is given by

$$\dot{\psi} = \frac{\partial \psi}{\partial \mathbf{F}^e} \dot{\mathbf{F}}^e + \frac{\partial \psi}{\partial \alpha} \dot{\alpha} \quad (15)$$

Using (11), (14) and (15), the dissipation in the bulk and crack plane reduces to

$$\mathbf{D} = \int_{\Omega} ((\mathbf{F}^e)^T \mathbf{S} \cdot \dot{\mathbf{F}}^p - \frac{\partial \psi}{\partial \alpha} \dot{\alpha}) dA + V \cdot \int_{\Gamma_{far}} [\psi \mathbf{I} - \mathbf{F}^T \mathbf{S}] \mathbf{N} dl \quad (16)$$

Next, according the relation of configurational body force, free energy potential and deformation gradient, we can calculate the configurational body force (5) as follows.

$$\mathbf{g} = (\mathbf{F}^e)^T \mathbf{S} \cdot \frac{\partial \mathbf{F}^p}{\partial \mathbf{X}} - \frac{\partial \psi}{\partial \alpha} \frac{\partial \alpha}{\partial \mathbf{X}} \quad (17)$$

After substituting (17) into (12) and transforming, it yields global configurational force balance formulation.

$$\int_{\Omega_0 - \Omega_\delta} ((\mathbf{F}^e)^T \mathbf{S} \cdot \frac{\partial \mathbf{F}^p}{\partial \mathbf{X}} - \frac{\partial \psi}{\partial \alpha} \frac{\partial \alpha}{\partial \mathbf{X}}) dA + \int_{\Gamma_{far}} (\psi \mathbf{I} - \mathbf{F}^T \mathbf{S}) \mathbf{N} dl = \int_{\Gamma_\delta} (\psi \mathbf{I} - \mathbf{F}^T \mathbf{S}) \mathbf{N} dl \quad (18)$$

Eq. (18) indicates when we consider a homogeneous elastic materials, free energy density is only related to elastic deformation gradient with  $\psi(\mathbf{F}^e)$  and  $\mathbf{F}^p = I$ , the configurational body force vanishes in (5) and results in the vanished 1st item of (18) too. This fact implies the path independence property of the J-integral. However, when we perform an analysis involving plastic deformation gradient and internal hardening phenomenon, the 1st item of (18) does not vanishes. This implies path independence property of the J-integral is not appropriate. For making designation easy, we call two curve integral of (19) effective J-integral defined at  $\Gamma_{far}$  and  $\Gamma_\delta$  in order to distinguish convectional J-integral and use the form given by

$$\int_{\Omega_0 - \Omega_\delta} ((\mathbf{F}^e)^T \mathbf{S} \cdot \frac{\partial \mathbf{F}^p}{\partial X} - \frac{\partial \psi}{\partial \alpha} \frac{\partial \alpha}{\partial X}) dA + J_{\Gamma_{far}}^{ef} = J_{\Gamma_\delta}^{ef} \quad (19)$$

### 2.3. Small strain plasticity

## 3. Numerical examples

The configurational force method is applied to evaluate crack driving force and dissipation for steady state crack growth in elastoplasticity materials. Crack growth is modeled using prefabricated crack method. We will examine the influence of crack length on the distribution of configurational force and plastic dissipation in quasi-static condition, meanwhile, effective J-integral and convectional J-integral are calculated at several different path surrounding crack tip.

### 3.1. The finite element geometry

The finite element (FE) model performed for the elastoplastic fracture problem is shown in Fig. 2. It is a C(T)-specimen with a prefabricated crack (thickness B=1000 mm, width W=50 mm, height H=120 mm, crack length a=10 mm, 15 mm, 20 mm, 25 mm, 30 mm, 35 mm and 40 mm). The material is an annealed mild steel with 16MnR. The material plastic deformation obeys Von-Mises yield principle and power law hardening constitute equation. The material mechanical parameters are Young's modulus E=210 GPa, Poisson's ratio  $\nu = 0.3$ , initial yield strength  $\sigma_y = 420MPa$ , average strain hardening coefficient n=0.2. The internal hardening variable  $\alpha$  is taken to be the equivalent plastic strain  $\bar{\epsilon}$ . The quasi-static displacement boundary is applied in the outer normal direction at the top and the bottom of the C(T)-specimen so that the specimen is in tension state. Hence Geometry model and loading boundary determine the problem is I mode fracture problem and plane strain condition is assumed. This problem is performed with ANSYS (Vers. 14) using a refined mesh near the crack tip and a coarse mesh near model boundary and standard four node element is adopted.

### 3.2. Numerical implementation

Solving the configurational force on FE mesh is an important step to evaluating the effective J-integral, dissipation in bulk and at crack and the distribution of configurational forces in the FE framework. According (17) key quantities that needs to be noticed specially is the deformation gradient of plastic strain components and equivalent plastic strain in nodal configurational force. As we know to differentiation procedure in numerical analysis method based on the FE mesh nodes, these quantities are computed only at the integration points in the standard displacement formulation of FE method. A simple method for obtaining the gradient involves first extrapolating the these quantities to the nodes. This step has been performed by ANSYS, next, what we need to do is just that calculating the gradient from the extrapolated nodal values by using standard FE interpolation method. Here, the modified central difference procedure is used as follows: given two vectors Y and X with  $Y = Y(X)$ , the derivative is found by averaging the slopes of two adjacent intervals. The formulation is referred to (20).

$$\frac{d}{dX} Y_{i+1} = \frac{\frac{Y_{i+2} - Y_{i+1}}{X_{i+2} - X_{i+1}} (X_{i+1} - X_i) - \frac{Y_{i+1} - Y_i}{X_{i+1} - X_i} (X_{i+2} - X_{i+1})}{X_{i+2} - X_i}, \quad i = 1, 2, \dots, n \quad (20)$$

with n designating total node number in FE mesh.

### 3.3. Results

The computations for the C(T)-specimen for deformation plasticity show that the configurational force vanishes in almost all regions of the body. Fig. 2 gives a contour of the configurational force x-component near the crack tip in a deformed body at a load line displacement  $D_{LL} = 0.5mm$ . Fig. 3 indicates the magnitude of the configurational force x-component in a deformed body. It implies that large value of configurational force x-component only lies near the crack tip. Fig. 4 presents the distribution of the configurational force vector near the crack tip as the same condition. It implies that configurational force is large directly at the crack tip node. Note that only the component of the configurational force in crack growth direction,  $\mathbf{f}_1 = \mathbf{f} \cdot \mathbf{e}$ , contributes to crack driving force. Fig. 5 indicates dissipation in bulk and crack plane decreases as crack growth, in contrast, effective J-integral as driving force increases by crack growth. When crack growth is of steady-state, both of them are the same values.

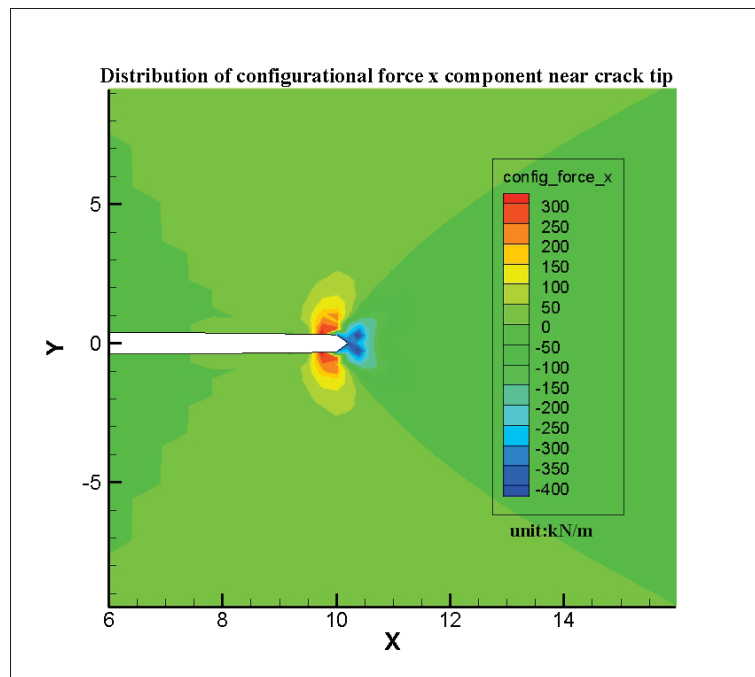


Figure 2: A contour of configurational force x-component in deformed body

## 4. Discussion and summary

A configurational force method is applied to evaluate crack driving force and dissipation for steady state crack growth in elastoplasticity materials. By using Helmholtz free energy characterized by internal variable and deformation gradient decomposition, nodal configurational forces and total dissipation in the body including crack tip due to the crack tip moving are derived based on Gurtin theories in finite strain setting. Specializations to isotropic hardening condition and homogeneous materials. It is shown that in steady-state growth case, distribution of nodal configurational forces is confined to local small area near crack plane. Furthermore, total dissipation in the body is related to nodal configurational forces. Theory and numerical simulations are applied to a steady state crack propagation in a C(T)-specimen. The variation of nodal configurational forces and total dissipation in the body in the process of crack growth are discussed.

## References

- Braun, M., 1997. Configurational forces induced by finite-element discretization. Proc. Estonian Acad. Sci. Phys. Math. 46 (1/2), 24-31.  
 Carka, D., Landis, C. M., 2011. On the path-dependence of the J-integral near a stationary crack in an elastic-plastic material. J. Appl. Mech. 78.

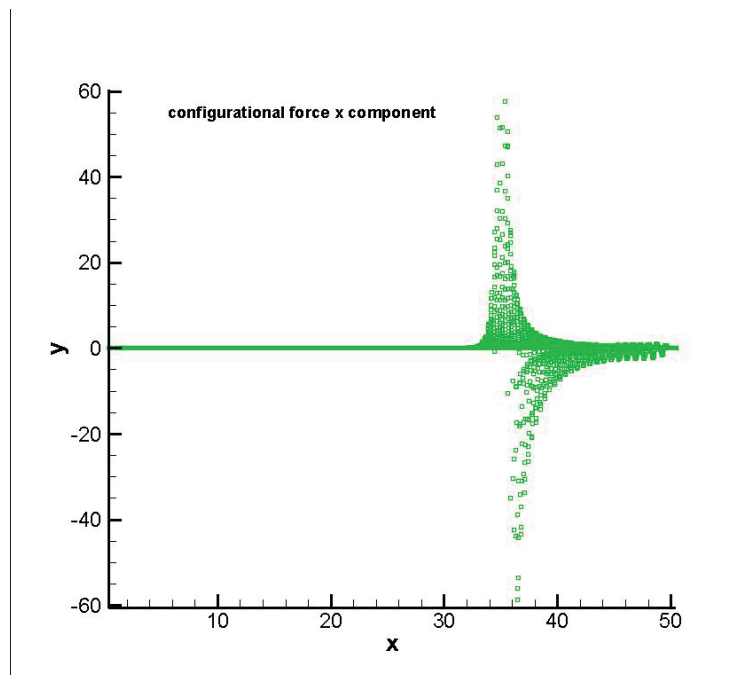


Figure 3: Magnitude of configurational force x-component in deformed body

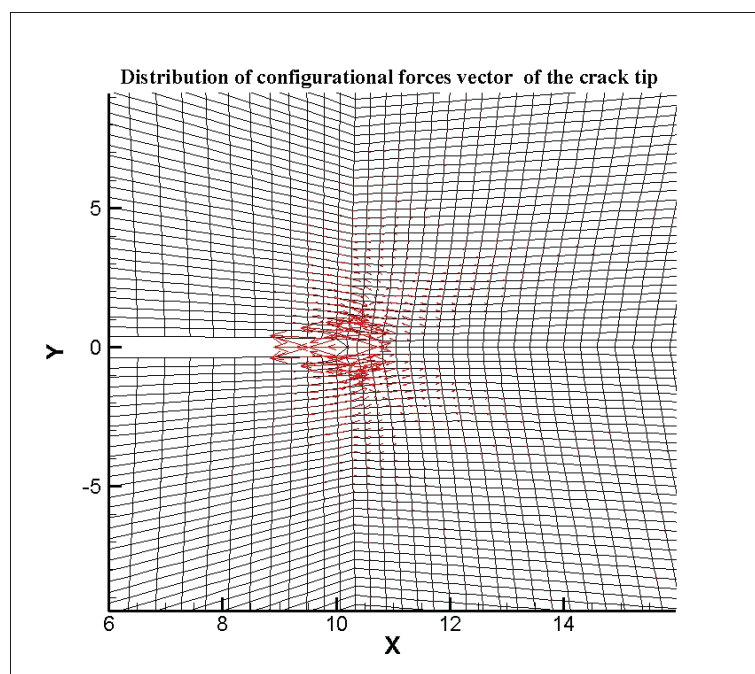


Figure 4: Distribution of configurational force vector in deformed body

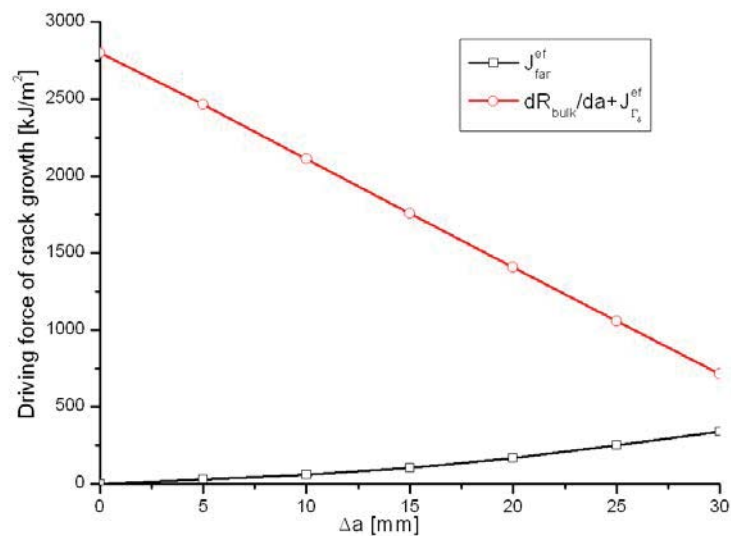


Figure 5: Distribution of configurational force vector in deformed body

- Cleja-Tigolu, S., Maugin, G.A., 2000. Eshelbys stress tensors in finite elastoplasticity. *Acta Mech.* 139, pp. 231-249.
- Eischen, J. W., Herrmann, G., 1987. Energy release rates and related balance laws in linear elastic defect mechanics. *ASME J. Appl. Mech.* 54, pp. 388-392.
- Epstein, M., Maugin, G.A., 1996. On the geometrical material structure of anelasticity. *Acta Mech.* 115, pp. 119-131.
- Epstein, M., 2002. The eshelby tensor and the theory of continuous distributions of inhomogeneities. *Mech. Res. Com.* 29, pp. 501C506.
- Eshelby, J., 1951. The force on an elastic singularity. *Philos. Trans. R. Soc. London A.* 244, 87-112.
- Eshelby, J., 1956. The continuum theory of lattice defects. In: Seitz, F., Turnbull, D. (Eds.), *Progress in Solid State Physics*, vol. 3. Academic Press, New York, pp. 79-114.
- Eshelby, J., 1970. Energy relations and the energy-momentum tensor in continuum mechanics. In: Kanninen, M.F., Adler, W.F., Rosenfield, A.R., Jaffe, R.I. (Eds.), *Inelastic Behavior of Solids*. McGraw-Hill, New York, p. 77-114.
- Eshelby, J. D., 1975. The elastic energy-momentum tensor. *J. Elast.* 5, 321-335.
- Fischer, F. D., Predan, J., Kolednik, O., Simha, N. K., 2007. Application of material forces to fracture of inhomogenous materials: illustrative examples. *Arch. Appl. Mech.* 77, pp. 95-112.
- Gross, D., Kolling, S., Mueller, R., Schmidt, I., 2003. Configurational forces and their application in solid mechanics. *Eur. J. Mech. A/solids.* 22, pp. 669-692.
- Gurtin, M.E., 1995. The nature of configurational forces. *Arch. Ration. Mech. Analysis* 131, 67-100.
- Gurtin, M.E., 2000. *Configurational forces as basic concepts of continuum physics*, Springer. Berlin.
- Kienzler, R., Herrmann, G., 1997. On the properties of the Eshelby tensor. *Acta Mech.* 125, pp. 73-91.
- Kienzler, R., Herrmann, G., 2000. *Mechanics of material space: with applications to defect and fracture mechanics*. Springer. Berlin.
- Kienzler, R., Herrmann, G., 2002. Fracture criteria based on local properties of the Eshelby tensor. *Mechanics Research Communications.* 29, pp. 521-527.
- Knowles, J.K., Sternberg, E., 1972. On a class of conservation laws in linearized and finite elastostatics. *Arch. Rational Mech. Anal.* pp. 187-211.
- Liebe, T., Denzer, R., Steinmann, P., 2003. Application of the material force method to isotropic continuum damage. *Comput. Mech.* 30, 171-184.
- Maugin, G. A., Trimarco, C., 1992. Pseudomomentum and material forces in nonlinear elasticity: variational formulations and application to brittle fracture. *Acta Mech.* 94, 1-28.
- Maugin, G. A., 1993. *Material inhomogeneities in elasticity*. London: Chapman Hall, 1993.
- Maugin, G. A., 1995. Material forces: concepts and applications. *Appl. Mech. Rev.* 48, pp. 213-245.
- Maugin, G. A., Trimarco, C., 1995. Dissipation of configurational forces in defective elastic solids. *Arch. Mech.* 47, pp. 81-99.
- Maugin, G. A., 2002. Remarks on the eshelbian thermomechanics of materials. *Mech. Res. Commun.* 29, 537-542.
- Mueller, R., Maugin, G., 2002. On material forces and finite element discretizations. *Comput. Mech.* 29(1), 52-60.
- Moran, B., Shih, C. F., 1987. Crack tip and associated domain integrals from momentum and energy balance. *Engineering Fracture Mechanics.* 27, pp. 615-542.
- Mueller, R., Kolling, S., Gross, D., 2002. On configurational forces in the context of the finite element method. *Int. J. Numer. Methods Engrg.* 53, 1557-1574.
- Naser, B., Kaliske, M., Muller, R., 2007. Material forces for inelastic models at large strains: application to fracture mechanics. *Comput. Mech.*

- 40, pp. 1005-1013.
- Nguyen, T.D., Govindjee, S., Klein, P.A., Gao, H., 2005. A material force method for inelastic fracture mechanics. *J. Mech. Phys. Solids* 53, 91-121.
- Rice, J. R., 1968. A path independent integral and approximate analysis of strain concentration by notches and cracks. *ASME J. Appl. Mech.* 35, 379-386.
- Rice, J. R., and Sorenson, E. P., 1978, Continuing crack-tip deformation and fracture for plane-strain crack growth in elastic-plastic solids. *J. Mech. Phys. Solids* 26, pp. 163-186.
- Simha, N.K., Fischer, F. D., Kolednik, O., Chen, C. R., 2003. Inhomogeneity effects on the crack driving force in elastic and elastic-plastic materials. *J. Mech. Phys. Solids*, 51, 209-240.
- Steinmann, P., 2000. Application of material forces to hyperelastic fracture mechanics. I. Continuum mechanical setting. *Int. J. Solids Structures* 37 (48-50), 7371-7391.
- Steinmann, P., Ackermann, D., Barth, F.J., 2001. Application of material forces to hyperelastic fracture mechanics. II. Computational setting. *Int. J. Solids Structures* 38 (32-33), 5509-5526.
- Steinmann, P., 2002. On spatial and material settings of hyperelastostatic crystal defects. *J. Mech. Phys. Solids* 50, 1743-1766.
- N. Y. Yu, Q. Li, Y. H. Chen., 2012. Experimental Evaluation of the M-integral in an Elastic-Plastic Material Containing Multiple. *J. Appl. Mech.* .

# Simulation of 2D Free-surface Potential Flows Using a Robust Local Polynomial Collocation Method

Nan-Jing Wu<sup>1</sup>, \*Ting-Kuei Tsay<sup>2</sup>, Yang-Yih Chen<sup>1,3</sup>, and I-Chen Tsu<sup>2</sup>

<sup>1</sup> Tainan Hydraulics Laboratory, National Cheng Kung University, Tainan City 70955, Taiwan.

<sup>2</sup> Department of Civil Engineering, National Taiwan University, Taipei City 10617, Taiwan.

<sup>3</sup> Department of Marine Environment and Engineering, National Sun Yat-sen University, Kaohsiung City 80424, Taiwan.

\*Corresponding author: tktsay@ntu.edu.tw

## Abstract

In this paper a mesh-free numerical model for simulating 2D free-surface potential flows is established. A Lagrangian time-marching scheme is chosen for the boundary conditions of the moving and deforming free surface while a local polynomial collocation method is applied for solving the Laplace equation at each time step. The collocation method is developed in a way that the governing equation is satisfied on boundaries as well as boundary conditions. At any free surface node, this gives accurate estimation of the derivatives of velocity potential, which represent components of the velocity vector at that specific node. Therefore, trajectories of the free surface nodes can be predicted precisely. The numerical model is applied to the simulation of free surface waves in the liquid sloshing of a swaying tank. Present model is verified by comparing the numerical results with experimental data. Fairly good agreements are observed.

**Keywords:** mesh-free, collocation, sloshing, free surface waves

## Introduction

For several decades, water wave problems are treated as potential flow problems governed by the Laplace equation subjected to two nonlinear free surface boundary conditions. Due to the deformation of the free surface, mesh re-generation is needed if one uses a grid-based method to solve this kind of problems. Mesh generation, which means construction of the connectivity among the nodes, is a tedious task. Because the governing equation is the Laplace equation, the Boundary Element Method (BEM, also denominated as Boundary Integral Equation Method, BIEM) is mostly employed to this kind of problems. (Longuet-Higgins and Cokelet, 1976; Grilli et al., 1989; Ohyama and Nadaoka, 1991; Grilli and Watts, 1999; Grilli et al., 2001, 2002)

A mesh-free method, which is named as Method of Fundamental Solutions (MFS), was applied to solve the Laplace equation in the fully nonlinear water wave problems. (Wu et al., 2006, 2008; Wu and Tsay, 2009) When using MFS, one has to place source points outside the domain. Because the values of the fundamental solutions are just related to the distances from the source points, fundamental solutions could be regarded as a Radial Basis Functions (RBF). Collocation is only needed on the boundaries, so MFS is a boundary type RBF collocation method. Though MFS could be employed to fully nonlinear water wave problems, its applicability is still limited because numerical blow up might occur when the free surface approaches too close to the source points.

Wu and Chang (2011) proposed a modified RBF Collocation Method that guarantees the accurate estimation of partial derivatives of the velocity potential on the free surface. By integrating with a Lagrangian time-marching scheme, the trajectories of the free surface nodes can be precisely predicted. However, the full matrix formed in that method limits its applicability to large-scale problems.

Besides treating water wave flows as potential flows, one could also choose Navier-Stokes equation or Reynolds Averaged Navier-Stokes equation models, such as models using Arbitrary Lagrangian-



Eulerian method (ALE) (Lo and Young, 2004), Volume of Fluid method (VOF) (Lin and Liu, 2008), Smoothed Particle Hydrodynamics (SPH) (Li and Liu, 2002), and Moving Particle Semi-implicit method (MPS) (Hori et al., 2011). Models using ALE or VOF are grid-based while models using SPH or MPS are meshless ones. Results of these models are more close to the real flow. However, these models are more time consuming and computer memory storage consuming.

Wu and Tsay (2013) proposed a local polynomial collocation method for the purpose of solving general partial differential equations. This method originates from the Finite Point Method (FPM) of Oñate et al. (1996a, b). It is a localized meshless method thus matrix formed in the collocation process is very sparse. The collocation method was developed in a way that the governing equation as well as boundary conditions is satisfied on boundaries. This method is more robust than conventional collocation methods.

Adopting the time-marching scheme for the free surface proposed by Wu and Chang (2011), and the local polynomial collocation method proposed by Wu and Tsay (2013), a numerical model for the fully nonlinear free surface potential flow is developed. In this paper, it is employed to simulate motions of liquid sloshing in a swaying tank.

### Mathematical description for free-surface potential flow

For inviscid, incompressible fluids, the governing equation of free-surface potential flow is the Laplace equation.

$$\nabla^2 \phi = 0 \quad (1)$$

where  $\phi$  is the velocity potential and the relation between velocity and velocity potential is  $\bar{v} = \nabla \phi$ . On the free surface, kinematic and dynamic boundary conditions are to be satisfied.

$$\nabla \phi = \frac{d\bar{x}}{dt} \quad (2)$$

$$\left. \frac{d\phi}{dt} \right|_{z=\eta} = -gz + \frac{1}{2} \nabla \phi \cdot \nabla \phi \quad (3)$$

where  $\eta$  is the free surface displacement,  $g$  is the gravitational acceleration. Both of them have been transformed onto the Lagrangian aspect. The boundary condition at the water-structure interface is the no-flux boundary condition, which can be expressed as

$$\bar{n} \cdot \nabla \phi = \bar{n} \cdot \bar{v}_b \quad (4)$$

where  $\bar{n}$  is the unit normal vector outward from the domain, and  $\bar{v}_b$  is the velocity of the moving solid boundary.

### Time marching scheme in the numerical model

For solving this kind of time-dependent problems, the time domain firstly has to be discretized. At each time step, the Laplace equation needs to be solved once to obtain the velocity potential for the entire domain thus to further determine the velocity. Boundary positions are updated by the given motion of the solid boundaries and the prediction from the time marching process of the free-surface boundary. Wu and Chang (2011) employed the second order central difference to Eq. 3.

$$(\phi|_{\bar{x}=\bar{x}_j})^{(n)} = (\phi|_{\bar{x}=\bar{x}_j})^{(n-2)} + 2\Delta t \left[ \left( -gz + \frac{1}{2} \nabla \phi \cdot \nabla \phi \right)_{\bar{x}=\bar{x}_j} \right]^{(n-1)} \quad (5)$$

where  $\bar{x}_j$  denotes the position of the  $j^{\text{th}}$  node and this equation is only valid in case the node is on the free surface. In this formulation, the required data on the right-hand side for seeking the velocity potential in the entire domain at the  $n^{\text{th}}$  time step, including the nonlinear terms, are already known. What one needs to do first is just to determine the position of each traced ‘particle’,  $\bar{x}_j^{(n)}$ . It was proposed to use the second-order finite difference scheme in the time domain.

$$\bar{x}_j^{(n)} = \bar{x}_j^{(n-2)} + 2\Delta t (\nabla \phi|_{\bar{x}=\bar{x}_j})^{(n-1)} \quad (6)$$

Here it should be noted that this equation is valid for all the nodes. When the velocity potential for the entire domain is obtained, the velocity at each of the nodes can be estimated accurately. The Crank-Nicolson formula is then applied for better numerical stability.

$$\bar{x}_j^{(n)} = \bar{x}_j^{(n-1)} + \frac{\Delta t}{2} \left[ (\nabla \phi|_{\bar{x}=\bar{x}_j})^{(n)} + (\nabla \phi|_{\bar{x}=\bar{x}_j})^{(n-1)} \right] \quad (7)$$

Note that there is no need to solve the Laplace equation again because there is barely difference between the free-surface velocity potential at  $\bar{x}_j^{(n)}$  predicted by using Eq. 6 and that predicted by using Eq. 7.

### Method for solving the Laplace equation

At each time step, the Laplace equation needs to be solved once. There are many methods for solving the Laplace equation numerically, either grid-based or mesh-free. In this study the local polynomial collocation method proposed by Wu and Tsay (2013) is chosen. It is a mesh-free method for solving general partial differential equations. It is so chosen to accommodate efficiently the deformation of the free surface boundary. Following gives a brief description of this meshless numerical method.

When solving a general 2-D linear second order PDE as

$$\mathcal{L}\{\phi\} = c_1 \phi + c_2 \frac{\partial \phi}{\partial x} + c_3 \frac{\partial \phi}{\partial y} + c_4 \frac{\partial^2 \phi}{\partial x^2} + c_5 \frac{\partial^2 \phi}{\partial y^2} + c_6 \frac{\partial^2 \phi}{\partial x \partial y} = s \quad (8)$$

subjected to the boundary conditions

$$\mathcal{B}\{\phi\} = q_1 \phi + q_2 \frac{\partial \phi}{\partial x} + q_3 \frac{\partial \phi}{\partial y} = f, \quad \bar{x} \in \Gamma_1 \quad (9)$$

$$\phi = \phi_b, \quad \bar{x} \in \Gamma_2 \quad (10)$$

where  $c_1, c_2, \dots, c_6, q_1, q_2, q_3, f$  and  $s$  are all functions of  $x$  and  $y$ . The boundary  $\Gamma_1$  could be non-smooth and then at a corner there could be more than one Robin condition. Therefore,  $q_1, q_2, q_3$ , and  $f$  could be multi-valued. Boundary condition can be expressed just as Eq. 9 for conciseness. It will be explained later on how boundary conditions will be treated at a point where more than one boundary condition exists. In seeking the numerical solutions, the entire domain is distributed with  $N$  nodes as needed. At each node,  $\phi$  is approximated as

$$\phi(\bar{x})|_{\bar{x} \approx \bar{x}_j} \approx \hat{\phi}_j(\bar{x}) = \sum_{i=1}^m \alpha_{ji} p_i(\bar{X}) \quad (11)$$

in which  $\bar{X} = \bar{x} - \bar{x}_j$  is the relative position vector,  $p_i(\bar{X})$  is the  $i^{\text{th}}$  monomial of the polynomial, and  $\alpha_{ji}$  are coefficients to be determined. The subscript  $j$  indicates that this approximation is valid only in the vicinity of  $\bar{x}_j$ . Once a new  $\bar{x}_j$  is chosen, there will be a new set of  $\alpha_{ji}$ . For a 2-D problem, the monomials are

$$\{p_i(\bar{X}), i=1 \sim m\} = \{1 \quad X \quad Y \quad X^2 \quad Y^2 \quad XY \quad \dots\} \quad (12)$$

in which  $\bar{X} = X \bar{i} + Y \bar{j}$ . The value of  $m$  is related to the chosen degree of the polynomial. Here the error residual of the local approximation around  $\bar{x} = \bar{x}_j$  is defined as

$$E_j = \sum_{l=1}^N \left( W_{jl} \left( \phi(\bar{x}_l) - \hat{\phi}_j(\bar{x}_l) \right)^2 \right) \quad (13)$$

where  $W_{jl}$  is a weighting factor determined by the distance between  $\bar{x}_j$  and  $\bar{x}_l$ . Usually, the normalized Gaussian function is selected for determining the weighting factor

$$W_{jl} = \begin{cases} \frac{\exp(-\varepsilon(r_{jl} / \rho_j)^2) - \exp(-\varepsilon)}{1 - \exp(-\varepsilon)} & , r_{jl} < \rho_j \\ 0 & , r_{jl} \geq \rho_j \end{cases} \quad (14)$$

where  $r_{jl}$  is the distance between  $\bar{x}_j$  and  $\bar{x}_l$  (i.e.  $r_{jl} = |\bar{x}_l - \bar{x}_j|$ ),  $\varepsilon$  is the shape parameter, and  $\rho_j$  is the supporting range measured from the point of  $\bar{x}_j$ . Considering only the non-zero terms, Eq. 13 can be rewritten as

$$E_j = \sum_{k=1}^n \left( W_{jk} \left( \phi(\bar{x}_k) - \hat{\phi}_j(\bar{x}_k) \right)^2 \right) \quad (15)$$

where  $k$  is the local index of  $\bar{x}_l$  in the  $j^{\text{th}}$  sub-domain and  $n$  is number of nodes inside the sub-domain. The coefficients of the local polynomial corresponding to the minimal error residual at the node  $\bar{x}_j$  under the condition that

$$\left( \mathcal{L}\{\phi\} - s \right)^2 + \left( \mathcal{B}_1\{\phi\} - f_1 \right)^2 + \dots + \left( \mathcal{B}_{n_{nd}}\{\phi\} - f_{n_{nd}} \right)^2 \rightarrow 0 \quad (16)$$

where  $n_{nd}$  is the number of non-Dirichlet boundary conditions at the node  $\bar{x} = \bar{x}_j$ , can be expresses as

$$[\alpha_j] = [\Lambda] \begin{bmatrix} \beta \\ \beta' \end{bmatrix} \quad (17)$$

in which

$$[\Lambda]_{m \times (n+n_{nd}+1)} = \left( \begin{bmatrix} [A]^T & [A] \\ [A'] & [A'] \end{bmatrix} \right)^{-1} \begin{bmatrix} [A]^T \\ [A'] \end{bmatrix} \quad (18)$$

$$[A]_{n \times m} = \begin{bmatrix} a_{11} & a_{12} & \cdots & \cdots & a_{1m} \\ a_{21} & \ddots & & & a_{2m} \\ \vdots & & a_{ki} & & \vdots \\ \vdots & & & \ddots & \vdots \\ a_{n1} & a_{n2} & \cdots & \cdots & a_{nm} \end{bmatrix} \quad (19)$$

$$[A']_{(n_{nd}+1) \times m} = \begin{bmatrix} w'c_1 & \cdots & \cdots & \cdots & w'c_p & 0 & \cdots & 0 \\ w'q_{1,1} & \cdots & w'q_{1,3} & 0 & \cdots & \cdots & \cdots & 0 \\ \vdots & & \vdots & \vdots & & & & \vdots \\ w'q_{n_{nd},1} & \cdots & w'q_{n_{nd},3} & 0 & \cdots & \cdots & \cdots & 0 \end{bmatrix} \quad (20)$$

$$[\beta]_{n \times 1} = [w_1\phi_1 \quad \cdots \quad w_k\phi_k \quad \cdots \quad w_n\phi_n]^T \quad (21)$$

$$[\beta']_{(n_{nd}+1) \times 1} = [w's \quad w'f_1 \quad \cdots \quad w'f_{n_{nd}}]^T \quad (22)$$

where  $w_k = \sqrt{W_{jk}}$ ,  $\phi_k = \phi(\bar{x}_k)$ ,  $a_{ki} = w_k p_i(\bar{x}_k - \bar{x}_j)$ , and  $w' = \sqrt{W'}$ . In case of  $n_{nd}$  in Eq. 16 is greater than 1, it obviously indicates that the collocation point rests on an edge or at a corner. At an internal node, there is only one term in Eq. 16 (i.e.  $n_{nd} = 0$ ). The symbol  $W'$  represents a penalty weighting factor whose value is much greater than 1. Assembling the local approximations into a global matrix system, one gets

$$[K]_{N \times N} [\phi]_{N \times 1} = [b]_{N \times 1} \quad (23)$$

In case that the value of  $\phi$  is known at  $\bar{x}_j$ , the entities in Eq. 23 are

$$\kappa_{jl} = \begin{cases} 1, & \text{if } j=l \\ 0, & \text{otherwise} \end{cases} \quad (24)$$

$$b_j = \phi_j \quad (25)$$

Otherwise,

$$\kappa_{jl} = \begin{cases} w_k \lambda'_{1k} - \delta_j(l), & \text{if } |\bar{x}_j - \bar{x}_l| < \rho_j \\ 0, & \text{otherwise} \end{cases} \quad (26)$$

$$\delta_j(l) = \begin{cases} 1, & \text{if } j=l \\ 0, & \text{otherwise} \end{cases} \quad (27)$$

$$b_j = - \sum_{k=1}^{n_{nd}+1} \lambda'_{1,(n+k)} \beta'_k \quad (28)$$

It should be noted that the symbol  $k$  in Eqs. 19, 21, 26 and 28 is the local index of  $\bar{x}_i$  in the  $j^{\text{th}}$  sub-domain. The approximated partial derivatives of the solution, which are related to the coefficients of the local polynomial approximation, can then be determined by

$$\begin{aligned} \phi|_{\bar{x}=\bar{x}_j} &\approx \hat{\phi}|_{\bar{x}=\bar{x}_j} = \alpha_{j1}, & \frac{\partial \phi}{\partial x}|_{\bar{x}=\bar{x}_j} &\approx \frac{\partial \hat{\phi}}{\partial x}|_{\bar{x}=\bar{x}_j} = \alpha_{j2}, & \frac{\partial \phi}{\partial y}|_{\bar{x}=\bar{x}_j} &\approx \frac{\partial \hat{\phi}}{\partial y}|_{\bar{x}=\bar{x}_j} = \alpha_{j3}, & \frac{\partial^2 \phi}{\partial x^2}|_{\bar{x}=\bar{x}_j} &\approx \frac{\partial^2 \hat{\phi}}{\partial x^2}|_{\bar{x}=\bar{x}_j} = 2\alpha_{j4}, \\ \frac{\partial^2 \phi}{\partial y^2}|_{\bar{x}=\bar{x}_j} &\approx \frac{\partial^2 \hat{\phi}}{\partial y^2}|_{\bar{x}=\bar{x}_j} = 2\alpha_{j5}, & \frac{\partial^2 \phi}{\partial x \partial y}|_{\bar{x}=\bar{x}_j} &\approx \frac{\partial^2 \hat{\phi}}{\partial x \partial y}|_{\bar{x}=\bar{x}_j} = \alpha_{j6}, & \dots \end{aligned} \quad (29)$$

The shape parameter  $\varepsilon$  in the normalized Gaussian function has been shown to be insensitive by Wu and Tsay (2013). Analyses of the convergence rate of nodal resolution were also carried out by Wu and Tsay (2013) while related analysis of nodal arrangement has been done by Wu et al (2013). The suggestions of Wu and Tsay (2013) for choosing the values of the shape parameter  $\varepsilon$ , the sub-domain size  $\rho_j$ , the penalty weighting factor  $W'$  are followed. Therefore, in this study,  $\varepsilon = 22$ ,  $\rho_j$  equal to 1.05 times of the distance from  $\bar{x}_j$  to its 25<sup>th</sup> nearest neighboring node, and  $W' = 10^4$  are used in all numerical computations.

## Applications and Verifications

### Description of the test problem

For testing their numerical model, Liu and Lin (2008) carried out a sloshing experiment. The layout of the experiment is shown in Figure 1. The non-breaking case with the strongest nonlinear effect in the experiment is chosen as the verification of present model. The period of the oscillation is 1.0372 sec. The amplitude of the oscillation is 0.5 cm.

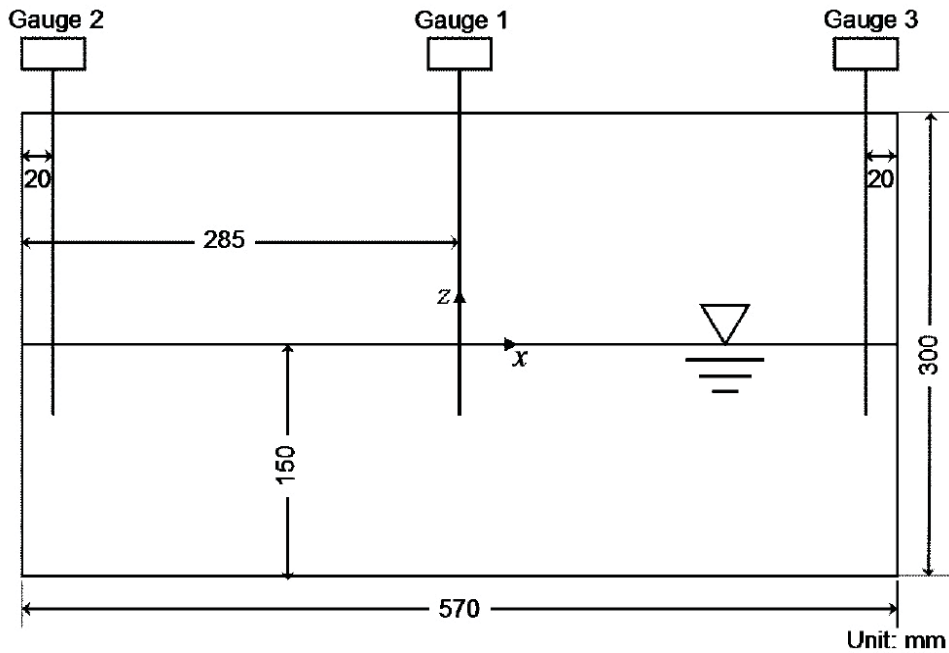
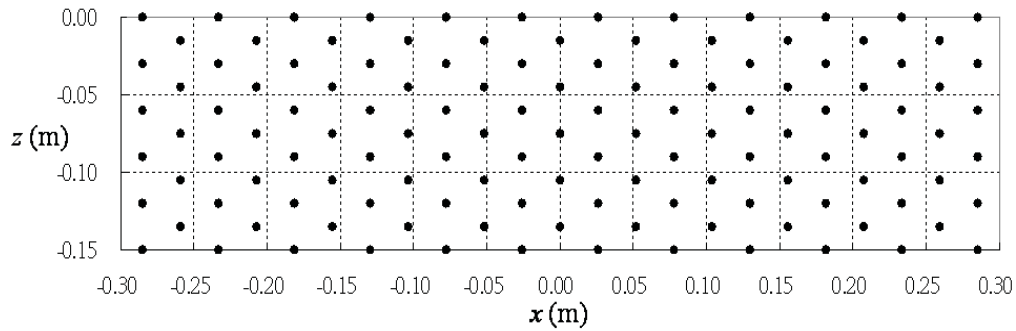


Figure 1. Layout of the sloshing experiment of Liu and Lin (2008)

### Model setup

Discretizing a wave length with at least 20 segments, the initial nodal spacing on the free surface is chose as 5.18 cm. The collocation points are initially distributed as a hexagonal close packing array so that the most compact nodal arrangement can be achieved. Therefore, the vertical nodal spacing on the side walls is 3 cm. Totally, there are 127 collocation points. The time step chosen in the simulation is 1/80 of the swaying period. The initial nodal distribution is shown in Figure 2.

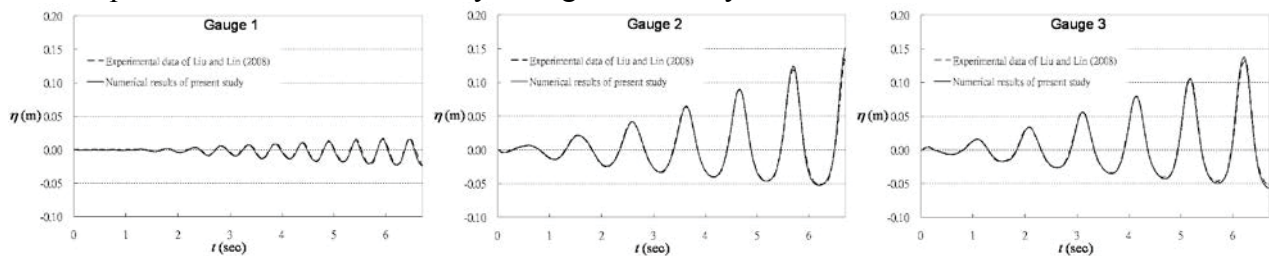


**Figure 2. Initial nodal distribution of the numerical model**

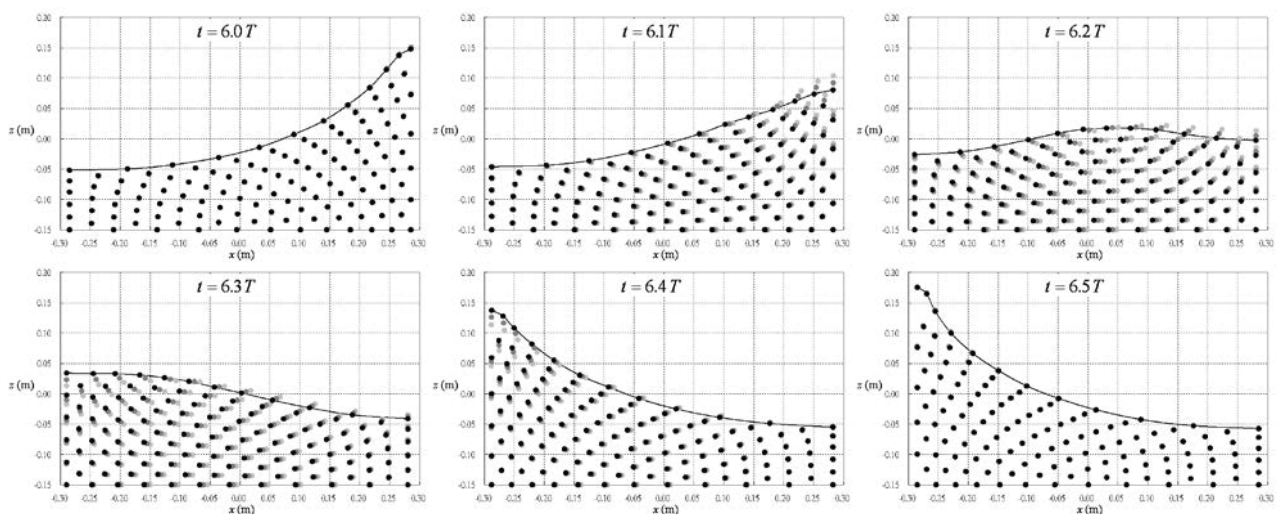
### Numerical results

Figure 3 shows the comparison of the numerical results with the experimental data. Very good agreement is found. It is also found that the higher the peak grows, the flatter the trough becomes. This indicates an increase of nonlinear effect as the tank oscillation continues. In the simulation the side walls are set to be infinitely high but in the experiment the tops of the two side walls are just 15 cm high from the still water level. It had not been mentioned in the paper of Liu and Lin (2008) what happened when the free surface elevation goes higher than the height of side walls. In present simulation, free surface elevation goes over the top of the right side wall at  $t = 6.184$  sec. This might be the reason why the simulated  $\eta$  in the last wave period are slightly higher than observed.

Figure 4 shows the positions of the traced fluid particles in the time interval of  $t = 6.0T \sim 6.5T$ . This figure shows that at the end of simulation, the run-up becomes much higher than the initial water depth. It is an indication of very strong nonlinearity on the free surface.



**Figure 3. Comparison of the numerical results with the experimental data**



**Figure 4. Snapshots of traced fluid particles in the time interval of  $t = 6.0T \sim 6.5T$**

Only 9 seconds is needed to simulate this case by using just one processing unit of Intel(R) Core™ i7-3370 CPU. The nodal spacing of present model is an order larger than the grid size in the model of Liu and Lin (2008). Present model is much more efficient in this case.

## Conclusions

A numerical model is presented in this paper by treating water wave phenomenon as potential flow of fluid motion with a free surface. The problem is governed by the Laplace equation and subjected to nonlinear free surface boundary conditions. The free surface boundary conditions are discretized by using the Lagrangian time-marching scheme of Wu and Chang (2011) so that Laplace equation is only required to be solved numerically once at each time step. The method chosen for solving the Laplace equation is the local polynomial collocation method proposed by Wu and Tsay (2013). Present model is applied to the simulations of liquid sloshing in a swaying tank. It is much more efficient in a testing problem because CPU time of the simulation takes only seconds. Fairly good agreement is found in the comparison with experimental data.

## Acknowledgement

The authors acknowledge the National Science Council of Taiwan for financial support (grant numbers: NSC 102-2911-I-006-302 and NSC 102-2221-E-002-155).

## References

- Grilli S.T., Skourup J., and Svendsen I.A. (1989), An efficient boundary element method for nonlinear water waves. *Engineering Analysis with Boundary Elements* 6, pp. 97–107.
- Grilli S.T. and Watts P. (1999), Modeling of waves generated by a moving submerged body. Applications to underwater landslides. *Engineering Analysis with Boundary Elements*, 23, pp. 645–656.
- Grilli S.T., Guyenne P., and Dias F. (2001), A fully nonlinear model for three-dimensional overturning waves over an arbitrary bottom. *International Journal for Numerical Methods in Fluids* 35, pp. 829 – 867.
- Grilli S.T., Vogelmann S., and Watts, P. (2002), Development of a 3d numerical wave tank for modeling tsunami generation by underwater landslides. *Engineering Analysis with Boundary Elements* 26, pp. 301–313.
- Hori C., Gotoh H., Ikari H., and Khayyer A. (2011), GPU-acceleration for Moving Particle Semi-Implicit Method. *Computers and Fluids* 51, pp. 174–183.
- Li S.F. and Liu W.K. (2002), Meshfree and particle methods and their applications. *Appl Mech Rev* 55, pp. 1–34.
- Liu D. and Lin P. (2008), A numerical study of three-dimensional liquid sloshing in tanks. *Journal of Computational Physics* 227, pp. 3921–3939.
- Lo D.C. and Young, D.L. (2004), Arbitrary Lagrangian–Eulerian finite element analysis of free surface flow using a velocity–vorticity formulation. *Journal of Computational Physics* 195, pp. 175 –201.
- Longuet-Higgins H.S. and Cokelet E.D. (1976), The deformation of steep waves on water, I, a numerical method of computation. *Proc R Soc Lond A* 350, pp. 1–26.
- Ohyama T. and Nadaoka K. (1991), Development of a numerical wave tank for analysis of nonlinear and irregular wave field. *Fluid Dynamic Research* 8, pp. 231–251.
- Oñate E., Idelsohn S., Zienkiewicz O.C., and Taylor R.L. (1996), A finite point method in computational mechanics. Applications to convective transport and fluid flow. *International Journal for Numerical Methods in Engineering* 39, pp. 3839–3866.
- Oñate E., Idelsohn S., Zienkiewicz O.C., Taylor R.L., and Sacco C. (1996), A stabilized finite point method for analysis of fluid mechanics problems. *Computer Methods in Applied Mechanics and Engineering* 139, pp. 315–346.
- Wu N.J., Tsay T.K., and Young D.L. (2006), Meshless simulation for fully nonlinear water waves. *International Journal for Numerical Methods in Fluids* 50, pp. 219–234.
- Wu N.J., Tsay T.K., and Young, D.L. (2008), Computation of nonlinear free-surface flows by a meshless numerical method. *Journal of Waterway, Port, Coastal and Ocean Engineering* 134, pp. 97–103.
- Wu N.J. and Tsay T.K. (2009), Applicability of the method of fundamental solutions to 3-D wave–body interaction with fully nonlinear free surface. *Journal of Engineering Mathematics* 63, pp. 61–78.
- Wu N.J. and Chang, K.A. (2011), Simulation of free-surface waves in liquid sloshing using a domain-type meshless method. *International Journal for Numerical Methods in Fluids* 67, pp. 269–288.
- Wu N.J. and Tsay T.K. (2013), A robust local polynomial collocation method. *International Journal for Numerical Methods in Engineering* 93, pp. 355–375.
- Wu N.J., Tsay T.K., Yang T.C., and Chang H.Y. (2013), Orthogonal grid generation of an irregular region using a local polynomial collocation method, *Journal of Computational Physics* 243, pp. 58–73.

## Multi-physics CFD simulation of three-phase flow with MPS method

**\*Ryouhei Takahashi<sup>1</sup>, Makoto Yamamoto<sup>2</sup> and Hiroshi Kitada<sup>1</sup>**

<sup>1</sup>CMS Corporation, Kasukabe, Saitama, Japan

<sup>2</sup>Department of Mechanical Engineering, Tokyo University of Science, Katsushika-ku, Tokyo, Japan

\*Corresponding author: yamamoto@rs.kagu.tus.ac.jp

### Abstract

Recently, the equipments to separate and classify nano-size particles are required in various areas. The target of the present study is a new solid-liquid separator, which enables us to separate and classify nano-size particles, to cut down the water content ratio of disposed particles and to accomplish extremely high collection efficiency. In the present investigation, we develop a numerical method to simulate a gas-liquid-solid three-phase flow, based of the MPS approach to clarify the flow field inside the separator and mechanism of particle separation. With using our method, some interactions of three phases, which are difficult to be simulated with the conventional grid methods, are successfully reproduced.

**Keywords:** Three-phase flow, Particle method, Particle separator, Nano-scale particle.

### Introduction

Nano-particle is expected to be very useful and promising as an advanced material in a great number of industries such as automobile, aeronautics, chemistry, pharmacy, food, military and so on. However, the production and collection of nano-particles are very difficult and cost consuming with current technologies. For example, the conventional particle separator, which is a so-called cyclone, can separate only few-micron-size particles from liquid (Stairmand(1985), Krishna et al. (2010)), and thus it cannot be applied to nano-particles separation. Therefore, we have to develop an innovative particle separator, and especially we need a specially-designed nano-particle separator. Conventionally, high performance separators adopt centrifugal force generated from a highly swirling flow or a rotating chamber, to separate particles from liquid. The flow is essentially of liquid-particle two-phase, highly swirling and turbulent. Moreover, the flow often has a liquid free surface in the core and air bubbles which are generated during the separation process. Since these complex flow natures prevent us from measuring and observing the flow and particle behaviours, the separation phenomena of particles from liquid have not been clarified yet. Hence, a numerical simulation is expected to be a useful analytical tool. However, the numerical procedure itself has not been established due to the difficulties in modelling and computing the multi-phase and multi-physics flow characteristics. Therefore, we need urgently and strongly to focus on the development of a new simulation technique that can sufficiently predict the complicated physics in a nano-particle separation process.

In the present study, taking into account the above backgrounds, we try to construct a new numerical modelling to reproduce the three-phase (i.e. liquid-particle-bubble) flow in a nano-particle separator. A specially-designed rotating-type particle separator is adopted as our computational target. It consists of coaxial rotating circular pipes. Particle-laden liquid is ingested from the top of the inner pipe. Since centrifugal force acting on particles in the liquid pushes the particles radially outward, the particles accumulate on the outer pipe surface, and the liquid forms a thick rotating film. It is noted that the centrifugal force can be about 3,000 times of the gravitational force (i.e. 3,000G). In this separation process, air bubbles are often generated in the liquid film on the outer pipe surface. The mechanism of the bubble generation has not been clarified. It is known



that the bubble formation degrades the separation performance. Finally, the accumulated particles are exhausted from the bottom of the outer pipe by the screw propeller mounted on the inner pipe. Figure 1 shows the schematic view of this separator. For this three-phase flow, a particle method is employed to model the motions of liquid, particle and air bubble by those of virtual particles. We use a MPS method as the base numerical procedure because of the simplicity and the relatively good predictability for liquid flow and free surface. In our modelling, different particles with different densities are assigned to particles representing liquid, particle and bubble. In the present study, as the first step of this research, we focus on the bubble formation region. Investigating the numerical results, it is confirmed that the bubble generation process is naturally and satisfactorily reproduced by the particle method proposed in the present study.

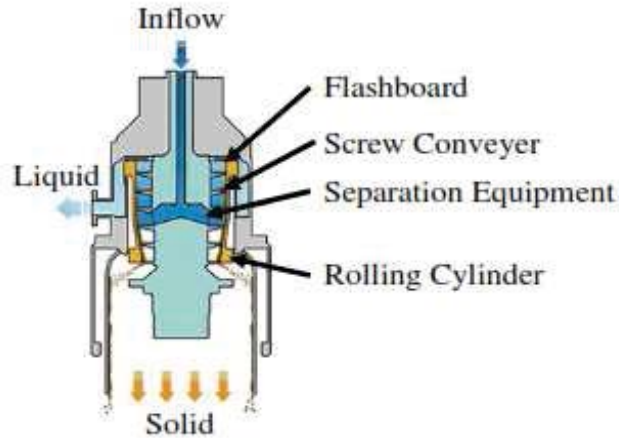


Figure1 Schematic view of nano-particle separator

### Numerical Procedures

The MPS method proposed by Koshizuka et al. (1995) is adopted as the basic method of our computation because of the simplicity and the feasibility for liquid flow and free surface. The governing equations are incompressible Navier-Stokes equations. They can be expressed as

$$\nabla \cdot \mathbf{u} = 0 \quad (1)$$

$$\frac{D\mathbf{u}}{Dt} = -\frac{1}{\rho} \nabla P + \nu \nabla^2 \mathbf{u} + \mathbf{F} . \quad (2)$$

In the MPS method, Navier-Stokes equation is divided into pressure part and other part as follows.

$$\left( \frac{D\mathbf{u}}{Dt} \right)^{\text{press}} = -\frac{1}{\rho} \nabla P \quad (3)$$

$$\left( \frac{D\mathbf{u}}{Dt} \right)^{\text{other}} = \nu \nabla^2 \mathbf{u} + \mathbf{F} \quad (4)$$

Time derivation of Equation(1) can be expressed by

$$\nabla \cdot \left( \frac{D\mathbf{u}}{Dt} \right)^{\text{press}} + \nabla \cdot \left( \frac{D\mathbf{u}}{Dt} \right)^{\text{other}} = 0. \quad (5)$$

Then the continuity equation is given by

$$\frac{D\rho}{Dt} + \rho \nabla \cdot \mathbf{u} = 0. \quad (6)$$

From Equations (3) to (6), the following equation

$$-\nabla \cdot \frac{1}{\rho} \nabla P = \frac{1}{\rho^0} \left( \frac{D^2 \rho}{Dt^2} \right) \quad (7)$$

can be obtained. In this equation, the relation that density  $\rho$  is equal to constant density  $\rho^0$  with incompressible fluid is taken into account.

These governing equations of Navier-Stokes and continuity equations involve gradient and Laplacian operators. In the MPS method, gradient and Laplacian models are prepared to solve the governing equations. The models can be given as follows

$$\nabla \phi = \frac{d}{n^0} \sum_j \frac{\phi_j - \phi_i}{|\mathbf{r}_{ij}|^2} \mathbf{r}_{ij} w_{ij} \quad (8)$$

$$\nabla^2 \phi = \frac{2d}{\lambda n^0} \sum_j (\phi_j - \phi_i) w_{ij} \quad (9)$$

where  $\phi$  is physical quantity,  $d$  is number of dimension,  $r_{ij}$  is interparticle distance  $r_{ij} = x_j - x_i$  and subscripts  $i$  and  $j$  are the numbers for particle identification.  $n_i$  is particle number density that is calculated by

$$n_i = \sum_j w_{ij} \quad (10)$$

and the particle number density calculated with initial particle position is  $n^0$ , and initial particle number density  $\lambda$  is calculated with regular particle position of initial state as follow

$$\lambda = \frac{\sum_j |\mathbf{r}_{ij}|}{\sum_j w_{ij}}. \quad (11)$$

$w_{ij}$  is a weighting function and weights the interaction according to the interparticle distance  $r_{ij}$ . The weighting function  $w_{ij}$  is generally given by

$$w_{ij} = \begin{cases} \frac{r_e}{|\mathbf{r}_{ij}|} - 1 & |\mathbf{r}_{ij}| < r_e \\ 0 & |\mathbf{r}_{ij}| \geq r_e \end{cases} \quad (12)$$

where  $r_e$  is influence radius. The closer particles are, the more influences take place between the particles with this weighting function. And particles having interparticle distance larger than influence radius  $r_e$  do not interact with each other.

Two-stage algorithm is employed in the MPS method and the time step is divided into two stages. In the first stage, all terms of Equation(2) except pressure gradient term are calculated and the temporal velocities  $u^*$  and positions  $x^*$  of all particles are predicted. Then, the temporal values are corrected by pressure term, and the actual velocities  $u^{k+1}$  and positions  $x^{k+1}$  are obtained in the second stage.

First, the value of Equation(4) is calculated with using Equation(9), and the temporal values are expressed as follows

$$\mathbf{u}^* = \mathbf{u}^k + \Delta t \left( \frac{D\mathbf{u}}{Dt} \right)^{\text{other}} \quad (13)$$

$$\mathbf{x}^* = \mathbf{x}^k + \Delta t \mathbf{u}^*. \quad (14)$$

Then, the right-hand side of Equation(7) becomes

$$\frac{1}{\rho^0} \left( \frac{D^2 \rho}{Dt^2} \right) = \frac{1}{\Delta t^2} \frac{n_i^* - n^0}{n^0} \quad (15)$$

where  $n_i^*$  is particle number density calculated from temporal values. Equation(15) is based on the concept that density is proportional to particle number density. Furthermore, by discretizing the left-hand side of Equation(7), pressure is calculated. At this time, pressure of the particles on the interface which satisfy

$$n_i < 0.8n^0 \quad (16)$$

is fixed to zero. And, if there are particles having negative pressure, pressures of the particles are corrected to zero. Then, Equation(3) is obtained with using Equation(8), and finally the velocities  $u^{k+1}$  and positions  $x^{k+1}$  are calculated as follows

$$\mathbf{u}^{k+1} = \mathbf{u}^* + \Delta t \left( \frac{D\mathbf{u}}{Dt} \right)^{\text{press}} \quad (17)$$

$$\mathbf{x}^{k+1} = \mathbf{x}^* + \Delta t^2 \left( \frac{D\mathbf{u}}{Dt} \right)^{\text{press}} \quad (18)$$

It should be noted that the above-described MPS method has been well validated in various flows.

In order to extend this MPS method to three-phase flows, firstly, we consider a liquid-gas two-phase flow. A two-phase flow simulation with the MPS method is performed by dividing the pressure computation into two steps. This computational technique is employed to prevent gas-phase particles from flying away (so-called explosion) by the continuous pressure gradient on the gas-liquid interface, and gas-phase and liquid-phase particles are calculated simultaneously with Equations(13) and (14).

That is, in the first step, only liquid-phase particles are computed ignoring the gas-phase particles. At this time, pressures of the liquid-phase particles on the gas-liquid interface are fixed to the pressure of neighbouring gas-phase particle. In this way, the influences of gas-phase are transfer to the neighbouring liquid-phase particles. In the second step, the liquid particles that are computed in the first step are treated as wall particles, and only the gas-phase computation is carried out. By separating the liquid-phase and gas-phase calculation like this technique, it is not necessary to treat gas-phase and liquid-phase particles that have large density difference at the same time, and the instability of computation caused from the large density difference, that is a severe problem for two-phase flow simulation with a MPS method, is completely avoided.

Finally, a three-phase flow can be simulated by combining the two-phase flow simulation described above and the trajectory computation of solid particles. The particle trajectories are calculated with a Lagrangian approach. Solid particles are assumed to be spherical and irrotational. Gravity and hydrodynamic drag are considered as the forces acting on the solid particles. The motion equation of a solid particle is given as

$$\frac{D\mathbf{u}}{Dt} = \mathbf{F}_G + \mathbf{F}_D \quad (19)$$

where  $F_G$  is gravitational force and  $F_D$  is aerodynamic (hydrodynamic) drag acting on a solid particle from gas-phase (liquid-phase). The drag can be expressed as follow

$$\mathbf{F}_D = \frac{3C_D \rho_f}{4\rho_s D_p} (\mathbf{u}_f - \mathbf{u}_p) |\mathbf{u}_f - \mathbf{u}_p| \quad (20)$$

$$\text{Re}_p = \frac{D_p |\mathbf{u}_f - \mathbf{u}_p|}{\nu_f} \quad (21)$$

$$C_D = \begin{cases} \frac{24}{\text{Re}_p} (1 + 0.15 \text{Re}_p^{0.687}) & (\text{Re}_p < 1000) \\ 0.44 & (\text{Re}_p \geq 1000) \end{cases} \quad (22)$$

where  $C_D$  is drag coefficient,  $D_p$  is particle diameter,  $\text{Re}_p$  is particle Reynolds number and subscripts  $f$  and  $s$  represent fluid (gas or liquid) and solid, respectively.

### Computational Conditions

In the present study, we conduct a numerical test for an air-bubble engulfment phenomenon with the gas-liquid-solid three-phase simulation procedure developed in the previous chapter. The computational conditions are listed in Table 1.

Table 1 Computational conditions

Particle spacing		0.12[m]
Gas-phase	Density	1.205[kg/m <sup>3</sup> ]
	Kinematic viscosity	15.12×10 <sup>-6</sup> [m <sup>2</sup> /s]
Liquid-phase	Density	998.2[kg/m <sup>3</sup> ]
	Kinematic viscosity	1.004×10 <sup>-6</sup> [m <sup>2</sup> /s]
Solid-phase	Density	2.2×10 <sup>3</sup> [kg/m <sup>3</sup> ]

In the air-bubble engulfment phenomena, free-fallen solid particles from certain height impact on the gas-liquid interface and the air-bubbles are engulfed into the water, as illustrated in Figure 2. This situation mimics the phenomenon occurred in the advanced particle separator (see Figure 1). The computational domain is exhibited in Figure 2, and the depth of the water  $L = 0.36$ [m] is assumed. The materials are air as the gas-phase, water as the liquid-phase and diatom earth as the solid-phase.

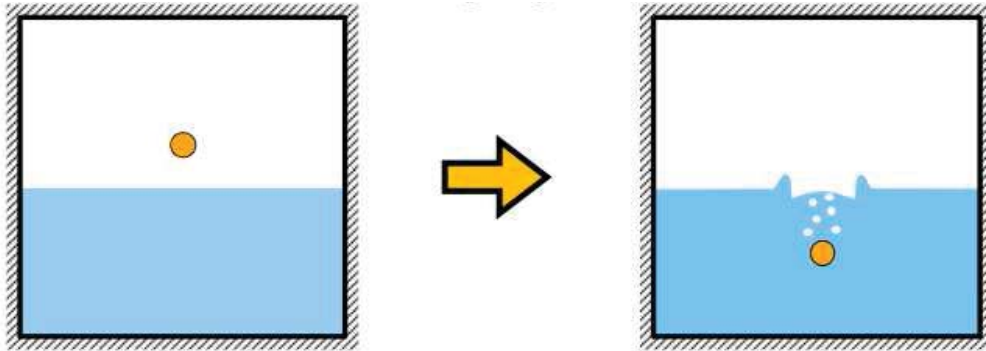


Figure 2 Schematic of air-bubble engulfment phenomenon

### Numerical Results and Discussion

For the validation of the developed code, a dam break problem was simulated under the single-phase and the two-phase conditions. Figure 3 compare the numerical results for the temporal position of water front with the experimental data measured by Koashizuka et al. (1995). From this figure, the predicted behaviours of single-phase and two-phase simulation represent the similar trend of the experiment. The difference between the single-phase and the two-phase simulations is derived from the maximum speed of interface. In the two-phase simulation, the maximum speed of interface is slightly larger than that of the single-phase one. In the two-phase simulation, there are gas-phase particles over the liquid-phase particles column and the liquid-phase particles are

accelerated more rapidly than the ones in the single-phase simulation at the earlier stage of dam breaking. In the same way, there are gas-phase particles between the interface and the right side wall, just before the liquid-phase particles reach the right side wall in the two-phase simulation. Because of these gas-phase particles, high pressure area is formed between the interface and the right side wall and liquid-phase particles decelerated more rapidly in the two-phase simulation than in the single-phase simulation. However, the global agreement is very good, and thus we confirmed that the developed code is sound.

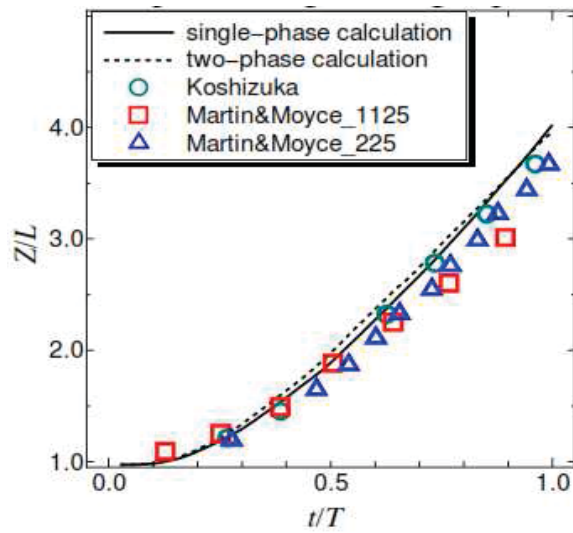


Figure 3 Validation of two-phase simulation

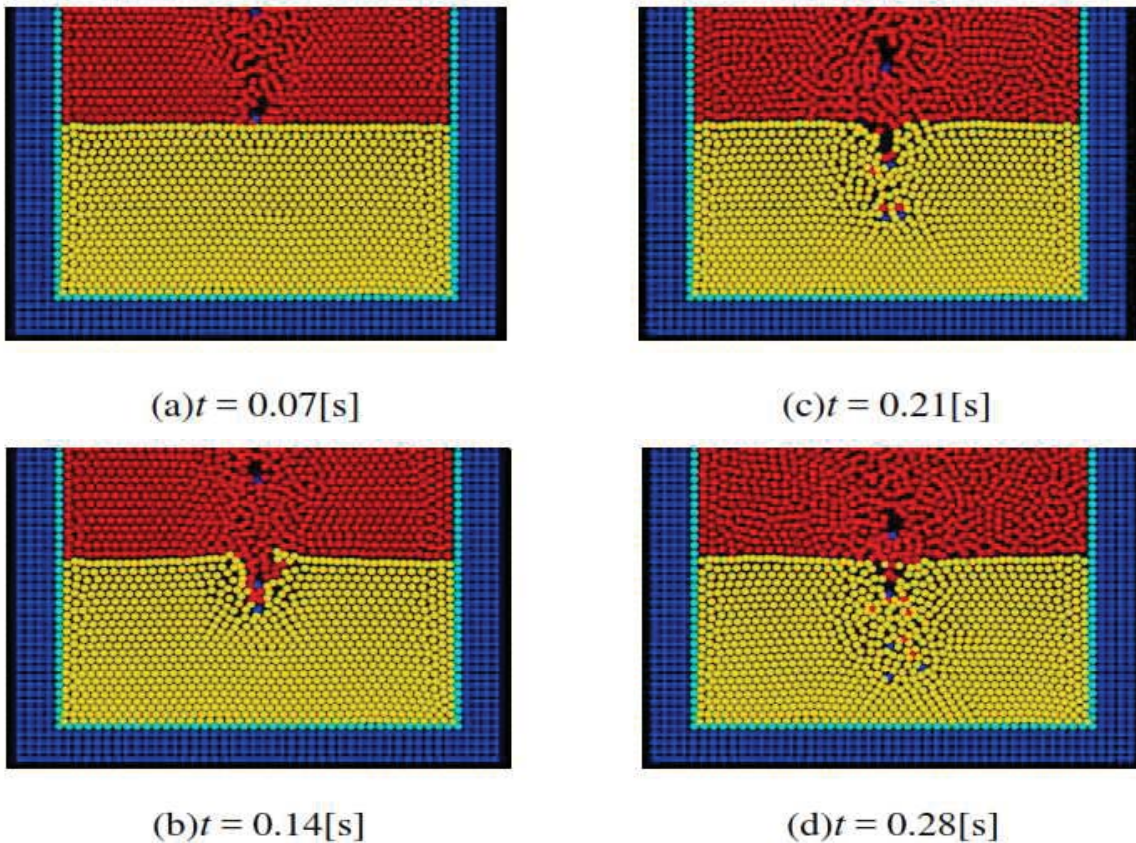


Figure 4 Engulfment of the air bubbles(red) into the water(yellow) by solid particle(blue)

The air-bubble engulfment phenomenon simulated with the gas-liquid-solid three-phase simulation is discussed here. The computational results are shown in Figure 4. Yellow, red, blue dots represent liquid-phase, gas-phase and solid-phase particles, respectively. In Figure 4, the engulfment of air bubbles are apparently observed. Also, the velocity changes of solid particles in gas and liquid-phase is satisfactorily reproduced (not shown here). The solid particles free-fall in gas-phase, then reduce their velocities rapidly with impacting to the gas and liquid-phase interface and sink by the density difference of solid and liquid in the liquid-phase. Furthermore, the interface is deformed by the impacts of solid particles. The interface bursts at the moment of solid particle impact, then the gas-phase particles go into the void space of liquid-phase particles. In this way, air bubbles are engulfed into the liquid-phase. These phenomena are difficult to be duplicated with use of the traditional grid methods, and thus it is confirmed that our developed method has the ability to reproduce the interferences of gas, liquid and solid phases. However, the response of the light particles (i.e. air) to the faster heavy particles are not completely predicted, and some no-particle spaces can be found behind the solid particles in Figure 4. This defect should be improved in our future works.

### Summary

In the present study, we developed a numerical method to simulate gas-liquid-solid three-phase flow, based of the MPS approach. We conducted some numerical tests with liquid single-phase, gas-liquid two-phase, gas-liquid-solid three-phase simulations. Those are the dam break problem with liquid single-phase and gas-liquid two-phase simulations and the air-bubble engulfment phenomenon with gas-liquid-solid three-phase simulation. In the dam break simulations, the code validation was fairly conducted, and both of the two computational results indicated reasonable agreement with the experimental results. In the air-bubble engulfment simulation, our numerical method reproduced the mutual interactions of gas, liquid and solid phases that are difficult to be predicted with the traditional grid methods.

In our future works, we are planning to improve the present numerical method, especially for the occurrence of blank region behind a heavy particle, and apply it to the actual particle separator, in order to clarify the three-phase flow characteristics and improve the separator performance.

### References

- Koshizuka S., Tamako H. and Oka Y., "A particle method for incompressible viscous flow with fluid fragmentation", *Computational Fluid Dynamics Journal*, 4, 29-46, 1995
- Krishna V., Sropriya R., Kumar V., Chakraborty S. and Meikap B.C., "Identification and Prediction of Air Core Diameter in a Hydro Cyclone by a Novel Online Sensor Based on Digital Signal Processing Technique", *Chemical Engineering and Processing: Process Intensification*, 49(2), 165-176, 2010
- Martin J.C. and Moyce W.J., "An experimental study of the collapse of liquid columns on a rigid horizontal plane", *Philos. Trans. Roy. Soc. London, Ser.A*, 244, 312-324, 1952
- Stairmand C.J., "The Design and Performance of Cyclone Separators", *Tans. Inst. Chemical Engineering*, 29, 356-383, 1985

## A Momentum Exchange-based Immersed Boundary-Lattice Boltzmann Method for Fluid Structure Interaction

Jianfei Yang<sup>1,2,3</sup>, Zhengdao Wang<sup>1,2,3</sup>, and \*Yuehong Qian<sup>1,2,3,4</sup>

<sup>1</sup>Shanghai Institute of Applied Mathematics and Mechanics, Shanghai University, 200072, China.

<sup>2</sup>Shanghai Key Laboratory of Mechanics in Energy Engineering.

<sup>3</sup>Shanghai Program for Innovative Research Team in Universities.

<sup>4</sup>Department of Mechanical and Aerospace Engineering, UC Irvine, CA 92617, USA

\*Corresponding author: qian@shu.edu.cn

### Abstract

A new immersed boundary-lattice Boltzmann method (IB-LBM) is proposed and validated in this work by its application to simulate incompressible viscous flows. The conventional IB-LBM based on the lattice Boltzmann equation with external forcing term, which contains a boundary velocity to represent the effect that the moving boundary exerts on the bounce-back distribution functions, whereas the present method use the boundary velocity to compute the momentum exchange in terms of the momentum theorem. Moreover, the momentum exchange based IB-LBM meets the Galilean invariance. Numerical examples show that the present method can provide very accurate numerical results.

**Keywords:** momentum exchange, immersed boundary, lattice Boltzmann method, fluid structure interaction.

### Introduction

In computational fluid dynamics(CFD), a primary issue is the development of accurate, efficient treatments of complex and moving boundaries. Many researchers have developed various numerical methods to resolve this issue. Conventional approaches such as finite difference, finite volume and finite element methods are generally used to accommodate complex geometries with tedious grid generation. However, the recently developed immersed boundary method (IBM) and lattice Boltzmann method (LBM) can handle complex geometry with the use of Cartesian mesh.

The IBM was introduced by Peskin (1977), it can be defined as a non-body-conformal grid method which adds a force density term either explicitly or implicitly to the flow governing equation to satisfy the no-slip condition on the boundary. The adoption of the structured non-body-conformal grid relieves the burden of meshing and reduces the amount of memory and CPU time used compared with unstructured body-conformal grids, and the accurate evaluation of the force density term maintains a high accuracy.

The LBM in previous work by Qian et al (1992) has achieved a great success in simulating complex fluid flows in the past decades. LBM is a particle-based numerical technique, it has two processes: streaming and collision. The major advantage of LBM is its simplicity, easy for implementation, algebraic operation and intrinsic parallel nature. No differential equation and resultant algebraic equation system are involved in the LBM.

In this paper, we couple the immersed boundary method and lattice Boltzmann method, presenting a Galilean invariant momentum exchange equation by introducing the relative velocity into the interfacial momentum transfer to compute the boundary force. The present method is validated by its application to simulate the steady flows past a circular cylinder. The obtained results are compared well with those available in the literature.

## Momentum Exchange-based Immersed Boundary-Lattice Boltzmann Method

### *Lattice Boltzmann model*

The Lattice Boltzmann model with single-relaxation time without a forcing term can be written as

$$f_\alpha(\mathbf{x} + \mathbf{e}_\alpha \Delta t, t + \Delta t) = f_\alpha(\mathbf{x}, t) - \frac{1}{\tau} [f_\alpha(\mathbf{x}, t) - f_\alpha^{eq}(\mathbf{x}, t)] \quad (1)$$

Where  $f_\alpha(\mathbf{x}, t)$  is the density distribution function at position  $\mathbf{x}$  and time  $t$ ,  $f_\alpha^{eq}$  is its corresponding equilibrium state,  $\tau$  is the single relaxation parameter,  $\mathbf{e}_\alpha$  is the particle velocity. For the D2Q9 model as shown in the work by Qian et al (1992), the velocity set is given by

$$\mathbf{e}_\alpha = \begin{cases} (0, 0) & \alpha=0 \\ c(\cos[(\alpha-1)\frac{\pi}{2}], \sin[(\alpha-1)\frac{\pi}{2}]) & \alpha=1,2,3,4 \\ \sqrt{2}c(\cos[(2\alpha-1)\frac{\pi}{4}], \sin[(2\alpha-1)\frac{\pi}{4}]) & \alpha=5,6,7,8 \end{cases} \quad (2)$$

Where  $c = \delta x / \delta t$ ,  $\delta x$  and  $\delta t$  are the lattice spacing and time step. For the case of  $\delta x = \delta t$ ,  $c$  is taken as 1. The corresponding equilibrium distribution is

$$f_\alpha^{eq} = \rho w_\alpha [1 + \frac{\mathbf{e}_\alpha \cdot \mathbf{u}}{c_s^2} + \frac{(\mathbf{e}_\alpha \cdot \mathbf{u})^2}{2c_s^4} - \frac{u^2}{2c_s^2}] \quad (3)$$

With  $w_0 = 4/9$ ,  $w_1 = w_2 = w_3 = w_4 = 1/9$ ,  $w_5 = w_6 = w_7 = w_8 = 1/36$ ,  $c_s = c/\sqrt{3}$  is the sound speed of the model. The density and velocity can be directly evaluated by taking the zeroth and first moments of particle density distribution functions, respectively:

$$\rho = \sum_\alpha f_\alpha = \sum_\alpha f_\alpha^{eq} \quad (4)$$

$$\rho \mathbf{u} = \sum_\alpha \mathbf{e}_\alpha f_\alpha = \sum_\alpha \mathbf{e}_\alpha f_\alpha^{eq} \quad (5)$$

and the kinematic viscosity  $\nu$  is determined by

$$\nu = (\tau - \frac{1}{2})c_s^2 \Delta t \quad (6)$$



When external forces exist, such as gravity. In the lattice BGK model, it is known that the whole force could be added to the lattice Boltzmann equation as shown in the work by Guo et al (2002). In the present model, the boundary force can be evaluated by momentum exchange method.

#### *Immersed boundary method*

The interaction between the boundary grid-points and fluid nodes in the immersed boundary method can be expressed as

$$\mathbf{F}(\mathbf{x}, t) = \int_{\Omega} \mathbf{g}(\mathbf{X}, t) \delta(\mathbf{x} - \mathbf{X}) ds \quad (7)$$

Where  $\mathbf{F}(\mathbf{x}, t)$  is the force generated by the boundaries onto the fluid,  $\delta(\mathbf{x} - \mathbf{X})$  is the Dirac delta function,  $\mathbf{X}(X, Y)$  is the coordinate of Lagrangian boundary points,  $\mathbf{g}(\mathbf{X}, t)$  is the Lagrangian force density.

The discretized form of Eq. (7) using a regularized discrete delta function  $D_{ij}$  are expressed as

$$\mathbf{F}(\mathbf{x}_{ij}, t) = \sum_l \mathbf{g}(\mathbf{X}_l, t) D_{ij}(\mathbf{x}_{ij} - \mathbf{X}_l) \Delta s_l \quad (8)$$

where  $\Delta s_l$  is the arc length of the boundary element.

The discrete delta function  $D_{ij}$  appearing in Eq. (8) is a smoothed approximation to the Dirac delta function  $\delta(\mathbf{x} - \mathbf{X})$ . The detailed derivation procedures and several forms were presented by Peskin (2002). We apply the common form as follows:

$$D_{ij}(\mathbf{x}_{ij} - \mathbf{X}_l) = \frac{1}{h^2} \delta_h\left(\frac{x_{ij} - X_l}{h}\right) \delta_h\left(\frac{y_{ij} - Y_l}{h}\right) \quad (9)$$

with

$$\delta_h(a) = \begin{cases} \frac{1}{4} (1 + \cos(\frac{\pi a}{2})) & |a| \leq 2 \\ 0 & \text{otherwise} \end{cases} \quad (10)$$

where  $h = \delta_x$  is the lattice spacing, the integral of function  $\delta_h(a)$  is equal to one.

#### *boundary force calculation*

In the conventional immersed boundary-lattice Boltzmann method, the penalty method in previous work by Feng et al (2004) or the direct forcing method as shown in the work by Fadlun et al (2000) was proposed to calculate the boundary force  $\mathbf{F}(\mathbf{X}, t)$ . Recently, a simple method for computing the boundary force was proposed as shown in the work by Niu et al (2006), in which the momentum exchange at the boundary is used to compute the force, however, the computed forces at the boundary have some oscillations. We use a novel momentum exchange at the boundary to compute the boundary force in the previous work by Wen (2013).

The force on the fluid-structure boundary can be written as

$$\mathbf{F}(\mathbf{X}_l, t) = \sum_{\alpha} [(\mathbf{e}_{\alpha} - \mathbf{u})f_{\alpha}(\mathbf{x}, t) - (\mathbf{e}_{\beta} - \mathbf{u})f_{\beta}(\mathbf{x}, t)] \quad (11)$$

Here  $f_{\alpha}(\mathbf{x}, t)$  indicates the mass component straming into the boundary and contributing a momentum increment  $(\mathbf{e}_{\alpha} - \mathbf{u})f_{\alpha}(\mathbf{x}, t)$  to the boundary, while  $f_{\beta}(\mathbf{x}, t)$  streams out of the boundary and contributes a momentum decrement  $(\mathbf{e}_{\beta} - \mathbf{u})f_{\beta}(\mathbf{x}, t)$ .

The total boundary force  $\mathbf{F}_T$  and the torque  $\mathbf{T}_T$  exerted on the boundary points are expressed as

$$\mathbf{F}_T(\mathbf{X}_l, t) = \sum_l \mathbf{F}(\mathbf{X}_l, t) \Delta s_l \quad (12)$$

$$\mathbf{T}_T = \sum_l (\mathbf{X}_l - \mathbf{R}) \times \mathbf{F}(\mathbf{X}_l, t) \Delta s_l \quad (13)$$

where  $\mathbf{R}$  is the mass center of the structure, and the summation runs over all the fluid structure boundary.

### Flows past a circular cylinder

In order to examine the accuracy and efficiency of the proposed immersed boundary-Lattice Boltzmann method (IB-LBM), numerical simulations of the viscous flow past a circular cylinder are carried out. The computational domain is set by  $22D \times 22D$ ,  $D$  is the diameter of circular cylinder, the free stream velocity  $u_{\infty}$  is taken as 0.05, and the free stream density  $\rho_{\infty}$  is set to be 1.0, The drag and lift coefficients are defined by

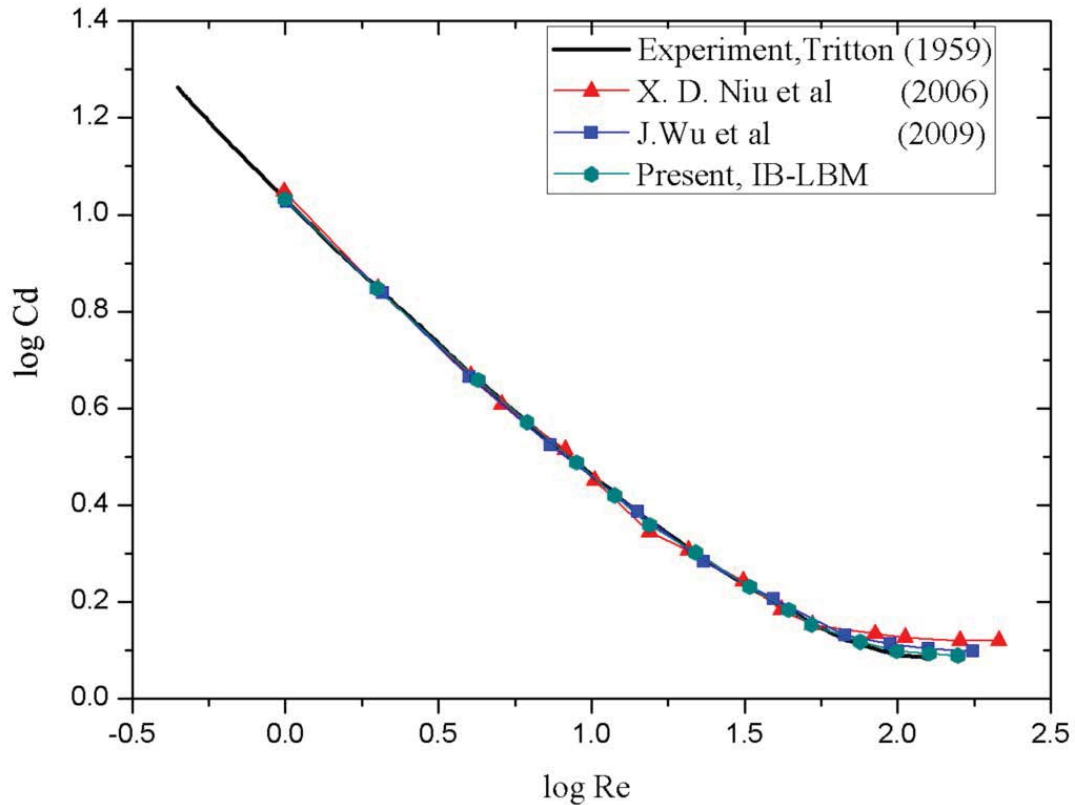
$$C_d = \frac{F_D}{0.5\rho u_{\infty}^2 D}, \quad C_l = \frac{F_L}{0.5\rho u_{\infty}^2 D} \quad (14)$$

Where the drag force  $F_D$  and the lift force  $F_L$  on the immersed body are calculated as

$$F_D = - \left\{ \frac{d}{dt} \left( \int_R u_1 dR \right) + \int_{\Omega} \left[ u_1 \mathbf{u} \cdot \mathbf{n} + pn_1 - \mu \left( \frac{\partial u_1}{\partial x_i} + \frac{\partial u_i}{\partial x_1} \right) \right] ds \right\} \quad (15)$$

$$F_L = - \left\{ \frac{d}{dt} \left( \int_R u_2 dR \right) + \int_{\Omega} \left[ u_2 \mathbf{u} \cdot \mathbf{n} + pn_2 - \mu \left( \frac{\partial u_2}{\partial x_i} + \frac{\partial u_i}{\partial x_2} \right) \right] ds \right\} \quad (16)$$

Where  $\mathbf{n}$  is the normal vector to the boundary of control surface, the subscripts 1 and 2 denote the  $x$ -direction and  $y$ -direction. Figure 1 shows the distribution of drag coefficients versus the Reynolds number in logarithmic scale. Obviously, the present results compare very well with the experimental data as shown in the work by Tritton (1959) and other numerical results by Niu et al (2006) and Wu et al (2009). Table 1 displays the comparison of non-dimensional length of recirculating eddy  $L/D$ , here  $L$  is the length of the recirculating region. Comparing the present method and other research work at  $Re = 20$  and  $Re = 40$ , we can see that our numerical results are in good agreement with previous ones.



**Figure 1. Comparison of drag coefficients**

**TABLE 1. Comparison of recirculating length (L/D) with previous studies**

Authors	Re=20	Re=40
Dennis and Chang (1959)	0.94	2.345
Nieuwstadt and Keller (1973)	0.893	2.179
Coutanceau and Bouard (1977)	0.93	2.13
Fornberg (1980)	0.91	2.24
He and Doolen (1997)	0.921	2.245
Tseng and Ferziger (2003)	--	2.21
Shu and Liu (2007)	0.90	2.20
Present	0.92	2.26

## Conclusions

we couple the immersed boundary method and lattice Boltzmann method, presenting a Galilean invariant momentum exchange equation by introducing the relative velocity into the interfacial momentum transfer to compute the boundary force. The present method preserves the merits of the LBM and the IBM by using two unrelated computational meshes, an Eulerian mesh for the flow domain and a Lagrangian mesh for the moving boundaries in the flow. The simplicity of the Eulerian mesh facilitates the numerical implementation of the LBM, and the generality of the Lagrangian mesh makes it easy to handle complex boundaries.

The present method is validated by its application to simulate the steady flows past a circular cylinder. The obtained results are in good agreement with available data in the literature.

### Acknowledgment

This work has been supported by Research on Lattice Boltzmann Method for Complex and Moving Boundary Problems (K.13-0401-13-001) from Shanghai University

### References

- [1] C.S. Peskin. (1977), Numerical analysis of blood flow in the heart, *J. Comput. Phys.* 25, 220.
- [2] Y. H. Qian, D. d'Humieres, P. Lallemand. (1992), Lattice BGK model for Navier-Stokes equation, *Europhys. Lett.* 17, 479-484.
- [3] Z. Guo, C. Zheng, B. Shi. (2002), Discrete lattice Boltzmann effects on the forcing term in the lattice Boltzmann method, *Phys. Rev. E* 65, 046308.
- [4] C. S. Peskin. (2002), The immersed boundary method, *Acta Numer.* 11, 479-517.
- [5] Z. Feng, E. Michaelides. (2004), The immersed boundary-lattice Boltzmann method for solving fluid particles interaction problems, *J.Comp.Phys.* 195, 602-628.
- [6] E. Fadlun, R. Verzicco, P. Orlandi, J. Mohd-Yusof. (2000), Combined immersed-boundary finite difference methods for three dimensional complex flow simulations, *J. Comp. Phys.* 161, 35-60.
- [7] X. D. Niu, C. Shu, Y.T. Chew, Y. Peng. (2006), A momentum exchange-based immersed boundary lattice Boltzmann method for simulating incompressible viscous flows, *Phys. Lett. A.* 354, 460-478.
- [8] B. H. Wen, C. Y. Zhang, Y. S. Tu, C. L. Wang, and H. P. Fang. (2013), Galilean Invariant Fluid-Solid Interfacial Dynamics in Lattice Boltzmann Simulations. Submitted to *Physical Review E*: e-print [arXiv:http://arxiv.org/abs/1303.0625](http://arxiv.org/abs/1303.0625).
- [9] D.J. Tritton. (1959), Experiments on the flow past a circular cylinder at low Reynolds number, *J. Fluid Mech.* 6, 547.
- [10] J. Wu, C. Shu. (2009), Implicit velocity correction-based immersed boundary-lattice Boltzmann method and its applications, *J. Comp. Phys.* 228, 1963-1979.
- [11] S.C.R. Dennis, G.Z. Chang. (1970), Numerical solutions for steady flow past a circular cylinder at Reynolds number up to 100, *J. Fluid Mech.* 42, 471.
- [12] F. Nieuwstadt, H.B. Keller. (1973), Viscous flow past circular cylinders, *Comput. Fluid* 1, 59.
- [13] M. Coutanceau, R. Bouard. (1977), Experimental determination of the main features of the viscous flow in the wake of circular cylinder in uniform translation. Part I. Steady flow, *J. Fluid Mech.* 79, 231.
- [14] B. Fornberg. (1980), A numerical study of steady viscous flow past a circular cylinder, *J. Fluid Mech.* 98, 819.
- [15] X. He, G. Doolen. (1997), Lattice Boltzmann method on curvilinear coordinates system: flow around a circular cylinder, *J. Comput. Phys.* 134, 306.
- [16] Y. H. Tseng, J.H. Ferziger. (2003), A ghost-cell immersed boundary method for flow in complex geometry, *J. Comput. Phys.* 192, 593.
- [17] C. Shu, N. Liu, Y. T. Chew. (2007), A novel immersed boundary velocity correction - lattice Boltzmann method and its application to simulate flow past a circular cylinder, *J. Comput. Phys.* 226, 1607-1622.

## A new scaled boundary finite element method using Fourier shape functions

Yiqian He<sup>1</sup>, Haitian Yang<sup>1</sup>, and \*Andrew J. Deeks<sup>2</sup>

<sup>1</sup>Department of Engineering Mechanics, Dalian University of Technology,  
Dalian 116024, P.R. China

<sup>2</sup> School of Engineering and Computing Sciences, Durham University,  
South Road, Durham, DH1 3LE, UK

\*Corresponding author: a.j.deeks@durham.ac.uk

### Abstract

The scaled boundary finite element method (SBFEM) is a semi-analytical method, whose versatility, accuracy and efficiency are not only equal to, but potentially better than the finite element method and the boundary element method for certain problems. This paper investigates the possibility of using Fourier shape functions in the SBFEM to form the approximation in the circumferential direction. The shape functions effectively form a Fourier series expansion in the circumferential direction, and are augmented by additional linear shape functions. The proposed method is evaluated by solving elastostatic problems. The accuracy and convergence of the proposed method is demonstrated, and the performance is found to be better than using polynomial elements or using an element-free Galerkin approximation for the circumferential approximation.

**Keywords:** Scaled boundary method; Fourier shape functions; computational accuracy; stress singularities; unbounded domains

### Introduction

The scaled boundary method (SBM) is a semi-analytical method developed relatively recently by Wolf and Song (Wolf and Song, 1996). The method introduces a normalised radial coordinate system based on a scaling centre and a defining curve (usually taken as the boundary). The governing differential equations are weakened in the circumferential direction and then solved analytically in the normalised radial direction. The SBM combines the advantages of the Finite Element Method (FEM) and the Boundary Element Method (BEM), and, unlike the BEM, no fundamental solution is required. In addition, the SBM has been shown to be more efficient than the FEM for problems involving unbounded domains and for problems involving stress singularities or discontinuities (Deeks and Wolf, 2002). Effective applications of this method have been demonstrated in various problem domains, including fracture problems and foundation problems.

In the scaled boundary method, the discretisation approach used in the circumferential direction has significant influence on the accuracy of the resulting solutions (Deeks and Augarde, 2005). The most commonly used method for performing this circumferential discretisation is the finite element approach, leading to the method called the scaled boundary finite element method (SBFEM). Vu and Deeks (Vu and Deeks, 2006, 2008a, 2008b) investigated the use of higher-order polynomial shape functions in the SBFEM, and demonstrated the SBFEM converged

significantly faster under p-refinement than under h-refinement. The development of meshless methods provided another approach to building circumferential approximations for the scaled boundary method. Deeks and Augarde (Deeks and Augarde, 2005) developed a Meshless Local Petrov-Galerkin method scaled boundary method (MLPG-SBM) and He et al (He et al, 2012) developed an Element-free Galerkin scaled boundary method (EFG-SBM). This work showed that these two meshless scaled boundary methods gave a higher level of accuracy and rate of convergence than the conventional SBFEM using linear or quadratic elements, with the EFG-SBM performing slightly better than the MLPG-SBM.

In this paper, the possibility of using shape functions based on the terms of a Fourier series for the circumferential approximation of the SBFEM is investigated. Fourier interpolations containing trigonometric functions have been applied to both the finite element method (FEM) and the boundary element method (BEM). For example, Guan et al. (Guan et al, 2006) developed a Fourier series based FEM for the analysis of tube hydroforming, and showed that this Fourier shape function reduced the number of degrees of freedom required. Javaran and Khaji (Javaran, 2011; Khaji and Javaran, 2013) applied Fourier radial basis functions into the BEM, and showed that the resulting BEM is much more accurate than the BEM using classic Lagrange shape functions. Although the advantages of Fourier based FEM and BEM have been illustrated in previous work, to date there has been no work reported on the use of Fourier shape functions in the SBFEM.

A new Fourier-based scaled boundary method (F-SBM) is presented in this paper. A set of shape functions based on Fourier series expansion is derived, and augmented with linear shape functions. The new shape functions provide good approximation to both trigonometric and polynomial functions in the circumferential direction of the scaled boundary system. In the numerical example, the F-SBM is used to solve a two-dimensional elastostatic problem. The accuracy and convergence of F-SBM is compared with the conventional SBFEM using both linear and quadratic elements and with the EFG-SBM. Superior performance in terms of both accuracy and convergence is demonstrated.

### A Fourier shape function

This paper employs shape functions obtained from the well-known Fourier series. Based on the theory of the Fourier series, any continuous function  $f(r)$  maybe represented by a series of trigonometric functions as

$$f(r) = a_0 + \sum_{n=1}^{\infty} \left( a_n \cos\left(\frac{n\pi}{L_{\max}} r\right) + b_n \sin\left(\frac{n\pi}{L_{\max}} r\right) \right) \quad (1)$$

where  $a_0$ ,  $a_n$ ,  $b_n$  and  $L_{\max}$  represent the Fourier series parameters.

Thus on the boundary at  $\xi = 1$ , the displacement can be approximated as

$$u_h(s) = a_0 + \sum_{j=1}^m \left( a_j \cos\left(\frac{j\pi}{L} s\right) + b_j \sin\left(\frac{j\pi}{L} s\right) \right) \quad (2)$$

where  $s$  is the circumferential coordinate in scaled boundary element,  $L$  is the length of the boundary and  $m$  represents the order of Fourier series.

To preserve  $C^0$  continuity between the edges or elements, linear polynomial functions terms are added into the standard Fourier approximation as

$$u_h(s) = \alpha_1 \frac{L-s}{L} + \beta_1 \frac{s}{L} + \sum_{j=1}^m \left( a_j \cos\left(\frac{j\pi}{L} s\right) + b_j \sin\left(\frac{j\pi}{L} s\right) \right) \quad (3)$$

where  $\alpha_1$  and  $\beta_1$  represent the values of the function at the end nodes of the element.

While it is possible to use the Fourier parameters as the unknown boundary parameters when solving the scaled boundary finite element equations, here the parameters in the Fourier expansion above are transferred to nodal values at equally spaced nodes along each element for ease of applying essential boundary conditions and enforcing  $C^0$  continuity between elements. If  $(2m+2)$  nodes are used, the nodal values vector  $\{u\}$  can be related to the parameters in Equations (3) by

$$\{u\} = [T]\{\hat{u}\} \quad (4)$$

where  $\{\hat{u}\} = \{\alpha_1 \ a_1 \ \dots \ a_m \ b_1 \ \dots \ b_m \ \beta_1\}^T$ , and  $[T]$  is a transfer matrix assembled as

$$T_{ij} = \psi_j(S_i) \quad i, j = 1, 2, \dots, 2m+2 \quad (5)$$

where  $S_i$  is the circumferential coordinate of the  $i^{\text{th}}$  node, and the component functions of the Fourier expansion are

$$\psi_i(s) = \begin{cases} \frac{L-s}{L} & i=1 \\ \cos\left(\frac{(i-1)\pi}{L}s\right) & 2 \leq i \leq m+1 \\ \sin\left(\frac{(i-1-m)\pi}{L}s\right) & m+2 \leq i \leq 2m+1 \\ \frac{s}{L} & i=2m+2 \end{cases} \quad (6)$$

Inverting Equation (4), the parameters  $\{\hat{u}\}$  in Equation (3) can be related to the nodal values  $\{u_h\}$  by

$$\{\hat{u}\} = [T]^{-1}\{u\} \quad (7)$$

Thus the approximation for displacement can be rewritten as

$$u_h(s) = \{\psi\}[T]^{-1}\{u\} \quad (8)$$

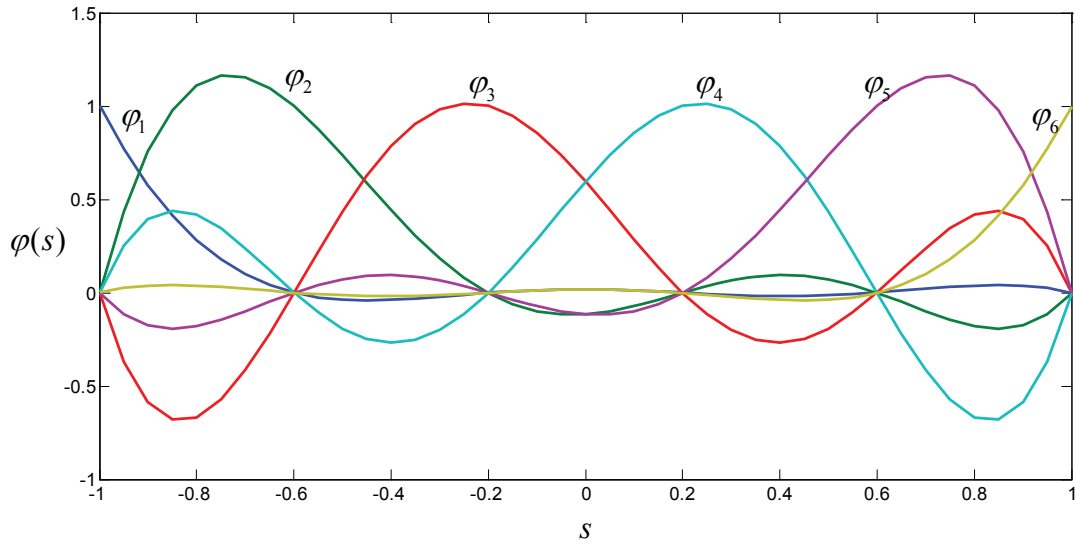
The shape functions relating to the nodal displacements are hence

$$\{\phi\} = \{\psi\}[T]^{-1} \quad (9)$$

and the shape function matrix for the scaled boundary method then becomes

$$[N(s)] = \begin{bmatrix} \phi_1(s) & 0 & \dots & \phi_{2m+2}(s) & 0 \\ 0 & \phi_1(s) & \dots & 0 & \phi_{2m+2}(s) \end{bmatrix} \quad (10)$$

Figure 3 plots these Fourier shape functions for  $m = 2$ , where 6 nodes are required.

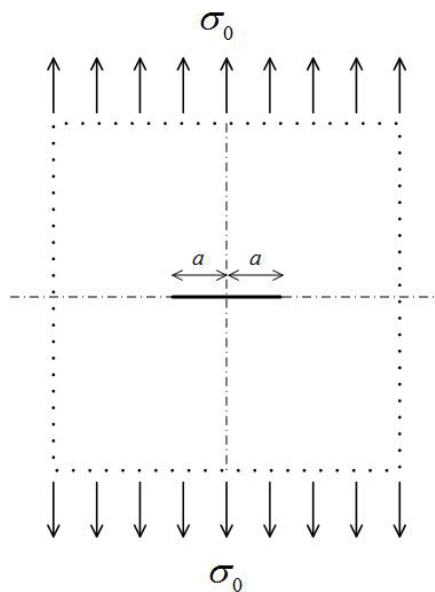


**Figure 1 The Fourier shape functions for order  $m = 2$**

**Performance of the method**

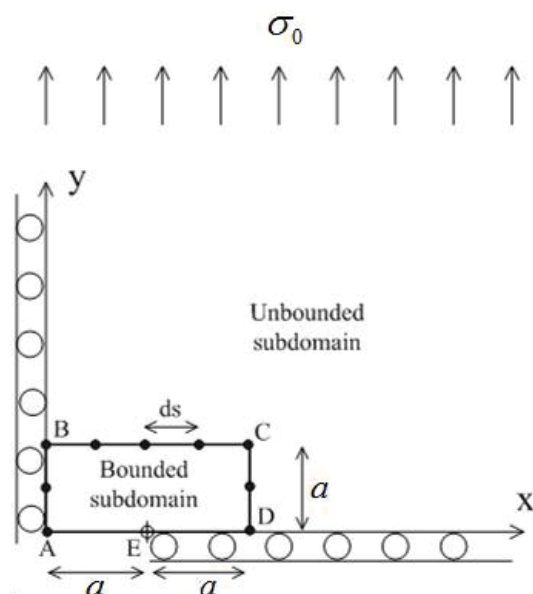
*An infinite plate with a through crack*

The example refers to the problem of determining the mode I stress intensity factor (SIF)  $K_I$  for a through crack in an infinite plate, as illustrated in Figure 9. The applied stress  $\sigma_0 = 1$ . Due to the symmetry, one quarter of the problem is modelled, as shown in Figure 3, with the model consisting of a bounded domain, with the scaling centre at the crack tip (point E), and an unbounded domain, with the scaling centre at the middle of crack (point A). The nodes are introduced on the edges AB, BC and CD with uniform spacing,  $ds$ . The problem has an exact solution,  $K_I = \sigma_0 \sqrt{2\pi a}$ .



**Figure 2 Infinite plate with a through crack: geometry and loads**





**Figure 3 Scaled boundary model of an infinite plate with a through crack.**

In Table 1 the F-SBM solutions are compared with the SBFEM with linear elements and the EFG-SBM with linear basis. The results show that the F-SBM achieves high accuracy for SIF, for example, a relative error as low as 0.0000555% can be obtained using 53 nodes. In comparison with SBFEM and EFG-SBM, it can be seen that F-SBM has higher accuracy when the same number of nodes are used.

**Table 1 The results of SIF using F-SBM**

Number of nodes	F-SBM	Error%	SBFEM (Linear)	Error%	EFG-SBM (Linear)	Error%	Exact Solutions
13	1.773047828	3.35e-2	1.765973947	3.65e-1	1.770648223	1.02e-1	
21	1.771909603	3.07e-2	1.770015354	1.37e-1	1.772806367	1.99e-2	
28	1.772534634	4.56e-3	1.771193770	7.11e-2	1.772432519	1.20e-3	
37	1.772441208	7.13e-4	1.771691632	4.30e-2	1.772372556	4.58e-3	1.772453851
45	1.772455534	9.49e-5	1.771443822	5.69e-2	1.772495119	2.33e-3	
53	1.772452866	5.55e-5	1.771456952	5.62e-2	1.772400534	3.01e-3	

## Conclusions

A new SBFEM using Fourier shape functions is presented in this paper. The shape functions are based on the Fourier series expansion and augmented with additional linear shape functions terms. By using a transfer matrix, the nodal values are related with Fourier parameters, and in this way the essential boundary conditions can be conveniently handled. In the numerical example, the new approach has been shown to yield higher accuracy and faster convergence in comparison with the SBFEM using linear or quadratic elements and the EFG-SBM using linear or quadratic basis.

## References

- Wolf, J. P and Song, Ch (1996), Finite-Element Modelling of Unbounded Media. John Wiley and Sons: Chichester.
- Deeks, A. J. and Wolf, J. P. (2002a), A virtual work derivation of the scaled boundary finite-element method for elastostatics, *Comput. Mech.* 28, pp. 489-504.
- Deeks, A. J. and Augarde, C. E. (2005), A meshless local Petrov-Galerkin scaled boundary method. *Comput. Mech.* 36, pp. 159–170.
- Guan, Y., Pourboghrat F. and Yu, W. R. (2006), Fourier series based finite element analysis of tube hydroforming: A axisymmetric model. *Engineering Computations* 23(7), pp. 697-728.
- He, Y. Q., Yang, H. T. and Deeks, A. J. (2012), An Element-free Galerkin (EFG) scaled boundary method, *Fin. Elem. Analy. Des.* 62, pp. 28-36.
- Javaran, H. S., Khaji N. and Moharrami H. (2011), A dual reciprocity BEM approach using new Fourier radial basis functions applied to 2D elastodynamic transient analysis. *Engineering Analysis with Boundary Elements* 35, pp. 85–95.
- Khaji N. and Javaran, H. S. (2013), New complex Fourier shape functions for the analysis of two-dimensional potential problems using boundary element method. *Engineering Analysis with Boundary Elements* 37, pp. 260–272.
- Vu, T. H. and Deeks, A. J. (2006), Use of higher order shape functions in the scaled boundary finite element method, *Int. J. Numer. Meth. Eng.* 65, pp. 1714-1733.
- Vu, T. H. and Deeks, A. J. (2008a), A p-hierarchical adaptive procedure for the scaled boundary finite element method, *Int. J. Numer. Meth. Eng.* 73, pp. 47-70.
- Vu, T. H. and Deeks, A. J. (2008b), A p-adaptive scaled boundary finite element method based on maximization of the error decrease rate, *Comput. Mech.* 41, pp. 441-455.

## Comparison of various numerical discretisation approaches for the scaled boundary method

Yiqian He<sup>1</sup>, Haitian Yang<sup>1</sup>, and \*Andrew J. Deeks<sup>2</sup>

<sup>1</sup>Department of Engineering Mechanics, Dalian University of Technology,  
Dalian 116024, P.R. China

<sup>2</sup> School of Engineering and Computing Sciences, Durham University,  
South Road, Durham, DH1 3LE, UK

\*Corresponding author: a.j.deeks@durham.ac.uk

### Abstract

The scaled boundary method is a semi-analytical method for solving linear partial differential equations. In the scaled boundary method, the discretisation approach used in the circumferential direction has significant influence on the accuracy of the resulting solutions. The most commonly used method for performing this circumferential discretisation is the finite element approach, leading to the method called the scaled boundary finite element method (SBFEM), and most previous work using the SBFEM has employed linear or quadratic isoparametric elements. In this paper, various alternative numerical discretisation approaches for the scaled boundary method developed by the authors are reviewed and compared, including higher-order finite elements, the meshless local Petrov-Galerkin approach, the Element-free Galerkin approach and Fourier shape functions. These approaches have significant advantages in accuracy and convergence compared with the conventional SBFEM with linear or quadratic elements. Numerical examples are provided to compare the above mentioned scaled boundary methods in terms of accuracy and convergence, and the performance of these various approaches in different cases will be discussed.

**Keywords:** Scaled boundary method, numerical discretisation approaches, computational accuracy, comparisons.

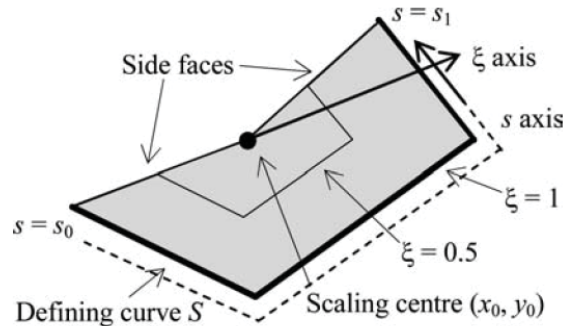
### Introduction

The scaled boundary method is a semi-analytical method developed relatively recently by Wolf and Song (Wolf and Song, 1996; Wolf, 2003). The method introduces a normalised radial coordinate system based on a scaling centre and a defining curve (usually taken as the boundary). The governing differential equations are weakened in the circumferential direction and then solved analytically in the normalised radial direction. Like the boundary element method, discretisation of the boundary only is required, but unlike that method no fundamental solution is required. The method has been shown to be more efficient than the finite element method for problems involving unbounded domains and for problems involving stress singularities or discontinuities (Deeks and Wolf, 2002a).

The Figure 1 shows a typical bounded scaled boundary coordinate system with a scaling centre  $(x_0, y_0)$ , radial coordinate  $\xi$  and circumferential coordinate  $s$ . An approximate solution for displacement is sought in the form

$$\{u_h(\xi, s)\} = \sum_{i=1}^n [N_i(s)] u_{hi}(\xi) = [N(s)] \{u_h(\xi)\} \quad (1)$$

This represents a discretisation of the part of the boundary located at  $\xi = 1$  with the shape function  $[N(s)]$ . The unknown vector  $\{u_h(\xi)\}$  is a set of  $n$  functions analytical in  $\xi$ . The shape functions apply for all lines with a constant  $\xi$ .



**Figure 1** A scaled boundary coordinate system

In the scaled boundary method, the discretisation approach used in the circumferential direction has significant influence on the accuracy of the resulting solutions. The most commonly used method for performing this circumferential discretisation is the finite element approach, leading to the method called the scaled boundary finite element method (SBFEM).

The scaled boundary method involves solution of a quadratic eigenproblem, the computational expense of which increases rapidly as the number of degrees of freedom increases. Therefore it is desirable to obtain solutions at a specified level of accuracy while using the minimum number of degrees of freedom necessary. Generally, there are two approaches to improve the accuracy of SBFEM. The first one is to use an adaptive approach to refining the discretisation of the boundary (Deeks and Wolf, 2002b). The second one is to use new shape functions, such as higher-order polynomial shape functions (Vu and Deeks, 2006, 2008a, 2008b) and meshless approaches (Deeks and Augarde, 2005; He et al., 2012) which may provide better performance in terms of convergence and smoothness of the solution.

This paper reviews various numerical discretisation approaches for the scaled boundary method. After a review of previous work in this field, the paper focuses on a comparison of the performance of these approaches and the conventional SBFEM through numerical examples. The accuracy and convergence of these approaches will be illustrated and compared, and discussions and conclusions will be provided.

## Review

### *Higher-order elements*

The use of higher-order elements ( $p > 2$ , where  $p$  represents the polynomial order of the shape functions) into the SBFEM is presented by Vu and Deeks (Vu and Deeks, 2006). Two approaches are examined: the spectral element approach with Lagrange shape functions interpolating for an increasing number of internal nodes; and a  $p$ -hierarchical approach where polynomial shape functions forming a hierarchical basis are employed to add new DOFs into the domain without changing the existing ones. It was proved that the SBFEM converged significantly faster with higher-order elements than linear or quadratic elements, and the performance of the two different types of higher-order elements is very similar. In order to take advantage of higher-

order elements, Vu and Deeks further developed the p-adaptive technique for SBFEM (Vu and Deeks, 2008a, 2008b) and demonstrated SBFEM converged significantly faster under p-refinement than under h-refinement.

### *Meshless approaches*

The meshless methods provide alternative approaches for SBFEM. The meshless methods are only based on nodes, and thus no mesh generation or remeshing is required. It has been shown that, compared with the finite element method, the meshless method (for example, the Element-free Galerkin method) has the advantages of high accuracy, rapid convergence, and a smooth stress solution can be obtained without post-processing. Deeks and Augarde (Deeks and Augarde, 2005) developed a Meshless Local Petrov-Galerkin method scaled boundary method (MLPG-SBM) and He et al (He et al, 2012) developed an Element-free Galerkin scaled boundary method (EFG-SBM). These works showed that these two meshless scaled boundary methods gave a higher level of accuracy and rate of convergence than the conventional SBFEM using linear or quadratic elements.

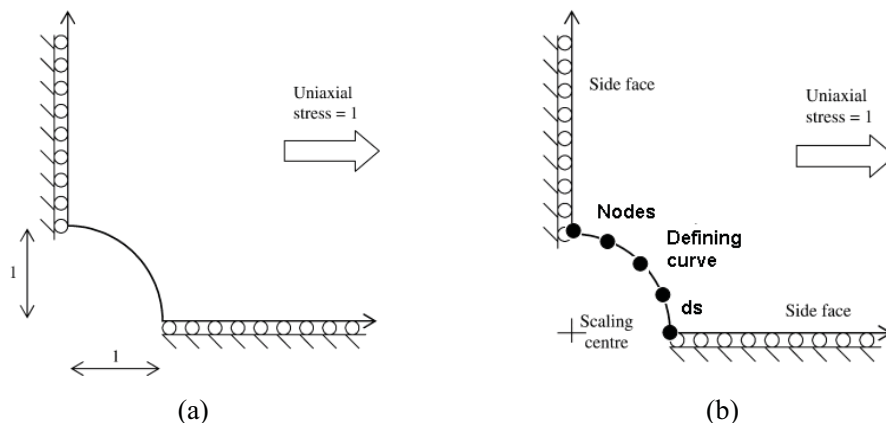
### *Fourier methods*

Fourier interpolation containing trigonometric functions has been demonstrated to be more accurate than the classic Lagrange shape functions in various studies of the BEM. He et al (He et al, 2013) investigated the possibility of using Fourier shape functions in the SBFEM to form the approximation in the circumferential direction. The shape functions effectively form a Fourier series expansion in the circumferential direction, and are augmented by additional linear shape functions. By solving benchmark elastostatic and steady-state heat transfer problems, it was demonstrated that the accuracy and convergence of Fourier interpolation based scaled boundary method has remarkable advantages in computational accuracy and convergence.

## **Examples for comparison**

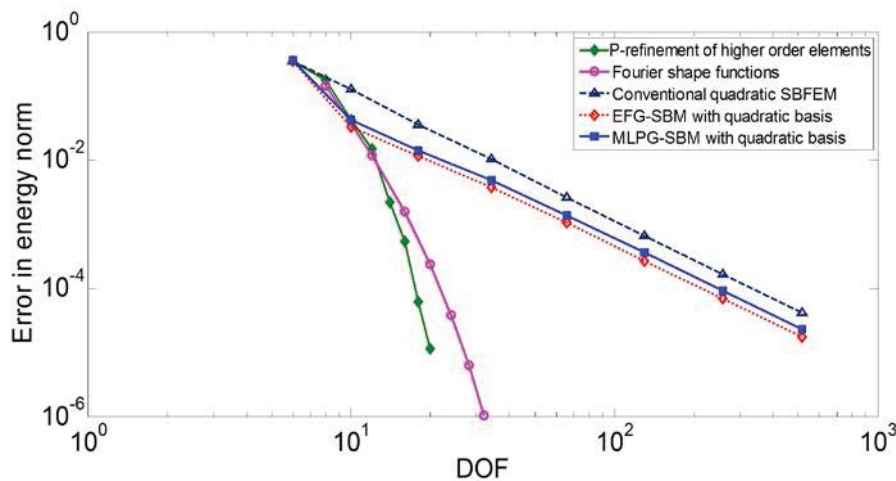
### *Example 1 - A plate of infinite extent subjected to a uniaxial stress*

The first example is a plate of infinite extent containing a hole of unit radius and subjected to a uniaxial stress of unity. Considering the symmetry of the problem, one quarter of the plate is represented (Figure 2(a)). The Young's modulus is taken as  $E = 1000$  and Poisson's ratio as  $\nu = 0.3$ . The boundary of the hole is considered as a single edge with the length  $l$  (Figure 2(b)). Uniform nodes are introduced along this edge, the nodes spacing is specified as  $ds$ . The centre of the hole is used as the scaling centre.



**Figure 2 A plate of infinite extent subjected to a uniaxial stress: (a) geometry and (b) scaled boundary model.**

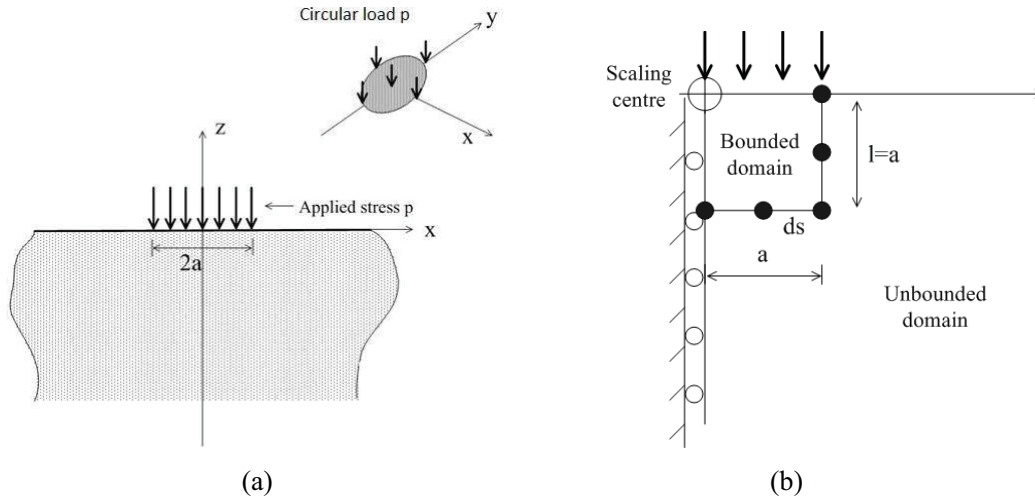
In order to evaluate the computed error in the domain, the relative error in energy norm is employed. Figure 3 shows the variation of the relative error in energy norm with degrees of freedom (DOF) in the domain  $\xi = [1, 3]$ . It is clear that the EFG-SBM and MLPG-SBM with quadratic basis are more accurate than conventional quadratic SBFEM with the same DOF, but the rate of convergence is similar. However, the higher-order elements and Fourier shape functions achieve a more rapid rate of convergence, showing that higher accuracy can be obtained under the same number of DOF compared with the conventional SBFEM and meshless SBM.



**Figure 3 The variation of error in energy norm with degrees of freedom**

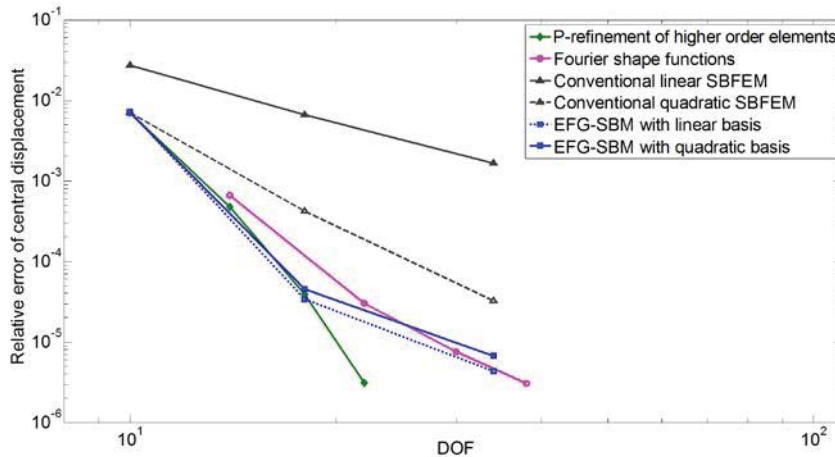
*Example 2 – Uniform circular load on homogeneous half-space*

The second example is the problem of a uniform load on an elastic homogeneous half-space, as shown in Figure 4(a). A vertical pressure  $p_0$  is applied uniformly over the circular region of radius  $a$  as shown. The Young's modulus is taken as  $E = 1000$  and Poisson's ratio as  $\nu = 0.3$ . This problem is axisymmetric. The scaled boundary model is illustrated in Figure 4(b), where the axis of symmetry runs along the left hand side of the domain. Two sub-domains are employed, sharing a common scaling centre, one bounded and one unbounded. Uniform nodes are distributed on the defining curve separating the two sub-domains, with node spacing  $ds$ . The stiffness matrix for each sub-domain is formed independently using the scaled boundary approach, and then the two stiffness matrices are assembled together. This problem has an analytical solution.



**Figure 4 Uniform circle/strip load on homogeneous half-space: (a) geometry and (b) scaled boundary model.**

In Figure 5, the variation of relative error for displacement on the central point ( $x=0, y=0, z=0$ ) is illustrated. It is seen that the EFG-SBM has better accuracy than conventional SBFEM using the same order of basis functions or elements, but the higher-order elements are still seen to have better convergence. The Fourier shape functions' performance is not quite so close to the higher order elements in this example.



**Figure 5 The variation of relative error for central displacement with degrees of freedom**

*Example 3 – Steady-state heat transfer in an L-shape domain*

The third example deals with the steady-state heat transfer problem in an L-shaped domain illustrated in Figure 6(a). The exact solution for this example contains a thermal singularity at the re-entrant corner, and is given in the polar coordinate system with the origin  $O$  by

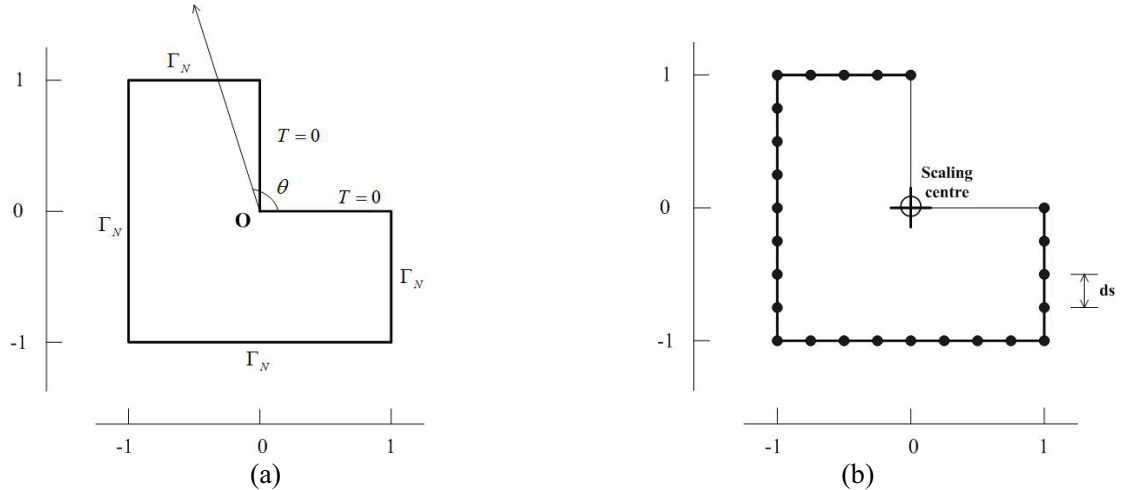
$$T(r, \theta) = r^{\frac{2}{3}} \sin\left(\frac{2\theta - \pi}{3}\right) \tag{2}$$

The specified boundary conditions are also indicated in Figure 6(a), with zero Dirichlet conditions at part of the boundary that lies on axis and Neumann conditions

determined by the exact solution  $T(r, \theta)$  elsewhere. The exact solution of heat flux on the radial direction  $q_r$  is

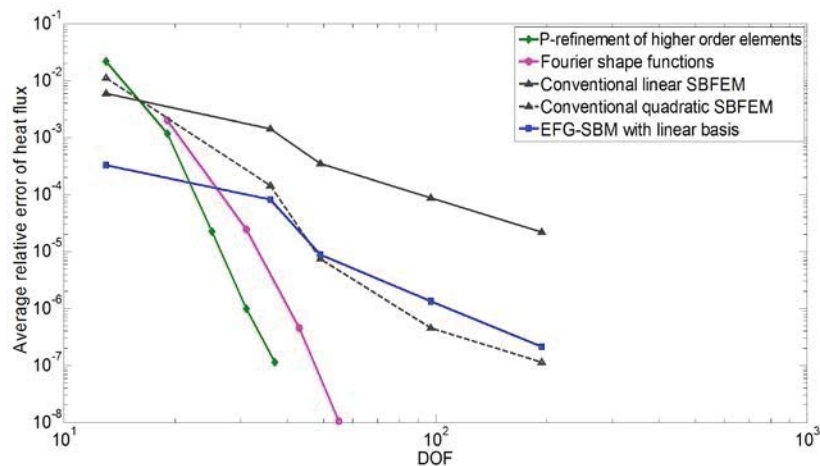
$$q_r = -k \cdot \frac{2}{3} r^{-\frac{1}{3}} \sin\left(\frac{2\theta - \pi}{3}\right) \quad (3)$$

where  $k$  is the thermal conductivity, taken as unit value in this example.



**Figure 6 Steady-state heat transfer in an L-shape domain: (a) geometry and (b) scaled boundary model.**

In order to evaluate the accuracy, the values of  $q_r$  are computed along the line with angle  $\theta = \pi$ , where ten points are located on radial coordinates  $r = 0$  and average relative error on these points are obtained to compare the performance of different shape functions, as illustrated in Figure 7. It is clearly demonstrated that the higher-order shape functions and Fourier shape functions are converge much more rapidly than the EFG-SBM and conventional SBFEM, and it is also shown that higher accuracy is obtained using the EFG-SBM with a linear basis compared with the linear SBFEM.

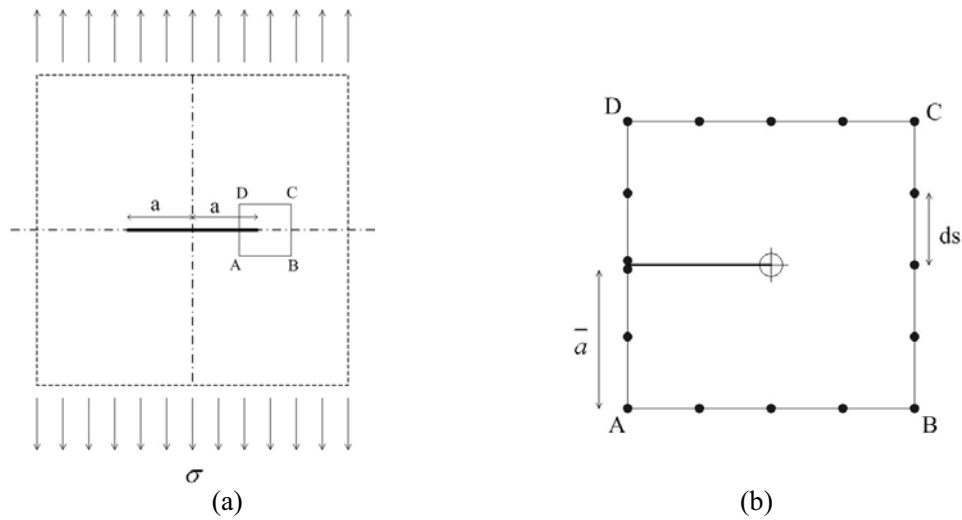


**Figure 7 The variation of relative error for central displacement with degrees of freedom**



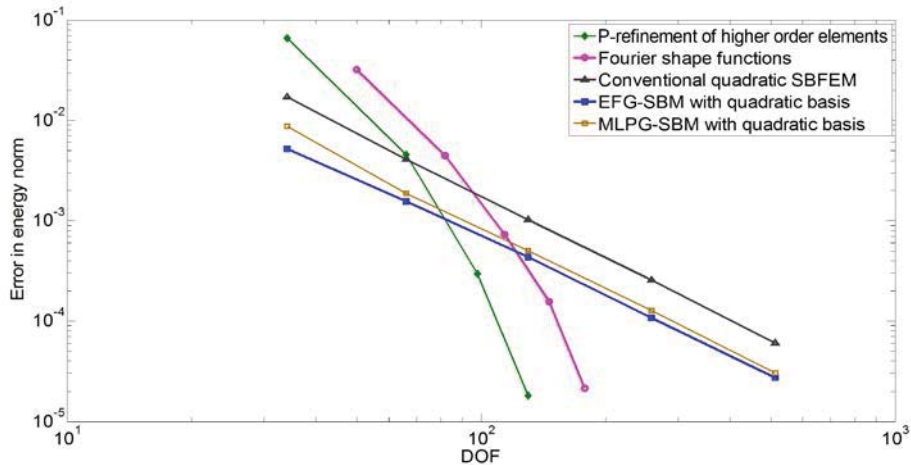
*Example 4 - Closed-form near-tip problem of an infinite plate with a through crack*

The example is an infinite plate containing a through crack and subjected to uniaxial tension in a direction normal to the crack, as illustrated in Figure 8(a). This is a mode I crack problem. The closed-form near-tip problem will be solved to investigate the performance of the scaled boundary method with different shape functions in solving for the stress field in a bounded domain around the crack tip when subjected to prescribed boundary displacements obtained from the exact solution. Along the boundary of square region ABCD with size  $\bar{a} = 0.01a$  in Figure 8(b), the closed-form near-tip displacements are imposed. The expression of the closed-form displacement and stress field can be found in [1]. The scaled boundary model is shown in Figure 8(b). Uniform nodes with spacing  $ds$  are used.



**Figure 8 Closed-form near-tip problem of an infinite plate with a through crack: (a) geometry and (b) scaled boundary model.**

The relative error in the energy norm used in Example 1 is also employed in this problem to evaluate the computational accuracy of the different approaches. Figure 9 shows that the results are similar to the results obtained for Example 1. The higher-order elements and Fourier shape functions have better convergence than the other approaches, and the higher-order elements are the best overall. The EFG-SBM has better performance than the conventional SBFEM and MLPG-SBM.



**Figure 9 The variation of error in energy norm with degrees of freedom**

## Conclusions

In this paper various numerical discretisation approaches for the scaled boundary method are reviewed, and numerical examples are provided to compare the accuracy and convergence of these approaches. Compared with the conventional SBFEM with linear or quadratic elements, these approaches have better performance in accuracy and convergence. For the meshless scaled boundary method (EFG-SBM and MLPG-SBM), higher accuracy can be obtained than the conventional SBFEM using the same number of nodes and order of elements or basis functions. For the higher-order elements and Fourier shape functions, significant advantages in convergence rate can be obtained, with very high accuracy obtained as more degrees of freedom are introduced. However, at lower numbers of degrees of freedom, the meshless approaches often give greater accuracy.

## References

- Deeks, A. J. and Wolf, J. P. (2002a), A virtual work derivation of the scaled boundary finite-element method for elastostatics, *Comput. Mech.* 28, pp. 489-504.
- Deeks, A. J. and Wolf, J. P. (2002b), An h-hierarchical adaptive procedure for the scaled boundary finite-element method, *Int. J. Numer. Meth. Eng.* 54, pp. 585-605.
- Deeks, A. J. and Augarde, C. E. (2005), A meshless local Petrov-Galerkin scaled boundary method. *Comput. Mech.* 36, pp. 159–170.
- He, Y. Q., Yang, H. T. and Deeks, A. J. (2012), An Element-free Galerkin (EFG) scaled boundary method, *Fin. Elem. Analy. Des.* 62, pp. 28-36.
- He, Y. Q., Yang, H. T. and Deeks, A. J. (2013), Use of Fourier shape functions in the scaled boundary method, Submitted to *CMAME*.
- Vu, T. H. and Deeks, A. J. (2006), Use of higher order shape functions in the scaled boundary finite element method, *Int. J. Numer. Meth. Eng.* 65, pp. 1714-1733.
- Vu, T. H. and Deeks, A. J. (2008a), A p-hierarchical adaptive procedure for the scaled boundary finite element method, *Int. J. Numer. Meth. Eng.* 73, pp. 47-70.
- Vu, T. H. and Deeks, A. J. (2008b), A p-adaptive scaled boundary finite element method based on maximization of the error decrease rate, *Comput. Mech.* 41, pp. 441-455.
- Wolf, J. P. and Song, C. (1996), *Finite-Element Modelling of Unbounded Media*. John Wiley and Sons, Chichester.
- Wolf, J. P. (2003), *The Scaled Boundary Finite Element Method*. John Wiley and Sons, Chichester, 2003.

# Performance Analysis of a High Order Immersed Interface Method for CFD Applications

\*P. C. V. Paino, M. A. F. de Medeiros

Universidade de São Paulo - Escola de Engenharia de São Carlos, Av. Trabalhador Sancarlene, 400, São Carlos - SP, Brazil

\*Corresponding author: paulopaino@usp.br

## Abstract

In Computational Fluid Dynamics, the physical representation of immersed objects within the computational domains leads to the loss of validity of the employed Finite Difference Schemes due to Jump Discontinuities. This paper analyses an Immersed Interface Method regarding its performance in High Order Schemes applications in the presence of such conditions. The error decay order of one 1D problem is observed. It is related to the computation of the first two derivatives of the Sin function. The results indicate eventual changes in the decay order of the original Finite Differences Schemes. This behaviour is investigated by a fragmented analysis of the method, which indicates a limitation of one of its numerical sub-steps. Finally, some remarks regarding restrictions to this method's applicability are presented.

**Keywords:** Immersed Interface Method, Immersed Boundary Method, Compact Schemes.

## Introduction

This article is intended to provide outlines and to investigate limitation(s) of the Immersed Interface Method, as proposed by (Linnick and Fasel, 2005) and (Wiegmann and Bube, 2000).

This method has been designed to provide for high-order (4th order and above) flow simulations around complex shape bodies. It's suited for problems such as the evolution of Tollmien-Schlichting waves and other problems that require high near-wall accuracy. One of its key advantages is the possibility of working with fixed, stationary grids, even if the immersed geometry moves within the domain. It's intended to significantly reduce the overall computational cost.

This method has been extensively analysed by the authors and, though its mathematical formulation does cope with the necessity of order maintenance, one of its inner steps seem to have restrictions regarding grid refinement. This is investigated through its employment to accomplish a simple calculation, that of the second derivative of a sine function over an uniform grid. The reason behind the selection of the sine function falls beyond the existence of an analytical solution to be compared with the numerical one. It lies on the fact that the sine function has an infinite number of derivatives. This is of particular importance not only in order to compare the final solutions, but also in order to perform individual tests throughout the IIM's substeps. This will become clearer later on.

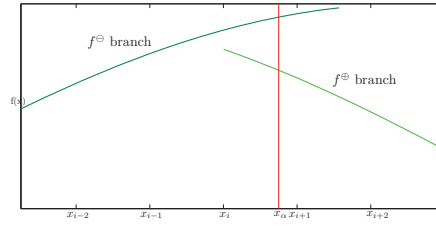
## The Immersed Interface Method

In general, Compact Schemes employed are based upon Taylor Series expansions. If the function is not continuous, these become not valid. Nevertheless, suitable corrections to them can still be applied. The IIM method described below builds upon the variant proposed by (Linnick and Fasel, 2005), which, in its turn, is based upon the original work from (Wiegmann and Bube, 2000). It provides the guidelines to calculate the aforementioned corrections when a function is subjected to Jump Discontinuities such as the one indicated at figure 1. The numerical discretization is performed here through the use of a fourth-order accurate Compact Scheme, in conjunction with the Immersed Interface Method, IIM.

The method is depicted here taking as an example the following approximation of a function's first derivative through the use of a Compact Scheme (second and higher order derivatives follow the same guidelines). Assuming that it consists of a set of equations of the form:

$$\begin{aligned} L_{1,i-1}f'(x(i-1)) + L_{1,i}f'(x(i)) + L_{1,i+1}f'(x(i+1)) = \\ = R_{1,i-1}f(x(i-1)) + R_{1,i}f(x(i)) + R_{1,i+1}f(x(i+1)) \end{aligned} \quad (1)$$

Where the coefficients  $L_{n,i+m}$  e  $R_{n,i+m}$  represent Padé Schemes coefficients, with  $n$  referring to the



**Figure 1. Jump Discontinuity Introduced at the point  $x_\alpha$**

$n$ -th order derivative (0 refers to the function value itself), and the letters  $L$  and  $R$  indicating left and right coefficients, respectively.

These equations are based upon Taylor Series expansions over different grid points. As those expansions presume function continuity, it becomes clear that the presence of Jump Discontinuities requires some kind of correction to be employed in order to maintain their validity.

Two situations might take place according to where the Jumps are placed, relatively to the interface.

Assuming a scheme centered at the point  $i$ , the point at which the function needs to be corrected can be either  $i + 1$  or  $i - 1$ . These situations are respectively represented as  $f^n, n = 0, 1, 2, 3, \dots$  superscripts  $\ominus$  and  $\oplus$ . The negative sign refers to the branch of function downstream the immersed interface, whereas the positive sign refers to the upstream branch.

*Jump Correction for the Downstream Branch Based Scheme*

Further simplifying the following terms:

$$f^{\ominus,\oplus}(x(i + 1)) = f_{i+1}^{\ominus,\oplus} \tag{2}$$

$$f'^{\ominus,\oplus}(x(i + 1)) = f'_{i+1}^{\ominus,\oplus} \tag{3}$$

The equation 1 then becomes:

$$L_{1,i-1}f'_{i-1}^{\ominus} + L_{1,i}f'_i{}^{\ominus} + L_{1,i+1}f'_{i+1}^{\ominus} = R_{1,i-1}f_{i-1}^{\ominus} + R_{1,i}f_i{}^{\ominus} + R_{1,i+1}f_{i+1}^{\ominus} \tag{4}$$

In this case, the Jump is introduced in the region  $x(i) < x_\alpha < x(i + 1)$ . This is imposed when boundary and interior conditions are applied to satisfy the presence of a physical object within the domain. With that particular introduction, the scheme, that was entirely based on downstream values, now computes two downstream (at points  $i - 1$  and  $i$ ) and one upstream value (at the  $i + 1$ -th grid point). With that in mind, and without any correction applied, the equation becomes:

$$L_{1,i-1}f'_{i-1}^{\ominus} + L_{1,i}f'_i{}^{\ominus} + L_{1,i+1}f'_{i+1}^{\oplus} = R_{1,i-1}f_{i-1}^{\ominus} + R_{1,i}f_i{}^{\ominus} + R_{1,i+1}f_{i+1}^{\oplus} \tag{5}$$

At this stage there's the need to introduce the Jump Correction Term, which intends to be a workaround to that problem. Following the definition provided by (Linnick and Fasel, 2005), this term shall, hereinafter, be represented as  $J_{\alpha,i+m}^n$ . Its meaning shall be elucidated below.

The next challenge is to find expressions for those corrections. Expanding  $f(x(i + 1))$  through Taylor Series both to the left and to the right side of the interface, and naming these expansions as  $f_{i+1}^{\ominus}$  and  $f_{i+1}^{\oplus}$ , one has:

$$f_{i+1}^{\oplus} = f_\alpha^{\oplus} + f_\alpha^{1\oplus} dx_\alpha^+ + \frac{f_\alpha^{2\oplus}(dx_\alpha^+)^2}{2!} + \dots + \frac{f_\alpha^{n\oplus}(dx_\alpha^+)^n}{n!} \tag{6}$$

$$f_{i+1}^{\ominus} = f_\alpha^{\ominus} + f_\alpha^{1\ominus} dx_\alpha^+ + \frac{f_\alpha^{2\ominus}(dx_\alpha^+)^2}{2!} + \dots + \frac{f_\alpha^{n\ominus}(dx_\alpha^+)^n}{n!} \tag{7}$$

With:

$$dx_\alpha^+ = x(i + 1) - x_\alpha \tag{8}$$

$$f_\alpha^{n\oplus,\ominus} = \lim_{x \rightarrow x_\alpha^{+,-}} f^n(x) \tag{9}$$

If one relates  $f_{i+1}^\oplus$  to  $f_{i+1}^\ominus$  then it's possible to equal this expression to a term called  $J_{\alpha,i+m}^{0\ominus}$ , which ultimately results in:

$$J_{\alpha,i+1}^{0\ominus} = f_{i+1}^\oplus - f_{i+1}^\ominus \tag{10}$$

This becomes, upon manipulation:

$$J_{\alpha,i+1}^{0\ominus} = [f_\alpha^0] + [f_\alpha^1]dx_\alpha^+ + [f_\alpha^2]\frac{(dx_\alpha^+)^2}{2!} + \dots + [f_\alpha^n]\frac{(dx_\alpha^+)^n}{n!} \tag{11}$$

With:

$$[f_\alpha^n] = \lim_{x \rightarrow x_\alpha^+} f^n(x) - \lim_{x \rightarrow x_\alpha^-} f^n(x)$$

After this procedure, it becomes obvious why the term  $J_{\alpha,i+1}^{0\ominus}$  is called Jump Correction Term, and one could proceed similarly to obtain an expression for  $J_{\alpha,i+m}^{1\ominus}$ :

$$J_{\alpha,i+1}^{1\ominus} = [f_\alpha^1] + [f_\alpha^2]dx_\alpha^+ + [f_\alpha^3]\frac{(dx_\alpha^+)^2}{2!} + \dots + [f_\alpha^n]\frac{(dx_\alpha^+)^{n-1}}{n-1!} \tag{12}$$

These manipulations lead to the corrected equation of the form:

$$\begin{aligned} L_{1,i-1}f'_{i-1}^\ominus + L_{1,i}f'_i^\ominus + L_{1,i+1}f'_{i+1}^\oplus &= \\ &= R_{1,i-1}f_{i-1}^\ominus + R_{1,i}f_i^\ominus + R_{1,i+1}f_{i+1}^\oplus - (R_{1,i+1}J_{\alpha,i+1}^{0\ominus} + L_{1,i+1}J_{\alpha,i+1}^{1\ominus}) \end{aligned} \tag{13}$$

*Jump Correction for the Upstream Branch Based Scheme*

The development for this case follows the same guidelines as those from the previous section. Considering an approximation to the first derivative:

$$L_{1,i-1}f'_{i-1}^\oplus + L_{1,i}f'_i^\oplus + L_{1,i+1}f'_{i+1}^\oplus = R_{1,i-1}f_{i-1}^\oplus + R_{1,i}f_i^\oplus + R_{1,i+1}f_{i+1}^\oplus \tag{14}$$

That becomes:

$$L_{1,i-1}f'_{i-1}^\ominus + L_{1,i}f'_i^\oplus + L_{1,i+1}f'_{i+1}^\oplus = R_{1,i-1}f_{i-1}^\ominus + R_{1,i}f_i^\oplus + R_{1,i+1}f_{i+1}^\oplus \tag{15}$$

Using the following Taylos Series expansions around  $x_\alpha$ :

$$f_{i-1}^\oplus = f_\alpha^\oplus - f_\alpha^{1\oplus}dx_\alpha^- + \frac{f_\alpha^{2\oplus}(dx_\alpha^-)^2}{2!} + \dots + [-1^{(n)}]\frac{f_\alpha^{n\oplus}(dx_\alpha^-)^n}{(n)!} \tag{16}$$

$$f_{i-1}^\ominus = f_\alpha^\ominus - f_\alpha^{1\ominus}dx_\alpha^- + \frac{f_\alpha^{2\ominus}(dx_\alpha^-)^2}{2!} + \dots + [-1^{(n)}]\frac{f_\alpha^{n\ominus}(dx_\alpha^-)^n}{(n)!} \tag{17}$$

$$f_{i-1}^{1\oplus} = f_\alpha^{1\oplus} - f_\alpha^{2\oplus}dx_\alpha^- + \frac{f_\alpha^{3\oplus}(dx_\alpha^-)^2}{2!} + \dots + [-1^{(n-1)}]\frac{f_\alpha^{n\oplus}(dx_\alpha^-)^{n-1}}{(n-1)!} \tag{18}$$

$$f_{i-1}^{1\ominus} = f_\alpha^{1\ominus} - f_\alpha^{2\ominus}dx_\alpha^- + \frac{f_\alpha^{3\ominus}(dx_\alpha^-)^2}{2!} + \dots + [-1^{(n-1)}]\frac{f_\alpha^{n\ominus}(dx_\alpha^-)^{n-1}}{(n-1)!} \tag{19}$$

Where:

$$dx_\alpha^- = x_\alpha - x(i-1) \tag{20}$$

$$f_\alpha^{n\oplus,\ominus} = \lim_{x \rightarrow x_\alpha^{+,-}} f^n(x) \tag{21}$$

And the following definitions:

$$J_{\alpha,i-1}^{0\oplus} = f_{i-1}^\ominus - f_{i-1}^\oplus \tag{22}$$

$$J_{\alpha,i-1}^{1\oplus} = f'_{i-1}^\ominus - f'_{i-1}^\oplus \tag{23}$$

The Jump Correction Terms are then written as:

$$J_{\alpha,i-1}^{0\oplus} = -[f_{\alpha}^0] + [f_{\alpha}^1]dx_{\alpha}^{-} - [f_{\alpha}^2]\frac{(dx_{\alpha}^{-})^2}{2!} + \dots + [-1^{(n+1)}][f_{\alpha}^n]\frac{(dx_{\alpha}^{-})^n}{n!} \quad (24)$$

$$J_{\alpha,i-1}^{1\oplus} = -[f_{\alpha}^1] + [f_{\alpha}^2]dx_{\alpha}^{-} - [f_{\alpha}^3]\frac{(dx_{\alpha}^{-})^2}{2!} + \dots + [-1^{(n)}][f_{\alpha}^n]\frac{(dx_{\alpha}^{-})^{(n-1)}}{(n-1)!} \quad (25)$$

Where:

$$[f_{\alpha}^n] = \lim_{x \rightarrow x_{\alpha}^{+}} f^n(x) - \lim_{x \rightarrow x_{\alpha}^{-}} f^n(x)$$

Finally, the corrected first derivative equation:

$$\begin{aligned} L_{1,i-1}f'_{i-1}{}^{\ominus} + L_{1,i}f'_i{}^{\oplus} + L_{1,i+1}f'_{i+1}{}^{\oplus} &= \\ &= R_{1,i-1}f_{i-1}{}^{\ominus} + R_{1,i}f_i{}^{\oplus} + R_{1,i+1}f_{i+1}{}^{\oplus} - (R_{1,i-1}J_{\alpha,i-1}^{0\oplus} + L_{1,i-1}J_{\alpha,i-1}^{1\oplus}) \end{aligned} \quad (26)$$

Nevertheless, it's yet to be shown how to obtain approximations to those Jump Terms. The only values known at each iteration of the method are function values themselves. So the only option available is to combine them in such a way that all derivatives at the immersed interface can be estimated accordingly. For the case depicted at this subsection, the desired system can be represented by:

$$\begin{aligned} f(x_{\alpha}) &= c_{\alpha,1}f(x_{\alpha}) + c_{i+1,1}f(x_{i+1}) + c_{i+2,1}f(x_{i+2}) + \dots + c_{i+n,1}f(x_{i+n}) \\ f^1(x_{\alpha}) &= c_{\alpha,2}f(x_{\alpha}) + c_{i+1,2}f(x_{i+1}) + c_{i+2,2}f(x_{i+2}) + \dots + c_{i+n,2}f(x_{i+n}) \\ &\vdots = \quad \vdots + \quad \vdots + \quad \vdots + \quad \vdots \\ f^n(x_{\alpha}) &= c_{\alpha,n}f(x_{\alpha}) + c_{i+1,n}f(x_{i+1}) + c_{i+2,n}f(x_{i+2}) + \dots + c_{i+n,n}f(x_{i+n}) \end{aligned} \quad (27)$$

With  $f^n(x_{\alpha}) = f_{\alpha}^n$  and  $f(x_{i+n}) = f_{i+n}^0$ , its matrix representation is:

$$\begin{pmatrix} f_{\alpha}^0 \\ f_{\alpha}^1 \\ \vdots \\ f_{\alpha}^{n-1} \end{pmatrix} = \begin{pmatrix} 1 & 0 & 0 & \dots & 0 \\ c_{\alpha,2} & c_{i+1,2} & c_{i+2,2} & \dots & c_{i+n,2} \\ \vdots & \vdots & \vdots & \vdots & \vdots \\ c_{\alpha,n} & c_{i+1,n} & c_{i+2,n} & \dots & c_{i+n,n} \end{pmatrix} \times \begin{pmatrix} f_{\alpha}^0 \\ f_{i+1}^0 \\ \vdots \\ f_{i+n}^0 \end{pmatrix} \quad (28)$$

The Weierstrass's theorem states that if a function  $f(x)$  is continuous over a finite interval  $a \leq x \leq b$  then it can be approximated as closely as wanted by a power polynomial, provided this polynomial's order is sufficiently large. So, one may want to represent the function values in successive points close to the immersed interface through Taylor Series expansions (according to (Linnick and Fasel, 2005), the first neighbor point shall be neglected):

$$\begin{pmatrix} f_{\alpha}^0 \\ f_{i+1}^0 \\ \vdots \\ f_{i+n}^0 \end{pmatrix} = \begin{pmatrix} 1 & 0 & 0 & \dots & 0 \\ 1 & (dx_{\alpha}^{+} + d_x) & \frac{(dx_{\alpha}^{+} + d_x)^2}{2!} & \dots & \frac{(dx_{\alpha}^{+} + d_x)^n}{n!} \\ \vdots & \vdots & \vdots & \vdots & \vdots \\ 1 & (dx_{\alpha}^{+} + nd_x) & \frac{(dx_{\alpha}^{+} + nd_x)^2}{2!} & \dots & \frac{(dx_{\alpha}^{+} + nd_x)^n}{n!} \end{pmatrix} \times \begin{pmatrix} f_{\alpha}^0 \\ f_{\alpha}^1 \\ \vdots \\ f_{\alpha}^{n-1} \end{pmatrix} \quad (29)$$

Using:

$$[C] = C_{n,n} = \begin{pmatrix} 1 & 0 & 0 & \dots & 0 \\ c_{\alpha,2} & c_{i+1,2} & c_{i+2,2} & \dots & c_{i+n,2} \\ \vdots & \vdots & \vdots & \vdots & \vdots \\ c_{\alpha,n} & c_{i+1,n} & c_{i+2,n} & \dots & c_{i+n,n} \end{pmatrix} \quad (30)$$

And:

$$[D] = D_{n,n} = \begin{pmatrix} 1 & 0 & 0 & \dots & 0 \\ 1 & (dx_{\alpha}^{+} + d_x) & \frac{(dx_{\alpha}^{+} + d_x)^2}{2!} & \dots & \frac{(dx_{\alpha}^{+} + d_x)^n}{n!} \\ \vdots & \vdots & \vdots & \vdots & \vdots \\ 1 & (dx_{\alpha}^{+} + nd_x) & \frac{(dx_{\alpha}^{+} + nd_x)^2}{2!} & \dots & \frac{(dx_{\alpha}^{+} + nd_x)^n}{n!} \end{pmatrix} \quad (31)$$

We can change between systems:

$$(f) = [D](f_\alpha^n) \tag{32}$$

$$[D]^{-1}(f) = [D]^{-1}[D](f_\alpha^n) \tag{33}$$

Upon close inspection, we conclude that [D] is always invertible. Finally:

$$[C] = [D]^{-1} \tag{34}$$

A brief discussion regarding the order maintenance of these expansions is found in (Linnick and Fasel, 2005). As for the fourth-order Compact Scheme used:

$$\begin{pmatrix} 1 & 11 & 0 & \dots & \dots & \dots \\ 1 & 10 & 1 & \dots & \dots & \dots \\ 0 & 1 & 10 & 1 & \dots & \dots \\ \vdots & \vdots & \vdots & \vdots & \vdots & \vdots \\ \dots & \dots & 1 & 10 & 1 & 0 \\ \dots & \dots & \dots & 1 & 10 & 1 \\ \dots & \dots & \dots & 0 & 11 & 1 \end{pmatrix} \text{ and } \begin{pmatrix} 39a & -81a & 45a & -3a & \dots & \dots \\ 1b & -2b & 1b & 0 & \dots & \dots \\ 0 & 1b & -2b & 1b & \dots & \dots \\ \vdots & \vdots & \vdots & \vdots & \vdots & \vdots \\ \dots & \dots & 1b & -2b & 1b & 0 \\ \dots & \dots & 0 & 1b & -2b & 1b \\ \dots & \dots & -3a & 45a & -81a & 39a \end{pmatrix}$$

With  $a = 1/3dx^2$  and  $b = 12/dx^2$ .

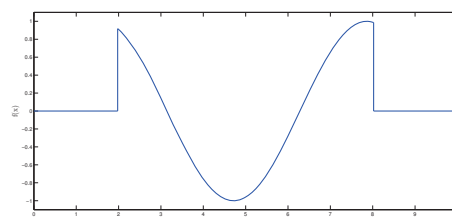
**Results**

Initial implementations of this method by the authors in full fledged CFD codes showed that the decay order of the solutions as the grid was progressively refined were not consistent with the order of the scheme. Considering that the method is modular, the necessity to investigate it in detail has arisen. The reader should observe that this paper does not compare distinct methods. This investigation regards only the decay order test of the Finite Difference when coupled to a particular IIM. The testing approach is only applicable in the following and similarly restrictive contexts. Therefore, it cannot provide ways of improving the method as proposed by (Linnick and Fasel, 2005) for general applications. From this perspective, a computational cost test was not taken into account.

From the mathematical formulation of the method, as presented by (Wiegmann and Bube, 2000), to the numerical application as proposed by (Linnick and Fasel, 2005), the main change regards the Jump Correction Terms. The former presents the mathematical correction needed to maintain a required scheme order. This is accomplished if all function jumps are known at each time step. This is true for functions with analytic solutions. If these jumps are not known, then there will be the necessity to provide approximations to them.

What is presented by (Linnick and Fasel, 2005) is that all Jump Terms can be approximated by linear combinations of the function value themselves. Taking all these considerations into account, a simple test has been conducted to precise the impact of the Jump Correction Terms approximations as presented by (Linnick and Fasel, 2005).

This has been achieved by the the application of the method to the calculation of the first two derivatives of the  $\sin(x)$  function over a domain length of  $L = 10$  (the selected profile is shown in figure . As seen on the figure, the curve is subjected to jump discontinuities at two domain points, namely  $x_{\alpha_1} = 1.97875$  and  $x_{\alpha_2} = 8.02125$ . These points have been purposely selected not to coincide with grid points even for the most refined grid.



**Figure 2. Jump Discontinuity Introduced at the points  $x_{\alpha_1}$  and  $x_{\alpha_2}$**

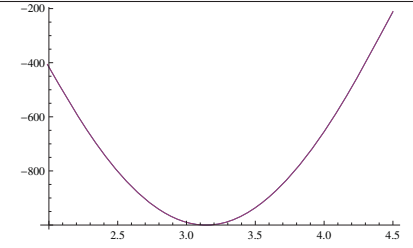
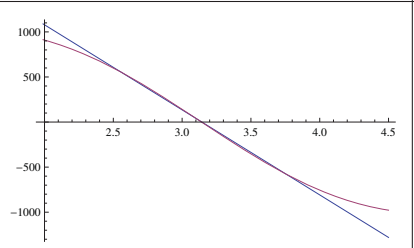
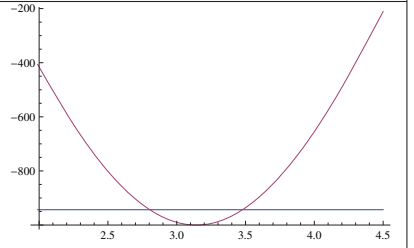
One of the key aspects of this approach is that all Jump Terms could be calculated not only by approximation of the function values themselves, but also by the analytical values of any of their derivatives (in fact, the Jump Correction Terms for the  $\sin(x)$  function could be calculated based upon polynomials as big as needed, once the function has infinity derivatives). The Jump Terms based upon exact derivatives would lead to the maintenance of the original scheme's order, according to the method introduced by (Wiegmann and Bube, 2000). The results presented here concentrate mainly on the analysis of the differences between these two applications. For the sake of this comparison, from now on a Jump Term will be simply named 'Analytical Jump Term' and the numerical one, 'Numerical Jump Term'. The reader should recall that The Numerical Jump Term, as already seen, is an approximation of the derivative by a linear combination of the function values themselves. One important note about this application is that this procedure has been executed for both the forward and the backward Taylor Series expansions, which are respectively representative of the two discontinuity points,  $x_{\alpha_1}$  and  $x_{\alpha_2}$ .

The first results regard an extensive check up of all these derivative approximations obtained by the matrix inversion process described. These were executed within the code and then compared to the same procedures executed by the commercial software Wolfram Mathematica. Tables 1 and 2 present results for given combinations of grid points and derivative order, at the point  $x_{\alpha_1}$ . In these tables, the 'Calculated value' field refers to the approximation calculated by the authors's code based upon the matrix inversion suggested by (Linnick and Fasel, 2005). The plots show two results from Wolfram Mathematica. The purple line indicates the analytical graphical values of the considered derivative, whereas the blue one indicates a fitted polynomial which best represent the function at the discontinuity point. The start of the x-axis is the point  $x_{\alpha_1}$ .

According to the precision order required (discussed in detail in (Linnick and Fasel, 2005)), each higher order derivative approximation can be calculated with a progressively decreasing order. Besides, this precision requirement implies the approximation of a number of derivatives for given scheme and derivative orders. In this case, 4th-order schemes are employed to the calculation of the first two derivatives of a function. Consequently, the Jump Correction Terms must include up to the fifth derivative approximation. The whole set of results has not been shown for the sake of available space. Nevertheless, it's important to note that this has been done for each derivative of each of the tested grids, at both points. The reader should also recall that this procedure should be done from the first to the fifth derivative, which are the required ones for the calculation of up to the second derivative with 4-th order.

**Table 1. First, fourth and fifth derivatives at  $x_{\alpha_1} = 1.989375$  - 21 points grid**

21 points grid					
1st Derivative		4th Derivative		5th Derivative	
Calculated value		Calculated value		Calculated value	
$-406.8457641830 \cdot 10^{-3}$		$1.0887651426$		$-943.4528052418 \cdot 10^{-3}$	
Analytical value		Analytical value		Analytical value	
$-406.4622438469 \cdot 10^{-3}$		$913.6675786778 \cdot 10^{-3}$		$-406.4622438469 \cdot 10^{-3}$	

The information from these tables show that the fitted polynomial obtained by the Wolfram Mathematica software agrees with the results obtained by the matrix inversion process employed by the authors' code at the jump point  $x_{\alpha_1} = 1.989375$ , and for all presented derivatives. As the grid is refined the numerical value approaches the analytical value. Of special attention is the behaviour exhibited for the 4th and 5th derivative, depicted by the second and third plots from the left. It shows that the polynomials fitted for all 4th derivatives are of 1st order, and the line for the the 5th derivatives are constant value lines. That is also an indication that each higher derivative is indeed calculated by



**Table 2. First, fourth and fifth derivatives at  $x_{\alpha_1} = 1.989375$  - 641 points grid**

641 points grid					
1st Derivative		4th Derivative		5th Derivative	
Calculated value		Calculated value		Calculated value	
$-406.4622443593 \cdot 10^{-3}$		$914.6222546697 \cdot 10^{-3}$		$-449.7330188751 \cdot 10^{-3}$	
Analytical value		Analytical value		Analytical value	
$-406.4622438469 \cdot 10^{-3}$		$913.6675786778 \cdot 10^{-3}$		$-406.4622438469 \cdot 10^{-3}$	

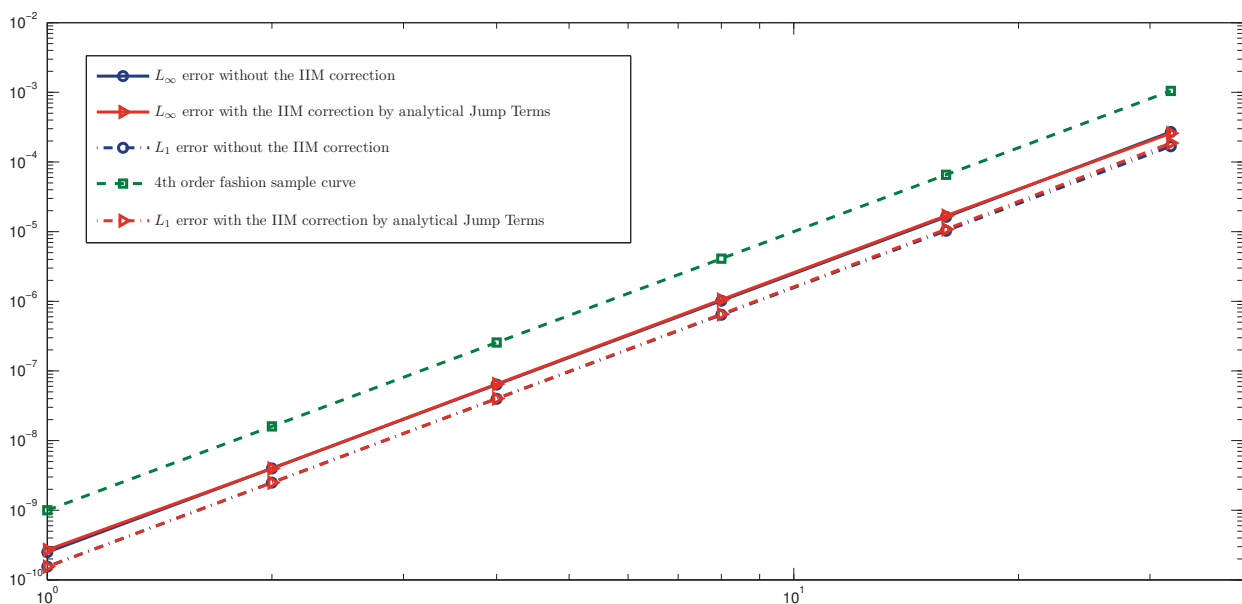
  

this process with a progressively lower order. Finally, it's also being demonstrated that this process implies a lot different than expected values for the derivatives at that point.

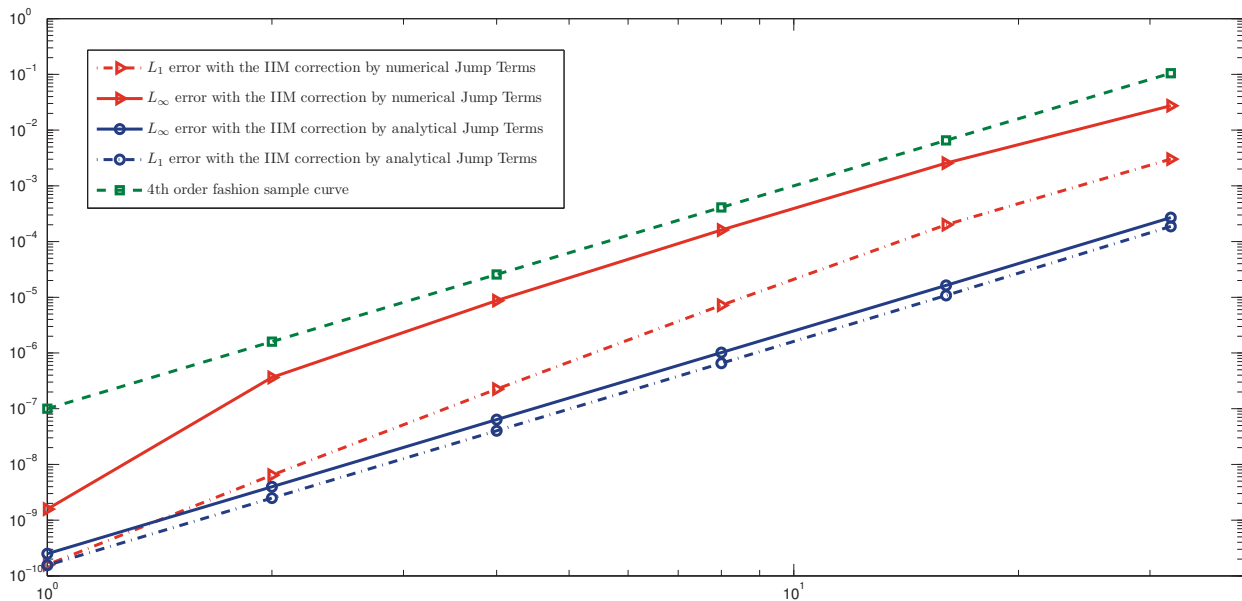
After this discussion, figures 4 and 3 show the results from the grid refinement test. This has begun with a 21 points grid and then has gotten progressively refined to the double of the previous points number, up to a 641 points grid. The errors' standards follow the definition found on (da Silva, 2008). That uses the error norms according to equations 35 and 36. The two plots show the errors  $L_\infty$  and  $L_1$  for different solutions, with the index  $n$  representing the number of grid points.

$$L_1 = \left[ \sum_{n=1}^j |f_{ex}(n) - f_{calc}(n)| \right] / j \tag{35}$$

$$L_\infty = \max |f_{ex}(n) - f_{calc}(n)| \quad ; \quad n = 1, 2, \dots, j \tag{36}$$



**Figure 3. Sin Function - Second Derivative Errors - Analytical Jump Terms (Grid Points Number vs. Error)**



**Figure 4. Sin Function - Second Derivative Errors - Numerical Jump Terms (Grid Points Number vs. Error)**

First, the plot from figure 3 shows the comparison between the results for the IIM with Analytical Jump Terms and the solution if no Jump Discontinuities were imposed (which implies that the function would be continuous for any  $x$  from 0 to 10). Comparing the error norms from both solutions to the green 4-th order sample curve it's shown that the decay order of the scheme is indeed maintained by the method. It is important to notice that the IIM based upon Analytical Jump Terms not only does that, decaying to the same order than the original scheme, but also agrees with it when it comes to absolute values. On the other hand, a direct comparison between the Analytical and the Numerical IIM (showed in figure 4), shows that the error norms of the IIM based upon the Numerical Jump Terms are not only considerably higher and inconsistent in terms of decay order, but they also start to match the Analytical IIM values only for the most refined grid, with 641 points. This behaviour rises the question of how effective is the approximation of those derivatives at points  $x_{\alpha_n}$  by the linear combination of the function values.

Closer inspection of the equations applied to those approximations shows that the method (as proposed by (Linnick and Fasel, 2005)) requires the same amount of neighbour points to be computed for each more refined grid, but one can immediately point out that their positions along the coordinate axis change as the grid becomes more refined. Compared to the domain length, this directly translates into a collection of points progressively more collapsed as we change from one grid to the next. This means that the portion of the curve that is actually being computed by this process, and therefore its shape, also changes from one grid to another.

All these discussion and results show that the method proposed by (Linnick and Fasel, 2005) is not capable of always maintaining the scheme's order in the same manner as the original mathematical formulation by (Wiegmann and Bube, 2000) does. This can have an ultimate effect on the grid refinement, requiring a great amount of points to reach a desirable error magnitude and diminishing the advantage of employing a High Order Scheme.

### Acknowledgements

The authors would like to thank CNPQ (Conselho Nacional de Desenvolvimento Científico e Tecnológico), which has fomented this paper's related research in the form of a scholarship.

**References**

- Wiegmann A., Bube K. P. (2000), The Explicit-Jump Immersed Interface Method: Finite Difference Methods for PDE's with Piecewise Smooth Solutions, *SIAM Journal on Numerical Analysis*, v.37 n.3, pp.827-862.
- Linnick M. K. and Fasel H. F. (2005), A high-order immersed interface method for simulating unsteady incompressible flows on irregular domains, *Journal of Computational Physics*, v.204, issue 1, pp.157-192.
- Da Silva H. G. (2008), Regime Não-linear de Trens de Ondas Modulados na Direção Transversal em um Escoamento de Poiseuille Plano, Tese de Doutorado, *Escola de Engenharia de São Carlos*.
- Kopal Z. (1961), Numerical Analysis, 2nd Edition, *Chapman & Hall*, London.

## Parallel Implementation of Grammatical Evolution

\*E. Kita<sup>1,2</sup>, Y. Lu<sup>1</sup>, H. Sugiura<sup>1</sup> and Y. Wakita<sup>1</sup>

<sup>1</sup>Department of Complex Science, Graduate School of Information Science, Nagoya University  
Nagoya, JAPAN

<sup>2</sup>Department of Computational Science, Graduate School of System Informatics, Kobe University  
Kobe, JAPAN

\*Corresponding author: kita@is.nagoya-u.ac.jp

### Abstract

Grammatical Evolution (GE) is one of the evolutionary computations, which determine function or program or program fragment satisfying the design objective, like Genetic Programming (GP). The interesting feature of GE is to define the translation rule from the genotype (bit-string) to the phenotype (function or program) in advance. The population of individuals (bit-strings) is evolved toward better individual by using the translation rule and Genetic Algorithm (GA) search process.

The aim of this study is to discuss the effectiveness of parallel implementation for GE. The parallel implementation is based on simple island model. The whole population is substituted into sub-populations. The evolution process is performed individually in subpopulations and some individuals are exchanged between subpopulations in any interval. Exchange of individuals is called as migration. Better individual migration and randomly selected individual migration are compared.

The symbolic regression problem is considered as a numerical example. The results show that, in random migration, longer migration interval is better for larger sub-population size and shorter migration interval is better for smaller sub-population size and that, in better individual migration, longer migration interval and larger sub-population size are better.

**Keywords:** Grammatical Evolution, Parallel Implementation, Island Model, Symbolic Regression Problem.

### Introduction

Evolutionary computations are algorithms based on the evolutionary process of living organism. Genetic Algorithm (GA) and Genetic Program (GP) are very popular algorithms in this field [1,2]. The aim of GA is to find the solution of the optimization problem. Potential solutions are represented by individuals as bit-strings. The population of individuals evolves to a better potential solution by genetic operators such as selection, crossover, mutation, and so on. Although GP comes from GA, their aims are different. GP is designed for finding the function, the program or the program fragment satisfying the design objective. The potential solutions, which are represented as the individuals in tree structure, evolve toward better solution by genetic operators.

GP has two difficulties. Firstly, the genetic operators are very complicated and the effect for the search process is not obvious. Secondly, during the GP search process, genetic operators often generate individuals which lead to invalid function or invalid program or invalid program fragment. For overcoming these difficulties, Grammatical Evolution (GE) was presented [3,4]. The interesting feature of GE is to define the translation rule from genotype (bit-string) to phenotype (function or program) in advance. The translation rule is written in Backus Naur Form (BNF). Once the valid translation rule is given, GE can generate the genotypes which lead to valid phenotypes. The search process of GE is as follows. Initial population of individuals is defined by randomly generated bit-strings. Genotypes are translated into the phenotype according to the translation rule and the fitness is estimated. According to the fitness, the population of individuals is evolved toward better solutions by the genetic operators.

Except for the use of the translation rule, the GE search process is very similar to simple GA. Therefore, the use of the improved GA algorithm can improve the search process of the original GE. The aim of this paper is to use parallel GA for GE. The parallel implementation of GA is studied widely [5]. The distributed Genetic Algorithm (DGA) based on Island model is employed in this study [6]. In DGA, the population is divided into sub-populations. GA is applied for each sub-population and then, individuals migrate from one sub-population to the other one at regular interval. It is reported that DGA based on island model can find better solution than traditional GA using single population. The algorithm is applied for symbolic regression problem in order to discuss the search performance.

Table 1: Example of translation rule

(A)	$\langle \text{expr} \rangle ::= \langle \text{expr} \rangle \langle \text{op} \rangle \langle \text{expr} \rangle$   $\langle \text{var} \rangle$	(A0) (A1)
(B)	$\langle \text{op} \rangle ::= +$   $-$   $*$   $/$	(B0) (B1) (B2) (B3)
(C)	$\langle \text{var} \rangle ::= X$   $Y$   $Z$	(C0) (C1) (C2)

## Grammatical Evolution

### Algorithm

The algorithm of the original GE is summarized as follows.

1. Translation rule is defined in Backus Naur Form (BNF).
2. Initial population is defined by randomly generated bit-strings.
3. Genotypes (bit-strings) are translated into phenotypes (function or program) according to the translation rule.
4. Phenotype fitness is estimated.
5. Population is updated by genetic operators such as selection, crossover and mutation.
6. If the convergence criterion is satisfied, the process is terminated. Otherwise, process goes to step 3.

### Translation from Genotype to Phenotype

We would like to explain the translation from genotype from phenotype. The translation rule in BNF syntax is shown in Table 1. It is shown from this table that the symbol  $\langle \text{expr} \rangle$  has two candidate symbols  $\langle \text{expr} \rangle \langle \text{op} \rangle \langle \text{expr} \rangle$  and  $\langle \text{var} \rangle$  and that the symbol  $\langle \text{op} \rangle$  has four candidate symbols  $+$ ,  $-$ ,  $*$  and  $/$  and that the symbol  $\langle \text{var} \rangle$  has three candidate symbols  $X$ ,  $Y$  and  $Z$ . The symbols  $+$ ,  $-$ ,  $*$  and  $/$  denote the four arithmetic operators and the symbols  $X$ ,  $Y$  and  $Z$  are variables. Since the symbol  $\langle \text{expr} \rangle \langle \text{op} \rangle \langle \text{expr} \rangle$  and  $\langle \text{var} \rangle$  should be replaced again, they are called as recursive symbols. The symbols  $+$ ,  $-$ ,  $*$ ,  $/$ ,  $X$ ,  $Y$  and  $Z$  are called as terminal rules because they are not replaced any more.

When the start symbol is  $\langle \text{expr} \rangle$  and the genotype is given as the binary 010001111101101110, the genotype is translated according to Table 1 as follows (Table 2).

1. The binary number 010001111101101110 is translated into the decimal number every 3bits as follows.

$$010001111101101110 \rightarrow 2 \ 1 \ 7 \ 5 \ 5 \ 6$$

2. The symbol  $\langle \text{expr} \rangle$  has two candidate rules and the first decimal number is 2. The remainder of the decimal number 2 with respect to the candidate symbol number 2 is 0. Then, the symbol  $\langle \text{expr} \rangle$  is replaced with  $\langle \text{expr} \rangle \langle \text{op} \rangle \langle \text{expr} \rangle$ .  
 $\langle \text{expr} \rangle \rightarrow \langle \text{expr} \rangle \langle \text{op} \rangle \langle \text{expr} \rangle$ .
3. Next replaced symbol is the leftmost recursive symbol  $\langle \text{expr} \rangle$ .
4. The symbol  $\langle \text{expr} \rangle$  has two candidate rules and the next decimal number is 1. The remainder of the decimal number 1 with respect to the candidate symbol number 2 is 1. Then, the symbol  $\langle \text{expr} \rangle$  is replaced with  $\langle \text{var} \rangle$ ;  
 $\langle \text{expr} \rangle \langle \text{op} \rangle \langle \text{expr} \rangle \rightarrow \langle \text{var} \rangle \langle \text{op} \rangle \langle \text{expr} \rangle$ .
5. According to the similar process, the function  $Y+X$  is obtained from the binary number 010001111101101110.

Table 2: Symbol replacement process

Decimal	Remainder	Target symbol	Selected symbol	Symbol after replacement
Start				$\langle \text{expr} \rangle$
2	0	$\langle \text{expr} \rangle$	$\langle \text{expr} \rangle \langle \text{op} \rangle \langle \text{expr} \rangle$	$\langle \text{expr} \rangle \langle \text{op} \rangle \langle \text{expr} \rangle$
1	1	$\langle \text{expr} \rangle$	$\langle \text{var} \rangle$	$\langle \text{var} \rangle \langle \text{op} \rangle \langle \text{expr} \rangle$
7	1	$\langle \text{var} \rangle$	Y	$Y \langle \text{op} \rangle \langle \text{expr} \rangle$
5	4	$\langle \text{op} \rangle$	+	$Y+ \langle \text{expr} \rangle$
5	1	$\langle \text{expr} \rangle$	$\langle \text{var} \rangle$	$Y+ \langle \text{var} \rangle$
6	0	$\langle \text{var} \rangle$	X	$Y+X$

## Parallel Grammatical Evolution

### Algorithm

In the present algorithm, the parallel implementation of Grammatical Evolution is performed according to Genetic Algorithm based on the island model. The whole population of the individuals is divided into sub-populations and then, the original GE is performed at each sub-population. The present algorithm is summarized as follows.

1. Translation rule is defined in Backus Naur Form (BNF).
2. Initial sub-populations are defined by randomly generated bit-strings.
3. Genotypes (bit-strings) are translated into phenotypes (function or program) according to the translation rule.
4. Individual fitness is estimated.
5. Sub-populations are updated by genetic operators such as selection, crossover and mutation.
6. If the convergence criterion is satisfied, the process is terminated. Otherwise, the process goes to next step.
7. Individuals are migrated from one sub-population to the other one at any interval.
8. Process goes to step 3.

### Migration

Migration operator exchanges the individuals between the sub-populations. In this study, two migration operators are compared.

The individuals to be migrated are selected as follows.

1. Random migration.  
Immigrant individuals are selected randomly from the sub-populations.
2. Better individual migration  
Immigrant individuals are selected from the sub-populations according to the descending order of the fitness value.

The migration frequency is given by the migration interval. The number of the migrated individuals is given as the product of the number of individuals and the migration rate. The migration topology is fixed.

Table 3: Translation rule

(A)	$\langle \text{expr} \rangle ::= \langle \text{expr} \rangle \langle \text{op} \rangle \langle \text{expr} \rangle$   $\langle \text{var} \rangle$	(A0) (A1)
(B)	$\langle \text{op} \rangle ::= +$   $-$   $*$   $/$	(B0) (B1) (B2) (B3)
(C)	$\langle \text{var} \rangle ::= X$   $Y$   $Z$	(C0) (C1) (C2)
(D)	$\langle \text{num} \rangle ::= 1$   $2$   $3$   $4$   $5$   $6$   $7$   $8$   $9$	(D1) (D2) (D3) (D4) (D5) (D6) (D7) (D8) (D9)

Table 4: Simulation parameters

Length of individual	800
Radix conversion bit-size	8 bit
Tournament size	3
Elite size	1
Crossover rate $\phi_c$	0.9
Mutation rate $\phi_m$	0.03
Number of sub-populations $n_s$	2, 5, 10
Migration rate $\eta_r$	0.1, 0.2, 0.5
Migration interval $\eta_i$	2, 4, 8, 16

## Numerical Example

### Symbolic Regression Problem

Symbolic regression problem is to find the function which can represent accurately the given data set;  $(x_1, y_1), (x_2, y_2), \dots, (x_N, y_N)$ . The real function is given as follows.

$$f(x) = 4x^2 - 12x + 9 \quad (1)$$

The variable  $x$  is given as  $\{x_1, x_2, x_{50}\} = \{-2.5, -2.4, \dots, -0.1, 0.1, \dots, 2.4, 2.5\}$ .

The fitness is estimated by the average least square error as follows.

$$E = \frac{1}{50} \sqrt{\sum_{i=1}^{50} \{f(x_i) - \bar{f}(x_i)\}^2} \quad (2)$$

The translation rule is shown in Table 3. The start symbol is <expr>. The tournament selection with tournament size 3, one-point crossover operators and elitist strategy are employed.

### Random Migration

Simulation parameters are shown in Table 4. Total number of individuals is 200. Maximum generation is 100. Simulations are performed 100 times. Success rates are shown Tables 5, 6 and 7. The success rate denotes, among 100 simulations, the percentage of simulations at which the exact function can be found.

In case of the migration rate  $\eta_r = 0.1$ , the fastest convergence is observed at the number of sub-populations  $n_s = 5$  and the migration interval  $\eta_i = 8$ . Second fastest convergence is at the number of sub-populations  $n_s = 2$  and the migration interval  $\eta_i = 8$  or at the number of sub-populations  $n_s = 10$  and the migration interval  $\eta_i = 2$ . In case of the migration rate  $\eta_r = 0.2$ , the fastest convergence is observed at the number of sub-populations  $n_s = 2$  and the migration interval  $\eta_i = 4$ . Second fastest convergence is at the number of sub-populations  $n_s = 5$  and the migration interval  $\eta_i = 8$ . In case of the migration rate  $\eta_r = 0.5$ , the fastest convergence is observed at the number of sub-populations  $n_s = 10$  and the migration interval  $\eta_i = 2$ . Second fastest convergence is at the number of sub-populations  $n_s = 5$  and the migration interval  $\eta_i = 8$ . It is concluded that longer migration interval is better for larger sub-population size and shorter migration interval is better for smaller sub-population size.

Table 5: Comparison of convergence speed (Random migration ; migration rate  $\eta_r = 0.1$ )

	$\eta_i = 2$	$\eta_i = 4$	$\eta_i = 8$	$\eta_i = 16$
$n_s = 2$	72	73	75	70
$n_s = 5$	68	73	76	72
$n_s = 10$	75	66	65	60

Table 6: Comparison of convergence speed (Random migration ; migration rate  $\eta_r = 0.2$ )

	$\eta_i = 2$	$\eta_i = 4$	$\eta_i = 8$	$\eta_i = 16$
$n_s = 2$	69	82	75	70
$n_s = 5$	73	79	81	65
$n_s = 10$	75	74	69	55

Table 7: Comparison of convergence speed (Random migration ; migration rate  $\eta_r = 0.5$ )

	$\eta_i = 2$	$\eta_i = 4$	$\eta_i = 8$	$\eta_i = 16$
$n_s = 2$	70	70	61	63
$n_s = 5$	73	74	81	74
$n_s = 10$	82	72	67	52

### Better Individual Migration

Simulation parameters are shown in Table 4. Total number of individuals is 200. Maximum generation at each simulation is 100. Simulations are performed 100 times. Success rates are shown Table 8, 9 and 10.

At the migration rate  $\eta_r = 0.1$ , the fastest convergence is observed at the number of sub-populations  $n_s = 2$  and the migration interval  $\eta_i = 4$ . Second fastest convergence is at the number of sub-populations  $n_s = 2$  and the migration interval  $\eta_i = 16$ . In case of the migration rate  $\eta_r = 0.2$ , the fastest convergence is observed at the number of sub-populations  $n_s = 2$  and the migration interval  $\eta_i = 8$ . Second fastest convergence is at the number of sub-populations  $n_s = 2$  and the migration interval  $\eta_i = 4$  or at the number of sub-populations  $n_s = 5$  and the migration



interval  $\eta_i = 16$ . In case of the migration rate  $\eta_r = 0.5$ , the fastest convergence is observed at the number of sub-populations  $n_s = 2$  and the migration interval  $\eta_i = 16$ . Second fastest convergence is at the number of sub-populations  $n_s = 2$  and the migration interval  $\eta_i = 4$ . It is concluded that longer migration interval and larger sub-population size are better.

Table 8: Comparison of convergence speed (Random migration; migration rate  $\eta_r = 0.1$ )

	$\eta_i = 2$	$\eta_i = 4$	$\eta_i = 8$	$\eta_i = 16$
$n_s = 2$	63	72	65	70
$n_s = 5$	62	60	62	61
$n_s = 10$	37	49	42	50

Table 9: Comparison of convergence speed (Random migration; migration rate  $\eta_r = 0.2$ )

	$\eta_i = 2$	$\eta_i = 4$	$\eta_i = 8$	$\eta_i = 16$
$n_s = 2$	54	67	68	61
$n_s = 5$	49	45	59	67
$n_s = 10$	37	46	46	39

Table 10: Comparison of convergence speed (Random migration; migration rate  $\eta_r = 0.5$ )

	$\eta_i = 2$	$\eta_i = 4$	$\eta_i = 8$	$\eta_i = 16$
$n_s = 2$	56	65	60	73
$n_s = 5$	44	57	58	55
$n_s = 10$	26	35	44	38

## Conclusion

Parallel implementation of Grammatical Evolution based was presented in this study. The algorithm is based on island model. The present algorithm was applied for the symbolic regression problem. In random migration, it is concluded that longer migration interval is better for larger sub-population size and shorter migration interval is better for smaller sub-population size. In better individual migration, longer migration interval and larger sub-population size are better. In the future, we would like to apply the present algorithm to industrial application problems.

## References

- [1] J. H. Holland. *Adaptation in Natural and Artificial Systems*. University of Michigan Press, 1975.
- [2] J. R. Koza. *Genetic Programming: On the Programming of Computers by Means of Natural Selection*. MIT Press, 1992.
- [3] C. Ryan, J. J. Collins, M. O'Neill. Grammatical Evolution: Evolving Programs for an Arbitrary Language. *Proceedings of 1st European Workshop on Genetic Programming*, pp.83-95, Springer, 1998.
- [4] C. Ryan, M. O'Neill. *Grammatical Evolution: Evolutionary Automatic Programming in an Arbitrary Language*, Springer, 2003.
- [5] E. Cantu-Paz. *Efficient and Accurate Parallel Genetic Algorithms*, Springer, 2000.
- [6] R. Tanese. Distributed Genetic Algorithms. *Proceedings of the 3rd International Conference on Genetic Algorithms*, pp.434-439, Morgan Kaufmann, 1989.

# Modeling of Wave Propagation in Unbounded Domains Using the Scaled Boundary Finite Element Method

\*Xiaojun Chen, Carolin Birk, Chongmin Song

School of Civil and Environmental Engineering, University of New South Wales, Australia.

\*Corresponding author: xiaojun.chen@unsw.edu.au

## Abstract

In this paper the dynamic soil-structure interaction problem is modeled using a scaled boundary finite element method (SBFEM) in the time domain. The original SBFEM formulation assumes a piece-wise constant approximation of the acceleration unit-impulse response matrix within one time step. A small maximum step size is required to make the algorithm stable. In this paper, the procedure is formulated in terms of the displacement unit-impulse response matrix, which leads two essential improvements: (1) the displacement unit-impulse response matrix is calculated using a more accurate and efficient approach, based on a piece-wise linear approximation; (2) the soil-structure interaction force described by the convolution integral is only calculated before a truncation time, which reduces the computational effort. Derivations of the corresponding efficient schemes will be presented and verified using numerical examples.

**Keywords:** dynamic soil-structure interaction, wave propagation, time domain, scaled boundary finite element method, displacement unit-impulse response matrix

## 1. Introduction

The numerical modeling of wave propagation in unbounded domains is required in a number of engineering applications, such as soil-structure interaction analysis or dam-reservoir interaction analysis. Here, the well-established finite element method cannot be used straightforwardly, since outgoing waves are reflected at the artificial boundaries of the finite element mesh, such that special measures have to be taken to prevent these reflections (Givoli, 1999), (Tsynkov, 1998). A popular method for the analysis of dynamic problems in unbounded media is the boundary element method, because the radiation condition is fulfilled explicitly by the fundamental solution (Beskos, 1987), (Beskos, 1997). The idea of extending the finite element mesh towards infinity has driven the development of infinite element techniques (Bettess, 1992). A recent technique, which is particularly suitable for modeling time-dependent problems in infinite media, is the scaled boundary finite element method (SBFEM) (Wolf & Song, 1997). This semi-analytical technique is based on a combination of a numerical solution in the circumferential directions with an analytical solution in the direction of wave propagation. Thus, radiation damping is modeled accurately.

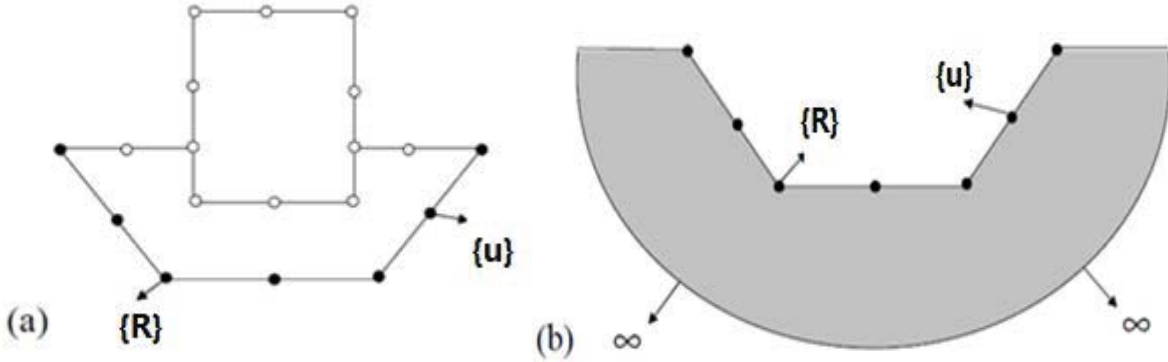
The structure (near field) can be modeled by either conventional finite element method or scaled boundary finite element method. The soil (far field) is modeled by scaled boundary finite element method. As shown in Figure 1, the connection between the near field and far field can be expressed in terms of the displacement vector  $\{u\}$  and the force vector  $\{R\}$ . In the frequency domain, the force displacement relationship is

$$\{R(\omega)\} = [S^\infty(\omega)]\{u(\omega)\}, \quad (1)$$

where  $[S^\infty(\omega)]$  is the dynamic stiffness matrix. In SBFEM, it can be calculated by (Wolf & Song, 1997),

$$([S^\infty(\omega)] + [E^1])[E^0]^{-1}([S^\infty(\omega)] + [E^1]^T) - (s - 2)[S^\infty(\omega)] - \omega[S^\infty(\omega)]_{,\omega} - [E^2] - \omega[M^0] = 0, \quad (2)$$

where  $[E^0]$ ,  $[E^1]$ ,  $[E^2]$  and  $[M^0]$  are the SBFEM coefficient matrices and  $s = (2 \text{ or } 3)$  is the spatial dimension (Wolf & Song, 1997), Equation (2) is called the SBFEM equation in dynamic stiffness matrix.



**Figure 1.** (a) Structure (near field); (b) Soil (far field).

In order to obtain the force-displacement relationship in the time domain, inverse Fourier transform needs to be applied to Equations (1) and (2). As  $[S^\infty(\omega)]$  is not square integrable, it contains a singular part  $[S_s^\infty(\omega)]$  and a regular part  $[S_r^\infty(\omega)]$ . In order to avoid numerical singularity, Equation (2) is alternatively expressed in terms of the acceleration dynamic stiffness matrix  $[M^\infty(\omega)] = [S^\infty(\omega)]/(i\omega)^2$  in the original SBFEM. This results in the force-acceleration relationship in the time domain,

$$\{R(t)\} = \int_0^t [M^\infty(\tau)]\{\ddot{u}(t - \tau)\}d\tau, \quad (3)$$

where  $[M^\infty(t)]$  is the acceleration unit-impulse response matrix, which is determined by

$$\int_0^t [m^\infty(t - \tau)][m^\infty(\tau)]d\tau + t \int_0^t [m^\infty(\tau)]d\tau + [e^1] \int_0^t \int_0^\tau [m^\infty(\bar{\tau})]d\bar{\tau}d\tau + \int_0^t \int_0^\tau [m^\infty(\bar{\tau})]d\bar{\tau}d\tau [e^1]^T - \frac{t^3}{6} [e^2]H(t) - t[m^0]H(t) = 0, \quad (4)$$

which is the transformed form of the equation for the acceleration unit-impulse response matrix (Wolf & Song, 1997). Equation (4) has to be solved by time discretization. The original time discretization scheme is based on a piece-wise constant variation of  $[m^\infty(t)]$ , and the time step size need to be set very small in order to keep the numerical results stable. Recently, a new time discretization scheme has been proposed by assuming  $[m^\infty(t)]$  to be piece-wise linear, and

introducing an extrapolation parameter  $\theta$ . This leads to improved stability and allows a larger time step size to be used (Radmanovic & Katz, 2010).

As  $[S_r^\infty(t)]$  converges to zero for later time, it is worthwhile to obtain an equation similar to Equation (4) for  $[S_r^\infty(t)]$ , and to employ a new similar time discretization scheme. In the time domain analysis, a truncation time can be introduced to reduce the total computational cost.

The objective of this paper is to first derive the SBF E equation for the displacement unit-impulse response matrix and propose the corresponding time discretization scheme. Then the time domain formulation is established while introducing the truncation at the same time.

The further outline of this paper is as follows. In Section 2, the SBF E equation for the displacement unit-impulse response matrix is derived and its time discretization scheme is proposed. The stability and efficiency of the method are investigated. In Section 3, algorithms for the interface force-displacement relationship are developed. In Section 4, numerical example is used to evaluate the new scheme. Concluding remarks are stated in Section 5.

## 2. SBF E equation for displacement unit-impulse response matrix

In this section a new numerical scheme for the computation of the displacement unit-impulse response matrix is derived. It starts from the transformed SBF E equation in dynamic stiffness  $[s^\infty(\omega)]$  in the frequency domain (Wolf & Song, 1997), which is given as:

$$([s^\infty(\omega)] + [e^1])([s^\infty(\omega)] + [e^1]^T) - (s - 2)[s^\infty(\omega)] - \omega[s^\infty(\omega)]_\omega - [e^2] - (i\omega)^2[\Lambda^2] = 0. \quad (5)$$

Equation (5) is obtained by performing the following eigenvalue decomposition:

$$[M^0][\Phi] = [E^0][\Phi][\Lambda^2]. \quad (6)$$

Details can be found in (Wolf & Song, 1998). Then,  $[s^\infty(\omega)]$  is decomposed as

$$[s^\infty(\omega)] = i\omega[c_\infty] + [k_\infty] + \frac{1}{i\omega}[a_1] + [s_r^*(\omega)], \quad (7)$$

where the first two terms comprise the singular part  $[s_s^\infty(\omega)]$ .  $[c_\infty]$  is the transformed dashpot matrix and  $[k_\infty]$  is the transformed spring matrix. The last two terms in Equation (7) comprise the regular part

$$[s_r^\infty(\omega)] = \frac{1}{i\omega}[a_1] + [s_r^*(\omega)]. \quad (8)$$

Substituting Equation (7) into Equation (5) leads to a polynomial in  $(i\omega)$ . Individual terms corresponding to different powers of  $(i\omega)$  must be equal to zero. The terms corresponding to  $(i\omega)^2$ ,  $(i\omega)^1$  and  $(i\omega)^0$  are used to calculate  $[c_\infty]$ ,  $[k_\infty]$  and  $[a_1]$  (Wolf J. , 2003). Setting the remaining terms equal to zero yields an equation for  $[s_r^*(\omega)]$ ,

$$\begin{aligned}
& [s_r^*(\omega)][s_r^*(\omega)] \\
& + [a_1] \frac{[s_r^*(\omega)]}{i\omega} + \frac{[s_r^*(\omega)]}{i\omega} [a_1] + ([k_\infty] + [e^1])[s_r^*(\omega)] + [s_r^*(\omega)]([k_\infty] + [e^1]^T) \\
& \quad + [c_\infty](i\omega[s_r^*(\omega)]) + (i\omega[s_r^*(\omega)])[c_\infty] \\
& \quad + \frac{1}{i\omega} \left( ([k_\infty] + [e^1])[a_1] + [a_1]([k_\infty] + [e^1]^T) \right) + \frac{1}{(i\omega)^2} [a_1]^2 \\
& \quad - (s-3) \frac{1}{i\omega} [a_1] - (s-2)[s_r^*(\omega)] - \omega[s_r^*(\omega)]_{,\omega} = 0,
\end{aligned} \tag{9}$$

Applying the inverse Fourier transform to Equation (9) yields:

$$\begin{aligned}
& \int_0^t [s_r^*(t-\tau)][s_r^*(\tau)]d\tau + [a_1] \left( \int_0^t [s_r^*(\tau)] d\tau \right) + \left( \int_0^t [s_r^*(\tau)] d\tau \right) [a_1] \\
& \quad + ([k_\infty] + [e^1])[s_r^*(t)] + [s_r^*(t)]([k_\infty] + [e^1]^T) + [c_\infty] \frac{d[s_r^*(t)]}{dt} \\
& \quad + \frac{d[s_r^*(t)]}{dt} [c_\infty] + t \frac{d[s_r^*(t)]}{dt} - (s-3)[s_r^*(t)] \\
& \quad + ([k_\infty][a_1] + [a_1][k_\infty] + [a_1][e^1]^T + [e^1][a_1] - (s-3)[a_1])H(t) \\
& \quad + t[a_1]^2 H(t) = 0,
\end{aligned} \tag{10}$$

Also applying the inverse Fourier transform to Equation (8) yields

$$[s_r^\infty(t)] = [a_1] + [s_r^*(t)], \quad \text{for } t \geq 0 \tag{11}$$

Substituting Equation (11) into Equation (10) yields

$$\begin{aligned}
& \int_0^t [s_r^\infty(t-\tau)][s_r^\infty(\tau)]d\tau + ([k_\infty] + [e^1])[s_r^\infty(t)] + [s_r^\infty(t)]([k_\infty] + [e^1]^T) + [c_\infty] \frac{d[s_r^\infty(t)]}{dt} \\
& \quad + \frac{d[s_r^\infty(t)]}{dt} [c_\infty] + t \frac{d[s_r^\infty(t)]}{dt} - (s-3)[s_r^\infty(t)] = 0,
\end{aligned} \tag{12}$$

Equation (12) is a first order ordinary differential equation with a convolution integral, with initial value (Wolf & Song, 1997)

$$[s_r^\infty(t=0)] = [a_1], \tag{13}$$

Generally, there is no analytical solution for Equation (12), so it needs to be solved by time discretization scheme, i.e. the total time history is discretized into a number of time steps  $t = t_n = n\Delta t$ , where  $\Delta t$  is the time step size. So the whole time history is divided into  $n$  time intervals:  $[(i-1)\Delta t, i\Delta t]$  ( $i = 1, 2, \dots, n$ ). It is assumed, that  $[s_r^\infty(t)] = \frac{d[s_r^\infty(t)]}{dt}$  changes linearly within each time interval. At each time step  $t_i = i\Delta t$ , the following procedures are used:

- a) An extrapolation parameter  $\theta \in [1, 2]$  is introduced. Equation (12) is evaluated at time  $t = (i-1 + \theta)\Delta t$ . The convolution integral in Equation (12) is discretized into  $i-1$

intervals of length  $\Delta t$  and one final interval of length  $\theta\Delta t$ . Within that extended interval  $[\dot{s}_r^\infty(t)]$  is assumed to vary linearly.

- b) The corresponding  $[s_r^\infty(t)]$  within the interval  $[(i-1)\Delta t, (i-1+\theta)\Delta t]$  has the following expression,

$$[s_r^\infty(t)] = [s_r^\infty]_{i-1+\theta} = [s_r^\infty]_{i-1} + \tau[\dot{s}_r^\infty]_{i-1} + \frac{\tau^2}{2\theta\Delta t}([\dot{s}_r^\infty]_{i-1+\theta} - [\dot{s}_r^\infty]_{i-1}), \quad (14)$$

where  $[s_r^\infty]_{i-1}$  is the value of  $[s_r^\infty(t)]$  at  $t = (i-1)\Delta t$ ,  $[\dot{s}_r^\infty]_{i-1}$  and  $[\dot{s}_r^\infty]_{i-1+\theta}$  are the value of  $[\dot{s}_r^\infty(t)]$  at  $t = (i-1)\Delta t$  and  $t = (i-1+\theta)\Delta t$ , respectively.  $\tau$  is the local coordinate  $\tau = t - (i-1)\Delta t$ ;

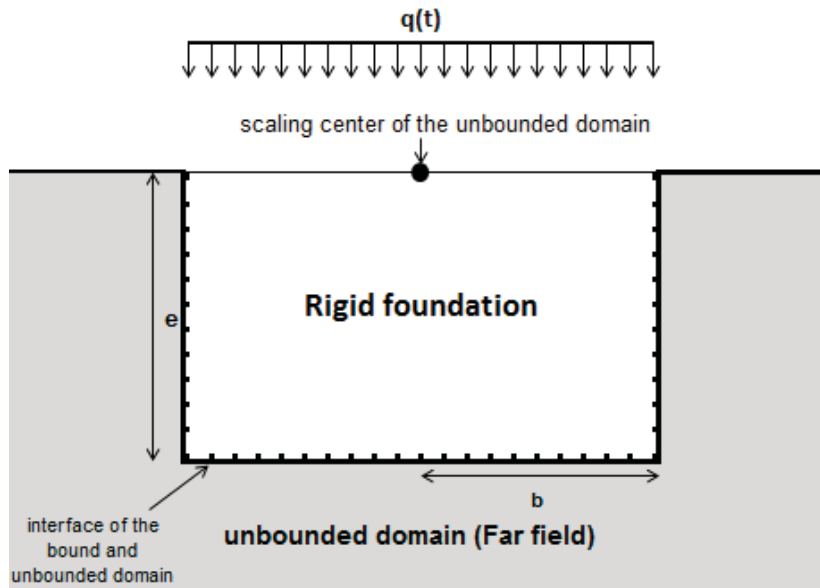
- c) The discretized formulation of Equation (12) is solved for  $[\dot{s}_r^\infty]_{i-1+\theta}$ . Then  $[s_r^\infty(t = i\Delta t)]$  is determined using,

$$[s_r^\infty(t = i\Delta t)] = [s_r^\infty]_i = [s_r^\infty]_{i-1} + \Delta t[\dot{s}_r^\infty]_{i-1} + \frac{\Delta t}{2\theta}([\dot{s}_r^\infty]_{i-1+\theta} - [\dot{s}_r^\infty]_{i-1}). \quad (15)$$

Steps (a) – (c) are repeated for each time step  $[s_r^\infty]_i$  ( $i = 1, 2, \dots, n$ ). Finally the displacement unit-impulse response matrix  $[S_r^\infty(t)]$  is calculated as,

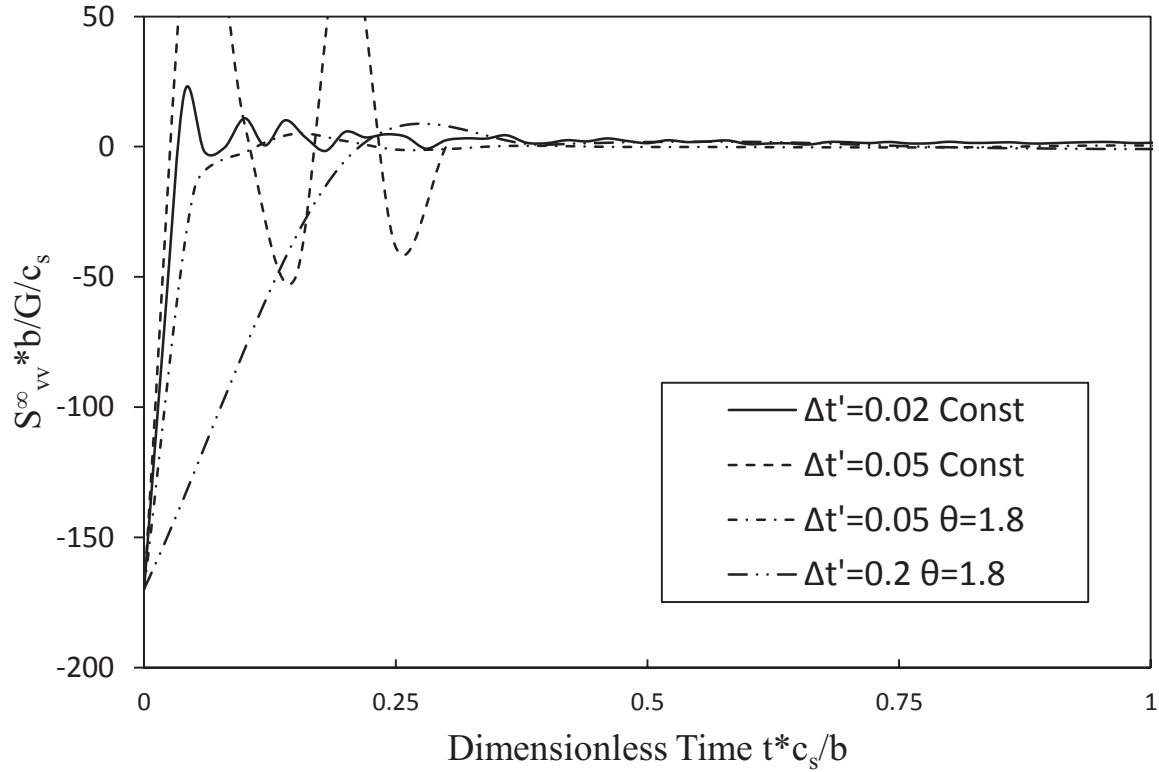
$$[S_r^\infty(t = i\Delta t)] = [\Phi]^{-T}[s_r^\infty]_i[\Phi]^{-1}. \quad (16)$$

In order to verify the stability of this algorithm, a two-dimensional example of a rigid strip foundation is analyzed (Figure 2). The displacement unit-impulse response matrix is calculated using the proposed method, and compared to the original constant scheme (Wolf & Song, 1998). In order to make the results comparable, a rigid vertical motion pattern  $\{\varphi\}$  is enforced on the displacement unit-impulse response, i.e.  $S_{vv}^\infty(t) = \{\varphi\}^T [S_r^\infty(t)] \{\varphi\}$ .  $S_{vv}^\infty(t)$  is then normalized by the factor  $b/(Gc_s)$  and plotted in Figure 3.



**Figure 2.** Two-dimensional rigid strip foundation embedded in isotropic and homogeneous half-space

It can be noted, that the original scheme (const) is stable for relatively small dimensionless time step size  $\Delta t' = \Delta t c_s/b = 0.02$ . For dimensionless time step size  $\Delta t' = 0.05$ , it becomes unstable very early, while for the proposed method with  $\theta = 1.8$ , the result is stable. Even if we choose large time step size  $\Delta t' = 0.2$ , no oscillation occurs in the solution. This example shows that the algorithm for the displacement unit-impulse response matrix can be used for larger time steps.



**Figure 3.** Comparison of the stability of the normalized unit-impulse response coefficient of the rigid foundation

### 3. Integration of the soil-structure interaction force

The soil-structure interaction force vector  $\{R(t)\}$  is given by the convolution integral (Wolf & Song, 1997)

$$\{R(t)\} = [C_\infty]\{\dot{u}(t)\} + [K_\infty]\{u(t)\} + \int_0^t [S_r^\infty(\tau)]\{u(t - \tau)\}d\tau, \quad (17)$$

where  $[C_\infty]$  and  $[K_\infty]$  are the constant dashpot and spring matrix, respectively, while can be calculated in advance. The displacement unit-impulse response matrix  $[S_r^\infty(t)]$  is given at discrete times:  $t_i = i\Delta t, (i = 0, 1, \dots, n)$ . The discretization size for  $\{u(t)\}$ , however, is controlled by the frequency range of the input loading, and normally smaller than the time step size for  $[S_r^\infty(t)]$ . Therefore, linear interpolation of  $[S_r^\infty(t)]$  is used to find intermediate values required to fit the smaller discretization size for  $\{u(t)\}$ . Thus, various time discretization schemes can be used to solve Equation (17), for example, the classical Newmark method.

In addition, as  $[S_r^\infty(t)]$  converges to zero at later time, a truncation time  $T = N\Delta t$  is introduced, i.e.  $[S_r^\infty(t)] = 0$  for  $t \geq T$ . Thus Equation (17) can be reformulated as,

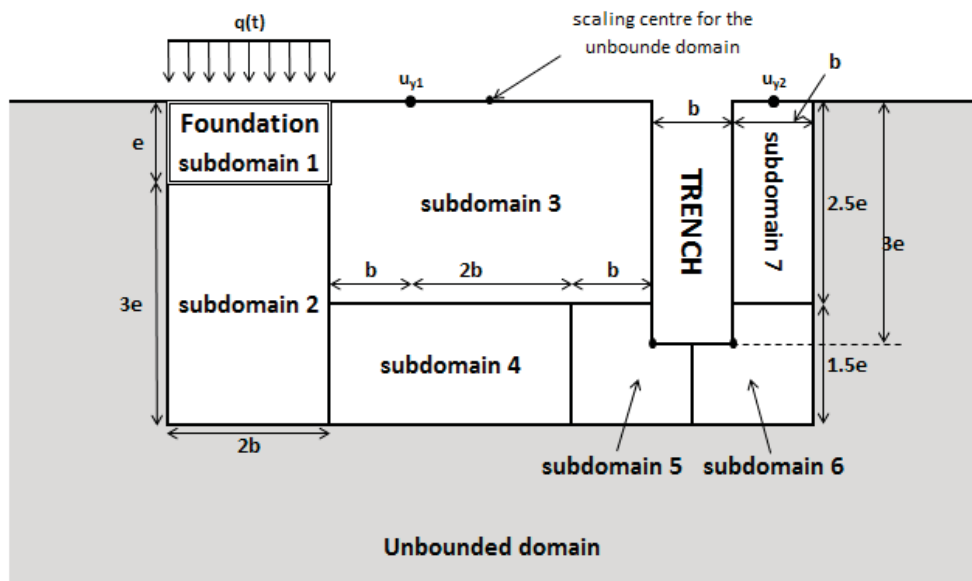
$$\{R(t)\} = [C_\infty]\{\dot{u}(t)\} + [K_\infty]\{u(t)\} + \int_0^T [S_r^\infty(\tau)]\{u(t - \tau)\}d\tau, \quad (18)$$

Therefore, after the truncation time  $T$ , the size of the convolution does not increase anymore and the computational cost is reduced. In the next section, a numerical example is used to demonstrate the efficiency of the method.

### 4. Numerical example

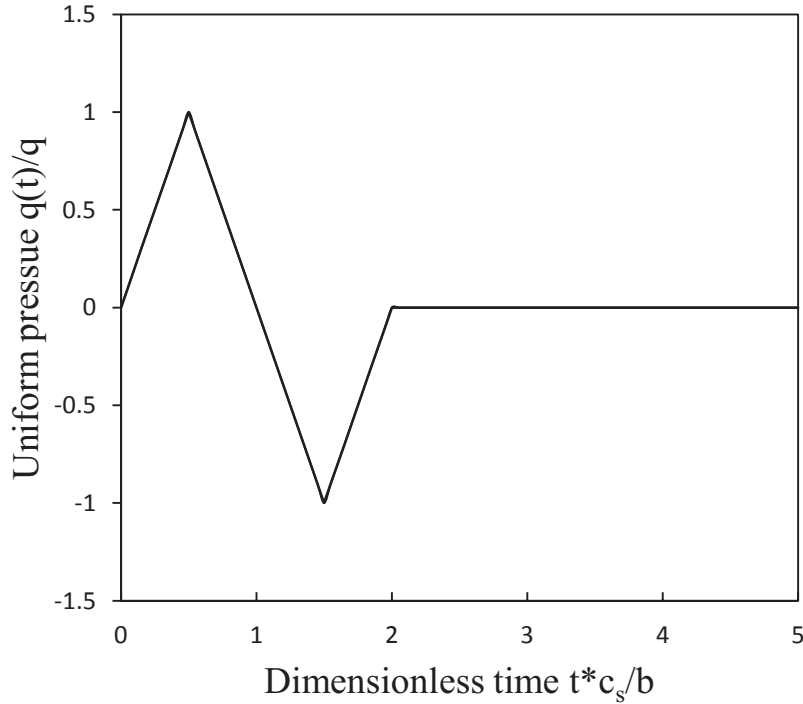
A flexible rectangular strip foundation embedded in homogeneous isotropic half-space, together with a deep trench next to the foundation is modeled (Figure 4). A uniformly distributed triangular pulse is applied on the surface of the foundation (Figure 5).

The near field includes the foundation and adjacent soil, and is divided into seven subdomains, which are modeled using the SBFEM described in (Song, 2009). The embedment ratio is  $e/b = 1$  and three-node line elements are used, whose length uniformly equals  $0.1b$ . The scaling center of the subdomains in the near field is located at the center of the rectangle, except for subdomain 5 and 6, whose scaling center is located at the corner of the trench, in order to avoid stress concentration. The far field is modeled with one unbounded subdomain, whose scaling center is located at the top center of the near field (shown in Figure 4). For the near field, each subdomain is modeled with continued fraction and the order of the continued fraction is 2 (Song, 2009), yields the total number of degree of freedom to be 1756. The foundation has a shear modulus  $G = 7GPa$ , mass density  $\rho = 2500kg/m^3$  and Poisson’s ratio  $\nu = 0.2$ , while for the soil,  $G = 0.125GPa$ ,  $\rho = 2300kg/m^3$  and  $\nu = 0.3$ .



**Figure 4.** Illustration of the flexible foundation embedded in isotropic and homogeneous half-space with a trench next to it





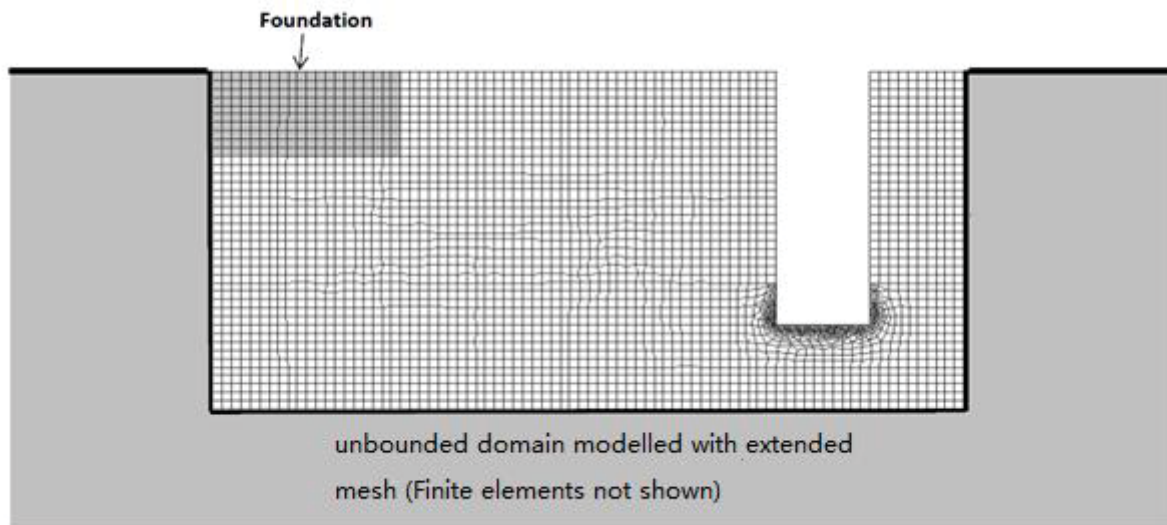
**Figure 5.** Time variation of uniformly distributed triangular pulse applied on top of the foundation

In order to verify the results, an extended mesh is analyzed using the finite element method. Figure 6 shows the meshing of the near field. Except in the region near the trench corner, eight-node isoparametric elements are used with the length and width equals to  $0.1b$ . In the region near the trench corner, due to stress concentration, a finer mesh is used. The far field up to the size of  $80b \times 40e$  is also discretized using eight-node isoparametric elements. Due to the large size of the far field, the meshing is not shown in the figure. The extended mesh is chosen to be large enough so that for the time duration of  $30b/c_s$ , the dilatational wave generated by  $p(t)$  does not reach its boundary. This extended finite element mesh results in 324713 elements

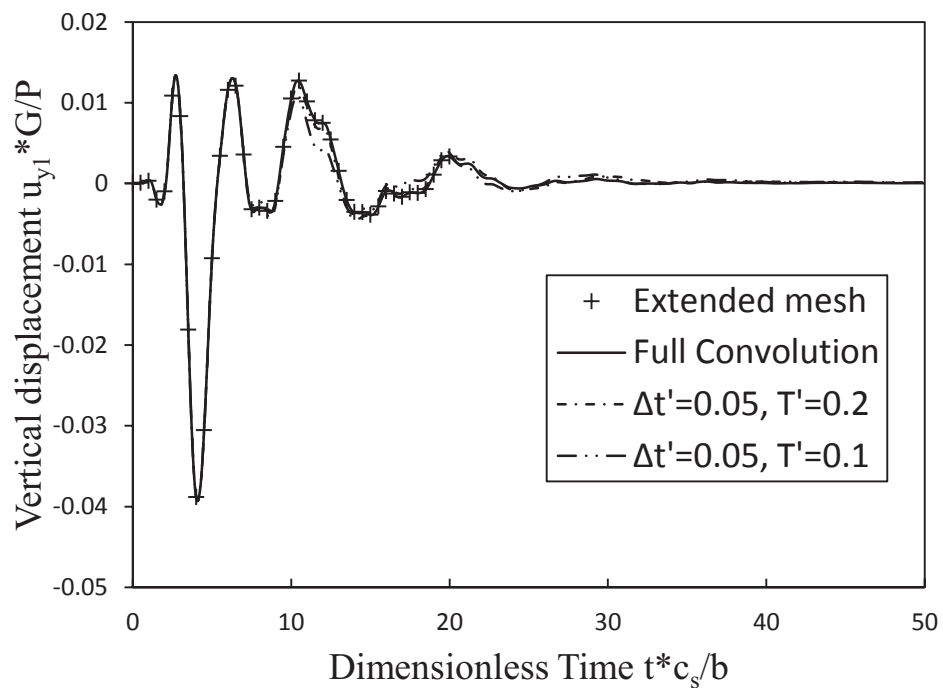
The dimensionless time step size for calculating the displacement unit-impulse response matrix is chosen as  $\Delta t' = \Delta t c_s / b = 0.05$ , while the time step size for the time domain analysis is  $0.01b/c_s$ . Therefore, 4 linear interpolation values need to be calculated within each time interval of the displacement unit-impulse response matrix. The vertical displacement  $u_{y1}$  in Figure 4 is calculated, first without truncation time, and then two different dimensionless truncation times  $T' = T c_s / b = 0.2$  or  $0.1$  are introduced. The results are plotted in Figure 7.

Figure 7 shows excellent agreement between the results obtained using the proposed method without truncation (full convolution) and the extended mesh. When a truncation time is introduced, the difference between the results with and without the truncation time is very small. Figure 8 shows the total CPU time (Intel i5-2500 @ 3.3 GHz, 8GB RAM) required for the computation up to a given dimensionless time. The original constant scheme is also used here as a comparison. It shows, the CPU time for the original method increases quadratically, since the total computational effort is proportional to  $n^2$ , where  $n$  is the number of time steps. For the new method without truncation, as a larger time step size is used for computing the displacement unit-impulse response matrix, the CPU time has been reduced significantly, although a quadratic increase is still observed. After the truncation time is introduced, the CPU time increases linearly, leading to a large saving of

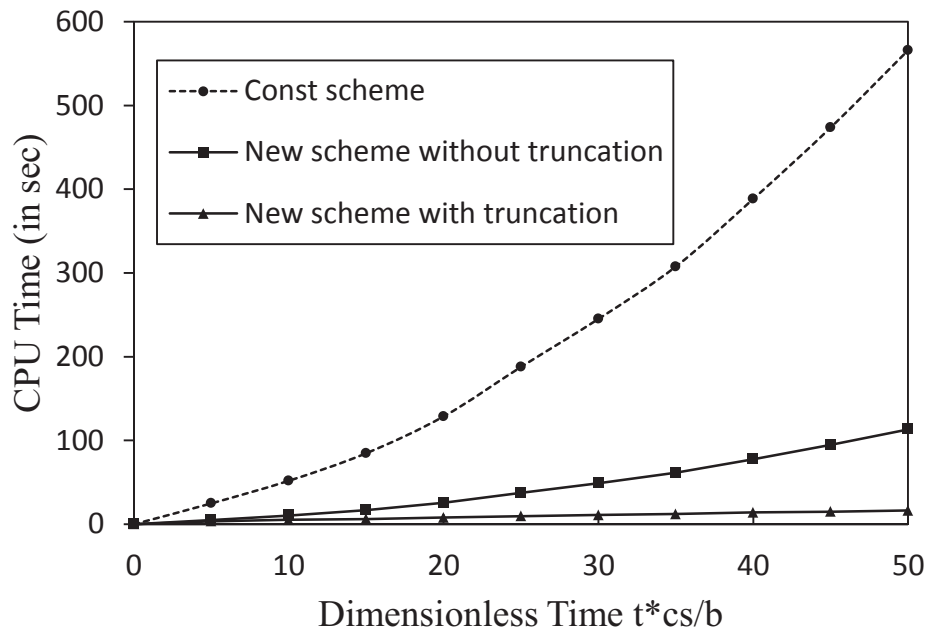
computational cost (as at  $t = 50b/c_s$ , the CPU time is reduced to only 2% of that of the original method).



**Figure 6.** Finite element mesh of the near field



**Figure 7.** Normalized vertical displacement response  $u_{y1}$



**Figure 8.** CPU time required for the computation

## 5. Conclusion

A new algorithm is developed which will be useful for the solution of dynamic soil-structure interaction problems in the time domain. The traditional SBFEM is based on approximating the acceleration unit-impulse response by a piece-wise constant function. Two essential improvements are proposed: (1) the displacement unit-impulse response is calculated instead of the acceleration unit-impulse response based on a piece-wise linear approximation; (2) the convolution integral in the soil-structure interaction force vector is truncated after a few steps. This leads to a significant reduction of computational effort. The accuracy and computational efficiency of the proposed algorithm have been verified by numerical examples. A wider range of applications of the new algorithm will be addressed in the near future.

## Reference

- Beskos, D. (1987). Boundary element methods in dynamic analysis. *Applied Mechanics Review*, 40,1-23.
- Beskos, D. (1997). Boundary elements methods in dynamic analysis: Part II. *Applied Mechanics Review*, 50,149-197.
- Bettess, P. (1992). *Infinite elements*. Sunderland: Penshaw Press.
- Givoli, D. (1999). Exact representations on artificial interfaces and applications in mechanics. *Applied Mechanics Reviews*, 52(22), 333-349.
- Radmanovic, B., & Katz, K. (2010). A high performance scaled boundary finite element method. *IOP Conf. Series: Materials Science and Engineering* 10.
- Song, C. (2009). The scaled boundary finite element in structural dynamics. *International Journal for Numerical Methods in Engineering*, 77,1139-1171.
- Tsynkov, S. (1998). Numerical solution of problems on unbounded domains: a review. *Applied Numerical Mathematics*, 27,465-532.
- Wolf, J. (2003). *The Scaled Boundary Finite Element Method*. John Wiley & Sons.
- Wolf, J., & Song, C. (1997). *Finite Element Modelling of Unbounded Media*. John Wiley & Sons.
- Wolf, J., & Song, C. (1998). Unit-impulse response of unbounded medium by scaled boundary finite element method. *Computer Methods in Applied Mechanics and Engineering*, 159,355-367.

## A quantitative method to determine the optimal stress field for 2D 8-node quadrilateral hybrid finite element

\*Canhui Zhang, Pei Liu, and Dongdong Wang

Department of Civil Engineering, Xiamen University, Xiamen, Fujian 361005, China

\*Corresponding author: chzhang@xmu.edu.cn

### Abstract

A quantitative method is developed to determine the optimal stress field for 2D 8-node quadrilateral hybrid stress element (HQ8). It provides a straightforward way as to that how and why the resulting element can improve its displacement response. A new inner product with material weighting matrix is defined to reveal the relationship in quantity of exact similarity degrees between different stress modes. It is different from the conventional energy product which can only qualitatively determine the orthogonality of stress and strain modes because they are considered as mathematical vectors without physical meaning. The proposed strategy includes two steps. Firstly, the basic stress modes are divided into a set of sub-modes. Secondly, the sub-mode with largest similarity degree with the basic mode is selected as the optimal assumed stress mode for a hybrid element. The optimal stress modes for HQ8 are determined when Poisson's ratio is larger than 1/9 which is the case for most materials.

**Keywords:** 8-node quadrilateral hybrid stress element; quantitative method; optimal assumed stress field; material weighting matrix based inner product; largest similarity degree

### Introduction

Since the displacement elements exhibit over rigidity, the hybrid stress element was first formulated by Pian (1964) to resolve this issue where the stress field was assumed independently as

$$\boldsymbol{\sigma} = \sum_{i=1}^M \boldsymbol{\sigma}_i \beta_i = \mathbf{P}\boldsymbol{\beta} \quad (1)$$

in which  $\boldsymbol{\sigma}_i$ 's are the assumed stress modes,  $\beta_i$ 's the corresponding stress parameters, and  $\mathbf{P} = \{\boldsymbol{\sigma}_1, \dots, \boldsymbol{\sigma}_M\}$  the stress matrix. Besides, the displacement field is assumed as  $\mathbf{u} = \mathbf{N}\mathbf{a}$ , where  $\mathbf{N}$  is the shape function matrix and  $\mathbf{a}$  the nodal displacement vector of the element. Then the element strain can be expressed as  $\boldsymbol{\varepsilon} = \mathbf{D}\mathbf{u} = \mathbf{B}\mathbf{a}$  where  $\mathbf{B} = \mathbf{D}\mathbf{N}$  is the geometry matrix in which  $\mathbf{D}$  is the matrix of differential operator. Thus the element stiffness matrix can be obtained via the Hellinger-Reissner variational principle as follows

$$\mathbf{K} = \mathbf{G}^T \mathbf{H}^{-1} \mathbf{G} \quad (2)$$

where

$$\mathbf{H} = \int_{V^e} \mathbf{P}^T \mathbf{S} \mathbf{P} dV, \quad \mathbf{G} = \int_{V^e} \mathbf{P}^T \mathbf{B} dV \quad (3)$$

Besides, the following relationships between the stress parameters and nodal displacements can also be obtained as

$$\boldsymbol{\beta} = \mathbf{H}^{-1} \mathbf{G}\mathbf{a} \quad (4)$$

In the hybrid finite element analysis, a stress subspace including all the assumed stress modes was introduced by Zhang, Feng and Huang (2002) as

$$\mathcal{S}_i = \left\{ \boldsymbol{\sigma} \in (L^2(V^e))^{n_d} \mid \boldsymbol{\sigma} = \sum_{k=1}^i \beta_k \boldsymbol{\sigma}_k, \beta_k \in \mathbb{R} \right\} \in \mathbb{R}^{n_d}, \quad i = 1, 2, \dots, M \quad (5)$$

where  $n_d$  is the dimension of  $\mathcal{S}$ , i.e.,  $n_d = 3$  for 2D and  $n_d = 6$  for 3D. To develop high performance hybrid stress elements, a number of approaches for obtaining the satisfactory stress modes have been presented such as Pian and Sumihara (1984), Han and Hoa (1993), Sze (1996), Wu and Cheung (1995). The concept of natural deformation modes for hybrid elements was introduced by Huang (1991). Unfortunately since these natural deformation modes are very complicated, an iterative numerical procedure has to be employed to find the relating natural stress modes. Pian and Chen (1983) presented the basic deformation modes to determine the necessary stress modes, but the shear components were ignored in their basic strains. Moreover, because the energy product is used, their method is limited to the qualitative analysis between the basic strain modes and the stress modes. Zhang and Wang (2006, 2010) proposed a selection method with basic deformation modes to improve the classification method by Feng et al. (1997). The complicated natural deformation modes are replaced by the simple basic deformation modes and the energy product was used to avoid the numerical modal analysis. Zhang et al. (2011) developed the basic deformation modes into the orthogonal basic deformation modes. Zhang et al. (2006) compared the performance of different elements with different assumed stress fields. For higher-order elements, Bilotta and Casciaro (2002) proposed a 2D 8-node hybrid element with 14 modes in his assumed stress field so the number of modes is larger than the least for the optimal requirement of 13 modes. Cen et al. (2011) proposed the stress functions to derive the assumed stress for hybrid-stress function plane element with high accuracy.

However, one existing problem is that there is still lack of rational way to find the satisfactory stress modes and tell that whether or not they are optimal for hybrid stress elements, particularly for those of higher-order. It is our attempt to find a suitable method to reveal the quantitative relationship between the different stress modes and obtain the optimal assumed stress modes for 8-node quadrilateral hybrid element (HQ8).

### A quantitative method to determine the optimal stress field

#### *Basic deformation modes and their relating basic stress modes*

For the hybrid element with  $n$  degrees of freedom including  $r$  rigid body motions and  $m = n - r$  deformations, following the procedures by Zhang and Wang (2006, 2010) the rigid body motions and pure deformations can be determined and separated. Thus the displacement field for pure deformation can be expressed as

$$\mathbf{u} = \sum_{i=1}^m \alpha_i \mathbf{u}_i = \bar{\mathbf{N}} \boldsymbol{\alpha}, \quad \bar{\mathbf{N}} = \{\mathbf{u}_1, \dots, \mathbf{u}_m\}, \quad \boldsymbol{\alpha} = \begin{Bmatrix} \alpha_1 \\ \vdots \\ \alpha_m \end{Bmatrix} \quad (6)$$

where  $\alpha_i$ 's are the independent coefficients and  $\mathbf{u}_i$ 's the basic displacements. The nodal displacement vectors for pure deformation can be readily obtained by substitution of the nodal coordinates into Eq. (6) as

$$\mathbf{a} = \sum_{i=1}^m \alpha_i \mathbf{a}_i = \mathbf{A} \boldsymbol{\alpha}, \quad \mathbf{A} = \{\mathbf{a}_1, \dots, \mathbf{a}_m\} \quad (7)$$

where  $\mathbf{a}_i$ 's are the basic deformation modes. By the geometry equation  $\boldsymbol{\varepsilon} = \mathbf{D}\mathbf{u} = \mathbf{B}\mathbf{a}$  with the basic displacements in Eq. (6), the hybrid element strain can be expressed as

$$\boldsymbol{\varepsilon} = \sum_{i=1}^m \alpha_i \boldsymbol{\varepsilon}_i = \bar{\mathbf{B}} \boldsymbol{\alpha}, \quad \bar{\mathbf{B}} = \mathbf{D}\bar{\mathbf{N}} = \{\boldsymbol{\varepsilon}_1, \dots, \boldsymbol{\varepsilon}_m\}, \quad \boldsymbol{\varepsilon}_i = \mathbf{B}\mathbf{a}_i \quad (8)$$

where  $\boldsymbol{\varepsilon}_i$ 's are the basic strain modes corresponding to the basic deformation modes. Because the basic deformation modes include all the  $m$  possibilities of the element to deform, they indeed can be used to describe any deformation of the element within these possibilities. In addition, since they are unique because of their linear independence, the derived basic strain modes were used to determine the zero-energy deformation modes in the element by Pian and Chen (1983) as well as Zhang and Wang (2006, 2010). However, in this paper we use the basic stress modes derived from

the basic strain modes to find the optimal stress modes for hybrid stress element. From Eq. (8) the following stress field can be expressed as

$$\boldsymbol{\sigma}' = \mathbf{C}\boldsymbol{\varepsilon} = \sum_{i=1}^m \alpha_i \boldsymbol{\sigma}'_i = \mathbf{P}'\boldsymbol{\alpha} = \mathbf{CBA}, \mathbf{P}' = \{\boldsymbol{\sigma}'_1, \dots, \boldsymbol{\sigma}'_m\} \quad (9)$$

where  $\boldsymbol{\sigma}'_i = \mathbf{C}\boldsymbol{\varepsilon}_i = \mathbf{CB}\mathbf{a}_i$  are the basic stress modes. In fact the stress field in Eq. (9) is that for the displacement element corresponding to the hybrid stress element. In other words, the stress field for the displacement counterpart can be expressed using the basic stress modes. That is because the basic deformation modes are derived directly from the displacement field (Zhang and Wang, 2006, 2010). As we know, the number of assumed stress modes for hybrid element should satisfy  $M \geq m = n - r$ . Because the number of the basic stress modes is equal to the degrees of freedom for element  $m = n - r$ , it is the least for the optimal requirement. However, inside the basic stress modes, some components are unnecessary. To verify this, we can take the basic stress modes as the assumed stress modes for hybrid element as  $\boldsymbol{\sigma}_i = \boldsymbol{\sigma}'_i, i = 1, 2, \dots, m$ , namely, the stress field for hybrid element is assumed as  $\boldsymbol{\sigma} = \mathbf{P}'\boldsymbol{\beta}'$ . Noting that  $\mathbf{S} = \mathbf{C}^{-1}$ , by Eq. (9) one has

$$\mathbf{H}' = \int_{V^e} \mathbf{P}'^T \mathbf{S} \mathbf{P}' dV = \mathbf{A}^T \mathbf{K}' \mathbf{A}, \mathbf{G}' = \int_{V^e} \mathbf{P}'^T \mathbf{B} dV = \mathbf{A}^T \int_{V^e} \mathbf{B}^T \mathbf{C} \mathbf{B} dV = \mathbf{A}^T \mathbf{K}' \quad (10)$$

where  $\mathbf{K}'$  is the stiffness matrix for the displacement counterpart as

$$\mathbf{K}' = \int_{V^e} \mathbf{B}^T \mathbf{C} \mathbf{B} dV \quad (11)$$

Equation (10) indicates that  $\mathbf{H}'$  represents the energies of the displacement counterpart corresponding to the basic deformation modes. Substituting Eqs. (10) into Eq. (4), the stress parameters for hybrid element can be calculated as

$$\boldsymbol{\beta}' = \mathbf{H}'^{-1} \mathbf{G}' \mathbf{a} = (\mathbf{A}^T \mathbf{K}' \mathbf{A})^{-1} (\mathbf{A}^T \mathbf{K}') \mathbf{A} \mathbf{a} = \boldsymbol{\alpha} \quad (12)$$

It is found that the stress parameters are exactly equal to the independent parameters for basic stress modes. So, consider Eq. (9), the stress field for hybrid element can be derived by Eq. (1) with Eq. (12) as

$$\boldsymbol{\sigma} = \mathbf{P}'\boldsymbol{\beta}' = \mathbf{P}'\boldsymbol{\alpha} = \boldsymbol{\sigma}' \quad (13)$$

It is exactly equal to its displacement counterpart. This implies that the resulting hybrid element cannot remove the over rigidity from its displacement counterpart. In other words, there are unnecessary components inside the basic stress modes even though the number of these modes is the least as required.

#### *Construction of optimal stress field for hybrid element*

On one hand, the shortcoming of over rigidity for displacement element implies that there are unnecessary factors coupled with the necessary factors inside its stress field, i.e., the basic stress field in Eq. (9). On the other hand, there is no denying that it has great success. Therefore, the necessary factors in the basic stress field are major while the unnecessary factors are minor. Since the basic stress field can be expressed by the basic stress modes, one can conclude that there are unnecessary components coupled with the necessary components in the basic stress modes, where the necessary components are major while the unnecessary components are minor. Our attempt is to obtain the necessary components and without the unnecessary components from the basic stress modes. For this purpose our procedure consists of two steps.

#### Step 1 (Breaking basic stress modes into sub-modes)

We take every component of the basic stress mode to construct a sub-mode. Thus the basic stress mode is broken into several sub-modes and can be expressed by the sum of them as

$$\boldsymbol{\sigma}'_i = \sum_{k=1}^3 (\boldsymbol{\sigma}'_i)_k \quad (i = 1, 2, \dots, m) \quad (14)$$

where  $(\boldsymbol{\sigma}'_i)_k = \bar{\alpha}_{ik} \bar{\boldsymbol{\sigma}}_j$  are the sub-modes in which  $\bar{\alpha}_{ik}$ 's are the constant coefficients dependent upon the material parameters and  $\bar{\boldsymbol{\sigma}}_j$ 's the stress modes of uni-axial stress or pure shear stress without any constant coefficient. Since all the sub-modes are uni-axial stress or pure shear stress, they can only be essential and not redundant.

### Step 2 (Comparing sub-modes with their basic stress mode)

The sub-modes are compared with their original basic stress mode. The sub-mode with larger similarity degree implies that it is more similar to the original basic stress mode than others, so it represents the main feature of this basic stress mode. Since the main features for the basic stress modes are good, the most similar sub-mode which reflects the main features can be selected as the optimal mode.

To investigate the quantitative relationship between the sub-modes with their basic stress modes, their similarity degree is needed which in general is defined as the cosine of the angle between vectors. According to the proposition by Zhang et al. (2007), the equivalent hybrid element can be resulted from the alternative assumed stress field in which an original mode is multiplied by a nonzero constant. It is easy to verify that the magnitude of this constant does not affect their angle while its sign does. In other words, the reverse direction of the sub-mode will change the cosine sign of its angle with original basic mode. For this sake, in this paper the similarity degree is defined as the absolute value of the cosine of the angle as

$$\text{Similarity degree} = |\cos \theta_{ik}| \quad (15)$$

where  $\theta_{ik}$  is the angle between  $(\boldsymbol{\sigma}'_i)_k$  and  $\boldsymbol{\sigma}'_i$ . Thus,  $|\cos \theta_{ik}| = 1$  when  $\theta_{ik} = 0^\circ$  or  $180^\circ$ , indicating  $\bar{\boldsymbol{\sigma}}_j$  is in the same direction as  $\boldsymbol{\sigma}'_i$  or in the reverse direction to  $\boldsymbol{\sigma}'_i$ . However, no matter which case,  $\bar{\boldsymbol{\sigma}}_j$  plays the same role to result in the hybrid elements equivalent to each other. On the other hand,  $|\cos \theta_{ik}| = 0$  when  $\theta_{ik} = 90^\circ$ , indicating  $(\boldsymbol{\sigma}'_i)_k$  and  $\boldsymbol{\sigma}'_i$  are orthogonal to each other so  $\bar{\boldsymbol{\sigma}}_j$  cannot be used to suppress the zero-energy mode for the element.

For the subsequent development, the following subspaces are defined as

$$\begin{aligned} \mathcal{D} &= \left\{ \mathbf{a} \in \mathbb{R}^n \mid \mathbf{a} = \sum_{i=1}^m \alpha_i \mathbf{a}_i, \alpha_i \in \mathbb{R} \right\}, & \mathcal{E} &= \left\{ \boldsymbol{\varepsilon} \in (L^2(V^e))^{n_d} \mid \boldsymbol{\varepsilon} = \mathbf{B}\mathbf{a}, \mathbf{a} \in \mathcal{D} \right\} \\ \mathcal{S}' &= \left\{ \boldsymbol{\sigma}' \in (L^2(V^e))^{n_d} \mid \boldsymbol{\sigma}' = \mathbf{C}\boldsymbol{\varepsilon}, \boldsymbol{\varepsilon} \in \mathcal{E} \right\}, & \bar{\mathcal{S}} &= \left\{ \bar{\boldsymbol{\sigma}} \in (L^2(V^e))^{n_d} \mid \bar{\boldsymbol{\sigma}} = \sum_{j=1}^M \bar{\beta}_j \bar{\boldsymbol{\sigma}}_j, \bar{\beta}_j \in \mathbb{R} \right\} \end{aligned} \quad (16)$$

where  $\mathcal{D} \subset \mathbb{R}^n$  is the deformation subspace by the basic deformation modes  $\mathbf{a}_i$ 's,  $\mathcal{E} \subset \mathbb{R}^{n_d}$  the basic strain subspace,  $\mathcal{S}' \subset \mathbb{R}^{n_d}$  the basic stress subspace, and  $\bar{\mathcal{S}} \subset \mathbb{R}^{n_d}$  the stress subspace by the mode  $\bar{\boldsymbol{\sigma}}_j$ 's of uni-axial stress or pure shear stress, in which  $n_d = 3$ ,  $m = 13$  and  $M = 18$  for 2D 8-node element. As discussed earlier, to find the optimal stress modes for hybrid element, the sub-modes have to be compared with their original basic modes using their similarity degrees. However, the similarity degree depends upon the inner product. It is well known for the energy product

$$\langle \boldsymbol{\varepsilon}_i, \boldsymbol{\sigma}_j \rangle = \int_{V^e} \boldsymbol{\varepsilon}_i^T \boldsymbol{\sigma}_j dV, \quad \boldsymbol{\varepsilon}_i \in \mathcal{E}, \boldsymbol{\sigma}_j \in \mathcal{S}' \quad (17)$$

This is a conventional inner product where both the strain modes and stress modes are considered as mathematical vectors. However, the strain and stress belong to different mechanical concepts, and their analysis should be in mechanics for our attempt. In addition, even though the inner product has the physical meaning of energy, there is not any physical meaning in the associated norms or generalized lengths of strains and stresses as

$$\|\boldsymbol{\varepsilon}_i\| = \left( \int_{V^e} \boldsymbol{\varepsilon}_i^T \boldsymbol{\varepsilon}_i dV \right)^{1/2}, \quad \|\boldsymbol{\sigma}_j\| = \left( \int_{V^e} \boldsymbol{\sigma}_j^T \boldsymbol{\sigma}_j dV \right)^{1/2} \quad (18)$$

In other words, the strain and stress are only considered as mathematical vectors without any physical meanings. Clearly, without appropriate norm and the relating inner angle, the comparison between the stress modes and basic strain modes is impossible. So, the further discussion is difficult, particularly for some stress modes of which the energy products with their related basic strain

modes are equal to each other. Therefore, the inappropriate energy product is found to be the big barrier to determine the optimal stress modes inside the basic stress field. To overcome this problem, the inner product with material matrix as weighting matrix is introduced as

$$\langle \boldsymbol{\sigma}'_i, \mathbf{S}(\boldsymbol{\sigma}'_i)_k \rangle = \int_{V^e} \boldsymbol{\sigma}'_i{}^T \mathbf{S}(\boldsymbol{\sigma}'_i)_k dV, \boldsymbol{\sigma}'_i, (\boldsymbol{\sigma}'_i)_k \in \mathcal{S}' \cup \overline{\mathcal{S}} \quad (19)$$

The associated norms are expressed as

$$\|\boldsymbol{\sigma}'_i\|_S = \left( \int_{V^e} \boldsymbol{\sigma}'_i{}^T \mathbf{S} \boldsymbol{\sigma}'_i dV \right)^{1/2} = \left( \int_{V^e} \boldsymbol{\varepsilon}'_i{}^T \mathbf{C} \boldsymbol{\varepsilon}'_i dV \right)^{1/2}, \|(\boldsymbol{\sigma}'_i)_k\|_S = \left( \int_{V^e} (\boldsymbol{\sigma}'_i)_k{}^T \mathbf{S} (\boldsymbol{\sigma}'_i)_k dV \right)^{1/2} \quad (20)$$

These norms have the specific physical significance as the flexibility of stress (or stiffness of strain), which is the square root of complementary energy (or deformation energy, in the case of linear elasticity they are equal to each other). It shows the relationship between two stress modes. So this inner product is more reasonable. For this sense, the inner product in Eq. (20) can be used for the quantitative analysis to calculate the similarity degree of the sub-modes with their basic stress mode. It should be noted that our inner product in Eq. (19) is the development from Zhang et al. (2002) where our inner product is defined in the mixed subspace of basic stress subspace  $\mathcal{S}'$  together with  $\overline{\mathcal{S}}$  in Eq. (16) rather than the assumed subspace  $\mathcal{S}$  in Eq. (5). Based on our inner product in Eq. (19), the sub-modes can be compared with their basic stress modes to determine the optimal mode according to their similarity degrees.

### Optimal stress field for 2D 8-node hybrid element

For the 2D 8-node quadrilateral hybrid element (HQ8) in Fig.1 where 5,6,7,8 are the mid nodes on the sides, there are  $n=16$  degrees of freedom including  $r=3$  rigid body motions and  $m=n-r=13$  deformations. The element displacement field in Eq. (6) can be written as

$$\begin{cases} u = A_0 + A_1x + A_2y + A_3xy \\ \quad + A_4x^2 + A_5y^2 + A_6x^2y + A_7xy^2 \\ v = B_0 + B_1x + B_2y + B_3xy \\ \quad + B_4x^2 + B_5y^2 + B_6x^2y + B_7xy^2 \end{cases} \quad (21)$$

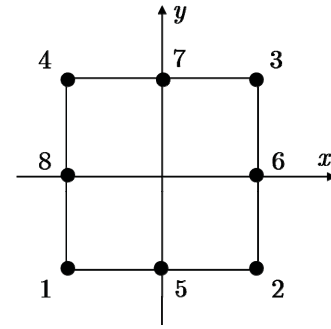


Fig.1 2D 8-node quadrilateral element

where  $A_i, B_i, i=0,1,\dots,7$  are the coefficients dependent upon the nodal displacements. Thus the basic strains modes in Eq. (8) can be derived as

$$\bar{\mathbf{B}} = \begin{bmatrix} 1 & 0 & 0 & y & 2x & 2xy & y^2 & 0 & 0 & 0 & 0 & 0 & 0 & 0 \\ 0 & 1 & 0 & 0 & 0 & 0 & 0 & x & 2y & 2xy & x^2 & 0 & 0 & 0 \\ 0 & 0 & 2 & x & 0 & x^2 & 2xy & y & 0 & y^2 & 2xy & 2y & 2x & 0 \end{bmatrix} \quad (22)$$

In addition, the basic stress modes in Eq. (9) can be obtained as

$$\mathbf{P}' = \begin{bmatrix} C & \nu C & 0 & Cy & 2Cx & 2Cxy & Cy^2 & \nu Cx & 2\nu Cy & 2\nu Cxy & \nu Cx^2 & 0 & 0 \\ \nu C & C & 0 & \nu Cy & 2\nu Cx & 2\nu Cxy & \nu Cy^2 & Cx & 2Cy & 2Cxy & Cx^2 & 0 & 0 \\ 0 & 0 & 2G & Gx & 0 & Gx^2 & 2Gxy & Gy & 0 & Gy^2 & 2Gxy & 2Gy & 2Gx \end{bmatrix} \quad (23)$$

in which  $C = E/(1-\nu^2)$ ,  $G = E/(2(1+\nu))$  for Young's modulus  $E$  and Poisson's ratio  $\nu$ . To take away the unnecessary components inside the basic stress modes in Eq. (23), they are broken into sub-modes in Eq. (14) with  $\bar{\boldsymbol{\sigma}}_j$ 's expressed as

$$\bar{\mathbf{P}} = \{\bar{\boldsymbol{\sigma}}_1, \bar{\boldsymbol{\sigma}}_2, \dots, \bar{\boldsymbol{\sigma}}_{18}\} = \{\mathbf{I}_3, x\mathbf{I}_3, y\mathbf{I}_3, xy\mathbf{I}_3, x^2\mathbf{I}_3, y^2\mathbf{I}_3\} \quad (24)$$

in which  $\mathbf{I}_3$  is the identity matrix of  $3 \times 3$ . Then sub-modes are compared with their original basic stress modes to select the optimal stress modes. The details are provided as follows:



(1) For  $\sigma'_1$ , it can be broken into its sub-modes as

$$\begin{Bmatrix} C \\ \nu C \\ 0 \end{Bmatrix} = \begin{Bmatrix} C \\ 0 \\ 0 \end{Bmatrix} + \begin{Bmatrix} 0 \\ \nu C \\ 0 \end{Bmatrix} = C \begin{Bmatrix} 1 \\ 0 \\ 0 \end{Bmatrix} + \nu C \begin{Bmatrix} 0 \\ 1 \\ 0 \end{Bmatrix} \quad (25)$$

namely,  $\sigma'_1 = (\sigma'_1)_1 + (\sigma'_1)_2 = \bar{\alpha}_{11}\bar{\sigma}_1 + \bar{\alpha}_{12}\bar{\sigma}_2$ , where  $\bar{\alpha}_{11} = C$  and  $\bar{\alpha}_{12} = \nu C$ . Based on our inner product in Eq. (19) the following similarity degrees can be calculated as

$$|\cos \theta_{11}| = \frac{\sqrt{E}}{d_0}, \quad |\cos \theta_{12}| = 0 \quad (26)$$

where  $d_0 = \sqrt{C}$ . Since  $|\cos \theta_{11}| > |\cos \theta_{12}|$ , one can conclude that  $(\sigma'_1)_1$  is more similar than  $(\sigma'_1)_2$  with  $\sigma'_1$ . It indicates  $(\sigma'_1)_1$  represents more features than  $(\sigma'_1)_2$  inside  $\sigma'_1$ . Therefore,  $\bar{\sigma}_1$  is selected as the optimal stress mode for hybrid element with respect to  $a_1$  as  $\sigma_1 = \bar{\sigma}_1$ . The cases for  $\sigma'_2$ ,  $\sigma'_5$ , and  $\sigma'_9$  are similar to  $\sigma'_1$  so that  $\sigma_2 = \bar{\sigma}_2$ ,  $\sigma_5 = \bar{\sigma}_4$ , and  $\sigma_9 = \bar{\sigma}_8$ .

(2) For  $\sigma'_3$ , since it is a pure shear stress mode as

$$\begin{Bmatrix} 0 \\ 0 \\ 2G \end{Bmatrix} = 2G \begin{Bmatrix} 0 \\ 0 \\ 1 \end{Bmatrix} \quad (27)$$

namely,  $\sigma'_3 = (\sigma'_3)_3 = \bar{\alpha}_{33}\bar{\sigma}_3$ , where  $\bar{\alpha}_{33} = 2G$ , the optimal stress mode is selected as  $\sigma_3 = \bar{\sigma}_3$ . The cases for  $\sigma'_{12}$ , and  $\sigma'_{13}$  are similar to  $\sigma'_3$  so that  $\sigma_{12} = \bar{\sigma}_9$  and  $\sigma_{13} = \bar{\sigma}_6$ .

(3) For  $\sigma'_4$ , it can be broken into its sub-modes as

$$\begin{Bmatrix} Cy \\ \nu Cy \\ 2Gx \end{Bmatrix} = \begin{Bmatrix} Cy \\ 0 \\ 0 \end{Bmatrix} + \begin{Bmatrix} 0 \\ \nu Cy \\ 0 \end{Bmatrix} + \begin{Bmatrix} 0 \\ 0 \\ 2Gx \end{Bmatrix} = C \begin{Bmatrix} y \\ 0 \\ 0 \end{Bmatrix} + \nu C \begin{Bmatrix} 0 \\ y \\ 0 \end{Bmatrix} + 2G \begin{Bmatrix} 0 \\ 0 \\ x \end{Bmatrix} \quad (28)$$

namely,  $\sigma'_4 = (\sigma'_4)_1 + (\sigma'_4)_2 + (\sigma'_4)_3 = \bar{\alpha}_{41}\bar{\sigma}_7 + \bar{\alpha}_{42}\bar{\sigma}_8 + \bar{\alpha}_{43}\bar{\sigma}_6$ , where  $\bar{\alpha}_{41} = C$ ,  $\bar{\alpha}_{42} = \nu C$ , and  $\bar{\alpha}_{43} = 2G$ . The following similarity degrees based on our inner product can be obtained as

$$|\cos \theta_{41}| = \frac{\sqrt{E}}{d_1}, \quad |\cos \theta_{42}| = 0, \quad |\cos \theta_{43}| = \frac{\sqrt{G}}{d_1} \quad (29)$$

where  $d_1 = \sqrt{C + G}$ . Due to the fact that the Poisson's ratio in general satisfies  $0 < \nu < 0.5$ , one has  $G < E$ . Thus by Eq. (29) one can obtain  $|\cos \theta_{41}| > |\cos \theta_{43}| > |\cos \theta_{42}|$ . Then we find the expected optimal mode for  $a_4$  as  $\sigma_4 = \bar{\sigma}_7$ . Obviously, by our systematic scheme, the parasitic shears  $\tau_{xy} = Gx$  in  $\sigma'_4$  are taken away automatically. The case for  $\sigma'_8$  is similar to  $\sigma'_4$  so that  $\sigma_8 = \bar{\sigma}_5$ .

(4) For  $\sigma'_6$ , it can be broken to its sub-modes as

$$\begin{Bmatrix} 2Cxy \\ 2\nu Cxy \\ Gx^2 \end{Bmatrix} = \begin{Bmatrix} 2Cxy \\ 0 \\ 0 \end{Bmatrix} + \begin{Bmatrix} 0 \\ 2\nu Cxy \\ 0 \end{Bmatrix} + \begin{Bmatrix} 0 \\ 0 \\ Gx^2 \end{Bmatrix} = 2C \begin{Bmatrix} xy \\ 0 \\ 0 \end{Bmatrix} + 2\nu C \begin{Bmatrix} 0 \\ xy \\ 0 \end{Bmatrix} + G \begin{Bmatrix} 0 \\ 0 \\ x^2 \end{Bmatrix} \quad (30)$$

namely,  $\sigma'_6 = (\sigma'_6)_1 + (\sigma'_6)_2 + (\sigma'_6)_3 = \bar{\alpha}_{61}\bar{\sigma}_{10} + \bar{\alpha}_{62}\bar{\sigma}_{11} + \bar{\alpha}_{63}\bar{\sigma}_{15}$ , where  $\bar{\alpha}_{61} = 2C$ ,  $\bar{\alpha}_{62} = 2\nu C$ , and  $\bar{\alpha}_{63} = G$ . The following similarity degrees based on our inner product can be obtained as

$$|\cos \theta_{61}| = \frac{4\sqrt{E}}{3d_2}, \quad |\cos \theta_{62}| = 0, \quad |\cos \theta_{63}| = \frac{2\sqrt{5G}}{5d_2} \quad (31)$$

where  $d_2 = \sqrt{4G/5 + 16C/9}$ . Since  $0 < \nu < 0.5$ , one has  $|\cos \theta_{61}|/|\cos \theta_{63}| = 2\sqrt{10(1+\nu)}/3 > 1$ . Thus  $|\cos \theta_{61}| > |\cos \theta_{63}| > |\cos \theta_{62}|$ . Then the expected optimal mode can be determined as  $\sigma_6 = \bar{\sigma}_{10}$ . The case for  $\sigma'_{10}$  is similar to  $\sigma'_6$  so that  $\sigma_{10} = \bar{\sigma}_{11}$ .

(5) For  $\sigma'_7$ , it can be broken to its sub-modes as

$$\begin{Bmatrix} Cy^2 \\ \nu Cy^2 \\ 2Gxy \end{Bmatrix} = \begin{Bmatrix} Cy^2 \\ 0 \\ 0 \end{Bmatrix} + \begin{Bmatrix} 0 \\ \nu Cy^2 \\ 0 \end{Bmatrix} + \begin{Bmatrix} 0 \\ 0 \\ 2Gxy \end{Bmatrix} = C \begin{Bmatrix} y^2 \\ 0 \\ 0 \end{Bmatrix} + \nu C \begin{Bmatrix} 0 \\ y^2 \\ 0 \end{Bmatrix} + 2G \begin{Bmatrix} 0 \\ 0 \\ xy \end{Bmatrix} \quad (32)$$

namely,  $\sigma'_7 = (\sigma'_7)_1 + (\sigma'_7)_2 + (\sigma'_7)_3 = \bar{\alpha}_{71}\bar{\sigma}_{16} + \bar{\alpha}_{72}\bar{\sigma}_{17} + \bar{\alpha}_{73}\bar{\sigma}_{12}$ , where  $\bar{\alpha}_{71} = C$ ,  $\bar{\alpha}_{72} = \nu C$ , and  $\bar{\alpha}_{73} = 2G$ . The following similarity degrees can be obtained as

$$|\cos \theta_{71}| = \frac{2\sqrt{5E}}{5d_2}, \quad |\cos \theta_{72}| = 0, \quad |\cos \theta_{73}| = \frac{4\sqrt{G}}{3d_2} \quad (33)$$

Since  $|\cos \theta_{71}|/|\cos \theta_{73}| = \sqrt{9(1+\nu)}/10$ , one can conclude  $\cos \theta_{71} > \cos \theta_{73}$  when  $\nu > 1/9$  which is the case for most materials. Then the expected optimal mode can be selected as  $\sigma_7 = \bar{\sigma}_{16}$ . The case for  $\sigma'_{11}$  is similar to  $\sigma'_7$  so that  $\sigma_{11} = \bar{\sigma}_{14}$ .

In summary, the final optimal stress modes are expressed as

$$\begin{aligned} \mathbf{P} = \{\sigma_1, \dots, \sigma_{13}\} &= \{\bar{\sigma}_1, \bar{\sigma}_2, \bar{\sigma}_3, \bar{\sigma}_7, \bar{\sigma}_4, \bar{\sigma}_{10}, \bar{\sigma}_{16}, \bar{\sigma}_5, \bar{\sigma}_8, \bar{\sigma}_{11}, \bar{\sigma}_{14}, \bar{\sigma}_9, \bar{\sigma}_6\} \\ &= \begin{bmatrix} 1 & 0 & 0 & y & x & xy & y^2 & 0 & 0 & 0 & 0 & 0 & 0 \\ 0 & 1 & 0 & 0 & 0 & 0 & 0 & x & y & xy & x^2 & 0 & 0 \\ 0 & 0 & 1 & 0 & 0 & 0 & 0 & 0 & 0 & 0 & 0 & y & x \end{bmatrix} \end{aligned} \quad (34)$$

Using the method by Zhang and Wang (2006, 2010), it is easy to verify that the element HQ8 constructed by the optimal stress modes in Eq. (34) is free of zero-energy mode.

## Numerical example

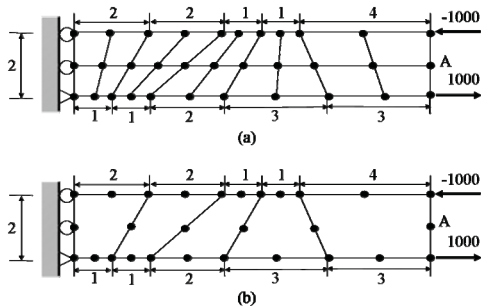


Fig 2. Cantilever beam (a) Q4 (b) Q8

Table 1 Tip deflections  $v_A$  for cantilever beams

$\nu$	0.25	0.49	0.499	0.4999
Q4	69.30	18.22	5.71157	2.713
Q8	93.34	73.79	65.3585	46.366
HQ4	93.23	75.20	74.2974	74.206
HQ8	93.72	75.49	74.5796	74.488
Exact	93.75	75.99	75.0999	75.010

A simple test for volume locking is given in Fig 2. This is an elastic plane-strain cantilever beam for  $E = 1500$  and different Poisson's ratio  $\nu$ . It is simply supported and subjected to pure bending. The results are provided in Table 1. It is shown that, when  $\nu$  tends to 0.5, the solution for improper elements show volumetric locking while HQ8 yields the most accurate solution for the tip deflection  $v_A$ . So the present element can overcome the volumetric locking successfully.

## Conclusions

A new inner product with the material matrix as the weighting matrix was introduced to study the relationship quantitatively between the different stress modes. Besides, the basic stress modes are considered instead of the basic strain modes in the conventional hybrid finite element formulation. They are broken into a set of sub-modes and these sub-modes are compared with their original basic stress modes to construct the optimal stress field for 2D 8-node quadrilateral hybrid element. The proposed method is straightforward to investigate the basic stress modes and determine the optimal stress modes, while the methods based on the conventional energy product as well as the modal technique can only be used to select the zero energy free stress modes.

## Acknowledgements

The support of this work by the National Natural Science Foundation of China (11222221) is gratefully acknowledged.

## References

- Bilotta, A. and Casciaro, R. (2002), Assumed stress formulation of high order quadrilateral elements with an improved in-plane bending behaviour, *Computer Methods in Applied Mechanics and Engineering*, 191, pp, 1523-1540.
- Cen, S., Zhou, M. J. and Fu, X. R. (2011), A 4-node hybrid stress-function (HS-F) plane element with drilling degrees of freedom less sensitive to severe mesh distortions. *Computers & Structures*, 89, pp, 517-528.
- Feng, W. and Hoa, S. V. and Huang, Q. (1997), Classification of stress modes in assumed stress fields of hybrid finite elements. *International Journal for Numerical Methods in Engineering*, 40, pp, 4313-4339.
- Han, J. and Hoa, S. V. (1993), A three-dimensional multilayer composite finite element for stress analysis of composite laminates. *International Journal for Numerical Methods in Engineering*, 36, pp, 3903-3914.
- Huang, Q. (1991), Modal analysis of deformable bodies with finite degree of deformation freedom-an approach to determination of natural stress modes in hybrid finite elements. In: Chien WZ, Fu ZZ, eds. *Advances in Applied Mathematics & Mechanics in China*, IAP, 3, pp. 283-303.
- Pian, T. H. H. (1964), Derivation of element stiffness matrices. *AIAA Journal*; 2, pp. 576-577.
- Pian, T. H. H. and Chen D. P. (1983), On the suppression of zero energy deformation modes. *International Journal for Numerical Methods in Engineering*, 19, pp. 1741-1752.
- Pian, T. H. H. and Sumihara, K. (1984), Rational approach for assumed stress finite elements, *International Journal for Numerical Methods in Engineering*, 20, pp. 1685-1695.
- Sze, Y. K. (1996), Admissible matrix formulation-from orthogonal approach to explicit hybrid stabilization, *Finite Elements in Analysis and Design*, 24, pp, 1-30.
- Wu, C. C. and Cheung, Y. K. (1995), On optimization approaches of hybrid stress elements, *Finite Elements in Analysis and Design*, 21, pp, 111-128.
- Zhang, C., Feng, W. and Huang, Q. (2002), The stress subspace of hybrid stress element and the diagonalization method for flexibility matrix H, *Applied Mathematics and Mechanics*, 23, pp. 1263-1273.
- Zhang, C., Huang, Q. and Feng, W. (2006), Deformation rigidity of assumed stress modes in hybrid elements. *Applied Mathematics and Mechanics*, 27, pp. 861-869.
- Zhang C. and Wang, D. (2006), Suppression of zero-energy modes in hybrid finite elements via assumed stress fields, *EPMESC-X*, pp, 21-23.
- Zhang, C., Wang, D., Zhang, J., Feng, W. and Huang, Q. (2007), On the equivalence of various hybrid finite elements and a new orthogonalization method for explicit element stiffness formulation. *Finite Elements in Analysis and Design*, 2007; 43, pp. 321-332.
- Zhang, C. and Wang, D. (2010), An assumed stress method for zero-energy mode suppression in hybrid finite elements. *Chinese Journal of Solid Mechanics*, 31, pp. 40-47.
- Zhang, C., Wang, D. and Li, T. (2011b), Orthogonal basic deformation mode method for zero-energy mode suppression of hybrid stress elements. *Applied Mathematics and Mechanics (English Edition)*, 32, pp. 83-96.

# Analytical solution for the transient response of functionally graded rectangular plates subjected to moving loads

Ta DuyHien<sup>1</sup>, Hyuk-Chun Noh<sup>1\*</sup>

<sup>1</sup>Department of Civil and Environmental Engineering, Sejong University, Seoul, South Korea.

\*Corresponding author: cpebach@sejong.ac.kr

## Abstract

An analysis scheme for the dynamic responses of functionally graded (FG) rectangular plates under moving loads is developed by using the third-order shear deformation plate theory (TSDT). It is assumed that material properties of the plate vary continuously in the thickness direction according to the power-law. The equations of motion are derived by using Hamilton's principle. Analytic solution of simply supported FG rectangular plates is presented by using state-space methods. The displacement and stresses are computed in the plates with various structural parameters, and the effects of these parameters, such as power-law exponent index, are discussed in detail. In addition, the effects of the moving load on the dynamic responses of the plates are investigated as well.

**Keywords:** Analytical solution, Dynamic response, functionally graded plate, moving loads.

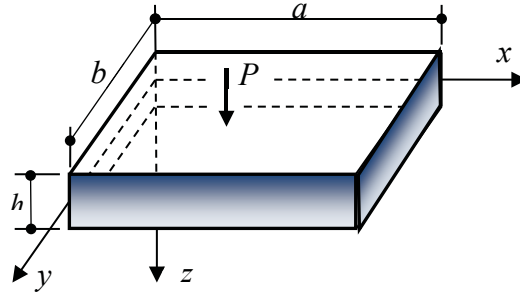
## 1. Introduction

The study of dynamic response of plates subjected to moving loads is of interest and of importance as well in the engineering field, as some of the results can be applicable to understand the dynamic behavior of bridge. Most of the previous studies on the plates subjected to moving loads have used the classical plate theory (CPT) or the first order shear deformation theory (FSDT). Hianget *al.*[5] used finite strip method to investigate the dynamic response of plate structure resting on an elastic foundation to moving loads. Lee *et al.*[7] investigated dynamic behaviors of single and two-span continuous composite plate structures subjected to multi-moving loads using finite element method. Vosoughi *et al.*[12] studies dynamic response of laminated rectangular plates on elastic foundation based on the higher order shear deformation theory and differential quadrature method. E.Ghafoori and M.Asghari[3] studied the dynamic response of laminated composite plates traversed by a moving mass or a moving force based on the first-order shear deformation theory using a finite element method. P.Malekzadeh *et al.*[8] used three-dimensional elasticity theory to investigate the dynamic response of cross-ply laminated thick plates subjected to moving load. Hao *et al.*[4] studied on nonlinear dynamic behavior of a simply supported functionally graded materials (FGMs) rectangular plate subjected to thermalmechanical loads. Qian *et al.*[9] studied a static and dynamic of rectangular functionally graded plate based on a higher-order shear and normal deformable plate theory by using a meshless local Petrov–Galerkin method. Akbarzadehet *et al.*[1] studies the dynamic response of a simply supported functionally graded rectangular plate subjected to thermomechanical loading by using the hybrid Fourier-Laplace transform method based on both the first-order and third-order shear deformation theories. Sun *et al.*[11] investigated the wave propagation and dynamic response of the rectangular FGM plates with completed clamped supports to consider the effects of transverse shear deformation and rotary inertia. However, the research works concerning the dynamic response of FG plates subjected to moving loads are still limited.

In the this paper, exact solutions for the transient response of FG rectangular plate are developed using the third-order shear deformation plate theory (TSDT) proposed by R.P. Shimpi[10]. The FG rectangular plate, with simply supported boundary conditions, is subjected to a concentrated moving load at the upper surface of the plate. Equations of motion are solved by using state-space methods and the effects of different parameters on the response of the plate are studied. The results are compared with finite element solutions for validation.

## 2. Equations of motion

Let us consider a functionally graded plate in Figure.1:



**Figure 1. Model of FG Plate**

We assume that the gradation of material properties along the plate thickness is represented by the profile for volume fraction variation:

$$E(z) = (E_c - E_m) \left( \frac{z}{h} + \frac{1}{2} \right)^p + E_m \quad (1)$$

$$\rho(z) = (\rho_c - \rho_m) \left( \frac{z}{h} + \frac{1}{2} \right)^p + \rho_m$$

where  $E, \rho$  denote generic properties of elastic modulus and mass density,  $E_c, \rho_c$  and  $E_m, \rho_m$  denote the properties on the top and bottom surfaces, respectively, and  $p$  is a parameter that dictates the material variation profile through the thickness. Poisson's ratios are assumed to be uniform.

The third-order shear deformation theory used in the present study is based on the following representation of the displacement field across the plate thickness as in Shimpi [10]:

$$U(x, y, z, t) = u(x, y, z, t) - z \frac{\partial w_b}{\partial x} + \left[ \frac{1}{4} z - \frac{5}{3} z \left( \frac{z}{h} \right)^2 \right] \frac{\partial w_s}{\partial x}$$

$$V(x, y, z, t) = v(x, y, z, t) - z \frac{\partial w_b}{\partial y} + \left[ \frac{1}{4} z - \frac{5}{3} z \left( \frac{z}{h} \right)^2 \right] \frac{\partial w_s}{\partial y} \quad (2)$$

$$W(x, y, z, t) = w_b(x, y, t) + w_s(x, y, t)$$

where  $(U, V, W)$  are the displacement components of a point  $(x, y, z)$  in the plate,  $(u, v, w_b, w_s)$  are the displacements of a point on the mid-plane at time  $t$ , respectively.

The strains are computed from displacement fields in Eq. (2), and can be used in constructing the strain energy and kinetic energy expressions. Hamilton's principle is used herein to derive the equations of motion; the equations of motion of plate are obtained as:

$$\delta u : \frac{\partial N_x}{\partial x} + \frac{\partial N_{xy}}{\partial y} = I_0 \ddot{u} - I_1 \frac{\partial \ddot{w}_b}{\partial x} - J_1 \frac{\partial \ddot{w}_s}{\partial x}$$

$$\delta v : \frac{\partial N_{xy}}{\partial x} + \frac{\partial N_y}{\partial y} = I_0 \ddot{v} - I_1 \frac{\partial \ddot{w}_b}{\partial y} - J_1 \frac{\partial \ddot{w}_s}{\partial y}$$

$$\delta w_b : \frac{\partial^2 M_x^b}{\partial x^2} + 2 \frac{\partial^2 M_{xy}^b}{\partial x \partial y} + \frac{\partial^2 M_y^b}{\partial y^2} + P = I_0 (\ddot{w}_b + \ddot{w}_s) + I_1 \left( \frac{\partial \ddot{u}}{\partial x} + \frac{\partial \ddot{v}}{\partial y} \right) - I_2 \nabla^2 \ddot{w}_b - J_2 \nabla^2 \ddot{w}_s$$

$$\delta w_s : \frac{\partial^2 M_x^s}{\partial x^2} + 2 \frac{\partial^2 M_{xy}^s}{\partial x \partial y} + \frac{\partial^2 M_y^s}{\partial y^2} + \frac{\partial Q_{xz}}{\partial x} + \frac{\partial Q_{yz}}{\partial y} + P = I_0 (\ddot{w}_b + \ddot{w}_s) + J_1 \left( \frac{\partial \ddot{u}}{\partial x} + \frac{\partial \ddot{v}}{\partial y} \right) - \hat{J}_2 \nabla^2 \ddot{w}_b \quad (3)$$

where  $P$  is the moving load and  $(N_i, Q_i, M_i^{b,s})$  are the stress resultants and the inertias  $(I_i, J_i, \hat{J})$  are defined by:

$$\begin{aligned} (N_x, N_y, N_{xy}) &= \int_{-h/2}^{h/2} (\sigma_x, \sigma_y, \sigma_{xy}) dz \\ (M_x^b, M_y^b, M_{xy}^b) &= \int_{-h/2}^{h/2} z (\sigma_x, \sigma_y, \sigma_{xy}) dz \\ (M_x^s, M_y^s, M_{xy}^s) &= \int_{-h/2}^{h/2} \hat{f} (\sigma_x, \sigma_y, \sigma_{xy}) dz \\ (Q_x, Q_y) &= \int_{-h/2}^{h/2} \hat{g} (\sigma_{xz}, \sigma_{yz}) dz \\ I_i &= \int_{-h/2}^{h/2} \rho(z) z^i dz, \quad (i=0,1,2,3,4,6) \\ J_i &= \int_{-h/2}^{h/2} \rho(z) z^i \hat{f} dz, \quad (i=1,2) \\ \hat{J}_2 &= \int_{-h/2}^{h/2} \rho(z) z^2 \hat{f}^2 dz \end{aligned}$$

The moving load is given as

$$P = P(t) \delta(x - x_{mov}(t)) \delta(y - y_{mov}(t))$$

where  $P(t)$  is the magnitude of the moving load;  $x_{mov}(t)$  and  $y_{mov}(t)$  are the coordinates of the location of the load. In this paper, it is assumed that  $P = P_0$ ,  $x_{mov}(t) = V_0 t$  and  $y_{mov}(t) = b/2$ .

### 3 Solution procedures

The state-space approach has been used generally in the area of control theory to determine the responses of given systems. The state-space representations [6] of the dynamic systems will be used to analyze the transient response of simply supported FG rectangular plates with side dimensions  $a$  and  $b$ . The Navier approach is used to derive the closed-form solutions of equations of motion. The sinusoidal function is chosen to satisfy all the boundary conditions as follows:

$$\begin{aligned} u(x, y, t) &= \sum_{n=1}^{\infty} \sum_{m=1}^{\infty} U_{mn}(t) \cos \alpha x \sin \beta y \\ v(x, y, t) &= \sum_{n=1}^{\infty} \sum_{m=1}^{\infty} V_{mn}(t) \sin \alpha x \cos \beta y \\ w_b(x, y, t) &= \sum_{n=1}^{\infty} \sum_{m=1}^{\infty} W_{bmn}(t) \sin \alpha x \sin \beta y \\ w_s(x, y, t) &= \sum_{n=1}^{\infty} \sum_{m=1}^{\infty} W_{smn}(t) \sin \alpha x \sin \beta y \end{aligned} \tag{4}$$

where  $\alpha = \frac{m\pi}{a}, \beta = \frac{n\pi}{b}$ .

Using (4), the expression in (3) can be written as follows:

$$\begin{bmatrix} S_{11} & S_{12} & S_{13} & S_{14} \\ S_{12} & S_{22} & S_{23} & S_{24} \\ S_{13} & S_{23} & S_{33} & S_{34} \\ S_{14} & S_{24} & S_{34} & S_{44} \end{bmatrix} \begin{bmatrix} U_{mn} \\ V_{mn} \\ W_{bmn} \\ W_{smn} \end{bmatrix} + \begin{bmatrix} m_{11} & 0 & m_{13} & m_{14} \\ 0 & m_{22} & m_{23} & m_{24} \\ m_{13} & m_{23} & m_{33} & m_{34} \\ m_{14} & m_{24} & m_{43} & m_{44} \end{bmatrix} \begin{bmatrix} \ddot{U}_{mn} \\ \ddot{V}_{mn} \\ \ddot{W}_{bmn} \\ \ddot{W}_{smn} \end{bmatrix} = \begin{bmatrix} 0 \\ 0 \\ F_{mn} \\ F_{mn} \end{bmatrix} \tag{5}$$

Here, we will use the following notations:

$$\begin{aligned} \mathbf{M} &= \{m_{ij}\}, \mathbf{S} = \{s_{ij}\} \\ \mathbf{F}^* &= \{0 \quad 0 \quad F_{mn} \quad F_{mn}\}^T \end{aligned}$$

where,

$$F_{mn} = \frac{4P_0}{ab} \sin(\alpha V_0 t) \sin\left(\frac{\beta b}{2}\right)$$

For solving (5) by using the state space methods, (5) is needed to be rewritten as:

$$\dot{\mathbf{Z}} = \mathbf{AZ} + \mathbf{b} \quad (6)$$

where

$$\mathbf{Z} = \{U_{mn} \quad V_{mn} \quad W_{bmn} \quad W_{smn} \quad \dot{U}_{mn} \quad \dot{V}_{mn} \quad \dot{W}_{bmn} \quad \dot{W}_{smn}\}^T$$

$$\mathbf{b} = \{0 \quad 0 \quad 0 \quad 0 \quad b_1 \quad b_2 \quad b_3 \quad b_4\}^T$$

and  $b_i$  are the term of the column matrix

$$\{b_1 \quad b_2 \quad b_3 \quad b_4\}^T = \mathbf{M}^{-1} \mathbf{F}^*$$

and block matrix A is

$$\mathbf{A} = \begin{bmatrix} 0 & \mathbf{I} \\ -\mathbf{M}^{-1} \mathbf{S} & 0 \end{bmatrix}$$

The solution of (6) is obtained as

$$\dot{\mathbf{Z}}(t) = e^{\mathbf{A}(t-t_0)} \mathbf{Z}(t_0) + \int_{t_0}^t e^{\mathbf{A}(t-\tau)} \mathbf{b}(\tau) d\tau \quad (7)$$

where  $t_0$  is the initial time,  $\mathbf{Z}(t_0)$  is the initial response, and the exponential matrix  $e^{\mathbf{A}(t-t_0)}$  can be expressed in terms of the matrix of eigenvectors and eigenvalues  $\lambda_i$  associated with the matrix A.

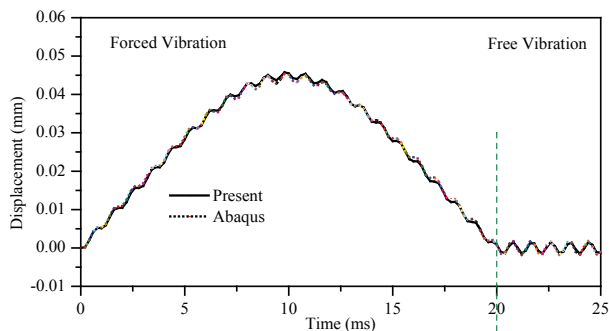
#### 4 Numerical examples

In order to investigate the legitimacy of the proposed method, an Al/Al<sub>2</sub>O<sub>3</sub> plate composed of aluminum (as metal) and alumina (as ceramic) is considered. The elastic moduli are chosen to be the same as given in [2]:  $E_m = 70 \text{ GPa}$ ,  $\rho_m = 2702 \text{ kg/m}^3$ ,  $E_c = 380 \text{ GPa}$ ,  $\rho_c = 3800 \text{ kg/m}^3$ . The Poisson's ratio of the plate is assumed to be constant through the thickness and is equal to 0.3. Consider a simply supported square FG plate with a side-length  $a = 0.3 \text{ m}$  and magnitude of load  $P_0 = 2 \times 10^3 \text{ N}$ .

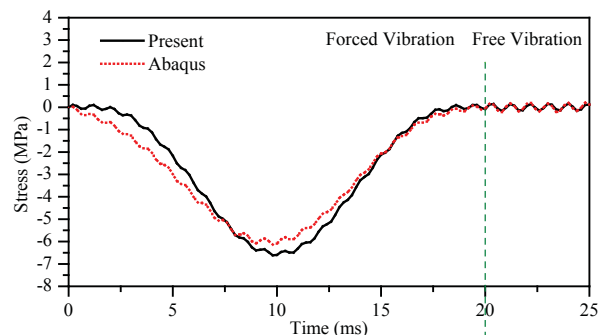
To validate the presented approach, the results are compared with those of finite element solution by using ABAQUS software. The time histories of central deflection and normal stress at top ( $z = -h/2$ ) as functions of time for simply supported square FG plate with  $p = 2$ ,  $h/a = 0.05$  and  $v = 15 \text{ m/s}$ , are plotted and compared in Figures 2 and 3. The results of this study are in good agreement with the finite element solutions.

Figure 4 contains plots of center transverse deflection as functions of time with parameter  $h/a = 0.05$  and  $v = 40 \text{ m/s}$  for the four cases with different power law index  $p = 0, 1, 2, 3$ , respectively. Figure 4 shows that the oscillation of the plate deflection increases if power law index  $p$  increases, which makes the flexural rigidity high.

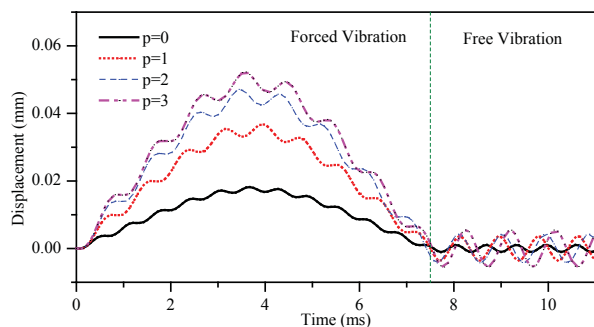
In order to investigate the effect of velocity of moving loads on the plate responses, we consider square FG plate with parameter  $a = 0.3 \text{ m}$ ,  $h/a = 0.05$  and  $p = 3$  for three cases of different velocities  $v = 1, 25, 50 \text{ m/s}$ , respectively. The effect of velocity of moving loads can be seen from Figure 5; the effect of velocity of moving loads is not so huge for the case of displacement. However, the effect of moving load velocity is significant from the viewpoint of vibration of the plate.



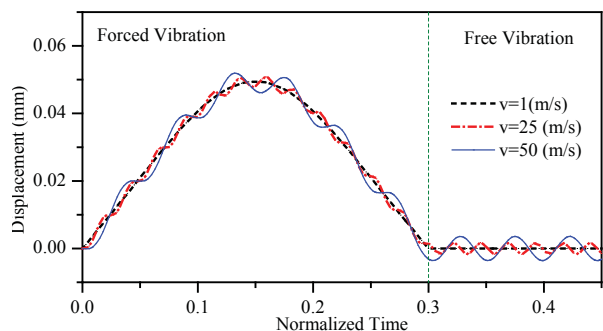
**Figure 2.** The time variations of the deflection at central plate



**Figure 3.** The time variations of the normal stress at top ( $z=-h/2$ ) of central plate



**Figure 4.** The time variations of the deflection at central plate with various power law  $p$



**Figure 5.** The time variations of the deflection at central plate with various velocity  $v$

## Conclusions

In this article, analytical solutions of dynamic responses are obtained for FG plates employing a third-order plate theory base on state-space approach. The dynamic responses are considered for both forced vibration and free vibration. Comparison with finite element solution shows that the results of present approach are acceptable. The volume fraction power law along the plate thickness has great influence on the dynamic behavior of FG plate, and the deflections of plate can be controlled by choosing proper values of  $p$ . The results also confirm that the effect of velocity of moving loads is negligible.

## References

- Akbarzadeh, A. H., Abbasi, M., Hosseini zad, S. K., Eslami, M. R., (2011), Dynamic Analysis of Functionally Graded Plates Using The hybrid Fourier-Laplace Transform under Thermomechanical Loading. *Meccanica*, 46 pp. 1373-1392.
- Benyoucef, S., Mechab, I., Tounsi, A., Fekrar, A., Ait Atmane, H., Adda Bedia, El Abbas, (2010), Bending of Thick Functionally Graded Plates Resting on Winkler–Pasternak Elastic Foundations. *Mechanics of Composite Materials*, 46 pp. 425-434.
- Ghafoori, E., Asghari, M., (2010), Dynamic Analysis of Laminated Composite Plates Traversed by a Moving Mass Based on a First-Order Theory. *Composite Structures*, 92 pp. 1865-1876.
- Hao, Y. X., Zhang, W., Yang, J., Li, S. Y., (2011), Nonlinear Dynamic Response of a Simply Supported Rectangular Functionally Graded Material Plate under the Time-Dependent Thermalmechanical Loads. *Journal of Mechanical Science and Technology*, 25 pp. 1637-1646.
- Huang, M., Thambiratnam, D., (2002), Dynamic Response of Plates on Elastic Foundation to Moving Loads. *Journal of Engineering Mechanics*, 128 pp. 1016-1022.
- Khdeir, A. A., Reddy, J. N., (1989), Exact-Solutions for the Transient-Response of Symmetric Cross-Ply Laminates Using a Higher-Order Plate-Theory. *Composites Science and Technology*, 34 pp. 205-224.
- Lee, S. Y., Yhim, S. S., (2004), Dynamic Analysis of Composite Plates Subjected to Multi-Moving Loads Based on a Third Order Theory. *International Journal of Solids and Structures*, 41 pp. 4457-4472.



- Malekzadeh, P., Fiouz, A. R., Razi, H., (2009), Three-Dimensional Dynamic Analysis of Laminated Composite Plates Subjected to Moving Load. *Composite Structures*, 90 pp. 105-114.
- Qian, L. F., Batra, R. C., Chen, L. M., (2004), Static and Dynamic Deformations of Thick Functionally Graded Elastic Plates by Using Higher-Order Shear and Normal Deformable Plate Theory and Meshless Local Petrov–Galerkin Method. *Composites Part B: Engineering*, 35 pp. 685-697.
- Shimpi, R. P., Patel, H. G., (2006), A Two Variable Refined Plate Theory for Orthotropic Plate Analysis. *International Journal of Solids and Structures*, 43 pp. 6783-6799.
- Sun, Dan, Luo, Song-Nan, (2011), The Wave Propagation and Dynamic Response of Rectangular Functionally Graded Material Plates with Completed Clamped Supports under Impulse Load. *European Journal of Mechanics - A/Solids*, 30 pp. 396-408.
- Vosoughi, A. R., Malekzadeh, P., Razi, H., (2013), Response of Moderately Thick Laminated Composite Plates on Elastic Foundation Subjected to Moving Load. *Composite Structures*, 97 pp. 286-295.

## 4D Model Reconstruction of Patient-Specific Cardiac Mesh from Segmented Contour Lines

\*Chi Wan Lim<sup>1</sup>, Yi Su<sup>1</sup>, Si Yong Yeo<sup>1</sup>, Gillian Maria Ng<sup>1</sup>, Vinh Tan Nguyen<sup>1</sup>, Liang Zhong<sup>2</sup>,  
Ru San Tan<sup>2</sup>, Kian Keong Poh<sup>3,4</sup>, Ping Chai<sup>3</sup>

<sup>1</sup> Institute of High Performance Computing, A\*STAR, Singapore

<sup>2</sup> National Heart Centre Singapore, Singapore

<sup>3</sup> Cardiac Department, National University Heart Center, National University Health System, Singapore

<sup>4</sup> Department of Medicine, Yong Loo Lin School of Medicine, National University of Singapore, Singapore

\*Corresponding author: limcw@ihpc.a-star.edu.sg

### Abstract

We propose an automatic algorithm for the reconstruction of a set of patient-specific dynamic cardiac mesh model with 1-to-1 mesh correspondence over the whole cardiac cycle. This work focus on both the reconstruction technique of the initial 3D model of the heart and also the consistent mapping of the vertex positions throughout all the 3D meshes. This process is technically more challenging due to the wide interval spacing between MRI images as compared to CT images, making overlapping blood vessels much harder to discern. We propose a tree-based connectivity data structure to perform a filtering process to eliminate weak connections between contours on adjacent slices. The reconstructed 3D model from the first time step is used as a base template model, and deformed to fit the segmented contours in the next time step. Our algorithm has been tested on an actual acquisition of cardiac MRI images over one cardiac cycle.

**Keywords:** Mesh Reconstruction, Cardiac, Patient-Specific, MRI, 4D

### Introduction

The cardiovascular diseases are becoming more commonplace in modern societies. One of the ways which physicians use to view the internal cross-sectional images patient's heart with cardiovascular diseases is by Magnetic Resonance Imaging (MRI). Inclusion of computational methods in cardiac analysis can allow us to further understand and visualize what we are unable to obtain from static 2D images, such as blood flow behavior (hemodynamics) in the chambers. To achieve this, the reconstruction of the 4D (spatial temporal) mesh model of the heart is an important and critical requirement. In this paper, we propose a framework to directly reconstruct a 4D right heart model from segmented contours drawn on MRI images.

### Related Work

Cardiac reconstruction, either static (3D) or dynamic (4D), has traditionally focused on the ventricular regions due to their simpler morphology and the relative ease of border delineation on CT and MRI scans, as compared to the atrial regions. This differentiation is further compounded for MRI-based methods due to its relatively large spatial intervals between slices. A comprehensive review of the different modeling techniques from cardiac images prior to 2001 was presented by Frangi et al. [1].

One of the first studies to directly construct a 3D model of the heart is by McQueen and Peskin [2], which employed idealized cones and ellipsoids for modeling the left and right ventricles for

simulating cardiac hemodynamics [3]. Using 3D echocardiography, Corsi et al. [4] employed the level set method and marching cubes algorithm to reconstruct a 3D model of the LV. Zhukov et al. [5] proposed to deform a sphere model using dynamic remeshing and curvature estimation methods to produce high quality meshes of the heart. Montagnat and Delingette [6] extended the deformable surface framework by introducing time-dependent constraints such as temporal smoothing and trajectory constraints. Sermesant et al. [7] fitted various image modality together using a non-rigid registration approach to create a mesh model of both the LV and RV (right ventricle) using the GHS3D commercial software. A noteworthy attempt to reconstruct a hugely detailed static animal heart model is presented by Plank et al. [8], which uses a 9.4T MR system that is able to generate MR datasets with isotropic resolution of up to  $20\mu m$ .

One of the biggest obstacles in 4D heart modeling has been the modeling of the passageways between the ventricles and the atriums and the complex vessels that connects them to the rest of the body. During cardiac contraction, these vessels deform, possibly in directions perpendicular to the imaging planes. This can cause difficulties during the 4D reconstruction process, as the vessels themselves moves in and out of the imaging planes, and thus their boundaries on these planes are manifested in a constant series of merging and splitting processes. In our work, we propose a methodology that aims to mitigate this issue by utilizing a tree structure to link and track the contours throughout the cardiac cycle, in order to reconstruct a 4D cardiac mesh model with 1-to-1 vertex correspondence.

## Overview of Method

The raw data input to this algorithm are the segmented contour lines, which are drawn on a set of short-axis MRI images over one cardiac cycle. We proceed to establish connectivity relationships between the segmented contours lines in two ways, inter-frame and intra-frame. Connectivities within the same time step (intra-frame) relates to the morphological structure of the heart in that particular time step; connectivities across adjacent time steps (inter-frame) provide information related to the motion of the heart across that time step.

The main challenge occurs during 2D contour topological changes, when there are no 1-to-1 inter-frame connections between contours. To handle this, we first collect the characteristics features of the 2D contour topological change, such as its vertical motion and the location of the ridge feature. Thereafter, we apply a 2D sine-based deformation function using the ridge feature as its center to induce the vertical motion, and therefore ensuring that the contours can be associated in a 1-to-1 manner across that time step.

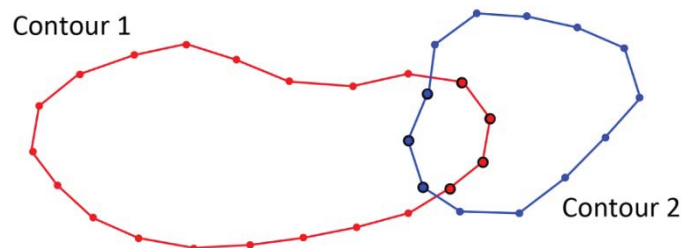
## Constructing a 3D model of the First Cardiac Frame

In this section we describe how we perform filtering to remove unwanted connections between segmented contours from adjacent slices, and then detail the reconstruction process of the 3D heart model, based on the MR images from the first time step.

### *Tree-Based Connectivity*

The set of connectivity relationship between contours from adjacent slices and across time steps are termed as a tree-based connectivity. The 3D reconstruction makes use of the connectivities between adjacent slices (intra-frame connectivities), while the deformation stage makes use of the connectivities between adjacent frames (inter-frame connectivities). Each contour can have four different types of connections, *above* and *below*, which are intra-frame connections; and *prev* and

*next*, which are inter-frame connections. The tree-based connectivity is established by comparing contours between adjacent slices (both inter- and intra-frame) based on a similarity index function. The similarity index is computed based on the proportion of the perimeter of the contour that lies within the interior of the other contour when both contours are superimposed on the same plane. The higher of the two proportion values is then taken as the similarity index (see Figure 1).



**Figure 1. Determining connectivity between contours. The similarity index based on the higher of the two proportions is 23.08% (3 out of 13 points from contour 2).**

In cases where there is only one pairing with non-zero similarity index, the assignment is straightforward. Otherwise, two situations could happen, either branching (intra-frame)/topological change (inter-frame) has occurred, or one of the similarity index is a very weak one. To decide between both potential situations, weak connections are filtered away by setting a minimum similarity index threshold of 30%.

#### *Reconstruction from Segmented Contour Lines*

For reconstruction of the 3D initial cardiac mesh model from the first frame, we extended the works of Barequet and Sharir [22] by incorporating the concept of contour connectivity into it such that only those contours that are connected will have a surface formed between them. One potential issue that might arise using their approach is that some of the reconstructed surface triangles might have all their three vertices belonging to the same contour, thereby making it flat when the contours are projected back. If another flat triangle exists on the other side of the contour, the resulting surface will contain a collapsed triangle-pair, thereby forming a disconnected internal volume. In order to prevent such problematic configuration, we inject new vertices into the triangulation before lifting by using the chordal axis transform (CAT) approach [23]. This CAT approach introduces new vertices which essentially act as a set of “lifting” points to break up the flat triangles to prevent a collapsed configuration. This also helps to create a relatively smoother volume.

#### **4D Morphing of the Heart Model**

The goal of the deformation process is to modify the heart model of a particular frame to fit the contours of the next frame without changing the mesh connectivity. To implement the deformation process, we split the heart model into logical sub-meshes using the MRI planes as the partitioning planes. As each sub-mesh (except the topmost and bottommost) is sandwiched between two partitioning planes (see Figure 2), we can compute the deformation for each sub-mesh independently. Using an example for illustration (see Figure 3), consider two adjacent contours  $X$  and  $X'$  that has a surface  $\zeta$  between them; we wish to find a mapping of the points on  $X$  (source points) onto the contour  $X'$  (target points). To achieve a good mapping, we project  $X$  and  $X'$  onto a common plane. Next, the intersection points between  $X$  and  $X'$  are then used as breaking points to

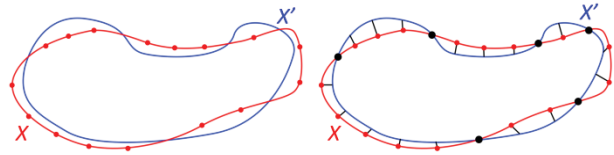
split both  $X$  and  $X'$  into segments. Each individual segment in  $X$  is then matched against its corresponding segment in  $X'$ , and the points in each segment are then mapped from  $X$  and  $X'$  proportionally. Using both sets of source points and target points, we generate a radial basis function (RBF) interpolant [32] of the form

$$\tilde{f}(x) = \sum_k^N w_k \phi(\|x - x_k\|),$$

where the kernel function  $\phi: \mathbb{R}^+ \rightarrow \mathbb{R}$  is univariate and radially symmetric, and  $w_k$  is a set of 3-dimensional weights. Our choice of the kernel function is the Hardy Multiquadric,  $\phi(r) = \sqrt{r^2 + c^2}$ , where  $c$  is a constant defined individually for each source point, based on the distance to its closest neighbor. By determining the weights of the RBF, we are able use it to interpolate where the new surface  $\zeta'$  lies on.



**Figure 2. A Sub-mesh is a subset of the 3D mesh that is bounded by a pair of contour lines.**



**Figure 3. Contour matching for generating a source-target point set.**

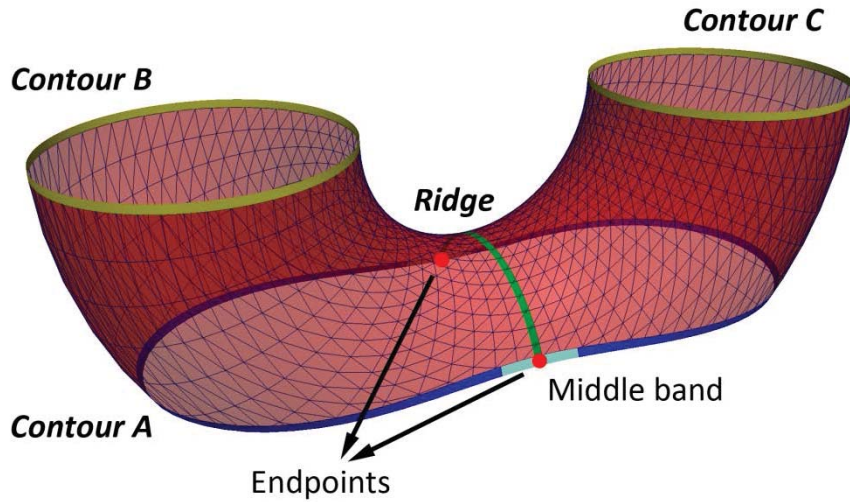
### Handling 2D Contour Topological Changes

A 2D contour topological change occurs when there is no 1-to-1 inter-frame matching of contours during the contour matching process. This contour slice is then referred to as the *incident* slice. For such situations, we first determine the direction of the vertical motion that is occurring at the contour, then locate the ridge feature, and finally apply a 2D sine-based deformation function centralized at the ridge feature. The goal is to make sure that there is a 1-to-1 inter-frame matching of all the contours.

In order to determine the direction of the vertical motion, we first need to detect the location of the ridge in both frames where the 2D contour topological change is deemed to have occurred. The location of the ridge can be easily determined by noting where a many-to-one (or one-to-many) intra-frame connectivity exists. By comparing the location of the ridge between the two adjacent frames, we can then determine the direction of the vertical motion, i.e., moving upwards or downwards. For the case of upward vertical motion, the slice below the *incident* slice is referred to as the *complement* slice. For the case of a downward vertical motion, the *complement* slice is the slice above the *incident* slice.

A ridge feature is a path described by a sequence of edges that are roughly equidistant from the two contours. The desired effect is to apply a stronger vertical deformation at the source of the branching, while gradually reducing the strength as we move further away from it. We use a 2D sine-based function, with its center localized along the ridge feature, as the vertical deformation function. To extract the ridge, we have to first locate the two end points of the ridge. Assuming that the *incident* slice contains contour  $A$  and the *complement* slice contains two contours,  $B$  and  $C$ , we

proceed to project all the three contours onto a common plane. For each vertex point on  $A$ , we compute its nearest distance to both  $B$  and  $C$ . For vertex points where its nearest distance to both  $B$  and  $C$  do not differ by more than 10%, we term it as the middle band (see Figure 4). Typically, two contiguous and disjointed middle bands will be formed. However, in the unlikely case where multiple contiguous middle bands are formed, we select the two largest bands and discard the rest. A point in each band is identified such that the difference between its distance to both  $B$  and  $C$  is the smallest. These two points are then selected as the end points of the ridge. The ridge is represented by the geodesic path computed between these two end points. A simple greedy algorithm that always select the next edge that result in closer distance to the end location is sufficient to extract the ridge. Figure 4 shows an idealized image of the ridge feature that is formed between two adjacent slices.



**Figure 4. Ridge Detection.**

To induce smooth vertical deformation, we have to expand the affected regions to include other sub-meshes around the incident slice. This allows the deformation to gradually spread its effect across several slices, thereby creating a smoother transition to the next frame. Hence, we considered two layers of adjacent sub-meshes above and below the incident sub-mesh. In total, six different slices are affected, labeled from 1 (topmost) to 6 (bottom). The deformation employs a 2D sine function, with its center located along the ridge feature. This allows us to apply the largest deformation at the ridge feature, while gradually reducing its effects, as we move away from the ridge. We proceed to project all the affected contours located on the six slices onto a common perpendicular plane, together with the ridge feature. On this perpendicular projection, the parameter  $\lambda$  is set to be the furthest 2D distance between the ridge and any point on the incident slice. We then use a 2D sine function to compute the amount of vertical displacement  $VD_p$  of each point  $p$  on the contour as a function of its 2D distance to the ridge  $D_{pr}$ .

$$VD_p = \begin{cases} \delta \left( \frac{R}{2} \right) \left[ \sin \left( \pi \left( \frac{2D_{pr} + \lambda}{2\lambda} \right) \right) + 1 \right] & \text{if } D_{pr} < \lambda \\ 0 & \text{if } D_{pr} \geq \lambda \end{cases}$$

The value  $R$  acts as a control variable to adjust the amount of deformation experienced by each individual contour. The parameter  $\delta$  refers to the inter-slice distance. An  $R$  value of 1 shifts a vertex by  $\delta$  upwards, while an  $R$  value of -1 does the opposite. By setting  $R$  independently, as illustrated in Table 1, we can then adjust and smooth the effect of the deformation across the slices. After

inducing the vertical motion, a 1-to-1 inter-frame correspondence can be established for each slice. We can then proceed using the standard deformation process to deform the mesh into the next time step.

**Table 1: Listing of applied R values.**

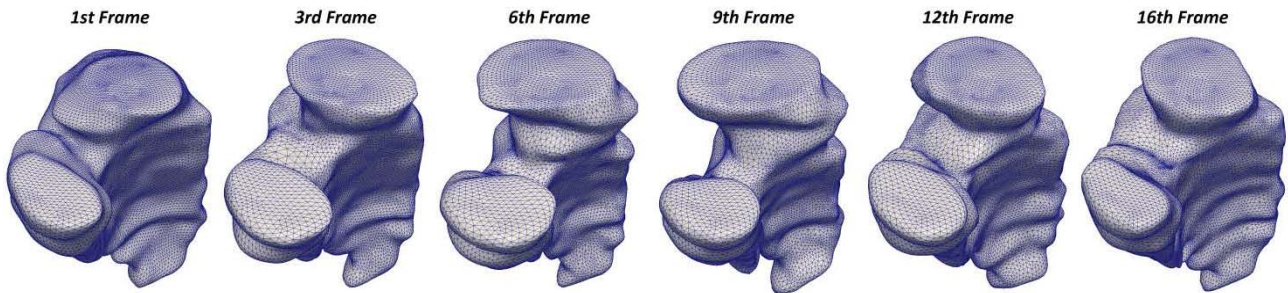
Slice Position	R Value	
	Upward	Downward
1	0.2	-0.2
2	0.4	-0.5
3	0.7 (Incident)	-1.2 (Complementary)
4	1.2 (Complementary)	-0.7 (Incident)
5	0.5	-0.4
6	0.2	-0.2

## Results and Discussion

We implemented the 4D heart deformation algorithm in C++ (with no multi-threading optimization) on an i7 core 3.07 GHz machine and tested it on a set of MRI scan of the right heart of a healthy patient. The MRI data was acquired using the steady state free precession sequence with retrospective electrocardiographic gating, and consists of 25 contiguous image slices 5 mm apart covering the mid of the right atrium to the apex of the right ventricle, with 25 frames per slice per heartbeat. The contours of the endocardial surface are segmented manually by a cardiologist using the CMRTools software developed by Cardiovascular Imaging Solutions Ltd.

### *Reconstructing a 4D Heart Model*

Using the MRI data from the first frame, we reconstruct a 3D mesh model of the right heart (17012 vertices with 34020 triangles). Using this 3D mesh model, we generate a 4D right heart model based on the deformation algorithm. Each of the 25 3D mesh model conforms to the corresponding input segmented contours lines and maintains vertex correspondence throughout. In Figure 5, a snapshot of the sequence of the 4D right heart model taken at different time steps is shown. We track the quality of the mesh model based on the conformity to the input contours and the quality of the surface triangles over the 25 time steps.



**Figure 5. 4D Right Heart Model Reconstruction.**

For tracking conformity, we sampled points along the input segmented contours at every 0.2mm interval and recorded its nearest distance (geometrical deviation) to the 3D mesh model. For each frame, we record the average geometrical deviation over all the input contours. Finally, we tabulate the mean and standard deviation of the averaged geometrical deviation over all the frames. The mean and standard deviation are 0.044mm and 0.003mm respectively. Taken as a percentage of  $\delta$  (5mm) for this dataset, this equate to around a mean deviation of around 0.89%, which is a very low percentage value and is unnoticeable visually.

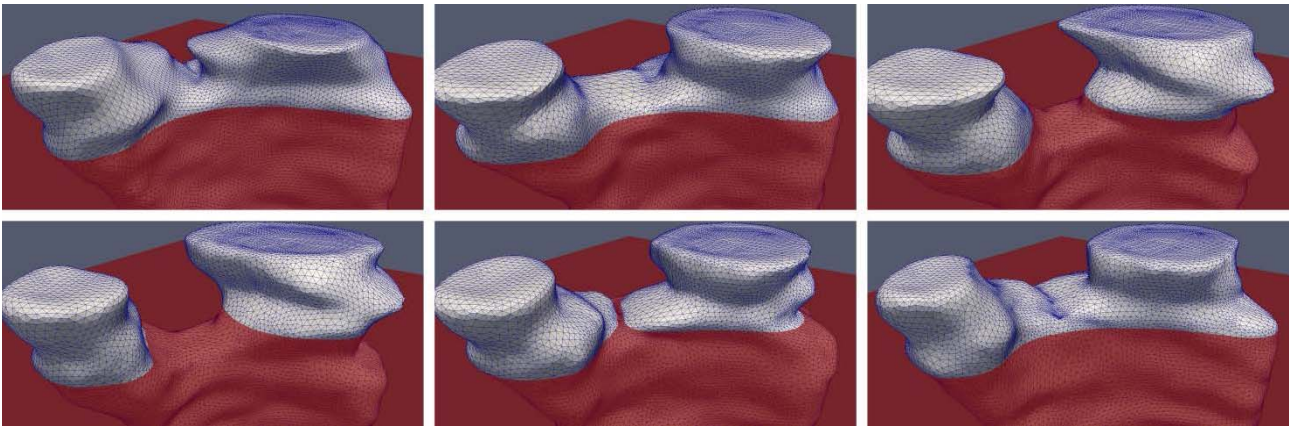
In terms of mesh quality, we can see from Table 2 that the majority of the triangles are within an acceptable quality range of between 40-80 degrees. Even as the 3D mesh deforms over the cardiac cycle and undergoing 2D contour topological changes with significant deformation, the percentage of acceptable quality triangles remains stable throughout (85% to 89%). On the other end of the spectrum, the number of bad quality triangle ( $< 20$  degrees) occurs at a very low rate of 0.88 per frame, or 0.002% of the total triangle count.

**Table 2: Distribution of Triangle Angle Quality.**

Dataset No		% of angles (in degrees) between				Total
		40-50	50-60	60-70	70-80	
1	First Frame	15.42%	30.67%	28.56%	15.01%	89.67%
	Mid Frame	17.07%	28.52%	26.76%	14.67%	87.02%
	Last Frame	18.16%	27.24%	25.84%	14.37%	85.61%

### *2D Contour Topological Changes*

From the dataset, 2D contour topological changes are found to occur at 4 different time steps. We illustrate how our algorithm is able to resolve it in a series of screen shots in Figure 6. In the figure, a red plane depicting the image scanning plane of the MRI, is shown to intersect with the 3D model. We observed the phenomenon of two distinct contours merging and splitting on the red plane, which is consistent with the drawn segmented contours in the dataset.



**Figure 6. Resolving 2D Contour Topological Changes.**

### *Computation Timing*

Generally, the average computational time is around 6.4 milliseconds per vertex for normal frames, and 7.8 milliseconds per vertex for frames with 2D contour topological changes. There is little timing variability among frames, with a standard deviation of 0.3 milliseconds and 0.17 milliseconds respectively. Typically, for a 3D mesh model with a vertex count of 20000, it would take approximately 2 minutes to complete a frame. To generate a 4D right heart model consisting of 20 frames would take around 40 minutes to complete, which is considered to be adequate for practical usage.



## Conclusion

In this paper, we presented a methodology for the automatic 4D reconstruction of a patient specific cardiac mesh model using segmented contour lines from MRI images. Our methodology is able to handle the inter-frame 2D contour topological changes that occur during the cardiac cycle and produces a sequence of good quality 3D mesh models with 1-to-1 vertex correspondence that conforms to the input contours. Such a model is useful for downstream computational simulation purposes.

## References

- Frangi AF, Niessen WJ, Viergever MA (2001) Three-dimensional modeling for functional analysis of cardiac images: A review. *IEEE Transaction on Medical Imaging* 20: 2–25.
- McQueen DM, Peskin CS (2000) A three-dimensional computer model of the human heart for studying cardiac fluid dynamics. *ACM SIGGRAPH Computer Graphics* 34: 56–60.
- Kovács SJ, McQueen DM, Peskin CS (2001) Modelling cardiac fluid dynamics and diastolic function. *Phil Trans R Soc Lond* 359: 1299–1314.
- Corsi C, Saracino G, Sarti A, Lamberti C (2002) Left ventricular volume estimation for real-time three-dimensional echocardiography. *IEEE Transaction on Medical Imaging* 21: 1202–1208.
- Zhukov L, Bao Z, Guskov I, Wood J, Breen D (2002) Dynamic deformable models for 3D MRI heart segmentation. *Proceedings of SPIE* 4684: 1398–1405.
- Montagnat J, Delingette H (2005) 4D deformable models with temporal constraints: Application to 4D cardiac image segmentation. *Medical Image Analysis* 9: 87–100.
- Sermesant M, Forest C, Pennec X, Delingette H, Ayache N (2003) Deformable biomechanical models: Application to 4D cardiac image analysis. *Medical Image Analysis* 7: 475–488.
- Plank G, Burton RAB, Hales P, Bishop M, Mansoori T, et al. (2009) Generation of histoanatomically representative models of the individual heart: tools and application. *Philosophical Transactions of the Royal Society A* 367: 2257–2292.
- Barequet G, Sharir M (1996) Piecewise-linear interpolation between polygonal slices. *Computer Vision and Image Understanding* : 251–272.
- Prasad L (2007) Rectification of the chordal axis transform skeleton and criteria for shape decomposition. *Image and Vision Computing* 25: 1557–1571.
- Roussos G, Baxter BJC (2005) Rapid evaluation of radial basis functions. *Journal of Computational and Applied Mathematics* 180: 51–70.

# Earthquake Response Analysis of a Gravity Dam Considering the Radiation

## Damping of Infinite Foundation

\* Y.S. Liu<sup>1</sup> and D.H. Chen<sup>2</sup>

<sup>1</sup>College of Hydraulic & Environmental Engineering, China Three Gorges University, China

<sup>2</sup>College of Civil Engineering & Architecture, China Three Gorges University, China

\*Corresponding author:ys850728@126.com

### Abstract

Two different earthquake input models are presented in the paper, i.e. massless foundation model and viscous-spring boundary. Based on the commercial nonlinear finite element code ANSYS, the user element subroutine of the viscous-spring boundary is implemented. The correctness of the viscous-spring boundary and its wave input model are validated by a numerical example. Finally, the viscous-spring boundary and wave input model are applied to the seismic analysis of the Longtan gravity dam-foundation system. The results show that the peak values of dam's dynamic responses are reduced by 4%~38% compared to the massless foundation model. The structural dynamic responses are overestimated to some extent utilizing the traditional massless model. The radiation damping effect of infinite foundation has a great influence to the structure's dynamic responses, and is very necessary to be considered.

**Keywords:** Dam-foundation dynamic interaction; Viscous-spring boundary; Wave input model; Longtan gravity dam

### Introduction

Dam-foundation dynamic interaction and the earthquake input mechanism are the key issues of safety evaluation of high dams. Clough (1980) proposed a massless foundation model and assumed that the foundation is linear elastic, massless, and the earthquake excitations act uniformly on the truncated boundary. It has been widely used in the practical engineering studies. But this model still has some limitations, which include: (1) The foundation is actually a mass of semi-infinite medium. The seismic wave energy will be dissipated to infinity. The infinite foundation plays a role in the absorption of the scattering seismic wave energy. (2) The high dams are usually built in narrow mountain valleys. There are apparent differences of the amplitude and phase of the earthquake along the interface of the dam foundation. It is difficult to reflect actual seismic responses for high dams when the ununiform earthquake excitations are neglected.

Many studies have been made to study the dam-foundation dynamic interaction. These include the viscous boundary (Lysmer and Kuhlemeyer, 1969), the viscous-spring boundary (Deeks and Randolph, 1994; Liu *et al.*, 2006), the transmitting boundary (Liao *et al.*, 1984), and the scaled boundary finite element method (Wolf and Song, 1996). The viscous-spring boundary is very efficient and convenient to incorporate it with the commercial finite element software and has sufficient accuracy without much increasing computational efforts.

This paper is organized as follows. Section 2 describes a viscous-spring boundary element and its seismic input model. Section 3 presents a numerical example to validate the correctness of the programme. Section 4 demonstrates the application of the proposed coupled method to the seismic analysis of the Longtan gravity dam-foundation system. Section 5 summarizes some major conclusions from this contribution.

## Viscous-spring boundary element and its seismic input model

### Viscous-spring boundary condition

A 2-D viscous-spring boundary is employed to absorb the wave energy radiating away from the dam. A sketch of the viscous-spring boundary used in the gravity dam-foundation system and the parallel-connected spring-dashpot system in each direction is shown in Fig. 1. The normal and tangential spring and damping coefficients (Du *et al.*, 2006) of the viscous-spring boundary are taken as

$$\begin{cases} K_{BN} = \frac{1}{1+\alpha} \frac{\lambda+2G}{2r_b}, C_{BN} = \beta\rho c_p \\ K_{BT} = \frac{1}{1+\alpha} \frac{G}{2r_b}, C_{BT} = \beta\rho c_s \end{cases} \quad (1)$$

where  $K_{BN}$  and  $K_{BT}$  are the normal and tangential stiffness coefficients, respectively.  $C_{BN}$  and  $C_{BT}$  are the normal and tangential damping coefficients, respectively.  $A$  is the total area of all elements around a node at the boundary.  $r_b$  is the distance from the scattering wave source to the artificial boundary point.  $c_s$  and  $c_p$  are the wave velocities of the S wave and P wave, respectively.  $G$  and  $\rho$  denote the medium's shear modulus and mass density, respectively.  $\alpha$  and  $\beta$  are dimensionless parameters, and are taken as 0.8 and 1.1, respectively (Du *et al.*, 2006).

The viscous-spring boundary is a continuous stress boundary that can be discretized with a common shape function. The shape function at the node  $i$  is

$$N_i(x) = 1 - \frac{x}{l}, \quad N_j(x) = \frac{x}{l} \quad (2)$$

The shape function for the displacements is expressed as

$$[N] = \begin{bmatrix} N_i(x) & 0 & N_j(x) & 0 \\ 0 & N_i(x) & 0 & N_j(x) \end{bmatrix} \quad (3)$$

The elastic matrix is taken as

$$[D] = \begin{bmatrix} K_{BT} & 0 \\ 0 & K_{BN} \end{bmatrix} \quad (4)$$

The stiffness matrix of a viscous-spring element is calculated using Eq. (5)

$$[K] = \int_0^l [N]^T [D] [N] dx dy \quad (5)$$

Thus, the stiffness matrix of the viscous-spring element is shown in Eq. (6)

$$[K]_B = \frac{l}{6} \begin{bmatrix} 2K_{BT} & 0 & K_{BT} & 0 \\ & 2K_{BN} & 0 & K_{BN} \\ & & 2K_{BT} & 0 \\ sym & & & 2K_{BN} \end{bmatrix} \quad (6)$$

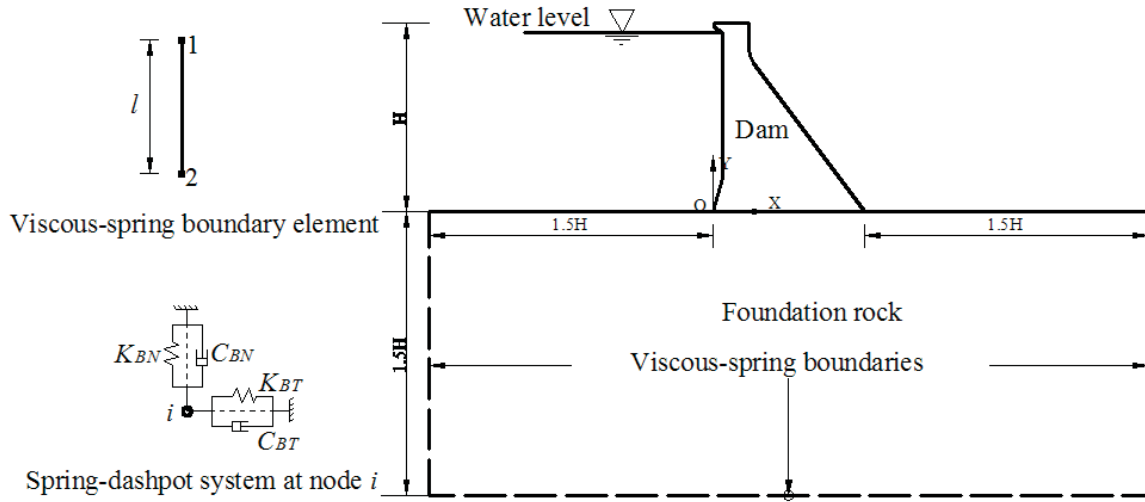
where  $l$  is the length of a viscous-spring boundary element. The damping matrix  $[C]_B$  has a similar form and is constructed from  $[K]_B$  by replacing  $K$  with  $C$ .

### The free field input model

The earthquake free field motions with viscous-spring elements can be translated into equivalent force loads at the truncated boundary of dam-foundation system using Eq. (7).

$$\mathbf{F}_B = \mathbf{K}_B \mathbf{u}_B^f + \mathbf{C}_B \dot{\mathbf{u}}_B^f + \boldsymbol{\sigma}_B^f \mathbf{n} \quad (7)$$

In Eq. (7), the subscript  $B$  denotes a boundary node at the viscous-spring boundary.  $K_B$  and  $C_B$  are the spring and damping coefficients, respectively, which are described in Eq. (1).  $u_B^f$  and  $\dot{u}_B^f$  are the free field displacement and velocity, respectively.  $\sigma_B^f$  is the free field stress and  $\mathbf{n}$  is outward normal direction cosine of the free field boundary.



**Fig.1 Viscous-spring boundary of dam-foundation system**

The free-field stress  $\sigma_B^f$  is obtained by elastic theory (He *et al.*, 2010).

$$\begin{Bmatrix} \sigma_{xx} \\ \sigma_{yy} \\ \sigma_{xy} \end{Bmatrix} = \begin{bmatrix} \lambda + 2G & \lambda & 0 \\ \lambda & \lambda + 2G & 0 \\ 0 & 0 & G \end{bmatrix} \begin{Bmatrix} \frac{\partial u}{\partial x} \\ \frac{\partial v}{\partial y} \\ \frac{\partial u}{\partial y} + \frac{\partial v}{\partial x} \end{Bmatrix} \quad (8)$$

When P waves are vertically propagated from the bottom boundary, the boundary conditions are  $u=0$  and  $v = v_0(t)$ . The free field displacement and velocity at height  $h$  are determined by the wave motion theory, which are composed of two parts, the incident wave and reflected wave,

$$\begin{cases} v = v_0(t - \frac{h}{c_p}) + v_0(t - \frac{2H-h}{c_p}) \\ \dot{v} = \dot{v}_0(t - \frac{h}{c_p}) + \dot{v}_0(t - \frac{2H-h}{c_p}) \\ \frac{\partial v}{\partial y} = -\frac{1}{c_p} \left[ \dot{v}_0(t - \frac{h}{c_p}) - \dot{v}_0(t - \frac{2H-h}{c_p}) \right] \end{cases} \quad (9)$$

where  $H$  is the distance from the bottom boundary to the free surface.

Substituting Eq. (9) into Eq. (8) and taking into account the boundary conditions  $h=0$  and  $\mathbf{n}=[0 \ -1]^T$ , the free field stress  $\sigma_B^f$  is calculated as

$$\begin{Bmatrix} \sigma_{xx} \\ \sigma_{yy} \\ \sigma_{xy} \end{Bmatrix} = \begin{Bmatrix} 0 \\ \rho c_p^2 \frac{\partial v}{\partial y} \\ 0 \end{Bmatrix} = \begin{Bmatrix} 0 \\ -\rho c_p \left[ \dot{v}_0(t - \frac{h}{c_p}) - \dot{v}_0(t - \frac{2H-h}{c_p}) \right] \\ 0 \end{Bmatrix} \quad (10)$$

Substituting Eq. (9) and (10) into Eq. (7), the equivalent load  $F_B$  can be expressed as

$$\begin{aligned} \begin{Bmatrix} F_{Bx} \\ F_{By} \end{Bmatrix} &= \begin{bmatrix} K_{BT} & 0 \\ 0 & K_{BN} \end{bmatrix} \begin{Bmatrix} 0 \\ v_0(t - \frac{h}{c_p}) + v_0(t - \frac{2H-h}{c_p}) \end{Bmatrix} + \begin{bmatrix} C_{BT} & 0 \\ 0 & C_{BN} \end{bmatrix} \begin{Bmatrix} 0 \\ \dot{v}_0(t - \frac{h}{c_p}) + \dot{v}_0(t - \frac{2H-h}{c_p}) \end{Bmatrix} \\ &+ \begin{Bmatrix} 0 \\ \rho c_p \left[ \dot{v}_0(t - \frac{h}{c_p}) - \dot{v}_0(t - \frac{2H-h}{c_p}) \right] \end{Bmatrix} \\ &= \begin{Bmatrix} 0 \\ K_{BN} \left[ v_0(t) + v_0(t - \frac{2H}{c_p}) \right] + C_{BN} \left[ \dot{v}_0(t) + \dot{v}_0(t - \frac{2H}{c_p}) \right] + \rho c_p \left[ \dot{v}_0(t) - \dot{v}_0(t - \frac{2H}{c_p}) \right] \end{Bmatrix} \end{aligned} \quad (11)$$

When the shear waves are vertically propagated from the bottom boundary, the boundary conditions are  $u=u_0(t)$  and  $v=0$ . The equivalent loads  $F_B$  are derived by the analogous method.

$$\begin{Bmatrix} F_{Bx} \\ F_{By} \end{Bmatrix} = \begin{Bmatrix} K_{BT} \left[ u_0(t) + u_0(t - \frac{2H}{c_s}) \right] + C_{BT} \left[ \dot{u}_0(t) + \dot{u}_0(t - \frac{2H}{c_s}) \right] + \rho c_s \left[ \dot{u}_0(t) - \dot{u}_0(t - \frac{2H}{c_s}) \right] \\ 0 \end{Bmatrix} \quad (12)$$

The corresponding equivalent force loads  $F_B$  of the free field stress at the lateral boundaries (Fig. 1) of the gravity dam-foundation system can also be easily derived by the aforementioned method.

The viscous-spring boundary element is implemented by the element type COMBIN14 in the commercial finite element software ANSYS 10.0. A macro file for the corresponding wave input is created using ANSYS Parametric Design Language (APDL).

### Numerical example

In order to verify the correctness of the viscous-spring boundary element and its wave input programme, an elastic half-space is studied. A vertically propagating S wave is analyzed, and the displacement equation of the input wave is

$$u(t) = \begin{cases} \sin(4\pi t) - 0.5 \sin(8\pi t) & 0 \leq t \leq 0.5 \\ 0 & t > 0.5 \end{cases} \quad (13)$$

The elastic medium has the following parameters: modulus of elasticity  $E=13.23$  GPa, Poisson's ratio  $\mu=0.25$ , mass density  $\rho=2700$  kg/m<sup>3</sup>, S-wave velocity  $c_s=1400.0$  m/s, and P-wave velocity  $c_p=2425$  m/s. The semi-unbounded foundation with an area  $762 \text{ m} \times 381 \text{ m}$  is analyzed, and four-node solid elements with  $2 \times 2$  Gauss integration points are adopted. The mesh size is 19.05 m, and there are a total of 800 elements and 946 nodes, of which there are 81 viscous-spring boundary elements on the bottom and lateral boundaries. The total calculation time is 2s. The fixed time step 0.005s is selected.

The horizontal displacement time histories of the free and bottom surfaces are shown in Fig. 2. It could clearly be seen that the maximum displacement of the free surface is nearly twice the corresponding amplitude of the input wave. Additionally, the displacements of the bottom points are basically the same, with the first half of the displacement time history showing the input wave

and the latter part of the displacement time history showing the reflection wave. The results are consistent with the theoretical solutions of wave motion. Therefore, it is concluded that the viscous-spring boundary element and wave input program are accurate.

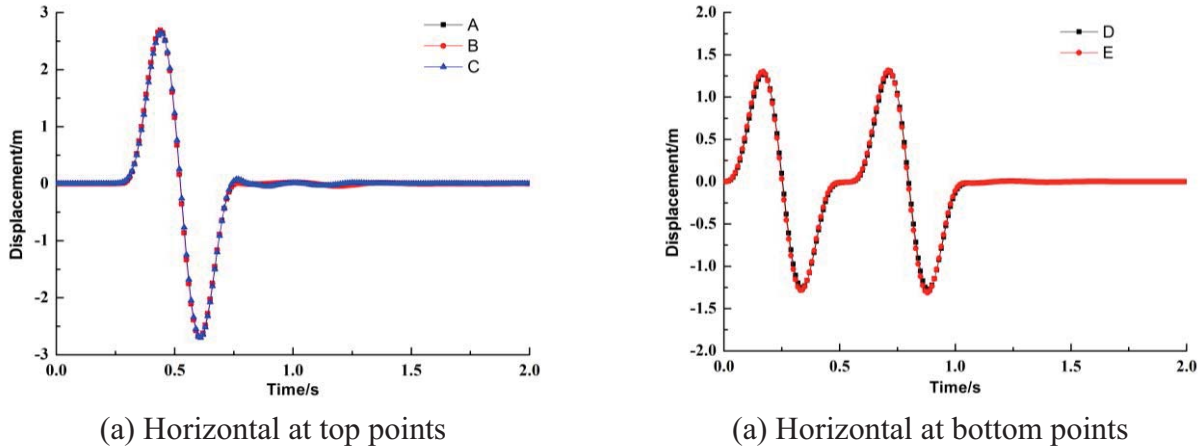


Fig.2 Time histories of the top and bottom displacements

### Engineering Application

The seismic response analysis of the Longtan gravity dam is selected as an engineering example. The Longtan hydropower station is mainly built for power generation in the upper reaches of the Hongshui River, China. The dam is a roller-compacted concrete (RCC) gravity dam with a crest elevation of 406.50 m. The maximum dam height is 216.50 m with a crest length of 849.44 m and downstream slope ratio of 1:0.75. The upstream slope ratio below the height of 270.00 m is 1:0.25. According to the research results from the Institute of Geology, State Seismological Bureau of China, the basic seismic intensity of the dam site is 7 degrees. The designed peak horizontal ground acceleration of the dam site is 0.2g.

The retaining water monolith of the dam as shown in Fig.3 is investigated in this paper. The four-node plane strain quadrilateral isoparametric elements with  $2 \times 2$  Gauss integration are adopted. The system is discretized with 4562 elements and 4737 nodes including 175 viscous-spring boundary elements on the bottom and lateral boundaries. Finite element discretization of the dam is shown in Fig.4.

The concrete has the following parameters: modulus of elasticity  $E_c=19.6$  GPa, Poisson's ratio  $\mu_c=0.167$ , the unit weight  $\gamma_c=24.0$  kN/m<sup>3</sup>, and the damping ratio  $\zeta=0.08$ . The rock mass has the following parameters: modulus of elasticity  $E_r=13.2$  GPa, Poisson's ratio  $\mu_r=0.25$ , the unit weight  $\gamma_r=27.0$  kN/m<sup>3</sup>. The dynamic elastic modulus of concrete and rock are taken as 1.3 times the corresponding static modulus (SETC, 2001). The artificial acceleration time history is simulated according to the design response spectrum (SETC, 2001). The total calculation time is 20s, and the fixed time step is  $\Delta t=0.01$ s. The input accelerations and response spectrum are shown in Fig.5.

Two earthquake input mechanisms are considered in this paper. The first one is the massless foundation model proposed by Clough. The foundation is considered massless. The dynamic load is uniformly applied to the dam body by inertia force. The second one is the viscous-spring boundary model. The dynamic loads are transformed into the bottom and lateral's equivalent nodal loads by Eq. (10), (11) and are applied to the truncated boundary. According to the numerical example in Section 3, the input wave of the bottom boundary would amplify nearly 1 time on the free surface. Thus, the input earthquake wave in the viscous-spring boundary model is taken as 0.5 times the

corresponding amplitude of Fig.5.

The peak values of the displacement and stress at key points are shown in Table 1. The comparisons of the displacements are shown in Fig.6. The comparisons of stresses at the key parts are shown in Fig.7. The results show that the peak values of dam’s dynamic responses are reduced by 4%~38% compared to the massless foundation model. The structural dynamic responses are overestimated to some extent utilizing the traditional massless model. The radiation damping effect of infinite foundation has a great influence to the structure’s dynamic responses, and is very necessary to be considered.

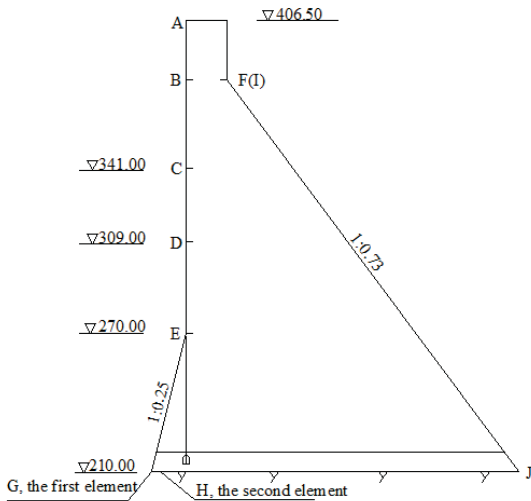


Fig.3 The retaining water section

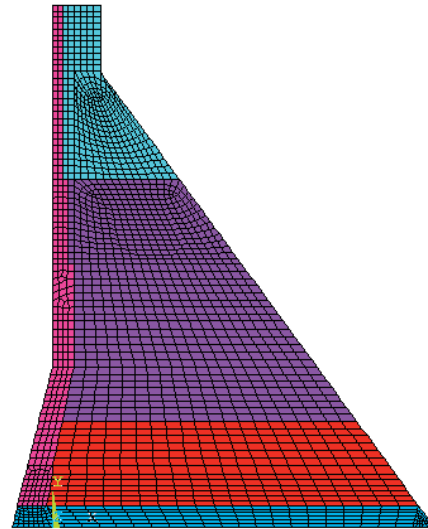


Fig.4 FE Mesh of the dam

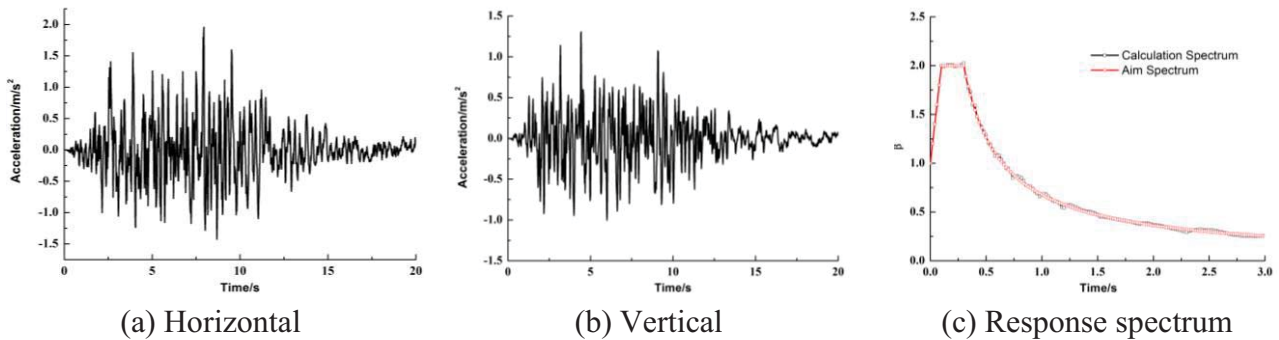


Fig.5 The input accelerations and response spectrum

Table 1 Comparisons of displacements and stresses at key points

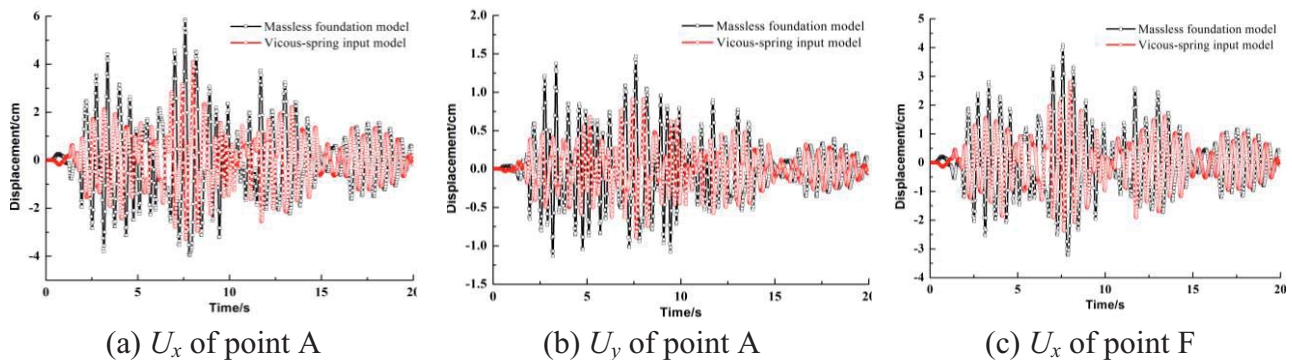
Feature points of the dam section	Massless foundation model	Viscous-spring boundary	Relative error
Horizontal displacements at point A $U_x/cm$	5.86	4.11	29.9%
Vertical displacements at point A $U_y/cm$	1.47	0.92	37.4%
Horizontal displacement at point F $U_x/cm$	4.09	2.80	31.5%
First principal stresses at point E $\sigma_1/MPa$	2.38	1.51	36.6%
First principal stresses at point F $\sigma_1/MPa$	2.32	2.23	3.9%
First principal stresses at point G $\sigma_1/MPa$	2.60	2.44	6.2%

Third principal stresses at point J  $\sigma_3$ /MPa

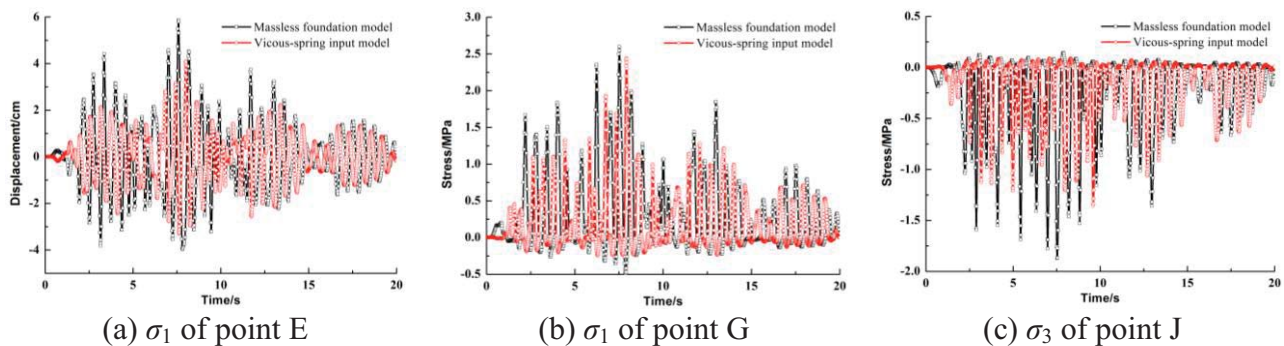
-1.87

-1.36

27.3%



**Fig.6 Comparisons of the displacements for the different seismic input models**



**Fig.7 Comparison of the stresses for the different seismic input models**

## Conclusion

Two different earthquake input models are presented in the paper, i.e. massless foundation model and viscous-spring boundary. Based on the commercial nonlinear finite element code ANSYS, the user element subroutine of the viscous-spring boundary is implemented. The correctness of the viscous-spring boundary and its wave input model are validated by a numerical example. Finally, the viscous-spring boundary and wave input model are applied to the seismic analysis of the Longtan gravity dam–foundation system. The results show that the peak values of dam’s dynamic responses are reduced by 4%~38% compared to the massless foundation model. The structural dynamic responses are overestimated to some extent utilizing the traditional massless model. The radiation damping effect of infinite foundation has a great influence to the structure’s dynamic responses, and is very necessary to be considered.

## References

- Clough, R.W. (1980), Nonlinear mechanisms in the seismic response of arch dams. Proceedings of International Research Conference on Earthquake Engineering, Skopje, Yugoslavia.
- Lysmer, J. and Kuhlemeyer, R. L. (1969), Finite dynamic model for infinite media. *Journal of Engineering Mechanics, ASCE*, 95, 759–877.
- Deeks, A. J. and Randolph, M. F. (1994), Axisymmetric time-domain transmitting boundaries. *Journal of Engineering Mechanics Division, ASCE*, 120, 25–42.
- Liu, J. B., Du, Y. X. and Du, X. L. (2006), 3D viscous-spring artificial boundary in time domain. *Earthquake Engineering and Engineering Vibration*, 5, 93–102.
- Liao, Z. P., Wong, H. L. and Yang B. (1984), A transmitting boundary for transient wave analyses. *Scientia Sinica Mathematica*, 27, 1063–1076.
- Wolf, J. P. and Song, C. (1996), *Finite-element modeling of unbounded media*. Wiley: New York.



- Du, X. L., Zhao, M. and Wang, J. T. (2006), A stress artificial boundary in FEA for near-field wave problem. *Chinese Journal of Theoretical and Applied Mechanics*, 38(1), 49–56. (in Chinese)
- He, J. T., Ma, H. F., Zhang B. Y. and Chen, H. Q. (2010), Method and realization of seismic motion input of viscous-spring boundary. *Journal of Hydraulic Engineering*, 41(8), 960–969. (in Chinese)
- State Economic and Trade Commission (SETC) (2001), *Specifications for Seismic Design of Hydraulic Structures DL 5073–2000*, China. (in Chinese)

## Simple Method of Calculation of Statically Indeterminate Trusses

\*J. Rębielak<sup>1</sup>

<sup>1</sup> Institute of Construction Design, Faculty of Architecture, Tadeusz Kosciuszko Cracow University of Technology, Cracow, Poland

\*Corresponding author: j.rebielak@wp.pl

### Abstract

The paper presents a very simple method, which in two stages enables to calculate the plane statically indeterminate truss by the application of one of methods used for the force calculation in members of the statically determinate trusses. The results are obtained in a very simple and quick way. Although the force values are approximated but they are relatively very close to those, which are determined by the exact methods. The point of the two-stage calculation process of the statically indeterminate trusses is to determine schemes of two independent and simple statically determined trusses, which after superposition of their patterns will give in the result a pattern of the initial, more complex form of the statically indeterminate truss. Each of the simple truss has to be of the same clear span and the load forces have to be of the half values and they have to be applied to the same nodes like in truss of the initial structural configuration.

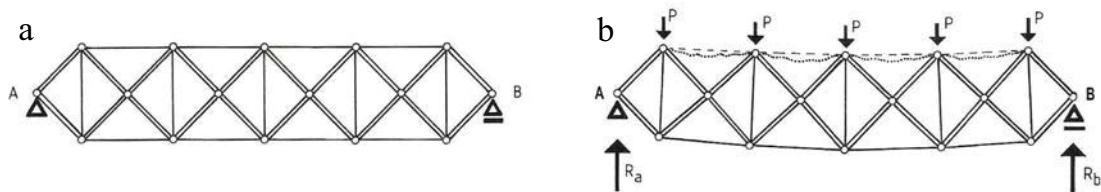
**Keywords:** Computational method, Static calculation, Truss structure, Principle of superposition.

### Introduction

A simple plane truss is built by means of an invariable, steady system of straight members, which are in a concentric way connected together by means of the theoretically articulated joints. It is obvious that a typical truss is supported and loaded by forces applied to these nodes. Economic reasons cause that most these nodes in the common practice are made as the rigid connections but due the usually big slenderness ratios of the truss members the influence of the node stiffness can be negligible. Simple forms of trusses are usually the statically determinate systems and for needs of calculation of the force values acting in their members one have to use e.g. the Cremona's method, the Ritter's method or the Culmann's method as shown in the works by the authors (Kolendowicz, 1993; Pyrak and Szulborski, 1994; Przewłocki and Górski, 2006; Allen and Zalewski, 2010). Trusses of the more complex patterns are usually the statically indeterminate systems, where the force transmission between their members depends also on stiffness of members connected in the same joint. The process of static analysis is then not so easy and it is necessary to use the suitable strain energy methods or taking into account e.g. displacements of joints, which methods requires application of the appropriate iterative or other suitable procedures as shown in the works by the authors (Timoshenko, 1953; Makowski, 1981). Modern numerical techniques together with a suitable software have made the processes of static calculations of even very complex trusses enormously fast and efficient. Structural analyses of the complex truss systems have to be repeated for new versions of the often modified shapes of trusses. Moreover an initial calculation of a very complex type of a space structure is required for the needs of the preliminary estimation of the force sizes acting in its members. In order to recognize the approximate force values and their distribution in the whole area of the designed structural system it is reasonable to apply instead of sophisticated a rather simple method of structural analysis. The proposed two-stage method of calculation of the statically indeterminate trusses was invented by the author during the preliminary analysis of a group of the spatial tension-strut structures what was shown in previous works by the author (Rębielak, 1985a; Rębielak, 2012).

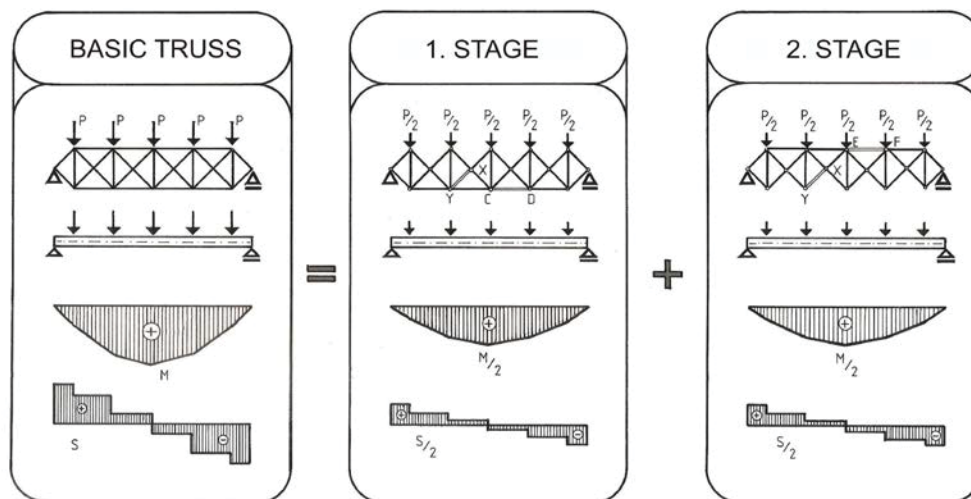
### Description of general concept of the two-stage method

The mentioned group of the multi-layer spatial tension-strut structures were previously developed also by the author (Rębielak, 1983). They are built by means of rigid bars, which constitute their cross-braces and by the slender tension members located mainly in the external layers, while some others are located vertically in space of these structures. A simplified scheme of their vertical cross-section presents Fig. 1a. It is obvious that structural system built in this way has to be suitable pre-stressed by means of e.g. appropriate shortening of the selected tension members.



**Figure 1. Simplified schemes of basic form of a tension-strut truss**

When to the truss are applied forces of too big values as it is allowed, what is conditioned by the appropriate pre-stressing, one can notice that some of the tension members, e.g. of the upper layer, do not participate in the force transmission, what is shown in Fig. 1b. From analysis of this figure follows, that a truss being the statically indeterminate system after the overloading is still able to take forces but it becomes a statically determinate truss. This remark brings to mind a following conclusion: if the overloaded structure remains a good acting truss, which can be calculated in an easy way, then maybe it could be possible – in order to calculate the force values acting in members of the more complex system – to apply equally easy and simple methods of static analyses. From the general, basic conditions of equilibrium follows, that the intended calculations have to be carried out in two suitable stages, see Fig. 2.



**Figure 2. Schemes of two stages of the proposed method of calculation**

The calculated truss, in each of the separated stages, has to be of the same clear span like the basic truss. Structural scheme of the truss considered in the both stages is obtained after removing appropriate number of members from the basic truss respectively from e.g. the upper chord and then from the lower chord. This number has to be equal to the degree of the statically indeterminacy of the basic truss. The

considered trusses in each stage have to be loaded by the forces two times smaller than forces applied to the basic truss. These forces should be applied to nodes of the same positions like in the basic truss. Below are presented results of successive calculations carried out for an exemplary basic truss shown in Fig. 2, having the clear span equals 5.00 meters and loaded by single forces of value equal to 1,00 kN applied to nodes of the upper chord. Length of each vertical member of this truss is equal to 1.00 meter. Results of the first stage of calculations are shown in Fig. 3, results of the second stage are presented in Fig. 4 while the final results are displayed in Fig. 5.

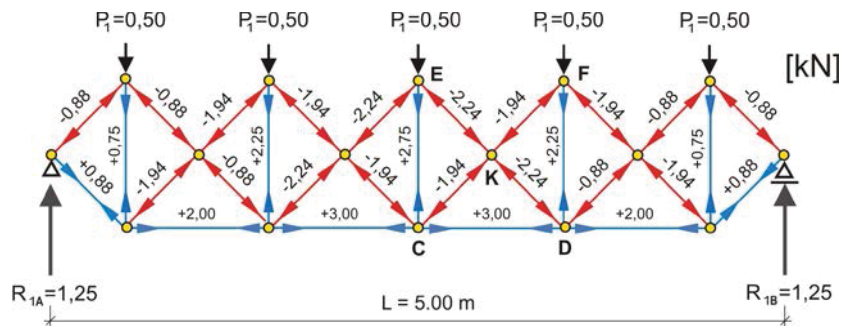


Figure 3. Arrangement of force values calculated in the first stage

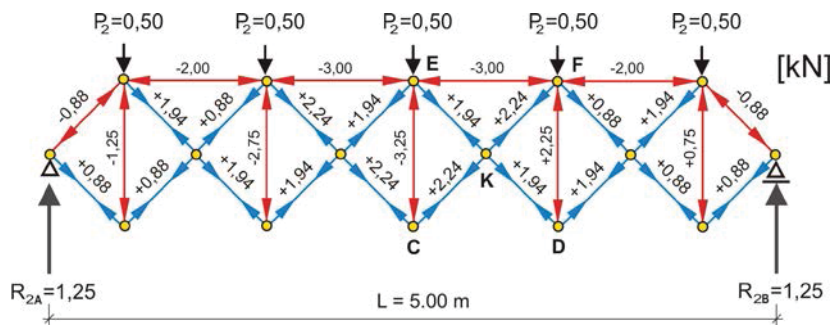


Figure 4. Arrangement of force values calculated in the second stage

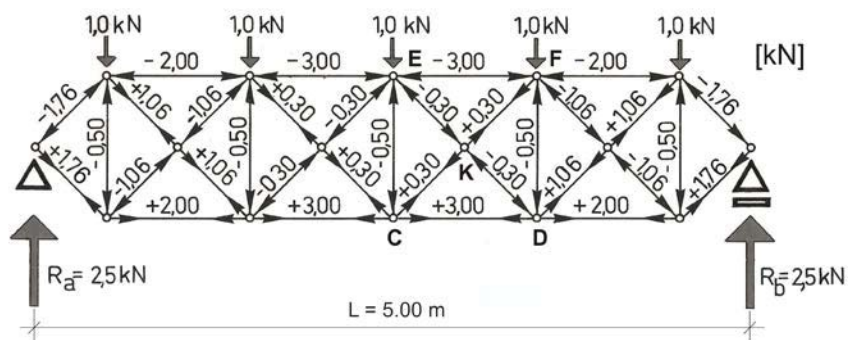


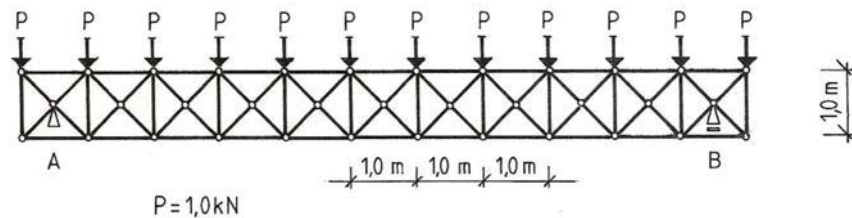
Figure 5. Values of forces obtained as a result of appropriate application of principle of superposition in the proposed two-stage method of calculation

The final values of forces acting in particular cross-braces are defined by sum up the suitable values obtained in each stage. For instance the final value - 0,30 kN of force acting in the cross brace KD, see Fig. 5, is a resultant of force - 2,24 kN calculated for the same member in the first stage, compare Fig. 3, and the value + 1,94 kN calculated for this member in the second stage, compare Fig. 4. Forces acting in

members of the lower chord are defined during the first stage of this method because they are removed in the second stage and in this case it is assumed, that in the second stage they are subjected to act forces of values equal to zero. It means that vector of the resultant force, which acts e.g. in member CD and equals + 3,00 kN, see Fig. 5, is determined for the same member in the first stage of calculation, compare Fig. 3, because the force vector obtained in the second stage is equal to zero. Similar remarks refer to the final values of forces defined in this two-stage method for members of the upper and lower chords of the considered sample of this simple truss.

### Comparison of results obtained in two different methods

In order to compare the force values calculated in the proposed two-stage method with values of forces determined in one of the methods considered as giving in result the exact force values there were undertaken two parallel calculations of the same statically indeterminate truss, scheme of which is shown in Fig. 6.



**Figure 6. Scheme of a plane statically indeterminate truss calculated in two compared methods**

In the both calculations the basic truss is of the same statically scheme, it's clear span equals 10.00 meters, the construction depth is equal to 1.00 meter and the same load forces are applied to nodes of exactly the same positions. As previously the load forces have the unit value equals 1,00 kN. The considered truss is built by the number of nodes "w" equals 35 and the number of members "p" equal to 78. Condition of the inner statical determinacy

$$p = 2 \times w - 3 \quad (1)$$

defines, that a plane truss consists of  $w = 35$  nodes has to be built by means of the following number of members

$$67 = 2 \times 35 - 3 . \quad (2)$$

It implies, that the basic truss is the eleven-fold statically indeterminate system. It means that in the first stage of the proposed method eleven members of e.g. the upper chord have to be removed in order to make this truss a statically determinate system. Because the truss is of symmetric shape and it is symmetrically loaded therefore process of calculations can be carried out only for its half. Results of the first stage of calculations, obtained by application of the Cremona's method, are shown in Fig. 7, while results determined in the second stage are presented in Fig. 8. The computer software ICES-STRUDL was applied for calculation of the statically indeterminate truss of scheme shown in Fig. 6, (Rębielak and Beranek and Hobbelman, 1985b). Final results of both compared methods are presented for a half of the truss in Fig. 9.

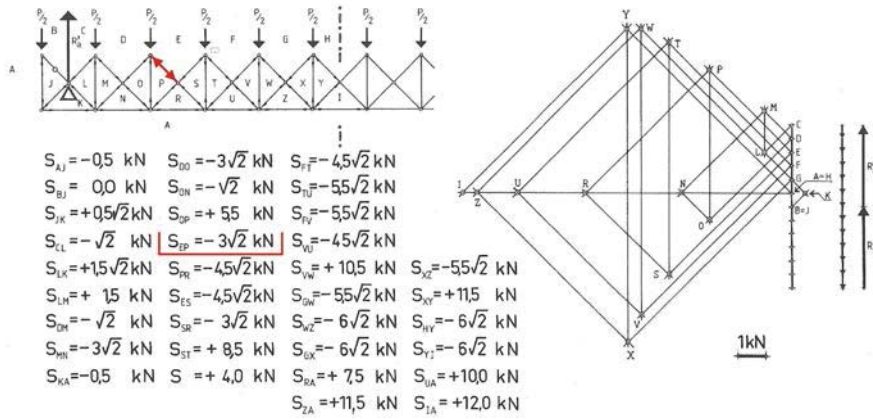


Figure 7. Values of forces obtained in the first stage of the proposed method of calculation

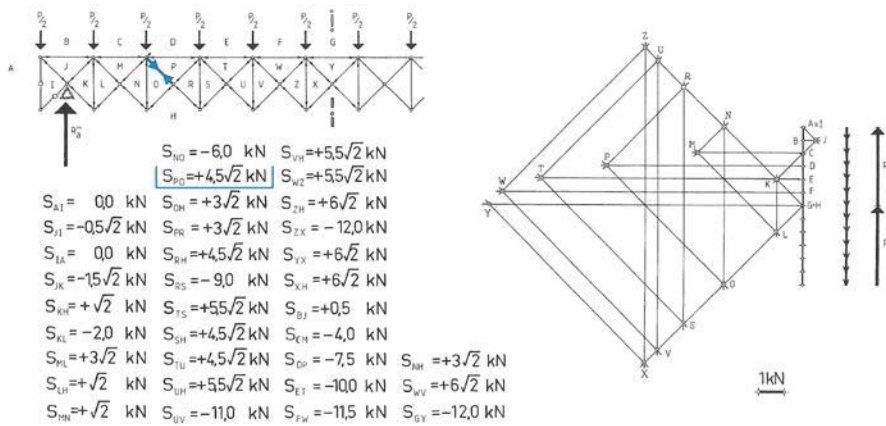


Figure 8. Values of forces obtained in the second stage of the proposed two-stage method of calculations of statically indeterminate trusses

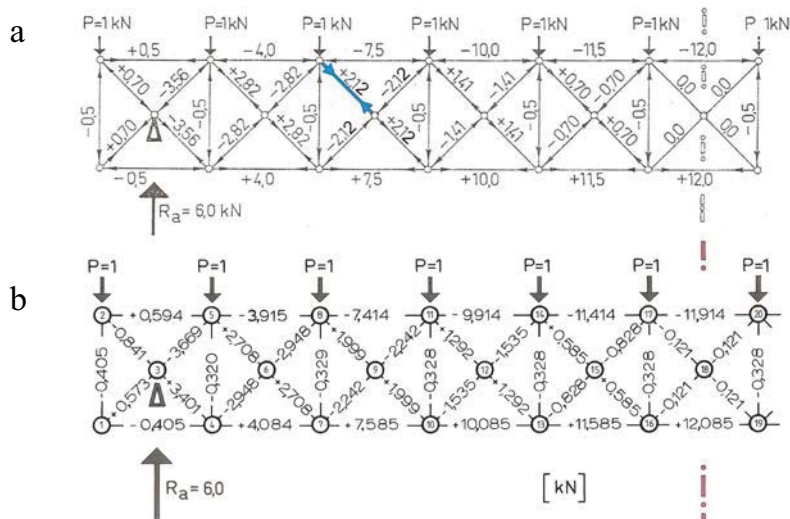


Figure 9. Final values of forces obtained a) in the proposed two-stage method of calculations, b) by application of the computer software ICES-STRUDL

In the computer aided process of the statically calculations it was assumed, that the truss is made of the steel members of the same Young's modulus (E), having the same area of the main cross-sections and the same value of the moment of inertia (I).

Comparison of results obtained in the proposed two-stage method to results determined by means of application of exact method used by the computer software ICES-STRUDL is carried out on example of a selected member of the truss. For instance the force value calculated in the first stage for a cross brace located between fields E and P equals ca.  $S_{EP} = -4,24$  kN, see Fig. 7, while in the second stage in the same member of this truss, placed now between fields P and O, acts a tension force equals ca.  $S_{PO} = +6,36$  kN, see Fig. 8. The resultant force vector acting in the same member of the basic indeterminate truss calculated in the two-stage method equals ca.  $+2,12$  kN, see Fig. 9a. The force value determined by means of the ICES-STRUDL computer software in the same member equals  $+1,999$  kN. However the difference between values calculated in the compared method is about of  $0,12$  kN, but it is relatively small in comparison to the total value of ca.  $2,00$  kN. In the proposed two-stage method there are not taken into consideration the differences between stiffness of members creating the structure. Therefore one should be aware that forces calculated in this way are of the approximate values in relation to the forces really acting in members of the considered truss. In spite of this feature the approximation is good enough for calculation of trusses built of members of not too much different lengths and having the same parameters of their cross-sections, what is also presented in works (Rębielak and Beranek and Hobbelman, 1985b), (Rębielak, 2013).

## Conclusions

Simplicity of the proposed two-stage method can be considered as the most important value of it that is why it can be especially useful for the preliminary static analyses of the statically indeterminate trusses. This method can give more exact results after application of suitable sets of special parameters, which in suitable way will take into account mutual differences between stiffness of the members creating the truss.

## References

- Kolendowicz T. (1993), *Mechanika budowli dla architektów*, Arkady, Warszawa.
- Pyrak S. and Szulborski K. (1994), *Mechanika konstrukcji dla architektów. Przykłady obliczeń*, Arkady, Warszawa.
- Przewłócki J. and Górski J. (2006). *Podstawy mechaniki budowli*, Arkady, Warszawa.
- Allen E. and Zalewski W. and Boston Structures Group (2010), *Form and Forces. Designing efficient, expressive structures*, John Wiley & Sons, Inc., Hoboken, New Jersey.
- Timoshenko S.P. (1953), *History of strength of materials*, McGraw-Hill Book Company Inc., New York-Toronto-London, 1953, Polish edition, Arkady, Warszawa, 1966.
- Makowski Z.S. (1981), *Analysis, design and construction of double-layer grids*, Applied Science Publishers, London.
- Rębielak J. (1983), *Przestrzenne struktury prętowo-ciężnowe. Konstrukcje nośne przekryć powłokowych*, *Architektura*, nr 1, pp. 69-70.
- Rębielak J. (1985a), *Dwuetałowa metoda obliczania kratownic statycznie niewyznaczalnych*, TH Delft, Afdeling der Bouwkunde, *Vakgroep 4, Project nr 4.1.2.1*.
- Rębielak J. and Beranek W.J. and Hobbelman G.J. (1985b), *Wielowarstwowe struktury przestrzenne. Zagadnienia statyczne i geometryczne*, TH Delft, Afdeling der Bouwkunde, *Vakgroep 4, III – 396, Raport Instytutu Architektury i Urbanistyki Politechniki Wrocławskiej*, Nr I-1/P-332/1985.
- Rębielak J. (2012), *A method of static calculation and shape of structural system developed by application of principles of superposition*, *Lightweight structures in civil engineering – contemporary problems*, Local seminar of IASS Polish Chapter, Warsaw, pp. 155-158.
- Rębielak J. (2013), *Metoda obliczania kratownic statycznie niewyznaczalnych w dwóch etapach (Method of calculation of statically indeterminate trusses in two stages – in Polish)*, XVII *Międzynarodowa Szkoła Komputerowego Wspomagania Projektowania, Wytwarzania i Eksploatacji*, Wojskowa Akademia Techniczna, Warszawa-Szczyrk, May 13-17, 2013, Vol 2, pp. 281-287 (paper is published on attached CD to the Journal *Mechanik* No 7, 2013, p. 599, electronic version, pp. 729-736).

## A computational model of bone-cell interactions taking into account bone specific surface

Ch. Lerebours<sup>\*,1</sup>, P.R. Buenzli<sup>2</sup>, C.D.L. Thomas<sup>3</sup>, J.G. Clement<sup>3</sup>, P. Pivonka<sup>1</sup>

<sup>1</sup>Northwest Academic Centre, Australian Inst. Musculoskeletal Science, University of Melbourne, VIC 3021, Australia.

<sup>2</sup>School of Mathematical Sciences, Monash University, VIC 3800, Australia.

<sup>3</sup>Melbourne Dental School, University of Melbourne, 720 Swanston Street, VIC 3053, Australia.

\*email: [chloe.lerebours@unimelb.edu.au](mailto:chloe.lerebours@unimelb.edu.au)

### Abstract

Bone cells are well-known to be regulated biochemically and biomechanically. The notion that the microscopic availability of bone surface affects bone remodelling is, however, less established. Bone-resorbing and bone-forming cells require a bone surface to attach to and initiate the matrix renewal. In this paper, we will extend a previous computational model of bone remodelling. This model includes several stages in the differentiation of bone cells, biochemical regulations and geometrical regulations. In particular a new calibration algorithm for uncommitted bone cells and activator/repressor functions is presented. This study is a necessary prerequisite to study endocortical bone loss due to aging in a spatio-temporal context.

**Keywords:** bone remodeling, specific surface, computational modeling, age-related bone loss

### Introduction

Bone has several important roles: (i) keeping its integrity and sustaining the mechanical loading applied on it, (ii) a source/sink of calcium and phosphate regulating mineral homeostasis, and (iii) a protected space for haematopoiesis. Like in all other materials, loads that are applied on bone every day, lead to fatigue damage and micro cracks. Those cracks have to be repaired, otherwise they will grow and lead to macroscopic fracture. This is the role of the bone remodelling process, i.e., to resorb bone matrix containing cracks and to form new bone matrix thereafter. Three kinds of cells are responsible for the remodeling process: osteocytes (i.e., the mechanoreceptors, detect the cracks and activate remodelling); osteoclasts resorb the bone matrix and osteoblasts refill the hole. These cells are spatially and temporally organized in functional structures called BMUs - Basic Multicellular Units (Parfitt 1994).

Few computational models have been developed representing bone cell behaviours and more generally the remodelling process (Lemaire, Tobin et al. 2004); (Pivonka, Zimak et al. 2008); (Pivonka, Zimak et al. 2010); (Scheiner, Pivonka et al. 2013) (Buenzli, Thomas et al. 2013; Pivonka, Buenzli et al. 2013). They included biochemical, biomechanical and simplified geometrical regulations.

The aim of this paper is to develop a computational model of bone remodelling taking into account a comprehensive description of geometrical feedback. Emphasis is on the recalibration of uncommitted bone cells and the activator/repressor functions.

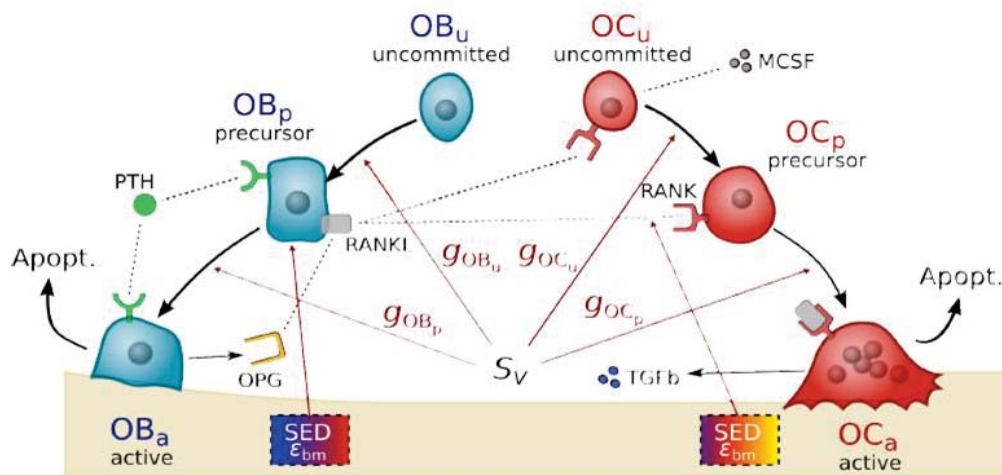
### Materials and Methods

This paper is a continuation of our previous work on bone remodelling (Pivonka, Zimak et al. 2008; Pivonka, Buenzli et al. 2013) and, hence, only mathematical expressions relevant for explaining the underlying model behaviour are given below. For a complete list of equations and respective parameter values the reader is referred to previous publications and the CELLML model repository (see link in references). In the following we describe the essential features of the model.



### Biochemical regulation

We modelled the interactions between osteoblasts and osteoclasts at various stages of differentiation using receptor-ligand binding reactions together with Hill-type functions (Figure 1); three stages in the differentiation of these bone cells are taken into account: uncommitted osteoclast and osteoblasts:  $OC_u$  and  $OB_u$ ; osteoclast and –blast precursor cells:  $OC_p$  and  $OB_p$  and active cells:  $OC_a$  and  $OB_a$ . The uncommitted cells represent bone marrow stromal cells ( $OB_u$ ) and hematopoietic stem cells ( $OC_u$ ) respectively from which all other cells derive. Active osteoblasts ( $OB_a$ ) produce bone matrix while active osteoclast ( $OC_a$ ) resorb the bone matrix.



**Figure 1 – Cell population model of bone remodeling including several developmental stages of osteoblasts and osteoclasts and their biochemical regulation, biomechanical regulation and geometrical regulation (Pivonka, Buenzli et al. 2013).**

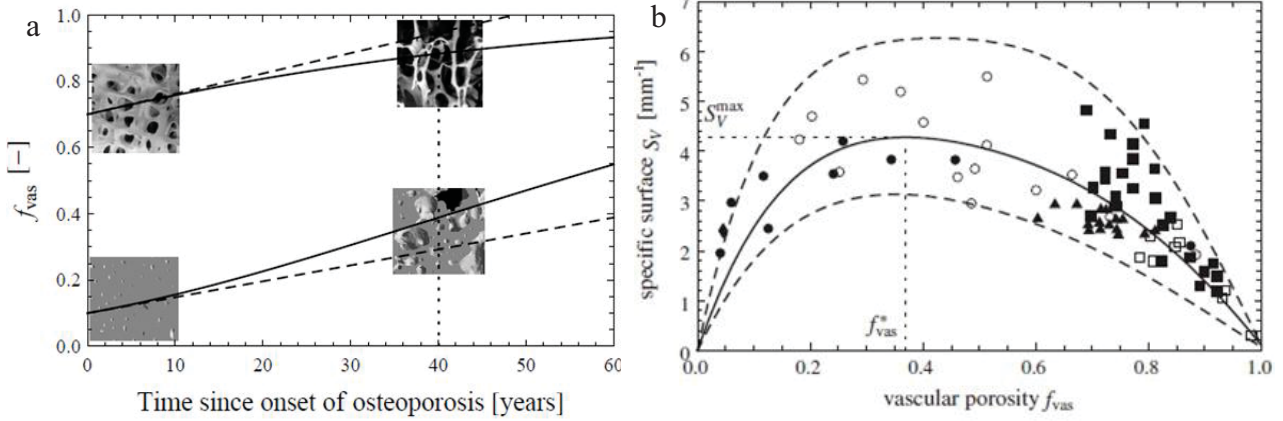
Communication between osteoblasts and osteoclasts enables a coordinated response to physiological demands, i.e., calcium and phosphate and the mechanical environment. Cells from the osteoclast lineage maintain a pool of osteoclast precursors through macrophage colony stimulation factor (MCSF, assumed constant) and RANKL (see next paragraph). Osteoclast precursor cells are then available for recruitment and differentiation into active osteoclasts.

Osteoblast lineage regulates the differentiation and the activity of osteoclasts. This pathway involves three major components: receptor activator of nuclear factor  $\kappa\beta$ : RANK, its ligand: RANKL and osteoprotegerin: OPG. RANK is expressed at the surface of uncommitted osteoclast and osteoclast precursor cells. RANKL is a polypeptide found at the surface of osteoblast precursor cells and can also be released as a soluble form (not modelled here). OPG is a decoy receptor molecule released by active osteoblastic cells. The differentiation of  $OC_p$  into  $OC_a$  requires binding of RANKL to RANK. The RANK - RANKL binding is inhibited by OPG which binds onto RANKL instead of RANK (Roodman 1999; Martin 2004). We sum up these interactions in the Figure 1.

### Geometrical regulation

As pointed out in the introduction, there is increasing evidence that bone surface availability, i.e., bone specific surface, may play an important role in bone remodeling and particular in age-related bone loss. Bone cells are “working” on the surfaces of the bone matrix and consequently bone morphology plays an important role in the remodeling process. Osteoclasts require attachment to a surface to be able to resorb the bone matrix while osteoblasts only secrete osteoid on existing bone surfaces.

Two types of bone are usually distinguished, i.e., cortical and trabecular bone based on their respective porosity. Martin (Martin 1984) highlighted the differences between cortical and trabecular bones in terms of bone specific surface. In the cortical bone, an increase of porosity will increase the available surface, where remodeling can proceed, and so increase remodeling. However, in trabecular bone, increasing the porosity will decrease the available surface and decrease the remodeling (see Figure 2.a).



**Figure 2 – a) Possible effect of geometrical feedback on the evolution of vascular porosity in osteoporosis, both in cortical and trabecular bone according to Martin (Martin 1972). Dashed curves show the changes in  $f_{vas}$  obtained without geometrical feedback. b) Relation between bone specific surface and vascular porosity investigated by Martin (Martin 1984)**

In order to introduce the effect of specific surface on bone cells we use a phenomenological function in the form of a polynomial similar as in (Pivonka, Buenzli et al. 2013):

$$g_i = \left( \frac{S_V}{S_{V_{t0}}} \right)^{k_i} \text{ with } S_{V_{t0}} = 1 \text{ mm}^{-1} \quad (1)$$

where  $S_V$  is the specific surface;  $k_i$  is a constant determined based on a parametric study presented in the next section and “i” refers to the particular cell on which the regulatory function is applied. We note that unlike in the paper (Pivonka, Buenzli et al. 2013)  $S_{V_{t0}}$  is set equal to 1 leading to a dimensionless quantity. We believe that the original formulation, while suitable for the extreme cases of trabecular and cortical bone may have problems in properly describing the transition from cortical to trabecular bone. Hence, this new more consistent formulation has been used. We note that this formulation requires recalibration of the steady state values of the model (see discussion below).

The specific surface is based on B.R. Martin’s equation (Martin 1984):

$$S_V(f_{vas}) = a \cdot f_{vas} + b \cdot f_{vas}^2 + c \cdot f_{vas}^3 + d \cdot f_{vas}^4 + e \cdot f_{vas}^5 \quad (2)$$

where a, b, c, d and e are constants and  $f_{vas}$  is the vascular porosity in cortical bone and the marrow porosity in trabecular bone.

This relation has been obtained from interpolating of experimental data from an investigation on slices of cortical and trabecular bones both in humans and in animals. We are currently investigating the relationship between cortical porosity and bone specific surface using high resolution micro-CT in more detail in order to verify the accuracy of Eqn.(2). For the purpose of this paper we will base our theoretical developments on the porosity versus specific surface relationship provided by Martin, i.e., Eqn.(2) shown in Figure 2.b. (Martin 1984).

Unlike, in previous models, we believe that the  $OC_u$  and  $OB_u$  cell densities are not constant, but depend on the available pore space. Assuming that these densities should be related to the

respective pore space and to the observed remodeling rates we assume  $OC_u = OC_u(f_{bm})$  and  $OB_u = OB_u(f_{bm})$ . Furthermore, we assume the shape of  $OC_u$  vascular density to follow a sigmoidal function. Indeed the vascular density is the density inside the pores. Hence, we assume the  $OC_u$  density to be higher where the porosity is low (i.e.,  $f_{bm} = 1$ ). Indeed, vascular pores in cortical bone are filled with blood vessels and BMUs. However, close to the marrow cavity, the trabecular pores are bigger but contain many other components such as bone marrow and fat. Hence, the density of bone cells in the vascular space is higher in cortical bone than in trabecular bone. Using suitable constraint conditions we then determine  $OB_u(f_{bm})$  at homeostasis (i.e., the equilibrium state). More details are found below.

### Bone cells equation

The evolution of bone cells is described mathematically based on “rate equations” (Lemaire, Tobin et al. 2004). The state variables are  $OB_p$ ,  $OB_a$ ,  $OC_p$  and  $OC_a$ , i.e., the cell densities. The Pi functions are Hill functions which represent the interaction – activation or repression – between a component (for example TGF $\beta$ ) and a cell.

$$\begin{aligned} \frac{dOB_p}{dt} &= g_{OB_u} * D_{OB_u} * \pi_{act,OB_u}^{TGF\beta} * OB_u(f_{bm}) + P_{OB_p} * \pi_{act,OB_p}^{mech} * OB_p - D_{OB_p} * \pi_{rep,OB_p}^{TGF\beta} * OB_p \\ \frac{dOB_a}{dt} &= D_{OB_p} * \pi_{rep,OB_p}^{TGF\beta} * OB_p - (D_{OB_a} + A_{OB_a}) * OB_a \\ \frac{dOC_p}{dt} &= g_{OC_u} * D_{OC_u} * \pi_{act,OC_u}^{MCSF} * \pi_{act,OC_u}^{RANKL} * OC_u(f_{bm}) - D_{OC_p} * \pi_{act,OC_p}^{RANKL} * OC_p \\ \frac{dOC_a}{dt} &= D_{OC_p} * \pi_{act,OC_p}^{RANKL} * OC_p - A_{OC_a} * \pi_{act,OC_a}^{TGF\beta} * OC_a \end{aligned} \quad (3)$$

where,  $D_i$  are the differentiation rates of the cell „i“;  $A_i$  the apoptosis rates and  $P_i$  the proliferation rates (see (Pivonka, Zimak et al. 2008) for details).

An important element in the remodeling process is the bone volume fraction:  $f_{bm}$ . It is the proportion of bone matrix in a volume of bone. Bone can be described as a two-phase material: the solid part, the matrix and the vascular part, the pores. With  $f_{vas}$  the proportion of pores we have:

$$f_{bm} = \frac{V_{bm}}{V_{total}} \quad \text{and} \quad f_{bm} + f_{vas} = 1 \quad (4 - 5)$$

(Martin 1972), in his work well explained how the porosity change during the remodeling process. The change in porosity is the difference between the total resorption of the osteoclasts and the total formation of the osteoblasts. And so, the changes of the bone matrix volume fraction over time can be represented by:

$$\frac{df_{bm}}{dt} = k_{form} * OB_a - k_{res} * OC_a \quad (6)$$

where  $k_{form}$  and  $k_{res}$  are the relative bone formation and resorption rates respectively. In a healthy (i.e., homeostatic) state, there is no change in the porosity/bone matrix volume fraction since the formation and the resorption are in equilibrium. In the following, this state will be referred to as the steady-state of the system.

The numerical simulation results are divided into two parts. The first part deals with simulations of the steady-state of the system which allows calculation of suitable initial conditions of uncommitted cell numbers and respective constants in the activator/repressor functions. The second set of simulations deal with age-related bone loss which is obtained by perturbing the initial healthy state. Based on this perturbation we can follow the temporal changes of cell numbers, regulatory factors and bone volume fractions.

## Results and discussion

### *Changing the geometrical feedback*

In the paper ref (Pivonka, Buenzli et al. 2013), the geometric regulation has been defined as in equation 1 where  $S_{V to}$  is the specific surface for the steady state. This type of normalization of  $g_i$  leads to  $g_i(t_0) = 1$ . Hence, no recalibration of the original model was required for estimating steady-states of the system. Whereas this formulation seems suitable for discrete states of cortical and trabecular bone it is not clear how a continuous transition as in a spatio-temporal setting can be achieved with this formulation.

For these reasons, we renormalize by  $S_{V to} = 1 \text{ mm}^{-1}$  in the current paper. We note that also in the model of Martin and others a similar approach has been applied. Introducing this normalization in Equation (1) would lead to changes in the differentiation rates. Indeed,  $S_{V to}$  varies between 0 and  $4 \text{ mm}^{-1}$ .

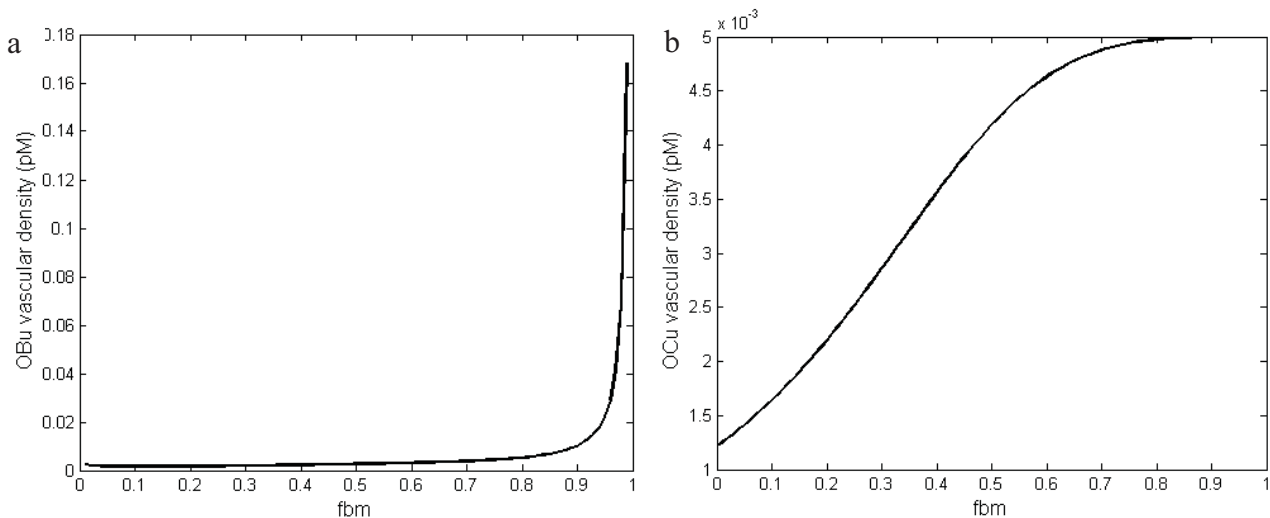
In order to have the same differentiation rates as in previous models, we renormalize the various differentiation rates according to the following relationship:

$$D_i^{\text{present model}} * g_i = D_i^{\text{previous model}} \quad (8)$$

### *Calibration of the uncommitted cell populations: porosity dependence*

Previously,  $OC_u$  and  $OB_u$  cell densities were considered constant and assumed to be large compared to the cell densities of the state-variables. Based on bone biology literature we take:  $k_{res} = 9.425 \cdot 10^{-6} \text{ mm}^3/\text{day}$  and  $k_{form} = 150 \mu\text{m}^3/\text{day}$  (Buenzli, Pivonka et al. 2013).

Here, we assume  $OB_u$  and  $OC_u$  densities to be porosity dependent. We impose  $OC_u(f_{bm})$ , as a sigmoidal function of  $f_{bm}$  in order to have approximately a 4 times change in the amplitude of  $OC_u$  ( $1.5 \cdot 10^{-3} \leq OC_u \leq 5 \cdot 10^{-3} \text{ pM}$ ). In the steady state,  $OB_u$  density is unknown. Using the equilibrium constraint, i.e. resorption equals formation; we obtain 5 equations for the 5 unknowns. We are solving these equations using the Newton algorithm. By solving this problem at discrete porosities for the entire range (from 0 to 100%), we determine  $OB_u(f_{bm})$  (see Figure 3a) at discrete points. These discrete values are then interpolated (using a linear interpolation) in order to obtain continuous functions of  $OB_u(f_{bm})$  and  $OC_u(f_{bm})$  which are then used for the subsequent dynamic simulations.



**Figure 3 – Dependence of uncommitted bone cells on bone matrix volume fractions  $f_{bm}$ . (a) Uncommitted osteoblasts, (computed function) and (b) Uncommitted osteoclasts (imposed function)**

The vascular density is the density inside the pores. This is why we assume this density to be higher where the porosity is low (i.e.,  $f_{bm} = 1$ ). Indeed, vascular pores in cortical bone are filled of blood vessels and BMUs. However, close to the marrow cavity, the trabecular pores are bigger but contains many other components. And so the density of bone cells in the vascular space is higher in cortical bone than in trabecular bone.

### Calibration of the Hill functions

Due to the novel model features some of the previously defined Hill functions require recalibration. One of the most important Hill function is:  $\pi_{act,OBu}^{TGF\beta}$ , i.e., the TGF $\beta$  activator function which promotes differentiation of bone marrow stromal cells (OB<sub>u</sub>s) into osteoblast precursor cells. Note that TGF $\beta$  is released from the bone matrix during osteoclastic resorption and provides a biochemical feedback on both osteoclastic and osteoblastic cells. The activator function is expressed as:

$$\pi_{act,OBu}^{TGF\beta} = \frac{\alpha \cdot k_{res} \cdot OC_a}{K_{rep} + \alpha \cdot k_{res} \cdot OC_a} \quad (9)$$

where  $\alpha$  is a proportionality constant expressing the TGF $\beta$  content stored in the bone volume and  $K_{rep}$  is the dissociation constant. In the original model  $K_{rep}$  has been calibrated such as to obtain a strong biochemical feedback response. In order to test the suitability of the choice of  $K_{rep}$  in the current model we investigate the case of age-related bone loss. Similar as in previous models we induce age-related bone loss by increasing the PTH concentration. Osteoporosis is characterized by an increase in porosity. To simulate OP in our model, we perturb the homeostatic state by increasing the RANKL/OPG ratio. This can be achieved by prescribing an excess of PTH concentration. This increase in PTH leads to an increase in RANKL and a decrease in OPG leading to an overall increase in the RANKL/OPG ratio. This increase promotes osteoclastic resorption and, hence, an increase in the TGF $\beta$  concentration. To obtain an increase in porosity of about 2%/year as assumed by Buenzli (Buenzli, Thomas et al. 2013), a continuous injection of PTH has been applied:  $P_{PTH}(t) = 15$  pM/day for all times  $t > t_0$ .

In Figure 4 we show the response of the TGF $\beta$  activator function for the case of age-related bone loss for different values of the dissociation constant ( $K_{rep}$ ). The red parts of these plots represent the temporal changes of  $\pi_{act,OBu}^{TGF\beta}$  over the simulation time ( $t_0 = 0$ ,  $t_{end} = 50$  years) while the black parts of the curves represent a larger interval of active osteoclast concentrations. Interestingly, we can see that use of the original value of  $K_{rep}$  (solid line) leads to an almost linear response of  $\pi_{act,OBu}^{TGF\beta}$  with negligible changes in values. On the other hand, using  $K_{rep} = 1 \cdot 10^{-3} \cdot K_{init}$  leads to a very strong non-linear response with values ranging between 0.40 and 0.77 for the investigated simulation time. Clearly the original  $K_{rep}$  value doesn't lead to a sensitive model response due to the introduced porosity dependent OB<sub>u</sub> and OC<sub>u</sub> values. Based on this parametric study we chose the  $K_{rep} = 1 \cdot 10^{-2} \cdot K_{init}$  (dashed lines) which leads to an intermediate response with values changing from 0.16 – 0.41.

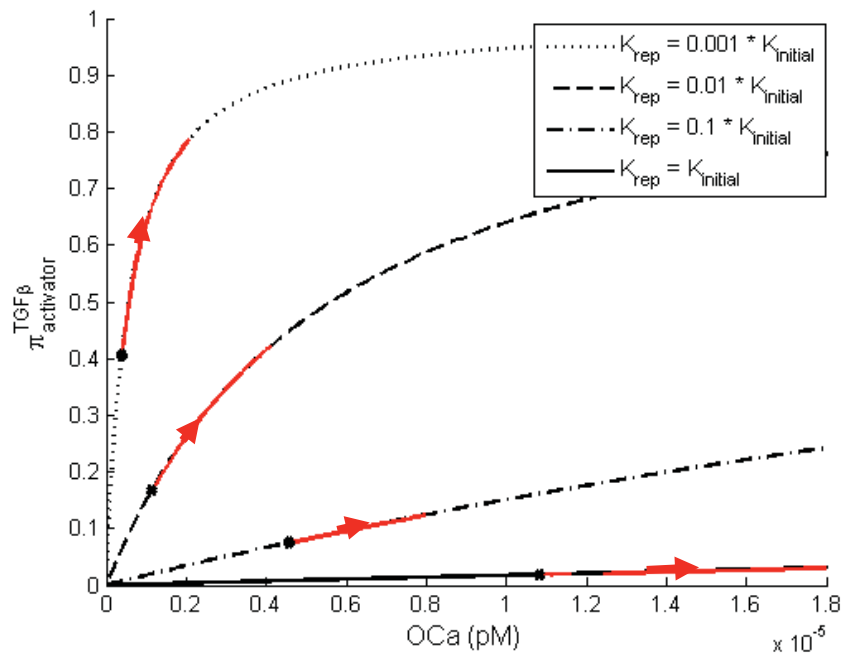


Figure 4 - Hill function for the regulation of TGF  $\beta$  depending on the active osteoclasts density. In red the portion of the curve where the osteoclasts density is in the model

Parametric study for the geometrical feedback

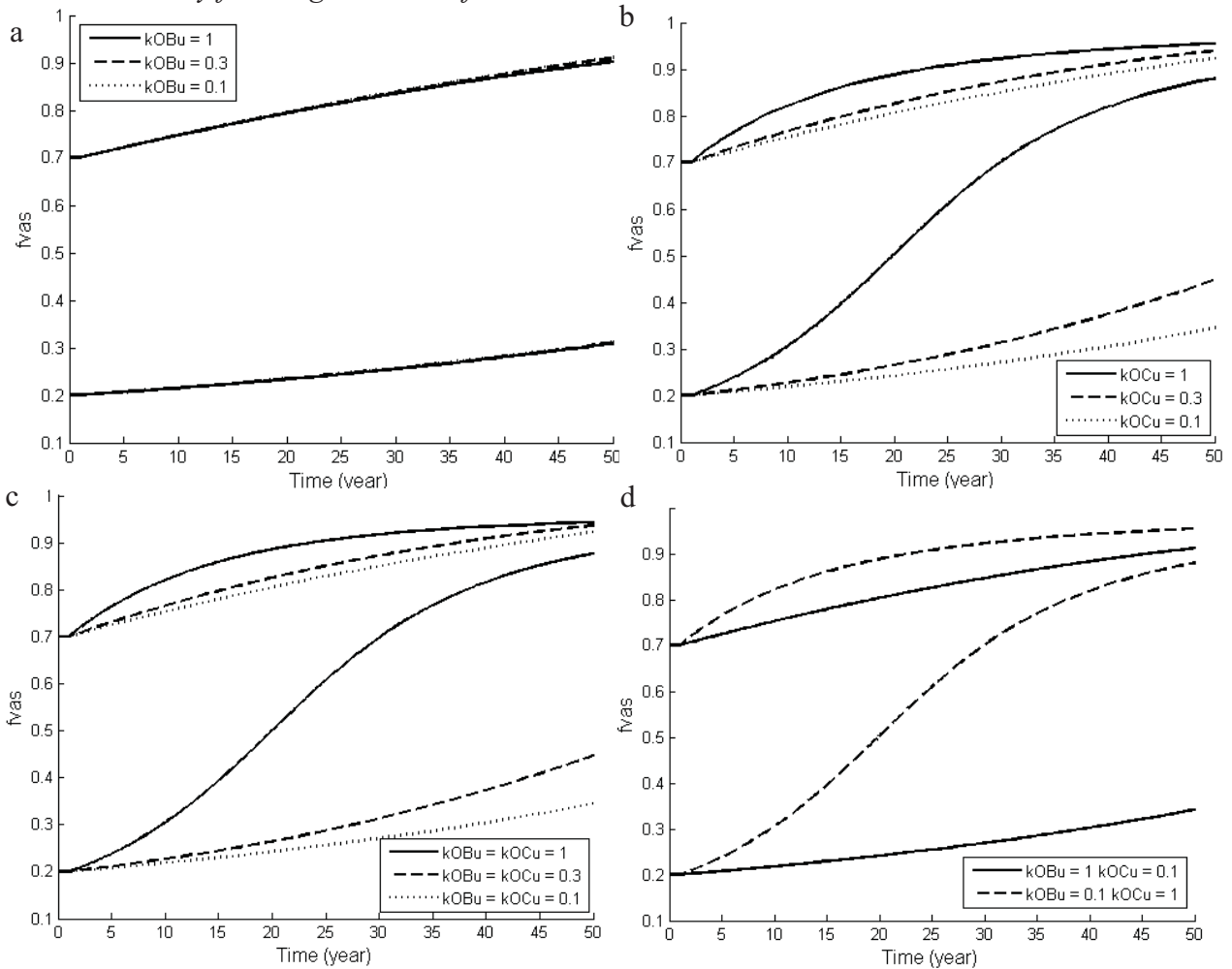


Figure 5 - Parametric study showing the evolution of the porosity depending on the time for several regulatory functions: a)  $g_{OBu}$  b)  $g_{OCu}$  c)  $g_{OBu} = g_{OCu}$  d)  $g_{OBu}$  and  $g_{OCu}$  differently regulated.

After having checked the suitability of the respective model parameters we are now in a position to study the effects of the different geometric regulatory functions  $g_i(f_{bm})$ , i.e., Eqn.(1) in more detail. In order to determine the effect of different choices of  $g_i$  with different values of  $k_i$  we apply a similar strategy as in (Pivonka, Buenzli et al. 2013). We tested:  $k_i = 0; 0.1; 0.3$  and 1 on both uncommitted osteoblasts and osteoclasts with different combinations.

The objective of introducing a geometrical feedback in the model is to observe the acceleration of bone loss in trabecular bones and deceleration in cortical bones. This idea has been introduced by (Martin 1972) and was further explored in (Pivonka, Buenzli et al. 2013).

The graphs in Figure 5 show that the geometrical regulation needs to be preferentially on  $OC_u$ . For the case  $k_{OC_u} = 0$  (Figure 5a). no acceleration of cortical bone loss is observed. For all other combinations, the expected behavior is observed indicating that the suggested model is capable of representing geometrical feedback. In the following, we chose  $k_{OB_u} = k_{OC_u} = 0.3$  as the combined regulation of both  $OB_u$  and  $OC_u$ , which leads to the anticipated geometrical behavior (Figure 5c). Indeed the other cases lead either to a too strong regulation ( $k_{OC_u} = 1$ ) or a not sufficiently strong regulation ( $k_{OC_u} = 0.1$ ).

## Conclusions

Here we presented a consistent bone cell population model which takes into account bone specific surface on bone remodeling. Indeed, this model is able to simulate age-related bone loss for all different initial conditions of porosity. The results are in good qualitative and quantitative agreement with data reported in the literature.

As a next model development we will introduce a mechanical feedback and apply this coupled model to assess spatio-temporal changes in a cortical bone cross section. Using this methodology will help to better understand the experimentally observed phenomenon of trabecularization.

## References

- Buenzli, P. R., P. Pivonka, et al. (2013). Bone refilling in cortical basic multicellular units: insights into tetracycline double labelling from a computational model. *Biomechanics and Modeling in Mechanobiology*.
- Buenzli, P. R., C. D. L. Thomas, et al. (2013). Endocortical bone loss in osteoporosis: The role of bone surface availability. *INTERNATIONAL JOURNAL FOR NUMERICAL METHODS IN BIOMEDICAL ENGINEERING*.
- Lemaire, V., F. L. Tobin, et al. (2004). Modeling the interactions between osteoblast and osteoclast activities in bone remodeling. *Journal of Theoretical Biology* **229**(3): 293-309.
- Martin, R. B. (1972). EFFECTS OF GEOMETRIC FEEDBACK IN DEVELOPMENT OF OSTEOPOROSIS. *Journal of Biomechanics* **5**(5): 447-&.
- Martin, R. B. (1984). POROSITY AND SPECIFIC SURFACE OF BONE. *Critical Reviews in Biomedical Engineering* **10**(3): 179-222.
- Martin, T. (2004). Paracrine regulation of osteoclast formation and activity: milestones in discovery. *Journal of Musculoskeleton Neuron Interact* **4**: 243-253.
- Parfitt, A. M. (1994). OSTEONAL AND HEMI-OSTEONAL REMODELING - THE SPATIAL AND TEMPORAL FRAMEWORK FOR SIGNAL TRAFFIC IN ADULT HUMAN BONE. *J. C. B.* **55**(3): 273-286.
- Pivonka, P., P. R. Buenzli, et al. (2013). The influence of bone surface availability in bone remodelling-A mathematical model including coupled geometrical and biomechanical regulations of bone cells. *Eng. Struct.* **47**: 134-147.
- Pivonka, P., J. Zimak, et al. (2008). Model structure and control of bone remodeling: A theoretical study. *Bone* **43**(2): 249-263.
- Pivonka, P., J. Zimak, et al. (2010). Theoretical investigation of the role of the RANK-RANKL-OPG system in bone remodeling. *Journal of Theoretical Biology* **262**(2): 306-316.
- Roodman, G. D. (1999). Cell biology of the osteoclast. *Experimental Hematology* **27**(8): 1229-1241.
- Scheiner, S., P. Pivonka, et al. (2013). Coupling systems biology with multiscale mechanics, for computer simulations of bone remodeling. *Computer Methods in Applied Mechanics and Engineering* **254**: 181-196.
- CELLML website: <http://models.cellml.org/exposure/51d04b5d2e2fe5abe8ac818a0c833b9c>

## Numerical Simulations of Shock Wave Reflection over Double Wedges

\*Z.L. Jiang and Y. Yang

State Key Laboratory of High-Temperature Gas Dynamics,  
Institute of Mechanics, CAS, Beijing 100190, China.

\*Corresponding author: zljiaang@imech.ac.cn

### Abstract

Shock wave reflection is a fundamental topic in aerodynamic research area and has a wide application in engineering. Three-dimensional shock reflections over two perpendicularly intersecting wedges are numerically investigated in this paper by using the finite volume method with the MUSCL-Hancock interpolation technique and self-adaptive unstructured mesh. Mach stem structures are demonstrated to be three-dimensional (3D) ones and have special configurations at different wedge angles. There are two different kinds of 3D Mach stem structures for the MR–RR interaction, namely the first and the second types of 3D Mach stem, respectively. The three-shock or four-shock configuration may occur in the intersecting corner for the MR–MR interaction. The four-shock one is consisting of the incident shock wave, the 3D Mach stem, the primary and secondary reflected shock waves. In the RR–RR interaction, the incident shock wave, the primary and secondary reflected shock waves meet at the same reflection point to combine a three-shock configuration.

**Keywords:** Shock waves, Double Wedges, Reflection, Mach Stem

### 1 Introduction

Shock wave reflection is a fundamental topic in aerodynamic research and engineering applications. The phenomena of shock wave reflection were first investigated by Mach<sup>[1]</sup> in 1870s and the well-known 'Mach reflection (MR)' was later named after him. Different types of MR configurations were further demonstrated by von Neumann<sup>[2,3]</sup> in 1940s. In recent decades, shockwave reflections have been studied systematically, e.g., shock wave reflections over wedges the hysteresis phenomena in steady shock wave reflections<sup>[4-7]</sup>, and the application of new experimental facilities<sup>[8]</sup>. However, the previous results are mainly on two-dimensional (2D) cases, and 3D shock wave reflection has not yet been investigated widely. This is mainly because the wave structures induced by 3D shock wave reflection are usually very complicated and thus difficult to be visualized clearly by the traditional visualization techniques.

Shock wave reflection over two perpendicularly intersecting wedges is schematically shown in Fig.1. This configuration of 3D shock reflection was first studied by Meguro et al.<sup>[9]</sup> experimentally, numerically and analytically. The 3D Mach stem was observed as well as its existence criterion according to the reflection types over each wedge, i.e., MR or regular reflection (RR). It was found that the 3D Mach stem definitely occurs for the MR–MR interaction, possibly occurs for the MR–RR interaction, but never occurs for the RR–RR interaction. The critical condition for whether or not the 3D Mach stem appears in the MR–RR interaction was analytically derived by the 2D theory of oblique shock wave reflection. In the case, as depicted in Fig.2, the 2D Mach stem on the vertical wedge was assumed to be two-dimensionally reflected over the horizontal wedge. Here,  $M_m$  denotes the Mach number of the Mach stem and  $\theta_m$  is the angle between the intersecting line of the two wedges and the horizontal wall of the shock tube.  $\theta_m$  corresponds to the inclination angle for the reflection of the Mach stem  $M_m$  over the horizontal wedge.  $M_m$  and  $\theta_m$  can be calculated by geometry relations:

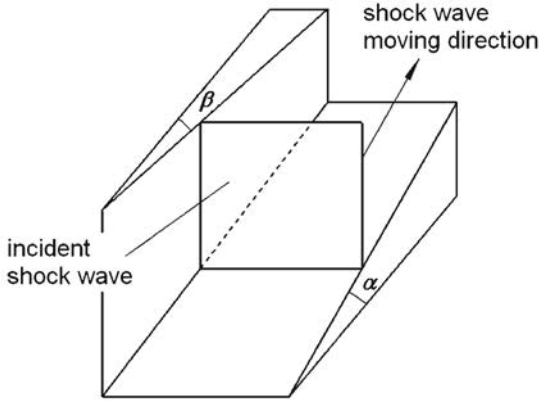
$$\theta_m = \arctan(\tan \alpha \cos \beta) \quad (1)$$

$$M_m = M_s \cos \chi_\beta / \cos(\chi_\beta + \beta) \quad (2)$$

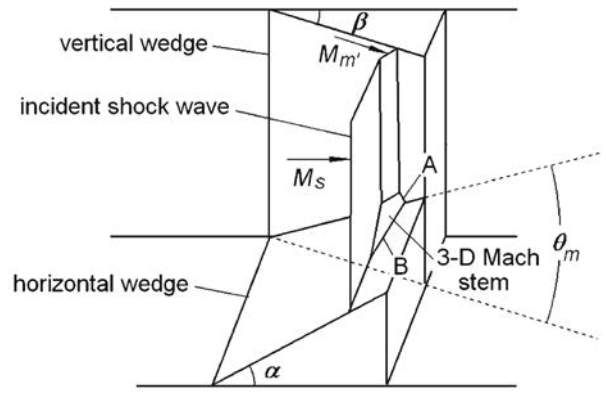
where  $\chi_\beta$  is the triple point trajectory angle of the Mach reflection over the vertical wedge. If the assumed 2D reflection forms a Mach stem, namely  $A$ , then the Mach stems  $A$  and  $B$  would interact with each other and eventually result in a 3D Mach stem. The 3D shock wave reflections and the



detailed interaction configurations are further investigated in this paper. Two kinds of 3D Mach stems and several types of shock wave reflection configurations are figured out. The existence criterion of the 3D Mach stem deduced from the 2D theory of shock wave reflection is re-examined using the computational results.



**Fig.1 Shock reflection over two perpendicularly intersecting wedges**



**Fig.2 Regular-Mach reflection interaction**

## 2 Governing equations and numerical methods

Assuming that viscosity effects on shock wave reflection are negligible, the governing equations are the hyperbolic system of three-dimensional conservation laws in Cartesian coordinates, which can be written as:

$$\frac{\partial U}{\partial t} + \frac{\partial F}{\partial x} + \frac{\partial G}{\partial y} + \frac{\partial H}{\partial z} = 0 \quad (3)$$

Where  $U$ ,  $F$ ,  $G$  and  $H$  denote the unknown variables and fluxes in the  $x$ -,  $y$ - and  $z$ -directions, respectively:

$$U = [\rho, \rho u, \rho v, \rho w, e]^T, \quad F = [\rho u, \rho u^2 + p, \rho uv, \rho uw, (e + p)u]^T,$$

$$G = [\rho v, \rho uv, \rho v^2 + p, \rho vw, (e + p)v]^T, \quad H = [\rho w, \rho uw, \rho vw, \rho w^2 + p, (e + p)w]^T$$

The primitive variables in the unknown  $U$  are density  $\rho$ , velocity components  $u$ ,  $v$  and  $w$ , and total energy per unit volume  $e$ . The equation of state for the perfect gas is given by:

$$e = \frac{p}{\gamma - 1} + \frac{1}{2} \rho (u^2 + v^2 + w^2) \quad (3)$$

where  $p$  is the pressure and the specific heat ratio  $\gamma = 1.4$ .

Using the finite volume method, the equations can be converted to the integral form over the governing volume:

$$\int_{\Omega} \frac{\partial U}{\partial t} dx dy dz + \int_{\Gamma} (F dy dz + G dx dz + H dx dy) = 0 \quad (4)$$

where  $\Omega$  and  $\Gamma$  denote the cubage and boundary of the governing volume, respectively. Hexahedron unit is adopted as the governing volume on the unstructured mesh and governing variables are fixed at the center of the unit. The HLLC scheme is applied to compute the fluxes on the governing unit boundaries and the second-order MUSCL scheme and the first-order time integral are used to reconstruct the governing variables at the unit center<sup>[10]</sup>.

In the present numerical simulations, the boundary conditions on the wedge surfaces, the upstream boundary, the downstream boundary and the mainstream boundary are set to be the slipping solid condition, the inflow condition, the outflow condition and the mirror condition, respectively. The air ahead of the incident shock wave is motionless and the air behind is calculated by the Rankine–Hugoniot relations for a given shock wave Mach number.

### 3 Validation of numerical algorithms

The numerical algorithms are validated by comparing the numerical flowfield with the experiment results. The experiment is conducted in the 100mm  $\times$  180mm diaphragmless shock tube in the ShockWave Research Center, Tohoku University, Japan. The shock waves are visualized with double exposure diffuse holographic interferometry. In order to show the 3D shock waves clearly, the interval between the first and second exposure is set to be 1  $\mu$ s.

Fig.3 shows the experimental and numerical results of the 3D shock wave reflection over two perpendicularly intersecting wedges. The incident shock wave Mach number is  $M_s = 2.0$  and the inclination angles of the horizontal and vertical wedges are  $\alpha = 43.5^\circ$  and  $\beta = 30^\circ$ , respectively. In Fig. 3a, it is obvious that the incident shock wave (I) is reflected over the wedges and a single-Mach reflection (R, M) appears over the horizontal wedge. Note that the reflected shock wave (R) over the vertical wedge is not as clear as the one over the horizontal wedge. It is mainly because the inclination angle of vertical wedge is relatively small and the reflected shock wave over it is relatively weak. However, it is still obvious that the reflection over the vertical wedge is a MR as the Mach stem (M) is visualized clearly. In the corner of the two intersecting wedges, the two Mach stems intersect each other forming a 3D forward-leaning Mach stem ( $M'$ ) followed by a secondary reflected shock wave ( $R'$ ). Fig.3b shows the numerical result, which consists of three translucent isopycnic surfaces and the isopycnic lines in all the computational boundary planes. The isopycnic surfaces denote the shock waves in the 3D reflection. All the wave structures, such as the incident shock wave (I), the Mach stems (M,M), the reflected shock waves (R,R), the secondary reflected shock wave ( $R'$ ) and the 3D Mach stem ( $M'$ ), can be identified clearly and agree well with the experimental result.

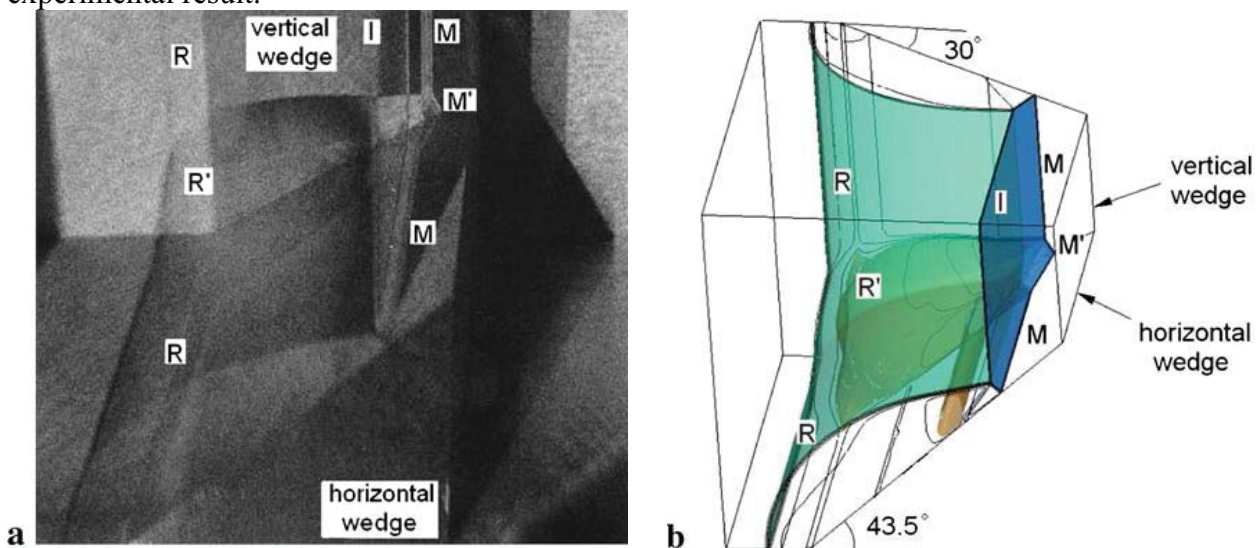


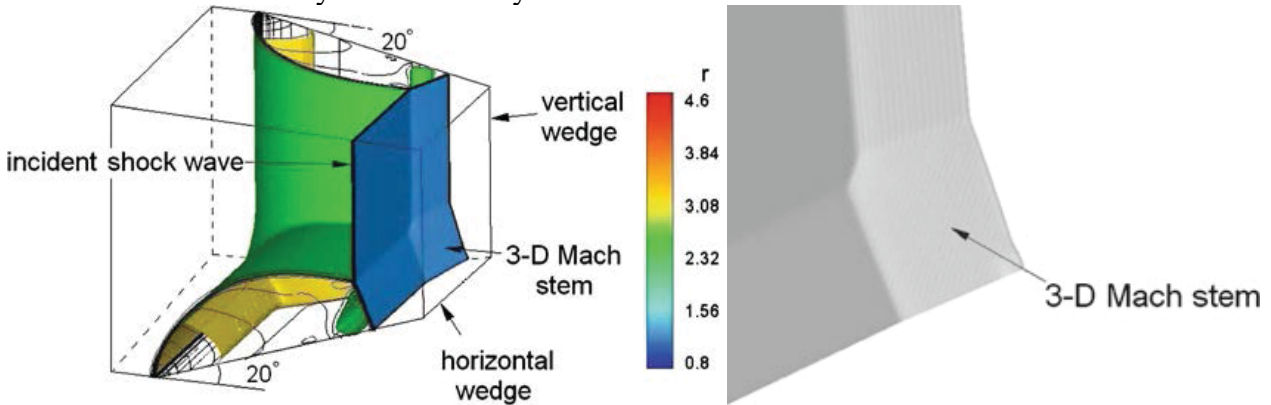
Fig. 3 Shock wave reflection over two intersecting wedges for  $\alpha = 43.5^\circ$ ,  $\beta = 30^\circ$  and  $M_s = 2.0$ :  
a) experimental result; and b) numerical result

## 4 Results and discussion

### 4.1 MR–MR interaction

The shockwave reflection for the wedge angles  $\alpha = \beta = 20^\circ$  and incident shock wave Mach number  $M_s = 3.0$  is shown in Fig. 4. Both of the patterns of the reflections over the vertical and horizontal wedges are single-Mach reflections. In the corner of the two intersecting wedges, the Mach stems intersect each other and a 3D Mach stem appears. It is obvious that the 3D Mach stem twists slightly and is approximately planar. Fig. 4 shows the 3D shock reflection from a different visual angle. In this figure the shockwave configuration in the corner of the two intersecting wedges can be observed clearly. The Mach stem on the vertical wedge is reflected over the horizontal wedge and a secondary MR appears. Similarly, the Mach stem on the horizontal wedge is also reflected over the vertical wedge and the other secondary MR appears. Accordingly, the two secondary MRs interact with each other to form the 3D Mach stem followed by the secondary

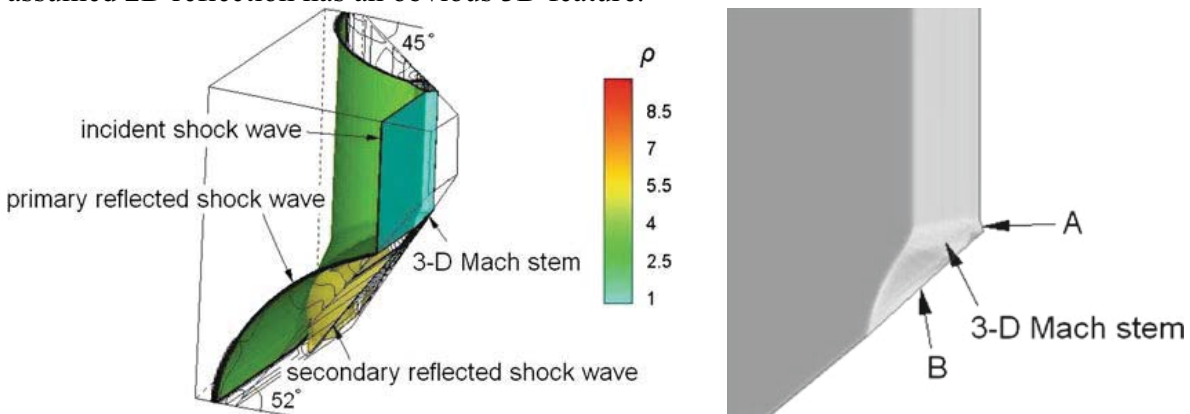
reflected shock wave surface in the wedge corner. Hence, in this condition a 3D four-shock configuration forms, consisting of the incident shock wave, the 3D Mach stem, the primary reflected shock wave and the secondary reflected shock wave. Meanwhile, a 3D slip surface is observed, which is similar to the slip line structure in a 2D MR. The 3D Mach stem leans forward indicating that it has a greater shock Mach number or higher shock intensity than both of the incident shockwave and the 2D Mach stems. Thus, for the flowfield enclosed in the secondary reflected shockwave surface, density, pressure and temperature are all higher than the ones in the flowfield outside, which are identical to the ones in a 2D reflection case. Therefore, the complex 3D wave configuration appears inside the secondary reflected shock wave surface while the shock wave reflection still obeys the 2D theory in the rest flowfield.



**Fig.4 Shock wave reflection over two intersecting wedges for  $\alpha = \beta = 20^\circ$  and  $M_s = 3.0$**

**4.2 MR–RR interaction**

Fig. 5 shows the interaction configuration over two intersecting wedges with  $\alpha = 52^\circ, \beta = 45^\circ$  and  $M_s = 3.0$ . A regular reflection appears on the horizontal wedge while a double-Mach reflection appears on the vertical wedge. According to the 2D analytical method aforementioned, the Mach stem on the vertical wedge is assumed to be two dimensionally reflected over the horizontal wedge with the shock Mach number  $M_{m'} = 4.51$  and inclination angle  $\angle \alpha_n = 42.15^\circ$ , as shown in Fig. 2. Coinciding with the 2D theory, such an assumed 2D reflection is a Mach reflection. The Mach stem *A* interacts with *B* resulting in a 3D Mach stem. However, the Mach stem *A* is much shorter as compared to the 2D reflection case under the same condition. This is because the horizontal wedge has a transverse inclination with regard to the Mach stem on the vertical wedge and thus it is not a complete 2D wedge in the secondary reflection. Actually, the velocity vector in the flowfield downstream the secondary reflected shock wave has a transverse component, which indicates this assumed 2D reflection has an obvious 3D feature.



**Fig.5 Shock wave reflection over two intersecting wedges for  $\alpha = 52^\circ, \beta = 45^\circ$  and  $M_s = 3.0$**

**4.3 RR–RR interaction**

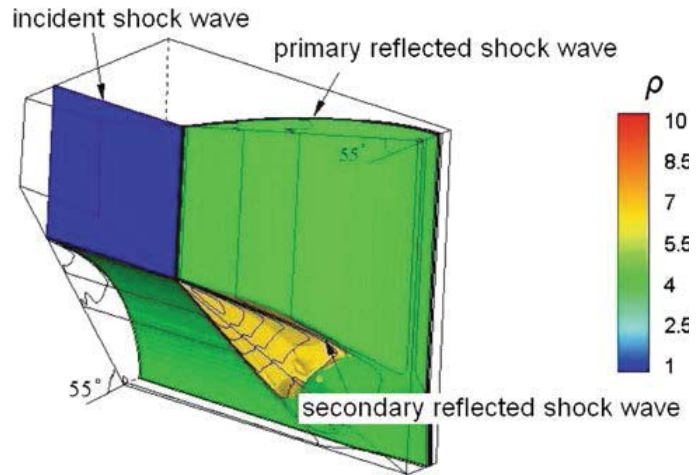
Fig. 6 shows the shock wave reflection over two intersecting wedges with the wedge angles  $\alpha = \beta = 55^\circ$  and incident shock wave Mach number  $M_s = 3.0$ . Two regular reflections appear

respectively over the two wedges. Obviously, there is not any 3D protuberance structure in the corner of the two intersecting wedges. Here, the primary and secondary reflected shock waves and the incident shock wave originate from the same reflection point which always locates on the wedge intersecting line. Therefore, a three-shock configuration is formed.

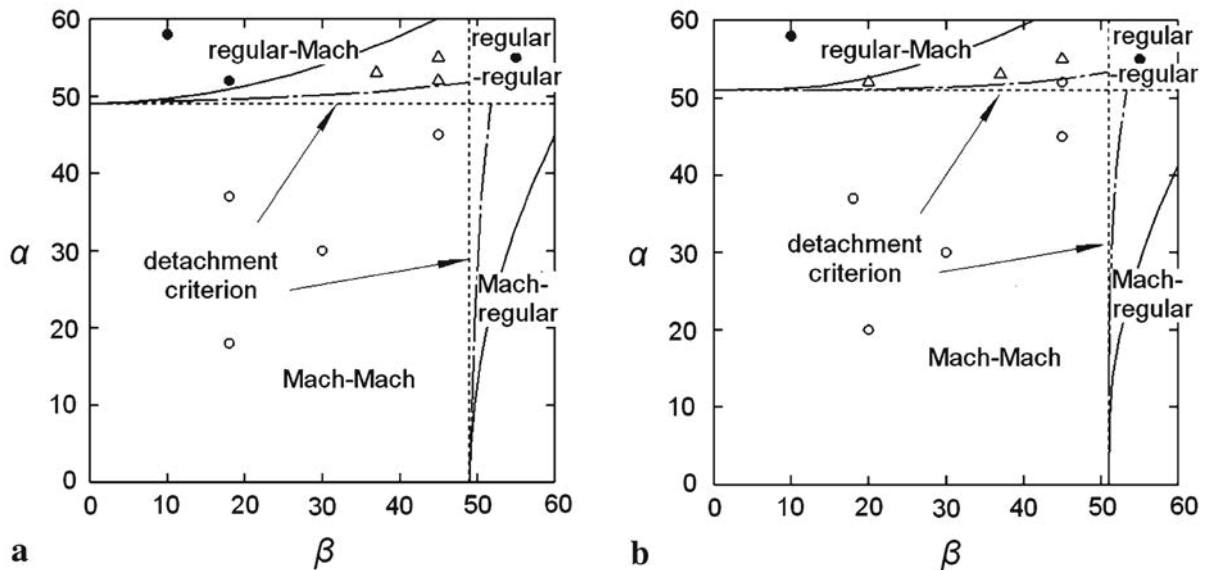
**4.4 The region of 3D Mach reflection**

In summary, analogous to 2D shock wave reflections, 3D shock wave reflections can be generally classified into two categories, i.e., RR and MR. Using 2D shock wave reflection theory, Meguro et al<sup>[12]</sup> derived the region where the 3D Mach stem exists. However, since the secondary reflection of the Mach stem in the 3D interaction zone is not completely two-dimensional, there are limitations in their derivation.

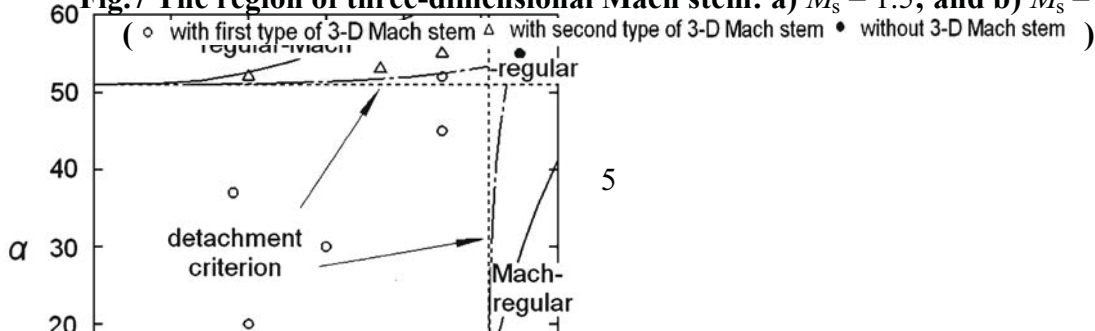
A different wave structure of 3D protuberance forms when an MR-RR interaction occurs in the corner, namely the second type of 3D Mach stem. Fig.7 shows the modified distribution of the 3D shock wave reflection pattern for  $M_s = 1.5$  and  $M_s = 3.0$ . The ordinate and abscissa are the inclination angles of the horizontal and vertical wedges, respectively. The dashed lines, which are derived from the detachment criterion, divide the diagrams into three regions: MR-MR interaction, MR-RR interaction and RR-RR interaction. The solid lines denote the boundaries between the solution domains without 3D Mach stem and with the second type of 3D Mach stem. Meanwhile, the dashed-dotted lines separate the solutions of the first and second type of 3D Mach stem. The plots denote the numerical results in the present study. Note that with the increase of the vertical wedge angle  $\beta$ , the dashed-dotted lines bend upward. It is mainly because that for the same  $\alpha$  the inclination wedge angle of the assumed 2D reflection,  $\alpha_n$  [see Fig.1] decreases with the increase of  $\beta$ . Therefore, the reflection of the Mach stem over the horizontal wedge is more likely a MR so that the first type of 3D Mach stem appears.



**Fig. 6 Shock wave reflection over two intersecting wedges for  $\alpha = \beta = 55^\circ$  and  $M_s = 3.0$**



**Fig.7 The region of three-dimensional Mach stem: a)  $M_s = 1.5$ ; and b)  $M_s = 3.0$**



## 5. Conclusions

The numerical results can be summarized as following:

1. It is found that there are two different kinds of 3D Mach stem structures for the MR–RR interaction, namely the first and the second types of 3D Mach stem, respectively.
2. The 3D Mach stem is a twist surface. If both wedge angles are relatively small, the 3D influence is relatively weak, and the 3D Mach stem twists slightly as a result. On the other hand, if the wedge angles are relatively great, the 3D influence is obvious to twist the 3D Mach stem much severely.
3. A 3D three-shock or four-shock configuration may occur in the intersecting corner. For the MR–MR interaction, the latter forms consisting of the incident shock wave, the 3D Mach stem, the primary and secondary reflected shock waves. In the RR–RR interaction, the incident shock wave, the primary and secondary reflected shock waves meet at the same reflection point to combine a three-shock configuration. For the MR–RR interaction, either of the configurations mentioned above may appear.

## Acknowledgments

The work is supported by Major Program of National Natural Science Foundation of China (90916028) and Main Direction Program of Knowledge Innovation of Chinese Academy of Sciences (KJCX2-EW-L05).

## References

- [1] Mach, E.: Über den Verlauf von Funkenwellen in der Ebene und im Raume. *Sitzungsbr Akad Wien* 78, 819–838 (1878)
- [2] von Neumann, J.: Oblique reflection of shocks, *Explos Res Rept* 12. Navy Dept Bureau of ordinance, Washington, DC (1943)
- [3] von Neumann, J.: Refraction, interaction and reflection of shock waves, *NAVORD Rep* 203-45. Navy Dept Bureau of ordinance,
- [4] Hornung, H.G., Oertel, H., Sandeman, R.J.: Transition to Mach reflexion of shock waves in steady and pseudosteady flow with and without relaxation. *J. Fluid Mech.* 90, 541–560 (1979)
- [5] Chpoun, A., Passerel, D., Li, H., Ben-Dor, G.: Reconsideration of oblique shock wave reflections in steady flows, Part 1. Experimental investigation. *J. Fluid Mech.* 301, 19–35 (1995)
- [6] Ivanov, M., Gimelshein, S., Beylich, A.: Hysteresis effect in stationary reflection of shock waves. *Phys. Fluids* 7, 685–687 (1995)
- [7] Hu, Z.M., Myong, R.S., Kim, M.S., Cho, T.H.: Downstream flow condition effects on the RR MR transition of asymmetric shock waves in steady flows. *J. Fluid Mech.* 620, 43–62 (2009)
- [8] Takayama, K.: Application of holographic interferometry to shock wave research. *Proc. SPIE* 398, 174–180 (1983) Washington, DC (1943)
- [9] Meguro, T., Takayama, K., Onodera, K.: Three-dimensional shockwave reflection over a corner of two intersecting wedges. *Shock Wave* 7, 107–121 (1997)
- [10] Li, H.H.: Experimental and numerical study on unsteady complex flow and wave interaction. PhD Thesis, University of Science and Technology of China, Hefei (2005)

# The distance sinh transformation for the numerical evaluation of nearly singular integrals over curved surface elements

\*Yu Miao<sup>1</sup>, Jiahe Lv<sup>1</sup>, Hongping Zhu<sup>1</sup>

<sup>1</sup>School of Civil Engineering and Mechanics, Huazhong University of Science and Technology, Wuhan 430074, China

\*Corresponding author: my\_miaoyu@163.com

## Abstract

This paper presents a new transformation termed as the distance sinh transformation for the numerical evaluation of nearly singular integrals arising in 3D BEM. The new transformation is an improvement of the previous sinh transformation. The original sinh transformation is only limited to planar elements. Moreover, when the nearly singular point is located outside the element, results obtained by the original sinh transformation combined with conventional subdivision method are not quite accurate. In the presented work, the sinh transformation combined with the distance function is proposed to overcome the drawbacks of the original sinh transformation. With the improved transformation, nearly singular integrals on the curved surface elements can be accurately calculated. Furthermore, an alternative subdivision method is proposed using an approximate nearly singular point, which is quite simple for programming and accurate results can be obtained. Numerical examples for both curved triangular and quadrangular elements are given to verify the accuracy and efficiency of the presented method.

**Keywords:** boundary element method, nearly singular integrals, numerical integration, distance function, sinh transformation

## Introduction

The implementation of the boundary element method (BEM) involves many numerical evaluations of line or surface integrals. For all the integrals, they can be categorized into three types depending on the position of the source point: non-singular integrals, singular integrals and nearly singular integrals. For non-singular integrals (the source point is away from the evaluation element), a straightforward application of Gaussian quadrature is sufficient to obtain accurate numerical values. For singular integrals (the source point is on the evaluation element), several transformation methods (Tanaka et al., 1994; Sladek, 1998; Guiggiani and Gigante, 1990; Guiggiani, 1992; Liu and Rudolphi, 1999; Liu, 2000; Gao, 2010) have been devised to improve the accuracy of the numerical evaluation. In this paper, the nearly singular integrals are concerned, which lie between the two types of integrals defined above as the source point is close to the interval of integration but not on it. Although the nearly singular integrals are actually regular in nature, they cannot be evaluated accurately by the standard Gaussian quadrature. The accurate numerical evaluation of nearly singular integrals plays an important role in many engineering applications. In general, these involve with the accurate solution near the boundary in potential and elasticity problems, such as the sensitivity problems (Zhang et al., 1999), unknowns around crack tips (Dirgantara and Aliabadi, 2000), contact problems (Aliabadi and Martin, 2000) and thin structures (Liu, 1998).

In the past decades, various numerical techniques have been proposed to remove the near singularities (Eberwien et al., 2005; Chen et al., 1995; Sladek et al., 1993; Zhou et al., 2008), among which the most popular approaches are based on the various nonlinear transformations, such as cubic polynomial transformation (Telles, 1987), coordinate optimization transformation (Sladek et al., 2000), rational transformation (Huang and Cruse, 1993), sigmoidal transformation (Johnston,

1999, 2000), distance transformation (Ma and Kamiya, 2001, 2002a, 2002b, 2003), the PART method (Hayami, 2005), exponential transformation (Zhang et al., 2009; Xie et al., 2011) and the sinh transformation (Johnston and Elliott, 2005; Elliott and Johnston, 2008; Johnston et al., 2007). The key aspect of the transformation methodology is to cluster more Gaussian points towards the ‘nearly singular point’ (the projection point of the source point to the element), which benefits from the strategies for singular integrals.

The previous sinh transformation, which automatically takes into account the position of the nearly singular point and the distance from source point to the element, is thought to be a promising method to deal with nearly singular integrals due to its high accuracy and straightforward implementation. However, the sinh transformation is only limited to planar elements so far. In this paper, we introduce the asymptotic distance function used in the distance transformation method into the sinh transformation. The combination of the distance function and the sinh transformation makes it suitable for curved surface elements. Besides, a new strategy using an approximate nearly singular point is proposed to deal with the case when the nearly singular point is located outside the element. Numerical results presented in this paper demonstrate the high efficiency and accuracy of the presented method.

This paper is organized as follows. The general forms of nearly singular integrals are described in Section 2. The sinh transformation using the distance function is developed in Section 3. Section 4 presents the subdivision method and a new simple and efficient method to deal with the case when the nearly singular point is located outside the element. Numerical examples for both curved triangular and quadrangular element are given in Section 5 to verify the efficiency and accuracy of presented method. The paper ends with conclusions in Section 6.

## General descriptions

Considering 3D potential problems in the domain  $\Omega$  enclosed by boundary  $\Gamma$ , the two boundary integrals concerned in the present work are written in the usual forms in terms of the potential  $u$  and the flux  $q$  on the boundary as follows:

$$c(\mathbf{y})u(\mathbf{y}) = \int_{\Gamma} q(\mathbf{x})u^*(\mathbf{x}, \mathbf{y})d\Gamma(\mathbf{x}) - \int_{\Gamma} u(\mathbf{x})q^*(\mathbf{x}, \mathbf{y})d\Gamma(\mathbf{x}) \quad (1)$$

$$c(\mathbf{y})u_k(\mathbf{y}) = \int_{\Gamma} q(\mathbf{x})u_k^*(\mathbf{x}, \mathbf{y})d\Gamma(\mathbf{x}) - \int_{\Gamma} u(\mathbf{x})q_k^*(\mathbf{x}, \mathbf{y})d\Gamma(\mathbf{x}) \quad (2)$$

where  $\mathbf{y}$  and  $\mathbf{x}$  are the source and the field point, respectively.  $c(\mathbf{y})$  is a coefficient depending on the smoothness of the boundary at  $\mathbf{y}$ .  $u^*(\mathbf{x}, \mathbf{y})$  represents the fundamental solution for 3D potential problems.

$$u^*(\mathbf{x}, \mathbf{y}) = \frac{1}{4\pi} \frac{1}{r(\mathbf{x}, \mathbf{y})} \quad (3)$$

and  $u_k^*(\mathbf{x}, \mathbf{y})$ ,  $q^*(\mathbf{x}, \mathbf{y})$  and  $q_k^*(\mathbf{x}, \mathbf{y})$  are the derived fundamental solutions

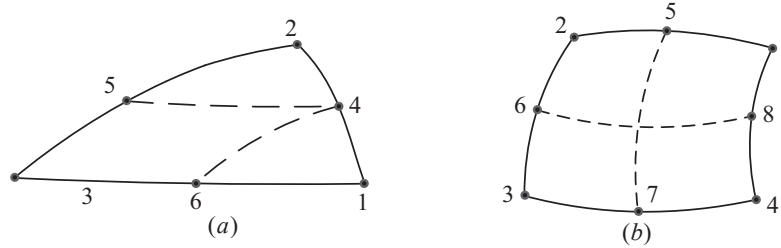
$$u_k^*(\mathbf{x}, \mathbf{y}) = \frac{\partial u^*(\mathbf{x}, \mathbf{y})}{\partial x_k}, \quad q^*(\mathbf{x}, \mathbf{y}) = \frac{\partial u^*(\mathbf{x}, \mathbf{y})}{\partial \mathbf{n}}, \quad q_k^*(\mathbf{x}, \mathbf{y}) = \frac{\partial q^*(\mathbf{x}, \mathbf{y})}{\partial x_k} \quad (4)$$

where  $r$  denotes the Euclidean distance between the source and the field point and  $\mathbf{n}$  is the unit outward normal on the boundary. When the source point  $\mathbf{y}$  moves towards the boundary, the boundary integrals in Eqs. (1) and (2) become nearly singular with different orders, namely, the nearly weak singularity with kernel  $u^*$ , the nearly strong singularity with the kernels  $q^*$  and  $u_k^*$  and the nearly hyper-singularity with the kernels  $q_k^*$ . After the boundary discretization and the coordinate transformation to the local system, the boundary integrals can be generalized into the following form:

$$I = \int_{-1}^{+1} \int_{-1}^{+1} \frac{f(\xi_1, \xi_2)}{r^\chi} d\xi_1 d\xi_2 \quad (5)$$

where  $\chi$  denotes the orders of singularities,  $\chi=1,2,3$  and  $f(\xi_1, \xi_2)$  is a well-behaved function, consisting of the shape function, Jacobian and coefficients from the derivation of the kernels.

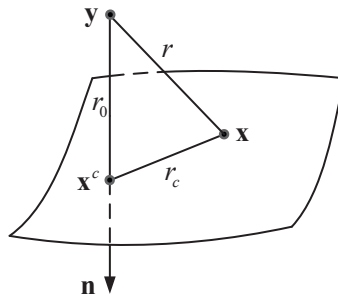
In this paper, both curved triangular and quadrangular elements are considered. The distributions of element nodes are shown in Fig.1. For each element, the global coordinates are interpolated through coordinates of the element nodes by the shape functions, which can be found in reference (Brebbia et al., 1984).



**Fig. 1 Curved surface element: (a) triangular element; (b) quadrangular element**

**Sinh transformation using distance function**

*Distance function*



**Fig. 2 The projection from the source point  $y$  to the curved element**

In this section, we will briefly review the asymptotic distance function defined in the local coordinate system  $(\rho, \theta)$ , which has been used to deal with nearly singular integrals successfully. Firstly, the projection from the source point  $y$  to the element is taken as shown in Fig. 2, where  $x^c$  is the projection point, herein we call it ‘the nearly singular point’ and  $r_0$  is the minimum distance from the source point to the element. By employing the one-order Taylor expansion in the neighborhood of the nearly singular point  $x^c$ , we have

$$\begin{aligned} x_k - y_k &= x_k - x_k^c + x_k^c - y_k \\ &= \frac{\partial x_k}{\partial \xi_1} \Big|_{\xi_1=c_1} (\xi_1 - c_1) + \frac{\partial x_k}{\partial \xi_2} \Big|_{\xi_2=c_2} (\xi_2 - c_2) + r_0 n_k(c_1, c_2) + O(\rho^2) \\ &= \rho A_k(\theta) + r_0 n_k(c_1, c_2) + O(\rho^2) \end{aligned} \quad (6)$$

where

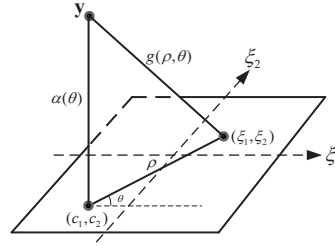
$$A_k(\theta) = \frac{\partial x_k}{\partial \xi_1} \Big|_{\xi_1=c_1} \cos \theta + \frac{\partial x_k}{\partial \xi_2} \Big|_{\xi_2=c_2} \sin \theta \quad (7)$$

and

$$\xi_1 = c_1 + \rho \cos \theta, \quad \xi_2 = c_2 + \rho \sin \theta \quad (8)$$



where  $(c_1, c_2)$  are the local coordinates of the nearly singular point  $\mathbf{x}^c$  as shown in Fig. 3.



**Fig. 3 The distance function  $g(\rho, \theta)$  in the local parametric system**

With the relation of Eq. (6), the real distance between the source and field points can be written in the following asymptotic form:

$$\begin{aligned} r^2(\rho, \theta) &= r_0^2 + \rho^2 A^2(\theta) + 2r_0 A_k(\theta) n_k(c_1, c_2) + O(\rho^3) \\ &= A^2(\theta) [\alpha^2(\theta) + \rho^2] + O(\rho^3) \end{aligned} \quad (9)$$

with

$$A(\theta) = \sqrt{A_k(\theta) A_k(\theta)} \quad (10)$$

$$\alpha(\theta) = \frac{r_0}{A(\theta)} \quad (11)$$

From Eq. (9), it can be found that the near singularities arise only in the radial direction in the polar system. To apply the distance function, the integration region should be split into sub-triangles at the nearly singular point in the local parametric system, which will be introduced in details in Section 4.

#### General Format Requirements

Using the distance function mentioned above, Eq. (5) can be rewritten as

$$I = \sum_{i=1}^n \int_{\theta_1}^{\theta_2} \int_0^{\rho_m(\theta)} \frac{f(\rho, \theta)}{A^z(\theta) [\alpha^2(\theta) + \rho^2]^{z/2}} \rho d\rho d\theta \quad (12)$$

where  $n$  is the total number of sub-triangles, and  $\theta_1$ ,  $\theta_2$  and  $\rho_m(\theta)$  represent the radial and the angular span for each sub-triangle, respectively. Note that the integrals all contain an argument of the form  $\alpha^2(\theta) + \rho^2$ , the previous sinh transformation can be applied in a straightforward fashion in the radial direction as follows:

$$\rho(s) = b \sinh(\mu_1 s - \eta_1) \quad (13)$$

where  $b$  is the minimum distance  $\alpha(\theta)$  in the local parametric system, and mapping  $[0, \rho_m(\theta)]$  into  $[-1, 1]$  gives

$$\mu_1 = -\eta_1 = \frac{1}{2} \operatorname{arcsinh} \frac{\rho_m(\theta)}{b} \quad (14)$$

Substituting the transformation of Eq. (13) into Eq. (12) yields

$$I = \sum_{i=1}^n \frac{b^{2-z} (\theta_2 - \theta_1)}{2} \int_{-1}^1 \int_{-1}^1 \frac{\mu_1 \sinh(\mu_1 s - \eta_1) f(s, \theta)}{A^z(\theta) \cosh^{z-1}(\mu_1 s - \eta_1)} ds d\phi \quad (15)$$

For the singular integrals of high order, a second sinh transformation is necessary, and a new variable  $u$  is introduced which satisfies

$$s(u) = a_1 + b_1 \sinh(\mu_2 u - \eta_2) \quad (16)$$

with  $a_1 = \frac{\eta_1}{\mu_1} = -1$  and  $b_1 = \frac{\pi}{2\mu_1}$ . Mapping  $-1 \leq u \leq 1$  into  $-1 \leq s \leq 1$  gives

$$\mu_2 = \frac{1}{2} \left( \operatorname{arcsinh} \frac{1+a_1}{b_1} + \operatorname{arcsinh} \frac{1-a_1}{b_1} \right) = \frac{1}{2} \operatorname{arcsinh} \frac{2}{b_1} \quad (17)$$

$$\eta_2 = \frac{1}{2} \left( \operatorname{arcsinh} \frac{1+a_1}{b_1} - \operatorname{arcsinh} \frac{1-a_1}{b_1} \right) = -\frac{1}{2} \operatorname{arcsinh} \frac{2}{b_1} \quad (18)$$

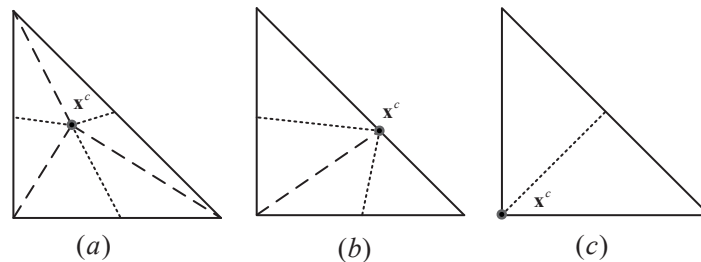
After the one or second sinh transformation, the kernel function has been transformed into a smooth one and the Gaussian quadrature can be used directly. Therefore, by combining the distance function, the sinh transformation will be suitable for curved boundary elements.

### Subdivision into sub-triangles

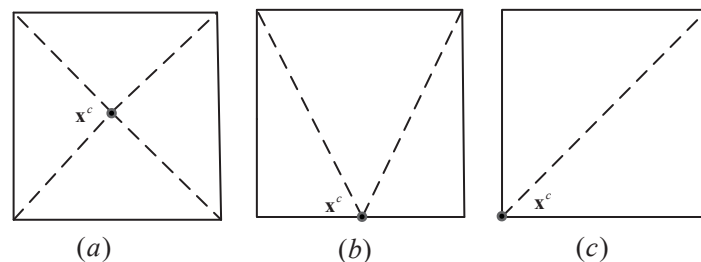
Before performing the sinh transformation, the integration region should be split into sub-triangles depending on the position of the nearly singular point in the parametric plane. We categories into two cases: case (i) the nearly singular point is located inside the element or on the sides/vertices of the element; case (ii) the nearly singular point is located outside the element. The subdivision method is described as follows.

#### Subdivision for case (i)

For triangular elements, when the nearly singular point is located inside the element, we initially split the triangle into three sub-triangles at the nearly singular point by drawing lines from the nearly singular point to each vertex of the triangle. If the sub-triangles contains angles greater than  $2\pi/3$ , poor result may be obtained (Scuderi, 2008). Therefore, we split these sub-triangles again by drawing lines from the nearly singular point to the midpoint of each side to ensure that every angle is less than  $2\pi/3$ . Similar results can be obtained when the nearly singular point is located on one of the sides or vertices as shown in Fig. 4. For quadrangular elements, we just connect the nearly singular point with the vertices as shown in Fig. 5, which is enough for the evaluation of nearly singular integrals.



**Fig. 4** Subdivision into sub-triangles for triangular elements when the nearly singular point is located (a) inside the element; (b) on one side; (c) on one vertex

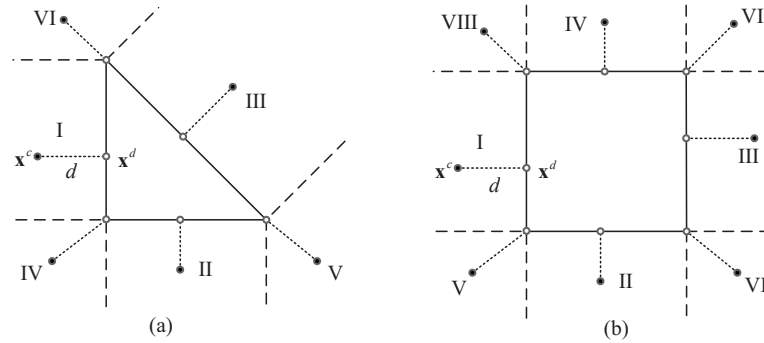


**Fig. 5** Subdivision into sub-triangles for quadrangular elements when the nearly singular point is located (a) inside the element; (b) on one side; (c) on one vertex

#### Subdivision for case (ii)

For the case when the nearly singular point is located outside the element, only a few literatures have been involved. The result obtained by the conventional subdivision method is not quite accurate. In this paper, an alternative method is proposed here using an approximate nearly singular point  $\mathbf{x}^d$ . The point  $\mathbf{x}^d$  is the nearest point from the nearly singular point  $\mathbf{x}^c$  to the element in the

parametric plane as shown in Fig. 6. For triangular elements, when  $\mathbf{x}^c$  is located in region I-III,  $\mathbf{x}^d$  is on the sides of the triangle, and on the vertices with region IV-VI. Similarly for quadrangular elements, when  $\mathbf{x}^c$  is located in region I-IV,  $\mathbf{x}^d$  is on the sides of the quadrangle, and on the vertices with region V-VIII. Then we use  $\mathbf{x}^d$  to subdivide the triangle element as mentioned in Section 4.1 instead of the nearly singular point  $\mathbf{x}^c$ , and the corresponding transformations can be applied in a straight fashion without introducing extra subdivision method. Therefore, this method is quite simple for programming and accurate results can be obtained as proved in Section 5.



**Fig. 6** The position of the approximate nearly singular point  $\mathbf{x}^d$

### Numerical examples

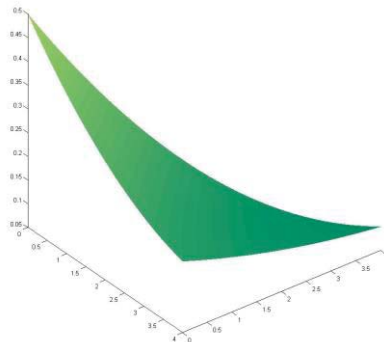
In this section, numerical examples for curved triangular and quadrangular elements are presented to verify the accuracy and efficiency of presented method. The relative distance from the nearly singular point to the element is given in terms of  $r_0/a^{1/2}$ , where  $r_0$  is the minimum distance as shown in Fig. 2 and  $a$  stands for the area of the element.  $r_0/a^{1/2}$  varies from  $10^{-1}$  to  $10^{-6}$ , which is thought to be enough for general computational applications. For the purpose of error estimation, the relative error is defined as follows:

$$\text{error} = \left| \frac{I_{num} - I_{ref}}{I_{ref}} \right| \quad (19)$$

where the subscripts *num* and *ref* refer to the numerical and reference solutions, respectively. The reference solutions are obtained by subdivision method with enough sub-elements and denoted as ‘Refer’ in the tables. Results obtained by one and second sinh transformation are denoted by ‘sinh1’ and ‘sinh2’, respectively. For each sub-triangle,  $10 \times 10$  Gaussian points are always used for the convenience of comparisons.

#### Example for curved triangular element

The first example considers nearly singular integrals on a curved triangular element with the node coordinates of  $(4.0, 0.0, 0.2)$ ,  $(0.0, 4.0, 0.0)$ ,  $(0.0, 0.0, 0.5)$ ,  $(2.0, 2.0, 0.1)$ ,  $(0.0, 2.0, 0.2)$ ,  $(2.0, 0.0, 0.3)$  as shown in Fig. 7. Two cases are discussed here regarding the position of the nearly singular point, namely, being inside and outside the element.



**Fig. 7 Curved triangular element**

For the first case, the nearly singular point is set at  $(0.2, 0.4)$  and the results obtained using sinh1 and sinh2 transformation with kernels  $u^*$ ,  $q^*$  and  $1/r^3$  are presented in Table 1. It can be found that for kernel  $u^*$ , the results obtained by sinh1 transformation is superior to that by sinh2 transformation. However, for kernels  $q^*$  and  $1/r^3$ , the sinh2 transformation is a better choice.

**Table 1 The relative errors of various nearly singular integrals over a curved triangular element when the source point is located inside the element**

Kernel	method	$10^{-1}$	$10^{-2}$	$10^{-3}$	$10^{-4}$	$10^{-5}$	$10^{-6}$
$u^*$	refer	0.62423927	0.73591934	0.74835201	0.74960801	0.74973374	0.74974631
	sinh1	1.9374E-10	7.6664E-10	9.0941E-10	4.0908E-09	3.2278E-08	1.5884E-07
	sinh2	2.0888E-10	3.7089E-08	2.5609E-06	4.2126E-05	3.1525E-04	1.4129E-03
$q^*$	refer	0.40331398	0.49728797	0.50695031	0.50791634	0.50801296	0.50802260
	sinh1	1.2967E-08	1.1528E-06	3.2355E-05	3.1065E-05	6.9237E-04	1.8707E-03
	sinh2	1.4616E-08	9.6723E-09	9.0818E-09	3.8001E-07	3.8444E-06	1.9117E-05
$1/r^3$	refer	17.6193421	216.651450	2207.92015	22120.57540	221247.13217	2212512.5976
	sinh1	1.3103E-08	1.1715E-06	3.2873E-05	3.1563E-05	7.0348E-04	1.9007E-03
	sinh2	1.4773E-08	9.6699E-09	6.0897E-10	8.3036E-09	8.7896E-08	1.3742E-07

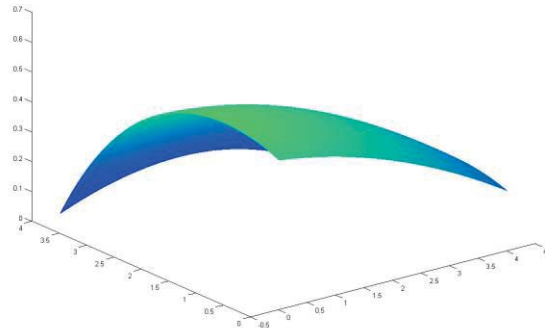
For the case when the nearly singular point is located outside the element, the nearly singular point is set at  $(-d, 0.5)$  and  $d$  is the minimum distance from the nearly singular point to the element as shown in Fig. 6. The results for various kernels with  $d = 0.1$  are given in Table 2. It can be seen that the proposed method to deal with the case when the nearly singular point is located outside element can get results with high precision, and for most cases, the results using sinh1 transformation are more accurate than that using sinh2 transformation.

**Table 2 The relative errors of various nearly singular integrals over a curved triangular element when the source point is located outside the element**

Kernel	method	$10^{-1}$	$10^{-2}$	$10^{-3}$	$10^{-4}$	$10^{-5}$	$10^{-6}$
$u^*$	refer	0.37206522	0.38178685	0.38181338	0.38180558	0.38180469	0.38180460
	sinh1	8.3749E-09	6.3887E-08	1.7829E-06	1.3955E-05	4.5094E-05	8.8765E-05
	sinh2	8.2805E-09	4.7014E-07	2.6679E-05	1.3762E-04	2.1755E-03	2.1777E-03
$q^*$	refer	0.07217142	0.01179206	0.00435905	0.00361427	0.00353980	0.00353235
	sinh1	1.0874E-07	2.5503E-06	4.1329E-06	4.6519E-05	4.5640E-05	2.9761E-04
	sinh2	1.0886E-07	1.0916E-05	3.1887E-04	3.4804E-04	1.6971E-04	1.2231E-03
$1/r^3$	refer	3.05253376	3.65695755	3.66185129	3.66161112	3.66157979	3.66157659
	sinh1	1.1426E-07	3.3912E-06	6.1869E-05	2.0772E-04	1.0925E-03	2.2873E-03
	sinh2	1.1440E-07	1.7043E-05	1.7932E-03	1.0238E-02	9.2299E-03	5.4256E-02

*Example for curved quadrilateral element*

The second example is computed over a curved quadrangular element with the node coordinates of (4.0, 4.0, 0.0), (0.0, 4.0, 0.0), (0.0, 0.0, 0.5), (4.0, 0.0, 0.2), (2.0, 3.9, 0.1), (-0.2, 2.0, 0.5), (2.0, 0.0, 0.4), (4.1, 2.0, 0.2) as shown in Fig. 8. Both the two cases are also concerned.



**Fig.8 Curved quadrangular element**

For the case when the nearly singular point is located inside the element, the nearly singular point is set at (-0.2, -0.6) and the results for various kernels are presented in Table 3. It can be seen that the results for kernel  $u^*$  obtained by sinh1 transformation is better than that by sinh2 transformation, and for kernels  $q^*$  and  $1/r^3$ , the sinh2 transformation can get more accurate results.

**Table 3 The relative errors of various nearly singular integrals over a curved quadrangular element when the source point is located inside the element**

Kernel	method	$10^{-1}$	$10^{-2}$	$10^{-3}$	$10^{-4}$	$10^{-5}$	$10^{-6}$
$u^*$	refer	0.85787103	1.02434449	1.04361476	1.04556977	1.04576555	1.04578513
	sinh1	1.4526E-07	1.8954E-08	3.1568E-07	5.8132E-07	1.9679E-06	3.9409E-06
	sinh2	1.5184E-07	3.7891E-07	4.1950E-06	8.0223E-05	2.1642E-04	1.0194E-04
$q^*$	refer	0.35050303	0.45562629	0.46704265	0.46818740	0.46830190	0.46831335
	sinh1	5.1083E-07	1.8517E-04	3.8064E-04	5.6334E-03	1.4731E-02	1.8315E-02
	sinh2	3.1023E-07	1.4415E-05	2.2084E-05	5.1677E-05	1.7026E-04	3.1543E-04
$1/r^3$	refer	11.4261730	149.337947	1531.96178	15358.37597	153622.53328	1536264.1079
	sinh1	4.7511E-07	1.7337E-04	3.5653E-04	5.2763E-03	1.3797E-02	1.7153E-02
	sinh2	2.8456E-07	1.3418E-05	1.7840E-05	6.5683E-05	2.0609E-04	3.5843E-04

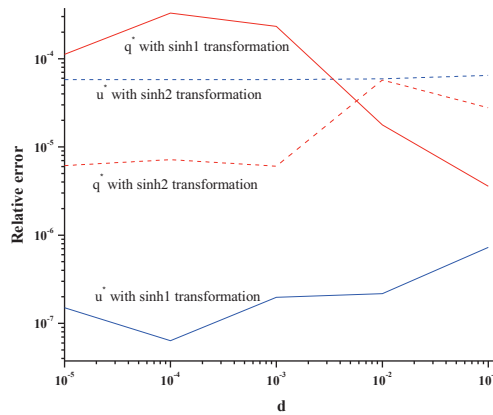
For the case when the nearly singular point is located outside the element, the nearly singular point is set at  $(1.0+d, 0.5)$  with  $d=0.1$ . The results for various kernels are given in Table 4. It can be concluded that the results for kernel  $u^*$  with sinh1 transformation is more accurate than that with sinh2 transformation. For kernel  $q^*$  and  $1/r^3$ , the results using sinh2 transformation are not as accurate as that using sinh1 transformation with  $r_0/a^{1/2}$  taking small values.

**Table 4 The relative errors of various nearly singular integrals over a curved quadrangular element when the source point is located outside the element**

Kernel	method	$10^{-1}$	$10^{-2}$	$10^{-3}$	$10^{-4}$	$10^{-5}$	$10^{-6}$
$u^*$	refer	0.58239266	0.62119294	0.62215256	0.62220180	0.62220626	0.62220670
	sinh1	5.5909E-08	5.4109E-08	7.2809E-07	6.6869E-08	2.2454E-05	2.2357E-05
	sinh2	5.7576E-08	3.5743E-06	6.4681E-05	3.2791E-04	5.5464E-04	3.0197E-03
$q^*$	refer	0.11681569	0.01239683	-0.01057018	-0.01290526	-0.01313883	-0.01316219
	sinh1	1.5373E-07	9.1195E-07	3.5908E-06	1.6050E-05	6.5228E-05	1.8545E-04

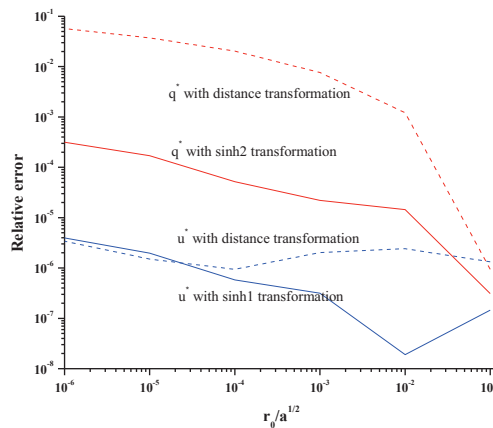
	sinh2	9.0428E-09	1.1085E-06	2.7760E-05	3.9627E-04	4.1489E-03	1.1711E-02
	refer	3.93249565	7.84157965	7.96907648	7.97201744	7.97221064	7.97222895
$1/r^3$	sinh1	1.3825E-07	4.4342E-07	2.9246E-05	2.6529E-04	4.3765E-04	2.4518E-03
	sinh2	7.4747E-09	1.8330E-07	2.3143E-04	1.0477E-03	5.5189E-03	4.7030E-02

In order to investigate the influence of  $d$ , nearly singular integrals with kernels  $u^*$  and  $q^*$  are evaluated as  $d$  varies from  $10^{-1}$  to  $10^{-5}$ .  $r_0/a^{1/2}$  is taken as  $10^{-3}$  and the results are plotted in Fig. 9. It can be observed that for kernel  $u^*$ , the sinh1 transformation can always get superior results. However, for kernel  $q^*$ , the sinh1 transformation can get better results when  $d \geq 10^{-2}$ , and as  $d$  becomes smaller, the sinh2 transformation is more competitive. Besides, both the two transformations can get acceptable results, which prove the stability and efficiency of the proposed method.



**Fig. 9** The relative errors for kernels  $u^*$  and  $q^*$  as  $d$  varies from  $10^{-1}$  to  $10^{-5}$

*Comparisons with distance transformation method*



**Fig. 10** Comparisons with the distance transformation method

In this section, comparisons with the distance transformation method are carried out for kernels  $u^*$  and  $q^*$  when the nearly singular point is located at  $(-0.2, -0.6)$ . The results for various values of  $r_0/a^{1/2}$  using different transformations are plotted in Fig. 10. It can be seen that for kernel  $u^*$ , as  $r_0/a^{1/2} \geq 10^{-4}$ , better results can be obtained using the sinh1 transformation, and results of the same

accuracy can also be got when  $r_0/a^{1/2}$  takes values of  $10^{-5}$  or  $10^{-6}$  compared with the distance transformation method. For kernel  $q^*$ , the sinh2 transformation is obviously superior to the distance transformation.

## Conclusions

In this paper, the previous sinh transformation based on the distance function is developed for the curved surface elements, which automatically takes into account the minimum distance from the source point to the element in the local parametric system. A new simple and efficient subdivision method is proposed to deal with the case when the nearly singular point is located outside the element. Numerical examples for both curved triangular and quadrangular elements are presented to validate the accuracy and efficiency of the proposed method. Comparisons with the distance transformation method are also performed to show the competitiveness of the sinh transformation. When the source point is located on the tangential plane, the distance from the source point to the element is 0. The sinh transformation cannot handle with this case so far, which will be the sequence work in the future.

## References

- Tanaka, M., Sladek, V., & Sladek, J. (1994). Regularization techniques applied to boundary element methods. *Applied Mechanics Reviews*, 47, 457.
- Sladek, V., & Sladek, J. (1998). *Singular integrals in boundary element methods*. Southampton: Computational Mechanics Publications.
- Guiggiani, M., & Gigante, A. (1990). A general algorithm for multidimensional Cauchy principal value integrals in the boundary element method. *Journal of Applied Mechanics*, 57(4), 906-915.
- Guiggiani, M., Krishnasamy, G., Rudolphi, T. J., & Rizzo, F. J. (1992). A general algorithm for the numerical solution of hypersingular boundary integral equations. *Journal of applied mechanics*, 59, 604.
- Liu, Y. J., & Rudolphi, T. J. (1999). New identities for fundamental solutions and their applications to non-singular boundary element formulations. *Computational mechanics*, 24(4), 286-292.
- Liu, Y. J. (2000). On the simple-solution method and non-singular nature of the BIE/BEM—a review and some new results. *Engineering analysis with boundary elements*, 24(10), 789-795.
- Gao, X. W. (2010). An effective method for numerical evaluation of general 2D and 3D high order singular boundary integrals. *Computer methods in applied mechanics and engineering*, 199(45), 2856-2864.
- Zhang, D., Rizzo, F. J., & Rudolphi, T. J. (1999). Stress intensity sensitivities via Hypersingular boundary integral equations. *Computational mechanics*, 23(5-6), 389-396.
- Dirgantara, T., & Aliabadi, M. H. (2000). Crack growth analysis of plates loaded by bending and tension using dual boundary element method. *International journal of fracture*, 105(1), 27-47.
- Aliabadi, M. H., & Martin, D. (2000). Boundary element hyper - singular formulation for elastoplastic contact problems. *International Journal for Numerical Methods in Engineering*, 48(7), 995-1014.
- Liu, Y. J. (1998). Analysis of shell-like structures by the boundary element method based on 3-D elasticity: formulation and verification. *International Journal for Numerical Methods in Engineering*, 41(3), 541-558.
- Eberwien, U., Duenser, C., & Moser, W. (2005). Efficient calculation of internal results in 2D elasticity BEM. *Engineering analysis with boundary elements*, 29(5), 447-453.
- Chen, H. B., Lu, P., Huang, M. G., & Williams, F. W. (1998). An effective method for finding values on and near boundaries in the elastic BEM. *Computers & structures*, 69(4), 421-431.
- Sladek, V., Sladek, J., & Tanaka, M. (1993). Regularization of hypersingular and nearly singular integrals in the potential theory and elasticity. *International Journal for Numerical Methods in Engineering*, 36(10), 1609-1628.
- Zhou, H., Niu, Z., Cheng, C., & Guan, Z. (2008). Analytical integral algorithm applied to boundary layer effect and thin body effect in BEM for anisotropic potential problems. *Computers & Structures*, 86(15), 1656-1671.
- Telles, J. C. F. (1987). A self - adaptive co - ordinate transformation for efficient numerical evaluation of general boundary element integrals. *International Journal for Numerical Methods in Engineering*, 24(5), 959-973.
- Sladek, V., Sladek, J., & Tanaka, M. (2000). Optimal transformations of the integration variables in computation of singular integrals in BEM. *International journal for numerical methods in engineering*, 47(7), 1263-1283.
- Huang, Q., & Cruse, T. A. (1993). Some notes on singular integral techniques in boundary element analysis. *International journal for numerical methods in engineering*, 36(15), 2643-2659.

- Johnston, P. R. (1999). Application of sigmoidal transformations to weakly singular and near - singular boundary element integrals. *International journal for numerical methods in engineering*, 45(10), 1333-1348.
- Johnston, P. R. (2000). Semi - sigmoidal transformations for evaluating weakly singular boundary element integrals. *International journal for numerical methods in engineering*, 47(10), 1709-1730.
- Ma, H., & Kamiya, N. (2001). A general algorithm for accurate computation of field variables and its derivatives near the boundary in BEM. *Engineering analysis with boundary elements*, 25(10), 833-841.
- Ma, H., & Kamiya, N. (2002a). Distance transformation for the numerical evaluation of near singular boundary integrals with various kernels in boundary element method. *Engineering analysis with boundary elements*, 26(4), 329-339.
- Ma, H., & Kamiya, N. (2002b). A general algorithm for the numerical evaluation of nearly singular boundary integrals of various orders for two-and three-dimensional elasticity. *Computational mechanics*, 29(4-5), 277-288.
- Ma, H., & Kamiya, N. (2003). Nearly singular approximations of CPV integrals with end-and corner-singularities for the numerical solution of hypersingular boundary integral equations. *Engineering analysis with boundary elements*, 27(6), 625-637.
- Hayami, K. (2005). Variable transformations for nearly singular integrals in the boundary element method. *Publications of the Research Institute for Mathematical Sciences*, 41(4), 821-842.
- Zhang, Y. M., Gu, Y., & Chen, J. T. (2009). Boundary layer effect in BEM with high order geometry elements using transformation. *Computer Modeling in Engineering and Sciences (CMES)*, 45(3), 227.
- Xie, G., Zhang, J., Qin, X., & Li, G. (2011). New variable transformations for evaluating nearly singular integrals in 2D boundary element method. *Engineering Analysis with Boundary Elements*, 35(6), 811-817.
- Johnston, P. R., & Elliott, D. (2005). A sinh transformation for evaluating nearly singular boundary element integrals. *International journal for numerical methods in engineering*, 62(4), 564-578.
- Elliott, D., & Johnston, P. R. (2008). The iterated sinh transformation. *International journal for numerical methods in engineering*, 75(1), 43-57.
- Johnston, B. M., Johnston, P. R., & Elliott, D. (2007). A sinh transformation for evaluating two - dimensional nearly singular boundary element integrals. *International journal for numerical methods in engineering*, 69(7), 1460-1479.
- Brebbia, C. A., Telles, J. C. F., & Wrobel, L. C. (1984). *Boundary element techniques: theory and applications in engineering* (Vol. 5). Berlin: Springer-Verlag.
- Scuderi, L. (2008). On the computation of nearly singular integrals in 3D BEM collocation. *International journal for numerical methods in engineering*, 74(11), 1733-1770.



## Numerical Simulation of Rigid Wheel Running Behavior on Sand Terrain

\*Mengyan Zang<sup>1</sup>, Chunlai Zhao<sup>1</sup>

<sup>1</sup>School of Mechanical & Automotive Engineering, South China University of Technology, Guangzhou, Guangdong 510640

\*Corresponding author: myzang@scut.edu.cn

### Abstract

The 3D discrete element method (DEM) and finite element method (FEM) were combined together to investigate the running behavior of rigid wheel on sand terrain. Firstly, an efficient method for the initial generation of discrete elements (DEs) which is suitable for the simulation of sand terrain was introduced. Then, the DEs were consolidated to a steady state to model the real condition of sand terrain. Afterwards, a 3D numerical model was established based on the soil bin experiment to model the running behaviour of the rigid wheel travelling from hard terrain to sand terrain, where the wheel, the hard terrain and the soil bin were solved by using FEM. Finally, a constant angular velocity and corresponding translational velocity were loaded to the rigid wheel to investigate its running behavior under different slip ratios. Corresponding running behavior parameters like net draw bar pull and sinkage were obtained. The overall trend of net draw bar pull versus slip ratio is qualitatively in agreement with current experimental results.

**Keywords:** DEM; FEM; running behavior; sand terrain; rigid wheel

### 1 Introduction

Off-road vehicles, which have been widely used in agricultural production, planetary exploration, and military field, usually work on discontinuous granular road such as sand terrain. The deformation and destruction of the soft road have large effects on the traction performance of vehicles. Thus, the research of the wheel-road system interactions is significant to the parameter match and design of off-road vehicles. Many researchers (Robert, Winnie and Tim 2005; Yang, Xu, Liang, Zhang, et al, 2011; Maciejewski and Jarzebowski, 2004; Hisanori, Nakashima, Takatsu, et al, 2010) had been working on this filed via experimental methods, but these methods have shortcomings like long development time and expensive cost. Recently, with the rapid development of computer technology, simulation methods had been widely used in the research of this filed.

Finite element method (FEM) as a traditional simulation method has been used by many researchers. And many achievements have been reported in various literatures. For example, in order to simulate the deformation behavior of soft terrain under a rolling wheel, Hiroma, Wanjii, Kataoka, et al (1998) regarded the soft soil as viscoelastic material; LIU and Wong (1996) implemented a modified critical state model in conjunction with a new nonlinear elastic law into the general purpose finite element program MARC; Xia (2011), Xia and Yang, (2012) took the soil as elastoplastic material and implemented the Drucker-Prager/Cap model into ABQUS as a user subroutine. Moreover, Hambleton and Drescher (2008 and 2009) analyzed the running behavior of the rigid wheel travels from hard terrain to soft terrain, where the two kinds of road were modeled by elastoplastic material with different material parameters. Although these studies used different materials to model the soft terrain, the traditional FEM technology is unable to describe the discontinuous features of granular materials such as sand terrain with sufficient accuracy. Moreover, the effect of the tread pattern on traction performance is also unable to be described clearly by FEM.

On the contrary, the discrete element method (DEM) shows a clear advantage to handle such problems. For example, Lav, Vilas, Salokhe, et al (2007) applied DEM to the investigation of the running performance of smooth rigid wheel rolling on coarse sand and medium sand under different vertical load conditions, Nakashima, Fujii, Oida, et al (2007 and 2010) and Li, Huang, Cui, et al

(2010) investigated the running behavior between lugged wheel and lunar regolith via 2D DEM. For further research, Zhang, Liu, Zeng, et al (2012), Knuth, Johnson, Hopkins, et al (2012) used 3D DEM to analyze the interaction between planet rover wheels and martain terrain. However, in these studies, the wheels, wheel lugs and granular terrain were all modeled by DEM, therefore, the deformation and the complex tread pattern structure of the tire could not be simulated reasonably.

Nakashima and Oida (2004), Nakashima, Takatsu, Shinone (2009) and Nakashima, Takatsu (2008) used the 2D finite element and discrete element method (FE-DEM) to investigate the wheel traction performance on sand terrain, where the rigid wheel was discretized by FEs and the sand terrain was modeled via DEs. This method compensated for the demerits of the two methods. However, it is obvious that the complex behaviors such as lateral force and steering performance of a rolling wheel are unable to be described by the current 2D method.

The purpose of this study is to apply 3D FE-DEM to the investigation of the wheel traction performance on sand terrain. Related program code is developed based on FORTRAN95 language. The numerical model of rigid wheel rolling from hard terrain to soft sand terrain is established based on the soil bin experiment, where the wheel, hard terrain and soil bin are all discretized by FEM, the sand terrain is modeled by DEM. The running behaviors of the rigid wheel under different slip ratios are analyzed.

This paper is organized as follows: in the next section, the basic equations of FE-DEM, including the motion equations of elements and the interaction forces among elements are introduced. The concept of analysis for the wheel-sand interaction in FE-DEM is also illustrated. Sect.3 illustrates an efficient way for the initial generation of the DEs which is suitable for sand simulation and the consolidation process of the DEs under self-weight is also shown. Sect. 4 presents the numerical model of the wheel-sand interaction system. The traveling process of the wheel under different slip ratios is modeled. And corresponding results are also illustrated and analyzed in this section.

## 2. The FE-DEM algorithm introduced

### 2.1 Equations of motion

For the 3D FE-DEM algorithm, the motions of the DEs and FEs are governed by the second Newton's law. For arbitrary element  $i$ , the equations are expressed by Eq. (1) (used for both DEs and FEs) and Eq. (2) (only used for DEs).

$$m_i(d^2\mathbf{u}_i / dt^2) = \mathbf{F}_i \quad (1)$$

$$I_i(d^2\boldsymbol{\theta}_i / dt^2) = \mathbf{M}_i \quad (2)$$

Where  $m_i$  and  $I_i$  are the mass and inertia moment of element  $i$ , respectively;  $\mathbf{u}_i$  and  $\boldsymbol{\theta}_i$  are the displacement and the rotation angle of element  $i$ , respectively;  $\mathbf{F}_i$  and  $\mathbf{M}_i$  are the total external force and centroidal moment of element  $i$ , respectively.

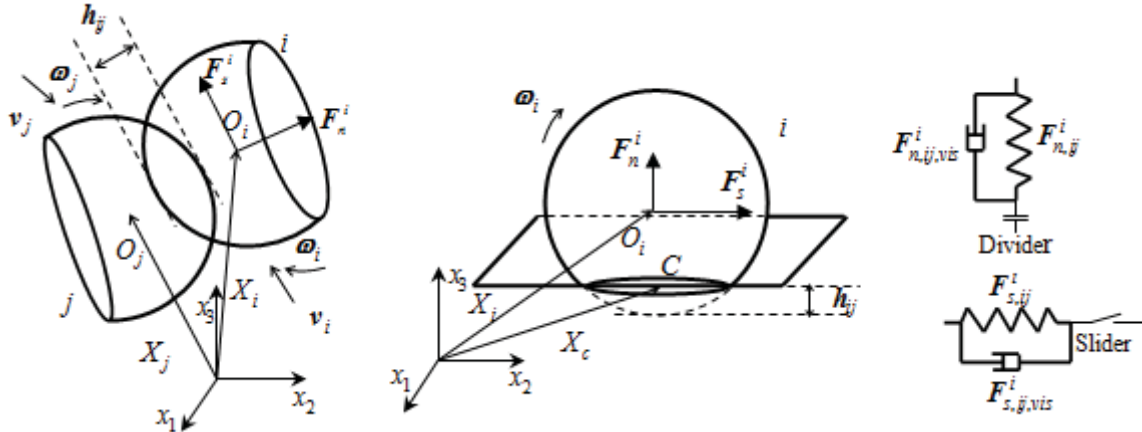
### 2.2 Interactions among elements and the wheel-sand system

Contact detection is the prerequisite for the calculation of interaction forces among elements. In this study, the C-grid detection method proposed by Williams, Perkins and Cook (2004) is used for DEs, and contact algorithm between 3D DEs and FEs has been previously developed by the authors (Zang, Gao, Lei, 2011). The contact models for elements are shown in Fig. 1. Where  $h_{ij}$  is the overlap of contacting elements;  $\mathbf{v}_i, \mathbf{v}_j, \boldsymbol{\omega}_i, \boldsymbol{\omega}_j$  are the velocity and angular velocity of element  $i$  and  $j$ , respectively;  $\mathbf{F}_n^i$  is the normal force, and  $\mathbf{F}_s^i$ , taken Coulomb friction law into account, is the tangential force of element  $i$ , which can be obtained from Eq. (3) and Eq. (4).

$$\mathbf{F}_n^i = \mathbf{F}_{n,ij}^i + \mathbf{F}_{n,ij,vis}^i \quad (3)$$

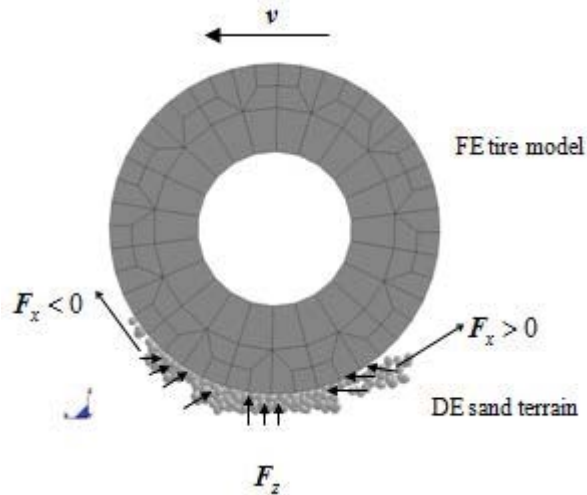
$$F_s^i = \begin{cases} F_{s,ij}^i + F_{s,ij,vis}^i & |F_s^i| < |F_n^i| \mu \\ F_n^i \mu & |F_s^i| \geq |F_n^i| \mu \end{cases} \quad (4)$$

Where  $F_{n,ij}^i$ ,  $F_{n,ij,vis}^i$ ,  $F_{s,ij}^i$ , and  $F_{s,ij,vis}^i$  are the normal spring force, the normal damping force, the tangential spring force and the tangential damping force of element  $i$ , respectively; These forces can be calculated via Hertz theory and Mindlin theory (Robertas, Algis, Rimantas, 2004);  $\mu$  is the friction coefficient. It should be noted that the FE was regarded as sphere with infinite radius (Han and Owen, 2000) when calculate the interaction force between FE and DE as illustrated in Fig. 1(b).



(a) Contact between DE and DE (b) Contact between FE and DE (c) Force between elements  
**Fig. 1 Contact models among elements**

Based on the theory mentioned above, the concept of analysis for the wheel-sand interaction by FE-DEM is illustrated in Fig. 2. The interactions among sand particles are solved via interactions of DEs (Fig. 1(a)), while the forces between tire and sand particles are calculated by interactions between FE and DE (Fig. 1(b)).



**Fig. 2 Description of wheel-sand system by FE-DEM**

The net draw bar pull  $N$ , normal reaction force  $P$  and slip ratio  $s$  are defined as follows:

$$N = G - |R| \quad (5)$$

$$P = \sum F_z \quad (6)$$

$$s = (1 - v / (r\omega)) \quad (7)$$

Where  $F$  is the contact force between FE wheel and DE terrain;  $G = \sum F_x^+$  and  $R = \sum F_x^-$  are the gross traction force and the resistance force, respectively;  $v$  and  $\omega$  are the translational speed and the angular velocity of the wheel;  $r$  is the free rolling radius of wheel.

2.3 Program flow

The simulation of the wheel running process is composed of following three steps: Step1, granular DEs compact to a steady state under self-weight; Step2, the FE wheel sink onto the FE road surface under vertical load including self-weight and external load until it reaches an equilibrium state; Step3, a constant angular velocity and corresponding translational velocities are loaded to the wheel center to analyze its traction performance under various slip ratios. And the wheel travels from FE hard road to DE soft terrain. The program flow chart is shown in Fig. 3.

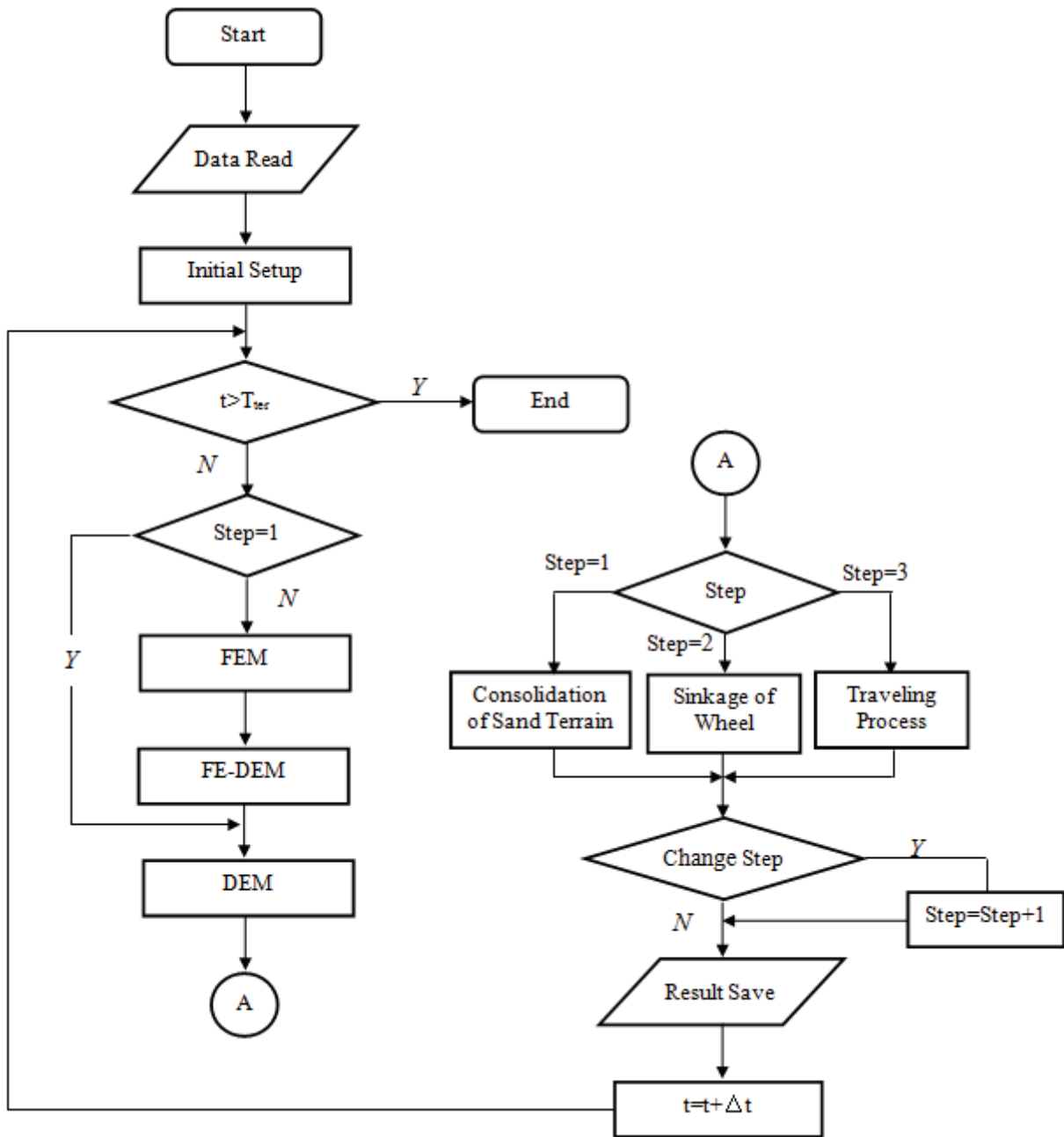


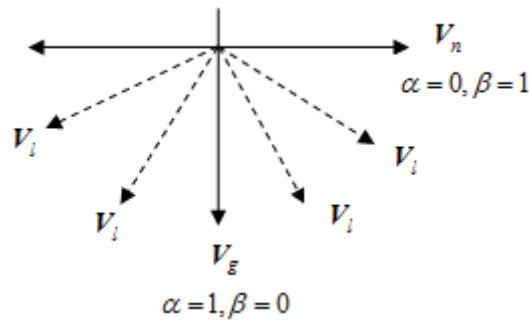
Fig. 3 Program flow chart

### 3 DE modeling of soft sand terrain

#### 3.1 Initial generation

The discontinuous characteristics of loose gravel terrain can be modeled effectively by DEM (Fujii, et al, 2010; Li, et al, 2010; Zhang, et al, 2012; Knuth, et al, 2012; Nakashima, et al, 2004 and Nakashima, et al 2009). Thus, we use the 3D DEM to model the sand terrain in this paper. The initial generation of the DEs is one of the main research topics. For this problem, Han, Feng, Owen (2005) proposed a method for the generation of spheres which randomly distributed in a given geometric domain with different sizes. The details are as follows:

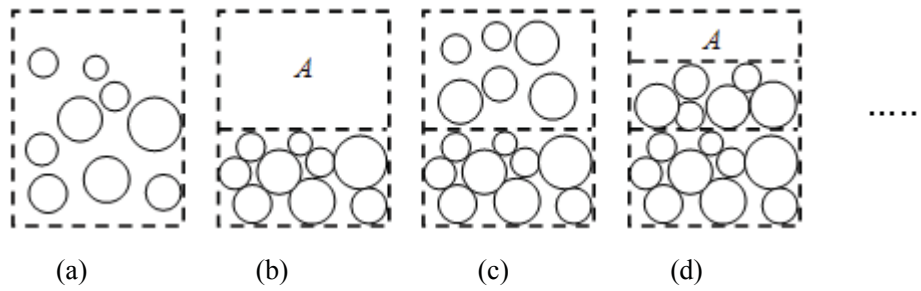
1. Various sizes of spheres which are randomly distributed in a given geometric domain are generated, and there are gaps among spheres.
2. Find out the neighbor spheres of each sphere. Calculate the distance between the target sphere and its neighbor spheres in a given direction (in this study is the vertical direction), and move the target sphere to the nearest neighbor sphere along the special direction, the moving distance is equal to the minimum distance.
3. Further compression is executed similar to step2 to improve the volume density of the spheres, where the compression direction  $V_i = \alpha V_g + \beta V_n$ , as illustrated in Fig. 4, changes in a given range.



**Fig. 4 Compression directions**

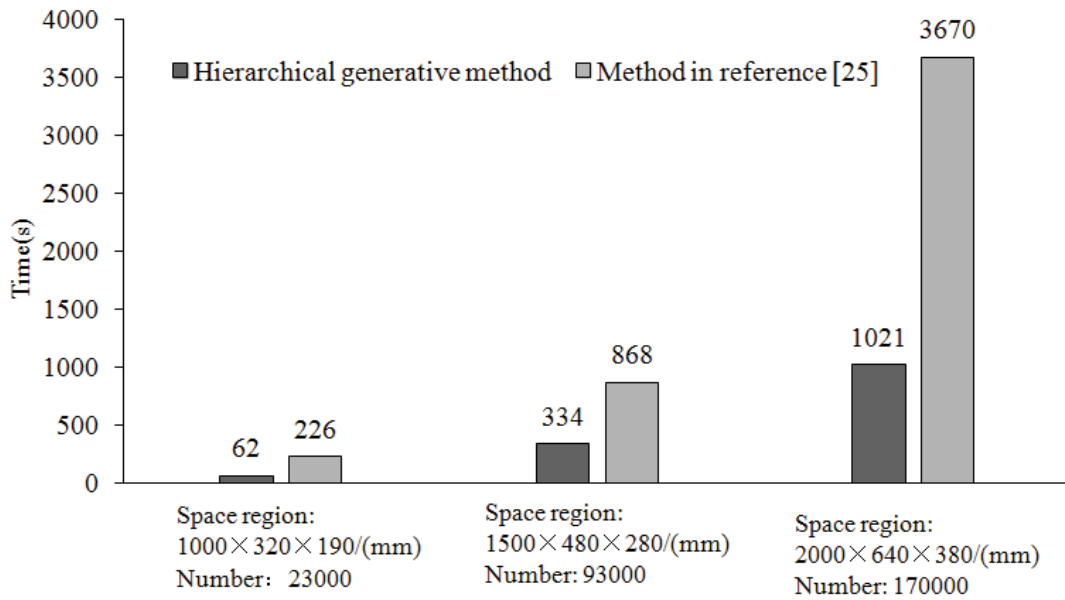
After the above steps are completed, a void will be produced on the upper part of the domain. In order to fill the void, a strategy of sphere insertion was adopted by Han, et al (2005): spheres were generated at the top of the domain and then dropped along the compression direction until they contact with the nearest existing sphere. During this procedure, it needs to loop over all the current spheres for the contact detection, which wastes a lot of computing time. With the increasing of the sphere number, the consumption of the computing resource is increased dramatically. For the sand terrain simulation problem, large amount of spheres need to be generated. What's more, considering that the spheres should be consolidated under self-weight to a steady state to model the real sand condition after the initial generation, we prefer the improving of efficiency to the increasing of volume density at the initial generate stage.

Hierarchical generative method is applied to enhance the efficiency of the initial generation in this study. A 2D schematic diagram is shown in Fig. 5. Firstly, various sizes of spheres are generated in a given geometric domain as illustrated in Fig. 5(a). Then, the spheres are compressed by using the method of Han, et al (2005), a new terrain  $A$  is created as shown in Fig. 5(b). Afterward, new spheres are generated and compressed in the new terrain  $A$ , as shown in Fig. 5(c), Fig. 5(d). Another new terrain  $A$  is produced as illustrate in Fig. 5(d). Repeat the above procedure until no sphere of given radius range can be generated. In this procedure, the contact detection only needs to be executed among spheres in the new domain  $A$  for every layer of generation.



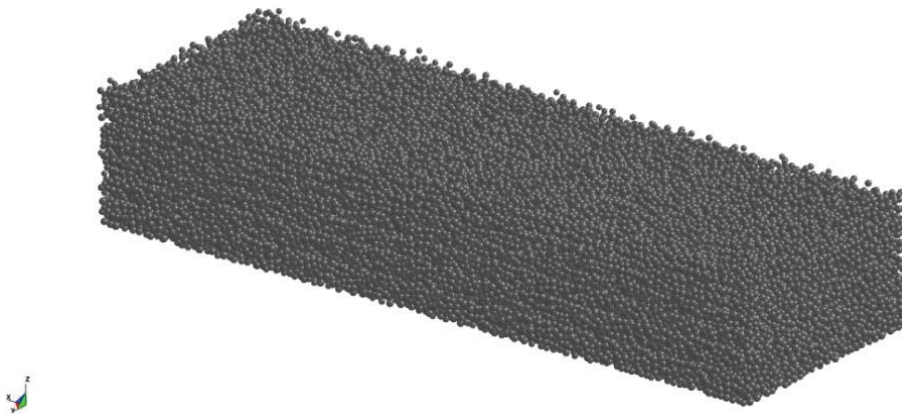
**Fig. 5 Hierarchical generate method**

In order to validate the superiority of the new method, a given number of spheres were generated in special geometric domains via hierarchical method and the method of Han, et al (2005), the results are shown in Fig. 6. It can be seen that the former method is more efficient than the latter one when generate same amount of spheres in a given geometric domain. With the increase of the computing scale, the efficiency is improved more significantly. For the geometric domain of  $2000 \times 640 \times 380\text{mm}$  and sphere number of 170000, the calculation efficiency can be improved by 60%.



**Fig. 6 Comparing of the computation time**

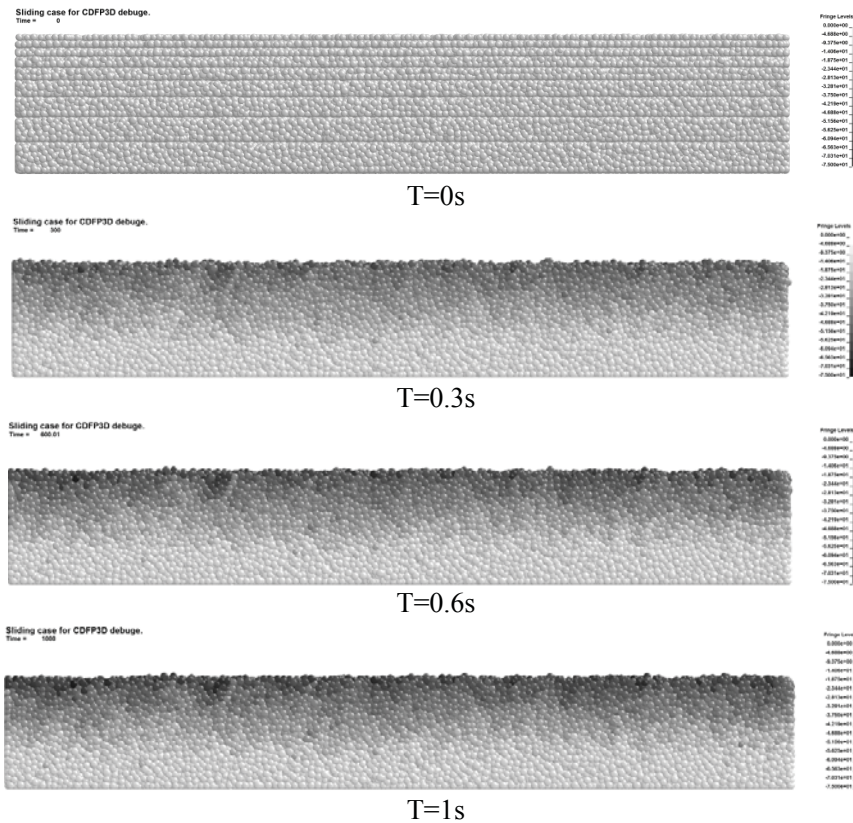
The initial configuration of the sphere DEs in the geometric domain of  $1500 \times 480 \times 280\text{mm}$  with sphere number of 93024 is shown in Fig. 7.



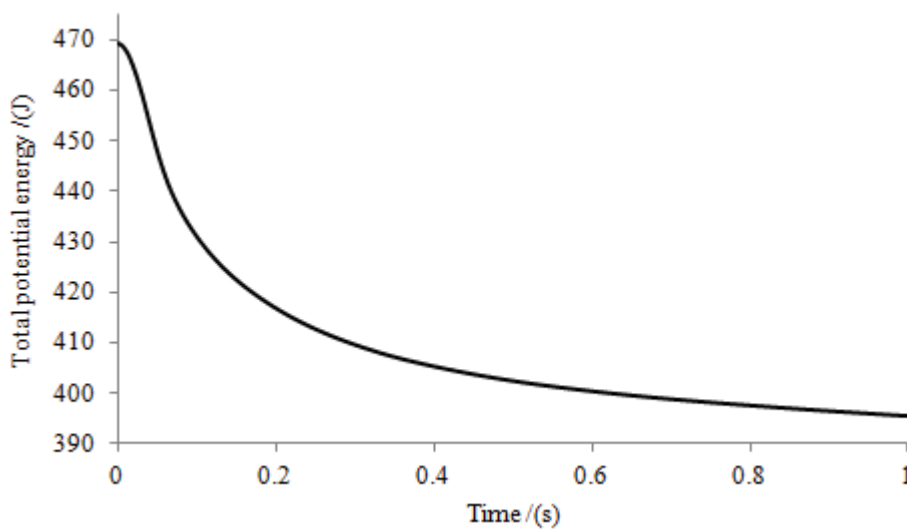
**Fig. 7 Initial configuration of the DEs in geometric domain of  $1500 \times 480 \times 280\text{mm}$**

### 3.2 DEs consolidation under self-weight

It should be noticed that there might be contact but no contact force among DEs after initial generation. This is different with the real state of the sand particles. Therefore, the DEs shown in Fig. 7 were placed into the soil bin with corresponding geometric size. Then, gravitational force was loaded to the DEs, and they were compacted to a stable state under self-weight. The displacement nephogram of the vertical direction during the compaction procedure is shown in Fig. 8. It can be seen that the displacements of the elements in the bottom of the soil bin are small, while the elements in the upper part of the soil bin show larger displacements.



**Fig. 8** Displacement nephogram of vertical direction of DEs during consolidation process



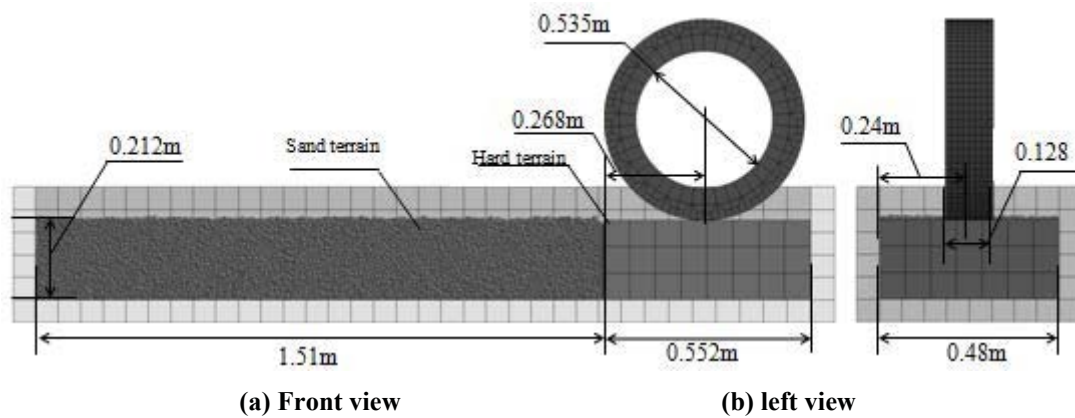
**Fig. 9** Time history of total potential energy of DEs

Total gravitational potential energy is used to estimate the consolidation state, and the time history of the total gravitational potential energy is illustrated in Fig. 9. It is obvious that the total potential energy decreases with the increasing of the computing time, and the trend tends to be flat. After 1s of consolidation, it tends to be stable, and the consolidation process is completed.

#### 4 Numerical simulation of running behavior

##### 4.1 Model introduced

Based on the soil bin experiment by Hisanori, et al (2010), considering that the wheel usually travels from hard terrain into soft terrain in practice, refer to papers of Hambleton, et al (2008 and 2009), the numerical model is established including hard terrain and soft terrain, as illustrated in Fig. 10, where the hard terrain, wheel and soil bin are discretized by FEs. The soft sand terrain is modeled by DEs with the geometric terrain of  $1500 \times 480 \times 280\text{mm}$  as illustrated in Fig7, and corresponding self-weight consolidation process is shown in Fig. 8, Fig. 9.



**Fig. 10 3D numerical model**

It should be noticed that we are focusing on the development 3D FE-DEM program in this paper, thus, the destruction of the tire, hard terrain and soil bin is neglected. The hard terrain and soil bin are modeled via elastic material. The radius range of the DEs is 5mm to 7mm. Time step for explicit calculation is  $10^{-5}\text{s}$ . Other parameters of the model are shown in Table1 and Table 2.

**Table 1 Material parameters**

	Wheel	Soil Bin	Hard Terrain	Sand Terrain
Number of Elements	1344	800	168	93024
Yong's Modulus (MPa)	2	$7.5 \times 10^4$	$7.5 \times 10^4$	$7.5 \times 10^4$
Poisson's Ratio	0.49	0.30	0.30	0.30
Density ( $\text{kg/m}^3$ )	$1.8 \times 10^3$	$2.4 \times 10^3$	$2.4 \times 10^3$	$2.4 \times 10^3$

**Table 2 Contact parameters**

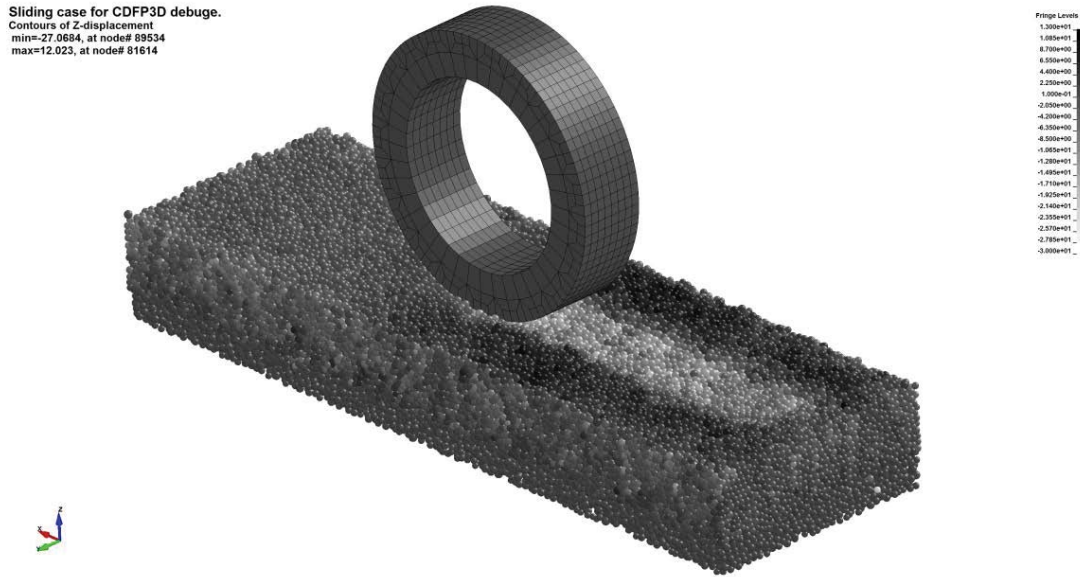
	Wheel-Sand	Wheel-Hard terrain	Soil-Bin
Normal Damping Coefficient (1/s)	40	50	50
Tangential Damping Coefficient (1/s)	35	45	45
Friction Coefficient	0.4	0.3	0.3

##### 4.2 The wheel traveling process

Firstly, according to the relevant experiment of Kyoto University (Hisanori, et al, 2010), vertical load of 1295N including self-weight and external load is loaded to the center of the wheel, and the wheel is sinking until reaches equilibrium state. Then, a constant angular velocity of 5rad/s and corresponding translational velocity are enforced to the center of the wheel to simulate its running

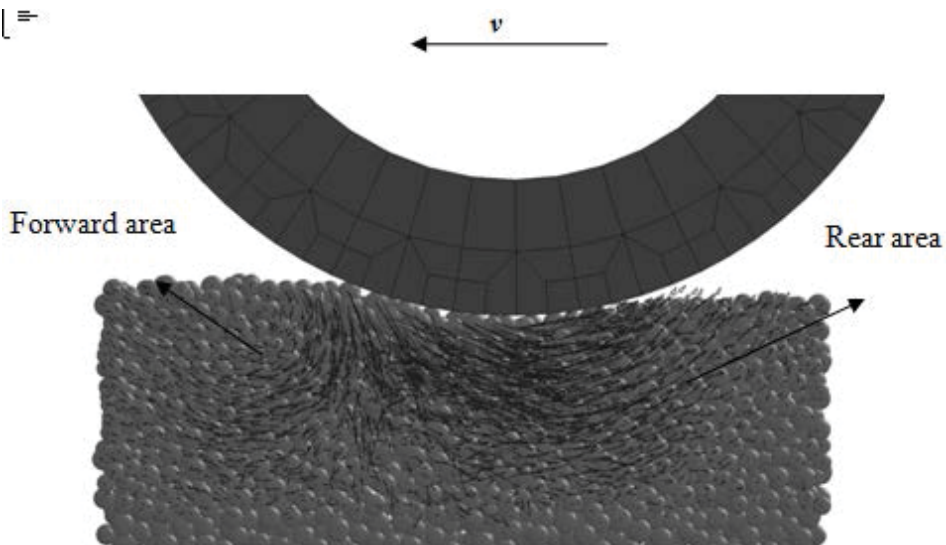


behavior under slip ratio of 30%. It should be noticed that the constant angular velocity value is set to 5rad/s, which is larger than that in Hisanori’s experiment, to reduce the running time of the wheel for a certain traveling distance because of the low computational efficiency of the program. And the improvement of the computational efficiency is our future work. The displacement nephogram of Z direction of the DEs is shown in Fig. 11. For better observation, the soil bin and the hard terrain is not shown. The figure shows that for the elements under the wheel track, with light color, the displacement values are negative, while on both sides of the trace, with dark color, the displacement values are positive. This phenomenon is consistent with the real condition.



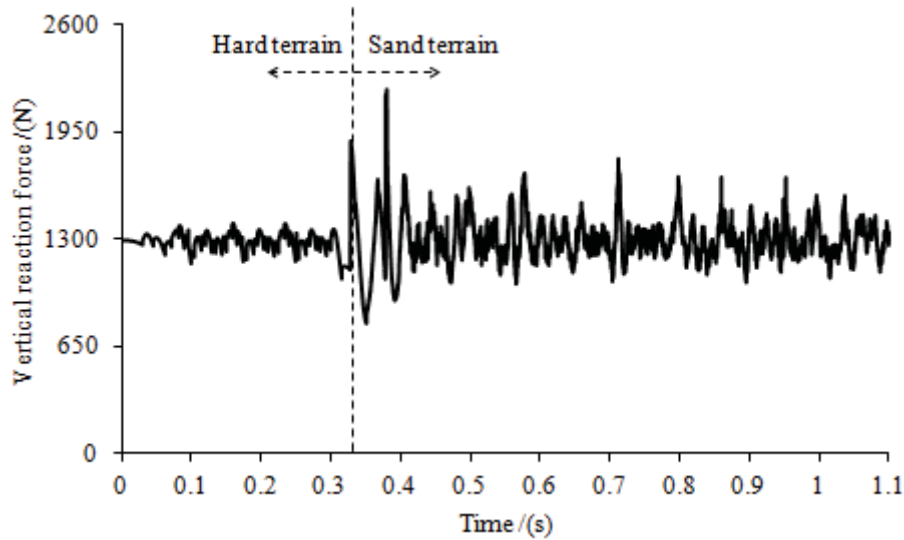
**Fig. 11 Displacement nephogram of Z direction of sand particles**

The flow of the sand particles has a great influence on running behavior of the wheel. Fig. 12 shows the flow trend of the particles at 0.74s, where the flow directions are described via velocity vectors. From the figure we can see that the flow trend of the particles can be divided into two areas, the forward flow in clockwise and the rear flow in anticlockwise. This phenomenon is consistent with the conclusions by Hambleton, et al (2009) and Zhuang (2002).



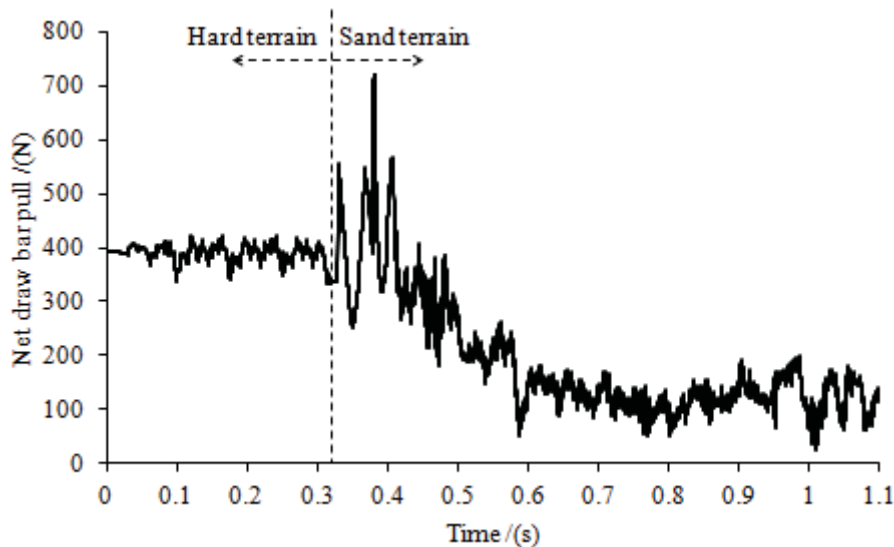
**Fig. 12 Configuration of sand flow trend**

Fig. 13 shows the time history of the vertical reaction force during the traveling process. It can be seen that the vertical reaction force fluctuates around the average value of 1300N, which is close to the given load value. The vertical reaction force on the soft sand terrain shows larger fluctuation than that on the hard terrain. The wheel starts to travel into the sand terrain at about 0.33s, and the vertical reaction force shows an abrupt fluctuation. The possible reason for this phenomenon is because of the sudden change of the support capacity of the road, the wheel sinks suddenly and the impact force leads to the fluctuation of the vertical reaction force.



**Fig. 13 Time history of the vertical reaction force**

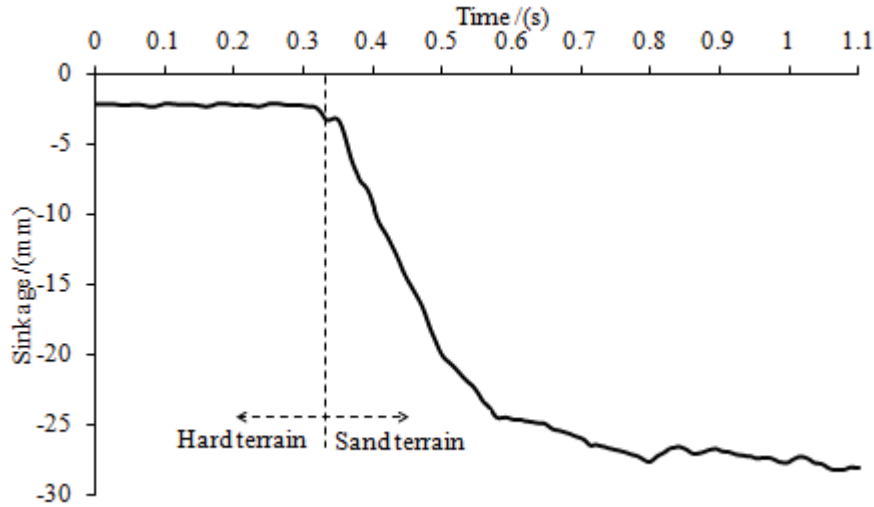
The time history of the net drawbar pull is shown in Fig. 14. It can be seen that the net draw bar pull on the hard terrain is larger than that on the soft sand terrain. As the wheel travels into the sand terrain after 0.33s, the average value of the net draw bar pull decreases dramatically from 380N to 110N. Analogous to the vertical reaction force shown in Fig. 13, the net draw bar pull of the soft sand terrain shows a larger fluctuation than that on the hard terrain. Similar mutation at the conjunction of two kinds of roads is also illustrated in the figure.



**Fig. 14 Time history of net draw bar pull**

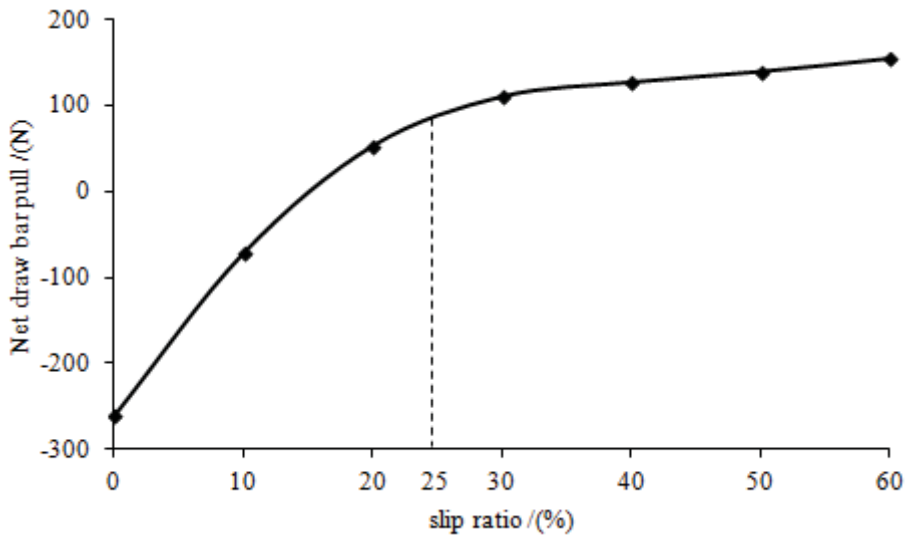
Fig. 15 shows the time history of the wheel sinkage. It can be seen that the wheel sinkage fluctuate in a small range on the hard road. As the wheel travels into the soft sand terrain after 0.33s, the

sinkage value increases dramatically because of the destruction of the terrain. Afterward, the trend tends to be flat and the value fluctuates in 24mm to 28mm.



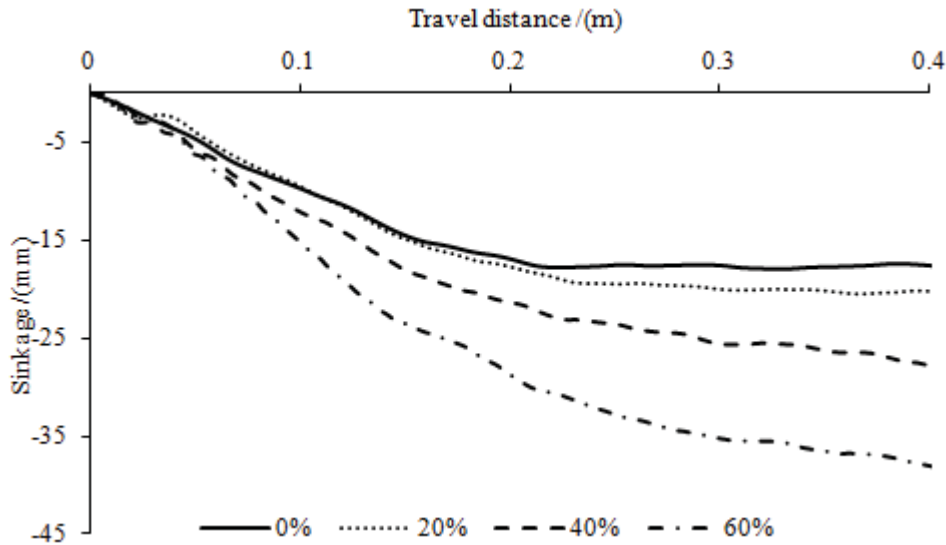
**Fig. 15 Time history of wheel sinkage**

In order to further analyze the effect of slip ratio on the running behavior of the wheel on sand terrain (net draw bar pull of hard terrain is not included), constant angular velocity of 5rad/s and corresponding translational velocity for different slip ratios according to Eq.(7) are enforced to the center of it. The average value of the net draw bar pull on the soft sand terrain is regarded as the equivalent value. The relation between the equivalent value of net draw bar pull and slip ratio is shown in Fig. 16. It is clearly that the value of the net draw bar pull rises with the increase of the slip ratio. And the trend is steeper when the slip ratio is less than 25%, then it shows a flat trend with the slip ratio larger than 25%,



**Fig. 16 Relation between net draw bar pull and slip ratio**

Fig. 17 shows the sinkage of the wheel with the traveling distance of 0.4m on sand terrain (sinkage on hard terrain is not included) under different slip ratio values. It can be seen that the value of the sinkage rises with the increase of the traveling distance. The sinkage value also rises with the increase of the slip ratio, for slip ratio value of 0% and 60%, the maximum values of the sinkage are 17.8mm and 37.9mm, respectively.



**Fig. 17 Relation between wheel sinkage and slip ratio**

#### 4.3 Simulation results discussion

From the above simulation, we can obtain the following results:

Hard terrain shows better traction performance than that of soft sand terrain, and the driving process is stable. During the process of running on sand terrain, the road is destructed, the net draw bar pull shows larger fluctuation, and the rut is clear. The main reason is because of the rolling and flow characters of the sand particles. Although we consider the frictions among DEs, the sphere shape of the elements is still inconsistent with the actual situation of sand particles. Various shape elements (Li, et al (2010), Chen, Zhao, Cui, et al (2012), Zhou, Hua, Ma, et al (2012)) and rolling resistance among elements (Iwashita, Oda (2000), Jiang, Yu, Harris (2006) ) will be considered in the future to improve current program.

As the wheel travels into soft sand terrain, the sinkage value increases dramatically. Meanwhile, the normal reaction force and the net draw bar pull show large fluctuations. The reason is because of the different support capacity between hard and sand terrain, this causes an unbalance force of the wheel in the vertical direction. Thus, the wheel sinks into the sand terrain and produces large impact force which leads to the fluctuation of vertical reaction force. Moreover, the average value of the traction force decreases gradually because of the rolling and flow of the sand particles.

On the soft sand terrain, the net draw bar pull shows a steeper trend when the slip ratio is less than 25%, and the trend is flat when the slip ratio is larger. With the same traveling distance, the sinkage value rises with the increase of the slip ratio. These conclusions agree qualitatively with the results proposed by Hisanori, et al (2010) and Li, et al (2010). In the mean time, there are still problems that the value of the net draw bar pull is larger than that in Hisanori's experimental results. The possible reason is because of the larger particle size and the larger angular velocity of the wheel. And this problem will be overcome after we develop the parallel computing program which can improve the computing efficiency.

#### 5 Conclusions

1. In this study, a 3D FE-DEM has been applied to model the interaction between wheel and sand, and corresponding procedure code was developed based on FORTRAN95 language.
2. An initial generation method named hierarchical generate method which was appropriate for the sand terrain simulation was developed. Corresponding numerical model was established to model the running behavior of the wheel travels from hard terrain to soft sand terrain. The time

history of normal reaction force, net draw bar pull and sinkage of the wheel were obtained. The damage of the sand terrain was also presented.

3. The overall trend of the net drawbar pull versus slip ratio is agreed qualitatively with the results of previous experiments, this indicates the effectiveness of the 3D FE-DEM in analysis the traction performance of rigid wheel travels on sand terrain.

Plans for the future work are to improve the accuracy and the efficiency of the method. The tread pattern will also be considered to simulate the real tire behavior.

### Acknowledge

This work was supported by the National Natural Science Foundation of China (NO. 10972079 and NO. 11172104) and The International Cooperation Project of the Ministry of Science and Technology of China (2013DFG60080).

### Reference

- Robert Bauer, Winnie Leung, Tim Barfoot (2005), Experimental and Simulation Results of wheel-soil interaction for planetary rovers. *IROS 2005*. PP. 586-591.
- Runhuai Yang, Min Xu, Xu Liang, Shiwu Zhang, et al. (2011), Experimental study and DEM analysis on rigid driving wheel's performance for off-road vehicles moving on loose soil. *ICMA 2011*. PP. 142-147.
- J. Maciejewski, A. Jarzebowski. (2004), Experimental analysis of soil deformation below a rolling rigid cylinder. *Journal of Terramechanics*, 41(4), PP. 223-241.
- Hisanori SHINONE, Hiroshi NAKASHIMA, Yuzuru TAKATSU, et al. (2010), Experimental Analysis of Tread Pattern Effects on Tire Tractive Performance on Sand using an Indoor Traction Measurement System with Forced-slip Mechanism. *Engineering in agriculture environment and food*, 3(2), pp. 61-66.
- T. Hiroma, S. Wanjii, T. Kataoka, et al. (1998), Stress analysis using FEM on stress distribution under a wheel considering friction with adhesion between a wheel and soil. *Journal of Terramechanics*, 34(4), pp. 225-233.
- Liu C H, Wong J Y. (1996), Numerical simulation of tire-soil interaction based on critical state soil mechanics. *Journal of Terramechanics*, 33(5), pp. 209-221.
- Kaiming Xia. (2011), Finite element modeling of tire/terrain interaction: Application to predicting soil compaction and tire mobility. *Journal of Terramechanics*, 48(2), pp.113-123.
- Kaiming Xia, Yunming Yang. (2012), Three-dimensional finite element modeling of tire/ground interaction. *International journal for numerical and analytical methods in geomechanics*, 36(4), pp. 498-516.
- J.P. Hambleton, A. Drescher. (2008), Modeling wheel-induced rutting in soils: Indentation. *Journal of Terramechanics*, 45(6), pp. 201-211.
- J.P. Hambleton, A. Drescher. (2009), Modeling wheel-induced rutting in soils: rolling. *Journal of Terramechanics*, 46(2), pp. 35-47.
- J.P. Hambleton, A. Drescher. (2009), On modeling a rolling wheel in the presence of plastic deformation as a three- or two-dimensional process. *International Journal of Mechanical Sciences*, 51(11-12), pp. 846-855.
- Lav R.Khot, Vilas M. Salokhe, H.P.W.Jayasuriya, et al. (2007), Experiment validation of distinct element simulation for dynamic wheel-soil interaction. *Journal of Terramechanics*, 12(44), pp. 429-437.
- H.Nakashima, H.Fujii, A.Oida, et al. (2007), Parametric analysis of lugged wheel performance for a lunar microrover by means of DEM. *Journal of Terramechanics*, 44(2), pp. 153-162.
- H.Nakashima, H.Fujii, A.Oida, et al. (2010), Discrete element method analysis of single wheel performance for a small lunar rover on sloped terrain. *Journal of Terramechanics*, 47(5), pp. 307-321.
- Wen Li, Yong Huang, Yi Cui, et al. (2010), Trafficability analysis of lunar mare terrain by means of the discrete element method for wheeled rover locomotion. *Journal of Terramechanics*, 47(3), pp. 161-172.
- Zhang Rui, Liu Fang, Zeng Gui-Yin, et al. (2012), Research on Dynamic Simulation System of Interactions between Irregular Rigid Wheel and Lunar Soil Simulant. *CMGM-2012*. pp. 438-443.
- M.A. Knuth, J.B. Johnson, M.A. Hopkins, et al. (2012), Discrete element modeling of a Mars Exploration Rover wheel in granular material. *Journal of Terramechanics*, 49(1), pp. 27-36.
- NAKASHIMA H, Oida A. (2004), Algorithm and implementation of soil-tire contact analysis code based on dynamic FE-DE method. *Journal of Terramechanics*, 41(2-3), pp. 127-137.
- Hiroshi NAKASHIMA, Yuzuru TAKATSU, Hisanori SHINONE. (2009), FE-DEM Analysis of the effect of tread pattern on the tractive performance of tires operating on sand. *Journal of mechanical systems for transportation and logistics*, 2(1), pp. 55-65.
- Hiroshi NAKASHIMA, Yuzuru TAKATSU. (2008), Analysis of tire tractive performance on deformable terrain by finite element-discrete element method. *Journal of computational science and technology*, 2(4), pp. 423-434.

- John R. Williams, Eric Perkins, Ben Cook. (2004), A contact algorithm for partitioning  $N$  arbitrary sized objects. *Engineering Computations*, 21(2/3/4), pp. 235-248.
- Zang MY, Gao W, Lei Z. (2011), A contact algorithm for 3D discrete and finite element contact problems based on penalty function method. *Computational Mechanics*, 48(5), pp. 541-550.
- Robertas Balevičius, Algis Džugys, Rimantas Kačianauskas. (2004), Discrete element method and its application to the analysis of penetration into granular media. *Journal of civil engineering and management*, 10(1), pp. 3-14.
- Han K, Perić, D.R.J. Owen. (2000), A combined finite/discrete element simulation of shot peening processes Part II: 3D interaction laws. *Engineering Computations*, 17(6), pp. 680-702.
- K. Han, Y.T. Feng, D.T.J. Owen. (2005), Sphere packing with a geometric based compression algorithm. *Powder Technology*, 155(1), pp. 33-41.
- ZHUANG Jide. (2002), Computational vehicle terramechanics. *China Machine Press*.
- Chen Youchuan, Zhao Yongzhi, Cui Zequn, et al. (2012), Study of Discrete Element Simulation of Non-Sphere Base on Superquadrics. CMGM-2012. pp. 76-85.
- Zhou Wei, Hua Jun-Jie, Ma Gang, et al. (2012), Study on Deformation Mechanism of Rockfill Dams during an Initial Impoundment Process. CMGM-2012. pp. 307-320.
- Kazuyoshi Iwashita, Masanobu Oda. (2000), Micro-deformation mechanism of shear banding process based on modified distinct element method. *Powder Technology*, 109(1-3). pp. 192-205.
- M. J. Jiang, H.S. Yu, D. Harris. (2006), Bond rolling resistance and its effect on yielding of bonded granulates by DEM analyses. *International Journal for Numerical and Analytical Methods in Geomechanics*, 30(8), pp. 723-761.

## Random Vibration Analysis for Impellers of Centrifugal Compressors Through the Pseudo-Excitation Method

\*Y.F. Wang<sup>1,2</sup>, S. J. Wang<sup>1,2</sup>, and L.H. Huang<sup>3</sup>

<sup>1</sup>Department of Engineering Mechanics, Dalian University of Technology, China.

<sup>2</sup>State Key Laboratory of Industrial Equipment, Dalian, China

<sup>3</sup>School of Construction and Infrastructures, Dalian University of Technology, China

\*Corresponding author: yfwang@dlut.edu.cn

### Abstract

Impellers of large centrifugal compressors are loaded by fluctuating aerodynamic pressure in operations. Excessive vibration of the impeller can be induced by unsteady airflows which may cause fatigue failures. Traditional vibration analyses require multiple load-step computations with input of pneumatic force in the time domain which are usually very time consuming. Hence, it is necessary to develop random vibration models and solve them in the frequency domain. In this paper, the finite element model is generated based on the result of unsteady CFD analysis for an unshrouded impeller. The pseudo-excitation method is used to obtain the power spectra density of the three-dimensional, dynamic displacement and stress of the impeller. Compared with the direct transient vibration analyses in time domain, the pseudo-excitation method provides accurate and fast estimation of dynamic response of the impeller, making it an applicable and efficient method for random vibration computation of impellers.

**Keywords:** Impeller, Random vibration, Aerodynamic load, Pseudo-excitation method

### Introduction

Impellers of centrifugal compressors play an important role in generating pressured air and gases for production lines in petroleum and chemical engineering. The impellers are designed to undertake loadings of mass imbalance, centrifugal forces as well as aerodynamic loads. The aerodynamic force provides distributed air pressure on the surface of blades, shroud and hub of the impeller, and is time variant since the condition of the flow of air inside the impeller is generally unsteady or even turbulent. A scheme of transient analysis based on the fluid-solid interaction is required to assess the stress of the impeller to ensure its structural integrity. Two kinds of multiple load-step analyses for the stress of solid and the pressure of fluid are incorporated in the scheme separately, and are combined with numerous rounds of real-time data exchange on the interacting boundary of the solid and the fluid domains (e.g. Bludszuweit 1995, Beckert and Wendland 2001, de Boer et al. 2007, Khelladi et al 2010). The full execution of this scheme is usually very time consuming due to the transient analyses for the impeller. Other options of dynamical stress analysis can be adopted from the standpoint of the frequency domain. Unsteady or turbulent forces can be treated as random loadings with statistic characteristics observed based on temporal records of the force (Tootkaboni and Graham-Brady 2010). In this way, the stress response arisen from the dynamic pressure can be formulated as a problem of random vibration and solved in the frequency domain.

In this paper, the transient stress analysis is performed as a random vibration problem through the Pseudo-Excitation Method (PEM, c.f. Lin and Zhang 2004). Based on an unsteady computational fluid dynamical analysis, the auto power spectral density of the air pressure is obtained. A solid, three dimensional finite element model is created using ANSYS. The random vibration analysis for the impeller is carried out through the PEM using a series of harmonic vibration solutions. A user-defined module incorporated with ANSYS is developed to apply the random loading of multiple

dimension and multiple points on the impeller structure. Based on the random vibration analysis, the spectral information of the stress response is obtained. Finally, the structural integrity of the impeller in terms of reliability index is computed. It is shown that the solution efficiency of the PEM-based random vibration is much higher than the conventional multiple step transient stress analysis, and thus is suitable for practical engineering.

### Mathematical formulation

The governing equation of motion of the impeller structure excited by unsteady, time variant force based on the finite element method can be written as:

$$\mathbf{M}\ddot{\mathbf{y}}(t) + \mathbf{C}\dot{\mathbf{y}}(t) + \mathbf{K}\mathbf{y}(t) = \mathbf{P}(t) \quad (1)$$

where  $\mathbf{M}$ ,  $\mathbf{C}$  and  $\mathbf{K}$  are matrices of mass, damping and stiffness of the impeller.  $\mathbf{P}$  is the vector of random nodal force applied at each degree of freedom of the model.  $t$  is the temporal variable. Herein, it is assumed that the time-invariant loads that contribute only to steady stress have been excluded from the load vector, and  $\mathbf{P}$  is stationary whose probabilistic function does not change with time.

Based on the PEM, the power spectral density  $S_{yy}(\omega)$  can be expressed as

$$S_{yy}(\omega) = |\mathbf{H}(\omega)|^2 S_{xx}(\omega) \quad (2)$$

where  $S_{xx}(\omega)$  is the power spectral density of a harmonic excitation denoted by  $\mathbf{x}(t)$  whose frequency is  $\omega$ ;  $\mathbf{H}(\omega)$  is the matrix of frequency-response function. Substituting a pseudo harmonic excitation vector  $\tilde{\mathbf{f}}(t) = \sqrt{S_{ff}(\omega)}e^{i\omega t}$  into Eq. (1) leads to a pseudo displacement vector denoted by  $\tilde{\mathbf{y}}(t)$ . It was proved that the auto power spectral density of the displacement  $\mathbf{y}(t)$  is related to  $\tilde{\mathbf{y}}(t)$  such that

$$S_{yy} = |\mathbf{H}|^2 S_{ff} = |\tilde{\mathbf{y}}|^2 \quad (3)$$

Following Eq. (3), the power spectral densities of strain and stress of each single element can be obtained as well using the conventional finite element method.

In the case of multiple dimensional, multiple pointed, totally coherent excitations, the matrix of auto power spectral density can be written as

$$\mathbf{S}(i\omega) = \begin{bmatrix} S_{11}(i\omega) & S_{12}(i\omega) & \cdots & S_{1m}(i\omega) \\ S_{21}(i\omega) & S_{22}(i\omega) & \cdots & S_{2m}(i\omega) \\ \vdots & \vdots & \ddots & \vdots \\ S_{m1}(i\omega) & S_{m2}(i\omega) & \cdots & S_{mm}(i\omega) \end{bmatrix} \quad (4)$$

where  $m$  is the number of excitations. The non-diagonal terms in the above matrix are sub-matrices of cross power spectral density that can be expanded along the three coordinate directions. Using the PEM again, the auto power spectral density matrix of displacement response can be obtained as

$$S_{yy}(\omega) = \sum_{j=1}^m \tilde{\mathbf{y}}_j^* \tilde{\mathbf{y}}_j^T \quad (5)$$

where  $\tilde{\mathbf{y}}_j$  is the  $j$ -th pseudo displacement vector generated by pseudo load vector  $\tilde{\mathbf{x}}_j = \boldsymbol{\varphi}_j^* \sqrt{\lambda_j} e^{i\omega t}$ . The subscripts \* and T represent complex conjugate and transposition of matrix, respectively.  $\lambda_j$  and  $\boldsymbol{\varphi}_j^*$  are the  $j$ -th eigenvalue and eigenvector of the auto power spectral density of  $x$ .

Assuming that the mean value of the loading is zero, the variance of the displacement response can be derived as



$$\sigma_y^2 = \int_{-\infty}^{+\infty} \mathbf{S}_{yy}(\omega) d\omega \quad (6)$$

Further, let the probabilistic densities of the structural resistance and loading be both normal (Gaussian) distributed, then the reliability index of structural integrity can be expressed as

$$\beta = (\mu_R - \mu_S) / \sqrt{\sigma_R^2 + \sigma_S^2} \quad (7)$$

where  $\mu_R$  and  $\mu_S$  are mean values of the resistance and loading, and  $\sigma_R$  and  $\sigma_S$  are their standard deviations, respectively. Notice all non-zero, time-invariant stresses resulted from mass imbalance and centrifugal force should be considered when  $\mu_S$  is computed.

### Scheme of PEM-based simulation incorporated with ANSYS

The random vibration analysis is carried out using finite element software ANSYS. A specialized user-defined module is developed to repeatedly run harmonic analysis for solution of auto power spectral densities with every single excitation frequency. The scheme of the numerical simulation can be summarized as follows.

1. Create the finite element model of the impeller and assign basic solution conditions.
2. Compute the matrix of power spectral density based on the given records of the air pressure in the time domain.
3. Specify appropriate range of frequency [ $\omega_{\min}$ ,  $\omega_{\max}$ ] and step size  $\Delta\omega$ .
4. Let frequency  $\omega = \omega_{\min} + i\Delta\omega$ . Generate the pseudo excitation and compute the pseudo displacement vector  $\tilde{y}_j$  using the harmonic analysis module provided by ANSYS, i.e. (ANTYPE, HARMIC).
5. Superpose for each pseudo displacement to obtain the power spectral density matrix related to frequency  $\omega$  according to Eq. (5). Compute the power spectral density matrix of the stress field.
6. Repeat steps 4 and 5 until  $\omega$  is equal to or greater than  $\omega_{\max}$ .
7. Compute the variances of displacement based on Eq. (6) and of stress at each element through conventional finite element method.
8. Compute the reliability index  $\beta$  according to Eq. (7).

### Example

Figure 1 shows the solid model of an unshrouded impeller of a centrifugal compressor. There are nineteen blades evenly distributed in the circumferential direction on the impeller. The whole impeller is meshed with the type solid186 by ANSYS as shown in Figure 2. Considering the axial symmetry of the structure, only a sector of one nineteenth of the model needs to be analyzed. The numbers of node and element for the sector are 7823 and 6283, respectively.

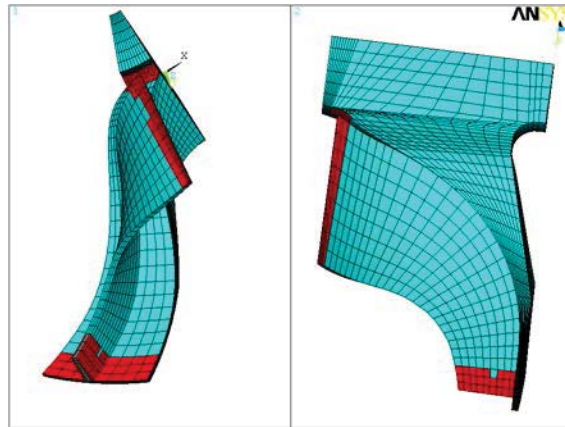


Figure 1. Solid model of the impeller



Figure 2. Meshed finite elements

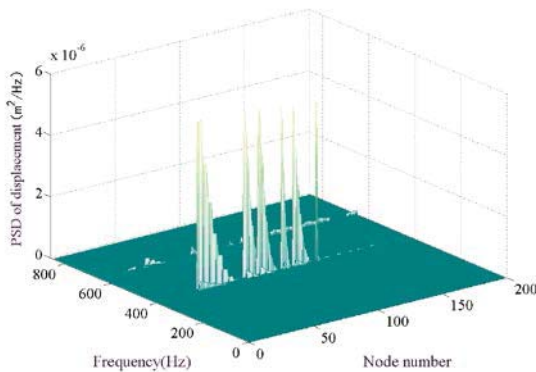
Further, a highlighted area colored in red is illustrated in Figure 3 to show the high stress zone of the impeller based on previous stress analysis using deterministic centrifugal loading. This area is believed the most vulnerable part of the whole impeller to structural failure of fatigue.



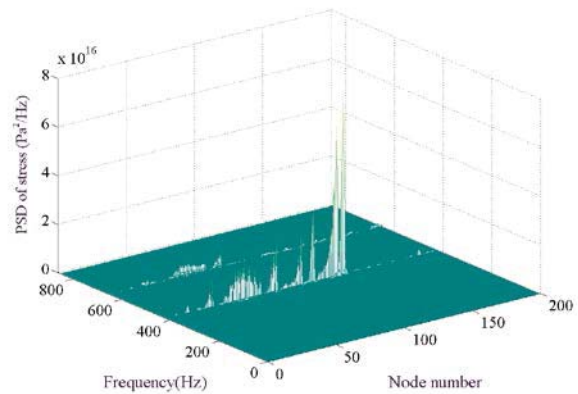
**Figure 3. High stress area**

The pulsating, unsteady air pressure on the surface of the impeller is obtained through computational fluid dynamics software NUMECA. The time history of the pressure contains 6,000 records and is converted into a three dimensional nodal force of the solid model using the method of radial basis function (Wu, Wang and Sun 2012). Then, the previously presented scheme of PEM-based simulation is carried out to obtain the auto power spectral densities of each nodal point of the impeller. The power spectral characteristics of von Mises stress can be computed as well.

Based on the steady-state stress analysis, the highly stressed area is composed of 200 nodes. Figures 4 and 5 show the auto power spectral densities (PSDs) of x-displacement and von Mises stress of these 200 nodes.



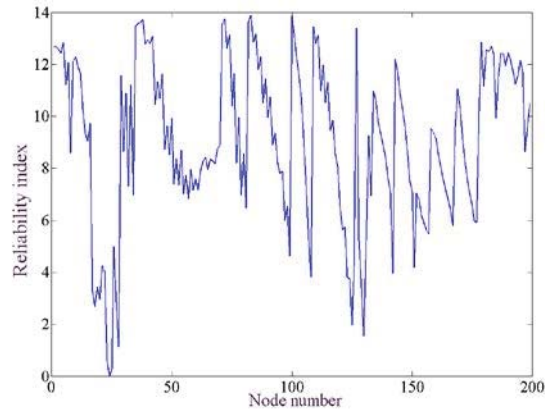
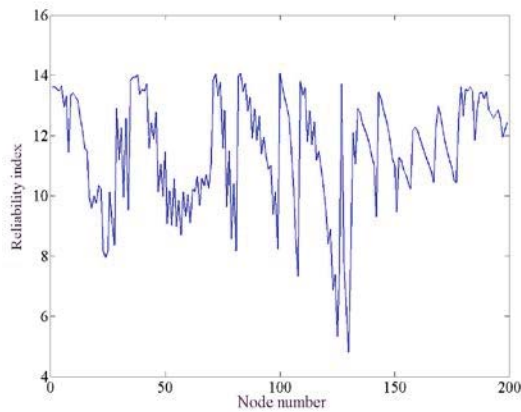
**Figure 4. auto PSDs of x-displacement**



**Figure 5. auto PSDs of von Mises stress**

Next, the reliability index of the impeller structure is computed following the above analysis for random vibration. Let the rotational speed of the impeller be  $\Omega=5373$  r/min, the mean value of stress  $\mu_s$  can be obtained for each node. The deviance of the nodal stress can be solved using Eq. (6). Assume  $\mu_R=1050$ MPa,  $\sigma_R=0.07$ , the reliability index of structural integrity can be determined through Eq. (7). The reliability indices of the 200 observed area is presented in Figure 6. The lowest value of the index is 4.79, which means the integrity of these highly stressed positions is guaranteed. By contrast, the indices drop drastically when the rotational speed is increased to 8594 r/min. The lowest value of the reliability index becomes 0.507 in this case, which suggests there will be a structural failure initiating from this position.

It is worth reporting that the solution efficiency of the presented random analysis is satisfactory. In this analysis 6000 records in the time domain and 4096 points of frequency sampling are used. The total computational lasts approximately 8 hours on a four-core workstation. Comparatively, the transient stress analysis in the time domain with 6000 load steps costs about 120 hours. This clearly shows the advantage of dynamical stress computation through the pseudo-excitation method.



**Figure 6. Reliability indices.  $\Omega=5373\text{r/min}$ . Figure 7. Reliability indices  $\Omega=8594\text{r/min}$ .**

## Conclusions

It has been demonstrated in this paper that dynamical stress analysis of impellers excited by unsteady aerodynamic force can be dealt with efficiently through random vibration analysis. A PEM based scheme incorporated with ANSYS is developed and executed to obtain the power spectral densities and deviances of stress and displacement. The reliability index of integrity is computed in the case of Gaussian distributions of structural resistance and air pressure. The advantage of the presented scheme in computational efficiency is demonstrated compared with transient stress analysis in the time domain.

## Acknowledgements

The authors are grateful for the sponsorships of the National Basic Research Program of China (Grants 2009CB724300 and 2011CB706504) and the SBW-DUT Key Scientific Research and Development Projects.

## References

- Beckert A. and Wendland H. (2001), Multivariate interpolation for fluid-structure-interaction problems using radial basis functions. *Aerospace Science and Technology*, 5, pp.125-134.
- Bludszuweit C. (1995), 3-Dimensional numerical prediction of stress loading of blood particles in a centrifugal pump. *Artificial Organs*, 19, pp. 590-596.
- de Boer A., van Zuijlen A. H. and Bijl H. (2007), Review of coupling methods for non-matching meshes. *Computer Methods in Applied Mechanics and Engineering*, 196, pp. 1515-1525.
- Khelladi S., Sarraf C., Bakir F., et al. (2010), Study of a high rotational speed shrouded centrifugal fan: aerodynamics and effects of a shroud-associated cavity on the performance. *Proceedings of the institution of Mechanical Engineers Part A-Journal of Power and Energy*, 224, pp. 691-700.
- Lin J. H. and Zhang Y. H. (2004), The pseudo excitation method for random vibrations. Beijing: Science Publisher.
- Poulimenos A., Spiridonakos M. and Fassois S. Parametric time-domain methods for non-stationary random vibration identification and analysis: An overview and comparison. *Proceedings of ISMA 2006: International Conference on Noise and Vibration Engineering*, Vols 1-8, 2006:2885-2905.
- Tootkaboni M. and Graham-Brady L. (2010). Stochastic direct integration schemes for dynamic systems subjected to random excitations. *Probabilistic Engineering Mechanics*, 25, pp.163-171.
- Wu Y. F., Wang Y. F. and Sun X. H. (2012), Interpolation schemes using radial basis functions for fluid-structure interaction analysis of impellers. *Fan Machines Technology*, 3, pp.34-39.

## Transient dynamical analysis of a dual-rotor system excited by a sudden loss of mass of blade

Jin Huang<sup>1</sup>, Yuefang Wang<sup>2</sup>

<sup>1</sup>Dalian University of Technology, Dalian116024, Liaoning, China

<sup>2</sup>Dalian University of Technology, Dalian116024, Liaoning, China

\*Corresponding author: yfwang@dlut.edu.cn

### Abstract

The transient dynamics of a high speed rotor assembly of a gas turbine is presented in this paper demonstrates that the blade loss will significantly influence to the rotor. To theoretically investigate the motion stability of the system, a reduced rigid Jeffcott rotor model with symmetrical short bearings is presented. The equations of motion are derived considering the nonlinear lubricant forces of bearings. The transient response of the rotor is numerically obtained through the Runge-Kutta scheme with adaptable step-sizes. It is shown that the equilibrium of the rotor is disturbed due to the sudden loss of mass. However, the stability of motion can be restored. Bifurcation diagrams are constructed to investigate the responses of the rotor at various the rotation speeds at a specific eccentricity. The largest Lyapunov exponent (LLE) diagram has been presented to indicate when the system evolves into chaos.

**Keywords:** blade loss; Jeffcott rotor; largest Lyapunov exponent

### Introduction

Rotors of gas turbines are required to operate at supercritical speeds. Structurally, most modern gas turbines are in form of twin spools and are composed of an axial compressor and a power turbine that rotates with different speeds and is supported by rolling bearings as well as intermediate bearings. Due to the complexity in both structure and loading of the rotor, it is very hard to obtain analytical solution of the rotor assembly. The transient response of the rotor is influenced by many loading effects. The most dominant of them is the loss of blades of the impellers. In practical operations of the gas turbine, there is a possibility that one blade of impellers breaks off which causes a sudden loss of mass. Consequently, an impulsive imbalance of mass is generated in the transverse direction of the rotor shafts. This unbalance leads to unexpected large motions. Hence, a detailed blade loss transient response of the rotor system should be conducted.

Since it is time consuming to obtain the dynamical characteristics of the rotor by performing various transient response analyses, the rotor is reduced to a 2-DOF Jeffcott system (Jing, 2004) in this study to obtain the essential dynamical properties of the system. The transient nonlinear lubricant force is necessary for obtaining transient response of the rotor system. The available approximate methods for the slide bearing can be classified as follows. The direct methods, such as difference or finite element method, tackle with the Reynolds equation directly to get the pressure distribution, and the transient oil film force can be obtained by integrating the acquired pressure of oil film. Based on variational method, the variational model (Xia and Qiao, 2009) has relatively high accuracy, but lots of variational iterations are needed to get the proper boundaries which will great reduce the efficiency. The approximate analytic methods claims simple and high accuracy for bearings with small length-to-diameter ratio and the Capone model (Adiletta, 1996) has been widely accepted which will also be implemented in this study.

In this paper, the dynamics of a dual rotor system is presented with specified unbalanced mass distribution on the rotor impellers. To simulate the situation of sudden loss of mass of blade, a concentrated mass imbalance is created and placed on the third impeller of the compressor. The Runge-Kutta method with adaptable step size is implemented to perform the numerical integration of the governing equation. It is demonstrated that the motion of the rotor system will be asymptotic stable when it is disturbed from the equilibrium position. With the journal center staying at the balanced position, a sudden step or ramp unbalance load is applied on the rotor, respectively, and

the motions of the system are investigated subsequently. The results show that in both cases a periodic orbit corresponding to a limit cycle will be generated with a slight difference between them. Bifurcation diagrams are generated based on the Poincaré section to present the responses of the rotor with varying rotational speeds. The results indicate that the system will enter the state of chaos through a complicate route when the rotation speed increases high enough. The largest Lyapunov exponent diagram has been presented to indicate when the motion of the system evolves into chaos.

### Transient response of a twin spool rotor

The twin-spool rotor of the gas turbine is shown in Fig.1(a), which was first studied by (Guangyoung and Palazzolo, 2008). The rotor is supported by six rolling element bearings numbered as #0 through #5 and composed of two parts, inner power turbine and outer compressor. Two intermediate bearings, i.e. IDB 1 and IDB 2 are used to connect the power turbine with the compressor. The parameters of stiffness and damping of the bearings are listed in Table 1. Fig.1(b) shows the finite element model created with software SAMCEF/Rotor using two dimensional axisymmetric elements. The total numbers of element and node are 477 and 269, respectively. Three concentrated masses are placed on points 1, 2 and 3 to represent the mass unbalances on the first three blades of the compressor. The place where the blade loss occurs coincides with the third mass unbalance. Their values are assigned in Table 2.

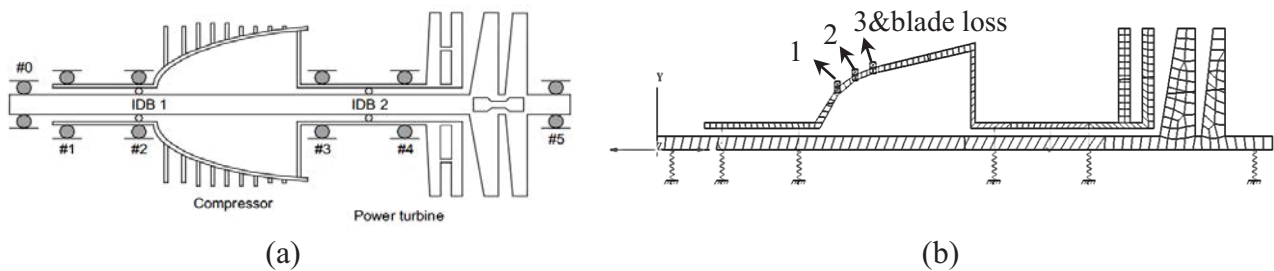


Figure 1 (a) Scheme of a twin spool rotor; (b) FEM model of the rotor.

The operating speeds of the power turbine and the compressor are 13,000rpm and 20,000 rpm, respectively. To get the transient response, a set of unbalanced masses are assigned to the impellers which are shown in Table 1 and their locations can be found as numbered points 1, 2, and 3 in Fig.1(b).

Table 1 Stiffness and damping coefficients of bearings

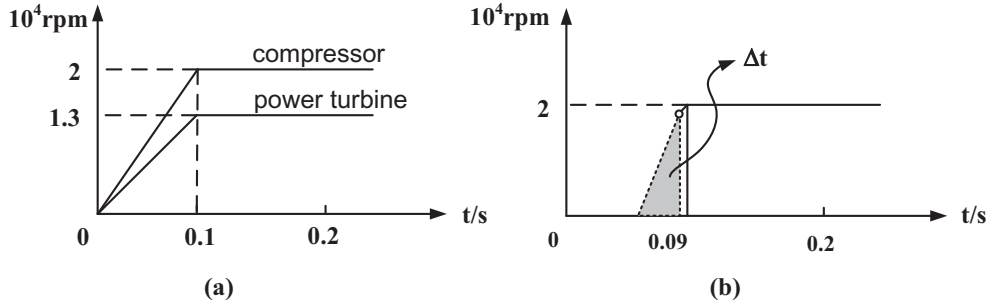
Bearing No.	Stiffness ( $10^8$ N/m)	Damping ( $10^3$ Ns/m)
#0~#5	1.75	1.75
IDB1	0.875	3.502
IDB2	0.875	3.502

Table 2 Unbalanced masses on impellers. "B.L." means blade loss.

Unbalance No.	Mass(kg)	Eccentricity (mm)	Phase (degree)
1	1.41	0.635	45
2	1.21	0.635	45
3	1.11	0.635	45
B.L.	1.11	3.175	45

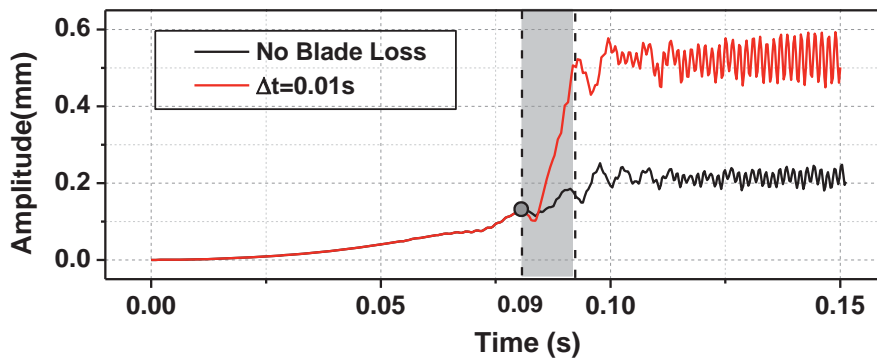
Fig.2(a) shows the operation speed profiles of start-up of the power turbine and compressor for creating the load of transient analysis. The speed profile is approximated by a series of straight lines for simplicity. Herein, it is assumed that the normal operation speed of the rotor remains unchanged

after the occurring of blade loss. The blade loss will result in a time-varying redistribution of the unbalances of the rotor system. An impulsive unbalance of mass is imposed on the rotor to simulate this process whose continuous effect to the system is achieved through the change of rotation speed with a different speed profile from the one of rotor.



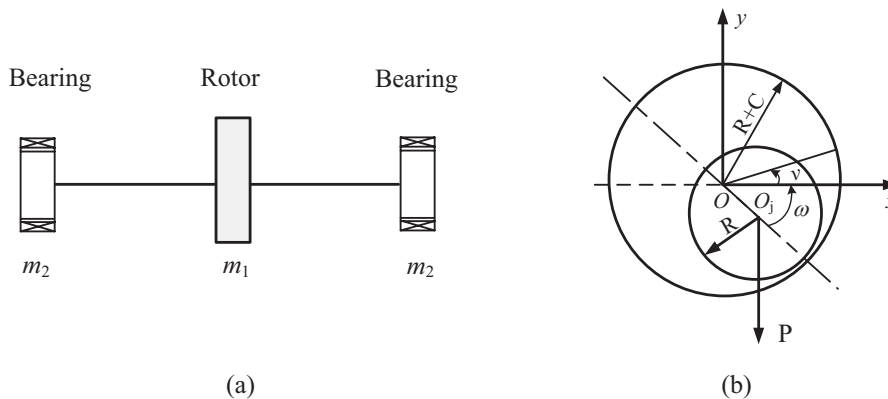
**Figure 2: (a) Profile of engine start-up and operation; (b) Profile of blade loss during start-up.  $\Delta t$  represents the duration of blade loss**

The transient response with  $\Delta t=0.01s$  compared to the case of without blade loss case is shown in Fig.3. The maximum amplitude of the transient response of the system occurs at 0.97s. The motion will decay to a steady state after a transient fluctuation. One can observe that the blade loss has generated a large amplitude transient response; hence it is of great importance to perform the blade loss response analyses for the rotor system.



**Figure 3 Transient responses at  $\Delta t=0.01s$ . The shadowy area represent the duration of the blade loss.**

**Transient response of a Jeffcott rotor**



**Figure 4: (a) Rotor system with short journal bearings; (b) Cross-section of the journal.**

Generally, it is time consuming to obtain the dynamical characteristics of the rotor by performing various transient response analyses; the rotor is reduced to a 2-DOF Jeffcott system in this study. The mass of the rotor is 120kg, the first order critical speed  $\omega_1=152\text{Hz}$ . Hence, the equivalent stiffness of the rotor is  $k_e = m\omega_1^2 = 1.1 \times 10^8 \text{ N/m}$ . The slide oil film bearings are included in the simplified model to investigate the transient dynamics of the system with nonlinear bearing forces. Fig.4(a) presents the rotor supported by symmetric bearings which is subjected to both static unbalance and external load. The equations of the motion of the journal center  $O_j$  are

$$\begin{cases} m_1 \ddot{X}_1 = -k_e(X_1 - X_2) + F_x, & m_1 \ddot{Y}_1 = -k_e(Y_1 - Y_2) + F_y - P_1 \\ m_2 \ddot{X}_2 = -2k_e(X_2 - X_1) + m_2 e \omega^2 \cos(\omega t), & m_2 \ddot{Y}_2 = -2k_e(Y_2 - Y_1) + m_2 e \omega^2 \sin(\omega t) - P_2 \end{cases} \quad (1)$$

where  $P_1$  and  $P_2$  are gravity loads,  $F_x$  and  $F_y$  are supporting forces to the rotor considering both the reaction force from the bending shaft and the oil-film forces from the bearings. The dimensionless form Eq.(3) of Eq. (1) can be obtained with the following substitutions:

$$\begin{cases} x = \frac{X}{C}, & y = \frac{Y}{C}, & \tau = \omega t, & \dot{x} = \frac{\dot{X}}{C\omega}, & \dot{y} = \frac{\dot{Y}}{C\omega}, & \ddot{x} = \frac{\ddot{X}}{C\omega^2}, & \ddot{y} = \frac{\ddot{Y}}{C\omega^2}, \\ \rho = \frac{e}{C}, & f_x = \frac{F_x}{\delta P}, & f_y = \frac{F_y}{\delta P}, & G = \frac{g}{\omega^2 C}, & m_{22} = \frac{m_2 \omega^2 C}{\delta}, & k = \frac{k_e}{\omega^2} \end{cases} \quad (2)$$

In this situation,  $f_x$  and  $f_y$  are dimensionless Journal supporting forces. The analytical form of the nonlinear journal force of the short bearing model proposed by Capone (Adiletta, 1996) is adopted in this study.

$$\begin{cases} \ddot{x}_1 = -\frac{2k}{m_1}(x_1 - x_2) + \rho \cos \tau, & \ddot{y}_1 = -\frac{2k}{m_1}(y_1 - y_2) + \rho \sin \tau - G \\ \ddot{x}_2 = -\frac{k}{m_2}(x_2 - x_1) + \frac{1}{m_{22}} f_x, & \ddot{y}_2 = -\frac{k}{m_2}(y_2 - y_1) + \frac{1}{m_{22}} f_y - G \end{cases} \quad (3)$$

The Runge-Kutta method with adaptable step size is implemented to perform the numerical integration of the governing equation.

The parameters listed in Table 3 are used to compute the transient responses of the rotor impulsively loaded by a step and a ramp mass unbalance load, respectively. The profiles of loads are given by Fig.5. Similar to the previous 2D case, the blade loss process is simulated by the continuous redistribution of the unbalance mass  $\rho$  with time, where the dimensional time is  $10/\pi \approx 3.2\text{s}$ .

For the case  $\rho=0$ , where the system only bear the gravity load under a specific speed, the orbit is illustrated in Fig.6(a). It is observed that the equilibrium positions of  $m_1$  and  $m_2$  are (0.4256, -0.3702) and (0.4256, -0.3824), from which we have  $x_1 = x_2$ . In light of Eq. (3), the  $x$ -acceleration is equal to zero and  $f_x$  should be and indeed is zero which ensures that  $m_2$  is in a balanced state. The fact that  $y_1$  and  $y_2$  are not equal is intended to generate lubricant forces to balance the gravity loads.

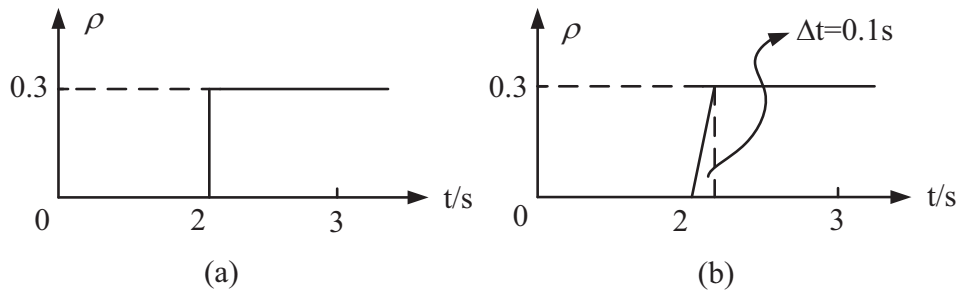


Figure 5 (a) Profile of step load, (b) Profile of ramp load

Table 3 Parameters of the rotor under gravity loads at a specific rotation speed

Item	Value
Rotor mass(kg)	114.4
Diameter(m)	0.08
Length(m)	0.03
Oil film gap(m)	0.0002
Kinetic oil viscosity( Pa·s)	0.0115
Rotation angular speed(rad/s)	$100\pi$
Computing time (dimensionless)	1000
Eccentricity $\rho$ of the load case	0.1
Stiffness of half shaft(N/m)	$1.1 \times 10^8$
Initial coordinate $(x_1, y_1, x_2, y_2)$ (dimensionless)	0.1, 0.1, 0.15, 0.15
Initial velocity $(\dot{x}_1, \dot{y}_1, \dot{x}_2, \dot{y}_2)$ (dimensionless)	-0.1, 0.1, -0.1, 0.1

From Fig.6(a) it is observed that the two orbits of  $m_1$  and  $m_2$  are almost overlap, hence in the following study only the orbit of  $m_1$  is selected as the research object. Fig.6(b) and (c) show the trajectories of the journal center when a sudden unbalance step or ramp load is applied after the journal converges to its equilibrium. The two load profiles are given by Fig.5(a). The unbalance force will push the journal away from the equilibrium center and eventually drives it to an orbit of stable limit cycle. Naturally, the ramp load case needs a longer time to progress to the limit cycle. From Fig.7, it is observed that the maximum transient amplitude of the step load be a little larger than the one of the ramp load and the rotor in both cases will evolve into an identical orbit in the end.

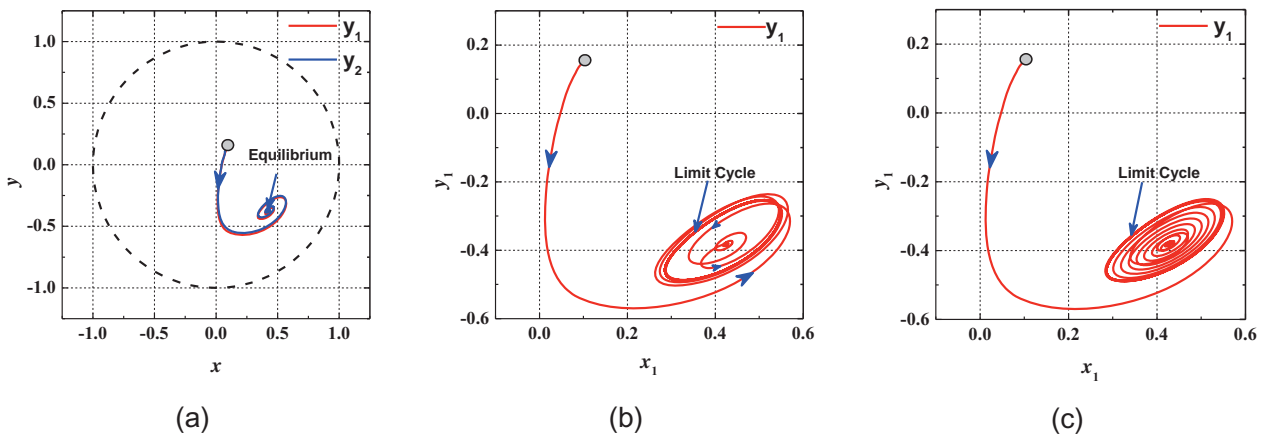
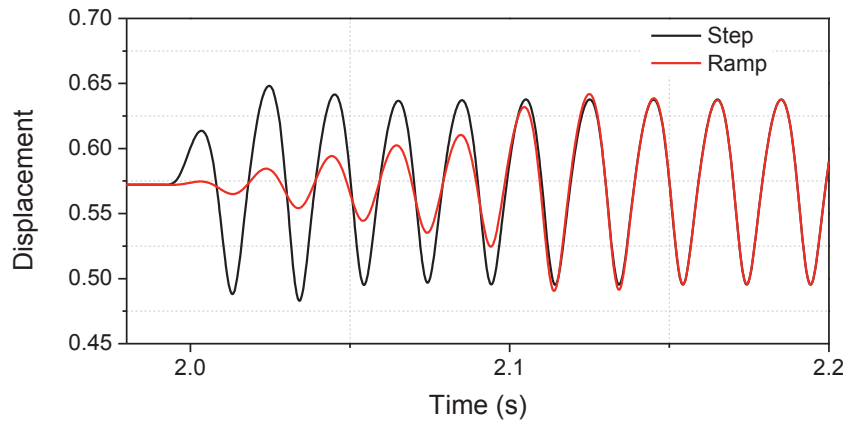


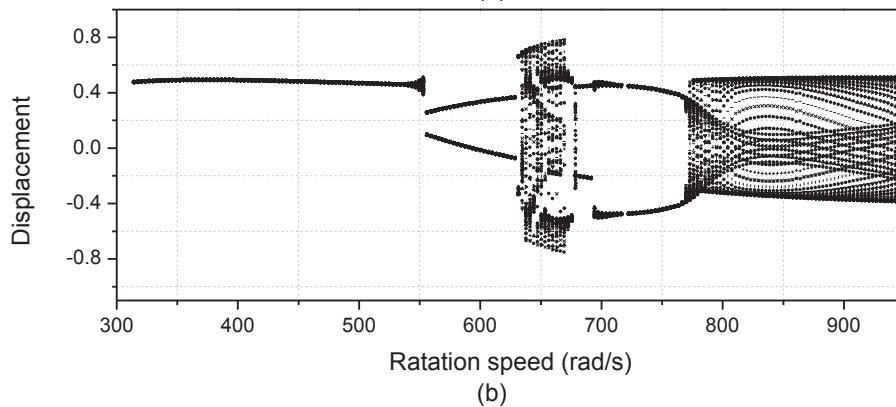
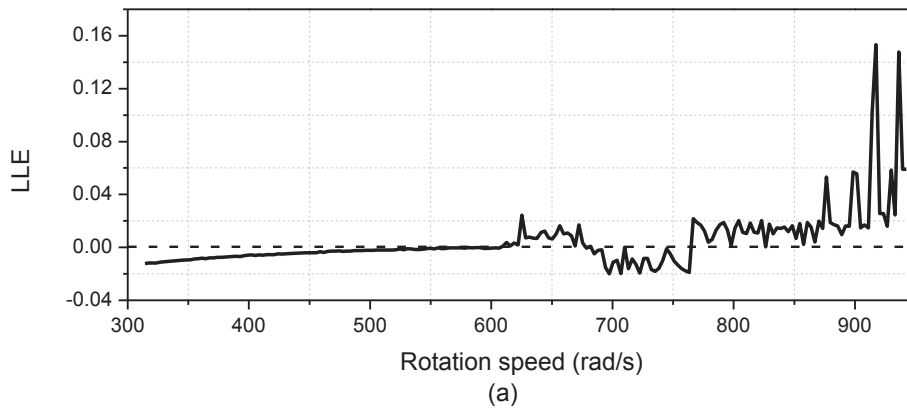
Figure 6 Results under different loads: (a) Orbit under gravity load; (b) Orbit under step load; (c) Orbit under ramp load.

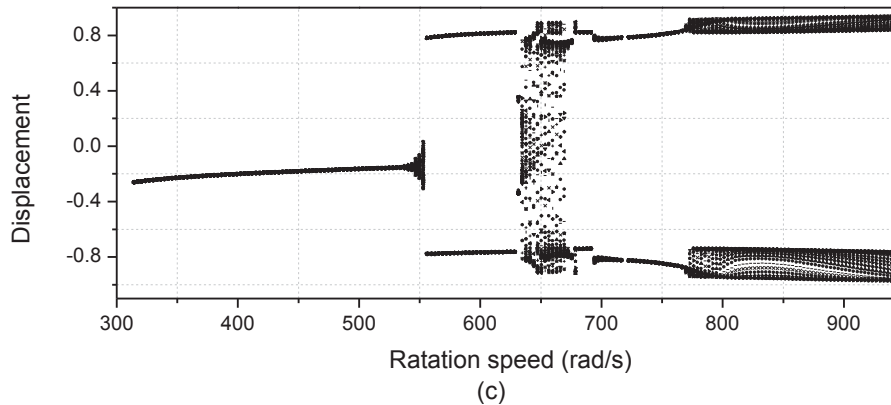




**Figure 7 Comparison of the transient response of the step load and ramp load**

At  $\rho=0.1$ , the LLE diagram (Fig.8(a)) is generated with the Benettin method (Benettin, G. and L. Galgani, 1980). The rotor is in chaotic state at the corresponding speed when the LLE is large than zero. It can be observed that the LLE diagram coincides with the two bifurcation diagrams. Two bifurcation diagrams shown in Fig.8(b) and (c) are designated to investigate the responses of the rotor with varying rotation speeds. The results show that the rotor undergoes small amplitude period motions orbiting around the equilibrium when the speeds less than 540 rad/s. After a short period of quasi-periodic evolution in the interval (540,556) rad/s, the rotor goes into a double-period orbit when the speed reaches 556 rad/s. After the speed rises up to 630rad/s, the rotor suddenly enters chaotic state at 680rad/s. Then, the rotor undergoes a short period of double period again before it evolves into another chaotic state at 768rad/s. On the whole, it is observed that the route of the state of the system from period motion to chaos is very complicated.





**Figure 8 Results of variation rotation speeds, (a) Largest Lyapunov exponent diagram; (b) bifurcation diagram of  $x_1$ ; (c) bifurcation diagram of  $y_1$ .**

## Conclusions

In this paper, two transient analyses of both a real engine rotor and a theoretical Jeffcott rotor have been conducted. A transient response analysis is conducted for start-up of the twin spool rotor shows that the blade loss will significantly influence the maximum transient response of the rotor.

Next, considering it is time consuming to perform lots of transient analysis with the 2D FEM model to get the dynamical properties of the rotor, a reduced Jeffcott rotor model supported by symmetrical slide bearings under step and ramp sudden unbalance loads has been investigated. The results show that the system will recover to a stable motion after undergoing unbalance impacts while the maximum amplitude resulting from the step load is larger than the one from ramp load. At a specific eccentricity, Poincaré sections have been constructed to investigate the responses of the rotor when the rotation speed changes. The bifurcation diagrams of displacements show that the route of the system evolves into chaos are complicated. The largest Lyapunov exponent diagram shows a good correspondence of the bifurcation diagram in indicating when the rotor evolves into chaos.

## Acknowledgments

The authors are grateful for the support from the State Key Development Program for Basic Research of China (Projects 2009CB724300 and 2011CB706504). The advice from Mr. Feng Guoquan in preparation of this paper is appreciated.

## References

- Adiletta G., Guido A. R., Rossi C. (1996), Chaotic motions of a rigid rotor in short journal bearings. *Nonlinear Dynamics*, 10, pp.251-26.
- Benettin, G. and Galgani L. et al. (1980), Lyapunov Exponents for smooth dynamical systems and for Hamiltonian systems; A method for computing all of them. Part 2: Numerical application. *Meccanica*, 15, pp. 21-30.
- Guangyoung, S. and A. Palazzolo, et al. (2008), Long duration blade loss simulations including thermal growths for dual-rotor gas turbine engine. *Journal of Sound and Vibration*, 316, pp. 147-163.
- Jing J. P. and Guan M., et al. (2004), On the non-linear dynamic behavior of a rotor–bearing system. *Journal of Sound And Vibration*, 274, pp. 1031-1044.
- Xia, Z. P. and Qiao G. et al. (2009). Nonlinear modeling and dynamic analysis of the rotor-bearing system. *Nonlinear Dynamics*, 57, pp. 559-577.

## 3D Elastostatic Boundary Element Analysis of Ultra-Thin Structures with Planar Surfaces

\*Y.C. Shiah<sup>1</sup>, Y.M. Lee<sup>2</sup>, and R.B. Yang<sup>2</sup>

<sup>1</sup> Department of Aeronautics and Astronautics  
National Cheng Kung University, Tainan 701, Taiwan.

<sup>2</sup> Department of Aerospace and Systems Engineering,  
Feng Chia University, Taichung 40724, Taiwan

\*Corresponding author: ycshiah@mail.ncku.edu.tw

### Abstract

This paper presents a regularization scheme for the nearly singular integrals used for 3D elastostatic boundary element analysis. For the regularization process, the local projection coordinates of the source point are first located via an iteration procedure. For planar elements, the boundary integrals are analytically integrated by parts to smooth the drastic fluctuations of their integrands so that the regularized forms can be numerically integrated by any conventional schemes in an usual manner. The validity of the formulations is numerically tested using the Gauss Quadrature scheme. The test shows the accuracy is satisfactory for the distance ratio (distance : element characteristic length) falling below micro-scale.

**Keywords:** Boundary integral regularization, 3D elastostatic BEM analysis

### Introduction

In these years, the boundary element method, usually abbreviated as BEM, has been widely applied to various engineering problems due to its distinctive feature that only the boundary needs discretisation. In particular, this is most advantageous in modeling three-dimensional problems with complicated geometry that demands heavy modeling efforts for the domain solution techniques, such as the finite element method (FEM) and the finite difference method. In engineering applications, ultra-thin structures are quite often applied that are characterized by their thickness dimensioned with several orders below their characteristic length. For yielding reliable results by the FEM analysis, the elements employed must have proper aspect ratios that are normally greater than 1:20. Due to this aspect-ratio constraint, the FEM-modeling of ultra-thin structures shall take tremendous amounts of elements, leading to overloading computations. Although no such issue is involved for the BEM, another difficulty of “near singularity” will arise. As has been well understood in the BEM community, approaching of the source point to the element under integration will lead to drastic fluctuation of the integrands near its projection place and cause difficulty of proper numerical integration.

Over the years, this topic of nearly singular integrals has attracted significant researches in the BEM community. The most known approaches for dealing with this issue can be referred to (e.g. Zozulya, 2010; Chen and Hong, 1999; Guz and Zozulya, 2001; Tanaka et al., 1994). For the BEM analysis, ultra-thin structures with flat or less-curved surfaces can be modeled by assemblage of planar elements. In this subcategory of planar elements, the main goal of the present work targets regularizing the boundary integrals for the BEM elastostatic analysis by an approach of “integration by parts”, abbreviated as IBP in this paper. There are too many articles to review as a complete for the topic of integral regularizations; only a few among them are mentioned herein as examples. Granados and Gallego (2001) proposed a kernels' complex regularization procedure, leading to a decomposition of the quasi-singular and quasi-hypersingular integrals in a series of simpler terms. Recently, Tomioka and Nishiyama (2010) presented a gradient field representation using an analytical regularization of a hypersingular boundary integral equation for the Helmholtz equation. For axisymmetric linear elasticity, de Lacerda and Wrobel (2001) presented a hypersingular boundary integral equation, which are regularized by employing the singularity subtraction technique. On applying the IBP, Shiah and Shi (2006) regularized the boundary integrals for the 2D anisotropic heat conduction problems. Furthermore, Shiah *et al.* (2007) applied this IBP technique to study the 2D interlaminar thermal stresses in thin layers of composites. To the authors' best

knowledge, no implementation of the IBP in 3D elastostatic BEM analysis has been reported in the open literature yet. The present work is to extend the IBP work (2006) for 2D cases to treat the boundary integrals of the 3D elastostatics for ultra-thin bodies with planar surfaces. For numerical tests, the regularized integrals of a typical case were evaluated using the conventional 14-point Gauss quadrature scheme and compared with the numerical results obtained by mathematical software. Before presenting the regularization scheme, a brief review of the boundary integral equation for 3D elastostatic analysis will be given next

### Boundary integral equation of 3D Elastostatics

In the direct formulation of BEM, the displacements  $u_i$  and the tractions  $t_i$  at the source point  $P$  and the field point  $Q$  on the surface  $S$  of an elastic body are related by the following integral equation,

$$C_{ij}(P) u_i(P) = \int_S t_i(Q) U_{ij}^*(P, Q) dS - \int_S u_i(Q) T_{ij}^*(P, Q) dS, \quad (1)$$

where  $C_{ij}$  are geometrically dependent coefficients at  $P$ ,  $q$  is an arbitrary field point inside the domain  $V$ ;  $U_{ij}^*$  and  $T_{ij}^*$  are respectively the fundamental solutions of the displacements and tractions, given for 2D isotropic elastic bodies by

$$U_{ij}^*(P, Q) = \frac{1}{16\pi G(1-\nu)r} [(3-4\nu)\delta_{ij} + r_{,i}r_{,j}], \quad (2a)$$

$$T_{ij}^*(P, Q) = \frac{-1}{8\pi(1-\nu)r^2} \left\{ r_{,k}n_k [(1-2\nu)\delta_{ij} + 3r_{,i}r_{,j}] - (1-2\nu)(r_{,i}n_j - r_{,j}n_i) \right\}, \quad (2b)$$

where  $\nu$  stands for the Poisson's ratio,  $G$  is the shear modulus,  $\delta_{ij}$  stands for the Kronecker delta defined as usual,  $n_i$  are the components of the outward normal vector, and  $r$  represents the radial distance between the source point at  $(x_1, x_2, x_3)$  and the field point at  $(xp_1, xp_2, xp_3)$  and  $r_{,i}$  represents taking partial differentiation of  $r$  with respect to  $x_i$ . They are calculated by

$$r = \sqrt{\sum_{l=1}^3 (x_l - xp_l)^2}, \quad r_{,i} = \frac{(x_i - xp_i)}{\sqrt{\sum_{l=1}^3 (x_l - xp_l)^2}}. \quad (3)$$

Apparently, when the source point approaches the field point i.e.  $r \approx 0$ , Eq.(2a) and (2b) reveal singularities with orders  $O(1/r)$  and  $O(1/r^2)$ , respectively. As the usual BEM process for solving Eq.(1), the boundary is discretized into a number of elements, say  $M$  elements, with  $k$  nodes on each one. As a result of interpolating the nodal values of  $u_i^{(c)}$ ,  $t_i^{(c)}$  by the shape functions  $N^{(c)}(\xi, \eta)$ , the displacements/tractions at  $Q$  can be written as

$$u_i(Q) = \sum_{c=1}^k N^{(c)}(\xi, \eta) u_i^{(c)}, \quad t_i(Q) = \sum_{c=1}^k N^{(c)}(\xi, \eta) t_i^{(c)}, \quad (4)$$

where  $(\xi, \eta)$  are the intrinsic local coordinates on each integration element. For an assemblage of  $M$ -elements, substitution of Eq.(4) into Eq.(1) yields a discretized integral equation as follows,

$$C_{ij}(P) u_i(P) = \sum_{m=1}^M \sum_{c=1}^k t_{i(m)}^{(c)} \int_{-1}^1 \int_{-1}^1 N^{(c)}(\xi, \eta) U_{ij}^* |J(\xi, \eta)| d\xi d\eta - \sum_{m=1}^M \sum_{c=1}^k u_{i(m)}^{(c)} \int_{-1}^1 \int_{-1}^1 N^{(c)}(\xi, \eta) T_{ij}^* |J(\xi, \eta)| d\xi d\eta, \quad (5)$$

where the subscript  $(m)$  is used to denote the  $m$ -th discretized element, and  $|J(\xi, \eta)|$  is the Jacobian transformation, defined by

$$|J(\xi, \eta)| = \sqrt{J_1^2 + J_2^2 + J_3^2}, \quad (6a)$$

$$J_1 = \left( \sum_{c=1}^k N_{,\xi}^{(c)} x_2^{(c)} \right) \left( \sum_{c=1}^k N_{,\eta}^{(c)} x_3^{(c)} \right) - \left( \sum_{c=1}^k N_{,\xi}^{(c)} x_3^{(c)} \right) \left( \sum_{c=1}^k N_{,\eta}^{(c)} x_2^{(c)} \right), \quad (6b)$$

$$J_2 = \left( \sum_{c=1}^k N_{,\xi}^{(c)} x_3^{(c)} \right) \left( \sum_{c=1}^k N_{,\eta}^{(c)} x_1^{(c)} \right) - \left( \sum_{c=1}^k N_{,\xi}^{(c)} x_1^{(c)} \right) \left( \sum_{c=1}^k N_{,\eta}^{(c)} x_3^{(c)} \right), \quad (6c)$$

$$J_3 = \left( \sum_{c=1}^k N_{,\xi}^{(c)} x_1^{(c)} \right) \left( \sum_{c=1}^k N_{,\eta}^{(c)} x_2^{(c)} \right) - \left( \sum_{c=1}^k N_{,\xi}^{(c)} x_2^{(c)} \right) \left( \sum_{c=1}^k N_{,\eta}^{(c)} x_1^{(c)} \right). \quad (6d)$$

In Eqs.(6b)-(6d), the superscript “(c)” denotes the  $c$ -th node on the  $m$ -th element;  $N_{,\xi}^{(c)}$ ,  $N_{,\eta}^{(c)}$  represent the derivatives of the shape functions taken with respect to  $\xi$  and  $\eta$ , respectively. For simplification, the integrals in Eq.(5) are symbolized by

$$E_{ij}^{(c)} = \int_{-1}^1 \int_{-1}^1 N^{(c)}(\xi, \eta) U_{ij}^* |J(\xi, \eta)| d\xi d\eta, \quad (7a)$$

$$F_{ij}^{(c)} = \int_{-1}^1 \int_{-1}^1 N^{(c)}(\xi, \eta) T_{ij}^* |J(\xi, \eta)| d\xi d\eta. \quad (7b)$$

Since quadratic elements are usually employed for BEM analysis, the following derivations will be presented only for this particular case using 8 nodes for a quadrilateral element, i.e.  $k=8$ . Also, it should be noted that the presented formulations may be applied to a triangular element treated as a degenerate quadratic element, where three nodes of a quadrilateral side are placed at the same vertex of the triangular element. For the 8-node quadrilateral element, the shape functions take the following forms,

$$\begin{aligned} N^{(1)} &= \frac{-1}{4}(1-\xi)(1-\eta)(1+\xi+\eta), & N^{(2)} &= \frac{1}{2}(1-\xi^2)(1-\eta), \\ N^{(3)} &= \frac{1}{4}(1+\xi)(1-\eta)(\xi-\eta-1), & N^{(4)} &= \frac{1}{2}(1+\xi)(1-\eta^2), \\ N^{(5)} &= \frac{1}{4}(1+\xi)(1+\eta)(\xi+\eta-1), & N^{(6)} &= \frac{1}{2}(1-\xi^2)(1+\eta), \\ N^{(7)} &= \frac{1}{4}(1-\xi)(1+\eta)(-\xi+\eta-1), & N^{(8)} &= \frac{1}{2}(1-\xi)(1-\eta^2). \end{aligned} \quad (8)$$

Next, the processes for regularizing these integrals with different singularity orders will be elaborated separately

### Integral regularization for $E_{ij}^{(c)}$

By substituting the fundamental displacements into the integrand and interpolating the coordinates using the 8-node shape functions, the integral can be expressed as

$$E_{ij}^{(c)} = \frac{1}{16\pi G(1-\nu)} \int_{-1}^1 \int_{-1}^1 \frac{N^{(c)} |J| [(3-4\nu)\delta_{ij} + r_i r_j]}{\sqrt{D(\xi, \eta)}} d\xi d\eta, \quad (9)$$

where  $D(\xi, \eta)$ , abbreviated simply as  $D$ , is defined by

$$D = \sum_{l=1}^3 \left( \sum_{m=1}^8 N^{(m)} x_l^{(m)} - x p_l \right)^2. \quad (10)$$

By substituting Eq.(3) into the integrand in Eq.(9), the integral can be rewritten as

$$E_{ij}^{(c)} = \frac{1}{16\pi G(1-\nu)} \left( \overline{E}_{ij}^{(c)} + \overline{\overline{E}}_{ij}^{(c)} \right), \quad (11)$$

where

$$\overline{E}_{ij}^{(c)} = (3-4\nu)\delta_{ij} \int_{-1}^1 \int_{-1}^1 \frac{N^{(c)} |J|}{\sqrt{D(\xi, \eta)}} d\xi d\eta, \quad (12a)$$

$$E_{ij}^{(c)} = \int_{-1}^1 \int_{-1}^1 \frac{N^{(c)} |J| \left( \sum_{m=1}^8 N^{(m)} x_i^{(m)} - xp_i \right) \left( \sum_{m=1}^8 N^{(m)} x_j^{(m)} - xp_j \right)}{\sqrt{D(\xi, \eta)^3}} d\xi d\eta . \quad (12b)$$

For a quadrilateral planar element depicted in Fig.1, the mid-point coordinates must satisfy

$$\begin{aligned} x_i^{(2)} &= (x_i^{(1)} + x_i^{(3)})/2, \quad x_i^{(4)} = (x_i^{(3)} + x_i^{(5)})/2, \\ x_i^{(6)} &= (x_i^{(5)} + x_i^{(7)})/2, \quad x_i^{(8)} = (x_i^{(1)} + x_i^{(7)})/2. \end{aligned} \quad (13)$$

As a direct consequence of substituting Eqs.(13) and the shape functions into Eq.(10), one obtains

$$D = \sum_{i=1}^3 A_i(\eta) \xi^2 + \sum_{i=1}^3 B_i(\eta) \xi + \sum_{i=1}^3 C_i(\eta), \quad (14)$$

where

$$A_i(\eta) = \left[ \left( x_i^{(\overline{1,3})} + x_i^{(\overline{5,7})} \right) \eta - \left( x_i^{(\overline{1,3})} - x_i^{(\overline{5,7})} \right) \right]^2 / 16, \quad (15a)$$

$$\begin{aligned} B_i(\eta) &= \left( \left( x_i^{(\overline{3,5})} \right)^2 - \left( x_i^{(\overline{1,7})} \right)^2 \right) \eta^2 / 8 + \left[ x_i^{(\overline{1,3})} \left( x_i^{(2)} - xp_i \right) + x_i^{(\overline{5,7})} \left( x_i^{(6)} - xp_i \right) \right] \eta / 2 \\ &\quad - \left( x_i^{(\overline{1,3})} - x_i^{(\overline{5,7})} \right) \left( x_i^{(2)} + x_i^{(6)} - 2xp_i \right) / 4 \end{aligned} \quad (15b)$$

$$C_i(\eta) = \left[ \left( x_i^{(2)} - x_i^{(6)} \right) \eta - \left( x_i^{(2)} + x_i^{(6)} - 2xp_i \right) \right]^2 / 4. \quad (15c)$$

and the  $\overline{x_i^{(m,n)}}$  is defined by

$$\overline{x_i^{(m,n)}} = x_i^{(m)} - x_i^{(n)}. \quad (16)$$

In brief, Eq.(10) is rewritten as

$$D = \overline{A}(\eta) \xi^2 + \overline{B}(\eta) \xi + \overline{C}(\eta), \quad (17)$$

where

$$\overline{A}(\eta) = \sum_{i=1}^3 A_i(\eta), \quad \overline{B}(\eta) = \sum_{i=1}^3 B_i(\eta), \quad \overline{C}(\eta) = \sum_{i=1}^3 C_i(\eta). \quad (18)$$

Recall the scheme of IBP, giving

$$\int_a^b U dV = U \cdot V \Big|_a^b - \int_a^b V dU. \quad (19)$$

For applying the IBP to Eq.(12a) with respect to  $\xi$ , one may let

$$U = N^{(c)} |J|, \quad dV = \frac{d\xi}{\sqrt{\overline{A}(\eta) \xi^2 + \overline{B}(\eta) \xi + \overline{C}(\eta)}}, \quad (20)$$

and the followings are obtained,

$$dU = NJ^{(c)} d\xi, \quad V = \frac{1}{\sqrt{\overline{A}(\eta)}} \ln \left( \frac{2\overline{A}(\eta) \xi + \overline{B}(\eta)}{\sqrt{\overline{A}(\eta)}} + 2\sqrt{D(\xi, \eta)} \right), \quad (21)$$

where

$$NJ^{(c)} = \partial \left( N^{(c)} |J| \right) / \partial \xi. \quad (22)$$

Thus, operation of the IBP by Eq.(19) yields

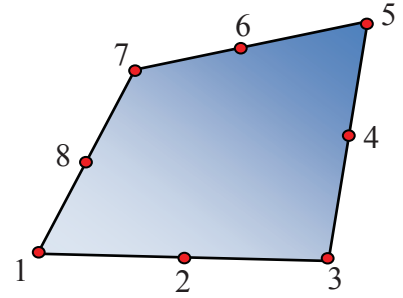


Fig.1: Nodes of a quadrilateral element

$$\int_{-1}^1 \int_{-1}^1 \frac{N^{(c)} |J|}{\sqrt{D(\xi, \eta)}} d\xi d\eta = \int_{-1}^1 G(\xi, \eta) \ln \left( \frac{2\bar{A}(\eta)\xi + \bar{B}(\eta)}{\sqrt{A(\eta)}} + 2\sqrt{D(\xi, \eta)} \right) \Big|_{\xi=-1}^{\xi=1} d\eta - \int_{-1}^1 \int_{-1}^1 F(\xi, \eta) \ln \left( \frac{2\bar{A}(\eta)\xi + \bar{B}(\eta)}{\sqrt{A(\eta)}} + 2\sqrt{D(\xi, \eta)} \right) d\xi d\eta \quad (23)$$

where

$$G(\xi, \eta) = \frac{N^{(c)} |J|}{\sqrt{A(\eta)}}, \quad F(\xi, \eta) = \frac{NJ'^{(c)}}{\sqrt{A(\eta)}}. \quad (24)$$

Still, both integrals on the right hand side of Eq.(23) reveal weak singularity that needs further regularization. For this, the single integral is expressed as

$$\int_{-1}^1 G(\xi, \eta) \ln \left( \frac{2\bar{A}(\eta)\xi + \bar{B}(\eta)}{\sqrt{A(\eta)}} + 2\sqrt{D(\xi, \eta)} \right) \Big|_{\xi=-1}^{\xi=1} d\eta = \int_{-1}^1 \left( \bar{G}(\xi', \eta) \Big|_{\xi'=1} - \bar{G}(\xi', \eta) \Big|_{\xi'=-1} \right) d\eta \quad (25)$$

where  $\bar{G}(\xi', \eta)$  is defined by

$$\bar{G}(\xi', \eta) = G(\xi', \eta) \ln \left( \frac{2\bar{A}(\eta)\xi' + \bar{B}(\eta)}{\sqrt{A(\eta)}} + 2\sqrt{D(\xi', \eta)} \right). \quad (26)$$

Firstly, the integral is rewritten as

$$\int_{-1}^1 \bar{G}(\xi', \eta) d\eta = \int_{-1}^1 \left( \bar{G}(\xi', \eta) \sqrt{\eta - \eta_0} \right) \frac{1}{\sqrt{\eta - \eta_0}} d\eta, \quad (27)$$

where  $\eta_0$  is the  $\eta$ -coordinate of the source projection on the integration element. Numerical determination of  $\eta_0$  will be elaborated later. For performing the IBP using Eq.(19), one may take

$$U = \bar{G}(\xi', \eta) \sqrt{\eta - \eta_0}, \quad dV = \frac{d\eta}{\sqrt{\eta - \eta_0}} \quad (28)$$

As a result of carrying out the IBP followed by some algebraic arrangements, one obtains

$$\int_{-1}^1 \bar{G}(\xi', \eta) d\eta = \bar{G}(\xi', \eta) (\eta - \eta_0) \Big|_{\eta=-1}^{\eta=1} - \int_{-1}^1 \bar{G}'_{\eta}(\xi', \eta) (\eta - \eta_0) d\eta, \quad (29)$$

where

$$\bar{G}'_{\eta}(\xi', \eta) = \frac{\partial \bar{G}(\xi', \eta)}{\partial \eta}. \quad (30)$$

Obviously, due to the presence of  $(\eta - \eta_0)$ , no more drastic fluctuation of the integrand will be present when the source point approaches the element at its projection coordinates  $(\xi_0, \eta_0)$  and thus, the single integral on the right hand side of Eq.(29) turns out to be regular.

Next, the effort is turned to regularize the double integral in Eq.(23). For using Eq.(19), the following substitutions are made,

$$U = F(\xi, \eta), \quad dV = \ln \left( \frac{2\bar{A}(\eta)\xi + \bar{B}(\eta)}{\sqrt{A(\eta)}} + 2\sqrt{D(\xi, \eta)} \right) d\xi. \quad (31)$$

Thus, it follows

$$dU = F'_\xi(\xi, \eta) d\xi, \quad V = \frac{2\bar{A}(\eta)\xi + \bar{B}(\eta)}{2\bar{A}(\eta)} \ln \left( \frac{2\bar{A}(\eta)\xi + \bar{B}(\eta)}{\sqrt{\bar{A}(\eta)}} + 2\sqrt{D(\xi, \eta)} \right) - \sqrt{\frac{D(\xi, \eta)}{\bar{A}(\eta)}}, \quad (32)$$

where  $F'_\xi(\xi, \eta) = \partial F(\xi, \eta) / \partial \xi$ . Consequentially, the use of IBP by Eq.(19) yields

$$\begin{aligned} & \int_{-1}^1 \int_{-1}^1 F(\xi, \eta) \ln \left( \frac{2\bar{A}(\eta)\xi + \bar{B}(\eta)}{\sqrt{\bar{A}(\eta)}} + 2\sqrt{D(\xi, \eta)} \right) d\xi d\eta \\ &= \int_{-1}^1 F(\xi, \eta) \left[ \frac{2\bar{A}(\eta)\xi + \bar{B}(\eta)}{2\bar{A}(\eta)} \ln \left( \frac{2\bar{A}(\eta)\xi + \bar{B}(\eta)}{\sqrt{\bar{A}(\eta)}} + 2\sqrt{D(\xi, \eta)} \right) - \sqrt{\frac{D(\xi, \eta)}{\bar{A}(\eta)}} \right]_{\xi=-1}^{\xi=1} d\eta \quad (33) \\ & - \int_{-1}^1 \int_{-1}^1 F'_\xi(\xi, \eta) \left[ \frac{2\bar{A}(\eta)\xi + \bar{B}(\eta)}{2\bar{A}(\eta)} \ln \left( \frac{2\bar{A}(\eta)\xi + \bar{B}(\eta)}{\sqrt{\bar{A}(\eta)}} + 2\sqrt{D(\xi, \eta)} \right) - \sqrt{\frac{D(\xi, \eta)}{\bar{A}(\eta)}} \right] d\xi d\eta \end{aligned}$$

Taking partial differentiation of  $D(\xi, \eta)$  defined in Eq.(17) yields

$$\partial D(\xi, \eta) / \partial \xi = 2\bar{A}(\eta)\xi + \bar{B}(\eta). \quad (34)$$

Under the circumstance when the source point approaches the element near its projection point  $(\xi_0, \eta_0)$ , one will have the following conditions:

$$D(\xi_0, \eta_0) \approx 0, \quad 2\bar{A}(\eta_0)\xi_0 + \bar{B}(\eta_0) = 0. \quad (35)$$

From the above conditions, it can be seen that the double integral on the right hand side of Eq.(33) are truly regular.

For the regularization of the integral in Eq.(12b) using Eq.(19), one may take

$$U = N^{(c)} |J| \left( \sum_{m=1}^8 N^{(m)} x_i^{(m)} - xp_i \right) \left( \sum_{m=1}^8 N^{(m)} x_j^{(m)} - xp_j \right), \quad (36a)$$

$$dV = \frac{d\xi}{\sqrt{\left( \bar{A}(\eta)\xi^2 + \bar{B}(\eta)\xi + \bar{C}(\eta) \right)^3}}. \quad (36b)$$

Following the similar IBP process as before, one may obtain

$$\begin{aligned} \bar{\bar{E}}_{ij}^{(c)} &= 2 \int_{-1}^1 \frac{\left[ 2\bar{A}(\eta)\xi' + \bar{B}(\eta) \right] H^{(c)}}{\left[ 4\bar{A}(\eta)\bar{C}(\eta) - \bar{B}(\eta)^2 \right] \sqrt{D(\xi', \eta)}} \Bigg|_{\xi'=-1}^{\xi'=1} d\eta \\ & - 2 \int_{-1}^1 \int_{-1}^1 \frac{\left[ 2\bar{A}(\eta)\xi + \bar{B}(\eta) \right] H'_\xi{}^{(c)}}{\left[ 4\bar{A}(\eta)\bar{C}(\eta) - \bar{B}(\eta)^2 \right] \sqrt{D(\xi, \eta)}} d\xi d\eta \end{aligned} \quad (37)$$

where

$$H^{(c)} = N^{(c)} |J| \left( \sum_{m=1}^8 N^{(m)} x_i^{(m)} - xp_i \right) \left( \sum_{m=1}^8 N^{(m)} x_j^{(m)} - xp_j \right), \quad H'_\xi{}^{(c)} = \frac{\partial H^{(c)}}{\partial \xi}. \quad (38)$$

It is noted that when the source point approaches the projection point  $(\xi_0, \eta_0)$ , one will have the following conditions,

$$H'_\xi{}^{(c)} \approx 0, \quad 2\bar{A}(\eta_0)\xi_0 + \bar{B}(\eta_0) \approx 0. \quad (39)$$

Thus, there is no spike-shape variation of the integrand of the double integral in Eq.(37). However, there is still relatively large variation of the integrands due to the presence of the term  $4\bar{A}(\eta)\bar{C}(\eta) - \bar{B}(\eta)^2$  in the denominator. This can be resolved by simply sub-dividing the integral range at the projection point without resorting to further regularization processes. Up to this point,



the  $E_{ij}^{(c)}$  may be numerically integrated using the regularized formulations presented above. Next, the task remains to treat the other integral by the similar IBP processes as before.

### Integral regularization for $F_{ij}^{(c)}$

As aforementioned, since hyper-singularity is present for the integral  $F_{ij}^{(c)}$ . numerical integrations by any conventional means shall fail to yield proper values. By substituting the fundamental solution in Eq.(2b) into the integrand, the integral is written as

$$F_{ij}^{(c)} = \frac{-1}{8\pi(1-\nu)} \int_{-1}^1 \int_{-1}^1 \frac{N^{(c)}(\xi, \eta) |J(\xi, \eta)|}{r^2} \left\{ \begin{array}{l} r_{,k} n_k [(1-2\nu)\delta_{ij} + 3r_{,i} r_{,j}] \\ -(1-2\nu)(r_{,i} n_j - r_{,j} n_i) \end{array} \right\} d\xi d\eta, \quad (40)$$

where  $n_i$ , the components of the unit outward normal vector, are given by

$$n_i = \frac{J_i}{|J(\xi, \eta)|}, \quad (41)$$

and for 8-node quadrilateral planar element,  $J_i$  are calculated by

$$J_i = \varpi_{i1}\xi + \varpi_{i2}\eta + \varpi_{i3}, \quad (42)$$

where

$$\varpi_{i1} = \frac{1}{8} \left( x_{i+1}^{(5,7)} x_{i+2}^{(1,3)} - x_{i+2}^{(5,7)} x_{i+1}^{(1,3)} \right), \quad (43a)$$

$$\varpi_{i2} = \frac{1}{8} \left( x_{i+1}^{(3,5)} x_{i+2}^{(1,7)} - x_{i+2}^{(3,5)} x_{i+1}^{(1,7)} \right), \quad (43b)$$

$$\varpi_{i3} = \frac{1}{8} \left( x_{i+1}^{(1,5)} x_{i+2}^{(3,7)} - x_{i+2}^{(1,5)} x_{i+1}^{(3,7)} \right). \quad (43c)$$

In Eqs.(43a)-(43c), the subscript “ $i$ ” follows the cyclic rule  $i=(i-3)$  for  $i>3$ . By substituting Eq.(41) and Eq.(42) into Eq.(40), one may sort out terms to rewrite the expression as

$$F_{ij}^{(c)} = \frac{-1}{8\pi(1-\nu)} \left[ (1-2\nu) \overline{F}_{ij}^{(c)} + 3 \overline{\overline{F}}_{ij}^{(c)} \right], \quad (44)$$

where

$$\overline{F}_{ij}^{(c)} = \int_{-1}^1 \int_{-1}^1 \frac{\overline{\Lambda}_{ij}^{(c)}(\xi, \eta)}{\sqrt{D^3}} d\xi d\eta, \quad (45a)$$

$$\overline{\overline{F}}_{ij}^{(c)} = \int_{-1}^1 \int_{-1}^1 \frac{\overline{\overline{\Lambda}}_{ij}^{(c)}(\xi, \eta)}{\sqrt{D^5}} d\xi d\eta, \quad (45b)$$

and  $\overline{\Lambda}_{ij}^{(c)}(\xi, \eta)$ ,  $\overline{\overline{\Lambda}}_{ij}^{(c)}(\xi, \eta)$  are given by

$$\overline{\Lambda}_{ij}^{(c)}(\xi, \eta) = N^{(c)} \delta_{ij} (X_k J_k) - X_i J_j + X_j J_i, \quad (45c)$$

$$\overline{\overline{\Lambda}}_{ij}^{(c)}(\xi, \eta) = N^{(c)} (X_k J_k) X_i X_j. \quad (45d)$$

In Eqs.(45a)-(45d),  $X_i$  is defined by

$$X_i = x_i - x p_i. \quad (46)$$

For analytically integrating the both integrals, they are re-expressed as

$$\overline{F}_{ij}^{(c)} = \int_{-1}^1 \int_{-1}^1 \frac{\sum_{m=0}^3 \Gamma_{ijm}^{(c)}(\eta) \xi^m}{\sqrt{D^3}} d\xi d\eta, \quad (47a)$$

$$\overline{\overline{F}}_{ij}^{(c)} = \int_{-1}^1 \int_{-1}^1 \frac{\sum_{m=0}^5 \Omega_{ijm}^{(c)}(\eta) \xi^m}{\sqrt{D^5}} d\xi d\eta, \tag{47b}$$

where  $\Gamma_{ijm}^{(c)}$ ,  $\Omega_{ijm}^{(c)}$  can be numerically determined by

$$\Gamma_{ijm}^{(c)}(\eta) = \frac{\left[ \partial^m \overline{\Lambda}_{ij}^{(c)}(\xi, \eta) / \partial \xi^m \right]_{\xi=0}}{m!}, \tag{48a}$$

$$\Omega_{ijm}^{(c)}(\eta) = \frac{\left[ \partial^m \overline{\overline{\Lambda}}_{ij}^{(c)}(\xi, \eta) / \partial \xi^m \right]_{\xi=0}}{m!}. \tag{48b}$$

In Eqs.(48a) and (48b), the partial differentiations can be performed using Eqs.(45c)-(45d) in a straightforward manner and thus, their explicit expressions are not presented here. As a result, analytical integration of Eq.(47a) with respect to  $\xi$  yields

$$\overline{F}_{ij}^{(c)} = \int_{-1}^1 \left\{ \frac{1}{\overline{A}\sqrt{D}} \left[ \frac{\Psi_{ij}^{(c)}(\xi', \eta)}{\overline{A}(4\overline{AC} - \overline{B}^2)} + \Gamma_{ij3}^{(c)} \xi'^2 \right] + \frac{(2\overline{A}\Gamma_{ij2}^{(c)} - 3\overline{B}\Gamma_{ij3}^{(c)})}{2\sqrt{\overline{A}^5}} \ln \left( \frac{2\overline{A}\xi' + \overline{B}}{\sqrt{\overline{A}}} + 2\sqrt{D} \right) \right\} \Bigg|_{\xi'=-1}^{\xi'=1} d\eta, \tag{49}$$

where

$$\Psi_{ij}^{(c)}(\xi', \eta) = \begin{bmatrix} 4\overline{A}^3 \Gamma_{ij0}^{(c)} - 2\overline{A}^2 (\overline{B}\Gamma_{ij1}^{(c)} + 2\overline{C}\Gamma_{ij2}^{(c)}) \\ -3\overline{B}^3 \Gamma_{ij3}^{(c)} + 2\overline{A}\overline{B} (\overline{B}\Gamma_{ij2}^{(c)} + 5\overline{C}\Gamma_{ij3}^{(c)}) \\ 2\overline{A}^2 (\overline{B}\Gamma_{ij0}^{(c)} - 2\overline{C}\Gamma_{ij1}^{(c)}) - 3\overline{B}^2 \overline{C}\Gamma_{ij3}^{(c)} \\ + 2\overline{A}\overline{C} (\overline{B}\Gamma_{ij2}^{(c)} + 4\overline{C}\Gamma_{ij3}^{(c)}) \end{bmatrix} \xi'. \tag{50}$$

It should be noted that near-singularity still appears in the integral in Eq.(49) due to

$$4\overline{A}(\eta_0)\overline{C}(\eta_0) - \overline{B}(\eta_0)^2 \approx 0, \tag{51}$$

and its associated integral is written as

$$\overline{f}_{ij}^{(c)} = \int_{-1}^1 \left[ \frac{\Psi_{ij}^{(c)}(\xi', \eta)}{\overline{A}^2 \sqrt{D}(4\overline{AC} - \overline{B}^2)} \right] \Bigg|_{\xi'=-1}^{\xi'=1} d\eta. \tag{52}$$

From the definitions of  $\overline{A}(\eta) \sim \overline{C}(\eta)$  given in Eqs.(15a)-(15c) and (18), it is clear that one may rewrite  $4\overline{A}(\eta)\overline{C}(\eta) - \overline{B}(\eta)^2$ , being represented by  $K(\eta)$ , into a quartic function of  $\eta$ , namely

$$K(\eta) = 4\overline{A}(\eta)\overline{C}(\eta) - \overline{B}(\eta)^2 = \sum_{m=0}^4 \alpha_m \eta^m. \tag{53}$$

Instead of explicitly sorting out all coefficients one by one, one may calculate the coefficients  $\alpha_m$  via the fundamental calculus processes as follows:

$$\alpha_m = \frac{\left[ \partial^m K(\eta) / \partial \eta^m \right]_{\eta=0}}{m!}. \tag{54}$$

For using Eq.(54), taking partial differentiation of  $\bar{A}(\eta) \sim \bar{C}(\eta)$  will be involved, which can be done in a straightforward manner. From the Ferrari's method,  $K(\eta)$  can be factored into a product of two quadratic polynomials, expressed as

$$K(\eta) = \alpha_4 H_1(\eta) H_2(\eta), \quad (55)$$

where

$$H_1(\eta) = (\eta^2 + \beta_1 \eta + \beta_0), \quad H_2(\eta) = (\eta^2 + \gamma_1 \eta + \gamma_0). \quad (56)$$

In Eqs.(57), the very explicit expressions for all coefficients, given in terms of  $\alpha_m$ , can be referred to (Wikipedia online). It is worth mentioning that only one of the two functions, either  $H_1(\eta)$  or  $H_2(\eta)$  but not both at the same time, shall approach null for the case of near singularity. Take it as an example when

$$|H_1(\eta_0)| < \varepsilon, \quad |H_2(\eta_0)| \gg \varepsilon, \quad (57)$$

where  $\varepsilon$  is a very small value. For regularization treatment, the integral in Eq.(53) is rewritten as

$$\int_{-1}^1 \frac{\Psi_{ij}^{(c)}(\xi', \eta)}{\bar{A}^2 \sqrt{D(4\bar{A}\bar{C} - \bar{B}^2)}} d\eta = \frac{1}{\alpha_4} \int_{-1}^1 \left[ \frac{\Psi_{ij}^{(c)}(\xi', \eta)}{\bar{A}^2 \sqrt{D} H_2(\eta)} \right] \frac{1}{H_1(\eta)} d\eta, \quad (58)$$

For the IBP process using Eq.(19), one may take

$$U = \left[ \frac{\Psi_{ij}^{(c)}(\xi', \eta)}{\bar{A}^2 \sqrt{D} H_2(\eta)} \right], \quad dV = \frac{d\eta}{H_1(\eta)}. \quad (59)$$

As a result of performing the IBP by Eq.(19), one obtains

$$\bar{f}_{ij}^{(c)} = \frac{-2}{\alpha_4 \sqrt{\beta_1^2 - 4\beta_0}} \left\{ \begin{array}{l} \Phi_{ij}^{(c)}(\eta) \tanh^{-1} \left( \frac{2\eta + \beta_1}{\sqrt{\beta_1^2 - 4\beta_0}} \right) \Big|_{\eta=-1}^{\eta=1} \\ - \int_{-1}^1 \Phi_{ij}^{(c)}(\eta) \tanh^{-1} \left( \frac{2\eta + \beta_1}{\sqrt{\beta_1^2 - 4\beta_0}} \right) d\eta \end{array} \right\}, \quad (60)$$

where

$$\Phi_{ij}^{(c)}(\eta) = \frac{\Psi_{ij}^{(c)}(\xi', \eta)}{\bar{A}^2(\eta) H_2(\eta) \sqrt{D(\xi', \eta)}} \Big|_{\xi'=-1}^{\xi'=1}, \quad \Phi_{ij}^{(c)'}(\eta) = \frac{\partial \Phi_{ij}^{(c)}(\eta)}{\partial \eta}. \quad (61)$$

Eventually, the integral  $\bar{F}_{ij}^{(c)}$  is thus given by

$$\bar{F}_{ij}^{(c)} = \bar{f}_{ij}^{(c)} + \int_{-1}^1 \left[ \frac{\Gamma_{ij3}^{(c)} \xi'^2}{\bar{A} \sqrt{D}} + \frac{(2\bar{A} \Gamma_{ij2}^{(c)} - 3\bar{B} \Gamma_{ij3}^{(c)})}{2\sqrt{\bar{A}^5}} \ln \left( \frac{2\bar{A} \xi' + \bar{B}}{\sqrt{\bar{A}}} + 2\sqrt{D} \right) \right]_{\xi'=-1}^{\xi'=1} d\eta. \quad (62)$$

Next, the similar regularization treatment can be carried out for  $\bar{\bar{F}}_{ij}^{(c)}$ , given in Eq.(47b). Analytical integration of the integral with respect to  $\xi$  leads to

$$\bar{\bar{F}}_{ij}^{(c)} = \bar{f}_{ij}^{(c)} + \int_{-1}^1 \left[ \frac{\Omega_{ij5}^{(c)} \xi'^4}{\bar{A} \sqrt{D^3}} + \frac{(2\bar{A} \Omega_{ij4}^{(c)} - 5\bar{B} \Omega_{ij5}^{(c)})}{2\sqrt{\bar{A}^7}} \ln \left( \frac{2\bar{A} \xi' + \bar{B}}{2\sqrt{\bar{A}}} + \sqrt{D(\xi', \eta)} \right) \right]_{\xi'=-1}^{\xi'=1} d\eta, \quad (63)$$

where

$$\overline{f}_{ij}^{(c)} = \int_{-1}^1 \frac{\sum_{k=0}^3 \Upsilon_{ijk}^{(c)} \xi^k / \sqrt{D^3} \Big|_{\xi^i=-1}^{\xi^i=1}}{3\overline{A}^3 (4\overline{AC} - \overline{B}^2)^2} d\eta, \quad (64)$$

and the  $\Upsilon_{ijk}^{(c)}$  is defined as follows:

$$\begin{aligned} \Upsilon_{ij3}^{(c)} = & 4\Omega_{ij5}^{(c)} \overline{AB} \left( 5\overline{B}^4 + 64\overline{A}^2 \overline{C}^2 - 37\overline{AC} \overline{B}^2 \right) - 16\Omega_{ij1}^{(c)} \overline{A}^5 \overline{B} \\ & - 8\Omega_{ij4}^{(c)} \overline{A}^2 \left( 8\overline{A}^2 \overline{C}^2 + \overline{B}^4 - 7\overline{AC} \overline{B}^2 \right) + 32\Omega_{ij0}^{(c)} \overline{A}^6, \end{aligned} \quad (65a)$$

$$\begin{aligned} & - 2\Omega_{ij3}^{(c)} \overline{A}^3 \overline{B} \left( 12\overline{AC} - \overline{B}^2 \right) + 4\Omega_{ij2}^{(c)} \overline{A}^4 \left( 4\overline{AC} + \overline{B}^2 \right) \\ \Upsilon_{ij2}^{(c)} = & 3\Omega_{ij5}^{(c)} \left( 16\overline{A}^2 \overline{B}^2 \overline{C}^2 + 64\overline{A}^3 \overline{C}^3 - 30\overline{B}^4 \overline{AC} + 5\overline{B}^6 \right) \\ & + \left( 6\Omega_{ij2}^{(c)} \overline{A}^3 \overline{B} - 12\Omega_{ij3}^{(c)} \overline{C} \overline{A}^3 \right) \left( 4\overline{AC} + \overline{B}^2 \right), \end{aligned} \quad (65b)$$

$$\begin{aligned} & + 6\Omega_{ij4}^{(c)} \overline{AB}^3 \left( 6\overline{AC} - \overline{B}^2 \right) - 24\Omega_{ij1}^{(c)} \overline{A}^4 \overline{B}^2 + 48\Omega_{ij0}^{(c)} \overline{A}^5 \overline{B} \\ \Upsilon_{ij1}^{(c)} = & 6\Omega_{ij5}^{(c)} \overline{BC} \left( 5\overline{B}^4 - 35\overline{AC} \overline{B}^2 + 52\overline{A}^2 \overline{C}^2 \right) - 48\Omega_{ij3}^{(c)} \overline{A}^3 \overline{BC}^2 \\ & + 12\Omega_{ij4}^{(c)} \overline{AC} \left( 7\overline{AC} \overline{B}^2 - 4\overline{A}^2 \overline{C}^2 - \overline{B}^4 \right) + 24\Omega_{ij2}^{(c)} \overline{A}^3 \overline{B}^2 \overline{C}, \end{aligned} \quad (65c)$$

$$\begin{aligned} & + \left( 12\Omega_{ij0}^{(c)} \overline{A}^4 - 6\Omega_{ij1}^{(c)} \overline{A}^3 \overline{B} \right) \left( 4\overline{AC} + \overline{B}^2 \right) \\ \Upsilon_{ij0}^{(c)} = & \Omega_{ij5}^{(c)} \overline{C}^2 \left( 15\overline{B}^4 - 100\overline{AC} \overline{B}^2 + 128\overline{A}^2 \overline{C}^2 \right) + 16\Omega_{ij2}^{(c)} \overline{A}^3 \overline{C}^2 \overline{B} \\ & + 2\Omega_{ij4}^{(c)} \overline{ABC}^2 \left( 20\overline{AC} - 3\overline{B}^2 \right) - 32\Omega_{ij3}^{(c)} \overline{A}^3 \overline{C}^3 \end{aligned} \quad (65d)$$

$$- 4\Omega_{ij1}^{(c)} \overline{A}^3 \overline{C} \left( 4\overline{AC} + \overline{B}^2 \right) + 2\Omega_{ij0}^{(c)} \overline{A}^3 \overline{B} \left( 12\overline{AC} - \overline{B}^2 \right)$$

Likewise, the integral in Eq.(64) still reveals near singularity under the condition as described in Eq.(51). For this, the integral is rewritten as

$$\overline{f}_{ij}^{(c)} = \frac{1}{3\alpha_4^2} \int_{-1}^1 \frac{\Lambda(\eta)}{H_2(\eta)^2} \frac{1}{H_1(\eta)^2} d\eta, \quad (66)$$

where  $\Lambda(\eta)$  is defined by

$$\Lambda(\eta) = \frac{\sum_{k=0}^3 \Upsilon_{ijk}^{(c)} \xi^k / \sqrt{D^3} \Big|_{\xi^i=-1}^{\xi^i=1}}{\overline{A}^3}. \quad (67)$$

For applying the IBP onto Eq.(66), one may let

$$U = \frac{\Lambda(\eta)}{H_2(\eta)^2}, \quad dV = \frac{d\eta}{H_1(\eta)^2}, \quad (68)$$

and thus, the use of Eq.(19) yields

$$f_{ij}^{(c)} = \frac{1}{3\alpha_4^2} \left( \frac{\Lambda(\eta')}{H_2(\eta')^2} \left[ \frac{4}{\sqrt{(4\beta_0 - \beta_1^2)^3}} \tan^{-1} \left( \frac{\beta_1 + 2\eta'}{\sqrt{4\beta_0 - \beta_1^2}} \right) + \frac{\beta_1 + 2\eta'}{H_1(\eta')(4\beta_0 - \beta_1^2)} \right] \right)_{\eta'=-1}^{\eta'=1} - \int_{-1}^1 Z(\eta) d\eta, \quad (69)$$

where  $Z(\eta)$  is defined by

$$Z(\eta) = \frac{\partial(\Lambda(\eta)/H_2(\eta)^2)}{\partial\eta} \left\{ \frac{4}{\sqrt{(4\beta_0 - \beta_1^2)^3}} \tan^{-1} \left( \frac{\beta_1 + 2\eta}{\sqrt{4\beta_0 - \beta_1^2}} \right) + \frac{\beta_1 + 2\eta}{H_1(\eta)(4\beta_0 - \beta_1^2)} \right\}. \quad (70)$$

Due to the following condition

$$\beta_1 + 2\eta_0 \approx 0, \quad (71)$$

the integrand defined in Eq.(70) is indeed regular when the source point approaches the element under integration. In the sequel, the resulting regularized integral can be calculated by Eq.(63) and Eq.(69). However, it should be noted that although the regularized forms may now be integrated by any conventional numerical schemes, relative higher integration order is still needed for yielding satisfactorily accurate results. This is mainly because the certain fluctuations of the integrands still remain, although not so drastic like the un-regularized forms. Nevertheless, the cost of greater integration order is minor since the integrations are performed only for single-integrals. Also, a good practice for improving the accuracy is to subdivide the integration element into 4 quadrants at the project point  $(\xi_0, \eta_0)$ . At this point, discussion about how to numerically determine the projection coordinates is elaborated next.

### Determination of the projection point

As explained earlier, under the nearly singular condition when the source point approaches the integration element, the integrand will become drastically large at its projection coordinates  $(\xi_0, \eta_0)$ . It is clear that when the source point approaches the element near  $(\xi_0, \eta_0)$ , the denominator of the integrand will be verging to null. Evidently, the numerical value of  $D(\xi_0, \eta_0)$  should be the minimum, leading to the following conditions:

$$D'_\xi(\xi_0, \eta_0) = \left. \frac{\partial D(\xi, \eta)}{\partial \xi} \right|_{\substack{\xi=\xi_0 \\ \eta=\eta_0}} = 0, \quad D'_\eta(\xi_0, \eta_0) = \left. \frac{\partial D(\xi, \eta)}{\partial \eta} \right|_{\substack{\xi=\xi_0 \\ \eta=\eta_0}} = 0. \quad (72)$$

For performing the partial differentiations described above, Eq.(17) is reformulated into the following form:

$$D(\xi, \eta) = \hat{A}(\xi)\eta^2 + \hat{B}(\xi)\eta + \hat{C}(\eta), \quad (73)$$

where

$$\hat{A}(\xi) = \frac{1}{16} \sum_{i=1}^3 \left[ \left( \hat{x}_i^{(1,7)} - \hat{x}_i^{(3,5)} \right) \xi - \left( \hat{x}_i^{(1,7)} + \hat{x}_i^{(3,5)} \right) \right]^2, \quad (74a)$$

$$\begin{aligned} \hat{B}(\xi) &= \sum_{i=1}^3 \left( \left\langle \hat{x}_i^{(5,7)} \right\rangle^2 - \left\langle \hat{x}_i^{(1,3)} \right\rangle^2 \right) \frac{\xi^2}{8} \\ &+ \sum_{i=1}^3 \left[ \hat{x}_i^{(1,7)} \left( \hat{x}_i^{(8)} - \hat{x}_{p_i} \right) - \hat{x}_i^{(3,5)} \left( \hat{x}_i^{(4)} - \hat{x}_{p_i} \right) \right] \frac{\xi}{2}, \\ &- \frac{1}{4} \sum_{i=1}^3 \left( \hat{x}_i^{(1,7)} + \hat{x}_i^{(3,5)} \right) \left( \hat{x}_i^{(2)} + \hat{x}_i^{(6)} - 2\hat{x}_{p_i} \right) \end{aligned} \quad (74b)$$

$$\hat{C}(\eta) = \frac{1}{4} \sum_{i=1}^3 \left[ (\hat{x}_i^{(8)} - \hat{x}_i^{(4)}) \xi - (\hat{x}_i^{(8)} + \hat{x}_i^{(4)} - 2\hat{x}p_i) \right]^2. \quad (74c)$$

Obviously, analytically solving the two simultaneous equations in Eqs.(72) is absolutely not an easy task. Alternatively, they can be numerically solved in an iterative manner. Firstly, one may adopt  $\xi_1=0$  as the initial shooting point and then, by use of Eqs.(72), perform the following repetitive iterations to yield a convergent solution:

$$\eta_i = \frac{-\hat{B}(\xi_i)}{2\hat{A}(\xi_i)}, \quad \xi_{i+1} = \frac{-\bar{B}(\eta_i)}{2\bar{A}(\eta_i)}, \quad (75)$$

where the subscript “ $i$ ” is used to denote the  $i$ -th iteration time. From the iterative process, fast convergence is assured to give the projection coordinates  $(\xi_0, \eta_0)$ .

Although the fully regularized integrals presented above are ideal substitutes for the original, their numerical evaluations shall cost more CPU-runtime as a tradeoff. For this reason, the computer code should be programmed in such a way that it can discriminate the special condition when the regularized integrals are supposed to be invoked. This can be easily achieved by use of the following criteria:

$$|D(\xi_0, \eta_0) / D_{ave}| \leq \varepsilon, \quad (76)$$

where  $\varepsilon$  is a small value chosen by the user and  $D_{ave}$  is the average value of  $D(\xi, \eta)$  for all element nodes. That is, under the regular condition, the integrals are evaluated in a conventional manner as usual; the regularized ones are used as the substitutes only when the criteria, Eq.(76), is met. In what follows, numerical examples will be studied for testing the accuracy of the regularized integrals.

### Numerical examples

For verifying the validity of the proposed formulations, consider a typical case assuming  $\nu=0.3$ , Young’s modulus=1000 (units) and an element with the following arbitrarily chosen nodal coordinates:

$$\begin{aligned} x_1^{(1)} &= -30, & x_2^{(1)} &= -50, & x_3^{(1)} &= 1, \\ x_1^{(3)} &= 50, & x_2^{(3)} &= -60, & x_3^{(3)} &= 1, \\ x_1^{(5)} &= 70, & x_2^{(5)} &= 30, & x_3^{(5)} &= 1, \\ x_1^{(7)} &= -40, & x_2^{(7)} &= 40, & x_3^{(7)} &= 1, \\ xp_1 &= 2, & xp_2 &= 1, & xp_3 &= 1 - \delta, \end{aligned} \quad (77)$$

where  $\delta$  is a small distance away from the element. For this test case, the average dimensional length of all four edges, denoted by  $L$ , is about 93.456371. By the iteration process as described earlier, a convergent solution  $(\xi_0 \approx -0.2248131, \eta_0 \approx 0.219465)$  was obtained for the projection coordinates.

Displayed in Table 1 are the computed values of  $E_{11}^{(c)}$ , serving to be a typical example of  $E_{ij}^{(c)}$ . Since all other components of  $E_{ij}^{(c)}$  have similar computation accuracy, they are not presented here. For providing a comparison base, the software MathCAD, employing the scheme of adaptive integration, was used to perform the numerical integrations. For the conventional numerical integrations, 14-point Gauss integrations of the both original and the regularized forms were carried out. Since the MathCAD has convergence difficulty for  $\delta \approx 10^{-3}$ , the distance  $\delta$  ranging from  $10^0$  to  $10^{-2}$  was used for the test, resulting the  $\delta/L$  as low as  $10^{-4}$  that is sufficiently small for most practical

applications. Also, as a typical example of  $F_{ij}^{(c)}$ , the numerical results of the computed  $F_{11}^{(c)}$  are tabulated in Table 2. As can be observed from these tables, with the decreasing  $\delta$ , Gauss integrations of the original forms will be getting off accuracy as compared with the MathCAD results, while the accuracies of the regularized integrations are satisfactory.

Table 1: Computed  $E_{11}^{(c)}$  for decreasing  $\delta$

$\delta$ ( $\delta L$ )		$10^0$ ( $\approx 1.7E-2$ )	$10^{-1}$ ( $\approx 1.7E-3$ )	$10^{-2}$ ( $\approx 1.7E-4$ )
$c$	$ D(\xi_0, \eta_0)/D_{ave} $	2.8614E-4	2.8623E-6	2.8623E-8
1	MathCAD	-7.4115E-3	-7.6819E-3	-7.7095E-3
	Original (% Diff.)	-7.0456E-3 (4.94%)	-7.0861E-3 (7.76%)	-7.0865E-3 (8.08%)
	Regularized (% Diff.)	-7.4109E-3 (0.01%)	-7.6924E-3 (0.14%)	-7.7036E-3 (0.08%)
2	MathCAD	1.6877E-2	1.7302E-2	1.7345E-2
	Original (% Diff.)	1.6311E-2 (3.36%)	1.6377E-2 (5.35%)	1.6377E-2 (5.58%)
	Regularized (% Diff.)	1.6877E-2 (0.00%)	1.7312E-2 (0.06%)	1.7326E-2 (0.11%)
3	MathCAD	-7.3512E-3	-7.6003E-3	-7.6257E-3
	Original (% Diff.)	-7.0161E-3 (4.56%)	-7.0540E-3 (7.19%)	-7.0544E-3 (7.49%)
	Regularized (%Diff.)	-7.3509E-3 (0.00%)	-7.6061E-3 (0.08%)	-7.6147E-3 (0.14%)
4	MathCAD	1.8390E-2	1.8814E-2	1.8857E-2
	Original (% Diff.)	1.7823E-2 (3.08%)	1.7890E-2 (4.91%)	1.7891E-2 (5.12%)
	Regularized (% Diff.)	1.8390E-2 (0.00%)	1.8824E-2 (0.05%)	1.8839E-2 (0.10%)
5	MathCAD	-6.9679E-3	-7.2379E-3	-7.2655E-3
	Original (% Diff.)	-6.6035E-3 (5.23%)	-6.6438E-3 (8.21%)	-6.6442E-3 (8.55%)
	Regularized (% Diff.)	-6.9676E-3 (0.00%)	-7.2442E-3 (0.09%)	-7.2535E-3 (0.17%)
6	MathCAD	2.3228E-2	2.3891E-2	2.3958E-2
	Original (% Diff.)	2.2348E-2 (3.79%)	2.2452E-2 (6.02%)	2.2453E-2 (6.28%)
	Regularized (% Diff.)	2.3227E-2 (0.00%)	2.3906E-2 (0.06%)	2.3929E-2 (0.12%)
7	MathCAD	-6.2830E-3	-6.5184E-3	-6.5425E-3
	Original (% Diff.)	-5.9644E-3 (5.07%)	-5.9992E-3 (7.96%)	-5.9996E-3 (8.30%)
	Regularized (% Diff.)	-6.2832E-3 (0.00%)	-6.5173E-3 (0.02%)	-6.5225E-3 (0.31%)
8	MathCAD	2.2970E-2	2.3639E-2	2.3707E-2
	Original (% Diff.)	2.2074E-2 (3.90%)	2.2179E-2 (6.17%)	2.2180E-2 (6.44%)
	Regularized (% Diff.)	2.2967E-2 (0.02%)	2.3701E-2 (0.26%)	2.3744E-2 (0.16%)

Table 2: Computed  $F_{11}^{(c)}$  for decreasing  $\delta$

$\delta$ ( $\delta L$ )		$10^0$ ( $\approx 1.7E-2$ )	$10^{-1}$ ( $\approx 1.7E-3$ )	$10^{-2}$ ( $\approx 1.7E-4$ )
$c$	$ D(\xi_0, \eta_0)/D_{ave} $	2.8614E-4	2.8623E-6	2.8623E-8
1	MathCAD	1.1214E-1	1.1818E-1	1.1879E-1
	Original (% Diff.)	3.6264E-2 (67.66%)	3.7705E-3 (96.81%)	3.7720E-4 (99.68%)
	Regularized (% Diff.)	1.1214E-1 (0.00%)	1.1810E-1 (0.07%)	1.2255E-1 (3.16%)
2	MathCAD	-1.7664E-1	-1.8440E-1	-1.8518E-1
	Original (% Diff.)	-5.8502E-2 (66.88%)	-6.0774E-3 (96.70%)	-6.0798E-4 (99.67%)
	Regularized (% Diff.)	-1.7664E-1 (0.00%)	-1.8426E-1 (0.08%)	-1.9103E-1 (3.16%)
3	MathCAD	1.0353E-1	1.0865E-1	1.0918E-1
	Original (% Diff.)	3.3860E-2 (67.29%)	3.5192E-3 (96.76%)	3.5206E-4 (99.68%)
	Regularized (%Diff.)	1.0353E-1 (0.00%)	1.0858E-1 (0.07%)	1.1263E-1 (3.16%)
4	MathCAD	-1.7810E-1	-1.8382E-1	-1.8440E-1
	Original (% Diff.)	-6.0295E-2 (66.14%)	-6.2557E-3 (96.60%)	-6.2580E-4 (99.66%)
	Regularized (% Diff.)	-1.7810E-1 (0.00%)	-1.8370E-1 (0.06%)	-1.9022E-1 (3.16%)
5	MathCAD	1.1154E-1	1.1806E-1	1.1870E-1
	Original (% Diff.)	3.5812E-2 (67.89%)	3.7251E-3 (96.84%)	3.7266E-4 (99.69%)
	Regularized (% Diff.)	1.1154E-1 (0.00%)	1.1798E-1 (0.07%)	1.2247E-1 (3.18%)
6	MathCAD	-2.7619E-1	-2.8812E-1	-2.8932E-1
	Original (% Diff.)	-9.2103E-2 (66.65%)	-9.5682E-3 (96.68%)	-9.5719E-4 (99.67%)
	Regularized (% Diff.)	-2.7619E-1 (0.00%)	-2.8795E-1 (0.06%)	-2.9847E-1 (3.16%)
7	MathCAD	9.7323E-2	1.0309E-1	1.0369E-1
	Original (% Diff.)	3.1168E-2 (67.98%)	3.2417E-3 (96.86%)	3.2429E-4 (99.69%)
	Regularized (% Diff.)	9.7323E-2 (0.00%)	1.0302E-1 (0.07%)	1.0696E-1 (3.16%)
8	MathCAD	-2.7985E-1	-2.9028E-1	-2.9134E-1
	Original (% Diff.)	9.3671E-2 (66.53%)	-9.7299E-3 (96.65%)	-9.7337E-4 (99.67%)
	Regularized (% Diff.)	-2.7985E-1 (0.02%)	-2.9009E-1 (0.07%)	-3.0054E-1 (3.16%)

For demonstrating the successful implementation in an existing BEM code, the second example considers a clamped-clamped thin plate subjected to uniform pressure as depicted in Fig.2. Also shown in this figure is the BEM discretization that employs 28 quadratic elements. Simply for the purpose of verification, the problem is fully modeled to check the symmetry of data output. For the material properties,  $E=1000$  (units) and  $\nu=0.3$  are used. The thickness ratio  $D/L$  is chosen to be 0.1 and 0.01 as two typical cases, testing the accuracy of our BEM analysis. Providing a comparison base, finite element analyses by ANSYS were also carried out. Figures 3(a) and 3(b) show the plots of the calculated transverse displacement ( $u_3/P$ ) along the centerline  $x_1=0$  for  $D/L=0.1$  and 0.01, respectively. As can be seen from these plots, for  $D/L=0.1$ , the both BEM approaches- the conventional and the regularization scheme provide consistent results as compared with the ANSYS analysis. However, for the  $D/L$  falling to 0.01, the conventional BEM approach fails to yield consistent results, while the present approach still gives ideal results in agreement with the ANSYS analysis.

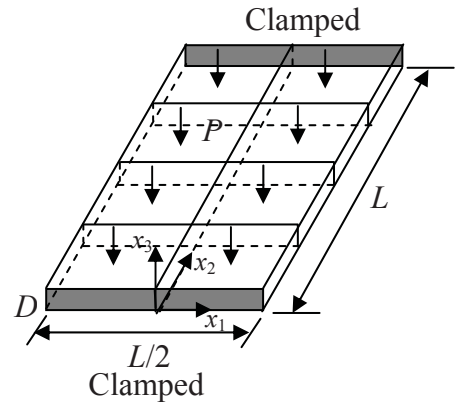


Fig.2: A clamped-clamped thin plate subjected to uniform pressure on top

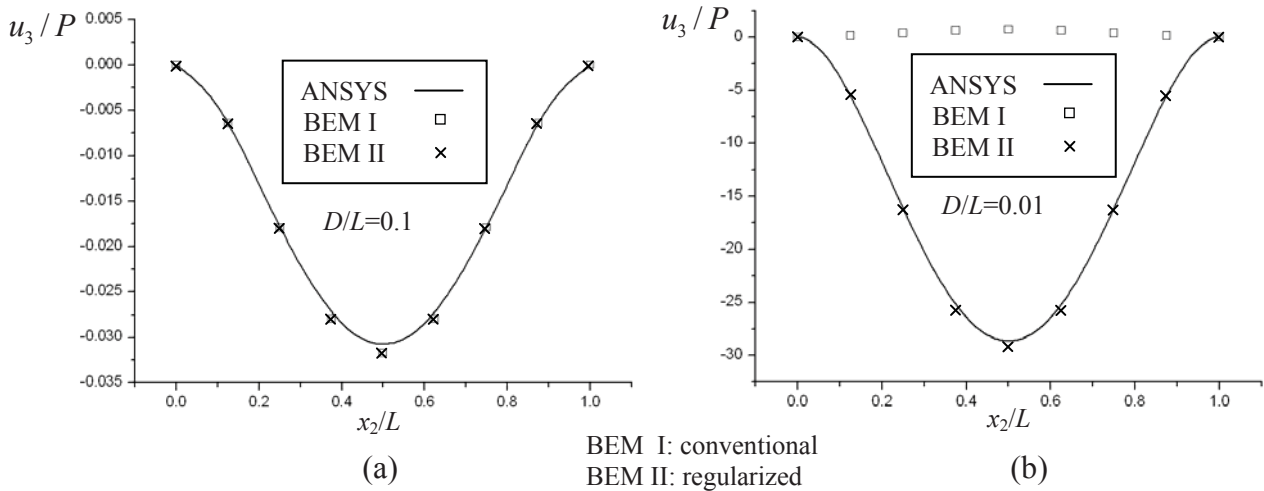


Fig.3: Normalized transverse displacement along the centerline of the thin plate for (a)  $D/L=0.1$  and (b)  $D/L=0.01$

**Conclusive remarks**

For analyzing the elastic field of thin bodies or at interior points near the boundary, integrations of the boundary integrals will have the numerical difficulty of so called "near singularity". This paper presents a regularization scheme, applying the approach of integration by parts, to regularize the strongly singular and hyper singular integrals for the elastostatic BEM analysis. In the past, this scheme has only been used for 2D problems; the present work is to demonstrate its extension to treat 3D elastostatic analysis. In this paper, only planar elements are treated, for which the associated integrals are integrated by parts to formulate regularized forms. As a typical example for the demonstration, derivations for quadrilateral elements are presented; nevertheless, the similar processes can be applied to a triangular element, treated as a degenerated quadrilateral element with three nodes of one side coincided at the same vertex. For verifying the validity of the regularized integrals, numerical tests were experimented for a typical example. The results show that the



regularized integral can be numerically integrated by the Gauss Quadrature scheme, although slightly more Gauss points are needed to guarantee satisfactory accuracy. The proposed regularization treatments have not been implemented to 3D BEM code yet. Further research is required for studying the accuracy of the BEM implementation and its computational efficiency.

### Acknowledgement

The authors gratefully acknowledge the financial support for this work from the National Science Council of Taiwan (NSC 99-2221-E-006-259-MY3).

### References

- Chen, J.T. and Hong, H-K. (1999), Review of dual boundary element methods with emphasis on hypersingular integrals and divergent series. *Applied Mechanics Reviews*, 52(1), pp.17-33.
- Granados, J.J. and Gallego, R. (2001), Regularization of nearly hypersingular integrals in the boundary element method, *Engineering Analysis with Boundary Elements*, 25 (3), pp. 165-184.
- Guz, A.N. and Zozulya, V.V. (2001), Fracture dynamics with allowance for a crack edges contact interaction, *International Journal of Nonlinear Sciences and Numerical Simulation*, 2(3), pp. 173-233.
- Lacerda, L.A. de and Wrobel, L.C., (2001), Hypersingular boundary integral equation for axisymmetric elasticity, *Int. J. Numer. Meth. Engng*, 52, pp.1337-1354.
- Reddy, J.N. (1984), *Energy and Variational Methods in Applied Mechanics: With an Introduction to the Finite Element Method*, John Wiley & Sons, p.346.
- Shiah, Y.C. and Shi, Yi-Xiao (2006), Heat conduction across thermal barrier coatings of anisotropic substrates, *International Communications in Heat and Mass Transfer*, 33 (7), pp.827-835.
- Shiah, Y.C., Chen, Y.H., and W.S. Kuo (2007), Analysis for the Interlaminar Stresses of Thin Layered Composites subjected to Thermal Loads, *Composites Science and Technology*, 67, pp.2485-2492.
- Tanaka, M., Sladek, V., and Sladek, J. (1994), Regularization techniques applied to boundary element methods. *Applied Mechanics Reviews*, 47(10), pp.457-499.
- Tomioka, Satoshi and Nishiyama, Shusuke (2010), Analytical regularization of hypersingular integral for Helmholtz equation in boundary element method, *Engineering Analysis with Boundary Elements*, 34 (4), pp. 393-404.
- Wikipedia online, [https://en.wikipedia.org/wiki/Quartic\\_function](https://en.wikipedia.org/wiki/Quartic_function).
- Zozulya, V.V. (2010), Divergent Integrals in Elastostatics: Regularization in 3-D Case, *CMES: Computer Modeling in Engineering & Sciences*, 70(3), 253-349.

## A modified SPH method for modeling explosion and impact Problems

\*M. B. Liu<sup>1</sup>, D. L. Feng<sup>1</sup> and Z. M. Guo<sup>2,3</sup>

<sup>1</sup>Institute of Mechanics, Chinese Academy of Sciences, Beijing 100190, China

<sup>2</sup>Laboratori de Càlcul Numèric (LaCàN), Universitat Politècnica de Catalunya (UPC),  
C. Jordi Girona 1-3, Campus Nord, 08034 Barcelona, Spain

<sup>3</sup>North University of China, Xueyuan Road 3, 030051 Taiyuan, Shanxi, China.

\*Corresponding author: liumoubin@imech.ac.cn

### Abstract

Explosion and impact problems are generally characterized by the presence of shock waves, intense localized materials response and intensive loadings. Most of the wave propagation hydro-codes for such problems use traditional grid based methods such as finite difference methods (FDM) and finite element methods (FEM). Though many successful achievements have been made using these methods, some numerical difficulties still exist. These numerical difficulties generally arise from large deformations, large inhomogeneities, and moving interfaces, free or movable boundaries. Smoothed particle hydrodynamics (SPH) is a Lagrangian, meshfree particle method, and has been widely applied to different areas in engineering and science. SPH method has been intensively used for simulating high strain hydrodynamics with material strength, due to its special features of meshfree, Lagrangian and particle nature. In this paper, some recent developments of the SPH in modelling explosion and impact problems will be introduced. A modified scheme for approximating kernel gradient (kernel gradient correction, or KGC) has been used in the SPH simulation to achieve better accuracy and stability. The modified SPH method is used to simulate a number of problems including 1D TNT detonation, linear shaped charge and explosively driven welding. The effectiveness of the modified SPH method has been demonstrated by comparative studies of the SPH results with data from other resources.

**Keywords:** Smoothed particle hydrodynamics (SPH), Explosion, Impact, Shaped charge, Explosive welding

### Introduction

Explosion and impact problems are generally characterized by the presence of shock waves, intense localized materials response and intensive loadings. A typical high explosive (HE) explosion consists of the detonation process through the HE and the later expansion process of the gaseous products to the surrounding medium (Liu et al., 2003c). For impact problems with different impacting speeds, solids under extreme situations behave like fluids. Two typical situations are high velocity impact (HVI) and penetration. In HVI, the kinetic energy of the system dominates and forces the solid material to deform extremely and the material actually “flows”. In the events of penetration, the materials can even be broken into pieces that “fly”, in addition to the extremely large deformation (Zukas, 1990).

Recently more and more analyses of explosion and impact problems are based on numerical simulations with the advancement of the computer hardware and computational techniques. Most of the applications are generally grid-based numerical methods such as the finite element methods (FEM) or finite difference methods (FDM). Though many successful achievements have been made for these methods in modeling explosion and impact problems, some numerical difficulties still exist. These numerical difficulties generally arise from large deformations, large inhomogeneities, and moving interfaces, movable boundaries when simulating explosion and impact problems including HE detonation and explosion of explosive gas, deformation of solid materials, and interaction of fluids and solids.

Smoothed particle hydrodynamics (SPH) method (Gingold and Monaghan, 1977; Liu and Liu, 2003) is a Lagrangian, meshfree particle method. In SPH, particles are used to represent the state of a system and these particles can freely move according to internal particle interactions and external forces. Therefore it can naturally obtain history of fluid/solid motion, and can easily track material

deformations, free surfaces and moving interfaces. During the last decades, SPH has been applied to modeling high explosive detonation and explosion, and hydrodynamics with material strength such as impact and penetrations (Monaghan, 1992; Randles and Libersky, 1996; Liu et al., 2003c; Liu et al., 2006; Liu and Liu, 2010). However, most of the existing works on SPH modeling of explosion and impact problems are based on conventional SPH method, which is believed to have poor performances especially in modeling problems with highly disordered particles (Liu and Liu, 2010). They usually lack quantitative and even qualitative comparisons with experimental results, and also lack validation and verification in energy conservation.

In this paper, we shall present a modified SPH model and the modified SPH model will be applied to a number of explosion and impact problems to demonstrate its effectiveness.

## SPH methodology

### *Basic concepts of SPH*

In conventional SPH method, there are basically two steps in obtaining an SPH formulation, kernel and particle approximations. The kernel approximation is to represent a function and its derivatives in continuous form as integral representation using the smoothing function and its derivatives. In the particle approximation, the computational domain is discretized with a set of particles. A field function and its derivative can then be written in the following forms (Monaghan, 2005)

$$\langle f(\mathbf{x}_i) \rangle = \sum_{j=1}^N \frac{m_j}{\rho_j} f(\mathbf{x}_j) W(\mathbf{x}_i - \mathbf{x}_j, h) \quad (1)$$

$$\langle \nabla f(\mathbf{x}_i) \rangle = \sum_{j=1}^N \frac{m_j}{\rho_j} f(\mathbf{x}_j) \nabla_i W_{ij} \quad (2)$$

where  $\langle f(\mathbf{x}_i) \rangle$  is the approximated value of particle  $i$ ;  $f(\mathbf{x}_j)$  is the value of  $f(\mathbf{x})$  associated with particle  $j$ ;  $\mathbf{x}_i$  and  $\mathbf{x}_j$  are the positions of corresponding particles;  $m$  and  $\rho$  denote mass and density respectively;  $h$  is the smooth length;  $N$  is the number of the particles in the support domain;  $W$  is the smoothing function representing a weighted contribution of particle  $j$  to particle  $i$ . The smoothing function should satisfy some basic requirements, such as normalization condition, compact supportness, and Delta function behavior (Liu and Liu, 2003; Liu et al., 2003a).

### *SPH equations of motion*

For hydrodynamics of fluids and solids with material strength, the following governing equations of continuum mechanics apply

$$\left\{ \begin{array}{l} \frac{D\rho}{Dt} = -\rho \frac{\partial \mathbf{v}^\beta}{\partial \mathbf{x}^\beta} \\ \frac{D\mathbf{v}^\alpha}{Dt} = \frac{1}{\rho} \frac{\partial \sigma^{\alpha\beta}}{\partial \mathbf{x}^\beta} \\ \frac{De}{Dt} = \frac{\sigma^{\alpha\beta}}{\rho} \frac{\partial \mathbf{v}^\alpha}{\partial \mathbf{x}^\beta} \\ \frac{D\mathbf{x}^\alpha}{Dt} = \mathbf{v}^\alpha \end{array} \right. \quad (3)$$

where the scalar density  $\rho$ , and internal energy  $e$ , the velocity component  $v^\alpha$ , and the total stress tensor  $\sigma^{\alpha\beta}$  are the dependent variables. The spatial coordinates  $x^\alpha$  and time  $t$  are the independent variables. The summation in equation (3) is taken over repeated indices, while the total time derivatives are taken in the moving Lagrangian frame. The total stress tensor  $\sigma^{\alpha\beta}$  in equation (3) is made up of two parts, one part of isotropic pressure  $p$  and the other part of shear stress  $S^{\alpha\beta}$ . The

hydrodynamic pressure is computed from an equation of state (EOS). For explosive gas, as the isotropic pressure is much larger than components of viscous shear stress, the viscous shear stress can be neglected. For solid materials, the shear stress can be computed from the constitutive equations of corresponding materials. Therefore using above-mentioned SPH approximations, the following SPH equations of motion can be obtained

$$\left\{ \begin{aligned} \frac{d\rho_i}{dt} &= \rho_i \sum_{j=1}^N \frac{m_j}{\rho_i} (\mathbf{v}_i^\beta - \mathbf{v}_j^\beta) \frac{\partial W_{ij}}{\partial x_i^\beta} \\ \frac{d\mathbf{v}_i^\alpha}{dt} &= - \sum_{j=1}^N m_j \left( \frac{\sigma_i^{\alpha\beta}}{\rho_i^2} + \frac{\sigma_j^{\alpha\beta}}{\rho_j^2} + \Pi_{ij} \right) \frac{\partial W_{ij}}{\partial x_i^\beta} \\ \frac{de_i}{dt} &= \frac{1}{2} \sum_{j=1}^N m_j \left( \frac{P_i}{\rho_i^2} + \frac{P_j}{\rho_j^2} + \Pi_{ij} \right) (\mathbf{v}_i^\beta - \mathbf{v}_j^\beta) \frac{\partial W_{ij}}{\partial x_i^\beta} + \frac{1}{\rho_i} S_i^{\alpha\beta} \varepsilon_i^{\alpha\beta} + H_i \\ \frac{d\mathbf{x}_i^\alpha}{dt} &= \mathbf{v}_i^\alpha \end{aligned} \right. \quad (4)$$

where  $\varepsilon^{\alpha\beta}$  is the strain rate tensor,  $\Pi$  and  $H$  stand for the component of the deviator stress tensor, the artificial viscosity and the artificial heat separately (Liu and Liu, 2003).

#### Kernel gradient correction

The conventional SPH method has been hindered with low accuracy and its accuracy is also closely related to the distribution of particles, selection of smoothing function and the support domain. Though different approaches have been proposed to improve the particle inconsistency and hence the SPH approximation accuracy, these approaches are usually not preferred for hydrodynamic simulations because the reconstructed smoothing function can be partially negative, non-symmetric, and not monotonically decreasing.

Explosion and impact involve fast expansion of explosive gas, rapid deformation and even liquefaction of solid materials, and quick damage on target materials. These lead to highly disordered particle distribution, which can seriously influence computational accuracy of SPH approximations. Hence an SPH approximation scheme, which is of higher order accuracy and is insensitive to disordered particle distribution, is necessary.

In this paper, the kernel gradient in SPH approximations is improved with a kernel gradient correction (KGC) technique (Shao et al., 2012). In the KGC technique, a modified or corrected kernel gradient is obtained by multiplying the original kernel gradient with a local reversible matrix  $L(\mathbf{r}_i)$ , which is obtained from Taylor series expansion method. In two-dimensional spaces, the new kernel gradient of the smoothing function  $\nabla_i^C W_{ij}$  can be obtained as follows

$$\nabla_i^C W_{ij} = L(\mathbf{r}_i) \nabla_i W_{ij} \quad (5)$$

$$L(\mathbf{r}_i) = \left( \sum_j \left( \begin{array}{cc} x_{ji} \frac{\partial W_{ij}}{\partial x_i} & y_{ji} \frac{\partial W_{ij}}{\partial x_i} \\ x_{ji} \frac{\partial W_{ij}}{\partial y_i} & y_{ji} \frac{\partial W_{ij}}{\partial y_i} \end{array} \right) V_j \right)^{-1} \quad (6)$$

where  $x_{ji} = x_j - x_i$ ,  $y_{ji} = y_j - y_i$ . It is found that for general cases with irregular particle distribution, variable smoothing length, and/or truncated boundary areas, the SPH particle approximation scheme with kernel gradient correction is of second order accuracy.

## Equations of state and constitutive modeling

### Equations of state

For ideal explosive, the standard Jones-Wilkins-Lee (JWL) equation (Lee et al., 1968) of state can be employed. The pressure of the explosive gas is given by

$$p = A\left(1 - \frac{\omega\eta}{R_1}\right)e^{-\frac{R_1}{\eta}} + B\left(1 - \frac{\omega\eta}{R_2}\right)e^{-\frac{R_2}{\eta}} + \omega\eta\rho_0 E \quad (7)$$

where  $\eta$  is the ratio of the density of the explosive gas to the initial density of the original explosive.  $e$  is the internal energy of the high explosive per unit mass.  $A, B, R_1, R_2$  and  $\omega$  are coefficients obtained by fitting the experimental data.  $E$  is the initial internal energy of the high explosive per unit mass. Values of the corresponding coefficients can be found in (Liu and Liu, 2003). For non-ideal explosive, the JWL++ equation of state can be used to model the detonation process with chemical reaction, while the pressure consists of the contributions from both reacted and non-reacted explosive.

The Tillotson equation (Katayama et al., 1999) is employed to describe pressure-volume-energy behavior of metals under high temperature, pressure and strain rate as follows

$$\begin{aligned} p_1 &= \left(a + \frac{b}{\omega_0}\right) \eta\rho_0 e + A\mu + B\mu^2 \\ p_2 &= \left(a + \frac{b}{\omega_0}\right) \eta\rho_0 e + A\mu \\ p_3 &= p_2 + \frac{(p_4 - p_2)(e - e_s)}{(e'_s - e_s)} \\ p_4 &= a\eta\rho_0 e + \left(\frac{b\eta\rho_0 e}{\omega_0} + A\mu e^{\beta x}\right) e^{-\alpha x^2} \\ \eta &= \frac{\rho}{\rho_0}, \mu = \eta - 1, \omega_0 = 1 + \frac{e}{e_0 \eta^2} \end{aligned} \quad (8)$$

where  $a, b, A, B, \alpha, \beta, e_0, e_s$  and  $e'$  are the parameters determined by the material, and  $p_1$  to  $p_4$  are the pressure of four different phases of material, e.g., the solid phase, the liquid phase, the vapor and liquid mixture, and the vapor phase (Katayama et al., 1999).

### Constitutive modeling

Johnson-Cook model (Johnson and Cook, 1983) is one of the most popular constitutive models for numerical simulations of impact and penetration, and which are usually associated with high strain rate. The model considers the effects of the stress hardening, strain rate and the temperature evolution. The yield stress in Johnson-Cook model can be written as

$$\sigma_y = (A + B\varepsilon^{p'}) (1 + C \ln \dot{\varepsilon}^*) (1 - T^{*m}) \quad (9)$$

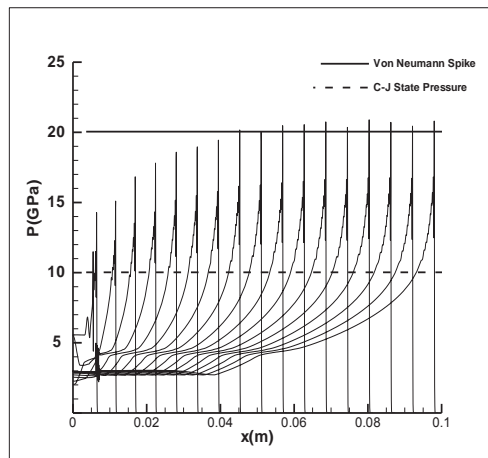
$$T^* = \frac{T - T_{room}}{T_{melt} - T_{room}} \quad (10)$$

where  $\varepsilon^{p'}$  is the effective plastic strain,  $\dot{\varepsilon}^*$  is a dimensionless strain rate, and  $T$  is the temperature.  $A, B, C, n$  and  $m$  are five parameters in the Johnson-Cook model that need to be determined from the torsion test under different strain rate, the Hopkinson Pressure Bar test with different temperatures, and the Standard static tensile test. Detailed parameters in the Johnson-Cook model for different metals can be found in (Feng et al., 2013).

## Applications

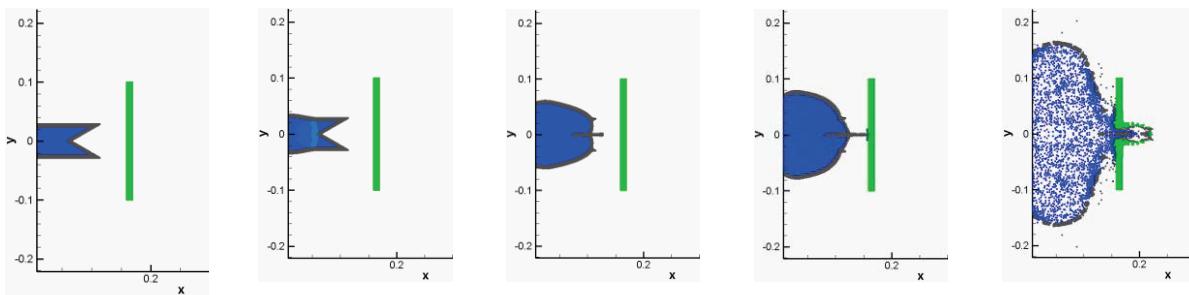
### *Detonation of a 1D ANFO bar*

The conventional SPH method was successfully applied to model the detonation of a 1D TNT bar, which is of idea explosive with a constant detonation speed (Liu et al., 2003c). In this work, the detonation process of a 1D ANFO bar is modeled using the method, while ANFO is a non-ideal explosive and the JWL++ equation of state is used. The ANFO bar is 0.1m long, and 4000 particles are used in the simulation. Figure 1 shows the pressure profiles along the slab at 1  $\mu$ s interval from 1 to 14  $\mu$ s. The von Neumann spike can be well captured in this simulation by using the JWL++ equation of state. Instead, if using the conventional JWL equation of state, it is only feasible to reach steady C-J pressure. The entire detonation process costs 17  $\mu$ s and the resultant detonation speed is 5725 m/s, which is very close to the experimental value of 5900 m/s.



**Figure 1: Pressure profiles along the 1D ANFO slab during the detonation process.**

### *Linear shaped charge*



**Figure 2: Shaped charge jet formation and penetration of a target plate.**

Shaped charge is a frequently used form of explosive charge for military and industrial applications. It can produce powerful metal jet and lead to stronger penetration effects onto targets than normal charges. After the explosion of high explosive, the detonation produced explosive gas can exert tremendous pressure on surrounding metal case and liner with very large deformation and even quick phase-transition. There are some preliminary works of using SPH to model shaped charges. For example, Liu et al. first simulated the detonation and explosion process of two-dimensional

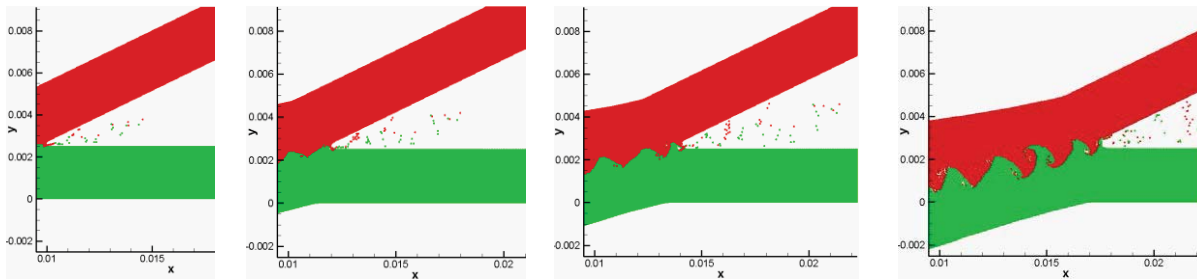
shaped charges with different shapes of cavity (Liu et al., 2003b) using SPH method. It is found that SPH can effectively model the explosive gas jet formation and dispersion. That work did not consider surrounding metal case and liner which present additional challenges in numerical simulation due to the existence of multi-material (explosive-metal) and multi-phase (solid-gas-liquid).

In this work, a practical linear shaped charge is modeled with metal case and liner. Figure 2 shows the entire process of HE detonation and explosion, explosion-driven metal deformation and jet formation as well the penetrating of a target aluminum plate at typical instants. The obtained snapshots with metal jet and penetrating effects agree well with experimental observations.

### *Explosive welding*

Explosive welding can be used to bond two dissimilar metal plates to obtain a metal composite with better performance. It is attractive when conventional fusion welding techniques are not able to combine two metal plates together.

Figure 3 shows the SPH simulation of explosive (TNT) welding of two steel plates. It is observed that with the detonation and explosion of TNT, the high pressure explosive gas drives the flyer plate, which impacts on and interacts with the substrate (base plate). As the detonation wave moves rightwards, the interaction of the flyer plate and substrate also move rightwards. A metal jet produces between the two steel plates and a wave-like welding pattern can be obtained during the explosive welding process, which is also observable in laboratory experiments. Figure 4 shows a full scale view of the wave-like welding pattern during the explosive welding process.



**Figure 3: SPH modeling of the explosive welding process.**



**Figure 4: A full scale view of the wave-like welding pattern.**

### **Conclusions**

In this paper, a modified SPH method with kernel gradient correction is developed for modeling explosion and impact problems. The modified SPH method has been applied to a number of applications including the detonation of a 1D ANFO bar, linear shaped charge jet formation and penetration effects on a target plate, and the explosive welding of two steel plates. The inherent physics can be well captured and the obtained numerical results are agreeable with experimental observations.

**Acknowledgement** This work has been supported by the National Natural Science Foundation of China (11172306) and the 100 Talents Programme of the Chinese Academy of Sciences.

## References

- Feng, D. L., Liu, M. B., Li, H. Q. and Liu, G. R. (2013), Smoothed particle hydrodynamics modeling of linear shaped charge with jet formation and penetration effects. *Computers & Fluids*, **(In press)**.
- Gingold, R. A. and Monaghan, J. J. (1977), Smoothed particle hydrodynamics-theory and application to non-spherical stars. *Monthly Notices of the Royal Astronomical Society*, **181**,pp. 375-389.
- Johnson, G. R. and Cook, W. H. (1983), A constitutive model and data for metals subjected to large strains, high strain rates and high temperatures. Proceedings of Seventh International Symposium on Ballistics. The Hague, Netherlands, International Ballistics Committee. **21**: 541-547.
- Katayama, M., Takeba, A., Toda, S. and Kibe, S. (1999), Analysis of jet formation and penetration by conical shaped charge with the inhibitor. *International Journal of Impact Engineering*, **23**(1),pp. 443-454.
- Lee, E. L., Hornig, H. C. and Kury, J. W. (1968), Adiabatic expansion of high explosive detonation products, California Univ., Livermore. Lawrence Radiation Lab.
- Liu, G. R. and Liu, M. B. (2003) Smoothed particle hydrodynamics: A meshfree particle method. World Scientific, Singapore.
- Liu, M. B. and Liu, G. R. (2010), Smoothed particle hydrodynamics (sph): An overview and recent developments. *Archives of Computational Methods in Engineering*, **17**(1),pp. 25-76.
- Liu, M. B., Liu, G. R. and Lam, K. Y. (2003a), Constructing smoothing functions in smoothed particle hydrodynamics with applications. *Journal Of Computational And Applied Mathematics*, **155**(2),pp. 263-284.
- Liu, M. B., Liu, G. R. and Lam, K. Y. (2006), Adaptive smoothed particle hydrodynamics for high strain hydrodynamics with material strength. *Shock Waves*, **15**(1),pp. 21-29.
- Liu, M. B., Liu, G. R., Lam, K. Y. and Zong, Z. (2003b), Meshfree particle simulation of the detonation process for high explosives in shaped charge unlined cavity configurations. *Shock Waves*, **12**(6),pp. 509-520.
- Liu, M. B., Liu, G. R., Zong, Z. and Lam, K. Y. (2003c), Computer simulation of high explosive explosion using smoothed particle hydrodynamics methodology. *Computers & Fluids*, **32**(3),pp. 305-322.
- Monaghan, J. J. (1992), Smoothed particle hydrodynamics. *Annual Review of Astronomy and Astrophysics*, **30**,pp. 543-574.
- Monaghan, J. J. (2005), Smoothed particle hydrodynamics. *Reports On Progress In Physics*, **68**(8),pp. 1703-1759.
- Randles, P. W. and Libersky, L. D. (1996), Smoothed particle hydrodynamics: Some recent improvements and applications. *Computer Methods in Applied Mechanics and Engineering*, **139**(1-4),pp. 375-408.
- Shao, J. R., Li, H. Q., Liu, G. R. and Liu, M. B. (2012), An improved sph method for modeling liquid sloshing dynamics. *Computers & Structures*, **100-101**,pp. 18-26.
- Zukas, J. A. (1990) High velocity impact dynamics. Wiley-Interscience.



## Contact analysis for an anisotropic half-domain with micropatterns considering friction

\*Hideo Koguchi<sup>1</sup>, Shuma Suzuki<sup>2</sup>, and Masahiro Taroura<sup>3</sup>

<sup>1</sup>Department of Mechanical Engineering, Nagaoka University of Technology, Japan.

<sup>2</sup>Graduate School of Nagaoka University of Technology, 1603-1 Kamitomioka, Nagaoka, Niigata, Japan.

<sup>3</sup>Taiheikogyo Co. Ltd. Tokai, Aichi 476-0003, Japan

\*Corresponding author: koguchi@mech.nagaokaut.ac.jp

### Abstract

In the present study, a contact problem between a spherical indenter and a half-anisotropic elastic region with a micropattern is solved under normal and tangential forces considering friction. Surface Green's function, the discrete convolution and the fast Fourier transform (DC-FFT) method are used to calculate displacements on a contact area, and the conjugate gradient (CG) method is employed for calculating a contact pressure, the contact area, shear tractions, and a stick-slip region, respectively. The influences of the shape and density (the ratio of the pattern area per a unit area) of the micropattern and of material anisotropy in the substrate on the friction property for the substrate are investigated. In this study, the substrate with circle- and square-micropatterns are used for the analysis. As the result, it is found that the shear traction concentrates at the edges and corners of circle- and square-patterns, respectively. The apparent friction coefficient varies with the direction of the anisotropic principal axis.

**Keywords:** Contact problem, Anisotropic material, Friction, Micropattern.

### Introduction

By machining a micropattern on the surface of material, the friction property on the surface is desired to control as we design. Then, the functional enhancement in various manufacturing processes can be promoted. For example, there are needs to control an inflow and a transformation to the die of the work piece partially by machining a micropattern for a surface of the press die and blank holder. However, we do not yet understand enough the effect of pattern shapes on friction properties or the advantage that give a micropattern. Therefore, the present study investigates the friction property through a contact analysis between a spherical indenter and a half-anisotropic elastic region with the micropattern. In particular, the normal and tangential forces are applied to the surface of the anisotropic and isotropic elastic body, and investigated the relationship between the frictional force and the micropattern. Vlassak et al. (2003) analyzed a contact problem, which the indenter in an arbitrary shape is penetrated in the normal direction for the surface of the anisotropic material. In addition, Lin et al. (2008) analyzed a contact problem of a three-dimensional rough surface, and He et al. (2004) performed a three-dimensional contact analysis of the rough surface with an arbitrary geometry. Cattaneo (1938) and Mindlin (1949) first established mathematical models for analyzing a partial slip problem in an elastic contact. They assumed that the magnitude of shear traction in a contact area could not exceed a static friction limit. Recently, Ciavarella (1998) extended Cattaneo-Mindlin's partial slip model to plane contact problems. However, the contact of dissimilar materials does not obey the classic theory of the Cattaneo-Mindlin model, in which the effects of shear tractions on the normal displacement were not considered. It is difficult to derive an analytical solution for the contact problems with coupled normal and tangential loads. Therefore, Kalker (1977) proposed the method for analysis using the variational principle, instead of solving a contact problem analytically. Moreover, Chen and Wang (2008) proposed a method for analysis in the case considering a partial slip on a three-dimensional contact problem. Dini et al. (2010) conducted a contact analysis to the surface with many hemispherical projections.

In the present paper, a partial slip contact problem on half-anisotropic elastic bodies with a micropattern is analyzed. The conjugate gradient (CG) method, the discrete convolution and the fast Fourier transform (DC-FFT) are used for the contact analysis. Distributions of contact area and contact pressure are calculated using the CG method. The surface displacement for a contact pressure is calculated using the DC-FFT method. Furthermore, the influence coefficient is obtained using a surface Green function in a three-dimensional anisotropic elastic body. As a result, a ratio of the apparent stick-slip area and the friction coefficient of the surface with a micropattern are obtained for various directions of horizontal external force. In addition, the apparent friction coefficient for the surface with patterns is analyzed.

## Theory and Descriptions

A model for contact problem between a rigid spherical ball and a surface with a micropattern is shown in Fig. 1. The  $x$ - and  $y$ -axes are set on the surface, while the  $z$ -axis directs towards the substrate. The ball indenter is pressed onto the substrate by a normal load,  $P_0$ , in the  $z$ -direction. Tangential loads,  $F_x$  and  $F_y$ , are applied to the ball in parallel directions to the  $x$ - and  $y$ - axes. The contact interaction results in a balance between normal pressure  $p$ , shear tractions  $q_x$  and  $q_y$  at the interface. The contact analysis of the semi-infinite isotropic elastic body considering friction was conducted by Mindlin (1949), and the validity of the result was checked in experiment, too. More general contact model is summarized as follows,

$$\begin{Bmatrix} u_x(x,y) \\ u_y(x,y) \\ u_z(x,y) \end{Bmatrix} - \begin{Bmatrix} \delta_x \\ \delta_y \\ \delta_z \end{Bmatrix} = \begin{Bmatrix} s_x(x,y) \\ s_y(x,y) \\ g(x,y) - h_0(x,y) \end{Bmatrix}, \quad (1)$$

where  $u_x$ ,  $u_y$ , and  $u_z$  are the surface displacement under external forces in the direction of three axes,  $\delta_x$ ,  $\delta_y$ , and  $\delta_z$  are the rigid body displacements, respectively,  $s_x$  and  $s_y$  the relative slip distance parallel to the  $x$ - and  $y$ -axes,  $h_0$  is the initial surface gap, and  $g$  the surface gap between the indenter and the substrate after loading. The meanings of variables are shown in Fig. 2. Furthermore, the rigid body displacements  $\delta_x$ ,  $\delta_y$ , and  $\delta_z$  for isotropic materials are derived from the equations below,

$$\delta_x = \delta_0 \left\{ 1 - \left( 1 - F_x / \mu_f P_0 \right)^{2/3} \right\}, \quad \delta_y = \delta_0 \left\{ 1 - \left( 1 - F_y / \mu_f P_0 \right)^{2/3} \right\}, \quad (2)$$

$$\delta_z = 9P_0^2 (1 - \nu^2) / 16RE^2, \quad (3)$$

where

$$\delta_0 = 3\mu_f P_0 (2 - \nu)(1 + \nu) / 8aE, \quad (4)$$

$a$  is a radius of the contact area,

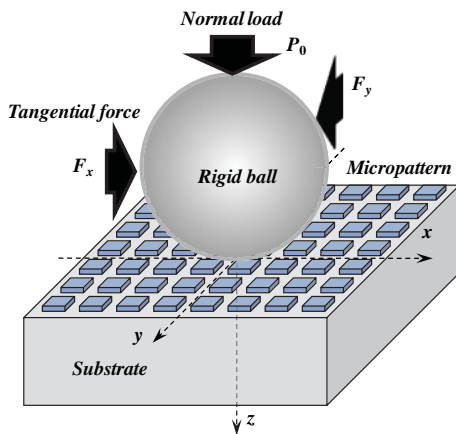


Figure 1. Model of contact analysis

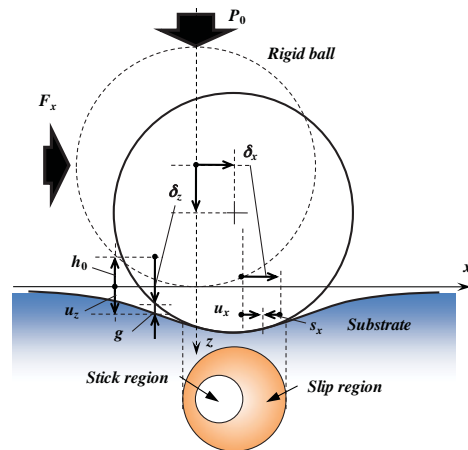


Figure 2. Description of contact situation

$$a = \left\{ 3RP_0(1-\nu^2)/4E \right\}^{1/3}, \quad (5)$$

$R$  is a radius of rigid ball,  $E$  is Young's modulus of elastic body, and  $\nu$  is a Poisson's ratio of elastic body.

In contact analysis, we determined the contact area, pressure and shear traction so as to satisfy the conditions of the following formula using Eq. (1).

Let

$$g(x, y) = h_0(x, y) - \delta_z + u_z(x, y). \quad (6)$$

The contact pressure  $p$  is thought as follows,

$$\begin{cases} g(x, y) = 0 : p(x, y) \geq 0 & \text{(In contact)} \\ g(x, y) > 0 : p(x, y) = 0 & \text{(In separation)}, \end{cases} \quad (7)$$

$$\int_{\Omega} p(x, y) dS = P_0, \quad (8)$$

where  $\Omega$  is the contact area, and  $P_0$  is the normal load.

The shear tractions in the stick and slip regions are assumed to obey the following conditions:

$$\text{In the stick region: } \sqrt{q_x^2(x, y) + q_y^2(x, y)} \leq \mu_f p, \text{ and } \sqrt{s_x^2(x, y) + s_y^2(x, y)} = 0 \quad (9)$$

$$\text{In the slip region: } \sqrt{q_x^2(x, y) + q_y^2(x, y)} = \mu_f p, \text{ and } \sqrt{s_x^2(x, y) + s_y^2(x, y)} \neq 0 \quad (10)$$

$$\int_{\Omega} q_i(x, y) dS = F_i, \quad i = x, y, \quad (11)$$

where the shear tractions  $q_i$  is the product of the friction coefficient  $\mu_f$  and the contact pressure  $p$ .

Furthermore, the elastic displacement in the contact region is calculated in order to perform contact analysis. If the force  $\mathbf{q} = (q_x, q_y, p)$  is applied to a contact surface, the surface displacement  $\mathbf{u}$  is calculated from the following equation,

$$\mathbf{u}(x, y) = \iint_{\Omega} \mathbf{K}(x - x_s, y - y_s) \mathbf{q}(x_s, y_s) dx_s dy_s \quad (12)$$

where  $(x, y)$  is an observation point,  $(x_s, y_s)$  is a source point of force,  $\mathbf{K}$  is the displacement of the observation point when unit concentration load acts to a source point. Generally,  $\mathbf{K}$  is expressed in a matrix form. The response function for displacement will be described later. Applying the two-dimensional Fourier transform to Eq.(12) yields  $\hat{\mathbf{u}} = \hat{\mathbf{K}} \cdot \hat{\mathbf{q}}$ , where the two-dimensional Fourier transform is defined by

$$\hat{f}(\eta_1, \eta_2) = \int_{-\infty}^{\infty} \int_{-\infty}^{\infty} f(x, y) e^{i(\eta_1 x + \eta_2 y)} dx dy \quad (13)$$

Calculation is carried out iteratively so that the normal load  $P_0$  and tangential forces  $F_x$  and  $F_y$  which are given as a prior condition may satisfy Eqs. (8)-(12). Moreover, the distributions of contact pressure  $p$  and shear tractions  $q_x$  and  $q_y$  in a contact region are calculated. In order to solve the basic equation for a contact problem, the field containing a contact surface is divided by a grid.

Grid intervals of the  $x$ - and  $y$ - directions are set to  $\Delta x$  and  $\Delta y$ . When the coordinates of an arbitrary grid point on the field are  $(i\Delta x, j\Delta y)$ , the coordinates of the point are represented as  $(i, j)$ . The algorithm for resolving the shear tractions proposed by Wang et al. (2010) is used in this study. This method is used for the repetitive calculation considering the coupling effect of contact pressure and shear traction. Furthermore, the stick-slip region and shear traction of the contact region are determined simultaneously.

In this study, the displacement in the contact area is calculated using the DC-FFT method. The displacement under the shear tractions  $q_x(i, j)$  and  $q_y(i, j)$  is obtained by the inverse Fourier transform of Eq. (13). Thus,

$$\begin{Bmatrix} u_x(i, j) \\ u_y(i, j) \\ u_z(i, j) \end{Bmatrix} = \text{IFFT} \left\{ \begin{bmatrix} \hat{K}_{q_x}^{u_x}(i, j) & \hat{K}_{q_y}^{u_x}(i, j) & \hat{K}_p^{u_x}(i, j) \\ \hat{K}_{q_x}^{u_y}(i, j) & \hat{K}_{q_y}^{u_y}(i, j) & \hat{K}_p^{u_y}(i, j) \\ \hat{K}_{q_x}^{u_z}(i, j) & \hat{K}_{q_y}^{u_z}(i, j) & \hat{K}_p^{u_z}(i, j) \end{bmatrix} \begin{Bmatrix} \hat{q}_x(i, j) \\ \hat{q}_y(i, j) \\ \hat{p}(i, j) \end{Bmatrix} \right\}, \quad (14)$$

where IFFT denotes the inverse Fourier transform, and  $\hat{\phantom{x}}$  expresses the Fourier transform of each function. Equating Eq. (14) to the  $x$ - and  $y$ - component of Eq.(1) yields

$$\text{IFFT} \left\{ \begin{bmatrix} \hat{K}_{q_x}^{u_x}(i, j) & \hat{K}_{q_y}^{u_x}(i, j) & \hat{K}_p^{u_x}(i, j) \\ \hat{K}_{q_x}^{u_y}(i, j) & \hat{K}_{q_y}^{u_y}(i, j) & \hat{K}_p^{u_y}(i, j) \end{bmatrix} \begin{Bmatrix} \hat{q}_x(i, j) \\ \hat{q}_y(i, j) \\ \hat{p}(i, j) \end{Bmatrix} \right\} - \begin{Bmatrix} \delta_x \\ \delta_y \end{Bmatrix} = \begin{Bmatrix} s_x(i, j) \\ s_y(i, j) \end{Bmatrix}, \quad (15)$$

where pressure distribution  $p(i, j)$  is provided from the contact problem of only normal load. Then, shear tractions  $q_x$  and  $q_y$  can be determined from Eq.(15) by using the CG method coupling with constraint conditions (Eqs.(9) and (10)).

Once the shear tractions  $q_x$  and  $q_y$  are obtained from the above procedure, the displacements  $u_z$  for  $q_x$  and  $q_y$ , respectively, can be determined in terms of the influence coefficients by using the DC-FFT method. Then, the surface vertical gap  $g$  is updated by adding the displacements due to the shear tractions. Furthermore, the CG method is also employed to renew the contact pressure, and the new pressure is used for further update of the shear tractions.

Now, we need to derive the influence function for a semi-infinite anisotropic region. We consider that a force  $\mathbf{f}=(f_x, f_y, f_z)$  is applied to the coordinate origin. The equilibrium equation for anisotropic materials can be expressed using the displacement,  $u_i$ :

$$C_{ijkl}u_{k,lj} = 0. \quad (16)$$

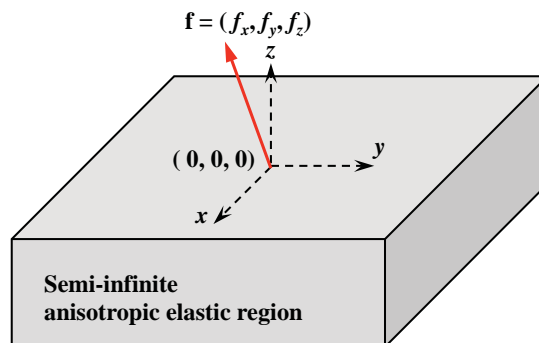


Figure 3. The coordinate system for an influence function

The two-dimensional spatial ( $x_1$ - $x_2$ ) Fourier transform is applied to Eq.(16). Then, an ordinary differential equation of displacement is derived. The general solution of the differential equation is assumed to be  $\hat{\mathbf{u}} = \mathbf{a}e^{-ip\rho x_3}$ . Where  $p$  and  $\mathbf{a}$  satisfy the following eigenrelation:

$$\{\mathbf{Q} + p(\mathbf{R} + \mathbf{R}^T) + p^2\mathbf{T}\}\mathbf{a} = 0 \quad (17)$$

where  $Q_{ik} = C_{ijks}n_jn_s$ ,  $R_{ik} = C_{ijks}n_jm_s$ , and  $T_{ik} = C_{ijks}m_jm_s$  with  $\mathbf{n} = [n_1, n_2, 0]^T = [\cos\theta, \sin\theta, 0]^T$ ,  $\mathbf{m} = [0, 0, 1]^T$ . The angle  $\theta$  is used in the variables  $(\eta_1, \eta_2) = (\rho n_1, \rho n_2)$  of the Fourier transform and taken from the  $\eta_1$  axis. Finally, the displacement obtained from the inverse Fourier transform is expressed as follows:

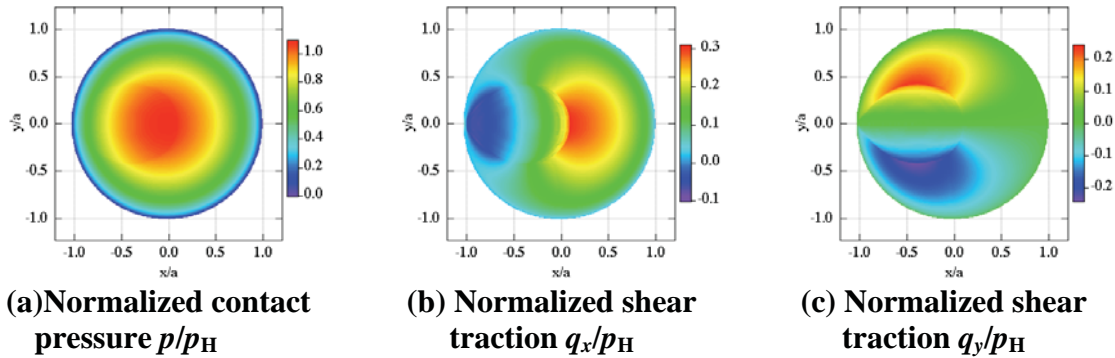
$$\mathbf{u}(x_1, x_2, x_3) = \frac{i}{4\pi^2} \int_{-\infty}^{\infty} \int_{-\infty}^{\infty} \frac{1}{\rho} \mathbf{A} \langle e^{-ip_s\rho x_3} \rangle \mathbf{B}^{-1} \mathbf{f} e^{-i(\eta_1 x_1 + \eta_2 x_2)} d\eta_1 d\eta_2 \quad (18)$$

where  $\mathbf{A} = [\mathbf{a}_1, \mathbf{a}_2, \mathbf{a}_3]$ ,  $\mathbf{B} = [\mathbf{b}_1, \mathbf{b}_2, \mathbf{b}_3]$ ,  $\langle e^{-ip_s\rho x_3} \rangle = \text{diag}[e^{-ip_1\rho x_3}, e^{-ip_2\rho x_3}, e^{-ip_3\rho x_3}]$ , and  $\mathbf{b}_j = (\mathbf{R}^T + p_j\mathbf{T})\mathbf{a}_j$ .

## Results and Discussions

### Result of isotropic material

For a verification of the validity of the result of analysis, the same problem as Wang et al. (2010) is analyzed. The condition for analysis is shown in Table 1(a). The Boussinesq's solution for an isotropic elastic body is used for calculating the response coefficient of traction and pressure. Distributions of the contact pressure and shear tractions are shown in Figs. 4(a) ~ (c). In addition, the contact pressure and shear tractions are normalized by the maximum pressure of Hertz contact theory,  $p_H = 860\text{MPa}$ , and coordinates are normalized by the contact radius of Hertz contact theory,  $a = 0.105\text{mm}$ . In this analysis, the displacement in a normal direction to the surface induced by the tangential force that acts on the surface of a half-infinite domain is also taken into consideration. Therefore, the maximum contact pressure causes at the position where the maximum shear traction  $q_x$  shown in Fig.4(b) occurs. The distributions of contact pressure and shear traction are agreed with the results of Wang et al. (2010).



**Figure 4. Contour plots of normalized contact pressure and shear tractions by  $p_H=860.03\text{MPa}$  and  $a=0.10537\text{mm}$**

### Results of anisotropic material

Distributions of the contact pressure and shear tractions on the plane of Fe(111) are shown in Figs. 5(a)~(c). Moreover, pressure and shear tractions were normalized by the maximum pressure of Hertz contact theory  $p_H = 931.62\text{MPa}$ , and coordinates were normalized by the contact radius of Hertz contact theory  $a = 0.10124\text{mm}$ . As compared with the result of isotropic material, the maximum and minimum values of the contact pressure and shear tractions in the anisotropic material are similar to those in the isotropic Fe. However, the shapes of the distribution are different,

but the difference of absolute values of the shear tractions is small. Here, Young's moduli and Poisson's ratio for anisotropic materials Fe(111), Cu(111) and Ni(111) are calculated using  $E_{(111)} = 4/(2s_{11} + 2s_{12} + s_4)$  and  $\nu_{(111)} = -(s_{11} + 5s_{12} - s_{44}/2) / (3s_{11} + 3s_{12} + 3s_{44}/2)$ , respectively, where  $s_{11}$ ,  $s_{12}$  and  $s_{44}$  are elastic compliance of materials.

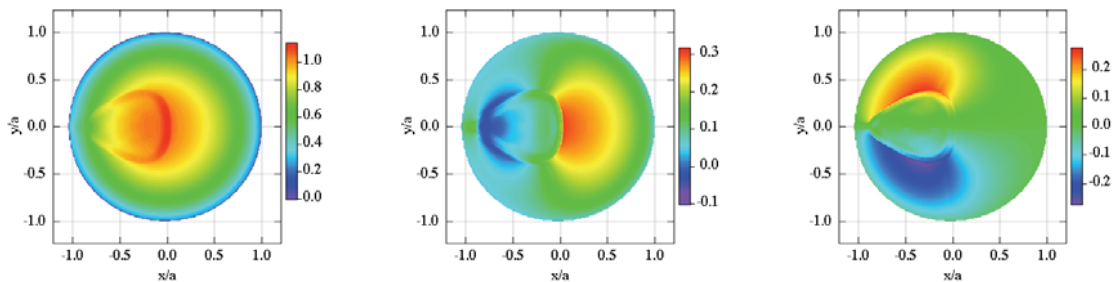
At first, a contact analyze for the surface of Cu (isotropy, anisotropy) and Ni (isotropy, anisotropy) which have four kinds of micropatterns shown in Fig.6 under the condition (c) shown in Table 1 is

**Table 1. Condition for analysis**

	(a)	(b)	(c)			
Material	Fe(Isotropy)	Fe(111)	Cu(Isotropy)	Ni(Isotropy)	Cu (111)	Ni (111)
Young's modulus $E$	210 GPa	220.41 GPa	128.73 GPa	220.64 GPa	128.53 GPa	227.34 GPa
Poisson's ratio $\nu$	0.3	0.391	0.345	0.302	0.503	0.423
Number of grid points	512 × 512		256 × 256			
Distance of grid points	0.5 μm		20.0 μm			
Shape	Plane		Circle( $\phi 400 \mu\text{m}$ ), Square( $\square 340 \mu\text{m}$ )			
Pattern	Pitch	-	-	1280 μm, 640 μm		
	Height	-	-	30.0 μm		
Radius of indenter $R$	18.0 mm		200 mm			
Coefficient of friction $\mu_f$	0.28571		0.3			
Normal load $P_0$	20 N		6.00 kN			
Tangent force $F_x (= 0.6\mu_f P_0)$	3.43 N		1.08 kN			

**Table 2. Material properties used in the analysis (GPa)**

	$C_{11}$	$C_{12}$	$C_{13}$	$C_{15}$	$C_{22}$	$C_{23}$	$C_{25}$	$C_{33}$	$C_{44}$	$C_{46}$	$C_{55}$	$C_{66}$
Fe(111)	300.1	111.6	97.26	20.26	300.1	97.26	-20.26	314.4	79.93	-20.26	79.93	94.25
Cu(111)	218.6	103.7	86.51	24.32	218.6	86.51	-24.32	235.8	40.25	-24.32	40.25	57.44
Ni(111)	325.7	129.0	103.2	36.58	325.7	103.20	-36.58	351.6	72.47	-36.58	72.47	98.33

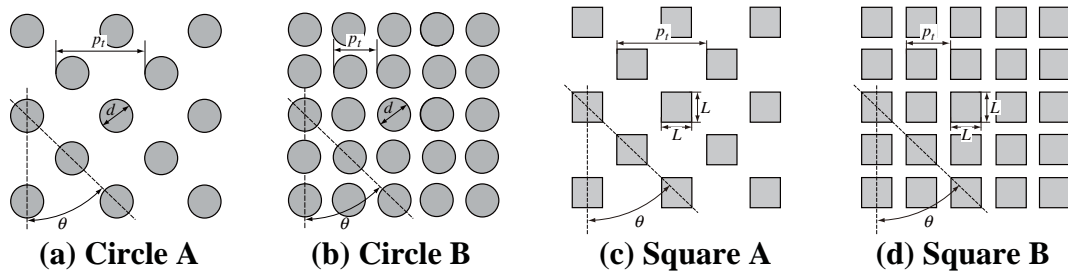


(a) Normalized contact pressure  $p/p_H$

(b) Normalized shear traction  $q_x/p_H$

(c) Normalized shear traction  $q_y/p_H$

**Figure 5. Contour plots of normalized contact pressure and shear tractions by  $p_H=931.62\text{MPa}$  and  $a=0.10124\text{mm}$**



(a) Circle A

(b) Circle B

(c) Square A

(d) Square B

**Figure 6. Geometry and size of micropatterns**

carried out, and the friction property for different micropatterns is investigated. Elastic constants for the anisotropic material are shown in Table 2. Figure 7 demonstrates the distributions of shear traction,  $q_x$ , and the contact pressure  $p$  on the surface of Cu(111). In case of Circle A, the shear traction  $q_x$  concentrates at the edge of each circle, and a positive shear traction occurs at the right side of the circle like Fig.4(b), since the external force which is applied to the rigid indenter directs in the positive direction of the  $x$ -axis. Large shear traction occurs near the center in the whole contact area. In case of Circle B, the shear traction  $q_x$  is less than that in Circle A (Fig.7(b)), and the concentration of  $q_x$  at the edge reduces moderately. This is attributed to the increase of pattern density. This is caused by the increase of contact area and the decrease of average contact pressure. There is no space to show the results for Squares A and B. Similar results are deduced for square patterns, furthermore, for Ni(111).

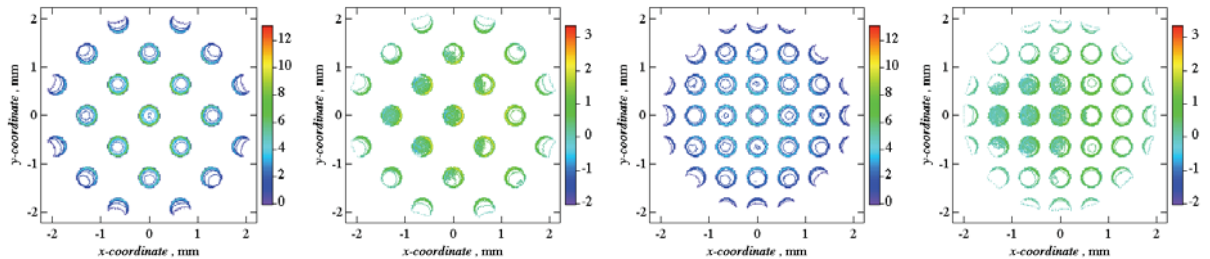
### Slip distance and stick region

The maps of slip distance,  $s_{xy}$ , for each surface pattern are shown in Fig.8. The stick region indicates the region of  $s_{xy}=0$ . For Circle A, it is found that the slip distance increases in the direction of the applied force within the region of a lower contact pressure, and the stick region exits at the opposite side of the slip region. Comparing the stick region with the distribution of shear tractions,  $q_x$  and  $q_y$ , it is found that the shear tractions vary significantly within the stick region. Figure 8(b) shows the map of slip distance for Circle B. It is found that the width of stick region in Circle B is less than that in Circle A. Next, comparing Fig.8(c) with Figs.8(a), (b) and (d), it is found that the stick region for square patterns is similar to that for circular patterns, and the width of stick region decreases with the increase of pattern density. Although the maximum slip distance does not so much vary for all patterns.

### Apparent friction coefficient

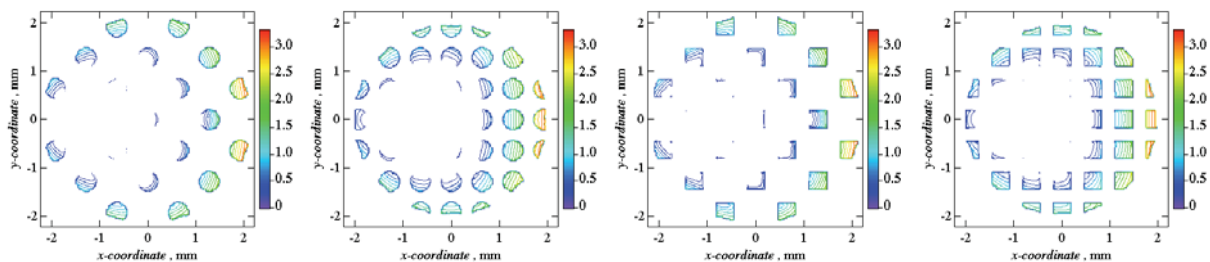
It is very hard to determine a friction property for each pattern due to the different tendency of the ratio of stick region against the pattern density. Then, a friction coefficient is investigated for the apparent contact area. An analytical solution for contact problem with anisotropic substrate considering friction cannot be available until now. So, the friction coefficient is estimated using the expression for isotropic materials in the study. When material is isotropic, the friction coefficient is obtained from

$$\mu_a = \delta_x a^3 K_E / \{P_0 (a^2 - c^2)\} \quad (19)$$



(a) Contact pressure  $p$  (GPa) : Circle A    (b) Shear traction  $q_x$  (GPa) : Circle A    (c) Contact pressure  $p$  (GPa) : Circle B    (d) Shear traction  $q_x$  (GPa) : Circle B

Figure 7. Contour maps of contact pressure and shear tractions : Cu(111)



(a) Circle A    (b) Circle B    (c) Square A    (d) Square B

Figure 8. Contour maps of slip distance : Cu(111)

where  $K_E = 8E\{3(1+\nu)(2-\nu)\}$ ,  $\nu$  is Poisson's ratio,  $E$  is Young's modulus for the isotropic substrate. When the substrate is an isotropic flat surface, the friction coefficient calculated using Eq.(19) is 0.3. When material is anisotropic,  $K_E$  is composed of anisotropic elastic moduli. We do not know the form until now. The value of  $K_E$  is determined from the data of the flat anisotropic substrate for different directions of applied force. The obtained values of  $K_E$  are shown in Fig.9(a). In the present analysis, the arrangement and direction of the patterns are fixed, and the direction of applied horizontal force is rotated  $15^\circ$  by  $15^\circ$  until  $180^\circ$  with respect to the  $z$ -axis. Then, the influence of pattern on the apparent friction coefficient,  $\mu_a$ , is investigated. The results are shown in Fig.9(b). It is found that the apparent friction coefficient for the surfaces with patterns is larger than that for the isotropic substrate with the flat surface. It is found that the value of friction coefficient for the surface with high pattern density is less than that with low pattern density. This is due to the increase of contact pressure in low pattern density. The influence of pattern shape on the friction coefficient can be a little observed.

## Conclusion

In the present study, a contact problem between a rigid spherical indenter and a half-anisotropic elastic region with the micropattern was analyzed under normal and tangential forces considering friction. Furthermore, the apparent friction property for the surface with a micropattern was investigated. From the results, the following conclusions can be drawn:

- (1) The difference of absolute values of the shear tractions between isotropic material and anisotropic material were not so much large. However, the shapes of the map for shear tractions were different.
- (2) For the surface with the micropattern, the contact pressure concentrated at the edge of each pattern, and the shear tractions also concentrated at the sites corresponding to the contact pressure.
- (3) The apparent friction coefficient for a high density of micropattern was less than that for a low density.

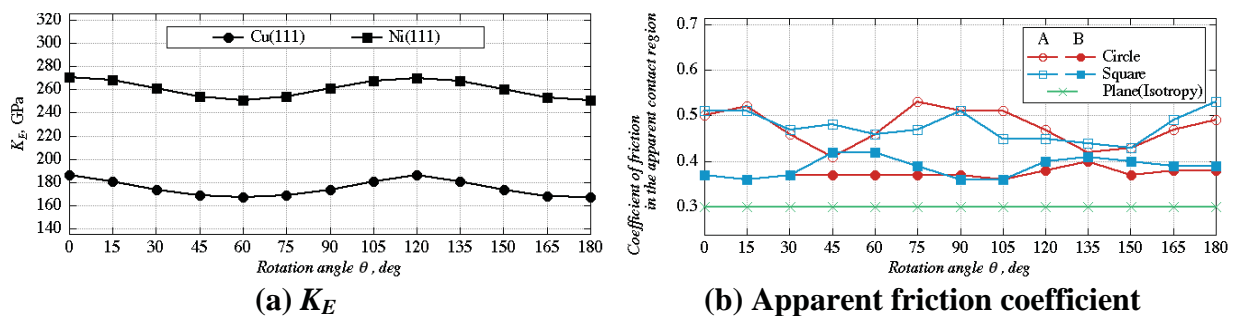


Figure 9. Variation of  $K_E$  and apparent friction coefficient

## References

- Vlassak, J.J., Ciavarella, M., Barber, J.R., Wang, X., (2003), The indentation modulus of elastically anisotropic materials for indenters of arbitrary shape, *J. Mech. Phys. Solids*, 51, pp.1701–1721.
- Lin Y. and Ovaert T.C., (2008), Three-dimensional rough surface contact model for anisotropic materials, *J. Tribol.*, 130, 021402.
- He L. and Ovaert T.C., (2004), A rough surface contact model for general anisotropic materials, *J. Tribol.*, 126, pp.41–49.
- Cattaneo, C., (1938), Sul Contatto Di Due Corpi Elastici: Distribuzione Locale Degli Sforzi, *Rend. Accad. Naz. Lincei*, 27, pp. 342–348, 474–478, 434–436.
- Mindlin, R. D., (1949), Compliance of Elastic Bodies in Contact, *J. Appl. Mech.*, 16, pp. 259–268.
- Ciavarella, M., (1998), The Generalized Cattaneo Partial Slip Plane Contact Problem. I—Theory, *Int. J. Solids Struct.*, 35(18), pp. 2349–2362.
- Kalker, J. J., (1977), Variational Principles in Contact Elastostatics, *J. Inst. Math. Appl.*, 20, pp. 199–219.
- Chen, W. W., and Wang, Q., (2008), A Numerical Model for the Point Contact of Dissimilar Materials Considering Tangential Tractions, *Mech. Mater.*, 40(11), pp. 936–948.
- Dini, D. Hill, D. A., 2009, Frictional Energy Dissipation in a Rough Hertzian Contact, *J. Tribol.*, 131(2), 021401.
- Wang, Z. J., Wang, W. Z., Wang, H., Zhu, D., and Hu, Y. Z., (2010), Partial Slip Contact Analysis on Three-Dimensional Elastic Layered Half Space, *J. Tribol.*, 132(2), 021403.



## Transition Phenomena in Turbulent Natural Convective Flow Using Subgrid Modeling

\*G.H. Yeoh<sup>1,2</sup>, G.E. Lau<sup>1</sup>, V. Timchenko<sup>1</sup> and J.A. Reizes<sup>1</sup>

<sup>1</sup>*School of Mechanical and Manufacturing Engineering, University of New South Wales,  
Sydney, NSW 2052, Australia.*

<sup>2</sup>*Australian Nuclear Science and Technology Organisation (ANSTO), PMB 1, Menai,  
NSW 2234, Australia.*

\*Corresponding author: g.yeoh@UNSW.EDU.AU

### Abstract

Turbulent natural convection in an enclosed cavity with two differentially heated opposite walls is investigated numerically by means of large-eddy simulation (LES). The dynamic global-coefficient subgrid-scale (SGS) model based on the “global equilibrium” approach for weakly compressible flows is applied. It can be shown that the physical mechanisms of the transition phenomena could be adequately captured. Tollmien-Schlichting waves persist along the hot and cold vertical walls. Nevertheless, the onset of transition occurs much earlier along the hot vertical wall in comparison to the cold vertical wall. Relaminarization flow regimes along the horizontal adiabatic top and bottom walls have been found to be distinctly different.

**Keywords:** Transition phenomena, turbulent natural convective flow, large eddy simulation, dynamic global model.

### Introduction

Turbulent natural convection in tall cavities with two differentially heated opposite walls has been the subject of numerous numerical studies due to its wide application in diverse industries. For example, cooling of electronic components or solar energy applications. In such configurations, two distinct patterns are usually observed in the flow structure – the boundary layers along the walls and the recirculating motion in the core. As succinctly indicated by Paolucci and Chenoweth (1989), the transition from a laminar to turbulent flow occurs at the critical Rayleigh number between  $10^7$  and  $10^8$ . A further increase in the Rayleigh number leads to a highly-turbulent motion in which wave-like structures may be found in the boundary layers (Paolucci, 1990, Trias et al., 2007).

One important feature of a buoyant flow in a tall cavity is the concurrent occurrence of laminar, transitional and turbulent regimes along the vertical walls as pointed out by Betts and Bokhari (2000) who have performed a number of experiments to investigate the buoyancy-driven flow in a rectangular cavity with an aspect ratio of 28. It was shown that the flow became fully turbulent in the downstream edges along both the heated and cooled vertical walls. Physical mechanisms involved in the transition process have been detailed by Paolucci (1990). Travelling waves in the distinctive “hook” pattern have been found to precede the transition process; a finding consistent with a number of experimental studies by Elder (1965) and Jaluria and Gebhart (1977). These characteristic folding waves have been found to closely resemble the Tollmien-Schlichting waves in forced convection boundary layers.

In this present study, the transition phenomena of turbulent natural convection in a tall cavity is elucidated via the consideration of the LES and SGS modeling of the dynamic procedure based on

“global equilibrium”. The concurrent occurrence of laminar, transitional and turbulent regimes along the vertical walls and relaminarization regimes along the horizontal walls are discussed.

## Mathematical Formulation

### Governing Equations

In LES, scale separation between large-scale structures and small-scale eddies can be achieved by spatially filtering the conservation equations of the mass, momentum and energy which in the present case are assumed to have variable transport properties. Adopting Favre averaging and neglecting acoustic waves, the fluid motion can be described by the filtered continuity, momentum, and energy equations for a weakly compressible flow as

$$\frac{\partial \bar{\rho}}{\partial t} + \frac{\partial (\bar{\rho} \tilde{u}_j)}{\partial x_j} = 0 \quad (1)$$

$$\frac{\partial (\bar{\rho} \tilde{u}_j)}{\partial t} + \frac{\partial (\bar{\rho} \tilde{u}_i \tilde{u}_j)}{\partial x_i} = -\frac{\partial \bar{p}}{\partial x_j} + \frac{\partial \tilde{\sigma}_{ij}}{\partial x_i} - \frac{\partial \tau_{ij}}{\partial x_i} + (\bar{\rho} - \rho_{ref}) g_i \quad (2)$$

$$\frac{\partial (C_p \bar{\rho} \tilde{T})}{\partial t} + \frac{\partial (C_p \bar{\rho} \tilde{u}_i \tilde{T})}{\partial x_i} = \frac{\partial}{\partial x_i} \left( \frac{\mu C_p}{Pr} \frac{\partial \tilde{T}}{\partial x_i} \right) - \frac{\partial h_i}{\partial x_i} \quad (3)$$

where  $\bar{\rho}$  and  $\tilde{T}$  are the filtered density and temperature respectively,  $\rho_{ref}$  is the reference density at reference temperature  $T_{ref}$ ,  $\tilde{u}_i$  and  $g_i$  are the respective filtered velocity and gravitational vectors,  $\bar{p}$  is the filtered pressure,  $Pr$  is the Prandtl number and  $\mu$  is the dynamic viscosity.

In Eq. (2),  $\tilde{\sigma}_{ij}$  is determined by the Stoke’s hypothesis as

$$\tilde{\sigma}_{ij} = \mu(T) \left( \frac{\partial \tilde{u}_i}{\partial x_j} + \frac{\partial \tilde{u}_j}{\partial x_i} \right) - \frac{2}{3} \mu(T) \frac{\partial \tilde{u}_k}{\partial x_k} \quad (4)$$

while the dynamic viscosity in Eq. (3) is calculated according to

$$\mu = 18.27 \times 10^{-6} \frac{291.15 + C}{\tilde{T} + C} \left( \frac{\tilde{T}}{291.15} \right)^{3/2} \quad (5)$$

where  $C$  is the Sutherland constant. For air,  $C$  and  $Pr$  are 120 and 0.71 respectively. The unresolved turbulent SGS momentum stress tensor  $\tau_{ij} = \bar{\rho} (u_i u_j - \tilde{u}_i \tilde{u}_j)$  in Eq. (2) is modelled through an SGS-viscosity model as

$$\tau_{ij} - \frac{1}{3} \tau_{kk} \delta_{ij} = -2 \mu_{sgs} \left( \tilde{S}_{ij} - \frac{1}{3} \tilde{S}_{kk} \delta_{ij} \right) \quad (6)$$

where  $\mu_{sgs}$  is the SGS viscosity and  $\tilde{S}_{ij} = (\partial \tilde{u}_i / \partial x_j + \partial \tilde{u}_j / \partial x_i) / 2$ . As detailed by Erlebacher et al. (1992),  $\tau_{kk}$  is assumed to be negligible for natural convective flows in which the effect of acoustic waves is considered to be small. The SGS thermal flux vector  $h_i$  is modelled by the SGS Prandtl number  $Pr_{sgs}$  as outlined by Eidson (1985):

$$h_i = \bar{\rho} \left( u_i T - \tilde{u}_i \tilde{T} \right) \approx - \frac{\mu_{sgs}}{Pr_{sgs}} \frac{\partial \tilde{T}}{\partial x_i} \quad (7)$$

It is noted that variation of the SGS thermal flux as represented by Eq. (7) accounts for variable thermal diffusion due to changing SGS viscosity.

#### *Dynamic Model Based on Global Equilibrium*

The dynamic global-coefficient model proposed by You and Moin (2007) which is based on ‘‘global equilibrium’’ between the SGS dissipation and viscous dissipation requires only a single-level test filtering procedure. In formulating this model, the test-filtered resolved-scale turbulent kinetic energy equation can be obtained as Subtracting test-filtered resolved-scale turbulent kinetic energy equation from the test-filtered total turbulent kinetic energy equation yields a transport equation for  $T_{ii} = \overline{\hat{\rho} u_i u_i} - \hat{\rho} \hat{u}_i \hat{u}_i$  and invoking the Germano identity, a transport equation for  $L_{ii} = T_{ii} - \hat{\tau}_{ii}$  is derived as

$$\begin{aligned} \underbrace{\frac{\partial \left( \overline{\hat{\rho} \tilde{u}_i \tilde{u}_i} - \hat{\rho} \hat{u}_i \hat{u}_i \right)}{\partial t}}_{\text{time variation}} &= \frac{\partial}{\partial x_j} \left\{ - \left( \overline{\hat{\rho} \tilde{u}_i \tilde{u}_i \tilde{u}_j} - \hat{\rho} \hat{u}_i \hat{u}_i \hat{u}_j \right) - 2 \left( \overline{\hat{p} \tilde{u}_j} - \hat{p} \hat{u}_j \right) \right. \\ &\quad + 2\mu \left[ \left( \tilde{u}_i \frac{\partial \tilde{u}_i}{\partial x_j} - \hat{u}_i \frac{\partial \hat{u}_i}{\partial x_j} \right) + \left( \tilde{u}_i \frac{\partial \tilde{u}_j}{\partial x_i} - \hat{u}_i \frac{\partial \hat{u}_j}{\partial x_i} \right) \right. \\ &\quad \left. \left. - \frac{2}{3} \left( \overline{\tilde{u}_i \frac{\partial \tilde{u}_k}{\partial x_k} - \hat{u}_i \frac{\partial \hat{u}_k}{\partial x_k}} \right) \delta_{ij} \right] - 2 \left( \overline{\tilde{u}_i \tau_{ij}} - \hat{u}_i T_{ij} \right) \right\} \\ &\quad + 2 \underbrace{\left( \overline{\hat{p}} \frac{\partial \tilde{u}_k}{\partial x_k} - \hat{p} \frac{\partial \hat{u}_k}{\partial x_k} \right)}_{\text{pressure dilatation}} \\ &\quad - 2\mu \left[ \left( \frac{\partial \tilde{u}_i}{\partial x_j} \frac{\partial \tilde{u}_i}{\partial x_j} - \frac{\partial \hat{u}_i}{\partial x_j} \frac{\partial \hat{u}_i}{\partial x_j} \right) + \left( \frac{\partial \tilde{u}_i}{\partial x_j} \frac{\partial \tilde{u}_j}{\partial x_i} - \frac{\partial \hat{u}_i}{\partial x_j} \frac{\partial \hat{u}_j}{\partial x_i} \right) \right. \\ &\quad \left. - \frac{2}{3} \left( \frac{\partial \tilde{u}_i}{\partial x_i} \frac{\partial \tilde{u}_k}{\partial x_k} - \frac{\partial \hat{u}_i}{\partial x_i} \frac{\partial \hat{u}_k}{\partial x_k} \right) \delta_{ij} \right] + 2 \left( \overline{\tau_{ij} \tilde{S}_{ij}} - T_{ij} \tilde{S}_{ij} \right) \end{aligned} \quad (9)$$

For a weakly compressible flow, the pressure dilatation term in Eq. (9) can be neglected following the observation of Vreman et al. (1995). Also, as detailed by Lee et al. (2010), the time variation term can be taken to be negligible in statistically steady turbulent flows. By taking volume averaging of Eq. (9) and assuming ‘‘global equilibrium’’, the model coefficient  $C_{DVME}$  can be obtained as

$$C_{DVME} = - \frac{\left\langle \mu \left[ \left( \alpha_{ij} \alpha_{ij} - \hat{\alpha}_{ij} \hat{\alpha}_{ij} \right) + \left( \alpha_{ij} \alpha_{ji} - \hat{\alpha}_{ij} \hat{\alpha}_{ji} \right) - \frac{2}{3} \left( \alpha_{ii} \alpha_{kk} - \hat{\alpha}_{ii} \hat{\alpha}_{kk} \right) \delta_{ij} \right] \right\rangle_V}{2 \left\langle \bar{\rho} \Pi^g \tilde{S}_{ij} \tilde{S}_{ij} - \hat{\rho} \Pi^t \hat{S}_{ij} \hat{S}_{ij} \right\rangle_V} \quad (10)$$

The SGS Prandtl number could also be determined dynamically using the ‘‘global equilibrium’’ hypothesis. Subtracting the transport equation for the Favre-filtered resolved temperature variance

from the Favre-filtered total temperature variance equation and the test-filtered transport equation for resolved temperature variance from test-filtered total temperature variance equation results in the transport equations for  $\theta_j = \bar{\rho}(TT - \tilde{T}\tilde{T})$  and  $\Theta_j = \bar{\rho}\tilde{T}\tilde{T} - \hat{\rho}\hat{\tilde{T}}\hat{\tilde{T}}$  which they can be expressed as

$$\begin{aligned} \frac{\partial}{\partial t}(C_p \theta_j) = \frac{\partial}{\partial x_j} & \left[ -C_p (\bar{\rho} u_j TT - \bar{\rho} \tilde{u}_j \tilde{T}\tilde{T}) + 2 \left( \overline{kT} \frac{\partial T}{\partial x_j} - \tilde{k}\tilde{T} \frac{\partial \tilde{T}}{\partial x_j} \right) + 2C_p \tilde{T} q_j \right] \\ & - 2 \left( k \frac{\partial T}{\partial x_j} \frac{\partial T}{\partial x_j} - \tilde{k} \frac{\partial \tilde{T}}{\partial x_j} \frac{\partial \tilde{T}}{\partial x_j} \right) - 2C_p q_j \frac{\partial \tilde{T}}{\partial x_j} \end{aligned} \quad (11)$$

$$\begin{aligned} \frac{\partial}{\partial t}(C_p \Theta_j) = \frac{\partial}{\partial x_j} & \left\{ -C_p (\bar{\rho} u_j TT - \hat{\rho} \hat{\tilde{u}}_j \hat{\tilde{T}}\hat{\tilde{T}}) + 2 \left( \overline{kT} \frac{\partial T}{\partial x_j} - \hat{\tilde{k}}\hat{\tilde{T}} \frac{\partial \hat{\tilde{T}}}{\partial x_j} \right) + 2C_p Q_j \hat{\tilde{T}} \right\} \\ & - 2k \left( \frac{\partial T}{\partial x_j} \frac{\partial T}{\partial x_j} - \frac{\partial \hat{\tilde{T}}}{\partial x_j} \frac{\partial \hat{\tilde{T}}}{\partial x_j} \right) - 2C_p Q_j \frac{\partial \hat{\tilde{T}}}{\partial x_j} \end{aligned} \quad (12)$$

where

$$q_j = -\frac{\mu_{sgs}}{Pr_{sgs}} \frac{\partial \tilde{T}}{\partial x_j} \quad (13)$$

$$Q_j = -\frac{\mu'_{sgs}}{Pr_{sgs}} \frac{\partial \hat{\tilde{T}}}{\partial x_j} \quad (14)$$

The transport equation for  $\mathcal{L}_j^\theta = \Theta_j - \hat{\theta}$  is derived as

$$\begin{aligned} \underbrace{\frac{\partial}{\partial t}(C_p \mathcal{L}_j^\theta)}_{\text{time variation}} = \frac{\partial}{\partial x_j} & \left\{ \underbrace{-C_p (\bar{\rho} \tilde{u}_j \tilde{T}\tilde{T} - \hat{\rho} \hat{\tilde{u}}_j \hat{\tilde{T}}\hat{\tilde{T}})}_{\text{redistribution}} + 2k \left( \tilde{T} \frac{\partial \tilde{T}}{\partial x_j} - \hat{\tilde{T}} \frac{\partial \hat{\tilde{T}}}{\partial x_j} \right) + 2C_p (q_j \tilde{T} - Q_j \hat{\tilde{T}}) \right\} \\ & - 2 \left( \tilde{k} \frac{\partial \tilde{T}}{\partial x_j} \frac{\partial \tilde{T}}{\partial x_j} - \hat{\tilde{k}} \frac{\partial \hat{\tilde{T}}}{\partial x_j} \frac{\partial \hat{\tilde{T}}}{\partial x_j} \right) + 2C_p \left( q_j \frac{\partial \tilde{T}}{\partial x_j} - Q_j \frac{\partial \hat{\tilde{T}}}{\partial x_j} \right) \end{aligned} \quad (15)$$

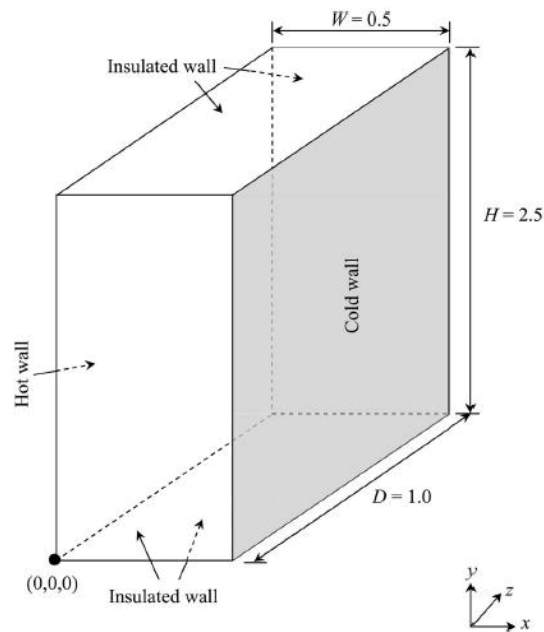
Assuming that time variation and redistribution terms are negligible, a global integration of Eq. (15) results in a dynamic evaluation of  $Pr_{DVME}$ :

$$Pr_{DVME} = -\frac{C_p \left\langle \mu_{sgs} \frac{\partial \tilde{T}}{\partial x_j} \frac{\partial \tilde{T}}{\partial x_j} - \mu'_{sgs} \frac{\partial \hat{\tilde{T}}}{\partial x_j} \frac{\partial \hat{\tilde{T}}}{\partial x_j} \right\rangle_V}{\left\langle \tilde{k} \frac{\partial \tilde{T}}{\partial x_j} \frac{\partial \tilde{T}}{\partial x_j} - \hat{\tilde{k}} \frac{\partial \hat{\tilde{T}}}{\partial x_j} \frac{\partial \hat{\tilde{T}}}{\partial x_j} \right\rangle_V} \quad (16)$$

For convenience, this model is termed DVME in the present article.

### Numerical Model

Turbulent natural convective flow is simulated in an enclosed cavity with two differentially heated opposite walls. The geometry is shown in Figure 1 which corresponds to the experimental apparatus used by King (1989) with an aspect ratio of  $H/W = 5$ . A hot wall ( $x = 0$ ) and a cold wall ( $x = W$ ) were maintained isothermal giving a temperature difference of  $45.8^\circ\text{C}$ . No-slip boundary condition is used for the velocities at all solid walls while Dirichlet boundary condition is applied at the hot and cold walls where  $T_{Hot} = 77.2^\circ\text{C}$  and  $T_{Cold} = 31.4^\circ\text{C}$ . This yields a Rayleigh number based on the cavity width as  $Ra = 4.56 \times 10^{10}$ . For the insulated walls, Neumann boundary condition is applied, i.e.  $\partial T/\partial n = 0$ , where  $n$  is the direction perpendicular to the wall. The predicted temperature field is validated against wall temperatures that have been measured via twenty thermocouples with an accuracy of  $\pm 0.2$  K. The predicted velocity field is validated against Laser Doppler Anemometer (LDA) measurements with uncertainty of the velocity measurements approximated to be about  $\pm 0.02$  m/s.



**Figure 1. Geometry of the cavity.**

Finite volume formulation is utilized to discretize the filtered equations on a collocated grid. The convective terms are approximated using the fourth-order central differencing scheme while the diffusion terms and other spatial derivatives are approximated using the second-order central differencing scheme. The numerical solution is advanced in time using an explicit two-step predictor-corrector approach. It involves a second-order Adams-Bashforth time integration scheme for the predictor stage and a second-order quasi Crank-Nicolson integration scheme for the corrector stage. Pressure correction steps which are incorporated in both the predictor and corrector stages involve the inversion of pressure correction Poisson equations and are solved by means of Krylov methods. Detailed derivation and implementation of the numerical method can be found in Lau et al. (2011).

Three grid resolutions are tested and their details are presented in Table 1 in wall units. From Table 1, it is clear that even the coarse mesh (DVME1) is sufficient to resolve the development of boundary layer in turbulent natural convection since the first mesh point lies within  $x^+ < 1.1$ ,

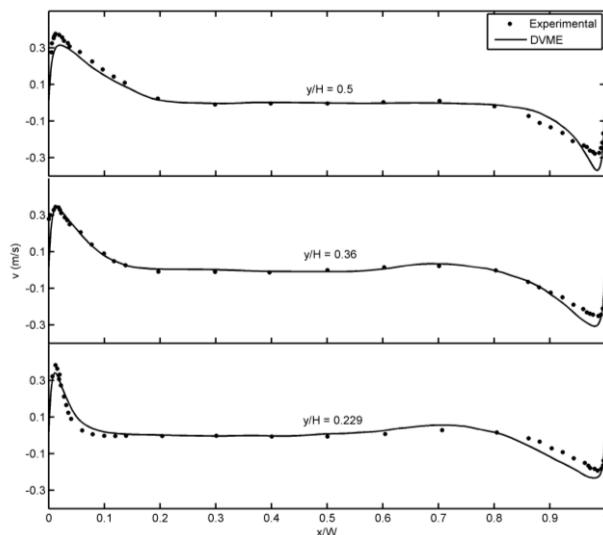
implying that viscous sublayer of the turbulent boundary layer is sufficiently resolved. It has been found that at least 6 mesh points are allocated in regions close to the wall to sufficiently capture formation of the turbulent structures in the cavity. A non-uniform mesh is applied where further from the walls the grid points are stretched geometrically toward the core of the cavity where the flow is expected to be highly stratified. Differences between the mean velocity profiles in the coarse (DVME1), medium (DVME2) and fine (DVME3) grid resolutions have been found to be small and do not exceed 4.2%. Thus in the following, numerical results are presented for the fine mesh unless mentioned otherwise. All simulations are carried out for approximately 25 000 time steps to allow initial transients to develop in the cavity before data are gathered from additional 100 000 time steps to satisfactorily capture the turbulent statistics. Stability of the numerical algorithm is ensured by employing a maximum Courant–Friedrichs–Lewy (CFL) criterion of 0.35 in all simulations.

**Table 1. Mesh Specification of Cases Simulated in Present Study**

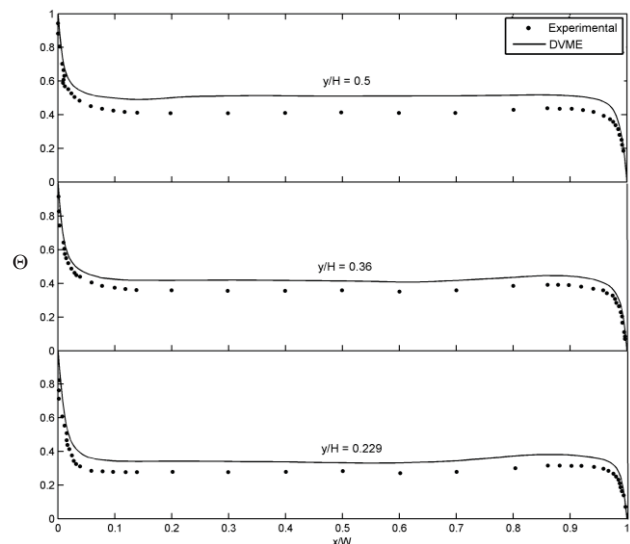
Case	Grid Points ( $x,y,z$ )	$x^+$	$\Delta y^+$	$\Delta z^+$
DVME1	(75,163,78)	$\leq 1.01$	$\leq 41$	$\leq 43$
DVME2	(112,204,94)	$\leq 0.67$	$\leq 34$	$\leq 39$
DVME3	(131,245,119)	$\leq 0.32$	$\leq 26$	$\leq 34$

## Results and Discussion

For validating the numerical model, Figs. 2 and 3 compare the evolution of time-averaged velocity and mean non-dimensional temperature  $\Theta = (\tilde{T} - T_{Cold}) / (T_{Hot} - T_{Cold})$  profiles along the height of the cavity in the central  $x$ - $y$  plane. Overall, good agreement is achieved between the predicted and measured profiles. Nevertheless, predicted temperatures are observed to be higher than the experimental data at  $y/H = 0.5$ . This discrepancy is consistent with the LES simulations performed by Barhaghi and Davidson (2007) on the same geometry where possibly heat loss could have occur in the experimental apparatus especially in the upper section of the cavity due to the imperfect insulation along the walls.



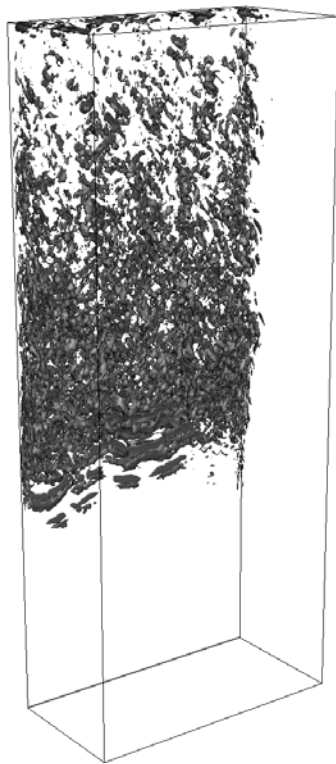
**Figure 2. Velocity profiles**



**Figure 3. Temperature profiles.**

In order to describe the transition phenomena of turbulent natural convective flow in the cavity, the onset of transition is primarily triggered by disturbances which propagate in hook-like structures along the boundary layer in the form of Tollmein-Schlichting waves. Figs. 4 and 5 depict the

formation of coherent structures are represented by iso-surfaces of the  $Q$ -criterion as was detailed by Hunt et al. (1988) for the hot and cold vertical walls respectively. Flow in the beginning portion of the hot wall is clearly laminar for a shorter period due to the absence of vortices in the height section  $0 < y/H < 0.2$ . However, the flow in the beginning portion of the cold wall remains rather laminar for a longer period due to the absence of vortices in the height section  $0.5 < y/H < 1.0$ . As the flow travels upwards along the hot vertical wall and downwards along the cold vertical wall, propagation of Tollmein-Schlichting waves which resemble the characteristic hook-like structures in the instantaneous isotherms ensues as disturbances began to amplify in the boundary layer. This distinctive hook pattern may be recognized as a series of vortex rolls in which faster moving fluid in the inner region of the waves are thrown out into the stratified core, leaving behind a region of lower pressure. As a result, fluid from the exterior whose temperature is lower than that in the inner region is decelerated and thereby entrained toward the wall, triggering a folding mechanism which progresses as the waves propagate. As time proceeds further, vorticity within these structures becomes excessively large that certain segments along a vortex roll starts to lift off from the wall, thereby disrupting the boundary layer and resulting in structures which are mostly irregular and disorganized

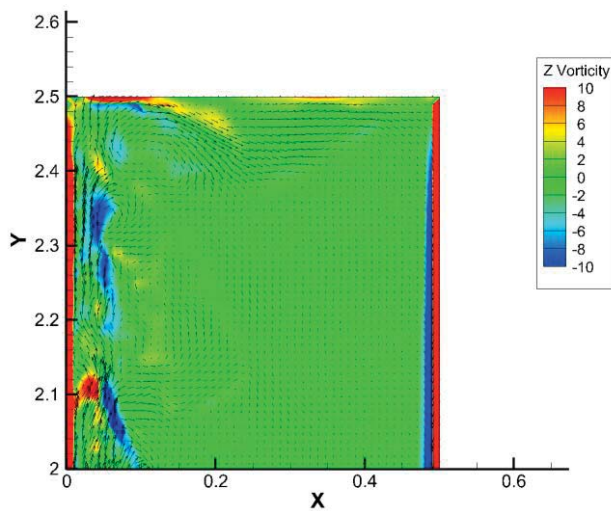


**Figure 4. Coherent structures near the hot wall.**

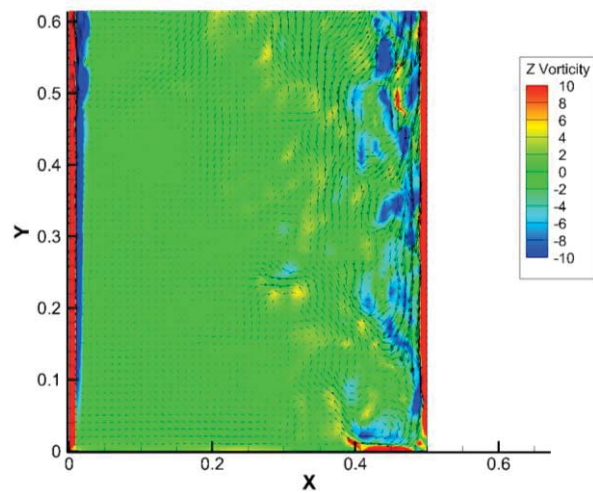


**Figure 5. Coherent structures near the cold wall.**

The transition phenomena due to relaminarization can also co-exist for turbulent natural convective flow in the cavity especially at the corners between hot and top walls and between cold and bottom walls. Figs. 6 and 7 illustrate the instantaneous isotherms of  $z$ -vorticity accompanied by the velocity vectors of the flow fields near these two regions. It can be clearly seen that the relaminarization behavior of the flow near the top horizontal adiabatic wall is distinctly different from the flow near the bottom horizontal adiabatic wall. Breakdown of coherent structures as the upward flow along the hot vertical wall hits the top horizontal adiabatic wall appears to be more gradual while the downward flow along the cold vertical wall hitting the bottom horizontal adiabatic wall augmented by the gravitational acceleration appears to be more abrupt.



**Figure 6. Relaminarization flow structures near the top wall.**



**Figure 7. Relaminarization flow structures near the bottom wall.**

## Conclusions

The dynamic procedure based on “global equilibrium” to determine the model coefficient of the Vreman SGS model in LES is applied to simulate the characteristics of turbulent natural convection in an enclosed cavity. The onset of transition of different flow regimes of the boundary layer is found to be prevalent along the hot and cold vertical walls as well as the flow turns at the top and bottom horizontal adiabatic walls. Essentially, propagation of Tollmein-Schlichting waves recognized as a series of vortex rolls exist along the hot and cold walls. The relaminarization behaviour is characterised by the breaking down of the coherent structures which occurs at the top and bottom horizontal adiabatic walls.

## References

- Betts, P. L. and Bokhari, I. H. (2000), Experiments on turbulent natural convection in an enclosed tall cavity. *Int. J. Heat Fluid Flow*, 21, pp. 675-683.
- Elder, J. W. (1965), Turbulent free convection in a vertical slot. *J. Fluid Mechanics*, 23, pp. 99-111.
- Erlebacher, G., Hussaini, M. Y., Speziale, V. G. and Zang, T. A. (1992), Towards the large-eddy simulations of compressible turbulent flows. *J. Fluid Mechanics*, 238, pp. 155-185.
- Hunt, J. C. R., Wray, A. A. and Moin, P. (1988), Eddies, streams, and convergence zones in turbulent flows. Proceedings of the Summer Program, Centre for Turbulence Research.
- Jaluria, Y. and Gebhart, B. (1977), On disturbance growth mechanisms in a buoyancy induced flow. *Int. J. Heat Mass Transfer*, 20, pp. 434-437.
- King, K. J. (1989), Turbulent natural convection in rectangular air cavities. Ph.D. Thesis, Queen Mary College, University of London, London.
- Lau, G. E., Yeoh, G. H., Timchenko, V. and Reizes, J. A. (2011), Large-eddy simulation of turbulent natural convection in vertical parallel-plate channels. *Num. Heat Transfer, Part B: Fundamentals*, 59, pp. 259-287.
- Lee, J., Choi, H. and Park, N. (2010) Dynamic global model for large eddy simulation of transient flow. *Phys. Fluids*, 22, pp. 125109.
- Paolucci, S. and Chenoweth, D. R. (1989), Transition to chaos in a differentially heated vertical cavity. *J. Fluid Mechanics*, 201, pp. 379-410.
- Paolucci, S. (1990), Direct numerical simulation of two-dimensional turbulent natural convection in an enclosed cavity. *J. Fluid Mechanics*, 215, pp. 229-262.
- Trias, F. X., Soria, M., Oliva, A. and Perez-Segarra, C. D. (2007), Direct numerical simulations of two- and three-dimensional turbulent natural convection flows in a differentially heated cavity of aspect ratio 4. *J. Fluid Mechanics*, 586, pp. 259-293.
- You, D. and Moin, P. (2007), A dynamic global-coefficient subgrid-scale eddy-viscosity model for large-eddy simulation in complex geometries. *Phys. Fluids*, 19, pp. 065110.



# A Finite Element Formulation of Minimization Problem for Steady Plastic Cycling

D.A. Tereshin

Department of Applied Mechanics, Dynamics and Strength of Machines, South-Ural State University,  
Lenin Avenue 76, Chelyabinsk City, Russia

denisat75@gmail.com

## Abstract

Direct approach was extended beyond the scope of elastic shakedown to determine the parameters (strain increments and stress state) of an arbitrary steady elasto-plastic cycle under prescribed loading in ratcheting, alternating flow or in combination of the both. The resulting convex constrained optimization problem was formulated making use of finite element discretization. The object function equals to the work of fictitious elastic stresses on the plastic strains subtracted from the energy dissipation, with both terms being integrated over the cycle time and spatially over the body. The constraint system includes equality constraints of plastic strain incompressibility, cycle closure and initial residual stress self-balance, which are enforced by means of quadratic penalties; and inequality ones ensuring that the total stress is admissible. For testing purposes the Bree problem was solved employing the optimization formulation, with the resulting plastic strains over each half-cycle agreeing well with the analytical solution to the problem, even though a cycle was discretized only by two time instants.

**Keywords:** Direct computation, Finite elements, Steady cycle, Plastic ratcheting, Inelastic shakedown

## Introduction

Elastic shakedown theory can be thought of as an extension of limit state theorems. The former allows determining the boundary between zone *II* of the Bree diagram (Bree 1967), shown in Fig. 1, and zones *III–V*. The further extension is the theory of steady inelastic structural response under repeated loadings (the response can be alternating flow – zone *III*, plastic ratcheting – zone *V* or the combination of the both – *IV*). Whereas in zone *II* of the Bree diagram a structure usually shakes down to purely elastic deformation over a relatively small number of cycles, stabilization to a steady cycle in excess of shakedown can proceed quite slowly and take many tens of cycles, with the structural behavior in steady condition being crucial for structural life assessments. The computations over loading history show that a slow stabilization usually occurs in severe alternating flow combined with incremental collapse (Abramov, Gadenin et al, 2011), which corresponds to the zone *IV* of in Fig. 1. In such case the whole stress-strain history can be very hard to compute using the step-by-step approach, with long loading history – not the amount of the degree of freedom unknowns – becoming the main trouble. This fact necessitates the development of an approach capable to find the steady cycle parameters (strain range and increment) directly. Although effective procedures for elastic shakedown have already been proposed and implemented, there are only few approaches being under development for steady plastic response, such as the algorithm by Chen and Ponter (2001), which is capable to capture the plastic shakedown boundary between zones *III* and *IV*, and the technique by

Spiliopoulos and Panagiotou (2012) employing the residual stress decomposition method to determine response for any kind of steady cycle.

In order to find the solution to a steady cycle problem, these approaches iteratively adjust either elastic constants or residual stress field. On the other hand, the problem of determining steady plastic response under prescribed cyclic loading can also be formulated as a convex constrained optimization problem (Gokhfeld and Cherniavsky, 1980). So the aim of the present study is to extend a mathematical optimization approach combined with finite element discretization to steady cycle state parameters for any region of the Bree diagram could be obtained.

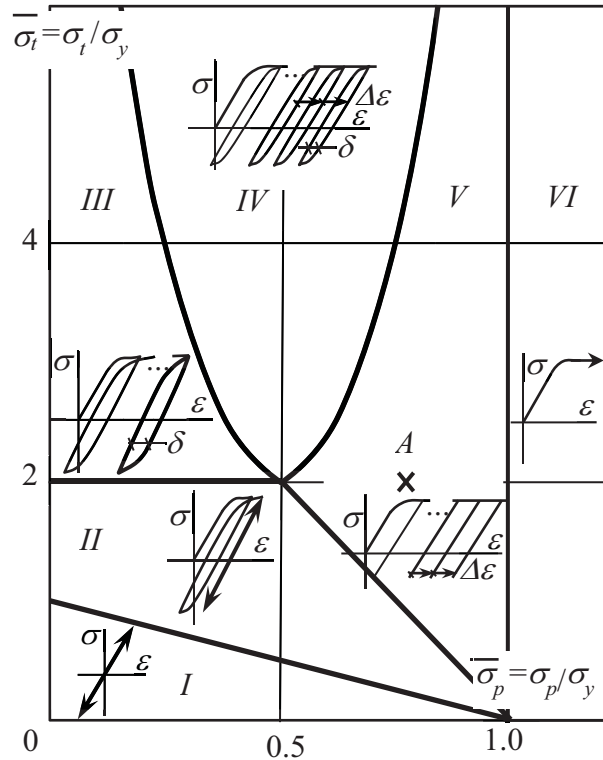


Figure 1. Bree problem

**Mathematical optimization problem formulation**

The system of expressions describing the deformation process in a steady state in terms of continuum mechanics can be written in the following way. The total stress is constituted by the fictitious elastic  $\sigma^e$  and residual  $\rho$  stresses, with the latter including the initial residual stresses  $\rho_0$  at the beginning of a cycle and the residual stress increment accumulated since then over time  $\tau$ :

$$\sigma = \sigma^e + \rho = \sigma^e + \rho_0 + \int_0^\tau \dot{\rho} d\xi. \tag{1}$$

The total strain rate is constituted by the elastic strain rate  $\dot{\epsilon}^e$  part, which is caused by the change in the fictitious elastic stress  $\sigma^e$ , and the parts due to the residual stress rate  $\dot{\rho}$  and the plastic strain rate  $\dot{\epsilon}^p$ :

$$\dot{\epsilon} = \dot{\epsilon}^e + \mathbf{E}^{-1} \cdot \dot{\rho} + \dot{\epsilon}^p, \tag{2}$$

with  $\mathbf{E}$  standing for the elastic stiffness matrix of the material.

The equilibrium for the fictitious elastic stress  $\sigma^e$  holds naturally. For the residual stress field  $\rho$ , equilibrium over a body and at the part of its surface  $S_p$  with prescribed tractions can be stated as follows:

$$\nabla \cdot \rho_0 = \mathbf{0} \text{ in } V, \quad \rho_0 \cdot \bar{n} = \mathbf{0} \text{ at } S_p; \tag{3}$$

$$\nabla \cdot \dot{\rho} = \mathbf{0} \text{ in } V, \quad \dot{\rho} \cdot \bar{n} = \mathbf{0} \text{ at } S_p. \tag{4}$$

Since the total strain rate and the elastic rate fields in Eq. (2) are compatible, the plastic strain rate field and the strain rate field caused by the residual stresses are also compatible to a displacement rate  $\dot{\mathbf{u}}$  field at every time moment:

$$\dot{\boldsymbol{\varepsilon}}'' + \mathbf{E}^{-1} \cdot \dot{\boldsymbol{\rho}} = \frac{1}{2} (\nabla \dot{\mathbf{u}} + \dot{\mathbf{u}} \nabla). \quad (5)$$

At each time instant in every material point the total stress is admissible: it lies inside or at the yield surface defined through a yield function  $f(\boldsymbol{\sigma})$ :

$$f(\boldsymbol{\sigma}) \leq 0. \quad (6)$$

The associated flow rule holds for plastic strain with a non-negative plastic multiplier  $\alpha \geq 0$ :

$$\dot{\boldsymbol{\varepsilon}}'' = \alpha \nabla f(\boldsymbol{\sigma}), \quad (7a)$$

$$\alpha f(\boldsymbol{\sigma}) = 0, \quad (7b)$$

$$\alpha \dot{f}(\boldsymbol{\sigma}) = 0. \quad (7c)$$

Steady cycle condition may be enforced either in terms of residual stresses by making them exactly repeat every steady cycle  $\boldsymbol{\rho}(\tau) = \boldsymbol{\rho}(\tau + T)$ , with  $T$  – cycle time period:

$$\Delta \boldsymbol{\rho}(T) = \int_0^T \dot{\boldsymbol{\rho}} d\tau = 0, \quad (8a)$$

or, equivalently, in terms of strains by ensuring the plastic strain field increment  $\Delta \boldsymbol{\varepsilon}''$  over a cycle to be compatible with displacement field increment  $\Delta \mathbf{u}$ :

$$\Delta \boldsymbol{\varepsilon}''(T) = \frac{1}{2} (\nabla(\Delta \mathbf{u}) + (\Delta \mathbf{u}) \nabla), \quad \Delta \boldsymbol{\varepsilon}''(T) = \int_0^T \dot{\boldsymbol{\varepsilon}}'' d\tau. \quad (8b)$$

Making use of Drucker's postulate, the system of equations and constraints (1–8) may be recast according to (Gokhfeld and Cherniavsky, 1980) to a convex mathematical optimization problem by retaining Eqs. (1–6,8) as a system of equality and inequality constraints and searching for the minimum of the functional  $J$ , which can be proved to be zero at the exact minimizer, in the optimization field variables  $\dot{\boldsymbol{\varepsilon}}''$ ,  $\boldsymbol{\rho}$  and  $\mathbf{u}$ :

$$J = \int_0^T d\tau \int_V (\bar{\boldsymbol{\sigma}} - \boldsymbol{\sigma}^e) \cdot \dot{\boldsymbol{\varepsilon}}'' dV, \quad (9)$$

with  $\dot{\boldsymbol{\varepsilon}}''$  associated to  $\bar{\boldsymbol{\sigma}}$  by the flow rule (7a,b).

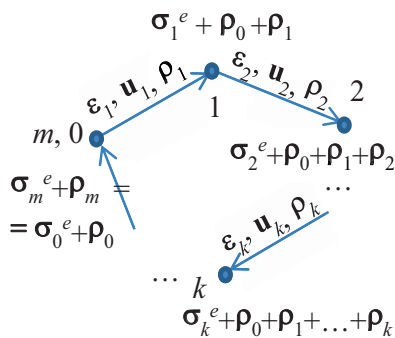


Figure 2. Time discretization

Let us make time discretization, as Fig. 2 shows, where time instant  $k$  is in the range from the beginning of a cycle ( $k=0$ ) to its end ( $k=m$ ), with the both coinciding by the fact the cycle is closed. The strain  $\boldsymbol{\varepsilon}_k$ , displacement  $\mathbf{u}_k$ , residual stress  $\boldsymbol{\rho}_k$  ( $k = \overline{1, m}$ ) have the meaning of increment,  $\boldsymbol{\rho}_0$  is initial residual stress, and the elastic stress  $\boldsymbol{\sigma}_k^e$  corresponds to the  $k$ -th instant.

Employing finite element spatial discretization, the

self-equilibrium condition (3) for the initial residual stress can be formulated as:

$$\mathbf{B}^T \boldsymbol{\rho}_0 \equiv \sum_{i=1}^{NG} w_i \mathbf{B}_i^T \boldsymbol{\rho}_{0i} = \mathbf{0}, \quad (10a)$$

where  $NG$  is the total number of the Gauss integration points,  $w_i$  is the integration weight of point  $i$ . From now on all vectors and matrices indexed by  $i$  or  $j$  imply local ones for the  $i$ -th or  $j$ -th point, whereas not indexed matrices – global ones. E.g., Hook's relation between the stress and strain for point  $i$  at time instant  $k$  is  $\boldsymbol{\sigma}_{ik}^e = \mathbf{E}_i \boldsymbol{\varepsilon}_{ik}^e$ , with  $\boldsymbol{\varepsilon}_{ik}^T = \{\varepsilon_x^{ik} \ \varepsilon_y^{ik} \ \varepsilon_z^{ik} \ 2\varepsilon_{xy}^{ik} \ 2\varepsilon_{yz}^{ik} \ 2\varepsilon_{zx}^{ik}\}$ , but the global relation is  $\boldsymbol{\sigma}_k^e = \mathbf{E} \boldsymbol{\varepsilon}_k^e$ .

Having plastic strain increment  $\boldsymbol{\varepsilon}_k''$ , in place of Eq. (5) one obtains the displacements induced  $\mathbf{u}_k$  by solving for the FE problem with global stiffness  $\mathbf{K}$  and deformation  $\mathbf{B}$  matrices:

$$\mathbf{u}_k = \mathbf{K}^{-1} \int_V \mathbf{B}^T \mathbf{E} dV \boldsymbol{\varepsilon}_k'', \quad (10b)$$

and then restores the residual stresses:

$$\boldsymbol{\rho}_k = \mathbf{E}(\mathbf{B}\mathbf{u}_k - \boldsymbol{\varepsilon}_k''). \quad (10c)$$

The total stress (1) evolves through the cycle points as Fig. 2 illustrates:

$$\boldsymbol{\sigma}_{ik} = \boldsymbol{\sigma}_{ik}^e + \boldsymbol{\rho}_{i0} + \sum_{l=1}^k \boldsymbol{\rho}_{il}. \quad (10d)$$

The cycle closure condition (8a) takes the form of

$$\sum_{k=1}^m \boldsymbol{\rho}_{ik} = \mathbf{0}, \quad (10e)$$

and the stress admissibility condition (6) is required to be satisfied for  $\forall k = \overline{1, m}$ ,  $i = \overline{1, NG}$ :

$$f(\boldsymbol{\sigma}_{ik}) \leq 0. \quad (10f)$$

Accepting von Mises yield condition the functional  $J$  becomes:

$$J = \sum_{k=1}^m \sum_{i=1}^{NG} \left[ \sqrt{2} w_i \tau_y \sqrt{\boldsymbol{\varepsilon}_{ik}''^T \mathbf{D}_i \boldsymbol{\varepsilon}_{ik}''} - w_i \boldsymbol{\sigma}_{ik}^{eT} \boldsymbol{\varepsilon}_{ik}'' \right], \quad (10g)$$

where  $\tau_y$  is the yield shear stress,  $\mathbf{D}_i = \text{Diag}\{1 \ 1 \ 1 \ 1/2 \ 1/2 \ 1/2\}$ .

Thus, the statement of mathematical optimization problem becomes: minimize  $J$  over  $\boldsymbol{\varepsilon}'', \boldsymbol{\rho}, \mathbf{u}$

subject to Eqs. (10a–f) satisfied for  $\forall k = \overline{1, m}$ ,  $\forall i = \overline{1, NG}$ , in addition to which, one has to impose incompressibility constraints on plastic strains:

$$\mathbf{D}_{Vi} \boldsymbol{\varepsilon}_{ik}'' = \mathbf{0}, \quad \forall k = \overline{1, m}, \quad \forall i = \overline{1, NG}, \quad (10h)$$

where  $\mathbf{D}_{Vi}$  is the diad projecting to the spherical part of tensor:  $\mathbf{D}_{Vi} = \frac{1}{3}(1 \ 1 \ 1 \ 0 \ 0 \ 0)^T(1 \ 1 \ 1 \ 0 \ 0 \ 0)$ .

In order to eliminate displacements, by substitution Eq. (10b) to Eq. (10c) one gets to:

$$\boldsymbol{\rho}_k = -\mathbf{E}\mathbf{P}\boldsymbol{\varepsilon}_k^{\prime\prime}, \quad \forall k = \overline{1, m} \quad (11)$$

with the matrix  $\mathbf{P} = \mathbf{I} - \mathbf{B}\mathbf{K}^{-1} \int_V \mathbf{B}^T \mathbf{E} dV$  projecting an arbitrary strain to the subspace of self-equilibrated strains.

For convenience's sake, let us accept the notation from Vu and Yan et al (2004), which simplifies energy relations:  $\mathbf{e}_{ik} = w_i \mathbf{D}_i^{1/2} \boldsymbol{\varepsilon}_{ik}$  – for strain increment vector;  $\hat{\mathbf{B}}_i = w_i \mathbf{D}_i^{1/2} \mathbf{B}_i$  – for deformation matrix, so that  $\sum_{k=1}^m \mathbf{e}_{ik} = \hat{\mathbf{B}}_i \mathbf{u}$ ;  $\mathbf{t}_{ik} = \mathbf{D}_i^{-1/2} \boldsymbol{\sigma}_{ik}^e$  and  $\boldsymbol{\beta}_{ik} = \mathbf{D}_i^{-1/2} \boldsymbol{\rho}_{ik}$  – for stress vectors. In these definitions  $\mathbf{D}_i^{-1/2}$  and  $\mathbf{D}_i^{1/2}$  are diagonal symmetric matrices such that:  $\mathbf{D}_i^{-1/2} = (\mathbf{D}_i^{1/2})^{-1}$  and  $\mathbf{D}_i = \mathbf{D}_i^{1/2} \mathbf{D}_i^{1/2}$ .

Von Mises yield condition (10f) can be presented in the form of Euclidian norm:

$$\left\| (\mathbf{I}_i - \mathbf{D}_{Vi}) \left( \mathbf{t}_{ik} + \boldsymbol{\beta}_{i0} + \sum_{l=1}^k \boldsymbol{\beta}_{il} \right) \right\| \leq \sqrt{2} \tau_y. \quad (12)$$

Let us define the matrix  $\mathbf{G}$  a component  $\mathbf{G}_{ij}$  of which relates plastic strain at point  $j$  to the induced residual stress at point  $i$ :

$$\boldsymbol{\beta}_{ik} = \mathbf{G}_{ij} \mathbf{e}_{jk}, \quad \forall k = \overline{1, m}, \quad \forall i, j = \overline{1, NG}, \quad (13)$$

where  $\mathbf{G}_{ij} = \mathbf{D}_i^{-1} \mathbf{E}_{-wi} \hat{\mathbf{B}}_i \mathbf{K}^{-1} \hat{\mathbf{B}}_j^T \mathbf{E}_{-wj} \mathbf{D}_j^{-1} - \mathbf{D}_i^{-1/2} \mathbf{E}_{-wi} \mathbf{D}_j^{-1/2} \delta_{ij}$  ( $\delta_{ij} = 1$  if  $i=j$ ,  $\delta_{ij} = 0$  if  $i \neq j$ ;  $\mathbf{E}_{-wi} = (1/w_i) \mathbf{E}_i$ ). In the new terms the optimization problem simplifies to:

$$\underset{\mathbf{e}_k, \boldsymbol{\beta}_{i0}}{\text{minimize}} \sum_{i=1}^{NG} \sum_{k=1}^m \left( \sqrt{2} \tau_y \sqrt{\mathbf{e}_{ik}^T \mathbf{e}_{ik} + \varepsilon_0^2} - \mathbf{t}_{ik}^T \mathbf{e}_{ik} \right) \quad (14a)$$

$$\hat{\mathbf{B}}_i^T \boldsymbol{\beta}_{i0} = \mathbf{0}, \quad (14b)$$

$$\sum_{j=1}^{NG} \mathbf{G}_{ij} \sum_{k=1}^m \mathbf{e}_{jk} = \mathbf{0}, \quad (14c)$$

$$s.t. \quad \mathbf{D}_{Vi} \mathbf{e}_{ik} = \mathbf{0}, \quad (14d)$$

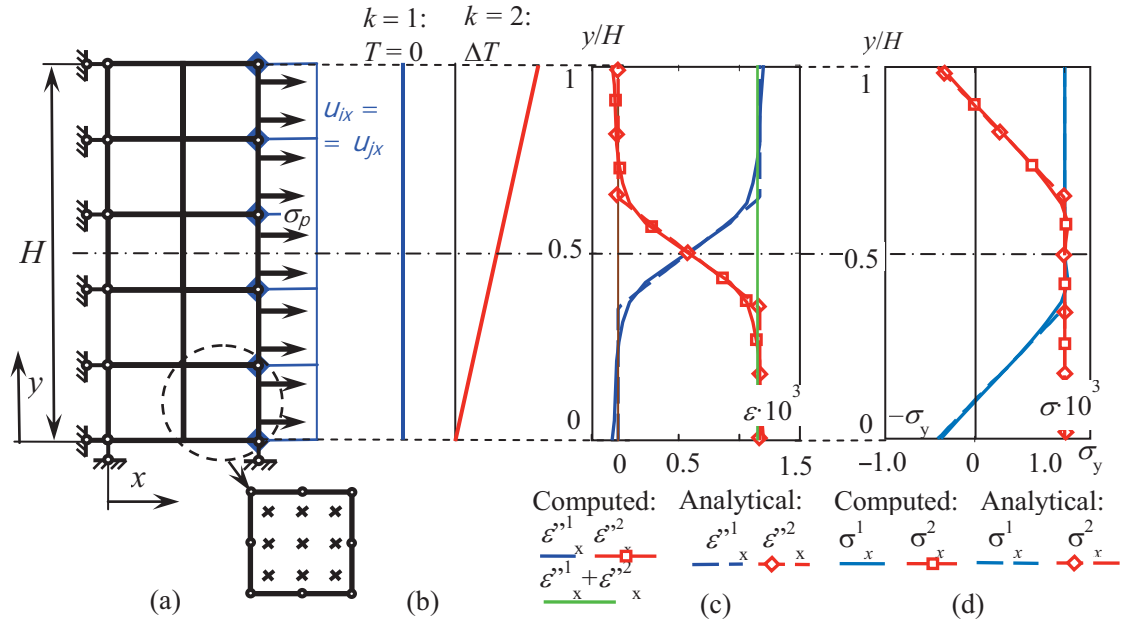
$$\left| f_{ik} = \left( \boldsymbol{\beta}_{i0} + \sum_{j=1}^{NG} \mathbf{G}_{ij} \sum_{l=1}^k \mathbf{e}_{jl} + \mathbf{t}_{ik} \right)^T (\mathbf{I}_i - \mathbf{D}_{Vi}) \left( \boldsymbol{\beta}_{i0} + \sum_{j=1}^{NG} \mathbf{G}_{ij} \sum_{l=1}^k \mathbf{e}_{jl} + \mathbf{t}_{ik} \right) - 2\tau_y^2 \leq 0, \right. \quad (14e)$$

for  $\forall i = \overline{1, NG}$ ,  $k = \overline{1, m}$ .

According to Vu and Yan et al (2004) a small regularization parameter  $\varepsilon_0$  was introduced to Eq. (14a) in order to make it differentiable at  $\mathbf{e}_{ik} = \mathbf{0}$ .

### Test problem

Since the Bree problem of pressurized thin-walled tube under repeated thermal loading has an analytical solution (Bree, 1967), it was used to prove the optimization



**Figure 3. Problem sketch (a), temperature distribution (b), a comparison of computed and analytical plastic strains (c) and total stresses (d)**

formulation (14) is capable of yielding the solution. If Tresca yield criterion is implied, the Bree problem is equivalent to the plain stress problem corresponding to a cross section of the tube under the same time-varying thermal stress  $\sigma_t$  and the constant stress  $\sigma_p$  equal to the hoop stress in the former problem caused by pressure. The structure was discretized with rectangular quadratic finite elements as Fig. 3a shows ( $0y$  points along a radial direction,  $0x$  – in a hoop one), each having nine integration points. The  $u_x$  displacement at the left edge is restrained, and all the nodes at the right edge have an identical value of  $u_x$ . In a cycle, temperature varies from uniform distribution at time point  $k=1$  to a linear distribution with the gradient directed along  $0y$  axis at the end of a cycle ( $k=2$ ) (see Fig. 3b). The constant applied stress  $\sigma_p$  amounts to  $0.75\sigma_y$ , the maximal thermal stress  $\sigma_t=2\sigma_y$ . The corresponding state is depicted by point  $A$  in the Bree diagram Fig. 1, at which pure incremental collapse is expected.

### Solution technique

The conditions of plastic incompressibility (14d), cycle closure (14c) and initial residual stress self-balance (14b) are enforced by means of quadratic penalties in an extended object function:

$$\begin{aligned}
 f_0 = & \sum_{i=1}^{NG} \sum_{k=1}^m \left( \sqrt{2}\tau_y \sqrt{\mathbf{e}_{ik}^T \mathbf{e}_{ik} + \epsilon_0^2} - \mathbf{t}_{ik}^T \mathbf{e}_{ik} \right) + \frac{c_1}{2} E \sum_{i=1}^{NG} \sum_{k=1}^m \mathbf{e}_{ik}^T \mathbf{D}_{Vi} \mathbf{e}_{ik} + \\
 & + \frac{c_2}{2E} \sum_{i=1}^{NG} \sum_{j=1}^{NG} \left( \sum_{l=1}^m (\mathbf{e}_{il})^T \left( \sum_{g=1}^{NG} \mathbf{G}_{gi}^T \mathbf{G}_{gj} \right) \sum_{k=1}^m (\mathbf{e}_{jk}) \right) + \frac{c_3}{2EL_e} \sum_{i=1}^{NG} \sum_{j=1}^{NG} \left( \hat{\boldsymbol{\beta}}_{i0}^T \hat{\mathbf{B}}_i \hat{\mathbf{B}}_j^T \hat{\boldsymbol{\beta}}_{j0} \right), \quad (15)
 \end{aligned}$$

where  $c_1, c_2, c_3$  are penalty coefficients,  $L_e$  – typical element size.

An unconstrained mathematical optimization problem is formulated using logarithmic barrier functions for the inequality constraints (14e):

$$\text{minimize } F_0, \quad (16)$$

$\mathbf{e}_k, \hat{\boldsymbol{\beta}}_{i0}$

in which  $F_0 = f_0 - \frac{1}{t} \sum_{i=1}^{NG} \sum_{k=1}^m \log(-f_{ik})$ .

Having denoted  $\mathbf{f}$  – the vector constituted by all the inequality constraint functions (14e), one obtains the stationary condition of  $F_0$  as central path conditions:

$$\begin{aligned} \nabla f_0 + \sum_{i=1}^{NG} \sum_{k=1}^m \lambda_{ik} \nabla f_{ik} &= \mathbf{0}, \\ -\mathbf{diag}(\boldsymbol{\lambda})\mathbf{f} - (1/t)\mathbf{I} &= \mathbf{0}, \end{aligned} \quad (17)$$

or, from another viewpoint, as the modified Karush-Khun-Tucker equations of the problem of minimization functional (15) subject to (14e) (Boyd and Vandenberghe, 2004), with the gradients being taken with respect to the primal variables  $(\mathbf{e}, \boldsymbol{\beta}_0)$ , and  $\boldsymbol{\lambda}$  being the dual variable vector. So solving Eqs. (17) one applies a simple primal-dual interior-point approach; and the greater the parameter  $t$ , the closer the solution of Eq. (17) to the solution to the original problem given by Eqs. (14a-e).

However, before solving Eqs. (17), one has to find a feasible point  $(\mathbf{e}, \boldsymbol{\beta}_0)$  satisfying all the inequality constraints (14e). This was done by means of a phase I method:

$$\begin{aligned} &\text{minimize } S \\ &\quad \mathbf{e}_k, \boldsymbol{\beta}_{i0} \\ &\text{s.t.} \left\{ \begin{array}{l} f_{ik}(\mathbf{e}_{ik}, \boldsymbol{\beta}_{i0}) \leq S, \quad i = \overline{1, NG}, \quad k = \overline{1, m}, \\ F_0 \leq M. \end{array} \right. \end{aligned} \quad (18)$$

For initialization  $S$  was taken such as to strictly satisfy all the inequality constraints, and  $M \approx 10|f_0(\mathbf{e} = \mathbf{0}, \boldsymbol{\beta}_0 = \mathbf{0})|$ . Having started with  $\varepsilon_0 = 10^{-4}$ , and small  $c_i = 10^{-5}$  so as not to pay much of attention to the equality constraints of the original problem (Eqs. (14b-d)) at this stage, the phase I method converges quite rapidly as inequality constraint functions expressed by Eqs. (14e) are quadratic, and the algorithm based on Newton's method described below performs at quadratically convergent stage immediately.

Eqs. (17) were solved by means of Newton's method using the analytical expressions of first and second derivatives to get primal and dual variable increments  $((\Delta\mathbf{e}, \Delta\boldsymbol{\beta}_0)$  and  $\Delta\boldsymbol{\lambda})$ . At the second stage exact line search was employed, as without line search, Newton's method experiences convergence difficulties when  $\|\mathbf{e}_{ik}\| \geq \varepsilon_0$ . The line search uses the extended object function  $F_0$  as a merit function and ensures  $\boldsymbol{\lambda} \succ \mathbf{0}$  and the incremented value of  $(\mathbf{e}, \boldsymbol{\beta}_0, \boldsymbol{\lambda})$  to be feasible. Basing on the value of surrogate duality gap  $\eta = -\mathbf{f}^T \boldsymbol{\lambda}$  the parameter  $t$  was determined in each iteration as:  $t = \mu \cdot NG \cdot m / \eta$ ; the more  $\mu$  is, the more aggressively  $t$  increases.

Convergence difficulties entailed by the sum of Euclidian norms term in the object function  $F_0$  were remedied by the proper choice of  $\mu$  value, combined with adjusting the regularization parameter  $\varepsilon_0$  and the penalty coefficients  $c_i$ . In general, the object function reduces successfully when  $\mu$  has a relatively small value of 1–5, and all of the four terms in Eq. (15) have nearly the same order of magnitude. However, approaching the boundary defined by inequality constraints Eqs. (14e), the method can drastically slow down (Wright, 1997). This obstacle was dealt with by a temporal reduction of  $\mu$  for several iterations to about 0.05, after which the point becomes repelled enough from the boundary for the object function to be reduced further.

At the end of the convergence process,  $\varepsilon_0$  was adjusted to be  $10^{-5}$ – $10^{-6}$  (2-3 order of magnitude less than maximal  $\|\mathbf{e}_{ik}\|$ ), and the coefficients  $c_i$  amounted to  $10^5$ – $10^{10}$  for the constraints given by Eqs. (14b-d) to be fulfilled well.

## Results

Three mesh patterns were used to solve the problem: 5 elements in column and 2 in row, as Fig. 3a depicts,  $10 \times 1$  elements, and  $5 \times 1$  elements. Only two instances were considered over cycle period ( $m = 2$ ) correspondent to no temperature applied and to the full thermal load.

The convergence process and results obtained in different cases of mesh patterns are nearly the same. One has to admit that in spite of the fact that the penalty coefficients  $c_i$  were increased gradually, and the regularization coefficient  $\varepsilon_0$  appearing in the sum of norms term was also reduced gradually, the convergence was neither fast nor stable since Newton's method is naturally not suited for the sum of norms problem. So it required about a hundred of iterations to converge.

Nevertheless, in spite of the fact that the cycle was discretized over time only by two time points, one can see a good agreement between the numerical solution (solid lines) and the analytical one (dashed lines) shown in Figs. 3c,d for strain  $\varepsilon_x$  and total stress  $\sigma_x$  distributions along  $0y$  axis (the stresses are normalized by the Young modulus  $E$ , e.g. the yield stress  $\sigma_y = 0.001$ ). Figure 3c also shows that the strain increment over the cycle is compatible, and the checks performed confirm that the residual stress  $\beta_0$  is self-balanced, and the plastic strain is deviatoric, which means the constraints presented by Eqs. 14b-d are satisfied.

## Conclusion

It has been shown that the general problem of steady cycle can be solved directly by stating it as a convex mathematical optimization problem with the use of finite element discretization.

This formulation has been proved to be able, in principle, to capture the proper results for all the parameters of a steady cycle such as plastic strains and residual stresses, even though the simple computational approach implemented in the study was used for demonstration only and is not claimed to be efficient for the real problem.

## References

- Abramov A.V., Gadenin M.M., Makhutov N.A., Evropin S.V., Cherniavsky A.O. and Cherniavsky O.F. (2011), Low-cycle deformation and fracture of structures. *Handbook. An engineering journal*, 11, 24p. (in Russian)
- Boyd S. and Vandenberghe L (2004), Convex optimization. *Cambridge University Press*.
- Bree J. (1967), Elastic-plastic behavior of thin tubes subjected to internal pressure and intermittent high-heat fluxes with application to fast nuclear reactor fuel elements. *J. Strain Anal.*, 2(3), pp. 226-238.
- Chen H. and Ponter A.R.S. (2001), A method for the evaluation of a ratchet limit and the amplitude of plastic strain for bodies subjected to cyclic loading. *Eur. J. Mech. A/Solids*, 20, pp. 555–571.
- Gokhfeld D.A. and Cherniavsky O.F. Limit analysis of structures at thermal cycling. *Sijthoff and Noordhoff, Leyden*, 1980.
- Spiliopoulos K.V. and Panagiotou K.D. (2012), A direct method to predict cyclic steady states of elastoplastic structures. *Comput. Methods Appl. Mech. Engrg.*, 223–224, pp. 186–198.
- Vu D. K., Yan A. M. and Nguyen-Dang H. (2004), A primal-dual algorithm for shakedown analysis of structures. *Comput. Methods Appl. Mech. Engrg.*, 193, pp. 4663-4674.
- Wright S.J. (1997), Primal-dual interior-point methods. *SIAM*.



## A multi-dimensional drift flux mixture model for gas-droplet two-phase flow

\*Zhi Shang, Hongying Li, Jing Lou

Institute of High Performance Computing (IHPC), Agency for Science, Technology and Research (A\*STAR), 1 Fusionopolis Way, #16-16 Connexis, Singapore 138632

\*Corresponding author: shangz@ihpc.a-star.edu.sg

### Abstract

A multi-dimensional drift flux mixture model was developed to simulate gas-droplet two-phase flows. The drift flux model was modified by considering the centrifugal force on the liquid droplets. Therefore the traditional 1D drift flux model was upgraded to multi-dimension, 2D and 3D. The slip velocities between the continual phase (gas) and the dispersed phase (liquid droplets) were able to calculate through multi-dimensional diffusion flux velocities based on the modified drift flux model. Through the numerical simulations comparing with the experiments and the simulations of other models on the backward-facing step and the water mist spray, the model was validated.

**Keywords:** drift flux mixture model, slip velocity, two-phase flow, droplet, spray.

### Introduction

Liquid spray systems are widely used in many chemical, petrochemical and biochemical industries, such as absorption, oxidation, hydrogenation, coal liquefaction and aerobic fermentation. The operation of these systems is preferred because of the simple construction, ease of maintenance and low operating costs. When the spray is injected from nozzle, it causes a turbulent stream to enable an optimum phase exchange. It is built in numerous forms of construction. The mixing is done by the liquid droplets and it requires less energy than mechanical stirring.

A good understanding of the liquid droplet dynamics of the spray will help the engineers to design the high efficient facilities under optimized operating parameters. Due to the complex two-phase or multi-phase flow and turbulence, normally the flow in spray system is under transient regime. The time average values of the parameters, such as liquid holdup distributions, liquid phase back mixing, gas-liquid interface disturbing, mass and heat transfer between gas and liquid phases, liquid droplet distributions, liquid droplet velocities etc., have to be considering the influence of turbulence. Although the operation of spray system is simple, the actual physical flow phenomena are still lack of complete understanding of the fluid dynamics (Husted, 2007).

Many experimental facilities and methods were introduced to study the multiphase flows in spray systems. Ruck and Makiola (1988) used a laser-Doppler anemometer (LDA) to study the gas-oil droplet passing over a backward facing step. Ferrand et al. (2003) used a phase Doppler and laser induced fluorescence technique to study the gas-droplet turbulent velocity and two-phase interaction through a jet with partly responsive droplets. Esposito et al. (2010) used a monochrome charge-coupled device CCD camera to study the growing of the droplets. The experimental methods can provide very useful information about the liquid droplets at certain measurement points, but they are difficult to show the details of the flow fields and parameters inside the spray.

Following the development of computer technology, it is already allowed to use the numerical method to do the researches in the recent decades (Shang et al., 2008). Therefore, many researchers employ the numerical method, called as computational fluid dynamics (CFD), to study the details of the flows. Griffiths et al. (1996) employed the coupled particle Lagrangian model with Eulerian continual fluid flow model to simulate a cyclone sampler and compared the numerical results with the empirical models. Barton (1999) used the stochastic Monte Carlo scheme coupled with k- $\epsilon$  turbulence model to study the particle trajectories in turbulent flow over a backward facing step. Husted (2007) used the Eulerian-Lagrangian model provided by FDS open source software to simulate a water mist spray system for the fully spray spreading and compared with experiments. Through the former studies of CFD method, it can be seen a good mathematical model will not only help to obtain the agreeable simulation results, but also to be simple, efficient and accurate.

A multi-dimensional drift flux mixture model was developed in this paper. This model was based on the idea of Yang et al. (1999) and Shang (2005). It employed a mixture model to describe the multi-phase flows based on Eulerian model. The slip velocity, which can be developed based on the extended 3D drift flux model. Owing to the the extended 3D drift flux model, the effects of gravity and centrifugal force were considered. Through comparisons with experiments and other model simulations on backward facing step and water mist spray, this model was validated.

### Mathematical Modeling

Considering a problem of turbulent multi-component multi-phase flow with one continuous phase and several dispersed phases, the time average conservation equations of mass, momentum and energy for the mixture model as well as the turbulent kinetic energy equation and the turbulent kinetic energy transport equation can be written as the following.

$$\partial \rho_m / \partial t + \nabla \cdot (\rho_m U_m) = 0 \quad (1)$$

$$\partial (\rho_m U_m) / \partial t + \nabla \cdot (\rho_m U_m U_m) = -\nabla p + \rho_m g + \nabla \cdot \left[ \left( \mu_m + \mu_t \right) (\nabla U_m + \nabla U_m^T) \right] - \nabla \cdot \sum \alpha_k \rho_k U_{km} U_{km} \quad (2)$$

$$\partial (\rho_m h_m) / \partial t + \nabla \cdot (\rho_m U_m h_m) = q + \nabla \cdot \left[ \left( \frac{\mu_m}{Pr} + \frac{\mu_t}{Pr_t} \right) \nabla h_m \right] - \nabla \cdot \sum \alpha_k \rho_k h_k U_{km} \quad (3)$$

$$\partial (\rho_m k) / \partial t + \nabla \cdot (\rho_m U_m k) = \nabla \cdot \left[ \left( \mu_m + \frac{\mu_t}{\sigma_k} \right) \nabla k \right] + G - \rho_m \varepsilon \quad (4)$$

$$\partial (\rho_m \varepsilon) / \partial t + \nabla \cdot (\rho_m U_m \varepsilon) = \nabla \cdot \left[ \left( \mu_m + \frac{\mu_t}{\sigma_\varepsilon} \right) \nabla \varepsilon \right] + \frac{\varepsilon}{k} (C_1 G - C_2 \rho_m \varepsilon) \quad (5)$$

in which

$$\rho_m = \sum \alpha_k \rho_k \quad (6)$$

$$\mu_m = \sum \alpha_k \mu_k \quad (7)$$

$$\rho_m U_m = \sum \alpha_k \rho_k U_k \quad (8)$$

$$U_{km} = U_k - U_m \quad (9)$$

$$G = \frac{1}{2} \mu_t \left[ \nabla U_m + (\nabla U_m)^T \right]^2 \quad (10)$$

$$\mu_t = C_\mu \rho_m \frac{k^2}{\varepsilon} \quad (11)$$

where,  $\rho$  is the density,  $U$  are the velocity vectors,  $\alpha$  is the volumetric fraction,  $p$  is pressure,  $g$  is the gravitational acceleration vector,  $U_{km}$  is the diffusion velocity vector of  $k$  dispersed phase relative to the averaged mixture flow,  $h$  is enthalpy,  $q$  is heat input,  $\mu$  is viscosity,  $\mu_t$  is turbulent viscosity,  $Pr$  is molecular Prandtl number,  $Pr_t$  is turbulent Prandtl number,  $G$  is stress production.  $C_\mu$ ,  $\sigma_k$ ,  $\sigma_\varepsilon$ ,  $C_1$ ,  $C_2$  are constants for standard  $k$ - $\varepsilon$  turbulence model (Launder & Spalding, 1974), shown in Table 1. The subscript  $m$  stands for the averaged mixture flow, and  $k$  stands for  $k$  dispersed phase.

Table 1 Constants of standard  $k$ - $\varepsilon$  turbulence model

variable	$C_\mu$	$\sigma_k$	$\sigma_\varepsilon$	$C_1$	$C_2$
constant	0.09	1.0	1.3	1.44	1.92

Additional to the above equations, the following conservation equation for each dispersed phase is also necessary.

$$\partial (\alpha_k \rho_k) / \partial t + \nabla \cdot (\alpha_k \rho_k U_m) = \Gamma_k - \nabla \cdot (\alpha_k \rho_k U_{km}) \quad (12)$$

where  $\Gamma_k$  is the generation rate of  $k$ -phase.

In order to closure the governing equations (1) ~ (12), it is necessary to determine the diffusion velocities  $U_{km}$ . The following equation is employed to covert the diffusion velocities to slip velocities that can be presented as  $U_{kl} = U_k - U_l$ .

$$U_{km} = U_{kl} - \sum \frac{\alpha_k \rho_k}{\rho_m} U_{kl} \quad (13)$$

Actually the above equation can be developed from the definition of the mixture density equation (6), the definition of mixture mass flux equation (8) and the diffusion velocity equation (9). Once the slip velocities are obtained, the whole governing equations will be closed.

Because the slip velocities present the difference of the movement between the dispersed phase for instance gas and the continuous phase for instance liquid. In gas-liquid two-phase flow, the slip velocity can be modeled through the drift flux model (Yang et al., 1999), shown in equation (14).

$$U_{gl} = \begin{cases} -1.53(1 - \alpha_1)^{1.5} \left[ \frac{\sigma(\rho_l - \rho_g)g'}{\rho_g^2} \right] \frac{g'}{|g'|}, & \alpha_1 < 0.1 \\ -1.53 \left[ \frac{\sigma(\rho_l - \rho_g)g'}{\rho_g^2} \right] \frac{g'}{|g'|}, & \alpha_1 \geq 0.1 \end{cases} \quad (14)$$

$$g' = g - \frac{dU_m}{dt} \quad (15)$$

$$U_m = (\alpha_g \rho_g U_g + \alpha_l \rho_l U_l) / (\alpha_g \rho_g + \alpha_l \rho_l) \quad (16)$$

where  $U_{gl}$  is the slip velocity between gas and liquid,  $\sigma$  is surface tension,  $g$  is gravity,  $U_m$  is mixture velocity.

In equation (14), the drift flux model is different from the traditional 1D drift flux model in Zuber and Findlay (1964) and Hibiki and Ishii (2002). It adopts the form as Yang et al. (1999) and Shang (2005). In Yang et al. (1999), the centrifugal force was induced by the mixture volumetric flux to revise the gravity considering the natural curve movement of gas bubbles. Owing to the concerns, the traditional 1D drift flux model (Zuber and Findlay, 1964; Hibiki and Ishii, 2002) was extended to 3D. Because of the extending, the revised 3D drift flux model is able to describe complex flow conditions and to be adopted by CFD. Further, in this paper, the gradient of mixture velocity, which is used to calculate the centrifugal force, is innovatively induced to revise and update Yang et al.'s (1999) 3D drift flux model. After the updating, the new terminal velocity model, shown in equations (14), (15) and (16), is able to suit the gas-droplet two-phase flows. Since the slip velocity is determined, the whole equations are closed to be solved.

## Numerical Procedures

In the simulations, the CFD technique was based on ANSYS FLUENT 13.0. In ANSYS FLUENT, during the numerical computing, all differential governing equations are solved by applying a finite volumes method (FVM). For the fluids, the spatial discretization was performed by upwind scheme of second order for all conservation equations and phase coupled SIMPLE scheme was used for coupling between the pressure and velocity. The overall spatial discretization was of the second order accuracy. The first order implicit scheme was used for the time discretization. During the numerical simulations, the pressure-based solver was employed because all the gas and liquid phases were considered as the incompressible fluids. The fixed time stepping method was employed to run the transient simulations.

The terminal velocity model was accomplished using the concept of user defined functions (UDF). This numerical solution was implemented as a subroutine and linked to the ANSYS FLUENT solver via a set of the original UDFs. The decision whether the UDFs of the coefficients should be used for the interfacial forces at the given calculation step was made automatically by the solver.

## Numerical Simulations

For the numerical simulations, two typical cases were chosen as the targets in this paper. They are 2D backward facing step and 3D water mist spray. The backward facing step is a kind of basic facility in many engineering applications, which can be used to investigate the fundamental understanding of important turbulent flow features such as flow separation, flow reattachment and free shear jet phenomena. 3D water mist spray is a very good case to be used to do the validations for the multi-dimensional (3D) drift flux mixture model.

### 4.1 Backward facing step

Ruck and Makiola (1988) did the experiment on a backward facing step using a laser-Doppler anemometer (LDA) measurement technology, shown in Fig. 1. Hereafter, the experiment data has been cited by other researchers (Tu, 1997; Barton, 1999; Tian, 2006). The backward facing step was with an expansion ratio of 1:2. The step height was 25 mm and the backward channel height after the step was 50 mm. During the experiment, the liquid droplets are kind of oil droplets which were of size of 1  $\mu\text{m}$  generated through an atomizer. The oil's density was of  $\rho_1 = 810 \text{ kg/m}^3$ . The flow Reynolds number (based on the step height  $h$ ) was of  $\text{Re} = 64000$ .

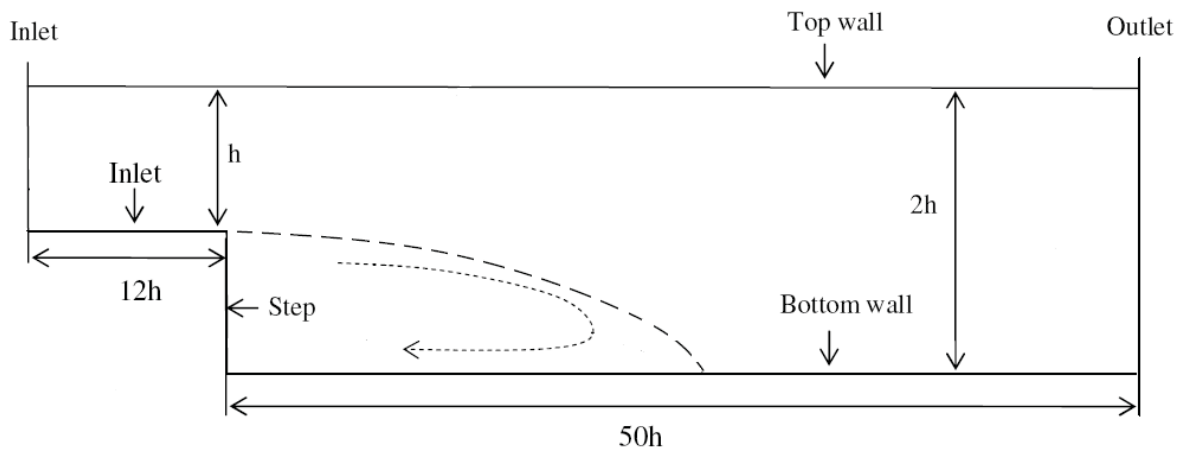


Fig. 1 Diagrammatic sketch of backward facing step

During the simulations, the numerical exercise was performed in a two-dimensional (2D) environment since only 2D representative measurements were available. All the parameters were used same as Ruck and Makiola (1988). The air and oil droplets were under atmospheric pressure. The grid size was employed same as Tian (2006). The computational domain had a size of  $12h \times 1h$  before the step and  $50h \times 2h$  after the step to ensure the flow was fully developed at the exit. Within the length of  $12h$  before the step, 100 (in the stream-wise direction)  $\times$  20 (in the lateral direction) uniform grid points have been allocated. Further downstream, the mesh is with 250 uniform grid points in the stream-wise direction and 40 uniform grid points in the lateral direction. Grid independence was checked by refining the mesh system through doubling the number of grid points along both of the stream-wise and the lateral directions.

Fig. 2 shows the comparisons of the simulation using current drift flux mixture model with the experiment data and the simulation by Tian (2006) using Eulerian-Lagrangian particle tracking model. The computed particle velocity profiles were against measurements for a Reynolds number of 64000, at locations of  $x/h = 0, 1, 3, 5, 7$  and  $9$  respectively behind the step. The velocity profiles are normalized by the free stream velocity  $u_0$  that is with value of 40 m/s.

From Fig. 2, it can be seen that the multi-dimensional drift flux mixture model is able to have the predictions similar with Eulerian-Lagrangian particle tracking model. At the location  $x/h \geq 3$ , the simulation results are even better than Eulerian-Lagrangian particle tracking model comparing with the experiment.

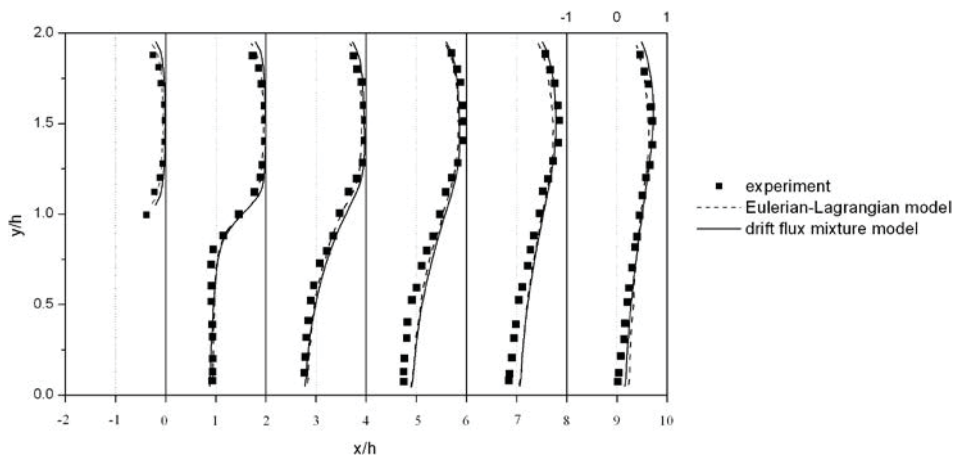


Fig. 2 Comparisons of particle velocities between experiments and simulations

#### 4.2 Water mist spray

Husted (2007) did the experiment on a water mist spray system using a particle image velocimetry (PIV), phase Doppler anemometer (PDA) and a high-speed camera measurement technology, shown in Fig. 3. In Husted's (2007) experiment, the water mist spray is used for fire extinguishing. The purpose of the experiment was to fill the lack of guidelines available for dimensioning water mist systems. The experiment data were good to be used to measure the modeling and numerical simulations. Therefore this experiment was chosen in this paper as the validation tool to validate the drift flux mixture model.

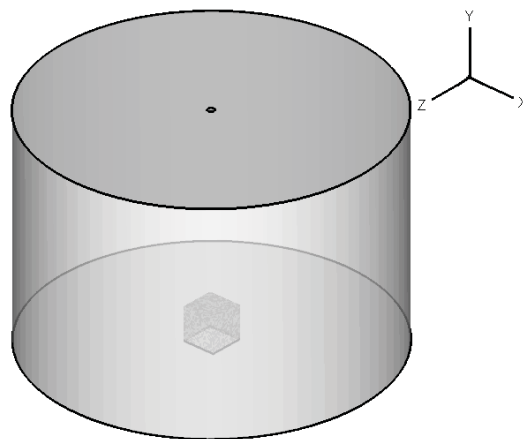


Fig. 3 Diagrammatic sketch of water mist nozzle

During the simulations, the numerical exercise was performed in a three-dimensional (3D) environment. All the parameters were used same as Husted (2007). Fig. 4 shows the mesh distribution. Before the formal simulations, the mesh cell sensitivity studies were carried out among the mesh cells from 154000 to 492000. Fig. 5 shows the comparisons of simulation results of the water mist velocities at different mesh cells. Through the comparisons, it can be seen that among the mesh cells of 154000, 328000 and 492000 the simulation results were not sensitive because there is no evident difference among the results. The averaged errors of the simulation results among the mesh cells were less than  $\pm 2.5\%$ . Considering both of the accuracy and the cost of computational time, the formal simulations were carried out by using the mesh cells of 328000. During the simulations, the time step was set as a constant of 0.01 seconds. The simulation time for every case lasted long enough until its steady state.

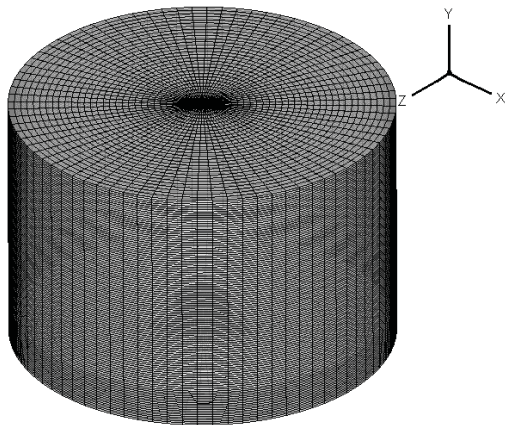


Fig. 4 Mesh distribution

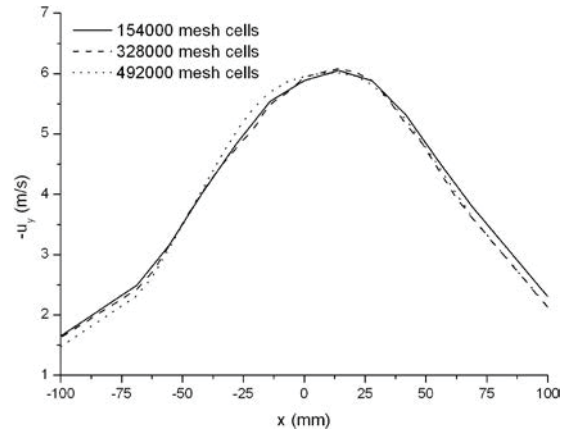
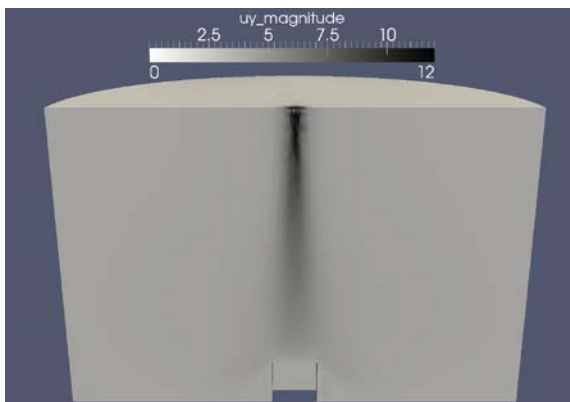
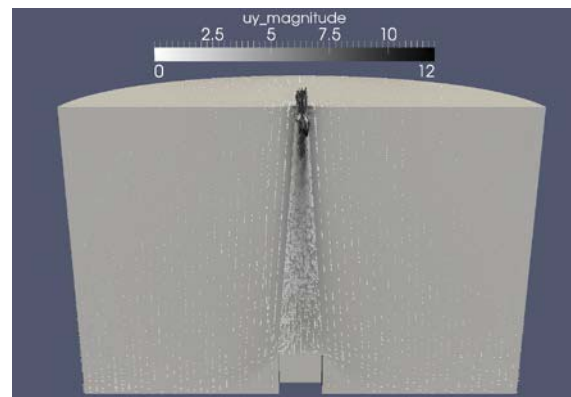


Fig. 5 Mesh sensitivity studies

Fig. 6 shows the distributions of the water mist droplet velocity vector long y coordinate at x-y cross section. From Fig. 6, it can be seen that the droplets flow down in the middle and gradually spreads like a cone shape down from the nozzle. According to the studied of Husted (2007), the stages of the development of the cone spray can be separated as initial conical zone, inflow zone, transition zone, turbulent zone and full cone zone. When the distance is far from 500 mm down from the nozzle, the spray is fully mixed and drop distribution is uniform. The drop velocity becomes flat.



(a) contour of  $u_y$  velocity



(b) vectors of  $u_y$  velocity

Fig. 6 Water mist droplet velocity vector at x-y cross section

Fig. 7 shows the comparisons of the water mist droplet velocity of the simulations with experiments along different positions down from the nozzle. In Fig. 7, the reference numerical simulations were carried out by Eulerian-Lagrangian particle tracking model in FDS4.0 (FDS, 2013). From the comparisons, it can be seen that the drift flux mixture model is able to capture the velocity profile same as experiments. The numerical predictions have not only the peak value is quite near experiment, but also the position is approaching experiment. The results are much better than the predictions by Eulerian-Lagrangian particle tracking model in FDS4.0.

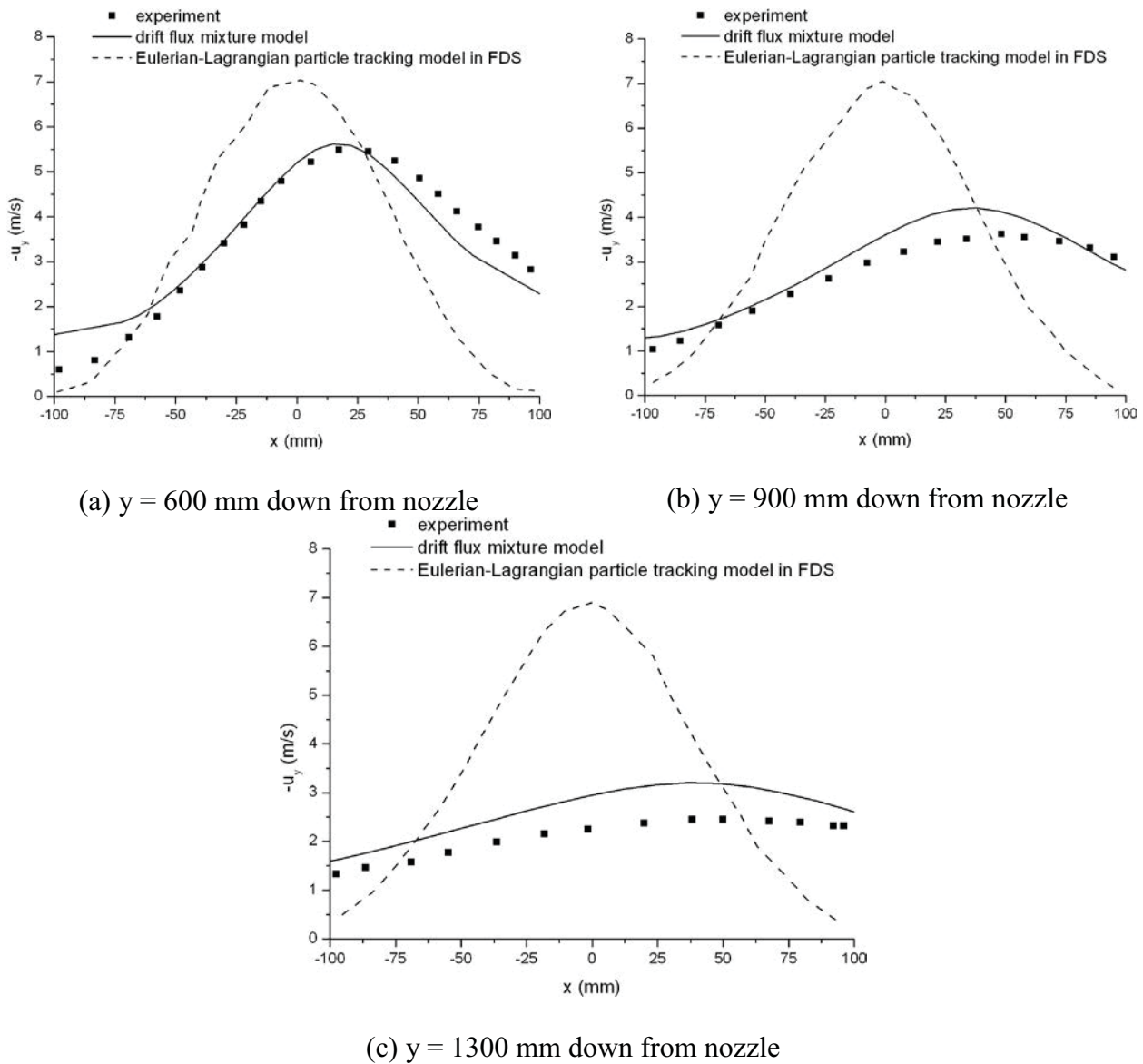


Fig. 7 Comparisons of water mist droplet velocity under different positions down from nozzle

**Conclusions**

The novel multi-dimensional drift flux mixture model is developed based on the mixture multiphase flow model. The diffusion velocity between the dispersed phase and the mixture is closed through the slip velocity. The slip velocity is developed through the drift flux model. Accordingly the multi-dimensional drift flux mixture model is different from the general homogenous model that treats the dispersed phase and the continuous phase flowing under same velocity on multiphase flow. Through the comparisons of the numerical simulations between the multi-dimensional drift flux

mixture model and experiments, the model is validated. Through comparisons of the numerical simulations between the multi-dimensional drift flux mixture model and the numerical simulations of Eulerian-Lagrangian particle tracking model, the efficiency and accuracy of the model is confirmed.

### Acknowledgements

The authors would like to thank the support by Multiphase Flow for Deep-Sea Oil & Gas Down-hole Applications - SERC TSRP Programme of Agency for Science, Technology and Research (A\*STAR) in Singapore (Ref #: 102 164 0075).

### References

- Barton, I. (1999), Simulation of particle trajectories in turbulent flow over a backward-facing step. *R & D Journal*, 15(3), pp. 65-78.
- Esposito, A., Montello, A. D., Guezennec, Y. G. and Pianese, C. (2010), Experimental investigation of water droplet-air flow interaction in a non-reacting PEM fuel cell channel. *Journal of Power Source*, 195, pp. 2691-2699.
- FDS (2013). <http://code.google.com/p/fds-smv>.
- Ferrand, V., Bazile, R., Boree, J. and Charnay, G. (2003), Gas-droplet turbulent velocity corrections and two-phase interaction in an axisymmetric jet laden with partly responsive droplets. *International Journal of Multiphase flow*, 29, pp. 195-217.
- Griffiths, W. D. and Boysan, F. (1996), Computational fluid dynamics (CFD) and empirical modeling of the performance of a number of cyclone samples. *Journal Aerosol Science*, 27(2), pp. 281-304.
- Hibiki, T. and Ishii, M. (2002), Distribution parameter and drift velocity of drift-flux model in bubbly flow. *International Journal of Heat and Mass Transfer*, 45, pp. 707-721.
- Husted, B. P. (2007), Experimental measurements of water mist systems and implications for modeling in CFD. PhD thesis, Lund University, Sweden.
- Launder, B. E. and Spalding, D. B. (1974), The numerical computation of turbulent flow. *Computer Methods in Applied Mechanics and Engineering*, 3, pp. 269-289.
- Ruck, B. and Makiola, B. (1988), Particle dispersion in a single-sided backward-facing step flow. *International Journal of Multiphase flow*, 14(6), pp. 787-800.
- Shang, Z. (2005), CFD of turbulent transport of particles behind a backward-facing step using a new model— $k-\epsilon$ -Sp. *Applied Mathematical Modelling*, 29, pp. 885-901.
- Shang, Z., Yao, Y. F. and Chen, S. (2008), Numerical investigation of system pressure effect on heat transfer of supercritical water flows in a horizontal round tube. *Chemical Engineering Science*, 63, pp. 4150-4158.
- Tu, J. Y. (1997), Computational of turbulent two-phase flow on overlapped grids. *Numerical Heat Transfer Part B Fundamental*, 32, pp. 175-195.
- Tian, Z. F. (2006), Numerical modelling of turbulent gas-particle flow and its applications. PhD thesis, RMIT University, Australia.
- Yang, R. C., Zheng, R. C., Wang, Y. W. (1999), The analysis of two-dimensional two-phase flow in horizontal heated tube bundles using drift flux model. *Heat and Mass Transfer*, 35, pp. 81-88.
- Zuber, N. and Findlay, J. A. (1964), The effects of non-uniform flow and concentration distributions and the effect of the local relative velocity on the average volumetric concentration in two-phase flow. Technical Report, GEAP-4592.



## **A semi-analytical model for predicting underwater noise radiated from offshore pile driving**

**Q. P. Deng, \*W. K. Jiang**

Institute of Vibration, Shock & Noise, Shanghai Jiao Tong University, China

\*Corresponding author: wkjiang@sjtu.edu.cn

### **Abstract**

It radiates high level of wideband underwater noise to drive large tubular piles into the seafloor by hydraulic impact hammers, which may detrimentally impact both fishes and marine mammals, such as dolphins and whales. Noise forecast and reduction is necessary in underwater engineering in order to protect the animals. In this study, a semi-analytical model is developed for predicting the vibration and the underwater sound radiation, where the pile is modeled as an elastic thin cylindrical shell. A modified variation methodology combined with the Reissner-Naghdi's thin shell theory is employed to formulate the mechanical model of the shell divided as several segments in axial direction. The sound pressures in both exterior and interior fluid fields are expressed as analytical series in frequency domain. The effect of the acoustic fluid on structural vibration is taken into consideration by incorporating the interface work done by the sound pressure into the total functional of the variation methodology. The underwater sound responses in both frequency domain and time domain are obtained from a case study. This mechanical model can be used to forecast underwater noise of piling and explore potential noise reduction measures to protect marine animals.

**Keywords:** Pile-driving, Cylindrical shell, Under-water noise, Structure-fluid interaction

### **Introduction**

Offshore constructions increase quickly over the world, such as wind power generation platforms, petroleum and gas platforms, artificial islands and oversea bridges. These produce severe undersea noise pollution which has raised serious concerns from environmental protection organizations and academic world. Pile-driving noise is generally considered as the most severe underwater noise which would influence, harm or even kill marine animals inhabiting around piling sites, such as fishes, dolphins and whales (Madsen et al., 2006; Jefferson et al., 2009; Slabbekoorn et al., 2010). Research and prediction on the vibration and sound radiation of the pile is urgent and significant for the sake of ocean exploration and animal protection.

Some attempts have been in recent years made on the topic of underwater piling noise. The experimental results by Robinson et al. (2007) showed that the relationship between acoustic pulse energy and hammer energy had an approximate linear dependence during the soft start period of the piling procedure. Pile-driving underwater noise was detected at ranges of up to 70 km and behavioral disturbance may occur up to a distance of 50 km for bottlenose dolphins (Bailey et al., 2010). Underwater pressure field at approximate 10 m from the pile was found to be depth dependent in the tests of the authors (Stockham et al., 2010). Reinhall and Dahl (2010, 2011) studied the underwater piling noise by using a finite element model for the sound generation and parabolic equation model for propagation and found that the dominant underwater noise from impact driving is from the Mach wave associated with the radial expansion of the pile that propagates down the pile after impact at supersonic speed. A semi-analytical model for the prediction of underwater piling noise was established by Tsouvalas and Metrikine (2013), in which

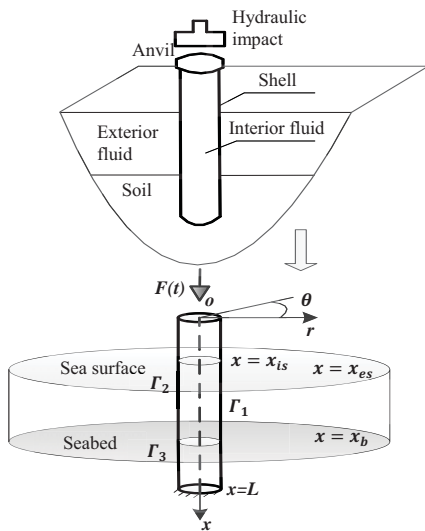
the displacements of the shell was expanded over the in-vacuo vibration modes and the seabed soil was simplified to be distributed springs and dashpots. However, further investigation is required to develop a mechanical model with higher computational efficiency and accuracy.

In this study, a semi-analytical mechanical model is established for predicting the levels of underwater piling noise. A modified variation methodology is employed to formulate the mechanical model of the shell divided as several segments in axial direction. The sound pressures in both exterior and interior fluid fields are expressed as analytical functions. The effect of the acoustic fluid on structural vibration is considered by incorporating the interface work done by the sound pressure into the total functional of the variation statement. The radiated underwater noise in both frequency domain and time domain is illustrated based on a case study.

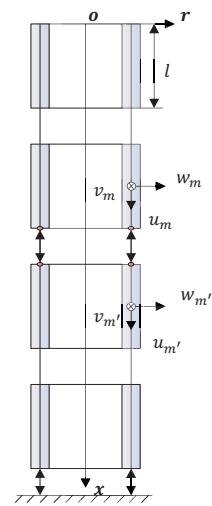
**Basic Theory**

*Description of the model*

The schematic diagram of the pile-driving model is illustrated in Figure 1. A pile is driving into the seabed by a hydraulic impact hammer. The pile is modeled as an elastic cylindrical shell with finite length and constant thickness. The hydraulic impact hammer is modeled as a force applied at the top of the pile. The seawater inside and outside the pile is assumed to be incompressible and inviscid. The effect of soil surrounding the pile is not taken into consideration and the pile is assumed to be fixed at the bottom. The sea surface  $\Gamma_2$  is assumed to be a pressure released boundary, which means sound pressure vanishes on this surface. For the seabed  $\Gamma_3$  two situations can be considered, i.e. a perfectly rigid boundary and a local impedance boundary. The constants  $E, \mu, \eta, \rho_s, L, h$  and  $R$  correspond to the modulus of elasticity, Poisson ratio, structural loss factor, the density, length, thickness and radius of the mid-surface of the cylindrical shell, respectively.  $c, \rho_f$  are sound velocity and density of the seawater. The pile fills up interior fluid at  $x_{is} < x < x_b$  and is surrounded by exterior fluid at  $x_{es} < x < x_b$ .



**Figure 1. Pile-driving model**



**Figure 2. Structure decomposition**

*Structure decomposition model of pile*

A modified variation methodology is used to establish the governing equations of the cylindrical shell. The methodology involves seeking the minimum of a modified functional as following equation (Qu, Chen et al., 2013).

$$\bar{\Pi}_{Total} = \int_{t_0}^{t_1} \sum_{i=1}^I (T_i - U_i + W_i) dt + \int_{t_0}^{t_1} \sum_{i,i+1} \Pi_{\lambda\kappa} dt + \int_{t_0}^{t_1} \bar{\Pi}_{\lambda\kappa} dt \quad (1)$$

A variation form in the boundary value problem is generally mathematically easier than solving the common differential governing equations directly. The total energy functional of the mechanical system has extreme or stationary value only when the actual movement occurs. The extreme or stationary value of the energy functional can be obtained by expressing the solutions of the shell as the summation of a set of admissible displacement functions. In order to obtain reliable computational accuracy of high-frequency vibration, the shell is decomposed into  $I$  sub-shells with equal length  $l$ , as showed in Fig. 2. The requirement of interface continuity between two adjacent sub-shells can be satisfied by incorporating the continuity constraint conditions into the total energy functional by interface forces and least-squares weighted parameters. The geometrical boundaries at the bottom of the pile can also be satisfied by incorporated modified energy terms. The modifications on the total energy functional make the selection of admissible displacement functions flexible: the interface continuity conditions and geometrical boundary conditions will not be imposed on the displacement functions, but eventually satisfied in the variation statement.

The subscript  $i$  in equation (1) is the sub-shell number.  $T_i$  and  $U_i$  are kinetic energy and strain energy of the sub-shell, respectively.  $W_i$  is the work done by external force.

$$W_i = \iint_{S_i} (f_{u_i} u_i + f_{v_i} v_i + f_{w_i} w_i) R dx d\theta \quad (2)$$

$\Pi_{\lambda\kappa}$  is modified energy term incorporated from interface continuity conditions and geometrical boundary conditions at pile bottom, respectively. The incorporated modified term  $\Pi_{\lambda\kappa}$  can be given as following form.

$$\begin{aligned} \Pi_{\lambda\kappa} = & \int_0^{2\pi} [N_x \Theta_u + \bar{N}_{x\theta} \Theta_v + \bar{Q}_x \Theta_w - M_x \Theta_r] R d\theta \\ & - \frac{1}{2} \int_0^{2\pi} [\kappa_u \Theta_u^2 + \kappa_v \Theta_v^2 + \kappa_w \Theta_w^2 - \kappa_r \Theta_r^2] R d\theta \end{aligned} \quad (3)$$

The function of the first integration term on the right side of equation (3) is to impose weak enforcement of kinematic interface continuity.  $\Theta_u, \Theta_v, \Theta_w, \Theta_r$  are the essential continuity equations on the interface between adjacent sub-shells and are defined as  $\Theta_u = u_i - u_{i+1}$ ,  $\Theta_v = v_i - v_{i+1}$ ,  $\Theta_w = w_i - w_{i+1}$ ,  $\Theta_r = \partial w_i / \partial x - \partial w_{i+1} / \partial x$ .  $N_x, \bar{N}_{x\theta}, \bar{Q}_x, M_x$  are the resultant force in  $x$  direction, circumferential shear resultant force, lateral Kelvin-Kirchhoff shear resultant force and bending moment resultant force at the interface between two sub-shells, respectively. According to Reissner-Naghdi's shell theory, they can be written as equations (4)~(7).

$$N_x = K \left[ \frac{\partial u_i}{\partial x} + \frac{\mu}{R} \left( \frac{\partial v_i}{\partial \theta} + w_i \right) \right] \quad (4)$$

$$\bar{N}_{x\theta} = \frac{1 - \mu}{2} \left[ K \left( \frac{1}{R} \frac{\partial u_i}{\partial \theta} + \frac{\partial v_i}{\partial x} \right) + \frac{D}{R^2} \left( \frac{\partial v_i}{\partial x} - 2 \frac{\partial^2 w_i}{\partial x \partial \theta} \right) \right] \quad (5)$$

$$\bar{Q}_x = D \left( \frac{1}{R^2} \frac{\partial^2 v_i}{\partial x \partial \theta} - \frac{\partial^3 w_i}{\partial x^3} - \frac{2 - \mu}{R^2} \frac{\partial^3 w_i}{\partial x \partial \theta^2} \right) \quad (6)$$

$$M_x = D \left[ -\frac{\partial^2 w_i}{\partial x^2} + \frac{\mu}{R^2} \left( \frac{\partial v_i}{\partial \theta} - \frac{\partial^2 w_i}{\partial \theta^2} \right) \right] \quad (7)$$

As shown in the second integrate term on the right side of equation (3), the least-squares weighted residual terms of the continuity equations are incorporated to further modify the total functional.

The functional of the least-squares weighted residual terms is to ensure a numerically stable operation for the structure decomposition methodology.

The incorporated modified term  $\bar{\Pi}_{\lambda\kappa}$  in equation (1) is incorporated from geometrical boundary conditions at the bottom of the pile.  $\bar{\Pi}_{\lambda\kappa}$  has the same form as  $\Pi_{\lambda\kappa}$  and it can be obtained by substituting interface continuity equations by continuity equations of the geometry boundary, i.e.  $\bar{\Theta}_u = u_l - \bar{u}$ ,  $\bar{\Theta}_v = v_l - \bar{v}$ ,  $\bar{\Theta}_w = w_l - \bar{w}$ , and  $\bar{\Theta}_r = \partial w_l / \partial x - \partial \bar{w} / \partial x$ .  $u_l, v_l, w_l$  and  $\partial w_l / \partial x$  are variables of the last sub-shell which is fixed at the bottom;  $\bar{u}, \bar{v}, \bar{w}, \partial \bar{w} / \partial x$  are corresponding variables of the boundary and equal zero in this work.

#### *Admissible displacement functions of shell*

The displacement components  $u_i, v_i, w_i$  in  $\bar{\Pi}_{\text{ToI}}$  can be expanded in terms of admissible displacement functions and generalized coordinates. Due to the incorporation of the modified terms, the admissible displacement functions of each sub-shell are not constrained to satisfy any continuity conditions or geometrical boundary conditions. They are only required to be linearly independent, complete and differentiable. In this model, Fourier series for circumferential expansion and Chebyshev orthogonal polynomials for axial expansion are employed as the admissible displacement functions. The displacement components of each sub-shell can be written as following form.

$$u_i(x, \theta, t) = \sum_{m=1}^M \sum_{n=0}^N \sum_{\alpha=0}^1 T_m(x) \cos\left(n\theta + \alpha \frac{\pi}{2}\right) \bar{u}_{mn\alpha}(t) = \mathbf{U}(x, \theta) \mathbf{u}_i(t) \quad (8)$$

$$v_i(x, \theta, t) = \sum_{m=1}^M \sum_{n=0}^N \sum_{\alpha=0}^1 T_m(x) \sin\left(n\theta + \alpha \frac{\pi}{2}\right) \bar{v}_{mn\alpha}(t) = \mathbf{V}(x, \theta) \mathbf{v}_i(t) \quad (9)$$

$$w_i(x, \theta, t) = \sum_{m=1}^M \sum_{n=0}^N \sum_{\alpha=0}^1 T_m(x) \cos\left(n\theta + \alpha \frac{\pi}{2}\right) \bar{w}_{mn\alpha}(t) = \mathbf{W}(x, \theta) \mathbf{w}_i(t) \quad (10)$$

where  $T_m(x)$  is the  $m$  order Chebyshev polynomials.  $M, N$  are the highest degrees taken in the polynomials and series, respectively.  $\mathbf{U}(x, \theta), \mathbf{V}(x, \theta), \mathbf{W}(x, \theta)$  are admissible displacement function vectors of the three directions.  $\mathbf{u}_i(t), \mathbf{v}_i(t), \mathbf{w}_i(t)$  are corresponding generalized coordinate vectors.

#### *Pressure in fluid domain*

Under some regular boundary conditions, fluid pressure in frequency domain can be expanded as a summation of analytical functions by applying variable separation technique in a circular cylindrical coordinates. The analytical expression of the fluid pressure allows one to examine qualitatively the influence of a number of parameters on the underwater sound radiation. For the fluid domain outside the pile, the fluid pressure and the velocity component normal to the surface of the shell can be given as equation (11) and (12) (Tsouvalas and Metrikine, 2013).

$$\tilde{p}_e(x, r, \theta) = -i\omega\rho_f \sum_{\alpha=0}^1 \sum_{n=0}^{\infty} \sum_{p=0}^{\infty} D_{np} H_n^{(2)}(k_{rp}r) \sin k_{xp}(x - x_{es}) \cos(n\theta + \alpha \frac{\pi}{2}) \quad (11)$$

$$\tilde{v}_{er}(x, r, \theta) = \sum_{\alpha=0}^1 \sum_{n=0}^{\infty} \sum_{p=0}^{\infty} D_{np} H_n^{(2)'}(k_{rp}r) \sin k_{xp}(x - x_{es}) \cos(n\theta + \alpha \frac{\pi}{2}) \quad (12)$$

where  $\rho_f$  is the density of the fluid.  $H_n^{(2)}$  is the Hankel function of the second kind and of order  $n$ .  $H_n'^{(2)}$  denotes its derivative with respect to  $r$ .  $k_{xp}$ ,  $k_{rp}$  are wave number in  $x$  direction and  $r$  direction respectively and they are determined by radian frequency  $\omega$  and boundary conditions at sea surface and seabed.  $D_{np}$  are unknown coefficients which can be determined by normal displacement on structure-fluid coupling interface  $\Gamma_1$ .

Assume there are  $I_e$  sub-shells submerged fully or partly in the exterior fluid. the  $i$ -th submerged sub-shell stretches over the axial coordinate interval  $[x_i, x_{i+1}]$ , and the coupling area on  $i$ -th submerged sub-shell occupies coordinate interval  $[\bar{x}_i, \bar{x}_{i+1}]$ . For fully submerged shell,  $[x_i, x_{i+1}]$  is expressed by  $[\bar{x}_i, \bar{x}_{i+1}]$ . Based on the normal displacement given in equation (10), the normal displacement on the entire shell-fluid coupling interface can be written as

$$w_r(x, \theta, t) = \sum_{i=1}^{I_e} w_{ri}(x, \theta, t) * [H(x - \bar{x}_i) - H(x - \bar{x}_{i+1})], \quad (x_{es} < x < x_b) \quad (13)$$

$$\text{With: } w_{ri}(x, \theta, t) = \sum_{m,n,\alpha} w_{imn\alpha} T_m(x - x_i) \cos\left(n\theta + \alpha \frac{\pi}{2}\right) e^{i\omega t}$$

$H(x - \bar{x}_i)$  is the Heaviside step function. On the coupling interface, the normal velocity continuity condition should be satisfied. Combining equations (12) and (13), the normal velocity continuity equations is given as

$$\begin{aligned} i\omega \sum_{i=1}^{I_e} \sum_{m,n,\alpha} w_{imn\alpha} T_m(x - x_i) \cos\left(n\theta + \alpha \frac{\pi}{2}\right) [H(x - \bar{x}_i) - H(x - \bar{x}_{i+1})] \\ = \sum_{\alpha=0}^1 \sum_{n=0}^{\infty} \sum_{p=0}^{\infty} D_{np} H_n^{(2)}(k_{rp}r) \sin k_{xp}(x - x_{es}) \cos(n\theta + \alpha \frac{\pi}{2}) \end{aligned} \quad (14)$$

By making use of orthogonality property of fluid modes, the unknown coefficient  $D_{np}$  can be obtained. Then the pressure in the exterior fluid domain can be expressed by analytical functions weighted by generalized coordinates of normal displacements, as shown in equation (15).

$$\begin{aligned} \tilde{p}_e(x, r, \theta, \omega) &= \sum_{\alpha=0}^1 \sum_{n=0}^{\infty} \sum_{i=0}^{I_e} \sum_{p=0}^{\infty} \sum_{m=1}^M w_{imn\alpha} \cdot \tilde{P}_{e,inmp\alpha} \quad \text{with:} \\ \tilde{P}_{e,inmp\alpha} &= \frac{\omega^2 \rho}{f_p} \frac{H_n^{(2)}(k_{rp}r)}{H_n'^{(2)}(k_{rp}R)} \cdot \sin k_{xp}(x - x_{es}) \cdot \cos(n\theta + \alpha \frac{\pi}{2}) \\ &\quad \cdot \int_{\bar{x}_i}^{\bar{x}_{i+1}} T_m(x - x_i) \cdot \sin k_{xp}(x - x_{es}) dx \end{aligned} \quad (15)$$

The derivation procedure of fluid pressure inside the pile is completely analogous as that of interior fluid pressure.

#### *Governing equations of shell-fluid coupling vibration*

Interaction between the pile wall and contiguous fluid has a profound influence on the magnitude and phase of the structural vibration. Use ‘fluid loading’ to describe the effect that the fluid has on the shell vibration (Fahy and Gardonio, 2007). The fluid pressure given in (15) is regarded as fluid loading acting on the pile wall. The work done by the exterior fluid pressure on the coupling interface is given as following equation

$$W_p = \int_0^{2\pi} \int_{x_s}^{x_b} -pw_r R dx d\theta \quad (16)$$

Fourier transform pairs with respect to time are introduced herein to transform variables between time domain and frequency domain. By substituting the work done by fluid pressure and the work done by hydraulic impact force into the total functional  $\bar{\Pi}_{Tot}$  and performing the variation operation with respect to the generalized coordinate vectors  $\mathbf{u}$ ,  $\mathbf{v}$ , and  $\mathbf{w}$ , the governing equations of motion of the pile can be obtained as

$$[-\omega^2 \mathbf{M} + (\mathbf{K} - \bar{\mathbf{K}}_\lambda + \bar{\mathbf{K}}_\kappa) - \mathbf{C}_e + \mathbf{C}_i] \mathbf{q}(\omega) = \mathbf{F}(\omega) \quad (17)$$

where  $\mathbf{M}$  and  $\mathbf{K}$  are mass matrix and stiffness matrix, respectively.  $\bar{\mathbf{K}}_\lambda$  and  $\bar{\mathbf{K}}_\kappa$  are the generalized interface stiffness matrixes introduced by the interface forces and the least-squares weighted residual parameters, respectively.  $\mathbf{C}_e$  and  $\mathbf{C}_i$  are coupling matrixes introduced by fluid pressure in exterior fluid domain and interior fluid domain.  $\mathbf{q}(\omega) = [\mathbf{u}_1^T, \mathbf{v}_1^T, \mathbf{w}_1^T, \mathbf{u}_2^T, \mathbf{v}_2^T, \mathbf{w}_2^T, \dots, \mathbf{u}_l^T, \mathbf{v}_l^T, \mathbf{w}_l^T]$  is the global generalized coordinate vector of the shell and  $\mathbf{F}(\omega)$  is the generalized force vector. Responses in time domain can be obtained by performing Fourier inverse transformation to frequency responses.

### Computational results and discussion

A pile with a certain geometry and material parameters is chosen for numerical case. The seabed is assumed to be perfectly rigid acoustic boundary. The hydraulic impact force is assumed to be an averagely distributed line force  $F(t)$ , which is parallel with  $x$  axis, acting on the intersecting line of the middle surface of the shell and cross section on the pile top. The material properties of the shell, geometry and parameters of the model are summarized in Table 1.

**Table 1. Model parameters**

Part	Parameters
Shell	Geometry: $L=16m, R=2.2m, h=50mm$ Material parameters: $E=2.1 \times 10^{11}, \rho_s=7800kg\ m^{-3}, \mu=0.3, \eta=0.005$ Decomposition parameters: $M=8, I=7, N=0$
Fluid	$c=1400m\ s^{-1}, \rho_f=1000kg\ m^{-3}, x_{es}=4, x_{is}=4, x_b=12$
Force	$F(t)=\begin{cases} 1 \times 10^5 N/m & (0 < t < 1\ ms) \\ 0 & (t \leq 0\ or\ t \geq 1\ ms) \end{cases}$

Fig. 3 shows the frequency spectrum and time history of sound pressure at observing position A which is located 4 meters under the sea surface and 8 meters away from the pile surface. As can be seen from the Figure, frequency spectrum of SPL at position A has 2 dominant peaks at 80 Hz and 140 Hz, respectively. The SPL curve has a remarkable nadir at around 1000 Hz. The history of sound pressure at position A sees its first peak at about 7 ms, which means it takes about 7 ms from the very beginning moment when the hydraulic impact acts on the pile top to the moment when the peak of the first pressure wave arrives at the position. Then the pressure decreases stably over the time axis, albeit with slight fluctuations.

Fig. 4 shows SPL distributions on the  $x-r$  plane at  $\theta=0\ rad$  for three different frequencies, i.e. 100 Hz, 200 Hz and 800 Hz. The pressure fields see an obvious attenuation trend as the radial distance increases and form distinct standing waves along the vertical axis. The sea surface plane and the seabed plane form an acoustic waveguide. Sound reflection in the acoustic waveguide produces standing waves in vertical direction. The existence of standing waves in vertical direction demonstrates that the fluid pressure is depth dependent.

From Fig. 4 the wavelength of the standing wave decreases as the frequency ascends. The dominant modes of high-frequency vibration have relatively small wavelengths in vertical direction for axisymmetric vibration. Therefore high-frequency sound has relatively small wavelengths in vertical direction due to the requirement of normal velocity continuity conditions.

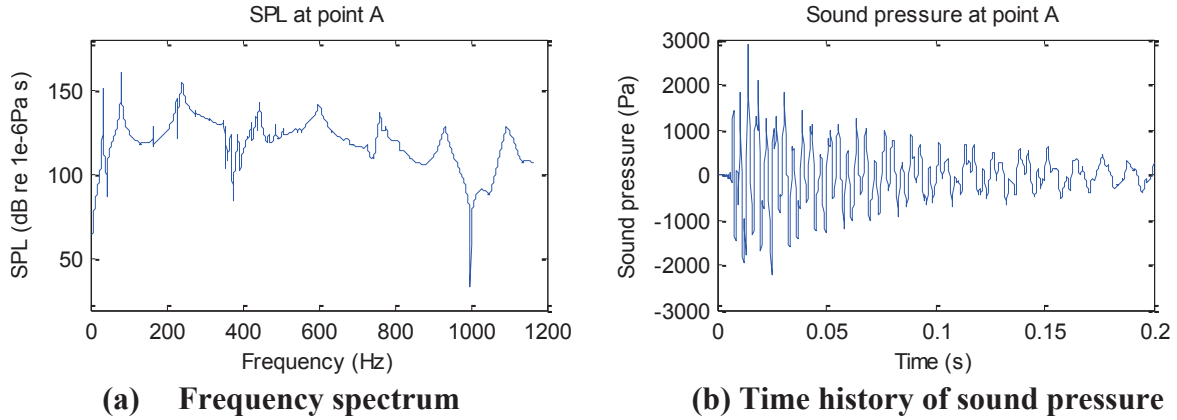


Figure 3. Sound at point A

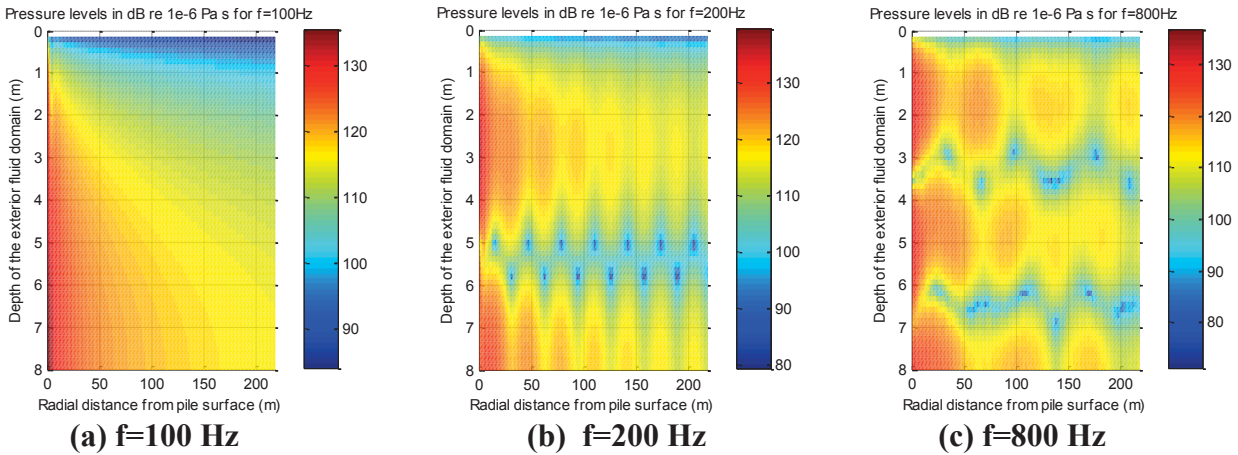


Figure 4. Distributions of sound pressure in the section plane

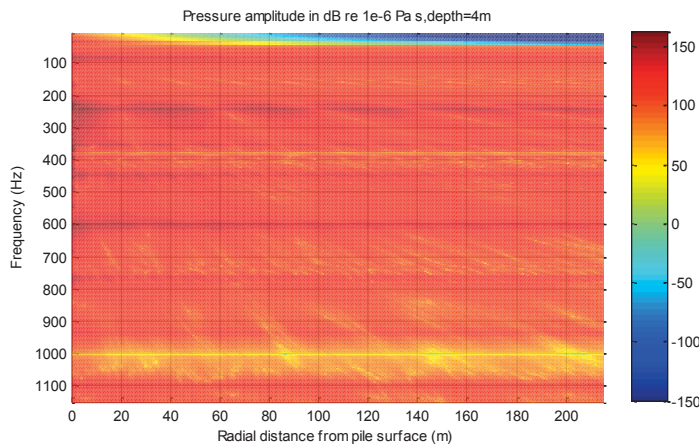


Figure 5. Sound pressure level vs. radial distance

Fig. 5 shows the attenuation of the pressure levels 4 meters under the sea surface for frequencies ranging from 5 Hz to 1150 Hz and for radial distances up to 215 m from the pile surface. It's obviously indicated at the top of the figure that no pressure waves can effectively propagate away

from the pile in the exterior fluid for frequencies lower than the cut-off frequency (about 42 Hz), which demonstrates the exterior fluid domain has a filtering function for relatively low frequencies. For perfectly rigid seabed, radial wavenumber can be expressed as  $k_{rp} = \sqrt{\left(\frac{\omega}{c}\right)^2 - \left[\frac{2p+1}{2(x_b-x_{es})}\right]^2}$ . The radiation condition at  $r \rightarrow \infty$  requires that  $Re(k_{rp}) \geq 0$  and  $Im(k_{rp}) \leq 0$ . According to equation (15), when  $Im(k_{rp}) < 0$ ,  $\tilde{P}_{e,inmp\alpha}$  will decrease along  $r$  axis nearly in the form of exponential attenuation. Hence the cut-off frequency can be given as  $f_c = \frac{c}{2\pi} \cdot \frac{2p_{min}+1}{2(x_b-x_{es})}$ . It is obvious that the cut-off frequency  $f_c$  is inversely proportional to the depth of the exterior fluid field.

As shown in Fig.5, sound pressures on frequencies around 80 Hz, 240 Hz, 450 Hz, 600 Hz and 760 Hz are dominant at this depth, while pressure level of 1000 Hz is much lower than pressure levels of other frequencies.

## Conclusions

A computationally efficient semi-analytical mechanical model has been established for predicting underwater noise radiated from offshore pile driving, in which the coupling effect between pile and fluid is taken into consideration. A modified variation methodology is employed to formulate the mechanical model and the shell is divided as several segments in axial direction. The methodology creates considerable flexibility in the selection of admissible displacement functions and significantly simplifies the solving progress of the coupling vibration. A case study shows that the pressure amplitude at the observing position declines steadily during the duration after the first pressure wave arrives, albeit with slight fluctuations. The fluid pressure in frequency domain form standing waves in vertical direction and the wavelengths of the standing waves descend as the frequency increases, which indicates that the underwater sound pressures are depth dependent. A cut-off frequency for sound propagating is found in the exterior fluid domain and it is inversely proportional to the depth of the exterior fluid field. No sound can propagate effectively away from the pile for frequencies lower than the cut-off frequency.

## References

- Madsen, P. T., Wahlberg, M., Tougaard, J., Lucke, K. and Tyack, P. (2006), Wind turbine underwater noise and marine mammals: implications of current knowledge and data needs. *Marine Ecology-Progress Series*, 309, pp. 279-295.
- Jefferson, T. A., Hung, S. K. and Wursig, B. (2009), Protecting small cetaceans from coastal development: Impact assessment and mitigation experience in Hong Kong. *Marine Policy*, 33(2), pp. 305-311.
- Slabbekoorn, H., Bouton, N., van Opzeeland, I., Coers, A., ten Cate, C. and Popper, A. N. (2010), A noisy spring: The impact of globally rising underwater sound levels on fish. *Trends in Ecology and Evolution*, 25(7), pp. 419-427.
- Robinson, S. P., Lepper, P. A. and Ablitt, J. (2007), The measurement of the underwater radiated noise from marine piling including characterisation of a "soft start" period. *OCEANS 2007-Europe*.
- Bailey, H., Senior, B., Simmons, D., Rusin, J., Picken, G. and Thompson, P. M. (2010), Assessing underwater noise levels during pile-driving at an offshore windfarm and its potential effects on marine mammals. *Marine Pollution Bulletin*, 60(6), pp. 888-897.
- Stockham, M. L., Dahl, P. H. and Reinhall, P. G. (2010), Characterizing underwater noise from industrial pile driving at close range. *2010 Oceans Mts/Ieee Seattle*.
- Reinhall, P. G. and Dahl, P. H. (2010), Acoustic radiation from a submerged pile during pile driving. *2010 Oceans Mts/Ieee Seattle*.
- Reinhall, P. G. and Dahl, P. H. (2011), Underwater Mach wave radiation from impact pile driving: Theory and observation. *Journal of the Acoustical Society of America*, 130(3), pp. 1209-1216.
- Tsouvalas, A. and Metrikine, A. V. (2013), A semi-analytical model for the prediction of underwater noise from offshore pile driving. *Journal of Sound and Vibration*, 332(13), pp. 3232-3257.
- Qu, Y. G., Chen, Y., Long, X. H., Hua, H. X. and Meng, G. (2013), Free and forced vibration analysis of uniform and stepped circular cylindrical shells using a domain decomposition method. *Applied Acoustics*, 74(3), pp. 425-439.
- Fahy, F. J. and Gardonio, P. (2007). Sound and Structural Vibratin: Radiation, Transmission and Response, *Elsevier Science*.



## Simulation to the Cyclic Deformation of Polycrystalline Aluminum Alloy Using Crystal Plasticity Finite Element Method

Juan Luo, Guozheng Kang\*, Mingxing Shi

School of Mechanics and Engineering, Southwest Jiaotong University, Chengdu 610031, China

\*Corresponding author: Kang GZ, E-mail address: guozhengkang@home.swjtu.edu.cn;

Tel: 86-28-87603794; Fax: 86-28-87600797

### Abstract

A crystal plasticity based finite element model (i.e., FE model) is used in this paper to simulate the cyclic deformation of polycrystalline aluminum alloy plates. The Armstrong-Frederick nonlinear kinematic hardening rule is employed in the single crystal constitutive model to capture the Bauschinger effect and ratcheting of aluminum single crystal presented under the cyclic loading conditions. A simple model of latent hardening is used to consider the interaction of dislocations between different slipping systems. The proposed single crystal constitutive model is implemented numerically into a finite element code, i.e., ABAQUS. Then, the proposed model is verified by comparing the simulated results of cyclic deformation with the corresponding experimental ones of a face-centered cubic polycrystalline metal, i.e., rolled 5083 aluminum alloy. In the meantime, it is shown that the model is capable of predicting local heterogeneous deformation in single crystal scale, which plays an important role in the macroscopic deformation of polycrystalline aggregates. Under the cyclic loading conditions, the effect of applied strain amplitude on the responded stress amplitude and the dependence of ratcheting strain on the applied stress level are reproduced reasonably.

**Keywords:** Crystal plasticity; Cyclic deformation; Finite element; Face-centered cubic metal

### Introduction

It is significant to study the cyclic deformation of metals for their extensive uses as engineering components subjected to cyclic loadings. In the last decades, many researches have been accomplished to observe the cyclic deformation of metals both experimentally and theoretically. However, many existing constitutive models are phenomenological versions, such as Chaboche and Dang Van (1979), Chaboche and Nouailhas (1989), and Abdel-Karim and Ohno (2000). These models do not give direct insight into the physical mechanism of cyclic plastic deformation. Recently, Cailletaud and Sai (2008) and Kang et al. (2010) proposed crystal plasticity based constitutive models to investigate the ratcheting of polycrystalline alloys by adopting explicit scale transition rules. However, the employed explicit scale transition rules are formulated with some simple assumptions, which cannot capture the real physical nature of elastic and plastic accommodations occurred between single crystal grains. To consider such accommodations reasonably, a crystal plasticity finite element method is a good candidate.

Therefore, in this work, based on the previous work done by Armstrong and Frederick (1966), Peirce et al. (1983) and Huang (1991), a micro-mechanically based cyclic single crystal viscoplastic constitutive model is implemented numerically into the finite element (FE) code ABAQUS, to predict the responses of polycrystalline metals under cyclic strain-controlled and stress-controlled loading. The model is verified by comparing the FE simulations with corresponding experimental results of face-centered cubic (FCC) polycrystalline aggregates, i.e., rolled 5083 aluminum alloy plate, carried out in the previous work by Lu et al. (2013).

### Single crystal constitutive model

In the framework of small perturbation, the total strain  $\boldsymbol{\varepsilon}$  is divided additively into an elastic part  $\boldsymbol{\varepsilon}^e$  and visco-plastic part  $\boldsymbol{\varepsilon}^{vp}$ , i.e.,

$$\boldsymbol{\varepsilon} = \boldsymbol{\varepsilon}^e + \boldsymbol{\varepsilon}^{vp} \quad (1)$$

The relation between the elastic strain  $\boldsymbol{\varepsilon}^e$  and the stress  $\boldsymbol{\sigma}$  is given by the Hooke's law

$$\boldsymbol{\varepsilon}^e = \mathbf{C}^{-1} : \boldsymbol{\sigma} \quad (2)$$

where  $\mathbf{C}$  is the fourth-rank tensor of elastic moduli. Since the dislocation slip is the main source of plastic deformation for the aluminum alloy at low temperatures, the visco-plastic strain rate can be obtained via the following expression,

$$\dot{\boldsymbol{\varepsilon}}^{vp} = \sum_{\alpha=1}^N \mathbf{P}^{\alpha} \dot{\gamma}^{\alpha} \quad (3)$$

$$\mathbf{P}^{\alpha} = \frac{1}{2} (\mathbf{m}^{\alpha} \otimes \mathbf{n}^{\alpha} + \mathbf{n}^{\alpha} \otimes \mathbf{m}^{\alpha}) \quad (4)$$

where  $\mathbf{P}^{\alpha}$  represents the orientation of the slip system  $\alpha$ ;  $\mathbf{m}^{\alpha}$  and  $\mathbf{n}^{\alpha}$  are the slip direction vector and the slip plane normal vector of the slip system  $\alpha$ , respectively. In the case of FCC materials, the number of active slip system  $N$ , is no more than the total slip system number, 12. The resolved shear stress  $\tau^{\alpha}$  acting on a particular slip system  $\alpha$ , i.e., the *Schmid stress*, is given by the relation

$$\tau^{\alpha} = \boldsymbol{\sigma} : \mathbf{P}^{\alpha} \quad (5)$$

The shear rate of each slip system  $\dot{\gamma}^{\alpha}$  can be related to the corresponding resolved shear stress  $\tau^{\alpha}$  via a power law expression,

$$\dot{\gamma}^{\alpha} = \left\langle \frac{|\tau^{\alpha} - x^{\alpha}| - Q^{\alpha}}{K} \right\rangle^n \text{sign}(\tau^{\alpha} - x^{\alpha}) \quad (6)$$

where  $x^{\alpha}$  and  $Q^{\alpha}$  are the kinematic and isotropic hardening variables of the slip system  $\alpha$ , and are called as back resolved shear stress and isotropic deformation resistance, respectively.  $K$  and  $n$  are the material parameters that control the viscosity of the material.

The isotropic hardening rule involves an interaction matrix  $H^{\alpha\beta}$  which represents the interaction between the systems  $\alpha$  and  $\beta$ . The evolution rule of the isotropic hardening variable is determined by the following formulation,

$$\dot{Q}^{\alpha} = \sum_{\beta=1}^N H^{\alpha\beta} |\dot{\gamma}^{\beta}| \quad (7)$$

The initial value of  $Q^{\alpha}$  means the initial shear yielding stress of each slip system, which is simply assumed as the same for all the slip systems in the model. The interaction hardening matrix  $H^{\alpha\beta}$  is obtained from a simplified rule as shown in the work by Asaro (1983), i.e.,

$$H^{\alpha\beta} = qH + (1 - q)H\delta_{\alpha\beta} \quad (8)$$

Whereas the nonlinear evolution rule of kinematic hardening is set to be similar to that proposed by Armstrong and Frederick (1966),

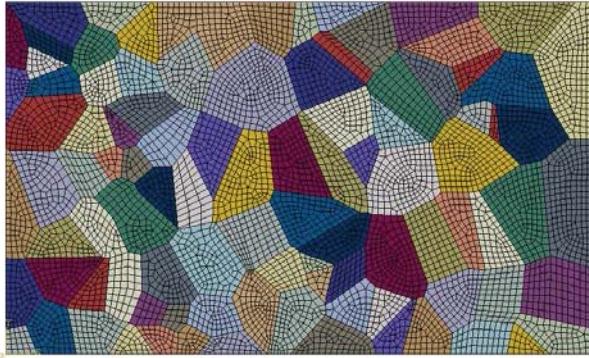
$$\dot{x}^{\alpha} = c\dot{\gamma}^{\alpha} - dx^{\alpha}|\dot{\gamma}^{\alpha}| \quad (9)$$

where  $c$  and  $d$  are the material parameters assumed to be the same for all slip systems. The fading memory term  $dx^{\alpha}|\dot{\gamma}^{\alpha}|$  makes it possible to describe the ratchetting behavior of materials.

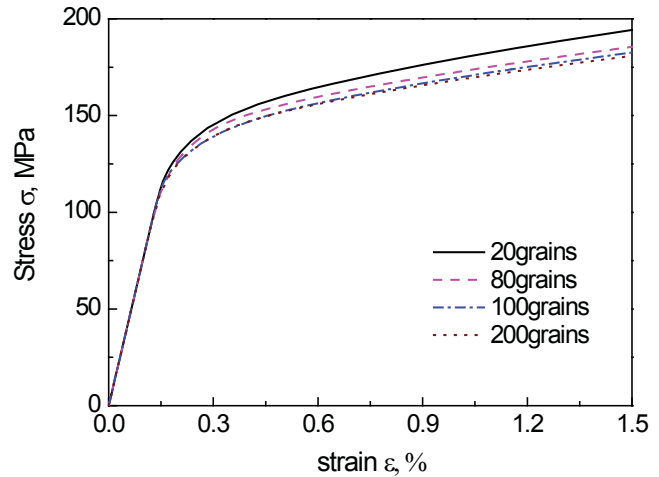
The proposed single crystal constitutive model is implemented numerically into the FE code ABAQUS via a user-defined material subroutine (UMAT), where the implicit integration is adopted.

### Finite element model

Polycrystalline 5083 Al alloy may be viewed as an aggregation of single crystal grains with random crystallographic orientations, thus a 2D aggregation model is generated by using the Voronoi tessellation technique (Okabe et al. 1993), as shown in Fig. 1, where different colors indicate the grains with different orientations. To be consistent with corresponding experiments, the FE model is constructed as a rectangle plate with a size of 10 mm×6 mm. The FE mesh consists of 7040 first-order plane-stress elements.



**Fig. 1. FE polycrystalline model (meshed)**



**Fig. 2. Effect of number of grains on the stress-strain response**

To eliminate the effect of random orientations as much as possible, sufficient number of grains is needed. A series of FE analyses containing 20, 80, 100, 200 grains are performed under monotonic tensile loading to assess the appropriate number of grains. It is seen in Fig. 2 that the further increase in the number of grains hardly influences the obtained stress-strain curves when the number of grains is larger than 100. Considering the computational efficiency, the following simulations are all based on the model containing 100 grains.

All material parameters used in the constitutive model for 5083 Al alloy are calibrated by trial-and-error method from the experimental results obtained under the monotonic tension, one of cyclic strain tests, and one of cyclic stress tests. The obtained material parameters are given in Table 1. Since there is no accurate anisotropic stiffness constant of 5083 Al alloy single crystal, and the main concern is focused on the macro responses of the polycrystalline alloy, the elastic parameters here are set to be isotropic. All the experimental results are carried out by Lu et al. (2013), and more details about experiments are referred to their work.

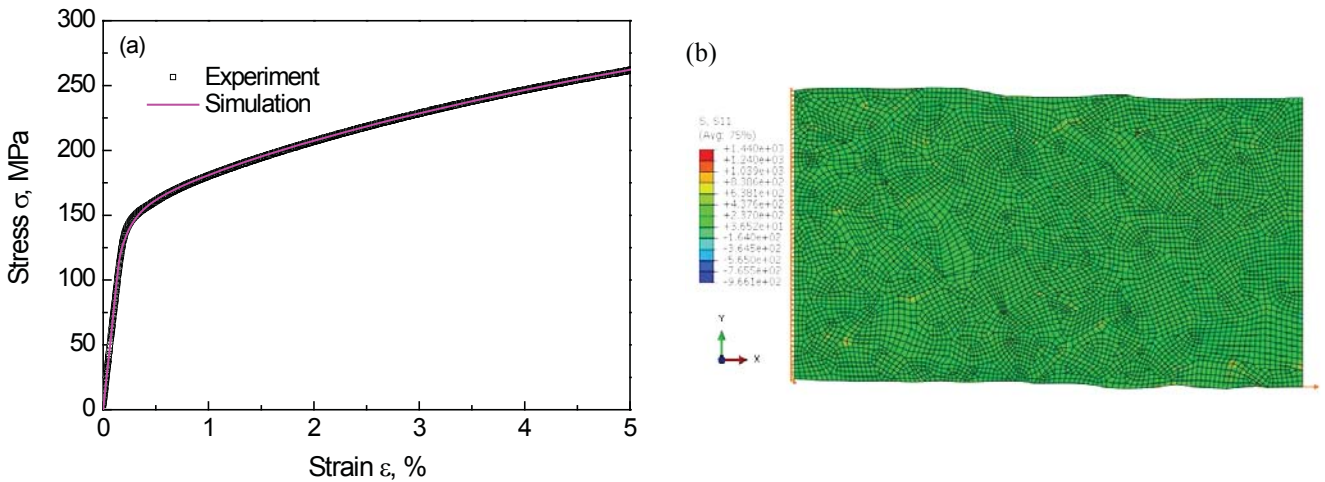
**Table 1. Material parameters**

Elasticity		Flow rule		Isotropic hardening	Interaction hardening	Kinematic hardening		
$E$ (MPa)	$\nu$	$n$	$K$ (MPa)	$Q_0$ (MPa)	$H$ (MPa)	$q$	$c$ (MPa)	$d$
70,000	0.3	50	20	34	100	0	880	15

### Simulation and discussion

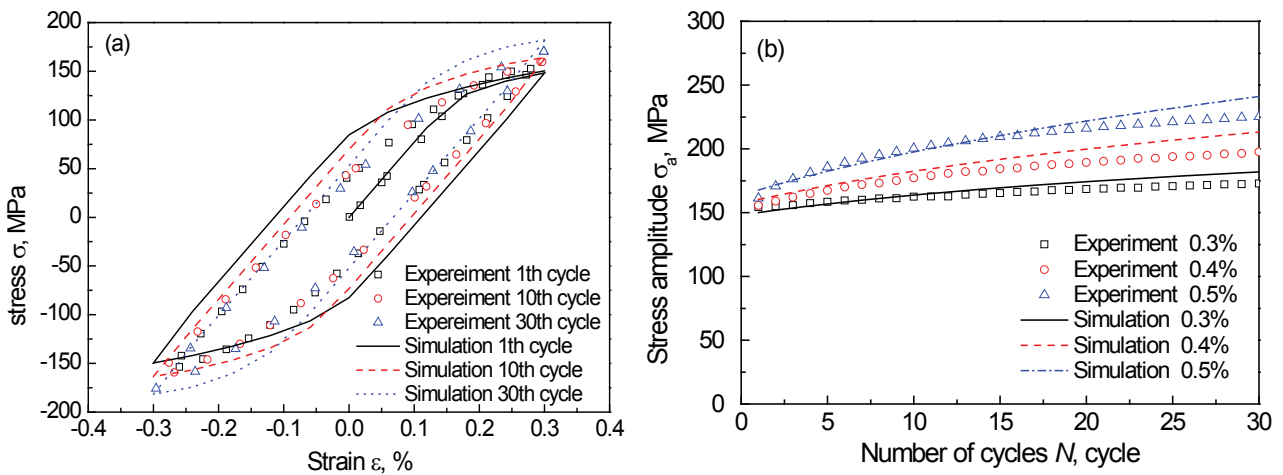
To verify the validation of the model, the simulated results by the FE technique are compared with experimental ones of 5083 Al alloy plates obtained in the monotonic tension, uniaxial strain- and stress-controlled cyclic tests, respectively.

The simulated and experimental monotonic tensile stress-strain responses of polycrystalline 5083 Al alloy are shown in Fig. 3a at a strain rate of 0.015%/s. Clearly, the model simulation agrees quite well with the test data of monotonic tension. Fig. 3b shows the distribution of stress in the tensile direction when the macro monotonic tensile strain is 5%. Due to the different orientations of grains, the deformation is heterogeneous at both the inter-granular and intra-granular scales. From Fig. 3b it is seen that although the macroscopic state is in a tensile stress state, the heterogeneity still leads to a local microscopic compressive stress state. The load direction is denoted in Fig. 3b by a small arrow in the lower corner of right sideline.



**Fig. 3. Monotonic tensile responses: (a) comparison of simulated and experimental stress-strain curves; (b) simulated stress contour in the tensile direction.**

The cyclic hardening behavior of 5083 Al alloy under uniaxial strain-controlled cyclic loading is then simulated and presented in Fig. 4 by plotting the stress-strain curves and variation of stress amplitude with the number of cycles. The strain rates in the load cases shown in Fig. 4 are fixed at 0.15%/s, the same as that used in the corresponding experiments.

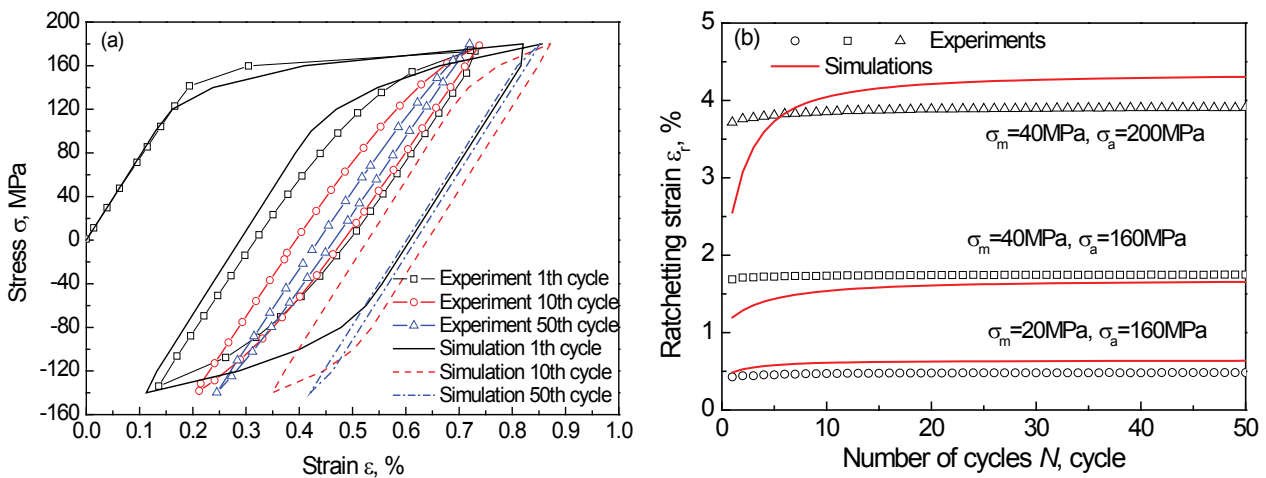


**Fig. 4. Simulated and experimental responses under the strain-controlled cyclic loading: (a) cyclic stress-strain curves with a strain amplitude of 0.3%; (b) responded stress amplitude vs. number of cycles with different strain amplitudes.**

Form Fig. 4a it can be found that the simulated hysteresis loops are a little wider than the experimental ones. This is caused by the delayed response of test machine and the practical peak strain cannot reach the prescribed value, especially in the first cycle. Fig. 4b shows the evolution curves of responded stress amplitude vs. number of cycles with three various applied strain

amplitudes. It is seen from Fig. 4b that the model provides a reasonable simulation to the cyclic hardening feature of the alloy, that is, the responded stress amplitude increases with the number of cycles, and the value of responded stress amplitude increases with the applied strain amplitude.

Finally, the ratchetting of 5083 Al alloy plates under the uniaxial stress-controlled cyclic loading with non-zero mean stress is predicted in the load cases with various mean stresses and stress amplitudes and compared with corresponding experiments. The results are shown in Fig. 5, and the stress rates in all the load cases are fixed at 80MPa/s, same as that used in the corresponding experiments. The comparison between simulated and experimental stress-strain hysteresis loops in the load case with a mean stress of 20MPa and stress amplitude of 160MPa is shown in Fig. 5a. It is seen from Fig. 5a that although the simulated loops are fatter than the experimental ones, the evolutionary process, that is the loops become narrower and narrower with the increasing number of cycles, is well simulated. The ratchetting strain obtained with various mean stresses and stress amplitudes are shown in Fig. 5b. It should be noted that the ratchetting strain  $\varepsilon_r$  is defined as  $\varepsilon_r = (\varepsilon_{\max} + \varepsilon_{\min})/2$ , where  $\varepsilon_{\max}$  and  $\varepsilon_{\min}$  are the maximum and minimum strains of each cycle, respectively. From Fig. 5b, it is concluded that the model can provide a reasonable simulation to the evolution of the uniaxial ratchetting and its dependence on the applied mean stress and stress amplitude. Or, specifically, the features include: (1) the ratchetting strain increases with the number of cycles, while its rate decreases as the number of cycles increases; (2) the ratchetting strain increases with the mean stress when the stress amplitude is fixed, and it also increases as the stress amplitude increases with a fixed mean stress; (3) after a certain number of cycles, the value of ratchetting strain hardly changes and the evolution of ratchetting falls into a stable state.



**Fig. 5. Simulated and experimental ratchetting under cyclic stressing: (a) cyclic stress-strain curves; (b) curves of ratchetting strain vs. number of cycles.**

## Conclusion

In this paper, a crystal plasticity based cyclic visco-plastic constitutive model is implemented numerically into the finite element code, to predict the mechanical responses of polycrystalline metals under cyclic loading. A two-dimensional finite element aggregation consisting of 100 randomly orientated grains constructed by the Voronoi tessellation method is used to represent the polycrystalline metal. By comparing the FE simulated results with corresponding experimental ones, it is demonstrated that the model provides fairly good simulations to the macroscopic stress-strain responses of 5083 Al alloy plates under monotonic tension, the cyclic hardening feature presented under the strain-controlled cyclic loading, and the ratchetting occurred under the stress-controlled cyclic loading. Additionally, a local heterogeneous deformation is observed due to the orientation mismatch between the neighboring grains.

## Acknowledgement

Financially supported by the projects for National Natural Science Foundation of China (11025210), Sichuan Provincial Youth Science and Technology Innovation Team (2013), China, and the project from National Key Laboratory of Traction Power (2011TPL-Z03).

## References

- Abdel-Karim, M., Ohno, N. (2000), Kinematic hardening model suitable for ratcheting with steady-state. *Int. J. Plast.*, 16, pp. 225-240.
- Armstrong, P. J., Frederick, C. O. (1966), A mathematical representation of the multiaxial Bauschinger effect. CEGB Report RD/B/N 731. Berkeley Nuclear Laboratories, Berkeley, UK.
- Asaro, R. J. (1983), Crystal plasticity. *ASME J. Appl. Mech.* 50, pp. 921-934.
- Cailletaud, G., Sai, K. (2008), A polycrystalline model for the description of ratchetting: Effect of intergranular and intragranular hardening. *Mater. Sci. Eng. A*, 480(1-2), pp. 24-39.
- Chaboche, J. L., Dang Van, K., Cordier, G. (1979), Modelization of the strain memory effect on the cyclic hardening of 316 stainless steel. SMiRT'5, Div. L, Berlin, L11/3.
- Chaboche, J. L., Nouailhas, D. (1989), Constitutive modeling of ratcheting effect: Part II, Possibilities of some additional kinematic rules. *ASME J. Eng. Mater. Technol.* 111, pp. 384-416.
- Huang, Y. G. (1991), A user-material subroutine incorporating single crystal plasticity in the ABAQUS finite element program. Harvard University Report, MECH 178.
- Kang, G. Z., Bruhns, O. T., Sai, K. (2011), Cyclic polycrystalline visco-plastic model for ratchetting of 316L stainless steel. *Comput. Mater. Sci.* 50(4), pp. 1399-1405.
- Lu, F. C., Kang, G. Z., Liu, Y. J., Shi, K. K. (2013) Experimental study on uniaxial cyclic deformation of rolled 5083Al alloy plate. 7th ICLCF, Aachen, Germany.
- Okabe, A., Boots, B., Sugihara, K. (1993), Spatial tessellations: concepts and applications of Voronoi diagrams. *Computers & Geosciences*, 19 (8), pp. 1209-1210.
- Peirce, D., Asaro, R. J., Needleman, A. (1983), Material rate dependence and localized deformation in crystalline solids. *Acta Metall*, 31, pp. 1951-1976.

## The power loss and efficiency analysis of a 3DOFs planetary gear box

\*H.B. Yin, S. L. Li, H. Zhang, X.Y. Zhao and J. Zhang

China North Vehicle Research Institute, Beijing, China

\*Corresponding author: yinhb201@163.com

### Abstract

The power loss and efficiency model of a planetary gear transmission system was built with a system modeling method. The method takes many transmission elements such as gear, planetary gear sets, hydraulic torque converter, friction disk, lubrication, sealing, bump and motor etc. into consideration and calculates non-load and load power loss for each element. The overall calculated power loss and efficiency is more accurate than the meshing power method. To make simulation more reliable it is compared with the test data. In the paper A planetary gearbox is selected and its power loss and efficiency were measured from the experiment. The power loss and efficiency of each gear of the planetary gearbox are compared and verified and corresponds well with the test data. The power loss error drop from 10% to 5% with the system method compared with meshing power method. It shows that the system method for power loss and efficiency analysis is more reliable. It provides important basis for engineers to improve design and reduces the power losses. It provides solutions to increase the planetary gear transmission efficiency and finally makes the whole vehicle lighter and the power density higher than before.

**Keywords:** power loss, efficiency, planetary gearbox, non load experiment, load experiment.

### Introduction

The gear transmission efficiency is one of most important factors in planetary gearbox design. It is related with additional heat generation within the gearbox. The more efficient gear transmission, the less heat generated, the less demands on the capacity and the size of the lubrication system. The amount and quality of the gearbox lubricant can easily meet the heat dissipation requirement with the improved efficiency. The problem now is how to calculate the gear transmission efficiency with much more accuracy? Up to now some formulas for efficiency ignored planetary gearbox structure details, gear relative speed, lubricant, temperature and friction disk slot type etc. These factors sometimes severely affect the power loss and efficiency of planetary gear transmission system. Taking these factors into consideration in efficiency calculation is important for engineers to improve their design shortcomings.

### The factors affecting power loss in the planetary gear transmission system

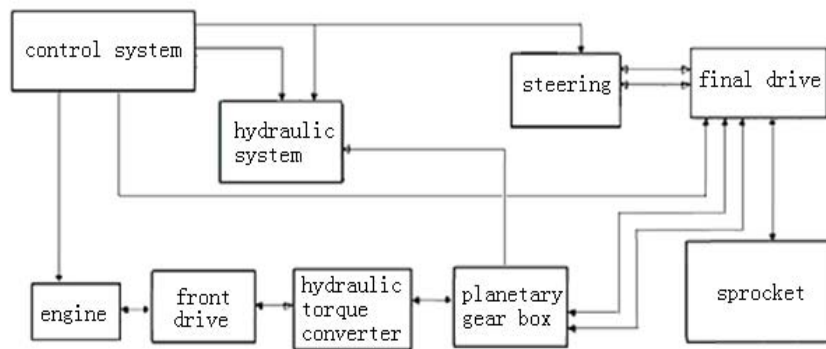
All the power losses in the gear transmission can be classified into non-load and load power loss. Non-load power losses occur when the output shaft is running free without power output and all the input power only maintains the transmission elements at a constant speed. Load-power losses depend on transmitted load, coefficient of friction and sliding velocity in the contact areas of the components. For nominal power transmission the load power losses of the gear mesh are typically dominant. For part load and high speed, non-load power losses dominate total losses. The gear, bearing, seals and auxiliaries generate non-load power losses. Gear and bearing also generate load power losses. In the planetary gearbox efficiency model building, these factors are included in the transmission element model.

The planetary transmission system, which is drawn out in the Fig.1, is made of hydraulic torque converter, planetary gearbox, hydraulic bump and motor, final drive and lubrication system. Its power losses include the planetary gear, friction disk, bearing, bump and lubrication etc. The

planetary gear power loss mainly consist of planetary gear non-load power losses, gear meshing power loss and churning power loss and bearing power loss. It is related with planetary gearbox structure, planetary gear number, gear angular speed, gear tooth width, lubrication type and oil etc. The friction disk power loss consists of non-load and load power loss. Its friction power losses are mainly associated with sliding velocity and load. It is related with friction disk numbers, its diameter, lubrication oil viscosity and transmitted torque. Bearing non power losses depend on bearing type and size, bearing arrangement, lubricant viscosity and supply. Bearing load dependent bearing losses depend also on bearing type and size, load and sliding conditions in the bearing and on lubricant type. Bump and motor power loss mainly includes the leakage power loss, overflow power loss, throttling power loss and friction power loss.

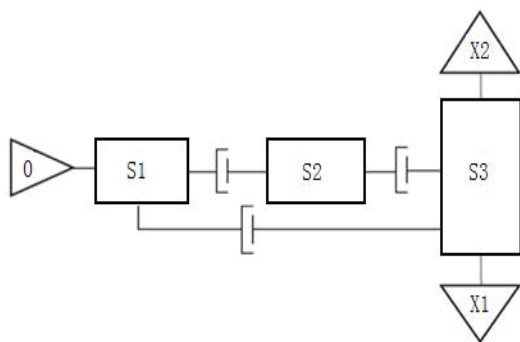
**The efficiency model building for the planetary gear transmission**

The whole transmission system of the vehicle comprises engine, front drive, hydraulic torque-converter, planetary gear box, electrical and hydraulic control system, hydraulic system, steering and final drive. All these sub systems in Fig. 1 contribute non-load and load power losses.

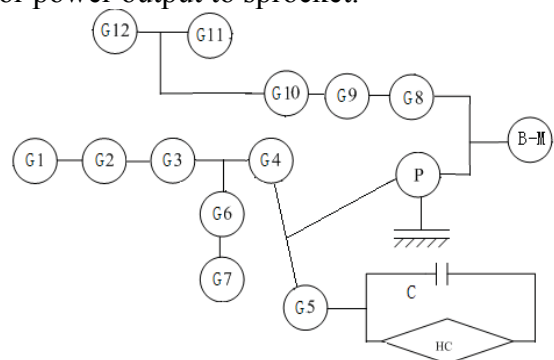


**Figure 1. The vehicle transmission system scheme**

In the efficiency model these sub systems are separated into three parts. The whole transmission system is separated into three sub-models in the efficiency model building. The kinematical scheme layout of planetary gearbox consists of three sub models S1, S2 and S3 showed in the Fig. 2. S1 stands for front drive, hydraulic torque converter and hydraulic system. S2 stands for gearbox and S3 stands for steering and final drive. X1 and X2 stand for power output to sprocket.



**Figure 2. The planetary gearbox efficiency model**



**Figure 3. The S1 efficiency model**

S1 sub efficiency model in Fig. 3 has 12 gear pairs G1 to G12, one planetary gear set P, lock-up clutch C, hydraulic torque converter HC and bump-motor system B-M. S2 sub efficiency model in Fig. 4 has four planetary gear sets D1 to D4, two clutches C1/C2 and four brakes B1 to B4. S3 efficiency model in Fig. 5 has four planetary gear sets P1 to P4, five gear pairs G1 to G5 and two power outputs to sprockets.



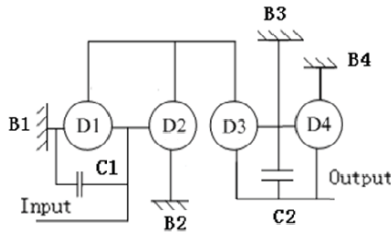


Figure 4. The S2 efficiency model

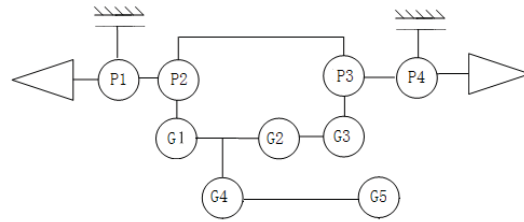


Figure 5. The S3 efficiency model

**Calculation and results analysis**

The each gear of the transmission is applied with four different loads, which are full load and three partial loads, 75%, 50% and 25%. When partial load is applied, it simply means the engine power outputs at the stated percentage of its full load output. This allows a more realistic validation of efficiency simulation results. In general the less load is exerted on, the less efficient the gear transmission system will be. In all these load cases, the 50% partial load is selected in this paper to test the power loss and efficiency at speed points 1500,2000,2500,3000,3500 and 4000 rpm. Through these tests, the simulation results can be verified and somehow become a reliable reference for design engineers.

*Non load power loss of the planetary gearbox and test validation*

Planetary gearbox power loss is the difference between its input power and output power. Non load power is the difference when output power equals zero. The non load power losses of five forward gear of the gearbox are tested and the results are recorded in Table 1 below. The theory calculation results and test results are drawn in the Fig. 6 to Fig. 10.

**Table 1. Non load power loss of the gearbox (kW)**

Speed (rpm)	1500	2000	2500	3000	3500	4000
1st gear Test	7.70	6.07	7.59	12.25	14.29	20.52
1st gear Theory	3.87	6.19	8.87	11.82	15.01	18.37
2nd gear Test	6.44	9.42	8.37	10.05	15.74	18.42
2nd gear Theory	4.04	6.38	9.1	12.07	15.24	18.57
3rd gear Test	9.56	11.51	10.99	13.19	15.74	30.56
3rd gear Theory	3.72	5.720	8.12	10.81	13.71	16.75
4th gear Test	6.44	9.42	12.3	19.46	26.38	30.56
4th gear Theory	4.15	6.32	9.34	12.55	16.23	17.97
5th gear Test	10.98	13.61	16.23	19.45	26.37	30.56
5th gear Theory	4.91	7.91	11.25	14.93	19.04	23.65

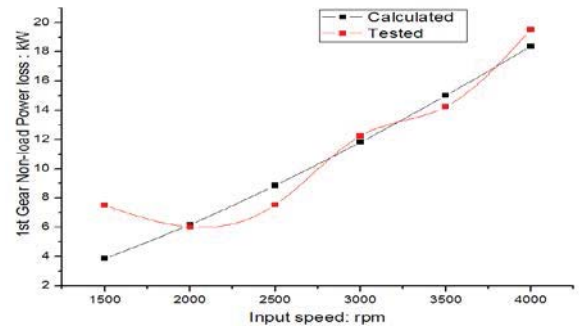


Figure 6. 1st gear non load power loss

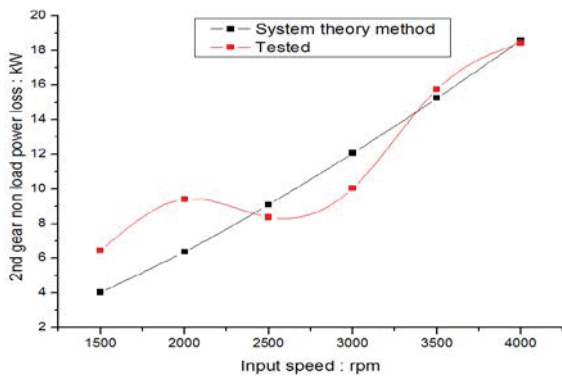


Figure 7. 2nd gear non load power loss

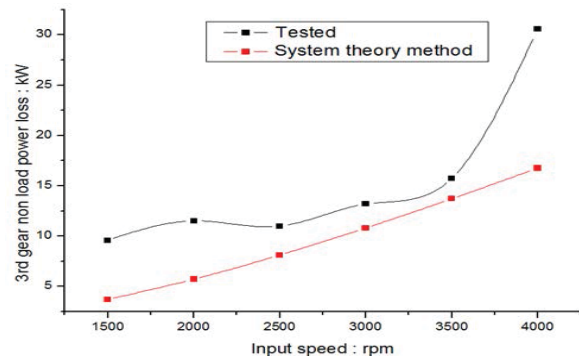


Figure 8. 3rd gear non load power loss

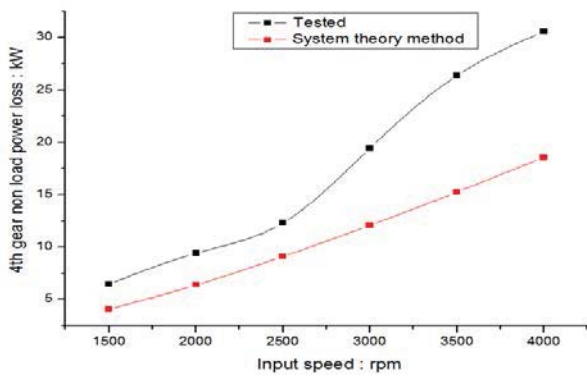


Figure 9. 4th gear non load power loss

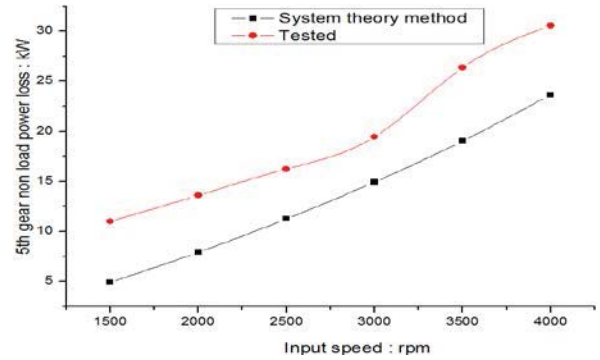


Figure 10. 5th gear non load power loss

From the above table and figure, the predicted power losses with the system theory correlated well the test results from speed 2000 rpm to 3500 rpm in 1st and 3rd gear. In the relatively lower and higher input speed the power losses of the 1st gear to the 4th gear have large errors with their theory predicted values. Whereas the 5th gear has not this phenomenon for the whole planetary gearbox rotates with the same speed.

*The efficiency of planetary gearbox with load power and test validation*

For the load power loss of the planetary gearbox, it is through each gear efficiency to evaluate. The efficiency is the ratio of input power to output power. The five gear efficiency of test and theory prediction are recorded in the Table 2. The each gear transmission efficiency obtained with different methods are drawn in the Fig.11 to Fig.15.

Table 2. Load power loss of the gearbox (kW)

Speed (rpm)	1500	2000	2500	3000	3500	
1st gear (%)	Test	87.8	88.18	87	86.47	85.37
	Theory		93.9	93.7	93.4	92.7
2nd gear (%)	Test	87.59	89.00	88.04	87.45	86.38
	Theory		94.65	94.39	94.03	93.25
3rd gear (%)	Test	86.19	87.40	89.07	88.71	87.27
	Theory		94.96	94.73	94.49	93.86
4th gear (%)	Test	91.04	91.65	89.16	86.37	87.36
	Theory		94.63	94.33	94.03	93.38
5th gear (%)	Test	88.53	89.70	92.30	86.27	79.42
	Theory		97.37	96.5	95.58	94.91

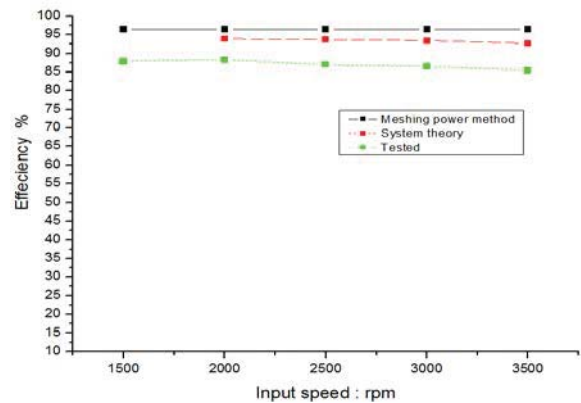


Figure 11. 1st gear efficiency

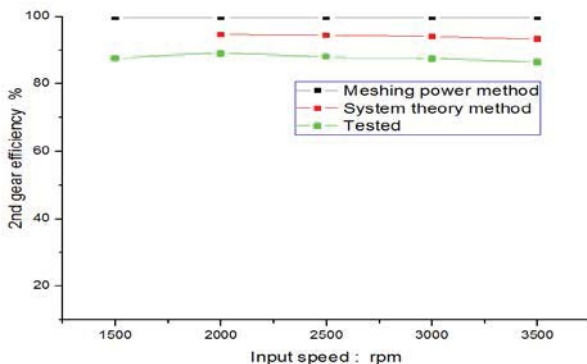


Figure 12. 2nd gear efficiency

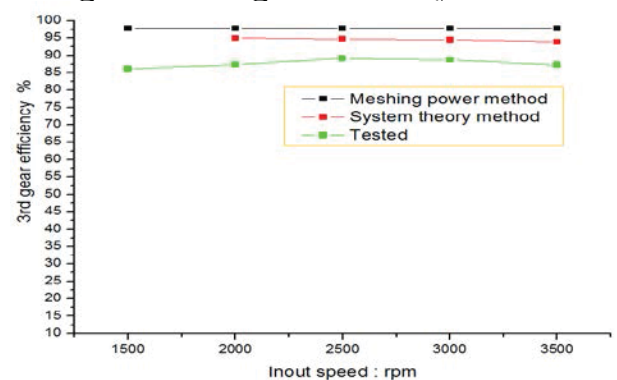


Figure 13. 3rd gear efficiency

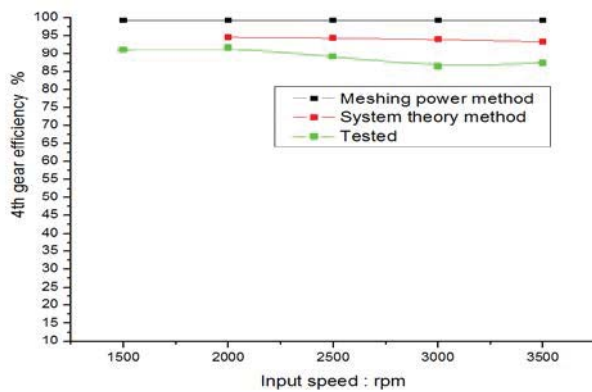


Figure 14. 4th gear efficiency

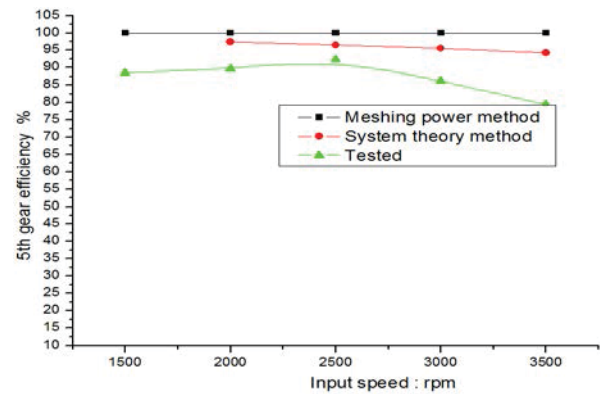


Figure 15. 5th gear efficiency

The error of 1st gear efficiency obtained with system theory method is 5.72% at speed 2000rpm and 7.33% at speed 3500rpm compared with the test data. It is 2.5% less and 3.7% less accordingly than the efficiency obtained with the meshing power method. It obvious more accurate than the meshing power method with reference to test data. The other gear efficiency has similar situation. The predicted efficiency with system method has an error from 3% to 8%. It is larger than test data and less than meshing power method. From the above comparison with the test and meshing power method, the system theory method in the paper is verified and can be a more reliable method to predict power loss and transmission efficiency.

## Conclusion

The efficiency model of an integrated transmission including planetary gearbox with system theory method was built in the paper. It calculated the speed, torque, power loss of every rotating element for each gear at different speed and engine throttle. Because of content requirement many calculation results are omitted. The 50% engine throttle load case is selected to test. The power loss and efficiency are verified from the test data. After the verification and validation of previous chapter, the system theory method in the paper takes many influence factors into consideration in the efficiency calculation and is much more accurate than the meshing power method. Finally the conclusion can be made that the system theory method with much more accurate formula for different kinds of power loss is more reliable and practical in transmission efficiency prediction. It provides a good solution for engineers to decrease the power loss and increase the efficiency of integrated transmission.

## References

- Satya S.(2009), An investigation of load-independent power losses of gear systems, *Dissertation of The Ohio State University*, pp.1-189.
- Höhn B.R., Klaus M. and Michael H(2009), Influence factors on gearbox power loss, *3rd International Conference on Integrity, Reliability and Failure, Porto/Portugal, 20-24 July*, pp.1-17.
- Al-Shibl, K., Simmons, K., and Eastwick, C. N.( 2007) , Modeling gear windage power loss from an enclosed spur gears, *Proceedings of the Institution of Mechanical Engineers, Part A, 221(3)*, pp. 331–341.
- Diab, Y., Ville, F., and Velez, P.(2006), Investigations on power losses in high speed gears, *Journal of Engineering Tribology*, 220, pp.191-298.
- Del Castillo J.M. (2002), The analytical expression of the efficiency of planetary gear trains, *Mech. Mach. Theory*, 37(2), pp.197-214.
- Anderson N. E., Loewenthal S. H.(1981), Effect of geometry and operating conditions on spur gear system power loss, *ASME J.Mech.Des.*, 103, pp.51-159.

# Grid deformation based on macro-element and partitioning techniques for flapping mechanism

\*J. H. Ko<sup>1</sup>, and T. Q. Le<sup>1</sup>

<sup>1</sup>Korea institute of ocean science and technology, Haean-ro, Ansan-si, Kyunggi-do

\*Corresponding author: jhko@kiost.ac

## Abstract

The grid deformation algorithms can be classified into linear algebra methods, elasticity-based approaches, and their hybrid forms. The methods in the first category have advantages in efficiency, but do not normally produce grids of sufficient quality. A spring analogy in the second category is known to cause grid irregularity for the large moving boundary problem and methods for improving the robustness of the grid regularity are subsequently required. The finite element method in the same category provides better quality than simple interpolation schemes, but become too expensive for large grids. Hybrid method using the macro-finite elements and interpolation reduced not only computational cost for finite element solution over entire grid, but also the disparity of mesh size, which causes bad effect on the grid quality.

However, the hybrid scheme is still needed to be improved for the flapping mechanism, which has the large deformation and motion. The failure during the grid deforming is mainly occurred near the moving object, namely the flapper. So the improvement should be focused on this region. Therefore, in this work, partitioning into body-fitted grid and other is enhanced on top of the hybrid scheme using the macro-element technique. In a little detail, the grid deformations are firstly computed in the body-fitted grid region because the highest performance is required. The deformations along the interface between the two regions are used as the boundary condition for the other domain. The hybrid scheme is then applied to the other region. The proposed grid deformation shows the better performance as compared to a conventional hybrid scheme in terms of grid orthogonality and its volume change in applications of flapping mechanisms.

**Keywords:** Grid deformation, Macro-element, Partitioning techniques, Flapping mechanism

## Introduction

In modern computational fluid dynamics, the moving boundary problem receives a great deal of attention, as it is mandatory in free surface flows, forced vibration problems, optimization, and fluid-solid interaction. A crucial part of this computation is the grid deformation at every step during the numerical time integration of the fluid analysis.

The finite macro-element based method for structured grids, which consists of fluid grids, computes the grid deformation along with interpolation scheme (Bartels, 2005). This reduced not only computational cost for finite element solution over entire mesh, but also the disparity of element size which causes bad effect on the grid quality.

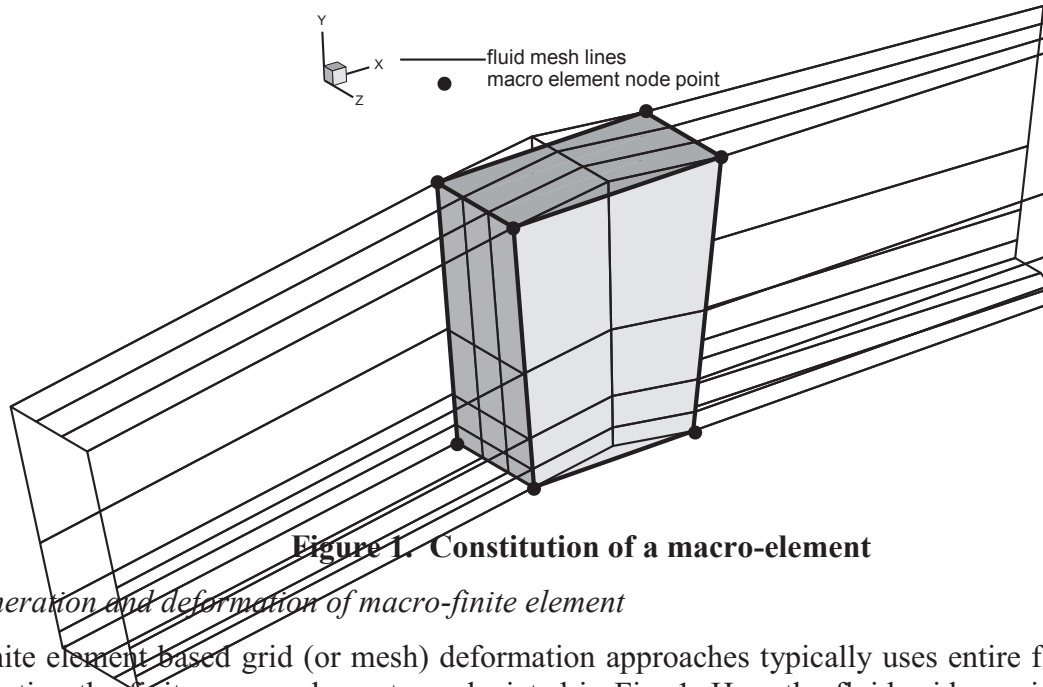
Recently, as an interesting type inspired by nature, flapping hydrofoil power generator from tidal stream have been developed in the UK: Stingray of Engineering Business Ltd and the newer Pulse stream 100 designed by Pulse Generation Ltd. in conjunction with IT Power Ltd. These system are known as echo-friendly systems (Glynn, 2006) compared to typical rotary turbines. Power extraction using the flapping mechanism requires large heave and pitch motion as well as structural deformation. Thus, higher performance in grid deformation is necessary.

Therefore, improvement methods were introduced such as the Jacobian option (Stein, Tezduyar and Benney, 2003) and partitioning method in which the verifications of the grid quality based on volume change and orthogonal change were adopted. In this paper, the performance of the finite macro-element based grid deformation is explored for large pitch and span flexure of a typical airfoil. The efficiency of power extraction is obtained by the approach.

## Methods

### A. Volume grid deformation (VGD)

To consider deformed shape effects, VGD (Volume Grid Deformation) code is developed in the overset grid Navier-Stokes solver as a mesh deformation code. The VGD code is developed based on the Ref. (Ko, 2010). The mesh deformation is divided into two main steps. First step is computing deformation from a finite macro-element model generated by fluid grid. The second step is transfinite interpolation that translates from the deformation of the macro-elements to whole fluid grids.



**Figure 1. Constitution of a macro-element**

### B. Generation and deformation of macro-finite element

Finite element based grid (or mesh) deformation approaches typically uses entire fluid grids in constituting the finite macro-elements as depicted in Fig. 1. How the fluid grids are included in a macro-element is important for the preservation of the grid regularity. Here, we use the condition that satisfies minimum distance and minimum grid index number of each edge line of the macro-element.

### C. Grid deformation by transfinite interpolation

Once the node displacements of the macro-elements are obtained from the finite element system, a transfinite interpolation is performed by using a blending function. The results are known to be a continuity of displacements at all macro-element boundaries, even if continuity of the derivative of the displacement is not ensured (Ko, 2010). A blending function in public domain, BLEND is employed. BLEND is coded by C and FORTRAN languages and is released in the function that interpolates corresponding fluid grids from a macro-element by using the deformations of the edge points. However, the moving boundary is composed of surfaces in three-dimension; thus we need to modify the original code for translating the fluid grids from given displacements over the surface of the macro element.

Through the two separate procedures, the large motions over the moving boundary successfully translate to the whole fluid grids. The grid deformation is developed only for three dimensional structured grids and is referred to as volume grid deformation (VGD).

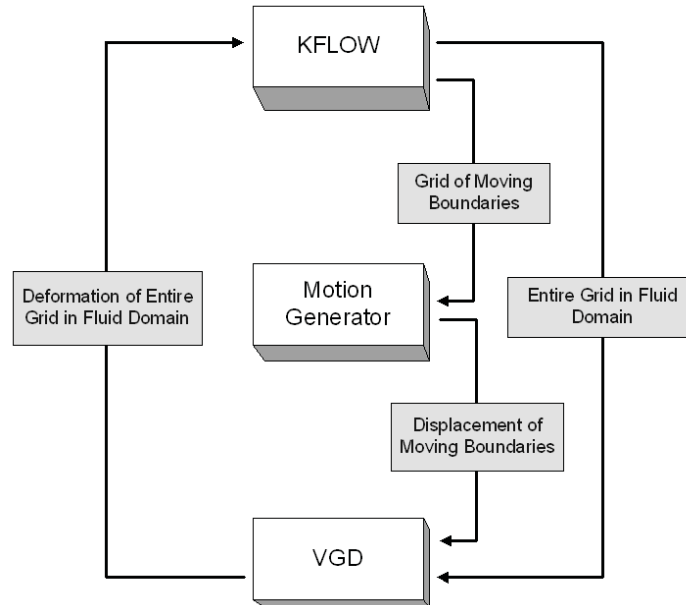
The Jacobian option was implemented by accounting for the Jacobian of the transformation from the mesh domain to the physical domain

$$\int_{\Xi} [\dots]^e J^e d\Xi = \int_{\Xi} [\dots]^e J^e \left( \frac{J^0}{J^e} \right)^{\chi} d\Xi \quad (1)$$

As another scheme for improving grid quality near wall, the partitioning method is adopted. The whole grid is separated into two subdomains. The first subdomain including the object is solved first and the second subdomain is solved with the boundary conditions computed from the first solution.

#### D. Computational fluid dynamic code and interface

As mentioned previously, numerical simulation for obtaining aerodynamic forces will be done by a computational fluid dynamics code. KFLOW, which we adopt, is an in-house code for the three-dimensional compressible, preconditioned Navier-Stokes analysis. Multi-block structured grid and automated interpolation point generation algorithm are implemented (Park 2003). Spatial discretization is done by finite volume method where discretization schemes with second and fourth order accuracy and WENO (Weighted Essentially Non-Oscillatory) scheme with fifth order accuracy are implemented. Spalart Allmaras, k- $\omega$  Wilcox, k- $\omega$  Wilcox Durbin (WD+), k- $\omega$  SST (Shear Stress Transport), and k- $\epsilon$



**Figure 2. Modules and data flow when VGD interfaces with KFLOW.**

The modules and data flow of VGD coupled with KFLOW are depicted in Fig. 2. For the CFD analysis of a flapping foil, the CFD solver should consider the large deformation of moving boundaries. As aforementioned, VGD plays a role in computing the deformation of the entire fluid grids from the displacement of the moving boundaries, which is made by a motion generator in Fig. 2.

## Results

### A. Performance measures of grid quality

The orthogonality change is calculated from the following equations with the edge vectors.

$$\begin{aligned}
\mathbf{v}_1 &= \mathbf{x}_{i+1,j,k} - \mathbf{x}_{i,j,k} \\
\mathbf{v}_2 &= \mathbf{x}_{i,j+1,k} - \mathbf{x}_{i,j,k} \\
\mathbf{v}_3 &= \mathbf{x}_{i-1,j,k} - \mathbf{x}_{i,j,k} \\
\mathbf{v}_4 &= \mathbf{x}_{i,j-1,k} - \mathbf{x}_{i,j,k} \\
q_k &= \frac{1}{4} \left\{ \frac{(\mathbf{v}_1 \cdot \mathbf{v}_2)^2}{v_1^2 v_2^2} + \frac{(\mathbf{v}_2 \cdot \mathbf{v}_3)^2}{v_2^2 v_3^2} + \frac{(\mathbf{v}_3 \cdot \mathbf{v}_4)^2}{v_3^2 v_4^2} + \frac{(\mathbf{v}_4 \cdot \mathbf{v}_1)^2}{v_4^2 v_1^2} \right\} \\
q_{i,j,k} &= 1.0 - \frac{q_i + q_j + q_k}{3} \\
q_{i,j,k}(t) - q_{i,j,k}(t=0) &/ q_{i,j,k}(t=0)
\end{aligned} \tag{2}$$

The volume change is simply calculated as follows:

$$(V_{i,j,k}(t) - V_{i,j,k}(t=0)) / V_{i,j,k}(t=0) \tag{3}$$

### B. Performance of grid quality

#### 1) Large pitch angles

Pitch angles are changed by 45, 60, and 75 degrees. Fig. 3 shows volumes changes when the number of time steps increases. The Jacobian option updates the stiffness of the macro elements that plays roll in resisting the deformation. That is the reason why the volume change decreases as the number of time steps increases.

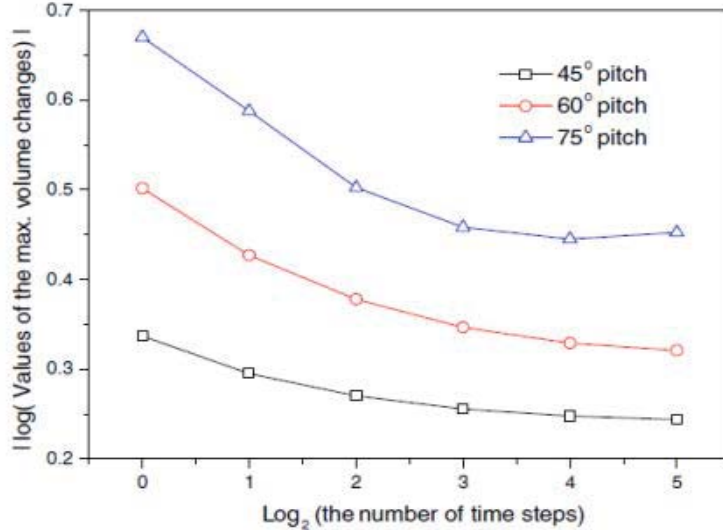
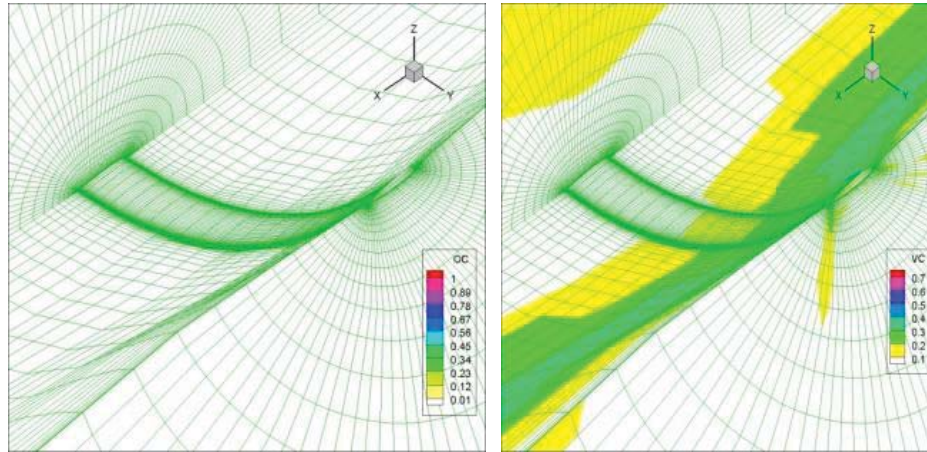


Figure 3 Volume change .vs. the number of time steps

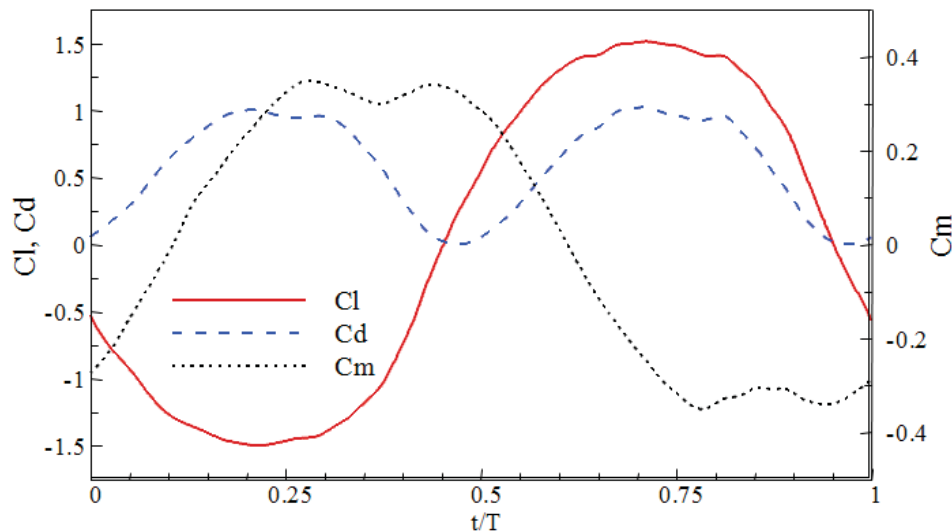
#### 2) Span flexure

Span flexure is given along the spanwise direction by a parabolic equation. The orthogonality and volume changes are depicted in Fig. 4. There are little orthogonality changes near the object while the some volume changes are existed. It is noted that the orthogonality change is more important than the volume change in order to obtain the accurate solution of the structured grid system.



**Figure 4 Orthogonality and volume change**

Numerical experiment of the power extraction is conducted with the 50 pitch angle amplitude and 0.5c heave amplitude given. The force and moment coefficients are shown in Fig. 5. The power efficiency  $C_p$  is calculated by 24% from the results as compared to flow energy with 2m/s flow speed.



**Figure 5 Force and moment coefficients versus time**

## Conclusion

Grid deformation based on macro element is able to preserve a good grid quality after a large deformation and rigid motion are given. Flapping mechanism for power extraction needs a much larger motion as well as structural deformation than that for propulsion applications. Hence, Jacobian option and partitioning schemes are enhanced. Here, the grid quality is measured by orthogonality and volume changes. Good grid quality is presented through validation for cases of large pitch and span flexure. Therefore, the grid deformation is usable for analyzing a flapping mechanism

## Acknowledgement

This work was supported by the New Researcher Program at Korea Institute of Ocean Science & Technology (PE98987).



**References**

- Bartels, R.E. (2005) Finite Macro-Element Mesh Deformation in a Structured Multi-block Navier-Stokes Code. *NASA Technical Memorandum*.
- Glynn, J. (2006), Design of Biomimetic Passive Control for Optimisation of Oscillating Hydrofoils in Tidal Energy Capture Master Thesis, University of Strathclyde.
- Ko, J. H.(2010) Finite macro-element-based volume grid deformation for large moving boundary problems, *Int. J. Numer. Meth. Biomed. Engng.* 26, pp.1656–1673
- Park, S. H. (2003) Prediction Methods of Dynamic Stability Derivatives Using the Navier-Stokes Equations, PhD thesis, Korea Advanced Institute of Science and Technology
- Stein, K., Tezduyar, T. and Benney, R. (2003) Mesh moving techniques for fluid-structure interactions with large displacements. *Journal of Applied Mechanics* 70(1), pp. 58-63.

# Tensile properties of graphene nanotube hybrid structures: a molecular dynamics study

H.F. Zhan, K. Xia and Y.T. Gu\*

School of Chemistry, Physics and Mechanical Engineering, *Queensland University of Technology*,  
*Brisbane, QLD 4001, Australia*

\*Corresponding author: yuantong.gu@qut.edu.au

## Abstract

Graphene has been reported with record-breaking properties which have opened up huge potential applications. A considerable research has been devoted to manipulate or modify the properties of graphene to target a more smart nanoscale device. Graphene and carbon nanotube hybrid structure (GNHS) is one of the promising graphene derivatives, while their mechanical properties have been rarely discussed in literature. Therefore, such a study is conducted in this paper basing on the large-scale molecular dynamics simulation. The target GNHS is constructed by considering two separate graphene layers that being connected by single-wall carbon nanotubes (SWCNTs) according to the experimental observations. It is found that the GNHSs exhibit a much lower yield strength, Young's modulus, and earlier yielding comparing with a bilayer graphene sheet. Fracture of studied GNHSs is found to fracture located at the connecting region between carbon nanotubes (CNTs) and graphene. After failure, monatomic chains are normally observed at the front of the failure region, and the two graphene layers at the failure region without connecting CNTs will adhere to each other, generating a bilayer graphene sheet scheme (with a layer distance about 3.4 Å). This study will enrich the current understanding of the mechanical performance of GNHS, which will guide the design of GNHS and shed lights on its various applications.

**Keywords:** graphene, nanotube, tension, Young's modulus, molecular dynamics simulation

## Introduction

The carbon nanotube (CNT) and graphene have grabbed appreciable scientific community attentions, owing to their excellent performance in the field of mechanics, photology, electronics and bio-sensing (Zhu et al. 2010; Wang 2005). Their record-breaking properties (e.g., enormous Young's modulus, fracture strength and low mass density) have enabled them with a wide promising applications in the nanoelectromechanical system (NEMS) including force, mass and position sensors, bio-sensors as well as high frequency resonators (Chen et al. 2009). Synthesising these two nanomaterials together, a graphene and nanotube hybrid structure (GNHS) is formed, which can be used to fabricate field-emitter devices and double layer capacity, demonstrating much improved performance over pervious designed CNT-bulk metal structures (Yan et al. 2012). Specifically, a combination of nanotube

and graphene layer extends the electric conductivity to three dimensions, which shows promising applications in solar cells (Yen et al. 2011; Wang, Zhi and Müllen 2008).

It is noticed that several works have been devoted to investigate the electrical and thermal properties of GNHS (Zhu et al. 2012; Varshney et al. 2010; Noakes, Urali and Rodeh 2010), while the studies of the mechanical performance, stability or durability of the hybrid structure are still lacking in literature. Typically, one relies on either experiments or numerical simulations to probe the mechanical properties of nanomaterials. While, it is generally accepted that experimental approach is usually suffering from several shortages, such as huge manipulation complex and experimental uncertainties. On the other hand, numerical simulation has been witnessed as an effective and efficient tool in investigating the performance and properties of nanomaterials or nano-device (Zhan and Gu 2011; Gu and Zhan 2012; Zhan, Gu and Park 2012), which could compensate certain experimental shortages, e.g., provides atomic-resolution deformation process of the material under loading in a degree of detail not possible experimentally.

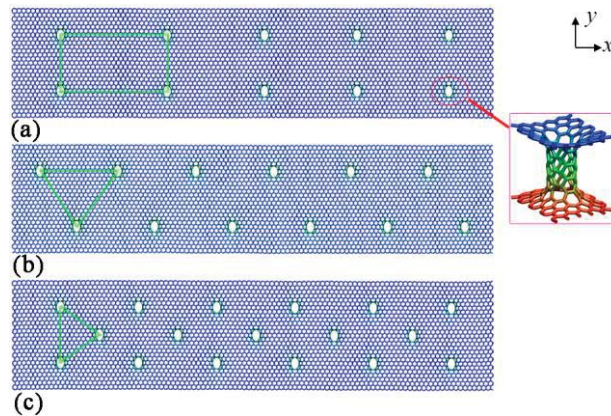
Therefore, in this work, the molecular dynamics (MD) simulation, as one of the popular simulation approaches, will be employed to unveil the tensile performance of GNHS. Emphasis will be placed on the Young's modulus, as well as the yield strength of different GNHSs that are constructed with different allocations of CNTs.

### Computational details

A series of large-scale MD simulations were carried out to investigate how the GNHS will perform when different allocations of CNTs are applied to connect two separate graphene layers. After several papers are viewed (Matsumoto and Saito 2002; Dimitrakakis, Tyliaakis and Froudakis 2008; Noakes, Urali and Rodeh 2010; Varshney et al. 2010), a specific cylindrical hole is made on the graphene to fit the selected CNT, which is armchair (4, 4) CNT with a height of 13.8 Å in our case. Different testing samples have an almost identical size around 24.7×5.6 nm<sup>2</sup>. Basically, five different allocations of CNTs have been used, including a rectangular allocation with 10 CNTs (denoted as R10-GNHS, shown in Fig. 1a), 12 CNTs (denoted as R12-GNHS) and 14 CNTs (denoted as R14-GNHS), a triangular allocation of 12 CNTs (denoted as T12-GNHS, shown in Fig. 1b) and 17 CNTs (denoted as T17-GNHS, shown in Fig. 1c).

In the MD simulation, the popularly applied reactive empirical bond order (REBO) potential (Brenner et al. 2002) was adopted to describe the interactions of C atoms, which has been shown to well represent the binding energy and elastic properties of graphene and CNT (Zhang et al. 2011). During the simulation, the GNHS was firstly relaxed to a minimum energy state using the conjugate gradient algorithm. We then used the Nose-Hoover thermostat (Hoover 1985; Nosé 1984) to equilibrate the GNHS at 1 K (NVT ensemble) for 500 ps at a time step of 1 fs. Finally, a constant velocity of

0.001 Å/ps was applied to one end of the GNHS along the length direction ( $y$ -axis in Fig. 1), while holding another end fixed. The equations of motion are integrated with time using a Velocity Verlet algorithm (Verlet 1967). No periodic boundary conditions have been applied. The system temperature was maintained at 1 K during the simulation to minimize the influence from thermal fluctuations. All simulations were performed using the open-source LAMMPS code (Plimpton 1995).



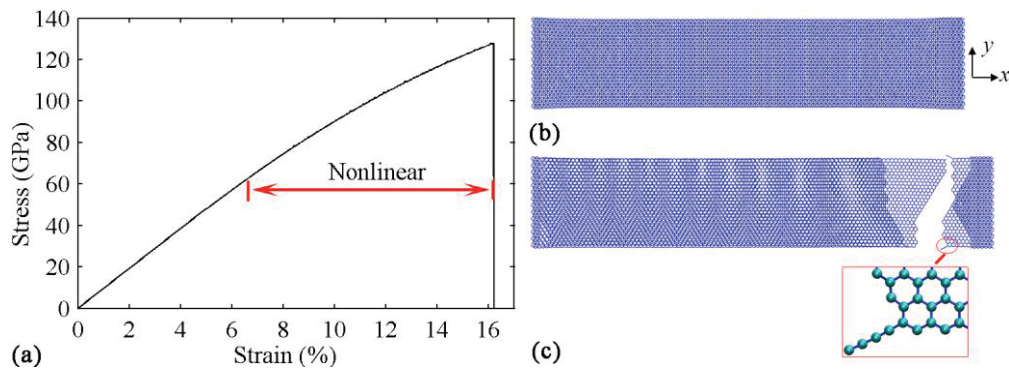
**Figure 1. Simulation models of different GNHSs. (a) A rectangular allocation of 10 CNTs between two separate graphene layers; (b) A triangular allocation of 12 CNTs; (c) A triangular allocation of 17 CNTs. Inset shows the bonds between graphene layer and CNT.**

## Results and discussion

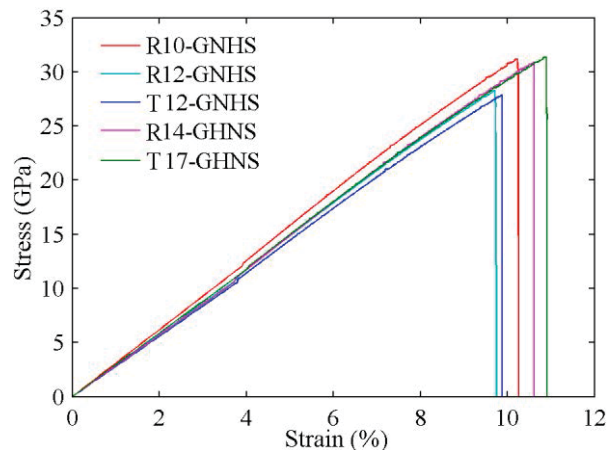
In the following, the tensile properties that extracted from the stress-strain curves will be discussed among different cases. Specifically, Young's modulus  $E$  will be calculated as the initial slope of the stress-strain curve within a strain of 5%. The yield strength and fracture strain are defined at the point where the peak stress is arrived. For the purpose of comparison and also validation, we studied the tensile properties of a bilayer graphene at the beginning. Figure 2a shows the simulation results for a bilayer GS. Young's modulus and the yield strength are estimated as 0.96 TPa and 128 GPa, respectively, which are consistent with that reported by previous researchers (Zhang et al. 2011). Figures 2b and 2c present the atomic configurations of the bilayer GS before and after failure, respectively. As is seen in Figure 2b, during the elastic deformation period, all the C-C bonds have been stretched in the loading direction. With the increasing strain, initial failure is found at the two edges of the bilayer GS which is caused by the bond breaking processes. Since the appearance of these breaking bonds, the bilayer GS is found to fail quickly as indicated by the sharp decrease of the stress after yield strain, signifying a brittle behaviour. It is found that after the failure of the sample, several short monatomic chains are formed at the front of the failure region, as shown in inset of Figure 2c.

We then turned to the tensile properties of different GNHSs. Figure 3 presents the stress-strain curves obtained from the MD simulations. Comparing with the bilayer

GS, an evident decrease of the yield strength and early yielding are observed. Rather than a nonlinear stress-strain curve of the bilayer GS at a higher strain during the elastic deformation region (shown in Figure 2), all GNHSs exhibit a linear stress-strain curve during the whole elastic deformation period. The brittle failure phenomenon is also observed in different GNHSs as indicated by the sharp decrease of stress after yielding in Figure 3.



**Figure 2. Numerical results from a bilayer GS: (a) Stress-strain curve; (b) Atomic configuration at 1996 ps; (c) Atomic configuration at 3870 ps. Inset shows the monatomic chain at the front of the failure region.**



**Figure 3. Stress-strain curves obtained from five different graphene and nanotube hybrid structures (GNHSs).**

The tensile properties of different GNHSs are summarised in Table 1. As aforementioned, a relatively smaller yield strength and earlier yielding are found in these GNHSs comparing with that of a bilayer GS. Specifically, the T12-GNHS exhibit the smallest yield strength of  $\sim 27.88$  GPa, which is only one fifth of bilayer GS's yield strength. The other four GNHSs also exhibit a similar low yield strength. In the other hand, the R12-GNHS shows the earliest yielding, at a strain of 9.71%, followed by the T12-GNHS with the yield strain as 9.88%. According to the results from the three GNHSs with rectangular allocations of CNTs, more connecting CNTs does not necessary mean a superior tensile property. While for the rest two cases with triangular allocation, better tensile properties are found for the one with more CNTs,

i.e., T17-GNHS. It can be concluded that the tensile properties of GNHS is determined by both the number and allocation schemes of the connecting CNTs.

**Table 1. Tensile properties of different GNHSs.**

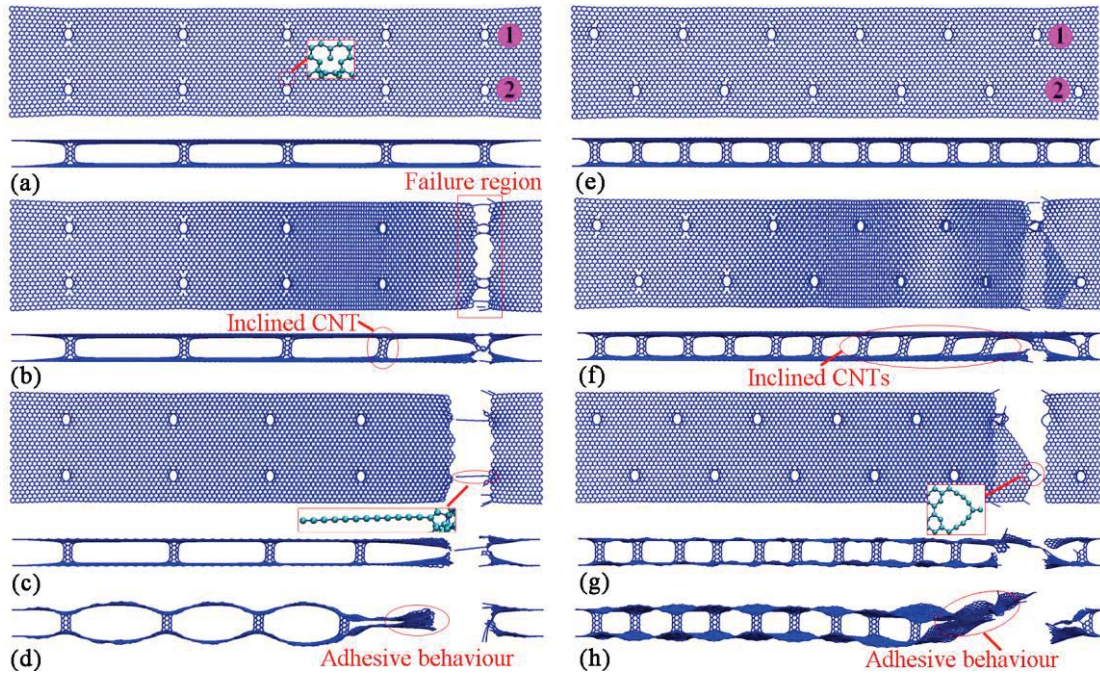
	Bilayer GS	R10- GNHS	R12- GNHS	T12- GNHS	R14- GNHS	T17- GNHS
Yield strength (GPa)	127.88	31.21	28.30	27.88	30.88	31.38
Yield strain (%)	16.12	10.23	9.71	9.88	10.60	10.90
Young's modulus (TPa)	0.96	0.31	0.28	0.28	0.28	0.29

To acquire the in-detail influence that induced by different allocations of CNTs, the atomic configurations of different GNHSs are compared at different simulation time. Figures 4a - 4d illustrate the atomic configuration of the R10-GNHS before and after failure. As illustrated in Figure 4a, the C-C bond that connecting the CNT and graphene is broken due to the high tensile strain. From Figure 4b, the fracture is occurred around the two connecting CNTs, and other CNTs that are adjacent to the fracture region are tilted by the tensile strain. Similar as the bilayer GS, several monatomic chains are formed at the failure region as revealed in Figure 4c. It is worth noting that the two GS layers adhere to each other because of the absence of connecting CNTs after fracture, which induce a local bilayer GS scheme with the initial layer distance reducing from the original 13.8 Å to approximate 3.4 Å. Such deformation processes are observed in other GNHSs with rectangular allocation of CNTs, i.e., R12-GNHS, R14-GNHS.

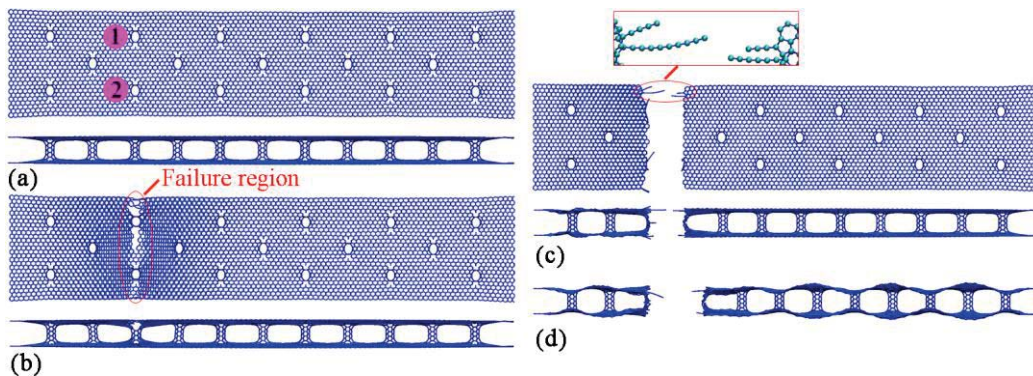
Simulation results have shown that the triangular allocation of CNT will endow the hybrid structure with different tensile behaviours. As presented in Figures 4f, for the T12-GNHS, more connecting CNTs have been tilted due to the increasing tensile stress, and the fracture occur around two CNTs. After fracture, two monatomic chain circles are formed at the locations of the corrupted CNTs, as shown in Figure 4g. Unlike previous cases with rectangular allocation of CNTs where the two graphene layers broke nearly at the same location, the two graphene layers of the T12-GNHS fracture differently as illustrated in Figure 4g. Consistently, we found the two graphene layers adhere to each other at the failure region due to the rupture of the connecting CNT.

Interestingly, for the T17-GNHS, the fracture is occurred around the region with two connecting CNTs rather than the area with only one CNT. After fracture, several monatomic chains are formed as illustrated in Figure 5c. We note that, the two CNTs have been spilt into two parts rather than rupture in previous cases, which leads the two GS layers still being separated with a relatively large distance (see Figure 5d). According to above discussions, it is concluded that the two GS layers connected by

CNTs will exhibit a much lower yield strength, Young's modulus and earlier yielding than a normal bilayer GS. The fracture or failure is usually occurred around the locations of connecting CNTs and the monatomic chains are normally observed at the failure region. Comparing with a bilayer GS, more monatomic chains are formed in the hybrid structures after yielding due to the failure of CNTs.



**Figure 4. Atomic configurations of HGNSs at different simulation time. R10-GNHS at: (a) 2562 ps, inset shows the broken C-C bonds around the connecting CNT, (b) 2568 ps, (c) 2586 ps, inset shows the formation of a monatomic chain, (d) 2616 ps; T12-GNHS at: (e) 2052 ps, (f) 2508 ps, inset shows the formation of a monatomic chain circle, (g) 2532 ps, (h) 2556 ps.**



**Figure 5. Atomic configurations of the T17-GNHS at different simulation time: (a) 2216 ps, (b) 2692 ps, (c) 2706 ps, inset shows the formation of four monatomic chains, (d) 2724 ps.**

## Conclusions

Basing on the large-scale MD simulation, the tensile properties of graphene carbon nanotube hybrids structures have been investigated. Discussions are emphasised on the yield strength, Young's modulus and the failure mechanisms. It is found that the GNHSs exhibit a much lower yield strength, Young's modulus, and earlier yielding comparing with a bilayer GS. Particularly, fracture of studied GNHSs is found to locate around connecting regions between CNTs and graphene. After failure, monatomic chains are normally observed at the front of the failure region, and the two graphene layers at the failure region without connecting CNTs will adhere to each other to generate a local bilayer GS scheme (i.e., the distance of the two layers reduces to a value of  $\sim 3.4 \text{ \AA}$ ). This study provides a fundamental investigation of the tensile properties of the graphene nanotube hybrid structures, which will benefit the design and also the applications of graphene-based hybrid materials.

## Acknowledgements

Support from the ARC Discovery Project (DP130102120) and the High Performance Computer resources provided by the Queensland University of Technology are gratefully acknowledged.

## References

- Brenner, Donald W, Olga A Shenderova, Judith A Harrison, Steven J Stuart, Boris Ni and Susan B Sinnott. 2002. "A second-generation reactive empirical bond order (REBO) potential energy expression for hydrocarbons." *Journal of Physics: Condensed Matter* 14 (4): 783.
- Chen, Changyao, Sami Rosenblatt, Kirill I Bolotin, William Kalb, Philip Kim, Ioannis Kymissis, Horst L Stormer, Tony F Heinz and James Hone. 2009. "Performance of monolayer graphene nanomechanical resonators with electrical readout." *Nature nanotechnology* 4 (12): 861-867.
- Dimitrakakis, Georgios K, Emmanuel Tylianakis and George E Froudakis. 2008. "Pillared graphene: a new 3-D network nanostructure for enhanced hydrogen storage." *Nano letters* 8 (10): 3166-3170.
- Gu, Y. T. and H. F. Zhan. 2012. "MD investigations for mechanical properties of copper nanowires with and without surface defects " *International Journal of Computational Methods* 9 (1): 1240003.
- Hoover, W.G. 1985. "Canonical dynamics: Equilibrium phase-space distributions." *Physical Review A* 31 (3): 1695-1697.
- Matsumoto, Takanori and Susumu Saito. 2002. "Geometric and electronic structure of new carbon-network materials: Nanotube array on graphite sheet." *Journal of the Physical Society of Japan* 71: 2765.
- Nosé, S. 1984. "A unified formulation of the constant temperature molecular dynamics methods." *The Journal of Chemical Physics* 81: 511.
- No aes, re derico , iccardo urali and Pablo r de n. 2010. "Electronic transport between graphene layers covalently connected by carbon nanotubes." *ACS nano* 4 (12): 7596-7602.
- Plimpton, S. 1995. "Fast parallel algorithms for short-range molecular dynamics." *Journal of Computational Physics* 117 (1): 1-19.
- Varshney, Vikas, Soumya S Patnaik, Ajit K Roy, George Froudakis and Barry L Farmer. 2010. "Modeling of thermal transport in pillared-graphene architectures." *ACS nano* 4 (2): 1153-1161.



- Verlet, Loup. 1967. "Computer 'experiments' on classical fluids. I. Thermodynamical Properties of Lennard-Jones Molecules." *Physical Review* 159: 98-103.
- Wang, Joseph. 2005. "Carbon - nanotube based electrochemical biosensors: A review." *Electroanalysis* 17 (1): 7-14.
- Wang, Xuan, Linjie Zhi and Klaus Müllen. 2008. "Transparent, conductive graphene electrodes for dye-sensitized solar cells." *Nano letters* 8 (1): 323-327.
- Yan, Zheng, Lulu Ma, Yu Zhu, Indranil Lahiri, Myung Gwan Hahm, Zheng Liu, Shubin Yang, Changsheng Xiang, Wei Lu and Zhiwei Peng. 2012. "Three-Dimensional Metal-Graphene-Nanotube Multifunctional Hybrid Materials." *ACS nano* 7 (1): 58-64.
- Yen, Ming-Yu, Min-Chien Hsiao, Shu-Hang Liao, Po-I Liu, Han-Min Tsai, Chen-Chi M Ma, Nen-Wen Pu and Ming-Der Ger. 2011. "Preparation of graphene/multi-walled carbon nanotube hybrid and its use as photoanodes of dye-sensitized solar cells." *Carbon* 49 (11): 3597-3606.
- Zhan, H.F. and Y.T. Gu. 2011. "Atomistic exploration of deformation properties of copper nanowires with pre-existing defects." *CMES: Computer Modeling in Engineering & Sciences* 80 (1): 23-56.
- Zhan, Haifei, Yuantong Gu and Harold S. Park. 2012. "Beat phenomena in metal nanowires, and their implications for resonance-based elastic property measurements." *Nanoscale* 4 (21): 6779-6785.
- Zhang, YY, CM Wang, Y. Cheng and Y. Xiang. 2011. "Mechanical properties of bilayer graphene sheets coupled by  $sp^3$  bonding." *Carbon* 49 (13): 4511-4517.
- Zhu, Yanwu, Shanthi Murali, Weiwei Cai, Xuesong Li, Ji Won Suk, Jeffrey R Potts and Rodney S Ruoff. 2010. "Graphene and graphene oxide: synthesis, properties, and applications." *Advanced Materials* 22 (35): 3906-3924.
- Zhu, Yu, Lei Li, Chenguang Zhang, Gilberto Casillas, Zhengzong Sun, Zheng Yan, Gedeng Ruan, Zhiwei Peng, Abdul-Rahman O Raji and Carter Kittrell. 2012. "A seamless three-dimensional carbon nanotube graphene hybrid material." *Nature Communications* 3: 1225.

## Recent Progress of NPLS Technique and Its Applications in Measuring Supersonic Flows

YI Shi-he, \*CHEN Zhi, HE Lin, ZHAO Yu-xin, TIAN Li-feng, WU Yu

College of Aerospace Science and Engineering, National University of Defense Technology, China

\*Corresponding author: gfkdcchenzhi@163.com

### Abstract

Experimental method is very important and effective to study supersonic turbulence. However, because of the complexity and instability of supersonic turbulence, measuring its fine structures is very difficult for most measurement methods. Nano-tracer planar laser scattering (NPLS) is a new flow visualization technique, which was developed by the authors' group in 2005. It can visualize temporal-resolved flow structure in a cross-section of instantaneous 3D supersonic flow at high spatiotemporal resolution. Many studies have demonstrated that NPLS is a powerful tool to study supersonic turbulence. In recent years, the authors of this paper have made great progresses in supersonic turbulence study using NPLS. And several techniques based on NPLS have been developed by the authors, such as NPLS-based density technique (NPLS-DT), which help us understand the density field of supersonic flows. This paper introduced NPLS technique for visualizing the fine structures of supersonic flows, and reviewed its applications in supersonic mixing layer, supersonic boundary layer, shock/boundary layer interaction, and so on. With its available application on measuring flow static parameters such as Reynold stress and turbulent kinetic energy, NPLS would contributes to the development of turbulence models for compressible flows.

Keywords: NPLS, supersonic turbulence, fine structure

### 0. Introduction

For the complexity and instability of the supersonic turbulence, measuring its fine structures becomes very difficult. The existing experimental methods have their own shortages for supersonic turbulence study, such as Schlieren, filtered Rayleigh scattering (FRS), and planar laser induced fluorescence (PLIF), and the main reasons are their low resolution and signal noise ratio (SNR) (YI 2009 a). NPLS, as a newly developed flow visualization technique by the authors' group, can visualize temporal-resolved flow structures in a cross-section of instantaneous 3D supersonic flow at high spatiotemporal resolution (ZHAO 2009 a). In recent years, Yi's many studies have demonstrating that NPLS is a powerful tool to study supersonic flow, especially for supersonic turbulence (YI 2009 a – YI 2006 c). In 2007, ZHAO et al visualized the flow structure of pressure unmatched supersonic mixing layer using NPLS, and discussed the influence of shock wave and expand wave on structures of mixing layer and the influence of pressure unmatched (ZHAO 2007 a). Based on NPLS, ZHAO Yu-xin, et al studied the shocklet in supersonic turbulent mixing layer, and in NPLS images the shocklets could be easily distinguished (ZHAO 2007 b). ZHAO et al studied the interaction between shock wave and turbulent mixing layer based on NPLS (ZHAO 2007 c), and observed the interaction between oblique shock wave and boundary layer and the influence of large vortex in mixing layer on oblique shock wave. In 2008, based on NPLS images of supersonic turbulent mixing layer, Yi et al studied the fractal dimension of transition region and turbulence region of supersonic mixing layer. And they found that in the transition region, the

fractal dimension increases with turbulence, and in the turbulence region, the fractal dimension doesn't vary apparently (ZHAO 2008). TIAN et al visualized the supersonic flow around a concave optical spheric conic model by NPLS, and the NPLS images revealed shock wave, expansion wave, turbulent boundary layer and wake in the flow ( TIAN 2009 a). In 2009, Yi et al studied a supersonic mixing layer with convective Mach number at 0.5. From the NPLS image of supersonic mixing layer, we can easily distinguish the fine structures, and estimate its transitional region. Based on the NPLS image, the control effect could be estimated easily (YI 2009 a). And based on the NPLS images, Yi et al analyzed geometrical character and temporal evolution of large-scale structure of turbulent boundary layer. In 2009, Yi Shi-he, et al introduced NPLS technique in detail (ZHAO 2009 a). Nanoparticles are used as NPLS tracer, and pulse planar laser is used as its light source. By recording location of the tracer particles with CCD, the flow structure with high spatiotemporal resolution can be imaged in NPLS image. In literature (ZHAO 2009 a), the flow-following ability and the scattering characteristics of nanoparticles were studied, and the results showed that the dynamic behavior and light scattering characteristics of nanoparticles make NPLS can image the supersonic flow structure at high spatiotemporal resolution and SNR.

Based on NPLS technique, several methods have been developed by the authors. In 2009, TIAN et al developed a density measurement method named NPLS-based density technique (NPLS-DT). This technique can measure planar instantaneous density field in 3D supersonic flow by calibrating the relationship between density field and gray of NPLS image, and has high spatiotemporal resolution (2009 b). In 2010, YI S H, et al proposed an aero-optical aberration measuring method – NPLS-based wavefront technique (NPLS-WT). This method has three significant innovations: (1) high spatiotemporal resolution; (2) it can avoid the integral effects and study the wavefront aberration induced by the flow field of interest locally; (3) it can avoid the influence from the test section wall boundary layers and environmental disturbances (TIAN 2010). Based on NPLS-DT and PIV techniques, measurements on Reynold stress of supersonic turbulence can be realized through special experimental arrangement.

## 1. NPLS Techniques

The authors have studies on measuring the structures of supersonic turbulence by non-intrusive method in recent years, including the traditional interferometry and the optical scattering. The results indicate that because of the influences of compressibility, shock wave, instability, and other factors, the traditional visualization and measurement methods encounter some difficulties. For supersonic flow, the flow visualization technique based on Mie scattering often cannot satisfy the requirement of following the flow faithfully, especially when there are shock waves. On the other hand, for the techniques based on molecule tracer, more expensive intensified CCD is necessary because of its weak signal. Thus, it is difficult to achieve high spatiotemporal resolution for these techniques.

Rapid developments and extensive applications of modern laser technology, imaging, image process technologies, and nanotechnology offer the opportunity for measuring the fine structures of supersonic flow. And in this condition, the authors developed NPLS technique several years ago, which can image fine structures of supersonic flow at high spatiotemporal resolution.

As shown in Fig. 1, the NPLS system is composed of light source system, nanoparticle generator, recording system, synchronization system, and a computer. The light source is a dual-cavity Nd: Yag laser, whose wavelength is 532nm, laser pulse width is 6ns, and pulse energy is 350mJ. A laser sheet with thickness about 0.5mm is formed by the sheet optics system, and then illuminates the flow region of interest. The nanoparticle generator is driven by high pressure, and the concentration

of the output particles can be adjusted. The recording system is an interline transfer CCD whose resolution is  $2048 \times 2048$  and the shortest time interval of double-exposure is  $0.2 \mu\text{s}$ . The synchronizer receive signals sent from the computer, and control the time sequences of laser and the CCD to make sure that the two laser beams are exposed in the frames of dual-exposure respectively. The computer not only sends synchronization signals to the synchronizer, but also stores and processes NPLS images. With the dual-exposure technique, NPLS can measure the instantaneous flow structure, and the temporal evolution of the flow between the two pulses also can also be yielded.

The flow-following ability of the NPLS tracer particle in supersonic flow was studied from particle dynamics by ZHAO Y X, et al (ZHAO 2009 a), and the particle diameter was measured with oblique shock wave calibration experiment, as shown in Fig. 2. The effective diameter of nanoparticle of NPLS is  $42.5 \text{ nm}$ , and its relaxation time is  $66.3 \text{ ns}$ . As a flow visualization technique, NPLS focuses on holistic scattering character of a cluster of particles, whose scattering character can be calculated from Mie scattering theory, and the results revealed that its scattering character is relative to scattering angle, wavelength of incident laser, its diameter and refractive index (ZHAO 2009 a).

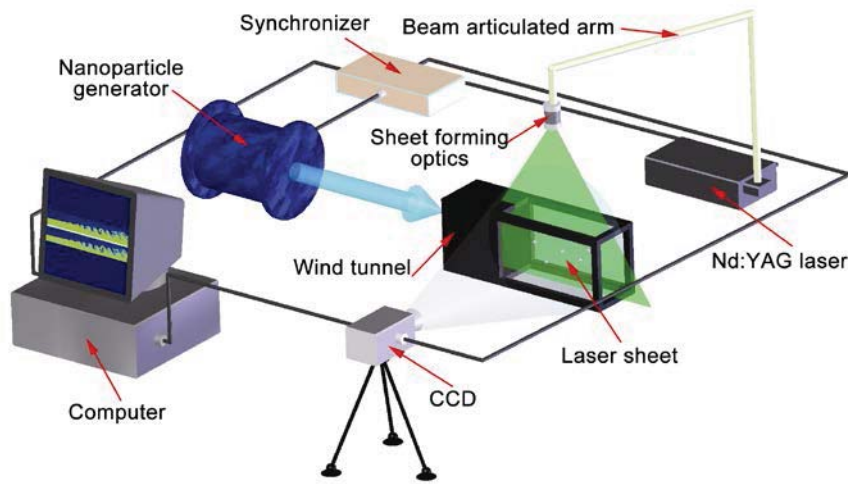
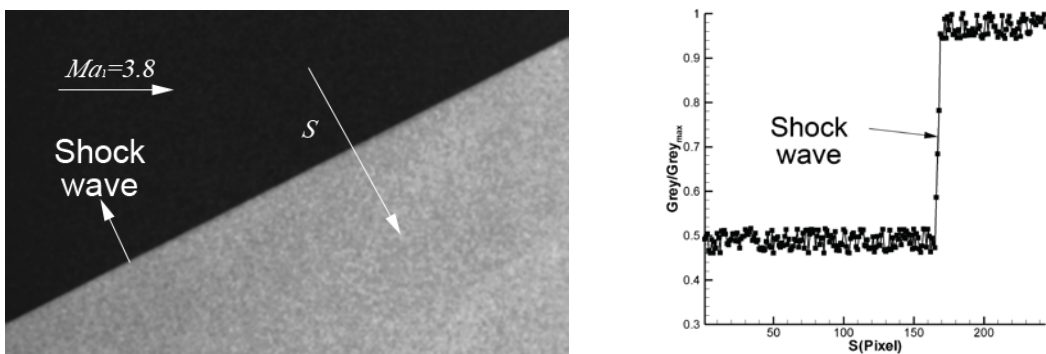


Fig. 1 The sketch of NPLS system



NPLS image of oblique shock wave (b) Relative grey along S  
 Fig. 2 NPLS image of shock wave and Relative grey across it

## 2. NPLS application in supersonic flows

For the advantages of NPLS in measuring fine structures of supersonic turbulence, several typical supersonic flows were studied, including supersonic mixing layer and boundary layer, shock/boundary layer interaction and the flow around a spheric conic model.

### 2.1 Supersonic mixing layer

In the past several years, spatiotemporal characteristic of supersonic mixing layers with convective Mach number 0.12, 0.21, 0.24, 0.32, 0.50 and 0.60 were studied by the authors (ZHAO 2008). The supersonic mixing layer wind tunnel is designed using double supersonic laminar nozzle and optical accesses for non-intrusive measurement, which can generate uniform flow filed with low noise, as shown in Fig.3. Changing the Mach number of the double nozzle, various convective Mach number can be gained for experimental study. The results revealed Kelvin-Helmholtz instable vortexes in the flow field. Its spatial features and temporal evolution can be yielded from NPLS images, which are shown in Fig. 4 and Fig. 5. ZHAO et al also studied its spanwise structure, and found the intriguing vortexes due to the secondary instability. Fig. 5 shows Reynold stress of supersonic mixing layer in this plane, which is quite valuable for constructing compressible turbulent models.

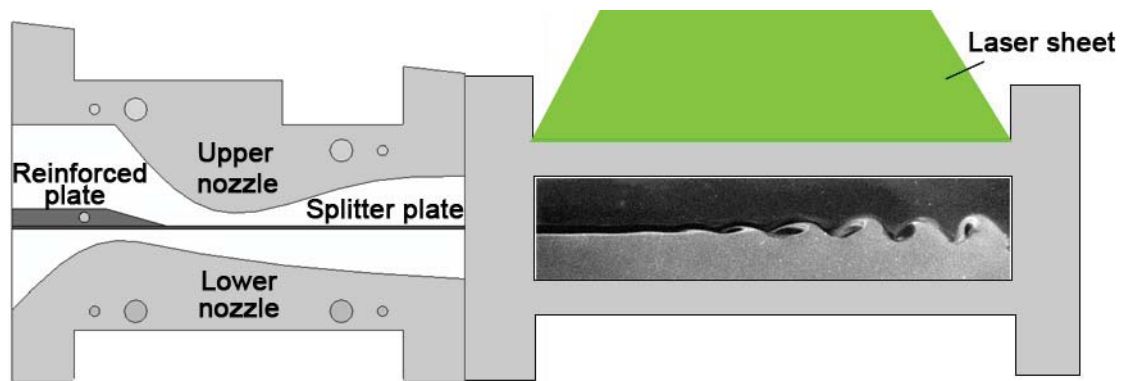


Fig. 3 Nozzle section and test section of the supersonic mixing layer wind tunnel

The NPLS technique has been widely used to study other important problems of supersonic mixing layer, including the velocity field of the transition process (ZHAO 2007 b), the turbulent structure with unmatched pressure (ZHAO 2007 a), the fractal characteristics of the mixing interface (ZHAO 2008), and the multiresolution analysis of the density field (ZHAO 2010).

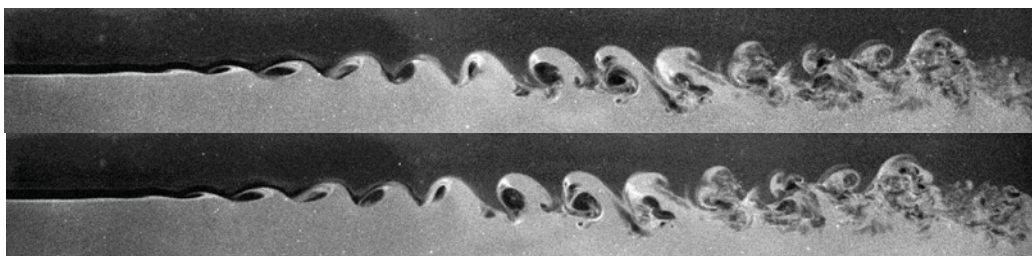


Fig. 4 NPLS images of K-H vortexes of supersonic mixing layer

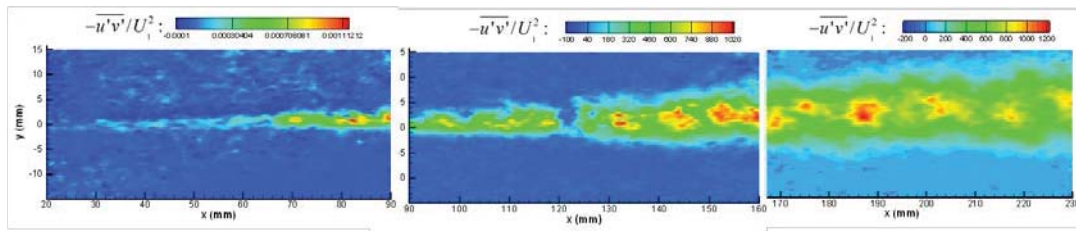


Fig. 5 Reynolds stress of supersonic mixing layer based on NPLS

## 2.2 Flow around a spheric conic model

The flow field around a spheric conic model in  $Ma=3.8$  flow was studied using NPLS, and its flow structure (TIAN 2009 a), density field (TIAN 2009 b), velocity field (TIAN 2010), and aero-optical effect (YI 2010) were studied. The structure of the flow around a spheric conic model is rather complex, which includes shock wave, expansion wave, boundary layer and wake. As shown in Fig. 6 are NPLS image of the flow field and the corresponding density field measured by NPLS\_DT. Compared with the results obtained by schlieren, the shock waves in NPLS image is much thinner. The reason is that the spatial resolution of the NPLS is much higher than that of schlieren. The density field in Fig.6 shows clearly the existence of flow structures mentioned above, and the transition of boundary layer.

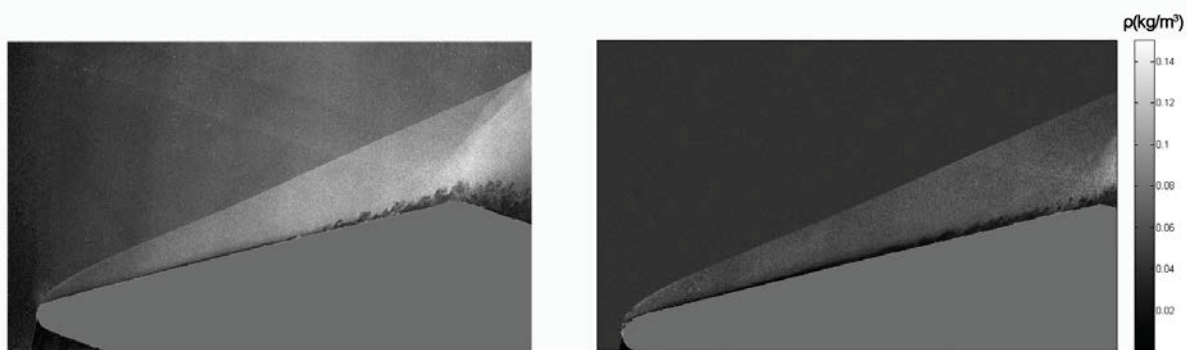


Fig. 6 NPLS image and corresponding density field of the flow around a spheric conic model in  $Ma=3.8$  flow

## 2.3 Supersonic boundary layer

Supersonic boundary layer, another typical flow, has been studying using NPLS in the past several years. The flow structure of the supersonic boundary layer in vertical plane and spanwise plane were captured by NPLS.

As shown in Fig. 7 is a NPLS image of flat plate boundary layer in vertical plane in  $Ma=3$  flow, and the flow region is 100-320mm from the leading edge of plate. Fig. 7 displays the whole transition process of the boundary layer. Until 180mm distant from the leading edge, the flow is still laminar. Then follows transition, and flow becomes fully developed from  $X=250$ mm. Fig. 8 and Fig. 9 are the flow regions within 170-250mm and 190-220mm from the leading edge of the plate, respectively. From these images, it is easy to find the development of instability and the emergence of hairpin vortexes. Fig. 10 is the NPLS image of fully developed turbulent boundary layer, whose flow region is 250-320mm from the leading edge. Compared with the cases in Fig. 8 Fig. 9, the flow structures in Fig. 10 are different absolutely and much more complex. However, the fine structures in the turbulent boundary layer were revealed clearly in Fig. 10 all the same. Fig. 11 (left)

shows the Spanwise NPLS image of supersonic boundary layer corresponding to Fig. 6. And in addition, the fully developed turbulent boundary layer of wind tunnel is different from that on a flat plate, as shown in Fig. 11 (right). By performing PIV technique, time-averaged streamwise velocity profiles at different locations and Reynolds stress distributions of turbulent boundary layer are present as shown in Fig. 12 to Fig. 14.

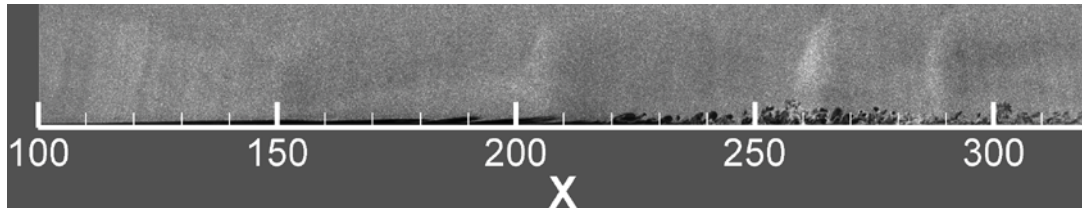


Fig. 7 NPLS image of supersonic boundary layer in Ma=3 flow

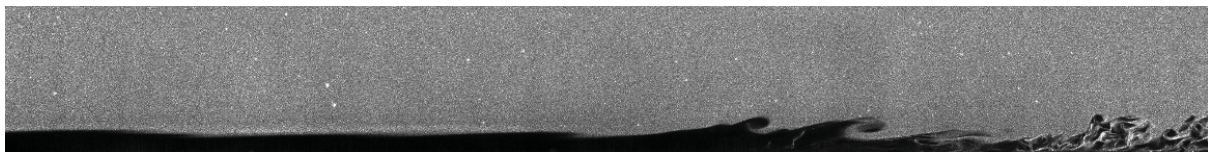


Fig. 8 NPLS image of supersonic boundary layer in the front of the plate

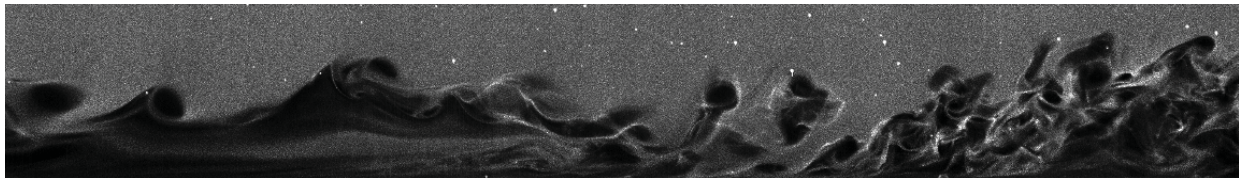


Fig. 9 NPLS image of supersonic boundary layer in the middle of the plate

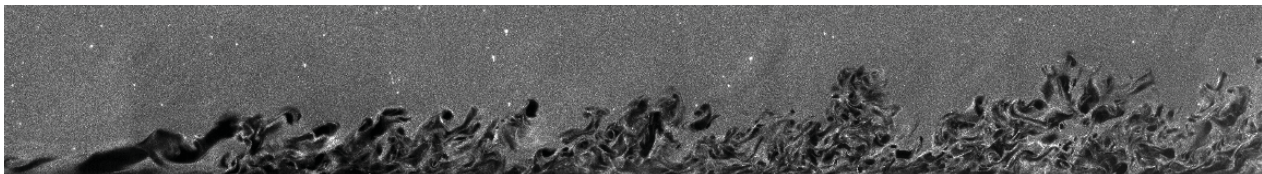


Fig. 10 NPLS image of fully developed supersonic turbulent boundary layer

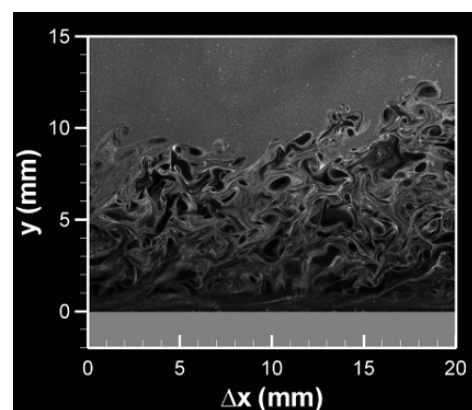
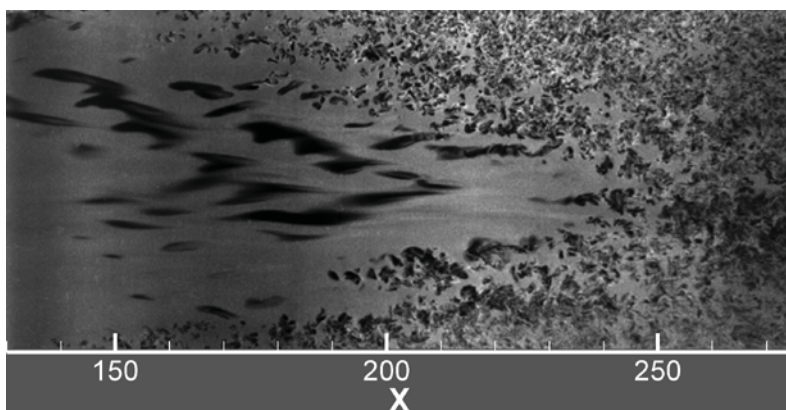


Fig. 11 Spanwise NPLS image of supersonic boundary layer in Ma=3 flow (left) and the fully developed supersonic turbulent boundary layer of wind tunnel (right)

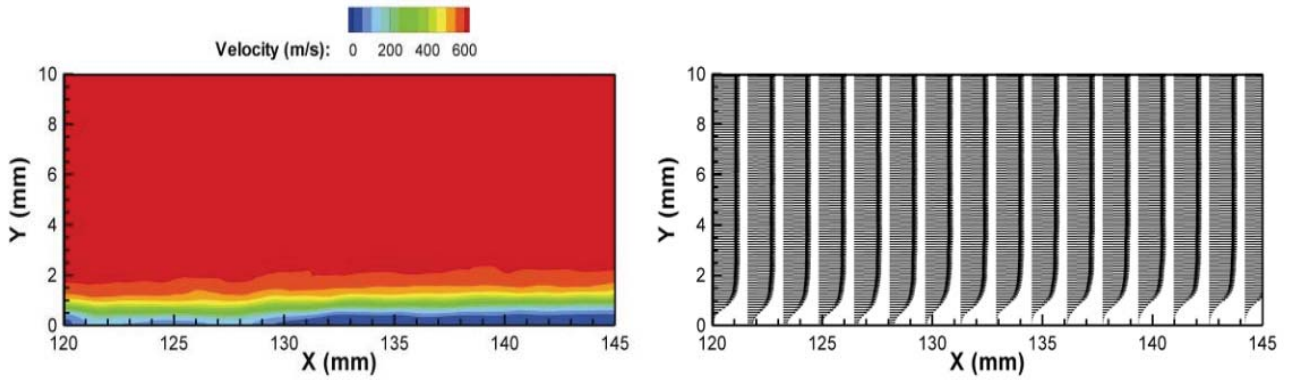


Fig. 12 Time-averaged velocity of supersonic boundary layer in the front of the plate corresponding to Fig.8

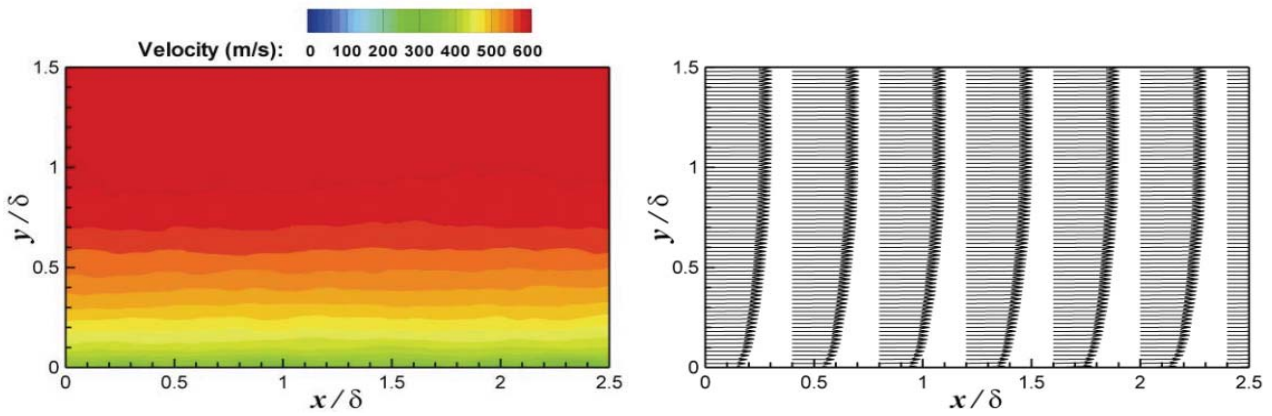


Fig. 13 Time-averaged velocity of fully developed supersonic turbulent boundary layer corresponding to Fig.10

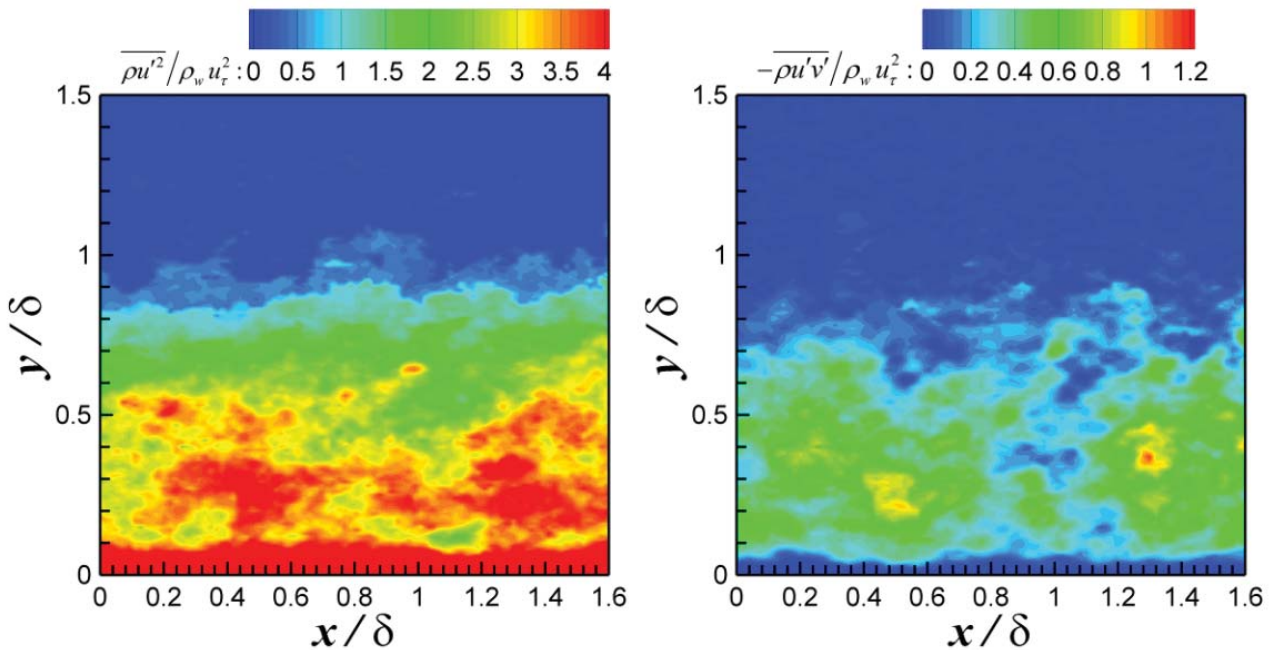


Fig. 14 Reynolds stress distribution of fully developed supersonic turbulent boundary layer corresponding to Fig.11 (right)



2.4 Shock/boundary layer interaction

Based on NPLS, the structure of shock/boundary layer interaction (SWBLI) was studied in this paper. As shown in Fig. 15 is the NPLS image of SWBLI in  $Ma=3$  flow, and its spatial resolution is  $43.5\mu\text{m}/\text{pixel}$ . The image revealed shock wave, expansion wave, turbulent boundary layer, and separation bubble. From the NPLS image, we can find that the vortex moves downstream, and its transfiguration is not obvious. Using NPLS\_DT, the density field of the flow field shown in Fig. 15 was measured at high spatial resolution. Density variation and temporal evolution of the SWBLI can be distinguished easily. Fig. 16 is the velocity field and the stream lines of the SWBLI flow field.

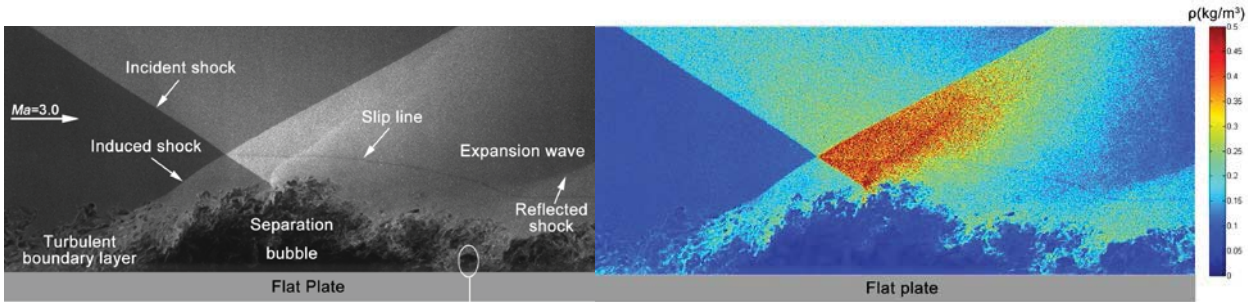


Fig. 15 NPLS image and the corresponding density field of shock/boundary layer interaction in  $Ma=3$  flow

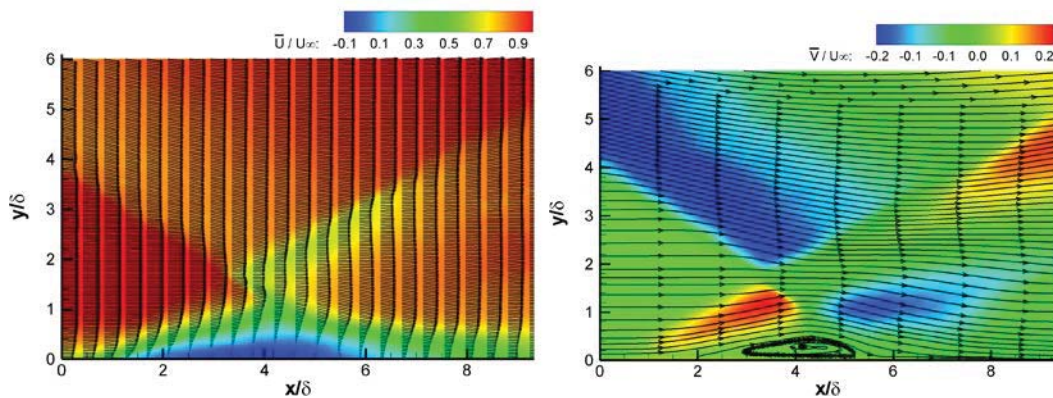


Fig. 16 Velocity field and the corresponding stream lines of the flow field as shown in 11

2.5 Supersonic Flow over a Compression Ramp

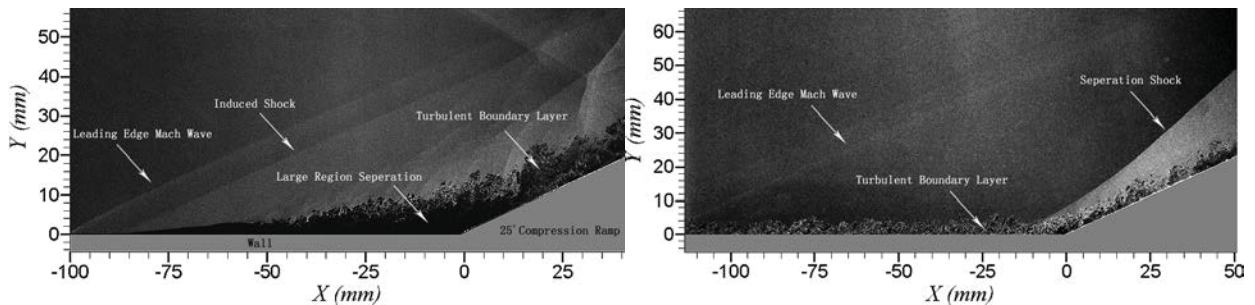


Fig. 17 Supersonic laminar flow (left) and supersonic turbulent flow (right) over a compression ramp

NPLS images of supersonic laminar/turbulent flow over a compression ramp are shown in Fig. 17, it can be seen distinctly from the images that there are obvious differences between the laminar flow

and the turbulent flow in compression ramp, even though the ramp angle is the same. For laminar flow, the development of the supersonic flow and its transition to turbulence are rapid. Flow separation occurs with the influence of adverse pressure gradient. Some typical flow structures such as K-H vortices, shear layer, separation shock and reattachment shock are visible clearly. However the thickness of turbulent boundary layer does not increase obviously and there is not evident separation in the flow field, as shown in Fig. 17 (right). The boundary layer adheres to the wall in the whole flow field. These experimental results of flow visualization have revealed that, compared with laminar flow, the performance of turbulent flow is more stable when suffering the effects of adverse pressure gradient, and is more difficult to separate.

### 3. Conclusions

From the results mentioned above, we can find that NPLS is a powerful tool to visualize the fine structures of supersonic turbulence and measure the corresponding instantaneous density and velocity field. A great number of experiments have been performed, and several important flow structures have been revealed by NPLS images. As a newly developed technique, however, NPLS and its application are still under development.

Currently, the measurement region of NPLS is only the scattering plane of laser pulse, and the temporal-resolved images are restricted to the pair obtained by frame, which prevents it from giving a more complete description of the flow structure. We are now updating the crucial components of the system to overcome these limitations, including employing multi-cavity laser to achieve high repetition frequency (hundreds of millions per second), employing proper CCD with very high recording speed and the synchronizer with accuracy of picosecond. Our ultimate goal is to synchronously measure several parameters (including density, velocity) of super flow with temporal correlation across many frames.

### Acknowledgement

The project is supported by National Basic Research Program of China (Grant NO. 2009 CB724100), National Natural Science Foundation of China (Grant NO. 11172326), innovation fund program for outstanding postgraduate students of NUDT (Grant NO. B120103) and Hunan Provincial Innovation Foundation for Postgraduate (CX2012B002).

### References

- YI S H, HE L and ZHAO Y X. (2009 a), A flow control study of a supersonic mixing layer via NPLS. *Sci China Ser G*, 2009, 52(12): 2001-2006.
- ZHAO Y X, YI S H, TIAN L F. (2009 a), Supersonic Flow imaging via nanoparticles. *Science China Ser E- Tech Sci*, 2009, 52(12): 3640-3648.
- ZHAO Y X, YI S H, TIAN L F. (2009 b), The quantificational measurement of supersonic mixing layer growth rate. *Journal of experiments in Fluid Mechanics*, 2009, 23(3): 100-103.
- YI S H, ZHAO Y X, TIAN L F. (2009 a), Recent advances of experimental study of supersonic mixing layer transition. *ACTA AERODYNAMICA SINICA*, 2009, 27: 114-119.
- TIAN L F, YI S H, ZHAO Y X. (2009 a) Flow visualization of supersonic flow around a concave optical bow cap model. *Journal of experiments in Fluid Mechanics*, 2009, 23(1): 15-17.
- ZHAO Y X, TIAN L F, YI S H. (2007 a) Experimental study of flow structure in pressure unmatched mixing layer [J]. *Journal of experiments in Fluid Mechanics*, 2007, 21(3): 14-17.
- ZHAO Y X, YI S H, HE L. (2007 b), The experimental research of shocklet in supersonic turbulent mix layer. *Journal of National University of Defense Technology*, 2007, 29(1): 12-15.
- ZHAO Y X, YI S H, HE L. (2007 c), The experimental study of interaction between shock wave and turbulence. *Chinese Science Bulletin*, 2007, 52(10): 1297-1301.
- ZHAO Y X, YI S H, HE L. (2008), The fractal measurement of experimental images of supersonic turbulent mixing layer. *Sci China Ser G-Phys Mech Astron*, 2008, 51(8): 1134-1143.

- ZHAO Y X. (2008), Experimental investigation of spatiotemporal structures of supersonic mixing layer. PhD Thesis, National University of Defense.
- YI S H, ZHAO Y X, TIAN L F. (2008), Advances of experimental study to transition of supersonic mixing layer. Proceedings of the 13th national symposium on shock wave and shock tube technology, ChangSha.
- YI S H, ZHAO Y X, HE L. (2006 a), Experimental study of temporal and spatial characters of the transition of supersonic mixing layer. Proceedings of the 12th national symposium on shock wave and shock tube technology, LuoYang.
- YI S H, ZHAO Y X, HE L. (2006 b), Fractal study of experiment images of supersonic mixing layer. Proceedings of the 12th national symposium on shock wave and shock tube technology, LuoYang.
- YI S H, ZHAO Y X, HE L. (2006 c), The quantificational measurement of supersonic mixing layer growth rate based on NPLS image. Proceedings of the 12th national symposium on shock wave and shock tube technology, LuoYang.
- ZHAO Y X, Yi S H, TIAN L F. (2009), An experimental study of aero-optical aberration and dithering of supersonic mixing layer via BOS. SCIENCE CHINA: Physics, Mechanics & Astronomy, 2009, 53(1): 81-93.
- TIAN L F, YI S H, ZHAO Y X. (2009 b), Study of density field measurement based on NPLS technique in supersonic flow. Sci China Ser G, 2009, 52(9):1357-1363.
- ZHAO Y X, YI S H, TIAN L F. (2010), Multiresolution analysis of density fluctuation in supersonic mixing layer. Sci China Tech Sci, 2010, 53(2): 584-591.
- YI S H, TIAN L F, ZHAO Y X. (2010), Aero-optical aberration measuring method based on NPLS and its application. Chinese Sci Bull, 2010, 55(31): 3545-3549.
- TIAN L F, YI S H, ZHAO Y X. (2010), PIV study of supersonic flow around an optical bow cap. Journal of experiments in Fluid Mechanics, 2010, 24(1): 26-29.
- ZHANG M L, YI S H, ZHAO Y X. (2007), The design and experimental investigations of supersonic length-shortened nozzle. ACTA AERODYNAMICA SINICA, 2007, 25(4): 500-503.
- HE L, YI S H, ZHAO Y X. (2010), The application of BOS in flow measurement. Journal of National University of Defense Technology, 2010, 31(1): 1-5.

## A study on the cloud effect on debris trajectory

C.K. Lee, \*J. Xu, and S.C. Fan

School of Civil & Environmental Engineering, Nanyang Technological University, Singapore.

\*Corresponding author: xu0003in@e.ntu.edu.sg

### Abstract

In this paper, the cloud effect on debris trajectory is investigated. The cloud effect discussed here refers to the reduction of the drag coefficients of debris at the initial stage of their trajectory after an internal explosion of an ammunition magazine, when the concrete magazine is just disintegrated into a cloud of closely packed concrete debris. The numerical results obtained with and without considering the cloud effect from the trajectory tracing tool DeThrow are used to study the influence on the debris initial landing position and kinetic energy. In addition, several different ways to simulate the influence of cloud effect are also discussed.

**Keywords:** debris trajectory, cloud effect, drag coefficient, DeThrow

### Introduction

Inhabited Building Distance (IBD) from an unexpected explosion of an earth-covered magazine traditionally attracts lots of interest from researchers and defense staff. The IBD depends on the trajectory of the debris generated from the explosion. Besides gravity, the flying motion of debris is influenced by air drag, lift force and moment of the debris, while the air drag depends on many factors such as debris size, shape, surface area, maximum section area perpendicular to the motion direction, and velocity (Baker 2007, Richards et al. 2008, Song and Ou 2010, Richards 2012). In the initial stage of explosion, the reinforced concrete (RC) structural members break into pieces as a debris cloud. The aerodynamic coefficients of the debris fragments are affected by the presence of other debris in their vicinities. This is especially the case, if one fragment is in the slipstream of another. As the fragments progress outward, such cloud interference effect on the aerodynamic coefficients is reduced significantly. In order to calculate the trajectories of debris more accurately, such cloud effect should be taken into account.

Van der Voort et al. (2010) proposed an approach in which a debris cloud is treated as an entire wall as the air passing through the cloud is very minor. The drag coefficient thus *increases* as the virtual large block has worse aerodynamic properties compared with each small piece of debris. Helland et al. (2007) found that the drag decreases in diluted cluster and increases when the cluster density is high. Schlüter et al. (2013) studied the interaction between two pieces of debris. In their study, the cloud effect is categorized into two types: side-by-side effect and trailing-leading effect. The side-by-side effect *increases* the air drag acting on debris, while the trailing-leading effect *decreases* the air drag.

In this study, a simplified approach is adopted to investigate the cloud effect on the debris flight trajectory. In the simplified approach, a reduction function is multiplied with the air drag coefficient to simulate the cloud effect. The simplified approach is

used in the Kasun test which is presented in (Fan et al. 2010) to study the cloud effect.

### Flight equation

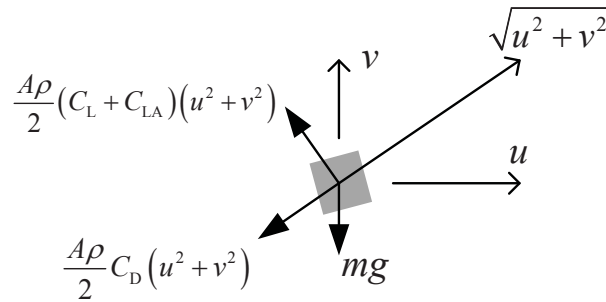
As shown in Figure 1, the flight equation can be written as (Tachikawa 1983, Tachihawa 1988, Chakraverty et al. 2001, Baker 2007):

$$M \frac{d^2x}{dt^2} = M \frac{du}{dt} = -\frac{A\rho}{2} (C_D \cos \alpha + (C_L + C_{LA}) \sin \alpha) (u^2 + v^2) \quad (1)$$

$$M \frac{d^2y}{dt^2} = M \frac{dv}{dt} = -\frac{A\rho}{2} (C_D \sin \alpha + (C_L + C_{LA}) \cos \alpha) (u^2 + v^2) - Mg \quad (2)$$

$$I \frac{d^2\theta}{dt^2} = M \frac{d\omega}{dt} = \frac{(C_M + C_{MA}) A l \rho}{2} (u^2 + v^2) \quad (3)$$

where  $\rho$  is the air density,  $A$  is the projected area facing the flow,  $C_D$ ,  $C_L$ ,  $C_{LA}$ ,  $C_M$  and  $C_{MA}$  are the coefficients of drag due to translational motion, lift due to translational motion, lift due to auto-rotation (magnus force), moment due to translational motion and moment due to auto-rotation (magnus moment), respectively.



**Figure 1. The flight state of debris**

In the present study, the effect from  $C_M$  and  $C_{MA}$  are excluded. The coefficients  $C_D$ ,  $C_L$  and  $C_{LA}$  are expressed as (Schlüter et al. 2013):

$$C_D = S_p C_{D,sphere} + (1 - S_p) C_{D,cube} \quad (4)$$

$$C_L = (1 - S_p) C_{L,cube} \quad (5)$$

$$C_{LA} = \frac{2\pi\omega R\alpha}{\alpha\sqrt{u^2 + v^2} + 190\pi\omega R} \quad (6)$$

In Eqs. (4) and (5),  $S_p = (V_{debris} - V_{cube}) / (V_{ellipsoid} - V_{cube})$  is the debris sphericity,  $C_{D,sphere}$  and  $C_{D,cube}$  are the drag coefficients for spherical and cubic debris, respectively, and  $C_{L,cube}$  is the lift coefficient for cubic debris. It should be noted that the lift coefficient for spherical debris is zero. In Eq. (6),  $R$  is the debris average radius,  $\alpha = 2R/L_p$  is the aspect ratio and  $L_p$  is the longest size of the debris along the rotation axis. The detailed expressions of  $C_{D,cube}$  and  $C_{L,cube}$  are referred to (Schlüter et al. 2013).

### Cloud effect

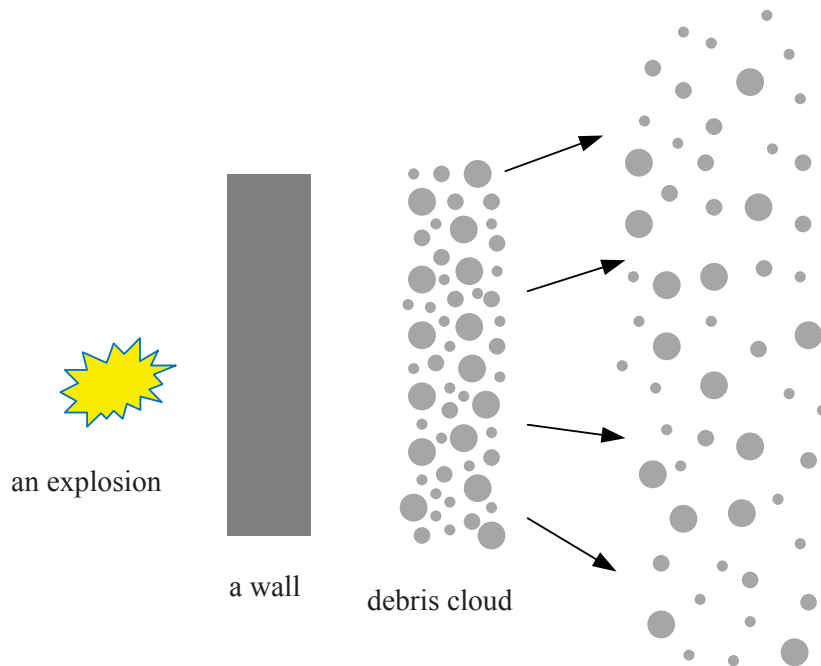
In a simulation, it is very hard to conduct a precise calculation on the air drag with cloud effect applying on each piece of debris. It is mainly due to the presence of a huge number ( $>100k$ ) of debris which makes it extremely costly to trace the distances between each two pieces of debris at every time step during trajectory calculation. Thus, a simplified approach is employed to consider the cloud effect in the present study.

In the present study, a correction parameter  $\chi$  is introduced into the algorithm. The coefficients of the air drag and lift with cloud effect can be written as

$$C_D = \chi C_{D,\text{free}}, C_L = \chi C_{L,\text{free}} \text{ and } C_{LA} = \chi C_{LA,\text{free}} \quad (7)$$

where the subscript 'free' refers to the coefficient for individual debris without cloud effect.

As shown in Figure 2, in the debris cloud, most of the debris hides behind the front debris and the drag on the back debris is very minor. Hence, when considering cloud effect, the drag coefficient and the lift coefficients for most of the debris should have a smaller value.



**Figure 2. The debris cloud**

In the present study, two kinds of reduction functions, namely a ramp function and a step function, are adopted to express the correction parameter  $\chi$  as:

The ramp function:

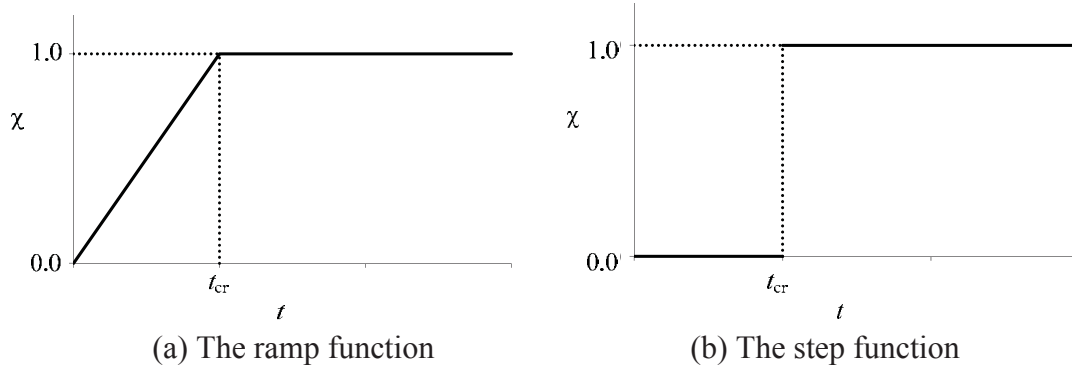
$$\chi = \begin{cases} t/t_{\text{cr}} & t \leq t_{\text{cr}} \\ 1.0 & t > t_{\text{cr}} \end{cases} \quad (8)$$

and

The step function:

$$\chi = \begin{cases} 0.0 & t \leq t_{cr} \\ 1.0 & t > t_{cr} \end{cases} \quad (9)$$

where  $t_{cr}$  is the critical time after which cloud effect is negligible. This parameter reflects the influence from the cloud effect on the air drag. The plots corresponding to Eqs. (8) and (9) are shown in Figure 3(a) and (b), respectively.



**Figure 3 The reduction function  $\chi$**

### Numerical results

In this section, the numerical simulation results are presented. The Kasun test presented in Fan et al. (2010) is employed in this study. The detonation is 2.5kg of TNT in the test. The numerical simulation for the disintegration of the magazine was conducted by the commercial package LS-DYNA. The numerical modelling was run for 0.008 second and the debris initial conditions at launching were collected for the present study.

Three cases are tested in the present study, including the case without cloud effect, the cases with the ramp function and the step function. For the two cases considering cloud effect, two critical time,  $t_{cr} = 0.1$  second and 1.0 second, are used. It is noted that in the case without cloud effect, the average time for the debris first impact on the ground is around 3.2 second from the numerical simulation. Hence,  $t_{cr} = 1.0$  second should be much greater than actual  $t_{cr}$  in the real test. However, as a numerical study on the influence from the parameter  $t_{cr}$ , the value of 1.0 can be regarded as an upper bound for the value of  $t_{cr}$ .

The two profiles of  $\chi$  (the ramp function and the step function) and the values of  $t_{cr}$  ( $t_{cr} = 0.1$ s and 1s) are studied. The average horizontal distances of debris flight for the different numerical cases are listed in Table 1. In Table 1, two distances are listed for each case, where  $d_c$  is the average distance with cloud effect and  $d_{nc}$  is the average distance without cloud effect. The first impact refers to the distance that debris first impact on the ground, while the final location includes the ricochet of debris impacting on the ground. In Table 1, the values in the bracket are the relative differences in percent which are calculated by  $\varepsilon = (d_c - d_{nc})/d_{nc} \times 100\%$ .

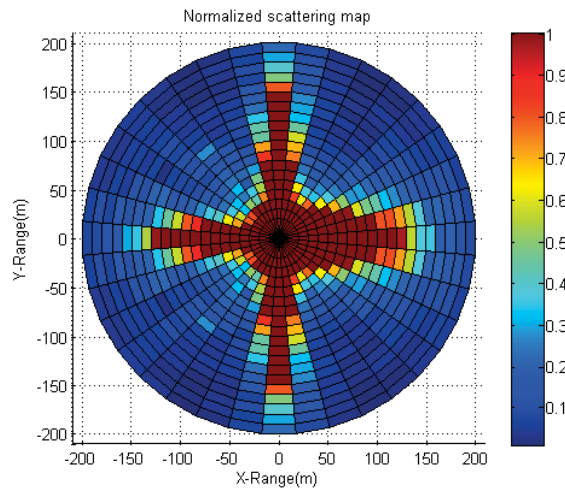
It can be found from Table 1 that the cloud effect has minor influence on the average horizontal distance of debris flight. The increase on the average distance is no more

than 8%, even when the upper bound of  $t_{cr}$  (1s) is employed. On the other hand, the profile of  $\chi$  does not influence on the average debris flight distance.

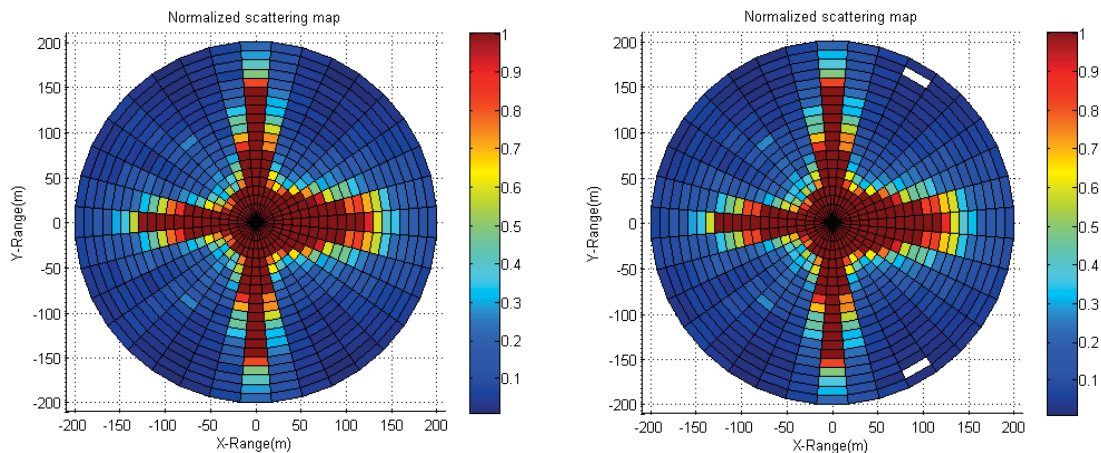
**Table 1. The average horizontal distance of debris**

	$t_{cr}$ (s)	$d_{nc}$ (m)	$d_c$ (m)	
			the ramp function	the step function
the first impact	0.1	94.88	95.83 (1.00%)	96.42 (1.62%)
	1		101.98 (7.48%)	101.04 (6.49%)
the final location	0.1	100.94	101.84 (0.89%)	102.00 (1.05%)
	1		108.18 (7.17%)	107.46 (6.46%)

The distributions of the location of debris first impact on the ground for cases without cloud effect, with cloud effect for  $t_{cr} = 0.1s$  and  $1s$  are shown in Figs. 4, 5 and 6, respectively.



**Figure 4. The location of the debris first hit without cloud effect**

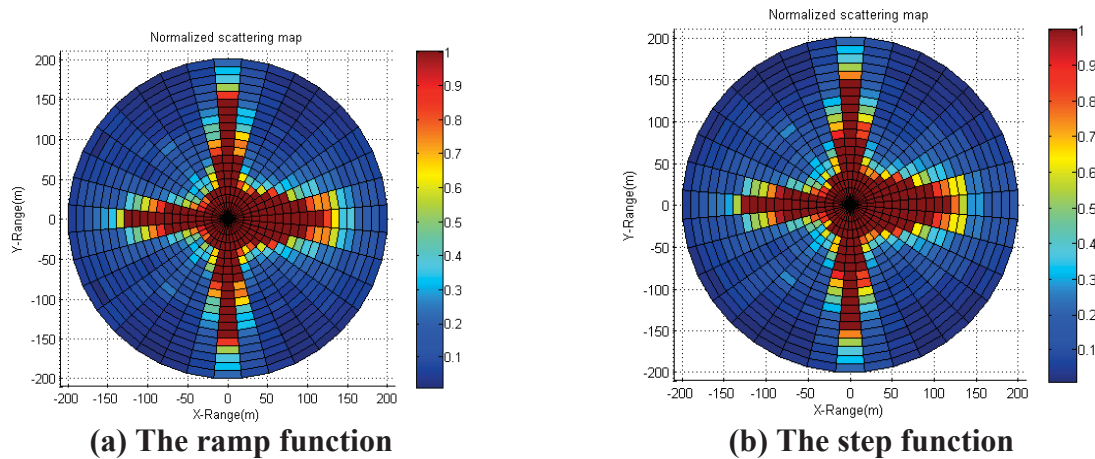


**(a) The ramp function**

**(b) The step function**

**Figure 5. The location of the debris first hit with  $t_{cr}=0.1s$**





**Figure 6. The location of the debris first hit with  $t_{cr}=1s$**

By comparing Figs. 5 and 6 with Fig. 4, it can also be found that the distribution of the debris first impact locations has shown a very minor change if the cloud effect is taken into account in the numerical analysis.

## Conclusions

In this study, the cloud effect on the debris trajectory after an explosion is presented. As it is very costly to simulate the cloud effect at every time step, a simplified approach is employed. In the simplified approach, a reduction function is used to consider the reduction of air drag on debris. It is found that the cloud effect has only limited influence on the distribution of the debris flight trajectory.

## Acknowledgements

This research was supported by a research grant provided by the Defence Science & Technology Agency (DSTA), Singapore, under the Protective Technology Research Centre, Nanyang Technological University, Singapore. Any opinions, findings and conclusions expressed in this paper are those of the writers and do not necessarily reflect the view of DSTA, Singapore.

## Reference

- Baker, C. J. (2007), The debris flight equations. *Journal of Wind Engineering and Industrial Aerodynamics* 95(5): 329-353.
- Chakraverty, S., I. Stiharu and R. B. Bhat (2001), Influence of aerodynamic loads on flight trajectory of spinning spherical projectile. *AIAA Journal* 39(1): 122-125.
- Fan, S. C., Q. J. Yu, Y. W. Yang, H. S. Lim and K. W. Kang (2010), Study of debris throw and dispersion after break-up of reinforced concrete structure under internal explosion. 34th DoD Explosive Safety Seminar. Portland, Oregon, USA.
- Helland, E., H. Bournot, R. Occelli and L. Tadrast (2007), Drag reduction and cluster formation in a circulating fluidised bed. *Chemical Engineering Science* 62(1-2): 148-158.
- M.M. van der Voort, R. J. M. v. A., Y.S. Khoe (2010), Ballistic Filtering for improved trajectory calculations in the KG software.
- Richards, P. J. (2012), Dispersion of windborne debris. *Journal of Wind Engineering and Industrial Aerodynamics* 104-106: 594-602.
- Richards, P. J., N. Williams, B. Laing, M. McCarty and M. Pond (2008), Numerical calculation of the three-dimensional motion of wind-borne debris. *Journal of Wind Engineering and Industrial Aerodynamics* 96(10-11): 2188-2202.
- Schlüter, J. U., A. Sarkar and S. R. Boopathy (2013), Prediction of explosion hazards from earth covered magazine, Nanyang Technological University.

- Song, F. and J. Ou (2010). Windborne debris damage prediction analysis. *Frontiers of Architecture and Civil Engineering in China* 4(3): 326-330.
- Tachihawa, M (1988). A method for estimating the distribution range of trajectories of wind-borne missiles. *Journal of Wind Engineering and Industrial Aerodynamics* 29: 175-184.
- Tachikawa, M. (1983), Trajectories of flat plates in uniform flow with application to wind-generated missiles. *Journal of Wind Engineering and Industrial Aerodynamics* 14(1-3): 443-453.
- Van Der Voort, M. M., van Amelsfort, R. J. M., and Khoe, Y. S. (2010), Ballistic Filtering for improved trajectory calculations in the KG software. *TNO report, TNO-DV 2010 C071*

# General Ray Method and Rotating Projection Algorithm for Fast Recognition of Discreet Micro Scale Compound Structures

**Grebennikov Alexandre**

Facultad de ciencias Físico Matemáticas  
Benemérita Universidad Autónoma de Puebla,  
Av. San Claudio y Río verde, Ciudad Universitaria, CP 72570, Puebla, MÉXICO  
[agrebe50@yahoo.com.mx](mailto:agrebe50@yahoo.com.mx)

## Abstract

A new fast method of high resolvability for identification of compound structures is proposed. Its mathematical model is constructed on the basis of General Ray Principle, proposed by the author for distribution of different, in particular electrostatic and thermostatic, fields. Proposed model leads to the classic Radon transformation that appears as specific element in new General Ray Method, constructed using explicit formulas and realized as a fast numerical algorithm. Proposed General Ray and Rotating Projection algorithms open possibility of high resolvability and fast computer recognition of compound structures with micro components. Computer simulation of developed scheme is realized as MATLAB software and justified by numerical experiments.

**Key-Words:** Micro Scale Compound Structures, General Ray Method, Rotating Projection algorithm.

## Introduction

In creation and construction of modern artificial materials it appears the necessity of recognition of compound structures with micro and nano-particles. Recognition of compound structures with elements that have different thermo-conductivities o electro-conductivities (permittivity) is possible by Computer Tomography (CT). In a plane case considering problem can be mathematically described (Williams, R.A. and Beck, M.S., 1995) as a coefficient inverse problem for the Laplace type equation, written in the divergent form

$$\frac{\partial}{\partial x}(\varepsilon(x, y)u'_x(x, y)) + \frac{\partial}{\partial y}(\varepsilon(x, y)u'_y(x, y)) = 0, \quad (1)$$

where  $(x, y) \in \Omega$  some limited open region on a plane,  $u(x, y)$  is a temperature or electrical potential, the function  $\varepsilon = \varepsilon(x, y)$  characterizes thermo-conductivity or electro-conductivity (permittivity) of a media.

In traditional statement (Williams, R.A. and Beck, M.S., 1995) it is supposed also that functions  $J_n(x, y)$ ,  $u^0(x, y)$  are known on the boundary curve  $\Gamma$  and the next boundary conditions are satisfied:

$$\varepsilon(x, y) \frac{\partial u(x, y)}{\partial n} = J_n(x, y), \quad (x, y) \in \Gamma, \quad (2)$$

$$u(x, y) = u^0(x, y), \quad (x, y) \in \Gamma, \quad (3)$$

where  $\frac{\partial}{\partial n}$  is the normal derivative in the points of the curve  $\Gamma$ .

Eq. (1) – (3) serve as the mathematical model of CT, if there is a family of boundary conditions that corresponds to different angles of scanning scheme. Traditional approach for resolving CT leads to nonlinear ill-posed problem.

### General Ray Method

To construct a new mathematical model for CT we use the General Ray Principle (Grebennikov, 2005), i.e., consider the physic field as the stream flow of "general rays". Each one of these rays corresponds to some straight line  $l$ . The main idea of the General Ray Principle consists in reduction a Partial Differential Equation to a family of Ordinary Differential Equations. Let the line  $l$  has the parametric presentation:

$$x = p \cos \varphi - t \sin \varphi, \quad y = p \sin \varphi + t \cos \varphi, \quad \text{where } |p| \text{ is a length of the perpendicular,}$$

passed from the centre of coordinates to the line  $l$ ,  $\varphi$  is the angle between the axis  $X$  and this perpendicular (Radon, J., 1917). Hence, using this parameterization for the line  $l$ , we shall consider the functions  $u(x, y)$  and  $\varepsilon(x, y)$  for  $(x, y) \in l$  as functions (traces)  $\bar{u}(t)$  and  $\bar{\varepsilon}(t)$  of variable  $t$ . Let suppose that domain  $\Omega$  is the circle of radius  $r$ . Considering Eq. (1) on the line  $l$ , we obtain for every fixed  $p$  and  $\varphi$  the ordinary differential equation for traces

$$\left( \bar{\varepsilon}(t) \bar{u}'_t(t) \right)' = 0, \quad |t| < \bar{t}, \quad \bar{t} = \sqrt{r^2 - p^2}. \quad (4)$$

We suppose that functions  $v(p, \varphi)$  and  $J(p, \varphi)$  are given and we can write boundary conditions

$$\bar{\varepsilon}(-\bar{t})\bar{u}'_t(-\bar{t}) = J(p, \varphi) , \quad (5)$$

$$\bar{u}(\bar{t}) - \bar{u}(-\bar{t}) = v(p, \varphi) . \quad (6)$$

Eq. (4) – (6) are considered as the new basic mathematical model for CT (Grebennikov, 2005).

If different components in the considered structure have the smooth distribution, therefore functions  $\bar{u}'_t(t)$  and  $(\bar{\varepsilon}(t)\bar{u}'_t(t))'$  are continuous. Out of the domain  $\Omega$  we define extensions of functions  $u(x, y)$ ,  $\varepsilon(x, y)$  and the function  $v(p, \varphi)/J(p, \varphi)$  as zero. Integrating twice the Eq. (4) on  $t$  and using boundary conditions (5) - (6), we obtain for  $\varepsilon(x, y)$  the next formula for scanning General Ray (*GR*) method

$$\varepsilon(x, y) = 1/R^{-1} \left[ \frac{v(p, \varphi)}{J(p, \varphi)} \right], \quad (7)$$

where  $R^{-1}$  is the inverse Radon transform operator (Radon, J., 1917). *GR*-method gives the explicit solution of the inverse coefficient problem for considering case. It is generalized and applied also for structures with piecewise constant characteristics (Reyes Mora, S. and Grebennikov, Alexandre I., 2009). We have constructed the numerical realization of Eq. (7) that we call "*GR*-algorithm". This algorithm is fast, because it does not require solving any equation and the Radon transform can be inverted by fast manner using discrete Fast Fourier Transform algorithm.

### Numerical Experiments with *GR*-algorithm

We tested scanning *GR*-algorithm on mathematically simulated model examples for structure with piecewise-constant permittivity. The scheme of solution of the corresponding example consists of the steps presented in details at papers (Reyes Mora, S. and Grebennikov, Alexandre I., 2009), (Grebennikov, 2011).

Here we considered a plane circle of radius 1mm with basic permittivity  $\mathcal{E}_0(x, y) = 1$  and two different internal elements as circles of radiuses  $r_i$ ,  $i=1,2$ , with permittivity  $\mathcal{E}_1(x, y) = 2$ ,  $\mathcal{E}_2(x, y) = 3$ .

At part (a) of Fig. 1, 2 the exact structures are shown; at part (b) – reconstructed structures, for  $r_1=0.05$  mm,  $r_2=0.005$  mm,  $r_1=0.0015$  mm,  $r_2=0.001$  mm correspondently. We have used discretization on the bi-dimensional red with  $N \times N$  nodes and made calculation at the PC with processor INTEL CORE 2 DUO T5250. For the first example  $N=1001$ , time of reconstruction – 207.1 sec; in the second example  $N=3001$ , time of reconstruction – 5950 sec.

So, we see that constructed algorithms needs for its realization a lot of time for the case of micro particles in simulated compound structure, because it requires

sufficiently large  $N$ . In paper (Grebennikov and others, 2007), it was proposed the simplified variant of scanning algorithm without application of the inverse Radon transform. We call it as Rotating Projection Algorithm (*RPA*). In (Grebennikov and others, 2007) this algorithm was applied for electric tomography. Here we use this idea and develop the approach for abstract Discrete Computer Tomography.

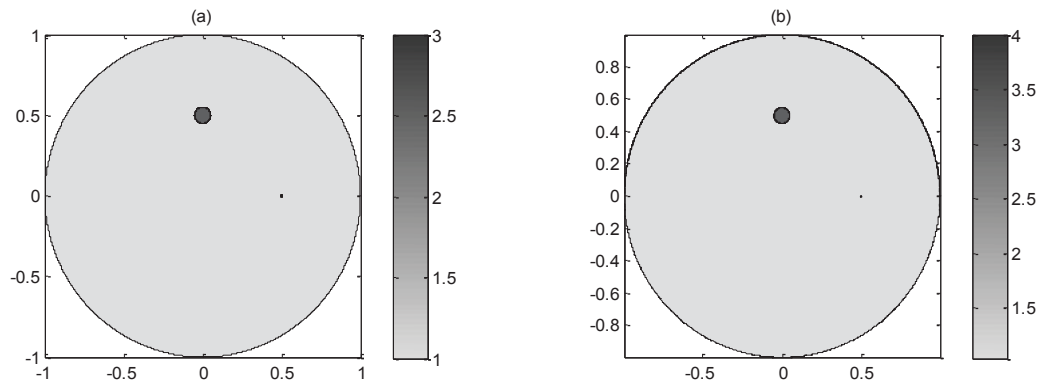


Figure 1. The first example,  $r_1=0.05$ ,  $r_2=0.005$ ;  
 (a)– exact distribution; (b) – reconstructed by GR-algorithm distribution.  
 $N=1001$ , time of reconstruction – 207.1 sec

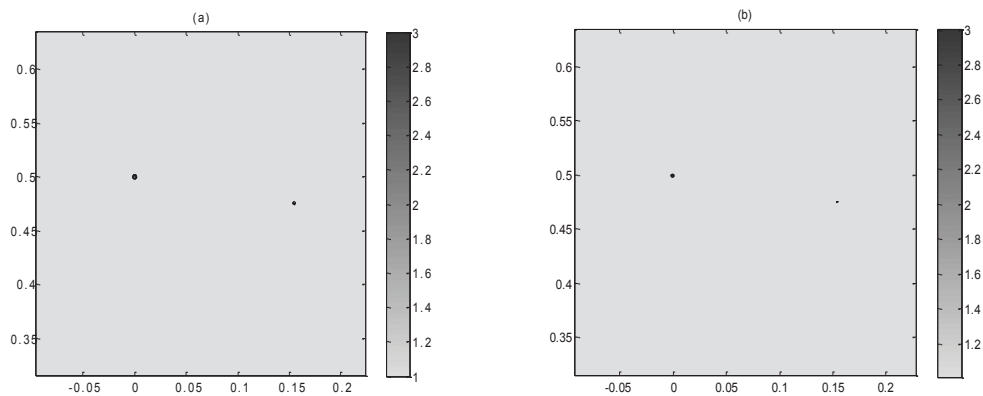


Figure 2. Scaled image of the second synthetic example;  $r_1=0.0015$ ,  $r_2=0.001$ ;  
 (a)– exact distribution; (b) – reconstructed by GR-algorithm distribution.  
 $N=3001$ , time of reconstruction – 5950 sec.

### Rotating Projection Algorithm and Numerical Experiments

Let us explain the idea of this algorithm in the plane case. Suppose that we know values of function  $\bar{v}(p, \varphi)$  (projections), which characterizes the intensiveness of rays, which have passed through the object for some fixed angles  $\varphi$  and all linear coordinates  $p$  of scanning. By another words, we know for some fixed angles

$\varphi_i, i=1, \dots, n$  corresponding number of one-dimensional images (projections), which present intensiveness as functions of one variable  $p$ .

We need the next steps.

1. Prolongation on a plane of calculated projections  $\bar{v}(p, \varphi_i)$  for every  $p$  along the direction, corresponding to angle  $\varphi_i$ , to obtain the extended two dimensional image.
2. Rotation, i.e., changing number  $i$  (scanning for different  $\varphi$ ) of prolonged projections and localization of the areas of intersection of projections with the same values of intensiveness.

In considering simulated numerical example we have homogeneous substance in the region and two elements with other characteristics. If we do not interesting in the exact geometrical form of the element and want to localize them as a rectangles, it is sufficient (Grebennikov and others, 2007) to use  $n=2$ . We suppose also that  $\varphi_1 = 0, \varphi_2 = 90 \text{ grad}$ , that means we have two orthogonal projections. So, our variable  $p$  is  $x$  for  $i=1$ , or  $y$  for  $i=2$ , and we can localize one dimensional images at exes X and Y, construct it's prolongations and realize the rotation with localization of intersections with the same intensiveness. To obtain the adequate entrance data we can use as  $\bar{v}(p, \varphi)$  recalculated function  $v(p, \varphi) / J(p, \varphi)$  in accordance to straight lines, at which corresponding projections appear. Graphical illustrations of calculations by MATLAB program realization of RPA are presented at Fig. 3 and 4. The time of reconstruction by RPA for the first example is 0.7628 sec., for the second example - 1.7972 sec.

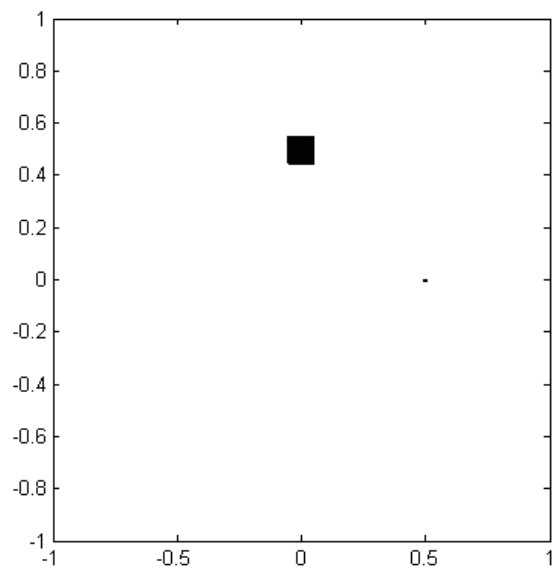


Figure 3. The structure of the first example, reconstructed by *RPA* for 0.7628 sec.

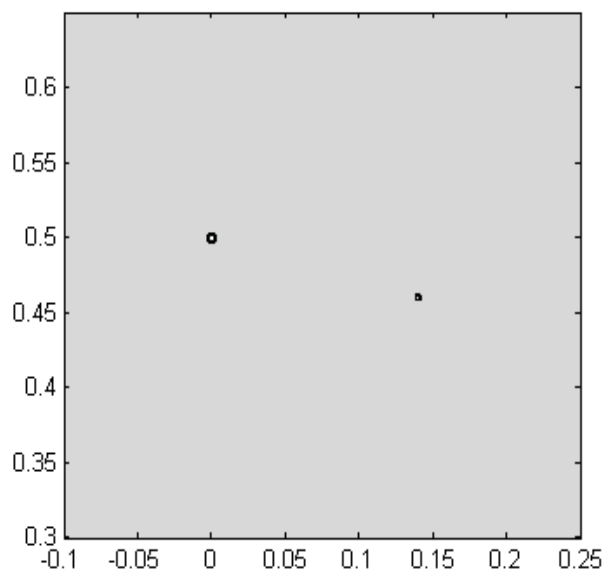


Figure 4. Scaled image of the second synthetic example, reconstructed by *RPA* for 1.7972 sec.

### Conclusions

A new mathematical model on the base of the *GRP* for recognition of compound structures by *CT* is considered. To resolve this model new *GR*- method, fast algorithms



and MATLAB software are constructed. The properties of the constructed algorithms and computer programs are illustrated by numerical experiments that demonstrate the possibility to reconstruct structures with micro-scale elements.

“Rotating Projection” algorithm is developed for the case of recognition of images on the base of data, obtained in computer tomography for objects that have the discreet structure. Good properties of the developed algorithm at recognition for very short time are demonstrated on numerical examples with simulated data.

### Acknowledges

The author acknowledges to CONACYT Mexico, Merited Autonomous University of Puebla Mexico and Aerospace School of Moscow Aviation Institute for approval of this investigation during the Probation Period at 2013 – 2014 years.

### References

- Williams, R.A. and Beck, M.S. (1995), *Process Tomography: Principles, Techniques and Applications*, Butterworth-Heinemann, Oxford.
- Grebennikov, A.I. (2005), A novel approach for solution of direct and inverse problems for some equations of mathematical physics. *Proceedings of the 5- th International conference on Inverse Problems in Engineering: Theory and Practice ( ed. D. Lesnic)*, Vol. II, Leeds University Press, Leeds, UK, chapter G04, pp. 1-10.
- Radon, J. (1917), *Über Die Bestimmung von Funktionen Durch Ihre Integrawerte Langs Gewisser Mannigfaltigkeiten*”, *Berichte Sachsische Academic der Wissenschaften, Leipzig, Math.-Phys.* K1. 69, pp. 262-267.
- Reyes Mora, S. and Grebennikov, Alexandre I. ( 2009), Unicidad de Solución del Problema Inverso de Identificación de Coeficiente en Ecuación de Tipo Laplace con Condiciones de Contorno Parcialmente Reducidos. *Boletín de la sociedad cubana de Matemática y Computación*, Numero especial Editorial de Universidad de Ciencias Pedagógicas “Enrique José Varona”, M-99.
- Grebennikov, A. (2011), General Ray Method for Solution of Inverse Coefficient Problems for Laplace Equation. *Proceedings of International Conference on Inverse Problems in Engineering*, May 4-6, 2011, Orlando, Florida, Centecorp Publishing, USA, pp. 7 – 13.
- Grebennikov, A. I., Vázquez Luna, J. G., Valencia Pérez, T. and Najera Enriquez, M. (2007), Realization of Rotating Projection Algorithm for Computer Tomography Using Visual Modeling Components of Matlab Package. *Proceedings of the VIII International Scientific-Technical Conference “Computing Modeling 2007”*, S.-Petersburg Polytechnic University, pp. 2-5.

## A Multi-Dimensional Limiter for Hybrid Grid

\* H. W. Zheng <sup>1</sup>

<sup>1</sup> State Key Laboratory of High Temperature Gas Dynamics, Institute of Mechanics, Chinese Academy of Sciences, Beijing 100190, China

\*Corresponding author: h.zheng@imech.ac.cn

### Abstract

For the finite volume method, the reconstruction step is employed to obtain the states for the calculation of numerical fluxes at the faces. To remove the non-physical oscillations, a limiting procedure is required. This limiting procedure is so important that it not only influence the numerical accuracy in the smooth regions but also affect the robustness of the solver. For the unstructured meshes, the design of the limiting procedure is not trivial. The well-known and wide-used limiting procedure is proposed by Barth and Jespersen in 1989 and lately improved by Venkatakrishnan in 1993. However, this method is too dissipative and the overshoot or undershoot phenomenon can still be observed. In this paper, a new limiter for hybrid grid is proposed. It limits the state variables of a face directly from the corresponding variables of this face's neighbor cells. It is so simple that it can be easily adopted in many solvers based on unstructured grid.

**Keywords:** finite volume, multi-dimensional limiter, hybrid grid.

### Introduction

A main computational challenge with nonlinear hyperbolic equations is the resolution of discontinuities. However, any linear scheme higher than first order accuracy cannot generate monotonic solutions. Hence, the non-linear limiting function is introduced to avoid numerical oscillations [1-5].

A good limiting function should be able to remove the non-physical oscillations nearby the shock and can also preserve the numerical accuracy in the smooth regions. Moreover, the limiter function should not affect the convergence to the steady state. Barth and Jespersen (1989) introduced the first limiter for unstructured grids. The Barth and Jespersen limiter is used to enforce a monotone solution. The main idea of their work is to avoid introducing oscillation is that no new local extrema are formed during reconstruction. The scheme consists of finding a value in each control-volume that will limit the gradient in the piecewise linear reconstruction of the solution. However, their method is rather dissipative which leads to smear discontinuities. Furthermore, the limiter may be active in smooth flow regions due to the numerical noise, which causes difficulties for steady state convergence. To improve the convergence, Venkatakrishnan (1993) proposed a smooth differentiable alternative of the minimum function in Barth-Jespersen. However, it does not preserve strict monotonicity, slight oscillations can be observed near shock discontinuities. Moreover, similar to Barth and Jespersen (1989), it is quite dissipative that predicted accuracy also cannot be guaranteed with the fixed stencil when these limiters are used.

In this work, a new multidimensional limiting procedure is proposed to limit the gradient in each direction independently. For each face of one cell, only the gradient along the direction between the two centroids is limited. This will reproduce a limited difference for each face. After having these limited differences, the unlimited differences and the limited differences for each face are limited secondly. This produces a new limited difference which is multidimensional in its very nature. The rest of paper is organized as follows. The governing equation and numerical method are described in section 2 and section 3 respectively. The numerical result and discussion is presented in section 4. The final section gives a summary about the main work of the paper.

## Governing equations

In this paper, the steady Favre-averaged Navier–Stokes equations with the two equation  $k-\omega$  turbulence model are considered,

$$\partial_t \int_{\Omega} U dV + \int_S F(U, \bar{n}) dS = 0 \quad (1)$$

$$\partial_t \int_{\Omega} \Xi dV + \int_S H(\Xi, \bar{n}) dS = \int_{\Omega} \Theta dV \quad (2)$$

Where  $U$  and  $\Xi$  are the state vectors,  $F$  and  $H$  are the normal flux vectors. They can be expressed as

$$U = \begin{pmatrix} \rho \\ \rho u \\ E \end{pmatrix}, F = F^c - F^v, F^c = u_n U + P \begin{pmatrix} 0 \\ \mathbf{n} \\ u_n \end{pmatrix}, F^v = \begin{pmatrix} 0 \\ [\tau] \cdot \mathbf{n} \\ ([\tau] \cdot u + q) \cdot \mathbf{n} \end{pmatrix}, \quad (3)$$

and

$$\Xi = \begin{pmatrix} \rho k \\ \rho \omega \end{pmatrix}, H = H^c - H^v, H^c = u_n \Xi, H^v = \begin{pmatrix} (\mu_L + \sigma_k \mu_{tur}) \nabla k \\ (\mu_L + \sigma_\omega \mu_{tur}) \nabla \omega \end{pmatrix} \cdot \mathbf{n}, \Theta = \begin{pmatrix} P_k - \rho \varepsilon \\ \alpha \omega P_k / k - \beta \rho \omega^2 \end{pmatrix}. \quad (4)$$

Here,  $\rho$  is the density,  $u$  is the velocity,  $E$  is the total energy,  $P$  is the pressure,  $[I]$  is the identity tensor,  $q$  is the heat flux,  $[\tau]$  is the stress tensor,

$$[\tau] = (\mu_L + \mu_{tur}) \left\{ \nabla \bar{u} + \nabla^T \bar{u} - \frac{2}{3} (\nabla \cdot \bar{u}) [I] \right\} \quad (5)$$

## Numerical Method and Limiters

The numerical semi-discretization of Eq. (1) is,

$$\frac{\partial}{\partial t} \int_{\Omega} U dV = R \approx \sum_f \left[ F_f^c(U_f^-, U_f^+, \bar{n}_f) - F_f^v(U_f^-, U_f^+, \bar{n}_f) \right] \cdot A_f \quad (6)$$

To increase the solution accuracy in space, the left and right states are constructed from extrapolated values from cell centers to cell interfaces and then used to construct fluxes (van Leer, 1979),

$$W_f^k = W^k + \Delta^k, \Delta^k = \bar{\nabla} W^k \cdot d\bar{r}^k, \quad k=-,+ \quad (7)$$

In order to make the solution be monotonic, the slope limiters are enforced in the extrapolation. For example, Barth-Jespersen's reconstruction (Barth and Jespersen, 1989) and limiter reads,

$$W_f^k = W^k + \Delta^{k,\text{lim}}, \Delta^{k,\text{lim}} = \phi^k \bar{\nabla} W^k \cdot d\bar{r}^k, \quad k=-,+ \quad (8)$$

with,

$$\phi^k = \min_{i \in N(k)} \phi^{ki}, \phi^{ki} = \begin{cases} \psi(1.0, \Delta_+ / \Delta_-), \Delta_+ = \max_{i \in N(k)} W^i - W^k & \text{if } \Delta_- > 0 \\ \psi(1.0, \Delta_+ / \Delta_-), \Delta_+ = \min_{i \in N(k)} W^i - W^k & \text{if } \Delta_- < 0 \\ 1.0 & \text{if } \Delta_- = 0 \end{cases} \quad (9)$$

In BJ's method (Barth and Jespersen, 1989), they use a non-differential limiter  $\psi(1,y)=\min(1,y)$ . This adversely affects the convergence properties of the solver. For this reason, Venkatakrishnan (1993) introduces a smooth alternative of the minimum function in Barth-Jespersen procedure,

$$\psi(1.0, \Delta_+ / \Delta_-) = \frac{(\Delta_+^2 + \varepsilon^2) + 2\Delta_- \Delta_+}{\Delta_+^2 + 2\Delta_-^2 + \Delta_- \Delta_+ + \varepsilon^2} \quad (10)$$

Although the Venkatakrishnan limiter is used to prevent the non-physical oscillations nearby the shock region, the overshoot or undershoot phenomenon can still be observed. Moreover, the numerical accuracy is degraded by using Venkatakrishnan limiter. Besides, it could be easily observed that the gradient in Barth-Jespersen's and Venkatakrishnan version is limited by multiplying a scalar limiter  $\phi$ . That is, the limiter is the same for each direction. This shows they may be too dissipative.

Hence, in this paper, a new multidimensional limiting procedure is proposed to limit the gradient in each direction independently. The main idea is to limit the gradient normal to the face direction for each face. For each face of one cell, only the difference along the direction between the two centroids is limited,

$$\Delta^{k,\text{lim}} = \chi^k L(\Delta^{k,-}, \Delta^{k,+}) \quad (11)$$

with

$$\Delta^{k,-} = 2\bar{\nabla} W^k \cdot (\bar{r}^i - \bar{r}^k) - (W^i - W^k), \quad (12a)$$

$$\Delta^{k,+} = W^i - W^k. \quad (12b)$$

This will reproduce a limited difference for each face. After having these limited differences, the unlimited differences and the limited differences for each face are limited secondly

$$\phi^k = \Upsilon(\Delta^{k,\text{lim}}, \Delta^k). \quad (13)$$

## Results and Discussion

To assess the performance of the proposed limiter, the case of flow around the transonic RAE2822 airfoil is chosen in this section. It is well known that the RAE 2822 airfoil is a supercritical airfoil. The measurements have been done for a variety of flow conditions by Cook et al. (1979). Hence, there are a lot of results for validation.

Here, case number 6 is considered. For this case, the Reynolds number based on a unit chord length is 6.5 million, the Mach number is 0.729, and the angle of attack is 2.31 degrees. It is a transonic speed case with a thin boundary layer attached to the aerofoil surface. The flow separation is not

expected. In this particular case, the results are expected to be primarily dictated by the RANS solver. The first grid spacing off the wall is about  $1 \cdot 10^{-5}$  chord length. The flow is assumed to be fully turbulent, i.e. transition is not specifically imposed. For the presented simulation, the Green-Gauss reconstruction technique is employed. The convective fluxes are based on the ROE scheme. A viscous wall boundary condition used over the surface of the airfoil, and a free-stream boundary condition used at the outer edge of the domain where the flow is everywhere subsonic. The flow is initialized using free stream values.

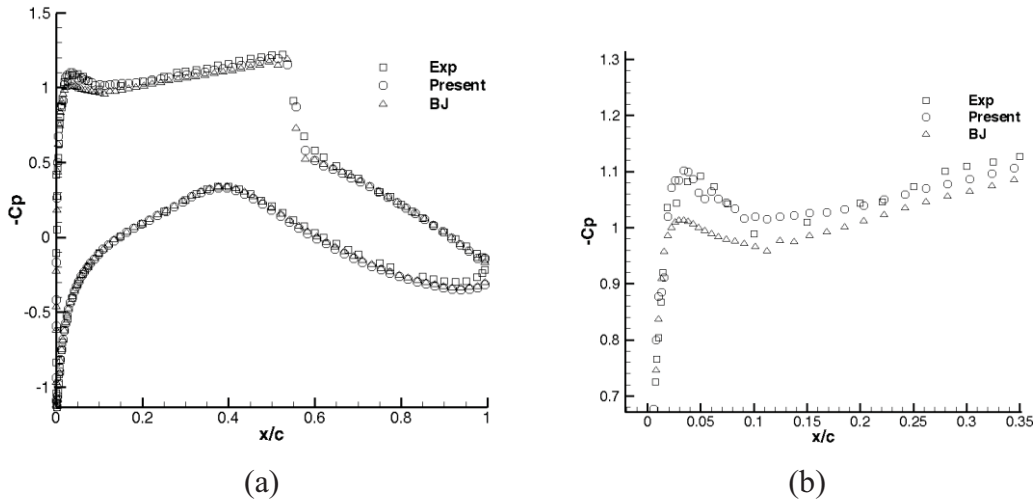


Figure 1. A plate

The distributions of the pressure coefficient and of the friction coefficient on the airfoil surface are plotted in figures 1 and 2. Both results agree well with the experimental data of Cook et al. (1979).

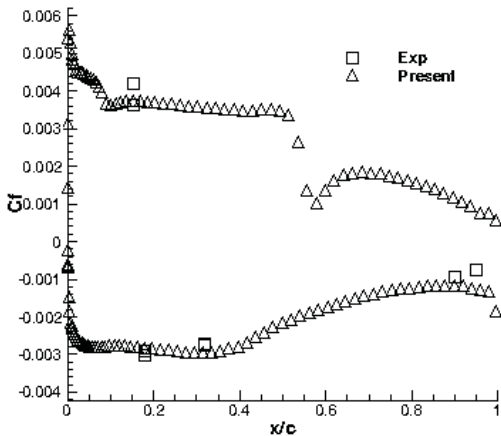


Figure 2. A plate

Besides, from Fig. 1, it is found that the distribution of  $C_p$  by present limiter is better than that by BJ limiter as compared to the experimental result. This can be clearly observed in Fig. 1 (b). The aerodynamic lift coefficient and the drag coefficient are predicted very accurately. This can be easily found in Table 1. The present results are better than those by BJ limiter as compared with the experimental data. All in all, the results show good performance the proposed limiter.

**Table 1. The aerodynamic Coefficients**

	CL	CD
Exp	0.743	0.0127
Present	0.753	0.0131
BJ	0.725	0.0144

### Conclusions

In this paper, a new limiter for hybrid grid is proposed. It is so simple that it can be easily adopted in many solvers based on unstructured grid. The numerical result around RAE2822 shows that it is less dissipative than BJ method.

### Acknowledgement

This research work was supported by the Natural Science Foundation for the Youth of China under Grant 11202220.

### References

- van Leer, B. (1979), Towards the ultimate conservative difference scheme. V, A second-order sequel to Godunov's Method, *J. Comput. Phys.*, 32, pp101-136.
- Venkatakrisnan, V. (1993), On The Accuracy of Limiters and Convergence to Steady State Solutions, Technical Report AIAA-93-0880.
- Barth, T. J. and Jespersen, D.C. (1989), The design and application of upwind schemes on unstructured meshes, AIAA Paper, 89-0366.
- Cook, P.H., McDonald, M.A., and Firmin, M.C.P. (1979), Aerofoil RAE 2822 - Pressure Distributions, and Boundary Layer and Wake Measurements, Experimental Data Base for Computer Program Assessment, AGARD Report AR 138.

## Snoring as Markers for Obstructive Sleep Apnea – A Computational Multiphysics Investigation

\*M.R. Rasani<sup>1</sup>, A.K. Ariffin<sup>1</sup>, and J.Y. Tu<sup>2</sup>

<sup>1</sup>Fakulti Kejuruteraan dan Alam Bina, Universiti Kebangsaan Malaysia, 43600 Bangi, Selangor, Malaysia.

<sup>2</sup>School of Aerospace, Mechanical and Manufacturing Engineering, RMIT University, PO Box 71, Bundoora, 3083 Victoria, Australia.

\*Corresponding author: rasidi@eng.ukm.my

### Abstract

Obstructive Sleep Apnea (OSA) influence daytime sleepiness and is linked with hypertension and cardiac problems. Diagnosis of obstructive sleep apnea involving sleep tests are expensive, cumbersome and not practical for large scale diagnosis. Therefore, this article presents a computational investigation of snoring as potential markers for identifying patients with obstructive sleep apnea. To that end, a coupling between the fluid and structural physics of a cantilevered plate inside an obstructed channel flow is undertaken, to idealize soft palate instability within an obstructed oropharynx. Unlike previous approach, a pressure-specified inlet and velocity-specified outlet boundary conditions in the channel are applied to closer replicate actual conditions. A parametric study on the effect of channel obstruction to cantilever plate instability suggest onset and variability in onset of snoring as potential markers to detect obstructive sleep apnea. This may be exploited for development of mass diagnosis of obstructive sleep apnea in the general population.

**Keywords:** Obstructive sleep apnea, Fluid-structure interaction, Snoring, CFD, FEM

### Introduction

Recurrence of complete or partial obstruction of the upper airway during sleep is associated with a condition called obstructive sleep apnea (OSA). This condition has the adverse affect of compromising sleep quality and reduction of oxygen saturation. Thus, leading to daytime sleepiness and has been linked to more serious disorders including hypertension and heart problems (Bertram, 2008).

Standard diagnosis of OSA through sleep tests are expensive, cumbersome and not practical for mass diagnosis in the general population. Therefore, this paper aims to explore a potential for cheaper and more practical detection of OSA by analyzing onset of soft palate snoring. Snoring is associated with flutter of the soft tissues in the upper airway (Huang et al., 1995). In order to investigate this soft palate flutter, following an approach by Balint and Lucey (2005), a simulation was undertaken where the upper airway was idealized as a 2-D channel and the soft palate was idealized as a cantilever plate. A multiphysics modeling was adopted by coupling the flow physics in the channel with the transient dynamic of the cantilever plate.

In this article, the governing fluid-structural physics and coupling approach are first presented in the following section. Next, simulation results for some obstructed cases are presented. Finally, the results are discussed in regards to difference in onset of snoring with severity of obstruction.

## Computational Method

### Fluid and Structural Equations

The fluid physics was modeled using standard laminar, incompressible, unsteady Navier-Stokes and continuity equations, described in the Arbitrary Lagrangian-Eulerian frame of reference:

$$\frac{\partial u_i}{\partial t} + (u_j - \hat{u}_j) \frac{\partial u_i}{\partial x_j} = -\frac{1}{\rho} \frac{\partial p}{\partial x_i} + \frac{\partial}{\partial x_j} \left[ \nu \left( \frac{\partial u_i}{\partial x_j} + \frac{\partial u_j}{\partial x_i} \right) \right] \quad (1)$$

$$\frac{\partial (u_i - \hat{u}_i)}{\partial x_i} = 0 \quad (2)$$

where density and dynamic viscosity for air is respectively,  $\rho = 1.185 \text{ kg/m}^3$  and  $\mu = 1.831 \times 10^{-5} \text{ kg/ms}$ , and  $\hat{u}_j$  represents the mesh velocity in an Arbitrary Lagrangian-Eulerian framework.

In addition, the transient dynamic of the cantilever plate was modeled using Cauchy's equation:

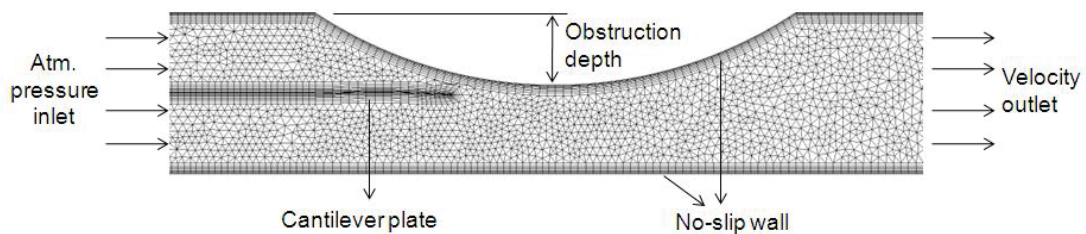
$$\nabla \cdot \sigma_{ij} + \mathbf{f} = \rho_s \frac{\partial^2 d_i}{\partial t^2} \quad (3)$$

where  $\sigma_{ij}$  is the stress tensor,  $d_i$  denote displacement of the cantilever plate and  $\mathbf{f}$  represents the aerodynamics forces applied on the cantilever plate, as calculated from the fluid computations. Density and Young's modulus of the cantilever plate is set to  $\rho_s = 2272.2 \text{ kg/m}^3$  and  $E = 880 \text{ MPa}$  respectively, giving a second mode frequency of 100 Hz (Balint and Lucey, 2005).

### Coupling and Numerical Approach

Soft palate flutter was investigated by introducing an initial perturbation in the form of initial deformation, corresponding to the second mode shape of the cantilever plate. Onset of flutter was predicted by examining growth (indicating instability) or reduction (indicating stability) of this cantilever plate deformation. The interaction between fluid and structure was implemented by successively transferring the aerodynamic forces calculated in the channel flow computation to the structural computation and then transferring the cantilever deformation to redefine the fluid domain in the fluid computation (ANSYS, 2010).

### Model and Boundary Conditions



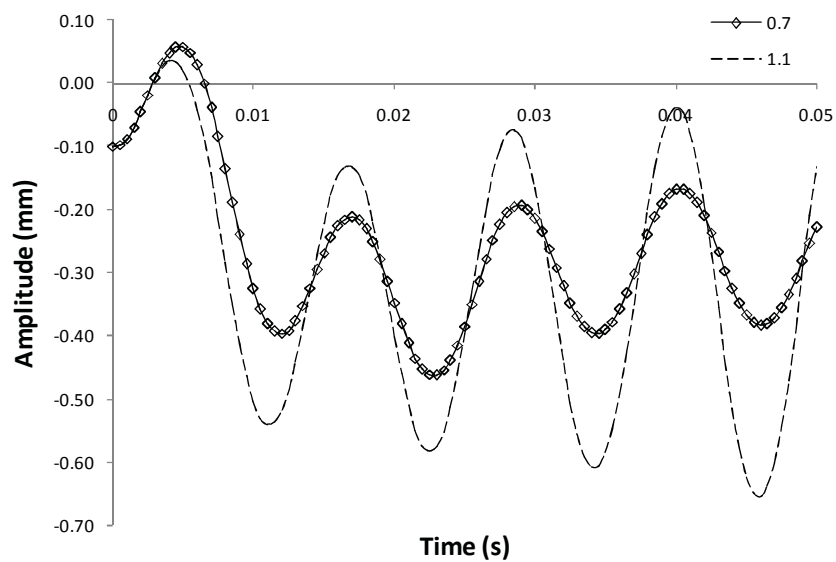
**Figure 1. Close-up of channel model (with mesh) and boundary conditions.**



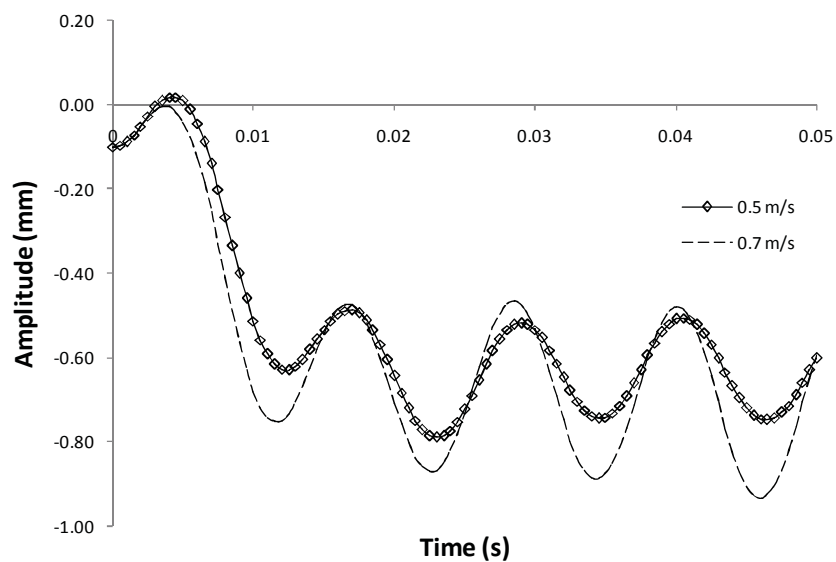
An obstruction was introduced in the 2-D channel to replicate partial obstruction of the upper airway. Two different obstruction depths (i.e. 2.0 mm and 4.5 mm) corresponding to respectively 20% and 45% obstruction of the channel, was simulated. The inlet of the channel was prescribed with atmospheric pressure, while the outlet of the channel was prescribed with velocities corresponding to typical inhalation flow rates. The remaining boundaries of the channel was set to no-slip walls. Fig. 1 shows geometry and boundary conditions of this model.

## Results

In the following, several plots of cantilever tip deformation over time, corresponding to different outlet velocities, are presented for each obstruction case. Fig. 2a and 2b shows the tip deformation history for channel with obstruction of 2.0 mm and 4.5 mm depth, respectively.



(a)



(b)

**Figure 2. Tip oscillation history for cantilever plate inside a channel with (a) 20% obstruction (b) 45% obstruction.**

For case with 20% obstruction, Fig. 2a shows that for outlet velocity = 0.7 m/s, the cantilever tip deformation decays over time, suggesting stable oscillation of the cantilever plate. While for outlet velocity = 1.1 m/s, the cantilever tip deformation grows with time, indicating instability in the cantilever plate oscillation. Therefore, we may conclude that the critical velocity for onset of flutter in this case, falls between 0.7 and 1.1 m/s of the outlet velocity.

Similarly, for case with 45% channel obstruction, Fig. 2b shows that cantilever tip deformation decays and grows for outlet velocities of respectively, 0.5 m/s and 0.7 m/s. As a result, in this case, critical velocity for onset of flutter is between 0.5 and 0.7 m/s of the outlet velocity.

## Discussion

Table 1 summarizes all our simulation results for each of the 20% and 45% channel obstruction cases.

**Table 1: Simulation results for each case**  
(‘x’ indicates instability, ‘✓’ indicates stability and ‘o’ indicates not performed)

Outlet velocities (m/s)	20% obstruction	45% obstruction
0.5	o	✓
0.7	✓	x
0.9	o	o
1.1	x	o

The critical outlet velocity for onset of flutter is different for each obstruction case. A lower critical velocity is predicted for case with more severe channel obstruction. This indicates that onset of flutter occurs at lower flow rates in obstructed channels.

As inhalation flow rates cycle somewhat sinusoidally over time during sleep (see for example, (Fenn and Rahn, 1964)), lower critical velocity means that flutter occurs earlier in the inhalation cycle. This may suggest that for more obstructed airways, the onset for soft palate snoring occurs earlier during the inhalation. As a result, the time lapse before start of soft palate snoring, may indicate the severity of obstruction in the vicinity of the soft palate region in the upper airway. It is proposed that this measured time to onset of snoring, may be exploited to detect localized obstruction during apnea.

Furthermore, OSA patients may experience varying degrees of airway collapse or occlusion during sleep. With varying severity of obstruction, onset of snoring is also expected to vary from inhalation to inhalation. As a result, the time lapse between snoring episodes may also be highly variable in OSA patients, which is consistent with previous clinical studies (see for example, (Cavusoglu et al., 2008)).

## Conclusions

In the present work, we investigated the onset of cantilever plate flutter in a partially obstructed channel. This was intended to idealize soft palate snoring in an obstructed upper airway, for a preliminary study on onset of snoring with respect to partial obstruction inside an upper airway. A multiphysics approach, coupling fluid and

structural computations, suggest lowering of critical velocity for onset of flutter with respect to increasing degree of channel obstruction. This may be linked to varying onset of snoring with respect to severity of OSA in patients, which may be further exploited as non-invasive markers of OSA.

Currently, the critical velocity for onset of flutter was determined by graphically identifying upper and lower bounds of plate stability. An improved method to accurately estimate this critical velocity is recommended for future work. It is recognized that current 2-D model is a very crude representation of the upper airway. Investigations using anatomically-accurate upper airway models should be undertaken in the future. Finally, clinical experiments to evaluate and validate this approach as markers for OSA would also need to be performed.

### References

- Bertram, C. D. (2008), Flow-induced oscillation of collapsed tubes and airway structures. *Respiratory Physiology & Neurobiology* **163**, pp. 256-265.
- Huang, Lixi, Quinn, S. James, Ellis, Peter D. M. and Williams, John E. Ffowcs. (1995), Biomechanics of snoring. *Endeavour* **19**, pp. 96-100.
- Balint, T.S. and Lucey, A.D. (2005), Instability of a cantilevered flexible plate in viscous channel flow. *Journal of Fluids and Structures* **20**, pp. 893-912.
- ANSYS Inc. (2010), *ANSYS CFX Solver Theory Guide - Release 12*.
- Fenn, W. O. and Rahn, H. (1964), *Handbook of Physiology: Respiration*. Washington: American Physiological Society.
- Cavusoglu, M., Ciloglu, T., Serinagaoglu, Y., Kamasak, M., Eroglu, O. and Akcam, T. (2008), Investigation of sequential properties of snoring episodes for obstructive sleep apnoea identification. *Physiological Measurement* **29**, pp. 879-898.

## Investigation of a Shock-Detecting Sensor for Filtering of High-Order Compact Finite Difference Schemes

M. Khoshab<sup>1</sup>, A. A. Dehghan<sup>1</sup>, H. Mahmoodi Darian<sup>2</sup>, and \*V. Esfahanian<sup>3</sup>

<sup>1</sup>Faculty of Mechanical Engineering, Yazd University, Yazd, Iran

<sup>2</sup>Department of Basic Engineering Science, College of Engineering, University of Tehran, Tehran, Iran

<sup>3</sup>Vehicle, Fuel, and Environment Research Institute, University of Tehran, Tehran, Iran

\*Corresponding author: evahid@ut.ac.ir

### Abstract

High-order simulation of flows containing shock waves is an extremely difficult task due to the discontinuous changes in flow properties across the shock. The present work investigates a shock-detecting sensor for filtering of high-order compact finite-difference schemes to examine the shock-capturing in direct simulation of Navier-Stokes solver. Based on the accuracy and minimum dissipation error, the shock-detecting sensor is selected for the DNS studies. The implementation of high resolution simulations using sixth-order compact schemes with a fourth-order two-register Runge-Kutta method is validated through selective test problems. Through several numerical experiments (including an inviscid shock/vortex interaction, a viscous shock/vortex interaction, and a shock/mixing layer interaction) the accuracy of the nonlinear filter is examined. The results indicate that the shock-detecting sensor works well, and can be used for future simulations of turbulent flows containing shocks.

**Keywords:** shock-detecting sensor, shock-capturing, nonlinear filter, high-order scheme.

### Introduction

Numerical investigation of high speed turbulent flows, including vortices and shocks, can be found in many engineering applications. In order to resolve a wide range of length and time scales in these flows, the compact methods proposed by Lele (1992) are typically used in DNSs of turbulent flows as well as in computational aeroacoustics (CAA). The compact schemes contain a smaller truncation error compared with non-compact schemes of the same order, and required smaller numerical stencil size.

As mention above, the accurate compact central scheme is required to preserve the vortical flow structures; however, it does not have shock capturing capability (Lo, Blaisdell, & Lyrantzis, 2010). Meanwhile, the traditional second-order accurate shock capturing schemes are usually not suitable for turbulence simulations due to dissipative feature. Therefore, high-order TVD schemes, the extension of Godunov algorithm using high-order reconstructions (Colella & Woodward, 1984; Van Leer, 1974) and the creation of essentially non-oscillatory (ENO) (Harten & Osher, 1985; Harten, Engquist, Osher, & Chakravarthy, 1987; Harten, Osher, Engquist, & Chakravarthy, 1986; Shu & Osher, 1988, 1989) and weighted essentially non-oscillatory (WENO) (Jiang & Shu, 1996; Liu, Osher, & Chan, 1994) schemes are developed to enhance the methods to have shock capturing ability. Assessment of the

WENO scheme for numerical simulations of compressible turbulence with shock waves shows that the WENO scheme can serve as a reliable tool for DNS of compressible turbulence (Chaudhuri, Hadjadj, Chinnayya, & Palerm, 2010; Johnsen et al., 2010).

The complicated algorithms of the above methods and some deficiencies encourage a few researchers to use high-order compact finite-difference schemes with a special kind of shock detecting sensor (Bogey, de Cacqueray, & Bailly, 2009; Hadjadj, Yee, & Sjögren, 2012; Mahmoodi Darian, Esfahanian, & Hejranfar, 2011; Sjögren & Yee, 2004; Visbal & Gaitonde, 2005; Yee, Sandham, & Djomehri, 1999; Yee & Sjögren, 2008). In other words, a shock-detecting sensor restricts the use of second-order filter to regions near shocks, therefore, the dissipation can be applied only in the large gradient regions (i.e. shocks) and the spatial higher-order filter is applied to other smooth regions instead. In addition, since these hybrid filters can be applied once to the solutions after each full time step, the computational cost is considerably less than that of traditional shock capturing schemes.

The motivation of the present work is to develop a reliable numerical solver in a fully compressible formulation using high-order accurate schemes and extending the shock-detecting sensor introduced by (Mahmoodi Darian et al., 2011) to the general curvilinear coordinates for simulation of subsonic turbulence, based on direct numerical simulation (DNS), and supersonic flows with vortical flows interacting with shocks waves.

## Numerical Methods

### *Governing Equation and Discretization Scheme*

Governing equations are the unsteady dimensionless compressible Navier-Stokes equations in curvilinear coordinates  $(\xi, \eta, \zeta)$ , are written in conservative form. The use of low-dissipation, high-order schemes is an essential ingredient when computing compressible flows. The objective is to avoid excessive numerical dissipating of the flow features over a wide range of length scales. For instance, the family of compact schemes can be a good choice to achieve this goal. The computation of all derivatives is carried out by a sixth-order compact central scheme (Lele, 1992). On near-boundary nodes, accurate non-central or one-sided compact schemes are considered. In this study, the time integration is performed by means of a fourth-order accurate Runge-Kutta method with two-register storage (Kennedy, Carpenter, & Lewis, 2000). In addition, non-reflecting boundary conditions for compressible flow in curvilinear coordinates (Chen & Zha, 2006) are used.

### *Description of the sensor and the nonlinear filter*

As the filter form introduced in (Mahmoodi Darian et al., 2011), the numerical filter equation in the conservative form is

$$\tilde{U}_j^{n+1} = U_j^{n+1} + \frac{\Delta t}{\Delta \xi} (\tilde{F}_{j+1/2} - \tilde{F}_{j-1/2}) \quad (1)$$

where  $\Delta t$  is the time-step and  $\Delta \xi$  is the grid size in  $\xi$  direction. The  $\Delta \xi$  and  $\Delta \eta$  is equal to 1. For a  $2m$  th-order explicit linear filter one can have:

$$\tilde{F}_{j+1/2}^{(m)} = (-1)^{m-1} \epsilon^{(m)} \tilde{\lambda}_\xi (\Delta \nabla)^{m-1} \Delta U_j \quad (2)$$

where  $\tilde{\lambda}_\xi$  is the modified characteristic velocity, in curvilinear coordinates,  $\epsilon^{(m)}$  is the dissipation coefficient and  $\Delta$  and  $\nabla$  are the forward and backward difference operators, which are defined by

$$\Delta U_j = U_{j+1} - U_j, \quad \nabla U_j = U_j - U_{j-1}$$

The modified characteristic velocity,  $\tilde{\lambda}_\xi$  is a weighted average between maximum characteristic velocity in the entire computational field,  $\lambda_{\max, global}$ , and local characteristic velocity,  $\lambda_{j+1/2}$ :

$$\lambda_\xi = \omega_\lambda \lambda_{\max, global} + (1 - \omega_\lambda) \lambda_{j+1/2}$$

where  $\lambda_j$  is the characteristic velocity (an eigenvalue of the flux jacobian).

There are good reasons that the second-order linear filter is suitable for discontinuous regions which is not the case for the higher-order linear filters. On the other hand, the high-order linear filters have desirable properties in smooth regions. Consequently, it is desirable to have a nonlinear filter which acts as a second-order linear filter near the discontinuities and behaves as a high-order linear filter in smooth regions (Bogey et al., 2009; Visbal & Gaitonde, 2005). In this regard, we write the numerical filter flux as a combination of the second- and a higher-order filter flux:

$$\tilde{F} = \omega_1 \tilde{F}^{(1)} + \omega_m \tilde{F}^{(m)}, \quad m > 1 \quad (3)$$

where  $\omega_1$  and  $\omega_m$  are the nonlinear weights controlling the amount of the second- and  $2m$  th-order filters. The proper design of these weights is essential to have high accuracy in smooth regions and to obtain non-oscillatory sharp discontinuities. The following weights are proposed by (Mahmoodi Darian et al., 2011):

$$\omega_1 = 1 - \exp(-c_e e_{j+1/2}^2), \quad \omega_m = \exp(-c_e e_{j+1/2}^2) \quad (4)$$

where  $c_e$  is a positive constant number. This definition ensures both  $\omega_1$  and  $\omega_m$  are between 0 and 1. Note that  $c_e = 0$  reduces the filter to the  $2m$  th-order linear filter and  $c_e \rightarrow \infty$  corresponds to the second-order linear filter. The term  $e_{j+1/2}$  is a kind of smoothness measurement which is defined as

$$e_{j+1/2} = \max(e_j, e_{j+1}), \quad e_j = \frac{|\hat{U}_j - U_j|}{D_j} \quad (5)$$

and  $\hat{U}_j$  is the interpolated value of  $U$  at the point  $x_j$  using the neighboring points  $\{U_{j\pm k}\}_{k=1, \dots, m'}$ , which is computed as

$$\hat{U}_j = U_j - \frac{(-1)^{m'}}{\binom{2m'}{m'}} (\Delta \nabla)^{m'} U_j, \quad \binom{2m'}{m'} = \frac{(2m')!}{(m')!(m')!} \quad (6)$$

Therefore, the numerator in (5) is the error of a  $2m'$  th-order interpolation. The denominator  $D_j$  is a scaling value. For more details see the (Mahmoodi Darian et al., 2011).

In equation (5) some sort of scaling is needed to have a measure to distinguish the large interpolation errors from the small ones. For this reason, we propose the following scaling

$$D_j = c_s S_g + (1 - c_s) S_l, \quad S_g = U_{\max}^g - U_{\min}^g, \quad S_l = U_{\max}^l - U_{\min}^l \quad (7)$$

where  $S_g$  and  $S_l$  are the global and local scales, respectively. Also,  $c_s$  is the scaling constant which is a positive number smaller than unity. The global and local maximum and minimum are defined as:

$$\begin{aligned} U_{\max}^g &= \max_k(U_k), & U_{\min}^g &= \min_k(U_k), & 1 \leq k \leq j_{\max} \\ U_{\max}^l &= \max_k(U_k), & U_{\min}^l &= \min_k(U_k), & j-m' \leq k \leq j+m' \end{aligned} \quad (8)$$

## Numerical Experiments

### 1D problems: Linear wave equation and Shock-tube

In the first test case, the linear wave equation is solved. The initial condition is a periodic function similar to work of Mahmoodi Darian et al., (2011). The equation is solved with a uniform grid of  $\Delta x = 1/200$  and a fixed time-step of  $\Delta t = 0.002$  up to  $t = 6$  corresponding to three time periods. Both linear and nonlinear filters produce nearly the same results in the smooth regions as shown in Fig. 1.

In the second test case, a well-known Riemann problem introduced by Sod (1978) is solved. The equations are the compressible one-dimensional Euler equations. The numerical solutions are obtained at  $t = 2$  with a uniform grid of 400 points and CFL=0.2. In Fig. 2 the results are compared with analytical solution.

In both test cases, it can be seen that the non linear filter capture discontinuities sharply.

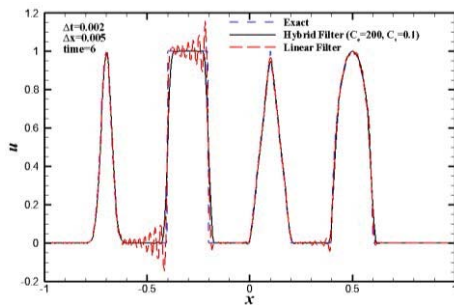


Figure 1. Linear wave equation

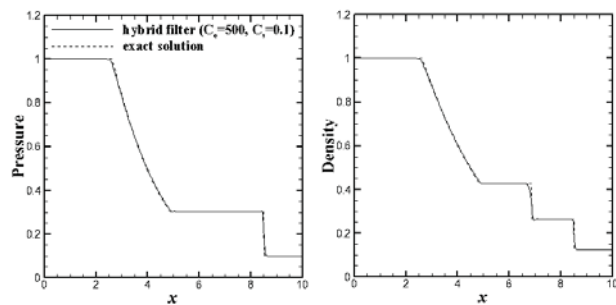


Figure 2. Pressure and density distribution

### 2D Inviscid Shock-Vortex interactions

This is a two-dimensional test case that describes the interaction between a stationary shock and a vortex (Jiang & Shu, 1996). A stationary Mach 1.1 shock is positioned at  $x = 0.5$  and normal to the  $x$ -axis similar to work of (Jiang & Shu, 1996).

The results are obtained with a uniform grid of  $251 \times 101$  and CFL=0.1. The coefficients  $c_e$ ,  $c_s$  and  $\omega_\lambda$  for the nonlinear filter are set to 200, 0.1 and 1, respectively. The non-reflecting far-field boundary conditions are applied in the top and bottom faces and the non-reflecting outflow boundary condition is set at the downstream. The pressure contours are displayed in Fig. 3. Eighteen contour lines from 0.59 to 0.78 are used. It can be seen that the sensor resolve the vortex properly. Fig. 4(a) displays the pressure distribution along the  $y = 0.5$  section at  $t = 0.6\sqrt{\gamma}M_\infty$  before and after the shock. The pressure distributions in some extreme zones are zoomed in figures 4(b)-4(d).

The effect of grid on the sensor resolution is presented in Fig. 5(a) by the pressure distribution along the  $y=0.5$  section. It can be seen that the shock is captured by nonlinear filter even in the coarse grid. The pressure distributions in some extreme zones are zoomed in figures 5(b)-5(d). The nonlinear sensor is designed for wide range of shock strength. In the Fig. 6(a), it can be seen that the strong shock is captured by nonlinear sensor properly. The pressure distributions in some extreme zones are zoomed in figures 6(b)-6(d). In the present case, the slip-wall (reflecting) boundary conditions are applied in the top and bottom faces due to investigation on the effects of shock reflection on the results.

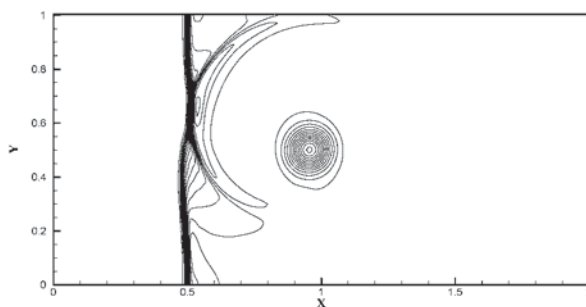


Figure 3. Pressure contours for the 2D shock-vortex interaction at  $t = 0.6\sqrt{\gamma}M_\infty$  (18 contours from 0.59 to 0.78).

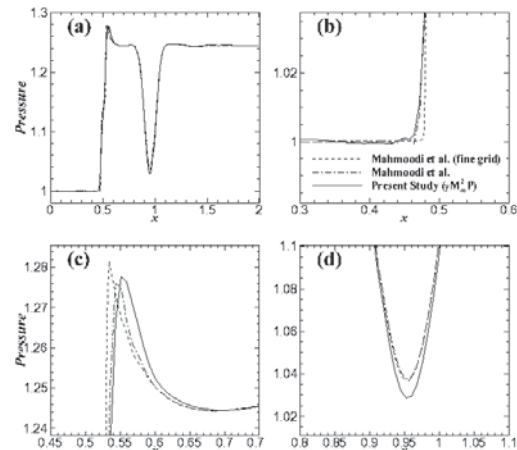


Figure 4. Pressure distribution along the  $y = 0.5$  section at  $t = 0.6\sqrt{\gamma}M_\infty$  for the Inviscid shock-vortex interaction.

### 2D Viscous Shock-Vortex interactions

This case is the two-dimensional compressible vortex convected through a normal shock. This is a typical test used to evaluate the diffusive or dispersive property of scheme i.e. used to evaluate of shock-capturing scheme. The configuration corresponds to an isolated Taylor vortex with a Mach number  $M_\infty = 1.1588$  and a Reynolds number  $Re = 2000$ , is initially superimposed on a uniform flow field aligned along the  $x$ -direction similar to (Lo et al., 2010). The CFL number is set to 0.1 with  $c_e = 200$ ,  $c_s = 0.1$  and  $\omega_\lambda = 1$  for the nonlinear filter. The non-reflecting far-field boundary conditions are applied in the top and bottom faces and the non-reflecting outflow boundary condition is used at the downstream.

The pressure contour at  $t = 0.7$  is shown in Fig. 7. Figure 8 shows the density distributions at  $t = 0.7$  along side of the results of (Lo et al., 2010). It can be seen that the sensor resolve the vortex properly in the viscous field. Along the line of  $y = 1$ , the vortex core at  $t = 0.7$  is located at  $x = 1.16$  and a downstream propagating acoustic wave is around  $x = 1.8$ .



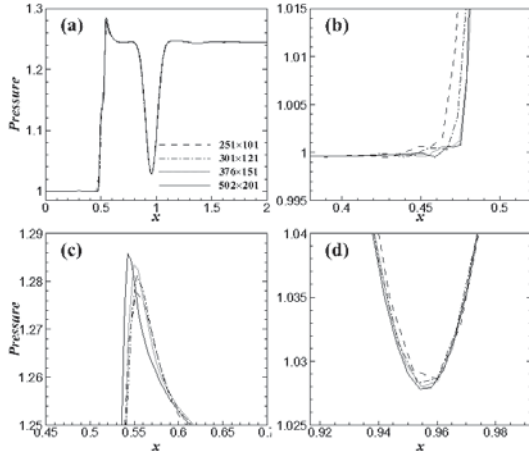


Figure 5. Effect of grid on the pressure distribution along the  $y = 0.5$  section at  $t = 0.6\sqrt{\gamma}M_\infty$ .

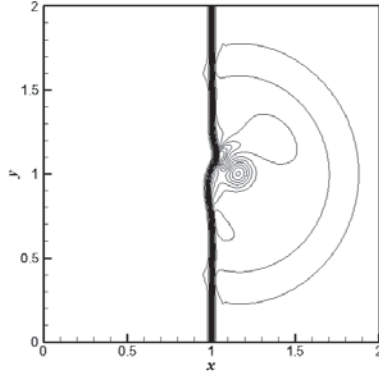


Figure 7. Pressure contours at  $t=0.7$  by a grid  $203 \times 203$  (20 contours from 0.527 to 0.817).

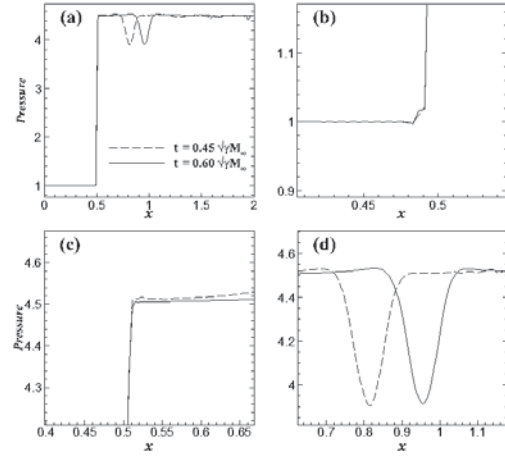


Figure 6. Pressure distribution along the  $y = 0.5$  section for strong shock  $M_\infty = 2.0$  (grid  $502 \times 201$ ).

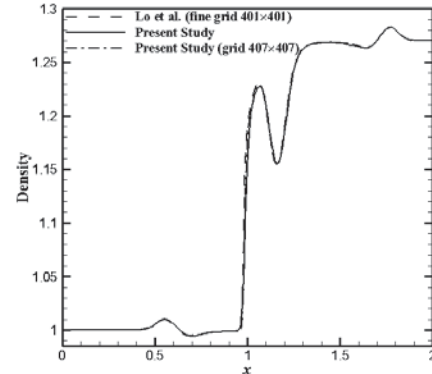


Figure 8. Instantaneous density distribution at  $t=0.7$  along  $y=1$  by a grid  $203 \times 203$  and  $407 \times 407$ .

### Shock-Mixing layer interactions

This case is used to evaluate the performance of the shock capturing schemes for interactions of shock waves and shear layers (Lo et al., 2010; Yee et al., 1999). Figure 9 shows the schematic view of the flow configuration. An oblique shock originating from the upper-left corner interacts with shear layers where the vortices arising from shear layer instability. This oblique shock is deflected by the shear layer and then reflects from the bottom slip wall. Simultaneously, an expansion fan forms above the shear layer and at the downstream, a series of shock waves form around the vortices. The outflow boundary has been arranged to be supersonic everywhere. The computational domain were taken to be  $L_x = 200$  and  $L_y = 40$ . The inflow boundary condition is specified with a hyperbolic tangent profile (see the stream (1) and (2) in Fig. 9).

$$u = 2.5 + 0.5 \tanh(2\hat{y}), \quad \text{with } \hat{y} = y - L_y / 2$$

The only transverse-velocity fluctuations are added to the inflow as:

$$v' = \sum_{k=1}^2 a_k \cos(2\pi kt / T) + \phi_k \exp(-\hat{y}^2 / b)$$

with the period  $T = \lambda / u_c$ , convective velocity  $u_c = 2.68$ , the wavelength  $\lambda = 30$  and the other constants are given by  $b = 10$ ,  $a_1 = a_2 = 0.05$ ,  $\phi_1 = 0$  and  $\phi_2 = \pi / 2$ , similar to (Yee et al., 1999). The two streams have the same inflow pressure and stagnation enthalpies. All properties are normalized by the properties of the stream (1).

For the left and top boundaries, supersonic inflow is imposed, whereas slip-wall conditions are assumed at the bottom boundary to avoid any boundary-layer formation and subsequent complexities arising from the shock/boundary layer interaction. At the outflow the non-reflecting outflow conditions are assumed. A grid dependency study using four different meshes, namely mesh-1:  $512 \times 128$  (uniform and non-uniform); mesh-2:  $1024 \times 256$ , mesh-3:  $2048 \times 512$  and mesh-4:  $4096 \times 1024$  (about 4.2 million points). Figures 10 show the Numerical schlieren based on density, pressure and shadowgraph contours. From the figures, it can be seen that the shapes of the vortices are resolved properly, and the shocklets generated by the vortices in the downstream region. The shock-detecting sensor provides high quality vortices and downstream shocklet resolution.

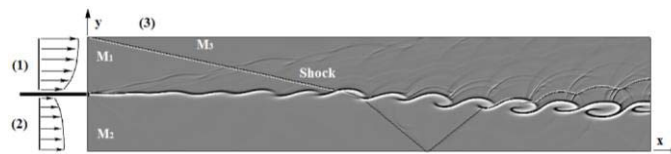


Figure 9. Schematic view of the shock/mixing-layer interaction configuration

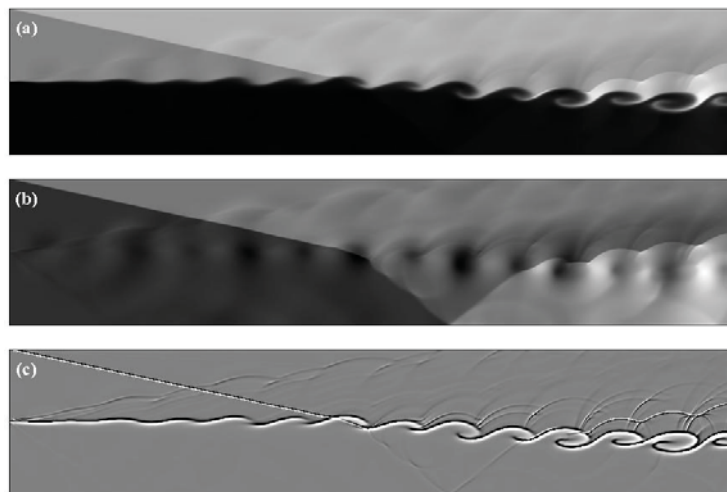


Figure 10. Numerical schlieren based on (a) density, (b) pressure, and (c) shadowgraph, for a  $2048 \times 512$  grid with  $c_e = 200$ ,  $c_s = 0.1$  and  $\omega_\lambda = 1$  for the filter.

## Conclusions

In the present study, a Navier-Stokes computational methodology for turbulent supersonic flows based on high-order compact finite-difference schemes is developed and the shock-detecting sensor has been extended and tested for several test cases. The sensor is based on an interpolation error scaled by a suitable scaling value which scales the large errors by their local scale and the small errors by a proportion of the global scale. The sensor is developed in curvilinear coordinates and tested through several test cases including a 2D stationary shock with a moving vortex, and a 2D shock/mixing layer interaction. The results indicate that the shock-detecting sensor works well, and can be used for future simulations of turbulent flows containing shocks.

## References

- Bogey, C., de Cacqueray, N., & Bailly, C. (2009). A shock-capturing methodology based on adaptive spatial filtering for high-order non-linear computations. *Journal of Computational Physics*, 228(5), 1447–1465.
- Chaudhuri, A., Hadjadj, A., Chinnayya, A., & Palerm, S. (2010). Numerical Study of Compressible Mixing Layers Using High-Order WENO Schemes. *Journal of Scientific Computing*, 47(2), 170–197.
- Chen, X., & Zha, G.-C. (2006). Implicit application of non-reflective boundary conditions for Navier–Stokes equations in generalized coordinates. *International Journal for Numerical Methods in Fluids*, 50(7), 767–793.
- Colella, P., & Woodward, P. R. (1984). The piecewise parabolic method (PPM) for gas-dynamical simulations. *Journal of computational physics*, 54(1), 174–201.
- Hadjadj, A., Yee, H. C., & Sjögreen, B. (2012). LES of temporally evolving mixing layers by an eighth-order filter scheme. *International Journal for Numerical Methods in Fluids*, 70, 1405–1427.
- Harten, A., & Osher, S. (1985). Uniformly high-order accurate non-oscillatory schemes, 1. *SIAM Journal on Numerical Analysis*, 24(2), 279–309.
- Harten, Ami, Engquist, B., Osher, S., & Chakravarthy, S. R. (1987). Uniformly high order accurate essentially non-oscillatory schemes. III. *Journal of Computational Physics*, 71(2), 231–303.
- Harten, Ami, Osher, S., Engquist, B., & Chakravarthy, S. R. (1986). Some results on uniformly high-order accurate essentially nonoscillatory schemes. *Applied Numerical Mathematics*, 2(3), 347–377.
- Jiang, G.-S., & Shu, C.-W. (1996). Efficient implementation of weighted ENO schemes. *Journal of Computational Physics*, 126(1), 202–228.
- Johnsen, E., Larsson, J., Bhagatwala, A. V., Cabot, W. H., Moin, P., Olson, B. J., ... Lele, S. K. (2010). Assessment of high-resolution methods for numerical simulations of compressible turbulence with shock waves. *Journal of Computational Physics*, 229(4), 1213–1237.
- Kennedy, C. A. C. A., Carpenter, M. H., & Lewis, R. M. (2000). Low-Storage, Explicit Runge-Kutta Schemes for the Compressible Navier-Stokes Equations. *Applied Numerical Mathematics*, 35(3), 177–219.
- Lele, S. K. (1992). Compact finite difference schemes with spectral-like resolution. *Journal of Computational Physics*, 103(1), 16–42.
- Liu, X. D., Osher, S., & Chan, T. (1994). Weighted Essentially Non-Oscillatory Schemes. *Journal of Computational Physics*, 115(1), 200–212.
- Lo, S., Blaisdell, G. A., & Lyrantzis, A. S. (2010). High-order shock capturing schemes for turbulence calculations. *International Journal for Numerical Methods in Fluids*, 62, 473–498.
- Mahmoodi Darian, H., Esfahanian, V., & Hejranfar, K. (2011). A shock-detecting sensor for filtering of high-order compact finite difference schemes. *Journal of Computational Physics*, 230(3), 494–514.
- Shu, C.-W., & Osher, S. (1988). Efficient implementation of essentially non-oscillatory shock-capturing schemes. *Journal of Computational Physics*, 77(2), 439–471.
- Shu, C.-W., & Osher, S. (1989). Efficient implementation of essentially non-oscillatory shock-capturing schemes. II. *Journal of Computational Physics*, 83(1), 32–78.
- Sjögreen, B., & Yee, H. C. (2004). Multiresolution wavelet based adaptive numerical dissipation control for high order methods. *Journal of Scientific Computing*, 20(2), 211–255.
- Sod, G. (1978). A survey of several finite difference methods for systems of nonlinear hyperbolic conservation laws. *Journal of Computational Physics*, 27, 1–31.
- Van Leer, B. (1974). Towards the ultimate conservative difference scheme. II. Monotonicity and conservation combined in a second-order scheme. *Journal of Computational Physics*, 14(4), 361–370.
- Visbal, M. R., & Gaitonde, D. V. (2005). Shock capturing using compact-differencing-based methods. In *43rd AIAA Aerospace Sciences Meeting and Exhibit* (p. 2005).
- Yee, H. C., Sandham, N. D., & Djomehri, M. J. (1999). Low-Dissipative High-Order Shock-Capturing Methods Using Characteristic-Based Filters. *Journal of Computational Physics*, 150(1), 199–238.
- Yee, H. C., & Sjögreen, B. (2008). Adaptive filtering and limiting in compact high order methods for multiscale gas dynamics and MHD systems. *Computers & Fluids*, 37(5), 593–619.

## An implicit multigrid solver for high-order compressible flow simulations on GPUs

\*V. Esfahanian<sup>1,2</sup>, M. Hedayat<sup>2</sup>, B. Baghapour<sup>2</sup>, M. Torabzadeh<sup>2</sup> and S.J. Hosseini<sup>2</sup>

<sup>1</sup>Vehicle, Fuel and Environment Research Institute, University of Tehran, Iran

<sup>2</sup>School of Mechanical Engineering, University of Tehran, Iran

\*Corresponding author: [e.vahid@ut.ac.ir](mailto:e.vahid@ut.ac.ir)

### Abstract

The multigrid method has proved to be effective for a large class of numerical methods. In this study, a strategy based on Full Approximation Storage (FAS) scheme is implemented together with Full Multigrid Algorithm (FMG) to accelerate convergence of steady state solutions of the two-dimensional compressible Euler equations on Graphics Processing Unit (GPU). The Beam and Warming linearization scheme in curvilinear coordinates is used to discretize the governing equation. The second-order central and the fourth-order compact finite-difference schemes are applied for spatial discretization. A high-performance GPU-implemented block-tridiagonal solver based on Block Cyclic Reduction (BCR) algorithm is utilized. The proposed BCR solver is applied to finite-difference discretization on structured grids via Alternating Direction Implicit (ADI) scheme. Attention is directed towards the computational performance of the V-cycle and W-cycle multigrid strategies in two and three grid levels using the NVIDIA GTX480 graphics card. Speedups between 2x–5.2x are achieved in comparison to the Intel Core i7-920 2.67GHz CPU for different grid sizes.

**Keywords:** Euler Equations, high-order method, Multigrid Acceleration, GPU computing, Block-tridiagonal solver

### Introduction

Among the different schemes that are proposed to accelerate convergence rate such as local time stepping, residual smoothing, multigrid method and most recently local preconditioning, the multigrid method has received great attention. In spite of time stepping schemes that efficiently damp high-frequency error components of numerical solutions, the multigrid method can accelerate the convergence rate by damping the low-frequency error components. This method was first introduced by Fedorenko (1962) and Bakhvalov (1966) and then developed by Brandt (1977). Although the multigrid theory was first developed for elliptic problems, it has been demonstrated in later works by (Ni, 1982; Jameson, 1983) that multigrid method can also greatly affect the convergence rate of numerical schemes applied to Euler equations. Recently, there have been some studies to implement the multigrid methods on high-order numerical discretization (Gupta, Kouatchou, & Zhang 1997; Sakurai, Aoki, Lee, & Kato 2002).

The multigrid method has also been developed for the implicit schemes, which enabled the utilization of the ADI methods (Jameson and Yoon, 1986). In this matter, the computational cost of block-structure matrix inversions is expensive. Therefore,

accelerating the linear system solution is an effective approach towards the computational performance improvement.

Recent developments on Graphics Processing Units (GPU) have led to a high computing power device with a GPU-oriented programming language (CUDA), which enables the applicability of GPU devices for accelerating a variety of CFD problems.

To accelerate the solution of block tridiagonal matrices, appeared in the ADI discretization of the multigrid method, on GPUs, the parallel Cyclic Reduction (CR) algorithm is at the center of attention. This algorithm was developed for block tridiagonal systems by Heller (1976). Performance of high-rank block cyclic reduction solver on distributed memory CPU cluster was reported in work by (Hirshman, Perumalla, Lynch, & Sánchez, 2010). A recent implementation of BCR algorithm on GPUs was done by (Stone, Duque, Zhang, Car, Owens, & Davis, 2011; Baghapour, Esfahanian, Torabzadeh, Mahmoodi Darian, 2013) for different CFD applications.

In the current work, a multigrid method based on FAS scheme is implemented beside a FMG scheme (Brandt, 1981) to accelerate convergence of steady state solutions of the two-dimensional compressible Euler equations. Alternate Directional Implicit (ADI) method is used for time advancement and the second-order central and fourth-order compact finite-difference schemes are applied to spatial discretization. The computational performance of the V-cycle and W-cycle multigrid strategies in two and three grid levels is investigated by using the NVIDIA GTX480 graphics card.

### Governing Equations

The two-dimensional Euler equations for a Cartesian coordinate system are given by:

$$\frac{\partial Q}{\partial t} + \frac{\partial F}{\partial \xi} + \frac{\partial G}{\partial \eta} = 0 \quad (1)$$

where,

$$Q = J^{-1} \begin{Bmatrix} \rho \\ \rho u \\ \rho v \\ E \end{Bmatrix}, F = J^{-1} \begin{Bmatrix} \rho U \\ \rho u U + \xi_x p \\ \rho v U + \xi_y p \\ (E + p)U \end{Bmatrix}, G = J^{-1} \begin{Bmatrix} \rho V \\ \rho u V + \eta_x p \\ \rho v V + \eta_y p \\ (E + P)V \end{Bmatrix} \quad (2)$$

and

$$U = \xi_x u + \xi_y v, \quad V = \eta_x u + \eta_y v, \quad J^{-1} = (x_{\xi} y_{\eta} - x_{\eta} y_{\xi}) \quad (3)$$

The variables  $p, \rho, T, u, v$ , and  $E$  are pressure, density, temperature, velocity components and total energy, respectively. Assuming air as an ideal gas, the equation of state is used to calculate the pressure and temperature:

$$p = (\gamma - 1)\rho \left[ E - \frac{u^2 + v^2}{2} \right], \quad T = \frac{p}{\rho R} \quad (4)$$

where  $\gamma$  is the ratio of specific heats and  $R$  is the gas constant.

## Numerical Method

### *Spatial Discretization*

For spatial discretization, the second-order central and the fourth-order compact finite difference schemes are applied. A general centered compact scheme (Lele, 1992) for the first derivative is the following:

$$\beta f'_{i-2} + \alpha f'_{i-1} + f'_i + \alpha f'_{i+1} + \beta f'_{i+2} = c \frac{f_{i+3} - f_{i-3}}{6\Delta x} + b \frac{f_{i+2} - f_{i-2}}{4\Delta x} + a \frac{f_{i+1} - f_{i-1}}{2\Delta x} \quad (5)$$

Herein,  $f$  and  $f'$  can be any flow variable and its derivative, respectively.  $\Delta x$  is the grid spacing in  $x$ -direction. Depending on the coefficients  $a$  and  $b$ , a tridiagonal or a pentadiagonal system will be produced. The compact method used in this study is as following:

$$f'_{i+1} + 4f' + f'_{i-1} = \frac{3}{\Delta x} (f_{i+1} - f_{i-1}) \quad (6)$$

### *Multigrid Method*

The FAS scheme for two grid levels with multigrid V-cycle is described as follows, where the fine grid is denoted by the  $h$  subscript.

- 1) Calculate the solution correction ( $\Delta Q_h$ ) on the fine grid and update the solution on the fine grid:  $Q_h^{n+1} = Q_h^n + \Delta Q_h$
- 2) Calculate the fine grid residual:  $R_h$
- 3) Transfer value of conservative variables to the coarse grid:  $q_{2h} = I_h^{2h} q_h$   
where  $q = JQ$  and  $I_h^{2h}$  is the restriction operator (Wesseling, 1995).
- 4) Collect the residuals on the fine grid for the coarse grid:  $R'_{2h} = I_h^{2h} R_h$
- 5) Calculate the residuals on the coarse grid using restricted conservative variables from the fine grid to the coarse grid:  $R_{2h}(Q_{2h}^{(0)})$ . To restrict flow variable from the fine grid to the coarse grid, a full-weighted restriction is used.
- 6) The forcing function is defined by:  $P_{2h} = R'_{2h} - R_{2h}(Q_{2h}^{(0)})$   
where,  $R'_{2h}$  is the residual that is restricted to the coarse grid ( $2h$ ) and  $R_{2h}(Q_{2h}^{(0)})$  is the residual evaluated by restricting  $Q_{2h}^{(0)}$  to the coarse grid from the fine grid.
- 7) The residual on the coarse grid is defined as:  $R_{2h} = P_{2h} + R_{2h}(Q_{2h}^{(0)})$

- 8) After one or several iterations, the solution on the coarse grid is updated. Then, the solution correction on the coarse grid is calculated as :  $Q_{2h}^{n+1} = Q_{2h}^n + \Delta Q_{2h}$
- 9) In order to update the solution on the fine grid ( $h$ ), the solution corrections are prolonged to the fine grid as follows:  $Q_h^{n+1} = Q_h^n + I_{2h}^h (Q_{2h}^{n+1} - Q_{2h}^{(0)})$
- where,  $Q_h^n$  is the solution before the restriction to the coarse grid and  $I_{2h}^h$  is the interpolation operator.

#### *Accuracy of Transfer Operator*

Orders of prolongation and restriction operators should satisfy the following equation in order to damp the frequency error (Hemker, 1990):

$$m_{\text{Res}} + m_{\text{Pro}} > m_{\text{Eqn}} \quad (7)$$

where,  $m_{\text{Res}}$ ,  $m_{\text{Pro}}$  and  $m_{\text{Eqn}}$  denote the order of restriction, prolongation operator and the order of spatial numerical discretization for the system of equations, respectively. A full-weighting restriction and fourth-order compact interpolation (Lele, 1992) that are used in this work will satisfy Eq. (7).

### **BCR algorithm and GPU implementation**

#### *CUDA architecture and GPU memory hierarchy*

In CUDA architecture, a kernel execution is divided among a batch of concurrent threads, which are partitioned in blocks of threads. The blocks are mapped to the stream multiprocessors (SM) of the GPU device for execution. The concurrent threads access data from different memory resources when executing on the GPU. Each thread within a group of blocks has access to the large global memory (Equal to the DRAM of the GPU) with high transaction latency. All threads have low latency access to 48KB of shared memory for thread communication within a block (CUDA, 2012). The NVIDIA GTX 480, used in this research, has 1536 MB of frame buffer global memory runs through a 384-bit bus and delivers 177.4 GB/s of memory bandwidth.

#### *The parallel Block Cyclic Reduction (BCR) algorithm*

The BCR algorithm is based on divide and conquer strategy. In the first level, the primary  $N \times N$  system of equations is divided into two decoupled  $N/2 \times N/2$  sub matrices. The two smaller sub matrices are consecutively divided again in the same way until the total number of  $N/2$  sub matrices of size  $2 \times 2$  are achieved in the last level, which can be solved in parallel. In each level of the BCR algorithm, the diagonals ( $L, M, U$ ) and the right-hand-side ( $D$ ) are calculated by Eq. (8). According to this above calculations consist of many small matrix multiplication and inversion operations. The basic approach to implement the above matrix operations on the GPU is to use different streams for parallel kernel execution (CUDA, 2012). However, this approach is bounded by 16 maximum concurrently running streams in CUDA architecture and cannot lead to performance improvements in large matrices. In order to benefit from the parallel nature of BCR algorithm together with the high computational throughput of the

GPU device, single GPU kernels are developed to perform all matrix multiplication and inversion operations in parallel. In both matrix kernels, the sub matrices are first loaded from the global memory to the shared memory, which is provided for each block of threads. Then the calculations on the sub matrices are obtained and the results are written back to the global memory. The number of offloading sub matrices to the shared memory of each block is optimized to avoid extra memory allocation than the 48KB limit and achieve the maximum performance on GPU.

$$\begin{aligned}
T_1^{level} &= L_i^{level} \left( M_{i-1}^{level} \right)^{-1}, T_2^{level} = U_i^{level} \left( M_{i+1}^{level} \right)^{-1} \\
R_i^{level+1} &= R_i^{level} - T_1^{level} R_{i-1}^{level} - T_2^{level} R_{i+1}^{level} \\
M_i^{level+1} &= M_i^{level} - T_1^{level} U_{i-1}^{level} - T_2^{level} L_{i+1}^{level} \\
U_i^{level+1} &= -T_2^{level} U_{i+1}^{level} \\
L_i^{level+1} &= -T_1^{level} L_{i-1}^{level}
\end{aligned} \tag{8}$$

## Results

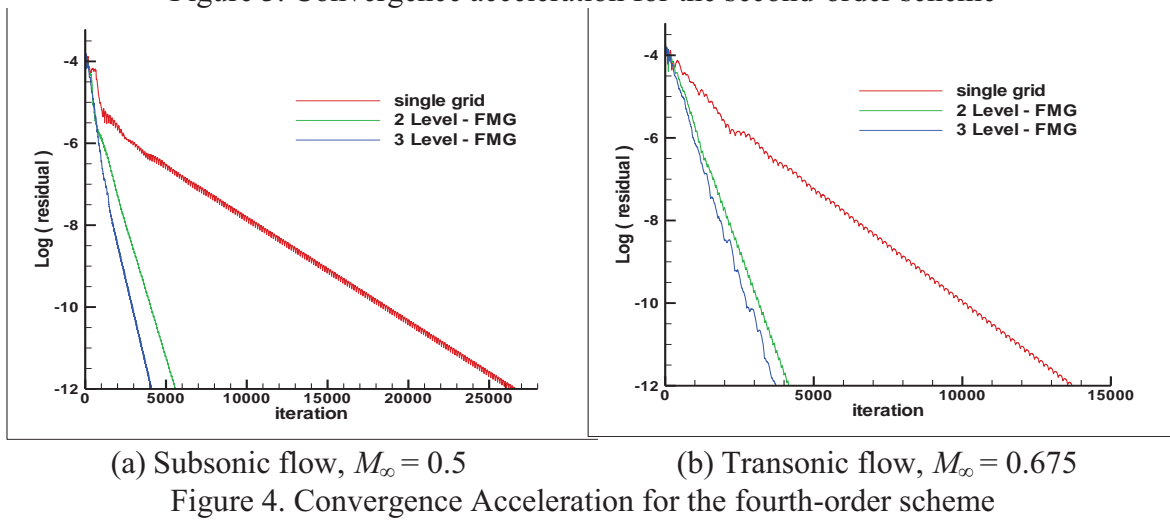
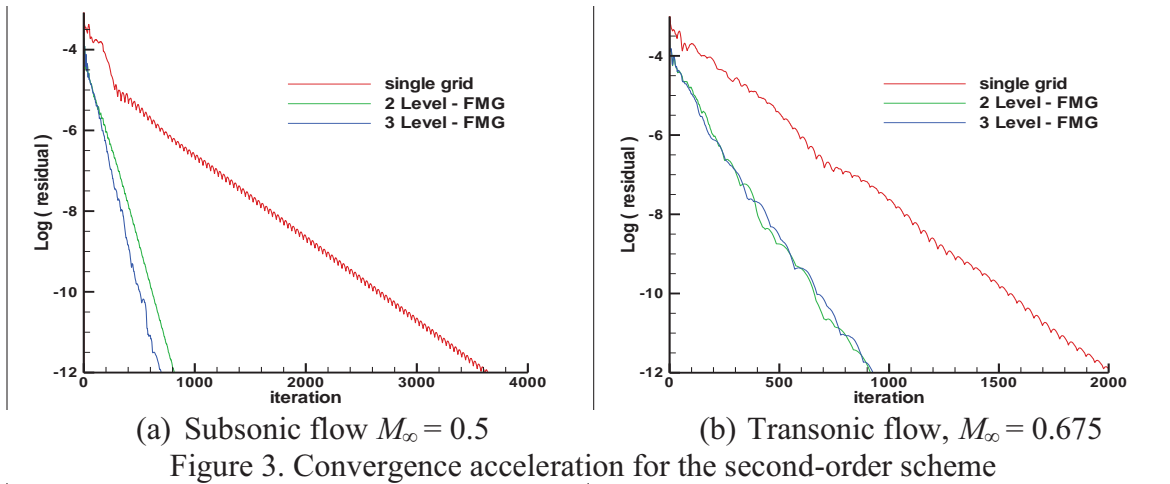
The double precision numerical results presented in this section demonstrate the accuracy and computational efficiency of the multigrid method for inviscid flows. The performance of the GPU-based multigrid solver with the implicit scheme is studied for two-dimensional circular arc bump. The thickness-to-chord ratio is 10% based on the standard test cases of the GAMM conference (Rizzi and Viviand, 1981). In the case of computations on two grid levels and three grid levels, the FMG method is applied to provide an initial solution for the fine grid. The CFL number of 0.6 is used on all grids so that larger time steps can be used on the coarse grid. Convergence is monitored using  $L_2$  norm of density residual. The performance of computations on GTX480 GPU (Core Clock rate: 700 MHz) is compared with a single core of Intel Core i7-920 2.67GHz CPU.

### *Multigrid performance*

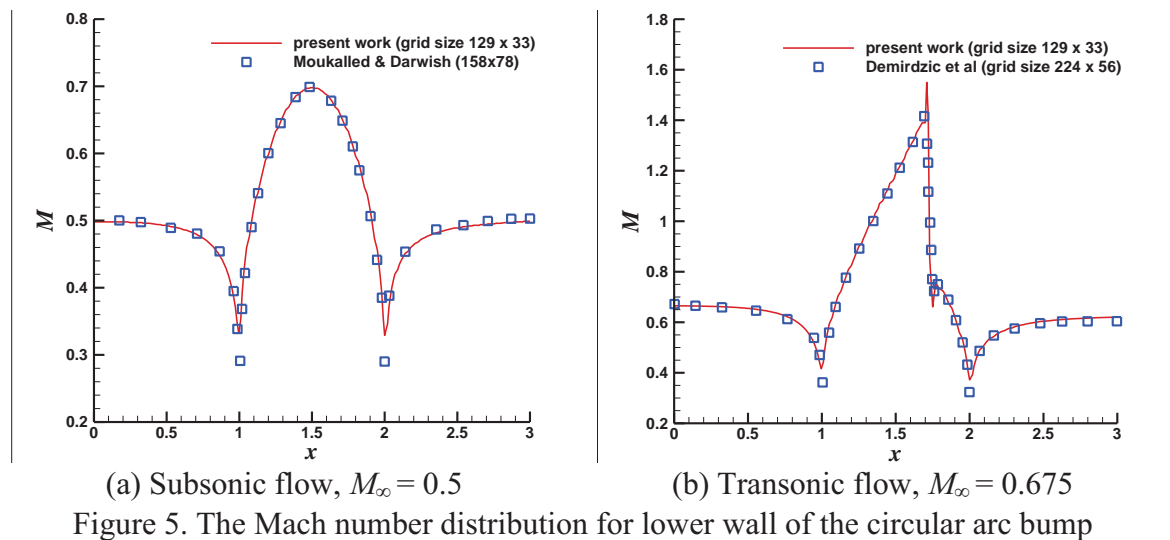
In first step, the performance of multigrid method for computational grid including  $33 \times 17$  cells at free stream Mach number for subsonic and transonic flows using second-order finite difference method is presented. Figure 3(a) and Fig. 3(b) compares the convergence rates between a single grid level, two grid levels and three grid levels multigrid with FMG for subsonic and transonic flow. Computations are performed using V-cycle procedure.

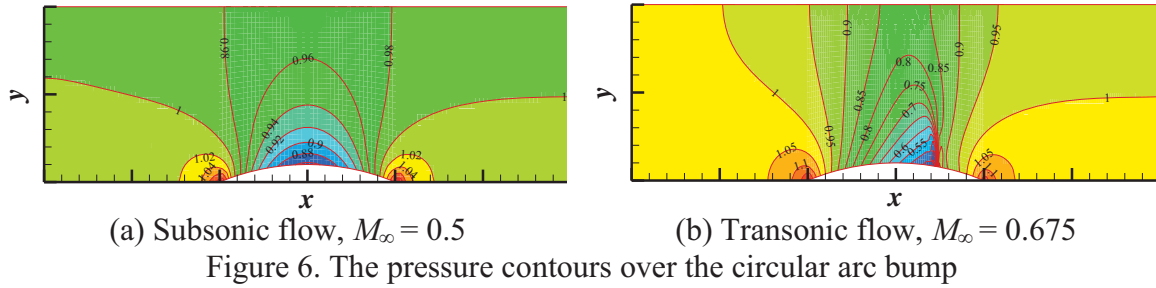
In the second step, the performance of multigrid method for the fourth-order compact method on the same geometry for both subsonic and transonic flows is investigated. . Figure 4(a) and Fig. 4(b) demonstrate the convergence rates between a single grid level, two grid levels and three grid levels multigrid with FMG for subsonic and transonic flow. Computations are performed using V-cycle procedure. It is worth mentioning that no significant difference between convergence rates of V-cycle and W-cycle computations is observed.





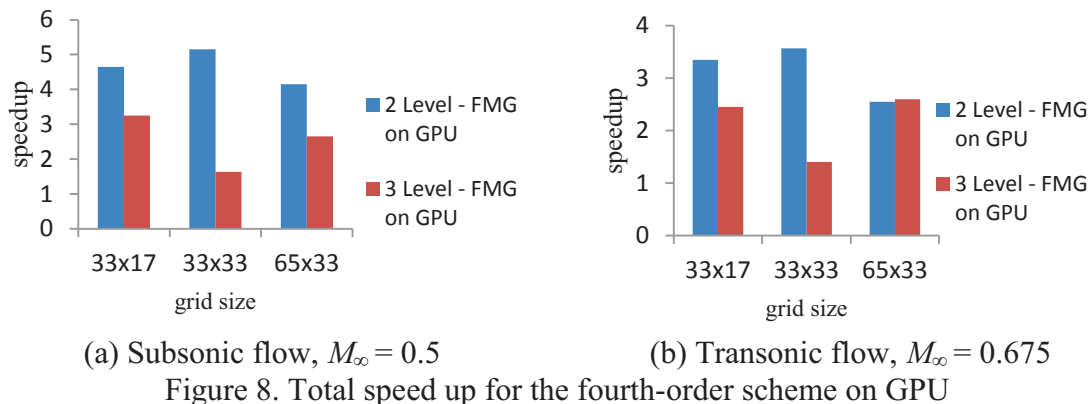
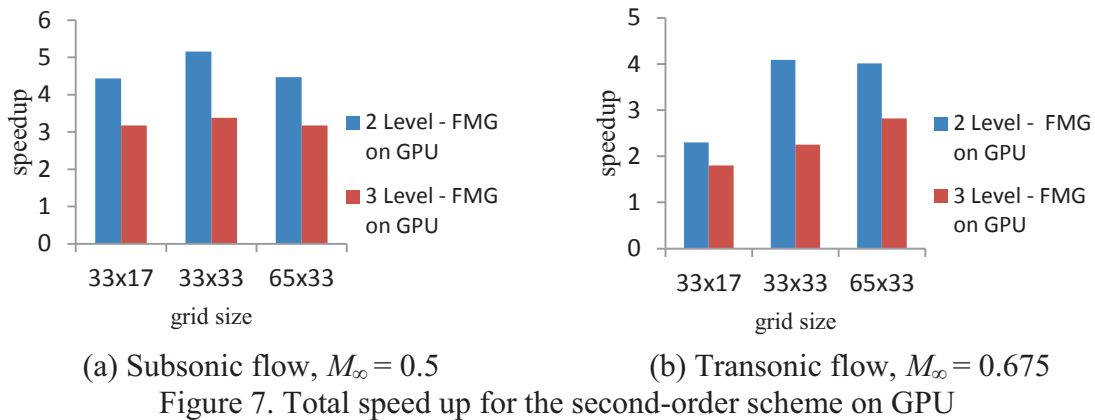
In Fig. 5(a) and Fig. 5(b) Mach number distribution of the present study compared to (Demirdžić, Lilek, & Perić, 1993). Figure 6(a) and Fig. 6(b) demonstrate the pressure contour for subsonic and transonic flow, respectively.





### Total performance

The total performance of the CFD code on the GPU, including the multigrid kernels and the BCR linear solver, is studied. Figure 7(a) and Fig. 7(b) show the overall GPU speedup of the two-dimensional subsonic and transonic flow test cases compared to the CPU platform for the second-order finite difference method. Figure 8(a) and Fig. 8(b) compare the solver speedup for the fourth-order compact finite difference method for  $M_\infty = 0.5$  and  $M_\infty = 0.675$ , respectively. Speedup term here is defined as the run time ratio obtained by single grid CPU- solver over the multigrid GPU-solver.



### Conclusion

A multigrid scheme is implemented on a two-dimensional Euler solver in order to accelerate convergence to steady state. Subsonic and transonic inviscid flows in a

channel with circular arc bump for both second-order central and fourth-order compact finite-difference methods are investigated as the test cases. The convergence acceleration obtained for second-order method is more than the fourth-order method. Moreover, the higher convergence rate for subsonic flow is observed in comparison to transonic flow. Total speedups between 2x–5.2x are achieved for different mesh sizes by implementing the GPU-based BCR solver in comparison to computations on the CPU platform.

## Acknowledgements

The authors would like to thank the Vehicle, Fuel and Environment Research Institute (VFERI) of University of Tehran for general support during this study.

## References

- Baghapour B., Esfahanian V., Torabzadeh M., Mahmoodi Darian H., (2013), A discontinuous Galerkin method with block cyclic reduction solver for simulating compressible flows on GPUs. *Submitted to Mathematics and Computers in Simulation*, MATCOM-S-13-00553.
- Bakhvalov, N. S. (1966), On the convergence of a relaxation method with natural constraints on the elliptic operator. *USSR Journal of Computational Mathematics and Mathematical Physics*, 6(5), 101-135.
- Brandt, A. (1977), Multi-level adaptive solutions to boundary-value. *problems. Mathematics of computation*, 31(138), 333-390.
- Brandt, A. (1981), Guide to Multigrid Development, Multigrid Methods I. *Lecture Notes in Mathematics*, 960, Springer Verlag.
- CUDA, C. (2012). Programming guide. NVIDIA Corporation.
- Demirdžić, I., Lilek, Ž., & Perić, M. (1993), A collocated finite volume method for predicting flows at all speeds. *International Journal for Numerical Methods in Fluids*, 16(12), 1029-1050.
- Fedorenko, R. P. (1962), A relaxation method for solving elliptic difference equations. *USSR Journal of Computational Mathematics and Mathematical Physics*, 1(4), 1092-1096.
- Gupta, M. M., Kouatchou, J. & Zhang, J. (1997), Comparison of second-and fourth-order discretizations for multigrid Poisson solvers. *Journal of Computational Physics*, 132(2), 226-232.
- Heller, D. (1976), Some aspects of the cyclic reduction algorithm for block tridiagonal linear systems. *SIAM Journal on Numerical Analysis*, 13(4), 484-496.
- Hemker, P.W. (1990), On the Order of Prolongations and Restrictions in Multigrid Procedures. *Journal of Computational and Applied Mathematics*, 32, pp. 423-429.
- Hirshman, S. P., Perumalla, K. S., Lynch, V. E., & Sánchez, R. (2010), BCYCLIC: A parallel block tridiagonal matrix cyclic solver. *Computational Physics*, 229(18), 6392-6404.
- Jameson, A. and Yoon, S. (1986), Multigrid Solutions of the Euler Equations using Implicit Schemes, " *AIAA J.*, 24, pp. 1737-1743.
- Jameson, A.(1983), Solution of the Euler Equations for Two-dimensional, Transonic Flow by a Multigrid Method. *Journal of Applied Mathematics and Computation*, 13, pp.327-356.
- Lele S. K. (1992), Compact finite difference schemes with spectral-like resolution. *Journal of Computational Physics* ;103:16–42.
- Ni, R.H. (1982), A multiple grid scheme for solving the Euler equations, *AIAA J.* 20, 1565-1571.
- Rizzi A. and Viviand H. (eds) (1981), Numerical methods for the computation of inviscid transonic flows with shock waves. *A GAMM workshop, in Notes on Numerical Fluid Mechanics Vieweg*, Braunschweig; 3.
- Sakurai, K., Aoki, T., Lee, W. H., & Kato, K. (2002), Poisson equation solver with fourth-order accuracy by using interpolated differential operator scheme. *Computers & Mathematics with Applications*, 43(6), 621-630.
- Stone, C. P., Duque, E. P., Zhang, Y., Car, D., Owens, J. D., & Davis, R. L. (2011). GPGPU parallel algorithms for structured-grid CFD codes. *InProceedings of the 20th AIAA Computational Fluid Dynamics Conference* (Vol. 3221).
- Wesseling, P. (1995), Introduction To Multigrid Methods (No. ICASE-95-11). *Institute for Computer Application in Science and Engineering Hampton VA*.

## Strong-stability-preserving explicit Runge-Kutta methods for SPH elastodynamics

\*L. He<sup>1</sup>, R.S. Crouch<sup>1</sup>, M. Seaid<sup>1</sup> and C.E. Augarde<sup>1</sup>

<sup>1</sup> School of Engineering and Computing Sciences,  
University of Durham,  
Durham DH1 3LE, UK

\* Corresponding author: lisha.he@durham.ac.uk

### Abstract

Developing an explicit time stepping scheme to accurately capture the dynamics in elastic materials is still a challenging problem. In the current study we investigate the accuracy and the stability of a family of explicit Runge-Kutta methods for the smoothed particle hydrodynamics (SPH) solution of equations in elastodynamics. The SPH method employs a purely meshless Lagrangian numerical technique for spatial discretization of the domain and it avoids many numerical difficulties related to re-meshing in mesh-based methods such as the finite element methods. The examined integration methods include the explicit Euler, explicit Runge-Kutta and explicit Runge-Kutta Chebyshev (RKC) schemes. Numerical results are presented for two test examples: shock-wave propagation in a one-dimensional problem and the velocity loading on a two-dimensional elastic plate. It is found that the proposed RKC scheme offers a robust and accurate approach for solving elastodynamics using SPH techniques.

**Keywords:** Elastodynamics, SPH method, explicit Runge-Kutta schemes, Numerical simulations

## Introduction

The Smoothed Particle Hydrodynamics (SPH) method was first developed by Lucy [6], Gingold and Monaghan [4]. In this method, the continuum domain is discretized into particles carrying the field variables. These variables are calculated from the contribution of the neighboring particles by means of a kernel function. The SPH is a truly meshless method based on the transformation of differential equations into integral ones which are then discretized using a distribution of moving particles. The SPH method has been traditionally applied to modeling fluid flows. In recent years, there has been a growing interest in applying SPH method to a wide variety of solid mechanics problems [5]. The main feature of SPH method is that it is a particle based technique and does not require any underlying grid structure to represent the problem geometry. This avoids the difficulties associated with traditional mesh-based methods (FEM, FVM and BEM), e.g. maintaining the integrity and quality of the mesh under large deformation. The mesh-free nature of the SPH method makes this method ideally suited to modeling processes that involve large deformations and discontinuities, such as fracture and fragmentation, metal forming, etc. It has given relatively good results in many applications in both fluid and solid dynamics.

The emphasis in this work is on the time integration of the resultant system of ordinary differential equations generated from the SPH space discretization of the transient elastodynamic problem. The

examined integration methods include the explicit Euler, explicit Runge-Kutta and explicit Runge-Kutta Chebyshev (RKC) schemes. In this paper, the SPH method is first explained, in relation to the discretization of the governing equations. Thereafter, time stepping techniques are employed to integrate the semi-discrete problem. After experiments with the different time integration schemes for a transient problem with known analytical solution, accuracy and efficiency of the different schemes are discussed. Numerical results are presented for two test examples: shock-wave propagation in a one-dimensional problem and velocity loading on a two-dimensional elastic plane. It is found that the proposed RKC scheme offers a robust and accurate approach for solving elastodynamics using SPH techniques.

## SPH Method in Elastodynamics

The governing equation in elastodynamics expresses of the conservation of momentum as follows

$$\frac{D\mathbf{v}}{Dt} = \frac{1}{\rho}\nabla\boldsymbol{\sigma}, \quad (1a)$$

where  $\nabla = (\frac{\partial}{\partial x}, \frac{\partial}{\partial y}, \frac{\partial}{\partial z})^T$  is the gradient operator,  $\rho$  the density,  $\mathbf{v}$  the velocity,  $\boldsymbol{\sigma}$  the stress tensor and  $(\frac{D}{Dt} = \frac{\partial}{\partial t} + \mathbf{v} \cdot \nabla)$  is the total derivative. In our case the density is constant in time and therefore no need to consider the energy equation. The mathematical model for small strains and displacements will be employed in this study. Thus,

$$\dot{\boldsymbol{\varepsilon}} = \frac{1}{2} \left( \nabla \cdot \mathbf{v} + (\nabla \cdot \mathbf{v})^T \right), \quad \dot{\boldsymbol{\sigma}} = \mathbf{D}^e \dot{\boldsymbol{\varepsilon}}, \quad (1b)$$

where the elastic constitutive matrix is given by

$$\mathbf{D}^e = \frac{E}{(1+\nu)(1-2\nu)} \begin{bmatrix} 1-\nu & \nu & \nu & 0 & 0 & 0 \\ \nu & 1-\nu & \nu & 0 & 0 & 0 \\ \nu & \nu & 1-\nu & 0 & 0 & 0 \\ 0 & 0 & 0 & \frac{1-2\nu}{2} & 0 & 0 \\ 0 & 0 & 0 & 0 & \frac{1-2\nu}{2} & 0 \\ 0 & 0 & 0 & 0 & 0 & \frac{1-2\nu}{2} \end{bmatrix}, \quad (2)$$

and  $E$  is Young's modulus,  $\nu$  is Poisson's ratio. Then we can reformulate the (1a) into another form,

$$\frac{1}{\rho}\nabla\boldsymbol{\sigma} = \nabla\left(\frac{\boldsymbol{\sigma}}{\rho}\right) + \frac{\boldsymbol{\sigma}}{\rho^2}\nabla\rho, \quad (3)$$

In the SPH method, the continuum domain  $\Omega$  is discretized into a set of  $N$  particles. The field variables and its spacial gradient can be determined from the contributions from the neighbouring particles

$$f_i = \sum_{j=1}^N \frac{m_j}{\rho_j} f_j \mathbf{W}_{ij}, \quad \nabla f_i = \sum_{j=1}^N \frac{m_j}{\rho_j} f_j \nabla \mathbf{W}_{ij}. \quad (4)$$

where  $W_{ij}$  is the smoothing (kernel) function. In the present work, we use the following B-spline function [7],

$$W(R, h) = \frac{15}{7\pi h^2} \begin{cases} \frac{2}{3} - 4R^2 + \frac{1}{2}(2R)^3, & \text{if } R < \frac{1}{2}, \\ 6(2 - 2R)^3, & \text{if } \frac{1}{2} \leq R < 1, \\ 0, & \text{if } R > 1, \end{cases} \quad (5)$$

with  $h$  is the smoothing length and  $R = \frac{|\mathbf{X}_i - \mathbf{X}_j|}{h}$ .

It is clear that for the particle near boundary, the support domain will lack neighbouring particles. To overcome this drawback we correct the approximation function using the procedure proposed in [1]. The correction forms are based on the principle that the smoothing function is normalised in the support domain  $\sum_{j=1}^N \frac{m_j}{\rho_j} W_{ij} = 1$ . Hence,

$$f_i = \frac{\sum_{j=1}^N \frac{m_j}{\rho_j} f_j W_{ij}}{\sum_{j=1}^N \frac{m_j}{\rho_j} W_{ij}} = \sum_{j=1}^N \frac{m_j}{\rho_j} f_j \tilde{W}_{ij}. \quad (6)$$

Since  $\nabla \mathbf{X}_i = \sum_{j=1}^N \frac{m_j}{\rho_j} \mathbf{X}_j \nabla W_{ij} = 1$  and  $\mathbf{X}_i \sum_{j=1}^N \frac{m_j}{\rho_j} \nabla W_{ij} = \sum_{j=1}^N \frac{m_j}{\rho_j} \mathbf{X}_i \nabla W_{ij} = 0$ , the equation (6) can be represented into two following forms,

$$\nabla f_i = \frac{\sum_{j=1}^N \frac{m_j}{\rho_j} f_j \nabla W_{ij}}{\sum_{j=1}^N \frac{m_j}{\rho_j} (\mathbf{X}_j - \mathbf{X}_i) \nabla W_{ij}} = \sum_{j=1}^N \frac{m_j}{\rho_j} f_j \tilde{\nabla} W_{ij}, \quad (7a)$$

$$\nabla f_i = \sum_{j=1}^N \frac{m_j}{\rho_j} (f_j - f_i) \tilde{\nabla} W_{ij}. \quad (7b)$$

Note that the second derivative of the kernel (5) is continuous, and the leading truncation error term is  $\mathcal{O}(h^2)$ . The finiteness of the kernel support means that only a limited number of neighbouring particles play a role in all the sums of conservation equations. This is used to reduce the computational time by building a link list between particles at each time step.

The artificial viscosity is always applied to reduce the unphysical oscillations and improve the numerical stability, which can be written as  $\Pi_{ij}$ . In this study we choose to apply the most popular expression of artificial viscosity which is developed by Monaghan [7],

$$\Pi_{ij} = \begin{cases} \frac{-\alpha_{\Pi} c_{ij} \phi_{ij} + \beta_{\Pi} \phi_{ij}^2}{\rho_{ij}}, & v_{ij} \cdot r_{ij} < 0, \\ 0, & v_{ij} \cdot r_{ij} \geq 0 \end{cases} \quad (8)$$

where we have  $\phi_{ij} = \frac{h_{ij} v_{ij} \cdot r_{ij}}{|r_{ij}|^2 + 0.01 h_{ij}^2}$ ,  $c_{ij} = \frac{c_i + c_j}{2}$ ,  $\rho_{ij} = \frac{\rho_i + \rho_j}{2}$ ,  $h_{ij} = 0.5(h_i + h_j)$ ,  $r_{ij} = r_i - r_j$  and  $v_{ij} = v_i - v_j$ .

Apply the SPH discretization into the elastodynamics system, the semi-discretized equations can be reformulated in a compact SPH form

$$\frac{D}{Dt} \begin{bmatrix} v_i^x \\ v_i^y \end{bmatrix} = \begin{bmatrix} \sum_{j=1}^N m_j \left( \frac{\sigma_j^{xx}}{\rho_j^2} + \frac{\sigma_i^{xx}}{\rho_i^2} - \Pi_{ij} \right) \frac{\partial \tilde{W}_{ij}}{\partial x} + \sum_{j=1}^N m_j \left( \frac{\sigma_j^{xy}}{\rho_j^2} + \frac{\sigma_i^{xy}}{\rho_i^2} \right) \frac{\partial \tilde{W}_{ij}}{\partial y} \\ \sum_{j=1}^N m_j \left( \frac{\sigma_j^{yx}}{\rho_j^2} + \frac{\sigma_i^{yx}}{\rho_i^2} \right) \frac{\partial \tilde{W}_{ij}}{\partial x} + \sum_{j=1}^N m_j \left( \frac{\sigma_j^{yy}}{\rho_j^2} + \frac{\sigma_i^{yy}}{\rho_i^2} - \Pi_{ij} \right) \frac{\partial \tilde{W}_{ij}}{\partial y} \end{bmatrix}. \quad (9a)$$

In practice, involving the difference of velocity between two interactive particles brings more accurate results than using single neighbouring particle's velocity. Then we can apply equation (7b) on the equation (1b),

$$\frac{D}{Dt} \begin{bmatrix} \sigma_i^{xx} \\ \sigma_i^{yy} \\ \sigma_i^{xy} \end{bmatrix} = \begin{bmatrix} \sum_{j=1}^N \frac{m_j}{\rho_j} \left( D_{11}v_j^x - D_{11}v_i^x \right) \frac{\partial \tilde{W}_{ij}}{\partial x} + \sum_{j=1}^N \frac{m_j}{\rho_j} \left( D_{12}v_j^y - D_{12}v_i^y \right) \frac{\partial \tilde{W}_{ij}}{\partial y} \\ \sum_{j=1}^N \frac{m_j}{\rho_j} \left( D_{21}v_j^x - D_{21}v_i^x \right) \frac{\partial \tilde{W}_{ij}}{\partial x} + \sum_{j=1}^N \frac{m_j}{\rho_j} \left( D_{22}v_j^y - D_{22}v_i^y \right) \frac{\partial \tilde{W}_{ij}}{\partial y} \\ \sum_{j=1}^N \frac{m_j}{\rho_j} \left( D_{33}v_j^y - D_{33}v_i^y \right) \frac{\partial \tilde{W}_{ij}}{\partial x} + \sum_{j=1}^N \frac{m_j}{\rho_j} \left( D_{33}v_j^x - D_{33}v_i^x \right) \frac{\partial \tilde{W}_{ij}}{\partial y} \end{bmatrix}, \quad (9b)$$

where  $D_{ij}$  are the entries of the elastic matrix  $\mathbf{D}$  for plane stress *i.e.*,  $\mathbf{D} = \frac{E}{(1-\nu^2)} \begin{bmatrix} 1 & \nu & 0 \\ \nu & 1 & 0 \\ 0 & 0 & \frac{1-\nu}{2} \end{bmatrix}$ .

## Strong-stability-preserving explicit Runge-Kutta methods

The solution procedure for equations (9) is completed when a time integration of the semi-discrete SPH equations is selected. This stage can be handled by any implicit ordinary differential equation (ODE) solver, since they are computationally without risk by virtue of their accuracy and linear unconditionally stability. This allows for larger time steps in the integration process. However, due to the large set of linear system of algebraic equations at each time step, these methods may be computationally inefficient. As an alternative, we use a class of explicit Runge-Kutta methods. Applied to the system (9), the SPH discretization can be reformulated in a compact system of ODE of this form

$$\frac{d\mathbf{U}}{dt} = \mathbf{F}(\mathbf{U}), \quad t \in (0, T], \quad (10)$$

where  $\mathbf{U} = [\sigma_{xx} \ \sigma_{yy} \ \sigma_{xy} \ v_x \ v_y]^T$  and the right-hand side  $\mathbf{F}(\mathbf{U})$  is defined accordingly to (9). It should be stressed that, because explicit time stepping schemes evaluate explicitly the right-hand side of the equation (10), then it has to satisfy a stability condition. This stability criterion can be reached based on the Courant-Friedrichs-Levy (CFL) condition

$$c \frac{\Delta t}{\Delta x} \leq 1, \quad (11)$$

where  $c = \sqrt{\frac{E}{\rho}}$  is the wave speed and  $\Delta x$  is the initial spacing between two particles. Difficulties often appear when the spectral radius of the Jacobian of  $\mathbf{F}$ ,  $\partial\mathbf{F}/\partial\mathbf{U}$ , has large eigenvalues. This may give rise to numerical stiffness. Thus, time integration schemes for (10) depend strongly on the spectral radius  $\rho(\partial\mathbf{F}/\partial\mathbf{U})$  and grid refinements, and for these reasons it is preferable that these schemes have to be either implicit or explicit with large stability regions. In the current work, we consider the RKC method studied for example in [2, 8, 3]. The RKC method has been designed for explicit time integration of systems of parabolic equations. To solve (10) the RKC scheme takes the

form

$$\begin{aligned}
 \mathbf{U}^{(0)} &= \mathbf{U}^n, \\
 \mathbf{U}^{(1)} &= \mathbf{U}^{(0)} + \tilde{\mu}_1 \mathbf{F}^{(0)} \\
 \mathbf{U}^{(j)} &= \mu_j \mathbf{U}^{(j-1)} + \nu_j \mathbf{U}^{(j-2)} + (1 - \mu_j - \nu_j) \mathbf{U}^{(0)} + \tilde{\mu}_j \mathbf{F}^{(j-1)} + \tilde{\gamma}_j \mathbf{F}^{(0)}, \quad 2 \leq j \leq s, \\
 \mathbf{U}^{n+1} &= \mathbf{U}^{(s)},
 \end{aligned} \tag{12}$$

where  $\mathbf{U}^n$  is the solution computed at time step  $t_n$ ,  $\mathbf{F}^{(j)}$  denotes the term  $\mathbf{F}(t_n + c_j \Delta t, \mathbf{U}^{(j)})$  and  $\mathbf{U}^{(j)}$  are internal vectors for RKC stages. The coefficients in (12) are available in analytical form for arbitrary  $s \geq 0$  from [2, 8]. For convenience of the reader we include the formulae for these coefficients. Consider the Chebyshev polynomial of the first kind of degree  $j$

$$T_j(z) = \cos(j \arccos z), \quad -1 \leq z \leq 1.$$

Then

$$\begin{aligned}
 \epsilon &= \frac{2}{13}, \quad q_0 = 1 + \frac{\epsilon}{s^2}, \quad q_1 = \frac{T'_s(q_0)}{T''_s(q_0)}, \\
 b_j &= \frac{T''_j(q_0)}{(T'_j(q_0))^2}, \quad (2 \leq j \leq s), \quad b_0 = b_2, \quad b_1 = b_2,
 \end{aligned}$$

and

$$\begin{aligned}
 \tilde{\mu}_1 &= b_1 q_1, \quad \mu_j = 2q_0 \frac{b_j}{b_{j-1}}, \quad \nu_j = -\frac{b_j}{b_{j-2}}, \quad \tilde{\mu}_j = 2q_1 \frac{b_j}{b_{j-1}}, \\
 \tilde{\gamma}_j &= (1 - b_{j-1} T_{j-1}(q_0)) \tilde{\mu}_j, \quad (2 \leq j \leq s).
 \end{aligned}$$

The coefficients  $c_j$  are

$$c_j = \frac{T'_s(q_0) T''_j(q_0)}{T''_s(q_0) T'_j(q_0)} \approx \frac{j^2 - 1}{s^2 - 1} \quad (2 \leq j \leq s), \quad c_1 = \frac{c_2}{T'_2(q_0)} \approx \frac{c_2}{4}, \quad c_s = 1.$$

It should be pointed out that two criteria have been taken into consideration for the calculation of the above coefficients namely, (i) the real stability boundary,  $\beta(s)$ , has to be as large as possible to obtain good stability properties for parabolic equations, and (ii) the application of the method with arbitrary number of stages should not damage the convergence properties, that is, the accumulation of local errors does not grow without bound. Observe that the number of stages  $s$  in our SPH method and the conventional RKC scheme varies with  $\Delta t$  such that, see [8],

$$s = 1 + \left\lceil \sqrt{1 + \frac{c \Delta t}{0.653 \Delta x}} \right\rceil, \tag{13}$$

where  $\lceil x \rceil$  denotes the integer part of  $x$  and  $c = \sqrt{\frac{E}{\rho}}$  is the wave speed.

## Numerical results

We then examine the performance of the proposed time stepping schemes for SPH method for a class of elastic problems in one and two dimensions. In the first example we solve the problem of propagation of a shock wave on a one dimensional elastic magnesium bar and the second example solve a large deformation problem in two dimensional elastic magnesium plate.



### One-dimensional shock-wave propagation

In this example we solve the problem of propagation of a shock wave on one-dimensional magnesium bar. The length of the bar  $L = 1m$  with material properties of  $\rho = 1738 \text{ kg/m}^3$  and the Young's modulus  $E = 45 \times 10^9 \text{ Pa}$ . Initial the bar is at rest with  $v = 0$  and  $\sigma = 0$ . The velocity at the right end of the bar is fixed ( $v = 0$ ) and we apply a compression stress on the left boundary  $\sigma_0 = 8.8436 \times 10^6 \text{ Pa}$ . The analytical velocity of the shock wave in this problem could be easily calculated by  $v_0 = \sigma_0/\sqrt{E\rho} = 1 \text{ m/s}$ . The wave will propagate through the bar with the wave speed  $c = \sqrt{E/\rho} = 5.0884 \times 10^3 \text{ m/s}$ . When the wave arrives the fixed right end of the bar, the stress at this point will double to become  $17.6872 \times 10^6 \text{ Pa}$ . In Figure 1(a), 1(b), 1(c) and 1(d), we

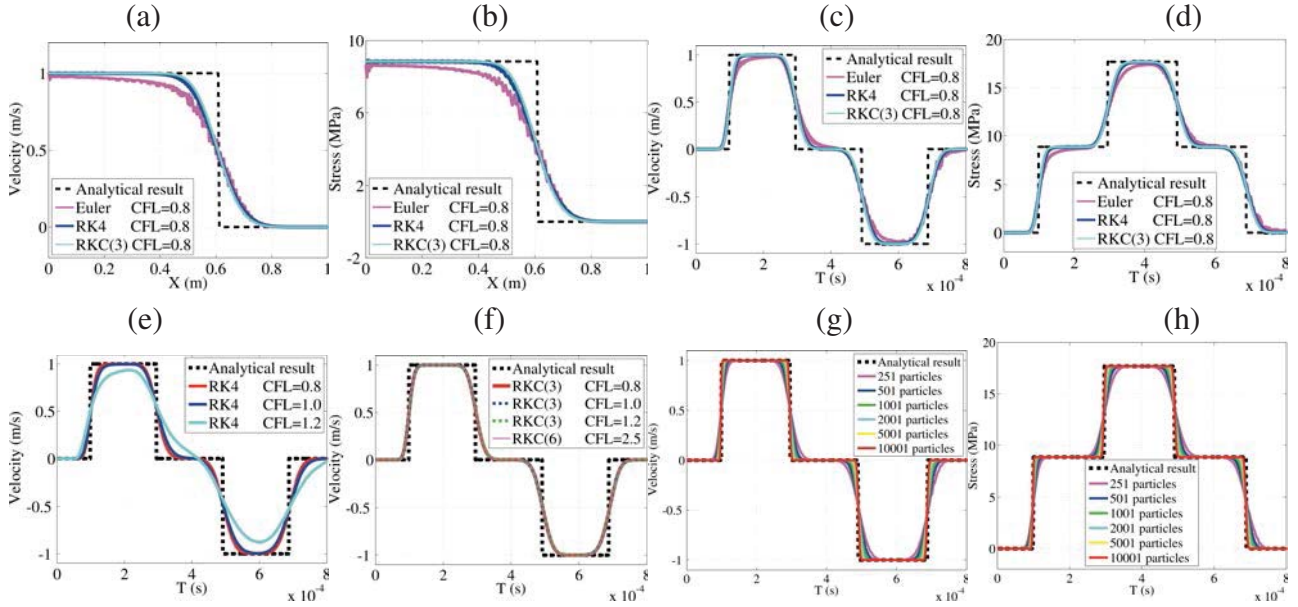


Figure 1: Numerical results for the shock-wave propagation problem.

present the velocity and the stress along the bar at time  $t = 1.2 \times 10^{-3} \text{ s}$  and the time evolution of velocity and stress at the mid point of the bar ( $x = L/2$ ), obtained using the considered time stepping schemes and 251 particles. It is evident from these results that the RKC scheme with 3 stages produces more stable and accurate results than the other considered schemes. As we know, the stability will decrease while increasing the value of CFL in normal time stepping schemes, like the RK4 scheme shown on Figure 1(e). However Figure 1(f) shows that the RKC scheme can still present stable results with a larger value of CFL in condition with increasing number of stages. To further examine the convergence of the RKC scheme applied in the SPH method, we then apply the RKC scheme with more particles, as shown on Figure 1(g) and 1(h). The error rates of using the SPH method for solving Example 1 with different time schemes are shown in Table 1, the error rate is obtained from the equation,

$$error_1 = \frac{\sum |u^{SPH} - u^{exact}|}{\sum |u^{exact}|}.$$

### Two-dimensional elastic plane

As a second example we consider a two-dimensional version of the previous example solved in the computational domain shown in Figure 2. The material properties of the plane are  $\rho = 2000 \text{ kg/m}^3$ ,

Table 1: Error rate of using the SPH method for solving Example 1 with different time schemes.

# nodes	CFL = 0.8			CFL=1.0			CFL=2.5		
	Euler	RK4	RKC	Euler	RK4	RKC	Euler	RK4	RKC
251	0.2417	0.1866	0.1661	-	0.2313	0.1655	-	-	0.1655
501	0.1676	0.1306	0.1165	-	0.1616	0.1165	-	-	0.116
1001	0.1157	0.092	0.082	-	0.1135	0.0821	-	-	0.0815
2001	0.0747	0.0651	0.0579	-	0.0802	0.0579	-	-	0.0574

the Youngs modulus  $E = 80 \times 10^6 Pa$  and the Poisson ratio  $\nu = 1/3$ . Fixed boundary conditions are applied on the upper and right sides of the plane, whereas, the velocity on the lowest left circular boundary is given as

$$v(t) = \begin{cases} 5 \text{ m/s}, & \text{if } t \leq 1.8 \times 10^{-3} \text{ s}, \\ 0 \text{ m/s}, & \text{otherwise.} \end{cases}$$

Based on the observations drawn from the previous example, we present numerical results obtained using the RKC scheme. We also examine the performance of our SPH method for three different node distributions exhibited in Figure 2. The corresponding node statistics along with the time steps used for each nodal distribution are summarized in Table 2. In this table we also include the minimum and maximum values of the principal stress obtained for the considered nodal distributions and a reference solution obtained on a very fine SHP nodal distribution.

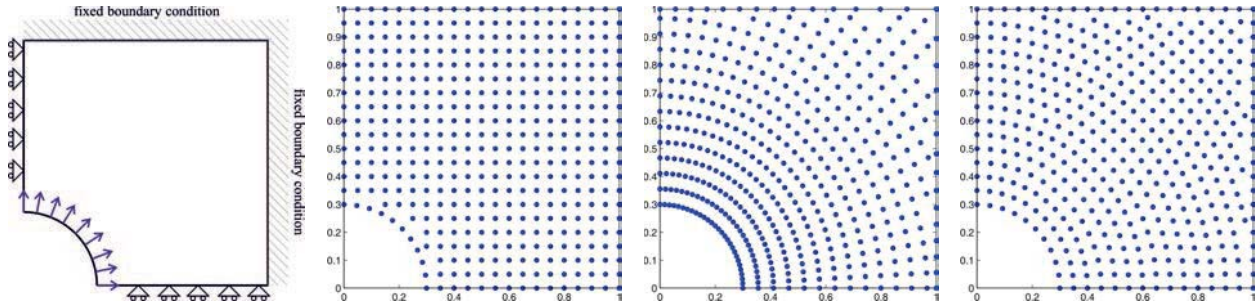


Figure 2: Computational domain and node collocations for Example 2.

Table 2: Nodal statistics and results for the principal stresses obtained using the SPH method for solving Example 2.

	# nodes	$\Delta t$	$t = 0.0018 \text{ s}$		$t = 0.003 \text{ s}$		$t = 0.0048 \text{ s}$	
			max $\sigma_p$	min $\sigma_p$	max $\sigma_p$	min $\sigma_p$	max $\sigma_p$	min $\sigma_p$
Reference	24170	1.25e-5	3.01e+6	0	1.87e+6	-1.26e+5	2.86e+6	-1.50e+6
Equal radial	2446	1.20e-4	2.95e+6	0	1.96e+6	-2.60e+5	2.96e+6	-1.96e+6
Uniform	2423	1.20e-4	3.23e+6	0	1.93e+6	-2.83e+5	2.64e+6	-3.83e+5
Radial	2376	1.19e-4	2.99e+6	0	1.64e+6	-1.21e+5	2.72e+6	-3.14e+5

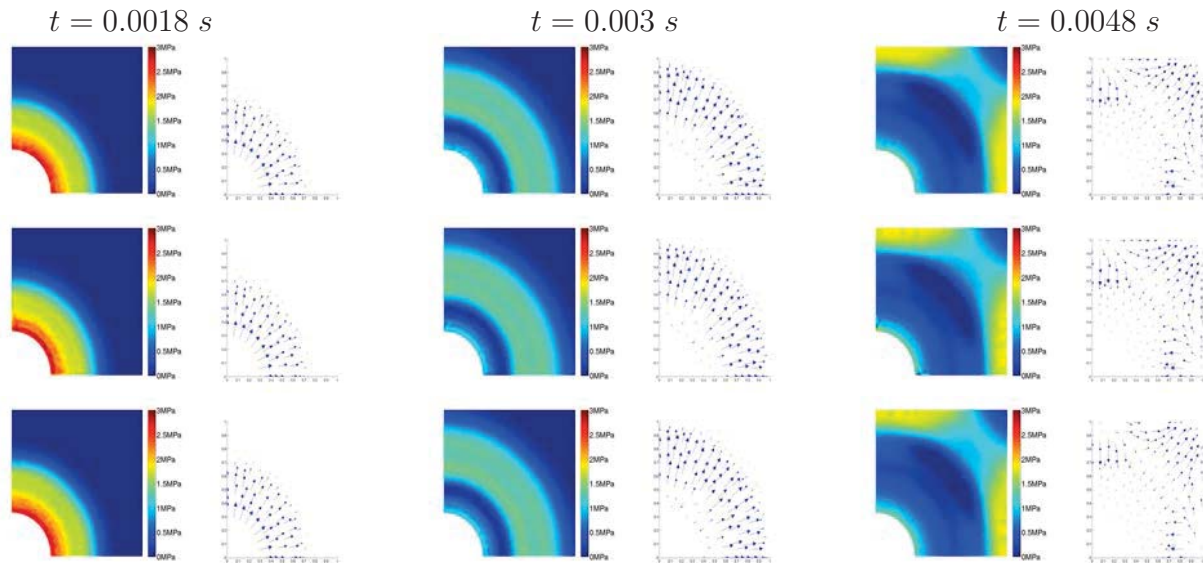


Figure 3: Stress distributions and velocity fields obtained for different node collocations and at three different simulation times. Uniform distribution (first row), radial distribution (second row) and equally radial distribution (third row).

In Figure 3 we present the stress distributions and velocity fields obtained for different node collocations and at three different simulation times namely  $t = 0.0018\text{ s}$ ,  $t = 0.003\text{ s}$  and  $t = 0.0048\text{ s}$ . At early simulation times, a shock wave is generated and propagates along the main diagonal in the computational domain. Reflections from fixed boundaries in the domain are also captured by the SPH method for all the considered nodal distributions. The reflection features are more visible in the velocity fields than the stress distributions at  $t = 0.0048\text{ s}$ . From the presented results it is evident that the nodal distribution in the considered SPH method affects quantitatively and qualitatively the simulated results. The artificial viscosity has been considered in all the analysis of example 2. It seems that, for the considered material properties and the boundary conditions, at the early stage  $t = 0.0018\text{ s}$ , the SPH method using the radial and equally radial nodal distributions produces more accurate results in term of both stress and velocity fields, because the distances between two nearest neighbouring particles near the curve boundary are similar in these two distributions, which bring more reasonable results. When the wave propagates to the fixed boundary and reflects ( $t = 0.0048\text{ s}$ ), the uniform distribution brings smoother results than others in terms of both stress and velocity, because the the distances between two nearest neighbouring particles near the fixed boundary are similar in uniform distribution, which can brings more accurate results.

## References

- [1] J. Bonet and S. Kulasegaram. Correction and stabilization of smooth particle hydrodynamics methods with application in metal forming simulations. *Int. J. Numer. Methods Eng*, 47:1189–1214, 2000.
- [2] P.J. Van der Houwen. Explicit Runge-Kutta formulas with increased stability boundaries. *Numer. Math.*, 20:149–164, 1972.

- [3] P.J. Van der Houwen and B.P. Sommeijer. On the internal stability of explicit, m-stage Runge-Kutta methods for large m-values. *Z. Angew. Math. Mech.*, 60:479–485, 1980.
- [4] R. A. Gingold and J. J. Monaghan. Smoothed particles hydrodynamics: theory and application to non-spherical stars. *Monthly Notices of the Royal Astronomical Society*, 181:375–389, 1977.
- [5] M. B. Liu and G. R. Liu. Smoothed particle hydrodynamics (sph): an overview and recent developments. archives of computational methods in engineering. *Monthly Notices of the Royal Astronomical Society*, 17(1):25–76, 2010.
- [6] L. B. Lucy. A numerical approach to the testing of the fission hypothesis. *Astronomical Journal*, 82(12):1013–1024, 1977.
- [7] J. J. Monaghan. Smoothed particle hydrodynamics. *Astro. Astrophys*, 30:543–574, 1992.
- [8] J.G. Verwer, W.H. Hundsdorfer, and B.P. Sommeijer. Convergence properties of the Runge-Kutta-Chebyshev method. *Numer. Math.*, 57:157–178, 1990.

## Nonparametric Reliability-based Design Optimization

### Using Sign Test on Limited Discrete Information

W. Lim, J. Jang, S. Park, E. Amalnerkar and \*T.H. Lee

Department of Automotive Engineering, Hanyang University, 222, Wangsimni-ro, Seongdong-gu, Seoul 133-791, Korea.

\*Corresponding author: thlee@hanyang.ac.kr

#### Abstract

Many methods for reliability analysis and reliability-based design optimization have been developed since the last decades. However, for most of these methods predicting the reliability, stochastic information of the variables has to be assumed as parameters like the mean (location parameter) and variance (scale parameter). This assumption cannot guarantee the accuracy of the reliability when information is limited. In this paper, we propose a nonparametric RBDO using sign test that does not consider the parameter but requires limited discrete information, like only sample data. We define the uncertainty of the reliability as the decision error of nonparametric hypothesis test due to limited information. We examine the tendency of the solution with respect to the reliability of a system and the uncertainty of the reliability through an example.

**Keywords:** Reliability analysis, Reliability-based design optimization, Uncertainty of reliability, Reliability error, Sign test, Limited discrete information

#### Introduction

In deterministic design optimization, since uncertainty of input variables does not considered, the reliability of a system cannot be evaluated. Thus, a safety factor has been employed to guarantee the reliability. To consider the reliability of a system, stochastic design optimization such as reliability-based design optimization (RBDO) has been developed. RBDO can provide an optimum point satisfying target the reliability of a system by using stochastic information of input variables.

There are many methods for reliability analysis such as the first and second order reliability method (Cornell, 1969; Breitung, 1984), moment-based method (Lee and Kwak, 2006; Rahman and Xu, 2004) and its implementation to RBDO (Shetty et al., 1998; Shan and Wang, 2007). Generally, in reliability analysis, uncertainty of a system is caused by uncertainty of input variables. In these methods, to treat the uncertainty, distribution of input variables has to be assumed as parameter such as statistical moments. However, in practical problems, information of input variables is often limited and discrete. Thus, the reliability of a system also has uncertainty because of the lack of information. Therefore, to treat the limited discrete information, we should consider the reliability of a system as well as the uncertainty of the reliability.

Recently, RBDO with confidence level under input model uncertainty is suggested (Noh et al., 2011). They assume that the uncertainty of the reliability is due to uncertainty of parameters of input variables and considered as a confidence level of the parameters. However, the method cannot quantify the uncertainty of the reliability but provides qualitative trends of the uncertainty of the reliability.

In this paper, we propose a new approach for nonparametric RBDO (NRBDO) using sign test. We assume that the uncertainty of the reliability is caused by the limited discrete information. A reliability analysis method, for instance, Akaike information criterion (AIC)-based reliability analysis method (Lim and Lee, 2012) is adopted to estimate the reliability of a system for discrete information. With the estimated reliability, we estimate the uncertainty of the reliability by using nonparametric sign test for limited discrete information. The proposed method can quantify the reliability of a system as well as the uncertainty of the reliability. For convenience, we name the reliability of a system and the uncertainty of the reliability as the first and second reliabilities, respectively. Using an example of RBDO with limited and discrete information of input variables, we evaluate the first and second target reliabilities.

We introduce AIC and sign test, then we formulate NRBDO in the second section. In the third section, we illustrate and compare deterministic design optimization (DDO), RBDO and NRBDO for a mathematical example. In the last section conclusions are summarized. When information of input variables is limited and discrete, the proposed method can obtain optimum point considering the reliability of a system as well as the uncertainty of the reliability.

### **Nonparametric Reliability-based Design Optimization**

In this section, we introduce AIC and sign test. AIC is adopted to estimate the reliability using discrete information. Then, considering limited discrete information, sign test is used to decide whether the second reliability namely the uncertainty of the reliability is acceptable or not. Combining these two concepts, we achieve an optimum result satisfying the first as well as the second reliabilities for limited discrete information.

#### *Reliability Analysis Using Akaike Information Criterion*

Akaike information criterion was introduced in 1973 by Akaike (Akaike, 1973) and has been developed and implemented on various fields of science such as statistics, ecology, engineering and reliability analysis (Lim and Lee, 2012; Hurvich et al., 1998; Pan, 2001; Spendelov et al., 1995; Al-Rubaie et al., 2007; Go et al., 2011).

AIC is a method that selects the best estimated distribution from candidate distributions provided by a user. The AIC is defined as follows (Sakamoto et al., 1986):

$$\varphi = -2(f_{ml} - n_{free}) \quad (1)$$

where  $f_{ml}$  is maximum log likelihood of a candidate distribution, and  $n_{free}$  stands for the number of parameters of a candidate distribution.

In this paper, we use six types of distribution: normal distribution, log-normal distribution, Gamma distribution, Weibull distribution, exponential distribution and generalized extreme value distribution. When the likelihood of a candidate distribution is approaching maximum, the probability of estimation becomes the highest. Hence, we choose the best estimated distribution with the smallest  $\varphi$ . Then we estimate the first reliability by integrating its probability density function.

### Second Reliability Analysis Using a Sign Test

The sign test is one of the oldest nonparametric hypothesis tests. In order to make a decision, whether to reject the null hypothesis or not, a binomial distribution is used to calculate the rejection or critical region (Conover, 1980).

Let  $P(+)$  and  $P(-)$  be the ratio of success and failure, respectively. Then the null and alternative hypothesis of sign test is given as follows:

$$H_0: P(+) \geq P(-) \quad (2)$$

$$H_a: P(-) < P(+)$$

As the number of successes increases, i.e.,  $P(+)$  increases, decreasing the chances of rejection of the null hypothesis. When we undertake a hypothesis test, a decision error always exists. In this case, there is a type II error since we do not reject null hypothesis. We decide a hypothesis using critical region calculated by integrating the binomial distribution. The probability mass function of binomial distribution is of form as follows:

$$y(x|n_t, p) = \binom{n_t}{x} p^x (1-p)^{n_t-x} \quad (3)$$

where  $n_t$  is the number of trials,  $p$  stands for success probability, and  $x$  is the number of successes which is a non-negative integer.

The critical region can be calculated by a summation of Eq. (3). The summation is of form as follows:

$$R_2 = \sum_{i=0}^{n_s} y(i|n_t, p) \text{ for non-negative integer } i \quad (4)$$

where  $n_s$  is the number of success and  $R_2$  stands for the second reliability. Also we can treat Eq. (3) on non-negative real number by using Gamma function. Then Eqs. (3) and (4) can be rewritten as follows:

$$y(x|n_t, p) = \frac{\Gamma(n_t+1)}{\Gamma(n_t-x+1)\Gamma(x+1)} p^x (1-p)^{n_t-x} \quad (5)$$

$$R_2 = \int_0^{n_s} y(x|n_t, p) dx \text{ for non-negative real number } x \quad (6)$$

We can estimate the first reliability using Akaike information criterion, and then estimate the number of success by Eq. (7).

$$n_s = R_1 n_t \quad (7)$$

where  $R_1$  is the first reliability, the reliability of a system. Then, the second reliability using Eq. (6) can be estimated and a decision not to reject the null hypothesis if the second reliability is greater than the second target reliability can then be made.

### Mathematical Example

We choose an example for optimization (Noh et al., 2011; Youn and Choi, 2004; Youn and Wang, 2008; Lee et al., 2013) consisting of two design variables and three constraint functions. The optimization formulation of the example is of form in Eq. (8)

Firstly, we find the optimum point using DDO. Secondly, we find the optimum point using RBDO with respect to target reliability. Finally, we find the optimum point

using NRBDO with respect to the reliability of a system and the uncertainty of the reliability. In this section, each of the results is illustrated.

$$\text{Find } x_1, x_2 \quad (8)$$

$$\text{to minimize } f(\mathbf{x}) = -x_1 + x_2$$

$$\text{subject to } g_1(\mathbf{x}) = 1 - \frac{x_1^2 x_2}{20}$$

$$g_2(\mathbf{x}) = 1 - \frac{(x_1 + x_2 - 5)^2}{30} + \frac{(x_1 - x_2 - 12)^2}{120}$$

$$g_3(\mathbf{x}) = 1 - \frac{80}{(x_1^2 + 8x_2 + 5)}$$

#### *Deterministic Design Optimization*

DDO problem is formulated in Eq. (8). It is easy to obtain the optimum point. We use 'fmincon' in MATLAB to solve the optimization problem. We can obtain minimum value of -5.9955 at  $\mathbf{x} = (7.7883, 1.7928)$ . The active constraint functions are  $g_2(\mathbf{x})$  and  $g_3(\mathbf{x})$  at the optimum point. However, DDO cannot consider the uncertainty of the input variables. Therefore, the optimum point can exist in infeasible region if any uncertainty of the input variables occurs.

#### *Reliability-based Design Optimization*

RBDO formulation is of form as follows:

$$\text{Find } x_1, x_2 \quad (9)$$

$$\text{to minimize } f = -x_1 + x_2$$

$$\text{subject to } \Pr[G_j(\mathbf{X}) \leq 0] \geq R_1^{\text{target}}, j = 1, 2, 3$$

$$G_1(\mathbf{X}) = 1 - \frac{X_1^2 X_2}{20}$$

$$G_2(\mathbf{X}) = 1 - \frac{(X_1 + X_2 - 5)^2}{30} + \frac{(X_1 - X_2 - 12)^2}{120}$$

$$G_3(\mathbf{X}) = 1 - \frac{80}{(X_1^2 + 8X_2 + 5)}$$

Generally, in deterministic design optimization, the uncertainty of the input variables cannot be considered. Therefore, to treat the uncertainty, we assume distribution of the input variables as the normal distribution, and then obtain  $10^6$  random samples from the distribution. The assumed distribution is as follows:

$$X_i \sim N(x_i, \sigma^2), i = 1, 2, \sigma = 0.3 \quad (10)$$

We use Monte Carlo simulation to estimate the reliability of a system using  $10^6$  samples. A genetic algorithm is used as the optimization algorithm.

When the first target reliability is 0.5, the result is similar to that of DDO. Because we assume the distribution of the input variables as the normal distribution, the probability of success is almost 1/2. However, if the first target reliability changes, the optimum point obviously changes. The results of optimum point and its objective value with respect to the first target reliability are shown in Table 1. If the design requires higher reliability, then the objective function should have a higher value.



*Nonparametric Reliability-based Design Optimization*

Using hypothesis test, NRBDO formulation can be written as follows:

$$\text{Find } x_1, x_2 \tag{11}$$

$$\text{to minimize } f = -x_1 + x_2$$

$$\text{subject to do not reject } H_0: \Pr[G_j(\mathbf{X}) \leq 0] \geq R_1^{\text{target}} \text{ with } R_2^{\text{target}}, j = 1, 2, 3$$

$$R_2^{\text{target}} = 1 - \text{type II error}$$

$$G_1(\mathbf{X}) = 1 - \frac{x_1^2 x_2}{20}$$

$$G_2(\mathbf{X}) = 1 - \frac{(X_1 + X_2 - 5)^2}{30} + \frac{(X_1 - X_2 - 12)^2}{120}$$

$$G_3(\mathbf{X}) = 1 - \frac{80}{(X_1^2 + 8X_2 + 5)}$$

In NRBDO, we obtain 50 random samples from Eq. (10). As explained above, if the number of samples is small, we cannot assure that the reliability of a system is accurate. Therefore, the uncertainty of the reliability must be considered due to limited information.

Results of NRBDO are summarized and illustrated in Table 2 and Figure 1, respectively. For the cases 1, 2 and 3, from the point of view of DDO, these optimum points are in infeasible region since the first target reliability is 0.1. For cases 2, 5 and 8, the second target reliability is 0.5, so results of these cases are similar to those of RBDO. For cases 4, 5 and 6, the first target reliability is 0.5 and the second target reliabilities are different. For case 4, optimum point is in infeasible region because the second reliability guarantees probability of 0.1. However, for case 6, optimum point is in feasible region because the second reliability guarantees probability of 0.9. From the result of optimum point, we can show the trend with respect to the first and second target reliabilities. Note that as the target reliability increases, objective value also increases.

Results of DDO, RBDO and NRBDO are shown in Table 3 with the first and second reliabilities of 0.5. When distribution of input variables is symmetric and the first target reliability is 0.5, RBDO result is similar to DDO result. However, in RBDO, since we do not consider the number of samples to estimate the distribution of input variables, we cannot quantify the uncertainty of the reliability. In NRBDO, since we consider the number of samples and the second target reliability as 0.5, NRBDO result is similar to RBDO result. So these result shows that the proposed method is slightly more feasible than other methods.

**Table 1. Comparison of RBDO results with respect to  $R_1^{\text{target}}$**

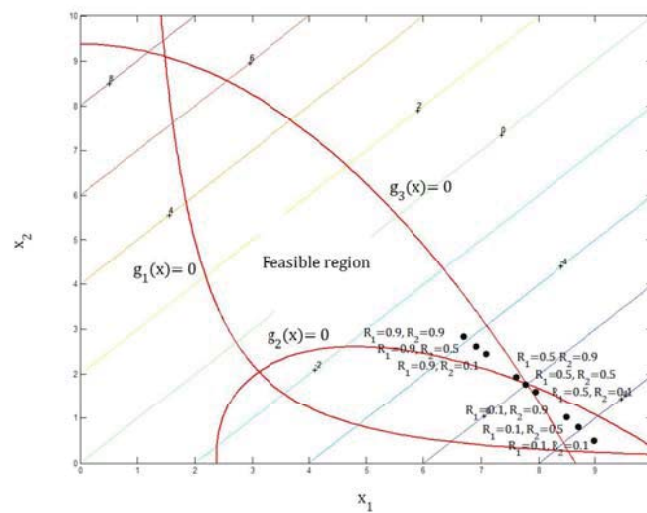
$R_1^{\text{target}}$	0.1	0.5	0.9
$x_1$	8.7014	7.7907	6.9316
$x_2$	0.8139	1.7866	2.5821
$f(\mathbf{x})$	-7.8874	-6.0041	-4.3495

**Table 2. Comparison of NRBDO results with respect to  $R_1^{\text{target}}$  and  $R_2^{\text{target}}$** 

Case	$R_1^{\text{target}}$	$R_2^{\text{target}}$	$x_1$	$x_2$	$f(x)$
1	0.1	0.1	8.9747	0.5026	-8.4721
2	0.1	0.5	8.7058	0.8054	-7.9003
3	0.1	0.9	8.4971	1.0322	-7.4640
4	0.5	0.1	7.9318	1.6221	-6.3096
5	0.5	0.5	7.7672	1.7870	-5.9802
6	0.5	0.9	7.6049	1.9475	-5.6573
7	0.9	0.1	7.0807	2.4582	-4.6225
8	0.9	0.5	6.9041	2.6318	-4.2723
9	0.9	0.9	6.6894	2.8483	-3.8411

**Table 3. Comparison of results of DDO, RBDO and NRBDO**

	DDO	RBDO	NRBDO
$n_t$	NA	$10^6$	50
$R_1^{\text{target}}$	NA	0.5	0.5
$R_2^{\text{target}}$	NA	NA	0.5
$x_1$	7.7883	7.7907	7.7672
$x_2$	1.7928	1.7866	1.7870
$f(x)$	-5.9955	-6.0041	-5.9802

**Figure 1. Nonparametric reliability-based design optimization result**

## Conclusions

In practical problems, the information of variables is often limited and discrete. However, recent studies of RBDO have to assume that the information of the input variables has a continuous distribution. Thus, the reliability estimated using recent methods has some uncertainty if we have only limited discrete information of the input variables. When we have limited discrete information, the uncertainty of the

reliability as well as the reliability of a system should be considered. In order to consider the uncertainty of the reliability, we proposed a new method of NRBDO.

We consider the reliability of a system and the uncertainty of the reliability as the first and second reliabilities, respectively. To estimate the first reliability, we adopt AIC. In AIC, we use six types of candidate distributions, and then we select the best estimated distribution by maximizing the likelihood function of each candidate distribution. Using the best estimated distribution, we estimate the first reliability. To treat the uncertainty of the reliability, we perform nonparametric hypothesis test using sign test. In the sign test, the rejection region is calculated from binomial probability mass function.

To verify the proposed method, we use a mathematical example. Firstly, deterministic design optimization is performed without stochastic information of input variables. Secondly, RBDO is performed with respect to the first target reliability of 0.1, 0.5 and 0.9, respectively. The optimum point of RBDO with the first target reliability of 0.5 converges to DDO result. Finally, NRBDO is performed with respect to the first and second target reliabilities of 0.1, 0.5 and 0.9. The NRBDO result converges to RBDO and DDO results if the first and second target reliabilities are 0.5. The result shows that the optimum point tends to exist in infeasible region if the first target reliability is less than half. Also, the result shows that if the second target reliability is less than half and the first target reliability is 0.5, the optimum point tends to exist in infeasible region. The proposed method finds the optimum point by considering the reliability of a system as well as the uncertainty of the reliability when the information of the input variables is given in a limited discrete form.

### Acknowledgments

This research was supported by the fundamental research subject (a study of the integrated framework for virtual design and analysis, no. GS-2) supervised by the ADD (Agency for Defense Development).

### References

- Akaike H. (1973), Information theory and an extension of the maximum likelihood principle. *Proceedings of the Second International Symposium on Information Theory*, pp. 267–281.
- Al-Rubaie KS, Godefroid LB, Lopes JAM. (2007), Statistical modeling of fatigue crack growth rate in Inconel alloy 600. *I J Fatigue*. 29(5), pp. 931–940.
- Breitung K. (1984), Asymptotic approximations for multinormal integrals. *ASCE J Eng Mech*. 110(3), pp. 357–366.
- Conover WJ. (1980), *Practical nonparametric statistics 2nd*. New York: John Wiley & Sons.
- Cornell CA. (1969), A probability-based structural code. *Journal of the American Concrete Institute*. 66(12), pp. 974–985.
- Go SJ, Lee MC, Park MK. (2001), Fuzzy sliding mode control of a polishing robot based on genetic algorithm. *J Mech Sci Tech*. 15(5), pp. 580–591.
- Hurvich CM, Simonoff JS, Tsai CL. (1998), Smoothing parameter selection in nonparametric regression using an improved Akaike information criterion. *J Royal Statistical Society Series B-Statistical Methodology*. 60, pp. 271–293.
- Lee I, Choi KK, Noh Y. (2013), Comparison study between probabilistic and possibilistic methods for problems under a lack of correlated input statistical information. *Struct Multidiscipl Optim*. 47(2), pp. 175–189.
- Lee SH, Kwak BM. (2006), Response surface augmented moment method for efficient reliability analysis. *Struct Saf*. 28(3), pp. 261–272.

- Lim W, Lee TH. (2012), Reliability-based design optimization using Akaike information criterion for discrete information. *Trans Korean Soc Mech Eng A*. 36(8), pp. 921–927.
- Noh Y, Choi KK, Lee I, Gorsich D, Lamb D. (2011), Reliability-based design optimization with confidence level under input model uncertainty due to limited test data. *Struct Multidiscipl Optim*. 43(4), pp. 443–458.
- Pan W. (2001), Akaike's information criterion in generalized estimating equations. *Biometrics*. 57(1), pp. 120–125.
- Rahman S, Xu H. (2004), A univariate dimension-reduction method for multi-dimensional integration in stochastic mechanics. *Probab Eng Mech*. 19(4), pp. 393–408.
- Sakamoto Y, Ishiguro M, Kitagawa G. (1986), *Akaike information criterion statistics*. Tokyo: KTK Scientific Publishers.
- Shan S, Wang GG. (2007), Reliable design space and complete single-loop reliability-based design optimization. *Rel Eng Sys Saf*. 93(8), pp. 1218–1230.
- Shetty NK, Soares CG, Thoft-Christensen P, Jensen FM. (1998), Fire safety assessment and optimal design of passive fire protection for offshore structures. *Rel Eng Sys Saf*. 61(1-2), pp. 139–149.
- Spendelow JA, Nichols JD, Nisbet ICT, Hays H, Cormons GD, Burger J, Safina C, Hines JE, Gochfeld M. (1995), Estimating annual survival and movement rates of adults within a metapopulation of roseate terns. *Ecology*. 76(8), pp. 2415–2428.
- Youn BD, Choi KK. (2004), An investigation of nonlinearity of reliability-based design optimization approaches. *J Mech Des*. 126(3), pp. 403–411.
- Youn BD, Wang P. (2008), Bayesian reliability-based design optimization using eigenvector dimension reduction (EDR) method. *Struct Multidiscipl Optim*. 36(2), pp. 107–123.

## Simulation of Thermal behavior of a Two-speed Dual Clutch Transmssion

\*Xingxing Zhou<sup>1</sup>, Paul Walker<sup>1</sup>, Nong Zhang<sup>1,2</sup>, Bo Zhu<sup>1,3</sup> Jiageng Ruan<sup>1</sup>

<sup>1</sup> School of Electrical, Mechanical and Mechatronic Systems Faculty of Engineering and Information Technology (FEIT) The University of Technology, Sydney (UTS), Sydney, Australia

<sup>2</sup> State Key Laboratory of Advanced Design and Manufacturing for Vehicle Design, Hunan University, Changsha, China 410082

<sup>3</sup> BAIC Motor Electric Vehicle Co Ltd BAIC Motor Electric Vehicle Co Ltd, Beijing, China

\*Corresponding author: Xingxing.Zhou@student.uts.edu.au

### Abstract

In order to study the thermal behaviour of a two-speed dual clutch transmission (DCT), mathematic calculation and simulation will be conducted. This paper presents a theoretical analysis of power losses and heat transfer in DCT. The power losses components include wet clutches, concentric shaft, power losses caused by gear meshing, gear windage, churning, and bearings. In order to demonstrate the effectiveness of the model, simulations are conducted based on the presented theoretical analysis and developed powertrain model using different vehicle test driving cycles. Thermal behaviour study can contribute to the optimization design of future transmissions and calculating its reliability.

**Keywords:** Thermal Capacity, heat dissipation, dual clutch transmission, DCT, Simulation.

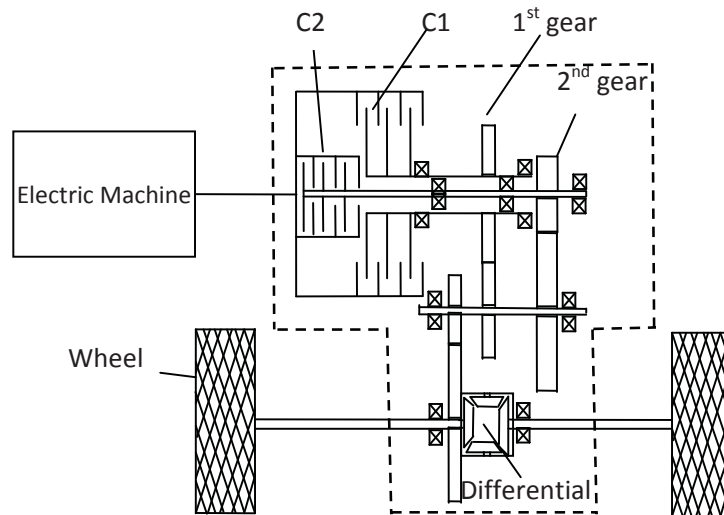
### Introduction

Pure EVs being currently widely used in the market are mainly equipped with single speed transmission, with tradeoffs between dynamic (such as climbing ability, top speed, and acceleration) and economic performance (driving range). Nowadays, more and more EV researchers and designers are paying attention to application of multiple speed transmissions instead of traditional single speed transmissions, expecting to improve the EV performance. The usage of multi-speed transmissions for electric vehicles is likely to improve average motor efficiency and range capacity, or even can reduce the required motor size. There are a number of multi-speed transmissions available for pure EVs, as shown by the author (Rudolph, 2007), indicating that DCTs have higher fuel efficiency than other automatic drives, making them extremely suitable.

It is necessary to point out that the vehicle performance improvement by using multi-gear transmissions for an electric vehicle is not as much as for an engine driven vehicle, as a result of significantly different characteristics of these two systems. In an engine driven system, the available output speed range of engine is narrower than that of electric motor. The inertia of motor is smaller than that of engine as well, usually smaller than a quarter of engine. And the motor speed is also more controllable than that of engine. Therefore, the number of gear ratios for a pure EV is not the more the better, as it will increase the transmission manufacture cost and the overall vehicle mass without contributing significantly to the overall performance of the vehicle. Consequently, the detailed performance difference between one-speed and two-speed EV can refer from our research work by the author (Zhou, 2012).

A general two-speed wet DCT is suggested to be equipped into a pure EV, as shown in Figure 1. It is made up of two clutches, C1 and C2. The two clutches have a common drum attached to the same input shaft from the

motor, and the friction plates are independently connected to 1st or second gear. C1 connects the inner input shaft engaged with 2<sup>nd</sup> gear, and C2 connects the outer input shaft, engaged with 1<sup>st</sup> gear. And there are no synchronisers in this two-speed DCT. Thus, the transmission can be looked at as two half manual transmission, and, in this sense, shifting is realised through the simultaneous shifting between these two half transmissions. For this special layout, it is the reason why that the author (Goetz, 2005) points out that vehicle equipped with DCT can change speed smoothly with nearly no power.



**Figure 1.** EV powertrain system equipped with two-speed wet DCT schematic

Computer calculations and simulations are now part of design new types of transmissions process, as prototype tests have become more and more expensive and time consuming as shown in the work by the author (Play, 1978). Thermal behaviour is not often considered in the preliminary design step as pointed by the author (Lechner, 1999). In fact, a thermal expansion of transmission cases, for example, can change gear axes geometry positions, gears clearances, lubricant types and film conditions, and consequently, dissipated heat during work. Furthermore, it is of great importance to know the temperature of oil lubricated transmission systems, and the quantity of demand cooling oil. The prediction of thermal behaviour of a transmission might be beneficial to evaluate cooling and lubricating conditions. Therefore, it appears necessary to develop numerical models to predict the transmissions thermal behaviours.

Some works (Changenet et al., 1996, Coe, 1989; Joule et al., 1988; Phillips, 1996) have been done considering the whole transmission system for thermal analysis. However, these approaches are mainly focus on manual or automatic transmission. There are limited, if any, publicised works and reports on dual clutch transmission thermal behaviours.

This paper performs a research of dual clutch transmission power losses and heat dissipation. Due to the particular structure of DCT, the power losses components include wet clutches, concentric shaft, power losses caused by gear meshing, gear windage, churning, and bearings. In order to demonstrate the effectiveness of the model, simulations are conducted based on the presented theoretical analysis and developed heat dissipation model using different assumed temperature and power losses. Thermal capacity study can contribute to the design of future transmissions and calculating its reliability.

## 1 Theoretical Analysis of Heat Dissipation of Dual Clutch Transmission

Given the rigorous development required for standards, the BS/ISO (2001) model is adopted to analysis the transmission heat dissipation.

The quantity of heat,  $Q_{Ca}$ , dissipated through the dual clutch transmission case by convection can be calculated by:

$$Q_{Ca} = kA_{ca}(T_{oil} - T_{en}) \quad (1)$$

where,  $k$  represents the heat transmission coefficient, which includes the internal heat transfer between oil and case, and the heat conduction through the case wall and the external heat transfer to the environment, usually surrounding air.  $T_{oil}$  and  $T_{en}$  mean the oil temperature and environment temperature respectively with unit of Kelvin.

$$\frac{1}{k} = \frac{1}{\alpha_{oil}} \frac{A_{ca}}{A_{oil}} + \frac{\delta_{wall}}{\lambda_{wall}} \frac{A_{ca}}{A_{oil}} + \frac{1}{\alpha_{ca}} \quad (2)$$

The heat dissipation via the DCT case is determined by the larger value air-side, i.e. external side, thermal resistance at the case surface. The front two terms in the above equation can then be neglected. For high air velocities and thus good external heat transfer, it will probably be necessary to also consider of the oil-side heat transfer. As a reference value, oil-side heat transfer coefficient,  $\alpha_{oil} = 200 \text{ W/m}^2\text{K}$ , can be assumed. But it requires for investigation and revision for different oil types. The heat conduction through the transmission case should only be considered in special cases, such as in the case of double-walled cases, cases with sound insulation and non-metallic cases. And the appropriate coefficient of thermal conduction,  $\lambda_{wall}$ , has to be expressed for the case material in question.

The air-side heat conduction,  $\alpha_{ca}$ , includes a convection part,  $\alpha_{con}$ , and a radiation part,  $\alpha_{rad}$ , which can performs as

$$\alpha_{ca} = \alpha_{con} + \alpha_{rad} \quad (3)$$

$$\alpha_{rad} = 0.23 * 10^{-6} \varepsilon \left( \frac{T_{wall}}{T_{en}} \right)^3 \quad (4)$$

where the emission ratio,  $\varepsilon$ , is assumed as 0.15.

The convection part can be divided into two parts, free and forced convection. According to the investigations by the author (Funck, 1985), the following can be presented:

$$\alpha_{con} = \alpha_{free} \left( 1 - \frac{A_{air}}{A_{ca}} \right) + \alpha_{forced} \frac{A_{air}}{A_{ca}} \eta^* \quad (5)$$

Where

$$\eta^* = \frac{T_{wall} - T_{air}}{T_{wall} - T_{en}} \quad (6)$$

As this DCT case without thermal finning, the free and forced convection can be followed as:

For free convection ( $V_{air} \leq 1.5\text{m/s}$ ):

$$\alpha_{free} = 18h_{ca}^{-0.1} \left( \frac{T_{wall} - T_{en}}{T_{en}} \right)^{0.3} \quad (7)$$

For forced convection ( $V_{air} > 1.5\text{m/s}$ ):

$$\alpha_{forced} = \frac{0.0086(R_e^*)^{0.64}}{l_x} \quad (8)$$

Where

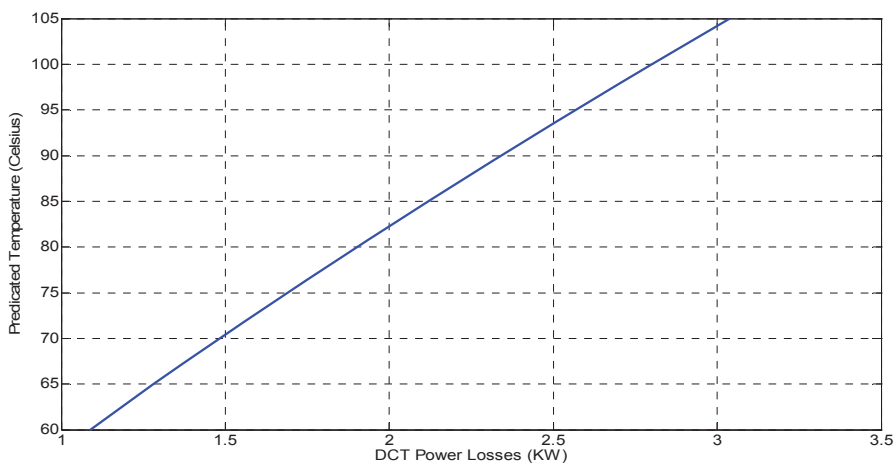
$$Re^* = \sqrt{Re^2 + \frac{Gr}{2.5}} \tag{9}$$

$$Re = \frac{v_{air} l_x}{\nu_{air}} \tag{10}$$

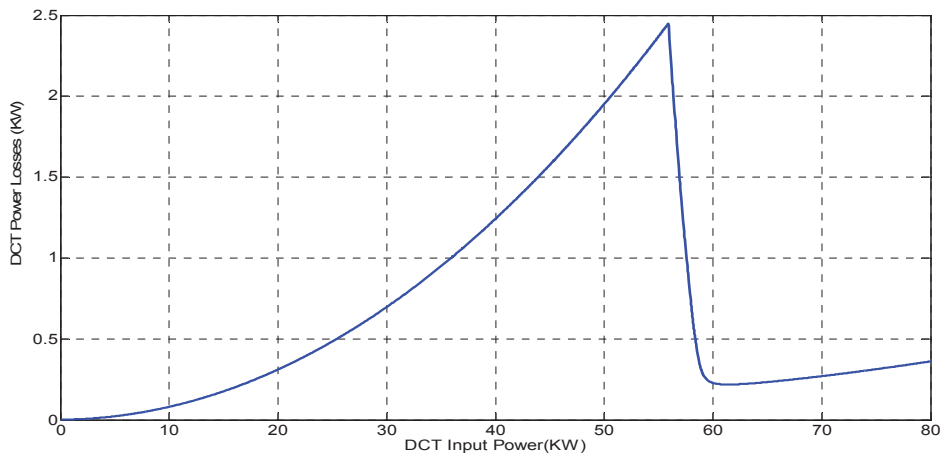
$$Gr = \frac{g h_{ca}^3 (T_{wall} - T_{en})}{T_{en} \nu_{air}^2} \tag{11}$$

## 2 Simulation Results and Discussion

The simulations present the relationship between DCT power losses and predicated temperature.

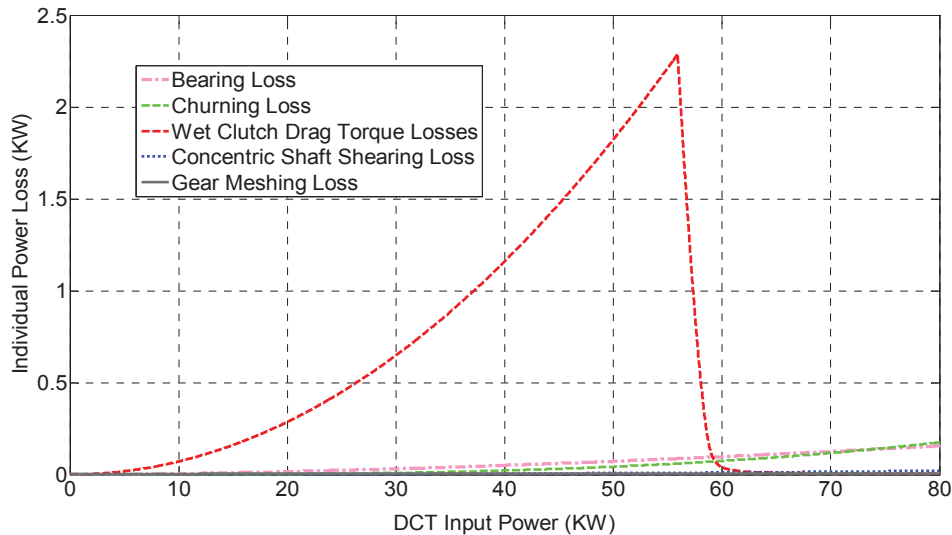


**Figure 2. Relationship between DCT power losses and predicated temperature**



**Figure 3. Relationship between input power and power losses**





**Figure 4. Individual DCT power losses verse input power**

Figure 2 shows that the predicated temperature linearly increases with the DCT power losses. Figure 3 indicates that the maximum power loss for DCT is approximate 2.4KW. Consider Figure 3 and Figure 4 together, the power loss decreased sharply is caused by the wet clutch. It is because that the effective wet clutch radius will decrease which is caused by increased centrifugal force during high speed. Figure 4 also shows that wet clutch drag torque loss domain the main power losses in the two-speed DCT. From Figure 2 and Figure 4, as the power losses is domain caused by wet clutch drag torque, it is not only necessary to consider the DCT thermal capacity but carefully to calculate the wet clutch pack thermal capacity as well.

## Conclusions

Thermal behaviour study can contribute to the design of future transmission prototypes and calculating its reliability avoiding unnecessary failures. It could help accelerating products development speed and save funds. Future research includes comparing power losses under different gears and operations, and using experiment to investigation the proposed model.

## References

- British Standards Institute BS ISO/TR 14179-2:2001. (2001), Gears-thermal capacity Part 2 : thermal Load carrying capacity.
- Changenet, C., Denis, M., and Nast, D. (1996), "Thermal Study of Railway Reduction Gears," *VDI BERICHTE NR1230*, pp.461-471.
- Coe, H. H. (1989), "Comparison of Predicted and Measured Temperatures of UH-60A Helicopter Transmission," *NASA, Tech. Report 89-C-010*, pp. 12.
- FUNCK, G. (1985), Wärmeabführung bei Getrieben unter quasistationären Betriebsbedingungen. Diss. TU München und FVA-Forschungsheft Nr. 197.
- Joule, D., Hinduja, S., and Ashton, J. N., 1988, "Thermal Analysis of a Spur Gearbox, Part 1: Steady State Finite Element Analysis. Part 2: Transient State Finite Element Analysis of the Gearbox Casing," *Proceedings of the Institution of Mechanical Engineers, Vol. 202 C4*, pp. 245-262.
- Lechner G. and Haunheimer H. (1999), *Automotive Transmissions: Fundamental, Selection, Design, and Application*, Springer, Germany.
- Goetz M. (2005), *Intergrated Powertrain Control for Twin Clutch Transmissions*, PHD thesis, University of Leeds.
- Play, D., 1978, Testing Alloys for Use in Heat Treatment Furnaces, *Tribology International*, June, pp. 193-196.
- Phillips, A. E., 1996, "The Development of a Practical Thermal Rating Method for Enclosed Gear Drives," *AGMA*, ISBN 1-55589-676-6.
- Rudolph F. Schafer M. Damm A. Metzner F T. and Steinberg I. (2007), The Innovative Seven Speed Dual Clutch Gearbox for Volkswagen's Compact Cars, *28th Internationales Wiener Motorensymposium*.
- Zhou X.X., Walker P.D., Zhang N., Zhu B., Ding F. (2012), The influence of transmission ratios selection on electric vehicle motor performance, *ASME 2012 International Mechanical Engineering Congress & Exposition, IMECE2012-85906*.

## Design Optimization of Structures using A Nodal Density-Based SIMP Method

**\*Y. Wang, Z. Luo, and N. Zhang**

School of Electrical, Mechanical and Mechatronic System, University of Technology Sydney  
Sydney, NSW 2007, Australia

\*Corresponding author: Yu.Wang-11@student.uts.edu.au

This paper proposes an alternative topology optimization method for the optimal design of continuum structures, which involves a multilevel nodal density-based approximant based on the concept of conventional SIMP (solid isotropic material with penalization) model. First, to construct a material density field with global smoothness over the design domain, a family of Shepard interpolation scheme is applied as a non-local nodal density interpolation. The new nodal density field possesses non-negative and range-bounded properties to ensure a physically meaningful approximation of topology optimization design. Second, the density variables at the nodes of finite elements are used to interpolate elemental densities, as well as corresponding element material properties. In this way, the nodal density field by using the non-local Shepard function method is transformed to a practical elemental density field via a local interpolation with the elemental shape function. The low-order finite elements are utilized to evaluate the displacement and strain fields, due to their numerical efficiency and implementation easiness. So, the proposed topology optimization method is expected to be efficient in finite element implementation, and effective in the elimination of numerical instabilities, e.g. checkerboards and mesh-dependency. A benchmark numerical example in topology optimization is employed to demonstrate the effectiveness of the proposed method.

**Keywords:** Topology optimization method, SIMP, nodal density-based approximant, Shepard function

### Introduction

In the area of structural optimization, topology optimization has experienced considerable development over the past two decades with a wide range of engineering applications (Bendsøe and Sigmund 1999). Topology optimization is essentially a systematic design methodology, which involves a numerical process to iteratively re-distribute a given amount of material inside the design domain subject to loads and boundary conditions, until a prescribed design objective is optimized under specified design constraints. Topology optimization has been recognised as the most promising but the most challenging approach in the conceptual stage of structural optimization. Many different methods have been developed for topology optimization of structures, including the homogenization method (Bendsøe and Kikuchi 1988), SIMP method (Zhou and Rozvany 1991; Mlejnek 1992; Bendsøe and Sigmund 1999), and level set-based methods (Sethian and Wiegman 2000; Wang et al. 2003; Allaire et al. 2004; Luo et al. 2008).

Topology optimization of continuum structures essentially belongs to a set of integer programming problems with a large number of discrete(0, 1) design variables. More efficient gradient-based optimization algorithms cannot be directly applied to solve such large-scale optimization problems due to the well-known combinatorial problem. To this end, the homogenization and SIMP methods have been widely employed to relax the discrete topology optimization problem, allowing the design variables taking intermediate densities from 0 and 1. In doing so, the original optimization

problem is changed to a regularized optimization problem with range-bounded continuous design variables. In particular, the SIMP, as an extension of the homogenization method, has won great popularity in topology optimization of solid mechanics problem, due to its conceptual simplicity and implementation easiness. In SIMP-based topology optimization methods, a ‘power-law’ criterion (Bendsøe and Sigmund 1999) is usually applied to penalize the intermediate densities of elements, to ensure the solution of the regularized 0-1 design close to the original binary (0,1) design as much as possible. In addition, numerical schemes such as filtering schemes (Sigmund 2001; Bourdin 2001; Luo et al. 2005) are required to be incorporated to eliminate numerical instabilities, e.g. the checkerboards and mesh-dependence (Sigmund 2001), in order to make a physically meaningful solution for topology optimization of continuum structures.

It can be found that most of the current SIMP approaches are based on element-wise design variables (Bendsøe and Sigmund 2003), which means that both the topological geometry of material distribution and the physical fields would be evaluated via elemental density variables which are piecewise constant. In topology optimization of continuum structures, the element-wise variables may be one of the reasons for the occurrence of numerical instabilities (Sigmund 2001), including checkerboards, local minima, and mesh-dependency. Moreover, the element-based topology optimization method may lead to zigzag non-smooth boundary. As a result, to overcome the shortcomings of conventional element-wise SIMP methods, several alternative methods have been proposed. More recently, there have been several approaches based on point-wise design variables (Rahmatalla and Swan 2004; Matsui and Terada 2004; Guest et al. 2004; Paulino and Le 2009; Kang and Wang 2011; Wang et al. 2012). According to these approaches, nodal densities of the finite elements are normally considered as the design variables, and subsequent element material properties are obtained in terms of nodal densities via interpolation schemes. For instance, Rahmatalla and Swan (2004) proposed several options to implement the point-wise interpolation for material density fields, although “layering” or “islanding” type numerical instabilities occurred in the design. Matsui and Terada (2004) studied a so-called CAMD (continuous approximation of material distribution) method based on the homogenization method, in which element material densities were interpolated via the nodal density values (design variables). Guest and et al. (2004) introduced nodal design variables and projection schemes into topology optimization to achieve minimum length-scale control and checkerboard-free characteristics. Nodal material densities are regarded as the design variables to calculate the element material densities and element stiffness matrices. Paulino and Le (2009) proposed a kind of hybrid low-order finite elements, in which the nodes for design variable vector are inconsistent with the nodes for displacement vector. Kang and Wang (2011) proposed a nodal density based topology optimization method, in which a non-local Shepard interpolation scheme and higher-order elements are applied to eliminate the numerical instabilities such as checkerboards.

This paper will propose a multilevel nodal density-based approximation scheme for topology optimization of continuum structures, based on the concept of SIMP method. In this study, regular Q4 (quadrilateral four-node) finite elements are applied to evaluate the displacement field vector, and the nodal densities of each Q4 element are considered as design variables. A family of Shepard functions is employed to implement a non-local density approximant with enhanced smoothness over the entire design domain. At the same time, nodal design variables are used to evaluate practical material properties of the finite elements.

### **Non-local Nodal Density Approximant**

The regular Q4 (4-node quadrilateral) element is considered for all implementations in this paper. A family of Shepard interpolation scheme is employed in this study in a form where performed as a non-local nodal density interpolation to construct a material density field with global smoothness

over the entire design space. Via this interpolation scheme, the density field includes both the contribution of the design variables of nodes with one element and the nodes related to the neighbouring nodes within an influential support. The Shepard interpolation method is introduced, firstly. Let  $\varphi_i (i=1,2,\dots,n_H)$  denote a set of  $n_H$  non-negative data values at the associated sampling points  $x_i = (X_i, Y_i)$  within the support radius  $r$  of an arbitrary point.  $(X_i, Y_i)$  defines the  $i$ th point location in the given Cartesian coordinate system. The approximation of the Shepard function method is stated as

$$\bar{\varphi}(x) = \sum_{i=1}^{n_H} \Theta_i(x) \varphi_i \quad (1)$$

Where  $n_H$  is the number of the nodes that is within the support radius  $r$  of the  $i$ th point. The Shepard function  $\Theta_i(x)$  is expressed as a normalized formulation

$$\Theta_i(x) = \frac{\omega_i(x - x_i)}{\sum_{j=1}^{n_H} \omega_j(x - x_j)} \quad (2)$$

$\omega_i(x - x_i)$  is the weight function, in the study which is a radially linear ‘hat’ function defined by [Bourdin (2001)], where  $x - x_i$  is the radial distance from point  $x$  to  $x_i$ .

Given  $D_i(x) = x - x_i = \sqrt{(X - X_i)^2 + (Y - Y_i)^2}$ , the weight function can be expressed as

$$\omega_i(x - x_i) = \frac{3}{\pi r^2} \max\left(0, 1 - \frac{D_i(x)}{r}\right) \quad (3)$$

The weight function is zero outside the domain of influential support, and decays linearly with the distance from the interest point  $x$ . It means that only nearby points are considered in computing any approximated value. In this way, the cost of computation is greatly saved by eliminating calculations with distant data points. The Shepard function  $\Theta_i(x)$  possesses the properties:

- (1)  $\sum_{i=1}^{n_H} \Theta_i(x) = 1$
- (2)  $\Theta_i(x) > 0$

It is apparent that the Shepard function has a mechanism similar to the smoothing effect of the density filtering schemes (Bourdin 2001; Luo et al. 2005). Meanwhile, the approximated values via the Shepard function are bounded between lower and upper values of the sampling points, which is essential property for a physically meaningful density field approximant in topology optimization.

### Local Nodal Density Interpolation Scheme

Here, a local nodal density-based interpolation will be presented to convert the nodal design variables into the elemental densities. In this study, the standard Lagrangian shape function in the finite element method is used to interpolate elemental material properties. The local nodal density-based interpolant is stated as

$$\rho_e = \sum_{n=1}^{n_e} N_n \bar{\rho}_n = \sum_{n=1}^{n_e} \left( N_n \sum_{i=1}^{n_H} \Theta_i(x_n) \rho_i \right) \quad (4)$$

where  $\rho_e$  is the elemental density,  $n_e$  is the number of the nodes of each element (4 in Q4 element), and  $N_n$  is the standard Lagrangian shape function. For simplicity,  $2 \times 2$  Gaussian points are utilized to compute the practical material properties and determine the displacement field.

Furthermore, elemental material properties, such as Young’s modules and elasticity constant, can then be expressed according to the proposed the multi-level approximation scheme, respectively, as

$$E_e = \sum_{n=1}^{n_e} N_n \bar{E}_n = \sum_{n=1}^{n_e} \left[ N_n \left( \sum_{i=1}^{n_H} \Theta_i(x_n) \rho_i \right)^p E_0 \right] \tag{5}$$

$$\mathbf{D}_e = \sum_{n=1}^{n_e} N_n \bar{\mathbf{D}}_n = \sum_{n=1}^{n_e} \left[ N_n \left( \sum_{i=1}^{n_H} \Theta_i(x_n) \rho_i \right)^p \mathbf{D}_0 \right] \tag{6}$$

From the above discussion, it can be found that the proposed multi-level interpolation scheme can be easily implemented and is numerically effective, due to the application of the standard low-order rather than the higher-order finite elements. The obtained nodal variables via the interpolant are bounded between [0, 1], which is crucial for generating a physically meaningful density field.

**Topology optimization problem**

According to the well-established theory proposed by Bendsoe and Sigmund (2003), the following structural mean compliance design is used for design sensitivity analysis. In the study, the topology optimization problem is stated as

$$\left\{ \begin{array}{l} \text{Minimize: } J = \mathbf{U}^T \mathbf{K} \mathbf{U} = \sum_{e=1}^{N_e} (\rho_e)^p \mathbf{u}_e^T \mathbf{k}_e \mathbf{u}_e \\ \text{Subject to: } \left\{ \begin{array}{l} V - f_v V_0 \leq 1 \\ \rho_{\min} \leq \rho_e \leq 1 \\ \mathbf{K} \mathbf{U} = \mathbf{F} \end{array} \right. \end{array} \right. \tag{7}$$

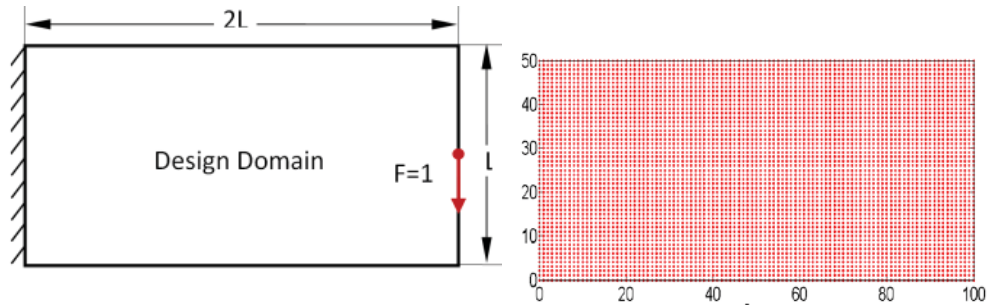
Where the objective function J is to be minimized, **U** is the displacement vector and **K** is the global stiffness matrix, **F** is the external vector.  $N_e$  is the number of total elements,  $\mathbf{u}_e$  is the elemental displacement vector, and  $\mathbf{k}_e$  is the elemental stiffness matrix. p is the penalty factor (p=3 in this study). V is the actual material volume and  $f_v$  is the specified volume fraction ratio, and  $V_0$  is the volume of the design domain.  $\rho_{\min} = 0.0001$  is the lower bound of elemental densities to avoid singularity in numerical implementation. The derivative of the objective function with respect to the nodal design variables is expressed as

$$\frac{\partial J(\rho_i)}{\partial \rho_i} = -\mathbf{U}^T \frac{\partial \mathbf{K}}{\partial \rho_i} \mathbf{U} = -\sum_{e \in n_i} \mathbf{u}_e^T \frac{\partial \mathbf{k}_e}{\partial \rho_i} \mathbf{u}_e \tag{8}$$

Where  $n_i$  is an index set containing indices of all the elements connected to the  $i$ th point (Kang 2011).

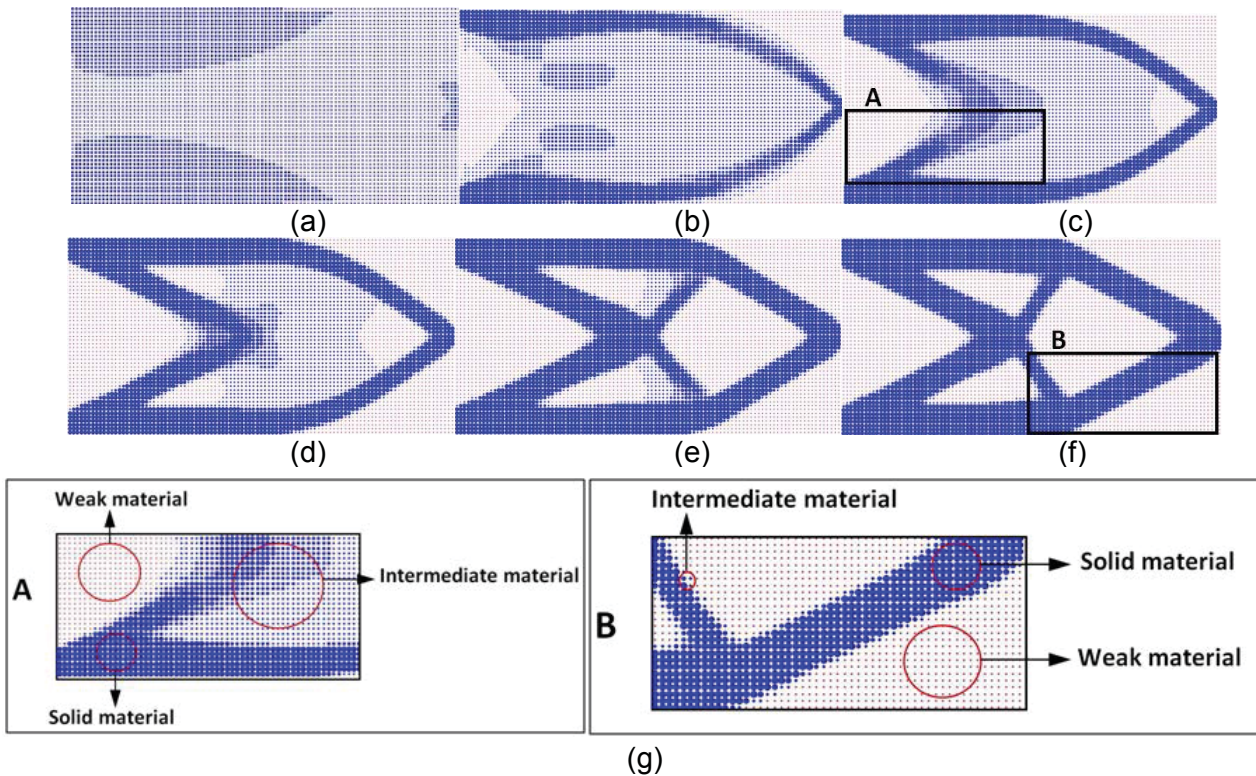
**Numerical ExampleS and Discussions**

To have an equitable assessment of the performance of the new interpolation scheme, the well-established minimum compliance problem is chosen (Bendsøe and Sigmund 2003). Fig.1 is the design domain of the cantilever beam with an aspect ratio of 2:1 corresponding to length over height. The left side of the domain is fixed as the Dirichlet boundary while the right side is treated as a non-homogenous Neumann boundary with a concentrated force F=1 vertically applied at the centre point. The objective function is to minimize the mean compliance, and mesh level (100 ×50) is adopted. As shown in Fig.1, the design domain is discretized with 100×50 Q4 elements and design variables are located at the corners of each element.

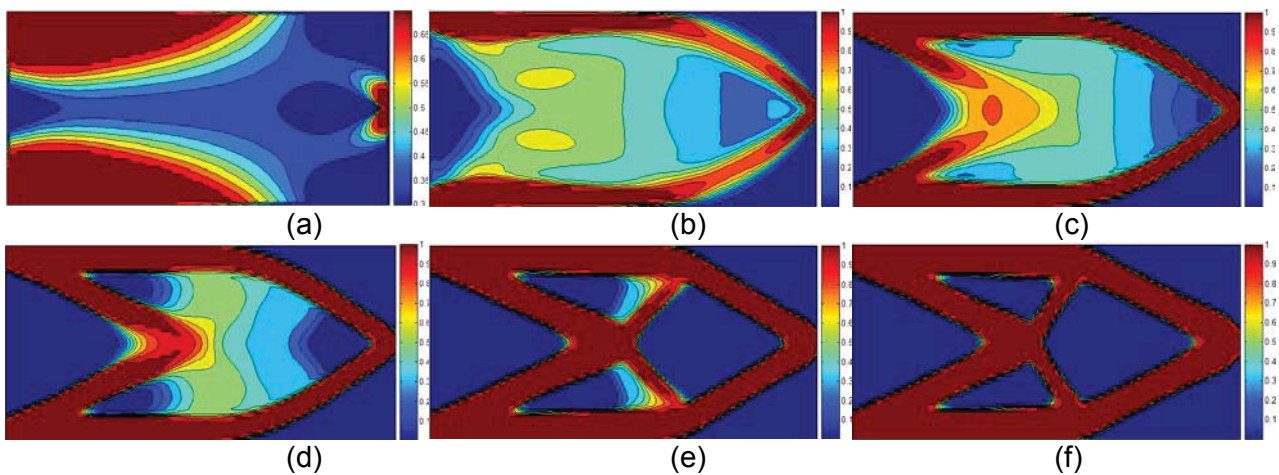


**Figure 1. Design domain of the cantilever beam (Left)**  
**Figure 2. FE nodes in the design domain(Right)**

The topology optimization is converged after 319 iterations, and the overall structural mean compliance is minimized from 319.136 to 66.519. Fig.3 shows the discrete plots of the nodal densities at different design stages, in which the first figure is the initial design, the last figure is the optimal design, and the rest are the intermediate designs. The corresponding contours of the design variables are displayed in Fig.4 that shows the design gradually moves towards the lower limit 0.0001 (weak material) and upper limit 1 (solid material) during the optimization. So it can be seen that the topology optimization in this study can actually be regarded as a numerically iterative process to re-distribute a number of material density points in the design space until the convergence criterion is satisfied.

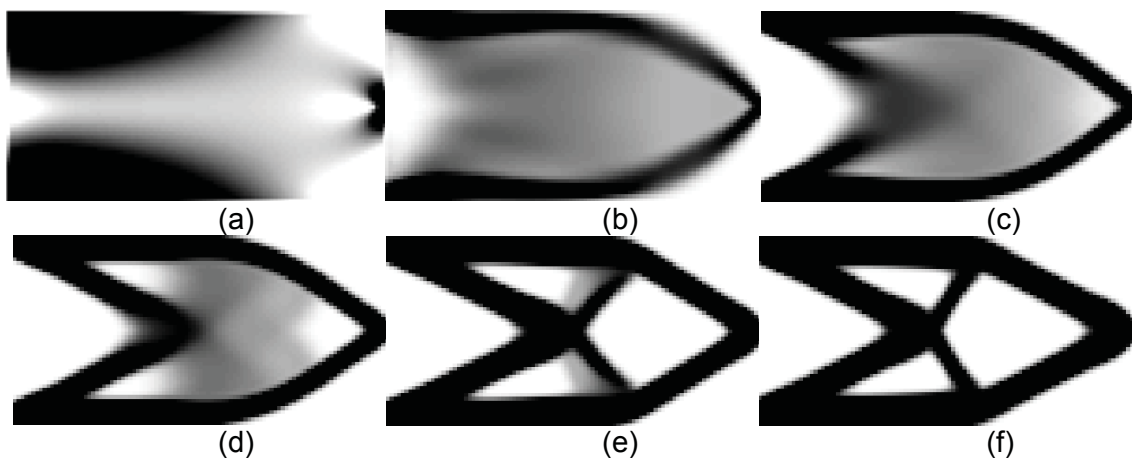


**Figure 3. Topology plots: (a) initial design, (b)-(e) intermediate designs, and (f) final solution, the size of the node denoting the magnitude of nodal density values. (g) Local zoom-out plots**

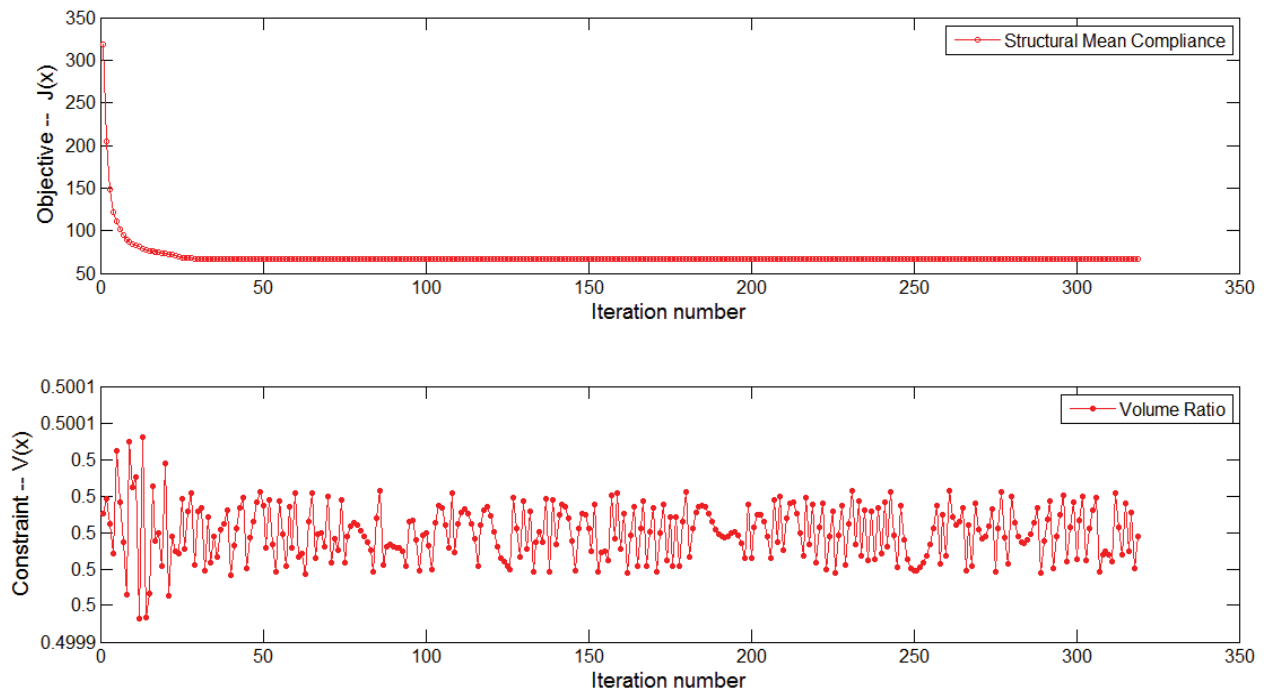


**Figure 4. Contour plots of nodal design variables**  
**(a) initial design, (b)-(e) intermediate designs, and (f) final solution**

Fig.5 displays the topology plots of the element stiffness at different design stages of the optimization. The optimization using the proposed nodal density-based method can result in checkerboard-free design, and the so-called “layering” or “islanding” numerical phenomenon (Rahmatalla and Swan 2004) can also be eliminated by using the present Shepard function approximant. Fig. 6 shows curves of the objective function and the volume constraint over the iterations. It is noted that the first 75 iterations are mainly employed to implement topological optimization, and the rest iterations are used to adjust local structural shapes until a uniform distribution of the strain energy in the structure is achieved. Since the proposed method has been proved to be mesh-independent, it is possible to use a coarser finite element mesh to improve computational efficiency. According to the curve of constraint, the proposed method is well mass conservative.



**Figure 5. Topology plots of nodal design variables:**  
**(a) initial design, (b)-(e) intermediate designs, and (f) final solution**



**Figure 6. Iteration histories of objective function and volume constraint**

## Conclusions

In this paper, an alternative SIMP scheme is proposed for topological optimization of structures based on a multi-level Shepard function approximant. In this method, the nodal variables are considered as the design variables, to implement structural topology changes. A nodal density field with enhanced smoothness is constructed by using the original set of design variables via a non-local Shepard function method. The new set of nodal variables is applied to evaluate the practical material properties of finite elements, via a local interpolation scheme of the standard Lagrangian shape function. Therefore, instead of using the time-consuming higher-order elements, the lower-order finite elements can be easily employed to improve computational efficiency. The proposed topology optimization methodology is able to eliminate the typical numerical instabilities in the topology optimization of continuum structures. It is straightforward to extend the proposed multi-level topology optimization method to more advanced mechanics problems.

## Acknowledgments

The research is partially supported by Chancellor's Research Fellowship (University of Technology, Sydney), and Australian Research Council, Discovery projects: DP1094451 and DP0988429.

## References

- Allaire, G., Jouve, F., Toader, A.M. (2004), Structural optimization using sensitivity analysis and a level-set method, *Journal of Computational Physics*, **194**, pp. 363-393.
- Bendsøe, M.P., Kikuchi, N. (1988), Generating optimal topologies in structural design using a homogenization method, *Computer Methods in Applied Mechanics and Engineering*, **71**, pp. 197-224.
- Bendsøe, M.P., Sigmund, O. (1999), Material interpolation schemes in topology optimization, *Archive of Applied Mechanics*, **69**, pp. 635-654.
- Bendsøe, M.P., Sigmund, O. (2003), *Topology optimization: Theory, Methods, and Applications*, Springer, Berlin Heidelberg.



- Bourdin, B. (2001), Filters in topology optimization, *International Journal for Numerical Methods in Engineering*, **50**, pp. 2143-2158.
- Guest, J.K., Prevost, J.H., Belytschko, T. (2004), Achieving minimum length scale in topology optimization using nodal design variables and projection functions, *International Journal for Numerical Methods in Engineering*, **61**, pp. 238-254.
- Kang, Z., Wang, Y. (2011), Structural topology optimization based on non-local Shepard interpolation of density field, *Computer Methods in Applied Mechanics and Engineering*, **200**, pp. 3515-3525.
- Luo, Z., Chen, L.P., Yang, J.Z., Zhang, Y.Q., Abdel-Malek, K. (2005), Compliant mechanism design using multi-objective topology optimization scheme of continuum structures, *Structural and Multidisciplinary Optimization*, **30**, pp. 142-154.
- Luo, Z., Wang, M.Y., Wang, S.Y., Wei, P. (2008), A level set-based parameterization method for shape and topology optimization, *International Journal for Numerical Methods in Engineering*, **76**, pp. 1-26.
- Matsui, K., Terada, K. (2004), Continuous approximation of material distribution for topology optimization, *International Journal for Numerical Methods in Engineering*, **59**, pp. 1925-1944.
- Mlejnek, H.P. (1992), Some aspects of the genesis of structures, *Structural and Multidisciplinary Optimization*, **5**, pp. 64-69.
- Paulino, G.H., Le, C.H. (2009), Modified Q4/Q4 element for topology optimization, *Structural and Multidisciplinary Optimization*, **37**, pp. 255-264.
- Rahmatalla, S.F., Swan, C.C. (2004), A Q4/Q4 continuum structural topology optimization implementation, *Structural and Multidisciplinary Optimization*, **27**, pp. 130-135.
- Sethian, J.A., Wiegmann, A. (2000), Structural boundary design via level set and immersed interface methods, *Journal of Computational Physics*, **163**, pp. 489-528.
- Sigmund, O. (2001), A 99 topology optimization code written in Matlab, *Structural and Multidisciplinary Optimization*, **21**, pp. 120-127.
- Wang, Y., Luo, Z., Zhang, N. (2012), Topological optimization of structures using a multilevel nodal density-based approximant, *CMES: Computer Modeling in Engineering & Sciences*, **84**(3): pp. 229-252.
- Wang, M.Y., Wang, X.M., Guo, D.M. (2003), A level set method for structural topology optimization, *Computer Methods in Applied Mechanics and Engineering*, **192**, pp. 227-246.
- Zhou, M., Rozvany, G.I.N. (1991), The COC algorithm, Part II: topological, geometry and generalized shape optimization, *Computer Methods in Applied Mechanics and Engineering*, **89**, pp. 197-224.

## Stability Problem of Stadium Roof

\*P. Rosko<sup>1,2</sup>, and A. Bekö<sup>2</sup>

4

<sup>1</sup>Center of Mechanics and Structural Dynamics, Vienna University of Technology, Austria

<sup>2</sup>Vienna Consulting Engineers, Vienna, Austria

\*Corresponding author: pr@allmech.tuwien.ac.at

### Abstract

The contribution deals with stability of existing stadium roof. The roof has elliptical shape in the plan view. The height of the roof is variable and is optimally designed according to minimum potential energy. The objective of the paper is the ultimate bearing capacity of the roof loaded with combination of dead loads, snow loads and wind loads. The investigation of the problem was carried out as a static analysis with large deformations. Only the amount of wind load was increased during the analysis. As an iteration procedure capable to handle bending and stability phenomena, the arc-length method was chosen. The solution procedure was stopped by snap-through.

**Keywords:** Stability, Snap-through, Arc-length method, Large deformation.

### Introduction

Big projects in civil engineering give opportunity for development of the theory and application methods. Study of stadium roof bearing capacity, additionally to solution of responsible tasks, brought new experiences, new knowledge in the field of non-linear numerical analysis. From the comprehensive static and dynamic analysis only part concerning stability of the structure is being published in this paper. For that reason, the numerical analysis is presented in application to the structure of the roof. Therefore, the structuring of this paper starts with construction description and continues with stability analysis illustrated with results.

### Structure

The contribution deals with stability of existing stadium roof. The bearing structure of the stadium roof is constructed from the steel beams connected with steel-concrete composite joints.

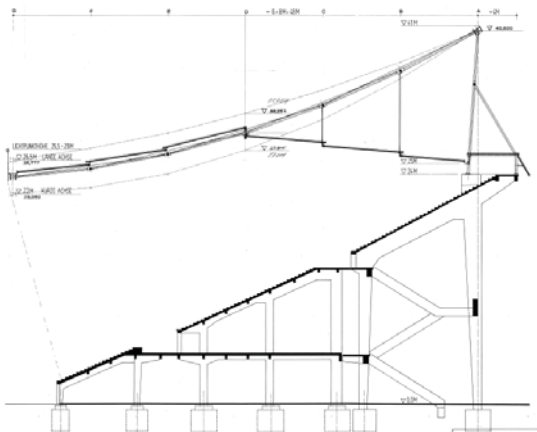


Figure 1. Sectional view of the structure

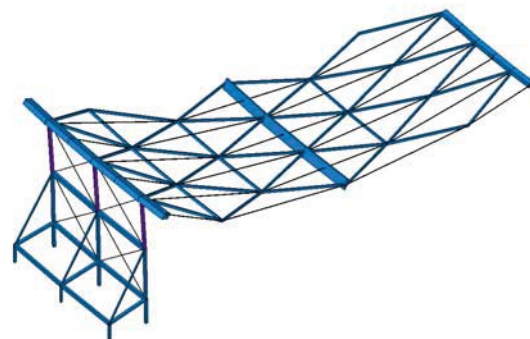
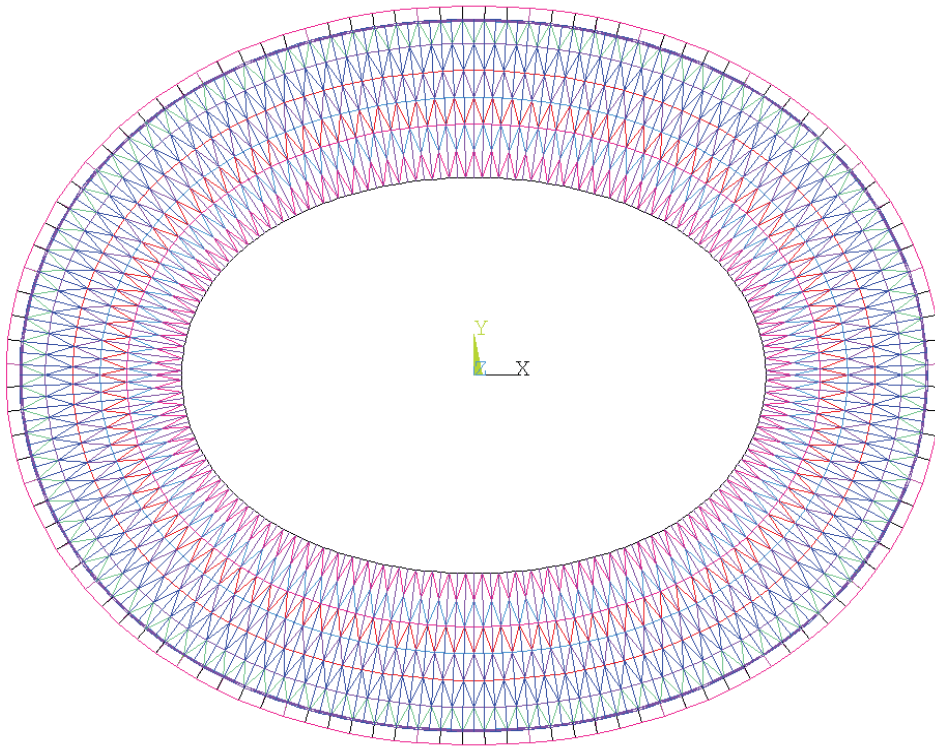
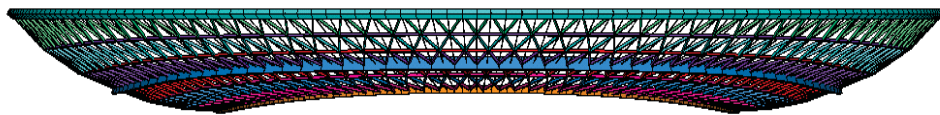


Figure 2. Section of stadium roof FE model

The roof has elliptical shape in the plan view. The height of the roof is variable and it is optimally designed according to minimum potential energy.



**Figure 3. Plan view of the stadium roof**



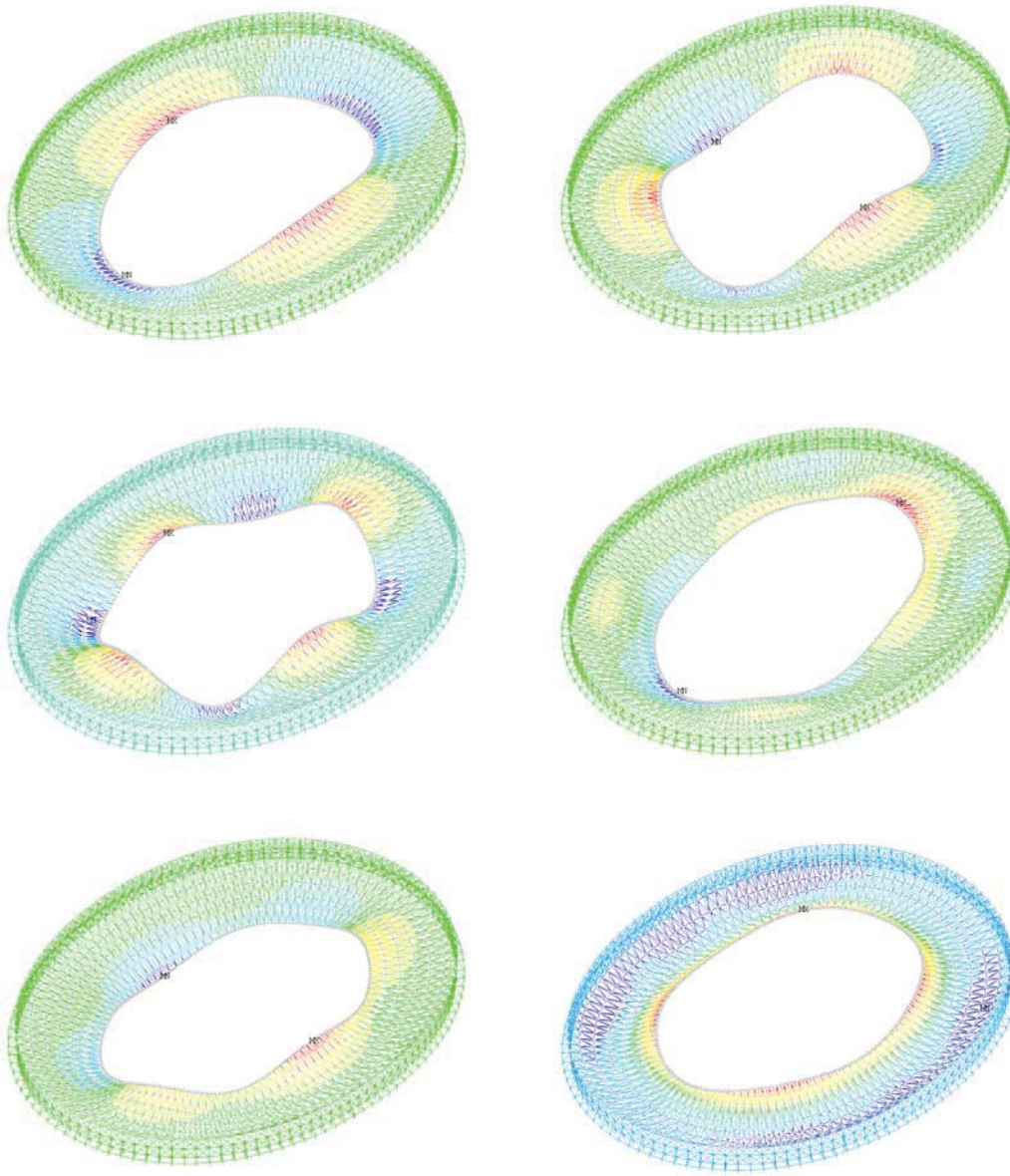
**Figure 4. Side view of the stadium roof**

### **Analysis**

The main task discussed in this paper is the proof of the ultimate bearing capacity of the stadium roof loaded with combination of dead loads, snow loads and wind loads on the base of Eurocode 1.

#### *Eigenvalue Analysis*

The first estimation of the critical loading was solved on the base of eigenvalue problem. The bifurcation point of linear (eigenvalue) buckling curve lies above the limit load obtained from nonlinear snap-through. First natural modes shown in Fig. 5 are useful for the comparison with the results of the nonlinear analysis.



**Figure 5. Shapes of 6 first natural modes**

### *Nonlineal Buckling Analysis*

The investigation of the snap-through problem was carried out.

### *Arc-length Method*

The arc-length method for structural analysis was originally developed by Riks (1972, 1979) and later modified by several authors. In arc-length method in comparison to traditional Newton-Raphson method the constraint curve has the arc geometry. That enables to follow buckling curves in force-displacement diagrams consisting of parts with increasing and decreasing displacement. Using the arc-length method, the equilibrium iterations convergence along an arc and thereby

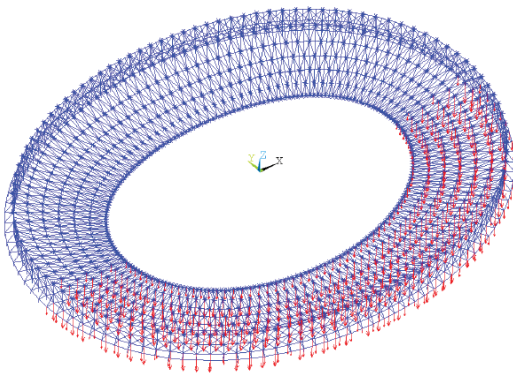
preventing divergence, even when the slope of the load vs. deflection curve becomes zero or negative. The quasi-Newton BFGS method (Broyden (1970), Fletcher (1970), Goldfarb (1970) and Shanno (1970)) uses approximate Jacobian instead of exact Jacobian for each iteration. Chang (1991) proposed periodically restarted quasi-Newton updates in constant arc-length method. Hellweg and Crisfield (1998) introduced the arc-length method for handling sharp snap-backs. Our analysis used the arc-length method with listed modifications.

#### *Application of the Arc-length Method*

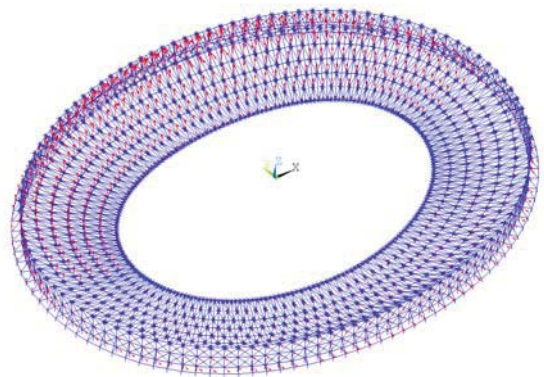
The load was applied gradually. At each substep the equilibrium iterations were performed to obtain a converged solution. The arc-length method was activated by sets of the minimum and maximum multipliers for the reference arc-length radius. The reference arc-length radius was calculated from the load increment of the first iteration. This increment was determined by total load divided by number of substeps. Lower and upper limit was calculated with help of factors multiplying the difference between reference arc and arc length radius. In each subsequent substep, a new arc-length radius was first calculated based on the arc-length radius of the previous substep and the solution behavior. Next, the newly calculated arc-length radius was further modified so that it falls between the range of the upper limit and lower limit. When the solution did not converge even when using the lower limit of the arc-length radius, the solution terminated.

#### *Loading of the Structure*

The reference model for the snap-through analysis the roof structure in static equilibrium was chosen. The loading was applied on the base of Eurocode 1: Actions on structures. Two critical load combinations were chosen: Combination 1: dead loads and wind loads and Combination 2: dead loads, snow loads and wind loads. The wind loads were stepwise added.

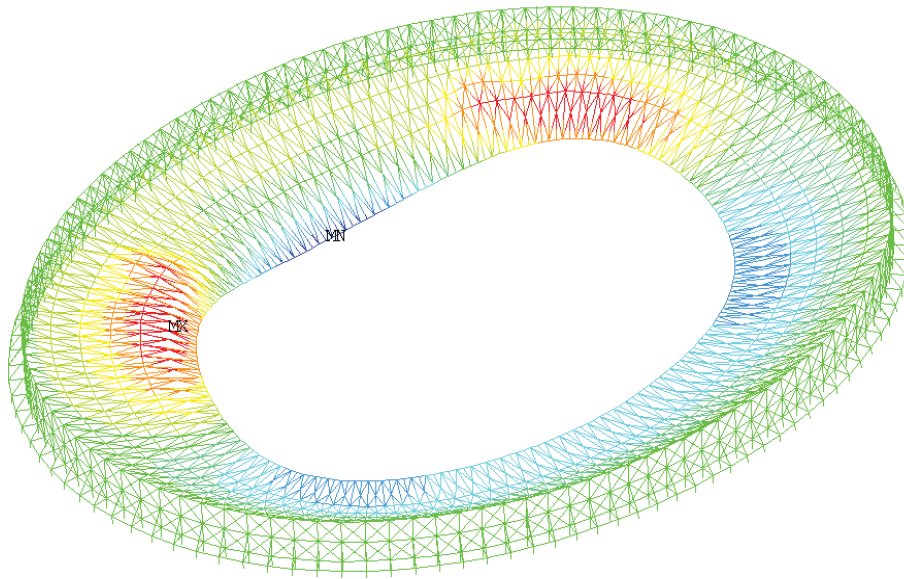


**Figure 5. Snow loading**

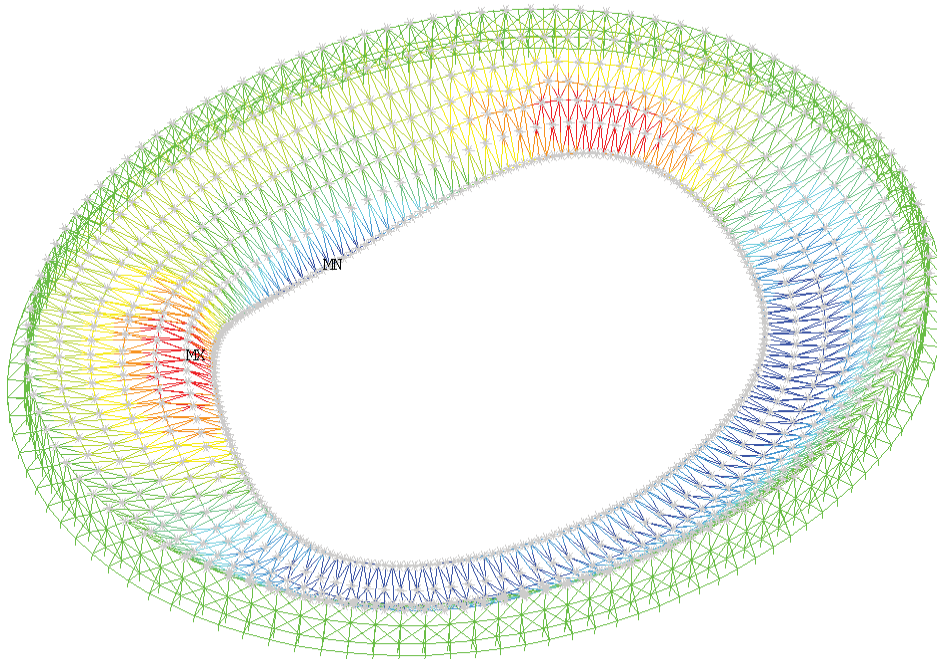


**Figure 6. Wind loads**

**Results**



**Figure 7. Shape of snap-through: combination 1 of dead loads and wind loads**



**Figure 8. Shape of snap-through: combination 2 of dead loads, snow loads and wind loads**

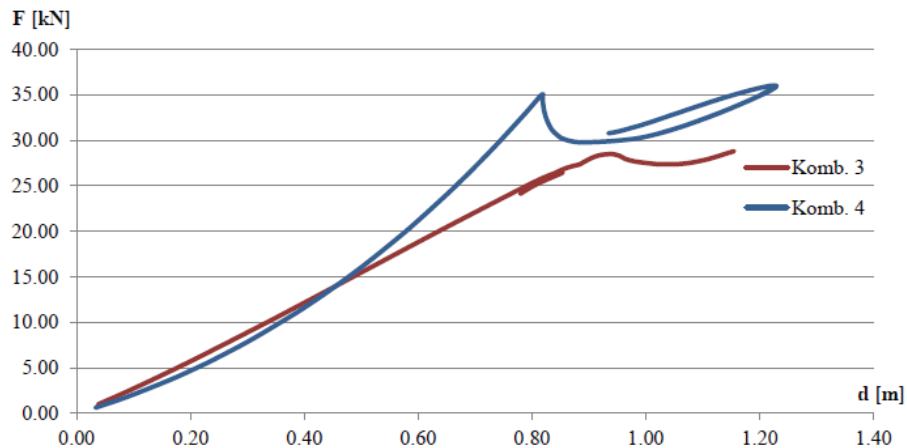


Figure 9. Force-displacement curve: load case 3 and load case 4 in most displaced nodes

Table 1. Identified results

Combination Value	Multiplicator for Wind	Max Vertical Displacement [m]
1	2,3	0.85
2	3,0	0.82

## Conclusions

Successful application of the arc-length method for the proof of the ultimate bearing capacity of real stadium roof loaded with combination of dead loads, snow loads and wind loads was presented. The arc-length method was adjusted for the stiffness of the structure defined on the base of the geometry and structural elements to achieve solution effectively. The ultimate bearing capacity was achieved by snap-through.

## References

- Riks, E. (1972), The application of Newton's method to the problem of elastic stability, *Journal of Applied Mechanics*, 39, pp. 1060-1065.
- Riks, E. (1979), An incremental approach to the solution of snapping and buckling problems, *International Journal of Solids and Structures*, 15, pp. 529-551.
- Crisfield, M. A. (1981), A fast incremental iterative solution procedure that handles snap-through, *Computers and Structures*, 13, pp. 55-62.
- Hellweg, H. B. and Crisfield, M.A. (1998), A new arc-length method for handling sharp snap-backs. *Computers and Structures*, Vol. 66 No. 5, pp. 705-709.
- Broyden, C. G. (1970), The convergence of a class of double-rank minimization algorithms. *Journal of the Institute of Mathematics and Its Applications*. 6, pp. 76-90.
- Fletcher, R. (1970), A new approach to variable metric algorithms. *Computer Journal*. 13, Nr. 3, pp. 317-322.
- Goldfarb, D. (1970), A family of variable metric updates derived by variational means. *Mathematics of Computation*. 24, Nr. 109, 1970, pp. 23-26.
- Shanno, D. F. (1970), Conditioning of quasi-Newton methods for function minimization. *Mathematics of Computation*. 24, Nr. 111, pp. 647-656.
- Chang, C. C. (1991), Periodically restarted quasi-Newton updates in constant arc-length method, *Computers and Structures*, Vol. 41 No. 5, pp. 963-972.
- APDL design language & ANSYS theory reference, Ebook, Asaha
- Eurocode 1 (2005): Actions on structures, Authority: The European Union Per Regulation, 2005.

# Meso-scale Fracture Modelling of Concrete Based on X-ray Computed Tomography Images

Wenyuan Ren<sup>1</sup>, \*Zhenjun Yang<sup>1,2</sup>, and Phil Withers<sup>3</sup>

<sup>1</sup>School of Mechanical, Aerospace and Civil Engineering, the University of Manchester, UK.

<sup>2</sup>College of Civil Engineering and Architecture, Zhejiang University, China.

<sup>3</sup>Manchester X-ray Imaging Facility, School of Materials, the University of Manchester, UK.

\*Corresponding author: zhjyang@zju.edu.cn

## Abstract

Meso-scale two-dimensional finite element models are developed for fracture modelling in concrete based on images from an in-situ microscale X-ray Computed Tomography test. In the models, the material heterogeneity is characterised by “real” multi-phases, namely, aggregates, cement and voids. Zero-thickness cohesive interface elements (CIEs) with normal/shear traction-separation constitutive laws are embedded within cement and on aggregate-cement interfaces to simulate potential cracks. Simulations of uniaxial tension tests were carried out. The results show good qualitative and quantitative agreement with experimental observations and simulations from literatures.

**Keywords:** Concrete, X-ray computed tomography, Image based modelling, Cohesive zone model, Meso-scale finite element model

## Introduction

Micro/meso-scale modelling of damage and fracture in quasi-brittle multiphase materials, such as concrete and fibre reinforced polymers, has received more and more attention, in order to obtain more accurate understanding of their failure mechanisms and evaluation of uncertainty and reliability due to random distribution of phases. There are basically two approaches in characterising random heterogeneity in materials numerically: direct approach and indirect approach. In the direct approach, different phases including matrices, inclusions and interfaces are explicitly modelled by finite elements (FE) with assigned properties. The randomness in the spatial distribution of different phases is realised by randomised positions and shapes of inclusions (Lilliu and van Mier, 2003; López *et al.*, 2008; Skarżyński and Tejchman, 2010; Yin *et al.*, 2012). In the indirect approach, the material properties are modelled as spatially-varying random fields with given correlation structures, so different phases are implicitly modelled (Xu, 2007; Xu and Chen, 2009; Yang *et al.*, 2009; Su *et al.*, 2010). However, most of these studies use assumed micro/meso-scale morphologies or random field properties, which are not direct and accurate representation of the internal structures of the materials. Therefore, the simulated micro/meso-scale damage and fracture processes cannot be directly and accurately validated, although macro-scale load-displacement curves can mostly be obtained.

More representative geometrical models can be constructed based on images obtainable from techniques such as digital cameras (Yue *et al.*, 2003) and microscopes (Michailidis *et al.*, 2010), and more recently, the X-ray Computed Tomography (XCT). The XCT, routinely used in hospitals, has now become attractive for characterising microstructures of materials, because of its high resolution, non-destructive nature, and clear visualisation. In the last decade, tremendous efforts have been made in applying the XCT to characterise microstructures and study evolutions of damage and fracture of a variety of materials, such as geological materials (rock, soil and fossils)



(Carlson WD, 2006), metals and alloys (Babout *et al.*, 2006; Marrow and Babout, 2006; Qian *et al.*, 2008), porous materials (Kerckhofs *et al.*, 2008), composites (Drummond *et al.*, 2005) and concrete (Garboczi, 2002; Wang *et al.*, 2003). However, XCT-image based modeling and analysis is only conducted occasionally, for example, by Hollister *et al.* (1994) for trabecular bones, Terada *et al.*, (1997) for metal matrix composites, Ali *et al.* (2009) and Sharma *et al.* (2012) for carbon/carbon composites, Mostafavi *et al.* (2013) for polygranular graphite, and Jivkov *et al.* (2013) for concrete, respectively. However, most of these studies carried out linear elastic stress analysis or calculated effective stiffness based on homogenisation method, and XCT image-based modelling of complicated fracture has hardly been conducted.

In this study, meso-scale 2D FE models are developed for fracture modelling in concrete based on images from an in-situ microscale XCT test (Yang *et al.*, 2013). In these models, the material heterogeneity is characterised by three phases, namely, aggregates, cement and voids. To model complicated fracture processes, zero-thickness cohesive interface elements (CIEs) with normal/shear traction-separation constitutive laws are embedded within cement and on aggregate-cement interfaces to simulate potential cracks, using an algorithm extended from a previous one for homogeneous materials (Yang *et al.*, 2009). Simulations of uniaxial tension tests were carried out. The influence of the inclusions' distribution on overall stress-displacement curves and crack patterns was investigated.

## Building of the meso-scale models

### Image processing

The segmented 37.2 mm concrete cube from the in-situ XCT test (Yang *et al.*, 2013) is shown in Figure 1, highlighting the locations of a few cross-sections to be studied. Figure 2 shows the image of cross-section 1, in which the dark, grey and white regions represent aggregates, cement and voids, respectively. The gray levels in this image are continuous (0-255) and roughly uniform in the regions of each colour. There are 372 pixels in each direction, so each pixel represents 0.1 mm. Before mesh generation, the image is processed into a binary one, by assigning 1 to aggregates and 2 to cement, after it is segmented into three phases using a proper threshold range of gray values for each, specifically, 0-120 for aggregates (dark areas), 121-220 for cement (grey areas) and 221-255 for voids (white areas). To simplify mesh generation, the phase value (1 or 2) of small regions with one pixel width (highlighted by red circles in Figure 2) is changed to be consistent with their surrounding regions. The image after processing is shown in Figure 3.

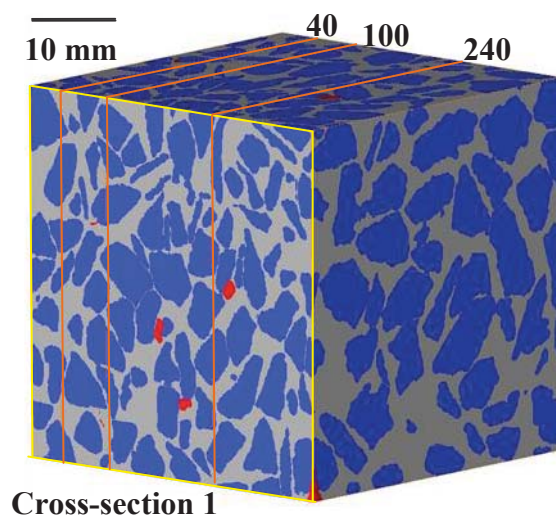


Figure 1. The segmented concrete cube

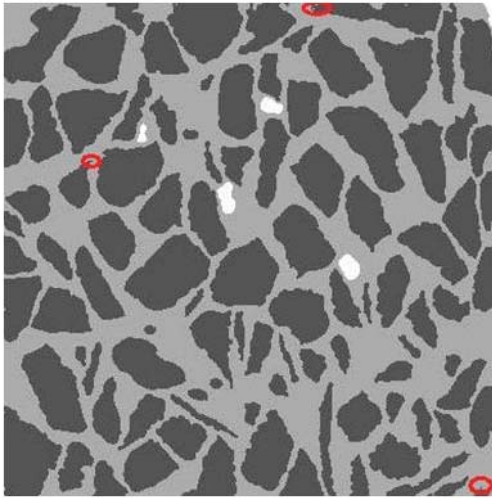


Figure 2. The image of cross-section 1

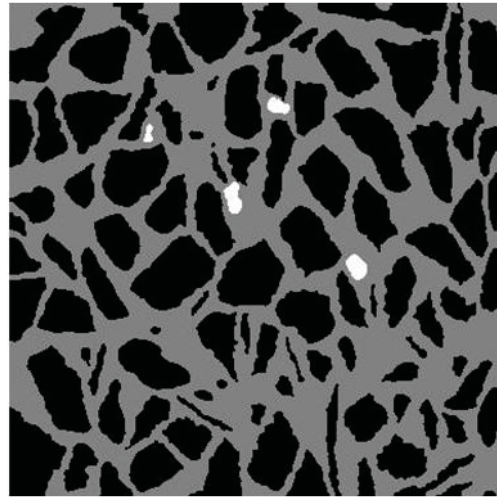
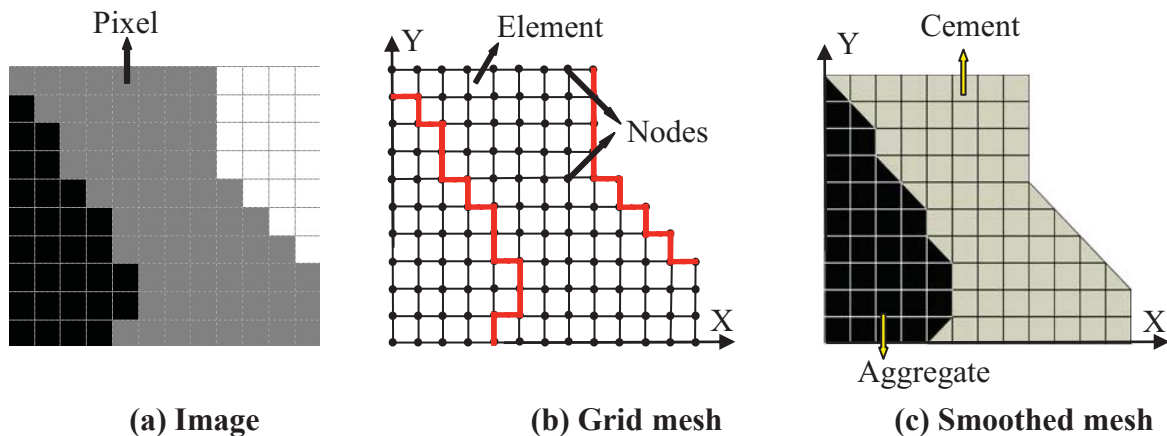


Figure 3. After image processing

### Initial mesh generation

The binary image in Figure 3 consists of an array of square pixels. Figure 4a shows a small part of Figure 3. Naturally, each pixel can be modelled by a quadrilateral element in the FE mesh. The resultant mesh is shown in Figure 4b, in which the boundaries between two phases are zigzagged. This situation is caused by image resolution and may not represent the real material interfaces. In addition, the stress concentration at the corner points may lead to numerical difficulties in FE simulations. Therefore, these inter-phase boundaries are further smoothed by dividing the corner elements into two triangles and assigning proper phase values. The smoothed mesh is shown in Figure 4c.



(a) Image

(b) Grid mesh

(c) Smoothed mesh

Figure 4. Transformation from pixel to mesh grid

### Cohesive interface elements insertion

In order to simulate realistic fracture processes, four-noded cohesive interface elements (CIEs) with zero in-plane thickness are inserted into the generated initial mesh. The detailed CIE insertion procedure devised for homogeneous materials in (Yang *et al.*, 2009) is extended to account for multi-phases and interfaces. Three sets of CIEs with different traction-separation softening laws are inserted, namely, CIE\_AGG inside the aggregates, CIE\_CEM inside the cement, and CIE\_INT on the aggregate-cement interfaces. As the aggregates have much higher strength than the cement and the interfaces, no cracks are allowed to initiate inside the aggregates by assuming elastic behaviour without damage to CIE\_AGG.

The final FE mesh after the insertion of CIEs based on the XCT image in Figure 3 is shown in Figure 5. It has 357,324 nodes and 291,875 elements including 141,505 solid elements and 150,370 CIEs. The CIE\_INT elements are highlighted as red lines.

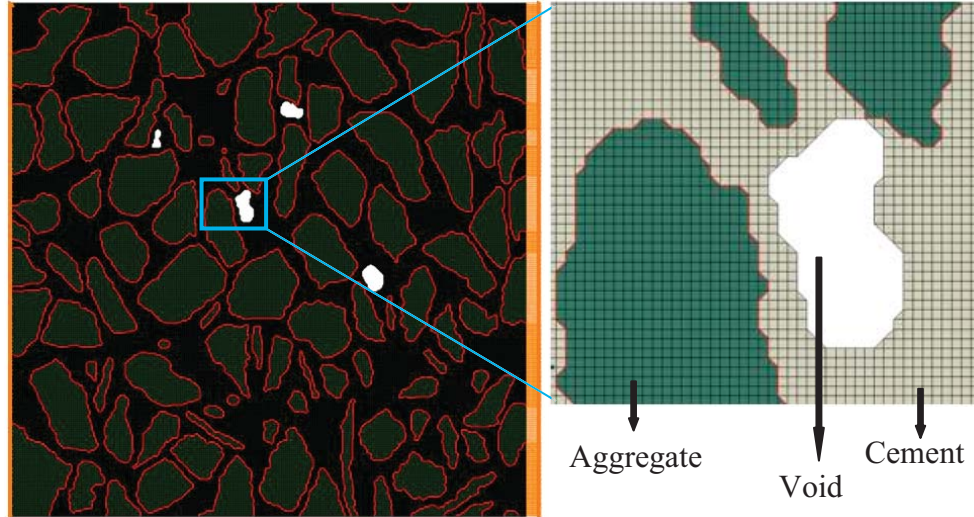


Figure 5. The FE mesh based on the XCT image in Figure 2

## Numerical simulations of uniaxial tension test

### Model parameters

The aggregates and cement are assumed to behave linear elastically. The linear tension/shear softening laws are used to model CIEs (Yang *et al.*, 2009) with quadratic nominal stress initiation criterion and linear damage evolution criterion. For comparison of results, the same material properties as used in (López *et al.*, 2008) are used in this study. They are listed in Table 1. Due to the lack of experimental data, the shear fracture properties are assumed to be the same as the normal ones.

Uniaxial tension tests are simulated. The image-based models are fixed at the left boundary and are subjected to a uniformly distributed displacement at the right boundary, i.e., a displacement-controlled loading scheme is used. All analyses are ended at a displacement  $d=0.2\text{mm}$ . The Abaqus/Explicit is used to solve the nonlinear equation systems with a step time of 0.01s, which is found long enough to ensure the quasi-static loading condition.

Table 1. Material properties

	Elastic modulus (GPa)	Poisson's ratio	Density ( $10^{-9}$ tone/ $\text{mm}^3$ )	Elastic stiffness (MPa/mm)	Tensile strength (MPa)	Fracture energy (N/mm)
Aggregate	70	0.2	2.5	/	/	/
Cement	25	0.2	2.2	/	/	/
CIE_AGG	/	/	2.5	$10^6$	/	/
CIE_CEM	/	/	2.2	$10^6$	6	0.06
CIE_INT	/	/	2.2	$10^6$	3	0.03

### Typical Results

The average stress ( $\sigma$ ) –displacement ( $d$ ) curve is plotted in Figure 6, together with the experimental curve (Hordijk, 1992) and the simulation results from an assumed meso-structure (López *et al.*, 2008). The average stress  $\sigma$  is calculated by dividing the total nodal reaction force of all the nodes on the left boundary by the specimen cross-section area. It can be seen that the peak loads and the post-peak parts of three curves are close. However, one should not intend to compare the curves in Figure 6 directly, as they are responses of specimens of very different sizes. A direct comparison of the present simulation with the in-situ XCT test (Yang *et al.*, 2013) is not available because the specimen is under compression rather than tension in the test.

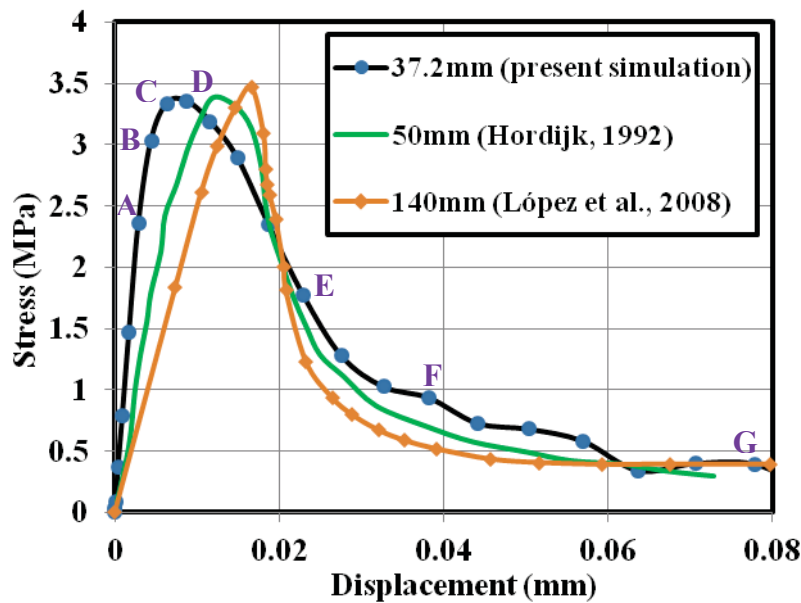


Figure 6. Average stress-displacement curves under uniaxial tension

Figure 7 illustrates the propagation of microcracks before the peak load, which are represented by the CIEs with scalar damage index (SDEG in ABAQUS) over 0.9. It should be noted that SDEG=1.0 means complete failure. All the predicted crack figures in this paper are shown using a displacement scale factor (DSF) =10. A few microcracks initiate on the aggregate-cement interfaces at low stress  $\sigma=2.36$  MPa (Figure 7a). More and more microcracks appear as the stress increases. At the end of the elastic behaviour stage at  $\sigma=3.03$  MPa at Point B in Figure 6, the microcrack pattern already looks complicated (Figure 7b). A crack pattern in the nonlinear stage ( $\sigma=3.34$  MPa at Point C) is shown in Figure 7c, which looks similar to that at the peak point D with  $\sigma=3.36$  MPa in Figure 7d. The predicted scenario in Figure 7 indicates that a large number of microcracks initiate very quickly at the early loading stage, and the crack pattern becomes gradually stable in the pre-peak nonlinear stage. It can also be seen that before the peak load is reached, the microcracks are not connected to form any dominant macrocracks. This is because most of them are on the aggregate-cement interfaces due to the relative low tensile strength (3MPa), and only a small number of them are inside the cement due to its high tensile strength (6MPa). It is also reconfirmed that the approach of pre-embedding CIEs is very flexible and powerful in modelling complicated fracture process.

The predicted post-peak crack propagation process is illustrated in Figure 8, in which the different phases are shown. It can be seen that at the peak load, there is still no evident macrocracks (Figure 8a). As the displacement increases, some aggregate-cement interfacial cracks continue to propagate and are gradually connected by newly formed cracks in the cement phase (Figure 8b and 8c). The

specimen fails with two main macrocracks (Figure 8d). It should be noted that the microcracks in Figure 7 still exist, but they are not shown in Figure 8 because their width is much smaller than that of the two macrocracks.

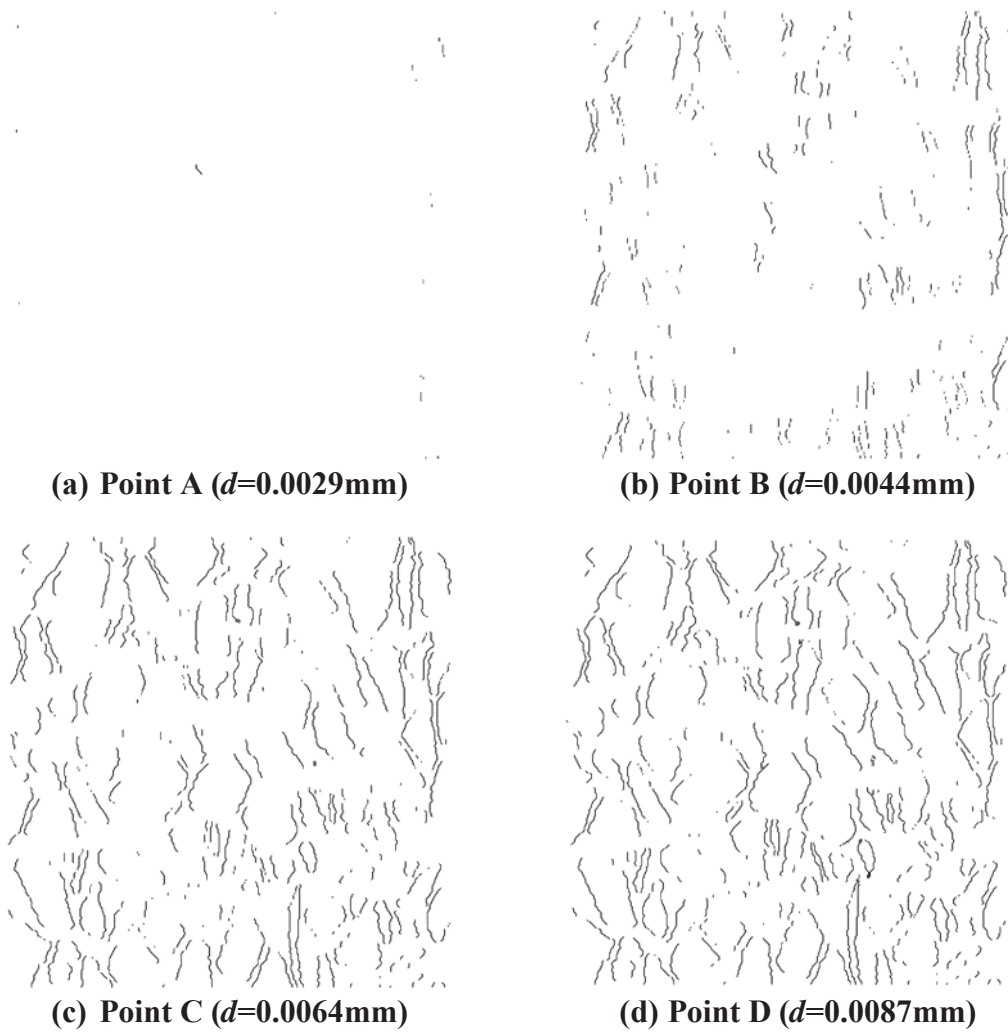
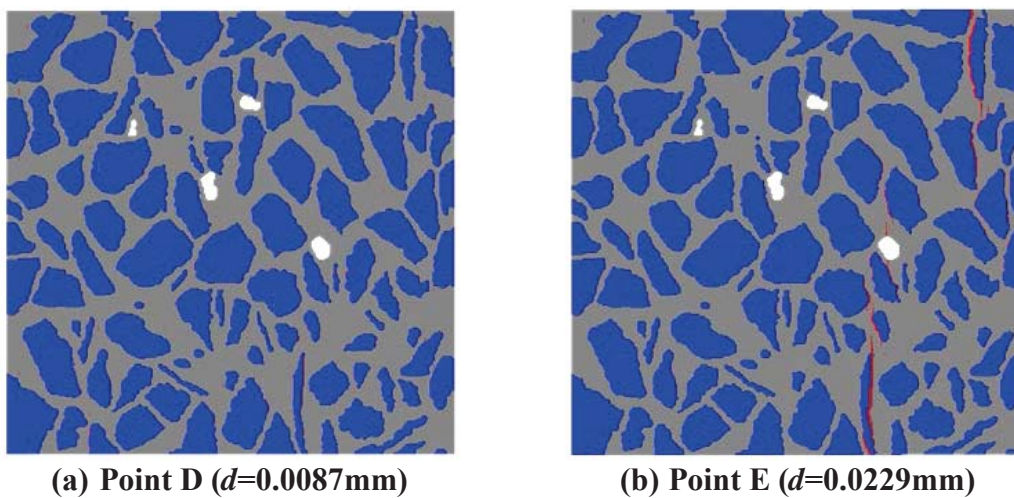
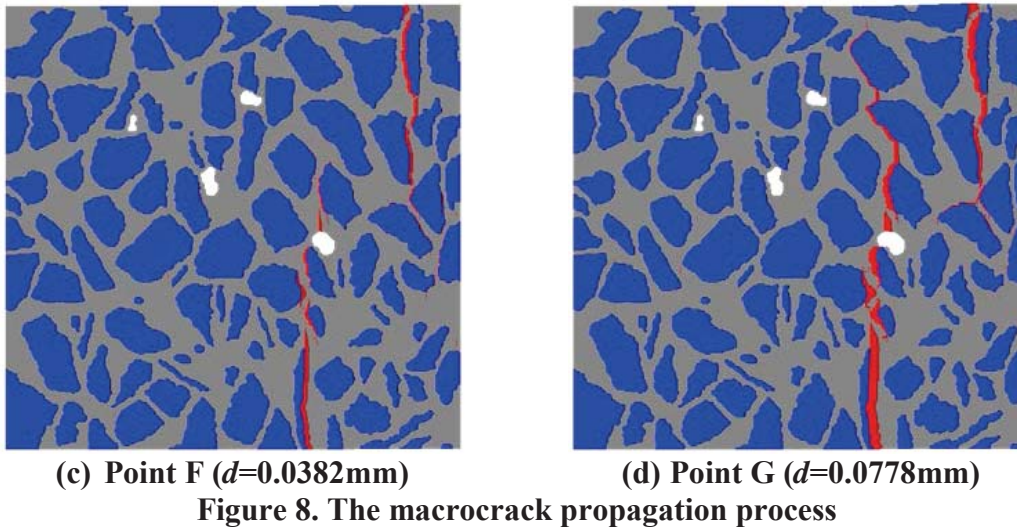


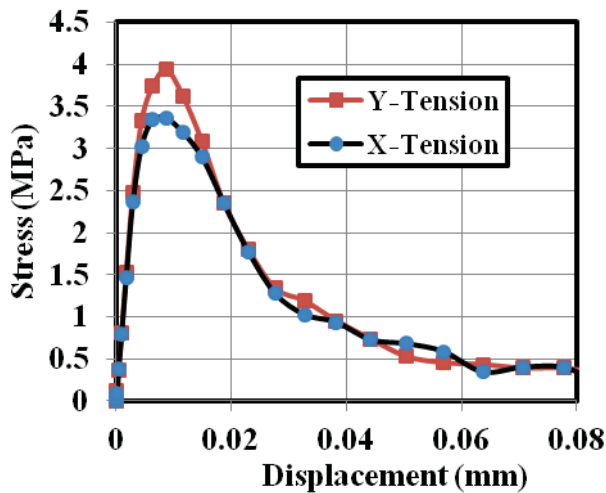
Figure 7. The pre-peak microcracking process



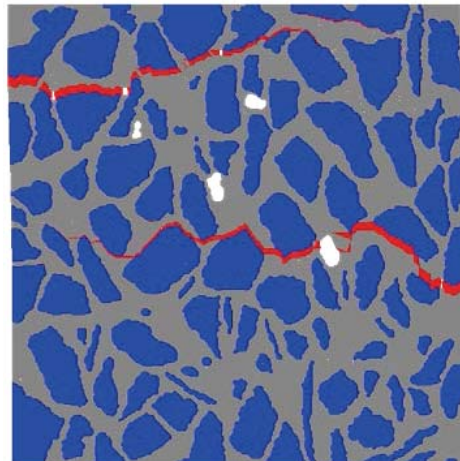


#### *Effects of loading direction*

The same model in Figure 5 is simulated under uniaxial tension in the vertical (Y) direction. The predicted average stress - displacement curves are shown in Figure 9. It can be seen that the predicted strengths of the same specimen differ about 11% (3.4MPa and 3.8MPa). A different crack pattern from Figure 8d is predicted, as shown in Figure 10. These differences are caused by different loading directions, or equivalently, by different distributions of phases of the same volume fractions under the same loading direction. The pre-peak elastic parts of the two curves in Figure 10 are identical and independent of the phase distribution, which has also been noticed in (Skarżyński and Tejchman, 2010) and (Yin *et al.*, 2013).



**Figure 9. Average stress-displacement curves under different tension directions**



**Figure 10. Crack pattern under vertical tension ( $d=0.0778\text{mm}$ )**

#### *Effects of image location*

Three more images on different cross-sections along another direction (shown in Figure 1) are transformed into 2D FE models which are simulated under uniaxial tension. The average stress - displacement curves are compared in Figure 11, with the final crack patterns shown in Figure 12-14 for the cross-section 40, 100 and 240, respectively. The very different load-carrying capacities and crack patterns at different locations in the same specimen reflect the effects of random distribution of phases of random shapes and sizes. This also demonstrates the limitations of 2D meso-scale

modelling and the necessity of 3D modelling, as there exists only one crack pattern in the physical test of one specimen.

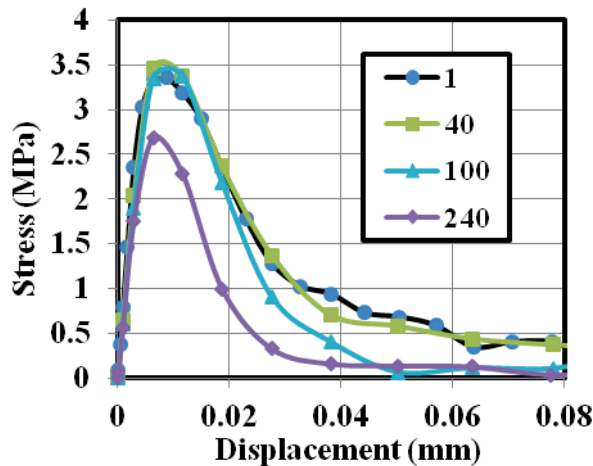


Figure 11. Average stress-displacement curves from different images

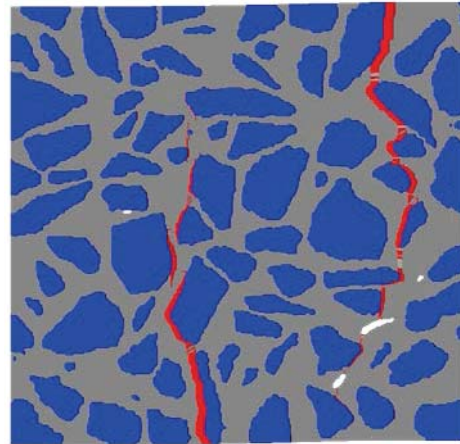


Figure 12. Crack pattern of cross-section 40 ( $d=0.0778\text{mm}$ )

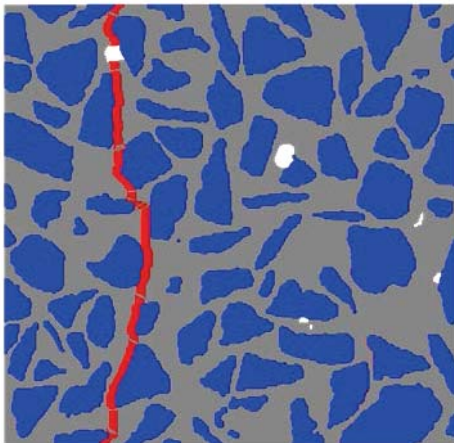


Figure 13. Crack pattern of cross-section 100 ( $d=0.0779\text{mm}$ )

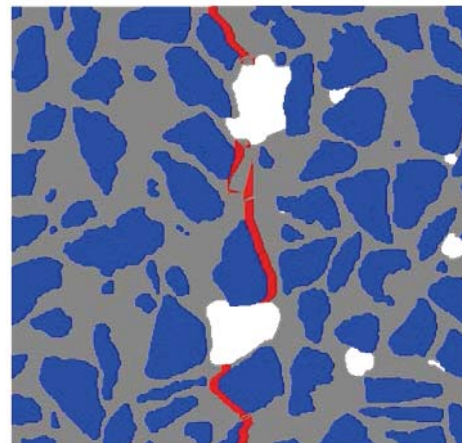


Figure 14. Crack pattern of cross-section 240 ( $d=0.0775\text{mm}$ )

## Conclusions

2D meso-scale FE models based on XCT images and the method of pre-embedding cohesive interface elements are built to simulate crack propagation processes in concrete under uniaxial tension loading. The flexibility and effectiveness of pre-embedding CIE technique in modelling realistic, complicated fracture processes is reconfirmed by good qualitative and quantitative agreement of predicted results with experimental observations and simulations from literatures. The very different crack patterns and load-carrying capacities on different cross-sections of the same specimen demonstrate not only the effects of random distribution of phases, but also the limitations of 2D modelling and the necessity of 3D modelling which is currently under way.

## Acknowledgement

The research is funded by a Royal Society Research Grant and an EPSRC grant (No. EP/J019763/1). Ren's PhD study in UoM is partially funded by China Scholarship Council. Yang would like to thank the Alexander von Humboldt Foundation, Germany for a Fellowship for Experienced Researchers.

## References

- Ali, J., Farooqi J. K., Buckthorpe D., Cheyne A. and Mummery P., (2009), Comparative study of predictive FE methods for mechanical properties of nuclear composites. *Journal of Nuclear Materials*, 383(3): 247-253.
- Babout, L., Marrow T.J., Engelberg D. and Withers P.J., (2006), X-ray microtomographic observation of intergranular stress corrosion cracking in sensitised austenitic stainless steel. *Materials Science and Technology*, 22(9):1068-1075.
- Carlson, W.D., (2006), Three-dimensional imaging of earth and planetary materials. *Earth and Planetary Science Letters*, 249(3-4):133-147.
- Drummond, J.L., De Carlo F and Super B.J., (2005), Three-dimensional tomography of composite fracture surfaces. *Journal of Biomedical Materials Research Part B-Applied Biomaterials*, 74B(2):669-675.
- Garboczi, E.J., (2002), Three-dimensional mathematical analysis of particle shape using X-ray tomography and spherical harmonics: Application to aggregates used in concrete. *Cement and Concrete Research*, 32(10): 1621-1638.
- Hollister, S.J., Brennan J.M. and Kikuchi N., (1994), A homogenization sampling procedure for calculating trabecular bone effective stiffness and tissue level stress. *Journal of Biomechanics* 27(4): 433-444.
- Hordijk, D.A. (1992). Tensile and tensile fatigue behaviour of concrete; experiments, modelling and analyses. *Heron*, 37(1): 1-79.
- Jivkov, A.P., Engelberg D.L., Stein R. and Petkovski M., (2013), Pore space and brittle damage evolution in concrete. *Engineering Fracture Mechanics*, In Press. DOI: <http://dx.doi.org/10.1016/j.engfracmech.2013.05.007>.
- Kerckhofs, G., Schrooten J., Cleynenvreugel T., Lomov S.V. and Wevers M., (2008), Validation of x-ray microfocus computed tomography as an imaging tool for porous structures. *Review of Scientific Instruments*, 79(1): Paper No. 013711.
- Lilliu, G. and van Mier J. G. M., (2003), 3D lattice type fracture model for concrete. *Engineering Fracture Mechanics*, 70(7-8): 927-941.
- López, C., Carol I. and Aguado A., (2008), Meso-structural study of concrete fracture using interface elements. I: numerical model and tensile behavior. *Materials and Structures*, 41(3): 583-599.
- Marrow, T.J., About L., Jivkov A.P., Wood P., Engelberg D., Stevens N., Withers P.J. and Newman R.C., (2006), Three dimensional observations and modelling of intergranular stress corrosion cracking in austenitic stainless steel. *Journal of Nuclear Materials*, 352(1-3):62-74.
- Michailidis, N., Stergioudi F., Omar H. and Tsipas D. N., (2010), An image-based reconstruction of the 3D geometry of an Al open-cell foam and FEM modeling of the material response. *Mechanics of Materials* 42(2): 142-147.
- Mostafavi, M., Baimpas N., Tarleton E., Atwood R.C., McDonald S.A., Korsunsky A.M. and Marrow T.J., (2013), Three-dimensional crack observation, quantification and simulation in a quasi-brittle material. *Acta Materialia*. 61(16): 6276-6289.
- Qian, L., Toda H., Uesugi K., Ohgaki T., Kobayashi M. and Kobayashi T., (2008), Three-dimensional visualization of ductile fracture in an Al-Si alloy by high-resolution synchrotron X-ray microtomography. *Materials Science and Engineering A-Structural Materials Properties Microstructure and Processing*, 483:293-296.
- Sharma, R., Mahajan P. and Mittal R.K., (2012), Fiber bundle push-out test and image-based finite element simulation for 3D carbon/carbon composites. *Carbon* 50(8): 2717-2725.
- Skarżyński, Ł. and Tejchman J., (2010), Calculations of fracture process zones on meso-scale in notched concrete beams subjected to three-point bending. *European Journal of Mechanics - A/Solids*, 29(4): 746-760.
- Su, X.T., Yang Z.J. and Liu G.H., (2010), Monte Carlo simulation of complex cohesive fracture in random heterogeneous quasi-brittle materials: A 3D study. *International Journal of Solids and Structures*, 47:2336-2345.
- Terada, K., Miura T. and Kikuchi N., (1997), Digital image-based modelling applied to the homogenization analysis of composite materials. *Computational Mechanics*, 20(4): 331-346.
- Wang, L.B., Frost J.D. and Voyadjis G.Z., (2003), Quantification of damage parameters using X-ray tomography images. *Mechanics of Materials*, 35: 777-790.
- Xu, X.F., (2007), A multiscale stochastic finite element method on elliptic problems involving uncertainties. *Computer Methods in Applied Mechanics and Engineering*, 196, 2723-2736.
- Xu, X.F. and Chen X., (2009), Stochastic homogenization of random elastic multi-phase composites and size quantification of representative volume element. *Mechanics of Materials*, 41-2, 174-186
- Yang, Z.J., Ren W.Y., Mostafavi M., McDonald S. A. and Marrow T. J., (2013), Characterisation of 3D fracture evolution in concrete using in-situ x-ray computed tomography testing and digital volume correlation. *VIII International Conference on Fracture Mechanics of Concrete and Concrete Structures*, Toledo, Spain, CIMNE.
- Yang, Z.J., Su X.T., Chen J.F. and Liu G.H., (2009), Monte Carlo simulation of complex cohesive fracture in random heterogeneous quasi-brittle materials. *International Journal of Solids and Structures*, 46(17): 3222-3234.
- Yin, A.Y., Yang X.H., Gao H. and Zhu H.P., (2012), Tensile fracture simulation of random heterogeneous asphalt mixture with cohesive crack model. *Engineering Fracture Mechanics*, 92(0): 40-55.



- Yin, A.Y., Yang X.H. and Yang Z.J., (2013), 2D and 3D Fracture Modeling of Asphalt Mixture with Randomly Distributed Aggregates and Embedded Cohesive Cracks. *Procedia IUTAM* 6(0): 114-122.
- Yue, Z.Q., Chen S. and Tham L.G., (2003), Finite element modeling of geomaterials using digital image processing. *Computers and Geotechnics* 30(5): 375-397.

## Computational Mechanics of a Coupled Flow-Structure Interaction Problem with Applications to Bio-inspired Micro Air Vehicles

**\*Rohan Banerjee<sup>1</sup>, \*Padmanabhan Seshaiyer<sup>2</sup>**

<sup>1</sup>Thomas Jefferson High School for Science and Technology, Alexandria, VA 22312, USA

<sup>2</sup>Mathematical Sciences, George Mason University, Fairfax, VA 22030, USA

\*Corresponding authors: rohan.b.banerjee@gmail.com, pseshaiy@gmu.edu

### Abstract

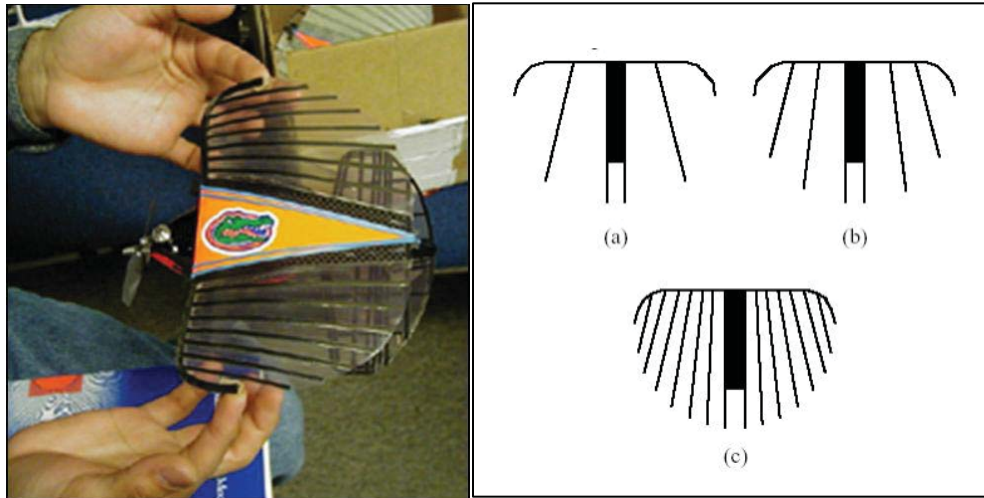
Micro Air Vehicles (MAVs) are small flying vehicles that are designed to fit certain size and weight constraints. MAVs are important because they have a variety of practical applications, including surveillance and weather imaging. MAVs fall into two major categories according to their lift mechanism, either fixed-wing or flapping-wing, and wing structure, either rigid or flexible. Much research has been devoted to fixed wing, flexible MAVs consisting of rigid stabilizing battens and a rigid central fuselage coupled with a flexible membrane. We used finite element software to implement a system of PDEs that represented the MAV wing. The goal of this study was to computationally verify qualitative results showing that varying the number of stabilizing battens and the angle of attack affected the wing deformation. The work will be extended to include rigorous stability estimates, which will provide a better understanding of flexible wing MAV aerodynamics, and nonlinear membrane models.

**Keywords:** Micro Air Vehicles, multiphysics, mechanics, PDE, finite element method

### Introduction

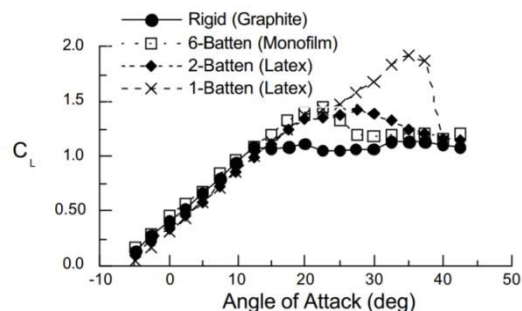
Applications in computational mechanics have expanded with the need to solve sophisticated fluid-structure applications using novel computational methodologies. Solving these coupled systems efficiently helps to understand complex non-linear interactions that arise in several applications such as blood flow interaction with arterial wall (Bathe and Kamm, 1999; Nobile, 2001) and computational aeroelasticity of flexible wing flying vehicles (Ferguson, 2006), where the structural deformation and flow field interact in a highly complex way. This study focuses specifically on the applications of computational mechanics to flexible-wing MAVs.

Micro Air Vehicles (MAVs) are small, autonomous flying vehicles which are designed for use in applications where human intervention would be either costly or dangerous. MAVs have the potential to be used in a large number of applications, including military reconnaissance and weather imaging. A number of variations on MAVs have been considered in computational and experimental studies. One type of MAV is the flexible-wing MAV, in which a flexible membrane is attached to a rigid body, allowing the wing to passively deform during the course of a flight. The other major type of MAV is the biologically-inspired flapping-wing MAV. A number of studies have been conducted which examine the thrust performance of flapping-wing mechanisms (La Mantia and Dabnichki, 2013). Unfortunately, constructing flapping-wing MAVs that satisfy power and stability requirements is often very difficult (Ifju et. al, 2002). Therefore, in this study, we computationally modeled the behavior of a particular variant of the flexible-wing MAV designed and tested by Ifju, et al.



**Figure 1. Flexible Wing MAV Model: (Left) 7-batten flexible wing MAV developed by the University of Florida (Ifju et. al, 2002); (Right) Schematic of one-batten (a), two-batten (b), and six-batten (c) flexible wing MAV designs (Ifju et. al, 2002)**

The Micro Air Vehicles developed by Ifju, et al. consist of a rigid skeleton consisting of a central fuselage and stabilizing battens which run perpendicular to the fuselage. Superimposed upon this rigid skeleton is a flexible membrane, typically constructed out of an extensible latex rubber membrane or an inextensible monofilm membrane. A number of different wings were theorized and tested by Ifju, of which the designs of note are displayed in Figure 1. In addition, Ifju et al. have conducted experimental studies that indicate the influence of the number of battens on the lift performance in relation to varying angles of attack (see Figure 2).



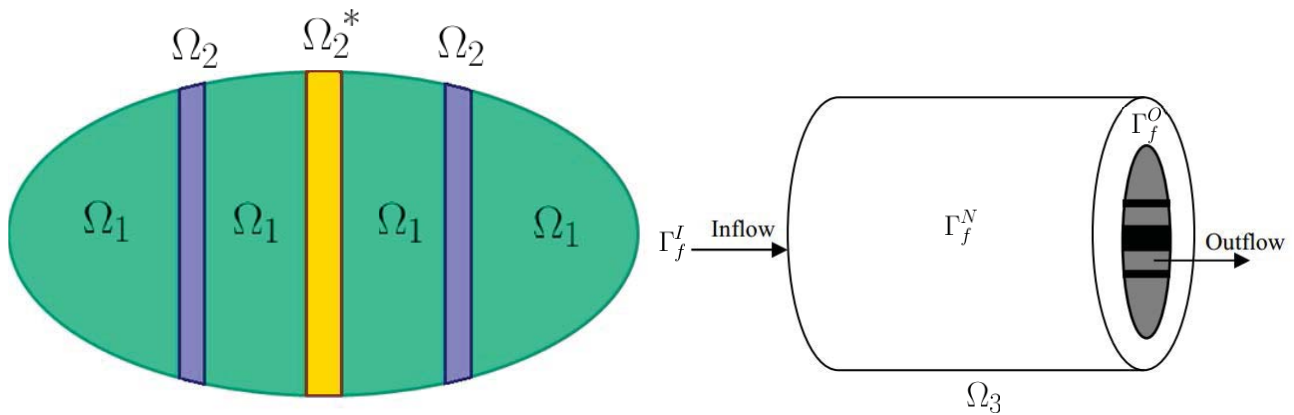
**Figure 2. Lift Coefficient vs. Angle of Attack for various MAV configurations (Ifju, et al)**

The major difference between the different designs is the number of stabilizing battens used, in addition to the type of membrane. One of the qualitative conclusions of the aforementioned study was that increasing the number of battens generally resulted in stiffer designs that exhibited smaller magnitudes of membrane vibration and deformation. The goal of this study was to computationally verify these qualitative experimental results and examine the role of the angle of attack on the membrane deflection.

## Models, Methods, and Governing Differential Equations

### Model Problem

In order to mathematically model the wing of the flexible-wing MAV, we first formulated a simplified geometry from which we subsequently imposed a system of partial differential equations. The geometry consisted of a 2D elliptical surface describing the underlying membrane, with 2D rectangles superimposed upon the ellipse which represented both the stabilizing battens and the central fuselage. The wing surface was superimposed on the face of a 3D cylinder, which represented a wind tunnel through which air could flow. The cylinder could be inclined to simulate different angles of attack, which describe at what angle the airflow makes contact with the MAV surface. A schematic showing the geometry and the different domains and boundaries of interest is shown in Figure 3.



**Figure 3. Subdomains of the wing structure for 1-batten MAV (top), schematic of airflow and 1-batten MAV wing placement (Nong et al., 2010) (bottom)**

In Figure 3, Note that  $\Omega_1$  represents the flexible membrane,  $\Omega_2$  represents the battens, and  $\Omega_2^*$  represents the fuselage (which differs from the battens only in elastic modulus). In addition,  $\Omega_3$  represents the entire 3D fluid domain,  $\Gamma_f^I$  represents the inflow face of the cylinder,  $\Gamma_f^N$  represents the rectangular outer face of the cylinder, and  $\Gamma_f^O$  represents the outflow face of the cylinder, not including the region where the MAV is placed.

### Governing PDE System

We modeled the deformation of the flexible membrane using a linear elastic membrane model based on Hooke's Law. This led to a PDE for the membrane which involved  $w$ , the transverse displacement of the membrane in space and time, shown below:

$$\rho_{s0} \frac{\partial^2 w}{\partial t^2} - E_0 \nabla^2 w = p \quad (\text{in } \Omega_1) \quad (1)$$

Note in equation 1 that the right hand side represents the fluid pressure, to be defined later. To model the stabilizing beams, we used Euler-Bernoulli beam theory, which gives another PDE involving  $w$ .

Adding the Euler-Bernoulli beam equation to the prior membrane equation yields the following set of PDEs (Nong et al., 2010):

$$\begin{aligned} (\rho_{s0} + \rho_{s1}) \frac{\partial^2 w}{\partial t^2} - E_0 \nabla^2 w + E_1 \frac{\partial^2 v}{\partial y^2} &= p \quad (\text{in } \Omega_2) \\ v &= \frac{\partial^2 w}{\partial y^2} + \epsilon \nabla^2 v \quad (\text{in } \Omega_1 \cup \Omega_2) \end{aligned} \quad (2)$$

Note the presence of an additional dependent variable  $v$ , which is an auxiliary variable used to facilitate the computational simulation of the system. The fuselage ( $\Omega_2^*$ ) satisfies in identical system of PDEs, only differing in the values of certain constants as previously mentioned.

We assumed that the fluid flow was incompressible, irrotational, and inviscid, allowing us to use the potential flow model for our airflow. This involved the introduction the velocity potential  $\phi$ , satisfying Laplace's equation:

$$\nabla^2 \phi = 0 \quad (\text{in } \Omega_3) \quad (3)$$

The fluid pressure is defined according to Bernoulli's Equation for flow, which relates the fluid velocity, density, pressure, and transverse displacement as follows:

$$p = -\rho_f \phi_t - \rho_f g w \quad (4)$$

#### *PDE Boundary Conditions*

We imposed certain boundary conditions on the MAV wing model and the wind tunnel cylinder to simulate realistic constraints. The bottom half of the MAV wing employed a Dirichlet boundary constraint to simulate a fixed, rigid beam, while the upper half of the MAV wing employed a Neumann boundary constraint to represent the free membrane, as follows:

$$\begin{aligned} w &= 0 \quad (\text{on lower boundary}) \\ \vec{n} \cdot \nabla w &= 0 \quad (\text{on upper boundary}) \end{aligned} \quad (5)$$

The inflow boundary condition for the fluid domain was specified by stating a constant value for the normal component of the fluid velocity on the inflow face. The normal fluid velocity on the outer, rectangular boundary of the cylinder was set to 0. The outflow boundary condition was specified using Sommerfeld's radiation condition (Schot, 1992), which relates the normal fluid velocity on the right face of the cylinder to the time partial derivative of the velocity potential. The boundary conditions for the cylinder are described in Equation 6:

$$\begin{aligned} \nabla \phi \cdot \vec{n} &= 0 \quad (\text{on } \Gamma_f^N) \\ \nabla \phi \cdot \vec{n} &= -c \quad (\text{on } \Gamma_f^I) \\ \nabla \phi \cdot \vec{n} &= -\alpha \frac{\partial \phi}{\partial t} \quad (\text{on } \Gamma_f^O) \end{aligned} \quad (6)$$

### Parameter Values

Table 1 contains the parameter values used in our model (all non-cited values are either fundamental constants or are defined by the authors):

**Table 1. Parameter Values**

Variable	Value
Density of Membrane ( $\rho_{s0}$ )	$10 \text{ kg} \cdot \text{m}^{-3}$
Density of Beams ( $\rho_{s1}$ )	$100 \text{ kg} \cdot \text{m}^{-3}$
Density of Air ( $\rho_f$ )	$1.293 \text{ kg} \cdot \text{m}^{-3}$ (Nave, 1999)
Young's Modulus Factor for Membrane ( $E_0$ )	$1 \text{ N} \cdot \text{m}^{-1}$
Young's Modulus Factor for Beams ( $E_1$ )	$10 \text{ N} \cdot \text{m}$
Young's Modulus Factor for Fuselage ( $E_3$ )	$1000 \text{ N} \cdot \text{m}$
Smoothing Factor ( $\epsilon$ )	$10^{-5} \text{ m}$
Acceleration of gravity ( $g$ )	$9.8 \text{ m} \cdot \text{s}^{-2}$
Inflow velocity ( $c$ )	$0.1 \text{ m} \cdot \text{s}^{-1}$
Sommerfeld Radiation Constant ( $\alpha$ )	$50 \text{ s} \cdot \text{m}^{-1}$

### Computational Results

#### Solution Methodology

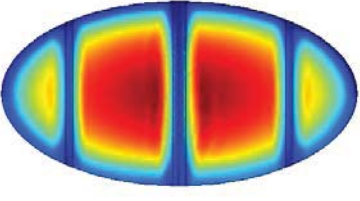
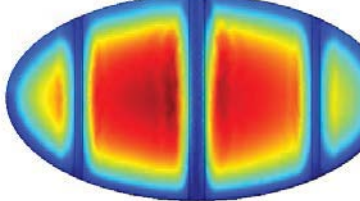
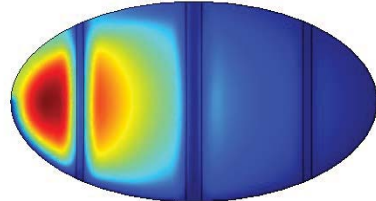
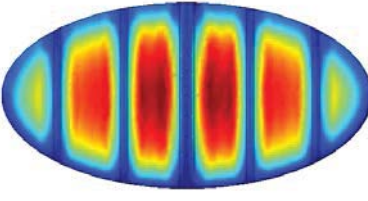
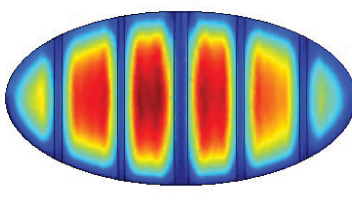
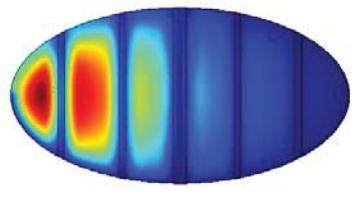
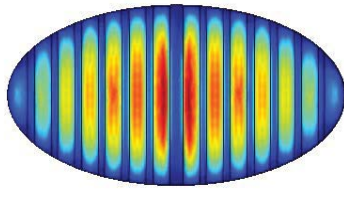
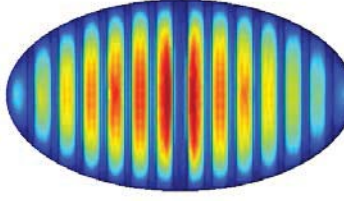
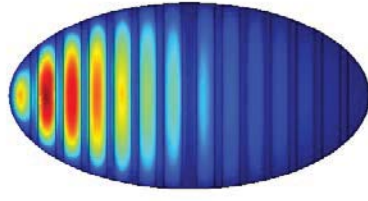
We then implemented computationally the PDE system described in Equations 1-4 and the boundary conditions described in Equations 5-6 using the finite element method. Specifically, we discretized Equations 1-4 and developed the weak formulation of the governing differential equations for the flow and the structure. These were coupled through interface variables that matched the velocity of the flow to the time derivative of the transverse displacement of the membrane-beam model.

This algorithm was implemented using the multiphysics software COMSOL. The software utilized a backward Euler scheme in time and used the UMFPACK (Unsymmetric Multifrontal Sparse LU Factorization Package) for solving the resulting linear systems. The geometry was discretized using triangular and tetrahedral elements.

#### Results

We conducted numerical simulations with the three batten configurations shown in Figure 1, consisting of one-batten, two-batten, and six-batten wing skeletons. Additionally, we investigated three different angles of attack for the fluid, namely  $90^\circ$ ,  $80^\circ$ , and  $15^\circ$ . We investigated the nine possible fluid-structure combinations and we have reproduced the results in the table below, showing the deflection of the MAV membrane at  $t = 1$  for varying numbers of battens and angles of attack as well as the maximum deflection of the MAV wing:

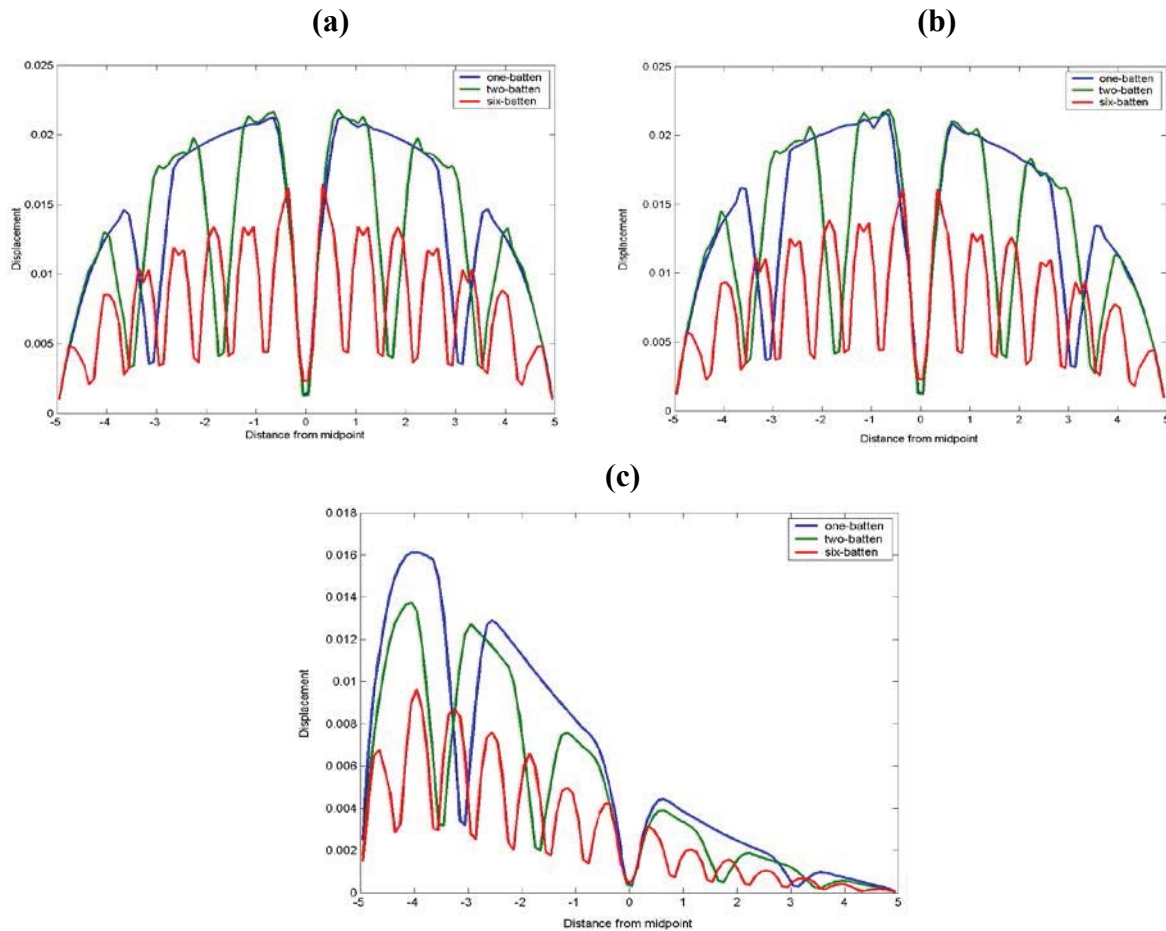
Table 2. Numerical Results

	90 degrees	80 degrees	15 degrees
1-batten	 <p>Maximum deflection: 0.0213</p>	 <p>Maximum deflection: 0.0217</p>	 <p>Maximum deflection: 0.0161</p>
2-batten	 <p>Maximum deflection: 0.0218</p>	 <p>Maximum deflection: 0.0138</p>	 <p>Maximum deflection: 0.0164</p>
6-batten	 <p>Maximum deflection: 0.0165</p>	 <p>Maximum deflection: 0.0161</p>	 <p>Maximum deflection: 0.0096</p>

Upon inspection of Table 2, there are two general trends of note. The first is that proceeding from top to bottom in each column of the matrix, which corresponds to increasing the number of battens while fixing the angle of attack, results in a general decrease in the maximum deflection of the MAV wing, with some irregularities. This seems to confirm the qualitative observations of Ifju et al., which stated that increasing the number of battens would increase the rigidity of the wing.

The second trend is that when proceeding from left to right in each row of the matrix, which corresponds to decreasing the angle of attack while fixing the number of battens, the maximum deflection also tends to decrease. Again, there are some irregularities, but overall this seems to confirm the expectation that lowering the angle of attack would decrease the maximum displacement. This presumably occurs because with smaller angles of attack, the normal component of the velocity is reduced, thus reducing the magnitude of the fluid pressure and therefore the magnitude of the deformation.

In order to gain another perspective on the deformation profile of the flexible wing MAVs, we have created the following set of graphs, shown in Figure 4:



**Figure 4. The effect of varying the number of battens on the deformation of the MAV wing for angle of attack  $90^\circ$  (a),  $80^\circ$  (b),  $15^\circ$  (c)**

The graphs in Figure 4 show the one-batten configurations in blue, the two-batten configurations in green, and the six-batten configurations in red. The graphs confirm that increasing the number of battens reduces the overall deformation, but they also reveal an interesting result: changing the number of battens from one to two actually increases the overall deformation slightly for the  $90^\circ$  and  $80^\circ$  angle-of-attack scenarios. The graphs also confirm the aforementioned observations about the angle of attack.

## Conclusion and Future Directions

In this paper, we have implemented the mathematical model initially investigated by Nong, et al, consisting of a PDE system that is meant to model the deformation of a flexible-wing MAV with multiple battens. We have been able to generally verify the qualitative observations made by Ifju, et al about the effect of altering the number of battens on wing deformation, with some exceptions.



Additionally, we have shown that decreasing the angle of attack of the MAV wing decreases the observed maximum deformation.

There are a number of potential future directions for this research. The first is to computationally validate the quantitative experimental results derived by Ifju, et al dealing with the coefficient of lift, which were shown in Figure 2. The tests to computationally verify Figure 2 will be done through a joint use of the COMSOL multiphysics software and a separate fluid dynamics package. Other modifications involve changing the material properties of the MAV wing to produce material non-linearity, which include considering non-linear elastic membrane models. Geometric non-linearity in the membrane and beam models will potentially be incorporated. Finally, a rigorous stability analysis for the coupled Fluid-Structure Interaction problem will be performed. This will involve a more complex model for the membrane which accounts for both axial (in-plane) and transverse displacements and will be based on establishing bounds for the mechanical energy of the MAV wing.

### References

- Bathe, M. and Kamm, R.D. (1999), A Fluid-Structure Interaction Finite Element Analysis of Pulsatile Blood Flow Through a Compliant Stenotic Artery. *Journal of Biomechanical Engineering*, 121, pp. 361–369.
- Ferguson, L. (2006), A computational model for flexible wing based micro air vehicles. Master's Thesis, Texas Tech University.
- Ifju, P.G., Jenkins, D.A., Ettinger, S., Lian, Y., & Shyy, W. (2002), Flexible-wing-based micro air vehicles. *American Institute of Aeronautics & Astronautics*, pp. 1-13.
- La Mantia, M., & Dabnichki, P. (2013), Structural response of oscillating foil in water. *Engineering Analysis with Boundary Elements*, 37(6), pp. 957-966.
- Nave, C. R. (1999), Densities of common substances. Retrieved from Hyperphysics: Department of Physics and Astronomy website: <http://hyperphysics.phy-astr.gsu.edu/hbase/tables/density.html>
- Nobile, F. (2001), Numerical approximation of fluid-structure interaction problems with application to haemodynamics, Ph.D. Thesis, EPFL, Lausanne.
- Nong, K., Aulisa, E., Garcia, S., Swim, E., & Seshaiyer, P. (2010), Computational methods for multi-physics applications with fluid-structure interaction. *Proceedings of the COMSOL Conference Boston*, 1-5.
- Schot, S.H. (1992). Eighty Years of Sommerfeld's Radiation Condition. *HISTORIA MATHEMATICA*, 19 (4), pp. 385-401.

## Modelling crack propagation using a non-matching SBFEM-FEM coupled method

X.F Wang<sup>1</sup>, \*Z.J Yang<sup>1,2</sup> and D.S Yin<sup>3</sup>

<sup>1</sup>School of Mechanical, Aerospace and Civil Engineering, the University of Manchester, Manchester, L13 9PL, UK

<sup>2</sup>College of Civil Engineering and Architecture, Zhejiang University, Hangzhou, 310058, China

<sup>3</sup>College of Hydraulic and Environmental Engineering, Three Gorges University, Yichang, 443002, China

\*Corresponding author: zhjyang@zju.edu.cn

### Abstract

A method coupling the scaled boundary finite element method (SBFEM) and the finite element method (FEM) is developed for linear elastic fracture modelling. A very simple but effective remeshing procedure based on the finite element mesh only is used to accommodate crack propagation. The crack-tip region is modelled by one SBFE subdomain whose semi-analytical displacement solutions are used to extract accurate stress intensity factors. The SBFE subdomain boundary is coupled with the surrounding FE mesh boundary through virtual interfaces so that the nodal discretisations of the two boundaries can be different. Two plane problems are modelled to validate the new method.

**Keywords:** scaled boundary finite element method, non-matching mesh, stress intensity factors, crack propagation, remeshing procedure, linear elastic fracture mechanics.

### 1. Introduction

The FEM is the most popular numerical method in simulating crack propagation because of the high generality and flexibility of finite elements in modelling structures with complex geometries, various boundaries and loading conditions, and complicated cracking patterns. The scaled boundary finite element method (SBFEM) (Song and Wolf 1997) is a semi-analytical method that is very efficient in modelling problems with discontinuities and singularities. This study proposes a non-matching SBFEM-FEM coupled method to simulate crack propagation problems based on the linear elastic fracture mechanics (LEFM). In this method, the SBFE subdomain boundary is coupled with the surrounding FE mesh boundary through virtual interfaces so that the nodal discretisations of the two boundaries can be different and only one SBFE subdomain is needed at a crack tip.

### 2. The Non-matching SBFEM-FEM Coupled method

#### 2.1. The Scaled Boundary Finite Element Method

Fig. 1 illustrates a two-dimensional (2D) SBFEM subdomain. The normalised radial coordinate  $\zeta$  and circumferential coordinate  $s$  form a local coordinate system used in the subdomain. They are related to the Cartesian coordinates  $(x, y)$  by the transformation Eqs. (Song and Wolf 1997)

$$x = x_0 + \zeta x_s(s) \quad y = y_0 + \zeta y_s(s) \quad (1)$$

The displacement vector at any point  $(\zeta, s)$  in a subdomain can be calculated as

$$\mathbf{u}(\zeta, s) = \mathbf{N}_b(\zeta, s) \mathbf{u}_b \quad (2)$$

where  $\mathbf{u}_b$  is the nodal displacement vector of the subdomain, and the shape function matrix  $\mathbf{N}_b$  is (Deeks and Wolf 2002)

$$\mathbf{N}_b(\zeta, s) = \mathbf{N}_b(s) \mathbf{\Phi} [\xi^\lambda] \mathbf{\Phi}^{-1} \quad (3)$$

where  $\mathbf{N}_b(s)$  is the one-dimensional shape function matrix as in FEM,  $[\lambda] = \text{diag}(\lambda_1, \lambda_2, \dots, \lambda_n)$  and  $\mathbf{\Phi} = \{\boldsymbol{\varphi}_1, \boldsymbol{\varphi}_2, \dots, \boldsymbol{\varphi}_n\}$  are the subset of positive eigenvalues and modal displacements obtained from

solving an eigenvalue problem (Deeks and Wolf 2002), and  $n$  is the degrees of freedom (DOFs) of the subdomain.

The stress field  $\boldsymbol{\sigma}(\boldsymbol{\xi}, s)$  in a subdomain is

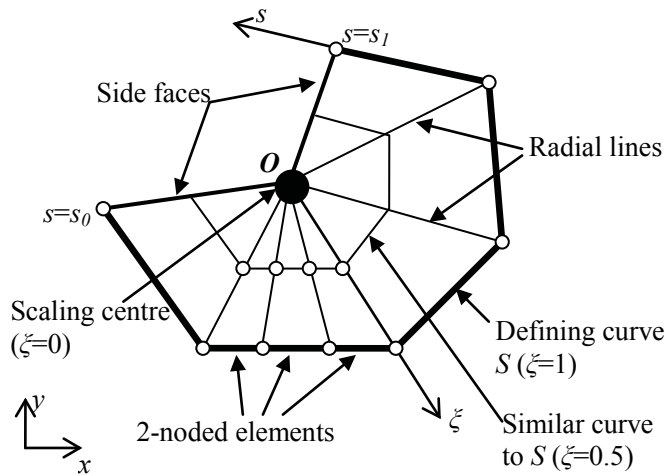
$$\boldsymbol{\sigma}(\boldsymbol{\xi}, s) = \mathbf{DB}^1(s) \left[ \sum_{i=1}^n c_i \lambda_i \boldsymbol{\xi}^{(\lambda_i-1)} \boldsymbol{\varphi}_i \right] + \mathbf{DB}^2(s) \left[ \sum_{i=1}^n c_i \boldsymbol{\xi}^{(\lambda_i-1)} \boldsymbol{\varphi}_i \right] \quad (4)$$

where  $c_i$  are constants dependent on boundary conditions,  $\mathbf{D}$  is the elastic matrix, and  $\mathbf{B}^1(s)$  and  $\mathbf{B}^2(s)$  are strain-displacement matrices (Deeks and Wolf 2002).

The stiffness matrix of the subdomain with respect to the boundary DOFs is

$$\mathbf{K}_b = \mathbf{E}^0 \boldsymbol{\Phi}[\boldsymbol{\lambda}] \boldsymbol{\Phi}^{-1} + \mathbf{E}^1 \quad (5)$$

where  $\mathbf{E}^0$  and  $\mathbf{E}^1$  are matrices dependent on the geometry and material properties of the subdomain only.



**Fig. 1. A subdomain in SBFEM**

## 2.2. Coupling SBFEM and FEM with non-matching meshes

Fig. 2a shows a domain  $\Omega$  with a crack, modelled by a FE part  $\Omega_{FE}$  away from the crack tip and an SBFE subdomain  $\Omega_{SB}$  surrounding the crack tip. Fig. 2b shows the virtual interface of zero in-plane thickness (the dashed line), which coincides with the defining curve  $S$  (with  $\zeta=1$ ) of the SBFE subdomain  $\Omega_{SB}$ .

For any point with circumferential coordinate  $s$  on the virtual interface  $S$ , there is a point 1 on the FE boundary and a point 2 on the SBFE boundary, possessing the same coordinates (plotted as white triangles in Fig. 2b). The displacement vector  $\mathbf{d}_1(s)$  of point 1 in the global coordinate system can be calculated by

$$\mathbf{d}_1(s) = \mathbf{N}_f(s) \mathbf{u}_f \quad (6)$$

where  $\mathbf{u}_f$  is the nodal displacement vector of the finite element  $f$  in which the point 1 is located, and  $\mathbf{N}_f(s)$  is the shape function matrix at point 1 in the finite element  $f$ , whose members are functions of the two local parametric coordinates of point 1 in the finite element  $f$ . The displacement vector  $\mathbf{d}_2(s)$  of point 2 can be calculated by Eq. (2) as

$$\mathbf{d}_2(s) = \mathbf{N}_b(s) \mathbf{u}_b \quad (7)$$

where  $\mathbf{N}_b(s)$  are functions of circumferential coordinate  $s$  only as  $\zeta=1$  on the defining curve  $S$ .

To simplify derivation, Eqs. (6) and (7) can be rewritten by expanding  $\mathbf{u}_f$ ,  $\mathbf{u}_b$ ,  $\mathbf{N}_f(s)$  and  $\mathbf{N}_b(s)$  to the global DOFs as

$$\mathbf{d}_1(s) = \mathbf{N}_1(s) \mathbf{u} \quad (8)$$

$$\mathbf{d}_2(s) = \mathbf{N}_2(s) \mathbf{u} \quad (9)$$

where  $\mathbf{u}$  is the nodal displacement vector of the whole model with  $N$  number of DOFs, and  $\mathbf{N}_1(s)$  and  $\mathbf{N}_2(s)$  are now both  $2 \times N$  matrices.

The relative displacements of points 1 and 2, with one component along the virtual interface and another normal to it, are

$$\bar{\mathbf{d}}(s) = \mathbf{L}(s)(\mathbf{d}_1(s) - \mathbf{d}_2(s)) \quad (10)$$

where

$$\mathbf{L}(s) = \begin{bmatrix} \cos\theta(s) & -\sin\theta(s) \\ \sin\theta(s) & \cos\theta(s) \end{bmatrix} \quad (11)$$

is the coordinate transformation matrix and  $\theta(s)$  is the inclination angle of the virtual interface at the point and measured clockwise from  $s$  direction to the positive  $x$  axis (see Fig. 2b).

Assuming that the relative displacements are sustained by two virtual springs with stiffness coefficients  $k_s$  along the virtual interface and  $k_n$  normal to it, the force vector on unit length transferred by the springs is

$$\mathbf{P}(s) = \mathbf{D}_c \bar{\mathbf{d}}(s) \quad (12)$$

with

$$\mathbf{D}_c = \begin{bmatrix} k_s & \\ & k_n \end{bmatrix} \quad (13)$$

The introduction of the virtual interface and the virtual springs leads to artificial gaps or penetrations along the shared boundary, and spurious potential energy which should be minimised. The potential energy on the whole virtual interface is

$$\Pi = \int_s \frac{1}{2} \mathbf{P}(s) \bar{\mathbf{d}}(s) ds \quad (14)$$

Substituting Eqs. (10) to (12) into Eq. (14) and using Eqs. (8) and (9) results in

$$\Pi = \int_s \frac{1}{2} \bar{\mathbf{d}}(s)^T \mathbf{D}_c \bar{\mathbf{d}}(s) ds = \frac{1}{2} \int_s \mathbf{u}^T (\mathbf{N}_1^T(s) - \mathbf{N}_2^T(s)) \mathbf{L}(s)^T \mathbf{D}_c \mathbf{L}(s) (\mathbf{N}_1(s) - \mathbf{N}_2(s)) \mathbf{u} ds \quad (15)$$

Calculating variation of Eq. (15) with respect to  $\mathbf{u}$  leads to

$$\delta \Pi = \delta \mathbf{u}^T \int_s \left[ \mathbf{N}_1^T(s) \bar{\mathbf{D}}_c(s) \mathbf{N}_1(s) + \mathbf{N}_2^T(s) \bar{\mathbf{D}}_c(s) \mathbf{N}_2(s) - \mathbf{N}_1^T(s) \bar{\mathbf{D}}_c(s) \mathbf{N}_2(s) - \mathbf{N}_2^T(s) \bar{\mathbf{D}}_c(s) \mathbf{N}_1(s) \right] ds \cdot \mathbf{u} \quad (16)$$

where

$$\bar{\mathbf{D}}_c(s) = \mathbf{L}(s)^T \mathbf{D}_c \mathbf{L}(s) \quad (17)$$

Thus the contribution of the virtual interface to the system stiffness matrix is (Zienkiewicz et al. 2005)

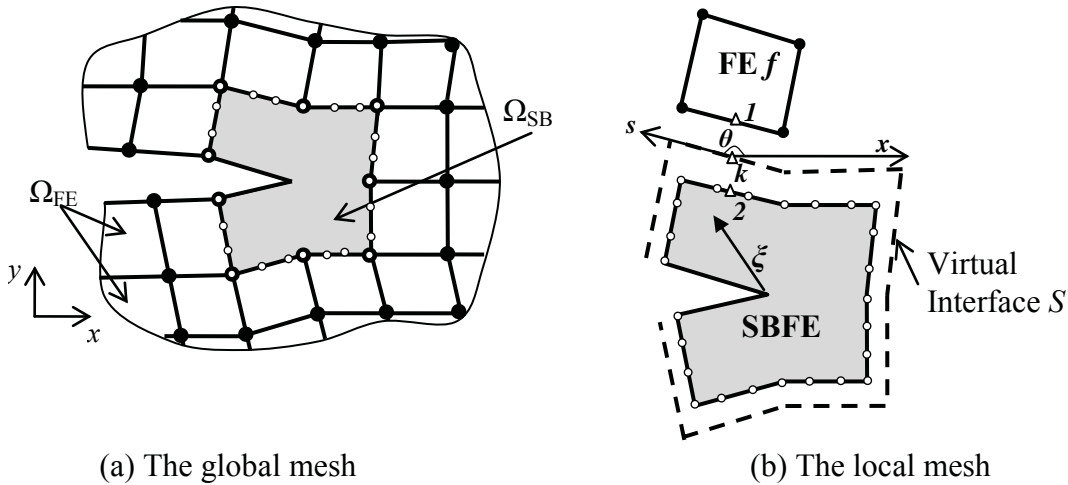
$$\mathbf{K}_c = \int_s \left[ \mathbf{N}_1^T(s) \bar{\mathbf{D}}_c(s) \mathbf{N}_1(s) + \mathbf{N}_2^T(s) \bar{\mathbf{D}}_c(s) \mathbf{N}_2(s) - \mathbf{N}_1^T(s) \bar{\mathbf{D}}_c(s) \mathbf{N}_2(s) - \mathbf{N}_2^T(s) \bar{\mathbf{D}}_c(s) \mathbf{N}_1(s) \right] ds \quad (18)$$

The system stiffness matrix is then obtained by assembling Eq. (5), Eq. (18) and the stiffness matrices of all the finite elements.

The spring stiffness coefficients  $k_s$  and  $k_n$  play a vital role in the accuracy of this coupling procedure. Too high values may lead to ill-posedness of the system equations and too low values cannot ensure displacement continuity across the virtual interface. The following is proposed in (Qiang et al. 2000) as a guideline

$$k_s = k_n = k = \frac{c(1-\nu)}{b(1+\nu)(1-2\nu)} E \quad (19)$$

where  $E$  and  $\nu$  are the Young's modulus and Poisson's ratio,  $b$  is the characteristic size of elements, and  $c$  is taken as 10~100 from the experience in (Qiang et al. 2000).



**Fig. 2. Coupling SBFE and FE meshes**

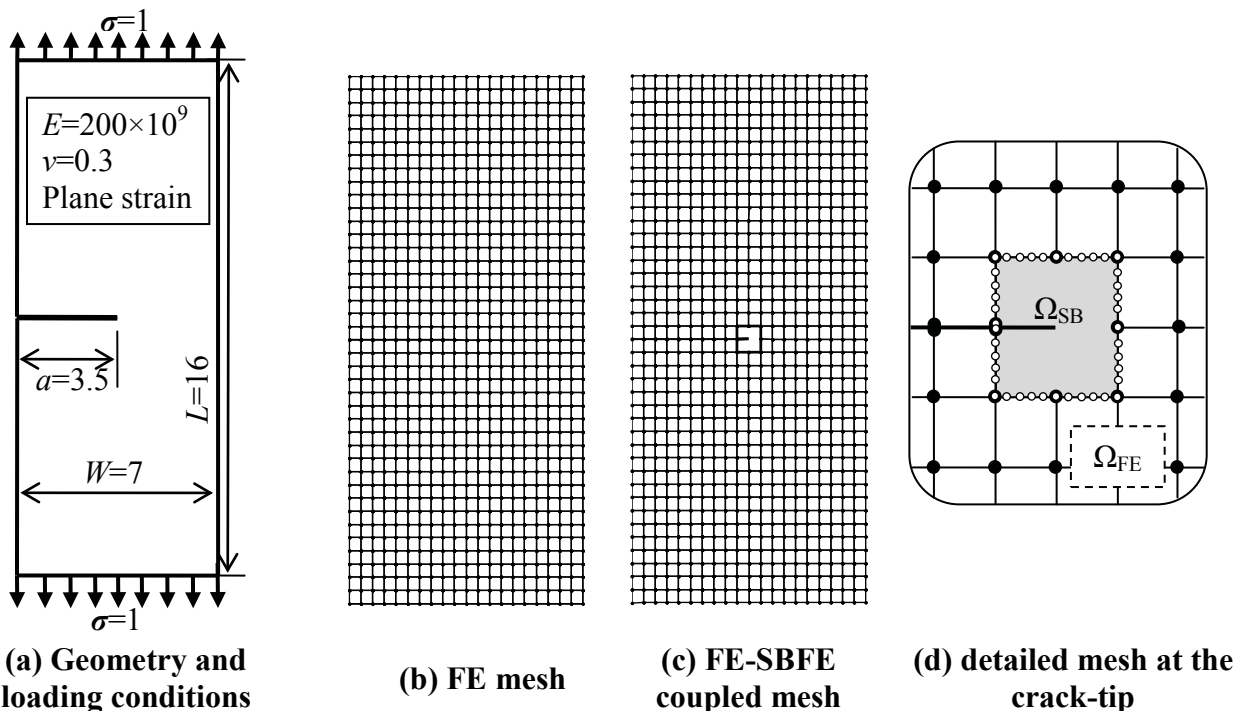
**3. Numerical examples**

When a crack is judged to propagate, a very simple, local remeshing procedure similar to the one in (Xie and Gerstle 1995) is used to accommodate its propagation. The crack propagation direction is calculated by the maximum circumferential stress theory in this study (Erdogan and Sih 1963). The SIFs are extracted directly from the displacement solutions (Chidgzey and Deeks 2005). Two problems are modelled to validate the developed method and demonstrate its capability.

*3.1. An edge-cracked plate under mode-I fracture*

The first example is an edge-cracked plate subjected to a far field unit stress ( $\sigma=1$ ) applied on the top and bottom. The geometry, boundary and loading conditions are shown in Fig. 3a. The exact solution of the mode-I SIF in this example is  $K_{Ie}= 9.37$  (Ingraffea et al. 1984).

To investigate the effects of the coupling parameter  $k$  in Eq. (19), structured FE meshes are modelled. Fig. 3b shows a mesh with  $20 \times 40$  4-noded quadrilateral elements. The FE-SBFE coupled mesh is shown in Fig. 3c, with the detailed region at the crack tip highlighted in Fig. 3d.



**Fig. 3. Example 1: a plate with an edge crack**

Fig. 4 plots the errors of  $K_I$  from three meshes as the virtual spring stiffness coefficient  $k$  varies. It is reconfirmed that too high or too low values of  $k$  lead to unsatisfactory accuracy. For this example, it is found that  $k=10^2E\sim 10^{10}E$  results in lower than 1% error in  $K_I$ . From the vertical displacement contours shown in Fig. 5 (20×40 mesh), the use of virtual interface between the FE and SBFE meshes does not affect the displacement continuity.  $k=100E$  is used in all the following examples, corresponding to  $c=26$  in Eq. (19).

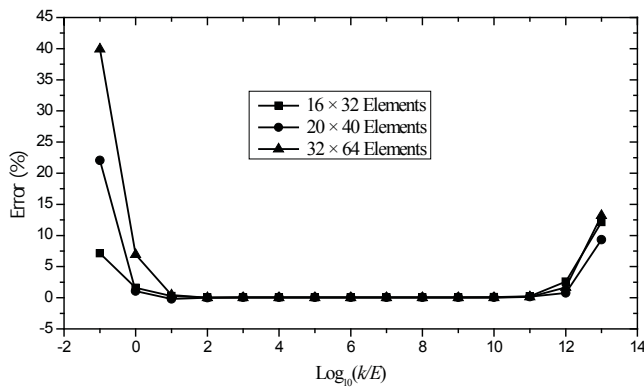


Fig. 4. Effects of virtual spring stiffness coefficient  $k$  on  $K_I$

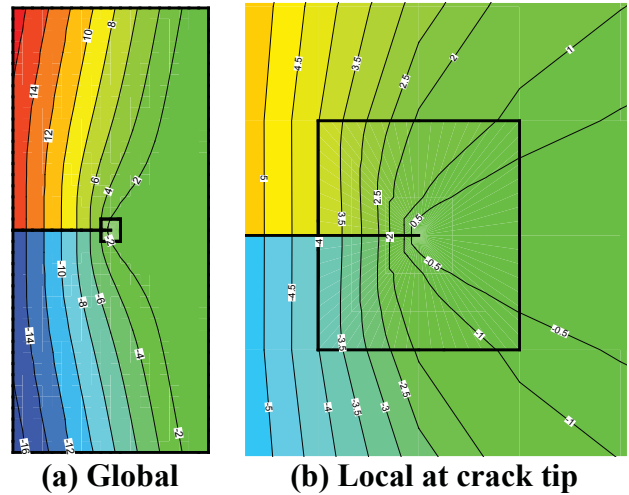


Fig. 5. Vertical displacement contours from structured 20×40 mesh ( $\times 10^{-11}$ )

Table 1 compares the relative error of  $K_I$  for five structured meshes using the FEM, the XFEM, the hybrid FE-SBFE method (Ooi and Yang 2010) and the present method. The results are also shown in Fig. 6, which indicate the much higher accuracy of the present method and the previous FE-SBFE hybrid method (Ooi and Yang 2010) over FEM and XFEM.

Table 1. Errors of  $K_I$  for the edge-cracked plate under mode-I loading

FEM			XFEM (Ooi and Yang 2010)			Hybrid method (Ooi and Yang 2010)			Present method		
No. Elements	No. DOF	Error ( $K_I$ )	No. Elements	No. DOF	Error ( $K_I$ )	No. Elements	No. DOF	Error ( $K_I$ )	No. Elements	No. DOF	Error ( $K_I$ )
4 × 8	94	25.0%	5 × 7	136	18.5%	4 × 8	222	7.4%	4 × 8	222	7.2%
8 × 16	314	14.3%	9 × 15	368	8.4%	8 × 16	442	3.5%	8 × 16	442	3.6%
16 × 32	1138	7.6%	17 × 31	1216	3.7%	16 × 32	1266	1.4%	16 × 32	1266	1.7%
20 × 40	1742	4.2%	21 × 39	1832	2.9%	20 × 40	1870	1.0%	20 × 40	1870	1.3%
32 × 64	4322	4.0%	33 × 63	4448	1.7%	32 × 64	4450	0.5%	32 × 64	4450	0.8%

The influence of the number of DOFs used to model the SBFE subdomain is shown in Fig. 7. It can be seen that using 30 nodes can achieve less than 1% error (32×64 elements).

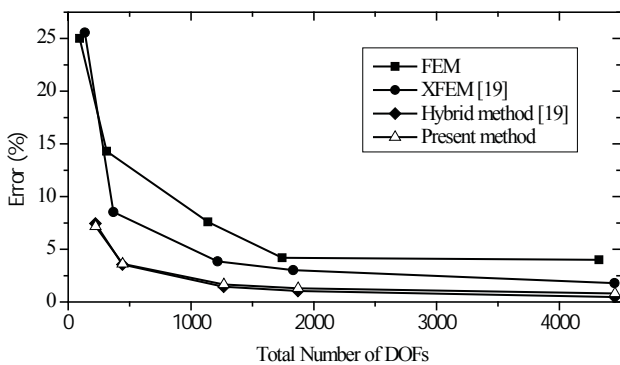


Fig. 6. Effects of total DOFs

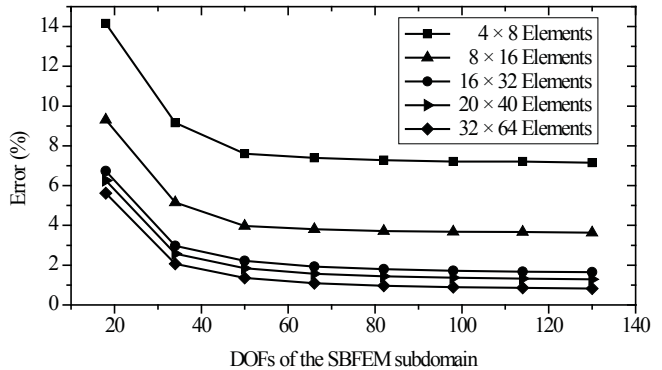
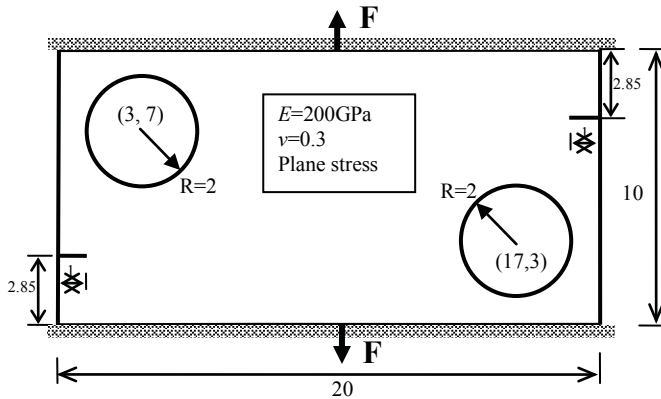


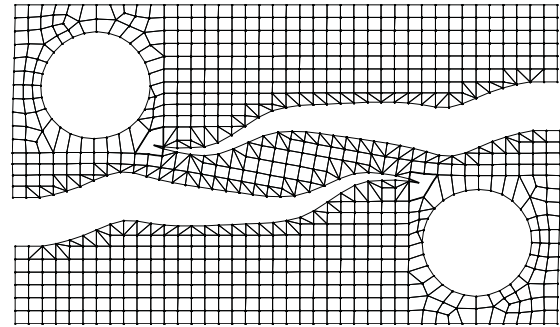
Fig. 7. Effects of DOFs of the SBFE subdomain

### 3.2. A double-edge notched plate with two holes

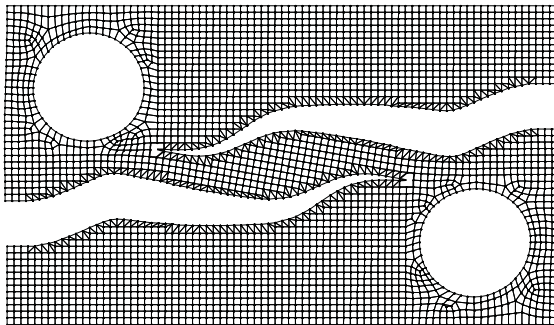
The second example is a plate with two holes and two edge cracks subjected to a uniform tensile test, shown in Fig. 8. Fig. 9 and Fig. 10 show two final FE-SBFE coupled meshes, with 1722 and 6208 DOFs, respectively. The predicted crack paths using the two meshes are very close. Fig. 11 compares the crack paths predicted by the present method with those obtained by the FEM in (Bouchard et al. 2003) and the polygon SBFEM in (Ooi et al. 2012).



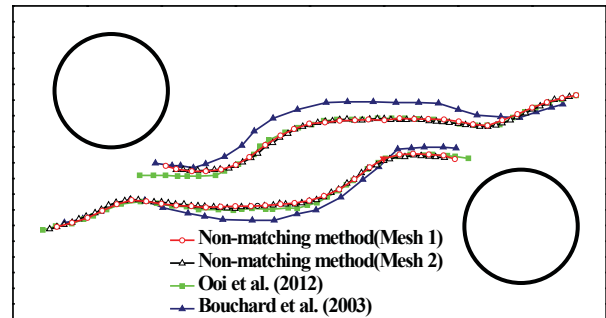
**Fig. 8. A plate with two holes and two edge cracks (unit: mm)**



**Fig. 9. Mesh 1, 772 finite elements, 861 nodes (displacement scale=50)**



**Fig. 10. Mesh 1, 772 finite elements, 861 nodes (displacement scale=50)**



**Fig. 11. Comparison of crack paths**

## 4. Conclusions

A non-matching SBFEM-FEM coupled method has been developed for modelling LEFM-based crack propagation. The stress singularities are accurately captured by crack-tip SBFE subdomains, making the FE-based remeshing procedure as simple as possible. The use of non-matching FE and SBFE meshes, whose displacement continuity is ensured by assigning sufficiently high stiffness on the virtual interface, makes remeshing even more flexible than other methods. The accuracy and effectiveness of the developed method has been demonstrated by modelling two fracture problems. It also paves the way for further development, such as the overlapping methods (Massing et al. 2012; Okada et al. 2005) in which the cracked subdomain floats on the global FE mesh, namely, the two meshes are completely independent. This will offer the highest flexibility in remeshing.

## 5. Acknowledgement

XF Wang is funded by an EPS Faculty PhD Studentship from the University of Manchester, UK. ZJ Yang would like to thank the Alexander von Humboldt Foundation, Germany for a Fellowship for Experienced Researchers. The discussion with Dr ET Ooi at the University of New South Wales is highly appreciated.

## References

- Bouchard, P.-O., F. Bay & Y. Chastel (2003), Numerical modelling of crack propagation: automatic remeshing and comparison of different criteria. *Computer methods in applied mechanics and engineering*, 192, 3887-3908.
- Chidgzev, S. R. & A. J. Deeks (2005), Determination of coefficients of crack tip asymptotic fields using the scaled boundary finite element method. *Engineering fracture mechanics*, 72, 2019-2036.
- Deeks, A. J. & J. P. Wolf (2002), A virtual work derivation of the scaled boundary finite-element method for elastostatics. *Computational Mechanics*, 28, 489-504.
- Erdogan, F. & G. Sih (1963), On the crack extension in plates under plane loading and transverse shear. *Journal of basic engineering*, 85, 519.
- Ingraffea, A. R., W. H. Gerstk, P. Gergely & V. Saouma (1984), Fracture mechanics of bond in reinforced concrete. *Journal of Structural Engineering*, 110, 871-890.
- Massing, A., M. G. Larson & A. Logg (2012), Efficient implementation of finite element methods on non-matching and overlapping meshes in 3D. *arXiv preprint arXiv:1210.7076*.
- Okada, H., S. Endoh & M. Kikuchi (2005), On fracture analysis using an element overlay technique. *Engineering Fracture Mechanics*, 72, 773-789.
- Ooi, E. T., C. M. Song, F. Tin-Loi & Z. J. Yang (2012), Polygon scaled boundary finite elements for crack propagation modelling. *International Journal for Numerical Methods in Engineering*, 91, 319-342.
- Ooi, E. T. & Z. J. Yang (2010), A hybrid finite element-scaled boundary finite element method for crack propagation modelling. *Computer Methods in Applied Mechanics and Engineering*, 199, 1178-1192.
- Qiang, T. C., X. D. Kou & W. Y. Zhou (2000), Three-dimensional FEM Interface Coupled Method and its Application to Arch Dam Fracture Analysis. *Chinese Journal of Rock Mechanics and Engineering*, 19, 562-566.
- Song, C. M. & J. P. Wolf (1997), The scaled boundary finite-element method—alias consistent infinitesimal finite-element cell method—for elastodynamics. *Computer Methods in Applied Mechanics and Engineering*, 147, 329-355.
- Xie, M. & W. H. Gerstle (1995), Energy-based cohesive crack propagation modeling. *Journal of engineering mechanics*, 121, 1349-1358.
- Zienkiewicz, O. C., R. L. Taylor & J. Z. Zhu (2005), The finite element method: its basis and fundamentals. *Butterworth-Heinemann*, Oxford.



## Calibration of Constitutive Adhesion Models

E. B. Albuquerque<sup>1</sup>, L.A. Borges<sup>1</sup> and \*D.A. Castello<sup>1</sup>

<sup>1</sup> Dept. of Mech. Eng., Coppe/UFRJ, Centro de Tecnologia Bloco G  
Sala 204 Cidade Universitária - RJ - Brasil

\*Corresponding author: castello@mecanica.ufrj.br

### Abstract

There has been an increase in the use of composite materials in engineering designs which motivated the development of reliable procedures to connect components with adhesives. As a consequence, there is a natural demand for reliable adhesion models that can be used in simulation based design environments. In this work we propose an approach to calibrate constitutive adhesion models. We chose to use the constitutive model proposed by Michel Raous which was built based on thermodynamics of irreversible processes with internal variables. The inverse problem associated to the model calibration is solved by means of Bayesian Inverse Approaches. Samples of the unknown model parameters are obtained via Population-Based Markov-Chain Monte Carlo combined with Adaptive Metropolis algorithms. Some numerical results are presented for situations in which we try to reproduce real-like operational\feasible conditions.

Keywords: Adhesion Model, Model Calibration, MCMC, Population Based, Adaptive Metropolis

### Introduction

The use of adhesives in Industrial applications has continuously increased in different Engineering fields. Their appropriate use in computer simulations demands accurate models to represent their physical behavior. Moreover, in several types of structural design analysis one should be able to reproduce mechanical adhesion.

Concerning adhesion models, the constitutive ones may be obtained with the formalism of the thermodynamics of irreversible processes with internal variables (Lemaitre, 1994). And, in particular, the model proposed by Raous et al. (Raous, 1999) seems to be quite appealing due to its consistence. This model is able to reproduce some adhesion physical behavior according to the proper choice of its constitutive parameters. Nevertheless, most of its model parameters cannot be estimated by direct measurements. Therefore, these parameters should be estimated by means of Inverse Methods (Kaipio, 2005).

Inverse Methods enable the estimation of model parameters once a set of measured data is available. More recently, due to the increase of computational resources, Statistical Inverse Problem formulations (Kaipio, 2005) have become feasible for different types of problems in a broad range of fields (Nichols, 2011).

The objective of this work is to propose an approach for calibration of the constitutive adhesion model proposed by Raous et al. (Raous, 1999). Here we use Statistical Inverse formulations. Furthermore, in this work we decided Population Based Markov Chain Monte Carlo (MCMC) (Jasra, 2007) in which each chain takes into account Adaptive Metropolis Hastings

(Haario, 2007). We present some simulation results for a situation which contains noise-corrupted data and modeling errors. . The following sections presents the constitutive adhesion model proposed by Raous, describe the inverse approach used for model calibration, some simulation results and final comments.

### Adhesion Model

The constitutive adhesion model proposed by Raous et al. (Raous, 1999) henceforth named RCCM model may be briefly described by the unilateral conditions with adhesion as shown in equation (1)

$$-R_n + C_n u_n \beta^2 \geq 0, \quad u_n \geq 0, \quad (-R_n + C_n u_n \beta^2) u_n \geq 0 \quad (1)$$

for which we assumed that only normal effects take place along the process. In equation (1)  $u_n$  and  $R_n$  correspond to normal displacement and normal reaction, respectively,  $C_n$  corresponds to original layer stiffness and  $\beta$  corresponds to an internal variable which is in charge of describing material degradation. The additional evolution equation for  $\beta$  is shown in equation (2)

$$\dot{\beta} = -\frac{1}{b} \langle (w - \beta(C_n u_n^2)) \rangle^{1/p} \quad (2)$$

in which the operator  $\langle Z \rangle$  is such that:  $\langle Z \rangle = 0$  if  $Z \geq 0$  and  $\langle Z \rangle = -Z$  if  $Z < 0$ . In equation (2),  $w$  and  $b$  corresponds to the adhesion energy and the viscosity of the interface, respectively, and parameter  $p$  comes from the choice of a power law for adhesion and could be adjusted accordingly to measured. It should be emphasized that  $b$ ,  $w$  and  $p$  would not possibly be obtained from direct measurements. Therefore, model calibration requires the use of Inverse Problem approaches (Kaipio, 2004).

### Parameter estimation

In this work the parameter estimation process is phrased as a Statistical Inverse Problem. In Statistical Inverse problem formulations all the variables are modeled as random and the solution consists in samples from the probability density functions of the unknown parameters. In particular, we have used some recent sampling algorithm named Population Based Markov Chain Monte Carlo (MCMC) (Jasra, 2007). Jasra et. al (Jasra, 2007) present comprehensive information about Population based MCMC. The basic idea is to obtain feasible samples of the unknown parameters along parallel chains which possesses exchange of data between them. For the sake of simplicity here we will simply present the results concerning the sampled parameters. The authors recommend Jasra et. al (Jasra, 2001) as a comprehensive reference about this subject.

### Mechanical System

Aiming at using a computational model containing the basic characteristics of an experiment designed for adhesion characterization we propose a mechanical system to be used in this work. The idea is use a simple mechanical system which is still realistic in a laboratory environment.

The system under analysis is composed of an elastic beam that is cantilevered on its left end ( $x=0$ ) and attached to the reference frame through an adhesive layer on its right end ( $x=L$ ) as shown in

Figure(1). We also consider that a controlled force  $P(t)$  is applied to a specific point of the beam ( $L/2$ ) and that both reaction and displacement histories are measured at the adhesion support located at  $x=L$ .

Given a force history  $P(t)$  the direct problem consist in determining the reaction and displacement of the system at the adhesion support located at  $x=L$ , Fig. 1. For this direct problem it is necessary the parameters that characterize the elastic beam and the parameters that characterize the adhesion model. The boundary condition at  $x=L$  is due to an adhesion layer between the beam and the support.

Here, motivated by the possibility of elaborating strategies that handle parameters that could be used for comparisons among different methodologies, we decided to work with dimensionless parameters. Therefore, after performing dimension analysis on the governing equations of the system shown in figure (1), ones gets to the following dimensionless parameters in equation (3):

$$W = \frac{48EI w}{L^3 P^2} ; \quad \mu = \frac{L^3 P^2}{48EI b} ; \quad K_{vn} = \frac{C_n L^3}{48EI} \quad (3)$$

in which  $w$ ,  $b$ , and  $C_n$  are the constitutive parameters presented in equations (1) and (2);  $E$ ,  $I$  and  $L$  are the modulus of elasticity, moment of inertia and length of the beam and  $P$  is the applied load.

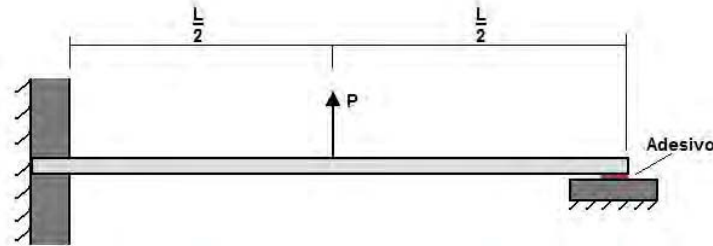


Figure 1. Elastic beam which is cantilevered at  $x=0$  and attached to the reference frame through an adhesive at  $x=L$ .

The normal reaction of the support and the relative displacement from the beam with the support are defined as:

$$R_n = P * r_n \quad (4)$$

$$U_n = \frac{L^3 P}{48EI} u_n \quad (5)$$

With the RCCM model and equations (3), (4) and (5) one may write the solution due to an applied force located at the center of the beam as shown in equations (6), (7) and (8)

$$\Delta\beta(t, \beta) = -\mu \left( W - K_{vn} u_n(t, \beta)^2 \beta \right) \quad (6)$$

For  $P_e(t) > 0$

$$\text{then } un = \frac{5P_e(t)}{1+16K_{vn}\beta^2}, \quad (7)$$

$$\text{and } rn = K_{vn}\beta^2 un(t, \beta) \quad (8)$$

## Results

In this section some results concerning the calibration of the RSSS constitutive adhesion model are presented. We refer to this as a pseudoexperiment inasmuch as it is completely based on numerical data. This pseudo experiment takes into account noise corrupted data, so the measured data  $y$  is obtained out of the model predictions summing up some random white noise  $\varepsilon$ . In fact we consider that the components of the measurement noise vector  $\varepsilon$  are such that:  $\varepsilon_k \sim N(0, \sigma^2)$  and  $\varepsilon_k$  and  $\varepsilon_r$  are independent for  $k$  different from  $r$ .

Henceforth in all the simulations the variance of the white noise is  $\sigma^2 = 0.042$ . For the simulations we considered the following constitutive parameters  $W = 0.05$ ,  $\mu = 0.3$  and  $K_{vn} = 0.5$ . A note worth to be mentioned is that we consider some error modeling analysis. This modeling error was taken into account as follows: (i) the experimental data consider the power  $p = 1$  and (ii) the model used for the inverse analysis assumes  $p = 1.1$  in equation (2).

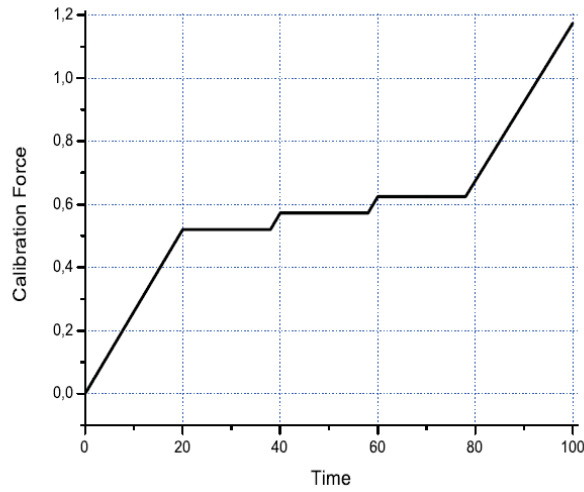


Figure 2. Force used for the calibration analysis.

In order to make visualization of the results more straightforward we decided to plot the results concerning the following scaling parameters

$$p_1 = \frac{W}{W_{exact}};$$

$$p_2 = \frac{\mu}{\mu_{exact}};$$

$$p_3 = \frac{K_{vn}}{K_{vn \text{ exact}}}$$

Figure (3) presents the sampled parameters for a 6000 sample-chain.

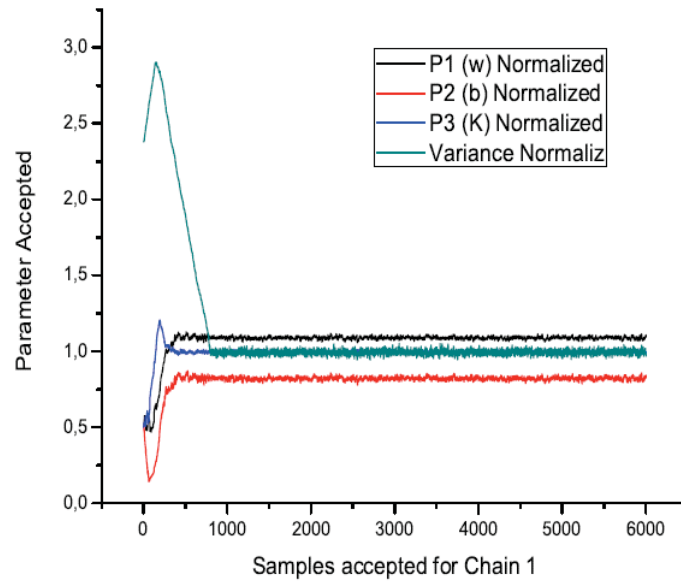


Figure 3. Parameter samples.

Figure (3) shows that accepted samples of the parameter  $Kv_n$  and the error variance  $\sigma$  achieve expected values approximately equal to their true values; accepted values of the viscous parameter  $b$  are underestimated; accepted values of the energy  $w$  is overestimated. It should be emphasized that the Inverse formulation took into account noise-corrupted data and some level of modeling error associated to the power  $p$ . These certainly affect accepted samples as we can see in figure (3). Further analysis concerning the effect of model uncertainty associated to the power  $p$  in equation (2) is currently being investigated and also the possibility of taking into account its uncertainty. Finally, it should be emphasized is that when we do not consider uncertainty in power  $p$  the expected value of the parameter samples are quite close to their true values.

### Final Remarks

The present work presented an approach for calibration of constitutive adhesion models. The constitutive adhesion model proposed by Michel Raous at al. was considered. We assumed in this work that only normal effects take place. A simple realistic mechanical system was proposed to analyze adhesion behavior within a system. Model calibration is performed using Bayesian Inverse Formulations. An illustrative numerical result was presented and the results are in favor of the approach. Further analysis have been investigated in order to describe model uncertainties effects on the results.

### References

- [1] J. Lemaitre, J-L. Chaboche. Mechanics of Solid Materials. s.l. : Cambridge University Press, 1994.
- [2] Raous, M. L. Cangémi, M. Cocou, 1999, "A consistent model coupling adhesion, friction and unilateral contact", Comput. Methods Appl. Mech. Engrg. 177, 383–399.

- [3] J. Kaipio and E. Somersalo. *Statistical and Computational Inverse Problems*. New York : Springer - Verlag, 2005. p. 339.
- [5] Haario H., Saksman E., Tamminen J., An Adaptive Metropolis Algorithm, *Bernoulli* 7(2), 223-242., 2001.
- [6] Jasra A., Stephens, D.A., Holmes. C.C., On population-based simulation for statistic inference. *Statistics and Computing* 17, 263-279, 2007.

## Some Considerations on the Appropriate Dimension in the Numerical Analysis of Geoengineering Structures

\*Ö. Aydan<sup>1</sup>, M. Geniş<sup>2</sup>, N. Tokashiki<sup>3</sup> and H. Tano<sup>4</sup>

<sup>1</sup>Institute of Oceanic Research and Development, Tokai University, Shizuoka, Japan.

<sup>2</sup>Department of Mining Eng., Bülent Ecevit University, Zonguldak, Turkey

<sup>3</sup>Department of Civil Eng. Dept, Ryukyu University, Okinawa, Japan

<sup>4</sup>Department of Civil Eng. Dept, Nihon University, Koriyama, Japan

\*Corresponding author: aydan@sccu-tokai.ac.jp

### Abstract

The selection of the appropriate dimension in numerical analyses of geo-engineering structures is always important issue. The first author realized the importance of this issue when he was doing some numerical analyses of an advancing tunnel in 1986, during which the data-preparation and visualization were extremely cumbersome. Although the memory size and processing speed of computers increased and pre-post processing of computational results become more convenient and less laboring since then, it is still a major issue how to select the appropriate dimension in numerical analyses of structures. In this article, the authors address this issue and compare several hypothetical and actual case history examples involving tunnel face advance, man-made and natural geoengineering structures

**Keywords:** Geoengineering, structures, dimension, numerical analysis, analytical.

### Introduction

How to select the appropriate dimension in numerical analyses of geo-engineering structures is always important issue. Every structure is three-dimensional in physical space. If time is considered, the problem becomes four-dimensional. When the first author did numerical analysis of an advancing tunnel in 1986, the data-preparation and visualization were extremely difficult at that time (Aydan et al. 1988). Furthermore, the memory size and computation speed were also severe problems. In 1986, the memory capacity of the super computer of Nagoya University was only 10 GB. The first author vividly remembers that he was asked by the computation center to have hardcopy outputs of the result of computation with a memory size of 2.5 GB and delete the computed output data files, immediately.

The present tiny notebook computers have now storage capacity of several TBs. Although the memory size and computation speed of computers increased and pre-post processing of computational results has become much more convenient and less laboring, it is still a major issue how to select the appropriate dimension in numerical analyses of structures. It is also fact that decisions in engineering design are still based on the rule of thumbs and/or one-dimensional analytical or numerical analysis of structures. In this article, the authors address this issue and compare several hypothetical and actual case histories involving tunnel face advance, man-made and natural geoengineering structures. The specific examples involve hypothetical tunnels, abandoned lignite mines, a karstic cave beneath Himeyuri Monument in Okinawa islands and steep cliffs and foundations.

### Underground Structures

#### *Tunnels*

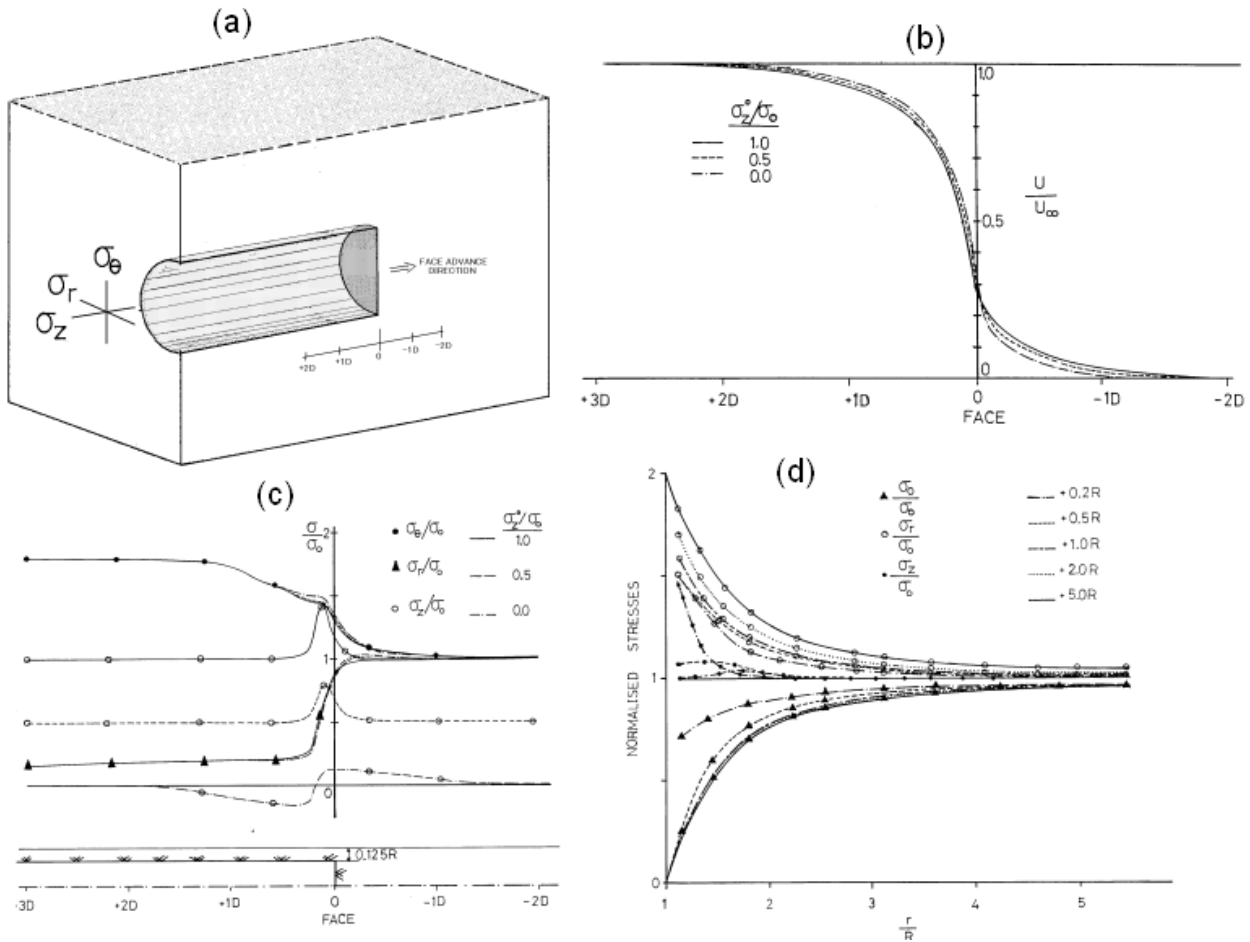
Advancing tunnels utilizing support systems consisting of rockbolts, shotcrete, steel ribs and concrete lining are three-dimensional complex structures and it is a dynamic process. However, tunnels are often modeled as a one-dimensional axisymmetric structure subjected to hydrostatic initial stress state as a static problem. The effect of tunnel face advance on the response and design of support systems is often replaced through an excavation stress release factor determined from pseudo three dimensional (axisymmetric) or pure three-dimensional analyses as given below

$$f = \frac{e^{-bx/D}}{1/B + e^{-bx/D}} \tag{1}$$

where  $x$  is distance from tunnel face and the values for coefficients  $B$  and  $b$  suggested by Aydan (2011) are 2.33 and 1.7, respectively.

Figure 1a illustrates an unsupported circular tunnel subjected to an axisymmetric initial stress state. The variation of displacement and stresses along the tunnel axis were computed using the elastic finite element method. The radial displacement at tunnel wall is normalized by the largest displacement and is shown in Figure 1b. As seen from the figure, the radial displacement takes place in front of the tunnel face. The displacement is about 28-30% of the final displacement. Its variation terminates when the face advance is about +2D. Almost 80% of the total displacement takes place when the tunnel face is about +1D. The effect of the initial axial stress on the radial displacement is almost negligible.

Figure 1c shows the variation of radial, tangential and axial stress around the tunnel at a depth of 0.125R. As noted from the figure, the tangential stress gradually increases as the distance increases from the tunnel face. The effect of the initial axial stress on the tangential stress is almost negligible. The radial stress rapidly decreases in the close vicinity of the tunnel face and the effect of the initial axial stress on the radial stress is also negligible. The most interesting variation is associated with the axial stress distribution. The axial stress increase as the face approaches, and then it gradually decreases to its initial value as the face effect disappears. This variation is limited to a length of 1R(0.5D) from the tunnel face. It is also interesting to note that if the initial axial stress is nil, even some tensile axial stresses may occur in the vicinity of tunnel face.



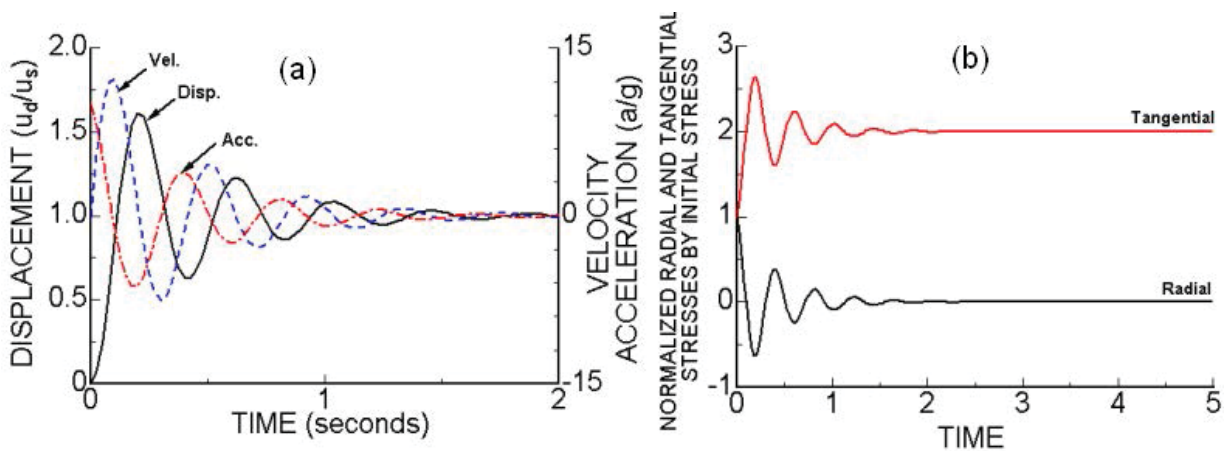
**Figure 1. (a) Computational model for elastic finite element analysis; (b) Normalized radial displacement of the tunnel surface; (c) Normalized stress components along tunnel axis at a distance of 0.125R; (d): The variation of stresses along r-direction at various distances from tunnel face**



Figure 1d shows the stress distributions along r-axis of the tunnel at various distances from the face when the initial axial stress is equal to initial radial and tangential stresses. As noted from the figure the maximum tangential stress is 1.5 times the initial hydrostatic stress and it becomes twice as the distance from the tunnel face is  $+5R$ , which is almost equal to theoretical estimations for tunnels subjected to hydrostatic initial stress state. The stress state near the tunnel face is also close to that of spherical opening subjected to hydrostatic stress state. The stress state seems to change from spherical state to the cylindrical state (Aydan 2011). It should be noted that it would be almost impossible to simulate exactly the same displacement and stress changes of 3D analyses in the vicinity of tunnels by 2D simulations using the stress-release approach irrespective of constitutive law of surrounding rock as a function of distance from tunnel (Aydan et al. 1988; Aydan and Geniş, 2010).

The effect of impulsive application of excavation force is evaluated for an axisymmetric cylindrical tunnel under initial hydrostatic stress by a dynamic visco-elastic finite element method. The responses of displacement, velocity and acceleration of the tunnel surface with a radius of 5m are plotted in Figure 2a. As noted from the figure, the sudden application of the excavation force, in other words, sudden release of ground pressure results 1.6 times the static ground displacement at the tunnel perimetry and shaking disappears almost at 2 seconds. As time progress, it becomes asymptotic to the static value and velocity and acceleration disappear.

The resulting tangential and radial stress components nearby the tunnel perimetry (25cm from the opening surface) are plotted in Figure 2b as a function of time. It is of great interest that the tangential stress is greater than that under static condition. Furthermore, very high radial stress of tensile character occur nearby the tunnel perimetry. This implies that the tunnel may be subjected to transient stress state, which is quite different than that under static conditions. However, if the surrounding rock behaves visco-elastically, they will become asymptotic to their static equivalents. In other words, the surrounding rock may become plastic even though the static condition may imply otherwise.

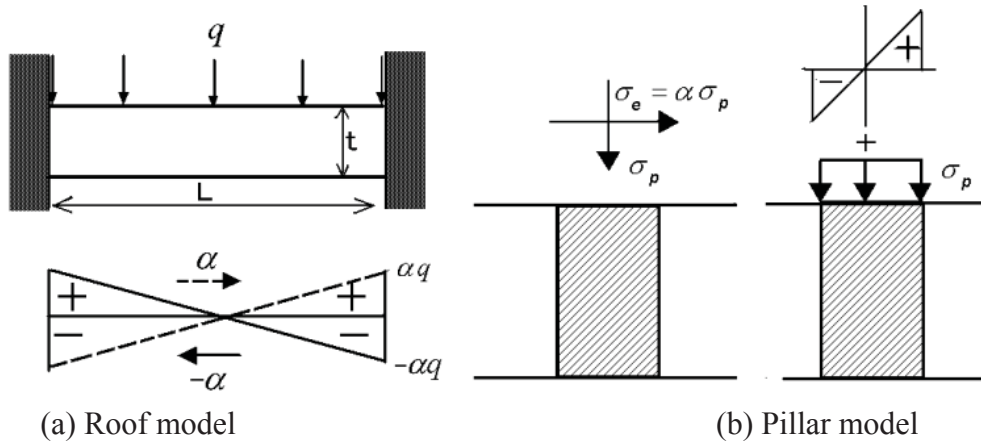


**Figure 2. (a) Responses of displacement, velocity and acceleration of the tunnel surface; (b) Responses of radial and tangential stress components nearby the tunnel surface**

### *Abandoned Lignite Mines*

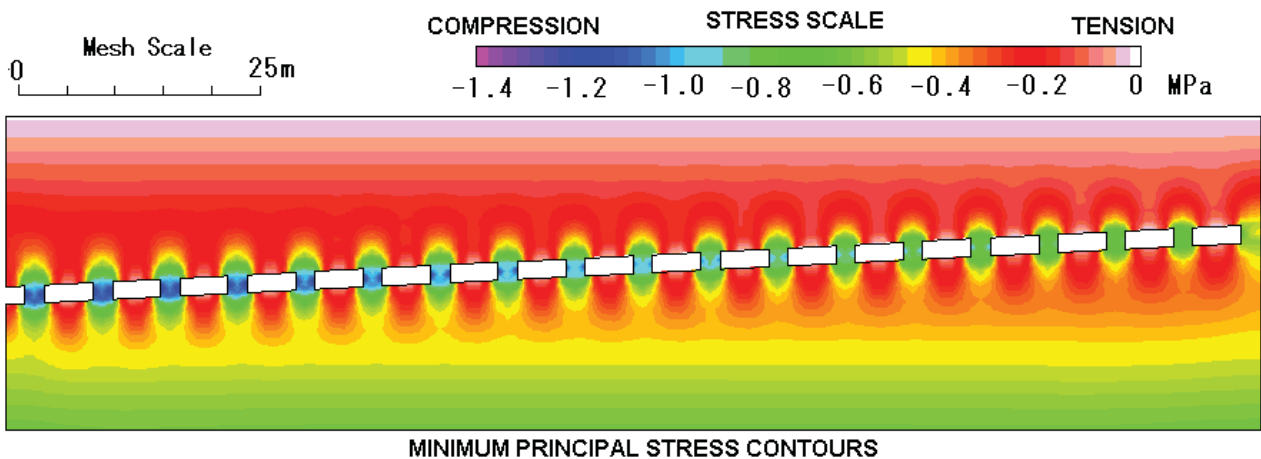
When abandoned lignite mines and quarries are of room and pillar type, their stability in short-term and long-term may be evaluated using some simple analytical techniques. Roof stability is generally evaluated using beam theory and/or arching theory under gravitational, earthquake and point loading (i.e. Coates, 1965; Obert and Duvall, 1967; Aydan 1989, 1994; Aydan and Tokashiki 2011). The tributary area method is quite widely used in mining engineering for assessing the pillar stability. Aydan and his co-workers (Aydan et al. 2008; Aydan and Geniş, 2008; Aydan and Tokashiki, 2011; Geniş and Aydan, 2008) extended to cover the effects of earthquake and point loading in addition to gravitational loading, creep and degradation of geomaterials to evaluate the stability of roof and pillars (Figure 3).

As shown by Aydan and Tokashiki (2011), simple analytical models and computations from two dimensional elastic finite element method yield very similar results. Nevertheless, stresses computed from the FEM in roof are less than those computed from the beam theory with built conditions. On the other hand, stresses computed from the FEM in pillars are slightly higher than those computed from the tributary area method. However, the stress state in the roof would be quite different if the opening depth increases. In such cases, the effects of gravitational load in the stress state of roof should be also taken into account. Nevertheless, the stability of pillars become more important than roof itself under such conditions and the tributary area method would yield quite reasonable values for the stress state in pillars for stability assessment.



**Figure 3. Models for roof and pillars (from Aydan and Geniş, 2008).**

Figure 4 shows the distribution of minimum principal stress (tension is positive) for an abandoned room and pillar mine beneath Kyowa Secondary School in Mitake Town of Gifu Prefecture, Japan. Although the maximum pillar stresses are slightly higher than those computed from the tributary area method, the quick stability assessment using the tributary area method should be quite acceptable.



**Figure 4. Contours of minimum principal stress beneath the Kyowa Secondary School.**

This area would be subjected to the anticipated Nankai-Tonankai-Tokai earthquake in future and there is a great concern about it. The authors have been involved with the stability assessment of the abandoned lignite mine beneath Kyowa Secondary School during the anticipated Nankai-Tonankai-Tokai earthquake (Aydan et al. 2012; Geniş and Aydan, 2013). The authors carried out 1D, 2D and 3D dynamic simulations for an estimated base ground motion data at Mitake Town obtained from the method of Sugito et al. (2001). Figure 5 illustrates the numerical model of the ground and abandoned lignite mine beneath the Kyowa Secondary School. Figure 6 shows the computed

responses from 1D and 3D numerical analyses. It is interesting to note that responses from 1D and 3D analyses are quite similar to each other.

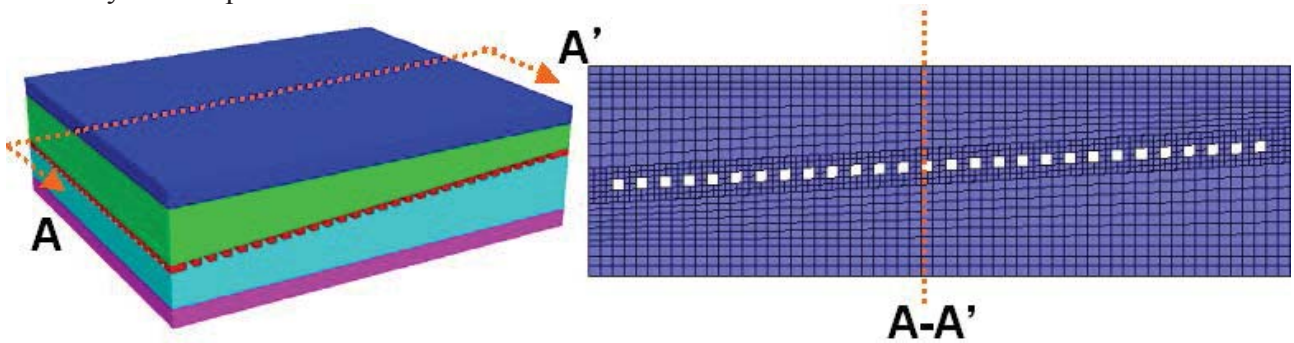


Figure 5. Illustration of models used in numerical analyses and selected section.

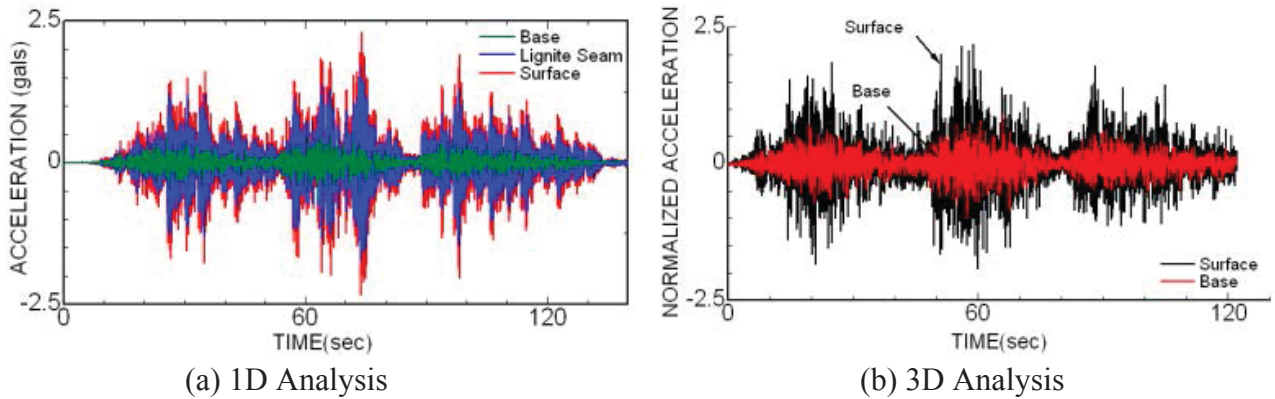
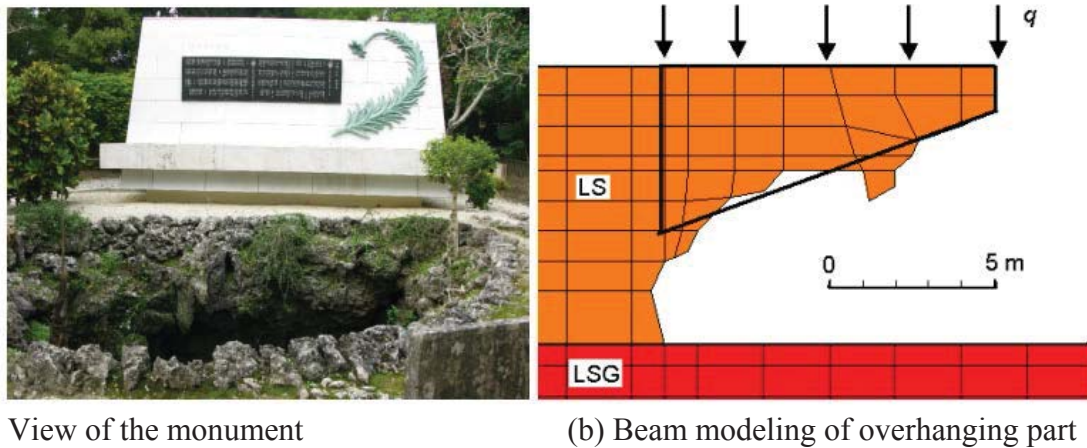


Figure 6. Acceleration responses at selected section from 1D and 3D numerical analyses.



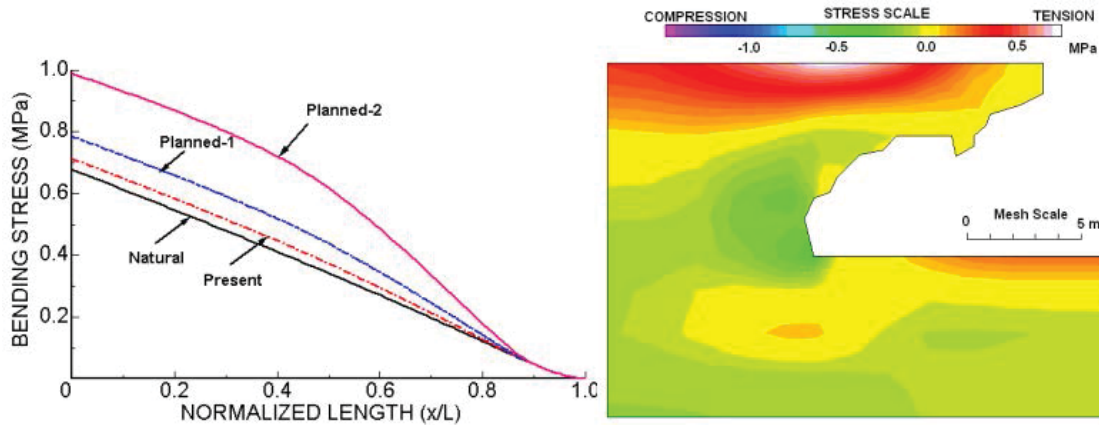
(a) View of the monument (b) Beam modeling of overhanging part  
**Figure 7. View and beam modeling of overhanging part.**

*Karstic Caves*

Karstic caves are quite common worldwide whenever limestone and evaporates deposits exist. In the coral limestone formation in Ryukyu Islands of Japan, there are many karstic caves, which present many geo-engineering problems. The authors are involved with the stability assessment of some karstic caves in relation to some engineering projects or preservation of some monumental structures (i.e. Tokashiki, 2011; Aydan and Tokashiki, 2011; Geniş et al. 2009). There is a huge karstic cave beneath the Himeyuri monument in Okinawa Island. The enlargement of the monument was considered and the authors were consulted if the karstic cave would be stable upon the enlargement. Figure 7 shows a view of the monument and the beam modelling of overhanging part. Table 1 and Figure 8 compares the maximum tensile and compressive stresses computed from beam theory and FEM. Despite some slight differences, the results are quite similar.

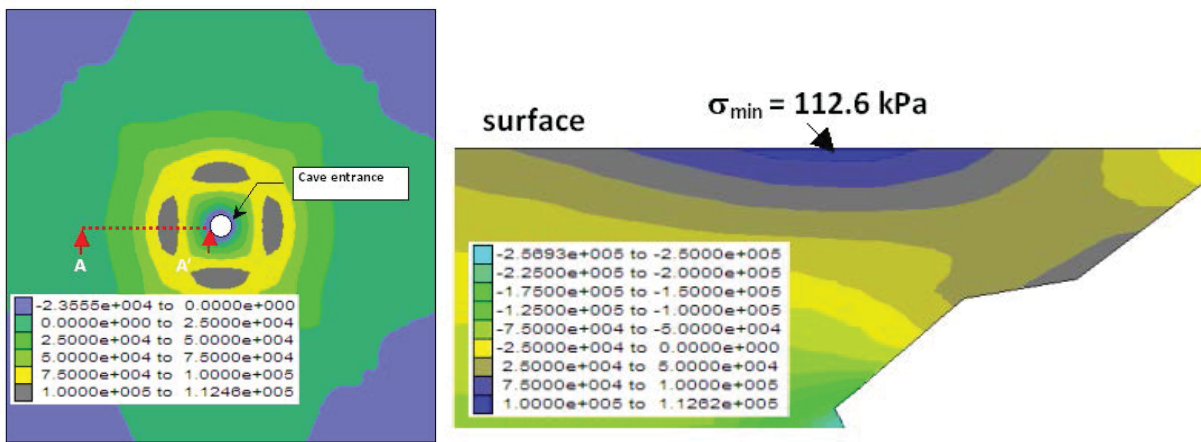
**Table 1. Comparison of maximum compressive and tensile stresses from FEM and bending theory.**

Loading Condition	Max. Tensile Stress (MPa)		Max. Compressive Stress (MPa)	
	FEM	THEORY	FEM	THEORY
Natural	0.557	0.677	-1.363	-0.677
Present	0.631	0.713	-1.402	-0.713
Planned-2	0.770	0.991	-1.478	-0.991



(a) Bending stress distribution from bending theory (b) Maximum principal stress from FEM  
**Figure 8. Comparison of stresses obtained from the bending theory and FEM.**

A 3D analysis of the vicinity of Himeyuri monument and the cave beneath was carried out with the consideration of surface loading due to the dead weight of the monument structure (Aydan et al. 2011). The cave was considered to be circular in plan view. The maximum tensile stress was much smaller than that computed from the bending theory and 2D FEM analysis. Additional axisymmetric FEM analysis was also performed and it yielded similar results. However, the cave has an ovaloid shape in plan and the actual stress state is expected to be closer to that of 2D analyses. Furthermore, there are some cross-joints in rock mass so that the actual stress state should be quite close to that of 2D-FEM analyses.



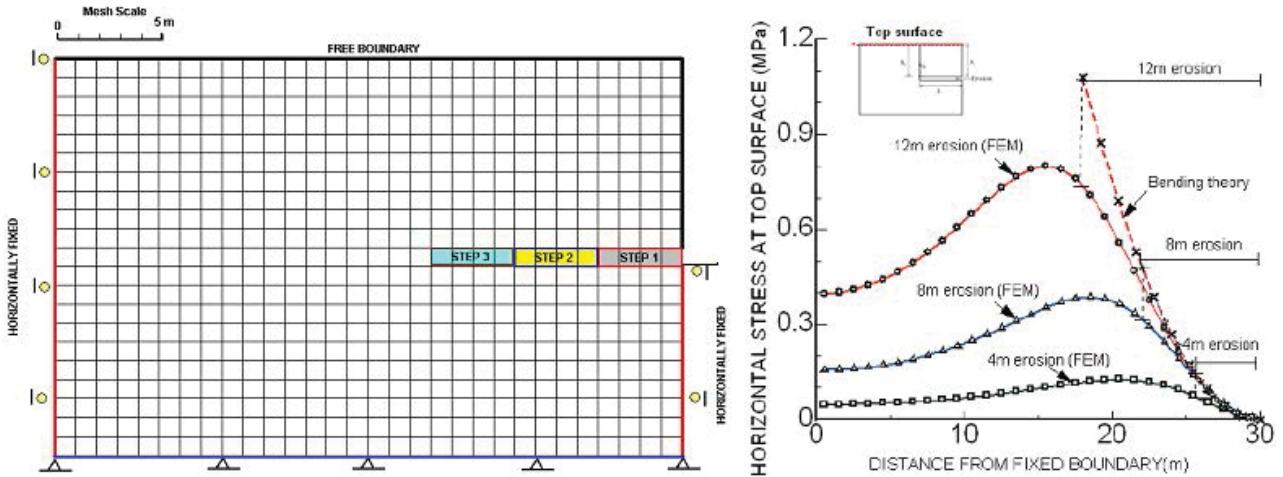
(a) Surface stresses (b) Maximum principal stress contours along A-A'  
**Figure 9. Computed maximum principal stress distributions from 3D numerical analysis.**

**Surface Structures**

*Cliffs*

Very steep cliffs are observed along the shorelines of Ryukyu Islands. The toe of the cliffs is often eroded by sea waves and they result in overhanging configurations. When the erosion depth reaches

to a certain distance, overhanging cliffs topple. Figure 10a shows the mesh used in FEM analyses for simulating erosion process while Figure 10b shows the distribution of tensile stress at top surface of the cliff for different erosion depths. The bending theory yields higher tensile stresses compared to those from the FEM analyses for different erosion depths (Tokashiki and Aydan, 2010). The maximum value of tensile stress obtained from the FEM analysis is about 75% of that computed from bending theory for the same erosion depth. Despite this slight difference, it may be quite acceptable to utilize the bending theory for quick assessment of the stability of cliffs.

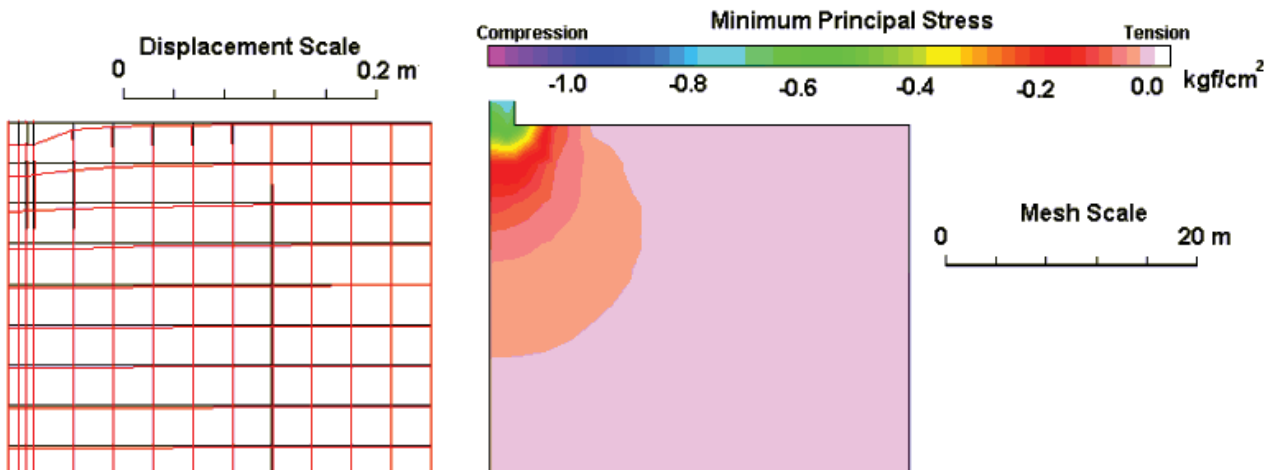


(a) 2D FEM mesh and simulation of toe erosion (b) Computed tensile stress at cliff surface

**Figure 10. Mesh used in simulation of the toe erosion of steep cliffs and computed stresses at the upper surface of the model.**

*Foundations*

Final example is concerned with settlement and stress state beneath foundations subjected to surcharge loads through relatively rigid foundation with a diameter of 3m, and it is modeled as an axisymmetric problem. Figure 11 shows the computed settlement and pressure contours beneath the foundation. The estimated settlement and pressure contours are generally in agreement with theoretical solutions by Timoshenko and Goodier (1951).



(a) Deformed configuration (b) Minimum principal stress contours

**Figure 11. Settlement and pressure contours beneath a circular foundation.**

**Conclusions**

The authors discussed how to select the appropriate dimension in numerical analyses of geo-engineering structures by considering some typical geo-engineering examples. There is no doubt

that 3D simulation of geo-engineering structures is desirable. Although the pre-post processing of 3D mesh generation and visualization of computed results for geo-engineering structures have become much easier with the advance of computer technology and computational techniques, it is still useful to utilize 1D or 2D simulations for quick assessments and decision making. Therefore, researchers and engineers should explore the power of 1D and 2D simulations as much as possible. If such simulations yield some uneconomical results, then 3D simulations should be implemented. Furthermore, if numerical simulations involve time dependent problems, particularly, hyperbolic type solution schemes, it may be imperative to utilize first 1D and later 2D numerical simulations before exploring the power of 3D simulations.

## References

- Aydan, Ö. (1989), The stabilisation of rock engineering structures by rockbolts. PhD Thesis, Nagoya University, 240 p.
- Aydan, Ö., (1994), Chapter 7: Rock Reinforcement and support in Introduction to Rock Mechanics, Industrial Pub. & Consul. Inc., Editors: V. Vutukuri, K. Katsuyama, pp. 193-247.
- Aydan, Ö., (2011), Some issues in tunnelling through rock mass and their possible solutions. Proc. First Asian Tunnelling Conference, ATS-15, pp. 33-44.
- Aydan, Ö., Geniş, M. (2008), Assessment of dynamic stability of an abandoned room and pillar underground lignite mine, Turkish Journal of Rock Mechanics, No.16, pp.23-44.
- Aydan, Ö., Geniş, M. (2010), A unified analytical solution for stress and stress fields about radially symmetric openings in elasto-plastic rock with the consideration of support system and long-term properties of surrounding rock. *International Journal of Mining and Mineral Processing*, Vol. 1, No.1, pp. 1-32.
- Aydan, Ö., Tokashiki, N. (2011), A comparative study on the applicability of analytical stability assessment methods with numerical methods for shallow natural underground openings. *The 13<sup>th</sup> International Conference of the International Association for Computer Methods and Advances in Geomechanics*, Melbourne, Australia, pp.964-969.
- Aydan, Ö., T. Kyoya, Y. Ichikawa, T. Kawamoto, T. Ito, Shimizu, Y. (1988), Three-dimensional simulation of an advancing tunnel supported with forepoles, shotcrete, steel ribs and rockbolts. *The 6th Int. Conf. on Num. Meths. in Geomechanics*, Innsbruck, Vol. 2, pp.1481-1486.
- Aydan, Ö., Tano, H., Geniş, M. (2008), Assessment of long-term stability of an abandoned room and pillar underground lignite mine. Turkish Journal of Rock Mechanics, No.16, pp.1-21.
- Aydan, Ö., Tokashiki, N., Geniş, M. (2011), Stability assessment of Himeyuri Monument and adjacent Karstic cave. The 10<sup>th</sup> Regional Rock Mechancis Symposium, ROCKMEC'2011, Ankara, pp. 39-46.
- Aydan, Ö., Geniş, M., Sugiura, K., Sakamoto, A. (2012), Characteristics of ground motions and amplifications above abandoned mines. International Symposium on earthquake Engineering, Vol.1, Tokyo.
- Coates, D.F. (1965), Rock Mechanics Principles, Mines Branch Monograph 874. Canadian Department of Energy, Mines and Resources, Ottawa,.
- Geniş, M., Aydan, Ö. (2008), Assessment of dynamic response and stability of an abandoned room and pillar underground lignite mine. *The 12<sup>th</sup> International Conference of International Association for Computer Methods and Advances in Geomechanics (IACMAG)*, Goa, India, pp. 3899-3906.
- Geniş, M., Aydan, Ö. (2013), A numerical study on ground amplifications above abandoned room and pillar mines and old longwal mines. EUROCK2013, Wroclaw, Taylor and Francis, pp. 733-737.
- Geniş, M., Tokashiki, N., Aydan, Ö. (2009), The stability assessment of karstic caves beneath Gushikawa Castle Remains (Japan). EUROCK 2010, pp. 449-454.
- Obert, L., Duwall, W. (1967), Rock Mechanics and Design of Structures in Rocks. Wiley, New York.
- Sugito, M., Furumoto, Y., Sugiyama, T. (2001), Strong Motion Prediction on Rock Surface by Superposed Evolutionary Spectra. 12th World Conference on Earthquake Engineering, 2111/4/A, CD-ROM.
- Timoshenko, S., Goodier, N. (1951), Theory of Elasticity. McGraw-Hill, 567p.
- Tokashiki, N. (2011), A Study on the Engineering properties of Ryukyu limestone and the evaluation of the stability of its rock mass and masonry structures. Doctorate, Thesis (in Japanese), Waseda University, .232 p..
- Tokashiki, N. Aydan, Ö. (2010), The stability assessment of overhanging Ryukyu limestone cliffs with an emphasis on the evaluation of tensile strength of Rock Mass. *Journal of Geotechnical Engineering, JSCE*, Vol. 66, No. 2, pp.397-406.

## **Wind Tunnel Tests of the Counter-Rotating Propeller of Stratospheric Airship**

Peiqing Liu<sup>1, a</sup>, Jingwei Sun<sup>2, b</sup> and Zhihao Tang<sup>3, c</sup>

School of Aeronautic Science and Engineering, Beijing University of Aeronautics and  
Astronautics, Beijing 100191, China

<sup>a</sup>charmingwei0703@gmail.com, <sup>b</sup>lpq@buaa.com, <sup>c</sup>sunjingwei59@sina.com

**Keywords:** stratospheric airship; counter rotating propeller; wind tunnel tests; advanced ratio

**Abstract:** *In this paper, a design of counter-rotating propeller (CRP) for stratospheric airship in low Reynolds number is tested in experiment for the first time. In consideration of stratosphere environment, a two-bladed counter-rotating propeller is designed for stratospheric airship. With the similarity theory of Reynolds number and advanced ratio, the experiment is conducted in low Reynolds number wind tunnel at Beihang University. The results indicate that counter-rotating propeller were 4%-7% percent more efficient than single-rotating propeller (SRP). This shows that for the counter-rotating propeller: 1) with the same diameter and power, the thrust coefficient is higher; 2) with the same thrust coefficient and power coefficient, the diameter could be reduced; 3) with the same thrust coefficient and diameter, the power coefficient could be reduced.*

## Introduction

Stratospheric airship is now received more and more attention. Stratospheric airship need to meet the requirements of long-endurance. So there are many methods are adopted: 1) improve the ability of energy storage; 2) use the lighter materials; 3) improve the airship aerodynamic configuration [1] [2]. As a fact, the propeller for stratospheric airship has low efficiency than the propeller for high speed aircraft. Due to the stratosphere atmospheric density is small, Reynolds number of stratosphere is an order of magnitude smaller than the ground. The propeller propulsion for the stratosphere airship has low efficiency[3] [4]. Some existing methods to raise the capacity of the propeller propulsion: At first, can by changing propeller diameter, but due to the stratosphere critical Mach number is small, blade tip is easy to produces shock resistance, bigger blades bring great difficulty to install; Secondly, increase the number of the propeller can effectively improve the overall thrust, but too much consider the layout and balance the propeller torque, installation also has a lot of difficulties; At last, the counter-rotating propeller (CRP) offers the potential of a higher efficiency, smaller diameter along with a reduction of reaction torque when compared with a single rotation propeller (SRP) for equal input horsepower. This is due to the recovery of swirl energy by the rear rotor and the partial cancellation of moments since they are in opposite directions on the front and the rear rotors although not equal in magnitude[5].

Biermann and Gray took a wind tunnel experiment for counter-rotating propeller with high Reynolds number, verified that counter-rotating propeller can significantly improve efficiency[6] [7]. Biermann and Hartman took an experiments prove that counter-rotating propeller propulsion system for the overall efficiency significantly increase applies to lower advance ratio[8] [9]. Airship propeller propulsion works at a low advance ratio. As the energy increasingly nervous today, counter-rotating propeller propulsion applied to stratosphere airship has a good prospect.

## Similarity Theory

Stratospheric air density is much smaller than the ground. How to simulation the low Re number environment on the ground must be studied first before taking the wind tunnel test. In this experiment, in order to ensure the movement similar and dynamic similar the advance ratio and Reynolds number similar conditions must be satisfied[10].

Advance ratio similarity determines the propeller working state movement is similar. The ratio of wind speed and the blade tip rotation speed is called advanced ratio.

$$\frac{V_{01}}{D_1 n_{s1}} = \frac{V_{02}}{D_2 n_{s2}} \quad (2.1)$$

Dynamic similarity requires that various forces acting on the fluid particle is proportional to the size and in the same direction. In general, the fluid particle by forces include: unsteady inertia force, viscous force, gravity, elastic force. Ma number is the ratio of elastic force and inertial force, and it is also the ratio of air velocity and speed of sound. The Ma number similar conditions are the same to the advanced ratio similarity. For air, the gravity can be neglected. As a result, the Re number similarity become the most important condition. Re number is the ratio of inertia force and viscous



force.

$$R_e = \frac{W_1 D_1}{\nu_1} = \frac{W_2 D_2}{\nu_2} \quad (2.2)$$

$W$  is the resultant velocity of the propeller blade element,  $\nu$  is the dynamic viscosity coefficient (20 km altitude:  $\nu = 16.1 \times 10^{-5} \text{m}^2/\text{s}$ , on the ground:  $\nu = 1.46 \times 10^{-5} \text{m}^2/\text{s}$ ). As the resultant velocity  $W$  is related to the blade tip speed, the formula (2.2) can be written as:

$$n_{s1} D_1^2 / \nu_1 = n_{s2} D_2^2 / \nu_2 \quad (2.3)$$

### Wind tunnel device

In this simulation, the propeller model is similar geometrical properties as those in reference [11] because of the lack of the appropriate data for low Re number CRP. The geometrical properties of this propeller were basically to achieve the highest single rotating propeller (SRP) efficiency and therefore it is not optimal for CRP[5]. Propeller diameter is 0.75m, SRP is two blade, CRP is  $2 \times 2$ . Low Reynolds number and high lift S1223 airfoils was chosen as the blade element. CRP  $2 \times 2$  propeller is shown in figure 1

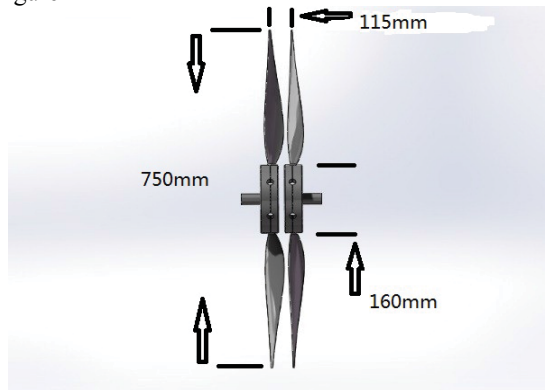


Figure. 1 counter-rotating propeller

This experiment was taken in low Reynolds number wind tunnel of buaa, as it is shown in figure 3.1. Experimental section diameter is 1.0m, the wind speed  $V_0=0\sim 20\text{m/s}$ , turbulence:  $k=1\%$ , contraction ratio  $\eta = 1.44$ .



Figure. 2 low Reynolds number wind tunnel

The motor speed and data collection were controlled by the "CRP experiment system" operated under the LabView. Servo motor is used to control the revolving speed of the propeller. Strain gauge balance is installed on the propeller shaft to measure the force and moment. The

result of a measurement is the averaging of 20 real-time signal value collected in the 4 seconds sampling period.

Experimental condition is shown on the chart1:space between two rotor is 150mm, setting angle of blade is  $28.3^\circ$ , two rotors used the same speed.

Chart. 1 experimental condition

Wind speed (m/s)	Rotate speed (rpm)	Time interval (rpm)
0	400~1500	50
5	400~1500	25
7.5	400~1500	25
10	700~1500	25
12.5	700~1500	25
15	1000~1500	25
17.5	1000~1500	25

### Error analysis

In this experiment, the force and torque was seven times repeated collection. As for multi-point measurement, each measuring point has the same repetitions and has the same accuracy. The formula for the uncertainty of multipoint measuring is shown in formula 4.1[12] [13]:

$$\sigma = \sqrt{\frac{\sum_{i=1}^k \sum_{j=1}^n (a_{ij} - \bar{a}_i)^2}{k(n-1)}} \quad (4.1)$$

The random uncertainty of the measurement is shown in formula 4.2:

$$\Delta = t_\alpha \cdot \sigma \quad (4.2)$$

{i} is the number of measuring points;

{n} is number of measurement of each measuring point;

{k} is total number of points;

{ $t_\alpha$ } is confidence interval, determined by measuring frequency and confidence probability.

The repetitions is 7,

k=1,

n=7,

confidence probability is 0.95.  $t_\alpha = 2.447$ .

The uncertainty of each u (M) and u (T) can be calculated.

Error transfer formula is shown in 4.3:

$$\Delta\eta = \sqrt{\left[\Delta T \frac{\partial(\eta)}{\partial(T)}\right]^2 + \left[\Delta n_s \frac{\partial(\eta)}{\partial(n_s)}\right]^2 + \left[\Delta V_0 \frac{\partial(\eta)}{\partial(V_0)}\right]^2 + \left[\Delta M \frac{\partial(\eta)}{\partial(M)}\right]^2} \quad (4.3)$$

In this experiment, the flow velocity error and rotate speed error is under 0.5%. The efficiency error distribution of each measuring point is shown in figure 3:

Field Code Changed

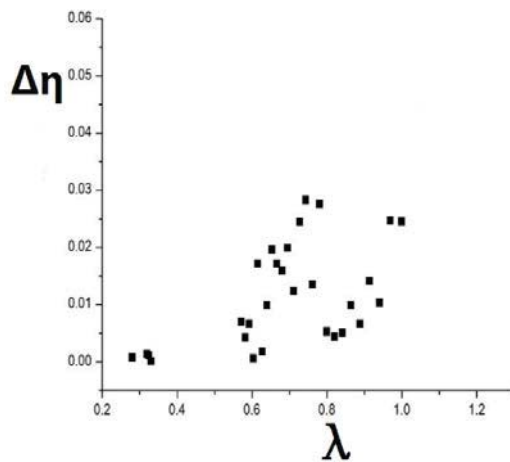


Figure. 3 propeller efficiency error distribution

Because the measurement of the force and torque has a fixed deviation, when the wind speed and rotate speed are low, the measurement precision is low. So the speed of measurement point is improved to improve the measurement accuracy. The higher rotate speed means better measurement accuracy. The maximum error is under 5%, and when it related to the low advance ratio region the maximum error is under 3%. The experiment is in a credible range error.

### Results analysis

Reynolds number can be determined by control the rotating speed of propeller and the speed of wind tunnel. After measured the aerodynamic force of SRP, front propeller and rear propeller, the dimensionless aerodynamic parameters could be determined. By definition, these parameter is as follows:

- (1) thrust coefficient of the propeller

$$C_t = \frac{t}{\rho n_s^2 D^4} \quad (1)$$

The t is the pull.

- (2) power of the propeller

$$C_p = \frac{P}{\rho n_s^3 D^5} \quad (2)$$

Power coefficient is power coefficient, p is the power.

- (3) efficiency of the propeller

$$\eta = \frac{tV_0}{P} = \frac{C_t}{C_p} \lambda \quad (3)$$

With the advanced ratio is determined from 0.6-1.0, the thrust coefficient could be raised by improve the wind speed of wind tunnel as it shown in figure 4.

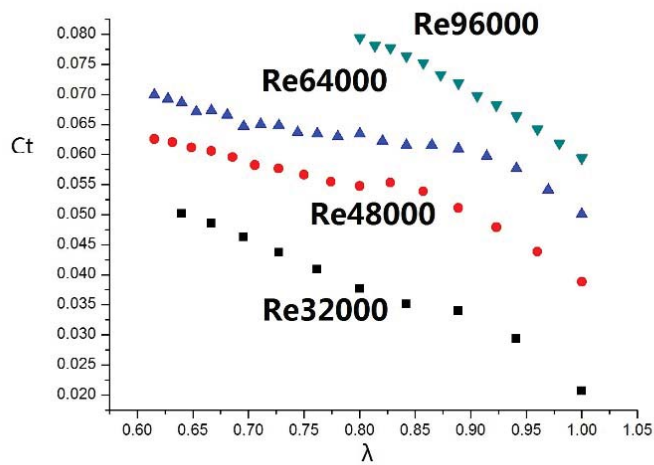


Figure. 4 Thrust coefficient with different wind speed

In general, as the Reynolds number increases, the thrust coefficient is improving. As the installation angle of propeller is fixed, the attack angle of the blade is determined by installation angle and advanced ratio. With the same advanced ratio, improve the wind speed, screw speed increase too. As it shown in figure 5, the efficiency could be increased by improving the Reynolds number. When Reynolds number is large, the efficiency curve is very near. The propeller's maximum efficiency is 72% when the advanced ratio is 0.8-1.0 and wind speed is 15m/s.

Chart. 2 the propeller efficiency

Wind speed/Re	$\lambda : 0.8$	0.88	0.91
5 (32000)	40.6%	42.4%	31.3%
7.5 (48000)	61.8%	63.0%	55.7%
10 (64000)	61.8%	64.3%	61.6%
12.5 (80000)	71.3%	64.6%	62.7%
15 (96000)	72.4%	72.6%	70.0%

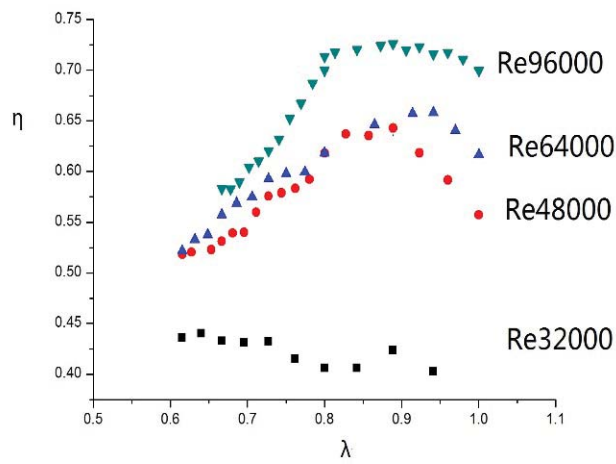


Figure. 5  $\eta$  with different wind speed

The efficiency of the rear propeller is significantly higher than SRP. At the same condition, the efficiency of the front propeller is lower than SRP. As the advanced ratio is 0.5-1.1, the CRP could improve the efficiency by 4%-6% in contrast with the SRP as it shown in figure 6.

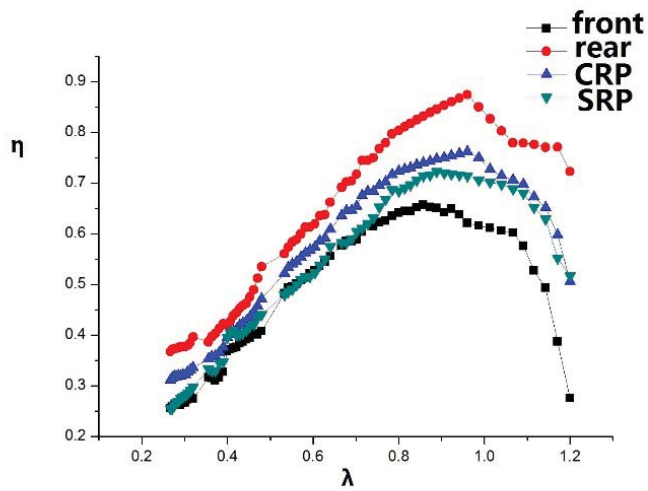


Figure. 6  $\eta$  with different wind speed

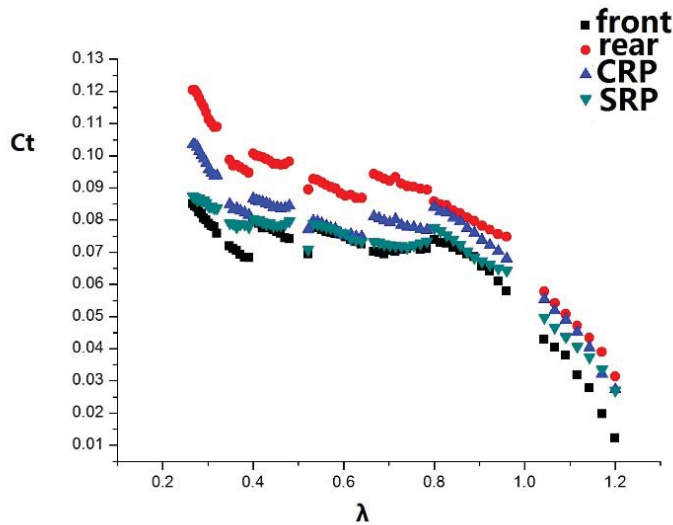


Figure. 7 Ct with different wind speed

In spite of the front propeller have the lowest thrust coefficient, the CRP has a higher thrust coefficient than SRP. The results indicate that the rear propeller have the highest thrust coefficient as it shown in figure 7.

### Summary

In contrast with SRP, the wind test show that CRP for stratospheric ship could improve the efficiency by 4%-7%. This result could be used to guide the design of stratospheric airship propulsion system.

### References

- [1] Xu Cao. Summary of the ISIS stratosphere airship. Beijing: China Academic Journal Electronic Publishing House
- [2] NIE wansheng., LUO shibin. Analysis of key technologies and development trend of near space vehicle. Journal of National University of Defense Technology. Vol.34 No.2 Apr.2012.
- [3] Bryan D. McGranahan and Michael S. Selig. "Surface Oil Flow Measurements on Several Airfoils at Low Reynolds Numbers". 21st AIAA Applied Aerodynamics Conference June 23–26, 2003/Orlando, FL, AIAA 2003-4067
- [4] R.J. Ong, J.T. Dawley and P.G. Clem: submitted to Journal of Materials Research (2003)
- [4] Jewel B Bar low, William H Rae Jr, Alan Pope. Low-Speed Wind Tunnel testing. New York: Wiley- Interscience Publication, 1991
- [5] S. Saito, H. Kobayashi. Performance Calculation of Counter Rotation Propeller. AIAA-87-1889
- [6] Lock, C, N, H., "Interference Velocity for a Close Pair of Contra-Rotating Airscrews, A & M 2084, July 1941.
- [7] Biermann, D. and Gray, W. H., "Wind Tunnel Tests of Single and Dual-Rotating Pusher Propellers Having from 3 to 8 Blades," NACA ARR (WRL-359), February 1942.
- [8] Biermann, D. and Hartman, E. P., "Wind Tunnel Tests of Four and Six Blade Single and Dual-Rotating Tractor Propellers," NACA Rept. 747, 1942.

- 
- [9] McHugh, J. G. and Pepper, E., "The Characteristics of Two Model 6-Blade Counterrotating Pusher Propellers of Conventional and Improved Aerodynamic Design," NACA ARR (WR L-404), June 1942.
- [10] LIU Pei-qing, MA Rong, Ground wind tunnel test study of propeller of stratospheric airships, Journal of Aerospace Power. Vol.26 No.8 Aug. 2011
- [11] Ronrbach, C. Meizger, F. B. Black, D. M. and Ladden, R. M. Evaluation of wind tunnel bladed propeller at Mach Numbers From 0.45 to 0.85, NASA CR 3505
- [12] Facek Mieloszyk, Cezary Galinski and Fanusz Piechna, Countra-rotating propeller for fixed wing MAV:Part 1, Aircraft Engineering and Aerospace Technology, ISSN 1748-8842
- [13] Facek Mieloszyk, Cezary Galinski and Fanusz Piechna, Countra-rotating propeller for fixed wing MAV:Part 2, Aircraft Engineering and Aerospace Technology, ISSN 1748-8842
- [14] LIU Pei-qing, Air propeller theory and its application. IBSN 7-81077-765-3

## Relevancy of Peak Parameter Plots in Estimating Effects of Ground Shock

J.H. Chew, and E.C. Leong\*

School of Civil & Environmental Engineering, Nanyang Technological University, Singapore.

\*Corresponding author: cecleong@ntu.edu.sg

### Abstract

Studies on correlations of ground shock parameters from explosions began since 1870. Many field tests of various scales have been conducted to obtain the correlation of these parameters. One example is the U.S. Army Corp of Engineer's TM 5-855-1 (1986). The objective of this paper is to evaluate the relevancy of the plots in TM 5-855-1 (1986) given that many advances have been made in computational modeling. In the paper, ground shock parameters such as pressure, velocity, acceleration, impulse and scaled distance are firstly expressed as dimensionless parameters to develop dimensionless counterpart plots of the TM5-855-1 (1986) plots. Next, data from ground shock studies in the literature are examined using the dimensionless plots. It is found that the dimensionless plots provide good indicative values of the parameters and it is also possible to know how the parameters will change as degree of saturation of the soil and soil type changes.

**Keywords:** Ground Shock, pressure, velocity, acceleration, impulse.

### Introduction

Ground shock parameters like pressure, velocity and density which are related to explosive detonation were investigated as early as 1870. The U.S. Army Corp of Engineers developed the TM 5-588-1 (1986) which provides correlations of peak parameters (pressure, velocity, acceleration, displacement and impulse) with variables like weight of explosive charge, distance and soil condition. However, the equations given by TM 5-855-1 (1986) are empirical based on field test data and do not take into consideration of consistency of units.

The objective of this paper is to evaluate the relevancy of the plots of ground shock parameters in TM5-855-1 (1986) given the current advances made in computational modeling. To achieve a sound basis, dimensionless ground shock parameters were firstly obtained using Buckingham's pi theorem. Using dimensionless ground shock parameters of TM5-855-1 (1986), data of ground shock studies from the literature are plotted. Through examination of these plots, a better understanding on how the peak ground shock parameters change with soil properties and soil type can be obtained.

### Background

The equations in TM5-855-1 (1986) for peak pressure  $P_0$ , peak velocity  $V_0$ , peak acceleration  $a_0$ , peak displacement  $d_0$  and impulse  $I_0$  are as follows:



Peak pressure: 
$$P_o = f \cdot (\rho c) \cdot 160 \cdot \left(\frac{R}{W^{1/3}}\right)^{-n} \tag{1.1}$$

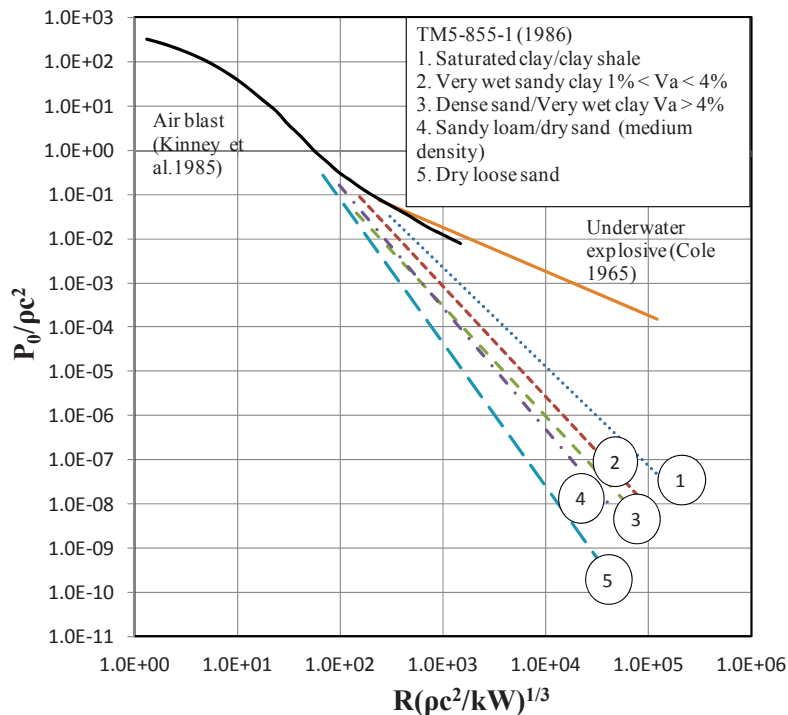
Peak acceleration: 
$$a_o W^{1/3} = f \cdot 50 \cdot c \cdot \left(\frac{R}{W^{1/3}}\right)^{-(n-1)} \tag{1.2}$$

Peak velocity: 
$$V_o = f \cdot 160 \cdot \left(\frac{R}{W^{1/3}}\right)^{-n} \tag{1.3}$$

Peak displacement: 
$$\frac{d_o}{W^{1/3}} = f \cdot 500 \cdot \frac{1}{c} \cdot \left(\frac{R}{W^{1/3}}\right)^{-(n+1)} \tag{1.4}$$

Impulse: 
$$\frac{I_o}{W^{1/3}} = f \cdot \rho_o \cdot 1.1 \cdot \left(\frac{R}{W^{1/3}}\right)^{-(n+1)} \tag{1.5}$$

R is the distance away from the explosion and W is the weight of the charge. It is noted that the weight of the charge is based on TNT equivalent. It is also noted that these equations are in imperial units and are not dimensionally consistent. Westine et al. (1983) suggested using dimensionless scaled pressure  $P_o/\rho c^2$  and dimensionless scaled distance  $R(\rho c^2/W)^{1/3}$ . Leong et al. (2006) also noted that W is in lb for imperial units and in newton for SI units and introduced a term k of 1m or 3.28ft in the dimensionless scaled distance  $R(\rho c^2/kW)^{1/3}$  so that there will be a seamless conversion from imperial units to SI units. Henceforth, the scaled distance shall be  $R(\rho c^2/kW)^{1/3}$ . If the coupling factor (f) is taken to be unity, it implies that the explosive energy is fully contained within the soil.



**Figure 1. Relationship of peak pressures with scaled distance using dimensionless parameters (modified from Leong et al. 2006)**

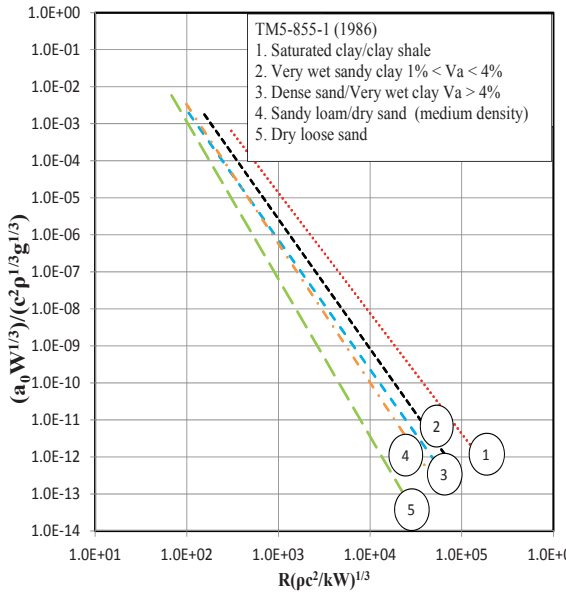
The TM5-855-1 (1986) plot for peak pressure is re-plotted with dimensionless parameters  $P_0/\rho c^2$  and  $R(\rho c^2/kW)^{1/3}$  as shown in Figure 1. The circled numbers represent the soil types as given by TM5-855-1 (1986) indicated in the legend of the plot. Leong et al. (2006) also suggested that the air blast and underwater explosion peak pressure curve be plotted in the dimensionless plot. The air blast peak pressure curves and underwater explosion peak pressure curve were obtained from Kinney's equation (Kinney and Graham, 1985) and Cole (1965), respectively. The air blast peak pressure curve merges with the underwater explosion curve and forms an upper boundary of the TM5-855-1 (1986) curves. Leong et al. (2006) observed that the peak pressure curves from TM 5-855-1 (1986) converged and merged into the air blast curve and fanned out with the increase in dimensionless scaled distance  $R(\rho c^2/kW)^{1/3}$  as shown in Fig. 1.

### Development of dimensionless plots

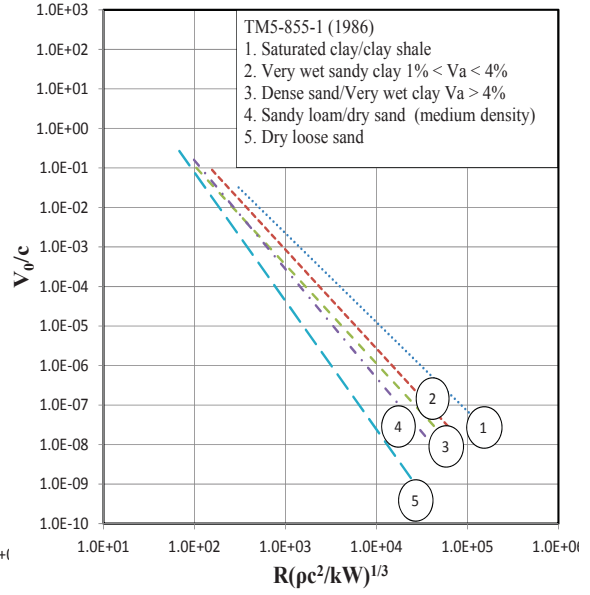
Buckingham's pi theorem was used to find dimensionless parameters for ground shock parameters of peak velocity, peak acceleration, peak displacement and impulse. Table 1 summarizes the dimensionless parameters of peak velocity, peak acceleration, peak displacement and impulse formed using Buckingham's pi theorem. The dimensionless parameters of peak pressure and scaled distance are also included in Table 1 for completeness. It is noted that both SI and imperial units can be used as long as the units are kept consistent. The dimensionless plots of peak acceleration, peak velocity, peak displacement and impulse with scaled distance for TM 5-85501 are shown in Fig. 2 to Fig. 5, respectively.

**Table 1: Correlation of peak pressure, velocity, acceleration, displacement and impulse with dimensionless parameters**

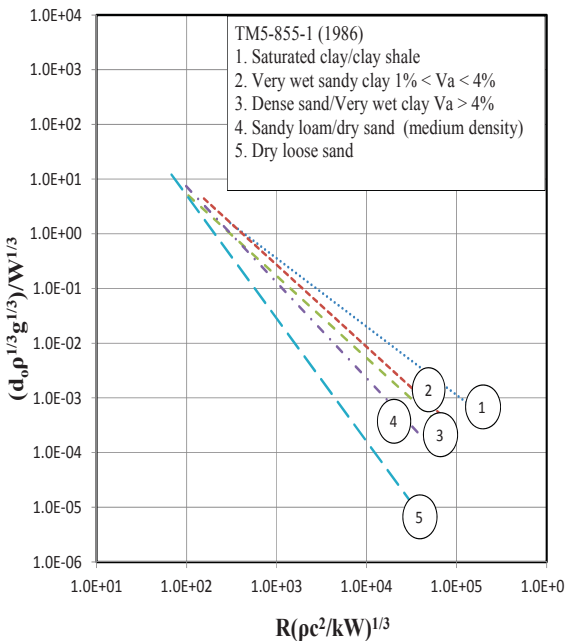
Parameter	Function	Dimensionless parameter
Peak pressure	$P_0 = f(\rho, c)$	$\frac{P_0}{\rho c^2}$
Peak acceleration	$a_0 W^{1/3} = f(\rho, c, g)$	$\frac{a_0 W^{1/3}}{c^2 \rho^{1/3} g^{1/3}}$
Peak velocity	$V_0 = f(c)$	$\frac{V_0}{c}$
Peak displacement	$d_0/W^{1/3} = f(\rho, g)$	$\frac{d_0 \rho^{1/3} g^{1/3}}{W^{1/3}}$
Impulse	$I_0/W^{1/3} = f(\rho, c, g)$	$\frac{I_0 g^{1/3}}{W^{1/3} \rho^{2/3} c}$
Scaled distance	$R/W^{1/3} = f(k, \rho, c)$	$R \left( \frac{\rho c^2}{kW} \right)^{1/3}$



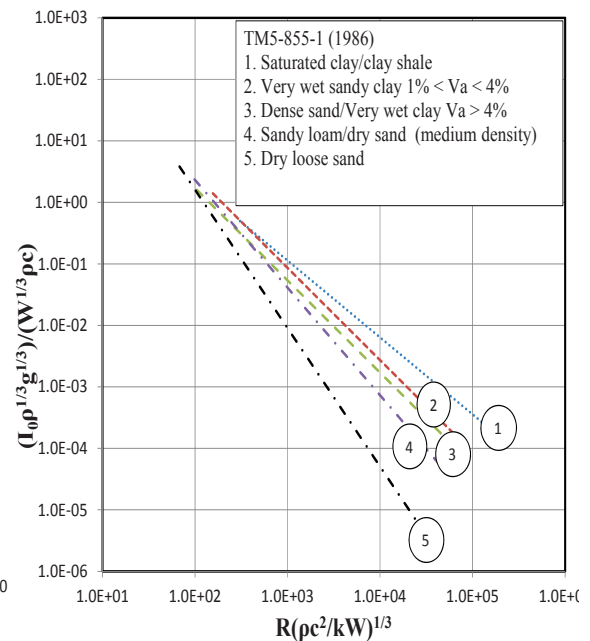
**Figure 2. Dimensionless of peak acceleration with scaled distance**



**Figure 3. Dimensionless plot of peak velocity with scaled distance**



**Figure 4. Dimensionless plot of peak displacement with scaled distance**



**Figure 5. Dimensionless plot of impulse with scaled distance**

**Observations and Discussions**

Ground shock data of peak pressure, peak velocity, peak acceleration and impulse were collated from the literature and plotted in the dimensionless plots. Peak displacement is not included as such data are not available in the literature. However, the data that are plotted into the plots are dependent on factors such as the placement

of the instruments, depth of burial of explosives and type of explosives used. For the purpose of measuring free-field ground shock parameters, the instruments should not be placed at the ground surface or poorly coupled to the ground as this will not accurately measure the ground shock waves. The depth of burial of the explosives determines the energy dissipated in the ground. Shallowly buried explosive does not have a coupling factor of one which is assumed in the dimensionless plot of the equations from TM5-855-1 (1986).

#### *Peak pressure versus scaled distance plots*

Leong et al. (2006) performed small scale tests using PETN in both wet and partially saturated soils with various charge weights (1, 4 and 10 kg) at various depths. The pressure gauges were located at the same level as the burial depth of the PETN charge. The burial depths of the PETN charge were 1kg at 2m depth, 4kg at 2.5m and 10kg at 2.5m. The test results are plotted in Fig. 6. The wet soil has a density of  $1900 \text{ kg/m}^3$  and wave velocity of 1380 m/s. The partially saturated soil has a density of  $1650 \text{ kg/m}^3$  and a wave velocity of 225 m/s. It is observed that the peak pressure for wet soil which was fully saturated is nearer to the underwater explosion curve by Cole (1948) compare to the peak pressure for partially saturated soil (85% saturated). The data from wet soil, composed of 93% clay and 7% sand, fall on the very wet sandy clay curve of TM5-855-1 (1986) whereas the data from the partially saturated soil, composed of 95% sand and 3% clay, fall on the sandy loam/dry sand curve. Both sets of data are observed to agree with the TM5-855-1 (1986) soil descriptions.

#### *Peak acceleration versus scaled distance plots*

Wu et al. (2003) performed a small scale test involving detonations of 2.5kg to 50kg of TNT with a depth of 14m in rock. The rock has a density of  $2610 \text{ kg/m}^3$  and wave speed of 5790 m/s. The accelerometers were placed on the surface and inside the rock mass at horizontal distances of 2.5m, 5m, 10m, 25m and 50m from the charge. The data in term of acceleration inside the rock mass are plotted in Fig. 7. It is observed from Fig. 7 that the peak acceleration data fall above the soil curves with a much lower attenuation. The explosive was detonated in a charged hole and the coupling factor may not be unity.

#### *Peak velocity versus scaled distance plots*

Charlie et al. (2007) performed a small scale test in a centrifuge and a field prototype test. The tests were carried out on Poudre valley sand which has a density of  $1635 \text{ kg/m}^3$ , wave speed of 170 m/s and degree of saturation ranging from 0 to 40%. The explosive used was 7 kg of TNT buried at a depth of 1.4 m. The experimental set-up and placement of accelerometers were not mentioned. The data are plotted in Fig. 8 and Fig. 9 for centrifuge test and prototype test, respectively. From Fig. 8 and Fig. 9, it is observed that as degree of saturation increases, the peak velocity data points move towards the saturated clay line of TM5-855-1 (1986). The data for both the centrifuge test and field prototype test are between the curves of dense sand and saturated clay from TM 5-855-1 (1986).

Peak impulse versus scaled distance plots

Grujicic et al. (2005) performed a numerical simulation using Autodyn (ANSYS INC). Buried C-4 explosives were assumed in the simulation. The modeled soil is assumed to have a density of 2000 kg/m<sup>3</sup> and a wave velocity of 700 m/s with different degrees of saturation ranging from 62.5 % to 100 %. It is observed from the impulse data in Fig. 10 that with the increase of degree of saturation, the data have a tendency to shift upwards towards the saturated clay curve of TM 5-855-1 (1986).

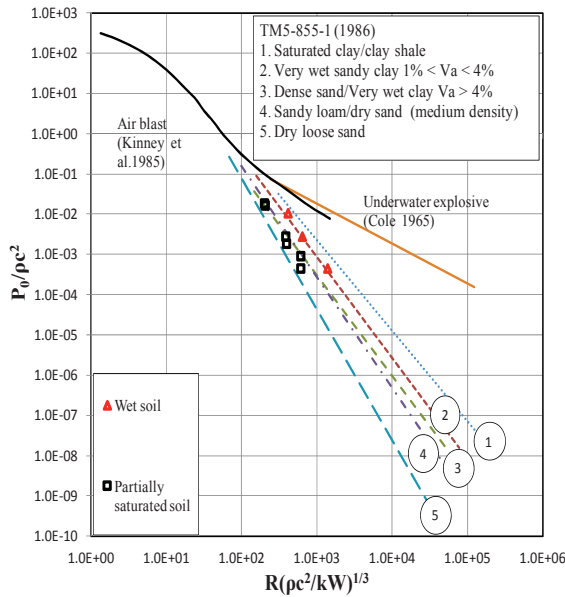


Figure 6. Peak pressure versus scaled distance plot for Leong et al. (2006) data

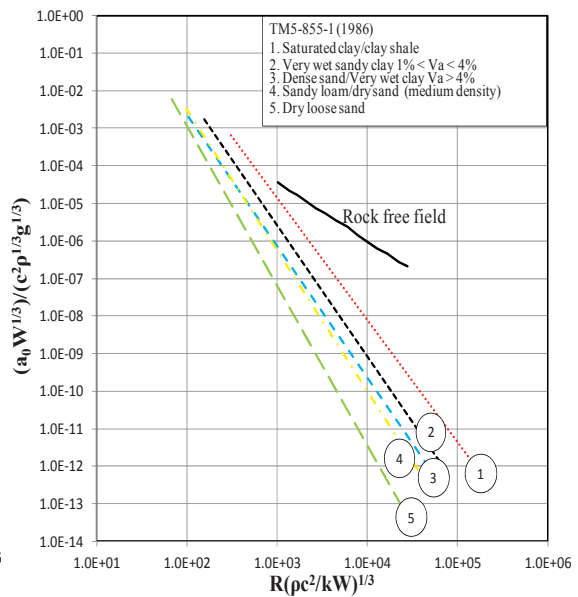


Figure 7. Peak acceleration versus scaled distance plot for Wu et al. (2003) data

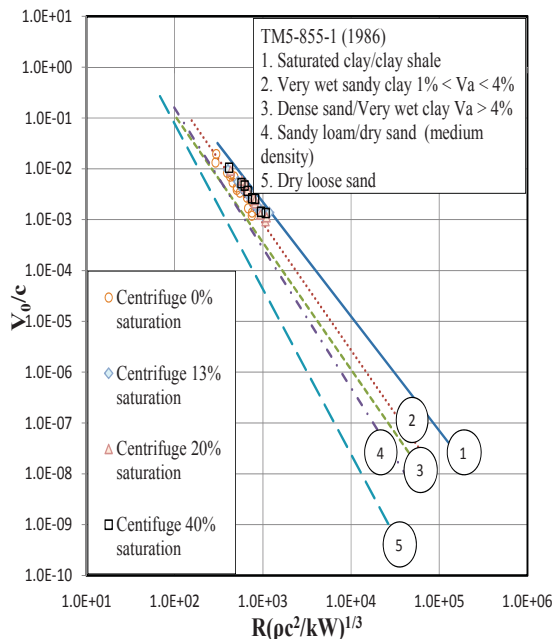


Figure 8. Peak velocity versus scaled distance plot for Charlie et al. (2007) centrifuge test data.

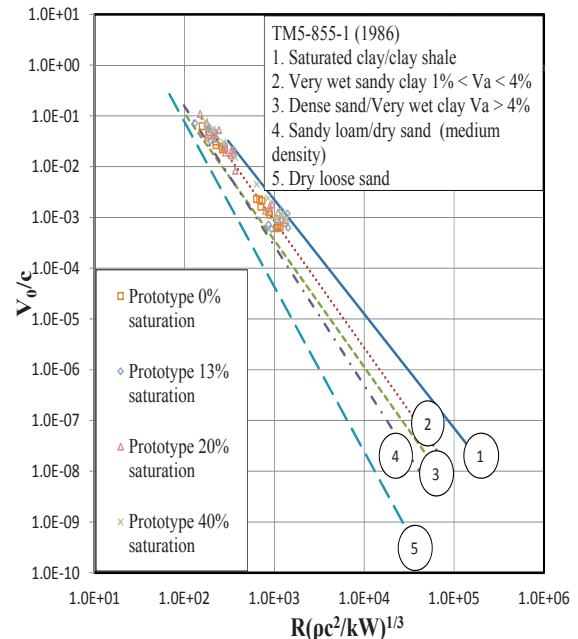
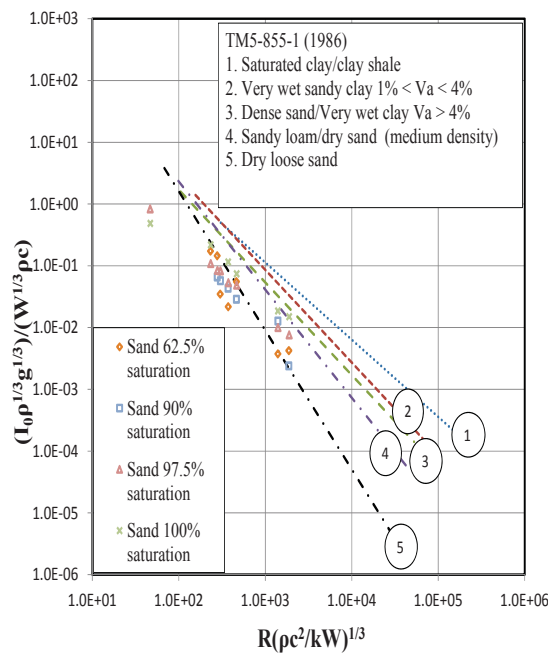


Figure 9. Peak velocity versus scaled distance plot for Charlie et al. (2007) prototype test data



**Figure 10. Impulse versus scaled distance plot for Grujicic et al. (2005) data**

## Conclusion

Peak velocity, peak acceleration, peak displacement and impulse were converted into dimensionless parameters using Buckingham's pi theorem. Dimensionless plots of these parameters with scaled distance of TM5-855-1 (1986) equations were presented. Data from field tests and numerical simulations were collated from the literature and plotted into the dimensionless plots. For peak pressure and peak velocity versus scaled distance, the soil description showed general agreement with TM5-855-1 (1986) soil description. However, for peak acceleration and impulse versus scaled distance, the data collated from the literature do not fall on any of the TM5-855-1 (1986) curves and they showed lower attenuation than the soil curves. It is observed in the peak pressure and peak velocity versus scaled distance dimensionless plots that the data have a tendency to shift towards the saturated clay curve with the increase in degree of saturation. The dimensionless plots of ground shock parameters versus scaled distance of equations from TM 5-855-1 (1986) can be used as benchmarks for numerical simulations.

## References

- Leong, E.C., Anand, S., Cheong, H.K. and Lim, C.H. (2007), Re-examination of peak stress and scaled distance due to ground shock, *International Journal of Impact Engineering*, 34, pp. 1487-1499
- Grujicic, M., Pandurangan, B. and Chessemann, B.A. (2005), The effect of degree of saturation of sand on detonation phenomena associated with shallow-buried and ground-laid mines, *Shock and Vibration*, 12, pp. 1-21
- Cole, R.H. (1965), *Underwater Explosions*, New York: Dover Publications
- TM 5-855-1 (1986), *Fundamentals of Protective Design for Conventional Weapons*, Department of Army, Washington DC, USA.

- Charlie, W.A., Dowden, N.A., Villano, E.J., Veyera, G.E. and Doehring, D.O. (2007), Blast-induced stress wave propagation and attenuation: centrifuge model versus prototype test, *Geotechnical Testing Journal*, 28, pp. 1-10.
- Wu, C., Hao, H., Lu, Y. and Zhou, Y. (2003), Characteristics of stress waves recorded in small-scaled filed blast tests on a layered rock-soil site, *Geotechnique*, 53, pp. 587-599
- Kinney, G.F. and Graham, K.J. (1985), *Explosive Shocks in Air*, Springer, Berlin.
- Westine, P.S. and Friesenhahn, G.J. (1983), Free-field ground shock pressures from buried detonations in saturated and unsaturated soils, *Proceedings of First Symposium on Interaction of Non-nuclear Munitions and Structures*, Florida University, Elgin AFB Graduate Engineering Center, U.S. Air Force Academy, Colorado, USA

## Two- and Three-Dimensional Validation of Icing Model

**\*Ryosuke Hayashi<sup>1</sup> and Makoto Yamamoto<sup>2</sup>**

<sup>1</sup>Graduate School of Mechanical Engineering, Tokyo University of Science  
6-3-1 Niiijyuku, Katsushika-ku, Tokyo, Japan

<sup>2</sup>Department of Mechanical Engineering, Tokyo University of Science

\*Corresponding author: j4512703@ed.tus.ac.jp

### Abstract

Ice accretion is a phenomenon where super-cooled water droplets impinge and accrete on a body. It occurs frequently on airplanes, windmills and conductor cables. In particular, when ice layer is formed on an aircraft wing, it affects on the aerodynamic performance by increasing drag and decreasing lift, and it may cause a serious accident. On a jet engine, ice accretion disturbs the inlet flow, and separated ice pieces can damage to the compressor and the casing, which leads to the severe performance degradation. There have been several accidents due to the ice accretion. Therefore, the estimation of ice accretion in the design phase is necessary to avoid accidents. The research on ice accretion phenomena has been conducted since early 1990's. The first icing simulation model was developed by Messinger in 1953. This model has been widely used in simulating ice accretion phenomena. Recently, Extended Messinger model was developed by Ozgen and Canibek in 2009. This model is more sensitive than Original Messinger model in suitably estimating the runback mass. The predictive performance for the runback mass has a huge influence on ice accretion phenomena in glaze ice condition. In this study, we conducted the validation of these icing models in two- and three-dimensional field. Finally, we indicated Extended Messinger model is more superior to Original Messinger model in simulating glaze icing.

**Keywords:** Multiphysics CFD, Ice Accretion, Jet Engine, Messinger Model

### Introduction

Ice accretion is a phenomenon where super-cooled water droplets impinge and accrete on a body. It has two types of ice shape. One is called 'rime ice' which is generated at very low temperature (less than -10 °C). On the rime ice condition, droplets in the air instantly freeze at the impingement point. The other is called 'glaze ice' which is generated at -10 to 0 °C. On the glaze ice condition, droplets gradually freeze with running along a body (so-called runback). This phenomenon is considerably important in simulating the glaze icing.

When ice layer is formed on an aircraft wing, it affects on the performance by increasing drag and reducing lift, and it may cause a serious accident. On a jet engine, ice accretion disturbs the inlet flow, and separated ice pieces can damage to the compressor and the casing, which leads to the severe performance degradation. There have been several instances of accidents due to ice accretion. Obviously, it is essential that the mechanisms of ice accretion are understood. The estimation of ice accretion is necessary to avoid accidents and useful to reduce the cost and the design time in the design phase of aircrafts and jet engines. However, the experimental investigations are very difficult, because it is not easy to set ice accretion conditions repeatedly in a wind tunnel. Therefore, it is expected computational fluid dynamics (CFD) will be a useful way to predict ice accretion phenomenon. CFD research of ice accretion phenomena has widely been conducted by agencies and universities, such as NASA [1], ONERA [2] and so on.



The first icing simulation model was developed by Messinger in 1953 [3]. This Original Messinger model has been widely used in the major research institution such as NASA, DRA and ONERA. The results predicted with the Original Messinger model is in good agreement with the experimental data in rime ice conditions. However, in glaze ice conditions, the predictive performance of the Original Messinger model is low, because the mass of the runback is underestimated. Therefore, the user specially modified the Original Messinger model in simulating glaze icing phenomena. Recently, Extended Messinger model was developed by Ozgen and Canibek in 2009. It is expected that the Extended Messinger model is more sensitive to glaze ice conditions than Original Messinger model, because it includes phase change condition from rime ice to glaze ice. However, the extended Messinger model has not been extensively validated yet.

In this study, we conducted the validation of these icing models two- and three-dimensional field. In the two-dimensional validation, we adopted the NACA 0012 airfoil because a lot of experimental data are available. In the three-dimensional validation, we adopted a fan rotor and FEGVs, because these components are easy to accrete ice. Finally, we indicated Extended Messinger model is more superior to Original Messinger model in simulating glaze icing.

## Numerical Procedure

Our icing simulation code is composed of iterative computations for fluid motion, droplet trajectory, thermodynamics and grid modification. Below each computational detail is explained.

### *Flow Field*

The flow field is assumed to be three-dimensional, compressible and turbulent. The governing equations are Favre-averaged continuity, Navier-Stokes and energy equations. Coriolis force and centrifugal force are added as body forces. The Kato-Launder  $k$ - $\varepsilon$  turbulence model (Kato and Launder, [4]) is applied to estimate turbulence. The governing equations are discretized using second-order upwind TVD scheme (Yee and Harten, [5]) for the inviscid terms, second-order central difference scheme for the viscous ones, and LU-ADI scheme (Fujii and Obayashi, [6]) for the time integration.

### *Droplet Trajectory*

Droplet trajectory calculation based on a Lagrangian approach is performed to obtain the droplet collection efficiency on a body. The calculation uses the following assumptions:

1. Droplet is spherical.
2. Droplet is sufficiently small, and thus it does not break up.
3. Forces acting on the droplet are drag, centrifugal force and Coriolis force.
4. Droplets do not interact with each other.
5. Droplets do not affect on the flow field (one-way coupling).
6. Initial droplet velocity is equal to the gas velocity at the release point.

The equation of droplet motion is

$$\frac{d\vec{U}_d}{dt} = \frac{3}{4} C_D \frac{\rho_f}{\rho_d} \frac{1}{d_d} \vec{U}_r |\vec{U}_r| - \left\{ 2\vec{\Omega} \times \vec{U}_d - \vec{\Omega} \times (\vec{\Omega} \times \vec{r}_d) \right\} \quad (1)$$

where  $t$  is the time,  $U_r$  is the relative velocity between the gas and the droplet,  $d_d$  is the droplet diameter, and  $\rho_f$  and  $\rho_d$  are the gas and the droplet density. The second term on the RHS represents

the centrifugal force and Coriolis force, where  $\Omega$  is the rotational speed, and  $r_d$  is the radial position of the droplet. The drag coefficient  $C_D$  is expressed as:

$$C_D = \frac{24}{\text{Re}_d} \left( 1 + 0.15 \text{Re}_d^{0.687} \right) \quad (2)$$

where  $\text{Re}_d$  is the Reynolds number of the droplet based on the diameter and the relative velocity between the gas and the droplet.

The droplet trajectory calculation is conducted to obtain the collection efficiency. The collection efficiency  $\beta$  is followed as:

$$\beta = \frac{A_{in} U_{in} LWC}{\rho_d MVD} \frac{N_{imp}}{N_{in} A_{imp}} \quad (3)$$

where  $A_{in}$  is the droplet inlet area,  $U_{in}$  is the droplet inlet velocity,  $LWC$  is the liquid water content,  $N_{imp}$  is the droplet impingement number,  $N_{in}$  is the droplet inlet number and  $A_{imp}$  is the droplet impingement area. The collection efficiency is one of the key parameters of the icing simulation.

#### *Original Messinger Model*

The Original Messinger model was developed by Messinger in 1953. This model is based on the mass and energy balance in a control volume. The governing equations is followed as:

$$m_{im} + m_{in} = m_{ac} + m_{e,s} + m_{out} \quad (4)$$

$$Q_{im} + Q_{in} + Q_{air} + Q_{fri} = Q_{ac} + Q_{e,s} + Q_{out} + Q_{con} \quad (5)$$

where  $m_{im}$ ,  $m_{in}$ ,  $m_{ac}$ ,  $m_{out}$  and  $m_{e,s}$  are the mass of impingement, runback-in, accretion, evaporating (or sublimating) and runback-out, respectively;  $Q_{im}$ ,  $Q_{in}$ ,  $Q_{air}$ ,  $Q_{fri}$ ,  $Q_{ac}$ ,  $Q_{e,s}$ ,  $Q_{out}$  and  $Q_{con}$  are the energy of impingement, runback-in, air, friction, accretion, evaporating (or sublimating), runback-out and convection. The freezing rate  $f$  can be derived from Eqs. (4) and (5).

$$f = \frac{m_{ac}}{m_{im} + m_{in}} \quad (6)$$

$$m_{out} = (1 - f)(m_{im} + m_{in}) - m_{e,s} \quad (7)$$

if  $f = 1$ , all mass in the control volume accretes, on the other hand, if  $f = 0$ , all mass in the control volume runbacks to the next cell.

#### *Extended Messinger Model*

Original Messinger model has a problem in the predictive performance of the runback mass, because the phase change from rime ice to glaze ice is instant. To get over this problem, Extended Messinger model was developed by Orgen and Canibak in 2009 [7]. This model is based on the Stefan problem, which is a standard method of the phase change problem. The governing equations are expressed as:

$$\frac{\partial T_i}{\partial t} = \frac{k_i}{\rho_i C_{pi}} \frac{\partial^2 T_i}{\partial h^2} \quad (8)$$

$$\frac{\partial T_w}{\partial t} = \frac{k_w}{\rho_w C_{pw}} \frac{\partial^2 T_w}{\partial h^2} \quad (9)$$

$$\rho_i \frac{\partial B_i}{\partial t} + \rho_w \frac{\partial B_w}{\partial t} = m_{im} + m_{in} - m_{e,s} \quad (10)$$

$$\rho_i L_F \frac{\partial B_i}{\partial t} = k_i \frac{\partial T_i}{\partial h} - k_w \frac{\partial T_w}{\partial h} \quad (11)$$

where Eqs. (8) and (9) are the energy equations in the ice and water layer respectively, Eq. (10) is the mass conservation equation and Eq. (11) is the phase change condition at the ice/water interface. In these equations,  $T_i$  and  $T_w$  are the temperatures of ice and water;  $B_i$  and  $B_w$  are the thicknesses of ice and water layers;  $k_i$  and  $k_w$  are the thermal conductivities of ice and water;  $C_{pi}$  and  $C_{pw}$  are the specific heats of ice and water;  $m_{im}$ ,  $m_{in}$  and  $m_{e,s}$  are impinging, runback and evaporating (or sublimating) water mass flow rates for a control volume, respectively;  $\rho_i$  and  $\rho_w$  are the density of ice and water;  $L_F$  denotes the latent heat of solidification of water. Ice density is assumed to have two different values for rime ice  $\rho_r$  and glaze ice  $\rho_g$ . The coordinate  $h$  is normal to the wall or ice surface.

## Two-dimensional validation

### Computational Target and Grid

We adopted a NACA 0012 airfoil in the two-dimensional validation, because a lot of experimental data are available in literatures. In this study, the overset grid method is applied to clarify the icing area around the leading edge, where it is easy to occur icing phenomena. The sub grid resolution is important for icing simulation. We checked relatively grid for the icing simulation by three type sub grids; the coarse grid resolution is 81 × 21, the medium grid resolution is 201 × 51 and the fine grid resolution is 301 × 81. The coarse grid has a margin of error in the icing limit point. Therefore, we adopted the medium grid in this study. The number of grid point in the main grid is 15,691 and that in the sub grid point is 10,251. The computational domain is 20 chord × 20 chord.

### Computational Condition

The computational condition is listed in Table 1. The LWC means the liquid water content, and the MVD is the median volume diameter of droplets. The number of validation cases is six. The number of inlet droplets is 1,000,000. The boundary conditions are followed as; in the inlet boundary, the flow angle, the volume flow rate and the total temperature are fixed and the Mach number is extrapolated; in the outlet boundary, the static pressure is fixed and the others are extrapolated; in the wall boundary, no-slip, adiabatic and wall function conditions are applied. Under the these conditions, we compared Original Messinger model with Extended Messinger model in the two-dimensional validation.

**Table 1. Computational Condition of 2D Validation**

	Chord [m]	Angle of Attack [deg.]	Velocity [m/s]	Static Temperature [°C]	Static Pressure [kPa]	LWC [g/m <sup>3</sup> ]	MVD [μm]	Exposure Time [s]
Run 1	0.530	4.0	58.10	-27.8	95.61	1.30	20.0	480.0
Run 2	0.530	4.0	58.10	-19.8	95.61	1.30	20.0	480.0
Run 3	0.530	4.0	58.10	-13.9	95.61	1.30	20.0	480.0
Run 4	0.530	4.0	58.10	-6.7	95.61	1.30	20.0	480.0
Run 5	0.530	4.0	58.10	-3.9	95.61	1.30	20.0	480.0
Run 6	0.530	4.0	58.10	-2.8	95.61	1.30	20.0	480.0

## Result and Discussion

We validated our icing simulation code by use of the NASA, DRA and ONERA simulation data and the experimental data [8]. These simulations were conducted by Original Messenger model. The ice shapes are seen in Fig. 1; (a)-(c) are under the rime ice condition, (d)-(e) are under the glaze ice condition. In the rime ice condition, the noticeable difference of the predictive performance between Original Messenger model and Extended Messenger model does not appear. This is why the runback phenomenon does not occur in the rime ice condition. On the other hand, there is considerable disagreement in the glaze ice condition. Extended Messenger model gives the results closer to the experimental data than Original Messenger model, because it is sensitive to the runback mass. However, the simulation results of NASA, DRA and ONERA can reproduce the glaze icing even if they use Original Messenger model. The reason why our icing simulation code of Original Messenger model is not modified unlike their icing models. Therefore, Original Messenger model need to be modified when simulate the glaze icing.

## Three-dimensional validation

### Computational Target and Grid

We validated our icing simulation code by use of a jet engine. The icing components of jet engine are the rotor fan, FEGV (fan exit guide vane), nose cone, splitter and low pressure compressor. In this study, we focused on a fan blade and FEGV, because these are more accreted ice area. The jet engine used in this study has twenty-four rotor blades and sixty stator vanes. For simplicity, only one rotor blade and two stator vanes are simulated, assuming the geometrical periodicity. The computational grid based on an overset grid method and a multi block method is exhibited in Fig. 2; (a) is the main

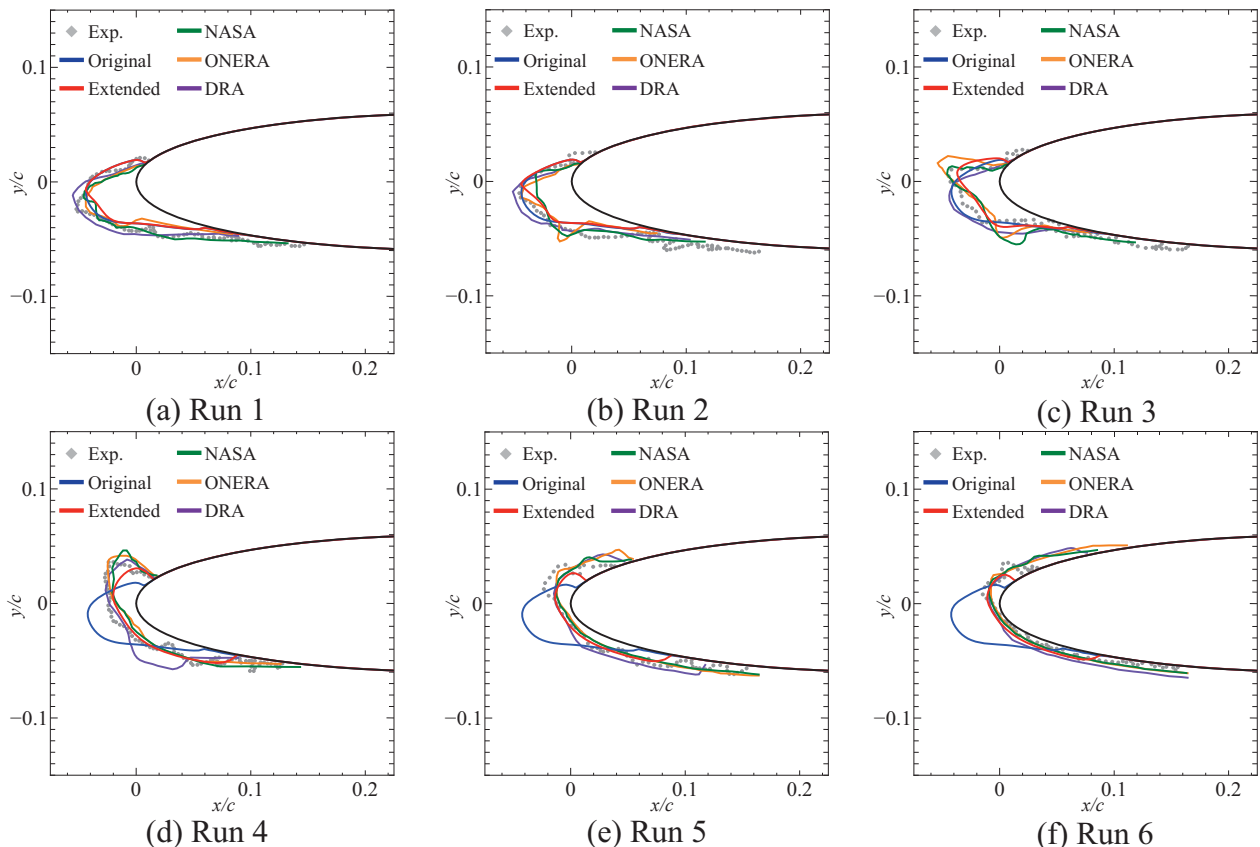


Figure 1. Icing Shape of 2D Validation

grid for the passage, (b) is the sub grid around the blade. The total number of the grid points is about 2.8 million.

### Computational Condition

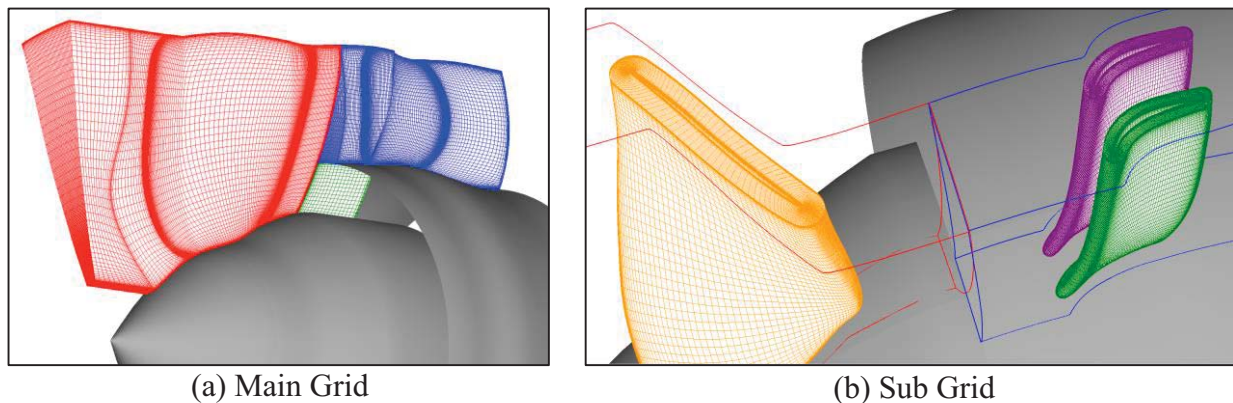
Computational conditions in this study are summarized in Table 2. We set three cases with different total temperature. In all cases, the mass flow rates are same. The droplet trajectory simulations are conducted for 1,000,000 droplets randomly and spatially distributed at the computational upstream boundary. The initial droplet velocity is equal to the local gas velocity. Total pressure, total temperature and flow angle are imposed, and Mach number is extrapolated at the upstream inflow boundary. The inflow turbulent kinetic energy is assumed by the 0.1 % turbulence of the free stream. Adiabatic, no slip and wall function boundary conditions are prescribed on the stationary and rotating surfaces. The exit static pressure is specified.

### Result and Discussion

Fig. 3 shows the static temperature distribution at the rotor midspan, which is a pitch-averaged. Around the leading edge of the rotor suction side, the static temperature is considerably low (about 200 K, Run 1) due to the high Mach number region. Even in the high temperature region such as the rotor wake, the stagnation point and the pressure surface on the FEGV, the temperature is below the freezing point. Therefore, ice accretion can occur if the super-cooled droplet impinges on the blade surface.

Fig. 4 indicates the collection efficiency in Run 3. A lot of droplets impinge on the rotor suction side, particularly, at the hub side. There are no impingement droplets on the rotor suction side. Some droplets impinge on the pressure side of the FEGV. Other simulation cases have a same tendency.

Finally, we show numerical results of the ice accretion. Ice thickness distributions are exhibited in Fig. 5. These figures are for the suction side of the rotor fan, because this is the thickest icing area. In all Extended Messinger model cases, icing area expanded to the tip side due to the centrifugal force.



**Figure 2. Computational Grid of 3D Validation**

**Table 2. Computational Condition of 3D Validation**

	Rotational Speed [rpm]	Mach Number	Total Pressure [MPa]	Total Temperature [K]	LWC [g/m <sup>3</sup> ]	MVD [μm]	Exposure Time [s]
Run 1	4291.0	0.44	0.1013	233.15	1.00	20.0	3.0
Run 2	4291.0	0.44	0.1013	243.15	1.00	20.0	3.0
Run 3	4291.0	0.44	0.1013	253.15	1.00	20.0	3.0

This tendency cannot be confirmed by use of Original Messenger model. This is caused by the predictive performance of the runback water. In the case of Extended Messenger model, the higher inlet temperature becomes, the more the runback mass becomes and the larger the icing area is. The ice volumes of all computational conditions are summarized in Fig. 6. In the low inlet temperature case, the icing models make no difference of the ice volume. However, in the high inlet temperature case, the difference between both icing models can be confirmed on the rotor fan icing. On the other hand, the icing on the FEGV is little distinction, because the runback hardly occur at the FEGV. Therefore, we recommend Extended Messenger model in simulating the ice accretion, because this model can reproduce runback phenomena in glaze ice conditions.

## Conclusion

We validated Original Messenger model and Extended Messenger model. The knowledge obtained in this study is described below:

- (1) In two dimensional validation, the icing model makes no difference on the icing phenomenon in the rime ice condition.
- (2) In two dimensional validation, Extended Messenger model is better agreement with the experimental data due to the higher predictive performance of the runback mass than Original Messenger model.
- (3) In three dimensional validation, there is no difference between Original Messenger model and Extended Messenger model in low inlet temperature case.
- (4) In three dimensional validation, Extended Messenger model can reproduce the span direction wider icing area in the spanwise direction on the rotor fan due to the centrifugal force in high inlet temperature case.

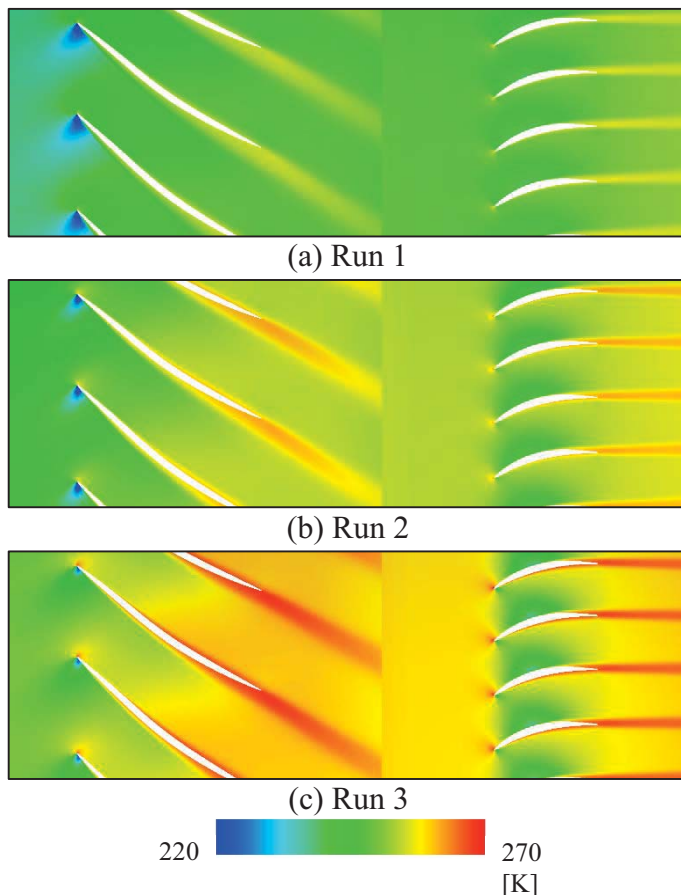


Figure 3. Static Temperature at Rotor Midspan

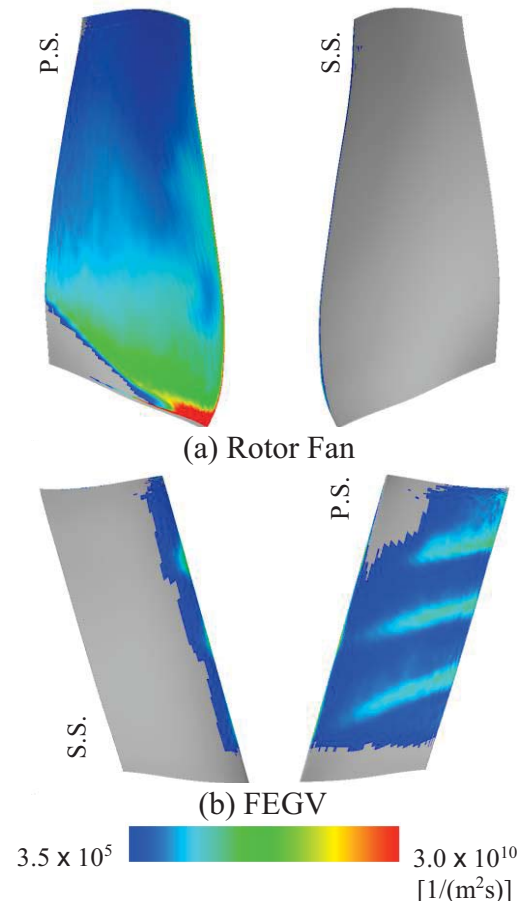
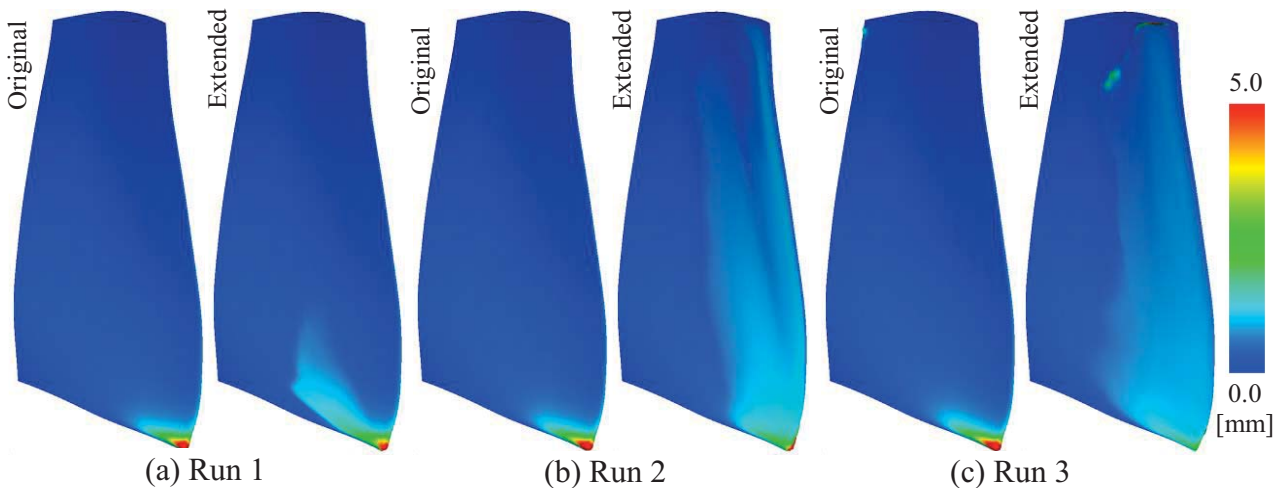


Figure 4. Collection Efficiency

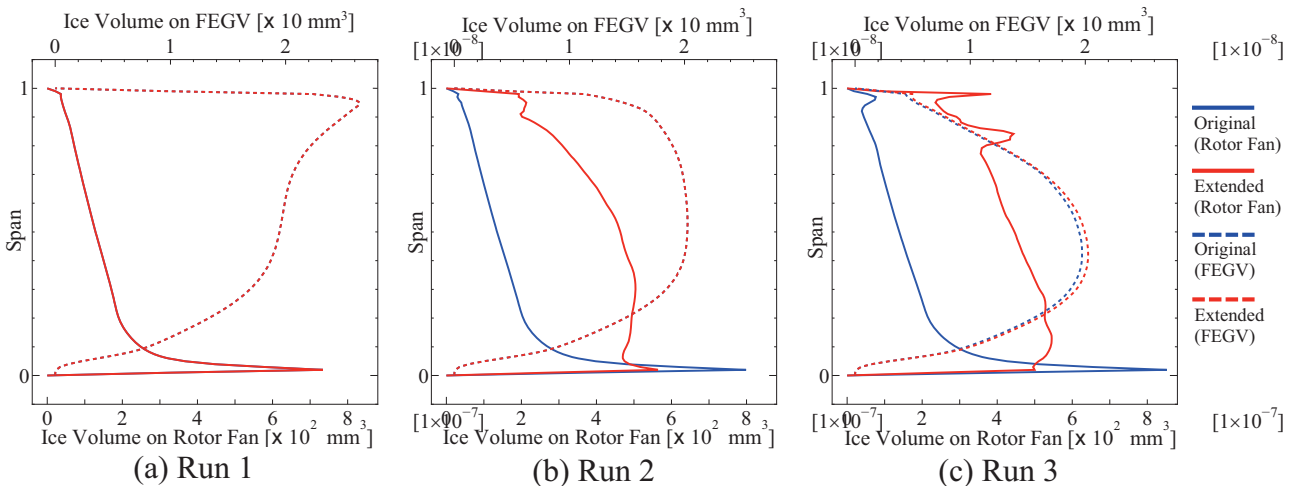
- (5) We recommend Extended Messinger model in simulating the icing phenomenon, because this model is superior to Original Messinger model in terms of the predictive performance of the runback mass.

**References**

[1] Bidwell, C. S. and Potapczuk, M. G., (1993), Users Manual for the NASA Lewice Three-Dimensional Ice Accretion Code (LEWICE3D), *NASA TM 105974*.  
 [2] Hedde, T. and Guffond, D., 1995, ONERA Three-Dimensional Icing Model, *Journal of AIAA*, Vol. 33, No. 6, pp. 1038–1045.  
 [3] Messinger, B. L., (1953), Equilibrium Temperature of an Unheated Icing Surface as a Function of Airspeed, *Journal of the Aeronautical Sciences*, vol. 20, no.1, pp. 29-42.  
 [4] Kato M., Launder B. E., (1993), The modeling of turbulent flow around stationary and vibrating square cylinder, *Proceedings of 8th Symposium on Turbulent Shear Flows*, 10-4-1-10-4-6.  
 [5] Yee H. C., (1987), Upwind and symmetric Shock-Capturing Schemes, *NASA TM 89464*.  
 [6] Fujii K. and Obayashi S., (1987), Practical application of improved LU-ADI scheme for the three-dimensional Navier-Stokes computations of transonic viscous flows, *AIAA Paper*, 86-0513.  
 [7] Ozgen S., Canibek M., (2009), Ice accretion simulation on multi-element airfoils using extended Messinger model, *Heat and Mass Transfer*, Vol. 45, pp. 305-322.  
 [8] William B. Wright, P. W. Gent and Didier Gufford, (1997), DRA/NASA/ONERA Collaboration on Icing Research, *NASA CR 202 34 9*.



**Figure 5. Ice Thickness at Suction Side of Rotor Fan**



**Figure 6. Ice Volume**

## Numerical and Fundamental Study on Ice Growth of Ice Crystal Accretion

\*Koharu Furuta<sup>1</sup> and Makoto Yamamoto<sup>2</sup>

<sup>1</sup>Graduate School of Mechanical Engineering, Tokyo University of Science  
6-3-1 Niijyuku, Katsushika-ku, Tokyo, Japan

<sup>2</sup>Department of Mechanical Engineering, Tokyo University of Science

\*Corresponding author: j4513645@ed.tus.ac.jp

### Abstract

This paper discusses a fundamental study on the ice crystal accretion. Ice accretion is a phenomenon to form ice layer on a body due to impingement of super-cooled water droplets. In recently years, it is known that ice accretion occurs in the engine core such as the low pressure compressor and the first stage of the high pressure compressor, where the temperature is about 30 degree C. The ice accretion in the engine core is called as "ice crystal accretion". It differs from rime and glaze ice accretion because these ice accretions occur under the temperature of the water freezing point. Some scenarios are given as a factor of the ice crystal accretion, but the mechanism has not been sufficiently clarified yet. Moreover, the current icing model is not available in the environment where the temperature is above the freezing point. In this paper, we present a new icing model which is applicable to a warm environment. The new icing model consists of four computations for turbulent flow, droplet/ice trajectory, thermodynamics of icing, and heat conduction within a wall, and is applied to for a flat plate instead of compressor blades as a basic study of the ice crystal accretion. The simulation results by use of the new model indicate that ice accretion occurs in the condition of the temperature even above the freezing point.

**Keywords:** Multi-physics CFD, Engine inner icing, Ice crystal accretion, Super-cooled water droplet

### Introduction

Ice accretion is a phenomenon that super-cooled water droplets in the atmosphere impinge on a body and form ice layer. When it occurs in a jet engine, the shape change of iced blades makes aerodynamic performance worse, and ingestion of shedding ice flakes causes serious mechanical damages to the fan and the compressor components. Since there is the risk to lead to the serious accidents such as crashes by an ice accretion on a jet engine as well as an aircraft, the prediction of ice accretion is necessary. Experimental investigations have been carried out to estimate the ice accretion, but it is too difficult to set actual icing condition. Therefore, computational fluid dynamics (CFD) is useful to predict the ice accretion. Engine components such as splitter, nose cone, fan blades and fan exit guide vane have been considered as icing area in a jet engine. However, it came to be confirmed that icing area expands to the low pressure compressor and the first grade of the high pressure compressor in the engine core [1]. The ice accretion in the engine core is called as ice crystal accretion. It causes the flame out of the engine because ice flakes shed from the compressor components flow into the combustor. There is a hypothesis that ice crystal accretion occurs mainly when the engine ingests ice particles. In addition to ice particles, super-cooled water droplets and mixture of ice particles and super-cooled water droplets have been advanced for ice crystal accretion. These three scenarios are given as a factor of ice crystal accretion, but the mechanism of ice crystal accretion is not clarified. It occurs in the environment where the ambient static temperature is at about 30 degree C, but the current icing model is unavailable in the environment where the temperature is above the freezing point. Therefore, a new



icing model which can be applied to such a warm environment is needed to find out the mechanism of the ice crystal accretion.

In this paper, as a basic study of the ice crystal accretion, we develop a new icing model which is applicable to the environment where the flow static temperature is above the freezing point. We simulate ice crystal accretion phenomena and predict the icing area and the icing mass by computing super-cooled water droplet impingements on an aluminum flat plate which has a high thermal conductivity. It comes out that the wall temperature of the flat plate can fall to the freezing point by interaction of the cooling with the super-cooled water droplets and the heat conduction in the flat plate. In addition, it becomes clear that ice accretion starts and grows where the wall temperature falls to the freezing point.

### Computational Approach

Fig. 1 shows the flow chart of the simulation procedure in this study. First, a flow field around a flat plate is computed. Then, properties of droplet trajectory, such as collision position and mass, are caught by a Lagrangian method. At last, temporal change of the plate temperature and the icing mass are computed by thermodynamic calculation. These computation approaches used in this study are described in detail below.

#### *Flow Field*

It is supposed that flow field is two-dimensional, compressive and turbulent. Favre-averaged mass, momentum and energy conservation equations are used as governing equations. Non-viscous terms and viscous terms in these equations are discretized by Yee-Harten's second-order upwind difference TVD scheme [2] and second-order central-difference scheme, respectively. Then, time integration is computed by LU-ADI method [3], turbulence is estimated by  $k-\varepsilon$  model with Kato-Launder modification [4].

#### *Droplet Trajectory*

Droplet trajectory computation based on a Lagrangian method is conducted to get properties of the droplet impingement on a flat plate. Force acting on droplets is only drag, and the other forces are not taken account. Also, droplet-droplet collision, evaporation, merge and break-up are ignored. It is supposed that droplets are complete sphere and do not make any effect on flow field (One-Way Coupling). The following B-B-O equation, which is simplified, is used as the governing equation:

$$\frac{d\vec{U}_w}{dt} = \frac{3}{4} C_D \frac{\rho_f}{\rho_w} \frac{1}{d_w} \vec{U}_r |\vec{U}_r| \quad (1)$$

where  $U_w$  is droplet velocity,  $U_r$  is relative velocity of gas and droplet,  $d_w$  is droplet diameter,  $\rho_f$  is density of gas, and  $\rho_w$  is density of droplet.  $C_D$  is drag coefficient and calculated from following formula. Then,  $Re_w$  is Reynolds number of a droplet.

$$C_D = \frac{24}{Re_w} \left( 1 + 0.15 Re_w^{0.687} \right) \quad (2)$$

#### *Ice Accretion*

Extended Messinger model [5] based on the Stefan problem is used for the ice accretion calculation. This model is governed by four equations; heat conduction equations in ice and water layers, a mass balance equation in the ice and water, and a phase change condition at the ice/water interface:

$$\frac{\partial T_i}{\partial t} = \frac{k_i}{\rho_i C_{pi}} \frac{\partial^2 T_i}{\partial y_w^2} \quad (3)$$

$$\frac{\partial T_w}{\partial t} = \frac{k_w}{\rho_w C_{pw}} \frac{\partial^2 T_w}{\partial y_w^2} \quad (4)$$

$$\rho_i \frac{\partial B_i}{\partial t} + \rho_w \frac{\partial B_w}{\partial t} = m_{im} + m_{in} - m_{e,s} \quad (5)$$

$$\rho_i L_F \frac{\partial B_i}{\partial t} = k_i \frac{\partial T_i}{\partial y_w} - k_w \frac{\partial T_w}{\partial y_w} \quad (6)$$

where  $T_i$  and  $T_w$  are the temperatures,  $B_i$  and  $B_w$  are the thicknesses,  $k_i$  and  $k_w$  are the thermal conductivities, and  $C_{pi}$  and  $C_{pw}$  are the specific heats of ice and water, respectively. In Eq. (5),  $m_{im}$ ,  $m_{in}$  and  $m_{e,s}$  are impinging, runback and evaporating (or sublimating) water mass flow rates for a control volume, respectively. In Eq. (6),  $\rho_i$  is density of ice,  $L_F$  is latent heat by solidification and  $y_w$  is distance from the wall. In Eqs. (3)-(6) are integrated on time by the fourth phase Runge-Kutta method. Each parameter used in upper equations is shown in Table 1.

### Heat Transfer

In order to estimate the temporal change of temperature within a flat plate, the heat conduction equation is employed:

$$\frac{\partial T_{in}}{\partial t} = a \left( \frac{\partial^2 T_{in}}{\partial x^2} + \frac{\partial^2 T_{in}}{\partial y^2} \right) \quad (7)$$

where  $T_{in}$  is temperature in a flat plate,  $a$  is thermal conductivity of a flat plate,  $x$  and  $y$  are horizontal and vertical coordinate in a flat plate, respectively. The material of plate used in this study is aluminum which has a high thermal conductivity.

## Computational Condition

### Computational Target and Grid

Computational domain in this study is shown in Fig. 2. Computational grid system has a sub grid based on the overset grid method to analyze the flow around the flat plate as indicated in Fig.3. The total number of the grid points is about 10,000.

### Computational Condition

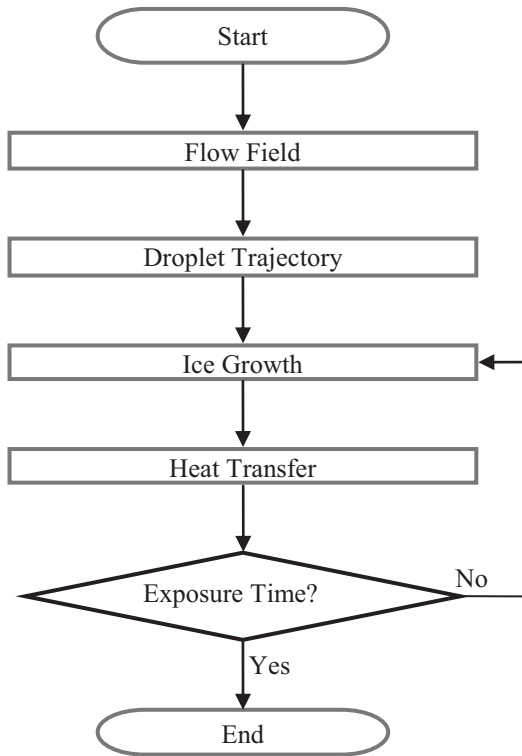
Computational conditions used in the ice accretion calculation are exhibited in Table 2. 100,000 droplets whose median volume diameter is 20 $\mu$ m are put in the inlet flow. Then, collision mass on the wall is computed and the ice accretion calculation for 15 sec. is performed.

In the inlet boundary, the total temperature and the total pressure are fixed and the Mach number is extrapolated. In the outlet boundary, the static pressure is fixed, other variables are extrapolated. The top and the bottom boundaries are periodic. The wall of the flat plate is under no-slip, wall function and adiabatic conditions. The inflow turbulent kinetic energy is assumed by the 0.1 % turbulence of the free stream. The temperature boundary condition at the wall in heat transfer calculation is adopted by Newton's law of cooling.

**Result and Consideration**

*Flow Field*

Static temperature and stream line are seen in Fig. 4 (a) and (b), respectively. The static temperature increases to about 309 K, around the stagnation point. Since ice accretion occurs on the windward wall of the plate, it is apparent that the plate wake does not have any remarkable influence on the icing phenomena.



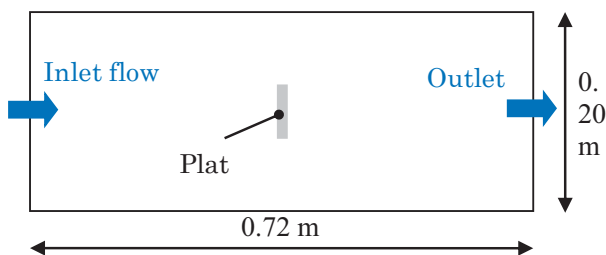
**Figure 1. Algorithm of Icing Simulation**

**Table 1. Parameter of Icing Model**

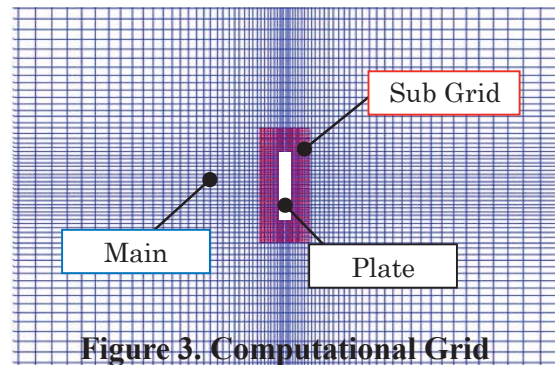
Specific Heat of Ice $C_{pi}$	2,050 J/kg K
Specific Heat of Water $C_{pw}$	4,218 J/kg K
Thermal Conductivity of Ice $k_i$	2.18 W/m K
Thermal Conductivity of Water $k_w$	0.571 W/m K
Latent Heat of Solidification $L_F$	$3.344 \times 10^5$ J/kg
Density of Glaze Ice $\rho_i$	917.0 kg/m
Density of Water $\rho_w$	1,000 kg/m
Heat Conductivity $a$	$9.73 \times 10^{-5}$ m <sup>2</sup> /s

**Table 2. Computational Conditions**

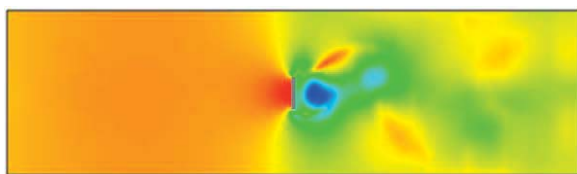
Inlet Mach Number	0.3
Inlet Total Pressure	0.1149 MPa
Inlet total Temperature	308.60 K
LWC (Liquid Water Content)	1.0 g/m <sup>3</sup>
Inlet Droplet Temperature	-20.0 °C
MVD (Median Volume Diameter)	20.0 μm
Plate Size	5.0 mm×40.0 mm
Exposure Time	15.0 sec.



**Figure 2. Computational Domain and Size**

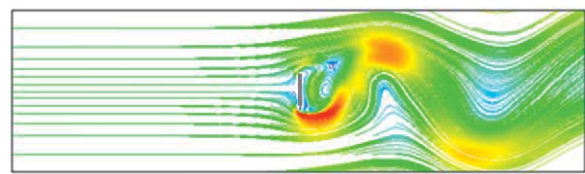


**Figure 3. Computational Grid**



294 309 [K]

(a) Static Temperature



0 157 [m/s]

(b) Stream Line

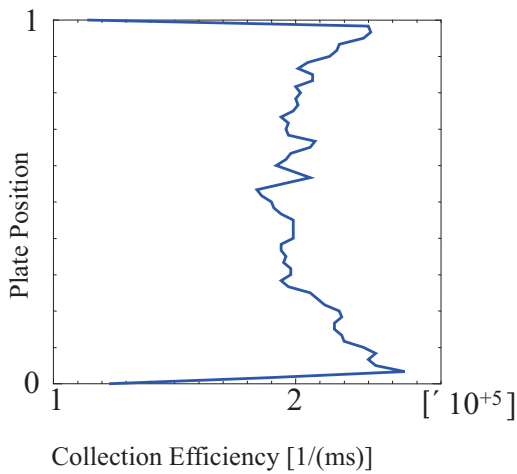
**Figure 4. Flow Field**

*Collection Efficiency*

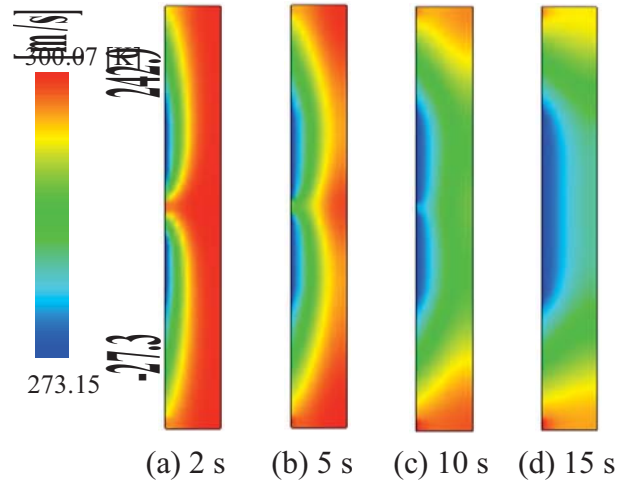
Collection efficiency on the plate is shown in Fig. 5. The collection efficiency is smaller at the stagnation point, because droplets tend to follow the flow streamline. Since droplets flow along the free stream, many droplets are collected near the edge of the plate.

*Mechanism of Ice Crystal Accretion*

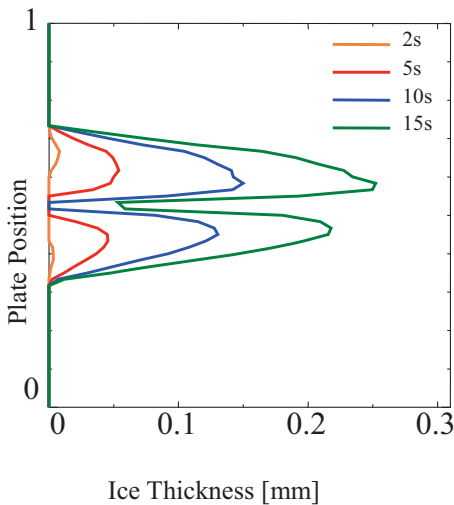
Temporal changes of the plate temperature are presented in Fig. 6. At first, temperature at the stagnation point of the wall is higher than the other area on the collision wall, but it is stable near 0 degree C as time passes. Then, temporal change of the ice thickness is exhibited in Fig. 7. The vertical axis in this figure represents the plate position, which is non-dimensionalized by the plate length. As Figs. 6 and 7, it is clear that ice accretion starts and grows around the region where the wall temperature fell to the freezing point. Ice accretion is related to not only collection efficiency but also wall temperature. With an existing icing model, ice accretion does not occur where the ambient fluid temperature is higher than the freezing point. Instead, with the new icing model developed in this study, ice accretion is observed around the region where the wall temperature falls to the freezing point due to heat transfer. Therefore, it is clear that the heat transfer computation in the plate and ice accretion calculation work each other.



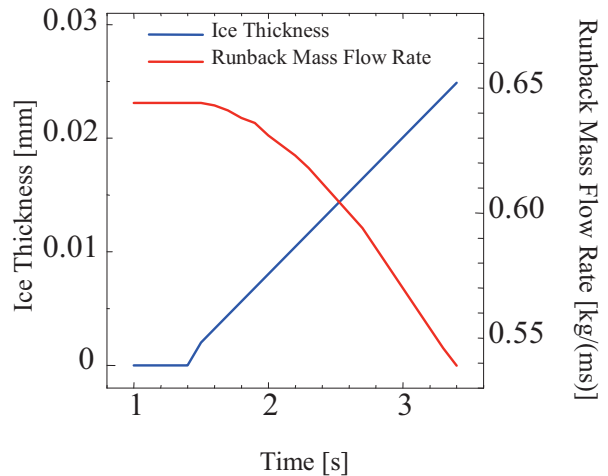
**Figure 5. Droplet Collection Property**



**Figure 6. Temporal Change of Plate Temperature**



**Figure 7. Temporal Evolution of Ice Thickness**



**Figure 8. Ice Thickness and Runback Mass Flow Rate**

Ice thickness and runback mass flow rate where ice accretion occurs for the first time are shown in Fig. 8. The collision wall certainly has water film, because the ambient static temperature is above the freezing point. Then, water film flows to the edge of the plate along the plate surface. When water film does not change to ice, the runback mass flow rate is constant even if time passes. However, from Fig.8, the runback mass flow rate decreases as ice thickness increases. Therefore, the runback mass changes into ice mass. In fact, ice accretes near the stagnation point rather than the icing area, because a part of water film which streams from the center of the plate changes to ice. Therefore, position of the maximum ice thickness approaches toward the stagnation point.

*Influence of Droplet Temperature*

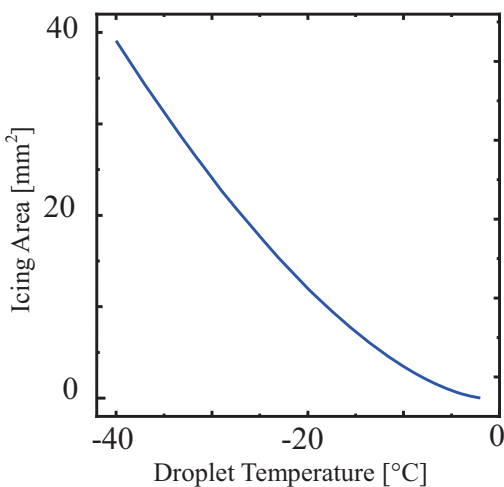
Icing area and time history of the plate temperature are shown in Figs. 9 and 10, respectively. The droplet temperature is changed from -40 to -2 degree C, every 1 degree C, exposure time is 60 sec. and the other computational conditions are not changed. As indicated in Fig. 9, the icing area increases as droplet temperature is lower. Also, the area of the temperature 0 degree C on the wall expands while droplet temperature is lower as seen in Fig. 10. The icing area increases when droplet temperature is lower, but the plate temperature is stable near the freezing point and no longer decreases. This is why most of energy droplets have is used for the ice growth.

**Conclusion**

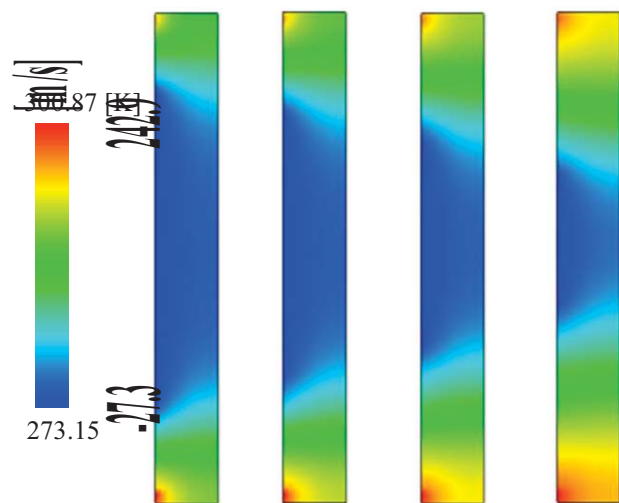
The research on the mechanism of ice crystal accretion is numerically performed. Insights obtained in this study are below.

- (1) Ice accretion occurs in the environment where the ambient static temperature is at 30 degree C when the wall temperature falls to the freezing point.
- (2) Ice grows where ice has accreted once, and the runback phenomenon becomes hard to occur in this area.
- (3) Icing wall temperature is stable near the freezing point and no more decreases.
- (4) The droplet temperature has an influence on the ice crystal accretion.

The future prospects include that the material and shape of the computational target should be changed from the aluminum flat plate to an actual compressor blade. In addition, the ingestion of not only super-cooled water droplets but also ice particles is taken into account. And a temporal change of the super-cooled droplet temperature will be computed in a jet engine core.



**Figure 9. Influence of Droplet Temperature**



**Figure 10. Influence of Droplet Temperature on Plate Temperature**  
 (a) -40 °C (b) -30 °C (c) -20 °C (d) -10 °C

**References**

- [1] Jeanne G. Mason, J. Walter Strapp, Philip Chow, (2006), "The Ice Particle Threat to Engines in Flight," 44<sup>th</sup> AIAA Aerospace Sciences Meeting and Exhibit, *AIAA* 2006-206.
- [2] Yee H. C., (1987), Upwind and symmetric Shock-Capturing Schemes, *NASA TM* 89464.
- [3] Fujii K. and Obayashi S., (1987), Practical application of improved LU-ADI scheme for the three-dimensional Navier-Stokes computations of transonic viscous flows, *AIAA Paper*, 86-0513.
- [4] Kato M., Launder B. E., (1993), The modeling of turbulent flow around stationary and vibrating square cylinder, *Proceedings of 8th Symposium on Turbulent Shear Flows*, 10-4-1-10-4-6.
- [5] Ozgen S., Canibek M., (2009), Ice accretion simulation on multi-element airfoils using extended Messinger model, *Heat and Mass Transfer*, Vol. 45, pp. 305-322.

# A rescaling method for generating inflow conditions in simulations of supersonic boundary layers

\*Ning Hu<sup>1</sup> and Han-Dong Ma<sup>1</sup>

<sup>1</sup>China Academy of Aerospace Aerodynamics, 100074 Mailbox 7201-56, Beijing, China.

\*Corresponding author: h\_ning@pku.org.cn

## Abstract

A method for generating turbulent inflow data for simulations of spatially developing boundary layers has been presented. The approach is based on solving for the turbulent mean velocity/temperature profile at the inlet station and mapping the fluctuations from a reference station to the inlet. The mean velocity profile is solved from the Favre-averaged mean momentum equation with the Reynolds stress calculated from a turbulent model proposed by Zhang *et al.* (2012). The mean temperature profile is obtained by applying a generalized Walz's law. LES of adiabatic zero pressure gradient flat plate boundary layer flows at Mach = 2.25 is carried out using fully spatial method with transition region from laminar to turbulent, and also using the inflow condition proposed herein. The boundary layer development and turbulent statistics obtained with the proposed method agree well with the fully spatial approach, with negligible transient section length.

**Keywords:** boundary layer, supersonic, turbulence, inflow condition

## Introduction

The simulation of turbulent boundary layers requires quite detailed inflow information since the resolved flow is unsteady and three-dimensional. Rather than simulating laminar and transitional regions arising near a leading edge, it is often more computationally efficient to formulate a fully turbulent inflow condition. To date, three types of methods for creating appropriate inflow conditions have been suggested: the random fluctuation method (Rai and Moin, 1993), the matching database method (Schlüter *et al.* 2003), and the recycling and rescaling method (Spalart, 1988; Lund *et al.*, 1998). Among those methods, the recycling method appears to establish a turbulent shear flow with a fairly short inlet buffer zone and provides accurate downstream profiles.

If the rescaling starts by using downstream data that are far from a correct turbulent state, the skin friction may decrease with time and make the achievement of the desired inflow turbulent state very difficult. To overcome the problem arising from unsuitable initial conditions, Lund *et al.* (1998) suggested making a correction to the resolved velocities during the early part of simulation. Spille-Kohoff and Kaltenbach (2001) suggested adding a source term to the resolved equation based on the desired Reynolds stress. The present paper proposes a new method for recycling and rescaling. In the present method, the position for mapping the reference turbulent field is determined from the value of the order function, instead of using the similarity laws. Without assumption of simple geometrical similarity, the method is easy to be extended to more general flows, with external effects such as pressure gradient or geometrical change, etc.

## Rescaling methods

### *Rescaling order function*

The rescaling method is based on the similarity of turbulent boundary layers. The turbulent field at a downstream position can be used as the inlet condition since they have similar turbulent fluctuation ensembles. Usually the rescaling is categorized into the inner scaling

$$U / u_{\tau} = y^{+} \quad (1)$$

and the outer scaling:

$$(U_\infty - U) / u_\tau = f_{\text{wake}}(\eta), \quad \eta = y / \theta \quad (2)$$

In the presence of pressure gradient, wall heating/cooling or other external forces, the two-layer description no longer holds, and it is difficult to find the correct corresponding position having the similar statistical properties. In this case more universal arguments are needed. According to the SED theory, the statistical properties of a turbulent ensemble can be described by the value of order functions. With a choice of proper order function, the corresponding vertical coordinates between the downstream reference position and the inlet position can still be found. Particularly, in the compressible turbulent boundary layers an order function, which is called Mach-invariant mixing length, can be defined (Zhang *et al.*, 2012):

$$\ell_{M,MI}^+ = \sqrt{\bar{\rho}^+} \mu^+ \ell_m^+ = \sqrt{\bar{\rho}^+} \mu^+ \frac{(-\overline{u''v''})^{1/2}}{\partial \tilde{u}^+ / \partial y^+} \quad (3)$$

This function has the length dimension, and describes the turbulent intensity of a vertical position. It is directly defined from Prandtl's mixing length theory but with a profile invariant with Mach number. This Mach-invariance is an important basis for van Driest transformation. According to the SED theory, an order function has multi-layer structure with scaling laws between each two layers, and can be formulated by the multiple of so-called SED base functions:

$$\left(1 + \left(\frac{y^+}{\delta}\right)^p\right)^{n/p} \quad (4)$$

For  $\ell_{M,MI}^+$ , Zhang *et al.* (2012) give the functional form as

$$\ell_{M,MI}^+ = 50 \left(1 - \left(1 - \left(\frac{y}{\delta_{vw}}\right)^5\right)\right) \left(1 + \left(\frac{y^+}{y_1}\right)^{-4}\right)^{-0.5/4} \left(1 + \left(\frac{y^+}{y_2}\right)^{-4}\right)^{1/4} \quad (5)$$

where  $\delta_{vw}$  is a boundary layer thickness defined as the vertical position where  $\langle v'^2 \rangle = \langle w'^2 \rangle$ ,  $y_1 = 12$  and  $y_2 = 85$  are the thicknesses of the sublayer and buffer layer, respectively. Zhang *et al.* (2012) point out that this definition of BL thickness best eliminates out the Mach number dependence.

### Velocity rescaling

Denote by subscript *in* the inflow condition and *ref* the condition at the reference *x*- position, the rescaling should guarantee same mean streamwise velocity at *y*- position with the same  $\ell_{MI}^+$ :

$$\frac{U_{in}}{U_{\tau,in}} (\ell_{MI,in}^+) U_{\tau,in}^\alpha = \frac{U_{ref}}{U_{\tau,ref}} (\ell_{MI,ref}^+) U_{\tau,ref}^\alpha \quad (6)$$

where  $\ell_{MI,ref}^+$  is calculated from statistics through the spanwise direction, and  $\ell_{MI,in}^+$  is given by the theoretical profile (5). The above formulation calls for a knowledge to the wall friction velocity and boundary layer thickness  $\delta_{vw}$  at the inlet position. When a RANS simulation is used as the inlet boundary, the wall friction velocity is easy to obtain. Here for convenience we just use the empirical law of White *et al.* (1974) instead. Further, since there is no turbulent fluctuation information from the upstream of inlet position, we simply take

$$\delta_{vw} \approx \delta_{99} \quad (7)$$

which is reasonably accurate according to DNS data.



### Temperature rescaling

When the mean velocity is properly rescaled, relationship between velocity and temperature rescaling can be used to rescale the temperature. For the mean temperature in a zero-pressure-gradient boundary layer, this relationship can be given by the Walz's equation:

$$\frac{T}{T_e} = \frac{T_w}{T_e} + \frac{T_r - T_w}{T_e} \left( \frac{U}{U_e} \right) - r \frac{\gamma - 1}{2} M_e^2 \left( \frac{U}{U_e} \right)^2 \quad (8)$$

where  $T_r$  is the recovery temperature, subscript e indicates a freestream quantity,  $M_e$  is the freestream Mach number,  $\gamma$  is the ratio of specific heats, and  $r$  is the recovery factor. To determine the wall temperature  $T_w$  we assume that the ratio between  $T_w$  and  $T_e$  varies with  $x$  in a linear way, which is well supported by the DNS data. Hence, the temperature ratio  $T_w/T_e$  can be obtained through the following relation:

$$\frac{T_{w,in}}{T_e x_{in}} - \left( \frac{T_w}{T_e} \right)_{\text{laminar}} = \frac{T_{w,ref}}{T_e x_{ref}} - \left( \frac{T_w}{T_e} \right)_{\text{laminar}} \quad (9)$$

This relationship decouples the mean streamwise velocity and the mean temperature. When fluctuations are small, to a first-order approximation, the mean temperature  $T$  and the mean density  $\bar{\rho}$  are related by the state equation  $T = p/R\bar{\rho}$  for perfect gas, where  $R$  is the gas constant. Thus, the rescaling of  $\bar{\rho}$  follows that of the mean temperature  $T$  is known.

### Implementation

The calculation of the mixing length profile requires mean quantities, wherefore a time average is needed to exclude the starting transient if the flow is initialized with a crude guess. In that case, the following formula is used:

$$U^{(m+1)} = w_1 U^{(m)} + w_2 \langle U^{(m+1)} \rangle_z \quad (10)$$

where  $U^{(m+1)}$  and  $U^{(m)}$  are the time-averaged mean at time step  $m + 1$  and  $m$ , respectively,  $\langle u^{(m+1)} \rangle_z$  is the average of  $u$  in the spanwise direction at time step  $m+1$ ,  $w_1$  and  $w_2$  are two weights satisfying  $w_1 > 0$ ,  $w_2 > 0$ ,  $w_1 \gg w_2$ , and  $w_1 + w_2 = 1$ . Lund *et al.* (1998) let  $w_1$  be  $1 - (\Delta t/\tau)$  and  $w_2$  be  $\Delta t/\tau$ , where  $\Delta t$  is the computational time step and  $\tau$  the characteristic time scale of the averaging interval. From formula (10), we know

$$U^{(m+1)} = w_1^{m+1} U^{(0)} + w_2 (w_1^m \langle u^{(1)} \rangle_z + w_1^{m-1} \langle u^{(2)} \rangle_z + \dots + \langle u^{(m+1)} \rangle_z). \quad (11)$$

At the beginning of the simulation, because  $m$  is small and  $w_1 \gg w_2$ ,  $U^{(0)}$  takes a very large fraction of  $U^{(m+1)}$ , as seen from Eq. (11). Thus, we provide a smooth mean profile from TDNS as  $U^{(0)}$  instead of using  $\langle u^{(0)} \rangle_z$ . We choose  $w_1$  so that when the mean information has propagated from the inlet to the recycling station,  $m$  is large enough for  $U^{(0)}$  to take almost no effect in  $U^{(m+1)}$ . After the transient, we increase  $w_1$  to run for  $N$  steps in order to stabilize the statistics and then switch to a usual running average, i.e.,  $w_1 = 1 - [1/(N + m - m_0)]$  and  $w_2 = 1 / (N + m - m_0)$ , where  $m_0$  is the step at which the running average begins. If  $U^{(0)}$  is very crude and  $w_1$  is not well attuned, the temporal starting transient can be very long before the right spatial behavior builds up over the boundary layer. If  $w_1$  is too small, a good mean profile  $U^{(m+1)}$  cannot be achieved due to insufficiency of effective samples for averaging, which leads to wrong scaling and thus wrong boundary layer mean behavior. A linear interpolation is used to evaluate the right-hand side of Eq. (6) at the mapped coordinates.

## Results and discussion

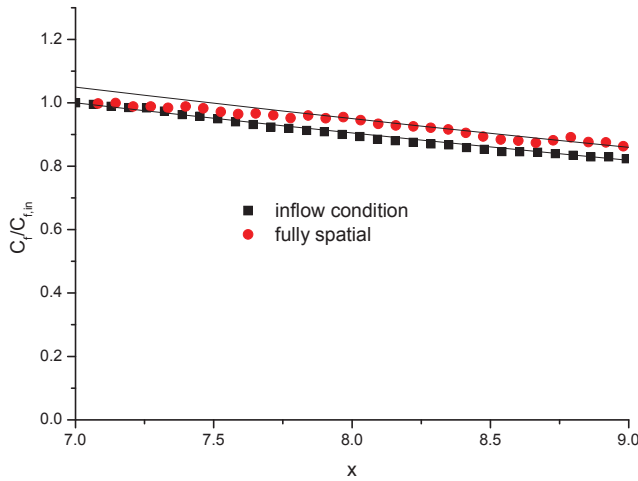
In order to evaluate this inflow method, a turbulent boundary layer with the conditions same with the DNS of Rai *et al.* (1995) is calculated. The freestream Mach number is 2.25. The Reynolds number based on freestream conditions is  $6.35 \times 10^5/\text{in}$ . The adiabatic wall temperature is  $580^\circ\text{R}$ , and the temperature at the freestream is  $305^\circ\text{R}$ .

Both fully spatial simulation and simulation using the proposed inflow condition are carried out. The size of the computational domain for both cases is 0.175 in spanwise, and 3 in wall-normal direction. For the fully spatial case, the computational domain consists of a transitional zone, a focus zone and a buffer zone. The transitional zone covers  $4 < x < 7$  in the streamwise direction, where  $x$  is the distance from the imagined flat plate leading edge. In this region the flow transitions from laminar inflow to turbulence, with blow/suction disturbance at the wall applied within  $4.5 < x < 5$ . The flow is considered as fully developed turbulence within the focus zone  $7 < x < 9$  where statistics are taken, and is followed by a buffer zone  $9 < x < 23$ . For the case with proposed inflow condition, there is no transitional zone, i.e., the computational domain begins at  $x = 7$ , and the other zones are the same with the fully spatial case. The reference plane is selected as  $x = 9$ , where the flow field is rescaled to form the inflow condition at  $x = 7$ .

**Table 1. Parameters of the numerical simulations.**

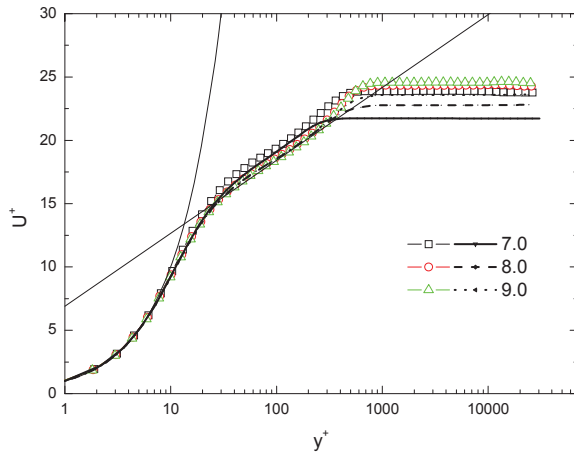
Case	$M_\infty$	$Lx \times Ly \times Lz$	$Nx \times Ny \times Nz$	$\Delta x^+ \times \Delta y^+ \times \Delta z^+$
A	2.25	$(3+2+14) \times 3 \times 0.175\text{in}$	$(586+1264+70) \times 55 \times 256$	<b><math>14.50 \times 1.05 \times 6.56</math></b>
B		$(2+14) \times 3 \times 0.175\text{in}$	$(1264+70) \times 55 \times 256$	<b><math>14.50 \times 1.05 \times 6.56</math></b>

The streamwise grid spacing  $\Delta x$  in the transition zone is no larger than  $6.9 \times 10^{-3}$  and gradually refined to smoothly link the focus zone, where  $\Delta x = 1.58 \times 10^{-3}$ . The buffer zone includes 70 grid points and is progressively coarsened in the streamwise direction. In the wall-normal direction the grid extends up to  $L_y = 3.0$ , with a minimum spacing  $\Delta y_w = 1.056 \times 10^{-4}$ . The grid is equally spaced in the spanwise direction, and the width of the domain is  $L_z = 0.175$ . In wall units (based on the boundary layer properties taken at  $x = 8.8$ ) the mesh spacings in the well-resolved region in the streamwise, wall normal, and spanwise directions are  $\Delta x^+ = 14.50$ ,  $\Delta y_w^+ = 1.05$ , and  $\Delta z^+ = 6.56$ , respectively.



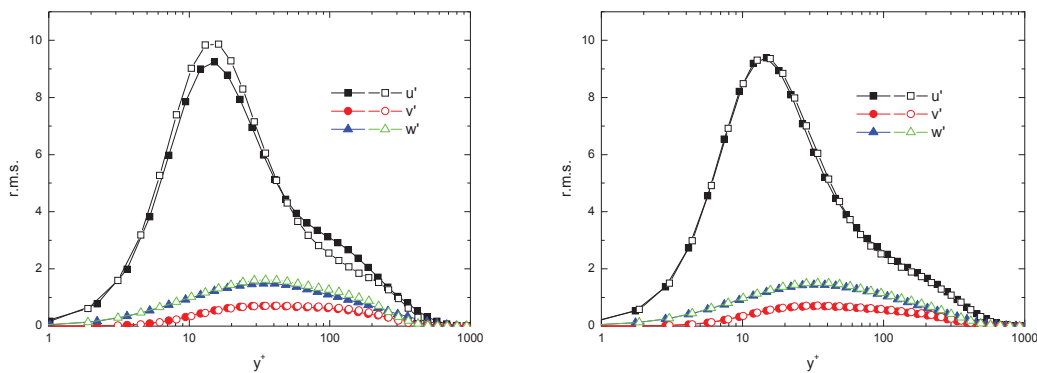
**Figure 3: spatial evolution of the friction coefficient  $C_f / C_{f,in}$**

The rescaling method results in a spatial boundary layer. Figure 3 shows the spatial evolution of the friction coefficient  $C_f$ . The rescaling method builds up the spatial boundary layer from the initial periodic flow field after the temporal transient is passed. The skin friction  $C_f$  is compared with the result of fully spatial DNS. The development of  $C_f$  deviates slightly from the fully spatial DNS. However, the variation of  $C_f$  seems to be faster after  $x = 8.0$  than before  $x = 8.0$  for the fully spatial



**Figure 5: van Driest transformed mean streamwise velocity profiles at three stations: lines: DNS with the proposed inflow condition; symbols: fully spatial DNS.**

Figure 5 shows the van Driest transformed mean streamwise velocity profiles at three stations. The wall-normal coordinate is also nondimensionalized using wall units. The profiles collapse very well using the transformation and scaling in the logarithmic region and they satisfy the theoretical logarithmic law. Near the inlet boundary, the mean streamwise velocity profiles from both inflow condition and fully spatial DNS deviate slightly from the log-law. However, the deviation of the result from the inflow condition is smaller.



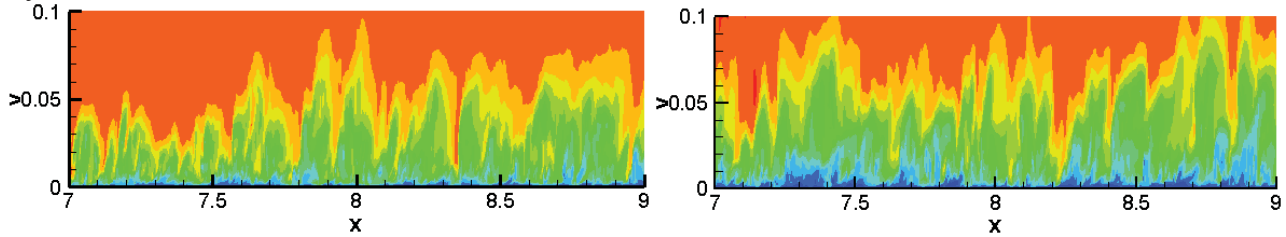
**Figure 6: profiles of turbulent intensities compared with DNS. Left: fully spatial; right: proposed inlet condition.**

Figure 6 shows the profiles of turbulent intensities at the inlet boundary and at a station within the fully developed region,  $x = 8.3$ . The profiles in the fully developed region agree well, but at the inlet boundary the two approaches differ. The profiles obtained with the inflow condition, especially the  $u'$  profile, are more similar to the fully developed ones.

The highly intermittent boundary layer edge with turbulent bursting events can be appreciated from density distributions in a longitudinal cross-section, Fig. 7. For the inflow condition case and  $x > 8$  of the fully spatial case, the virtual boundary thickness does not change much. The structures of the inflow condition case throughout the simulation region have similar shapes. We can say that the

DNS, although they are using the same fine grid. This implies that there may be an “early phase” of the turbulent state in the fully spatial DNS where the transition process still has an effect on the flow. After  $x = 8.0$   $C_f$  decays exponentially with the coefficient  $-0.1$ . For the simulation using the proposed inflow condition, the exponential decay is valid throughout the whole focus region. Therefore we may consider the development after  $x = 8.0$  in the fully spatial DNS as fully developed, and the proposed method yields fully developed result for the whole field.

proposed method provides good inflow condition for spatial simulation of the turbulent boundary layer.



**Figure 7: density distributions in a longitudinal cross-section. Left: fully spatial; right: proposed inlet condition.**

## Conclusions

A method for generating turbulent inflow data for simulations of spatially developing boundary layers has been presented. The approach is based on mapping the time-dependent velocity data from a reference station to the position with the same value of an order function at the inflow station. The selected order function,  $\ell_{M,MI}^+$ , is Mach number dependent as proposed by Zhang *et al.* (2012). This function has a multi-layer structure with scaling behaviors which describes the structure ensemble properties in each layer. Therefore the position for mapping the reference turbulent field is determined from the value of the order function, instead of using the similarity laws. Direct numerical simulations of a supersonic adiabatic zero pressure gradient flat plate boundary layer flow at Mach = 2.25 are carried out using fully spatial method with transition region from laminar to turbulent, and also using the inflow condition proposed in this paper. The boundary layer development and turbulent statistics obtained with the proposed method agree well with the results of the fully spatial approach, with negligible transient section length. Without assumption of simple geometrical similarity, the method is easy to be extended to more general flows. When subjected to external effects such as pressure gradient or geometrical change, the lengths of scaling regions and the scaling exponents will change, but the turbulent structural ensembles are still characterized by the same order function.

## References

- Lund T. S., Wu X. and Squires K. D. (1998), Generation of turbulent inflow data for spatially-developing boundary layer simulation. *J. Comput. Phys.* 140, pp. 233.
- Rai, M. M. and Moin P. (1993), Direct numerical simulation of transition and turbulence in a spatially evolving turbulence. *J. Comput. Phys.* 109, pp. 169.
- Rai M. M., Gatski T. B. and Erlebacher G. (1995) Direct numerical simulation of spatially evolving compressible turbulent boundary layers. *AIAA Paper* 95-0583,.
- Schlüter, J. U., Pitsch H. and Moin P. (2003), On boundary conditions for LES in coupled simulations. *AIAA Paper* 2003-0069,.
- Spalart P. R. (1988), Direct numerical simulation of turbulent boundary layer up to  $Re_\theta = 1410$ . *J. Fluid Mech.* 187, pp. 61.
- Spille-Kohoff A. and Kaltenbach H. -J. (2001), Generation of turbulent inflow data with a prescribed shear-stress profile, in: 3rd AFOSR Conference, Arlington, TX, pp. 319.
- White F. M. (1974), *Viscous Fluid Flow*. McGraw-Hill Book Company.
- Zhang, Y.S., Bi, W.T., Hussain, F., Li, X. L., She, Z. S. (2012), A Mach number invariant mean velocity profile of compressible turbulent boundary layers. *Phys. Rev. Lett.* 109, pp. 054502

## Analysis of Acoustic-Fields generated by Supersonic Jet Impinging on an Inclined Flat Plate and a Curved Plate

\*Yuki Nagata<sup>1</sup>, Taku Nonomura<sup>2</sup>, Kozo Fujii<sup>3</sup>, Makoto Yamamoto<sup>4</sup>

<sup>1</sup> Graduate School of Engineering, Tokyo University of Science, Japan

<sup>2</sup> Assistant professor, Japan Aerospace Exploration Agency, Japan

<sup>3</sup> Professor, Japan Aerospace Exploration Agency, Japan

<sup>4</sup> Professor, Tokyo University of Science, Japan

\*Corresponding author: j4513639@ed.tus.ac.jp

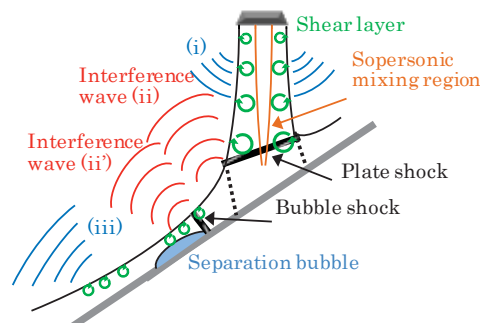
### Abstract

Flow and acoustic-fields of a supersonic jets impinging on an inclined flat plate and an inclined arc plate are computationally analyzed toward the prediction of the rocket plume acoustic waves. Effects to acoustic-field by changing plate angle and curvature of arc plate are investigated. A weighted compact nonlinear scheme is employed to solve 3-dimensional compressible Navier-Stokes equations. The results show that two acoustic waves generated near the jet impinging point affect the magnitude of sound pressure level near the fairing of the rocket and over-all sound pressure level becomes larger when curvature of arc plate increases.

**Keywords:** Mach wave, Interference wave, Shock wave, Separation bubble

### Introduction

When launching a rocket, strong acoustic waves are generated from a jet plume impinging on the rocket launch site and they have bad influence on the satellite in the rocket. The report NASA-SP8072<sup>1</sup>, proposed by NASA in 1971, is used for predicting acoustic waves over the world. However, it is based on the empirical model and its accuracy is not good enough for especially a new rocket launch site. It is necessary to understand the generation mechanism of acoustic waves for further improvements of the prediction model. Recently, analysis of acoustic waves of a rocket plume by using CFD has been conducted energetically at JEDI/JAXA, but it is limited to the practical one that simulates a real launch site for the support of the project in JAXA. Thus, fundamental knowledge has not been obtained. On the other hand, Nonomura et al<sup>2</sup>. and, Honda et al<sup>3</sup>. performed analyses of acoustic waves from a supersonic jet impinging on inclined flat plate. As a result, they classified variety of acoustic wave and obtained knowledge of a sound source for each acoustic wave. Main acoustic waves which have strong directivity are Mach waves generated from



**Figure 1. Schematic of jet flow and acoustic wave**

shear layers of supersonic region (Figure.1 (i),(iii)) and an interference wave generated by interference of turbulence and a shock wave generated at the region where the supersonic jet impinges on the wall or flow separates from the wall (Figure.1 (ii),(ii')). However, influence on the rocket by these acoustic waves have not been discussed. The purpose of this paper is, therefore, to understand the flow and acoustic fields for the prediction of acoustic waves. Moreover, we analyze

the influences of flat plate angle and plate curvature on flow and acoustic fields by conducting the computations with different value of those parameters.

### Program settings

In the present study, air (specific heat ratio  $\gamma$  of 1.4) is used as fluid and an ideally-expanded jet is assumed. Thus, flowing three conditions; the ideally expanded Mach number  $M_j$ , the Reynolds number  $Re$ , and the temperature ratio  $TR_c$ . These parameters are related to the jet chamber condition and the ambient conditions by the assumption of isentropic expansion for the chamber to the nozzle exit.

$$M_j = \frac{u_j}{a_j} = \sqrt{\frac{2}{\gamma-1} \left\{ \left( \frac{p_c}{p_\infty} \right)^{\frac{\gamma-1}{\gamma}} - 1 \right\}} \quad (1)$$

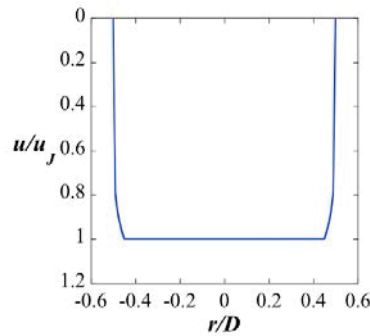
$$Re = \frac{\rho_j u_j D}{\mu_\infty} \quad (2)$$

$$TR_c = \frac{T_c}{T_\infty} \quad (3)$$

where  $u$ ,  $a$ ,  $p$ ,  $\rho$  and  $T$  denote the  $x$ -direction velocity, the speed of sound, the pressure, the density, and the temperature, respectively. Subscriptions  $J$ ,  $c$ , and  $\infty$  denote the nozzle exit condition (which is equivalent to the ideally expanded condition in this study), the chamber condition, and the ambient condition, respectively.  $M_j$  and  $Re$  are set to 2.0 and 100.000, respectively. Both Mach and Reynolds numbers are set to be lower values than those of rocket plumes, but high enough for the qualitative discussion for acoustic waves from rocket plumes.<sup>4</sup>

Figure.2 shows the jet profile used in this study. This profile consists of two parts, a center flat part and a boundary part which simulates the turbulent boundary layer with  $(1/7)^5$  power law. Here, 99% thickness is  $0.05D$  and the momentum thickness is approximately  $0.006D$ .

Definitions of geometric parameters and the coordinate system are shown in Figure 2. In this study, flat plate angles  $\theta$  are set to be 25 deg. to 70 deg. every 5 deg.. Here,  $TR_c$  is set to be 1.0. From previous work, we set the parameters to clearly observe an interference wave (ii).



**Figure 2. JET-profile**

The Strouhal number and the sound pressure level(SPL) are defined as follows.

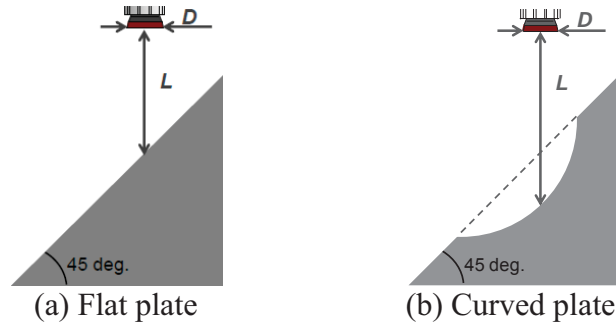
$$St = \frac{fD_j}{u_j} \quad (4)$$

$$SPL[dB] = 20 \log_{10} \frac{\tilde{p}}{\tilde{p}_{ref}} \quad (5)$$

where  $f$  is frequency,  $\tilde{p}$  is effective pressure fluctuation and  $\tilde{p}_{ref}$  is the reference SPL in our computation which is defined as follows.

$$\tilde{p}_{ref} = \frac{2 \times 10^{-5} [pa]}{101300 [Pa]} \times p_{\infty} \quad (6)$$

In this study, computational cases are plate angle  $\theta=25$  deg. to 70 deg.(every 5 deg.) and  $L/D$  is 5.0 for the case with an inclined flat plate,  $5D$  radius and  $L/D$  is approximately 7.5 $D$  for the case with curved plate. Figure.3 shows schematic of flat and curved plates.

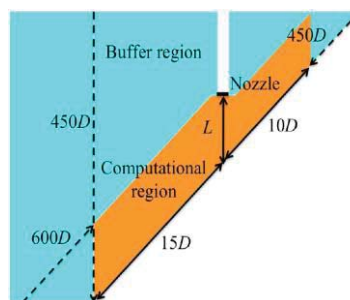


**Figure 3. Schematic of launch site**

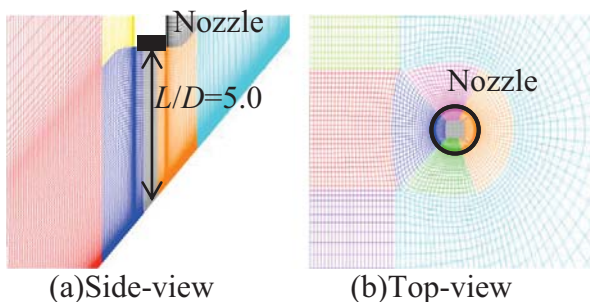
**Computational approach**

*Computational grids*

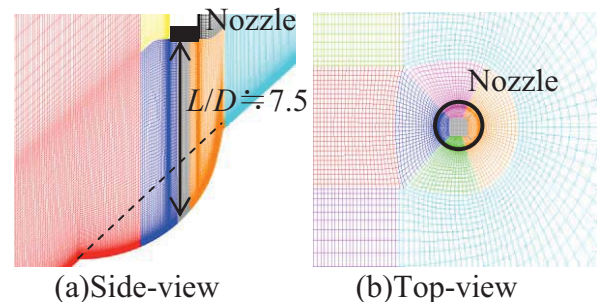
Figure 4 shows computational domain. Orange area is computational domain, and the outside, buffer region<sup>6</sup>(sky blue region in Fig.4) stretched to prevent acoustic wave from nonphysical reflecting and generating is set up. Stretching ratio of grid is 1.03 on a boundary of computational domain, and raised the ratio gradually to 1.2 as far from computational domain. Figures.5 and 6 show computational grids. In this study, it is important how to resolve downstream flow after impinging. Therefore, fine grids are required for those regions. In this study, entire computational domain is divided into 11 zones, and physical quantities are interpolated between each grids. However, grid points are over-lapped by 16 points, thus, no error due to interpolation are produced. A number of grid points is 150 on the center line of nozzle ( $x$ -direction), 106 in the direction apart from the axis(upstream-direction), 206(downstream-direction), and 197 in the direction around circumference. Total grid points are approximately 8 million.



**Figure 4. Computational domain**



**Figure 5. Computational grids(Flat plate)**



**Figure 6. Computational grids(Arc plate)**

### Computational scheme

Government equation is three-dimension compressible Navier-Stokes equation non-dimensionalized by diameter of the nozzle, the ambient density, and the ambient sound speed<sup>7</sup>. Seventh order weighted compact nonlinear scheme (WCNS) and sixth order central difference are used for discretization of convective and viscous terms, respectively. Here, WCNS was developed by Deng<sup>8</sup> as mixture of weighted essentially non-oscillatory (WENO) scheme<sup>9</sup> and compact difference scheme.<sup>10</sup> Although the original WCNS is 5th order, recently it is extended to 9th order by Nonomura et al<sup>11</sup>, Zhang et al<sup>12</sup>, independently. The resolution of WCNS is higher than WENO method in terms of resolution. Besides, WCNS method have merits that it can hold freestream.<sup>13</sup> Simple high resolution upwind scheme<sup>14</sup> is used to evaluate flux in WCNS method. In this study, below devise is used to raise computational velocity. When seeking physical quantity  $\tilde{U}_{j+1/2}^L$  at cell boundary, computing is conducted as follows:

$$\tilde{U}_{j:k}^{(n)} = \left( \frac{1}{\Delta x} \right)^n \sum_{l=0}^{r-1} \alpha_{k:l}^n U_{j-r+k+l} \quad (7)$$

$$\tilde{U}_{j+1/2:k}^L = U_j + \sum_{n=1}^{r-1} \left( \frac{\Delta x}{2} \right)^n \left( \frac{1}{n!} \right) \tilde{U}_{k:l}^{(n)} \quad (8)$$

$$IS_{j:k} = \sum_{n=1}^{r-1} \left( \tilde{U}_{j:k}^{(n)} \right)^2 \square IS_{j:k} = \begin{cases} IS_{j:k} & \frac{\max(IS_{j:l})}{\min(IS_{j:l})} > R \\ 0 & \frac{\max(IS_{j:l})}{\min(IS_{j:l})} < R \end{cases} \quad (9)$$

$$\alpha_k = \frac{C_k}{(IS_k + \varepsilon)^p} \quad (10)$$

$$w_k = \frac{\alpha_k}{\sum_{i=1}^r \alpha_i} \quad (11)$$

$$\tilde{U}_{j+1/2}^L = \sum_{k=1}^r w_k \tilde{U}_{j+1/2:k}^L \quad (12)$$

Here,  $w_k$  is a non-linear weight.

Monotonicity integrated large-eddy simulation is adopted<sup>15</sup> and that the numerical viscosity of upwind difference scheme is used for turbulence eddy viscosity as the subgrid scale model of LES. Therefore, any explicit subgrid scale models are not used. For the time integration, second order backward difference scheme is converged using an implicit method and inner iterations. For an implicit method, alternative directional implicit symmetric Gauss-Seidel scheme<sup>17</sup> which adopt the upwinding by the spectral radius to each direction of lower-upper alternative directional implicit scheme<sup>16</sup> is used. Three inner iterations employed. Time step is set so that the maximum CFL number is approximately 10 (near the shock wave and shear layer, less than 1), the non-dimensional integration time is 400, and the minimum resolved Strouhal number is approximately 0.02(cold jet),0.007(hot jet) considering the sound pressure oscillation is included more than 10 periods in integration times. Regarding the boundary condition, static pressure is set to be the ambient condition at the exit boundary and no-slip condition is used at the wall surface. For evaluation of the sound pressure, the pressure fluctuation is analyzed as the sound pressure in the computational domain. On the other hand, in the far field, after fast Fourier transform of the integral surface, the Kirchhoff method<sup>18</sup> is used to predict the sound pressure in frequency domain. An integral surface is set to be the outside of the computational domain, and this domain is enough far to pick up no pressure fluctuation due to the flow motion (pseudo sound wave) in near field. However, the sound pressure level of acoustic waves generated in the present computation is very high, and it seems that non-linearity seems to be included in acoustic wave propagation. Since the Kirchhoff method does not allow non-linear propagation of acoustic waves, it seems that the correct sound pressure level

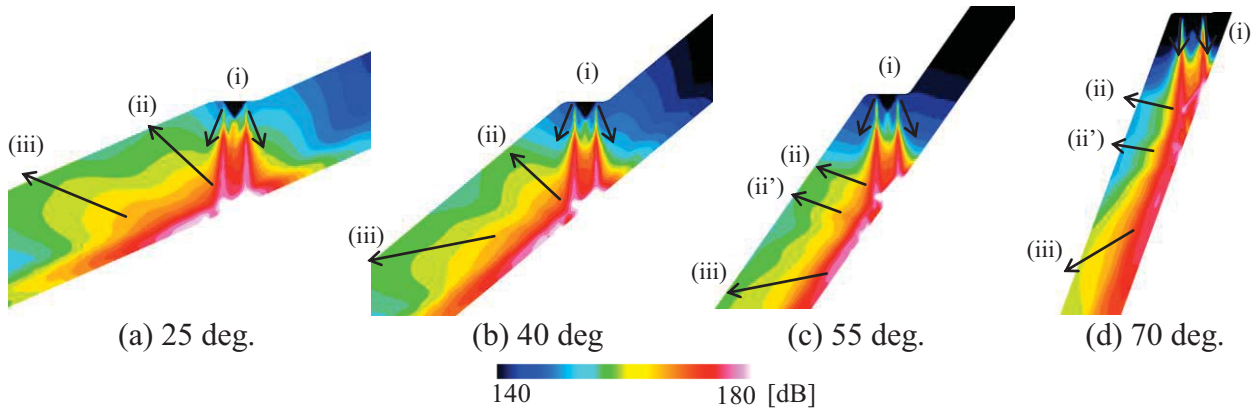


distribution is not obtained quantitatively. However, it does not matter for the objective of the present study: the qualitative reorganization of mechanism of acoustic wave generation.

## Results and discussion

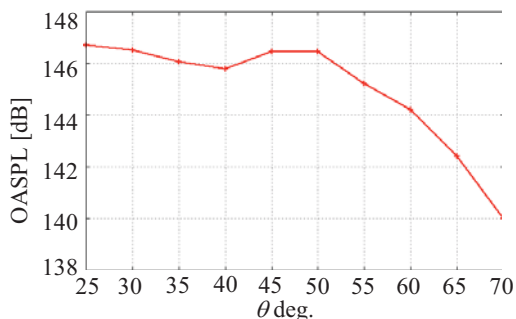
### Effect of changing angle of inclined flat plate

Figure 7 shows sound pressure level distribution for the cases with different plate angles. It shows that Mach waves (i) generated from the shear layer before impinging, interference waves (ii) are generated by interference of the shear layer and the shock wave. Moreover, when the plate angle exceed 45 deg., acoustic wave (ii') generated by the bubble shock is observed.

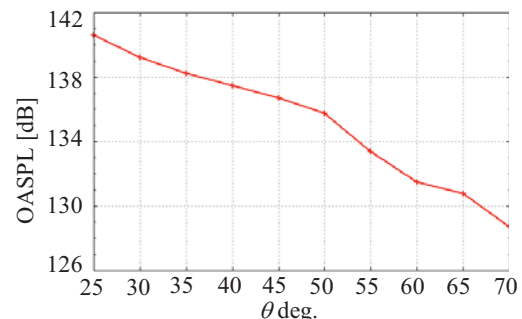


**Figure 7. OASPL Distribution of Symmetry plane**

The location of source of interference wave (ii) overlaps with that of (ii') in near field, As a result, these two acoustic waves seem to behave as one kind of acoustic waves in far field. Since it may have main influence on a rocket, it is focused on in this study. Figure 8 shows peak OASPL(Over all Sound Pressure Level) of this kind of acoustic waves at  $20D$  from the point of jet impinging. The horizontal axis shows the plate angle,  $\theta$ . It shows that OASPL has the local maximum at 50 deg.. Since interference wave (ii) is weaker as the plate angle rises<sup>19</sup>, interference wave (ii) is dominant at 40 deg., on the other hand, interference wave (ii') is dominant from 45 deg. to 50 deg.. Figure 9 shows OASPL at  $20D$  vertically from the point of jet impinging (this point is located at the rocket fairing). It can be seen that OASPL decreases as  $\theta$  increases. Moreover, when  $\theta$  is over 50 deg., OASPL decreases sharply. It seems that the superposition of interference wave (ii) and (ii') has the significant effects on the sound pressure at the rocket fairing because OASPL of superposition of interference wave (ii) and (ii') is also decreased sharply over 50 deg.. However, further investigation is necessary to conclude this.



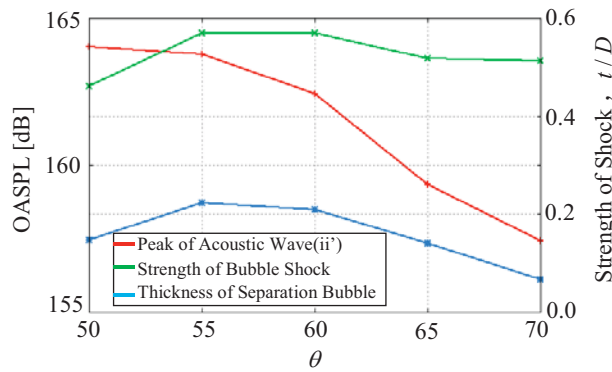
**Figure 8. Superposition of interference wave (ii),(ii') at  $20D$**



**Figure 9. OASPL at the rocket fairing**

Figure 10 shows three quantities for the cases with flat plate. Firstly, the vertical axis at left side shows the peak OASPL of interference wave (ii') at  $1.5D$  from the wall surface. The vertical axis at

the right side shows the others, strength of the bubble shock (pressure ratio before and after bubble shock) and thickness of separation bubble. It can be seen that strength of the bubble shock and thickness of a separation bubble have similar trend and become the maximum at 55 deg., together (this is same in all angles less than 50 deg.). Therefore, it seems that the thicker separation bubble makes bubble shock stronger. Since the stronger shock wave makes the acoustic waves caused by the shock stronger, the strength of bubble shock seems to be correlated with the interference wave (ii'). However, OASPL of the interference wave (ii') becomes maximum at 50 deg.. At 50 deg., it may be that the interference wave (ii) influenced on the interference wave (ii') because the position of occurrence of interference wave (ii') is nearer to interference wave (ii) than the other angles in the horizontal axis of Fig.10.

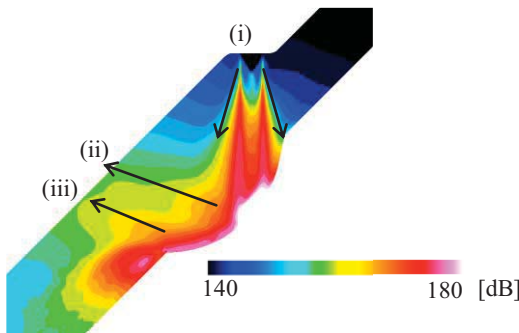


**Figure 10. Relation of Acoustic Wave(ii') and Flow Factor**

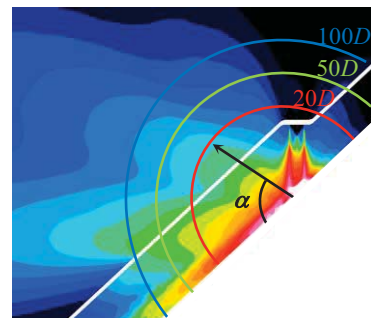
*Effect of launch site's curvature*

Effect of curvature of launch site is discussed by comparing the case with a curved plate with the case with a flat plate. The cases with 45 deg. inclined flat plate and curved plate of curvature of 5D (angle of flat plate part is 45 deg.) are considered, respectively. Distance from the nozzle exit to the impinging point is 5.0D for the case with the flat plate, approximately 7.5D for the case with the curved plate. Figure 11 shows that SPL distribution at near field of the case with curved plate. It can be seen that acoustic waves are generated similar to the case with the flat plate.

Here, OASPL of flat plate at the rocket fairing is 134.7 dB, on the other hand, that of curved plate is 135 dB. Goto et al.<sup>20</sup> confirmed that OASPL of acoustic wave decreases as L/D becomes larger for flat plate cases. Though the case with the curved plate has larger L/D (approximately 7.5) than the case with the flat plate (5.0), OASPL of curved plate at the rocket fairing is larger. Figure 13 shows these two cases of OASPL on arc of radius 20D, 50D, 100D, around impinging point (see Figure 12, though it is not exactly scaled). The horizontal axis  $\alpha$  is the angle measured from the wall in a downstream side. It shows that a rise in OASPL due to interference wave (ii), (ii'), and



**Figure 11. OASPL distribution of symmetry plane**



**Figure 12. Measurement position of SPL**

Mach wave (iii).both cases. In the case with a curved plate, one OASPL peak can be observed,

although they are two peaks in flat plate case. It is thought that the Mach wave (iii) overlapped with interference wave (ii) and (ii') because the Mach wave (iii) propagates upward by a curvature of wall surface.

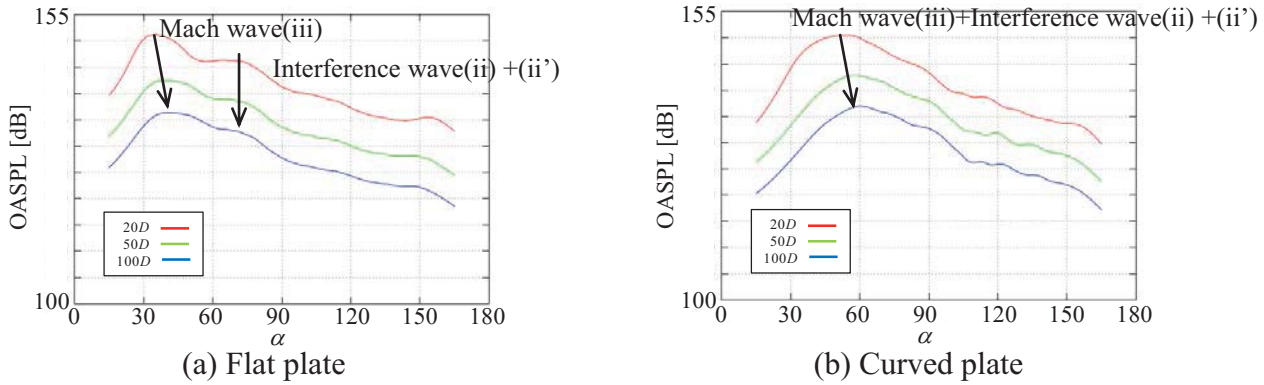


Figure 13. Far field directivity

Figure 15 shows the spectra of SPL at the points defined in Figure 14. Points A, B, and C are located at the position for Mach wave(iii), superposition of interference wave(ii) and (ii'), and rocket fairing, respectively. At the point A,  $\alpha$  is 32.5 deg. for the flat plate. At the point B,  $\alpha$  is 61 deg. for the flat plate, 52.5 deg. for the curved plate. At the point C,  $\alpha$  is 135 deg. It can be seen that the case with a curved plate has lower peak in the Strouhal number of the spectrum than the case with a flat plate in terms of Strouhal number of the spectrum peak from Figure 15. Figure 16 shows spectra of the Mach wave (iii) and superposition of the interference wave (ii) and (ii') at 20D from the impinging point for the case with flat plate of 45 deg.. It can be seen that the frequency of the Mach wave is generally lower than that of the interference wave. Moreover, also it can be seen that the peak of spectrum of acoustic waves in the case of the curved plate is lower than that of the case with the flat plate in terms from Figure 17. Therefore, it may be that Mach wave(iii) has influence on the sound pressure level at the rocket fairing in the case with the curved plate.

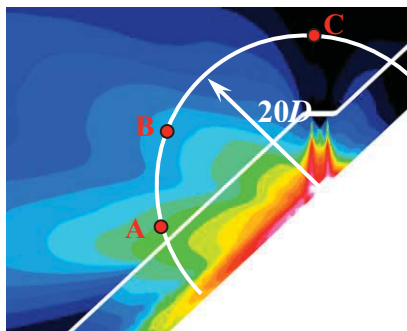


Figure 14. Measurement point of spectra of SPL

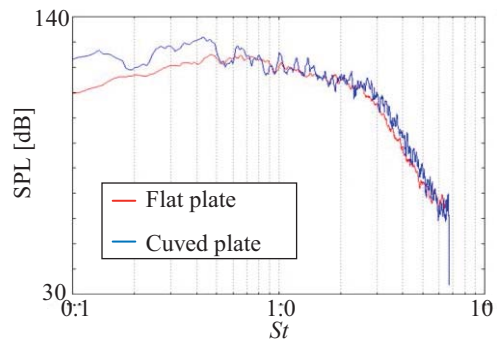


Figure 15. Spectra of SPL at pointB

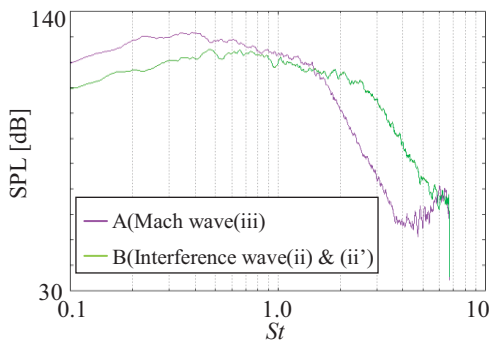


Figure 16. Spectra of SPL at pointA, B

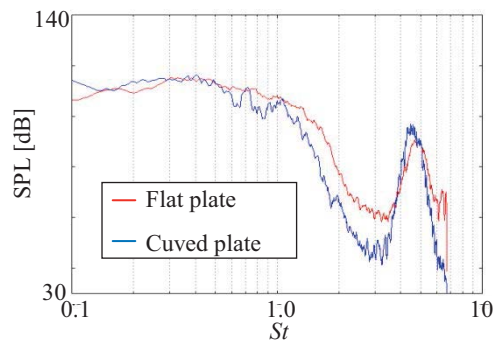


Figure 17. Spectra of SPL at pointC(rocket fairing)

## Conclusion

Analysis for flow and acoustic fields of a supersonic jet impinging on an inclined flat plate and a curved plate was conducted and, as a result, following knowledge was obtained.

- (a) Interference waves (ii) overlaps with (ii') in near field, as a result, they behaves as one kind of acoustic waves in far field, and OASPL of this kind of acoustic waves are according to magnitude of interference wave(ii) and (ii').
- (b) Sound pressure level of superposition of the interference waves (ii) and (ii') is sharply changed when the plate angle becomes more than 50 deg..
- (c) Making the plate angle more than 50 degrees significantly reduces OASPL at the rocket fairing.
- (d) A launch site with no curvature prevents the Mach waves (iii) propagating into the rocket fairing.

## References

- (1) Eldred, S. (1971) "Acoustic Loads Generated by Propulsion System," NASA SP-8072(1971).
- (2) Nonomura ,T. , Goto ,Y. , Fujii ,K. "Acoustic Waves from a Supersonic Jet Impinging on an Inclined Flat Plate," AIAA paper 2011-476(2010)
- (3) Honda ,H. , Nonomura ,T. , Fujii ,K. , Yamamoto ,M. "Effects of Plate Angles on Acoustic Waves from a Supersonic Jet Impinging on an Inclined Flat Plate," AIAA paper 2011-3260(2011).
- (4) Nonomura, T., Characteristics of Acoustic Waves Generated by Flow Instability of Supersonic Jets, Ph.D. thesis, University of Tokyo, 2008.
- (5) Pope, S. B., Turbulent Flows, Cambridge University Press, 2000
- (6) Borre, S., Bogey, C. and Baily, C. (2006), "Computation of the Noise Radiated by Jets with Laminar/Turbulent nozzle-exit conditions," AIAA-paper 2006-2443.
- (7) T, Colonius, S. K. Lele and P. Moin, "Boundary Condition for Direct Computation of Aerodynamics Sound Generation," AIAA Journal, vol. 31, No. 9(1993).
- (8) Fujii ,K., "Numerical Methods for Computational Fluid Dynamics (1994).
- (9) Deng, X. G. and Zhang, H., "Developing high-order weighted compact nonlinear schemes," Journal of Computational Physics, 165(2000), pp.22-44.
- (10) Jiang, G.-S. and Shu, C.-W., "Efficient implementation of weighted ENO schemes", J. Comput. Phys, 126, (1996), pp. 200-212.
- (11) Lele, S. K., "Compact Finite Difference Schemes with Spectral-Like Resolution," Journal of Computational Physics, 103(1992), pp. 16-42.
- (12) Nonomura, T., Iizuka, N. and Fujii, K., 2007, "Increasing Order of Accuracy of Weighted Compact Non-Linear Scheme." AIAA Paper 2007-0468(2007).
- (13) Zhang, S., Jiang, S. and Shu, CW., "Development of nonlinear weighted compact scheme with increasingly higher order accuracy," Journal of Computational Physics, 227(2008), pp. 7294-7321.
- (14) Nonomura, T., Iizuka, N. and Fujii, K., "Uniform preserving property of higher order upwind finite difference scheme on generalized coordinate system," Proceedings of 4th International Conference of Computational Fluid Dynamics.(2006).
- (15) Boris, J. P., Grinstein, F. F., Oran, E.S. and Kolbe, R. J., 1992, "New Insights Into Large Eddy Simulation," Fluid Dynamics Research, Vol. 10, pp. 199-288.
- (16) Fujii, K. and Obayashi, S., "Practical Applications of New LU-ADI Scheme for the Three-Dimensional Navier-Stokes Computation of Transonic Viscous FLOws" AIAA paper 86-0513(1986).
- (17) Fujii, K., "The frontier of finite volume method-Recent trend of High-speed air flow numerical methods", JSCES journal, Volume 3, Item 3 pp. 158-166
- (18) Pan, F.L., Uzun, A. and Lyrintzis, A. S., "Refraction Corrections for Surface Integral Methods in Jet Aeroacoustics," AIAA paper 2004-2873(2004).
- (19) Ted, A., Manning, "A NUMERICAL INVESTIGATION OF SOUND GENERATION IN SUPERSONIC JET SCREECH " (1999)
- (20) Goto ,Y. , Nonomura ,T. , Fujii ,K. , "Relation between Jet Potential Core Length and Nozzle-Plate Distance for Acoustic Waves from a Supersonic Jet Impinging on an Inclined Flat Plate," JSASS paper U-7(2009).

# Displacement Function Method of Space Problem for Transversely Isotropic Foundation Based on Damage Theory

**\*Wang Baoshi<sup>1</sup>, Liu Junqing<sup>1</sup>, Chen Chengcheng<sup>1</sup>**

School of Science, Xi'an University of Architecture and Technology, China

\*Corresponding author: wang-baoshi@126.com

## Abstract

This paper investigates the solution of space problem for transversely isotropic foundation based on damage theory. Firstly, the modified Galerkin's displacement function is introduced into the basic equations of the transversely isotropic elastomer space problem. Secondly, employing Hankel integration transform and Bessel function theory, we obtain a general three-dimensional solution in the image field by the displacement function method. Finally, by means of the Hankel integration inversion shift theory, the fundamental expressions of strain and stress in the transversely isotropic foundation are presented for different cases that the characteristic roots were equal or not. The solution could be used to solve some specific axisymmetric and asymmetrical problems in semi-infinite space under different boundary conditions.

**Keywords:** transversely isotropic foundation, damage, displacement function method, Hankel integral transform, stress.

## 1 Introduction

The research achievements of many researchers at home and abroad and a large number of engineering practice show that it is feasible and more representative that the cohesive soil foundation is simplified transversely isotropic elastic half-space model in many cases. Since the transversely isotropic foundation model was put forward, many domestic and foreign researchers have carried out in-depth research on the model. In 1940, a general solution of axisymmetric problem about the transversely isotropic body of revolution was firstly solved by Soviet scholar Lekhnitskii. And then, Elliott derived a particular solution about a three-dimensional problem that can be degenerated to Lekhnitskii solution in the axisymmetric condition by means of two harmonic functions in 1948. Based on the equilibrium equation of displacement expression, Eubanks and Sternberg obtained the Lekhnitskii solution systematically in 1954, and proved the completeness of Elliott solution. The detailed analytic solution expression of the surface and interior of the transversely isotropic half-space under point loads or circular loads was given by C.M.Gerrard(1980). And by referencing the three displacement functions, Pan and Chou(1979) made use of the Green's function method to obtain the whole expressions of fundamental solution of transversely isotropic semi-infinite body.

Interiorly, it is Hu haichang who studied that problem first. In 1953, he obtained the general solution of space problem of transversely isotropic elastic body by means of two potential functions, specifically discusses the problems of transversely isotropic semi-infinite elastic body, and got the fundamental solution when  $s_1 \neq s_2$ . Ding Haojiang, through the Hu Haichang's solution, used integral method to obtain the fundamental solution of axisymmetric problems of transversely isotropic materials, which can be directly degenerated to the fundamental solution of

axisymmetric problems of isotropic materials. Dun zhiling and his graduates, by modifying Love displacement function in isotropic elastic mechanics, made use of displacement method and Hankel integral-transform theory to get the general solution of transversely isotropic foundation in image field. And by using the inversion of Hankel integral, the analytical solutions of displacement and stress of semi-infinite foundation under several common loads were obtained and the results of numerical calculation were given. Based on the basic equations of transversely isotropic elastic body and Hankel transform, the generation solutions of displacement and stress of space problem of layered transversely isotropy under non-axisymmetric loads were solved by using transfer matrix method(Chen guangjing and Zhao xihong, 1998). The Biot's wave equations of transversely isotropic saturated poroelastic media excited by non-axisymmetrical harmonic source were solved by means of Fourier expansion and Hankel transform. Then the components of total stress in porous media are expressed with the solutions of Biot's wave equations.( Zhang Yinke and Huang Yi, 2001).

Based on the theory of damage mechanics, the elastic damage of transversely isotropic foundation was considered and a general three-dimensional solution for transversely isotropic foundation in the image field was strictly obtained by the displacement function method. The Galerkin's displacement function for isotropic elasticity was modified, and Hankel integration transform and Bessel function theory were employed in the solution. With the Hankel integration inversion shift theory, the analytical expressions of stress and displacement in the transversely isotropic foundation were presented.

## 2 Damage theory

Shen Zhujiang put forward that the damage characteristics of the material are described by the cementitious bar element. The linear elastic damage model is adopted to simulate the transverse isotropic soil. This model is a single-spring model, which is composed of cementitious bar and spring and includes a lot of cementitious node. The soil of the mechanical process is analyzed as a synthetic material including undisturbed and damage soil. With the increase of deformation, cementitious nodes will be gradually destroyed and mechanical properties of soil gradually deteriorate.

The effective stress in damage mechanics is called the equivalent stress in this article to distinguish the concept of effective stress in soil mechanics. According to Lemaitre equivalent strain principle, the stress-strain relationship of one-dimensional damaged soil is as follows:  $\varepsilon = \sigma / \tilde{E} = \tilde{\sigma} / E = \sigma / E(1 - D)$  (1)

Where  $\tilde{\sigma}$  is equivalent stress,  $E$  is the elastic modulus of non-destructive materials,  $\tilde{E}$  is effective elastic modulus, and  $D$  is damage variable.

For the three-dimensional anisotropic damage, equivalent stress can be expressed as:

$$\tilde{\sigma} = M(D) : \sigma \quad (2)$$

In the formula,  $M(D)$  is the damage effective tensor. considering the matrix is symmetric and can be reduced to an matrix of isotropic damage problem, so damage tensor  $M(D)$  is elected:

$$[M(D)] = \begin{bmatrix} \frac{1}{1-D_1} & & & & & \\ & \frac{1}{1-D_1} & & & & \\ & & \frac{1}{1-D_2} & & & \\ & & & \frac{1}{\sqrt{(1-D_1)(1-D_2)}} & & \\ & & & & \frac{1}{\sqrt{(1-D_1)(1-D_2)}} & \\ & & & & & \frac{1}{(1-D_1)} \end{bmatrix} \quad (3)$$

where  $D_1, D_2$  respectively respect the damage variable of the horizontal plane and the vertical plane. The damage variables can be determined according to the literature[15].

### 3 The general solution of space problem for transversely isotropic foundation based on damage theory

#### 3.1 The equivalent stress of transversely isotropic space problem in cylindrical coordinate

In cylindrical coordinate  $(r, \theta, z)$ , it is assumed that the z-axis is perpendicular to the isotropic plane of physical properties, so elasticity is isotropic in the plane  $(r, \theta)$ . Let  $u$ ,  $v$ ,  $w$  be the displacement of points along the three directions  $r$ ,  $\theta$ ,  $z$ . The geometric equation of transversely isotropic space problem in cylindrical coordinate is as follows:

$$\{\varepsilon\} = \{\varepsilon_r, \varepsilon_\theta, \varepsilon_z, \gamma_{\theta z}, \gamma_{rz}, \gamma_{r\theta}\}^T = \left\{ \frac{\partial u}{\partial r}, \frac{u}{r} + \frac{1}{r} \frac{\partial v}{\partial \theta}, \frac{\partial w}{\partial z}, \frac{\partial v}{\partial z} + \frac{1}{r} \frac{\partial w}{\partial \theta}, \frac{\partial u}{\partial z} + \frac{\partial w}{\partial r}, \frac{1}{r} \frac{\partial u}{\partial \theta} + \frac{\partial v}{\partial r} - \frac{v}{r} \right\}^T \quad (4)$$

Therefore the relationship of stress components and displacement components of undamaged foundation can be expressed by the displacement in cylindrical coordinates:

$$\{\tilde{\sigma}\} = \{\tilde{\sigma}_r, \tilde{\sigma}_\theta, \tilde{\sigma}_z, \tilde{\sigma}_z, \tilde{\tau}_{rz}, \tilde{\tau}_{r\theta}\}^T = [C]\{\varepsilon\} = [C] \left\{ \frac{\partial u}{\partial r}, \frac{u}{r} + \frac{1}{r} \frac{\partial v}{\partial \theta}, \frac{\partial w}{\partial z}, \frac{\partial v}{\partial z} + \frac{1}{r} \frac{\partial w}{\partial \theta}, \frac{\partial u}{\partial z} + \frac{\partial w}{\partial r}, \frac{1}{r} \frac{\partial u}{\partial \theta} + \frac{\partial v}{\partial r} - \frac{v}{r} \right\}^T \quad (5)$$

Where

$$[C] = \begin{bmatrix} c_{11} & c_{12} & c_{13} & & & \\ c_{12} & c_{11} & c_{13} & & & \\ c_{13} & c_{13} & c_{33} & & & \\ & & & c_{44} & & \\ & & & & c_{44} & \\ & & & & & c_{66} \end{bmatrix}, \lambda = E_2 / [(1 + \mu_1)(1 - \mu_1 - 2n\mu_2^2)], c_{11} = \lambda n(1 - n\mu_2^2),$$

$c_{12} = \lambda n(\mu_1 + n\mu_2^2)$ ,  $c_{13} = \lambda n\mu_2(1 + \mu_1)$ ,  $c_{33} = \lambda(1 - \mu_1^2)$ ,  $c_{44} = G_2$ ,  $c_{66} = E_1 / [2(1 + \mu_1)]$ ,  $n = E_1 / E_2$ ,  $E_1$  and  $E_2$  is the modulus of elasticity in a horizontal plane and a vertical plane respectively;  $\mu_1$  and  $\mu_2$  is the Poisson ratio in a horizontal plane and a vertical plane respectively;  $G_2$  is the shear modulus in a vertical plane.

From Eq.(2), the stress of transversely isotropic foundation with damage can be obtained by the stress of undamaged foundation in the follow form as

$$\{\sigma\} = \begin{bmatrix} \tilde{c}_{11} & c_{12} & c_{13} & & & \\ c_{12} & \tilde{c}_{11} & c_{13} & & & \\ c_{13} & c_{13} & \tilde{c}_{33} & & & \\ & & & \tilde{c}_{44} & & \\ & & & & \tilde{c}_{44} & \\ & & & & & \tilde{c}_{66} \end{bmatrix} \left\{ \frac{\partial u}{\partial r}, \frac{u}{r} + \frac{1}{r} \frac{\partial v}{\partial \theta}, \frac{\partial w}{\partial z}, \frac{\partial v}{\partial z} + \frac{1}{r} \frac{\partial w}{\partial \theta}, \frac{\partial u}{\partial z} + \frac{\partial w}{\partial r}, \frac{1}{r} \frac{\partial u}{\partial \theta} + \frac{\partial v}{\partial r} - \frac{v}{r} \right\}^T \quad (6)$$

Where  $\tilde{c}_{11} = \lambda n(1 - n\mu_2^2)(1 - D_1)$ ,  $\tilde{c}_{33} = \lambda(1 - \mu_1^2)(1 - D_2)$ ,

$$\tilde{c}_{44} = G_2 \sqrt{(1 - D_1)(1 - D_2)}, \tilde{c}_{66} = E_1(1 - D_1) / [2(1 + \mu_1)]$$

#### 3.2 The Displacement Function Method of transversely isotropic space problem in cylindrical coordinate

When analyzing elastic semi-infinite body and non-axisymmetric problem of the thick plate in 1960, Ruki R introduced two displacement functions  $\varphi$  and  $\psi$ :

$$u = -\frac{\partial^2 \varphi}{\partial r \partial z} - \frac{1}{r} \frac{\partial \psi}{\partial \theta} \quad v = -\frac{1}{r} \frac{\partial^2 \varphi}{\partial \theta \partial z} + \frac{\partial \psi}{\partial r} \quad w = 2(1-\mu) \nabla^2 \varphi - \frac{\partial^2 \varphi}{\partial z^2} \quad (7)$$

These are the general expression of the isotropic spatial problems. And they can be used to solve the isotropic spatial problem in a variety of different boundary conditions specifically.

Based on damage theory, the relation between the displacement components and the displacement function for transversely isotropic spatial problem can be obtained through complex calculations (specific process can be seen in reference [6], [16] and [17]). And it is the revised Galerkin's displacement function.

$$u = -\frac{\partial^2 F}{\partial r \partial z} - \frac{1}{r} \frac{\partial \varphi}{\partial \theta} \quad v = -\frac{1}{r} \frac{\partial^2 F}{\partial \theta \partial z} + \frac{\partial \varphi}{\partial r} \quad w = \left( \tilde{a} \nabla^2 + \tilde{b} \frac{\partial^2}{\partial z^2} \right) F \quad (8)$$

where,  $\tilde{a} = \frac{\tilde{c}_{11}}{c_{13} + \tilde{c}_{44}}$ ,  $\tilde{b} = \frac{\tilde{c}_{44}}{c_{13} + \tilde{c}_{44}}$ ,  $\nabla^2 = \frac{\partial^2}{\partial r^2} + \frac{\partial}{r \partial r} + \frac{\partial^2}{r^2 \partial \theta^2}$  is Laplace Operator.  $F$

and  $\varphi$  is two displacement function for transversely isotropic body. Hu Haichang proved that the displacement function,  $F$  and  $\varphi$ , represents a complete solution of the space problem.

What's more,  $F$  and  $\varphi$  should go for the following compatible equation.

$$\left( \frac{\partial^2}{\partial r^2} + \frac{\partial}{r \partial r} + \frac{\partial^2}{r^2 \partial \theta^2} + \frac{\partial^2}{\tilde{s}_1^2 \partial z^2} \right) \cdot \left( \frac{\partial^2}{\partial r^2} + \frac{\partial}{r \partial r} + \frac{\partial^2}{r^2 \partial \theta^2} + \frac{\partial^2}{\tilde{s}_2^2 \partial z^2} \right) F = 0, \quad \left( \frac{\partial^2}{\partial r^2} + \frac{\partial}{r \partial r} + \frac{\partial^2}{r^2 \partial \theta^2} + \frac{\partial^2}{\tilde{s}_3^2 \partial z^2} \right) \varphi = 0 \quad (9)$$

$$\begin{aligned} \text{Where } \tilde{s}_1 &= \sqrt{(\tilde{c}_{13} - c_{13})(\tilde{c}_{13} + c_{13} + 2\tilde{c}_{44})/4\tilde{c}_{33}c_{44}} + \sqrt{(\tilde{c}_{13} + \tilde{c}_{13})(\tilde{c}_{13} - c_{13} - 2\tilde{c}_{44})/4\tilde{c}_{33}\tilde{c}_{44}} \\ \tilde{s}_2 &= \sqrt{(\tilde{c}_{13} - c_{13})(\tilde{c}_{13} + c_{13} + 2\tilde{c}_{44})/4\tilde{c}_{33}\tilde{c}_{44}} - \sqrt{(\tilde{c}_{13} + c_{13})(\tilde{c}_{13} - c_{13} - 2\tilde{c}_{44})/4\tilde{c}_{33}\tilde{c}_{44}} \\ \tilde{s}_3^2 &= \frac{\tilde{c}_{66}}{\tilde{c}_{44}} \quad \tilde{c}_{13} = \sqrt{\tilde{c}_{11}\tilde{c}_{33}} \end{aligned} \quad (10)$$

In order to obtain the expression of stress and displacement components, the derivative of the Eq. (8) for  $r$ ,  $\theta$  and  $z$  are substituted into Eq. (6). Then we can obtain the expression of the stress components in cylindrical coordinates.

$$\begin{aligned} \sigma_r &= \frac{(c_{12} - \tilde{c}_{11})}{r} \frac{\partial^2 \varphi}{\partial r \partial \theta} + (ac_{13} - \tilde{c}_{11}) \frac{\partial^3 F}{\partial r^2 \partial z} + \frac{(c_{12} - \tilde{c}_{11})}{r^2} \frac{\partial \varphi}{\partial \theta} + \frac{(ac_{13} - c_{12})}{r} \frac{\partial^2 F}{\partial r \partial z} + \frac{(ac_{13} - c_{12})}{r^2} \frac{\partial^3 F}{\partial \theta^2 \partial z} + bc_{13} \frac{\partial^3 F}{\partial z^3} \\ \sigma_\theta &= \frac{(\tilde{c}_{11} - c_{12})}{r} \frac{\partial^2 \varphi}{\partial r \partial \theta} + (ac_{13} - c_{12}) \frac{\partial^3 F}{\partial r^2 \partial z} - \frac{(\tilde{c}_{11} - c_{12})}{r^2} \frac{\partial \varphi}{\partial \theta} + \frac{(ac_{13} - \tilde{c}_{11})}{r} \frac{\partial^2 F}{\partial r \partial z} + \frac{(ac_{13} - \tilde{c}_{11})}{r^2} \frac{\partial^3 F}{\partial \theta^2 \partial z} + bc_{13} \frac{\partial^3 F}{\partial z^3} \\ \sigma_z &= (a\tilde{c}_{33} - c_{13}) \frac{\partial^3 F}{\partial r^2 \partial z} + \frac{1}{r} (a\tilde{c}_{33} - c_{13}) \frac{\partial^2 F}{\partial r \partial z} + \frac{1}{r^2} (a\tilde{c}_{33} - c_{13}) \frac{\partial^3 F}{\partial \theta^2 \partial z} + b\tilde{c}_{33} \frac{\partial^3 F}{\partial z^3} \\ \tau_{\theta z} &= \frac{\tilde{c}_{44}}{r} (\tilde{b} - 1) \frac{\partial^3 F}{\partial \theta \partial z^2} + \tilde{c}_{44} \frac{\partial^2 \varphi}{\partial r \partial z} + \frac{\tilde{c}_{44}}{r} \tilde{a} \left( \frac{\partial^3}{\partial \theta \partial r^2} + \frac{1}{r} \frac{\partial^2}{\partial \theta \partial r} + \frac{1}{r^2} \frac{\partial^3}{\partial \theta^3} \right) F \\ \tau_{zr} &= \tilde{c}_{44} (b - 1) \frac{\partial^3 F}{\partial r \partial z^2} - \frac{\tilde{c}_{44}}{r} \frac{\partial^2 \varphi}{\partial \theta \partial z} + \tilde{a} \tilde{c}_{44} \left( \frac{\partial^3}{\partial r^3} + \frac{1}{r} \frac{\partial^2}{\partial r^2} - \frac{1}{r^2} \frac{\partial}{\partial r} + \frac{1}{r^2} \frac{\partial^3}{\partial \theta^2 \partial r} - \frac{2}{r^3} \frac{\partial^2}{\partial \theta^2} \right) F \\ \tau_{r\theta} &= \tilde{c}_{66} \left( -\frac{2}{r} \frac{\partial^3 F}{\partial r \partial \theta \partial z} - \frac{1}{r^2} \frac{\partial^2 \varphi}{\partial \theta^2} + \frac{2}{r^2} \frac{\partial^2 F}{\partial \theta \partial z} + \frac{\partial^2 \varphi}{\partial r^2} - \frac{1}{r} \frac{\partial \varphi}{\partial r} \right) \end{aligned} \quad (11)$$

Eq. (8) and Eq. (11) are the general solution of transversely isotropic space problem and they are represented by  $F$  and  $\varphi$ . As can be seen from the expression, if displacement function,  $F$  and  $\varphi$ , is determined appropriately, we can determine the corresponding displacement components and stress components. Therefore, Hankel



integration transform is introduced and displacement functions,  $F$  and  $\varphi$ , are expressed in the form of series as the following.

$$F = F(r, \theta, z) = \sum_{k=0}^{\infty} F_k(r, z) \cos k\theta, \quad \varphi = \varphi(r, \theta, z) = \sum_{k=0}^{\infty} \varphi_k(r, z) \sin k\theta \quad (12)$$

After Eq. (12) put into Eq. (9), we obtain:

$$\left( \frac{\partial^2}{\partial r^2} + \frac{\partial}{r \partial r} - \frac{k^2}{r^2} + \frac{\partial^2}{\tilde{s}_1^2 \partial z^2} \right) \cdot \left( \frac{\partial^2}{\partial r^2} + \frac{\partial}{r \partial r} - \frac{k^2}{r^2} + \frac{\partial^2}{\tilde{s}_2^2 \partial z^2} \right) F_k = 0, \quad \left( \frac{\partial^2}{\partial r^2} + \frac{\partial}{r \partial r} - \frac{k^2}{r^2} + \frac{\partial^2}{\tilde{s}_3^2 \partial z^2} \right) \varphi_k = 0 \quad (13)$$

$$\text{Let } \bar{F}_k(\xi, z) = \int_0^{\infty} r F_k(r, z) J_k(\xi r) dr, \quad \bar{\varphi}_k(\xi, z) = \int_0^{\infty} r \varphi_k(r, z) J_k(\xi r) dr \quad (14)$$

Then using the Hankel transform and the nature of Bessel functions

$$\int_0^{\infty} \left( \frac{\partial^2}{\partial r^2} + \frac{\partial}{r \partial r} - \frac{n^2}{r^2} \right) f(r) J_n(\xi r) dr = -\xi^2 \bar{f}(\xi) \quad (15)$$

After k-order Hankel transform is applied to, the Eq. (13) can be transformed into as follows:

$$\left( \frac{\partial^2}{\tilde{s}_1^2 \partial z^2} - \xi^2 \right) \left( \frac{\partial^2}{\tilde{s}_2^2 \partial z^2} - \xi^2 \right) \bar{F}_k = 0, \quad \left( \frac{\partial^2}{\tilde{s}_3^2 \partial z^2} - \xi^2 \right) \bar{\varphi}_k = 0 \quad (16)$$

The inversion formula of Hankel transform is :

$$F_k(r, z) = \int_0^{\infty} \xi \bar{F}_k(\xi, z) J_k(\xi r) d\xi, \quad \varphi_k(r, z) = \int_0^{\infty} \xi \bar{\varphi}_k(\xi, z) J_k(\xi r) d\xi \quad (17)$$

After the Eq. (17) put into Eq. (11), the displacement function can be expressed as:

$$F_k(r, \theta, z) = \sum_{k=0}^{\infty} \int_0^{\infty} \xi \bar{F}_k(\xi, z) J_k(\xi r) \cos k\theta d\xi, \quad \varphi_k(r, \theta, z) = \sum_{k=0}^{\infty} \int_0^{\infty} \xi \bar{\varphi}_k(\xi, z) J_k(\xi r) \sin k\theta d\xi \quad (18)$$

According to the nature of Bessel functions, we can obtain its derivative express

$$\frac{d}{dr} J_k(\xi r) = \xi J_{k-1}(\xi r) - \frac{k}{r} J_k(\xi r), \quad \frac{d^2}{dr^2} J_k(\xi r) = -\xi^2 J_k(\xi r) + \xi \left[ \frac{k+1}{2r} J_{k+1}(\xi r) + \frac{k-1}{2r} J_{k-1}(\xi r) \right] \quad (19)$$

Using Eq. (19), we can calculate the derivative of the displacement Eq. (18) for  $r$ ,  $\theta$  and  $z$ . And after putting them into the Eq. (8) and Eq. (11) respectively, the general solution of transversely isotropic spatial problems within quadrants is obtained (only  $u$ 、 and  $\tau_{\theta z}$  was listed).

$$u = -\sum_{k=0}^{\infty} \int_0^{\infty} \xi^2 \frac{d\bar{F}_k}{dz} J_{k-1}(\xi r) \cos k\theta d\xi + \sum_{k=0}^{\infty} \frac{k}{r} \int_0^{\infty} \xi \left( \frac{d\bar{F}_k}{dz} - \bar{\varphi}_k \right) J_k(\xi r) \cos k\theta d\xi$$

$$\tau_{\theta z} = \sum_{k=0}^{\infty} \int_0^{\infty} \left[ \frac{\tilde{c}_{44}}{r} (1-\tilde{b}) k \frac{d^2 \bar{F}_k}{dz^2} - \frac{\tilde{c}_{44}}{r} k \frac{d\bar{\varphi}_k}{dz} + \frac{\tilde{c}_{44}}{r} \tilde{a} k \xi^2 \bar{F}_k \right] \xi J_k(\xi r) \sin k\theta d\xi + \tilde{c}_{44} \sum_{k=0}^{\infty} \int_0^{\infty} \xi^2 \frac{d\bar{\varphi}_k}{dz} J_{k-1}(\xi r) \sin k\theta d\xi \quad (20)$$

### 3.3 The displacement components and the stress components of space problems for transversely isotropic foundation

The Eq. (20) shows that, if the functions  $\bar{F}_k$  and  $\bar{\varphi}_k$  can be obtained, we can get the analytical expressions of displacement components and stress components of the elastic space problem that is transversely isotropic. According to the material characteristic roots of transversely isotropic body,  $s_1$  and  $s_2$ , the situation can be divided into  $s_1=s_2$  and  $s_1 \neq s_2$  when solving  $\bar{F}_k$  and  $\bar{\varphi}_k$  and getting their derivatives for  $z$ . Because the anisotropy of most foundation rock materials can be reflected by  $s_1 \neq s_2$ , the solution of  $\tilde{s}_1 \neq \tilde{s}_2$  is only solved as follow.

When  $\tilde{s}_1 \neq \tilde{s}_2$ , the solution of ordinary differential equation of Eq. (16) is

$$\bar{F}_k(\xi, z) = A_\xi e^{-\tilde{s}_1 \xi z} + B_\xi e^{-\tilde{s}_2 \xi z} + C_\xi e^{\tilde{s}_1 \xi z} + D_\xi e^{\tilde{s}_2 \xi z}, \bar{\varphi}_k(\xi, z) = E_\xi e^{-\tilde{s}_3 \xi z} + F_\xi e^{\tilde{s}_3 \xi z} \quad (21)$$

Put the Eq. (21) and its derivative for z into Eq. (20). when  $\tilde{s}_1 \neq \tilde{s}_2$ , the general expression of displacement components and stress components can be obtained (only  $u$ 、 and  $\tau_{\theta z}$  were listed).

$$\begin{aligned} u = & -\sum_{k=0}^{\infty} \int_0^{\infty} \frac{1}{2} [(-\tilde{s}_1 A e^{-\tilde{s}_1 \xi z} - \tilde{s}_2 B e^{-\tilde{s}_2 \xi z} + \tilde{s}_1 C e^{\tilde{s}_1 \xi z} + \tilde{s}_2 D e^{\tilde{s}_2 \xi z}) + (E_\xi e^{-\tilde{s}_3 \xi z} + F_\xi e^{\tilde{s}_3 \xi z})] J_{k-1}(\xi r) \cos k\theta d\xi \\ & + \sum_{k=0}^{\infty} \frac{k}{r} \int_0^{\infty} \frac{1}{2} [(-\tilde{s}_1 A e^{-\tilde{s}_1 \xi z} - \tilde{s}_2 B e^{-\tilde{s}_2 \xi z} + \tilde{s}_1 C e^{\tilde{s}_1 \xi z} + \tilde{s}_2 D e^{\tilde{s}_2 \xi z}) - (E_\xi e^{-\tilde{s}_3 \xi z} + F_\xi e^{\tilde{s}_3 \xi z})] J_{k+1}(\xi r) \cos k\theta d\xi \\ \tau_{\theta z} = & \sum_{k=0}^{\infty} \int_0^{\infty} \left\{ \frac{\tilde{c}_{44}}{2} [\xi(1-\tilde{b}) (\tilde{s}_1^2 A e^{-\tilde{s}_1 \xi z} + \tilde{s}_2^2 B e^{-\tilde{s}_2 \xi z} + \tilde{s}_1^2 C e^{\tilde{s}_1 \xi z} + \tilde{s}_2^2 D e^{\tilde{s}_2 \xi z})] \right. \\ & + \tilde{s}_3 \xi (E_\xi e^{-\tilde{s}_3 \xi z} - F_\xi e^{\tilde{s}_3 \xi z}) + \tilde{a} \xi (A e^{-\tilde{s}_1 \xi z} + B e^{-\tilde{s}_2 \xi z} + C e^{\tilde{s}_1 \xi z} + D e^{\tilde{s}_2 \xi z}) \left. \right\} J_{k+1}(\xi r) \sin k\theta d\xi \quad (22) \\ & + \sum_{k=0}^{\infty} \int_0^{\infty} \left\{ \frac{\tilde{c}_{44}}{2} [\xi(1-\tilde{b}) (\tilde{s}_1^2 A e^{-\tilde{s}_1 \xi z} + \tilde{s}_2^2 B e^{-\tilde{s}_2 \xi z} + \tilde{s}_1^2 C e^{\tilde{s}_1 \xi z} + \tilde{s}_2^2 D e^{\tilde{s}_2 \xi z})] \right. \\ & - \tilde{s}_3 \xi (E_\xi e^{-\tilde{s}_3 \xi z} - F_\xi e^{\tilde{s}_3 \xi z}) + \tilde{a} \xi (A e^{-\tilde{s}_1 \xi z} + B e^{-\tilde{s}_2 \xi z} + C e^{\tilde{s}_1 \xi z} + D e^{\tilde{s}_2 \xi z}) \left. \right\} J_{k-1}(\xi r) \sin k\theta d\xi \end{aligned}$$

The analytic expressions of displacement components and stress components expressed in the Eq. (22) apply to space issues for transversely isotropic foundation with injury under a variety of non-axisymmetric loads. For the specific space problem of transversely isotropic foundation, when it is known that the specific boundary conditions of transversely isotropic foundation and five independent engineering elastic constants,  $E_1$ 、  $E_2$ 、  $\mu_1$ 、  $\mu_2$ 、  $G_2$ , and damage variable  $D_1$ 、  $D_2$ , displacement and stress field distribution in the corresponding boundary conditions can be obtained through using the result.

### 4 The example analysis

In order to verify the validity of these theoretical approaches and indicate the impact on transversely isotropic foundation when damage considered, the engineering elastic constants of transversely isotropic foundation in the reference[9] was selected:  $E_1 = 35.6\text{MPa}$  ,  $E_2 = 20.8\text{MPa}$  ,  $G_2 = 9.09\text{MPa}$  ,  $\mu_1 = 0.299$  ,  $\mu_2 = 0.146$  , The foundation bears the circular uniform unidirectional horizontal load. Its load collection degree, p, is 10kPa. And the load radius r is 1m. Because of space limitations and time constraints, this numerical example just makes the comparative analysis of the shear stress component in the z-axis,  $\tau_{\theta z}|_{r=0}$ , for transversely isotropic foundation without injury. The mathematical software used is Matlab.

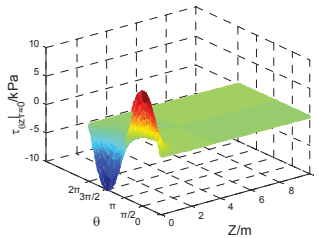


Figure1 Spatial distribution of shear stresses as  $r=0$

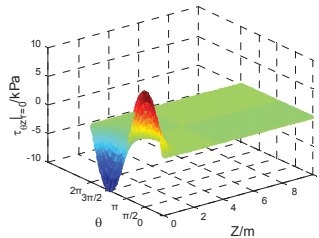


Figure2 Spatial distribution of shear stress as  $r=0$  and  $D_1=0.2$

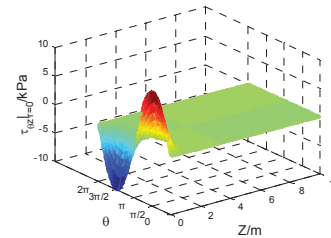


Figure3 Spatial distribution of shear stress as  $r=0$  and  $D_1=0.2$

Fig. 1, Fig. 2 and Fig. 3 show that the spatial distribution curves of the shear stress component in the z-axis,  $\tau_{\theta z}|_{r=0}$ , for transversely isotropic foundation with damage or not, are almost identical with the changing of the depth  $z$  and the polar angle  $\theta$ . Then we can make a qualitative analysis of the difference of foundation shear stress  $\tau_{\theta z}|_{r=0}$  in two different situations when choosing two kinds of the plane state.

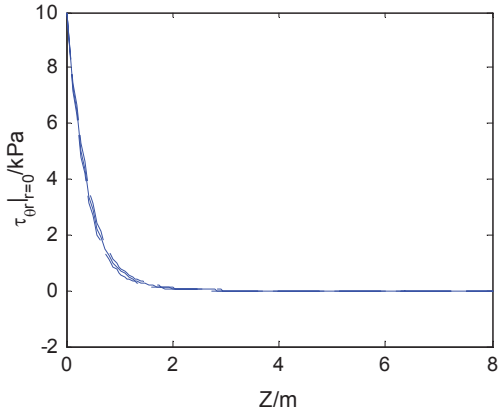


Figure 4 The comparison of shear stress as  $\theta=\pi/2$  for two kind of foundation

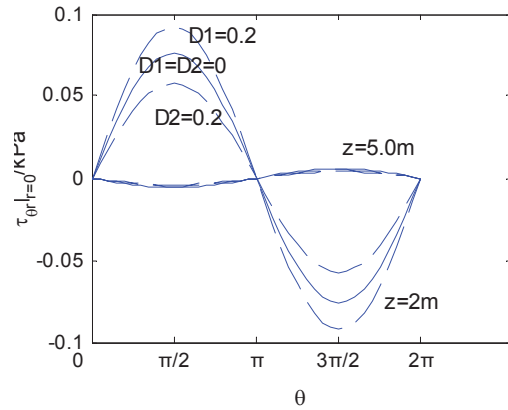


Figure 5 The comparison of shear stress as  $z=2m$  and  $z=5m$  for two kind of foundation

(Note: The dotted line represents damage foundation and solid line represents the foundation without damage in figures)

Fig. 4 and Fig. 5 show that: ① When  $\theta$  fixed, with the  $z$  value increases, the foundation's shear stress  $\tau_{\theta z}|_{r=0}$  in three cases is continuously attenuated. And when the depth  $z$  is smaller than 4m (equivalently 4 times of circular load's radius), the attenuation is in a fast rate. When  $z$  is greater than 4m, the attenuation speed becomes slower. And with the increasing of the depth, three shear stress values are close to equal ultimately; ② When  $z$  is constant, the foundation's shear stress  $\tau_{\theta z}|_{r=0}$  in three cases, conforms with the sinusoidal line as  $\theta$  changing. In view of  $D_1$ , The shear stress  $\tau_{\theta z}|_{r=0}$  of transversely isotropic foundation is greater than that without damage, while it is smaller than that in view of  $D_2$ . And when the depth is to 4m (equivalently 4 times of circular load's radius), the shear stress is almost equal in three cases. Thus the damage has an impact on the transversely isotropic foundation's shear stress within the scope of 4 times of load's radius, but the impact can be negligible beyond the scope. This conclusion is identical to the results of practical engineering test, which can describe that the displacement function method here is reasonable and effective.

### 5 Conclusions

In this paper, it is a important work that the Galerkin displacement potential function has been revised. Base on this, a general solution of the transversely isotropic elastic space's problem is obtained in the image field, which is based on the elastic damage theory. Moreover, The analytic solution expression of displacement and stress components for the space problem of transversely isotropic foundation is derived. The solution doesn't only apply to solve both axisymmetric and non-axisymmetric problem of the transversely isotropic elastic space no matter whether or not the damage is considered., but also plays a important role in studying

displacement and stress field of transversely isotropic foundation under specific boundary conditions.

### Acknowledgement

This work was financially supported by the National Natural Science Foundation (51178387) and the Youth Natural Science Foundation of Xi'an University of Architecture and Technology (QN1240).

### References

- [1] LEKHNITSKII S G. Theory of elasticity of an anisotropic body. Moscow: Mir Publishers, 1981
- [2] Elliontt H A. Three-Dimensional stress distributions in hexagonal aeolotropic crystals. Proc, Cambridge Phil. Soc. 1948, Vol.44, pp. 522-553
- [3] Eubanks R A, Sternberg E. On the axisymmetric problem of elasticity theory equations for a media with transversely isotropy. *Journal of Rational Mechanics Analysis*, 1954, Vol.3, pp.89-101
- [4] C M Gerrard. Solutions for point loads and generalized circular loads applied with cross-anisotropic half-space, CSIRO Aust, Division of applied Geomechanics technical paper.1980, No.28
- [5] Pan Y C, Chou T W. Green function solutions for semi-infinite transversely isotropic materials. *International Journal Of Engineering Science*. 1979, Vol.17, pp. 545-551
- [6] Hu Haichang. On the three-dimensional problems of the theory of elasticity of a transversely isotropic body. *Journal of Physics*, 1953, 9(2): pp.130-147.(in Chinese)
- [7] Hu Haichang. On the equilibrium of a transversely isotropic elastic half space. *Journal of Physics*, 1954,10(3): pp. 239-258.(in Chinese)
- [8] Ding Haojiang, Chi Yuwei. Fundamental solutions of axisymmetric problems of transversely isotropic materials. *Chinese Journal of Applied Mechanics*,1999, 16(4): pp. 114-120
- [9] Dun Zhilin, Liu Ganbin, Chang Xiangyang. Displacement function method of axisymmetrical problem with transversely isotropic layers. *Journal of Jiaozuo Institute of Technology*, 2002,21(6): pp. 420-426.(in Chinese)
- [10] Dun Zhilin, Liu Ganbin. Analytical solution for axial symmetric problems of transversely isotropic foundation under several common loads. *Engineering Mechanics*, 2003,20(6): pp. 187-194.(in Chinese)
- [11] Chen Guangjing, Zhao Xihong,et al.. A nalytic solutions of non-axisymmetric load applied to layered cross-anisotropic elastic body. *Journal of Tongji University*, 1998,26(5): pp. 105-108.(in Chinese)
- [12] Zhang Yinke, Huang Yi. The non-axisymmetrical dynamic response of transversely isotropic saturated poroelastic media. *Applied Mathematics and Mechanics*, 2001,22(1): pp. 56-70
- [13] Shen Zhujiang. Simulation of damage mechanics deformation characteristics of soil. The fifth national conference on numerical analysis and analytical method of rock and soil mechanics, 1994
- [14] Chow C.L. and Wang J. An anisotropic theory of elasticity for continuum damage mechanics. *International Journal of Fracture*, 1987, 33, pp. 3-16.
- [15]Zhao Xihong, Sun Hong, Luo Guanwei. Damage Soil Mechanics. Shanghai: Tongji University Press, 2000.
- [16] Ding Haojiang. The transverse isotropic elastic mechanics. Hangzhou: Zhejiang University Press, 1997
- [17] Li Jie. The analysis of stress and displacement about space problem for transversely isotropic foundation. Jiaozuo: Henan Polytechnic University, 2005. (in Chinese)

## Analysis of Steel Moment Frames subjected to Vehicle Impact

Hyungoo Kang<sup>1</sup>, Jeongil Shin<sup>1</sup>, Jinkoo Kim<sup>2\*</sup>

<sup>1</sup>Graduate Student, Department of Civil-Architectural and Environmental System Engineering,  
Sungkyunkwan University, Suwon, Korea.

<sup>2</sup>Professor, Department of Civil and Architectural Engineering, Sungkyunkwan University, Suwon, Korea

\*Corresponding author: jkim12@skku.edu

### Abstract

Structures are often subject to vehicle collision which can be accidental or intentional as in the case of a terrorist attack. This study investigates the performance of a 2D and a 3D steel moment frame subjected to vehicle collision at a first story column using LS-DYNA. The finite element models of vehicles provided by the National Crash Analysis Center (NCAC) are used for numerical analysis. Nonlinear dynamic time history analysis of the 2D model structure is carried out based on the arbitrary column removal scenario and the vertical displacement of the damaged structure is compared with that obtained from collision analysis. The analysis results show that the model structure remain stable when the speed of the car is 40km/h. However at the speed of 80 and 120 km/h both the 2D and 3D structures collapse by progressive collapse. The vertical displacement of the damaged joint obtained from collision analysis is significantly larger than the displacement computed based on the arbitrary column removal scenario.

**Keywords:** Vehicle Collision, Progressive Collapse, FEM Explicit Analysis, LS-DYNA®.

### 1. Introduction

Recently the collision of vehicles with structures has increased due either to accidents or to terrorist attack. It has been reported that there has been a shift in terrorist modus operandi from a parked vehicle-borne improvised explosion to a penetrative attack (Cormie et al. 2009). In this regard it is necessary to investigate the damage and collapse behavior of structures subjected to vehicle collision. Borovinsek et al. (2007) presented the results of computational simulations of road safety barrier behavior under vehicle crash conditions mandated by the European standard EN 1317. Itoh et al. (2007) simulated the progressive impact of a heavy truck on a concrete barrier using LS-DYNA, and compared the accuracy of the FEM models with full scale on-site testing results. Liu (2011) investigated the dynamic crushing behaviors of steel box beams focusing on the effect of strain hardening and strain rate effects. Sharma et al. (2012) developed a framework for estimation of the dynamic shear force capacity of an RC column subject to vehicle impact. Tay et al. (2012) carried out vehicular crash test of a security bollard, and compared the results with those of numerical simulations using two different loading approaches in LS-DYNA.

The damage caused by vehicle collision may result in progressive collapse in structures. U.S. Department of Defense has issued guidelines for evaluating the progressive collapse potential (UFC, 2013). Many researchers such as Kim and Choi (2013) evaluated the progressive collapse resisting capacity of structures based on the arbitrary column removal scenario specified in the UFC guidelines.

This study investigates the performance of steel moment frames subjected to vehicle collision at a first story column through numerical simulation using LS-DYNA®. The finite element models of vehicles provided by the National Crash Analysis Center (NCAC) are used for numerical analysis. Nonlinear dynamic time history analyses are carried out with three bay 2D and 3D steel structures subjected to a car impact in a first story column. The vertical displacements of the damaged structure obtained from the collision and the arbitrary column removal method recommended in the UFC guidelines are compared.

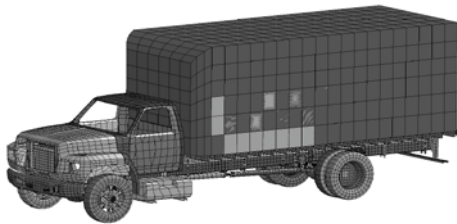
## 2. Analysis modeling

Materials can behave very differently at the higher strain rates typical of moderate to high-speed dynamic events such as impact. In this study high strain rate effect is accounted for using the Cowper-Symonds model which scales the yield stress by the strain rate dependent factor as follows:

$$\sigma_y = \left[ 1 + \left( \frac{\dot{\varepsilon}}{C} \right)^{1/p} \right] \cdot \sigma_0 \quad (1)$$

where,  $\dot{\varepsilon}$  is the strain rate during dynamic crushing,  $C$  and  $p$  are the Cowper-Symonds strain rate parameters. In the impact analysis the original yield strength  $\sigma_0$  is replaced by the dynamic flow stress  $\sigma_y$  considering the strain rate effects.

The automobile used in the impact analysis is the eight-ton single unit truck shown in Fig. 1 provided by the NCAC (National Crash Analysis Center), and the detailed finite element modeling information is shown in Table 1. The vehicle is built on a main longitudinal rail structure that acts as its backbone. The material of the rails is specified in the Service Manual as the High Strength Low Alloy (HSLA) steel of yield point 350 MPa. The yield stress of the steel forming the surface of the truck is 155MPa, and that of the other components is 270 MPa. The mass density and elastic modulus of steel used in the model are 7.85 kN/m<sup>2</sup>/g and 205,000MPa, respectively. It was assumed that 2.8ton of mass is loaded on the truck, which leads to total mass of 8.035 ton. The material data available from the Auto/Steel Partnership [4] and American Iron and Steel Institute [5] was used to enhance the existing material model.



**Figure 1. F800 FEM truck model**

**Table 1. Information of truck FEM model**

Number of element	Shell	19,479
	Solid	1,248
	Beam	124
Weight of vehicle [kg]		8035
Elastic modulus [MPa]		205,000
Impact velocity [km/h]		40, 80, 120
Vehicle geometry [B x H x L, mm]		2,400 x 3,200 x 8,500

## 3. Analysis of single steel column

Impact analysis is carried out on a single steel column with fixed boundary conditions at both ends. The analysis results of columns with a hollow circular (C-column), a square (S-column), and a H section shown in Fig. 2 are compared. The columns have the same length and are designed for the same loading condition. The steel columns are modeled with solid elements, and the contact condition between the column and the automobile is defined by \*CONTACT\_AUTOMATIC\_SURFACE\_TO\_SURFACE function in LS-Dyna. The friction coefficient between the ground and the wheels is assumed to be 0.01. The \*CONTACT\_INTERIOR condition is used to prevent the occurrence of negative volume due to large deformation of the automobile. Fig. 3 shows the stress-strain relationship of the A572 steel of which the columns are made.

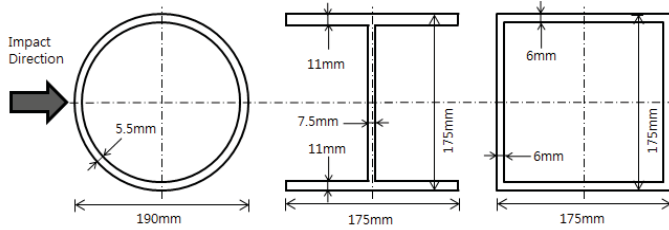


Figure 2. Cross-section of steel column

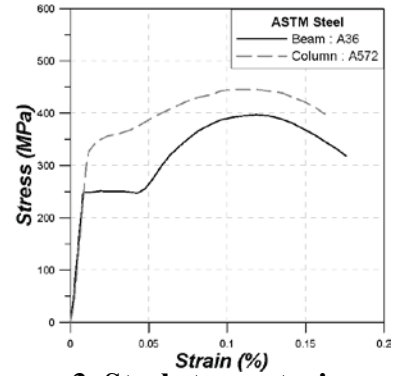
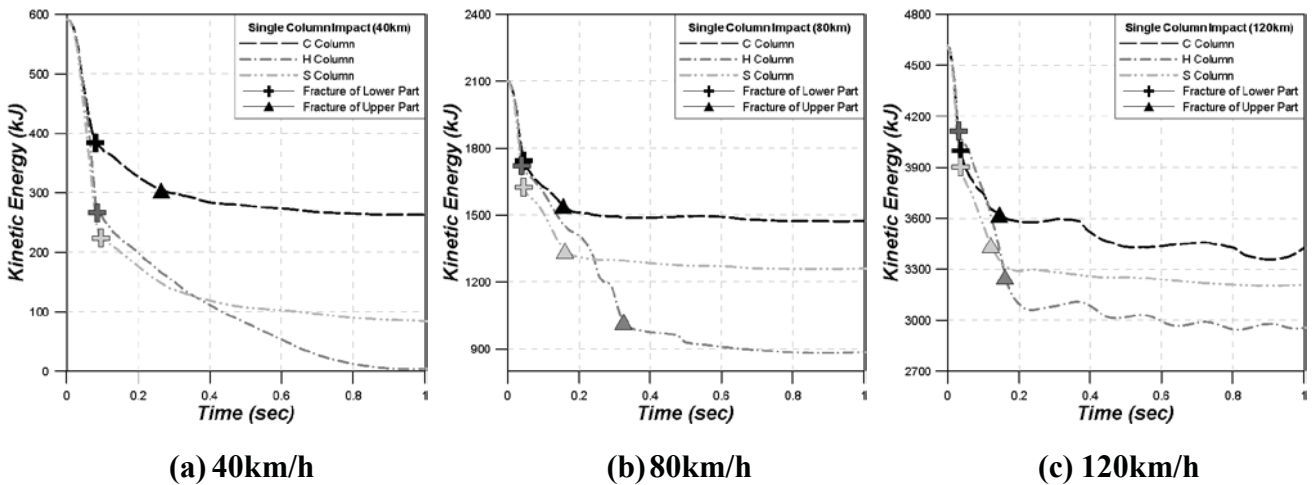


Figure 3. Steel stress-strain curve



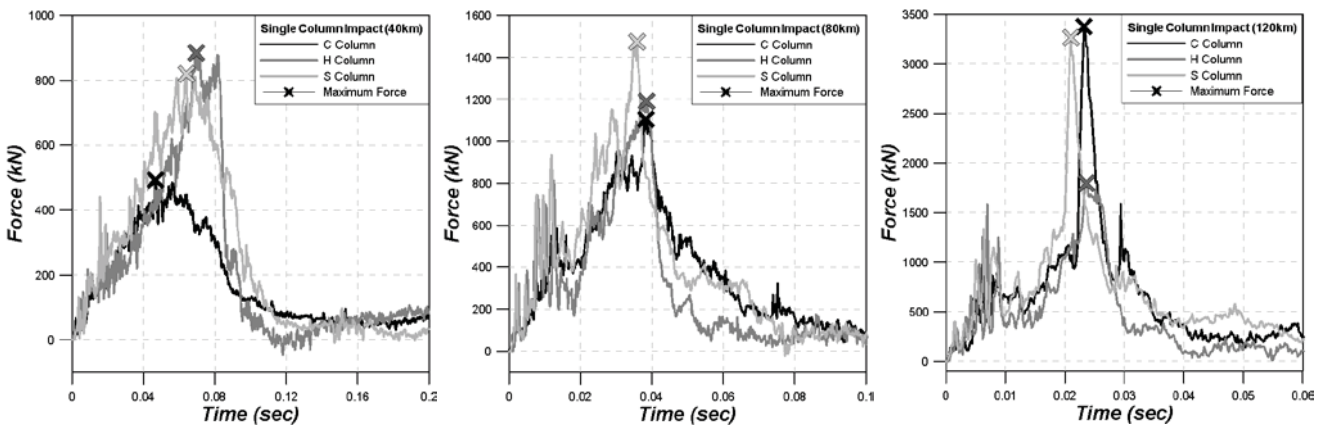
(a) 40km/h

(b) 80km/h

(c) 120km/h

Figure 4. Variation of kinetic energy

The impact simulation is carried out with three different car speeds: 40, 80, and 120 km/h. Fig. 4 depicts the variation of kinetic energy generated during the collision. The analysis results show that in every case the rate of decrease in kinetic energy (i.e. the rate of decrease in car speed after impact) is smallest in the circular column. The kinetic energy decreases most rapidly in the H-shaped column which has the largest cross sectional area. When the speed is 40km/h the kinetic energy associated with the collision to the H-shaped column becomes zero at 1.0 second after the impact, which implies that the car stopped completely due to the collision. On the other hand the existence of kinetic energy at 1.0 second in other columns implies that the columns are completely destroyed by the car crash and the car is still moving.



(a) 40km

(b) 80km

(c) 120km

Figure 5. Variation of impact force for different car speeds

Figure 5 shows the variation of impact force for three different car speeds and the maximum values are summarized in Table 2. The impact force is smallest in the circular column when the car speed is lowest. However in the highest speed the impact force of the circular column turns out to be highest. The opposite is observed in the H-shaped column.

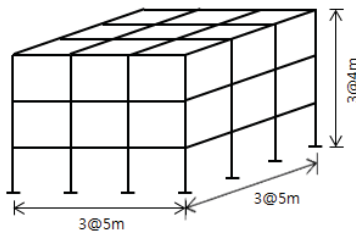
**Table 2. Maximum force generated during the collision**

Velocity [km/h]	FEM analysis result [kN]		
	Circular column	H column	Square column
40	493.14	883.68	820.05
80	1105.60	1189.98	1475.38
120	3377.45	1798.69	3263.19
Rate of increase	680.9%	203.5%	397.9%

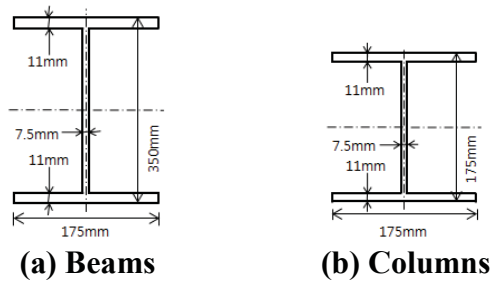
**4. Analysis of a moment frame structure subjected to car impact**

*4.1 Model structure*

The analysis model structure is a three-story three-bay moment resisting frame with 5m span length and 4m story height as shown in Fig. 6. The beams and columns are designed with steel H-shaped members with A36 and A572 steel, respectively. The cross-sectional information is shown in Fig. 7. The structure is designed with dead and live loads of 5 and 3 kN/m<sup>2</sup>, respectively. The structure is modeled in the LS\_Dyna with 416,224 solid elements. The columns are modeled to be continuous throughout the stories and the beams are welded to columns. Two horizontal continuity plates are located between column flanges across the connections at the level of beam flanges. The limit strain or the elongation at break is assumed to be 0.2, 0.18, and 0.1 for beams, columns, and connections, respectively, in the analysis. Table 3 shows the material properties of the model structure, and the stress-strain curves for beams and columns are depicted in Fig. 3. Fig. 8 depicts the finite element mesh of a typical beam-column joint.



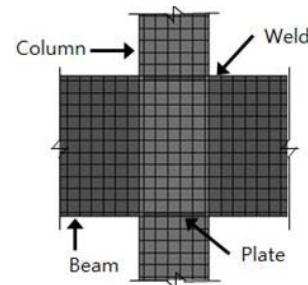
**Figure 6. 3D model structure**



**Figure 7. Cross-section of elements**

**Table 3. Modeling information of frame**

Yield Stress	Beams	250 (MPa)
	Columns	345 (MPa)
Elongation at break	Beams	0.2
	Columns	0.18
	Weld	0.1
Elastic modulus		205,000 (MPa)
Poisson's ratio		0.3



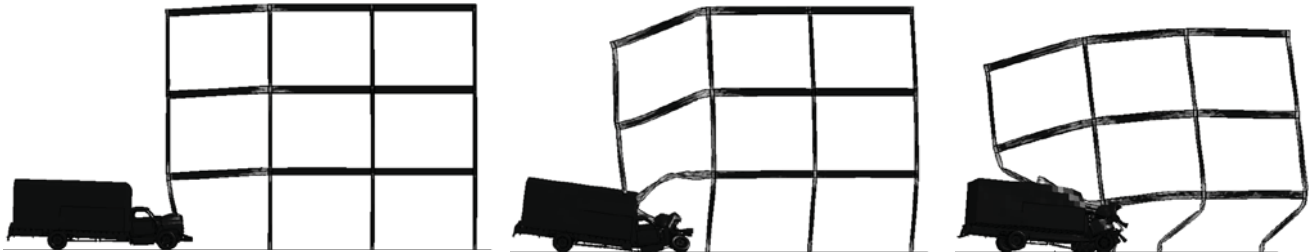
**Figure 8. FE mesh generation of a connection**

*4.2 Analysis results of 2D frame structure*

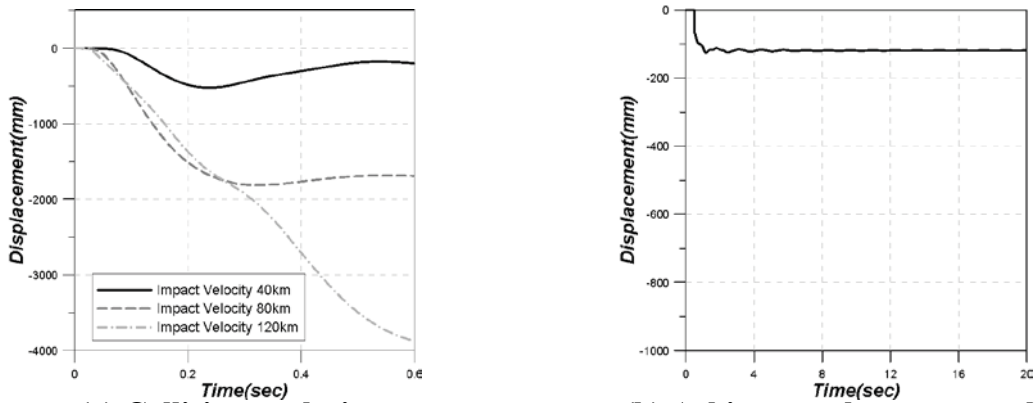
Collision analysis is carried out with one of the internal frame separated from the 3D model structure shown in Fig. 6. Fig. 9 shows the deformed shapes of the structure 1.0 second after



collision. It is observed that when the speed of the truck is 40km/h only the exterior column is severely damaged due to the collision with the truck but is not separated from the joint. When the car speed is increased to 80km/h the bottom of the collided column is completely separated from the joint and the left-hand-side bay collapses due to progressive collapse. At the speed of 120km/h the truck goes through the exterior column and collides with the adjacent interior column. The other first story columns are also severely damaged due to large lateral displacement.



(a) 40km/h (b) 80km/h (c) 120km/h  
**Figure 9. 2D frame impact simulation results (t=1 sec.)**



(a) Collision analysis (b) Arbitrary column removal  
**Figure 10. Vertical displacement obtained from collision analysis and arbitrary column removal method**

Figure 10(a) shows the vertical displacement of the first story exterior beam-column joint obtained from the collision analysis with three different car speed. It can be observed that at the speeds of 40 and 80km/h the collision results in significant vertical displacements but the vertical displacements remain stable. However at the speed of 120km/h the vertical displacement decreases almost unbounded, which implies collapse of the structure. Fig. 10(b) depicts the vertical displacement at the same point obtained by arbitrary sudden removal of the first story column. Compared with the results of the collision analysis, the vertical displacement obtained by the arbitrary removal of the column is significantly smaller. This is due to the fact that after collision the catenary force caused by the large bending deformation of the column pulls the joint down, which cannot be considered in the arbitrary column removal scenario.

4.3 Analysis result of 3D framed structure

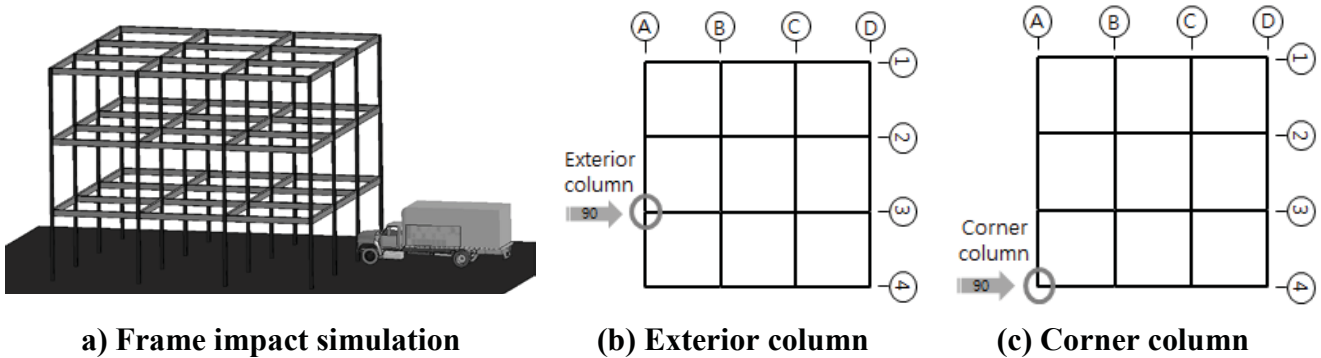


Figure 11. Steel frame impact simulation and impact direction on plane condition

Figure 11 shows the collision of the truck to the exterior and corner column of the 3D analysis model, and the analysis results for car speed of 120km/h are shown in Fig. 12. It is observed that the bottom of the exterior column is completely separated from the joint at 0.03 second after the impact. After passing through the exterior column the car continues to move until colliding with the adjacent interior column at t=0.19 second. As in the 2D model, the car collision results in progressive collapse. The vertical displacement of the upper joint of the impacted column is shown in Fig. 12(a), where it can be observed that the vertical deflection oscillate after the first impact to the exterior column and keeps decreasing after the second impact to the interior column. Fig. 12(b) depicts the deformed second story floor plan with respect to the original configuration. It can be observed that due to the series of collisions the second story is displaced laterally in significant amount and many floor beams suffers moderate to severe damage based on the failure criteria of ASCE (1000) shown in Table 4. The deformed configuration of the structure at the final stage of analysis is shown in Fig. 12(c), where it can be observed that the first story columns of the two right-hand-side frames are severely damaged and the structure is significantly tilted. Fig. 13 depicts the collision analysis results of the structure subjected to the car impact to the corner column. The vertical deflections at the joints increase monotonically after the first impact as shown in Fig. 13(a), which implies that the structure collapses progressively due to the collision to the corner column. This can be confirmed by the deformed configuration of the structure depicted in Fig. 13(b), which shows that all the first story exterior columns in the right-hand-side frame are severely damaged and the exterior frame is collapsed. Compared with the results of collision to the exterior column shown in Fig. 12, the car collision to the corner column results in more severe damage to the impacted part of the structure.

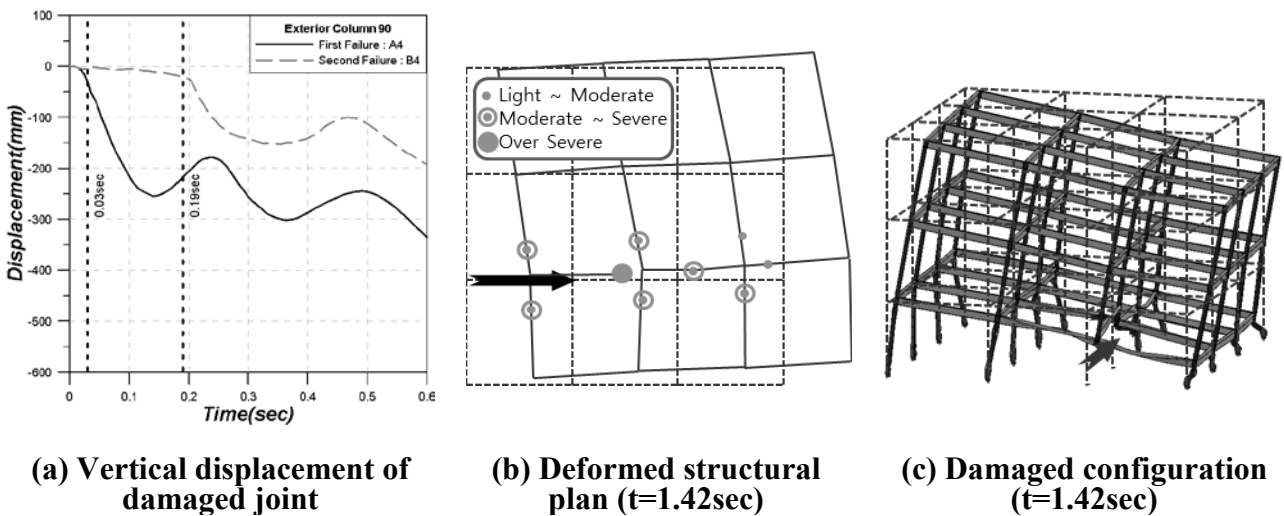
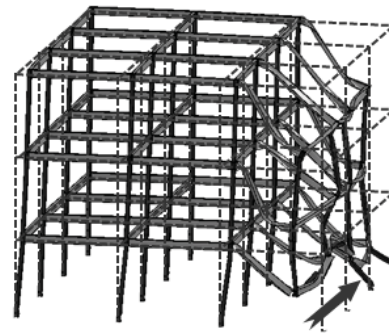
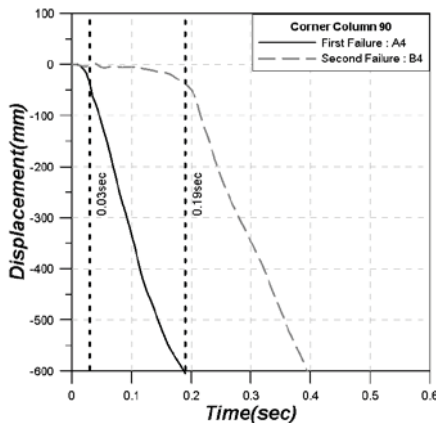


Figure 12. Analysis results for exterior column collision

**Table 4. Failure criteria for Steel members (ASCE, 1999)**

Element	Material Properties	Failure Type	Criteria	Damage		
				Light	Moderate	Severe
Beam	Steel	Bending/Membrane Response	$\delta / L$	5%	12%	25%
		Shear	$\gamma_v$	2%	4%	8%
Column		Compression	$\Delta L / L$	2%	4%	8%

- $\delta / L$  : Ratio of center line deflection to span
- $\gamma_v$  : Average shear strain across section
- $\Delta L / L$  : Ratio of shortening to height



**(a) Vertical displacement of damaged joint      (b) Deformed configuration of the structure**  
**Figure 13. Analysis results for corner column collision**

**5. Summary**

This study investigated the performance of a steel moment frame subjected to vehicle collision at a first story column using LS-DYNA. Nonlinear dynamic time history analyses were carried out with three bay 2D and 3D steel structures subjected to a car impact in a first story column with three different impact speeds.

The analysis results of the 2D frame and the 3D frame with collision to the exterior column showed that the model structure remain stable when the speed of the car is 40km/h. It was observed that only the exterior column was damaged before the car finally stopped. However at the speed of 80 and 120 km/h both the 2D and 3D structures were severely damaged by progressive collapse after the car pass through the exterior or the corner column and collided with the adjacent column in its path. The damage caused by the collision to the corner column was far greater than the damage due to collision to the exterior column. It was also observed that the vertical displacement of the model structure caused by the automobile collision is significantly larger than that obtained by the arbitrary column removal method specified in the UFC (2013) provisions. Therefore the arbitrary column removal method applied to investigate the progressive collapse potential of a structure may underestimate the actual structural response for automobile collision.

**Acknowledgement**

This research was financially supported by a grant (Code# 09 R&D A01) funded by the Ministry of Land and Transport of Korean government, and by the Korean Government (NRF-2013-Global Ph.D. Fellowship Program).

**References**

ASCE (1999), Structural design for physical security: State of the practice, *American Society of Civil Engineers*.  
 Borovinssek M, Vesenjck M, Ulbin M, Ren Z., Simulation of crash tests for high containment levels of road safety barriers, *Engineering Failure Analysis* 14 (2007) 1711–1718  
 Cho B, Jee N (2009), A study on the mechanical properties of structural steels by welding at high temperature. *Architectural Institute of Korea - Structure & Construction*, Vol. 25, Issue. 12, pp. 97-104

- Cormie D, Mays G, and Smith P. (2009). Vehicle-borne threats and the principles of hostile vehicle mitigation, Blast effects on buildings (2nd edition), Thomas Telford Limited
- Ferrer B, Ivorra S, Segovia E, Irlas R (2009), Impact load in parking steel column: Code review and numerical approach. *ECCOMAS Thematic Conference on Computational Methods in Structural Dynamics and Earthquake Engineering*, pp. 1-9
- Han H, Taheri F, Pegg N (2007), Quasi-static and dynamic crushing behaviors of aluminum and steel tubes with a cutout. *Thin-Walled Structures* 45, pp. 283-300.
- HSE (2001), Elevated temperature and high strain rate properties of offshore steels. (Offshore Technology Report 020), *Steel Construction Institute for the Health and Safety Executive*.
- Itoh Y, Liu C, Kusama R (2007), Dynamic simulation of collisions of heavy high-speed trucks with concrete barriers. *Chaos, Solitons and Fractals* 34, pp. 1239-1244.
- Kim J, Lee S, Choi H (2013), Progressive collapse resisting capacity of moment frames with viscous dampers. *The Structural Design of Tall and Special Buildings* 22, pp. 299-414.
- Liu Y (2011), Study of thin-walled box beams crushing behavior using LS-DYNA. *11<sup>th</sup> International LS-DYNA® Users Conference* 13, pp.31-40.
- LS-DYNA (2006), Theory manual version 971, © *Livemore Software Technology Corporation*.
- NCAC (2010), *National Crash Analysis Center*, <http://www.ncac.gwu.edu>
- NCHRP (1993), Recommended procedures for the safety performance evaluation of highway features. (Report 350), *National Cooperative Highway Research Program*.
- NIST (2005), Analysis of aircraft impacts into the world trade center towers. (NIST NCSTAR 1-2B), *National Institute of Standards and Technology*.
- Perform3D (2006), Nonlinear analysis and performance assessment for 3D structures-User Guide, *Computer & Structures, INC, Berkeley, CA*.
- UFC (2013), Unified Facilities Criteria. Design of buildings to resist progressive collapse. (UFC 4-023-03), *Department of Defense, USA*.
- Sharma H, Hurlbaeus S, Gardoni P (2012), Performance-based response evaluation of reinforced concrete columns subject to vehicle impact. *International Journal of Impact Engineering*. 43, pp. 52-62.
- Sherif EI-Tawil (2004), Vehicle collision with bridge piers. *Final Report*. Department of Civil and Environmental Engineering, University of Michigan.
- Tay SK, Lim B, NG SH (2012), Crash Impact Modelling of Security Bollard. *12th International LS-DYNA® Users Conference* 13, pp.1-10.

## Formulation and development of the cell-based smoothed discrete shear gap plate element (CS-FEM-DSG3) using three-node triangles

\*T. Nguyen-Thoi<sup>1,2</sup>, P. Phung-Van<sup>1</sup>, H. Nguyen-Xuan<sup>1,2</sup>

<sup>1</sup>Division of Computational Mechanics, Ton Duc Thang University, Hochiminh City, Vietnam

<sup>2</sup>Faculty of Mathematics & Computer Science, University of Science, Hochiminh City, Vietnam

\*Corresponding author: [ngttrung@hcmus.edu.vn](mailto:ngttrung@hcmus.edu.vn) ; [thoitrung76@gmail.com](mailto:thoitrung76@gmail.com)

### Abstract

The paper presents the formulation and recent development of the cell-based smoothed discrete shear gap plate element (CS-FEM-DSG3) using three-node triangles. In the CS-FEM-DSG3, each triangular element will be divided into three sub-triangles, and in each sub-triangle, the original plate element DSG3 is used to compute the strains and to avoid the transverse shear locking. Then the cell-based strain smoothing technique (CS-FEM) is used to smooth the strains on these three sub-triangles. Due to its superior and simple properties, the CS-FEM-DSG3 has been now developed for some different analyses such as: flat shells, stiffened plates, FGM plates, and piezoelectricity composite plates, etc.

Keywords: Reissner-Mindlin plate, smoothed finite element methods (S-FEM), cell-based smoothed finite element method (CS-FEM), cell-based smoothed discrete shear gap method (CS-FEM-DSG3), strain smoothing technique.

### Introduction

In the past 50 years, many of plate bending elements based on the Mindlin–Reissner theory and the first-order shear deformation theory (FSDT) have been proposed. Such a large amount of elements can be found in literatures [Reddy (2006)]. In formulations of a Mindlin–Reissner plate element using the FSDT, the deflection  $w$  and rotations  $\beta_x$ ,  $\beta_y$  are independent functions and required at least to be  $C0$ -continuous. In practical applications, lower-order displacement-based Reissner-Mindlin plate elements are preferred due to their simplicity and efficiency. These elements usually possess high accuracy and fast convergence speed for displacement solutions [Ayad *et al.* (2002)]. In addition, the main difficulty encountered of these elements is the phenomenon of shear locking which induces over-stiffness as the plate becomes progressively thinner.

In order to avoid shear locking, many new numerical techniques and effective modifications have been proposed and tested. Recently, the Discrete-Shear-Gap (DSG) method [Bletzinger *et al.* (2000)] which avoids shear locking was proposed. The DSG method works for elements of different orders and shapes and has several superior properties [Bletzinger *et al.* (2000)]. However, the element stiffness matrix in the DSG still depends on the sequence of node numbers, and hence the solution of DSG is influenced when the sequence of node numbers changes, especially for the coarse and distorted meshes.

In the front of the development of numerical methods, Liu *et al.* have recently integrated the strain smoothing technique [Chen *et al.* 2001] into the point interpolation method (PIM) [Liu *et al.* (2003, 2004a, 2004b)] to create a series of smoothed PIM (S-PIM) [Liu *et al.* (2006a, 2006b, 2013), Zhang *et al.* (2007)], as well as into the FEM to

create a series of smoothed FEM (S-FEM) [Liu *et al.* (2010a)] such as the cell/element-based smoothed FEM (CS-FEM) [Liu *et al.* (2007a, 2007b), Dai *et al.* (2007a, 2007b)], the node-based smoothed FEM (NS-FEM) [Liu *et al.* (2009a)], the edge-based smoothed FEM (ES-FEM) [Liu *et al.* (2009b)] and the face-based smoothed FEM (FS-FEM) [Nguyen-Thoi *et al.* (2009a)]. Each of these smoothed FEM has different properties and has been used to produce desired solutions for a wide class of benchmark and practical mechanics problems. Several theoretical aspects of the S-FEM models have been provided in Refs [Liu *et al.* (2007a, 2010b)]. The S-FEM models have also been further investigated and applied to various problems such as plates and shells [Nguyen-Xuan *et al.* (2009a,b), Nguyen-Thoi *et al.* (2013a)], piezoelectricity [Nguyen-Xuan *et al.* (2009c)], visco-elastoplasticity [Nguyen-Thoi *et al.* (2009b)], limit and shakedown analysis for solids [Nguyen-Xuan *et al.* (2012)], fracture mechanics [Liu *et al.* (2010c)], and some other applications [Nguyen-Thoi *et al.* (2013b,c)], etc.

Among these S-FEM models, the CS-FEM [Liu *et al.* (2007a, 2007b), Dai *et al.* (2007a, 2007b)] shows some interesting properties in the solid mechanics problems. Extending the idea of the CS-FEM to plate structures, Nguyen-Thoi *et al.* (2012) have recently formulated a cell-based smoothed discrete shear gap method (CS-FEM-DSG3). In the CS-FEM-DSG3, each triangular element will be divided into three sub-triangles, and in each sub-triangle, the original plate element DSG3 [Bletzinger *et al.* (2000)] is used to compute the strains and to avoid the transverse shear locking. Then the cell-based strain smoothing technique (CS-FEM) is used to smooth the strains on these three sub-triangles. The numerical results showed that the CS-FEM-DSG3 is free of shear locking and achieves the high accuracy compared to the exact solutions and others existing elements.

This paper hence aims to present a brief outline of the CS-FEM-DSG3 and its recent developments in some different analyses such as: flat shells [Nguyen-Thoi *et al.* (2013d)], stiffened plates [Nguyen-Thoi *et al.* (2013e)], FGM plates [Phung-Van *et al.* (2013a)] and piezoelectricity plates [Phung-Van *et al.* (2013b)], etc.

### Weakform for the Reissner-Mindlin plate

Consider a plate under bending deformation. The middle surface of plate is chosen as the reference plane that occupies a domain  $\Omega \subset R^2$  as shown in Figure 1.

Let  $w$  be the transverse displacement (deflection), and  $\boldsymbol{\beta}^T = [\beta_x \ \beta_y]$  be the vector of rotations, in which  $\beta_x, \beta_y$  are the rotations of the middle plane around  $y$ -axis and  $x$ -axis, respectively, with the positive directions defined as shown in Figure 1.

The unknown vector of three independent field variables at any point in the problem domain of the Reissner-Mindlin plates can be written as  $\mathbf{u}^T = [w \ \beta_x \ \beta_y]$ . The curvature of the deflected plate  $\boldsymbol{\kappa}$  and the shear strains  $\boldsymbol{\gamma}$  are defined, respectively, as

$$\boldsymbol{\kappa} = \mathbf{L}_d \boldsymbol{\beta} \ ; \ \boldsymbol{\gamma} = \nabla w + \boldsymbol{\beta} \quad (1)$$

where  $\nabla = [\partial/\partial x \ \partial/\partial y]^T$ , and  $\mathbf{L}_d$  is a differential operator matrix.

The standard Galerkin weakform of the static equilibrium equations for the Reissner-Mindlin plate can now be written as:

$$\int_{\Omega} \delta \boldsymbol{\kappa}^T \mathbf{D}^b \boldsymbol{\kappa} \, d\Omega + \int_{\Omega} \delta \boldsymbol{\gamma}^T \mathbf{D}^s \boldsymbol{\gamma} \, d\Omega = \int_{\Omega} \delta \mathbf{u}^T \mathbf{b} \, d\Omega \quad (2)$$

where  $\mathbf{b}$  is the distributed load applied on the plate. The matrices  $\mathbf{D}^b$  and  $\mathbf{D}^s$  are the material matrices related to the bending and shear deformation.

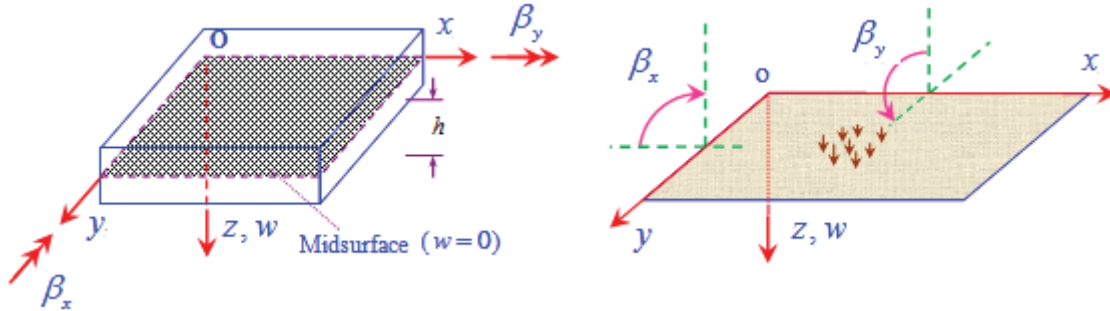


Figure 1. Mindlin plate and positive directions of deflection  $w$  and rotations  $\beta_x, \beta_y$

### Formulation of the CS-FEM- DSG3

*A brief outline on the formulation of DSG3*

Using a mesh of  $N_e$  triangular elements such that  $\Omega = \bigcup_{e=1}^{N_e} \Omega_e$  and  $\Omega_i \cap \Omega_j = \emptyset, i \neq j$ ,

the approximation  $\mathbf{u}^h = [w \ \beta_x \ \beta_y]^T$  for a three-node triangular element  $\Omega_e$  shown in Figure 2 for the Reissner-Mindlin plate can be written, at the element level, as

$$\mathbf{u}_e^h = \sum_{I=1}^3 \underbrace{\begin{bmatrix} N_I(\mathbf{x}) & 0 & 0 \\ 0 & N_I(\mathbf{x}) & 0 \\ 0 & 0 & N_I(\mathbf{x}) \end{bmatrix}}_{\mathbf{N}_I(\mathbf{x})} \mathbf{d}_{eI} = \sum_{I=1}^3 \mathbf{N}_I(\mathbf{x}) \mathbf{d}_{eI} \quad (3)$$

where  $\mathbf{d}_{eI} = [w_I \ \beta_{xI} \ \beta_{yI}]^T$  are the nodal degrees of freedom of  $\mathbf{u}_e^h$  associated to node  $I$  and  $N_I(\mathbf{x})$  is linear shape functions in a natural coordinate defined by

$$N_1 = 1 - \xi - \eta, \quad N_2 = \xi, \quad N_3 = \eta \quad (4)$$

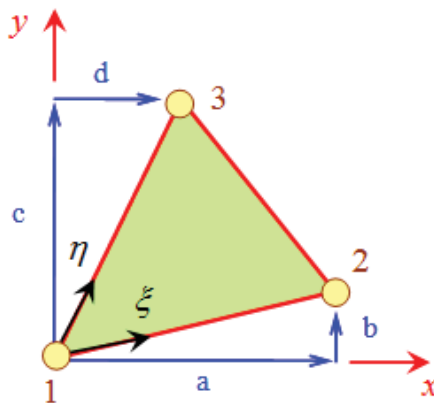


Figure 2. Three-node triangular element and local coordinates in the DSG3.

The bending and shear strains can be then expressed in the matrix forms as:

$$\boldsymbol{\kappa} = \mathbf{B}\mathbf{d}_e, \quad \boldsymbol{\gamma} = \mathbf{S}\mathbf{d}_e \quad (5)$$

where  $\mathbf{d}_e = [\mathbf{d}_{e1} \quad \mathbf{d}_{e2} \quad \mathbf{d}_{e3}]^T$  is the nodal displacement vector of element,  $\mathbf{B}$  and  $\mathbf{S}$  contain the derivatives of the shape functions that are constants such as

$$\mathbf{B} = \frac{1}{2A_e} \begin{bmatrix} 0 & b-c & 0 & 0 & c & 0 & 0 & -b & 0 \\ 0 & 0 & d-a & 0 & 0 & -d & 0 & 0 & a \\ 0 & d-a & b-c & 0 & -d & c & 0 & a & -b \end{bmatrix} = \frac{1}{2A_e} [\mathbf{B}_1 \quad \mathbf{B}_2 \quad \mathbf{B}_3] \quad (6)$$

$$\mathbf{S} = \frac{1}{2A_e} \begin{bmatrix} b-c & A_e & 0 & c & ac/2 & bc/2 & -b-bd/2 & -bc/2 \\ d-a & 0 & A_e & -d & -ad/2 & -bd/2 & c & ad/2 & ac/2 \end{bmatrix} = \frac{1}{2A_e} [\mathbf{S}_1 \quad \mathbf{S}_2 \quad \mathbf{S}_3] \quad (7)$$

with  $a, b, c, d$  are geometric distances as shown in Figure 2 and  $A_e$  is the area of the element  $\Omega_e$ .

Substituting Eqs. (3) and (5) into Eq.(2), the global stiffness matrix now becomes

$$\mathbf{K} = \sum_{e=1}^{N_e} \mathbf{K}_e \quad (8)$$

where  $\mathbf{K}_e$  is the element stiffness matrix and is computed by

$$\mathbf{K}_e = \int_{\Omega_e} \mathbf{B}^T \mathbf{D}^b \mathbf{B} d\Omega + \int_{\Omega_e} \mathbf{S}^T \mathbf{D}^s \mathbf{S} d\Omega = \mathbf{B}^T \mathbf{D}^b \mathbf{B} A_e + \mathbf{S}^T \mathbf{D}^s \mathbf{S} A_e \quad (9)$$

Basing on the formulation, it is seen that the element stiffness matrix in the DSG3 depends on the sequence of node numbers of elements, and hence the solution of DSG3 is influenced when the sequence of node numbers of elements changes, especially for the coarse and distorted meshes. The CS-FEM-DSG3 is hence proposed to overcome this drawback and also to improve the accuracy as well as the stability of the DSG3.

#### Formulation of CS-FEM-DSG3

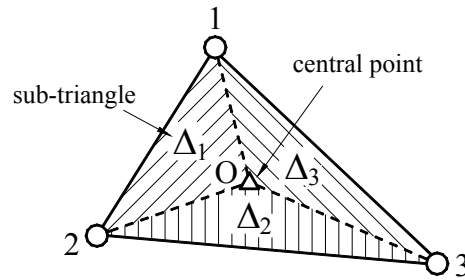
In the CS-FEM-DSG3 [Nguyen-Thoi *et al.* (2012)], the domain discretization is the same as that of the DSG3 [Bletzinger *et al.* (2000)] using  $N_n$  nodes and  $N_e$  triangular elements. However in the formulation of the CS-FEM-DSG3, each triangular element is divided into three sub-triangles by connecting the central point  $O$  of the element to three field nodes as shown in Figure 3. Using the DSG3 [Bletzinger *et al.* (2000)] formulation for each sub-triangle, the bending and shear strains in 3 sub-triangles are then obtained, respectively, by

$$\boldsymbol{\kappa}_e^{\Delta_j} = \mathbf{B}^{\Delta_j} \mathbf{d}_e, \quad j = 1, 2, 3 \quad (10)$$

$$\boldsymbol{\gamma}_e^{\Delta_j} = \mathbf{S}^{\Delta_j} \mathbf{d}_e, \quad j = 1, 2, 3 \quad (11)$$

where  $\mathbf{d}_e$  is the vector containing the nodal degrees of freedom of the element;  $\mathbf{B}^{\Delta_j}$ ,  $\mathbf{S}^{\Delta_j}$ ,  $j = 1, 2, 3$ , are bending and shearing gradient matrices by the DSG3 [Bletzinger *et al.* (2000)] of  $j^{\text{th}}$  sub-triangle, respectively.





**Figure 3. Three sub-triangles ( $\Delta_1$ ,  $\Delta_2$  and  $\Delta_3$ ) created from the triangle 1-2-3 in the CS-FEM-DSG3 by connecting the central point O with three field nodes 1, 2 and 3.**

Now, applying the cell-based strain smoothing operation in the CS-FEM [Liu *et al.* (2010a)], the bending and shear strains  $\kappa_e^{\Delta_j}$ ,  $\gamma_e^{\Delta_j}$ ,  $j=1,2,3$  are, respectively, used to create element smoothed strains  $\tilde{\kappa}_e$  and  $\tilde{\gamma}_e$  on the triangular element  $\Omega_e$ , such as:

$$\tilde{\kappa}_e = \tilde{\mathbf{B}}\mathbf{d}_e \quad ; \quad \tilde{\gamma}_e = \tilde{\mathbf{S}}\mathbf{d}_e \quad (12)$$

where  $\tilde{\mathbf{B}}$  and  $\tilde{\mathbf{S}}$  are the smoothed strain gradient matrices, respectively, given by

$$\tilde{\mathbf{B}} = \frac{1}{A_e} \sum_{j=1}^3 A_{\Delta_j} \mathbf{B}^{\Delta_j} \quad ; \quad \tilde{\mathbf{S}} = \frac{1}{A_e} \sum_{j=1}^3 A_{\Delta_j} \mathbf{S}^{\Delta_j} \quad (13)$$

Therefore the global stiffness matrix of the CS-FEM-DSG3 is computed by

$$\tilde{\mathbf{K}} = \int_{\Omega} \tilde{\mathbf{B}}^T \mathbf{D}^b \tilde{\mathbf{B}} d\Omega + \int_{\Omega} \tilde{\mathbf{S}}^T \mathbf{D}^s \tilde{\mathbf{S}} d\Omega = \tilde{\mathbf{B}}^T \mathbf{D}^b \tilde{\mathbf{B}} A_e + \tilde{\mathbf{S}}^T \mathbf{D}^s \tilde{\mathbf{S}} A_e \quad (14)$$

### Advantages of CS-FEM-DSG3

Through the formulation of CS-FEM-DSG3 [Nguyen-Thoi *et al.* (2012)], it is seen that the method is simple and only based on three-node triangular elements without adding any additional DOFs. The CS-FEM-DSG3 is free of shear locking and pass the patch test. The method can be seen as an effective tool for analyses of Mindlin plates. Through the numerical examples of CS-FEM-DSG3 [Nguyen-Thoi *et al.* (2012)], the method shows four superior properties such as: (1) be a strong competitor to many existing three-node triangular plate elements in the static analysis; (2) can give high accurate solutions for problems with skew geometries in the static analysis; (3) can give high accurate solutions in free vibration analysis; (4) can provide accurately the values of high frequencies of plates by using only coarse meshes.

### Extension of the CS-FEM-DSG3 to some others applications

Due to its superior and simple properties, the CS-FEM-DSG3 has been extended quickly to some different analyses.

First, by adding three degrees of freedom of the membrane and rotation displacements, together using the coordinate transformation matrix, the CS-FEM-DSG3 is easy to extend to the flat shell element [Nguyen-Thoi *et al.* (2013d)]. This extension hence highlights the advantage of the method which uses only triangular elements,

because the geometry of shell structures is often much more complicated than that of the plate structures.

Next, by combining with a membrane element and stiffened by a thick beam element Timoshenko, the CS-FEM-DSG3 is extended to the stiffened plates [Nguyen-Thoi *et al.* (2013e)]. In this element, the eccentricity between the plate and the beam is included in the formulation of the beam. The compatibility of deflection and rotations of stiffeners and plate is assumed at the contact positions.

Next by using 7 degrees of freedom, the CS-FEM-DSG3 is extended to the  $C^0$ -type high-order shear deformation plate theory for the static and free vibration analyses of functionally graded plates (FGPs) [Phung-Van *et al.* (2013a)]. In the FGPs, the material properties are assumed to vary through the thickness by a simple power rule of the volume fractions of the constituents. In the static analysis, both thermal and mechanical loads are considered and a two-step procedure is performed including a step of analyzing the temperature field along the thickness of the plate and a step of analyzing the behavior of the plate subjected to both thermal and mechanical loads.

And recently, by combining the degrees of membrane displacement and electric potential, the CS-FEM-DSG3 is further extended for the static, free vibration analyses and dynamic control of composite plates integrated with piezoelectric sensors and actuators [Phung-Van *et al.* (2013b)]. In the piezoelectric composite plates, the electric potential is assumed to be a linear function through the thickness of each piezoelectric sublayer. A displacement and velocity feedback control algorithm is used for the active control of the static deflection and the dynamic response of plates through the closed loop control with bonded or embedded distributed piezoelectric sensors and actuators.

## Conclusions

The paper presents a brief outline and recent developments of the CS-FEM-DSG3 using three-node triangles. In the original plate element, each triangular element will be divided into three sub-triangles, and in each sub-triangle, the original plate element DSG3 is used to compute the strains and to avoid the transverse shear locking. Then the cell-based strain smoothing technique (CS-FEM) is used to smooth the strains on these three sub-triangles. Through the formulation and numerical examples, it is seen that the CS-FEM-DSG3 is an effective tool for analyses of Mindlin plates. And due to its superior and simple properties, the CS-FEM-DSG3 has been extended quickly to some different analyses such as flat shells, stiffened plates, FGM plates, and piezoelectricity composite plates, etc.

## Acknowledgements

This research is funded by Vietnam National University Hochiminh City (VNU-HCM) under grant number B-2013-18-03.

## References

- Ayad, R., Rigolot, A. (2002), An improved four-node hybrid-mixed element based upon Mindlin's plate theory. *International Journal for Numerical Methods in Engineering*, 55, pp. 705–731.
- Bletzinger, K. U., Bischoff, M., Ramm, E. (2000), A unified approach for shear-locking free triangular and rectangular shell finite elements. *Computers and Structures*, 75, pp. 321–334.

- Chen, J. S., Wu, C. T., Yoon, S., You, Y. (2001), A stabilized conforming nodal integration for Galerkin mesh-free methods. *International Journal for Numerical Methods in Engineering*, 50, pp. 435–466.
- Dai, K.Y., Liu, G.R., Nguyen-Thoi, T. (2007a), An n-sided polygonal smoothed finite element method (nSFEM) for solid mechanics. *Finite elements in analysis and design*, 43, pp. 847-860.
- Dai, K.Y., Liu, G.R. (2007b), Free and forced vibration analysis using the smoothed finite element method (SFEM). *Journal of Sound and Vibration*, 301 (3-5), pp. 803 -820.
- Liu, G.R., Dai, K.Y., Lim, K.M., Gu, Y.T. (2003), A radial point interpolation method for simulation of two-dimensional piezoelectric structures. *Smart Materials and Structures*, 12 (2), pp. 171.
- Liu, G. R., Gu, Y. T., Dai, K. Y. (2004a), Assessment and applications of point interpolation methods for computational mechanics. *International Journal for Numerical Methods in Engineering*, 59(10), pp. 1373-1397.
- Liu, G. R., Dai, K. Y., Lim, K. M. (2004b), Static and vibration control of composite laminates integrated with piezoelectric sensors and actuators using the radial point interpolation method. *Smart Materials and Structures*, 13, pp. 1438-1447.
- Liu, G.R., Zhang, G.Y., Dai, K.Y., Wang, Y.Y., Zhong, Z.H., Li, G.Y., Han, X. (2006a), A linearly conforming point interpolation method (LC-PIM) for 2D solid mechanics problems. *International Journal of Computational Methods*, 2, pp. 645–665.
- Liu, G.R., Li, Y., Dai, K.Y., Luan, M.T., Xue, W. (2006b), A linearly conforming radial point interpolation method for solid mechanics problems. *International Journal of Computational Methods*, 3, pp. 401–428.
- Liu, G. R., Dai, K. Y., Nguyen-Thoi, T. (2007a), A smoothed finite element for mechanics problems. *Computational Mechanics*, 39, pp. 859-877.
- Liu, G. R., Nguyen-Thoi, T., Dai, K. Y., Lam, K. Y. (2007b), Theoretical aspects of the smoothed finite element method (SFEM), *International Journal for Numerical Methods in Engineering*, 71, pp. 902–930.
- Liu, G.R., Nguyen-Thoi, T., Nguyen-Xuan, H., Lam, K.Y. (2009a), A node-based smoothed finite element method (NS-FEM) for upper bound solution to solid mechanics problems, *Computers and Structures*, 87, pp. 14-26.
- Liu, G.R., Nguyen-Thoi, T., Lam, K.Y. (2009b), An edge-based smoothed finite element method (ES-FEM) for static, free and forced vibration analyses in solids, *Journal of Sound and Vibration*, 320, pp. 1100-1130.
- Liu, G. R., Nguyen Thoi Trung. (2010a), *Smoothed Finite Element Methods*, CRC Press, Taylor and Francis Group, NewYork.
- Liu, G. R., Nguyen-Xuan, H., Nguyen-Thoi, T. (2010b), A theoretical study on NS/ES-FEM: properties, accuracy and convergence rates. *International Journal for Numerical Methods in Engineering*, 84, pp. 1222–1256.
- Liu, G. R., Chen, L., Nguyen-Thoi, T., Zeng, K., Zhang, G.Y. (2010c), A novel singular node-based smoothed finite element method (NS-FEM) for upper bound solutions of cracks. *International Journal for Numerical Methods in Engineering*, 83, pp. 1466–1497.
- Liu, G.R., Zhang, G.Y. (2013), *Smoothed Point Interpolation Methods: G Space Theory and Weakened Weakforms*, World Scientific Publishing Company, Singapore.
- Nguyen-Thoi, T., Liu, G.R., Lam, K.Y., Zhang, G.Y. (2009a), A Face-based Smoothed Finite Element Method (FS-FEM) for 3D linear and nonlinear solid mechanics problems using 4-node tetrahedral elements, *International Journal for Numerical Methods in Engineering*, 78, pp. 324-353.
- Nguyen-Thoi, T., Liu, G. R., Vu-Do, H. C., Nguyen-Xuan, H. (2009b), A face-based smoothed finite element method (FS-FEM) for visco-elastoplastic analyses of 3D solids using tetrahedral mesh. *Computer Methods in Applied Mechanics and Engineering*, 198, pp. 3479-3498.

- Nguyen-Thoi, T., Phung-Van, P., Nguyen-Xuan, H., Thai-Hoang, C. (2012), A cell-based smoothed discrete shear gap method using triangular elements for static and free vibration analyses of Reissner–Mindlin plates. *International journal for numerical methods in Engineering*, 91, pp. 705:741.
- Nguyen-Thoi, T., Phung-Van, P., Luong-Van, H., Nguyen-Van, H., Nguyen-Xuan, H. (2013a), A cell-based smoothed three-node Mindlin plate element (CS-MIN3) for static and free vibration analyses of plates. *Computational Mechanics*, 50(1), pp. 65-81.
- Nguyen-Thoi, T., Phung-Van, P., Rabczuk, T., Nguyen-Xuan, H., Le-Van, C. (2013b), Free and forced vibration analysis using the n-sided polygonal cell-based smoothed finite element method (*n*CS-FEM). *International Journal of Computational Methods*, 10(1), pp. 1340008.
- Nguyen-Thoi, T., Phung-Van, P., Rabczuk, T., Nguyen-Xuan, H., Le-Van, C. (2013c), An application of the ES-FEM in solid domain for dynamic analysis of 2D fluid-solid interaction problems. *International Journal of Computational Methods*, 10(1), pp. 1340003.
- Nguyen-Thoi, T., Phung-Van, P., Thai-Hoang, C., Nguyen-Xuan, H. (2013d), A cell-based smoothed discrete shear gap method (CS-DSG3) using triangular elements for static and free vibration analyses of shell structures. *International Journal of Mechanical Sciences*, 74, pp. 32-45.
- Nguyen-Thoi, T., Bui-Xuan, T., Phung-Van, P., Nguyen-Xuan, H., Ngo-Thanh, P. (2013e), Static, free vibration and buckling analyses of stiffened plates by CS-FEM-DSG3 using triangular elements. *Computers and Structures*, 125, pp. 100-113.
- Nguyen-Xuan, H., Liu, G. R., Thai-Hoang, C., Nguyen-Thoi, T. (2009a), An edge-based smoothed finite element method with stabilized discrete shear gap technique for analysis of Reissner-Mindlin plates. *Computer Methods in Applied Mechanics and Engineering*, 199, pp. 471-489.
- Nguyen-Xuan, H., Nguyen-Thoi, T. (2009b), A stabilized smoothed finite element method for free vibration analysis of Mindlin-Reissner plates. *International Journal for Numerical Methods in Biomedical Engineering*, 25, pp. 882 – 906.
- Nguyen-Xuan, H., Liu, G. R., Nguyen-Thoi, T., Nguyen-Tran, C. (2009c), An edge-based smoothed finite element method (ES-FEM) for analysis of two-dimensional piezoelectric structures. *Smart Materials and Structures*, 18, pp. 065015.
- Nguyen-Xuan, H., Rabczuk, T., Nguyen-Thoi, T., Tran, T. N., Nguyen-Thanh, N. (2012), Computation of limit and shakedown loads using a node-based smoothed finite element method. *International Journal for Numerical Methods in Engineering*, 90, pp. 287-310.
- Phung-Van, P., Nguyen-Thoi, T., Tran V. Loc., Nguyen-Xuan, H. (2013a), A cell-based smoothed discrete shear gap method (CS-DSG3) based on the  $C^0$ -type higher-order shear deformation theory for static and free vibration analyses of functionally graded plates. *Computational Materials Science*, 79, pp. 857–872.
- Phung-Van, P., Nguyen-Thoi, T., Le-Dinh, T., Nguyen-Xuan, H. (2013b), Static, free vibration analyses and dynamic control of composite plates integrated with piezoelectric sensors and actuators by the cell-based smoothed discrete shear gap method (CS-FEM-DSG3). *Smart Materials and Structures*, 22, pp. 095026.
- Reddy, J. N. (2006), *Theory and analysis of elastic plates and shells*, CRC Press: Taylor and Francis Group, NewYork.
- Zhang, G.Y., Liu, G.R., Wang, Y.Y., Huang, H.T., Zhong, Z.H., Li, G.Y., Han, X. (2007) A linearly conforming point interpolation method (LC-PIM) for three-dimensional elasticity problems. *International Journal for Numerical Methods in Engineering*, 72, pp. 1524 – 1543.

## A High-Order Unstructured Mixed Method for Aerodynamic Applications

Min Kyu Jung<sup>1</sup> and \*Oh Joon Kwon<sup>1</sup>

<sup>1</sup>Department of Aerospace Engineering, KAIST, Korea.

\*Corresponding author: ojkwon@kaist.ac.kr

### Abstract

A flow solver based on a mixed mesh paradigm is developed for resolving flows in a high-order accurate manner. The proposed mesh topology involves unstructured tetrahedral/prismatic mesh in the near-body region and adaptive Cartesian-based unstructured mesh in the off-body region. The body-conforming near-body unstructured mesh offers a great flexibility in treating complex geometries, and also ensures proper mesh resolution for capturing the boundary layer. For the Cartesian mesh in the off-body region, a high-order accurate WENO scheme was adopted to better resolve the detailed flow features. A multi-level mesh adaptation scheme with a tree-based data structure was also employed directly on the Cartesian cells to further enhance the accuracy of the solution. To transfer the flow information between the two mesh topologies, an overset mesh technique was applied. The accuracy and performance of the flow solver were validated for fixed-wing and rotary-wing configurations.

**Keywords:** Mixed Unstructured Mesh, Overset Mesh, High-order WENO scheme, Adaptive Mesh Refinement

### Introduction

Accurate prediction of unsteady flow fields around rotorcrafts still remains as one of the most challenging problems in the field of applied aerodynamics. One of the key aspects of the rotorcraft flow simulation is in the accurate capturing of near-field rotor wake that has significant impacts on the blade aerodynamic loading, overall vehicle performance, vibration, and noise (Datta et al., 2008; Caradonna et al., 1988; Harihanan et al., 2012). At the same time, prediction of the unsteady off-body phenomena, such as the far-wake development, vortex or pressure wave propagation, and their interactions with other bodies, is also very critical. Therefore, to accurately assess the aerodynamic performance of rotorcrafts, elaborate flow simulations are required, along with an ability of handling complex geometric configurations and the relative motion between the rotorcraft sub-components.

The main difficulty involved in the rotorcraft aerodynamic simulations is in the fact that the trailed tip vortices typically have very small core size, and convect over a relatively long distance (Pulliam et al., 2009). To capture these tip vortices accurately with less numerical dissipation at given order of accuracy of the scheme, dense cells need to be distributed along their trajectories. However, this may result in a very large number of cells, and thus require an excessive computational cost. To avoid this problem, solution-adaptive mesh refinement methods based on feature detection techniques, so-called h-adaptation, are sometimes adopted to locally enhance the density of the grids (De Zeeuw, 1993; Kamkar et al., 2011). However, this may be a difficult task for structured grids because of the regularity of the point distribution. Thus, on the structured mesh frameworks, mesh adaptation is usually performed on block or patch bases. Meanwhile, for unstructured mesh topologies, direct cell-based mesh adaptation is easily applicable. Another approach of better resolving the tip vortices and avoiding excessive numerical dissipation is to use high-order accurate numerical schemes, sometimes coupled with solution-adaptive mesh refinement/coarsening.

To overcome the shortcomings of using single mesh strategies and to achieve high-order accuracy, dual-mesh methods have been proposed. The OVERFLOW solver has been developed by adopting structured body-fitted grids in the near-body region, and multi-level Cartesian grids in the off-body

region (Buning, 2003). The two grid zones are coupled with an overset mesh scheme by using a domain connectivity module. OVERFLOW adopts spatial accuracy up to sixth-order using central differencing and allows adaptive mesh refinement by a multi-block approach. The solver offers good computational results, but the geometry modeling with structured body-fitted grids is still difficult and is time-consuming, particularly for complex configurations. Recently, the Helios flow solver has been developed based on a hybrid grid paradigm by adopting unstructured meshes in the near-body region to allow more flexible geometry modeling (Wissink et al., 2008). Helios employs coupling of a set of several existing codes, the parallel unstructured mesh NSU3D flow solver for the near-body region and the serial high-order structured ARC3D flow solver for the solution on the Cartesian grids at the off-body region, through a Python infrastructure (Mavriplis et al., 1997; Hornung et al., 2006; Pulliam, 1984; Schluter et al., 2005). The CHIMPS software is used for the communication between the overlapped two mesh systems. While the flux calculation in the near-body unstructured mesh region is performed with second-order accuracy, high-order accuracy is achieved up to sixth-order in the off-body Cartesian grid region. Even though the flow solver was successfully used for solving several rotor flow problems, the file-based data exchange between the two independent heterogeneous mesh solvers is known to degrade the solution efficiency and the parallel scalability of the coupled solver. Also, mesh adaptation in the off-body Cartesian mesh region can be achieved only by multi-block bases because of the nature of the structured grids.

In the present study, a new mixed-type unstructured mesh flow solver is developed for solving flows around fixed- and rotary-wing configurations in a high-order accurate manner. The proposed mixed mesh paradigm involves prismatic/tetrahedral unstructured mesh in the near-body region and adaptive Cartesian-based unstructured mesh in the off-body region. The two mesh domains are coupled using an overset mesh topology. Unlike the Helios flow solver, the present flow solver is implemented by adopting a same unstructured mesh finite-volume topology, and thus is a unified solver. In the off-body Cartesian mesh region, to better resolve the detailed flow features away from the body, a high-order WENO scheme was achieved by utilizing the regularity of the Cartesian mesh cells. Also, a multi-level tree-based mesh adaptation scheme was employed directly on cells to further enhance the accuracy of the solution in the Cartesian mesh region. In the near-body prismatic/tetrahedral mesh region, second-order accuracy was maintained. The flow solver was validated against the NACA0015 wing in a steady flow condition and the Caradonna-Tung rotor in a hovering flight condition. The results were compared with the available experimental data, and the effect of the order of accuracy in the flow solution was discussed.

## Numerical Method

The fluid motion is modeled by the three-dimensional, compressible Reynolds-averaged Navier-Stokes equations. The equations can be written in an integral form for arbitrary computational domain  $V$  with boundary  $\partial V$  as

$$\iint_{\Omega} \frac{\partial}{\partial t} \bar{Q} dV + \oint_{\partial\Omega} (\bar{F} \cdot \bar{n}) dS = \oint_{\partial\Omega} (\bar{G} \cdot \bar{n}) dS + \iint_{\Omega} S dV \quad (1)$$

where  $\bar{Q}$  is the vector of the primitive variables, and  $\bar{F}(Q)$  and  $\bar{G}(Q)$  denote the inviscid and viscous fluxes of these variables, respectively. The governing equations were discretized using a vertex-centered finite-volume method in the near-body region. In the off-body Cartesian mesh region, a cell-centered scheme was applied. The convective flux term was evaluated by employing the flux-difference splitting scheme of Roe, whereas the diffusive flux term was computed by adopting a modified central-difference method. An implicit time integration algorithm based on a linearized second-order Euler backward differencing coupled with dual-time stepping was used to advance the solution in time. The linear system of equations was solved at each time step using a

point Gauss-Seidel method. The Spalart-Allmaras one-equation turbulence model was adopted to consider the turbulent eddy viscosity in the calculations.

#### *Near-Body Flow Solver*

For the near-body region, body-fitted unstructured tetrahedral and prismatic unstructured mesh is constructed. This mesh offers the flexibility of treating complex geometries and resolving the viscous shear layers, such as the boundary layers. In this near-body region, a vertex-centered finite-volume method is adopted. The flow domain is divided into a finite number of control volumes surrounding each vertex, which are made of non-overlapping median-dual cells. For the inviscid flux calculations, a second-order spatial accuracy is achieved through a linear reconstruction procedure based on either the least-square method or the Green-Gauss reconstruction technique. To achieve numerical stability along the steep gradient region, such as the shock discontinuities, a slope limiter proposed by Venkatakrisnan was adopted.

#### *Off-Body Flow Solver*

The off-body region is modeled with unstructured Cartesian mesh generated by a tree-data structure. In the present study, the volume mesh generation in the off-body region is conducted by a simple and robust procedure of cell division. Starting with a coarse background mesh or a single root cell, hexahedral elements are repeatedly subdivided to resolve emerging features of the flow (Aftosmis, 1997). The off-body region is discretized by using a cell-centered finite-volume method to comply with the regularity and the orthogonality of Cartesian meshes. The flow calculation is performed in a high-order accurate manner by adopting WENO (Weighted Essentially Non-Oscillatory) scheme to better resolve the detailed flow features. WENO scheme utilizes the weights of sub-stencils based on the local smoothness of the numerical solution to automatically achieve high-order accuracy and non-oscillatory approximation of the solution around flow discontinuities. To further enhance the accuracy of the flow solution, a solution-adaptive mesh refinement/coarsening methodology is also applied in the off-body region. In the present study, two types of feature detection method were adopted. To capture the flow discontinuities such as the shock and the contact surface, the total velocity difference was applied, while the non-dimensional Q-criterion was utilized for vortex-driven flows (De Zeeuw, 1993; Kamkar et al., 2011).

## **Results and Discussion**

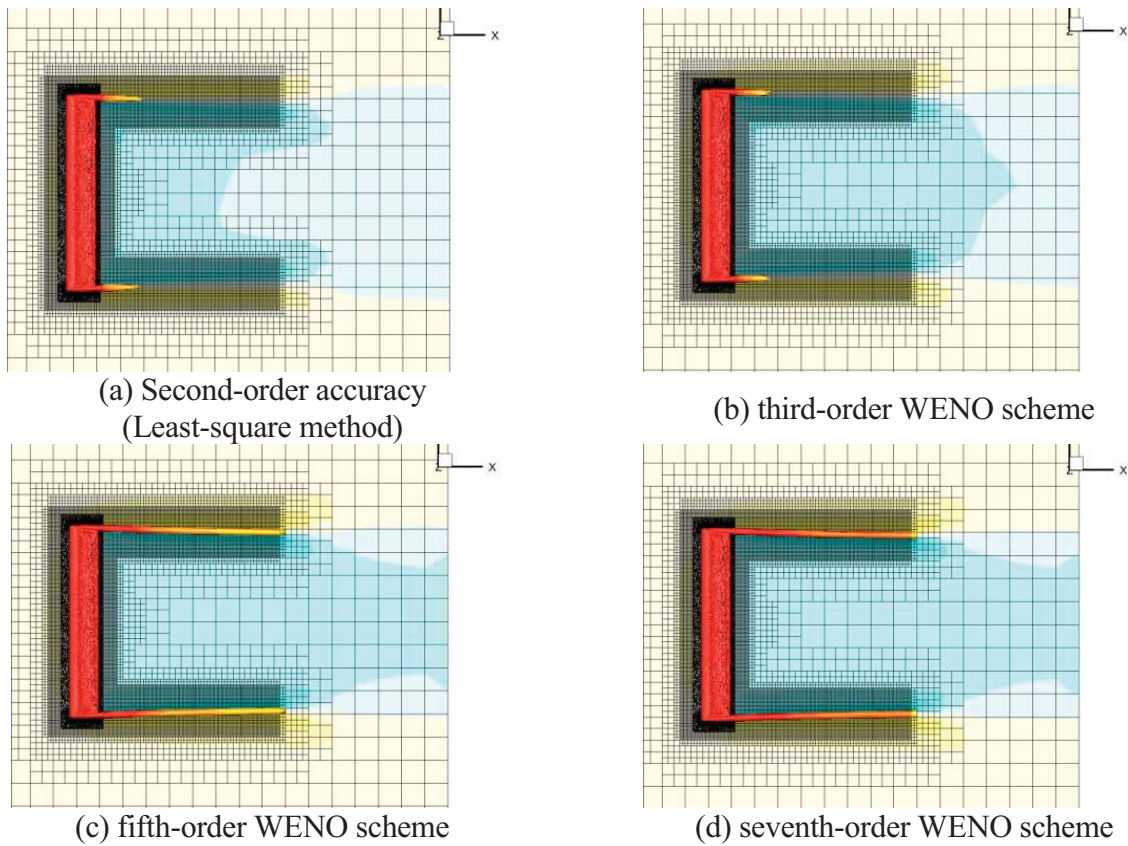
The present flow solver was applied to typical fixed-wing and rotary wing configurations, and the effects of the order of accuracy and the mesh adaptation on the results are discussed. The order of accuracies tested are the second-order adopting a least-square method, and the third-, fifth-, and seventh-order WENO schemes. The results with and without the adaptive mesh refinement were also compared.

#### *Steady Flow around an NACA0015 Wing*

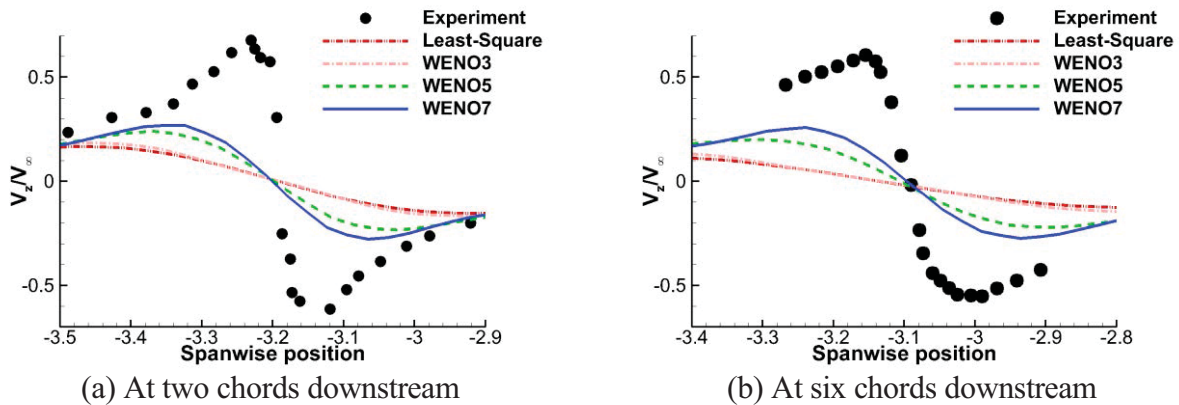
A steady flow around an NACA 0015 rectangular wing was simulated to compare the tip vortex resolution by adopting the high-order scheme and the solution adaptive mesh refinement. The present test case was experimentally studied at a freestream Mach number of 0.1235, a Reynolds number of 1.5 million, and a positive angle of attack of 12 degrees (McAllister and Takahashi, 1991). The wing has an aspect ratio of 3.3 with a square tip.

Figure 1 shows the predicted wake structures for the different order of accuracies represented by the iso- $\lambda_2$  surface colored by vorticity magnitude. The minimum cell size is  $\Delta x = 0.05c$ , and the small cells are initially clustered around the wing and the vortex shedding region. It is shown that in the cases of second- and third-order accurate solutions, the tip vortices are evolved from the wing tips, but are quickly diffused due to numerical dissipation. On the other hand, the numerical results of the

fifth- and seventh-order WENO schemes show that the tip vortices are well-developed to further downstream and the strength is well maintained along the fine cells. To quantify the difference of the wake resolution by the order of accuracy, non-dimensional  $z$ -direction velocity distributions are presented at two- and six-chord lengths downstream of the trailing edge in Fig. 2. The results are compared with the experimental data. It is shown that improved velocity distributions are obtained with high-order schemes by better preserving the wake structure, even though the numerical solutions are not close enough to the experimental data.



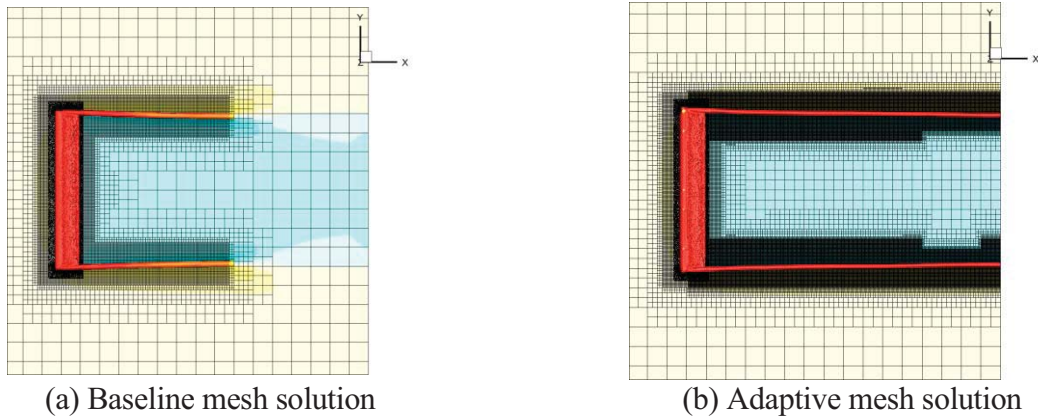
**Figure 1. Wake structure represented by iso- $\lambda_2$  surface for NACA 0015 Wing. (a) L-S method; (b) WENO3; (c) WENO5; (d) WENO7.**



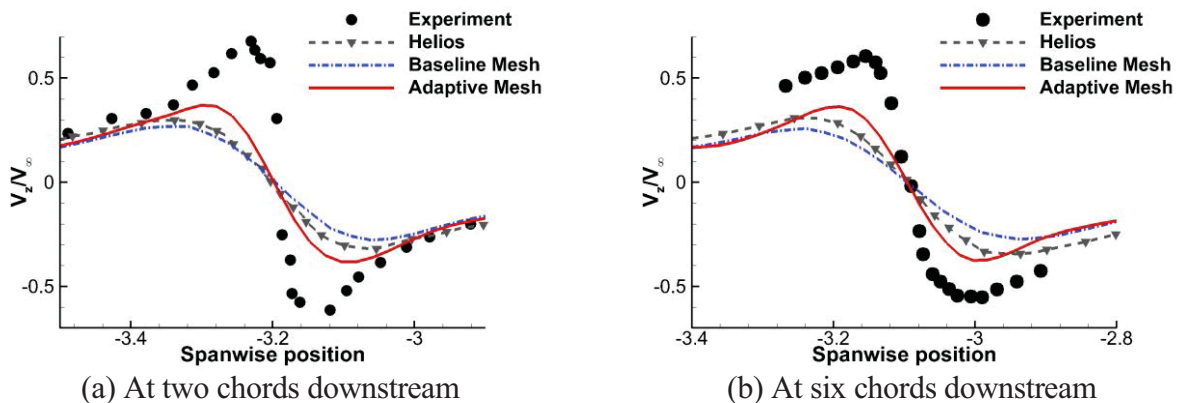
**Figure 2. Comparison of normalized  $z$ -directional velocity distributions in wake region for NACA 0015 wing. (a) Two chords from trailing edge; (b) Six chords from trailing edge.**



To further enhance the flow resolution of the tip vortex, the solution-adaptive mesh refinement was performed by using the non-dimensional Q-criterion. The wake structures are represented by the iso- $\lambda_2$  surface for the initial and adaptive meshes in Fig. 3. The results of seventh-order accuracy previously shown in Fig. 1 were utilized as the baseline solution for the mesh adaptation. The additional flow calculation was performed by maintaining the same seventh-order accuracy, and the mesh adaptation was conducted up to the second refinement level such that the typical cell size becomes  $\Delta x = 0.0125c$ . It is shown in Fig. 3 that the mesh adaptation was well implemented along the downstream from the wing tip, and the tip vortices are preserved better until they reach the downstream boundary. In Fig. 4, the resultant normalized z-direction velocity distributions are presented, along with the experiment and the Helios prediction (Wissink et al, 2010). The Helios is a hybrid mesh flow solver which uses sixth-order central difference with  $\Delta x = 0.025c$  grid spacing in the off-body. Both numerical results show similar velocity distributions, but the adaptive mesh solution shows better resolution by employing the higher order scheme and more fine meshes. It is shown that the adaptive mesh refinement additionally improves the flow resolution significantly, demonstrating that for accurate flow simulations a proper mesh resolution is also essential in addition to high-order accurate numerical schemes.



**Figure 3. Wake structure for NACA 0015 Wing with 7<sup>th</sup>-order accuracy. (a) Baseline mesh solution; (b) Adaptive mesh solution.**

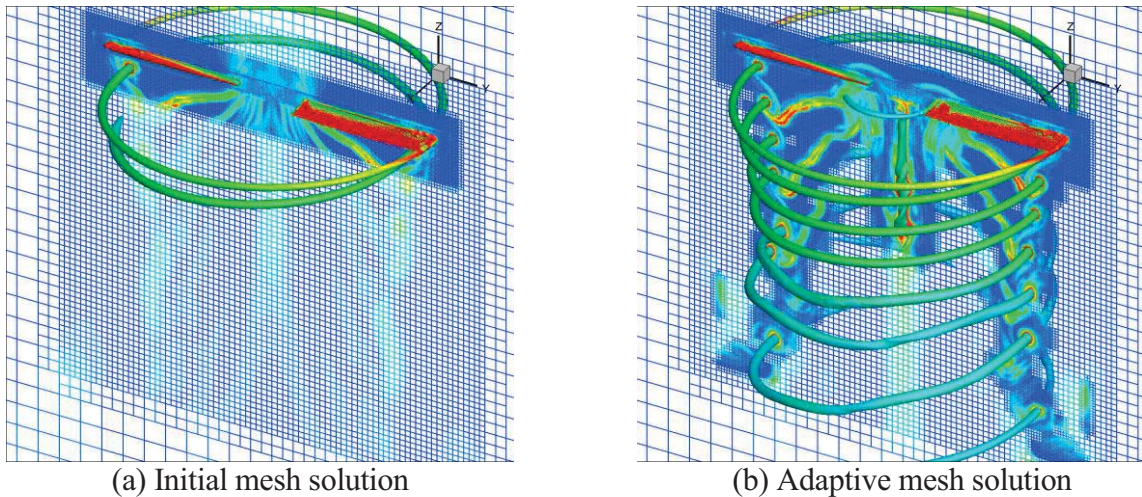


**Figure 4. Effect of mesh adaptation on normalized z-directional velocity distributions for NACA 0015 wing. (a) Two chords from trailing edge; (b) Six chords from trailing edge.**

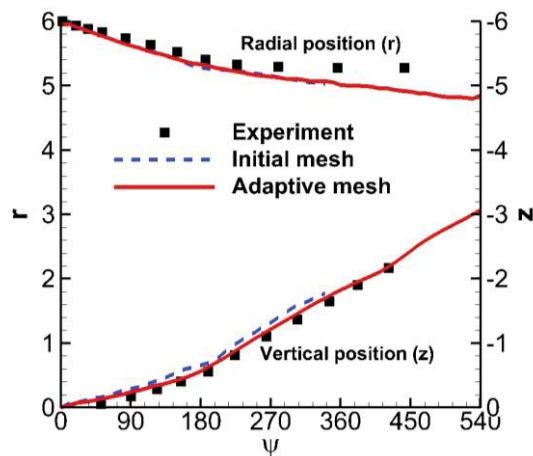
### Hovering Flight of Caradonna-Tung Helicopter Rotor

Next, the Caradonna-Tung rotor in hovering flight, which was experimentally tested (Caradonna and Tung, 1981), was simulated. The rotor has two blades, and the blades are made of NACA0012 airfoil sections with an untwisted and non-tapered planform of an aspect ratio of six. The flow simulation is conducted at a tip Mach number of 0.877, a Reynolds number of 3.93 million, and a collective pitch angle of eight degrees. To improve the tip vortex resolution, the adaptive mesh refinement was utilized by using the non-dimensional Q-criterion. Mesh adaptation was conducted up to the second refinement level after the flow solution is fully converged.

Figure 5 shows comparison of the wake structures represented by the iso- $\lambda_2$  surface for the initial and adaptive meshes with the seventh-order WENO scheme in the off-body Cartesian mesh region. The far boundary size is five times of the rotor radius, and the typical minimum cell size at the initial off-body Cartesian mesh is  $\Delta x = 0.05c$ . In the case of the initial mesh solution, the wake vortices are emanated from the rotor blade tips, but are quickly diffused, even at seventh-order accuracy. After applying the adaptive mesh refinement scheme, it is observed the wake structures are much better resolved further downstream in the far wake by maintaining the shape and the strength along the adaptively refine cells.



**Figure 5. Predicted wake structures for Caradonna-Tung rotor with 7<sup>th</sup>-order accurate method. (a) Initial mesh solution; (b) Adaptive mesh solution.**



**Figure 6. Predicted and experimental vortex trajectories of Caradonna-Tung rotor.**

In Fig. 6, the predicted and experimental vortex trajectories of the Caradonna-Tung rotor in the hovering flight condition are compared between with and without the mesh adaptation. The trajectories are presented for both the radial and vertical positions for the rotor azimuthal angle from 0 to 540 degrees. In the initial mesh solution, the vortex trajectory was obtained only up to 350 degrees due to the numerical dissipation caused by the lack of fine cells. However, for the adaptive mesh solution, the vortex trajectory was well captured over 540 degrees, and are overall in good agreements with the experimental data for both the radial and vertical positions.

## Conclusions

In the present study, a new mixed-type unstructured mesh flow solver is developed to obtain high-resolution for vortex-driven flows. For this purpose, prismatic/tetrahedral unstructured meshes are used in the near-body region, and adaptive Cartesian-based unstructured meshes are adopted in the off-body region. Unstructured prismatic/tetrahedral meshes enable to resolve the viscous shear flows near the body surface and easily handle complex geometric configurations. On the other hand in the off-body region, coupled high-order numerical scheme and solution-adaptive mesh refinement method were adopted to enhance the flow resolution by utilizing the nature of Cartesian meshes.

To assess the solution ability of the developed flow solver, an NACA0015 wing in steady flow and the Caradonna-Tung helicopter rotor in hovering flight were calculated. It was found that the present methodology is well capable of capturing and preserving the wake vortices. It was concluded that high-order scheme coupled with a proper adaptive mesh refinement method is indispensable elements for improving the off-body solution resolution containing highly vertical flow features.

## Acknowledgments

This work was supported by the National Research Foundation of Korea (NRF) of grant funded by the Korean government (MSIP) (No. 2009-0083510). The authors also would like to acknowledge the support from National Research Foundation of Korea (NRF) Grant by the Korean government (No. 2011-0029094)

## References

- Datta, A. and Johnson, W., (2008), An Assessment of the State-of-the-art in Multidisciplinary Aeromechanical Analysis. American Helicopter Society Technical Specialist's Meeting.
- Caradonna, F. X., Strawn, R. C., and Kholodar, D., (1988), An Experimental and Computational Study of Rotor-Vortex Interaction, *Vertica*, 12, pp. 315-327.
- Hariharan, N., Potsdam, M., and Wissink, A., (2012), Helicopter Rotor Aerodynamic Modeling in Hover Based on First-Principles: State-of-the-Art and Remaining Challenges. AIAA paper 2012-1066.
- Pulliam, T. H., and Jaspersen, D. C., (2009) Large Scale Aerodynamic Calculation on Pleiades. 21<sup>st</sup> International Conference on Parallel CFD.
- De Zeeuw, D. A., (1993), A Quadtree-Based Adaptively-Refined Cartesian-Grid Algorithm for Solution of the Euler Equations. PhD Thesis, University of Michigan.
- Kamkar, S., Wissink, A., Sankaran, V., and Jameson, A., (2011), Feature-driven Cartesian Adaptive Mesh Refinement for Vortex-dominated Flows, *J. of Computational Physics*, 230, pp. 6271-6298.
- Buning, P. G., et al, (2003), OVERFLOW User's Manual. NASA Langley Research Center.
- Wissink, A. M., Sitaraman, J., Sankaran, V., Mavriplis, D. J., and Pulliam, T. H., (2008), A Multi-Code Python-Based Infrastructure for Overset CFD with Adaptive Cartesian Grids. AIAA paper 2008-927.
- Mavriplis, D. J., and Venkatakrishnan, V., (1997), A Unified Multigrid Solver for the Navier-Stokes Equations on Mixed Element Meshes. *International Journal for Computational Fluid Dynamics*, 8, pp. 247-263.
- Hornung, R. D., Wissink, A. M., and Kohn, S. R., (2006), Managing Complex Data and Geometry in Parallel Structured AMR Applications. *Engineering with Computers*, 22, pp. 181-195.
- Pulliam, T. H., (1984), Euler and Thin-Layer Navier-Stokes Codes: ARC2D and ARC3D. Computational Fluid Dynamics User Workshop.

- Schluter, J. U., Wu, X., Weide, E., Hahn, S., Alonso, J. J., and Pitsch, H., (2005), Multi-Code Simulations: A Generalized Coupling Approach. AIAA paper 2005-4997.
- Aftosmis, M., J., (1997), Solution Adaptive Cartesian Grid Methods for Aerodynamic Flows with Complex Geometries. Von Karman Institute for Fluid Dynamics, Lecture Series 1997-02.
- McAllister, K., and Takahashi, R., (1991), NACA0015 Wing Pressure and Trailing Vortex Measurements. NASA Technical Paper 3151, AVSCOM Technical Report 91-A-003.
- Wissink, A. M, Kamkar, S., Pulliam, T. H., Sitaraman, J., and Sankaran, V., (2010), Cartesian Adaptive Mesh Refinement for Rotorcraft Wake Resolution. AIAA paper 2010-4554.
- Caradonna, F. X. and Tung, C., (1981), Experimental and Analytical Studies of a Model Helicopter Rotor in Hover. NASA TM 81232.

# Investigation of Residual Stress Effect on Fatigue Life of Butt Weld Joints Subjected to Cyclic Bending

\* Ali Gharizadeh, Bijan Samali, Ali Saleh

School of Civil and Environmental Engineering, Faculty of Engineering and Information Technology,  
University of Technology Sydney, P.O. Box 123, Broadway, NSW 2007, Australia

\*Corresponding author: Ali.Gharizadeh@student.uts.edu.au

This paper investigates the impact of the Residual Stress (RS) effect on high-cycle fatigue compared with low-cycle fatigue for a butt weld connection subjected to the cyclic bending load. A procedure to estimate the fatigue life based on Strain-Life method by using ANSYS software and two dimensional structural solid finite elements is described. Finite element analysis is carried out to obtain the elasto-plastic stress and strain distribution caused by the combination of RS and loading in the welded joint and subsequently, the stress and strain fields are used to assess the fatigue life at the critical region. Applying different RS fields as the initial conditions in finite element modelling while each one is subjected to different loadings, shows that the presence of RS has significant effect on fatigue life in high cycle cases while in low cycle fatigue situations, it is almost unimportant and negligible.

**Keywords:** Residual stress, High-cycle fatigue, Low-cycle fatigue, Finite element analysis, Strain-Life method, Butt weld.

## Introduction

Welded zones are usually the weakest section of a structure. One of the most serious challenges in construction industry is welded steel structures failure and the majority of these mechanical failures in welded structures are due to fatigue. Cyclic loading is a major concern to produce fatigue damage in welded components of a steel structure. To design safer components, engineers are eager to deal with welds with consistently higher fatigue strength and reasonable cost. Thus, better understanding of the low-cycle and high-cycle fatigue behaviour, as the most important damage criterion, is necessary. Heating locally, highly non-uniform temperature distribution and sudden cooling cause severe thermal stresses. These thermal stresses in the form of RS will remain in the welding zone. The presence of residual stresses in welded structures will increase the probability of failure during external cyclic loading; this will have significant effect on the fatigue behaviour (Taljat, 1998). The fatigue design philosophy for welded components was first introduced in design guidelines for tubular joints in offshore structures, based on the hot spot stress concept (Structural welding code, 1990). The best approach to study the fatigue failure especially in low cycle case is strain-life method which is based on occurring plastic strain at a local discontinuity that caused stress concentration. At the discontinuity, plastic strains will appear when the stress level exceeds the elastic limit.

### *Strain-life method*

Basquin (1910) worked on the relationship between the elastic strain amplitude and number of cycles to failure and also Manson (1963) and Coffin (1962) proposed an

equation relating the plastic strain to the cycles. There are different models to modify the strain-life model proposed by Basquin and Manson-Coffin. Smith–Watson–Topper (1970) modified Manson–Coffin equation and suggested the following equations:

$$\sigma_{\max} \frac{\Delta \varepsilon}{2} = \frac{\sigma_f'^2}{E} (2N)^{2b} + \sigma_f' \varepsilon_f' (2N)^{b+c} \quad (1)$$

Where,  $\sigma_{\max}$  is the maximum stress,  $\frac{\Delta \varepsilon}{2}$  is strain amplitude,  $\sigma_f'$  is fatigue strength coefficient,  $\varepsilon_f'$  is fatigue ductility coefficient,  $E$  is modulus of elasticity,  $N$  is the number of cycles to failure,  $b$  and  $c$  are fatigue strength and fatigue ductility exponents. In completely reversed cycling case  $\varepsilon_{\max}$  is employed as strain amplitude as follow:

$$\sigma_{\max} \varepsilon_{\max} = \frac{\sigma_f'^2}{E} (2N)^{2b} + \sigma_f' \varepsilon_f' (2N)^{b+c} \quad (2)$$

Dowling (2004) shows that S-W-T equation will be acceptable choice for study of fatigue in steel.

#### *Residual Stress*

Incompatible internal permanent strain is the main reason for RS. In engineering structures or components, the presence of residual stresses may have significantly useful or harmful effects on the fatigue behaviour during external cyclic loading depending on its type, magnitude and distribution. Only tensile stresses can cause fatigue failures by helping increase the growth of the fatigue crack. In weld fabricated structures, due to local plastic deformation from thermal and mechanical operations and also large volume changes because of the phase transformation during the manufacturing, residual stresses are present. These stresses near welds will be tensile with maximum values of equal to or more than the yield strength of the base plate (Deaconu, 2007).

Teng et al. (2003) studied thermo-mechanical behaviour of welding process and evaluated the residual stress magnitude and distribution along weld line with various types of welding sequence in single-pass, multi pass butt welded plates and circular patch welds. For analysis of the single pass butt weld, they used specimens with material steel SAE 1020.

It is impossible to add linearly the RS to the actual stress. When the local stress and stress at the crack tip exceeds the yield limit, they do not show a linear behaviour. Neuber (1946) suggested a method to determine the actual elasto-plastic stress and strain at the notch tip which is well-known as Neuber rule.

### **ANSYS Modelling**

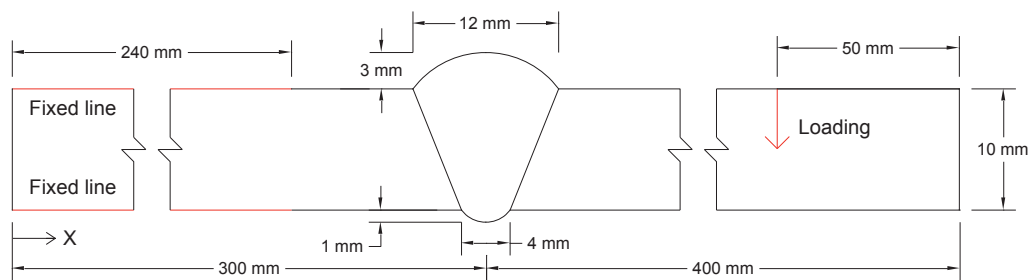
#### *Mechanical Properties*

The mechanical properties and fatigue parameters for SAE-1008 used in the modelling are: ultimate strength: 351MPa, yield strength: 198 MPa, elastic modulus: 207.5 GPa, elongation: 20%, fatigue strength coefficient ( $\sigma_f'$ ): 1346.3 MPa, fatigue

strength exponent ( $b$ ): -0.1614, fatigue ductility coefficient ( $\varepsilon'_f$ ): 0.2264, fatigue ductility exponent ( $c$ ): -0.4457 and also the mechanical properties for weld zone are ultimate strength: 585.4 MPa, yield strength: 488.8 MPa, elastic modulus: 1200 GPa and Elongation: 26.25% which are regular properties produced by welding electrodes grade E80.

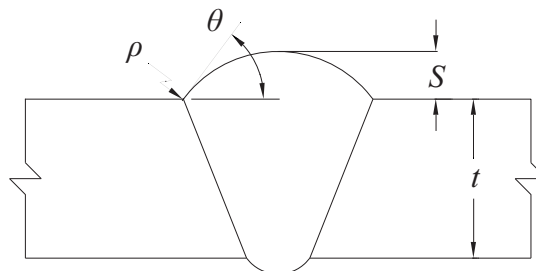
### Geometry and meshing

“SOLID183” has been chosen for this study. It is an 8-node 2D solid element with quadratic displacement behaviour. Capability for applying an initial stress state via the INISTATE command is an advantage of this element type. To model the cross section of a welded joint, a 2D finite element solid model of the specimen is prepared and shown in Fig 1.



**Figure 1. Model geometry**

Fatigue cracks tend to initiate at stress concentrations in structures. A welded joint introduces remarkable stress concentrations due to the geometrical discontinuities and the abrupt change in section at the weld toe. The stresses in the vicinity of a welded joint rise very rapidly and nonlinearly until the weld toe. The Stress Concentration Factor (SCF) due to the notch at the weld toe is a function of the weld shape and weld toe geometry which are defined by the weld toe angle and the weld toe radius, as given in Fig 2.



**Figure 2. Weld geometry parameters**

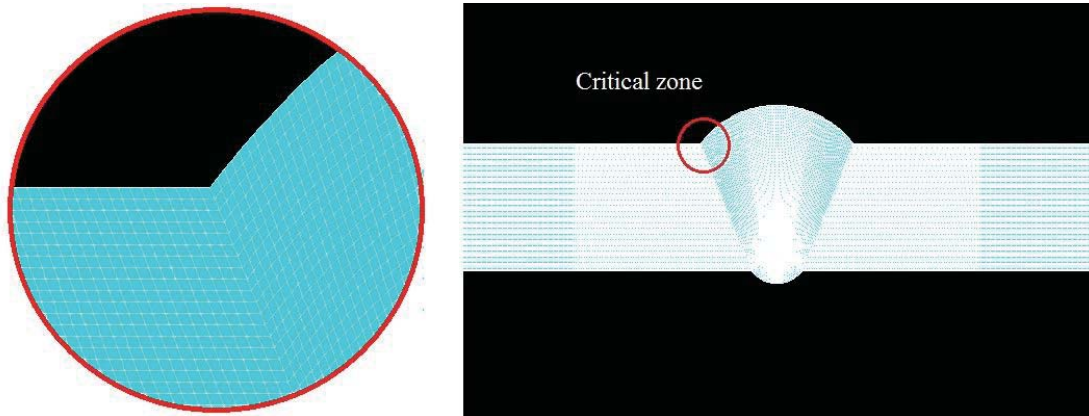
Niu and Glinka (1987) proposed the following relationship for the notch SCF at a weld toe:

$$K_w = 1 + 0.5121(\theta)^{0.572} \left( \frac{t}{\rho} \right)^{0.469} \quad \text{For} \quad \frac{\pi}{6} \leq \theta \leq \frac{\pi}{3} \quad \text{and} \quad 15 \leq \frac{t}{\rho} \leq 50 \quad (3)$$

Where  $K_w$  is the notch SCF due to the weld profile,  $\theta$  is the local weld angle,  $\rho$  is the weld toe radius and  $t$  is the plate thickness.

Eq. (3) illustrates that the weld toe SCF will be reduced by increasing the toe radius and decreasing the weld toe angle. For this model,  $\theta = 0.93$  radians, thus,  $2.75 \leq K_w \leq 4$ . If the weld toe radius is assumed as 0.5 mm, the weld notch SCF will

be 3. Since the angles at the weld connection zone in this model are completely sharp, with decreasing element edge length, the SCF tends to infinity. Therefore, the mesh size which produces weld notch SCF near 3 is acceptable. The elements edge size of 0.1 mm produce  $K_w = 2.97$  while for size 0.2 mm  $K_w = 2.38$ . Fig. 3 shows the finite element mesh with element edge length 0.1 mm around the weld toe. The node on the base plate surface and connection between plate and weld which has more potential to initiate and propagate fatigue crack is the critical node.



**Figure 3. Finite element mesh**

#### *Residual stress modelling*

After version 12, the capabilities to define initial strain and initial stress have been added to ANSYS by INISTATE command. These capabilities allow defining a primary situation at the start of an analysis. This new improvement provides a noticeable capability to use a stress-strain field as residual stress-strain state from previous loadings.

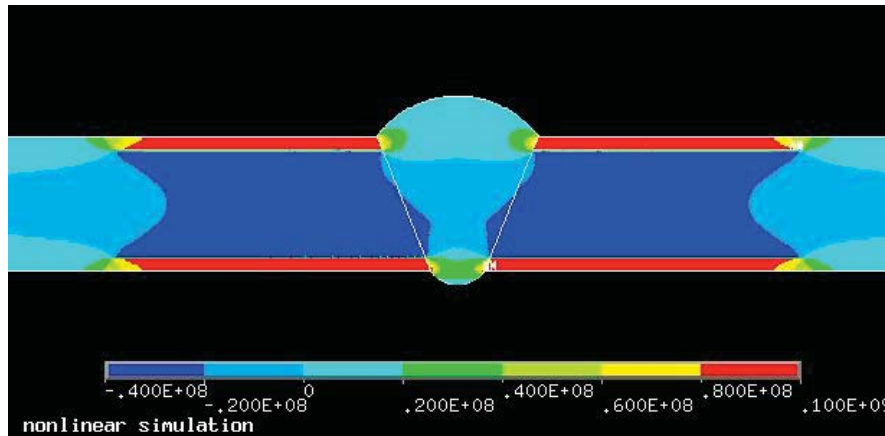
Since the RS has a self-equilibrium characteristic, the initial state applied to the model would not be the desired RS because each element shares the stress with its neighbours until the whole specimen is balanced. Therefore, after analysing the model with initial state, the results as the balanced stress-strain field would be the demanded RS. Applying an initial strain equal 0.00164 with 1 mm depth and over 20 mm in X direction around the weld toe produces RS field in Fig.4 that shows the X direction stress field as the desired RS generated by INISTATE command. It is clear that the residual stresses in the weld toe and plate thickness have been ignored and only the surfaces around the weld toe have been considered to apply RS because these areas are locations for initiation and propagation of fatigue induced cracks and the stress due to bending would be more severe there. In addition, welding zone material has much higher stiffness than base plate so that in high quality welding and pure bending situation, failure always occurs in base plate not in weld toe.

#### *Effect of adding RS*

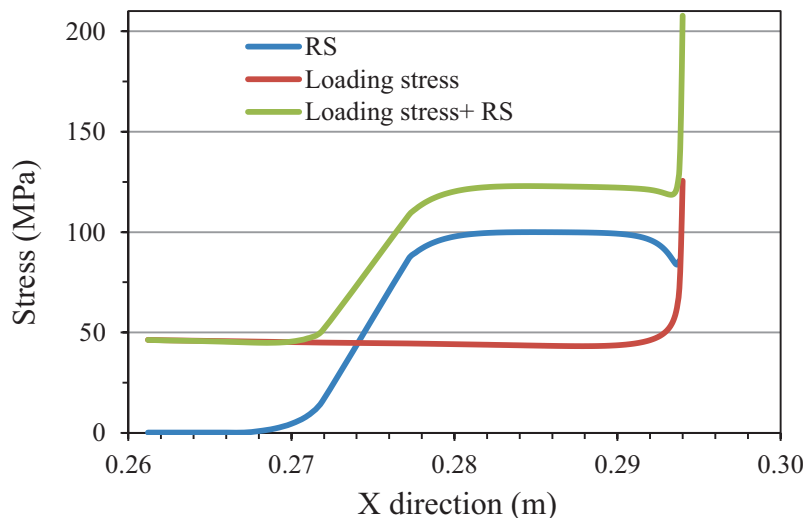
Fig. 5 shows the distribution of transverse residual stress  $\sigma_x$  at the surface of plate near the weld toe along X direction which has good agreement in shape with results presented by Finch (1992) and Teng (2003). The maximum RS produced this way is almost half the yield strength of steel SAE-1008. The stress distribution due to pure bending and also combination of loading and RS are given in Fig. 5. The stress



concentration effect is clear in loading stress curve for loading of 2 kN so that the normal stress at the connection node between base plate and weld ( $x=0.294$ ,  $y=0.01$ ) is 43.2 MPa but due to SCF the real stress will be 125.5 MPa and also, it can be clearly seen that it is not true to add linearly the RS amounts to the pure loading stress data. The stress produced by bending in  $0.28 < x < 0.29$  is approximately 44 MPa and this amount for stress because of RS is 100 MPa while the combination of loading and RS will be 123 MPa.

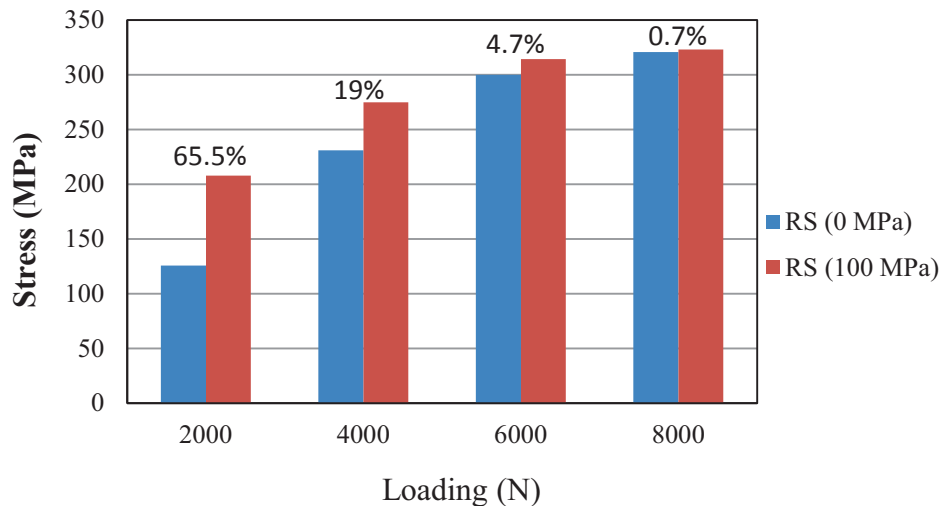


**Figure 4. Residual stress produced by applying the strain of 0.00164 at elements near the weld toe**



**Figure 5. Residual stress, pure loading stress and combination of residual stress and loading distribution along X direction**

Four reversible loadings with amplitudes (2, 4, 6 and 8 kN) were applied on the model for two conditions, in the presence and in the absence of the RS. Fig. 6 shows the stress amplitudes at the critical point ( $x=0.294$ ,  $y=0.01$ ) for different loadings when the RS is 100 MPa and when the RS does not exist. The comparison between the two conditions clarify that in lower loading, RS has more effect on critical stress. Therefore, in loading of 2 kN, RS causes 65.5% rise in stress while this amount for 8 kN of loading will cause only 0.7% increase.



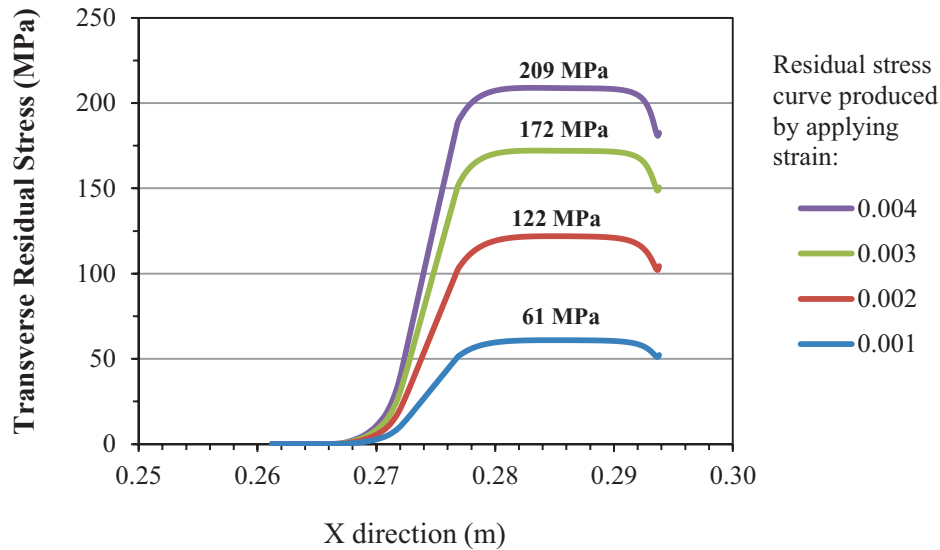
**Figure 6. Comparison between stresses in the critical point when RS exists and does not exist for loadings of 2, 4, 6 and 8 kN**

In Table 1 the amounts of stress and strain and also the number of fatigue cycles that are generated by S-W-T equation (Eq. (2)) are shown for four different loadings in the absence and in the presence of RS at the critical point. Although the presence of RS reduces the fatigue cycles in all cases, its effect is more significant when lower loads are applied and the number of cycles is in high-cycle fatigue range. By eliminating RS the weld fatigue life enhances from 43,000 cycles to 510,000 cycles in loading of 2 kN while this improvement in 8 kN loading and in low-cycle fatigue range will be from 750 cycles to 1100 cycles.

**Table 1. Comparison between stresses and strains and number of cycles in the critical point when RS exists and does not exist for loadings of 2, 4, 6 and 8 kN**

Loading (kN)	Stress (MPa)			Strain ( $\mu\epsilon$ )		No. of Cycles	
	RS (0 MPa)	RS (100 MPa)	Relative change (%)	RS (0 MPa)	RS (100 MPa)	RS (0 MPa)	RS (100 MPa)
2	125.5	207.7	65.5	1348.6	2543.4	510,000	43,000
4	230.9	274.9	19	3072.4	4145.1	25,000	6,000
6	300.1	314.2	4.7	5788.3	7244.8	4,200	2,500
8	320.8	323.1	0.7	10856	13498	1,100	750

The RS value near the weld zone is equal to or more than the yield strength and also, after welding process there are some ways to reduce or eliminate the RS. Therefore, we may be faced with a wide range of values for RS from zero to yield strength or even more. Four RS fields were prepared with maximum values 61 MPa, 122 MPa, 172 MPa and 209 MPa by applying initial strain of 0.001, 0.002, 0.003 and 0.004, respectively as before. Fig. 7 shows four RS distributions at the surface of model along X-direction. Since the yield strength for this modelling is 198 MPa, the residual stress with maximum value of 209 MPa is more than yield strength.



**Figure 7. Distribution of four RS along X-direction generated by applying initial strains**

The fatigue life predicted by S-W-T equation for different RS and loadings are given in Table 2. If we assume that the RS existing in weld zone is 209 MPa and the maximum of applied reversible load is 2 kN, with decreasing RS to 172 MPa the fatigue life is improved from 4,000 cycles to 9,000 cycles and decreasing the stress 50 MPa again to 122 MPa, enhances the life from 17,000 cycles to 26,000 cycles. By completely eliminating RS, it is possible to reach a noticeable improvement in fatigue life from 4,000 to 510,000 for the same loading, which is more than a hundred times improvement while this trend is smoother when the loading is increased. This improvement for reversible bending load 4 kN is more than 15 times and for 6 kN is approximately 6 times. Although it seems the life enhancement for reversible bending load of 8 kN is nearly 4 times, it should be noted that this improvement is just about 800 cycles which is not much and the specimen will still be in low-cycle fatigue category.

**Table 2. Number of fatigue life cycles predicted by S-W-T equation**

Loading (kN)	Residual Stress (MPa)				
	0	61	122	172	209
2	510,000	130,000	26,000	9,000	4,000
4	25,000	16,000	7,000	3,000	1,500
6	4,200	3,100	2,000	1,000	700
8	1100	800	700	400	300

## Conclusions

A procedure to evaluate the fatigue life for a butt weld joint subjected to cyclic reversible bending loads in the presence of residual stress was presented in this paper. The evaluation is based on Strain-Life method and used ANSYS software employing 2D structural solid finite elements. By means of finite element analysis, the elasto-plastic stress and strain distributions were obtained and used to estimate the fatigue life at the critical region. The findings of this project show that RS has significant

effect on fatigue life in high-cycle fatigue situations so that by eliminating the RS, it is possible to achieve more than hundred times improvement in welded joint fatigue life. It means eliminating or even decreasing the RS will be efficient and economical. While in low cycle fatigue situations, the RS effect is almost unimportant and negligible. Therefore, any efforts to eliminate the RS may not be too profitable and useful.

### References

- Basquin, O. H. (1910), The Experimental Law of Endurance Tests, Proc. ASTM, Vol. 10, Part 11, pp. 265-269.
- Neuber, H. (1946), Kerbspannungslehre, Springer-Verlag, Berlin, 1937 (in German); also Theory of Notches, J.W. Edwards, Ann Arbor, MI.
- Tavernelli, J. F. and Coffin, L. F. (1962), Experimental Support for Generalized Equation Predicting Low Cycle Fatigue, Trans. ASME, J. Basic Eng., Vol. 84, No. 4, pp. 533-38.
- Manson, S. S. and Hirschberg, M. H. (1963), Fatigue behaviour in strain cycling in low- and intermediate cycle range, Sagamore Army Matls Research conference, pp.133-178.
- Smith, K. N., Watson, P. and Topper, T. H. (1970), A stress-strain function for the fatigue of metals, Journal of Materials, ASTM, Vol. 5, No. 4, 5(4), pp.767-778.
- Niu, X. and Glinka, G. (1987) The Weld Profile Effect on Stress Intensity Factors in Weldments, Int. J. Fracture, 35, pp. 3-20.
- Structural Welding Code (1990), steel. ANSI/AWS D1, pp.1-90
- Finch, D. M. and Burdekin, F. M. (1992) Effects of welding residual stresses on significance of defects in various types of welded joint, Engineering Fracture Mechanics Vol. 41, No. 5, pp. 721-735.
- Taljat, B., Radhakrishnan, B. and Zacharia, T. (1998), Numerical analysis of GTA welding process with emphasis on post-solidification phase transformation effects on residual stresses, Materials Science and Engineering, Volume 246, Issues 1-2, pp. 45-54.
- Teng, T. L., Chang, P. H. and Tseng, W. C. (2003), Effect of welding sequences on residual stresses, Computers and Structures, 81, , pp. 273-286.
- Dowling, N. E. (2004), Mean Stress Effects in Stress-Life and Strain-Life Fatigue, In: Society of Automotive Engineers, fatigue 2004: proceedings of the third international sae fatigue congress, Sao Paulo, Brazil.
- Deaconu, V. (2007), Finite Element Modelling of Residual Stress – A Powerful Tool in the Aid of Structural Integrity Assessment of Welded Structures, 5th Int. Conference Structural Integrity of Welded Structures (ISCS2007), Timisora, Romania

## Sequential Projection Maximin Distance Sampling Method

J. Jang<sup>1</sup>, W. Lim<sup>1</sup>, S. Cho<sup>1</sup>, M. Lee<sup>2</sup>, J. Na<sup>3</sup>  
and \*T.H. Lee<sup>1</sup>

<sup>1</sup>Department of automotive engineering, Hanyang University, 222 Wangsimni-ro, Seongdong-gu, Seoul, Korea

<sup>2</sup>Korea Institute of Ocean Science and Technology, 32-1312 beon-gil, Yuseong-daero, Yuseong-gu, Daejeon, Korea

<sup>3</sup>GMKorea, 199-1 Cheongcheon 2-dong, Bupyeong-gu, Incheon 403-714, Korea

\*Corresponding author: thlee@hanyang.ac.kr

### Abstract

Design optimization for engineering problems often requires severe computer simulations. Thus, to perform a design optimization efficiently, surrogate models replacing the time-consuming simulator by using the adequate number of computer experiments, i.e., design and analysis of computer experiments (DACE) have been developed. Our goal in this paper is to propose a sequential design of experiments to construct a global surrogate model. The proposed method employs the priority of variables defined from non-linearity, contribution ratio or global sensitivity. The priority gives a chance to have better projective property to more important variable, because relatively more important variable significantly influences on the accuracy of surrogate model. Consequently this causes a decrease in the error of surrogate model and a reduction of the total number of sample points. The proposed method is compared with sequential maximin distance design and optimal Latin hypercube design with two examples.

**Keywords:** Design of experiment (DOE), Sequential design, Maximin distance design, Space filling design, Projective property, Surrogate model

### Introduction

In engineering problems, design often requires computer simulations to evaluate design objectives and constraints. If a single simulation is severe time-consuming, design optimization becomes impossible because it often requires the considerable number of simulations. One way of alleviating this burden is to employ surrogate models, for instance, response surface model (RSM), radial basis function (RBF) and kriging model. The basic concept of surrogate model is to approximate relation between input and output for predicting responses at untried input within the adequate number of computer experiments. This can reduce the computational cost by replacing the high-fidelity simulator. However, since inaccurate surrogate model can give incorrect responses, appropriate design of experiment is necessary to generate accurate surrogate model. Thus, many studies have been performed to suggest criteria of superior design of experiment and to implement the algorithm to enhance the efficiency. Among many criteria, we focus on two criteria such as space filling and projective property. And as a method for enhancing efficiency, sequential design method is adopted. In the following paragraphs, we briefly review earlier researches for two criteria and sequential design methods.

One of representative criteria for computational experiment is the space filling that sampling points fill design space uniformly. The space filling criterion has been developed to obtain information effectively on the overall design domain because

computational experiment is deterministic. Many researchers have proposed different criteria to define the space filling design. Thus, the criteria provide optimal sample set accompanied with optimization algorithm and a sample set can be different according to the criteria in spite of the same number of sample points. One of these criteria is maximin distance that tries to maximize the smallest Euclidean distance between any two sets of points over design domain (Johnson, 1990). It is simple and easy to implement, so it is widely used in practice. Maximum entropy design was introduced (Shewry and Wynn, 1987). Entropy is defined as the matrix that consists of entropy function value of each sample point such as Gaussian form. By maximizing determinant of entropy, evenly distributed sample set can be achieved. As a further study, to reduce its computation cost and resolve singularity problem, maximin eigenvalue design was suggested (Lee and Jung, 2004). In general, however, above space filling criteria cannot simultaneously consider projective property that is a space filling in terms of each axis. Fig. 1-(a) shows the best space filling, but projective property is not considered at all, i.e., collapsing arose. In addition, the criteria cannot reflect the behavior of output but consider only relations of input. Thus, to obtain more information of an important variable, the scaled maximin distance design was proposed (Jin Chen, 2002) that gives dimensional weighting to more important variable but it still could not solve the problem of overlapping of sample points as shown in Fig. 1-(b).

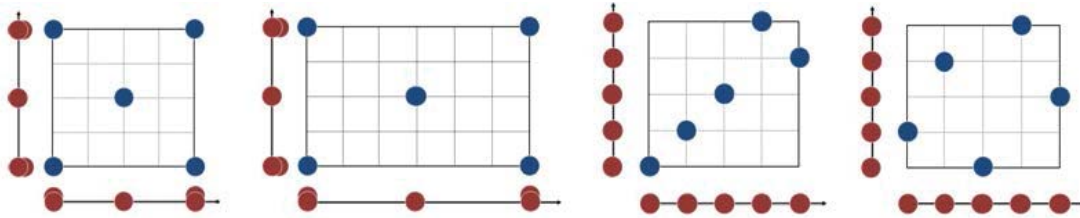
Another criterion is projective property. It is also called non-collapsing or non-overlapping property. It is important to consider distances that are projected to axis of each variable. If a certain variable ' $x_i$ ' has no influence on the output, two design points that are only different a coordinate of the variable ' $x_i$ ' are considered as the same point. Therefore, two design points should not share any coordinate values. In the early days, design method considering projective property were used in the field of safety diagnosis, reliability analysis or uncertainty propagation. Latin hypercube design (LHD) is representative method (Mckay, 1979). Even now, various design method based on LHD have been steadily proposed. However, there are some problems in LHD whose sample points are biased, distorted or clustered as shown in Fig. 1-(c). In order to resolve this problem, optimal Latin hypercube design (OLHD) was developed by employing optimization concept in previous work (Morris and Mitchell, 1995; Park, 1994). OLHD compromises between optimal criterion such as entropy and Latin hypercube with the good projection properties. However, depending on increase of the number of sample points and variables, it takes too much time to optimize and optimal sample set can be unstable. And design based on LHD is difficult to employ sequential design since area of one sample point is determined in advance according to the number of sample points and variables.

Meanwhile, most of the authors are concerned these criteria as one shot approach that sample points are selected over the design space in advance. However, since a simulator is nonlinear and complex, a designer is hard to predict how many sample points are necessary to achieve the sufficient accuracy of surrogate model. Thus, in order to solve this problem, sequential design methods have been proposed. It allows the sampling process to be stopped as soon as there is sufficient information as data accumulate. Also, it takes information such as predicted response, contribution, nonlinearity of variables and mean squared error (MSE) gathered from existing surrogate model updated sequentially with new sample points and the associated

response evaluations. These are significantly advantageous compared to one shot approach.

Sequential design can be used for both global surrogate model and surrogate model-based design optimization. Sequential design for global surrogate model focuses on sequentially improving the accuracy of a surrogate model over the entire design space, but sequential design for surrogate model-based design optimization finds promising area where optimum point can be exist. The latter is also called infilling sampling method that gives up space filling. As one of the latter method, mean squared error gathered from kriging model based design of experiment (Sacks and Welch, 1989). And expected improvement (EI) was suggested in work by Mockus, Tiesis, and Zilinskas (1978), and has been popularized in work by Jones, Schonlau, and Welch (1998) as an efficient global optimization (EGO) algorithm. EI is the function whereby points that have either low objective function value or high uncertainty are preferred.

This paper focuses on a global surrogate model by using sequential design method. To enhance the efficiency, the priority of variables is defined, that derived from output information, i.e., nonlinearity of variable, contribution of variable, global sensitivity or even intuition of a designer. In addition, both space filling and projective property is simultaneously considered to improve the accuracy quickly. At last, the proposed method, sequential projection maximin distance design, overcome drawbacks of earlier space filling design and projective property based design. The proposed method is compared with sequential maximin distance design and optimal Latin hypercube design with two examples.



(a) space filling design, (b) scaled space filling design, (c) LHD, (d) OLHD  
**Figure 1. Examples of existing design methods: sample points on 2-D (blue) and those projected to axis (red)**

### Sequential projection maximin distance design

#### *Formulation of the proposed method*

Sequential projection maximin distance design is proposed based on maximin distance design. Original maximin distance design doesn't use output information gathered from existing surrogate model but use only input information, i.e., distance between pre-sampled points. Thus, to select a new sample point(s), we introduce sequential projection maximin distance design. The proposed method employs priority of variables. If one variable is more important than the other variables, priority should be assigned to that variable. The priority gives chance to have better projective property to more important variable. In other word, relatively less important variable's projective property does not significantly influences on accuracy of surrogate model. Thus, according to priority, each variable is sequentially optimized in iteration. And in order to satisfy space filling criterion, first optimized

variables continually influence on an objective function, i.e. modified distance. The steps of new method are:

Step 1 Define priority measure and gather information of priority from existing surrogate model.

Step 2 Maximize the proposed criterion made up of Min.  $l_1$  norm of 1<sup>st</sup> priority variable

Step 3 Maximize the proposed criterion made up of Min.  $l_2$  norm and Min.  $l_1$  norm of 2<sup>nd</sup> priority variable with optimized 1<sup>st</sup> priority variable.

Step 4 Repeat step 3 until the last variable.

Above steps can be formulated as Eq. (1)

$$\begin{aligned}
 & \text{Find } \mathbf{x}_{new} \\
 & \mathbf{i} \in \text{a set of priority order, } \mathbf{i} = \{i | 1, 2, \dots, n_d\} \\
 & \text{while } i \leq n_d \\
 & \quad \text{if } i = 1, \text{ Maximize } \min \|\mathbf{x}_E^i, \mathbf{x}_{new}^i\|_1, i = i + 1 \\
 & \quad \text{else, while } i = \text{Maximize } \frac{1}{\sqrt{n_d}} \min \|\mathbf{x}_E^j, \mathbf{x}_{new}^j\|_2 + \min \|\mathbf{x}_E^i, \mathbf{x}_{new}^i\|_1, \mathbf{j} = [1, \dots, i], i = i + 1 \\
 & \text{end}
 \end{aligned} \tag{1}$$

where  $\mathbf{x}_E$  are existing sample points and  $n_d$  is the number of variables.

In this method, it is important to define the priority since it decisively determines accuracy of surrogate model. The priority of variable can be defined from nonlinearity of variable, contribution of variable, global sensitivity or even intuition of designers. Among them, we employ the nonlinearity of variable that can be alternated by correlation parameters,  $\theta_k$ , in kriging model. The correlation parameters indicate smoothness of  $x_k$  coordinate. The smaller  $\theta_k$  linear effect on the response of the variable, impact on the response is non-linear as the  $\theta_k$  increases.

#### *Proposed method comparison with sequential maximin distance design and OLHD*

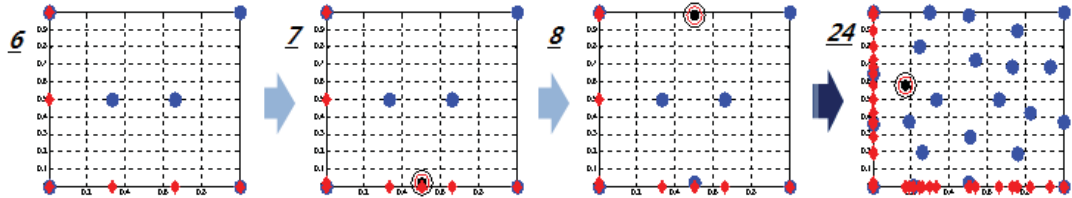
The proposed method is compared with sequential maximin distance design and OLHD in order to show or not it meets above criteria, space filling and projective property. Experiments are carried out sequentially one by one on 2-dimensional domain from initial 6 sample points, 4 on vertex and 2 on center. And since OLHD cannot provide sequential design, we perform experiments at the same number of sample points in order to compare the surface of distribution of sample points. We use genetic algorithm as an optimizer provided by matlab R2011 to select a new point, and OLHD is also designed by matlab toolbox.

Fig. 2-(a) show results of sequential maximin distance design. We can check a first optimized sample point is located in bottom line. It is the best position as an aspect of space filling, but it can be the worst position in terms of vertical axis. A second optimized sample point also similar. Also after adding 18 points, the trend of result is same.

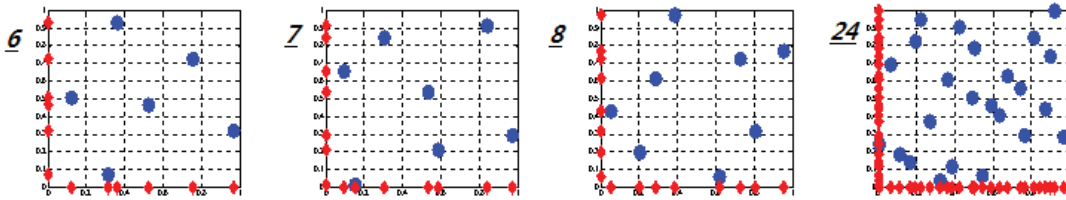


The results of OLHD in Fig. 2-(b) are the opposite of the results of sequential maximin distance design. While projective property is sufficiently conscious, space filling is poor.

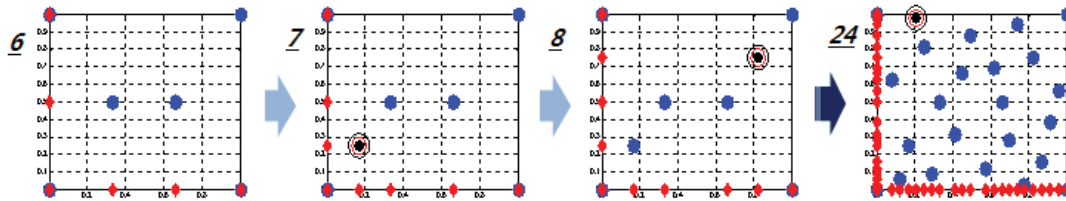
Even if one sample point is selected, the results of the proposed method in Fig 2-(c) show its characteristic well. The first optimized point satisfies projective property both horizontal and vertical axis. And after adding 18 points likewise above method, while not lose space filling, projective property is maintained very well.



(a) Sequential maximin distance design (sequentially sampled from 6 to 24)



(b) OLHD (one shot approach)



(c) Sequential projection maximin distance design (sequentially sampled)

Figure 2. Surface of distribution of samples using three methods: pre-sampled points (blue), projected points (black) and a new point (red)

### Examples

The two examples are utilized in order to show the performance of proposed method. Since we focus on build up accurate global surrogate modeling, the accuracy, i.e. error is used as a performance measure.

#### Mathematical example

The first example is a mathematical example in 2-D that can easily obtain responses and know real response. The equation of example is as following;

$$f(\mathbf{x}) = 2\cos(8\pi x_1) + 0.25\cos(\pi x_2) + 12, 0 \leq x_1, x_2 \leq 1 \quad (2)$$

The experiment is carried out in the following procedure.

Step 1 Select initial sample points.

Step 2 Build up surrogate model, i.e. kriging model with initial sample points.

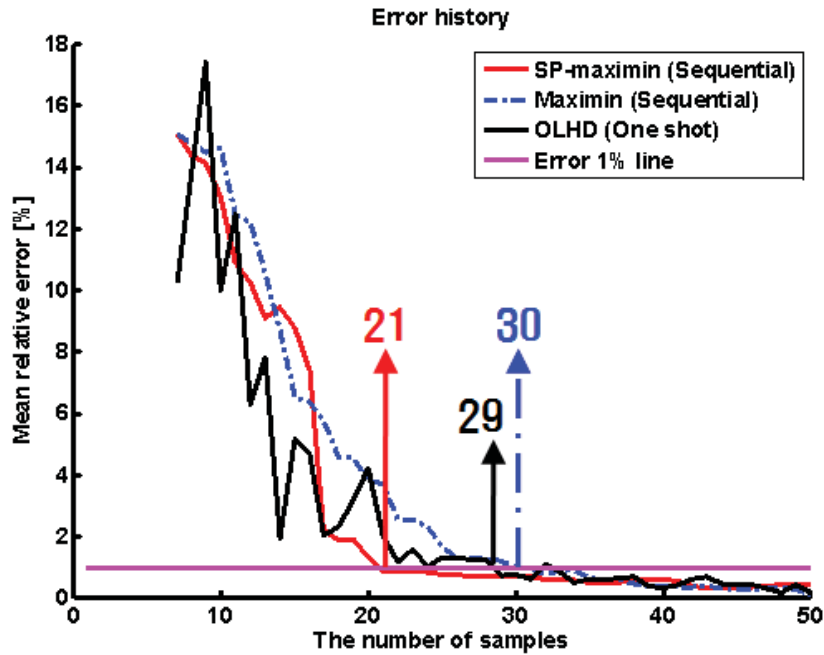
Step 3 Predict responses at validation points, and measure the error.

Step 4 Select a new sample point according to each method.

Step 5 Repeat steps 2~4 until pre-defined maximum iteration and skip step 4 in last iteration.

Validation points are  $9^2$  from full factorial design (FFD) and we employ a mean relative error (MRE) as follows;

$$MRE[\%] = E \left[ \frac{Y - \hat{Y}}{Y} \right] \times 100 \tag{3}$$



**Figure 3. History of error for mathematical example as adding sample points; 21, 29 and 30 mean the first number of sample point satisfying 1% error**

Errors of kriging model made by the three methods are decrease as adding sample points. It means that kriging model becomes more accurate as added pre-sampled points. However, error using the proposed method (SP-maximin) considering projective property according to priority of variables decreases faster than two other methods. Thus, the proposed method can reduce 8 or 9 experiments. Errors of OLHD as the one shot approach fluctuate since its distribution of sample points is change.

*Engineering example*

The second example is an engineering example with 10 design variables that takes more time and cost. Target model is a front cradle in a passenger vehicle released by GM Korea. 10 thickness values are considered as design variables. Analysis purpose is to make plastic deformation of front cradle under target value. Abaqus is used as analyzer. The experiment is carried out in the following procedure.

- Step 1 Select initial sample points.
- Step 2 Build up surrogate model, i.e. kriging model with initial sample points.
- Step 3 Predict responses at validation points.
- Step 4 Measure the error.
- Step 5 Stop if error is under 1% five times in a row.
- Step 6 Select a new sample point according to each method. And go step. 2

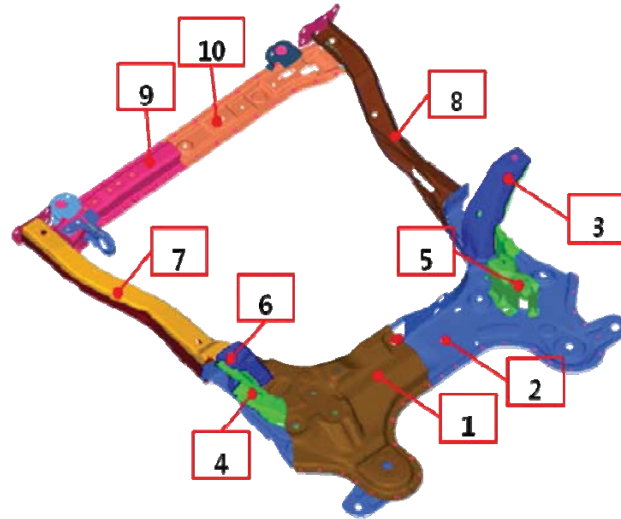


Figure 4. Finite element model of a front cradle

Cross validation (one-leave-out) is employed since adding points is also time-consuming. Initial sample points are obtained from OLHD and they are used for validation points. Lastly OLHD is not considered in this example.

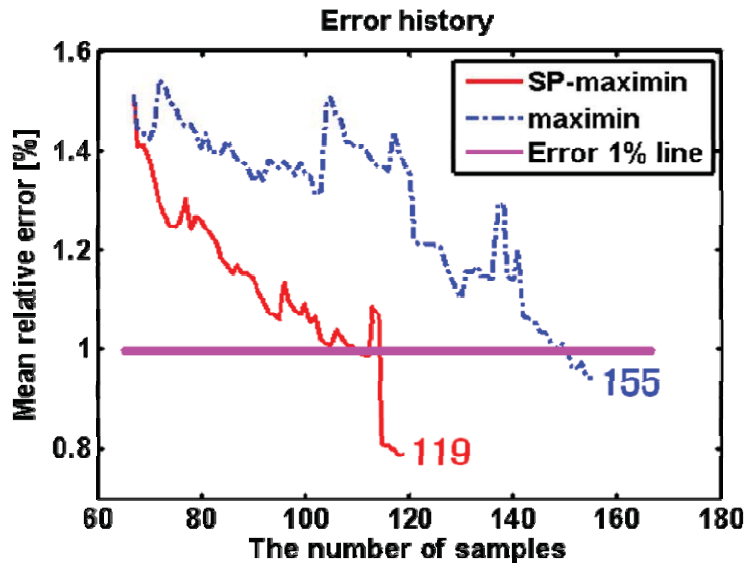


Figure 5. . History of error for an engineering example as adding sample points: 53 and 89 mean the last number of sample point satisfying 1% error 5 times in a row

Likewise a mathematical example, the error of the propose method decreases faster while the proposed method reduce the total number of sample points. It means the proposed method save about 6 hours since 1 simulation takes about 10 minute.

**Conclusions**

The sequential design method to create global surrogate model accurately is proposed in this paper. The proposed method employs the priority of variables defined from non-linearity, contribution ratio or global sensitivity. The priority gives a chance to have better projective property to more important variable. Consequently more

information of variables in the priority can be obtained by using the proposed method. This decreases the error of surrogate model and reduces the total number of sample points. In order to show the performance of the proposed method, kriging model is introduced and correlation coefficients of kriging model are considered as a criterion defining the priority. And sequential maximin distance design and optimal Latin hypercube design are used for comparison. The mathematical example that consists of a highly nonlinear variable and a moderately linear variable shows an advantage of the proposed method well. And there is a remarkable difference between the convergence histories. This is because a curve of the highly nonlinear variable is well fitted when projective property of it is fully represented. Even if the response is unpredictable, this merit still exists. In engineering example, the finite element model of front cradle in the vehicle, a sampling with the proposed method is stopped after 53th iteration under defined stop criterion. In other word, the proposed method uses 119 sample points to create a sufficiently accurate surrogate model and it uses less 36 sample points than using sequential maximin distance design. In terms of time, an engineer can save 6 hours since 1 simulation takes about 10 minute. As a result, the sequential projection maximin distance design helps engineers to solve the problems in that only a part of variables are important.

## References

- Johnson, M., Moore, L. and Ylvisaker, D., (1990), Minimax and maximin distance designs. *Journal of Statistical Planning and Inference*. 26, pp. 131–148.
- Shewry, M.C, and Wynn, H.P (1987), Maximum entropy sampling. *Journal of Applied Statistics*. 40(4), pp. 165–170.
- Lee, T.H., and Jung, J.J. (2004), Maximum eigenvalue sampling of kriging model. 10th AIAA/ISSMO Multidisciplinary Analysis and Optimization Conference. Albany, New York, August, AIAA 2004-4488.
- Morris, M. D. and Mitchell, T. J. (1995), Exploratory designs for computational experiments. *Journal of Statistical Planning and Inference*. 43(3), pp.381-402.
- McKay, M.D., Beckman, R.J. and Conover, W.J. (1979), A comparison of three methods for selecting values of input variables in the analysis of output from a computer code. *Technometrics*. 21(2), pp.239-245.
- Park, J.S. (1994), Optimal Latin-hypercube designs for computer experiments. *Journal of statistical planning and Inference*. 39(1), pp.95-111.
- Sacks, J., Welch, W.J., Mitchell, T.J. and Wynn, H.P. (1989), Design and analysis of computer experiments. *Statistical Science*. 4, pp.409–435.
- Mockus, J., Tiesis, V. and Zilinskas, A. (1978), The application of Bayesian methods for seeking the extremum. *Towards Global Optimisation*. North Holland, Amsterdam, 2, pp.117–129.
- Jones, D.R., Schonlau. M., and Welch, W.J (1998), Efficient global optimization of expensive black-box functions. *Journal of Global Optimization*. 13, pp455-492.
- Jin, R., Chen, W., and Sudjianto, A. (2002), On sequential sampling for global metamodeling for in engineering design. *Proceedings ASME 2002 Design Engineering Technical Conferences and Computer and Information in Engineering Conference*, Montreal, Canada, September, DETC2002/DAC-34092.
- Crombecq , K., Laermans, E. and Dhaene, T. (2011), Efficient space-filling and non-collapsing sequential design strategies for simulation-based modeling. *European Journal of Operation Research*. 214(3), pp683-696.
- Xiong, F., Xiong, Y., Chen, W. and Yang, S. (2009), Optimizing Latin Hypercube design for sequential sampling of computer experiments. *Engineering Optimization*. 41(8), pp793-810.
- Timothy W. S., Dennis, K. J. Lin, Chen, W. (2001), Sampling strategies for computer experiments: design and analysis. *International Journal of Reliability and Applications*. 2(3), pp209-240.
- Jin, R., Chen, W., Sudjianto, A. (2005). An efficient algorithm for constructing optimal design of computer experiments. *Journal of Statistical Planning and Inference*.134, pp268–287.
- van Dam, E.R., Husslage, B., den Hertog, D., Melissen, H. (2007). Maximin latin hypercube design in two dimensions. *Operations Research*. 55, pp158–169.

## Computational Fluid Dynamics (CFD) Simulations of Dispersed Flow of Viscous Oil in Water in a Horizontal Pipe

\*Robin Yap Miao Sin, Cary K Turangan

Institute of High Performance Computing, 1 Fusionopolis Way, #16-16 Connexis, Singapore

\*Corresponding author: yapmsr@ihpc.a-star.edu.sg

### Abstract

Heavy oil is a type of crude oil that has higher viscosity and heavier molecular composition than conventional oil, which make heavy oil very challenging to transport by means of pipelines. Our objective is to study and establish a methodology via Computational Fluid Dynamics (CFD) simulations on transportation of viscous oil in pipes in the form of dispersed oil droplets in water. Numerical simulations with *Eulerian-Eulerian* scheme are performed to model experimental tests of oil-in-water dispersed flow. In the simulations, two parameters (lift coefficient  $C_L$  and oil droplet diameter  $d$ ) are assumed to be constant. Oil superficial-velocity,  $J_o$ , is also kept constant at 0.64m/s, and water superficial-velocity,  $J_w$ , ranges from 2.20m/s to 2.60m/s. Simulation shows that positive  $C_L$  and large oil droplet diameters gives results resembling the experimental observation. In particular,  $C_L$  of 0.01 and oil drop diameter  $d$  of 4.0mm or 8.0mm show a good agreement with the experiment. The results show some valuable insights into the mechanisms of dispersed oil-in-water flow to provide further understanding on its flow mechanism.

**Keywords:** Viscous oil, dispersed oil-in-water, CFD simulations, pipe flow

### 1. Introduction

Heavy oil is a type of oil which is characterized by its heavier molecular composition and higher viscosity, which makes transportation difficult along pipeline. At present, it is estimated that heavy oil accounts for 70% of the global crude oil reserves (Alboudwarej *et al.*, 2006). As conventional crude oil reserve is scarce, heavy oil becomes more attractive alternative. The present research efforts associated with heavy crude oil have been on the extraction, transportation and production. In practice, the most common method of transporting heavy oil is via dispersed flow of oil in water. It has also been suggested that core-annular flow where the oil core is flowing at the core of the pipe and surrounded by a water layer flowing in the annulus can be another promising alternative (Bannwart *et al.*, 2012). Core-annular flow is considered a revolutionary method but still needs further development in terms of flow initiation and control. For dispersed flow, oil droplets are normally dispersed in water. Our main focus in the present work is to investigate the flow of viscous oil that represents heavy oil via dispersed flow along a horizontal pipe using numerical simulations.

There have been substantial experimental works on the two-phase flow of oil and water in horizontal and vertical pipelines including those on two-phase flow of low viscosity oil conducted by Lovick and Angeli (2004) and Hu and Angeli (2006). Lovick and Angeli (2004) studied the dual continuous flow pattern in oil-water flows in a 38.0mm-diameter, horizontal, stainless steel pipe using water and oil (oil viscosity  $\mu_o = 6\text{mPa}\cdot\text{s}$ , oil density  $\rho_o = 828\text{kg/m}^3$ ). Measurements were made for mixture velocities from 0.8m/s to 3.0m/s and input oil volume fractions from 0.1 to 0.9. They found that velocity ratio increased with increasing input oil fraction, and for high oil fractions it was above 1.0. At the highest mixture

velocities, it was reduced to values below 1.0. Hu and Angeli (2006) studied co-current upward and downward oil-water flows in a vertical stainless steel pipe of 38.0mm in diameter. Oil ( $\mu_o = 5.5\text{mPa}\cdot\text{s}$ ,  $\rho_o = 828\text{kg}/\text{m}^3$ ) and tap water were used as test fluids. The flow pattern changed from water-in-oil dispersion to oil-in-water dispersion. The mixture velocity was varied from 1.5m/s to 2.5m/s for upflow and downflow. Oil input-ratio was varied from 0 to 1.0. The in-situ oil hold-up and velocity ratio were investigated at different mixture velocity and input oil fraction.

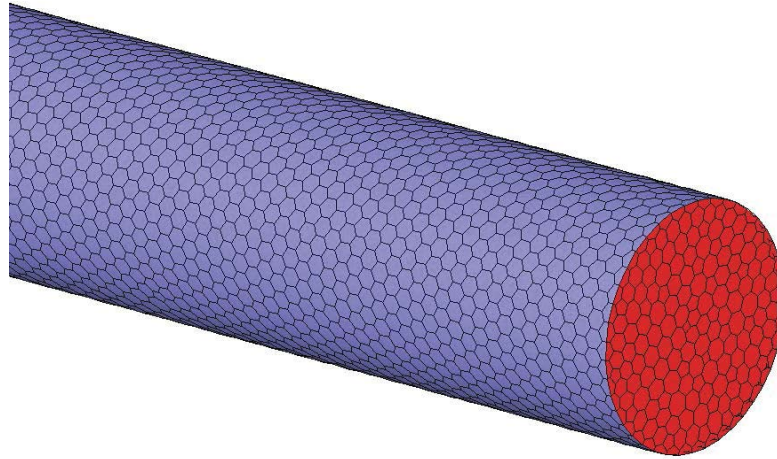
Other works on two-phase flow of high viscosity oil and water were conducted by Charles *et al.* (1961), Bai *et al.* (1992), Bannwart *et al.* (2004), Sotgia *et al.* (2008) and Wang *et al.* (2011). Charles *et al.* (1961) investigated two-phase flow of high viscosity oil and water in a horizontal pipe of 26.4mm (1.04in) in diameter. Oil with viscosities of {0.00629, 0.0168, 0.065} Pa.s was used. Flow patterns, holdup ratios and pressure gradients were investigated for a range of superficial oil velocity,  $J_o$ , from 0.0152m/s to 0.914m/s and a range of superficial water velocity,  $J_w$ , from 0.0305m/s to 0.107m/s with input oil-water ratios ranging from 0.1 to 10.0.

Bai (1992) investigated the upflow and downflow of oil and water in a vertical pipe. Oil ( $\rho_o = 905\text{kg}/\text{m}^3$ ,  $\mu_o = 0.601\text{kg}/\text{ms}$ ) and water ( $\rho_w = 995\text{kg}/\text{m}^3$ ,  $\mu_w = 0.001\text{kg}/\text{ms}$ ) are used as test fluids. The flow pattern changes from oil bubbles in water to dispersions. Dimensionless pressure gradient as a function of input ratio for various values of water flow velocity from 0.101m/s to 0.853m/s were investigated. Bannwart *et al.* (2004) studied the flow patterns formed by heavy crude oil ( $\rho_o = 925.5\text{kg}/\text{m}^3$ ,  $\mu_o = 488\text{mPa}\cdot\text{s}$  at 20°C) inside vertical and horizontal pipe of 2.84cm in diameter. The annular flow pattern (“core annular flow”) was observed in both horizontal and vertical test sections at low water input fractions.

Sotgia *et al.* (2008) performed an experimental study of water continuous oil-water flow in horizontal pipes using mineral oil ( $\mu_o = 0.919\text{Pa}\cdot\text{s}$ ,  $\rho_o = 889\text{kg}/\text{m}^3$  at 20°C) and tap water ( $\mu_w = 1.026 \times 10^{-3}\text{Pa}\cdot\text{s}$ ). The oil-water interfacial tension is  $\sigma = 20 \times 10^{-3}\text{N}/\text{m}$ . A set of seven different pipes of Pyrex and Plexiglas with diameters ranging from 21.0 to 40.0 mm were used. Flow patterns for  $J_o = 0.50\text{m}/\text{s}$  and  $J_w = 0.11\text{m}/\text{s}$  to 2.51m/s were observed in the 26.0mm Plexiglas tube. In addition, flow patterns for  $J_o = 0.48\text{m}/\text{s}$  and  $J_w = 0.05\text{m}/\text{s}$  to 1.11m/s were observed in the 40.0mm Pyrex tube. Pressure drop reduction factor,  $R$  were measured in the 26.0mm Plexiglass for  $J_o = 0.21\text{m}/\text{s}$  to 0.97m/s at water input ratio,  $\varepsilon_w$ , from 0.1 to 0.9.

## 2. Computational domain and methodology

The computational domain of the simulations presented here is modelled after the experimental set-up by Sotgia *et al.* (2008). The length of the pipe,  $L$ , is 5.0m and inner diameter,  $\Phi$ , is 26.0mm. The geometry was meshed using polyhedral cells of approximately 470 thousand cells (Figure 1). The boundary condition for the inlet is *velocity inlet* and the outlet is *pressure outlet*. The water input ratio is  $\varepsilon_w = J_w / (J_w + J_o)$ , where  $J_w$  and  $J_o$  are water and oil superficial velocity, respectively. At outlet, the (gauge) pressure was set to 0. The actual velocity of the phase is  $V_p = J_p / \alpha_p$ , where  $J_p$  is the superficial velocity of the phase and  $\alpha_p$  volume fraction of the phase.



**Figure 1.** A plot of the computational mesh on the surface of the pipe showing polyhedral cell types. The pipe was discretized using 470 thousand polyhedral cells. Pipe length  $L = 5.0$  m and diameter  $\Phi = 26.0$  mm.

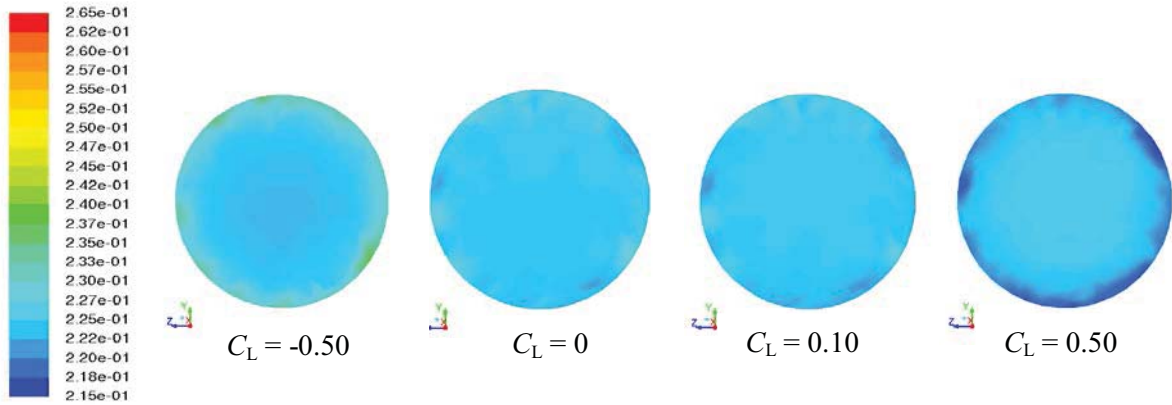
The flow physics inside the pipe was solved using computational fluid dynamics (CFD) solver ANSYS Fluent. The steady state simulations were performed, and gravitational force was taken into account. As the simulation involved interaction between two fluids, Eulerian multiphase model was implemented. For this model, water is assumed to be the continuous phase, and the oil is represented using droplets with finite diameters. It is also assumed that the droplets are spherical in shape throughout the simulations. Because for this particular flow conditions, the flow is turbulent,  $k-\varepsilon$  turbulence model of *Realizable* type was used.

Thermodynamic properties of oil and water follow those given by Sotgia *et al.* (2008). For oil, the density and viscosity are  $\rho_o = 889\text{kg/m}^3$  and  $\mu_o = 0.919\text{Pa.s}$ , respectively. For water, the density and viscosity are  $\rho_w = 998\text{kg/m}^3$  and  $\mu_w = 1.026 \times 10^{-3}\text{Pa.s}$ , respectively. The oil-water interfacial tension  $\sigma = 20 \times 10^{-3}\text{N/m}$ . The oil drops were assumed to be spherical in shape with constant diameter ranged from 1.0mm to 8.0 mm. The lift coefficient,  $C_L$ , on the oil drop ranged from -0.50 to 0.50. In addition, the drag coefficient,  $C_D$ , was also taken into account.

### 3. Results and Discussions

#### 3.1. Effects of lift coefficient, $C_L$

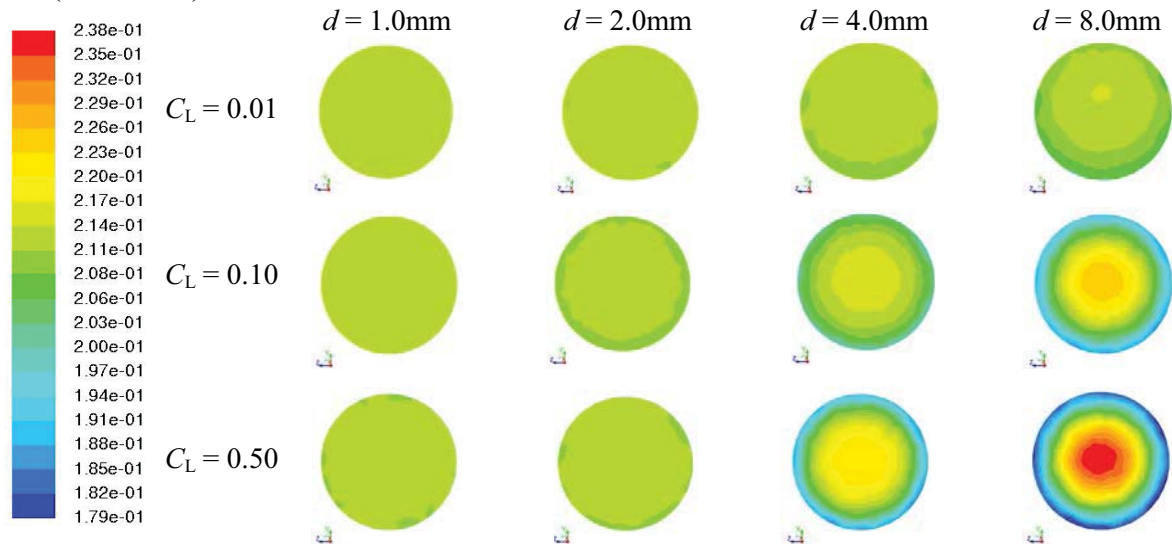
The effects of lift coefficient,  $C_L$ , on dispersed flow were investigated at oil superficial velocity  $J_o = 0.64\text{m/s}$  and water superficial velocity  $J_w = 2.20\text{m/s}$ . The oil drop diameter was kept constant at 1.0mm. Simulation was done for  $C_L = -0.50, 0, 0.10$  and 0.50. Figure 2 shows the phase contour of the cross section of the pipe at 4.5m from the inlet. At  $C_L = -0.50$ , water is at the core and oil is at the annulus of the pipe. At  $C_L = 0$ , oil appears to be scattered with a greater concentration of water ( $\alpha_w = 0.775$ ) at the core. At  $C_L = 0.10$ , oil appears to be scattered with a greater concentration of oil ( $\alpha_o = 0.23$ ) at the core. At  $C_L = 0.50$ , oil is at the core and water is at the annulus of the pipe. The results at  $C_L = 0.10$  and 0.50 are more consistent with the experiment as the phase contour shows dispersed flow with a greater concentration of oil at the core as compared with the annulus. From the results, we may deduce that the lift coefficient acting on the oil droplets may be between 0.10 and 0.50 for an oil drop diameter of 1.0mm.



**Figure 2.** Plot of volume fraction of oil at different  $C_L$  for dispersed flow of oil drop diameter  $d = 1.0$  mm. Positive  $C_L$  resembles more closely with experiment as compared with negative  $C_L$ .

3.2. *Effects of oil drop diameter,  $d$*

The effects of oil drop diameters,  $d$ , for different lift coefficient,  $C_L$ , on dispersed flow were further investigated. The oil drop diameter was kept constant and ranges from 1.0mm, 2.0mm, 4.0mm and 8.0mm. The effects of lift coefficient,  $C_L$  on dispersed flow were investigated at 0.01, 0.10 and 0.50. The plot of the phase contours from the simulation results are shown in Figure 3. At  $C_L = 0.01$  and  $d = 1.0$ mm or 2.0mm, the oil drop appears to be scattered ( $\alpha_o = 0.214$ ). At  $C_L = 0.01$  and  $d = 4.0$ mm, there is a higher concentration oil at the core ( $\alpha_o = 0.214$ ) as compared with the annulus ( $\alpha_o = 0.211$ ) and the core is displaced vertically upwards. The oil core was surrounded by a higher concentration of water. At  $C_L = 0.01$  and  $d = 8.0$ mm, oil appears to be concentric at the core ( $\alpha_o = 0.217$ ) which is displaced vertically upwards. The oil core was surrounded by an annulus having a lower concentration of oil ( $\alpha_o = 0.208$ ).



**Figure 3.** Plots of volume fraction of oil at different oil drop diameter,  $d$  and  $C_L$  for dispersed flow.  $C_L = 0.01$  and  $d = 4.0$ mm or 8.0mm resemble more closely with the experiment as oil core is displaced vertically upwards.

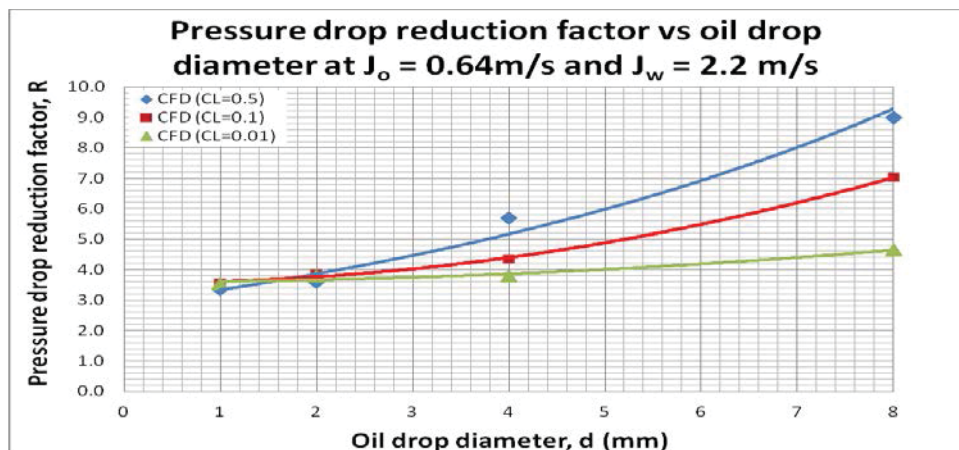
At  $C_L = 0.10$  and  $d = 1.0$ mm, oil appears to be scattered. At  $C_L = 0.10$  and  $d = 2.0$ mm, there is a higher concentration of oil at the core ( $\alpha_o = 0.214$ ) as compared with the annulus ( $\alpha_o =$



0.208). At  $C_L = 0.10$  and  $d = 4.0\text{mm}$ , there is a higher concentration of oil at the core ( $\alpha_o = 0.217$ ) as compared with the annulus ( $\alpha_o = 0.208$ ). At  $C_L = 0.10$  and  $d = 8.0\text{mm}$ , there is a higher concentration of oil at the core ( $\alpha_o = 0.226$ ) as compared with the annulus ( $\alpha_o = 0.182$ ).

At  $C_L = 0.50$  and  $d = 1.0\text{mm}$  or  $2.0\text{mm}$ , oil appears to be scattered ( $\alpha_o = 0.214$ ). At  $C_L = 0.50$  and  $d = 4.0\text{mm}$ , there is a higher concentration of oil at the core ( $\alpha_o = 0.223$ ) as compared with the annulus ( $\alpha_o = 0.194$ ). At  $C_L = 0.50$  and  $d = 8.0\text{mm}$ , there is a higher concentration of oil at the core ( $\alpha_o = 0.381$ ) as compared with the annulus ( $\alpha_o = 0.182$ ). From the results, we can deduce that when the oil drop diameter increases, there is a higher tendency for oil to coagulate at the core displacing water to the annulus. This displacement effect is more significant when the lift coefficient increases from 0.10 to 0.50 and the oil drop diameter increases from 1.0mm to 8.0mm. However, at  $C_L = 0.10$  or 0.50, the oil core remains at the centre which does not resemble closely with the experiment.

The plot of pressure drop reduction factor versus oil drop diameter at  $J_o = 0.64\text{m/s}$  and  $J_w = 2.20\text{m/s}$  is shown in Figure 4. The pressure drop reduction factor,  $R$  as given in the work by Sotgia *et al.* (2008) is defined as  $R = \Delta P_o / \Delta P_{ow}$ , where  $\Delta P_{ow}$  is the calculated pressure drop of the two-fluid flow and  $\Delta P_o$  is the pressure drop calculated using the Hagen-Poiseuille law for the single-phase laminar flow of oil having the same flow rate as the oil phase in the two-phase flow. The Hagen-Poiseuille law is given by the following equation:  $\Delta P = (128 \mu L Q) / (\pi D^4)$ , where  $\Delta P$  is the pressure drop,  $L$  is the length of pipe,  $\mu$  is the dynamic viscosity,  $Q$  is the volume flow rate and  $D$  is the pipe diameter.



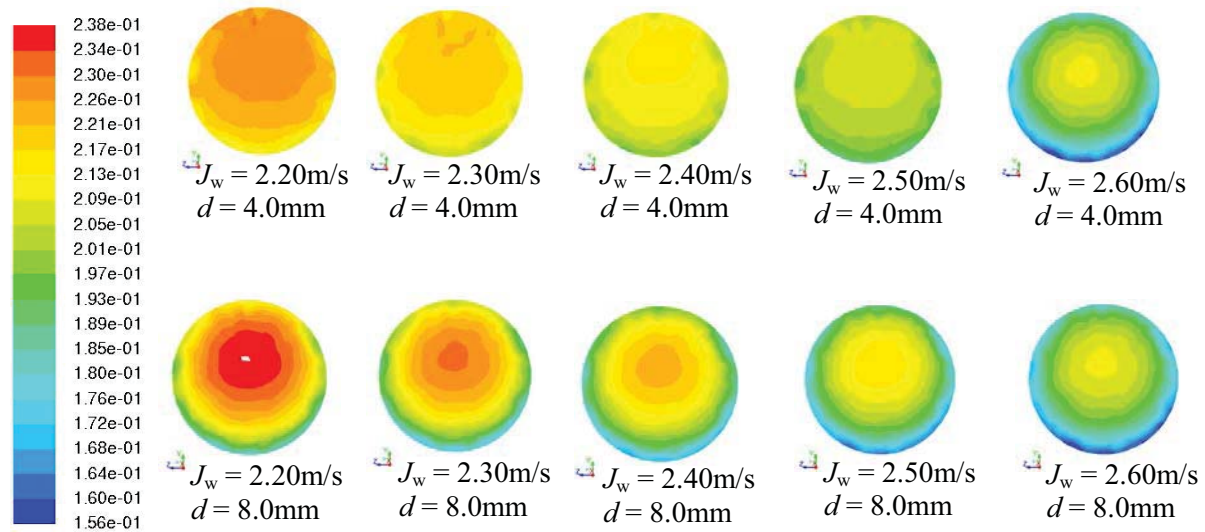
**Figure 4. Plot of pressure drop reduction factor versus oil drop diameter at  $J_o = 0.64\text{m/s}$  and  $J_w = 2.20\text{m/s}$  for dispersed flow. For all  $C_L$ , when oil drop diameter,  $d$  increases from 4.0mm to 8.0 mm, pressure drop reduction factor,  $R$  also increases. The increase in  $R$  is more significant for higher  $C_L$ .**

In general, when the oil drop diameter is between 1.0mm to 2.0mm, the lift coefficient,  $C_L$  does not appear to have a significant effect on the pressure drop reduction factor. When the oil drop diameter is between 2.0mm and 8.0mm and the lift coefficient is increased from 0.01 to 0.50, the pressure drop reduction factor increases. This is because when the lift coefficient increases, there is a higher tendency for the oil droplets to coagulate at the core which is lubricated by a higher concentration of water at the annulus. This reduces the pressure gradient, causing the pressure drop reduction factor to increase. However, it should be noted that a lift coefficient of 0.50 is only for inviscid flow. It is suggested that the lift coefficient to be between 0.01 and 0.10 (Madhavan, 2005) for low viscosity oil.

In comparison with the oil-water distribution from experiment, the phase contour at  $C_L = 0.01$  and  $d = 4.0\text{mm}$  or  $8.0\text{mm}$  is more consistent with the experiment as compared with the phase contour at  $C_L = 0.10$  or  $0.50$ . At  $C_L = 0.10$  or  $0.50$  and  $d = 4.0\text{mm}$  or  $8.0\text{mm}$ , the oil core is concentric at the core. However, at  $C_L = 0.01$  and  $d = 4.0\text{mm}$  or  $8.0\text{mm}$ , the oil core was displaced vertically upwards from the centre. From the results, we may draw the conclusion that the lift coefficient for viscous oil may be  $0.01$  with an equivalent oil drop diameter between  $4.0\text{mm}$  to  $8.0\text{mm}$ .

### 3.3. Effects of mixture velocity

The effects of mixture velocity on pressure drop reduction factor were investigated at  $J_o = 0.64\text{ m/s}$  and  $J_w = 2.20\text{m/s}$ ,  $2.30\text{m/s}$ ,  $2.40\text{m/s}$ ,  $2.50\text{m/s}$  and  $2.60\text{m/s}$ . The plot of volume fraction of oil at different mixture velocities for  $C_L = 0.01$  and oil drop diameter  $d = 4.0\text{mm}$  and  $8.0\text{mm}$  is shown in Figure 5. For  $d = 4.0\text{mm}$ , when water superficial velocity increases from  $2.2\text{m/s}$  to  $2.6\text{m/s}$ , the volume fraction of oil at the core decreases from  $0.226$  to  $0.213$  respectively. The volume fraction of oil at the annulus decreases from  $0.213$  to  $0.156$  respectively. For  $d = 8.0\text{mm}$ , when the water superficial velocity increases from  $2.2\text{m/s}$  to  $2.6\text{m/s}$ , the volume fraction of oil at the core decreases from  $0.238$  to  $0.213$  respectively. The volume fraction of oil at the annulus decreases from  $0.197$  to  $0.156$  respectively. The results show that when the mixture velocity increases, the volume fraction of oil at the core and annulus decreases. This can be attributed to the fact that when the mixture velocity increases, the higher turbulence effect of water causes the oil droplets to become more dispersed.



**Figure 5.** Plots of oil volume fraction for different water superficial velocities  $J_w$ . Oil drop diameters  $d = 4.0\text{mm}$  and  $8.0\text{mm}$ . Constant parameters are lift coefficient  $C_L = 0.01$  and oil superficial velocity  $J_o = 0.64\text{m/s}$ . When  $J_w$  increases from  $2.20\text{m/s}$  to  $2.60\text{m/s}$ , oil concentration decreases. There is a tendency the oil droplets to congregate at the centre of the pipe forming a core-annular-like flow.

In addition, when the oil drop diameter increases from  $4.0\text{mm}$  to  $8.0\text{mm}$ , the volume fraction of oil at the core increases but that at the annulus remains constant. This can be attributed to the fact that when the oil drop diameter increases, there is a higher tendency for the oil droplets to concentrate at the core. For all flow regimes, the oil core is displaced vertically upwards from the centre which is consistent with the flow pattern in experiments. CFD

simulations also show that when the water superficial velocity,  $J_w$ , increases, the pressure drop reduction factor,  $R$ , increases marginally. In addition, when the oil drop diameter,  $d$ , increases from 4.0mm to 8.0mm, the pressure drop reduction factor,  $R$ , also increases. It appears that it is more desirable to increase the water superficial velocity as this helps to increase the pressure drop reduction factor. In addition, it is also more desirable to have a larger oil drop diameter as this helps to promote coagulation of the oil droplets at the core, which helps to increase the pressure drop reduction factor (i.e. reduce the pressure gradient). These are interesting observations which has not been reported before in other works. This knowledge is of practical importance for oil industry as it helps to reduce the overall energy required to transport viscous oil along horizontal pipes.

### 3.4. Effects of water input ratio, $\epsilon_w$

Figure 6 shows the plot of pressure drop reduction factor,  $R$ , versus water input ratio,  $\epsilon_w$ , for dispersed flow with  $d = 4.0\text{mm}$  and  $8.0\text{mm}$ . The lift coefficient  $C_L$  is kept constant at 0.01. The oil superficial velocity is kept constant at  $0.64\text{m/s}$  and water superficial velocity is between  $2.2\text{m/s}$  to  $2.6\text{m/s}$ . The simulation results show that when the water input ratio,  $\epsilon_w$  increases from 0.775 to 0.800, there is a marginal increase in the pressure drop reduction factor,  $R$ . This is consistent with the flow physics as when the water input ratio increases, the superficial velocity of water also increases which increases the turbulent intensity of the mixture. The higher turbulence effect of water causes greater dispersion of oil in water. Hence, the pressure gradient decreases and pressure drop reduction factor,  $R$  increases.

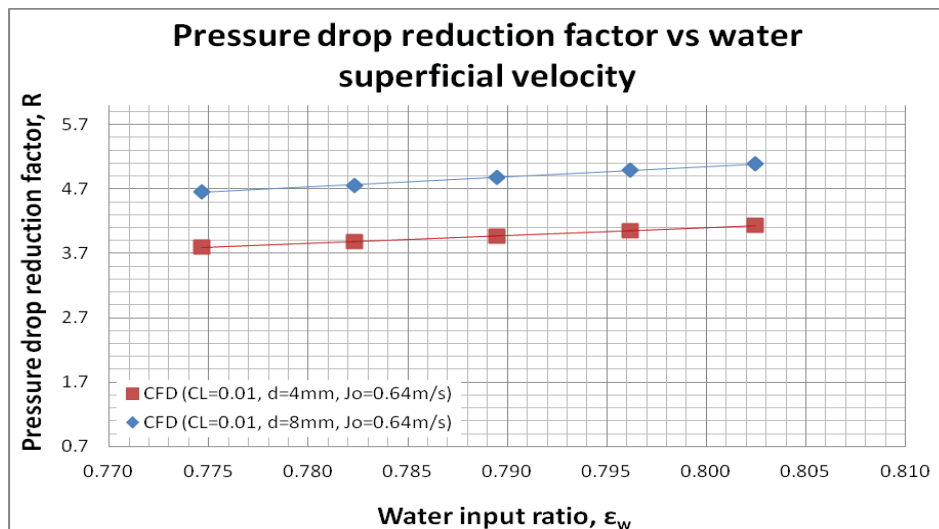


Figure 6. Plot of pressure drop reduction factor versus water input ratio for dispersed flow. Oil superficial velocity,  $J_o$ , is kept constant at  $0.64\text{m/s}$  and water superficial velocity,  $J_w$ , varies from  $2.2\text{m/s}$  to  $2.6\text{m/s}$ .

## 4. Conclusions

Dispersed flow of viscous oil and water in a horizontal pipe of  $5.0\text{m}$  long and  $26.0\text{mm}$  in diameter were simulated using the Eulerian-Eulerian multiphase model. The water is treated as the continuous phase and the oil is treated as the dispersed phase modeled as spheres with finite diameters. For the low volume fraction of oil in the system ( $\sim 0.225$ ), the mixture is assumed to be of Newtonian fluid. The simulations suggest that positive lift coefficient,  $C_L$ ,

on the oil droplet is more consistent with experimental observation. In particular, when  $C_L = 0.01$  and oil drop diameter,  $d = 4.0\text{mm}$  or  $8.0\text{mm}$ , the phase contour of the dispersed phase at the core is displaced vertically upwards which is more consistent with experiment. The CFD simulation results also show that it is desirable to have a larger oil drop diameter as this helps to increase the pressure drop reduction factor. When the oil superficial velocity,  $J_o$ , remains constant at  $0.64\text{m/s}$  and water superficial velocity,  $J_w$ , increases from  $2.20\text{m/s}$  to  $2.60\text{m/s}$ , the volume fraction of oil for the dispersed phase decreases due to the higher turbulence effect of water. In addition, it appears that it is more desirable to have a higher water superficial velocity as this helps to increase the pressure drop reduction factor,  $R$  marginally. This reduces the overall pressure gradient which helps to improve the efficiency of transportation of viscous oil.

### References

1. Alboudwarej, H, Felix, J, Taylor, S, 2006. Highlighting Heavy Oil. Oilfield Review.
2. Bannwart, A.C., Rodriguez, O.M.H., Carvalho, C.H.M., Wang, I.S. and Vara, R.M.O., 2004. Flow Patterns in Heavy Crude Oil-Water Flow. Trans. ASME, 126, pp. 184 – 189.
3. Bannwart, A.C., Rodriguez, O.M.H. and Biazussi, J.L., 2012. Water-assisted Flow of Heavy Oil in a Vertical Pipe: Pilot-scale Experiments. Int. J. Chem. Reactor Eng., 10, pp. 1 – 16.
4. Hu, B. and Angeli, P., 2006. Phase inversion and associated phenomena in oil-water vertical pipeline flow. The Canadian J. Chem. Eng., 84, pp. 1 – 14.
5. Sogtia, G., Tartarini, P. and Stalio, E., 2008. Experimental analysis of flow regimes and pressure drop reduction in oil-water mixtures. Int. J. Multiphase Flow 34, pp. 1161 – 1174.
6. Lovick, J. and Angeli, P., 2004. Experimental studies on the dual continuous flow pattern in oil-water flows. Int. J. Multiphase Flow, 30, pp. 139 – 157.
7. Charles, M.E, Govier, G.W. and Hodgson, G.W., 1961. The horizontal pipeline flow of equal density oil-water mixtures. The Canadian J. Chem. Eng., 39, pp. 27 – 36.
8. Bai, R.Y., Chen, K.P and Joseph, D.D., 1992. Lubricated pipelining: Stability of core-annular flow. Part 5. Experiments and comparison with theory. J. Fluid Mech., 240, pp. 97 – 132.
9. Madhavan, S., 2005. CFD Simulation of Immiscible Liquid Dispersions. MSc Thesis, Dalhousie University, Canada.
10. Wang, W., Gong, J. and Angeli, P., 2011. Investigation on heavy crude-water two phase flow and related flow characteristics. Int. J. Multiphase Flow, 37, pp. 1156 – 1164.

## Grid Generation for Screw Compressors with Variable Geometry Rotors

\*A. Kovacevic, S. Rane and N. Stosic

City University London, Northampton Square, EC1V 0HB London, United Kingdom  
tel: +44 20 7040 8780, fax: +44 20 7040 8566

\*Corresponding author: a.kovacevic@city.ac.uk

### Abstract

An algebraic grid generation algorithm presented in this paper is applicable for Computational Fluid Dynamics (CFD) calculation of twin screw compressors with variable rotor geometry. It is based on the method previously developed by authors for standard uniform pitch rotors with constant cross-section profile. The new algorithm allows the rotors with variable pitch and/or variable rotor profiles to be analysed. Performance predictions are obtained by commercial CFD solver ANSYS CFX for three variants of an oil-free 3/5 screw compressor, namely uniform helical rotors, variable pitch rotors and variable profile rotors. The variable pitch and variable profile rotors achieve steeper internal pressure rise, lower leakage rate due to reduced sealing line length in high pressure domains and a larger discharge area for the same pressure ratio. This work will allow analysis of the existing and novel compressor configurations.

**Keywords:** Algebraic Grid Generation, Computational Fluid Dynamics, Twin Screw Compressor, Variable Pitch Rotors, Variable Profile Rotors.

### Introduction

Twin screw compressors contain helically lobed rotors with profile optimized for an efficient compression process. These usually have a constant pitch. The pitch of screw compressor rotors is defined as an axial distance between tips of consecutive lobes. Figure 1 shows CAD model of a twin screw compressor consisting of the compression chamber formed by the helical rotors and casing. Such domain includes the main chamber, leakage paths, and rotor ports. Rotors with variable pitch were patented by Gardner in 1969. These are still rarely used due to lack of efficient and economical manufacturing techniques for their production.

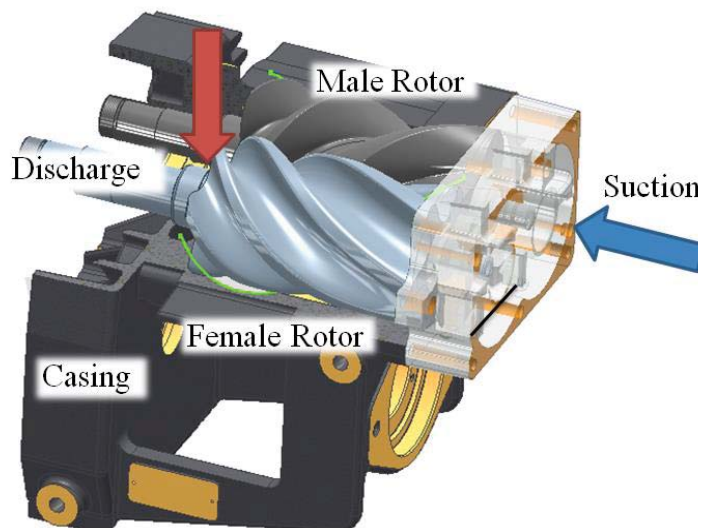


Figure 1. Sectioned view of a Twin Screw Compressor

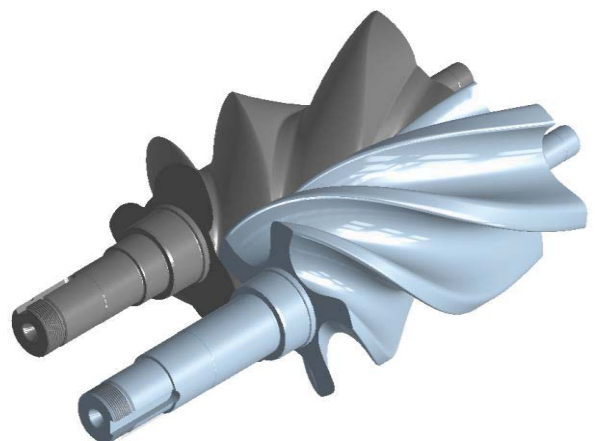


Figure 2. Variable Pitch Screw Rotors

Figure 2 shows configuration of twin screw rotors with variable pitch. It has been shown in the literature that for the same rotor lengths, diameter, wrap angles and lobe profiles, variable pitch rotors can provide higher pressure ratio and larger discharge port opening areas with reduced throttling losses than the equivalent rotors of a constant pitch (Gardner, 1969). Even higher compression ratios could be achieved with rotors of variable diameter.

Twin screw machines are today often analysed by use of Computational Fluid Dynamics (CFD). The prerequisite for successful CFD is appropriate space discretisation by a suitable numerical grid. Three main mathematical methods are used to generate such grids, namely algebraic methods, differential methods and variational methods, as described in (Eiseman et. al., 1994; Liseikin, 1999; Samareh and Smith, 1992; Shih et. al., 1991; Soni, 1992 and Thompson, 1999).

Kovacevic et. al. (2000, 2002, 2005 and 2007) have successfully used algebraic grid generation method to produce numerical mesh for twin screw machines with constant pitch rotors. This has been implemented in the custom made program called Screw Compressor Rotor Grid Generator – SCORG<sup>®</sup>. Figure 3 shows an example of the grid in one cross-section produced by SCORG<sup>®</sup>.

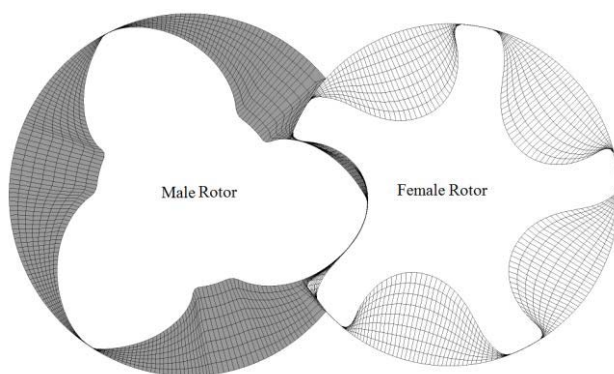


Figure 3. Numerical grid in a cross section

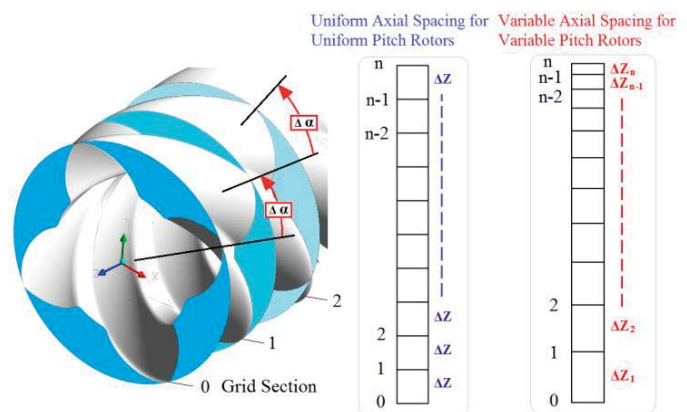


Figure 4. Cross sectional spacing for uniform and variable pitch rotors

## Grid Generation

Rotors with uniform pitch and constant rotor profile have a fixed relationship between the lead and the rotor rotation angle. This allows for the numerical grids generated in one cross section at different angular positions in time to conveniently be used for spatial definition of rotors along the rotor axis.

The challenge in generating a numerical grid for variable lead rotors is in establishing the relationship of the axial distance between consecutive cross sections and the angular rotation of the rotor. The uniform rotation does not correspond to the uniform axial spacing of cross sections in variable pitch rotors. Figure 4 shows the difference in grid spacing for the constant and variable pitch rotors. The existing procedure used in SCORG<sup>®</sup> has been reformulated and adapted for the variable pitch and variable profile screw rotors as presented in this paper.

The rotor pitch is usually constant. However it can also change linearly, non-linearly or in steps. The former is often used for screw vacuum pumps while the latter is applied in some car superchargers. The change in the pitch can be expressed through following equations:

*Constant Pitch*

$$p = \text{constant} \tag{1}$$

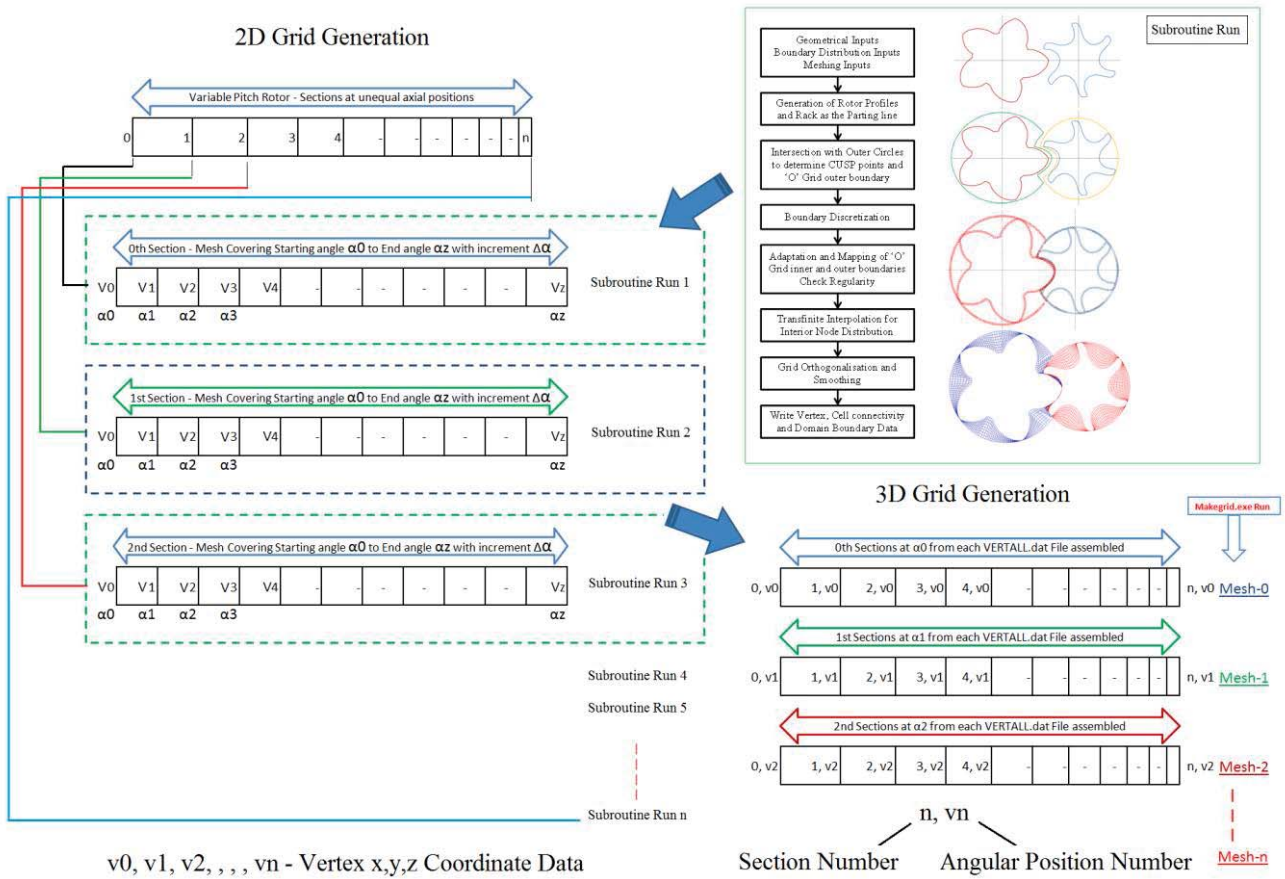
*Linear Pitch*

$$p = \left(\frac{P_e - P_s}{L}\right)z + p_s \tag{2}$$

*Quadratic Pitch*

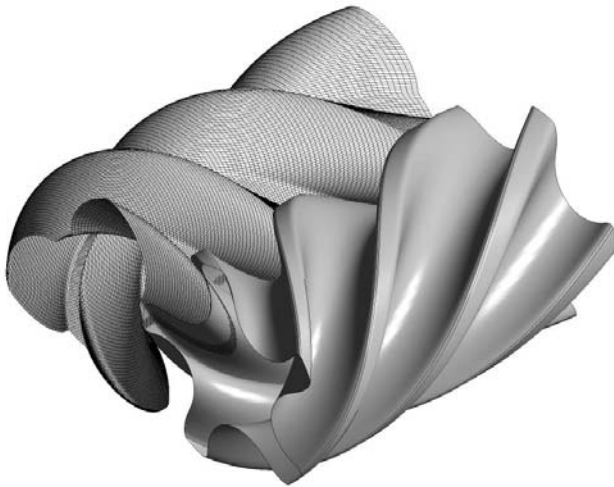
$$p = \left(\frac{P_e - P_s}{L^2}\right)z^2 + p_s \tag{3}$$

Authors developed two approaches for grid generation for machines with variable pitch rotors, as described in detail in previous publications (Rane et. al., 2013).

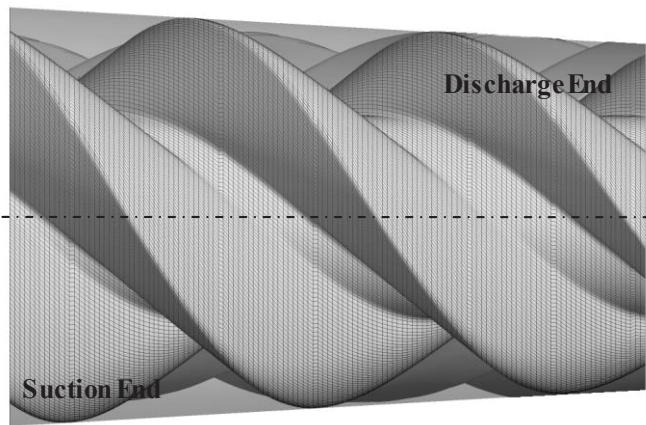


**Figure 5. Variable Pitch and Variable Profile Grid Generation**

The first approach uses relations like (1) to (3) to define corresponding axial distance at different axial positions of a cross section  $\Delta Z_n$  which will relate to a uniform rotation of a rotor  $\Delta\alpha$ . It does not allow change of a profile along the rotor axis. The second approach shown in Figure 5 is more general. In it, it is assumed that screw compressor rotors form a conjugate pair in each cross section. Therefore each section can be calculated independently using its specific rotor profile. The procedure is described in detail in Rane et. al. (2013). Once 2D grids are generated for all time steps in each cross section, these could be assembled to form a set of rotor flow domain grids for every time step. An example of the constant rotor profile with variable pitch rotors is shown in Figure 6 while the grid for variable rotor geometry and uniform pitch is shown in Figure 7.



**Figure 6. Numerical grid for variable pitch screw rotors**



**Figure 7. Numerical grid for uniform pitch, variable profile rotors**

### CFD Analysis

Numerical analysis was carried out by use of ANSYS CFX solver with objectives to validate the grid generation approach for variable rotor profile and to study performance of compressors with various configurations. The male rotor has 3 lobes with 127.45mm outer diameter, L/D ratio 1.6 and wrap angle  $\Phi_w$  of  $285^\circ$ . The female rotor is with 5 lobes and the rotor centre distance is 93mm. Both rotors are rack generated 'N' profiles. The compressor speed is 8000 rpm with pressure ratio of 2.0 and 3.0. Three test cases were calculated.

**Case 1.** Uniform pitch and uniform profile rotors with built in volume index  $V_i$  of 1.8.

**Case 2.** Variable pitch with uniform profile rotors and built in volume index  $V_i > 1.8$ . The Suction side pitch was 130mm and Discharge side pitch was 40mm. The wrap angle of  $\Phi_w$   $285^\circ$  was maintained.

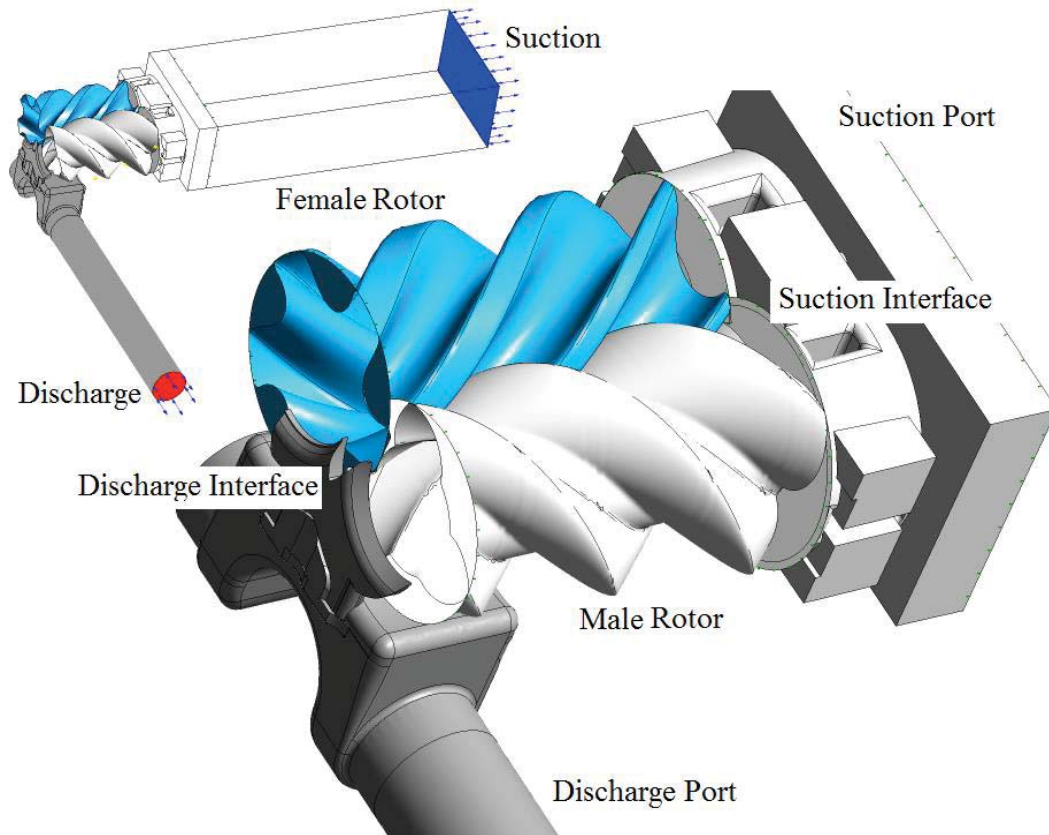
**Case 3.** Variable profile and uniform pitch rotors. Rotor profile in successive sections is generated using rack generation procedure by variation of addendum on the defining racks (Stosic et. al., 2005). Addendum on the suction end of the rotors was 33mm while on the discharge side it was reduced to 21mm. The addendum on the uniform profile rotors had constant value 28.848mm. Due to the variation of addendum the outer diameter of the male rotor is changing while the inner diameter remains constant and vice versa for the female rotor as shown in Figure 7. The displacement of these rotors is smaller than for the uniform profile rotors.

For the purpose of comparison, same suction and discharge ports were used for all three cases. Each rotor configuration was analysed on three different grid sizes. Table 1 shows the number of computational nodes in each case. Stationary compressor ports were meshed by use of the commercial grid generator. Figure 8 shows the compressor domain decomposed into three main regions; the suction port, the discharge port and the rotor domains.

**Table 1. Size of refined grids, number of nodes**

Case	Uniform	Variable Pitch	Variable Profile
<b>Coarse</b>	691174	648190	675918
<b>Medium</b>	838378	915184	889794
<b>Fine</b>	1214418	1344944	1297434





**Figure 8. Compressor model with variable profile rotors**

The working fluid is air following an ideal gas law. The suction pressure in all cases was 1.0 bar. The discharge pressures were 2.0 bar and 3.0 bar. The target convergence criterion is  $1.0 \times 10^{-3}$ . During solution, r.m.s residuals were between  $1.0 \times 10^{-3}$  and  $5.0 \times 10^{-3}$  for the momentum equation, while for continuity and energy equations the convergence criteria was always achieved. The calculations were run sufficiently long to allow a cyclic repetition of flow and pressure at boundaries. Each case was calculated with both Laminar and SST k-Omega Turbulence model.

## Results and Discussion

### *Pressure field*

Figure 9 shows the pressure field on the variable pitch rotors – Case 2 with discharge pressure of 2.0 bar. The red colour indicates higher pressure while the blue colour is the lower pressure. The indicator diagrams for all three cases calculated on fine grid with SST turbulence model are shown in Figure 10. The increase of internal pressure is steeper for the variable pitch and variable profile rotors. The vertical dashed lines show the angle of rotation of the male rotor at which the working chamber is exposed to suction and discharge port. Since the same discharge port is used for all three cases, the variable geometry rotors, Case 2 and Case 3 achieve full internal compression for the case of 3 bar discharge pressure while in that case constant geometry rotors under-compress making them more inefficient for this higher pressure. In the case of the 2bar discharge pressure, the constant geometry rotors achieve full internal compression while variable geometry rotors over-compress. This will make them less efficient in case of lower discharge pressures. Depending on the geometry, variable profile rotors may have smaller displacement than the uniform rotors. Therefore these are better suited for high pressure applications.

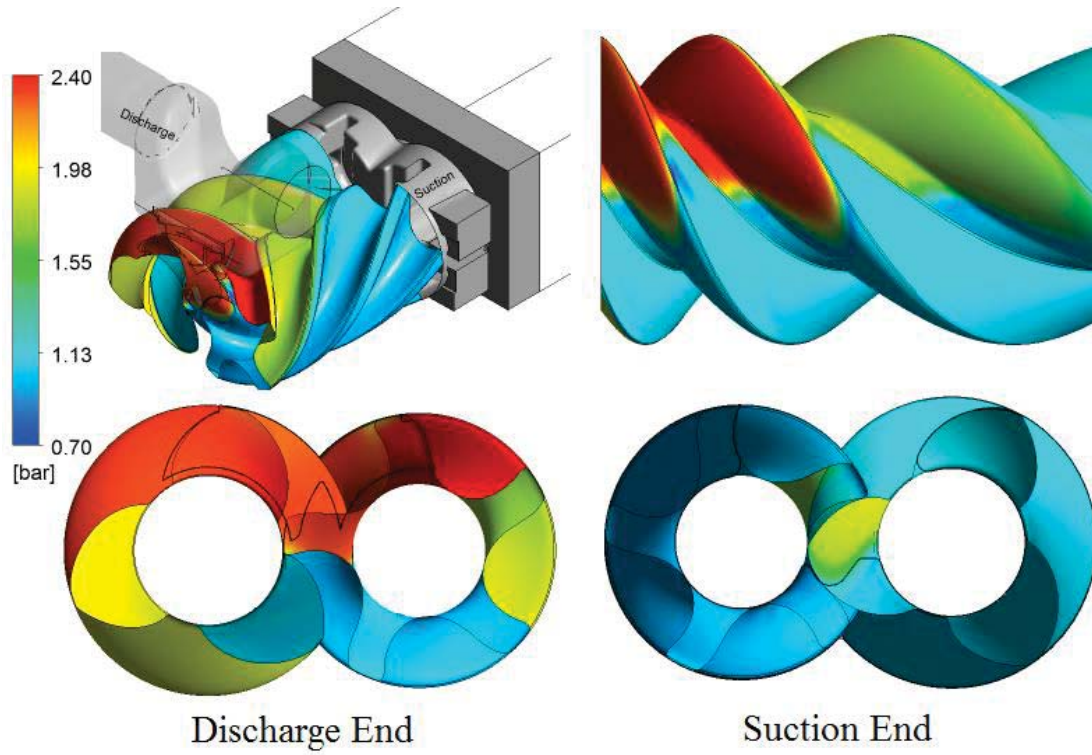


Figure 9. Pressure variations in the variable pitch rotors with discharge pressure 2.0 bar

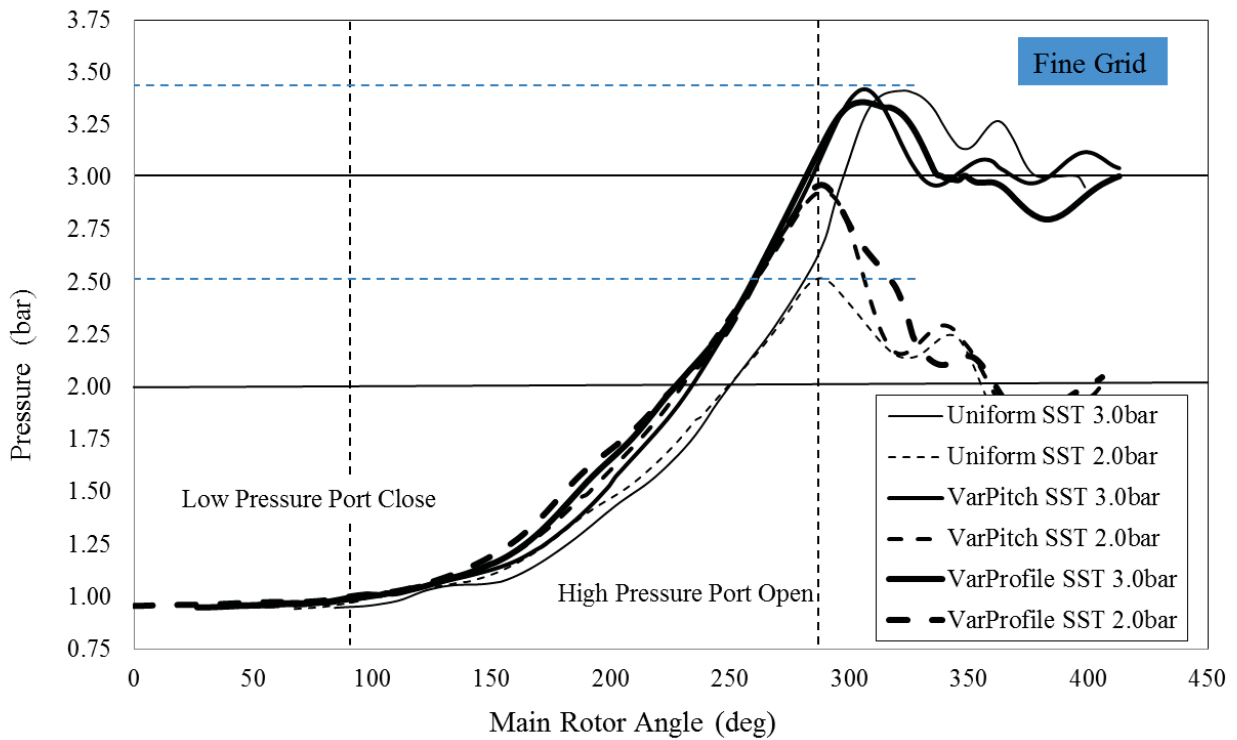
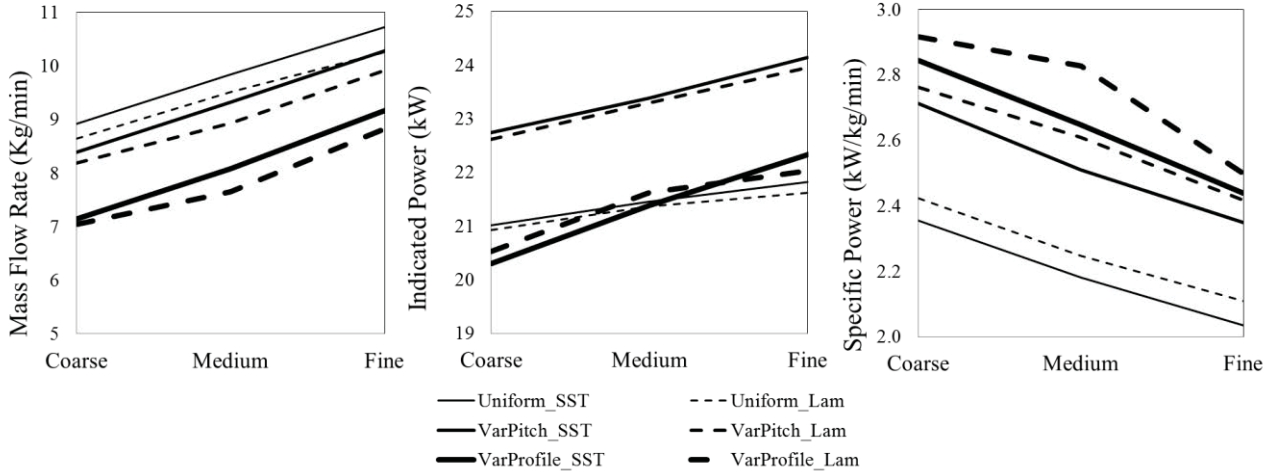


Figure 10. Indicator diagram

*Influence of Grid Refinement*

Figure 11 shows the effect of grid refinement on the prediction of integral quantities such as the mass flow rate, indicated power and specific power. The cases presented in the figure are with 2 bar discharge pressure. The increase in mass flow rate is observed with grid refinement in all cases. The

difference between each consecutive refined grids is around 10%. This indicates that the rotor geometry is captured better with finer grids, which results in better representation of leakage losses which are progressively reduced with grid refinement. Similarly, indicated power increases for 2-5% each time the grid is refined.



**Figure 11. Effect of grid refinement on integral parameters**

*Influence of Turbulence Model*

As shown in Figure 11, the higher mass flow rates are achieved when the turbulence model is applied. Indicated power is also increases as the consequence of increased mass flow. However, specific power is reduced for turbulent cases and is closer to the expected values. This suggests that the appropriate turbulence model must be applied for calculation of screw compressor performance. For variable profile rotors, the results obtained on the finest grid are contradictory which may be consequence of the grid generation method used in this case. This needs to be investigated further.

*Sealing Line Length*

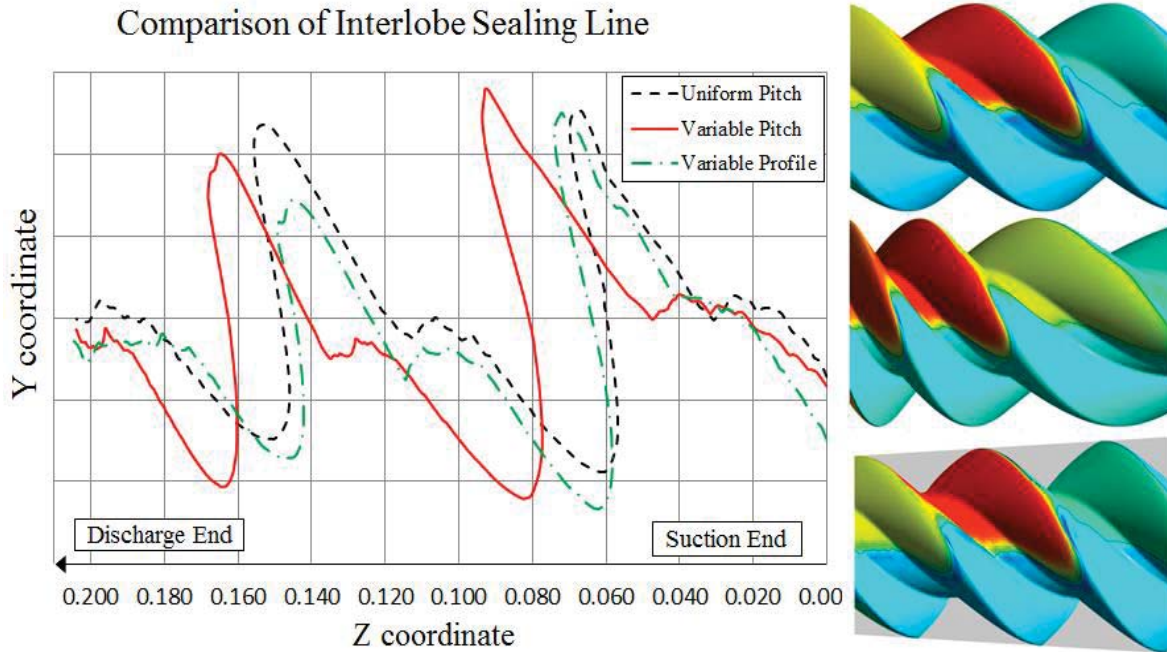
The interlobe sealing line is the line of closest proximity between two rotors. The leakage of gas through the interlobe gap is proportional to the length of the sealing line and the size of the clearance normal to the profile (Fleming and Tang, 1994; Hanjalic and Stosic, 1997 and Stosic et. al., 2005). Contours of pressure distribution on the rotor can be established from numerical calculations. The line which divides the high and the low pressures between the rotors represents the sealing line. The comparison of the sealing line lengths for three calculated cases is shown in Figure 12 and in Table 2.

**Table 2. Comparison of Interlobe Sealing Line Length [mm]**

Interlobe No	Uniform	Variable Pitch	Difference	Var. Prof	Difference
1	145.8	175.9	-30.1	158.4	-12.6
2	170.3	164.0	+6.4	162.2	+08.1
3 (part)	069.1	056.8	+12.2	068.4	+00.6
Total	385.2	396.6	-11.5	389.1	-03.9

The sealing line for the uniform pitch rotors has the same length for each interlobe space along the rotor. At the suction end on the variable pitch rotors the sealing line is 30mm longer than for the uniform case. It decreases towards the discharge end of rotors by 12mm. This helps to reduce leakage as the largest pressure difference across the sealing line is at the discharge end. In the case

with variable profile the suction end is longer by 12mm and discharge end has very small difference compared with the uniform profile.



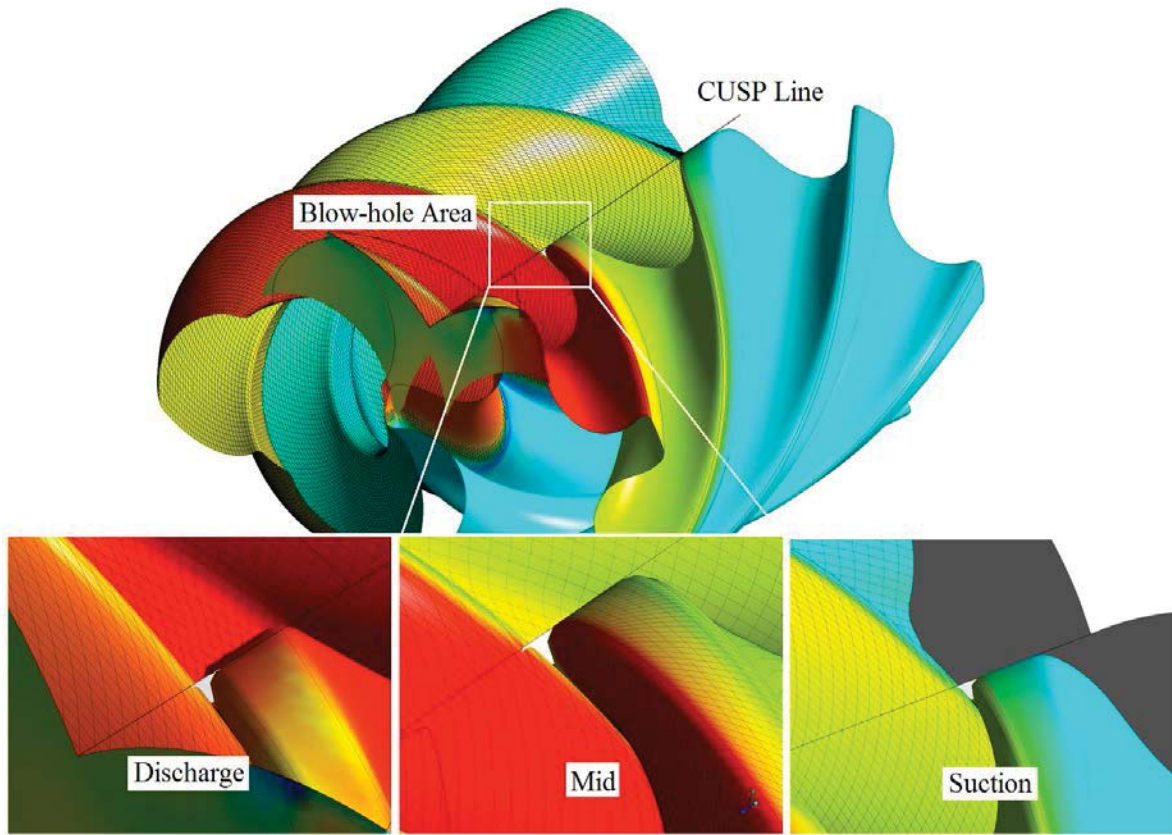
**Figure 12. Comparison of interlobe sealing line lengths**

*Blow-hole area*

Blow-hole area is the leakage area formed between the male and female rotors and the casing at the rotor cusp as shown in Figure 13. The blow-hole area on the high pressure side is important for leakage due to the pressure difference between adjacent compression chambers. A smaller blow-hole area is desired for improved performance of the machine. Table 3 shows the blow-hole areas measured on the medium size grid for different calculated cases at different positions in the rotor. The blow-hole area for the uniform rotors remains constant along the length of the rotors. In the variable pitch rotors, the suction side blow-hole area is larger than in the uniform rotors but the discharge side blow-hole area is smaller than for the uniform rotors. In the variable profile rotors, the suction side blow-hole area is nearly the same as that of the uniform rotors but the discharge blow-hole area is smaller than for the uniform rotors. Proportionally, the reduction of blow-hole area towards the discharge side rotors is most pronounced in the case of variable pitch rotors.

**Table 3. Comparison of Blow-hole area [mm<sup>2</sup>]**

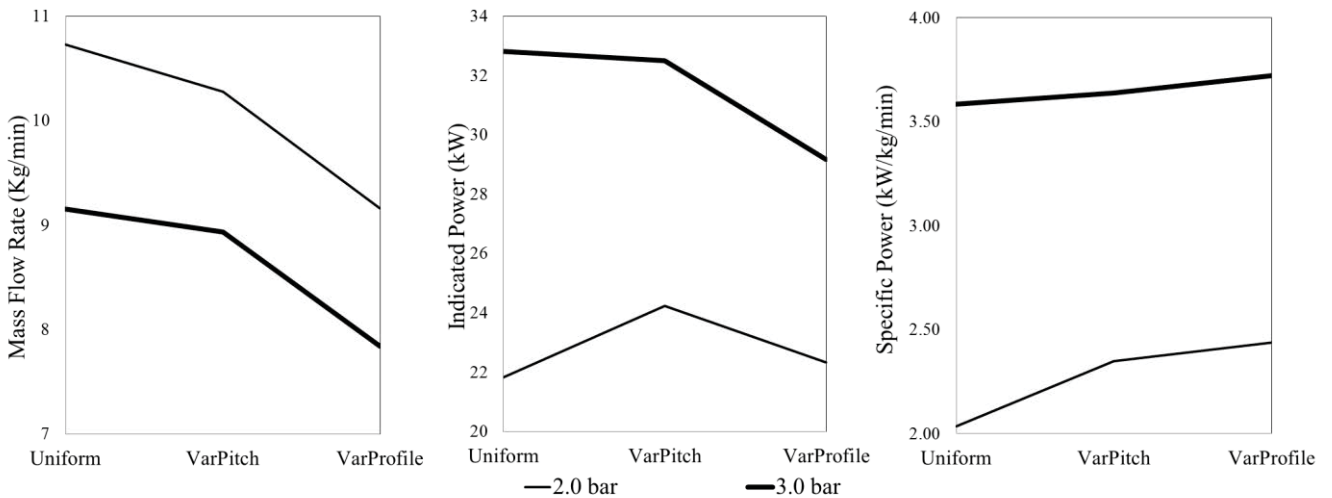
Position	Uniform	Var. Pitch	Diff %	Var. Profile	Diff %
Suction	9.817	12.49	-27.2	9.83	-0.15
Mid	9.908	9.263	6.51	9.35	5.64
Discharge	9.701	6.562	32.3	9.19	5.29



**Figure 13. Comparison of Blow-hole area**

*Overall performance*

The influence of the discharge pressure on the compressor performance for three analysed cases is shown in Figure 14. Uniform rotors have a highest flow rate and lowest specific power for both pressures. However the difference in the specific power between uniform and variable geometry rotors is much reduced at higher pressures. This further confirms that the variable geometry rotors are more suitable for high pressure applications.



**Figure 14. Influence of discharge pressure on overall compressor performance**

## Conclusions

The procedure for grid generation of twin screw compressors with variable pitch and variable cross section profile rotors was implemented successfully. Examples of grids and CFD results with variable lead and variable profile have been presented.

By varying the rotor lead continuously from the suction to discharge or by varying the rotor profile to reduce the cross section area towards the discharge, it is possible to improve compression characteristics and achieve a steeper internal pressure rise. The variable lead rotors additionally reduce the sealing line length and blow-hole area in the high pressure difference zone.

The grid generation enhancements allow use of CFD for novel compressor performance analysis.

## Nomenclature

L – Rotor Length	$\Delta Z$ – Increment in Axial distance
D – Male Rotor Outer Diameter	$p_s$ – Starting Pitch
$\Phi_w$ – Male Rotor Wrap Angle	$p_e$ – Ending Pitch
$\alpha$ – Male rotor rotation angle	$z_1$ – Number of lobes on the Male rotor
$\Delta\alpha$ – Increment in Male rotor angle	$z_2$ – Number of lobes on the Female rotor
Z – Axial distance along the rotors	$V_i$ – Built in Volume Index

## References

- Eiseman, P. R., Hauser, J., Thompson J. F. and Weatherill, N. P. (1994), Numerical Grid Generation in Computational Field Simulation and Related Fields, Proceedings of the 4th International Conference, Pineridge Press, Swansea, Wales, UK.
- Fleming, J. S. and Tang Y. (1994), The Analysis of Leakage in a Twin Screw Compressor and its Application to Performance Improvement, Proceedings of IMechE, Part E, Journal of Process Mechanical Engineering, 209, 125.
- Gardner, J. W. (1969), US Patent No 3,424,373 – Variable Lead Compressor. Patented 1969.
- Hanjalic, K. and Stosic, N. (1997), Development and Optimization of Screw machines with a simulation Model – Part II: Thermodynamic Performance Simulation and Design Optimization”. ASME Transactions. Journal of Fluids Engineering. 119, 664.
- Kovacevic, A., Stosic, N. and Smith, I. K. (2000), Grid Aspects of Screw Compressor Flow Calculations, Proceedings of the ASME Advanced Energy Systems Division, 40, 83.
- Kovacevic, A. (2002), Three-Dimensional Numerical Analysis for Flow Prediction in Positive Displacement Screw Machines, Ph.D. Thesis, School of Engineering and Mathematical Sciences, City University London, UK.
- Kovacevic, A. (2005), Boundary Adaptation in Grid Generation for CFD Analysis of Screw Compressors, Int. J. Numer. Methods Eng., 64(3): 401-426.
- Kovacevic, A., Stosic, N. and Smith, I. K. (2007), *Screw compressors - Three dimensional computational fluid dynamics and solid fluid interaction*, ISBN 3-540-36302-5, Springer-Verlag Berlin Heidelberg New York.
- Liseikin, V. D. (1999), *Grid Generation Methods*, ISBN 3-540-65686-3, Springer-Verlag.
- Samareh, A. J. and Smith, R. E. (1992), A Practical Approach to Algebraic Grid Adaptation, Computers & Mathematics with Applications, 24(5/6): 69-81.
- Shih, T. I. P., Bailey, R. T., Ngoyen, H. L. and Roelke, R. J. (1991), Algebraic Grid Generation for Complex Geometries, Int. J. Numer. Meth. Fluids, 13, 1-31.
- Soni, B. K. (1992), Grid Generation for Internal Flow Configurations, Computers & Mathematics with Applications, 24(5/6): 191-201.
- Rane, S., Kovacevic, A., Stosic, N. and Kethidi, M. (2013), CFD grid generation and analysis of screw compressor with variable geometry rotors, International conference on compressors and their systems, London, C1390/139, 2013.
- Steinhorsson, E., Shih, T. I. P. and Roelke, R. J. (1992), Enhancing Control of Grid Distribution in Algebraic Grid Generation, Int. J. Numer. Meth. Fluids, 15, 297-311.
- Stosic, N., Smith, I. K. and Kovacevic, A. (2005), *Screw Compressors: Mathematical Modeling and Performance Calculation*, Springer Verlag, Berlin, ISBN: 3-540-24275-9.
- Thompson, J. F., Soni, B. and Weatherill, N. P. (1999), *Handbook of Grid generation*, CRC Press.

## Neural Network Prediction of Nonlinear Elastic Unloading for High Strength Steel

\*M. R. Jamli<sup>1,2</sup>, A. K. Ariffin<sup>1</sup>, and D. A. Wahab<sup>1</sup>

<sup>1</sup>Department of Mechanical and Materials Engineering, Faculty of Engineering and Built Environment, Universiti Kebangsaan Malaysia 43600, Bangi, Selangor, Malaysia

<sup>2</sup>Department of Manufacturing Process, Faculty of Manufacturing Engineering, Universiti Teknikal Malaysia Melaka, Hang Tuah Jaya, 76100, Durian Tunggal, Melaka, Malaysia

\*Corresponding author: ridzuanjamli@utem.edu.my

### Abstract

In achieving accurate results, current nonlinear elastic recovery applications of finite element (FE) analysis have become more complicated for sheet metal springback prediction. In this paper, an artificial neural network (ANN) was used to mimic the nonlinear elastic recovery and provides a generalized solution in the FE analysis. The nonlinear elastic recovery was processed through back-propagation networks. This approach is able to perform pattern recognition and create direct mapping of the elastically-driven change after plastic deformation. The FE program for nonlinear elastic recovery experiment was carried out with the integration of ANN. The results obtained at the end of the FE analyses were closed to the measured data.

Keywords: Finite element, neural network, non-linear recovery, springback prediction

### Introduction

One of the problems in the sheet metal forming process is the springback phenomenon. This phenomenon occurs due to the elastic recovery, which is influenced by the elastic properties and the plastic flow of the sheet metal material. Although the elastic recovery contributes only small strain if compared to the plastic strain, the final shape of a sheet metal forming product is significantly affected due to the accumulative small strain in corner radii and sidewall of curved surface (Kim et al. 2013). Most of the current finite element (FE) method practices still utilize the classic elastoplasticity theory, which assumes that the unloading modulus after plastic deformation is parallel to the initial Young's modulus. However, several investigations have shown that the unloading modulus is influenced by accumulated plastic strain (Cleveland and Ghosh 2002; Li et al. 2002; Yoshida et al. 2002; Andar et al. 2010). Furthermore, several investigations have found that the unloading stress-strain curve actually shows nonlinear elastic recovery (Cleveland and Ghosh 2002; Cáceres et al. 2003; Andar et al. 2010; Chatti and Hermi 2011; Sun and Wagoner 2011). The development of an additional surface in the yield surface (Eggertsen and Mattiasson 2010) and the transition of the elastic to the plastic model (Quasi-Plastic-Elastic model) (Sun and Wagoner 2011) have been proposed for the description of nonlinear elastic recovery in constitutive modeling. However, due to the complexity of developing the nonlinear recovery model, the variable elastic modulus achieves a relatively wider range of application in springback predictions (Chatti and Hermi 2011; Zhu et al. 2012).

The applications of an artificial neural network (ANN) as the parameters identification tool for the FE springback analysis provide solution without solving the nonlinearity problems (Aguir et al. 2008; Kazan et al. 2009; Veera Babu et al. 2010;

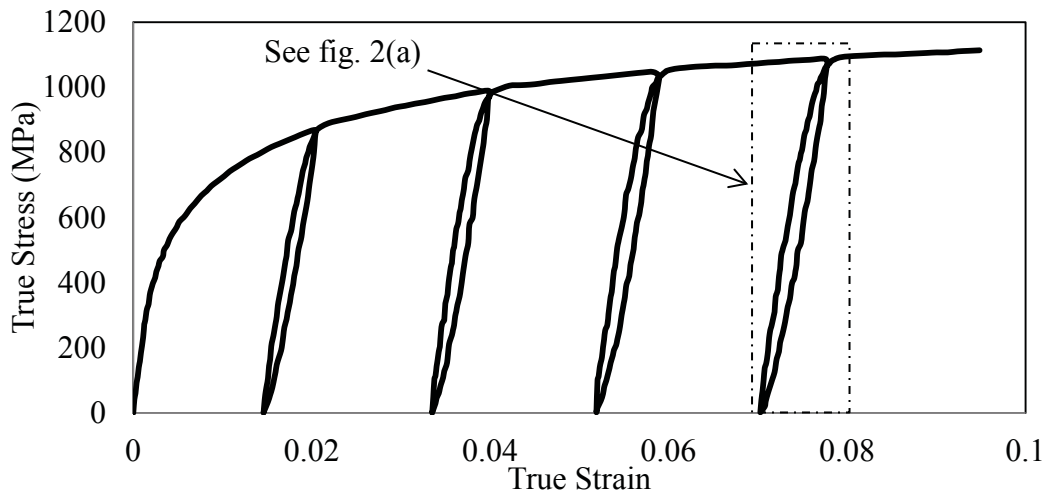
Aguir et al. 2011). Thus in this paper, ANN was used to mimic the nonlinear elastic recovery and provides a generalized solution in the FE analysis. The implementation of ANN in the constitutive model of the FE software requires an additional technique to achieve better generalization. This is to ensure that the developed ANN model is utilizable in a wide range of the FE springback analysis.

## Methodology

The application of ANN is split into the curve regeneration and interpolation coefficient parts. A new curve is generated from the raw experimental data and the output is used as an input to the interpolation coefficient part. This procedure is discussed further in the next subsection.

### 3.1 The Database and its Regeneration

This study utilized the experimental data that have been published by (Sun and Wagoner 2011). The published data were chosen based on their comprehensiveness in providing information from the identification of material parameters until the measurement of springback. Figure 1 shows the tensile test result for a DP 980 steel sheet with intermediate unloading cycles. The hysteresis loops are noticeable significantly as the flow stresses increase prior to unloading. Figure 2a shows the magnified view of the fourth cycle from Figure 1. A chord modulus ( $E_{av}$ ) of 145GPa and an initial Young's modulus ( $E_0$ ) of 208GPa are shown for comparison. It is shown that the current elastic modulus ( $E_c$ ) varied at different normalized stress points ( $\sigma_1/\sigma_0$ ). Figure 2b shows the regeneration of the unloading curve by the first ANN, whose architecture was investigated in two cases, as shown in Table 1. The true strain and true stress are the input and the output of the network.



**Figure 1. Tensile test result for DP 980 steel with intermediate unloading cycles**

### 3.2 Determination of Interpolation Coefficient

In the second ANN, the input and output data of the network are formed based on the regenerated curve in Figure 2b. An interpolation model is applied to interpolate the range between  $E_{av}$  and  $E_0$  at every normalized stress point ( $\sigma_1/\sigma_0$ ) as shown in Eq.(1).

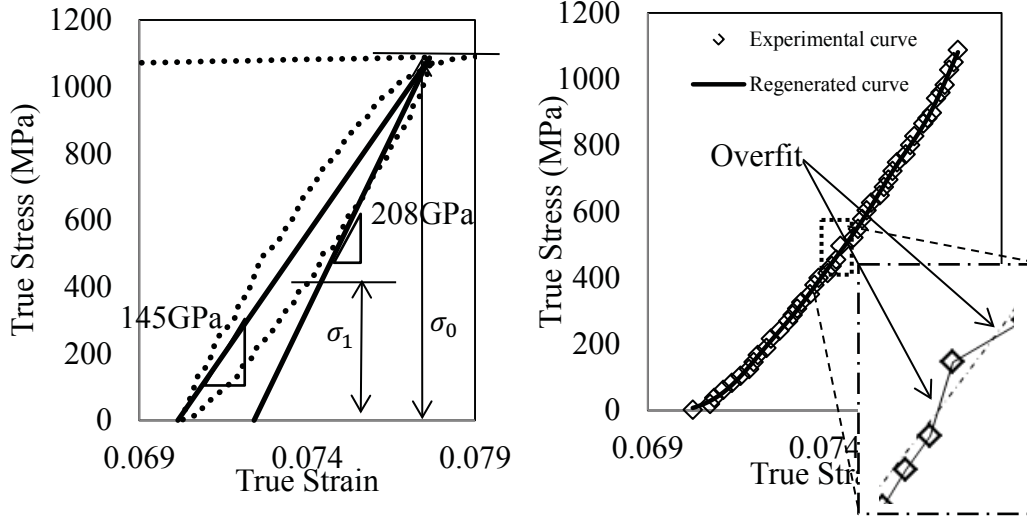
$$C_e = \frac{E_c - E_{av}}{E_0 - E_{av}} \quad (1)$$

where  $\sigma_1/\sigma_0$  and  $C_e$  are the input and output of the network training.



**Table 1. Neural network training parameters**

Parameters	Case 1	Case 2
Training function	Trainlm (LM)	Trainlm (LM)
Hidden layer	3	3
Neuron per layer	20, 20, 20	2, 2, 2



**Figure 2. (a) Magnified view of the fourth unloading-reloading with  $E_0$  and  $E_{av}$  (Sun and Wagoner 2011) (b) new unloading curve regenerated by first ANN**

### 3.3 ANN to FE analysis link establishments

The second ANN is completely trained and the neuron weights and biases are extracted in the form of matrices. A feedforward network from the matrices is implemented into the user defined material subroutine. In the FE analysis,  $E_c$  need to be updated at every increment of the unloading/reloading process. The function of the feedforward-network-based constitutive model in the FE model at every increment is as follows:

- (i) For  $(i + 1)$ th strain increment, the input of the network is the value of the normalized stress point,  $\sigma_1/\sigma_0$ , where  $\sigma_1$  and  $\sigma_0$  are given by the current stress and current yield stress. To distinguish the input between unloading and reloading processes, the input is expressed as  $(1 - \sigma_1/\sigma_0)$  and  $(\sigma_1/\sigma_0)$
- (ii)  $E_c$  is then calculated by reversing Eq. (1) as:

$$E_c = C_e * (E_0 - E_{av}) + E_{av} \quad (2)$$

## Results and Discussion

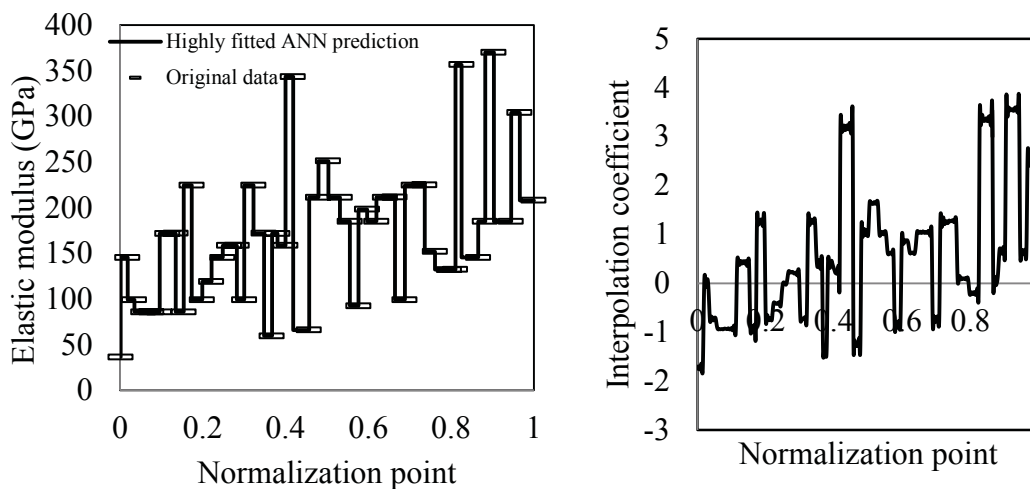
The variation of the unloading elastic modulus is a function of plastic pre-strain and it contributes to the size of hysteresis loops, as shown in Figure 1. Therefore, ANN prediction of the unloading curve cannot be utilized in the constitutive model if it is only based on the true strain and true stress as the input and output of the network.

This is due to the stresses along the unloading curve that need to be updated at every iteration as a product of  $E_c$  and true strain. By determining the relation of  $E_c$  with  $E_0$  and  $E_{av}$  at the fourth loop, the product of Eq.(1) is able to represent all other loops based on the provided  $E_0$  and  $E_{av}$ .

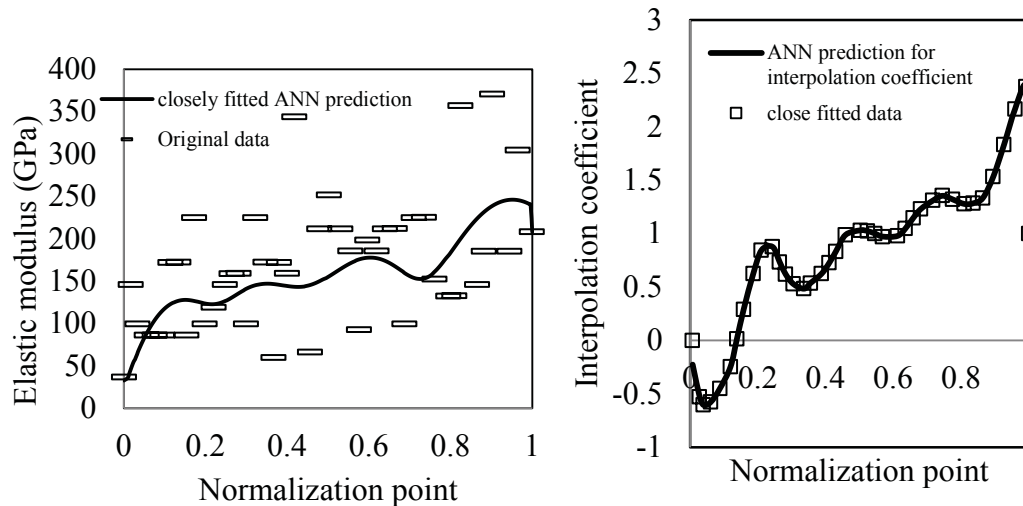
Figure 2b shows the result of the curve regeneration which consists of a closely fitted curve and a highly fitted curve by the first ANN. This fitting accuracy has a significant effect on the architecture of the second ANN. In the first case, the first ANN regenerates the unloading curve with high accuracy. A fluctuating step curve is produced when the slope determination is based on the highly fitted unloading curve, as shown in Figure 3a. In the second ANN part, high accuracy is essential as the result was utilized directly into the FE analysis. Therefore, a network training with a highly fitted training set requires 20 neurons in its first, second, and third hidden layer. This network consumes a very high computational cost and time. Furthermore, the prediction of  $C_e$  experiencing distortions at every step curves, as shown in Figure 3b. The distortions are the source of error when the predictions were transferred into FE analysis.

In the second case, the first ANN regenerates the unloading curve with a closely fitting accuracy and it results in quite a smooth curve, as shown in Figure 4a. In order to obtain such a smooth curve, the selection of network architecture with low number of neurons is essential, which determines the accuracy of the model with regard to the particular set of data. In the second ANN part, a network training with a closely fitted training set only requires eight neurons in its first, second, and third hidden layer, which results in low computational consumption. In addition, the prediction of  $C_e$  experiencing a smooth mapping, as shown in Figure 4b.

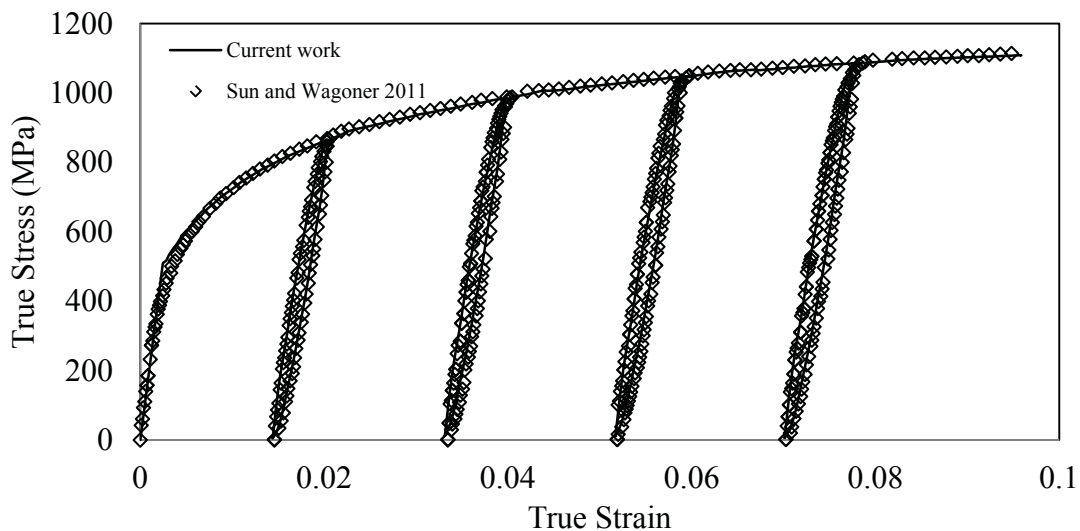
Figure 5 shows a comparison of the overall fit by the FE analysis using the current model with the experimental data. Although the network training was based on the fourth cycle, the overall prediction fit obtained was adequate. The result also shows that a closely fitting ANN prediction was adequate to achieve closeness to the experimental data in the FE analysis.



**Figure 3. Case 1:(a) Elastic modulus determination;(b)interpolation coefficient prediction**



**Figure 4. Case 2:(a) Elastic modulus determination;(b)interpolation coefficient prediction**



**Figure 5. Comparison of overall fit by the FE analysis by using ANN prediction model**

## Conclusions

The above work demonstrates the ability of ANN to predict the relation between the nonlinear elastic modulus, the initial Young's modulus, and the chord modulus. It is shown that the model is well implemented in the finite element analysis to achieve closeness to the experimental data. With its generalization, this approach is suitable to be used in other finite element model of sheet metal forming to predict springback.

## References

- Aguir, H., BelHadjSalah, H., et al. (2011), Parameter identification of an elasto-plastic behaviour using artificial neural networks-genetic algorithm method. *Materials & Design* 321, pp.48-53.
- Aguir, H., Chamekh, A., et al. (2008), Identification of Constitutive Parameters using Hybrid ANN multi-objective optimization procedure. *International Journal of Material Forming* 10, pp.1-4.

- Andar, M. O., Kuwabara, T., et al. (2010), Elastic&Plastic and Inelastic Characteristics of High Strength Steel Sheets under Biaxial Loading and Unloading. *ISIJ International* 504, pp.613-619.
- Cáceres, C. H., Sumitomo, T., et al. (2003), Pseudoelastic behaviour of cast magnesium AZ91 alloy under cyclic loading–unloading. *Acta Materialia* 5120, pp.6211-6218.
- Chatti, S. and Hermi, N. (2011), The effect of non-linear recovery on springback prediction. *Computers & Structures* 8913-14, pp.1367-1377.
- Cleveland, R. M. and Ghosh, A. K. (2002), Inelastic effects on springback in metals. *International Journal of Plasticity* 185-6, pp.769-785.
- Eggertsen, P.-A. and Mattiasson, K. (2010), On the Modeling of the Unloading Modulus for Metal Sheets. *International Journal of Material Forming* 30, pp.127-130.
- Kazan, R., Firat, M., et al. (2009), Prediction of springback in wipe-bending process of sheet metal using neural network. *Materials & Design* 302, pp.418-423.
- Kim, H., Kim, C., et al. (2013), Nonlinear elastic behaviors of low and high strength steels in unloading and reloading. *Materials Science and Engineering: A* 5620, pp.161-171.
- Li, X., Yang, Y., et al. (2002), Effect of the material-hardening mode on the springback simulation accuracy of V-free bending. *Journal of Materials Processing Technology* 1232, pp.209-211.
- Sun, L. and Wagoner, R. H. (2011), Complex unloading behavior: Nature of the deformation and its consistent constitutive representation. *International Journal of Plasticity* 277, pp.1126-1144.
- Veera Babu, K., Ganesh Narayanan, R., et al. (2010), An expert system for predicting the deep drawing behavior of tailor welded blanks. *Expert Systems with Applications* 3712, pp.7802-7812.
- Yoshida, F., Uemori, T., et al. (2002), Elastic–plastic behavior of steel sheets under in-plane cyclic tension–compression at large strain. *International Journal of Plasticity* 185-6, pp.633-659.
- Zhu, Y. X., Liu, Y. L., et al. (2012), Development and application of the material constitutive model in springback prediction of cold-bending. *Materials & Design* 420, pp.245-258.

**Prediction of solid recirculation rate and solid volume fraction in an ICFB****\*Ravi Gujjula<sup>1</sup>, Narasimha Mangadoddy<sup>1</sup>.**<sup>1</sup>Department of Chemical Engineering, Indian Institute of Technology Hyderabad, Ordnance Factory Estate, 502205, Andhra Pradesh, India.

\*Corresponding author: narasimha@IITH.AC.IN

**Abstract**

This paper presents a numerical study of gas and solid flow in an internally circulating fluidized bed (ICFB). The gas and solid hydrodynamics have been simulated by using two-fluid model. 2D & 3D geometry was used to represent key parts of a laboratory ICFB. In ICFB, the two-fluid Eulerian model with kinetic theory of granular flow option and the various drag laws used to predict the hydrodynamic behavior of ICFB. The simulation results by four drag laws show that the Gidaspow and Arastoopour drag models predict the fluidization dynamics in terms of flow patterns, void fractions and axial velocity fields were compared with experimental data. The effect of superficial gas velocity, presence of draft tube on solid hold-up distribution, solid circulation pattern, and variations in gas bypassing fraction for the 3D ICFB investigated through CFD simulations. The mechanism governing the solid circulation in an ICFB has been explained based on gas and solid dynamics obtained from the simulations. Predicted total granular temperature distributions in the draft tube and annular zones qualitatively agree with experimental data. The total granular temperature tends to increase with increasing solids concentrations and decrease with an increase of solids concentration.

Key words: ICFB; Two fluid model; Solid recirculation rate; Gas solid granular flow; Drag law models; Fluidization, Hydrodynamics.

\*Corresponding author: ch09p002@iith.ac.in, Fax: +91 4023016032

## 1. Introduction

Gas-solid fluidization by conventional circulating fluidized beds (CFB) are common in various industrial operations such as coal combustion and gasification, incineration of municipal solid waste, catalyst regeneration, thermal cracking and drying (Yang et al., 2008; Kim et al., 1997,2000; Burugupalli 1988). They require very long tall column as a solids raiser and accompanying additional external circulation of solids through a cyclone. In order to avoid external circulation accessories, a compact internally circulating fluidized bed (ICFB) is developed, which is a modified spouted fluidized bed with a draft tube inside the column to avoid problem of gas bypassing. An ICFB is having a centrally located draft tube that divides the bed into two or more sections and thus promotes solid circulation within a single vessel (Kim et al., 1997, 2000; Burugupalli, 1988; Yang & Keairns, 1978). This ICFB reactor has many advantages such as its compact size and the annular section act as heat sink because riser is located inside the vessel (Jeon & Kim, 2010). The ICFB reduces the height of conventional CFB riser and construction cost, solves the problems of CFB, makes highly efficient and low pollution combustion for a wide range of fuels. In ICFB, the draft tube (or riser) was fixed directly to the gas distributor of the riser section.

In recent years due to advances in high performance computers and numerical algorithms, the computational fluid dynamics (CFD) technique is become a fundamental element of research in simulating gas–solid multiphase flow systems (Mujumdar, & Wu, 2008). Thus many researchers have put considerable effort in validating the CFD models in order to achieve fundamental and accurate model for these systems. One of the difficulties to validate CFD models using experimental measurements is the computational effort needed to perform three-dimensional (3D) simulations of dynamic behavior of industrial scale fluidized beds. Several drag models have been developed to calculate the inter-phase momentum exchange in fluidized bed, such as the Wen and Yu, Syamlal & O'Brien and Gidaspow drag models (Wen & Yu, 1966; Syamlal, & O'Brien, 1989; Gidaspow, 1994). The effect of various drag models on hydrodynamics behavior of gas–solid fluidized beds was also compared by (Van Wachem et al., 2001). They found that the expression suggested by Syamlal–O'Brien (Syamlal, & O'Brien, 1989) model under predicts the pressure drop, bed expansion and bubble diameter compared to the experimental data. The work reported in this paper aimed at the development of a CFD-model for the hydrodynamics of 3D- ICFB reactor. With the help of this CFD model the instantaneous and the time-averaged profiles of pressure drop and volume fractions within the draft tube and the annulus section of ICFB calculated. Further, the flow fields, i.e. volume fractions and velocity distributions predicted for different size particles in the range of 86  $\mu\text{m}$ -250  $\mu\text{m}$ . Additionally 2D-ICFB CFD simulations run to validate the CFD model predictions. These predictions are then compared to the experimental data of Ahuja, & Patwardhan, (2008).

## 2. Methodology

### 2. 1. Eulerian–Eulerian model equations for gas–solid flow with KTGF

The partial differential TFM equations for explaining particle and fluid flows in the fluidized bed (Patankar, 1980) are adopted for the ICFB. The continuity equation in the absence of mass transfer between phases is give for each phase as follows

$$\frac{\partial}{\partial t}(\varepsilon_g \rho_g) + \nabla \cdot (\varepsilon_g \rho_g v_g) = 0 \quad (1)$$

$$\frac{\partial}{\partial t}(\varepsilon_s \rho_s) + \nabla \cdot (\varepsilon_s \rho_s v_s) = 0 \quad (2)$$

$$\varepsilon_g + \varepsilon_s = 1 \quad (3)$$

Momentum conservation equations

$$\frac{\partial}{\partial t}(\varepsilon_g \rho_g v_g) + \nabla \cdot (\varepsilon_g \rho_g v_g v_g) = \nabla \cdot \tau_g + \varepsilon_g \rho_g g - \varepsilon_g \nabla P + \beta(v_g - v_s) \quad (4)$$

$$\frac{\partial}{\partial t}(\varepsilon_s \rho_s v_s) + \nabla \cdot (\varepsilon_s \rho_s v_s v_s) = \nabla \cdot \tau_s + \varepsilon_s \rho_s g - \nabla P_s - \varepsilon_s \nabla P + \beta(v_g - v_s) \quad (5)$$

The solid pressure is composed of a kinetic term and a second term due to particle collisions as follows (Luna et al., 1984)

$$P_s = \varepsilon_s \rho_s \Theta_s + 2\rho_s(1+e_s)\varepsilon_s^2 g_0(\varepsilon_s)\Theta_s \quad (6)$$

$$\tau_s = \varepsilon_s \mu_s (\nabla v_s + (\nabla v_s)^\top) + \varepsilon_s (\lambda_s - \frac{2}{3}\mu_s)(\nabla \cdot v_s)I \quad (7)$$

$$\tau_g = \varepsilon_g \mu_g (\nabla v_g + (\nabla v_g)^\top) - \frac{2}{3}\varepsilon_g \mu_g (\nabla \cdot v_g)I \quad (8)$$

$$\lambda_s = \frac{4}{3}\varepsilon_s \rho_s d_p g_0(\varepsilon_s)(1+e_s)\sqrt{\frac{\Theta_s}{\pi}} \quad (9)$$

## 2.2. Drag models

The mathematical formulations of the four drag models that have been used in this work are shown below.

**Gidaspow's drag model (1994).**

$$\beta_{Wen-Yu} = \frac{3C_D \varepsilon_s \varepsilon_g \rho_g |v_g - v_s|}{4d_p} \varepsilon_g^{-2.65}, \quad \varepsilon_g \geq 0.8 \quad (10)$$

$$\beta_{Ergun} = 150 \frac{\varepsilon_s^2 \mu_g}{\varepsilon_g d_p^2} + 1.75 \frac{\varepsilon_s \mu_g |v_g - v_s|}{d_p}, \quad \varepsilon_g < 0.8 \quad (11)$$

$$C_D = \begin{cases} \frac{24}{\text{Re}_p} [1 + 0.15(\text{Re}_p)^{0.687}], & \text{Re}_p < 1000 \\ 0.44 & , \quad \text{Re}_p > 1000 \end{cases} \quad (12)$$

$$\text{Re}_p = \frac{\varepsilon_g \rho_g d_p |\nu_g - \nu_s|}{\mu_g}, \quad \text{Particle Reynolds Number} \quad (13)$$

**Arastoopour's drag model (1990)**

$$\beta_{gs} = \left( \frac{17.3}{\text{Re}_p} + 0.336 \right) \frac{\rho_g |\nu_g - \nu_s|}{d_p} (1 - \varepsilon_g) \varepsilon_g^{-2.8} \quad (14)$$

**Syamlal–O'Brien (1989) is expressed as**

$$\beta_{gs} = \frac{3 \varepsilon_g \varepsilon_s \rho_g}{4 \nu_{rs}^2 d_p} C_D \left( \frac{\text{Re}_p}{\nu_{rs}} \right) |\nu_g - \nu_s| \quad (15)$$

$$C_D = \left( 0.63 + \frac{4.8}{\sqrt{\text{Re}_p / \nu_{rs}}} \right)^2 \quad (16)$$

$$\text{Re}_p = \frac{\rho_g d_p |\nu_g - \nu_s|}{\mu_g} \quad (17)$$

$$\nu_{rs} = 0.5 \left[ A - 0.06 \text{Re}_p + \sqrt{(0.06 \text{Re}_p)^2 + 0.12 \text{Re}_p (2B - A) + A^2} \right] \quad (18)$$

$$A = \varepsilon_g^{4.14}, B = \begin{cases} 0.8 \varepsilon_g^{1.28} & \text{for } \varepsilon_g \leq 0.85 \\ \varepsilon_g^{2.65} & \text{for } \varepsilon_g \geq 0.85 \end{cases} \quad (19)$$

Fig.1. shows the relationship between the fluid-solid phase exchange coefficient, which is estimated for the available drag models in the literature as a function of solids volume fraction. For the various drag models at fixed slip velocity of 0.5 m/s and for the 86  $\mu\text{m}$ , 170  $\mu\text{m}$ , 250  $\mu\text{m}$  & 853  $\mu\text{m}$  particles used in the present study calculations of Fig.1. It is evident that the Syamlal–O'Brien drag model predicts larger values of gas-solids exchange coefficient at a higher values of solids concentration. This means that the Syamlal and O'Brien drag model predictions are significant near the walls and drag coefficient will have the greatest influence on the model. Fig.1 shows the quantitative comparison of various drag models at fixed slip velocity of 0.5 m/s and for the 853 $\mu\text{m}$  particles used in the present study as part of validation. No significant difference between



drag coefficients predicted by the models at all values of solid volume fraction for the coarsest particles, i.e. 853  $\mu\text{m}$ .

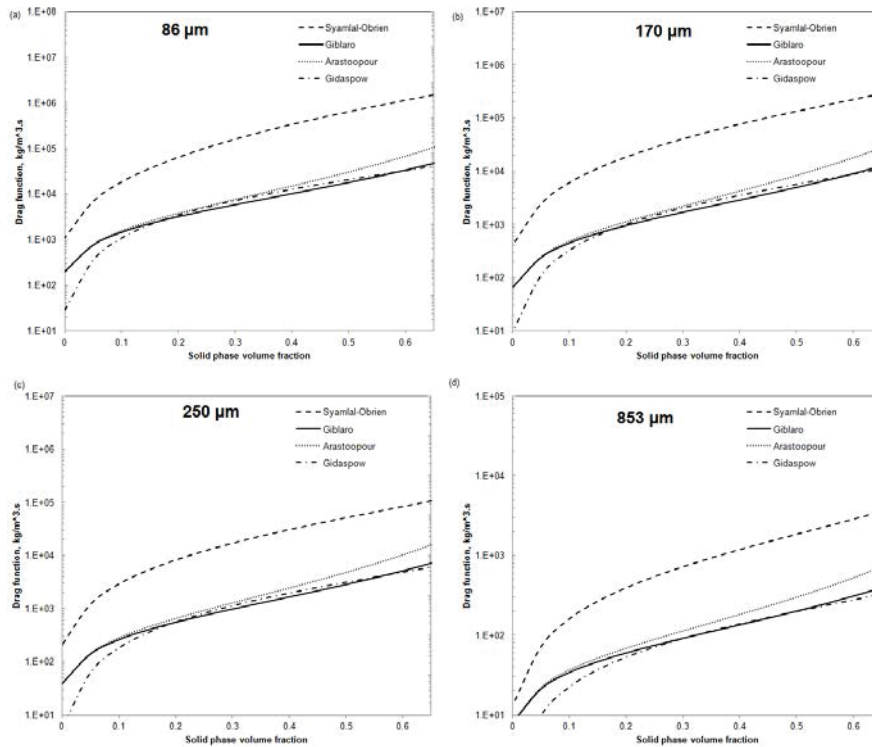


Fig. 1. Comparison of different drag models for (a) 86  $\mu\text{m}$  particles (b) 170  $\mu\text{m}$  particles (c) 250  $\mu\text{m}$  particles (d) 853  $\mu\text{m}$  particles at a slip velocity of 0.5 m/s.

### 3. Simulation strategy and conditions

This paper simulates two different fluidization geometries consist an internal draft tube. First geometry, 2D ICFB is considered from Ahuja & Patwardhan, (2008) work, used for validation of the CFD model. The second geometry, 3D ICFB from IITH's 30 cm diameter fluidization rig is used for parametric analysis. Ahuja & Patwardhan, (2008) experimented solid-gas flow patterns in ICFB with a small geometry (Column 0.186 m X 1.2 m with a draft tube of 0.10 m X 0.158 m) by considering a particular case as partial sparging with a draft tube, 2D simulations are performed using Eulerian–Eulerian two-fluid model along with No-slip boundary conditions were used for both phases at the ICFB walls. Solids volume fraction was defined as 0.62 with a maximum packing limit of 0.65. Simulation was initiated with uniform inlet superficial gas velocity of 1.041 m/s. In this work the 3D geometry of ICFB ( 0.3 mX 3.0 m & draft tube 0.1mX 0.9 m) height of draft tube as shown in Fig. 2(b). Grid consists of total 46536 nodes and two cell zones. The initial bed height as 0.86 m considered and the initial solid volume fraction was defined as 0.62 with a maximum packing of 0.65. Simulation was initiated with uniform inlet superficial gas velocity to the draft tube was set as 0.8, 1.25, 1.5 and 1.75 m/s with a constant uniform gas velocity of 0.2 m/s as an input to the annular section.

### 4. Results and discussion

#### 4.1 2D ICFB model predictions & validation

In the current study, Gidaspow, Syamlal–O'Brien, Gibilaro and Arastoopour drag models are tested and compared with the experimental data to identify the suitable drag model for modelling the turbulent fluidization for gas-solid particles. This present work assumes two cases of experiments having partial and complete sparging for 2D ICFB CFD runs operating at a 1.0425 m/s superficial velocity.

**Table 1**

Simulation and model parameter	
Parameter Description	Value
Particle density	2500 (kg/m <sup>3</sup> )
Air density	1.225 (kg/m <sup>3</sup> )
Mean particle diameter	86,170 and 250 (μm)
Initial solid packing	0.62
Superficial air velocity	0.8, 1.0, 1.25, 1.5, 1.75 (m/s)
Fluidized bed column dimension	0.3 (m) x 3.0 (m)
Static bed height	0.8 (m)
Restitution coefficient	0.95
Boundary Condition	Outlet- pressure, walls-No slip

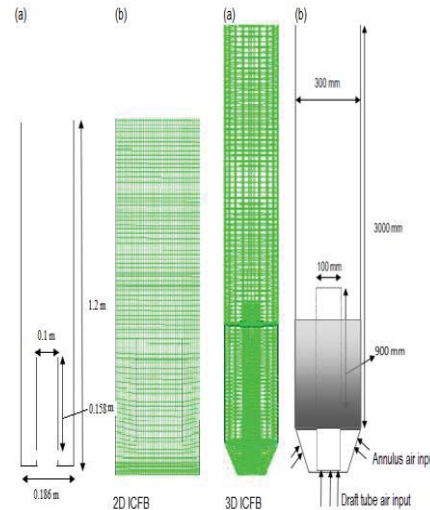


Fig. 2. Schematic diagrams of 2D ICFB (a) Geometry (b) Grid and 3D ICFB (a) Grid (b) Geometry.

The simulated results of the 2D ICFB are presented in Fig. 3-4 in terms of solid volume fraction and flow field. In Fig. 3, comparison between the various drag models based on solid volume fraction snapshot have made in terms of bed height and shape of fluidization pattern. It can be observed that the Arastoopour and Gidaspow drag models show the best results in simulating the bed height. The Gibilaro drag model prediction represents the lowest bed expansion and gas void fraction comparatively with other drag model predictions. The CFD models of Gidaspow, Syamlal-O'Brien and Arastoopour predict lean solids zone just above the gas distributor as seen in the Fig.3. Whereas in the case of Gibilaro drag model, predicts dense zone at the bottom of draft tube which is just above the gas distributor. In Fig.4 the predictions by Syamlal-O'Brien drag model based CFD model shows an improvement over the Gibilaro model.

#### 4.2 Pressure drop in 3D ICFB

The mean  $\Delta p$  value is plotted to compare pressure difference at different locations along with 3D ICFB column as shown in the Fig. 5. The pressure drop in the draft tube passed through minima with an increase of gas superficial velocity. In the low velocity region the pressure drop decreases steadily. After minimum fluidization stage, once transport of solids moves upward then the pressure drop decreases with an increase of superficial velocity due to the lean solids holdup in the draft tube.

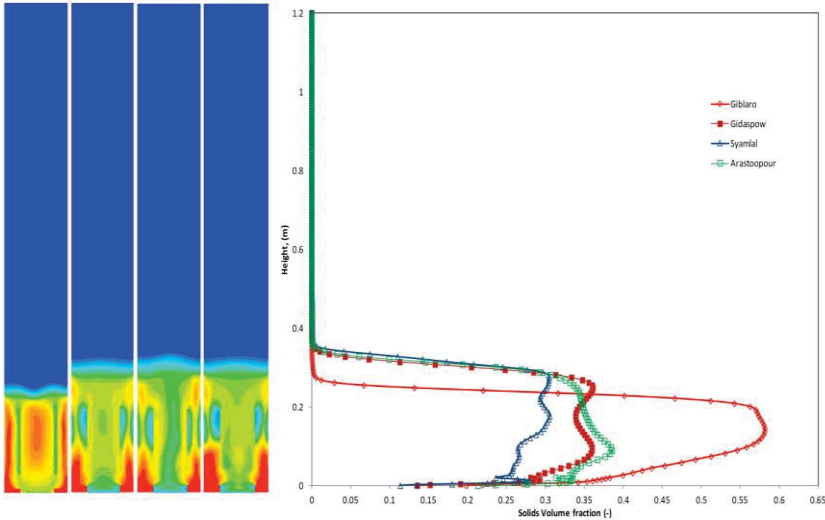


Fig. 3. The Simulated solid volume fraction contours for various drag models for partially sparging with a draft tube ( $U_o=1.0425$  m/s) (a) Giblaro drag model (b) Gidaspow drag model (c) Syamlal-O'Brien drag model and (d) Arastoopour drag model.

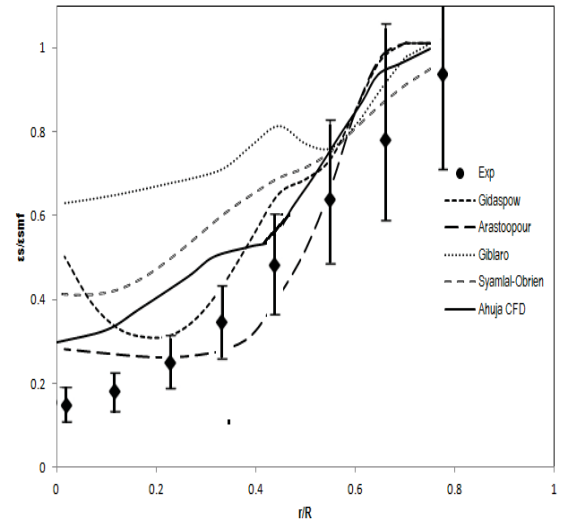


Fig. 4. Solids hold-up profiles for partial sparging with a draft tube: Comparison of different drag models of 853  $\mu$ m particles.

The pressure drop at different heights of draft tube is following a decline trend with an increase of superficial gas velocity except at location of 0.25 m, which is just above the air distributor. At 0.25 m location, part of draft tube gas gets into by passing; the  $\Delta p$  seems unchanged at this gap area.

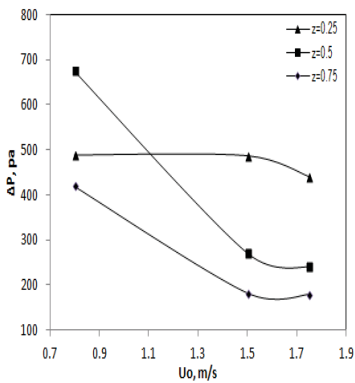


Fig. 5. Pressure drop vs draft tube velocity for the silica particle size  $d_p=86$   $\mu$ m .

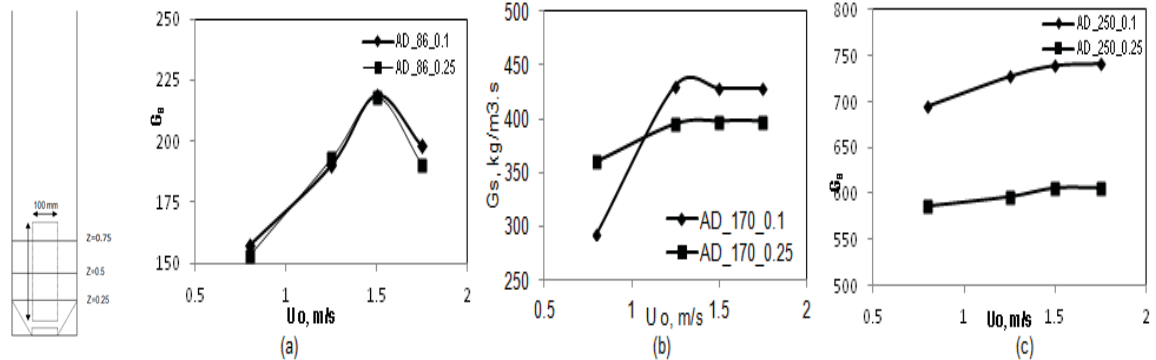


Fig. 6. Solids circulation rate vs draft tube velocity (a) 86  $\mu$ m (b) 170  $\mu$ m (c) 250  $\mu$ m.

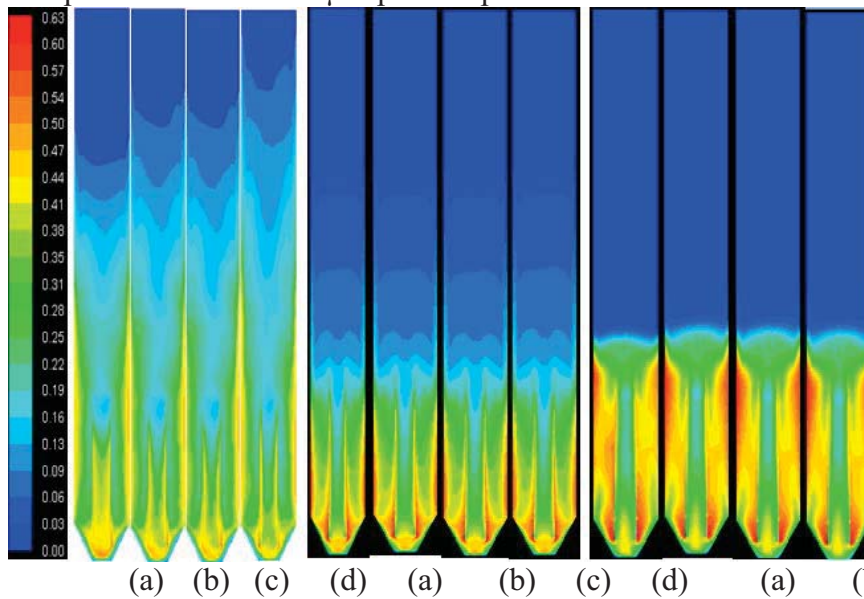
### 4.3 Solid Circulation Rate

Solid recirculation rate  $G_s$  is an important parameter to design 3D ICFB reactor with a suitable draft tube configuration. The effect of superficial gas velocity ( $U_o$ ) on solid recirculation rate is shown in Fig. 6. Solids recirculation rate  $G_s$  was calculated based on the product of mean volume fraction of solids, density of solids and the solid velocity

magnitude.  $G_s$  increases with  $U_o$  due to the increase in the driving force for the circulation of solids between the draft tube and annular moving bed is observed through increased bed voidage in the draft tube. It can be seen in the Fig.6 (a), (b )and (c), that the solid circulation rate of smaller particles increases with the increase of superficial velocity.

4.4 Mean Volume fraction contour plots

Using the Arastoopour drag, contours of solid phase volume fractions are shown in Fig.7 ,10 & 11 for 86  $\mu\text{m}$  170  $\mu\text{m}$  and 250  $\mu\text{m}$  size silica particles at gas superficial velocities at 0.8, 1.25 and 1.5 m/s respectively. The bed expansion for different size particles is clearly distinguished from these contour plots. Fig. 7 is the simulation result of particle diameter 86 $\mu\text{m}$  size with the Arastoopour drag model. It is found that the bed expansion is low at low superficial gas velocities. There exist a dense phase zone in the lower part of the ICFB and a dilute phase zone in the upper zone. However the dense phase bed level increases gradually with increasing superficial gas velocity from 0.8 to 1.5 m/s. Similar behavior is also observed in the case of particles 170  $\mu\text{m}$  and 250  $\mu\text{m}$  as shown in the Fig. 8 & 9 respectively. In the case of 250  $\mu\text{m}$  size particles as expected, due to the increase effective weight of the particles, the height of the bed expansion is lower compared to 170 and 86  $\mu\text{m}$  particle profiles.



**Fig. 7.** (a) Contour plot of solids volume fraction with different gas velocities of Silica particles of size 86  $\mu\text{m}$  at a constant annulus input velocity (With Arastoopour drag model)  $U_a=0.2$  m/s.(a)  $U_d=0.8$  m/s (b)  $U_d=1.0$  m/s (c)  $U_d=1.25$  m/s (d)  $U_d=1.5$  m/s.

**Fig. 8.** Contour plot of mean solids volume fraction with different gas velocities of Silica particles size 170  $\mu\text{m}$  at constant annulus input velocity  $U_a=0.2$  m/s (With Arastoopour drag model).(a)  $U_d=0.8$  m/s.(b)  $U_d=1.25$  m/s.(c)  $U_d=1.5$  m/s.(d)  $U_d=1.75$  m/s.

**Fig. 11.** Contour plot of mean solids volume fraction with different gas velocities of Silica particles size 250  $\mu\text{m}$  at constant annulus input velocity  $U_a=0.2$  m/s (With Arastoopour drag model). (a)  $U_d=0.8$  m/s. (b)  $U_d=1.25$  m/s. (c)  $U_d=1.5$  m/s. (d)  $U_d=1.75$  m/s.

## 5. Conclusion

The hydrodynamic characteristic of 2D & 3D ICFB with solid particle was studied by an Eulerian-Eulerian CFD model with the kinetic theory of granular flow. Four drag models considered for the simulations. Syamlal and O'Brien, Gidaspow, Arastoopour and Gibilaro drag models are implemented into Fluent through the User Defined Functions (UDF). 2D simulation of an internally circulating gas-solid fluidized bed with polypropylene particles was run based on Ahuja & Patwardhan, (2008) case. The resulting hydrodynamic properties are compared to Ahuja & Patwardhan, (2008) data. The simulation results by four different drag models show that the Gidaspow & Arastoopour models can accurately predict the flow pattern, voidage profiles, and velocity profiles in the ICFB. With the Arastoopour drag model the simulations are giving the best fits to the experimental data. The draft tube superficial gas velocity and the solids circulation rate have significant effects on the solid fraction in each region. Increasing the draft tube superficial gas velocity can decrease solid fraction in the draft tube but has little effect in the annulus zone.

## 6. References

- Ahuja, G.N., & Patwardhan, A.W. (2008). CFD and experimental studies of solids hold-up distribution and circulation patterns in gas–solid fluidized beds. *Chemical Engineering Journal*, 143 147–160.
- Arastoopour H., Pakdel, P., & Adewumi M. (1990) Hydrodynamic analysis of dilute gas–solids flow in a vertical pipe. *Powder Technology*, 62, 163–170.
- Burugupalli, V.R. (1988). Process analysis of a twin fluidized bed biomass gasification system. *Industrial and Engineering Chemistry Research*, 27, 304–312.
- Gibilaro, L.G., Di Felice, R., & Waldram, S.P. (1985). Generalized friction factor and drag coefficient correlations for fluid–particle interactions. *Chemical Engineering Science*, 40, 1817–1823.
- Gidaspow, D. (1994). Multiphase flow and fluidization: Continuum and kinetic theory description. New York : Academic Press.
- Gidaspow, D., Jonghwun, J., & Singh, R.K. (2004). Hydrodynamics of fluidization using kinetic theory: an emerging paradigm-2002 Flour–Daniel lecture. *Powder Technology*, 148, 123–141.
- Gidaspow, D., & Mostofi, R. (2003). Maximum carrying capacity and granular temperature of A, B, and C particles, *AIChE Journal*, 49, 831–843.
- Jeon, J. H., & Kim, S.D (2010). Hydrodynamic Characteristics of Binary Solids Mixtures in a Square Internally Circulating Fluidized Bed. *Journal of Chemical Engineering of Japan*, 43(2), 26-131.
- Kim, Y.T., Song, B.H., & Kim, S.D. (1997). Entrainment of solids in an internally circulating fluidized bed with draft tube. *Chemical Engineering Journal*, 66, 105-110.
- Kim, Y.J., J.M. Lee and S.D. Kim, (2000). Modeling of Coal Gasification in an Internally Circulating Fluidized Bed Reactor with Draught Tube. *Fuel*, 79, 69-77.
- Lun, C.K.K., Savage, S.B., Jeffrey, D.J., and Chepur, N. (1984). Kinetic theories for granular flow: inelastic particles in Couette flow and slightly inelastic particles in a general flow field. *Journal of Fluid Mechanics*, 140, 223–256.
- Mujumdar, A.S., & Wu, Z. (2008). Thermal drying technologies Cost-effective innovation aided by mathematical modeling approach. *Drying Technology*, 26, 146–154.
- Patankar, S.V. (1980). Numerical Heat Transfer and Fluid Flow. Hemisphere Publishing Corporation.
- Syamlal, M., Rogers, W., & O'Brien, T.J. (1993). MFIX documentation: theory guide, Technical Report DOE/METC-9411004, NTIS/(DE9400087) Morgantown Energy Technology Centre, Morgantown, West Virginia.
- Syamlal, M & O'Brien, T.J. (1989). Computer simulation of bubbles in a fluidized bed. *AIChE Symposium Series*, 85, 22–31.

- Van Wachem, B.G.M., Schouten, J.C., Krishna, R., Van den Bleek, C.M., & Sinclair, J. L. (2001). Comparative analysis of CFD models of dense gas–solid systems,” *AIChE Journal*, 47,1035–1051.
- Wen, Y.H., & Yu. (1966). Mechanics of fluidization.*Chemical Engineering Progress Symposium Series*, 62, 100–111.
- Yang, W.C., & Keairns, D.L. (1978). Design of recirculating fluidized beds for commercial applications. *AIChE Symposium Series*, 74, 218–228.
- Yang, T., Zhang, T., & Bi, H. T. (2008). A novel continuous reactor for catalytic reduction of NO<sub>x</sub> – Fixed bed simulation. *The Canadian Journal of Chemical Engineering*, 86(3), 395-402.

## **Coupled Reliability and S-version Finite-Element Model for Probabilistic Distribution of Surface Crack Growth under Constant Amplitude Loading**

**\*M.R.M. Akramin<sup>1</sup>, A.K. Ariffin<sup>2</sup>, Masanori Kikuchi<sup>3</sup>, S. Abdullah<sup>2</sup>, and N. Nikabdullah<sup>2</sup>**

<sup>1</sup>Universiti Malaysia Pahang, 26600 Pekan, Pahang, Malaysia.

<sup>2</sup>Universiti Kebangsaan Malaysia, 43600 UKM Bangi, Selangor, Malaysia.

<sup>3</sup>Tokyo University of Science, 2641 Yamazaki, Noda, Chiba 278-8510, Japan.

\*Corresponding author: akramin@ump.edu.my

### **Abstract**

This research work was focused on probabilistic finite-element analysis of a surface crack growth distribution and its sustainability. Implementation of S-version Finite Element Model (s-FEM) performs an improvement in the finite-element analysis. The application of s-FEM was by superposed the local dense finite-element mesh on the global coarse finite-element mesh. An adaptive mesh refinement method implemented to provide local mesh refinement without introducing a transition region. The Monte Carlo method embeds with s-FEM for reliability analysis of the structural system with a combination of random parameters. The generated random parameters by Monte-Carlo method activate as an input in the s-FEM sampling process. In order to improve the sampling process, Latin hypercube was implemented and validated with Monte Carlo. Probabilistic research was conducted based on s-FEM results and presented the uncertainty in the model. Numerical example was showed that probabilistic analysis based on s-FEM simulation provides accurate estimation of crack growth distribution. The comparison shows that the association between s-FEM analysis and probabilistic analysis provide an effortless and faithful of quantify the failure probability.

**Keywords:** Surface crack, S-version Finite Element, Probabilistic, Monte Carlo, Reliability.

### **Introduction**

A crack shape development was first discovered by (Newman Jr and Raju 1981). An assumption was made for an initial semi-elliptical surface crack. It will maintain their shape until a fracture occurs with an increment of crack was based on Paris law (Hou 2011). Numerous studies have investigated the evolution of crack shape through the alternative current field measurement technique, various aspect ratios and the stress intensity factor of corner cracks and round bars. The growth rate of the crack shape has a tendency to slow down at the free surface, and hence the usage of a semi-elliptical crack shape in the simulation process allowed it to evolve in a way that was close to reality. Then the crack shape evolution was independent of the semi-elliptical shape.

Predictions of crack shape and failure of a structure were a challenging problem in fatigue analysis. This was due to the uncertainty in parameter, complicated meshing technique and expensive computation process. Traditionally, the randomness of parameters was considered in safety factor approach and re-meshing process was constructed for the whole domain. It leads to time consuming computing process when the whole structure was involved in a re-meshing process for each crack growth. Therefore, analysis that considers any variation in parameter with feasible meshing technique is needed.

The development of the two-dimensional finite-element analysis has been established for the last few decades (Hou 2004). Nonetheless, modelling intricate geometries is one of the major

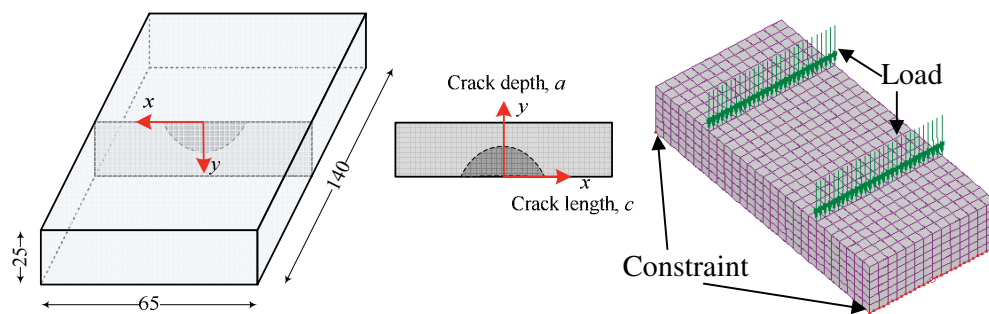
challenges, due to the high gradient solution in a complex geometry. In order to enhance the finite element solution, adaptive  $h$ - and  $p$ -methods are introduced. The  $h$ -method keeps the order of the elements' approximation and subdivides them into smaller sizes. Meanwhile, the  $p$ -method increases the order of the approximation while maintaining element size. The efficiency of these methods still needs to be improved by subdividing the finite element mesh using the  $h$ -method and increasing the degree of the polynomial using the  $p$ -method. Therefore, (Fish 1992) introduced  $hp$  procedures, in order to integrate the improvement of polynomial order and mesh refinement. The  $hp$ -method, the so-called S-version of Finite Element Model (S-FEM) consists of superimposing elements between a local and a global finite element mesh.

The S-FEM has been applied to a diverse range of applications such as heat-affected zone material (Kikuchi et al. 2010; Kikuchi et al. 2012), corrosion cracking (Kikuchi et al. 2011), the crack closure effect (Kikuchi et al. 2010) and composite material (Angioni et al. 2012). Various types of load behaviours (Kikuchi et al. 2010; Kikuchi et al. 2010; Kikuchi et al. 2010; Kikuchi et al. 2011) have become an issue in numerical implementation. The most remarkable is fatigue loading since it represents actual loading cases in practice. Fatigue loading is a leading cause of fracture in structures due to long-term cyclic loading. The integrity of the structure can be questioned when a crack is discovered in a structure. The sustainability of the structure needs to be evaluated in order to avoid a disaster, especially when a crack is detected. Surface cracks are frequently found in aeronautical panels, extrusion press cylinders, riveted aeronautic reinforcements and pressure vessels due to random loading, material, the environment, and so on.

In this paper, probabilistic S-FEM (ProS-FEM) was developed together with fatigue analysis of surface cracking. The main objective of this paper was to evaluate the growth of surface cracks under bending cyclic loads while considering uncertainty in the parameters. A fatigue load was applied throughout the three-dimensional simulation model. The calculation of the stress intensity factor was based on the virtual crack closure technique. The prediction of the crack growth rate was based on Paris's law. In order to predict the range of crack shape development, a new approach is presented in this paper. Experimental works were carried out to validate the simulation data. A comparison between crack growth obtained by the above technique and experimentally is presented and discussed.

### Probabilistic s-FEM Finite Element Model

A model as shown in Figure 1 was used in the simulation process. The model was selected based on the actual problem of an aircraft wing (Iyyer et al. 2007). A surface crack was introduced at the centre of the model. Span of loading points was 70 mm length with surface crack at the centre. Two constraints were applied at the bottom end of the model.



**Figure 1. Geometry of the model in mm and axis identification.**



Figure 2 shows the concept of S-FEM implementation in crack surface analysis. A coarser mesh was generated for the global mesh while a denser mesh was used in the vicinity of the crack tip area. During the implementation of the global mesh,  $\Omega^G$  implementation, the crack tip area was neglected temporarily to allow mesh generation for the whole domain. Subsequently, the mesh around the crack tip area was taken into account during the implementation of the local mesh. Then, the local mesh,  $\Omega^L$ , was overlaid on the global mesh. Finally, the complete structure was ready for analysis. Deciding on the size of the local mesh area was crucial since the propagation of the crack was affected by the calculation of the displacement function. The displacement in the overlaid area was calculated from the global and local meshes as shown below:

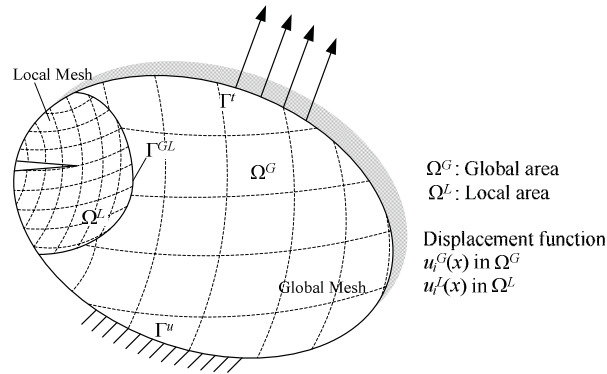
$$u(x) = \begin{cases} u^G(x) & x \in \Omega^G - \Omega^L \\ u^G(x) + u^L(x) & x \in \Omega^L \end{cases} \quad (1)$$

On the other hand, the strain of the superimposed area was calculated as below:

$$\varepsilon(x) = \varepsilon^G(x) + \varepsilon^L(x) \quad (2)$$

The final matrix form for S-FEM was:

$$\begin{bmatrix} K_{GG} & K_{GL} \\ K_{LG} & K_{LL} \end{bmatrix} \begin{Bmatrix} u_G \\ u_L \end{Bmatrix} = \begin{Bmatrix} F_G \\ F_L \end{Bmatrix} \quad (3)$$



**Figure 2. Concept of S-FEM**

The  $[K^{GL}]$  matrix represents the stiffness matrix of the superimposed area. By computing the final form of the S-FEM matrix, the displacement can be obtained for each node. The displacement was calculated simultaneously for the global and local meshes for each node. The global mesh was not affected by the changing of the local mesh size. A re-meshing process can be generated for the local area alone since the region of interest is in the area of the crack tip. During the crack growth simulation, the local mesh's size was expanded and the stress intensity factor (SIF) was calculated.

Since the structure is subject to a fatigue load, the crack growth rate is expressed by Paris's law equation:

$$\frac{da}{dN} = C(\Delta K_{eq})^n \quad (4)$$

where  $a$  and  $N$  are crack length and number of cycles, respectively. The  $C$  and  $n$  coefficients are material constants. The value of  $\Delta K_{eq}$  is the parameter associated with the fatigue crack growth

rate under mixed-mode conditions. Numerous parameters have been proposed for this purpose, but the equivalent stress intensity factor,  $\Delta K_{eq}$  was used in this research work. The equivalent stress intensity factor,  $\Delta K_{eq}$  based on Richard's criterion is expressed by:

$$\Delta K_{eq} = \frac{\Delta K_I}{2} + \frac{1}{2} \sqrt{\Delta K_I^2 + 4(1.155\Delta K_{II})^2 + 4(\Delta K_{III})^2} \quad (5)$$

Furthermore, the crack growth angle was calculated according to the criterion proposed by (Richard et al. 2005):

$$\varphi_o = \mp \left[ 140^\circ \frac{|K_{II}|}{K_I + |K_{II}| + |K_{III}|} - 70^\circ \left( \frac{|K_{II}|}{K_I + |K_{II}| + |K_{III}|} \right)^2 \right] \quad (6)$$

where  $\varphi_o < 0^\circ$  for  $K_{II} > 0$  and  $\varphi_o > 0^\circ$  for  $K_{II} < 0$  and  $K_I \geq 0$ .

The probabilistic analysis was performed using the Monte-Carlo method (Beer and Liebscher 2008). The material parameters and the initial crack size were deemed to be the random variables. The parameters' distribution was varied for each variable as shown in Table 1. The fatigue analysis was performed in ProS-FEM utilizing the crack closure effect and the appropriate four-point bending model. The embedded probabilistic and fatigue analyses in S-FEM produced a new contribution entitled ProS-FEM.

The parameters for the input-induced closure model for the aluminium alloy 7075-T6 were based on the work by (Liu and Mahadevan 2009). The distributions of the input parameters were developed from available literature data for aluminium alloy 7075-T6. In the probabilistic analysis, the Paris coefficient,  $C$  of Al 7075-T6 was represented by a mean of  $6.54 \times 10^{-13}$  m/cycle with a standard deviation of  $4.01 \times 10^{-11}$  m/cycle. The distribution was assumed to be lognormal based on the assumptions made in the literature (Liu and Mahadevan 2009). There was no standard deviation for the fatigue power parameter  $n$  since it was set as deterministic. The reason for this was to control the acceleration of the crack growth in the numerical calculation.

**Table 1. Input distribution for the model.**

Variable	Distribution	Mean	Standard deviation
Tensile Strength, Ultimate	Deterministic	572 MPa	0
Fatigue power parameter, $n$	Deterministic	3.8863	0
Tensile Strength, Yield	Deterministic	691 MPa	0
Young's modulus, $E$	Normal	71.7 GPa	10.34
Paris coefficient, $C$	Lognormal	$6.54 \times 10^{-13}$ m/cycle	$4.01 \times 10^{-13}$
Threshold value, $\Delta K_{th}$	Lognormal	$5.66 \text{ MPa.m}^{0.5}$	0.268
Initial crack length, $da$	Lognormal	0.23 mm	0.05

Once the random variable had been generated, based on its distribution, ProS-FEM started to process the SIF calculation. A random variable of each parameter was generated for one sample. Each sample maintained the same value of the generated variable until the end of crack growth.

Consequently, the calculation of the cycle proceeded with a random maximum crack length  $da_{max}$ . Therefore, based on Paris's law, the mean of the cycle can be obtained as

$$E[dN] = \frac{E[da_{max}]}{E[C](\Delta K_{eq_{max}})^n} \quad (7)$$

The equivalent stress  $\Delta K_{eq_{max}}$  treated as deterministic since a deterministic load was applied in the analysis. The deterministic load produces constant values of  $\Delta K_I, \Delta K_{II}$  and  $\Delta K_{III}$  and reflected to the equivalent stress  $\Delta K_{eq_{max}}$ .

Since  $da_{max}$  and  $C$  are independent variables, the variance of  $dN$  can be calculated as

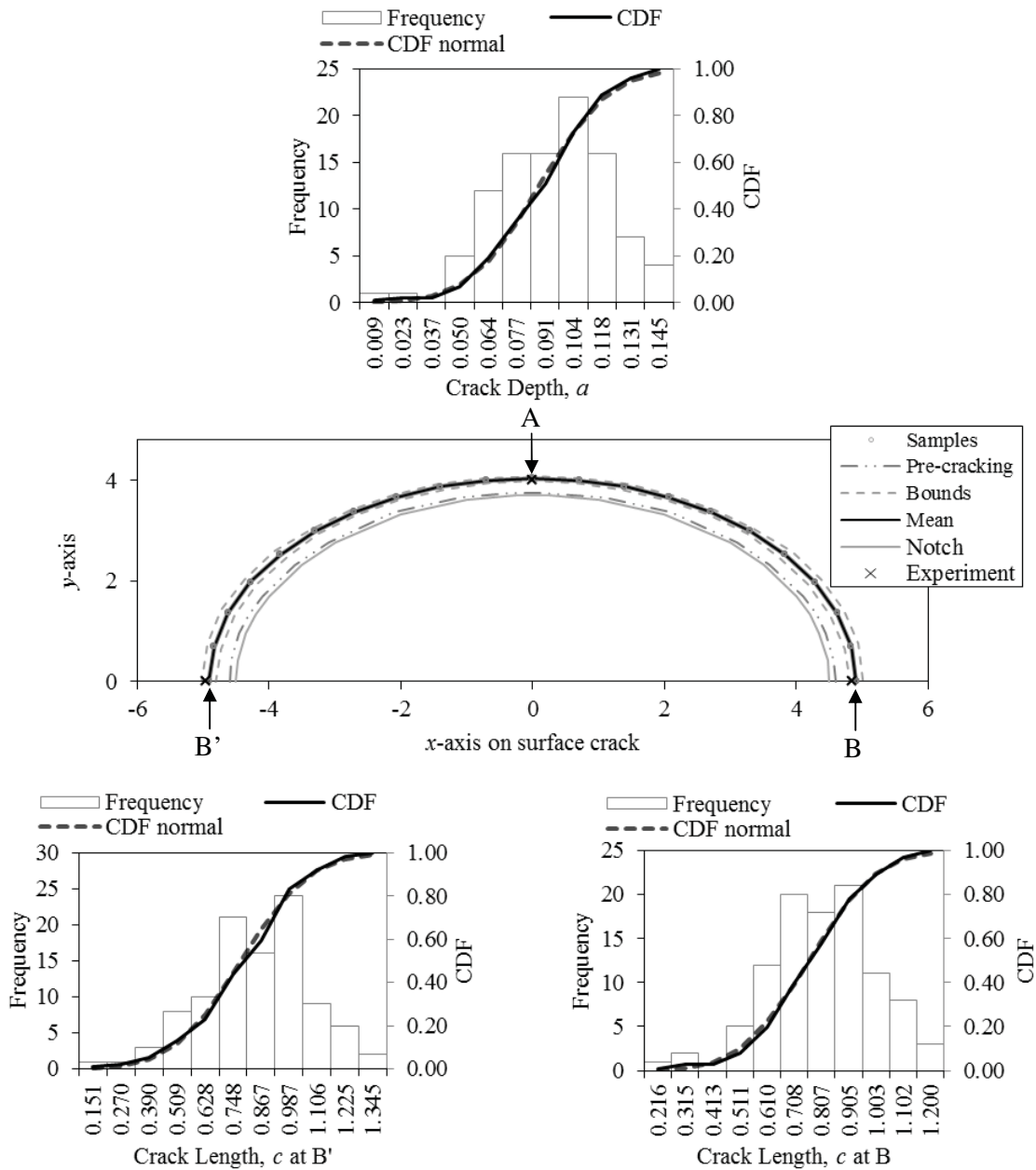
$$Var[dN] = \left[ \frac{1}{(\Delta K_{eq_{max}})^n} \right]^2 \times \left[ E[da_{max}]^2 Var\left[\frac{1}{C}\right] + E\left[\frac{1}{C}\right]^2 Var[da_{max}] + Var[da_{max}] Var\left[\frac{1}{C}\right] \right] \quad (8)$$

The random crack length of the crack front was calculated based on the cycle and variance from the random  $da_{max}$ . Crack shape development took place after the crack length calculation of each node at the crack front. The process continued with looping of the generation of the random variable for the next sample. The uncertainty quantification analysis can be produced after a number of samples have been simulated. From the results of the quantification of uncertainty, the reliability analysis was conducted.

In order to improve the sampling process, Latin hypercube was develop. The generation of Monte Carlo samples focused around the mean value, and the distribution was scattered within the range of two standard deviations. Meanwhile, the sampling process for the Latin hypercube was scattered within a number of portions. A sample was taken from each portion to generate the input parameter. In this way, all samples covered every part of the distribution. Otherwise, the Monte Carlo technique covers part of the distribution and most of the outliers are neglected. The effect of the sampling technique affected the results, as described in the following section.

## Results and Discussion

The simulation results for growth of the surface crack are compared with the experimental work was shown in Figure 3. A notch introduced in the early stage of the experimental process for the initiation of crack growth is shown clearly. After a cyclic load was applied to the specimen, the pre-cracking was generated as shown in the plot. The pre-cracking area was drawn approximately on the graph. Crack growth in the experimental work started to be observed after the pre-cracking took place. The same initial boundary conditions were introduced for the numerical model. The size of the pre-cracking area was modelled in a local mesh. The variations in crack growth as a result of the randomness of uncertain parameters are shown in this figure. It shows all possibilities of crack growth. The trends of crack depth and crack length distribution are presented in this graph. The trends of crack depth and length show the highest frequency in the middle of the distribution. This is due to the effect of randomness in input distribution. As the input distribution was scattered over a range with the highest frequency at the mean, it reflected the crack to growth in the middle of the distribution.

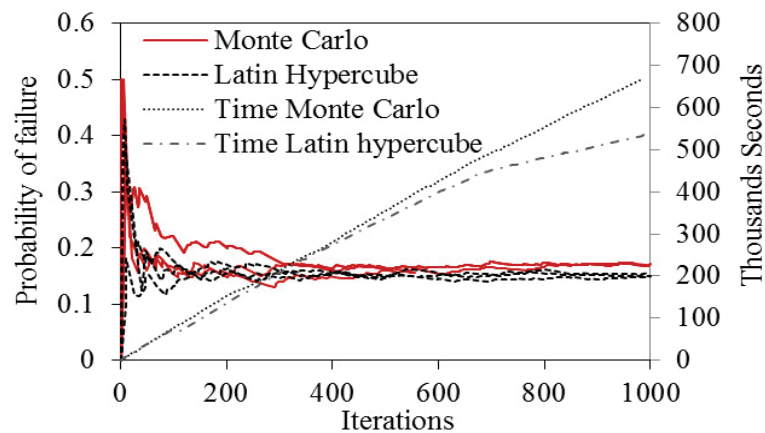


**Figure 3. Crack growth on surface crack with length and depth distribution.**

Figure 4 shows the reliability result of a four-point bending structure. The failure probability of this structure was 0.18. In general, the number of failed samples increased in proportion to the total number of samples, with a failure rate of 18%. In this case, the load's magnitude plays a major role. The strength of the model could sustain a minimum load but the minimum load fluctuated according to the uncertainty in a parameter. Thus, the failed or safe samples in a model varied probabilistically.

Both the Monte Carlo and the Latin hypercube method need more samples at the beginning of the simulation before they converge to a level of failure probability. After more than 500 samples were generated by the system, the failure probability of the Monte Carlo simulation converged at 0.18,

while the Latin hypercube converged after the generation of just 300 samples. As the Latin hypercube could reduce the sample number, the simulation time could be shortened.



**Figure 4. Probability of failure and simulation time for the Monte Carlo and Latin hypercube.**

## Conclusions

The ProS-FEM simulation technique was developed with auto-mesh generation and a fully automatic fatigue crack growth system. A probabilistic model was developed for four-point bending geometry. The probabilistic scenario of fatigue loading was simulated by treating the Young's modulus, Paris coefficient, threshold value, and initial crack length as variables with distributions. The probabilistic prediction shows good agreement with the experimental results. Furthermore, ProS-FEM provides the distribution of crack length and depth, highlighting the CDF of crack growth. In order to determine the minimum and maximum extent of growth, the mean and bounds of crack growth were generated by ProS-FEM. This shows that the randomness of parameters was modelled successfully in the simulation process. ProS-FEM performed robustly, providing valuable information for analysing high-risk component.

## References

- Aguilar Espinosa, A. A., Fellows, N. A., et al. (2013), Experimental measurement of crack opening and closure loads for 6082-T6 aluminium subjected to periodic single and block overloads and underloads. *International Journal of Fatigue* 470, pp.71-82.
- Angioni, S. L., Visrolia, A., et al. (2012), Combining X-FEM and a multilevel mesh superposition method for the analysis of thick composite structures. *Composites Part B: Engineering* 432, pp.559-568.
- Beer, M. and Liebscher, M. (2008), Designing robust structures – A nonlinear simulation based approach. *Computers & Structures* 8610, pp.1102-1122.
- de Matos, P. F. P. and Nowell, D. (2009), Experimental and numerical investigation of thickness effects in plasticity-induced fatigue crack closure. *International Journal of Fatigue* 3111–12, pp.1795-1804.
- Fish, J. (1992), The s-version of the finite element method. *Computers & Structures* 433, pp.539-547.
- Hou, C.-Y. (2004), Three-dimensional finite element analysis of fatigue crack closure behavior in surface flaws. *International Journal of Fatigue* 2611, pp.1225-1239.
- Hou, C.-Y. (2011), Simulation of surface crack shape evolution using the finite element technique and considering the crack closure effects. *International Journal of Fatigue* 335, pp.719-726.
- Iyyer, N., Sarkar, S., et al. (2007), Aircraft life management using crack initiation and crack growth models – P-3C Aircraft experience. *International Journal of Fatigue* 299–11, pp.1584-1607.
- Kikuchi, M., Maitireymu, M., et al. (2010), Study on fatigue crack growth criterion 1st report, paris' law of a surface crack under pure mode I loading. *Nihon Kikai Gakkai Ronbunshu, A Hen/Transactions of the Japan Society of Mechanical Engineers, Part A* 76764, pp.516-522.
- Kikuchi, M., Wada, Y., et al. (2010), *Closure effect on interaction of two surface cracks under cyclic bending*. American Society of Mechanical Engineers, Pressure Vessels and Piping Division, Bellevue, Washington, USA.

- Kikuchi, M., Wada, Y., et al. (2010), *Effect of  $K_{III}$  on fatigue crack growth behavior*. American Society of Mechanical Engineers, Pressure Vessels and Piping Division, Bellevue, Washington, USA.
- Kikuchi, M., Wada, Y., et al. (2012), Crack growth analysis in a weld-heat-affected zone using S-version FEM. *International Journal of Pressure Vessels and Piping* 90–910, pp.2-8.
- Kikuchi, M., Wada, Y., et al. (2010), *Crack growth analysis in weld-heat affected zone using S-Version FEM*. American Society of Mechanical Engineers, Pressure Vessels and Piping Division, Bellevue, Washington, USA.
- Kikuchi, M., Wada, Y., et al. (2011). Stress corrosion cracking analysis under thermal residual stress field using S-FEM, *Key Engineering Materials*. **462-463**: 431-436.
- Kikuchi, M., Wada, Y., et al. (2011), Surface crack growth simulation under mixed mode cyclic loading condition. *Procedia Engineering* 10, pp.427-432.
- Kikuchi, M., Wada, Y., et al. (2010), Effect of  $K_{III}$  on fatigue crack growth behavior (factory roof and fatigue crack growth rate). *Nihon Kikai Gakkai Ronbunshu, A Hen/Transactions of the Japan Society of Mechanical Engineers, Part A* 76772, pp.1674-1680.
- Kim, C.-Y., Choi, J.-M., et al. (2013), Fatigue crack growth and closure behavior under random loadings in 7475-T7351 aluminum alloy. *International Journal of Fatigue* 470, pp.196-204.
- Liu, Y. and Mahadevan, S. (2009), Probabilistic fatigue life prediction using an equivalent initial flaw size distribution. *International Journal of Fatigue* 313, pp.476-487.
- Newman Jr, J. C. and Raju, I. S. (1981), An empirical stress-intensity factor equation for the surface crack. *Engineering Fracture Mechanics* 151-2, pp.185-192.
- Richard, H. A., Fulland, M., et al. (2005), Theoretical crack path prediction. *Fatigue & Fracture of Engineering Materials & Structures* 281-2, pp.3-12.
- Savaidis, G., Savaidis, A., et al. (2010), Mode I fatigue crack growth at notches considering crack closure. *International Journal of Fatigue* 3210, pp.1543-1558.
- Song, P. S. and Shieh, Y. L. (2004), Crack growth and closure behaviour of surface cracks. *International Journal of Fatigue* 264, pp.429-436.

## Left Ventricle Segmentation by Circular Shape Constrained Clustering Algorithm

\*Xulei Yang<sup>1</sup>, Si Yong Yeo<sup>1</sup>, Yi Su<sup>1</sup>, Calvin Lim<sup>1</sup>, Min Wan<sup>2</sup>, Liang Zhong<sup>2</sup>, and Ru San Tan<sup>2</sup>

<sup>1</sup>Computing Science Department, Institute of High Performance Computing, A\*STAR, 1 Fusionopolis Way #16-16 Connexis, Singapore 138632.

<sup>2</sup>National Heart Centre Singapore, 17 Third Hospital Avenue, Mistri Wing, Singapore 168752.

\*Corresponding author: yangx@ihpc.a-star.edu.sg

### Abstract

This study presents a novel clustering algorithm for the automatic segmentation of the left ventricle (LV). A circular shape function is incorporated into the dissimilarity measure of the objective function of the well-known fuzzy c-means (FCM) clustering algorithm. In that way, the proposed circular shape constrained FCM (CS-FCM) algorithm integrates both intensity related feature and spatial shape information into the clustering procedure. As a result, pixels having similar intensity information but located in different regions (LV region and non-LV region) can be differentiated. A weighting parameter is introduced to adjust the weight of the spatial distance against the intensity feature, which increases the flexibility of the proposed CS-FCM algorithm. The experimental results on benchmark cardiac magnetic resonance (CMR) images show two obvious advantages of the proposed CS-FCM over the standard clustering algorithms: it successfully distinguishes the LV from other structures which have similar intensity as the LV. Also, it correctly segments the LV even when the papillary muscles are adjacent to or fall inside the LV region.

Keywords: Left Ventricle, Cardiac Image Segmentation, Fuzzy Clustering, Fuzzy C-Means, Circular Shape Function.

### 1. Introduction

Cardiovascular disease is the leading cause of death for both men and women in most developed countries. The early detection of cardiovascular diseases plays a very important role in the clinical management pathway. Cardiac Magnetic Resonance (CMR) is a popular non-invasive imaging modality used to diagnose cardiovascular diseases. The clinical CMR imaging modality produces 3D and 3D+time images of the heart. To diagnose cardiovascular diseases, doctors commonly assess the functionality of the left ventricle (LV) over the whole cardiac cycle. Quantitative indicators such as ejection fraction and cardiac output are used to assist in the assessment. To derive these metrics, the two boundaries describing the LV (i.e., the endocardial and epicardial borders) need to be extracted from a patient scan. Traditionally, this is done manually by doctors. However, manual analysis is no longer feasible due to the large quantity of data in 3D and 3D+time images. Moreover, manual annotation is prone to inter- and intra-observer variability which can affect the reliability and repeatability of cardiovascular diseases diagnosis. Therefore, an automatic segmentation solution is needed to address this practical problem.

A variety of segmentation techniques have been proposed for LV segmentation over the last few decades. While earlier approaches were often based on heuristics, recent studies employ more sophisticated and principled techniques. We refer the reader to the two recently published survey papers (Kang, 2012) and (Petitjean, 2011) for detailed review of this topic. Previously published automatic methods for this segmentation task have various disadvantages for routine clinical use (Cocosco, 2008): They are often computationally demanding, potentially unstable for subjects with

pathology, require additional images to be acquired, or need complex shape and/or gray-level appearance models. Such models need to be constructed (“learned”) from many manually segmented images, which is labour intensive, and are of limited use due to anatomical variability and image contrast variability. Moreover, most prior work has been devoted to segmenting cardiac data given a reasonable initialization, or an accurate manual segmentation of a subset of the image data. To achieve full automation and eliminate inter- and intra-observer variability, initialization should also be automatic. Despite several efforts, there is currently still a need for a fast and robust initialization procedure.

Many of the automatic medical image segmentation techniques rely on a combination of information directly derived from the image and information provided by prior models of anatomy and its appearance in the image. Due to the limitations and the construction cost of prior models, methods that rely primarily on image information have distinct advantages. In this study, we present a new CMR image segmentation method based on fuzzy image segmentation that is predominantly image-driven: it does not use any prior knowledge, and makes only plausible assumptions about the image and the imaged heart. In the last decade, fuzzy segmentation methods, especially the fuzzy c-means (FCM) algorithm (Bezdek, 1981), have been widely used in image segmentation. Its success is mainly attributed to the introduction of fuzziness for the “belongingness” of each image pixel. Unlike hard segmentation methods, such as K-means (Macqueen, 1967), which impose that pixels belong exclusively to one class, fuzzy segmentation methods allow pixels to belong to multiple classes with varying degrees of membership. This enables fuzzy segmentation methods to retain more information from the original image than hard segmentation methods (Pham, 2000). Some fuzzy clustering methods that have been used for LV segmentation in the literature are (Boudraa, 1997; Lynch, 2006; Cocosco, 2008).

In this study, a novel fuzzy clustering algorithm is proposed for the automatic segmentation of the LV endocardial border in CMR images. A circular shape function is incorporated into the dissimilarity measure of the objective function of the FCM clustering algorithm. In this way, the proposed circular shape constrained FCM (CS-FCM) algorithm integrates both intensity related feature and spatial shape information into the clustering procedure. As a result, pixels having similar intensity information but located in different regions (LV region and non-LV region) can be differentiated. A weighting parameter is introduced to adjust the weight of the spatial distance against the intensity feature, which increases the flexibility of the proposed CS-FCM algorithm. Experimental results on real CMR images show two obvious advantages of the proposed CS-FCM over the standard clustering algorithms like FCM: It successfully distinguishes the LV from other structures which have similar intensity as the LV; and it correctly segments the LV even when papillary muscles are adjacent to or fall inside the LV region.

The rest of this paper is organized as follows: Section 2 describes the proposed CS-FCM image segmentation algorithm. The experimental results of the proposed approach are reported in Section 3. Finally, the conclusion is given in Section 4.

## 2. Methodology

In this section, we provide a brief review of the fuzzy c-means (FCM) algorithm. This is followed by a description of the proposed circular shape constrained fuzzy c-means (CS-FCM) algorithm.

### 2.1 Standard Fuzzy C-Means (FCM)

Mathematically, the FCM algorithm [1] is used to minimize the objective function  $J_{fcm}$  with respect to the membership function  $u_{k|ij}$  and the cluster centre  $v_k$ , such that



$$J_{fcm} = \sum_{x_{ij} \in I} \sum_{k=1}^K (u_{k|ij})^m \cdot d_{kij} \quad \text{subjected to} \quad \sum_{k=1}^K u_{k|ij} = 1, \forall x_{ij} \in I \quad (1)$$

where  $m$  is the weighting exponent on the fuzzy memberships. A value of  $m = 2$  is known to give good results with the FCM algorithm. The parameter  $u_{k|ij}$  is the membership of the  $(i,j)$ th pixel  $x_{ij}$  in the  $(k)$ th cluster, and  $d_{kij}$  is the squared Euclidean distance between the pixel  $x_{ij}$  and the cluster centre  $v_k$  where

$$d_{kij} = \|x_{ij} - v_k\|^2 \quad (2)$$

The minimization of (1) gives the updating equations for the membership  $u_{k|ij}$  and cluster centre  $v_k$ , which are given by

$$u_{k|ij} = \frac{(x_{ij} - v_k)^{-2/(m-1)}}{\sum_{k=1}^K (x_{ij} - v_k)^{-2/(m-1)}} \quad \text{and} \quad v_k = \frac{\sum_{x_{ij} \in I} u_{k|ij}^m x_{ij}}{\sum_{x_{ij} \in I} u_{k|ij}^m} \quad (3)$$

The FCM algorithm is summarized as follows:

- 1) Fix the cluster number  $K$ ; Initialize the cluster centres  $\{v_k\}_{k=1}^K$  and set the threshold  $\varepsilon$  to a small positive value, e.g.,  $\varepsilon = 0.001$ .
- 2) Alternatively update the membership function and cluster centre by using (3) until  $\|v_{new} - v_{old}\| \leq \varepsilon$ .

## 2.2 Circular Shape Constrained FCM (CS-FCM)

Let  $f(i,j,s)$  represents the geometric circular shape function. By incorporating it into (2), we have the new dissimilarity measure  $\hat{d}_{kij}$ , as shown below

$$\hat{d}_{kij} = d_{kij} + \alpha f(i, j, s) \quad (4)$$

where  $\alpha$  is the weighting parameter used to adjust the weight of the spatial shape information against the intensity related feature. The circular shape function  $f(i,j,s)$  is expressed as

$$f(i, j, s) = \left[ \frac{(i - x_c)^2 + (j - y_c)^2}{r} \right]^{\beta_k} \quad (5)$$

where  $s = \{x_c, y_c, r\}$  is a unique clique that denotes the circular shape,  $x_c$  and  $y_c$  denote the geometric  $x$ - and  $y$ -coordinates of the centre of circular shape, and  $r$  denotes the radius of the circular shape. The exponent parameter  $\beta$  ensures a small value for the pixels within the  $k$ th cluster and a large value for the pixels outside the cluster. In this study, we set  $\beta = 2$  for the LV region, and  $\beta = -2$  for the non-LV region.

The circular shape function  $f(i,j,s)$  is an overall geometric information and its influence in the objective function is controlled by the weighting parameter  $\alpha$ . The dissimilarity measure  $\hat{d}_{kij}$  consists of a measure of the intensity dissimilarity between the  $(i,j)$ th pixel  $x_{ij}$  and the  $(k)$ th centre  $v_k$  in the intensity space as well as a distance dissimilarity in the spatial space. With the inclusion of the circular shape information, several advantages are achieved: 1) pixels with similar intensity but

located in disjointed region can be differentiated; and 2) a large membership for the cluster associated with the LV region can be obtained.

By using the newly defined dissimilarity measure (4), the proposed CS-FCM algorithm is formulated as the minimization of the following objective function

$$J_{cs-fcm} = \sum_{x_{ij} \in I} \sum_{k=1}^K (u_{k|ij})^m \cdot \hat{d}_{kij} \quad (6)$$

The partial derivative of  $J_{cs-fcm}$  with respect to membership  $u_{k|ij}$  and cluster centre  $v_k$  yields the following updating equations

$$u_{k|ij} = \frac{\hat{d}_{kij}^{-1/(m-1)}}{\sum_{k=1}^K \hat{d}_{kij}^{-1/(m-1)}} \quad \text{and} \quad v_k = \frac{\sum_{x_{ij} \in I} u_{k|ij}^m \cdot x_{ij}}{\sum_{x_{ij} \in I} u_{k|ij}^m} \quad (7)$$

The partial derivative of  $J_{cs-fcm}$  with respect to  $s$  gives

$$x_c = \frac{\sum_{x_{ij} \in I} i \cdot u_{k|ij}^m}{\sum_{x_{ij} \in I} u_{k|ij}^m} \quad \text{and} \quad y_c = \frac{\sum_{x_{ij} \in I} j \cdot u_{k|ij}^m}{\sum_{x_{ij} \in I} u_{k|ij}^m} \quad (8)$$

And

$$r = \sum_{x_{ij} \in LV} (i - x_c)^2 + (j - y_c)^2 \quad (9)$$

The CS-FCM algorithm is summarized as follows,

- 1) Fix the cluster number  $K$ . Initialize the cluster centres  $\{v_k\}_{k=1}^K$  and set the threshold  $\varepsilon$  be a small positive value, e.g.,  $\varepsilon = 0.001$ .
- 2) Update the membership function and cluster centre by using (7).
- 3) Update the circular shape by using (8) and (9).
- 4) Repeat Steps 2 to 3 until  $\|v_{new} - v_{old}\| \leq \varepsilon$ .

### 3. Experimentation

To demonstrate and evaluate the performance of the proposed CS-FCM method on cardiac LV segmentation, we apply it to real CMR images obtained from the RV Challenge website (<http://www.litislabs.eu/rvsc>). For the purpose of qualitative comparison, all the images are also subjected to the standard FCM algorithm. In all examples, we fix the cluster number as  $K = 2$  (i.e., one cluster for LV region and the other for non-LV region) and the weighting parameter as  $\alpha = 0.3$  for the CS-FCM.

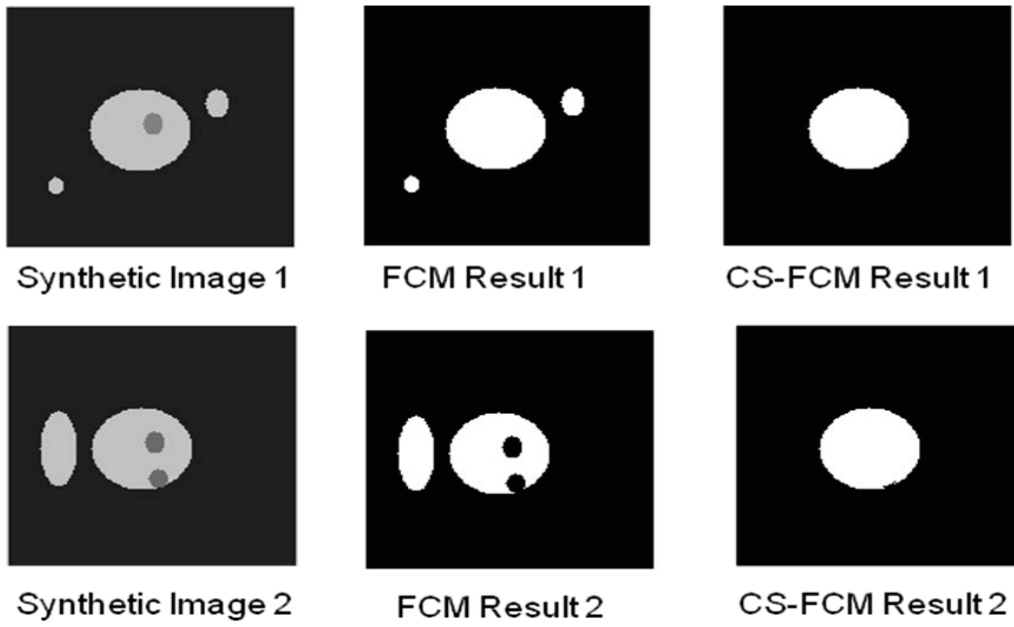


Fig.1 Segmentation results of the FCM and CS-FCM on two synthetic images.

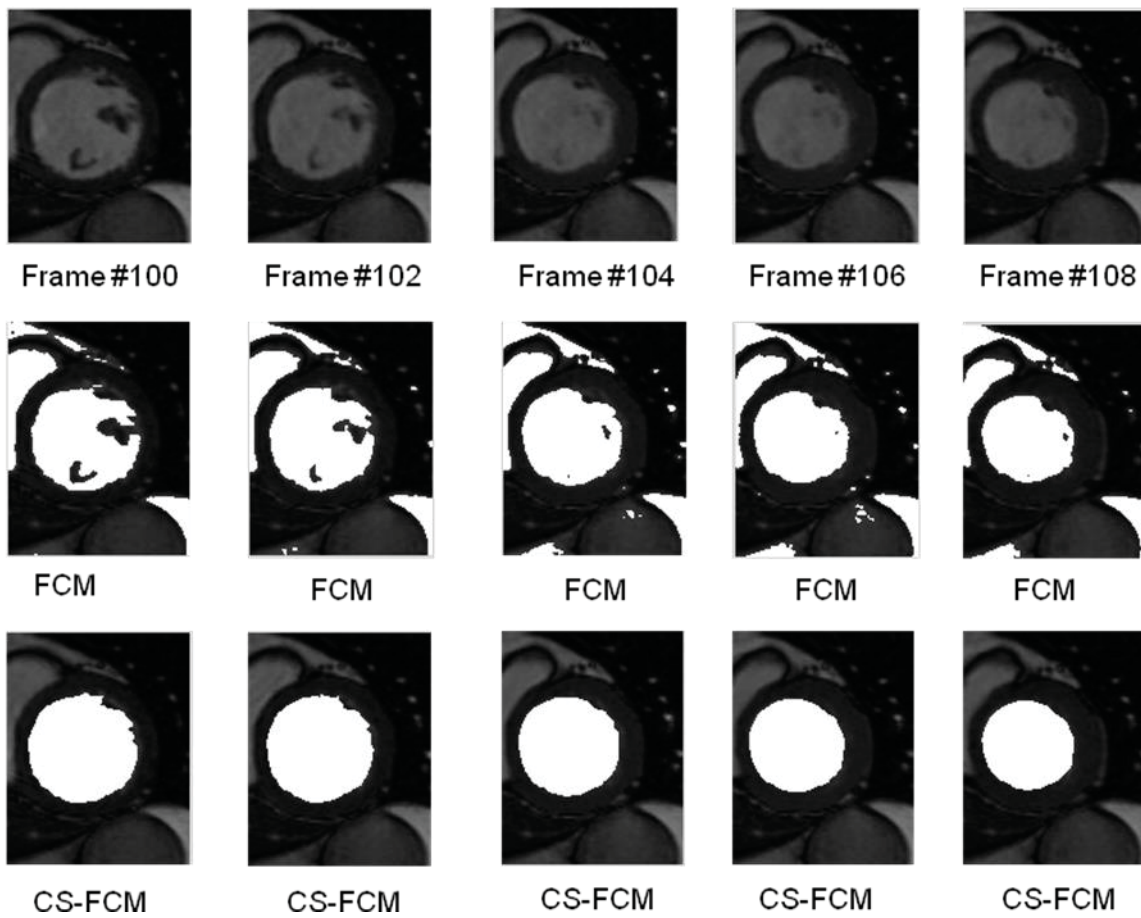
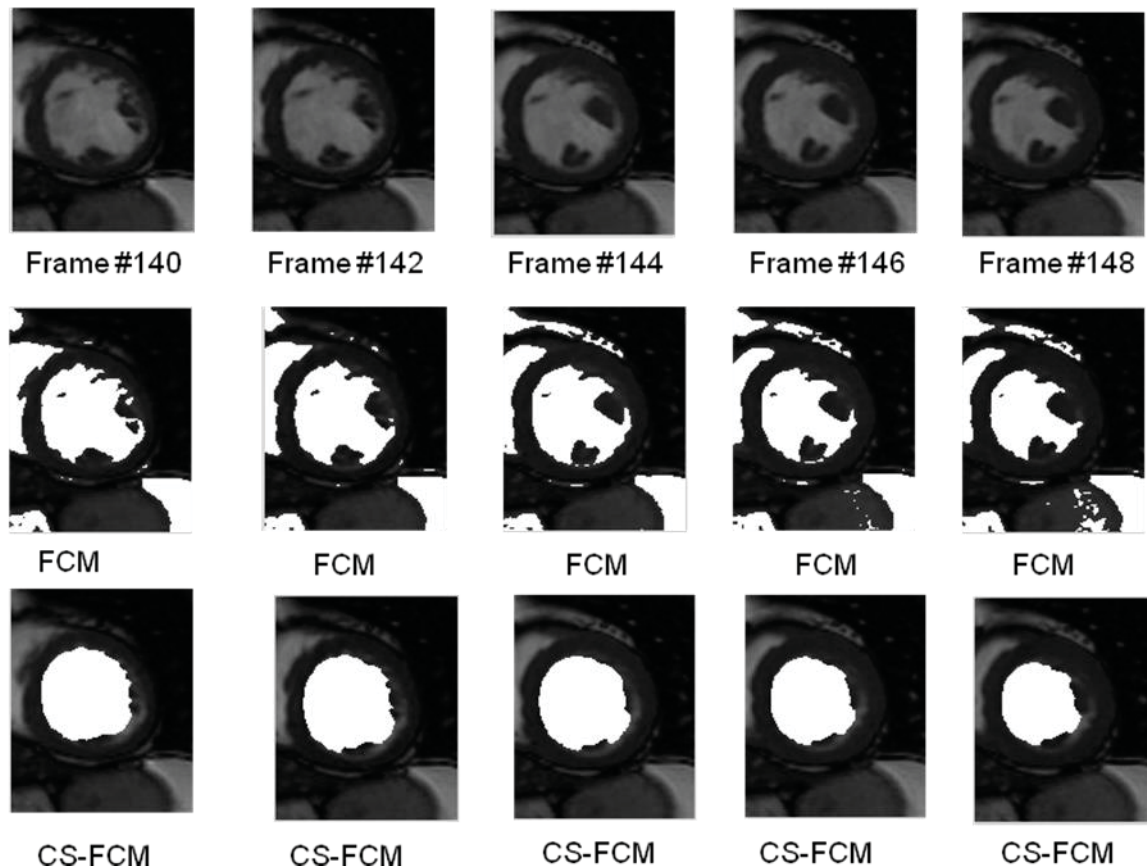


Fig.2 Segmentation results of the FCM and CS-FCM on real CMR images (Frames #100 to #119). Five frames are shown here.



**Fig.3 Segmentation results of the FCM and CS-FCM on real CMR images (Frames #140 to #159). Five frames are shown here.**

Before performing the segmentation on the CMR images, we demonstrate the effectiveness of the proposed CS-FCM on some synthetic images. As shown in Fig.1, there are two synthetic images in the first column, the target is to separate the big bright ball from others. The segmentation results of FCM are shown in the second column, it can be seen that the FCM partitions several other bright objects with the ball into one cluster. In terms of intensity feature only, the FCM will cluster all the objects with similar intensity into one cluster regardless of their locations. In contrast, the proposed CS-FCM integrates the spatial shape information into the clustering procedure, such that objects with similar intensity but located in different regions can be differentiated. As shown in the third column, the proposed CS-FCM successfully partitions the bright ball with one cluster.

Fig.2 and Fig.3 show the segmentation results of the standard FCM and the proposed CS-FCM on the CMR images from the RV Challenge. The test is performed on data from Patient #1, Frames #100 to #119 (one cardiac cycle) in Fig.2 and Frames #140 to #159 (another cardiac cycle) in Fig.3. The segmentation results of the standard FCM are shown in the second row in Fig.2 and Fig.3. It can be observed from the figures that the standard FCM failed to separate the LV region from the image: The LV region is partitioned into one cluster together with other objects having bright intensities. In contrast, as shown in the last row, the proposed CS-FCM achieves much better results: it successfully distinguishes the LV from other structures which have similar intensity as the LV; and it correctly segments the LV even when papillary muscles are adjacent to or fall inside the LV region.

#### 4. Conclusion

In this study, a novel clustering approach called the CS-FCM is proposed for cardiac LV endocardial border segmentation. The basic idea is to integrate the circular shape function into the standard FCM algorithm, such that pixels having similar intensity but located in different regions can be differentiated. The experimental results of the LV segmentation on real CMR images illustrate the superiority of the proposed approach over the standard FCM algorithm.

#### References

- Kang, D., Woo, J., Slomka, P.J., Dey, D., Germano, G. and Jay-Kuo, C. (2012), Heart chambers and whole heart segmentation techniques: review, *SPIE Journal of Electronic Imaging*, 21, pp. 131-139.
- Petitjean, C. and Dacher, J.N. (2011), A review of segmentation methods in short axis cardiac MR images, *Medical Image Analysis*, 15, pp. 169-184.
- Cocosco, C., Wiro, W.N., Netsch, T., Vonken, E.-J., Lund, G., Stork, A., Viergever, M. (2008), Automatic image-driven segmentation of the ventricles in cardiac cine MRI. *Journal of Magnetic Resonance Imaging*, 28, pp. 366–374.
- Bezdek, J.C. (1981), *Pattern Recognition with Fuzzy Objective Function Algorithms*, Plenum Press, New York.
- Macqueen, J.B. (1967), Some methods for classification and analysis of multivariate observations, *proceedings of 5<sup>th</sup> Berkley Symposium on Mathematical Statistics and Probability*, pp. 281-297.
- Pham, D.L., Xu, C. and Prince, J.L. (2000), Current Methods in Medical Image Segmentation, *Annual Review of Biomedical Engineering*, 2, pp. 315-337.
- Boudraa, A.-E.-O. (1997), Automated detection of the left ventricular region in magnetic resonance images by fuzzy C-means model. *International Journal of Cardiac Imaging*, 13, pp. 347–355.
- Lynch, M., Ghita, O., Whelan, P. (2006), Automatic segmentation of the left ventricle cavity and myocardium in MRI data. *Computers in Biology and Medicine*, 36, pp. 389–407.

## Research on Energy-saving for two Different Cutter-head Drive System of Shield Tunneling Machine

\*H.Y. Liu<sup>1</sup>, J.H. Bu<sup>2</sup>, S.N. Wang<sup>3</sup>, and Y.T. Sun<sup>4</sup>

China Academy of Aerospace Aerodynamics (CAAA), China

\*Corresponding author: lhykm1985@163.com

### Abstract

The cutter-head system driven by hydraulics is a key part of shield tunneling machine. In this article, two cutter-head systems of shield tunneling machine are illuminated and a test rig is built for simulating the actual cutter-head system of shield. Two driving systems and hydraulic loads are used in the test rig in the research on the energy-saving characteristics of cutter-head drive system, and the rules of energy transmission of variable speed and variable displacement systems are studied. The contrast experiments of two cutter systems are done to compare two control methods under different cutter-head revolution speed and different load conditions. The results show that the variable speed pump control system has higher efficiency than the variable displacement pump control system in the same working condition. These results would provide the theoretical reference for developing the next generation of shield tunneling machine with energy-saving.

Keywords: Cutter-head system, Shield tunneling machine, Energy-saving, Variable displacement, Variable speed

### Introduction

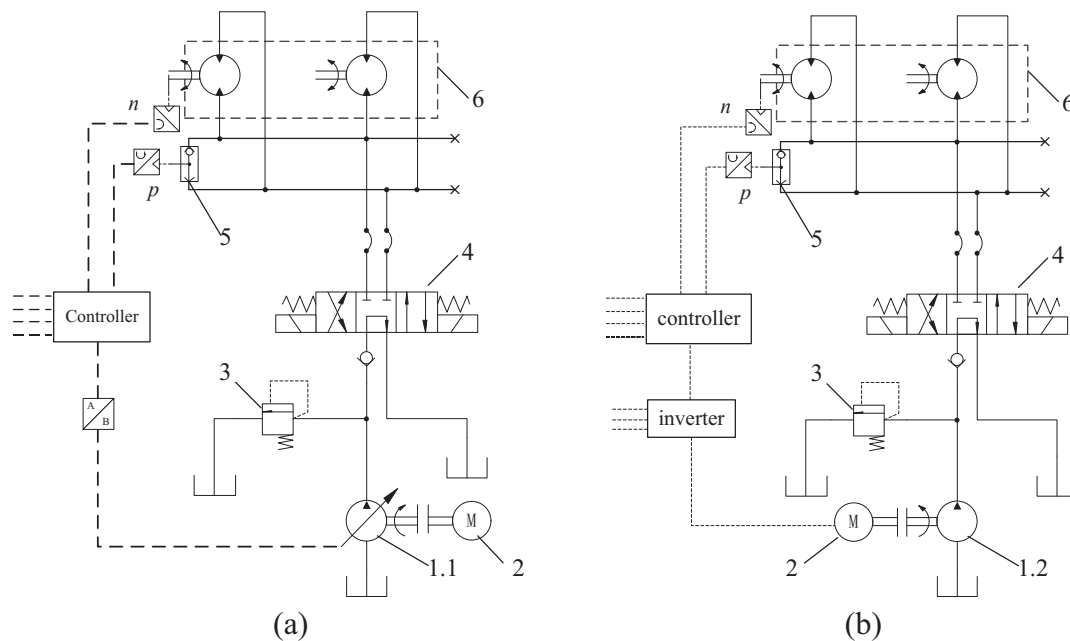
Shield tunneling machine is a modern construction machinery widely employed in tunneling field, which is famous for high efficiency and safe operation environment compared with the conventional excavation methods. The cutter-head drive system, as one of the most important parts of shield, is usually driven by hydraulic system because of its high installed power. It not only performs the task of cutting soils before shield during tunneling but also holds the excavated face in position.

Generally, the hydraulic system is designed according to its highest power, but the machine does not operate in this state constantly. So for most of the working time, the system is partially loaded, all forms of energy are ultimately converted into heat. In practice, when shield tunneling machine is tunneling in different geological conditions, in which the excavated site tend to be complex and uncertain, the torque and speed of cutter-head are different and output power required is discrepant. Those variable working conditions necessitate a great requirement of increasing the overall efficiency of the cutter-head drive system. During tunneling, the cutter-head drive should adapt itself to the front soil condition and keep collaborating with other parts of the shield, which make it necessary to regulate revolution speed of the cutter-head under variable load conditions for reducing energy consumption. Up to now, the speed regulation drive system commonly used in shield cutter-head system is the variable displacement pump control system, which uses electro-hydraulic proportional control technology to change the displacement of pump for regulating the rotation speed of motors. The variable speed pump control system is a new type of speed regulation system, which changes the output flow by varying the rotation speed of the fixed-displacement pump.

This paper takes the simulation cutter-head system of shield tunneling machine as research object which simulate the actual conditions encountered on the working process. A test rig is built including the design of principle. Experiment is done based on the test rig and energy analysis on the variable speed control and variable displacement control of the cutter-head system is carried out in different load conditions.

### Working principle of two different cutter-head drive systems

The working principles of two cutter-head hydraulic systems of the shield machine can be simplified as illustrated in Fig. 1 (a) and Fig. 1 (b). Fig. 1 (a) shows the model of variable displacement control system, and Fig. 1 (b) shows the model of variable speed control system.



1.1 Variable-displacement pump 1.2 Fixed-displacement pump 2.Motor 3.Relief valve 4. Directional valve 5. Shuttle valve 6. Hydraulic motors

**Figure 1. Two type hydraulic drive modes of the cutter system in shield machine**

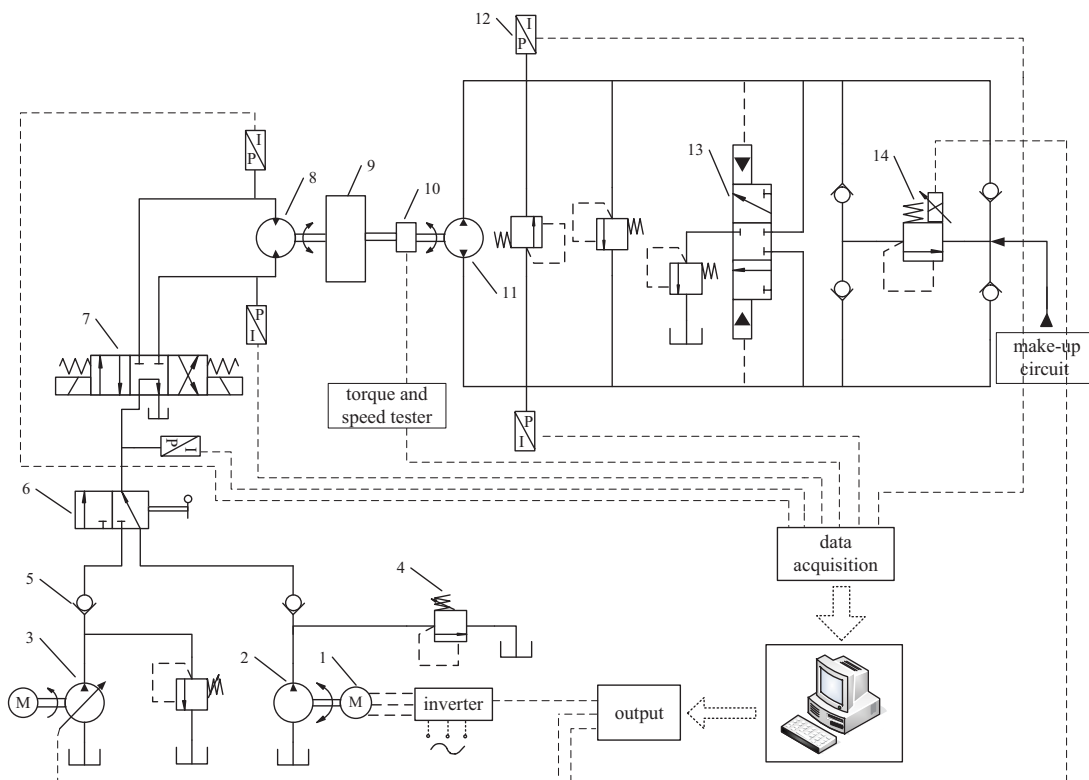
The two hydraulic systems adopt the pump control motor mode and the hydraulic motor drives the cutter-head via a reducer. The hydraulic motor 6 are two fixed-displacement hydraulic motors. The directional valve 4 is an electro-hydraulic valve used to change the rotate direction of the cutter-head. The shuttle valve 5 is used to the pressure control of the hydraulic system, and the relief valve 3 sets the safety pressure. During excavating, the rotational speed of the hydraulic motor  $n$  is sensed by speed measuring device while the working pressure  $p$  is measured by pressure sensor. The speed and pressure signals are sent back to the controller to implement control with the appropriate control strategy.

In the variable displacement control system, the output signal of controller is delivered to the controllers directly mounted at the variable-displacement pump 1.1, and then stroking mechanism of the pump is regulated by desired signals to adjust the displacement of pump accordingly. In the variable speed control system, because the oil supply pump 1.2 is of fixed displacement, the output signal of controller is delivered to the inverter. The rotational speed of the cutter-head is regulated by converter motor 2 controlled with the inverter.

The only difference between the two control systems is the power source. The output speed and torque of the cutter-head are controlled by varying the rotation speed of the fixed-displacement pump in the variable speed pump control system, while the output speed and torque of the cutter-head are controlled by varying displacement of the variable-displacement pump in the variable displacement pump control system.

### Hydraulic test rig for the cutter-head system

It is the most appropriate method to compare the energy-saving effect of two control systems by analyzing testing dates of the actual tunneling machine. However, field test is likely to be costly and risky, thus it is very significant to conduct physical simulation test to simulate the field working conditions. In this paper, a semi-physical simulation test rig with a set of variable speed and variable displacement control system which can be switched each other to control the cutter-head has been built, which include two pumps with different control methods, proportional relief valve, pressure sensor and flow meter, etc. Three loads of clay, sand and gravel soil which are typical working conditions in the process of excavating are simulated with hydraulic loads to analyze the energy consumption of two drive systems under the same condition. The hydraulic principle diagram of the test rig is shown in Fig. 2. In accordance with the actual working condition of shield tunneling machine, the simulation system mainly contains two parts: cutter-head drive module and simulative loads module. The cutter-head is simulated with motor 8, and cutter-head loads are simulated by motor 11.



1. Converter motor 2. Fixed-displacement pump 3. Variable-displacement pump 4. Relief valve 5. Check valve 6. Ball valve 7. Directional valve 8. Hydraulic motor 9. Inertia wheel 10. Torque and speed transducer 11. Two-way fixed-displacement pump 12. Pressure transducer 13. Oil controlled valve 14. Proportional relief valve

**Figure 2. The hydraulic principle diagram of simulation test rig for cutter-head drive system**



The test system adopts parallel drive in two ways: variable speed and variable displacement, which can be switched between the two modes according to experiment requirements through a three-way ball valve 6. When the system is working, the high pressure oil pass through check valve 5, three-way ball valve 6 and directional control valve 7 taking charge of the cutter-head rotation in two rotational directions. The motor 8 is connected rigidly with inertia wheel, speed and torque transducer and two-way fixed-displacement pump via a coupling. The motor 11, whose ports are connected with the proportional relief valve 14, is used to simulate the loads the shield machine may encounter. By regulating the pressure of the proportional relief valve 14, which ranges from 0 to 315bar, we can simulate different working torques.

In addition to the primary loop, the experiment system also includes electric control system and oil compensating circuit in which the oil compensating pressure is 2MPa. In the part of load simulation, the simulation cutter-head 8 and loading pump 11 need bi-directional rotation constituting a small closed hydraulic circuit. Electric control module adopts acquisition cards and an industrial PC to complete the data acquisition, processing and output.

The main parameters of the test rig for cutter-head drive system are given in Table 1 below.

**Table 1. The main parameters of the simulation test rig for cutter-head drive system**

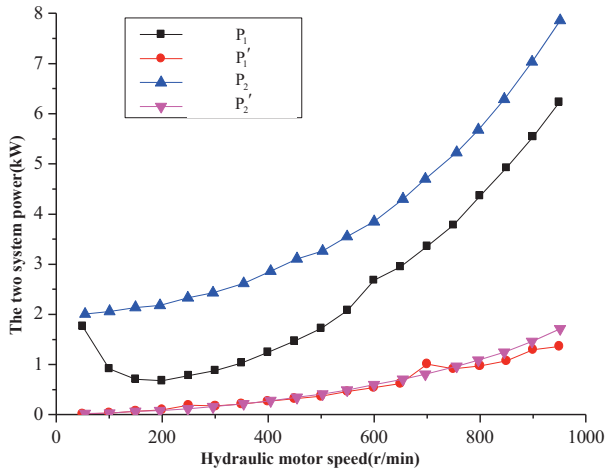
	motor power	displacement	speed
fixed-displacement pump	55kW	40 ml/r	0-1500 r/min
variable-displacement pump	45kW	45 ml/r	1500 r/min
hydraulic motor		40 m/r	

## Results and analysis

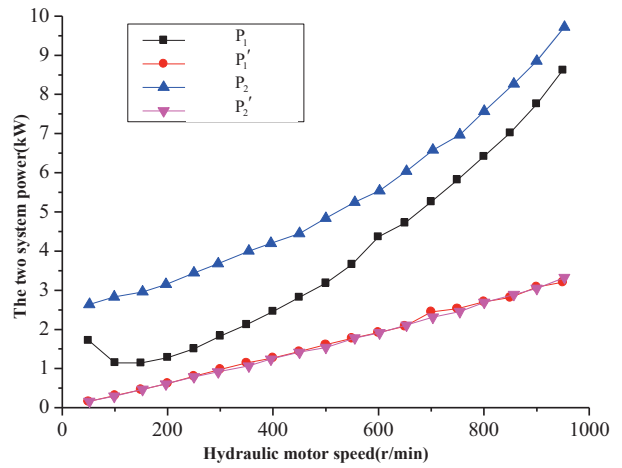
The energy-saving contrast experiment of two cutter-head hydraulic system is carried out in the test rig as shown in Fig. 2.

In order to compare energy-saving characteristics of two drive systems, the experiment should be conducted in the condition of the same load condition and motor speed. When tunneling in different geological conditions, the cutter-head torque of shield tunneling machine is also different. The relief valve pressure is set to 5MPa, 10MPa and 15MPa which are three kinds of typical pressure levels for simulating three different cutter-head loads on the motor rotation speed increasing from 0 to 1000 r/min. In addition, the working condition in the pressure of 0MPa is also taken into account in order to deeply compare the energy consumption characteristics of two kinds of systems.

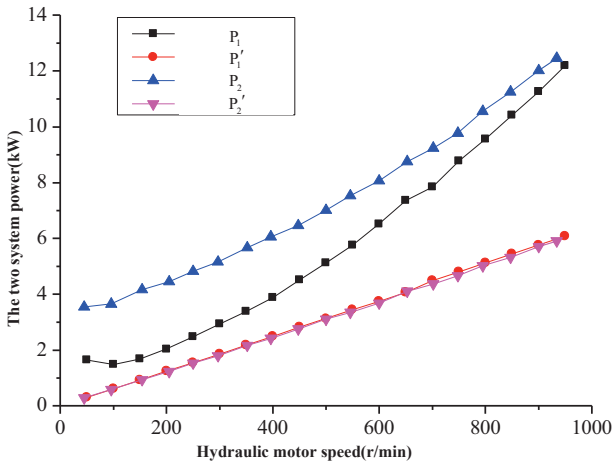
Input and output power curves of variable speed and variable displacement system under different load pressures are plotted respectively, as shown from Fig. 3 to Fig. 6. Where  $P_1$  is the input power of variable speed control system,  $P_1'$  is the output power of variable speed control system,  $P_2$  is the input power of variable displacement control system,  $P_2'$  is the output power of variable displacement control system.



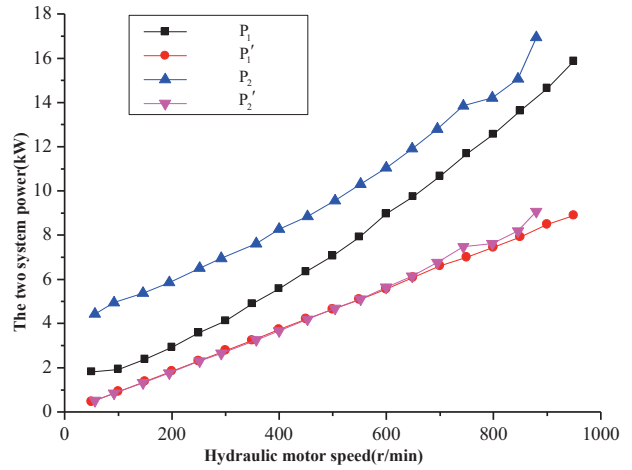
**Figure 3. Power contrast of two control system in 0MPa load condition**



**Figure 4. Power contrast of two control system in 5MPa load condition**



**Figure 5. Power contrast of two control system in 10MPa load condition**



**Figure 6. Power contrast of two control system in 15MPa load condition**

We can safely draw some conclusions from the above curves:

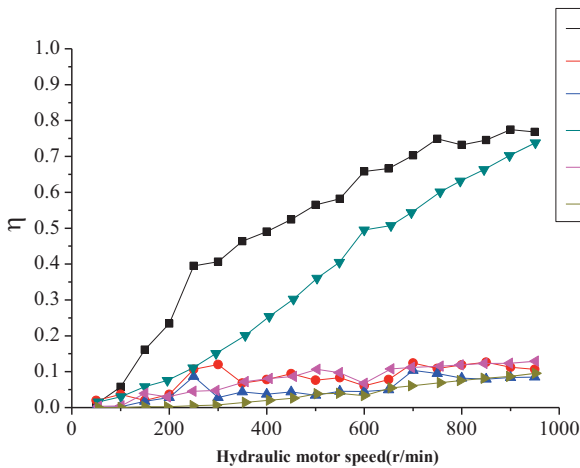
(1) When the load pressure is zero, the input and output power are increasing gradually with the increase of motor rotational speed, this is because the viscous friction resistance of the rotating parts increases as the rotational speed increases. Meanwhile, the large flow in the hydraulic lines also lead to the increased oil resistance in the working condition of high speed, eventually making the actual power presents increasing trend.

In addition, the difference of input power between the variable displacement system and variable speed system in low-speed working condition is larger than one in high-speed working condition under the same load pressure. In the low-speed condition, the pump motor in the variable speed system has low rotational speed and low friction loss, while the pump motor speed in the variable displacement system keep the high rotational speed always.

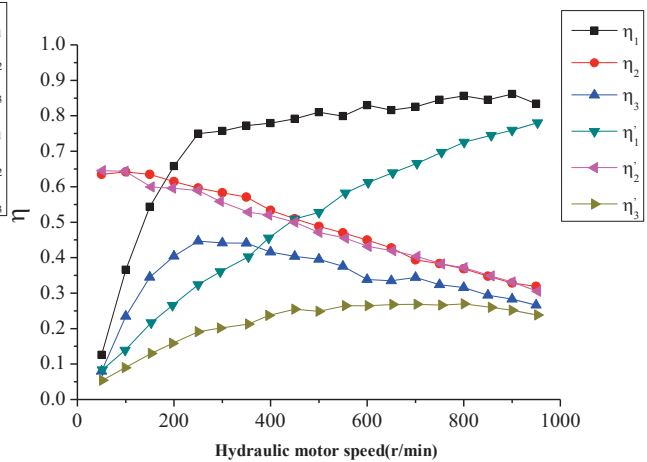
(2) The output powers of two systems are basically the same because they have the same loading pressures, while the input powers of two systems namely motor power are different. For the variable speed control system, the curves of motor input power have a good match with the curves of system output power. The lower the motor speed, the better the match and the smaller power loss.

For the variable displacement control system, although the input power of the system increases with the increase of output power, but the input power is greater than the power required compared with the variable speed control system.

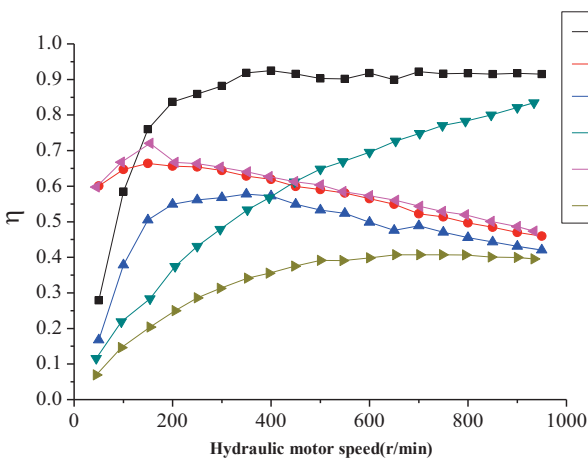
The Fig. 7-10 are work efficiency of variable speed and variable displacement control systems under different load pressures. In order to detail the contrast, the motor efficiency, the hydraulic system efficiency as well as the whole system are drawn. In the variable speed control system,  $\eta_1$  is the motor efficiency,  $\eta_2$  is the hydraulic efficiency, and  $\eta_3$  is the overall efficiency. In the variable displacement control system,  $\eta'_1$  is the motor efficiency,  $\eta'_2$  is the hydraulic efficiency, and  $\eta'_3$  is the overall efficiency.



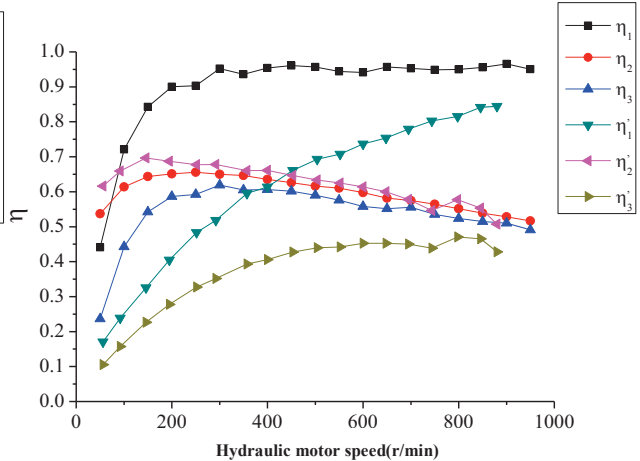
**Figure 7. Efficiency contrast of two control system in 0MPa load condition**



**Figure 8. Efficiency contrast of two control system in 5MPa load condition**



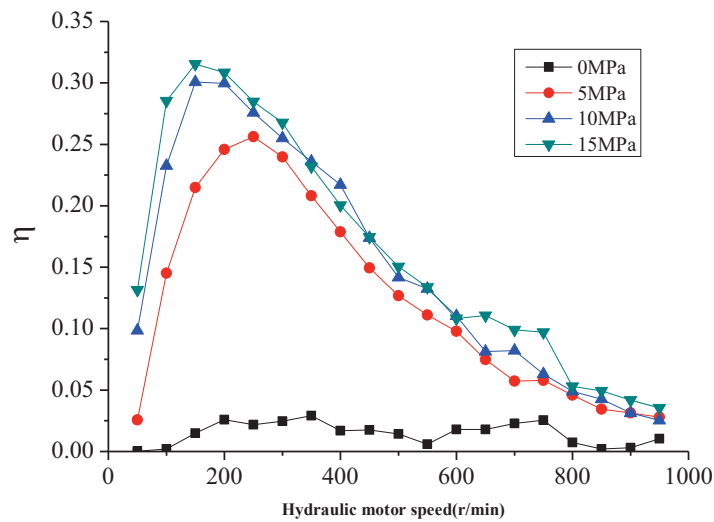
**Figure 9. Efficiency contrast of two control system in 10MPa load condition**



**Figure 10. Efficiency contrast of two control system in 15MPa load condition**

As can be seen from the figures that the efficiency of hydraulic module declines with the increase of the hydraulic motor speed in the same working conditions. This is because the efficiency of hydraulic module includes the overall transfer efficiency of motor, loading pump and mechanical connection among them. Therefore, the higher the motor speed, the bigger the friction torque, which increases the load indirectly causing the working pressure increase, along with the leakage of the hydraulic system.

In addition, the motor efficiency of the variable speed control system has high efficiency at low speed, and keeps the high efficiency with the increase of the hydraulic motor speed. While the motor efficiency of the variable displacement control system is very low at low speed, and increases gradually with the increase of the hydraulic motor speed, and is close to the variable speed control system at higher speed. This is because the converter motor has a mechanical characteristic curve and an efficiency curve at a certain frequency, and the efficiency curve changes along with the external load. When the external load reaches the rated load of the frequency, the motor efficiency reaches the maximum value. The converter motor efficiency increases with the increase of load if the external load is lower than the rated load. Furthermore, the converter motor speed is low when the hydraulic motor speed is low, thus reducing the mechanical loss of the converter motor, compared with the ordinary motor of variable displacement control system running in the rated speed always. From what have been discussed above, we can draw the conclusion that the variable speed pump control system is a global type energy-saving control mode.



**Figure 11. Efficiency improvement of two control system in different load conditions**

In order to further demonstrate the efficiency comparison of two speed control systems, the efficiency improvement value of two systems is drawn, which make a difference between the overall efficiency of two systems, as shown in Fig. 11. It can be seen clearly in Fig. 11 that the overall efficiency of two systems increases with the increase of the load pressure, and the variable speed control system is more efficient than the variable displacement control system under the different loads. The efficiency of the variable speed control system is higher than the variable displacement control system up to 30% at the speed of 100~200r/min. It also can be seen in Fig. 11 that the hydraulic motor speed should be not too high or too low which are disadvantageous for the efficiency improvement of the variable speed control system.

## Conclusions

In this paper, based on the semi-physical simulation platform, the contrast experiment of the efficiency between the variable speed and variable displacement control system was carried out in three different pressure loads, and the efficiency improvement of the variable speed control system applied in cutter-head drive system was analyzed. These experimental curves proved the superiority of variable speed control system in energy saving, especially in larger load or low speed condition.

The experimental results show that the shield cutter-head hydraulic drive system with variable speed control technology is more energy-saving, regardless of the varying geological conditions. The maximum magnitude of energy reduction reaches approximately 30% by using the variable speed control system rather than the variable displacement one under the same working condition. The research would provide the theoretical reference for the actual application of the energy-saving shield tunneling machine.

#### References

- Yang, H. Y. and Gong, G. F. (2004), Shield TBM and its applications of hydraulic technology. *Hydraulics Pneumatics & Seals*, vol. 1, pp. 27–29.
- Peng, T. H. (2003), Research on variable frequency pump-control-motor speed governing and compensation characteristics, *Dissertation*, Zhejiang University.
- Yang, H.Y. and Xu, B. (2004), Computational simulation and experimental research on speed control of VVVF hydraulic elevator, *Control engineering practice*, pp. 563–568.
- Xing, T. (2008), Research on Hydraulic Drive and Control System of the Cutter Head in Shield Tunneling Machine, *Dissertation*, Zhejiang University.

## Simulation of Bubbly Flow in a Vertical Pipe Using Discrete Phase Model

\*H.Y. Li<sup>1</sup>, J. Lou<sup>1</sup>, Z. Shang<sup>1</sup> and H. Tang<sup>2</sup>

<sup>1</sup>Institute of High Performance Computing (IHPC), Agency for Science, Technology and Research (A\*STAR), 1 Fusionopolis Way, #16-16 Connexis, Singapore 138632

<sup>2</sup>School of Mechanical & Aerospace Engineering, Nanyang Technology University, 50 Nanyang Avenue, Singapore 639798

\*Corresponding author: lih@ihpc.a-star.edu.sg

### Abstract

Bubbly flow is widely encountered in many engineering applications, such as those in chemical and nuclear systems, bubble column reactors and oil transportation pipes. Therefore, understanding of bubbly flow in a bubble-liquid flow system is extremely important. In this paper, bubbly flow involved with thousands of bubbles in a vertical pipe is numerically simulated. The motions of the bubbles are tracked using a Discrete Phase Model (DPM) and bubble-bubble interactions are simulated through the model of discrete element method (DEM). The effects of bubble diameter on the bubble flow trajectories are studied. Comparisons are made on the flow field with and without considering bubble-bubble collision.

**Keywords:** Bubbly flow, Discrete phase model, Bubble trajectory, DEM collision.

### 1. Introduction

Bubbly flow is widely encountered in many engineering applications, such as oil and gas pipes, chemical and nuclear systems (Oolman and Blanch, 1986; Chen et al., 1994) and bubble column reactors (Jakobsen, 2001). In these systems, millions of bubbles are dispersed into a continuous phase which is the carrier fluid. The movements of these bubbles have significant effects on the flow fields as well as the pressure drops in the systems. Therefore, understanding the dynamics of the bubbles is essentially important to know bubbly flow.

Experimental investigation of bubbly flow has been performed extensively (Liu and Bankoff, 1993a, 1993b; Gnotke et al., 2003; Daeseong et al., 2010). For experimental study, it generally requires large length scale test rig and high resolution measuring instruments to provide convincing data. These would lead to an extremely high cost. Meanwhile, it is rather difficult to capture the physical phenomenon occurred for each individual bubble in the experiments. In view of this, theoretical studies, in particular numerical simulations, play an essential complementary role in understanding the bubble dynamics in bubbly flow.

Bubbly flow generally involves two phases which are the carrier fluid and the bubbles. The carrier fluid is usually treated as the continuous phase in the numerical simulation. Bubbles can be treated either as a continuous phase or a discrete phase based on the methods bubbles are handled. These methods include Eulerian-Eulerian (EE) two fluid method, Lagrangian-Eulerian (LE) method and Direct Numerical Simulation (DNS) (Hirt and Nichols, 1981; Unverdi and Tryggvason, 1992; Shan, 1997; Osher and Sethian, 1988; Quan and Schmidt, 2007). EE (Drew, 1983; Enwald, 1996) two fluid model assumes bubble as another continuous phase which the average size and average velocity are chosen to represent the information for all the ranges of bubbles. Although EE model can be applied in the large scale system with both spatial and time, it is not able to represent two streams of bubbles with different velocities at the same location. The interactions among bubbles are usually not considered either. This results in the unrealistic simulations of the physical phenomena observed in the bubbly flow. Unlike EE model, LE model and DNS treat the bubbles as a discrete phase. DNS can reveal the useful detailed insights of bubble behavior and bubble interactions. Generally, it can only be applied in a system where a small number of bubbles are considered. For bubbly flow which involves thousands of bubbles, LE could be the most appropriate choice. In LE model, bubbles are represented in a Lagrangian reference frame while the carrier phase is represented in an Eulerian frame. Under such a treatment, the movement for each individual bubble in bubbly flow could be traced. The interactions among bubbles such as bubble

collision can also be included. The advantage of this method has been well documented in the paper of Subramaniam (2013).

In LE model, the trajectories of bubbles are predicted by integrating the force balance on the bubbles. The interactions between bubble and the continuous phase are achieved by the additional forces such as drag force, virtual mass force and lift force. This method has been used by Laín et al. (2002), Buwa et al. (2006), Pang et al. (2010) and Ashraf Ali and Pushpavanam (2011), to name a few, for simulation of the system with two phase flow. Zhang et al. (2005) and Xu et al. (2013) also adopted this method to investigate the dynamics of three phases including gas, liquid and particle in a multiphase system. Laín et al. (2002) evaluated the fluctuating energy existing in a bubble column system. They found that the source term in the turbulent  $\kappa$ - $\epsilon$  equations is the main issue which governs the hydrodynamic behavior of the bubbles. Buwa et al. (2006) studied the effects of geometric parameters and gas velocity on the bubble volume fraction. It is found that the recirculation flow which is observed in the experiment in the bubble columns is breakdown due to the numerical diffusion as well as the unrealistic lift force added in the simulation. Pang et al. (2010) investigated the air-water flow in a vertical channel using LE model. Their results show that most bubbles accumulated near the wall while water velocity increases at the center of the channel. Ashraf Ali and Pushpavanam (2011) compared both EE and LE model for two-phase flow in a rectangular tank. The two models agree well with each other when the gas volume fraction is low.

Bubbly flow is one of the most important flow patterns in the two phase flow in both horizontal and vertical pipes. The other flow patterns can be transited through bubbly flow by varying factors such as the bubble velocity, the bubble diameters, bubble distributions as well as the physical properties of two phases. Therefore, the effects of these parameters are extremely important for achieving a stable bubbly flow. Interesting and surprisingly, to the best knowledge of the authors, the effect of bubble diameter as well as the collision among bubbles on the flow field in the bubbly flow has not been investigated based on LE. The present work intends to fill in this gap. This paper studies air-water bubbly flow in a vertical pipe using discrete phase model which is based on LE. The flow field and bubble dynamics under different bubble diameters are investigated. In addition to this, the effect of bubble collision on the bubbly flow system is also studied.

## 2. Problem Description

The schematic diagram of the simulation domain is show in Fig.1(a). The radius of the cylinder  $R$  is 0.1m and the height is 10m. 25 air bubbles are injected into the domain at the bottom of the cylinder with a constant interval of 0.0005s. The distribution of the injected air bubble is shown in Fig. 1(b). 12 bubbles are distributed uniformly at radius of 0.07m and 0.03m, respectively. There is also another bubble located in the center of the domain. Initially, water flows into the domain with a constant speed of 1m/s. Once steady state solution of water flow is achieved, air bubbles are then injected. The injection velocity of air bubble is 0.1m/s. Driven by the buoyancy force, these air bubbles move upwardly and drive water adjacent flowing faster.

out

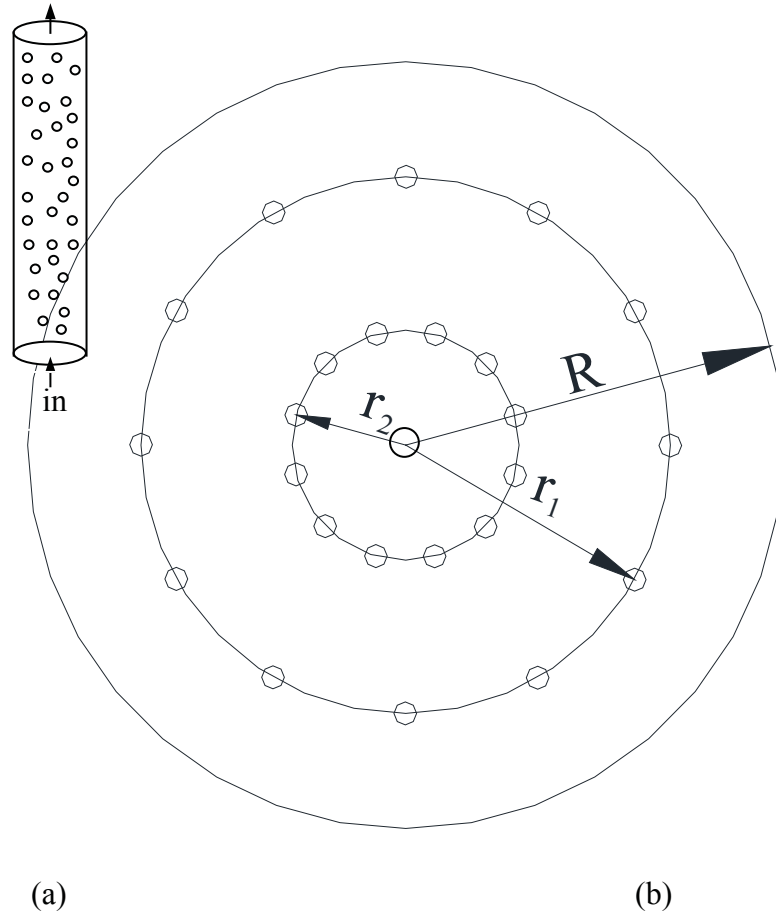


Fig. 1(a) Schematic diagram of simulation domain (b) distribution of 25 injected air bubbles

### 3. Numerical Model

#### 3.1 Mathematical Formulation

The trajectory of the air bubble was predicted through the integration of the force balance on the bubble based on the Lagrangian reference frame (Cundall and Strack, 1979). The mathematical formulation for bubble movement is:

$$\frac{du_{ib}}{dt} = F_D(u_{ib} - u_i) + \frac{g_i(\rho_b - \rho)}{\rho_b} + F_i \quad (1)$$

The subscript  $i$  represents the components of the axis.  $u_b$  and  $u$  are the bubble and water velocity, respectively.  $F_D$  is the drag force exerted on water by the air bubble.  $F_i$  is the other forces involved such as virtual force and pressure gradient force. As suggested by Sokolichin et al. (2004), we do not include lift force in the current work since we have no clear experimental evidence on the information of the lift force. The mathematical expression of  $F_D$  is:

$$F_D = \frac{18\mu}{\rho_b d_b^2} + \frac{C_D \text{Re}}{24} \quad (2)$$

Where  $C_D$  is the drag force coefficient and  $\text{Re}$  is the Reynolds number.  $d_b$  is the bubble diameter. The expression for  $C_D$  and  $\text{Re}$  are, respectively:



$$C_D = a_1 + \frac{a_2}{\text{Re}} + \frac{a_3}{\text{Re}^2} \quad (3)$$

$$\text{Re} = \frac{\rho d_b |u_{ib} - u|}{\mu} \quad (4)$$

$a_1$ ,  $a_2$  and  $a_3$  are constants which can be applied for spherical bubbles for all ranges of Re (Morsi and Alexander, 1972). The expressions of these constants are:

$$a_1, a_2, a_3 = \begin{cases} 0, 24, 0 & 0 < \text{Re} < 0.1 \\ 3.69, 22.73, 0.0903 & 0.1 < \text{Re} < 1 \\ 1.222, 29.1667, -3.8889 & 1 < \text{Re} < 10 \\ 0.6167, 46.50, -116.67 & 10 < \text{Re} < 100 \\ 0.3644, 98.33, -2778 & 100 < \text{Re} < 1000 \\ 0.357, 148.62, -47500 & 1000 < \text{Re} < 5000 \\ 0.46, -490.546, 578700 & 5000 < \text{Re} < 10000 \\ 0.5191, -1662.5, 5416700 & \text{Re} \geq 10000 \end{cases} \quad (5)$$

$$F_i = 0.5 \frac{\rho}{\rho_b} \frac{d(u_i - u_{ib})}{dt} + \frac{\rho}{\rho_b} u_{ib} \frac{\partial u_{ib}}{\partial x_i} \quad (6)$$

The bubbles are carried by a flowing fluid. To model the continuous phase flow, the incompressible forms of the continuity and the Navier-Stokes with considering turbulent flow equations are employed for the simulation domain.

$$\frac{\partial \rho}{\partial t} = \frac{\partial}{\partial x_i} (\rho u_i) \quad (7)$$

$$\frac{\partial}{\partial t} (\rho u_i) + \frac{\partial}{\partial x_j} (\rho u_i u_j) = -\frac{\partial p}{\partial x_i} + \frac{\partial}{\partial x_j} \left[ \mu \left( \frac{\partial u_i}{\partial x_j} + \frac{\partial u_j}{\partial x_i} \right) - \frac{2}{3} \delta_{ij} \rho \kappa \right] + \frac{\partial}{\partial x_j} \left( -\rho \overline{u_i u_j} \right) \quad (8)$$

The turbulent flow is simulated through  $\kappa$ - $\varepsilon$  model which is embedded in FLUENT.

### 3.2 Geometry Mesh

The geometry of the simulation domain is meshed using GAMBIT 2.4. A uniform mesh size of 5 mm and a total of 2.8 million cells are used for the whole domain. Such mesh is chosen based on the grid independency study among the mesh cells of 1.8 million, 2.8 million and 4.2 million.

### 3.3 Boundary conditions

The current simulation is performed using ANSYS FLUENT 14. Initially, water single-phase flow under steady state simulation is carried out. Once the steady state solution of water flow is achieved, air bubbles are then injected into the domain. Bubbles are tracked in a transient basis with a time step size of 0.0005s. The inlet velocity of water is 1m/s and the inlet velocity of bubble is 0.1m/s. An atmosphere pressure is set at the outlet boundary. No slip boundaries are applied on the walls for water. For air bubbles on the walls, reflection with no energy loss is assumed.

## 4. Results and Discussion

### 4.1 Validation

The current numerical simulation is validated with the experimental work done by Ohnuki and Akimoto (2000). Figure 2 shows the comparison of pressure drop under different air inlet velocity. The inlet water velocity is fixed at 1.06m/s. Generally, the increase of air velocity increases its volume fraction. This leads to a low pressure drop in a vertical pipe. Good agreement was achieved between the experimental data and simulation results.

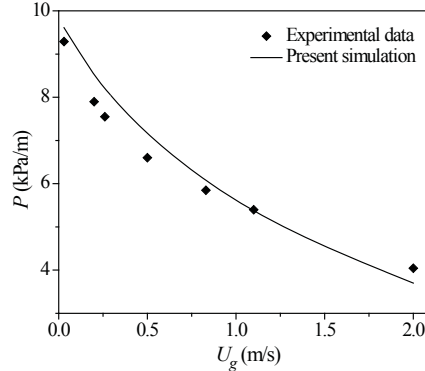


Fig. 2 Comparison of pressure drop under different air velocity

#### 4.2 Air bubble and water velocity without considering bubble collision

Figure 3(a) and 3(b) show the bubble and water velocity at different locations, respectively. As the bubbles are tracked in a transient basis, bubble velocity is shown at different times. Figure 3(a) shows the bubble velocity at  $t = 2s$  at  $r = 0, 0.03m$  and  $0.07m$ .  $r = 0$  is the center of the pipe. The diameter of bubbles introduced into the pipe is  $300\mu m$ . A significant increase of bubble velocity is observed as seen from Fig. 3(a) in a short time once bubbles are injected into the domain. This is due to the dominance of buoyancy force at the initial stage in the bubble rising process. Such velocity increases to its maximum value of  $3.2m/s$  at around  $t = 0.05s$  and after that, bubble velocity decreases. The increase of bubble velocity increases the drag force between bubble and water. When the drag force becomes dominated, bubble velocity starts to decrease. Similar trends have been found for the bubble velocity at different locations before  $t = 0.1s$ . This is not what observed thereafter. After  $t = 0.1s$ , a slightly increase of bubble velocity is found for the bubbles at the center of the domain while a further decrease of bubble velocity is seen at  $r = 0.03$  and  $0.07m$ . Water velocity at  $t = 2s$  is shown in Fig. 3(b). Compared with water single phase flow at different locations, water velocity with air bubble inside shows significantly difference from its corresponding partner before  $4.5m$  along the height of the pipe. The length of  $4.5m$  actually is the travel distance for the air bubbles in the duration of  $2s$ . With air bubbles injected into the domain, these bubbles rise quickly given the buoyancy force. They exert high drag force to water and drive water surrounding moving faster. Therefore, water velocity increases. However, the injection of air bubbles in water enhances the instability of the flow field. As a consequence, water velocity exemplifies fluctuated styles which reveal the random and chaotic flow behavior once bubbles are introduced. Water velocity is higher than its counterpart at  $r = 0$  while at the other two locations, water velocity is lower than its counterpart after the length of  $1m$ . Unlike velocity in the length of  $4.5m$ , water velocity is less affected by air bubble in the pipe length where air bubble has not reached. Those lines are overlapped together with its counterpart at different locations upon achieving to the end of the pipe.

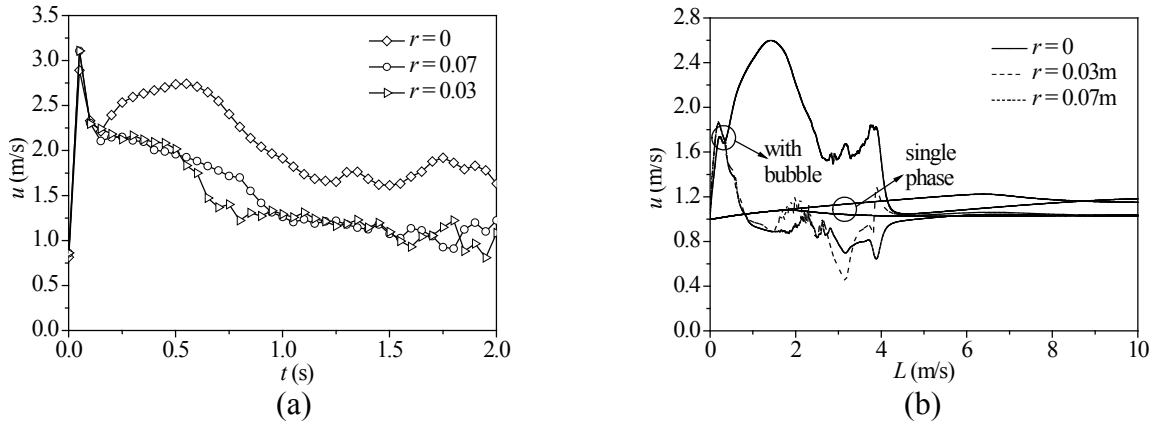


Fig. 3 Variations of (a) particle velocity under different times, (b) water velocity along the pipe at  $t = 2s$

Figure 4(a) and 4(b) show air bubble and water velocity at different radial locations at  $t = 4.5s$ , respectively. Fluctuations of the air bubble velocity is seen after  $t = 3.0s$ . Bubble flow in water actually increases the intensity of turbulent flow which leads to the fluctuation of both water and air bubble velocity. Such fluctuation is generally irregular and chaotic. A dramatic fluctuation in water velocity is initially observed at the center of the pipe and then it propagates to other locations. The travel distance for bubbles at  $t = 4.5s$  is around 9m which is indicated by the variation of water velocity in Fig. 4(b).

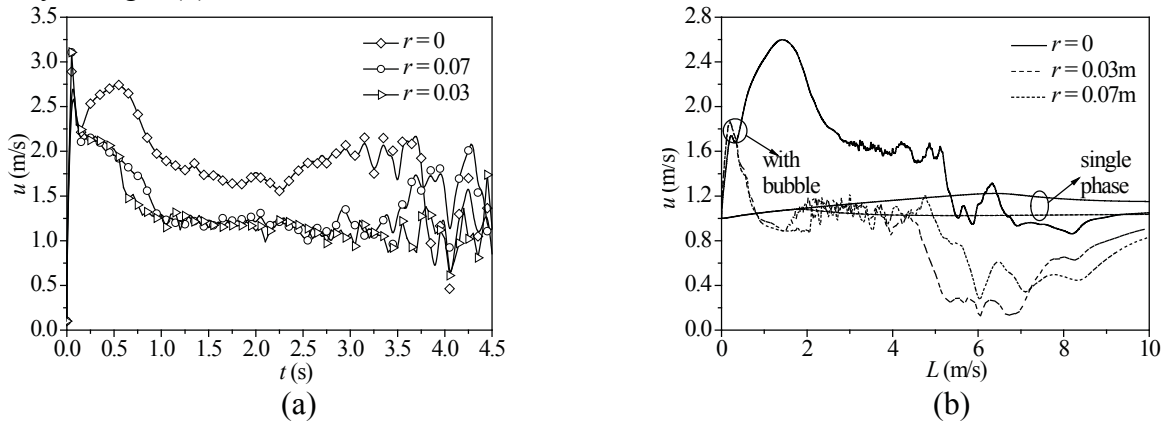


Fig. 4 Variations of (a) particle velocity under different times, (b) water velocity along the pipe at  $t = 4.5s$

Figure 5(a) and 5(b) show air bubble and water velocity at  $t = 10s$  at different locations, respectively. At this time, the number of bubbles entering and escaping from the pipe is almost equivalent. The number of bubble reside in the pipe is around 36 thousand. The flow field become much more chaos as can be seen from the fluctuation of both water and air bubble velocity. Generally, air bubble and water velocity at the center of the pipe is larger than those at other radial locations. This is not the situation when fluctuations occur. The existence of bubble changes the flow dynamic significantly.

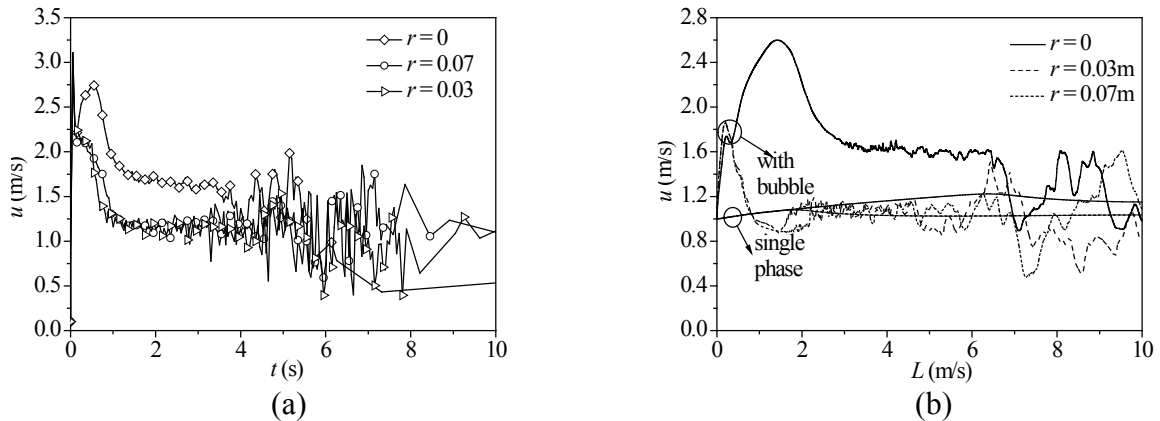


Fig. 5 Variations of (a) particle velocity under different times, (b) water velocity along the pipe at  $t = 10$ s

The effect of bubble diameter on water flow velocity at  $r = 0$  is shown in Fig. 6. Such water velocity is chosen when the number of bubble entering and escaping from the pipe is the same. It is surprised to find water velocity with considering bubbles is the same as that without considering bubbles when the bubble diameter is  $3\mu\text{m}$ . This implicates there is a critical bubble diameter under which the flow filed acts as no bubbles involved. For the case where the bubble diameter is above the critical value, there is no much difference on the water velocity along the length of 2.5m of the pipe under different bubble diameters. Thereafter, water velocity fluctuates. Generally, the larger the bubble diameter, the higher the fluctuation is.

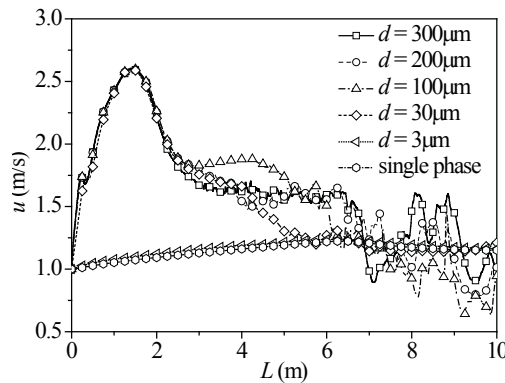


Fig. 6 Effect of bubble diameter on water velocity at  $r = 0$

#### 4.3 The effect of bubble collision on the air bubble and water velocity

Bubble collision is simulated based on the spring collision law where no energy loss is considered. Bubble and water velocity at  $r = 0.07\text{m}$  with and without considering collision model under different bubble diameters is shown in Fig. 7(a) and 7(b), respectively. For bubble diameter of  $3\mu\text{m}$ , the inclusion of the bubble collision has no effects on both the bubble and water velocity. This is not the case for bubble diameter of  $300\mu\text{m}$ . For bubble diameter of  $300\mu\text{m}$ , bubble collision is not significant at initial time as both bubble and water velocity are overlapped together first. Since then, large differences are found. The inclusion of bubble collision enhances the chaotic of the bubble dynamics. Therefore, a large fluctuation of bubble velocity is expected as seen from Fig. 7(a) after  $t = 3$ s. The large fluctuation of bubble increases the fluctuations of the water velocity simultaneously.

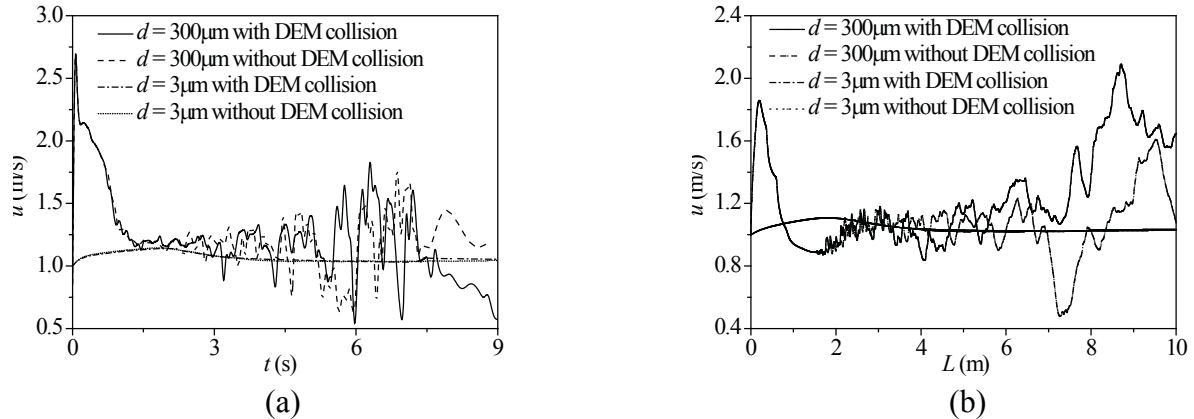


Fig. 7 Comparison of (a) bubble, and (b) water velocity with and without bubble collision at  $r = 0.07\text{m}$

Drag force is another important force in the bubbly flow. The comparison of drag force coefficient along the pipe with and without considering bubble collision is shown in Fig. 8. Given the fluctuation of the bubble and water velocity, the drag coefficient also shows a fluctuated mode. A higher fluctuation is observed with considering bubble collision compared with that without considering bubble collision.

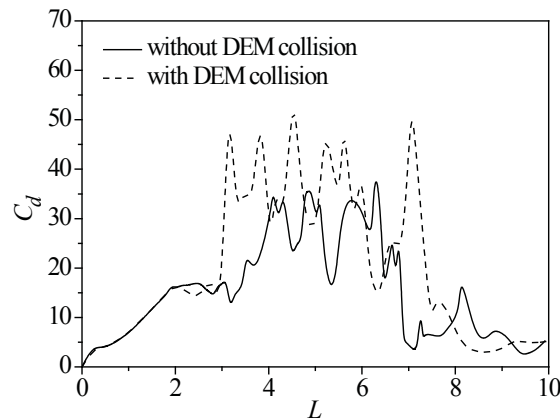


Fig. 8 Comparison of drag coefficient for  $d = 300\mu\text{m}$

## 5. Conclusions

In this paper, bubbly flow is simulated through DPM based on LE model. The effect of bubble diameter as well as bubble collision on the flow field is investigated. It is found that the involvement of the bubbles forces the flow field fluctuated. A high fluctuation is observed under large bubble diameter. However, when the bubble diameter is sufficiently small, the dynamic of bubble in the flow filed has no effect on the fluid flow even bubble collision is considered. The inclusion of the bubble collision enhances the fluctuation of the flow filed as well.

## References

- Ashraf Ali, B. and Pushpavanam, S. (2011), Analysis of unsteady gas-liquid flows in a rectangular tank: comparison of Euler-Eulerian and Euler-Lagrange simulations. *International Journal of Multiphase Flow*, 37, pp. 268-277.
- Buwa, V.V., Deo, D.S. and Ranade, V.V. (2006), Eulerian-Lagrangian simulations of unsteady gas-liquid flows in bubble columns, *International Journal of Multiphase Flow*, 32, pp. 864-885.
- Chen, R.C., Reese, J. and Fan, L.S. (1994), Flow structure in three-dimensional bubble column and three-phase fluidized bed. *AIChE Journal*, 42, pp. 1093-1104.
- Cundall P.A. and Strack O.D.L. (1979), A discrete numerical model for granular assemblies. *Géotechnique*, 29, pp. 47-65

- Daeseong, J., Shripad, T. and Revankar, T. (2010), Effect of coalescence and breakup on bubble size distributions in a two-dimensional packed bed. *Chemical Engineering Science*, 65, pp. 4231-4238.
- Drew, D. A. (1983), Mathematical modeling of two-phase flow. *Annual Review of Fluid Mechanics*, 15, pp. 261-291.
- Enwald, H., Peirano, E., Amstedt, A.E. (1996), Eulerian two-phase flow theory applied to fluidization. *International Journal of Multiphase Flow*, 22, pp. 21-66.
- Gnotke, O., Benk, H. and Loth, R. (2003), Experimental study on the number density distribution function in turbulent bubbly flows with coalescence and break-up. *Experimental Thermal and Fluid Science*, 27, pp. 803-816.
- Hirt, C. W. and Nichols, B. D. (1981), Volume of fluid /VOF/ method for the dynamics of free boundaries. *Journal of Computational Physics*, 39, pp. 201-225.
- Jakobsen, H.A. (2001), Phase distribution phenomena in two-phase bubble column reactors. *Chemical Engineering Science*, 56, pp. 1049-1051.
- Laín, S., Bröder, D., Sommerfeld, M. and Göz, M.F. (2002), Modeling hydrodynamics and turbulence in a bubble column using the Euler-Lagrange procedure. *International Journal of Multiphase Flow*, 28, pp. 1381-1407.
- Liu, T.J. and Bankoff, S.G. (1993a), Structure of air-water bubbly flow in a vertical pipe, I. liquid mean velocity and turbulence measurement. *International Journal of Heat and Mass Transfer*, 36, pp. 1049-1060.
- Liu, T.J. and Bankoff, S.G. (1993b), Structure of air-water bubbly flow in a vertical pipe, II. void fraction, bubble velocity and bubble size distribution. *International Journal of Heat and Mass Transfer*, 36, pp. 1061-1072.
- Moris, S.A. and Alexander, A.J. (1972), An investigation of particle trajectories in two-phase flow systems. *Journal of Fluid mechanics*, 55, pp. 193-208.
- Ohnuki, A. and Akimoto, H. (2000), Experimental study on transition of flow pattern and phase distribution in up-ward air-water two-phase flow along a large vertical pipe. *International Journal of Multiphase Flow*, 26, pp. 367-386.
- Oolman, T. and Blanch, H.W. (1986), Bubble coalescence in air-sparged bioreactor. *Biotechnology and Bioengineering*, 28, pp. 578-584.
- Osher, S. and Sethian, J.A. (1988), Fronts Propagating with Curvature-Dependent Speed: Algorithms Based on Hamilton-Jacobi Formulations. *Journal of Computational Physics*, 79, pp. 12-49.
- Pang, M.J., Wei, J.J. and Yu, B. (2010), Numerical study of bubbly upflows in a vertical channel using the Euler-Lagrange two-way model. *Chemical Engineering Science*, 65, pp. 6215-6228.
- Quan, S.P. and Schmidt, D.P. (2007), A moving mesh interface tracking method for 3D incompressible two-phase flows. *Journal of Computational Physics*, 221, pp. 761-780.
- Shan, X. (1997), Simulation of Rayleigh-Bénard convection using a Lattice Boltzmann Method. *Physical Review E*, 55, pp. 2780-2788.
- Sokolichin, A., Eigenberger, G. and Lapin, A. (2004), Simulation of buoyancy driven bubbly flow: established simplifications and open questions. *Fluid Mechanics and Transport Phenomena*, 50, pp. 24-45.
- Subramaniam, S. (2013), Lagrangian Eulerian methods for multiphase flows. *Progress in Energy and Combustion Science*, 39, pp. 215-245.
- Unverdi, S. O. and Tryggvason, G. (1992), A front-tracking method for viscous, incompressible, multi-fluid flows. *Journal of Computational Physics*, 100, pp. 25-37.
- Xu, Y.G., Liu, M.Y. and Tang, C. (2013), Three-dimensional CFD-VOF-DPM simulations of effects of low-holdup particles on single-nozzle bubbling behavior in gas-liquid-solid system. *Chemical Engineering Journal*, 222, pp. 292-306.
- Zhang X., Ahmadi, G. (2005), Eulerian\_lagrangian simulations of liquid-gas-solid flows in three-phase slurry reactors, *Chemical Engineering Science*, 60, pp. 5089-5104.

# Numerical Studies of Gas-Liquid-Fueled Two-Phase Detonation by Using Improved CE/SE method

D. L. Zhang

*State Key Laboratory of High Temperature Gas Dynamics, Institute of Mechanics, CAS,*

*15 Beisihuanxi Road, Haidian District, Beijing 100190, China*

*\*Corresponding author. Email: DLZhang@imech.ac.cn*

**Abstract:** The gas-liquid-fueled two-phase detonation has very complex phenomena and characters. Until now they are studied mainly by experiments, because complex interactions between the two phases and chemical reactions models make numerical simulations very difficult. In the paper, numerical simulations of gas-liquid-fueled two-phase detonation have been performed by using an improved Space-Time Conservation Element and Solution Element (CE/SE) method. The Eulerian Two-Fluid Model and Eulerian-Lagrangian Particle-Trace Model were adopted already. Numerical results were compared with some experiments and characters of gas-liquid-fueled two-phase detonation were analyzed. All of them show that the complex phenomena of gas-liquid-fueled two-phase detonation can be simulated. The improved CE/SE scheme has the features of high resolution, simple form and robustness.

*Keywords: gas-liquid-fueled two-phase flow; detonation; chemical reactions; CE/SE method;*

## 1 Introduction

The formation and propagation of detonation is a very complicated phenomenon [1] [2]. For a long time the detonation phenomena are studied mainly by experiments. However, in the last 25 years the numerical simulations have improved immensely as a result of major progress in both computational methods and available computer. Especially in last recent decades of development, the mechanism recognition of detonations in gaseous fuel-oxidizer mixtures has made large progresses and its numerical simulation can be basically achieved [3]. But our understanding of the initiation, formation, structure and stability of detonations in gas-liquid-fueled two-phase mixtures are still more primitive than for detonations in gaseous fuel-oxidizer mixtures [4].

The lack of knowledge of the features of gas-liquid-fueled detonations can be partly ascribed to the fact that the governing parameters of gas-liquid-fueled mixtures are far more than that of gaseous mixtures. Indeed, apart from the chemical composition and initial pressure and temperature of the mixture, one should take into account atomization, droplet breakup and vaporization, droplet size and shape as well as droplet distribution, etc. The latter effects may play a major role in gas-liquid-fueled two-phase detonations [5]. They will induce that the detonation processes are very complex and detonation zone thickness is at least a few times larger than that in gaseous fuel-oxidizer mixtures. All these features result in mathematical and physical difficulties.

The difficulties of numerical simulation of gas-liquid-fueled detonation are mainly due to its complex physical and chemical phenomena as well as determination for governing parameters of gas-liquid-fueled mixtures. In the simulations of gas-liquid-fueled detonation there are two primary factors: One is the strong discontinuity surface in detonation waves; another is the process of energy release in the flow field. These factors depend on numerical schemes and chemical reaction models respectively [6] [7].

In this paper an efficient and accurate Eulerian-Lagrangian Particle-Trace Model for

gas-liquid-fueled two-phase detonations was constructed and compared with the normal Eulerian Two-Fluid Model. A new two-dimensional CE/SE scheme with two-order accuracy with a hexahedral mesh was deduced. The simplified chemical reaction models were adopted. The gas-liquid-fueled two-phase detonation in liquid-fueled  $C_6H_{14}$ -air system and liquid-fueled  $C_{10}H_{22}$ - $O_2$ /air systems were simulated. The numerical results were discussed and compared with corresponding results by C-J theory and experiments. All of these show that Eulerian Two-Fluid Model, Eulerian-Lagrangian Particle-Trace Model and the improved CE/SE schemes with two-order accuracy are reasonable and feasible. The main features and characters of complex gas-liquid-fueled two-phase detonation can be successfully simulated.

## 2 Governing Equations and Chemical Reaction Model

### 2.1 Governing Equations

In this paper, an Eulerian-Lagrangian Particle-Trace Model is introduced for treating the gas-liquid-fueled two-phase detonations. The droplet phase is considered as continuous and homogeneous medium and all droplets can be traced by Lagrangian method.

Following assumptions are made about present model: the gas phase behaves as an ideal gas; the temperature of all gaseous species is the same; there are no process of collision, coalescence and fragmentation in droplet phase; the shape of droplets always keeps to be spherical; the temperature distribution in droplet phase is uniform; the volume occupied by droplets is negligible when it compares with the volume of gas; chemical reactions occur only in the gas phase; if chemical reaction occurs, the chemical energy is absorbed only by gas.

Under the above assumptions, the gas-phase is governed by Eulerian equations:

$$\frac{\partial \mathbf{Q}}{\partial t} + \frac{\partial \mathbf{E}}{\partial x} + \frac{\partial \mathbf{F}}{\partial y} = \mathbf{S}. \quad (1)$$

In Eq. (1),  $\mathbf{Q}$  is the vector of conserved variables,  $\mathbf{E}$  and  $\mathbf{F}$  are the conservation flux vectors in x- and y-directions,  $\mathbf{S}$  is the source term vector. Combined with chemical reaction and phase transition, the expressions of  $\mathbf{Q}$ ,  $\mathbf{E}$ ,  $\mathbf{F}$ ,  $\mathbf{S}$  are as follows

$$\mathbf{Q} = \begin{pmatrix} \rho_i \\ \rho u \\ \rho v \\ e \end{pmatrix}, \quad \mathbf{E} = \begin{pmatrix} \rho_i u \\ \rho u^2 + p \\ \rho uv \\ (e + p)u \end{pmatrix}, \quad \mathbf{F} = \begin{pmatrix} \rho_i v \\ \rho uv \\ \rho v^2 + p \\ (e + p)v \end{pmatrix}$$

$$\text{and } \mathbf{S} = \begin{pmatrix} \omega_i + \delta \sum_1^{N_p} \frac{I_{pk}}{dV_k} \\ \sum_1^{N_p} \frac{-f_{xk} + u_{pk} I_{pk}}{dV_k} \\ \sum_1^{N_p} \frac{-f_{yk} + v_{pk} I_{pk}}{dV_k} \\ \sum_1^{N_p} \frac{-q_{dk} - (u_{pk} f_{xk} + v_{pk} f_{yk}) + \left( e_{pk} + \frac{u_{pk}^2 + v_{pk}^2}{2} \right) I_{pk}}{dV_k} \end{pmatrix}. \quad (2)$$

The Lagrangian governing equations for the  $k$ -th droplet are as follows:



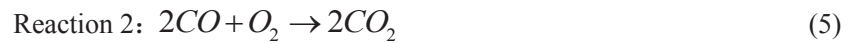
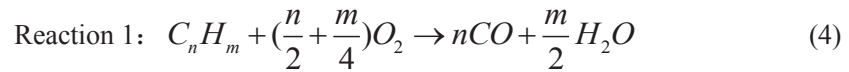
$$\left\{ \begin{array}{l} \frac{dm_{pk}}{dt} = -I_{pk} \\ \frac{dx_{pk}}{dt} = u_{pk} \\ \frac{dy_{pk}}{dt} = v_{pk} \\ m_{pk} \frac{du_{pk}}{dt} = f_{xk} \\ m_{pk} \frac{dv_{pk}}{dt} = f_{yk} \\ C_v \frac{dT_{pk}}{dt} = q_{dk} \end{array} \right. \quad (3)$$

Here  $\rho_i$  ( $i$  from 1 to  $Ns$ ) is the mass density of the  $i$ -th species (especially,  $\rho_1$  is defined as the density of fuel gas),  $Ns$  is the number of considered species,  $\omega_i$  is the production rate of the  $i$ -th species.  $\rho$ ,  $u$ ,  $v$ ,  $p$  and  $e$  are the total density, the velocity components of  $x$ -direction and  $y$ -direction, the pressure, and the total energy per unit volume of gas phase, respectively. Accordingly,  $m_{pk}$ ,  $x_{pk}$ ,  $y_{pk}$ ,  $u_{pk}$ ,  $v_{pk}$ ,  $T_{pk}$ ,  $e_{pk}$  and  $I_{pk}$  denote the mass, the position coordinates components and the velocity components, temperature, the internal energy per unit mass and atomization rate of the  $k$ -th ( $k$  from 1 to  $Np$ ) droplet, respectively.  $Np$  is the number of initial droplets, which is determined by the equivalence ratio of gas-liquid-fueled mixture.  $f_{xk}$  and  $f_{yk}$  are the force components acting on the  $k$ -th droplet.  $q_{dk}$  is the convection heat transfer between gas mixtures and the  $k$ -th droplet.  $C_v$  is the capacity of liquid fuel.  $dV_k$  is the volume of gas phase influenced by the  $k$ -th droplet, which is related to the Euler grid. When  $i=1$ ,  $\delta=1$ , otherwise,  $\delta=0$ .

The dynamic interaction of droplets with the gaseous flow could bring to instability of the interface and atomization of droplets. According to boundary layer theory, the atomization rate of droplets and the force components acting on the  $k$ -th droplet as well as convection heat transfer between gas mixtures and the  $k$ -th droplet were derived by references [8] [9].

## 2.2 Chemical Reaction Models

$CO$ ,  $CO_2$  and  $H_2O$  are the main product of the chemical reaction between hydrocarbon and oxygen. In present study, to avoid complicate the problem and save computing resources, the following three main global reaction involving five species are considered:



The expression of each chemical reaction rate  $RP_k$  is available in Ref. [10-11]. Then, production rate of each chemical species  $\omega_i$  is expressed as:

$$\omega_i = W_i \sum_{k=1}^{Nr} (v_{ki}'' - v_{ki}') RP_k, \quad (7)$$

where  $W_i$  is the molecular weight of the  $i$ -th species,  $Nr$  is the number of chemical reactions,  $v_{ki}'$

and  $v_{ki}''$  are the stoichiometric coefficients of the  $i$ -th species in the  $k$ -th chemical reaction.

### 3 Improved CE/SE Scheme

The CE/SE method was originally proposed by Chang and co-workers [12-13], which is a completely new numerical framework for solving hyperbolic conservation equations. According to principle of Chang designed two grid types, we design more general structures of two-dimensional CEs and SEs (Fig.1) [14]. New two-dimensional CE/SE schemes can be constructed sententiously and three-dimensional scheme can be extend easily.

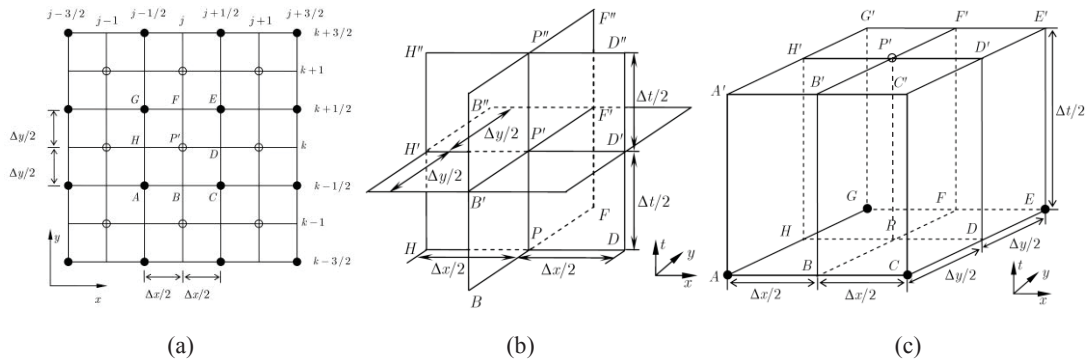


Fig.1 (a) Mesh points projection on  $xy$  plane (b)SE (c)CEs (in this work)

#### 3.1 Improved CE/SE Scheme with the second order accuracy

Consider the two-dimensional conservation equations:

$$\frac{\partial \mathbf{Q}}{\partial t} + \frac{\partial \mathbf{E}}{\partial x} + \frac{\partial \mathbf{F}}{\partial y} = 0, \quad (8)$$

Then because Eq. (8) can be expressed as  $\nabla \cdot \mathbf{H} = 0$  with  $\mathbf{H} = (\mathbf{Q}, \mathbf{E}, \mathbf{F})$ . The Gauss' divergence theorem in the space-time  $E_3$  implies that Eq. (8) is the differential form of the integral conservation law:

$$\int_{S(V)} \hat{\mathbf{s}} \cdot \mathbf{H} \, d\sigma = 0 \quad (9)$$

where  $S(V)$  is the boundary of an arbitrary space-time region  $V$  in  $E_3$ ;  $d\mathbf{s} = d\sigma \cdot \mathbf{n}$  with  $d\sigma$  and  $\mathbf{n}$ , respectively, being the area and the unit outward normal vector of a surface element on  $S(V)$ .

For an arbitrary grid point  $P'$ , we define a solution element SE ( $P'$ ) that constituted by the three vertical planes intersecting at  $P'$  as demonstrating in Fig. 1 (b). Assuming that  $\mathbf{E}$ ,  $\mathbf{F}$  and  $\mathbf{Q}$  at point  $(x, y, t)$  in SE ( $P'$ ) are approximated by the second-order Taylor's expansions at  $P'(j, k, n)$ :

$$\begin{aligned} \mathbf{Q}(\delta x, \delta y, \delta t)_{P'} &= (\mathbf{Q})_{P'} + (\mathbf{Q}_x)_{P'} \delta x + (\mathbf{Q}_y)_{P'} \delta y + (\mathbf{Q}_t)_{P'} \delta t \\ &\quad + \frac{1}{2} (\mathbf{Q}_{xx})_{P'} (\delta x)^2 + \frac{1}{2} (\mathbf{Q}_{yy})_{P'} (\delta y)^2 + \frac{1}{2} (\mathbf{Q}_{tt})_{P'} (\delta t)^2, \\ &\quad + (\mathbf{Q}_{xy})_{P'} \delta x \delta y + (\mathbf{Q}_{xt})_{P'} \delta x \delta t + (\mathbf{Q}_{yt})_{P'} \delta y \delta t \end{aligned} \quad (10)$$

$$\begin{aligned} \mathbf{E}(\delta x, \delta y, \delta t)_{P'} &= (\mathbf{E})_{P'} + (\mathbf{E}_x)_{P'} \delta x + (\mathbf{E}_y)_{P'} \delta y + (\mathbf{E}_t)_{P'} \delta t \\ &\quad + \frac{1}{2} (\mathbf{E}_{xx})_{P'} (\delta x)^2 + \frac{1}{2} (\mathbf{E}_{yy})_{P'} (\delta y)^2 + \frac{1}{2} (\mathbf{E}_{tt})_{P'} (\delta t)^2, \\ &\quad + (\mathbf{E}_{xy})_{P'} \delta x \delta y + (\mathbf{E}_{xt})_{P'} \delta x \delta t + (\mathbf{E}_{yt})_{P'} \delta y \delta t \end{aligned} \quad (11)$$

$$\begin{aligned} \mathbf{F}(\delta x, \delta y, \delta t)_{P'} &= (\mathbf{F})_{P'} + (\mathbf{F}_x)_{P'} \delta x + (\mathbf{F}_y)_{P'} \delta y + (\mathbf{F}_t)_{P'} \delta t \\ &\quad + \frac{1}{2} (\mathbf{F}_{xx})_{P'} (\delta x)^2 + \frac{1}{2} (\mathbf{F}_{yy})_{P'} (\delta y)^2 + \frac{1}{2} (\mathbf{F}_{tt})_{P'} (\delta t)^2, \\ &\quad + (\mathbf{F}_{xy})_{P'} \delta x \delta y + (\mathbf{F}_{xt})_{P'} \delta x \delta t + (\mathbf{F}_{yt})_{P'} \delta y \delta t \end{aligned} \quad (12)$$

Where  $\delta x=x-x_{P'}$ ,  $\delta y=y-y_{P'}$ ,  $\delta t=t-t_{P'}$ ,  $x_{P'}$ ,  $y_{P'}$  and  $t_{P'}$  are the position coordinates of point  $P'$ , but  $(V)_{P'}$ ,  $(V_x)_{P'}$ ,  $(V_y)_{P'}$ ,  $(V_t)_{P'}$ ,  $(V_{xx})_{P'}$ ,  $(V_{yy})_{P'}$ ,  $(V_{tt})_{P'}$ ,  $(V_{xy})_{P'}$ ,  $(V_{xt})_{P'}$  and  $(V_{yt})_{P'}$  are the constant values of  $V$ , its first-order and second-order derivative on  $x$ ,  $y$  and  $t$  directions at point  $P'$ , respectively, in which  $V$  denotes  $\mathbf{Q}$ ,  $\mathbf{E}$  and  $\mathbf{F}$ . Substituting Eq. (10), (11) and (12) into Eq. (8), it can obtain:

$$\begin{cases} (\mathbf{Q}_t)_{P'} = -(\mathbf{E}_x)_{P'} - (\mathbf{F}_y)_{P'} \\ (\mathbf{Q}_{xt})_{P'} = -(\mathbf{E}_{xx})_{P'} - (\mathbf{F}_{xy})_{P'} \\ (\mathbf{Q}_{yt})_{P'} = -(\mathbf{E}_{xy})_{P'} - (\mathbf{F}_{yy})_{P'} \\ (\mathbf{Q}_{tt})_{P'} = -(\mathbf{E}_{xt})_{P'} - (\mathbf{F}_{yt})_{P'} \end{cases} \quad (13)$$

The above equations imply that the variables required in computation are  $(\mathbf{Q})_{P'}$  and its first and second order space derivatives  $(\mathbf{Q}_x)_{P'}$ ,  $(\mathbf{Q}_y)_{P'}$ ,  $(\mathbf{Q}_{xx})_{P'}$ ,  $(\mathbf{Q}_{yy})_{P'}$  and  $(\mathbf{Q}_{xy})_{P'}$ .

Assuming flux vectors in every CE satisfy the integral conservation law, and the integrating Eq. (9) on the surfaces of CE ( $P'$ ) with the aid of Eq. (10), (11) and (12), we can obtained:

$$(\mathbf{Q})_{P'} + \frac{\Delta x^2}{24} (\mathbf{Q}_{xx})_{P'} + \frac{\Delta y^2}{24} (\mathbf{Q}_{yy})_{P'} = \frac{1}{4} \left( \bar{\mathbf{Q}} + \frac{\Delta t}{\Delta x} \bar{\mathbf{E}} + \frac{\Delta t}{\Delta y} \bar{\mathbf{F}} \right) \quad (14)$$

Define the following functions as:

$$\begin{aligned} \hat{\mathbf{Q}}(\delta x, \delta y, \delta t)_{P'} &= (\mathbf{Q})_{P'} + (\mathbf{Q}_x)_{P'} \delta x + (\mathbf{Q}_y)_{P'} \delta y + (\mathbf{Q}_t)_{P'} \delta t \\ &\quad + \frac{1}{6} (\mathbf{Q}_{xx})_{P'} (\delta x)^2 + \frac{1}{6} (\mathbf{Q}_{yy})_{P'} (\delta y)^2 + (\mathbf{Q}_{xy})_{P'} \delta x \delta y \\ \hat{\mathbf{E}}(\delta x, \delta y, \delta t)_{P'} &= (\mathbf{E})_{P'} + (\mathbf{E}_x)_{P'} \delta x + (\mathbf{E}_y)_{P'} \delta y + (\mathbf{E}_t)_{P'} \delta t \\ &\quad + \frac{1}{6} (\mathbf{E}_{yy})_{P'} (\delta y)^2 + \frac{1}{6} (\mathbf{E}_{tt})_{P'} (\delta t)^2 + (\mathbf{E}_{yt})_{P'} \delta y \delta t \\ \hat{\mathbf{F}}(\delta x, \delta y, \delta t)_{P'} &= (\mathbf{F})_{P'} + (\mathbf{F}_x)_{P'} \delta x + (\mathbf{F}_y)_{P'} \delta y + (\mathbf{F}_t)_{P'} \delta t \\ &\quad + \frac{1}{6} (\mathbf{F}_{xx})_{P'} (\delta x)^2 + \frac{1}{6} (\mathbf{F}_{tt})_{P'} (\delta t)^2 + (\mathbf{F}_{xt})_{P'} \delta x \delta t \end{aligned} \quad (15)$$

So the  $\bar{\mathbf{Q}}$ ,  $\bar{\mathbf{E}}$  and  $\bar{\mathbf{F}}$  in Eq. (14) can be expressed as:

$$\begin{aligned} \bar{\mathbf{Q}} &= \hat{\mathbf{Q}}\left(\frac{\Delta x}{4}, \frac{\Delta y}{4}, 0\right)_A + \hat{\mathbf{Q}}\left(-\frac{\Delta x}{4}, \frac{\Delta y}{4}, 0\right)_C + \hat{\mathbf{Q}}\left(-\frac{\Delta x}{4}, -\frac{\Delta y}{4}, 0\right)_E + \hat{\mathbf{Q}}\left(\frac{\Delta x}{4}, -\frac{\Delta y}{4}, 0\right)_G \\ \bar{\mathbf{E}} &= \hat{\mathbf{E}}\left(0, \frac{\Delta y}{4}, \frac{\Delta t}{4}\right)_A - \hat{\mathbf{E}}\left(0, \frac{\Delta y}{4}, \frac{\Delta t}{4}\right)_C - \hat{\mathbf{E}}\left(0, -\frac{\Delta y}{4}, \frac{\Delta t}{4}\right)_E + \hat{\mathbf{E}}\left(0, -\frac{\Delta y}{4}, \frac{\Delta t}{4}\right)_G \\ \bar{\mathbf{F}} &= \hat{\mathbf{F}}\left(\frac{\Delta x}{4}, 0, \frac{\Delta t}{4}\right)_A + \hat{\mathbf{F}}\left(-\frac{\Delta x}{4}, 0, \frac{\Delta t}{4}\right)_C - \hat{\mathbf{F}}\left(-\frac{\Delta x}{4}, 0, \frac{\Delta t}{4}\right)_E - \hat{\mathbf{F}}\left(\frac{\Delta x}{4}, 0, \frac{\Delta t}{4}\right)_G \end{aligned} \quad (16)$$

From Eq. (14) the current space second-order derivatives  $(\mathbf{Q}_{xx})_{P'}$  and  $(\mathbf{Q}_{yy})_{P'}$  at  $P'$  must be known firstly for solving  $(\mathbf{Q})_{P'}$ . With the estimated value in SE ( $P'$ ) approximated from the last half time step, the current second-order can be expressed as:

$$\begin{aligned} (\mathbf{Q}_{xx})_{P'} &= \frac{(\hat{\mathbf{Q}}_x)_C - (\hat{\mathbf{Q}}_x)_A + (\hat{\mathbf{Q}}_x)_E - (\hat{\mathbf{Q}}_x)_G}{2\Delta x} \\ (\hat{\mathbf{Q}}_x) &= (\mathbf{Q}_x) + \frac{\Delta t}{2} (\mathbf{Q}_{xt}) \end{aligned} \quad (17)$$

$$(\mathbf{Q}_{yy})_{P'} = \frac{(\hat{\mathbf{Q}}_y)_C - (\hat{\mathbf{Q}}_y)_A + (\hat{\mathbf{Q}}_y)_E - (\hat{\mathbf{Q}}_y)_G}{2\Delta y} \quad (18)$$

$$(\hat{\mathbf{Q}}_y) = (\mathbf{Q}_y) + \frac{\Delta t}{2} (\mathbf{Q}_{yt})$$

The cross derivatives  $(\mathbf{Q}_{xy})_{P'}$  and  $(\mathbf{Q}_{yx})_{P'}$  are:

$$(\mathbf{Q}_{xy})_{P'} = (\mathbf{Q}_{yx})_{P'} = \frac{(\mathbf{Q}_{xy})'_{P'} + (\mathbf{Q}_{yx})'_{P'}}{2} \quad (19)$$

Where

$$(\mathbf{Q}_{xy})'_{P'} = \frac{(\hat{\mathbf{Q}}_x)_C - (\hat{\mathbf{Q}}_x)_A + (\hat{\mathbf{Q}}_x)_E - (\hat{\mathbf{Q}}_x)_G}{2\Delta y} \quad (20)$$

$$(\mathbf{Q}_{yx})'_{P'} = \frac{(\hat{\mathbf{Q}}_y)_C - (\hat{\mathbf{Q}}_y)_A + (\hat{\mathbf{Q}}_y)_E - (\hat{\mathbf{Q}}_y)_G}{2\Delta x}$$

Using the continuous condition at point  $A'$ ,  $C'$ ,  $E'$  and  $G'$ , the left and the right derivatives of  $(\mathbf{Q})_{P'}$  in  $x$  and  $y$  direction can be gained as

$$(\mathbf{Q}_x)_{P'}^- = -\frac{1}{\Delta x} \left[ \mathbf{Q} \left( 0, 0, \frac{\Delta t}{2} \right)_A + \mathbf{Q} \left( 0, \frac{\Delta t}{2}, 0 \right)_G - 2(\mathbf{Q})_{P'} \right]$$

$$(\mathbf{Q}_x)_{P'}^+ = +\frac{1}{\Delta x} \left[ \mathbf{Q} \left( 0, 0, \frac{\Delta t}{2} \right)_C + \mathbf{Q} \left( 0, 0, \frac{\Delta t}{2} \right)_E - 2(\mathbf{Q})_{P'} \right]$$

$$(\mathbf{Q}_y)_{P'}^- = -\frac{1}{\Delta y} \left[ \mathbf{Q} \left( 0, 0, \frac{\Delta t}{2} \right)_A + \mathbf{Q} \left( 0, 0, \frac{\Delta t}{2} \right)_C - 2(\mathbf{Q})_{P'} \right]$$

$$(\mathbf{Q}_y)_{P'}^+ = +\frac{1}{\Delta y} \left[ \mathbf{Q} \left( 0, 0, \frac{\Delta t}{2} \right)_E + \mathbf{Q} \left( 0, 0, \frac{\Delta t}{2} \right)_G - 2(\mathbf{Q})_{P'} \right] \quad (21)$$

To avoid numerical instability in the case of discontinuity, the derivatives are written in form of weighted average:

$$(\mathbf{Q}_x)_{P'} = W[(\mathbf{Q}_x)_{P'}^-, (\mathbf{Q}_x)_{P'}^+, \alpha] \quad (22)$$

$$(\mathbf{Q}_y)_{P'} = W[(\mathbf{Q}_y)_{P'}^-, (\mathbf{Q}_y)_{P'}^+, \alpha]$$

where  $\alpha$  is an adjustable constant and usually equals 1~2 and the weighted equation  $W$  is expressed

as

$$W[x_-, x_+, \alpha] = \frac{|x_+|^\alpha x_- + |x_-|^\alpha x_+}{|x_+|^\alpha + |x_-|^\alpha} \quad (23)$$

### 3.1 Treatments of Stiff Source

The  $\mathbf{S}$  is the source term vector of governing equations (1), which are consisted of the production rates of each species. In a reacting flow, the characteristic time of chemistry and flow have a scale gap. The magnitude of stiffness problem can be weighted by the Damkohler number which is defined as the ratio of the maximum characteristic time scale and the minimum's in a

system. For detonation problems:

$$Da = \frac{\tau_{flow}}{\tau_{chem}} \quad (24)$$

where  $\tau_{flow}$  and  $\tau_{chem}$  are the characteristic time scale of flow and chemistry reaction, respectively.

Decoupling method was applied to treat the stiff source in this study [15], namely we decoupled the chemistry reaction from governing equations (1), So in one time step, we frozen the reaction and solved the flow field first, then solved the variation of the each species by source

items. And  $Da=30$  in this study.

### 4 Verification of our Improved CE/SE Scheme

In order to verify our improved CE/SE scheme with the second-order accuracy deduced by new structure of CEs and SEs, a detonation propagating in a stoichiometric  $H_2-O_2$  gas was computed. In this case the initial pressure and temperature were 1 atm and 298 K, respectively. Detonation wave was generated by igniting in the left with high initial pressure and temperature 28 atm and 3874 K, respectively. The detailed chemically reacting model was adopted. An mechanism with the eight-species ( $H_2, O_2, H, O, HO, HO_2, H_2O, H_2O_2$ ) and twenty chemical reactions for hydrogen-oxygen combustion was used [16].

Fig. 2 is the developing process of pressure and temperature simulated. From Fig.2 it can show that deflagration-to-detonation transition (DDT) process completes in very short time and can be ignored. Fig. 3 gives out the numerical results compared with experimental and theoretical results for detonation velocity and CJ pressure. The compared results indicate that they are limited in 3% and the results are very agreement.

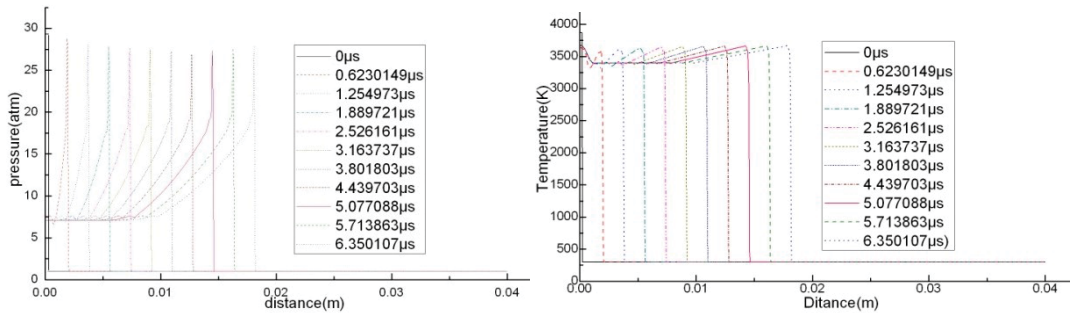


Fig.2 Developing process of pressure and temperature

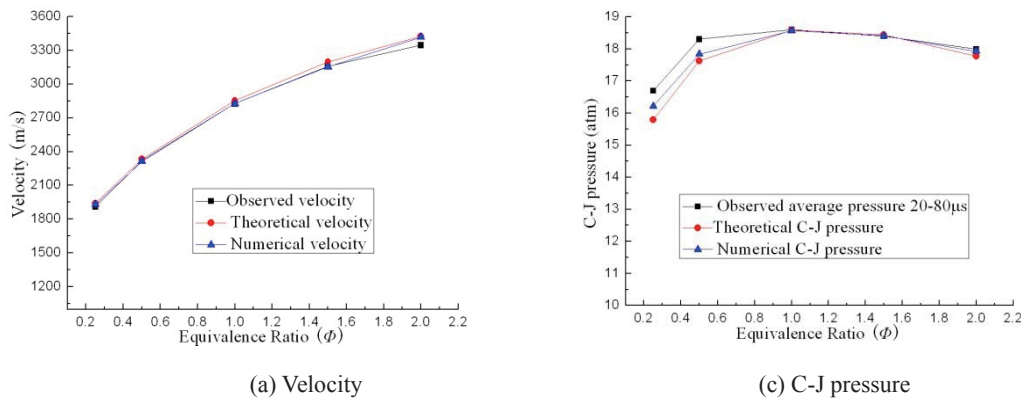


Fig.3. Numerical results compared with experimental and theoretical results

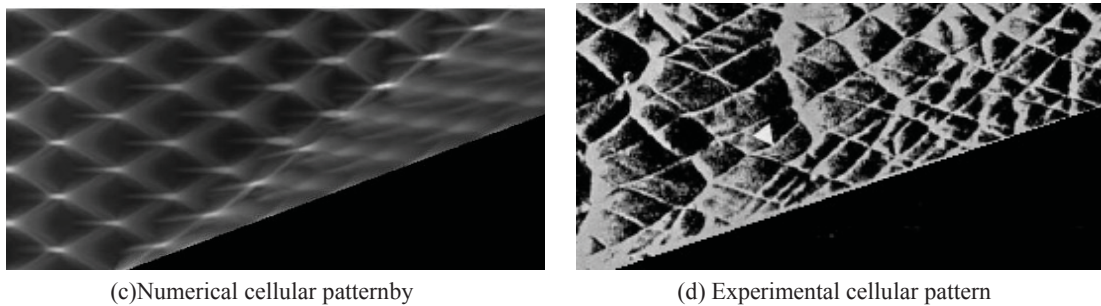


Fig. 4 Cellular pattern of a detonation wave on a 19.3° wedge

Fig.4 shows the cellular patterns produced by the reflection of  $H_2-O_2$  detonation wave over a

19.3° wedge by experiment [17]. The numerical results can agree well with the experiment and numerical results can draw up the basic feature of detonation wave reflection over wedge clearly.

## 5 Numerical Results

We have completed the numerical simulation of gas-droplet-fueled two-phase detonation by using the Eulerian Two-Fluid Model and Eulerian-Lagrangian Particle-Trace Model and the CE/SE method with the second order accuracy. Their numerical results were compared and analyzed briefly.

### 5.1 Gas-Droplet-Fueled Detonations with Eulerian-Lagrangian Particle-Trace Model

In the Eulerian-Lagrangian Particle-Trace model it assumed that both droplet phase and gas phase are the continuous and homogeneous medium. The gas phase is governed by Eulerian Eq. (1). However, droplet phase is consisted of particles system and all droplets are traced by using Lagrangian method. Each particle in droplet phase is governed by Lagrangian Eq. (3).

The detonations in liquid  $C_{10}H_{22}$ - $O_2$ /air systems with different fuel droplet radii and equivalence ratios ( $\Phi$ ) have been simulated. Initial pressure and temperature of the mixtures are 1 atm and 298 K, respectively. Detonation wave is generated by igniting in the left with a high initial pressure and temperature as 10 atm and 2980 K, respectively. The other computing parameters are given as below:  $\lambda=0.1 \text{ W}\cdot\text{K}^{-1}\cdot\text{m}^{-1}$ ,  $\rho_f=730 \text{ kg/m}^3$ ,  $\mu=2.07\times 10^{-5} \text{ Pa}\cdot\text{s}$ ,  $\mu_f=3.5\times 10^{-4} \text{ Pa}\cdot\text{s}$ ,  $C_v=2.1\times 10^3 \text{ J}\cdot\text{kg}^{-1}\cdot\text{K}^{-1}$ ,  $P_f=0.74$ . In the present simulations, the velocity and temperature of the droplets are set to 0 if the radii of the droplets are decreased to 0.

Tang and Nicholls et al. [18] has systematically studied the detonations in a  $C_{10}H_{22}$  spray with 200  $\mu\text{m}$  radius droplets in air and oxygen using a vertical shock tube. In order to verify the accuracy of the present model, the detonations in a  $C_{10}H_{22}$  spray with 200  $\mu\text{m}$  radius droplets in air and oxygen have been simulated by using Eulerian-Lagrangian Particle-Trace model. The numerical results are compared with theoretical prediction values and experimental data mentioned above. Fig. 6 (a) and (b) show that calculated detonation velocities in our simulation is consistent with the experimental data in trends. Just the calculated results are higher than experimental data.

Meanwhile, we can also find that all theoretical prediction values are agree well with experiment data for mixtures with lean fuel. However, it is worth noting that, for mixtures with rich fuel, all the theoretical prediction values are contrary with experimental value in trends.

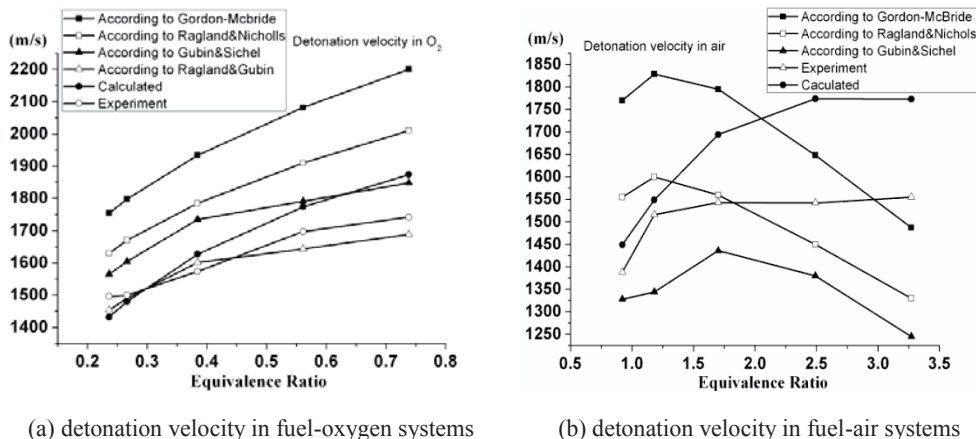


Fig. 6. Comparison of detonation velocity in fuel-oxygen/air systems derived by different methods

Fig. 7 shows the comparison of calculated detonation velocities with C-J theory for all gaseous mixtures. It can be seen that the detonation velocities in O<sub>2</sub> has a similar trend as that in air. Just the detonation velocities in O<sub>2</sub> is higher than that in air.

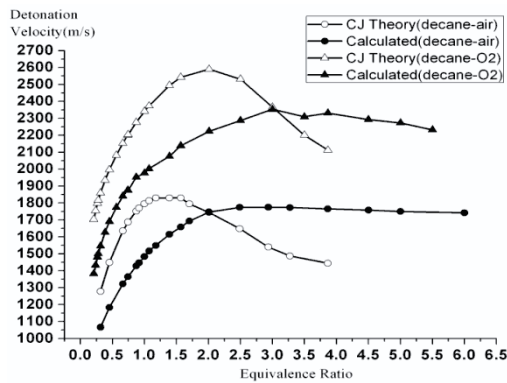


Fig. 7. Comparison of calculated detonation velocity with C-J theory for all gaseous mixtures

### 5.2 Gas-Droplet-Fueled Detonations with the Eulerian Two-Fluid Model

In order to compare the numerical results obtained with using the Eulerian-Lagrangian Particle-Trace model, we simulated numerically also the Gas-Droplet-Fueled Detonations with the Eulerian Two-Fluid Model.

In the Eulerian Two-Fluid Model it assumed that both droplet phase and gas phase are the continuous and homogeneous medium. The governing equations of gas phase and droplet phase are both Eq. (1): for the gas phase:  $\mathbf{Q}=(\rho, \rho u, \rho v, E)^T$ ,  $\mathbf{E}=(\rho u, \rho u^2+p, \rho uv, (E+p)u)^T$ ,  $\mathbf{F}=(\rho v, \rho uv, \rho v^2+p, (E+p)v)^T$ ,  $\mathbf{S}=(I_d, -F_x+u_d I_d, -F_y+v_d I_d, -(u_d F_x+v_d F_y)+((u_d^2+v_d^2)/2+q_r)I_d)^T$ , for droplet phase:  $\mathbf{Q}=(\rho_d, \rho_d u_d, \rho_d v_d, N)^T$ ,  $\mathbf{E}=(\rho_d u_d, \rho_d u_d^2, \rho_d u_d v_d, Nu)^T$ ,  $\mathbf{F}=(\rho_d v_d, \rho_d u_d v_d, \rho_d v_d^2, N)^T$ ,  $\mathbf{S}=(I_d, -F_x+u_d I_d, -F_y+v_d I_d, 0)^T$ , where  $\rho_d$  is the density of droplet phase,  $u_d$  and  $v_d$  are the velocity components of droplet phase,  $N$  is the droplet numbers per unit volume,  $I_d$  is the density variation by the phase change,  $F_x$  and  $F_y$  are the forces components acting on droplets, the total energy density  $E=p/(\gamma-1)+\rho u^2/2$ . The detail of the reduced reaction mechanism can be found in Ref. [19].

The detonations in liquid C<sub>6</sub>H<sub>14</sub> fuel-air system with different equivalence ratios ( $\Phi$ ) have been simulated. Figure 5 show the detonation velocities of C<sub>6</sub>H<sub>14</sub> fuel at different equivalence ratios by experiments, C-J theory [20, 21] and simulations, respectively. The numerical results are more accurate than the C-J theoretical values and can agree well with the experimental data. However, the C-J theoretical values are higher than that of the experimental data.

From the results mentioned above we can find that the general trend of the detonations velocities obtained with the Eulerian Two-Fluid Model is consistent with that of the Eulerian-Lagrangian Particle-Trace model.

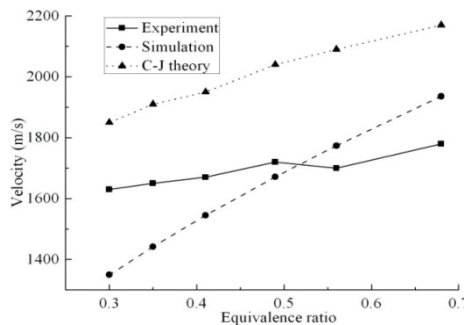


Fig.5 Detonation velocities of C<sub>6</sub>H<sub>14</sub> fuel at different equivalence ratios

## 6 Conclusions

The gas-liquid-fueled two-phase detonation is very complex phenomenon, until now we are still the lack of knowledge of the features for gas-liquid-fueled two-phase detonation. In this paper, The Eulerian Two-Fluid Model and Eulerian-Lagrangian Particle-Trace model have been developed and a new framework of the two-dimensional CE/SE method was proposed and deduced. Numerical simulations of detonations in liquid  $C_6H_{14}$  fuel-air and  $C_{10}H_{22}$  fuel- $O_2$ /air systems have been achieved. Comparison of numerical simulation with theoretical values and experimental data was completed. Compared results indicate that our simulating results agree well with experimental data in trends. Numerical results obtained by using Eulerian-Lagrangian Particle-Trace model are more accurate than that obtained with Eulerian Two-Fluid Model. However the general trend of the detonations velocities obtained with the Eulerian Two-Fluid Model is consistent with that of the Eulerian-Lagrangian Particle-Trace model.

It is proved that the two models and an improved CE/SE method we proposed above can be successful to simulate gas-liquid-fueled two-phase detonation. Our improved CE/SE scheme has the features of high resolution, simple form and robustness.

## References

- [1] Fickett W, Davis W.C, Detonation: Theory & Experiment, Berkeley CA: University of California Press, (1979).
- [2] John H.S. Lee, The Detonation Phenomenon, Cambridge University Press, (2008).
- [3] Charles C Mader, Numerical Modeling of Detonations (LS Series in Basic and Applied Science), University of California Press, (1979).
- [4] Charles C Mader, Recent Advances in Numerical Modeling of Detonations, Propellants, Explosives, Pyrotechnics 11(6) (1986) 163–166.
- [5] Charles C Mader, Numerical Modeling of Explosive & propellants (Third Editions) CRC Press, (2007).
- [6] Dabora E. K., E. K. Weinberger E. K., Present Status of Detonations in Two-Phase Systems, Acta. Astronaut. 1 (3-4) (1974) 361-372.
- [7] Burcat A., Eidelman S., Evolution of a Detonation Wave in a Cloud of Fuel Droplets II. Influence of Fuel Droplets, AIAA J. 18 (10) (1980) 1233-1236.
- [8] Ranger A. A., Nicholls J. A., Aerodynamic Shattering of Liquid Drops, AIAA Journal. 7 (2) (1969) 285-290.
- [9] Eidelman S., Burcat A., Evolution of a Detonation Wave in a Cloud of Fuel Droplet: Part I. Influence of Igniting Explosion, AIAA J. 18 (9) (1980) 1103-1109.
- [10] Westbrook C. K., Dryer F. L., Simplified Reaction Mechanisms for the Oxidation of Hydrocarbon, Combust. Sci. Technol. 27 (1981) 31-43.
- [11] Kiehne T. M., Matthews R. D., et al, An Eight Step Kinetics Mechanism for High Temperature Propane Flames, Combust. Sci. Technol. 54 (1987) 1-23.
- [12] S.C. Chang S.C., The Method of Space-Time Conservation Element and Solution Element-A New Approach for Solving the Navier-Stokes and Euler Equations, J. Comput. Phys. 119 (2) (1995) 295-324.
- [13] Chang S. C., Wang X. Y., Chow C. Y., The Space-Time Conservation Element and Solution



- Element Method: A New High-Resolution and Genuinely Multidimensional Paradigm for Solving Conservation Laws, *J. Comput. Phys.* 156 (1) (1999) 89-136.
- [14] Wang G., Zhang D. L., Liu K. X., An Improved CE/SE Scheme and Its Application to Detonation Propagation, *Chin. Phys. Lett.* 24 (2007) 3563-3566.
- [15] Shiro T., Toshi F., Numerical Simulation on the Establishment of Gaseous Detonation, *Progress in Astronautics and Aeronautics*, **94** (1984) 186-200.
- [16] Wang G., Zhang D. L., Liu K. X., Numerical Study on critical Wedge Angle of Cellular Detonation Reflections, *Chin. Phys. Lett.* 27 (2010) 024701.
- [17] C. M. Guo, D. L. Zhang, W. Xie, The Mach Reflection of a Detonation Based on Soot Track Measurements, *Combustion and Flame*, **127** (2001) 2051-2058.
- [18] Tang M. J., Nicholls J. A., Sichel M., Lin Z. C., The Direct Initiation of Detonation in Decane-Air and Decane-Oxygen Sprays, Gas dynamics laboratories, report No. UM-018404-1, October 1983.
- [19] Wang T.S., Thermophysics characterization of kerosene combustion, AIAA 2000-2511, 2000.
- [20] E.K. Dabora E.K., Ragland K.W., Nicholls J.A., A study of heterogeneous detonations, *Astronautica Acta* 12 (1966) 9-16.
- [21] Roy G.D., Frolov S.M., Borisov A.A., Netzer D.W., Pulse detonation propulsion: challenges, current status, and future perspective, *Progress in Energy and Combustion Science* 30 (2004) 545-672.

## **A dual-reciprocity boundary element method for axisymmetric thermoelastodynamic deformations in functionally graded solids**

**\*W. T. Ang and B. I. Yun**

Division of Engineering Mechanics, School of Mechanical and Aerospace Engineering, Nanyang Technological University, Singapore.

\*Corresponding author: wtang@pmail.ntu.edu.sg

### **Abstract**

A dual-reciprocity boundary element method is outlined for solving a class of initial-boundary value problems concerning axisymmetric thermoelastodynamic deformations in functionally graded materials. The time derivatives of the temperature and the displacement, which appear in the governing partial differential equations, are suppressed by using the Laplace transformation technique. In the Laplace transform domain, the problem under consideration is formulated in terms of integral equations which contain both boundary integrals and domain integrals. The dual-reciprocity method is used together with suitably constructed interpolating functions to reduce the domain integrals approximately into boundary integrals. The problem under consideration is eventually reduced to linear algebraic equations which may be solved for the numerical values of the Laplace transforms of the temperature and the displacements at selected points in space. The temperature and the displacement in the physical time domain are approximately recovered by using a numerical method for inverting Laplace transforms. To check that the numerical procedure presented is valid, it is applied to solve a specific test problem which has a closed-form analytic solution.

**Keywords:** Boundary element method, Dual-reciprocity method, Interpolating functions, Laplace transformation, Axisymmetric thermoelasticity, Functionally graded materials.

### **Introduction**

In recent years, there has been considerable interest in the analysis of axisymmetric materials possessing material properties that are graded continuously along the axial and radial directions. For example, Clements and Kusuma (2011) studied the axisymmetric deformation of an elastic half space having elastic moduli that vary as a quadratic function of the axial coordinate; Matysiak, Kulchytsky-Zhyhailo and Perkowski (2011) considered the Reissner-Sagoci problem for a homogeneous layer bonded to an elastic half space with a shear modulus that varies axially in accordance with a simple power law; and Keles and Tutuncu (2011) calculated the dynamic displacement and stress fields in hollow cylinders and spheres with material properties that are functionally graded along the axial direction by a simple power law.

In the present paper, the dual-reciprocity boundary element approach and the interpolating functions proposed in Yun and Ang (2012) for solving an axisymmetric thermoelastostatic problem involving functionally graded materials is extended to thermoelastodynamic deformations. The material properties vary with the axial and radial coordinates following sufficiently smooth functions in general forms.

It may be of interest to note that a boundary element solution of the corresponding two-dimensional thermoelastodynamic problem for functionally graded solids may be found in a very recent paper by Ekhlov. Khay, Zhang, Sladek and Sladek (2012).

### Basic equations of axisymmetric thermoelastodynamics

With reference to the cylindrical polar coordinates  $r$ ,  $\theta$  and  $z$ , the temperature  $T$  and the displacement  $\underline{\mathbf{u}}$  in an isotropic solid that is symmetrical about the  $z$  axis is independent of  $\theta$  and the only non-zero components of the displacement  $\underline{\mathbf{u}}$  are given by  $u_r$  and  $u_z$ . If the material properties of the solid are radially and axially graded using sufficiently smooth functions of  $r$  and  $z$ , the governing partial differential equations of axisymmetric thermoelastodynamics are given by

$$\underline{\nabla} \cdot (\kappa \underline{\nabla} T) + Q = \beta T_0 \frac{\partial}{\partial t} \left[ \frac{\partial u_r}{\partial r} + \frac{u_r}{r} + \frac{\partial u_z}{\partial z} \right] + \rho c \frac{\partial T}{\partial t}, \quad (1)$$

$$\begin{aligned} & \nabla_{\text{axis}}^2 u_r - \frac{u_r}{r^2} + \frac{1}{1-2\nu} \frac{\partial}{\partial r} \left( \frac{\partial u_r}{\partial r} + \frac{u_r}{r} + \frac{\partial u_z}{\partial z} \right) \\ &= \frac{1}{\mu} \left\{ \beta \frac{\partial T}{\partial r} + \frac{\partial \beta}{\partial r} (T - T_0) - F_r - \frac{\partial \mu}{\partial z} \left( \frac{\partial u_r}{\partial z} + \frac{\partial u_z}{\partial r} \right) \right. \\ & \quad \left. - 2 \frac{\partial \mu}{\partial r} \left[ \frac{\partial u_r}{\partial r} + \frac{\nu}{1-2\nu} \left( \frac{\partial u_r}{\partial r} + \frac{u_r}{r} + \frac{\partial u_z}{\partial z} \right) \right] + \rho \frac{\partial^2 u_r}{\partial t^2} \right\}, \end{aligned} \quad (2)$$

$$\begin{aligned} & \nabla_{\text{axis}}^2 u_z + \frac{1}{1-2\nu} \frac{\partial}{\partial z} \left( \frac{\partial u_r}{\partial r} + \frac{u_r}{r} + \frac{\partial u_z}{\partial z} \right) \\ &= \frac{1}{\mu} \left\{ \beta \frac{\partial T}{\partial z} + \frac{\partial \beta}{\partial z} (T - T_0) - F_z - \frac{\partial \mu}{\partial r} \left( \frac{\partial u_r}{\partial z} + \frac{\partial u_z}{\partial r} \right) \right. \\ & \quad \left. - 2 \frac{\partial \mu}{\partial z} \left[ \frac{\partial u_z}{\partial z} + \frac{\nu}{1-2\nu} \left( \frac{\partial u_r}{\partial r} + \frac{u_r}{r} + \frac{\partial u_z}{\partial z} \right) \right] + \rho \frac{\partial^2 u_z}{\partial t^2} \right\}, \end{aligned} \quad (3)$$

where  $\nabla_{\text{axis}}^2 \equiv \frac{\partial^2}{\partial r^2} + \frac{1}{r} \frac{\partial}{\partial r} + \frac{\partial^2}{\partial z^2}$ ,  $t$  is the time coordinate,  $T_0$  is a constant reference temperature at which the body does not experience any thermally induced stress, the coefficients  $\kappa$ ,  $\beta$ ,  $\rho$ ,  $c$ ,  $\nu$  and  $\mu$  are respectively the thermal conductivity, stress-temperature coefficient, density, specific heat capacity, Poisson's ratio and shear modulus of the isotropic body,  $F_r$  and  $F_z$  are respectively the  $r$  and the  $z$  components of the body force, and  $Q$  is the internal heat generation term. Note that  $\kappa$ ,  $\beta$ ,  $\rho$ ,  $c$  and  $\mu$  are, in general, functions of  $r$  and  $z$  and the Poisson's ratio  $\nu$  is assumed to be constant. The body force components  $F_r$  and  $F_z$  and the internal heat generator  $Q$  are, in general, functions of the axisymmetric coordinates  $r$  and  $z$  and the time coordinate  $t$ .

Details on the basic equations of thermoelasticity may be found in Nowacki (1986).

### Boundary-domain integral equations

The governing partial differential equations in (1), (2) and (3) in terms of the boundary-domain integral equations

$$\begin{aligned}
& \gamma(r_0, z_0) \sqrt{\kappa(r_0, z_0)} T(r_0, z_0, t) \\
&= \int_{\Gamma} \left\{ T(r, z, t) [\sqrt{\kappa(r, z)} G_1(r, z; r_0, z_0; n_r, n_z) - \frac{\partial \sqrt{\kappa(r, z)}}{\partial n} G_0(r, z; r_0, z_0)] \right. \\
&\quad \left. - \sqrt{\kappa(r, z)} G_0(r, z; r_0, z_0) q(r, z, t; n_r, n_z) \right\} r ds(r, z) \\
&+ \int_{\Omega} G_0(r, z; r_0, z_0) \left[ -\frac{Q(r, z, t)}{\sqrt{\kappa(r, z)}} + T(r, z, t) \cdot \nabla_{\text{axis}}^2 (\sqrt{\kappa(r, z)}) \right. \\
&\quad \left. + \frac{\rho(r, z) c(r, z)}{\sqrt{\kappa(r, z)}} \frac{\partial T(r, z, t)}{\partial t} \right. \\
&\quad \left. + \frac{\beta(r, z) T_0}{\sqrt{\kappa(r, z)}} \frac{\partial}{\partial t} \left[ \frac{\partial u_r(r, z, t)}{\partial r} + \frac{u_r(r, z, t)}{r} + \frac{\partial u_z(r, z, t)}{\partial z} \right] \right] r dr dz \\
&\quad \text{for } (r_0, z_0) \in \Omega \cup \Gamma,
\end{aligned} \tag{4}$$

and

$$\begin{aligned}
& \gamma(r_0, z_0) u_K(r_0, z_0, t) \\
&= \int_{\Gamma} (\Phi_{JK}(r, z; r_0, z_0) p_J(r, z, t; n_r, n_z) \\
&\quad - \Psi_{JK}(r, z; r_0, z_0; n_r, n_z) u_J(r, z, t)) r ds(r, z) \\
&+ \int_{\Omega} \frac{1}{\mu(r, z)} \Phi_{JK}(r, z; r_0, z_0) \left\{ -\beta(r, z) \frac{\partial}{\partial x_J} [T(r, z, t)] \right. \\
&\quad \left. - \frac{\partial}{\partial x_J} [\beta(r, z)] (T(r, z, t) - T_0) + F_J(r, z, t) \right. \\
&\quad \left. + \frac{\partial}{\partial x_J} [\mu(r, z)] \frac{2\nu}{(1-2\nu)r} [u_r(r, z, t)] \right. \\
&\quad \left. + X_{JN}(r, z) \frac{\partial}{\partial z} [u_N(r, z, t)] + Y_{JN}(r, z) \frac{\partial}{\partial r} [u_N(r, z, t)] \right\} \\
&\quad - \rho(r, z) \frac{\partial^2 u_K(r, z, t)}{\partial t^2} \} r dr dz \\
&\quad \text{for } (r_0, z_0) \in \Omega \cup \Gamma \quad (K = r, z),
\end{aligned} \tag{5}$$

where  $\Omega$  is the solution domain on the  $Orz$  plane,  $\Gamma$  is the boundary of  $\Omega$  (excluding the part that lies on the  $z$  axis),  $n_r$  and  $n_z$  are respectively the  $r$  and  $z$  components of the unit normal outward vector to curve  $\Gamma$  at the point  $(r, z)$ ,  $G_0(r, z; r_0, z_0)$  is the fundamental solution of axisymmetric Laplace's equation,  $G_1(r, z; r_0, z_0; n_r, n_z)$  is the normal derivative of  $G_0(r, z; r_0, z_0)$  along the direction of the vector  $[n_r, n_z]$ , the uppercase Latin subscripts (such as  $K$ ) are assigned values  $r$  and  $z$  and

summation over those values are implied for repeated subscripts,  $\Phi_{JK}(r, z; r_0, z_0)$  is the fundamental solution of the partial differential equations for axisymmetric elastostatics,  $\Psi_{JK}(r, z; r_0, z_0; n_r, n_z)$  is the traction function corresponding to  $\Phi_{JK}(r, z; r_0, z_0)$ , and  $p_J(r, z, t; n_r, n_z)$ ,  $X_{JN}(r, z)$  and  $Y_{JN}(r, z)$  are defined by

$$\begin{aligned} p_r(r, z, t; n_r, n_z) &= 2\left(\frac{\partial u_r}{\partial r} + \frac{\nu}{1-2\nu}\left[\frac{\partial u_r}{\partial r} + \frac{u_r}{r} + \frac{\partial u_z}{\partial z}\right]\right)n_r(r, z) \\ &\quad + \left(\frac{\partial u_r}{\partial z} + \frac{\partial u_z}{\partial r}\right)n_z(r, z), \\ p_z(r, z, t; n_r, n_z) &= \left(\frac{\partial u_r}{\partial z} + \frac{\partial u_z}{\partial r}\right)n_r(r, z) \\ &\quad + 2\left(\frac{\partial u_z}{\partial z} + \frac{\nu}{1-2\nu}\left[\frac{\partial u_r}{\partial r} + \frac{u_r}{r} + \frac{\partial u_z}{\partial z}\right]\right)n_z(r, z), \end{aligned} \quad (6)$$

$$\begin{aligned} X_{rr}(r, z) &= \frac{\partial \mu(r, z)}{\partial z}, \quad X_{rz}(r, z) = \frac{2\nu}{1-2\nu} \frac{\partial \mu(r, z)}{\partial r}, \\ X_{zr}(r, z) &= \frac{\partial \mu(r, z)}{\partial r}, \quad X_{zz}(r, z) = \frac{\partial \mu(r, z)}{\partial z} \frac{2(1-\nu)}{1-2\nu}, \\ Y_{rr}(r, z) &= \frac{\partial \mu(r, z)}{\partial r} \frac{2(1-\nu)}{1-2\nu}, \quad Y_{rz}(r, z) = \frac{\partial \mu(r, z)}{\partial z}, \\ Y_{zr}(r, z) &= \frac{2\nu}{1-2\nu} \frac{\partial \mu(r, z)}{\partial z}, \quad Y_{zz}(r, z) = \frac{\partial \mu(r, z)}{\partial r}. \end{aligned} \quad (7)$$

The functions  $p_J(r, z, t; n_r, n_z)$  are related to the axisymmetric tractions  $t_J(r, z, t; n_r, n_z)$  through

$$\begin{aligned} t_J(r, z, t; n_r, n_z) &= \mu(r, z)p_J(r, z, t; n_r, n_z) \\ &\quad - \beta(r, z)[T(r, z, t) - T_0]\delta_{JL}n_L(r, z), \end{aligned} \quad (8)$$

where  $\delta_{JN}$  is the Kronecker-delta.

The boundary-domain integral equations in (4) and (5) for the corresponding case of axisymmetric thermoelastostatic deformations are given in Yun and Ang (2012) where the details of the functions  $G_0(r, z; r_0, z_0)$ ,  $G_1(r, z; r_0, z_0; n_r, n_z)$ ,  $\Phi_{JK}(r, z; r_0, z_0)$  and  $\Psi_{JK}(r, z; r_0, z_0; n_r, n_z)$  are explicitly written out.

### Dual-reciprocity boundary element method

The dual-reciprocity method in Partridge, Brebbia and Wrobel (1992) may be employed to approximate the domain integrals over  $\Omega$  in the integral equations (4) and (5) in terms of boundary integrals over the curve  $\Gamma$  by using interpolating functions centered about selected collocation

points in  $\Omega \cup \Gamma$ . As in Yun and Ang (2012), the collocating functions centered about the  $n$ -th collocation point, denoted by  $\chi^{(n)}(r, z)$ ,  $\phi^{(n)}(r, z)$ ,  $\chi_{rJ}^{(n)}(r, z)$  and  $\phi_{rJ}^{(n)}(r, z)$ , are assumed to be sufficiently smooth and are required to satisfy the partial differential equations

$$\begin{aligned} \nabla_{\text{axis}}^2 \chi^{(n)}(r, z) &= \phi^{(n)}(r, z), \\ \nabla_{\text{axis}}^2 \chi_{rJ}^{(n)}(r, z) - \frac{\chi_{rJ}^{(n)}(r, z)}{r^2} \\ &+ \frac{1}{1-2\nu} \frac{\partial}{\partial r} \left( \frac{\partial}{\partial r} [\chi_{rJ}^{(n)}(r, z)] \right) + \frac{\chi_{rJ}^{(n)}(r, z)}{r} + \frac{\partial}{\partial z} [\chi_{zJ}^{(n)}(r, z)] = \phi_{rJ}^{(n)}(r, z), \\ \nabla_{\text{axis}}^2 \chi_{zJ}^{(n)}(r, z) \\ &+ \frac{1}{1-2\nu} \frac{\partial}{\partial z} \left( \frac{\partial}{\partial r} [\chi_{rJ}^{(n)}(r, z)] \right) + \frac{\chi_{rJ}^{(n)}(r, z)}{r} + \frac{\partial}{\partial z} [\chi_{zJ}^{(n)}(r, z)] = \phi_{zJ}^{(n)}(r, z). \end{aligned}$$

(9)

In Agnantiaris, Polyzos and Beskos (2001) and Wang, Mattheij and ter Morsche (2003), the interpolating functions  $\chi^{(n)}(r, z)$ ,  $\phi^{(n)}(r, z)$ ,  $\chi_{rJ}^{(n)}(r, z)$  and  $\phi_{rJ}^{(n)}(r, z)$  are constructed by integrating axially selected radial basis functions in three-dimensional space. The interpolating functions thus constructed are well defined at  $r = 0$ , but they are in highly complicated forms and are expressed in terms of special functions given by the elliptic integrals.

To construct interpolating functions expressed in terms of relatively simple elementary functions, one may choose  $\chi^{(n)}(r, z)$  and  $\chi_{rJ}^{(n)}(r, z)$  to be sufficiently smooth functions of  $\sqrt{(r-r_0^{(n)})^2 + (z-z_0^{(n)})^2}$ , where  $(r_0^{(n)}, z_0^{(n)})$  is the  $n$ -th collocation point, and determine  $\phi^{(n)}(r, z)$  and  $\phi_{rJ}^{(n)}(r, z)$  using (9). Nevertheless, the interpolating functions  $\phi^{(n)}(r, z)$  and  $\phi_{rJ}^{(n)}(r, z)$  constructed in this manner are not well defined at  $r = 0$ . This poses a problem if the  $z$  axis is part of the solution domain  $\Omega$ . In Yun and Ang (2012), the singular behaviors of  $\phi^{(n)}(r, z)$  and  $\phi_{rJ}^{(n)}(r, z)$  at  $r = 0$  are removed by modifying  $\chi^{(n)}(r, z)$  and  $\chi_{rJ}^{(n)}(r, z)$  in such a way that  $\chi^{(n)}(r, z)$  and  $\chi_{rJ}^{(n)}(r, z)$  behave as  $O(r^2)$  for small  $r$ . Specifically,  $\chi^{(n)}(r, z)$  and  $\chi_{rJ}^{(n)}(r, z)$  are taken to be

$$\begin{aligned} \chi^{(n)}(r, z) &= \frac{1}{9} \{ [\sigma(r, z; r_0^{(n)}, z_0^{(n)})]^3 + [\sigma(r, z; -r_0^{(n)}, z_0^{(n)})]^3 \}, \\ \chi_{rr}^{(n)}(r, z) &= \chi^{(n)}(r, z) - \frac{2}{9} [\sigma(0, z; r_0^{(n)}, z_0^{(n)})]^3, \\ \chi_{zr}^{(n)}(r, z) &= \chi_{rz}^{(n)}(r, z) = 0, \quad \chi_{zz}^{(n)}(r, z) = \chi^{(n)}(r, z), \end{aligned} \tag{10}$$

where  $\sigma(r, z, r_0, z_0) = \sqrt{(r-r_0)^2 + (z-z_0)^2}$ .

For a numerical procedure for solving initial-boundary value problems governed by (1), (2) and (3), we apply the Laplace transformation on the boundary-domain integral equations (4) and (5) to suppress the time derivatives of  $T$ ,  $u_r$  and  $u_z$ , use the dual-reciprocity method together with the

interpolating functions constructed using (10) to approximate the domain integrals in the resulting boundary-domain integral equations in terms of boundary integrals, and discretize the boundary  $\Gamma$  into elements to develop a boundary element procedure for finding the temperature and the displacement in the Laplace transform domain. The temperature and the displacement in the physical domain may be recovered by using a numerical method for inverting Laplace transforms.

### Test problem

The coefficients of the partial differential equations in (1), (2) and (3) are chosen to be given by  $\rho = r^2 + z^2$ ,  $c = 2$ ,  $\beta = r^2 + z^2$ ,  $\mu = r + z$ ,  $\kappa = (r^2 + z^2)^2$ ,  $\nu = 3/10$ , and

$$\begin{aligned}
 Q(r, z, t) &= -\frac{r^2 + z^2}{r} \{ \sin(t)[16r^3z - r^2 + 4r + 4rz^3 + z^2] \\
 &\quad - 2r^3z \cos(t) + 16r^3z + 4rz^3 \}, \\
 F_r(r, z, t) &= -\frac{1}{2r^2} \{ \cos(t)[4r^5 + 2r^4z^2 + 4r^3z^2 - 4r^3 \\
 &\quad + 2r^2z^2 + 20r^2 + r^2z - 4rz^2 - 7z^3] \\
 &\quad + (1 + \sin(t))[-8r^5z - 4r^3z^3] + 4r^3 \}, \\
 F_z(r, z, t) &= \frac{1}{2r^2} \{ \cos(t)[2r^4z - 4r^3 + 7r^2 + 2r^2z^3 \\
 &\quad - 10rz - 4rz^2 - 12r - 11z^2] \\
 &\quad + (1 + \sin(t))[2r^5 + 6r^3z^2] - 4rz \}.
 \end{aligned}$$

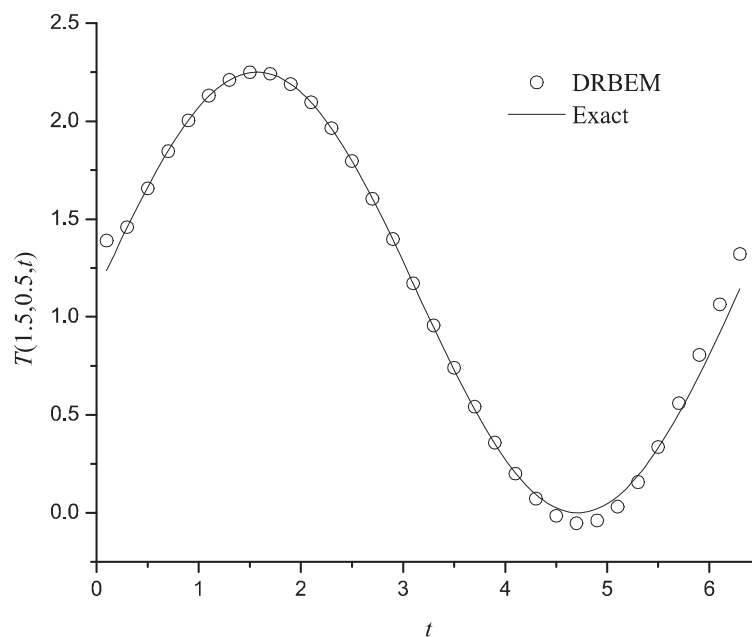
It is easy to check that a solution of the partial differential equations is given by

$$\begin{aligned}
 T(r, z, t) &= r^2z(\sin(t) + 1), \\
 u_r(r, z, t) &= (z^2 + 2r)\cos(t), \\
 u_z(r, z, t) &= (2 - rz)\cos(t).
 \end{aligned} \tag{11}$$

For a specific initial-boundary value problem as a test problem, take the solution domain  $\Omega$  to be  $1 < r < 2$ ,  $0 < z < 1$ , which is a rectangular region on the  $Orz$  plane, and use the solution in (11) to generate the following initial and boundary data – (a) initial values of  $T$ ,  $u_r$ ,  $u_z$ ,  $\frac{\partial u_r}{\partial t}$  and  $\frac{\partial u_z}{\partial t}$  at time  $t = 0$  at points  $(r, z)$  in  $\Omega \cup \Gamma$ , (b) boundary values of the displacement  $(u_r, u_z)$  on the entire boundary of  $\Omega$  for time  $t > 0$ , (c) boundary values of  $T$  on the sides of the rectangular region where  $z = 0$  and  $z = 1$  for time  $t > 0$ , and (d) boundary values of  $\frac{\partial T}{\partial r}$  on the sides of the rectangular region where  $r = 1$  and  $r = 2$  for time  $t > 0$ .

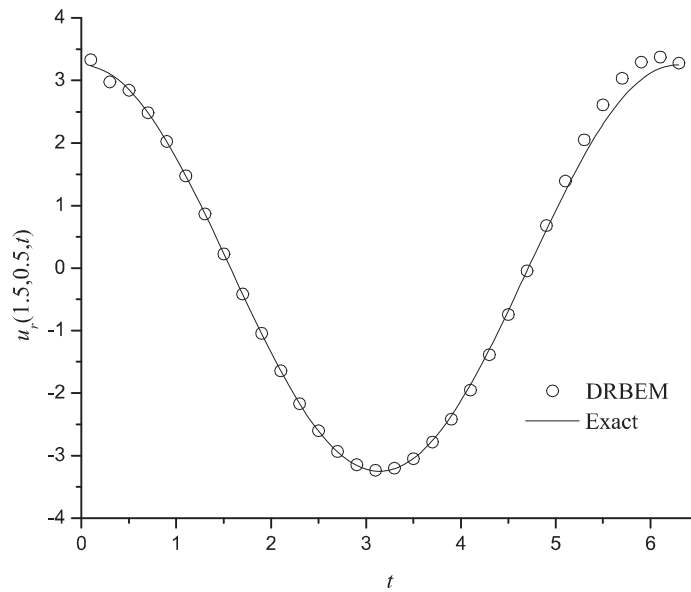
For the boundary element procedure, the sides of the rectangular region are discretized into 80 straight line elements. The Laplace transforms of the temperature, heat flux, displacement and traction on the boundary elements are approximated using discontinuous linear functions. As many as 121 well distributed collocation points in  $\Omega \cup \Gamma$  (including those on the boundary elements) are used in the dual-reciprocity method for converting approximately the domain integrals in the integral formulation of the initial-boundary value problem into boundary integrals. We use the numerical method in Stehfest (1970) to invert the Laplace transforms in order to recover the temperature and the displacement in the physical domain.

Numerical values of  $T$ ,  $u_r$  and  $u_z$  obtained using the dual-reciprocity boundary element method (DRBEM) are plotted against  $t$  ( $0 < t < 6$ ) at  $(r, z) = (1.5, 0.5)$  in Figures 1, 2 and 3 respectively. The numerical values agree well with the analytical solution in (11), showing that the interpolating functions given in (9) and (10) are employed successfully to treat the domain integrals in the boundary-domain integral equations in (4) and (5).

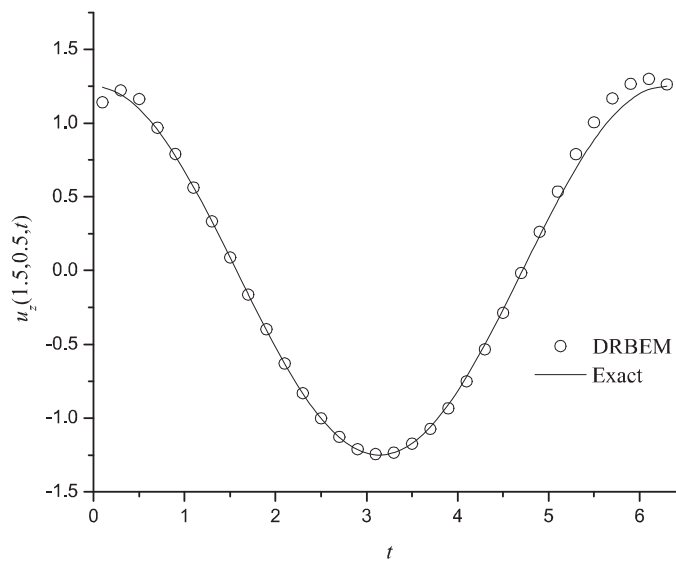


**Figure 1.** A comparison of the numerical and exact  $T$  at  $(r, z) = (1.5, 0.5)$  for  $0 < t < 6$ .





**Figure 2.** A comparison of the numerical and exact  $u_r$  at  $(r, z) = (1.5, 0.5)$  for  $0 < t < 6$ .



**Figure 3.** A comparison of the numerical and exact  $u_z$  at  $(r, z) = (1.5, 0.5)$  for  $0 < t < 6$ .

## References

- Agnantiaris, J. P., Polyzos, D. and Beskos, D. E. (2001), Free vibration analysis of non-axisymmetric and axisymmetric structures by the dual-reciprocity BEM, *Engineering Analysis with Boundary Elements*, 25, pp. 713-723.
- Clements, D. L. and Kusuma, J. (2011), Axisymmetric loading of a class of inhomogeneous transversely isotropic half-spaces with quadratic elastic moduli, *Quarterly Journal of Mechanics and Applied Mathematics*, 64, pp. 25-46.
- Ekhlakov A. V., Khay, ). M., Zhang Ch., Sladek, J. and Sladek V. (2012), A DBEM for transient thermoelastic crack problems in functionally graded materials under thermal shock, *Computational Material Science*, 57, pp. 30-37.

- Keles, I. and Tutuncu, N. (2011), Exact analysis of axisymmetric dynamic response of functionally graded cylinders (or disks) and spheres, *Journal of Applied Mechanics*, 78, 061014.1-7.
- Matysiak, S. J., Kulchytsky-Zyhailo, R. and Perkowski, D. M. (2011), Reissner-Sagoci problem for a homogeneous coating on a functionally graded half-space, *Mechanics Research Communications*, 38, pp. 320-325.
- Nowacki, W. (1986), *Thermoelasticity*, Warsaw and Pergamon Press, Oxford.
- Partridge, P. W., Brebbia, C. A. and Wrobel, L. C. (1992), *The Dual Reciprocity Boundary Element Method*, Computational Mechanics Publications, London.
- Stehfest, H. (1970), Numerical inversion of the Laplace transform, *Communications of ACM*, 13, pp. 47-49 (see also p624).
- Wang, K., Mattheij, R. M. M. and ter Morsche, H. G. (2003), Alternative DRM formulations, *Engineering Analysis with Boundary Elements*, 27, pp. 175-181.
- Yun, B. I. and Ang, W. T. (2012), A dual-reciprocity boundary element method for axisymmetric thermoelastostatic analysis of nonhomogeneous materials, *Engineering Analysis with Boundary Elements*, 36, pp. 1776-1786.

# OPTIMIZATION OF THE GAS FLOW IN A GEM CHAMBER AND DEVELOPMENT OF THE GEM FOIL STRETCHER

Francesco NOTO<sup>1,2</sup>, Valerie DE SMET<sup>5</sup>, Vincenzo BELLINI<sup>1,2</sup>, Evaristo CISBANI<sup>3,4</sup>, Francesco LIBRIZZI<sup>2</sup>, Francesco MAMMOLITI<sup>1,2</sup>, Maria Concetta SUTERA<sup>2</sup>

<sup>1</sup>*Dipartimento di Fisica ed Astronomia, Università di Catania, via Santa Sofia 64, 95123 Catania, Italy*

<sup>2</sup>*INFN - Sezione di Catania, via Santa Sofia 64, I-95123 Catania, Italy*

<sup>3</sup>*INFN - Sezione di Roma – Sanità group, P.le Aldo Moro, 2 I-00185 Roma, Italy*

<sup>4</sup>*Istituto Superiore di Sanità, viale Regina Elena 299, I-00161 Roma, Italy*

<sup>5</sup>*Haute Ecole Paul - Henri Spaak, ISIB, Brussels, Belgium*

Corresponding Author: Francesco Noto, Dipartimento di Fisica e Astronomia, Università di Catania, Via Santa Sofia 64, I-95123 Catania, Italy. Email address: francesco.noto@ct.infn.it

The Gas Electron Multiplier (GEM) technology has been proven to tolerate rate larger than 50 MHz/cm<sup>2</sup> without noticeable aging and to provide sub millimeter resolution on working chambers up to 45x45 cm<sup>2</sup> [1]. A new GEM-based tracker is under development for the Hall A upgrade at Jefferson Lab. The chambers of the tracker have been designed in a modular way: each chamber consists of 3 adjacent GEM modules, with an active area of 40x50 cm<sup>2</sup> each [2]. We optimized the gas flow inside the GEM module volume, using the COMSOL physics simulator framework; the COMSOL-based analysis includes the design of the inlet and outlet pipes and the maximization of the uniformity of the gas flow.

We have defined the procedures for the assembling of the GEM modules and designed a mechanical system (TENDIGEM) that will be used to stretch the GEM foils at the proper tension (few kg/cm); the TENDIGEM is based on the original design developed at LNF [3].

**Keywords:** GEM foil, TENDIGEM, Fluid dynamic, Simulation, SBS Tracker

## 1. Introduction

In late 2014 the CEBAF electron beam at Jefferson Lab is expected to complete the energy upgrade to 12 GeV. JLab will become one of the most important experimental facilities for the study of the nucleon structure, in terms of form factors, transverse momentum distributions of the constituent partons and generalized parton distributions. New experimental equipment is under development for an optimal exploitation of the full potentiality of the new beam; a new hybrid tracker able to operate with luminosity as large as 10<sup>39</sup> s<sup>-1</sup>cm<sup>-2</sup> is part of this development. The tracker will provide an average single hit resolution better than 80 μm and an event readout rate of about 20 kHz.

The tracker is made of two types of detectors: 40x50 cm<sup>2</sup> GEM modules and 10x20

cm<sup>2</sup> silicon microstrips. The former will be used as basic building blocks of large (~0.60 m<sup>2</sup>) chambers that will seat behind a momentum analyzing spectrometer, while the latter will be positioned close to the scattering chamber, thus extending considerably the useful tracking arm. The hybrid design is aiming at a balance between cost and performance. The modular design of the GEM chambers (up to 6) intends to maximize reconfiguration on the existing or planned spectrometers of Hall A; each 40x50 cm<sup>2</sup> GEM module has its own high voltage supply and gas inlet/outlet as well as front-end electronics. Mechanics and gas flow have been investigated and optimized by Finite Element Analysis. The single module is made of 3 GEM foils and double layer x/y strip readout with 400 μm strip pitch. The modules are connected in a way to minimize the dead area and are supported by an external service frame.

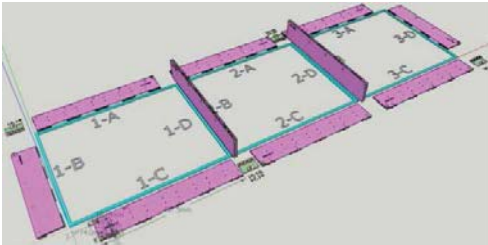


Figure 1: The triple GEM

## 2. Gas Input design

The role played by the gas mixture in the GEM detector is important. The avalanche process creates ions that pollute the gas degrading the performance of the detector. Thus the gas has to be constantly and relatively quickly replaced. The GEM structure being very thin, gas inlet and outlet pipes are limited in diameter. Hereafter we present a calculation of the minimal diameter of the pipes as a function of the rate of renewing. The characteristic number that measures the ratio between inertial and viscous forces is the Reynolds number:

$$Re := \frac{\rho V D}{\mu} \quad (1)$$

where  $\rho$  is the density (expressed in  $\text{kg/m}^3$ ),  $V$  is the gas velocity (expressed in  $\text{m/s}$ ),  $D$  is the diameter of the pipe (in  $\text{m}$ ) and  $\mu$  the dynamic viscosity of the gas (in  $\text{Pa}\cdot\text{s}$ ). If we denote by  $\Phi = \pi D^2 V / 4$  the flux of the gas (expressed in  $\text{m}^3/\text{s}$ ), we obtain that, at fixed Reynolds number, the diameter of the pipe is given by:

$$D = \frac{4}{\pi} \frac{\rho \Phi}{Re \mu} \quad (2)$$

To insure a laminar flow, the Reynolds number must not be greater than about 2300. With a mixture of  $\text{Ar}/\text{CO}_2$  (70/30), and a renewing of the gas of 10 times per hour, we find for the 10 cm x 10 cm test detector (using  $\rho = 1.7 \text{ kg/m}^3$  and  $\mu = 2 \times 10^{-5} \text{ Pa}\cdot\text{s}$  and a thickness of 9 mm) a minimum diameter of  $3 \times 10^{-4} \text{ mm}$ .

The diameter will vary linearly with the dimensions of the detector and with the rate of refreshing of the gas, and in inverse proportion to the viscosity of the gas. It will also depend on the temperature as the density decreases as  $T^{-1}$ , while to first approximation the dependence of the viscosity on the temperature is given by the Sutherland empirical law:

$$\mu = \mu_0 \frac{T_0 + C}{T + C} (T/T_0)^{3/2} \quad (3)$$

Here  $C$  is the Sutherland's constant, which depends on the nature of the gas and is of the order of 200 ( $C_{\text{Ar}}=144$ ;  $C_{\text{CO}_2}=240$ ). To first approximation the computed diameter will behave like  $(T_0/T)^{5/2}$  as a function of the temperature, and thus will vary by a factor of the order of 0.9 between 15 °C and 25 °C. Another parameter that must be taken into account is the dependence of the flux on the diameter of the pipe,  $\Phi \propto D^4$  in laminar regime, but this effect can be compensated by adjusting the pressure gradient. This dependence of the flux on the diameter of the pipes justifies its optimization.

## 2. Simulation

Permanent gas flow in a module is required to provide the expected gain and signal timing, to evacuate gas that contaminates the mixture and to prevent fast aging of the detector due to radiation-induced chemical reactions in the gas. The gas flow should be spatially uniform in order to guarantee a homogeneous and stable detector response. Therefore, the goal of our study was to optimize the design of the frame separating two GEM foils in order to obtain the optimal gas flow uniformity over the active area of the module.

## 3. Use of Finite Element Method

The Finite Element Method (FEM) approximates a Partial Differential Equations problem with a discretization of the original problem based on a mesh, which is a partition of the geometry into small units of simple shape called mesh elements. The FEM method looks for a solution in the form of a piecewise polynomial function, each mesh element defining the domain for one "piece" of it. Such a piecewise polynomial function will be expressed as a linear combination of a finite set of predefined basis functions. Let us consider for example a 2-dimensional problem with a single dependent variable  $p(x,y)$ . We would like to solve this problem based on a mesh with quadratic triangular elements. The expression "quadratic elements" refers to the fact that on each mesh element the sought piecewise polynomial function  $p^*(x,y)$  is at most a quadratic polynomial. In this case, the solution is expressed as:

$$p(x, y) \cong p^*(x) = \sum_{i=1}^n p_i \varphi_i(x, y) \quad (4)$$

where  $i$  refers to a node of the mesh,  $p_i$  are the degrees of freedom,  $\varphi_i(x, y)$  are the basis functions and  $n$  is the total number of nodes, under the assumption that each triangle of the mesh possesses six nodes: three corner nodes and three mid-side nodes [4]. A basis function  $\varphi_i(x, y)$  has here the restriction to be a polynomial of degree at most 2 such that its value is 1 at node  $i$  and 0 at all other nodes [5]. The degree of freedom  $p_i$  is thus the value of  $p^*(x, y)$  at node  $i$ . The definition of the basis function associated to each node of the mesh can be derived using for example a general method introduced by Silvester in 1969 [6].

### 3.1. Simulations development

All the details on the selection of the physical parameters in the design of the GEM are taken from ref. [5].

The geometry of the frame separating two GEM foils has been constructed in 2 dimensions, whereas the third dimension, which corresponds to the gas film thickness, has been inserted as a parameter of the physical model. Actually, two separate Thin-Film Flow models have been defined in order to account for the two different film thicknesses in the problem: 2 mm in between two GEM foils and 1 mm inside the openings of the frame's spacers and inside the inlets and the outlets.

As far as the inlets and outlets are concerned, it has not been possible to define their exact configuration, because this requires to use a physical model that can be applied to a geometry constructed in 3 dimensions. Therefore, we have defined inlets and outlets as 8x5 mm rectangular zones with a uniform film thickness of 1 mm.

Typical flow in gas detectors corresponds to  $\frac{1}{3}$  volume renewals per hour. If the 3 GEM modules of one chamber are connected to each other in series with respect to the gas flow, the total gas volume for a 2 mm thick "floor" of the chamber is approximately  $3 \cdot 0.4 \cdot 0.5 \cdot 0.002 = 0.0012 \text{ m}^3$ , so  $\frac{1}{3}$  volume renewals per hour correspond in our case to a gas flow between 20  $\text{cm}^3/\text{min}$  and 60  $\text{cm}^3/\text{min}$ . Nearly all our simulations have therefore been made with a total flow of 60  $\text{cm}^3/\text{min}$  imposed at the inlets. In a frame with 2 inlets, each having a cross-section

of 8  $\text{mm}^2$ , the mean entrance velocity is then  $U_e = 0.0625 \text{ m/s}$ . If one wants to evaluate whether such a stationary gas flow is incompressible or not, the mean velocity should be compared to the speed of sound in the same medium [4]. For an ideal gas, the speed of sound is given by the following formula:

$$U_s = \sqrt{\frac{\gamma RT}{M}} \quad (5)$$

where  $\gamma$  is the adiabatic constant of the gas,  $R = 8.314 \text{ J}/(\text{mol} \cdot \text{K})$  is the universal gas constant,  $T$  is the temperature and  $M$  is the molecular mass of the gas. In our case, we consider that  $\gamma \approx 5/3$  since argon is the main component of the gas mixture;  $T = 293 \text{ }^\circ\text{K}$  and  $M \approx 0.70 \cdot 0.03995 + 0.30 \cdot 0.04401 = 0.04117 \text{ kg/mol}$ . For the speed of sound, we thus obtain  $U_s \approx 314 \text{ m/s} \gg U_e = 0.0625 \text{ m/s}$ . Therefore, it has been assumed that the gas flow is incompressible and a constant value for the density  $\rho$  has been used. Somehow, it is useful to get rid of the density's dependence on the pressure. The ambient pressure  $p_a$  has been set to 1 atm. However, the solution for the velocity field does not depend on this value. The obtained velocity field does not depend either on the value of the constant density  $\rho$  which, for a Ar-CO<sub>2</sub> (70/30) mixture at 20 °C and 1 atm, can be computed using the densities at 20 °C and 1 atm of respectively argon and carbon dioxide ( $\rho_{\text{Ar}} = 1.7837 \text{ kg/m}^3$  and  $\rho_{\text{CO}_2} = 1.9770 \text{ kg/m}^3$ ), with the following formula:

$$\rho = (0,30 \cdot \rho_{\text{CO}_2} + 0,70 \rho_{\text{Ar}}) = 1,8417 \frac{\text{kg}}{\text{m}^3} \quad (6)$$

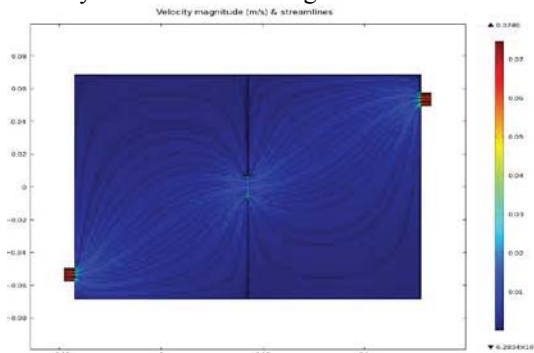
To compute the dynamic viscosity at 20 °C and 1 atm of the gas mixture, we have used the Reichenberg's formula [7] with parameters from literature and we have obtained:

$$\mu = 1.9696 \cdot 10^{-5} \text{ Pa} \cdot \text{s} \quad (7)$$

In the two defined Thin-Film Flow Models, instead of considering two moving solid structures, we have forced the normal displacements,  $\Delta h_m$  and  $\Delta h_b$ , and the tangential velocities,  $u_m$  and  $u_b$ , of these structures to zero, so that the film thickness  $h$  would remain constant at its initial value  $h_0$ . We have also assumed in the first place that the fluid can be treated as a continuum. Actually, the Knudsen number obtained with our no-slip models was around  $5 \cdot 10^{-5}$ , which is indeed negligible with respect to 0.1. In our case, the ambient pressure  $p_a$  has been set to 1 atm. As boundary conditions:

- We have imposed a uniform perpendicular velocity (e.g. 0.0625 m/s) on the external 8 mm side of the inlets.
- On the external 8 mm side of the outlets, we have forced the additional pressure  $p_f$  to zero.
- “Walls” have been inserted on the sectors of the geometry that represent surfaces of the frame. This imposes the standard wall boundary condition  $\vec{U} = \vec{0}$  on these sectors.

When simulating a system that is quite complex, it’s advisable to start with a strongly simplified geometry and increase progressively the complexity of the model, as one’s understanding of the simulation improves [4]. We have started by simulating a frame with only two sectors, separated by a spacer containing just one opening of length 15 mm. One inlet (with velocity 0.0625 m/s) and one outlet have been defined. The problem has been treated as stationary and a predefined mesh type of COMSOL (“Normal”) has been used, which in our case is made up of 24182 unstructured quadratic triangular elements. The obtained velocity field is shown in Figure 2.



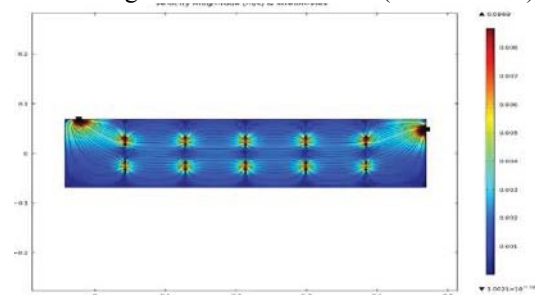
**Figure 2: Velocity magnitude on a linear scale and streamlines of the velocity field obtained in the case of a frame with 2 sectors, 1 inlet at the left and 1 outlet at the right. The two sectors communicate through a central opening of 15 mm.**

In a next step, we have simulated six adjacent sectors of the frame and included two 15 mm openings in each spacer. It has been useful to define a time-dependent model in which the inlet velocity increases smoothly from 0 to 0.0625 m/s. We are however not mainly interested in this evolution and we focus on the results obtained for the final state (Figure 3). In this simulation, we have also tried out a more complex mesh, consisting of a predefined “Fine”

unstructured quadratic triangular mesh in the central regions (133276 elements) and a “Boundary Layer”, made up of parallel rectangular quadratic elements along the borders of the geometry (39252 elements). Note that on Figure 3, the scale has been cut at a tenth of the maximum velocity.

Based on these results, we have tried to modify some aspects of the frame’s design in order to reduce, in number and/or in size, the zones with particularly high or low velocities. The optimization of the frame design has been realized by gradually modifying the simulated geometry and comparing each time the new results with those from previous simulations.

In all our simulations of full-sized frame versions, we have used the time-dependent model but without working with the same type of mesh as in the six-sectors simulation, because of the too large number of elements (over 500000).



**Figure 3: Velocity magnitude on a linear scale and streamlines of the velocity field obtained in the case of a frame with 6 sectors, 1 inlet (left) and 1 outlet (right).**

We have defined another type of customized mesh consisting of three predefined unstructured quadratic triangular mesh types:

- in the inlets and outlets, as well as in a 16 x 10 mm<sup>2</sup> rectangular zone in front of each of them, we have defined a “Finer” (“Extremely fine”) mesh, in the first two (last four) simulations.
- in the central openings we have defined a “Fine” (“Extra fine”) mesh, in the first two (last four) simulations.
- in the rectangles left over in the center of the several frame sectors, we have defined a “Normal” (“Finer”) mesh, in the first two (last four) simulations.

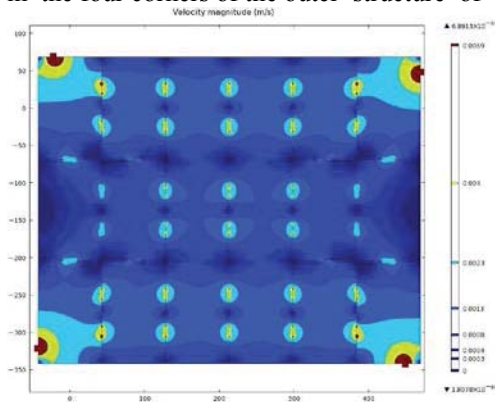
Furthermore we have performed all six simulations using either 15 mm or 20 mm thicknesses for the central openings.

In this way, we have tried to refine our meshes without exceeding 250000 elements. Since the geometry is different in each simulation, in order to assess in some way the precision of our different simulations we have compared for each simulation the inlet and the outlet total fluxes based on the computed velocity field. Since the flow is supposed to be conserved, these fluxes should in theory be equal and, of course, correspond to the initially imposed value (e.g. 60 cm<sup>3</sup>/min).

### 3.1.1 Analysis and results

#### 3.1.1.1 Simulation 1: Full frame in its first prototype version

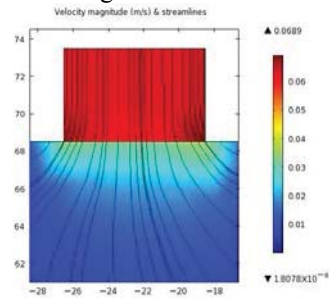
In its first prototype version, the frame separating two GEM foils possesses 18 sectors, 2 inlets and 2 outlets. Two adjacent sectors along the longest side of the module communicate through 2 openings of 15 mm, while two adjacent sectors along the other direction communicate through a single 15 mm opening. In our simulation, the uniform velocity imposed on both inlets is 0.0625 m/s, which corresponds to a total flow of 60 cm<sup>3</sup>/min. Note that the scale has been cut at a tenth of the maximum velocity. A contour plot with logarithmic scale of the velocity magnitude is also given in Figure 4. As expected, the zones with lower velocities are found mainly in corners where spacers cross each other or reach the border of the frame, and in the four corners of the outer structure of the



**Figure 4: Simul. 1 – Contour plot with logarithmic scale of the velocity magnitude obtained in the case of the full frame in its first prototype version.**

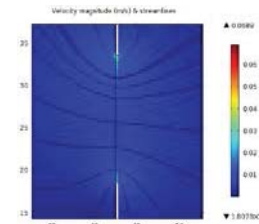
frame. However, our attention has also been drawn towards two large low-flux zones at the

extremities of the central 6-sectors row, which contains no inlets and outlets. For this reason, in our next simulation we included an extra inlet and outlet, placed at the level of this central row. Zones with higher velocities correspond to inlets, outlets and openings in the spacers, especially in the spacers parallel to the shortest side of the module. Figure 5 shows a close-up on one of the inlets. Although our simulation isn't the most appropriate to estimate the actual velocity field in the region of inlets and outlets,



**Figure 5: Simul. 1 – Velocity magnitude on a linear scale and streamlines of the velocity field obtained for one of the two inlets in the first prototype version.**

we can realize from it that the 90 degree angles between an inlet (or outlet) and the borders of sectors are responsible for particularly high velocities, which are in fact also much higher than in the openings of spacers (Figure 6). The maximum velocity computed by the simulation (0.0689 m/s) is indeed found on these edges at the inlets and outlets. Thereupon, we decided also to replace in our next simulation these 90 degrees edges by circular joints of radius 1.5 mm.



**Figure 6: Simul. 1 – Velocity magnitude on a linear scale and streamlines of the velocity field obtained for an opening in a spacer of the full frame in its first prototype version.**

#### 3.1.1.2 Simulation 2: Modifications to the inlet and outlet configuration

In this second simulation, one inlet and one outlet have been added with the aim to improve the uniformity of the gas flow in the central 6-sectors row of the frame. The exact positions of these inlet and outlet have been selected based on the available space in the detector. For all inlets and outlets, the aforementioned circular joints of radius 1.5 mm have also been introduced. The 60 cm<sup>3</sup>/min flow has been

maintained, resulting in an inlet velocity of 0.04167 m/s. In Figure 6, the obtained velocity magnitude is shown on a linear scale (cut to a tenth of the maximum velocity), together with the streamlines. Figure 8 is a contour plot of the velocity magnitude with a logarithmic scale. On a qualitative basis, the overall uniformity of the velocity magnitudes looks improved by the added inlet and outlet. It seems that in this configuration we obtain in the six-sectors rows three relatively independent and similar flows. In order to show the effect of the circular joints at inlets and outlets (cf. Figure 8), we have also run the same simulation using the initial geometry of the inlets and outlets.

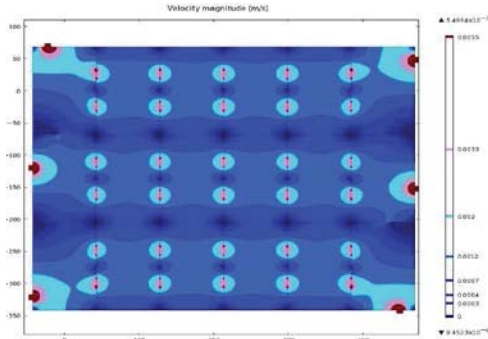


Figure 7: Simul. 2 – Contour plot with logarithmic scale of the velocity magnitude obtained for an 18-sectors frame with 3 inlets (left) and 3 outlets (right).

Figures 9 and 8 share the same color scale, so that the slight reduction of the high velocities inside the sector is visible in the design with circular joints. It will help avoiding their separation from the walls and thus avoiding possible small turbulence areas near the inlets and outlets.

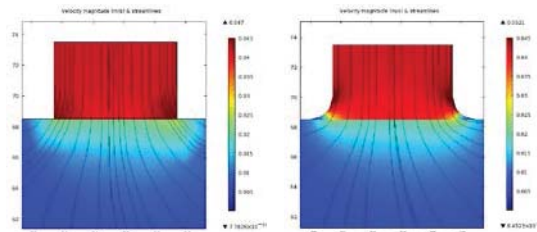


Figure 8: Simul. 2 bis – Inlet without circular joints  
 Figure 9: Simul. 2 – Inlet with 1.5 mm radius circular joints

**3.1.1.3 Simulation 3: Reduction of the number of sectors from 18 to 12**

Since low velocity zones are found where spacers intersect each other or reach the border of the frame, reducing for example the number of spacers would be a way to reduce these “stagnation” zones, which might thus improve the overall uniformity of the gas flow. A sector of a GEM-foil glued to its frame can be modeled as a built-in rectangular thin plate of area  $S$ , being isotropically stretched by a uniform force per unit length  $T$  at its circumference, and undergoing a normal pressure  $P$ . The maximum deformation  $u_{max}$  of such a plate is given by the following expression:

$$u_{max} = k(\zeta) = \frac{PS}{T} \quad (8)$$

where the geometrical factor  $\kappa(\zeta)$  is an increasing function of the ratio  $\zeta \in ]0, 1]$  of the rectangle sides. For a square plate,  $\kappa$  reaches a maximum value of nearly 0.074. In our case, we want the maximum deformation  $u_{max}$  to remain lower than 1% of the 2 mm thick gap between two GEM-foils, at a pressure  $P$  up to 10 N/m<sup>2</sup>, when a tension of 1 kg/cm ( $T = 9.81$  N/cm) is applied to the GEM-foil. If we consider in first approximation a geometrical factor  $\kappa$  of 0.074, the maximum allowable area  $S$  of a sector should thus be:

$$S = \frac{u_{max}T}{\kappa P} = \frac{2 \cdot 10^{-5} \cdot 9.81 \cdot 10^2}{0.074 \cdot 10} = 2.65 \cdot 10^{-2} m^2 \quad (9)$$

Based on these assumptions, it would have been feasible to reduce the number of sectors to only 9 (using 2 spacers along both directions), since the area of each sector would have been equal to  $\frac{0.2}{9} m^2 = 2.22 \cdot 10^{-2} m^2$ . However, a more conservative choice of 12 sectors (2 spacers along the long side and 3 spacers along the short one) has been made, which results in sectors of about  $0.125 \times 0.133 m^2 = 1.66 \cdot 10^{-2} m^2$ . In the simulation results for a frame with 12 sectors, the overall uniformity of the gas flow seems indeed improved by the reduction of the number of spacers along the shortest side of the module.

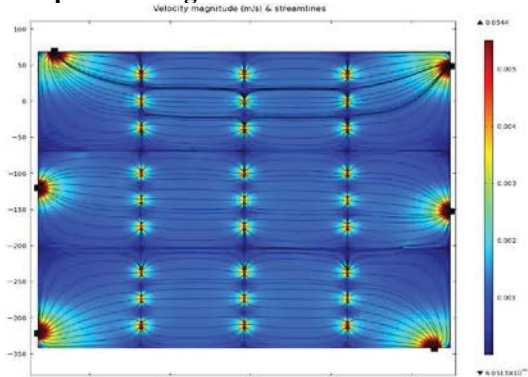
**3.1.1.4 Simulation 4: Enlargement of some openings in the spacers**

With the hope to further improve the flow uniformity, especially in the sectors possessing an inlet or an outlet, we have made a simulation in which the openings in the spacers that delimit these particular sectors are enlarged from 15 to 20 mm. The results have however not been so



convincing. For this reason, the idea of modifying the width of the openings in spacers has been abandoned.

### 3.1.1.5 Simulation 5: Nine openings in the spacers along the short side of the module

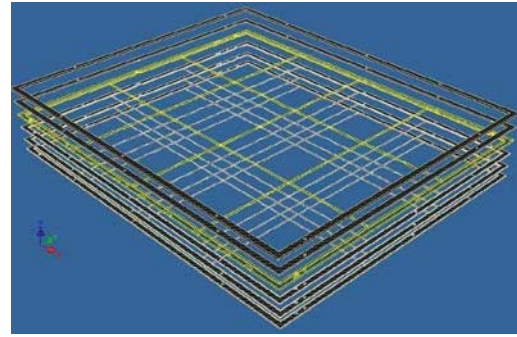


**Figure 10: Simulation 5 – Velocity magnitude on a linear scale and streamlines of the velocity field obtained for a 12-sectors frame with 3 inlets (left) and 3 outlets (right), having nine 10 mm openings in the spacers along the short side of the module.**

Good results have been obtained with nine openings of 10 mm instead of six openings of 15 mm for the spacers along the short side of the module. When comparing Figure 10, with the figures from previous simulations, we notice a reduction in size of the low velocity zones where spacers cross each other and where the short spacers reach the longest border of the frame.

### 3.1.1.6 Simulation 6: Doubling the openings in the spacers along the long side of the module

After the results of Simulation 5, we have tried to find out whether doubling the number of 15 mm openings in the spacers along the longest side would decrease the size of the large low velocity zones near the shortest borders of the frame. However, these long spacers are parallel to the main direction of the gas flow, instead of being perpendicular to it like the short spacers. For this reason, increasing the number of openings in the long spacers does not produce the same positive effect on the flow uniformity. We have therefore decided to stick with the frame design of Simulation 5, since in Simulation 6 we have not found a sufficient improvement of the flow uniformity to justify



adding openings in the long spacers and thus weakening the mechanical support they provide.

**Figure 11: All frames of the module assembled**

The finally chosen new frame designs is the one yielding the simulations results shown in figure 10.

## 4. TENDIGEM TENSION CONTROL SYSTEM

TENDIGEM is a tool designed to stretch a GEM-foil before gluing it to the frame that will hold the foil. This tool is a sensor-based device which uses load cells to measure the tension. The load cells of the TENDIGEM monitor the tension on the different sides of the foil. It is important to stretch the foils properly because if a GEM foil shrivels, it can touch another foil. So when the foils are not stretched properly, there is a big chance that an electrical short will occur in the foil, which would make the detector useless. The GEM-foil will be placed in the TENDIGEM by using the clips that are provided. There are 14 clips in total as shown in fig. 11. Only half of the clips are connected with the load-cells. After a foil is correctly stretched, the frame will be glued on it. Fiducial metal pins located on the sides of the TENDIGEM and corresponding holes in the frames are arranged asymmetrically in order to easily match the appropriate sides of either one. The frame is then glued with polymeric glue to the GEM-foil and allowed to dry for 24 hours. Once the glue has dried they are removed from the TENDIGEM. At this point the frame and foil are ready to use in a GEM-chamber. To improve the GEM detector assembly method an electronic control system is used. In the TENDIGEM the goal is to create the correct tension on a GEM-foil before it is glued to the frame.

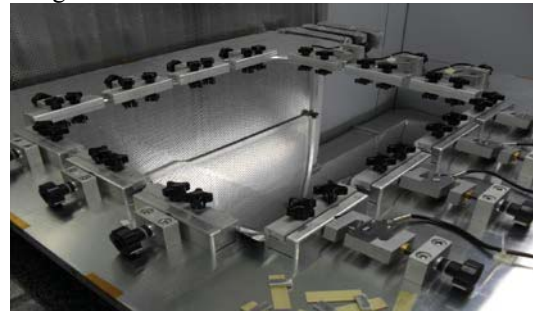
There are different ways to put tension in a controlled way on a system, like Sensor Based Tension Control or Open Loop Tension Control. The Sensor Based Tension Control uses load

cells that measure the tension in a point and compare it with the desired tension level. If it is necessary the load cells will induce the controller to do some adjustments. This is an example of a closed loop control system and has an accuracy of 1-2%. In an Open Loop Tension Control System there is no feedback. The system only estimates what the value at the output will be. The accuracy for an Open Loop Tension Control System is 8-10%. In the TENDIGEM the system used is Sensor Based Tension Control (Fig.12) that uses load cells.

## 5. CONCLUSION

Our goal has been to obtain a better spatial uniformity (over the active area of the module) of the continuous Ar-CO<sub>2</sub> (70/30) gas flow in the 2 mm gap between two GEM foils, since this gas flow should be spatially uniform in order to guarantee a homogeneous and stable detector response. With a frame geometry defined in two dimensions, we have used the built-in Thin-Film Flow Model, which treats the laminar and isothermal flow of a thin fluid film between two large solid structures and solves the corresponding Reynolds equation. We have defined a typical total gas flow of about 3 chamber-volume renewals per hour (60 cm<sup>3</sup>/min) and this gas flow has been considered incompressible. The optimization of the frame design has been presented through six main simulations, showing incremental modifications of the simulated geometry. The initially defined geometry corresponds to the first prototype version of the frame, possessing eighteen sectors, two inlets and two outlets. A second simulation has shown that adding a third inlet and a third outlet improves the overall flow uniformity, as the flows in the three six-sector rows become rather independent and similar. High velocity zones near inlets and outlets have also been reduced by replacing 90 degrees edges with 1.5 mm radius circular joints. In a third simulation, the number of stagnation zones has been decreased by reducing the number of short spacers from five to three, leading to a frame with twelve sectors which still meets the mechanical requirements related to the planarity of the GEM foils. The fourth simulation, in which openings in the spacers near the inlets and outlets have been enlarged from 15 mm to 20 mm, has not yielded a significant improvement of the gas flow

uniformity. However, the fifth simulation has shown that introducing in the short spacers nine openings of 10 mm, instead of six openings of 15 mm, decreases the size of various stagnation zones. Finally, we have concluded from a sixth simulation that doubling the number of 15 mm openings in the long spacers does not significantly improve the flow uniformity and thus the geometry of the fifth simulation has been selected as the basis for a new frame design.



**Figure 12: The TENDIGEM Tension Control System**

## 6. REFERENCES

- [1] M. Alfonsi et al “ Activity of CERN and LNF groups on large area GEM detectors” Nucl. Instr. Meth. A 617 (2010) 151.
- [2] J. Alcorn et al - “Basic instrumentation for Hall A at Jefferson Lab”, Nucl. Instr. Meth. A 522 (2004) 294.
- [3] G. Bencivenni, “The GEM detector activity at the Frascati Laboratory,” Nucl. Phys. A 827 (2009) 614C1. Author, Article title, *Journal*,
- [4] Felippa C.A., Introduction to Finite Element Methods, lecture notes, Department of aerospace engineering sciences of the University of Colorado, Boulder, 2004.
- [5] COMSOL Multiphysics User’s Guide v4.1, COMSOL A B, 2010.
- [6] Lewis R.W., Nithiarasu P. & Seetharamu K.N., Fundamentals of the Finite Element Method for Heat and Fluid Flow, New York, John Wiley & Sons, 2004.
- [7] Alfonsi M. et al., Aging measurements on triple-GEM detectors operated with CF<sub>4</sub>-based gas mixtures, Proceedings of the 9<sup>th</sup> Topical Seminar on Innovative Particle and Radiation Detectors, Nucl. Ph. B – Proceedings Supplements, Vol. 150, pages 159-163, BIBLIOGRAPHY 119 January 2006.

## Simulation of passive myocardium of rabbit ventricles, using selective smoothed finite element method(S-FEM)

C. Jiang<sup>1</sup>, Zhi-Qian Zhang<sup>2</sup>, \*X. Han<sup>1</sup>, G.R. Liu<sup>3</sup>

<sup>1</sup> State Key Laboratory of Advanced Technology of Design and Manufacturing for Vehicle Body, Hunan University, P.R. China, 410082

<sup>2</sup> Institute of High Performance Computing, A\*STAR, Singapore, 138632

<sup>3</sup> Department of Aerospace Engineering and Engineering Mechanics, University of Cincinnati, 2851 Woodside Dr, Cincinnati, OH 45221, USA

\*Corresponding author: hanxu@hnu.edu.cn

### Abstract

A selective smoothed finite element method (Selective S-FEM) is developed for dynamic 3D analysis of extremely large deformation of incompressible bio-tissues, using the simplest 4-node tetrahedron elements. In the present selective S-FEM, face-based Smoothed FEM (FS-FEM) and node-based Smoothed FEM (NS-FEM) are, respectively, used for the deviatoric and volumetric parts of the deformation of incompressible bio-tissues. Therefore the “overly-soft” feature of the NS-FEM is made use of for mitigating the volumetric locking that may occur in bio soft tissue. Because the FS-FEM can provide close-to-exact stiffness, our selective S-FEM can provide an accurate solution. In the current formulation, the soft tissue is modeled using the hyperelastic constitutive law. Numerical examples are presented to simulate a passive filling process of anatomical rabbit ventricles. It is demonstrated that the Selective S-FEM possess good potential for accurately simulating the behavior of bio-tissues for reliable solution..

**Keywords:** Finite Element Method, Smoothed Finite Element Method, Gradient Smoothing, Incompressibility, Anisotropy, Myocardium, Tetrahedral, Large Deformation, Explicit time integration

### Introduction

The explicit dynamic Finite Element Method (FEM) has been successfully applied to solve transient nonlinear responses of various material and structural systems with large deformation and strain, impact-contact and metal forming problems in automotive, aerospace, and bioengineering (Goudreau and Hallquist 1982; Belytschko, Liu, and Moran 2000; Miller et al. 2006). In explicit dynamics analyses using FEM, four-node quadrilateral element (Q4) and eight-node hexahedron element (H8) are the most frequently used with single quadrature point for efficiency, which requires a hourglass control to remedy hourglass instability (spurious zero-energy modes) (Belytschko, Liu, and Moran 2000). In addition, the one-point quadrature technique can also mitigate the volumetric locking in nearly incompressible solids.

When quadrilateral and hexahedral elements are used, it is laborious and time-consuming in pre-processing and the remeshing for distorted elements, because of the difficulties in automatically meshing with these types of elements. It is much easier to automatically create and refine, when using Triangular and Tetrahedral mesh (T-mesh) are used in complicated geometry. In fact, there are now many commercial and open-source softwares, have been developed for automotive generating T-meshes. However, in the FEM based on the standard weak formulation, the performance of T-mesh is usually very poor for its overly stiff behavior. This is in particular true for incompressible solids where volumetric locking may occur.

Many efforts have been made to enhance the capability of T-mesh in handling the incompressibility, including the F-bar method (De Souza Neto et al. 1996), the method using hydrostatic pressure as an additional independent variable (Zienkiewicz et al. 1998), nodal pressure average treatment (Bonet and Burton 1998), Hu-Washizu three fields variational theorem (Taylor 2000), and nodal averaging treatment of deformation gradient tensor (Bonet, Marriott, and Hassan 2001). The node-based strain smoothing has also been successfully applied to meshfree methods for stabilization (Chen, Yoon, and Wu 2002).

Models using smoothed strains can have a theoretical foundation on G space theory (Liu and Zhang 2009; Liu 2009; Liu and Zhang 2013). Because the G space theory allows the use of discontinuous functions, such a formulation is also termed as weakened weak (or W2) forms. Typical W2 formulation method is the Smoothed Point Interpolation Methods (S-PIM) (Liu and Zhang 2013). When functions in a FEM space are used in a W2 formulation, the so-called the smoothed finite element method or S-FEM. In terms of the way to construct the smoothing domains, S-FEM can have a family of methods of unique properties, which can be classified as cell-based smoothed FEM (CS-FEM) (Liu, Dai, and Nguyen 2006), node-based smoothed FEM (NS-FEM) (Nguyen-Thoi et al. 2010), edge-based S-FEM (ES-FEM) (Liu, Nguyen-Thoi, and Lam 2009) for 2D problems, and face-based S-FEM (FS-FEM) for 3D problems (Nguyen-Thoi et al. 2009). In these S-FEM methods, the NS-FEM has an unique property of volumetric locking free, due to its strong softening effects. However, spurious non-zero-energy eigen-modes and temporal instabilities arise for NS-FEM, despite the fact that it is proven spatially stable (Liu 2009; Liu, Dai, and Nguyen 2006). Differing from NS-FEM, the ES-FEM or FS-FEM that uses edge-based or face-based smoothing domains are found both spatial and temporal stable, because of using more smooth domains. However, ES-FEM or FS-FEM usually produces slightly overestimated stiffness, and hence it can also suffer from the volumetric locking. A method using selective gradient-smoothing technique, so called Selective S-FEM, has been proposed in order to eliminate volumetric locking, at the same time, improve the performance of the simplex TRI3 and TET4 elements. The employment of the combined edge-based and node-based smoothing operations enables effective handling of element distortion in extremely large deformation with low computation cost.

Biological tissues, like skin, myocardium, arterial layer, can often treated as hyperelastic material. This is because they can undergo very large deformation, and after unloading, they can recover to original state. These strain energy functions can be divided into two groups by their variables. The first group is the strain-based strain energy functions, such as the Fung form for arterial layer (Chuong and Fung 1986) and the McCulloch exponential form for myocardium (Vetter and McCulloch 2000), which regard strains as independent variables. The another group is the invariant-based strain energy functions, like the Hozapfel-Gasser-Ogden form for arterial layer (Gasser, Ogden, and Holzapfel 2006), the Lin form (Lin and Yin 1998) for rabbit heart, and the Ogden form (Ogden 1972) for extremely large deformation.

In this paper, we first introduce the basic formulations of explicit dynamic nonlinear Selective S-FEM in Section 1, and then briefly review the strain energy functions of bio-tissues in Section 2. Following numerical examples of transversely isotropic hyperelastic plate and passive bi-ventricles in Section 3, conclusions are drawn in Section 4.

### **Explicit Dynamic nonlinear Selective S-FEM**

In dynamic analysis, inertia and damping effects must be considered, and the discrete form of the governing equation can be given in general as follow

$$\mathbf{M}\ddot{\mathbf{u}} + \mathbf{C}\dot{\mathbf{u}} + \mathbf{F}_{\text{int}} = \mathbf{F}_{\text{ext}} \quad (1)$$

where  $\mathbf{u}$  is nodal displacements vector, and  $\mathbf{M} = \int_{\Omega} \mathbf{N}^T \rho \mathbf{N} d\Omega$  ( $\rho$  is mass density vector),  $\mathbf{C} = \int_{\Omega} \mathbf{N}^T \mathbf{c} \mathbf{N} d\Omega$  ( $\mathbf{c}$  is damping coefficient vector),  $\mathbf{F}_{\text{ext}} = \int_{\Omega} \mathbf{N}^T \mathbf{b} d\Omega + \int_{\Gamma_t} \mathbf{N}^T \mathbf{t} d\Gamma_t$ .

In general S-FEM, nodal internal forces should be computed from smoothed strain matrix and smoothed stress,

$$\mathbf{F}_{\text{int}} = \int_{\Omega} \tilde{\mathbf{B}}^T \tilde{\boldsymbol{\sigma}} d\Omega \quad (2)$$

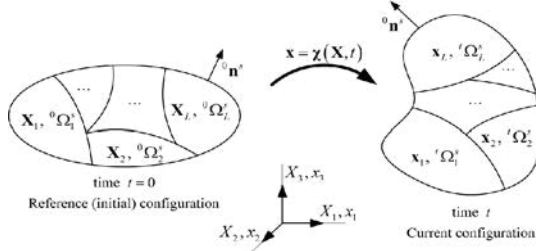


Figure 1. Configuration and motion of a continuum body, and smoothing domains

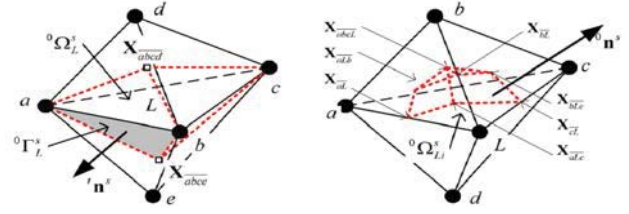


Figure 2. Illustrations of smoothing domains of (left) FS-FEM-TET4 (right) NS-FEM-TET4

In this paper, total Lagrange formulation is employed to solve geometrical nonlinearity. The initial reference configuration of material point in a body  $\Omega$  is denoted by  $\mathbf{X}$ , and displacement at time  $t_n$  is denoted as  $\mathbf{u}_n$  then the current deformed configuration is expressed as

$$\mathbf{x}_n = \mathbf{X} + \mathbf{u}_n \quad (3)$$

There is the deformation gradient tensor of  $\mathbf{X}$  which is the measure of deformation from reference configuration, as in Figure 1. It is given by

$$\mathbf{F}_n = \frac{\partial \mathbf{x}_n}{\partial \mathbf{X}} \quad (4)$$

In our S-FEM, the deformation gradient tensor needs also be written in smoothed version, as below

$$\tilde{\mathbf{F}}_{ij} = \frac{1}{A_L^s} \int_{\Omega_L^s} \tilde{F}_{ij}(\mathbf{X}_L) d\Omega = \frac{1}{A_L^s} \int_{\Gamma_L^s} u_i^0 n_j^s d\Gamma + \delta_{ij} = \tilde{e}_{ij}(\mathbf{X}_L) + \delta_{ij}, \quad (5)$$

where  $A_L^s$  is the area of initial smooth domains.

For hyperelastic incompressible biology material, the corresponding strain energy function is often split into volumetric part and deviatoric part. The smoothed second Piola-Kirchhoff (PK2) stress tensor can be calculated by given strain energy function and smoothed deformation gradient as follows

$$\tilde{\mathbf{S}}_{ij} = \frac{\partial \Psi}{\partial \tilde{E}_{ij}} = 2 \frac{\partial \Psi}{\partial \tilde{C}_{ij}} = 2 \frac{\partial \Psi^{\text{vol}}}{\partial \tilde{C}_{ij}^{\text{NS-FEM}}} + 2 \frac{\partial \Psi^{\text{dev}}}{\partial \tilde{C}_{ij}^{\text{FS-FEM}}} \quad (6)$$

where  $\tilde{E}_{ij}$  is the *Green strain tensor*, the smoothed *right Cauchy-Green strain tensor*  $\tilde{C}_{ij} = \tilde{F}_{ki} \tilde{F}_{kj}$ .

After getting the PK2 stress tensor, substitute it into Eq.(2) to get internal nodal force vector.

In the Selective S-FEM, its strain smoothing is performed using a combination of edge-based smoothing in 2D problem (face-based smoothing in 3D) and node-based smoothing. These two types of smooth domains in Selective S-FEM used here are plotted in Figure 2. In Selective S-FEM, volumetric part of PK2 stress is computed by the ‘‘over-softly’’ NS-FEM, and the deviatoric part of

PK2 stress is handled by more precise ES-FEM using smoothed deformation gradient tensor from Eq.(5).

For the time integration, the well-established explicit central differential method is used. Although explicit scheme is conditional stable, it is much easier in programming and no need to form the global tangent stiffness matrix. The time increments are defined as

$$\Delta t^{n+1/2} = t^{n+1} - t^n, \quad t^{n+1/2} = (t^{n+1} + t^n) / 2, \quad \Delta t^n = t^{n+1/2} - t^{n-1/2}. \quad (7)$$

The displacement and velocity can be update by

$$\mathbf{u}^n = \mathbf{u}^{n+1} + \mathbf{v}^{n+1/2} \Delta t^{n+1/2}, \quad (8)$$

$$\mathbf{v}^{n+1/2} = \mathbf{v}^{n-1/2} + \Delta t^n \mathbf{a}^n, \quad (9)$$

The acceleration  $\mathbf{a}^n = \ddot{\mathbf{u}}^n$  is obtained by solving the following equation

$$\mathbf{M} \mathbf{a}^n = \mathbf{f}^{ext}(\mathbf{u}^n, t^n) - \bar{\mathbf{f}}^{int}(\mathbf{u}^n, t^n) - \mathbf{C} \mathbf{v}^n. \quad (10)$$

If a lumped mass matrix is employed in Eq.(10),  $\mathbf{M}$  becomes a diagonal matrix, and  $\mathbf{a}^n$  can be computed via trivial operations without invoking a linear algebra equation solver.

### Hyperelastic strain energy functions for bio-tissue

Hyperelastic constitutive laws are often employed to model the mechanical response of bio-tissues. Based on experimental data, variety of isotropic and anisotropic strain energy functions have been proposed in recent years. In all these forms of strain energy function, they can be grouped into two categories, in terms of their independent variables. The first group is *the strain-based forms* group, which is expressed directly in terms of the components of suitable strain tensor (often is Green strain tensor  $\mathbf{E}$ ). The general decoupled form of this group is given below

$$\Psi = \Psi^{dev}(\mathbf{E}) + \Psi^{vol}. \quad (11)$$

In the beginning of the development of biomechanics, almost all strain energy functions are formed using Green strain tensor, like Fung's form (Chuong and Fung 1986), "Pole-zero" form (Nash and Hunter 2000), and McCulloch form (Vetter and McCulloch 2000). Although these forms are the naturally transited from elastic constitutive law, they are boring in finding the material parameters and constructing the local material coordinate systems for their needs of an orthogonal coordinate system.

Another group is *the invariant-based forms* group, strain energy functions are expressed in terms of invariants of right Cauchy-Green strain tensor  $I_1, I_2$  and fiber directions  $I_i (i=4,5,\dots)$ , and the general form is given as below

$$\Psi(I_1, I_2, J, I_4, \dots) = \Psi^{dev}(I_1, I_2, I_4, \dots) + \Psi^{vol}(J), \quad (12)$$

where  $J$  is the volume ratio and  $J = \sqrt{I_3}$ . Note that in S-FEM, all invariants should use the smoothed version. Material parameters of invariant-based form are less than strain-based form and often just need the fiber orientation. With these advantages, this type is more and more popular in biomechanics, like the recently proposed Holzapfel-Gasser-Ogden (H.G.O) form (Gasser, Ogden, and Holzapfel 2006) for adventitial layers.

There is also a group of strain energy function in terms of *principal stretches*, such as the Ogden form (Ogden 1972). Although they should be categorized in another group for its variables, the principal stretches can be derived from invariants of right Cauchy-Green strain tensor, so we regard they are just special version of the invariant-based forms.

**Numerical examples**

*1. Transversely isotropic hyperelastic plate under uniform pressure*

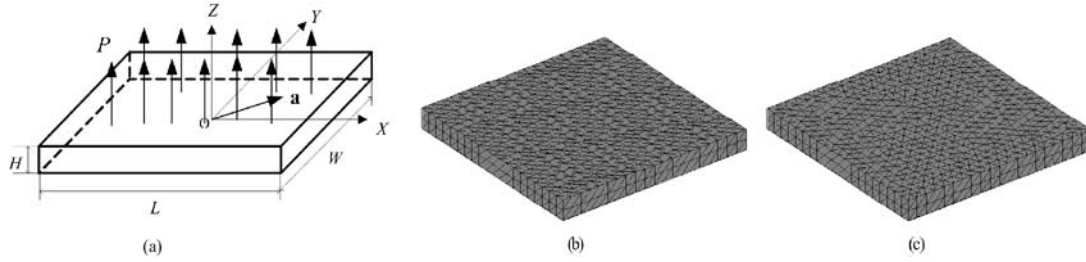


Figure 3. (a) Problems settings of example 3, regular mesh (b) and irregular mesh (c) at initial configuration

The model configuration of one family of fiber-reinforced hyperelastic plate is showed in Figure 3, where  $L = 1\text{m}$ ,  $W = 1\text{m}$ ,  $H = 0.1\text{m}$ , and  $\mathbf{a}$  is the unit vector in fiber orientation. The regular mesh and one kind of irregular mesh are plotted in Figure 3(b)(c). Nearly-incompressible Mooney-Rivlin model is employed as the isotropic part of strain energy with the parameters:  $C_{10} = 1\text{kPa}$ ,  $C_{01} = 0.5\text{kPa}$ ,  $\kappa = 1000\text{mPa}$  and density  $\rho_0 = 1000\text{kg/m}^3$ . Weiss polynomial form (Weiss, Maker, and Govindjee 1996) is employed as deviatoric part of strain energy function with parameter:  $A_1 = 5\text{kPa}$ . This strain energy function can be written in following form.

$$\Psi(I_1, I_2, J, I_4, \dots) = \Psi_{iso}^{dev}(I_1, I_2) + \Psi_{ani}^{dev}(I_1, I_2, I_4, \dots) + \Psi^{vol}(J),$$

$$\Psi_{iso}^{dev}(I_1, I_2) = C_{01}(I_1 - 3) + C_{10}(I_2 - 3), \Psi_{ani}^{dev}(I_1, I_2, I_4, I_5) = \frac{A_1}{2}(I_4 - 1)^2. \quad (13)$$

The boundary condition and initial condition are given as follows. *Initial condition:*  $\mathbf{v}^0 = \mathbf{0}$  and  $\mathbf{u}^0 = \mathbf{0}$ . *Boundary condition:* on the four lateral surface  $u_x^n = u_y^n = u_z^n = 0$ . *Loading:* on the upper surface, a given uniform pressure is applied. This example is aimed to illustrate the ability S-FEM to solve large anisotropic deformation caused by transversely isotropic constitutive law.

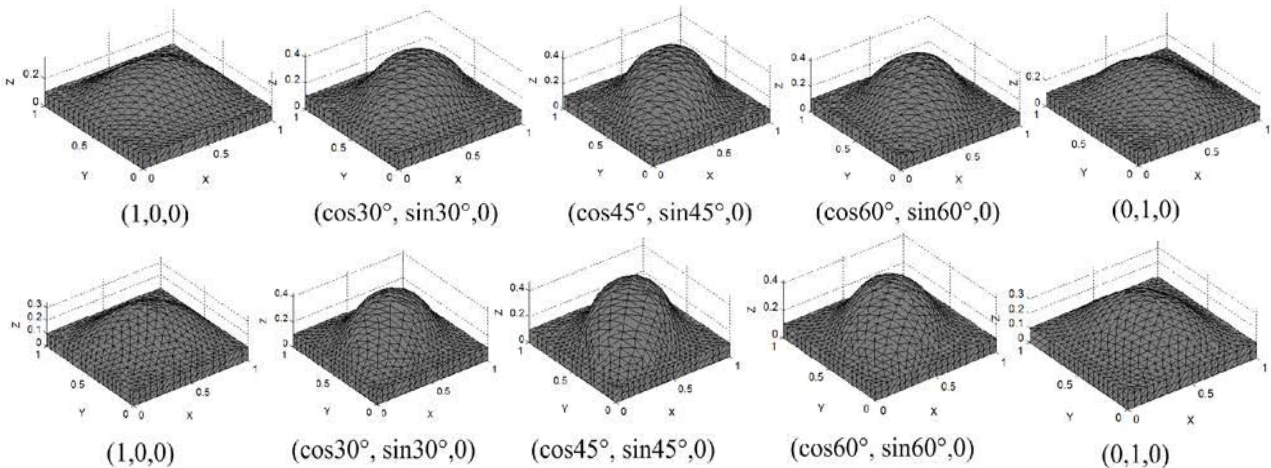


Figure 4. Deformed configurations for regular (above) and irregular meshed (below) example 1 with different fiber directions

Explicit analyses with conventional dynamic relaxation technique are only performed using Selective S-FEM with 7058 TET4 elements (5088 nodes) to achieve the quasi-static solutions. Five different fiber orientations cases are calculated here, and the corresponding orientation vectors

are  $(\cos 0^\circ, \sin 0^\circ, 0)$ ,  $(\cos 30^\circ, \sin 30^\circ, 0)$ ,  $(\cos 45^\circ, \sin 45^\circ, 0)$ ,  $(\cos 60^\circ, \sin 60^\circ, 0)$ , and  $(\cos 90^\circ, \sin 90^\circ, 0)$ . The deformation configurations of different cases are plotted in Figure 4. It is obvious that different embedded fiber direction will lead to a quite different deformation. Moreover, according to definition of transversely isotropic, deformation configurations of cases with fiber direction  $(\cos 0^\circ, \sin 0^\circ, 0)$  and  $(\cos 90^\circ, \sin 90^\circ, 0)$  should be identical, so as to  $(\cos 30^\circ, \sin 30^\circ, 0)$  and  $(\cos 60^\circ, \sin 60^\circ, 0)$ . For clear demonstration of this phenomenon, displacements of Z-axis in the two upper face diagonal lines are plotted in Figure 5. In Figure 5, nodes with the same distance to the center of plate will have the same deflections in every different fiber direction cases. Also in this figure, results of regular and irregular mesh are matched very well. This example demonstrates that the present selective S-FEM using TET4 is capable to handle the transversely isotropic hyperelastic material in large deformation.

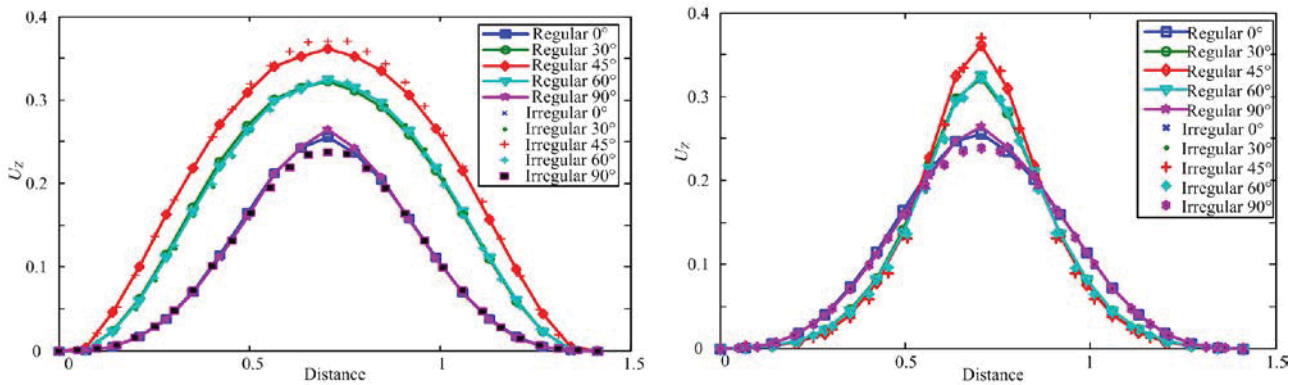


Figure 5. The deflections on the diagonal line  $(0, 0, 0.1) - (1, 1, 0.1)$  (left) and  $(1, 0, 0.1) - (0, 1, 0.1)$  (right) versus distances to point  $(0, 0)$  of regular and irregular meshed cases with different fiber orientations.

## 2. Passive filling of rabbit ventricles

Heart, as the most important organ in any species of animals, pumps blood to other organs and muscles by repeated, rhythmic contractions and expansions. Two phases can be divided in the cardiac cycle; one is the contraction period, referred as *ventricular systole*, another is the *ventricular diastole* which the heart is relaxed and refilled for the next cycle.

This heart pump depends mainly on the active mechanical property of left ventricle myocardium. Here for the sake of simplicity, the passive filling process is calculated to approximate the *diastole* phase, because of its easier passive mechanical property and loading. Usually, myocardium is fiber-reinforced, and its fibers are complex distributed. According to reference (Lin and Yin 1998) and reference (Vetter and McCulloch 2000), they provide a invariant-based transversely isotropic strain energy function for rabbit myocardium and corresponding equibiaxial stress-strain curves. Luckily, because *the correlation of the fiber and crossfiber strain-stress curves is 0.998631*, anisotropy can be ignored. Ignoring the anisotropy of fiber architecture really can reduce many works on reconstructing the fiber orientations. We fit these two curves into Ogden form strain energy function (Ogden 1972) as in Figure 6. In Figure 6, the

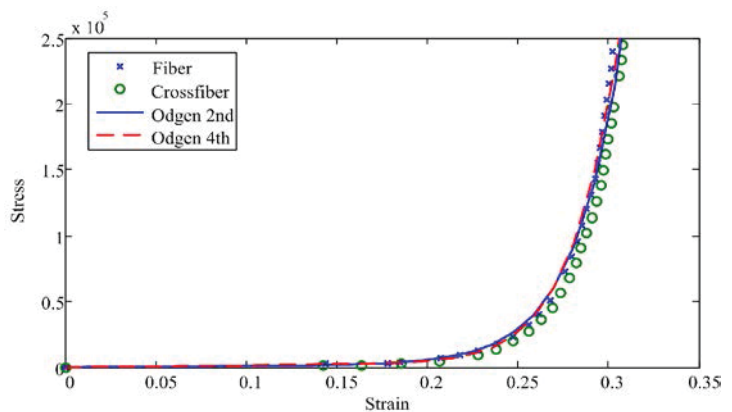


Figure 6. Stress-strain curves of fiber, cross fiber and fitted Ogden forms.



2nd and 4th order Ogden forms can well approximate the curves in the fiber direction and cross fiber direction. For the sake of less parameters, the 2nd Ogden form here is employed as the constitutive law, the decoupled form is

$$\Psi = \sum_{i=1}^N \frac{2\mu_i}{\alpha_i^2} (\bar{\lambda}_1^{\alpha_i} + \bar{\lambda}_2^{\alpha_i} + \bar{\lambda}_3^{\alpha_i} - 3) + \frac{1}{2} \kappa (J-1)^2 \quad (14)$$

where modified principal stretches  $\bar{\lambda}_a = J^{-1/3} \lambda_a$  ( $a=1,2,3$ ),  $N=2$  for 2nd Ogden form,  $\mu_i$  (Pa) and  $\alpha_i$  are the material coefficients,  $\kappa$  is the bulk modulus. Here, for the rabbit myocardium,  $\mu_1 = 1803.71\text{Pa}$ ,  $\alpha_1 = -0.924$ ,  $\mu_2 = 5.96\text{Pa}$ ,  $\alpha_2 = -25.0$ , and  $\kappa = 35590.19\text{Pa}$ .

To validate our Selective S-FEM, standard FEM with TET10 elements is employed here to do a comparison. The rabbit ventricle model is discretized by 39142 elements, 9069 nodes for Selective S-FEM, 62239 nodes for FEM, see it in Figure 7 (left). *Boundary condition*: LV and RV endocardial base is constrained the longitude ( $X$ -direction) displacements, epicardial base are fixed constrained. *Loading*: The 25mmHg pressure is smoothly applied on the LV surface to simulate the passive filling process, and the RV is unloaded here.

A slice of rabbit ventricles in  $X$ - $Y$  plane is drew in Figure 7 (Right) as a simple validation of TET4 Selective S-FEM and TET10 FEM. In Figure 7 (Right), the blue dash curve is the undeformed outline of TET10 FEM slice, the red dot curve is the deformed outline of TET10 FEM slice, but the contour of displacement magnitude belongs to TET4 FS/NS-FEM. The two deformed outline match with each other very well, except some mismatches in the septum. This example shows the near quadratic tetrahedron element accuracy of Selective S-FEM.

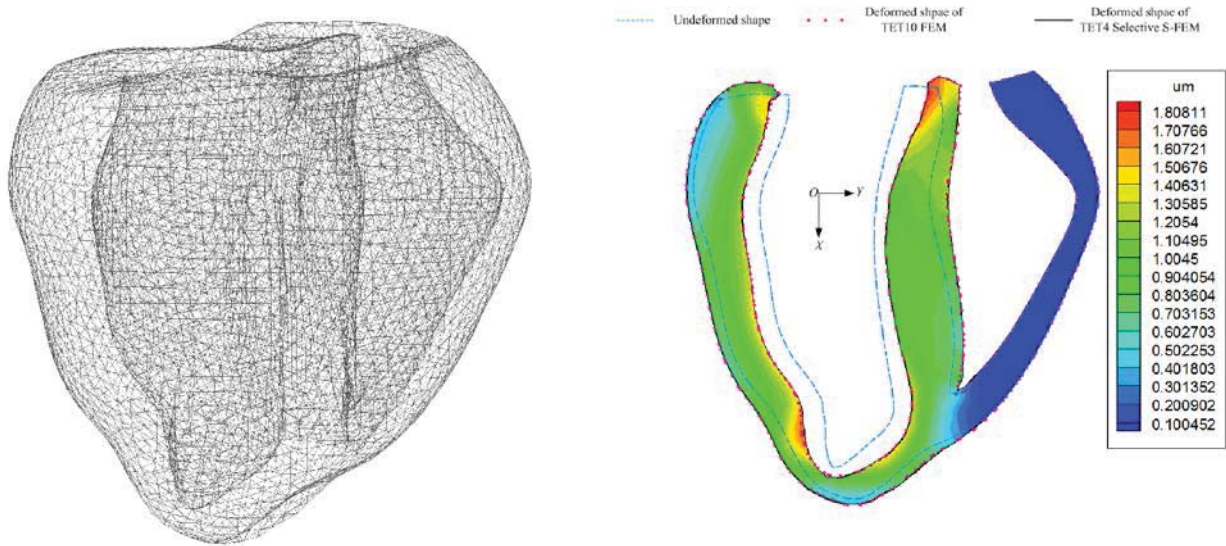


Figure 7. Mesh of rabbit ventricles (left) and a slice in  $X$ - $Y$  plane (right, outline belongs to FEM TET10, contour belongs to FS/NS-FEM).

## Conclusions

In this paper, Selective FS/NS-FEM is applied into isotropic and anisotropic incompressible bio-tissues. Several conclusions can be derived from this paper.

- (1) Selective S-FEM using TET4 element can easily mesh complex geometry, such as ventricles.
- (2) FS-FEM is ideal for the deviatoric part of deformation of incompressible isotropic or anisotropic solids, so as to greatly improve the performance of the linear elements.

- (3) NS-FEM is ideal for the volumetric part of deformation of incompressible solids, and can effectively mitigate the volumetric locking in incompressible materials, even if linear elements are used.
- (4) Selective S-FEM is capable to handle the large rotation of fibers in anisotropic bio-tissues with regular or irregular mesh.
- (5) Selective S-FEM can enhance the accuracy of linear TET4 element to be closer to quadratic TET10 element.

## References

- Belytschko, Ted, W.K Liu, and B. Moran. (2000). *Nonlinear Finite Elements for Continua and Structures*. Wiley.
- Bonet, J., and A. J. Burton. (1998). A Simple Average Nodal Pressure Tetrahedral Element for Incompressible and Nearly Incompressible Dynamic Explicit Applications. *Communications in Numerical Methods in Engineering*. 14. (5).pp: 437–449.
- Bonet, J., H. Marriott, and O. Hassan. (2001). An Averaged Nodal Deformation Gradient Linear Tetrahedral Element for Large Strain Explicit Dynamic Applications. *Communications in Numerical Methods in Engineering*. 17. (8).pp: 551–561.
- Chen, Jiun-Shyan, Sangpil Yoon, and Cheng-Tang Wu. (2002). Non-linear Version of Stabilized Conforming Nodal Integration for Galerkin Mesh-free Methods. *International Journal for Numerical Methods in Engineering*. 53. (12).pp: 2587–2615.
- Chuong, C. J., and Y. C. Fung. (1986). On Residual Stresses in Arteries. *Journal of Biomechanical Engineering*. 108. (2).pp: 189.
- Gasser, T Christian, Ray W Ogden, and Gerhard a Holzapfel. (2006). Hyperelastic Modelling of Arterial Layers with Distributed Collagen Fibre Orientations. *Journal of the Royal Society, Interface / the Royal Society*. 3. (6).pp: 15–35.
- Goudreau, G.L., and J.O. Hallquist. (1982). Recent Developments in Large-scale Finite Element Lagrangian Hydrocode Technology. *Computer Methods in Applied Mechanics and Engineering*. 33. (1-3).pp: 725–757.
- Lin, D. H. S., and F. C. P. Yin. (1998). A Multiaxial Constitutive Law for Mammalian Left Ventricular Myocardium in Steady-State Barium Contracture or Tetanus. *Journal of Biomechanical Engineering*. 120. (4).pp: 504.
- Liu, G. R. (2009). A G Space Theory and a Weakened Weak (W 2 ) Form for a Unified Formulation of Compatible and Incompatible Methods: Part II Applications to Solid Mechanics Problems. *International Journal for Numerical Methods in Engineering*.pp: n/a–n/a.
- Liu, G. R., K. Y. Dai, and T. T. Nguyen. (2006). A Smoothed Finite Element Method for Mechanics Problems. *Computational Mechanics*. 39. (6).pp: 859–877.
- Liu, G. R., and G. Y. Zhang. (2009). A Normed G Space and Weakened Formulation of a Cell-based Smoothed Point Interpolation Method. *International Journal of Computational Methods*. 06. (01).pp: 147–179.
- Liu, G.R., T. Nguyen-Thoi, and K.Y. Lam. (2009). An Edge-based Smoothed Finite Element Method (ES-FEM) for Static, Free and Forced Vibration Analyses of Solids. *Journal of Sound and Vibration*. 320. (4-5).pp: 1100–1130.
- Liu, G.R., and G.Y. Zhang. (2013). *The Smoothed Point Interpolation Methods – G Space Theory and Weakened Weak Forms*. WorldScientific.
- Miller, Karol, Grand Joldes, Dane Lance, and Adam Wittek. (2006). Total Lagrangian Explicit Dynamics Finite Element Algorithm for Computing Soft Tissue Deformation. *Communications in Numerical Methods in Engineering*. 23. (2).pp: 121–134.
- Nash, M P, and P J Hunter. (2000). Computational Mechanics of the Heart. *October*. 61. (1).pp: 113–141.

- Nguyen-Thoi, T., G. R. Liu, K. Y. Lam, and G. Y. Zhang. (2009). A Face-based Smoothed Finite Element Method (FS-FEM) for 3D Linear and Geometrically Non-linear Solid Mechanics Problems Using 4-node Tetrahedral Elements. *International Journal for Numerical Methods in Engineering*. 78. (3).pp: 324–353.
- Nguyen-Thoi, T., H.C. Vu-Do, T. Rabczuk, and H. Nguyen-Xuan. (2010). A Node-based Smoothed Finite Element Method (NS-FEM) for Upper Bound Solution to Visco-elastoplastic Analyses of Solids Using Triangular and Tetrahedral Meshes. *Computer Methods in Applied Mechanics and Engineering*. 199. (45-48).pp: 3005–3027.
- Ogden, R. W. (1972). Large Deformation Isotropic Elasticity - On the Correlation of Theory and Experiment for Incompressible Rubberlike Solids. *Proceedings of the Royal Society A: Mathematical, Physical and Engineering Sciences*. 326. (1567).pp: 565–584.
- De Souza Neto, E.A., D. Perić, M. Dutko, and D.R.J. Owen. (1996). Design of Simple Low Order Finite Elements for Large Strain Analysis of Nearly Incompressible Solids. *International Journal of Solids and Structures*. 33. (20-22).pp: 3277–3296.
- Taylor, Robert L. (2000). A Mixed-enhanced Formulation Tetrahedral Finite Elements. *International Journal for Numerical Methods in Engineering*. 47. (1-3).pp: 205–227.
- Vetter, FJ, and AD McCulloch. (2000). Three-dimensional Stress and Strain in Passive Rabbit Left Ventricle: a Model Study. *Annals of Biomedical Engineering*. 28.ppp: 781–792.
- Weiss, Jeffrey A., Bradley N. Maker, and Sanjay Govindjee. (1996). Finite Element Implementation of Incompressible, Transversely Isotropic Hyperelasticity. *Computer Methods in Applied Mechanics and Engineering*. 135. (1-2).pp: 107–128.
- Zienkiewicz, O. C., J. Rojek, R. L. Taylor, and M. Pastor. (1998). Triangles and Tetrahedra in Explicit Dynamic Codes for Solids. *International Journal for Numerical Methods in Engineering*. 43. (3).pp: 565–583.

## Theoretical and Numerical Analysis of Heat Transfer in Pipeline System

Xiaowei Zhu, Hui Tang, \*Hua Li, Jiahua Hong, Songyuan Yang

School of Mechanical & Aerospace Engineering, Nanyang Technological University, Singapore 639798.

\*Corresponding author: lihua@ntu.edu.sg

### Abstract

In this paper, analysis is conducted in both theoretical and numerical aspects on the heat transfer in a pipeline system via three steps: (1) Development of a theoretical model based on the heat transfer theory and existing work from literature; (2) Development of a corresponding MATLAB-based software for the evaluation of heat loss within the pipeline system; (3) Validation of the software via three-dimensional computational fluid dynamics (CFD) simulations using ANSYS FLUENT. It is concluded that the software can provide in-depth understanding of the heat transfer phenomena in pipelines and can be used for fast assessment of the heat loss in pipeline systems.

**Keywords:** Pipeline system; Software; Heat transfer.

### Nomenclature

$\dot{m}$	Mass flow rate (kg/s)	$\lambda$	Thermal conductivity of liquid or gas (W/m·K)
$q$	Heat transfer rate (W)	$t$	Temperature (K)
$h$	Convection heat transfer coefficient (W/m <sup>2</sup> ·K)	$r$	Radius (m)
$H'$	Specific enthalpy (kJ/kg)	$x$	Steam dryness
$Re$	Reynolds number	$\rho$	Density (kg/m <sup>3</sup> )
$Pr$	Prandtl number	$R_f$	Fouling factor (W/m <sup>2</sup> ·K)
$Nu$	Nusselt number	$L$	Length (m)
$k$	Thermal conductivity of solid (W/m·K)	$\eta$	Viscosity (kg/s·m)

### Subscripts

$in$	Inlet	$i$	Inside
$out$	Outlet	$o$	Outside
$eq$	Equivalent	$S$	Sub-pipe

### Introduction

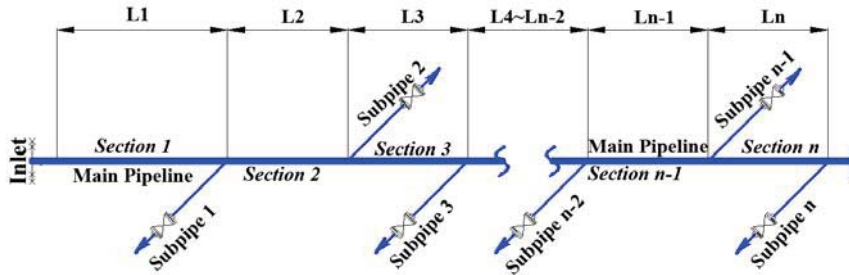
Overhead pipelines were used extensively in both industrial and civic heat supply engineering (Zhang and Lu, 1998). Since pipeline systems are complex and the ambient environment is highly variable, how to quickly determine the heat loss of a pipeline system is a difficult problem for engineers and pipe network designers. Firstly, the pipeline structure and the mass flow distribution influence significantly on the convection heat transfer inside the pipeline (Yang, 2009). Secondly, the pipe material, the cladding material and the insulation have great effects on the heat conduction inside the pipe wall. Thirdly, the variable environmental parameters are challenges to the analysis of convection heat transfer outside the pipeline. Therefore, the heat transfer through the pipeline system is an interesting but challenging research topic.

In the present paper, based on the heat transfer theory, a theoretical model is established, and then the corresponding software is developed in MATLAB. In order to validate the software, several numerical case studies are carried out via a CFD code in ANSYS FLUENT. In addition, an example of application is presented to demonstrate the capability of the software. It is shown that the

software can assess the heat loss with acceptable accuracy and improve the computing efficiency significantly. It is thus a useful tool for engineers and pipe network designers

**Theoretical model**

As shown in Figure 1, the pipeline system in the present work consists of a main pipeline and several sub-pipelines, which is a common structure in industrial and civic heat supply engineering.



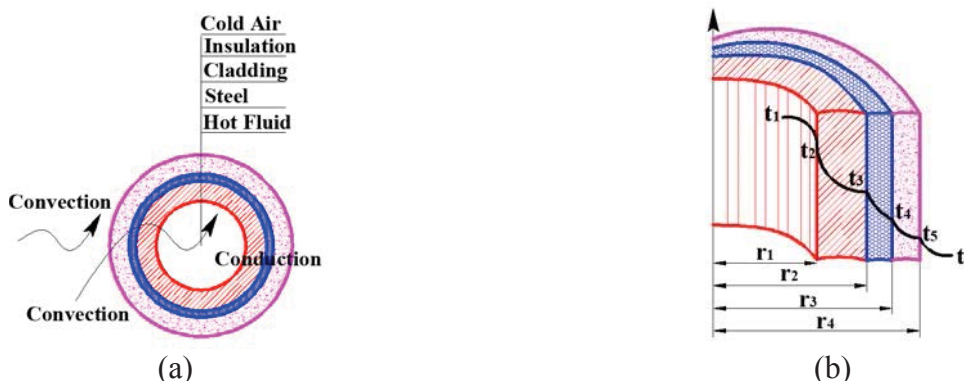
**Figure 1. Structure of the pipeline system.**

The mass flow rate in the main pipeline is a variable, which varies along the flow direction because of bypass flows. In order to solve this problem, the main pipeline is divided into several sections. Within each section the mass flow rate remains constant. Equation (1) shows the mass flow rate of each section, in which  $\dot{m}_1$  represents the mass flow rate of Section 1,  $\dot{m}_2$  the mass flow rate of Section 2,  $\dot{m}_n$  the mass flow rate of Section n, and so on.

$$\begin{aligned}
 \dot{m}_2 &= \dot{m}_1 - \dot{m}_{S1} \\
 \dot{m}_3 &= \dot{m}_2 - \dot{m}_{S2} \\
 &\dots\dots\dots \\
 \dot{m}_{n-1} &= \dot{m}_{n-2} - \dot{m}_{Sn-2} \\
 \dot{m}_n &= \dot{m}_{n-1} - \dot{m}_{Sn-1}
 \end{aligned}
 \tag{1}$$

*Heat transfer process*

Figure 2 shows a part of the pipeline, where the inner and outer surfaces are exposed to hot fluid and cold air respectively. The heat transfer process includes the convection inside the pipe, the conduction through the pipe, and the convection outside the pipe. The heat transfer process is presented in Figure 2 (a) and the distribution of temperature in Figure 2 (b).



**Figure 2. Heat transfer process and temperature distribution through pipe wall.**

According to the thermal resistance theory, the heat transfer rate through the pipe wall is presented as (Bergman, Incropera *et al.*, 2011)

$$q = \frac{t_1 - t_6}{\frac{1}{2\pi r_1 L h_i} + \frac{\ln\left(\frac{r_2}{r_1}\right)}{2\pi k_1 L} + \frac{\ln\left(\frac{r_3}{r_2}\right)}{2\pi k_2 L} + \frac{\ln\left(\frac{r_4}{r_3}\right)}{2\pi k_3 L} + \frac{1}{2\pi r_4 L h_o} + R_f} \quad (2)$$

where  $t$  stands for the temperature,  $r$  the radius,  $k$  the thermal conductivity,  $h$  the convection heat transfer coefficient, and  $L$  the length respectively. In practical analysis, although the outside air temperature  $t_6$  is usually considered as a constant, the inside fluid temperature  $t_1$  is a variable since it varies along the flow direction. By analysis and calculation, it is concluded that the temperature difference ( $t_1 - t_6$ ) may be assumed to be the log mean temperature difference. As a result, Equation (2) is modified to

$$q = \frac{\frac{t_{in} - t_{out}}{\ln\left(\frac{t_{in} - t_{air}}{t_{out} - t_{air}}\right)}}{\frac{1}{2\pi r_1 L h_i} + \frac{\ln\left(\frac{r_2}{r_1}\right)}{2\pi k_1 L} + \frac{\ln\left(\frac{r_3}{r_2}\right)}{2\pi k_2 L} + \frac{\ln\left(\frac{r_4}{r_3}\right)}{2\pi k_3 L} + \frac{1}{2\pi r_4 L h_o} + R_f} \quad (3)$$

In Equation (3), there are three unknowns, i.e. the inside heat transfer coefficient  $h_i$ , the outside heat transfer coefficient  $h_o$ , and the outlet temperature  $t_{out}$ , which will be figured out by analyses of convection heat transfer inside and outside the pipeline.

#### *Heat transfer inside the pipeline*

In industrial and civic heat supply engineering, the most common fluid inside includes hot water and steam. Although the heat transfers of these two fluids are all forced convection, the phase change of steam gives more challenge to the analysis in steam pipeline systems. In addition, the heat transfer inside the pipeline is an internal convection, such that another important characteristic is that the fluid is confined by the surface wall of the pipeline. As a result, the heat transfer phenomena inside pipeline are thus closely associated with the characteristic of the hot fluid and the dimension of the pipeline.

For hot water, the Dittus-Boelter equation as a classical expression for computing the Nusselt number of fully developed turbulent flow in a circular tube is given as (Tao, 2001),

$$Nu_{water} = 0.023 Re^{0.8} Pr^n \quad (4)$$

where  $n = 0.4$  for heating and  $n = 0.3$  for cooling.

By Equation (4) and the definition of the Nusselt number (Tao, 2001), the inside convection heat transfer coefficient for water  $h_{i-water}$  is thus expressed as

$$h_{i-water} = 0.023 \frac{\lambda}{d_{in}} Re^{0.8} Pr^{0.3} \quad (5)$$

while  $Re$  stands for the Reynolds number, and  $Pr$  the Prandtl number respectively.

For steam, the condensation of steam has to be considered in the heat transfer process. Condensation is a phase change process from vapor to liquid. It occurs when the steam strikes the pipe wall whose surface is at a temperature below the steam saturation temperature and the steam releases latent heat and converts to a liquid phase immediately (Tandon, Varma *et al.*, 1995). Several empirical and semi-empirical correlations were suggested and one of the most widely used correlations is the Ackers Equation as follows (Yang and Webb, 1996).

$$Nu_{steam} = C Re_{eq}^n Pr_{liquid}^{\frac{1}{3}} \quad (6)$$

where  $C = 0.0265$ ,  $n = 0.8$  for  $Re_{eq} > 5 \times 10^4$ , and  $C = 5.03$ ,  $n = 1/3$  for  $Re_{eq} < 5 \times 10^4$ .

In Equation (6), the equivalent Reynolds number  $Re_{eq}$  is given by (Yang and Webb, 1996)

$$Re_{eq} = \frac{\dot{m}_{eq} d_{in}}{\eta_{liquid}} \quad (7)$$

where  $\dot{m}_{eq}$  stands for the equivalent mass flow rate,  $d_{in}$  the inside diameter,  $\eta_{liquid}$  the viscosity of the liquid. Equation (8) gives the expression of  $\dot{m}_{eq}$ , in which  $x$  means the steam dryness and  $\rho$  the density.

$$\dot{m}_{eq} = \dot{m} \left[ (1-x) + x \left( \frac{\rho_{liquid}}{\rho_{vapor}} \right)^{\frac{1}{2}} \right] \quad (8)$$

The inside convection heat transfer coefficient for steam  $h_{i-steam}$  is thus obtained as

$$h_{i-steam} = C \frac{\lambda_{liquid}}{d_{in}} Re_{eq}^n Pr_{liquid}^{\frac{1}{3}} \quad (9)$$

### Heat transfer outside the pipeline

The heat transfer from pipe wall to outside air is an external heat convection between solid boundary and moving fluid. In general, pipeline systems are exposed to the surrounding, such that the meteorological conditions have a great influence on the heat loss of the pipeline systems. A well-known empirical correlation contributed by Hilpert is presented as (Rathore and Kapuno, 2011)

$$Nu = C Re^n Pr^{\frac{1}{3}} \quad (10)$$

while  $Re$  stands for the Reynolds number, and  $Pr$  the Prandtl number respectively.  $C$  and  $n$  are constants and tabulated in Table 1 at various Reynolds numbers. This empirical correlation is widely used for  $Pr \geq 0.7$ .

**Table 1. The values of  $C$  and  $n$  (Rathore and Kapuno, 2011)**

$Re$	$C$	$n$
0.4~4	0.989	0.330
4~40	0.911	0.385
40~4000	0.683	0.466
4000~40000	0.193	0.618
40000~400000	0.0266	0.805

According to Equation (10) and the definition of the Nusselt number (Tao, 2001), the outside convection heat transfer coefficient  $h_o$  is thus presented as

$$h_o = C \frac{\lambda}{d} Re^n Pr^{\frac{1}{3}} \quad (11)$$

#### *Energy equation*

Considering the pipeline and the inside fluid as a whole system, when using the first law of thermodynamics, the energy equation for water pipelines is obtained as

$$q_{water} = \dot{m} (H'_{in} - H'_{out}) \quad (12)$$

For steam pipelines, the condensation has to be considered and the energy equation becomes

$$q_{steam} = \dot{m} x (H'_{steam-in} - H'_{steam-out}) + \dot{m} (1-x) (H'_{water-in} - H'_{water-out}) \quad (13)$$

while  $q$  stands for the energy,  $H'$  the specific enthalpy,  $m$  the mass flow rate, and  $x$  the steam dryness.

Equations (1) ~ (13) represent the entire heat transfer process through the pipeline such that the theoretical model for assessing heat loss of the present pipeline system is established.

#### **Development of the software**

Based on the theoretical model of the present pipeline system, a software is written and debugged using MATLAB R2012b, under Windows operating system. MATLAB is a high-level technical computing language and interactive platform for algorithm development, data visualization, data analysis, and numeric computation (Özgü Arısoy and Dikmen, 2011).

All the equations in the theoretical model as mentioned above are formulated first with MATLAB source code, in which an iterative computational technique is used to solve the problem. After that, Graphical User Interface (GUI) is adopted to create the user-friendly interface. Furthermore, the testing and debugging of the module are conducted backstage as MATLAB is internally packaged



with an editing and debugging functionality (Sen and Shaykhian, 2009). Finally, the software is published as an executable file that can be used in normal computers, even without MATLAB installed.

Figure 3 shows the main user interface of the software, which includes Parameter Input, Control Function, Output Display, and Database. Parameter Input is used to input basic parameters, including hot fluid parameters, pipeline structures, environmental parameters, and so on. Control Function is used for start or stop of the calculation, modification of the input data, and quit from the software. Output Display is designed for exporting the computational results. The clear and concise user interface enable user to operate the software easily and thus significantly improve the efficiency.

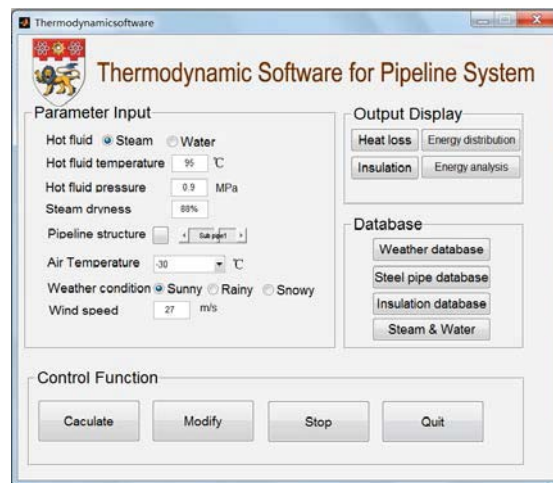


Figure 3. Main user interface of the software.

### Validation of the software

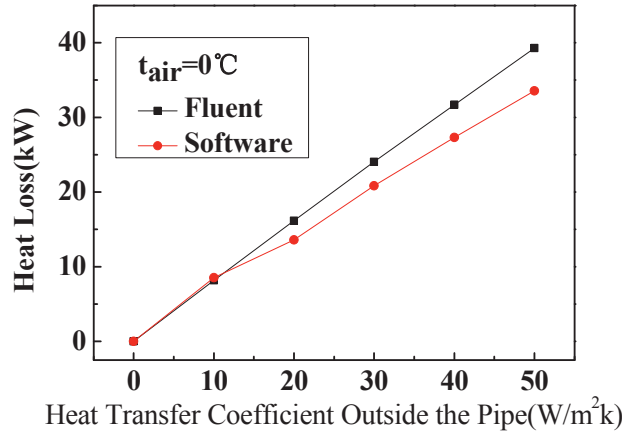
As well known, ANSYS FLUENT as a CFD tool has a long history for simulation of the pipeline heat transfer process and for optimization of the pipeline structure (Li, Zhao *et al.*, 2012). Therefore, it is adopted to simulate the fluid flow and temperature field in the present pipeline system for validation of the software developed. In the present work, a model containing a main pipeline and two sub-pipelines is created and analyzed numerically. The fluid is hot water with the inlet temperature 85 °C and the inlet pressure 0.5 MPa. The ambient air temperature is set to be 0 °C, and the outside convection heat transfer coefficient  $h_o$  is set as 10, 20, 30, 40, 50 W/m<sup>2</sup>·K, respectively.

In the simulation, SOLIDWORKS is used to create the 3-D geometry model of this pipeline system. The grid selected has achieved its convergence through a sensitivity study. The Pressured-Based solver in steady heat transfer approach is used for simulation. The Standard  $k-\varepsilon$  model is adopted to model the turbulence in the pipe flow. Through simulation, the temperature distribution of the pipeline is obtained, and the heat loss of the pipeline system is then calculated according to the enthalpy difference of the fluid at the inlet and the outlet, by (Moran, Shapiro *et al.*, 2010).

$$q = \dot{m}(H'_{in} - H'_{out}) \quad (17)$$

where  $q$  stands for the heat loss,  $H'$  the specific enthalpy, and  $m$  the mass flow rate.

The results from ANSYS FLUENT and the software are compared. As shown in Figure 4, the difference is generally less than 15%, and less than 10% when the outside heat transfer coefficient ranges from 10 to 30 W/m<sup>2</sup>·K, which are usual values in practical applications. It is thus concluded that the software can achieve results with acceptable accuracy and can be used in practical applications.

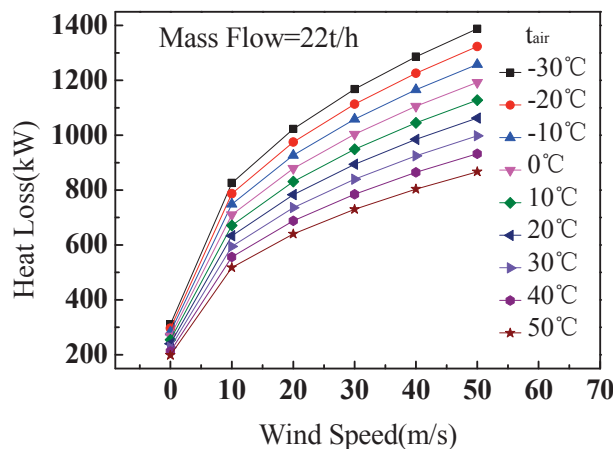


**Figure 4. Comparison of the results between FLUENT and the software.**

**Case study**

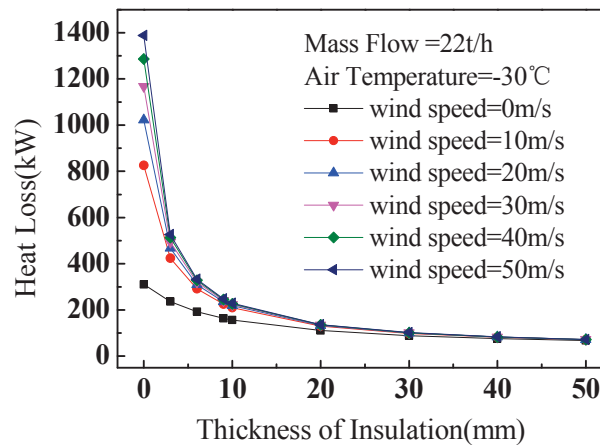
In this section, a steam pipeline in a cargo heating system is employed to demonstrate the function and capability of the software. In the cargo heating system, the pipeline plays a role of conveying steam from boiler to cargo tanks continuously. The fluid in this case study is saturated steam with the inlet temperature of 181 °C and the pressure of 0.9 MPa. The structure of the present pipeline system includes a main pipeline and 12 sub-pipelines. By inputting the basic information into the software, the heat loss of the pipeline system with various outside parameters is obtained.

Figure 5 shows the effects of the wind speed on the heat loss of the pipeline system subject to different air temperatures. The heat loss of the pipeline system increases sharply with the increase of wind speed. The reason is that the wind speed enhances the convection heat transfer outside the pipe and thus more heat transfers to the cold environment (Rohsenow, Hartnett *et al.*, 1998).



**Figure 5. Effects of wind speed on the heat loss of the pipeline system.**

As shown in Figure 6, the heat loss of the pipeline system decreases sharply with the increase of insulation thickness, even with just several millimeters. This is because the additional insulation increases the conduction resistance significantly, resulting in less heat transfers to the ambient air (Lin, Guo *et al.*, 2005). Such that it is strongly recommended that the present pipeline system needs to be insulated for about 20 mm for energy saving. It is also observed that there is only a marginal effect when the insulation thickness is more than 30 mm. This study indicates that this software can be used for the optimization of the pipeline insulation.



**Figure 6. Effects of insulation on the heat loss of the pipeline system.**

## Conclusions

Based on the heat transfer theory, a theoretical model is established, and its corresponding MATLAB-based software is developed for assessment of the heat loss of pipeline systems. The software can obtain results with acceptable accuracy as the comparison between the software and ANSYS FLUENT shows a reasonable agreement. The software can save analysis time significantly when compared with the ANSYS FLUENT based models. It also has a user-friendly interface, which ensures the easy use for engineers and other customers without thermodynamics background. In summary, the software not only provides an easy way for fast assessment of the heat loss, but also offers a useful tool for the optimal design and energy saving analysis of pipeline systems.

## References

- Bergman, T. L., Incropera, F. P., Lavine, A. S., and DeWitt, D. P. (2011). *Fundamentals of heat and mass transfer*: John Wiley & Sons.
- Li, G., Zhao, F., and Li, X. (2012). Application of Computational Fluid Dynamics in Piping Design. *Pipeline Technique and Equipment* 03(0014), 14-15.
- Lin, T. R., Guo, B., Song, S., Ghalambor, A., and Chacko, J. (2005). *Offshore pipelines*: Access Online via Elsevier.
- Moran, M. J., Shapiro, H. N., Boettner, D. D., and Bailey, M. (2010). *Fundamentals of engineering thermodynamics*: Wiley.
- Özgü Arısoy, M., and Dikmen, Ü. (2011). Potensoft: MATLAB-based software for potential field data processing, modeling and mapping. *Computers & Geosciences*, 37(7), 935-942.
- Rathore, M. M., and Kapuno, R. (2011). *Engineering heat transfer*: Jones & Bartlett Publishers.
- Rohsenow, W. M., Hartnett, J. P., and Cho, Y. I. (1998). *Handbook of heat transfer* (Vol. 3): McGraw-Hill New York.
- Sen, S. K., and Shaykhian, G. A. (2009). MatLab tutorial for scientific and engineering computations: International Federation of Nonlinear Analysts (IFNA); 2008 World Congress of Nonlinear Analysts (WCNA). *Nonlinear Analysis: Theory, Methods & Applications*, 71(12), e1005-e1020.
- Tandon, T., Varma, H., and Gupta, C. (1995). Heat transfer during forced convection condensation inside horizontal tube. *International journal of refrigeration*, 18(3), 210-214.
- Tao, W. (2001). *Numerical heat transfer*. Xi'an: Xi'an Jiao Tong University Publishing Company.

- Yang, C. (2009). *The Analysis and Research For The 72000DWT Crude Oil Tanker Heating and Insulation Process Operation System*. Master Degree Thesis, Dalian Maritime University, Dalian, China.
- Yang, C., and Webb, R. (1996). Condensation of R-12 in small hydraulic diameter extruded aluminum tubes with and without micro-fins. *International Journal of Heat and Mass Transfer*, 39(4), 791-800.
- Zhang, D., and Lu, Y. (1998). Displacement calculation of thermal overhead pipeline. *Oil and Gas Storage and Transportation*, 17(11), 17-21.

**Simulation on separation flowing around cylinders with lattice****Boltzmann method****Z.D.Wang<sup>1,2,3</sup>, J.F.Yang<sup>1,2,3</sup>, Y.H.Qian<sup>1,2,3,4</sup>**<sup>1</sup>Shanghai Institute of Applied Mathematics and Mechanics, Shanghai University, Shanghai, China<sup>2</sup>Shanghai Key Laboratory of Mechanics in Energy Engineering, Shanghai, China<sup>3</sup>Shanghai Program for Innovative Research Team in Universities, Shanghai, China<sup>4</sup>Department of Mechanical and Aerospace Engineering, UC Irvine, CA 92617, USA

\*Corresponding author: qian@shu.edu.cn

**Abstract**

In computational fluid dynamics, traditional methods show low rate of convergence on low speed flow, while lattice Boltzmann method performed well on it. In this report, we use lattice Boltzmann method to simulate cylinder flow, which cylinders are in many shapes. These results will be important to further study on control of cylinder flow.

**Keywords:** cylinder flow, separation flow, lattice Boltzmann method

**Introduction**

Lattice Boltzmann method (LBM) has been widely used in computational fluid dynamics (CFD), different from other traditional methods, which need to solve Jacobian matrix, LBM solves Boltzmann method with single variable particle distribution function  $f(\mathbf{x}, \xi, t)$  instead of Navier-Stokes equations. When simulating low speed flow, traditional methods show low rate of convergence. LBM is explicit scheme, which can solve equations fast. Normally, LBM uses Cartesian coordinate. When treating with curved boundaries, lattice will be broken into different parts. It is hard to describe the curved boundaries. At very first, A.J.C.Ladd (1994) suggests to use Link Bounce-Back scheme to treat the curved boundaries, but this treatment will change the curved boundaries into “coarse lattice boundary”. Later, O.Filippova and D.Hänel (1998) propose a new boundary treatment for curved boundaries. But the stability is not so good. Then R.Mei et al. (1999) improved its stability, but when treating with low Reynolds flow, the stability is still not enough. In 2002, Z.L.Guo et al. (2002) proposed an extrapolation method for curved boundaries. Lately, Z.D. Wang et al. (2013) proposed a new extrapolation treatment, which improve the accuracy and stability in low Reynolds flow.

**Governing Equation**

Lattice Boltzmann method solves the following discretization equation:

$$f_i(x_\alpha + c_{i\alpha}\delta t, t + \delta t) = f_i(x_\alpha, t) - \omega [f_i^{eq}(x_\alpha, t) - f_i(x_\alpha, t)] \quad (1)$$

where  $f$  is the density distribution function of particles,  $c_{i\alpha}$  is the discretized velocities and  $\alpha$  represents Cartesian coordinate. We simulate the low speed flow using D2Q9 model, which is one of the DdQb models proposed by Y.H. Qian et al. (1992). The equilibrium equation is chosen as follows:

$$f_i^{\text{eq}}(\mathbf{x}, t) = w_i \rho \left\{ 1 + \frac{c_{i\alpha} u_\alpha}{c_s^2} + \frac{u_\alpha u_\beta}{2c_s^2} \left( \frac{c_{i\alpha} c_{i\beta}}{c_s^2} - \delta_{\alpha\beta} \right) \right\} \quad (2)$$

where  $\rho$  and  $u_\alpha$  represent the density and velocity of the fluid particle at position  $\mathbf{x}$  and time  $t$ ,  $c_s$  is the speed of sound, the index  $i$  denotes different particles' dimensionless velocity and  $\delta_{\alpha\beta}$  is the Kronecker operator.  $w_i$  and  $c_s$  is chosen as

$$w_i = \begin{cases} \frac{4}{9}, & i = 0, \\ \frac{1}{9}, & i = 1 \sim 4, \\ \frac{1}{36}, & i = 5 \sim 8 \end{cases} \quad c_s = \frac{1}{\sqrt{3}} \frac{\delta x}{\delta t}. \quad (3)$$

To simulate the Newtonian fluid,  $\omega$  is related to the shear viscosity, which can be driven by Chapman-Enskog expansion as

$$\frac{1}{\omega} = \frac{\nu}{c_s^2 \delta t} + \frac{1}{2}. \quad (4)$$

### Boundary Condition

On the boundary, we use the boundary treatment proposed by WANG et al. This boundary treatment divide the fictitious particle distribution into the equilibrium part and nonequilibrium part as follows:

$$f_i(\mathbf{x}_b, t) = f_i^{(\text{eq})}(\mathbf{x}_b, t) + f_i^{(\text{neq})}(\mathbf{x}_b, t) \quad (5)$$

where  $f_i^{(\text{eq})}(\mathbf{x}_b, t)$  is set as

$$f_i^{(\text{eq})}(\mathbf{x}_b, t) = w_i \rho(\mathbf{x}_b, t) \left[ 1 + \frac{c_{i\alpha} u_{b,\alpha}}{c_s^2} + \frac{(c_{i\alpha} u_{b,\alpha})^2}{2c_s^4} - \frac{u_b^2}{2c_s^2} \right] \quad (6)$$

where  $\rho(\mathbf{x}_b, t) = 2\rho(\mathbf{x}_f, t) - \rho(\mathbf{x}_{ff}, t)$  and  $\mathbf{u}_b = \frac{2\lambda}{1+\lambda} \mathbf{u}_f - \frac{\lambda}{2+\lambda} \mathbf{u}_{ff}$ .

For the nonequilibrium part, we define  $f_i^{(\text{neq})}(\mathbf{x}_b, t)$  as follows:

$$f_i^{(\text{neq})}(\mathbf{x}_b, t) = 2f_i^{(\text{neq})}(\mathbf{x}_f, t) - f_i^{(\text{neq})}(\mathbf{x}_{ff}, t). \quad (7)$$

### Simulations

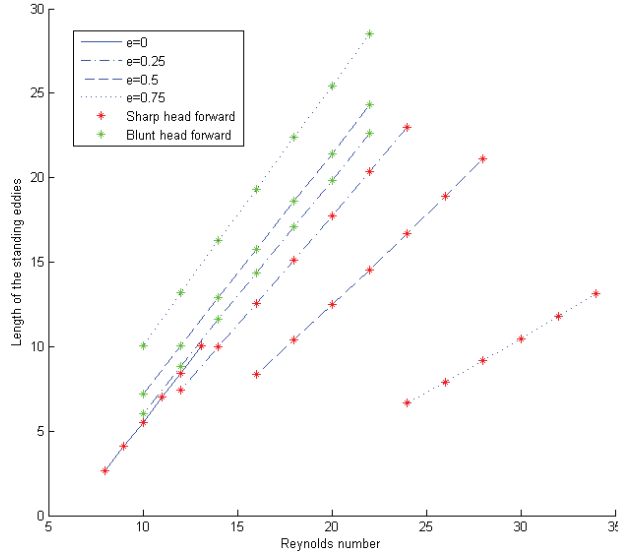
In this report, polygonal cylinders and oval cylinders with different eccentricities are simulated. Because of the resolution, the critical flow when it separated cannot be simulated. To find the critical Reynolds number, higher Reynolds number flows are simulated and extrapolated to critical Reynolds number.

The Reynolds number is define as:

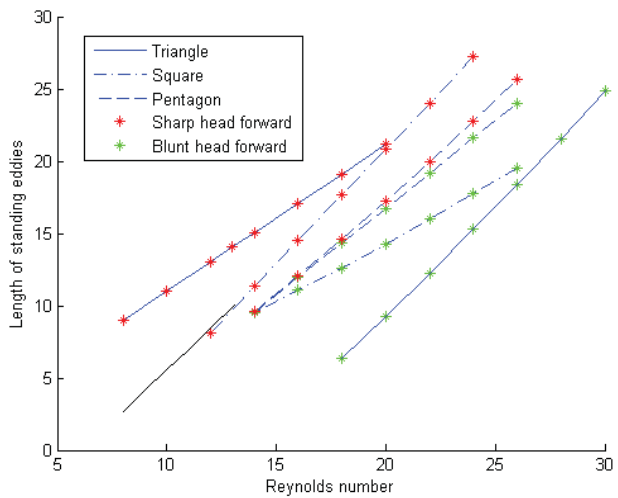
$$\text{Re} = \frac{UL}{\nu} \quad (8)$$

In flows around polygonal cylinders,  $L$  is the diameter of their circumcircles. In flows around oval cylinders,  $L$  is the length of major axis.

As experiment assembled by Milton Van Dyke (1988) reported, the length of standing eddies increases linearly with Reynolds number. The results of simulations are shown below:



**Figure 1. Eddies’ lengths of ovals**

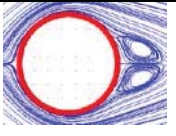
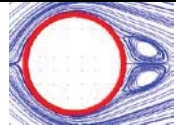
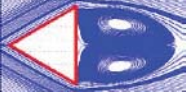
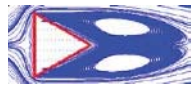

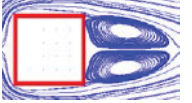

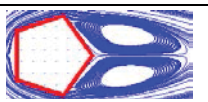



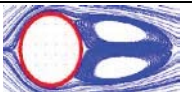




**Figure 2. Eddies’ lengths of polygons. The black solid line represents circle cylinder**

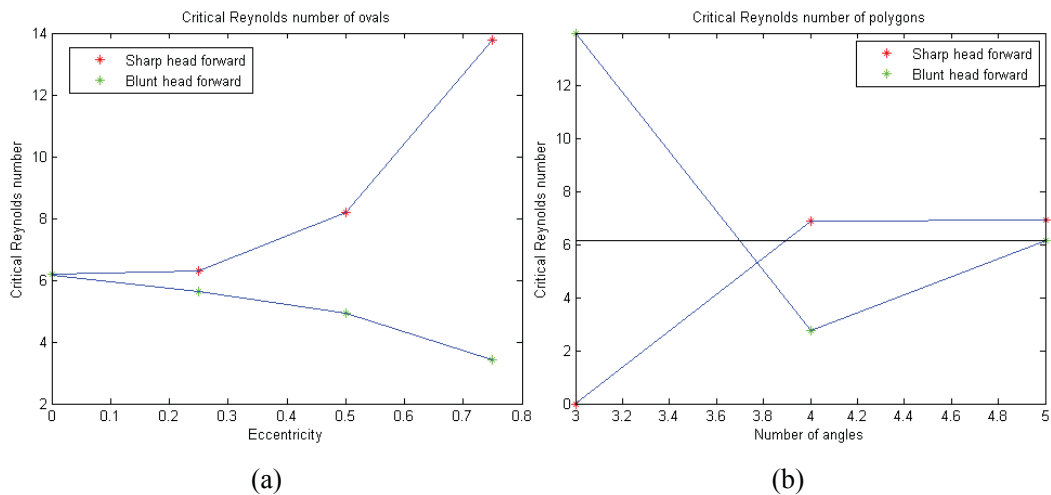
The two figures above show the exact linear relationship between the length and Reynolds number, which agrees with the experiment results. The slopes of these straight lines in the figures above are different. It shows how separating vortex changes after separated. We consider it is relative to aspect ratio of each cylinder. The slope increases as the aspect ratio increases.

The critical Reynolds number is shown in the table below:

**Table 1. Critical Reynolds number and streaming pattern**

	Sharp head forward	Blunt head forward	Streamlines pattern (sharp head forward)	Streamlines pattern (blunt head forward)
Circle	6.1758	6.1758		
Triangle	0	13.9904		
Square	6.9117	2.7690		
Pentagon	6.9461	6.1410		
Oval (e=0.25)	6.2908	5.6197		
Oval (e=0.5)	8.2046	4.9342		
Oval (e=0.75)	13.7695	3.4372		

The variation tendency of oval cylinders is shown below:



**Figure 3. Tendency of critical Reynolds numbers**

When sharp head point forward, the tendency of critical Reynolds number of oval cylinders monotone increases as the eccentricity increases. When blunt head point



forward, critical Reynolds number monotone decrease as the eccentricity decreases. As the number of angles increasing, the critical Reynolds number of polygonal cylinders is approaching that of circle cylinder (the black line in Figure 3(b)).

### Conclusions

We successfully simulated the flows around various cylinders and get some preliminary result. We find the separation flow has two important characteristics: critical Reynolds number and the slopes.

### Acknowledgment

This work has been supported by Research on Lattice Boltzmann Method for Complex and Moving Boundary Problems (K.13-0401-13-001) from Shanghai University.

### References

- [1] A.J.C. Ladd. (1994), Numerical simulations of particulate suspensions via a discretized Boltzmann equation. *J. Fluid Mech.* 271, pp.285-310.
- [2] Milton van Dyke. (1988), An album of fluid motion. *Stanford: The Parabolic Press.*
- [3] O. Filippova and D. Hänel. (1998), Grid refinement for lattice-BGK Models. *J. Comput. Phys.* 147, pp.219-228.
- [4] R. Mei, L.S. Luo, and W. Shyy. An accurate curved boundary treatment in the lattice Boltzmann method. *J.Comput. Phys.* 155, pp.307-330.
- [5] Y.H. Qian, D. d’Humières and P. Lallemand. (1992), Lattice BGK models for Navier-Stokes equation. *Europhys Lett.*, 17, pp. 479–484.
- [6] Z.D. Wang, J. F. Yang, Y. K. Wei and Y. H. Qian. (2013), A new extrapolation treatment for boundary conditions in lattice Boltzmann method. *Chin.Phys.Lett.* 30, pp.094703-1–094703-5.
- [7] Z.L. Guo,C.G. Zheng, and B.C. Shi. (2002) An extrapolation method for boundary condition in lattice Boltzmann method. *Phys. Fluids* 14, pp.2007-2010.

# Symbolic Calculation of Free Convection for Porous Material of Quadratic Heat Generation in a Circular Cavity

Kamyar Mansour

Amirkabir University of technology, Tehran , Iran, 15875-4413

[mansour@aut.ac.ir](mailto:mansour@aut.ac.ir)

**Keywords:** Free convection flow, nonlinear equations, Symbolic calculations

**Abstract** We consider the two-dimensional problem of steady natural convection in a circular cavity with quadratic volumetric generation filled with porous material. We use Darcy's law for this cavity filled with porous material. The solution is governed by dimensionless parameter Darcy-Rayleigh number. The solution is expanded for low Darcy-Rayleigh number as was done by [1] and extended to 18 terms by computer. Analysis of these expansions allows the exact computation for arbitrarily accuracy up to 50000 figures. Although the range of the radius of convergence is small but Pade approximation leads our results to be good even for higher value of the similarity parameter.

## Introduction

We consider the two-dimensional problem of steady natural convection in a circular cavity with linear volumetric heat flux filled with porous material. We use Darcy's law for this cavity filled with porous material. The solution is governed by dimensionless parameter Darcy-Rayleigh number. The solution is expanded for low Darcy-Rayleigh number as was done by [1], [2],[3] and extended to 18 terms by computer. Analysis of these expansions allows the exact computation for arbitrarily accuracy up to 50000 figures. Although the range of the radius of convergence is small but Pade approximation leads our result to be good even for higher value of the similarity parameter. This investigation is in a porous circular cavity driven by heating in the horizontal direction is our interest. We use Darcy's law for this cavity filled with porous material. The solution is governed by dimensionless parameter Darcy-Rayleigh number. The solution is expanded up to 18 terms by computer in powers of Darcy-Rayleigh number. Analysis of these expansions allows the exact computation for arbitrarily accuracy up to 50000 figures. Although the range of the radius of convergence is small but Pade approximation leads our result to be good even for higher value of the similarity parameter. The analysis yields a solution for all values of Rayleigh number from zero to finite value in a continuous fashion. The natural convection in a cavities filled with porous medium has received much attention because of the theoretical interest of [4], [5], [6], [7] for isothermal surfaces and [8] for isothermal inner and sinusoidal outer boundaries. As far as the numerical works for the case of isothermal surfaces a parameter study of diameter-ratio effects on the heat transfer coefficient was performed by [4] and angle of heating by [8] and other related problem of Natural Convection Non-Darcy effect by [9] and finally experimental work of [4]. The question of Hydrodynamic instability induces steady or oscillatory flows have been subject of many studies for example [4] and [10]. I hope the present exact solution of steady flow will help to answer such question more clearly. We recently have done the same present approach of symbolic calculation for laminar flow through heated horizontal pipe [3] and similar work done for concentrically spheres [11]. The similar approach was done for rectangular cavity by [12] and they found boundary limit solution from their regular perturbation for small Darcy-Rayleigh number.

## Statement of Problem

The governing equations for porous materials with Darcy's law can be written in dimensionless form as:

$$\nabla \dot{V} = 0 \tag{1}$$

$$\dot{V} = -\frac{K}{\mu}(\nabla \dot{P} - \rho g J) \tag{2}$$

$$q''' + \rho c(V \cdot \dot{V})\dot{T} = k\nabla^2 \dot{T} \tag{3}$$

$$\rho = \rho_r(1 - \beta(T - T_r))$$

Where  $\dot{V}$  is the velocity vector,  $\rho$  density, temperature,  $\mu$  viscosity,  $\dot{P}$  pressure  $J = (\cos \theta, -\sin \theta)$  is a unit vector in the direction of gravity and  $\lambda = \frac{g\beta\Delta T_q(KK)R}{\nu\alpha}$  is defined the internal Rayleigh number. The equations (5), (6) have been non-dimensionalized by scaling length, velocity and temperature using the inner radius of cavity as the length scale,  $\frac{k}{R(\rho c)_r}, \Delta T_q, \Delta T_q$  Is calculated from uniform heat generation  $q''', \Delta T_q \sim \frac{q'''R^2}{\alpha}$  is somehow certain gradient of temperature across the cavity,  $\beta$  the coefficient of volumetric expansion of the fluid) and  $g$  the acceleration due to gravity. Introducing the stream function in order to satisfy Eq. (1), eliminating the pressure from Eq. (2) and writing the resulting equation in cylindrical polar coordinates leads to the dimensionless equations as used in [13].

We consider the two-dimensional problem of steady natural convection Mansour [1]. We introduced cylindrical coordinates  $(r, \theta)$   $\theta$  measured from upward vertical.

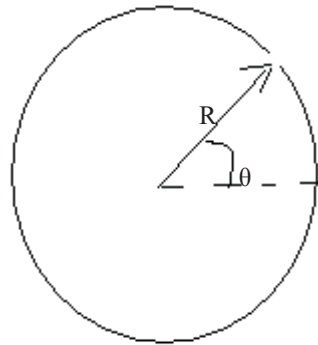


Fig.1 Geometry of the Problem

We mainly follow Mansour’s notation [1]. Then the velocity component  $U, V, W$  in the fluid are functions of  $r$  and  $\theta$  only. The continuity equation can be satisfied by introducing a Stokes stream function  $\psi$  for the cross flow The governing equations for porous materials with Darcy’s law can be written in dimensionless form as:

$$\nabla^2 \psi = -\lambda \left( \sin \theta \frac{\partial T}{\partial r} + \frac{\cos \theta}{r} \frac{\partial T}{\partial \theta} \right) \tag{4}$$

$$\nabla^2 T = \frac{1}{r} \left( -\frac{\partial \psi}{\partial \theta} \frac{\partial T}{\partial r} + \frac{\partial \psi}{\partial r} \frac{\partial T}{\partial \theta} \right) + 9r \tag{5}$$

$$\nabla^2 = \frac{\partial^2}{\partial r^2} + \frac{1}{r} \left( \frac{\partial}{\partial r} \right) + \frac{1}{r^2} \left( \frac{\partial^2}{\partial \theta^2} \right) \tag{6}$$

The corresponding boundary conditions expressing the impermeability of the wall, the no-slip conditions, and imposed temperature distribution are respectively:

1467

$$\psi = 0, \quad \text{at } r = 1$$

$$\partial\psi/\partial r = 0 \quad \text{at } r = 1$$

$$T = 1 \quad \text{at } r = 1,$$

$\lambda = \frac{g\beta\Delta T_0(KK)R}{\nu\alpha}$  is the Rayleigh number. Coordinates are non-dimensionalized by using the radius of cavity as the length scale. Here  $\Delta T_0$  is imposed temperature difference ( $\nu$  is kinematics viscosity,  $\beta$  the coefficient of volumetric expansion of the fluid) and  $g$  the acceleration due to gravity.

### Series Derivation and Computer Extension

In this work we delegated the mounting algebra to the computer and, for our boundary condition (9) one can systematically improve on this approximation).

$$\left\{ \begin{array}{l} T = T_0 + \left(\frac{\lambda}{32}\right) T_1 + \left(\frac{\lambda}{32}\right)^2 T_2 + \left(\frac{\lambda}{32}\right)^3 T_3 + \dots \\ \psi = \left(\frac{\lambda}{32}\right) \psi_1 + \left(\frac{\lambda}{32}\right)^2 \psi_2 + \left(\frac{\lambda}{32}\right)^3 \psi_3 + \dots \end{array} \right. \quad (7)$$

We substitute the expansions (7) into our simplified equations (4) and (5) then equating like powers of  $\lambda$  Gives for  $T_0$  the equation:

$$\frac{\partial^2 T_0}{\partial r^2} + \frac{1}{r} \frac{\partial T_0}{\partial r} = 16r^2$$

Subject to boundary condition, It is easy to show that  $T_0 = r^4$  and  $\psi_0 = 0$ . Therefore, the basic solution is the state of simple conduction. Substituting and equating like powers of  $\lambda$  yields this sequence of successive linear equations, together with boundary conditions

$$\psi_1 = \left(\frac{16}{3}\right) * r * (-1 + r^4) * \cos(\theta)$$

$$\psi_2 = \left(-\left(\frac{16}{45}\right)\right) * r^2 (4 - 5 * r^4 + r^8) \sin(2\theta)$$

$$\psi_3 = \left(\frac{1}{42525}\right) * (32 * (3 * r * (1517 - 1995 * r^2 + 665 * r^6 - 217 * r^{10} + 30 * r^{14}) \cos(\theta) - 35 * r^3 * (-19 + 27 * r^4 - 9 * r^8 + r^{12}) * \cos(3\theta)))$$

$$\psi_4 = -\left(\frac{1}{7016625}\right) * (16 * (2 * r^2 * (-706043 + 800560 * r^2 + 250305 * r^4 - 457380 * r^6 + 139920 * r^{10} - 30030 * r^{14} + 2668 * r^{18}) \sin(2\theta) - 5 * r^4 * (14495 - 23100 * r^4 + 10593 * r^8 - 2156 * r^{12} + 168 * r^{16}) \sin(4\theta)))$$

$$\psi_5 = \left(\frac{1}{948191619375}\right) * (32 * (6 * r * (-26649918834 + 46048261255 * r^2 - 19049830800 * r^4 - 9882692820 * r^6 + 11124883770 * r^8 + 1553442891 * r^{10} - 3856272420 * r^{12} + 831228255 * r^{16} -$$

1468

$$\begin{aligned}
 & 127869742 * r^{20} + 8768445 * r^{24}) \text{Cos}(\theta) - \\
 & r^3 * (57276117182 - 57801113370 * r^2 - \\
 & 37637043444 * r^4 + 47328421140 * r^6 + \\
 & 4509995490 * r^8 - 17437955535 * r^{10} + \\
 & 4400505252 * r^{14} - 684018335 * r^{18} + \\
 & 45091620 * r^{22}) \text{Cos}(3\theta) + \\
 & 99 * r^5 * (-15241026 + 27220700 * r^4 - 16041025 * r^8 + \\
 & 4711980 * r^{12} - 692125 * r^{16} + 41496 * r^{20}) * \\
 & \text{Cos}(5\theta))
 \end{aligned}$$

$$T_1 = \left(-\frac{4}{45}\right) * r * (7 - 10 * r^4 + 3 * r^8) \text{Sin}(\theta)$$

$$\begin{aligned}
 T_2 = & \left(\frac{1}{14175}\right) * (4 * (4 * (368 - 735 * r^2 + 595 * r^6 - 273 * r^{10} + \\
 & 45 * r^{14}) - 105 * r^2 * (-3 + r^4)^2 * (-1 + r^4) * \\
 & \text{Cos}(2\theta)))
 \end{aligned}$$

$$\begin{aligned}
 T_3 = & -\left(\frac{1}{7016625}\right) * (8 * (33 * r * (-31227 + 44730 * r^2 + \\
 & 15170 * r^4 - 43400 * r^6 + 19334 * r^{10} - \\
 & 5145 * r^{14} + 538 * r^{18}) \text{Sin}(\theta) - \\
 & 10 * r^3 * (9175 - 17325 * r^4 + 10593 * r^8 - \\
 & 2695 * r^{12} + 252 * r^{16}) * \text{Sin}(3\theta)))
 \end{aligned}$$

$$\begin{aligned}
 T_4 = & -\left(\frac{1}{316063873125}\right) * \\
 & (4 * (10 * r^2 * (7377934765 - 8889961080 * r^2 - \\
 & 6272840574 * r^4 + 10723280568 * r^6 + \\
 & 1052332281 * r^8 - 5412390984 * r^{10} + \\
 & 1711184904 * r^{14} - 313196884 * r^{18} + \\
 & 23657004 * r^{22}) * \text{Cos}(2\theta) - \\
 & 3003 * (22 * (-1 + r^2)^3 * (826973 - 29841 * r^2 - \\
 & 696192 * r^4 + 59260 * r^6 + 380115 * r^8 + \\
 & 29721 * r^{10} - 105442 * r^{12} - 25374 * r^{14} + \\
 & 10995 * r^{16} + 3665 * r^{18}) + \\
 & 5 * r^4 * (-196994 + 418780 * r^4 - 317295 * r^8 + \\
 & 113916 * r^{12} - 19775 * r^{16} + 1368 * r^{20}) * \\
 & \text{Cos}(4\theta))))
 \end{aligned}$$

(It is possible to introduce the quantity average of temperature defined as:

$$\begin{aligned}
 T_{\text{ave}} &= \frac{1}{\pi} \int_{r=0}^1 \int_0^{2\pi} T r d\theta \\
 T_{\text{ave}} &= 4 + \frac{40 * \left(\frac{\lambda}{32}\right)^2}{27} - \frac{178784224 * \left(\frac{\lambda}{32}\right)^4}{91216125} + \frac{33127587128816 * \left(\frac{\lambda}{32}\right)^6}{9050920003125} - \frac{415246476669183596492032 * \left(\frac{\lambda}{32}\right)^8}{52421427336744481640625} + \\
 & \frac{13856116561981926942506797974752 * \left(\frac{\lambda}{32}\right)^{10}}{743816806230851380283115234375} - \\
 & \frac{2589929811683749738873764604340745236900296 * \left(\frac{\lambda}{32}\right)^{12}}{56030187988183353122363351673196142578125} \\
 & + \dots
 \end{aligned}$$

Of course for lack of space we omit showing the calculation further than this order if any reader interested to have more calculation please contacts the author.

**Analysis of Series and Discussion**

Pade approximants has been used in original forms to enable us to increase the range of applicability of the series as has been used in the works of Mansour [2] and Mansour [3]. This method does not necessarily require any information about the radius of convergence. The Pade approximants provide an approximation that is invariant under an Euler transformation of the independent variables. The theory of Pade approximants has been used extensively in Mansour [1]. Briefly stated, the Pade approximant is the ratio  $P(\lambda)/Q(\lambda)$  of polynomials P and Q of degree m and n, respectively, that, when expanded, agrees with the given series through terms of degree m+n, and normalized by  $P(0)/Q(0)=1$ . Such rational fractions are known to have remarkable properties of analytic continuation. The coefficients of the power series must be known to degree m+n. By equating like power of  $g(\lambda)$  and  $P(\lambda)/Q(\lambda)$ , the linear system of m+n+1 equation must be solved to obtain the coefficients in the functional form  $P(\lambda)/Q(\lambda)$  Pade approximation of orders [1/2], [2/3] and [3/4] for  $T_{ave}$  series are respectively:

pade[1/2]:

$$\frac{4}{1 - \frac{10 * (\frac{\lambda}{32})^2}{27}}$$

pade[2/3]:

$$\frac{4 + \frac{114417112 * (\frac{\lambda}{32})^2}{16891875}}{1 + \frac{22348028 * (\frac{\lambda}{32})^2}{16891875}}$$

pade[3/4]:

$$\frac{4 + \frac{(12026891273204)}{(1419129742275)} (\frac{\lambda}{32})^2}{1 + \left( \frac{2481119210051 * (\frac{\lambda}{32})^2}{1419129742275} - \frac{(4315769032925186)(\frac{\lambda}{32})^4}{(27396299674618875)} \right)}$$

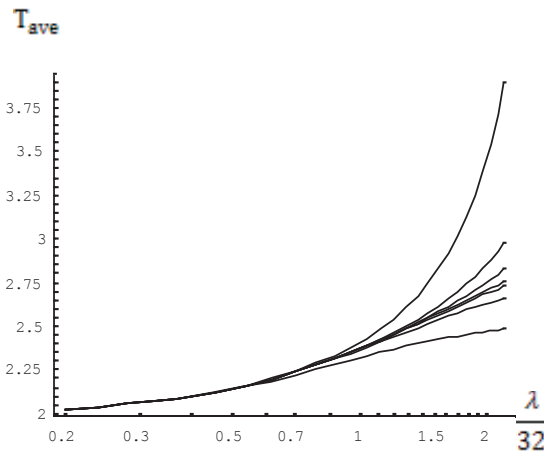


Fig.2. Plots of [8/9], [7/8],[6/7],[5/6 ],[4/5], [3/4]and [2/3] of the Pade approximants for  $T_{ave}$  versus  $\frac{\lambda}{32}$

When we form the ratios [8/9], [7/8], [6/7],[5/6], [4/5], [3/4]and [2/3] of the Pade approximants, It can be shown, they agreed up to the value  $\frac{\lambda}{32}=7$ . This conclusion is confirmed as is plotted in Figure 2.

**Summary**

This is problem of the two-dimensional problem of steady natural convection in a horizontal cylinder filled with porous medium due to quadratic volumetric generation. The solution is expanded for low Darcy-Rayleigh number and the series extended by means of symbolic calculation up to 18 terms. Analysis of these expansions allows the exact computation for arbitrarily accuracy up to 50000 figures. Although the range of the radius of convergence is small but Pade approximation leads our

result to be good even for much higher value of the similarity parameter we have found extending terms exactly by means of symbolic calculation up to 18th order. Then we tried to make analytic continuation by using Pade approximation. In other words, we have solved the nonlinear partial differential equation exactly by means of computer and that is a real success. Finally we mention recent work of [14] with viscous fluid for micro gap which shows our analytical approach more attractive and successful.

## References

- [1] Mansour, K. 1993 “Using Stokes Expansion For Natural Convection inside a two-dimensional cavity”. *Fluid Dynamics Research*, 1-33
- [2] Mansour, K. 1985 “Laminar flow through a slowly rotating straight pipe”. *Journal of Fluid Mech.* 150, 1-24.
- [3] Mansour, K. 2004 “Using Symbolic Calculation For Solving laminar Flow Through Heated Horizontal Pipe ” *Proceeding of 2nd BSME – ASME International conference on Thermal Engineering*, 2-4 January 2004 Dhaka, Bangladesh.
- [4] Caltagirone, J.P. 1976 “Thermo convective instabilities in a porous medium bounded by two concentric horizontal cylinders” *Journal of Fluid Mech.* 76, part 2, 1-24.
- [5] Bau, H. H. 1984 “Thermal Convection in a Horizontal, eccentric Annulus containing a Saturated Porous Medium—an extended perturbation expansion” *Int. J. Heat Mass Transfer*, Vol. 27, No. 12, pp. 2277-2287.
- [6] Bau, H. H. 1984 “Low Rayleigh Number Thermal Convection in a Saturated Porous Medium bounded by two horizontal, eccentric cylinders” *Trans. ASME* Vol. 106, pp. 166-175.
- [7] Himasekhar, K. & Bau, Haim. H. 1988 “Two Dimensional Bifurcation Phenomena in Thermal Convection in Horizontal concentric Annuli containing a Saturated Porous media”. *Journal of Fluid Mech.* Vol. 187, 267-300.
- [8] Prudhomme, M., Robillard, L., Vasseur, P., 1986 “Free convection in a two Dimensional Porous Loop” *Journal of Heat Transfer*, Vol. 108, pp. 277-283.
- [9] Muralidhar, K., Kulacki, F.A. 1988 “Non- Darcy Natural Convection in a Saturated Horizontal Porous Annulus” *Journal of Heat Transfer*, Vol. 110, pp. 133-139.
- [10] Fant, D.B., Prusa, J., Rothmayer, A. P. 1990 “Unsteady Multi cellular Natural Convection in a narrow Horizontal Cylindrical annulus” *Journal of Heat Transfer*, Vol. 112, pp. 379-385.
- [11] TeBeest, K. G., Trogdon, S. A., Douglass, R. W., 1993 “Natural Convection Within Spherical Annuli by Symbolic Algebra” *Journal of Heat Transfer*, Vol. 115, pp. 807-809.
- [12] Walker, Ken L., Homsy, George M., “Convection in a porous Cavity,” *Journal of Fluid Mech.*, 87, 449, 1978.
- [13] Vasseur, P, Nguyen, T.H., Robillard, L, Tong Thi, V.K., Natural Convection Between Horizontal Concentric Cylinders Filled with a Porous Layer With Internal Heat Generation, *Int. J. Heat Mass Transfer*, Vol. 27, No. 12, pp.337-349, 1984.
- [14] Kamyar Mansour, The Analytical Solution of Natural Convection in a Micro Size Horizontal Cylindrical Annulus with Periodic Volumetric Heat Flux, *Heat Transfer Asian Research*, Vol. 40, pp.26-40 Wiley, 2011.

## Combined explicit and implicit algorithms for dynamic problems using the numerical manifold method

X.L. Qu<sup>1</sup> and \*G.W. Ma<sup>1</sup>

<sup>1</sup>School of Civil and Resource Engineering, The University of Western Australia, WA 6009, Australia

\*Corresponding author: ma@civil.uwa.edu.au

### Abstract

The efficiency and accuracy are usually regarded as two general indices to check capability of a numerical method with respect to the time integration. The traditional numerical manifold method (NMM) employs implicit scheme to obtain high computational accuracy, but the efficiency is relatively low, especially when the iterations of contacts are involved. In this paper, the temporal coupled explicit-implicit (E-I) algorithm is proposed, in which the time integration schemes, transfer algorithm and contact algorithm are studied, respectively. A few numerical examples are simulated using the proposed coupled algorithms, in which one calibration example is studied with respect to the coupled temporal based on the cover system. The simulated results are well agreement with the implicit and explicit algorithms simulations, but the efficiency is improved evidently. It is predicted that the proposed couple E-I algorithm can be applied for larger scale engineering systems to combine the merits of both the implicit and the explicit algorithms of the NMM.

**Keywords:** Computational efficiency; Computational accuracy; Explicit algorithm; Implicit algorithm; Numerical manifold method.

### Introduction

The efficiency and accuracy are usually regarded as two indices to check capability of a numerical method in terms of time integration for dynamic problems. In general, there are two classes of time integration algorithms for dynamic problems: implicit and explicit (Gelin et al, 1995). Implicit algorithms possess such as the continuum-based finite element method (FEM) and discontinuum-based discontinuous deformation analysis (DDA), explicit algorithms such as finite difference method (FDM) and discrete element method (DEM). It is noted when more contact problems are involved in the discontinuum-based methods such as DDA and DEM, the efficiency is significantly declined. Thus, how to treat the contact problems balancing the efficiency and accuracy, an appropriate time integration algorithm is required.

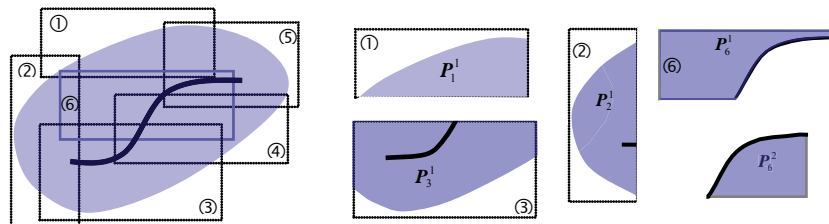
In the present study, the numerical manifold method (NMM) is considered to combine the both time integration algorithms. The traditional NMM is originally proposed by Shi (1991, 1992). It employs the implicit time integration and open-close contact iteration for the simulations of complicated dynamic problems. Since the implicit scheme requires the assembling of the coupled global stiffness matrix for the governing equations, which may involve many thousand DOFs, especially when such more contact problems and nonlinear problems are encountered, the computational cost can be increased dramatically. Thus, the choice of an appropriate algorithm is essential to ensure efficiency and robustness of the numerical simulations, but the difficulty resides in being able to combine robustness, accuracy, stability and efficiency of the algorithms. The distinction between explicit and implicit where we have considered is that the explicit uses a diagonal mass matrix and the implicit applies a consistent inertia matrix (Liu and Belytschko, 1982). Then, a temporal



coupled E-I algorithm for the NMM based on the dual cover system is proposed, in which different time steps, time integration schemes are applied in temporal discretization. Then, some calibration examples and numerical simulations are studied to validate the coupled E-I algorithms.

**Basic Concept of the NMM and Its Dual Cover System**

In the traditional NMM, one manifold element is generated through a set of overlapping covers, which is the distinct characteristic differs from other numerical methods. As shown in Figure 1(a), the mathematical cover system, which is united by six rectangle patches denoted by ①, ②, ③, ④, ⑤ and ⑥ respectively. The overlapping patches cover the whole material domain  $\Omega$  without considering any physical properties, so any arbitrary shape of mathematical cover can be chosen. And then, physical covers can be obtained from these mathematical covers intersect with the physical domain  $\Omega$ , a manifold element can be produced as the common area of physical covers. Each small rectangle patch is termed as a mathematical cover (MC), denoted by  $M_i$  ( $i= 1, 2, 3, \dots, 6$ ). External boundary and internal joints or cracks may intersect one MC into several separate sub-patches, then each one within the material domain is termed as a physical cover (PC), denoted by  $P_j^i$  ( $j \in N$ ). As can be seen in Figure 1(b), material domain  $\Omega$  is intersected by patch ① to generate one PC within its material domain, denoted by  $P_1^1$ . When the internal discontinuities (i.e. cracks or joints) are taken into accounted in the NMM, each discontinuous boundary is considered as one special material domain to form a new PC. If the crack passes through the whole patch within the material domain, two isolated PCs form by the crack surface just as  $M_4$  and  $M_6$ , two separated PCs, denoted by  $P_4^1, P_6^1$  based on  $M_4$  and  $P_6^1, P_6^2$  based on  $M_6$ , respectively. On the other case, when the crack cuts MC partially, only one PC forms within the material domain, which can be seen by  $M_2, M_3$  and  $M_5$ , only one PC generates denoted by  $P_2^1, P_3^1$  and  $P_5^1$  respectively. Furthermore, the common area of several overlapping PCs is termed as a manifold element (ME).



(a) General cover system in the NMM; (b) Generation of physical covers for the NMM

**Figure 1. Cover system of the NMM.**

For convenience, a regularly structured mesh is employed in the NMM which is similar as that in the FEM. A regularly-patterned triangular mesh is employed, in which each MC is defined through six triangular elements sharing a common node (i.e. nodal star). Each cover has two degree of freedom is similar as node property in the FEM, each element formed by the overlapping of three neighboring hexagonal covers has six degree of freedom for the second order time integration. The mathematical mesh covers the whole physical domains form PC system. The common areas are formed by the neighboring three hexagonal MCs combined with the material domains. When the linear triangular element weight function is applied based on cover system, the global displacement function over a ME can be expressed as

$$u_e(x, y) = \sum_{i=1}^3 \psi_i(x, y) U_i(x, y), \quad (x, y) \in \Omega_e \quad (1)$$

where  $\psi_i(x, y)$  is the weight function over the three associated mathematical covers,  $U_i(x, y) = \begin{Bmatrix} u_i(x, y) \\ v_i(x, y) \end{Bmatrix}$  is the displacement function on the three associated PCs. Here, it is the cover system makes the solution for both continuous and discontinuous problems practicability without any re-meshing technique used in the FEM.

### Temporary Coupled Explicit-Implicit Algorithm in the NMM

#### The Coupled Explicit-Implicit Algorithm

For the different problems, there are two types of coupled approaches can be considered: implicit-explicit (E-I) algorithm and explicit-implicit (I-E) algorithm. When different approaches are employed, the different step time scale can be applied into the corresponding time integration scheme. To investigate the temporal couples algorithm, the E-I algorithm is taken into account in the present study. Furthermore, the Newmark- $\beta$  methods (Newmark, 1959) with two characteristic parameters  $\beta$  and  $\gamma$  for all sub-domains are assumed here. As is shown in Figure 2, initial diagonal mass matrix and force vector are constructed for the explicit algorithm (Ma and Qu, 2013), then the explicit central difference method, i.e. the Newmark method with the parameters  $\beta_1 = 0$  and  $\gamma_1 = 1/2$ , is employed from the initial step time  $t_0$  to  $t_n$  at the step number  $n$  to simulate the high frequency part of the dynamic problems. And then, the explicit integration algorithm switches to the implicit, in which the transfer algorithm is proposed in order to achieve the conservation of the kinematic energy from the explicit to implicit integration, and  $D_E = D_I$ ,  $V_E = V_I$  and  $\sigma_E = \sigma_I$  are satisfied for the coupled E-I integration without the element and node partition. Thus, it is convenient to achieve in the programming. In the part of the implicit integration from step time  $t_{n+1}$  to  $t_{n+r}$ , the constant acceleration method with the parameters  $\beta_2 = 1/2$  and  $\gamma_2 = 1$  is used in the implicit integration by the end of step  $(n+r)$  for the low frequency and quasi-static problems. Continuing the explicit procedure, the initial inertial, stiffness matrix and force vector for the implicit integration are require to construct again as the difference items in the equations of motion. It is noted that different step time sizes are adopted before and after the transition in the couples E-I algorithm in terms of the numerical stability and accuracy, respectively. Normally, the step time size  $\Delta t_I$  in the implicit algorithm is larger than  $\Delta t_E$  in the explicit algorithm, which denotes  $\Delta t_I = \alpha \cdot \Delta t_E$ ,  $\alpha > 1$  is the coefficient to describe the scale between the implicit and explicit integrations. Sequentially, the transfer algorithm of the coupled E-I integration is exposed and discussed in the following section.

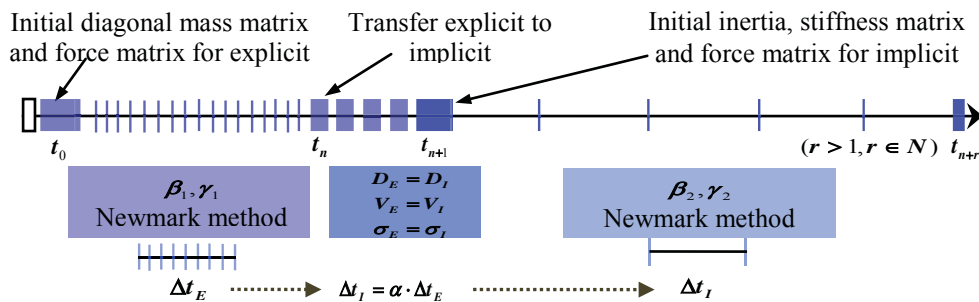


Figure 2. Transfer algorithm from the explicit to implicit scheme.

### Transfer Algorithm for the E-I Algorithm

In the coupled E-I method, we employ the explicit algorithm to model motion of the system at the early stage, followed by the implicit algorithm to simulate the subsequent motions of the system. Thus, an explicit physical model in the NMM will be transferred to the implicit one at a certain time so that the coupled method is more efficient. In the transition, the geometric configurations, physical and mechanical parameters, and status, including stress state and velocities, are consistent and continue. Therefore, the transfer algorithm is required to satisfy the kinetic energy and potential energy conservation from the explicit integration to the implicit one, which can be represented as

$$\frac{1}{2} \sum_{i=1}^n M_i^E (v_x^E{}^2 + v_y^E{}^2) = \frac{1}{2} \sum_{i=1}^n M_i^I (v_x^I{}^2 + v_y^I{}^2) \quad (2a)$$

$$\prod_e^E (\sigma_x^E, \sigma_y^E, \tau_{xy}^E) = \prod_e^I (\sigma_x^I, \sigma_y^I, \tau_{xy}^I) \quad (2b)$$

where  $M_i^E$  and  $M_i^I$  are the  $i$ -th explicit and implicit element mass, respectively;  $v_x^E, v_y^E$  and  $v_x^I, v_y^I$  are the velocity components of an explicit element and implicit element in the  $x$  and  $y$  directions, respectively;  $\prod_e^E (\sigma_x^E, \sigma_y^E, \tau_{xy}^E)$  and  $\prod_e^I (\sigma_x^I, \sigma_y^I, \tau_{xy}^I)$  are the explicit and implicit element potential energy, in which  $\sigma_x^E, \sigma_y^E, \tau_{xy}^E$  and  $\sigma_x^I, \sigma_y^I, \tau_{xy}^I$  are stress components of the explicit and implicit elements respectively. Furthermore, equations of  $M_i^E = M_i^I, v_x^E = v_x^I, v_y^E = v_y^I, \sigma_x^E = \sigma_x^I, \sigma_y^E = \sigma_y^I, \tau_{xy}^E = \tau_{xy}^I$  are satisfied in the transfer algorithm to ensure the parameters of the terms are consistent and the computation is continuous.

### Contact Algorithm for the Coupled Scheme

#### Contact Force Calculation

As previously mentioned, contact detection and contact force calculations are done by the NMM. Once contacts have been detected, a contact interaction algorithm is employed to evaluate contact forces between the contact elements. A thorough discussion and formulations of these approaches can be found in (Munjiza, 2004).

For a discrete block system involving  $m$  elements, there are  $N$  contact pairs have been detected to an element  $i$  ( $i=1,2,\dots,m$ ). Here, we assume one element denoted by  $j$  ( $j=1,2,\dots,N$ ) and  $i$  are detected in contact state,  $[K^c]$  between  $i$  and  $j$  can be expressed as

$$[K^c] = \begin{bmatrix} [K_{ii}^c] & [K_{ij}^c] \\ [K_{ji}^c] & [K_{jj}^c] \end{bmatrix} \quad (3)$$

in which  $[K_{ij}^c]$  is defined by the contact spring between the contact elements  $i$  and  $j$ , and the value is zero if the elements  $i$  and  $j$  have no contact. Since each element is consisted by three associated PCs, thus the matrix  $[K_{ij}^c]$  is a  $6 \times 6$  sub-matrix and the derivation of the matrix  $[K_{ij}^c]$  will be discussed in detail at the following section. It is noted that the displacement  $\{D_{n+1}\}$  on the three associated PCs can be predicted using the Verlet algorithm by the previous step  $n$ . Then, contact forces associated with  $[K_{ij}^c]$  on the contact element  $i$  are assembled as

$$\{\mathbf{I}_i^c\} = -\sum_{j=1}^m [\mathbf{K}_{ij}^c] \cdot \{\mathbf{D}_{i(r)}\}, \quad j = 1, 2, \dots, N; r = 1, 2, 3 \quad (4)$$

The total internal forces on the element  $i$  can be represented as

$$\{\tilde{\mathbf{I}}_i\} = [\mathbf{K}_{ii}^e] \cdot \{\mathbf{D}_{i(r)}\} + \{\mathbf{I}_i^c\} = \left( [\mathbf{K}_{ii}^e] + \sum_{j=1}^N [\mathbf{K}_{ij}^c] \right) \cdot \{\mathbf{D}_{i(r)}\}, \quad j = 1, 2, \dots, N; \quad r = 1, 2, 3 \quad (5)$$

in which  $\{\tilde{\mathbf{I}}_i\}$  is the element internal force vectors and  $[\mathbf{K}_{ii}^e]$  is the stiffness matrix of element. Since each element is formed by the three associated PCs, thus  $\{\tilde{\mathbf{I}}_i\}$  can be rewritten as

$$\{\tilde{\mathbf{I}}_i\} = \begin{Bmatrix} \tilde{\mathbf{I}}_{i(1)} \\ \tilde{\mathbf{I}}_{i(2)} \\ \tilde{\mathbf{I}}_{i(3)} \end{Bmatrix} \quad (6)$$

in which  $\{\tilde{\mathbf{I}}_{i(1)}\}$  maps the first PC associated the element, the subsequent  $\{\tilde{\mathbf{I}}_{i(2)}\}$  and  $\{\tilde{\mathbf{I}}_{i(3)}\}$  map the second and third PCs, respectively. Then,  $\{\tilde{\mathbf{I}}_i\}$  at each PC can be assembled by the associated  $\{\tilde{\mathbf{I}}_i\}$  on the cover system.

#### *Damping Algorithm*

It is noted that the explicit scheme employs dynamics method to solve the uncoupled equations, in which the generated kinetic energy can not be neglected. To the static or quasi-static problems, it requires the physical damping to adsorb the kinetic energy of the systems so that the systems achieve stable condition. As in reference (Cundall, 1982), we suggest an alternative scheme to simulate the damping, in which the damping force with the unbalance force or inertial force is in direction proportion, and the damping item of each MC in the NMM can be expressed as

$$\{\mathbf{F}_d\} = -\zeta [\mathbf{M}_e] \{\ddot{\mathbf{D}}_e |_{t_0}\} \quad (7)$$

where  $\{\mathbf{F}_d\}$  is the damping force matrix,  $\{\ddot{\mathbf{D}}_e |_{t_0}\}$  is the element initial acceleration vector at the start of the time step. The total potential energy from the damping item is summered by each element, which can be written as

$$\Pi_d = \sum_e \zeta \{\mathbf{D}_e\}^T [\mathbf{M}_e] \{\ddot{\mathbf{D}}_e |_{t_0}\} \quad (8)$$

Substituting Equation (8) using the variational principle, the equivalent damping force matrix can be described as

$$[\mathbf{F}_d] = -\frac{\partial \Pi_d}{\partial \{\mathbf{D}_e\}} = -\zeta [\mathbf{M}] \{\ddot{\mathbf{D}}_e |_{t_0}\} \quad (9)$$

which is a  $6 \times 1$  matrix to produce external force item.

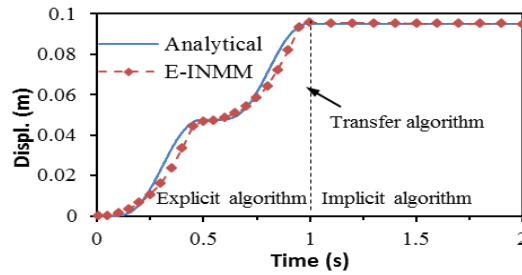
## **Numerical Examples**

### *Calibration of the Coupled Algorithm*

In order to calibrate the proposed coupled E-I algorithm for the temporal problems, one Newmark sliding modelling of block sliding under input horizontal acceleration  $\mathbf{a}_H$  is studied here. A block rests on an inclined plane is taken into account as a first approximation of the Newmark sliding model. The angle of the plane is  $31.47^\circ$ . And a sinusoidal seismic acceleration  $\mathbf{a}_H$  is employed to impose the fixed point as expressed in Equation (10), where  $\mathbf{g}$  is the gravity acceleration,  $\mathbf{t}$  is the simulation duration for

the simulation. In this study, we assume the frictional angle  $\phi = 30^\circ$ , the total displacement of analytical solutions can be referred in (Newmark, 1959; An et al, 2011), then the simulated results of the proposed E-I NMM can be obtained as shown in Figure 3. It is noted that when the E-I algorithm is considered, the proposed transfer algorithm is employed from the explicit to implicit algorithm at the time of  $t = 1s$ , and the final results of the simulations are well agreement with the analytical solution.

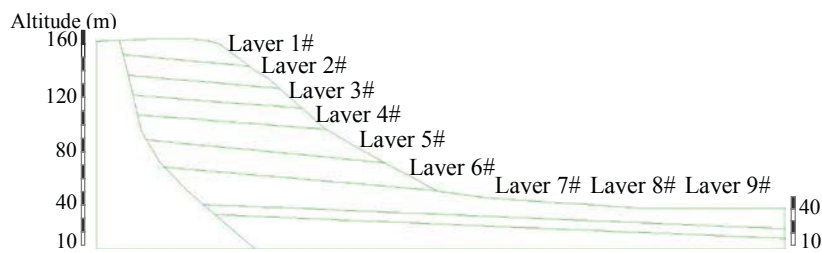
$$a_H = \begin{cases} 0.1g \sin 4\pi t & t \leq 1s \\ 0 & t > 1s \end{cases} \quad (10)$$



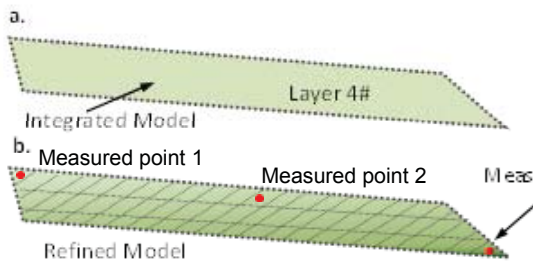
**Figure 3. Block displacement under horizontal ground acceleration.**

*Open-pit Mining Stability Analysis*

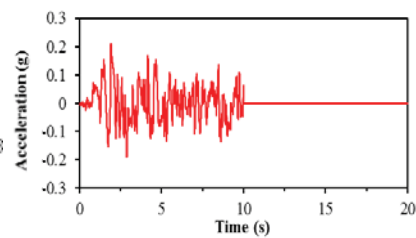
In this simulation, one open-pit mine slope modeling is assumed to study the stability using the proposed E-I algorithm. As shown in Figure 4, there are 9 layers denoted by 1# to 9# separate the whole modeling, in which we assume the layer 4# is the fracture zone constituted by many discontinuous joints. The inclined angle of the slope is  $42^\circ$  and drop is 120 m. In order to investigate the effect of the fracture zone to stability of the slope, two models of layer 4# are represented in Figure 5. Integrated Model considers the whole layer as one domain, on the other hand, Refined Model adds more joints into the layer to approach the realistic condition, in which a set of joints with orientation of  $32.47^\circ$  are constructed as seen Figure 5 to simulate the fractured zone of the open-pit slope.



**Figure 4. Geology section of the open-pit mining.**



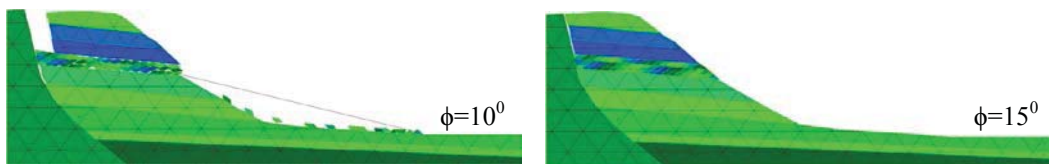
**Figure 5 Study model of the layer 4#.**



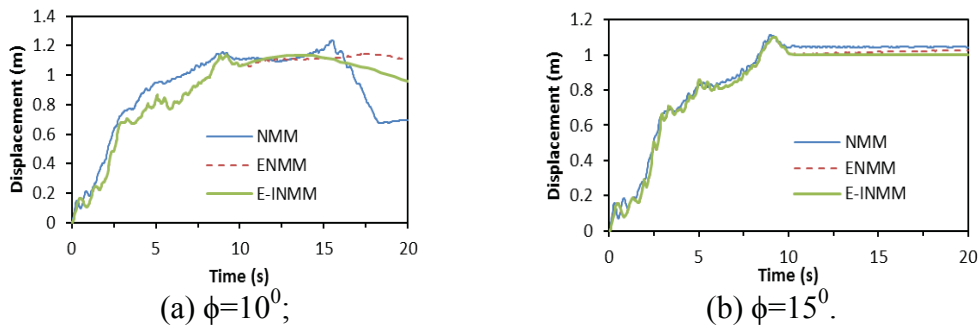
**Figure 6 Input seism acceleration.**

Traditional methods apply to the slope stability analysis is to determine the factor of stability (FoS) of the slope using the limit equilibrium method (LEM) without considering the effect of the dynamic loading with time history (i.e. seismic loading, blasting loading, etc). Here, the FoS is computed using the LEM to the integrated model, FoS can be determined as 1.436 and 2.182 by cases of  $10^0$  and  $15^0$  of joint frictional angle. To further investigate the stability of the slope under the earthquake, a stochastic horizontal seismic acceleration with maximum value of 0.2g is applied as shown in Figure 6. The detailed of physical parameters such as unit weight is 26.0 kN/m<sup>3</sup>, Young's modulus is 1.0 GPa, Poisson's ratio is 0.2, Joint normal stiffness is 1.0 GPa and Joint shear stiffness is 0.5 GPa, respectively.

To investigate the instability of the fracture zone under earthquake loading, the measure points selected in the fracture zone and the displacements of them at both cases of  $\phi=10^0$  and  $\phi=15^0$  are presented in Figure 7 and 8, respectively. It is verified that the proposed E-INMM satisfies the computational accuracy comparing with the original NMM. We can find that the slope is instable at the case of  $\phi=10^0$  whether static or dynamic states, but the slope approaches to be stable after the seismic loading at the case of  $\phi=15^0$ . Thus, the fractured zone should be taken into account to the design of the open-pit slope to improve the stability of slope.



**Figure 7. Simulations for Refined Model (Total time: 20s).**



**Figure 8. Measured point 1 in the Refined Model.**

With respect to the efficiency of the proposed algorithms, CPU time is taken into consideration to check the computational cost of the algorithms. All three algorithms are run on the same computer with the system configuration: processor speed = 4.0 GHz and RAM = 4.0 GB. As represented in Table 1, the proposed E-I algorithm is more efficient comparing the explicit and implicit algorithms in the refined model with both cases of  $\phi=10^0$  and  $\phi=15^0$ . In particular, E-I algorithm can be considered as one computational criteria for the large scale engineering as it combines the merits of both the explicit and implicit algorithms in terms of accuracy and efficiency of the computations dramatically.

**Table 1. CPU cost for the different cases (hr.).**

Study Case	10°			15°		
	$CPU^I$	$CPU^E$	$CPU^{E-I}$	$CPU^I$	$CPU^E$	$CPU^{E-I}$
Refined Model	1.467	1.376	0.882	1.816	1.515	0.911

## Conclusions

The temporal coupled explicit and implicit algorithm for the numerical manifold method (NMM) is proposed in this paper. The time integration schemes, transfer algorithm, contact algorithm and damping algorithm are studied in the temporal coupled E-I algorithm to combine both merits of the explicit and implicit algorithms in terms of efficiency and accuracy. Then, some numerical examples are simulated using the proposed coupled algorithms, in which one calibration example is studied with respect to the coupled temporal based on the dual cover system. One numerical example of open-pit slope seismic stability analysis using the coupled E-I algorithm is investigated as well. The simulated results are well agreement with the implicit and explicit algorithms simulations, but the efficiency is improved evidently. It is predicted that the couple E-I algorithm proposed in the present paper can be applied into larger scales engineering systems to combine the merits of both the implicit and explicit algorithms in the NMM.

## References

- An, X. M., Ning, Y. J., Ma, G. W. and Zhao, Z. Y. (2011). Seismic stability analysis of rock slopes using the numerical manifold method. *12th International Congress on Rock Mechanics, Beijing*, pp. 693-698.
- Cundall, P. A. (1982), Adaptive density-scaling for time-explicit calculations. *Proceedings of the 4th international conference on numerical methods in geomechanics, Rotterdam: A. A. Balkema*, pp. 23-26.
- Gelin, J. C., Boulmance, L. and Boisse, P. (1995), Quasi-static implicit and transient explicit analyses of sheet-metal forming using a c0 three-nodes shell element. *Journal of material processing technology*, pp. 395-409.
- Liu, W. K. and Belytschko, T. (1982), Mixed-time implicit-explicit finite elements for transient analysis. *Journal of computers and structures*, Vol.15 (4), pp. 445-450.
- Ma, G. W. and Qu, X. L. (2013), An explicit version of the numerical manifold method and its applications. *Proc. Eleventh Int. Conf. Analysis of Discontinuous Deformation (ICADD-11), Fukuoka Japan*, pp. 315-321.
- Munjiza, A. (2004), *The combined Finite-Discrete Element Method*. John Wiley & Sons Ltd.
- Newmark, N.M. (1959), A method of computation for structural dynamics. *Journal of Engineering and Mechanics Division*, 85, pp. 67-94.
- Shi, G. H. (1988), Discontinuous deformation analysis: A new numerical method for the static and dynamic of block system. *PhD dissertation*, Dep. of Civ. Engrg., University of California, Berkeley, Calif.
- Shi, G. H. (1991), Manifold method of material analysis. In: *Transactions of the 9th army conference on applied mathematics and computing, Minneapolis, Minnesota*, pp. 57- 76.
- Shi, G. H. (1992), Modeling rock joints and blocks by manifold method. In: *Proceedings of the 33rd US rock mechanics symposium, Santa Fe, New Mexico*, pp. 639- 648.

## AUTHORS INDEX

<b>Authors</b>	<b>Page No</b>	<b>Authors</b>	<b>Page No</b>
<i>Abdullah, S.</i>	18, 1382	<i>Chai, Yingbin</i>	383
<i>Akramin, M.R.M.</i>	1382	<i>Chen, Chengcheng</i>	1300
<i>Albuquerque, E.B.</i>	1240	<i>Chen, D.</i>	8
<i>Alibrandi, U.</i>	752	<i>Chen, D.H.</i>	977
<i>Amalnerkar, E.</i>	1188	<i>Chen, Ding</i>	73
<i>Ang, W. T.</i>	1425	<i>Chen, Jiangyi</i>	604
<i>Aoki, K.</i>	432	<i>Chen, Shenyan</i>	406
<i>Aono, H.</i>	877	<i>Chen, Xiaojun</i>	945
<i>Arai, Masahiro</i>	858	<i>Chen, Y.H.</i>	885
<i>Ariffin, A.K.</i>	1158, 1366, 1382	<i>Chen, Yang-Yih</i>	895
<i>Armfield, Steven W.</i>	498, 641	<i>Chen, Zhi</i>	1129
<i>Arrifin, A.K.</i>	18	<i>Chen, Zhi-Hua</i>	80
<i>Asai, Mitsuteru</i>	470, 736	<i>Cheng, Gengdong</i>	314
<i>Augarde, C.E.</i>	1179	<i>Cheng, Xiaoli</i>	440, 550
<i>Aydan, Ö.</i>	1246	<i>Chew, J.H.</i>	1263
<i>Baghapour, B.</i>	1171	<i>Cho, S.</i>	1340
<i>Banerjee, Rohan</i>	1225	<i>Cisbani, Evaristo</i>	1434
<i>Becker, W.</i>	27	<i>Clement, J.G.</i>	991
<i>Bekö, A.</i>	1209	<i>Colaço, M.J.</i>	567
<i>Bellini, Vincenzo</i>	1434	<i>Crouch, R.S.</i>	1179
<i>Birk, Carolin</i>	8, 945	<i>Cui, K.</i>	51
<i>Borges, L.A.</i>	1240	<i>Dai, S.</i>	8
<i>Bradford, Mark A.</i>	633, 648	<i>Darian, H. Mahmoodi</i>	1163
<i>Bu, J.H.</i>	1397	<i>de Medeiros, M.A.F.</i>	930
<i>Bu, Junhui</i>	73, 104	<i>De Smet, Valerie</i>	1434
<i>Buenzli, P.R.</i>	991	<i>Deeks, Andrew J.</i>	916, 922
<i>Calo, V.M.</i>	151	<i>Dehghan, A.A.</i>	1163
<i>Cao, H.</i>	322	<i>Deng, Huaxia</i>	760, 769
<i>Cao, Hui</i>	344	<i>Deng, Q.P.</i>	1096
<i>Castello, D.A.</i>	1240	<i>Dey, A.</i>	222
<i>Chai, Ping</i>	969	<i>Ding, H.</i>	788



<i>Djamaluddin, F.</i>	18	<i>H, Nguyen-Xuan</i>	1316
<i>Do, Duy Minh</i>	483	<i>Hamasaki, E.</i>	863
<i>Dogan, N.F.</i>	129	<i>Hamasaki, Toru</i>	793
<i>Dong, G.</i>	124	<i>Han, Xu</i>	1442
<i>Dong, K.</i>	116	<i>Hasebe, Tadashi</i>	799, 812, 834
<i>Du, Xiaoxu</i>	185	<i>Hasegawa, M.</i>	807
<i>Ejima, Kou</i>	720	<i>Hayashi, Ryosuke</i>	1271
<i>Esfahanian, V.</i>	1163, 1171	<i>He, L.</i>	1179
<i>Estumano, D.C.</i>	567	<i>He, Lin</i>	1129
<i>Fajisaki, Wataru</i>	281	<i>He, Xindang</i>	236
<i>Fan, Bao-Chun</i>	80, 124	<i>He, Yiqian</i>	916, 922
<i>Fan, S.C.</i>	302, 1139	<i>Hedayat, M.</i>	1171
<i>Feng, D.L.</i>	1057	<i>Hinago, Takuya</i>	820
<i>Fontes, E.F. Jr</i>	575	<i>Holmes, David W.</i>	641
<i>Fu, S.</i>	542	<i>Homma, S.</i>	584
<i>Fujihashi, Daiki</i>	842	<i>Hong, Jiahua</i>	1451
<i>Fujii, Kozo</i>	877, 1292	<i>Hosseini, S.J.</i>	1171
<i>Fujiwara, Y.</i>	207	<i>Hu, Ning</i>	1286
<i>Fumuro, Taiki</i>	688	<i>Hu, S.C.</i>	51
<i>Furuta, Koharu</i>	1279	<i>Hu, Zhimao</i>	344
<i>Gajda-Zagórska, E.</i>	273	<i>Hua, Jianmin</i>	344
<i>Gao, L.</i>	611	<i>Huang, Cheng</i>	448
<i>Gao, W.</i>	648	<i>Huang, Cheng</i>	559
<i>Gao, Wei</i>	483, 589, 597, 633	<i>Huang, F.</i>	744
<i>Gao, Y.</i>	116	<i>Huang, Fei</i>	440, 550
<i>Geniş, M.</i>	1246	<i>Huang, Hai</i>	406
<i>Gharizadeh, Ali</i>	1332	<i>Huang, Jin</i>	1035
<i>Grebennikov, Alexandre</i>	1146	<i>Huang, L.H.</i>	1030
<i>Gu, Yuantong</i>	215, 463, 656, 1121	<i>Ijima, Katsushi</i>	249, 257
<i>Gui, M.Y.</i>	124	<i>Imiya, Kazuhiro</i>	812, 834
<i>Gujjula, Ravi</i>	1372	<i>Inthavong, Kiao</i>	535
<i>Guo, Z.M.</i>	1057	<i>Ishibashi, K.</i>	249
<i>Guo, Zaoyang</i>	400	<i>Ishii, Yoshikazu</i>	672
<i>Gurgul, P.</i>	850	<i>Iu, V.P.</i>	414
		<i>Jamli, M.R.</i>	1366
		<i>Jang, J.</i>	1188, 1340

<i>Jia, D.</i>	619	<i>Koguchi, Hideo</i>	1064
<i>Jiang, Bingyan</i>	64	<i>Koh, C.G.</i>	752
<i>Jiang, C.</i>	1442	<i>Kondo, K.</i>	877
<i>Jiang, Jun</i>	185, 361	<i>Kou, K.P.</i>	414
<i>Jiang, W.K.</i>	1096	<i>Kovacevic, A.</i>	1356
<i>Jiang, Z.L.</i>	999	<i>Kuba, Shunichi</i>	672
<i>Jiang, Z.Y.</i>	338	<i>Kurata, M.</i>	627
<i>Ju, Yuan-Yuan</i>	110	<i>Kuźnik, K.</i>	151
<i>Jung, J.D.</i>	27	<i>Kwon, Oh Joon</i>	1324
<i>Jung, Min Kyu</i>	1324	<i>Lam, C.C.</i>	414
<i>Kagami, T.</i>	807	<i>Lau, G.E.</i>	1072
<i>Kageyama, Akira</i>	704	<i>Le, T.Q.</i>	1115
<i>Kajishima, Takeo</i>	696	<i>Lee, C.K.</i>	302, 1139
<i>Kajiwara, Naoki</i>	834	<i>Lee, M.</i>	1340
<i>Kambayashi, A.</i>	207	<i>Lee, T.H.</i>	1188, 1340
<i>Kanber, B.</i>	129, 137	<i>Lee, Y.M.</i>	1042
<i>Kang, Guozheng</i>	1104	<i>Lei, Ming</i>	383
<i>Kang, Hyungoo</i>	1308	<i>Leong, E.C.</i>	1263
<i>Kashiyama, Kazuo</i>	680, 688, 704, 712, 720	<i>Lerebours, Ch.</i>	991
<i>Katagiri, Yukinori</i>	672	<i>Li, Dongfang</i>	406
<i>Katori, Toru</i>	455	<i>Li, G.L.</i>	51
<i>Kawabe, Takeshi</i>	712	<i>Li, H.</i>	611
<i>Kawaguchi, Atsushi</i>	793	<i>Li, H.X.</i>	519
<i>Kawasaki, Fumiya</i>	826	<i>Li, H.Y.</i>	1405
<i>Kawasaki, Noriaki</i>	257	<i>Li, Hongying</i>	1088
<i>Khoshab, M.</i>	1163	<i>Li, Hua</i>	1451
<i>Kikai, S.</i>	807	<i>Li, Huiyu</i>	604
<i>Kikuchi, Masanori</i>	1382	<i>Li, L.</i>	310
<i>Kim, Jinkoo</i>	1308	<i>Li, P.G.</i>	611
<i>Kimata, M.</i>	807	<i>Li, Q.</i>	885
<i>Kirkpatrick, Michael P.</i>	641	<i>Li, Q.B.</i>	542
<i>Kita, E.</i>	939	<i>Li, S.L.</i>	1110
<i>Kitada, Hiroshi</i>	903	<i>Li, S.M.</i>	331
<i>Ko, J. H.</i>	1115	<i>Li, Wei</i>	383
<i>Kobori, Hiromu</i>	858	<i>Li, Weihua</i>	760
		<i>Li, Xiaoyu</i>	367

<i>Li, Xiwei</i>	294	<i>Ma, Han-Dong</i>	1286
<i>Liao, He</i>	64	<i>Ma, J.</i>	597
<i>Liao, Jun</i>	64	<i>Mammoliti, Francesco</i>	1434
<i>Librizzi, Fancesco</i>	1434	<i>Mangadoddy, Narasimha</i>	1372
<i>Lim, Calvin</i>	193, 1390	<i>Mansour, Kamyar</i>	1465
<i>Lim, Chi Wan</i>	969	<i>Mao, Yadan</i>	664
<i>Lim, W.</i>	1188, 1340	<i>Matsuda, Hiroki</i>	243
<i>Lin, Wenxian</i>	498, 641	<i>Matsuda, Tetsuya</i>	826, 858, 869
<i>Liu, G.R.</i>	383, 1442	<i>Matsumoto, Yoichiro</i>	506
<i>Liu, H.Y.</i>	1397	<i>Mendis, P.</i>	1
<i>Liu, J.</i>	780	<i>Miao, Wenbo</i>	440, 550
<i>Liu, Junqing</i>	1300	<i>Miao, X.H.</i>	619
<i>Liu, Moubin</i>	1057	<i>Miao, Yu</i>	1005
<i>Liu, Nengguang</i>	589	<i>Miramini, S.</i>	1
<i>Liu, Pei</i>	955	<i>Mitadera, Takayuki</i>	672
<i>Liu, Peiqing</i>	1254	<i>Miyachi, Hideo</i>	712
<i>Liu, Rumeng</i>	177	<i>Mojsilović, N.</i>	200
<i>Liu, T.</i>	322	<i>Morimoto, Takashi</i>	375
<i>Liu, Wei</i>	294	<i>Morimoto, Toshihiro</i>	470
<i>Liu, Y.P.</i>	338	<i>Muramatsu, Mayu</i>	230
<i>Liu, Y.S.</i>	977	<i>Na, J.</i>	1340
<i>Liu, Yang</i>	144	<i>Nagasao, Tomohisa</i>	96
<i>Liu, Z.J.</i>	338	<i>Nagata, Yuki</i>	1292
<i>Liu, Zhuli</i>	604	<i>Nan, Hua</i>	236
<i>Lou, J.</i>	1405	<i>Nayanajith, P.G.H.</i>	656
<i>Lou, Jing</i>	1088	<i>Ng, Gillian Maria</i>	969
<i>Lu, Y.</i>	939	<i>Nguyen, Vinh Tan</i>	969
<i>Luo, Juan</i>	1104	<i>Nguyen, Trung Dung</i>	463
<i>Luo, K.</i>	648	<i>Nikabdullah, N.</i>	1382
<i>Luo, Rongmo</i>	88	<i>Nizam, Z.M.</i>	249, 257
<i>Luo, Xingwen</i>	511	<i>Noh, Hyuk-Chun</i>	963
<i>Luo, Zhen</i>	728, 1201	<i>Nonomura, T.</i>	877
<i>Lv, Jiahe</i>	1005	<i>Nonomura, Taku</i>	1292
<i>Lv, Junming</i>	550	<i>Nopiah, Z.M.</i>	18
<i>Ma, C.Y.</i>	752	<i>Noto, Fancesco</i>	1434
<i>Ma, Guowei</i>	1471	<i>Obiya, H.</i>	249

<i>Obiya, Hiroyuki</i>	257	<i>Richardson, M.</i>	1
<i>Oide, Kohei</i>	826	<i>Rosko, P.</i>	1209
<i>Okawa, Hiroshi</i>	712	<i>Ruan, Jiageng</i>	1196
<i>Okazawa, Shigenobu</i>	793	<i>Saha, S.C.</i>	215, 656
<i>Okuda, Tatsuya</i>	812	<i>Sakai, Seigo</i>	169
<i>Oloyede, A.</i>	1	<i>Sakakiabara, T.</i>	627
<i>Orlande, H.R.B.</i>	567	<i>Sakuma, Atsushi</i>	476
<i>Oshima, Kento</i>	230	<i>Sakuraba, Masaaki</i>	680
<i>Owada, Shuji</i>	35, 842	<i>Saleh, Ali</i>	1332
<i>Oyama, A.</i>	877	<i>Salmanpour, A.H.</i>	200
<i>P., Phung-Van</i>	1316	<i>Samali, Bijan</i>	1332
<i>Paino, P.C.V.</i>	930	<i>Santiago, J.A.F.</i>	575
<i>Pan, Guang</i>	185, 361	<i>Sauret, E.</i>	215
<i>Pang, F.Z.</i>	619	<i>Sawant, M.B.</i>	222
<i>Pardo, D.</i>	151, 273	<i>Schaefer, R.</i>	273
<i>Park, S.</i>	1188	<i>Seaid, M.</i>	1179
<i>Paszyński, M.</i>	151, 273	<i>Seshaiyer, Padmanabhan</i>	1225
<i>Paszyński, M.</i>	850	<i>Shang, Yidan</i>	535
<i>Peng, Xiongqi</i>	400	<i>Shang, Zhi</i>	1088, 1405
<i>Pi, Y.L.</i>	648	<i>Shen, Feng Jing</i>	104
<i>Pi, Yong-Lin</i>	633	<i>Shi, Guangyu</i>	353
<i>Pirpiris, M.</i>	1	<i>Shi, Mingxing</i>	1104
<i>Pivonka, P.</i>	991	<i>Shi, Xue</i>	633
<i>Poh, Kian Keong</i>	969	<i>Shi, Yao</i>	185, 361
<i>Qian, D.J.</i>	619	<i>Shiah, Y.C.</i>	1042
<i>Qian, Y.H.</i>	1460	<i>Shimoda, Masatoshi</i>	144, 286, 375
<i>Qian, Yuehong</i>	910	<i>Shimura, Masayuki</i>	720
<i>Qin, Dongchen</i>	604	<i>Shin, Jeongil</i>	1308
<i>Qin, Qing H.</i>	490	<i>Shiomi, T.</i>	207
<i>Qu, X.L.</i>	1471	<i>Shoji, Hirokazu</i>	476
<i>Qu, Z.P.</i>	51	<i>Shu, C.</i>	788
<i>Rane, S.</i>	1356	<i>Sieniek, M.</i>	850
<i>Rasani, M.R.</i>	1158	<i>Sladek, J.</i>	527
<i>Rębielak, J.</i>	985	<i>Sladek, V.</i>	527
<i>Reizes, J.A.</i>	1072	<i>Slamet, Samuel Susanto</i>	96
<i>Ren, Wenyuan</i>	1215	<i>Smołka, M.</i>	273

<i>Soares, D. Jr.</i>	43	<i>Tanaka, Satoyuki</i>	793
<i>Song, Baowei</i>	185	<i>Tanaka, Seizo</i>	688
<i>Song, Chongmin</i>	483, 589, 597, 945	<i>Tang, Hui</i>	1405, 1451
<i>Song, S.Y.</i>	310	<i>Tang, L.Q.</i>	338
<i>Sonoda, Yoshimi</i>	470, 736	<i>Tang, Zhihao</i>	1254
<i>Stewart, Nicholas J.</i>	641	<i>Tangaramvong, S.</i>	424
<i>Stosic, N.</i>	1356	<i>Tanigawa, Masaki</i>	720
<i>Su, Yi</i>	193, 969, 1390	<i>Tano, H.</i>	1246
<i>Suetugu, T.</i>	281	<i>Taroura, Masahiro</i>	1064
<i>Sugiura, H.</i>	939	<i>Telles, J.C.F.</i>	575
<i>Sun, Jingwei</i>	1254	<i>Tereshin, D.A.</i>	1080
<i>Sun, Shuaishuai</i>	760	<i>Thomas, C.D.L.</i>	991
<i>Sun, Shulei</i>	400	<i>Tian, Jiandong</i>	448
<i>Sun, Tao</i>	104	<i>Tian, Li-Feng</i>	1129
<i>Sun, Yong-Tang</i>	104, 1397	<i>Timchenko, V.</i>	1072
<i>Sutera, Maria Concetta</i>	1434	<i>Tin-Loi, F.</i>	424, 597
<i>Suzuki, Shuma</i>	1064	<i>Tokashiki, N.</i>	1246
<i>T., Nguyen-Thoi</i>	1316	<i>Tokoro, Chiharu</i>	35, 842
<i>Ta, DuyHien</i>	963	<i>Tokubuchi, Ryota</i>	249, 257
<i>Tahara, Kazuki</i>	35, 842	<i>Torabzadeh, M.</i>	1171
<i>Takahashi, Ryouhei</i>	903	<i>Torii, Naoki</i>	476
<i>Takahashi, Yusuke</i>	680	<i>Toriu, D.</i>	432
<i>Takaki, Tomohiro</i>	230, 627	<i>Touhei, Terumi</i>	820
<i>Takano, Naoki</i>	96	<i>Tran, D.</i>	744
<i>Takashima, M.</i>	281	<i>Tsay, Ting-Kuei</i>	895
<i>Takeuchi, N.</i>	207, 863	<i>Tsu, I-Chen</i>	895
<i>Takeuchi, Shintaro</i>	696	<i>Tsunazawa, Yuki</i>	35, 842
<i>Tamura, Yoshiaki</i>	506	<i>Tsurumi, Nobuo</i>	506
<i>Tamura, Yuta</i>	793	<i>Tsutsumi, Kazutoshi</i>	243, 455
<i>Tan, Ru San</i>	193, 969, 1390	<i>Tsutsumi, Takaaki</i>	696
<i>Tan, S.</i>	542	<i>Tu, J.Y.</i>	1158
<i>Tanabe, Shoichi</i>	736	<i>Tu, Jiyuan</i>	535
<i>Tanaka, Satoshi</i>	704	<i>Tufik, O.M.</i>	137
		<i>Turangan, Cary K.</i>	1348
		<i>Uematsu, Motoki</i>	799
		<i>Unnisa, Y.</i>	744

<i>Ushijima, S.</i>	432	<i>Xia, K.</i>	1121
<i>Wahab, D.A.</i>	1366	<i>Xie, Guizhong</i>	159
<i>Wakita, Y.</i>	939	<i>Xu, Dafu</i>	64
<i>Walker, Paul</i>	1196	<i>Xu, J.</i>	302
<i>Wan, Min</i>	193, 1390	<i>Xu, J.</i>	1139
<i>Wang, Baoshi</i>	1300	<i>Xue, Yanni</i>	263
<i>Wang, Bin</i>	448	<i>Yagi, T.</i>	863
<i>Wang, Dongdong</i>	294, 955	<i>Yamamoto, Makoto</i>	877, 903, 1271, 1279, 1292
<i>Wang, H.</i>	490	<i>Yamamura, K.</i>	863
<i>Wang, H.L.</i>	885	<i>Yamanaka, Yuki</i>	869
<i>Wang, Lifeng</i>	177	<i>Yamane, Koichi</i>	286
<i>Wang, Peiyan</i>	367	<i>Yan, Kun</i>	314
<i>Wang, S.J.</i>	1030	<i>Yang, B.</i>	338
<i>Wang, S.N.</i>	1397	<i>Yang, Haitian</i>	263, 916, 922
<i>Wang, Tie-Jing</i>	104	<i>Yang, J.F.</i>	1460
<i>Wang, Wei</i>	73	<i>Yang, Jianfei</i>	910
<i>Wang, X.C.</i>	519	<i>Yang, R.B.</i>	1042
<i>Wang, X.F.</i>	1233	<i>Yang, Songyuan</i>	1451
<i>Wang, X.R.</i>	619	<i>Yang, Xulei</i>	193, 1390
<i>Wang, Xiaodan</i>	353	<i>Yang, Y.</i>	414
<i>Wang, Y.</i>	1201	<i>Yang, Y.</i>	999
<i>Wang, Y.F.</i>	1030	<i>Yang, Zhenjun</i>	511, 1215, 1233
<i>Wang, Ying</i>	73	<i>Yang, Zhidong</i>	185
<i>Wang, Yue</i>	769	<i>Yao, Huiju</i>	236
<i>Wang, Yuefang</i>	1035	<i>Yap, Robin Miao Sin</i>	1348
<i>Wang, Z.D.</i>	1460	<i>Yashiki, Tatsuro</i>	672
<i>Wang, Zhengdao</i>	910	<i>Yeo, Si Yong</i>	193, 969, 1390
<i>Withers, Phil</i>	1215	<i>Yeoh, G.H.</i>	1072
<i>Wu, J.Y.</i>	310	<i>Yi, Shi-he</i>	1129
<i>Wu, Jian</i>	88	<i>Yin, D.S.</i>	1233
<i>Wu, Jinglai</i>	728	<i>Yin, H.B.</i>	1110
<i>Wu, Nan-Jing</i>	895	<i>Yoshida, Tomohiko</i>	672
<i>Wu, T.</i>	611		
<i>Wu, Y.L.</i>	788		
<i>Wu, Yu</i>	1129		
<i>Wünsche, M.</i>	527		

<i>Yue, Zhufeng</i>	367	<i>Zhang, Qing-Ming</i>	110
<i>Yun, B.I.</i>	1425	<i>Zhang, Xi</i>	559
<i>Zang, Mengyan</i>	1016	<i>Zhang, Z.Q.</i>	780
<i>Zhan, H.F.</i>	1121	<i>Zhang, Zhi-Qian</i>	1442
<i>Zhang, B.H.</i>	885	<i>Zhao, Chunlai</i>	1016
<i>Zhang, Canhui</i>	955	<i>Zhao, Shiyu</i>	760
<i>Zhang, Chuanzeng</i>	414, 527	<i>Zhao, X.Y.</i>	1110
<i>Zhang, D.L.</i>	1414	<i>Zhao, Y.</i>	116
<i>Zhang, Feng</i>	236	<i>Zhao, Yu-Xin</i>	1129
<i>Zhang, H.</i>	1110	<i>Zheng, H.W.</i>	1153
<i>Zhang, Hanjie</i>	294	<i>Zheng, Xing</i>	344
<i>Zhang, Hui</i>	80	<i>Zhong, Liang</i>	193, 969, 1390
<i>Zhang, J.</i>	1110	<i>Zhou, Laijun</i>	760
<i>Zhang, Jianming</i>	159	<i>Zhou, X.</i>	310
<i>Zhang, Jin</i>	760, 769	<i>Zhou, Xingxing</i>	1196
<i>Zhang, L.</i>	1	<i>Zhu, B.</i>	519
<i>Zhang, Liang</i>	440	<i>Zhu, Bo</i>	1196
<i>Zhang, Ling</i>	559	<i>Zhu, Hongping</i>	1005
<i>Zhang, Nong</i>	589, 728, 1196, 1201	<i>Zhu, Xiaowei</i>	1451